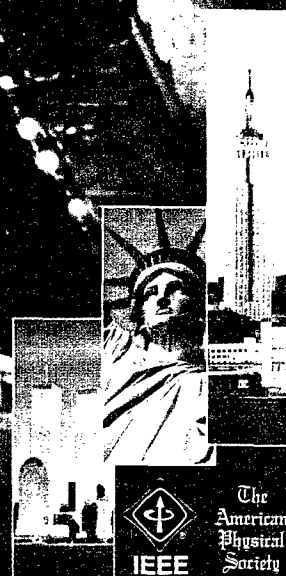


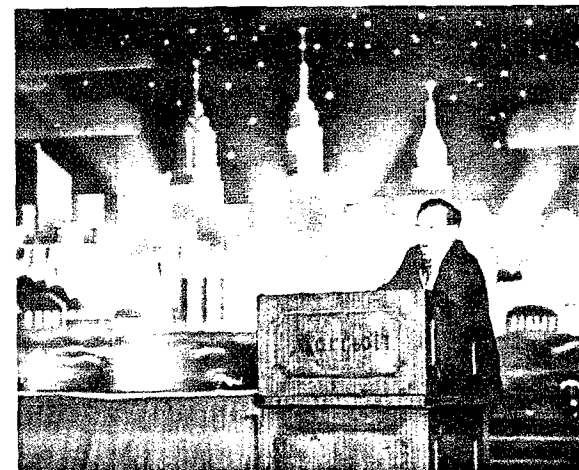
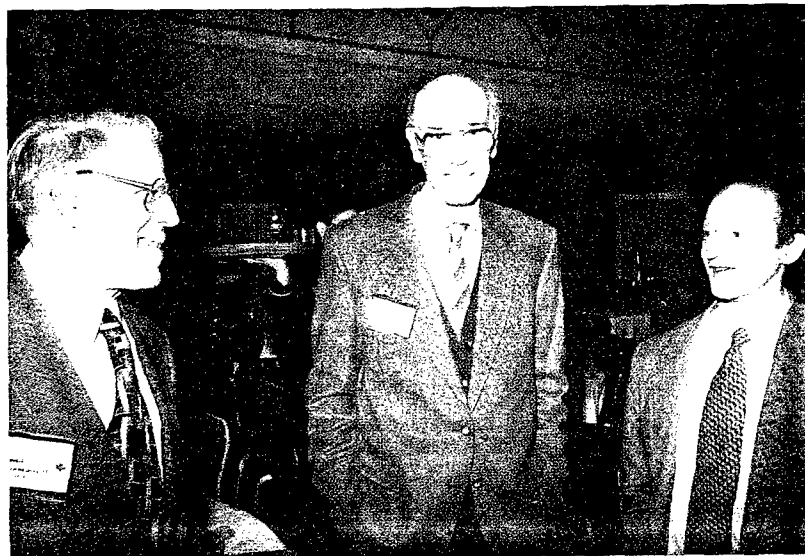
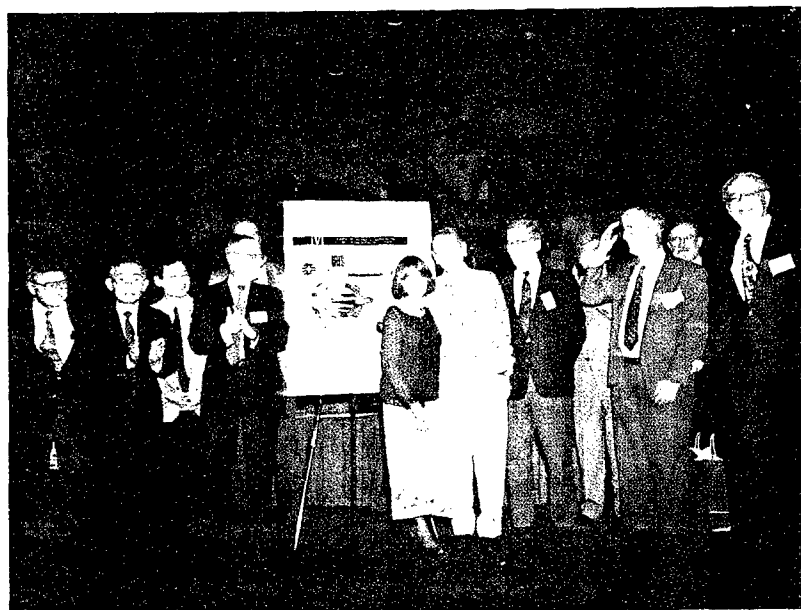
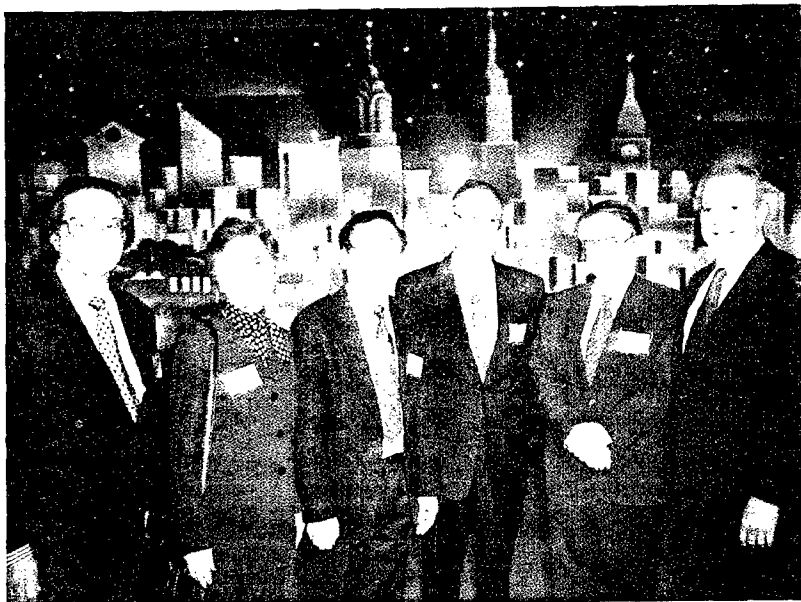
PROCEEDINGS OF THE 1999 PARTICLE ACCELERATOR CONFERENCE

VOLUME 3 OF 5

PAGES 1477 - 2258



BROOKHAVEN NATIONAL LABORATORY
Brookhaven Science Associates



REPORT DOCUMENTATION PAGE			Form Approved OMB No. 0704-0188	
Public reporting burden for this collection of information is estimated to average 1 hour per response, including the time for reviewing instructions, searching existing data sources, gathering and maintaining the data needed, and completing and reviewing the collection of information. Send comments regarding this burden estimate or any other aspect of this collection of information, including suggestions for reducing this burden, to Washington Headquarters Services, Directorate for Information Operations and Reports, 1215 Jefferson Davis Highway, Suite 1204, Arlington, VA 22202-4302, and to the Office of Management and Budget, Paperwork Reduction Project (0704-0188), Washington, DC 20503.				
1. AGENCY USE ONLY (Leave Blank)	2. REPORT DATE June 1999	3. REPORT TYPE AND DATES COVERED Final; March 27 - April 2, 1999		
4. TITLE AND SUBTITLE Proceedings of the 1999 Particle Accelerator Conference Volumes 1 through 5		5. FUNDING NUMBERS G		
6. AUTHORS A. Luccio, W. MacKay - editors				
7. PERFORMING ORGANIZATION NAME(S) AND ADDRESS(ES) Brookhaven National Lab P.O. Box 500 Upton, NY 11973		8. PERFORMING ORGANIZATION REPORT NUMBER		
9. SPONSORING / MONITORING AGENCY NAME(S) AND ADDRESS(ES) U.S. DOE National Science Foundation Office of Naval Research		10. SPONSORING / MONITORING AGENCY REPORT NUMBER		
11. SUPPLEMENTARY NOTES				
12a. DISTRIBUTION / AVAILABILITY STATEMENT Available to public		12b. DISTRIBUTION CODE		
13. ABSTRACT (Maximum 200 words) Papers for the eighteenth biennial Particle Accelerator conference, an international forum on accelerator science and technology held March 27-April 2, 1999 in New York City, organized by Brookhaven National Lab.				
14. SUBJECT TERMS			15. NUMBER OF PAGES 3779	
			16. PRICE CODE	
17. SECURITY CLASSIFICATION OF REPORT Unclassified	18. SECURITY CLASSIFICATION OF THIS PAGE Unclassified	19. SECURITY CLASSIFICATION OF ABSTRACT Unclassified	20. LIMITATION OF ABSTRACT UL	

NSN 7540-01-280-5500

Standard Form 298 (Rev. 2-89)
Prescribed by ANSI Std. Z39-1
298-102

20000209019



BROOKHAVEN
NATIONAL LABORATORY

The
American
Physical
Society

Proceeding of the 1999 Particle Accelerator Conference

(Editors: A. Luccio, W. MacKay)

Volume 3 of 5

Pages 1477 – 2258

DISTRIBUTION STATEMENT A
Approved for Public Release
Distribution Unlimited

Papers from the eighteenth biennial Particle Accelerator Conference, an international forum on accelerator science and technology held March 27 – April 2, 1999 in New York City, organized by Brookhaven National Laboratory. Sponsored by the Institute of Electrical and Electronics Engineers Nuclear and Plasma Sciences Society and the American Physical Society Division of Physics of Beams, and with support from the U.S. Department of Energy, the National Science Foundation, the Office of Naval Research, and Brookhaven Science Associates (BSA).

DTIC QUALITY INSPECTED 3

20000229 019

**Proceedings of the
1999 IEEE Particle Accelerator Conference**

Abstracting is permitted with credit to the source. Libraries are permitted to photocopy, beyond the limits of U.S. Copyright law for private use of patrons, those articles in this volume that carry a code at the bottom of the first page, provided the per-copy fee indicated in the code is paid through the copyright Clearance Center, 222 Rosewood Drive, Danvers, MA 01923. For other copying, reprint, or republication permission, write to the IEEE Copyright Manager, IEEE Service Center, 445 Hoes Lane, P.O. Box 1331, Piscataway, NJ 08855-1331. All rights reserved. Copyright ©1999 by the Institute of Electrical and Electronics Engineers, Inc.

**IEEE Catalog Number: 99CH36366
Library of Congress Number: 88-647453**

**ISBN Softbound: 0-7803-5573-3
Casebound: 0-7803-5574-1
Microfiche: 0-7803-5575-X
CD-Rom: 0-7803-5576-8**

Additional copies of this publication are available from:

**IEEE Service Center
445 Hoes Lane
Piscataway, NJ 08854-4150, USA**

**1-800-678-IEEE (1-800-678-4333)
1-732-981-1393
1-732-981-9667 (FAX)
e-mail: customer.service@ieee.org**

VOLUME 3: CONTENTS

(A DETAILED TABLE CAN BE FOUND IN VOLUME 1)

Volume 3: POSTER, pp. 1477 – 2258

PULSED POWER TECHNOLOGY.....	1477
LINEAR AND NON LINEAR ORBIT THEORY	1518
TRANSVERSE AND LONGITUDINAL INSTABILITIES AND CURES.....	1596
BEAM-BEAM INTERACTION	1668
BEAM COOLING.....	1698
HIGH CURRENT DYNAMICS.....	1725
PARTICLE SOURCES	1878
RF GUNS AND LINACS INJECTORS	1997
BEAM DIAGNOSTICS INSTRUMENTATION	2048

PROJECT OF SEMICONDUCTOR HIGH-POWER HIGH-REPETITION RATE COMPACT ACCELERATOR

E. Galstjan*, L. Kazanskiy, MRTI,
 Warszawskoe Shosse 132, Moscow 113519, Russia

Abstract

The paper describes project of a compact accelerator (120 kV, 2 kA, 15-25 ns pulse duration, 1 kHz - repetition rate). To attract an attention of accelerator community to abilities of modern power fast semiconductors, this device is suggested to create by using modern high-power super-fast semiconductor switches.

1 INTRODUCTION

The tendency of the last years in the field of development of high-power pulse and accelerating facility is the maximum extension of possible areas of its application. It demands development simple in circulation, reliable in maintenance, and, principal, whenever possible of compact devices. On the other hand, for the last two decades of research in the field of a solid state physics have resulted in creation of semiconductor devices [1-2], which parameters have allowed to create generators of high-voltage high-power impulses working in a repetitive mode [1, 2]. However, till now these semiconductor devices have not found the place directly in development of accelerating facility. The presented paper is devoted to exposition of idea of possible usage of modern semiconductor devices [2] for creation of a compact accelerator device, which, on our opinion, can find rather broad application. In the basis of this device the principle stating lies that the inductive storage of electrical energy combined with possibilities of modern semiconductors, is most perspective for creation of high-power pulse devices working with a high repetition rate. Instead of gas discharges, which limit a pulse-repetition rate and have enough wide jitter in a response time, it is offered to use new semiconducting switches. These switches are capable to reconnect for extremely short time (0,1 - 1 ns) currents by magnitude 1 - 10 kA at an operation voltage 10 - 100 kV [2]. In addition, the process of switching is controlled with split-hair accuracy, as the jitter in operation of keys does not exceed 20 ps. Thus the repetition rates of switching limits only by conditions of heat rejection from the device and can reach tens of megahertz.

*) E-mail address: galstjan@aha.ru

2 ACCELERATOR PROJECT

Let's consider more in detail principle of operation of the accelerator. In Fig. 1 one section of the device is shown. A toroidal inductor L_p is inserted in a transmission line

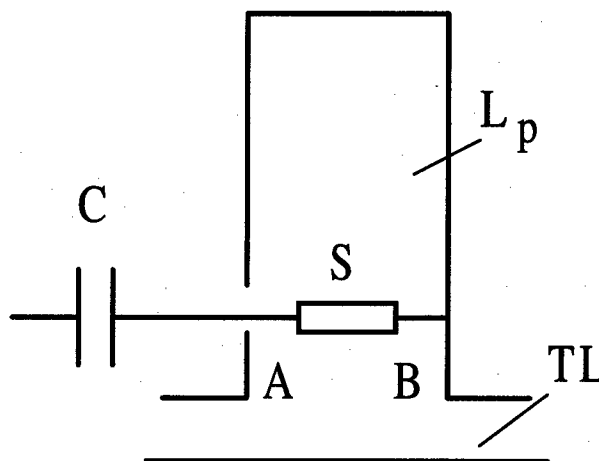


Figure 1: Principal schematic of the accelerator section

TL, which generally can be a coaxial line or can be loaded with a beam of charged particles. Originally capacitor C is charged by an external source up to primary voltage U_1 , reaching several kilovolt, then it starts to be discharged through walls of the inductor connected by a semiconducting switch S. There is a transfer of the energy, accumulated in the capacitor, in an energy of a magnetic field of the inductor and at reaching a maximum value of a current in the inductor, when the voltage on the capacitor C becomes equal to zero, the switch S is turned off, switching the inductor on a load. Thus on the gap AB there is a high voltage U_2 , which generates electric pulse in a coaxial line or accelerates charged particles of a beam.

The simple estimates display, that at small time of switching Δt the maximum voltage on the gap AB has magnitude $U_2 = U_1 \cdot t_1 / t_2$, where $t_1 = (L_p \cdot C)^{1/2}$, $t_2 = L_p / Z$ - reference times of charging and discharging of the inductor. The front of high-voltage impulse is determined by time of a rupture of a current Δt , and its duration - discharge time of the inductor t_2 . Thus, though scheme of the section reminds to section used in linear electron accelerators, actually it works

completely in another way. In usual linear accelerator the energy, transforming in accelerating impulse, is stored in capacitors, and in our accelerator - directly in the inductor of the section, that allows effectively generating short (10 - 15 ns) high-power electric pulses. Besides it is possible to shape very short impulses (3 - 5 ns) of rectangular form by using matched radial lines as the inductors.

However incarnation of all these ideas in actual devices requires a solution of a lot of engineering problems. For this purpose now in Institute of Experimental Physics (Sarov, Russia) in cooperation with the authors the construction of an accelerator grounded on the above-described principles is developed. This accelerator is designed to operate with the cold explosive-emission cathode, for which it is necessary to create an operation voltage not less than 100 kV. Therefore, a series connection of several described above sections is supposed. As the first variant it is supposed to connect sequentially such three sections. At primary voltage $U_1 = 4$ kV and the relation $t_1/t_2 = 10$, the output voltage on the cathode should be 120 kV at pulse duration about 15 - 25 ns, working current up to 2 kA and repetition rate of working impulses 1 kHz. On this accelerator it is supposed to decide engineering problems, bound up with a construction, an electrical circuit, matched operation all sections etc.

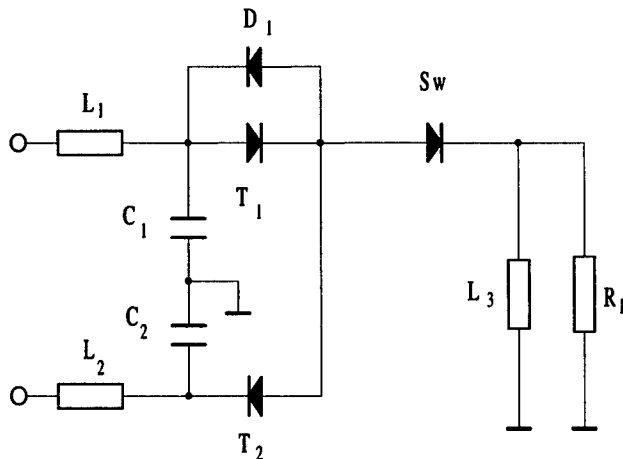


Figure 2: Electrical circuit of the section.
($C_1 = C_2 = 0.4 \mu\text{F}$, $L_1 = L_2 = 30 \mu\text{H}$,
 $L_3 = 0.2 \mu\text{H}$, $R_1 = 10 \text{ Ohm}$)

In fig. 2 one of possible variants of the principle electrical circuit of a section of the above-described accelerator is shown. A semiconductor switch, first of all, defines the view of this circuit, as it demands initial pump by electrical carriers in a forward direction, and the rupture of a current happens at opposite direction of a current, when it reaches a maximum value. In addition, the charge, which is flowing past through the switch in a forward direction, should coincide with the charge that has flowed past

in the opposite direction. This condition also determines choice of the circuit. The circuit operates as follows. Originally the capacitors C_1 and C_2 , connected in series, are charged through inductances L_1 and L_2 up to the primary voltage. Further capacitor C_1 is used for direct pump of the semiconductor switch. For this purpose the thyristor T_1 is turned on at a closed thyristor T_2 , and the capacitor C_1 is completely recharged through the inductor and the switch. After the recharge process is over, the thyristor T_2 is turned on and, as a result, capacitors C_1 and C_2 are connected in parallel. It results in that the above-stated condition of equality of an amount of the flowed past charges is fulfilled for a quarter of phase of oscillation of a reverse current. At a maximum value of a current in the inductor L_3 , the switch produces cutoff of this current and the voltage pulse is shaped on a load resistance R_1 .

It is necessary to mark that the selected operational mode of semiconductor switches in the given circuits is far from limiting on output voltage. For this reason, expected rate of acceleration can reach only moderate magnitude $\sim 0.2 \text{ MV/m}$, but this value may be gained. Besides it is known, that an electron beam generated by a cold cathode with an explosive emission, has no enough high quality. It limits its applications, for example, in Free Electron Lasers. In our variant of the accelerator the generated beam could be additionally accelerated up to a necessary energy in a set of the same sections, loaded on the beam. In this case, quality of the beam could be essentially improved.

Thus, usage of modern semiconductor switches allows creating the compact device both a generator of power electric pulses, and an accelerator of charged particles. The generator of electric pulses can be used in medicine and biology, where a possibility of selective action of short electric pulse on a cell now is researched [3].

The accelerating devices, assembled from above described sections, are good sources of charged particle (electrons, protons, and ions) bunches, which can be used for generation of electromagnetic radiation, for surface treatment, in an ecology etc. Besides it is possible to gather classical Linacs with a possibility of acceleration of bunches up to large energies.

3 REFERENCES

- [1]. Lyubutin S. K., Mesyats G. A., Rukin S. N., et al. In Proc.: XI Int. Conf. on High Power Particle Beams. Prague, Czech Republic, 1996. V.1. P.1211-1214.
- [2]. Efanov V.M., Karavaev V.V., Kardo-Sysoev A.F., Tchaashnikov I.G. Fast ionization dynistor (FID) - a new semiconductor superpower closing switch. // In Proc.: XI IEEE Int. Pulsed Power Conf. Baltimore, USA, 1997. P. 988-991.
- [3]. Schoenbach H. et al. The effect of pulsed electrical fields on biological cells. // In Proc.: XI IEEE Int. Pulsed Power Conf. Baltimore, USA, 1997. P. 73-78.

THE ITEP-TWAC INJECTION AND EXTRACTION KICKER

V. Krasnopolsky, S. Krylov, G. Mamaev^{*}, S. Mamaev, S. Poutchkov,

I. Tenyakov, V. Fedorov, MRTI RAS, Moscow

A. Sidorov, JINR, Dubna

N. Alekseev, ITEP, Moscow

Abstract

The system multi-turn injection and fast extraction for installation ITEP-TWAC is developing in MRTI RAS. In this paper one kicker in injection ring and one extraction kicker in storage ring are described. In both kickers rise time of magnetic field is not more 300 ns, and platen duration 300-500 ns. The total length of the injection kicker is 1.8 m, aperture is 0.1×0.1 m and kicker strength is 0.16 T·m. The total length of the extraction kicker is 1.5 m, aperture is 0.09×0.09 m and kicker strength is 0.14 T·m. Both kickers are situated outside vacuum chamber and consisted of number uniform sections 0.3 m length. In each section ferrite magnet, pulse former line, matched resistor 2.5 Ohm and 50 kV ceramic metal thyatron with grounded grid are used. Pulse current in each magnet achieves 7-8 kA in order to magnetic field not more 0.1 T. In each former line concentration capacitors and inductance in order to storage energy and pulse correction are used. The compact pulse power supply system in each section gives the possibility connection with magnet short feed buses without low-impedance 2.5 Ohm cable.

1 GENERAL DESIGN

The kicker of the injection ring (kicker 1) and the kicker of the storage ring (kicker 2) are parts of installation ITEP-TWAC [1]. A performance specification for the kickers is given in table 1 and table 2.

Table 1: The specification of the kicker 1.

Magnet total length	1.812 m
Magnetic field	0,0883 T
Rise time (1-95%)	300 ns
Flat top	(300-500) ns
Fall time	Unlimited
Flat top tolerance	± 5%
Repetition period	1 s
Beam aperture in magnet	80 mm-diam.
Field uniformity in half-aperture	± 3%

Table 2: The specification of the kicker 2.

Magnet total length	1,51 m
Magnetic field	0,0947 T
Rise time (1-95%)	300 ns
Flat top	(300-500) ns
Fall time	Unlimited
Flat top tolerance	± 5%
Repetition period:	1 s
Beam aperture in magnet	70 mm- diam.
Field uniformity in half-aperture	± 3%

Series parameters each kicker is near parameters kicker for installation "Mirabel" [2]. For this reason each magnet consist of sections like "Mirabel" magnets and each section is connected to self-contained pulse supply unit. Kicker 1 consist of six sections, kicker 2 consist of five sections. The ceramic beam tube is used in kickers because the vacuum in the installation ITEP-TWAC is very high ($10^{-10} - 10^{-13}$ torr).

2 MAGNETS

The cross section of magnets is shown in Fig. 1.

Kicker1: $h = 100$ mm; $s = 100$ mm, $D = 80$ mm.

Kicker2: $h = 90$ mm; $s = 90$ mm, $D = 70$ mm.

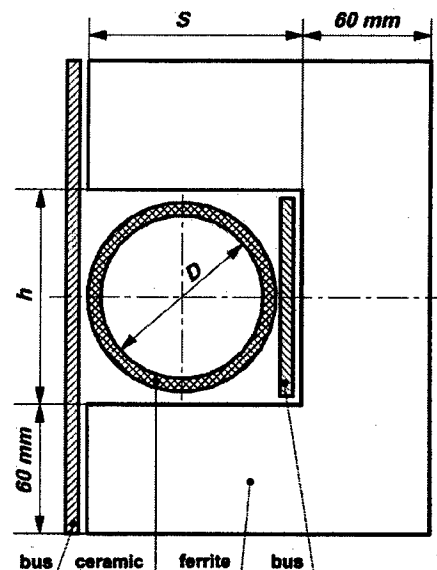


Figure 1: Cross-section of magnets.

*E-Mail: mamaev_g@mail.sitek.ru

The length of each section of each magnet is equal to 300 mm, and ratio h/s of each section is equal to 1. In the results the inductance of each section is equal to 400 nH. The magnetic circuit consist of ferrite 600 NN. The thickness of ferrite plate is 20 mm. Epoxy compound is used for gluing. The feed buses are manufactured from aluminium. For target magnetic field we have to receive the current near to 8 kA in feed buses. The ferrite and feed buses are situated in air and in the result the air-cooling is possible.

(Look right for continue).

3 PULSE SUPPLY UNIT

The rise time of pulse 300 ns gives the possibility to use in forming line concentrated capacitors and inductances [3]. The commutator for current 8 kA is the main problem in our case. The thyatron TGI1-2500/50 is used. It works at voltage 40-50 kV and connected on the circuit with a grounded grid [4,5]. In this circuit the main current of a load going through the gap anode-grid and the gap grid-cathode is used only for initial pulse. In this case the oxide-coated cathode is not destroy. Each of magnet section connected to self-contained pulse supply unit, which electric circuit is shown in Fig. 2.

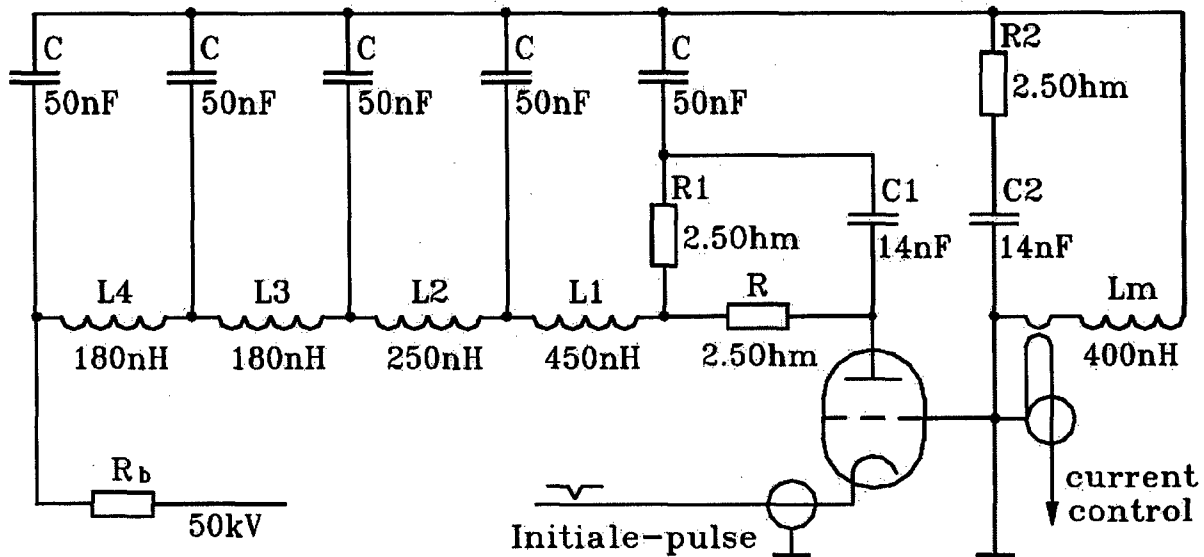


Figure 2: Electric circuit pulse supply unit in connection of the magnet.

Own inductances of capacitors and buses are not shown in Fig. 2, but were considered in the pulse current calculation. Own inductance of a magnet L_m fulfils functions of inductance of the first cell. Common number of cells is equal to five. The small number of cells has required for optimization of the form of pulse to use forming line with various inductances L_1 - L_4 in cells. For correction of front of pulse two additional cells R_1 C_1 and R_2 C_2 were added also. The matched resistor $R=2,5$ Ohm is connected between anode of the thyatron and output of line. The small value of resistor $R=2.5$ Ohm could make difficulty for connection of a forming line with magnet by a long cable with a low impedance $Z=2,5$ Ohm. Taking into account difficulties of using of such cable we decided to place each unit near to appropriate section of the magnet and to use for connection the pair of short buses. Buses are connected to the grounded grid of the thyatron and to another output of line. Their inductance is not more than 180 nH. Due to this the high voltage on buses is absent during charging a line and on a flat top when $U=L_m \cdot di/dt \sim 0$. The voltage arises only during the rise time and the fall time of pulse and is not more than 25 kV. It simplifies

the high-voltage insulation of buses and ferrite in magnet located on an air.

During development one or two type ceramic and oil capacitors were tested. As a result oil capacitors IK100-0.05 were used in cells of line C and ceramic capacitors KVI-3 were used in cells R_1 C_1 , R_2 C_2 .

The experimental model of the unit kicker1 was manufactured as a result of development. It consists of the pulse supply unit and the section of magnet. The general view of the model is shown in Fig. 3.

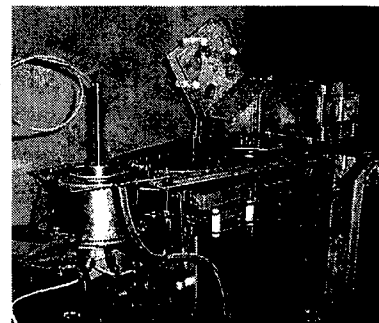


Figure 3: Experimental model of the unit kicker1.

4 EXPERIMENTAL RESULTS AND FUTURE DEVELOPMENTS

On experimental model electrical durability, form of pulse of a current in buses of a magnet and pulse of a magnetic field in a working clearance and also uniformity of a magnetic field were investigated. Single break-down in air on constant charge voltage were observed only 35 kV up, nevertheless they have not hindered to lift charge voltage up to 47 kV and to achieve the calculated current 8 kA. There were no breakdowns in insulation of buses of a magnet during pulse voltage. The form of pulse of a current in buses of a magnet and pulse of a magnetic field in clearance was further defined. The measurements were carried out by two types of monitors and have shown satisfactory coincidence with calculated form of pulse.

The outcome is shown in Fig. 4.

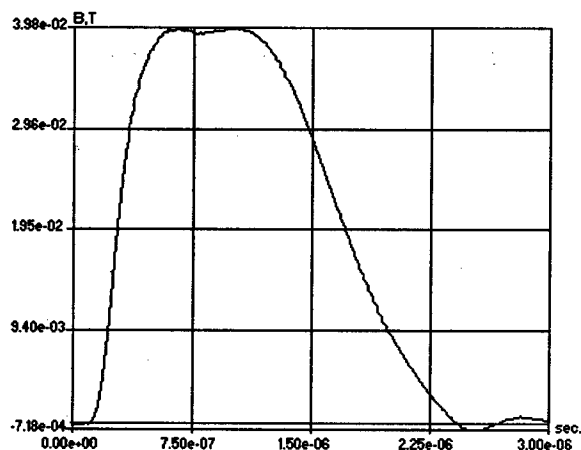


Figure 4: Magnetic field pulse in the median plane (charge voltage $U=20$ kV).

The necessary charge voltage was defined as the result of measurements. For kicker 1 it is equal 48 kV, for kicker 2 it is equal 46 kV. The oil insulation in a power supply unit was decided to use for the guaranteed electrical reliability. This oil insulation is used for all parts of unit, where constant charge voltage is, including a thyatron. The construction of a power supply unit with oil insulation is developed.

Preliminary measurements the uniformity of a magnetic field in the median plane were made also. At the distance 15 mm from the center of ceramic tube the uniformity is equal (2.0 - 2.5)%.

The test of the power supply unit with oil insulation and the measurement uniformity of a magnetic field in full aperture are planed for nearest future.

5 ACKNOWLEDGMENTS

We sincerely thank O. Kurnaev for valuable consultations and advise.

6 REFERENCES

- [1] N. Alekseev, D. Koshkarev, B. Sharkov et. al., "Modernization of the Accelerator-storage Facility in ITEP-project ITEP-TWAC, 15* Russian Charged Particle Accelerator Workshop, v.2, p. 319., Protvino, 1996
- [2] A. Aseev, A. Afonin, A. Drogdin et. al., "Proton Quick Ejection from 70 GeV Accelerator for Liquid Hydrogen Chamber "Mirabel", Proceedings 3d Charged Particle Accelerator Workshop, v.2, p. 160, M., "Science", 1978
- [3] Y. Vahrushin, A. Anackiy, "Line Induction Accelerators", M. Atomisdat, 1978, p. 78-82.
- [4] Ceramic Metal grid Thyratrons, EGG Electro-Optical Division, Data sheet H5003B-1, 1974, p.1-3, USA
- [5] A. Belaev et. al., "Investigations of the Start and Commutation Thyratrons TGI1-2500/50, JINR, 9-10313, Dubna, 1976

INFLUENCE OF THE TECHNOLOGICAL PROCESS CONDITIONS TO PARAMETERS OF MAGNETIC CORES FROM RIBBON AMORPHOUS ALLOYS*

I. Bolotin, G. Mamaev^{*}, S. Mamaev, S. Poutchkov, A. Ctcherbakov,
MRTI RAS, Moscow

Abstract

In an electrical engineering and items of powerful impulse engineering are actively applied amorphous magnetically soft alloys, which can substitute electrotechnical steel, permalloy and ferrite. A high specific electrical resistance and low specific losses, especially in items working on high frequencies characterize the amorphous alloys. The characteristics of items from amorphous magnetically soft alloys essentially depend on chemical structure of a ribbon as cast and conditions of technological processing (winding, applying of interlayer insulation coating, thermomagnetic processing and measurements).

Especially this dependence appears on properties of magnetic cores, intended for use in magnetic pulse compression circuit, magnetic switches, inductors for linear accelerators, high voltage pulse transformers etc.

The outcomes of researches on controlled effect through the technological process on parameters of magnetic cores from amorphous and nanocrystalline alloys are reduced.

The properties of magnetic cores are investigated in two frequency ranges: on frequency 50 Hz and of large speeds of magnetic reversal - up to 30 T/μs (in this range the losses in cores are analyzed).

1 INTRODUCTION

The influence of an interlayer insulation to properties of manufactured cores from amorphous alloys is now well explored. It is known, the coat by thickness ~ 1 micron for a theoretically smooth tape allows to yield a core with record low losses. Substantially tapes have inhomogeneities (salients, peaks, nicks-and-burrses), resulting in necessities of thickening of a coat. It gives in diminution of a pack factor and magnification of losses. We have tried to find requirements of a manufacturing process permitting to reach an optimum relation between these parameters.

The analysis of influence of requirements of a manufacturing process on the most relevant parameters of cores was carried out on cores intended for usage in switching devices, i.e. having a so-called rectangular

hysteresis curve. All cores had been manufactured of an amorphous tape (2605SA1, 2605SC from AlliedSignal, (USA), 30KCP, 9KCP, 2HCP, 5BDSR from Amet (Russia)) of width 20-25 mm and thickness 25±10 μm. The cores were made with insulation interlayer based of a fluid soda-ash glass (technology MRTI RAS) and annealed in a longitudinal magnetic field. Mass of cores were from 0.2 up to 2 kg.

2 RESULTS AND DISCUSS

It is easy to effect on the mentioned above two basic criterions of quality of cores by thickness of interlayer insulation and by tension during winding of the cores.

The influence of tape tension at winding on magnetic parameters of the cores is well-studied [1]. Is exhibited that the overflow of gain of a tension of quantity in 10 N carries on to slope of parameter Br, therefore opportunity of magnification of a pack factor at the expense of gain of a tension is restricted. Thus, the searching of an optimum relation between the indicated criterions of quality of the core was reduced to a finding of minimally permissible thickness of coating using an opportunity to change thickness of coating available by MRTI RAS technology.

It was explored influence of thickness of the coating to losses in cores manufactured from a widely known alloy 2605SA1. The cores with different coating, which had the values of breakdown voltage from 10 up to 40 V, were wound with gain of a tension in 10N and were tested. The cores were manufactured on special installation, which allow to realize the whole chain of the process (winding, coating, annealing, test measuring of parameters) [2].

The estimation of dependence of losses in cores from a value insulation breakdown voltage at magnetization rates of about 19 T/μs and 12 T/μs was done. The master data obtained during experiments at different magnetization rates are represented in Fig. 1 and 2 accordingly.

As display the diagrams in Fig. 1 and 2, the dependence of losses in cores from a breakdown voltage value has the exponential character. The fracture of an exponential curve is in region 15 - 20V of the breakdown voltage of insulation. Therefore reduction rate of losses in the core at increasing of the thickness of insulation at

* Work supported in part by LLNL

* E-mail: mamaev_g@mail.sitek.ru

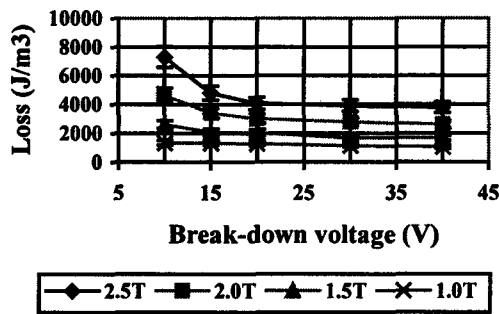


Figure 1: Core losses at $dB/dt \sim 19$ T/ μ s

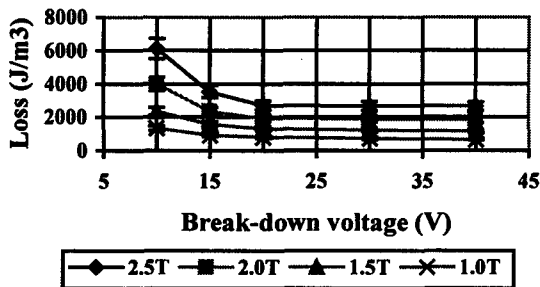


Figure 2: Core losses at $dB/dt \sim 12$ T/ μ s

breakdown voltage greater 20V will be less than reduction rate of the packing factor. We consider that optimum for the insulation is the insulation providing breakdown voltage not less than 20V. With such thickness of the insulation (20V of a breakdown voltage coated on technique MRTI RAS), we reached on alloys 2605SA1 and 2605SC the magnitude of a packing factor more than 80%. In Fig. 3 dependence of losses in cores from of alloys 2605SA1 (thickness of tape - 22 μ m) and 2605SC (thickness of tape - 17 μ m) wound with tension in 10N with insulation,

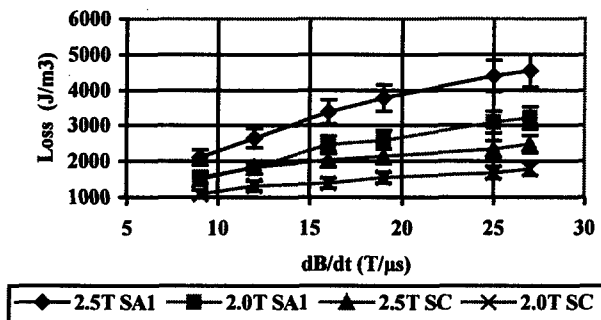


Figure 3: Losses for 2605SA1 and 2605SC for flux swings 2.0T and 2.5T.

on 20V of a breakdown voltage, depending from magnetization rate from 8 up to 27 T/ μ s are shown.

In Fig. 4 the graphs of change of losses in cores manufactured of such iron-based alloys of the Russian production as 30KCP, 9KCP, 2HKCP with insulation for 20V, depending on magnetization rate function are given.

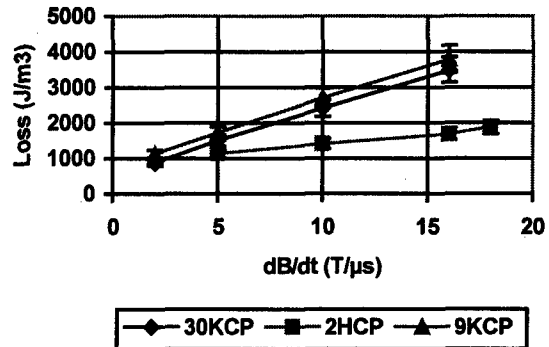


Figure 4: Losses for 30KCP, 9KCP and 2HKCP for flux swing 2.5T

The major contribution for reaching of the good results is given by surface quality and geometry (squareness of section) of the tape. The preliminary grinding of a tape as cast helps considerably to improve total parameters of cores from the tapes with medial and poor surface quality and geometry. The preliminary grinding also allows to reduce thickness of insulation without magnification of losses in the core. The results of measuring of losses in the cores manufactured from a customary and ground tapes from a cheap electrotechnical alloy 9KCP with insulation, calculated on 10V of a breakdown voltage are shown in Fig. 5.

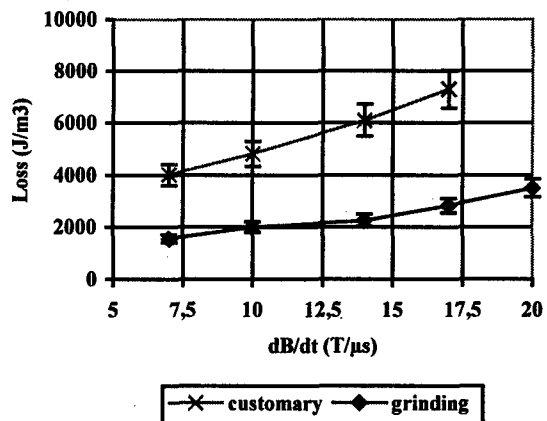


Figure 5: Losses for customary and grinding 9KCP for flux swing 2.5T

As it is clear from the graphs, the values of losses in the core from the ground tape are comparable with losses in the core from the alloy 2605SC, distinguished by extremely low losses.

It is necessary to mark essential influence to losses in cores of a magnetic annealing, which one should be conducted with a major exactitude (temperature, time of annealing and cooling) to receive optimum properties and to not suppose a partial crystallization, which one reduces greatly the magnetic properties. It is necessary to mark advantages, which one can obtained with using the modern nanocrystalline alloys (5BDSR from Russia).

Nanocrystalline alloys have the minimum losses, low coercive force and constant of magnetostriction. The alloy does not contain such scarce materials, as a nickel and cobalt. The 5BDSR alloy has a coercive force and value of a magnetic permeability comparable with the according values of precision amorphous alloys 82K3XCP and 82K2XCP (Russia) containing more of 80% of a cobalt, also the value of an induction B_s for an alloy 5BDSR is much higher (1.2 against 0.5). For these alloys the procedure of annealing became rather simple – the only critical parameter is the holding period of the core at fixed temperature $\sim 540^\circ\text{C}$.

In a Fig. 6 results of measuring of losses in the core manufactured from nanocrystalline alloy 5BDSR in comparing with losses in the core manufactured from an alloy 2605SC with insulation, calculated on 20V, at flux swing 1T are represented.

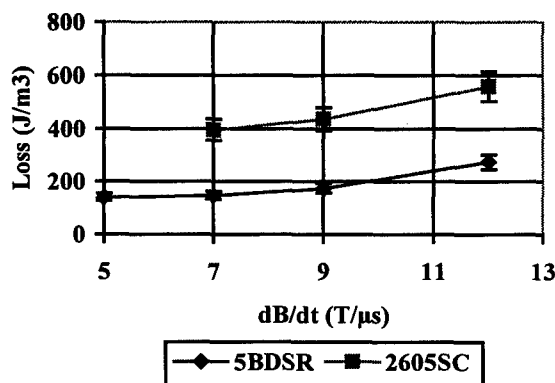


Figure 6: Losses for 2605SC and 5BDSR for flux swing 1T

As it is visible from the graphs the losses in the core from 5BDSR are two times less than in the core from 2605SC. But the nanocrystalline alloy has the low induction of saturation $B_s=1.2\text{T}$. However Russian manufacturers assert that they can raise an induction of saturation of this alloy up to $B_s=1.5-1.65\text{T}$. The cost of an alloy 5BDSR of the same order, as well as amorphous alloys with the small content of a cobalt $\sim 40-50$ $\$/\text{kg}$. At the ordering of major lots (order 2-5 tons) the cost can diminish till 10-15 $\$/\text{kg}$.

Thus, if the information on the opportunity of magnification of an induction of saturation up to 1.5 - 1.65T will be confirmed, the alloy 5BDSR has indisputable advantage before usual amorphous alloys.

2.1 Technique of monitoring and measuring of parameters

On a high frequency (the magnetization rate up to 30 T/ μ s) installation shaping high-current one-time impulse of a discharge current beforehand of the charged capacitor is applied. For deriving results PC with built-in double-channel 8 bit analog-digital converters with a frequency of sampling 100 MHz is applied. On data of measuring of magnetization field magnitude and the inductions in the cores curves of a hysteresis are created. The further analysis will be carried out on obtained hysteresis curves. The accuracy of such combined measurements - is not worse than 10 %.

3 CONCLUSION

The opportunity of reaching the optimum relations between magnitudes of a packing factor and interlayer insulation thickness is exhibited.

The advantages of usage of modern nanocrystalline alloys to production of cores are shown.

4 REFERENCES

- [1] D.M.Nathasingh, C.H.Smith and A.Datta IEEE Trans. Mag. **MAG-20**, 5 (1984)
- [2] <http://www.triumf.ca/PAC97/papers/pdf/7P095.pdf>

RESULTS OF START OF THE 150 KV MAGNETIC PULSE COMPRESSOR

S. Krylov, G. Mamaev*, S. Mamaev, T. Latypov, S. Poutchkov,
I. Tenykov, V. Fedorov, MRTI RAS, Moscow,
A. Sidorov, JINR, Dubna

Abstract

The powerful pulse generator with target parameters 150 kV, 37 kA and duration of a pulse 150 nsec was described in article [1]. The magnetic cores from amorphous alloys with ratio B_r/B_s more than 0.9 were used as the key elements in the generator. We have carried out process of start, adjustment and have obtained the designed parameters. The researches on improvement of electrical durability of installation and the researches of losses in cascades of the generator have been carried out. The greatest attention devoted to the research of work and modernization of the second step of compression, to the reduction of its inductance with the

purpose of to reduce built-up time of a pulse. We managed to receive built-up time (at a level from 0.1 up to 0.9) of the generator pulse about 40 nsec.

1 GENERAL DESIGN

The general parameters of the generator are:

Output voltage	150 kV
Output impedance	4 Ohm
Output pulse duration	150 ns
Build-up time	40 ns
Pulsed-oscillator starting time (jitter)	10 ns
Repetition rate	1 pulse/min

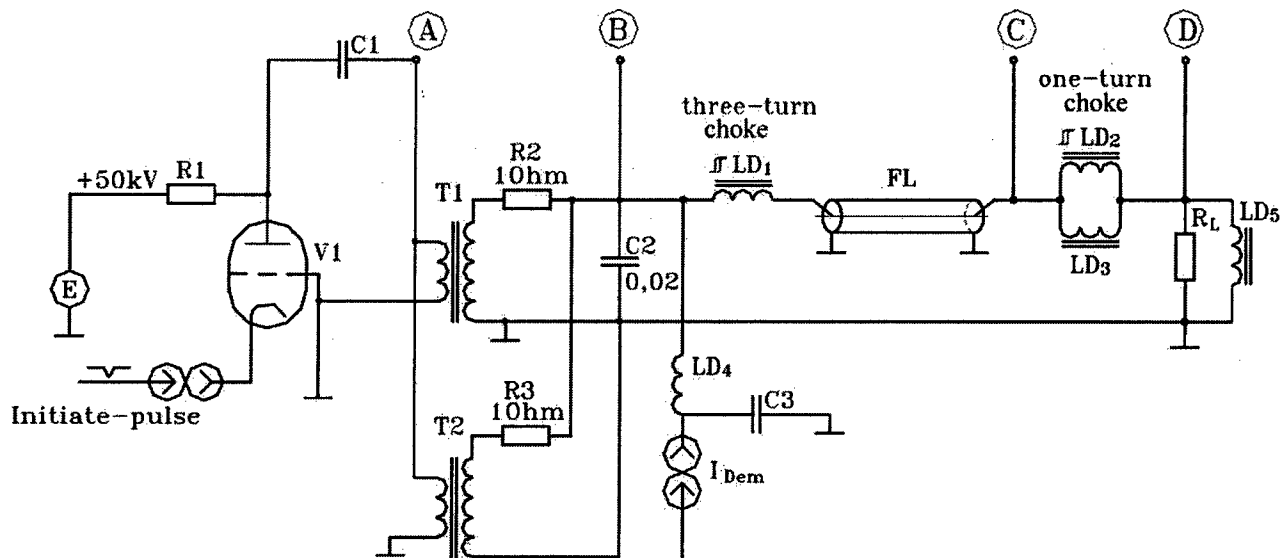


Figure 1: The generator design.

The generator includes an energy store C1, thyatron switch V1 and step-up transformer (there were used two transformers T1 and T2 connected in parallel). The secondary energy store C2 is connected to secondary winding of transformer. By means of saturable choke LD1, energy of the store supplied to pulse forming line (PFL). Charged PFL connects to load R_L by means of second saturable choke LD2. After each pulse, the demagnetization of the cores of the transformers and

chokes is performed. After that the induction of all cores is equal to maximum residual induction - B_r . The demagnetization pulse current I_{dem} is creating by the demagnetization unit, which is not shown in Fig. 1. The choke LD4 and capacitor C3 forms a filter for the protection of the demagnetization unit from high voltage of the secondary windings of T1 and T2.

The demagnetization current branches on 2 parts. First saturates transformer cores. Its magnitude is limited by resistor R2, R3. The second part saturates a circuit of the series connected chokes LD1, LD3, LD4, LD5. The

* Email: mamaev_g@mail.sitek.ru

choke LD5 shunts a load. It allows reducing demagnetization unit power. As this circuit is saturated after saturation of transformers, it is not necessary to limit this current.

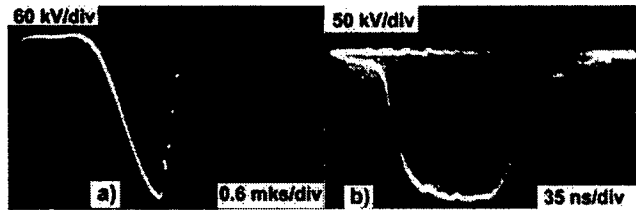


Figure 2: The basic voltage diagrams.

Below there are the results of starting up of the generator.

1.1 Primary circuit

It is the battery of store capacitors (C1) and charged – discharged circuits, connected to it. We had the breakdowns near capacitor buses at the 50 kV voltage level. To achieve calculated high-voltage durability the heating of the oil in pumping out vessels was made. We have achieved breakdown voltage of the oil 65-70 kV (before drying it was 30-35 kV) on VDE0370 measurement, which is equivalent - 58 kV on VTE. We have to improve the high voltage buses and other elements with the purpose to reduce strength of the field, and also to improve the reliability threading joints, as the discharge current exceeded 50 kA.

1.2 The circuit of transmission of energy to the secondary store

We used two transformers connected in parallel in order to receive the necessary power using one of our transformer design and also with desire to reduce the weight of each unit. In Fig. 3 the basic elements of the first step of a generator - primary energy store, thyatron unit, step-up transformer and also choke are shown. Basic work, which was carried out with the transformer, is an optimization of its factor of transformation with the purpose of deriving on the secondary store C2 of necessary voltage - 300-310 kV. In Fig. 2a the oscillogram of voltage on the secondary store C2 is shown. As to duration of charging pulse, this parameter has not caused the problems; i.e. the time was close to calculated one - about 1.5 microsecond. The voltage on C2 had appeared a little less than expected on 10-15%. The research has shown that it was connected to active losses in an outline of transmission of energy. For localization of losses the work of the first stage of a generator with disconnected second stage was investigated and it was shown that the main losses were the losses in capacitors. On resonance frequency ($f = 300$ kHz) their quality factor $Q = 7$. Quality factor of the transformer together with buses is 80.

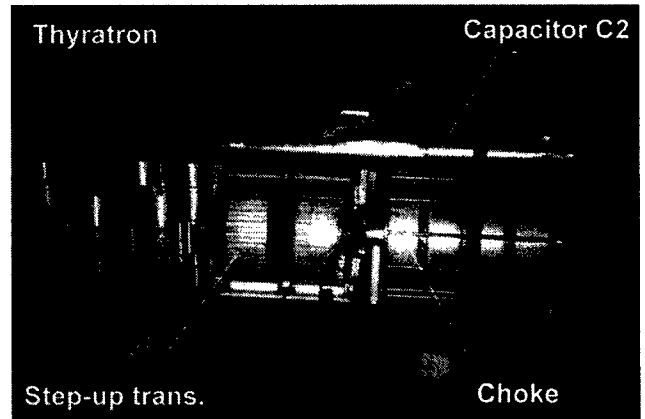


Figure 3: The basic elements of the generator first step.

For achieving the voltage 300-310 kV we have to raise transformation ratio from 7 up to 8.5 and the same time the conditions of transmission of the energy had been improved a little.

The reduced value of capacity C2 to the primary winding of the transformer with new factor became closer to capacity of a primary store, than before.

After testing the efficiency of the first step, which is equal to ratio of energy of secondary and primary stores became 0.7.

1.3 Choke of the first step L1

Choke of the first step has three turns wound around ferromagnetic core with rectangular square loop of a hysteresis (material 9KCP). The cross section of the steel $S = 290$ cm², weight of a material of the core - 200 kg. The choke is realized from 4 in series connected sections. It was made with the purpose of a voltage reduction between choke turns (Fig. 4).

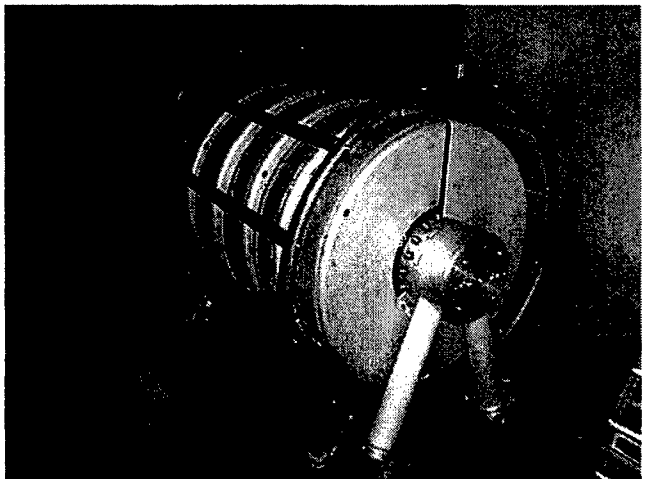


Figure 4: The view of the first step choke.

At the beginning of the work there were the breakdowns between the turns of output section because of non-uniform distribution voltage along sections. After saturation of the choke water line is charged during 0.5

microsecond. The stray capacitance, which is derived by last section on a grounded screen, is charged up to 300 kV. The terminal of the last section connected to a water line after it discharging appears under a zero potential, that means that on winding of the section there is a full voltage - 300 kV. For it elimination the capacity divider was installed, which aligned voltage along sections. Also the clearance between the first and third turns in last section was enlarged. After these changing the choke worked reliable. The calculated time of charging of a water line 0.45 - 0.5 microsecond was obtained without additional regulation and adjustment. The moment of saturation choke L1 approximately corresponded to a maximum of a charge of a secondary store without additional regulations.

1.4 Choke of the second step L2

Originally installed double-turn choke with additional sharpener of voltage was replaced by two connected in parallel single-turn chokes. We used additional material, but simplified deriving a necessary sharpness of the front of impulse. A cross-section of the steel is equal 237 cm². Chokes were made from the same type of the ferromagnetic cores, using material 9KCP. The voltage waveform on a load (4 Ohm) is shown in Fig. 2b.

Efficiency of installation as a whole, defined by a ratio of output pulse energy to energy of a primary store is equal about 0.5. If to take into account, that the efficiency of the first step is equal 0.7, it is received, that in the second step the efficiency is 0.7. The reason of losses in the second step was not investigated, since losses were not the defining factor for the installation.



Figure 5: The view of the second step loads area.

Nevertheless, the losses can be explained by some mismatching of the water line and load, and also by incomplete transmission of the energy from a secondary store to PFL. In Fig. 5 the chokes of the second step with an on-line load are represented.

1.5 Diagnostics

In a construction of a generator the measuring voltage dividers and also measuring transformers of a current are installed.

The measuring voltage divider is connected in a parallel way to capacitor C2 (Fig. 3). Two measuring voltage dividers are built in the water line. The resistive divider is connected in a parallel way to the load of the generator. Measuring transformers of the current are installed on the input and output of the PFL. In Fig. 4 the resistive divider and also measuring transformer included in one of six parallel resistors of a load of the type TBO-60 are shown.

2 REFERENCES

- [1] G. Mamaev, S. Mamaev, T. Latypov, S. Poutchkov, A. Ctcherbakov, I. Tenyakov, «150 kV Magnetic Pulse Compressor», Vancouver, PAC'97

A PULSED MODULATOR POWER SUPPLY FOR THE g-2 MUON STORAGE RING INJECTION KICKER*

J. Mi, Y.Y. Lee, W. M. Morse, C.I. Pai, G.C. Pappas,
R. Sanders, Y.K. Semertzidis D. Warburton, and R. Zapasek, BNL, Upton, NY, USA
K. Jungmann, HU, Heidelberg, Germany, L. Roberts, BU, Boston, MA, USA

Abstract

This paper describes the pulse modulator power supplies used to drive the kicker magnets that inject the muon beam into the g-2 storage ring that has been built at Brookhaven National Laboratory. Three modulators built into coaxial structures consisting of a series circuit of an energy storage capacitor, a damping resistor and a fast thyatron switch are used to energize three magnets that kick the beam into the proper orbit. A 100 kV charging power supply is used to charge the capacitor to 95kV. The damping resistor shapes the magnet current waveform to a 450 nanosecond half-sine to match the injection requirements. This paper discusses the modulator design, construction and operation.

INTRODUCTION

The goal of high energy physics experiment AGS 821 is to make precision measurements of the muon g-2 value. These measurements require the use of a super-conducting storage ring to store a circulating muon beam. The muon beam intensity in the storage ring is increased by moving the beam into the proper orbit with three kicker magnets after injection.

The kicker magnets are located in the ring, down stream of the inflector. Each of the three kicker magnets is driven by its own pulse modulator power supply. The kicker system deflects the 3.094GeV/c momentum beam 10 mrad¹.

The initial development of the pulse modulator can best be described as long and arduous. The first prototype model used a sparkgap as a switch. While the modulator was able to produce the correct current amplitude and waveform, switch life was limited to at most one million pulses². The spark gaps of various manufacturers were tested with no improvement in switch life. Many months of R&D were invested into looking for causes and a solution to electrode deterioration. The gap electrodes were replaced with electrodes of different materials but they failed because of metal migration, pitting and sputtering.

The prototype structure was modified and the sparkgap was replaced by a high voltage thyatron. The modulator was pulsed over three million times without failure.

The modulator is a simple low inductance coaxial structure consisting of a grounded cathode thyatron in series with a damping resistor, an energy storage capacitor and the kicker magnet. The capacitor is charged by a resonant charging power supply. The series discharge resistor provides a load for the circuit. The resistor value was chosen to limit the thyatron current during discharge and to reduce the pulse reverse voltage.

Because of the sensitivities of other systems and instrumentation associated with the storage ring, much thought was given to electromagnetic compatibility (EMC). Consideration was given to the isolation and grounding of all parts of the system. Prevention of electromagnetic interference (EMI), from the high energy circuits was accomplished by using a totally enclosed outer conductor of the modulator and the magnet chamber. Power supply and magnet currents are kept inside to provide a continuous low noise grounding circuit with no external conducted or radiated EMI. All power-wiring conductors are filtered. Instrumentation shields and cabinets also required planning and carefully placed point grounds.

The associated trigger timing system, auxiliary power supplies, and controls are located inside the g-2 ring adjacent to the modulators.

DESIGN AND SIMULATION

The modulator is required to generate a nominal 450 nsec half-sine 4.3 kA peak current pulse in the kicker magnet. It must operate in a burst mode of six pulses at a 30 Hz rate with a 2.5 second period. Future requirements include doubling the number of pulses to 12.

Computer simulations were used to optimize the simple RLC circuit so that the current amplitude and pulse length requirements could be met with realizable

* Work performed under the auspices of the U.S. Department of Energy

components. The kicker magnet consists of a single turn aluminum conductor in vacuum. The inductance of the kicker magnet and its high voltage feedthrough is $1.1 \mu\text{H}$. The inductance of the coaxial line section and thyatron is $0.4 \mu\text{H}$. The simulations confirmed the need for an energy storage capacitor of 10 nF , a damping resistor of 11.5 ohms and a charging voltage of 95 kV . The simplified circuit model is shown in Figure 1.

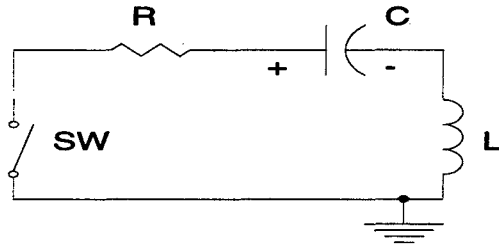


Figure 1. Simplified simulation circuit model.

HIGH VOLTAGE DISCHARGING CIRCUIT ASSEMBLY

The discharge switch is an EEV type CX1699 four gap hydrogen thyatron shown in Figure 2. It is rated at a 130 kV maximum peak forward anode voltage. The 10 nF storage capacitor is rated for 100 kV . The dumping resistor is a stack assembly consisting of 12 each, 3.75 inch in diameter by 1 inch thick Cesiwid washer resistors sandwiched between copper cooling fin disks for improved internal cooling. The Damping resistor stack is shown in Figure 3.

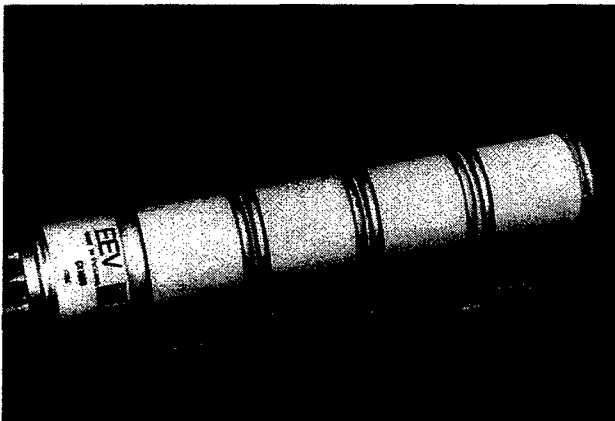


Figure 2. EEV type CX1699 thyatron.

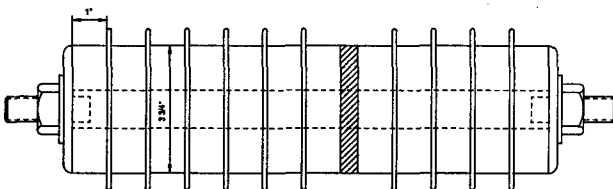


Figure 3. Damping resistor stack assembly.

The capacitor and resistor stack are coaxially mounted in an aluminum pipe filled with a silicon insulating fluid. The thyatron is housed in an accessible rectangular box section filled with the same fluid, at one end of the coaxial line. The other end of the line is provided with a ceramic high voltage feedthrough insulator in a separate section filled with Flourinert FC40 insulating liquid. This insulator provides an interface between the modulator and the magnet vacuum chamber. The outer pipe of the line section is the magnet return conductor. Figure 4 shows the modulator and kicker magnet assembly.



Figure 4. Modulator and kicker magnet assembly.

RESONANT CHARGING SYSTEM

The system repetition rate of 30 Hz requires a timing sequence that will allow charging of the energy storage capacitor to the operating voltage in 28 msec , and then fire the thyatron 3 msec later. This requirement is accomplished by using a resonant charging power supply. Figure 5 shows the resonant charging power supply. It consists an $85 \text{ to } 1$ step-up transformer with a resonant secondary, that is pulse driven by a lower voltage power supply with energy storage and a switching SCR. The low voltage power supply is inhibited when the SCR and thyatron are conducting.

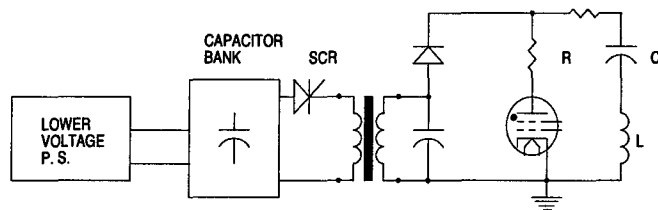


Figure 5. Resonant charging power supply

TRIGGER TIMING SYSTEM

The operation of the power supplies depends on proper timing and triggering. The major system components are

located in both the g-2 control room and in the center of the g-2 ring as shown in Figure 6. Fiber optic and transformer links are used where it is necessary to provide noise isolation.

A real time pulse, "AGS Pre-pulse" which is converted to a 27ms charge gate for the ALE charging supplies by a digital delay generator, initiates the kicker cycle. An SCR firing trigger is internally generated one millisecond after the end of this gate. The SCR discharges a storage capacitor bank into the resonant charge transformer, charging the main discharge capacitor. At approximately 2 ms after the charging, an AGS "beam request" trigger which is synchronous to the beam rf phase is received and delayed by approximately 56 μ s. Then, it is fanned out to three individually variable channels (to accommodate individual tube characteristics) and sent to a three channel sequential delay chassis used to minimize timing variations over the 6 burst pulses. These signals are then sent to the MOSFET trigger amplifiers that are transformer coupled to the thyatron grids firing the tubes.

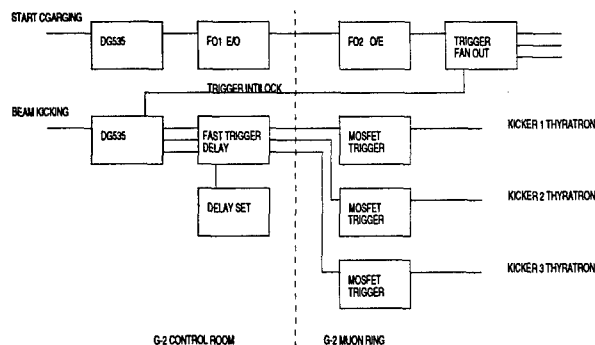


Figure 6. Trigger timing system.

TEST RESULT DATA AND CONCLUSION

The three modulators and their kicker magnets have been operating successfully without failure for the August 1998 and also the January and February 1999 g-2 physics runs. They have been running at 92 kV. Figure 7 shows a typical magnet current pulse at 95kV. The present operating mode is a six pulse burst. In the future the experiment will go to a 12 pulse burst. The modulator has already been tested successfully with 12 pulses. Figure 8 shows a complete system diagram.

ACKNOWLEDGEMENTS

The authors would like to express their appreciation to A. Soukas, J. Sandberg, W. Zhang, R. Lockey and A. Dunbar for their valuable engineering advice. Also, they would like to thank P. Rosas, J. Makoulis and F. Toldo for their design assistance. Finally, they would like to thank J.

Adessi, P. Benjamin, K. Hartmann, S. Kochis, S. Perlstein and D. Vonlintig for their expeditious help in manufacturing and assembly.

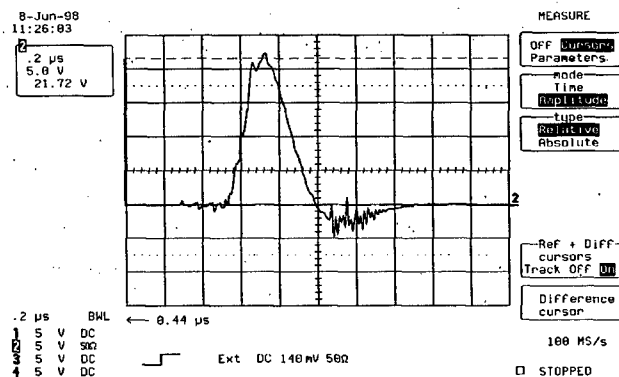


Figure 7. Kicker magnet current waveform (1kA/div, 200nS/div)

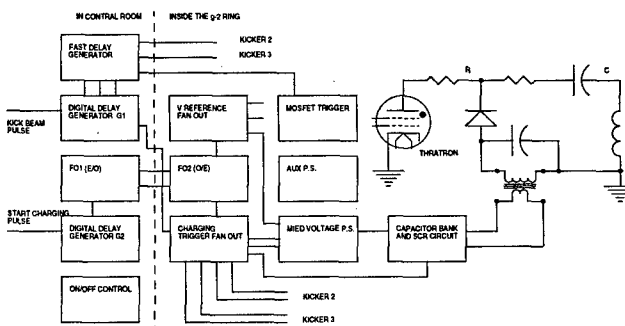


Figure 8. Modulator power supply diagram.

REFERENCE

1. Muon g-2 Design Report, AGS 821 July 1992, Brookhaven National Laboratory, AUI.
2. "Some High voltage Spark Gap Test Rest Results From The g-2 Kicker Modulator Power Supply" J. Mi, Y.Y. Lee, R. Sanders... 98' High Voltage Workshop October 22-23, 1998

SOLID STATE MODULATOR APPLICATIONS IN LINEAR ACCELERATORS

M.P.J. Gaudreau, J.A. Casey, T.P. Hawkey, J.M. Mulvaney, M.A. Kempkes, P. Ver Planck
Diversified Technologies, Inc. 35 Wiggins Ave., Bedford, MA 01730

1. ABSTRACT

The next generation of linear colliders will require an order of magnitude leap in pulsed power to millions of volts at thousands of amperes, delivered at much higher efficiency than is presently available. The current technology base of thyratrons, PFNs, etc., is inherently limited in scaling to meet these new requirements.

Diversified Technologies, Inc. (DTI), has had tremendous success since 1993 in the application of high

from 50A-1200A continuous. They also feature the very low drive current requirements of Field Effect Transistors (thus the Insulated Gate). This eliminates the need for cascaded stages of bipolar drives required by the low betas of early high current bipolar circuit designs.

To use IGBTs for high voltage switching, many devices

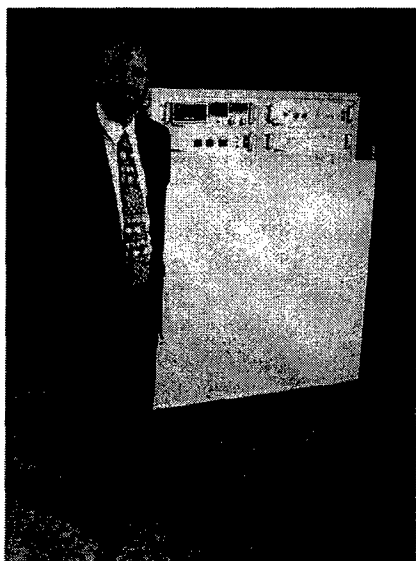


Figure 1 DTI's HVPM 100-500 100 kV, 50 MW Peak Pulse Modulator.

voltage IGBT devices to large, high-voltage and high-current modulator systems. DTI has sold commercial solid-state modulators capable of 20 to 160 kV and 150 to 2000 A for customer applications ranging from RF tube testing to ion-implantation. This technology is rapidly becoming the preferred alternative to conventional vacuum tube modulators and switches for future accelerator designs.

2. BACKGROUND

2.1 IGBTs

Solid state devices are, in general, low voltage devices. Recent advances in Insulated Gate Bipolar Transistors (IGBTs) have improved the voltage and current handling characteristics considerably. Typical devices have voltage ratings from 1200V-3300V and current ratings

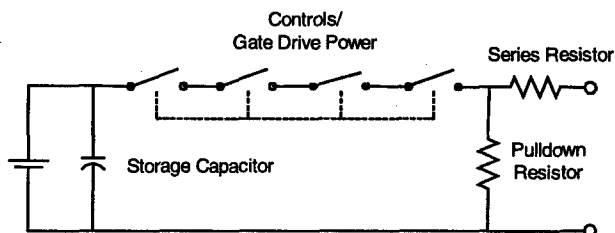


Figure 2: Solid State Modulator Components

must be cascaded in series. (Figure 2). This concept provides the flexibility of a modular design, with no inherent limit to voltage handling. However, it also necessitates the formidable task of ensuring that the load is shared equally between devices so that no single device sees harmful or destructive voltages. The gate drives must be highly synchronized to accomplish this. DTI has developed and patented the technology to achieve this synchronization, which has been demonstrated at up to 160 IGBTs in series, and up to six IGBTs in parallel.

The benefits of solid-state switching of high voltage include high reliability, significantly higher efficiency, and fast, repeatable switching characteristics. Our analyses have shown that these solid state systems are capable of providing 15x improvements in power efficiency during switching, and orders of magnitude improvements in reliability compared to vacuum tube and thyatron based switches.

3. SOLID STATE MODULATOR PRINCIPLES

3.1 Simple Switch – Ideal Pulse

Ideally, a modulator acts as a simple switch between a high voltage power supply and its load (such as a klystron). The desired properties of such an ideal switch would be infinite voltage holdoff, infinite off-resistance, zero on-resistance, and full immunity to transients and voltage reversals.

Achieving, as closely as possible, this ideal pulse is critical to the performance of a number of pulsed power applications. Generating pulses which closely approach this ideal pulse is typically a critical objective of high pulsed power system design.

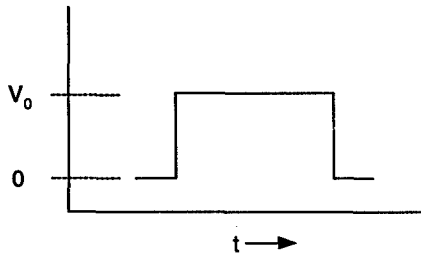


Figure 3: Ideal Pulse

Historically, vacuum switch tubes or thyratrons, alone, or in combination with Pulse Forming Networks (PFNs) and pulse transformers, have been used for this purpose. The non-ideal behavior of these conventional

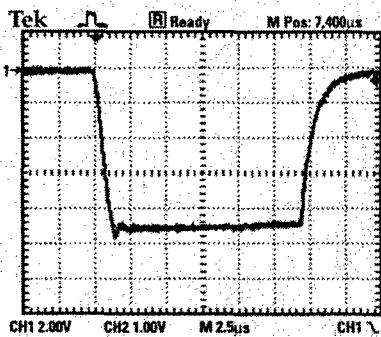


Figure 4: Nearly Ideal HVPM 100-500 Pulse 80 kV, 90A Into Water Resistor

switches includes a large effective voltage drop, limited current capability and speed, high maintenance, and complex driving and protection circuitry. As future system requirements extend to higher voltage and power, the use of vacuum tubes becomes increasingly impractical due to the inherent voltage and current limits of these devices.

4. APPLICATIONS

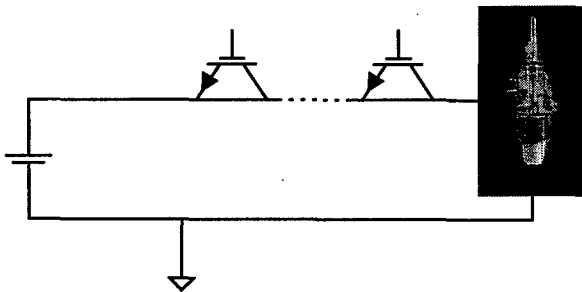


Figure 5: Cathode Modulator / Crowbar Replacement

4.1 Cathode Modulator

There are two principal approaches to applying high voltage solid-state modulators to accelerators. First, very high voltage and moderate current operation can be used to switch microwave devices directly. This also has the direct benefit eliminating the need for a separate crowbar circuit, since the switch can open rapidly in the event of an arc. Alternately, lower switch voltages at high currents can be used in conjunction with pulse transformers to provide pulses of energy. In either case, very fast risetimes and falltimes are required for operational and cost efficiency reasons. Furthermore, these basic circuits can be used either as cathode modulators or mod-anode modulators in typical accelerator systems.

4.2 Crowbar Replacement

The response time of DTI's technology provides a new level of protection to sensitive high power electronics, such as vacuum tubes. A typical crowbar, at 100 kV and 100 A current, will allow 20 J of energy through the arc even with a fast 2 μ S response- below the 50 J which may cause damage, but enough to degrade the lifetime of the tube.

DTI's switches can open and close in less than 0.5 μ S. This fast response allows these switches to operate as effective 'fast fuses'. Under the conditions described above, the energy available to cause tube damage is reduced by 75% to 5 J. Unlike a typical crowbar, however, the solid state switch can be closed again almost immediately. Furthermore, this cycle can be repeated indefinitely.

4.3 Mod-Anode Modulator

The same switching solid state switching technology can be applied to mod-anode modulators – either directly (hard switched) or in conjunction with a pulse

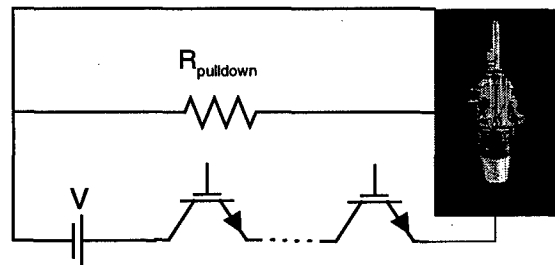


Figure 6: Mod-Anode Modulator

transformer. Typically, the lower power required for mod-anode modulation allows very fast operation. DTI has demonstrated a 20 kV mod-anode modulator for a Navy radar application capable of 400 kHz operation.

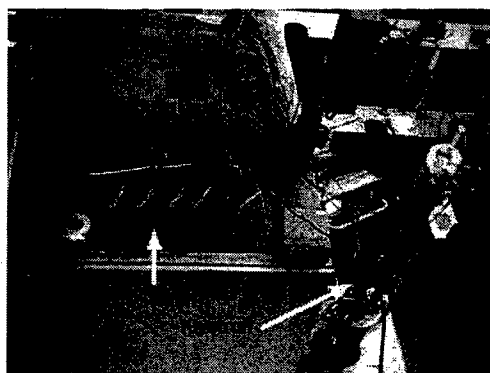


Figure 7: 45 kV, 30 A DTI Solid State Switch with Klystron at SLAC

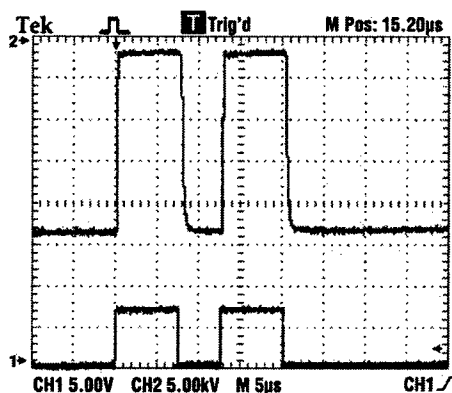


Figure 8: SLAC Prototype 45 kV, 30 A Switch Result @ 22 kV, 80 A Into Resistive Load

5. BENEFITS

The primary benefit of a full voltage (cathode) switch for advanced accelerators will be economic. The principal power loss in a direct switched system is the fCV^2 losses to the parasitic capacitance. The fast risetime capability of a direct switch will reduce power lost on ramp-up and settling time. A PFN or hybrid modulator/transformer approach will generally have a slower risetime because of series inductance, as well as additional magnetizing current and parasitic capacitance in the magnetics. This also allows fully programmable pulse-width, and the adaptability of the accelerator system to varying physics requirements.

5.1 Increased Efficiency

Switch tubes have an inherently high voltage drop across them. At high peak power, this results in significant power loss across the tube, and drives the need for substantial cooling systems for the tube itself.

5.2 Higher Reliability

Due to arcing and emissions/outgassing within the tube itself and short cathode life, vacuum tubes have an inherently limited lifetime. Although improvements have been made in tube manufacturing since WWII, tube lifetime is still limited to the thousands (tens of thousands in some case) of hours.

DTI's solid state modulators provide nearly infinite flexibility in pulse parameters (pulsewidth, PRF, peak current, voltage, and duty cycle). Typical rise / fall times for DTI's PowerMod™ Systems are $<0.5 \mu s$ for high power (MWs) pulses.

Line modulators and PFNs use resonant circuits to achieve high power pulses. These systems are designed to provide a very narrow range of PRFs and pulsewidths.

5.3 Increased Current Handling Capability

With DTI's solid state modulators, maximum current capability is a design parameter. DTI has built modulators capable of handling 2000A, and placing switch modules in parallel can accommodate higher currents.

5.4 Ruggedness

DTI's PowerMod™ solid state modulators are inherently rugged, isolated from external conditions, and able to provide consistent performance over a wide range of conditions. High voltage tubes, by virtue of their construction, are relatively fragile and susceptible to variations in performance due to operating conditions.

5.5 Safety from X-rays

High voltage power tubes produce X-rays due to inherent grid emission leakage or primary electron conduction. Shielding of the tube is required for safe operation. DTI's PowerMod™ systems do not create X-rays.

The combination of the technology required for advanced accelerators, and DTI's ongoing efforts to move to higher voltages, peak power, and frequency, provides both our government and commercial customers significant advantages in future high voltage, high power systems.

(wd)

A SOLID STATE INDUCTION MODULATOR FOR SLAC NLC*

R.L. CASSEL, G.C. PAPPAS, M.N. NGUYEN, J.E. DeLAMARE

Stanford Linear Accelerator Center

Abstract

The Next Linear Collider accelerator proposal at SLAC requires a high efficiency, highly reliable, and low cost pulsed-power modulator to drive the 500 kV, 260A X band klystrons. With a pulse width of less than 1.5 microseconds, it is difficult for the present SLAC type modulator with conventional pulse transformer to have a high efficiency due primarily to the inherently slow rise and fall time of the video pulse. The proposed induction modulator utilizes a pulse transformer similar to an induction accelerator driven by Solid State high voltage IGBTs. The performance of the IGBTs, induction cores and a low voltage model will be discussed as well as the design and construction of a prototype modulator capable of driving up to 8 of the X band klystrons

1.0 Design consideration efficiency, availability & cost

The major problem with the conventional PFN type modulator use at SLAC and around the world for the Next Linear Collider (NLC) is the efficiency of the modulator for short pulse operation. The leakage inductance for the pulse transformer and the stray inductance of the switching circuit inherently limit the rise and fall time of the klystron voltage waveform. To reach the efficiency goals of $> 75\%$ for the modulator for the NLC it is necessary to have a rise and fall time of the klystron voltage pulse of less than 200 ns. With the high voltage of the NLC klystron of 500 kV and large stray capacitance of > 100 pfd per klystron (RC time constant of 200 ns.) it is difficult to obtain a fast rise time with a matched impedance PFN modulator.

The operational availability of the standard SLAC type modulator is limited by the failure rate of hydrogen thyatron used for switching. In addition thyatron are subject to a high incidents of spontaneous triggering, which effects the overall accelerator availability.

The peak power of thyatron and circuit & PFN impedance limits the practical peak power of a SLAC type modulator to about 300 megawatts peak, or capability of driving more than two NLC klystron at one time. This makes the cost of modulators $>100k\$$ per klystron for the conventional SLAC modulator expensive to build.

1.2) Configuration Selection

To obtain a low leakage inductance, the pulse transformer configuration selected was the fractional turn transformer

with a one turn secondary. This configuration is similar to an induction accelerator with a conductor in place of the beam. The resulting secondary leakage inductance is extremely low ($<1 \mu\text{hy}$). The major part of the leakage induction coming from the multiple primary connections and the drivers.

To obtain 500 kV for 1.5 usec. (0.75 volt seconds) with one turn secondary requires a large magnetic core cross sectional area. To drive the core without using a matched PFN requires a switch that can not only turn on fast at high power levels but also turn off. This switching devices now exists in the form of IGBT's (Isolated Gate Bipolar Transistors). IGBT's are now available from several manufactures which can switch on and off in < 100 ns to power levels of 5 megawatts per device. High voltage devices capable of switch > 10 megawatts for 1.5 μsec . are under development.

The use of one turn secondary fractional turn transformer combined with high current IGBT allows for the driving of 8 klystron with one modulator or approximately 1000 megawatts of power for 1.5 μsec . The larger number of klystrons per modulator reduces the overall cost and size of the modulator. Figure 1.

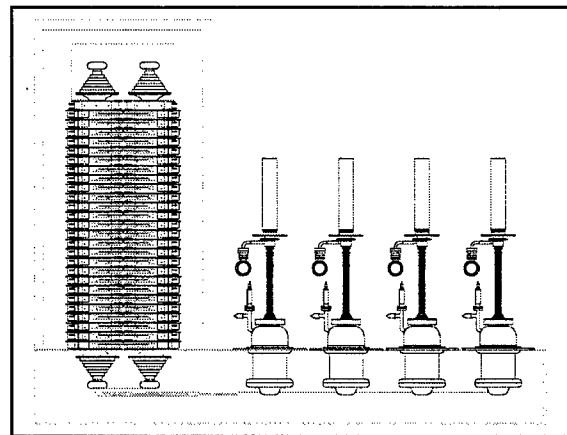


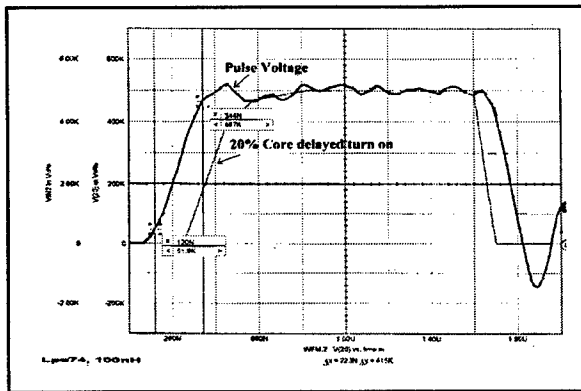
Figure 1. Induction Modulator Layout

1.3 Induction Modulator Specification

• NUMBER OF NLC KLYSTRONS	8 EACH
• OPERATING PULSED VOLTAGE	500 kV
• OPERATING PULSED CURRENT	2120 AMPS
• REPETITION RATE	120 Hz
• VOLTAGE REGULATION FLAT TOP	$<\pm 1.0 \%$
• RISE /FALL TIME	$<200 \text{ ns}$
• PULSE DURATION FLAT TOP	1.5 μsec
• ENERGY EFFICIENCY	$>75\%$
• NUMBER SECONDARY TURNS	1

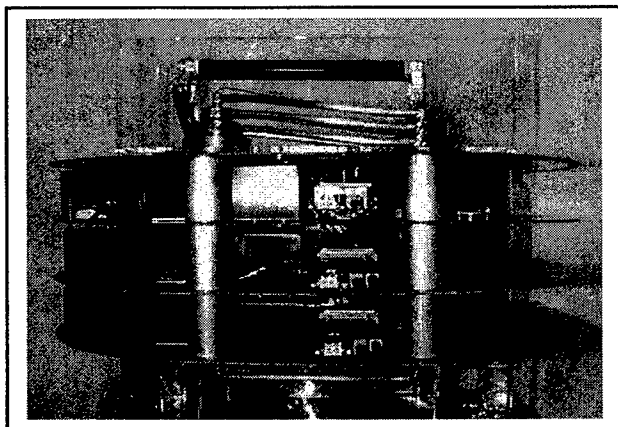
*Work supported Department of Energy contract DE-AC03-76SF515

Spice simulations were made on the induction modulator driving eight klystron with a 100 cell induction modulator using the turn on and turn off characteristics of the EUPEC IGBTs. The resulting waveform had a small amount of overshoot ringing. By delaying turn on of less than 20 % of the cells the waveform performance can be improved. Figure 4. The Spice simulations did not adequately take into account the losses introduced by the transformer cores, which should help in reducing the waveform ringing. The resulting rise time was approximately 200 ns. The resulting waveform power efficiency of better than 89%, which indicates the possibility of reaching the 75% efficiency goal. Figure 6.

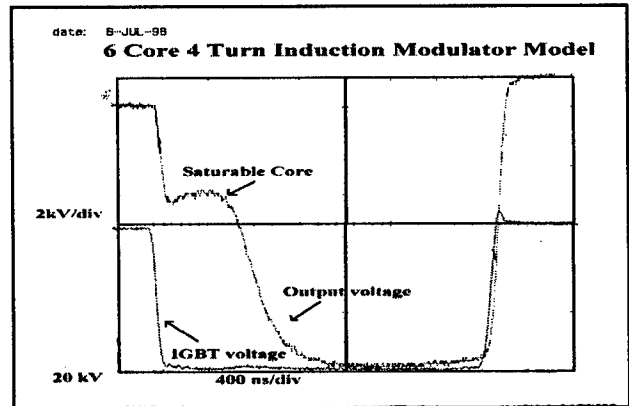


1.7 Model of Induction modulator

A model of the induction modulator was fabricated to study the performance of the cores and IGBT's. It consisted of 6 core with 0.004 Volt-Second driven from 6 1700 volt IGBTs. There were 4 secondary turns. In addition there was a saturated core to increase the rise time and lower the IGBT losses. Figure 7.



The model demonstrated that the concept was workable. The total reset of the magnetic cores, allowed for one or more of the IGBTs to be not functional or shorted with only a reduction in the output voltage in the overall performance of the system. Figure 8.



1.8 Induction modulator advantages

There are several additional advantages of the Solid State induction modulator over the conventional modulator. All of the high voltage parts are inside the transformer core and not exposed. The core drivers are at ground potential with only the IGBTs collector and the capacitor are at moderate voltages. The addition of more driver cells then are required for the 500 kv results in redundancy so that an individual driver or core could fault without effecting the overall operation of the modulator. The pulse duration is only determined by the volt-seconds in the core so that a shorter pulse can be obtained by timing for conditioning of the klystron or accelerator or if operated at a lower voltage a longer pulse is available.

1.9 Conclusions

From the modelling, measurement of core, and IGBT and calculation it appears that the induction modulator is feasible and practical. It has the potential of high efficiency and reliability and low cost. Figure 9.

		joules	120hz watts	100 watts/cell
Total Power 500KV * 2120 A * 1.5 usec		1,590.0	190,800	
Efficiency	76.5%	487.6	58,506	
Pulse wave form (200 nsec)	88.5%	182.9	21,942	
Core loss Total	95.4%	72.4	8,688	87
Power Supply 5Kv 250Kw	95.0%	80.0	9,600	96
Solid State (IGBT + diodes)	95.7%	68.6	8,232	82
Stray Impedance	96.3%	58.4	7,008	70
Capacitor & Snubbers	98.4%	25.3	3,036	30
		joules	watts	watts/cell
Total power used		2,077.6	249,306	366

The R&D on a prototype modulator is underway with a collaboration of SLAC and LLNL to produce a working unit by the end of FY 00.

FAST SCR THYRATRON DRIVER*

M. N. Nguyen

Stanford Linear Accelerator Center
Stanford, California 94309

Abstract

As part of an improvement project on the linear accelerator at SLAC, it was necessary to replace the original thyatron trigger generator, which consisted of two chassis, two vacuum tubes, and a small thyatron. All solid-state, fast rise, and high voltage thyatron drivers, therefore, have been developed and built for the 244 klystron modulators. The rack mounted, single chassis driver employs a unique way to control and generate pulses through the use of an asymmetric SCR, a PFN, a fast pulse transformer, and a saturable reactor. The resulting output pulse is 2 kV peak into 50 Ω load with pulse duration of 1.5 μ s FWHM at 180 Hz. The pulse risetime is less than 40 ns with less than 1 ns jitter. Various techniques are used to protect the SCR from being damaged by high voltage and current transients due to thyatron breakdowns. The end-of-line clipper (EOLC) detection circuit is also integrated into this chassis to interrupt the modulator triggering in the event a high percentage of line reflections occurred.

1 INTRODUCTION

The original thyatron driver had been designed and used since the beginning of SLAC modulator operations in the middle sixties. It could generate up to 5 kV at 1.5 μ s pulses. However, it was large and heavy, required frequent intervention, and used PCB dielectric capacitors and unreliable thyatron and vacuum tubes. In 1992, a

modulator reliability improvement project was established, and one phase was to replace these original drivers with solid-state trigger drivers utilizing modern components and packaging techniques. Besides meeting certain electrical and mechanical requirements, the new trigger generator reliability and manufacturing cost were of major concerns. Fast and extremely stable thyatron drivers had been designed and built for the kicker systems at SLAC [1-2], but they were quite expensive because of high part and assembly costs. This report describes the design and performance of an economical, reliable, fast, and high voltage thyatron driver.

2 DESIGN

A simplified circuit diagram of the driver is shown in figure 1. The basic pulse generating circuit consists of four essential components. They include a pulse transformer, a PFN, a thyristor, and a saturable reactor.

The pulse transformer T2 was commercially made by Stangenes Industries. It has a turns-ratio of 6 to 1 with a primary leakage inductance of only 100 nH.

The PFN, which comprises C2, C3, and L1, is a 1-section voltage-fed network that simulates an open-ended transmission line [3]. Its characteristic impedance, Z_n , was designed to match with the load impedance reflected through the transformer. Lumped parameters were determined as follows.

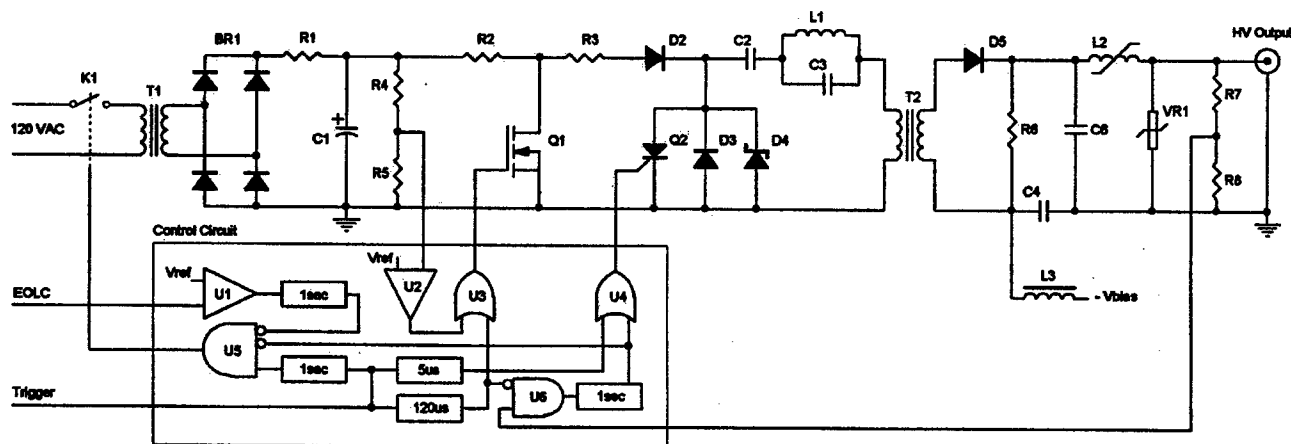


Fig. 1: Simplified circuit diagram.

* Work supported by the Department of Energy under contract No. DE-AC03-76SF00515.

$$\begin{aligned} C2 &= Cn \\ C3 &= Cn / 2 \\ L1 &= 2 L_n / \pi^2 \end{aligned}$$

where network capacitance Cn and inductance L_n were derived from the desired 50Ω load impedance and $1.5 \mu s$ pulse duration.

$$\begin{aligned} Z_n &= Z_{load} / N^2 \\ &= 50 / 6^2 \cong 1.4 \Omega \end{aligned}$$

$$\begin{aligned} C_n &= \tau / 2 Z_n \\ &= 1.5 \times 10^{-6} / 2 \times 1.4 \cong 0.6 \mu F \end{aligned}$$

$$\begin{aligned} L_n &= C_n Z_n^2 \\ &= 0.6 \times 10^{-6} \times 1.4^2 \cong 1.2 \mu H \end{aligned}$$

The thyristor Q2 is an asymmetric SCR from Mitel model ACR44. It is rated at 1200 V, 69 A RMS, and was particularly selected for its high di/dt rate of 2000 A/ μs .

The saturable reactor L2 reduces the output risetime by a factor of three. It has a volt-second product of 225 V μs , which was determined from the capacitor C6 charging voltage. Fair-Rite 43 NiZn material was used because of its relatively high magnetic flux density and low cost. An off-the-shelf ferrite bead P/N 2643540202 was then selected to fit in the available space on the PC board. The core o.d., i.d., and length h is 14.3 mm, 6.35 mm, and 13.8 mm respectively. From common transformer equations, the number of turns (N), the current required at saturation (I_s), and the saturated inductance (L_s) were calculated as follows.

$$N = E_p t_s / \Delta B A_c$$

where:

$$\Delta B = B_s = 0.275 \text{ T at } H_s = 795 \text{ A/m}$$

$$A_c = h (od - id) / 2 = 55 \times 10^{-6} \text{ m}^2$$

$$l_e = 2\pi (od + id) / 4 = 32 \times 10^{-3} \text{ m}$$

$$N = 225 \times 10^{-6} / 0.275 \times 55 \times 10^{-6} \cong 14 \text{ Turns}$$

and:

$$I_s = H_s l_e / N$$

$$= 795 \times 32 \times 10^{-3} / 14$$

$$= 1.8 \text{ A} \approx 5\% \text{ load current}$$

and:

$$L_s = \mu N^2 A_c / l_e$$

where:

$$\mu = \mu_0 \mu_{sat} = 1.256 \times 10^{-6} \times 2 = 2.5 \times 10^{-6} \text{ H/m}$$

$$L_s = 2.5 \times 10^{-6} \times 14^2 \times 55 \times 10^{-6} / 32 \times 10^{-3} = 0.85 \mu H$$

The following is brief description of the circuit operation.

Low-level voltages simultaneously trigger three retriggerable monostables of 1 second, 120 μs , and 5 μs wide pulses. The first pulse of 1 second, which is gated by U5, switches on solid-state relay K1 for the high

voltage power supply. Subsequent pulses of 5 μs and 120 μs are then used to trigger SCR Q2 and MOSFET Q1. While the MOSFET serves to turn off the SCR by shunting anode current, it is also used as a switching element to regulate the PFN charging voltage by way of error amplifier U2. Figure 2 shows waveforms of Q1 switching regulation and PFN charging voltages. Comparator U1 monitors peak and average currents of the modulator EOLC, and turns off the power supply when these currents exceed a predetermined value.

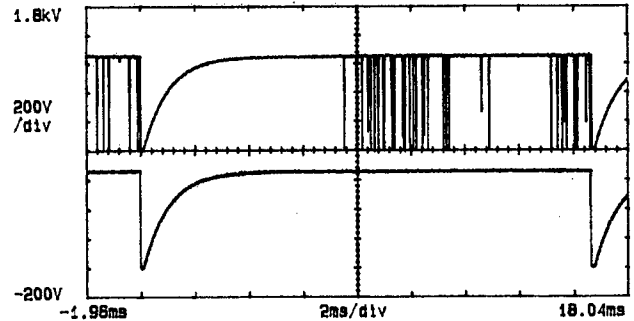


Fig. 2: Typical MOSFET and PFN charging voltages.

When the AC line supplies 120 V to power transformer T1, the secondary voltage is rectified and filtered and shunt-regulated to ≈ 640 VDC by BR1, C1, R1, R2, and Q1. The PFN is resistively charged at the same time by the regulated voltage via R2, R3, and D2. Once Q2 is turned on, the PFN discharges one-half of its voltage into the primary of pulse transformer T2. The secondary voltage is then applied to saturable reactor L2 which, when saturated, sharpens the output voltage rise. The resulting pulse output of 2 kV peak into 50Ω resistive load (4 kV open circuit) at 1.4 μs FWHM is shown in figure 3.

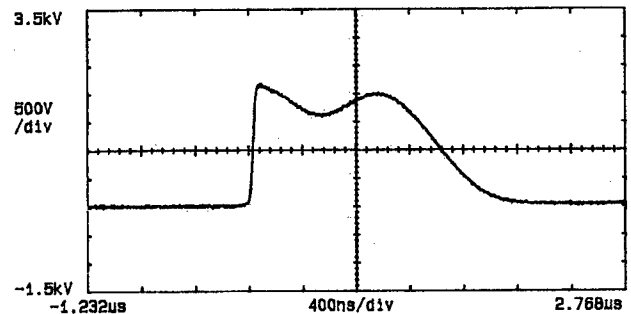


Fig. 3: Output voltage waveform.

Figure 4 shows the effect of saturable reactor on output risetime. A 1-stage pulse sharpener shortens the voltage rise as shown from 119 ns (10 – 90%) to 36 ns. A second stage, which has been tested with CMD-5005 core but not been implemented on this chassis, further reduces the risetime to 12 ns.

Thyratron breakdowns as a result of either misadjusted reservoir voltages or aging thyratrons [4] can generate destructive transient voltage and current for the SCR; therefore, several SCR protection devices are necessary.

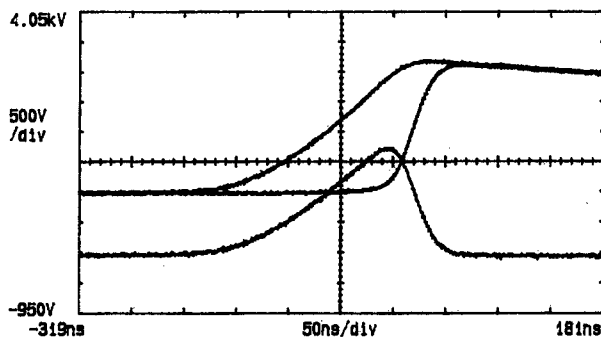


Fig. 4: Voltage rises before and after 1-stage sharpener, and saturating reactor voltage.

Fast turn-on diode D3 and transorb D4 are used to limit the anode reverse and forward blocking voltages. On the output side, VR1, which consists of two series GE metal-oxide varistors rated 180 joules at 1.2 kV each, clamps down transient voltages while diode D5 blocks the reverse current. To further reduce the chance of an SCR failure by a soft turn-on due to high ground potentials, which can sometimes build up on the gate after a rapid set of thyatron fire-throughs, an active feedback scheme is employed. A portion of the output voltage is gated through U6 with the 120 μ s command trigger pulse. A thyatron arc that randomly occurs outside this timing window would immediately turn on the SCR and shut off the high voltage supply for a period of 1 second before returning to normal operation.

For ease of manufacture and low assembling cost, all connectors and electrical components were mounted on a single 0.093 inches thick PC board. One exception was the output HN connector that must be mounted directly on the chassis for mechanical strength. The driver was simply constructed by fitting together the PC board, front, rear, and side panels of a standard 19 x 5.25 x 8 inches rackmount chassis. Figure 5 shows a photograph of the complete trigger generator PC board.

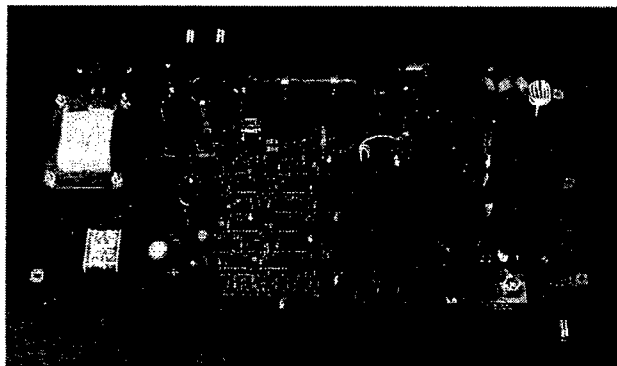


Fig. 5: Photograph of the complete driver on PC board.

3 PERFORMANCE

Jitter and long-term timing drift were measured with SR-620 Universal Time Interval Counter. The test conducted

at 120 Hz with a sample size of 5000 shots. A typical result of jitter distribution is shown in figure 6. The graph displays a peak-to-peak jitter of 320 ps with standard deviation or RMS jitter of 72 ps. Throughput delay, defined as the timing difference (on rising edges at half maximum) between the trigger input and the pulsed output, is 580 ns. A 24-hrs run test at 20°C temperature excursion resulted in a timing drift of less than 3 ns.

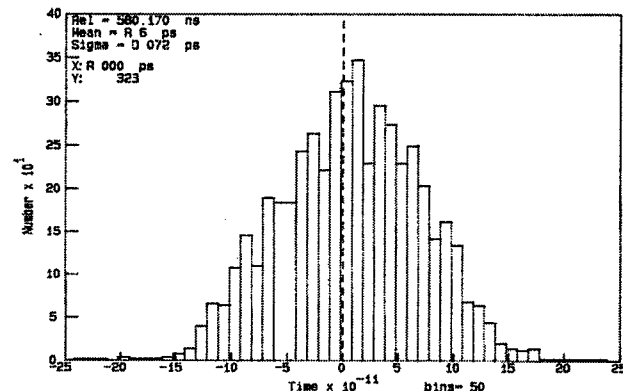


Fig. 6: Histogram of jitter distribution.

The mean time to failure (MTTF) rate, which was calculated based on actual data collected over several years, is 195,000 hours. More detailed discussions of the modulator reliability can be found in the report [5].

4 CONCLUSION

New thyatron drivers for the 244 SLAC klystron modulators have been economically built and operated since 1994. In several years of operation, these drivers have contributed to the modulator stability and proven to be very reliable.

5 ACKNOWLEDGMENTS

The author wishes to thank R. Cassel for his valuable comments, A. Donaldson for support and editing help, and the AMW crew for their hard work in bringing this project to a successful completion.

6 REFERENCES

- [1] T. Mattison *et al.*, "Status of the SLC Damping Ring Kicker Systems", Proc. of the 1991 IEEE Particle Accelerator Conf., San Francisco, pp. 2955 - 7.
- [2] M. Nguyen and R. Cassel, "Fast Thyatron Driver", Proc. of the 1991 IEEE Particle Accelerator Conf., San Francisco, pp. 3153-5.
- [3] G. N. Glasoe and J. V. Lebacqz, "Pulse Generators", New York and London, 1948, McGraw-Hill Book Company, Inc.
- [4] A. R. Donaldson *et al.*, "Kicker Experience from SLC", Proc. of the 1991 IEEE Particle Acc. Conf., San Francisco, pp. 3165 - 7.
- [5] A. R. Donaldson, "SLAC Modulator System Improvements and Reliability Results", Proc. of the 1998 International Power Modulator Symposium, Rancho Mirage, pp. 74 - 9.

Damping Ring Kickers for the Next Linear Collider*

C. Pappas, R. Cassel
Stanford Linear Accelerator Center

ABSTRACT

The Next Linear Collider (NLC) uses a damping ring for the electron beam, a pre-damping ring and a main damping ring for the positron beam to reduce the beam emittances. The requirements of the main damping ring kickers are to bend a 2 GeV beam by an angle of 2 mrad over a length of 1.2 m. This results in a required field of 139 G. The magnet aperture is 30×30 mm. The pre-damping ring kicker requirements are based on a 2 GeV beam with a bend angle of 8 mrad in 1.2 m, or a field of 308 G. The magnet aperture is 62×45 mm (H×V). A pulse width is 130 ns with rise and fall times of less than 60 ns is the same for both the pre-damping ring and main damping ring kickers. The three rings operate at a 180 Hz repetition rate¹.

The kicker magnets being developed to meet these requirements consist of two strip line conductors in the vacuum chamber, for the pre-damping ring kickers they may be loaded with ferrite, to give a matching impedance of 25 Ω . The buses are separated from magnetic flux linkage by a grounded flux excluder, which also serves as a low impedance return for the beam current. Both busses of the magnet are driven in parallel from the same modulator and are grounded at the end opposite the feed. The modulator uses two IGBT stacks which both act as opening switches in order to meet the rise time requirements.

1. Damping Ring Kicker Magnets

Several types of magnets were considered to meet the difficult rise time parameters for the damping ring kickers. An air core, strip line, matched impedance magnet was decided upon because of its simplicity, low cost, and it uses no non-linear materials². The magnet is made from a slotted pipe which is housed in the vacuum chamber. A metal strip is brazed onto the top and bottom of the slotted pipe to prevent magnetic coupling between the two busses during the pulse rise time. A drawing of the magnet is shown in Figure 1. This magnet was analyzed with the electro-magnetic field solver MAXWELL. The impedance of the magnet was calculated to be 32 Ω , and the one way transit time to be 3.49 ns per meter. A plot of the B field magnitude with a drive current of one ampere is shown in Figure 2.

*Work supported by Department of Energy contract DE-AC03-76SF515.

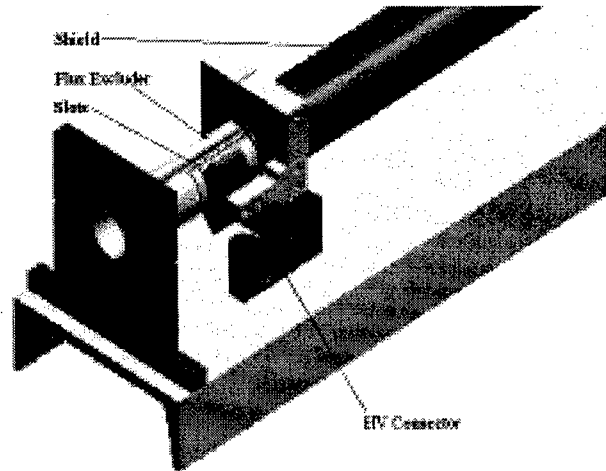


Figure 1. Proto type slotted kicker magnet.

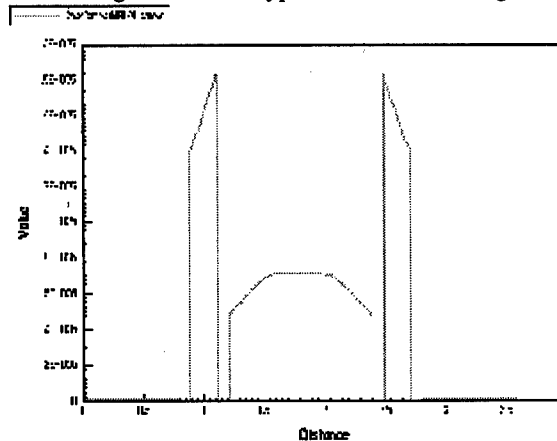


Figure 2. Calculated B field magnitude.

A one meter long, stainless steel magnet was built and tested. An oscillograph of the magnet current, B dot, and the B field are shown in Figure 3. It can be noted from this data that the current in the magnet is constant while the B field rises as time progresses. After eliminating the B dot probe, electric fields, digitization error, and other measurements errors, it was determined that the slope of the B field might be explained by skin depth effects caused by the stainless steel. Because the resistivity of stainless is approximately fifty times greater than copper, the steel magnet structure will allow the currents to penetrate further into the conductors, essentially increasing the width of the slits, and hence the magnetic field. The magnetic field was recalculated allowing the currents to penetrate further into the magnet busses by increasing the permeability of the conductors. It was found that the magnetic field intensity increased by a

factor of approximately 12 % with a decrease in the permeability of the conductors used in the calculations for 0.001 to 0.01. Based upon these calculations the magnet was plated with 10 mils of copper, and tested again. The results of this testing are shown in Figure 4, where it is clearly seen that the **B** field no longer increases during the pulse.

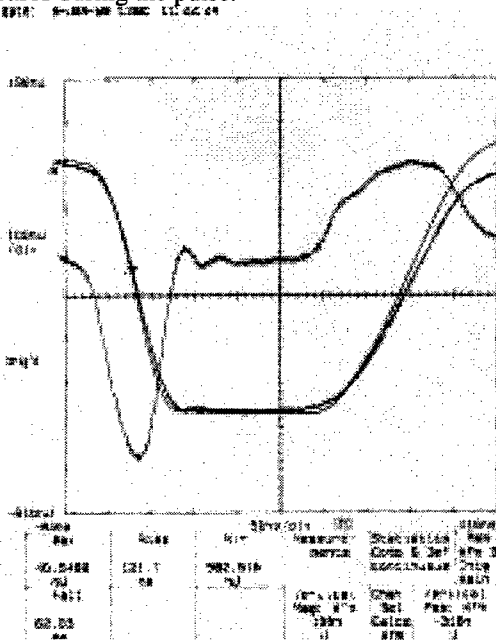


Figure 3. **B** field and current in the stainless steel magnet.

Further measurements were then made both with and without the shield in place, and the results were compared with the calculated values of the magnetic gain. The **B** dot probe was rotated 180 ° for each measurement and the traces were subtracted to eliminate the effects of electric field. Figure 5 shows the magnet current, and integrated **B**·**l** curve with the shield, and Figure 6 shows the same curves without the shield. The measured gain of the magnet with the shield is approximately 69 mG/A, while the calculated gain is approximately 71 mG/A. With the shield removed the gain is measured to be approximately 118 mG/A, and the computed gain is 117 mG/A.

The impedance of the magnet was then measured with a TDR and compared with the calculated values. The measured impedance with the shield was approximately 35 Ω and the computed impedance was 32 Ω. Without the shield we measured the impedance to be 61 Ω, and calculated it to be greater than 53 Ω. Initial beam impedance measurements performed at Lawrence Berkeley National Laboratory indicate that the magnet structure will not seriously impact beam performance.

2. The IGBT Based Modulator

A solid state modulator which uses a set of IGBTs as the switching element is being developed. A schematic of the

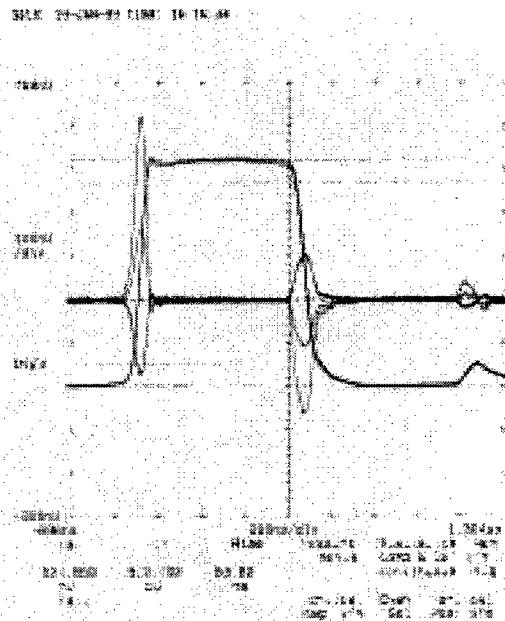


Figure 4. **B** field and current of the copper plated magnet.

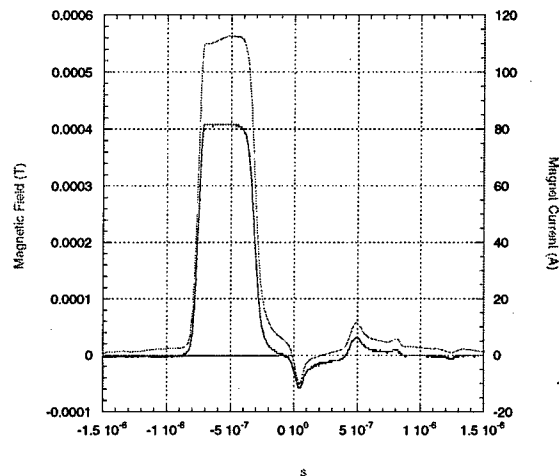


Figure 5. Magnet current and integrated field with shield.

circuit is shown in Figure 7. The operation of the circuit is as follows. The IGBT stack to the right is turned on to begin charging of the capacitors through the diodes. When the capacitors are fully charged the IGBT stack to the left is turned on, putting the full voltage across the saturable reactor. Just as the core of the reactor saturates, the IGBTs to the right are opened, transferring the current to the load. The pulse is ended by opening the IGBT stack on the left. This switching scheme is done to utilize the opening characteristics of the IGBT modules, which are faster than the closing speed. A model of the circuit has been built which uses three Eupec BSM-300GA-170DN2S, 1700 V, IGBTs in each stack. The circuit has been fully tested, and was used as the pulser for the data in this paper³. Higher voltage devices (3300 V) have also been purchased, and have been found to have better

switching characteristics. We are currently waiting delivery of 6500 V devices⁴.

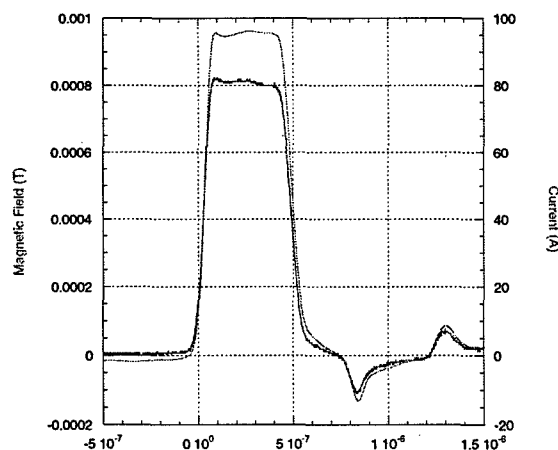


Figure 6. Magnet current and integrated field without shield.

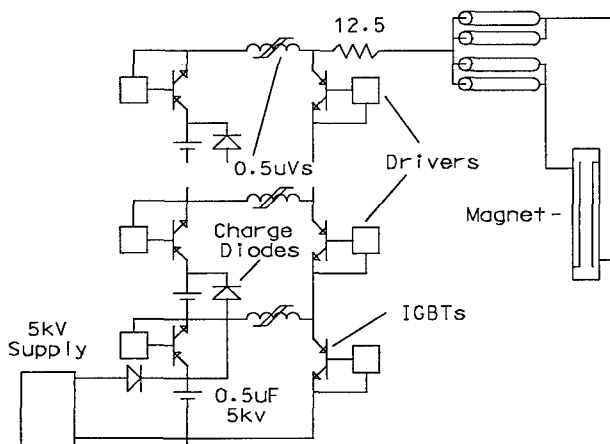


Figure 7. Schematic of solid state modulator.

3. The Pre-damping Ring Kickers.

Work has begun on the pre-damping ring kickers, with several different types of magnets under consideration. A slotted pipe kicker similar to the one above, a similar magnet which would be ferrite loaded, and a traveling wave C-magnet similar to the SLAC damping ring kickers⁵ are being studied. With the simple geometry shown in Figure 8, the magnetic gain and impedance of both an air core, and ferrite loaded kicker magnet have been calculated. For the air core magnet the gain is approximately 35 mG/A, with an impedance of 46 Ω . This magnet would therefore require the IGBT to switch 4400 A, if a circuit similar to Figure 7 were used. When the magnet is loaded with ferrite, the magnetic gain is increased to approximately 160 mG/A, and the impedance is reduced to 27 Ω , therefore the IGBT current would be reduced to 963 A. The field is also slightly more uniform if the magnet is load with ferrite. One

problem with a ferrite loaded magnet, besides complexity and cost, is that some method would have to be incorporated to make sure that there are no large air gaps between the ferrite and the conductors. The ferrite could be put into the vacuum chamber and sandwiched between the conductors and a sheet of soft metal such as indium, or the ferrite could be potted between the busses, which would necessitate a ceramic beam pipe. Another problem is that he ferrite would load the beam, which would require cooling for the ferrite.

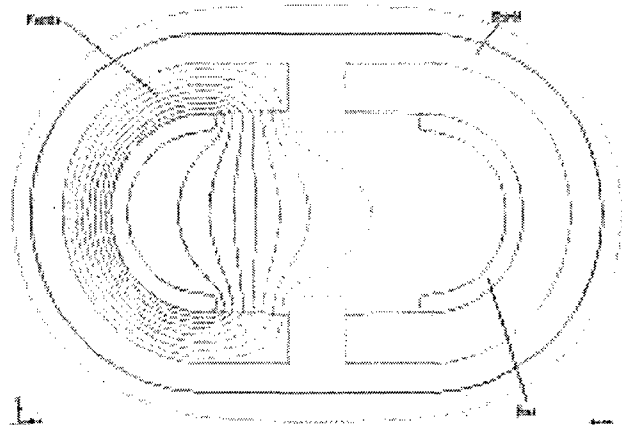


Figure 8. Magnetic flux lines in ferrite loaded kicker.

4. Conclusions

A slotted pipe kicker magnet is being developed at SLAC for the NLC damping rings, which does not appear to have any major problems. It can be driven by a solid state, IGBT based modulator. The overall cost and reliability of such a kicker system should be much better than for a conventional type of kicker system. Development of a pre-damping ring kicker system has begun, with several options available. Further research is required before a decision can be reached as to which technology is preferable.

5. References

- [1] *The Next Linear Collider Damping Ring Complex*, M. Ross, etal, this conference.
- [2] *A Slotted-pipe Kicker for High-current Storage Rings*, G. Blokesch, etal, Nuclear Instruments and Methods in Physics Research A 338 (1994).
- [3] *A Solid State Induction Modulator for SLAC SLC*, R. Cassel, etal, this conference.
- [4] *Eupec Electronic Data Book, 1999*, Eupec Inc., Lebanon, NJ.
- [5] *Kicker Systems for the Stanford Linear Collider*, T. Mattison, etal, 1990 Journal, Particle Accelerators.

IMPLICATIONS OF NEW INDUCTION CORE MATERIALS AND COATINGS FOR HIGH POWER INDUCTION ACCELERATORS *

A. W. Molvik⁺, W. R. Meier, R. W. Moir, LLNL, Livermore, CA;
A. Faltens, LBNL, Berkeley, CA

Abstract

Two recent developments enable induction accelerators to achieve better and more consistent performance with higher efficiency. First, better and more consistent performance is achieved with insulating coatings that allow magnetic cores to be annealed after winding. Second, losses are reduced by a factor of 2-3 with nanocrystalline alloys, while the flux swing is only slightly reduced to 2.0 T compared with 2.3 T with economical amorphous alloys. One metric for selecting between the alloys is the cost-of-electricity, COE. A systems code optimizes an accelerator and compares the COE for higher flux-swing amorphous and higher-efficiency nanocrystalline materials and for several variations in assumptions.

1 INTRODUCTION

Heavy ion inertial fusion (HIF) has attractive prospects for generating electrical power at reasonable cost, with high availability, safety, and low activation.[1,2] These advantages are, in large part, due to the use of thick liquid walls of Flibe, a lithium-containing, low-activation molten salt.[2] The liquid walls shield the vacuum chamber solid walls from neutrons and gamma rays and also generate tritium in a continuously replaced blanket that eliminates the need to shutdown for blanket replacement, thereby providing high availability.

Induction accelerators have been selected by the U.S. HIF program because their high current and high power capability eliminates the need for one or more storage rings to accumulate, then rapidly extract the ion beams. Acceleration occurs from pulsing a voltage across the primary winding of a magnetic core, which then couples through an insulating vacuum barrier to induce a voltage along the beam. By timing the pulsers to reach full amplitude as the beam arrives, the ion beam experiences a succession of D.C. accelerating fields.

Induction cores and pulsers form one of the major cost areas[3] for HIF: to achieve GeV range ion energies and several MJ beam energy per pulse requires of the order of 10^7 kg of magnetic alloy tape. The coupling of the cores to the beams is determined by Faraday's Law, which for our purposes is conveniently expressed as

$$V_C \Delta t = A \Delta B$$

*Work performed under the auspices of the U.S. Department of Energy under contract No. W-7405-ENG-48 (LLNL) and DE-AC03-76F00098 (LBNL).

⁺ Email: molvik1@llnl.gov

where V_C is the voltage induced across an insulated gap for a time Δt , by a core with a cross-sectional area (equivalent solid metal area) A , and a magnetic flux swing ΔB .

Short pulse performance is strongly degraded by interlaminar eddy currents, unless interlaminar insulation is provided. By applying Faraday's law to a single lamination (15-25 μm thick and 0.025-0.2 m wide) with a flux swing of $\Delta B=2.3$ T for durations between ~ 0.2 μs and 20 μs , we find the average interlaminar voltage can reach ~ 60 V. The difficulty of insulating cores is increased by the necessity of magnetic annealing (at 300-550° C in ~ 80 A-turns/m magnetic field parallel to the laminations and perpendicular to the core axis) in order to maximize ΔB and minimize the core losses. The insulation must not only withstand the temperature but must not apply significant mechanical stress to the alloy during cool-down, or the performance will be degraded.

We have used mica-paper insulation, co-wound with METGLAS 2605SC,[4] and proprietary inorganic insulating coatings supplied by core manufacturers in the tests described here. After surveying a variety of alloys,[5] we selected two distinct types to examine with a driver and power plant systems code.[3] The alloys are 2605SC from Allied Signal, selected for a larger usable flux swing of 2.3 T and moderately low losses, and the nanocrystalline alloy Finemet FT-1H from Hitachi (VITROPERM 800F from VACUUMSCHMELZE is similar), selected for a moderate flux swing of 2.0 T and very low losses, as shown in Fig. 1 and listed in Table 1. Core losses account for most of the pulsed energy losses in an induction linac, so minimizing the core loss decreases the capital costs of

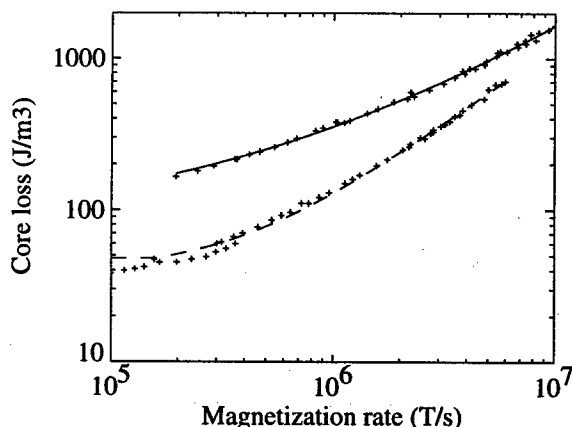


Figure 1: Loss data (plus) and fits for 2605SC amorphous (solid line) and FT-1H nanocrystalline (dashed line) cores.

Table 1: Loss coefficients and loss in J/m³ for two pulse durations 0.42 and 1.0 μ s.

Alloy	Loss coef.	Loss(0.42,1.0)
2605SC	81, 193, 119	1044, 577
+bias	89, 213, 132	1433, 782
FT-1H	51, -49, 200	565, 241
+ bias	55, -54, 220	855, 363

pulsers and increases the accelerator efficiency. Core losses are fit by[6]

$$U\left(\frac{J}{m^3}\right) = C_1\left(\frac{\Delta B}{2.5}\right) + C_2\left(\frac{\Delta B}{2.5}\right)\left(\frac{dB}{dt}\right)^{0.5} + C_3\left(\frac{\Delta B}{2.5}\right)^2\left(\frac{dB}{dt}\right)$$

where B is in Tesla, dB/dt is in T/ μ s, and the coefficients are listed in Table 1.

We use \$5/kg as a cost goal for assembled cores of 2605SC. Based on estimated niobium costs of ~\$30/kg, the 3% Nb in nanocrystalline materials would add ~\$1/kg to the cost, so we assume \$6/kg for assembled nanocrystalline cores.

2 ACCELERATOR SYSTEMS STUDY

The accelerator design parameters are chosen to satisfy constraints imposed by the fusion target design. For this paper, we design to a close-coupled target[7] which minimizes accelerator costs by requiring less beam energy (3.3 MJ) to deliver a yield of 430 MJ vs. 5.9 MJ to deliver a yield of ~400 MJ with a previous distributed radiator design.[8] The disadvantage of using the close coupled target is that each elliptical beamlet must be focused to an area with an equivalent circular spot radius of 1.7 mm, as compared with 2.7 mm for the distributed radiator target. The close-coupled target calculation used a lead ion beam, but the systems code finds lower costs with lower mass ions.

Systems studies have shown that lower M/Q ions with their lower ion energy will shorten the accelerator and reduce costs.[9] The target performance is essentially invariant to the beam-ion mass, if the ion energy is adjusted to keep the range (stopping distance) constant, and the pulse duration and beam energy (MJ) remain the same. The optimum is below M/Q=50, but the higher beam current requires better space-charge neutralization[10] in order to focus the beam to the 1.7 mm spot radius required on target. Kr⁺ was chosen as a compromise: it is near the minimum cost for present concepts of induction linacs, without requiring the maximum neutralization. The target requirements are met with a 1.3 GeV Kr⁺ main pulse ion beam to deliver 2.8 MJ in 8 ns and a 0.85 GeV Kr⁺ prepulse ion beam to deliver 0.5 MJ in 30 ns. A lower ion mass could further reduce the costs by ~20%.

The accelerator architecture is simplified by transitioning to magnetic quadrupole focusing at a low energy of 1.6 MeV, and omitting beam combining.

Several optimizations by the systems code for 2605SC are shown in Fig. 2, where the cost multiplier is plotted

vs. the reference value multiplier. The nominal energy at which the beam radius becomes fixed at 0.01 m, rather than continuing to decrease with energy, is 500 MeV. Allowing the radius to decrease further reduces costs by decreasing the core volume at fixed area, but magnetic quadrupole construction and beam alignment become more difficult. Even the minimum radius of 0.01 m, assumed here, is quite challenging. Increasing the number of beams to beyond 140 (30 in the prepulse and 110 in the main beam) does not decrease costs because not only is the minimum beam radius fixed, but the beam-to-wall distance, and the thickness of cryo-insulation are also fixed. The cost vs. initial pulse duration apparently optimizes near 24 μ s, but beyond 20 μ s, the spot size on target exceeds the required 1.7 mm, so 20 μ s is the usable optimum. (The beam duration is reduced to 200 ns as rapidly as possible after injection. It then remains constant for the rest of the accelerator, where the core pulse duration has a minimum of 420 ns.) Finally, increasing the quadrupole magnetic field decreases the core inner radii, until the superconducting cable thickness builds up faster than the beamlet radius decreases.

The current per beamlet of the prepulse (main pulse) is 1.0 A at the injector, 96 (97) at the end of the accelerator, and 650 (2450) at the target. The prepulse beam is separated from the main pulse beams at 0.85 GeV. The main pulse beams are then accelerated further to 1.30 GeV. A velocity tilt is applied to the beams near the end of the accelerator to compress them to 30 (8) ns over a drift compression distance of a few hundred meters. During drift compression, the beams are also split into 2 groups that impinge on the target from opposite directions.

The core geometry is optimized, subject to constraints on the axial voltage gradient. The core costs scale with the core mass or metal volume V, which is given by

$$V = \pi \epsilon_{PF} L \Delta R (2R_i + \Delta R)$$

where ϵ_{PF} is the packing fraction, L is the length, R_i the inner radius, and ΔR the radial build up. Since the cross-sectional area $A = \epsilon_{PF} L \Delta R$ must satisfy Faraday's Law, the acceleration voltage V_c from a core is

$$V_c = (\epsilon_{PF} L \Delta R) \Delta B / \Delta t$$

The core efficiency η_c in terms of core loss is

$$\begin{aligned} \eta_c &= (I V_c \Delta t) / (I V_c \Delta t + \text{Loss}(\Delta B, \Delta t) V) \\ &= (I \Delta B) / (I \Delta B + \text{Loss} \pi (2R_i + \Delta R)), \end{aligned}$$

so high beam current and low losses increase efficiency. The pulser efficiency η_p is taken as 75% or 50%.

Our results, comparing 2605SC with nanocrystalline materials, are shown in Table 2. We find that, as expected for its higher flux swing, 2605SC requires less mass of cores, and has lower direct costs; whereas nanocrystalline materials have lower losses for higher efficiency and reduced circulating power in the driver. These effects

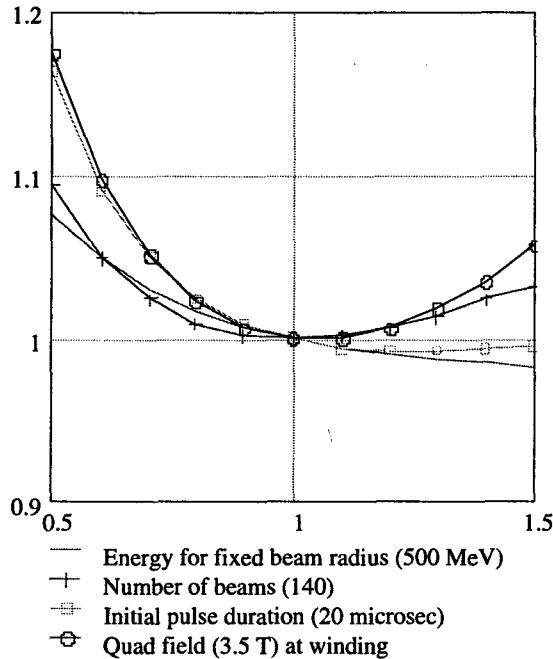


Figure 2: Accelerator optimizations

partially cancel, leaving 2605SC with a lower cost-of-electricity, COE, by 3.3%. Increasing the flux swing slightly by back-biasing the cores reduces the COE for 2605SC by 0.4%, and for FT-1H by 1.1%, resulting in 2605SC still 2.6% lower. The COE, quoted in Table 2, are relatively low for a 1 GWe fusion plant. Economies of scale reduce the COE to 3.4 cents/kWh for a 2 GWe plant. These are competitive with other sources of power except natural gas without carbon sequestration.

Three design choices lead to the low costs with an increase in the technical risk: (1) The low-mass ion Kr⁺ requires a lower energy, higher current accelerator, only 1000 m long; but requires 99% beam neutralization at final focus. (2) The close-coupled target has lower beam energy requirements, but a demandingly small focus radius of 1.7 mm and tighter tolerances on beam-target aiming. Focus and neutralization are costed at \$8 M.[3] Target injection experiments to date show an ability to determine target position in the target chamber to within 0.22 mm.[11] (3) The beam radius is only 0.01 m in the accelerator. The minimum beam radius is determined by alignment accuracy, cryo-insulation thickness, quadrupole magnet design (typically 0.05 m radius), and other issues.

The direct costs for the driver are \$600 M, compared with \$1400 M for a 5.9 MJ Pb⁺ accelerator.[3] This shows the high cost-leverage of developing effective beam-neutralization techniques combined with a precise final focus and target injection and steering techniques.

The sensitivity of the COE to our assumptions about the core and pulser parameters is listed in Table 3. Engineering studies, by industry, of thyratrons and capacitors concluded that redesign for quantity production could reduce costs by factors of several. Pulser costs then drop from \$10/J [3] to \$2/J, both values are listed in Table 3. With these changes, the pulsed power accounted for only

Table 2: Systems code results, second value is for back-biased core.

	2605SC	FT-1H
Flux swing, Tesla	2.3, 2.43	2.0, 2.15
Core mass 10 ⁶ kg	15.5, 14.4	18.5, 16.9
Ave. core eff., %	50.4, 47.9	57.5, 54.4
Accelerator direct costs, \$M	612, 602	669, 650
COE, cents/kWh	4.55, 4.53	4.70, 4.65

 Table 3: Sensitivity of COE (Cents/kWh) to core alloy, pulsed power efficiency η_p and cost C, and back-biasing.

	COE	% Change
Base case 2605SC, $\eta_p=75\%$, $C=\$2/J$	4.55	0.0
Lower pulser efficiency, $\eta_p=50\%$	4.62	+1.5
Higher pulser cost, $C=\$10/J$	4.79	+5.3
Both, $\eta_p=50\%$, $C=\$10/J$	4.99	+9.7
Base case, back-biased 2605SC	4.53	-0.4
Use Finemet FT-1H @ \$6/kg	4.70	+3.3
Use FT-1H with $\eta_p=50\%$ and $C=\$10/J$	5.08	+11.6
Finemet FT-1H @ \$5/kg	4.62	+1.5
Back-bias FT-1H @ \$5/kg	4.58	+0.7

12% of the costs in the magnetic focus portion of the accelerator, down from 40% in earlier studies.[3]

Core efficiency becomes more important with more expensive and lower efficiency pulsers, as shown in Table 3. The lower flux swing of the nanocrystalline material is as important as its higher price in increasing the COE: at core costs of \$5/kg, the COE still increases by 1.5%. Back-biasing either material results in a slight decrease in the COE, assuming that the pulser cost increase is only due to increased energy storage. Because the COE difference is small between amorphous and nanocrystalline materials, and because their magnetic performance and impedance variations are distinctly different, these other characteristics may also play a significant role in the selection decision.

3 REFERENCES

1. R. O. Bangerter, *Il Nuovo Cimento* **106 A**, 1445 (1993).
2. R. W. Moir, et al., *Fusion Technology* **25**, 5 (1994); and *Fusion Technology* **30**, 1613 (1996).
3. W. R. Meier, R. O. Bangerter, A. Faltens, *Nuclear Instrum. and Methods in Physics Research A* **415**, 249 (1998).
4. A. W. Molvik, A. Faltens, L. Reginato, M. Blaszkiewicz, C. Smith, and R. Wood, *NIM A* **415**, 315 (1998).
5. A. W. Molvik, W. R. Meier, A. Faltens, L. Reginato, and C. Smith, "Induction Core Performance", in *Proc. of Linac98 Conf.* (1998).
6. Carl Smith, *J. Appl. Phys.* **67**, 5556 (1990).
7. D. A. Callahan-Miller, submitted to *Nuclear Fusion*.
8. M. Tabak, D. A. Callahan-Miller, D. Ho, G. B. Zimmerman, *Nuclear Fusion* **38**, 509 (1998).
9. W. R. Meier, ANS Nashville. "Systems Modeling and Analysis of Heavy Ion Drivers for Inertial Fusion Energy," LLNL Report UCRL-JC-130954 (May 1998). Accepted for publication in *Fusion Technology*.
10. C. L. Olson, *J. Fusion Energy* **1**, 309 (1982). D. A. Callahan, "Chamber Propagation Physics for Heavy Ion Fusion," *Proc. HIF Symp.*, Princeton, NJ, 1995.
11. R. W. Petzoldt, *Fusion Technology* **34**, 831 (1998).

A HIGH POWER LINEAR SOLID STATE PULSER

Boris Yen, Brent Davis, Bechtel Nevada – Livermore/Las Vegas Operations
Rex Booth, E2 Consulting Engineers

Abstract

Particle accelerators usually require high voltage and high power. Typically, the high voltage/power generation utilizes a topology with an energy store and switching mechanisms to extract that stored energy. The switches may be active or passive devices. Active switches are hard or soft vacuum tubes, or semiconductors. When required voltages exceed tens of kilovolts, numerous semiconductors are stacked to withstand that potential. Such topologies can use large quantities of crucial parts that, when in series, compromise a system's reliability and performance. This paper describes the design of a linear, solid state amplifier that uses a parallel array of semiconductors, coupled with unique transmission line transformers. This system can provide output signals with voltages exceeding 10 kV (into 50-ohms), and with rise and fall times (10-90 percent amplitude) that are less than 10-ns. This solid state amplifier is compact, modular, and has both hot-swap and soft-fail capabilities.

1 INTRODUCTION

Development of the High Power Linear Solid State Pulser (HPLSSP) is a continuation of kicker modulator work at Livermore, CA. The present hybrid solid state and planar triode kicker modulator [1] is being upgraded; the solid state complimentary stage hybrid microcircuit (HMC) will replace the first stage (YU-176 planar triodes) that drives the grids of the Y-820 output tubes.

Recent advances in high power impedance "matchers" [2], [7] (Transmission Line Transformers or TLTs)

encouraged us to develop an all, solid state, linear pulser. This pulser uses Coplanar Kelvin leaded MOSFETs [3] in an open loop, delayed feedback architecture, and relies upon distortion compensation [4] to assure an acceptable output. Figure 1 is a simplified block diagram of that system. All of the signal paths from the 84X splitter to the 50-ohm load are in transmission line configurations.

2 SYSTEM RELIABILITY

Key to the success of any system is reliability; reliability is dependent upon operating time and failure rate. Failure rate is related to the number of crucial parts that must function in order for the system to perform its mission. For applications (such as beam splitting) in large scientific machines, down time translates into wasted expenditures. Reliability can be enhanced by 1) Pre-screening components. 2) Pre-testing components and modules, 3) Reducing the quantity of critical serial parts, 4) Designing redundancy into the operating system, and 5) Using passive components when possible.

A parallel, modular system with passive voltage multiplying TLTs is especially attractive for highly reliable systems. Such a system's reliability or probability of success can be expressed mathematically [5] as:

$$P_N = 1 - (1 - P_0)^N$$

Where: P_N = Success Probability of N parallel systems.

P_0 = Success Probability for one system.

N = Number of parallel systems.

The current HPLSSP system has a 20% redundancy. There are six parallel channels in each module (five active and one backup) and 14 modules (12 active modules) in this system. This topology, however, will adapt to any number of parallel modules/systems, limited only by time and cost constraints.

Should one of a module's active five channels fail, the system computer will inhibit the defective channel, activate that module's backup channel through an impedance-matched switch, SW1. If a second channel fails in that same module, the computer will power down the entire module and disconnect it from the system (by disengaging its transmission line edge connector). One of the system's two redundant modules will then be put into service (see Figure 1). With each configuration change due to component/module failure, new predetermined distortion compensating information is downloaded to the computer to compensate for any differences between the failed and the backup components/modules. This modular system will tolerate failures in any two of its twelve

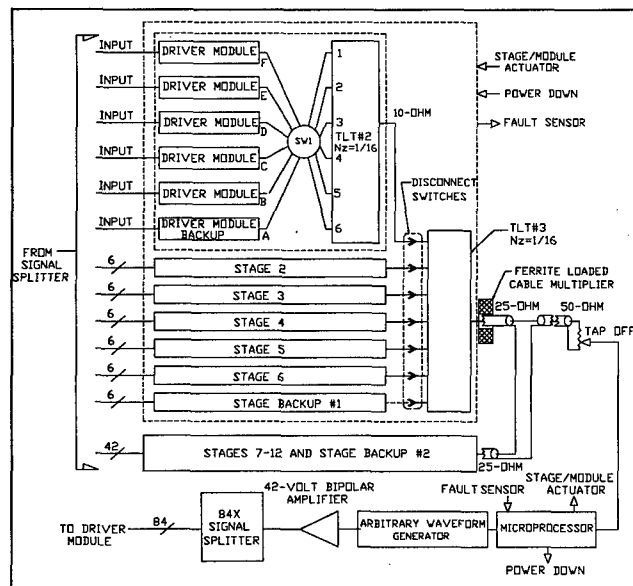


Figure 1: Simplified HPLSSP system block diagram

modules without service interruptions. The system also has hot swapping capabilities for servicing and maintenance.

Compactness and weight advantages of the HPLSSP make it attractive for airborne and space applications. These advantages are possible because of parallel-ground referenced modules, open loop architecture and high ratio impedance TLTs that use less magnetic material than conventional TLTs. See section 4 for TLT descriptions.

3 SOLID STATE MODULE

A simplified block diagram of the solid state module is shown in Figure 2. It has three stages; 1) An Operational Trans-conductance Amplifier (OTA), 2) A TLT, and 3) The MOSFET pair.

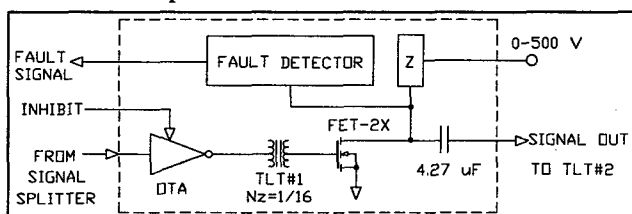


Figure 2: Solid State Module simplified circuit.

Within the OTA stage is a voltage-to-current (V/I) converter, video amplifier, two bipolar transistors and a high bandpass RF transistor. A current source is necessary because of the large dynamic changes to the video amplifier's input impedance during its operation. The V/I converter can supply ± 75 ma. The OTA's video amplifier is biased from the dc rails (to avoid signal saturation) and has a fixed voltage gain of about 20. Its output signal swings from 5 to 75 volts. The ac coupled final stages of the OTA (the complimentary pair and R.F. transistor) are all in emitter-follower configurations. Their rise and fall times (10-90%) are less than 3-ns. The maximum linear output from the OTA is about 2.4-amps into 25-ohms.

RF techniques are used in the PC board's layout and in its construction. The output of the OTA's is through two edge-launched, 50-ohm connectors whose center conductor merge to provide a 25-ohm input to TLT1. The OTA stage is driven by a 500-mV signal from the system's 84-way splitter. Figure 3 depicts the display of a typical output signal from the OTA.

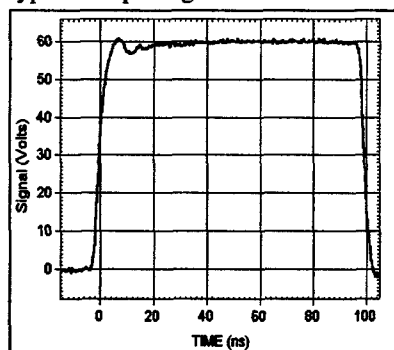


Figure 3: OTA Signal Output

TLT1 has a 16:1 impedance ratio (25-ohms input, 1.6-ohms output). See section 4 for more details on TLT1. The low impedance from TLT1 is used to charge and discharge the gate capacitance of two parallel MOSFETs

(from Directed Energy, Inc). This particular MOSFET is chosen specifically because of its physical and thermal attributes that are conducive to high speed and power applications [3]. The MOSFET parallel combination will deliver over 400-volts into a 3.2-ohm load. The MOSFET footprint (excluding leads) is 1.80-cm x 2.54-cm.

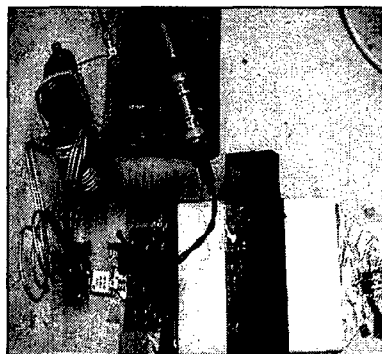


Figure 4: Single channel setup of Solid State Module

The MOSFET operates at less than 450-volts (it is a 500-volt device). A 4.27- μ F signal coupling capacitor isolates the 450-volts from all components downstream of the MOSFET. Figure 4 is a photograph of the test setup used to duplicate one of the Solid State Module's five active channels.

The TLT for this experiment is oversized, but the output impedance is the same as that of TLT1. Figure 5

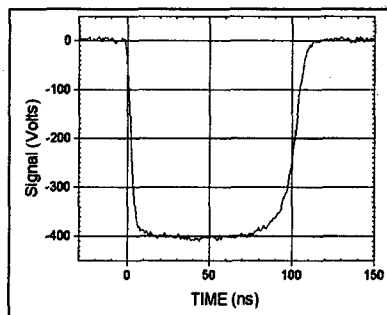


Figure 5: Single channel output of Solid State Module

graphically depicts the signal output from that simulated channel. The data were acquired by driving the gates of the MOSFET pair to about 15-volts with a series, 0.5-ohm gate resistor while having a 450-volt drain voltage, and a 3.2-ohm load.

The signal's fall time is about five nanoseconds. This test clearly demonstrates the Solid State Module's ability to deliver an acceptable input to TLT2.

4 NEW TLTs

The TLTs described in this paper differ significantly from traditional TLTs [6] by combining both strip and semi-rigid transmission cables so that signal propagation is uninterrupted by segmented, coaxial connectors or lines. Moreover, not all of the new TLT's transmission lines need magnetic cores. These improved TLTs can have impedance ratios as high as 250:1 with sub-nanosecond response even at relatively high power levels. They use balanced windings of both strip and semi-rigid coaxial transmission lines on cores of Mn-Zn ferrite. Figure 6 shows the general winding diagrams of TLT1, TLT2 and TLT3. The winding turns, T, are relative opposed to absolute numbers. The core's physical dimensions are 2.54 x 3.18 x 0.64 cm. for TLT1 and 6.45 x 8.08 x 2.40 cm for both TLT2 and TLT3.

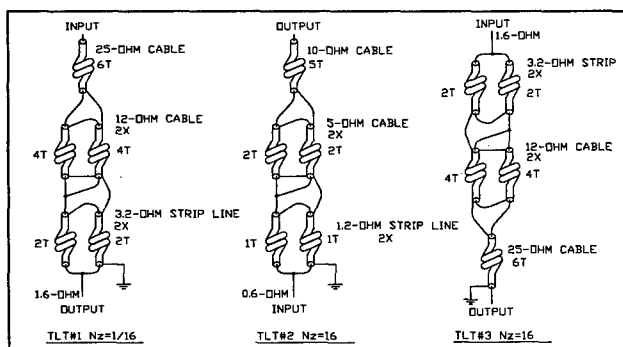


Figure 6: Diagrams of TLT1, TLT2 & TLT3

TLT1 provides a 1.56-ohm drive from the OTA. This low impedance allows a rapid charge and discharge of the FET gate capacitance (includes the Miller effect). Rise and fall times of TLT1 are less than 600-ps, i.e. TLT1 has only minor effects on the system's overall bandpass. This is also true for TLT2 and TLT3.

TLT2 increases the 400-volt signal from the FET to about 1.6 kV. TLT2's input and output characteristic impedance is 0.6 and 10.0-ohms respectively. A TLT similar to TLT2, but with a 16:1 impedance ratio, was evaluated relative to signal droop caused by core non-linearity and/or saturation. Figure 7 (input) and Figure 8 (output) show the experimental results. Note that this particular TLT inverts the input signal. Without core biasing, its output signal follows the input signal for almost 800-ns before core effects become evident.

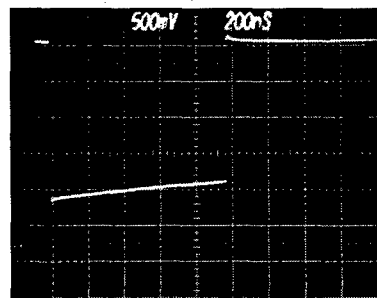


Figure 7: TLT Input Signal

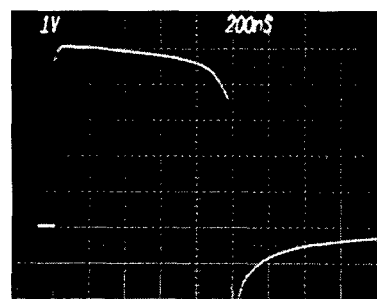


Figure 8: TLT Output Signal

TLT3 steps up the 1.6 kV signal output from TLT2 to about 6.4 kV. This signal amplification is possible because of the TLT's characteristic impedance change from an input of 1.6-ohms to a 25-ohms output.

A cable multiplier sums the two TLT3 output signals into 50-Ohms resulting in a final output of about 12 kV.

5 COMPUTER CONTROL

The front end of the Solid State Module needs optimizing to bring the temporal behavior of its signal into acceptable parameters – to “linearize” the signal. We implement defined, pre-distortion to the input signal to obtain sharp rise and fall times of the solid-state module's output signal. A similar algorithm [1], [4] is used to linearize the

main amplifier. The parameters for these algorithms are predetermined and stored for access by the HPLSSP's computer. Whenever the HPLSSP is operated, the main input signal controlling the arbitrary waveform generator is initiated only after the correct parameters are accessed for the solid state modules, and the overall system.

The same computer that provides predetermined input distortions to the input signals of the HPLSSP will also repeatedly check for the operational integrity of the Solid State Modules. Shown in the block diagram of Figure 1 (of section 1) is a fault sensor network for each module of the HPLSSP. As describe in section 2, if components or modules malfunction within the system, the computer will sense the problem and replace the faulty components or modules with their spares through electrical inhibitors and actuators.

6 SUMMARY

We have presented the description and supporting data for an ultra reliable, computer-controlled, HPLSSP. With proper linearization the HPLSSP performs as a high powered (10-kV, 200-amp), fast rise and fall time (<10-ns) arbitrary waveform generator with the following features:

- 1) A ground referenced, low voltage, parallel component, modular system
- 2) A low cost, easily fabricated/maintained system using state-of-art components.
- 3) A passive, high bandpass (sub-nanosecond rise time), V/I multiplying TLT design.
- 4) A graceful degrading system with low component count.
- 5) An open loop, computer controlled pulser.

7 ACKNOWLEDGMENTS

We acknowledge the BN/LLNL ETA II team for their valuable support and express appreciation to Mr. J. Pigg (Project Manager) for his encouragement and guidance.

8 REFERENCES

- [1] R. Buckles, B. Davis, B. Yen, A Linear Hybrid Kicker Modulator for ETA-II, proc. 11th IEEE international Pulsed Power Conference, MD July, 1997.
- [2] R. Booth, High Power Impedance Matchers with 100 ps Risetime, UCID-21632 LLNL, Dec. 19, 1989.
- [3] Directed Energy, Inc. DE-Series Fast Power MOSFET TM, An Introduction, Fort Collins, CO, Oct 1998.
- [4] B. Yen, Solid State High Power Pulse Modulator --Demonstration to Varian Oncology, Palo Alto, CA, Sep 27, 1996.
- [5] R.F. Graf, Electronic Databook 3rd edition, Lake Publishing Corp. Libertyville, IL, 1983.
- [6] C.N. Winnigstad, Nanosecond Pulse Transformers, IRE trans. Nuc. Sci. 6, 26, 1959.
- [7] Patent pending, Laminated Mn Zn Ferrite Magnetic Cores and Toroids, R. Booth, 1999.

HIGH VOLTAGE MEASUREMENTS ON A PROTOTYPE PFN FOR THE LHC INJECTION KICKERS

M.J. Barnes, G.D. Wait*, TRIUMF, Vancouver, B.C., Canada

E. Carlier, L. Ducimetière, G.H. Schröder, E.B. Vossenberg, CERN, Geneva, Switzerland

Abstract

Two LHC injection kicker magnet systems must produce a kick of 1.3 T.m each with a flattop duration of 4.25 μ s or 6.5 μ s, a rise time of 900 ns, and a fall time of 3 μ s. The ripple in the field must be less than $\pm 0.5\%$. The electrical circuit of the complete system has been simulated with PSpice[3]. The model includes a 66 kV resonant charging power supply (RCPS), a 5 Ω pulse forming network (PFN), a terminated 5 Ω kicker magnet, and all known parasitic quantities. Component selection for the PFN was made on the basis of models in which a theoretical field ripple of less than $\pm 0.1\%$ was attained. A prototype 66 kV RCPS[1,6] was built at TRIUMF and shipped to CERN. A prototype 5 Ω system including a PFN[2], thyatron switches, and terminating resistors, was built at CERN. The system (without a kicker magnet) was assembled as designed without trimming of any PFN component values. The PFN was charged to 60 kV via the RCPS operating at 0.1 Hz. The thyatron timing was adjusted to provide a 30 kV, 5.5 μ s duration pulse on a 5 Ω terminating resistor. Measurement data is presented for the prototype PFN, connected to resistive terminators. A procedure has been developed for compensating the probe and oscilloscope amplifier calibration errors. The top of the 30 kV pulse is flat to $\pm 0.3\%$ after an initial oscillation of 600 ns total duration. The post-pulse period is flat to within $\pm 0.1\%$ after approximately 600 ns from the bottom of the falling edge of the pulse. A calculation was performed in which a measured 27.5 kV pulse with a 5.5 μ s flattop was fed into a PSpice model of a kicker magnet with a 690 ns delay length. The resultant predicted kick rise time, from 0.2% to 99.8%, is 834 ns and the fall time 2.94 μ s, for a field pulse with a flattop of 4.69 μ s and a ripple of less than $\pm 0.2\%$.

1 INTRODUCTION

The European Laboratory for Particle Physics (CERN) is designing a Large Hadron Collider (LHC) to be installed in an existing 27 km circumference tunnel. The LHC will be equipped with Injection Kicker Systems, devices for providing a fast deflection of the incoming particle beams onto the accelerator's circular trajectory. Two pulsed systems, of 4 magnets and 4 PFN's each, are required for injection. The injection sequence, during normal operation, consists of 12 pulses with a period of 16.8 s.

Fig. 1 shows a schematic of the prototype LHC injection kicker system. The 5 Ω PFN consists of two lumped element delay lines, each of 10 Ω impedance, connected in parallel. There are two thyatron switches connected to the PFN, referred to as a main switch (MS) and a dump switch (DS). Each 10 Ω PFN consists of 23 seven-turn cells, a five-turn cell at the DS end, and a nine-turn cell at the MS end. A cell consists of a series inductor, a damping resistor connected in parallel, and a capacitor connected to ground. Each capacitor is mounted in a coaxial housing to minimise parasitic inductance. The prototype PFN capacitors are selected in pairs from a batch of capacitors with $\pm 5\%$ tolerance to provide an effective tolerance of $\pm 0.5\%$ for each pair [2]. Each capacitor per pair is mounted in the same corresponding cell of the parallel lumped element delay lines. The capacitance values are graded linearly from the MS to the DS with a gradient of +0.09% per cell [7]. Two, 3.85 m long, 175 turn coils are mounted on rigid fibreglass coil formers: The total inductance variation per pair of 7 turn coils over the length of the coils is 3%.

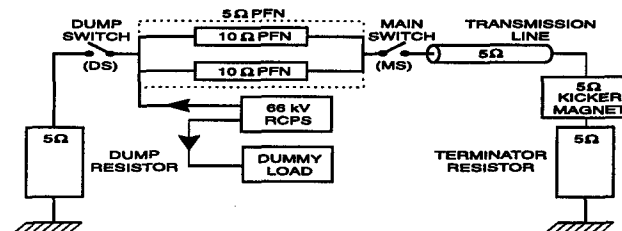


Figure 1: Prototype LHC injection kicker system.

Fig. 1. of reference [6] shows a simplified schematic of the prototype RCPS. The prototype RCPS consists of a 2.6 mF storage capacitor bank (C_{storage}) charged up to 2.8 kV. A GTO [5] was used to switch the energy on the storage capacitor bank onto the primary of a 1:23 step-up transformer of low leakage inductance. The output of the secondary is connected to each of two loads through a cable, a 70 Ω resistor and a diode stack. Each 5 Ω PFN can be considered as a 0.96 μ F capacitor during the charge cycle, which will later be discharged through a kicker magnet using thyatron switches. The MS thyatron is a CX2003[4] and the DS thyatron is a CX1171A[4]. Since there is only one prototype PFN, the test set-up included a dummy load (a 0.96 μ F capacitor with a parallel 500 k Ω discharge resistor) connected in place of a second PFN. Thus the RCPS was properly loaded. The DS thyatron connects one end of the prototype PFN, via 10 parallel 50 Ω coaxial cables to the 5 Ω prototype dump

* Email: wait@triumf.ca

resistor. The MS connects the other end of the PFN via 10 parallel 50 Ω cables, to a kicker magnet (not installed for these tests) terminated with a 5 Ω MS resistor.

2 MEASUREMENTS

The prototype PFN was charged to various voltages up to 60 kV and the timing of the thyatron trigger pulses were varied. The stability and the pulse to pulse reproducibility of the PFN voltage, the ripple of the flat-top of the pulse and the ripple in the post pulse period were measured with high precision. A calibration procedure was developed to provide measurements on the ripple of a 30 kV pulse to a precision of $\pm 0.1\%$ [12].

2.1 Stability

The overall stability of the RCPS and PFN was determined by measuring the magnitude of the flat-top voltage on the MS terminator voltage divider (VD), on successive pulses. A TDS744A oscilloscope [8] was used to determine the average value of the flat-top of the MS VD voltage over a 4 μ s time window, permitting 5 figures of accuracy to be displayed on the oscilloscope. Although the absolute value of voltage is not known to such a high precision, the relative value is mainly of interest. The value of the average voltage was noted for several consecutive pulses, under a variety of conditions, such as a cold start-up, and also after operation for several hours. The maximum excursion of the MS VD voltage for 20 consecutive pulses, with the PFN pre-charged to 60 kV, was $\pm 0.035\%$, compared with a goal of $\pm 0.2\%$.

2.2 Probe Calibration

A 1 kV FET, precision, calibration pulse generator [9] with a transition time of 30 ns (5% to 95%) has been designed and built at TRIUMF. This pulse generator was used to obtain calibration data for a freon filled P6015 [8] high voltage probe connected to a TDS744A oscilloscope. The calibration of a 6015A (freon free) probe was found to be sensitive to slight changes in parasitic capacitance to ground of the surroundings. A PSpice model of the precision pulser shows that the output waveform is flat to within $\pm 0.1\%$, 100 ns after the start of the pulse. The required compensation can not be achieved using the available adjustments in the P6015 probe compensation box. Thus a procedure was developed to provide a relative precision of $\pm 0.1\%$ for a 6015 probe as follows:

- Use a FET based pulse generator to generate a "known" waveform. Compensate the probe and store this reference waveform digitally. The compensation at this stage is only approximate.
- Comparison of the reference and "known" waveforms gives the calibration curve (for a given waveform shape), as a function of time, for the probe and oscilloscope amplifier (for a given gain).

The calibration depends on the oscilloscope amplifier gain and on the waveform shape. Thus the calibration pulse must have approximately the same duration, rise time and fall time as the pulse to be measured, and the oscilloscope settings must be the same for the calibration data collection as for the PFN pulse data collection [12]. The 30 kV MS terminator pulse was measured across one of ten series resistor disks that make up the MS terminating resistor. Thus the P6015 probe was used to measure a 3 kV pulse, and was calibrated with a 600 V pulse with the same amplifier gain settings on the TDS744A oscilloscope.

2.3 Flat-top

Fig. 2 shows a measured 29 kV pulse, after compensation for the 6015 probe and the oscilloscope amplifier, with the DS not turned on. The waveform has been corrected to account for the calibration. The top of the measured voltage pulse is flat to within $\pm 0.3\%$ 600 ns after the end of a rise time of approximately 60 ns, without any adjustments of the PFN.

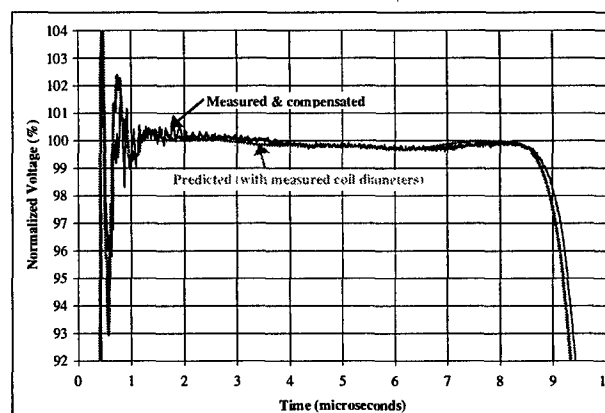


Figure 2: Measured and predicted flat-top portion of PFN voltage pulse each normalised to 100%.

Measurements on a 7 turn section of the PFN coil showed that the copper tube from which the coil is made was no longer round. The outside diameter of the tube on the length of the helix was between 0.2 mm and 0.3 mm larger than the nominal 8 mm. Since the coil former has grooves to fit the 8 mm circular cross section of copper tubing, the coil diameter is slightly too large. Detailed measurements of the outside diameter of the PFN coils at each cell, showed that the average mean coil diameter is 1.4% greater than the designed mean diameter, giving rise to an average increase in inductance of 2.8%. The average diameter of the cells near the centre of the PFN is 1.5% and 0.8% greater than at the MS and DS ends, respectively. The prediction in Fig. 2 is a PSpice calculation with measured coil diameters used to scale the PFN cell inductance. A PSpice prediction for an ideal PFN coil (constant diameter) gives a waveform that is flat from an elapsed time of 1.2 μ s through to 8 μ s. The variation in

the coil diameter explains the small dip in the voltage waveform at approximately 6 μ s in Fig. 2.

Analysis of measurements made at low voltage, (up to 50 V) indicate that the inductance of each cell of the PFN is approximately 4% greater than predicted for an ideal (constant radius) coil. Thus there is still an unexplained anomaly of 1.2% error in the total PFN inductance. The relative difference between the predicted flattop ripple and the actual measured waveform is $\pm 0.2\%$, from 1400 ns after the start of the flattop of the pulse.

The field strength was calculated from a measured 27.5 kV pulse with a 5.5 μ s flattop, fed to the model of the kicker magnet with a 690 ns delay length. The resultant predicted kick rise time from 0.2% to 99.8%, is 834 ns and the fall time is 2.94 μ s, for a field pulse with a flattop of 4.69 μ s and a ripple of less than $\pm 0.2\%$.

2.4 Post Pulse

It was thought that the 3 stage thyratrons would block reverse voltages up to a few kV and would conduct at higher reverse voltages[10]. In order to confirm that small reverse voltages are blocked, the post pulse period of a waveform was measured at the MS terminator for two different values of DS terminating resistor. The results are shown in Figure 3 for a 27.5 kV pulse.

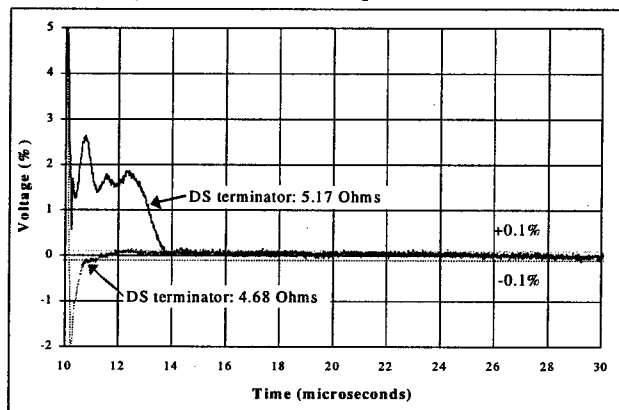


Figure 3. Post pulse voltage for a positive and a negative reflected pulse from the DS terminator.

Assuming that the PFN impedance is exactly 5Ω at the DS end, then with a DS resistor of 5.17Ω , the reflection coefficient is $+1.7\%$ and there is a small positive pulse reflected back to the MS terminator which shows up in as a positive distortion during the post pulse period (Fig. 3). However with a DS resistor of 4.68Ω , the reflection coefficient is -3.3% and there is a negative pulse reflected back which would show up as a negative pulse, with a magnitude of approximately -3.3% . However there is only a small and short negative pulse (Fig. 3), which confirms that the MS thyatron (CX2003) blocked a reverse voltage of 6.6% (ie: 1.8 kV due to pulse doubling). This means that the precision of the DS terminator does not have to be very high (e.g. $5\Omega \pm 0\% - 6\%$). The small negative pulse (Fig. 3) is thought to be due to the cleanup current from

the MS thyatron. There is also a probe calibration error, since the calibration pulser fall time is 30 ns and the fall time of the measured pulse is approximately 1 μ s. A new calibration pulser has been designed to permit calibration with pulses of representative fall time [11].

3 CONCLUSION

The top of the 29 kV pulse is flat within $\pm 0.3\%$ after 600 ns from the start of the flattop of the pulse. The post-pulse period is flat to within $\pm 0.1\%$ after a period of approximately 600 ns from the bottom of the falling edge of the pulse, providing the resistance of the DS terminator is slightly less than 5Ω . The PSpice calculations of the system are accurate to the 0.2% level and thus the theoretical model can be applied with confidence to evaluate future PFNs and RCPSSs. A kicker magnet is being fabricated, and measurements will be carried out to confirm that the field pulse can meet the stringent requirements. The prototype PFN and RCPSS have met the design specifications so TRIUMF can now proceed to fabricate 9 PFNs and 5 RCPSSs for installation into the LHC.

4 REFERENCES

- [1] M.J. Barnes, G.D. Wait, E. Carlier, L. Ducimetière, G.H. Schröder, E.B. Vossenberg, "Measurements on a Fast 66kV Resonant Charging Power Supply", Proc. of EPAC 1998, Stockholm Sweden, June 1998, pp2278-2280.
- [2] M.J. Barnes, G.D. Wait, L. Ducimetière, G.H. Schröder, E.B. Vossenberg, "Kick Sensitivity Analysis for the LHC Inflectors", Proc. 23rd Power Modulator Symposium, California, June 1998, pp96-99.
- [3] OrCAD, 9300 SW Nimbus Ave., Beaverton, OR 97008 USA.
- [4] EEV Limited, Waterhouse Lane, Chelmsford, Essex CM1 2QU, United Kingdom.
- [5] Westcode Semiconductors, "Gate Turn-Off Thyristor (Symmetrical blocking type.) Types WG15026Rxx to WG15045Rxx", August 1996, Rat.Rep.96G9, Issue-3.
- [6] M.J. Barnes, G.D. Wait, L. Ducimetière, E. Carlier, U. Jansson, G.H. Schröder, E.B. Vossenberg, "Design and Optimisation of a 66kV Resonant Charging Power Supply for the LHC Inflectors", Proc. of 11th IEEE Pulse Power Conference, Baltimore, June 1997, pp1309-1314.
- [7] M.J. Barnes, G.D. Wait, L. Ducimetière, U. Jansson, G.H. Schröder, E.B. Vossenberg, "Kick Stability Analysis of the LHC Inflectors", 5th EPAC, Barcelona, June 10-14, 1996, pp2591-2593
- [8] Tektronix Inc., Wilsonville, Oregon 97070-1000, USA.
- [9] M.J. Barnes, G.D. Wait, L. Ducimetière, G.H. Schröder, E.B. Vossenberg, "Construction and 60kV Tests of the Prototype Pulser for the LHC Injection Kicker System", to be presented at 12th IEEE Int. Pulsed Power Conference, California, June 1999.
- [10] Private communication with Ron Sheldrake, EEV Limited, Waterhouse Lane, Chelmsford, Essex CM1 2QU, United Kingdom
- [11] Michael Barnes & Gary Wait, "Design of a FET Based Push-Pull Pulse Generator for Probe Calibration", Design note TRI-DN-99-02, January 29, 1999.
- [12] Michael Barnes & Gary Wait, "Obtaining and Utilising Calibration Data for High Precision Voltage Pulse Measurements", Design note TRI-DN-98-15, October 2, 1998.

DESIGN OPTIMIZATION AND CONSTRUCTION OF THE THYRATRON/PFN BASED COST MODEL MODULATOR FOR THE NLC*

Roland Koontz rkap@slac.stanford.edu, Saul Gold, Anatoly Krasnykh, John Eichner,
Bin #33 SLAC P. O. Box 4349, Stanford, CA 94309

Abstract

As design studies and various R&D efforts continue on Next Linear Collider (NLC) systems, much R&D work is being done on X-Band klystron development, and development of pulse modulators to drive these X-Band klystrons. A workshop on this subject was held at SLAC in June of 1998, and a follow-up workshop is scheduled at SLAC June 23-25, 1999. At the 1998 workshop, several avenues of R&D were proposed using solid state switching, induction LINAC principles, high voltage hard tubes, and a few more esoteric ideas. An optimised version of the conventional thyatron-PFN-pulse transformer modulator for which there is extensive operating experience is also a strong candidate for use in the NLC. Such a modulator is currently under construction for base line demonstration purposes. The performance of this "Cost Model" modulator will be compared to other developing technologies. Important parameters including initial capital cost, operating maintenance cost, reliability, maintainability, power efficiency, in addition to the usual operating parameters of pulse flatness, timing and pulse height jitter, etc. will be considered in the choice of a modulator design for the NLC. This paper updates the progress on this "Cost Model" modulator design and construction.

1 INTRODUCTION

The history of conventional modulator development for the NLC is covered in previous papers enumerated in the references. A brief description of the NLC concept is repeated here for reader's benefit. The NLC is a 1TEV, electron-positron linear collider, wherein two 500GEV linear accelerators are aimed at each other. Each LINAC is 10 km long, and operates at X-band, (11.424 GHz). Each LINAC employs over 3,000 75 MW klystrons, two klystrons per modulator. LINACS are divided into Sectors, each Sector containing 72 klystrons and 36 modulators in the Base Line configuration. An 8-pack induction modulator concept described in the Cassel paper in this conference could reduce the modulator count per sector to 9, each modulator powering 8 klystrons. This is new technology, however, so at the present time, both conventional modulator and induction modulator developments are moving ahead in the NLC R&D.

Efficiency, reliability and performance are major elements in the design requirements. SLAC's cost model modulator is based upon conventional technology and components that exist today, with the idea of optimising

the components to meet the design criteria [2]. In the last year, various pulse discharge capacitors have been evaluated. These results indicate that at present, a conventional polypropylene design with attention to reducing series inductance is the best compromise where power transfer efficiency and reliability are prime considerations. Some work has been done by thyatron manufacturers to develop an appropriate thyatron having a 50,000-hour MTBF (mean time between failure). There is an effort to develop or co-ordinate development of a high voltage charging power supply with 95+% efficiency. A solid state on-off switch is being considered as a replacement for the thyatron-PFN in a conventional modulator design. For a conventional modulator, a proposed physical size and layout has been developed which is being used in other areas of the NLC design efforts that interact with modulators.

Table 1 delineates the latest requirements for the klystron-modulator assembly. It is expected that these parameters can be achieved using current component technology.

Table 1 Baseline Modulator Requirements

Parameter	Value
Peak Klystron Voltage	500 kV
Total Peak Current	530 A
Pulse Width(usable FT)	1.5 μ s
Pulse Top Flatness	2%
Pulse Top Ripple	2%
Pulse-pulse Ripple	0.25%
Pulse-pulse Jitter	10ns
P.R.F.	120 Hz
Charging Voltage	80kV max.
Charging Supply Power.	75 kW
Charging Supply Efficiency.	90%
Overall Efficiency	61.5%
Reliability (MTBF)	8,100hr

2 ENERGY STORAGE CAPACITORS

Pulse shape can be very dependent on the type of energy storage capacitor used. A fast rate of rise of current can be limited by the internal inductance of the capacitor itself, especially during a high current discharge. R. Cassel and Saul Gold have tested film and ceramic capacitors for their internal inductance and found inductance of greater than 100nHy in most designs. A Sicond solid dielectric capacitor from Russia [2] was tested and found to have less than 30nHy of internal inductance, but at the expense of increased losses. After all of this testing, a standard polypropylene capacitor with

special attention to end connections to minimise series inductance has been chosen for the "Cost Model" development.

3 THYRATRON SWITCHES

There is a long history of thyatron operation at SLAC. Presently, high power thyatrons have an average lifetime in excess of 15,000 hours [4]. A lifetime of 50,000 hours is desired for the NLC. Discussions with EEV, Litton and Triton, the three main thyatron manufacturers, have indicated that life increases with decreasing peak and average current. The 80kV charging voltage of the "Cost Model" modulator dictates a peak thyatron current at about 7500 amperes and an average current below 2 amperes. Three gap thyatrons are currently being developed by all three manufacturers to meet these requirements. The "Cost Model" modulator design will accept any of these three new thyatron models. In the next two years, samples of these thyatrons will be operated continuously in the SLAC LINAC and Klystron Test Lab to establish basic lifetime and reliability profiles.

4 PULSE TRANSFORMERS

Pulse transformer design, for the most part, is a mature technology, which can produce high reliability, relatively low loss voltage step-up to klystron cathode pulse potential. For most prior applications, energy transfer efficiency, and pulse rise time were not primary requirements of the transformer design. In the case of the NLC, these two parameters are of significant interest as they affect the operating cost of the two LINACs. Both Stangenes Industries and North Star Research have supplied SLAC with prototype NLC transformers. The testing results of these two units are given in [5]. Out of this initial testing, a new transformer design is emerging which will be used in the first version of the "Cost Model" modulator.

5 PHYSICAL TANK LAYOUT

The physical layout of the modulator is of critical importance to performance, reliability and maintainability and manufacturability. The sheer numbers of modulators required demands a layout, which affords ease of manufacturing and cost minimisation. We have built a full-scale partial mock-up of the modulator tank to help in this design effort, and have further modified it as the design was optimised. A photo of this mock-up is shown in the adjacent column.

The cross-section view of the modulator tank is shown in Fig 3. All components that are part of the pulse power delivery system are housed in a single tank, which also mounts the two X band klystrons. The two klystrons and modulator tank assembly forms a single maintenance unit that will be removed to a repair facility when any of the modulator components, or the klystrons fail. This removes the need to handle oil in the Klystron Alcoves.

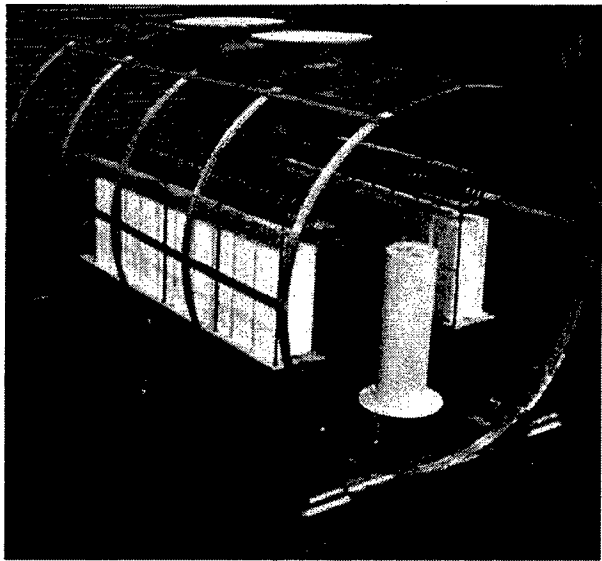


Fig.2 Modulator Tank Physical Mock-up

One exception to this procedure may be the replacement of the thyatron if that unit requires more frequent replacement. The tank design is such that the thyatron can be plugged and unplugged through the oil expansion column on the top of the tank without removal of the oil.

A key to designing a fast rise time, electrically quiet modulator is to take into account, and minimise, all interconnecting impedances and stray capacitance that do not show up on the schematic diagram. The component layout in this tank design is based on minimising these loss-producing elements. Each high current path is mapped separately and isolated to its intended circuit via very low impedance connections, and ferrite isolated supports. Circuit elements that move up and down in voltage with the pulsing are designed to have minimum capacity to the grounded walls of the tank. Voltage hold-off margins are adequate for 500 kV pulses, but excessive size and spacing which leads to inductive or capacitive losses are minimised.

Most of the components needed to build the first version of the "Cost Model" modulator are on hand. A detailed design of the tank assembly was completed and given to tank fabricators for costing. The resulting cost for a prototype unit was much higher than expected, so at this time, the design is being modified to reduce the fabrication cost. It is expected that an order for a reduced scope modulator tank will be placed in the next two months, and a "Cost Model" modulator will be in operation by the end of this fiscal year.

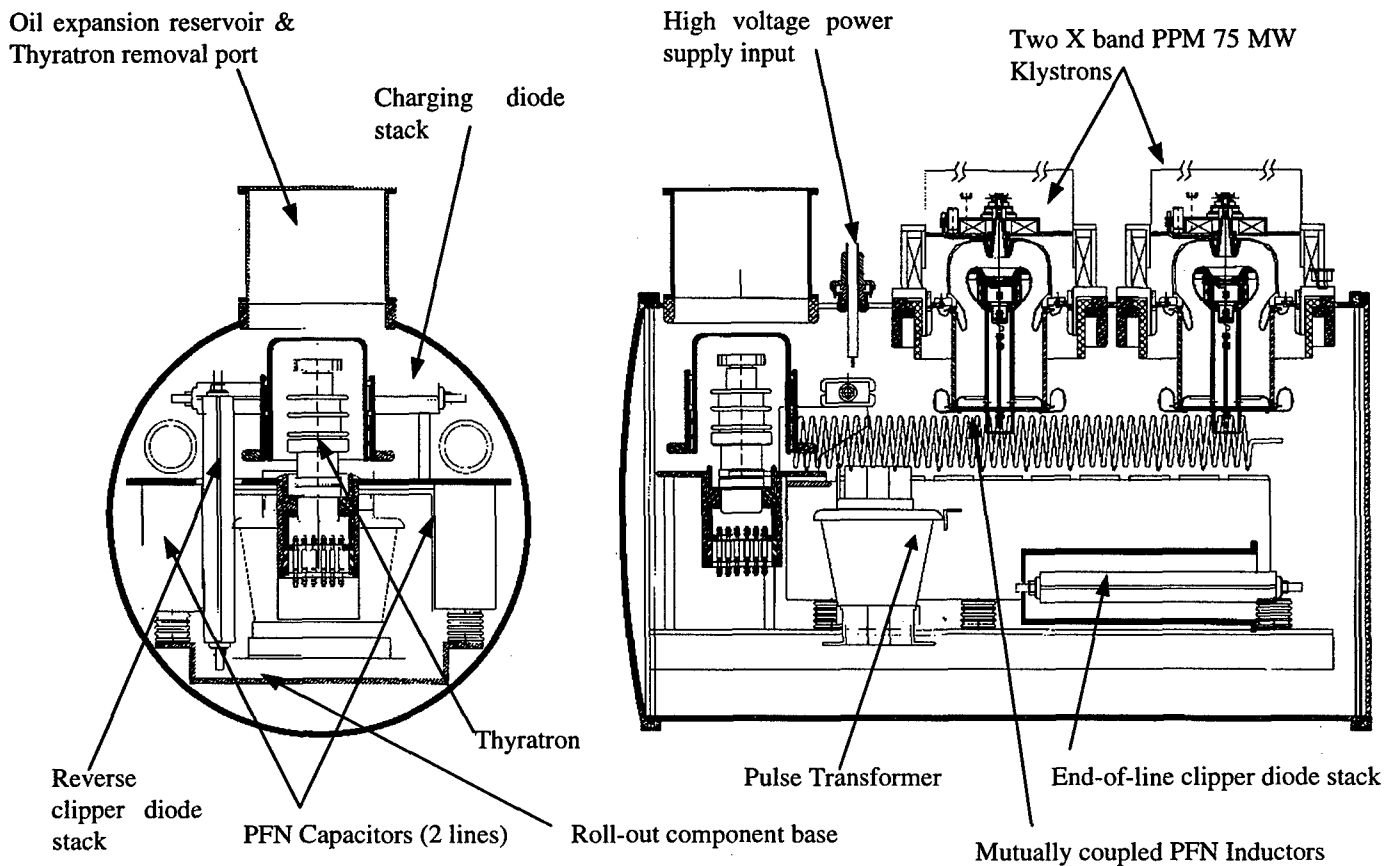


Figure 3: Cross-section views of modulator components in tank

*Work supported by Department of Energy contract
DE-AC03-76SF00515.

References

- [1] The NLC design group: 'Zeroth-Order Design Report for the Next Linear Collider', SLAC-474, 1996.
- [2] R. Koontz, M. Akemoto, S. Gold, A. Krasnykh, Z. Wilson: 'NLC Klystron Pulse Modulator R&D at SLAC', Proceeding of 1997 Particle Accelerator Conference, Vancouver, B.C Canada, 1997.
- [3] M. Akemoto, S. Gold: 'Optimization of a PFN with Mutual Coupling', to be published.
- [4] D.B. Ficklin Jr.: 'An Updated History of the Thyatron Lifetimes at the Stanford Linear Accelerator Center', 23 International Modulator Symposium, Rancho Mirage, CA, 1998.
- [5] S.L. Gold, J.P. Eichner, R.F. Koontz, A. Krasnykh 'Developments in the NLC Modulator R&D Program at SLAC' 23rd Pulse Modulator Symposium 1998
- [6] This paper can be obtained from SLAC Publications as SLAC-PUB-8073

TRIGGER CONTROL AND FAULT REACTION CIRCUITRY FOR THE SOLID-STATE SWITCH MODULATOR DECK AT THE MIT-BATES S-BAND TRANSMITTER

R. Campbell, A. Hawkins, W. North (Consultant), L. Solheim, C. Wolcott[#],
A. Zolfaghari, MIT Bates

Abstract

This paper describes the trigger control and fault reaction circuitry for the new solid-state switch modulator at the MIT Bates Linear Accelerator Center. This new circuitry has been designed and built to control the new cathode-switching solid-state modulator that replaces the old vacuum-tube technology modulator. The old modulator used a start signal to commence its pulses and a separate stop signal to end its pulses. The new system uses a single gate signal to control the modulator pulse.

The trigger control circuit is a stand-alone control unit that can operate in a local (manual) mode or a remote mode. In the local mode the unit uses its own oscillator to run the transmitter. In the remote mode the accelerator-control computer can turn triggers on or off (enable the triggers), can reset the unit, and can send the gate signal that triggers the modulator. There is no microprocessor fault control of the transmitter. The trigger control chassis receives all necessary signals from the transmitter and performs all necessary trigger control and fault reaction functions by itself. These fault reactions can be to turn off the solid-state switch, to fire the crowbar, or simply to light LEDs. The main accelerator-control microprocessor receives report signals from the trigger control unit to alert the accelerator operators to the status of the transmitter.

The trigger control circuitry limits the modulator pulse width to 5 microseconds longer than the gate signal up to a maximum of 55 microseconds and limits the pulse repetition frequency to under 2 kHz. All the circuitry is designed with noise suppression techniques and with a high level of noise immunity (5 volts or more) to ensure fault-free operation in a noisy, transient-filled environment.

1 INTRODUCTION

The MIT-Bates Linear Accelerator is powered by six RF transmitter stations that each contain two RF amplifying klystrons. The old modulator design, which pulses high-voltage across the klystrons, uses vacuum-tube technology that is prone to failures and is difficult to maintain. This design consists of a center-deck and two outboard switch-tube decks that each hold two parallel-connected L-5097 Beam Switch Tubes (BSTs) that are in series with each klystron and the High-Voltage Power Supply (HVPS)

output. The center deck contains the power supplies and various vacuum-tube power-circuitry that sends high-voltage pulses to the BSTs modulating anodes. These pulses "turn on" the BSTs to the desired current-regulation level and allow a current pulse to be sent through each klystron. The klystron current pulses are initiated by a Start trigger signal and cut off by a Stop trigger signal. The new modulator system creates two separate modulators, one for each klystron, using the existing switch-tube decks and BSTs. The center deck is eliminated. At the heart of the new design is a 20kV, 100Amp solid-state switch (built by Diversified Technology, Inc. in Bedford, MA) which is connected to the parallel BSTs in a cathode switching configuration. A 0-20kV DC power supply is connected between the negative high voltage of the HVPS and the modulating anodes of the BSTs to set them for the desired current pulse amplitude. A fiber-optic gate signal is used to close the switch. When light is transmitted, the switch closes until the light is removed. With the closing of the switch, the cathodes of the BSTs are taken to the negative high-voltage (-180kV) of the transmitter and the klystrons are pulsed. When the switch opens, the BSTs stop conducting, thereby blocking the current through the klystrons.

Because of the basic differences between the two systems, and due to new fault monitoring devices, a new approach was needed to trigger the new modulator. Therefore, a new trigger control chassis was designed and a prototype built. The control circuitry was designed at Bates and ModPower, Inc. in Taunton, MA designed the power supply and built the complete prototype system. The system contains its own power supply, power monitoring, remote and local trigger control, trigger filtering, modulator fault detection and latches, crowbar control, and fail-safe safety features. The circuitry is designed with noise suppression techniques with a high level of noise immunity (5 volts or more) to ensure fault-free operation in a noisy, transient-filled environment.

2 POWER SUPPLY

The main power to the chassis is 120 VAC. The AC input is first fused then bypassed from line to neutral by back to back zener diodes and a 1 μ F capacitor (cap). The AC is then filtered with a line filter. The filter output is bypassed from line to neutral by a 1 μ F cap, back to back zener diodes

[#] Email: CWOLCOTT@MIT.EDU

and a 100k resistor. The line filter output from line to ground is bypassed by a 4.7nF cap as is the output from neutral to ground. A power switch switches the AC on to the power supply. The power supply outputs are +5VDC, +7.5VDC, +10VDC, +12VDC, +15VDC, and +20VDC. These voltages are used to power Integrated Chips (ICs), pulse fiber-optic transmitters, and as reference voltages for Comparators (LM339s). Comparators were used because of their high noise immunity features. Each DC voltage is produced from a separate fused transformer whose output is full-wave rectified and then filtered. An adjustable regulator with an adjustable reference set by a 12-turn potentiometer (pot) sets the voltages precisely. Every IC power supply input travels through a ferrite bead and is bypassed by a 0.1 μ F and 10 μ F cap. The power supply is self-monitoring and if any DC voltage fails, the crowbar is fired and the modulators are latched off, stopping all transmitter operation. If this occurs a red LED is lit to show which voltage has failed. As with any fault the trigger control needs to be reset (either locally or by remote) to resume operation. As long as the power supply is functioning properly a green LED is lit to indicate a good power supply.

3 TRIGGER CONTROL

The primary function of the trigger control chassis is to gate the modulator on and off in a controlled fashion. This can be done by two sources: a remote gate signal or a gate signal from the local oscillator. A front panel break-before-make switch labeled Remote/Local selects the trigger source. If the remote source is selected (a computer generated signal transmitted from the control room via fiber optic cable) the control room's gate signal will run the modulator. The remote trigger is input to the circuitry through a pulse transformer to ensure galvanic isolation. The gate signal then undergoes two filtering processes. The first filter blocks any pulse that is longer than 55 μ s. If any remote gate signal longer than 55 μ s is sent it is cut off at 55 μ s, the modulator is latched off, and an LED is lit to show that a remote width fault has occurred. The second filter is a pulse repetition frequency (PRF) filter. It blocks any frequencies higher than 2kHz. If any pulse is detected within 500 μ s of another (2kHz), the pulse is blocked, the modulator is latched off, and a red LED is lit to indicate a remote PRF fault. If a gate signal gets past these filters it passes through the Remote/Local switch and then to the Enable Triggers circuit. The transmitter system has many interlocks that must be satisfied before the main high-voltage can be turned on. If all these interlocks are satisfied, and high voltage is turned on, a 24 VDC signal is sent to the trigger control chassis. If this signal is not present the triggers cannot be enabled and the gate signal cannot get past the enable circuit. If the 24VDC signal is present, a green LED labeled "Ready for Triggers" is lit. Only then can the triggers be enabled, either remotely or by a local pushbutton. When the triggers have been enabled

the gate can pass through the enable circuit to gate a transistor. This transistor switches 15 VDC to a pair of parallel-connected fiber-optic transmitter circuits (one for each modulator). In each path are five fiber optic transmitters (one for each module of the solid-state switch), a resistor, and a switch that allows for the manual shut-off of either modulator so that one klystron can be pulsed while the other is not used. When the gate signal switches the transistor on, current flows through the fiber optic transmitter LEDs. The lights are transmitted via fiber optic cables to the solid state switch. The switch closes and pulses current through the klystron. At the bottom of each fiber-optic transmitter string is a viewing resistor that develops a voltage whenever current is flowing through the fiber-optic transmitters. A front panel BNC bulkhead is connected across each resistor to allow monitoring of the trigger signals. This signal is also connected to a panel-mounted meter that displays the PRF of the modulators, and is also sent to the switch-status fault detection circuit discussed below.

If the local oscillator is selected to gate the modulator, the signal is taken from an oscillator circuit inside the chassis. This circuit supplies a gate that is variable from 3-55 μ s long with a PRF variable from 0-2kHz. These parameters are controlled by panel mounted potentiometers.

4 FAULT DETECTION

The trigger control chassis must monitor many modulator signals to protect the modulator and klystrons from system faults. Besides the remote width, remote PRF, and power supply faults already discussed the system monitors each modulator's BST difference current, each klystron's body current and collector current, and the total ground current of the entire transmitter. These signals are sent from current monitor transformers via coaxial cables that pass through pulse baluns to attenuate any shield noise. The circuitry also monitors the status of each module in both solid-state switches to verify its operation.

As stated, each modulator deck contains two parallel-connected BSTs. If one of the BSTs arcs there will be a huge difference between the current in the arcing tube and the current in the non-arcing tube. This difference current is monitored, and if a large enough difference is detected the system crowbar is fired and the triggers are disabled. The collector current of each klystron is compared to a width window that is the original gate signal plus 5 μ s. If any collector current in either klystron is detected outside this window, indicating a wide pulse or spontaneous current, the crowbar is fired and the triggers are latched off. The body current of each klystron is monitored and if either exceeds 10 Amps the triggers are latched off. In this way, if a klystron arcs, but the BSTs do not, the klystron arc can be extinguished by simply shutting off the solid-state switch. The body current signal will be a very useful new tool. The total ground current fault is more

complicated. Because it is desirable not to fire the crowbar in the event of a klystron arc, the ground current fault detection circuit must be slowed down slightly. A klystron arcs to ground and this shows up as both klystron body current and ground current. Therefore, if the ground current detection circuit is allowed to fire the crowbar instantly, the switch will not have time to extinguish the arc. So a delay of 10 μ s was introduced into the ground current detection circuit. However, if the detected ground current is still present after the 10 μ s delay, indicating a problem other than a klystron arc, the crowbar is fired. All of these fault detection circuits have their own latches and LEDs that will indicate what fault occurred. Each circuit latches a set of relay contacts which alerts the control room computer to the fault condition. Each one of these signals can be monitored by an oscilloscope from front panel BNC connections.

Another set of signals that is monitored is the switch status signals from the solid-state switch. The switch contains 5 switch modules connected in series. Each module sends back a fiber-optic signal indicating if it is open or closed. Every switch status signal is compared to each gate signal to check for proper operation. If a fault occurs, an LED is lit to indicate which module is bad and an overall switch fault signal is sent to the control room by a relay contact.

5 CROWBAR CONTROL

The crowbar control chassis receives a signal from the trigger control chassis and then sends a high-voltage pulse (15kV) to a large step-up pulse transformer which fires the system crowbar and dumps the high-voltage of the transmitter. Because the old crowbar control chassis will be replaced eventually, two crowbar firing circuits were built into the trigger control chassis; one for the old crowbar chassis and one for the new. The circuit for the old crowbar chassis sends a 15VDC pulse. Because the old system requires a pulse it was not possible to make it fail-safe. The new system, however, will be fail safe. A current sinking field-effect transistor (FET) will hold a voltage generated in the new crowbar chassis down through an interconnecting cable. If the cable is removed, if the trigger control chassis is shut off, or if the FET drive fails the crowbar will fire rendering the system safe for equipment and personnel. In the event of a fault requiring a crowbar the FET is turned off and the crowbar will fire. A Crowbar Test button is mounted on the front panel that sends a high signal to all the fault detection circuits and not only fires the crowbar but tests all the latches as well.

6 FAIL-SAFE FEATURES

The trigger control circuitry was designed to be as fail safe as possible. When the unit is turned on or off, all the faults are set to ensure that no spurious signals occur. All the current transformers inside the transmitter actually sink

voltage because of their low impedance. If either end of any coaxial cable that carries fault signals is disconnected, the trigger control will act as if that fault occurred; either by firing the crowbar or shutting of the triggers. Also, every comparator, transistor, latch, or logic gate in any fault circuit sinks current or voltage in its "good" condition. If any IC is removed, loses power, or if any connection is misaligned or broken, the circuit will act as though that fault had occurred.

7 CONCLUSION

Because the old modulator has become obsolete and unreliable and has proven to be too difficult to maintain, we have the chance to greatly improve the entire transmitter. Simplicity, safety, and reliability have driven the new modulator and trigger control system design. An entirely new strategy for running the transmitter will be implemented. The control circuitry is noise free, robust, and fail-safe. It uses old and new modulator signals that will allow for better fault control strategies, better monitoring and easier troubleshooting. It has been designed to interface with a central computer but does not depend on a microprocessor or software for equipment and personnel safety. The combination of a new modulator system with the new trigger control circuitry will replace obsolete and failing technology and significantly improve the reliability and performance of the accelerator and the RF transmitters.

PRODUCTION OF HALO PARTICLES BY COLLECTIVE MODE EXCITATIONS IN HIGH INTENSITY CHARGED PARTICLE BEAMS

Sean Strasburg and Ronald C. Davidson, Princeton Plasma Physics Laboratory

Abstract

This paper examines the effects of self-consistent collective oscillations excited in a high-intensity ion beam on the motion of a test particle in the beam core. Even under ideal conditions, assuming a constant transverse focusing force (smooth focusing approximation), and perturbations about a uniform-density, constant-radius beam, it is found that collective mode excitations, in combination with the applied focusing force and the equilibrium self fields, can eject particles from the beam core to large radii.

1 INTRODUCTION

It is increasingly important to develop improved theoretical models of halo production and control for charged-particle beam propagation in high-intensity accelerators and transport systems[1], with applications to spallation neutron sources, heavy ion fusion, nuclear waste treatment, and tritium production. While halo formation mechanisms, such as beam mismatch and nonlinearities associated with nonuniform space-charge forces have been explored both analytically and numerically[2, 3], a fundamental understanding of halo production is incomplete. In this paper, we consider a *new mechanism* for the production of halo particles. Namely, we consider, for the first time, the effects of self-consistent collective oscillations excited in a high-intensity ion beam on the motion of a test particle in the beam core. Even under ideal conditions, assuming a constant transverse focusing force (smooth focusing approximation), and perturbations about a uniform-density, constant-radius beam, it is found that collective mode excitations, in combination with the applied focusing force and the equilibrium self fields, can eject particles from the beam core to large radii.

2 THEORETICAL MODEL AND ASSUMPTIONS

We consider an intense nonneutral ion beam with characteristic beam radius R and axial momentum $\gamma_b m \beta_b c$ propagating in the z -direction with average axial velocity $V_b = \beta_b c = \text{const.}$ The applied transverse focusing force in the *smooth focusing* approximation is modeled by $\mathbf{F}_{fo}(\mathbf{x}) = -\gamma_b m \omega_f^2 (x \hat{x} + y \hat{y})$. The effects of self-electric and self-magnetic fields on the particle dynamics are retained in a self-consistent manner, consistent with the paraxial approximation, and the assumption that Budker's parameter satisfies $\nu_B = N_b (Ze)^2 / mc^2 \ll \gamma_b$. Here, N_b is the number of beam ions per unit axial length, related to the number density of beam ions $n_b(x, y, s)$ by $N_b = \int dx dy n_b$, where $s = \beta_b ct$. The wavenumber equivalent

to the transverse focusing frequency, the transverse focusing coefficient κ , is defined by $\sqrt{\kappa} = \omega_f / \beta_b c$, which has units of inverse length. We further assume axisymmetric unbunched beam propagation ($\partial/\partial\theta = 0 = \partial/\partial z$), and introduce the normalized dimensionless self-field potential ψ defined by $\psi(r, s) = Ze \phi(r, s) / \gamma_b^3 m \beta_b^2 c^2$.

We assume a kinetic or warm-fluid[4] Kapchinskij-Vladimirskij (KV) beam equilibrium, and for this case the equilibrium density profile $n_b^0(r, s)$ has the uniform value $N_b / \pi R^2$ in the beam interior and is equal to zero outside the beam, defined by $r > R(s)$, where $R(s)$ is the solution to the envelope equation[2]. We further assume a matched, constant-radius beam equilibrium with $R(s) = R_0$, a constant, given by $(\kappa - K/R_0^2)R_0 = \epsilon^2/R_0^3$. Here ϵ is the unnormalized transverse emittance, and K is the self-field perveance defined by $K = 2N_b(Ze)^2/\gamma_b^3 m(\beta_b c)^2$. The "depressed" oscillation wavenumber $\bar{\nu}$ (dimensionless units) is defined in terms of the transverse focusing coefficient κ , perveance K , and equilibrium beam radius R_0 , by $\bar{\nu}^2 = 1 - K/\kappa R_0^2$. The "depressed" oscillation wavenumber ω (dimensional units) is given by $\omega^2 = \kappa \bar{\nu}^2$.

A key focus of the present analysis is to investigate the motion of a *test ion* in the combined force of the applied focusing field \mathbf{F}_{fo} , the equilibrium self fields, and the perturbed self fields associated with self-consistent collective oscillations excited in the beam. We express the *total* self-field potential as $\psi(\bar{r}, s) = \psi_0(\bar{r}) + \delta\psi(\bar{r}, s)$, where $\psi_0(\bar{r})$ is produced by the step-function equilibrium density profile and $\bar{r} = r/R_0$ is the normalized radial coordinate. For the perturbed potential $\delta\psi(\bar{r}, s)$, we make use of the warm-fluid model developed by Lund and Davidson[4]. This model, simplified by the assumptions of cylindrical symmetry, predicts an infinite class of collective modes $\delta\psi_n$, vanishing outside the beam core, with purely radial dependence, and stably oscillating with eigenfrequency ω_n . The radial eigenfunction $\delta\psi_n(\bar{r})$ in the beam interior ($0 \leq \bar{r} < 1$) is defined in terms of the Legendre polynomials (of the first kind), $P_{n-1}(x)$ and $P_n(x)$, by $\delta\psi_n(\bar{r}) = \frac{1}{2} A_n [P_{n-1}(1 - 2\bar{r}^2) + P_n(1 - 2\bar{r}^2)]$, where $\{A_n\}$ are constant amplitudes. The normal-mode oscillation wavenumbers $\{\omega_n\}$ are defined in Ref. [4] by $\omega_n^2 = \kappa[2 + 2^{-\nu^2}(2n^2 - 1)]$.

It is readily shown that the equation of motion in the applied and equilibrium self fields, together with the oscillating collective modes, is given by

$$\frac{d^2 \bar{r}}{ds^2} + \left(\kappa + \frac{2}{R_0^2} \frac{\partial \psi}{\partial \bar{r}^2} \right) \bar{r} = \frac{\bar{P}_\theta^2}{\bar{r}^3}, \quad (1)$$

where \bar{P}_θ is the (normalized) canonical angular momentum, $R_0^2 \bar{P}_\theta = xy' - yx'$, which is a constant of the motion. Here $\psi(\bar{r}, s) = \psi_0(\bar{r}) + \delta\psi(\bar{r}, s)$, where the eigenfunctions

are the Legendre polynomials defined above and the eigenfrequencies are $\{\omega_n\}$. Equation (1) is a valid description of the test ion motion, both inside the beam ($\bar{r} < 1$) and outside the beam ($\bar{r} > 1$).

For test-particle motion inside the beam, we obtain[6]

$$\frac{d^2\bar{r}}{ds^2} + \omega^2\bar{r} - \frac{\bar{P}_\theta^2}{\bar{r}^3} = \frac{K}{R_0^2} \sum_{n=1}^{\infty} A_n \delta\psi'_n(\bar{r}) \cos \omega_n s. \quad (2)$$

On the other hand, for particle motion outside the beam, Eq. (1) reduces to the nonlinear autonomous equation

$$\frac{d^2\bar{r}}{ds^2} + \left(\kappa - \frac{K}{R_0^2 \bar{r}^2} \right) \bar{r} - \frac{\bar{P}_\theta^2}{\bar{r}^3} = 0. \quad (3)$$

For case of vanishing angular momentum (*meridional* particles), setting $\bar{P}_\theta = 0$ in Eqs. (2) and (3) and replacing \bar{r} with $\bar{x} = x/R_0$ yields the appropriate equations.

Equations (2) and (3), supplemented by the associated definitions of $\delta\psi_n$, $\{\omega_n\}$, etc., constitute the final forms of the test-particle orbit equations to be investigated analytically and numerically in Secs. 3 and 4.

3 THEORY OF THE DYNAMICAL SYSTEMS

In this section we examine several features of the test ion motion analytically, using numerical solutions as verification.

3.1 Resonant Behaviour

Meridional Test Ions We begin by considering *meridional* particles with $\bar{P}_\theta = 0$ in a beam supporting a single collective mode with eigennumber n . The functional relationship between the n^{th} mode frequency ω_n and the depressed transverse oscillation frequency ω makes fundamental and principal resonances “inaccessible” for all mode numbers n . The Hamiltonian expansions predict resonances for the n^{th} mode at $\omega_n/\omega = \pm 2m$ for integers $m \leq n$. Using $\{\omega_n\}$, we can easily obtain an expression for $\omega_n^2/\omega^2 \equiv g_n^2$. The minimum of g_n occurs at $\bar{\nu}^2 = 1$ at which $g_n = 2n$, the uppermost resonance. However, as this resonance is approached, the coefficient which multiplies the mode amplitude, $K/R_0^2 = \kappa(1 - \bar{\nu}^2)$, approaches zero.

Equation (2) for meridional particles inside a beam supporting an $n = 1$ mode is a Mathieu equation, the same as that generated by an envelope oscillation $R(s) = R_0(1 + \frac{1}{2}\delta_e \cos \omega_e s)$ in the limit of small δ_e , taking $\delta_e = \delta_1$ and $\omega_e = \omega_1$. However, it is important to distinguish what constitutes *inside* the beam for the two cases. The fluid modes are derived for perturbations about a constant radius beam, so *inside the beam* corresponds to $|\bar{x}| < 1$, or $|x| < R_0$. The mismatched ripple, however, requires $|x| < R(s) = R_0(1 + \frac{1}{2}\delta_e \cos \omega_e s)$. Since $R(s)$ is the projection of an energy level, particles initially inside the energy shell of the beam will remain confined in the interior of a mismatched beam for all time, whereas the beam

edge R_0 of a beam with an $n = 1$ mode is not a node of the perturbed potential, and so particles may escape.

Test Ions With Nonzero Angular Momentum As a simple example for particles with nonzero angular momentum $\bar{P}_\theta \neq 0$, we consider perturbations around an interior *circular* orbit with constant radius $\bar{r}_c = r_c/R_0$, requiring that $\bar{P}_\theta^2 = \bar{r}_c^4 \omega^2$. The frequency of small radial oscillations about the equilibrium orbit is found to be $\omega_c = 2\omega$, independent of the equilibrium radius \bar{r}_c . If these orbit oscillations resonate with the collective mode, the particle will experience a significant energy change.

The linearization for small radial oscillations has fundamental and principal resonances when the ratio $\omega_1/\omega_c = 1, 2m$ for integers $m \leq n$. For $n = 1$, the fundamental resonance is at $\bar{\nu}^2 = 1$, and the Mathieu (or principal) resonance is at $\bar{\nu}^2 = \frac{1}{4}$. Both have important effects on the dynamics of a single particle.

3.2 Non-Resonant Behaviour

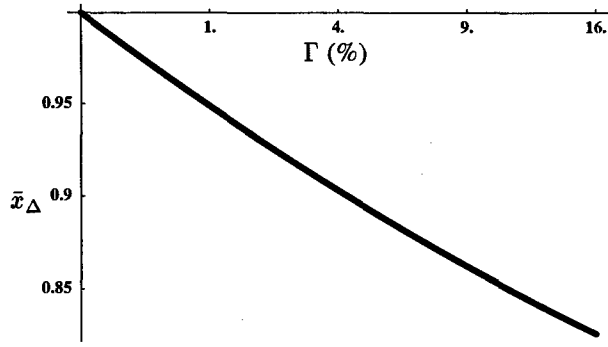
It is also possible for a test particle to nonresonantly gain enough energy in the beam interior to escape the beam, disrupting the process of giving the energy back. All particles with sufficient energy in the unperturbed case to attain a radius greater than $\bar{x}_\Delta < 1$ will be ejected by the collective modes into the highly nonlinear region exterior to the beam at some point of their trajectory. This minimum expelled radius \bar{x}_Δ is a strong function of the mode amplitude strength Γ , defined as the rms field energy in the n^{th} mode divided by the rms electrostatic energy in the beam core. The function \bar{x}_Δ may be calculated for low n by transforming the perturbation in the Hamiltonian to higher-order[5], yielding a new energy-like invariant, the new action \bar{J} , whose maximum is directly related to the maximum excursion of the perturbed particle trajectory. For $n = 2$, the unperturbed maximal radius which will just reach the beam edge due to the collective mode is given by[6]

$$\bar{x}_\Delta^2 = \frac{-(1 + \epsilon c_2) \pm [(1 + \epsilon c_2)^2 + 2\epsilon c_1 \omega]^{\frac{1}{2}}}{\epsilon \omega c_1}. \quad (4)$$

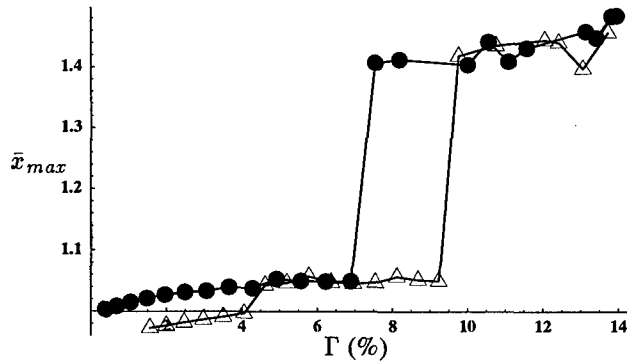
The values c_1 and c_2 depend only on the depressed transverse frequency and the ratio $\alpha \equiv \omega_2/\omega$, which in turn depend only on $\bar{\nu}$, and are given by $c_1 = c_3(21\alpha - \frac{3}{4}\alpha^3)$ and $c_2 = c_3\omega(-16\alpha + \alpha^3)$, where $c_3^{-1} = \omega^3(64 - 20\alpha^2 + \alpha^4)$. Here, we define $\epsilon = (K/R_0)\sqrt{\Gamma}$. This expression gives, within a few percent over a wide range of parameters, the extent of the region near the beam edge which will be ejected from the beam at some point of the trajectory. Figure 1 shows \bar{x}_Δ as a function of normalized mode energy Γ in a range over which it is an accurate approximation.

4 NUMERICAL RESULTS

The dynamics become more complicated when a trajectory spends time both inside and outside the beam, and numerical solutions of the equations are easiest under these conditions.

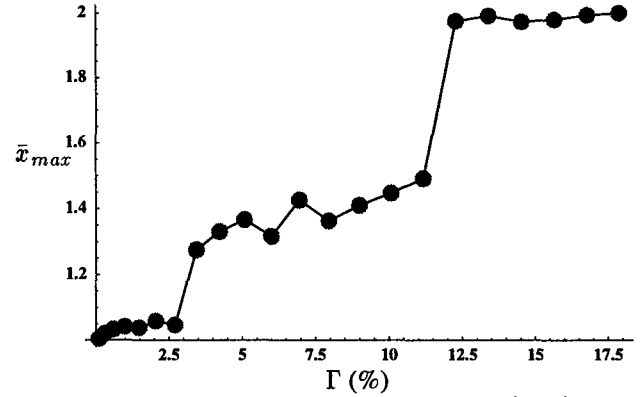

 Figure 1: Plot of \bar{x}_Δ versus Γ (%) for $\bar{\nu}^2 = \frac{1}{4}$.

Particles whose energy corresponds to a maximum *unperturbed* trajectory, which we denote \bar{x}_0 , between \bar{x}_Δ and 1 will be ejected from the beam at some point, with the possibility of large energy gains. In general, ejected particles either (i) experience negligible energy gains, or (ii) obtain a well-defined maximum excursion $\bar{X}_1 \simeq 1.5$. This behaviour is a function of space-charge depression $\bar{\nu}$, rms field energy in the n^{th} mode relative to rms electrostatic energy in the beam core $\Gamma \equiv \mathcal{E}_n/\mathcal{E}_0$, and the ejected particle's unperturbed maximum radius \bar{x}_0 .


 Figure 2: Plot of \bar{x}_{max} versus Γ (%) for $\bar{\nu}^2 = \frac{1}{3}$ with $\bar{x}_0 = 0.99$ (●) and $\bar{x}_0 = 0.95$ (△).

For mode energies less than a certain critical energy $\Gamma_1(\bar{\nu}, \bar{x}_0)$, particles go no further than a few percent of R_0 outside of the beam; for energies greater than Γ_1 , particles consistently travel as far out as $\bar{X}_1 \simeq 1.5$ (see Fig. 2). The value of Γ_1 decreases as the beam becomes more intense, ranging from less than 2% at $\bar{\nu}^2 = \frac{1}{5}$ to 15% at $\bar{\nu}^2 = \frac{1}{2}$. In addition, particles with \bar{x}_0 further from the beam edge have slightly higher critical energies, and of course particles with $\bar{x}_0 < \bar{x}_\Delta$ never leave the beam. The value of \bar{X}_1 gradually increases with Γ , and depends weakly on $\bar{\nu}$. Since \bar{X}_1 does *not* depend on \bar{x}_0 , this is the largest radius any particle initially in the beam can escape to, and functions as a KAM curve, giving an indication of the phase space structure in the halo region.

Finally, for intense beams with sufficiently large amplitude modes, this phase-space spanning curve can be destabilized and break into islands. Above a critical energy Γ_2 ,


 Figure 3: Plot of \bar{x}_{max} versus Γ (%) for $\bar{\nu}^2 = \frac{1}{5}$.

particles can explore out to $\bar{X}_2 \simeq 2$ (see Fig. 3). It is plausible that, for extremely intense beams, larger collective mode amplitudes would make accessible even greater regions of phase space.

5 CONCLUSIONS

We have explored the range of particles capable of being expelled from the beam core by collective mode excitations, and the maximum radii they can attain as KAM surfaces are successively destabilized with increasing perturbation strength. These processes occur under even ideal conditions, assuming constant transverse focusing force and a uniform-density matched-beam equilibrium.

6 ACKNOWLEDGEMENTS

This research was supported by the Department of Energy and the Department of Defense.

7 REFERENCES

- [1] R. C. Davidson, *Physics of Nonneutral Plasmas* (Addison-Wesley Publishing Co., Reading, MA, 1990); M. Reiser, *Theory and Design of Charged-Particle Beams* (Wiley, NY, 1994); and references therein.
- [2] *Space Charge Dominated Beams and Applications of High Brightness Beams*, ed. S. Y. Lee, AIP Conf. Proc. 377 (AIP, NY, 1996), and references therein.
- [3] R. Gluckstern *et al.*, Phys.Rev.Lett. **75**, 2835 (1995); R. Gluckstern, Phys.Rev.Lett. **73**, 1247 (1994). A. Riabko *et al.*, Phys.Rev. E **51**, 3529 (1995).
- [4] S. Lund and R. C. Davidson, Phys. Plasmas **5**, 3028 (1998).
- [5] A. J. Lichtenberg and M. A. Lieberman, *Regular and Chaotic Dynamics*, 2nd ed. (Springer-Verlag, NY, 1992), and references therein.
- [6] S. Strasburg and R. C. Davidson, to be published.

SIMPLIFIED THEORY OF THE HEAD-TAIL INSTABILITY OF COLLIDING BUNCHES

E. A. Perevedentsev, Budker Institute of Nuclear Physics, Novosibirsk, 630090, Russia

Abstract

A proposed theoretical model incorporates in an averaged form both the conventional head-tail effect in a single bunch (due to impedance elements in the machine), and the linear part of the coherent beam-beam interaction, with the account of the finite bunch length.

1 INTRODUCTION

For the strong head-tail effect in the beam-beam system we construct here an *averaged version* of the space-time domain formalism [1, 2], aiming at clarity and solvability, at the sacrifice of localized interaction effects. This holds in situations when all the mode spectrum of interest lies far off the (half)integer tunes, i.e. for machines where the synchrotron tune and collective tunes are much less than fractional betatron tune.

Applied to strong-strong collisions, the new theory predicts the coherent dipole beam-beam instability of head-tail type; estimates show that the chromaticity is effective in control of its increments.

2 CIRCULANT EQUATIONS

The main difficulty of multi-particle models in the space-time domain is seen already in the educational 2-particle model in A. Chao's text [3]: the wake acts in alternating mode on either the 1st or the 2nd particle, resulting in time-dependent coefficients in the equations of motion even with the constant wake.

The model employed in [2] and here is not based on real macroparticles which move longitudinally. It considers the synchrotron phase circle¹ divided into N fixed equal boxes with *fixed* longitudinal position in the bunch, see Fig. 1. These boxes are uniformly populated with particles each carrying its transverse dipole moment.

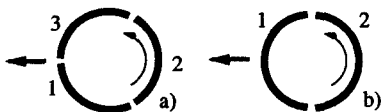


Figure 1: Division of the synchrotron phase into boxes, populated with particles; a) 3 divisions, CE3 formalism; b) 2 divisions for the CE2 formalism.

A variable dipole moment d_i is ascribed to each i th box, $i = 1, \dots, N$. The synchrotron oscillation just transports

¹For the needs of this paper the *hollow beam model* will suffice, i.e. all the particles are assumed to have the same amplitude of the synchrotron oscillation.

the dipole moment around the circle, across the boxes, and we follow variations of d_i in each box: no need to interchange the boxes when evaluating their interaction.

The dipole moments obey the betatron oscillation equation in the Courant-Snyder normalization, with the coupling in the RHS:

$$\ddot{d}_i + \omega_b^2 d_i = -2\omega_b D_{ik} d_k. \quad (1)$$

Here ω_b is the betatron frequency, the machine azimuth is used as quasi-time, and the dynamic matrix D_{ik} approximates the integral linear operator of collective interaction. First of all we use the ansatz $d_i = a_i e^{-i\omega_b t} + \text{c.c.}$ and standard averaging to get rid of a_i^* in the shortened equations:

$$i \dot{a}_i = D_{ik} a_k. \quad (2)$$

N complex amplitudes a_i of oscillating dipole moments sitting in each box, form a complete set of dynamic variables of the averaged problem. In fact, a_i are sampled values of the continuous function of the synchrotron phase φ : $a_i = a(\varphi_i, t)$, its total time derivative

$$\dot{a}(\varphi, t) = \frac{\partial a}{\partial t} + \dot{\varphi} \frac{\partial a}{\partial \varphi} = \frac{\partial a}{\partial t} + \omega_s \frac{\partial a}{\partial \varphi}$$

should be represented in our difference equations with a correct N -point approximation of $\partial a(\varphi, t)/\partial \varphi \rightarrow \gamma_{ik} a_k$. For periodic functions, γ is known to be a special *circulant matrix*; we define another circulant $C = -i\omega_s \gamma$, and finally come from (2) to new equations

$$i \dot{a}_i = (C_{ik} + D_{ik}) a_k. \quad (3)$$

In what follows we will refer to Eqs. (3) as *Circulant Equations*, with the notation CE3 and CE2, for 3 and 2 boxes, respectively. Their remarkable feature is that the circulant matrix C responsible for the free synchrotron motion, and the interaction matrix D on the RHS are *additive*.

The *synchrotron mode spectrum* emerging from CE should first be checked for free oscillation. We start with $N = 3$, Fig. 1a, and accordingly define the proper mode numbers m as $-1, 0, +1$. The 3-point circulant is:

$$C_3 = \frac{i\omega_s}{\sqrt{3}} \begin{pmatrix} 0 & -1 & 1 \\ 1 & 0 & -1 \\ -1 & 1 & 0 \end{pmatrix}. \quad (4)$$

Substituting for the proper modes $a_i(t) = v_i e^{-i\Omega t}$ in (3), with $D_{ik} = 0$, we find the mode frequencies Ω and eigenvectors v from the eigensystem of C_3 :

$$\begin{aligned} \Omega_0 &= 0, & v_0^T &= (1, 1, 1); \\ \Omega_{+1,-1} &= \pm\omega_s, & v_{+1,-1}^T &= (1, e^{\pm 2\pi i/3}, e^{\pm 4\pi i/3}) \end{aligned} \quad (5)$$

Indeed, the free oscillation mode spectrum comprises the betatron frequency and two its synchrotron sidebands: $\omega_b, \omega_b \pm \omega_s$. Mind that all frequencies in the shortened equations are counted from ω_b , e.g. those in (5). The mode eigenvectors v give sampling of the Fourier harmonics $e^{im\varphi}$, with $m = +1, 0, -1$ (cf. [3], Eq. (6.185)), at 3 equidistant values of φ_k according to division into 3 boxes.

In many cases coupling of only two modes in all the spectrum is important, those with the least separation in frequencies. $N = 2$ boxes (Fig. 1b) then suffice to represent them. Coupling of these two modes to the other ones is neglected. Thus we come to the extremely simple circulant equation CE2, where free motion of the only two modes in question is given by (3) with $D = 0$, and the 2×2 circulant:

$$C = \frac{\omega_s}{2} \begin{pmatrix} -1 & 1 \\ 1 & -1 \end{pmatrix}. \quad (6)$$

Its eigensystem reads:

$$\Omega_{0,-1} = 0, -\omega_s; \quad v_{0,-1}^T = (1, \pm 1).$$

The mode spectrum here consists of the betatron frequency ω_b and only one sideband $\omega_b - \omega_s$ with exceptionally simple mode structure. It is convenient to take $\omega_s = 1$ hereafter, i.e. to measure all the frequencies in the units of ω_s .

3. BEAM-BEAM MODES

Now our task is to study the linear coherent dipole beam-beam oscillations of longitudinally non-rigid bunches with finite length and incoherent synchrotron motion. We have to perform the same division into boxes in the both colliding bunches, like in Fig. 1, thus the set of variables a_i in (2) is duplicated. All the matrices of the previous section have to be replaced accordingly, i.e.:

$$C \rightarrow \begin{pmatrix} 1 & 0 \\ 0 & 1 \end{pmatrix} \otimes C,$$

since they are relevant to each of the two bunches.

The beam-beam matrix B (written for 2 boxes in each bunch) represents the linearized beam-beam force:

$$B = -\frac{bI}{2} \begin{pmatrix} -2 & 0 & 1 & 1 \\ 0 & -2 & 1 & 1 \\ 1 & 1 & -2 & 0 \\ 1 & 1 & 0 & -2 \end{pmatrix}.$$

We consider here equal currents I in each bunch, b is the beam-beam tune slope in units of the synchrotron tune, $bI = \xi/Q_s$, ξ is the conventional beam-beam parameter. Four proper modes, doubly degenerate, are given by the eigensystem of $C + B$:

$$\begin{aligned} 0\pi) \quad \Omega_{0\pi} &= 2bI & v_{0\pi}^T &= (1, 1, -1, -1), \\ 0\sigma) \quad \Omega_{0\sigma} &= 0 & v_{0\sigma}^T &= (1, 1, 1, 1), \\ -1\sigma) \quad \Omega_{-1\sigma} &= bI - 1 & v_{-1\sigma}^T &= (1, -1, 1, -1), \\ -1\pi) \quad \Omega_{-1\pi} &= bI - 1 & v_{-1\pi}^T &= (1, -1, -1, 1). \end{aligned}$$

In the basis of these beam-beam modes all the matrices of Section 4 are blockwise diagonal: the interaction preserves orthogonality of the σ -modes subset to the subset of π modes. Thus the characteristic equation of our 4-mode system always breaks up into a pair of quadratic equations, in CE2 formalism (a pair of cubic equations in CE3), making the mode analysis so clear.

Finite bunch length l of the order of the beta-function value β^* at the IP, results in substantial betatron phase slippage over the interaction length. We include this effect in the phase lag parameter y ($0 < y \approx l/2\beta^* < 1$), and modify the beam-beam matrix:

$$B_y = \text{diag}\{1, e^{2iy}, 1, e^{-2iy}\} \cdot B \cdot \text{diag}\{1, e^{2iy}, 1, e^{2iy}\}.$$

Eigenvalues of $C + B_y$ give the new mode tunes², see (8) with $w = 0$. The mode coupling results in repulsion between the mode tunes; they are always real and never merge. Thus, *no instability* can appear in this beam-beam model, unless we introduce some impedance elements.

4. BEAM-BEAM INSTABILITY

The impedance element(s) inevitably present in the machine act on each of the colliding bunches individually; in CE2 formalism they are plugged in the wake matrix W , e.g. for the constant wake³ we have:

$$W = -\frac{wI}{2} \begin{pmatrix} 1 & 0 \\ 0 & 1 \end{pmatrix} \otimes \begin{pmatrix} 1 & 0 \\ 2 & 1 \end{pmatrix}, \quad (7)$$

I is the beam current, w is the coherent tune slope.

The chromaticity χ will cause the chromatic phase lag $2x \propto -\chi$, (cf. [3], Eq. (4.88)), of the trailing box oscillation with respect to the leading one; we have to modify the wake matrix accordingly:

$$W_x = \text{diag}\{1, e^{-2ix}, 1, e^{-2ix}\} \cdot W \cdot \text{diag}\{1, e^{2ix}, 1, e^{2ix}\}.$$

In combination with the beam-beam interaction, impedance elements completely change the situation. Consider first the case of very short bunches, $y \ll 1$. The mode tunes are eigenvalues of $C + B + W$, put $x = y = 0$ in (8). The beam-beam tunes shift results in reduction of the modes $0\sigma, -1\sigma$ merge threshold: $(b + 2w)I_{th} = 1$, the closest one. The head-tail + beam-beam problem corresponding to this short bunch limit was studied numerically in the 2×2 -particle model [4], predictions on possible reduction of the head-tail threshold due to beam-beam collisions and some of the results agree with ours.

The betatron phase slippage accounting for the finite bunch length in the beam-beam matrix B_y gives a new instability, when acts in combination with wakes; we can see

²Saving the space, we omit here expressions for the mode tunes since they are available from the general formula (8) presented at the end of Section 4, being its particular cases.

³With a known wake function other than constant the coefficients in W are available from the complete theory [2]. Or they may be considered as phenomenological coefficients, to be tuned to fit experimentally known head-tail parameters for a particular machine.

this from the eigenvalues of $C + B_y + W$ (put $x = 0$ in (8)). Simple analysis shows that modes 0σ and -1π are *unstable* without a current threshold, as if in conventional head-tail instability, see Fig. 2, left. However, their increments δ start quadratically at low beam current: $\delta_{0\sigma, -1\pi} = \text{Im}\Omega \approx bwI^2 \sin y \cos y$; $\delta_{-1\sigma, 0\pi} = -\delta_{0\sigma, -1\pi}$. Changing our normalized units to ordinary ones, we have: $\delta \rightarrow \omega_s \delta$, $bI \rightarrow \xi/Q_s$, $wI \rightarrow \Delta Q_{coh}/Q_s$ and rewrite the increment via the revolution period T_0 :

$$\delta \approx bwI^2 \sin y \cos y \rightarrow 2\pi\xi\Delta Q_{coh}/T_0Q_s.$$

One should take here $Q_s > \xi$, ΔQ_{coh} large enough, to stay in the validity range of our 2-mode model. At high currents $\delta \sim \omega_s$ roughly, we deal with a *fast* instability.

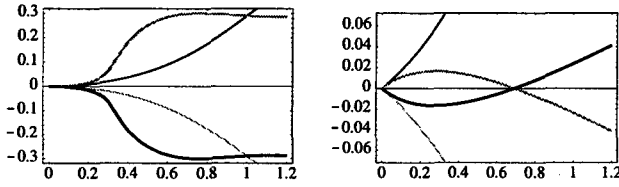


Figure 2: Effect of the positive chromaticity on the mode increments (plotted vs. the beam current) for combined action of the wake and betatron phase slippage in collision. Left: $x = 0$, right: $x = -1.42$. Parameters in (8): $y = 0.2$, $b = 1.1$, $w = 1$. All the σ modes are shown in thick lines, π modes in thin lines, the 0 modes in green, the -1 modes in black.

Physically, the phase slippage is somewhat similar to the chromatic phase effect. So, the chromaticity tuning gives us a possible cure of this instability. The chromatic phase lag x is involved in both beam-beam and impedance action, and therefore the eigenvalues of $C + B_{x+y} + W_x$ are now needed:

$$\begin{aligned} \Omega_{0\pi, -1\pi} &= -\frac{1}{2}(1 - (3b - w)I \mp (1 + bIe^{2i(x+y)})^{\frac{1}{2}}) \\ &\quad \times (1 + (be^{-2iy} - 2w)Ie^{-2ix})^{\frac{1}{2}}, \\ \Omega_{0\sigma, -1\sigma} &= -\frac{1}{2}(1 - (b - w)I \mp (1 - bIe^{2i(x+y)})^{\frac{1}{2}}) \\ &\quad \times (1 - (be^{-2iy} + 2w)Ie^{-2ix})^{\frac{1}{2}}. \end{aligned} \quad (8)$$

Due to zero sum of the increments, tuning chromaticity at a given phase slippage y cannot stabilize all the modes, when $y \neq 0$. However, it strongly changes the increment partition: at positive chromaticities ($x < 0$) we can keep the increments of the both σ modes reasonably small in a certain range of currents, see Fig. 2, right.

Fig. 3 shows how strongly absolute values of the decrements depend on the chromaticity knob; the optimum where the σ and π modes both have small decrements differs for the cases of shorter (Fig. 3, top) and longer (Fig. 3, bottom) bunches, and varies with the current. An overall trend is that $x_{opt} \sim -1$, i.e. an elevated positive value of the chromaticity would help.

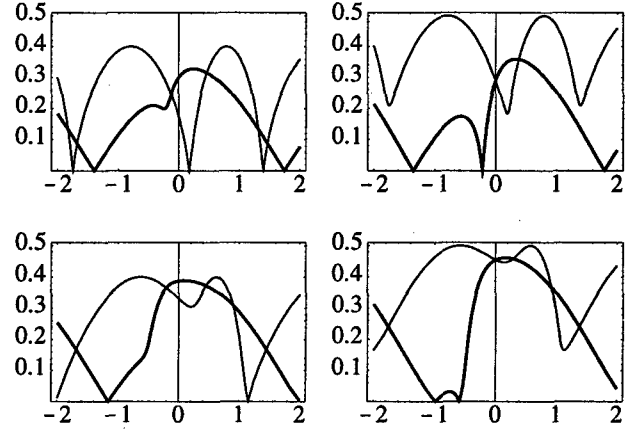


Figure 3: $|\text{Im}\Omega|$ vs. the chromatic phase x at two fixed beam currents I , left column: $I = 0.8$, right column: $I = 1$; for two bunch lengths y , top row: $y = 0.2$, bottom row: $y = 0.5$. Other parameters are the same as in Fig. 2. All the σ modes are shown in thick lines, π modes in thin lines.

5 CONCLUSION

A new formalism with Circulant Equations predicts stability of coherent dipole oscillations of non-rigid colliding bunches with finite length, in the linear beam-beam force model. Adding wakefields to the above strong-strong model, we find in such a combination a *new beam-beam instability* of head-tail type, arising without any current threshold. Its *possible cure* is the positive chromaticity.

Indeed, rather *large positive chromaticities* are known to help in improvement of the beam-beam performance on existing machines, e.g. VEPP-2M.

Any instability found in a linear theory is not necessarily lethal for a highly nonlinear beam-beam system. The amplitude growth is most likely to saturate at a certain level, but the onset of the instability may be a detriment to a low emittance regime.

Discussions with V.Parkhomchuk who has drawn my attention to the beam-beam problem with non-rigid bunches, are gratefully acknowledged.

6 REFERENCES

- [1] V.V.Danilov and E.A.Perevedentsev, "Strong Head-Tail Effect and Decoupled Modes in the Spacetime Domain", in: Proc. 15th Int. Conf. on High Energy Accelerators, Hamburg, (1992), vol. 2, 1163.
- [2] V.V.Danilov and E.A.Perevedentsev, "Feedback System for Elimination of the Transverse Mode Coupling Instability", CERN Report SL/93-38(AP), (1993).
V.V.Danilov and E.A.Perevedentsev, *NIM*, A 391, (1997), 77.
- [3] A.W.Chao, *Physics of Collective Beam Instabilities in High Energy Accelerators*, (Wiley, 1993).
- [4] K.Cornelis, "TMC Threshold as a Function of Beam-Beam Interaction", CERN SL/Note 93-39(OP), (1993).
G.X.Li and K.Cornelis, "Calculation of TMC Threshold in the Presence of Beam-Beam Force", CERN Report SL/94-85(AP), (1994).

ON SELF-CONSISTENT β -FUNCTIONS OF COLLIDING BUNCHES

A. V. Otboev and E. A. Perevedentsev

Budker Institute of Nuclear Physics, Novosibirsk, 630090, Russia

Abstract

The flip-flop effect with the linearized beam-beam force is formulated through self-consistent β -functions and equilibrium emittances which are both affected by collision. We give the results of two models of emittance dependence. The effect of finite bunch length is also discussed.

1 INTRODUCTION

From many observations of the beam-beam effects on existing e^+e^- colliders, it is known that under some conditions the sizes of opposing bunches become very different. This phenomenon is called the flip-flop effect. Such a state is not stable and the bunches may exchange their sizes. The flip-flop effect leads to reduction of the luminosity, because of the difference in bunch sizes resulting in reduction of the effective interaction area.

The problem is greatly simplified by *linearization* of the beam-beam force; it has been studied in terms of evolution of the 2nd moments of the beam distribution, involving the radiation effects: damping and quantum excitation [1, 2, 3].

Another way to understand this problem is formulation in terms of self-consistent dynamic β -functions of colliding beams at the interaction point (IP) [4]. The equilibrium emittances of the bunches are affected by the linear part of the beam-beam force: action of the opposing bunch is roughly equivalent to insertion of a (thin) lens modifying the arc lattice [5]. So, a correct account for these *dynamic* emittance variations should be done in a self-consistent way.

This paper gives results of the self-consistent model for round colliding beams, and calculation of the equilibrium radiation emittance with the thin lens insertion. We also discuss the simple model representing the bunch length effect.

2 SELF-CONSISTENT β -FUNCTIONS

Consider a collider lattice with one IP and the betatron phase advance on the arc $\mu_0 = 2\pi\nu$. We can get the resulting matrix of one revolution $M = M_0 \cdot F$ multiplying the arc matrix M_0 by the thin lens matrix F , involving the size of the opposing bunch and its intensity expressed through the nominal beam-beam parameter ξ_0 . From M we obtain new values of μ and β -function, modified by collision. Let us consider equal intensities of the colliding bunches (equal ξ_0). After simple calculations [4], using a convenient notation: $x = 2\pi\xi_0$, $c = \cot 2\pi\nu$, $b_i = \beta^*/\beta_i$, and e_i for the normalized emittances (here $i = 1, 2$ refer to the two bunches in collision), we get equations on self-consistent

β -functions in the special case of round beams:

$$\begin{aligned} b_1^2 &= 1 + 2xc \frac{b_2}{e_2} - x^2 \frac{b_2^2}{e_2^2} \\ b_2^2 &= 1 + 2xc \frac{b_1}{e_1} - x^2 \frac{b_1^2}{e_1^2}. \end{aligned} \quad (1)$$

The problem is periodic in ν with the period $1/2$, therefore we only consider $0 < \nu < 1/2$ in what follows.

We start with the case of constant emittances. Unequal solutions of (1) b_i correspond to the flip-flop situation. They are real and positive when $\nu \in (0, 1/4)$ and x belongs to the interval:

$$\sqrt{\frac{2 + 3c^2 + c\sqrt{8 + 9c^2}}{2(1 + c^2)}} < x < c + \sqrt{1 + c^2}. \quad (2)$$

For $\nu \in (1/4, 1/2)$ the inequalities should be reversed. Small ν are of predominant interest for a high beam-beam performance. One can obtain the threshold value of x for small ν by taking the limit $c \rightarrow \infty$ in the LHS of (2): $x_{th} = \sqrt{3}$.

This is a very large and unrealistic value of x , which corresponds to $\xi_0 \simeq 0.26$.

Another way to get x_{th} is the graphical method [6], applied to (1): we consider b_1 as function of b_2 , and evaluate the derivative $\partial b_1 / \partial b_2$ at the point of equal b_i , thus inspecting a possibility for unequal solutions to appear. Then the flip-flop threshold $x = x_{th}$ satisfies the equation:

$$\left. \frac{\partial b_1}{\partial b_2} \right|_{b_1=b_2} = -1, \quad (3)$$

yielding the same x_{th} as in the LHS of (2).

In contrast to the above solution, one may expect a *non-round* flip-flop state, e.g. a cross-shaped one: $b_{1x} = b_{2y}$, $b_{1y} = b_{2x}$. Using (3) we obtain this threshold:

$$x \geq x_{th} = \sqrt{\frac{4 + 5c^2 + c\sqrt{24 + 25c^2}}{2(1 + c^2)}}$$

It appears to be even higher than that for the round flip-flop state: the round beam shape seems to be "flip-proof", cf. [7].

3 RADIATION EMITTANCE

Assuming the emittances unchanged by collision, we see from the above section that the flip-flop thresholds are rather high in terms of ξ_0 .

Let us now evaluate the radiation emittance of the bunch with a thin lens insertion at the IP, representing the linear

effect of collision. Zero dispersion at the IP is assumed for simplicity.

The equilibrium emittance is determined by the one-turn average of the Courant-Snyder quadratic form with the dispersion function:

$$H(s) = \beta(s) \eta'(s)^2 + 2\alpha(s) \eta(s) \eta'(s) + \gamma(s) \eta(s)^2.$$

The lens insertion modifies the Twiss parameters involved in $H(s)$ thus changing the radiation emittance. In the Floquet parametrization $H(s) = |W(s)|^2$, the appropriate Wronskian reads:

$$W(s) = \begin{vmatrix} \eta(s) & w(s) \\ \eta'(s) & w'(s) + i/w(s) \end{vmatrix} e^{i\phi},$$

and the modified Floquet function $w(s) e^{i\phi}$ should be decomposed via the basis of the unperturbed Floquet vectors at the IP, then propagated through the unperturbed arc to get the modified vector on the current azimuth of integration s . Thus we obtain the effect of collision:

$$\frac{H(s)}{H_0(s)} = \frac{1 + p \cot 2\pi\nu + p \csc 2\pi\nu \cos 2(\arg W_0(s) - \pi\nu)}{\sqrt{1 + 2p \cot 2\pi\nu - p^2}}$$

where $p = P\beta^*/2$ is the normalized strength of the lens, and the 0 subscript marks the quantities relevant to the unperturbed lattice.

The $1 + p \cot 2\pi\nu$ term in the numerator gives positive definite contribution to the radiation emittance, and compares to the result of [5]. But the 2nd term, proportional to $\cos 2(\arg W_0(s) - \pi\nu)$, depends on the arc lattice, and generally its contribution to the radiation integral does not vanish. It may well override the effect the 1st term in some particular lattices, resulting in a linear slope of either sign in the emittance dependence on ξ_0 , contradicting to [2, 5].

4 MODELS OF EMITTANCE VARIATION

We can implement the above conclusion in simple models of variable emittance, to be used jointly with (1) for the self-consistent analysis.

The 1st model assumes the linear variation of emittance with the strength of the lens of the opposite bunch: we have then for the normalized emittances:

$$\begin{aligned} e_1 &= 1 + k \frac{b_2}{e_2} \\ e_2 &= 1 + k \frac{b_1}{e_1}, \end{aligned} \quad (4)$$

k is the linear slope coefficient; it should be kept not too large for our model to be valid. We solve (4) for e_1 and e_2 first, substitute these solutions into (1) to obtain two equations on the two variables (b_1, b_2) :

$$\begin{aligned} b_1^2 &= 1 + \frac{4b_2x(c(1 + (b_1 - b_2)k + \sqrt{D}) - b_2x)}{(1 + (b_1 - b_2)k + \sqrt{D})^2} \\ b_2^2 &= 1 + \frac{4b_1x(c(1 + (b_2 - b_1)k + \sqrt{D}) - b_1x)}{(1 + (b_2 - b_1)k + \sqrt{D})^2} \end{aligned} \quad (5)$$

where $D = 4b_2k + (1 + (b_1 - b_2)k)^2$.

Now we may solve the problem using method [6]. With $k > 0$, the flip-flop situation appears only at high values of $x = 2\pi\xi_0$ (Fig.1). In this case the values of the self-consistent β -functions are small enough and the emittances exceed their nominal values.

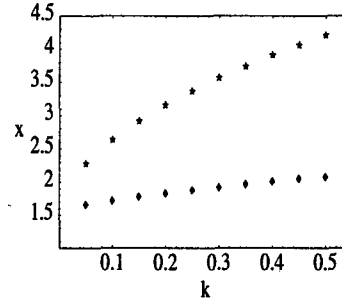


Figure 1: The flip-flop threshold x_{th} vs. the positive slope k in (5), $\nu = 0.01$ (top), $\nu = 0.1$ (bottom).

The case $k < 0$ is more interesting. There is some limiting value of x , which depends on the values of k and ν . If x is above this limit, the system (5) has no solutions. And when x is close to its threshold, there is a range of x , where (5) has two different solutions with equal b_i . We may avoid this situation by increasing the value of ν . Before x approaches its maximal value, (5) has one solution with equal b_i .

The 2nd model: we assume linear variation of the beam sizes with the strength of the lens of opposite bunch. After some calculations, this model is expressed by equations

$$\begin{aligned} e_1 &= b_1(1 + kx \frac{b_2}{e_2})^2, \\ e_2 &= b_2(1 + kx \frac{b_1}{e_1})^2, \end{aligned} \quad (6)$$

reducible to 2 variables e_1/b_1 and e_2/b_2 only. Hence, we solve (6) for these and substitute into (1) to obtain solutions for b_i .

The resultant of two equations in (6) has simple factorization:

$$R = (e_2^2 + 2b_2e_2kx + b_2^2k^2x^2 - b_2e_2k^2x^2) \times (e_2^3 - b_2e_2^2 - 2b_2^2e_2kx - b_2^3k^2x^2).$$

The first factor gives two solutions:

$$e_2 = \frac{1}{2}b_2kx(kx - 2 \pm \sqrt{kx(kx - 4)}). \quad (7)$$

So, for $k > 0$ the flip-flop threshold is high: we need $kx > 4$ for $e_{1,2}$ to be real. The second factor in R has one real root, if $k > 0$. It corresponds to normal solution $b_1 = b_2$.

Another situation is in the case of $k < 0$. Now (7) are always real and positive and correspond to the flip-flop solutions. After substitution (7) into (1) we get $b_{1,2}^2$ and require

that they be positive; this yields the condition on existence of the flip-flop solutions:

$$x < x(k) = \tan \pi \nu (\cot \pi \nu + 1/k)^2; \quad \tan \pi \nu < -k.$$

These expressions indicate how to avoid the unwanted flip-flop situation: at some x and a given value of k in the linear dependence of emittances, we may raise the tune to shift it in the area of only equal solutions, crossing the flip-flop border shown in Fig 2.

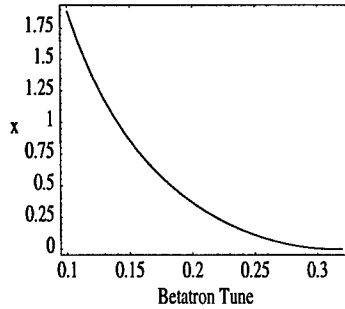
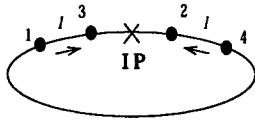


Figure 2: The flip-flop threshold x_{th} vs. the tune ν in the case of $k < 0$ in (6), $k = -0.8$. The flip-flop area lies under the curve.

5 EFFECT OF THE BUNCH LENGTH

In this section we present the constant emittance model, accounting for the effect of bunch length in collision by splitting either of the colliding bunches into 2 equal infinitely short ones spaced by l (in units of β_0):



The interaction process then has three phases: 1) collision of particles 2 and 3 at the IP; then 2a) collision of 2 and 1, and 2b) collision of 3 and 4 at the points positioned at the distance of $\mp l/2$ from the IP; finally, 3) collision of particles 1 and 4 at the IP. All values of the Twiss parameters α and β for each particle are taken at the IP and traced to the respective collision point.

From the matrix of one revolution for each particle M_i ($i = 1..4$) we get the new values of the phase advance μ , β - and α -functions and then obtain the equations on the self-consistent β -functions. This system is very complicated and can only be studied numerically. The first conclusion: if $l \neq 0$, there is no situation, when all β -functions are equal. We have the state in our system, when parameters of front and back particles are equal. We define the flip-flop situation when all the 4 parameters are different; the threshold for these solutions to appear is high (Fig.3). Therefore we conclude that the finite bunch length effect is not detrimental in the round beam case.

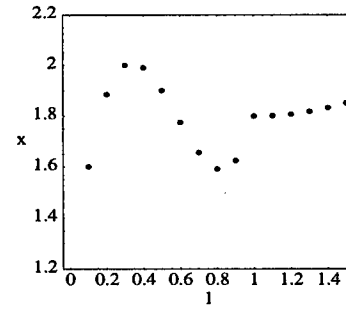


Figure 3: The flip-flop threshold x_{th} vs. l in the model of the bunch length.

6 CONCLUSION

The flip-flop effect is studied in terms of self-consistent β -function in the case, when the emittances of colliding bunches are influenced by the linear part of the beam-beam force. Evaluation of the radiation emittance of the bunch is presented in the case of one additional thin lens at the IP, with the emphasis on the term omitted in [5].

We have presented two models of variable emittances. One of them, when the emittance has a linear dependence on the strength of the lens of opposite bunch, gives high flip-flop thresholds in the area of positive slope k in (4) and no but equal sizes of colliding bunches if $k < 0$ and the beam intensity is below a certain limit. The second model (6) also predicts low flip-flop thresholds only when we assume $k < 0$, i.e. the size of the bunch is decreased by the force of opposite lens. We can avoid the flip-flop situation here by the working point manoeuvre. However, lattices with $k > 0$ seem to be generally preferable against the flip-flop effect.

The influence of the bunch length on the flip-flop effect thresholds in our simple model is weak.

We acknowledge useful discussions of the subject with P.M.Ivanov, I.A.Koop, I.N.Nesterenko and D.V.Pestrikov.

7 REFERENCES

- [1] M.A. Furman, K.Y. Ng and A.W.Chao, SSC-174 (1988).
- [2] K. Hirata and F. Ruggiero. Treatment of Radiation for Multiparticle Tracking in Electron Storage Rings, *Part. Acc.*, **28**, 137-142, 1990.
- [3] S. Matsumoto and K. Hirata. Quadrupole Modes in Linearized Beam-Beam Interaction in e^+e^- Colliding Rings. KEK Report 91-12, 1992.
- [4] D.V. Pestrikov. Self-consistent β -functions in Asymmetric Colliders. <http://www.gsi.de/struck/contrib.html>, 1996, or in GSI Report 97-07, GSI, 1997.
- [5] K. Hirata and F. Ruggiero. Treatment of Radiation in Electron Storage Rings. LEP Note 611 (1988).
- [6] A.B. Temnykh. Phenomenological Model of Flip-Flop Effect in Colliding Beams. Preprint INP 82-148. Novosibirsk, 1982.
- [7] D.V. Pestrikov. Flip-flop Effect with Variations of Bunch Aspect Ratios. KEK Preprint 98-230, 1999.

METHODS AND COMPLEX OF PROGRAMS FOR RADIATING PARTICLE 3DOF NONLINEAR DYNAMICS ANALYSIS

Y.Alexahin[#], JINR, Dubna, Russia

Abstract

The Lie-transform perturbation theory for non-autonomous non-Hamiltonian systems and its implementation in a complex of *Mathematica* programs are described. On the example of LEP 108/90 lattice the radiation effects are shown to play an important effect on particle stability at high energies.

1 INTRODUCTION

To meet the strict requirements on the beam quality and lifetime in high energy e^+e^- rings used as circular colliders, synchrotron radiation sources and damping rings of linear colliders, a tool for nonlinear dynamics analysis is necessary which takes into account the synchrotron radiation and coupling of all three degrees of freedom in the presence of errors.

An efficient tool bringing a Hamiltonian dynamical system to the normal form with the help of the Lie-transform perturbation theory was presented in [1]. It permits to evaluate separately contributions of various sources of nonlinearity (kinetic energy, magnetic multipoles, RF field) to the resonance excitation (with a possibility to keep some multipole strengths in symbolic form); the transformation generating function being known all over the lattice may be important for analysis of the off-resonance "smear" and nonlinear emittance production in the case of weak synchrotron radiation.

In the case of strong synchrotron radiation (such as LEP2) the dependence of the radiation reaction force in quadrupoles on the transverse coordinates introduce strong *radiative beta-synchrotron coupling* [2] which should be included in the normalization process. The corresponding generalization of the Lie-transform perturbation theory is outlined in the present report, as well as its implementation in a complex of *Mathematica* notebooks permitting to study high order nonlinear effects in machines as complicate as LEP or HERA-e.

2 PERTURBATION THEORY

2.1 Equation of motion of radiating particle

Introducing 6D phase space column vector of coordinates and momenta

$$z = (x, p_x, y, p_y, \sigma, \delta_p)^T \quad (1)$$

and $\theta = s/R$ we have the following equation of motion

$$\dot{z} = \frac{d}{d\theta} z = F = S \cdot \frac{\partial}{\partial z} \mathcal{H} + F^{(rad)}, \quad (2)$$

$$S = S_2 \oplus S_2 \oplus S_2, \quad S_2 = \begin{pmatrix} 0 & 1 \\ -1 & 0 \end{pmatrix}, \quad (3)$$

which is driven by the Hamiltonian and radiation reaction $F^{(rad)}$, which can be decomposed into the mean (classical) and fluctuating (quantum) parts [3]:

$$F^{(rad)} = F^{(c)} + F^{(q)}. \quad (4)$$

We will proceed as follows: solve for the nonlinear dynamics in the Hamiltonian and classical radiative fields and then add the quantum field, $F^{(q)}$, to find the distribution of an ensemble of particles.

2.2 Linear normal modes

The first step is subtraction of the finite closed orbit due to misalignments and (the mean part of) the energy losses (see e.g.[4]). We assume it to have been performed so that the power series expansion of the Hamiltonian starts with quadratic terms in the dynamical variables, whereas the mean part of the radiative force starts with linear terms.

For the next step we ignore nonlinearities and introduce eigenvectors w_n and eigenvalues λ_n of the 1-turn transfer matrix $M(2\pi+\theta, \theta)$. They form three complex conjugate pairs which we numerate as follows

$$\lambda_n = \exp[2\pi(iQ_n - \gamma_n)], \quad \lambda_{n+1} = \lambda_n^*, \quad n = 1, 3, 5 \quad (5)$$

Alternatively we will use Greek indices for numbering the normal modes, so that $Q_1 = Q_I, Q_3 = Q_{II}, Q_5 = Q_{III}, Q_{III} < 0$ above the transition energy.

We use the normalization

$$w_\mu^+ \cdot S \cdot w_\mu = i \quad (6)$$

at $\theta=0$ and then propagate the eigenvectors so that to make them 2π -periodic:

$$w_n(\theta) = e^{-(iQ_n - \gamma_n)\theta} M(\theta, 0) \cdot w_n(0), \quad (7)$$

Using the eigenvectors we can build a matrix, W , with the elements $W_{in} = (w_n)_i$ and expand the phase space vector as follows

$$z = W(\theta) \cdot \underline{a} \quad (8)$$

The 6-tuple of the coefficients

$$\underline{a} = \{a_I, a_I^*, a_{II}, a_{II}^*, a_{III}, a_{III}^*\}^T \quad (9)$$

may be regarded as a new phase space vector. In the absence of nonlinearities

$$a_\mu(\theta) = \sqrt{I_\mu} \exp[i(Q_\mu - \gamma_\mu)\theta] \quad (10)$$

with I_μ being the initial values of the action variables of the linear normal modes.

2.3 Nonlinear normalization

In the presence of nonlinearities we may use (8) just as a linear change of variables after which the equation of motion becomes

$$\dot{\underline{a}} = \Lambda^{(0)} \cdot \underline{a} + \underline{R}^{(c)}(\underline{a}, \theta; \epsilon), \quad (11)$$

[#] Email: alexahin@sunse.jinr.ru

where $\Lambda^{(0)}$ is a diagonal matrix with elements $\Lambda^{(0)}_{kk} = iQ_k - \gamma_k$, vector

$$\underline{R}^{(c)} = \varepsilon W^{-1} \cdot [S \cdot (W^{-1})^T \cdot \frac{\partial}{\partial \underline{a}} \mathcal{H}_{\text{hot}} + \underline{F}^{(c)}] \quad (12)$$

includes terms of order 2 in \underline{a} and higher (subscript "hot" standing for higher order terms), ε is the perturbation parameter (introduced here in the simplest way).

We may try to treat the nonlinear problem (11) with the method of averaging [5] which does not involve canonical transformations, however it is not convenient for practical calculations in higher orders in the perturbation parameter.

In the Hamiltonian case there is an efficient Lie-transform based algorithm, Deprit's algorithm (see e.g. [6]), which in principle permits to perform calculations to an arbitrarily high order in an automated way. Here we present its generalization for the non-Hamiltonian case.

Let us look for a continuous set of transformations

$$\underline{A} = \underline{A}(\underline{a}, \theta; \varepsilon) \equiv \hat{T}(\underline{a}, \theta; \varepsilon) \underline{a}, \quad \hat{T}(\underline{a}, \theta; 0) = I, \quad (13)$$

which renders equation of motion in the new dynamical variables

$$\dot{\underline{A}} = \underline{G}(\underline{A}, \theta; \varepsilon), \quad \underline{G}(\underline{A}, \theta; 0) = \Lambda^{(0)} \cdot \underline{A}, \quad (14)$$

as simple as possible. Defining the transformation by the equation

$$\frac{\partial}{\partial \varepsilon} \underline{A}(\underline{a}, \theta; \varepsilon) = \underline{V}(\underline{A}(\underline{a}, \theta; \varepsilon), \theta; \varepsilon), \quad (15)$$

\underline{V} being called a *Lie-dragging field*, we obtain the equation for the inverse operator

$$\frac{\partial}{\partial \varepsilon} \hat{T}^{-1} = -\hat{L}_V \hat{T}^{-1}, \quad \hat{L}_V \equiv \underline{V}^T \cdot \frac{\partial}{\partial \underline{a}} \quad (16)$$

Arbitrary vector fields are transformed with the help of the matrix operator

$$\hat{T}^{-1} = \hat{T}^{-1} \frac{\partial \underline{A}}{\partial \underline{a}}, \quad (17)$$

which satisfies the equation

$$\frac{\partial}{\partial \varepsilon} \hat{T}^{-1} = -\hat{L}_V \hat{T}^{-1}, \quad \hat{L}_V \underline{U} \equiv \hat{L}_V \underline{U} - \hat{L}_V \underline{V} = -\hat{L}_V \underline{V}, \quad (18)$$

The Lie-dragging field \underline{V} is related to the original and new vector fields by the following basic equation [1]

$$\frac{\partial}{\partial \theta} \underline{V} + \hat{L}_{\underline{G}^{(c)}} \underline{V} = \frac{\partial}{\partial \varepsilon} \underline{G}^{(c)} - \hat{T}^{-1} \frac{\partial}{\partial \varepsilon} \underline{R}^{(c)}, \quad (19)$$

which in principle permits to find \underline{V} for a given $\underline{G}^{(c)}$ or *vice versa*. But it is not clear in advance for which $\underline{G}^{(c)}$ solution of (19) may exist. Perturbation theory allows to specify $\underline{G}^{(c)}$ in the process of normalization so as to assure existence of the (formal) solution.

Expanding everything in power series

$$\underline{V} = \sum_{n=0}^{\infty} \frac{\varepsilon^n}{n!} \underline{V}_{n+1}, \quad \underline{G}^{(c)} = \sum_{n=0}^{\infty} \frac{\varepsilon^n}{n!} \underline{G}_{n+1}^{(c)}, \quad \underline{R}^{(c)} = \sum_{n=0}^{\infty} \frac{\varepsilon^n}{n!} \underline{R}_{0n}^{(c)}, \dots \quad (20)$$

we can reduce general equation (19) to the following set of homology equations

$$\frac{\partial}{\partial \theta} \underline{V}_n + \hat{L}_{\underline{G}_0^{(c)}} \underline{V}_n = \underline{G}_n^{(c)} - \underline{R}_{0n}^{(c)} + \underline{\Sigma}_n \quad (21)$$

where

$$\underline{\Sigma}_n = \sum_{m=1}^{n-1} \left\{ \binom{n-1}{m-1} \hat{L}_{\underline{V}_m} \underline{G}_{n-m}^{(c)} - \binom{n-1}{m} \underline{R}_{m,n-m}^{(c)} \right\}, \quad \underline{R}_{m,n}^{(c)} = - \sum_{j=1}^m \binom{m-1}{j-1} \hat{L}_{\underline{V}_j} \underline{R}_{m-j,n}^{(c)}$$

Eqs.(21) for the autonomous system ($\partial/\partial\theta=0$) were first obtained by Kamel [7]. In the Hamiltonian case they reduce to Deprit's equations [6].

Introducing unit 6-vectors \underline{e}_i with the components $(\underline{e}_i)_k = \delta_{ik}$ we can build the vector basis functions

$$\underline{\Phi}_{k,m} = \underline{e}_k \prod_i A_i^{m_i}, \quad \hat{L}_{\underline{G}_0} \underline{\Phi}_{k,m} = \left(\sum_i m_i \Lambda_{ii}^{(0)} - \Lambda_{kk}^{(0)} \right) \underline{\Phi}_{k,m}, \quad (22)$$

to solve eqs.(21) by expansion in them. We may set $\underline{G}_n^{(c)}$ to zero unless $(\underline{R}_{0n}^{(c)} - \underline{\Sigma}_n)$ contains a term with the basis function which eigenvalue is close to an integer times i , these being the detuning ($m_{2i} = m_{2i-1}$, $i \neq k$, $m_{2k} = m_{2k-1} - 1$) and the resonance terms. The corresponding Fourier harmonics of such terms should be added to $\underline{G}_n^{(c)}$ to avoid small denominators in \underline{V}_n .

If no close resonance is encountered in the orders of interest, we will obtain in the result of the normalization process

$$\underline{G}^{(c)}(\underline{A}, \theta; \varepsilon) = \Lambda(|A_i|^2, |A_{ii}|^2, |A_{iii}|^2; \varepsilon) \cdot \underline{A}, \quad (23)$$

where Λ is again a diagonal matrix independent of θ . Having solved eq.(14) for \underline{A} , we can transform back to the original variables as follows:

$$\underline{a} = \sum_{n=0}^{\infty} \frac{\varepsilon^n}{n!} \underline{A}_n^{-1}(\underline{A}, \theta), \quad \underline{A}_0^{-1} = \underline{A}, \quad \underline{A}_n^{-1} = - \sum_{m=1}^n \binom{n-1}{m-1} \hat{L}_{\underline{V}_m} \underline{A}_{n-m}^{-1} \quad (24)$$

2.4 Distribution of radiating particles

Let us now consider the fluctuating part of the radiative field $\underline{F}^{(q)}$ as a perturbation of the deterministic motion. Transforming and expanding it on the analogy of the classical radiative field in (12), (20) (note that expansion in ε now starts with zero order) we can project it onto the normal form coordinates \underline{A} by the following recursion scheme:

$$\underline{G}_n^{(q)} = \underline{R}_{0n}^{(q)} + \sum_{m=1}^n \binom{n}{m} \underline{R}_{m,n-m}^{(q)}, \quad \underline{R}_{m,n}^{(q)} = - \sum_{j=1}^m \binom{m-1}{j-1} \hat{L}_{\underline{V}_j} \underline{R}_{m-j,n}^{(q)}. \quad (25)$$

In the result of this projection additional nonlinear transverse components of the fluctuating force can appear from the longitudinal component enhancing diffusion in the transverse planes.

To find particle distribution in the phase space, \mathcal{F} , one should resort to the Fokker-Planck equation which has the standard form [3] in the complex variables as well.

With known \mathcal{F} we can obtain the *true emittance* of nonlinear normal modes, $\varepsilon_{\mu}^{(\text{true})} = \langle |A_{\mu}|^2 \rangle$, and, with the help of (24), the *apparent emittance* of linear normal modes, $\varepsilon_{\mu}^{(\text{app})} = \langle |a_{\mu}|^2 \rangle$, related to the observable beam characteristics via eq.(8).

3 COMPLEX OF PROGRAMS

The described above theory was implemented in a complex of *Mathematica* notebooks (see Fig.1). One group of the notebooks perform symbolic computations and generate analytical expressions for subsequent numerical calculations.

Another group of the notebooks find linear eigenvectors with radiation, components of the Lie-dragging field, resonance and diffusion coefficients for a particular lattice. As the starting point it uses the closed orbit due to imperfections and classical radiation and the linear eigenvectors of the Hamiltonian motion around it computed by *MAD* [8]. Employing *Mathematica* for numerical calculations permits to operate with nonlinear element strengths in symbolic form which may be convenient for determination of the multipole correctors strength. At present the treatment is limited to the second order effects in the thin lens approximation.

4 LEP2 108/90 LATTICE

The lattice with phase advances in the arc cells $\mu_x/\mu_y=108^\circ/90^\circ$ was once considered as a strong candidate for LEP operation at the highest energy. However some problems were encountered with this lattice tested at the beam energy of 86 GeV: sporadic onsets of particle losses and by almost a factor of three larger vertical emittance than expected from the linear theory (0.5 nm vs. 0.2nm). Though the large vertical emittance (but not particle losses) was obtained also in simulation by quantum tracking with *MAD* [9], the physics is not still clear. To get an insight the developed methods were applied for the particular misaligned lattice used in [9].

Table 1

resonance	$ v_1 ^2$	$ v_3 ^2$	$ v_5 ^2$
$Q_x - Q_y - Q_s $	2.76	2.41	$1.50 \cdot 10^6$
$Q_y - 2 Q_s $	-	$4.94 \cdot 10^{-3}$	6.11
$(1-1) Q_x - Q_s$	42.6	-	$1.55 \cdot 10^7$
$(1-1) Q_y - Q_s$	-	205.	$5.02 \cdot 10^5$

Table 1 presents for some resonances squared absolute values of the first order Lie-dragging field components averaged over the arcs. One can see that the influence of the transverse motion on the longitudinal one is much stronger than *vice versa*, which is a manifestation of the *radiative beta-synchrotron coupling* [2]. Also, the nearest to the working point $Q_x=102.280$, $Q_y=96.192$, $|Q_s|=0.107$ synchro-betatron resonances appear too weak to produce noticeable vertical emittance.

Table 2

	$\partial/\partial I_I$	$\partial/\partial I_{II}$	$\partial/\partial I_{III}$
Λ_I	-509+51261 i	-74 - 34702 i	-0.10 - 80 i
Λ_{II}	-11- 34329 i	56 +35806 i	0.01 - 1.2 i
Λ_{III}	928 + 4949 i	-127 + 1124 i	-0.02 + 8.5 i

The second order perturbation theory gives dependence of the tunes and damping rates on the oscillation amplitudes. Table 2 presents derivatives of $\Lambda_\mu = iQ_\mu - \gamma_\mu$ w.r.t. the action variables of the nonlinear normal modes I_ν . Due to large derivative $\partial \text{Re}(\Lambda_{III})/\partial I_I$ the longitudinal damping fails at $I_I=2.9 \mu\text{m}$. Though this value exceeds the dynamic aperture ($\sim 2.5 \mu\text{m}$), the

weakened longitudinal damping can contribute to particle losses at smaller I_I .

5 REFERENCES

- [1] Y.Alexahin, in Proc. HEACC'98, Dubna, 1998.
- [2] J.Jowett, in Proc. 4th Workshop on LEP Performance, Chamonix, 1994, p.47.
- [3] J.Jowett, SLAC-PUB-4033, Stanford, 1986; AIP Conf. Proc. 153 (1987).
- [4] Y.Alexahin, DESY HERA 99-02, Hamburg, 1999.
- [5] J.Ellison, H.-J.Shih, in AIP Conf. Proc. 326 (1995).
- [6] L.Michelotti, "Intermediate Classical Dynamics with Applications to Beam Physics". J.Wiley, 1995.
- [7] A.Kamel, *Celestial Mech.*, v.3, p.90 (1970).
- [8] H.Grote, F.Iselin, "The MAD program. Version 8.21. User's Reference Manual", 1997.
- [9] J.Jowett, in Proc. 7th Workshop on LEP Performance, Chamonix, 1997, p.76.

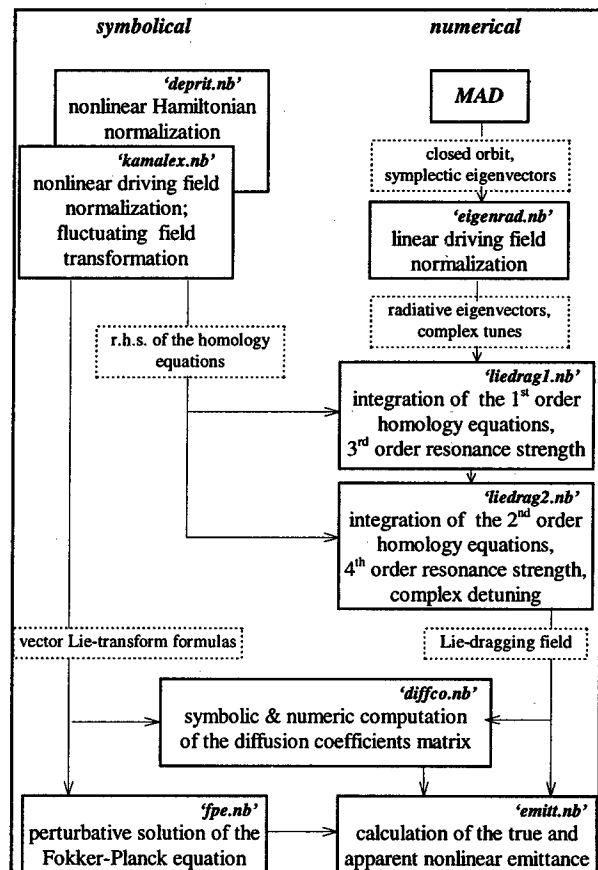


Figure 1. Structure of the complex of programs.

CORRECTION OF THE BETATRON COUPLING BY LOCAL ORBIT CROSS TALK

A. Loulergue, J. Payet

CEA/DSM/DAPNIA/SEA, Saclay, 91191, Gif-sur-Yvette Cedex, France.

Abstract

Analytical expressions, in presence of skew quadrupoles errors, have been derived to estimate the betatron coupling contribution to the vertical beam size and emittance [1]. The treatment of the betatron coupling is based on the matrix transport perturbation and related eigen vectors. The advantage of this approach is to be free of the usual resonant approximation and to allows a compact formulation of the vertical emittance. In addition, this approach gives a fast analytical statistical analysis. From this analytical expressions, we propose a new scheme of the betatron coupling correction also based on the closed cross orbit correction [2]. This method, called local cross orbit correction, improve the correction of the betatron coupling with few judicious measurements [3]. It allows also to fully uncoupled the beam locally on the lattice.

1 INTRODUCTION

The third generation synchrotron machine are designed with a very small beam emittance to produce very high brilliance beams of synchrotron radiation in the VUV and soft X-ray regions. This requires relatively strong focusing, and magnet errors will therefore introduce large distortions in closed orbit (C.O.) as well as residual dispersion and large betatron coupling. To achieve these performances we need to control the coupling value, define by the ratio of the vertical emittance ϵ_z by the horizontal emittance ϵ_x , in a range from few 0.1 % to about 10 %. We have studied the correction of the spurious vertical dispersion and betatron coupling on the SOLEIL [4] and ESRF [5] machine from an analytical and statistical point of view, using the BETA-LNS code.

2 COUPLING SOURCES

The vertical emittance is generated in two ways, directly when a photon is radiated in a region where there is nonzero vertical dispersion, or by betatron coupling between the two planes horizontal and vertical. This two sources of vertical emittance are induced by the presence of misalignment errors and by the resulting closed orbit.

Noting Δ_{zj} the vertical kick in j , $\Delta\Phi_q$ the tilt of the quadrupoles and Δz_s the vertical misalignment of the sextupoles, we have for the vertical corrected closed orbit and the vertical spurious dispersion in i :

$$z_i^{CO} = \sum_j C_{ij}^z \Delta_{zj} \quad \text{with} \quad C_{ij}^z = c_{ij}^z + \sum_{cor} c_{ic}^z d_{ic}$$

$$D_i^z = \sum_{quad} c_{iq}^z [(2KLD)_q \Delta\Phi_q - (KL)_q z_i^{CO}]$$

$$+ \sum_{sext} c_{is}^z (2SLD)_s [\Delta z_s + z_i^{CO}] - z_i^{CO}$$

c_{ij} is the vertical response matrix from j to i . We generalize this response matrix C_{ij} including the sum over the correctors : each element d_{ic} represents the value of the corrector c induced by the default j . K, S, L and D are respectively, the strength of the quadrupoles, sextupoles, their length and the horizontal unperturbed dispersion.

To derive a complete analytical formulation of the beam envelop and emittance induced by betatron coupling between the two transverse planes in presence of synchrotron radiation, we study the eigen vectors of the one turn transport coupled matrix. After a tedious calculation, we find that we could simply estimate analytically the coupling K in presence of misalignment by the means of the vertical dispersion and the two complex function A and B with [1] :

$$K = \sqrt{\frac{(\sin\mu_+)^2 |B|^2 + (\sin\mu_-)^2 |A|^2}{(4\sin\mu_+ \sin\mu_-)^2} + \frac{U_3}{\epsilon_x^0}} - \left[\frac{|AB|}{8\sin\mu_+ \sin\mu_-} \right]^2$$

$$\mu_+ = \frac{\mu_x + \mu_z}{2} \quad \text{and} \quad \mu_- = \frac{\mu_x - \mu_z}{2}$$

μ and ϵ_x^0 are the tune and the horizontal emittance. Using the same notation than for the spurious dispersion, with β and φ the optical function and phase advance, the two complex functions A and B are :

$$A = \sum_{quad} \sqrt{\beta_{xq} \beta_{zq}} e^{i(\varphi_{xi} + \varphi_{zi})} [(2KL)_q \Delta\Phi_q]$$

$$+ \sum_{sext} \sqrt{\beta_{xs} \beta_{zs}} e^{i(\varphi_{xi} + \varphi_{zi})} (2SL)_s [\Delta z_s + z_s^{CO}]$$

$$B = \sum_{\text{quad}} \sqrt{\beta_{xq} \beta_{zq}} e^{i(\varphi_{xi} - \varphi_{zi})} [(2KL)_q \Delta\Phi_q] \\ + \sum_{\text{sext}} \sqrt{\beta_{xs} \beta_{zs}} e^{i(\varphi_{xi} - \varphi_{zi})} (2SL)_s [\Delta z_s + z_s^{\text{CO}}]$$

U_3 is the second invariant at four dimension (Courant and Snyder invariant) in average in the bending magnets. This term is function of A, B and the vertical dispersion.

Once we have develop the dispersion and the two function A and B over the errors, it is straight forwards to estimate their rms and mean values. The coupling K being a quadratic function of the errors, its mean value, $\langle K \rangle$, can be expressed in function of the square standard deviation of the errors [1].

In summarize, the relevant items concerning the betatron coupling are :

1. All the quantities such as the tree moments and the vertical emittance induced by the betatron coupling are only dependent of the tow functions A and B and their respective complex conjugates A^* and B^* . They are the generating functions of the linear betatron coupling.
2. All the cross terms of the one-turn transverse transport matrix T are only dependent of A and B and their complex conjugates A^* and B^* .
3. This four functions A, B, A^* and B^* are s dependent (along the lattice) and are independent one to each other. We need at least also four skew correctors to cancel them in one location in the lattice. If we cancel this four functions on one point, we have :

⇒ an uncoupled one turn transport matrix T
 ⇒ an uncoupled beam matrix (or optical functions)
 ⇒ the two vertical and horizontal emittances are equal to their respective invariant

4. The two quantities $B/\sin\mu_-$, $A/\sin\mu_+$ are the sum of all the coupling resonances.

5. Near the two resonances, the K coupling tend to :

⇒ difference resonance ($2\mu_- = \mu_x - \mu_z \rightarrow 2n\pi$)

$$K \rightarrow \frac{|B|^2}{(\sin\mu_-)^2} \left(1 + \frac{J_x}{J_z} \right)$$

⇒ sum resonance ($2\mu_+ = \mu_x + \mu_z \rightarrow 2n\pi$)

$$K \rightarrow \frac{|A|^2}{(\sin\mu_+)^2} \left(1 + \frac{J_x}{J_z} \right)$$

6. The two quantities $|A|^2$ and $|B|^2$ are constant along the lattice except at each skew errors (or correctors), where they have a jump. This jump tends to cancel near the resonance.

3 COUPLING CORRECTION

In order to correct the coupling, we have to reduced the two sources of vertical emittance : the vertical dispersion and the betatron coupling. In both case the correctors are skew quadrupoles. The vertical dispersion is corrected at each Beam Plot Monitor (BPM) using a Singular Value Decomposition (SVD) in a similar manner than the closed orbit. In addition we prospect few techniques to correct simultaneously the betatron coupling. The principal difficulties in correcting the betatron coupling is to be able to estimate and to measure his contribution to the vertical emittance. Actually, among others, two schemes used to correct the betatron coupling are : correction of the two resonances, sum and difference, and correction of Cross Talk Orbit (OCT) at each BPM (closed orbit induced by the kick of a steerer in the other plane via the skew errors [2]).

The resonance correction need to shift the tunes to set the machine on the two resonances. It is generally not sufficient to reach the desired coupling. From the analytical point of view, it corresponds to correct the two square modules of the functions A and B (items 4 and 5) once the tunes are shifted. The OCT corrections tend to improve the coupling correction, but the relation between the OCT and the coupling was not clear [5]. It could be shown that there is only a one way relation between a segment of the Cross Orbit induced by a steerer and the two generating functions A and B. The concerned segment is the part of the orbit near the steerer free of skew errors (figure 1). This relation is no longer valid elsewhere.

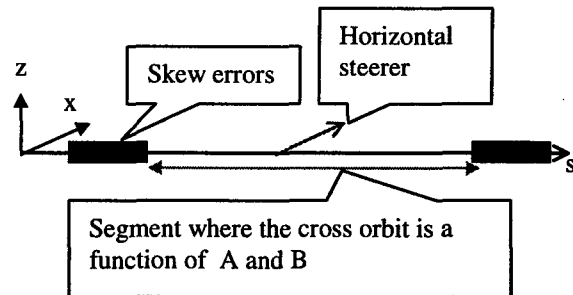


Figure 1

For a better targeting of the betatron coupling, one can only correct the cross orbit at the nearest BPM from the steerer (one steerer one BPM). At best, if there is no skew errors between the BPM and the steerer (both located on the same straight section for instance), one will correct the

betatron coupling via the correction of the cross orbit (item 1).

To test this new technique of correction, we compared the mean resulting coupling of the four betatron correction methods :

1. Theoretical via direct correction of the square module of A and B in each dipoles, named AB.
2. The tow resonances correction, named RES.
3. All the OCT correction at each BPM, named OCT
4. All the OCT corrected only at the nearest BPM, a Local Cross Talk Orbit (LOCT) correction, named LOCT.

on the SOLEIL (table 1) and ESRF (table 2) machine. In each case, we correct a weighted function of both dispersion and betatron coupling using one of the above technique varying the number of correctors. In order to simplify the computation, we only set tilted quadrupoles (2.10^{-4} rad rms) and sextupoles vertical displacement (1.10^{-4} m rms). Without any correction, the mean coupling of the SOLEIL and ESRF machine are respectively of $1.4 \cdot 10^{-2}$ and $17 \cdot 10^{-2}$.

	4	8	16
AB+Disp	$0.75 \cdot 10^{-2}$	$0.18 \cdot 10^{-2}$	$0.63 \cdot 10^{-3}$
RES+Disp	$0.76 \cdot 10^{-2}$	$0.20 \cdot 10^{-2}$	$0.16 \cdot 10^{-2}$
LOCT+Disp	$0.78 \cdot 10^{-2}$	$0.22 \cdot 10^{-2}$	$0.15 \cdot 10^{-2}$
OCT+Disp	$0.91 \cdot 10^{-2}$	$0.33 \cdot 10^{-2}$	$0.22 \cdot 10^{-2}$

Table 1 : Mean coupling on SOLEIL for the four schemes of correction versus the number of skew correctors.

	16*	16**	32
AB+Disp	$0.62 \cdot 10^{-2}$	$0.26 \cdot 10^{-2}$	$0.41 \cdot 10^{-2}$
RES+Disp	$4.00 \cdot 10^{-2}$	$0.32 \cdot 10^{-2}$	$0.10 \cdot 10^{-2}$
LOCT+Disp	$0.72 \cdot 10^{-2}$	$0.28 \cdot 10^{-2}$	$0.64 \cdot 10^{-3}$
OCT+Disp	$2.50 \cdot 10^{-2}$	$0.36 \cdot 10^{-2}$	$0.88 \cdot 10^{-3}$

Table 2 : Mean coupling on ESRF for the four schemes of correction versus the number of skew correctors.

*Standard corrector setting ** New corrector setting [6]

One observes that the LOCT correction improve by 20 to 30 % the coupling correction compared to the OCT scheme. In the first case on the ESRF machine one gets an improvement of a factor 3.5 (from 2.5 to 0.72 %). An other advantage is to notably reduce the amount of data to handle by only using one BPM per steerer. For instance on the SOLEIL machine, if one wants to correct the vertical closed cross orbits induced by the 48 horizontal steerers at the 112 BPM, the number of constraints is $48 \times 112 = 5376$. By using one BPM per steerer, the number of constraints is reduced to only 48. This improvement of the coupling correction came simply from the fact that, by locally correcting the Cross Orbit we correct the

generating functions, A and B, of the betatron coupling (item 1).

An other application of the one way relation between the Cross talk Orbit and the two functions A and B, is the possibility to fully uncouple the beam (item 4) (and the one turn transport matrix (item 3)). By correcting the Cross Orbit induced by two steerers on two BPM judiciously localized (figure 2), we get four constraints (function of A and B) that can be cancelled with four skew correctors.

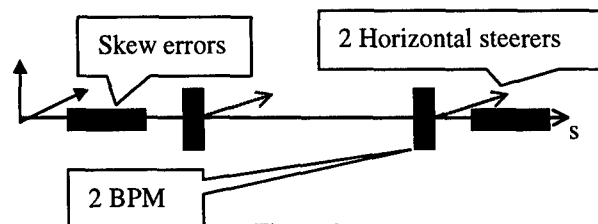


Figure 2

A numerical test of such a Cross Orbit correction on the SOLEIL machine with four correctors effectively cancel the local coupling as well as the one turn transport matrix.

4 CONCLUSION

From a complete analytical treatment of the betatron coupling, we proposed a new technique of the coupling correction based on the local cross talk orbit minimization. By simply correct the cross orbit to the nearest BPM from the active steerer, we improve notably the reduction of the coupling induced by the betatron coupling by a better targeting of the correction. An other advantage of this technique, is to reduce the amount of constraints to handle.

5 REFERENCES

- [1] A. Loulergue, J. Payet, Traitement analytique et statistique du couplage betatron, Internal Report, DAPNIA/SEA 99/02.
- [2] J. Safranek, S. Krinsky, Plans to Increase Source Brightness of NSLS X-Ray Ring, PAC 93 Proceedings.
- [3] A. Loulergue, J. Payet, Correction du couplage betatron dans un anneau synchrotron, Internal report DAPNIA/SEA 99/03.
- [4] M.P. Level et al, Status of the SOLEIL Project, EPAC 98 Proceeding.
- [5] R. Nagaoka, L. Farvacque, Workshop on coupling correction, ESRF Grenoble, 21-09-1998.

THE EFFECT OF NONLINEAR SYNCHROTRON MOTION ON THE SOLEIL ENERGY ACCEPTANCE *

A. Nadji[†], J.-L. Laclare, M.-P. Level, A. Mosnier, P. Nghiem,
Projet SOLEIL, DRIF CNRS, Av. de la Terrasse, Bât. 5, 91198 Gif sur Yvette, France
G. Flynn, LURE, Centre Universitaire Paris-Sud, Orsay, France

Abstract

The lengthening of the trajectory is determined by the momentum compaction factor α and the betatron oscillation contribution term $\frac{\Delta C}{C_0}$. When the first order term of the momentum compaction factor α_1 is small, the second order term α_2 and $\frac{\Delta C}{C_0}$ have to be included in the longitudinal equations of motion. In this case, the RF bucket form changes and the energy acceptance can be significantly reduced. This leads to a decrease in Touschek beam lifetime. In this paper we show that the value of α_2 in the standard low emittance lattice of SOLEIL is large and can reduce the energy acceptance of the machine. We discuss the magnitude of this reduction and the difficulties encountered in minimizing the value of α_2 in the case of a low emittance lattice. We also show that the lengthening of the trajectory induced by horizontal and vertical betatron oscillations vanishes when the chromaticities are corrected to zero.

1 INTRODUCTION

In a storage ring, the Touschek relevant energy acceptance may be determined by the RF bucket momentum height, by the physical aperture or by the dynamic aperture associated with off momentum particles if the induced amplitude after a Touschek scattering event exceeds one of these two transverse limits. In the case of the SOLEIL project, a great effort has been made to increase the dynamic aperture for off-momentum particles leading to a transverse energy acceptance of up to $\pm 6\%$ [1]. The Touschek beam lifetime calculations take into account the higher order effects in energy which become important for such large values [2]. The use of superconducting cavities with a peak voltage fixed at 3.8 MV insures a longitudinal energy acceptance larger than $\pm 6\%$. Nevertheless, this value was determined using the first order momentum compaction factor, α_1 , thus assuming that the other momentum factor terms are negligible. In our case, the second order term of the momentum compaction factor α_2 is significant and must be considered in the equations of longitudinal motion. The expected problem is that the synchrotron motion being nonlinear, the buckets become asymmetric which can reduce the RF energy acceptance and therefore the Touschek beam lifetime.

2 NONLINEAR LONGITUDINAL MOTION

The momentum compaction factor is defined as the relative change in orbit path length, $\frac{\Delta l}{l_0}$, with relative particle energy, $\delta = \frac{\Delta p}{p_0}$:

$$\alpha = \frac{d(\Delta l/l_0)}{d\delta} \quad (1)$$

where p_0 is the momentum of the reference particle and l_0 the length of the reference orbit.

The expression for particle position contains betatron oscillation, closed orbit distortion and off momentum orbit terms:

$$x = x_\beta + x_{co} + \eta_1 \delta + \eta_2 \delta^2 + \dots \quad (2)$$

η_1 and η_2 are respectively the first and the second order terms of the dispersion function. Assuming that $x_{co} \approx 0$, the resulting variation in orbit length with energy (up to the second order) and betatron amplitudes, can be written in the following way:

$$\frac{\Delta l}{l_0} = \frac{\Delta C}{C_0} + \alpha_1 \delta + \alpha_2 \delta^2 \quad (3)$$

where

$$\frac{\Delta C}{C_0} = \frac{1}{l_0} \oint \left(\frac{x_\beta}{\rho} + \frac{x_\beta'^2}{2} \right) ds \quad (4)$$

$$\alpha_1 = \frac{1}{l_0} \oint \frac{\eta_1}{\rho} ds \quad \alpha_2 = \frac{1}{l_0} \oint \left(\frac{\eta_2}{\rho} + \frac{\eta_1'^2}{2} \right) ds \quad (5)$$

$\frac{\Delta C}{C_0}$ is the term representing lengthening effects due to betatron oscillations, α_1 and α_2 are respectively the first and the second order terms of the momentum compaction factor.

The longitudinal motion equations including these terms can then be written as:

$$\frac{d\varphi}{dt} = -\omega_{rf} \left[\alpha_1 \delta + \alpha_2 \delta^2 + \frac{\Delta C}{C_0} \right] \quad (6)$$

$$\frac{d\delta}{dt} = \frac{eV_{rf}}{ET} [\sin \varphi - \sin \varphi_s]$$

they can be derived from the following Hamiltonian:

$$H(\delta, \varphi) = \frac{\Delta C}{C_0} \delta + \alpha_1 \frac{\delta^2}{2} + \alpha_2 \frac{\delta^3}{3} + \quad (7)$$

$$\frac{eV_{rf}}{ET} (\cos \varphi - \cos \varphi_s + (\varphi - \varphi_s) \sin \varphi_s)$$

* Work supported by CNRS-CEA-MENESR.

[†] Email: Nadji@lure.u-psud.fr

where ω_{rf} is the angular frequency of the RF cavity, V_{rf} is the RF peak voltage, E is the particle energy and T the revolution period, φ_s and φ are respectively the phases of the reference and the test particles.

In the case where $\alpha_2 \neq 0$ and $\frac{\Delta C}{C_0} \neq 0$ we obtain two stable fixed points and two unstable fixed points which correspond to the existence of a second zone of stability in addition to the well-known stable linear RF-bucket. According to the values of α_2 and $\frac{\Delta C}{C_0}$, the synchrotron diagram presents different aspects, particularly the separatrices are no longer symmetric in $+\delta$ and $-\delta$ [3],[4].

3 THE CASE OF THE SOLEIL OPTICS

The small beam emittance is obtained by increasing the amount of horizontal focusing. The dispersion in the bending magnets is then very small and consequently we find naturally small values of α_1 . At its nominal energy, 2.5 GeV, the lattice has a horizontal emittance of 3 nm.rad. In this case α_1 is about 4.722×10^{-4} and using the values of the sextupoles corresponding to the optimized dynamic aperture the value of the α_2 term is about 4.513×10^{-3} .

Figure 1 shows the longitudinal phase space diagram corresponding to these two values but assuming that $\frac{\Delta C}{C_0} = 0$.

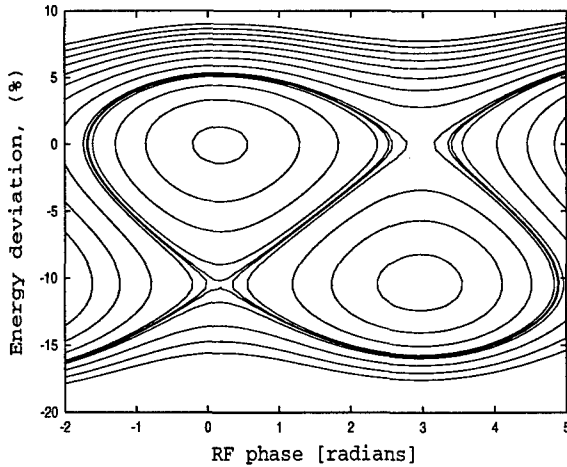


Figure 1: Longitudinal phase space.

We can see that the effect of α_2 is important. The RF-bucket, centered around $\delta = 0$, is asymmetric in energy, the upper limit is at +5.2 % ($|\frac{\alpha_1}{2\alpha_2}|$) and the lower limit is at -10.5 % ($-\frac{\alpha_1}{\alpha_2}$). The impact of this asymmetry can be understood by inspecting figure 2 which shows the dynamic and physical apertures calculated as a function of δ . We recall that in the linear case, the RF bucket height is about ± 6 %. In figure 2, one can see that a particle with an energy deviation of +6 % is still inside the lowest transverse aperture (the vacuum chamber aperture) when its energy deviation changes to -6 %. Unfortunately, the low value of α_1 renders significant the contribution of the term α_2 and

the synchrotron motion becomes in fact nonlinear. A particle with a positive energy deviation of +5.2 % for example can be lost because its separatrix can bring it to a negative energy deviation as high as -10.5 %.

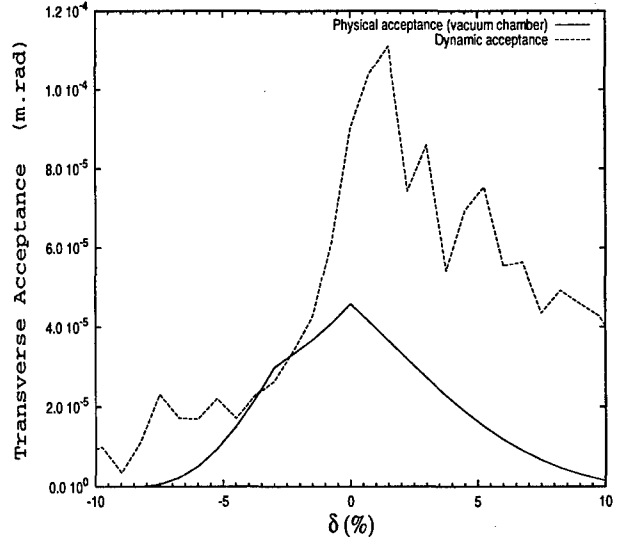


Figure 2: Horizontal dynamic and physical acceptances as a function of δ .

The energy acceptance/Touschek lifetime module of the BETA code [5], described in detail in [2] has been modified to take into account the non-linear synchrotron motion. Instead of assuming, as we did in [2] that a particle having been Touschek scattered to δ will oscillate between δ and $-\delta$ during one synchrotron period, we now calculate the mapping, by integration of the longitudinal equations (6), from δ to the maximum opposing energy $\delta_{max}(\delta)$ which occurs one half synchrotron period later. Expression (3) of [2] then becomes :

$$A(\delta) = \min_{\delta' \in [\delta, \delta_{max}(\delta)]} \{ \min[A_{phys}(\delta'), A_{dyn}(\delta')] \}. \quad (8)$$

We also take into account the asymmetric longitudinal acceptance which is determined during the process of calculating $\delta_{max}(\delta)$.

Figure 3 presents the results for the energy acceptance along one period of the ring. The corresponding value of the Touschek beam lifetime is about 26 hours instead of 40.5 hours in the linear case. This calculation is performed for multibunch operation using the following parameters : the bunch current is 1.26 mA, the horizontal-vertical coupling is 0.01 and the natural bunch length is 11.6 ps.

To reduce synchrotron motion nonlinearity and thus recuperate some extra beam lifetime, we must reduce the value of α_2 . The expression giving this term shows that, due to the $\eta_1'^2$ contribution, α_2 is always positive in a linear machine. η_2 can be made positive or negative with sextupoles and can compensate the term $\eta_1'^2$. The adjustment of α_2 by the sextupoles can be made as follows :

$$\Delta\alpha_2 = -\frac{\Delta S \eta_1'^2}{I_0} \quad (9)$$

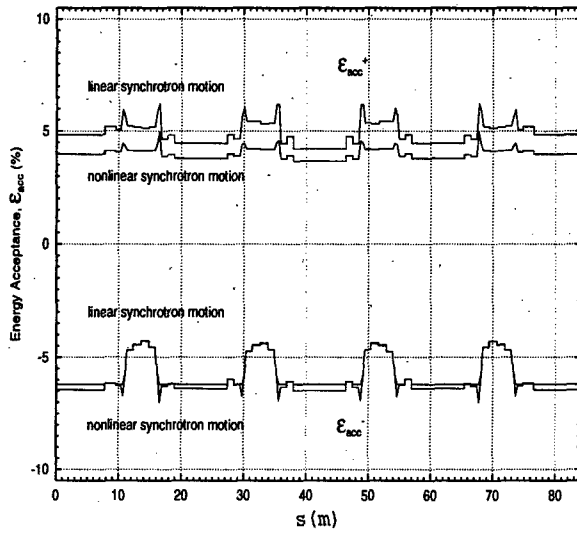


Figure 3: Energy acceptances.

where $\Delta S(m^{-2})$ is the change in the sextupole strength, $\eta_1(m)$ is the horizontal dispersion at the sextupole and $l_0(m)$ is the orbit length. Even if we take the sextupole (S4) [1], where the dispersion is maximum (0.27 m), its efficiency in reducing α_2 is small. As an example, increasing the strength of the 16 type S4 sextupoles by a factor 2 would reduce α_2 by only a factor 2, which is not nearly enough to restore the linearity of the longitudinal motion. The objective is to reduce the term α_2 while compensating the two transverse chromaticities and obtaining a very good dynamic aperture. This seems to be extremely difficult in the case of a very low emittance lattice for which the dispersion is low and the circumference is large. Up to now, we have not performed an exhaustive study in this direction.

4 EFFECT OF THE TERM $\frac{\Delta C}{C_0}$

When $\frac{\Delta C}{C_0} \neq 0$, the longitudinal equations (6) have the following stable fixed points :

$$\delta_{1,2} = -\frac{\alpha_1}{2\alpha_2} \left(1 \pm \sqrt{1 - \frac{4\alpha_2}{\alpha_1^2} \frac{\Delta C}{C_0}} \right) \quad (10)$$

whose locations depend on the value of the betatron amplitude and the closed orbit. In order for the fixed points to be real we must require :

$$\frac{\Delta C}{C_0} < \frac{\alpha_1^2}{4\alpha_2}; \quad \frac{\Delta C}{C_0} < 1.235 \times 10^{-5} \quad (11)$$

First, we can determine the maximum RF frequency variation, by taking into account the well-known relation $\frac{\Delta C}{C_0} = -\frac{\Delta f_{rf}}{f_{rf}}$ and using expression (11), we can see that there is a limit for $\frac{\Delta f_{rf}}{f_{rf}} < 0$. This limit is $|\Delta f_{rf}| < 4.3 \text{ kHz}$.

Secondly, in a linear machine (i.e. sextupoles and higher multipoles off), the betatron motion can be represented by $x_\beta(s) = \sqrt{a_0 \beta_x(s)} \cos \varphi_x(s)$. Introducing this expression and its derivative into formula (4), one can easily obtain an average value for the term $\frac{\Delta C}{C_0}$ which is in this case always positive :

$$\frac{\Delta C}{C_0} = \frac{x_\beta^2}{4\beta_x} < \gamma_x > \quad (12)$$

During the injection of the beam or after a Touschek collision for example, the particle can undergo large amplitude betatron oscillations, the combination of equations (11) and (12) gives an upper limit to x_β .

This could have been a problem without the fortunate effect of chromatic sextupoles. In fact, using the BETA code, we have calculated the variation of $\frac{\Delta C}{C_0}$ as a function of the amplitude x_β for the case where the two transverse chromaticities are corrected to zero. In contrast to the linear case, the average value (over several turns) of $\frac{\Delta C}{C_0}$ is very near to zero. The analytical developments taking into account the presence of sextupoles corroborate perfectly the simulations performed with the BETA code which show that the term $\frac{\Delta C}{C_0}$ is on average zero when the transverse chromaticities of a storage ring are corrected to zero. In fact the analytical result gives in this case the following expression :

$$\frac{\Delta C}{C_0} = -\pi \frac{x_\beta^2}{\beta} [\xi_{\text{sextupoles}} + \xi_{\text{quadrupoles}}] \quad (13)$$

where $\xi_{\text{quadrupoles}}$ is the natural chromaticity of the ring and $\xi_{\text{sextupoles}}$ is that due to the chromatic sextupoles. As is well known a zero chromaticity corresponds to $\xi_{\text{quadrupoles}} + \xi_{\text{sextupoles}} = 0$.

5 CONCLUSION

Because of the very low emittance, the effect of α_2 is significant in the SOLEIL lattice. It reduces the Touschek lifetime by a factor 1.5. Although the correction of α_2 term seems to be difficult in such lattice, further reflexions on how to reduce its effect are needed.

6 REFERENCES

- [1] P. Nghiem, et. al., "Optics for SOLEIL at 2.5 GeV", Proceedings 6th European Particle Accelerator Conference, Stockholm, (1998).
- [2] A. Nadji et. al., "Energy acceptance and Touschek lifetime calculations for the SOLEIL project", Proceedings 6th European Particle Accelerator Conference Stockholm, (1998).
- [3] A. Nadji, et. al., "Quasi-isochronous experiments with the Super-ACO storage ring", N.I.M. A378 (1996) 376.
- [4] J. P Bardin, "Thesis, 1973".
- [5] J. Payet, "BETA-LNS code".

OPTIMIZATION OF DAΦNE BEAM-BEAM PERFORMANCE

M.E. Biagini, C. Biscari, A. Ghigo, S. Guiducci, G. Mazzitelli, C. Milardi, M.A. Preger,
F. Sannibale, M. Serio, G. Vignola, M. Zobov, INFN-LNF, Frascati, Italy
M. Boscolo, Univ. La Sapienza, Roma, Italy and INFN-LNF, D. Shatilov, BINP, Novosibirsk, Russia

Abstract

The Φ -factory DAΦNE is an electron-positron collider with a design luminosity of $5.2 \cdot 10^{32} \text{ cm}^{-2} \text{ s}^{-1}$ at the energy of the Φ -resonance (1020 MeV c. m.) [1]. In order to achieve the design luminosity high current multibunch electron and positron beams are stored in two separate rings and collide in two common interaction regions. Since the beams arrive at the interaction points from the different rings, a careful longitudinal timing and precise transverse scan of the colliding bunches are necessary to optimize the collider luminosity. In this paper we describe luminosity measurement techniques adopted in DAΦNE, discuss measures aimed at maximizing the luminosity in the beam-beam collisions and report the achieved results. The experimental data are compared with the results of numerical simulations.

1 INTRODUCTION

We describe DAΦNE beam-beam performance optimization at the commissioning stage before the installation of the experimental detectors. A beam-beam interaction study at this stage was necessary to check and calibrate all the luminosity measurement set-ups, to study and apply methods and techniques for luminosity improvement and to demonstrate DAΦNE's capability of achieving the high luminosity goals in both the single and multibunch modes. In Section 2 we describe the main set-ups used for the luminosity measurements such as the single bremsstrahlung and the beam-beam tune split detectors. Section 3 deals with the techniques and methods applied to optimize the luminosity performance. In particular, longitudinal timing, transverse scanning and the phase jump procedure are discussed. Finally, the results achieved so far in both single and multibunch beam interaction modes are given in Section 4.

2 LUMINOSITY MEASUREMENTS

The DAΦNE luminosity monitors [2] (see Fig. 1) are based on the measurement of the photon production in the single bremsstrahlung (SB) electromagnetic reaction at the interaction point during the collisions. Among other possible reactions, SB has been selected for DAΦNE since its high counting rate allows to perform "on line" luminosity measurements which are very useful during machine tune-up. Moreover, the sharp SB angular distribution significantly simplifies the geometry of the detector and makes the counting rate almost independent from the position and angle of the beams at the Interaction Point (IP).

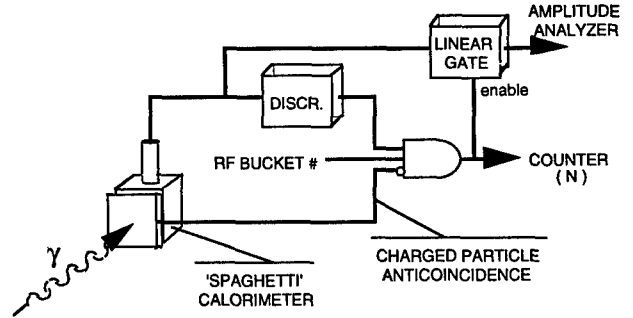


Figure 1: Schematic layout of the luminosity monitor.

The detector is a proportional counter consisting of alternated layers of lead and scintillating fibers with photomultiplier read-out. The charge signal from the photomultiplier is proportional to the photon energy. The data acquisition system provides energy analysis and photon counting.

The main background affecting the measurement is due to photons from bremsstrahlung on the residual gas (GB). This contribution is statistically subtracted by measuring the GB rate while beams are longitudinally separated, obtaining the SB counting rate \dot{N} and the luminosity:

$$L = \frac{\dot{N}}{\left[\int_{E_T}^{E_{\max}} dE \int_{\Omega_T} d\Omega \frac{\partial^2 \sigma_{SB}}{\partial E \partial \Omega} \right]}$$

where E_{\max} is the maximum photon energy; σ_{SB} is the SB theoretical cross section; Ω_T is the solid angle covered by the detector, defined by a collimator placed in front of the proportional counter. The minimum photon energy E_T accepted by the system is found by a calibration procedure using the GB spectrum.

The direct luminosity measurements with the luminosity monitors were supported and cross-checked by the coherent tune split measurements which allow to estimate the space charge tune shift parameters. The fractional part of the vertical and horizontal tunes were measured simultaneously in both the positron and the electron rings during the beam-beam collisions.

The betatron tunes are measured by exciting the beam at RF frequency with transverse stripline kickers and measuring the beam response in the excitation plane with a transverse pick-up. Two different setups have been adopted to perform the tune measurements: in the first one a Network Analyzer HP 4195A (10 Hz - 500 MHz) RF output, amplified up to 100 W by class A amplifiers,

provides the sweeping excitation. The horizontal and vertical coherent beam response is picked-up by strip line pairs and detected with the Network Analyzer. In the second system the other beam is excited with white noise and the beam oscillations signal, from a dedicated beam position monitor (BPM), is sent to a Spectrum Analyzer (HP 70000 system) operating in zero span (detector) mode. The Spectrum Analyzer IF output is down-converted with a HP 89411 module and processed by a real time FFT analyzer HP 3587S.

The knowledge of the tune shift parameter ξ_y contributes to the luminosity evaluation from the following expression:

$$L = f \frac{N_p}{2r_e} \frac{\xi_y}{\beta_y} \left(1 + \frac{\sigma_y}{\sigma_x} \right)$$

Here the beta function at the IP β_y is found from lattice measurements; the beam size ratio is measured by the DAΦNE synchrotron light monitors [3] while the number of particles per bunch N_p is calculated from the current measured by a DCCT. The results from the two kinds of measurement are in agreement.

3 LUMINOSITY OPTIMIZATION

For the collider commissioning two provisional Interaction Regions (IR) with seven conventional quadrupoles were installed in the experimental pits. One of the quadrupoles is placed at the IP. Such a scheme allows to reduce the machine chromaticity.

The beam orbit measurements in the IRs are performed by seven BPMs distributed along each IR. Since the position of both beams is measured by the same monitors, monitor offsets cancel out. One of the BPMs in each IR is installed at the IP position. This simplified beam superposition and beta functions measurements at the IP during collision tuning. Averaging over 100 BPM readings provided precise beam position measurements in the IRs with a standard deviation below 10 μm .

In order to achieve high luminosity the longitudinal and transverse positions of the two beams must be adjusted to provide maximum overlap at the IP. Moreover, the waists of the vertical beta functions should be the same for the two rings and coincide with the crossing point. Since the IP is not a symmetry point of the machine, the tuning of the IR optics has been done iteratively to obtain symmetric beta functions with equal minima for the two rings.

The longitudinal overlap of colliding bunches at the nominal IP has been synchronized by monitoring the distance between the combined signals of the two beams on two sets of symmetric BPMs on either side of the IP. The final precise longitudinal timing has been achieved by varying the RF phase of one of the two beams in order to maximize the luminosity monitor signal.

In Figure 2 we can see an image from the luminosity monitor showing the counting rate as a function of time

(full scale is equal to 10 min.). The dip in the counting rate corresponds to the beam separation obtained with an RF phase change.

Closed orbit bumps in the IR with four correctors have been applied to adjust angle and displacement at the IP and overlap the beams. Bumps have been also used to separate vertically the beams in one of the IRs when colliding in only one IP. In the horizontal plane the crossing angle has been set to be 25 mrad and the horizontal orbit displacement has been adjusted to be much smaller than the horizontal beam size of 2.1 mm at the IP. Since the vertical beam size is much smaller than the horizontal one ($\sim 20 \mu\text{m}$), fine tuning of the vertical orbit has been performed by changing the position at the IP in steps of 5 μm and the angle in steps of 50 μrad . The optimal collision configuration has been found by scanning the beam in the vertical plane looking for maximum luminosity monitor signal.

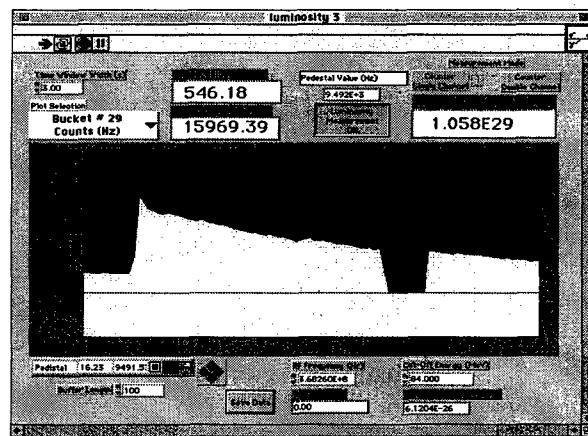


Figure 2: Luminosity monitor output.

It has been observed that during injection in the collision mode the intensity of the beam being injected saturated below the nominal level. This has been explained by the fact that the injected bunch performs both longitudinal and transverse oscillations during a time comparable with the radiation damping one. Such a bunch interacting with an opposite, already stored bunch, loses current. A "phase jump" procedure has been adopted to fix this problem [4]. Initially, the two bunches are injected into non-interacting RF buckets in order to avoid beam-beam interactions during accumulation. Then, when the nominal intensity is reached, the stored bunches are brought into collision by changing rapidly the phase of one of the two RF cavities. In this way the orbit length in one of the main rings is changed for a short time to cancel the initial longitudinal separation of the bunches. If the phase shift is performed with a fast ramp (of the order of few synchrotron oscillation periods) the bunch follows the RF phase and no synchrotron oscillations are excited. The procedure has proved to be efficient in both single and multibunch collision modes. The highest luminosity values reached so far have been achieved by applying the "phase jump" technique.

4 NUMERICAL SIMULATIONS AND EXPERIMENTAL RESULTS

During commissioning it was decided to run on the working point (5.15; 5.21) situated farther from integers than the one (5.09; 5.07) proposed earlier [5]. This choice was based on beam-beam numerical simulations with the LIFETRAC code [6] and dictated by several reasons taken into account during machine start up. Among these:

(a) closed orbit distortions are less sensitive to machine errors for working points situated far from the integers;

(b) the second order chromaticity responsible for the parabolic tune variation as a function of the particle momentum deviation is much smaller for these points;

(c) the dynamic aperture is large enough for this working point even without switching on the dedicated sextupoles for the dynamic aperture correction;

(d) it is easier to correct machine coupling during the initial operation when the vacuum pressure is higher than the design value of 10^{-9} Torr.

According to the numerical simulations, the maximum luminosity in single bunch collisions which can be reached on this working point without remarkable beam blow up is $2.2 \cdot 10^{30} \text{ cm}^{-2} \text{ s}^{-1}$ [7]. This value corresponds to tune shift parameters $\xi_{x,y}$ of 0.03. The equilibrium density contours on this working point are shown in Fig. 3 (b).

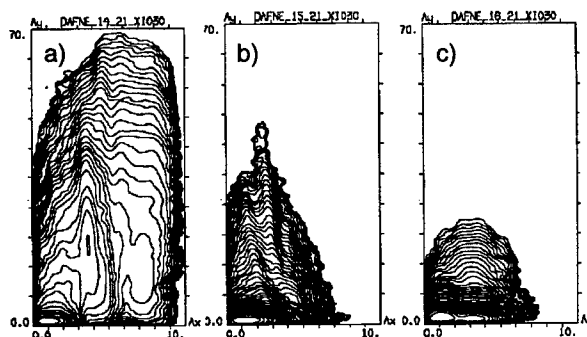


Figure 3: Equilibrium density in the normalized betatron amplitudes space. Adjacent contour levels are at a constant ratio \sqrt{e} .

As it can be seen, the tails of the distributions are well within the machine dynamic aperture, which is $10 \sigma_x$ times $70 \sigma_y$ for a machine coupling of 1%. Experimentally, a good lifetime and the present maximum achieved single bunch luminosity of $1.6 \cdot 10^{30} \text{ cm}^{-2} \text{ s}^{-1}$ have been reached at this working point. The measured luminosity is somewhat smaller than that predicted numerically since the collisions have been performed at somewhat lower currents with smaller tune shift parameters.

The results of all single bunch luminosity measurements during different machine shifts are shown in Fig. 4, where the luminosity is given as a function of the product of the electron times positron bunch currents. The dashed line shows the luminosity calculated with the design parameters at the same currents.

We have performed a luminosity scan changing the tunes around the working point (5.15; 5.21) with steps of 0.01 in both horizontal and vertical directions. The experimental results are in a good qualitative agreement with the numerical ones. For example, an increase of the horizontal tune from 5.15 to 5.16 resulted in a substantial increase of the horizontal beam size observed on the synchrotron light monitor while the lifetime was improved, in agreement with the simulations. In fact, for the point (5.16; 5.21) (see Fig. 3 (c)) the beam core is blown up horizontally and the vertical distribution tails are shorter than for the point (5.15; 5.21). In turn, by decreasing the vertical tune to 5.14 a sharp degradation of the lifetime was observed, as foreseen from the tail growth predicted numerically in Fig. 3 (a).

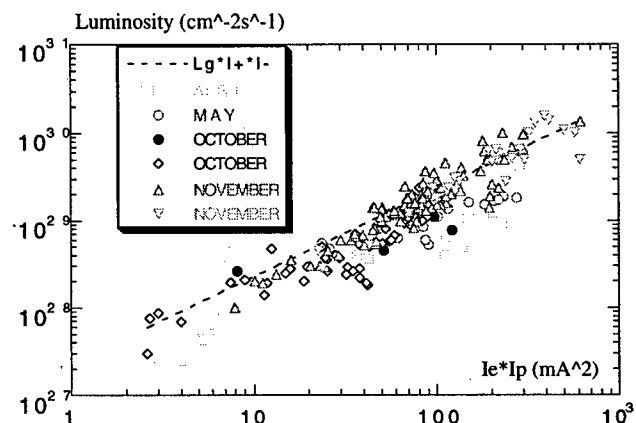


Figure 4: Measured luminosity versus beam current.

Only two days were dedicated to multibunch beam collision operation. During these days a luminosity in the range of $10^{31} \text{ cm}^{-2} \text{ s}^{-1}$ was obtained by accumulating about 200 mA in 13 bunches in each beam and applying the "phase jump" procedure. Just a first attempt has been made to collide the bunches at the two IPs simultaneously. The reached luminosity per IP was lower than in the single IP configuration. At present, a simulation study [7] has been performed to find optimal working conditions for two IP interactions and the lattice adjustments have been prepared for the next shifts with two experiments in DAΦNE.

REFERENCES

- [1] G. Vignola and DAΦNE Project Team, EPAC96, pp. 22-26 (1996); S. Guiducci, WEAR1, these Proceedings.
- [2] G. Di Pirro et al., BIW98, pp. 485 - 493 (1998).
- [3] A. Ghigo et al., BIW94, pp. 238 - 244 (1994).
- [4] A. Gallo et al., MOP84, these Proceedings.
- [5] K. Hirata and M. Zobov, EPAC96, pp. 1158 - 1160 (1996).
- [6] D. Shatilov, Part. Acc. 52, 65 (1996).
- [7] M. Zobov et al., DAΦNE Technical Note, G-51 (1999).

COMPUTING TRANSFER FUNCTIONS OF MULTIPOLE DEVICES DIRECTLY FROM MAGNETIC FIELD DATA, INCLUDING FRINGE FIELD EFFECTS AND HIGHER ORDER ABERRATIONS

R.M.G.M. Trines^{1,2}, J.I.M. Botman², S.J.L. van Eijndhoven¹
H.L. Hagedoorn², T.J. Schep³

Abstract

The scalar and vector potentials of a magnetic multipole device are described in terms of magnetic field measurements gathered on either a cylindrical surface or a median plane [1]. Fringe field effects and multipole contributions of arbitrary order, as well as the discrete nature of the field measurements, are taken into account. This description has been used to calculate the transfer function of the device, directly in terms of the field measurements. The method as described in this paper can be applied to single beam guiding elements as well as to clusters of elements, and can be extended to calculate the transfer function for a complete beam line setup or a storage ring. The accuracy of the results is only limited by the accuracy of the field measurements.

1 INTRODUCTION

From Maxwell's equations for the static electromagnetic field, we find that, for a magnetic field \vec{B} in a region without free charges or currents, there exists a scalar potential u , and a vector potential \vec{A} , satisfying:

$$\text{grad } u = \vec{B} = \text{curl } \vec{A}, \quad (1)$$

$$\Delta u = 0, \quad (2)$$

$$\text{curl curl } \vec{A} = \vec{0}. \quad (3)$$

The vector potential \vec{A} will be chosen such that $\text{div } \vec{A} = 0$. In this case, we have $\Delta \vec{A} = \vec{0}$.

We apply these equations to the magnetic field inside a magnetic multipole device which has the z -axis as its central axis. Our region of interest G is, in cylindrical coordinates, given by: $G : 0 \leq r < R, -\pi \leq \varphi \leq \pi, -\infty < z < \infty$, with boundary $\Gamma : r = R$. Here, $R > 0$ is a convenient maximal radius of the multipole device, e.g. the aperture radius. We assume u to be known at Γ , and introduce dimensionless coordinates $r^* = r/R, z^* = z/R$. The potential problem for u is then given by (we drop the stars for convenience):

$$\begin{cases} \frac{\partial^2 u}{\partial r^2} + \frac{1}{r} \frac{\partial u}{\partial r} + \frac{1}{r^2} \frac{\partial^2 u}{\partial \varphi^2} + \frac{\partial^2 u}{\partial z^2} = 0 & \text{on } G, \\ u(1, \varphi, z) = U(\varphi, z) & \text{on } \Gamma. \end{cases} \quad (4)$$

In order to have a unique solution to this problem, we have to impose the additional conditions

$$\begin{cases} \lim_{z \rightarrow \pm\infty} u(r, \varphi, z) = C_{\pm} < \infty, & 0 \leq r \leq 1, \\ \lim_{|z| \rightarrow \infty} u_z(r, \varphi, z) = 0, & 0 \leq r \leq 1. \end{cases} \quad (5)$$

Here, C_+ and C_- are constants such that $\lim_{z \rightarrow \pm\infty} u(r, \varphi, z) = C_{\pm}$. For non-solenoidal fields (no φ -independent terms), we have $C_{\pm} = 0$. In practical cases, the conditions (5) will always be satisfied.

2 FIELD DESCRIPTION

The general solution to (4) can be expanded into $2m$ -pole contributions [1]:

$$u = \sum_{m=0}^{\infty} J_m(r \frac{d}{dz}) (A_m(z) \cos(m\varphi) + B_m(z) \sin(m\varphi)),$$

while the associated vector potential \vec{A} is given by:

$$A_r = \sum_{m=1}^{\infty} J_{m+1}(r \frac{d}{dz}) (B_m \cos(m\varphi) - A_m \sin(m\varphi)),$$

$$A_{\varphi} = \sum_{m=0}^{\infty} J_{m+1}(r \frac{d}{dz}) (A_m \cos(m\varphi) + B_m \sin(m\varphi)),$$

$$A_z = \sum_{m=1}^{\infty} J_m(r \frac{d}{dz}) (-B_m \cos(m\varphi) + A_m \sin(m\varphi)).$$

The functions $A_m(z)$ and $B_m(z)$ are to be determined from the boundary conditions at $r = 1$. Let $V_m(z)$ and $W_m(z)$ denote the Fourier coefficients of $U(\varphi, z)$, then

$$J_k(r \frac{d}{dz}) A_m(z) = \int_{-\infty}^{\infty} g_m^k(r, z - \zeta) V_m(\zeta) d\zeta. \quad (6)$$

A similar result holds for $J_k(r \frac{d}{dz}) B_m(z)$. The basic function $g_m^k(r, z)$ is given by

$$g_m^k(r, z) = \frac{1}{2\pi} \int_{-\infty}^{\infty} \frac{I_k(\omega r)}{I_m(\omega)} i^{k-m} e^{i\omega z} d\omega.$$

Any field-related quantity can be expressed in the same manner as the potentials by differentiating or integrating this basic function.

¹Eindhoven University of Technology, Den Dolech 2, P.O.Box 513, 5600 MB Eindhoven, The Netherlands, Department of Mathematics and Computer Science

²Eindhoven University of Technology, Department of Applied Physics

³FOM Institute for Plasma Physics "Rijnhuizen", P.O.Box 1207, 3430 BE Nieuwegein, The Netherlands

3 FITTING THE MULTIPOLE FIELD

3.1 Boundary conditions known

In practice, we obtain approximations of V_m or its derivatives by interpolating a discrete set of measurements by a piecewise constant or linear function. First, assume V_m is piecewise constant. Then there are pairs (λ_i, z_i) with $\sum_i \lambda_i = 0$ such that $U'_m = \sum_i \lambda_i \delta(z - z_i)$. Then, after integration,

$$J_k(r \frac{d}{dz}) A_m(z) = \sum_i \lambda_i G_m^k(r, z - z_i), \quad (7)$$

where $G_m^k(r, z) = \int_0^z g_m^k(r, \zeta) d\zeta$. If V_m is supposed to be piecewise linear, then $U'_m = \sum_i \lambda_i \delta(z - z_i)$, in which case we need to replace $G_m^k(r, z)$ by $\tilde{G}_m^k(r, z) = \int_0^z G_m^k(r, \zeta) d\zeta$. As was shown above, related quantities can easily be derived by replacing the functions G_m and \tilde{G}_m by functions related to these quantities, while retaining the pairs (λ_i, z_i) .

The values for λ_i are obtained from measurements. For example, assume B_z has been measured at the points $(1, \varphi_j, w_i)$. The Fourier coefficients of $B_z(1, \varphi, z)$ are U'_m and W'_m ; these are obtained from the measurements using Fourier series theory. Employing a piecewise constant approximation for U'_m , we write $\lambda_i = U'_m(w_{i+1}) - U'_m(w_i)$, and $a_m(r, z) = \sum_i \lambda_i \tilde{G}_m(r, z - z_i)$, where $z_i = \frac{1}{2}(w_{i+1} - w_i)$. Measurements of other components can be treated in the same way.

It should be noted that, in order to determine the $2m$ -pole contribution, one needs measurements performed at $2m$ different angles φ_i .

The errors in $a_m(r, z)$ are limited by those in V_m :

$$\sup_{z \in \mathbb{R}} |\delta a_m(r, z)| \leq r^m \sup_{z \in \mathbb{R}} |\delta V_m(z)|,$$

This justifies the use of the given approximations.

3.2 Boundary conditions unknown

Expressions for the potential can also be obtained in case measurements were performed at points not on the surface $r = 1$. Assume measurements of $u(r, \varphi, z)$ were taken at the points with scaled coordinates (r_k, φ_i, w_j) , $k = 1, \dots, M$, $i = 1, \dots, P$, $j = 1, \dots, N$. In this case, we are able to fit at most M different multipole contributions simultaneously; in most cases, the $2m$ -pole contributions corresponding to $m = 1, \dots, M$, will be fitted. If less than M multipole coefficients are fitted, the remaining data can be used to improve the statistics of the fit.

As an example, assume that u contains dominant normal-oriented quadrupole and sextupole contributions, and that all higher order contributions are negligible:

$$u(r, \varphi, z) = a_2(r, z) \cos(2\varphi) + a_3(r, z) \cos(3\varphi).$$

The coefficients a_2 and a_3 are then approximated by

$$a_2(r, z; \lambda) \doteq \sum_{l=1}^N \lambda_l G_2(r, z - z_l),$$

$$a_3(r, z; \mu) \doteq \sum_{l=1}^N \mu_l G_3(r, z - z_l),$$

where $z_l = \frac{1}{2}(w_l + w_{l+1})$. This corresponds to a piecewise constant approximation of the multipole coefficients of u at $r = 1$. We denote the measured value of u at (r_k, φ_i, w_j) by f_{kij} , and define the quantity $M(\lambda, \mu)$ by:

$$M(\lambda, \mu) = \sum_{k=1}^M \sum_{i=1}^P \sum_{l=1}^N (f_{kij} - u(r_k, \varphi_i, w_j))^2.$$

The optimal values for λ, μ are then obtained by minimizing $M(\lambda, \mu)$ under the conditions $\sum_l \lambda_l = \sum_l \mu_l = 0$. Again, knowledge of the values for λ, μ completely determines the corresponding multipole contribution.

There are a few remarks to be made concerning this example:

- Measurements at at least two different angles are needed to fit both normal and skew multipole contributions.
- A surplus of angles and/or radii can be used to improve on statistics.
- The w_i -values at which signal is dominant over noise should be used to define $M(\lambda, \mu)$; the remaining w_i -values only serve to improve on statistics.
- Further improvement on the statistics can be obtained by using a weighted average for the sum of squares in the definition of $M(\lambda, \mu)$.

It should also be noted that the former method yields better results for individual multipole contributions, while the latter yields a better approximation of the total field, distributing higher order multipole contributions among the lower order multipole coefficients.

4 TRANSFER FUNCTIONS

4.1 Numerical calculation

Having obtained a complete field description in terms of field measurements, we show how to obtain the transfer function from numerical integration of the equations of motion. The system of Hamiltonian equations of motion for a charged particle in the field can be written in the following form:

$$(q', p')(z) = \underline{f}(\underline{q}, \underline{p}, \vec{A}(\underline{z}, \underline{q}), \frac{\partial \vec{A}}{\partial \vec{x}}(\underline{z}, \underline{q})). \quad (8)$$

Here, $\underline{q} = (r, \varphi, t)$, $\underline{p} = (p_r, p_\varphi, p_z)$, and $\vec{x} = (r, \varphi, z)$.

As derived in the previous section, the components of \vec{A} and their partial derivatives all take the form as in (7).

The system (8) will be solved by means of a finite difference method. The discrete version of (8) reads:

$$(q, p)(w_{i+1}) = (q, p)(w_{i-1}) + (w_{i+1} - w_{i-1}) \times f(q(w_i), p(w_i), \vec{A}(w_i, q(w_i)), \frac{\partial \vec{A}}{\partial \vec{x}}(w_i, q(w_i))). \quad (9)$$

We apply the initial condition $(q, p)(w_0) = (q_0, p_0)$, and calculate $(q, p)(w_1)$ from

$$(q, p)(w_1) = (q, p)(w_0) + (w_1 - w_0) \times f(q_0, p_0, \vec{A}(w_0, q_0), \frac{\partial \vec{A}}{\partial \vec{x}}(w_0, q_0)).$$

We then find (q_f, p_f) by repeated application of (9), described in terms of (q_0, p_0) and the field measurements. By varying (q_0, p_0) , we can calculate the complete transfer function of the device, directly in terms of these measurements.

Since the steps of this finite difference method are located precisely at the points $z = w_i$, where the field measurements were performed, we find that there are no interpolation errors in the values for \vec{A} used in the calculations. By optimizing the interpolation of the boundary values at $r = 1$, such that not only the boundary values, but also their z -derivatives are matched at the points $z = w_i$, we can also remove interpolation errors from the values of the partial derivatives of \vec{A} for better results.

Note that for the numerical scheme, we need a best possible overall approximation of the magnetic vector potential, so the least squares method is preferred over direct integration of the boundary values in this case.

4.2 Analytical results

In the past, aberration coefficients for the transfer functions of many magneto-optical devices have been derived analytically. (See Smith [2], Lee-Whiting [3], Matsuda & Wollnik [4], Nakabushi & Matsuo [5].) Often, these coefficients are expressed in the on-axis r -derivatives of the field of such devices. The methods presented here can be used to obtain these gradients directly from field measurements away from the z -axis.

By expanding the functions g_m into powers of r , one can expand the coefficients a_m and b_m into powers of r . For example:

$$\begin{aligned} a_m(r, z) &= \sum_{l=0}^{\infty} \alpha_{ml}(z) r^{m+2l}, \\ \alpha_{ml}(z) &= \int_{-\infty}^z g_{ml}(z - \zeta) V_m(\zeta), \\ g_{ml}(z) &= \frac{1}{4^l l! (m+l)! \pi} \int_0^{\infty} \frac{\omega^{m+2l}}{I_m(\omega)} \cos(\omega z) d\omega. \end{aligned}$$

The z -dependent coefficients of these power series and their derivatives are used in the expressions for the aberration

coefficients. The aberration coefficients for a normal-oriented magnetic quadrupole, for example, are all expressed in terms of the quantity $k_2(z)$ and its derivatives, which are, for a particle with charge q and momentum p_0 , given by

$$(k_2^2)^{(l)}(z) = \frac{q}{p_0} 4^l l! (l+2)! \alpha_{2,l}(z).$$

From this, we find that we can avoid measuring the on-axis r -derivatives of the magnetic field, and obtain k_2 , and thus the aberration coefficients, directly from measuring the magnetic field away from the z -axis, which is easier. The same holds for the aberration coefficients corresponding to higher order multipole contributions.

Note that, in order to calculate the various aberration coefficients properly, we need a best possible approximation of the individual multipole coefficients, so direct integration of the boundary values is the preferred method to obtain them.

5 CONCLUSIONS

The magnetic field inside a magnetic multipole, and its harmonic scalar and vector potentials, have been explored in the area $0 \leq r < 1$ and $-\infty < z < \infty$. The various multipole contributions to these quantities have been fitted using field measurements at the boundary $r = 1$ and shifted basic functions. An alternative least-squares method has been developed for measurements not at the boundary. The same set of measurements and shiftings can be used to fit many field-related quantities.

The developed procedure is independent of the exact form of the boundary conditions and can be used to fit the field of one device or various consecutive devices.

The procedure works for any order multipole contribution, but will be most useful for lower order multipole contributions, since higher order multipole contributions are more difficult to obtain from measurements and their effect on particle trajectories will often be small.

A numerical method for calculating the transfer functions from the field description has been derived. The field description has also been applied to existing analytical results. The least squares method is preferred in the first, direct integration of the boundary values in the second case.

6 REFERENCES

- [1] R. Trines et al., EPAC-98 Conf. Proc. (1998), p. 1969.
- [2] D.L. Smith, *Nucl. Instr. and Meth.* **79** (1970), p. 144; G.E. Lee-Whiting, *Nucl. Instr. and Meth.* **99** (1972), p. 609.
- [3] G.E. Lee-Whiting, *Nucl. Instr. and Meth.* **83** (1970), p. 232.
- [4] H. Matsuda & H. Wollnik, *Nucl. Instr. and Meth.* **103** (1972), p. 117.
- [5] H. Nakabushi & T. Matsuo, *Nucl. Instr. and Meth.* **198** (1982), p. 207.

STUDIES ON IMPERFECTIONS IN THE SLS STORAGE RING

M. Böge, A. Streun, M. Muñoz, Paul Scherrer Institute, Switzerland

Abstract

Studies on linear and nonlinear imperfections in the SLS storage ring operated at 2.4 GeV are presented. The influence of spurious vertical dispersion and linear coupling on the vertical emittance and possible correction schemes are discussed. The deterioration of the Dynamic Aperture caused by higher order multipoles is investigated based on field calculations. Furthermore the influence of ground waves on the orbit stability is estimated.

1 THE MACHINE MODEL

For a successful operation of the SLS storage ring [1] it is crucial to keep the tolerances on linear and nonlinear imperfections as small as possible. Correction schemes have to compensate for the remaining errors. In order to simulate the imperfect SLS ring a realistic machine model has been developed utilizing the 6D code TRACY[2][3].

Horizontal and vertical alignment errors, magnet tilts, strength distortions and higher order multipoles are included. The fact that the elements are mounted on girders and the dipoles are chaining adjacent girders introduces a correlation which has to be taken into account in the simulation. The elements on the girders are assumed to have an rms alignment error of $50\mu\text{m}$, the girders themselves $300\mu\text{m}$ and the girder joints $100\mu\text{m}$.

The roll of the girders is controlled to $25\mu\text{rad}$ by a hydrostatic leveling system. Individual elements are allowed to have residual rolls of $100\mu\text{rad}$ rms. In order to get a proper statistics 200 different error sequences (seeds) have been chosen in the simulation. It should be noted that all assigned errors are gaussian distributed with a cut at two sigma.

2 ORBIT CORRECTION

Once the errors have been assigned a first turn steering algorithm ("threader") is used to find the initial closed orbit. After setting the sextupoles to 50% of their strength a closed orbit correction is performed which is based on the information of beta functions and phases for the ideal optics. This is followed by another correction loop at full sextupole strength until the monitors have zero readings.

For the orbit correction two schemes are considered. One is based on the Singular Value Decomposition (SVD) algorithm. The other involves interleaved three corrector bumps "sliding" around the machine.

The global SVD scheme has the advantage of being able to handle an unequal number of monitors and correctors in the case of faulty monitors and/or saturated correctors and is therefore very flexible. On the other hand the

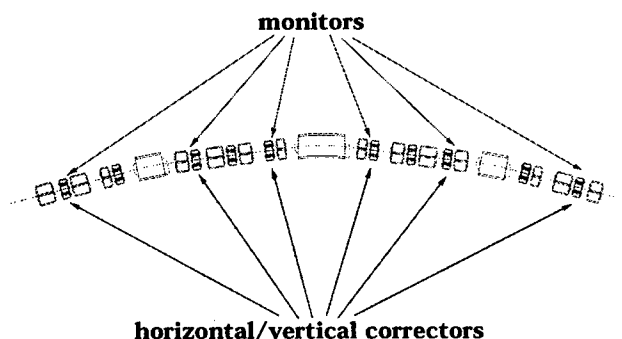


Figure 1: Corrector/Monitor layout of one sector (1/12th) of the SLS storage ring

SVD scheme requires a good knowledge of the linear machine optics in order to determine the inverse of the corrector/monitor correlation matrix A^{-1} .

For the envisaged monitor and corrector layout (72 monitors and 72 correctors at the same locations in both planes) (see Figure 1) the SVD and the sliding bump orbit correction scheme converge to the same correction state. This can be explained by the fact that A^{-1} is a sparse tridiagonal matrix containing the kick ratios of interleaved three corrector bumps. It should be noted that the properties of A^{-1} have implications on the implementation of the fast global orbit feedback [4].

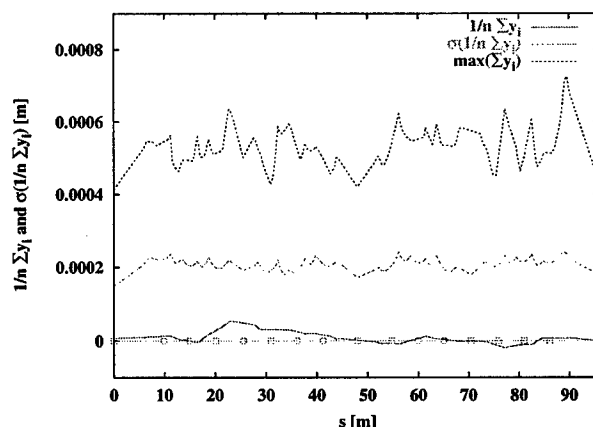


Figure 2: Mean, rms and maximum vertical orbit for 200 seeds for 1/3rd of the lattice.

After the correction rms values of about $200\mu\text{m}$ (zero monitor readings) are observed in both planes. As an example Figure 2 visualizes the mean, rms and maximum orbit in the vertical plane. The maximum corrector kicks needed are 50% below the design maximum of $\approx 1\text{ mrad}$.

In the vertical direction about 20% more corrector strength is needed than in the horizontal plane although the rms horizontal kick is about 30% larger. This can be explained by a 50% less efficient correction in the vertical plane.

3 COUPLING CORRECTION

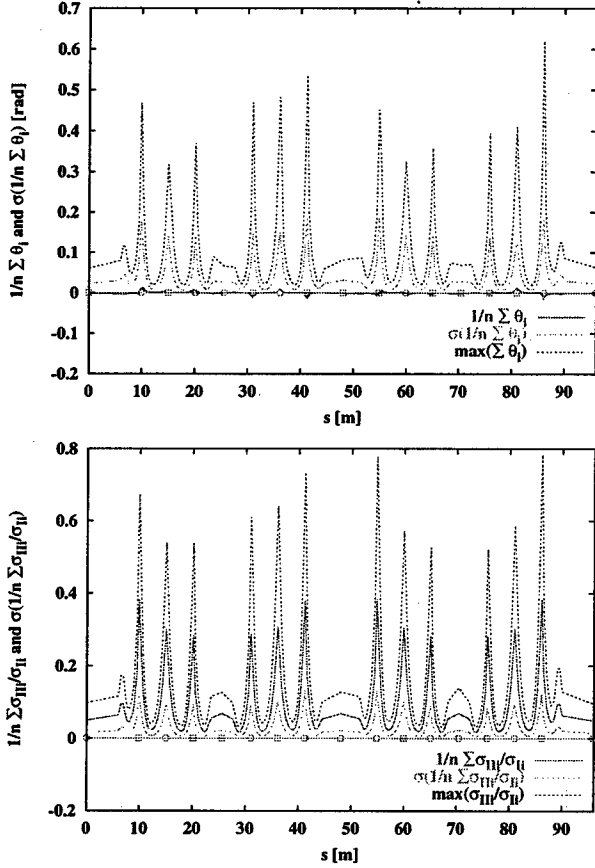


Figure 3: Top: Mean, rms and maximum beam ellipse twist θ for 200 seeds for 1/3rd of the lattice, bottom: corresponding sigma ratio σ_{II}/σ_I .

Betatron and emittance coupling have been estimated from the calculation of generalized emittances and sigma matrices [5]. The beam ellipse twist in the straight sections of the SLS storage ring has been found to be ≈ 40 mrad (see top graph of Figure 3).

The corresponding value for the emittance coupling in mode D1 which allows 5-8 cm horizontal dispersion in the straight sections is calculated to be 0.2% and 1% in the zero dispersion mode D0. This relatively large coupling factor for the latter mode can be explained by the fact that the vertical working point had been initially chosen very close to the integer ($\nu_y = 7.08$) in order to optimize the Dynamic Aperture. At the same time this results in a significant increase of the spurious vertical dispersion. A change of the vertical tune to $\nu_y = 8.28$ (D2A lattice) leads to a reduction of the emittance coupling to 0.25%. The bottom graph of Figure 3 shows the sigma ratios σ_{II}/σ_I for

1/3rd of the D2A lattice after the tune change. The contribution from quadrupoles is nicely compensated by the dispersion generated by the nearly adjacent orbit correctors in the sextupoles. Thus the remaining vertical dispersion of 0.3 cm is mainly induced by sextupoles. Another source of emittance coupling is the feeddown of horizontal dispersion through skew quadrupole components induced by nonzero vertical orbits in sextupoles and quadrupole roll errors. This contribution can be minimized utilizing dedicated skew quadrupoles. Foreseen are three families with two magnets per family paired around the three long straight sections. The idea is to use the foreseen additional corrector windings on the sextupoles to generate the necessary field. The effectiveness of the correction scheme has been tested for the 200 seeds. The resulting histograms for the emittance ratio κ are depicted in Figure 4. It can be seen that the mean κ value is reduced from 0.25% (see curve labeled *sextupoles+tilt error+no correction*) to 0.1% (see curve labeled *sextupoles+tilt error+correction*). Furthermore the κ spread has been reduced from 0.16% to 0.06%. It can be also deduced from the graph that magnet tilt errors have only a marginal influence on κ (see curves labeled *sextupoles+tilt error+(no) correction*). Switching of the sextupoles results in a κ of 0.02% (see curve labeled *no sextupoles+tilt error+correction*) which illustrates that the residual coupling is dominated by sextupoles. Quadrupoles plus correctors alone account for a κ of 0.01% (see curve labeled *no sextupoles+no tilt error*).

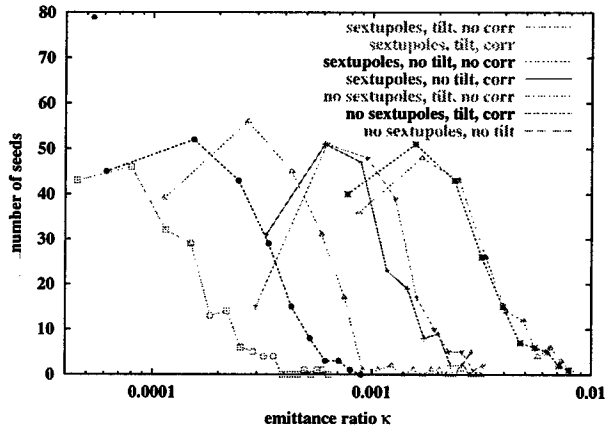


Figure 4: Histograms of the emittance ratio κ for 200 seeds with and without coupling correction.

4 MULTIPOLE ERRORS

Results from 2D field calculations [11] for quadrupoles and dipoles have been investigated concerning the impact on Dynamic Aperture [10]. Alignment errors and orbit correction have been included. It has been found that the multipoles cut off all Dynamic Aperture outside the physical aperture which is simply due to the fact, that the multipole decomposition is only valid within the pole inscribed radius. Tracking including physical limits virtually does

not show any Dynamic Aperture deterioration. Subsequent tests using data from 3D field calculations for quadrupoles and sextupoles have confirmed this result.

The vertical correctors with dipole coefficient b_1 which are integrated into the sextupoles create a large decapole component b_5 . The ratio of the multipole coefficients b_5/b_1 is calculated to be $5.25 \cdot 10^5 \text{ m}^{-4}$. Assuming a linear scaling of b_5 with b_1 the Dynamic Aperture has been calculated for 200 distorted and orbit corrected machines operated in the D0 lattice mode. It has been shown that the Dynamic Aperture is only reduced for large momentum deviations $dp/p > 2\%$.

5 GROUND WAVES

The magnets of the SLS storage ring are mounted onto 48 girders with the 36 bending magnets of the 12 TBAs sitting on the ends of two adjacent girders [7]. The amplitude of stored beam orbit oscillation excited by groundwaves is calculated by convolution of the seismic spectrum on site, damping by the concrete slab of the hall, girder mechanical amplification factors, closed orbit distortion amplification factors and attenuation factors of the fast feedback system [4].

For a rough worst case estimate the following assumptions are made:

- The largest ground noise observed was recorded while a heavy truck was passing by on the nearby road. Peaks of 300 nm at 30 Hz and 30 nm at 60 Hz [8] were found. Continuous ground noise however is at least one order of magnitude lower.
- Within the worst case estimate the damping effect of the hall's 40 cm concrete slab are neglected.
- The mechanical amplification factors of the girder were measured to be ≤ 10 on resonance horizontally and vertically over a frequency range from 0...50 Hz [9].
- Amplification factors for the closed orbit with and without girders are shown in Fig. 5. With girders one sees horizontal [vertical] amplification factors of 8 [5] at 30 Hz and 25 [5] at 60 Hz.
- The attenuation provided by the fast feedback system is about -55 dB at 30 Hz and -35 dB at 60 Hz (assuming that there is only one dominant peak) [4].

Multiplying these numbers one arrives at rms average orbit distortions of 25 [15] μm horizontally [vertically] at 30 Hz and 7.5 [1.5] μm at 60 Hz without feedback. Including the feedback the orbit distortions are well below 1 μm over the whole frequency range.

With this as the result of a worst case estimate we are looking forward to achieve a rather quiet beam at SLS.

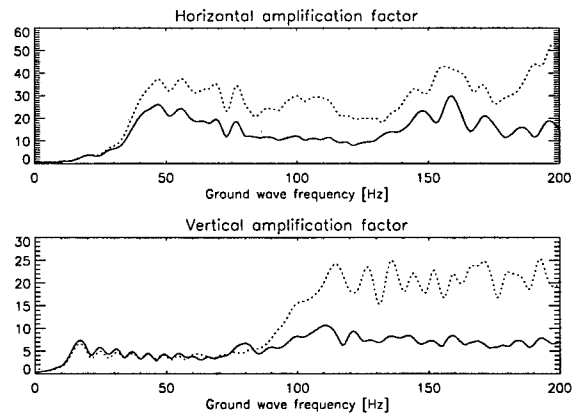


Figure 5: Amplification factors defined as ratio of closed orbit (averaged over ground wave incident angle and phase) to ground wave amplitude for single elements (dotted) and elements mounted on girders (solid). For high frequency the factors approach the values from random magnet misalignments which are for single elements, girder to girder and girder absolute alignment given by 58, 22, 6 horizontally and 25, 4, 3 vertically. An increase of the factors is observed where λ equals the betatron wavelength, which occurs at 36 Hz for the horizontal and at 14 Hz for the vertical. Speed of sound was assumed to be 500 m/s (soft ground).

6 REFERENCES

- [1] M. Böge *et al.*, "The Swiss Light Source Accelerator Complex: An Overview", Proc. of EPAC-98, Stockholm, (1998).
- [2] J. Bengtsson, "TRACY-2 User's Manual", Internal SLS document, (1997).
- [3] M. Böge, "Update on TRACY-2 Documentation", SLS-TME-TA-1999-0002, (1999).
- [4] M. Böge *et al.*, "Fast Closed Orbit Control in the SLS Storage Ring", Contribution to this Conference.
- [5] A. W. Chao, J. Appl. Phys. 50, (1979).
- [6] M. Böge *et al.*, "Beam lifetime studies for the SLS storage ring", Contribution to this Conference.
- [7] M. Böge *et al.*, "SLS Lattice Finalization and Magnet Girder Design", Proc. of EPAC-98, Stockholm, (1998).
- [8] C. Markovits, "Erschütterungsmessungen des Schweiz. Erdbendienstes am Ort der geplanten Synchrotronlichtquelle SLS auf dem Gelände des PSI West", SLS-TME-TA-1994-0006, (1994).
- [9] S. Zelenika, Private Communication.
- [10] A. Streun, "SLS Dynamic Acceptance Degradation due to Magnet Multipole Errors", SLS-TME-TA-1998-0002, (1998).
- [11] BINP Novosibirsk, Internal Design Report.

DIFFUSION MECHANISM OF PARTICLE BEAMS IN THE PRESENCE OF PHASE MODULATION IN DOUBLE RF SYSTEMS*

M. Ball, J. Budnick, C. M. Chu[†], K. M. Fung, B. Hamilton, D. Jeon, X. Kang, L. L. Kiang, S. Y. Lee, A. Pei, T. Sloan, Indiana University, Bloomington, IN
K. Y. Ng, FNAL, Batavia, IL

Abstract

The particle diffusion mechanism due to phase modulation on one of the rf cavities in a double rf system is studied. We find that the Einstein relation is satisfied if there is a global chaos in the phase space. On the other hand, the existence of dominant parametric resonances forces the particles streaming along the separatrix, which may result in *anomalous diffusion* process. The particle tracking simulations based on the Hamiltonian for the double rf system is employed to reveal the essential diffusion mechanism. Also for the first time, a coherent octuple mode has been observed in the bunch beam excitation. The phase space evolution of the octuple mode is displayed.

1 INTRODUCTION

Controlled particle beam diffusion has many applications in beam physics such as phase space painting for beam injection, beam dilution for minimizing the growth due to the collective instabilities, stochastic beam scraping and stochastic slow beam extraction. Practically, the diffusion process is dominated by the chaos generated by overlapping resonances[1]. Particles in the existence of Langevin force diffuse in the phase space following the Einstein relation: $\sigma^2 \simeq Dt$, where σ^2 is the mean square of the beam bunch, D is the diffusion coefficient and t is the evolving time. However, there are anomalous diffusion processes that do not follow the Einstein relation. They occur in plasma physics, Lévy dynamics, turbulent flow and space charge dominated beams [2]. Understanding the causes and detail dynamics of the anomalous diffusion is particularly important in those areas.

Experimentally, We studied the particle diffusion processes in phase space by applying a phase modulation on one on a double rf system at the Indiana University Cyclotron Facility (IUCF) Cooler ring. The experiment data alone with in-depth beam tracking simulation will be presented in this paper.

2 SYNCHROTRON EQUATION OF MOTION

The normalized conjugate phase space coordinates are defined as

$$\phi = -h_1(\theta - \theta_s) \quad (1)$$

$$\delta = (h_1|\eta|/\nu_s)(\Delta p/p_0) \quad (2)$$

where h_1 is the harmonic number of the rf cavity, θ and θ_s are respectively the orbiting angles of a non-synchronous and synchronous particles, η is the phase slip factor, p_0 is the momentum of a synchronous particle, $\Delta p = p - p_0$ is the momentum deviation, $\nu_s = (h_1 e V |\eta| / 2\pi \beta^2 E)^{1/2}$ is the synchrotron tune, V is the voltage, e is the particle's electric charge, and β and E are the Lorentz velocity factor and energy of the particle. the synchrotron motion of a particle in a double-rf system with phase modulation can then be written as

$$\dot{\delta} = -\nu_s [\sin(\phi + \Delta\phi_1) - r \sin(h\phi + \Delta\phi_2)] - \lambda\delta + D\xi, \quad (3)$$

$$\dot{\phi} = \nu_s \delta \quad (4)$$

where $r = V_2/V_1$ is the ratio of the primary and secondary rf voltages, $h = h_2/h_1$ is the ratio of harmonic numbers where V_1 and V_2 are the voltage gains for the primary and secondary rf systems, respectively, h_1 and h_2 are the harmonic numbers for the primary and secondary rf system, respectively, λ is the damping decrement, the white Gaussian noise ξ where $\langle \xi(\theta)\xi(\theta') \rangle = \delta(\theta - \theta')$ with $\langle \xi \rangle = 0$, and D is the amplitude of the white noise. At the Cooler ring, typically λ and D are set about 3×10^{-6} and 2×10^{-4} . The phase modulation term in Eq.3 is given by

$$\Delta\phi_1(t) = A_1 \sin(\nu_{m1}\theta), \quad (5)$$

$$\Delta\phi_2(t) = A_2 \sin(\nu_{m2}\theta) + \Delta\phi_0 \quad (6)$$

where A_i and $\nu_{mi} = f_{mi}/f_s$ are the modulation amplitudes and the modulation tunes, respectively, where $i = 1$ and $i = 2$ represent primary and secondary cavities, respectively, f_{mi} is the modulation frequency and f_s is the synchrotron frequency with primary cavity alone; and $\Delta\phi_0$ is a relative phase difference between the two rf systems. Without damping and fluctuation terms, the double rf system with phase modulation can be described in the following Hamiltonian form

$$\tilde{H}_0 = \frac{1}{2}\nu_s\delta^2 + \nu_s\{1 - \cos(\phi + \Delta\phi_1) + \frac{r}{h}[1 - \cos(h\phi + \Delta\phi_2)]\}. \quad (7)$$

*Work supported by U.S. Department of Energy DE-FG02-92ER40747 and National Science Foundation PHY-9512832.

[†]Email: cmchu@iucf.indiana.edu

Multi-particle tracking simulation follows Eq.3 and 4. We focus on several important factors, namely, mean square of beam width, averaged beam center and the Poincaré surfaces of section of the system.

3 EXPERIMENTS

The main purpose for our experiment was to systematically study the beam dilution mechanism in the presence of phase modulation of a double rf system. The IUCF Cooler ring is a 6-sided proton storage ring with electron cooling and two rf acceleration cavities. The primary MPI cavity operates at a harmonic number $h_1 = 1$, and the secondary PPA cavity operates at the harmonic number $h_2 = 9$. The ring can accelerate protons from 45 to 500 MeV in kinetic energy. In this experiment, the beam current was between 100 to 500 μA for a 45 MeV single bunch proton beam in the ring.

After injection, the proton beam was cooled by an electron beam cooling system to reduce its momentum spread and transverse emittances. The electron cooling rate for the Cooler ring was measured to be about $3 \pm 1 \text{ s}^{-1}$ at this energy [3]. The accelerator cycle time was set at 10 s, and the secondary rf system and the data acquisition system were turned on 3 s after the completion of injection, which was much longer than the needed 300 ms cooling time. The cooled beam bunch rms length was about $15 \sim 20 \text{ ns}$ with a momentum spread less than 0.1%. The primary rf voltage was set at about 300 V, which resulted in a synchrotron frequency, f_s , of about 705 Hz while operating with the primary rf cavity alone.

Beam profile was taken from a BPM sum signal passing through a low loss cable, and recorded by a fast digital scope which was set at a sampling rate of 1 GHz for a total of 512 or 1024 channels for each turn. The bunch profiles were digitized every 25 to 75 turns. A pretrigger to start data recording was set at least 100 ns prior to the arrival of the beam bunch. This sampling rate can provide the detailed evolution of beam profile in the diffusion process.

4 DATA ANALYSIS

We tried to understand the diffusion mechanism by looking at physics quantities such as mean square of longitudinal beam size, Fast Fourier Transform (FFT) spectra of mean square beam size and averaged beam center position and actual beam evolution profiles. The evolution of the beam profile can be characterized by the mean square bunch length $\langle \sigma^2 \rangle$ which is defined as

$$\langle \sigma^2 \rangle = \frac{1}{N} \sum_{j=1}^N (\phi_j - \phi_{\text{avg}})^2, \quad (8)$$

where N is the number of particles in a beam bunch and $\phi_{\text{avg}} = \frac{1}{N} \sum_{j=1}^N \phi_j$ is the average value of ϕ and where ϕ_j is the ϕ value of the j -th particle.

Fig. 1 summarizes our data for modulation on the secondary rf cavity, where the final beam width is plotted as

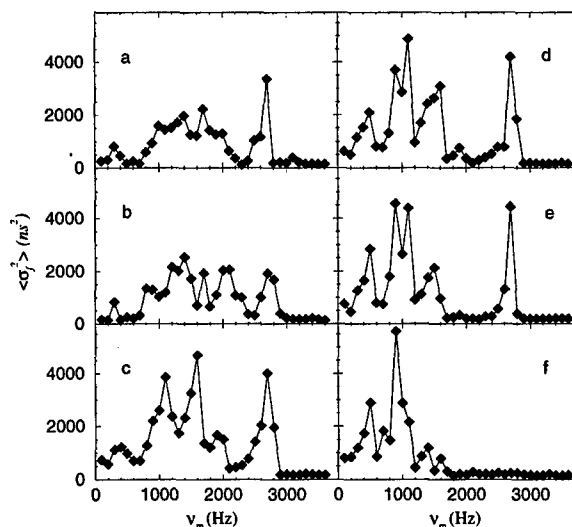


Figure 1: Averaged final rms beam size versus modulation frequency for various modulation amplitude (on the secondary rf cavity). This is done by averaging the rms beam size over the last 1 ms of the data taking $\langle \sigma_f^2 \rangle$. The alphabetic letters indicate the modulation amplitudes, A_2 , where a: 60° , b: 100° , c: 125° , d: 150° , e: 175° , and f: 200° .

a function of the modulation frequency for the modulation amplitudes 60° , 100° , 125° , 150° , 175° , and 200° . Since our results indicate that the beam response appeared to be important at the modulation frequencies above and near the harmonics of the synchrotron frequency [4]. The data analysis is mostly focused on the modulation frequencies about integer factors of the synchrotron frequency. Fig. 2 shows that by properly adjusting the parameters, f_s , $\Delta\phi_0$ and α , the tracking results match quite well with the data.

The sensitivity of beam diffusion mechanism on the modulation frequency can be visualized by the FFT spectra of experimental data. Fig. 3 shows the FFT spectra of the rms beam widths of all data with a modulation amplitude of 150° . A direct response line is visible diagonally across the figure. Furthermore, the quadruple and the octuple modes arising from the dominant parametric resonances are particularly strong when the modulation frequencies are driven at $2f_s$ and $4f_s$. We note also that when the beam is driven into chaotic sea, the data show characteristic strong low frequency response.

5 CONCLUSION

Our experimental data show that the linear growth of mean square of beam width, $\langle \sigma^2 \rangle$, with time arises from the diffusion process in a complete chaotic region in the phase space. If the phase space possess a layer of chaotic sea with invariant tori embedded inside, $\langle \sigma^2 \rangle$ will show characteristics of anomalous diffusion. On the other hand, if stable islands still exist in the chaotic background as shown in a and f of Fig. 4, the evolution of $\langle \sigma^2 \rangle$ will be strongly

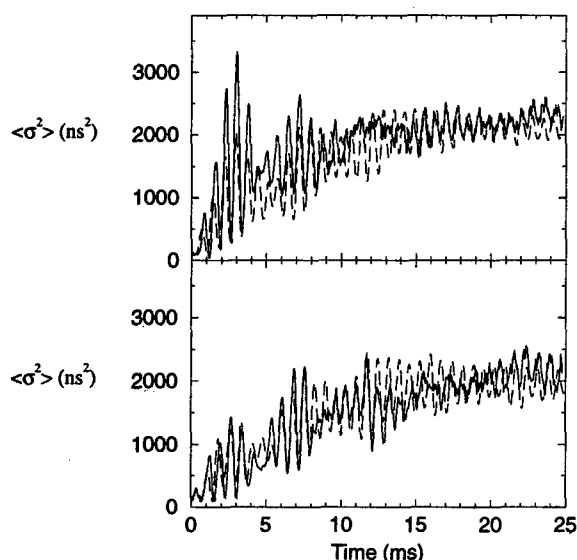


Figure 2: Comparison between data (solid curves) and simulation (dashed curves) for modulation on the secondary cavity near 2:1 resonance. The set parameters are $f_{m2} \simeq 1200$ Hz, $A \simeq 100^\circ$ and $r \simeq 0.11$. The parameters used in tracking are $f_s = 719$ Hz. The only difference between the two figures is for the top one $\Delta\phi_0 = 215^\circ$ and for the bottom one $\Delta\phi_0 = 143^\circ$.

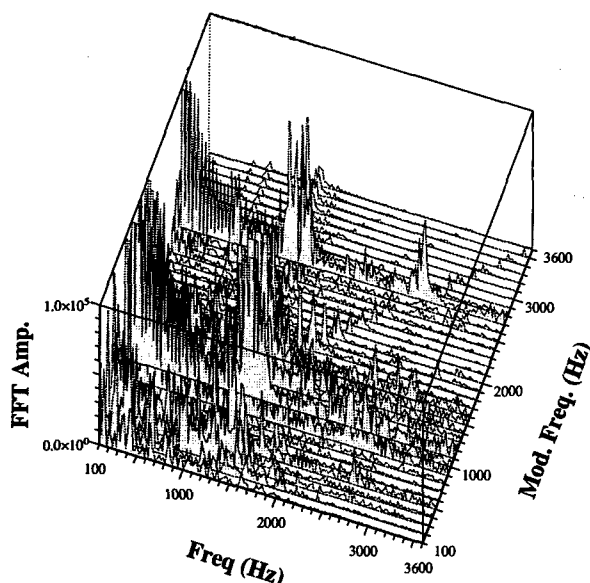


Figure 3: The FFT spectra of the experimental data of mean square beam widths for the modulation amplitude of 150° . We note that the low frequency response in the data arises from the chaotic sea, the quadruple and octuple modes arises from strong parametric resonances.

oscillatory. Our experiments, with numerical simulations, have systematically verified these conditions. The understanding of the signature of the beam phase space evolution can be used to diagnose sources of emittance dilution mechanisms in high brightness beams and space charge

dominated beams.

We have experimentally measured the evolution of beam distribution as a function of rf parameters in a storage ring. These parameters are the ratio of rf voltages r , the modulation frequency f_{m2} , the modulation amplitude A_2 , and the relative phase $\Delta\phi_0$. We have found that the evolution of the bunch beam can be divided into a fast process that is related to particle diffusion along the dominate parametric resonances, and a slow process that particles diffuse inside the chaotic sea.

We have also observed for the first time the coherent octuple excitation in beam. The corresponding phase space evolution for the octuple excitation has been clearly measured. Particles stream through the separatrix of the 4:1 parametric resonance, and then diffuse into the chaotic sea. The signature of the beam signal can easily be identified by comparing the data and tracking simulation shown in Fig.4, which also clearly indicates that the chaotic area strongly depends on $\Delta\phi_0$.

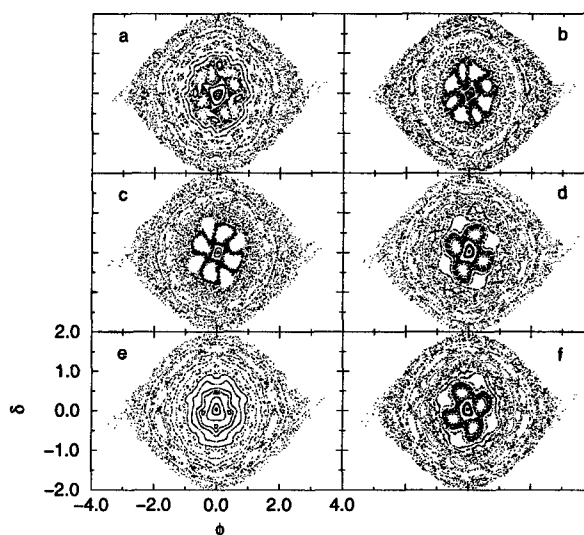


Figure 4: The Poincaré surfaces of section for the modulation frequency of 2700 Hz with different relative phases, $\Delta\phi_0$, where a: 20° , b: 60° , c: 100° , d: 140° , e: 180° and f: 220° . Note that the chaotic structure arises mainly from the overlapping resonances of 4:1 parametric resonances.

6 REFERENCES

- [1] D. Jeon *et al.*, Phys. Rev. Lett. **80**, 2314 (1998).
- [2] See e.g., C.L. Bohn, Phys. Rev. E **50**, 1516 (1994); J. Struckmeier, Phys. Rev. E **54**, 830 (1996) and references therein.
- [3] M. Ellison *et al.*, Phys. Rev. Lett. **70**, 591 (1993); H. Huang *et al.*, Phys. Rev. E **48**, 4678 (1993); D. Li *et al.*, Phys. Rev. E **48**, R1638 (1993); D. Li *et al.*, Nucl. Inst. Methods A **364**, 205 (1995).
- [4] see e.g. S.Y. Lee, in *Accelerator physics at the SSC*, AIP Proceedings No. 326, edited by Y. Yan and M. Syphers, p.13 (AIP, N.Y. 1995).

Beam Motions Near Separatrix*

M. Ball¹ B. Brabson¹ J. Budnick¹ C.M. Chu¹ D.D. Caussyn¹ J. Collins¹ V. Derenchuk¹
G. East¹ M. Ellison¹ D. Friesel¹ K.M. Fung¹ B. Hamilton¹ W.C. Hsi¹ H. Huang²
W.P. Jones¹ S.Y. Lee¹ D. Li³ K.Y. Ng⁴ X. Pei⁵ A. Riabko¹ and T. Sloan¹

¹Indiana University, Bloomington, IN 47405, ²Brookhaven National Laboratory,

³Lawrence Berkeley national Laboratory, ⁴Fermilab, ⁵Lucent Technology.

Abstract

Experimental data on particle motion near the separatrix of the one dimensional (1-D) fourth-integer islands are analyzed. When the beam bunch is initially kicked to the separatrix orbit, we observed a strong decoherence in the coherent betatron motion. We find that, through intensive particle tracking simulation analysis, the decoherence has resulted from the beam being split into beamlets in the betatron phase space. However, we also observe an unexpected recoherence of coherence signal, which may result form a modulated closed orbit or the homoclinic structure near the separatrix.

1 INTRODUCTION

Particle motion along the separatrix is important in the stochastic slow beam extraction. Since the stochasticity layer at the separatrix orbit is further enhanced by the time dependent dipole and quadrupole modulations [1, 2], the study of particle motion near separatrix can provide needed information on the dynamical aperture and lifetime of stored beam particles. Thus it is important to study the dynamics of particle motion near the separatrix.

In our previous studies [3, 4], we studied particle motion at the fourth order resonance, and examined the effects of tune modulation on particle motion inside the island. We mapped out a boundary of stability by analyzing our experimental data on the tune modulation to the particle trapped at the center of the resonance islands. This paper studies the dynamics of particle motion near separatrix.

Although the particle motion near the separatrix is complicated by rapid decoherence and inherent finite beam size in our experiments, we can re-analyze our data to explore the effects of inherent noise for particle motion near separatrix because we have made many progresses in understanding the dynamics of particle motion near the separatrix. [2] The paper is organized as follows. Section 2 outlines our experimental setup and gives a brief review of the nonlinear Hamiltonian model. Section 3 discusses the data analysis. The conclusion is given in Sec 4.

2 NONLINEAR BETATRON RESONANCE AND EXPERIMENTAL METHOD

Particle motion in accelerators is governed by the linear Hill's equation, where dipoles provide a closed orbit, and quadrupoles provide linear focusing for beam stability. However, sextupole and higher multipoles are needed to correct chromatic aberration, and are inherent components in magnets. By design, the nonlinear perturbation in accelerator is small except when the nonlinear resonance condition is encountered, i.e. $m\nu_x + n\nu_z = \ell$, where m, n and ℓ are integers. This paper studies the $4\nu_x = 15$ resonance.

Near an isolated single resonance ($m\nu = \ell$, hereafter, the subscript is neglected) in the resonance rotating frame, the Hamiltonian can be approximated by [5]

$$H \approx \delta J + \frac{1}{2}\alpha J^2 + gJ^{\frac{m}{2}} \cos(m\psi), \quad (1)$$

where J and ψ are the conjugate action-angle variables, $\delta = \nu - (\ell/m)$ is the resonance proximity parameter, ν is the betatron tune, α is the nonlinear detuning parameter arising from higher-order multipoles, and g is resonance strength. The phase ψ in the resonance rotating frame is related to the betatron phase ϕ by

$$\psi = \phi - \frac{\ell}{m} \theta + \frac{\chi}{m}.$$

The θ is orbit angle serving as the time coordinate and χ is the resonance phase that depends on the measurement location.

This Hamiltonian is time-independent. A torus is the Hamiltonian flow at a constant 'energy,' i.e. $H(J, \psi) = E$. Hamilton's equations of motion are

$$\begin{aligned} \dot{\psi} &= \delta + \alpha J + \frac{m}{2} g J^{\frac{m}{2}-1} \cos(m\psi), \\ \dot{J} &= m g J^{\frac{m}{2}} \sin(m\psi) \end{aligned} \quad (2)$$

where the overdot corresponds the derivative with respect to the time coordinate θ .

2.1 Experimental setup at the IUCF Cooler Ring

The procedure of our experiments is as follows. The 90 MeV H_2^+ beam was stripped injected into the Cooler for

*Work supported by U.S. Department of Energy DE-FG02-92ER40747 and National Science Foundation PHY-9512832.

attaining 45 MeV protons. The cycle time was 10 s. The beam was electron cooled for 3 s before we started our experiments. The cooling time was about 0.3 s. Typical, we had about 3×10^8 protons per bunch with a bunch length of about 5.4 m (or 60 ns) FWHM. The revolution period was 969 ns, and the rf cavity was operating at a frequency $f_0 = 1.03168$ MHz with the harmonic number $h = 1$. The 95% emittance was about 0.3π mm-mrad, and the stability of the horizontal close orbit was smaller than 0.05 mm FWHM. Details of our experimental setup have been published [6].

To study the nonlinear resonance at $4\nu_x = 15$, we adjusted our horizontal betatron tune to the resonance line. A ferrite kicker with the rise and fall time of about 100 ns and a flat top of about 700 ns was used to impart a transverse angular kick to the beam. The subsequent beam positions were tracked and digitized by two beam position monitors. The data $(x_1, x_2)_i$ are transformed to the normalized phase space $(x, p_x)_i$ with known betatron amplitude functions, and BPM calibrations. Figure 1 shows the Poincaré maps for some typical Hamiltonian tori with five different kicker amplitudes. The separatrix orbit is also drawn to compare our experimental data. Properties of this fourth-integer resonances have been successfully explored [3].

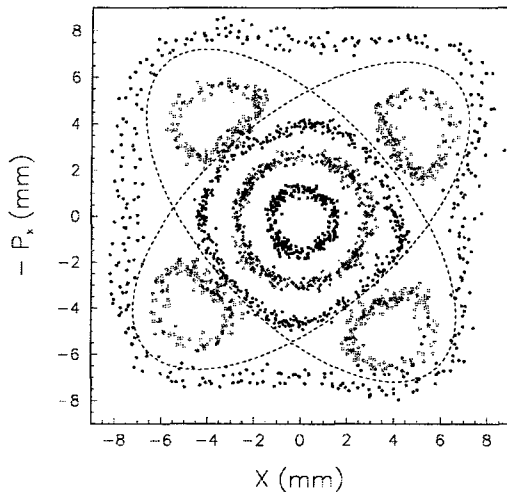


Figure 1: Poincaré map shows beam sampling the nonlinear fourth-integer resonance by exciting particles with five different kicker amplitudes, increasingly kicker amplitudes corresponding the larger radius contours. The line is the predicted separatrix. Beam motion close to separatrix is evident.

2.2 Multiparticle Simulation Model

Our experiments were intended to explore the single particle motion near a betatron resonance. However, the beam bunch in accelerators is composed of many particles. Because of the electron cooling, and the random noises inherent in all accelerators, the beam bunch reaches an equilib-

rium emittance [7]:

$$\rho(x, p_x) = C e^{-H/kT} = \frac{1}{2\pi\sigma^2} e^{(x^2 + p_x^2)/2\sigma^2}, \quad (3)$$

where C is the normalization constant, H is the Hamiltonian, " kT " is the effective thermal energy, x and p_x are the normalized conjugate phase space coordinates, and $\sigma^2 = \beta_x \epsilon_{rms}$ with an rms emittance ϵ_{rms} . Here, we have assumed a linear Hamiltonian at the center of the phase space.

The phase space evolution of Eq. (2) can be attained by the symplectic map:

$$\begin{aligned} \psi_{n+1} &= \psi_n + \delta + \alpha J_n + \frac{m}{2} g J_n^{\frac{m}{2}-1} \cos(m \psi_n), \\ J_{n+1} &= J_n + m g J_n^{\frac{m}{2}} \sin(m \psi_{n+1}), \end{aligned} \quad (4)$$

which preserves the phase space area. For particle motion near the separatrix, two hundred steps is used for each orbital revolution. Typically, 4000 test particles with a Gaussian distribution, distributed in 3σ region of the phase space are used in our numerical simulations.

3 DATA ANALYSIS

First, we analyze Poincaré maps that are outside the resonance region and obtain a consistent set of betatron amplitude functions, and the phase difference between two BPMs. This procedure establishes the method of transforming our digitized data to the normalized phase space coordinates. Our results are shown in Fig. 1. Since the Hamiltonian of Eq. (1) is a quadratic equation, the separatrix is given by two intersecting ellipses.

The decoherent of betatron motion a beam with finite emittance can be used to determine the nonlinear detuning parameter α . Similarly, the FFT spectra and the size of the resonance islands can be used to determine the resonance proximity parameter, and the resonance strength g . These analysis provide us a self consistent set of data for the effective nonlinear Hamiltonian.

3.1 Motion Near the Separatrix

Figure 2 shows the centroid of beam motions a 300 revolutions when the beam is kicked onto the separatrix, where solid points correspond to the first 50 revolutions. To understand the rapid decoherence, we carry out multiparticle simulations. Figure 3 shows the beam distribution after 500 revolutions for a beam with an initial emittance of 0.3π -mm-mrad. The decoherence arises from the fact that the beam bunch splits into beamlets under the action of the separatrix. Particles inside the separatrix move in one direction, while the particles inside the resonance island are trapped. Such a rapid decoherence is very sensitive to the emittance of the beam. Our multiparticle simulations show that the beam emittance of 0.3π mm-mrad describes very well the strong decoherence.

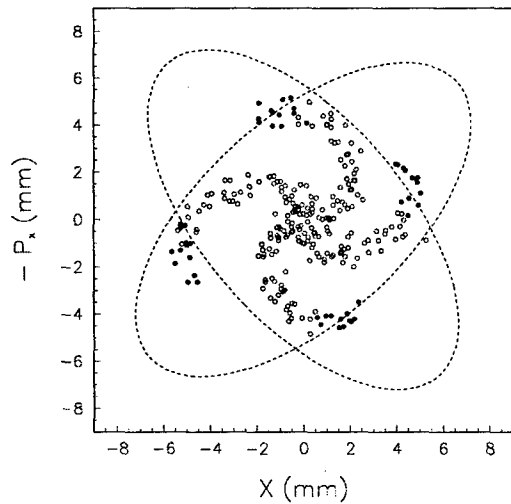


Figure 2: Poincaré map shows the data of the first 300 revolutions, where the first 50 revolutions is shown as solid points. Decoherence is due to the fact beam particles move along separatrix. The separatrix of Fig. 1 is also drawn for reference.

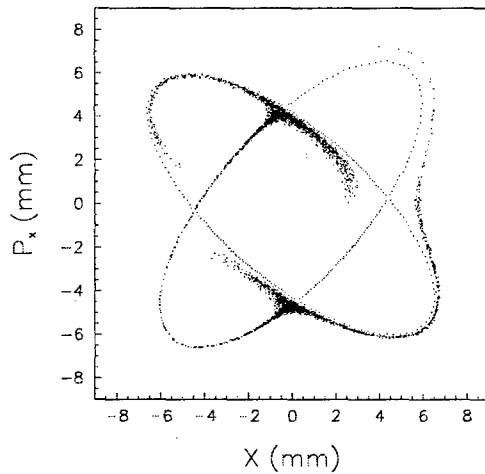


Figure 3: The plot shows the final beam distribution at 500 revolutions.

It is worth noting that our long-term experimental data shows significant recoherence of the coherent betatron motion shown in Fig. 4. Our model can not explain such a rapid recoherence, instead, it predicts a very strong recoherence at 1600 revolutions. The sizable early recoherence may arise from either closed orbit modulation of the order of 0.2 mm or the sensitivity of particle motion (homoclinic structure) near the UFP.

4 CONCLUSIONS

In conclusion, we have analyzed the data for the beam motion near the separatrix, and find that the decoherence of the beam signal arises from the beam being split at the UFP. We observe a significant recoherence in our data, that can not be explained by our model.

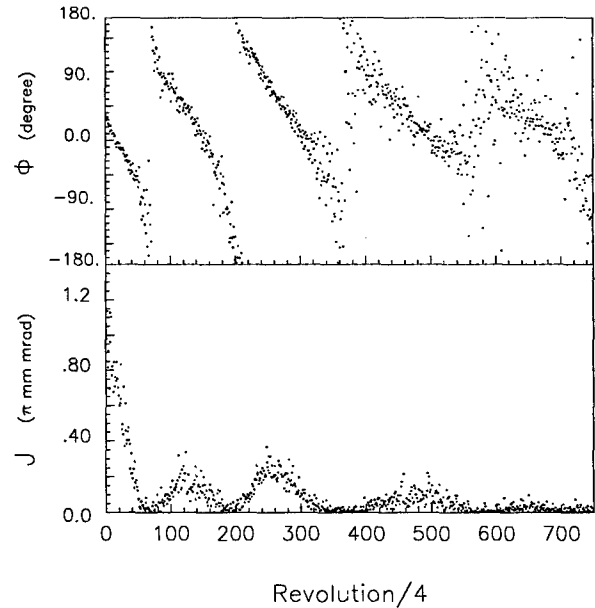


Figure 4: The rapid decoherence of coherent betatron motion in Fig. 2 is displayed in the betatron phase (top) and betatron action (bottom). Complete decoherence is observed to occurs at 240 revolutions. We note, however, that there is a significant recoherence in the coherence betatron motion at 520 and 1000 revolutions. The recoherence is associated with a phase where particles reaggregate into the unstable fixed points. Numerical simulation has not been able to reproduce the recoherence of the experimental data.

In general, there are many time-dependent terms in the actual nonlinear Hamiltonian. Our model of the Hamiltonian (1) should include these terms in the simulations. The stochasticity near the separatrix orbit arises from these time dependent terms in the Hamiltonian. A more realistic numerical simulation is need for modelling the beam motion. The experimental data offer a unique challenge for the understanding of particle diffusion process in accelerators.

5 REFERENCES

- [1] F. Vivaldi, Rev. Mod. Phys., **56**, 737 (1984).
- [2] S.Y. Lee, *Nonlinear Beam Dynamics Experiments at IUCF Cooler Ring, Accelerator physics at the SSC*, AIP Proceedings No. 326, edited by Y. Yan and M. Syphers, p.13 (1995).
- [3] M. Ellison et al., in *Stability of Particle Motion in Storage Rings*, AIP Conf. Proc. No 292 (AIP New York 1992), p. 170.
- [4] Y. Wang et al., Phys. Rev. E **49**, 5697 (1994).
- [5] S.Y. Lee, *Accelerator Physics*, (World Scientific, Singapore, 1999).
- [6] S.Y. Lee et al., Phys. Rev. Lett. **67**, 3768 (1991); D.D. Caussyn et al., Phys. Rev. A **46**, 7942 (1992).
- [7] M. Bai et al., Phys. Rev. E **55**, 3493 (1997).

USING MARYLIE WITH THE PARTICLE BEAM OPTICS LABORATORY

George H. Gillespie, Barrey W. Hill, Hendy Martono, John M. Moore
G. H. Gillespie Associates, Inc., P.O. Box 2961, Del Mar, CA 92014, U.S.A.

Alex J. Dragt

Department of Physics, University of Maryland, College Park, MD 20742, U.S.A.

Abstract

A MARYLIE module has been developed for a new version of the Particle Beam Optics Laboratory (PBO Lab™). MARYLIE is an optics code based on a Lie algebra formulation of charged particle trajectory calculations and is particularly useful for particle tracking and for the analysis of linear and nonlinear lattice properties. The PBO Lab provides an intelligent graphic user interface based upon the Multi-Platform Shell for Particle Accelerator Related Codes (S.P.A.R.C. MP), a software framework developed specifically to support accelerator modeling, simulation and training. Transport element icons are selected from a palette and assembled into beamlines by graphical construction. Optical cells and lattices composed of element groups may be defined as sublimes, and elements or sublimes can be replicated using an alias element. An icon-based description of MARYLIE commands and procedural processes has also been developed. The icon-based beamlines and commands generate entries for the MARYLIE Master Input File (MIF). Frequent computations are encapsulated into interactive commands which create the needed entries in the MIF, call MARYLIE to execute the required computations, and then return output data to the graphic interface for display. Use of the PBO Lab MARYLIE module is described and illustrations from the Windows95 implementation are presented.

1 INTRODUCTION

The MARYLIE program [1] is a powerful tool for studying nonlinear optics. The version of MARYLIE 3.0 described in [2] is being integrated with PBO Lab 2.0 [3] to provide a unique graphical environment for beamline studies. PBO Lab provides an easy-to-use graphic user environment, customized to the needs of the accelerator community for both particle optics education [4] and beamline design [5]. This paper discusses selected features of the new MARYLIE Module.

2 MARYLIE MODULE FOR PBO LAB

The use of the PBO Lab MARYLIE Module is perhaps best illustrated via an example: designing and then studying the performance of a four-cell, second-order achromatic bend. (It should be noted that MARYLIE can also be used to design a third-order achromat.) The basic layout of the example beamline is illustrated in Figure 1, using the iconic representation provided by the PBO Lab

graphical beamline construction kit. The beamline is composed of four identical cells, with each cell containing a sector bend, two quadrupoles and two sextupoles, all interspersed with drifts. Figure 1 also illustrates two approaches (described below) for using the MARYLIE Module to fit magnet strengths.

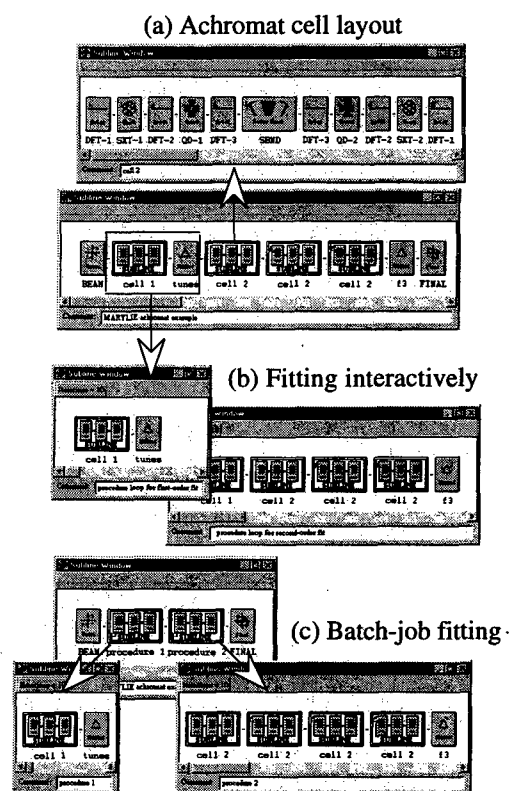


Figure 1. Selected images from the PBO Lab MARYLIE Module showing icon representations of: (a) the four-cell achromat, (b) creation of MARYLIE procedure loops used to fit first-order and second-order optical constraints interactively, and (c) the use of two MARYLIE procedure loops to fit both sets of conditions as a "batch job." All images are from the Windows95/98/NT implementation.

The construction of a scalable version of this type of achromatic bend had been discussed previously [5,6]. With the PBO Lab, formulas can be used to incorporate dependent parametric relationships between elements [5], while intelligent alias elements replicate either identical or near-identical elements with no redundant data [3,6]. The graphical construction of a beamline defines all data necessary to run any of the particle optics modules

installed in the PBO Lab. The PBO Lab takes care of all I/O requirements for each code, with no knowledge required of the user concerning command syntax, file formats, or similar code-specific details.

The principal design tasks are to determine: (a) the quadrupole strengths that are necessary for each cell to have phase advances of 90° in both transverse directions (i.e. quarter-wave transformer), and (b) the sextupole strengths that are required to eliminate (second-order) chromatic aberrations. The primary performance studies involve simulating beams with different momentum spreads passing through the beamline. MARYLIE can perform both of these functions (as well as many more). The remainder of this paper illustrates how this is done using the PBO Lab.

2.1 Solving Fitting Problems

Fitting with MARYLIE is done using procedure loops [1]. A procedure loop is readily defined graphically in the PBO Lab: the user selects (with the mouse) a beamline segment containing one or more Marker Pieces, and then chooses the "Create Procedure Loop" option from the Commands menu. The steps are similar to the actions used to interactively create a Map Piece [6]. Figure 1(b) illustrates the selection of elements and creation of the procedure loop for fitting the first-order properties of the achromat. Desired optical conditions are set using Marker Pieces in a procedure loop, while the parameters to be varied are set using "S" buttons in the Piece Windows of elements, similar to those of the PBO Lab TRANSPORT Module [5]. The first Marker Piece is used to specify the desired phase advances for the first cell, and the field gradients of the first two Quad Pieces are selected as variation parameters. MARYLIE uses tunes ν , related to the phase advances μ by $\nu = \mu/(2\pi)$, so for transverse phase advances of $\pi/2$ the MARYLIE fitting aims are:

$$\nu_x = 0.25 \quad \text{and} \quad \nu_y = 0.25 \quad (1)$$

The first-order fit may be carried out interactively, and then the Lie Map coefficients examined to select the largest non-linear terms to minimize as a second step. This is easily done using a graphic display of the polynomial coefficients for a Map Piece of the beamline. The desired fitting conditions for second-order are:

$$f_3(33) = 0 \quad \text{and} \quad f_3(67) = 0 \quad (2)$$

The first procedure loop is removed and a second procedure loop containing all four cells is then defined. This loop is also shown in Figure 1(b), with the aims (2) specified using the Marker Piece at the end of the achromat, and the first two sextupole strengths selected as fitting variables. Alternatively, two separate procedure loops may be created as illustrated in Figure 1(c), to define a single "batch job," which will sequentially carry out both the first- and second-order fitting using a single interactive command.

2.2 Comparison of Results to Other Calculations

The results from MARYLIE may be readily compared to results from any other code integrated with PBO Lab 2.0. The ease of carrying out such comparisons is difficult to over-emphasize. For example, to compare beamline transfer maps or output beam distributions, one simply selects a different sub-menu from the Commands Menu [3] and executes an appropriate command. The PBO Lab takes care of correctly formatting the input to each code, executing the selected command, and displaying the results. Appropriate TRANSPORT fitting constraints equivalent to those given by (1) and (2) are easily defined with PBO Lab [5]:

$$R_{11} + R_{22} = 0 \quad \text{and} \quad R_{33} + R_{44} = 0 \quad (3)$$

$$T_{126} = 0 \quad \text{and} \quad T_{346} = 0 \quad (4)$$

Table 1 summarizes the fitting results obtained for the quadrupole and sextupole field strengths using the MARYLIE and TRANSPORT Modules of PBO Lab 2.0.

Table 1. Comparison of quadrupole and sextupole fitting results using the MARYLIE and TRANSPORT Modules with PBO Lab 2.0 for the achromatic bend described in reference [5]. Tolerances for all aims were set at 10^{-6} .

Computation Engine	Quadrupole 1 (B')		Quadrupole 2 (B')		Sextupole 1 (S)		Sextupole 2 (S)	
MARYLIE	9.6843595	T/m	-10.180100	T/m	107.41	T/m ²	-146.74	T/m ²
TRANSPORT	9.6843590	T/m	-10.180092	T/m	107.04	T/m ²	-145.67	T/m ²

2.3 Performance Simulations of Beamlines

Once the fitting tasks are complete, MARYLIE may then be used to simulate the performance of the achromat for different initial beam conditions. Several ray tracing and tracking options are available in MARYLIE. Figure 2 illustrates results using the element-by-element ray tracing command. Six output beam cross sections are shown: three for the achromat with the sextupole correctors turned-off, and three with the sextupole strengths set to the

values given in Table 1. The initial beam for all cases was a 6-D uniformly filled ellipsoid of 1000 particles with semi-axes parameters from Table 1 of reference [7]. Results are shown for three different initial momentum spreads. The second-order achromat performs very well for this beam with a 9% momentum spread, nearly identical to that for a beam with 3% momentum spread, and may be adequate for use with momentum spreads up to 27%, depending upon the application.

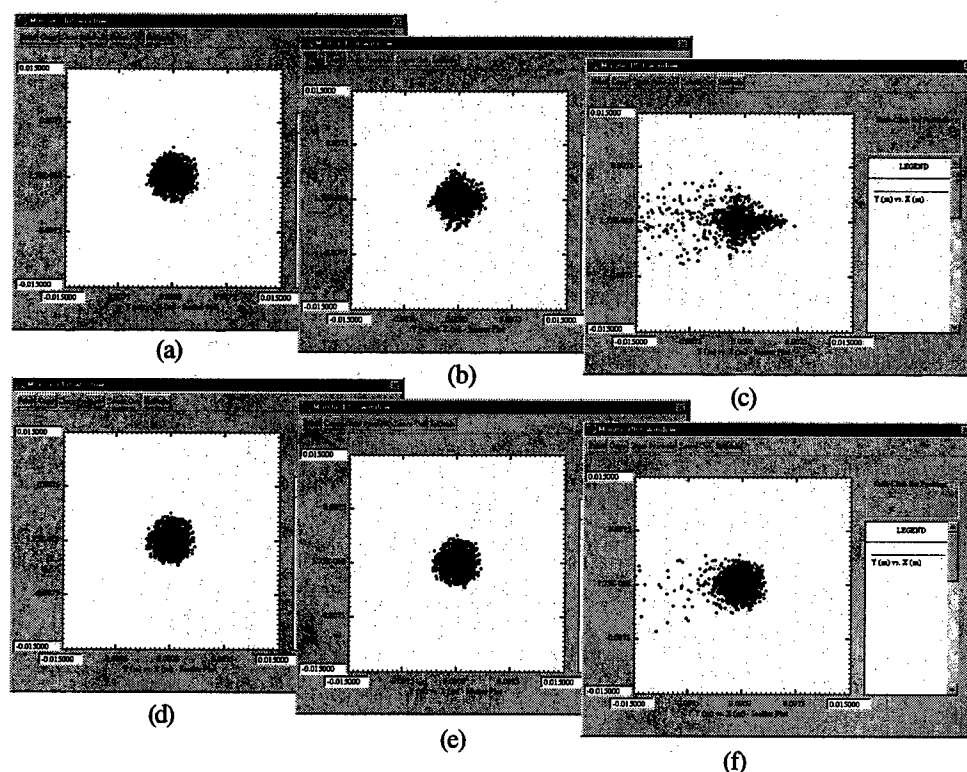


Figure 2. Two-dimensional scatter plots of the beam cross-section at the end of the achromatic bend, without sextupole correctors [top (a)-(c)] and with sextupole correctors [bottom (d)-(f)]. In both cases, results are shown for three different values of the initial momentum spread δ : 3%, 9% and 27%, increasing from left to right. Window images are from the PBO Lab 2.0 MARYLIE Module as implemented for Windows95/98/NT platforms.

3 SUMMARY

An innovative MARYLIE Module for the PBO Lab [8] has been developed that provides an easy-to-use graphic interface for setting up problems and executing commands. The unique S.P.A.R.C. MP framework [3] provides both for the graphical construction of beamlines and for graphically formulating MARYLIE procedures.

ACKNOWLEDGEMENTS

Work supported in part by the U. S. Department of Energy under Small Business Innovation Research (SBIR) Grant No. DE-FG03-95ER81975.

REFERENCES

- [1] A. J. Dragt, D. R. Douglas, F. Neri, C. T. Mottershead, R. D. Ryne, E. Forest, L. M. Healy, P. Schutt and J. van Zeijts, "MARYLIE 3.0 User's Manual, A Program for Charged Particle Beam Transport Based on Lie Algebraic Methods," February draft, 721 pages (1999).
- [2] A. J. Dragt, "Release of MARYLIE 3.0," this conference (1999).
- [3] B. W. Hill, H. Martono, J. M. Moore and J. S. Gillespie, "An Application Framework and Intelligent Graphic User Interface for Multiple Accelerator Codes," to be published in the proceedings of the International Computational Accelerator Physics Conference (Monterey), 4 pages (1998).
- [4] N. A. Brown, G. H. Gillespie, B. W. Hill, M. C. Lampel, H. Martono and J. M. Moore, "The Particle Beam Optics Laboratory (PBO LAB™): A New Education and Training Aid," Proc. 1998 European Particle Accelerator Conference, 1183-1185 (1998).
- [5] G. H. Gillespie, B. W. Hill, H. Martono, J. M. Moore, M. C. Lampel, and N. A. Brown, "Using the Particle Beam Optics Laboratory (PBO LAB™) for Beamline Design and Simulation," to be published in the proceedings of the 15th International Conference on Cyclotrons and Their Applications, 4 pages (1998).
- [6] G. H. Gillespie, B. W. Hill, M. C. Lampel, H. Martono, J. M. Moore, A. J. Dragt, "Multi-Platform Graphic User Interface for MARYLIE Charged Particle Beam Transport Code," to be published in the proceedings of the International Computational Accelerator Physics Conf. (Monterey), 5 pages (1998).
- [7] G. H. Gillespie, B. W. Hill and M. C. Lampel, "Using 3-D Perspectives as a Visualization Tool for Phase Space Data," to be published in the proceedings of the International Computational Accelerator Physics Conference (Monterey), 5 pages (1998).
- [8] The PBO Lab™ is available from AccelSoft Inc., www.gnga.com/accelsoft.

FREQUENCY MAPS OF LHC MODELS

Y. Papaphilippou*

CERN, CH-1211 Geneva 23, Switzerland

Abstract

The Frequency Map Analysis method is applied in models of LHC optics versions 5 and 6 in order to study their non-linear dynamics. The maps present a global picture of the resonance structure of the phase space. They enable us to view the dangerous zones tracing the limits of the dynamic aperture. This approach, assisted by detailed resonance analysis, is used as a guide for exploring possible correction schemes, which are subsequently verified by long-term tracking.

1 INTRODUCTION

The long term stability of the beam is the major concern for the design of a hadron collider, as the LHC [1]. Especially during long injection period of more than 10^7 turns needed to fill the LHC with 2835 bunches per beam, particle trajectories are perturbed strongly by non-linear magnet fields, mainly attributed to the multipole errors of the superconducting magnets. In order to estimate the dynamic aperture (D.A.), the region of the phase space where particles survive after a long time, particle tracking is usually employed, with codes optimised for this task [2, 3]. Nevertheless, even in the upgraded multiprocessor system now available at CERN [4], tracking studies of the full injection plateau are extremely time consuming. Simulations are thus limited to 1% of the total injection period and a reduction factor of 7% [5, 6] is taken into account for the estimation of the D.A. [7]. Beside the numerical difficulties, the main drawback comes from the fact that tracking cannot provide enough information about the system's phase space structure. The application of high-order perturbation theory has been extensively used in beam physics [8, 9] in order to give some insight regarding the systems' non-linear dynamics. However, the construction of some optimal set of variables (normal forms or action-angle) for the evaluation of the phase space distortion cannot be applied in the parts of the phase space which are close to instabilities, such as resonances or chaotic regions. In fact, an approach giving in a direct way a global view of the phase space structure is needed. This later can be achieved by the Frequency Map Analysis (F.M.A), a method extensively used in celestial mechanics [10, 11] and in Hamiltonian toy models [12–14] but only recently in real accelerators, as the ALS [15] or the LHC [7]. The method relies on the high precision calculation [18] of another fixed feature of KAM orbits, the associated frequencies of motion and can be directly applied in short term tracking data. Moreover, the variation of the frequencies over time [7, 13, 14] can provide an early stability indicator as good as, if not better

than, the Lyapounov exponent.

After a brief introduction to the method (Sect. 2), we display in frequency maps the global dynamics for cases of interest of LHC optics version 5 and 6, show many interesting features of the phase space structure and demonstrate the efficiency of the method in comparing different designs through a diffusion quality factor (Sect. 3). The last section is devoted to the final conclusions and perspectives.

2 FREQUENCY MAPS

The first step is to derive through the NAFF algorithm [10] or variants of this code (e.g. SUSSIX [17]), a quasi-periodic approximation, truncated to order N ,

$$f'_j(t) = \sum_{k=1}^N a_{j,k} e^{i\omega_{j,k}t}, \quad (1)$$

with $f'_j(t)$, $a_{j,k} \in \mathbb{C}$ and $j = 1, \dots, n$, of a complex function $f_j(t) = q_j(t) + ip_j(t)$, formed by a pair of conjugate variables of a n degrees of freedom Hamiltonian system, which are determined by usual numerical integration, for a finite time span $t = \tau$. The next step is to retain from the quasi-periodic approximation the frequency vector $\nu = (\nu_1, \nu_2, \dots, \nu_n)$ which, up to numerical accuracy [18], parameterises the KAM tori in the stable regions of a non-degenerate Hamiltonian system. Then, the construction of the frequency map can take place [12–15], by repeating the procedure for a set of initial conditions which are transversal to the orbits of interest. As an example, we may keep all the q variables constant, and explore the momenta p to produce the map \mathcal{F}_τ :

$$\mathcal{F}_\tau : \begin{array}{ccc} \mathbb{R}^n & \longrightarrow & \mathbb{R}^n \\ p|_{q=q_0} & \longrightarrow & \nu \end{array} \quad (2)$$

The dynamics of the system is then analysed by studying the regularity of this map.

3 APPLICATION TO THE LHC

The F.M.A is applied to the short-term tracking data ($\tau = 10^3$ turns) issued by SIXTRACK [3], for a large number of initial conditions ($\approx 10^4$). We select an arbitrary section of the phase space, setting the initial transverse momenta to zero. The particle coordinates are chosen equally spaced in the transverse linear Courant-Snyder invariants I_{x0} and I_{y0} , at different ratios I_{x0}/I_{y0} . Hence, we construct the map

$$\mathcal{F}_\tau : \begin{array}{ccc} \mathbb{R}^2 & \longrightarrow & \mathbb{R}^2 \\ (I_x, I_y)|_{p_x, p_y=0} & \longrightarrow & (\nu_x, \nu_y) \end{array}, \quad (3)$$

and proceed to the dynamical analysis of the accelerator model.

*Email: yannis@mail.cern.ch

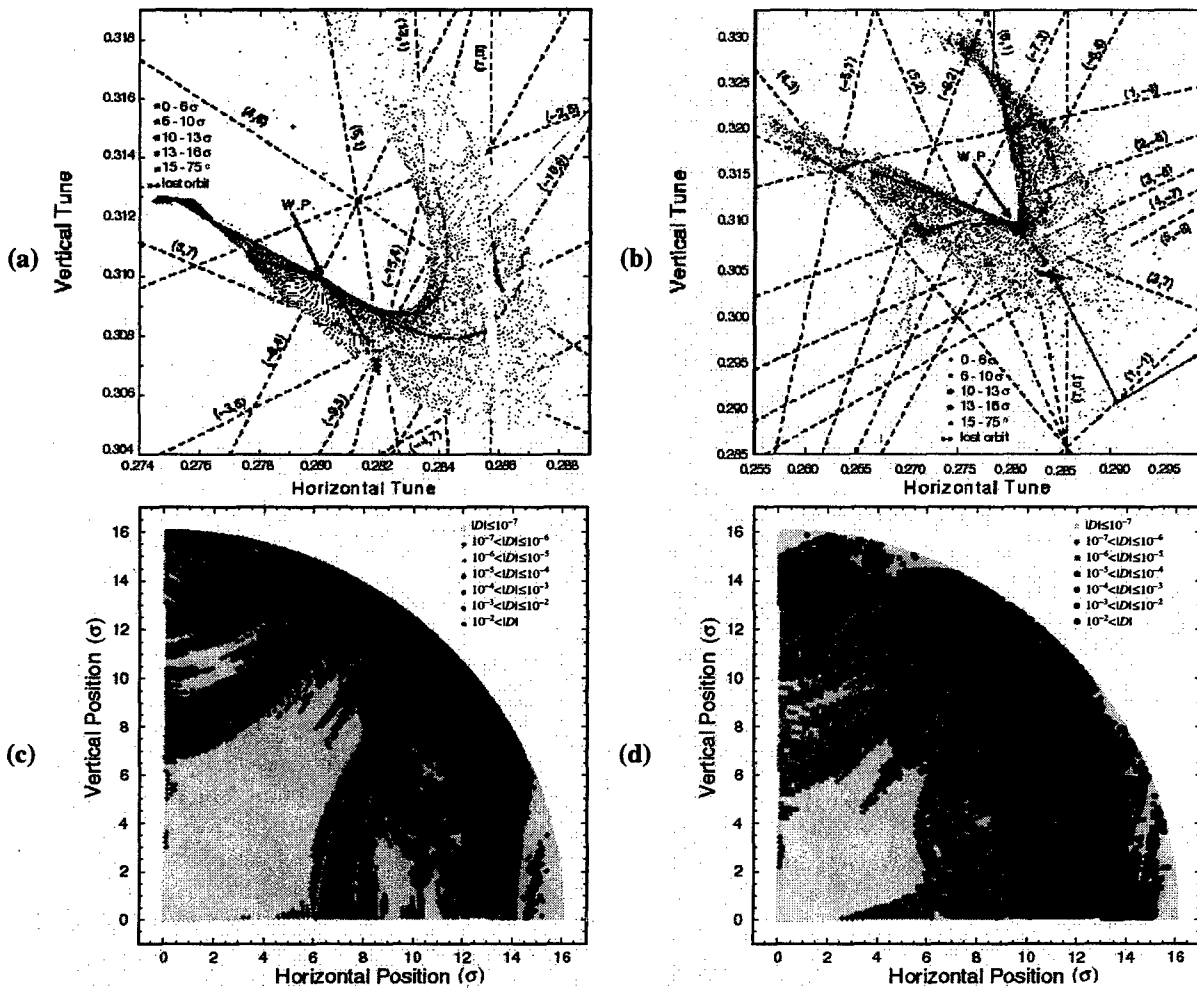


Figure 1: Frequency and amplitude maps for LHC optics version 5 target table without ((a),(c)) and with ((b),(d)) the high a_4 value of error table 9712 on the dipoles.

In order to reach the target D.A. of 12σ for the LHC injection optics, giving a necessary safety factor of 2 with respect to the position of the collimators at 6σ , a target error table was proposed. A frequency map for optics version 5 with this error table and for the nominal working point ($Q_x = 63.28$, $Q_y = 59.31$) is shown in Fig. 1a. This specific machine gives an average D.A. over 11 different invariant ratios of 13.1σ and a minimum of 12.1σ (at $\arctan(I_{y0}/I_{x0}) = 15^\circ$), values which are close to the average and minimum D.A. over all the 60 random realisation of the magnet errors ("seeds") usually produced for 6D tracking. Each point in the frequency space corresponds to a different orbit. The different colours in the map correspond to orbits with different initial amplitude $I = \sqrt{I_x^2 + I_y^2}$ (from $0 - 16\sigma$) and the black dots label initial conditions with different ratios (from 15° to 75°). The orderly spaced points correspond to regular orbits whereas the dispersed points to chaotic ones. This plot is a snapshot of the so called Arnold web, the complicated network of resonances $a\nu_x + b\nu_y + c = 0$, which appear as distortion of the map (empty and filled lines) and can be easily identified. For example, we put in evidence the importance of three 7th order resonances ($(a, b) = (7, 0)$, $(6, -1)$ and $(-2, 5)$). Especially, the crossings of the

resonant lines are "hot spots", from which particles can easily diffuse: as an example, we show the evolution of the frequency of an orbit starting close to the crossing of the $(7, 0)$ with the $(-3, 6)$ and $(4, 6)$ resonances. The orbit diffuses along the unstable manifold of the 7th order resonance and is lost after a few thousand turns. This is a clear demonstration of the importance of this resonance with respect to the D.A. of this model.

One of the main issues in the specification of the LHC injection optics, is the correction of the systematic part of the lowest order multipole errors of the super-conducting dipoles, which limit the D.A. [6]. This is usually done by magnetic coils ("spool pieces") placed at the ends of the dipoles. In the case of the last 9712 error table, where biases of the normal and skew octupoles have been significantly raised, there was an important loss of the dynamic aperture [19] with respect to the target error table. A frequency map for the same "seed" as for the previous case with the skew octupole error of the 9712 table in the dipoles is shown in Fig. 1b. The phase space now looks much more distorted. The most remarkable feature concerning the system's dynamics is the explosion of the detuning, to the point that particles, especially the ones with initial amplitude ratio of 45° are diffusing towards the diagonal

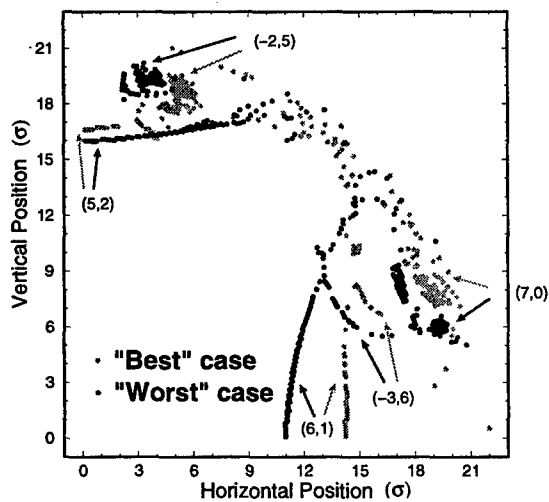


Figure 2: Positioning of the main resonances the initial amplitude space for two different correction schemes of the b_4 , b_5 error on the main dipoles of LHC optics version 6.

(1, -1) in the right corner of the map. On the other hand, particles close to horizontal motion at the top of the map are approaching the (0, 3) resonance and the ones close to vertical motion the (4, 0). This finding has been confirmed with Normal Form analysis. The dynamic aperture could be recovered by tuning the skew octupole spool pieces such as to cancel the (1, -1) resonance [19]. The global dynamics of these two cases can be also displayed in the physical space of the system by mapping each initial condition with a diffusion indicator: the tune can be calculated for two equal and successive time spans which correspond to half of the total integration time τ , giving a diffusion vector:

$$D|_{t=\tau} = \nu|_{t \in (0, \tau/2]} - \nu|_{t \in (\tau/2, \tau]}, \quad (4)$$

the amplitude of which can be used for characterising the instability of each orbit. In Figs. 1c and d, we plot the points in the (I_{x0}, I_{y0}) -space with a different colour corresponding to different diffusion indicators in logarithmic scale: from grey for stable ($|D| \leq 10^{-7}$) to black for strongly chaotic particles ($|D| > 10^{-2}$). Through this representation we are able to view the traces of the resonances in the physical space, and set a pessimistic threshold for the minimum D.A.. Moreover, we can compute a diffusion quality factor defined as the average of the local diffusion coefficient to the initial amplitude of each orbit, over a domain R of the phase space:

$$D_{QF} = \left\langle \frac{|D|}{(I_{x0}^2 + I_{y0}^2)^{1/2}} \right\rangle_R. \quad (5)$$

This quantity can be used for the comparison of different designs and the optimisation of the correction schemes proposed. For example, for the normal octupole and decapole correction of LHC optics version 6, five schemes were proposed, regarding the positioning of the “spool pieces”. In Fig. 2, we display the strongly excited resonances (four of 7th and one 9th order) in the amplitude space for the best and worst case, as suggested by the diffusion quality factor. The best one corresponds to the nominal scheme, where the

“spool pieces” are positioned in every dipole and correct the average value of b_4 and b_5 systematic per arc, whereas the worst machine corresponds to a correction with spool pieces in every second dipole. In both cases only the systematic per arc b_4 and b_5 errors are switched on, which explains the relatively weak distortion of the phase space for small amplitudes. On the other hand, in the “bad” case, the dangerous resonances are shifted towards lower amplitudes, as the detuning is higher, especially for horizontal motion. In fact, this correction option is not good for the LHC, due to the odd number of dipoles per half cell.

4 CONCLUSIONS

The F.M.A. was employed for the thorough study of the dynamics of different LHC machines with the injection optics version 5 and 6. All the fine details of the systems' phase space are directly viewed in frequency maps. Through the evolution of the tunes with time, the drifting of chaotic orbits is followed in the frequency space and different types of diffusion are shown. Moreover, the tune difference for two successive time spans enables the representation of the resonance structure and phase space distortion on the initial amplitude space. This instantaneous diffusion coefficient allows the computation of a global quality factor which can be efficiently used for comparison of different accelerator models with respect to their phase space stability. The method can be applied to the study of many open problems regarding the LHC non-linear dynamics, as the beam-beam effect, the optimal choice of the working point and its sensitivity to small variations or the influence of tune modulation. For this, it is envisaged to extend the approach to the full 6D phase space. Indeed, the challenge will be to establish the statistical correlation of early indicators such as the frequency variation with the beam lifetime.

5 REFERENCES

- [1] The LHC Study Group, CERN/AC/95-05(LHC), (1995).
- [2] H. Grote and F.C. Iselin, CERN-SL-90-13-AP, (1990).
- [3] F. Schmidt, CERN-SL-94-56-AP, (1994).
- [4] E. McIntosh, et al., LHC95 Workshop, Montreux, (1995).
- [5] M. Böge and F. Schmidt, PAC'97, Vancouver, (1997).
- [6] J.P. Koutchouk, this conference.
- [7] M. Giovannozzi, et al., Part. Accel. 56, 195, (1997).
- [8] M. Berz, et al., Part. Accel. 24, 91 (1989).
- [9] A. Bazzani, et al., CERN Yellow Report, 94-02, (1994).
- [10] J. Laskar, Astron. Astroph. 198, 341, (1988).
- [11] J. Laskar, Icarus 88, 266, (1990).
- [12] J. Laskar, et al., Physica D 56, 253, (1992).
- [13] J. Laskar, Physica D 67, 257 (1993).
- [14] H.S. Dumas and J. Laskar, Phys. Rev. Let. 70, 2975, (1993).
- [15] J. Laskar and D. Robin, Part. Acc. 54, 183, (1996).
- [16] E. Todesco, et al., EPAC'96, Barcelona, (1996).
- [17] R. Bartolini and F. Schmidt, CERN-SL-98-17-AP, (1998).
- [18] J. Laskar, NATO-ASI, S' Agaro, Spain, unpublished.
- [19] Y. Papaphilippou, et al., LHC Project Report 253, (1998).

MEASUREMENT OF RESONANCE DRIVING TERMS FROM TURN-BY-TURN DATA

R. Bartolini, L.H.A. Leunissen, Y. Papaphilippou, F. Schmidt, A. Verdier
CERN, Geneva, Switzerland

Abstract

It has been shown that the Fourier analysis of recorded turn-by-turn tracking data can be used to derive resonance terms of an accelerator. Beside the resonance driving terms, the non-linear one-turn map can be obtained with all non-linearities arising from magnetic imperfections and correction elements. This could be interesting for the LHC which will be a machine dominated by strong non-linear fields. The method works very well for tracking data and is expected to work equally well for turn-by-turn beam data. The precision to which these terms can be determined relies on the frequency analysis tool. To demonstrate the feasibility of the method, measurements of real accelerators are presented in which the beam is kicked once and the beam oscillations are recorded over several thousand turns. Besides the tune, the strengths of resonance driving terms have been measured and the results are compared with numerical calculations.

1 INTRODUCTION

The application of perturbative techniques for the analysis of tracking and also of experimental data has proven to be difficult since it requires a detailed knowledge of all the magnetic elements in the accelerator lattice. Checking such a model experimentally [1] may prove even more difficult.

More recently it has been shown [2] that frequency analysis à la Laskar [3] of tracking data does allow to derive all driving and Hamiltonian terms in an order-by-order procedure without any knowledge of the accelerator model [4].

In 1998, first experiments at the SPS and LEP have been performed to show the feasibility of this method using turn-by-turn data from pickups instead of tracking. Eventually, the goal is to measure simultaneously the following information:

1. Phase advance between pickups
2. β -beating
3. Linear coupling [5]
4. Detuning versus amplitude
5. Driving terms of resonances
6. Full non-linear model of the accelerator

Once the method has been proven to work reliably in the case of real accelerators, it will be possible to use it for feed-back control of linear coupling, but also for the planned LHC b_3 and b_5 spool piece correction.

2 EXPERIMENTS

Several measurements were carried out in 1998. One with LEP and two with the SPS [6, 7]. We show the detuning as a function of the linear invariant $I_x = \epsilon_x/2$ and the three first-order horizontal spectra lines which are due to sextupoles in both machines. These are the (3,0) resonance (f_{3000} term) and the (1,0) resonance (f_{2100} and f_{1200} term) [2].

2.1 SPS experiment

The SPS is an ideal test bed for this kind of investigation. The machine has practically no multipolar components so that particles exhibit mainly linear oscillations. Moreover, closed orbit, linear coupling and chromaticity have been well corrected. This "ideal" machine is made non-linear with the use of eight strong sextupoles.

In the experiment, the beam is kicked to various amplitudes and the turn-by-turn data is recorded by all pickups in one sixth of the machine (to which the SPS turn-by-turn recording system is presently limited).

As expected from earlier experiments [1] the detuning as a function of the linear invariant (Fig. 1a) is very well predicted by tracking (all solid lines in Fig. 1 are tracking results obtained with SIXTRACK [8]). Very promising is the agreement between the tracking and the experiment for the (3,0) resonance (Fig. 1b), the experimental data are systematically lower by a few percent only. When studying the first (1,0) resonance (Fig. 1c) a problem of the closed orbit measuring system becomes apparent. This line is the amplitude dependent offset of the FFT signal after the kick. To calculate this line one has to measure and subtract the signal offset before the kick which was not possible with sufficient precision. Moreover, the number of data samples were limited to 170 turns and there had been unavoidable electronic spikes. Lastly, we present the other (1,0) resonance (Fig. 1d) which should suffer less from the limitations of the measurement system. Indeed, we find less noise signals in that case. However, there is a significant discrepancy with the tracking data which remains to be understood.

2.2 LEP experiment

The electron storage ring LEP was used for another experiment. Five different cases were studied with the 90/60 optics used for physics runs in 1997: one tune close to the (3,0) resonance and two tunes at increasing distance to that resonance. In the latter two cases the beam was kicked to 2

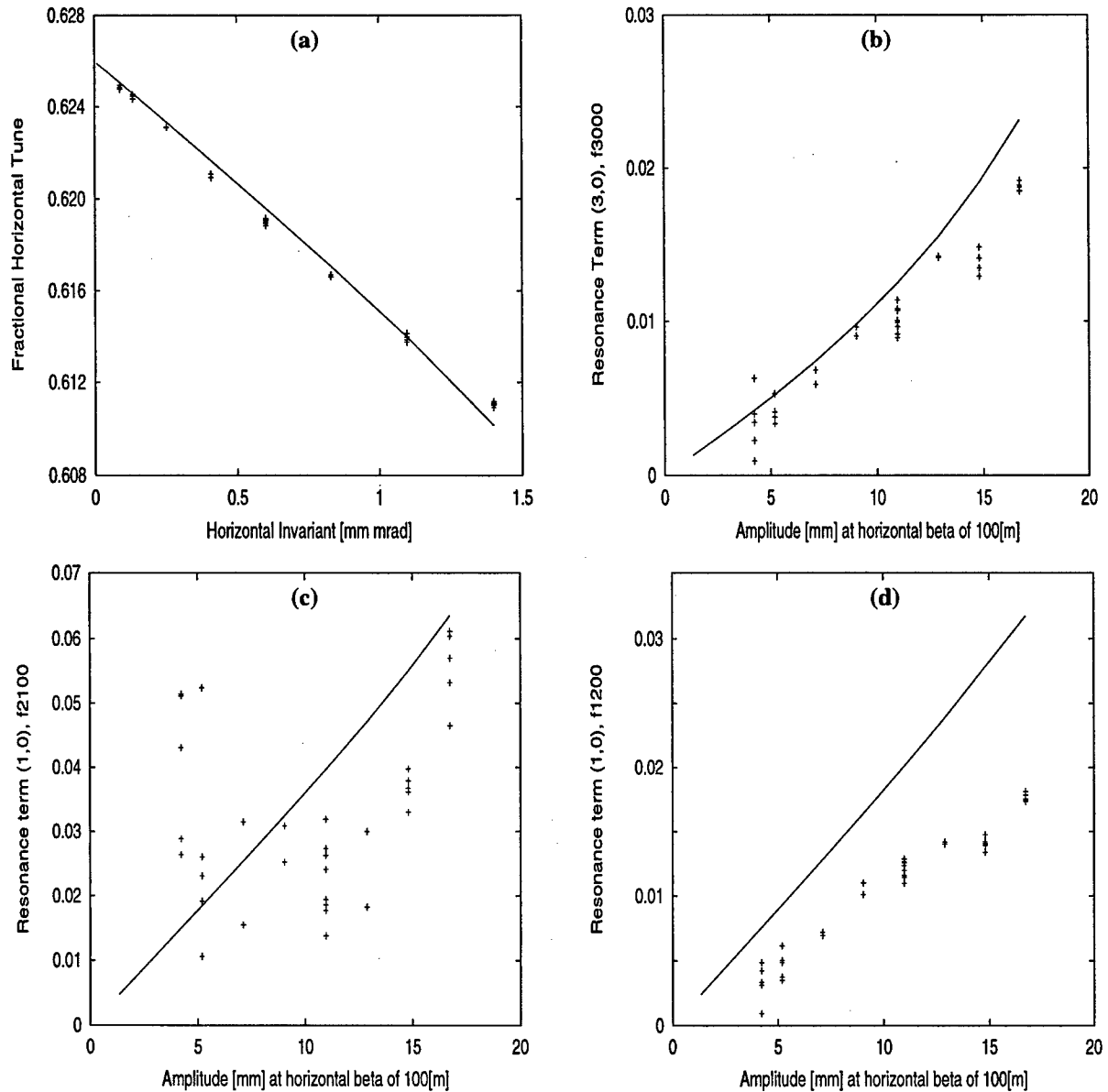


Figure 1: Detuning and First Order Sextupole Driving Terms
 Part (a): Detuning versus linear Invariant I_x ; Part (b): (3, 0) Resonance versus Amplitude;
 Part (c): (1, 0) Resonance (f_{2100}) versus Amplitude; Part (d): (1, 0) Resonance (f_{1200}) versus Amplitude;
 -Lines are from tracking -Symbols are experimental data

different amplitudes (each case is represented by another symbol in Fig. 2). In Fig. 2a the detuning curves are recorded with a sliding window in time for two different kick strengths. Both curves lie fairly well on top of each other. The effect of radiation can be directly observed and there is no sign of filamentation [9]. Moreover, the detuning is well predicted by tracking (solid line as calculated with MAD [10]). Both terms of the (1,0) resonance (part (c) and (d) of Fig. 2) show good agreement between the tracking and the experiment after inclusion of radiation (the straight curve in part (c) is obtained without radiation). However, the (3,0) resonance has a significant discrepancy with the tracking data even when radiation is properly treated. We find almost a factor 10 between experiment and tracking. Although we do not yet have a full

understanding of the cause of this difference it can probably be addressed to random sextupole components which are not included in the tracking.

3 CONCLUSIONS

Since the detuning versus amplitude can be well predicted from tracking (for the SPS as well as LEP) we are confident that our model includes the proper systematic part of the non-linearities. With respect to the first-order sextupole resonances the results are promising, but not yet conclusive. In the case of the SPS one resonance (3,0) is well predicted, but only one of the (1,0) resonances can be measured with sufficient precision but is wrong by a factor of two. For LEP the (3,0) resonance is largely underestimated,

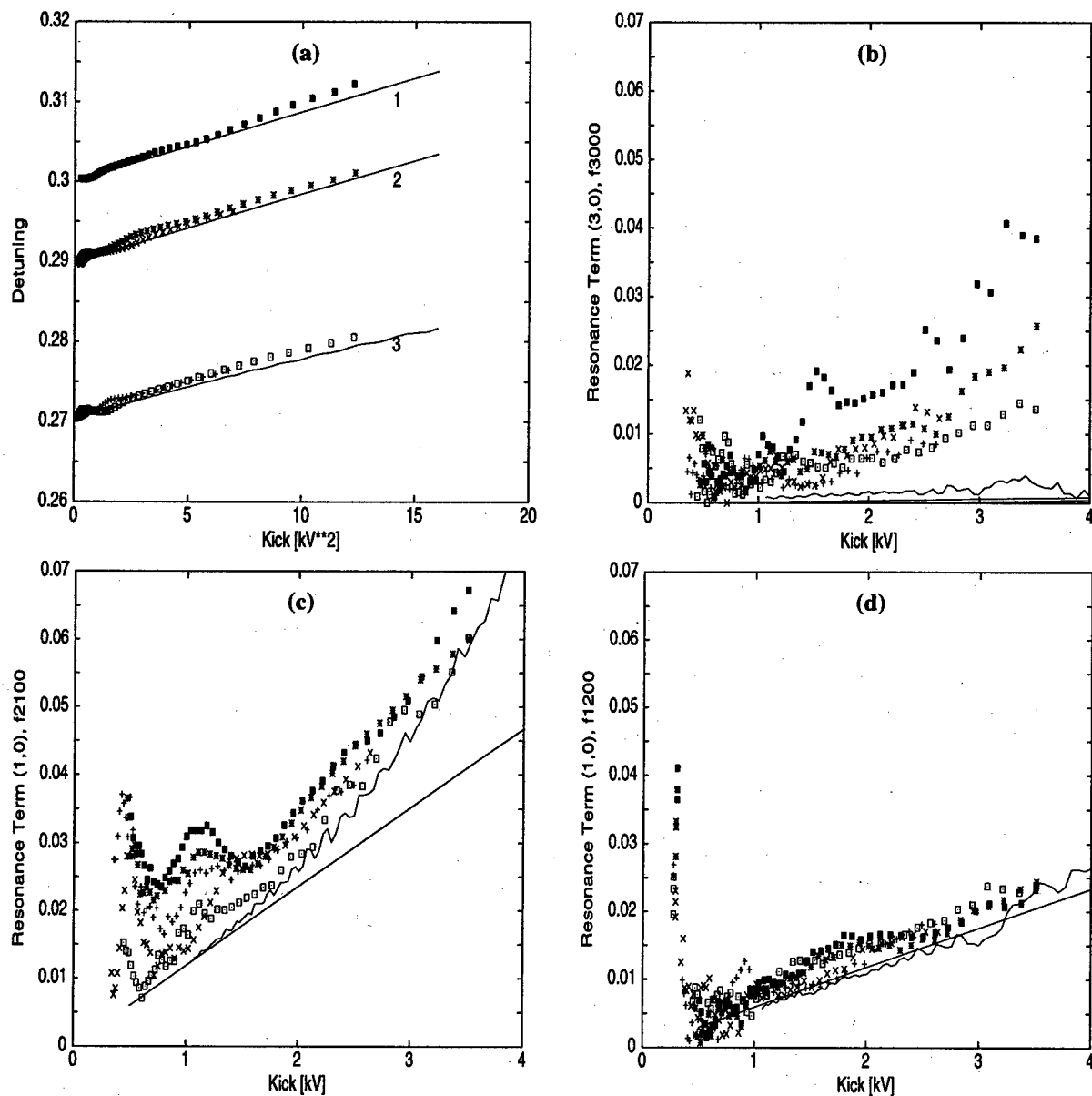


Figure 2: Detuning and First Order Sextupole Driving Terms

Part (a): Detuning versus kick amplitude [kV^2]; Part (b): (3, 0) Resonance versus Amplitude;

Part (c): (1, 0) Resonance (f_{2100}) versus Amplitude; Part (d): (1, 0) Resonance (f_{1200}) versus Amplitude;

—Lines are from tracking —Symbols are experimental data

probably due to the effect of the machine errors which increase the driving terms by more than one order of magnitude as shown in Ref. [11], while the two parts of the (1,0) resonances are in good agreement with the tracking.

We can conclude that there is a large potential for this method. However, more experimental studies and better tracking models are needed to make it a useful tool to measure and correct non-linear effects in real machines.

4 ACKNOWLEDGEMENTS

We thank the SPS operations team and equipment specialists. We also like to thank A.-S. Müller and J. Wenninger for helping us taking data from LEP.

5 REFERENCES

- [1] W. Fischer et al., Phys. Rev. E Vol. 55, no. 3, 3507 (1995).
- [2] R. Bartolini and F. Schmidt, Part. Accel. 59, 93 (1998).
- [3] J. Laskar, Physica D 57, 257 (1993).
- [4] R. Bartolini and F. Schmidt, CERN SL/Note 98-017 (AP).
- [5] F. Zimmermann et al., SLAC-AP-113 (1998).
- [6] X. Altuna et al., CERN SL/Note 98-045 MD.
- [7] X. Altuna et al., CERN SL/Note 99-017 MD.
- [8] F. Schmidt, CERN SL 94-56 (AP).
- [9] A.-S. Müller, 7th LEP Perf. Workshop, CERN SL 97-06 (DI).
- [10] H. Grote and C.H. Iselin, CERN SL 90-13 (AP).
- [11] J. Jowett, 7th LEP Perf. Workshop, CERN SL 97-06 (DI).

EFFECTS OF SEXTUPOLE TIME DEPENDENCE ON THE LHC DYNAMIC APERTURE

Y. Papaphilippou, F. Schmidt and F. Zimmermann, CERN, Geneva, Switzerland

Abstract

A primary concern regarding the LHC dynamic aperture is the time dependence of persistent-current sextupole fields in the superconducting magnets. Decaying slowly during injection, these fields are reinduced rapidly at the start of the acceleration ("snap-back"). If uncompensated, this snap-back would cause a chromaticity change by some 130 units. We investigate how this time dependence and the ramp rate affect the stability of particle motion and we evaluate the efficiency of different correction schemes.

1 INTRODUCTION

Superconducting magnets provide high magnetic fields at low operating costs. Therefore, they are the magnets of choice for the present and next-generation highest-energy proton storage rings, *e.g.*, for the Large Hadron Collider (LHC) now under construction at CERN [1]. The superconducting magnets exhibit large nonlinear field errors. These are partly caused by the geometry of the superconducting coils, and partly due to "persistent currents" (p.c.), which are eddy currents in the superconducting cable. The nonlinear field errors are expected to limit the LHC "dynamic aperture" (the stable region of phase space where particles are not lost) at injection energy.

In order to ensure an adequate dynamic aperture of 6σ as required by the collimation system [1], the effect of the strongest magnet nonlinearities, such as the normal sextupole component, will be compensated by dedicated multipole correctors. At the injection plateau, where the magnet field quality is most critical, the p.c. errors decay in time [2, 3]. This decay is caused both by a slow flux creep in the superconductor and, more importantly, by a current redistribution between the strands of the superconducting cable. At the start of the acceleration the p.c. fields are reinduced rapidly, a phenomenon called the "snap-back" [2].

During acceleration a new kind of eddy current is induced in the loops formed by the twisted strands in the superconducting cable [4, 5]. The resulting dynamic field imperfections are proportional to the ramp rate and inversely proportional to the inter-strand resistance.

In this report we employ particle tracking to investigate the influence of the persistent-current decay, the snap-back and the ramp-induced field imperfections on the dynamic aperture, and we estimate the implied tolerances on chromatic correction and ramping speed.

2 PARAMETERS

The LHC, a double storage-ring with a circumference of 26.7 km, is designed to collide two 7-TeV proton beams. Relevant parameters at injection energy are compiled in

Table 1. It will take about 7 minutes to inject both LHC beams; a three times longer time period is required for acceleration to top energy.

The tracking simulation with the SIXTRACK code [6] models a time-span of 10^5 turns, which corresponds to approximately 1% of the total injection period. Initial particle coordinates are chosen equally spaced in the transverse linear Courant-Snyder invariants I_{x0} and I_{y0} , at a constant ratio of I_{x0}/I_{y0} (usually 1). The initial transverse momenta are set to zero and the initial energy error is $\delta = 1.6\sigma$ (or 7.5×10^{-4}), roughly 75% of the rf bucket half size. Twin particles with slightly different initial conditions are tracked in order to determine the onset of chaotic motion by computing the Lyapunov exponent [7]. The tracking is repeated for 10 random seeds of the multipole errors, and we infer both the average and the minimum dynamic aperture over all error seeds. Throughout this report, the dynamic aperture a refers to a simultaneous amplitude in both transverse planes, in units of the rms beam size. The aperture is calculated from the transverse phase space areas $A_{x,y}$ inscribed by a particle during its betatron motion, via $a = \sqrt{(A_x + A_y)/(2\pi)}$.

Our simulation study assumes a realistic set of nonlinear field components for the main dipoles known by the acronym "9712". The strengths of the sextupole field errors for this error set are given in Table 2. Higher multipoles and their variation up to order 11 (not listed in the table) are also taken into account. The simulation is performed for LHC optics version 6, with a 4-integer tune split between the horizontal and vertical plane. The linear optics is considered to be constant. Thus, changes of dipole and quadrupole fields or feeddown from higher-order multipoles for off-center orbit are disregarded.

Table 1: LHC injection parameters.

parameter	symbol	value
proton energy	E	450 GeV
transv. norm. emittance	$\gamma\epsilon_{x,y}$	$3.75 \mu\text{m}$
transv. rms beam size in arc	$\sigma_{x,y}$	$\sim 1.2 \text{ mm}$
rms energy spread	σ_δ	4.7×10^{-4}
rms bunch length	σ_z	13 cm
betatron tunes	$Q_{x,y}$	63.28, 59.31

3 CHROMATICITY

The decrease of the average sextupole fields due to persistent-current decay at injection energy, if uncompensated, results in a huge chromaticity variation of $\Delta Q'_x \approx +144$, and $\Delta Q'_y \approx -129$ (where Q' is defined as

$\Delta Q/(\Delta p/p)$). The opposite chromaticity change occurs, in less than 1 minute, during the snap-back. To permanently maintain a small net chromaticity, sextupole correction coils must be powered synchronized with the accelerating cycle. It is of interest to estimate the correction accuracy required.

Table 2: Normal and skew sextupole components in the main LHC dipoles, assumed in this study. The errors are quoted in units of 10^{-4} , normalized to the main dipole field, for a reference radius of 17 mm. The different rows show the field errors due to p.c. decay, geometry & iron, persistent currents, and acceleration at the nominal ramp rate of 8T/20min, respectively. In each case the first number is the mean change, the second the uncertainty (the rms difference between octants), and the third the rms variation between magnets. The table does not show the multipole errors of order $n = 4$ to 11, which were also included in the simulation.

contribution	mean	uncert.	rms
normal sextupole b_3			
p.c.	-10.7	1.1	0.3
p.c. decay	3.2	0.4	1.0
geometry & iron	2.9	0.9	1.4
ramp	1.0	0.2	0.3
skew sextupole a_3			
p.c.	0.0	0.0	0.2
p.c. decay	0.0	0.3	0.7
geometry & iron	0.0	0.9	0.4
ramp	0.0	0.2	0.3

Figure 1 presents the simulated dynamic aperture at the start of LHC injection as a function of equal and opposite-sign chromaticity in the two transverse planes. The case of opposite-sign chromaticity, which naturally occurs during p.c. decay or snap-back, shows a stronger effect on the dynamic aperture. In either case a chromaticity of a few units seems acceptable. Larger chromatic variations could seriously reduce the dynamic aperture which scales roughly inversely with the chromaticity.

In Fig. 2 we depict the dynamic aperture after the persistent current decay, near the end of the injection plateau. Comparing with Fig. 1 (top) shows that the effect of the p.c. decay on the dynamic aperture is insignificant, provided that the chromaticity is held constant. The smallness of this effect can be attributed to the fact that, firstly, an increase of either random or systematic sextupole components leads to a comparable reduction of the dynamic aperture (see Fig. 3) and that, secondly, during the p.c. decay the systematic sextupole decreases while the random component increases, by roughly 40% and 22%, respectively (see Table 2).

A frequency map analysis [8, 9] of the two cases, before and after p.c. decay, reveals that resonances are encountered at approximately the same amplitudes as illustrated in Fig. 4. This implies that these resonances remain fixed

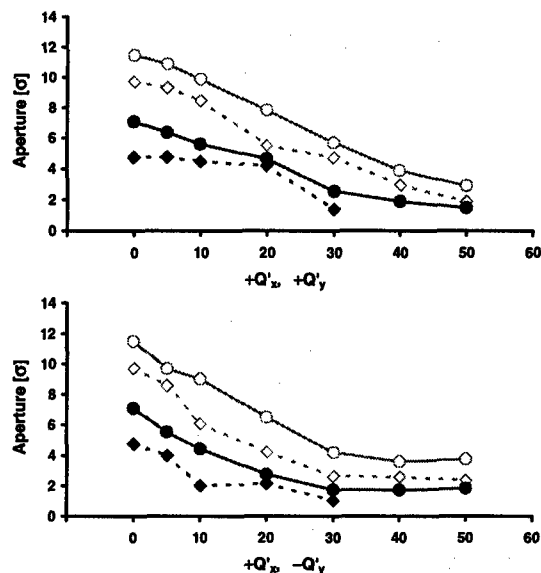


Figure 1: Dynamic aperture as a function of uncorrected chromaticity, at the start of the injection plateau. Top: equal sign for horizontal and vertical chromaticity, bottom: opposite sign. Shown are the mean (circles) and the minimum (diamonds) amplitudes beyond which particles are lost in less than 10^5 turns (open symbols) and beyond which the particle motion is found to be chaotic (closed symbols). The chromaticity was varied by changing the strength of the main sextupoles.

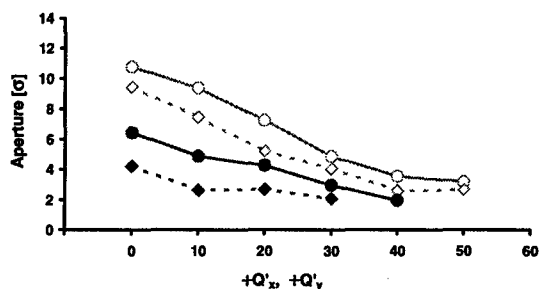


Figure 2: Dynamic aperture as a function of uncorrected chromaticity, at the end of the injection plateau (after the p.c. decay), considering equal horizontal and vertical chromaticity. The plotting symbols are the same as in Figure 1.

during the entire decay process. Hence, the dynamic aperture should not be influenced by the time dependence.

A correction of the chromaticity change due to p.c. decay (or snap-back) can be performed either locally with the spool pieces in the dipole magnets or with the main lattice sextupoles. Figure 5 shows that the two correction methods would provide about the same aperture.

It should be mentioned that a large negative chromaticity may induce the fundamental-mode head-tail instability. To insure beam stability at nominal current, the chromaticity should be larger than -1 unit. On the other hand for positive values, the chromaticity is limited to a few units to avoid the $m = 1$ head-tail mode [10] and to restrict the tune footprint.

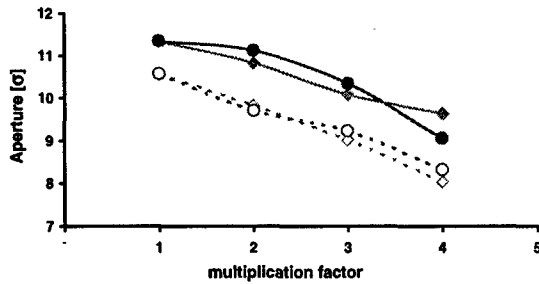


Figure 3: Dynamic aperture as a function of random (diamonds) and systematic (circles) sextupole components in units of the nominal strength. Solid lines represent the mean value, dashed lines the minimum over all seeds.

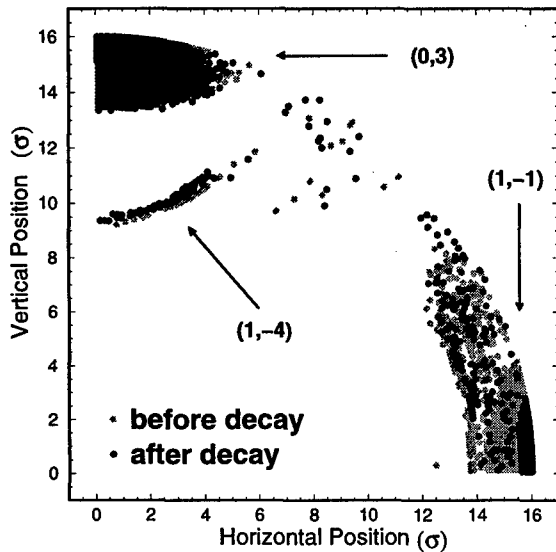


Figure 4: Initial amplitudes of particles locked to three strong resonances, determined by tracking and frequency map analysis [8].

4 RAMP RATE

The additional imperfections caused by interstrand coupling during acceleration are proportional to the ramp rate (see Table 2 for the change in sextupole field). Figure 6

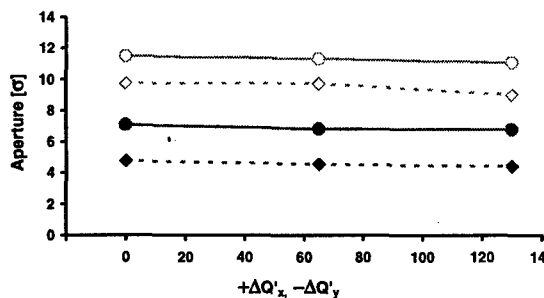


Figure 5: Dynamic aperture after half and full snapback corresponding to $\Delta Q'_y \approx -\Delta Q'_x \approx +65$ and $+130$ units, respectively and its correction with the lattice sextupoles (instead of using the spool pieces). The plotting symbols are the same as in Figure 1

demonstrates that the dynamic aperture is not much affected by these additional field errors, up to ramp rates four times larger than nominal.

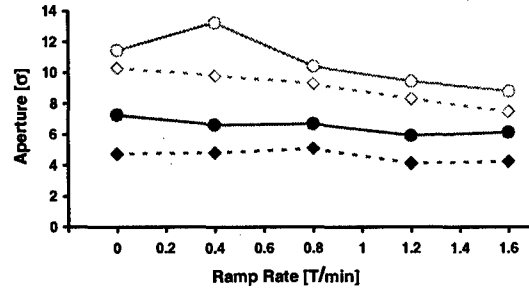


Figure 6: Dynamic aperture during acceleration as a function of ramp rate, close to the injection energy. The plotting symbols are the same as in Figure 1. The chromaticity is corrected for all points.

5 CONCLUSIONS

Assuming the linear optics stays constant, we found that the time variation of the higher-order field errors—induced by p.c. decay at injection or by the subsequent snap-back—has only minor effects on the LHC dynamic aperture, as long as the overall chromaticity is corrected and remains within a few units. Under the same assumptions, the dynamic aperture during acceleration shows little dependence on the ramp rate. Correcting the chromaticity with the main arc sextupole magnets is about as effective as correcting it with the sextupole spool pieces in the bending magnets.

6 ACKNOWLEDGEMENTS

We thank L. Bottura and R. Wolf from the CERN LHC division for discussions on the persistent-current decay and the snap-back, and J. P. Koutchouk for helpful suggestions.

7 REFERENCES

- [1] The LHC Study Group, CERN/AC/95-05 (1995).
- [2] L. Bottura, et al., 1996 Applied Supercon. Conference.
- [3] K.H. Meß, P. Schmüser, and S. Wolf, "Superconducting Accelerator Magnets", World Scientific (1996).
- [4] A.P. Verweij and R. Wolf, CERN AT-MA/AV 94-07 (1994).
- [5] A. Faus-Golfe, LHC Project Note 9 (1995).
- [6] F. Schmidt, CERN-SL-94-56-AP (1994).
- [7] F. Schmidt, et al., Part. Accel. 35, 249 (1991).
- [8] J. Laskar, Physica D 67, 257 (1993); J. Laskar and D. Robin, Part. Acc. 54, 183 (1996).
- [9] Y. Papaphilippou, this conference.
- [10] S. Berg, LHC Project Report 100 (1997).

OPTIMISATION OF THE LHC DYNAMIC APERTURE VIA THE PHASE ADVANCE OF THE ARC CELLS

F. Schmidt and A. Verdier
SL Division

Abstract

The phase advances of the arc cells of storage rings are traditionally chosen to be simple fractions of π in order to take advantage of second order achromats they constitute.

For the LHC, such a choice is not relevant because of the existence of high order systematic multipole components in the main dipoles. In this case it is better to choose the phase advances to cancel the driving term for the largest possible number of non-linear resonances, which is straightforward for an ensemble of identical cells. This can also be achieved for an actual LHC arc featuring dispersion suppressors. The associated improvement of the dynamic aperture is shown in this paper.

1 INTRODUCTION

The working point in the tune diagram is usually determined by a systematic scanning. The SPEAR upgrade projects is a good example [1].

A more subtle approach consists of building a machine from blocs which do not contribute to the excitation of non-linear resonances. The details are explained in [2] and the application to the LHC is shown in section 2 below.

In order to have a basis for comparison, several LHC optics have been constructed. Their characteristics are given in section 3.

In order to help the understanding the resonance strengths have been computed by Normal Form [4]. Lastly, tracking results, performed with SIXTRACK [3], are presented for these optics.

2 A "RESONANCE FREE" LHC ARC

The main problem associated with multipole errors in the LHC arises from the arc dipoles. These dipoles are constructed by several different firms. Each fabrication line may produce dipoles with different systematic multipole errors. As the number of fabrication lines is comparable with the number of LHC arcs, which is eight, the concept of "systematic multipole per arc" comes naturally into the game. Such a component takes a constant value over a given arc and this value varies randomly from arc to arc.

In this context it is attractive to design the arc optics such that it does not contribute to the excitation of low order resonances [2]. To this end both cell phase advances have to be set to the values $k_1 \cdot 2\pi/N_c$ in the horizontal plane and $k_2 \cdot 2\pi/N_c$ in the vertical plane. Under these conditions

only those resonances are excited which satisfy,

$$n_x k_1 + n_y k_2 = k_3 N_c, \quad (1)$$

where k_3 is any integer.

N_c is determined for the LHC as follows. Each arc is composed of 23 FODO cells plus one dispersion suppressor at each end. Each cell is composed of two quadrupoles and six dipoles. The dispersion suppressors consist of four quadrupoles and eight dipoles. Thus, a dispersion suppressor is a little longer than one cell, it has a larger phase advance and it contains one third more dipoles. Even though, each dispersion suppressor is taken as one cell. The number of cells is therefore 25 (23 cells plus 2 dispersion suppressors).

The phase advance of the arc cells must be close to 90° because the quadrupole gradient and the aperture of the vacuum chamber have been designed in view of these phase advances. This leaves two possibilities for (k_1, k_2) : (7,6) or (6,5). Nevertheless there remain systematically excited single resonances satisfying equation (1). Below order 10 they are: 4,8,9 and 5,6,9 for these two cases respectively. The pair (7,6) has been kept for tracking studies due to its lower β functions.

3 LHC OPTICS STUDIED

In order to have a relevant basis of comparison, several optics have been constructed:

1. A simple model with 25 FODO cells and at each end a transfer matrix to simulate a LHC arc
2. An optics with a tune-split of 5 ($Q_x=64.28$, $Q_y=59.31$). A tune-split of 5 has been chosen as the nominal LHC lattice version 6.
3. An optics which minimises some adverse effects of non-linearities for multipole components which have the same value in all dipoles $Q_x=65.28$, $Q_y=58.31$ [5]. Such an optics is likely not to bring any improvement in the case where the systematic by arcs dominate.
4. A "resonance free" lattice with the phase advances per cell: $\mu_{x,c} = \frac{7}{25} \times 2\pi$ and $\mu_{y,c} = \frac{6}{25} \times 2\pi$. $Q_x=68.28$, $Q_y=59.31$. The phase advance in the cells has been set and the insertions have been rematched using the minimum number of variable parameters. Then the tunes have been adjusted by means of IR4 and IR6 to the closest values with the same fractional

parts as above. For this lattice, the resonances are not cancelled as they should be for the case of 25 FODO cells, nevertheless their driving term is substantially reduced compared with other lattices.

4 RESONANCE COMPUTATION

In order to test the efficiency of the resonance cancellation procedure, the resonance driving terms have been computed by means of the formalism in ref. [4].

At first this has been done for the simple model composed of 25 cells and two insertions for which the resonance driving term is exactly zero. It is found to have a value smaller by five order of magnitude compared with the other cases. This shows the validity of the computation and the consistency between the two approaches, namely perturbation calculation and map transformation to calculate resonance driving terms.

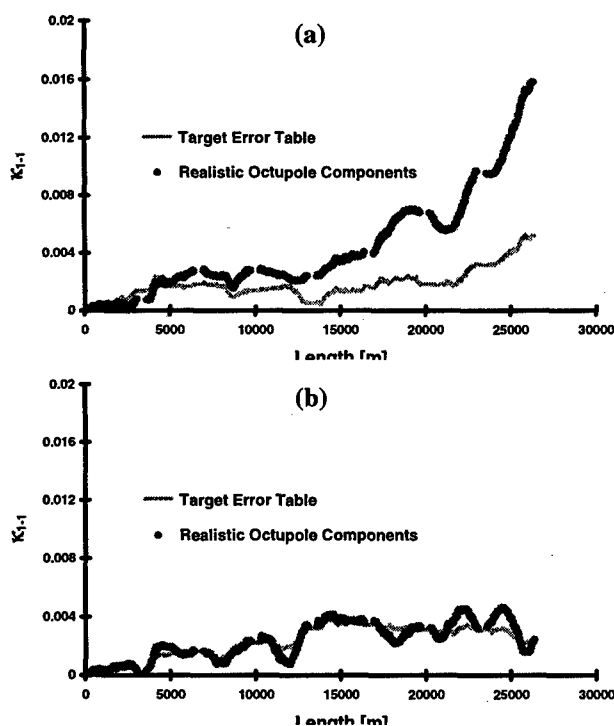


Figure 1: Build-up of the driving term of the (1012) sub-resonance over the length of the LHC. The light gray (green) curve is associated with the "target error table" [6]. The dark gray (red) curve is obtained with larger b_4 and a_4 systematic by arc multipole components, respectively 0.35 and 0.555 in units of 10^{-4} and at a reference radius 17mm. Part (a) Case 2 in section 2. Part (b) Case 4 in section 2.

The build-up of the resonance driving term along the LHC lattice is shown in figure 1(a) for the optics with a tune-split of 5 and in figure 1(b) for the "resonance free" lattice respectively. The multipole errors introduced in the

lattice are: systematic per arc and random. The error tables can be found in ref. [6]. The resonance cancellation per octant appears quite clearly in figure 1(b): the value of the driving term at the end of the lattice is the same both with and without realistic octupole components.

5 DYNAMIC APERTURE

For the simple model, trajectories have been tracked over 1000 turns without synchrotron oscillations. The maximum initial amplitudes with zero slopes for which the trajectory remains stable are shown on figure 2.

For realistic lattices (case 2, 3 and 4 in section 2), trajectories have been tracked for 10^5 turns with two sets of initial conditions. One set has identical coordinates in both planes, the other set has an amplitude ratio of $\tan(15^\circ)=0.27$, the two trajectory slopes are zero. Both β -functions have the value of 18m at the starting point. The beam emittance is 3.75nm at 1σ . Synchrotron oscillations with an initial relative momentum deviation of 0.00075 are included. 60 different realizations of the multipole errors have been studied in order to achieve a 95% confidence level of the minimum dynamic aperture.

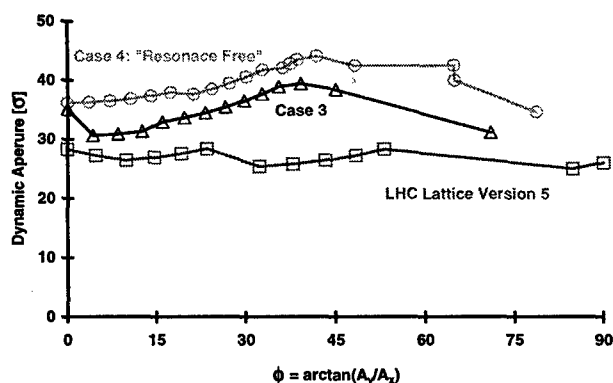


Figure 2: 1'000 turn dynamic aperture of the LHC model for three phase advances per cell: LHC lattice version 5, case 3 and case 4 of section 2. The dynamic aperture is defined as the ensemble of points in the $\{x,y\}$ plane for which the trajectories starting with the initial coordinates x and y and zero slopes at the beginning of the lattice where both α 's are zero, are stable over 1000 turns. Both horizontal and vertical β functions are equal to 1m at the starting point. The multipole errors are $b_4=0.5$, $a_4=0.5$ and $b_5=1.4$ in units of 10^{-4} and at a reference radius 17mm.

The tracking results are shown in table 1. For the "target error table" (the first three cases) we observe no difference in the values for the dynamic apertures. When realistic octupole components b_4 and a_4 are introduced the dynamic aperture is not changed for quasi horizontal motion ($y_0 = 0.27x_0$). For equal amplitudes ($y_0 = x_0$) there is a 10% reduction of the minimum dynamic aperture for the

cases 3 and 4 in section 2. This reduction is fully recovered for the “resonance free” lattice.

Case	Realistic b_4 & a_4	$y_0 = x_0$		$y_0 = 0.27x_0$	
		min.	av.	min.	av.
3 (V6 nom.)	off	12.4	14.6	11.3	12.7
4		12.4	14.5	11.0	12.8
5 (Res. free)		12.5	14.8	11.3	12.6
3 (V6 nom.)	on	10.9	13.4	11.1	12.8
4		11.3	13.8	11.3	12.9
5 (Res. free)		12.6	14.5	10.8	12.7

Table 1: Minimum and average dynamic aperture in units of r.m.s. beam size for a series of 60 distributions of errors, both random and systematic per arc. For the first three cases, the values are taken from the “target error table”. For the following three cases the errors are the same except for the systematic by arc octupole components which have been set to the more realistic values of $a_4=0.555$ and $b_4=0.35$ (in units of 10^{-4} at a reference radius of 17mm) without compensation. From our current experience, the dynamic apertures can be overestimated by 0.2 for the average and 0.5 for the minimum.

In order to observe the beneficial effect of the resonance suppression the same exercise was repeated with values of the realistic b_4 and a_4 components increased threefold. The efficiency of the “resonance free” lattice appears clearly in table 2.

From these three sets of tracking results we conclude that the dynamic aperture of the “target error table” is far from being dominated by low order resonances driven by systematic multipoles.

Case	$y_0 = x_0$		$y_0 = 0.27x_0$	
	min.	av.	min.	av.
3 (V6 nom.)	7.7	10.3	7.6	10.8
5 (Res. free)	10.2	13.5	10.3	12.5

Table 2: Minimum and average dynamic aperture in units of r.m.s. beam size for a series of 60 distributions of errors, both random and systematic per arc. The values are taken from the “target error table” except the octupole errors which have been set to three times their realistic values.

In order to check that there is no artifact in the “resonance free” lattice, the dynamic aperture has been evaluated for 12 ratios of initial amplitudes. The results are shown on figure 3. The maximum dynamic apertures (the two upper curves) are both at the level we expect from the random components only [7], the resonance suppression has obviously no effect in this case. The average dynamic apertures (medium two curves) show an improvement of

some 2σ for all amplitude ratios. The minimum dynamic apertures (lower two curves) show a sizable improvement except for quasi vertical motion. This lack of improvement is probably due to higher order effects.

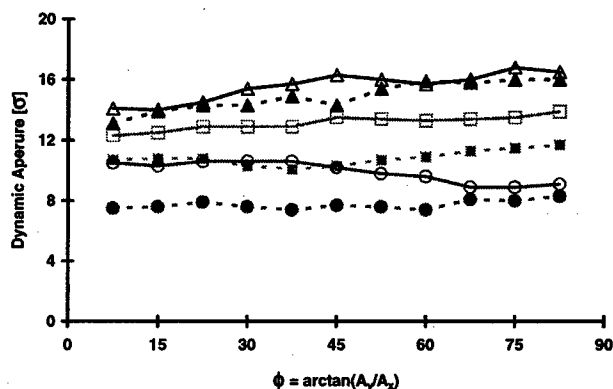


Figure 3: Dynamic aperture in the x,y plane for the two cases of table 2.

6 CONCLUSION

We have demonstrated, for the case of the LHC, that the dynamic aperture can be increased by a suppression of first order resonances with a proper choice of the cell phase advances in the arcs. This is closely associated with the fact that we expect large systematic per arc multipole components to dominate the dynamic aperture.

This optimisation of the cell phase advances provides a large safety margin against unexpected large systematic components of the LHC dipoles.

7 REFERENCES

- [1] J. Corbett et al., “Design of the SPEAR3 magnet lattice”, 6th European Particle Accelerator Conference, Stockholm, Sweden, June 1998. Also SLAC-PUB-7882.
- [2] A. Verdier, “Resonance free lattices for A.G. machines”, this conference.
- [3] F. Schmidt, “SIXTRACK, Version 1.2, Single Particle Code treating Transverse Motion with synchrotron oscillations in a symplectic manner”, CERN SL/94-56(AP) (Rev. 4).
- [4] M. Berz, E. Forest and J. Irwin, “Normal form methods for complicated periodic systems: a complete solution using differential algebra and Lie operators”, Part. Acc. Vol. 24, Number 2 (1989), pp. 91-107, ISSN 0031-2460.
- [5] R. Talman, “Tune optimisation for maximum dynamic acceptance, II”, LHC Project Report 233 (August 1998).
- [6] Y. Papaphilippou, F. Schmidt and L. Jin, “Improvement of LHC Dynamic Aperture via Octupole Spool Pieces for the Nominal Tunes”, LHC Project Report 253.
- [7] M. Böge, F. Schmidt and G. Xu, “Comparison of Tracking Results with Ziemann’s Conjecture for the LHC Dynamic Aperture”, LHC Project Note 170.

SIMULATION OF GROUND MOTION INDUCED PROTON BEAM ORBIT VIBRATION IN HERA

C. Montag, DESY, Hamburg, Germany*

Abstract

A ground motion model based on realistic spectra and correlation properties has been developed in order to simulate ground motion induced beam orbit vibration. This model has been used to simulate the motion of the HERA proton beam. Simulation results and comparisons with orbit measurements will be presented.

1 INTRODUCTION

Ground motion induced beam jitter plays an important role for many kinds of accelerators, like future linear colliders, synchrotron radiation sources or storage rings. The resulting beam orbit vibration potentially leads to luminosity degradation in colliding beam facilities due to beam offset at the interaction point and/or emittance growth.

The sensitivity of beam orbits to quadrupole motion depends strongly on the correlation length of ground motion at a specific frequency. Quadrupole motion with a correlation length exceeding the betatron wavelength has only little influence on beam jitter [1]. Therefore any simulation of ground motion effects has to take into account not only the power spectrum of motion at a single point but also the coherence properties of ground motion.

This paper presents a ground motion simulation model which has been originally developed for linear accelerators [2]. It is based on measured power spectra and coherence properties of ground motion. This model is extended to circular machines in order to simulate ground motion induced beam jitter in the HERA proton ring.

2 THE SIMULATION MODEL

As measurements at different geographical locations show, the power spectrum $P_{\text{tot}}(\omega)$ of ground motion at a single point can be roughly approximated as [3]

$$P_{\text{tot}}(\omega) = \frac{B}{\omega^4}, \quad (1)$$

where B is some proportionality constant characteristic of the site, and $\omega = 2\pi f$. According to the *ATL* rule [4], the power spectrum $\rho(\omega, L)$ of the uncorrelated motion of two points at a distance L is [3]

$$\rho(\omega, L) = \frac{A \cdot L}{\omega^2}. \quad (2)$$

Obviously, the uncorrelated part of motion must be smaller than the total motion, thus

$$\rho(\omega, L) \leq P_{\text{tot}}(\omega) \text{ for all } \omega. \quad (3)$$

According to Equations (1) and (2), this is violated for frequencies $\omega > \sqrt{B/(A \cdot L)}$. Therefore Equation (2) can only be valid for frequencies below this limit, while it has to be modified in the frequency domain above. This is achieved by a redefinition of $\rho(\omega, L)$ as

$$\rho(\omega, L) = \begin{cases} \frac{A \cdot L}{\omega^2}, & \omega < \sqrt{B/(A \cdot L)} \\ \frac{B}{\omega^4}, & \omega \geq \sqrt{B/(A \cdot L)}. \end{cases} \quad (4)$$

For the description of transverse motion of N quadrupoles in a circular accelerator, we start with $N + 1$ independent time series $x_n(t)$, each of them having the same power spectrum $P_n = P_{\text{tot}} = B/\omega^4$.

The coherent part of the motion of the $(n + 1)$ st magnet with respect to the n th one can be calculated by applying a first order lowpass filter with cutoff frequency $\omega_0 = \sqrt{B/(A \cdot L)}$ to the motion $y_n(t)$ of the n th magnet. The resulting power spectrum of this correlated motion in terms of the Laplace variable $s = i\omega$ is

$$\begin{aligned} P_{\text{corr},n+1}(\omega) &= \left| \frac{\omega_0}{s + \omega_0} \right|^2 \cdot P_{\text{tot},n}(\omega) \\ &= \left| \frac{\omega_0}{s + \omega_0} \right|^2 \cdot \frac{B}{\omega^4}. \end{aligned} \quad (5)$$

The corresponding uncorrelated part of motion of the $(n + 1)$ st magnet with respect to the n th one is calculated applying a first order high pass filter with the same cutoff frequency ω_0 to an independent motion signal $x_{n+1}(t)$ with power spectrum P_{n+1} , resulting in

$$P_{\text{uncorr},n+1}(\omega) = \left| \frac{s}{s + \omega_0} \right|^2 \cdot P_{n+1}(\omega). \quad (6)$$

In the low frequency limit, this spectrum reflects the *ATL* rule:

$$\lim_{\omega \rightarrow 0} P_{\text{uncorr},n+1} = \frac{A \cdot L_{n+1}}{\omega^2}, \quad (7)$$

where L_{n+1} is the distance between the n th and the $(n + 1)$ st magnet.

As can be shown, $P_{\text{corr},n+1} + P_{\text{uncorr},n+1} = P_{n+1} = P_{\text{tot}} = B/\omega^4$, while the resulting coherence $|\gamma_{n+1}|$ is calculated as [2]

$$\begin{aligned} |\gamma_{n+1}| &= \sqrt{\frac{P_{\text{corr},n+1}}{P_{\text{uncorr},n+1}}} / \left(1 + \frac{P_{\text{corr},n+1}}{P_{\text{uncorr},n+1}} \right) \\ &= \sqrt{\frac{\omega_0^2}{|s|^2 + \omega_0^2}} \\ &= \sqrt{\frac{B/(A \cdot L)}{|s|^2 + B/(A \cdot L)}}. \end{aligned} \quad (8)$$

*Email: christoph.montag@desy.de

This scheme is repeated for all N magnets, starting with $y_1(t) = x_1(t)$. To reflect the periodicity of the circular accelerator, the motion $y_{N+1}(t)$ of an $(N + 1)$ st magnet is formally calculated from the motion $y_N(t)$ of the N th magnet by application of the corresponding filters, with L_{N+1} being the distance between the N th and the 1st magnet. Obviously, the motion of the $(N + 1)$ st magnet has to be identically the same as the motion of the 1st magnet. Therefore all magnet positions $y_n(t)$ are corrected according to

$$y_n^*(t) = y_n(t) - \frac{y_{N+1}(t) - y_1(t)}{L_{\text{tot},N+1}} \cdot L_{\text{tot},n}. \quad (9)$$

Here $L_{\text{tot},n} = \sum_{k=2}^n L_k$ is the total distance between the 1st and the n th magnet, i. e. $L_{\text{tot},N+1}$ is the circumference of the machine.

To get a more realistic model, the experimentally obtained ground motion data in the HERA tunnel at DESY are fitted as [2]

$$P_{\text{tot}} = \left| \frac{B}{\omega^4} \right| + \left| \frac{4.225 \cdot 10^{-14}}{s^2} \right| \text{m}^2 \cdot \text{Hz} + \left| \frac{7 \cdot 10^{-6}}{s^2 + 9.425 \text{ Hz} \cdot s + 246.74 \text{ Hz}^2} \right|^2 \text{m}^2 \text{Hz}^3 + \left| \frac{7 \cdot 10^{-7}}{s^2 + 0.528 \text{ Hz} \cdot s + 0.774 \text{ Hz}^2} \right|^2 \text{m}^2 \text{Hz}^3. \quad (10)$$

In the low frequency limit this spectrum is dominated by the B/ω^4 term, thus leading to an ATL -like behaviour of the uncorrelated motion. The second term represents some additional cultural noise at high frequency, while the third and the fourth term reflect some 2.5 Hz resonance of the upper earth's crust and the microseismic peak at 1/7 Hz, respectively.

3 RESULTS

The ground motion model described in the previous section has been applied to the vertical motion of the HERA proton ring, using $A = 4 \cdot 10^{-6} \mu\text{m}^2/(\text{m} \cdot \text{sec})$ as obtained on the DESY site [5]. The parameter B is chosen at $B = 3 \cdot 10^{-2} \mu\text{m}^2 \cdot \text{Hz}^3$, resulting in good agreement of the power spectrum (Eq. (10)) as well as the coherence (Eq. (8)) with measured data.

Starting with a perfectly aligned machine, the orbit change is obtained by tracking a single particle, with initial conditions being on the design orbit, while the transverse quadrupole positions $y^*(t)$ are changed from turn to turn. For this tracking, only linear elements are taken into account. The resulting beam motion is monitored at a single point in such a way that the motion of this "monitor" itself is subtracted. This motion signal is normalized to a β -function of $\beta_{\text{mon}} = 1 \text{ m}$. Figure 1 shows the resulting power spectrum, which has been averaged over several samples. As a comparison with measured data (Fig. 2)

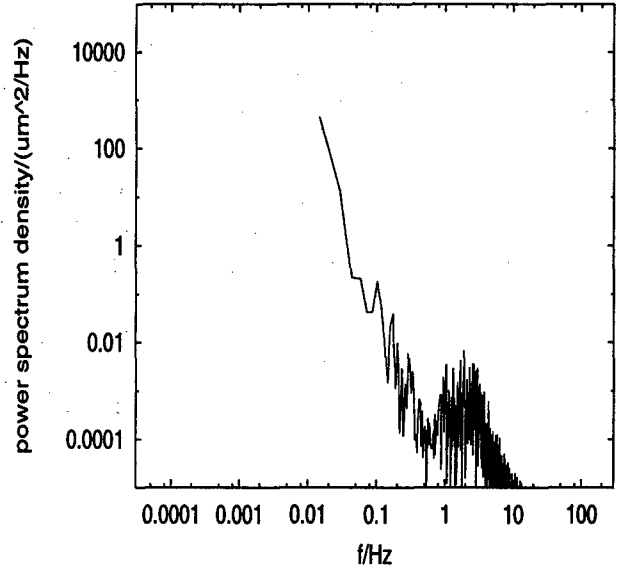


Figure 1: Power spectrum of simulated vertical beam jitter in HERA-p, normalized to $\beta_{\text{mon}} = 1 \text{ m}$.

shows, the simulated spectrum reflects the general properties of observed beam motion. The enhancement of orbit vibration amplitudes around 2.5 Hz is clearly seen in both spectra, but the frequency region in which this enhancement occurs stretches to higher frequencies (up to 50 Hz) in the measured beam motion. This can possibly be explained by mechanical resonances of magnet supports which are not reflected by the ground motion spectrum used for simulation. The same argument also holds for the clearly visible 50 Hz peak caused by either mechanical vibration of some electric equipment or by direct noise on the cables.

In both spectra the microseismic peak at 1/7 Hz almost vanishes due to the large correlation length of this low-frequency motion.

Quantitatively, both power spectra agree within a factor of 10, which corresponds to a factor of $\sqrt{10}$ in amplitude. This difference can possibly be explained by the uncertainties in the parameters A and B .

4 CONCLUSION

As has been shown, simulated ground motion induced beam orbit vibration amplitudes in the circular accelerator HERA agree within a factor of about 3 with measured data. For a more realistic simulation, mechanical resonances of the magnet supports, for example, should be taken into account in order to achieve a better agreement in the frequency region above a few Hertz.

5 ACKNOWLEDGEMENTS

The author is indebted to B. Holzer for many helpful discussions, and to M. Minty for reading the manuscript.

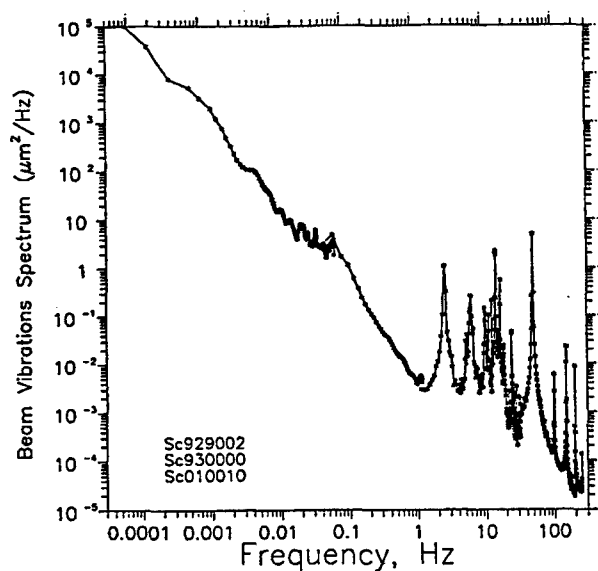


Figure 2: Measured power spectrum of vertical beam motion in HERA-p, normalized to $\beta_{\text{mon}} = 1 \text{ m}$ [6].

6 REFERENCES

- [1] J. Rossbach, Closed-Orbit Distortions of Periodic FODO Lattices Due to Plane Ground Waves, Part. Acc. 23 (1988) pp. 121-132
- [2] C. Montag, Active Stabilization of Mechanical Quadrupole Vibrations in a Linear Collider Test Facility, DESY 97-030
- [3] A. Sery, O. Napoly, Influence of Ground Motion on the Time Evolution of Beams in Linear Colliders, Phys. Rev. E 63 (1996)
- [4] B. Baklakov et al., Investigation of Seismic Vibrations for Linear Collider VLEPP, Sov. Phys. ZhTF., Vol. 63, No. 10 (1993) (in Russian)
- [5] R. Brinkmann, J. Rossbach, Observation of Closed Orbit Drift at HERA Covering 8 Decades of Frequency, Nucl. Instr. Meth. A 350 (1994)
- [6] V. Shiltsev, B. Baklakov, P. Lebedev, C. Montag, J. Rossbach, Measurements of Ground Vibrations and Orbit Motion at HERA, DESY HERA 95-06

NEWS ON BEAM DYNAMICS AT SUPER-ACO*

P. Brunelle[#], J.-C. Besson, L. Cassinari, J.-M. Cousin, J. Darpentigny, G. Flynn, F. Girault,
J.-F. Lamarre, A. Nadji, B. Rieul, M. Sommer

LURE, Université Paris-Sud, Bât. 209A, BP 34, 91898 Orsay Cedex, France

Abstract

The 0.8 GeV storage ring Super-ACO is now fully equipped with undulators. Two new undulators have been recently installed. Their effects on beam dynamics have been studied. In addition, new developments are continuously in progress in order to optimize the beam performances for the users. A beam position feedback system is now operational. A 500 MHz RF cavity allows to reduce the bunch length and increase the FEL gain. A feedback system on betatron tunes has been tested using a very precise detection. Some experiments on beam dynamics have been performed in order to understand and improve beam lifetime. The variation of tunes with momentum has been measured, for several configurations of undulators (up to 6 undulators closed), and compared with computed results.

1. INTRODUCTION

Since three years, the LURE machine group has developed new equipments for the Super-ACO storage ring. A 500 MHz cavity is now operational and used for Free Electron Laser (FEL) operation in addition to the 100 MHz cavity. Two undulators have been installed in the two last free straight sections of the ring. A feedback system on beam position is fully tested and will be used routinely this year. A feedback system on horizontal and vertical tunes has been developed in order to compensate for tune variation introduced by field variations in undulators. In parallel, studies on beam dynamics have been performed in order to evaluate undulator field tolerances and to improve the optical model of the machine.

2. THE 500 MHz HARMONIC CAVITY

A new active 500 MHz fifth harmonic RF cavity was installed on Super-ACO in January 1997 primarily for the purpose of reducing bunch length for FEL and time-resolved synchrotron radiation experiments [1]. To date bunch length reduction factors up to 3.5 have been obtained but many single-bunch coherent beam instability phenomena are observed with very short bunches [2]. Nevertheless, significant improvements in FEL performance have been obtained [3].

In the future we will attempt to operate the harmonic RF system at higher power levels (25 kW rather than 14 kW currently) and observe the effect on beam stability and bunch length. In addition we will attempt to use the cavity in a bunch-lengthening mode in the hope of improving beam lifetime in normal operation. This will require operating the cavity at very low field levels (roughly 1/5 of the principal RF voltage) of about 34 kV. In this configuration a direct RF feedback system will be needed to avoid type II Robinson instability. Tests of such a system are currently underway both on the principal and harmonic RF systems.

3. INSERTION DEVICES

The two last undulators installed on Super-ACO are SU8 (a planar symmetric hybrid undulator made by Danfysik) and OPHÉLIE (an electromagnetic crossed overlapped undulator). The design, construction and commissioning of OPHÉLIE are described in [4]. The SU8 characteristics are $B_{\max} = 0.48$ T, $N \times \lambda = 21.5 \times 100$ mm with a minimum gap of 39 mm. This undulator has no field integral default at any gaps. The transverse peak field homogeneity was limited to 50 T.m^{-2} in order to avoid strong non linear effects. An automatic global compensation of its strong focusing effect ($\Delta v_{z\max} = 2.8 \cdot 10^{-2}$) is made at each gap using two quadrupole families. An increase of the vertical chromaticity, due to the beta-function beat, was measured at minimum gap, with a 10 % reduction of the beam lifetime [5].

4. BEAM POSITION FEEDBACK

A fast global feedback system is used on Super-ACO in order to improve beam stability [6]. The feedback uses all the 16 machine BPMs and 8 correctors in each plane to correct the orbit at a 16 kHz rate. The goal is to provide a correction from DC to 100 Hz, both in horizontal (x) and vertical (z) plane. The BPM signal processors are Bergoz developed heterodyne receivers working at 200 MHz (twice the RF frequency) with a resolution of $0.5 \mu\text{m}/\sqrt{\text{Hz}}$. The fast corrections are computed by 8 DSP boards which acquire the x and z signals from the 16 BPM processors (2 BPMs per DSP). The 8 DSP boards are linked via a fast high rate digital serial link and form a ring controlled by a DSP master board. It takes 60 μs to complete the whole acquisition, transmission, checking and calculation cycle for the 32 data (16 x and 16 z).

*Work supported by CNRS, CEA and MENESR.

[#] Email : brunelle@lure.u-psud.fr.

The correction kicks are produced by 8 coils in each plane, located inside quadrupole magnets. They are powered by current-controlled wideband power amplifiers.

Two correction algorithms have been tested, a harmonic based method, and a direct inversion of the response matrix using the SVD method.

The achieved bandwidth of the feedback is 40 Hz in the horizontal plane, and 150 Hz in the vertical plane. Additional tests are being carried out in order to have the feedback operational during user sessions.

5. BETATRON TUNE FEEDBACK

Slow Feedback : This system uses a data processing microcontroller to analyze the video signal output of a spectrum analyzer. The feedback is made by dialog with the quadrupole power supply control system [7] (Fig. 1). The correction is made every 1.2 s with a resolution of $\pm 10^{-4}$. A typical response is shown in figure 2 where the feedback compensates the tune shift due to the gap variation of the SU3 undulator of Super-ACO.

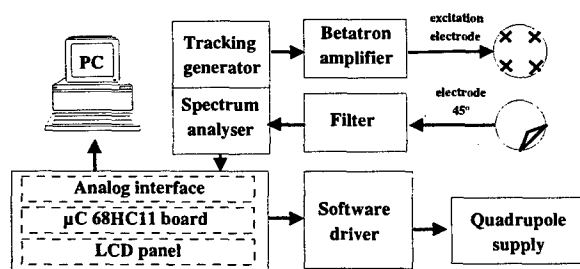


Fig. 1. Slow feedback system simplified schematic.

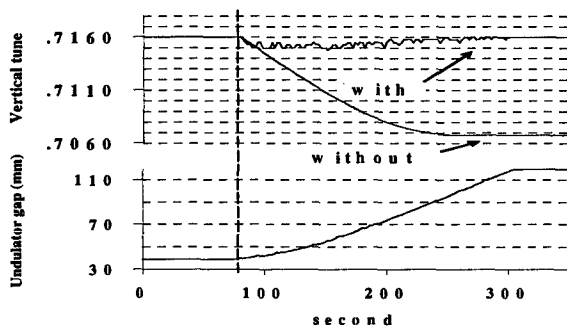


Fig. 2. Slow feedback system typical response.

Fast feedback : Two fast feedback systems are currently being developed. The first is based on digital analysis of the signal using a DSP while the second uses a phase locked loop.

Digital system (DSP) [8] : A TMS320C6201 DSP is used to determine the betatron tunes by FHT of a beam electrode signal. A tune resolution of 10^{-4} (416 Hz) is obtained by acquiring 32 000 samples. With a processing

power of 1 600 Mips the DSP computes a spectrum every 10 ms, with the possibility of speeding up to every 1 ms (Fig. 3). This system is able to operate with low stored beam current or with a low excitation level.

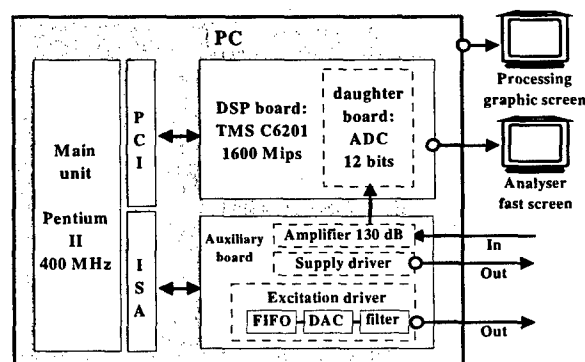


Fig. 3. Fast digital feedback system simplified schematic.

Analog system (PLL) : The measurement presented here uses an analogy with a resonant electronic circuit (Fig. 4).

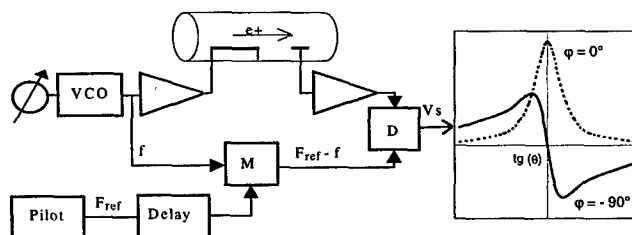


Fig. 4. Fast analog feedback system simplified schematic.

The signal delivered by the generator (VCO) at the frequency f is sent simultaneously to the beam excitation amplifier and to a mixer (M) which transposes this frequency to the value $F_{ref} - f$. A synchronous demodulator (D) compares this voltage to the detected signal and delivers a signal proportional to $V_s = \cos \theta \cos [\phi - \theta]$. In this expression θ represents the difference in phase with regard to the resonance and ϕ is given by the sum of the phase shifts and delays of the various loop elements. If $\phi = -90^\circ$ and is independent of f one obtains a phase locked loop by using the output voltage, V_s to control the generator frequency. The generator is then locked to the betatron frequency. On DCI [9] the precision obtained is 10^{-4} and the response time is 1 ms. The system currently under development acts on the two betatron tunes independently and is driven by a microcontroller. The tune information obtained from this system in either digital or analog form will be used to directly control the storage ring magnetic element power supplies thus providing the feedback.

6. TUNE VARIATION WITH MOMENTUM

On Super-ACO, for large momentum deviations ($dp/p > 0.3\%$), tune variations are no longer linear and take into account non linear effects due to higher order field components and undulator fields. The aim of this study was double : compare the tune variation computed with the BETA code [10] to the one measured on the ring when undulators are all open, and measure the effect of undulators in order to understand energy acceptance limitation. The experimental tune variation [11] was measured using RF frequency variations up to ± 30 kHz ($dp/p = \pm 2\%$). The higher order field components of magnetic elements have been deduced from magnetic measurements and introduced in the BETA code as thin lenses. Figure 5 shows that the maximum stable dp/p values are larger than the RF energy acceptance ($\pm 1.8\%$). The computed v_x variation is rather different from the experimental one for $dp/p > 0$ while the agreement is quite good for v_z variation. A good agreement for v_x can be obtained by adjusting the decapolar component generated by sextupoles.

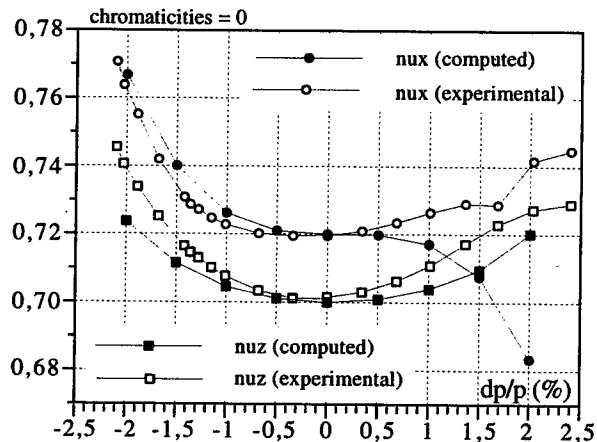


Fig. 5. Tune variation with momentum (open undulators).

Figure 6 shows the measured effect of the first four undulators (SU2, SU3, SU6, SU7) closed at nominal gap, in the positive chromaticity operation mode. The non linearities occur essentially in the vertical plane (undulator field plane) and reduce the maximum stable dp/p values (beam losses have been observed near the $3v_z = 5$ resonance). The measurements have been performed for two optics with the same tunes : a 4 fold symmetry optic and a quasi 8 fold symmetry obtained with equal β -functions in the 8 straight sections. The symmetrization reduces the undulator effect and leads to an increase of beam lifetime because the maximum stable dp/p values are larger. Tune variation versus momentum introduced by the two last undulators (SU5 and SU8) was found to be negligible.

Other tests have shown that an increase of v_z leads to a beam lifetime reduction when the Touschek effect is dominant. In fact, when v_z is increased, the effect of the $3v_z = 5$ resonance does not occur any more for large negative dp/p values. But the $4v_z = 7$ resonance, excited by undulators, becomes a limitation for positive dp/p values.

All these experimental results show the influence of the tune variation with momentum in the Touschek lifetime behaviour.

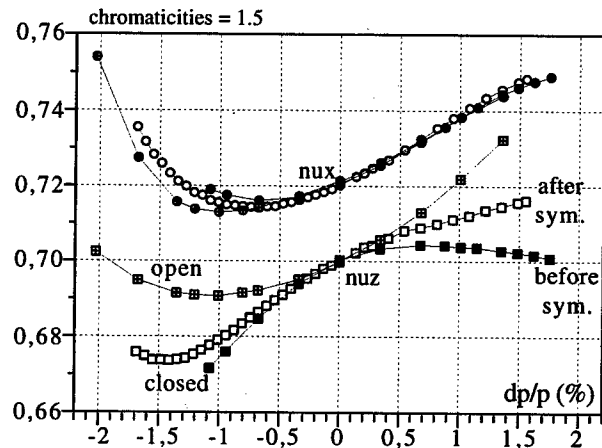


Fig. 6. Effect of undulators.

7. ACKNOWLEDGEMENTS

It is a pleasure to thank all the members of the technical and operation staff of Super-ACO for their collaboration.

8. REFERENCES

- [1] G. Flynn et al., EPAC 98, pp. 1767-1769.
- [2] G. Flynn et al., EPAC 98, pp. 954-956.
- [3] D. Nutarelli et al., EPAC 98, pp. 670-672.
- [4] M. Corlier et al., this conference.
- [5] P. Brunelle, internal report, Super-ACO/97-05.
- [6] L. Cassinari et al., this conference.
- [7] J.-M. Cousin et al., internal reports, RT/99-01, Super-ACO/99-03.
- [8] J.-M. Cousin et al., internal report, RT/99-03.
- [9] J.-F. Lamarre and H. Zyngier, inter. rep. NI/96-21.
- [10] J. Payet, BETA-LNS code.
- [11] P. Brunelle, internal report, Super-ACO/99-04.

NONLINEAR DIAGNOSTICS USING AC DIPOLES *

S. Peggs, BNL, Upton, NY

There are three goals in the accurate nonlinear diagnosis of a storage ring. First, the beam must be moved to amplitudes many times the natural beam size. Second, strong and long lasting signals must be generated. Third, the measurement technique should be non-destructive.

Conventionally, a single turn kick moves the beam to large amplitudes, and turn-by-turn data are recorded from multiple beam position monitors (BPMs) [1-6]. Unfortunately, tune spread across the beam causes the center of charge beam signal to “decohere” on a time scale often less than 100 turns. Filamentation also permanently destroys the beam emittance (in a hadron ring). Thus, the “strong single turn kick” technique successfully achieves only one out of the three goals. AC dipole techniques can achieve all three. Adiabatically excited AC dipoles slowly move the beam out to large amplitudes. The coherent signals then recorded last arbitrarily long. The beam maintains its original emittance if the AC dipoles are also turned off adiabatically, ready for further use.

The AGS already uses an *RF dipole* to accelerate polarized proton beams through depolarizing resonances with minimal polarization loss [7]. Similar AC dipoles will be installed in the horizontal and vertical planes of both rings in RHIC [8]. The RHIC AC dipoles will also be used as spin flippers, and to measure linear optical functions [9].

1 LINEAR MOTION

Horizontal motion is described using complex phasors

$$z \equiv x' + ix = a e^{i\phi} \quad (1)$$

so that the unperturbed one turn motion is just

$$z_{t+1} = R z_t \quad (2)$$

where $R = \exp(i 2\pi Q_X)$. Here Q_X is the betatron tune, and the normalized coordinates x and x' both have the dimensions of length. An AC dipole just after the reference point gives a real normalized angular kick on turn t of

$$\Delta z_t = \Delta x' = \delta \cos(2\pi Q_D t + \psi_0) \quad (3)$$

where Q_D is the drive tune and ψ_0 is the initial phase. The AC dipole strength is $\delta = (BL/(B\rho))\beta_D$, where BL is the integrated field amplitude, $(B\rho)$ is the rigidity, and β_D is the Twiss function at the dipole.

If $z = z_0$ just before the first dipole kick, then the net displacement phasor on turn T is

$$z_T = R^T z_0 + (R^T \Delta z_0 + R^{T-1} \Delta z_1 + \dots + R^1 \Delta z_{T-1}) \quad (4)$$

* Work supported by the DoE.

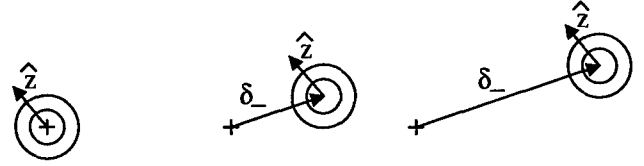


Figure 1: Adiabatic excitation of an AC dipole, in the rotating frame. The circles represent single particle motion.

The *exact* general solution for linear motion is [10]

$$z_T = \hat{z} e^{i 2\pi Q_X T} + \delta_- e^{i 2\pi Q_D T} - \delta_+ e^{-i 2\pi Q_D T} \quad (5)$$

where $\hat{z} = z_0 - \delta_- + \delta_+$ is a constant given by the initial conditions, and the complex AC dipole strengths are

$$\begin{aligned} \delta_- &= \frac{\delta}{4} \frac{\exp(-i[\pi Q_- - \psi_0])}{\sin(\pi Q_-)} \\ \delta_+ &= \frac{\delta}{4} \frac{\exp(i[\pi Q_+ - \psi_0])}{\sin(\pi Q_+)} \end{aligned} \quad (6)$$

where $Q_- = Q_D - Q_X$ and $Q_+ = Q_D + Q_X$.

The *oscillating closed orbit* is defined as that orbit which exactly repeats itself after one modulation period. The solution on turn T is obtained by putting $\hat{z} = 0$, so that

$$z_{CO} = \delta_- e^{i 2\pi Q_D T} - \delta_+ e^{-i 2\pi Q_D T} \quad (7)$$

generally following a tilted ellipse, *not* a circle, in normalized phase space. The semi-minor and semi-major axes are $||\delta_-| - |\delta_+||$ and $|\delta_-| + |\delta_+|$ long. In practice the aspect ratio of the ellipse is close to 1 when the AC dipole is driven at a tune close to the fractional betatron tune ($Q_- \approx 0$). When $|\delta_-| \gg |\delta_+|$ the approximate motion is

$$z_T \approx \hat{z} e^{i 2\pi Q_X T} + \delta_- e^{i 2\pi Q_D T} \quad (8)$$

Motion in the *rotating frame*, which rotates with the AC dipole drive at $2\pi Q_D$ per turn, is denoted by over-bars. Assuming the previous approximation to be accurate,

$$\bar{z}_T = \delta_- + \hat{z} e^{-i 2\pi Q_- T} \quad (9)$$

That is, a test particle slowly circulates the vector δ_- at a radius of constant length $|\hat{z}|$, as illustrated in Fig. 1.

When a bunch is considered, a distribution of \hat{z} values must be used. A smoothly distributed beam has $\langle \hat{z} \rangle = 0$ and $\langle \hat{z}^2 \rangle = 2\beta\epsilon_u$ where $\langle \rangle$ represents a bunch average, and ϵ_u is the unnormalized root mean square emittance. The center of charge motion in the non-rotating frame is just

$$\langle z_T \rangle = \delta_- e^{i 2\pi Q_D T} \quad (10)$$

Thus, the coherent bunch response to an adiabatically driven AC dipole has a constant amplitude

$$a_{COH} = |\delta_-| = \frac{1}{4} \left| \frac{\delta}{\sin(\pi Q_-)} \right| \quad (11)$$

This has been quantitatively confirmed in the AGS [7].

Any bunch tune spread (due to non-zero chromaticity or nonlinear detuning) trivially modifies the rate of advance around the δ_- vector for different particles. Less trivially, the tune spread also modifies δ_- , which is a function of Q_- (see Eqn. 6). This is not a practical problem if Q_D is sufficiently far outside the bunch tune spectrum.

2 SHEAR MOTION - DETUNING

The total *approximate* one turn difference map is

$$\Delta J = \frac{\delta}{\sqrt{\beta_D}} \sqrt{2J} \cos(2\pi Q_D t) \cos(\phi) \quad (12)$$

$$\Delta \phi = -\frac{\delta}{\sqrt{\beta_D}} \frac{1}{\sqrt{2J}} \cos(2\pi Q_D t) \sin(\phi) + 2\pi(Q_{X0} + \alpha J) \quad (13)$$

where ψ_0 is set to 0, and the action $J = a^2/2\beta_D$ has the dimensions of length. Detuning with action is present, proportional to αJ , since (if $\delta = 0$)

$$Q_X(J) \equiv \langle \Delta \phi \rangle / 2\pi = Q_{X0} + \alpha J \quad (14)$$

where $\langle \rangle$ represents a time average. A *one turn discrete Hamiltonian* H_1 concisely describes this motion, through

$$\begin{pmatrix} \Delta J \\ \Delta \phi \end{pmatrix} = \begin{pmatrix} -\partial H_1 / \partial \phi \\ \partial H_1 / \partial J \end{pmatrix} \quad (15)$$

Since H_1 represents a *difference* map, and not continuous *differential* motion, it is not (necessarily) even approximately a constant of the motion. In the case at hand

$$H_1 = 2\pi(Q_{X0}J + \frac{\alpha}{2}J^2) - \frac{\sqrt{2}\delta}{\sqrt{\beta_D}} J^{1/2} \cos(2\pi Q_D t) \sin(\phi) \quad (16)$$

This Hamiltonian is marred by its time dependence.

A canonical transformation to the rotating frame is achieved by applying the generating function

$$W(\bar{J}, \phi, t) = \bar{J}\phi - 2\pi Q_D t \bar{J} \quad (17)$$

New and old action-angle coordinates are related through

$$\begin{aligned} J &\equiv \partial W / \partial \phi = \bar{J} \\ \bar{\phi} &\equiv \partial W / \partial \bar{J} = \phi - 2\pi Q_D t \end{aligned} \quad (18)$$

If one turn motion is small ($Q_- \approx 0$), the transformation $\bar{H}_1 \equiv H_1 + \partial W / \partial t$ (averaged over many turns) yields

$$\bar{H}_1 = 2\pi \left(\frac{\alpha}{2} \bar{J}^2 - Q_- \bar{J} \right) - \frac{\delta}{\sqrt{2\beta_D}} \bar{J}^{1/2} \sin(\bar{\phi}) \quad (19)$$

\bar{H}_1 is independent of time, and is a good approximation to a constant of the motion. The fixed points are given by

$$\bar{\phi}_{FP} = \pm \frac{\pi}{2} \quad (20)$$

$$0 = 2\pi(\alpha \bar{J}_{FP} - Q_-) \mp \frac{\delta}{2\sqrt{2\beta_D}} \frac{1}{\bar{J}_{FP}^{1/2}}$$

In general there is either one stable fixed point, or one unstable and two stable fixed points [7]. When detuning is absent ($\alpha = 0$) the fixed point amplitude is

$$a_{FP} = \frac{1}{4\pi} \left| \frac{\delta}{Q_-} \right| \quad (21)$$

agreeing with Eqn. 11 when Q_- is small!

3 NONLINEAR MOTION IN 2-D

The action-angle time series $(J_x, \phi_x, J_y, \phi_y)_t$ is derived from turn-by-turn data $(x_1, x_2, y_1, y_2)_t$ recorded at 2 horizontal and 2 vertical BPMs. This requires the empirical adjustment of the β function ratio of each BPM pair, of the phase advance of each pair, and of the closed orbit error at every BPM, in a process which also corrects for the elliptical motion of the oscillating closed orbit [1, 3, 6].

The general 2-D one turn discrete Hamiltonian is

$$\begin{aligned} H_1 &= 2\pi Q_{X0} J_x + 2\pi Q_{Y0} J_y \\ &+ \sum_{ijkl} V_{ijkl} J_x^{i/2} J_y^{j/2} \sin(k\phi_x + l\phi_y + \phi_{ijkl}) \end{aligned} \quad (22)$$

where the appropriate set of indices $(ijkl)$ depends on the dominant nonlinearities [2]. Only in the simplest of models can V_{ijkl} and ϕ_{ijkl} be predicted analytically. The horizontal action time series is then

$$J_x(t) = J_{x0} - \sum_{ijkl} \frac{k V_{ijkl} J_{x0}^{i/2} J_{y0}^{j/2}}{2 \sin[\pi Q_{kl}]} \sin(2\pi Q_{kl} t + \phi_{0ijkl}) \quad (23)$$

A single harmonic dominates if $Q_{kl} = kQ_X + lQ_Y$ approaches an integer for some (k, l) pair. With coherent bunch motion, Q_X and Q_Y represent the drive tunes of simultaneous horizontal and vertical AC dipoles, and J_{x0} and J_{y0} represent the average (fixed point) actions.

The Discrete Fourier Transform (DFT) of a long action time series generates *action harmonic coefficients*

$$D_{xkl} = \frac{-k}{2 \sin[\pi Q_{kl}]} \sum_{ij} V_{ijkl} J_{x0}^{i/2} J_{y0}^{j/2} e^{i\phi_{0ijkl}} \quad (24)$$

The value of a coefficient (D_{xkl} or D_{ykl}) depends on the J_{x0} and J_{y0} values used in that measurement. Multiple measurements on a grid of (J_{x0}, J_{y0}) values can be used to recover a complete set of V_{ijkl} and ϕ_{0ijkl} values.

Sometimes the motion is summarized by *smear* statistics [2]. The horizontal smear s_{xx} is given by

$$s_{xx}^2 \equiv \frac{\langle a_x a_x \rangle}{\langle a_x \rangle \langle a_x \rangle} - 1 = \sum_{ijkl} \frac{k^2 V_{ijkl}^2 a_{x0}^{2i-4} a_{y0}^{2j}}{2^{i+j+3} \sin^2[\pi Q_{kl}]} \quad (25)$$

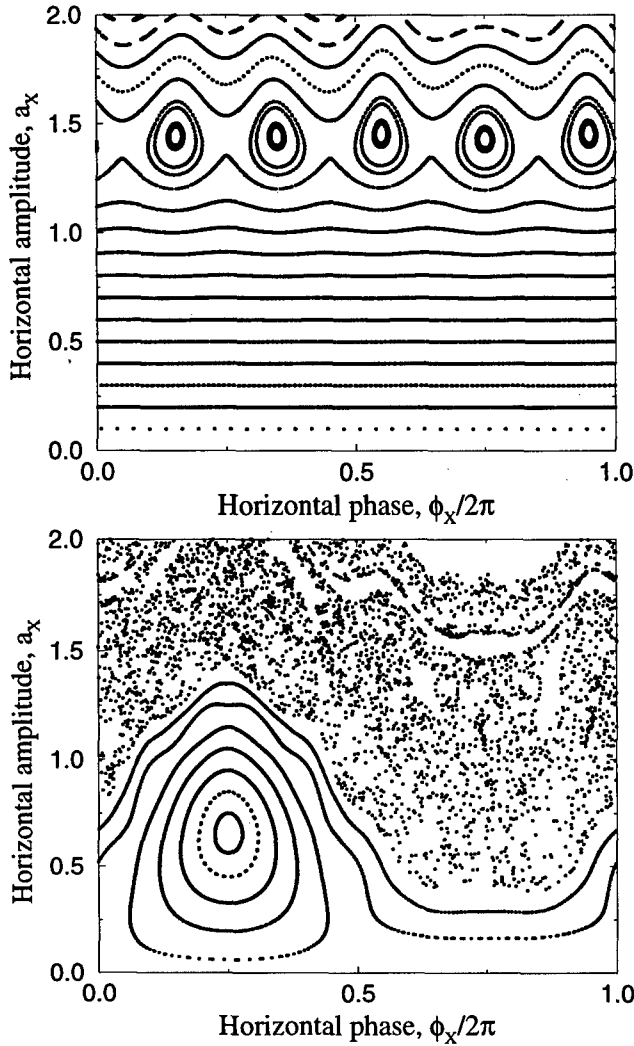


Figure 2: 1-D motion near a decapole driven resonance with an AC dipole OFF (TOP) or ON (BOTTOM).

(assuming $\beta_x = \beta_y = 1$). Similar expressions exist for the vertical and correlation smears, s_{yy} and s_{xy} . Predicted and measured smears agree well in controlled experiments with a small number of dominant nonlinearities [3, 4].

4 A NUMERICAL EXPERIMENT

Figure 2 illustrates a simple 1-D numerical experiment. Detuning (from $Q_x = 0.591$ to 0.609 between $a_x = 0$ and 2.0) is driven by three octupoles, arranged to minimize octupole driven resonances [6]. A single decapole drives the $Q_x = 3/5$ resonance, generating a chain of 5 islands at $a_{RES} \approx 1.4$ in the TOP figure. The AC dipole tune $Q_D = 59/101 \approx 0.584$ allows a plotting period of 101 turns to be used in the BOTTOM figure. A coherent AC dipole ON signal is simulated by launching a single particle at the fixed point in the BOTTOM figure, to generate a turn-by-turn "BPM" time series. The goal is to show that this time series closely resembles that obtained with the same launch coordinates, but with the AC dipole OFF.

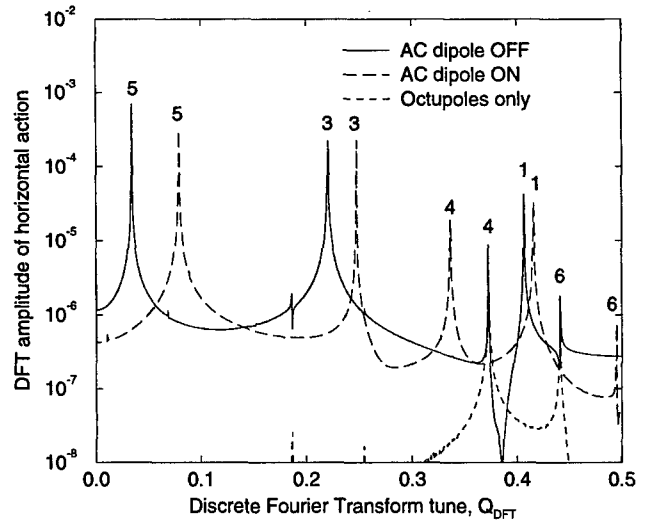


Figure 3: Discrete Fourier Transforms of the horizontal action of a test particle in the numerical experiment.

Figure 3 shows action DFTs with the AC dipole OFF and ON. The harmonic peaks shift because $Q_x \approx 0.593(0.584)$ in the OFF (ON) case. Nonetheless, the D_{x50} and D_{x30} values derived from both data sets are closely consistent, after correcting for the $1/\sin[\pi Q_{k0}]$ dependence in Eqn. 24. This implies that single particle Hamiltonian values V_{ijkl} and ϕ_{0ijkl} can indeed be derived from measurements of coherent motion driven by AC dipoles.

5 ACKNOWLEDGMENTS

Many thanks to Mei Bai, Rhianna Bianco, Wolfram Fischer, Todd Satogata, and Chunmei Tang.

6 REFERENCES

- [1] A. Chao et al, PRL 61 (1987) 2752; T. Chen et al, PRL 68 (1992) 33; T. Satogata et al, PRL 68 (1992) 1838
- [2] S. Peggs, Proc. 2nd ICFA workshop, CERN 88-04, and SSC-175 (1988)
- [3] N. Merminga, Ph.D. Thesis, U. Michigan (1989)
- [4] M.Y. Li, Ph.D. Thesis, U. Houston (1990)
- [5] S.Y. Lee et al, PRL 67 (1991) 3768; D.D. Caussyn et al, PRA 46 (1992) 7942; W. Fischer, Dissertation, U. Hamburg (1995); W. Fischer et al, PRE 55 (1997) 3507
- [6] T. Satogata, Ph.D. Thesis, Northwestern U. (1993)
- [7] M. Bai et al, PRE 56 (1997) 6002; M. Bai, Ph.D. Thesis, U. Indiana (1999); M. Bai et al, Beam manipulation with an RF dipole, these proceedings (1999)
- [8] B. Parker et al, Design of an AC dipole for use in RHIC, these proceedings (1999)
- [9] P. Castro-Garcia, Doctoral Thesis, U. de Valencia (1996)
- [10] S. Peggs and C. Tang, RHIC/AP/159, Upton, (1998)

BNL-BUILT LHC MAGNET ERROR IMPACT ANALYSIS AND COMPENSATION

V. Ptitsin*, S. Tepikian, J. Wei, BNL, Upton, NY

Abstract

Superconducting magnets built at the Brookhaven National Laboratory will be installed in both the Insertion Region IP2 and IP8, and the RF Region of the Large Hadron Collider (LHC). In particular, field quality of these IR dipoles will become important during LHC heavy-ion operation when the β^* at IP2 is reduced to 0.5 meters. This paper studies the impact of the magnetic errors in BNL-built magnets on LHC performance at injection and collision, both for proton and heavy-ion operation. Methods and schemes for error compensation are considered including optimization of magnet orientation and compensation using local IR correctors.

1 INTRODUCTION

An important part of the USA contribution to the Large Hadron Collider (LHC) project is the construction of superconducting magnets for the interaction and RF regions of the future collider. The half of the total number of IR triplet quadrupole magnets will be produced by FNAL which is also responsible for the assembling another half of IR quads produced by KEK into cryostat. The BNL constructs superconducting dipole magnets for LHC experimental and RF insertions.

In the previous paper[1] we analysed the impact of magnet field errors in the IR quadrupoles and dipoles on LHC collision performance for proton collisions at top energy. In this article the accent is made on the evaluation of the impact coming from the errors of BNL-made dipoles both at collision and injection and on the case of heavy ion collision lattice with additional low-beta interaction point at IP2 in comparison with the proton collision lattice. The basic parameters of proton and ion lattices used at the analysis are listed in Table 1.

Table 1: Lattice parameters.

Quantity	p inj.	p coll.	ion coll.
E [GeV]	450	7000	7000 per charge
ν_x/ν_y	63.28/59.31	63.31/59.32	63.31/59.32
ξ_x/ξ_y	2/2	2/2	2/2
ϵ_N [m·r]	3.75×10^{-6}	3.75×10^{-6}	1.5×10^{-6}
σ_p	4.7×10^{-4}	1.1×10^{-4}	1.14×10^{-4}

Two beam dynamic characteristic quantities are used to evaluate the error impact: the dynamic aperture (DA) and the tune footprint. The target values for the LHC are more than 12σ of average DA, more than 10σ minimum DA and less than 10^{-3} tune spread.

* Email: vadimp@bnl.gov

2 TRACKING SETUP

Fortran version of TEAPOT code was used for tracking studies. We restricted our investigation to 1000 turn tracking. Previous study indicates that 10^5 turn tracking further reduces DA by $0.5 - 1\sigma$.

Ten seeds of magnet errors were created based on the error tables for all studied magnets (the errors of warm D1 dipoles at IR1 and IR5 also were included). We excluded from the consideration only skew quadrupole component of the errors assuming that the coupling is completely compensated.

The working point at collision ($\nu_x = 63.31, \nu_y = 59.32$) and injection ($\nu_x = 63.28, \nu_y = 59.31$) are both close enough to the third integer resonance condition. Thus to avoid the decrease in dynamic aperture the machine has to be retuned to the nominal working point after the magnet errors are introduced to the lattice. Also the arc sextupoles are used to correct the chromaticity to the nominal values of 2.0 in both X and Y planes.

The tracking is 6 dimensional with the RF system operating at nominal values of RF voltage. The particles to track are taken with the initial 2.5σ energy deviation.

3 DIPOLE ERROR ANALYSIS

BNL superconducting dipoles include interaction region beam separation magnets D1 for IR2 and IR8, interaction region magnets D2 for all 4 IRs, and RF insertion magnets D3A, D3B, D4A, D4B (Fig.1). The magnet design is based on the RHIC arc dipole. However, due to the specific LHC requirements the magnets D2, D4A, D4B utilize 2-in-1 design with two magnet apertures in one yoke. Examples of 1-in-1 and 2-in-1 magnet designs from BNL-built dipoles are shown in Figure 2.

The expected dipole error sets for D1 and D3 magnets at injection and collision used at the analysis are shown in Tables 2, 3 where b_2, a_2 present quadrupole components. The twin aperture magnets (D2, D4) have slightly different the error set with $b_3 = -5.7$ at injection and $b_3 = -0.48$ at collision.

The big value of b_3 at injection is caused by the effect of persistent current. In comparison with RHIC case this effect is relatively large. The magnet design was optimized initially for RHIC but the current of RHIC magnet at injection is about 600 A while the magnets for LHC would use the current as low as 300 A which leads to increasing persistent sextupole component. The analysis showed the persistent b_3 at the arc LHC dipoles is of the same value as shown in Table 4. The contribution of the the RF region dipoles (D3, D4) to the chromaticity variation is small in comparison with the total contribution from the large

Table 2: Expected D1 & D3 errors at collision. $R_0 = 17$ mm

n	Normal			Skew		
	$\langle b_n \rangle$	$d(b_n)$	$\sigma(b_n)$	$\langle a_n \rangle$	$d(a_n)$	$\sigma(a_n)$
Body	[unit]					
2	0.07	0.54	0.19	0.43	2.4	1.1
3	-1.5	1.6	0.84	-0.12	0.27	0.10
4	0.00	0.08	0.03	0.01	0.34	0.13
5	0.11	0.17	0.09	-0.01	0.04	0.01
7	0.11	0.02	0.01	-0.00	0.01	0.00
9	0.00	0.01	0.00	-0.00	0.00	0.00
LE	[unit-m]	(Length=0.73 m)				
2	-0.3	1.5	0.7	-1.0	2.9	1.2
3	10.3	1.4	0.5	-4.6	0.5	0.2
5	-0.1	0.2	0.1	0.5	0.1	0.0
RE	[unit-m]	(Length=0.73 m)				
2	0.2	1.2	0.5	0.6	3.1	1.3
3	2.8	1.2	0.5	0.1	0.5	0.2

amount of arc dipole magnets and does not require special corrections. Furthermore, no noticeable impact was found from the saturation of b_3 component at collision.

Compensation measures have been taken to diminish the effect of the errors of interaction region dipole D1 on beam dynamics. They include:

1. Magnet Orientation Optimization: D1 lead end is oriented towards the interaction points where a b_3 corrector is located.
2. Body-End Compensation for the systematic b_3 :

$$b_3(\text{Body}) = -0.095 B_3(\text{LE}) - 0.116 B_3(\text{RE}) = -1.3[\text{u}]$$

Tracking studies were performed for the proton LHC lattice both at injection and collision with the whole set of errors from dipole error tables. The studies indicated no

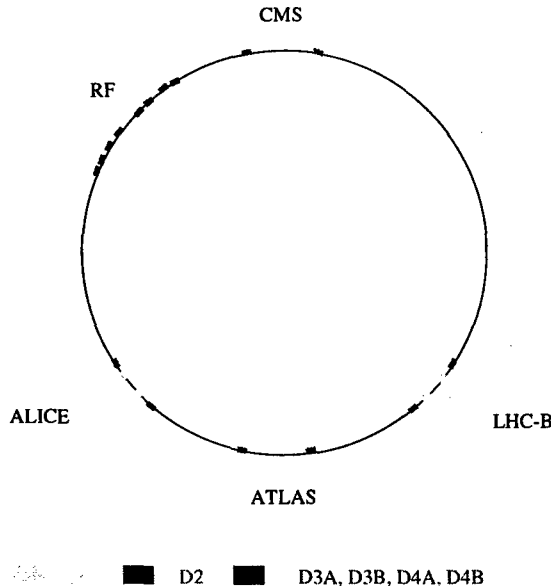


Figure 1: BNL-made dipoles at LHC ring

 Table 3: Expected D1 & D3 errors at injection. $R_0 = 17$ mm

n	Normal			Skew		
	$\langle b_n \rangle$	$d(b_n)$	$\sigma(b_n)$	$\langle a_n \rangle$	$d(a_n)$	$\sigma(a_n)$
Body	[unit]					
2	0.08	0.51	0.19	0.14	2.8	1.1
3	-6.3	2.5	0.92	-0.03	0.24	0.09
4	-0.02	0.07	0.03	0.04	0.37	0.13
5	0.14	0.18	0.09	-0.01	0.04	0.01
7	-0.04	0.02	0.01	0.0	0.01	0.0
9	0.01	0.01	0.0	0.0	0.0	0.0
LE	[unit-m]	(Length=0.73 m)				
2	-0.2	1.5	0.7	-1.6	2.9	1.1
3	8.7	1.3	0.5	-4.6	0.5	0.2
5	-0.1	0.2	0.1	0.5	0.1	0.0
RE	[unit-m]	(Length=0.73 m)				
2	0.2	1.3	0.5	-0.2	3.1	1.1
3	1.8	1.1	0.5	0.1	0.5	0.2

Table 4: Persistent current contribution from D3,D4 dipoles versus arc dipoles

Quantity	Arc dipoles	D3,D4
Persistent b_3 [u]	-9	-6
Dispersion [m]	1.5	0.1
Chromaticity	500	0.03

noticeable impact of the dipole errors on the beam dynamics. If only BNL dipole errors are taken into the account the resulting dynamic aperture is beyond the physical aperture. Figure 3 shows no difference in 11σ footprint at the injection energy for the cases with and without the BNL dipole errors.

4 HEAVY-ION OPERATION

Heavy-ion collision lattice uses low- β^* IP2 in addition to low- β^* collisions at IP1 and IP5. This produces large values of β functions in corresponding IR triplet quadrupoles and D1 dipoles. Furthermore, all interaction regions utilize orbit separation and crossing angle schemes. Such schemes lead to large orbit excursion inside IR quads and dipoles thus shifting the beam to the field regions with larger nonlinearity. The interaction region configuration for ion lattice used at the tracking studies is shown in Table 5. The worst case is considered with the crossing angle of $\pm 150 \mu\text{rad}$ at each low- β interaction points.

The tracking used the two possible schemes of IR

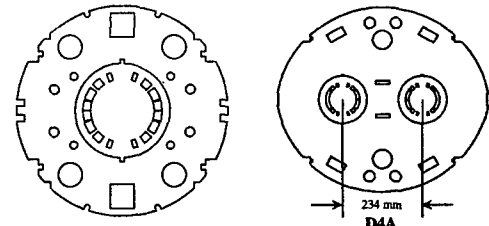


Figure 2: Magnet body cross section of BNL-built D1 and D4A.

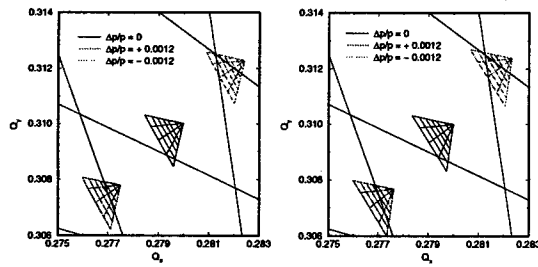


Figure 3: 11σ tune footprints with and without the errors in D1,D2,D3,D4 magnets.

Table 5: Interaction region configuration parameters

	IP1	IP2	IP5	IP8
sep. [mm]	0	0	0	1.5 h
angle[μ rad]	± 150 v	± 150 v	± 150 h	± 100 v
β_x^*, β_y^* [m]	0.5,0.5	0.5,0.5	0.5,0.5	33,33

quadrupole arrangement. In the *unmixed* scheme KEK-built magnets are installed at IR1, IR2 and FNAL-built magnets at IR5, IR8. In the *mixed* scheme the each interaction region contains both KEK-built (Q1,Q3) and FNAL-built (Q2A,Q2B) quadrupoles. The most tracking has been done for the mixed scheme. Table 6 presents a summary of the tracking results.

Table 6: Effects of MQX and dipole errors in terms of 10^3 -turn 6D DA.

Case	DA (σ_{xy})	Min. DA
Unmixed case:		
Full error	8.3 ± 1.8	$5\sigma_{xy}$
Errors at IR2 only	9.7 ± 2.4	$6\sigma_{xy}$
Quad error at IR2 only	11.8 ± 3.7	$6\sigma_{xy}$
Mixed case:		
Full error	8.5 ± 1.5	$5\sigma_{xy}$
Full error, no cross.angle	13.1 ± 2.1	$9\sigma_{xy}$
Quad error only	8.9 ± 1.6	$6\sigma_{xy}$
Errors at IR2 only	10.2 ± 2.3	$6\sigma_{xy}$
Quad error at IR2 only	11.7 ± 3.5	$6\sigma_{xy}$
Systematic only	9.5 ± 0.8	$8\sigma_{xy}$
Random only	12.4 ± 2.2	$8\sigma_{xy}$
Without $n = 3, 4$ errors	9.1 ± 1.8	$6\sigma_{xy}$
Without $n = 5, 6$ errors	11.4 ± 1.4	$7\sigma_{xy}$
Without $n = 7, 8$ errors	8.1 ± 2.5	$5\sigma_{xy}$
Without $n = 9, 10$ errors	9.0 ± 1.7	$6\sigma_{xy}$
IR dipole error only	> physic.apert.	

The beam dynamic characteristics are mainly determined by the errors in IR quadrupoles. The dipoles, especially cold D1 at IR2, enhance the impact by further reducing the DA by up to 2σ . The mixed quad arrangement scheme provides slightly better results for DA as well as for the 6σ footprint size:

scheme	footprint [10^{-3}]	max.footprint [10^{-3}]
mixed	2.7 ± 1.5	4.9
separated	3.6 ± 1.9	6.6

The important case is when the errors were installed only at IR2 quads and dipoles. The resulting average DA of

10.2σ and minimum DA of 6σ are below the acceptable values. It indicates that the non-linear correctors would also be useful at IR2 in order to achieve the target value of DA at the ion operation. The rms values of the results for DA with the errors at IR2 only are quite large. It is explained by the big difference between horizontal and vertical dynamic aperture in this case. Vertical DA is about 4-5 σ smaller.

In order to understand how effectively the local IR correction schemes compensate for the IR magnet errors the tracking has been done with the non-linear correctors on. The present correction strategy includes 3 correctors per each triplet at IR1 and IR5. It is still under discussions and studies what the best choice of the layers of correction elements to be put into these correctors. The following corrector configuration was considered:

corrector place	harmonic layers
between Q2A and Q2B	b_4, b_5
between Q2B and Q3	a_3, a_4, a_6
between Q3 and D1	$b_3, b_6, (b_{10})$

In order to compensate for IR2 magnet errors the same corrector scheme was put also into IR2. The results obtained for the cases with and without correctors at IR2 confirmed the conclusion that the presence of the correctors at IR2 considerably improves the nonlinear dynamics characteristics:

Case	DA (σ_{xy})	Min. DA
Correctors only at IR1,IR5	10.5 ± 3.0	$6\sigma_{xy}$
With IR2 correctors	17.0 ± 1.7	$13\sigma_{xy}$

5 CONCLUSION

Field quality of BNL dipoles is adequate for nominal proton operation both for injection and collision lattices.

In the case of the ion lattice the contribution from IR2 magnets are considerable. The use of the non-linear correctors at IR2 is preferable if the crossing angle as large as $\pm 150\mu$ rad to be used.

6 ACKNOWLEDGEMENTS

We thank J.-P. Koutchouk, O. Brüning and R. Ostojic for lattice assistance and discussions, and many others, including A. Jain, M. Harrison, S. Peggs, S. Plate, J. Strait, R. Talman and E. Willen.

7 REFERENCES

- [1] J. Wie et al., "US-LHC IR magnet error analysis and compensation", EPAC 1998 Proceedings, (1998) p.380.
- [2] J. Wei et al., "Insertion region local correction for the Large Hadron Collider", these proceedings.

NEW CAPABILITIES OF THE SPIN TRACKING CODE *SPINK**

A.Luccio[#], A.Lehrach, J.Niederer, T.Roser, M.Syphers, and N.Tsoupas, BNL, Upton, NY

Abstract

The code *SPINK*, originally written to track polarized protons in RHIC, underwent several modifications and additions that have added substantial new capabilities to it.

1 BASIC FEATURES OF *SPINK*

A tracking code: *SPINK* [1] was written for the RHIC SPIN project at Brookhaven [2] to study the behavior of polarized protons in the Relativistic Collider during injection, acceleration and storage at fixed energy. From the output of *MAD* [3] *SPINK* reads the first order matrices for each machine element and the second order Transport maps as well as the Twiss functions along the lattice. Then, a subset of matrices is being created, where all elements that do not generate any spin rotation or any bend in the trajectory are lumped together. To the newly created elements a keyword is attached, such as BEND, QUAD, SEXT, HELIX, SNAKE, RFCAV, etc. Particle orbits are tracked through the first and second order maps (thick elements, with edge effects, as described in *MAD*). The spin of each proton, represented by a real 3-dimensional vector of length one, is also tracked using spin rotation matrices created by the code. At the present, with the exception of Helices, spin rotation matrices are for thin elements.

SPINK has been used for years, both in RHIC and the AGS, in particular to study the survival of the spin polarization in passing through resonances. The most significant new features of the code are described below.

2 LATTICE ERRORS

Angle, position and field errors in the machine lattice generate a distorted closed orbit. Since the strength of spin resonances depends on the average distance of a particle from the design equilibrium orbit, depolarization at a resonance is affected by lattice errors. In an actual accelerator the closed orbit distortions are being corrected with the use of horizontal and vertical steering magnets, whose currents are calculated with various algorithms. Orbit correction in *MAD* is accomplished through the Micado algorithm, that solves in the least square approximation an under constrained system of equations.

To correctly track phase space and spin, we had to transmit from *MAD* to *SPINK* the information related to the errors (measured or randomly assumed) of each machine element, and displace and rotate accordingly the relevant orbit transport maps. This task is accomplished using the BNL version of *MAD* [4].

Results of proton spin tracking in the RHIC lattice in the presence of errors for two intrinsic resonances, for an ideal orbit (no lattice errors), and for errors in the lattice but with a corrected orbit (to 0.2 mm), are shown in

Fig.1. Here, we assumed random errors of the order of 1 mm and 1 mrad in position and angle of all magnets, respectively. The momentum spread in the beam was 0.03%.

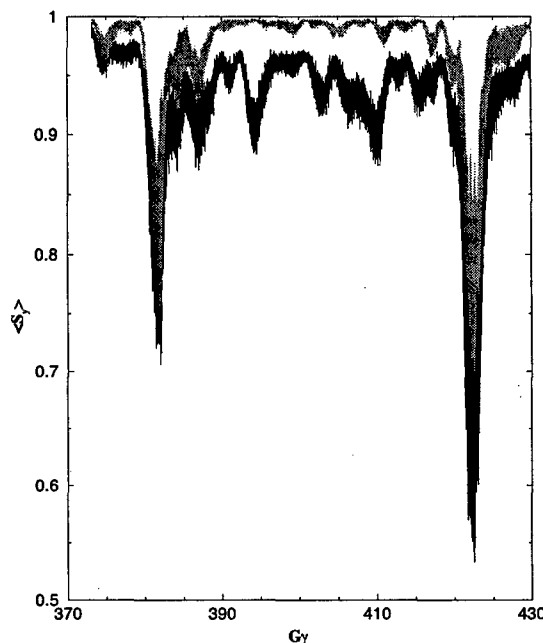


Figure 1: Spin tracking in RHIC, crossing the $Gy = 381.82$ and 422.18 intrinsic resonances. The upper curve is for an ideal orbit. The lower, for a distorted orbit due to lattice errors. Average over a few hundred particles tracked.

3 SECOND ORDER EFFECTS

Second order effects in *SPINK* are dealt with using the second order Transport maps from *MAD*. Important effects on spin resonances arise from crossing of sextupoles and higher order multipoles in the lattice.

Since in building maps for orbit tracking some elements are lumped together as explained in Sec. 1, matrices have to be multiplied, and also second order maps are convoluted to produce an overall map for the new element. This is done using the expression

$$T_{ijk} = \sum_{n=1}^6 \left(R''_{in} T'_{nj} + \sum_{m=1}^6 T''_{im} R'_{mj} R'_{mk} \right) \quad (1)$$

Where R and T are the first order and the second order orbit Transport maps, respectively, and the index (') or (") denotes the order in which maps are taken.

* Work supported by the U.S. Department of Energy
[#] luccio@bnl.gov

Two comments are necessary: (i) Second order tracking considerably reduces the speed of calculation, which is an unpleasant factor when many particles for many turns are tracked. (ii) Second order Transport maps are truncated and therefore non-symplectic.

In conclusion, in performing second order tracking one has to exercise caution when the conservation of quantities like the emittance is an important issue. Using of better maps, like the one derived with Lie algebra will be implemented in the future.

4 BEAM-BEAM EFFECTS

In RHIC, the two acceleration chambers intersect at six locations around the circumference, where the counter rotating beams can be brought to collide. Collisions affect both orbit and spin dynamics, since the electric and magnetic field of a beam exercise forces on the particles of the other beam, producing defocusing and spin rotation.

In *SPINK*, we modeled one beam as a Gaussian distribution of charges in motion and we studied the effect of the fields on the single particles of the other beam [5]. The expression of the resulting betatron tune shift in a collision is

$$\Delta\nu = -\frac{\xi}{u^2} \left[1 - e^{-u^2} I_0(u^2) \right] \quad (2)$$

where $u = r/2\alpha$, and ξ is the tune shift on axis, proportional to the number of particles per bunch n and inversely to the normalized emittance. E.g. for $n = 2 \times 10^{11}$, emittance 10π mm-mrad and $\beta^* = 1$ m, it is on axis $\xi = -0.015$. Tune distribution in the beam can be calculated by Eq. (2). *SPINK* tracking agreed very well with Eq. (2) and was also used to calculate the effect of beam-beam on spin. Fig. 3 shows how the vertical component of the spin is affected by beam-beam at fixed energy corresponding to $G\gamma = 261$, close to the strong intrinsic spin resonance at $G\gamma = 232 + \nu_y$.

For this simulation run, the beams are first accelerated, then brought to constant energy and made to collide.

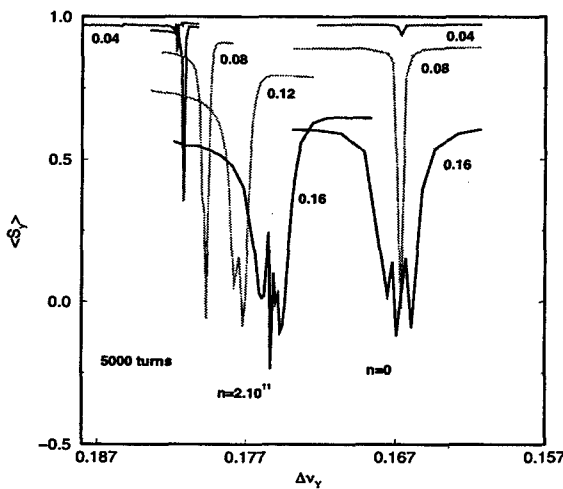


Figure 2: Beam-beam in a resonance crossing. The tune of particles at various vertical distances from axis determines the resonance strength. No space charge, and $n=2 \times 10^{11}$.

5 STABLE SPIN AXIS. SPIN TUNE

For each position along the accelerator lattice and for each position in phase space, there is a stable spin axis. If the spin of a proton is initially aligned along this direction, it will remain stable, if it isn't, it will precess in a cone around this direction. Finding the stable spin cone corresponding to a given phase space distribution of the particles in the beam is particularly important at injection, since we should make it coincide with the spin cone of the injected beam.

On the closed orbit the spin tune for a polarized particle is the number of spin precessions per turn in an accelerator. It is measured by the quantity $G\gamma$, and increases with the energy of the beam. When, during the acceleration cycle, the spin tune crosses some specific values, spin-depolarizing resonances appear. Siberian snakes in the lattice make the spin tune independent of energy. For RHIC, with two Siberian snakes, the spin is made equal to one. This means that the spin pattern should remain identical and repeat at each turn.

To calculate the stable spin axis direction, *SPINK* uses the method of Stroboscopic Average [6], as implemented in the code *SPRINT* [7]. A number of protons with different initial spin directions are tracked for a certain number of turns, then only one proton with the average spin is tracked back to reach the initial phase space location. The spin at this starting point, averaged over the multiple passages through the same location in the lattice, is applied to the proton, and the process continues with forward and backward tracking until the process eventually converges.

Fig. 3 shows an example of calculated stable spin axis in RHIC for very small emittance of the beam, at injection ($G\gamma = 41.5$). The two snakes were set for spin rotation of 180° and 100° , respectively, around several settings of mutual perpendicular axes. This arrangement produces a stable spin axis on a cone of semi-aperture $\theta = 40^\circ$. For each snake axis orientation there is a corresponding angle ϕ for the stable spin axis.

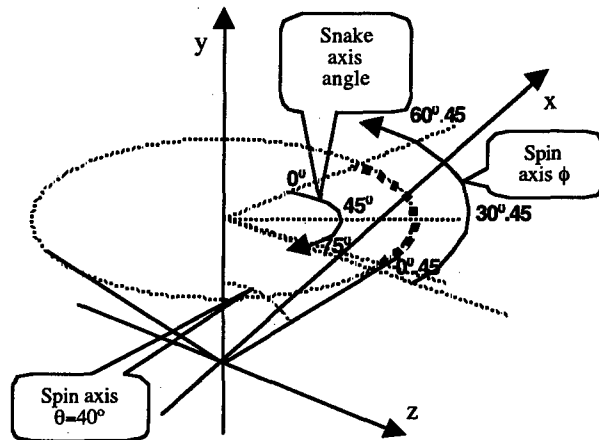


Figure 3: stable spin axis for spin rotation 180° and 100° in two snakes around different axis settings

For the same example, Fig. 4 shows the pattern of the three components of the stable spin axis along the circumference of RHIC. The vertical component of the spin axis is flipped at the two locations of the snakes.

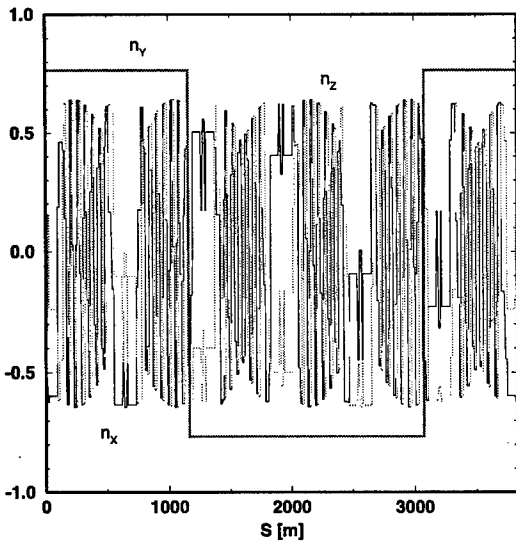


Figure 4. Stable spin axis components in RHIC. Two snakes with spin rotation of 180° and 100° , and axes at $+45^\circ$ and -45° , respectively.

6 MAP-GENERATED MATRICES FOR HELICAL SNAKES

RHIC will be equipped with helical Siberian snakes and Spin rotators. *SPINK* has three ways to treat helical devices of this kind (i) Synthetic Snakes, (ii) Analytical Snakes, and (iii) Map Snakes.

In the first mode, snakes and rotators are represented for orbit tracking as thin passive elements (*MAD* Markers), and for spin tracking by a matrix that effectively represents a rotation of the spin vector by a given angle and around a given axis.

Analytical helical devices are represented by a formalism that produces the transport of orbit and spin coordinates through the field of helices, expanded to first order [8].

Map helical devices is implemented by transformations up to third order of the coordinates, whose coefficients have been numerically calculated by tracking by numerical integration a distribution of particles in phase space and spin space through magnetic field maps for the actual devices. The first order part of these maps has been made symplectic [9].

For the first mode, input of *SPINK* is the spin rotation and axis angles. For the second, values of the nominal field and characteristic angles for the helices are used. For the third, a set of numerical coefficients.

Fig. 5 shows the geometry of a 4-helix Siberian snake for RHIC [10] and the trajectories of protons used to calculate the transport maps by third-order fitting.

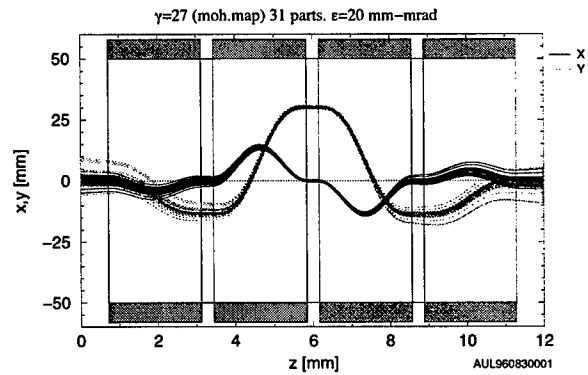


Figure 5: Envelope of trajectories used to calculate *R* and *T* orbit and spin maps in a 4-helices Siberian snake.

7 REFERENCES

- [1] A.U.Luccio in "Trends in Collider Spin Physics", Trieste, Italy, 5-8 Dec. 1995, p.235.
A.U.Luccio, T.Katayama and H. Wu, Proc. of PAC97, Vancouver, BC, Canada, May 12-16, 1997, p.92
- [2] T.Roser "The Acceleration of Polarized Protons to High Energies", these Proceedings
- [3] H.Grote and F.C.Iselin, "The MAD Program Vers. 8.16" CERN/SL/90-13, Geneva, Switzerland, May, p 26, 1995
- [4] J.Niederer, "Z Twiss Tracking Matrix File" BNL MAD Programming Note, Upton, NY, updated March 1999
- [5] A.U.Luccio and M.Syphers AGS/RHIC/SN No.068, Upton, NY, Nov. 25, 1997
- [6] K.Heinemann and Hoffstätter, Phys.Rev. E54, 4240
- [7] D.P.Barber and M.Vogt, Proc. of the EPAC98, Stockholm, Sweden, 22-26 June 1998, p. 1362
- [8] E.D.Courant, AGS/RHIC/SN No. 004, Upton, NY, Nov.8 1994.
M.J.Syphers AGS/RHIC/SN No.020, Upton, NY, Feb. 1996
- [9] A.U.Luccio, "Field Map Generated Matrices for Spin Tracking", Riken-AF-NP-235, Wako, Japan, October 1996
- [10] V.I.Pitsin and Yu.M.Shatunov, in "Proc Third Workshop on Siberian Snakes and Spin Rotators" (A.Luccio and Th.Roser Eds.), BNL-52453, Upton, NY Sept. 12-13, 1994, p. 15.

DYNAMIC APERTURE MEASUREMENTS AT THE ADVANCED LIGHT SOURCE *

W. Decking[†], D. Robin, LBNL, Berkeley, USA

Abstract

A large dynamic aperture for a storage ring is of importance for long lifetimes and a high injection efficiency. Measurements of the dynamic aperture of the third generation synchrotron light source Advanced Light Source (ALS) using beam excitation with kicker magnets are presented. The experiments were done for various accelerator conditions, allowing us to investigate the influence of different working points, chromaticities, insertion devices, etc.. The results are compared both with tracking calculations and a simple model for the dynamic aperture yielding good agreements. This gives us confidence in the predictability of the nonlinear accelerator model. This is especially important for future ALS upgrades as well as new storage ring designs.

1 DEFINITION OF THE APERTURE

The aperture of an electron storage ring is the maximum transverse and/or longitudinal deviation from the design orbit an electron can experience without being lost. The size of the aperture can effect both injection and lifetime. At the ALS where one injects horizontally offset from the stored beam the on-momentum aperture has to be large enough to accept the injected electron beam. From the point of view of lifetime it is important to have both sufficiently large on-momentum and off-momentum apertures. In particular the lifetime of a low energy, low emittance electron storage ring like the ALS¹ is usually given by the scattering of electrons within a bunch (Touschek effect) and/or by elastic and inelastic scattering of electrons with the residual gas.

When electrons scatter within a bunch, they may transfer enough momentum to be outside the momentum aperture of the storage ring. Depending on the dispersion function at the scattering position, scattered electrons start a betatron oscillation in addition to the momentum offset. An electron with a large betatron amplitude usually reaches the off-momentum aperture at smaller momentum deviations. Elastic scattering of electrons with the residual gas excites betatron oscillations. The elastic scattering lifetime is thus proportional to the on-momentum aperture. For more details about aperture measurements using lifetime investigations see [1], [2].

The aperture can be limited by several effects. The linear transverse motion of electrons is limited by the vacuum chamber aperture x_{vc} . In the presence of disper-

sion η this aperture is reduced by the off-momentum orbit. The invariant physical horizontal aperture is the minimum around the ring of $A_{phys,x}(\delta) = (x_{vc}(s) - \eta(s)\delta)^2 / \beta_x(s)$ with $\delta = \frac{dP}{P_0}$ the relative momentum deviation. Dispersion is usually only present in the horizontal plane leaving the vertical physical aperture $A_{phys,y}$ momentum independent. The longitudinal motion of electrons is limited by the height of the rf-bucket provided by the accelerating voltage in the cavity.

The electron motion is also confined by dynamic effects, leading to resonant or chaotic amplitude growth. The border of this motion is called the dynamic aperture $A_{dyn,x}(\delta)$ and depends on the relative momentum deviation. The dynamic aperture is often estimated through tracking calculations.

One can also estimate the dynamic aperture using a simple model in the following way: Electrons are lost when their tune satisfies a resonance condition. From knowing the tune shift terms with amplitude, $\frac{\partial \nu_y}{\partial A_x}$, $\frac{\partial \nu_y}{\partial A_y}$, and momentum deviation, $\frac{\partial \nu_y}{\partial \delta}$, $\frac{\partial^2 \nu_y}{\partial \delta^2}$, one can compute the tune shift due to momentum and transverse deviations:

$$\Delta \nu_y = \frac{\partial \nu_y}{\partial A_x} A_{dyn,x} + \frac{\partial \nu_y}{\partial A_y} \kappa A_{dyn,x} + \frac{\partial \nu_y}{\partial \delta} \delta + \frac{\partial^2 \nu_y}{\partial \delta^2} \delta^2 + \dots \quad (1)$$

where $\Delta \nu_y$ is the distance to the closest 'deadly' resonance, and κ is the emittance coupling factor. Knowing the distance to the resonance defines a momentum dependent dynamic aperture.

From equation 1 several ways to increase the dynamic aperture can be seen:

- Increase the distance to the closest 'deadly' resonance by choosing a 'good' working point.
- Decrease the tune shift for large amplitude electrons. This is addressed in the design phase by adequately distributing the nonlinear elements. During operation one can lower the chromaticity $\frac{\partial \nu_y}{\partial \delta}$ to small numbers.
- Avoid excitation of resonances, which is achieved in high periodicity machines, where a large number of identical basic cells decreases the number of excitable resonances.

The total aperture is the minimum of all the aperture limitations discussed above. It is often difficult to distinguish clearly between dynamic and physical limits in the measurements. Only good knowledge of the vacuum chamber dimensions, the optical functions and the emittance coupling allows the separation of the two effects. We will thus only use the term dynamic aperture in the following if we can exclude physical limits.

* This work was supported by the Director, Office of Energy Research, Office of Basic Energy Sciences, Materials Sciences Division, of the U.S. Department of Energy, under Contract No. DE-AC03-76SF00098.

[†] Now at DESY, Hamburg, Germany.

¹ The ALS is operated with an energy of 1.5 – 1.9 GeV and an emittance of $3.5 - 5.6 \times 10^{-9}$ radm.

2 MEASUREMENTS OF THE APERTURE

A tool for aperture measurements is a beam kicker magnet. This is a fast magnet which permits the kicking of the beam over a single turn. A criteria for the aperture could be to increase the kick amplitude until the beam is lost. A measurement of this maximum kick amplitude as a function of an artificial aperture limit (horizontal scraper) is shown in figure 1. This measurement serves as a calibration for the kicker voltage. It also shows that at a certain point the kick amplitude is independent of the scraper position. This is when the kicked beam hits another aperture in the ring.

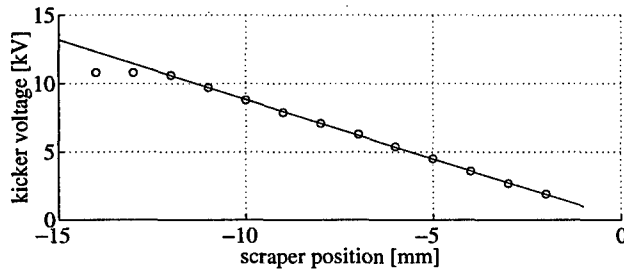


Figure 1: Maximum kicker voltage versus horizontal scraper position.

To measure the aperture for off-momentum electrons, the storage ring rf-frequency is changed to change the storage ring energy. This simulates a 'static' off-momentum situation, as the bunch centroid is not performing synchrotron oscillations. If the main reason for the dynamic aperture is the tune shift with momentum deviation, this 'static' measurement should be sufficient.

Figure 2 shows a measurement of the aperture versus momentum deviation. The measured aperture is asymmetric in momentum due to higher order tune shift terms, which shift the lower momentum electrons faster towards the integer resonance. At a momentum deviation of ≈ -0.03 one can see a dip in the curve, which is interpreted as a resonance which is overcome for lower momentum electrons when the tune is shifted beyond this resonance. To estimate the dynamic aperture with synchrotron oscillations, the dynamic aperture is assumed to be the smallest envelope fitting into the measured aperture. With synchrotron oscillations it may be possible for electrons to cross through resonances like the one at $\delta \approx -0.03$ in figure 2. The synchrotron tune at the ALS is $\nu_s \approx 0.008$ or approximately 125 turns per synchrotron oscillation. Therefore the dashed-dotted line, representing the inner envelope, is a somewhat pessimistic approximation of the dynamic aperture including synchrotron oscillations.

Figure 3 shows a comparison of the measured aperture with tracking calculations and with the tune-shift model. Electrons were tracked through the ALS lattice with a six-dimensional symplectic integrator². The following errors

²The tracking code TRACY2 was used.

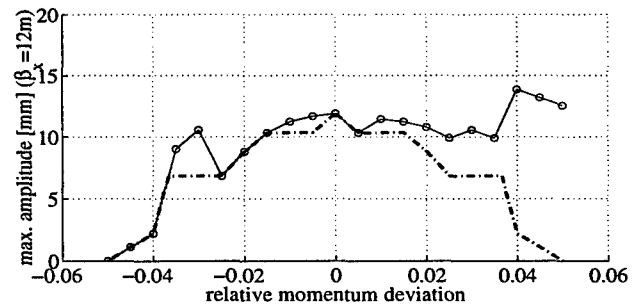


Figure 2: Maximum kick amplitude versus momentum deviation at the following storage ring conditions: $\nu_x = 0.31$, $\nu_y = 0.22$, $\xi_x \approx 0.5$, $\xi_y \approx 0.5$. The solid line is the raw measurement, while the dashed dotted line shows the derived dynamic aperture assuming synchrotron oscillations.

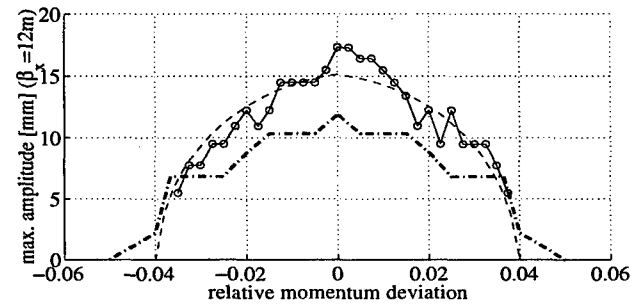


Figure 3: Comparison of measured aperture (dashed-dotted line), tracking calculations (solid line / circles), and tune-shift model with a $\Delta\nu_y = -0.14$. The tune was $\nu_x = 14.31$, $\nu_y = 8.22$.

and constraints were included in the model to simulate the realistic machine:

- Physical aperture borders were included in the tracking to prevent electron oscillations outside the realistic vacuum chamber. This is important because large amplitude electrons may perform large, but stable oscillations which would be outside the physical aperture but not lead to a loss of the electron in the tracking.
- Linear field errors are simulated according to the optics measurements done at the ALS with the response-matrix fitting method [3]. These errors lead to a β -beat and thus a break in periodicity.
- Random skew quadrupole errors were distributed in all quadrupoles of the lattice and adjusted to obtain a 1% coupling.
- The wiggler (see below) was simulated as a chain of hard edge dipoles obtaining the correct linear focusing and longitudinal dynamics properties.

The tune-shift $\Delta\nu_y$ for the tune-shift model was chosen to fit the measured aperture. Measurements, tracking and the tune-shift model agree rather well for large off-momentum electrons. For on-momentum electrons the measurement

shows smaller horizontal amplitudes. The horizontal physical aperture of the ALS is ≈ 20 mm, thus the measurement (and the tracking) show that the horizontal aperture is limited through dynamic effects.

To investigate the dependence on the tune, the tune is moved towards the integer resonance, parallel to the $\nu_x - \nu_y$ coupling resonance. Figure 4 shows the aperture for this tune setting, again compared with tracking calculations and the model. The measured dynamic aperture is only slightly smaller than in the previous case (figure 3) and the tracking and tune-shift model agree better with the measurements. The integer resonance defines a clear limit for the dynamic aperture. The tracking thus shows the expected behavior (increase of dynamic aperture with distance to the integer resonance) while the measurements indicate that on-momentum electrons are lost at almost the same large transverse amplitudes. Large transverse amplitude particles are for instance more sensitive to additional nonlinear fields, which we have not included in the tracking.

The effect of periodicity breaking in a highly periodic machine can be shown with the insertion of a wiggler³ in the ALS lattice. The vertical focusing effect of the wiggler is locally compensated, which leaves a breaking of the ideal 12-fold symmetry. The aperture measurement shows a slight degradation of the dynamic aperture when the wiggler is closed (see figure 5 compared with figure 4). This is in good agreement with tracking calculations.

To show the importance of coupling, an aperture measurement was performed with the skew quad circuits powered. This should decrease the on-momentum dynamic aperture considerably, because electrons with large horizontal amplitudes are coupled in the vertical plane, where they are lost at the small gap vacuum chambers⁴. This situation was also modeled in the tracking. The results are displayed in figure 6. The agreement between measurement and tracking is good. The tune-shift model fails in this case, because it does not take into account the vertical aperture limit.

3 CONCLUSION

The aperture of the ALS was measured with the help of a horizontal kicker magnet. The results of this measurement agree very well with previous measurements using lifetime techniques [1], [2]. The dynamic aperture is also derived from tracking studies and from a rather simple model. The agreement between measurement and tracking is good. The nonlinear accelerator model has to be improved to predict the behavior of large transverse amplitude particles. The simple model can be used to understand the tracking data and to optimize the operating conditions of the ALS.

³The wiggler has a peak field of 2 T, 0.16 m period length, and 3 m total length.

⁴The smallest vacuum chamber gap in the ALS has a full height of ≈ 8 mm at $\beta_y = 4$ m.

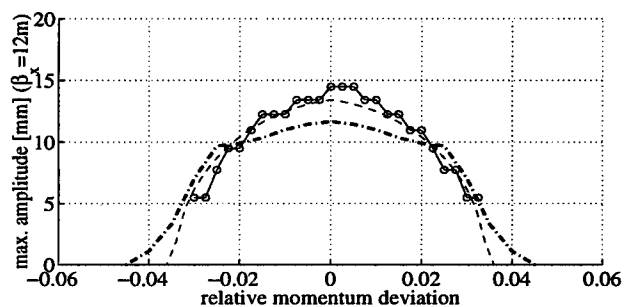


Figure 4: Comparison of measured aperture (dashed-dotted line), tracking calculations (solid line / circles), and tune-shift model with a $\Delta\nu_y = -0.11$. The tune was shifted to $\nu_x = 14.27$, $\nu_y = 8.18$.

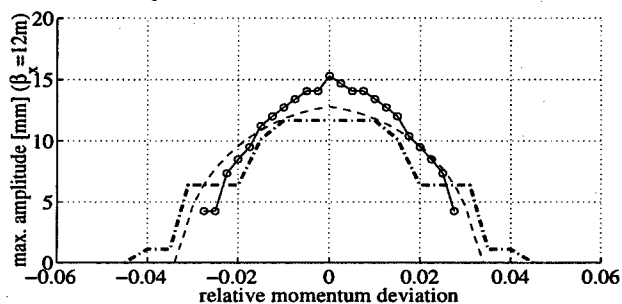


Figure 5: Comparison of measured aperture (dashed-dotted line), tracking calculations (solid line / circles), and tune-shift model with a $\Delta\nu_y = -0.1$. The tune was $\nu_x = 14.27$, $\nu_y = 8.18$ and the wiggler was closed.

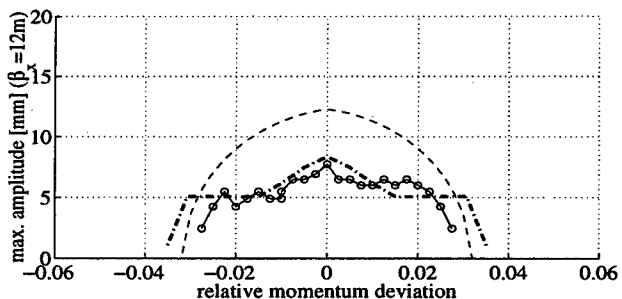


Figure 6: Comparison of measured aperture (dashed-dotted line), tracking calculations (solid line / circles), and tune-shift model with a $\Delta\nu_y = -0.09$. The tune was $\nu_x = 14.27$, $\nu_y = 8.18$ and the wiggler was closed. In addition the skew quadrupole circuit was powered.

4 REFERENCES

- [1] W. Decking et al., "Lifetime Studies at the Advanced Light Source", EPAC98, Stockholm, 1998.
- [2] W. Decking, D. Robin, "Momentum Aperture of the Advanced Light Source", EPAC98, Stockholm, 1998, and ICFA Workshop on Nonlinear and Collective Phenomena in Beam Physics, Arcidosso, 1998.
- [3] D. Robin et al., "Model Calibration and Symmetry restoration of the Advanced Light Source", EPAC96, Sitges, 1996.

OPTICS CHARACTERIZATION AND CORRECTION AT PEP-II*

J. Safranek[†], M. H. Donald, SLAC, Stanford, CA

Abstract

The linear optics of both the high energy ring (HER) and low energy ring (LER) for SLAC's PEP-II B-Factory were characterized with two algorithms: analysis of the measured closed orbit response matrix and analysis of betatron phase advance measurements. The results of the two analyses were in good agreement. When the HER was first run in a low β optics in autumn 1997, the measured β functions showed more than a factor of two discrepancy from the design. The source of the optics distortion was diagnosed and corrected using these methods.

1 INTRODUCTION

The PEP-II collider consists of two storage rings - a high energy ring (HER) for 9 GeV electrons and a low energy ring (LER) for 3 GeV positrons. The storage rings are each 2.2 km long, and they intersect at a single interaction point (IP) to produce collisions for high energy physics experiments.

In order to maximize luminosity, the LER and HER optics were designed with small β functions at the IP. When the HER was first commissioned in this low β optics during the autumn of 1997, the measured β_y showed a large discrepancy from the design model. Fig. 1 compares the measured and design model β_y in the region of the ring ± 60 meters from the IP. The beam size is large in the final focus doublet (QD4 and QF5), and the beam is focused tightly at the IP. The measured β_y data points were generated by measuring the tune shifts, $\Delta\nu_y$, from small changes in integrated quadrupole gradients, ΔKL .

$$\beta_y = 4\pi \frac{\Delta\nu_y}{\Delta KL} \quad (1)$$

The measured β_y differed by as much as a factor of 2.5 from the design model. The error in β_y was seen throughout the ring. The measured β_x agreed much better with the design.

Two methods were applied to investigate the source of this optics distortion - analysis of the measured closed orbit response matrix, and analysis of betatron phases determined using turn-by-turn measurements of betatron oscillations.

* This work was performed under the auspices of the U.S. Department of Energy.

[†] Email: safranek@slac.stanford.edu

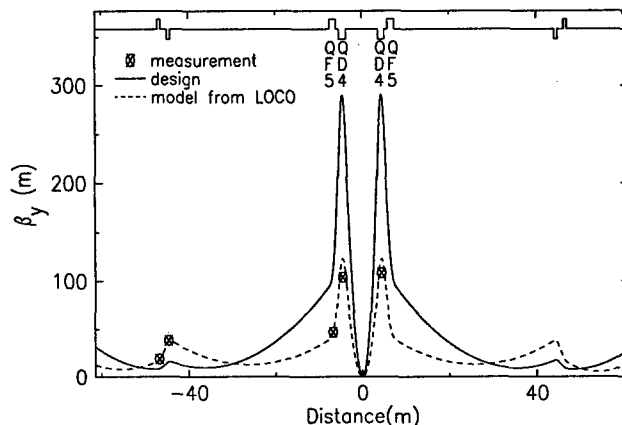


Figure 1: The β_y measured at quadrupoles compared to the design and to the model fit by LOCO. The IP is at the center of the graph.

2 LOCO FOR HER

2.1 Method

The closed orbit response matrix is the shift in orbit at each BPM for a change in strength of each steering magnet. The HER has 144 horizontal and 143 vertical steering magnets with about 150 horizontal and 150 vertical BPMs, so the HER orbit response matrix has more than 40,000 data points. Differences between the model and measured response matrix can arise from quadrupole gradient errors, BPM gain errors, and steering magnet calibrations errors.

The computer code LOCO[1] (Linear Optics from Closed Orbits) was used to vary the quadrupole gradients, BPM gains, and steering magnet calibrations in a computer model of the HER to minimize the χ^2 difference between the model and measured response matrices. In total about 770 parameters were varied to fit the model to the 40,000 measured data.

The HER has about 300 quadrupoles. The number of BPMs in the ring and the accuracy of the BPM measurements are not sufficient to accurately calibrate the gradient in each of these quadrupoles independently. For this reason it was assumed that all quadrupoles driven by the same power supply had the same gradient. Also the gradients of the two QD4's as well as the two QF5's were assumed to be the same, even though each of these quadrupoles are powered with its own supply. In total this gave 68 families of

quadrupoles varied.

The β_y for the model fit to the response matrix is included in Fig. 1. The prediction of the measured β_y is greatly improved. The fit model also accurately reproduced the measured β_x . The difference between the fit and design model gradients, ΔK , is plotted as a function of position around the ring in Fig. 2 for all 300 HER quadrupoles. Rather than simply plotting ΔK , the plot shows $\beta_y \Delta K L$, the integrated quadrupole gradient error multiplied by β_y at each quadrupole. $\beta_y \Delta K L$ is the contribution to β_y distortion from each quadrupole gradient error. (The β_y distortion from a single quadrupole gradient error, $\Delta K L$, is [2]

$$\frac{\Delta \beta_y(s)}{\beta_y(s)} = \beta_y(s_0) \Delta K L \frac{\cos 2[|\phi(s) - \phi(s_0)| - \pi \nu]}{2 \sin 2\pi \nu}, \quad (2)$$

where the quadrupole is at position s_0 .) The LOCO fit indicated that errors in the IP doublet quadrupoles, QD4 and QF5, drove nearly all of the β_y distortion.

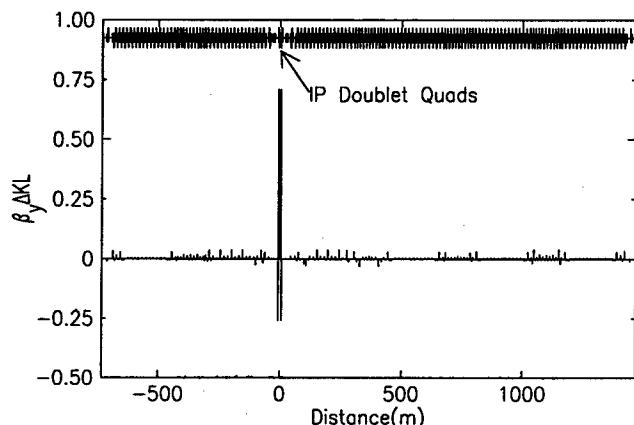


Figure 2: The magnitude of the driving term for β_y distortion as a function of position around the ring according to the LOCO fit.

2.2 Error Analysis

Once LOCO had converged to find the model with the best statistical fit to the data, the rms difference between the measured and model response matrices was $88 \mu\text{m}$ horizontal and $32 \mu\text{m}$ vertical. The accuracy of the fit was considerably worse than the noise level of the closed orbit measurements ($4 \mu\text{m}$), presumably due to systematic errors associated with gradients from horizontal orbit offsets in sextupoles as well as variation in gradients of quadrupoles powered by the same power supply. The steering magnet kicks used to measure the response matrix gave rms orbit shifts of 1.7 mm , so the model orbit shifts fit the measured shifts to 5% and 2% horizontally and vertically.

Figure 3 shows the error bars for Fig. 2 from the $4 \mu\text{m}$ random BPM measurement error. The error bars were calculated analytically assuming a normal measurement error distribution. The error bars are quite small, indicating the quadrupoles on individual supplies around the IP can be

calibrated to about 1 part in 10,000., and the QD and QF quadrupoles in the arcs with many magnets on one supply can be calibrated to 5 parts in a million. Of course, with systematic errors included, the error bars are much larger. (Not to mention that the QD and QF power supplies are not even stable to this level.)

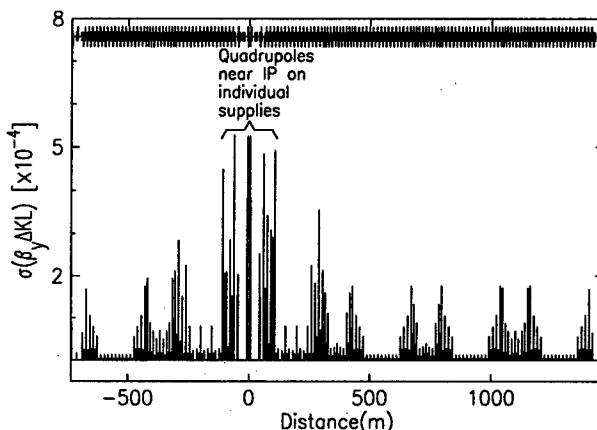


Figure 3: The error bars for Fig. 2 due to the random $4 \mu\text{m}$ BPM measurement error.

Nonetheless, Fig. 3 is useful in demonstrating that the expected error bars on $\beta_y \Delta K L$ for quadrupoles on individual supplies tend to be the same order of magnitude from quadrupole to quadrupole. In other words, QD4 and QF5 sticking out like sore thumbs in Fig. 2 indicates a real problem with these quadrupoles, not just uncertainty in the fit parameters.

2.3 Optics Correction

Starting from the fit optics model and reducing QD4 and QF4 by .60% and .49% restored the optics to design. QD4 and QF5 were reduced in the ring, and measurements confirmed that the design optics were restored. No good explanation of the gradient errors was found. It was noted that longitudinal displacement of the IP doublets 3 cm closer to the IP would give nearly the same optics distortion as the strength errors. Measurements of the quadrupole positions indicated no such large position errors.

When the IP was rebuilt during the installation of the LER, the effective error in the IP doublet strengths was greatly diminished, to about 0.13%.

3 PHASE FITTING

Using buffered data acquisition of Beam Position Monitor (BPM) data, which records beam position for 1024 consecutive turns, the relative phase of the betatron motion between the BPMs may be found. The phase fitting is now available on-line [4]. Because of beta function mismatch, this phase will be different from the ideal (model) phase between the BPMs. It is possible to fit this phase error using errors in the strength of quadrupole families as the fit-

ting variable. We used the program LEGO [5] as the fitting code.

The results obtained by such fitting were consistent with the LOCO results. The whole table of quadrupole gradient errors showed some correlation between the two methods but was conclusive only when the beta functions were taken into account. The comparison between the errors found by the two methods is given in Table 1.

Table 1: Comparison of results obtained by LOCO and phase fitting method

	phase fit results	LOCO results
QD	0.20	0.18
QF	-0.04	-0.04
QD4	0.55	0.60
QF5	0.69	0.49

Figures 4 and 5, and show the measured phase differences before the fitting.

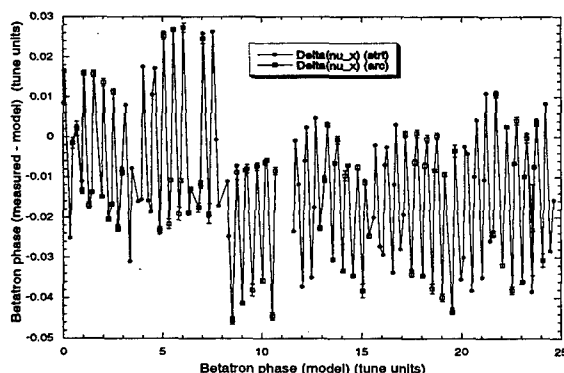


Figure 4: Error in the horizontal betatron phase. The phase error (measured - model) is plotted as a function of horizontal phase advance. The phase is in tune units i.e. $\mu/2\pi$.

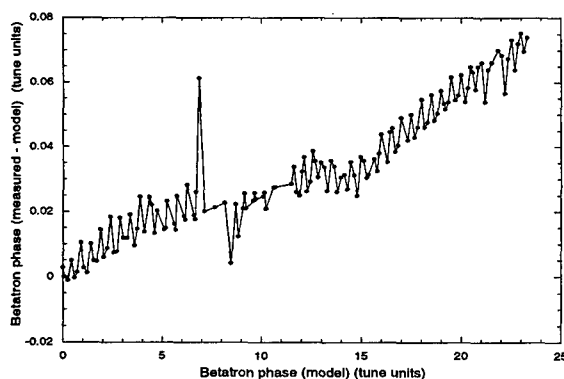


Figure 5: Error in the vertical betatron phase. The phase error (measured - model) is plotted as a function of vertical phase advance. The phase is in tune units i.e. $\mu/2\pi$.

Figures 6 and 7 are phase differences between the same measured data and a "new" model with fitted values for

quadrupole strengths in the interaction region and the main QD,QF strings.

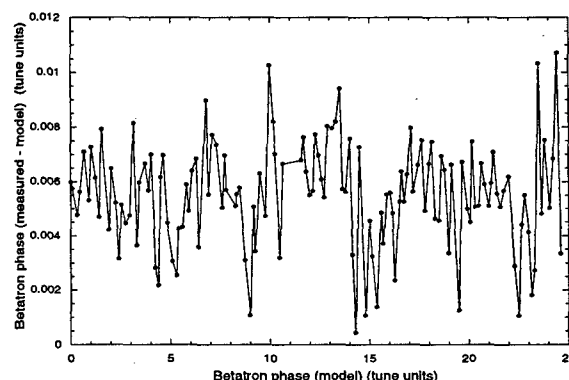


Figure 6: Error in the horizontal betatron phase. The phase error (measured - model) is plotted as a function of horizontal phase advance. The phase is in tune units i.e. $\mu/2\pi$.

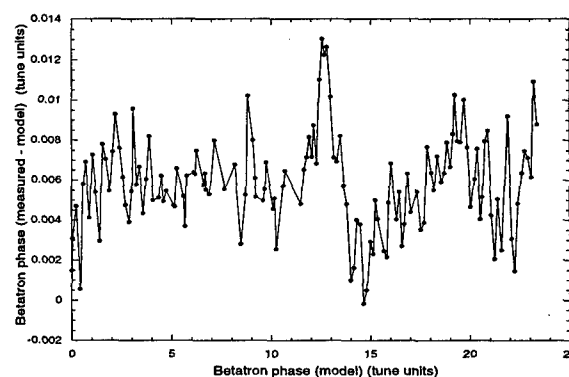


Figure 7: Error in the vertical betatron phase. The phase error (measured - model) is plotted as a function of vertical phase advance. The phase is in tune units i.e. $\mu/2\pi$.

4 ACKNOWLEDGMENTS

We would like to thank many people on the PEP-II team, in particular Y. Cai, T. Himel, W. Kozanecki, A. Kulikov, M. Lee, J. Seeman U. Wienands, and F. Zimmermann.

5 REFERENCES

- [1] J. Safranek, "Experimental determination of storage ring optics using orbit response measurements", *Nucl. Instr. and Meth. A* 388, (1997) pg. 27.
- [2] J. Murphy, "Synchrotron Light Source Data Book, Version 4", BNL note 42333, (1996).
- [3] J. Borer et al., "Harmonic Analysis of Coherent Bunch Oscillations in LEP", EPAC92 (1992).
- [4] T. Himel et al., "Measuring the Betatron Phase Advance in PEP-II with 1000 Turn BPM Measurements", These proceedings.
- [5] Y. Cai, M. Donald, J. Irwin and Y. Yan, "LEGO: A modular Accelerator Design Code", SLAC-PUB-7642, (Aug 1997)

MEASUREMENT OF SEXTUPOLE ORBIT OFFSETS IN THE APS STORAGE RING *

M. Borland, E.A. Crosbie, and N.S. Sereno ANL, Argonne, IL

Abstract

Horizontal orbit errors at the sextupoles in the Advanced Photon Source (APS) storage ring can cause changes in tune and modulation of the beta functions around the ring. To determine the significance of these effects requires knowing the orbit relative to the magnetic center of the sextupoles. The method considered here to determine the horizontal beam position in a given sextupole is to measure the tune shift caused by a change in the sextupole strength. The tune shift and a beta function for the same plane uniquely determine the horizontal beam position in the sextupole. The beta function at the sextupole was determined by propagating the beta functions measured at nearby quadrupoles to the sextupole location. This method was used to measure the sextupole magnetic center offset relative to an adjacent beam position monitor (BPM) at a number of sextupole locations. We report on the successes and problems of the method as well as an alternate method.

1 INTRODUCTION

Given the strong sextupoles present in third-generation light sources, miscentering of the beam in the sextupoles can seriously impact one's ability to model the machine's behavior. This affects one's ability to correct the orbit, adjust the tunes, and perform other corrections that tend to make use of data from modeling. It may also have an adverse effect on dynamic aperture and injection.

There are several possible sources of such miscentering. First, a sextupole may simply be improperly aligned. Second, an unknown or mistaken value for a BPM offset may result in steering off axis in the sextupole. Third, the beam may be moved deliberately to steer for a user. (At APS, final beam alignment for users is performed by steering of the electron beam.) Fourth, since some sextupoles are in dispersion areas, a systematic miscentering may result from a particular choice of the rf frequency.

At APS, many BPM offsets are derived using a scanning technique using a quadrupole and a corrector bump [1]. This permits finding the offsets relative to quadrupoles for those BPMs that are adjacent to quadrupoles. The method relies on the fact that if the beam is centered in a quadrupole, then changing the strength of that quadrupole does not change the orbit. Because this method is relatively straightforward to implement, we used it as the definition of our BPM offsets. The assumption was that the sextupoles were well-aligned relative to the quadrupoles, so that steering to the center of quadrupoles would also center the beam in the sextupoles.

However, we encountered persistent disagreements between our model of the ring and measurements of the beta functions. Hence, a program to measure the beam position in sextupoles directly was undertaken. Note that while we sometimes speak of measuring sextupole "offsets" or "positions" and of "sextupole miscentering," we are in fact measuring the position of the beam relative to the sextupole center for a particular lattice configuration and steering.

2 PRINCIPLE OF THE MEASUREMENT

The measurement relies on the quadrupole field component generated by a displaced sextupole magnet. It also makes use of the existence of individual power supplies for the 280 sextupoles and 400 quadrupoles in the APS. The effective geometric focusing strength (K_1) seen by a beam displaced by x from the magnetic center of a sextupole of geometric strength K_2 is just K_2x . If the sextupole strength is changed between states 1 and 2 with no change in orbit, then the tune change is related to the change in K_2 by a well-known [2] equation, giving

$$\Delta\nu = \pm \frac{\beta \Delta K_2 x L_s}{4\pi}, \quad (1)$$

where L_s is the length of the sextupole, the $+$ ($-$) sign is used if horizontal (vertical) tune data is used, and the β function should be for the same plane as the tune change. In order to determine x , we change the strength of the sextupole and measure the change in tune. To make the tune change as large as possible, we chose to change the sextupole from zero to maximum current. The value of $\Delta K_2 L_s$ is then 4.974 m^{-2} [3] for APS sextupoles.

In order to eliminate spurious tune changes due to orbit motion elsewhere in the ring caused by the change in the sextupole field, we employed continuous orbit correction and a settling period (30-60s) to allow correction of any orbit perturbation. Typical perturbations were 20-30 μm peak and were easily corrected.

The beta function value needed to compute x was originally taken from the model. Later, we implemented a refinement of the technique that involves using measured beta functions from two quadrupoles that bracket the sextupole.

3 MEASUREMENT TECHNIQUE AND DATA ANALYSIS

The principle of this measurement is clearly quite simple, and it was readily implemented using existing software tools, notably the SDDS (Self-Describing Data Sets) toolkit [1, 4, 5]. The measurement is available via a GUI interface built using the Tcl/Tk script language. The script uses SDDS tools for data collection, analysis, and display.

* Work supported by U.S. Department of Energy, Office of Basic Energy Sciences, under Contract No. W-31-109-ENG-38.

The tune measurements were taken with a Hewlett-Packard Vector Signal Analyzer (HP VSA), which has low noise and fast averaging compared to a typical network analyzer, using a frequency chirp to drive the beam. To save time and allow higher tune measurement resolution, we narrowed the span of the analyzer to include only one of the tunes. We chose to use the vertical tune for most measurements as this increases $\Delta\nu$, given that we have $\beta_y > \beta_x$ at most of the sextupoles of interest. Further, the vertical tune is less subject to drift and wobble than the horizontal tune.

The script reads the tune spectra from the HP VSA for the two sextupole settings (0 and full current). Typical spectra are shown in Figure 1. The script processes the tune spectra using either a smoothing and peakfinding algorithm or a correlation-based algorithm. The results are very close for the two algorithms, with maximum differences being equivalent to about $30 \mu\text{m}$ in sextupole position.

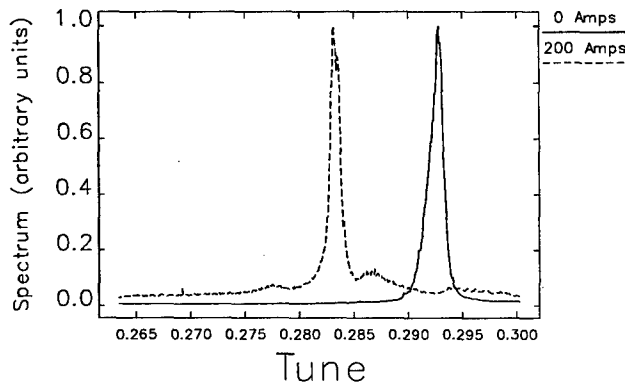


Figure 1: Typical spectra from a measurement of beam position in a sextupole

The same instrument and software tools are used for the beta function measurements. Indeed, the equation underlying the beta function measurement is simply a variant of Eq. (1), namely $\beta = \Delta K_1 \beta L_S / (4\pi)$. We have verified using simulations that this equation is accurate when used for a single quadrupole at a time or for groups of up to 40 quadrupoles; that is, any perturbation of the lattice due to the measurement is negligible. The beta function measurement script takes five tune measurements for five different values of the quadrupole strength. The beta function is computed from the slope of the tune vs quadrupole strength, where the strength itself is deduced from the excitation curve of the magnet. The script restores the tunes by iteratively adjusting the quadrupole current, so that the lattice is not perturbed by successive measurements. This means we do not have to rely on knowing the hysteresis behavior of the magnet in order to restore the lattice.

Figure 2 shows a histogram of the measurements made to date, for S2 and S3 sextupoles, that bracket the dipoles in our double bend acromat (DBA) lattice. The mean position is $-0.25 \pm 0.04 \text{ mm}$. For the S2 sextupoles (which are in a nominally zero-dispersion location), the mean is $-0.13 \pm 0.05 \text{ mm}$. For the S3 sextupoles (in a dispersion location), the mean is $-0.37 \pm 0.05 \text{ mm}$. This suggests that we are

systematically off-center in the sextupoles largely due to the particular value of rf frequency we use.

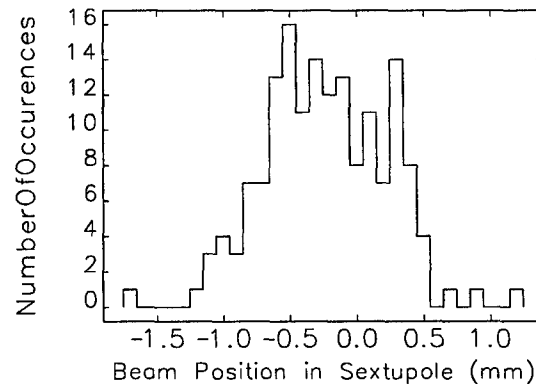


Figure 2: Histogram of measured beam positions in sextupoles

As mentioned in the introduction, one reason for wanting to know the beam position in the sextupoles is to evaluate the effect on the lattice. Although we have only made measurements for 160 of the 280 sextupoles, it is interesting to compute the beta function resulting from the beam offsets in these sextupoles. This is shown in Figure 3. In practice, such beats are corrected using a singular value decomposition (SVD) technique [6] that does not require knowing the beam position in the sextupoles. However, application of that technique does not provide an explanation of the presence of beta beats. Although our data is incomplete and cannot be taken to represent the actual beta function modulation, it does demonstrate the possibility that any such modulations may be due to the position of the beam in the sextupoles.

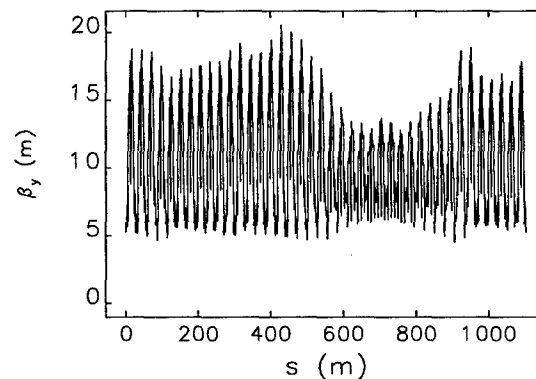


Figure 3: Computed vertical beta function for the APS due to beam positions in the 160 sextupoles for which measurements were done. APS has 280 sextupoles plus other potential sources of focusing errors, so this figure does not purport to represent the actual beta function.

4 TESTS OF THE METHOD

We tested the method in two ways: First, we checked the reproducibility of the measurement; when repeated within

a short time, this was very good, with successive measurements reproducing at the $2\text{-}\mu\text{m}$ level imposed by our tune measurement resolution. Second, we checked the linearity and slope by making successive measurements with the beam deliberately steered to different positions in a sextupole. This was done for two sextupoles. The linearity was generally good, but the data showed slope errors; i.e., the change in BPM reading over the change in position deduced from the sextupole-based measurement was not unity. For example, in one case we found a reproducible 30% error in the slope, as seen in Figure 4. In another case we found a 50% error. Possible sources of this error are the various calibrations of the BPM, sextupole, and quadrupole, plus the particular bump shape that was used.

There is evidence from response matrix measurements of 15-25% errors in the calibration of the two BPMs in question. Since this is based on comparing a measured matrix [7] to a computed matrix using a model that matches the average beta functions [8], it is not necessarily accurate for a given sector. However, because 30-50% of magnet calibration errors are difficult to conceive, we believe that BPM calibration accounts for most of the discrepancy. If this is correct, then the beam position measurements in the sextupoles are reliable. These measurements do not rely on BPMs, but only on tune measurement.

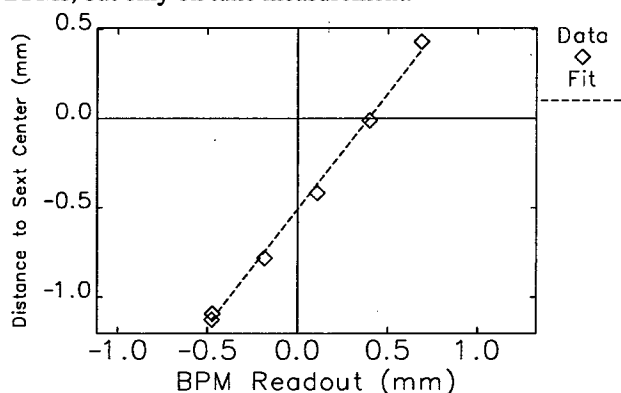


Figure 4: Linearity test of measurement of beam position in a sextupole

Even if the position measurements are accurate, the discrepancy makes it impossible to use the data to center the beam in the sextupoles. Because of this, we have developed a different technique that obviates the need to know the magnet calibrations. Specifically, we will use beam bumps in the sextupoles to steer the beam until the tune change due to changing a sextupole current is nulled out. The readout of the nearest BPM tells us where to steer the beam in order to center it in the sextupole. As long as the BPM calibration is not changed, this data could be used for beam centering even if the calibration is not good in absolute terms. This method also requires no measurement of beta functions and, being iterative, it does not rely on the linearity of the BPMs. An initial test of this method showed that it converged to the accuracy of our tune measurements after three to four iterations.

One problem discovered when doing the linearity tests was that the results depended on the type of beam bump used (i.e., the location and coefficients of the corrector magnets). We interpret this to mean that different types of local bumps may have sufficiently different shapes that the relationship between the position at the nearest BPM and the position in the sextupole changes appreciably. Hence, in choosing the beam bump to use for the new method, care needs to be taken that the beam is moved in a parallel fashion through the sextupole and nearby BPMs. This also implies that we may have a practical difficulty in steering precisely to the center of all sextupoles, as such bumps are likely to move the beam in several sextupoles.

5 CONCLUSION

A method of measuring the beam position in sextupoles by measuring the tune shift caused by a change in sextupole strength has been presented. The method is shown to be linear with respect to BPM readout, although the slope was in error by 30-50%. This implies that our measured positions may have errors of this magnitude; however, we believe much of the error in the two cases studied is attributable to BPM calibration and hence that the measured positions are accurate. The error in each individual measurement was found to reproduce at the $2\text{-}\mu\text{m}$ level (the limit imposed by the tune measurements) when measurements were taken in quick succession. A modified technique that directly finds the beam-centering value to which to steer on a nearby BPM was also discussed.

6 REFERENCES

- [1] M. Borland, L. Emery, N. Sereno, "Doing Accelerator Physics Using SDDS, UNIX, and EPICS," Proc. 1995 ICALEPCS, Oct. 30 - Nov. 3, 1995, Chicago, Illinois, pp. 382-391 (1996).
- [2] M. Sands, "The Physics of Electron Storage Rings: An Introduction," SLAC-121, Stanford Linear Accelerator Center, May 1979.
- [3] C. Doose, ANL/APS, private communication.
- [4] M. Borland, "A Self-Describing File Protocol for Simulation Integration and Shared Postprocessors," Proc. 1995 PAC, May 1-5, 1995, Dallas, Texas, pp. 2184-2186 (1996).
- [5] M. Borland, "A Universal Postprocessing Toolkit for Accelerator Simulation and Data Analysis," Proc. 1998 ICAP Conference, Sept. 14-18, 1998, Monterey, California, to be published.
- [6] L. Emery, "Dispersion and Betatron Function Correction in the APS Storage Ring Using Singular Value Decomposition," these proceedings.
- [7] J. Carwardine, ANL/APS, private communication.
- [8] L. Emery, ANL/APS, private communication.

SCALING OF THIRD-ORDER QUADRUPOLE ABERRATIONS WITH FRINGE FIELD EXTENSION*

M. Venturini†

Physics Department, University of Maryland, College Park, Maryland 20742

Abstract

We present a simplified analytical model that shows how fringe field aberrations depend on a quadrupole magnet aperture. It is found that for a fixed magnet length and focal length the fringe field aberrations are smaller if the magnet aperture is larger (i.e. if the fringes are more extended).

1 INTRODUCTION

In spite of the progress made in understanding the effects of magnet fringe fields there still seems to be some confusion about the way the aberrations scale with the fringe extension. A popular belief in the accelerator physics community is that the fringe extension should be contained as much as possible. Although there may be some good reasons for that belief, limiting the strength of aberrations is not one of them. A source for this misconception may have been the fact that the intrinsic aberrations associated with the fringes increase as the length of a magnet decreases. That is, given for instance two quadrupoles with the same focal length and same aperture, the aberrations are larger for the magnet with shorter length. Short magnets are associated with relatively more extended fringe fields and this fact may have generated the wrong perception that the more extended the fringes are the higher the aberrations. In fact the opposite turns out to be true. A clarification of this issue is desirable because short-length, large-aperture magnets are increasingly being used in a number of applications. In this paper we calculate and compare the third order aberrations associated with the fringes of quadrupole magnets having the same length and same integrated on-axis gradient but different apertures (and therefore different extension of the fringes). The calculation is done for a simplified 1D model for which one can calculate the third order aberrations associated with the fringes analytically. The approximated analytical formulas are compared with an exact numerical computation carried out using MARYLIE [1]. We find that the aberrations decrease exponentially with the square root of the magnet aperture.

2 TRANSFER MAP COMPUTATION

A convenient way to represent the dynamics of a charged particle through a magnet is to write the associated transfer map in the Lie form [2]:

$$\mathcal{M} = \cdots \exp(: f_5 :) \exp(: f_4 :) \exp(: f_3 :) \mathcal{M}_2. \quad (1)$$

* Work supported by the U.S. Department of Energy.

† venturin@physics.umd.edu

The linear content of the dynamics is described by \mathcal{M}_2 while the nonlinear part is represented by the Lie generators f_n . The f_n are homogeneous polynomials of order n in the dynamical variables and $: f_n :$ are the Lie operators associated with f_n , i.e. $: f_n : g = [f, g]$ with $[\cdot, \cdot]$ being the Poisson brackets.

A map can be calculated by solving the canonical equation $\mathcal{M}' = \mathcal{M} : -H :$. In particular the linear part of the map is a solution of

$$\mathcal{M}'_2 = \mathcal{M}_2 : -H_2 :. \quad (2)$$

Here H_2 denotes the quadratic part of the Hamiltonian, which we assume can be written as a series $H = H_2 + H_3 + H_4 + \cdots$ with H_3 being the cubic part, H_4 the quartic part etc. . It can be shown that H_2 contributes to \mathcal{M}_2 and all the f_n ; H_3 contributes to the f_n with $n = 3$ and higher and so on. For the case considered in this paper $H_3 = 0$, and therefore the first nonlinear generator is f_4 . It can be shown [2] that:

$$f_4 = - \int_{z_i}^{z_f} \mathcal{M}_2^{z_i \rightarrow z} H_4(z) dz, \quad (3)$$

where with $\mathcal{M}_2^{z_i \rightarrow z}$ we indicate the solution of (2) from $z = z_i$ (some point before the magnet entry) to z_f (some point past the magnet exit). The generator f_4 contributes to the third and higher order aberrations that appear in a Taylor representation of the transfer map. We now consider a 1-D model of charged particle dynamics in a quadrupole magnet described by the Hamiltonian:

$$H = \frac{p_x^2}{2} + \frac{x^2}{2} k(z) + \frac{p_x^4}{8} + \frac{x^4}{12} k''(z) + \frac{x^3 p_x}{4} k'(z). \quad (4)$$

The focusing function $k(x)$ equals the magnetic rigidity times the on-axis gradient: $k(x) = (q/p^o) \mathcal{G}(z)$. Apart from the reduced dimensionality and omission of chromatic terms the Hamiltonian above is exact through 4th order. By indicating with $m_{ij}(z)$ the matrix representation of the linear part of the map, the 4th order Lie generator can be written as $f_4 = f_4^{geom} + f_4^{dyn}$ where:

$$f_4^{geom} = -\frac{1}{8} \int_{z_i}^{z_f} (m_{21}x + m_{22}p_x)^4 dz. \quad (5)$$

and

$$f_4^{dyn} = -\frac{1}{4} \int_{z_i}^{z_f} \left[\frac{k''(z)}{3} \mathcal{M}_2 x^4 + k'(z) \mathcal{M}_2 p_x x^3 \right] dz. \quad (6)$$

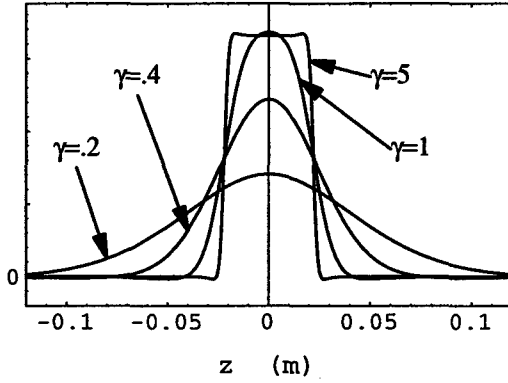


Figure 1: Profiles of the focusing function (9) for different values of the aspect ratio $\gamma = l/R$; the quadrupole semi-length is $l = .022$ m. The integrals of the various curves are the same.

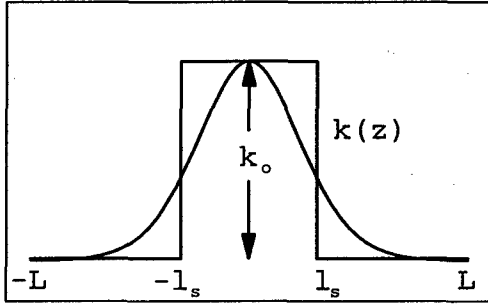


Figure 2: Approximation of the focusing function with a stepwise function.

After an integration by parts, use of Eq. (2) and the relationship

$$: H_2 : x^4 = [H_2, x^4] = \left[\frac{1}{2} p_x^2 + \frac{1}{2} k(z) x^2, x^4 \right] = -4x^3 p_x, \quad (7)$$

finally yield

$$\begin{aligned} f_4^{dyn} &= \frac{1}{12} \int_{z_i}^{z_f} k'(z) \mathcal{M}_2 x^3 p_x dz \\ &= \frac{1}{12} \int_{z_i}^{z_f} k'(z) (m_{11}x + m_{12}p_x)^3 (m_{21}x + m_{22}p_x) dz. \end{aligned} \quad (8)$$

Because f_4^{geom} does not depend on the quadrupole fields, in the following we consider f_4^{dyn} only. Our goal is now to evaluate the integral (8) for a specific choice of $k(z)$.

3 COMPUTING THE ABERRATIONS

Consider a family of quadrupoles with focusing function

$$k(z, R) = g_0 [G(z+l) - G(z-l)], \quad (9)$$

and

$$G(t) = \frac{1}{2} \frac{R^4 t}{(R^2 + t^2)^{5/2}} + \frac{1}{3} \frac{t(3R^2 + 2t^2)}{(R^2 + t^2)^{3/2}}, \quad (10)$$

where R and l are the magnet aperture and semilength. A focusing function of the form (9) is typical of iron-free quadrupole magnets like those used in the Electron Ring under construction at the University of Maryland [3]. Here we are interested in comparing quadrupole magnets that have the same length $2l$ but different aperture $2R$. The function (9) is defined in such a way that the z -integral (and therefore the magnet focal length in first approximation) does not depend on the quadrupole aperture: $\int k(z, R) dz = 8g_0 l/3$. Physically this is achieved by powering the magnets in a way dependent on their aperture. The profiles for 4 different choices of the apertures are shown in Fig 1. The 'aspect ratio' γ is defined as the ratio between the magnet length and aperture: $\gamma = l/R$. Notice that $\gamma \rightarrow \infty$ (i.e. $R \rightarrow 0$) represents the hard edge limit. In order to compute the integral (8) we first need to find the linear part of the map. We do the calculation in an approximated manner by assuming that we can represent $k(z)$ as a stepwise function, (see Fig. 2). Two parameters need to be specified: the length l_s and the peak value k_o of $k_{step}(z)$. A constraint we impose is that the integral of $k(z)$ equals that of $k_{step}(z)$. Therefore we need to specify either k_o or l_s , for any given value of the aspect ratio. We can expect that as the aspect ratio decreases and the extension of the fringes increases, l_s should become larger and k_o smaller. A possible choice is to use the standard definition of a magnet effective length and write: $k_o = k(z=0, R)$. Instead we use a slightly modified expression

$$k_o = k(z=0, R(1 + \gamma\gamma_1^{-1})) \quad (11)$$

to allow for the presence of a free parameter γ_1 to be determined later. The length l_s is then determined by requiring that $l_s k_o$ is the same as the integrated gradient. With these assumptions the elements m_{ij} of the transfer matrix from $z = -L$ to $z \in [-l_s, l_s]$ are $m_{11} = \cos \omega(z + l_s)$, $m_{21} = -\omega \sin \omega(z + l_s)$, etc., with $\omega = \sqrt{k_o}$. As a further approximation we assume that these expressions for the elements of the transfer matrix can be extended to $|z| > l_s$. This is plausible because the error we introduce in this way is small as $k(z)$ decays rapidly for $|z| > l_s$. For the same reason we can approximate $z_i = -L \simeq -\infty$ and $z_f = L \simeq \infty$ in the the integral (8). The Lie generator for the third order aberrations for the motion in the x plane consists of 5 monomials:

$$\begin{aligned} f_4^{dyn} &= x^4 f_{x^4}^{dyn} + x^3 p_x f_{x^3 p_x}^{dyn} + x^2 p_x^2 f_{x^2 p_x^2}^{dyn} \\ &\quad + x p_x^3 f_{x p_x^3}^{dyn} + p_x^4 f_{p_x^4}^{dyn}. \end{aligned} \quad (12)$$

Let us focus on $f_{x^4}^{dyn}$. By using the approximations we have indicated above we have:

$$f_{x^4}^{dyn} \simeq \frac{-1}{12} \int_{-\infty}^{\infty} k'(z) [\cos \omega(z + l_s)]^3 [\omega \sin \omega(z + l_s)] dz. \quad (13)$$

This integral can be expressed in terms of the modified Bessel functions K_0 and K_1 . Having introduced the defin-

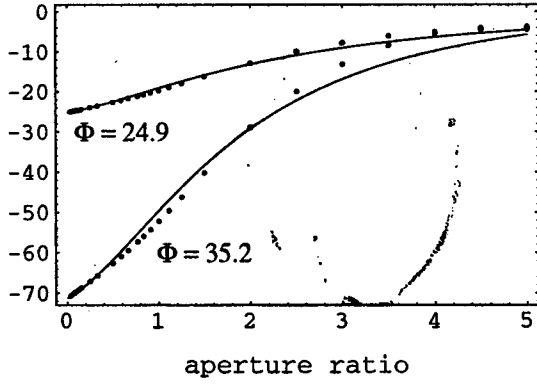


Figure 3: Lie generator $f_{x^4}^{dyn}$ (in units of m^{-4}) as a function of the aperture ratio R/l for various values of the phase advance Φ (expressed in deg). The solid lines represent Eq. (15), the dots are from the MARYLIE calculation.

ition of the function $I(\Omega)$

$$I(\Omega) \equiv \int_{-\infty}^{\infty} k'(z) \sin(\Omega z) dz = \frac{-4l}{3} g_o \Omega R \sin(\Omega l) \times \{ [4 + (\Omega R)^2] K_1(\Omega R) + 2(\Omega R) K_0(\Omega R) \}, \quad (14)$$

we find

$$f_{x^4}^{dyn} \simeq \frac{\omega}{48} [I(2\omega) \cos \Phi + \frac{1}{2} I(4\omega) \cos 2\Phi], \quad (15)$$

where $\Phi = 2\omega l_s$ is the phase advance between $z = -l_s$ and $z = l_s$. In a similar way we can calculate

$$f_{x^3 p_x}^{dyn} \simeq -\frac{I(2\omega)}{24} [\sin \Phi + 2(L - l_s) \omega \cos \Phi] - \frac{I(4\omega)}{24} [\sin 2\Phi + (L - l_s) \omega \cos 2\Phi], \quad (16)$$

as well as the remaining coefficients in (12) which we not report here. They all contain terms proportional to either $I(2\omega)$ or $I(4\omega)$. From the expression above one can recover the aberrations in the hard edge limit $R \rightarrow 0$ (with l kept fixed). We have

$$\lim_{R \rightarrow 0} I(\Omega) = -\omega^2 \sin(\Omega l), \quad (17)$$

and hence for example:

$$f_{x^4}^{dyn} = -\frac{\omega^3}{48} [\sin 2\Phi + \frac{1}{2} \sin 4\Phi]. \quad (18)$$

In the hard edge limit the quantities ω and Φ appearing in the expressions above are related by $2\omega l = \Phi$ because $l_s = l$. In the hard edge limit these expressions are exact and are consistent with the analytical formulas found in the literature. The limiting form in the infinitely soft limit can also be written using

$$\lim_{R \rightarrow \infty} I(\Omega) = -\frac{4l}{3} g_o \sqrt{\frac{\pi}{2}} \sin(\Omega l) \exp(-\Omega R) \times [4(\Omega R)^{\frac{1}{2}} + 2(\Omega R)^{\frac{3}{2}} + (\Omega R)^{\frac{5}{2}}] \quad (19)$$

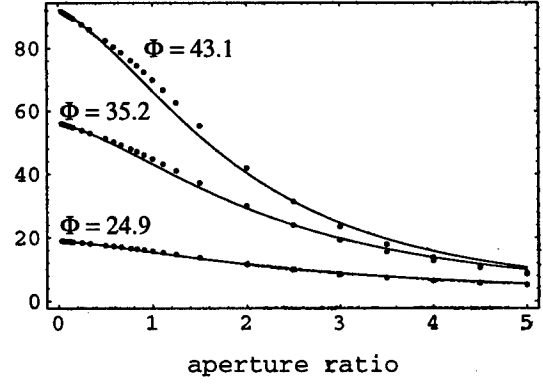


Figure 4: Lie generator $f_{x^3 p_x}^{dyn}$ (in units of m^{-3}) as a function of the aperture ratio R/l for various values of the phase advance Φ (expressed in deg). The solid lines represent Eq. (15) the dots are from the MARYLIE calculation.

Notice that the aberrations decrease exponentially with ΩR . For large values of R we have $\omega \propto 1/\sqrt{R}$ and therefore $I(2\omega) \propto \exp(-\sqrt{R} \times \text{const})$. The limiting expression (19) deviates less than a few percents from the exact expression (14) for $\Omega R \geq 2$. The Lie generators $f_{x^4}^{dyn}$ and $f_{x^3 p_x}^{dyn}$ as functions of the magnet aperture ratio ($= R/l$, i.e. the inverse of the aspect ratio γ) are shown in Figs. 3 and 4. The solid lines are plots of the analytical formulas for various values of the phase advance Φ [corresponding to various choices of the constant g_o in the expression (9) for $k(z)$]. Comparison is made with an exact numerical calculation of the transfer map carried out with MARYLIE (dots). The best agreement is obtained with a value $\gamma_1 = 1/1.17$ for the free parameter γ_1 . Notice how the qualitative dependence of the generators on the aperture ratio is well described by the analytical formulas.

4 CONCLUSION

The conclusion of this paper is that for the kind of quadrupole magnets considered here less extended fringes carry larger aberrations. The integral (6) defining the strength of the aberrations depends on two opposing factors: the size of the fringe field region (i.e. the interval in z in which the integral is non vanishing) and the derivatives of the focusing function. As a quadrupole magnet aperture decreases the fringe extension decreases but the derivative of the focusing function increases, and between the two the latter prevails.

5 REFERENCES

- [1] A. Dragt, Release of MARYLIE 3.0, these proceedings.
- [2] A. Dragt, Lie Methods for Nonlinear Dynamics with Applications to Accelerator Physics, University of Maryland Physics Department Report (1999).
- [3] M. Reiser et al., The Maryland Electron Ring for Investigating Space-Charge Dominated Beams in a Circular FODO System, These Proceedings.

COMPUTING TRANSFER MAPS FROM MAGNETIC FIELD DATA*

M. Venturini[†] and A. Dragt,

Physics Department, University of Maryland, College Park MD 20742

Abstract

In many cases the most accurate information about fields in a magnet comes either from direct measurement (using for example spinning coils) or from a numerical computation done with a 3D electromagnetic code. In this paper we show how this information can be used to compute transfer maps with high accuracy. The resulting transfer maps take into account all effects of real beamline elements including fringe-field and multipole error effects. The method we employ automatically incorporates the smoothing properties of the Laplace Green function. Consequently, it is robust against both measurement and electromagnetic code errors. The method has been implemented in the code MARYLIE as a pair of user-defined routines.

1 INTRODUCTION

The motion of charged particles through any beam-line element is described by the transfer map \mathcal{M} for that element. Through aberrations of order $(n - 1)$ such a map has the Lie representation [1, 2]

$$\mathcal{M} = \mathcal{R}_2 \exp(: f_3 :) \exp(: f_4 :) \cdots \exp(: f_n :). \quad (1)$$

The linear map \mathcal{R}_2 and the Lie generators f_i are determined by the equation of motion $\dot{\mathcal{M}} = \mathcal{M} : -H :$ where $H = H_2 + H_3 + H_4 + \cdots$ is the Hamiltonian expressed in terms of deviation variables and expanded in a homogeneous polynomial series. The deviation variable Hamiltonian H is determined in turn by the Hamiltonian K . In Cartesian coordinates with z taken as the independent variable, and in the absence of electric fields, K is given by the relation

$$K = -[p_t^2/c^2 - m^2 c^2 - (p_x - qA_x)^2 - (p_y - qA_y)^2]^{1/2} - qA_z$$

Here A is the magnetic vector potential. We therefore need a Taylor expansion for the vector potential components A_x , A_y , A_z in the deviation variables x and y . How can the coefficients of the Taylor expansion for the vector potential be determined from a knowledge of the magnetic field? In this paper we review the method we proposed in [3]. The method uses information about the fields coming from either direct measurement or numerical computation done with a 3D electromagnetic code. It is based on the calculation of Fourier integrals with suitable kernels derived from the Green function of the Laplace equation. Our approach is different from and more accurate than other methods based on numerical differentiation (e.g. [4]). A pleasant feature is relative insensitivity to the presence of noise

in the magnetic field data, which makes the method capable of providing accurate computations of high order terms in the desired Taylor expansion. An additional advantage is that it applies, with minor modifications, to both magnet data obtained by numerical computation and measured data found with spinning coils (see [3] for more details).

2 DETERMINATION OF THE VECTOR POTENTIAL

In a current-free region the magnetic field B can be described most simply in terms of a *scalar* potential ψ (with $B = \nabla\psi$) obeying the Laplace equation $\nabla^2\psi = 0$. In cylindrical coordinates the general solution to this equation (that is regular for small ρ) has the expansion

$$\psi = \sum_{m=0}^{\infty} \int_{-\infty}^{\infty} dk e^{ikz} I_m(k\rho) [\hat{b}_m \sin m\phi + \hat{a}_m \cos m\phi], \quad (2)$$

where the functions $\hat{a}_m = \hat{a}_m(k)$ and $\hat{b}_m = \hat{b}_m(k)$ are arbitrary, and I_m is the modified Bessel function. This is a "cylindrical multipole" expansion, where m is related to the order of the multipole, and should not be confused with a spherical multipole expansion. The first term on the RHS of (2) describes a purely solenoidal field ($m = 0$). The other terms in the series correspond to the dipole ($m = 1$), quadrupole ($m = 2$), \cdots components. For simplicity we will treat the terms with $m \geq 2$. The solenoidal term requires a separate, but analogous, treatment that entails no new complications. The dipole case is more complicated. In the sometimes restrictive case that the sagitta of the design orbit does not exceed the radius R introduced in Sec. 3, the methods of this paper also apply. However other methods are required if the sagitta is larger. If ψ is given in the form (2), a suitable corresponding vector potential is easily found. Since there is gauge freedom, a possible convenient choice, in the absence of a solenoidal component, is to work in a gauge satisfying $A_\phi = 0$. Suppose ψ as given by (2) is rewritten in the form

$$\psi = \sum_{m=1}^{\infty} \psi_{m,s}(\rho, z) \sin m\phi + \psi_{m,c}(\rho, z) \cos m\phi \quad (3)$$

with

$$\psi_{m,s}(\rho, z) = \int_{-\infty}^{\infty} dk e^{ikz} I_m(k\rho) \hat{b}_m(k). \quad (4)$$

[$\psi_{m,c}$ has the same form, with $\hat{a}_m(k)$ replacing $\hat{b}_m(k)$.] Then it is easily verified that the remaining components of

* Work was supported by the US Department of Energy.

[†] venturin@physics.umd.edu

the vector potential are given by the relations

$$\begin{aligned} A_\rho &= \sum_{m=1}^{\infty} \frac{\cos(m\phi)}{m} \rho \frac{\partial}{\partial z} \psi_{m,s} - \frac{\sin(m\phi)}{m} \rho \frac{\partial}{\partial z} \psi_{m,c}, \\ A_z &= \sum_{m=1}^{\infty} -\frac{\cos(m\phi)}{m} \rho \frac{\partial}{\partial \rho} \psi_{m,s} + \frac{\sin(m\phi)}{m} \rho \frac{\partial}{\partial \rho} \psi_{m,c}. \end{aligned}$$

From the two equations above it is clear that finding Taylor expansions for the vector potential components A_x , A_y , and A_z (what we need) is equivalent to finding Taylor expansions for $\psi_{m,s}$ and $\psi_{m,c}$ in the variable ρ . This is easily done by a two-step process: first, we expand the modified Bessel functions $I_m(k\rho)$ appearing in (4) as Taylor series in the quantity $(k\rho)$. Doing so produces an expansion in powers of ρ with coefficients that involve integrations over various powers of k . Second, we observe that the powers of k can be replaced by multiple differentiation with respect to the variable z . The net results of these two steps are the relations ($\alpha = c, s$)

$$\psi_{m,\alpha}(\rho, z) = \sum_{\ell=0}^{\infty} \frac{(-1)^\ell m!}{2^{2\ell} \ell! (\ell + m)!} C_{m,\alpha}^{[2\ell]}(z) \rho^{2\ell+m}. \quad (5)$$

The index $[2\ell]$ indicates the 2ℓ derivative with respect to the longitudinal variable z . The functions $C_{m,\alpha}^{[0]}(z)$ are the generalized on-axis gradients. Note that the generalized gradients depend on the longitudinal variable z . For fields produced by long well-made magnets, however, the z dependence will be significant only at the ends. We conclude that the dynamics of a charged particle passing through a region of space occupied by a magnetic field described by the scalar potential (2) is completely determined by a knowledge of the generalized on-axis gradient functions $C_{m,\alpha}^{[0]}(z)$ and their derivatives.

3 COMPUTATION OF GENERALIZED GRADIENTS FROM FIELD DATA

Suppose the radial component of the magnetic field B_ρ is known, either by measurement or computation, on the surface of some infinitely long cylinder of radius R . Moreover, suppose that the field is given in terms of an angular Fourier series,

$$B_\rho = \sum_{m=1}^{\infty} B_m(R, z) \sin(m\phi) + A_m(R, z) \cos(m\phi). \quad (6)$$

It can be shown [3] that the generalized on-axis gradients appearing in the expansion coefficients for the scalar potential (8) can be written as

$$C_{m,s}^{[n]}(z) = \frac{i^n}{2^m m!} \frac{1}{\sqrt{2\pi}} \int_{-\infty}^{\infty} dk e^{ikz} \frac{k^{m+n-1}}{I'_m(kR)} \tilde{B}_m(R, k). \quad (7)$$

The expression for $C_{m,c}^{[n]}(z)$ has $\tilde{A}_m(R, k)$ replacing $\tilde{B}_m(R, k)$. Here $\tilde{B}_m(R, k)$ and $\tilde{A}_m(R, k)$ are the Fourier

transforms of $B_m(R, z)$ and $A_m(R, z)$, e.g.,

$$\tilde{B}_m(R, k) = \frac{1}{\sqrt{2\pi}} \int_{-\infty}^{\infty} dz e^{-ikz} B_m(R, z). \quad (8)$$

In the case where the magnetic field is produced by an iron dominated magnet, and is therefore localized in space, the integrals (8) can be considered to have, in practice, finite limits of integration. With some care, an effective cut-off can also be found even if the fields extend to infinity since they fall off sufficiently rapidly at infinity. Also, since the generalized Bessel function $I'_m(w)$ increases exponentially for large $|w|$, there is also, in effect, a cut-off in k for the integral (7) defining the generalized gradients.

4 TESTS AND EXAMPLES

The method described in Section 3 has been implemented in the code MARYLIE [2] as a pair of user-defined routines. Versions of the two routines exist for both MARYLIE 3.0, which has recently been released [5] and MARYLIE 5.0, which is still under development. The first routine, 'usr15', reads the magnetic field data from an external file and computes the functions $A_m(R, z)$ and $B_m(R, z)$. The second routine, 'usr16', uses the output of 'usr15' to calculate the corresponding transfer map. In the input file one has to provide a listing of the B_x and B_y components of the magnetic field together with the coordinates (x, y, z) of the points on the cylindrical surface of radius R on which the field is defined. For a fixed z , there are n_ϕ equally distributed points along a circumference of radius R centered in z and there are n_z such slices. A user-defined routine in MARYLIE is invoked in the master input file like any other MARYLIE command, together with the required parameters. For example, for 'usr15' there are two sets of parameters one needs to specify. The first set consists of the file number containing the magnetic field data, the numbers n_ϕ and n_z , a scaling factor for the z coordinate and the magnetic field and the radius R . The second parameter set contains the numbers of files in which to write the normal and skew harmonics, and the values of the integrated harmonics respectively. An excerpt of a MARYLIE master input file containing a setting for 'usr15' is shown below:

```
#menu
  hrmnscs   usr15
    1  501  101  0.001  1  0.03
  hrmpsl1 ps1
    40  42   12  0  0  0
#lines
  harm
    1*hrmpsl1 1*hrmnscs
```

In order to test both the routines and the method we treated the case of an ideal iron-free Lambertson quadrupole. The use of this case as an example has the virtue that the various $C_{m,\alpha}^{[n]}(z)$ can also be determined analytically (see [3]) given a knowledge of the location of the conductors. Results are shown in Figs. 1 and 2. In Fig. 1 the dashed

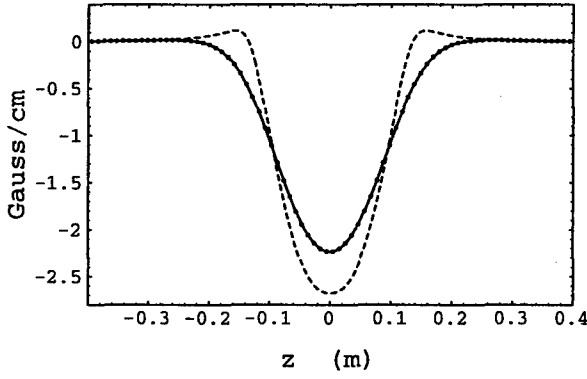


Figure 1: Plot of the scaled harmonic $B_2(R, z)/R$ (dashed line) and the on-axis gradient $2C_{2,s}^{[0]}(z)$ as calculated from surface data (dots) and analytically (solid line) for an ideal Lambertson quadrupole.

line is the function $B_2(R, z)/R$ as calculated numerically by using the Biot-Savart law. The solid line represents the on-axis gradient, which is equal to $2C_{2,s}^{[0]}(z)$, as calculated analytically, while the dots represent the same function as calculated from the surface data. The deviation between $B_2(R, z)/R$ and $2C_{2,s}^{[0]}(z)$ is due to terms in the multipole expansion containing derivatives of $2C_{2,s}^{[0]}(z)$. These terms are the so called pseudo-multipoles. This can be seen by writing the multipole expansion for B_ρ through 6th order in ρ :

$$B_\rho = \left(2C_{2,s}^{[0]}\rho - \frac{1}{3}C_{2,s}^{[2]}\rho^3 + \frac{1}{64}C_{2,s}^{[4]}\rho^5 \right) \sin 2\phi + 6C_{6,s}^{[0]}\rho^5 \sin 6\phi. \quad (9)$$

In Fig. 2, as an indication of the reliability of the method, we report the 8th derivative of the generalized gradient (needed for a 9th order code) calculated from the surface data (dots) compared to the analytical profile (solid line).

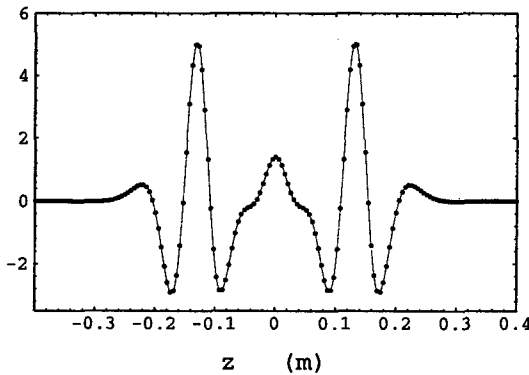


Figure 2: Function $C_{2,s}^{[8]}(z)$ (in units of 10^{-5} Gauss/cm⁹) as calculated from surface data (dots) and analytically (solid line) for an ideal Lambertson quadrupole.

Finally as an example of application, Figs. 3 and 4 show the result of magnetic field analysis for the Return end of a

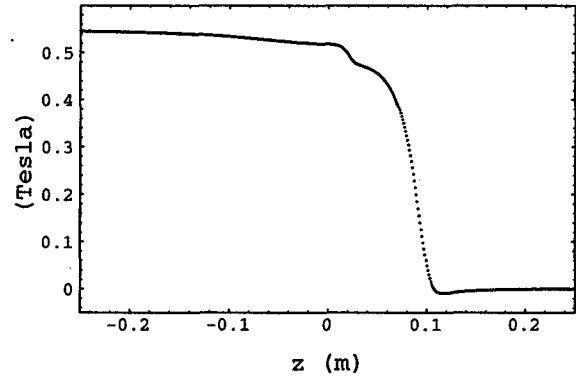


Figure 3: Harmonic $B_2(R, z)$ (quadrupole field component) for the Return End; $R=3$ cm.

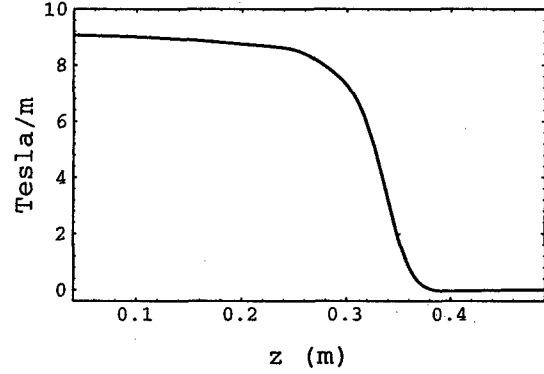


Figure 4: Generalized gradient $C_{2,s}(z)$ for the Return End, ($z = 25$ cm in this picture corresponds to $z = 0$ of Figs. 3).

High Gradient quadrupole in LHC [6].

5 ACKNOWLEDGEMENTS

We thank P. Walstrom for helpful discussions and for sharing his Fourier integration and Bessel function routines with us.

6 REFERENCES

- [1] A. Dragt, Lie Methods for Nonlinear Dynamics with Applications to Accelerator Physics, University of Maryland Physics Department Report (1998).
- [2] A. Dragt, F. Neri, G. Rangarajan, D. Douglas, L. Healy, and R. Ryne, Ann. Rev. Nucl. Part. Sci. **38** (1988) pp. 455-96.
- [3] M. Venturini and A. Dragt, Accurate Computation of Transfer Maps from Magnetic Field Data, to be published in NIM-A.
- [4] S. Caspi, M. Helm, and L.J. Laslett, IEEE Trans. on Magnetics, vol.30, no. 4, (1994).
- [5] A. Dragt, Release of MARYLIE 3.0, these proceedings.
- [6] G. Sabbi, HGQSO3 End Field Analysis, Fermilab Report TD-98-010 (1998); Private Communication.

RESEARCH ON DC-CLEARING ELECTRIC FIELD AND CHANGES OF FOCUSING STRUCTURE PARAMETERS OF STORAGE RING

X.Q. Wang*, Y.J. Pei, X.L. Dong, H.L. Xu, L. Shang, L. Wang,

K.J. Fan, G.C. Wang, C.G. Yao, S.M. Hu, X.F. Luo

NSRL, USTC, P.O. Box 6022, Hefei, Anhui 230029, China

Abstract

This paper presents DC clearing field to clear ions in vacuum pipe of Hefei ring. It also presents changes of focusing structure parameters caused by the clearing field. It concludes that tune shifts caused by the field are related to real-time close orbit of the beam. The paper points out that the field asymmetrically distributed along the ring destroys the symmetry of focusing structure and decreases the ring acceptance, which has negative effect to injection and accumulation process in certain condition.

1 INTRODUCTION

Some clearing field patterns to suppress instability are reported by the papers¹⁻⁴. One of them is produced by DC-clearing electrode in circular tube, its function was described⁵⁻⁸, but the potential reported in paper 9 and 10 isn't analytic in two-dimension boundary problem. The force and potential functions presented in this paper are analytic; the data are taken from Hefei ring. There are thirteen electrodes in the tubes installed asymmetrically along the ring, their length is 17.9 meters that is 1.86 times the length of all quadrupole magnets. They have played an important role in clearing ion, suppressing ion instability and storing beam since 1989^{5-8,11,12}. These electrodes destroy the lattice symmetry, research on linear influence of the field to betatron tunes of beam was presented^{1-4,9}. This paper only discusses the influence of the dipole and quadrupole of DC clearing field on beam: Twiss parameters¹³, ring acceptance and multi turn injection.

2 ANALYTIC EXPRESSIONS

Analyze the DC field in uniaxial bicylindrical surface-boundary, the analytic expressions of potential and field caused by inner wire in circular pipe¹¹ can be get,

$$\varphi(x, z) = -\frac{V_{dce}}{\ln(ar/R\delta)} \cdot \ln \left[\frac{R\sqrt{x^2 + (z+a)^2}}{a\sqrt{x^2 + (z+b)^2}} \right] \quad (1a)$$

$$\psi_+(x, z) = -\frac{V_{dce}}{\ln(ar/R\delta)} \cdot \arctg \left[\frac{x^2 + z^2 + z(b+a) + R^2}{x(b-a)} \right] (x > 0) \quad (1b)$$

$$\psi_-(x, z) = +\frac{\pi V_{dce}}{\ln(ar/R\delta)} - \psi_+(-x, z) \quad (x < 0) \quad (1c)$$

$$a = a_0 + \delta, \quad b = \frac{R^2}{a_0 + \delta}$$

$$\delta = \frac{2a_0 R^2}{R^2 + a_0^2 - r^2 + \sqrt{(R^2 + a_0^2 - r^2)^2 - 4a_0^2 R^2}} - a_0$$

Here, the coordinate origin is on pipe axis. x is radial coordinate (horizontal on the cross section). z is vertical. R is inner radius of the pipe, and r is radius of the wire. a_0 is the distance from the wire to the pipe axis, and V_{dce} is DC clearing voltage. The unit of V_{dce} is DC clearing voltage and other units are meter. The two-dimension schematic diagrams of the clearing field are shown in Fig.1 for an example. The figure presents equipotential lines and field lines.

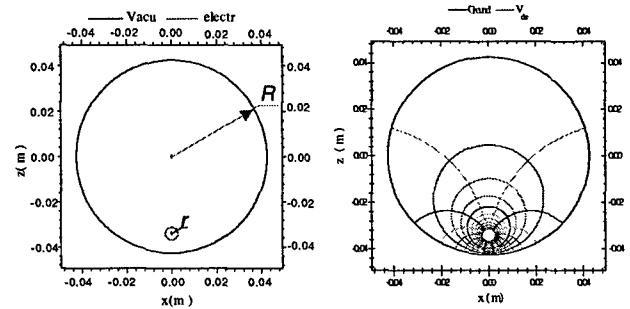


Fig.1 Schematic diagram of equipotential lines and field lines of the DC clearing field

3 TUNE SHIFTS NEAR AXIS OF PIPE

There is focusing effect due to quadrupole of the field¹¹.

3.1 Linear formulation

The focusing effect of the field quadrupoles is

$$K_E = K_z(0,0) = -K_x(0,0) = \frac{-e(b^2 - a^2)}{E_c R^4 \ln(ar/R\delta)} \cdot V_{dce} \quad (2)$$

in first-order approximation. The unit of K_E is m^{-2} , E_c is eV and e is an electronic charge. So the quadrupole of field is focusing (defocusing) on beam in vertical (horizontal), and second-order differential equations are

$$\frac{d^2 x}{ds^2} + (K_Q - K_E)x = 0, \quad (3a)$$

$$\frac{d^2 z}{ds^2} - (K_Q - K_E)z = 0. \quad (3b)$$

Here, the unit of K_Q , focusing strength of quadrupole magnets, is m^{-2} . The K_E is always less than K_Q . Thus, the tune shifts of beam are

* wangxq@ustc.edu.cn, xwang@ssrl.slac.stanford.edu (only before June 3, 1999)

$$\Delta v_x = \frac{e(b^2 - a^2) \int_{L_{dce}} \beta_x(s) ds}{4\pi E_c R^4 \ln\left(\frac{ar}{R\delta}\right)} \cdot V_{dce}, \quad (4a)$$

$$\Delta v_z = -\frac{e(b^2 - a^2) \int_{L_{dce}} \beta_z(s) ds}{4\pi E_c R^4 \ln\left(\frac{ar}{R\delta}\right)} \cdot V_{dce}. \quad (4b)$$

L_{dce} implies that integrates in the clearing field sections. It's obvious that tunes are linear relevance to voltage. The coefficients rely only upon the lattice mode and the electrode structure, and their sign reverse in different direction. The relevance is illustrated in fig.2 and fig.3 (circle dot is calculated, square dot is measured). The horizontal coordinates show applied voltage and the vertical show tune. Here, the straight line segments being

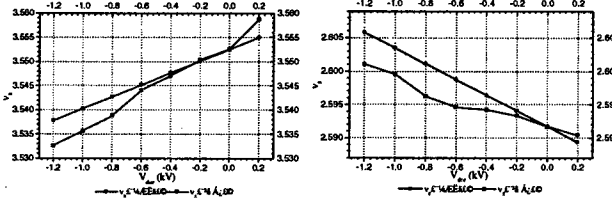


Fig.2 Schematic change of tune in hori. Direction Fig.3 Schematic change of tune in verti. Direction

approximately beeline is based on the (4), and another line segments is based on measured data. We have three conclusions from the figures. First, there is defocusing in vertical and focusing in horizontal based on the (4) or the measured data. Second, the tune shifts always increase as the voltage rises based on numerical calculation or the measured data. Third, relevance between the tune shifts and voltage is nonlinear based on measured data, which are different from the (4).

3.2 Nonlinear formulation

Fig.2 and 3 show that tune shift is larger in vertical than in horizontal at the same DC voltage. In linear formulation, the effect of the quadrupoles of field on the beam is calculated along the pipe axis. Neglect higher order quantities such as $(x/a)^2$, $(x/b)^2$, $(z/a)^2$ and $(z/b)^2$ in the denominators, we can derive second-order nonlinear differential equations,

$$\frac{d^2 x}{ds^2} + \left[K_Q - K_E \left(1 - 2 \cdot \frac{a^2 + ab + b^2}{R^2(a+b)} z \right) \right] x = 0, \quad (5a)$$

$$\frac{d^2 z}{ds^2} - (K_Q - K_E) z = -\frac{eV_{dce}(b-a)}{E_c R^2 \ln(ar/R\delta)}. \quad (5b)$$

3.3 Relevance on close orbit

The right of (5b) is an analogue of close orbit displacement. There is always a vertical dipole of the field on the vertical symmetry plane^{11,12}, so the stored beam leave from the central orbit, that is why the real focusing strength is smaller than K_E based on (4). The displacement between close orbits is shown in fig.4, which is respectively with or without DC-septum magnetic field (electrons energy is 200MeV or 800MeV),

the DC voltage is -1kV, the baseline (square dot) is the beam close orbit (energy of 800MeV) without DC-septum magnetic field. The horizontal axes denote the longitudinal coordinate of the ring. The difference among the real orbits can be observed obviously in the fig.4.

B. Autin defined tune is the mean value of betatron oscillations per turn over a great number of turns¹⁴. The differential equation (5b) contains the correction term related to close orbit, the correction term sign indicates vertical orientation of close orbit. Thus, we may calculate accurately tune shift so long as we know close orbit along ring. But, it's only a rough calculation if without enough accuracy of monitor system.

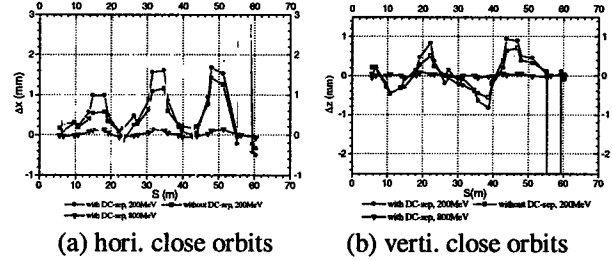


Fig.4 The relative displacement measured

The tune shifts change obviously as close orbit moves based on the nonlinear formulation. The vacuum chamber of Hefei ring was opened at the first of 1997. When it was closed, the injection working point changed and the accumulation capability was bad when a couple of electrodes didn't operate, the machine runs well after all electrodes operated again..

4 CORRECTION OF RING LATTICE

Fig.5 shows the fitting curves of β and η functions of the GPLS mode without clearing field, the starts of curves are the midpoint of fourth long linear section.

4.1 asymmetric distribution

Regarding whole ring as one period, by the help of MULIN code (developed in the NSRL), the β and η functions of the GPLS mode with DC-clearing field can be calculated, the DC voltage is -1.0kV, and other parameters are the same as those without clearing field. There are three cases: first, all of thirteen electrodes operate; next, two of them turn off; last, fifteen electrodes operate after Phase two project will be completed. These β and η functions are shown in the fig.6, 7 and 8. Obviously, the symmetry of GPLS mode is distorted and β and η functions become asymmetry along the ring as the electrodes operate in the fig.6 and 7. If fifteen electrodes are in operation, the symmetry of GPLS mode will approach those without clearing electrode.

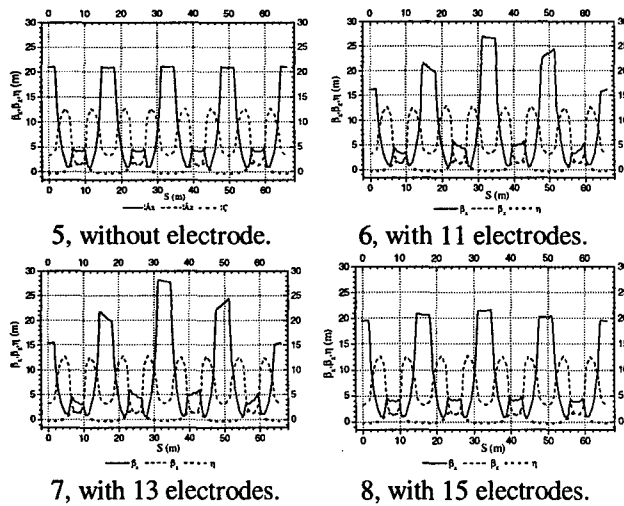


Fig.5-8 Twiss parameter curves along the ring

4.2 Ring acceptance

The β_x distribution in each long linear section is same without the electrode. When electrodes work, the β_x in the fourth long linear section decreases while increases in the second long linear section, see Fig.6 and 7. The β_x in the second section midpoint is larger than that of the first one, their ratios are 1.31 in Fig.6 and 1.37 in Fig.7, that means the amplitude of betatron oscillation increases respectively 15% and 17%, in other words, the ring acceptances decrease. Simply, neglect energy spread and consider the dynamic aperture is large enough, study the influence of clearing field on ring acceptance. Without electrode, the injection bottleneck of GPLS mode is the restrict of the strip of pulse septum near injection point, the acceptance $81 \text{ nm} \cdot \text{rad}$. The bottleneck maybe in the second long section when electrodes work, the acceptance is $66 \text{ nm} \cdot \text{rad}$, that means the acceptance will decrease 19% if DC electrodes in operation asymmetrically.

It will increase commissioning complicity if the vacuum chamber aperture in second straight section decreases. The horizontal half width of the chamber is 40 mm after superconducting wiggler was installed. The ring acceptance decreases 30%, down to $57 \text{ nm} \cdot \text{rad}$ when the electrodes work. If 15 electrodes are in operation, The acceptance of the GPLS is $75 \text{ nm} \cdot \text{rad}$, only decrease 7%, the limit of ring acceptance is the effective horizontal half width near the septum strip, and the acceptance will restore to $79 \text{ nm} \cdot \text{rad}$ if the chamber width remains its size.

Deduce from this, the double symmetry of HBLS mode is also destroyed when the electrodes work. So the beam envelop becomes larger where β function increases. abnormally, the electrons lose easily and the accumulation becomes difficult, that's why the commissioning of the HBLS mode is so difficult now. The symmetry of the HBLS mode will be recovered and beam accumulation will be improved after fifteen DC clearing electrodes work.

5 CONCLUSION

Three conclusions can be drawn. First, the clearing electrodes can cause tune shifts. Second, the relativity between tune shifts and DC voltage is linear and can be calculated if no perturbation of closed orbit. Tune shifts will be affected by real-time closed orbit if the orbit is distorted, and can be calculated only based on nonlinear the asymmetrically distributed electrodes can destroy the periodic symmetry of Twiss parameters and decrease ring acceptance, which will do some bad effect on injection. If these electrodes are distributed symmetrically, these bad effects will decrease. Therefore, clearing electrodes should be installed symmetrically as possible.

Reference

- [1] R D Kohaupt, In. Bericht DESY H1-71/2, 1971.
- [2] T Kasuga et al., IEEE NS-32 (5) (1985) 2550.
- [3] T Kasuga et al., J. Jour. of A. Phys. **24** (9) (1985) 1212.
- [4] T Kasuga, J. Jour. of A. Phys. **25**(11) (1986) 1711.
- [5] Duohui He, Int. Jour. Mod. Phys. A(P. S.) **2A** (1993) 552.
- [6] Y J Pei, Proc. of 1st Taiwan Straits Symp. on SR, 1993, p.40.
- [7] C Y Yao & Y J Pei, AIP Confer. Proc. **326**, 1993, p.197.
- [8] Y J Pei, J. of China of S. and T. **25** (1995) 64.
- [9] L Chen et al., Proc. of the Workshop on Beam Ins. in Storage Rings, 1994, p.65.
- [10] L Chen et al., Jour. of Shenzhen Uni. (S. & E.) **13** (1~2) (1996) 1.
- [11] X Q Wang et al., Jour. of China Uni. of S. & T. **27** (2) (1997) 228.
- [12] X Q Wang et al., Jour. of China Uni. of S. & T. **28** (2) (1998) 166.
- [13] E D Courant & H S Snyder, Annals of Physics **3** (1958) 1.
- [14] B Autin, AIP Confer. Proc. **153**(1), 1985, p.288.

ON THE SANDS AND REES MEASUREMENT METHOD OF THE LONGITUDINAL COUPLING IMPEDANCE

A. Argan, INFN- LNF; L. Palumbo⁺, Dip. di Energetica-Roma;
M.R. Masullo, INFN- Napoli; V.G. Vaccaro, INFN- Napoli/Dip. Sci. Fisiche

Abstract

By means of a general theory we examine the Sands and Rees method of measurement of the longitudinal coupling impedance between a particle beam and the vacuum chamber components. We discuss the validity limits of the method in relation to the presence of the central wire which simulates the beam.

1 INTRODUCTION

The longitudinal coupling impedance (LCI) of an ultrarelativistic point charge q , travelling on a beam pipe axis, is defined as:

$$Z(\omega) = -\frac{1}{q} \int_{-\infty}^{+\infty} E_{sz}(r=0, z; \omega) e^{jk_0 z} dz \quad (1)$$

where \vec{E}_s is the Fourier transform of the longitudinal electric field on the pipe axis and $k_0 = \omega/c$. The impedance is often measured by means of the transmission Scattering (S) parameter of the device. This method has been proposed in 70's on the ground of intuitive considerations. The basic idea is that the relativistic beam fields in the vacuum chamber can be simulated by means of a TEM wave propagating thanks to the presence of a central wire [1,2,3]. Several formulae have been proposed to express the LCI as function of the transmission S-parameter. The first in order of time is the so called relation of Sands and Rees suggested for the estimate of $Z(\omega)$ when the wire radius is very small [4]:

$$Z(\omega) = 2R_0 \left(\frac{S_{2,1}^{REF} - S_{2,1}^{DUT}}{S_{2,1}^{REF}} \right) \quad (2)$$

$S_{2,1}^{DUT}$ is the transmission parameter of the component under test, $S_{2,1}^{REF}$ the parameter of a portion of unperturbed coaxial line of the same length and R_0 is the characteristic impedance of the transmission line.

An improved relation valid for a single lumped impedance has been provided by Hahn and Pedersen [5] where $S_{2,1}^{REF}$ at the denominator of (2) has been replaced by $S_{2,1}^{DUT}$. Other expressions have been proposed for distributed impedances [6,7] for which the Hahn and Pedersen formula breaks down.

Aim of this paper is to give a more rigorous proof of the relation (2) when the wire radius approaches zero. All the results have been obtained using only the Schelkunoff's Field Equivalence Principle and the Lorentz Reciprocity Theorem.

2 LONGITUDINAL COUPLING IMPEDANCE BELOW CUTOFF

A point charge q moving, with velocity $v = \pm c \hat{i}_z$, along z axis of a conducting beam pipe of radius b has a current density spectrum given by:

$$\vec{J}_q^\pm(\vec{r}, z; \omega) = \pm q \frac{\delta(r)}{2\pi r} e^{\mp jk_0 z} \hat{i}_z \quad (3)$$

and produces electromagnetic fields \vec{E}_q^\pm and \vec{H}_q^\pm on the pipe walls given by:

$$\vec{E}_q^\pm(r=b, \varphi, z; \omega) = Z_0 \frac{q}{2\pi b} e^{\mp jk_0 z} \hat{i}_r \quad (4)$$

$$\vec{H}_q^\pm(r=b, \varphi, z; \omega) = \pm \frac{q}{2\pi b} e^{\mp jk_0 z} \hat{i}_\varphi \quad (5)$$

where Z_0 is the characteristic impedance of the vacuum.

Let the beam pipe have an aperture S_A on the conducting wall which in general can couple to an external structure. By using the Schelkunoff's Field Equivalence Principle, we may consider a system of equivalent magnetic currents \vec{J}_{ms} on the aperture surface S_A . The electromagnetic fields into the waveguide can be written as:

$$\vec{E} = \vec{E}_q^+ + \vec{E}_s \quad \vec{H} = \vec{H}_q^+ + \vec{H}_s \quad (6)$$

where \vec{E}_s and \vec{H}_s are the fields scattered by the aperture, i.e., the fields radiated by the surface currents \vec{J}_{ms} inside the pipe.

In order to calculate the LCI as function of the magnetic currents \vec{J}_{ms} [8,9] we can apply the Lorentz Reciprocity Theorem relating the fields \vec{E}_q^-, \vec{H}_q^- to the fields \vec{E}_s, \vec{H}_s of the unperturbed structure. Below the cutoff frequency, for an infinite pipe, we get [10]:

$$-\frac{1}{q} \int_{-\infty}^{+\infty} E_{sz}(r=0, z) e^{jk_0 z} dz = -\frac{1}{q} \iint_{S_A} \vec{H}_q^- \cdot \vec{J}_{ms} dS \quad (7)$$

which recalling the definition (1) becomes:

$$Z(\omega) = \frac{1}{2\pi q b} \iint_{S_A} J_{ms\varphi} e^{jk_0 z} dS \quad (8)$$

3 BEAM SIMULATED BY A WIRE

We assume, now, that in the same pipe a perfectly conducting wire of radius a is stretched along the z axis. The beam pipe so modified becomes a transmission line. In this new configuration, we consider a generator which excites a TEM wave \vec{E}_q^+, \vec{H}_q^+ reproducing the field \vec{E}_q^+, \vec{H}_q^+ of the charge in the unperturbed waveguide. We have, then:

$$\vec{E}_q^+ = \frac{qZ_0}{2\pi r} e^{-jk_0 z} \hat{i}_r \quad \vec{H}_q^+ = \frac{q}{2\pi r} e^{-jk_0 z} \hat{i}_\phi \quad (9)$$

Calling, now, \vec{E}_A the electric field on the aperture and \vec{J}'_{ms} the equivalent magnetic surface currents, we have that:

$$\vec{J}'_{ms} = \hat{i}_r \times \vec{E}_A \quad (10)$$

The electromagnetic field inside the coaxial line can be expressed by the relations:

$$\vec{E}' = \vec{E}_q^+ + \vec{E}_s' \quad \vec{H}' = \vec{H}_q^+ + \vec{H}_s' \quad (11)$$

where \vec{E}_s' and \vec{H}_s' are the fields scattered by the aperture.

Below the cutoff frequency of the coaxial line mode $TE_{1,1}$, the fields \vec{E}_s' and \vec{H}_s' at a sufficient distance from the aperture can be represented by means of the TEM components only:

$$\vec{E}_s'^{\pm} = \frac{\alpha^{\pm}}{r} e^{\mp jk_0 z} \hat{i}_r \quad \vec{H}_s'^{\pm} = \pm \frac{\alpha^{\pm}}{Z_0 r} e^{\mp jk_0 z} \hat{i}_\phi \quad (12)$$

In order to calculate the coefficients α^+ and α^- we apply the Lorentz Reciprocity Theorem to the volume V_1 (fig.1), getting:

$$\alpha^{\pm} = \mp \frac{1}{4\pi b \ln\left(\frac{b}{a}\right)} \iint_{S_A} J'_{ms\phi} e^{\pm jk_0 z} dS \quad (13)$$

We observe that the TEM components of the fields scattered by the aperture vanish as the wire radius a tends to zero. Furthermore the eigenfunctions of the coaxial line approach the cylindrical waveguide modes for $a \rightarrow 0$, therefore, the surface currents \vec{J}'_{ms} tend to the \vec{J}_{ms} . Thus we can express the longitudinal coupling impedance:

$$\lim_{a \rightarrow 0} Z(\omega) = \frac{1}{2\pi q b} \iint_{S_A} J'_{ms\phi} e^{jk_0 z} dS \quad (14)$$

Multiplying and dividing the right-hand side of the above equation by the quantity $2Z_0 \ln(b/a)$ it is readily found that:

$$\frac{1}{2\pi q b} \iint_{S_A} J'_{ms\phi} e^{jk_0 z} dS = -2 \frac{R_0 \alpha^+}{qZ_0/2\pi} \quad (15)$$

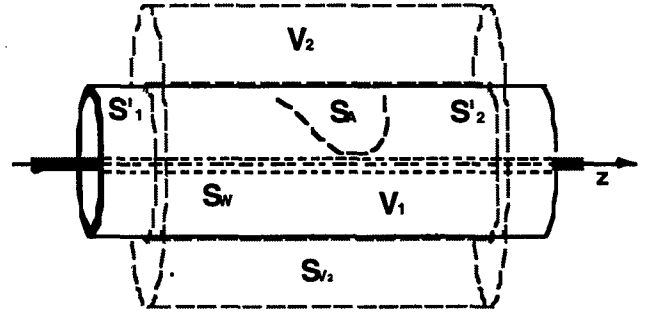


Figure 1: Geometry of the structure.

Regarding the coaxial structure as a two-port network, it is possible to express the right-hand side of the equation (16) by means of the circuital parameters of such device. In fact, if the output line is terminated in a matched load and on the input side we put a generator, matched to the line, such as to produce the incident wave provided by (9), the transmission parameter of the S-matrix is given by:

$$S_{2,1}^{DUT} = \frac{V_2^-}{V_1^+} \Big|_{V_2^+=0} = \frac{(qZ_0/2\pi + \alpha^+)}{qZ_0 e^{-jk_0 z_1}/2\pi} e^{-jk_0 z_2} = \left(1 + \frac{\alpha^+}{qZ_0/2\pi}\right) e^{-jk_0 l} \quad (16)$$

where $l = z_2' - z_1'$.

For a portion of unperturbed coaxial line of length l , we have:

$$S_{2,1}^{REF} = e^{-jk_0 l} \quad (17)$$

Then, using (16) and (18), we obtain:

$$Z(\omega) = -2 \frac{R_0 \alpha^+}{qZ_0/2\pi} = 2R_0 \left(\frac{S_{2,1}^{REF} - S_{2,1}^{DUT}}{S_{2,1}^{REF}} \right) \quad (18)$$

4 IMPEDANCE FOR A SMALL BUT FINITE RADIUS OF THE WIRE

Our aim is now to account for the effect of the central conductor with a small but finite radius.

Applying twice the Reciprocity Theorem in relation to the volumes V_2 and V_1 (fig.1), with the equivalent currents $(-\vec{J}'_{ms}, -\vec{J}_{ms})$ in V_2 and $(\vec{J}'_{ms}, \vec{J}_{ms})$ in V_1 as fields sources, and using the fields given by eqs.(8) and (11) we get the equations:

$$Z(\omega) + Z^*(\omega) = \frac{1}{q^2} \left[\iint_{S_{V_2}} (\vec{E}'^* \times \vec{H} + \vec{E} \times \vec{H}'^*) \cdot d\vec{S} - \iint_{S_A} \vec{H}_s'^* \cdot \vec{J}_{ms} dS - \iint_{S_A} \vec{H}_s \cdot \vec{J}_{ms}'^* dS \right] \quad (19)$$

$$\iint_{S_A} \vec{H}_s^* \cdot \vec{J}_{ms} dS + \iint_{S_A} \vec{H}_s \cdot \vec{J}_{ms}^* dS = - \iint_{S_w} \hat{i}_r \times \vec{H}_s^* \cdot \vec{E}_s dS \quad (20)$$

where $Z'(\omega)$ is the impedance in presence of the wire and S_w is the whole wire surface.

For very small wire radius, we may put $\vec{E}_s(r=a, \varphi, z) \approx \vec{E}_s(r=0, z)$ and, assuming the aperture smaller than the wavelength, the equations (19) and (20) give:

$$Z(\omega) + Z'^*(\omega) - \frac{Z'^*(\omega)Z(\omega)}{2R_0} = \frac{1}{q^2} \iint_{S_2} (\vec{E}'^* \times \vec{H} + \vec{E} \times \vec{H}'^*) d\vec{S} \quad (21)$$

In this expression the perturbed terms are unknown and depend on the wire thickness. Assuming that for small radius, there is a little difference between the perturbed and unperturbed fields, we will consider two perturbative approaches:

4.1 Substitution $(\vec{E}, \vec{H}) \rightarrow (\vec{E}', \vec{H}')$

We obtain:

$$Z(\omega) = \frac{4R_0^2}{4R_0^2 - |Z'(\omega)|^2} \left[Z'(\omega) - \frac{|Z'(\omega)|^2}{2R_0} \right] \quad (22)$$

which can be expressed by means of the transmission S -parameters:

$$Z(\omega) = \frac{2R_0}{1 - |S_{2,1}^{REF} - S_{2,1}^{DUT}|^2} \left[\frac{S_{2,1}^{REF} - S_{2,1}^{DUT}}{S_{2,1}^{REF}} - |S_{2,1}^{REF} - S_{2,1}^{DUT}|^2 \right] \quad (23)$$

We observe that when the wire radius a tends to zero the above equation approaches the Sands and Rees formula.

4.2 Substitution $(\vec{E}', \vec{H}') \rightarrow (\vec{E}, \vec{H})$

We get:

$$Z(\omega) = \frac{2R_0}{2R_0 - Z'^*(\omega)} \left[Z'(\omega) - \frac{|Z'(\omega)|^2}{R_0} \right] \quad (24)$$

which can be express by means of the transmission S -parameters as:

$$Z(\omega) = \frac{2R_0 S_{2,1}^{DUT} S_{2,1}^{REF*}}{|S_{2,1}^{DUT}|^2} \left[\frac{S_{2,1}^{REF} - S_{2,1}^{DUT}}{S_{2,1}^{REF}} - 2|S_{2,1}^{REF} - S_{2,1}^{DUT}|^2 \right] \quad (25)$$

We observe that also this relation tends to the Sands and Rees formula when the wire radius approaches zero. Neglecting the second order term in the square brackets, it can be rewritten as:

$$Z(\omega) = 2R_0 \frac{S_{2,1}^{REF} - S_{2,1}^{DUT}}{S_{2,1}^{DUT}} \left(\frac{qZ_0/2\pi + \alpha^+}{qZ_0/2\pi + \alpha^{+*}} \right) \quad (26)$$

which becomes similar to the Hahn and Pedersen formula for a small radius.

5 COMPARISON WITH EXPERIMENTAL DATA

We have performed measurements with the coaxial wire method on a device similar to fig.1 with four narrow slots as aperture [10]. The results are shown in fig.2, where the curves corresponding to: a) ref. [4]; b) ref. [5]; c) eq. (23); d) eq. (25). We notice that there are no visible difference between a) and c), and b) and d).

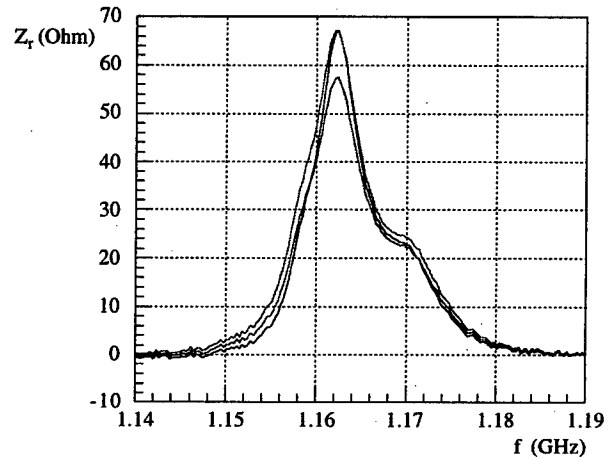


Figure 2: Real part of impedance calculated using the expressions given by: a) • ref. [4]; b) • ref. [5]; c) • eq. (23); d) • eq. (25).

6 REFERENCES

- [1] M. Sands and J. Rees, SLAC-Report PEP-95, (1974).
- [2] G. Lambertson, unpublished, (1987).
- [3] F. Caspers, Proc. of the Workshop on impedance and current limitations, (ERSF-Grenoble, France, oct 1988), CERN PS/88-59.
- [4] L. Palumbo and V. G. Vaccaro, LNF-89/035(P), (1989).
- [5] H. Hahn, F. Pedersen, BNL 50870, Particle Accelerators and High-Voltage Machines TID-4500, (1978).
- [6] L. S. Walling et al., NIM A 281, pp. 433-447, (1989).
- [7] V. G. Vaccaro, INFN/TC-94/023, (1994).
- [8] R. L. Gluckstern, Physical Rev. A, vol.46, pp. 1106-1115, (1992).
- [9] S. S. Kurennoy, Report SSLC-636, (1983).
- [10] A. Argan, "L'impedenza longitudinale negli acceleratori: teoria e misura", laurea thesis 1998.

The Ion Produced Transverse Instabilities in SRRC Storage Ring

J. C. Lee and M. H. Wang

SRRC, Hsinchu Science-Based Industrial Park, Hsinchu, Taiwan, ROC

Abstract

The ions captured by the electron beam potential can introduce transverse instabilities and deteriorate the beam quality. For SRRC storage ring, the transverse instabilities due to trapped ions are found since commissioning and affect the beam performance. In this paper, we summarize the measurements of transverse instabilities which related to the ions. The efforts used to reduced the instabilities are also presented in the paper.

1 INTRODUCTION

The SRRC storage ring is a dedicated synchrotron light source in the VUV and soft X-ray. It was design and operated at 1.3 GeV. While it was upgraded to 1.5 GeV in 1996 to increase the emitted photon energy and the beam performance. Since commissioning of the ring, the transverse instabilities were found occasionally. The trapped ions effect was one of the suspicious. Since then measurements were performed to study these effects. They includes the general investigations from the conventional ion points of view, the tried cures and the venting H_2 gas studies. For effects of fast beam ion instability, the measurements are very few due to instrument issues. Since the dust trapping has relations to the ions, this phenomenon is also discussed in the paper.

From the commissioning phase till now, many efforts were down to improve the ring performance. Among them, the energy upgrade and the improvement in vacuum pressure reduce the instabilities by reducing the driven force from ions. In contrast to the reduction of ion driven force, the systems such as damper, beam shaking and clean electrode etc, eliminate the instability by interfering the beam. There are the third kind methods such as empty gap in the bunch train and strong chromaticities. Most of the curing methods would be discussed in the paper.

2 DUST TRAPPING

During the commissioning of the ring, the vacuum pressure was gradually pumped down as the increasing of beam dosage. While at that time the beam current and lifetime had a sudden jump occasionally. In the latter operation the sudden beam lost became not obvious while the lifetime still had a dip. This effect was suspicious from the dust trapping phenomenon. To identify this assumption the bremsstrahlung emitted from the beam was measured by Cherenkov counter. As the beam encountered the massive dust, electron beam will interact with the protons in the dust such that the beam would be bent and accelerated

to emit bremsstrahlung. Figure 1 shows the consistence from the dip in beam lifetime and the sudden increasing in counter readings. The dust trapping phenomenon was verified at commissioning phase. While this phenomenon disappeared as the vacuum conditions getting better.

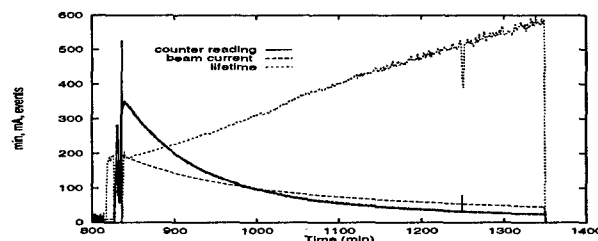


Figure 1: Indication of dust trapping from the dip of beam lifetime and the corresponding reading increasing in Cherenkov counter.

3 OBSERVATIONS IN CONVENTIONAL ION EFFECTS

In the commissioning phase the transverse instabilities were found from the pickup signal of stripline electrode, as shown in figure 2 for a all of buckets uniformly filled pattern. The spontaneous betatron sidebands in horizontal and vertical indicate the instabilities. The longitudinal sidebands is accompanied with the peaks of revolution and betatron sidebands. The emitted photon beam was observed as the instrument was ready. It was found the beam size pulsed as there were the spontaneous betatron sidebands. Many efforts were tried to understand these instabilities. The ion trapping effect was one of the suspicious. It was found a very big empty gap in the filling pattern can reduce and dismiss the oscillation peaks. A big enough empty gap in the filled bunch train is the typical curing method for the ion trapping phenomenon. Since then the ion trapping phenomenon was studied and reported[1].

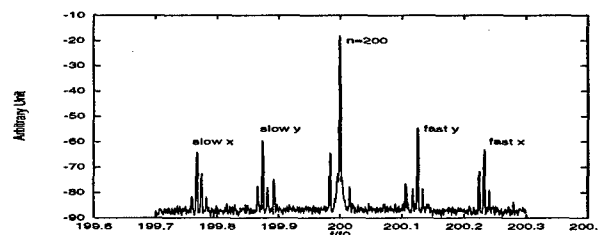


Figure 2: Spontaneous oscillation peaks at the revolution of $n=200$ for a all of buckets filled pattern.

From the residual gas analyzer data, H_2 and CO are the

than 90% population and CO only takes about 4%. While since the ionization rate for CO is larger than that for H₂, these two species were suspicious for the ion instabilities at the beginning. From the experimental results of how big of the empty gap to avoid the spontaneous transverse peaks and from theoretic prediction, the H₂ ion is the major contributor for the ion instabilities. This is also verified by the venting H₂ gas experiments recently^[2].

The trapped ions will introduce an additional quadrupole force on beam, which implies the lattice will be perturbed a little bit such that the betatron tune will be shifted by the ion force. This was basically confirmed by the measurements of tune versus different empty gap.

For more understandings, a pattern was filled to have the possibility to trap ions and chromaticities were applied to damp the instabilities at the normal operation pressure. The ion driven force was then increased by the trapped ion density, which is increased from the increasing of vacuum pressure by turning off some of the pumps. It was found that the vertical betatron sideband showed up first at around 12 ntorr and then the horizontal sideband at higher vacuum pressure. It was also found the transverse betatron peaks have threshold current limits. The current limit for the vertical is smaller than that for horizontal.

4 THE TRIED REMEDY METHODS

4.1 Empty gap and chromaticity

For the possible cures the empty gap in the filling pattern is an easy method to be applied. While the gap needed to avoid trapping was large, around 120 or bigger from the 200 RF buckets at 250mA. The beam lifetime became small since beam population per bunch getting large in big empty gap operation. The compromise was the small empty gap, say 20 to 40 buckets, with the damping mechanism from chromaticities. The chromaticities were found very effective to damp the transverse peaks in both planes. For big gap operation only small chromaticities were needed to damp transverse peaks. If the gap was big enough, there were no transverse peaks even at zero chromaticities. While the chromaticities should be increased up to +6.5 for all of the buckets filled one at 1.3 GeV. The bad effect of applying strong chromaticities is that it increases the sextupole strength such that the beam lifetime and the dynamic aperture reduced.

4.2 Clean electrode

The clean electrodes were also tried to remove ions. One button type electron beam position monitor and one 15cm long stripline electrode were modified for this studies. The remedy is clearly shown from the reduction of tune and tune spread as the clean voltage applied. While the clean ability is not enough for only two electrodes.

The beam shaken at the betatron sidebands was effective to remove the instabilities from ions^[3]. In this studies one 50cm long stripline electrode was modified to input the power to shake the beam periodically. As the beam was proper shaken the transverse peaks were dismissed. The beam pulsation disappeared and the beam size reduced. While the lifetime increased for around 2 hours at 1.3GeV. The studies also show the shaken frequency is not only effective at coherent betatron sidebands but also at the betatron sidebands of which no coherent oscillation peaks showed up. The shaking frequency was applied by sweeping a range from 0 to 34 MHz. It was found the frequency of betatron sidebands within this range are almost effective to damp the instabilities. But it is more effective for the sidebands of coherent oscillation. It was also found that slow betatron sidebands were more effective than fast sidebands.

Though the goal of longitudinal beam modulation by the second synchrotron sideband is try to cure the longitudinal instabilities^[4], the transverse oscillation peaks are also reduced or damped, dependent on the operation conditions. The pulsation and beam size are reduced in the modulation process. These phenomena are similar to that of the transverse shaking at the betatron sidebands.

4.4 Other improvements

These improvements include the beam energy upgrade from 1.3 GeV to 1.5 GeV^[5] and the improvement in vacuum^[6]. Though the authors were not engaged in these two improvements, while the impacts were considerable. Increased beam energy will benefit beam stabilities from reducing the ion driven force as well as the other driven sources such as the force of wake field etc. The improvement on vacuum pressure can also reduce the ion driven force by reducing the trapped ion density. Another method of reducing ion driven force is to increase the beam size. In the past year a high emittance lattice was operated for the users with the diluted beam size to reduce the instabilities. This can be taken as the example for increasing beam size. While the emitted photon intensity is reduced in this diluted beam size operation.

5 OBSERVATION IN FAST BEAM ION EFFECTS

The fast beam ion effect was proposed^[7] and studied^[8,9] in other laboratories. Due to the instrument issue, we can't observe the bunch by bunch motion directly. For the undirect measurement, the scraper was used to scrape the beam with a 75/200 filled pattern at 40mA to avoid conventional ion trapping. Before scraping there were some of missing bunches within the bunch train and the population in head bunches is smaller than that of the tail bunches. While the tail bunches are roughly uniformly filled. This experiment was down as the vacuum chamber were replaced in January 1998. The local pressure of the replacing section was

ter scraping is shown in figure 3 for the less population in the tail of the bunch train, which indicates the increasing of instability along the train. This result is similar to that in ALS^[6].

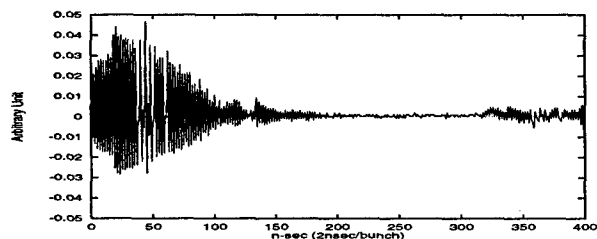


Figure 3: Beam population along the bunch train after scraping the beam.

6 VENTING H₂ GAS EXPERIMENT

Since the H₂ ion is the dominate species in the ring and would cause instability, the venting H₂ gas experiments were performed at 1.5GeV recently to increase the H₂ density in different cases^[3]. From the studied results the H₂ ion is confirmed to be the dominate source again for the ion instability. The coherent peaks from the button electrode is identified to be the H₂ ion oscillation frequency as the gap is not big enough or as the local pressure of H₂ increased up to around 60 ntorr. The coherent peaks seem have periodic structure with the period of revolution. As the vacuum pressure as high up to 500 ntorr, additional peaks show up besides the coherent frequency peak of H₂ ion even at a 75/200 buckets filled pattern of which no ions could be trapped from the conventional theory prediction and no coherent oscillation before and after venting H₂ gas. Similar spectrum, as shown in figure 5, was found for a all of buckets filled pattern at 1.3GeV in the normal operation vacuum pressure. Compared above two results, the coherent peaks have a little different due to different operation conditions. While ion driven force is increased for these two cases, which implies that the ion driven force could be the key point for the instability. Increasing the vacuum pressure, reducing the beam energy and operated with the pattern of all of buckets filled arrive the same destinate. That is increasing the driven force from ions. The known theories can't fully explain these additional peaks. Therefore the 'impedance like' idea for the ion force is introduced to explain these phenomena. While more works will be done in the future, including the theory and experiments.

7 DISCUSSION

The ion produced instabilities were investigated in the SRRS storage ring. From the studied results the driven force from ions is the key for the instabilities. As the empty gap is not big enough in the bunch train the trapped ions would cause instability. While if the empty gap is big enough to reduce the trapping and the driven force was de-

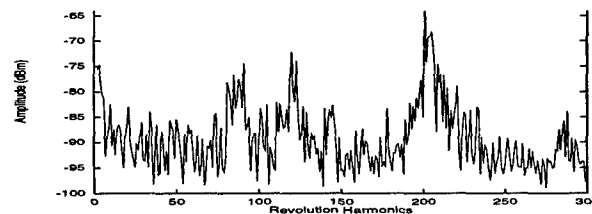


Figure 4: Measurement of vertical slow sideband for all of buckets filled at 1.3GeV and 138mA in the normal operation vacuum pressure.

creased by increasing the beam energy, diluting the beam size or reducing the trapped ion density from the improvement on vacuum, the instability from ions could be dismissed. The shaking method knock out the ions by driving the beam oscillated at some particular frequency. The electron bunch is also redistributed from shaking. The electron density within bunches becomes smaller and less trapping potential from electron beam resulted. Ion produced instability is also reduced from this bunch redistribution process.

The damping mechanism from chromaticities complete the instability. If chromaticities are strong enough, the instability from ion driven force could be eliminated. From the transverse spectrum data, the coherent peaks of H₂⁺ oscillation frequency show up first as the ion force cause instability. While as the ion driven force getting larger, additional peaks appear from the indication of venting H₂ gas experiment. This feature can't be fully explained from conventional ion and fast beam ion theory. The impedance like behavior was suggested to explain this phenomenon. While more works would be down in the future to verify this assumption.

8 REFERENCES

- [1] J. C. Lee et al., Proceedings of the European Particle Accelerator Conference, p1159, 1994.
- [2] J. C. Lee et al., Investigation of Ion Effects in SRRS Storage Ring by Venting H₂ gas, This Proceedings.
- [3] J. C. Lee et al., Proceedings of the Particle Accelerator Conference, p2968, 1995.
- [4] M. H. Wang et al., Experiment of RF Voltage Modulation at SRRS, This Proceedings.
- [5] G. H. Luo et al., Proceedings of the Particle Accelerator Conference, p853, 1997.
- [6] Y. J. Hsu et al., Proceedings of the European Particle Accelerator Conference, p2175, 1998.
- [7] T. O. Raubenheimer and F. Zimmermann, Phys. Rev. E 52, p5487, 1995.
- [8] J. Byrd et al., Phys. Rev. Lett., p79, 1997.
- [9] J. Y. Huang et al., Phys. Rev. Lett., p4388, 1998.

INVESTIGATION OF ION EFFECTS IN THE SRRC STORAGE RING BY VENTING H₂ GAS

J. C. Lee, M. H. Wang, G. Y. Hsiung, K. T. Hsu and J. R. Chen
SRRC, Hsinchu Science-Based Industrial Park, Hsinchu, Taiwan, ROC

Abstract

The instabilities produced by ions are one of the issues in the electron storage ring. At SRRC, H₂ ion is the dominate species. Comparing with other species, H₂ ions are uneasy to be trapped from the conventional ion points of view for its small atomic mass. While H₂ ions could introduce fast beam ion instabilities. In order to understand more details of the ion produced instabilities in the ring, H₂ gas was intentionally vented into the ring chamber. In this paper, the instabilities which relate to the H₂ ions are described and the physics is also discussed.

1 INTRODUCTION

As ions are trapped by the electron potential, the beam and the ions are mutually interacted with each other and perform two beam oscillations. The linear equations of motion are

$$y_e''(s, t) + \omega_{\beta e}^2 y_e(s, t) = \frac{2\lambda_i r_e}{\gamma} \frac{y_i(s, t) - y_e(s, t)}{\sigma_y(s, t)(\sigma_y(s, t) + \sigma_x(s, t))} \quad (1)$$

$$\ddot{y}_i(s, t) + \omega_i^2 y_i(s, t) = \omega_i^2 y_e(s, t) \quad (2)$$

in which the subindex e and i indicate the motion of electron and ion respectively. The derivative of y_e'' is w.r.t. coordinate s and \dot{y}_i to time. Also λ_i is ion charge density, γ the electron beam energy, $\sigma_{x,y}$ the horizontal or vertical beam size and $\omega_{\beta,i}$ the angular frequency for the beam and ions respectively.

From equation (1) it is clear that the driven force from ions is proportional to the trapped ion density and is inversely proportional to the beam size and beam energy. Equation (2) can be treated with the help of periodic passing of the beam bunches to obtain stable conditions of ion motion. From the stable conditions ions trapped by beam potential can be investigated. It depends on the operation conditions and ion atomic mass. For the smaller atomic mass and the bigger empty gap the less ion trapping in the ring. The ring operated with a big enough empty gap to avoid ion trapping is the well known method^[1,2,3,4] in the world. While there is the possibility for the massive ions to be trapped. It is also not easy to control the ion species in the ring. For the SRRC storage ring even H₂⁺ ion has the possibility to be trapped^[5]. While unfortunately the H₂ ion is the dominate species in the SRRC storage ring. This stimulated the studies by increasing the trapped density of H₂⁺ ion from venting H₂ gas into the ring.

There is another kind of ion produced instability which is called fast beam ion instabilities^[6,7]. This kind of instability is very fast such that the ions accumulated by the previous bunch could affect the next coming bunches. Due to the instrument issues, no much measurements were down about this kind of instability. While some discussions are given in the paper.

2 VENTING SETUP

The venting port is around 140mm down steam Q₂ quadrupole magnet in the R6 section. High purity H₂ gas was vented into the ring by using the electropolished tube. For vacuum consideration, TMP, ion pump and NEG were installed in the bottom of the venting port. During the studies the pressure was increased across a local area, depends on how much venting, and no pressure increasing outside this local area. The H₂ gas was intentionally increased in the experiment and the other species were neglected small compared with the population of H₂. For the normal operation the averaged vacuum pressure is around 0.3 ntorr and is around 0.7 ntorr in the local vented area. While the local pressure is under 1×10^{-7} ntorr in the local vented area for most cases as H₂ gas vented.

3 EXPERIMENTAL MEASUREMENT

The experiments were all performed at 1.5GeV. During the experiments the global orbit feedback and transverse damper systems are off to avoid unexpected driven on the beam. But the large positive chromaticities are set to damp instabilities in reasonable levels. The experiment was first performed at 122mA with a pattern of big enough empty gap, 120/200 buckets filled, to avoid conventional ion trapping (case A). The beam is stable for there are no transverse peaks. Then the H₂ gas was vented into the ring up to 60 ntorr in the local vented area. The coherent oscillation peak in the vertical plane showed up. By measuring the slow betatron sideband at each revolution, the coherent spectrum is obtained, as shown in figure 1. This coherent peak has the periodic structure with the period of revolution. This peak frequency is identified to the H₂ ion oscillation frequency according to^[6]

$$\omega_i = \left(\frac{4N_e r_p C^2}{3L_{sep} \sigma_y (\sigma_x + \sigma_y) A} \right)^{1/2} \quad (3)$$

where N_e is the number of electrons per bunch, r_p the classical proton radius, A the atomic number and L_{sep} the separation of bunches. The vertical beam size is dilute a little

bit but no significant changing in horizontal. These results are similar to that of ALS fast ion observations^[7].

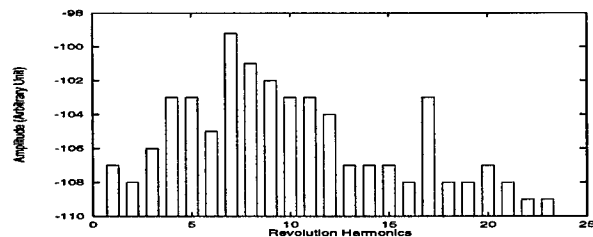


Figure 1: Coherent spectrum corresponding to the H_2^+ ion oscillation frequency.

In order to understand more details, a pattern with all of the RF buckets filled was employed in the studied at 200mA (case B). In this case the transverse coherent peaks were showed up, horizontally and vertically, and the beam pulsed. The betatron tune peak shifted randomly across a range of 3kHz. These features indicate the convention ion effect plays an important role in this all buckets filled case. The H_2 gas was then intentionally vented into the ring up to around 70 ntorr in the local vented area. It is found that a) there are still the transverse coherent peaks and pulsation on beam size, b) the betatron tune peak is also shifted in a more wider range, and c) the frequency of the coherent peaks are almost the same as that of the before venting one under almost the same beam size which is pulsed on both cases, d) the vertical beam size increased as the increasing of H_2 gas but no significant variation in horizontal, as shown in figure 2. The fluctuation on the vertical beam size shows the instability in the vertical plane.

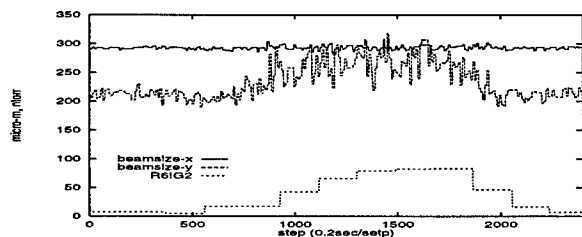


Figure 2: Beam size variation versus the vacuum pressure in the local vented area.

Form the results in case B it can conclude that the coherent peaks are produced by the H_2 ions before and during venting H_2 gas. It is also verified by the theoretical calculation of H_2^+ oscillation frequency from ring parameters.

The experiments were reproduced with a big empty gap in the pattern, around 125/200 buckets filled, to have vertical coherent oscillation peaks before venting H_2 gas (case C). The results of venting H_2 gas are the same as that of all of RF buckets filled one but with the less strength in coherent peaks. The tune is also shifted in a range of 2KHz for without venting one and of 2.5KHz for venting H_2 gas due to instabilities. The averaged results of these shifted tune peaks give the 'averaged' tune spread for the instability, as shown in figure 3 for venting and without venting.

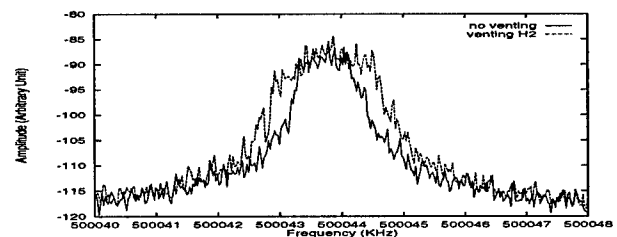


Figure 3: Vertical tune spread with and without venting H_2 gas.

From conventional points of view, case A has no conventional ion effects before venting H_2 gas. The instabilities during venting is coming from fast beam ion effects. While if we compare the venting results of case A with case B, there are no big differences between two cases except the coherent oscillation amplitude is bigger for case B, in which the conventional ion effect is important. From the similar results of cases B and C it indicates the conventional ion effects play an important role in these two cases. Also from the facts of venting H_2 gas and the frequency information of the coherent oscillation, it concludes that the H_2 ion is the suspicion of the ion instability for case C without venting. For the routine operation in SRRC storage ring, the empty gap is smaller than that of case C, about 20 to 40 gap. While the transverse oscillation behavior in routine operation is similar to that of case C when the feedback systems are off. Hence we arrives the following understandings from above results. There are a) the H_2 ion is the dominate source for the conventional ion instability in SRRC storage ring, which is consistent with our previous estimation^[5], b) the increased density of H_2 gas (or ions) is to enhance the instability, c) the vertical beam size increasing and no increasement in horizontal from venting H_2 gas are common features for the fast beam ion (case A) and conventional ion (cases B and C) effects.

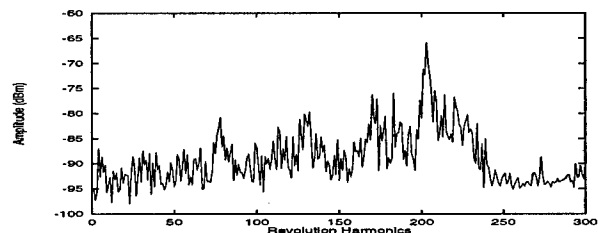


Figure 4: Measurements of the vertical slow sideband for 95/200 filled pattern at 156mA as H_2 gas vented.

While the H_2 ion is very easy to escape from trapping for its small atomic mass. In order to understand more details, the partial pressure of H_2 was increased further by venting more gas into the ring, which was operated at 156mA with around 95 buckets filled (case D). There were no coherent peaks before venting. It is found that lots of the transverse peaks show up, as shown in figure 4, besides the coherent peak of H_2^+ oscillation frequency, about 9.9MHz, as the local pressure increased up to 5×10^{-7} torr. The empty-gap

of case D is smaller than that of case A. Therefore there is no conventional ion effects also. While the results are quite different during venting. The additional peaks shown in figure 4 would not coming from other species for the frequency of these additional peaks are larger than the coherent peak of H_2^+ and other species will give smaller frequency peaks for the large atomic mass.

The electric potential produced by the electron beam would not be changed by the vacuum pressure. That means the trapping ability is almost the same for different pressure. If the pattern is filled such that the beam can accumulate ions, then the instabilities enhanced by the pressure is reasonable for more ions are trapped in the higher vacuum pressure. But if empty gap is big enough to avoid trapping why there are additional peaks in high vacuum. One possible answer is that the theory we followed is only linear one. It is valid for small amplitude. For the cases of drastic oscillation, the high order terms need to be included^[8]. People could criticized that the ions are trapped in cases A and D since the instabilities could be damped off by the strong chromaticities in the experiments. While since the empty gap is larger than that for trapping this possibility is excluded.

If we investigate what shown in figure 4, there is something like the features of impedance. The idea of impedance provides a trace to follow. The new idea is similar to that of the fast beam ion instability with the ions accumulated by previous bunch does affect on the following coming bunches by the very fast time. But the period of the affect time is larger than the revolution. If we compare this new idea with the physics of impedance from wake field, they are quite similar. The wake force affects on the beam with the help of vacuum chamber. While the ion force is coming from the interaction of beam and ions. If the idea of impedance like behavior is accepted then what shown in figure 4 and the above results are reasonable. Hence we can arrive the following understandings (maybe suspicious only): the ion effects on the beam have some kind of impedance behavior.

4 DISCUSSION

From above experimental results, it clear that the coherent peaks shows up during venting H_2 gas are due to the H_2 ions. By comparing the frequency of the coherent peaks with and without venting H_2 gas it concludes the coherent oscillations appeared in the no venting cases are mainly from the H_2 ion. This is also verified by theoretical calculation of ion frequency from ring operation parameters. From what shown in above experimental results, especially in case C, H_2 ion is the major contributor for the ion instability in SRRC storage ring. For case D with around half buckets filled and no coherent peaks before venting, it would not have conventional ion effects. While there are lots of the coherent peaks besides that of the H_2^+ frequency as the vacuum was increased up to 5×10^{-7} torr by venting H_2 gas. Does these peaks come from the fast beam ion in-

stabilities? However it is assumed the ions will lost in the gap for the fast ion one. Otherwise it is difficult to distinguish the fast ion and the conventional ion effects. While if the impedance idea is introduced for the ion effects this problem can be solved and the behavior shown in figure 4 could be explained also.

This 'impedance like' behavior not only occurs in the high vacuum but also found in the low vacuum. It is found in SRRC storage ring at normal operation vacuum pressure at 1.3 GeV with a all of buckets filled pattern^[9]. From these facts it imply that the impedance like behavior could happen as the ion driven force become large. This is understood from the driven term in equation (1), in which less beam energy and high vacuum pressure enhance the driven force. Ring operated with all of the buckets filled will increase the trapping ability. Though the ion could introduce impedance like behavior, while the quantitative measurements are still in progress. In the next step the direct measurement on the impedance will be important.

From the additional peaks show up by the large driven force, it imply there is the rise time issue. The instabilities at some of the frequency could be damped by the radiation damping, chromaticities etc. While the rise time could be faster than above damping mechanism as the driven force increased.

From the experiments the coherent peak of ion frequency shows up first and then the additional peaks as the driven force getting large. These peaks have the periodic structure with the period of revolution. This fact is obvious for the coherent frequency peak of H_2^+ . While the theory in conventional ion and fast beam ion instabilities can't explain these coherent modes. Hence the theoretical studies and the further measurements will be important in the future.

5 ACKNOWLEDGEMENT

The author would like to thank J. Chen and H. J. Tsai for the help in data acquisition.

6 REFERENCES

- [1] Mark Q. Barton, Nucl. Instr. and Meth., A243, p278, 1986.
- [2] H. Kobayakawa et al., Nucl. Instr. and Meth. A248, p565, 1986.
- [3] Y. Baconnier and G. Brianti, CERN/SPS/80-2 (DI), 1980.
- [4] S. Sakanaka et al. Nucl. Instr. and Meth., A256, p184, 1987.
- [5] J. C. Lee et al., Proceedings of the European Particle Accelerator Conference, p1159, 1994.
- [6] T. O. Raubenheimer and F. Zimmermann, Phys. Rev. E 52, p5487 (1995).
- [7] J. Byrd et al., Phys. Rev. Lett. p79, 1997.
- [8] J. C. Lee, Proceedings of the European Particle Accelerator Conference, p1117, 1996.
- [9] J. C. Lee and M. H. Wang, The Ion Produced Transverse Instabilities in SRRC Storage Ring, This Proceedings.

TRANSVERSE BEAM STABILITY WITH "ELECTRON LENS"*

A. Burov, V. Shiltsev, FNAL, Batavia, IL
V. Danilov, ORNL, Oak Ridge, TN

Abstract

Stability analysis is presented for an antiproton beam interacting with an electron beam of an "electron lens" proposed as a beam-beam tune shift compensator. Coherent antiproton-electron interaction causes coupling of the antiproton synchrotron modes which may lead to a transverse mode coupling instability (TMCI). Analytical studies and numerical simulations of this effect are presented.

1 INTRODUCTION

An "electron lens" was proposed to compensate beam-beam tune shift in the Tevatron collider [2]. A tune shift of antiprotons on electron beam with total current J_e , radius a_e , length L_e , is equal to

$$\xi_{x,y}^e \approx -\frac{\beta_{x,y}}{4\pi} \frac{2(1+\beta_e)J_e L_e r_{\bar{p}}}{e v_e a_e^2 \gamma_{\bar{p}}}, \quad (1)$$

here $r_{\bar{p}} = e^2/(M_{\bar{p}} c^2) \approx 1.53 \cdot 10^{-18} \text{ m}$ is the (anti)proton classical radius, $\gamma_{\bar{p}}$ is relativistic antiproton factor, $v_e = c\beta_e$ is electron beam velocity, $\beta_{x,y}$ is the beta function at the set-up location.

The electron beam create a transverse impedance that can result in collective instabilities of the antiproton bunch. The electron beam is generated by an electron gun cathode, transported through the interaction region, and absorbed in the collector. Therefore, each portion of electrons passes through the \bar{p} beam only once, and only short distance transverse wake fields are of interest. When the bunch head collides off the electron beam center, it causes electron motion and, as a result, the electron beam acquires a displacement at the moment when it interacts with the tail of the \bar{p} bunch. This interaction can lead to the strong head-tail instability. To suppress it, a longitudinal magnetic field in the interaction region is assumed to be applied. The magnetic field couples the electron transverse degrees of freedom, transforming a kick in one direction into an offset in another. In the result, the magnetized electron medium creates both conventional and skew wakes.

2 TWO-MODE MODEL

To find the dipole wake function, let us consider a thin antiproton slice with a charge q and transverse offset Δx traveling through the electron beam. After interaction with the slice, electrons acquire a transverse velocity

$$v_{xe} = \frac{2eq\Delta x}{a^2 \gamma_e m c}, \quad (2)$$

where m is the electron mass. Such a kick causes transverse Larmor oscillations in a longitudinal magnetic field B , and

after a time interval t , the resulting electron transverse offsets are:

$$x_e = \frac{v_{xe}}{\omega_L} \sin(\omega_L t); \quad y_e = \frac{v_{xe}}{\omega_L} (1 - \cos(\omega_L t)), \quad (3)$$

where $\omega_L = eB/(\gamma_e m c)$ stands for the Larmor frequency. The originally horizontal displacement Δx resulted in both horizontal and vertical displacements. The antiprotons at the distance s behind the slice will experience momentum changes

$$\begin{aligned} \Delta p_x(s) &= -\frac{eq}{c} (W_d(s)\Delta x - W_s(s)\Delta y) \\ \Delta p_y(s) &= -\frac{eq}{c} (W_s(s)\Delta x + W_d(s)\Delta y) \end{aligned} \quad (4)$$

where we introduced direct wake function $W_d(s)$ and skew $W_s(s)$ wake function:

$$\begin{aligned} W_d(s) &= W \sin(ks), \quad W_s(s) = W(1 - \cos(ks)), \text{ for } s > 0 \\ W &= 4\pi n_e L_e / (Ba^2), \quad k = \omega_L / ((1 + \beta_e)c) \end{aligned} \quad (5)$$

Depending on the parameters, one or the other of the two wake functions (5) can give a dominant influence on the antiproton beam stability. The direct wake effects are suppressed if there are many Larmor oscillations periods over the \bar{p} bunch length σ_s , while the skew force impact decreases with increasing the $x - y$ detuning.

For the parameters under study, the skew wake is found to be more dangerous. To damp the instability, the longitudinal magnetic field B has to be high enough; a two-mode model gives the threshold condition as

$$B \geq B_{th} \approx 2.0 \frac{e N_{\bar{p}} \sqrt{\xi_x \xi_y}}{a^2 \sqrt{\Delta \nu \min(\Delta \nu, 2.4 \nu_s)}}. \quad (6)$$

For $\xi_x = \xi_y = 0.01$, $N_{\bar{p}} = 6 \cdot 10^{10}$, $\nu_s = 0.001$, $\Delta \nu = 0.01$, $a = 1 \text{ mm}$ it comes out $B_{th} = 12 \text{ kG}$.

In addition to these simplified analytical calculations, A multi-mode numerical algorithm of Ref. [3] was applied for the stability study. Typical eigenvalues behavior is presented in Fig. 1.

Fig.2 shows the tune shift threshold ξ_e for the first coupling modes versus the tune split in units of the synchrotron tune $\Delta \nu = (\nu_x - \nu_y)$ while the vertical tune is equal to .555. The threshold grows linearly until $\Delta \nu \approx (2 - 2.5)\nu_s$ and then is approximately proportional to $\sqrt{\Delta \nu}$ - in a good agreement with the two mode model formula (6).

Transverse widening of the electron beam was found to suppress the instability, decreasing the threshold field as $B_{th} \propto a_e^{-2}$.

3 TRACKING SIMULATIONS

Three dimensional numerical simulations of the effects have been done with ECWAKE code written in FORTRAN.

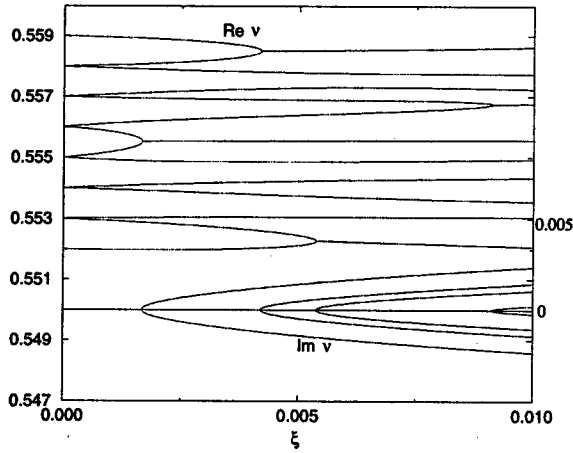


Figure 1: Eigenfrequencies (tunes) of the antiproton bunch oscillation modes versus the antiproton betatron tune shift due to electron beam ξ_e (horizontal axis). Vertical scale on the left is for fractional part of the tunes $Re \nu$ (upper series of lines), the right side scale is for imaginary part of the tunes $Im \nu$ (lower series of lines).

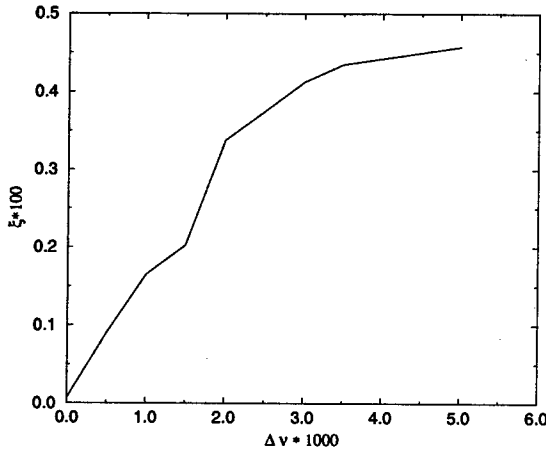


Figure 2: Threshold antiprotons tune shift ξ_e (vertical axis) due to the electron beam versus the difference of antiproton horizontal and vertical tunes $\Delta \nu = \nu_x - \nu_y$. $B = 10$ kG, $\nu_s = 0.001$, $N_{\bar{p}} = 6 \cdot 10^{10}$.

Fig.3 shows the threshold strength of solenoidal magnetic field B_{thr} vs. electron beam intensity parameter ξ_e for antiproton bunch population equal to $N_{\bar{p}} = (1, 6, 10) \cdot 10^{10}$ - lower, middle and upper curves, respectively. We define the threshold as the value of B which results in more than 10-fold increase of the initial centroid betatron amplitude over the first 10,000 turns. One can see, that the field is approximately proportional to both ξ_e and $N_{\bar{p}}$ in accordance with Eq.(6).

Dependence of the threshold on the synchrotron tune ν_s

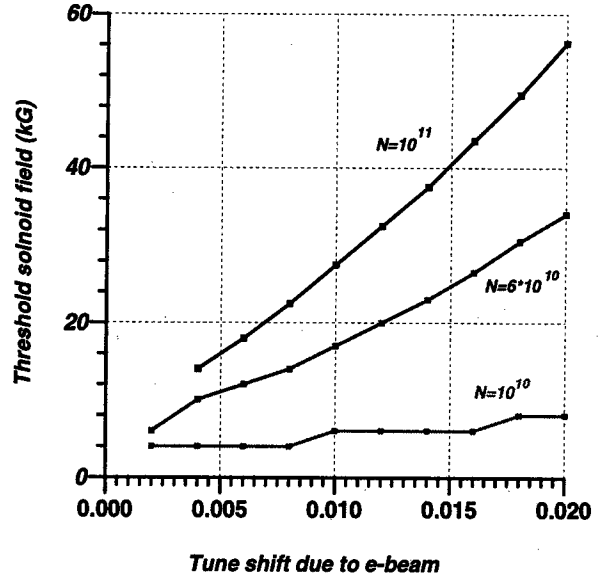


Figure 3: Threshold solenoid field B_{thr} vs tune shift due to electrons $|\xi_e|$ at different bunch populations $N_{\bar{p}} = 1, 6, 10 \cdot 10^{10}$. Focusing lattice tunes $\nu_x = 0.585$, $\nu_y = 0.575$, synchrotron tune $\nu_s = 0.0012$, maximum tune spread $\delta \nu = 0$, the rms size of \bar{p} beam $\sigma_{\bar{p}} = 0.7$ mm.

is depicted in Fig.4. Dots are simulation results with $\nu_x = 0.585$, $\nu_y = 0.575$, $\xi_e = -0.01$, $\delta \nu = 0.002$, $N_{\bar{p}} = 6 \cdot 10^{10}$, $\sigma_{\bar{p}} = 0.7$ mm. The solid line represents a fit $B_{thr} = 17.5[kG]/\sqrt{\nu_s}/0.001$ in line with the two-mode prediction Eq.(6).

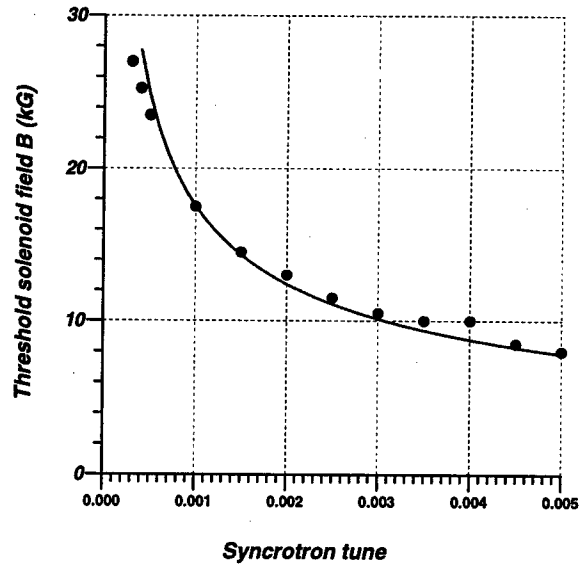


Figure 4: Threshold magnetic field vs synchrotron tune ν_s . Solid line is for $B_{thr} = 12.4[kG]/\sqrt{\nu_s}$. $\nu_x = 0.585$, $\nu_y = 0.575$, $\xi_e = -0.01$, $\delta \nu = 0$, $N_{\bar{p}} = 6 \cdot 10^{10}$, $\sigma_{\bar{p}} = 0.7$ mm.

In order to evaluate importance of the oscillation part of the wakes Eq.5, we performed similar scan without constant

part of the skew wake, i.e. with $W_d(s) = W \sin(ks)$ and $W_s(s) = -W \cos(ks)$ and found that about 5 times smaller solenoid field is required for stability. It confirms decisive role of the the constant part of skew wake that is a basic assumption of the two-mode model in Section II.

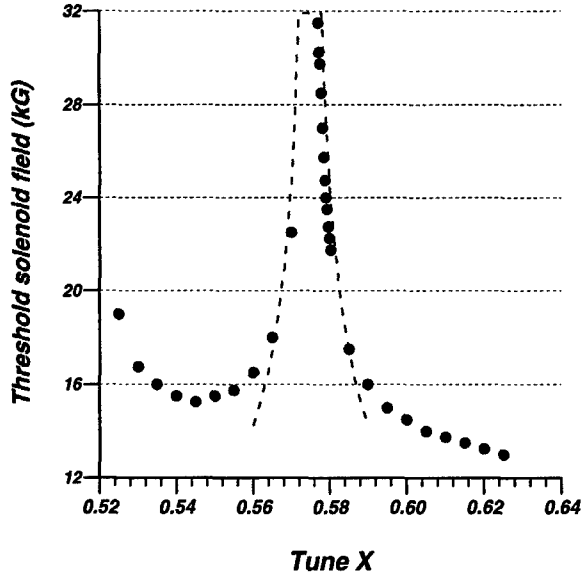


Figure 5: Threshold magnetic field vs horizontal tune ν_x . Dashed line corresponds to $B_{thr} \propto 1/\sqrt{|\nu_x - \nu_y|}$; $\nu_y = 0.575$, $\nu_s = 0.001$, $\xi_e = -0.01$, $\delta\nu = 0.0$, $N_{\bar{p}} = 6 \cdot 10^{10}$, $\sigma_{\bar{p}} = 0.7$ mm.

It is found that the TMCI threshold greatly depends on operation point ν_x, ν_y . Fig.5 presents results of scanning of the horizontal tune ν_x from 0.52 to 0.63 while the vertical tune is $\nu_y = 0.575$. In close vicinity of the coupling resonance $\Delta\nu = |\nu_x - \nu_y| \leq 15\nu_s$ the threshold magnetic field depends on ν_s approximately as $\propto 1/|\Delta\nu|^\kappa$, where $2/5 < \kappa < 1/2$. The threshold also goes up near half-integer resonance $\nu_x \rightarrow 0.5$.

In order to compare with the two mode model, one can fit B_{thr} in the form similar to Eq.(6):

$$B_{th} \approx \frac{0.95eN_{\bar{p}}\xi_e}{\sigma_{\bar{p}}^2 \sqrt{|\nu_x - \nu_y|} \nu_s} = \frac{17.5[kG] \frac{N_{\bar{p}}}{6 \cdot 10^{10}} \frac{|\xi_e|}{0.01}}{\left(\frac{\sigma_{\bar{p}}[mm]}{0.7}\right)^2 \sqrt{\frac{\nu_s}{0.001} \frac{|\Delta\nu|}{0.01}}}, \quad (7)$$

- see also dashed line in Fig.5.

These results are in a reasonable agreement with the two-mode analysis and the coupled-mode calculations. The difference ($\approx 40\%$) in numerical factors between Eq.(7) and Eq.(6) lies within the accuracy limits of the wake calculations and two-mode model.

4 CONCLUSIONS.

We have considered strong head-tail instability of the Tevatron antiproton bunch due to the beam-beam compensation set-up. The head-tail interaction takes place because of the fact that the electron beam is not rigid enough

and can be displaced transversely by the bunch head particles. The resulting direct and skew wake forces act on the tail particles and, thus, can lead to the instability. We pursue three approaches to study the instability: a two-mode model with analytical calculations, more sophisticated multi-mode analysis which requires numerical solution of eigenmode equations, and straightforward macroparticle tracking. The results coincide qualitatively and rather well quantitatively agree with each other. For the parameters of the planned Tevatron beam-beam compensation experiment the \bar{p} bunch intensity $eN_{\bar{p}} = 6 \cdot 10^{10}$ and its rms size $\sigma_{\bar{p}} = 0.7$ mm, the tune shift due to electron beam $\xi_e = -0.01$, the distance to the coupling resonance $\Delta\nu = |\nu_x - \nu_y| = 0.01$, and the synchrotron tune $\nu_s = 0.001$, the instability takes place if the longitudinal magnetic field in the set-up is below threshold of about $B_{thr} = 17.5$ kG. Essential features of the instability are:

- the constant skew wake plays a major role in the mode coupling;
- the threshold solenoid field B_{thr} is proportional to the transverse charge density of the electron beam, to the transverse charge density of the antiproton beam, and inversely proportional to the product $\sqrt{\nu_s |\nu_x - \nu_y|}$ in vicinity of the coupling resonance $\nu_x - \nu_y = \text{integer}$;

Having the electron beam wider than the antiproton beam results in lower threshold magnetic field $B_{thr} \propto (\sigma_{\bar{p}}/a_e)^2$.

We plan to continue investigations of the instability in order to clear some inadequacies of the present studies. In particular, the following effects have to be taken into consideration:

1. non-linear forces with general current distributions in the electron and antiproton beams;
2. instability suppression due to betatron and synchrotron tune spreads;
3. higher order transverse mode coupling.

We acknowledge stimulating discussions with Vasily Parkhomchuk, Andrei Sery, Gerry Jackson and David Finley.

5 REFERENCES

- [1] * An extended version: A. Burov, V. Danilov and V. Shiltsev, Phys. Rev E, **59**, p. 3605 (1999).
- [2] V.Shiltsev, V.Danilov, D.Finley, A.Sery, FNAL-Pub-98/260 (1998), submitted to Phys. Rev. ST Accel. Beams.
- [3] V.V.Danilov and E.A.Perevedentsev, NIMA, **391** (1997), 77.

INSTABILITIES IN THE SNS*

M. Blaskiewicz[†], BNL, Upton, NY

Abstract

The 2MW Spallation Neutron Source (SNS) will have a D.C. beam current of 40 A at extraction, making it one of the worlds most intense accelerators. Coherent instabilities are a major concern and efforts to predict beam behavior are described.

1 INTRODUCTION

For 2 MW operation the SNS will accumulate 2×10^{14} , 1 GeV protons over 1 ms via charge exchange injection. The machine circumference is 220 m with a transition energy of $\gamma_t = 4.9$ and betatron tunes around 5.8[1]. The baseline design calls for natural chromaticities ~ -1 , but chromatic control is likely in the final design. The machine impedance below 200 MHz has been characterized[2, 3], and measurements of the extraction kicker impedance are in progress.

2 LONGITUDINAL INSTABILITIES

Two methods have been used to characterize longitudinal stability in the SNS. First assume a coasting beam with a rectangular energy distribution and do first order perturbation theory on the Vlasov equation with

$$I = I_0 + I_1 \exp(in(\theta - \omega_0 t) - i\Omega t).$$

The dispersion relation is given by,

$$\frac{\Omega^2}{\omega_0^2 n^2} = \hat{v}^2 + i \frac{q I_0 \eta}{2\pi E_0 \beta^2} \frac{Z_{\parallel}(\Omega + n\omega_0)}{n} \quad (1)$$

where $\eta = -0.193$ is the frequency slip factor, $E_0 = \gamma mc^2$, q is the proton charge, and $\hat{v} = |\eta| \max(E - E_0)/E_0 \beta^2 \approx 1 \times 10^{-3}$. With $I_0 = 40A$ the terms on the right hand side are equal for $Z_{\parallel}/n = i650\Omega$. The space charge impedance is $Z_{\parallel}/n = i150\Omega$ and dominates the magnitude of the impedance. Taking the square root of eq(1) and assuming the second term is small compared to the first yields

$$Im(\Omega) \approx \frac{\omega_0}{2\hat{v}} \frac{e I_0 \eta}{2\pi E_0 \beta^2} Re(Z_{\parallel}). \quad (2)$$

When all objects other than the extraction kicker are included in the impedance budget the growth rate of the most unstable mode below 700 MHz is $\lesssim 2/ms$, which is benign. Near the cutoff frequency for transverse magnetic microwave propagation ≈ 1 GHz, codes such as ABCI [6]

predict strong, narrow, resonant impedances. These will be considered in the future.

Instabilities of the sort predicted by eq (1) and (2) are rare or nonexistent below transition. The reason can be inferred from a simple bunched beam model. Assume a "brick wall" barrier bucket rf system. The bunch has length τ_b (radians) and peak current I_0 . The particles undergo perfect reflection at the edges of the bunch and the impedance is given by $Z = R - i\omega L$. Use the machine azimuth θ as the time-like variable. Let $\tau = \omega_0 t - \theta$ and $v = d\tau/d\theta$ be the dynamical variables. Assume the unperturbed phase space density is given by

$$\Psi_0(\tau, v) = \frac{1}{2\hat{v}\tau_b}$$

for $0 < \tau < \tau_b$ and $|v| < \hat{v}$, and zero otherwise. This neglects the effect of R on the unperturbed distribution. Assume a solution to the Vlasov equation of the form

$$\Psi(\tau, v, \theta) = \Psi_0(\tau, v) + e^{-iQ\theta} \Psi_1(\tau, v).$$

The perturbation satisfies

$$-iQ\Psi_1 + v \frac{\partial \Psi_1}{\partial \tau} = F_1(\tau) (\delta(v - \hat{v}) - \delta(v + \hat{v}))$$

where

$$\Psi_1(\tau, v) = \Psi_+(\tau)\delta(v - \hat{v}) + \Psi_-(\tau)\delta(v + \hat{v}) \quad (3)$$

$$F_1(\tau) = \kappa \left(R + \omega_0 L \frac{d}{d\tau} \right) (\Psi_+(\tau) + \Psi_-(\tau)) \quad (4)$$

and

$$\kappa = \frac{-\eta q I_0}{4\pi \hat{v} \beta^2 E_0}$$

The equations for $\Psi_+(\tau)$ and $\Psi_-(\tau)$ are first order with constant coefficients. To solve these equations let $U - iV = \kappa(R - i\omega_0 L)$, $S(\tau) = \Psi_+(\tau) + \Psi_-(\tau)$, and $D(\tau) = \Psi_+(\tau) - \Psi_-(\tau)$. Then

$$-iQS + \hat{v} \frac{dD}{d\tau} = 0, \quad (5)$$

$$-iQD + (\hat{v} - 2V) \frac{dS}{d\tau} = 2US. \quad (6)$$

For perfect reflection at $\tau = 0$ and $\tau = \tau_b$ the boundary conditions are $D(0) = D(\tau_b) = 0$, so

$$D(\tau) = \exp(\lambda_+ \tau) - \exp(\lambda_- \tau).$$

Equations (5) and (6) give

$$\lambda_{\pm} = \frac{U}{\hat{v} - 2V} \pm \sqrt{\frac{U^2}{(\hat{v} - 2V)^2} - \frac{Q^2}{\hat{v}(\hat{v} - 2V)}}$$

* Work supported by US Department of Energy

[†] Email: mmb@bnl.gov

The boundary condition at τ_b gives $\lambda_+ - \lambda_- = 2\pi i k / \tau_b$ with $k \neq 0$ an integer. Solving for $\Omega = \omega_0 Q$ gives

$$\Omega^2 = \omega_0^2 \hat{v} (\hat{v} - 2V) \left\{ \frac{k^2 \pi^2}{\tau_b^2} + \frac{U^2}{(\hat{v} - 2V)^2} \right\} \quad (7)$$

The right hand side of (7) is positive as long as $\hat{v} > 2V$ or

$$-\frac{qI_0\eta}{2\pi E_0\beta^2}\omega_0 L < \hat{v}^2.$$

This is very different from the coasting beam result. For the SNS space charge dominates ($L < 0$) and we are below transition $\eta < 0$ so no amount of resistance makes the beam unstable. For a resonator impedance there are 4 coupled ODEs and numerical techniques apply [5]. Figure 1 shows the eigentunes for a wake potential given by

$$W(\tau) = W_0(1 - 10\pi\tau/\tau_b)e^{-10\pi\tau/\tau_b},$$

corresponding to a critically damped resonator with a frequency of 8 MHz in SNS. The tunes are in units of $2\tau_b/\hat{v}$ and are plotted versus the tune shift obtained by assuming $D(\tau) = \sin(\pi\tau/\tau_b)$. The system appears stable for all val-

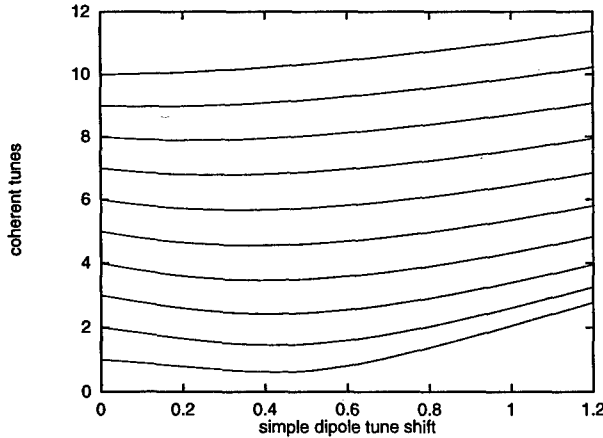


Figure 1: Exact coherent tunes versus tune shift for the dipole mode in the weak coupling approximation

ues of W_0 , not just those shown. This too is a curious result and independent confirmation would be appreciated.

For long range wakefields the residual fields from previous turns must be included in the equations of motion. Studies in this direction continue and growth rates of order the synchrotron frequency are expected. Since the entire SNS cycle is about half a synchrotron period no serious instabilities are expected.

The final type of longitudinal stability is related to the rf system. With large beam current the coupling between the beam, cavity and power amplifier is a major consideration in rf design. For SNS we have simulated the effects of beam loading with realistic amplifier passbands and delays. As of now the delays are large enough to keep the feedforward and feedback amplifiers outside the tunnel. The amplifiers will go into the tunnel if needed.

3 TRANSVERSE INSTABILITIES

Both coasting and bunched beam approximations have been used to study transverse stability. The space charge tune shift reaches ≈ 0.2 while $\Delta p/p \lesssim 0.01$. For a coasting beam with a parabolic energy distribution a normalized chromaticity ≈ -16 is needed to Landau damp low frequency oscillations[7]. Such a chromaticity would have a strong impact on dynamic aperture so no Landau damping due to chromaticity will be assumed. A similar statement applies to octupoles. Landau damping due to frequency slip becomes effective for mode numbers $n \gtrsim 4 \times 0.2/\hat{v} \approx 800$. This frequency is above cutoff for transverse electric microwave propagation ≈ 800 MHz where the transverse impedance may have narrow resonances. Therefore, a cold coasting beam dispersion relation is appropriate and the growth rate is[7]

$$Im(\Omega) = \frac{qcI_{peak}Re(Z_{\perp}(n - Q_{\beta}))}{4\pi E_0 Q_{\beta}} = 2.12I_A Z_{KS}^{-1}, \quad (8)$$

where $Q_{\beta} \approx 5.8$, I_A is the current in amps, Z_K is the transverse impedance in k Ω /m, and $n > 0$ for instability. For the narrow band resistive wall growth rate $I_A = 40$ and $Im(\Omega) = 1.1$ /ms, which is benign. The stripline beam position monitors (BPMs) have a transverse resistance of 25k Ω /m near 100 MHz and a large bandwidth. Taking $I_A = 100$ gives $Im(\Omega) = 5.3$ /ms. This is a large growth rate, but the wide bandwidth of the BPM impedance requires that the finite bunch length be taken into account.

Bunched beam stability calculations have been done assuming an air bag longitudinal distribution in a square well [4, 5]. The impedance budget includes the resistive wall, BPMs, extraction kicker, bellows, and transitions. The high frequency narrow band resonances associated with the latter were ignored. The extraction kicker impedance was modeled using a slightly modified version of the Nassibian Sacherer formula[8].

$$Z_{\perp}(\omega) = \frac{-iNcL}{g^2} \frac{Z_g/L}{Z_g/L - i\omega},$$

where N is the number of kicker modules, L is the inductance per module, g is the aperture in the kick direction, and Z_g is the generator impedance of the pulse forming network. This formula differs from [8] in that $Z_{\perp} \rightarrow 0$ as $\omega \rightarrow \infty$ here. Both have identical expressions for $Re(Z_{\perp})$.

Table 1 shows the growth rate of the most unstable mode as a function of space charge tune shift and kicker generator impedance. The growth rates are for 2×10^{14} protons and should be multiplied by 0.5ms to obtain the number of e-folding times in the cycle. In the worst case there are 2.5 e-folding times in the SNS cycle. An initial offset of 1mm yields 1.2cm at extraction.

4 ELECTRON PROTON INSTABILITY

Very fast, high frequency, transverse instabilities have been observed in the Los Alamos PSR and the AGS Booster.

Table 1: Transverse bunched beam growth rates as a function of space charge tune shift and kicker generator impedance.

ΔQ_{sc} 1	$Z_g = \infty$ $10^3 s^{-1}$	$Z_g = 500\Omega$ $10^3 s^{-1}$	$Z_g = 50\Omega$ $10^3 s^{-1}$	$Z_g = 5\Omega$ $10^3 s^{-1}$
0.00	1.27	1.41	2.01	3.85
0.05	1.37	1.52	4.58	3.69
0.10	1.37	3.14	4.87	3.70
0.15	1.37	4.27	4.99	3.70
0.20	1.37	4.99	5.05	3.70

The e-folding times (~ 10 turns) require a transverse resistance or order $1M\Omega/m$ which is significantly larger than can be accounted for by the lattice. Additionally, the frequency of the instability depends strongly on beam parameters like betatron frequency ω_β , which requires a broad band impedance. An alternate driving mechanism is the electrostatic interaction between the proton beam and electrons within the beam pipe [9, 10, 11, 12].

Assume a coasting proton beam of radius a with vertical offset

$$Y_p(\theta, t) = \hat{Y}_p \exp[in(\theta - \omega_0 t) + i(\omega_\beta + \delta\omega_\beta)t]$$

where θ is the machine azimuth and $\delta\omega_\beta$ is the betatron frequency shift. Let an electron cloud be trapped by the beam with vertical offset

$$Y_e(\theta, t) = \hat{Y}_e \exp[in\theta - i(\omega_e + \delta\omega_e)t]$$

where

$$\omega_e = \sqrt{\frac{eIZ_0}{2\pi\beta m_e a^2}}$$

is the incoherent transverse frequency for electrons trapped within the proton beam. Of course $\delta\omega_e = -\delta\omega_\beta + (n\omega_0 - \omega_\beta - \omega_e)$. The equations of motion are given by

$$\ddot{Y}_p = -\omega_\beta^2 Y_p + \omega_p^2 (Y_e - Y_p) \quad (9)$$

$$\ddot{Y}_e = \omega_e^2 (Y_p - Y_e) \quad (10)$$

where

$$\omega_p^2 = f \frac{m_e}{\gamma m_p} \omega_e^2$$

with f being the fractional neutralization due to the electrons. Assuming $\delta\omega_\beta \ll \omega_\beta$ and $\delta\omega_e \ll \omega_e$

$$2i\omega_\beta \delta\omega_\beta Y_p = \omega_p^2 Y_e, \quad -2i\omega_e \delta\omega_e Y_e = \omega_e^2 Y_p$$

Solving for $\delta\omega_\beta$ yields

$$\delta\omega_\beta = \frac{\Delta\omega}{2} \pm \sqrt{\left(\frac{\Delta\omega}{2}\right)^2 - \frac{\omega_p^2 \omega_e}{4\omega_\beta}}$$

where $\Delta\omega = n\omega_0 - \omega_\beta - \omega_e$. For unstable conditions the ratio of proton to electron amplitudes is given by

$$\left| \frac{\hat{Y}_p}{\hat{Y}_e} \right| = \frac{\omega_p}{\sqrt{\omega_e \omega_\beta}}$$

Since $|\Delta\omega| \leq \omega_0/2$ for some n the beam will be unstable if $\omega_p^2 \geq \omega_0^2 \omega_\beta / 4\omega_e$ which gives $\hat{Y}_p \sim \omega_0 \hat{Y}_e / \omega_e \ll \hat{Y}_e$.

Electrons with $\hat{Y}_e = b$ (the pipe radius) will be created by the familiar slow loss mechanisms. As f increases the beam goes unstable and the electron amplitudes grow. An electron striking the beam pipe leads to secondary emission which can cause an electron cascade and beam loss. A key parameter is the kinetic energy the electron has when it strikes the wall. This is easily estimated by assuming the electron grazes the wall on one oscillation and hits it on the next. If only one side of the vacuum chamber is involved the electron velocity on impact is given by

$$v_e = b\sqrt{4\pi\omega_e\omega_I} \left(1 + O(\sqrt{\omega_I/\omega_e})\right)$$

where $\omega_I = Im(\delta\omega_e)$. Assuming $\Delta\omega = 0$, the electron kinetic energy when striking the wall is

$$KE_e = \pi m_e (\omega_e b)^2 \sqrt{\frac{f m_e \omega_e}{\gamma m_p \omega_\beta}}. \quad (11)$$

Table 2 summarizes the observations of the instability in the AGS Booster and PSR. For $f = 1\%$ the electrons hit the wall with an energy greater than 100eV, which results in a secondary emission coefficient greater than one for most metals. With $f = 1$ both machines have $|\hat{Y}_p/\hat{Y}_e| < 0.1$ so strong multipactoring is required for fast beam loss.

Table 2: Coasting beam instability parameters

machine	$\omega_e/2\pi$ MHz	$\omega_\beta/2\pi$ MHz	b cm	γ	KE_e/\sqrt{f} keV
PSR	100	6.0	5	1.85	1.24
Booster	80	4.1	6	1.21	1.52

5 REFERENCES

- [1] W.T. Weng *et. al.* PAC97, p953.
- [2] M. Blaskiewicz SNS Tech note 46 (1998).
- [3] S. Y. Zhang SNS Tech note *in preparation*.
- [4] V.V. Danilov, E.A. Perevedentsev, 15th ICHEA p1163 (1992).
- [5] Blaskiewicz M., *PRSTAB* Vol 1, 044201 (1998).
- [6] Y.H. Chin, ABCI version 9.2.1, (1995).
- [7] J. L. Laclare CERN 85-19 p377 (1985).
- [8] G. Nassibian, F. Sacherer, CERN/ISR-TH/77-61 (1977).
- [9] B.V. Chirikov, *Sov. Atomic Energy*, **19** p1149 (1965).
- [10] E. Keil, B. Zotter, CERN/ISR-TH/71-58, (1971).
- [11] D. Neuffer *et. al.* *NIM A321* p1 (1992).
- [12] A. Ruggiero, M. Blaskiewicz, PAC 97 p1581 (1998).

NONLINEAR ACCELERATOR PROBLEMS VIA WAVELETS:

1. ORBITAL MOTION IN STORAGE RINGS

A. Fedorova, M. Zeitlin, IPME, RAS, St. Petersburg, Russia * †

Abstract

In this series of eight papers we present the applications of methods from wavelet analysis to polynomial approximations for a number of accelerator physics problems. In this part, according to variational approach we obtain a representation for orbital particle motion in storage rings as a multiresolution (multiscales) expansion in the base of well-localized in phase space wavelet basis. By means of this "wavelet microscope" technique we can take into account contribution from each scale of resolution.

1 INTRODUCTION

This is the first part of our eight presentations in which we consider applications of methods from wavelet analysis to nonlinear accelerator physics problems. This is a continuation of our results from [1]-[8], which is based on our approach to investigation of nonlinear problems – general, with additional structures (Hamiltonian, symplectic or quasicomplex), chaotic, quasiclassical, quantum, which are considered in the framework of local (nonlinear) Fourier analysis, or wavelet analysis. Wavelet analysis is a relatively novel set of mathematical methods, which gives us a possibility to work with well-localized bases in functional spaces and with the general type of operators (differential, integral, pseudodifferential) in such bases. In the parts 1-8 we consider applications of wavelet technique to nonlinear dynamical problems with polynomial type of nonlinearities. In this part we consider this very useful approximation in the case of orbital motion in storage rings. Approximation up to octupole terms is only a particular case of our general construction for n-poles. Our solutions are parametrized by solutions of a number of reduced algebraical problems one from which is nonlinear with the same degree of nonlinearity and the rest are the linear problems which correspond to particular method of calculation of scalar products of functions from wavelet bases and their derivatives.

* e-mail: zeitlin@math.ipme.ru

† <http://www.ipme.ru/zeitlin.html>; <http://www.ipme.nw.ru/zeitlin.html>

2 ORBITAL MOTION IN STORAGE RINGS

We consider as the main example the particle motion in storage rings in standard approach, which is based on consideration in [9]. Starting from Hamiltonian, which described classical dynamics in storage rings $\mathcal{H}(\vec{r}, \vec{P}, t) = c\{\pi^2 + m_0^2 c^2\}^{1/2} + e\phi$ and using Serret-Frenet parametrization, we have after standard manipulations with truncation of power series expansion of square root the following approximated (up to octupoles) Hamiltonian for orbital motion in machine coordinates:

$$\begin{aligned} \mathcal{H} = & \frac{1}{2} \cdot \frac{[p_x + H \cdot z]^2 + [p_z - H \cdot x]^2}{[1 + f(p_\sigma)]} \\ & + p_\sigma - [1 + K_x \cdot x + K_z \cdot z] \cdot f(p_\sigma) \\ & + \frac{1}{2} \cdot [K_x^2 + g] \cdot x^2 + \frac{1}{2} \cdot [K_z^2 - g] \cdot z^2 - N \cdot xz \\ & + \frac{\lambda}{6} \cdot (x^3 - 3xz^2) + \frac{\mu}{24} \cdot (z^4 - 6x^2 z^2 + x^4) \\ & + \frac{1}{\beta_0^2} \cdot \frac{L}{2\pi \cdot h} \cdot \frac{eV(s)}{E_0} \cdot \cos \left[h \cdot \frac{2\pi}{L} \cdot \sigma + \varphi \right] \end{aligned} \quad (1)$$

Then we use series expansion of function $f(p_\sigma)$ from [9]: $f(p_\sigma) = f(0) + f'(0)p_\sigma + f''(0)p_\sigma^2/2 + \dots = p_\sigma - p_\sigma^2/(2\gamma_0^2) + \dots$ and the corresponding expansion of RHS of equations corresponding to (1). In the following we take into account only an arbitrary polynomial (in terms of dynamical variables) expressions and neglecting all nonpolynomial types of expressions, i.e. we consider such approximations of RHS, which are not more than polynomial functions in dynamical variables and arbitrary functions of independent variable s ("time" in our case, if we consider our system of equations as dynamical problem).

3 POLYNOMIAL DYNAMICS

The first main part of our consideration is some variational approach to this problem, which reduces initial problem to the problem of solution of functional equations at the first stage and some algebraical problems at the second stage. We have the solution in a compactly supported wavelet basis. Multiresolution expansion is the second main part of our construction. The solution is parameterized by solutions of two reduced algebraical problems, one is nonlinear

and the second is some linear problem, which is obtained from the method of Connection Coefficients (CC).

3.1 Variational Method

Our problems may be formulated as the systems of ordinary differential equations

$$dx_i/dt = f_i(x_j, t), \quad (i, j = 1, \dots, n) \quad (2)$$

with fixed initial conditions $x_i(0)$, where f_i are not more than polynomial functions of dynamical variables x_j and have arbitrary dependence of time. Because of time dilation we can consider only next time interval: $0 \leq t \leq 1$. Let us consider a set of functions $\Phi_i(t) = x_i dy_i/dt + f_i y_i$ and a set of functionals

$$F_i(x) = \int_0^1 \Phi_i(t) dt - x_i y_i \Big|_0^1, \quad (3)$$

where $y_i(t)(y_i(0) = 0)$ are dual variables. It is obvious that the initial system and the system

$$F_i(x) = 0 \quad (4)$$

are equivalent. In the following parts we consider an approach, which is based on taking into account underlying symplectic structure and on more useful and flexible analytical approach, related to bilinear structure of initial functional. Now we consider formal expansions for x_i, y_i :

$$x_i(t) = x_i(0) + \sum_k \lambda_i^k \varphi_k(t) \quad y_j(t) = \sum_r \eta_j^r \varphi_r(t), \quad (5)$$

where because of initial conditions we need only $\varphi_k(0) = 0$. Then we have the following reduced algebraical system of equations on the set of unknown coefficients λ_i^k of expansions (5):

$$\sum_k \mu_{kr} \lambda_i^k - \gamma_i^r(\lambda_j) = 0 \quad (6)$$

Its coefficients are

$$\begin{aligned} \mu_{kr} &= \int_0^1 \varphi'_k(t) \varphi_r(t) dt, \\ \gamma_i^r &= \int_0^1 f_i(x_j, t) \varphi_r(t) dt. \end{aligned} \quad (7)$$

Now, when we solve system (6) and determine unknown coefficients from formal expansion (5) we therefore obtain the solution of our initial problem. It should be noted if we consider only truncated expansion (5) with N terms then we have from (6) the system of $N \times n$ algebraical equations and the degree of this algebraical system coincides with degree of initial differential system. So, we have the solution of the initial nonlinear (polynomial) problem in the form

$$x_i(t) = x_i(0) + \sum_{k=1}^N \lambda_i^k X_k(t), \quad (8)$$

where coefficients λ_i^k are roots of the corresponding reduced algebraical problem (6). Consequently, we have a parametrization of solution of initial problem by solution of reduced algebraical problem (6). The first main problem is a problem of computations of coefficients of reduced algebraical system. As we will see, these problems may be explicitly solved in wavelet approach. The obtained solutions are given in the form (8), where $X_k(t)$ are basis functions and λ_k^i are roots of reduced system of equations. In our case $X_k(t)$ are obtained via multiresolution expansions and represented by compactly supported wavelets and λ_k^i are the roots of corresponding general polynomial system (6) with coefficients, which are given by CC construction. According to the variational method to give the reduction from differential to algebraical system of equations we need compute the objects γ_a^j and μ_{ji} , which are constructed from objects:

$$\begin{aligned} \sigma_i &\equiv \int_0^1 X_i(\tau) d\tau, \quad \nu_{ij} \equiv \int_0^1 X_i(\tau) X_j(\tau) d\tau, \\ \mu_{ji} &\equiv \int_0^1 X'_i(\tau) X_j(\tau) d\tau, \\ \beta_{klj} &\equiv \int_0^1 X_k(\tau) X_l(\tau) X_j(\tau) d\tau \end{aligned} \quad (9)$$

for the simplest case of Riccati systems (sextupole approximation), where degree of nonlinearity equals to two. For the general case of arbitrary n we have analogous to (9) iterated integrals with the degree of monomials in integrand which is one more bigger than degree of initial system.

3.2 Wavelet Computations

Now we give construction for computations of objects (9) in the wavelet case. We present some details of wavelet machinery in part 2. We use compactly supported wavelet basis (Fig. 1, for example): orthonormal basis for functions in $L^2(\mathbb{R})$.

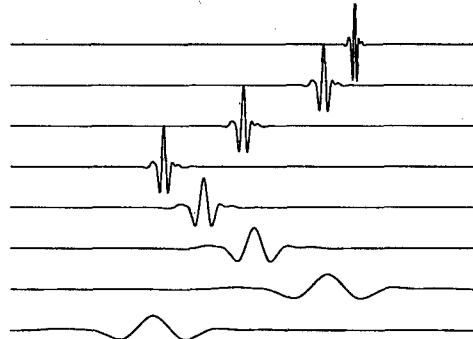


Figure 1: Wavelets at different scales and locations

Let be $f: \mathbb{R} \rightarrow \mathbb{C}$ and the wavelet expansion is

$$f(x) = \sum_{\ell \in \mathbb{Z}} c_\ell \varphi_\ell(x) + \sum_{j=0}^{\infty} \sum_{k \in \mathbb{Z}} c_{jk} \psi_{jk}(x) \quad (10)$$

If in formulae (10) $c_{jk} = 0$ for $j \geq J$, then $f(x)$ has an alternative expansion in terms of dilated scaling functions only $f(x) = \sum_{\ell \in \mathbb{Z}} c_{J\ell} \varphi_{J\ell}(x)$. This is a finite wavelet expansion, it can be written solely in terms of translated scaling functions. Also we have the shortest possible support: scaling function DN (where N is even integer) will have support $[0, N - 1]$ and $N/2$ vanishing moments. There exists $\lambda > 0$ such that DN has λN continuous derivatives; for small N , $\lambda \geq 0.55$. To solve our second associated linear problem we need to evaluate derivatives of $f(x)$ in terms of $\varphi(x)$. Let be $\varphi_\ell^n = d^n \varphi_\ell(x)/dx^n$. We consider computation of the wavelet - Galerkin integrals. Let $f^d(x)$ be d-derivative of function $f(x)$, then we have $f^d(x) = \sum_\ell c_\ell \varphi_\ell^d(x)$, and values $\varphi_\ell^d(x)$ can be expanded in terms of $\varphi(x)$

$$\varphi_\ell^d(x) = \sum_m \lambda_m \varphi_m(x), \quad (11)$$

where $\lambda_m = \int \varphi_\ell^d(x) \varphi_m(x) dx$ are wavelet-Galerkin integrals. The coefficients λ_m are 2-term connection coefficients. In general we need to find ($d_i \geq 0$)

$$\Lambda_{\ell_1 \ell_2 \dots \ell_n}^{d_1 d_2 \dots d_n} = \int_{-\infty}^{\infty} \prod \varphi_{\ell_i}^{d_i}(x) dx \quad (12)$$

For Riccati case (sextupole) we need to evaluate two and three connection coefficients

$$\begin{aligned} \Lambda_\ell^{d_1 d_2} &= \int_{-\infty}^{\infty} \varphi^{d_1}(x) \varphi_\ell^{d_2}(x) dx, \\ \Lambda^{d_1 d_2 d_3} &= \int_{-\infty}^{\infty} \varphi^{d_1}(x) \varphi_\ell^{d_2}(x) \varphi_m^{d_3}(x) dx \end{aligned} \quad (13)$$

According to CC method [10] we use the next construction. When N in scaling equation is a finite even positive integer the function $\varphi(x)$ has compact support contained in $[0, N - 1]$. For a fixed triple (d_1, d_2, d_3) only some $\Lambda_{\ell m}^{d_1 d_2 d_3}$ are nonzero: $2 - N \leq \ell \leq N - 2$, $2 - N \leq m \leq N - 2$, $|\ell - m| \leq N - 2$. There are $M = 3N^2 - 9N + 7$ such pairs (ℓ, m) . Let $\Lambda^{d_1 d_2 d_3}$ be an M -vector, whose components are numbers $\Lambda_{\ell m}^{d_1 d_2 d_3}$. Then we have the first reduced algebraical system: Λ satisfy the system of equations ($d = d_1 + d_2 + d_3$)

$$\begin{aligned} A \Lambda^{d_1 d_2 d_3} &= 2^{1-d} \Lambda^{d_1 d_2 d_3}, \\ A_{\ell, m; q, r} &= \sum_p a_p a_{q-2\ell+p} a_{r-2m+p}. \end{aligned} \quad (14)$$

By moment equations we have created a system of $M + d + 1$ equations in M unknowns. It has rank M and we can obtain unique solution by combination of LU decomposition and QR algorithm. The second reduced algebraical system gives us the 2-term connection coefficients. For non-quadratic case we have analogously additional linear problems for objects (12). Solving these linear problems we obtain the coefficients of nonlinear algebraical system (6)

and after that we obtain the coefficients of wavelet expansion (8). As a result we obtained the explicit time solution of our problem in the base of compactly supported wavelets with the best possible localization in the phase space, which allows us to control contribution from each scale of underlying multiresolution expansions.

In the following parts we consider extension of this approach to the case of (periodic) boundary conditions, the case of presence of arbitrary variable coefficients and more flexible biorthogonal wavelet approach.

We are very grateful to M. Cornacchia (SLAC), W. Herrmannsfeldt (SLAC), Mrs. J. Kono (LBL) and M. Laraneta (UCLA) for their permanent encouragement.

4 REFERENCES

- [1] Fedorova, A.N., Zeitlin, M.G. 'Wavelets in Optimization and Approximations', *Math. and Comp. in Simulation*, **46**, 527-534 (1998).
- [2] Fedorova, A.N., Zeitlin, M.G., 'Wavelet Approach to Polynomial Mechanical Problems', *New Applications of Nonlinear and Chaotic Dynamics in Mechanics*, Kluwer, 101-108, 1998.
- [3] Fedorova, A.N., Zeitlin, M.G., 'Wavelet Approach to Mechanical Problems. Symplectic Group, Symplectic Topology and Symplectic Scales', *New Applications of Nonlinear and Chaotic Dynamics in Mechanics*, Kluwer, 31-40, 1998.
- [4] Fedorova, A.N., Zeitlin, M.G. 'Nonlinear Dynamics of Accelerator via Wavelet Approach', *AIP Conf. Proc.*, vol. **405**, 87-102, 1997, Los Alamos preprint, physics/9710035.
- [5] Fedorova, A.N., Zeitlin, M.G., Parsa, Z., 'Wavelet Approach to Accelerator Problems', parts 1-3, *Proc. PAC97*, vol. **2**, 1502-1504, 1505-1507, 1508-1510, IEEE, 1998.
- [6] Fedorova, A.N., Zeitlin, M.G., Parsa, Z., 'Nonlinear Effects in Accelerator Physics: from Scale to Scale via Wavelets', 'Wavelet Approach to Hamiltonian, Chaotic and Quantum Calculations in Accelerator Physics', *Proc. EPAC'98*, 930-932, 933-935, Institute of Physics, 1998.
- [7] Fedorova, A.N., Zeitlin, M.G., Parsa, Z., 'Variational Approach in Wavelet Framework to Polynomial Approximations of Nonlinear Accelerator Problems', *AIP Conf. Proc.*, vol. **468**, 48-68, 1999. Los Alamos preprint, physics/9902062.
- [8] Fedorova, A.N., Zeitlin, M.G., Parsa, Z., 'Symmetry, Hamiltonian Problems and Wavelets in Accelerator Physics', *AIP Conf. Proc.*, vol. **468**, 69-93, 1999. Los Alamos preprint, physics/9902063.
- [9] Dragt, A.J., *Lectures on Nonlinear Dynamics*, CTP, 1996,
- [10] Latto, A., Resnikoff, H.L. and Tenenbaum E., *Aware Technical Report AD910708*, 1991.

NONLINEAR ACCELERATOR PROBLEMS VIA WAVELETS: 6. REPRESENTATIONS AND QUASICLASSICS VIA FWT

A. Fedorova, M. Zeitlin, IPME, RAS, St. Petersburg, Russia * †

Abstract

In this series of eight papers we present the applications of methods from wavelet analysis to polynomial approximations for a number of accelerator physics problems. In this part we consider application of FWT to metaplectic representation (quantum and chaotical problems) and quasiclassics.

1 INTRODUCTION

This is the sixth part of our eight presentations in which we consider applications of methods from wavelet analysis to nonlinear accelerator physics problems. This is a continuation of our results from [1]-[8], in which we considered the applications of a number of analytical methods from nonlinear (local) Fourier analysis, or wavelet analysis, to nonlinear accelerator physics problems both general and with additional structures (Hamiltonian, symplectic or quasicomplex), chaotic, quasiclassical, quantum. Wavelet analysis is a relatively novel set of mathematical methods, which gives us a possibility to work with well-localized bases in functional spaces and with the general type of operators (differential, integral, pseudodifferential) in such bases. In contrast with parts 1-4 in parts 5-8 we try to take into account before using power analytical approaches underlying algebraical, geometrical, topological structures related to kinematical, dynamical and hidden symmetry of physical problems. In part 2 according to the orbit method and by using construction from the geometric quantization theory we construct the symplectic and Poisson structures associated with generalized wavelets by using metaplectic structure. In part 3 we consider applications of very useful fast wavelet transform technique (FWT) (part 4) to calculations in quasiclassical evolution dynamics. This method gives maximally sparse representation of (differential) operator that allows us to take into account contribution from each level of resolution.

2 METAPLECTIC GROUP AND REPRESENTATIONS

Let $Sp(n)$ be symplectic group, $Mp(n)$ be its unique two-fold covering – metaplectic group [9]. Let V be a sym-

plectic vector space with symplectic form (\cdot, \cdot) , then $R \oplus V$ is nilpotent Lie algebra – Heisenberg algebra: $[R, V] = 0$, $[v, w] = (v, w) \in R$, $[V, V] = R$. $Sp(V)$ is a group of automorphisms of Heisenberg algebra. Let N be a group with Lie algebra $R \oplus V$, i.e. Heisenberg group. By Stone-von Neumann theorem Heisenberg group has unique irreducible unitary representation in which $1 \mapsto i$. Let us also consider the projective representation of symplectic group $Sp(V)$: $U_{g_1} U_{g_2} = c(g_1, g_2) \cdot U_{g_1 g_2}$, where c is a map: $Sp(V) \times Sp(V) \rightarrow S^1$, i.e. c is S^1 -cocycle. But this representation is unitary representation of universal covering, i.e. metaplectic group $Mp(V)$. We give this representation without Stone-von Neumann theorem. Consider a new group $F = N' \ltimes Mp(V)$, \ltimes is semidirect product (we consider instead of $N = R \oplus V$ the $N' = S^1 \times V$, $S^1 = (R/2\pi Z)$). Let V^* be dual to V , $G(V^*)$ be automorphism group of V^* . Then F is subgroup of $G(V^*)$, which consists of elements, which acts on V^* by affine transformations. This is the key point! Let $q_1, \dots, q_n; p_1, \dots, p_n$ be symplectic basis in V , $\alpha = pdq = \sum p_i dq_i$ and $d\alpha$ be symplectic form on V^* . Let M be fixed affine polarization, then for $a \in F$ the map $a \mapsto \Theta_a$ gives unitary representation of G : $\Theta_a : H(M) \rightarrow H(M)$. Explicitly we have for representation of N on $H(M)$: $(\Theta_q f)^*(x) = e^{-iqx} f(x)$, $\Theta_p f(x) = f(x - p)$. The representation of N on $H(M)$ is irreducible. Let A_q, A_p be infinitesimal operators of this representation

$$A_q = \lim_{t \rightarrow 0} \frac{1}{t} [\Theta_{-tq} - I], \quad A_p = \lim_{t \rightarrow 0} \frac{1}{t} [\Theta_{-tp} - I],$$

$$\text{then } A_q f(x) = i(qx)f(x), \quad A_p f(x) = \sum p_j \frac{\partial f}{\partial x_j}(x)$$

Now we give the representation of infinitesimal basic elements. Lie algebra of the group F is the algebra of all (non-homogeneous) quadratic polynomials of (p, q) relatively Poisson bracket (PB). The basis of this algebra consists of elements $1, q_1, \dots, q_n, p_1, \dots, p_n, q_i q_j, q_i p_j, p_i p_j$, $i, j = 1, \dots, n$, $i \leq j$,

$$PB \text{ is } \{f, g\} = \sum \frac{\partial f}{\partial p_j} \frac{\partial g}{\partial q_i} - \frac{\partial f}{\partial q_i} \frac{\partial g}{\partial p_j}$$

$$\text{and } \{1, g\} = 0 \text{ for all } g,$$

$$\{p_i, q_j\} = \delta_{ij}, \quad \{p_i q_j, q_k\} = \delta_{ik} q_j,$$

$$\{p_i q_j, p_k\} = -\delta_{jk} p_i, \quad \{p_i p_j, p_k\} = 0,$$

$$\{p_i p_j, q_k\} = \delta_{ik} p_j + \delta_{jk} p_i, \quad \{q_i q_j, q_k\} = 0,$$

$$\{q_i q_j, p_k\} = -\delta_{ik} q_j - \delta_{jk} q_i$$

* e-mail: zeitlin@math.ipme.ru

† http://www.ipme.ru/zeitlin.html: http://www.ipme.nw.ru/zeitlin.html

so, we have the representation of basic elements $f \mapsto A_f$:
 $1 \mapsto i, q_k \mapsto ix_k,$

$$p_l \mapsto \frac{\partial}{\partial x^l}, p_i q_j \mapsto x^i \frac{\partial}{\partial x^j} + \frac{1}{2} \delta_{ij},$$

$$p_k p_l \mapsto \frac{1}{i} \frac{\partial^k}{\partial x^k \partial x^l}, q_k q_l \mapsto ix^k x^l$$

This gives the structure of the Poisson manifolds to representation of any (nilpotent) algebra or in other words to continuous wavelet transform. According to this approach we can construct by using methods of geometric quantization theory many "symplectic wavelet constructions" with corresponding symplectic or Poisson structure on it. Then we may produce symplectic invariant wavelet calculations for PB or commutators which we may use in quantization procedure or in chaotic dynamics (part 8) via operator representation from section 4.

3 QUASICLASSICAL EVOLUTION

Let us consider classical and quantum dynamics in phase space $\Omega = R^{2m}$ with coordinates (x, ξ) and generated by Hamiltonian $\mathcal{H}(x, \xi) \in C^\infty(\Omega; R)$. If $\Phi_t^{\mathcal{H}} : \Omega \rightarrow \Omega$ is (classical) flow then time evolution of any bounded classical observable or symbol $b(x, \xi) \in C^\infty(\Omega, R)$ is given by $b_t(x, \xi) = b(\Phi_t^{\mathcal{H}}(x, \xi))$. Let $H = Op^W(\mathcal{H})$ and $B = Op^W(b)$ are the self-adjoint operators or quantum observables in $L^2(R^n)$, representing the Weyl quantization of the symbols \mathcal{H}, b [9]

$$(Bu)(x) = \frac{1}{(2\pi\hbar)^n} \int_{R^{2n}} b\left(\frac{x+y}{2}, \xi\right) e^{i\langle x-y, \xi \rangle / \hbar} u(y) dy d\xi,$$

where $u \in S(R^n)$ and $B_t = e^{iHt/\hbar} B e^{-iHt/\hbar}$ be the Heisenberg observable or quantum evolution of the observable B under unitary group generated by H . B_t solves the Heisenberg equation of motion $\dot{B}_t = (i/\hbar)[H, B_t]$. Let $b_t(x, \xi; \hbar)$ is a symbol of B_t then we have the following equation for it

$$\dot{b}_t = \{\mathcal{H}, b_t\}_M, \quad (1)$$

with the initial condition $b_0(x, \xi, \hbar) = b(x, \xi)$. Here $\{f, g\}_M(x, \xi)$ is the Moyal brackets of the observables $f, g \in C^\infty(R^{2n})$, $\{f, g\}_M(x, \xi) = f \sharp g - g \sharp f$, where $f \sharp g$ is the symbol of the operator product and is presented by the composition of the symbols f, g

$$(f \sharp g)(x, \xi) = \frac{1}{(2\pi\hbar)^{2n}} \int_{R^{4n}} e^{-i\langle r, \rho \rangle / \hbar + i\langle \omega, \tau \rangle / \hbar} \cdot f(x + \omega, \rho + \xi) \cdot g(x + r, \tau + \xi) d\rho d\tau dr d\omega.$$

For our problems it is useful that $\{f, g\}_M$ admits the formal expansion in powers of \hbar :

$$\{f, g\}_M(x, \xi) \sim \{f, g\} + 2^{-j} \cdot \sum_{|\alpha+\beta| \geq 1} (-1)^{|\beta|} \cdot (\partial_\xi^\alpha f D_x^\beta g) \cdot (\partial_\xi^\beta g D_x^\alpha f),$$

where $\alpha = (\alpha_1, \dots, \alpha_n)$ is a multi-index, $|\alpha| = \alpha_1 + \dots + \alpha_n$, $D_x = -i\hbar \partial_x$. So, evolution (1) for symbol $b_t(x, \xi; \hbar)$ is

$$\dot{b}_t = \{\mathcal{H}, b_t\} + \frac{1}{2j} \sum_{|\alpha|+|\beta|=j \geq 1} (-1)^{|\beta|} \cdot \hbar^j (\partial_\xi^\alpha \mathcal{H} D_x^\beta b_t) \cdot (\partial_\xi^\beta b_t D_x^\alpha \mathcal{H}). \quad (2)$$

At $\hbar = 0$ this equation transforms to classical Liouville equation

$$\dot{b}_t = \{\mathcal{H}, b_t\}. \quad (3)$$

Equation (2) plays a key role in many quantum (semiclassical) problem. We note only the problem of relation between quantum and classical evolutions or how long the evolution of the quantum observables is determined by the corresponding classical one [9]. Our approach to solution of systems (2), (3) is based on our technique from [1]-[8] and very useful linear parametrization for differential operators which we present in the next section.

4 FAST WAVELET TRANSFORM FOR DIFFERENTIAL OPERATORS

Let us consider multiresolution representation $\dots \subset V_2 \subset V_1 \subset V_0 \subset V_{-1} \subset V_{-2} \dots$ (see our other papers from this series for details of wavelet machinery). Let T be an operator $T : L^2(R) \rightarrow L^2(R)$, with the kernel $K(x, y)$ and $P_j : L^2(R) \rightarrow V_j$ ($j \in Z$) is projection operators on the subspace V_j corresponding to j level of resolution: $(P_j f)(x) = \sum_k \langle f, \varphi_{j,k} \rangle \varphi_{j,k}(x)$. Let $Q_j = P_{j-1} - P_j$ is the projection operator on the subspace W_j then we have the following "microscopic or telescopic" representation of operator T which takes into account contributions from each level of resolution from different scales starting with coarsest and ending to finest scales [10]: $T = \sum_{j \in Z} (Q_j T Q_j + Q_j T P_j + P_j T Q_j)$. We remember that this is a result of presence of affine group inside this construction. The non-standard form of operator representation [10] is a representation of an operator T as a chain of triples $T = \{A_j, B_j, \Gamma_j\}_{j \in Z}$, acting on the subspaces V_j and W_j : $A_j : W_j \rightarrow W_j, B_j : V_j \rightarrow W_j, \Gamma_j : W_j \rightarrow V_j$, where operators $\{A_j, B_j, \Gamma_j\}_{j \in Z}$ are defined as $A_j = Q_j T Q_j, B_j = Q_j T P_j, \Gamma_j = P_j T Q_j$. The operator T admits a recursive definition via

$$T_j = \begin{pmatrix} A_{j+1} & B_{j+1} \\ \Gamma_{j+1} & T_{j+1} \end{pmatrix},$$

where $T_j = P_j T P_j$ and T_j works on $V_j : V_j \rightarrow V_j$. It should be noted that operator A_j describes interaction on the scale j independently from other scales, operators B_j, Γ_j describe interaction between the scale j and all coarser scales, the operator T_j is an "averaged" version of T_{j-1} . The operators A_j, B_j, Γ_j, T_j are represented by matrices $\alpha^j, \beta^j, \gamma^j, s^j$

$$\alpha_{k,k'}^j = \iint K(x, y) \psi_{j,k}(x) \psi_{j,k'}(y) dx dy$$

$$\beta_{k,k'}^j = \int \int K(x,y) \psi_{j,k}(x) \varphi_{j,k'}(y) dx dy \quad (4)$$

$$\gamma_{k,k'}^j = \int \int K(x,y) \varphi_{j,k}(x) \psi_{j,k'}(y) dx dy$$

$$s_{k,k'}^j = \int \int K(x,y) \varphi_{j,k}(x) \varphi_{j,k'}(y) dx dy$$

We may compute the non-standard representations of operator d/dx in the wavelet bases by solving a small system of linear algebraical equations. So, we have for objects (4)

$$\begin{aligned} \alpha_{i,\ell}^j &= 2^{-j} \int \psi(2^{-j}x - i) \psi'(2^{-j}x - \ell) 2^{-j} dx \\ &= 2^{-j} \alpha_{i-\ell} \end{aligned}$$

$$\begin{aligned} \beta_{i,\ell}^j &= 2^{-j} \int \psi(2^{-j}x - i) \varphi'(2^{-j}x - \ell) 2^{-j} dx \\ &= 2^{-j} \beta_{i-\ell} \end{aligned}$$

$$\begin{aligned} \gamma_{i,\ell}^j &= 2^{-j} \int \varphi(2^{-j}x - i) \psi'(2^{-j}x - \ell) 2^{-j} dx \\ &= 2^{-j} \gamma_{i-\ell}, \end{aligned}$$

where

$$\alpha_\ell = \int \psi(x - \ell) \frac{d}{dx} \psi(x) dx$$

$$\beta_\ell = \int \psi(x - \ell) \frac{d}{dx} \varphi(x) dx$$

$$\gamma_\ell = \int \varphi(x - \ell) \frac{d}{dx} \psi(x) dx$$

then by using refinement equations we have in terms of filters (h_k, g_k) :

$$\alpha_j = 2 \sum_{k=0}^{L-1} \sum_{k'=0}^{L-1} g_k g_{k'} r_{2i+k-k'},$$

$$\beta_j = 2 \sum_{k=0}^{L-1} \sum_{k'=0}^{L-1} g_k h_{k'} r_{2i+k-k'},$$

$$\gamma_i = 2 \sum_{k=0}^{L-1} \sum_{k'=0}^{L-1} h_k g_{k'} r_{2i+k-k'},$$

where $r_\ell = \int \varphi(x - \ell) \frac{d}{dx} \varphi(x) dx$, $\ell \in Z$. Therefore, the representation of d/dx is completely determined by the coefficients r_ℓ or by representation of d/dx only on the subspace V_0 . The coefficients r_ℓ , $\ell \in Z$ satisfy the following system of linear algebraical equations

$$r_\ell = 2 \left[r_{2\ell} + \frac{1}{2} \sum_{k=1}^{L/2} a_{2k-1} (r_{2\ell-2k+1} + r_{2\ell+2k-1}) \right]$$

and $\sum_\ell \ell r_\ell = -1$, where $a_{2k-1} = 2 \sum_{i=0}^{L-2k} h_i h_{i+2k-1}$, $k = 1, \dots, L/2$ are the autocorrelation coefficients of the filter H . If a number of vanishing moments $M \geq 2$ then this linear system of equations has a unique solution with finite number of non-zero r_ℓ , $r_\ell \neq 0$ for $-L+2 \leq$

$\ell \leq L-2$, $r_\ell = -r_{-\ell}$. For the representation of operator d^n/dx^n we have the similar reduced linear system of equations. Then finally we have for action of operator $T_j(T_j : V_j \rightarrow V_j)$ on sufficiently smooth function f :

$$(T_j f)(x) = \sum_{k \in Z} \left(2^{-j} \sum_{\ell} r_\ell f_{j,k-\ell} \right) \varphi_{j,k}(x),$$

where $\varphi_{j,k}(x) = 2^{-j/2} \varphi(2^{-j}x - k)$ is wavelet basis and

$$f_{j,k-1} = 2^{-j/2} \int f(x) \varphi(2^{-j}x - k + \ell) dx$$

are wavelet coefficients. So, we have simple linear parametrization of matrix representation of our differential operator in wavelet basis and of the action of this operator on arbitrary vector in our functional space. Then we may use such representation in all preceding sections.

We are very grateful to M. Cornacchia (SLAC), W. Herrmannsfeldt (SLAC) Mrs. J. Kono (LBL) and M. Laraneta (UCLA) for their permanent encouragement.

5 REFERENCES

- [1] Fedorova, A.N., Zeitlin, M.G. 'Wavelets in Optimization and Approximations', *Math. and Comp. in Simulation*, **46**, 527-534 (1998).
- [2] Fedorova, A.N., Zeitlin, M.G., 'Wavelet Approach to Polynomial Mechanical Problems', *New Applications of Nonlinear and Chaotic Dynamics in Mechanics*, Kluwer, 101-108, 1998.
- [3] Fedorova, A.N., Zeitlin, M.G., 'Wavelet Approach to Mechanical Problems. Symplectic Group, Symplectic Topology and Symplectic Scales', *New Applications of Nonlinear and Chaotic Dynamics in Mechanics*, Kluwer, 31-40, 1998.
- [4] Fedorova, A.N., Zeitlin, M.G. 'Nonlinear Dynamics of Accelerator via Wavelet Approach', *AIP Conf. Proc.*, vol. **405**, 87-102, 1997, Los Alamos preprint, physics/9710035.
- [5] Fedorova, A.N., Zeitlin, M.G., Parsa, Z., 'Wavelet Approach to Accelerator Problems', parts 1-3, *Proc. PAC97*, vol. **2**, 1502-1504, 1505-1507, 1508-1510, IEEE, 1998.
- [6] Fedorova, A.N., Zeitlin, M.G., Parsa, Z., 'Nonlinear Effects in Accelerator Physics: from Scale to Scale via Wavelets', 'Wavelet Approach to Hamiltonian, Chaotic and Quantum Calculations in Accelerator Physics', *Proc. EPAC'98*, 930-932, 933-935, Institute of Physics, 1998.
- [7] Fedorova, A.N., Zeitlin, M.G., Parsa, Z., 'Variational Approach in Wavelet Framework to Polynomial Approximations of Nonlinear Accelerator Problems', *AIP Conf. Proc.*, vol. **468**, 48-68, 1999. Los Alamos preprint, physics/9902062.
- [8] Fedorova, A.N., Zeitlin, M.G., Parsa, Z., 'Symmetry, Hamiltonian Problems and Wavelets in Accelerator Physics', *AIP Conf. Proc.*, vol. **468**, 69-93, 1999. Los Alamos preprint, physics/9902063.
- [9] G.B. Folland, 'Harmonic Analysis in Phase Space', Princeton, 1989.
- [10] G. Belykin, R.R. Coifman, V. Rokhlin, *Comm. Pure and Appl. Math.*, **44**, 141-183, 1991.

NONLINEAR ACCELERATOR PROBLEMS VIA WAVELETS: 7. INVARIANT CALCULATIONS IN HAMILTON PROBLEMS

A. Fedorova, M. Zeitlin, IPME, RAS, St. Petersburg, Russia * †

Abstract

In this series of eight papers we present the applications of methods from wavelet analysis to polynomial approximations for a number of accelerator physics problems. In this paper we consider invariant formulation of nonlinear (Lagrangian or Hamiltonian) dynamics on semidirect structure (relativity or dynamical groups) and corresponding invariant calculations via CWT.

1 INTRODUCTION

This is the seventh part of our eight presentations in which we consider applications of methods from wavelet analysis to nonlinear accelerator physics problems. This is a continuation of our results from [1]-[8], in which we considered the applications of a number of analytical methods from nonlinear (local) Fourier analysis, or wavelet analysis, to nonlinear accelerator physics problems both general and with additional structures (Hamiltonian, symplectic or quasicomplex), chaotic, quasiclassical, quantum. Wavelet analysis is a relatively novel set of mathematical methods, which gives us a possibility to work with well-localized bases in functional spaces and with the general type of operators (differential, integral, pseudodifferential) in such bases. In contrast with parts 1-4 in parts 5-8 we try to take into account before using power analytical approaches underlying algebraical, geometrical, topological structures related to kinematical, dynamical and hidden symmetry of physical problems. We described a number of concrete problems in parts 1-4. The most interesting case is the dynamics of spin-orbital motion (part 4). In section 2 we consider dynamical consequences of covariance properties regarding to relativity (kinematical) groups and continuous wavelet transform (CWT) (in section 3) as a method for the solution of dynamical problems. We introduce the semidirect product structure, which allows us to consider from general point of view all relativity groups such as Euclidean, Galilei, Poincare. Then we consider the Lie-Poisson equations and obtain the manifestation of semiproduct structure of (kinematic) symmetry group on dynamical level. So, correct description of dynamics is a consequence of correct understanding of real symmetry

of the concrete problem. We consider the Lagrangian theory related to semiproduct structure and explicit form of variation principle and corresponding (semidirect) Euler-Poincare equations. In section 3 we consider CWT and the corresponding analytical technique which allows to consider covariant wavelet analysis. In part 8 we consider in the particular case of affine Galilei group with the semiproduct structure the corresponding orbit technique for constructing different types of invariant wavelet bases.

2 DYNAMICS ON SEMIDIRECT PRODUCTS

Relativity groups such as Euclidean, Galilei or Poincare groups are the particular cases of semidirect product construction, which is very useful and simple general construction in the group theory [9]. We may consider as a basic example the Euclidean group $SE(3) = SO(3) \ltimes \mathbb{R}^3$, the semidirect product of rotations and translations. In general case we have $S = G \ltimes V$, where group G (Lie group or automorphisms group) acts on a vector space V and on its dual V^* . Let V be a vector space and G is the Lie group, which acts on the left by linear maps on V (G also acts on the left on its dual space V^*). The Lie algebra of S is the semidirect product Lie algebra, $s = \mathcal{G} \ltimes V$ with brackets $[(\xi_1, v_1), (\xi_2, v_2)] = ([\xi_1, \xi_2], \xi_1 v_2 - \xi_2 v_1)$, where the induced action of \mathcal{G} by concatenation is denoted as $\xi_1 v_2$. Let $(g, v) \in S = G \times V$, $(\xi, u) \in s = \mathcal{G} \times V$, $(\mu, a) \in s^* = \mathcal{G}^* \times V^*$, $g\xi = Ad_g \xi$, $g\mu = Ad_{g^{-1}}^* \mu$, ga denote the induced left action of g on a (the left action of G on V induces a left action on V^* — the inverse of the transpose of the action on V), $\rho_v : \mathcal{G} \rightarrow V$ is a linear map given by $\rho_v(\xi) = \xi v$, $\rho_v^* : V^* \rightarrow \mathcal{G}^*$ is its dual. Then adjoint and coadjoint actions are given by simple concatenation: $(g, v)(\xi, u) = (g\xi, gu - (g\xi)v)$, $(g, v)(\mu, a) = (g\mu + \rho_v^*(ga), ga)$. Also, let be $\rho_v^* a = v \diamond a \in \mathcal{G}^*$ for $a \in V^*$, which is a bilinear operation in v and a . So, we have the coadjoint action: $(g, v)(\mu, a) = (g\mu + v \diamond (ga), ga)$. Using concatenation notation for Lie algebra actions we have alternative definition of $v \diamond a \in \mathcal{G}^*$. For all $v \in V$, $a \in V^*$, $\eta \in \mathcal{G}$ we have $\langle \eta a, v \rangle = - \langle v \diamond a, \eta \rangle$.

Now we consider the manifestation of semiproduct structure of symmetry group on dynamical level. Let F, G be real valued functions on the dual space \mathcal{G}^* , $\mu \in \mathcal{G}^*$. Functional derivative of F at μ is the unique ele-

* e-mail: zeitlin@math.ipme.ru

† <http://www.ipme.ru/zeitlin.html>; <http://www.ipme.nw.ru/zeitlin.html>

ment $\delta F/\delta\mu \in \mathcal{G}$: $\lim_{\epsilon \rightarrow 0} [F(\mu + \epsilon\delta\mu) - F(\mu)]/\epsilon = \langle \delta\mu, \delta F/\delta\mu \rangle$ for all $\delta\mu \in \mathcal{G}^*$, \langle, \rangle is pairing between \mathcal{G}^* and \mathcal{G} . Define the (\pm) Lie-Poisson brackets by $\{F, G\}_{\pm}(\mu) = \pm \langle \mu, [\delta F/\delta\mu, \delta G/\delta\mu] \rangle$. The Lie-Poisson equations, determined by $\dot{F} = \{F, H\}$ or intrinsically $\dot{\mu} = \mp ad_{\delta H/\delta\mu}^* \mu$. For the left representation of G on $V \pm$ Lie-Poisson bracket of two functions $f, k : s^* \rightarrow \mathbb{R}$ is given by

$$\begin{aligned} \{f, k\}_{\pm}(\mu, a) &= \pm \langle \mu, [\frac{\delta f}{\delta\mu}, \frac{\delta k}{\delta\mu}] \rangle \\ &\pm \langle a, \frac{\delta f}{\delta\mu} \frac{\delta k}{\delta a} - \frac{\delta k}{\delta\mu} \frac{\delta f}{\delta a} \rangle, \end{aligned} \quad (1)$$

where $\delta f/\delta\mu \in \mathcal{G}$, $\delta f/\delta a \in V$ are the functional derivatives of f . The Hamiltonian vector field of $h : s^* \in \mathbb{R}$ has the expression $X_h(\mu, a) = \mp(ad_{\delta h/\delta\mu}^* \mu - \delta h/\delta a \diamond a, -\delta h/\delta\mu a)$. Thus, Hamiltonian equations on the dual of a semidirect product are [9]:

$$\dot{\mu} = \mp ad_{\delta h/\delta\mu}^* \mu \pm \frac{\delta h}{\delta a} \diamond a, \quad \dot{a} = \pm \frac{\delta h}{\delta\mu} a \quad (2)$$

So, we can see the explicit contribution to the Poisson brackets and the equations of motion which come from the semiproduct structure.

Now we consider according to [9] Lagrangian side of a theory. This approach is based on variational principles with symmetry and is not dependent on Hamiltonian formulation, although it is demonstrated in [9] that this purely Lagrangian formulation is equivalent to the Hamiltonian formulation on duals of semidirect product (the corresponding Legendre transformation is a diffeomorphism). We consider the case of the left representation and the left invariant Lagrangians (ℓ and L), which depend in addition on another parameter $a \in V^*$ (dynamical parameter), where V is representation space for the Lie group G and L has an invariance property related to both arguments. It should be noted that the resulting equations of motion, the Euler-Poincare equations, are not the Euler-Poincare equations for the semidirect product Lie algebra $\mathcal{G} \ltimes V^*$ or $\mathcal{G} \ltimes V$. So, we have the following:

1. There is a left representation of Lie group G on the vector space V and G acts in the natural way on the left on $TG \times V^* : h(v_g, a) = (hv_g, ha)$. 2. The function $L : TG \times V^* \rightarrow \mathbb{R}$ is the left G -invariant. 3. Let $a_0 \in V^*$, Lagrangian $L_{a_0} : TG \rightarrow \mathbb{R}$, $L_{a_0}(v_g) = L(v_g, a_0)$. L_{a_0} is left invariant under the lift to TG of the left action of G_{a_0} on G , where G_{a_0} is the isotropy group of a_0 . 4. Left G -invariance of L permits us to define $\ell : \mathcal{G} \times V^* \rightarrow \mathbb{R}$ by $\ell(g^{-1}v_g, g^{-1}a_0) = L(v_g, a_0)$. This relation defines for any $\ell : \mathcal{G} \times V^* \rightarrow \mathbb{R}$ the left G -invariant function $L : TG \times V^* \rightarrow \mathbb{R}$. 5. For a curve $g(t) \in G$ let be $\xi(t) := g(t)^{-1}\dot{g}(t)$ and define the curve $a(t)$ as the unique solution of the following linear differential equation with time dependent coefficients $\dot{a}(t) = -\xi(t)a(t)$, with initial condition $a(0) = a_0$. The solution can be written as $a(t) = g(t)^{-1}a_0$.

Then we have four equivalent descriptions of the corresponding dynamics: 1. If a_0 is fixed then Hamilton's variational principle $\delta \int_{t_1}^{t_2} L_{a_0}(g(t), \dot{g}(t))dt = 0$ holds for variations $\delta g(t)$ of $g(t)$ vanishing at the endpoints. 2. $g(t)$ satisfies the Euler-Lagrange equations for L_{a_0} on G . 3. The constrained variational principle $\delta \int_{t_1}^{t_2} \ell(\xi(t), a(t))dt = 0$ holds on $\mathcal{G} \times V^*$, using variations of ξ and a of the form $\delta\xi = \dot{\eta} + [\xi, \eta]$, $\delta a = -\eta a$, where $\eta(t) \in \mathcal{G}$ vanishes at the endpoints. 4. The Euler-Poincare equations hold on $\mathcal{G} \times V^*$

$$\frac{d}{dt} \frac{\delta \ell}{\delta \xi} = ad_{\xi}^* \frac{\delta \ell}{\delta \xi} + \frac{\delta \ell}{\delta a} \diamond a \quad (3)$$

So, we may apply our wavelet methods either on the level of variational formulation or on the level of Euler-Poincare equations.

3 CONTINUOUS WAVELET TRANSFORM

Now we need take into account the Hamiltonian or Lagrangian structures related with systems (2) or (3). Therefore, we need to consider generalized wavelets, which allow us to consider the corresponding structures instead of compactly supported wavelet representation from parts 1-4. In wavelet analysis the following three concepts are used now: 1). a square integrable representation U of a group G , 2). coherent states (CS) over G , 3). the wavelet transform associated to U . We consider now their unification [10]-[12]. Let G be a locally compact group and U_a strongly continuous, irreducible, unitary representation of G on Hilbert space \mathcal{H} . Let H be a closed subgroup of G , $X = G/H$ with (quasi) invariant measure ν and $\sigma : X = G/H \rightarrow G$ is a Borel section in a principal bundle $G \rightarrow G/H$. Then we say that U is square integrable $mod(H, \sigma)$ if there exists a non-zero vector $\eta \in \mathcal{H}$ such that $0 < \int_X |\langle U(\sigma(x))\eta | \Phi \rangle|^2 d\nu(x) < \infty$, $\forall \Phi \in \mathcal{H}$. Given such a vector $\eta \in \mathcal{H}$ called admissible for (U, σ) we define the family of (covariant) coherent states or wavelets, indexed by points $x \in X$, as the orbit of η under G , though the representation U and the section σ [10]-[12]: $S_\sigma = \eta_{\sigma(x)} = U(\sigma(x))\eta$, $x \in X$. So, coherent states or wavelets are simply the elements of the orbit under U of a fixed vector η in representation space. We have the following fundamental properties: 1. Overcompleteness: the set S_σ is total in $\mathcal{H} : (S_\sigma)^\perp = 0$. 2. Resolution property: the square integrability condition may be represented as a resolution relation: $\int_X |\eta_\sigma(x) \rangle \langle \eta_\sigma(x)| d\nu(x) = A_\sigma$, where A_σ is a bounded, positive operator with a densely defined inverse. Define the linear map $W_\eta : \mathcal{H} \rightarrow L^2(X, d\nu)$, $(W_\eta \Phi)(x) = \langle \eta_{\sigma(x)} | \Phi \rangle$. Then the range H_η of W_η is complete with respect to the scalar product $\langle \Phi | \Psi \rangle_\eta = \langle \Phi | W_\eta A_\sigma^{-1} W_\eta^{-1} \Psi \rangle$ and W_η is unitary operator from \mathcal{H} onto H_η . W_η is Continuous Wavelet Transform (CWT). 3. Reproducing kernel. The orthogonal projection from $L^2(X, d\nu)$ onto H_η is an integral operator K_σ and H_η is a reproducing kernel Hilbert space of functions:

$\Phi(x) = \int_X K_\sigma(x, y) \Phi(y) d\nu(y)$, $\forall \Phi \in \mathcal{H}_\eta$. The kernel is given explicitly by $K_\sigma(x, y) = \langle \eta_{\sigma(x)} A_\sigma^{-1} \eta_{\sigma(y)} \rangle$, if $\eta_{\sigma(y)} \in D(A_\sigma^{-1})$, $\forall y \in X$. So, the function $\Phi \in L^2(X, d\nu)$ is a wavelet transform (WT) iff it satisfies this reproducing relation. **4. Reconstruction formula.** The WT W_η may be inverted on its range by the adjoint operator, $W_\eta^{-1} = W_\eta^*$ on \mathcal{H}_η to obtain for $\eta_{\sigma(x)} \in D(A_\sigma^{-1})$, $\forall x \in X$ $W_\eta^{-1} \Phi = \int_X \Phi(x) A_\sigma^{-1} \eta_{\sigma(x)} d\nu(x)$, $\Phi \in \mathcal{H}_\eta$. This is inverse WT. If A_σ^{-1} is bounded then S_σ is called a frame, if $A_\sigma = \lambda I$ then S_σ is called a tight frame. This two cases are generalization of a simple case, when S_σ is an (ortho)basis.

The most simple cases of this construction are:

1. $H = \{e\}$. This is the standard construction of WT over a locally compact group. It should be noted that the square integrability of U is equivalent to U belonging to the discrete series. The most simple example is related to the affine $(ax + b)$ group and yields the usual one-dimensional wavelet analysis $[\pi(b, a)f](x) = \frac{1}{\sqrt{a}} f(\frac{x-b}{a})$. For $G = SIM(2) = \mathbf{R}^2 \rtimes (\mathbf{R}_+^* \times SO(2))$, the similitude group of the plane, we have the corresponding two-dimensional wavelets. **2.** $H = H_\eta$, the isotropy (up to a phase) subgroup of η : this is the case of the Gilmore-Perelomov CS. Some cases of group G are: **a).** Semisimple groups, such as $SU(N)$, $SU(N|M)$, $SU(p, q)$, $Sp(N, \mathbf{R})$. **b).** the Weyl-Heisenberg group G_{WH} which leads to the Gabor functions, i.e. canonical (oscillator) coherent states associated with windowed Fourier transform or Gabor transform (see also part 6): $[\pi(q, p, \varphi)f](x) = \exp(i\mu(\varphi - p(x - q))) f(x - q)$. In this case H is the center of G_{WH} . In both cases time-frequency plane corresponds to the phase space of group representation. **c).** The similitude group $SIM(n)$ of \mathbf{R}^n ($n \geq 3$): for $H = SO(n - 1)$ we have the axisymmetric n -dimensional wavelets. **d).** Also we have the case of bigger group, containing both affine and Weyl-Heisenberg group, which interpolate between affine wavelet analysis and windowed Fourier analysis: affine Weyl-Heisenberg group [12]. **e).** Relativity groups. In a nonrelativistic setup, the natural kinematical group is the (extended) Galilei group. Also we may add independent space and time dilations and obtain affine Galilei group. If we restrict the dilations by the relation $a_0 = a^2$, where a_0, a are the time and space dilation we obtain the Galilei-Schrodinger group, invariance group of both Schrodinger and heat equations. We consider these examples in the next section. In the same way we may consider as kinematical group the Poincare group. When $a_0 = a$ we have affine Poincare or Weyl-Poincare group. Some useful generalization of that affinization construction we consider for the case of hidden metaplectic structure in part 6. But the usual representation is not square-integrable and must be modified: restriction of the representation to a suitable quotient space of the group (the associated phase space in our case) restores square-integrability: $G \rightarrow$ homogeneous space. Our goal is applications of these results to problems of Hamiltonian dynamics and as consequence we need to take into account symplectic nature of our dynamical problem. Also, the symplectic and wavelet structures must be consistent

(this must be resemble the symplectic or Lie-Poisson integrator theory). We use the point of view of geometric quantization theory (orbit method) instead of harmonic analysis. Because of this we can consider (a) – (e) analogously. In next part we consider construction of invariant bases.

We are very grateful to M. Cornacchia (SLAC), W. Herrmannsfeldt (SLAC) Mrs. J. Kono (LBL) and M. Laraneta (UCLA) for their permanent encouragement.

4 REFERENCES

- [1] Fedorova, A.N., Zeitlin, M.G. 'Wavelets in Optimization and Approximations', *Math. and Comp. in Simulation*, **46**, 527-534 (1998).
- [2] Fedorova, A.N., Zeitlin, M.G., 'Wavelet Approach to Polynomial Mechanical Problems', *New Applications of Nonlinear and Chaotic Dynamics in Mechanics*, Kluwer, 101-108, 1998.
- [3] Fedorova, A.N., Zeitlin, M.G., 'Wavelet Approach to Mechanical Problems. Symplectic Group, Symplectic Topology and Symplectic Scales', *New Applications of Nonlinear and Chaotic Dynamics in Mechanics*, Kluwer, 31-40, 1998.
- [4] Fedorova, A.N., Zeitlin, M.G. 'Nonlinear Dynamics of Accelerator via Wavelet Approach', *AIP Conf. Proc.*, vol. **405**, 87-102, 1997, Los Alamos preprint, physics/9710035.
- [5] Fedorova, A.N., Zeitlin, M.G., Parsa, Z., 'Wavelet Approach to Accelerator Problems', parts 1-3, *Proc. PAC97*, vol. **2**, 1502-1504, 1505-1507, 1508-1510, IEEE, 1998.
- [6] Fedorova, A.N., Zeitlin, M.G., Parsa, Z., 'Nonlinear Effects in Accelerator Physics: from Scale to Scale via Wavelets', 'Wavelet Approach to Hamiltonian, Chaotic and Quantum Calculations in Accelerator Physics', *Proc. EPAC'98*, 930-932, 933-935, Institute of Physics, 1998.
- [7] Fedorova, A.N., Zeitlin, M.G., Parsa, Z., 'Variational Approach in Wavelet Framework to Polynomial Approximations of Nonlinear Accelerator Problems', *AIP Conf. Proc.*, vol. **468**, 48-68, 1999. Los Alamos preprint, physics/9902062.
- [8] Fedorova, A.N., Zeitlin, M.G., Parsa, Z., 'Symmetry, Hamiltonian Problems and Wavelets in Accelerator Physics', *AIP Conf. Proc.*, vol. **468**, 69-93, 1999. Los Alamos preprint, physics/9902063.
- [9] Marsden, J.E., *Park City Lectures on Mechanics, Dynamics and Symmetry*, CALTECH, 1998.
- [10] Antoine, J.-P., UCL, 96-08, 95-02.
- [11] Kalisa, C., and Torresani, B., CPT-92 P.2811 Marseille, 1992.
- [12] G.B. Folland, 'Harmonic Analysis in Phase Space', Princeton, 1989.

KINETIC DESCRIPTION OF ELECTRON-PROTON INSTABILITY IN HIGH-INTENSITY LINACS AND STORAGE RINGS

Ronald C. Davidson, Hong Qin, and W. Wei-li Lee
 Plasma Physics Laboratory
 Princeton University, Princeton, NJ 08543
 Tai-Sen F. Wang
 Los Alamos National Laboratory
 Los Alamos, NM 87545

Abstract

The Vlasov-Maxwell equations are used to investigate properties of the electron-ion two-stream instability for a continuous, high-intensity ion beam propagating in the z -direction with directed axial velocity $V_b = \beta_b c$ through a background population of (stationary) electrons. The analysis is carried out for arbitrary beam intensity, consistent with transverse confinement of the beam particles, and arbitrary fractional charge neutralization. Stability properties are calculated for dipole perturbations with azimuthal mode number $\ell = 1$ about monoenergetic ion and electron distribution functions.

1 INTRODUCTION

Periodic focusing accelerators and transport systems[1, 2] have a wide range of applications ranging from basic scientific research, to applications such as spallation neutron sources, tritium production, and heavy ion fusion. For a *one-component* high-intensity beam, considerable progress has been made in describing the self-consistent evolution of the beam distribution function $f_b(\mathbf{x}, \mathbf{p}, t)$ and the self-generated electric and magnetic fields in kinetic analyses[1, 3, 4, 5, 6] based on the Vlasov-Maxwell equations. In many practical accelerator applications, however, an (unwanted) second charge component is present. When a second charge component is present, it has been recognized for many years[7, 8, 9, 10, 11, 12] that the relative streaming motion of the high-intensity beam particles through the background charge species provides the free energy to drive the classical *two-stream* instability[13].

In the present analysis, we apply the Vlasov-Maxwell equations[1, 14] to describe the self-consistent interaction of the ion and electron distribution functions with the applied field and the self-generated electric and magnetic fields. The analysis can be applied to ion beams ranging from the emittance-dominated, moderate-intensity proton beams in proton linacs and storage rings, to the low-emittance, space-charge-dominated ion beams in heavy ion fusion.

2 THEORETICAL MODEL AND ASSUMPTIONS

The present analysis [14] considers a continuous ion beam with distribution function $f_b(\mathbf{x}, \mathbf{p}, t)$, and characteristic radius r_b and axial momentum $\gamma_b m_b \beta_b c$ propagating in the z -direction through a background population of electrons with distribution function $f_e(\mathbf{x}, \mathbf{p}, t)$. The ions have directed axial velocity $V_b = \beta_b c$, and the background electrons are assumed to be nonrelativistic and stationary with $\int d^3 p p_z f_e \simeq 0$ in the laboratory frame. The *applied* focusing force on a beam ion is modeled by

$$\mathbf{F}_{foc} = -\gamma_b m_b \omega_{\beta b}^2 \mathbf{x}_{\perp}, \psi \quad (1)$$

where $\mathbf{x}_{\perp} = x\hat{e}_x + y\hat{e}_y$ is the transverse displacement, $(\gamma_b - 1)m_b c^2$ is the ion kinetic energy, m_b is the ion rest mass, c is the speed of light *in vacuo*, and $\omega_{\beta b} = \text{const.}$ is the effective betatron frequency for the applied focusing field. Assuming that the ion density exceeds the background electron density, the space-charge force on an electron, provides transverse confinement of the background electrons by the electrostatic potential $\phi(\mathbf{x}, t)$. It is further assumed that the ion motion in the beam frame is nonrelativistic. The electrostatic potential $\phi(\mathbf{x}, t)$ is determined self-consistently from Poisson's equation $\nabla^2 \phi = -4\pi e(Z_b n_b - n_e)$, and the z -component of vector potential $A_z(\mathbf{x}, t)$ is determined self-consistently from $\nabla^2 A_z = -4\pi Z_b e \beta_b n_b$, where the electrons are assumed to carry zero axial current in the laboratory frame. Here, $n_b(\mathbf{x}, t) = \int d^3 p f_b(\mathbf{x}, \mathbf{p}, t)$ and $n_e(\mathbf{x}, t) = \int d^3 p f_e(\mathbf{x}, \mathbf{p}, t)$ are the ion and electron densities, respectively.

Finally, the stability analysis assumes perturbations with sufficiently long axial wavelength and high frequency that $k_z^2 r_b^2 \ll 1$, $|\omega/k_z - \beta_b c| \gg v_{Tbz}$, and $|\omega/k_z| \gg v_{Tez}$. Here, $v_{Tbz} = (2T_{bz}/\gamma_b m_b)^{1/2}$ and $v_{Tez} = (2T_{ez}/m_e)^{1/2}$ are the axial thermal speeds of the beam ions and the background electrons, respectively. Furthermore, the perturbed axial forces are treated as negligibly small, and the analysis neglects the effects of Landau damping due to axial momentum spread.

We make use of these assumptions to simplify the theoretical model[14]. First, we introduce the reduced distribution functions defined by $F_j(\mathbf{x}, \mathbf{p}_{\perp}, t) = \int dp_z f_j(\mathbf{x}, \mathbf{p}, t)$

for $j = b, e$. Because $\int dp_z p_z f_e \simeq 0$ for the electrons, the nonlinear Vlasov equation for $F_e(\mathbf{x}, \mathbf{p}_\perp, t)$ is given by

$$\left\{ \frac{\partial}{\partial t} + \frac{\mathbf{p}_\perp}{m_e} \cdot \frac{\partial}{\partial \mathbf{x}_\perp} + (e\nabla_\perp \phi) \cdot \frac{\partial}{\partial \mathbf{p}_\perp} \right\} F_e(\mathbf{x}, \mathbf{p}_\perp, t) = 0, \quad (2)$$

where $-e$ is the electron charge, and $\nabla_\perp \equiv \hat{\mathbf{e}}_x \partial/\partial x + \hat{\mathbf{e}}_y \partial/\partial y$. The ions, however, have large directed axial velocity $V_b \simeq \beta_b c$, and the Vlasov equation for $F_b(\mathbf{x}, \mathbf{p}_\perp, t)$ becomes

$$\left\{ \frac{\partial}{\partial t} + V_b \frac{\partial}{\partial z} + \frac{\mathbf{p}_\perp}{\gamma_b m_b} \cdot \frac{\partial}{\partial \mathbf{x}_\perp} - (\gamma_b m_b \omega_{\beta b}^2 \mathbf{x}_\perp + Z_b e \nabla_\perp \psi) \cdot \frac{\partial}{\partial \mathbf{p}_\perp} \right\} F_b(\mathbf{x}, \mathbf{p}_\perp, t) = 0. \quad (3)$$

Here, $+Z_b e$ is the ion charge, and $\psi(\mathbf{x}, t) \equiv \phi(\mathbf{x}, t) - \beta_b A_z(\mathbf{x}, t)$. The self-field potentials $\phi(\mathbf{x}, t)$, and $\psi(\mathbf{x}, t)$ in Eqs. (2) and (3) are determined self-consistently from

$$\begin{aligned} \left(\frac{\partial^2}{\partial x^2} + \frac{\partial^2}{\partial y^2} \right) \phi &= -4\pi e \left(Z_b \int d^2 p F_b - \int d^2 p F_e \right), \\ \left(\frac{\partial^2}{\partial x^2} + \frac{\partial^2}{\partial y^2} \right) \psi &= -4\pi e \left(\frac{Z_b}{\gamma_b^2} \int d^2 p F_b - \int d^2 p F_e \right). \end{aligned} \quad (4)$$

We assume that the beam propagates axially through a perfectly conducting cylindrical pipe with radius $r = r_w$. Enforcing $[E_\theta]_{r=r_w} = [E_z]_{r=r_w} = [B_r]_{r=r_w} = 0$ readily gives $\phi(r = r_w, \theta, z, t) = 0$, and $\psi(r = r_w, \theta, z, t) = 0$. Here, the constant values of the potentials at $r = r_w$ have been taken equal to zero.

3 EQUILIBRIUM PROPERTIES

Under quasisteady equilibrium conditions with $\partial/\partial t = 0$, we assume axisymmetric beam propagation and negligible variation with axial coordinate ($\partial/\partial \theta = 0 = \partial/\partial z$). The equilibrium distribution functions for the beam ions and background electrons are of the general form $F_b^0 = F_b^0(H_{\perp b})$ and $F_e^0 = F_e^0(H_{\perp e})$, where

$$\begin{aligned} H_{\perp b} &= \frac{1}{2\gamma_b m_b} \mathbf{p}_\perp^2 + \frac{1}{2} \gamma_b m_b \omega_{\beta b}^2 r^2 + Z_b e [\psi^0(r) - \hat{\psi}^0], \\ H_{\perp e} &= \frac{1}{2m_e} \mathbf{p}_\perp^2 - e [\phi^0(r) - \hat{\phi}^0]. \end{aligned} \quad (5)$$

Here, $r = (x^2 + y^2)^{1/2}$ is the radial distance from the beam axis, $H_{\perp b}$ and $H_{\perp e}$ are exact single-particle constants of the motion, and $\hat{\psi}^0 \equiv \psi^0(r = 0)$ and $\hat{\phi}^0 \equiv \phi^0(r = 0)$ are constants.

There is wide latitude in specifying the functional forms of the equilibrium distribution functions[14]. In the present analysis, we assume monoenergetic ions and electrons, with distribution functions

$$\begin{aligned} F_b^0(H_{\perp b}) &= \frac{\hat{n}_b}{2\pi\gamma_b m_b} \delta(H_{\perp b} - \hat{T}_{\perp b}), \\ F_e^0(H_{\perp e}) &= \frac{\hat{n}_e}{2\pi m_e} \delta(H_{\perp e} - \hat{T}_{\perp e}). \end{aligned} \quad (6)$$

Here, \hat{n}_b and $\hat{n}_e \equiv f Z_b \hat{n}_b$ are positive constants corresponding to the ion and electron densities, $f = \text{const.}$ is the fractional charge neutralization, and $\hat{T}_{\perp b}$ and $\hat{T}_{\perp e}$ are constants corresponding to the on-axis ($r = 0$) values of the transverse ion and electron temperatures, respectively. Without presenting details[14], some algebraic manipulation of Eqs. (4) – (6) gives the step-function density profiles $n_j^0(r) = \hat{n}_j = \text{const.}$, for $0 \leq r < r_b$, and $n_j^0(r) = 0$ for $r_b < r \leq r_w$, and $j = b, e$. Here, the beam radius r_b is related to other equilibrium parameters by $\hat{\nu}_b^2 r_b^2 = 2\hat{T}_{\perp b}/\gamma_b m_b$ and $\hat{\nu}_e^2 r_b^2 = 2\hat{T}_{\perp e}/m_e$, where the (depressed) betatron frequencies $\hat{\nu}_b$ and $\hat{\nu}_e$ are defined by

$$\begin{aligned} \hat{\nu}_b^2 &= \omega_{\beta b}^2 - \frac{1}{2} \left(\frac{1}{\gamma_b^2} - f \right) \hat{\omega}_{pb}^2 = \text{const.}, \\ \hat{\nu}_e^2 &= \frac{1}{2} \frac{\gamma_b m_b}{Z_b m_e} (1 - f) \hat{\omega}_{pb}^2 = \text{const.}, \end{aligned} \quad (7)$$

and $\hat{\omega}_{pb}^2 = 4\pi\hat{n}_b Z_b^2 e^2 / \gamma_b m_b$ is the ion plasma frequency-squared.

4 STABILITY ANALYSIS AND DISPERSION RELATION

For small-amplitude perturbations, a stability analysis proceeds by linearizing Eqs. (2)–(4). Perturbed quantities are expressed as $\delta\psi(\mathbf{x}, t) = \delta\psi^l(r) \exp(ik_z z + il\theta - i\omega t)$, $\delta F_b(\mathbf{x}, \mathbf{p}_\perp, t) = \delta\hat{F}_b^l(r, \mathbf{p}_\perp) \exp(ik_z z + il\theta - i\omega t)$, etc., where $Im\omega > 0$ is assumed, corresponding to instability (temporal growth), k_z is the axial wavenumber, and l is the azimuthal harmonic number. The linearized Vlasov equations are formally integrated by using the method of characteristics[14]. For perturbations about the monoenergetic ion and electron distribution functions in Eq. (6), we obtain[14] the kinetic dispersion relation

$$\begin{aligned} \left[\frac{2}{1 - (r_b/r_w)^{2\ell}} + \frac{\hat{\omega}_{pb}^2}{\ell\gamma_b^2 \hat{\nu}_b^2} \Gamma_b^\ell(\omega - k_z V_b) \right] \left[\frac{2}{1 - (r_b/r_w)^{2\ell}} \right. \\ \left. + \frac{\hat{\omega}_{pe}^2}{\ell\hat{\nu}_e^2} \Gamma_e^\ell(\omega) \right] = \frac{\hat{\omega}_{pe}^2}{\ell\hat{\nu}_e^2} \cdot \frac{\hat{\omega}_{pb}^2}{\ell\hat{\nu}_b^2} \Gamma_e^\ell(\omega) \Gamma_b^\ell(\omega - k_z V_b). \end{aligned} \quad (8)$$

where $\hat{\omega}_{pe}^2 = 4\pi\hat{n}_e e^2 / m_e$. Here, the ion and electron susceptibilities are defined by[14]

$$\begin{aligned} \Gamma_b^\ell(\omega - k_z V_b) &= -\frac{1}{2^\ell} \sum_{m=0}^{\ell} \frac{\ell!}{m!(\ell-m)!} \times \\ &\quad \frac{(\ell-2m)\hat{\nu}_b}{[(\omega - k_z V_b) - (\ell-2m)\hat{\nu}_b]}, \\ \Gamma_e^\ell(\omega) &= -\frac{1}{2^\ell} \sum_{m=0}^{\ell} \frac{\ell!}{m!(\ell-m)!} \frac{(\ell-2m)\hat{\nu}_e}{[\omega - (\ell-2m)\hat{\nu}_e]}, \end{aligned} \quad (9)$$

for general azimuthal harmonic number l .

A careful examination[14] of Eq. (8) for $\hat{n}_e \neq 0$ shows that the strongest instability (largest growth rate) occurs for azimuthal mode number $\ell = 1$, corresponding to a simple

(dipole) displacement of the beam ions and the background electrons. For $\ell = 1$, we find $\Gamma_e^1(\omega) = -\hat{v}_e^2/[\omega^2 - \hat{v}_e^2]$ and $\Gamma_b^1(\omega - k_z V_b) = -\hat{v}_b^2/[(\omega - k_z V_b)^2 - \hat{v}_b^2]$, and introduce the collective oscillation frequencies defined by

$$\begin{aligned}\omega_e^2 &\equiv \hat{v}_e^2 + \frac{1}{2}\hat{\omega}_{pe}^2 \left(1 - \frac{r_b^2}{r_w^2}\right) = \frac{1}{2}\frac{\gamma_b m_b}{Z_b m_e}\hat{\omega}_{pb}^2 \left(1 - f\frac{r_b^2}{r_w^2}\right) \\ \omega_b^2 &\equiv \hat{v}_b^2 + \frac{\hat{\omega}_{pb}^2}{2\gamma_b^2} \left(1 - \frac{r_b^2}{r_w^2}\right) = \omega_{\beta b}^2 + \frac{1}{2}\hat{\omega}_{pb}^2 \left(f - \frac{1}{\gamma_b^2}\frac{r_b^2}{r_w^2}\right)\end{aligned}\quad (10)$$

where use is made of $\hat{\omega}_{pe}^2 = (\gamma_b m_b/Z_b m_e)f\hat{\omega}_{pb}^2$. Substituting into Eq. (8) and rearranging terms, the $\ell = 1$ dispersion relation can be expressed in the compact form

$$[(\omega - k_z V_b)^2 - \omega_b^2][\omega^2 - \omega_e^2] = \omega_f^4, \quad (11)$$

where ω_f is defined by

$$\omega_f^4 \equiv \frac{1}{4}f \left(1 - \frac{r_b^2}{r_w^2}\right)^2 \frac{\gamma_b m_b}{Z_b m_e}\hat{\omega}_{pb}^4. \quad (12)$$

In the absence of background electrons ($f = 0$ and $\omega_f = 0$), Eq. (11) gives stable collective oscillations of the ion beam with frequency $\omega - k_z V_b = \pm\omega_b$, where ω_b is defined in Eq. (11). For $f \neq 0$, however, the ion and electron terms on the left-hand side of Eq. (11) are coupled by the ω_f^4 term on the right-hand side, leading to one unstable solution with $\text{Im}\omega > 0$ for a certain range of axial wavenumber k_z . It is important to recognize that the dispersion relation (11) is applicable over a wide range of normalized beam intensity and fractional charge neutralization. That is, Eq. (11) can be applied to the emittance-dominated, moderate-intensity ion beams ($\hat{\omega}_{pb}^2/\omega_{\beta b}^2 \lesssim 0.2$, say) in proton linacs and storage rings. On the other hand, Eq. (11) can also be applied to the low-emittance, very high-intensity ion beams ($\hat{\omega}_{pb}^2/\omega_{\beta b}^2$ approaching $2\gamma_b^2$, for $f = 0$) envisioned for heavy ion fusion.

A careful examination of Eq. (11) shows that the unstable, positive-frequency branch has frequency and wavenumber (ω, k_z) closely tuned to the values (ω_0, k_{z0}) defined by $\omega_0 = +\omega_e$ and $\omega_0 - k_{z0}V_b = -\omega_b$. In this regime, expressing $\omega = \omega_0 + \delta\omega$ and $k_z = k_{z0} + \delta k_z$, and assuming $|\delta\omega| \ll 2\omega_e$, the dispersion relation (11) is given to good approximation by

$$\begin{aligned}\delta\omega(\delta\omega - \delta k_z V_b)[1 - (\delta\omega - \delta k_z V_b)/2\omega_b] \\ = -\Gamma_0^2 \equiv -\frac{\omega_f^4}{4\omega_e\omega_b}.\end{aligned}\quad (13)$$

At moderate beam intensities with $\Gamma_0^2 \ll 1$, the unstable solution to Eq. (13) satisfies $|\delta\omega - \delta k_z V_b| \ll 2\omega_b$. In this regime, Eq. (13) can be approximated by the quadratic form $\delta\omega(\delta\omega - \delta k_z V_b) = -\Gamma_0^2 \equiv -\omega_f^4/4\omega_e\omega_b$. This quadratic dispersion relation supports an unstable solution with growth rate $\text{Im}\delta\omega = \Gamma_0[1 - (\delta k_z V_b/2\Gamma_0)^2]^{1/2}$ for δk_z in the (symmetric) interval, $-2\Gamma_0 < \delta k_z V_b < 2\Gamma_0$. The maximum growth rate is $(\text{Im}\delta\omega)_{\max} = \Gamma_0 \equiv$

$\omega_f^2/2(\omega_e\omega_b)^{1/2}$, which occurs for $\delta k_z = 0$. For example, for a proton beam ($Z_b = 1$, $m_b/m_e = 1836$) with relativistic mass factor $\gamma_b = 1.85$, a moderate value of normalized beam intensity $\hat{\omega}_{pb}^2/\omega_{\beta b}^2 = 0.1$, large wall radius $r_w/r_b \rightarrow \infty$ and fractional charge neutralization $f = 0.1$, we obtain $(\text{Im}\delta\omega)_{\max} = 0.127\omega_{\beta b}$, corresponding to a particularly virulent growth rate for the electron-proton (e-p) instability. For this choice of system parameters, the central oscillation frequency and wavenumber are $\omega_0 = 13.03\omega_{\beta b}$ and $k_{z0}V_b = 14.03\omega_{\beta b}$.

5 CONCLUSIONS

The general kinetic formalism[14] outlined here can also be applied to perturbations about a wide range of non-monoenergetic equilibrium distribution functions. A detailed, self-consistent stability analysis based on Eqs. (2)–(4) for continuously varying profiles is beyond the scope of the present article. It is sufficient to note that the spread in (depressed) betatron frequencies[7, 14] associated with continuously varying profiles is expected to lead to a *threshold* in beam intensity and/or fractional charge neutralization for the onset of instability.

6 ACKNOWLEDGEMENT

This research was supported by the Department of Energy and the APT Project and LANSCE Division of Los Alamos National Laboratory.

7 REFERENCES

- [1] R. C. Davidson, *Physics of Nonneutral Plasmas* (Addison-Wesley Publishing Co., Reading, MA, 1990), and references therein.
- [2] T. P. Wangler, *Principles of RF Linear Accelerators* (John Wiley & Sons, Inc., New York, 1998).
- [3] T. -S. Wang and L. Smith, *Part. Accel.* **12**, 247 (1982).
- [4] J. Struckmeier and I. Hofmann, *Part. Accel.* **39**, 219 (1992).
- [5] R. C. Davidson, *Physics of Plasmas* **5**, 3459 (1998).
- [6] R. C. Davidson and C. Chen, *Part. Accel.* **59**, 175 (1998).
- [7] D. Koshkarev and P. Zenkevich, *Part. Accel.* **3**, 1 (1972).
- [8] E. Keil and B. Zotter, CERN-ISR-TH/71-58 (1971).
- [9] L. J. Laslett, A. M. Sessler, and D. Möhl, *Nuclear Instruments and Methods* **121**, 517 (1974).
- [10] D. Neuffer, E. Colton, D. Fitzgerald, T. Hardek, R. Hutson, R. Macek, M. Plum, H. Thiessen, and T. -S. Wang, *Nuclear Instruments and Methods in Phys. Res.* **A321**, 1 (1992).
- [11] J. Byrd, A. Chao, S. Heifets, M. Minty, T. O. Roubenheimer, J. Seeman, G. Stupakov, J. Thomson and F. Zimmerman, *Phys. Rev. Lett.* **79**, 79 (1997).
- [12] K. Ohmi, *Phys. Rev.* **E55**, 7550 (1997).
- [13] See, for example, pp. 240–271 of Ref. 1.
- [14] “Kinetic Description of Electron-Proton Instability in High-Intensity Proton Linacs and Storage Rings Based on the Vlasov-Maxwell Equations,” R. C. Davidson, H. Qin, P. H. Stoltz, and T. -S. Wang, submitted for publication (1999).

3D MULTISPECIES NONLINEAR PERTURBATIVE PARTICLE SIMULATION OF INTENSE PARTICLE BEAMS

Hong Qin, Ronald C. Davidson, and W. Wei-li Lee
Plasma Physics Laboratory
Princeton University, Princeton, NJ 08543

Abstract

The Beam Equilibrium Stability and Transport (BEST) code, a 3D multispecies nonlinear perturbative particle simulation code, has been developed to study collective effects in intense charged particle beams described self-consistently by the Vlasov-Maxwell equations. This code provides an effective numerical tool to investigate collective instabilities, periodically-focused beam propagation in in alternating-gradient focusing fields, halo formation, and other important nonlinear process in intense beam propagation.

1 INTRODUCTION AND THEORETICAL MODEL

For accelerator applications to spallation neutron sources, tritium production, and heavy ion fusion, space-charge effects on beam equilibrium, stability, and transport properties become increasingly important. To understand these collective process at high beam intensity, it is necessary to treat the nonlinear beam dynamics self-consistently using the nonlinear Vlasov-Maxwell equations[1, 2, 3]. Recently, the δf formalism, a low-noise, nonlinear perturbative particle simulation technique, has been developed for intense beam applications, and applied to matched-beam propagation in a periodic focusing field[4, 5, 6, 7, 8] and other related problems. This paper reports recent advances in applying the δf formalism to simulate the nonlinear dynamics of an intense beam. The BEST code described here is a 3D multispecies nonlinear perturbative particle simulation code, which can be applied to a wide range of important collective processes in intense beams, such as the electron-ion two-stream instability[9, 10], periodically-focused beam propagation[11, 12], and halo formation. In the the theoretical model[9, 10, 13], we consider a thin, continuous, high-intensity ion beam ($j = b$), with characteristic radius r_b propagating in the z -direction through background electron and ion components ($j = e, i$), each of which is described by a distribution function $f_j(x, p, t)$. The charge components ($j = b, e, i$) propagate in the z -direction with characteristic axial momentum $\gamma_j m_j \beta_j c$, where $V_j = \beta_j c$ is the directed axial velocity, $\gamma_j = (1 - \beta_j^2)^{-1/2}$ is the relativistic mass factor, e_j and m_j are the charge and rest mass, respectively, of a j -th species particle, and c is the speed of light in *vacuo*. For each component ($j = b, e, i$), the transverse and axial particle velocities in a frame of reference moving with axial velocity

$\beta_j c \hat{e}_z$ are assumed to be *nonrelativistic*. While the nonlinear δf formalism outlined here is readily adapted to the case of a *periodic* applied focusing force, for present purpose we make use of a *smooth-focusing* model in which the applied focusing force is described by

$$F_j^{foc} = -\gamma_j m_j \omega_{\beta j}^2 x_{\perp}, \quad (1)$$

where $x_{\perp} = x \hat{e}_x + y \hat{e}_y$ is the transverse displacement, and $\omega_{\beta j} = \text{const}$ is the effective betatron frequency for transverse oscillation. For example, in the absence of background ions ($f_i = 0$), to describe the two-stream interaction between the beam ions ($j = b$) and background electrons ($j = e$), we normally assume $V_e = \beta_e c \simeq 0$. The space-charge intensity is allowed to be arbitrarily large, subject only to transverse confinement of the beam ions by the applied focusing force, and the background electrons are confined in the transverse plane by the space-charge potential $\phi(x, t)$ due to the excess ion charge. In the electrostatic approximation, we represent the self-electric and self-magnetic fields by $E^s = -\nabla \phi(x, t)$ and $B^s = \nabla \times A_z(x, t) \hat{e}_z$, respectively. For present purpose, assuming perturbations with long axial wavelength ($k_z^2 r_b^2 \ll 1$) and neglecting the perturbed axial force on the charge components, the nonlinear Vlasov-Maxwell equation in the five-dimensional phase space (x, p_{\perp}) can be approximated by[9, 10, 13]

$$\left\{ \frac{\partial}{\partial t} + v \cdot \frac{\partial}{\partial x} - [\gamma_j m_j \omega_{\beta j}^2 x_{\perp} + e_j \nabla_{\perp} (\phi - \beta_j A_z)] \cdot \frac{\partial}{\partial p_{\perp}} \right\} f_j(x, p_{\perp}, t) = 0, \quad (2)$$

and

$$\begin{aligned} \nabla_{\perp}^2 \phi &= -4\pi \sum_j e_j \int d^2 p f_j(x, p_{\perp}, t), \\ \nabla_{\perp}^2 A_z &= -4\pi \sum_j e_j \beta_j \int d^2 p f_j(x, p_{\perp}, t). \end{aligned} \quad (3)$$

Here, $\nabla_{\perp} = \hat{e}_x \partial / \partial x + \hat{e}_y \partial / \partial y$ and $v = V_j \hat{e}_z + (\gamma_j m_j)^{-1} p_{\perp}$.

2 NONLINEAR δf SIMULATION METHOD AND THE BEST CODE

In the nonlinear δf formalism, we express the total distribution function as $f_j = f_{j0} + \delta f_j$, where f_{j0} is a *known* solution to the nonlinear Vlasov-Maxwell equations (2) and

(3), and determine the detailed evolution of the perturbed distribution function $\delta f_j \equiv f_j - f_{j0}$. This is accomplished by advancing the weight function defined by $w_j \equiv \delta f_j / f_j$, together with the particles' positions and momenta. The equations of motion for the particles, obtained from the characteristics of the nonlinear Vlasov equation (2), are given by

$$\begin{aligned} \frac{d\mathbf{x}_{ji}}{dt} &= V_j \hat{e}_z + (\gamma_j m_j)^{-1} \mathbf{p}_{\perp ji}, \\ \frac{d\mathbf{p}_{\perp ji}}{dt} &= -\gamma_j m_j \omega_{\beta j}^2 \mathbf{x}_{\perp ji} - e_j \nabla_{\perp} (\phi - \beta_j A_z). \end{aligned} \quad (4)$$

Here the subscript "ji" labels the i-th simulation particle of the j-th species. The weight functions w_j , as functions of phase space variables, are carried by the simulation particles, and the dynamical equations for w_j are easily derived from the definition of w_j and the Vlasov equation (2). Following the algebra in Refs. [4, 5, 6, 7], we obtain

$$\begin{aligned} \frac{dw_{ji}}{dt} &= -(1 - w_{ji}) \frac{1}{f_{j0}} \frac{\partial f_{j0}}{\partial \mathbf{p}_{\perp}} \cdot \delta \left(\frac{d\mathbf{p}_{\perp ji}}{dt} \right), \\ \delta \left(\frac{d\mathbf{p}_{\perp ji}}{dt} \right) &\equiv \frac{d\mathbf{p}_{\perp ji}}{dt} \Big|_{(\phi, A_z) \rightarrow (\delta\phi, \delta A_z)}, \end{aligned} \quad (5)$$

where $\delta\phi = \phi - \phi_0$ and $\delta A_z = A_z - A_{z0}$. Here, the equilibrium solutions (ϕ_0, A_{z0}, f_{j0}) solve the steady-state $(\partial/\partial t = 0)$ Vlasov-Maxwell equations (2) and (3) with $\partial/\partial z = 0$ and $\partial/\partial \theta = 0$. A wide variety of axisymmetric equilibrium solutions to Eqs. (2) and (3) have been investigated in the literature. The perturbed distribution δf_j is obtained through the weighted Klimontovich representation

$$\delta f_j = \frac{N_j}{N_{sj}} \sum_{i=1}^{N_{sj}} w_{ji} \delta(\mathbf{x} - \mathbf{x}_{ji}) \delta(\mathbf{p}_{\perp} - \mathbf{p}_{\perp ji}), \quad (6)$$

where N_j is the total number of actual j-th species particles, and N_{sj} is the total number of simulation particles for the j-th species. Maxwell's equations are also expressed in terms of the perturbed fields and perturbed density according to

$$\begin{aligned} \nabla_{\perp}^2 \delta\phi &= -4\pi \sum_j e_j \delta n_j, \\ \nabla_{\perp}^2 \delta A_z &= -4\pi \sum_j e_j \beta_j \delta n_j, \\ \delta n_j &= \int d^2 p \delta f_j(\mathbf{x}, \mathbf{p}_{\perp}, t) = \frac{N_j}{N_{sj}} \sum_{i=1}^{N_{sj}} w_{ji} U(\mathbf{x}, \mathbf{x}_{ji}). \end{aligned} \quad (7)$$

Here, $U(\mathbf{x}, \mathbf{x}_{ji})$ represents the method of distributing particles on the grids in configuration space. The nonlinear particle simulations are carried out by iteratively advancing the particle motions, including the weights they carry, according to Eqs. (4) and (5), and updating the fields by solving the perturbed Maxwell's equations (7) with appropriate boundary conditions at the cylindrical conducting

wall. Even though it is a perturbative approach, the δf method is fully nonlinear and simulates the original nonlinear Vlasov-Maxwell equations. Compared with conventional particle-in-cell simulations, the noise level in δf simulations is significantly reduced. In addition, the δf method can be used to study linear stability properties provided the factor $(1 - w_{ji})$ in Eq. (5) is approximated by 1, and the forcing term in Eq. (4) is replaced by the unperturbed force (i.e., advancing particles along the unperturbed orbits). Implementation of the 3D multispecies nonlinear δf simulation method described above is embodied in the BEST code at the Princeton Plasma Physics Laboratory. The code advances the particle motions using a 4th-order Runge-Kutte method, and solves Maxwell's equations by a fast Fourier transform and finite-difference method in cylindrical geometry. Written in Fortran 90/95, the code utilizes extensively the object-oriented features provided by the computer language. The NetCDF scientific data format is implemented for large-scale diagnostics and visualization. The code has achieved an average speed of $40 \mu\text{s}/(\text{particle} \times \text{step})$ on a DEC alpha personal workstation 500au computer.

3 SIMULATION RESULTS

For brevity, we present here illustrative simulation results for a single-species thermal equilibrium ion beam in a constant focusing field. In this case, equilibrium properties depend on the radial coordinate $r = (x^2 + y^2)^{1/2}$. The thermal equilibrium distribution function is given by

$$\begin{aligned} f_{b0}(r, \mathbf{p}_{\perp}) &= \frac{\hat{n}_b}{2\pi\gamma_b m_b T_b} \\ &\times \exp \left\{ -\frac{p_{\perp}^2/2\gamma_b m_b + \gamma_b m_b \omega_{\beta b}^2 r^2/2 + e_b(\phi_0 - \beta_b A_{z0})}{T_b} \right\} \end{aligned} \quad (8)$$

where \hat{n}_b is the density of beam particles at $r = 0$, and T_b is the transverse temperature of the beam ions in energy units. It is also assumed that the beam is centered inside a cylindrical chamber with perfectly conducting wall located at $r = r_w$. The equilibrium self-field potentials ϕ_0 and A_{z0} can be determined numerically from Maxwell's equations (3). First, we examine the nonlinear propagation properties of the beam. A random initial perturbation is introduced into the system, and the beam is propagated from $t = 0$ to $t = 500\tau_{\beta}$, where $\tau_{\beta} \equiv \omega_{\beta b}^{-1}$. The simulation results show that the perturbations do not grow and the beam propagates quiescently, which agrees with the nonlinear stability theorem [14, 15] for the choice of equilibrium distribution function in Eq. (8). Shown in Fig. 1 is a plot of the change in transverse emittance-squared (normalized by $V_b^2/\omega_{\beta b}^2$), $\delta\epsilon^2 = \epsilon^2(t) - \epsilon_0^2$, versus normalized time t/τ_{β} , for perturbations about the thermal equilibrium distribution in Eq. (8). The system parameters in Fig. 1 correspond to protons with $\gamma_b = 1.85$, and normalized beam intensity $K\beta_b c\tau_{\beta}/\epsilon_0 = 0.025$, where $K = 2N_b e^2/\gamma_b^3 m_b \beta_b^2 c^2$ is the self-field perveance, and N_b is the number of beam ions per

unit axial length. The amplitudes of the initial random perturbation in weights in Fig. 1 is 10^{-4} , which leads to the very small offset in $\delta\epsilon^2$. It is evident from Fig. 1 that the variations in beam emittance, $\delta\epsilon^2$, remain extremely small for perturbations about a thermal equilibrium beam. As a

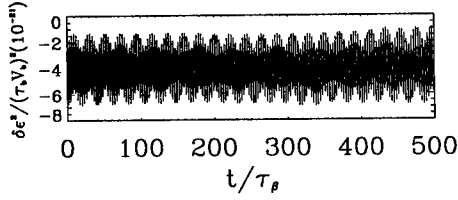


Figure 1: Plot of $\delta\epsilon^2$ versus t/τ_β

second example, we study the linear surface mode for perturbations about a thermal equilibrium beam in the space-charge-dominated regime, with flat-top density profile and $K\beta_b c\tau_\beta/\epsilon_0 \gg 1$. These modes are of practical interest because they can be destabilized by a two-stream electron-ion interaction when background electrons are present[9, 10]. The BEST code, operating in its linear stability mode, has recovered very well-defined eigenmodes with mode structures and eigenfrequencies which agree well with theoretical predictions. For $K\beta_b c\tau_\beta/\epsilon_0 \gg 1$, and azimuthal mode number $l = 1$, the dispersion relation for these modes is given by[1, 9, 10]

$$\omega = k_z V_b \pm \frac{\hat{\omega}_{pb}}{\sqrt{2}\gamma_b} \sqrt{1 - \frac{r_b^2}{r_w^2}}, \quad (9)$$

where r_b is the radius of the beam edge, and r_w is location of the conducting wall. In Eq. (9), $\hat{\omega}_{pb}^2 = 4\pi n_b e_b^2/\gamma_b m_b$ is the ion plasma frequency-squared, and $\hat{\omega}_{pb}/\sqrt{2}\gamma_b \simeq \omega_{pb}$ in the space-charge-dominated limit. Shown in Fig. 2 is the comparison between plots of the eigenfrequency versus r_w/r_b obtained from the simulations (diamonds and triangles) and that predicted by Eq. (9) (solid curves). The parameters for this case are chosen close to the space-charge limit with $K\beta_b c\tau_\beta/\epsilon_0 = 6.59$, and the perturbation has normalized axial wavenumber $k_z V_b/\omega_{pb} = 2\pi$. It is clear from Fig. 2 that the simulation results agree well with theory.

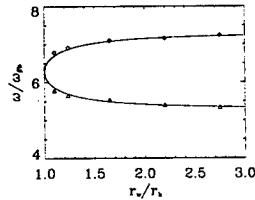


Figure 2: Eigenfrequency versus r_w/r_b .

4 CONCLUSION AND FUTURE WORK

The BEST code has been tested and applied in different scenarios. As a 3D multispecies perturbative particle sim-

ulation code, it provides several unique capabilities. Since the simulation particles are used to simulate only the perturbed distribution function and self-fields, the simulation noise is reduced significantly. The perturbative approach also enables the code to investigate different physics effects separately, as well as simultaneously. The code can be easily switched between linear and nonlinear operation, and used to study both linear stability properties and nonlinear beam dynamics. These features, combined with 3D and multispecies capabilities, provide us with an effective tool to investigate the electron-ion two-stream instability, periodically focused solutions in alternating focusing fields, halo formation, and many other important problems in nonlinear beam dynamics and accelerator physics. Finally, the BEST code is readily adapted to the case where the applied focusing force, F_j^{foc} , corresponds to a periodic focusing quadrupole field or solenoidal field, and the effects of the axial self-field $F_{jz}^s = -\hat{e}_z e_j \partial\phi(x, t)/\partial z$ on the particle dynamics are retained self-consistently. Results of these studies will be reported in future publications.

5 ACKNOWLEDGMENT

This research was supported by the Department of Energy and the APT Project and LANSCE Division of Los Alamos National Laboratory.

6 REFERENCES

- [1] R. C. Davidson, *Physics of Nonneutral Plasmas* (Addison-Wesley Publishing Co., Reading, MA, 1990), and references therein.
- [2] T. P. Wangler, *Principles of RF Linear Accelerators* (John Wiley & Sons, Inc., New York, 1998).
- [3] M. Reiser, *Theory and Design of Charged Particle Beams* (John Wiley & Sons, Inc., New York, 1994).
- [4] W. W. Lee, Q. Qian, and R. C. Davidson, *Phys. Lett. A* **230**, 347 (1997).
- [5] Q. Qian, W. W. Lee, and R. C. Davidson, *Phys. Plasmas* **4**, 1915 (1997).
- [6] P. H. Stoltz, W. W. Lee, and R. C. Davidson, *Nucl. Instrum. Methods Phys. Res.* **415**, 433 (1998).
- [7] P. H. Stoltz, R. C. Davidson, and W. W. Lee, *Phys. Plasmas* **6**, 298 (1999).
- [8] Alex Friedman, private communication.
- [9] R. C. Davidson, H. Qin, and T. -S. Wang, *Phys. Lett. A* **252**, 213 (1999).
- [10] "Kinetic Description of Electron-Proton Instability in High-Intensity Proton Linacs and Storage Rings Based on the Vlasov-Maxwell Equations," R. C. Davidson, H. Qin, P. H. Stoltz, and T. -S. Wang, submitted for publication (1999).
- [11] P. J. Channell, *Physics of Plasmas* **6**, 982 (1999).
- [12] R. C. Davidson, H. Qin, and P. J. Channell, to be published (1999).
- [13] R. C. Davidson and C. Chen, *Parti. Accel.* **59**, 175 (1998).
- [14] R. C. Davidson, *Physical Review Letters* **81**, 991 (1998).
- [15] R. C. Davidson, *Physics of Plasmas* **5**, 3459 (1998).

Periodically-Focused Solutions to the Nonlinear Vlasov-Maxwell Equations for Intense Beam Propagation Through an Alternating-Gradient Quadrupole Field

Hong Qin and Ronald C. Davidson

Plasma Physics Laboratory

Princeton University, Princeton, NJ, 08543

Paul J. Channell

Los Alamos National Laboratory

Los Alamos, NM 87545

Abstract

This paper considers an intense nonneutral ion beam propagating in the z -direction through a periodic focusing quadrupole field with transverse focusing force, $\mathbf{F}_{foc} = -\kappa_q(s)(x\hat{e}_x - y\hat{e}_y)$, on the beam ions. A third-order Hamiltonian averaging technique using a canonical transformation is employed to transform away the rapidly oscillating terms. This leads to a Hamiltonian, $\mathcal{H}(\tilde{X}, \tilde{Y}, \tilde{X}', \tilde{Y}', s) = (1/2)(\tilde{X}'^2 + \tilde{Y}'^2) + (1/2)\kappa_{fq}(\tilde{X}^2 + \tilde{Y}^2) + \psi(\tilde{X}, \tilde{Y}, s)$, in the transformed variables $(\tilde{X}, \tilde{Y}, \tilde{X}', \tilde{Y}')$, where the focusing coefficient κ_{fq} is constant, and many solutions and properties of the Vlasov-Maxwell system are well known.

1 INTRODUCTION

It is important to be able to investigate, based on the nonlinear Vlasov-Maxwell equations, the equilibrium and stability properties of general distribution functions for periodically-focused beams[1, 2, 3]. Despite its limited practical interest due to the unphysical distribution in phase space, the Kapchinskij-Vladimirskij (KV) beam equilibrium[1, 4, 5, 6], including its recent generalization to a rotating beam in a periodic focusing solenoidal field[7, 8], has been the *only* known periodically-focused equilibrium solution to the nonlinear Vlasov-Maxwell equations describing an intense beam propagating through a periodic focusing field. The difficulty of solving the nonlinear Vlasov-Maxwell system in general lies in the fact that the Hamiltonian for the motion of an individual beam particle is time dependent. Channell[9] and Davidson *et al*[10] have recently developed a third-order Hamiltonian averaging technique using a canonical transformation to average over the fast time scale associated with the betatron oscillations. This procedure is expected to be valid for sufficiently small phase advance ($\sigma \lesssim 60^\circ$, say). In the present analysis, we apply this technique to the Vlasov-Maxwell system for intense beams propagating through a periodic focusing lattice. Under the thin-beam assumption, the applied transverse focusing force on a beam particle is $\mathbf{F}_{foc} = -\kappa_q(s)(x\hat{e}_x - y\hat{e}_y)$. The Vlasov-Maxwell equations for the distribution function

$f_b(x, y, x', y', s)$ and the normalized self-field potential $\psi(x, y, s) = Z_b e \phi(x, y, s) / \gamma_b^3 m_b \beta_b^2 c^2$ can be expressed as[1, 7]

$$\left\{ \frac{\partial}{\partial s} + x' \frac{\partial}{\partial x} + y' \frac{\partial}{\partial y} - \left(\kappa_q(s)x + \frac{\partial \psi}{\partial x} \right) \frac{\partial}{\partial x'} - \left(-\kappa_q(s)y + \frac{\partial \psi}{\partial y} \right) \frac{\partial}{\partial y'} \right\} f_b = 0, \quad (1)$$

and

$$\left(\frac{\partial^2}{\partial x^2} + \frac{\partial^2}{\partial y^2} \right) \psi = -\frac{2\pi K_b}{N_b} \int dx' dy' f_b. \quad (2)$$

Here,

$$K_b = \frac{2N_b Z_b^2 e^2}{\gamma_b^3 m_b \beta_b^2 c^2} \text{ and } N_b = \int dx dy dx' dy' f_b \quad (3)$$

are the self-field perveance and the number of beam ions per unit axial length, respectively.

2 CANONICAL TRANSFORMATION

Because of the oscillatory time dependence of $\kappa_q(s)$, there is no general analytical method to solve the nonlinear Vlasov-Maxwell equations. However, we can average over the fast time scale associated with the betatron oscillations when the phase advance is sufficiently small. The averaging process is accomplished by introducing a canonical coordinate transformation from the laboratory coordinate system (x, y, x', y') to a new coordinate system (X, Y, X', Y') . In the laboratory coordinates, the single-particle Hamiltonian $H(x, y, x', y', s)$ is

$$H = \epsilon \left[\frac{1}{2}(x'^2 + y'^2) + \frac{1}{2}\kappa_q(s)(x^2 - y^2) + \psi(x, y, s) \right], \quad (4)$$

where ϵ is a small dimensionless parameter proportional to the focusing field strength. We use a near-identity canonical transformation $T : (x, y, x', y') \mapsto (X, Y, X', Y')$ that is generated by a generating function of the Von Zeipel form, i.e.,

$$S(x, y, X', Y', s) = xX' + yY' + \sum_{n=1}^{\infty} \epsilon^n S_n(x, y, X', Y', s). \quad (5)$$

Consequently, the transformed Hamiltonian in the new variables $\mathcal{H}(\tilde{X}, \tilde{Y}, \tilde{X}', \tilde{Y}', s)$ is given by

$$\mathcal{H} = \sum_{n=1}^{\infty} \epsilon^n \mathcal{H}_n = H + \frac{\partial}{\partial s} S(x, y, X', Y', s). \quad (6)$$

The corresponding coordinate transformation is given by

$$\begin{aligned} X &= \frac{\partial S}{\partial X'} = x + \sum_{n=1}^{\infty} \epsilon^n \frac{\partial}{\partial X'} S_n(x, y, X', Y', s), \\ x' &= \frac{\partial S}{\partial x} = X' + \sum_{n=1}^{\infty} \epsilon^n \frac{\partial}{\partial x} S_n(x, y, X', Y', s). \end{aligned} \quad (7)$$

The equations for Y and y' are similar in form.. We choose, order by order, the generating function S_n in such a way that \mathcal{H}_n is independent of the fast time scale associated with oscillations in $\kappa_q(s)$, and solve for the coordinate transformation iteratively when S_n is known. Following the detailed algebra presented in Ref. [10], we obtain the transformed Hamiltonian correct to order ϵ^3 ,

$$\mathcal{H} = \frac{1}{2}(\tilde{X}'^2 + \tilde{Y}'^2) + \frac{1}{2}\kappa_{fq}(\tilde{X}^2 + \tilde{Y}^2) + \psi(\tilde{X}, \tilde{Y}, s), \quad (8)$$

where we have set $\epsilon = 1$. Here, κ_{fq} is defined in Eq. (11), and we have introduced the additional (canonical) fiber transformation to shifted velocity coordinates defined by

$$\begin{aligned} \tilde{X} &= X, \quad \tilde{X}' = X' - \langle \alpha_q \rangle X, \\ \tilde{Y} &= Y, \quad \tilde{Y}' = Y' + \langle \alpha_q \rangle Y. \end{aligned} \quad (9)$$

Similarly, correct to order ϵ^3 , we calculate the inverse coordinate transformation, $x = X + \epsilon x_1 + \epsilon^2 x_2 + \epsilon^3 x_3$, $x' = X' + \epsilon x'_1 + \epsilon^2 x'_2 + \epsilon^3 x'_3$, etc. Setting $\epsilon = 1$, this gives [10]

$$\begin{aligned} x(\tilde{X}, \tilde{Y}, \tilde{X}', \tilde{Y}', s) &= [1 - \beta_q(s)]\tilde{X} + 2\left(\int_0^s ds \beta_q(s)\right)\tilde{X}', \\ x'(\tilde{X}, \tilde{Y}, \tilde{X}', \tilde{Y}', s) &= [1 + \beta_q(s)]\tilde{X}' + \left\{-\alpha_q(s) + \langle \alpha_q \rangle \right. \\ &\quad \left. + \langle \alpha_q \rangle \beta_q(s) - \alpha_q(s)\beta_q(s) - \left(\int_0^s ds [\delta_q(s) - \langle \delta_q \rangle]\right)\right\}\tilde{X} \\ &\quad \left. + \left(\int_0^s ds \beta_q(s)\right) \frac{\partial}{\partial \tilde{X}} \left(\tilde{X} \frac{\partial \psi(\tilde{X}, \tilde{Y})}{\partial \tilde{X}} - \tilde{Y} \frac{\partial \psi(\tilde{X}, \tilde{Y})}{\partial \tilde{Y}}\right)\right\}. \end{aligned} \quad (10)$$

The coordinate transformation can be easily obtained by solving Eq. (10) for \tilde{X} and \tilde{X}' in terms of x and x' . The expressions for y and y' are identical in form to Eq. (10) provided we make the replacements $(x, x') \rightarrow (y, y')$ and $(\tilde{X}, \tilde{Y}, \tilde{X}', \tilde{Y}') \rightarrow (\tilde{Y}, \tilde{X}, \tilde{Y}', \tilde{X}')$ and reverse the signs of $\alpha_q(s)$ and $\beta_q(s)$. In the above equations, $\alpha_q(s)$, $\beta_q(s)$, and $\delta_q(s)$ are defined in terms of the lattice function $\kappa_q(s)$, which is assumed to have zero average, $\int_0^S ds \kappa_q(s) =$

0, and odd half-period symmetry with $\kappa_q(s - S/2) = -\kappa_q[-(s - S/2)]$. The definitions are given by

$$\begin{aligned} \alpha_q(s) &= \int_0^s ds \kappa_q(s), \quad \beta_q(s) = \frac{1}{S} \int_0^s ds [\alpha_q(s) - \langle \alpha_q \rangle], \\ \langle \dots \rangle &\equiv \frac{1}{S} \int_0^S ds (\dots), \quad \delta_q(s) = \alpha_q^2(s) - 2\kappa_q(s)\beta_q(s), \\ \kappa_{fq} &= \langle \delta_q \rangle - \langle \alpha_q \rangle^2 = \frac{3}{S} \int_0^S ds [\alpha_q^2(s) - \langle \alpha_q \rangle^2]. \end{aligned} \quad (11)$$

In addition, $\alpha_q(s)$ and $\langle \alpha_q \rangle$ are of order ϵ ; $\beta_q(s)$ is of order ϵ^2 ; and $\langle \alpha_q \rangle \beta_q(s)$, $\alpha_q(s)\beta_q(s)$, $(\int_0^s ds \beta_q(s))$, and $(\int_0^s ds [\delta_q(s) - \langle \delta_q \rangle])$ are of order ϵ^3 .

3 VLASOV-MAXWELL EQUATIONS IN THE TRANSFORMED VARIABLES

Because the transformation leading to the new Hamiltonian in Eq. (8) is canonical, the nonlinear Vlasov-Maxwell equations for the distribution function $F_b(\tilde{X}, \tilde{Y}, \tilde{X}', \tilde{Y}', s)$ and self-field potential $\psi(\tilde{X}, \tilde{Y}, s)$ in the transformed variables are given by

$$\begin{aligned} \left\{ \frac{\partial}{\partial s} + \tilde{X}' \frac{\partial}{\partial \tilde{X}} + \tilde{Y}' \frac{\partial}{\partial \tilde{Y}} - \left(\kappa_{fq} \tilde{X} + \frac{\partial \psi}{\partial \tilde{X}} \right) \frac{\partial}{\partial \tilde{X}'} \right. \\ \left. - \left(\kappa_{fq} \tilde{Y} + \frac{\partial \psi}{\partial \tilde{Y}} \right) \frac{\partial}{\partial \tilde{Y}'} \right\} F_b = 0, \end{aligned} \quad (12)$$

and

$$\left(\frac{\partial^2}{\partial \tilde{X}^2} + \frac{\partial^2}{\partial \tilde{Y}^2} \right) \psi = -\frac{2\pi K_b}{N_b} \int d\tilde{X}' d\tilde{Y}' F_b, \quad (13)$$

where $\kappa_{fq} = \text{const.}$ is defined in Eq. (11). Variables in laboratory-frame coordinates can be obtained through the pull-back transformation \tilde{T}^* associated with the coordinate transformation

$$\tilde{T} : (x, y, x', y') \mapsto (\tilde{X}, \tilde{Y}, \tilde{X}', \tilde{Y}'). \quad (14)$$

Here, \tilde{T}^* pulls (transforms) functions on $(\tilde{X}, \tilde{Y}, \tilde{X}', \tilde{Y}')$ back into functions on (x, y, x', y') . For example, the distribution function transforms according to

$$\begin{aligned} \tilde{T}^* : F_b(\tilde{X}, \tilde{Y}, \tilde{X}', \tilde{Y}', s) &\mapsto f_b(x, y, x', y', s) \\ &\equiv F_b(\tilde{T}(x, y, x', y'), s). \end{aligned} \quad (15)$$

In addition, we obtain the following pull-back equation for the beam density correct to order ϵ^3 ,

$$\begin{aligned} n_b(x, y, s) &= \int d\tilde{x} d\tilde{y} d\tilde{x}' d\tilde{y}' f_b \delta(\tilde{x} - x) \delta(\tilde{y} - y) \\ &= \int d\tilde{X} d\tilde{Y} d\tilde{X}' d\tilde{Y}' F_b \delta(\tilde{T}^{-1} \tilde{X} - x) \delta(\tilde{T}^{-1} \tilde{Y} - y) \\ &= \left\{ \int d\tilde{X}' d\tilde{Y}' [1 - (x_2 + x_3) \frac{\partial}{\partial \tilde{X}} \right. \\ &\quad \left. - (y_2 + y_3) \frac{\partial}{\partial \tilde{Y}}] F \right\}_{(\tilde{X}, \tilde{Y}) \rightarrow (x, y)}. \end{aligned} \quad (16)$$

Here, x_2 , y_2 and x_3 , y_3 , defined by Eq. (10), are the second-order and third-order inverse coordinate transformations expressed as functions of $(\tilde{X}, \tilde{Y}, \tilde{X}', \tilde{Y}')$.

Because of the simple form of the Vlasov-Maxwell equations in the transformed variables, with constant focusing coefficient $\kappa_{fq} = \text{const.}$, a wide range of literature developed for the constant focusing case[1, 11, 12, 13] can be applied virtually intact in the transformed variables. For example, it is readily shown that any distribution function of the form

$$F_b^0(\tilde{X}, \tilde{Y}, \tilde{X}', \tilde{Y}') = F_b^0(\mathcal{H}^0), \quad (17)$$

where $\mathcal{H}^0 = (1/2)(\tilde{X}'^2 + \tilde{Y}'^2) + (1/2)\kappa_{fq}(\tilde{X}^2 + \tilde{Y}^2) + \psi^0(\tilde{X}, \tilde{Y})$ is the single-particle Hamiltonian, is an exact equilibrium solution to the Vlasov-Maxwell equations (12) and (13) with $\partial/\partial s = 0$. There is clearly enormous latitude[1, 7] in specifying the functional form of $F_b^0(\mathcal{H}^0)$ in the transformed variables, with equilibrium examples[10] ranging from the KV distribution, to the waterbag equilibrium, to thermal equilibrium, to mention a few examples. Once the functional form of $F_b^0(\mathcal{H}^0)$ is specified, and ψ^0 is calculated self-consistently from Eq. (13), periodically-focused equilibrium properties in the laboratory coordinates, such as the density profile and the transverse temperature profile, can then be determined by the pull-back transformation. For example, to the leading order, the density profile is of the form[10]

$$n_b(x, y, s) = n_b^0\left(\frac{x}{1 - \beta_q(s)}, \frac{y}{1 + \beta_q(s)}\right), \quad (18)$$

where $n_b^0(\tilde{X}, \tilde{Y}) = \int d\tilde{X}' d\tilde{Y}' F_b^0(\tilde{X}, \tilde{Y}, \tilde{X}', \tilde{Y}')$.

4 CONCLUSIONS

To summarize, the formalism developed here represents a powerful framework for investigating the kinetic equilibrium and stability properties of an intense nonneutral ion beam propagating through an alternating-gradient quadrupole field. First, the analysis applies to a broad class of equilibrium distributions $F_b^0(\mathcal{H}^0)$ in the transformed variables. Second, the determination of (periodically-focused) beam properties in the laboratory frame is relatively straightforward. Third, the analysis applies to beams with arbitrary space-charge intensity, consistent only with requirement for radial confinement of the beam particles by the applied focusing field ($\kappa_{fq}\beta_b^2 c^2 > \hat{\omega}_{pb}^2/2\gamma_b^2$). Finally, the formalism can be extended[10] in a straightforward manner to the case of a periodic-focusing solenoidal field $\mathbf{B}_{sol}(\mathbf{x}) = B_z(s)\hat{\mathbf{e}}_z - (1/2)B_z'(s)(x\hat{\mathbf{e}}_x + y\hat{\mathbf{e}}_y)$, and to the case where weak nonlinear corrections to the focusing force are retained in the analysis.

5 ACKNOWLEDGEMENT

This research was supported by the Department of Energy.

6 REFERENCES

- [1] R. C. Davidson, *Physics of Nonneutral Plasmas* (Addison-Wesley Publishing Co., Reading, MA, 1990), and references therein.
- [2] T. P. Wangler, *Principles of RF Linear Accelerators* (John Wiley & Sons, Inc., New York, 1998).
- [3] M. Reiser, *Theory and Design of Charged Particle Beams* (John Wiley & Sons, Inc., New York, 1994).
- [4] I. Kapchinskij and V. Vladimirkij, in *Proceedings of the International Conference on High Energy Accelerators and Instrumentation* (CERN Scientific Information Service, Geneva, 1959), p. 274.
- [5] R. L. Gluckstern, in *Proceedings of the 1970 Proton Linear Accelerator Conference*, Batavia, IL, edited by M. R. Tracy (National Accelerator Laboratory, Batavia, IL, 1971), p. 811.
- [6] T. -S. Wang and L. Smith, *Particle Accelerators* **12**, 247 (1982).
- [7] R. C. Davidson and C. Chen, *Particle Accelerators* **59**, 175 (1998).
- [8] C. Chen, R. Pakter, and R. C. Davidson, *Phys. Rev. Lett.* **79**, 225 (1997).
- [9] P. J. Channell, *Physics of Plasmas* **6**, 982 (1999).
- [10] R. C. Davidson, H. Qin, and P. J. Channell, to be published (1999).
- [11] R. C. Davidson, W. W. Lee, and P. H. Stoltz, *Phys. Plasmas* **5**, 279 (1998).
- [12] R. C. Davidson, *Physical Review Letters* **81**, 991 (1998).
- [13] R. C. Davidson, *Physics of Plasmas* **5**, 3459 (1998).

Simulation of Longitudinal Multibunch Instabilities in CESR*

D. B. Fromowitz, CESR, LNS, Cornell University†

Abstract

A tracking simulation predicts beam current thresholds in CESR (Cornell Electron-positron Storage Ring) based on the longitudinal dynamics of multibunch beams in RF cavities. The simulated thresholds are found to have a very strong dependence on the frequencies of the HOM cavity wakefields and are consistent with CESR measurements. Fourier transforms of simulated data are also consistent with observed spectral lines in CESR. After the phase III upgrade to SRF (Superconducting RF) cavities is completed in 1999, a significant increase in the thresholds is predicted.

1 INTRODUCTION

A new tracking code called "*Oscil*"[1] was created to study how beam current thresholds are affected by longitudinal motion in CESR. "*Oscil*" has no transverse degrees of freedom.

Section 2 lists some of the parameters and discusses the physics used in *Oscil*. Section 3 shows how the simulated thresholds depend on particle and lattice variables. Finally, Section 4 states the theory connecting the growth rates with Fourier spectra of the longitudinal motion.

2 TRACKING DETAILS

The *Oscil* code considers a single beam in a storage ring. Other than RF cavities, there are no explicit optics; the momentum compaction factor α represents all other accelerator elements. Synchrotron radiation effects are included and treated as continuous. Many parameters are specified at run time including, but not limited to, the number of bunches, the bunch current, the number of macroparticles comprising each bunch, and the quantities that define RF cavity modes: ω , R/Q , and Q_L .

2.1 Dynamics

There are four processes that fuel the longitudinal phase space motion of the simulated bunches. The first three processes modulate the bunch energy. First, the bends in the ring cause synchrotron radiation losses. Next, the drive (generator) voltage waveform changes the bunch energy. The third source of energy variations is the cavity wakefields left by previous bunches. This third process is the only way that different bunches (or even macroparticles within a bunch) interact in *Oscil*. The last phase space ef-

fect is the change in the longitudinal displacement between cavities due to a nonzero α .

3 SIMULATION RESULTS

3.1 Longitudinal Oscillation Envelopes

Using a nine-train, two-bunch (9x2) configuration, the envelope of the longitudinal displacement time evolution may be obtained for a variety of conditions. First, if the bunches are pointlike and only fundamental cavity mode wakefields are allowed (i.e. there are no HOM's), then the envelope at 72 mA total current is that seen in Fig. 1. The beam is highly damped and remains small. (All four cavities have parameters corresponding to copper CESR cavities in this simulation.)

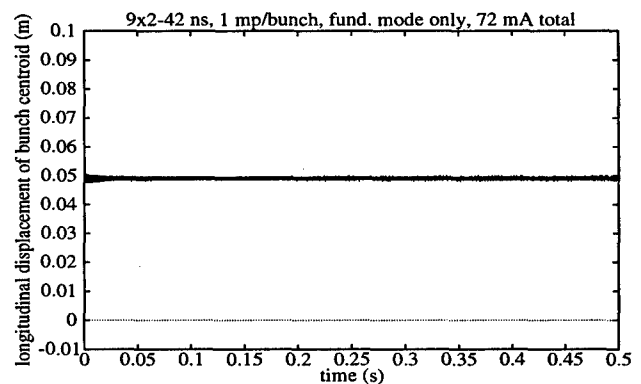


Figure 1: Envelope of longitudinal oscillations of 18 pointlike bunches (with a 42-ns intratrain interbunch spacing) at 72 mA total current. The only wakefield is that due to the fundamental mode. The interior of the envelope is darkened for clarity.

When the total beam current is increased to 144 mA, the longitudinal displacement undergoes a series of pulses as seen in Fig. 2. (The RF drive wavelength is about 0.60 m.) Although the fundamental cavity and klystron drive frequencies are set such that the machine is Robinson stable, the presence of multibunch modes causes the displacement amplitude to grow occasionally.

As the current is increased even higher, both the period and the amplitude of the oscillations become erratic. At 216 mA total current, chaos ensues as illustrated in Fig. 3. Remember that this chaos is caused by the fundamental cavity mode alone because there are no HOM's!

Representing a bunch by many macroparticles instead of just one greatly increases the execution time. However, it is necessary to examine multiparticle bunches to see how the behavior changes. When each of the 18 pointlike bunches

* Work supported by the NSF.

† Email: dbf5@cornell.edu

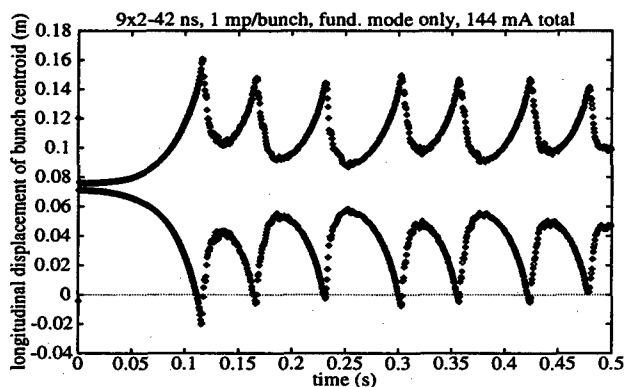


Figure 2: Longitudinal oscillation envelope at 144 mA total current.

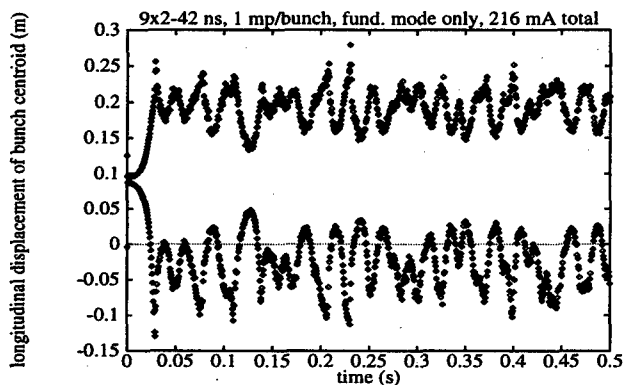


Figure 3: Longitudinal oscillation envelope at 216 mA total current.

is instead represented by 200 macroparticles, the longitudinal displacement envelope (of the bunch centroid) becomes narrower in several places as a result of Landau damping among the macroparticles.

3.2 Beam Current Thresholds

The CESR RF cavities are in the process of being replaced by SRF cavities so that the thresholds may be increased. The main differences between the NRF (normal RF) and SRF cavities are shown in Table 1. The cavity voltage amplitude V_c is one quantity that may vary quite a bit. Table 1 only shows a typical value.

There are two types of thresholds observed with the *Oscil* code. The lower-current threshold is the current at which the always-damped longitudinal motion (as seen in Fig. 1) turns to a pulsed-amplitude motion (as seen in Fig. 2). This "damping-to-pulses" threshold is plotted in Fig. 4 as NRF cavities are replaced with SRF cavities in a simulation that includes the fundamental and 1399.8 MHz cavity modes. This HOM of about 1400 MHz is used because it has a high R/Q in both NRF and SRF cavities. Parameters of this mode are shown in Table 1.

The most notable feature is that the current thresholds rise as each NRF cavity is replaced with an SRF cavity

Table 1: Differences between normal and superconducting RF cavities in CESR.

Quantity	NRF (Cu) Cavity	SRF (Nb) Cavity
fundamental Q_L	6000	200,000
fundamental R/Q	427 Ω/m	145 Ω/m
typical V_c	1.5 MV	1.9 MV
cells per cavity	5	1
1400 MHz Q_L	1100	13.0
1400 MHz R/Q	12.6 Ω/m	4.7 Ω/m

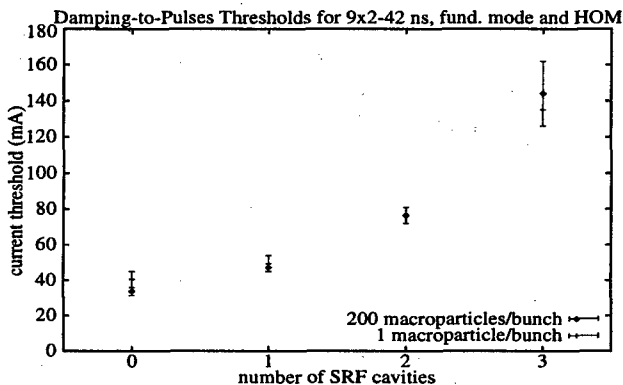


Figure 4: Damping-to-Pulses thresholds for the fundamental mode and a HOM (1399.8 MHz) for pointlike bunches and for bunches of 200 macroparticles.

(with the total number of cavities constant at four). The thresholds are very similar for 1- and 200-macroparticle bunches.

The higher-current threshold is the boundary between the pulsed-amplitude motion (as seen in Fig. 2 or 3) and a higher-current beam where the initial growth rate is so large that the beam immediately diverges. This threshold is coined the "pulses-to-divergence" threshold and is illustrated in Fig. 5.

The pulses-to-divergence threshold also increases with the number of SRF cavities. However, this threshold is markedly higher with multiparticle bunches than with pointlike bunches. The thresholds shown in Fig. 5 for the zero-, one-, and two SRF cavity cases are close to what has been observed in CESR.

3.3 Cavity Voltage

The current thresholds recently observed in CESR with one or two SRF cavities were not noticeably higher than when there were no SRF cavities. The reason is that the cavity voltages have often been *lowered* in CESR as NRF cavities were replaced with SRF cavities. The thresholds introduced in Section 3.2 were based on simulations using the typical V_c from Table 1 as the voltages for the cavities. If actual CESR voltages are used in the *Oscil* simulation, then the simulated thresholds follow the trends of CESR.

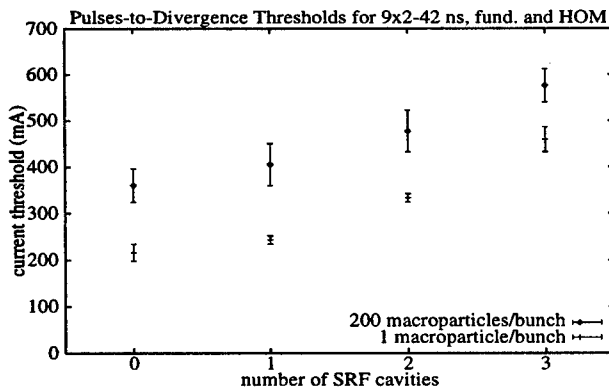


Figure 5: Pulses-to-Divergence thresholds for the fundamental mode and a HOM (1399.8 MHz) for pointlike bunches and for bunches of 200 macroparticles. Compare with the Damping-to-Pulses thresholds of Fig. 4.

3.4 Effect of HOM's

The precise values for the thresholds in CESR are not easily duplicated over time. Part of the reason is due to all the different cavity cells present and the differences in temperature of each cell. In reality, there are many different HOM's, and even one particular HOM, such as the 1399.8 MHz mode, will have a slightly different center frequency in each cell. When the pulses-to-divergence threshold is found for two different HOM conditions, one with all cells having a HOM center frequency of 1399.8 MHz, the other condition having 1398.8 MHz for all cells, it is seen that the threshold depends strongly on the HOM frequency, as shown in Fig. 6. Also shown are measured CESR thresholds for zero and one SRF cavity. The 1-SRF-cavity threshold is for 28 ns spacing and would be higher for 42 ns and with a higher cavity voltage as explained in Section 3.3.

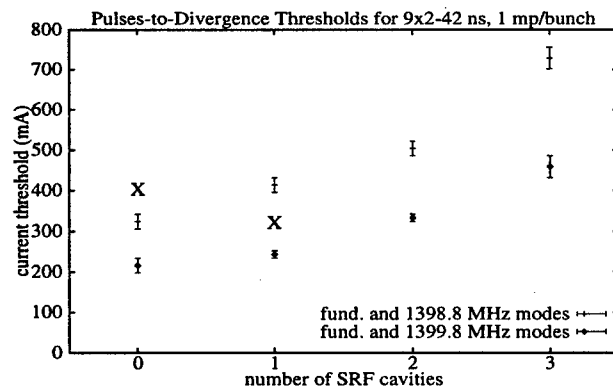


Figure 6: Pulses-to-Divergence thresholds for pointlike bunches with the fundamental cavity mode and one HOM. The upper data set is for a 1398.8 MHz HOM; the lower set for 1399.8 MHz. The X's are measured CESR data, the rightmost X having a 28 ns interbunch spacing.

This 1 MHz HOM shift corresponds to a 44 K change in a given cell. Although this is a large temperature fluctuation,

the actual temperature *and shape* differences from cell to cell do amount to several MHz variations, causing a significant threshold variation in time.

4 GROWTH RATES

The level of the thresholds are partially explained by the longitudinal growth rates of the beam. Application of a growth rate formula from Chao[2] shows that the initial growth rate is related to the spectral sidebands $(h-1)\omega_0 + \omega_s$ and $(h+1)\omega_0 - \omega_s$ where h is the harmonic number of CESR, ω_0 is the revolution frequency, and ω_s is the synchrotron frequency.

If at the first cavity the longitudinal displacement is recorded for every pass of every particle (rather than just for the envelope), then the data may be Fourier transformed to find the sidebands. A spectrum of the first 1 ms of longitudinal displacement data from the 216 mA beam represented by Fig. 3 is shown as Fig. 7.

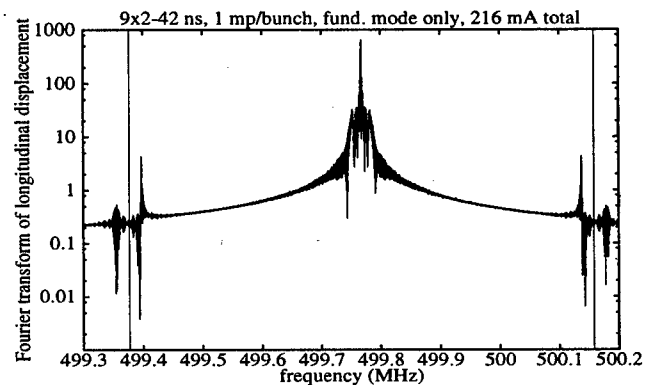


Figure 7: Magnitude of the Fourier transform of the longitudinal displacement of a 216 mA beam. The vertical lines indicate the $(h \pm 1)\omega_0$ revolution harmonics.

The sidebands mentioned are significantly higher than the surrounding features. As a comparison, a spectrum of the 72 mA beam would show that the indicated sidebands are slightly *smaller* than the sidebands on the other side of the $(h \pm 1)\omega_0$ revolution harmonics. This effect is evidence that the observed instability is associated with the sidebands.

5 ACKNOWLEDGMENTS

I appreciate the help and guidance of my research adviser, David Rubin. I thank Zippi Greenwald, Sasha Temnykh, and Sergey Belomestnykh for cavity mode data.

6 REFERENCES

- [1] D. B. Fromowitz, CBN 98-18 (Laboratory of Nuclear Studies internal paper), Cornell University, 1998.
- [2] A. W. Chao, "Coherent Instabilities of a Relativistic Bunched Beam," *Physics of High Energy Particle Accelerators* **105**, 1983.

NEW THEORY OF SINGLE BUNCH STABILITY IN A LINAC WITH QUADRUPOLE DISPLACEMENTS.

G. Guignard, J. Hagel, CERN, Geneva, Switzerland

Abstract

The analytical treatment previously described [1] has been extended to include the important effect of magnetic quadrupole transverse displacements, the chromatic variation of the magnetic focusing, the energy spread along the bunch and possible microwave quadrupoles, the last two in relation to BNS damping. Both, the longitudinal and transverse equations of motion are solved, the second by using the perturbation method with partial expansions developed for this theory. The localized nature of the quadrupole displacements is preserved by using thin lenses and the superposition principle for the kick effects. The causality principle applied to the downstream beam oscillations due to the kicks is introduced via Heaviside functions. The treatment presented [2] provides formulae for the tunes shift in the bunch and first-order solutions for the transverse beam off-sets within the bunch. It presents a break-through in the recent efforts [3] to solve the problem of the bunch stability theoretically, with realistic beam and linac models.

1 EQUATIONS OF MOTION

The equations of motion for the longitudinal and transverse (vertical) plane in a linac with longitudinal and transverse wakefields is given in the form of two semicoupled partial and linear integro-differential equations [4] as:

$$\frac{\partial \gamma(s, z)}{\partial s} = \frac{eU}{m_0 c^2} \cos(k_{RF} z - \bar{\Phi}_{RF}) - C \int_0^z \rho(z^*) [W_{L0} + \frac{W_{L1} - W_{L0}}{l_B} (z - z^*)] dz^* \quad (1)$$

$$\frac{\partial^2 x(s, z)}{\partial s^2} - K(s)[1 + \Delta k(z)]x = \frac{W_{T0} C}{\gamma_0} \int_0^z \rho(z^*) (z - z^*) x(s, z^*) dz^* + K(s)[1 + \Delta k(z)]x_Q(s) \quad (2)$$

The initial conditions are:

$$x(0, z) = 0 \quad (3)$$

$$\frac{\partial x}{\partial s}(s=0) = 0 \quad (4)$$

The independent variables s and z represent the distance along the linac and the coordinate inside the bunch. z is zero at the head and equal to the bunch length l_B at the tail

of the truncated bunch. The unknowns $\gamma(s, z)$ and x are the energy Lorentz factor as well as the vertical transverse displacement along the bunch at a given linac position. A piecewise constant energy of the bunch along the different linac sectors is assumed so that no acceleration term proportional to $\frac{\partial x}{\partial s}$ appears in the equation of motion. In addition, a linear variation of the wakefield level along the bunch in both planes is assumed. While W_{L0} and W_{L1} represent the longitudinal wakefield (W_L) at the head and tail of the bunch, W_{T0} stands for the transverse wakefield (W_T) at the tail. We use a 4-th order Chebyshev expansion of a normalized Gaussian charge distribution in the range of $\pm 2\sigma_z$ given by:

$$\rho(z) \simeq \frac{75}{46l_B} \left[\frac{1}{20} \left(\frac{4z}{l_B} - 2 \right)^4 - \frac{41}{100} \left(\frac{4z}{l_B} - 2 \right)^2 + 1 \right] \quad (5)$$

The quantity $\Delta k(z)$ in Eq. (2) represents a variation of the focusing force inside the bunch which is caused by the energy dependent focusing (chromatic effect) as well as by the application of RF quadrupoles in order to reduce the emittance blowup caused by the presence of wakefields. The constant C is defined as $C = 4\pi\epsilon_0 r_e N$ where ϵ_0 is the permittivity of free space, N the number of particles in the bunch and r_e the classical electron radius. The function $x_Q(s)$ represents the actual quadrupole misalignments as function of the position s . This function is either random or given by recurrence relations representing a trajectory correction [2].

2 SOLUTION OF THE LONGITUDINAL EQUATION

Eq. (2) can be solved in a straightforward way by simple integration w.r.t the independent variable s . This yields

$$\gamma(s, z) = \gamma_0 + \frac{eUs}{m_0 c^2} \cos(k_{RF} z - \bar{\Phi}_{RF}) - 4\pi\epsilon_0 r_e N s R(z) \quad (6)$$

with

$$R(z) = \int_0^z W_L(z - z^*) \rho(z^*) dz^* \quad (7)$$

In this notation, Φ_{RF} is the acceleration phase at the head of the bunch. The function $R(z)$ can easily be found by using the linear variation of W_L inside a single bunch and the Chebyshev model (5) for the gaussian distribution.

With the definition $\zeta = \frac{z}{l_B}$, $R(z)$ is given by

$$R(z) = W_{L0} \times \left(-\frac{16}{23}\zeta^6 + \frac{144}{23}\zeta^5 - \frac{559}{46}\zeta^4 + \frac{157}{23}\zeta^3 + \frac{6}{23}\zeta \right) + W_{L1} \times \left(\frac{16}{23}\zeta^6 - \frac{48}{23}\zeta^5 + \frac{79}{46}\zeta^4 + \frac{1}{23}\zeta^3 + \frac{3}{23}\zeta^2 \right) \quad (8)$$

The energy spread $\delta(s, z)$ inside the bunch is defined in the usual way as $\delta(s, z) = (\gamma(s, z) - \gamma(s, 0))/\gamma(s, z)$. However, as a simplification, only the asymptotic limit given as $\delta(z) = \lim_{s \rightarrow \infty} \delta(s, z)$ is used. In this way the z -dependent detuning force $\Delta k(z)$ is given by

$$\Delta k(z) = -\delta(z) + \alpha_0 \sin(k_{RF}z - \bar{\Phi}_{RFQ}) \quad (9)$$

where α_0 is the maximum focusing strength of the RF quadrupole and $\bar{\Phi}_{RFQ}$ its phase at the head of the bunch.

3 SOLUTION OF THE TRANSVERSE EQUATION

The linear partial integro-differential equation for the transverse bunch displacement (2) can be solved in an easier way by separating two types of solution, one only depending on s and one on both independent variables, s and z . Hence, the solution is decomposed as

$$x(s, z) = X(s) + y(s, z) \quad (10)$$

and two new equations are obtained, one for the coherent part (independent of z) and one for the incoherent part (depending on s and z) of the bunch oscillation:

$$\frac{d^2 X(s)}{ds^2} - K(s)X(s) = K(s)x_Q(s) \quad (11)$$

$$\begin{aligned} \frac{\partial^2 y(s, z)}{\partial s^2} - K(s)[1 + \Delta k(z)]y(s, z) = X(s) \times \\ \times \left[K(s)\Delta k(z) + \frac{CW_{T0}}{\gamma_0 l_B} \int_0^z \rho(z^*)(z - z^*)dz^* \right] + \\ + \frac{CW_{T0}}{\gamma_0 l_B} \int_0^z \rho(z^*)(z - z^*)y(s, z^*)dz^* + \\ + K(s)\Delta k(z)x_Q(s) \end{aligned} \quad (12)$$

While Eq. (11) represents the betatron motion in the absence of wakefields and acceleration, Eq. (12) contains chromatic contributions as well as terms responsible for creating dispersion induced by the quadrupole misalignments. The weak focusing approximation is now introduced with the average tune defined by $\bar{q} = 1/\bar{\beta}$. However, this is used in the focusing forces but not in the terms containing the quadrupole misalignments, to keep their discrete nature. Computing the β functions from the transfer

matrices gives the dependence of \bar{q}

$$\bar{q}(z) = \frac{3(1 + \Delta k(z))}{L(3 - (1 + \Delta k(z))^2 \sin^2 \frac{\mu}{2})} \times \sqrt{(1 - \cos \mu)[2 - (1 + \Delta k(z))^2(1 - \cos \mu)]} \quad (13)$$

In the case of the coherent equation (11) the tune follows by substituting $\Delta k(z) = 0$ in the above equation [4],

$$q = \left[L \left(\cot \frac{\mu_{cell}}{2} + \frac{2}{3} \tan \frac{\mu_{cell}}{2} \right) \right]^{-1} \quad (14)$$

In this way, the actual equations of motion become

$$\frac{d^2 X}{ds^2} + q^2 X = K(s)x_Q(s) \quad (15)$$

$$\begin{aligned} \frac{\partial^2 y}{\partial s^2} + \bar{q}^2(z)y = X(s) \times \\ \times \left[\frac{CW_{T0}}{\gamma_0 l_B} \int_0^z \rho(z^*)(z - z^*)dz^* - (q^2 - \bar{q}^2(z)) \right] + \\ + \frac{CW_{T0}}{\gamma_0 l_B} \int_0^z \rho(z^*)(z - z^*)y(s, z^*)dz^* + \\ + K(s)\Delta k(z)x_Q(s). \end{aligned} \quad (16)$$

3.1 Solution for the coherent motion

The coherent equation (15) describing the betatron motion in the absence of wakefields and under the influence of quadrupole misalignments can be solved by assuming localized kicks for the actual quadrupole displacements. In between these kicks the solution is sinusoidal and its amplitude is defined by the effects of the kicks **upstream** of the position considered. In order to describe this limitation to upstream quadrupoles, the Heaviside Function $H(s - s_k)$ is used which has the property to be strictly zero for negative arguments and equal to unity for positive ones. Here s_k denotes the k -th quadrupole position given by $s_k = kL$ if L is half a FODO period. In addition to this causality principle, the method of superposition of all the solutions due to single kicks is used. This is justified by the linearity of the equation and the use of thin lenses. The solution is then:

$$X = \frac{2}{qL} \sin \frac{\mu}{2} \sum_k (-1)^k x_k \sin [q(s - s_k)] H(s - s_k) \quad (17)$$

The x_k are the actual quadrupole misalignments at position s_k . In Fig. 1, a typical solution is shown for X in a FODO lattice with misaligned quadrupoles with an RMS displacement of $10 \mu m$, when $\mu = 105^\circ$. The resonant behaviour of the solution arises from the continuity of the frequency spectrum of a random function which contains the unperturbed betatron frequency on the left side of Eq. (15).

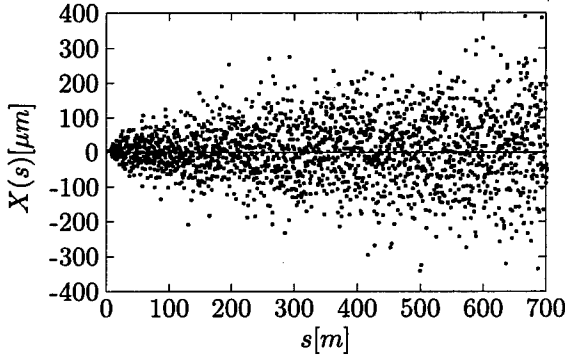


Fig. 1 Solution $X(s)$ in the presence of quadrupole misalignments

3.2 Solution for the incoherent motion

Equation (16) can be rewritten as

$$\frac{\partial^2 y}{\partial s^2} + \bar{q}^2(z; E \Delta k(z)) y = A(z) X(s) + K(s) \Delta k(z) x_Q(s) + \epsilon \frac{CW_{T0}}{\gamma_0 l_B} \int_0^z \rho(z^*) (z - z^*) y(s, z^*) dz^* \quad (18)$$

with

$$A(z) = \left[\frac{CW_{T0}}{\gamma_0 l_B} \int_0^z \rho(z^*) (z - z^*) dz^* - (q^2 - \bar{q}^2(z)) \right] \quad (19)$$

Using the approximation (5) for $\rho(z)$ the coefficient function $A(z)$ becomes a sixth order polynomial. The formal perturbation parameters E and ϵ multiply small contributions such as the wakefields. However, the expansion is only made with respect to one of them, namely ϵ in order to keep the z dependent tune \bar{q} to any order and in this way avoid the occurrence of secular terms. Hence $y = y^{(0)}(s, z; E) + \epsilon y^{(1)}(s, z; E) + O(\epsilon^2)$. Already the lowest order contribution $y^{(0)}(s, z)$ has been proven to describe the solution sufficiently well for the case of the CLIC main linac. The equation for $y^{(0)}$ is

$$\frac{\partial^2 y^{(0)}}{\partial s^2} + \bar{q}^2(z) y^{(0)} = X(s) A(z) + K(s) x_Q(s) \Delta k(z) \quad (20)$$

and this linear inhomogeneous second order equation is solved as usual by adding the homogeneous solution y_h to the particular one found applying Green's formula.

$$y^{(0)}(s, z) = y_h + \frac{\sin \bar{q}s}{\bar{q}} \int_0^s \cos \bar{q}s^* g(s^*) ds^* - \frac{\cos \bar{q}s}{\bar{q}} \int_0^s \sin \bar{q}s^* g(s^*) ds^* \quad (21)$$

where $g(s)$ represents the right hand side of Eq. (20). After integration the final result becomes

$$y^{(0)}(s, z) = y_0 \cos \bar{q}(z)s + \frac{y'_0}{\bar{q}(z)} \sin \bar{q}(z)s + A(z) \sum_{k=1}^{N_Q} \frac{2}{Lq\bar{q}(z)} \sin(\mu/2) (-1)^k x_k H(s - s_k) \times$$

$$\times [\sin \bar{q}(z) s I_1(s, s_k) - \cos \bar{q}(z) s I_2(s, s_k)] + \Delta k(z) \frac{2}{Lq\bar{q}(z)} \sin(\mu/2) \times \sum_{k=1}^{N_Q} (-1)^k x_k \sin \bar{q}(z)(s - s_k) H(s - s_k) \quad (22)$$

where

$$I_1(s, s_k) = \int_{s_k}^s \cos \bar{q}s^* \sin q(s - s_k) ds^* \quad (23)$$

$$I_2(s, s_k) = \int_{s_k}^s \sin \bar{q}s^* \sin q(s - s_k) ds^*. \quad (24)$$

Evidently $I_{1,2}$ permit a closed form solution and these expressions contain denominators of the form $q^2 - \bar{q}^2(z)$ which clearly exhibit the near resonance dynamics of the single bunch problem with wakefields.

Fig. 2 shows a comparison of the perturbative analytical solution $y^{(0)}$ to a numerical one obtained by the code MUSTAFA [5] for CLIC main linac parameters of $N = 6 \cdot 10^9$ and an RMS bunch length of $\sigma_z = 200 \mu m$ at the linac position $s = 1000 m$.

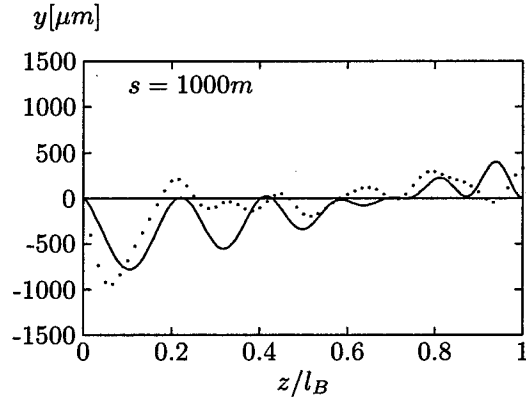


Fig.2 Comparison of the analytical and the numerical result for $y(z)$ at $s = 1000 m$.

To conclude, it can be pointed out that the agreement in amplitude and frequency of the analytical (full line) and numerical result (points) is very good. The local differences in phase mainly originate from the fact that MUSTAFA uses a strong focusing model while the theory is based on the weak focusing approximation. In addition the sequence of random numbers chosen in both examples is different although both sequences have the same RMS value.

4 REFERENCES

- [1] G. Guignard, J. Hagel, CERN-SL-98-015 AP (1998)
- [2] G. Guignard, J. Hagel, CERN-SL-99-006 AP (1999), 'Theory of Single Bunch Stability and Dynamics in Linacs with Strong Wakefields and Misalignments, submitted to Nuclear Instruments and Methods in Physics Research A.
- [3] G.V. Stupakov, SLAC-AP-108 (1997)
- [4] T. Raubenheimer, CLIC Note 347 (1997)
- [5] G. Guignard, J. Hagel, CERN-SL-98-002 AP (1998)

Preliminary Design of the CLIC Drive-Beam Transfer Line.

T.E. d'Amico and G. Guignard, CERN, 1211 Geneva 23, Switzerland.

ABSTRACT

In the drive-beam generation complex of CLIC there is an important beam transfer line between the drive-beam accelerator and the drive-beam decelerators, where the 30 GHz RF power is generated in the decelerator structures. The design proposed for this transport system is based on building blocks or beam optics subsystems, which have been individually studied in detail and can be combined in order to cover specific functions. One function consists of bending the beams wherever required by the geometrical layout, so as to preserve the bunch length and keep the bending arc compact and compatible with acceptable synchrotron radiation. Other functions are to adjust the path length of each drive beam for synchronism with the main-linac beam and to compress or stretch the bunch according to the needs. Furthermore, there are vertical and horizontal beam translations, isochronous or acting as a compressor, and β -function transformers for matching the optics. All these functions are necessary in the drive-beam transfer that precedes injection into the decelerators.

1 MAIN FUNCTION DESCRIPTION

The different parts of the beam transport system between the drive-beam accelerator and the many drive-beam decelerators (making up the CLIC RF power source [1]) must in general terms cover four types of functions:

1. Bending the beams where required in order to follow the geometrical lay-out of the drive beam generation complex, in such a way that the bunch length is preserved and the bending arc is as compact as possible, compatible with tolerable synchrotron radiation effects.
2. Adjusting the path length of each individual drive beam in order to regulate of the synchronism of the beams with the main linac beam, when they are injected into the separated decelerating sections.
3. Compressing and also stretching the bunch length according to the needs at the different stages of the beam acceleration and multiplication.
4. Vertical or horizontal beam translation, isochronous or combined in specific cases with a bunch compression.

Each of the four functions have been studied and are present in various places of the drive beam generation complex. Function 1 appears each time the beam has to be bent, for instance after the pre-acceleration, between the combining rings and mainly in the "turn-around" loop preceding the injection in the decelerator. Function 2 is

only required before the injection into the decelerator while Function 3 is essential into the accelerating linac and immediately after the "turn-around" loop in order to satisfy the conditions assumed for the bunch length, considering the drive beam stability. Function 4 serves mainly for the vertical translation needed after the turn-around because of the geometry adopted in the tunnel, but also for the incoming drive beam which has to be lifted up to the level of the "turn-around" loop. The whole complex which requires the four functions is briefly described below.

2 OVERVIEW OF THE TURN AROUND.

The drive beam accelerator and the combiner rings are planned to be in a central position with respect to the two main linacs of the collider, which means that all the drive beams have to be first transported in a direction opposite to the main beams, before being turned around through a 360° loop and injected into the different decelerators [1] where they travel parallel to the main beams. The transport line for the beam going upstream is of course situated in the same tunnel as the decelerators, near the highest point in order to minimise the loss of space in the accessible area (Fig. 1). This position offers the advantage of keeping the "turn-around" loops near the roofs of the tunnel and of the alcoves which will house the loops. This prevents geometrical interference with the main linac and the decelerators which are placed on a common concrete support (Fig. 1), at about 1 m above the level of the tunnel floor. The difference in elevation of the beams going upstream and downstream (1.5 m approximately) imposes the need for vertical bends to bring the drive beams down before their injection in the decelerators. In addition, the up-going beam is not exactly above the down-going beam of the power-linac, since the two have to run anti-parallel over a short distance near the roof (where the path-length chicane is foreseen); they are horizontally separated by 0.75 m. In addition, the transport line carrying the up-going drive-beams must run without interruption all the way to the starting point of the main linac (also the injection-point of the first drive-beam). This transport line must therefore be placed slightly below the level of the turn-around loop (0.25 m) to avoid a crossing at the same level. Each drive-beam entering its specific loop is therefore deflected vertically. The relative vertical positions of the different beam lines are shown in Fig. 1 and in the elevation of Fig. 2. The latter shows the location of the vertical bends bringing the beam from roof-level to decelerator level just above the beam-dump line of the preceding drive-beam.

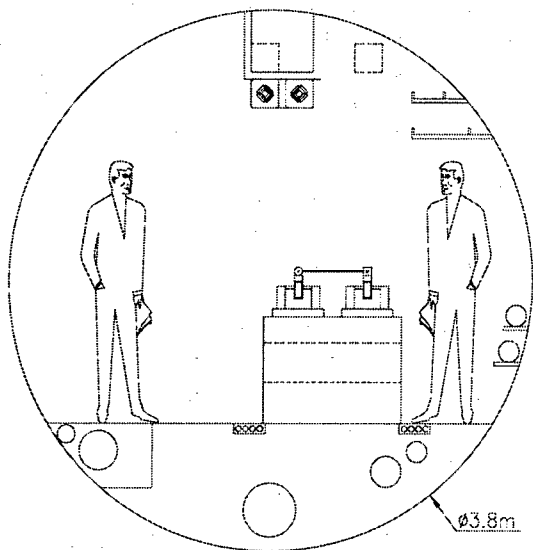


Figure 1 Tunnel cross-section with the transfer lines.

This compact design minimises the space lost for power transfer. The various elements of the turn-around appear in the plan view of Fig. 2. The up-going drive-beam comes from the left through a FODO line. After a vertical deflection, the selected drive-beam pulse enters the 360° loop, consisting of a 90° right-turn followed by three 90° left-turns. Drifts are added to adjust the geometry and separate the axes of the down- and up-going beams. After the loop, the beam traverses a special kind of chicane or "dipole-snake" that serves to adjust the path

length and compress the bunch. It then goes through a dipole that is only turned on in case of emergency to deviate the beam onto a dump. The drive beam pulse is then bent down to reach the decelerator injection-point. A further bunch compression is done in this downward bend. Fig. 2 also shows part of the previous decelerator section (coming from the right) which ends with a dipole and half-quadrupoles to bend the spent beam (with a large energy spread) into the same dump. The various elements or optics-modules of this area are described below.

The size of the alcove containing the turn-around as well as its relative position in the tunnel are shown in Fig.2. There are as many alcoves as there are drive beam pulses; they can also be used to house electronics racks.

3 TURN-AROUND LATTICE.

As seen in Section 2, the turn-around consists of four modules, each with a 90° bend. These modules are designed to be isochronous ($R_{56} = 0$) in order to preserve the bunch length and are based on the design concept elaborated for such applications with compact lattice and acceptable synchrotron radiation effects [2]. A module includes three dipoles of equal length, two quadrupole doublets between them to control dispersion as well as beam focusing and one triplet to join the modules. The dispersion is adjusted such that the integral of $D(s)/\rho(s)$ is zero in the bending magnets (of bending radius ρ) and D vanishes in the triplet. An optimisation of the magnet- and drift-length provides compact modules with reasonable β -amplitudes and magnetic fields. Fig. 3 gives a sketch of one module as well as the β -functions and the

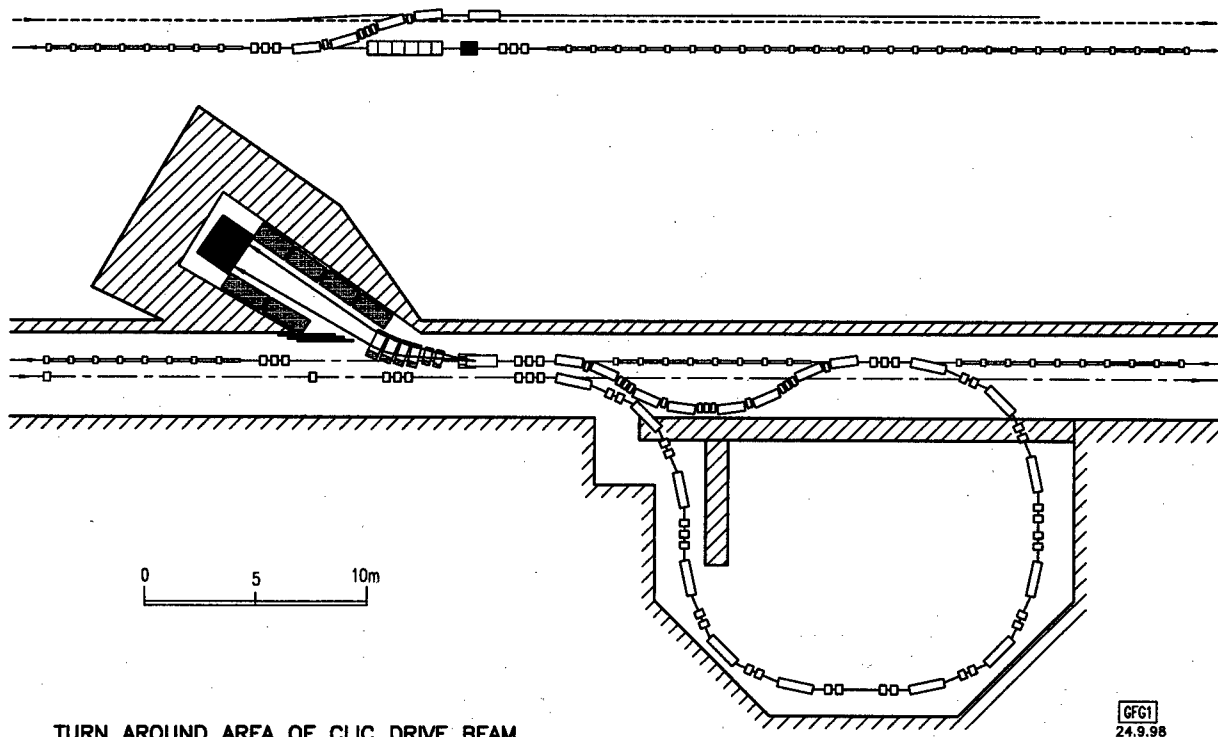


Figure 2 – Sketched Layout of the transfer lines.

dispersion achieved. Table 1 lists the main parameters.

Table 1 - Isochronous module parameters.

Bending magnet length	[m]	1.6
Bending magnet fields	[T]	1.0 / 1.8
Bending angle per dipole	[deg.]	23.5 / 43
Bending radius	[m]	3.9 / 2.15
Quadrupole length	[m]	0.3
Quadrupole gradient	[T/m]	26.0
Module length	[m]	11.0
Transfer matrix coefficient R_{56}	[m]	0.00

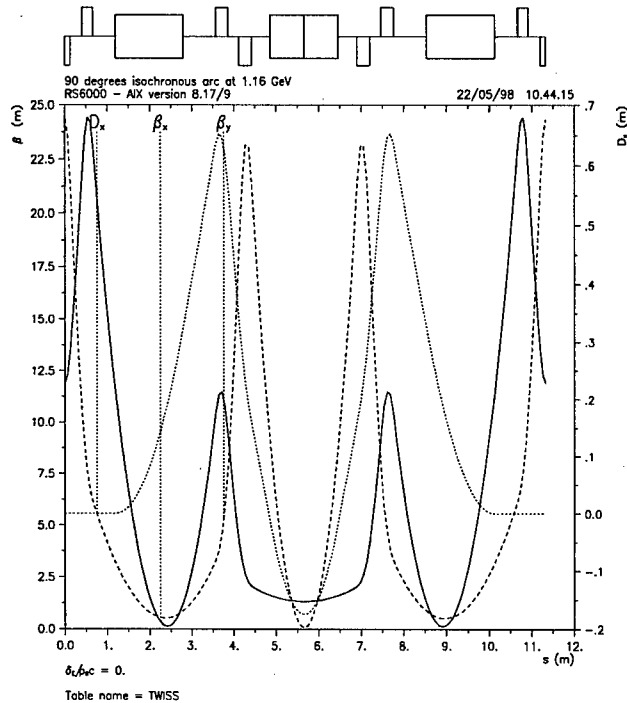


Figure 3 Optical functions of one isochronous module.

The total circumference of the turn-around is near 45 m. The coherent synchrotron radiation effect at 1.24 GeV is tolerable. The path length variation within the bunch, for a momentum spread $\Delta p/p$ of ± 0.025 , is strongly reduced with one family of sextupoles placed near the doublets, where the dispersion is relatively large.

4 OTHER BEAM TRANSFER MODULES

To adjust the phasing of each drive beam requires a fine **tuning of the path length** before injection into the decelerator and the addition of a kind of special chicane or "dipole-snake", after the "turn-around" loop. This chicane has to provide a non-zero R_{56} coefficient in order to introduce a correlation between the path-length variation Δl and a change $\Delta\theta$ of the deviation angle in the "snake", around a finite average value θ_0 for the dipoles. The sign of R_{56} is not important since the sign of $\Delta\theta$ is free, but its amplitude must allow an adjustment Δl between ± 2 mm and ± 5 mm (i.e., half the RF period at 30 GHz). R_{56} has therefore been chosen such as to achieve

most of the **bunch compression** needed in addition, i.e. $R_{56} = 0.13$ m, the remaining compression of 0.03 m being provided by the vertical translation that follows. In the drive-beam accelerator, the head of the bunch has an energy above average and the tail below. Such a correlation requires a positive R_{56} for bunch compression and the consequent use of a double-bend with two dipoles deflecting the beam in the same direction, i.e. with p and θ_0 of the same sign. To provide the desired R_{56} value, it is necessary to have a succession of four double-bends arranged in a geometry that looks like a long chicane (Fig. 2). A single quadrupole between the two bends controls the dispersion and a triplet of quadrupoles focuses the beam in the two transverse planes. The following parameters were selected to give $R_{56} = 0.13$ m and $\Delta l = 0.5$ mm/mrad:

$$\theta_B = 16^\circ, l_B = 1.23 \text{ m}, B = 0.88 \text{ T}, l_Q = 0.2 \text{ m}, G_Q = 20 \text{ T/m}$$

A path-length adjustment of 2 mm implies a change in the bending angle of 4 mrad with $l_{\text{drift}} = 0.5$ m.

The elevation difference of 1.5 m between the upstream- and downstream-going beams (Fig. 2) implies a **vertical translation** that can be combined with some compression of the bunch, using double-bends again. This function is achieved by half a "dipole-snake", i.e. two double-bends separated by a drift given by the geometry, and bending the beam into opposite directions. The coefficient R_{56} of this module is equal to 0.03 m in order to give with the path length module the total of 0.16 m that is required. The following parameters have been obtained for these two vertical double-bends:

$$\theta_B = 11^\circ, l_B = 1.23 \text{ m}, B = 0.6 \text{ T}, l_Q = 0.2 \text{ m}, G_Q = 38 \text{ T/m}$$

The drift in the middle of the module, containing a matching quadrupole triplet, has a total length equal to 1.0 m, to satisfy the translation amplitude required.

At various locations of the drive beam transport system, **matching Twiss functions** at zero-dispersion is needed. This happens at the junction between the transport line of the incoming beam and the first 90° isochronous module, between the turn-around and the path-length module, the latter and the vertical translation, and this translation and the drive-beam decelerator. In most cases, it is an adjustment to a FODO type lattice or between two FODO type lattices. This is best achieved by using quadrupole triplets of the type "FODO transformer" (that transforms a β -crossing with equal and opposite derivatives into a different β -crossing with opposite slopes also), the properties of which have been studied elsewhere [3].

5 REFERENCES

- [1] H. Braun and 14 co-authors, rep. CERN/PS 98-011 (LP) and Proc. EPAC98, Stockholm, 1998.
- [2] T.E. d'Amico and G.Guignard, rep. CERN/SL 95-021 (AP) and Proc. PAC95, Dallas, 1995.
- [3] T.E. d'Amico and G.Guignard, rep. CERN/SL 980-14 (AP) and Proc. EPAC98, Stockholm, 1998.

MEASUREMENTS OF THE ELECTRON CLOUD IN THE APS STORAGE RING

K. C. Harkay* and R. A. Rosenberg, Advanced Photon Source
Argonne National Laboratory, Argonne, IL 60439 USA

Abstract

Synchrotron radiation interacting with the vacuum chamber walls in a storage ring produce photoelectrons that can be accelerated by the beam, acquiring sufficient energy to produce secondary electrons in collisions with the walls. If the secondary-electron yield (SEY) coefficient of the wall material is greater than one, as is the case with the aluminum chambers in the 7-GeV Advanced Photon Source (APS) storage ring, a runaway condition can develop. As the electron cloud builds up along a train of stored positron or electron bunches, the possibility exists that a transverse perturbation of the head bunch will be communicated to trailing bunches due to interaction with the cloud. In order to characterize the electron cloud, a special vacuum chamber was built and inserted into the ring. The chamber contains 10 rudimentary electron-energy analyzers, as well as three targets coated with different materials. Measurements show that the intensity and electron energy distribution are highly dependent on the temporal spacing between adjacent bunches and the amount of current contained in each bunch. Furthermore, measurements using the different targets are consistent with what would be expected based on the SEY of the coatings. Data for both positron and electron beams are presented.

1 MOTIVATION

Postulation of an electron-cloud instability (ECI) arose from observations with stored positron beams at the KEK Photon Factory [1]. Similar results were later obtained at BEPC [2] and possibly at CESR [3]. Theoretical simulations predict large amplitude motions produced in the tail of positron bunch trains, leading to beam loss [4]. Although results from the models are consistent qualitatively with the observations, the electrons had not been directly measured. The goal of the measurements at the APS storage ring is to characterize the electron cloud (EC) so as to better predict conditions leading to a possible electron-cloud instability. Of particular interest is to provide realistic limits on critical input parameters in the models: the SEY of different surfaces in a real chamber and the influence of single or multiple reflections of the photons.

2 EXPERIMENTAL SETUP

In order to measure the properties of the electron cloud, a special 5-m vacuum chamber, equipped with rudimen-

tary electron energy analyzers, beam position monitors (BPMs) and targets, was built and installed in a field-free region in the APS storage ring [5] in May 1998. The locations of the components are shown in Fig. 1. EA6 is a copper end absorber designed to intercept high-energy photons to protect the downstream surfaces. Given that the chamber is straight, the bending magnet synchrotron radiation fan penetrates slightly farther into the channel at the downstream detectors.

The electron detector consists of two mesh grids in front of a collector: the outermost grid is grounded, and a bias voltage can be applied to the shielded grid. The collector is graphite-coated to lower the secondary-electron yield (SEY) and is biased at +45 V with a battery to maximize its collection efficiency. The average detector resolution is 4% fwhm, measured using 100-eV electrons from an electron gun.

The detectors are mounted on a 2-3/4 in. flange on a standard-aperture vacuum chamber as close to directly opposite the antechamber channel as its geometry will allow, as shown in Fig. 1. The channel allows most of the high-energy photons to escape without interacting with the chamber walls. The penetration into the vacuum chamber for the detectors was slotted for rf shielding and coupling impedance considerations. A standard BPM is mounted opposite a detector at three locations for comparison. The BPM surface area and the detector aperture are both ~ 1 cm². A removable, water-cooled, target is shown inserted in the channel to the right. Data were collected by measuring the collector current with a picoammeter as a function of bias applied to the retarding grid.

3 MEASUREMENTS

Amplification of the electron cloud due to secondary production is expected to be the most serious factor leading to a possible EC instability. Machine studies at the APS storage ring were designed to characterize and distinguish among the various contributions to the electron cloud. For a fixed beam energy, the average total number of photoemitted electrons (PE) will be linear with beam current and independent of the temporal distribution of the beam. This contribution includes photoelectrons and secondaries produced in the collision of the photons with the walls. In the absence of multipactoring effects, the electron density will depend primarily on the distance from the main electron source, the EA6 absorber, and in a minor way on electrons produced by the bending magnet radiation and x-rays that are emitted by fluorescence from EA6. In con-

* Email: harkay@aps.anl.gov

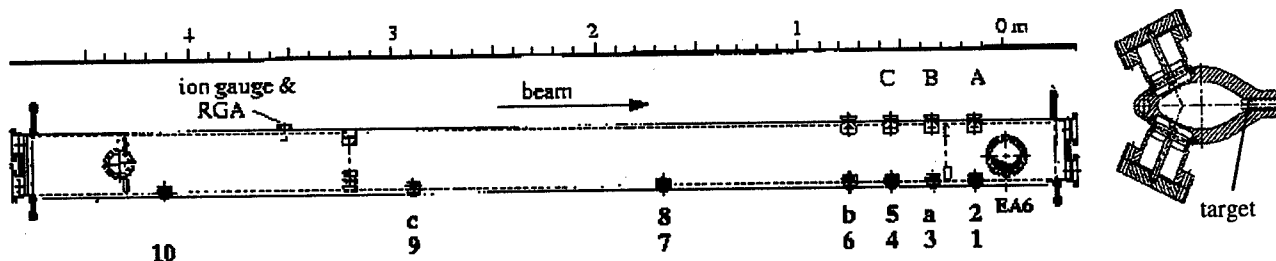


Figure 1: Modified chamber (top view) showing locations of: electron detectors 1-10; BPMs a, b, and c; and targets A, B, and C. On the right is a cross-section schematic showing target and mounting of detectors.

trast, the total number and energy distribution of secondary electrons (SE), produced in collisions with the walls by EC electrons accelerated by the beam, will be highly dependent on the bunch charge and spacing, since this determines the acceleration of the electrons (the SEY is energy-dependent).

3.1 Positrons

A typical measurement of the detector current, normalized to the total beam current, as a function of bias voltage (I-V) is shown in Fig. 2 for four of the detectors. In this example, 20 mA are stored in 10 bunches spaced at 128 rf buckets, or 0.36 μ s. The +45 V bias on the collector assures that all the electrons are collected when the bias grid voltage is positive, i.e., the peak of the I-V curve is the total number of electrons integrated over all energies. The normalized electron current at this large spacing is identical to that with a single bunch; therefore, this I-V signature is believed to be determined mostly by the PE.

The dependence on the detector location is seen in Fig. 3. As expected, EA6 is the primary source of electrons, dominating the signal at detectors 1-2 (< 0.3 m). The nearly linear slope of the normalized current at the 128-bucket spacing for detectors 4-9 (> 0.5 m) is consistent with their location.

Beam-induced Multipactoring

A dramatic amplification of the signal is observed at a 7-bucket bunch spacing (~ 20 ns), shown in Fig. 3. This can be attributed to the SE contribution. Detectors 6-9 (> 1.4 m from EA6) show a higher amplification, which we speculate comes from multiple scattering of electrons originating from the absorber. A scan in the bunch spacing (10 bunches total) gives a peak in the normalized electron current at a spacing between 8-10 buckets, shown in Fig. 4. In addition, there is a factor of 2.6 increase in the normalized electron current when increasing the beam current from 10 to 20 mA, although the position of the peak remains roughly constant. A fine scan between 1-10 bucket spacing reveals sharp peaks at 7 and possibly 9, shown in the insert. A beam instability, likely unrelated to ECI, limited the bunch current at short spacings. Figures 3 and 4 give evidence of a beam-induced multipactoring effect [6]; the bunch spacing at the peak current equals the wall-to-wall time-of-flight in the vertical direction (full height 42 mm) of electrons with an average energy of 8-12 eV.

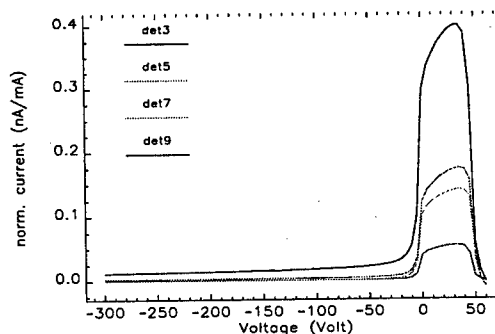


Figure 2: Normalized detector current vs. bias voltage for 10 bunches spaced by 128 buckets.

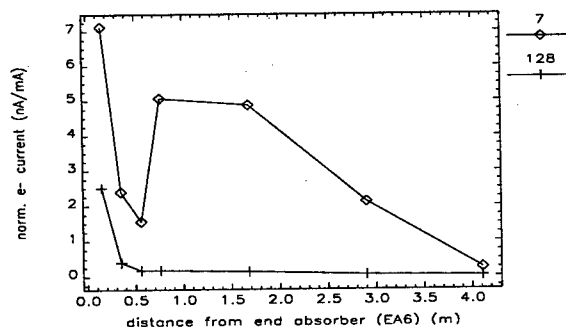


Figure 3: Total, normalized electron current per detector vs. distance from EA6 as a function of bunch spacing (10 bunches, 20 mA).

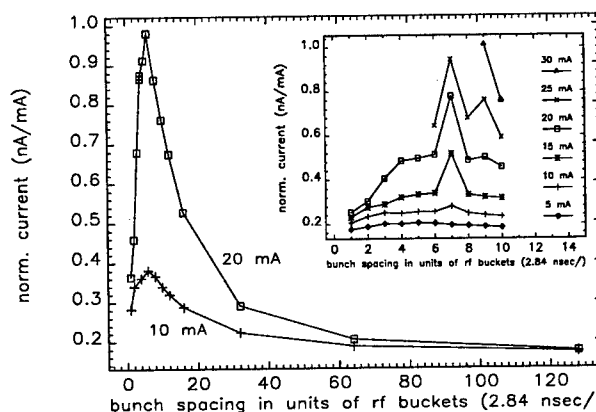


Figure 4: Comparison of normalized electron current as a function of bunch spacing and current (10 bunches total).

The electron energy distribution is dominated by low-energy electrons, seen in the derivative of the I-V curves (Fig. 5). The derivatives have been normalized to high-

light the differences in the energy distributions. The bunch spacing affects the shape of the high-energy tail, giving a longer tail for the multipactoring conditions.

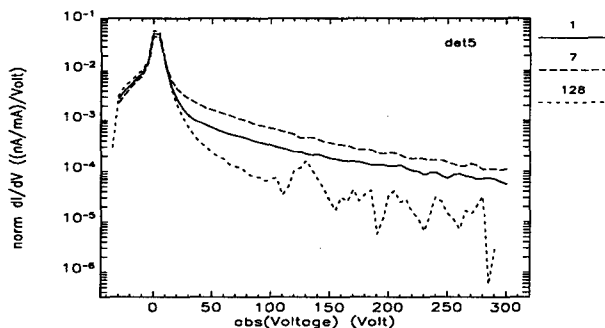


Figure 5: Electron energy distribution vs. bunch spacing.

The buildup of the EC was measured for bunch trains of varying lengths. As expected, the buildup was most pronounced at the 7-bucket spacing, and the most dramatic increases occurred for detectors farthest from EA6. Figure 6 shows the normalized current for detector 9 for bunch trains of varying length, with 1-2 mA/bunch. The total amplification at 2 mA/bunch is a factor of 360 in normalized current, and 50 times higher still in absolute electron current. A pressure rise of a factor of 20 was observed for these conditions over the pressure without multipactoring (0.5 nTorr), indicative of enhanced desorption induced by the secondary electrons, and giving independent evidence of the multipactoring effect [6]. A saturation effect is observed beyond a certain number of bunches, beyond which the increases becomes linear.

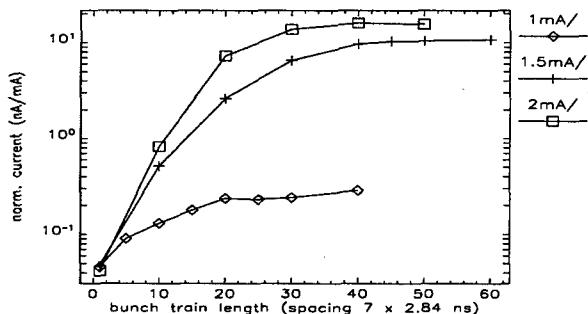


Figure 6: Amplification of EC over bunch trains.

The variation with target SEY was measured by inserting each of the targets (Cu, oxidized Al, and TiN) separately. Ratios of the detector current at 7-bucket spacing (maximum SE) and 128-bucket spacing (minimum SE) were obtained. The ratio was greatest for Al and about the same for Cu and TiN, which is roughly consistent with the relative SEY. The differences, however, were small, which is to be expected since the surface areas of the targets are small compared to that of the chamber.

The maximum, normalized detector currents decreased over time for the same beam conditions as the walls became conditioned after installation of the chamber. After an integrated current of 62.5 A-h, the PE-dominated signal

decreased by 20% and the SE-dominated signal decreased by 45%. This suggests that as the oxidized Al surface becomes more metallic as a result of conditioning, the SEY is lowered, which affects the SE to a greater degree compared to the PE.

3.2 Electrons

Conversion to electrons in Sept. 1998 allowed comparison of the electron cloud data with a positron beam. The results are qualitatively very similar. There is a peak in the normalized electron current with bunch spacing, although it occurs at an 11-bucket spacing. This is not unexpected, as the trajectories of low-energy electrons accelerated by an electron beam will differ from those by a positron beam. The buildup of the electron cloud was also observed over long trains of bunches, with a similar saturation effect. The amplification is more modest: a factor of 14 at 50 bunches with 2 mA/bunch.

4 SUMMARY

Dramatic amplification has been observed in the electron cloud in the APS storage ring under certain stored beam conditions. Beam-induced multipactoring effects gave rise to amplification factors up to 18,000 in long positron bunch trains with 2 mA/bunch, spaced at 7 rf buckets (~20 ns). A pressure rise of an order of magnitude was observed for these conditions, over that without multipactoring. More modest amplifications were seen for long electron bunch trains, but at a spacing of 11 buckets. Although the electron cloud instability is not a resonant phenomenon, beam-induced multipactoring appears to be an important effect in the amplification and buildup of the electron cloud. Preliminary results with targets of different materials show a reduction in the SE production for Cu or TiN surfaces compared to oxidized Al. Comparisons of these data with simulations are planned, with the goal of developing an empirical model for realistic chamber geometries. A detailed report is in preparation.

5 ACKNOWLEDGEMENTS

The authors would like to thank J. Galayda for the inspiration for these studies, and G. Goepfner, J. Gagliano, J. Warren, M. McDowell, and B. Yang for their technical assistance. This work was supported by the U.S. Department of Energy, Office of Basic Energy Sciences, under Contract No. W-31-109-ENG-38.

6 REFERENCES

- [1] M. Izawa, Y. Sato, T. Toyomasu, Phys. Rev. Lett. 74, 5044 (1995)
- [2] Z.Y. Guo et al., Proc. of 1997 PAC, 1566 (1998) and Proc. of 1998 EPAC, 957 (1998)
- [3] J.T. Rogers, KEK Proc. 97-17, 42 (Dec. 1997)
- [4] K. Ohmi, Phys. Rev. Lett. 75, 1526 (1995)
- [5] ANL Report Nos. ANL 87-15 (1987) and ANL/APS/TB-26 (1996)
- [6] O. Gröbner, Proc. of 10th Int'l Conf. on High Energy Accel., Protvino, 277 (1977)

IMPEDANCE AND THE SINGLE BUNCH LIMIT IN THE APS STORAGE RING

K. C. Harkay^{*}, M. Borland, Y.-C. Chae, L. Emery, Z. Huang, E. S. Lessner,
A. H. Lumpkin, S. V. Milton, N. S. Sereno, B. X. Yang, Advanced Photon Source
Argonne National Laboratory, Argonne, IL 60439 USA

Abstract

The single-bunch current limit and tune shift with current have been documented over time in the 7-GeV Advanced Photon Source (APS) storage ring as a function of lattice, chromaticity, and number of small-gap insertion device (ID) chambers. The contribution to the machine coupling impedance of the 8-mm-gap ID chambers was reported earlier [1]. One 5-mm-gap ID chamber was installed in December 1997. This required changing the lattice to preserve the vertical acceptance. The new lattice reduced the average vertical beta function at the 5-mm chamber as well as at all the other ID chambers and so has also lowered the effect of the vertical coupling impedance. As additional 8-mm and 5-mm chambers are planned, a more detailed characterization of the impedance is essential. This includes separating the effects of the transitions between the small-gap chambers and the standard chambers from the resistive wall impedance of the small-gap chambers themselves. In this paper, we report on the transverse instabilities and thresholds observed in the vertical and horizontal planes. From these observations, various contributions to the coupling impedance are derived.

1 INTRODUCTION

The maximum single-bunch current achieved in the APS storage ring under standard operating conditions is 18 mA. This current limit is most sensitive to the chromaticity, $\xi = \Delta v / \Delta p / p$. For these conditions, the chromaticity was (4, 7), where the parentheses indicate ξ_x and ξ_y in that order. The low β_y lattice installed for use with the 5-mm-gap ID chamber lowers the vertical coupling impedance, but reduces the effectiveness of the chromaticity-correcting sextupoles. The chromaticities are presently about (1.5, 4). The single-bunch current limit is subsequently reduced to ~6 mA, determined by the transverse instability threshold.

Typical multibunch user operations require less than 2 mA per bunch in "triplets" mode, and about 4 mA/bunch in "singlets" mode. Although present operations are not limited by the single-bunch current limit, additional 8-mm and 5-mm chambers are planned, which will increase the machine coupling impedance. Experimental studies were undertaken to characterize the single-bunch instabilities, and theoretical studies (modeling) are being carried out to determine the impedance model that best fits these data.

The instability threshold, growth rate, and current limit were studied as a function of chromaticity, rf voltage (bunch length), rf frequency, and orbit position. The growth rate was also measured as a function of current. The instability was monitored using beam position monitor (BPM) history modules, a streak camera, and the tune measurement system.

2 TUNE SLOPE

The present complement of twenty 5-m-long small-gap chambers results in tune slopes of -0.0026 per mA vertically and -0.0008 per mA horizontally. The vertical tune slope was reduced by 40% after reducing $\langle \beta_y \rangle$ in the ID chambers by 60%. Figures 1 and 2 show the vertical and horizontal tune waveforms, respectively, as a function of current. These were obtained by increasing the current in small steps, while using an HP89440A vector signal analyzer to record the beam response to a chirped rf signal.

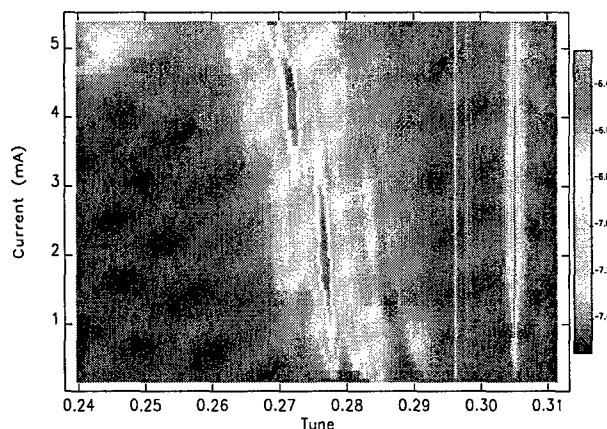


Figure 1: Vertical tune vs. single-bunch current.

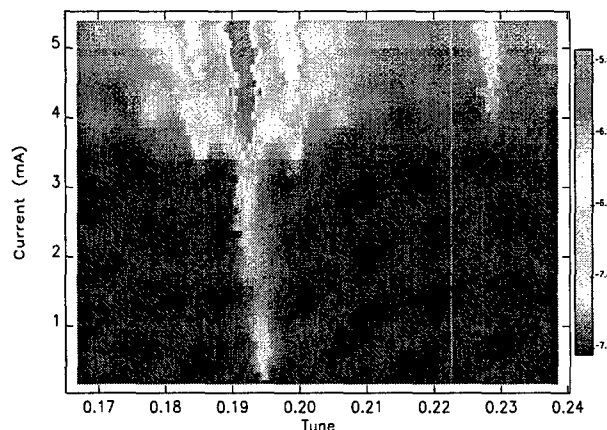


Figure 2: Horizontal tune vs. single-bunch current.

^{*} Email: harkay@aps.anl.gov

The tune waveforms show rich details of the current-dependent beam response. In the vertical plane, the tune (mode 0 is 0.285 at low current) crosses two synchrotron sidebands as the current increases. The synchrotron tune is 0.007 at the nominal rf voltage of 9.4 MV. The tune appears to just reach mode -3 at the current limit of 5.5 mA. In the horizontal plane, a self-excited tune appears above 3.5 mA. The tune shift over the range is about -0.005 (mode 0 is 0.195 at low current), approximately equal to the synchrotron tune. It appears that the horizontal tune begins to couple to mode -1 near the current limit. At large signal amplitudes, the tune is itself modulated at the synchrotron frequency, which appear as sidebands.

The APS was switched from positron to electron operations in Sept. 1998, and no significant differences in the transverse instability limits were seen.

3 VERTICAL

In order to study the transverse planes independently, the vertical chromaticity was reduced while keeping the horizontal almost constant: (1.0, 1.4). The single-bunch limit was reduced to 1.9 mA, the lifetime was severely shortened, and the vertical modes 0 and -1 collided. This is consistent with the tune "map" in Fig. 1.

4 HORIZONTAL

Observations of the horizontal instability reveal a higher degree of complexity compared to the vertical. It is characterized by a self-excited horizontal tune at a threshold of about 4 mA. Above 4.7 mA (nominal conditions), a periodic blowup of betatron oscillations of the bunch centroid occurs. This can be seen in Fig. 3, which shows a BPM history recording the x-position over 16,000 turns (acquired every turn) with 5.2 mA. The maximum, self-limiting amplitude of the instability is 800 μm . This is roughly 1.9 times the horizontal rms beam size.

This observation is confirmed using a visible streak camera to image the bending magnet radiation. Figure 4 shows an image acquired in dual-sweep mode. The horizontal beam profile was captured on two time scales: T_1 , which is fast compared to the betatron period, and T_2 , which is slow compared to the instability rise time. Two cycles are seen of the periodic betatron oscillations. Notably, σ_x does not appear to blow up as the coherent centroid motion decays. Within the spatial resolution, no head-tail motion was detected using streak camera imaging of the x-t plane in synchroscan mode.

The instability growth rate, $1/\tau_g$, was computed as a function of current by fitting the initial blowup in data such as in Fig. 3, and using $1/\tau_{\text{fit}} = 1/\tau_g - 1/\tau_d$, where τ_d is the transverse radiation damping time of 9.46 ms at 7 GeV. The results are shown in Fig. 5. A preliminary analysis of the amplitude-dependent tune shift was made by performing a fast Fourier transform on the BPM history data in 512-point slices. The horizontal tune peak was

fitted to find the frequency. The tune variation with amplitude appears to match a quadratic fit.

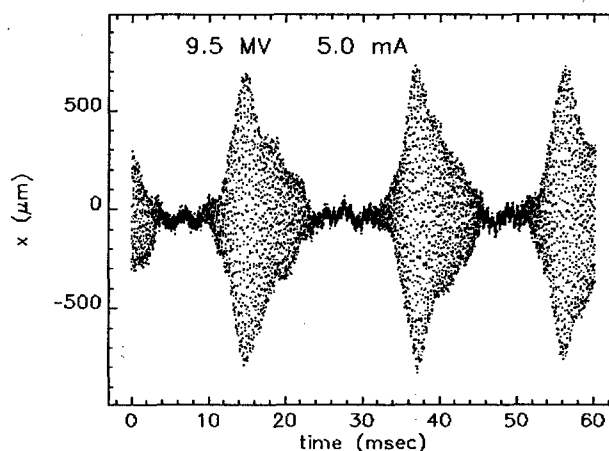


Figure 3: Periodic blowup of horizontal centroid motion.

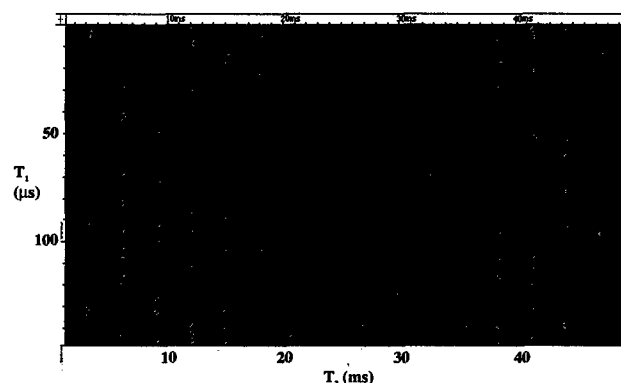


Figure 4: Horizontal oscillations observed using a streak camera in dual-sweep mode.

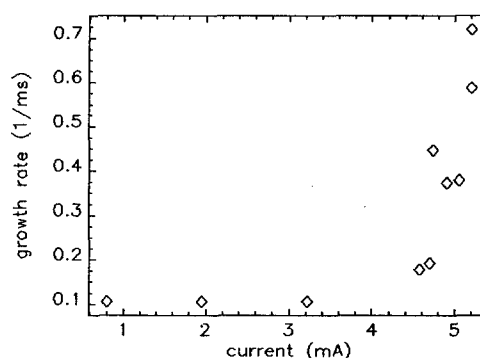


Figure 5: Instability growth rate vs. current.

4.1 Chromaticity

At the threshold of 4.7 mA, the periodic instability mode could be stabilized with a $\Delta\xi_x$ of 0.6 above nominal. The instability growth rate increased approximately linearly with negative changes in ξ_x . The instability threshold was not sensitive to even large variations in the tune.

4.2 Rf voltage

The rf voltage was reduced from 9.5 MV to 7.1 MV, resulting in a 20% increase in the bunch length at 5 mA. The

current limit increased slightly, from 5.0 mA at 9.5 MV to 5.5 mA at 7.9 MV and 5.7 mA at 7.1 MV. More interestingly, with 7.9 MV, the beam underwent periodic blowups around 4.7 mA, but this changed to steady-state, fixed-amplitude betatron oscillations at higher currents up to the limit of 5.5 mA (see Fig. 6). The amplitude of the motion at this limit was about 2/3 of the peak value in the blowup mode. At 7.1 MV, only steady-state oscillations were seen; no blowups were observed at any current up to the limit. In all cases, the threshold for the onset of the self-excited horizontal tune remained about the same.

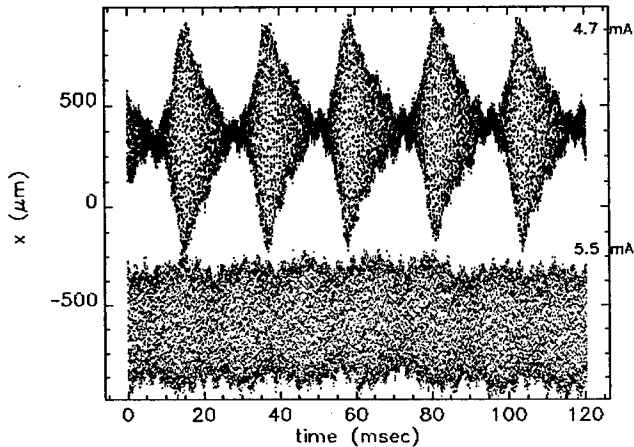


Figure 6: Instability as a function of current at 7.9 MV (plotted offset for clarity).

4.3 Rf frequency and orbit

Orbit bumps were used to couple more strongly to the transverse impedance at various places in the ring: 5-mm-gap chamber, 19-mm-gap chamber with unique transitions to the standard-aperture chambers, rf cavities, and injection region (septum magnet and kicker chambers.) No changes were seen in the instability growth rate for either vertical or horizontal orbit bumps with one exception. A +1.5 mm vertical bump in the 5-mm gap chamber stabilized the periodic instability mode horizontally. In addition, changes of ± 110 Hz in the rf frequency also stabilized this mode.

5 SIMULATIONS

Tracking simulations employed the 6-D tracking program *elegant* [2]. Resonator impedances are implemented using the following algorithm. A histogram of current density (or its first moment for transverse impedances) is first made. The resonator voltage vs. bin is then obtained by summing the phasor contributions of particles in preceding bins. Particles see only one-half their own induced voltage (fundamental theorem of beam-loading). The voltage is propagated turn-to-turn as a damped sinusoidal oscillation. Tests show excellent agreement with analytical wakefield expressions. *elegant* includes synchrotron radiation damping and quantum excitation, implemented

approximately using the nominal damping decrements and excitation rates.

Simulations of a broad-band resonator (BBR) impedance model ($Q=1$) reproduced the measured tune slopes, namely, $-0.0008/\text{mA}$ in the horizontal, and $-0.0026/\text{mA}$ in the vertical plane. Cutoff frequencies of 5 GHz in the horizontal and 25 GHz in the vertical plane were assumed, determined by the small-gap chambers. The simulations assumed a linear lattice (zero chromaticity) to save computation time. The best fit to the measured values were obtained for a shunt impedance, R_s , of $0.2 \text{ M}\Omega/\text{m}$ in the horizontal plane and $1.2 \text{ M}\Omega/\text{m}$ in the vertical plane. The vertical impedance agrees well with the $53 \text{ k}\Omega/\text{m}$ per chamber effective impedance value estimated in [1].

A mode-coupling instability (between modes 0 and -1) occurs around 4.4 mA (horizontal) and 2.2 mA (vertical), nearly reproducing the experimental observations under low chromaticity conditions. Preliminary simulations using a BBR and a fully nonlinear lattice at the nominal chromaticities show some of the instability features, but do not reproduce the periodic blowup seen experimentally.

6 SUMMARY

The single-bunch current limit is believed to be dominated by a horizontal instability because of the smaller ξ_x , compared to ξ_y . Attempts to raise the instability threshold by raising the chromaticity is hampered by the sextupole current limit. The vertical tune slope ($\propto \langle \beta \rangle R_s$) is larger than in the horizontal plane, but the beam is stable to mode -3 with $\xi_y = 4$. In the horizontal plane, mode -1 is unstable with $\xi_x = 1.5$. The instability exhibits two modes: periodic blowup and steady-state. The current threshold of the periodic mode decreases with both smaller chromaticity (i.e., tune spread) and shorter bunches (i.e., higher peak current), and the instability growth rate changes linearly with the current. Simulations reproduce the current-dependent tune shift and mode-coupling instability thresholds using a BBR model. The periodic instability mode will be further explored through fully nonlinear simulations. Future machine studies include: additional chromaticity correction, measure the bunch length on the instability time scale, test a single-bunch feedback system and its effect on the instability threshold, and repeat the studies at lower energy.

7 ACKNOWLEDGEMENTS

The authors would like to thank E. Crosbie for ongoing lattice calculations. This work was supported by the U.S. Department of Energy, Office of Basic Energy Sciences, under Contract No. W-31-109-ENG-38.

8 REFERENCES

- [1] N. S. Sereno, Y.-C. Chae, K. C. Harkay, A. H. Lumpkin, S. V. Milton, B. X. Yang, Proc. of 1997 PAC, 1700 (1998)
- [2] M. Borland, User's Manual for *elegant*, v. 12.4, ANL Note LS-231 (1995), also www.aps.anl.gov/asd/oag/oagSoftware.shtml

EFFECTS OF A HARMONIC CAVITY AT THE ESRF

J. Jacob, O. Naumann, W. Beinhauer, ESRF, Grenoble, France

Abstract

The installation of a harmonic cavity to provide bunch lengthening and thereby increase the Touschek lifetime is considered for the ESRF storage ring. Simulations with a particle tracking code have shown that for few bunch operation - where the current per bunch is large - a strong lengthening already results from the coupling with the broad band impedance of the vacuum chamber. Therefore the net gain with an additional harmonic cavity is only moderate. For multibunch operation, however, where the current per bunch is small, a harmonic cavity is expected to increase the bunch length by up to a factor six, with a corresponding increase in Touschek lifetime. The Landau damping provided by the additional non-linearity of the RF voltage has also been studied in detail. As an important and somewhat surprising result, it turns out that the thresholds for longitudinal coupled bunch instabilities may even be reduced when the operation parameters of the harmonic cavity are optimised to provide a maximum bunch lengthening.

1 INTRODUCTION

The installation of more and more narrow gap insertion devices at the ESRF has increased the transverse impedance of the storage ring. Since this has lowered the head-tail stability limits, higher chromaticities have to be used as a remedy. This, however, reduces the dynamic aperture and the energy acceptance, with the further consequence of a lower Touschek lifetime, especially in single and few bunch filling, where the current per bunch is high. To optimise the Touschek lifetime in few bunch operation, the acceleration voltage used to date at the ESRF is around 8 MV instead of the possible 12 MV: this maximises the bunch length without penalising the energy acceptance. Lengthening the bunches also has the beneficial side effect of an increased head-tail stability limit, since the overlap of the beam spectrum with the broadband impedance is smaller for longer bunches.

A precise control of the bunch length without reduction of the RF-acceptance should be possible with a higher harmonic cavity. This paper summarises the possible performance upgrade with such a cavity for the ESRF storage ring. Section 2 describes the achievable bunch lengthening as a function of the harmonic number n and a deviation from the optimum working point. The expected gain in bunch length for single and few bunch operation is presented in section 3, taking into consideration the already strong effect from the impedance of the

storage ring. The results from a detailed analysis of the effect on longitudinal coupled bunch instabilities, taking into account Landau damping which results from the non-linearity in the RF-voltage, are given in section 4.

2 BUNCH LENGTHENING WITH A HARMONIC CAVITY

A double RF-system allows to shape the accelerating voltage at the time of passage of the synchronous particle [1]. Both the relative phase and the harmonic voltage level V_H can be used to adjust the harmonic system. Two conditions allow the determination of the operation values for optimum bunch lengthening: firstly, for maximum bunch length the slope of the accelerating voltage has to be horizontal at the bunch centre and, secondly, the accelerating voltage should not be curved at this point, to avoid the forming of micro-bunches. In order to maintain the same time of synchronous passage, it is additionally necessary to adjust the amplitude of the normal voltage by a factor slightly different from unity. All these quantities can be expressed in terms of the time of synchronous passage and the harmonic number n .

Fig. 1 shows how the zero current bunch length varies in the case of the ESRF as a function of the harmonic voltage level V_H . Since the maximum bunch lengthening factor, of approximately 6 for $n=3$, is reached only very close to the optimum value V_{OPT} for V_H , finding and maintaining a good working point is likely to become a delicate operation as very precise control of the cavity parameters is necessary.

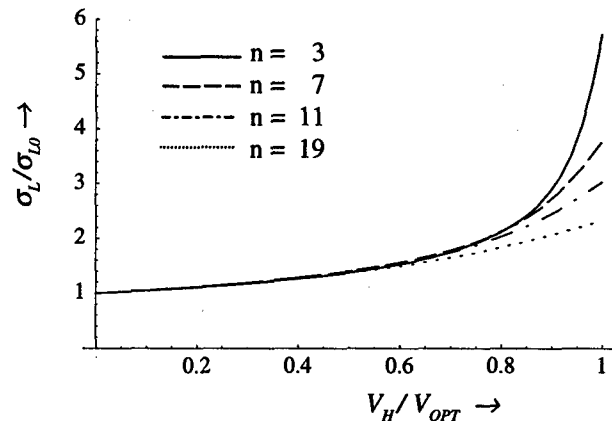


Figure 1: Bunch length σ_L as a function of the harmonic voltage level (σ_{L0} : bunch length for $I_b=0$ and $V_H=0$)

Fig. 1 also shows how a variation of the harmonic number n influences the dependency of the bunch

lengthening factor on the harmonic voltage. Although values of $n > 7$ are of merely academic interest, the comparison shows how the choice of a higher value for the harmonic number n reduces the sensibility on the harmonic cavity parameters. This means easier operation conditions, but limits the maximum possible increase in bunch length.

3 PARTICLE TRACKING FOR HIGH CURRENT PER BUNCH

With increasing current per bunch, several effects occur. Firstly, transverse head-tail instabilities have to be mastered by operating the storage ring with an increased chromaticity, which unfortunately also reduces the dynamic energy acceptance and the associated lifetime. Secondly, the higher charge density increases the Touschek effect, leading to an overall lifetime of the order of 4 hours in single bunch operation at 15 mA and about 9 hours in 16 bunch operation at 90 mA. This already takes into account the high natural bunch lengthening due to the interaction with the broadband impedance of the ring, as well as the choice of a rather low accelerating voltage of 8 MV, as a compromise between a maximum bunch length and sufficient RF-acceptance.

The gain in bunch length that could be obtained with a third harmonic cavity has been evaluated by adapting a multiple particle tracking code. It solves the synchrotron equation turn by turn, taking into account the broadband resonator model BBR ($Q=1$, $R=42 \text{ k}\Omega$, $f_r=30 \text{ GHz}$) of the ESRF storage ring [2]. For the present study, the code has been modified to incorporate the harmonic voltage distortion, assuming an optimum amplitude and phase of the modulating voltage.

Table 1

Current per bunch	10 mA	15 mA	25 mA
Lengthening factor from BBR only	3.6	4.2	5.4
Lengthening factor from BBR and 3 rd harmonic cavity	6.2	6.6	7.6
Net gain in bunch length with a harmonic cavity	+ 72 %	+ 57 %	+ 41 %

In the limit of zero current, the simulations confirmed the theoretical bunch lengthening by a factor 6 for $n=3$ in Fig. 1. They also confirmed that the energy spread is only affected by the BBR and not influenced by the presence of a harmonic cavity. As shown in table 1, for the nominal single bunch current of 15 mA, the interaction with the BBR already lengthens the bunch by a factor 4.2, so that a harmonic cavity would at best give 57% additional lengthening.

If a passive cavity is to be used, it must exhibit a shunt resistance of the order of several 100 M Ω in order

to provide the optimum harmonic voltage with a driving current of about 10 mA. The only feasible options would therefore be either a passive superconducting or an active normal conducting cavity. The final choice, however, needs further investigations.

4 EFFECT ON MULTIBUNCH OPERATION

The effect of main interest in the application for multi-bunch operation is the increase of the Touschek lifetime, that accompanies the increased bunch length, especially in the case where the effect of an increased energy acceptance has an upper limit, as is the case at the ESRF. In multi-bunch operation the per-bunch current intensity is small (of the order of tenths of mA), therefore single-bunch effects such as the head-tail instability play only a minor role. Still, the additional bunch lengthening should allow a further reduction of the chromaticity.

As far as the effect on multi-bunch instabilities is concerned, it is commonly assumed that the spread in synchrotron frequencies within a bunch due to the distorted RF-voltage leads to increased stability limits because of the additional Landau damping. A closer investigation, however, reveals that this need not necessarily be the case.

4.1 Effect on the synchrotron frequency density

The density ρ of the synchrotron frequency f_s can be calculated using the formula

$$\rho(f_s) = -T^2(H)\psi(H)\left(\frac{dA}{dH}\right)\left/\left(\frac{dT}{dH}\right)\right.$$

where A and T are the quantities defined on page 3 of [1]. Inverting the relation $T(H)$ gives a function in $f_s = 1/T(H)$.

Curve parameter, from left to right:

$V_H/V_{OPT} = 100\%, 87\%, 75\%, 66\%, 50\%, 33\%, 25\%, 0\%$

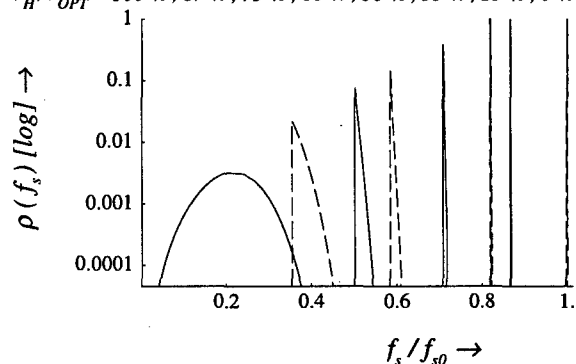


Figure 2: Synchrotron frequency distributions for various levels of harmonic voltage and $n = 3$

Fig.2 shows a sequence of densities for the case $n=3$. The natural frequency density spread for $V_H=0$ is extremely small, because the non-linearity is weak. With

a change in operation parameters, the centre of the distribution is shifted towards smaller frequencies and the spread increases, although only considerably so close to the optimum choice of operation parameters. This can be explained from the fact, that - especially for a small harmonic number - the accelerating voltage is distorted on a scale much larger than the bunch. Thus, switching on the modulation changes the voltage slope for all particles in almost the same way, the bunch being too short to profit from the additional non-linearity. Consequently the synchrotron frequency density is not spread out, but is shifted in the mean because of the overall reduced slope. It is only as the optimum voltage is approached, that the bunch becomes large enough for some particles to reach the region of increased non-linearity, which then increases the frequency spread.

4.2 Dispersion relation and threshold current

In order to determine the net effect on longitudinal multi-bunch instability thresholds due to cavity higher order modes (HOM), a dispersion relation has to be solved. The values entering into it are the impedance Z_{HOM} and the resonance frequency f_{HOM} of the HOM and several machine parameters: α (momentum compaction), E_0 (energy), T_0 (revolution time), and δ_n (natural radiation damping).

$$1 = j \frac{\alpha 2\pi f_{HOM} Z_{HOM} I_b}{T_0 E_0 / e} \int \frac{\rho(\omega'_s) d\omega'_s}{\omega'^2_s - \omega^2 + 2j\delta_n \omega}$$

This has to be solved for the real coherent synchrotron frequency ω and the beam current I_b in order to determine the threshold current I_{th} [3].

The threshold current I_{th} can be plotted as a function of V_H by applying this formula, as is shown in Fig. 3. Increasing V_H , one first observes a decrease of I_{th} , up to a turning point, which is reached earlier the larger n is, but in any case a valley of decreased stability always has to be crossed.

4.3 Application to the ESRF

Investigating the values for the optimum operation parameters that can be seen on Fig 3, we discover that a value of $n > 7$ would at least allow to break even as far as thresholds are concerned. However, in order to provide real protection against instabilities, a much higher value would be necessary. Then, of course, one has to pose the question of how to construct a harmonic cavity with a high n . Such a choice would also be discouraged as the optimum gain in bunch length would be much smaller (Fig. 1).

Therefore, one important result is that for the practical choices of $n=3$ or 5, additional means to damp or tune HOMs away from synchrotron sidebands are necessary, if a harmonic cavity is not to seriously

compromise the multi-bunch instability thresholds. At the ESRF, this can be achieved with the recently commissioned highly accurate temperature control system for the accelerating cavities (error < 0.1°C).

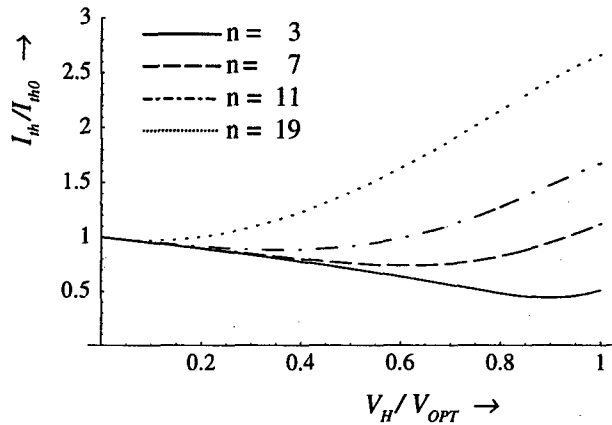


Figure 3: Multibunch instability threshold I_{th} as a function of the harmonic voltage (I_{th0} : value for $V_H = 0$)

An interesting alternative would be to operate the harmonic system at a frequency of a multiple of the RF-frequency plus the revolution frequency ("harmonic plus one" cavity). This modulates the RF-voltage around the circumference of the storage ring and provides a bunch-to-bunch frequency spread, which has a much stronger Landau damping effect [4]. This, however, still requires some investigation.

5 SUMMARY AND CONCLUSIONS

A harmonic cavity at the ESRF would provide only a limited net increase of the bunch length for single and few bunch operation, because of the already strong lengthening due to the broadband impedance. For standard multi-bunch operation, however, the net increase can be much larger. The somewhat higher sensitivity to multi-bunch instabilities can easily be overcome by means of the cavity temperature control.

6 REFERENCES

- [1] A. Hofmann and S. Myers, "Beam Dynamics in a double RF System", In W.S. Newman, editor, Proc. Of the 11th International Conference on High Energy Accelerators, pp 610-614, Boston, (1980)
- [2] G. Besnier, T.F. Günzel, J.-L. Laclare, C. Limborg, "Simulation of the Evolution of a Bunch due to the Machine Impedance", 10th ICFA Beam Dynamics Panel Workshop on 4th Generation Light Sources, Grenoble, (1996)
- [3] O. Naumann and J. Jacob, "Fractional Filling Induced Landau Damping of Longitudinal Instabilities at the ESRF", PAC'97, Vancouver, (1997)
- [4] O. Naumann and J. Jacob, "Landau Damping of Longitudinal Instabilities for the Operation of the ESRF Storage Ring", EPAC'98, Stockholm, (1998)

OPTIMAL BEAM OPTICS IN THE TTF-FEL BUNCH COMPRESSION SECTIONS: MINIMIZING THE EMITTANCE GROWTH

M. Dohlus, A. Kabel*, T. Limberg
Deutsches Elektronen-Synchrotron DESY
Notkestr. 85, D-22607 Hamburg, Germany

Abstract

In the bunch compressing sections of the Tesla Test Facility Free Electron Laser, short bunches travel on trajectories with small bending radii. Thus, coherent synchrotron radiation (CSR) will play a significant role in beam dynamics. The energy loss of the bunch will vary longitudinally as well as transversally across the bunch and will induce an emittance growth. This emittance growth will affect the projective as well as the slice emittance (i.e., the emittance of sub-ensembles of particles with equal longitudinal position). The computer code TraFiC⁴ is a significantly augmented version of WAKE, which calculates these effects from first principles. One result of simulations is the observation that the slice emittance growth depends crucially on the initial Twiss parameters chosen for the beam. We discuss the mechanisms leading to this dependence. Simulation results for a range of optics will be given.

1 INTRODUCTION

The Tesla Test Facility (TTF) aims to conduct a proof-of-principle experiment for a self-amplified spontaneous emission free electron laser. (SASE FEL). For FEL operation, high peak currents and low transversal emittances are crucial. To reach these quality conditions, the bunch has to be compressed longitudinally after it leaves the gun. In the case of the TTF FEL experiment, this is done in magnetic chicanes. Bunch Compressor II, which has been commissioned recently [1], is the only chicane to be used for the proof-of-principle experiment.

All subsequent calculation are for the BC II design values; i. e. $E = 140\text{MeV}$, $Q = 10^{-9}\text{As}$, $\sigma_{l,\text{initial}} = 1\text{mm}$, $\sigma_{l,\text{final}} = 250\mu\text{m}$. The initial emittance used is $\epsilon_{N,i} = 0.85 \cdot 10^{-6}\text{m}$, in accordance with simulations¹ for the FEL Gun emittance.

A further stage of FEL operation, using smaller wavelengths, higher energy and a longer undulator, requires another stage of compression (Bunch Compressor III) [2]. The low-energy stage Bunch Compressor I will not be used for FEL operation.

When a short charged bunch travels on a bent trajectory, coherent interaction of the bunch's tail with its head (as opposed to usual wake field behavior) may occur. This is

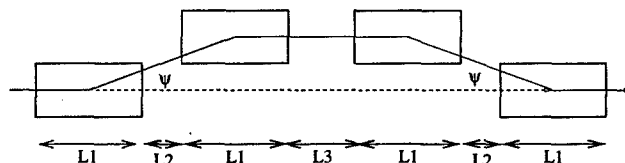


Figure 1: Geometry of BC II: $L_1 = L_2 = 0.5\text{m}$, $L_3 = 1.3\text{m}$, $\psi = 17^\circ \dots 21^\circ$

expected to be the main cause of emittance dilution in the TTF bunch compression sections [3, 4, 5, 6].

2 SLICE EMITTANCE GROWTH

TraFiC⁴ is a code written by the authors which allows the numerical computation of these emittance-diluting mechanisms. It is a full three-dimensional tracking code which calculates the fields acting on the particles from first principles. It allows for the calculation of the slice emittance, i. e., the emittance of a longitudinally small sub-ensemble of the bunch. In the FEL process, only particles from within a certain *slippage length* interact. The saturation length of the process will be affected by the transverse emittance of the sub-ensemble within that slice, while the overall (or *projective*) emittance only affects beam optics and the brightness of the FEL photon beam. Thus, the slice is the primary quantity to use to judge beam quality. The TTF FEL requires a slice emittance of $\epsilon_N < 2 \cdot 10^{-6}\text{m}$. (In this paper, we use the normalized statistical slice emittance ϵ_N with a slice length of $10\mu\text{m}$ and its counterpart ϵ_N^β (which is conserved even in dispersive regions for $\delta' = 0$), where $(x, x')^\beta = (x, x') - \delta(\eta, \eta')$. (x refers to the bending plane of motion.)

When one considers a true slice, i. e. an ensemble whose correlation matrix projects to the, x, x' subspace, a linear transformation would not generate a dependence of emittance growth on initial Twiss parameters.

Doing exact tracking calculations, however, one finds quite a different behavior: the slice emittance growth depends sensitively on the initial correlation matrix of the incoming slice. We thus can infer that nonlinear effects are an important source of emittance growth.

This fact can also be concluded from typical phase-space portraits of the chicane, indicating an effective sextupole moment in the transport map.

Consequently, the TraFiC⁴ code has been augmented to

*E-Mail: andreas.kabel@desy.de

¹Zhang Min, private communication

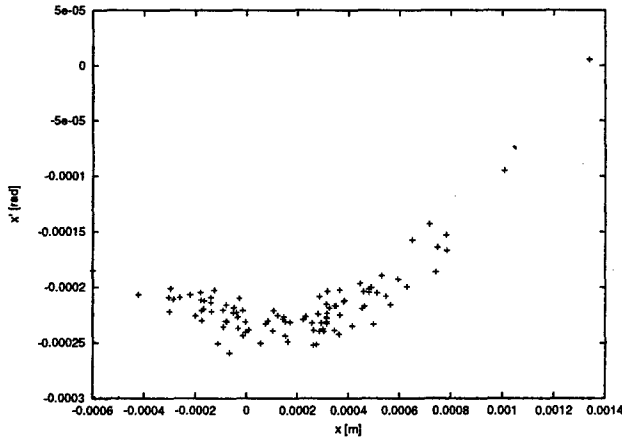


Figure 2: Transverse phase-space portrait of an initially ellipsoidal-gaussian bunch after traveling through the chicane. $\beta_i = 30\text{m}$, $\epsilon_{N,i} = 10^{-6}\text{m}$, $\alpha_i = 0$, $Q = 10^{-9}\text{As}$.

extract nonlinear matrix elements from the transport of the slice through the chicane under the influence of the self-field.

Expanding the transfer map into a power series, one has

$$\bar{x}_i = \sum_{n=0}^{\infty} \sum_{k_1 \dots k_n=1}^6 C_{k_1 \dots k_n}^{(n)} x_{k_1} \dots x_{k_n},$$

where C^1 is the usual linear transport matrix.

The coefficients $C^{(n)}$ can be read off the transport function through the chicane by tracking an appropriate number of polynomially independent particles and approximating derivatives by difference quotients. For the time being, we are restricted to coefficients up to second order, for which this procedure is quite straightforwardly implemented.

Looking at the dominant coefficients for transverse movement, one finds that, for example, C_{111}^2 is in the order of magnitude of $10^5/\text{m}$, resulting in a significant contribution for realistic beam dimensions.

2.1 EMITTANCE GROWTH MECHANISMS

While traveling on the bent trajectory, the test particles will experience collective radiative forces of the bunch as a whole. One has a force longitudinal to the direction of motion, which will induce an energy change, and a transverse force, which will kick the particle of its design orbit. The former causes an angular kick in the dispersive region. Both forces lead to slice emittance growth; in the case of BC II, the growth is clearly dominated by the longitudinal forces, which can be seen by turning off the transverse kicks in the TraFiC⁴ tracking simulations. Thus, the problem is virtually planar, i. e. the motion of the bending plane is decoupled from the one perpendicular to it, in which emittance growth is benign, and we will ignore (y, y') space in the sequel.

2.2 OPTICS DEPENDENCE

We can expect emittance growth due to non-linear dependence of the perturbing fields on the phase space coordinates. In principle, making the bunch extension as small as possible in all directions cures all non-linear effects and we are left with the linear part of emittance growth, so a beam approaching zero-emittance should be left with only the linear effects acting on the emittance.

Starting with a finite-emittance beam, however, the Twiss parameters must be subject to optimization. Making $\langle x^2 \rangle$ as small as possible will minimize sampling the nonlinear force component F_{\parallel} components, due to both the reduced size of the sampling slice in the transverse and longitudinal direction.

There are two trade-offs, however: (1) higher $\langle x'^2 \rangle$ will lead to an induced uncorrelated energy spread, because, to first order, $p_0 \delta' = F_{\parallel} + x' F_{\perp}$ (where the subscripts refer to the design orbit, not the individual particles). Thus, at some point the effects due to the transverse force F_{\perp} will be stronger than the ones due to the variation of F_{\parallel} . One can estimate this break-even point to be at $\beta_{\min} \approx \frac{R(F_{\perp})}{\langle F_{\parallel} \rangle}$, which is well below 10cm for BC II. (2) The chicane behaves (in the horizontal plane) basically like a drift space, i.e., a low minimum β will lead to a high variation in β and thus to uncompensated (see below) sampling of non-linear field components.

The matter is further complicated by the fact that the change in beam dimensions changes not only the sampling range of the test particles, but also the shape of the sampled fields. It turns out, however, that the latter dependence is quite weak as long as the bunch is slim.

The longitudinal fields vary both longitudinally and transversally (for analytic expressions for special cases, cf. [4]). The longitudinal fields scales with the bunch length as $l^{-\frac{4}{3}}$, so one can expect the dominant contribution in the 3rd magnet (where the bunch reaches its final length) and 4th magnet (where the dispersion is closed).

Thus, reduction of the slice emittance growth can be achieved by minimizing the longitudinal dimensions of the bunch as it travels along the chicane. A slice can acquire longitudinal dimension by its initial uncorrelated energy spread and due to its betatron movement. For the transverse slice, where $\eta^2 \langle \delta^2 \rangle \ll \langle x^2 \rangle$, the slice length is dominated by the β function.

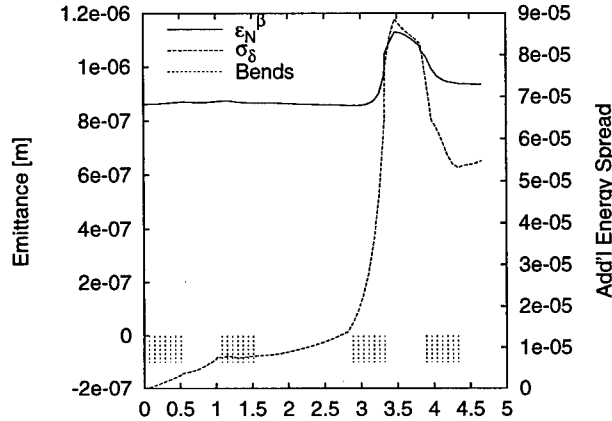
Since in a quadrupole-less magnetic chicane the curvatures of the bending magnets have signature $+- - +$, the sign of the transverse gradient of the longitudinal field between the magnets changes. A test particle on the concave side of the 3rd bend will be on the convex side of the 4th bend, so in principle the net transverse energy spread will average out.

As the bunch length of the field-generating bunch and its longitudinal distribution changes between magnets, the sampling particles change their relative longitudinal position with respect to the generated field. The field itself will grow in magnitude, as the bunch shortens. Thus, one can-

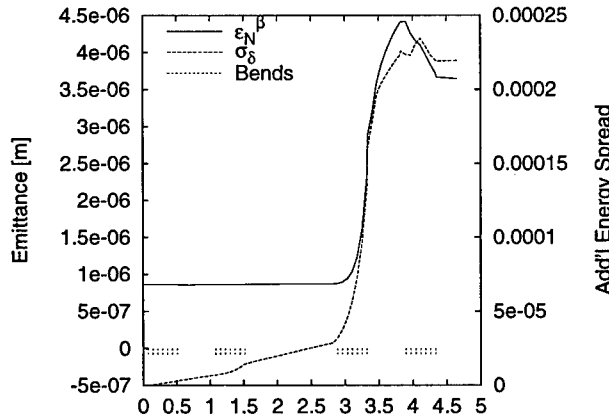
not expect this cancellation to be complete.

However, the energy spread can actually decrease within the compressor, which may lead to a decreasing induced angular spread and, consequently, a subsequent lowering of the emittance, which may—in principle—go down to its initial value again. Due to the non-linear components of $F_{||}$, this mechanism depends on beam dimensions. This mechanism can be observed in figures 2.2,2.2. Similar effects have been exploited in [7].

$\langle \delta^2 \rangle$ and ϵ_N^β along the beam line of BC II: $\alpha_i = 1, \beta_i = 15\text{m}$



$\langle \delta^2 \rangle$ and ϵ_N^β along the beam line of BC II. $\alpha_i = 3, \beta_i = 3\text{m}$

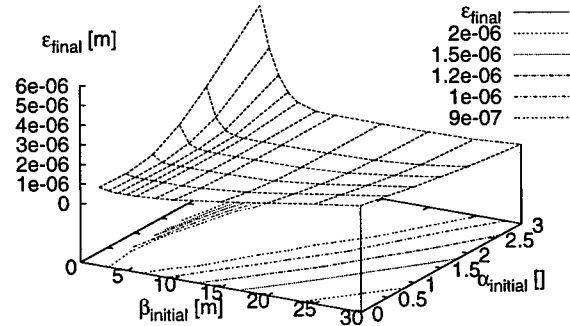


3 RESULTS

The TraFiC⁴ code was used to calculate the emittance growth for a transverse slice of test particles for a range of initial Twiss parameters. The design parameters of BC II were used. The results are shown in fig. 3. As could be expected from the discussion above, a range of low emittance growth is enclosed by high emittance dilutions both for large and for small β functions.

In terms of beam envelopes, the low ϵ region corresponds to flat $\langle x^2 \rangle(s)$ behavior. The waist of the advantageous $\langle x^2 \rangle(s)$ functions is near the 3rd and 4th magnet,

Figure 3: Final emittances for a scan of initial Twiss parameters.



thus causing compensation of energy kicks and minimizing sampling of non-linearities in the region of high field amplitudes.

4 CONCLUSION

We have shown that the slice emittance growth in a magnetic chicane can depend heavily on the initial beam parameters chosen, contrary to naïve expectations based on linear estimates. The nonlinear part of the slice emittance growth can be reduced by an appropriate choice of the initial Twiss parameters. For the case of BC II at TTF, the design parameter set should allow a feasible set of optic parameters compatible with the requirements of FEL operation.

5 REFERENCES

- [1] M. Geitz, A. Kabel, G. Schmidt for the TTF collaboration, "Commissioning of BCII", this conference (unpublished)
- [2] D. A. Edwards (Ed.), TESLA Test Facility LINAC - Design Report, DESY Print March 1995, TESLA 95-01
- [3] Ya. S. Derbenev, J. Rossbach, E. L. Saldin, V. D. Shiltsev, "Microbunch Radiative Tail - Head Interaction". DESY PRINT-98-023, Sep 1995. 12pp.
- [4] Ya. S. Derbenev, V. D. Shiltsev, "Transverse Effects of Microbunch Radiative Interaction". SLAC-PUB-7181, May 1996.
- [5] M. Dohlus, A. Kabel, T. Limberg, "Wake Fields of a Bunch on a General Trajectory Due to Coherent Synchrotron Radiation", DESY-M-97-10J, August 1997
- [6] M. Dohlus, A. Kabel, T. Limberg, "Uncorrelated Emittance Growth in the TTF-FEL Bunch Compression Sections Due to Coherent Synchrotron Radiation and Space Charge Effects", Proceedings of the 6th European Particle Accelerator Conference, 1998
- [7] P. Emma, R. Brinkmann "Emittance Dilution Through Coherent Energy Spread Generation in Bending Systems", SLAC-PUB-7554, May 1997

LONGITUDINAL IMPEDANCE TUNER USING HIGH PERMEABILITY MATERIAL

K.Koba¹, D.Arakawa, M.Fujieda, K.Ikegami, Y.Ishi, Y.Kanai, C.Kubota, S.Machida, Y.Mori, C.Ohmori, K.Shinto, S.Shibuya, A.Takagi, T.Toyama, T.Uesugi, T.Watanabe, M.Yamamoto, T.Yokoi, and M.Yoshii, *KEK, Tsukuba, Japan*

Abstract

We have succeeded in canceling longitudinal space charge effects using the 'impedance tuner'[1][2][3] at the KEK-PS. The impedance tuner consists of the new material, 'FINEMET'[4][5][6][7] which has large permeability over the beam spectrum region. A frequency shift of coherent quadrupole mode is measured to infer the modified impedance. It turns out that nonlinearity unavoidable in a longitudinal rf bucket has to be treated carefully in order to digest observed beam signals. We will describe how to measure the impedance from the beam signal, how to analyze the effect of impedance tuner, and how to succeed in canceling space charge effects.

1. INTRODUCTION

In a high intensity proton synchrotron, some of the emittance growth and beam instabilities are caused by space charge effects. In the longitudinal phase space, the space charge forces weaken the rf focusing force. When a short bunch is required, for example in a proton driver of a muon collider, the effects are further enhanced and they limit the minimum bunch length.

An inductive device in a ring should be able to cancel the space charge force. Recently a very high permeability material, FINEMET, becomes available. It turns out that the material has enough permeability at the beam frequency region and possibly cancels the space charge impedance. We designed a device, and named it "impedance tuner". It consists of FINEMET cores and is installed in the KEK PS main ring.

2. ESTIMATE OF IMPEDANCE

The space charge impedance is negative inductance and written as,

$$\frac{Z_{sc}}{n} = -j \frac{g_0 Z_0}{2\beta\gamma^2}, \quad (1)$$

where Z_0 is the free space impedance, β and γ are Lorentz factors, and g_0 is a form factor defined by

$$g_0 = 1 + 2 \ln \frac{a}{b}. \quad (2)$$

Here a is the radius of beam pipe and b is the transverse beam radius.

On the other hand, FINEMET has positive inductive impedance. The inductive impedance is expressed as

$$\frac{Z_{ind}}{n} = j\omega_0 L, \quad (3)$$

where $\omega_0 = 2\pi f_0$ and f_0 is the revolution frequency (667

¹ koba@psacw01.kek.jp

kHz), and L is the inductance at that frequency.

The impedance tuner is installed in the KEK PS main ring. Let us first calculate the space charge impedance. Since the size of beam pipe is about 150 mm and the average beam size is about 60 mm, the form factor g_0 becomes 2.8. Together with the other parameters of a 500 MeV beam, the space charge impedance becomes $-j310\Omega$.

In order to observe space charge effects and its compensation with the impedance tuner, an experiment was carried out using beams at the injection energy.

We take the revolution frequency and characterize the impedance by it because we observe the effects of the impedance tuner on a single bunch whose fundamental frequency is the revolution. In order to cancel space charge impedance of $-j310\Omega$ completely, the total inductance of 73.7 μH should be prepared with FINEMET.

The FINEMET is wound to a toroidal core with the outer diameters of 340 mm, the inner diameter of 140 mm, and the thickness of 25 mm. We measured the inductance of FINEMET as a function of frequency is inductive impedance is about $j25.5\Omega$ at the injection revolution frequency. Therefore, the total of 12 pieces of FINEMET core are necessary to fully compensate space charge impedance.

3. EXPERIMENTAL SET UP

The impedance tuner consists of identical three units and each unit has 4 pieces of FINEMET core, ceramic gaps and cooper shields as shown in Fig.1. All of the FINEMET cores are placed outside of the ceramic gaps. There are short to observe the difference between with and without the short bars. The total length is 1.2m.



Fig.1 Impedance tuner installed in the KEK PS.

4. RADIATION EFFECT

This is the first time to apply FINEMET to an accelerator. It may happen that radiation due to beam loss causes a deterioration in the characteristic of FINEMET. We have proved that the radiation dose not affect the impedance of FINEMET with the following procedure. A small sample of FINEMET was placed for three weeks at the section of the beam extraction where the radio activation becomes maximum in the main ring. Then the impedance was measured with a network analyzer. The same procedure was repeated every three weeks.

Figure 2 show the imaginary part of the impedance. For nine week, the total neutron flux applied to FINEMET was $1.83 \times 10^{12} [n \cdot cm^{-2}]$. We could conclude that the impedance of the FINEMET was not changed by the total neutron flux of $1.83 \times 10^{12} [n \cdot cm^{-2}]$. The impedance tuner were installed in the place where the beam loss was much less than the beam extraction section.

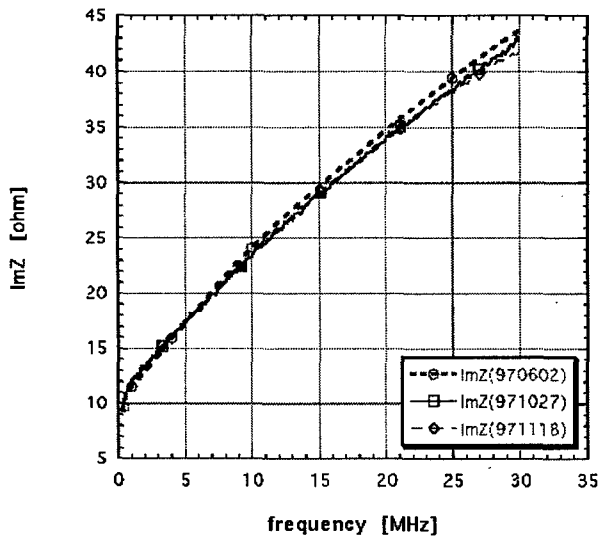


Fig.2 Imaginary impedance of the FINEMET.

5. MEASUREMENT

The frequency f_{s0} of synchrotron oscillations is perturbed with the potential of the space charge and the inductive impedance. We will measure the shift of synchrotron frequency Δf_s as a function of beam intensity and obtain total impedance as a coefficient.[8]

In fact, the shift of incoherent synchrotron oscillations can not be measured directly. However, the incoherent frequency shift can be inferred from the coherent quadrupole oscillations. If we take Δf_{s2} as a frequency shift of the quadrupole oscillations, there is the following relation with the incoherent shift[9].

$$\frac{\Delta f_{s2}}{f_{s20}} \approx \frac{1}{4} \frac{\Delta f_s}{f_{s0}} \quad (4)$$

where f_{s20} is the coherent quadrupole frequency at zero beam intensity.

The frequency of the quadrupole oscillations is measured as the envelope oscillations of a bunch signal from a wall current monitor.

The frequency of the quadrupole oscillations was measured as a function of beam intensity using impedance tuner and shown in Fig.3. The solid line is a fitted line of the data when all of the ceramic gap were shorted. The dashed line is the one when one ceramic gap was shorted and the rest of the gaps were opened. The long-dashed line is the one when all of the gaps were opened.

We estimate the non-perturbed quadrupole frequency f_{s20} by extrapolating the measured frequency to that of zero beam intensity, and list the results on the Table1. The average synchrotron frequency is 10.27 kHz. The reactive impedance on each condition is derived from the slope using the average synchrotron frequency and listed in Table2. As expected, the more inductance is installed, the lower magnitude of impedance is obtained. That demonstrates the space charge impedance is compensated with the impedance tuner.

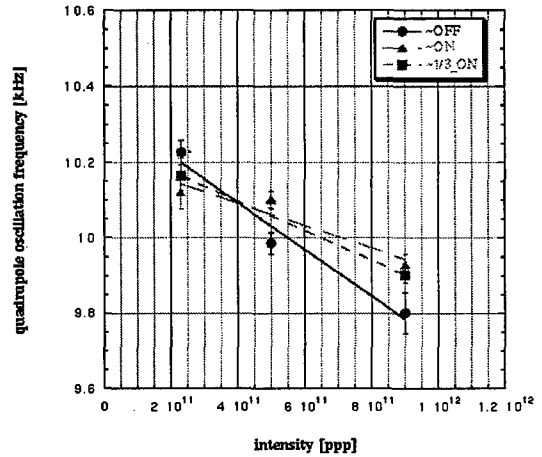


Fig.3 Quadrupole oscillation frequency estimated from the bunch envelope measurement.

Table1: synchrotron frequency (at zero intensity)

condition	f_0 [kHz]
without cores	10.34
with 1/3 of total cores	10.25
with total cores	10.21

Table2: Reactive impedance on each condition is derived from the slope.

condition	reactive impedance [Ω]
without cores	$-j2475$
with 1/3 of total cores	$-j1554$
with total cores	$-j1182$

6. EFFECT OF THE RF NONLINEAR FIELD

We have observed that the measured space charge impedance was reduced from $-j2475\Omega$ to $-j1182\Omega$ by the impedance tuner which consisted of 12 pieces of the

FINEMET cores. However, the measured impedance of $-j2475\Omega$ was 8 times as large as the impedance of $-j310\Omega$ obtained from the calculation. Moreover, the quadrupole frequency at the zero beam intensity was lower than the frequency, 12.44kHz, estimated by the following equation (5) and Table 3.

$$f_{s0} = 2 \times f_{s0} = 2 \times f_{rev} \sqrt{\frac{-\eta h}{2\pi\beta^2 \epsilon_s} eV_0 \cos \phi_s} \quad (5)$$

Table 3: Nominal values of the KEK PS main ring at injection.

symbol	nominal value
R ; machine average radius	54m
η ; slippage factor	-0.42
V_0 ; RF voltage	120kV
h ; harmonic number	9
ϕ_s ; synchronous phase	0deg
f_{rev} ; revolution frequency	667kHz

These two inconsistencies were caused by the nonlinearity of the RF field. The equation (4) and (5) are based on the assumption that an RF field is linear. The eq.(4) also assumes that the particles distribution matches to the RF bucket shape. However, the bunch occupies the most of the RF bucket area and not matches to it under the operational condition of the KEK PS main ring. We have examined the difference between linear and non-linear effects by the multiparticle simulation. The results of the simulation are shown as follows.

6.1 Simulation with linear field

Assuming a linear field without space charge (zero intensity), the frequency of the envelope oscillation (the coherent quadrupole frequency f_{s20}) is twice frequency of the single particle motion in the bunch (incoherent frequency f_{s0}), which is 12.46kHz.

Assuming a linear field with space charge, the relation of the frequency shift agree with the eq.(4).

6.2 Simulation with non-linear field

It turns out that assuming the non-linear field without space charge, the envelope oscillation frequency f_{s20} dose not agree with that estimated by eq.(5). We found that the frequency obtained by the envelope oscillation becomes an average frequency $\langle f_{s0} \rangle$, which is 10.60kHz, because each particle has each incoherent synchrotron frequency as a function of the amplitude. This value is consistent with the result of the measurement.

Assuming a non-linear field with space charge, the frequency shift is written by eq.(6) rather than (4)

$$\frac{\Delta f_{s2}}{f_{s20}} \approx \frac{1}{2} \frac{\Delta f_s}{f_{s0}} \quad (6)$$

As a result of these examinations, we know that if the bunch

is influenced by the RF nonlinear field strongly, the impedance has been over estimated.

We have tried again the impedance analysis considering the RF non-linear effect. As a result, the impedance became $-j697\Omega$ and was closed to the result of the calculation as shown in Fig.4. The detail has been discussed in ref.[10].

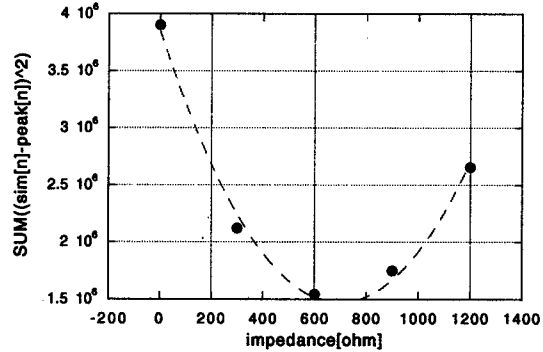


Fig.4 Analyzed impedance including RF non-linearity.

7. SUMMARY

We designed the impedance tuner consisting of the inductive material, FINEMET, to cancel the space charge impedance in the longitudinal direction. It was installed in the KEK PS main ring.

We observed the frequency shift of the coherent quadrupole oscillations and inferred the shift of the incoherent synchrotron oscillation. Total reactive impedance can be estimated as the coefficient between the shift and beam intensity. The measured impedance is reduced from $-j2475\Omega$ to $-j1182\Omega$ by the impedance tuner which consists of 12 pieces of the FINEMET cores. We demonstrated the space charge impedance is compensated by the impedance tuner.

This is the first time for FINEMET to be equipped with as an accelerator component. We have proved that the radiation dose not affect the FINEMET even with the total neutron dose of $1.83 \times 10^{12} [n \cdot cm^{-2}]$, which is considered as the highest dose of the main ring.

We have analyzed the RF non-linear effect in detail with calculation and simulation.

8. REFERENCES

- [1] K.Koba et al., Proceedings of the 11th Symposium on Accelerator Technology and Science, 1997, pp.409-411.
- [2] K.Koba et al, Proceedings of the APAC,1998.
- [3] K.Koba et al, RSI, to be published.
- [4] T.Uesugi et al., JHF internal report, JHP-31, 1997.
- [5] Y.Yoshizawa et al., Journal of Applied Physics, vol.64, 1988, pp.6044-6046.
- [6] Y.Yoshizawa et al., IEEE, vol.25, No5, 1989, pp.3324-3326.
- [7] Y.Mori et al., Proceedings of the EPAC,1998, pp.299-301.
- [8] S.Hansen, IEEE vol.NS-22, NO.3, 1975.
- [9] F.Sacherer, CERN/SI-BR/72-5, 1972.
- [10] K.Koba, doctor thesis, 1999.

CALCULATION OF PARTICLE MOTIONS AT THE HEAD AND TAIL OF A BUNCH FOR THE UNIVERSITY OF MARYLAND ELECTRON RING *

Y. Li[#], R. Kishek, M. Reiser and J.G. Wang^a,

Institute for Plasma Research, University of Maryland, College Park, MD 20742

Abstract

The end effect in a bunched beam is caused by the space-charge forces, which accelerate particles at the bunch head and decelerate particles at the bunch tail. It occurs in high-current linear accelerators and rings [1]. In the University of Maryland Electron Ring (UMER) project [2,3,4], the energy of particles at the very ends of a rectangular bunch is 15% different from that of the main part of the bunch. Assuming a negligible transverse space charge effect at the edge of the bunch, one dimensional single particle calculation is performed by a matrix formalism [6] to estimate the ratio of particle loss due to the end effect. Two possible cases are examined: with no induction gap, and with three induction gaps. If three induction modules are used, for a small number of turns, the particle loss is less than 0.15%, which is small enough to be acceptable. Simulation by code CIRCE [8] is in progress.

1 INTRODUCTION

A compact electron ring, UMER, [2,3,4] is designed and being developed at the University of Maryland for transport of a low-energy, highly space-charge dominated beam in a circular lattice. A 10 keV, 100 mA, 50 ns electron beam is injected into the ring from the injector. The ring has 36 dipoles and 36 FODO focusing periods to keep the beam along the designed orbit.

When a bunch with a rectangular current profile is transported, the strong longitudinal space charge force causes an edge erosion and large energy spread [5]. Three induction gaps are used to restore the pulse shape. The energy of the bunch edge varies periodically due to the longitudinal expansion and restoration. In UMER, the maximum energy difference between the edge and the main part of the bunch is as large as 1.5 keV, which is 15% of the beam energy. This large energy difference leads to a serious deviation from the desired beam orbit when these edge particles go through a circular lattice with dispersion. Also, the focusing function of quadrupoles, which depends on the particle energy, will be different to the edge particles. Therefore, the head and tail particles have different behaviour and may be lost.

For a rectangular bunch with a uniform velocity distribution, when the beam length is much larger than

the beam radius, the variation of the line charge density λ and relative velocity v_r can be found in [5]. The typical erosion process and formation of head and tail are shown in Figure 1, where \tilde{V}_0 is the space charge wave velocity, with V_0 the beam center velocity.

Before reaching the "cusp" point, the expanded bunch can be restored by an "ear field" produced by induction gaps. After the bunch is contracted back into a rectangular shape, it will repeat the expansion. Thus, the energy of the head particles vary periodically from 1.5 keV higher than the beam to 1.5 keV lower than the beam, with the same time-average value as particles in the main part of the beam.

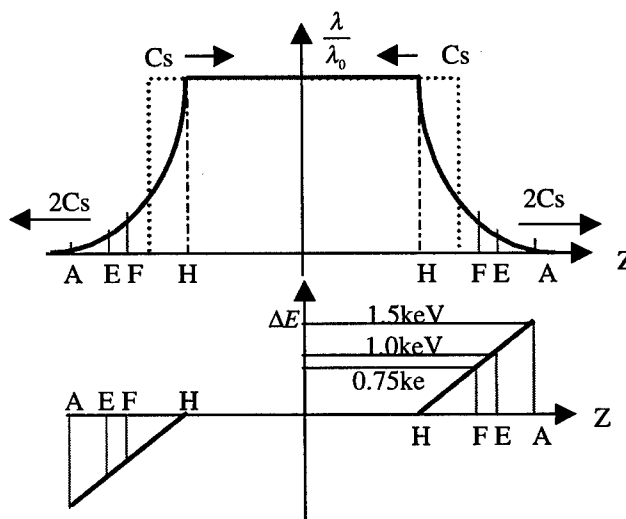


Figure 1: Bunch expansion process.

2 MODEL USED IN CALCULATION

In this paper, a simple one-dimensional model is developed to estimate the ratio of particle loss due to the end effect. It is supposed that the transverse space charge effect can be neglected due to the relatively small line charge density at the edge of the bunch. And the longitudinal space charge only changes the energy of particles, and therefore, the focus function of quadrupoles and the bending radius in the dipole. The particle motion is tracked by the matrix formalism [6].

The hard edge approximation is made for the quadrupoles and dipoles. The focusing function of the quadrupole is determined by the energy of the particle at the time it passes through the quadrupole. The particle gets a kick in the horizontal direction when it goes

*Work supported by the US Department of Energy.

^aEmail: liyun@glue.umd.edu

[#]: Present Address: ORNL and Visiting at BNL.

through the dipole; the strength of the kick depends on the particle energy. A MATLAB program is written to calculate the particle trajectory by using the matrix formalism.

The particles whose oscillation amplitude is larger than 20mm are considered lost, and whose amplitude is less than 20mm will remain in the beam pipe. By varying the initial condition (x, x') of the particle at some longitudinal location z and observing the maximum deviation, the stable area in the phase space at the location z for that particle is obtained. After comparing the stable area with the matched beam distribution in the phase space, the ratio of particle loss at the position z is known. Several particles were picked up in calculation according to their longitudinal positions in the bunch. These particles are marked in Figure 1. They are: head A, head E, tail A, tail E, and tail F.

There are three induction gaps in one revolution and 12 FODO periods between two adjacent induction gaps. One period is defined as from the middle of the long drift section to the middle of the next long drift section. The matrix elements are as following [6]:

- Drift space:

$$\begin{pmatrix} x \\ x' \end{pmatrix}_{out} = \begin{bmatrix} 1 & S \\ 0 & 1 \end{bmatrix} \begin{pmatrix} x \\ x' \end{pmatrix}_{in}$$

- Quadrupole:

$$\begin{pmatrix} x \\ x' \end{pmatrix}_{out} = \begin{bmatrix} \cos kl & \frac{\sin kl}{k} \\ -k \sin kl & \cos kl \end{bmatrix} \begin{pmatrix} x \\ x' \end{pmatrix}_{in} \quad \text{for focusing}$$

$$\text{or } \begin{pmatrix} x \\ x' \end{pmatrix}_{out} = \begin{bmatrix} \cosh kl & \frac{\sinh kl}{k} \\ k \sinh kl & \cosh kl \end{bmatrix} \begin{pmatrix} x \\ x' \end{pmatrix}_{in} \quad \text{for defocusing}$$

$$\text{With } k^2 = \frac{B'q}{m_0 c \beta \gamma}$$

- Dipole:

$$\begin{pmatrix} x \\ x' \end{pmatrix}_{out} \approx \begin{bmatrix} 1 & \rho \sin \theta \\ 0 & 1 \end{bmatrix} \begin{pmatrix} x \\ x' \end{pmatrix}_{in} + \begin{pmatrix} \rho(1 - \cos \theta) \\ \theta \end{pmatrix} \delta$$

Where $\delta = \frac{\Delta P}{P}$ is the relative momentum error.

3 CALCULATION RESULTS

The matched beam distribution in phase space is obtained by TRACE-2D [7]. It is further supposed that the beam is uniformly distributed inside the ellipse of the matched beam distribution in phase space.

The acceptance is obtained by sending an ideal particle with initial condition (x, x') into the FODO lattice, and observing its maximum amplitude of betatron oscillation. The initial conditions (x, x') which corresponding to maximum amplitude of 20 mm compose the acceptance ellipse. For 10keV ideal particle, the acceptance is shown in Figure 2 (the large ellipse) with the matched beam distribution (the small ellipse).

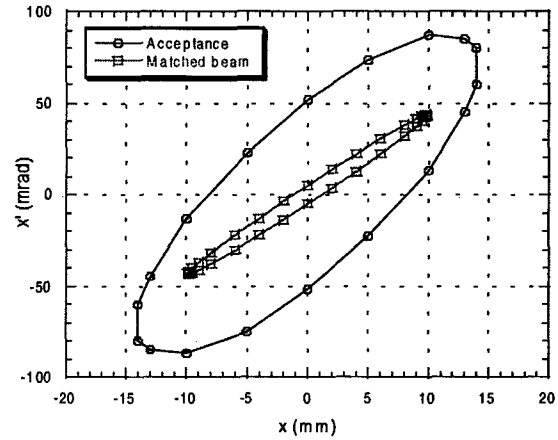


Figure 2: Matched beam distribution and the acceptance.

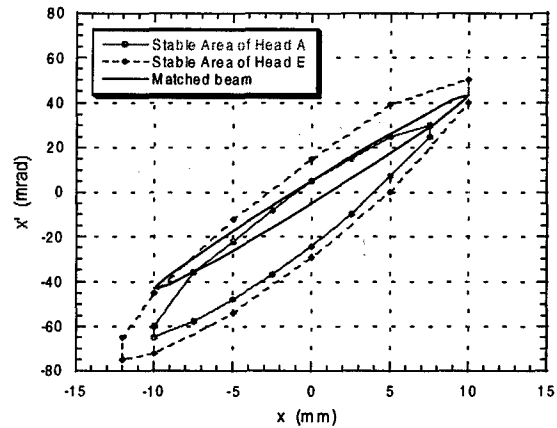


Figure 3: Stable Area of Head A and Head E, with 3 gaps.

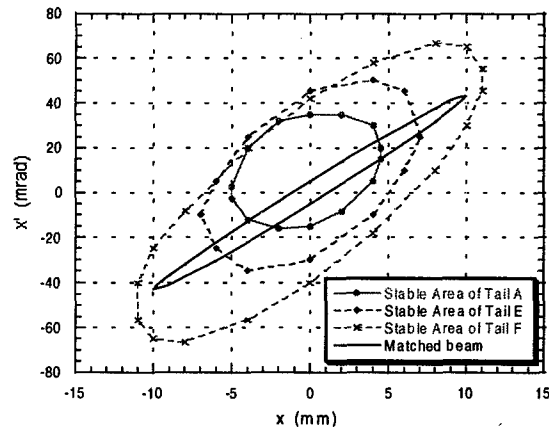


Figure 4: Stable area of tail A, tail E and tail F, with 3 gaps.

In order to know the ratio of the particle loss, the stable area is compared with the matched beam

distribution. The stable area of the head particles and tail particles are shown in Figure 3 and Figure 4. The ellipses are corresponding to the initial condition (x, x') that causes 20 mm deviation; so the particles outside of the stable area ellipse will be lost.

From Figure 3, the ratio of particle loss for particle head A and head E are 0.4 and 0. So the ratio of particle loss in bunch head is less than

$$\frac{\text{\# of particles between AE}}{\text{\# of particles between AH}} \cdot 0.4 = 3.7\% \cdot 0.4 = 1.5\%$$

From Figure 4, the ratio of particle loss for particle tail A, tail E, and tail F are respectively 0.5, 0.3 and 0. So the ratio of particle loss in bunch tail is less than

$$\frac{\text{\# of particles between AE}}{\text{\# of particles between AH}} \cdot 0.5 + \frac{\text{\# of particles between EF}}{\text{\# of particles between AH}} \cdot 0.3 = 3.7\% \cdot 0.5 + (12.5\% - 3.7\%) \cdot 0.3 = 4.5\%$$

There is 5% of particles located in the head and tail. So, the total ratio of particle loss is less than $5\% \times 4.5\% + 5\% \times 1.5\% + 2 = 0.15\%$

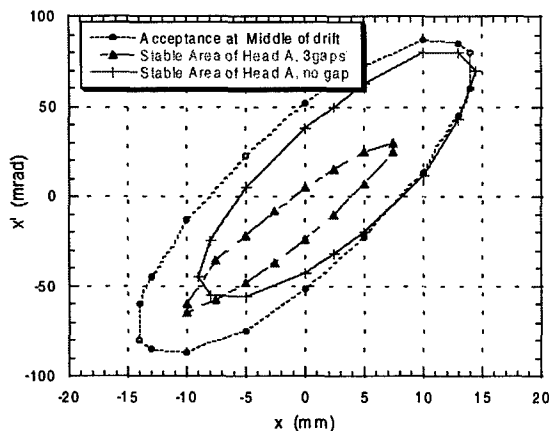


Figure 5: Comparison of stable area of particle head A in 2 cases: with 3 gaps and with no gap.

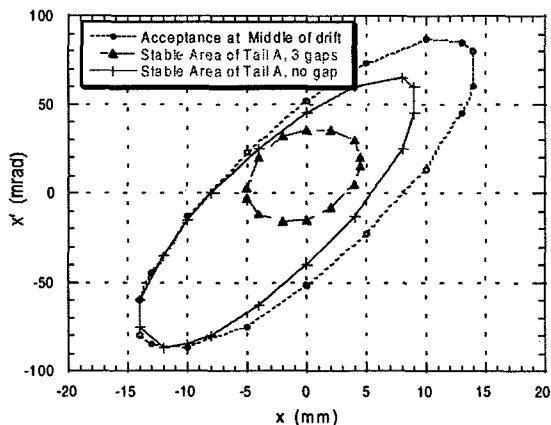


Figure 6: Comparison of stable area of particle tail A in 2 cases: with 3 gaps and with no gap.

In some experiments when we care more about beam position, the induction gaps will be changed into resistive beam position monitors, resulting in no periodic energy variation. In Figure 5 and Figure 6, the stable area in this case is compared with that of three induction gaps. From the comparison we know that the stable area is larger if there is no induction gap. The ratio of loss is smaller compared to the case with three induction gaps. However, this model only applies to the first three turns before the "cusp" point. After that the model is no longer correct.

Simulation by code CIRCE [8] is going on. But there is no final result yet. The first author would like to acknowledge Bill Sharp of LLNL for his great help in using this code.

4 SUMMARY

The calculation results show that the end effect is not of serious concern in UMER. In the case of no induction gaps, for the first three turns considered here, the particle loss rate is negligibly small. In the case of three induction gaps, less than 0.15% particles will be lost for a small number of turns. This number is small enough so that no special arrangement is needed to overcome this effect during the initial operation of UMER.

5 REFERENCES

- [1] D. A. Edwards and M. J. Syphers, "An Introduction to the Physics of High Energy Accelerators", Wiley, New York, 1992.
- [2] M. Reiser, et al., "The Maryland Electron Ring for Investigating Space-Charge Dominated Beams in a Circular FODO System," in these proceedings.
- [3] J.G. Wang, S. Bernal, P. Chin, R. A. Kishek, Y. Li, M. Reiser, M. Venturini, Y. Zou, T. Godlove, I. Haber, and R. C. York, Nucl. Instrum. Methods Phys. Res. A. (1998), vol. 415, no. 1-2, p.422-7.
- [4] <http://www.ipr.umd.edu/ebte/ring>.
- [5] D.X. Wang, J.G. Wang, and M. Reiser, "Restoration of Rectangular Pulse shape after Edge Erosion for a Space-Charge Dominated Electron Bunch", Phys. Rev. Lett. 73(1), 66 (1994).
- [6] M. Reiser, "Theory and Design of Charged Particle Beams", Wiley, New York, 1994.
- [7] K. R. Crandall and D. P. Rusthoi, "TRACE 3-D Documentation", LA-UR-90-4146, Los Alamos National Laboratory.
- [8] Bill Sharp, private communications.

OBSERVATION OF NONLINEAR BEHAVIOR OF LOCALIZED SPACE-CHARGE WAVES IN SPACE-CHARGE DOMINATED ELECTRON BEAMS*

J. G. Wang^a, Y. Zou, H. Suk^b, and M. Reiser

Institute for Plasma Research, University of Maryland, College Park, MD 20742

Abstract

We present an experimental observation of the abnormal growth of localized nonlinear fast space-charge waves in space-charge dominated electron beams passing through a dissipative channel. High-perveance electron beams with localized perturbations are launched from a gridded electron gun and transported through a short resistive-wall channel consisting of a resistive-film coated glass tube inside a long solenoid providing uniform focusing. The energy width of the space-charge waves developed from the perturbations is measured on both ends of the channel. The experiments have shown that the localized fast space-charge wave appears to grow under nonlinear perturbations; in the linear regime, as expected, the energy width of slow waves increases, while the energy width of fast waves decreases when they pass through the resistive channel.

1 INTRODUCTION

The longitudinal instability of charged particle beams, caused by the growth of slow space-charge waves due to interaction with a dissipative wall, is an important issue in particle accelerators, microwave generators, and plasmas. We have been studying this instability in space-charge dominated electron beams by perturbing the beams with localized perturbations and transporting them in a resistive environment. In the previous studies, linear waves were employed and the experiment demonstrated the growth of localized slow space-charge waves and the decay of fast space-charge waves. The growth/decay rates of the slow/fast waves were measured and the experiment was compared with theory [1]. In this paper, we report an unexpected observation that the energy width of localized fast space-charge waves appears to grow in a resistive channel if the perturbations are highly nonlinear.

2 EXPERIMENTAL SETUP AND METHOD

The experimental setup, as shown in Fig. 1, consists of a short-pulse electron beam injector, a resistive-wall channel, and diagnostics. The injector [2] contains a gridded electron gun, which can produce desired beam parameters with localized perturbations. The key component of the resistive-wall channel is a glass tube of

about 1 m in length and 3.81 cm in inner diameter. The inner surface of the glass tube is coated with Indium-Tin-Oxide (ITO). The total resistance of the tube employed in the experiments is 5.44 k Ω , which corresponds to 0.673 k Ω per square. The beam is focused by a 1.4-m long uniform solenoid coaxial to the resistive-wall tube. Three short solenoidal lenses are employed in the injector to match the beam into this channel. The diagnostics includes two retarding-field energy analyzers at the entrance and the exit of the resistive tube to measure the energy of beam particles and space-charge waves. Typical beam parameters are 2-8 keV in energy, 20-100 mA in current, and about 100 ns in the pulse duration.

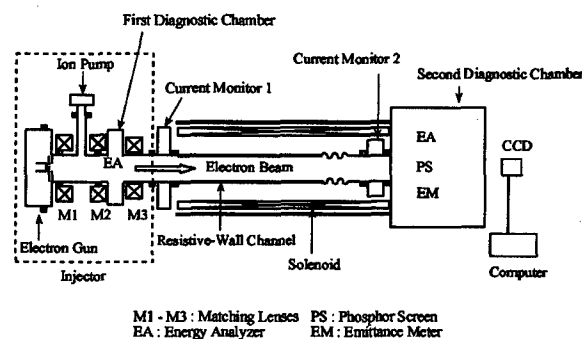


Fig. 1 Setup of resistive-wall instability experiment.

In the experiment, electron beams with localized perturbations are generated in the gridded electron gun and transported through the resistive-wall channel. Single slow or fast waves can be developed on these beam pulses by applying the technique described in a previous letter [3]. The energy width of space-charge waves is measured and compared at the both ends of the resistive-wall channel. This is done as the follows: by increasing the retarding voltage in the energy analyzers, the beams and space-charge waves can be gradually suppressed in the analyzer output. In this way, the energy levels of the beam and the energy width of space-charge waves can be determined. A typical measurement with the energy analyzers is shown in Fig. 2. The beam is suppressed at a retarding high voltage of 3.595 kV. The remaining signal on the top trace is a fast wave in which the particles have a higher energy than the beam average energy. When the retarding high voltage further increases, the space-charge wave signal decreases and eventually disappears at 3.608 kV. This results in an energy width of 13 eV for the fast wave.

*Work supported by the U.S. Department of Energy.

^a Email: jgwang@bnl.gov

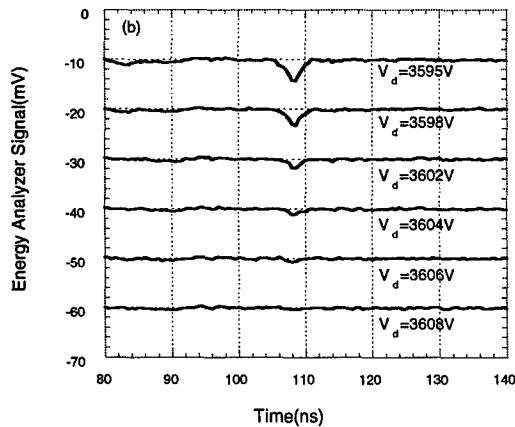


Fig. 2 Fast wave signals from an energy analyzer at different retarding high voltage.

3 EXPERIMENTAL OBSERVATIONS

The measurement with the two energy analyzers for a slow wave on a beam of about 2.5 keV and 39.2 mA is shown in Fig. 3. Here the relative amplitude of the wave from the two energy analyzers is plotted against the difference between the retarding voltage and beam voltage. The energy width of the slow wave increases from 28 eV to 43 eV due to the instability, corresponding to a spatial growth rate of 0.45/m. Another measurement for a fast wave is performed at a beam energy of 3.595 kV and a beam current of 19.8 mA. The result is shown in Fig. 4. The energy width of the fast wave decreases from 21 eV to 13 eV, giving a spatial decay rate of -0.50/m.

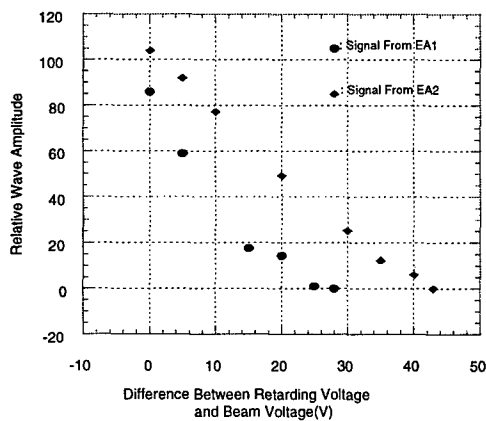


Fig. 3 Relative amplitude of a slow space-charge wave vs. the difference between the retarding voltage and beam voltage, where EA1 and EA2 are the energy analyzer before and after the resistive wall, respectively.

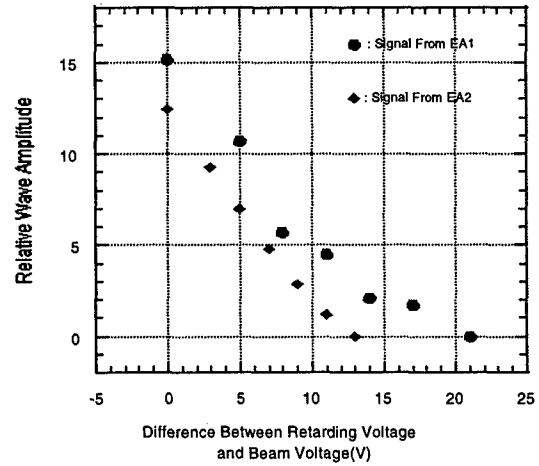


Fig. 4 Energy width of a fast wave from EA1 and EA2.

Measurements with the energy analyzers are also performed in the nonlinear regime where a rather large line-charge density perturbation is introduced on the beams. This is done by introducing a strong voltage perturbation on the grid-cathode pulse of the electron gun, that results in large line-charge density and current perturbation on the beam. Figure 5 shows such a case, where it can be seen that a beam current signal modulated with a large localized space-charge wave, measured before the resistive wall. The ratio of the wave amplitude over the average beam current is nearly 40%, a highly nonlinear case ! Under such nonlinear perturbations, the energy width of a localized slow wave always increases when the wave passes through the resistive channel. This is shown in Fig. 6, where the growth rate of slow waves vs. the perturbation strength is plotted.

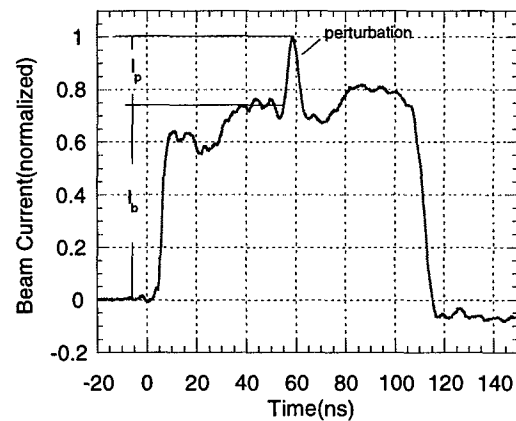


Fig. 5 Beam current signal with a highly nonlinear space-charge wave.

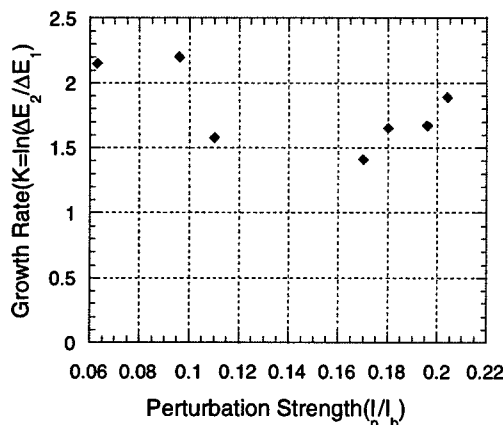


Fig. 6 Growth rates vs. perturbation strength for slow waves.

Nevertheless, the results for localized fast waves are totally unexpected and counter-intuitive. The energy width of the fast waves appears to increase under nonlinear perturbations in the resistive wall channel. This is shown in Fig. 7. Measurements have been performed for fast waves under different perturbation strength. In the linear regime, the fast wave decays, as expected. When the perturbation is strong enough, a transition from decay to growth takes place. The growth rate eventually levels off for the strongest perturbations in the experiments.

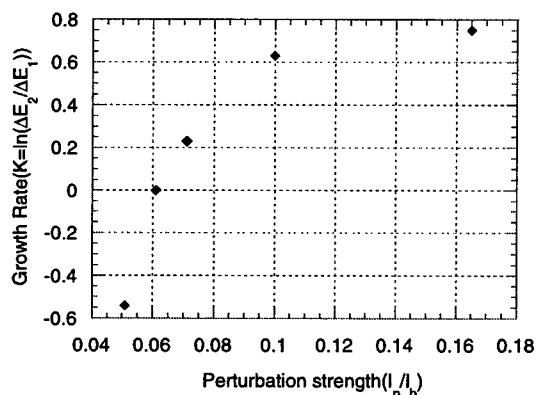


Fig. 7 Growth rates vs. perturbation strength for fast waves in a resistive-wall channel.

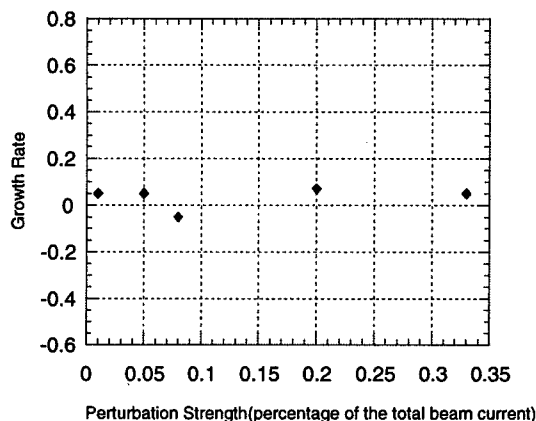


Fig. 8. Growth rates vs. perturbation strength for fast waves in a conducting wall pipe.

We are so far not able to interpret this unexpected phenomenon by the nonlinear dynamics, including the solitary waves, explosive instability, etc. In order to eliminate possible errors in the diagnostics, the resistive wall is replaced by a conducting tube and any other conditions remain the same. In this case, no growth or decay is observed for the fast wave, as expected. The results are plotted in Fig. 8.

4 REFERENCES

^aPresent Address: ORNL and Visiting at BNL.

^bPresent Address: Dept. of Physics, UCLA.

- [1] J. G. Wang, H. Suk, and M. Reiser, *Phys. Rev. Lett.* **79** (6), 1042 (1997).
- [2] J. G. Wang, D. X. Wang, and M. Reiser, *Nucl. Instr. & Meth. in Phys. Res. A* **316**, 112 (1992).
- [3] J. G. Wang, D. X. Wang, and M. Reiser, *Phys. Rev. Lett.*, **71**(12), 1836 (1993).

MICROWAVE INSTABILITY AND IMPEDANCE MODEL

A. Mosnier, SOLEIL, Gif/Yvette (France)

Abstract

Tracking simulations, with the aim of studying the microwave regime with short and intense bunches, suggest different instability mechanisms, according to the impedance model. In order to get a better insight of the source of the instability, i.e. azimuthal or radial mode coupling, we chose to follow the Vlasov-Sacherer approach to investigate the stability of the stationary solution. The generalized Sacherer's integral, including mode coupling and potential well distortion, was then solved by using the "step function technique" for the expansion of the radial function, as proposed by Oide and Yokoya. For illustration, the effect of the resonant frequency of a broadband resonator in the SOLEIL storage ring was studied. When the resonator frequency is much higher than the bunch spectrum width, azimuthal mode coupling can occur before radial mode coupling. When the resonator frequency is lower, radial mode coupling comes usually first, but two or more bunchlets are produced at relatively low current. The diffusion process between the bunchlets, which leads to the well-known "saw-tooth" behaviour, originates actually from a fast growing microwave instability. Lastly, the beneficial effect of an harmonic cavity on the microwave instability is estimated and discussed.

1 INTRODUCTION

The Vlasov-Sacherer approach is chosen to investigate the onset of the microwave instability, leading to abnormal bunch-lengthening and energy spread widening in electron storage rings. As soon as the potential well distortion, due to wakefields induced in the vacuum chamber, is significant, single-particle trajectories are no longer ellipses and the spread in synchrotron frequency must be taken into account in the stability study of the stationary distribution, given by the Haissinski's equation [1]. The Sacherer's integral equation with mode coupling [2] is then generalized to [3]

$$(\Omega - m\omega(J))R_m(J) = -m\omega(J)\psi_o(J)k \sum_{m'} \int G_{mm'}(J, J') R_{m'}(J') dJ' \quad (1)$$

As the synchrotron motion is strongly nonlinear, the action-angle variables (J, ϕ) have been used. ψ_o and ω are the amplitude-dependent distribution and synchrotron frequency of the equilibrium state. The perturbation distribution oscillates with the coherent frequency Ω and has been expanded into the usual radial functions R_m . The Kernel is an integral over the frequency, involving the impedance :

$$G_{mm'}(J, J') = \int \frac{Z(\omega)}{i\omega} K_m^*(\omega, J) K_{m'}(\omega, J') d\omega \quad (2)$$

where K_m is an integral over the phase variable. The integral equation (1) was solved by expanding the radial function R_m .

$$R_m(J) = \sum_n C_{mn} h_n(J) \quad (3)$$

according to the "mesh technique", as suggested by Oide and Yokoya [4]. This method uses step functions for $h_n(J)$ which takes the constant value $1/\Delta J_n$ in the strip around the n -th mesh with the thickness ΔJ_n , and zero elsewhere, and converts (1) into an eigenvalue's problem..

For illustration, the parameters of the SOLEIL storage ring [5] are used throughout the paper, as well as a broadband resonator as impedance model of the vacuum chamber. The shunt impedance was fixed to 3.6 k Ω , but since the feature of the impedance, as seen by the beam, changes with the resonant frequency, we resolved to vary the resonator frequency on a wide frequency range, from 10 to 30 GHz, in order to study the effect on the phase space topology and, above threshold, on the origin of the microwave instability.

2 HIGH RESONANT FREQUENCY

The potential well distortion is first calculated by solving the Haissinski's equation for a 30 GHz resonator (Fig.1).

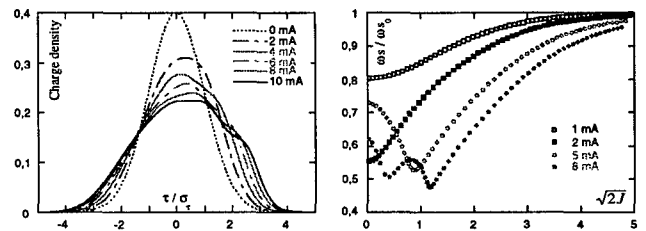


Figure 1: Charge distributions (top) - bunch head on the right side - and synchrotron frequency (bottom) for different beam currents (30 GHz resonator).

As usual, the distribution becomes asymmetric due to the resistive part of the impedance and the bunch shifts forward (positive momentum compaction) to compensate for the energy loss. The actual synchrotron frequency starts below the zero-current frequency due to the inductive part of the impedance. However, above 3 mA, instead of raising monotonically towards unity as the amplitude increases, it reaches a minimum due to the resistive component.

The next task consists in studying the stability of the stationary distribution. Looking first for eventual radial mode coupling by calculating the eigenvalues for each azimuthal mode m , separately, we find that the modes

$m=3$ to 5 are unstable above 5 mA. Fig. 2 shows for example the power spectra of the sextupole mode, calculated by means of the eigenvectors just before and after the instability threshold. The overlap of the resistance with the power density is higher at positive frequencies than at negative frequencies above 5.5 mA, confirming the emergence of a radial mode coupling. If now we pursue the analysis by solving the system with pairs of azimuthal modes, we find a strong coupling between the modes $m=1$ and $m=2$ at relatively low intensity

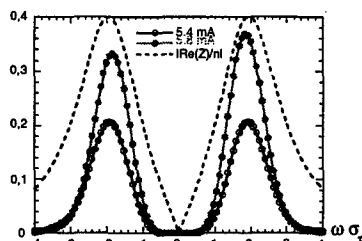


Figure 2: Power spectra the $m=3$ mode just before and after the instability threshold of 5.5 mA.

Lastly, the coherent frequency is plotted in Fig. 3, when more azimuthal modes than enough are taken into account ($m=1$ to 6). A complete mixing occurs at relatively low current, after a rapid spread. The growth rate increases dramatically with a current around 5 mA, which represents the onset of the instability. For higher intensity, the growth rate is larger than the radiation damping rate of the SOLEIL ring. Several types of instability - identified by solid circles - develop simultaneously, the nature of the most unstable modes changing with intensity: at the threshold of 5 mA, the microwave instability is induced by a radial coupling of the sextupole mode and a coupling of the dipole and quadrupole modes; these instabilities are finally overtaken by the radial $m=5$ mode coupling above 8 mA; an octupole mode can be also identified, but with a smaller growth rate.

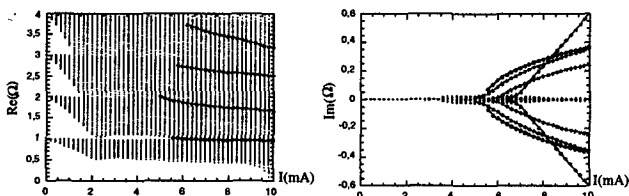


Figure 3: $\text{Re}(\Omega)$ and $\text{Im}(\Omega)$ vs. current ($m=1$ to 6).

3 LOW RESONANT FREQUENCY

Similarly, potential well distortion is first calculated for a lower resonant frequency 11 GHz resonator (Fig. 4). The bunch becomes much more distorted than before and two peaks appear above 3.5 mA, as soon as there are two or more stable fixed points, forming distinct islands in the phase space (Fig. 5). We note that the synchrotron frequency is vanishing on the separatrix, whereas it is

about equal to the zero-current frequency at the center of the first island and twice the zero-current frequency at the center of the second island.

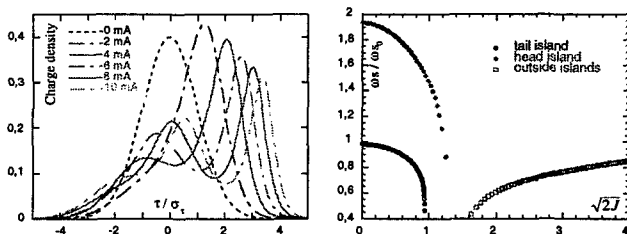


Figure 4: Charge distributions (top) - bunch head on the right side - and synchrotron frequency (bottom) for different beam currents (11 GHz resonator).

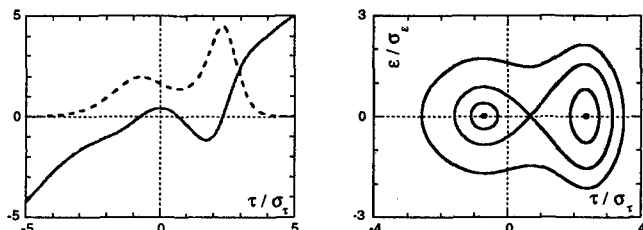


Figure 5: Norm. net voltage (left - solid line) and constant- H contours in phase space (right) at 5 mA.

The next task consists in studying the stability of the stationary distribution. The imaginary and real parts of Ω , calculated for with a sufficient number of modes, are plotted as a function of bunch current in Fig. 6. The growth rate looks more chaotic than for the higher frequency resonator, because of the rapid change of the topology of the phase space, perturbed by the formation of two or more bunchlets. Above 4 mA, which can be considered as a threshold, two mode families with regular growth rate increase (identified by solid circles on the figure), stand out nevertheless. It is worth noting the sudden change of behaviour at a current of 6 mA.

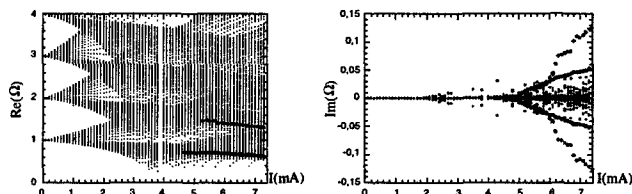


Figure 6: $\text{Re}(\Omega)$ and $\text{Im}(\Omega)$ vs. current ($m=1$ to 6).

Again, tracking simulations confirmed a threshold of 4 mA, although some premonitory fluctuation of energy spread can be observed slightly before, as predicted. However, the so-called sawtooth instability, already observed in existing machines appears suddenly at 6 mA. Tracking results show a quick increase of both energy spread and bunch length, followed by a slower decrease, with a recurrence of about 150 Hz (Fig. 7).

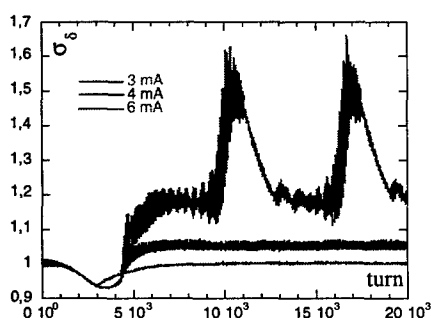


Figure 7: Energy spread widening as a function of the number of turns.

A density-plot of the most unstable distribution, calculated from the eigenvectors, is given in Fig.8 at the limit of emergence of the sawtooth behaviour (6 mA). The azimuthal pattern reveals a pure dipole mode inside the trailing bunchlet. It is worthwhile noting that this unstable dipole mode widens so far as to reach the separatrix of the tail island. Particles can diffuse through the unstable fixed point and populate the head bunchlet, leading to relaxation oscillations. A phenomenological description of the sawtooth behaviour was suggested in [6], but the diffusion process was assumed to originate from the random emission of radiation, instead of a strong instability.

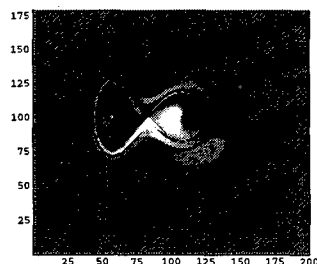


Figure 8: Density-plot of the dipole mode (6 mA).

4 CONCLUSION

The threshold of the microwave instability has been estimated over a wide frequency range of the broadband resonator. Although the source of the instability, radial or azimuthal mode coupling, is changing and although the azimuthal mode number is differing greatly (from $m=1$ or 2 at low frequency to $m=5$ or 6 at high frequency), the onset of the instability does not change a lot from 5 GHz to 30 GHz. It is plotted in Fig. 9 as a function of the frequency $\omega_r \sigma_r$ and has a broad minimum between 1 and 1.5. However, the threshold is not the only criterion; in particular, lower frequency resonators are more harmful since they can induce dipole or quadrupole oscillations of large amplitude and sawtooth type instabilities can develop, owing to the formation of micro-bunches.

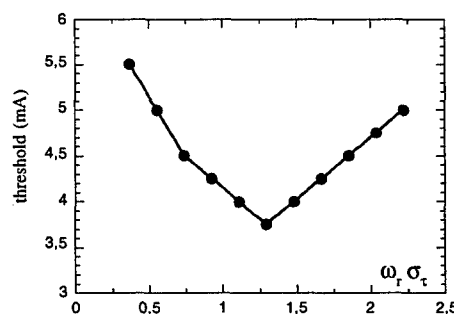


Figure 9: Microwave instability threshold as function of normalized resonator frequency.

Although the primary goal of an harmonic cavity, operating in the bunchlengthening mode, is to increase beam lifetime in Synchrotron Light Sources, it has also a beneficial effect on the microwave instability. As the use of the harmonic cavity reduces strongly the peak current, we could expect a large increase of the instability threshold. Besides, since the final voltage, including the wake potential, is smoothed off, it will suppress multiple bunchlets, which would appear at relatively low current. However, we found [3] that, even though the particle density is divided by a factor of about 4, the instability threshold enhancement is only a factor two. This efficiency loss can be explained by the lower synchrotron frequency spread due to a lower potential well distortion (Fig.10). In case of short bunches, the non-linearity and then the Landau damping effect of an harmonic cavity, even operating at the third harmonic, is much smaller than the wakefield's one.

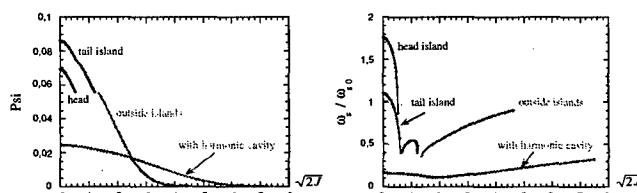


Figure 10: Magnitude ψ_0 (left) and synchrotron frequency (right) of the stationary distribution vs. \sqrt{J} .

REFERENCES

- [1] J. Haissinski, *Il Nuovo Cimento* 18 B, 72 (1973).
- [2] F. Sacherer, "Bunch lengthening and microwave instability", *IEEE Trans. Nucl. Sci.*, NS-24, 1393 (1977).
- [3] A. Mosnier, "Microwave Instability Study in the SOLEIL Ring", SOLEIL Report 98-11, 1998.
- [4] K. Oide and K. Yokoya, "Longitudinal single-bunch instability in electron storage rings", KEK Preprint 90-10, April 1990.
- [5] M.P. Level et al, "Status of the SOLEIL Project", *Proc. of the 6th European Part. Acc. Conf.*, Stockholm, June 1998.
- [6] R. Baartman and M. D'Yachkov, "Simulations of Sawtooth Instability", PAC95, 3119 (1995).

Single Bunch Monopole Instability*

Boris Podobedov and Sam Heifets

Stanford Linear Accelerator Center, Stanford University, Stanford, CA 94309

Abstract

We study single bunch stability with respect to monopole longitudinal oscillations in electron storage rings. Our analysis is different from the standard approach based on the linearized Vlasov equation. Rather, we reduce the full nonlinear Fokker-Planck equation to a Schrödinger-like equation which is subsequently analyzed by perturbation theory. We show that the Haissinski solution [3] may become unstable with respect to monopole oscillations and derive a stability criterion in terms of the ring impedance.

1 INTRODUCTION

Single bunch longitudinal instability often limits the performance of electron storage rings. Theoretical analysis of this instability is usually based on the Fokker-Planck equation that includes the effects of both Hamiltonian and stochastic forces. The Hamiltonian part describes the synchrotron motion while radiation terms account for the much slower effects of the synchrotron radiation and define the beam size at low intensity. A stationary solution of the Fokker-Planck equation was first obtained in 1973 by J. Haissinski [3]. Since then much of the instability analysis was done utilizing the linearized Vlasov equation technique, where the Fokker-Planck equation is linearized with respect to the Haissinski solution. In this approach the Haissinski solution is also used to introduce the action-angle variables that make the Haissinski Hamiltonian independent of angle. The linearized Vlasov technique leads to the concept of azimuthal phase space modes, which are the components of the perturbation to the Haissinski solution with certain azimuthal symmetry. The first three of such modes are sketched in Fig. 1. Neglecting the possibility of several potential well minima we assume that action-angle variables can be defined uniformly across the whole plane.

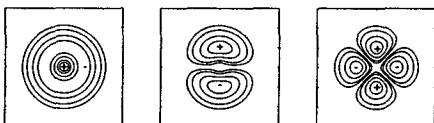


Figure 1: Example contour plots of the monopole, dipole and quadrupole modes

As seen from Fig. 1 the monopole mode is special because its physical space projection does not change significantly during a synchrotron period. This argues that ra-

diation rather than Hamiltonian forces define the dynamics of this mode. Since the monopole mode has the same azimuthal structure as the Haissinski solution it is normally omitted from the standard linearized Vlasov analysis. There the radiation terms in the Fokker-Planck equation define the Haissinski solution and then only Hamiltonian terms remain in the linearized Vlasov equation. The possibility that a perturbation is monopole, but with radial structure different from the Haissinski solution, is neglected.

In this paper we are exploring the possibility that an instability can be associated with the monopole mode. Rather than extending the linearized Vlasov technique we find it more convenient to transform the Fokker-Planck equation to a Schrödinger-like equation and analyze the latter using the Haissinski solution as a basis. Advantages of this approach are that it is tractable and it allows us to use some well known facts about Schrödinger equation solutions.

We assume below that the monopole mode can be considered separately from other modes. The validity and consequences of this assumption are discussed in [1].

2 NOTATION AND BASIC EQUATIONS

For a relativistic bunch longitudinal dynamics is often described in dimensionless variables

$$x = z/\sigma_0, \quad p = -\delta/\delta_0, \quad \tilde{\tau} = \omega_{s0}t, \quad (1)$$

where z is the position of a particle with respect to the bunch centroid ($z > 0$ in the head of a bunch), δ is the relative energy spread, ω_{s0} is the synchrotron frequency, and the subscript "0" refers to zero-current quantities. The Fokker-Planck equation for the distribution function $\rho(x, p, \tilde{\tau})$ can be written [2] as

$$\frac{\partial \rho}{\partial \tilde{\tau}} + \{H, \rho\}_{p,x} = \frac{\gamma_d}{\omega_{s0}} \frac{\partial}{\partial p} \left(\frac{\partial \rho}{\partial p} + p\rho \right), \quad (2)$$

where $\{\dots\}$ denotes the Poisson brackets, γ_d is the radiation damping rate, $H(x, p, \tilde{\tau})$ is the self-consistent Hamiltonian

$$H(x, p, \tilde{\tau}) \equiv \frac{p^2}{2} + \frac{x^2}{2} + \Lambda \int dx' dp' \rho(x', p', \tilde{\tau}) S(x' - x), \quad (3)$$

and ρ is normalized to 1. We have neglected the nonlinearities of RF potential and defined the parameter

$$\Lambda \equiv Nr_0(C\gamma\alpha\delta_0^2)^{-1}, \quad (4)$$

where N is the number of particles in a bunch, r_0 is the classical electron radius, C is the ring circumference and α is the momentum compaction. We have also defined a dimensionless function $S(x) \equiv \sigma_0 \int_0^x dx' W(\sigma_0 x')$ in terms of the wakefield $W(z)$ for two particles separated by z .

* Work supported by Department of Energy contract DE-AC03-76SF00515.

The Fokker-Planck equation (2) has a steady-state Haissinski solution [3]

$$\rho_H(x, p) = Z_H e^{-H_H(x, p)}. \quad (5)$$

where Z_H is a normalizing factor and H_H is defined by (3) with ρ replaced by ρ_H .

Canonical transformation from x, p to action-angle variables J, ϕ can be defined to make the Hamiltonian H_H phase independent, $H_H(x, p) \rightarrow H_H(J)$. Ignoring non-zero azimuthal modes by assuming $H = H(J, \bar{\tau})$, $\rho = \rho_0(J, \bar{\tau})$ the dynamics of the monopole mode is described by (2) transformed to J, ϕ variables and averaged over phase. This can be done using the invariance of the Poisson brackets [4]. Introducing the diffusion coefficient

$$D(J) \equiv J/\omega_H(J), \quad (6)$$

and renormalizing time to the damping rate $\tau \equiv \gamma_d t$ we can transform (1) equation (2) to the form

$$\frac{\partial \rho}{\partial \tau} = \frac{\partial}{\partial J} \left(D(J) \left[\frac{\partial \rho}{\partial J} + \omega(J, \tau) \rho \right] \right), \quad (7)$$

where $\omega_H(J) \equiv \frac{\partial H_H(J)}{\partial J}$ and $\omega(J, \tau) \equiv \frac{\partial H(J, \tau)}{\partial J}$.

3 TRANSFORMATION TO A SCHRÖDINGER-LIKE EQUATION

The Fokker-Planck equation (7) has a standard form that permits transformation to a Schrödinger-like equation [5]. Let us introduce a new independent variable

$$y \equiv y(J) = \int_0^J dJ' / \sqrt{D(J')} \quad (8)$$

and two functions

$$f(y, \tau) \equiv \frac{1}{\sqrt{D(J(y))}} e^{\Phi(y, \tau)/2} \rho(J(y), \tau), \quad (9)$$

$$\Phi(y, \tau) \equiv H(J(y), \tau) - (1/2) \ln D(J(y)), \quad (10)$$

where $J(y)$ is given implicitly by (8). Now the Fokker-Planck equation (7) takes the form

$$\frac{\partial f}{\partial \tau} = \frac{\partial^2 f}{\partial y^2} - U_S(y, \tau) f + \frac{1}{2} \dot{\Phi}(y, \tau) f, \quad (11)$$

where

$$U_S(y, \tau) \equiv [\Phi'(y, \tau)/2]^2 - \Phi''(y, \tau)/2 \quad (12)$$

and dot and prime denote partial derivatives with respect to τ and y . Eq. (11) is nonlinear since Φ is related to f by a self-consistency condition ([1]) that follows from (3).

Note, that $f_H(y) \equiv Z_H \sqrt[4]{D(J(y))} e^{-H_H(J(y))/2}$ is the steady-state solution of (11) and it corresponds to the Haissinski solution. Without the last term (11) can be thought of as a Schrödinger equation for a particle in the potential well $U_S(y, \tau)$. Since this term is zero for the Haissinski solution, one can neglect it for solutions that are close to f_H . This includes the case of the early time behavior of a system initialized with the Haissinski distribution at $\tau = 0$.

4 SCHRÖDINGER EQUATION ANALYSIS

After neglecting the $\dot{\Phi}$ term equation (11) reads

$$\frac{\partial f}{\partial \tau} = \frac{\partial^2 f}{\partial y^2} - U(y, \tau) f. \quad (13)$$

First, we solve a linear problem for which $\omega(J) = \omega^0$ is a constant. In this case $y = 2\sqrt{\omega^0 J}$ and the Schrödinger potential is simply

$$U_S^0(y) = \frac{y^2}{16} - \frac{1}{2} - \frac{1}{4y^2}, \quad (14)$$

which makes (13) a solvable eigenvalue problem. The solution is

$$f^0(y, \tau) = \sum_{m=0}^{\infty} \psi_m^0(y) e^{-\lambda_m^0 \tau}, \quad (15)$$

$$\psi_m^0(y) = (y/2)^{1/2} e^{-y^2/8} L_m(y^2/4), \quad (16)$$

where $\lambda_m^0 = m = 0, 1, 2, \dots$ are the eigenvalues and L_m is the Laguerre polynomial of order m . As expected, the linear problem does not have unstable solutions. Any initial distribution exponentially approaches the Haissinski solution $\psi_0^0(y)$ on the time-scale defined by radiation damping.

For the general case, $\omega(J) \neq \text{const}$, asymptotic behavior of the solutions of (11) is described by the solutions to the linear problem (14), (16). In spite of the singularity in the potential the eigenvalues λ_m are bounded from below [1]. Furthermore, because $f_H(y)$ does not have zeros, this solution has the lowest eigenvalue $\lambda_0 = 0$ and the rest of λ_m are positive. Therefore, in this approximation, the Haissinski solution is stable.

5 PERTURBATION THEORY

How much the conclusion above depends on the assumption that the $\dot{\Phi}$ term in (11) is negligible can be analyzed by a perturbation technique. The approach is summarized below and the details can be found in [1]. We assume small deviation from the Haissinski solution. This deviation is expanded over $\psi_m(y)$ that are orthogonal eigenfunctions of (13). Now (11) together with the self-consistency condition result in an infinite linear system for the expansion coefficients. Looking for exponentially varying solutions $\propto e^{\mu \tau}$ transforms this system to a matrix equation. Its solutions are given by the roots of the determinant for the infinite matrix

$$M \equiv \delta_{n,k} + 2\Lambda \frac{\kappa_{n,k} \lambda_k}{\mu + \lambda_k}, \quad (17)$$

where

$$\kappa_{n,k} = i \frac{2\sigma_0}{Z_0} \int \frac{d\nu}{2\pi} \frac{Z(\nu)}{\nu} F_n(\nu) F_k^*(\nu), \quad (18)$$

$$F_n(\nu) \equiv \int dJ d\phi \frac{\psi_n(y(J))}{\sqrt[4]{D(J)}} e^{-\frac{H_H(J)}{2} + i\nu \sigma_0 x(J, \phi)/c} \quad (19)$$

and Z_0 is the impedance of free space. Positive roots $\mu > 0$ mean instability to monopole excitation of a bunch.

Since the off-diagonal terms of $\kappa_{n,k}$ are small and the others quickly converge to zero, a good approximation for the roots μ can be found by truncating the matrix M . If we truncate it to the lowest nontrivial rank 2 then zero determinant occurs for $\mu = -\lambda_1(1 + 2\Lambda\kappa_{1,1})$. Because $\lambda_1 > 0$, this root is positive when

$$2\Lambda\kappa_{1,1} < -1, \quad (20)$$

and this may be viewed as the criterion for the onset of the monopole instability.

The sign of $\kappa_{1,1}$ is given by the odd part of the impedance, $\text{Im}Z(\nu)$ which is negative for inductive impedance. As a result, for the most common case of positive α and inductive impedance, $\Lambda\kappa_{1,1} > 0$ and the Haissinski solution is stable.

The situation is different for negative momentum compaction or in the case of capacitive impedance. Each of these have been proposed to get shorter bunches and as a remedy against longitudinal instabilities. For illustration, we use a broadband ($Q = 1$) resonator impedance model (e.g. [6]) with shunt impedance R_s and resonator frequency ω_R . Using (18)-(19) we numerically compute the quantity $2\Lambda\kappa_{1,1}$ as a function of normalized bunch length $\sigma \equiv \omega_R\sigma_0/c$ at intensity $I \equiv 4\pi\Lambda R_s/Z_0 = -1$, where minus is due to $\alpha < 0$. The result and the threshold given by (20) are plotted in Fig. 2. It shows that a bunch is monopole unstable at this intensity provided σ_0 exceeds about 1/12 of the resonator wavelength. Note, that this intensity is not too high. For example, for $\sigma = 3$, it only leads to about 5% increase in the incoherent frequency spread [1].

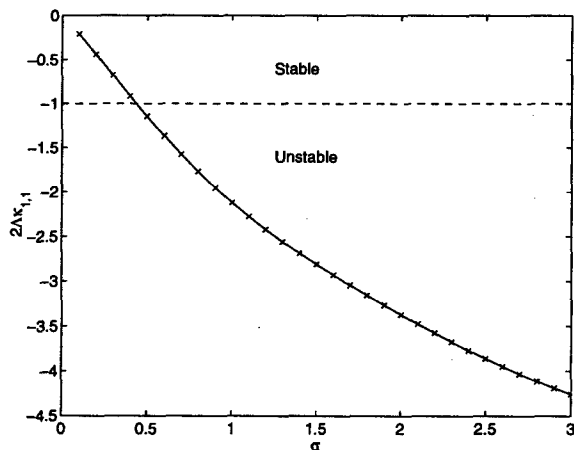


Figure 2: Monopole instability criterion (20) for broadband resonator impedance for $\alpha < 0$ and intensity $|I| = 1$.

6 DISCUSSION

We have investigated single bunch stability with respect to longitudinal monopole oscillations. These oscillations may

become unstable as a result of an imbalance between radiation excitation and damping. Since this effect falls beyond the scope of the linearized Vlasov approach, we employed a different method that has not been used for instability analysis. This method involves the transformation of the phase-averaged Fokker-Planck equation to a Schrödinger-like equation which is analyzed by perturbation analysis.

Utilizing this technique we have obtained a criterion, (20) for the onset of monopole instability. We have found that this instability does not appear in the most common case of storage ring operation with positive momentum compaction when the impedance is largely inductive. However, for $\alpha < 0$ bunches may become monopole unstable at modest intensity. We expect a similar behavior for the case of predominantly capacitive impedance and $\alpha > 0$.

The monopole instability could be one of the factors preventing high current operation of storage rings with negative momentum compaction. Many attempts of such operation have been tried (e.g. [7], [8]) mainly to shorten a bunch and to avoid the microwave instability [6]. Usually only the static bunch shape and the energy spread measurements are reported and it is hard to infer what particular effect was the limitation. However, in some cases, it appears that there is something other than the microwave instability, because the threshold increase predicted [9] for this instability is not observed. An evidence of monopole instability might include growth of the longitudinal beam size, in the absence of synchrotron sidebands to the rotation harmonics of a beam position monitor signal.

We hope that the technique described in this paper can be applied to other problems in accelerator physics that lead to the one dimensional Fokker-Planck equation.

7 ACKNOWLEDGMENTS

We thank Alex Chao, Albert Hoffman, Dave Pritzkau, Bob Siemann, and Dave Whittum for insightful discussions.

8 REFERENCES

- [1] S. Heifets, B. Podobedov, Phys. Rev. ST-AB (to be published).
- [2] H. Bruck, in *Accelérateurs circulaires des particules*, (Presses Universitaires de France, Paris, 1966).
- [3] J. Haissinski, *Nuovo Cimento* 18B, 72, (1973).
- [4] J. Schonfeld, *Ann. Phys.* 160, 149, (1985).
- [5] H. Risken, in *The Fokker-Planck Equation*, (Springer, Berlin, 1988).
- [6] A. Chao, *Physics of Collective Beam Instabilities in High Energy Accelerators*, (J. Wiley & Sons, Inc, New York, 1988).
- [7] M. Hosaka et. al., *Nuclear Instr. and Meth. in Physics Research A* 407 (1998) 234-240.
- [8] A. Nadji et. al., *Proc. EPAC-96, Barcelona*, 676, (1996).
- [9] S.X. Fong et. al., *KEK Preprint* 94-190, (1994).

HIGH ENERGY BEAM-BEAM EFFECTS IN CLIC

D. Schulte, CERN, 1211 Geneva 23, Switzerland

Abstract

In order to achieve high luminosity, the Compact Linear Collider (CLIC) has to be operated in the high-beamstrahlung regime at centre-of-mass energies in the few TeV range. Beam-beam effects for this case are simulated. The dependence of luminosity, luminosity spectrum and background conditions on the different beam parameters is investigated. In particular the effect of beam size, waist shift and offsets are considered; as well as the background due to beamstrahlung and secondary electro-magnetic and hadronic processes.

1 INTRODUCTION

The beams in future linear colliders must have very small transverse dimensions at the interaction point. This leads to strong transverse electro-magnetic beam fields. In the case of electron positron collision, the field of each beam focuses the other beam. Therefore the luminosity is enhanced. The bending of the trajectories causes the beam particles to emit photons, the beamstrahlung. This effect is comparable to synchrotron radiation and is described by the beamstrahlung parameter $\Upsilon = 2/3 \cdot E_c/E$, where E_c is the average critical energy of the emitted photon spectrum and E is the beam energy. The CLIC parameters for different centre-of-mass energies are shown in Table 1. The main focus of the paper is on the version with a centre-of-mass energy $E_{cm,0} = 3$ TeV. The designs with $E_{cm,0} \leq 1$ TeV have $\Upsilon \ll 1$, while for higher energies $\Upsilon \gg 1$ is used in order to achieve the required luminosity. As a result, the average energy loss δ of a beam particle due to beamstrahlung varies from a small correction (3.6 % at $E_{cm,0} = 0.5$ TeV) to a strong effect (42 % at $E_{cm,0} = 5$ TeV).

With large Υ the background due to the coherent pair production process is also drastically increased. The additional charge due to this process starts to affect the beam-beam interaction itself. This process has therefore been implemented into the program GUINEA-PIG [4].

2 COHERENT PAIRS

In a strong external field a photon can turn into an electron-positron pair [1]. This coherent pair creation is strongly suppressed for small values κ

$$\kappa = \frac{\hbar\omega}{mc^2} \frac{B}{B_c} = \frac{\hbar\omega}{E} \Upsilon$$

where $\hbar\omega$ is the photon energy, m the electron mass, B the magnetic field and $B_c = m^2c^2/(e\hbar)$. The coherent pair production is thus small if $\Upsilon \ll 1$ as it is the case for the colliders at centre-of-mass energies of 1 TeV or below. The number of coherent pairs is given in Table 1. It is negligible at $E_{cm} = 0.5$ TeV. At $E_{cm} = 1$ TeV it is a possible source of background, while at centre-of-mass energies of $E_{cm} \geq 3$ TeV it plays a very important role, since $\Upsilon \gg 1$.

The number of particles is, in the latter case, not only important as a background but is not negligible even compared to the number of beam particles. The simulation code had thus to be modified to also include the contribution of these particles to the beam fields.

Since the two particles in the pair have opposite charge and fly in the same direction their electro-magnetic fields neutralise immediately after production. If the particles move in the direction of the electron beam they will not experience a significant force from the electron beam since the electric and magnetic forces cancel. The electron is however focused by the oncoming positron beam while the positron is deflected to the outside. The different charges will thus separate. The equivalent is true for a pair moving in the direction of the positron beam. Effectively the charges of the bunch centres are thus increased.

The effect on the other background sources is not straightforward. While the total luminosity and number of photons is increased the number of high-energy photons is decreased since these have a larger probability of turning into pairs.

3 RESULTS

The luminosity spectra for the different parameters in Table 1 are shown in Fig. 1. As expected the higher relative energy loss at higher centre-of-mass energies leads to more degraded spectra, but even at $E_{cm} = 5$ TeV the fraction of the luminosity with $E_{cm} > 0.99E_{cm,0}$ remains significant.

The spectrum of produced coherent pair particles is shown in Fig. 2 and their angular distribution after the collision in Fig. 3. The particles are concentrated in small angles, so they would enter a mask that covers the final quadrupoles at the two ends of the detector. However, if they hit material inside these masks—like the final quadrupoles—they would produce secondaries, especially photons and neutrons that could penetrate the mask. Due to the enormous flux of particles this could lead to unacceptable background. It is therefore necessary to have an exit hole of about 10 mrad so that the particles can leave

Table 1: The beam parameters of CLIC at different centre-of-mass energies. All background numbers are per bunch crossing. The values for $E_{cm} \geq 3$ TeV differ from previous ones in [4] due to the inclusion of coherent pair production.

centre-of-mass energy	E_{cm}	[TeV]	0.5	1	3	5
repetition frequency	f_{rep}	[Hz]	200	100	75	50
bunches per train	N_b		150	150	150	150
particles per bunch	N	$[10^9]$	4	4	4	4
emittances	$\gamma\epsilon_x/\gamma\epsilon_y$	$[\mu\text{m}]$	1.88/0.1	1.48/0.07	0.6/0.01	0.58/0.01
transverse beam sizes	σ_x^*/σ_y^*	[nm]	196/4.52	123/2.7	40.4/0.58	26.7/0.45
bunch length	σ_z	$[\mu\text{m}]$	50	50	30	25
beamstrahlung parameter	Υ		0.18	0.56	8.7	26.4
luminosity(wo/w coh. pairs)	\mathcal{L}	$[10^{33}\text{cm}^{-2}\text{s}^{-1}]$	6.3	13.6	133/146	186/246
luminosity($E_{cm} > 0.99E_{cm,0}$)	\mathcal{L}_1	$[10^{33}\text{cm}^{-2}\text{s}^{-1}]$	4.5	5.1	40	44.5
average energy loss	δ	[%]	3.6	9.2	32	42
photons prod. per beam particle	n_γ		0.8	1.1	2.5	4.4
coherent pairs	N_{coh}		3.4	$2 \cdot 10^5$	$8 \cdot 10^8$	$2.9 \cdot 10^9$
pair p. ($\theta > 0.15, p_\perp > 20$ MeV/c)	N_\perp		2.9	8.0	135	314
hadronic events ($E_{cm} > 5$ GeV)	N_H		0.022	0.15	7.8	24
minijet pairs ($p_\perp > 10$ GeV/c)	N_{MJ}		$2.3 \cdot 10^{-5}$	$3.9 \cdot 10^{-4}$	0.13	0.75

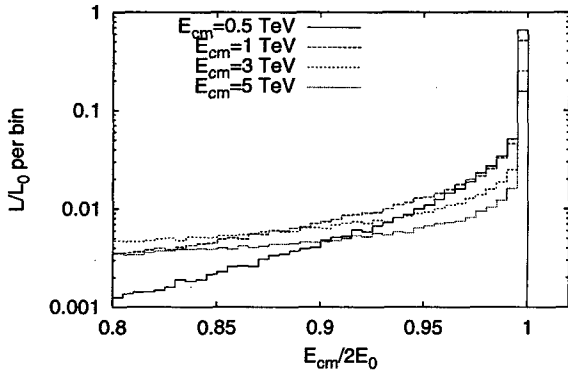


Figure 1: Normalised luminosity spectra for the different centre-of-mass energies.

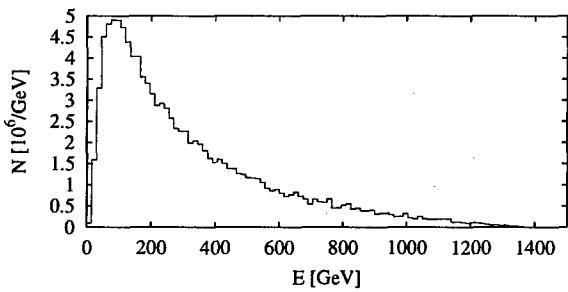
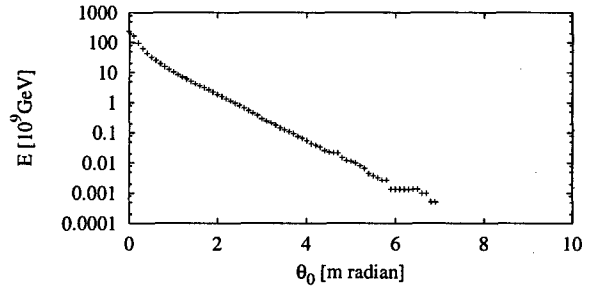
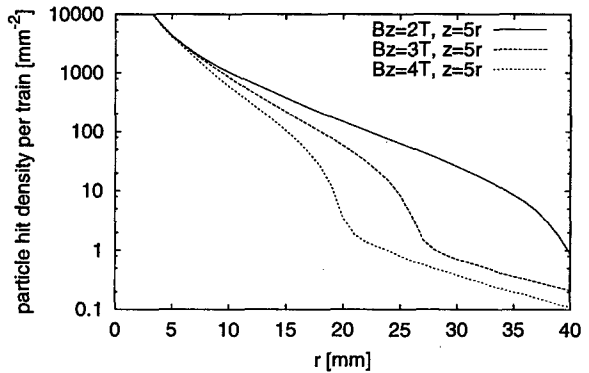


Figure 2: Spectrum of the produced coherent pairs (sum for both beams).

the detector.

4 INCOHERENT PAIR BACKGROUND

Electron positron pairs can also be produced via incoherent processes. The main contributions are the Breit-Wheeler process $\gamma\gamma \rightarrow e^+e^-$, the Bethe-Heitler pro-


 Figure 3: Total energy of the coherent pair particles of one beam with an angle of more than θ_0 .

 Figure 4: Number of particles that hit a vertex detector for different radii and magnetic fields. The angular coverage was kept constant at $\cos \theta = 0.98$.

cess $e\gamma \rightarrow e^+e^-$ and the Landau-Lifshitz process $ee \rightarrow ee + e^+e^-$. The photons are the ones from the beamstrahlung. The last two processes can be calculated replacing the beam particle e^\pm with an equivalent spectrum of virtual photons which are treated as being real.

The energy of the resulting pair particles is lower than those from the coherent process. While they are deflected the same way by the beam fields, they can have large initial angles. Therefore they can hit a vertex detector and complicate the reconstruction of the trajectories from physics events. Figure 4 shows the number of particles that hit the inner layer of a vertex detector with an opening angle of 200 mrad. Since the crossing angle is not optimised its small effect on the necessary radius is ignored.

5 HADRONIC BACKGROUND

Two photon collisions can also result in the production of hadrons. Except for the direct process $\gamma\gamma \rightarrow q\bar{q}$, also the one once resolved and twice resolved processes are possible. In these one or both of the photons interact as hadrons. The ansatz for the total cross section follows reference [3]

$$\sigma_H = 211 \text{ nb} \cdot \left(\frac{s}{\text{GeV}^2} \right)^{0.0808} + \sigma_2 \cdot \left(\frac{s}{\text{GeV}^2} \right)^{-0.4525}$$

Here, $\sigma_2 = 215 \text{ nb}$ is expected and $\sigma_2 = 297 \text{ nb}$ the most pessimistic value, which is normally used for the calculation of the number of hadronic events comparing different colliders [4]. The calculated number of events per bunch crossing for the 3 TeV design is 7.8.

An estimate of the hard transverse hadronic background can be found by calculating the number of minijet pairs with a transverse momentum $p_\perp > 10 \text{ GeV}/c$. For the reference design 0.13 events per bunch crossing are found, see Table 1.

6 VARIATION OF THE BEAM PARAMETERS

Without disruption, the optimal positions of the waists of the beam lay in the symmetry plane of the collision $z = 0$. With strong disruption, it is advantageous to have the vertical waists of the two beams before this plane [2]. In the case of CLIC this effect is visible, but the difference in luminosity is very small.

Changing the horizontal spot size has a significant impact on the average energy loss of the beam particles during collision. Figure 6 shows the luminosities with a centre-of-mass energy larger than a fraction $f = 0, 0.95, 0.99$ of the nominal one. While the luminosity in the high-energy peak of the spectrum depends weakly on the horizontal spot size, the total luminosity does so very strongly. At small σ_x also the number of coherent pairs increases drastically, their contribution to the total luminosity becomes significant. Depending on the requirements of the experiments, total luminosity can be traded against sharpness of the luminosity spectrum.

7 CONCLUSION

At high centre-of-mass energies, CLIC can achieve high luminosity with a spectrum that is still reasonably peaked

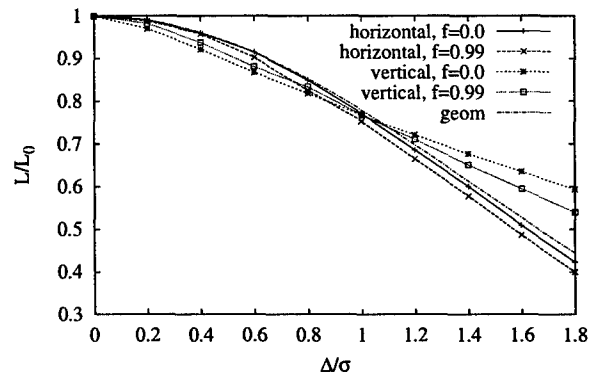


Figure 5: Relative luminosity for different offset normalised to the beam size. The curves correspond to total luminosity, luminosity of collision with $E_{cm} > 0.95E_{cm,0}$ and $E_{cm} > 0.99E_{cm,0}$.

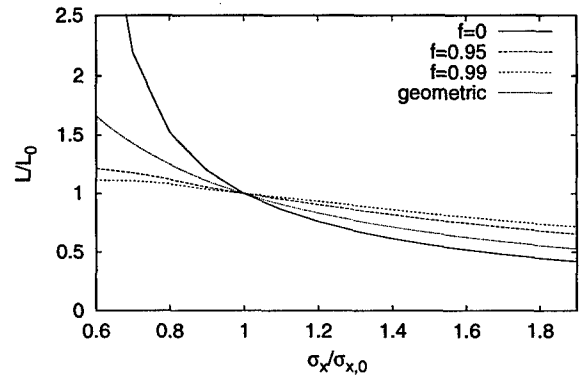


Figure 6: Luminosity for different horizontal spot sizes. The curves correspond to total luminosity, luminosity of collision with $E_{cm} > 0.95E_{cm,0}$ and $E_{cm} > 0.99E_{cm,0}$. For comparison the variation of the geometric luminosity is also shown.

at nominal energy. In contrast to lower energy machines, the coherent pair production plays an important role and not only as a background source. It also begins to affect the dynamics of the beam-beam interaction itself. An analysis of the impact the calculated electro-magnetic and hadronic background have on the detector components and on physics experiments remains to be done.

8 REFERENCES

- [1] P. Chen and K. Yokoya. "Beam-beam phenomena in linear colliders". *KEK Prepr. 91-2* (1992).
- [2] D. Schulte. "Study of Electromagnetic and Hadronic Background in the Interaction Region of the TESLA Collider". *TESLA-97-08* (1996).
- [3] G. A. Schuler and T. Sjöstrand. "A scenario for high-energy gamma gamma interactions". *Z. Phys. C*, **37** (1997) 677–688.
- [4] D. Schulte. "Beam-beam simulations with GUINEA-PIG". *ICAP 1998 and CERN-PS-99-014 (LP)*.

MEASUREMENT OF ELECTROMAGNETIC CROSS SECTIONS IN HEAVY ION INTERACTIONS AND ITS CONSEQUENCES FOR LUMINOSITY LIFETIMES IN ION COLLIDERS

P. Grafström*, CERN, CH, S. Datz, H.F. Krause, C.R. Vane, Oak Ridge, TN, U.S., H. Knudsen, U. Mikkelsen, Aarhus Univ., Aarhus, DK, R.H. Schuch, MSL, Stockholm, S, C. Scheidenberger, GSI, Darmstadt, D, Z. Vilakazi, Witwatersland Univ. Johannesburg, S. Africa.

1. INTRODUCTION

One of the principal limitations to the luminosity lifetime in high energy heavy ion colliders is the loss of beam particles due to the large cross section for beam-beam interactions. At very high energies there are essentially three processes that contribute to the losses: Electron capture, electromagnetic dissociation and hadronic processes.

The electron capture proceeds through several different mechanisms. In Radiative Electron Capture (REC) the ion picks up a target electron and simultaneously emits a photon. The capture can also be non-radiative (NRC) when an electron bound to an atom is picked up. However at very high energies a third mechanism is dominant. Electron-positron pairs are created in the strong electromagnetic pulse produced when the ion passes near the target nucleus and with a certain probability the electron can be captured (ECPP; Electron Capture via Pair Production). This later process, contrary to the two others, does not require an electron in the initial state, and thus the reaction can take place between two initially bare ions. This fact, together with the large cross section, which increases with energy, makes ECPP a potential limiting factor for high energy heavy ion colliders.

The strong electromagnetic field between the ions is also the origin of a possible nuclear dissociation of one or both of the ions in the interaction. The electromagnetic dissociation proceeds via photon excitation of the nucleus followed by decay through particle emission. These electromagnetic processes dominate at large impact parameters of the collisions. However contributions from hadronic interactions in more central collisions are not negligible even for very relativistic energies.

In this paper we report measurements on the total cross section for electron capture and measurements of the sum the total nuclear loss cross section through electromagnetic dissociation and hadronic interactions.

The experiment was performed at the CERN Super Proton Synchrotron (SPS) with completely stripped Pb^{82+} ions at 33 TeV (158 GeV/A). These measurements were mainly motivated by their theoretical importance as a test ground of QED under nonperturbative conditions. However, using the data and extrapolating to the energies of the RHIC and LHC colliders, limits on the beam lifetimes can also be estimated. Similar estimates have

been done previously [1,2,3,4], though our limits are based upon the first measurements made in an energy regime where the simple reliable scaling laws should be valid [5].

2. DESCRIPTION OF THE EXPERIMENT

The SPS external beam lines are used to transport the 33 TeV Pb^{82+} beam from the extraction points, via magnetic beam splitters, to a number of different experiments located between 500 m and 1 km away. The beam lines are comprised of a large number of bending magnets and quadrupoles. In our application we used the whole system of magnetic elements of one of the beam lines as a spectrometer for charge and mass selection.

The first set of main bends of the beam line are used to clean up the Pb^{82+} beam. There are contaminations of different species in the Pb^{82+} beam on the level of permille. The source of this contamination is mainly interaction in the steel of the beam splitters and in the material of the beam monitors. Using the first part of the beam line the contaminant species are identified and eliminated with a collimator located at a position of maximum dispersion. Thus a pure Pb^{82+} beam impinges on the target located in the middle of the transfer tunnel.

The second part of the beam line was used to analyse the different masses and charge states exiting the target. This was done by scanning a collimator slit across the beam phase space at a point which had a large momentum dispersion with a horizontal and vertical focus. The transmitted ions were counted in a Cerenkov counter at the end of the beam line. The momentum resolution of the system was $\sim 7 \times 10^{-4}$ and the different species could easily be separated and identified.

3. RESULTS

a) Electron capture

The cross section for electron loss is known to be several orders of magnitude bigger than the electron capture cross section. To separate the two cross sections it is necessary to measure the yield of Pb^{81+} ions as a function of different thicknesses for each target type. Beyond a certain target thickness, equilibrium between the number of Pb^{82+} and Pb^{81+} ions will be established. It is important to choose the

thicknesses of the target such that the Pb^{81+} growth curve is sampled below the equilibrium. Figure 1 gives an example of the measured fraction of Pb^{81+} ions versus thickness for Au targets.

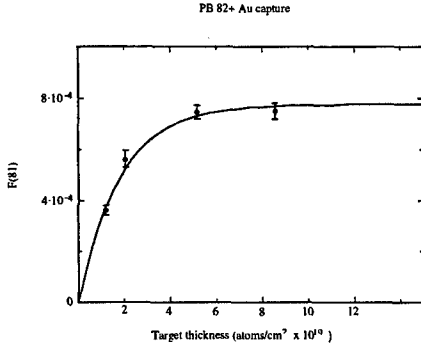


Figure 1: Fraction of Pb^{81+} ions for different thicknesses of Au targets.

The data of Figure 1 can be used to determine both the capture cross section (σ_c) and the cross section for electron loss (σ_e) by fitting the data using a two-state model [6]:

Table 1: Capture (σ_c) and electron loss (σ_e) cross sections. σ_{ECPP} is derived from σ_c (see text).

Target	Z	σ_c (kbarn)	σ_e (barn)	σ_{ECPP} (barn)
Be	4	0.15	0.23	0.18
C	6	0.31	0.44	0.36
Al	14	1.4	1.6	1.5
Ar	18	2.0	2.9	2.6
Cu	29	8.0	7.2	6.8
Kr	36	7.4	10.1	9.6
Sn	50	21	19.2	18
Xe	54	16	20.7	20
Au	79	53	44.3	43

As mentioned in the introduction three different reaction mechanisms contribute to the total capture cross section. Each of the processes has a different scaling behaviour relative to the target atomic number (Z_T) and the relativistic Lorentz factor of the incoming ion (γ). The radiative capture scales as Z_T/γ and the non-radiative capture has a Z_T^5/γ scaling. On the other hand, the capture from pair production scales as $Z_T^2 \ln \gamma$ [5] which makes this process dominate at high enough energies. In order to separate the ECPP contribution, which is the only one relevant for estimation of lifetimes in colliders, the calculated REC and NRC contributions [7] have been subtracted from the measured total capture cross section. The ECPP cross sections obtained in this way are indicated in Table 1 and plotted in figure 2. A dependence close to Z_T^2 is clearly seen.

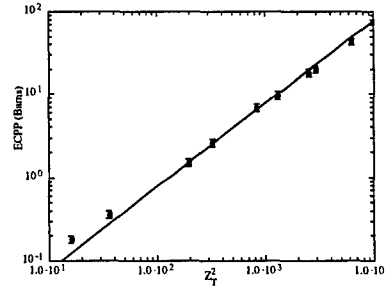


Figure 2: The measured σ_{ECPP} cross sections as a function of Z_T^2 .

b) Electromagnetic dissociation

In this case the full beam line optics and the slits were tuned for Pb^{82+} ions and the total cross section was determined from the measured attenuation in the target. The attenuation was obtained by integrating the transmitted beam intensities for a number of targets with different thicknesses

The total experimental cross sections obtained for the five targets are shown in Table 2.

The hadronic cross section and the electromagnetic cross section have very different energy and Z behaviours. Thus, it is necessary to separate the two contributions in order to be able to make an extrapolation to higher energies and other species. This has been done by a theoretical estimate of the hadronic contribution [8]. The calculated values of σ_h for the different targets are listed in Table 2. The table also lists a small contribution to the electromagnetic dissociation cross section from bound electrons in the target [8]. This contribution has to be subtracted as it will not be present in a collider. The last column of Table 2 lists the electromagnetic dissociation cross section from ion-ion interaction as obtained from our measurement, subtracting the hadronic and the small electron contribution.

Table 2: Measured total loss cross sections (σ_{meas}).

Target	Z	σ_{meas} (barn)	σ_h (barn)	σ_e (barn)	σ_{dis} (barn)
C	6	4.5	3.4	0.051	1.05
Al	14	7.4	4.3	0.13	2.97
Cu	29	15.2	5.5	0.28	9.43
Sn	50	31.0	6.6	0.48	23.9
Pb	82	64.0	7.9	0.78	55.3

4. CONSEQUENCES FOR LHC AND RHIC

The luminosity lifetime of high energy heavy ion collider is determined by the blow up of the beams due to the intra-beam scattering and the losses in the interaction(s) points due to beam-beam interactions. The intra-beam scattering is machine dependent while the losses due to interactions exclusively depend on the underlying physics processes. Here we will only consider the ultimate machine independent limit set by the physics processes.

To estimate the effect we have to extrapolate the relevant cross sections from SPS energies to RHIC and LHC energies. The Lorentz factor must be taken in a system where one of the nuclei is at rest and we get

$$\gamma = 2 \gamma_{\text{coll}}^2 - 1 \quad (1)$$

The effective Lorentz factor γ at RHIC and LHC with 100 GeV/u and 2.76 GeV/u, respectively, becomes $\gamma_{\text{RHIC}} = 2.3 \cdot 10^4$ and $\gamma_{\text{LHC}} = 1.7 \cdot 10^7$. This should be compared to $\gamma = 168$ at the SPS.

The electron capture from pair production cross section has been shown to scale as $A \ln \gamma + B$ [5] where A and B are independent of γ at $\gamma = \sim 100$. Including both perturbative and nonperturbative contributions, B is estimated to be -24 barn [9]. Applying this scaling to our measured cross section of Pb^{82+} on Au from Table 1 and making a small correction for the Z-dependence going to a symmetric Au or Pb system we obtain $\sigma_{\text{capture}}^{\text{RHIC}} = 94$ barn and $\sigma_{\text{capture}}^{\text{LHC}} = 204$ barn, respectively. For the target we applied a Z_T^2 scaling and a Z_p^5 behaviour was assumed for the projectile.

The scaling of the electromagnetic dissociation cross section is somewhat less straightforward. The strong electromagnetic field is simulated by an equivalent photon spectrum and the cross section is essentially determined by this spectrum folded with the photo-nucleon dissociation cross section. The calculation has to be done integrating over all photon energies. The energy dependence is slightly different depending on what part of the photon spectrum is considered [10]. The dominant contribution comes from the giant dipole resonance in the energy region up to 40 MeV and this part has a simple $\ln \gamma$ scaling [10]. At SPS energies this part constitutes 85 % of the total electromagnetic dissociation cross section [8]. Thus we have taken 85 % of our measured cross section from Table 2 and scaled it to higher energies. For the remaining 15 % we rely upon the calculation in Ref. [11] and adding this contribution we get $\sigma_{\text{dis}}^{\text{RHIC}} = 123$ barn and $\sigma_{\text{dis}}^{\text{LHC}} = 225$ barn.

The energy dependence of the hadronic cross section is taken from a dispersion relation calculation based on measurements of σ_{tot} and of the parameter p (ratio of real to imaginary part of the forward amplitude) for proton-proton interactions [12]. This calculation predicts an increase of the cross section by a factor 1.2 for RHIC and 2.4 for LHC relative to SPS energies. Assuming the same energy dependence for Au or Pb interactions we get $\sigma_{\text{had}}^{\text{RHIC}} = 9.5$ barn and $\sigma_{\text{had}}^{\text{LHC}} = 19$ barn.

Adding the three cross sections together, we get $\sigma_{\text{tot}}^{\text{RHIC}} = 227$ barn and $\sigma_{\text{tot}}^{\text{LHC}} = 448$ barn. It should be pointed out that these cross sections are somewhat larger than what was originally used for RHIC and LHC estimates.

The beam loss due to beam-beam interaction is proportional to σ_{tot} , the instantaneous luminosity and the number of interaction points n . With N being the number of ions in the beam we have:

$$dN/dt = -L(t) \sigma_{\text{tot}} n \quad (2)$$

Since L is proportional to $N(t)^2$ we get as solution to (3)

$$N(t) = N_0 / (1 + t/t_b), \quad (3)$$

where t_b is given by

$$t_b = N_0 / (L_0 \sigma_{\text{tot}} n). \quad (4)$$

Defining the luminosity lifetime as if the decay were exponential we have

$$t_{1/2} = \ln 2 / 2 t_b. \quad (5)$$

Using the above formulae and taking the values of the initial luminosity and number of ions in the beam from the RHIC and LHC design reports [1,2] we can calculate the luminosity half-life due to beam-beam interactions. We get a luminosity half-life of 7.3 hrs at RHIC and 5.8 hrs at LHC. These values are not far from those stated in the design reports which were 14 hrs and 6.7 hrs, respectively. They also are quite similar to those calculated by Baltz et al. in Ref. [4]. These previous estimates were based upon extrapolations from low energy data in combination with theoretical considerations. Our measurement at SPS energies, where the $\ln \gamma$ scaling is supposed to be valid, basically confirms that the assumptions made earlier were reasonable.

ACKNOWLEDGEMENT

Authors (H.F. Krause, C.R. Vane and S. Datz) acknowledge support by the U.S. Department of Energy, Office of Basic Energy Sciences, Division of Chemical Sciences under contract No: DE-ACO5-96OR22464 with Lockheed Martin Energy Research Corporation. H. Knudsen and U. Mikkelsen acknowledge support of the Danish Natural Science Research Council. We also would like to acknowledge preparation of the solid targets used in the electron capture measurements to the GSI target shop.

REFERENCES

- [1] LHC Conceptual Design, CERN/AC/95-05 (1995).
 - [2] RHIC Design Manual, BNL-52195 (1989).
 - [3] D. Brandt et al. CERN SL/94-04(AP).
 - [4] A.J. Baltz et al. Phys. Rev. **E54**, 4233 (1996).
 - [5] A.J. Baltz et al. Phys. Rev. **A44**, 5569 (1991).
 - [6] H.F. Krause et al. Phys. Rev. Lett. **80**, 1190 (1998).
 - [7] R. Anholt and U. Becker, Phys. Rev. **A36**, 4628 (1987).
 - [8] S. Datz, et al. Phys. Rev. Lett. **79**, 3355 (1997).
 - [9] A.J. Baltz et al. Phys. Rev. **A50**, 4842 (1994).
 - [10] G. Baur, C.A. Bertulani, Nucl. Phys. **A505** 835 (1989).
 - [11] M. Vidovic et al. Phys. Rev. **C48**, 2011 (1993).
 - [12] C. Augier et al., Phys. Lett. **B316** (1993) 448.
- #Email: per.grafstrom@cern.ch

STUDIES OF THE BEAM-BEAM INTERACTION FOR THE LHC[#]

S. Krishnagopal*, Centre for Advanced Technology, Indore, INDIA

M. A. Furman and W. C. Turner, LBNL, Berkeley, CA, USA

Abstract

We have used the beam-beam simulation code CBI to study the beam-beam interaction for the LHC. We find that for nominal LHC parameters, and assuming only one bunch per beam, there are no collective (coherent) beam-beam instabilities. We have investigated the effect of sweeping one of the beams around the other (a procedure that could be used as a diagnostic for head-on beam-beam collisions). We find that this does not cause any problems at the nominal current, though at higher currents there can be beam blow-up and collective beam motion.

1 THE CODE CBI

The code CBI (for Collective Beam-beam Interactions) is a self-consistent code that models the transverse beam-beam dynamics of beams of arbitrary distribution and ellipticity. It is a Particle-in-Cell (PIC) code that calculates the beam-beam force on a two-dimensional (transverse) Cartesian grid. The code is evolving and presently has the following features:

- (a) there is only one bunch per beam and there is only one collision point;
- (b) the beams are ultra-relativistic;
- (c) longitudinal dynamics is not modeled;
- (d) arc transport is linear;
- (e) radiation damping and fluctuations are put in once a turn and at one point in the ring;
- (f) there is no crossing angle;
- (g) transverse dimensions and distributions of the beams can be completely arbitrary.

Details of the code can be found in Refs. 1 and 2.

The code, as described above, is a strong-strong beam-beam code that is best suited for studying collective beam-beam effects in storage-ring e^+e^- colliders, particularly quadrupole effects (that affect the beam sizes). To our knowledge, quadrupole collective effects have never been studied for hadron colliders, and it seemed interesting and relevant to undertake this study for the Large Hadron Collider (LHC). In particular, in light of a proposal for sweeping one beam around the other as a diagnostic for head-on collisions [3], it seems relevant to look at possible beam-size blow-up and distortion as a consequence of quadrupole collective effects.

2 RESULTS

2.1 Nominal LHC Parameters

LHC parameters used in the simulations are given below in Table 1.

Table 1: Parameters for the LHC simulations.

Parameter	Value
Energy (TeV)	7.0
Revolution period (μ s)	88.9
Emittance (nm-rad)	0.5
Beta function (m)	0.5
Tunes (H, V)	(0.28, 0.31)
Nominal bunch current (mA)	0.2
Number of bunches	1

As can be seen from Table 1, the simulations use the nominal LHC parameters [4], except for the fact that we assume one bunch per beam, and therefore do not model parasitic beam-beam collisions. This is a feature we hope to incorporate into the code in the future.

We first ran our simulation for nominal LHC parameters, with the nominal bunch current of 0.2 mA, and with an idealized feedback system that takes out all collective dipole effects (centroid motion). For reasons of computer time, the simulations were run for only 90,000 turns. Figure 1a shows the rms beam sizes for the last 20,000 turns of the simulation: it is clear that for nominal LHC parameters there are no collective quadrupole effects that could affect the performance. Beam sizes are pretty much equal to their nominal value, and there is no sizable beam blow-up. When the current is increased to 1 mA (Fig. 1b) there is some beam blow-up, but all beam sizes are the same, and there is no indication of collective behavior.

* Work supported by the US Department of Energy under contract No. DE-AC-03-76SF00098.

* Email: skrishna@cat.ernet.in

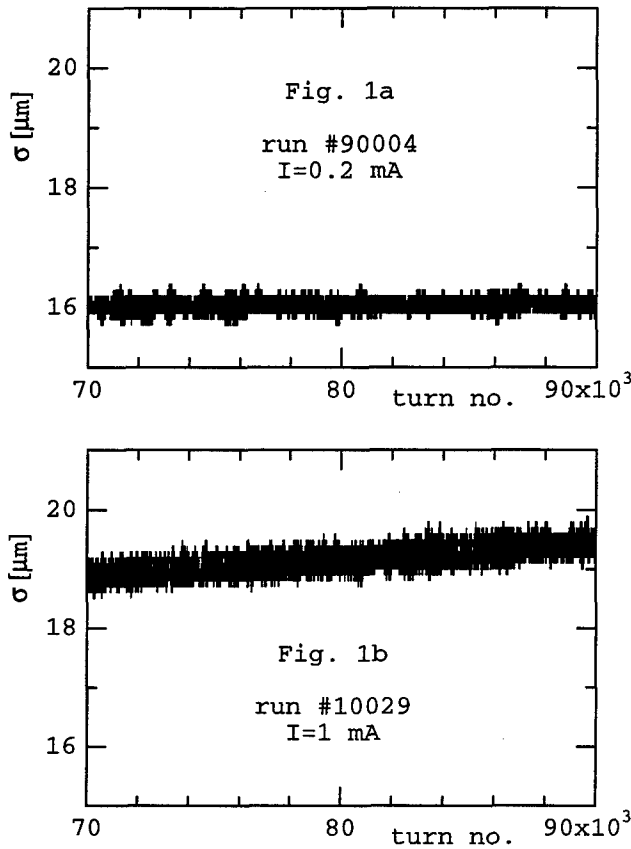


Figure 1: For nominal LHC parameters, plot of beam sizes as a function of turn number for the last 20,000 turns; (a) for the nominal current of 0.2 mA, and (b) for a current of 1 mA.

2.2 Sweeping One Beam Around The Other

We next looked at the effect of sweeping one beam around the other. We chose to sweep beam 1 around beam 2. In this case, after each turn, as before, the centroids of the two beams are zeroed, implementing the idealized feedback system. Then the centroid of beam 1 is displaced a fixed radial distance from the zero position. Two input parameters govern this displacement: the displacement and the rotation period (in number of turns). The latter is the number of turns taken to sweep beam 1 once around beam 2.

In the simulations described here, we fixed the rotation period at 10 turns, and looked at the effect on the beam sizes of different displacements and different currents. We looked at two different displacements, $\sigma/5$ and $\sigma/10$, where σ is the nominal size of the beams (15.8 μm). We looked at five different currents, starting from 0.1 mA, up to 2 mA. All simulations were run for 90,000 turns, and with the idealized feedback system turned on. Note that only one bunch is simulated in each beam: there are no parasitic collisions.

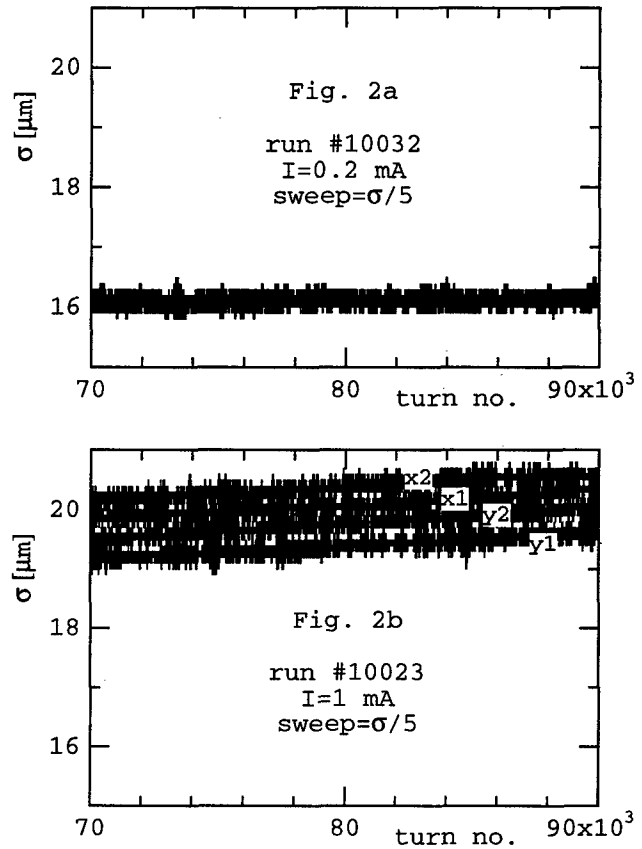


Figure 2: Beam size as a function of turn number for beam 1 being swept around beam 2 with a radial displacement of $\sigma/5$; (a) at $I = 0.2$ mA, and (b) at $I = 1$ mA.

Figure 2 shows the beam-sizes as a function of turn number, for the last 20,000 turns, when the displacement is $\sigma/5$. One can see that for the nominal current of 0.2 mA the beam-sizes are all equal, and equal to the nominal size of 15.8 μm , indicating that there are no deleterious collective beam-beam effects. At a current of 1 mA, however, it is clear that the beams are being blown-up, and by unequal amounts: in other words, the beams are becoming elliptical, and there is a flip-flop developing. This is a signature of quadrupole collective beam-beam effects. The same picture is seen in Figure 3, for a displacement of $\sigma/10$. Again, at a current of 0.2 mA the picture is benign, but at 1 mA a flip-flop has clearly set in.

Table 2 below gives a clearer picture of how the dynamics evolve with current. At a current of 0.1 mA, there is no discernible blow-up of the beam, and no collective motion; all beam sizes are equal, and equal to the nominal size of 15.8 μm . When the bunch current is increased to the nominal LHC value of 0.2 mA, there is slight beam blow-up, but all beam sizes are still equal, which indicates there is no collective motion. At a current of 0.5 mA there are the first signs of collective motion. All beam sizes are no longer equal: a flip-flop instability

has developed. As the current is increased further, the beam blow-up as well as the flip-flop become larger.

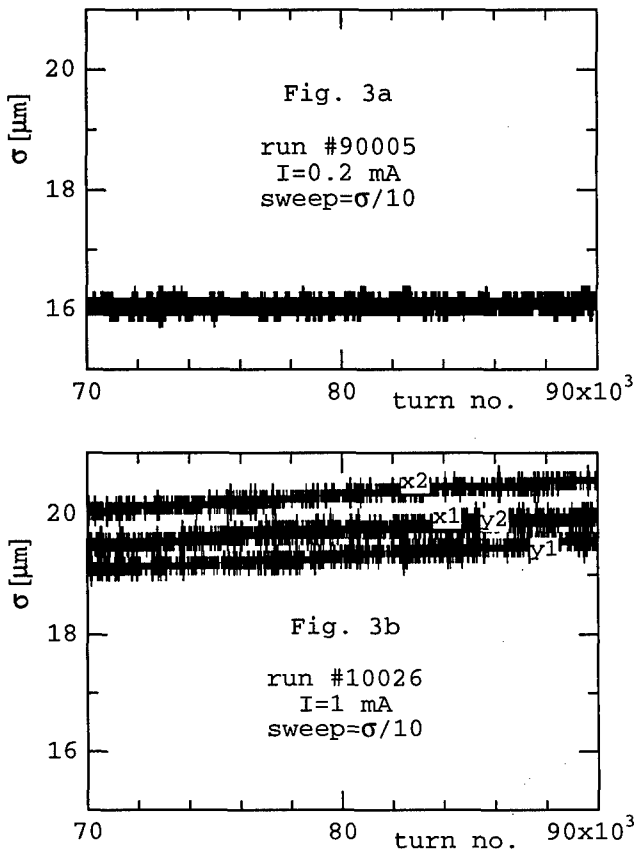


Figure 3: Beam size as a function of turn number for beam 1 being swept around beam 2 with a radial displacement of $\sigma/10$; (a) at $I = 0.2$ mA, and (b) at $I = 1$ mA.

Table 2: All beam sizes at the end of the simulation (after 90,000 turns), at different currents, for a displacement of $\sigma/5$. Nominal beam size is $15.8 \mu\text{m}$. Recall that beam 1 is being swept around beam 2.

Current (mA)	σ_{x1} (μm)	σ_{y1} (μm)	σ_{x2} (μm)	σ_{y2} (μm)
0.1	15.8	15.8	15.8	15.8
0.2	16.2	16.1	16.1	16.1
0.5	17.4	17.4	17.1	16.9
1.0	20.6	20.0	20.4	19.6
2.0	28.1	25.4	27.6	25.1

3 DISCUSSION AND CONCLUSIONS

It is clear from Figs. (1a), (2a) and (3a), that for nominal LHC parameters, particularly the nominal bunch current of 0.2 mA, there is little beam blow-up, and no collective motion, whether or not one beam is swept around the other. When one beam is swept around the other, collective effects are seen from a bunch current of around 0.5 mA (over twice the nominal value), though at this current they are still small.

It should be emphasized that our simulations do not model multiple bunches and therefore parasitic collisions. These could have a significant impact on collective beam-beam dynamics. We plan to extend the code to handle these effects.

In the simulations reported here dipole motion is removed by modeling an ideal feedback system in which the centroids of the two beams are zeroed every turn. The consequences of turning off this feedback, particularly on collective dipole motion, need to be explored. We plan to do this in the near future.

In conclusion, we have studied the beam-beam interaction at the LHC using the code CBI. We find that for nominal LHC parameters, collective quadrupole effects should not be an issue. If one beam is swept around the other, for diagnostic purposes, then collective issues still are unimportant at the nominal bunch current of 0.2 mA, though they could become important at currents around and above twice the nominal value.

One of us (SK) would like to thank the other two for an invitation to visit the Lawrence Berkeley National Laboratory during the summer of 1998, when most of this work was done. We are grateful to NERSC for supercomputer support.

4 REFERENCES

- [1] S. Krishnagopal, Phys. Rev. Lett. **76**, 235 (1996).
- [2] S. Krishnagopal, Centre for Advanced Technology Internal Report, CAT-95/5 (1995).
- [3] *Luminosity Instrumentation for the Absorbers in the Low Beta Insertions of the LHC*, W. C. Turner, LBNL-42180 (Aug. 1998), submitted for publication to PRST-AB.
- [4] *The Large Hadron Collider: Conceptual Design*, CERN/AC/95-05 (LHC), 20 October 1995.

Effect of the Beam-Beam Interactions on the Dynamic Aperture of the LHC at Collision *

N. Gelfand, C. Johnstone, T. Sen,[†] and W. Wan, FNAL, Batavia, IL 60510

Abstract

The dynamic aperture of the LHC at collision energy is limited by the field errors in the IR quadrupoles being built at FNAL and KEK. The $300\mu\text{rad}$ crossing angle, incorporated in the design to reduce the effect of the long-range beam beam interactions, enhances the effect of the multipoles on the dynamic aperture. We have investigated the possibility of a different crossing angle with a more accurate modelling of the long-range interactions. Tune scans have been done to determine if a better choice of the tunes exists.

1 INTRODUCTION

At collision energy, nonlinear fields in the interaction region (IR) quadrupoles are the most important in determining the dynamic aperture of the LHC. The field quality "seen" by the beam while traversing these quadrupoles depends on the crossing angle of the beams at the IP. A study of the dynamic aperture, taking into account only the nonlinearities of the IR quadrupoles [1], had assumed a crossing angle of $300\mu\text{rad}$. This was based on an earlier study [2] which had determined this to be the optimum value when both the IR quadrupole fields and beam-beam interactions were included.

On each side of the IP, there are fifteen long-range interactions, six of which occur in the drift space before the first quadrupole while the remaining nine occur in the triplet quadrupoles or in the drift spaces between them. Over the drift region the beams are round and the dimensionless separation D_{sep} between the beams (measured in units of the rms beam size) stays nearly constant and equal to the crossing angle measured in units of the beam divergence at the IP. Once the beams are focused by the triplets, D_{sep} is no longer constant. Figure 1 shows, for example, that with a crossing angle of $300\mu\text{rad}$, the separation varies between 7.8σ to 13.6σ . In addition within the triplets, the beams are no longer round and the aspect ratio varies between 0.6 to 1.9. The phase advance from the IP to the locations of the long-range kicks varies from 82° to 89° through the drift section while within the triplets, it remains nearly constant at 90° . In order to reduce tracking time, earlier studies of the impact of the beam-beam interactions on the dynamic aperture made several approximations in treating the long-range interactions, viz. i) the phase advances between the long range kicks are negligible, ii) the beams are round at all locations of the long range kicks, and iii) the dimensionless beam separation stays constant. As we have seen, these assumptions break down in different regions within the IRs.

* Work supported by the U.S. Department of Energy under contract No. DE-AC02-76HO3000

[†] email: tsen@fnal.gov

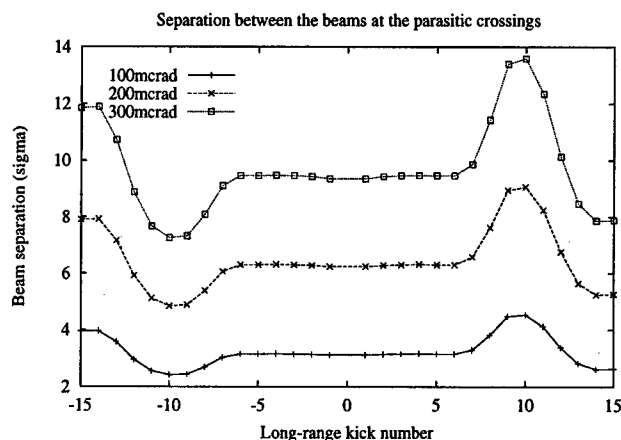


Figure 1: The separation between the two beams at each of the 30 parasitic crossings in a high luminosity IR for total crossing angles of 100, 200 and $300\mu\text{rad}$. The separation, measured in units of the rms size of a beam, stays constant within the drift section (kicks from -6 to +6) but varies within the triplet quadrupoles.

In order to determine the optimum crossing angle more accurately, we have not made any of these approximations. Another reason for a second look at this issue is that the error harmonics in the IR quadrupoles have changed significantly since the last study was done. Specifically, reduced measurement errors have lowered estimates of high order harmonics by nearly an order of magnitude.

Among the several issues associated with the crossing angle geometry are: reduction in luminosity, orbit offset in IR quadrupoles which reduces the physical aperture, dispersion wave generated by the orbit offset, increase in the strength of the coupling, change in the beam-beam tune spreads, excitation of synchro-betatron resonances etc. The optimal crossing angle will ultimately be determined during operations. Our aim here is to study the impact of the choice of crossing angle on the required field quality of the IR quadrupoles and the complexity of correction schemes.

2 LATTICE DESCRIPTION

The version used is derived from the MAD lattice V5.1. The only lattice nonlinearities are the chromaticity correcting sextupoles and the systematic and random errors of the body harmonics of the triplet quadrupoles but not the uncertainties in the systematic nor the errors in the ends. Two different codes TEVLAT and MAD were used for tracking to 10^3 turns.

Sixteen of the thirty two IR quadrupoles are to be built at

n	Normal	Skew
	$[(b_n), db_n, \sigma(b_n)]$ FNAL/KEK1	$[(a_n), da_n, \sigma(a_n)]$ FNAL/KEK1
3	0, .3, .8/0, .51, 1.0	0, .3, .8/0, .51, 1.0
4	0, .2, .8/0, .29, .57	0, .2, .8/0, .29, .57
5	0, .2, .3/0, .19, .38	0, .2, .3/0, .19, .38
6	0, .6, .6/0, .5, .19	0, .05, .1/0, .10, .19
7	0, .06, .06/0, .05, .06	0, .04, .06/0, .05, .06
8	0, .05, .05/0, .02, .03	0, .03, .04/0, .02, .03
9	0, .03, .03/0, .01, .01	0, .02, .02/0, .01, .01
10	0, .03, .03/-1.0, .03, .01	0, .02, .03/0, .01, .01

Table 1: Design field harmonics, at a reference radius of 17mm, of the IR quadrupoles to be built at FNAL and KEK. KEK1 refers to the first version. In the revised version (KEK2), $|(b_{10})| \leq 0.25$. Harmonics are expressed in units of 10^{-4} .

Fermilab [3] and the other half will be built at KEK [4]. The designs of the cross-sections of the quadrupoles at the two laboratories differ and so do the expected error harmonics. Earlier plans had called for the magnets in one of the high luminosity insertions IR5 to be built at Fermilab while the magnets in the other high luminosity insertion IR1 would be from KEK. In part due to the non-zero design value of $\langle b_{10} \rangle$ in the KEK magnets, it is presently proposed that the outer magnets Q1 and Q3 of each triplet be KEK magnets and the inner two magnets Q2a and Q2b (where the beam size is large) be Fermilab magnets.

3 DYNAMIC APERTURE

It is desirable to keep the minimum beam separation greater than 5σ so the crossing angle must be greater than $100\mu\text{rad}$. We have calculated the dynamic aperture for various scenarios with crossing angles ϕ in the range $100\mu\text{rad} \leq \phi \leq 300\mu\text{rad}$.

In the initial studies, particles were tracked assuming that the error harmonics of all the triplet quadrupoles were those of the Fermilab quadrupoles. Subsequently the first, and later second, version of the KEK error harmonics was incorporated in the lattice. Table 2 shows the dynamic aperture calculated for all these different cases at a constant crossing angle of $300\mu\text{rad}$ but without the beam-beam interaction. The large value of $\langle b_{10} \rangle = -1$ in KEK1 leads to a significant drop in the dynamic aperture of about 2σ . The reduced value $\langle b_{10} \rangle = -0.25$ in KEK2 improves the dynamic aperture by about 2σ . Mixing the magnets as described earlier further increases the dynamic aperture by $.6\sigma$. In the following, all tracking calculations assume the mixed magnets scenario.

The beam-beam interactions are modelled in a similar fashion in TEVLAT and MAD, e.g. each kick is treated individually with the proper beam separation and the Bassetti-Erskine expressions are used for kicks from non-round beams. As a check, the tune footprint with only the beam-

IR Magnet Description	$\langle DA \rangle \pm \sigma_{\langle DA \rangle}$
FNAL only	11.2 ± 1.7
FNAL + KEK1 ($\langle b_{10} \rangle = -1$)	$9.0 \pm .9$
FNAL + KEK2 ($\langle b_{10} \rangle = -0.25$) (no mixing)	11.1 ± 1.1
FNAL + KEK2 ($\langle b_{10} \rangle = -0.25$) (with mixing)	11.7 ± 1.2

Table 2: Dynamic aperture (with TEVLAT) with only systematic and random errors in the body of the IR quadrupoles and without the beam-beam interaction.

beam interactions at a crossing angle of $300\mu\text{rad}$ was calculated with TEVLAT at amplitudes up to 6σ and compared with that found by MAD [6]. The tune shifts with amplitude agreed to within 10%.

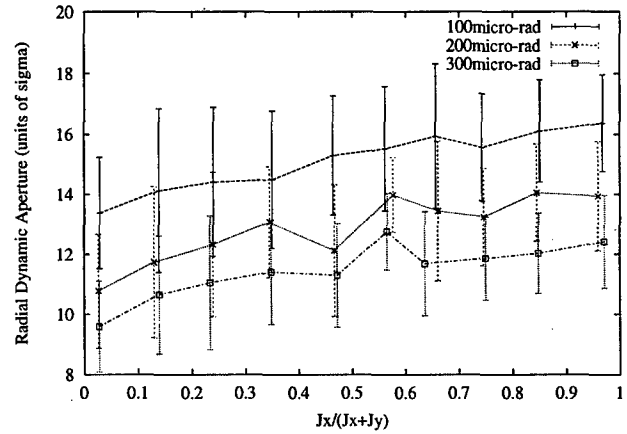


Figure 2: The dynamic aperture (in units of the rms beam size) calculated with TEVLAT at different aspect ratios in emittance space for different crossing angles. Triplet errors and the beam-beam interactions are included. The dynamic aperture clearly decreases with increasing crossing angle.

Figure 2 shows the dynamic aperture, averaged over 20 seeds, as a function of the transverse emittance ratio for three crossing angles. We observe that as the crossing angle increases from 100 to $300\mu\text{rad}$, the dynamic aperture decreases. We have also calculated the dynamic aperture at crossing angles of 150, 225 and $250\mu\text{rad}$. Taken together, our results show that the dynamic aperture, even after including the beam-beam interactions, decreases nearly monotonically at all emittance ratios as the crossing angle increases.

Two different distributions of 20 random seeds were used with TEVLAT and MAD. Table 3 shows that the results from the two codes, both without and with the beam-beam interaction, are within 1-1.5 σ of each other. Some of these differences may be due to the different seeds used and are within the statistical uncertainties of the averages. Both of these codes show clearly that the dynamic aperture decreases with increase in crossing angle. This table also

ϕ (μ rad)	$\langle DA \rangle \pm \sigma_{\langle DA \rangle}$ TEVLAT Beam-beam OFF/ON	$\langle DA \rangle \pm \sigma_{\langle DA \rangle}$ MAD Beam-beam OFF/ON
100.0	$15.0 \pm 0.9 / 14.7 \pm 1.1$	$13.8 \pm 1.1 / 13.3 \pm 1.0$
200.0	$13.8 \pm 0.8 / 12.4 \pm 1.1$	$12.9 \pm 1.2 / 12.7 \pm 1.1$
300.0	$11.7 \pm 1.2 / 11.0 \pm 1.1$	$11.6 \pm 1.6 / 12.0 \pm 1.3$

Table 3: Dynamic aperture without and with the beam-beam interaction calculated with TEVLAT and MAD at different crossing angles. The averages are over emittance space and over 20 random seeds.

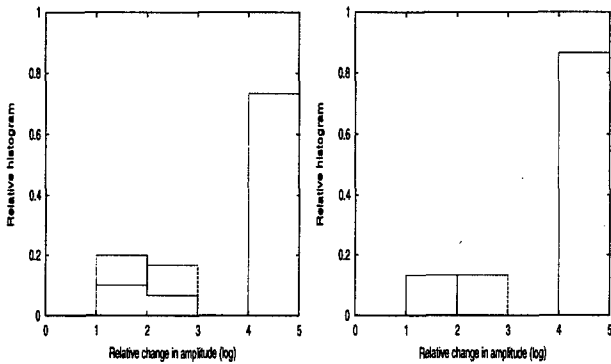


Figure 3: Normalized histograms of the relative amplitude growth (shown on a log scale) due to the resonances $2\nu_x + \nu_y = 186$ (left) and $2\nu_x + 2\nu_y = 245$ (right). The histograms represent data from tracking with 30 seeds.

shows that the effect of the beam-beam interactions is always small compared to that of the IR quadrupole fields.

At a crossing angle of $300\mu\text{rad}$, tracking results have shown that higher order multipoles beyond b_{10}, a_{10} also have an impact on the dynamic aperture [5]. We expect that the higher orders will have a smaller effect at smaller crossing angles due to the reduced feed-down.

4 RESONANCES AND TUNE SCANS

Among the low order resonances we have identified two, the skew third order resonance $2\nu_x + \nu_y$ and the normal fourth order resonance $2\nu_x + 2\nu_y$, as being driven strongly by the IR quadrupole nonlinearities. Figure 3 shows the normalized histograms, obtained with 30 seeds, of relative amplitude growth due to these resonances. For example, in more than 85% of the cases, the $2\nu_x + 2\nu_y$ resonance leads to a larger than 10^4 fold amplitude growth. Compensating these resonances with the MCBX and MCQS correctors may improve the dynamic aperture. Since the beam-beam interactions do not have a significant impact on the dynamic aperture at the crossing angles of interest, any correction scheme devised to correct for the nonlinearities of the IR quadrupoles should be adequate even when the beams col-

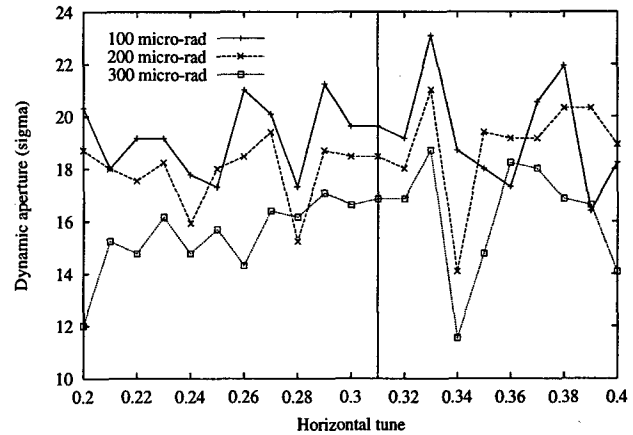


Figure 4: Tune scan of the dynamic aperture with a constant tune split, $\nu_y - \nu_x = 0.01$. The vertical line represents the design tune, $\nu_x = 0.31, \nu_y = 0.32$.

lide.

A tune scan along the diagonal in emittance space and averaged over 10 seeds is shown in Figure 4. The tune split is kept constant at $\nu_y - \nu_x = 0.01$. This figure suggests there exist possible tunes with dynamic apertures larger than at the chosen tunes. More detailed tracking studies, including tracking for off-momentum particles undergoing synchrotron oscillations, will be required to confirm the preliminary results shown here.

5 CONCLUSIONS

Our results suggest that the target dynamic aperture of 12σ can be achieved with a $200\mu\text{rad}$ crossing angle, use of nonlinear correctors and the present design harmonics of the IR quadrupoles. It is currently expected that tuning shims will not be included in the final cross section design given the continuing improvement in field quality seen in the first model magnets [7]. At $200\mu\text{rad}$, the shims are even less of a requirement and also the nonlinear correctors strengths are reduced. Our tune scans suggest that the dynamic aperture may be improved by a different choice of working point.

Thanks to J. Gareyte, H. Grote, J. Kerby, J.P. Koutchouk, M. Lamm, S. Peggs, R. Ostojic, F. Ruggiero, J. Strait, J. Wei and A. Zlobin.

6 REFERENCES

- [1] J. Wei, et.al. Proc. EPAC 1998, p 380
- [2] W. Chou, D. Ritson, Proc. PAC 1997
- [3] J. Kerby et.al. Proc. ASC 1998, R. Bossert et.al., this conference
- [4] Y. Ajima et.al., Proc. EPAC 1998, p 2047
- [5] N. Gelfand, this conference
- [6] H. Grote, O. Meincke, LHC Project Note 161 (1998)
- [7] J. Kerby, personal communication.

REALISTIC PREDICTION OF DYNAMIC APERTURE AND OPTICS PERFORMANCE FOR LEP

John M. Jowett*, CERN, Geneva, Switzerland

Abstract

Over the two-decade lifetime of the LEP project, techniques for evaluating the quality of optical configurations have evolved considerably to exploit the growth in computer power and improved modelling of single-particle dynamics. These developments have culminated in a highly automated Monte-Carlo evaluation process whose stages include the generation of an ensemble of imperfect machines, simulation of the operational correction procedures, correlation studies of the optical functions and parameters of (both) beams, 4-dimensional dynamic aperture scans and tracking with quantum fluctuations to determine the beam core distribution. We outline the process, with examples, and explain why each step is necessary to realistically capture essential physics affecting performance. The mechanisms determining the vertical emittance, radial beam distribution and dynamic aperture are especially important. As a storage ring in which an unusual variety of optics have been tested, LEP provides a valuable test case for the predictive power of the methodology.

1 INTRODUCTION

Persistent disagreement of, say, a factor of two between computed and measured dynamic apertures would invalidate computation as a rational means of assessing the quality of a storage ring optics.

However, the potential of an optical configuration only becomes clear after some weeks of operational performance maximisation (and may also require hardware changes). Such tests are expensive in large machines like LEP. Accurate computational appraisal is therefore vital to estimate not only dynamic aperture but also—and consistently—the gamut of optical quantities culminating in the beam sizes at the collision points.

The conceptual framework and tools brought to bear on the problem of performance prediction for LEP have evolved considerably over some 20 years. Rather than review the history (traceable through the citations), this paper will describe current best efforts to model the various LEP optics, emphasising recent high energy operation (LEP2) where the synchrotron radiation effects are strong.

2 CONCEPTS AND METHODOLOGY

In this paper, **computing the linear machine** is shorthand for the calculation of the 6D closed orbit including radiation, the eigenvectors of linear oscillations around it (hence all optical functions and the canonical transformations to

the eigenmodes), the 3 tunes, energy loss, damping rates, emittances, etc. Usually, the eigenmodes correspond approximately to (1,2) horizontal and vertical “betatron” oscillations and (3) “synchrotron” oscillations. These calculations are implemented in the program MAD [1].

In MAD’s tracking, radiation damping and quantum excitation arise naturally [2] because all particle momentum changes are computed locally, according to the distribution of $\gtrsim 300$ RF cavities and the canonical co-ordinates of the particle in each multipole magnet.

The **dynamic aperture** is the *basin of attraction of the closed orbit* in deterministic tracking with radiation damping [2] (without quantum fluctuations). This definition is computationally unambiguous and independent of the number of turns tracked beyond a certain minimum (for LEP2, 100 turns are ample).

The dynamic aperture of LEP is essentially determined by three classes of intentional non-linear elements: chromaticity sextupoles, RF cavities and focusing quadrupoles. Although quadrupoles provide linear focusing, their non-linear radiation terms are responsible for the ultimate dynamic aperture limit. (Higher order multipole errors are less important.)

A **dynamic aperture scan** is carried out by varying the action variables $(I_1, I_2, I_3) \in (\mathbb{R}^+)^3$ over a spherical polar grid $\mathbb{R}^+ \times [0, \pi/2]^2$. At each point, the phase $\phi_3 \in [0, 2\pi)$ of the third mode is also scanned. A dynamic aperture is typically the result of tracking 1000–2000 particles and is returned as a surface in the 3D action space [3].

The correction procedures applied are designed to *emulate the real operational procedures*, as responses to measured quantities without knowledge of the imperfections, rather than the best that could be done computationally.

In outline, the optics evaluation procedure is:

1. Generate ideal machine with detector solenoids, RF, and radiation switched off.
2. Install vacuum chamber elements in all quadrupoles to provide aperture limitations in tracking.
3. Compute solenoid compensation with tilted quadrupoles, to be applied in calculations with the solenoids on.
4. Compute linear machine and dynamic aperture scan of ideal machine (with solenoids, RF and radiation on) as a reference.
5. Generate an ensemble (typically 30) of machines with typical random misalignments, tilts and field errors in all dipoles, quadrupoles and sextupoles.

For each machine in the ensemble,

- (a) Correct the non-radiating closed orbit independently in the two planes (to $\sqrt{\langle x^2 \rangle} = 0.6$ mm,

* John.Jowett@cern.ch, <http://wwwslap.cern.ch/~jowett/>

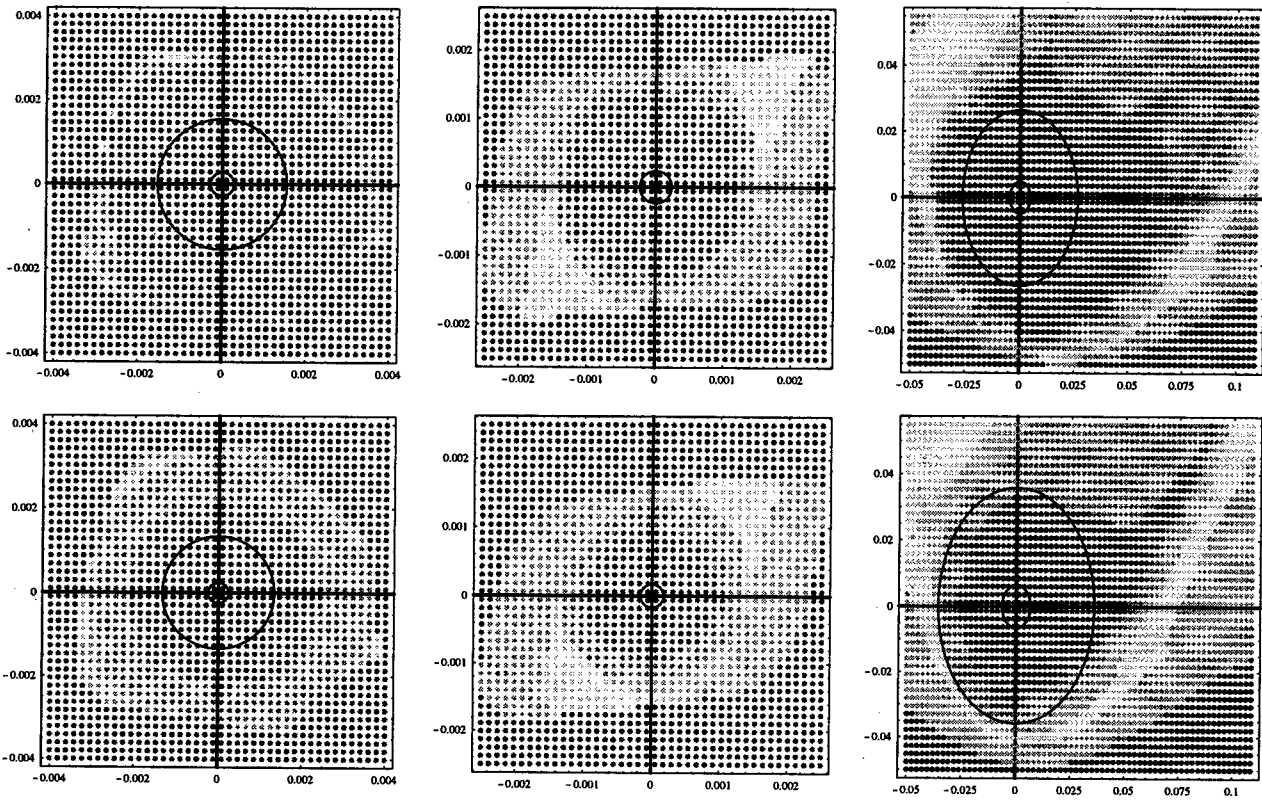


Figure 1: Shrinking of the dynamic aperture at the ultimate energy: the upper row shows survival plots in the normalised phase planes (all co-ordinates in \sqrt{m}) of the 3 normal modes at 94 GeV with $J_x = 1$ and a comfortable $V_{RF} = 2961$ MV. The lower row shows the same imperfect machine at 100 GeV with $J_x = 1.5$ and $V_{RF} = 3265$ MV just sufficient. Contours of 1 and 5.5σ of the notional gaussian distributions are shown to give the scale. Most of these 6400 particles rotate *anti-clockwise* from the initial conditions shown. Initial conditions are coloured with a hue indicating survival time, ranging from violet (dark central stable zone) to red (loss in one turn).

$$\sqrt{\langle y^2 \rangle} = 0.4 \text{ mm}.$$

- (b) Switch on solenoids, RF and radiation. For the e^+ beam, correct the IP optics (β_y^*) and tunes using “knobs” as in operation.
- (c) Save all the imperfections and their corrections, reverse the ideal machine structure and rebuild the *physically equivalent* machine for the e^- beam. Thus, some corrections appropriate for the positrons are applied to the electron beam and may enhance the differences between the beams. Tune splits between beams can be $\gtrsim 0.01$, depending on the distribution of V_{RF} .
- (d) Compute the linear machine and carry out a dynamic aperture scan for each beam.
- (e) Track with quantum fluctuations [2] (for $\gtrsim 200$ damping times) to estimate non-linear effects on the emittances and beam sizes.

This process involves $\gtrsim 1000$ multifarious runs of MAD, all managed by a Mathematica [4] notebook interface that prepares the input and absorbs the results into a structured database of function definitions.

Other notebooks load the database to display and correlate machine parameters or generate comprehensive re-

ports [6] on an optics. These include orbit and optics at key elements, emittances, tunes, survival data and dynamic apertures and differences between beams. The environment is open-ended and congenial: it is easy to compute derived quantities such as beam-overlaps or centre-of-mass energies at the experiments; several databases can be loaded to make comparisons across optics, etc.

3 SAMPLE RESULTS

3.1 Dynamic aperture

LEP has operated with several optical configurations [3, 7] with varying arc cell phase advances (μ_x, μ_y). Dynamic aperture measurements have been made, where possible, with two or three different methods.

For certain optics, results of tracking with radiation are quantitatively in agreement with earlier calculations without radiation. This is the hallmark of certain physical mechanisms, e.g., detuning with amplitude onto an integer resonance. Including radiation, or even imperfections, makes little quantitative difference although the radiative beta-synchrotron coupling instability (RBSC) [2, 3] effect always steps in to accelerate initial amplitude growth. In

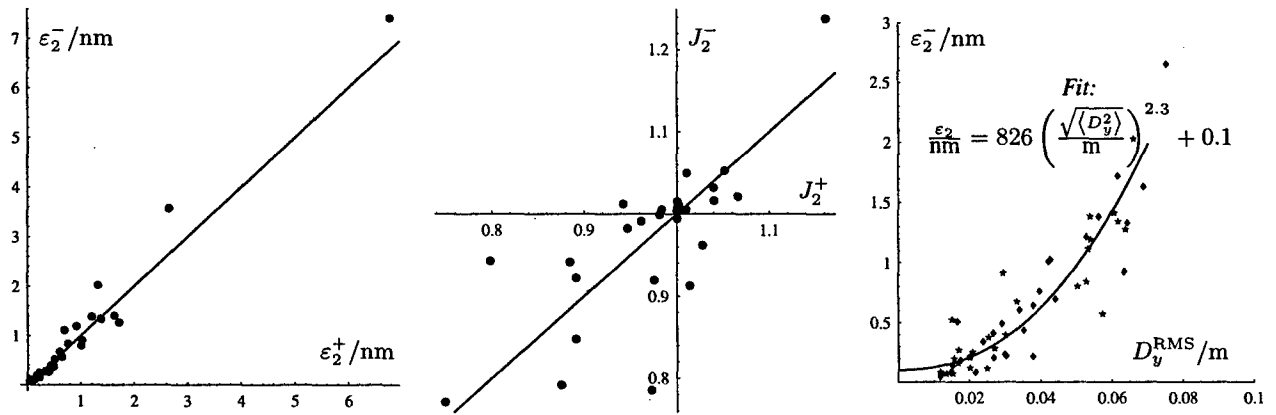


Figure 2: Correlation of vertical emittance and damping partition numbers between e^+e^- ; correlation of vertical emittance (both beams) and RMS vertical dispersion, D_y^{RMS} . The fit tests the hypothesis $\epsilon_2 \simeq a(D_y^{\text{RMS}})^2/J_2 + \epsilon_c = a(D_y^{\text{RMS}})^p + \epsilon_c$.

other cases, e.g., higher order resonances or pure RBSC, radiation and imperfections are important, the dynamic aperture has a spread and is less than for an ideal machine. Radiation effects are essential in all cases to determine the stability limit of mode 3 (“momentum acceptance”).

There is no space to discuss measurements here. However a recent survey [8, 5] showed that calculation and measurement agree within about 10 % in all cases where satisfactory measurements have been made.

Figure 1 has been computed for the present optics with $(\mu_x, \mu_y) = (102^\circ, 90^\circ)$ to show the effect of moving from a situation with a reserve of RF voltage to “ultimate” LEP parameters at 100 GeV where V_{RF} is just sufficient according to the conventional quantum lifetime calculation. *All details of this figure can be understood* by analysing the orbits of individual particles. At 94 GeV, the stability limit of mode 1 is determined by the cross-detuning effect: Q_2 moves down to the integer resonance with increasing I_1 . The boundary between stability and loss in one turn is sharp. At 100 GeV, the transverse dynamic apertures are sharply reduced because the limit is now determined by the RBSC instability. Since the growth time of this instability is $\simeq 2/Q_3 \simeq 20$ turns, a “ghost” of the former dynamic aperture remains visible. Similar effects are visible in mode 2 which was already limited by RBSC.

In mode 3, the dynamic aperture becomes simpler in shape although this example shows why a scan of ϕ_3 is essential. It is clear that the approximations underlying existing analytic approaches to the calculation of quantum lifetime are inadequate in this regime.

3.2 Vertical emittance

The emittance of mode 2, ϵ_2 , is a crucial parameter determining luminosity. It is determined almost entirely by machine imperfections and so can only be estimated statistically. Figure 2 shows predictions for the same optics at 94 GeV. A mismatch of ϵ_2 between beams can arise, partly because the damping partition numbers J_2 can be different. Fitting shows that ϵ_2 is determined mainly by the RMS ver-

tical dispersion. The dependence is stronger than quadratic because J_2 tends to decrease with the dispersion (because of combined dispersion and closed orbit in quadrupoles).

The statistical distribution of vertical emittance in the ensemble is typical of measurements during the life-cycle of an optics. Operational procedures seem to select corrections that reduce ϵ_2 to the smallest values.

Synchro-betatron resonances can increase ϵ_2 further. Such effects can be estimated by tracking particles with quantum fluctuations [5].

4 CONCLUSIONS

By carefully constructing ensembles of model machines, simulating the operational correction procedures and using a physically faithful model of single particle dynamics, it is possible to predict the distribution of beam parameters and their differences between the beams in LEP. Dynamic aperture can be predicted to within about 10 % in a variety of optical configurations.

At the highest accessible energies, the dynamic aperture of LEP will be sharply reduced by the RBSC instability.

Acknowledgements: I thank A. Verdier for valuable collaboration, K. Goral for help with software development.

5 REFERENCES

- [1] F.C. Iselin, http://wwwslap.cern.ch/~fci/mad/mad_home.html
- [2] F. Barbarin, et al, Proc. 4th European Particle Accelerator Conference (EPAC'94), World Scientific, p. 193.
- [3] Y. Alexahin et al, EPAC'96, Sitges, IOP Publishing, 1996.
- [4] S. Wolfram, *Mathematica*, Cambridge Univ. Press, 1996.
- [5] J.M. Jowett, Proc. 8th LEP Performance Workshop, CERN SL/98-006 (1998).
- [6] J.M. Jowett, CERN-SL Notes 97-84, 98-020, 98-072 (1997–98). See also [5].
- [7] D. Brandt et al EPAC'98, Stockholm, IOP Publishing, 1998.
- [8] H. Burkhardt, Proc. 8th Workshop on LEP Performance, CERN-SL-98-006 (1998).

INFLUENCE OF VERTICAL DISPERSION AND CROSSING ANGLE ON THE PERFORMANCE OF THE LHC

L.H.A. Leunissen,* CERN, Geneva, Switzerland

Abstract

Misalignments, magnetic field deviations and the beam crossing angle induce closed orbit deviations and residual dispersion at the interaction points of the LHC. These in turn excite synchro-betatron resonances. We present a numerical investigation of these effects and their influence on the luminosity. Bunch length effects are important and are included in the model by means of the numerical code BBC [1]. The crossing angle excites resonances that increase particle amplitudes when the tunes are near resonance while vertical dispersion changes the resonance strength. The influence on the beam core size is studied. For the nominal LHC working point, a 13th-order resonance may be crossed by the particles in the beam. The width of the synchrotron sidebands are evaluated.

1 INTRODUCTION

At collision energy in the LHC, local orbit bumps are used to separate the beams or make them cross at an angle. These bumps have the unwanted side effect of creating dispersion at the interaction points (IPs). Besides this, the random misalignments and imperfections of the machine generate further random components of the dispersion at the IPs. The crossing angle and dispersion in turn modify the beam-beam interaction at the IPs through the excitation of synchro-betatron resonances.

The calculations in this paper can be divided into two main classes: To study *optical effects*, we calculate the vertical dispersion that can be expected to arise from the sources and its effect on the beam size. For these calculations, we use the MAD [2] model of LHC Version 5 with error table 9607. Two different types of calculations are carried out:

1. Misalignments are introduced and the resulting closed orbit deviations are corrected to RMS values of 1 mm in both horizontal and vertical planes (simulating the typical quality of correction in a real machine).
2. The crossing angles and separation bumps are then introduced at IP1, IP2, IP5 and IP8, modifying the closed orbit again. The linear coupling is corrected in both cases again simulating the quality of correction in a real machine and the residual dispersion in the horizontal and vertical plane is calculated. In Table 1 the machine parameters of immediate interest are summarised.

To study the *beam-beam effects* we use the tracking program BBC [1]; it includes an appropriate model of a single

beam-beam interaction but treats the rest of the machine in linear approximation.

The dispersion at the RF cavities is assumed to be zero, so that this is not an additional source of synchro-betatron resonances.

Where it is possible to do so, the results of BBC are compared with existing analytical theory and other models. Further details are given in [3].

Relativistic factor γ	7461
Normalised emittance ϵ_n	$3.75 \cdot 10^{-6}$ m.rad
bunch length σ_s	0.077 m
relative energy spread σ_e	$1.11 \cdot 10^{-4}$
Particles per bunch N_b	$1.05 \cdot 10^{11}$
Number of bunches k_b	2835
Revolution frequency f_r	11245.5 Hz
β^* (IP1, IP2, IP5, IP8)	(0.5 m, 250 m, 0.5 m, 33 m)
Q_x, Q_y, Q_s	63.31, 59.32, 0.00212
Q'_x, Q'_y	2.0, 2.0

Table 1: Beam parameters of the LHC at collision energy.

2 PARASITIC DISPERSION DUE TO THE CLOSED ORBIT

The dispersion functions for the ideal machine are zero at the IPs. In Table 2 the horizontal and vertical dispersion are shown at the experimental interaction points together with the calculated standard deviation over the ensemble of 20 closed orbit calculations.

I.P.	D_x [m]	D_y [m]
IP1	-0.001 ± 0.008	-0.006 ± 0.028
IP2	0.003 ± 0.169	-0.087 ± 0.508
IP5	-0.002 ± 0.009	0.004 ± 0.015
IP8	0.006 ± 0.071	-0.029 ± 0.213

Table 2: Horizontal and vertical dispersion at the four experimental interaction points from residual closed orbit.

3 PARASITIC DISPERSION DUE TO THE CROSSING ANGLE

The dispersion created at the IPs by orbit bumps were calculated with MAD. They are presented in Table 3.

* Email: Leonardus.Leunissen@cern.ch

I.P.	D_x [m]	D_y [m]
IP1	0.021	-0.006
IP2	-0.087	-0.035
IP5	-0.002	-0.005
IP8	0.059	-0.028

Table 3: Horizontal and vertical dispersion at the four experimental interaction points from crossing angle.

4 LUMINOSITY CHANGE WITH THE BEAM CROSS SECTION

Dispersion will contribute to the beam size in the following way:

$$(\sigma_z^*)^2 = \epsilon_z \beta_z^* + (\sigma_e D_z^*)^2. \quad (1)$$

Here, σ_z , D_z^* and β_z^* are the beam size, the dispersion and the β -function value at the interaction point with $z \in \{x, y\}$. The energy spread of the beam is denoted by σ_e .

The increase of the beam size leads to a change in the luminosity approximated by:

$$L = \frac{N_b^2 k_b f_r}{4\pi \sigma_x^* \sigma_y^*} \frac{1}{\sqrt{1 + \delta^2}} \text{ and } \delta = \frac{\phi \sigma_s}{2\sigma_z^*}. \quad (2)$$

This equation holds when the crossing angle ϕ is small and the β^* does not vary much near the interaction point.

Inserting Eq. 1 in Eq. 2 and then Taylor expanding with respect to D_y shows that \mathcal{L} decreases.

$$\mathcal{L} = \mathcal{L}_0 \left(1 - \frac{2\sigma_e^2 D_y^2}{4\epsilon_y \beta_y^* + \phi^2 \sigma_s^2} + \mathcal{O}(D_y^4) \right). \quad (3)$$

The design luminosity is $\mathcal{L}_0 = 10^{34} \text{ cm}^{-2} \text{ s}^{-1}$. The luminosity changes at most by about 5% due to the changes of horizontal and vertical beam size at the IP.

5 RESONANCE EFFECT OF CROSSING ANGLE

The effect of one single beam-beam interaction is studied with the program BBC. This FORTRAN code analyses a beam-beam collision with a crossing angle in a symplectic way in 6 dimensions. The bunch length effect influences the synchro-betatron resonances. To represent this, the strong beam is split into several longitudinal slices. The parameters $R = \sigma_s / \beta_z^*$ and $\Phi = \phi \sigma_s / \sigma_z$ (Piwinski angle) show the necessity of the slicing. For $R \geq 1$, the hourglass effect (depth of focus) [4] is important. This means that bunch length effects need to be included in the calculations by using slices. When $\Phi \geq 1$, the tilt effect is important. For the LHC $R=0.15$ and $\Phi=0.5$ (at IP1 the crossing angle is $\pm 150 \mu\text{rad}$), the same order of magnitude. One might expect that the bunch length effects are not important, but the numerical results show that this is not the case. Calculations show that it is necessary to split the beam into five slices [3].

A separate numerical simulation was carried out to calculate the coupling of the transverse and longitudinal oscillations. This program is based on the equations of motion as derived from a Hamiltonian [5].

The tracking was done with both programs over 10000 turns. The largest amplitude during this number of turns was recorded. The resonance $q Q_z \pm r Q_s = 4$ is scanned ($q = 13$) in this study.

The following plots (Figure 1 and 2) compare the maximum amplitude on the resonance as a function of the initial betatron amplitude as found by BBC calculation and the simulation with the equations of motion. Because of the symmetry of the beam-beam potential the satellites with even $q + r$ are stronger than those with odd $q + r$.

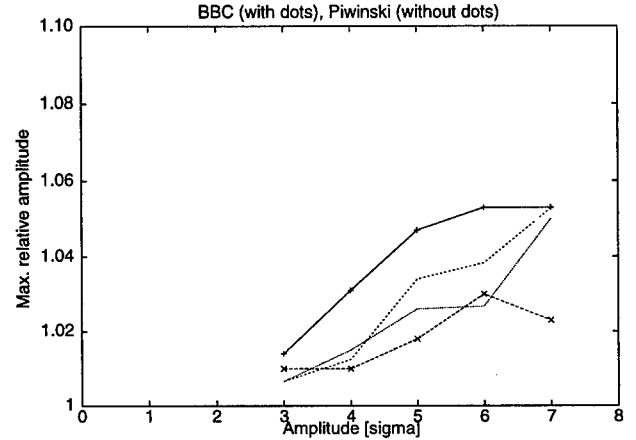


Figure 1: Resonance strength of $13Q_x \pm 3Q_s = 4$ as a function of the initial amplitude of the particles.

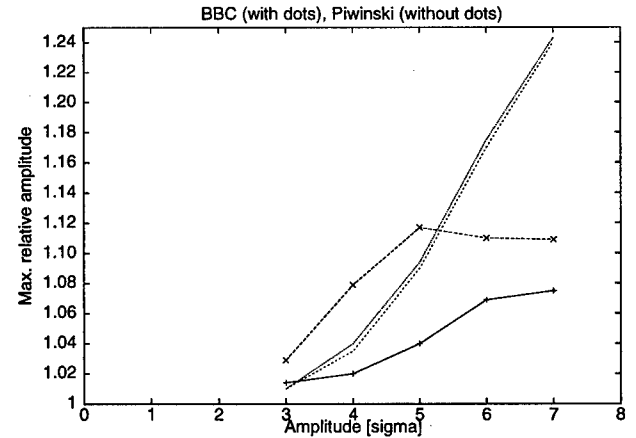


Figure 2: Resonance strength of $13Q_x \pm Q_s = 4$ as a function of the initial amplitude of the particles.

6 RESONANCE EFFECT OF DISPERSION

The effect of dispersion is similar to that of a crossing angle: it excites the same synchrotron satellites close to each

beam-beam resonance. The strength of the satellites are the same in both cases when the dispersion at the IP is equal to [5]:

$$D_{IP} = \phi \frac{\alpha_M \bar{R}}{2Q_s} \quad (4)$$

where α_M is the momentum compaction factor and \bar{R} is the mean radius of the accelerator. For a dispersion of about 10 cm the resonances would be excited with the same strength as with the nominal crossing angle. In Figure 3 the four resonance lines described earlier ($r \in \{1, 3\}$) are recalculated including a 10 cm vertical dispersion at the IP.

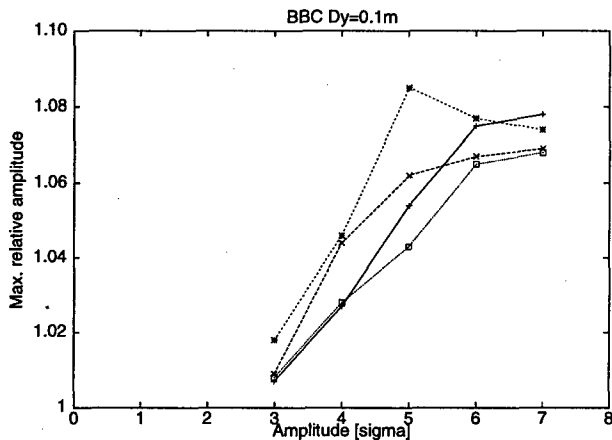


Figure 3: Resonance strength of $13Q_x \pm rQ_s = 4$ as a function of the initial amplitude of the particles with $r \in \{1, 3\}$ and $D_y = 0.1m$.

The two outer resonances become stronger and the two inner are weakened, resulting in a global equal strength of the four resonance lines. The initial amplitude is increased by about 7.5% with respect to the resonance free part.

Numerical calculations show that the width of the resonances $13Q_\beta \pm 3Q_s = 4$ is 1×10^{-4} (BBC). The other program yields 9×10^{-5} . The resonances $13Q_\beta \pm Q_s = 4$ have a width of about 1.5×10^{-4} (BBC) whereas the other program yields 2×10^{-4} . First-order theoretical investigations [5] result in a width of the resonance islands of 6×10^{-5} .

7 CORRECTION OF VERTICAL DISPERSION

The closed orbit in quadrupoles and sextupoles is the driving term for the parasitic vertical dispersion. Special vertical orbit bumps can create vertical dispersion to compensate the dispersion generated by the beam crossing scheme at the IP or the closed orbit deviations. Usually a closed orbit bump starts at the beginning of one arc and is closed at the end of the same arc. To cancel the dispersion wave a second orbit bump (in the following arc) is used. In the case of a vertical dispersion of 6 mm (at IP1 and IP5) orbit

bumps of about 2 mm have to be used. The correction magnets can generate kicks of at most $70\mu\text{rad}$. This generates a maximum dispersion of 2 cm at IP1 and IP5 (leaving the dispersion at all other IPs zero).

8 CONCLUSIONS

The random closed orbit deviations due to misalignments and magnetic field errors result in a few cm of residual dispersion at the interaction points of the LHC. The local orbit bumps in the interaction region are a further deterministic source of dispersion. This dispersion increases the beam size by less than 10%.

Higher-order resonances will still be crossed by particles in the tail of the beam (large amplitudes). Their influence has been studied in detail, by tracking particles with initial amplitudes of 3, 4, 5 and 6σ , both with BBC and with another program based on the equations of motion derived in [5]. Without dispersion, both methods gave similar results for the studied resonances. For example, the sidebands of the 13th order betatron resonance ($13Q_\beta \pm rQ_s = 4$ with $r \in \{1, 3\}$) have a width of approximately 1.5×10^{-4} . The crossing angle increases the amplitude of the particle oscillation by less than 10%. BBC shows that the nominal crossing angle combined with vertical dispersion of 10 cm at the IP changes the strength of the resonance, giving an increase of amplitudes of 7.5% with respect to the unperturbed case. Thus, the strengths of some sidebands are *reduced*.

Correction of residual dispersion at the IP is possible with closed orbit bumps in the arcs. The dispersions at IP1 and IP5 can be changed independently of each other by ± 2 cm without affecting the dispersion at the other IPs. They can therefore be used to correct the dispersion arising from the beam crossing angle.

9 REFERENCES

- [1] K. Hirata, "BBC User's Guide; A Computer Code for Beam-Beam Interaction with a Crossing Angle, version 3.4", SL-Note 97-57 AP (1997)
- [2] H. Grote and F.C. Iselin, The MAD program (Methodical Accelerator Design) version 8.16, User's reference manual, CERN/SL/90-13(AP) (rev.4) (1995)
- [3] L.H.A. Leunissen, Influence of Vertical Dispersion and Crossing Angle on the Performance of the LHC, LHC Project report, to be published
- [4] G.E. Fisher, Measurements on beam-beam interaction at Spear, IEEE Trans Nucl. Sci. NS-20 (1973) p.838
- [5] A. Piwinski, Limitation of the Luminosity by Satellite Resonances, DESY 77/18 (1977)

ODYSSEUS: DESCRIPTION OF AND RESULTS FROM A STRONG-STRONG BEAM-BEAM SIMULATION FOR STORAGE RINGS

E. B. Anderson *, T. I. Banks, J. T. Rogers, LNS, Cornell University, Ithaca, NY

Abstract

ODYSSEUS is a simulation of the beam-beam interaction in e^+e^- storage ring colliders which is specifically intended to reveal the dynamic collective behavior of the colliding beams. This program is a true six-dimensional strong-strong simulation in which the electromagnetic fields of longitudinal slices of the colliding beams are recalculated for each slice collision. Broadband wake fields are included. No constraints are placed on the distribution of particles in the beams. The program achieves its speed through adaptively choosing between alternative electromagnetic field calculation methods. Benchmarking tests and various results will be presented.

1 INTRODUCTION

In storage ring colliders the beam-beam forces produce changes in the distribution of particles that can be important to the stability of the beams and the luminosity. Because the beam-beam force is strongly nonlinear, exact calculations are difficult and particle tracking simulations are more suitable. Strong-strong simulations, in which the force exerted on each beam by the opposing beam is calculated, are capable of generating self-consistent charge distributions and have been used to examine the collective behavior of round beams [1, 2], charge-compensated round beams [3], and beams of arbitrary ellipticity [4]. These simulations are very time-intensive because of the need to repeatedly calculate the electromagnetic field of each beam, and previous unconstrained strong-strong simulations have therefore included only transverse degrees of freedom.

This paper presents a new beam-beam simulation program, ODYSSEUS (Optimized DYNAMIC Strong-Strong E-plus e-minus Simulation). To the authors' knowledge, ODYSSEUS is the first six-dimensional strong-strong beam-beam simulation in which no constraints are placed on the beams and is the first to include wake fields. These features make it possible to investigate any mode of oscillation of the colliding beams, including head-tail modes.

ODYSSEUS is capable of rapidly calculating the electromagnetic field of a beam divided into many longitudinal slices because it adaptively chooses from a variety of different field computation methods. Different algorithms are used for the core, the transverse tails, and the longitudinal tails of the beam. The parameters of the program can be changed to model flat or round beams. Further, inclusion of the longitudinal degree of freedom and wake fields allows the investigation of previously inaccessible physics.

* Email: eba1@cornell.edu

ODYSSEUS is written in Fortran77 for portability.

2 PARTICLE TRACKING

2.1 The Storage Ring

On each simulated turn through the storage ring, each macroparticle is propagated from the collision point and back again through the linear optics of the storage ring, including chromaticity, synchrotron radiation excitation and damping, RF phase focusing, and wake field deflections. Macroparticles which have migrated past a transverse aperture are no longer considered in the simulation. Longitudinal and transverse short-range wake fields are included in the simulation. An input file contains a list of longitudinal and transverse resonators with values for the resonant frequency ω_R , shunt impedance R_s , and quality factor Q of each resonator.

2.2 Collisions

During its passage through the opposing bunch, the transverse position of each macroparticle may change appreciably because the vertical interaction point beta function, β_v^* , in CESR and many other colliders is comparable to the bunch length, σ_z . ODYSSEUS handles the longitudinal variation of the electromagnetic field of the beam by dividing the beam into slices. The simulation collides each pair of slices sequentially, updating the transverse momenta and positions of each macroparticle after each pairwise collision of slices. For each slice collision the slice electromagnetic field is calculated by one of the methods described below. Macroparticles undergoing longitudinal oscillations may migrate from slice to slice, so on each turn the macroparticles are sorted according to their longitudinal position and reassigned to slices.

3 ELECTROMAGNETIC FIELD CALCULATION

3.1 Beam core

If the number of macroparticles, N , within a slice is very small, the integrated field at a probe beam macroparticle is calculated from the exact radius vector from each opposing source beam macroparticle. The field must be calculated at the position of each macroparticle in the probe beam, so the number of calculations goes as N^2 , making this method efficient only for $N < 50$.

For larger values of N , the electromagnetic field is calculated on a rectangular grid using pre-calculated Green's functions for charges on the grid points. The macroparticle

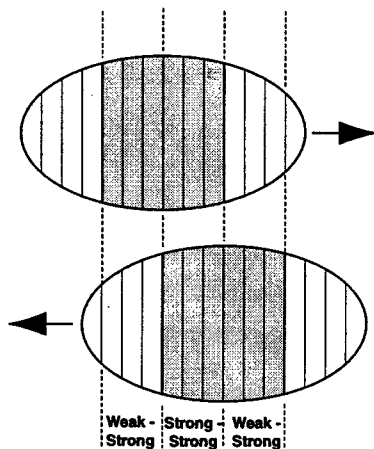


Figure 1: The beam is divided into longitudinal slices and the collision of each pair of slices is simulated in sequence. Slices are marked as either "weak" (white) or "strong" (gray) and the appropriate technique is applied when they interact. No two weak slices ever interact.

charge is assigned to the grid points using one of two area-weighted techniques described in below. If the number of grid points N_g is less than about 200, the convolution of the charge density and Green's function is done as a summation in real space. The number of calculations required for this convolution goes as N_g^2 .

For larger values of N_g , the convolution of the Green's functions and charge density is done as a simple multiplication in wavenumber space. The speed of this method is limited by the speed of the necessary Fourier transform to wavenumber space and the inverse transform back to real space. The number of calculations goes as $N_g \log_2 N_g$. To suppress edge effect problems in the Fourier transforms, the size of the wavenumber space can be doubled in both directions and padded with zeros [5] although this is found to be unnecessary for a typical, Gaussian-like, charge distribution.

3.2 Beam tails

The tails of the beam, typically taken to be particles with a displacement of more than $(10/3)\sigma$ in any direction, are treated differently than the core particles. The tail particles have very little effect on the beam-beam force. They do, however, respond to the beam-beam force, so a weak-strong calculation is used.

Longitudinal tail particles are subject to forces from the core of the opposing beam. This is a weak-strong calculation. A full calculation of the field from the opposing (strong) beam slice is performed, but the tails are assumed to have no effect on the other beam. All slices may be treated as strong-strong slices if the user so chooses.

The transverse tail particles are subject to a beam-beam force of similar magnitude to that experienced by the core particles. The fine structure of the charge distribution of the

core has little influence on the field in the transverse tails, so the core is assumed to be a two-dimensional Gaussian charge distribution with the same total charge and transverse moments as the slice. The field from this Gaussian charge distribution is calculated from the rational approximation of Talman and Okamoto [7].

3.3 Interpolation techniques

Whenever a grid-based technique is used, it is necessary to interpolate from the fields on a grid to arbitrary particle locations and from the particle locations to the grid when depositing charge. ODYSSEUS gives the user a choice between two interpolation methods: a four-point Cloud-In-Cell (CIC) technique and a nine-point extension of the Triangular-Shaped Cloud (TSC) technique[5]. Higher order interpolation schemes tend to blur the detail in the charge distribution. In ODYSSEUS a "sharpening function" is used during the convolution of the charge density and Green's function in wavenumber space [6].

4 PRE- AND POST-PROCESSING

A user interface, PENELOPE, has been written to produce the input files used by ODYSSEUS. Parameters may be read from existing files and modified, or may be entered through the keyboard. PENELOPE works with a set of accelerator parameters which is convenient for the user, but which is larger than the set of independent parameters. As new parameters are entered, derived parameters are calculated and displayed. Thus, self-consistency between parameters is enforced, unless the user specifically chooses otherwise.

ODYSSEUS was designed to investigate the coherent oscillations of the bunch, so post-processing to analyze the bunch spectrum is necessary. Post-processing is done in a *Mathematica* [8] notebook designed to look at beam-beam modes and their growth and damping rates.

5 SPEED AND ACCURACY CONSIDERATIONS

5.1 Field error due to transverse grid

For round beams a field calculation grid can be constructed out of square cells with equal numbers of cells in each dimension. This construction allows for accurate field calculation with low numbers of grid squares. In contrast, the often extreme aspect ratios of flat beams force the use of either large numbers of cells or individual cells with poor aspect ratios. When trying to model flat beams with a minimum number of grid cells, one may give the grid cells an aspect ratio other than unity, but there are dangers in this choice. If a potential is used to calculate the fields, then the choice of the value of the Green's function at the origin is important. ODYSSEUS uses a separate Green's function for each component of the electric field and the maximum aspect ratio usually allowed is 1.4.

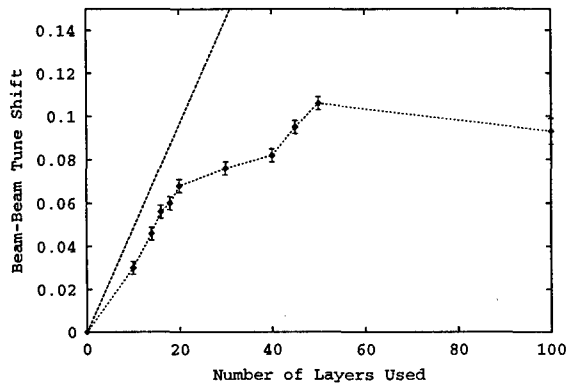


Figure 2: The figure above shows the vertical beam-beam tune shift, $\Delta\nu_y$, as a function of the number of slices. The straight line is an estimate of the maximum beam-beam parameter, ξ_y , from slicing errors alone (See Equation 1).

5.2 Field error due to longitudinal slicing

Previous investigators [9] had indicated that few slices, five or less, are necessary to model the colliding beams. We instead found that the error introduced by slicing increases the simulated emittance of the beam, so that the simulation produces a maximum value of ξ . This limit is severe when β_y^* is so small that it is comparable to the bunch length σ_z . In a particle-tracking simulation using longitudinal slices of uniform width, particles at the front and back of each slice receive a different deflection than would actual beam particles. From this we find that a horizontal tune shift can be produced due to the finite slice length. We find this to be:

$$\xi_{y,max} = \frac{4\sqrt{3}}{\pi} \frac{\beta_y^*}{\Delta z} \sqrt{\delta}. \quad (1)$$

Other physical or numerical effects may further reduce ξ_y . Fig. 2 shows the vertical beam-beam tune split as a function of the number of slices. The behavior supports the result of Eq. 1 that there is a maximum tune split that is inversely proportional to the slice length. Simulations of storage rings with a small natural vertical emittance require a large number of slices. Slices of non-uniform length [9] may reduce the effect.

5.3 Speed

ODYSSEUS is currently being run on a farm of 500 MHz Alpha-chip personal computers running Linux. The fast Fourier transform takes almost 90% of the time taken by the code for a typical run. The speed of ODYSSEUS may be compared to that of a non-adaptive PIC-only calculation by running with PIC-only options and comparable parameters. The calculation takes five times longer than a calculation with the optimized code.

6 CONCLUSIONS

There are a number of computational advances represented in ODYSSEUS. Its adaptive nature allows it to run several times faster than a code using PIC methods alone. The Green's function grid used in the PIC calculations is pre-generated and recalculated as necessary. Approximations are used in the transverse and longitudinal tails in order to save time on calculations. ODYSSEUS incorporates wake fields, enabling the user to calculate collective instability thresholds for colliding beams. Runs can be done in reasonable amounts of time, ranging from an hour to a few days depending on the approximations used and beam shape.

Three unexpected results became evident during this work. The first is the necessity for grid aspect ratios close to 1:1 when using an electric field Green's function, and exactly 1:1 when using an electric potential Green's function. The second was the discovery of a minimum (simulated) emittance due to the nonzero longitudinal slice width. The third was that using zero-padding in the Fourier transform was not the most efficient means to minimize errors.

Three interesting results have already been found. The ratio between the beam-beam parameter and the coherent tune split has been calculated, the shift in head-tail mode frequencies for colliding beams have been investigated, and the effect of additional wiggler magnets on CESR's luminosity approximated.

7 ACKNOWLEDGMENTS

This work was supported by the National Science Foundation. The authors extend their thanks to R. Talman, G. Codner, J. Irwin, R. Siemann, M. Furman, S. Krishnagopal, R. Ryne, R. Ng, and R. Helmke.

8 REFERENCES

- [1] S. Krishnagopal, Ph.D. Thesis, 1991, Cornell University.
- [2] S. Krishnagopal and R. Siemann, *Phys. Rev. Lett.* **67** (1991) 2461.
- [3] B. Podobedov and R.H. Siemann, *Phys. Rev. E* **52** (1995) 3066.
- [4] S. Krishnagopal, *Phys. Rev. Lett.* **76** (1996) 235.
- [5] R.W. Hockney and J.W. Eastwood, *Computer Simulation Using Particles*, Hilger, Bristol, U.K., 1988.
- [6] E. B. Anderson, *ODYSSEUS: A Dynamic Strong-Strong Beam-Beam Simulation for Storage Rings*, Ph.D. Dissertation, Cornell University (1998); Available at <http://www.ruph.cornell.edu/edwin/>.
- [7] Y. Okamoto and R. Talman, Cornell Laboratory of Nuclear Studies report CBN 80-13 (1980).
- [8] *Mathematica*, Wolfram Research, Inc., Champaign, Illinois, USA.
- [9] M. Furman, A. Zholents, T. Chen, and D. Shatilov, Lawrence Berkeley National Laboratory report PEP-II/AP Note 95.39/LBL-37680/CBP Note-152 (1995).

ENERGY RESOLUTION AT INTERACTION POINT FOR ASYMMETRIC BEAMS

S. Petracca*, K. Hirata†, KEK, Tsukuba, Japan

Abstract

The monochromatic scheme adopted in the tau-charm factories uses a large dispersion at interaction point to obtain a very high collision energy resolution.

Due to the presence of dispersion, however, the beam-beam interaction induces the synchro-betatron coupling. Even if in the linear regime, it can lead to potentially serious effects. One of the most serious is the rapid decrease of the energy resolution when the beam-beam parameter increases, even if the motion is stable. In this paper we study this effect in detail either for symmetric and asymmetric beams and give formula for the energy resolution.

1 INTRODUCTION

Recently the monochromatization has been considered seriously for future tau-charm factories [1], where a rather large dispersion exists at the IP with opposite signs for both beams. In this case, the dispersion effects can no longer be discussed in the perturbative sense as in the conventional colliders [2, 3]. In a previous paper [4] we discussed the effects of the dispersion at the IP paying enough attention to the mutual interaction between the betatron and the synchrotron degrees of freedom, and the possible problems associated with the monochromatization within the linear approximation of the beam-beam force.

The purpose of the monochromatization is to make the spread σ_ϵ of the collision energy much smaller than the nominal one σ_ϵ^0 . Thus this quantity gives the figure of merit of the machine as well as the luminosity. The monochromatic scheme uses beams with opposite dispersion D , and realizes a distribution (centered at the IP) in vertical position y analogue (Gaussian) to that one (centered at E_0) in energy E . In this way the particles with energy $E_0 - \epsilon$ collide with those at the same quote in the other beam but with different energy $E_0 + \epsilon$, then getting as collision energy $E_{CM} \sim 2 E_0$.

2 ENERGY RESOLUTION

For simplicity we consider the synchrotron motion and one betatron (vertical) oscillation degree of freedom only. The physical variables of a particle for the betatron and synchrotron motions are $\mathbf{x}_\pm = (y_\pm, p_{y\pm}, z_\pm, \epsilon_\pm)$, where y_\pm is the vertical coordinate, $p_{y\pm}$ the vertical momentum normalized by the (constant) momentum p_0 of the reference particle, z_\pm the time advance relative to the reference particle multiplied by the light velocity c , and $\epsilon_\pm =$

$(E_\pm - E_0)/E_0$ is the energy deviation from the nominal value E_0 and normalized by it.

In the monochromatization, as well as the luminosity L , the spread σ_w of the collision energy $w - 2E_0 \equiv \epsilon_+ + \epsilon_-$ is important. The luminosity can be expressed as

$$L = \text{const} \times \int f_+(y, \epsilon_+) f_-(y, \epsilon_-) dy d\epsilon_+ d\epsilon_- \quad (1)$$

Here $f_\pm(y_\pm, \epsilon_\pm)$ is the distribution function in the (y_\pm, ϵ_\pm) space. If we assume

$$f_\pm(y, \epsilon_\pm) = \frac{\exp\left(\frac{-A_{22}^\pm y^2 + 2A_{12}^\pm y\epsilon_\pm - A_{11}^\pm \epsilon_\pm^2}{2 \det A_\pm}\right)}{2\pi \sqrt{\det A_\pm}} \quad (2)$$

with A being

$$A_\pm = \begin{pmatrix} \langle y^2 \rangle_\pm & \langle y\epsilon \rangle_\pm \\ \langle y\epsilon \rangle_\pm & \langle \epsilon^2 \rangle_\pm \end{pmatrix}, \quad (3)$$

we get

$$L = \text{const} \times \frac{1}{\sqrt{2\pi}} \frac{1}{\sqrt{A_{11}^+ + A_{11}^-}} \quad (4)$$

The luminosity density with respect to w is defined as [10]

$$\Lambda(w) = \frac{1}{L} \int f_+(y, \epsilon_+) f_-(y, \epsilon_-) \delta(w - \epsilon_+ - \epsilon_-) dy d\epsilon_+ d\epsilon_- \quad (5)$$

Here w stands for the deviation of the collision energy from the nominal one ($2E_0$). Then we have

$$\Lambda(w) = \frac{1}{\sqrt{2\pi\sigma_w^2}} \exp\left(-\frac{w^2}{2\sigma_w^2}\right), \quad (6)$$

and the formula for the energy resolution for asymmetric beams is

$$\sigma_w^2 = \frac{A \det A_+ \det A_-}{A_{11}^+ + A_{11}^-} \quad (7)$$

with

$$A = \left(\frac{A_{11}^+}{d_+} + \frac{A_{11}^-}{d_-}\right) \left(\frac{A_{22}^+}{d_+} + \frac{A_{22}^-}{d_-}\right) - \left(\frac{A_{12}^+}{d_+} - \frac{A_{12}^-}{d_-}\right)^2 \quad (8)$$

If we assume that two beams are modified symmetrically, we have $A_{11}^+ = A_{11}^-$, $A_{22}^+ = A_{22}^-$, and $A_{12}^+ = -A_{12}^-$, $A_\pm = A$ and the formula for the energy resolution becomes

$$\sigma_w^2 = \frac{2 \det A}{A_{11}} \quad (9)$$

In the absence of collision ($\xi_0 \simeq 0$) we can assume the following:

$$A_\pm = \begin{pmatrix} \beta_y^0 \epsilon_y^0 + D_0^2 (\sigma_\epsilon^0)^2 & \pm D_0 (\sigma_\epsilon^0)^2 \\ \pm D_0 (\sigma_\epsilon^0)^2 & (\sigma_\epsilon^0)^2 \end{pmatrix} \quad (10)$$

* On leave of absence from Università del Sannio, Benevento and I.N.F.N. Salerno, Italy

† Graduate University for Advanced Studies, Hayama, Japan

which implies [10]

$$\sigma_w^2 = \frac{2(\sigma_\epsilon^0)^2}{1 + \frac{D_0^2(\sigma_\epsilon^0)^2}{\beta_y^0 \epsilon_y^0}}. \quad (11)$$

3 EQUILIBRIUM ENVELOPE

The equilibrium value of the envelope matrix σ , where

$$\sigma_{ij} = \langle (x_i - \bar{x}_i)(x_j - \bar{x}_j) \rangle, \quad (12)$$

is determined by the following equation [9]:

$$\sigma = M_{bb}^{1/2} [\bar{\Lambda} M_{arc} \sigma (\bar{\Lambda} M_{arc})^t + (I - \bar{\Lambda}^2) \bar{E}] (M_{bb}^t)^{1/2}, \quad (13)$$

where

$$\bar{\Lambda} = H_0 B_0 \Lambda (H_0 B_0)^{-1}, \quad \bar{E} = H_0 B_0 E (H_0 B_0)^t, \quad (14)$$

$$\Lambda = \text{diag}(\lambda_y, \lambda_y, 1, \lambda_z^2), \quad E = \text{diag}(\epsilon_y^0, \epsilon_y^0, \epsilon_z^0, \epsilon_z^0). \quad (15)$$

$\lambda_{y,z} = \exp(1/T_{y,z})$ being the damping constants and $\epsilon_{y,z}^0$ the nominal emittances. The one turn matrix from IP ($s = 0$) to IP is [5]:

$$M = M_{bb}^{1/2} M_{arc} M_{bb}^{1/2} \quad (16)$$

where:

$$M_{arc} = M(0_-, 0_+) = H_0 B_0 \hat{M}_{arc} B_0^{-1} H_0^{-1}, \quad (17)$$

$$\hat{M}_{arc} = \text{diag}(r(\mu_y^0), r(\mu_z^0)), \quad B_0 = \text{diag}(b_y^0, b_z^0), \quad (18)$$

with

$$r(\mu_{y,z}^0) = \begin{pmatrix} \cos \mu_{y,z}^0 & \sin \mu_{y,z}^0 \\ -\sin \mu_{y,z}^0 & \cos \mu_{y,z}^0 \end{pmatrix}, \quad (19)$$

$$b_{y,z}^0 = \text{diag}(\sqrt{\beta_{y,z}^0}, 1/\sqrt{\beta_{y,z}^0}),$$

$$H_0 = \begin{pmatrix} I & h_0 \\ h_0 & I \end{pmatrix}, \quad h_0 = \begin{pmatrix} 0 & D_0 \\ 0 & 0 \end{pmatrix}. \quad (20)$$

$\mu^0 = 2\pi\nu^0$, ν^0 being the nominal tune, $\beta_{y,z}^0$ the nominal betatron functions at IP ($\beta_z^0 \equiv \sigma_z^0/\sigma_\epsilon^0$, σ_z^0 being the nominal bunch length), and D_0 the dispersion at IP. Note that H_0 , B_0 , and M_{arc} are symplectic. Finally the beam-beam interaction is described as a linear kick

$$M_{bb} = \begin{pmatrix} 1 & 0 & 0 & 0 \\ -4\pi\xi_0/\beta_y^0 & 1 & 0 & 0 \\ 0 & 0 & 1 & 0 \\ 0 & 0 & 0 & 1 \end{pmatrix}, \quad (21)$$

with ξ_0 being the vertical (nominal) beam-beam parameter

$$\xi_0 = \frac{2\pi\gamma r_e N \beta_y^0}{2\pi\gamma\sigma_y^0(\sigma_y^0 + \sigma_x^0)}. \quad (22)$$

Note that the nominal synchrotron tune ν_z^0 is negative for conventional electron machines with positive momentum compaction factor α_p , and we have assumed that there is only one IP which is a symmetric point with respect to betatron and synchrotron motions. We have also implicitly assumed that dispersion does not exist in cavities.

4 DISCUSSIONS

In Fig. 1 we show that the energy resolution σ_w increases rapidly with ξ_0 and approaches its nominal value σ_ϵ^0 , then making the monochromatization less effective or even useless. This, obviously, gives a more stringent limit for the maximum value of ξ_0 than the single particle instability [4].

Furthermore, from Fig. 1, it is clear that this effect weakly depends on the betatron tunes and is almost independent on the synchrotron ones.

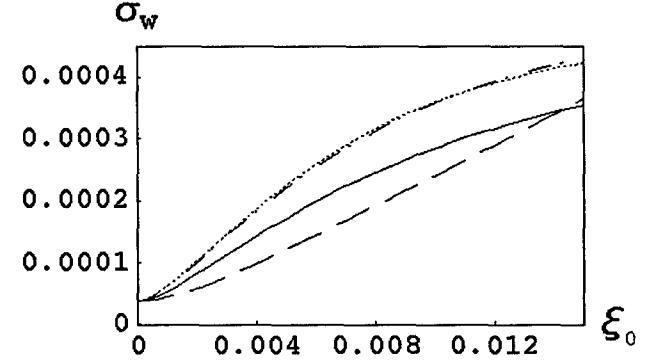


Figure 1: The energy resolution σ_w versus ξ_0 with $D_0 = 0.4\text{m}$ and other parameters are in Table 2.

Table 1: Legend of Figure 1

line	ν_y^{0+}	ν_y^{0-}	ν_z^{0+}	ν_z^{0-}	beams
dash-dot	0.05	0.05	0.03	-0.03	asymmetric
dash	0.1	0.05	0.03	-0.08	asymmetric
solid	0.1	0.05	0.03	0.03	asymmetric
dot	0.05	0.05	0.03	0.03	symmetric

Table 2: Parameters for both beams

β_y^0	0.03m	β_z^0	26.3m
ϵ_y^0	410^{-9}m	ϵ_z^0	3.810^{-6}m
σ_ϵ^0	3.810^{-4}	σ_z^0	0.01m
T_y	1000	T_z	500

The reason of the rapid growth of the energy resolution with ξ_0 is due to one of σ_{11} and in particular of σ_{22} [8], hence of the vertical and longitudinal emittances respectively. They increase in a similar manner regardless of the sign of ν_z^0 , even if for negative ν_z^0 the increase might be easier to understand, because the system is unstable [4].

The emittances are obtained from the envelope matrix σ as follows:

$$\text{Eigenvalues}[J\sigma] = \{i\epsilon_y, -i\epsilon_y, i\epsilon_z, -i\epsilon_z\}. \quad (23)$$

In Fig.2 we plot the emittances $\epsilon_{y,z}$ as functions of ξ_0 , for $\nu_z^0 = 0.08$. This shows that the longitudinal emittance ϵ_z is

influenced considerably by the the beam-beam force. This effect has been usually overlooked in the literature where the synchrotron oscillation is assumed to be unaffected. Also, the vertical emittance ϵ_y grows up quite rapidly.

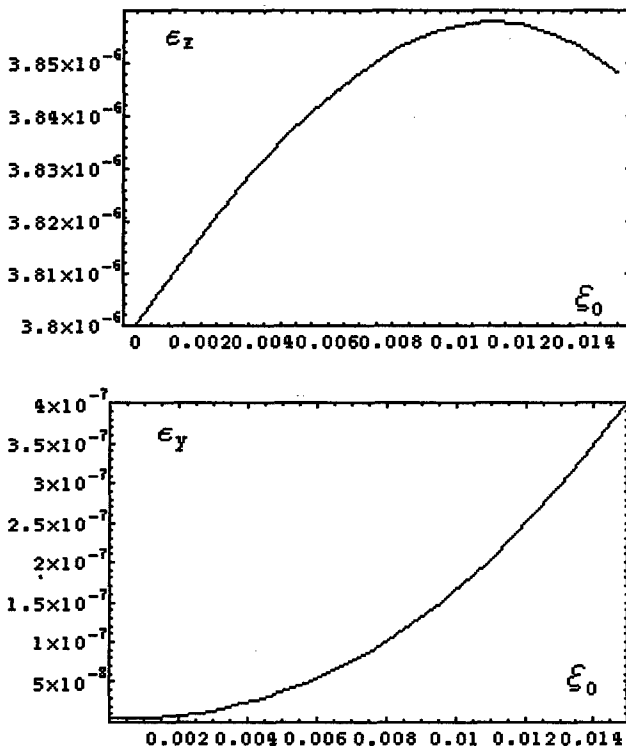


Figure 2: The synchrotron emittance ϵ_z (top) and the betatron one ϵ_y (bottom) as functions of ξ_0 with $\nu_{z0} = 0.08$ and all other parameters are listed in Table 2.

As conclusion, within the linear analysis used in this paper, it seems difficult to avoid this dangerous effect. However there can be some other effects in nonlinear regime which is worth to study. In deciding the machine parameters one should pay enough attention to the energy resolution.

5 REFERENCES

- [1] IHEP-BTCF Report-01, Dec. (1995) (unpublished); Yu. I. Alexahin A. N. Dubrovin and A. A. Zholents, Proc. of 2nd EPAC, 398 (1990); A. A. Zholents, AIP Conf. Proc. **214**, 592 (1990); A. Faus-Golfe and J. Le Duff, Nucl. Inst. Meth. A **372**, 6 (1996); P. F. Beloshitsky, JINR, EP-92-187, Dubna (1992)(unpublished); J. M. Jowett, *Frontiers of Particle Beams: Factories with e+e- Rings*, eds. M. Denies, M. Month, B. Strasser, S. Turner, Springer Verlag (1994), and references given there.
- [2] A. Renieri, INF-75/6(R), February 1975. A. Piwinski, DESY 77/18, 1977, and DESY H1/71-1, (1971) (unpublished).
- [3] Y. Kamiya and A. W. Chao, SLAC/AP-10, (1983) (unpublished).
- [4] S. Petracca and K. Hirata, Phys. Rev. D**59**, 1, R 40 (1999).
- [5] K. Ohmi, K. Hirata and K. Oide, Phys. Rev. E-**49**, 751 (1994).
- [6] S. X. Fang et al. Part.Acc. **51**, 15 (1995).
- [7] K. Hirata, H. Moshhammer and F. Ruggiero, Part. Acc. **40**, 205 (1993).
- [8] S. Petracca and K. Hirata, KEK Preprint 97-28 (1996).
- [9] K. Hirata and F. Ruggiero, Part. Acc., **28**, 137 (1990).
- [10] M. Bassetti and J. M. Jowett, IEEE Proc. of the PAC 1987, 115 (1987).

Electron Beam Distortions in Beam-Beam Compensation Setup

V. Shiltsev, FNAL, Batavia, IL 60510
and A. Zinchenko, JINR, Dubna, Russia

Abstract

This article is devoted to electron beam distortions in the "electron compressor" setup for beam-beam compensation in the Tevatron collider. The distortions are due to interaction of the electron beam with impacting elliptical antiproton beam. We estimate of longitudinal magnetic field necessary to keep the distortions low.

1 INTRODUCTION

Compensation of the beam-beam effects in the Tevatron with use of high current, low energy electron beam is discussed in [1]. The electron beam travels in the direction opposite to the antiproton beam and interacts with an antiproton bunch via its space charge forces. The proton beam has to be separated from the electron and antiproton beams. A 10 kV electron beam about 2-m long, 2-mm diameter, with 1-2 Amperes of current is to be installed in a place with large beta-function (~100m), away from the main interaction points. Experimental results from an "electron lens" prototype set-up are discussed in [2]. The electron beam is born on an electron gun cathode, transported through the interaction region, and absorbed in the collector. Strong longitudinal magnetic field plays a significant role in maintaining stability of both electron and antiproton beams. It also suppresses the electron beam current distribution distortions and, therefore, the electron space charge force distortions.

This article is focused on the time-dependent deviations of the electron beam shape due to interaction with antiproton beam in the "electron lens" [3].

2 ELECTRON BEAM DISTORTIONS

ZBEAM code [4] is used for tracing electron trajectories. This is essentially two dimensional code which takes into account only transverse components of the electric and magnetic forces. It is a good approximation for the forces due to ultra-relativistic \bar{p} bunch. The electrons are non-relativistic, but their space charge forces are mostly transverse, too. The code tracks number of particles by integrating their equations of motion over successive small time steps.

Interaction with round \bar{p} bunch in strong magnetic field conserves axial symmetry and radial size of the electron beam. As the result, the electron beam space charge forces are the same for antiprotons at the head and at the tail of the \bar{p} bunch. That is no longer true if electron or antiproton beam is not round. Roundness of the electron beam can be assured by using round cathode in the electron gun and by

appropriate choice of the magnetic field in the transport section of the set-up. In opposite, the \bar{p} beam roundness can be achieved in very few Tevatron locations where vertical and horizontal beta-functions are the same $\beta_x = \beta_y$ (vertical and horizontal emittances of 1000 GeV beams in the Tevatron are approximately equal $\varepsilon_{x,y}^{rms} \approx 3.3\pi \text{ mm} \cdot \text{mrad}$). This condition can not be fulfilled *a priori*. E.g., at present stage we consider to install one of the "electron lens" devices at the Tevatron F48 location which is characterized by $\beta_x = 101.7 \text{ m}$ and $\beta_y = 30.9 \text{ m}$, and, consequently, the rms bunch sizes are $\sigma_x = 0.61 \text{ mm}$ and $\sigma_y = 0.31 \text{ mm}$ [2].

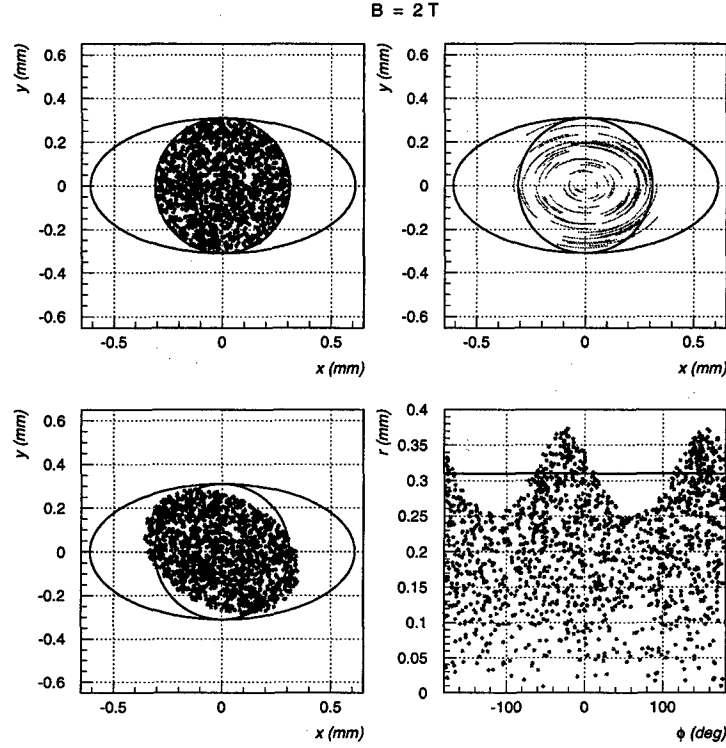
Fig.1 shows what happens with round electron beam (radius $a_e = 0.31 \text{ mm}$) when it interacts with such an antiproton beam being in 2T solenoid field. *ZBEAM* code is used for the electric field calculations and electron tracing. Top left plot shows an ellipse which corresponds to 1σ of the Gaussian \bar{p} bunch and a circle of the electron beam cross section uniformly filled with electron macroparticles before the interaction with \bar{p} -s. Top right plot demonstrates traces of the electrons under impact of asymmetric electric field of the antiproton bunch. Resulted macroparticle positions and the shape of the electron beam in $x - y$ and $r - \phi$ planes are shown in lower left and right plots of Fig.1 respectively. One can see that the electron beam becomes a rotated ellipse to the moment when the tail of antiproton bunch passes through it, while the head of the bunch sees originally undisturbed round electron beam. This might be of concern because of two reasons: 1) there appears a "head-tail" interaction in the \bar{p} bunch via higher than dipole wake fields propagating in the electron beam; 2) in addition to useful defocusing effect, electric fields of the elliptic electron beam produce effective $x - y$ coupling of vertical and horizontal betatron oscillations in the \bar{p} beam.

Distortion of electron density. The continuity equation for the electron charge density $\rho(x, y, z, t)$ can be written as $\frac{\partial \rho}{\partial t} + \vec{v}_d \cdot \vec{\nabla} \rho_0 = 0$, where ρ_0 stands for initial charge density, and drift velocity of an electron in crossed electric and magnetic fields \vec{E} and \vec{B} is equal to $\vec{v}_d = c \frac{[\vec{E} \times \vec{B}]}{B^2}$. The resulted distortion due to elliptic Gaussian relativistic \bar{p} beam is given by [3]:

$$\delta \rho(x, y, t) = \frac{z}{(1 + \beta_e)c} \left(\int_{-\infty}^z \lambda(z') dz' \right) \times \times \frac{2eN_{\bar{p}}}{B} \frac{d\rho_0(r^2)}{d(r^2)} \cdot \frac{xyI(x, y)(\sigma_x^2 - \sigma_y^2)}{\sigma_x^2 \sigma_y^2}, \quad (1)$$

where now z is the coordinate inside the \bar{p} bunch¹ and

¹i.e. $z = -\infty$ is for the bunch head and $\int_{-\infty}^z \lambda(z') dz'$ is proportional to the antiproton charge which passed through the given part of the electron beam.


 Figure 1: Narrow electron beam distortion due to \bar{p} bunch.

$$I(x, y) = \int_0^\infty dq \frac{e^{-\frac{x^2}{2\sigma_x^2(1+qR)} - \frac{y^2}{2\sigma_y^2(1+q/R)}}}{(1+qR)^{3/2}(1+q/R)^{3/2}},$$

$$I(0, 0) = \frac{2R}{(1+R)^2}, \quad R = \frac{\sigma_y}{\sigma_x}. \quad (2)$$

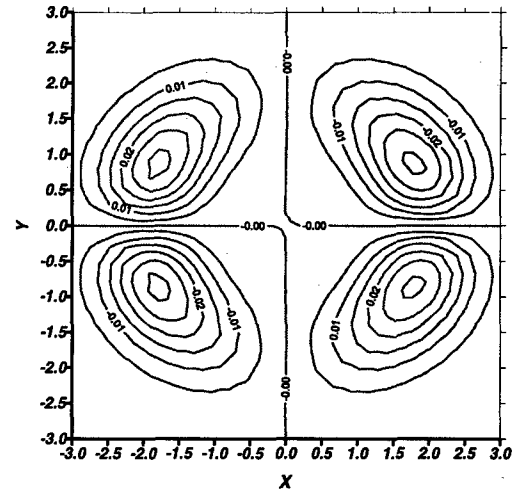
Now we can see major features of the resulted distortion:

- a) it is absent in the case of round \bar{p} beam when $\sigma_x = \sigma_y$;
- b) it performs two variations over azimuth $\delta\rho \propto xy \sim \sin(2\theta)$;
- 3) it vanishes with the solenoid field B increase, or with decrease of antiproton intensity $N_{\bar{p}}$;
- 4) most of the distortion takes place at the radial edge of the electron beam, and, since $d\rho_0(r^2)/d(r^2) \simeq \rho_0^{\max}/a_e^2$, then wider electron beam gets smaller density distortions during the interaction.

Finally, the scaling of the maximum distortion strength is:

$$\frac{\delta\rho^{\max}}{\rho_0^{\max}} \sim \frac{0.2eN_{\bar{p}}}{a_e^2 B} \approx \frac{0.6[N_{\bar{p}}/6 \cdot 10^{10}]}{a_e^2 [\text{mm}] B [\text{kG}]}, \quad (3)$$

and value of 0.2 comes from geometrical factor $\propto xy \cdot I(x, y)$. For example, the distortion is about 3% for 1 mm radius electron beam in $B = 20\text{kG}=2\text{T}$ solenoid field. As soon as the elliptic distortion is excited, it starts the rotation drift in the crossed fields of the electron space charge and the solenoid field. Under conditions of the Tevatron beam-beam compensation setup the rotation is small. E.g., one gets that over time of the \bar{p} bunch passage $\pm 2\sigma_z/c = 2\text{ns}$, the angle in the field of $B = 20\text{kG}$ is about $\theta_d \approx 4j\sigma_z a_e / \beta_e B \approx 0.1\text{rad}$.


 Figure 2: Distortions $\delta\rho/\rho$ of an electron beam wider than antiproton beam $a_e = 2.5 \cdot \sigma_x$. x and y coordinates are given in units of σ_x .

Distortion of other than constant electron density can be calculated analytically with use of Eq.(1). For example, Fig.2 shows contour lines of the electron beam distortion $\delta\rho/\rho$ in the case when initial density is $\rho_0(r) = \frac{1}{1+(r/a_e)^{2\mu}}$, $\mu = 3$, with $a_e = 2.5 \text{ mm}$, $\sigma_x = 0.61 \text{ mm}$, $\sigma_y = 0.31 \text{ mm}$, the antiproton bunch population $N_{\bar{p}} = 6 \cdot 10^{10}$, the magnetic field $B = 4\text{kG}$. Resulted distortion $\delta\rho/\rho$ is now less than 0.05.

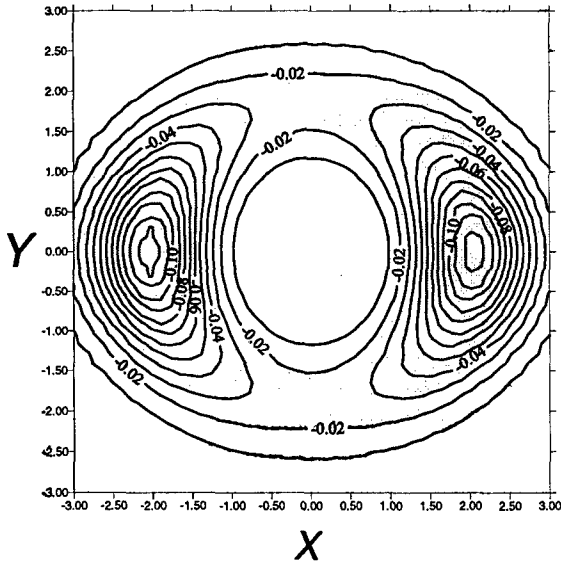


Figure 3: Coupling function $S(x, y)$ for antiproton betatron oscillations with a wide electron beams.

Coupling due to distorted electron beam. Electric and magnetic fields of the elliptic electron beam lead to effective $x - y$ coupling of vertical and horizontal betatron oscillations in the \bar{p} beam. Since originally the electron beam is round, the head of the \bar{p} bunch experiences no coupling force. But, as the electron density distortion grows as $\int^z \lambda(z') dz'$, the coupling grows proportionally. Particles in the head and in the tail of the bunch change their positions while performing synchrotron oscillations, thus, an average coupling effect is half of the maximum coupling spread. The average coupling can be corrected in the Tevatron, while there are no tools to compensate the spread in coupling. Therefore, the spread has to be small enough in order not to affect \bar{p} beam dynamics.

The tunes of a small amplitude particle can be written as

$$\nu_{\pm} = \frac{(\nu_x + \Delta\nu_x) + (\nu_y + \Delta\nu_y)}{2} \pm \sqrt{\frac{[(\nu_x + \Delta\nu_x) - (\nu_y + \Delta\nu_y)]^2}{4} + |\kappa + \Delta\kappa|^2}, \quad (4)$$

where ν_x and ν_y are the unperturbed horizontal and vertical tunes, in the current Tevatron lattice they are 0.585 and 0.575 correspondingly. κ is a complex number describing the coupling. For a satisfactory operation of the Tevatron collider, the global coupling is corrected down to value of $|\kappa| \approx 0.001$ [5]. Δ 's in Eq.(4) represent the changes of these quantities that arise from the interaction with the electron beam. E.g., the horizontal tune shift due to electron lens is about $\Delta\nu_x = -0.01$. The maximum coupling shift can be calculated from Eq.(1):

$$|\kappa| \approx |\Delta\nu_x| \frac{eN_{\bar{p}}}{2\sqrt{3}\sigma_x^2 B} \cdot \langle S(x, y) \rangle$$

$$\approx \frac{0.84[N_{\bar{p}}/6 \cdot 10^{10}]}{\sigma_x^2[mm]B[kG]} \cdot \langle S(x, y) \rangle. \quad (5)$$

Brackets $\langle \dots \rangle$ denote averaging over antiproton betatron oscillations. In the above equation we used an approximate relation $\beta_x \approx 3\beta_y$. Fig.3 shows numerical factor $S(x, y)$ for electron distributions $\rho_0(r) = \frac{1}{1+(r/a_e)^{2\mu}}$, $\mu = 3$, with $a_e = 2.5\sigma_x$. The maximum value of this factor of $S^{max}(x, y) = 0.13$. The coupling vanishes for small betatron amplitude particles and at very large amplitudes. The effect is larger in the plane of the longer antiproton ellipse axis (horizontal in our case).

For example, having parameters $\sigma_x = 0.61mm$, $N_{\bar{p}} = 6 \cdot 10^{10}$, $\Delta\nu_x \approx 0.01$ we get maximum numerical factor is about $\langle S(x, y) \rangle^{max} \approx 0.5 \cdot S^{max}(x, y)$, i.e. 0.065 for $a_e = 2.5\sigma_x$. Now, with solenoid field of $B = 2T$, one gets the maximum coupling spread $|\kappa| \approx 7 \cdot 10^{-5}$ for the electron beam. The value is rather small with respect to the Tevatron global coupling correction goal of about 0.001.

3 CONCLUSION.

We have considered distortions of the electron beam density due to interaction with an antiproton beam in the beam-beam compensation set-up. For a given number of antiprotons per bunch, both the electron density distortion and the coupling due to the distortion are inversely proportional to the magnetic field B in the set-up. In the case when the transverse sizes of the electron and antiproton beams are about the same (as it should be in the nonlinear electron lens for compensation of nonlinear beam-beam effects in the Tevatron), one needs more than 2T longitudinal field to keep the electron charge distribution distortions less than 3% with respect to original axisymmetric distribution and the spread of the coupling $|\kappa|$ less than $4 \cdot 10^{-4}$. Electron beam in the linear electron lens (for compensation of the bunch-to-bunch tune spread) has to be 2-3 times wider than the antiproton beam, and because of that in the same field of $B = 2T$ the distortion $\delta\rho/\rho$ is smaller, less than 1%, and the coupling spread in the antiproton bunch becomes negligible $|\kappa| < 7 \cdot 10^{-5}$.

We acknowledge stimulating and fruitful discussions with V. Parkhomchuk, S. Danilov, A. Sery, P. Bagley, and A. Burov.

4 REFERENCES

- [1] V.Shiltsev, *et. al*, "Compensation of Beam-Beam Effects in the Tevatron with Electron Beams", FNAL-Pub-98/260 (1998), see also these Proceedings.
- [2] C.Crawford, *et. al*, "Prototype "Electron lens" Set-up for the Beam-Beam Compensation", these Proceedings.
- [3] V.Shiltsev, A.Zinchenko, *Phys.Rev. ST - Accel. Beams*, **1**, 064001 (1998).
- [4] E.Tsyganov, A.Zinchenko, SSCL-Preprint-618 (1993).
- [5] P.Bagley and J.Annala, private communication.

BEAM-BEAM STUDY IN BEPC MINI- β SCHEME

Sheng Wang*, Shouxian Fang, Chuang Zhang
Institute of High Energy Physics, Beijing 100039

Abstract

For performing mini- β colliding on Beijing Electron Positron Collider(BEPC), high RF voltage is supplied for shortening the bunch length, but beam experiments show that high RF voltage results in the luminosity decrease. The conclusions of detailed study are that, for BEPC, the averaging over the betatron phase during the collision has occurred. The ratio of bunch length over beta function at interaction point is too small, and the mitigating of averaging over the betatron phase causes the luminosity decreases.

1 INTRODUCTION

Mini- β scheme is one of the most important way of Beijing Electron Positron Collider(BEPC) luminosity upgrades. For performing Mini- β scheme on BEPC, high RF voltage is supplied for shortening the bunch length. But the abnormal phenomenon was observed during machine study [1]. For 2.015GeV colliding mode, the vertical beam size σ_y increases with the RF voltage increasing and result in the luminosity decrease. Learned from the machine study that the increase of σ_y is correlated with the beam-beam interactions, but we did not know why and how to overcome it. This abnormal phenomenon seriously influenced on the performance of the Mini- β scheme. Here, authors are aiming to explain the abnormal phenomenon and overcome it.

The higher RF voltage not only shorten the bunch length, but also increase the synchrotron frequency. Here, our study are concentrated on the effects of bunch length, and for the change of the synchrotron frequency induced by the RF voltage, as shown in the later simulation and machine study, do not influence on the vertical beam size and luminosity obviously. We also can know from the beam experiments that the synchrotron betatron resonance is not the reason of the abnormal phenomenon.

The "hourglass" effect lets the luminosity increase with the increasing of the ratio β_y^*/σ_s , where β_y^* is the vertical β function at the interaction point, and σ_s is the bunch length. On the other hand, there is another bunch length effect on beam-beam interaction, i.e. effect of averaging over the betatron phase. In BEPC, this effect occurred.

For the finite bunch length, the beam-beam force experienced by a particle does not act on a betatron phase point, but a phase interval. The total beam-beam force is "averaged" by the phase interval. For the resonance

$$p\nu_y = m \quad p, m \text{ integer}, \quad (1)$$

in which ν_y is the betatron tune, the effect of averaging decreases the resonance strength. Roughly speaking, the effect is proportional to the size of the interval. The size of phase interval is

$$\Delta\phi = \int_{-\sigma_s}^{\sigma_s} \frac{1}{\beta(s)} ds \approx \frac{2\sigma_s}{\beta^*} \quad (2)$$

one can obtain that the smaller β_y^*/σ_s contributed more to increase the effect of the averaging over betatron phase as well as to decrease of the resonance strength. This agrees to the result of theoretic derivation [2].

In BEPC machine study, we found that for 2.015GeV mini- β mode, when the nominal value of β_y^* is 5cm, the measurement value is about 8.7cm, and $\beta_y^*/\sigma_s > 1.5$. Just under this condition, the special phenomenon that the σ_y increase with increasing of RF voltage, resulting in the decrease of the luminosity. So we infer that the increase of the vertical beam size resulting from high RF voltage is related to the decrease of the effect of averaging over betatron phase resulting from the compression of the bunch length. This reference is supported by the later simulation and results of machine study.

2 SIMULATION

The code BBC(Beam Beam with Crossing angle) [4], with little modification, was used in beam-beam interaction simulations. The bunch length used in simulation is calculated by the following scaling law,

$$\sigma_s \text{ (cm)} = 0.651 * \left(\frac{I_b \text{ (mA)} \alpha_p}{E \text{ (GeV)} v_s^2} \right)^{\frac{1}{3.49}} \quad (3)$$

which is given by the bunch length measurement with stream camera, and α_p is momentum compaction factor.

* The works supported by President Foundation of Chinese Academy of Sciences and Post Doctor Science Foundation of China.

* E-mail: wangs@bepc5.ihep.ac.cn

2.1 Simulation results of 2.015GeV

In the first two figures give simulation results of total 6 different working point, $v_x=5.81$, v_y is from 6.75 to 6.80, with step 0.01, and under the different RF voltage, compare the luminosity.

Fig.1 shows the simulation results with parameters of $E=2.015\text{GeV}$, $\beta_y^*=8.7\text{cm}$, bunch intensity $I_b=35\text{mA}$. One can obtain from Fig.1 that the luminosity with RF voltage 0.9MV is higher than the one with RF voltage 1.5MV, except one working point. So when β_y^* is larger than nominal value, luminosity decrease with RF voltage increase. Then if we set $\beta_y^*=5\text{cm}$ (nominal value), how about the results?

Fig.2 shows the simulation results with same parameter as Fig.1, except $\beta_y^*=5\text{cm}$. One can learn from Fig.2 that luminosity increase with RF voltage increase, totally contrary to the Fig.1.

In Fig.1 and Fig.2, all the parameters except β_y^* are same, but the results are totally different. From this we also can draw another conclusion that the synchrotron frequency changed with RF voltage do not influence the luminosity obviously.

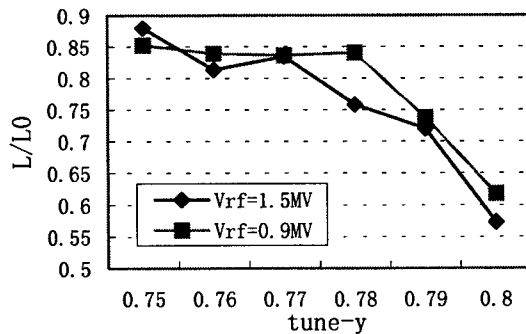


Fig.1 Luminosity vs. RF voltage with $E=2.0\text{GeV}$, $\beta_y^*=8.7\text{cm}$

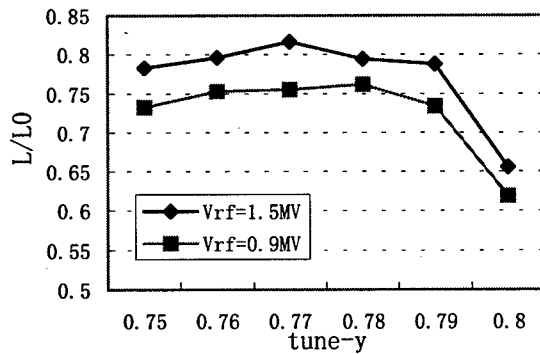


Fig.2 Luminosity vs. RF voltage with $E=2.0\text{GeV}$, $\beta_y^*=5\text{cm}$

2.2 Simulation results of 1.548 GeV mode

The simulation results of 2.0GeV colliding mode are given in the above section. We are more interesting in the 1.548GeV mini- β colliding mode, because now BEPC is

running on J/ψ (1.548GeV) energy region, and the later machine study are also at 1.548GeV colliding mode. So we can compare the machine study results with the simulation here directly.

Fig.3 shows the simulation results with $E=1.548\text{GeV}$, $\beta_y^*=5\text{cm}$, bunch intensity $I_b=15\text{mA}$, and gives simulation results of total 6 different working point, $v_x=5.81$, v_y is from 6.73 to 6.78, with step 0.01. One can obtain that the luminosity with RF voltage 0.85MV is higher than the one with RF voltage 0.30 MV, except one working point (5.81,6.71), which close to resonance $3v_x+2v_y+2v_s=4$.

Fig.4 gives the simulation results with $\beta_y^*=8.5\text{cm}$, same energy and bunch intensity as Fig.3. Totally 10 working points, $v_x=5.81$, v_y is from 6.67 to 6.76, with step 0.01, are involved in the simulation. The figure tell us that the result here is not only different from Fig.3, but also different from Fig.2. The luminosity do not vary with RF voltage regularly. From Fig.5 in the later section, we can get the answer: under this condition, β_y^*/σ_y is too large to observe varying of luminosity with different RF voltage.

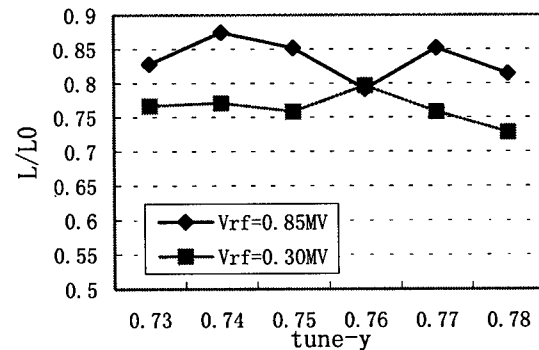


Fig.3 Luminosity vs. RF voltage, $E=1.5\text{GeV}$, $\beta_y^*=5\text{cm}$

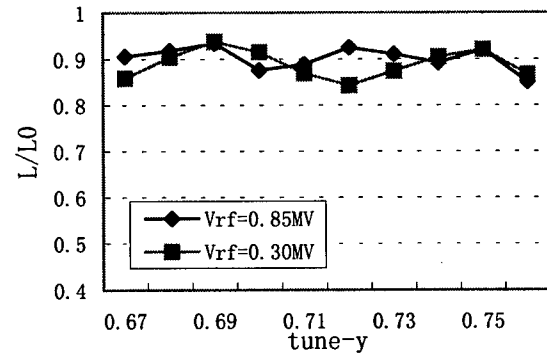


Fig.4 Luminosity vs. RF voltage, $E=1.5\text{GeV}$, $\beta_y^*=8.5\text{cm}$

2.3 Simulation study on the relation between luminosity and σ/β_y^* in BEPC

In the above simulation study, our purpose is to observe how the luminosity change with higher and lower RF voltage, and so only two RF voltage value(bunch length)

were simulated. According to the theoretic analysis, for the existing of "hourglass" effect and averaging over betatron phase, how will the luminosity vary with σ_s/β_y^* continuously? For BEPC, is there the most optimal σ_s/β_y^* which give highest luminosity? If there is, what its value is? To answer these questions, a group of simulations were done. Different from the above simulations, here synchrotron frequency ν_s do not change with RF voltage.

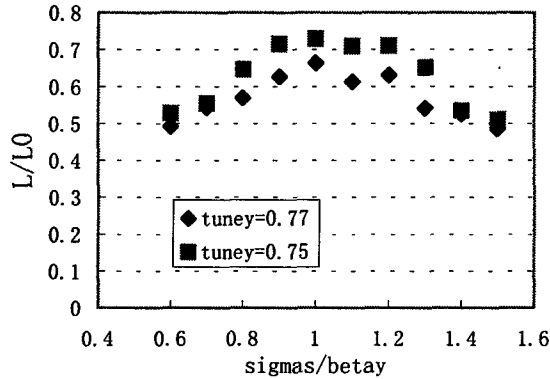


Fig.5 Relations between luminosity and σ_s/β_y^* in BEPC

Fig.5 shows the simulation results of two working points (5.81,6.75) and (5.81,6.77). We can obtain that the most optimal value of σ_s/β_y^* is about 0.9~1.1.

3 MACHINE STUDY

Machine study is done at 1.548GeV mode. Under the condition of $\beta_y^*=8.5\text{cm}$ and $\beta_y=5\text{cm}$, change RF voltage, and observe the change of luminosity. RF voltage was changed from 0.35MV to 0.85MV. For each given RF voltage, five luminosity readings are recorded to reduce the measurement error of luminosity. The bunch intensity should decrease during the changing of the RF voltage, and this change are corrected by $L \propto I_b^2$ when process data. In the following figures the line indicates the average value.

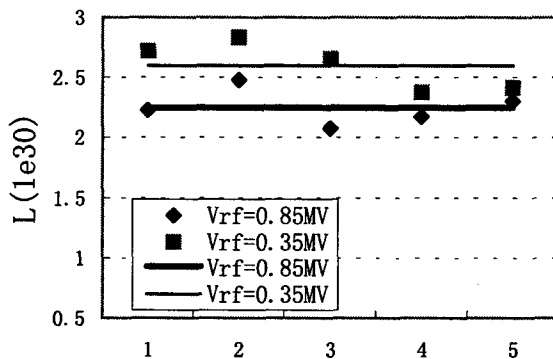


Fig.6 Machine study results, $E=1.548\text{GeV}$, $\beta_y^*=8.5\text{cm}$

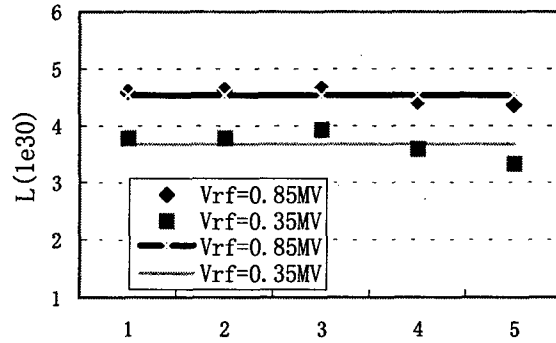


Fig.7 Machine study results, $E=1.548\text{GeV}$, $\beta_y=5\text{cm}$

The machine study results of $\beta_y^*=8.5\text{cm}$ mode are shown in Fig.6, in which the luminosity decrease with the increase of RF voltage. Fig.7 shows the results of $\beta_y=5\text{cm}$, the luminosity increase with the increase of RF voltage, as predicted by theoretic analysis and simulations.

4 CONCLUSIONS

The study on problem of the beam-beam effects which come from mini- β scheme BEPC luminosity upgrades draws the following conclusions:

For BEPC, the bunch length σ_s influences the beam-beam interaction mainly through the "hourglass" effect and averaging over the betatron phase during the collision, and these two contrary effects make the luminosity be maximum only when σ_s/β_y^* is near the optimal value. If σ_s/β_y^* is more than the optimal value, the luminosity decreases resulting from the hourglass effect, and if the σ_s/β_y^* is less than the optimal value, the luminosity decreases resulting from mitigating of averaging over the betatron phase as well as the increasing of resonance strength. The most optimal value of σ_s/β_y^* for BEPC given by the simulation is about 0.9~1.1. All the recorded machine study results about bunch length influencing on luminosity agree to the theoretic analysis and simulations. At the suitable range of σ_s/β_y^* , the luminosity can be increased by shortening the bunch length, for BEPC, as well as increasing of RF voltage.

5 REFERENCES

- [1] Li Ma etc., BEPC/MD/95.
- [2] S. Krishnagopal and R. Siemann, Physics, Review D, Volume 41, No.7, April 1990.
- [3] Yingzhi Wu, Guangxiao Li and Aimin Xiao, Proceeding of the Workshop in on BEPC Luminosity Upgrades, Beijing, June, 1991.
- [4] K. Hirata, Nucl. Instr. Meth. A269(1988) 7.
- [5] C. Zhang and K. Hirata, KEK, Preprint 96-91.

NEW PROJECTS AT CRYRING

H. Danared, G. Andler, L. Bagge, A. Källberg, P. Löfgren, A. Paál, K.-G. Rensfelt, Ö. Skeppstedt,
A. Simonsson, M. af Ugglas, Manne Siegbahn Laboratory, Stockholm, Sweden
H. Cederquist, H. T. Schmidt, S. H. Schwartz, Stockholm University, Stockholm, Sweden

Abstract

Major recent developments at CRYRING include the installation of a superconducting gun solenoid on the electron cooler one and a half years ago, the construction of a gas target for studies of fast ion-atom collisions that will be operating in the late spring of this year, and an ECR ion source on a high-voltage platform that will be used as an additional injector into CRYRING. Smaller projects relate to the continuous requests for new atomic and molecular ions in the ring, including now negative ions, which leads to a demand for new detector positions and, since these ions often are difficult to produce in an ion source, also to improvements of the diagnostics of weak beams in injection lines and in the ring.

1 ELECTRON COOLER

The electron cooler was rebuilt during the summer of 1997 for the installation of a superconducting gun solenoid and a new electron gun of 4 mm diameter [1]. The aim with this modification was to reduce the transverse electron temperature further and to improve the conditions for experiments with electron-ion recombination.

The superconducting magnet has a nominal maximum field of 5 T, but it is usually run at 3 T together with 300 G in the rest of the cooler magnets. This gives an adiabatic electron-beam expansion with a factor of 100 and, theoretically, a reduction of the transverse energy spread of the electrons from 100 meV to 1 meV. With the new electron gun of 4 mm diameter, the electron-beam diameter in the cooling section will then be 40 mm as before the introduction of the beam expansion.

Some measurements of the longitudinal drag force with the 100 times beam expansion have been performed. They showed an increase in the drag force compared with the data for 10 times beam expansion by 25–50% at relative velocities in the vicinity of the drag-force maximum. This increase is presumably larger than the measurement errors, but it is possible that the longitudinal electron temperature in the new measurements was lower than in those with 10 times expansion since the new electron gun is of a different construction. This may then explain some of the effect. The longitudinal drag force thus still agrees reasonably well with a binary-collision model with a value of kT_{\perp} approximately equal to 3 meV [2]. Note, however, that this model does not include the effect of the magnetic field in the cooler, and the com-

parison thus does not necessarily mean that kT_{\perp} actually is 3 meV.

Preliminary studies with the new cooler where the expansion ratio has been changed have also been made, and here the difference between 10 and 100 times expansion was of the same size as the measurement errors.

To some extent, information about the transverse drag force can be obtained by studying so-called transverse Hopf bifurcations [3–4]. When an angle is introduced between the ion and the electron beam, a transverse instability will occur at an angle where the transverse electron velocity (relative to the ion beam) exceeds the velocity where the transverse drag force has its maximum. The ions will then start to perform transverse oscillations with an amplitude that depends on the electron-beam angle.

We measured the oscillation amplitude using a beam profile monitor and compared the measured profile with tracking results. These profiles have the form of two distinct peaks whose separation corresponds to the oscillation amplitude and weaker intensity between the peaks. The tracking program uses a drag force calculated in three dimensions according to the model described in ref. [2] and include such effects as betatron oscillations, dispersion, the space charge of the electron beam, and the position and alignment of the electron beam relative to the ion beam.

Figure 1 shows a preliminary comparison between measurements and tracking simulations. The shape of the curves are reasonably similar, showing a sharp threshold for the onset of the transverse oscillations, and again the measurements seem to agree with the binary-collision model with a kT_{\perp} somewhere in between 1 and 10 meV.

The most accurate way of measuring the electron temperature is to look at the peak shape of sharp recombination resonances. The asymmetry of such peaks that occur provided that the relative energy between ions and electrons is sufficiently low makes it possible to determine the transverse and longitudinal temperature simultaneously. In order to be sensitive to temperatures as low as around 1 meV, the recombination resonances should be at a relative energy of at most 10 meV, preferably lower. In addition, the peak should be well apart from other resonances and must have a narrow natural line width. The best systems studied so far at CRYRING is C^{3+} [5] and F^{6+} [6], where the two latter criteria are essentially fulfilled, but where the resonance energy is somewhat too high (0.17 and 0.12 meV, respectively). Although the high

resonance energy gives some uncertainty, the best fits to the peak shapes gave a transverse electron-energy spread of about 3 meV in both cases.

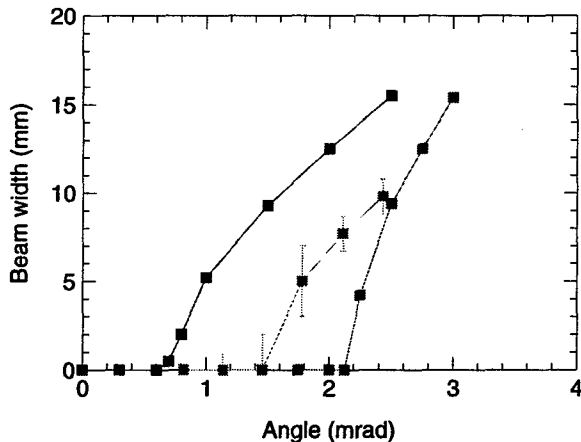


Figure 1: Beam width, defined as the peak separation (see text), as a function of electron-beam misalignment. The left curve is tracking results with a theoretical drag force and $kT_{\perp}=1$ meV and the right curve with $kT_{\perp}=10$ meV. The middle curve represents measured values.

Several facts thus points at a transverse energy spread that is higher than the expected 1 meV, but there remains to make a conclusive measurement. It could also be noted that we do not expect that the straightness of the magnetic field in the cooling solenoid (which was carefully measured when the cooler was built) or a misalignment between ion and electron beams could explain the observed transverse temperature.

2 ECR ION SOURCE

An ECR ion source has now been installed at the laboratory. The source as such has been tested, and work with the beamlines that will connect it to the experimental facilities is in progress. We expect that it will be able to deliver ions to the storage ring next year.

The ion source is a single stage HYPERNANOGAN device delivered by Pantechnik. It has an operating frequency of 14.5 GHz and a maximum rf power of 2 kW. The solenoidal field is generated by an electromagnet, while the hexapolar field is given by permanent magnets. The magnetic structure enables a future upgrade to 18 GHz. Extraction voltages of up to 30 kV can be used.

The ECR source with its cw beams of heavy ions in intermediate charge states will serve as a complement to the present EBIS source both for injection into the ring and for atomic collision and surface physics with the ions directly from the source. It will also be able to deliver singly charged atomic and molecular ions, for which the high-voltage platform will facilitate injection into the ring in some cases.

In order to improve the injection into the ring and to allow a wider range of experiments using ions directly

from the source, the ECR is mounted on a 300 kV high-voltage platform. On the platform, and separated from the source by an einzel lens, is a 102° double-focusing analysing magnet. Due to space restrictions and ripple and leakage current considerations, the 300-kV platform is separated into two units. The 350-kVA motor-generator unit and the 300-kV 2.5-mA Glassman high-voltage supply are placed in another hall and connected to the ECR platform by 40 m long high-voltage cables. The platform will be fully enclosed in a metal cage, and in order to limit the risk for flashover and to protect personnel, the inner cage will in addition be enclosed in an outer cabinet, separated by a least 60 cm from the inner shield.

After installation on the platform, an acceptance test of the source was performed. The three injection systems, gas only (Ar), furnace for molten metals (Pb), and sputtering for metals and compounds (Ta) were tested, and the currents obtained were in fair agreement with the values guaranteed by the manufacturer. Table 1 shows some of the results of these tests, as well as the result when the source was running in the so-called afterglow mode.

Table 1: Examples of measured ion currents in electrical μ A during the acceptance test for various charge states q . *Afterglow mode in which case the current in continuous mode was 24 μ A.

q	8	11	12	14	20	24	25
Ar	300	125	60	8			
Ta					26	24	
Pb							30
Ar*		60					

3 GAS TARGET

A gas-jet target to be installed in CRYRING later this spring has been designed and constructed in a collaboration between the Physics Department of Stockholm University, the Manne Siegbahn Laboratory, Frankfurt University, GSI, and Freiburg University [7]. The main purpose of the gas-jet target is detailed investigations of collisions between the fast CRYRING ions and the molecules or noble-gas atoms of the gas jet by means of the technique of COLd Target Recoil-Ion-Momentum Spectroscopy (COLTRIMS).

The target is designed for helium for which the aim is to create a cold (<5 mK) target with a density of about 10^{12} cm $^{-3}$ in a 1.0 mm narrow jet at the point of intersection with the ion beam. At the same time the ultra-high vacuum of the CRYRING should remain unaffected.

The target operates such that precooled (30 K) gas expands through a 30 μ m nozzle from a container with a helium pressure of $p_0=2$ bar into an expansion chamber, where a pressure of the order of 10^{-3} mbar is maintained by means of a 1000 l/s turbomolecular pump. After this a

beam is formed by narrow skimmers before the interaction region is reached. Finally the jet is disposed of in a three-stage differentially pumped jet dump.

The target has been tested off-line with the helium-gas container at room temperature. In one particular test, the load of helium in the collision chamber was measured by means of a commercial He leak detector while the jet was running. In this way, the load of helium gas lost to the collision chamber and thereby affecting the CRYRING vacuum was found to be less than 5×10^{-10} mbar l/s, which with the increased helium pumping capacity (as discussed below) corresponds to a pressure increase of less than 10^{-12} mbar in CRYRING. This load is expected to increase by a factor of $10^{1/2}$ when the gas is pre-cooled to 30 K.

By blocking the jet with a scraper in the collision chamber, the full load of the jet (2×10^6 mbar l/s) was measured by the leak detector, and the jet diameter was determined by considering the load as a function of the scraper position. The diameter of the jet was found to be 1.0 mm as expected. From the full jet load, the diameter and the expected jet velocity, the He density at the intersection point was found to be about 3×10^{10} cm⁻³. The density is expected to increase by a factor of 10 when the gas is pre-cooled to 30 K, so it seems that we will not quite achieve the desired density with this choice of gas-target parameters. On the other hand, with this parameter choice we are on the safe side regarding the CRYRING vacuum conditions, and a density of 3×10^{11} cm⁻³ will be sufficient for all planned experiments. If, at a later stage, a higher density is needed, a wider nozzle and improved pumping of the expansion chamber seem to be the most feasible alternative.

4 OTHER PROJECTS

The rest gas in CRYRING, where the average pressure is around 1×10^{-11} mbar, consists to 90% of hydrogen. However, it is to a large extent the remaining 10% that reduces beam lifetime and increases the experimental background in studies of processes like ion-electron recombination. Furthermore, with the use of helium in the gas-jet target, there will inevitably be some increase in the helium pressure in the ring, and this helium is not pumped efficiently neither by the NEG (non-evaporable getter) pumps nor by the ion pumps used at present. In fact, the memory effects of the ion pumps will lead to an increased helium background even long after the gas target has been turned off.

For these reasons, the vacuum system of the ring will be upgraded with eight high-compression turbomolecular pumps. On the high-pressure side of each of these pumps a smaller turbo pump will be connected, providing a backing pressure of around 10^{-6} mbar, and mechanical forepumps to each of these turbo-pump assemblies. On the low-pressure side there will be NEG strips to reduce the outgassing of H₂ from the turbo pumps themselves.

A complete reconstruction of the vacuum chambers after the electron cooler (the dipole chamber behind the cooler and the straight section up to the following dipole) has been made in order to allow detection of a wider range of ions that have undergone charge exchange in the cooler. Now there are detector positions that allow the interception of almost all ions with charge states from 1 to around 55 that have decreased the charge by one unit in the cooler. There are also manipulators in the dipole magnet after the cooler for the detection of ions that have increased their charge state (i.e. that bend more than the primary beam in the dipole), and for ions whose charge has changed sign (that bend in the opposite direction). These detector positions are particularly interesting for the study of charged fragments produced in dissociative recombination of molecular ions.

Since several years there have been proposals for experiments with negative ions in CRYRING. When the ring was constructed, this option was foreseen, and it is fairly straightforward to change the polarity of magnets and electrostatic deflectors. Tests with negative ions in the ring will be performed during the spring, and if these tests are successful, a dedicated ion source for negative atomic and molecular ions will be purchased.

Finally the efforts to improve the sensitivity of the diagnostics in the beam lines and in the ring are continuing. These include the installation of sensitive electronics for strip detectors in the injection lines [8], the use of integrating CCD cameras with image processing at fluorescent screens, and improvement of the noise level of the amplifiers for the electrostatic pickups in the ring. For the latter, the use of state-of-the-art integrated-circuit amplifiers and an input stage with several low-noise field-effect transistors in parallel have reduced the noise level to less than $1 \text{ nV/Hz}^{1/2}$.

5 REFERENCES

- [1] H. Danared, A. Källberg, L. Liljeby, and K.-G. Rensfelt, Proc EPAC'98, eds. S. Myers, L. Liljeby, Ch. Petit-Jean-Genaz, J. Poole, and K.-G. Rensfelt (Inst. of Publishing, London, 1998), p. 1031.
- [2] H. Danared, Nucl. Instr. Meth, A391 (1997) 24.
- [3] D. D. Caussyn et al, Phys. Rev. E51, (1995) 4947.
- [4] K. Hedblom and L. Hermansson, Nucl. Instr. Meth, A391 (1997) 37.
- [5] R. Schuch, W. Zong, W. Spies, P. Glans, and H. Danared, Hyperfine Int., 115 (1998) 123.
- [6] P. Glans et al., Nucl. Instr. Meth, in press.
- [7] H. T. Schmidt et al., Hyperfine Int., 108 (1997) 339, H. T. Schmidt et al., Phys. Scr, in press.
- [8] S. Leontein and E. Westlin, Proc. EPAC'98, p. 1550.

Optical Notch Filter for the Stochastic Cooling System of COSY

U. Bechstedt, J. Dietrich, K. Henn, A. Lehrach, R. Maier, D. Prasuhn, A. Schnase, H. Schneider, R. Stassen*, H. Stockhorst, R. Toelle, Forschungszentrum Juelich GmbH, D-52425 Juelich

Abstract

Two cooling methods are installed in the cooler synchrotron COSY. The electron cooler is used for stacking and cooling of proton beams with energies between 45 MeV and 180 MeV. After last year's commissioning the stochastic cooling system became a standard tool for beam cooling in the momentum range of 1.5-3.3 GeV/c. The stochastic cooling pickups also serve for precision measurements of the chromaticity [6]. One advantage of COSY is the possibility to set up different machine settings in a 'supercycle'. Internal experiments can take data below, close at and far above the threshold in one supercycle. The transversal stochastic cooling system was updated using the COSY software timing system to allow cooling in all three experiments. For longitudinal cooling a new notch-filter was fabricated. The delay-line of the notch-filter was substituted by an optical delay line. We will present the characteristics of the optical notch filter and the enhancement of the beam quality for an internal gas target using the longitudinal cooling system with the new notch-filter. In order to use the longitudinal cooling in a 'supercycle' the optical delay line has been further improved. A part of the optical signal path is carried free through an air section. This section is adjusted according to the beam travelling time with the aid of a motor-driven prism.

1 INTRODUCTION

The transversal stochastic cooling system operates in the frequency range from 1 to 3 GHz divided into two bands. [1]. The stochastic cooling has been used for the internal gas cluster target experiment COSY11. The cycle length has been increased up to 1 hour. Less than 10% of the stored protons were lost. The cooling system reached an

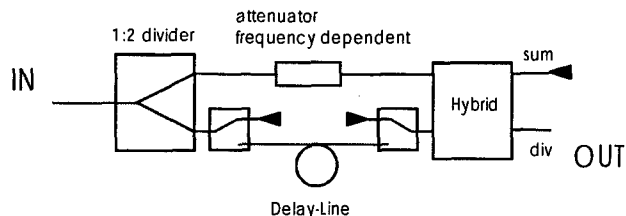


Fig. 1: Notch filter for the longitudinal cooling

equilibrium state after 20 minutes, where the energy loss of the protons through the gas target was compensated by

* Email: r.stassen@fz-juelich.de

the longitudinal cooling system. The shape of the distribution remains unchanged until the end of the spill [3,4].

The longitudinal cooling was realized by using the vertical band 1 system in sum mode including a simple notch filter (fig. 1) [2]. The attenuator in the short branch compensates the loss of the delay-line especially its frequency dependence. This attenuator is fixed once. There is no remote control of the value and the frequency slope.

2 STOCHASTIC COOLING IN A 'SUPERCYCLE'

The possibility to group up different machine settings within a 'supercycle' is a major advantage of COSY [5]. The transversal stochastic cooling system has been upgraded using the COSY timing system to allow transversal cooling in all settings. The installed programmable delay-lines allow a change of proton momentum from 2.15 to 3.4 GeV/c or with an additional fixed length of 5 m from 1.68 to 2.15 GeV/c in one supercycle with transversal stochastic cooling. Longitudinal cooling in a supercycle needs a system adjusting the length of the delay-line in the notch-filter. Both accuracy and resolution are required to be in the order of $1 \cdot 10^{-6}$. An envisaged realization using commercial RF components seems to consume too much time and costs. The solution transferring the RF signals into the terahertz region of a laser source was more praiseworthy [3].

3 OPTICAL NOTCH-FILTER

The first version of the notch-filter was fabricated in a similar structure like our coaxial notch-filter. The delay line was substituted by an optical structure (Fig. 2).

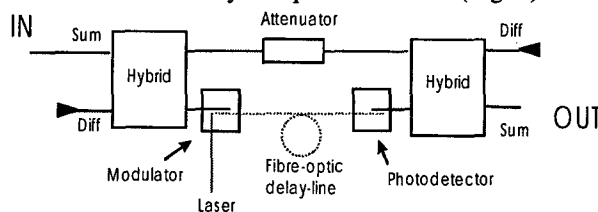


Fig. 2: Optical delayed notch filter

The modulator attenuates the laserlight synchronously to the longitudinal RF signal of the pick-up. The infrared signal is delayed by a fibre optic coil. The RF signal is afterwards reconstructed by the photodetector. The equal phase power divider [2] was substituted by a hybrid

having a better decoupling between the short and the long branch of the notch filter. The frequency dependence of the attenuation in the optical delayed branch is negligible because the small relative bandwidth required of the optical system is around $3 \cdot 10^{-6}$ at the RF frequency band of 1-1.8 GHz. Therefore, the RF attenuator in Fig. 2 is now a frequency independent one. Equalizing the attenuation between the short and the long branch of the notch filter is simply fulfilled by regulating the power of the laser light.

The longitudinal cooling was improved by the optically delayed notch filter in the following items:

The notch depths over the whole frequency band exceed values of 35 dB compared to 25 dB of our first RF delayed filter. The dispersion of the optical notch filter can be neglected. Frequency shifts of only 25 Hz relating to the proton revolution frequency were measured at the RF band end caused by small phase deviations between both branches of the notch filter. The dispersion of the coaxial line used for the delay in the coax notch filter is essentially larger.

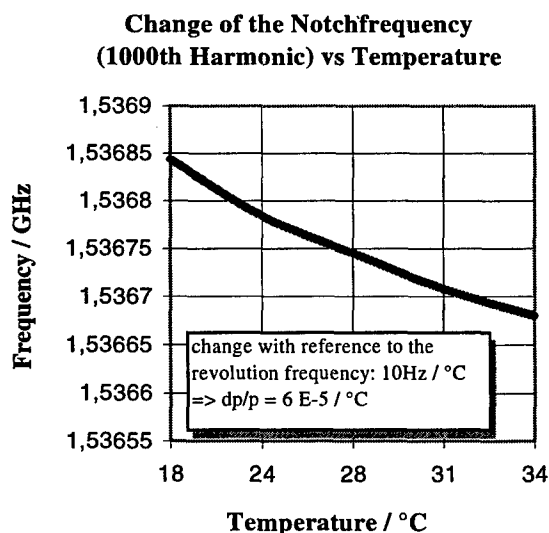


Fig. 3: Temperature behaviour of the optical delayed notch filter

The temperature behaviour of the optical notch filter was measured. Fig. 3 shows the change of the notch-frequency versus temperature. The frequency change is so small that no further steps like the use of a temperature stabilized fibre optic has to be taken [7].

The horizontal Band 1 cooling system was extended by a new path for the longitudinal optical cooling system. Amplitude and phase of this new signal path have been adjusted by automated BTF measurements. The optical notch filter was installed and tested with beam. After several minutes most of the particles are concentrated at the momentum given by the frequency of the notch filter. Fig. 4 shows the resulting Schottky signal measured at the revolution frequency over 1.5 h.

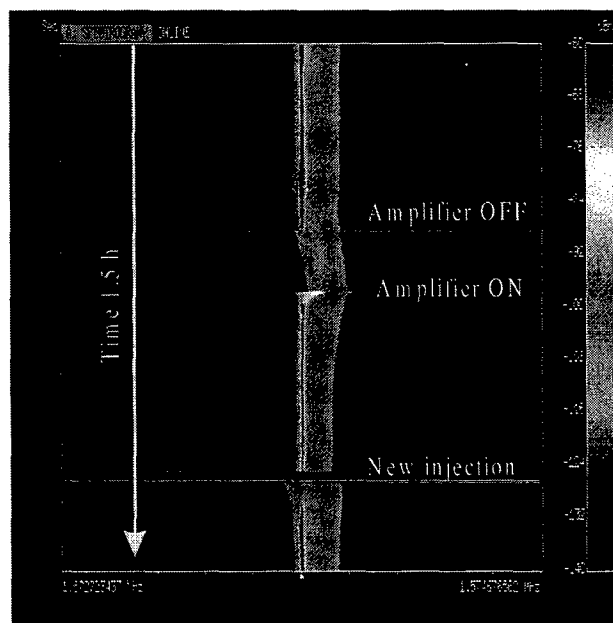


Fig. 4: Longitudinal Schottky scan

When the amplifier of the cooling system are switched off the distribution would be shifted upwards in frequency due to energy loss in the target. The resulting frequency distribution is smaller compared to the old notch filter. Both longitudinal cooling systems (the old notch filter of commercially available RF components and the optical one) were used alternately in a COSY11 run time at different energies.

The cycle lengths were successfully increased up to 2 hours with the aid of the optical notch-filter. After filling the COSY ring for the COSY11 experiment the beam of the cyclotron was used for radionuclide production during these 2 hours.

3.1 Adjustable notch filter

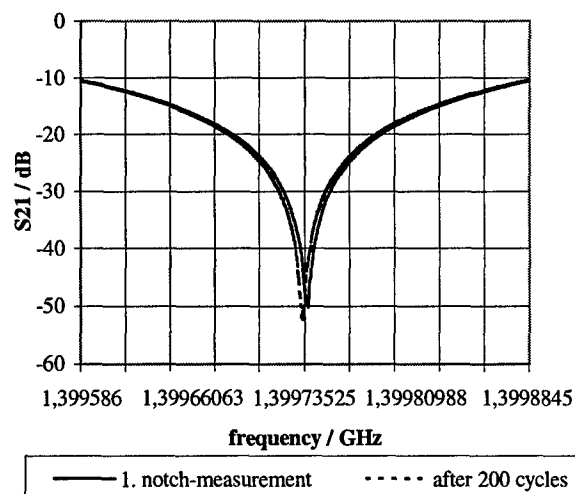


Fig. 5: Accuracy of the repeatability of the adjustable notch filter

We added an adjustable delay line to the notch filter in order to use the longitudinal cooling system in a supercycle. Fig.6 shows the implemented changes of the

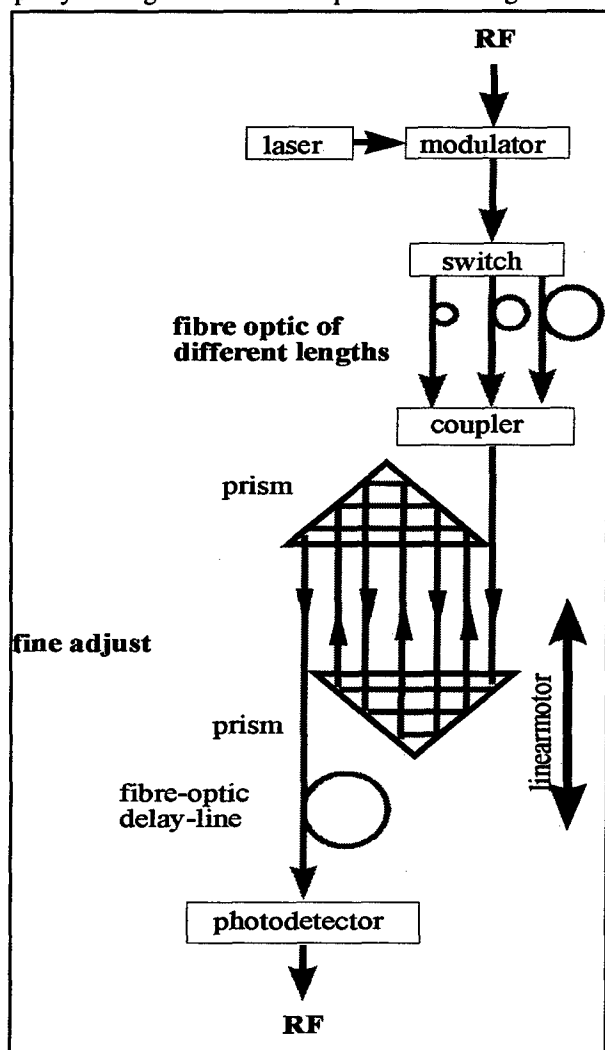


Fig. 6: Adjustable delay line

optical delay line. The system for the fine adjustment was fabricated with a planned adjustable length of about 5m. This length difference is realized by an air section. This section is adjustable according to the beam travelling time with the aid of a motor-driven prism.

Fig. 5 presents the first measurements of the adjustable notch filter around the 900th-harmonic of the beam-revolution frequency.

The motored prism was moved 200 times over the moving range and back. 200 cycles are a realistic number for a 1 week COSY11 user run of a cycle length of 1 hour. We reached a reproducibility of $1.5 \cdot 10^{-6}$.

The temperature changes of the system are now very critical. Small variations of the room temperature caused a displacement of the laser spot after the air-section. The laser light is not coupled completely into the 50 μ m multi-mode fibre-optic. The amplitude of the demodulated RF-signal decreased and changed the notch depth rapidly to smaller values.

A regulating circuit compensates this loss of the laser-light by adjusting the laser light according to the monitored photo current of the diode in the photodetector. The vertical position of the incoupling collimator is additionally motored with a accuracy of 1 μ m. If the available laser power reaches its highest limit the vertical direction will be adjusted to reach the optimal RF-power.

4 CONCLUSION

The fine adjustment of the optical notch filter has been installed in the COSY ring and successfully used in COSY11 user run at 3.2 GeV/c. The experiments can now take data below, close at and far above the threshold with a stochastically cooled beam in one 'supercycle'. The adjustable notch filter allows longitudinal cooling in the momentum range from 3.4 GeV/c down to 2.6 GeV/c in one supercycle. Different momentum ranges down to 1.5 GeV/c will be available by adding different lengths of additional fibre optics. The signal paths of the transversal cooling systems can be adjusted within a similar momentum range. The beam size of $1 \cdot 10^{10}$ protons is reduced by a factor of two although the gas target is permanently heating the beam.

5 ACKNOWLEDGMENT

We like to thank R.Hartung (FZJ-ZEL) and F.Häsing (FZJ-ZEL) for their great design and fabrication work concerning the optical system.

6 REFERENCES

- [1] R. Maier, Cooler Synchrotron COSY – Performance and Perspectives, Nuclear Instruments & Methods in Physics Research A 390, 1997
- [2] R. Stassen et al., The Stochastic Cooling System and its Application to Internal Experiments at the Cooler Synchrotron COSY, EPAC98, Stockholm 1998
- [3] H. Stockhorst et al, Commissioning of the Stochastic Cooling System and Application to an Internal Target Experiment, IKP Ann.Rep. 1997, p.160
- [4] S. Brauksiepe et al., COSY-11 – an Internal Experiment Facility for Threshold Measurements, Nucl. Inst. & Methods A 376, 1996, p.397-410
- [5] H. Stockhorst et al., The Cooler Synchrotron Cosy Facility, PAC97, San Francisco, 1997
- [6] H. Stockhorst et al., The Performance of COSY, EPAC98, Stockholm 1998
- [7] R. Pasquinelli, Electro Optical Technology Applied to Accelerator Beam Measurement and Control, PAC93

ELECTRON COOLING ASSISTED BEAM ACCUMULATION IN THE HEAVY ION SYNCHROTRON SIS BY REPEATED MULTITURN INJECTION

M. Steck, L. Groening, K. Blasche, H. Eickhoff, B. Franczak, B. Franzke, T. Winkler,
GSI Darmstadt, Germany; V.V. Parkhomchuk, BINP Novosibirsk, Russia

Abstract

The heavy ion synchrotron SIS has been equipped with an electron cooling system for fast beam accumulation at the injection energy. Optimization of injection and cooling resulted in synchrotron pulses with more than an order of magnitude higher intensity. For highly charged ions the intensity is limited by recombination with free electrons. The rate coefficients have been measured thus allowing a selection of the most favorable charge state in order to maximize the beam intensity for highly charged ions.

1 INTRODUCTION

The heavy ion synchrotron SIS [1] is filled by horizontal multiturn injection which results in a horizontal emittance $\epsilon_x \simeq 150 \pi$ mm mrad. It can presently not be operated with highly charged ions up to the space charge limit. The intensity for beams of highly charged heavy ions is limited by the ion source and the low energy section of the injector linac. In order to facilitate beam accumulation by repeated multiturn injection with interspersed cooling an electron cooling system has been designed [2].

Short transverse cooling times allow fast repetition of multiturn injection into the outer part of the horizontal ring acceptance, while the inner part is reserved for the cooled accumulated ion beam. As the typical synchrotron cycle times are a few seconds and transverse cooling times of order 100 ms are aimed at the intensity gain can be up to one order of magnitude. The cooling time decreases proportional to A/q^2 promising the highest intensity gain for the heaviest ions which can be injected with the lowest intensities.

After an intensity upgrade of the linac the electron cooler will be ready for accumulation of beams of rare isotopes and preparation of high quality beams.

2 ELECTRON COOLING SYSTEM

The electron cooling system was designed and manufactured in a collaboration between GSI and BINP, Novosibirsk. The design parameters of the electron cooling system [2] were specified according to the requirement of transverse cooling times for ions with mass numbers $A \geq 100$ of around 100 ms. Use of adiabatic magnetic expansion for reduction of the transverse electron temperature and for matching of the electron beam diameter to the ion beam size was included in the design. Cooling at an

electron energy	6.3 keV
cathode diameter	25.4 mm
cathode temperature	~ 1200 K
gun perveance	$2.9 \mu\text{P}$
maximum electron current	1.5 A
relative loss current	$\leq 1 \times 10^{-4}$
magn. expansion factor	3
magn. field strength in cool. section	0.06 T
magn. field parallelism in cool. section	$\leq 1 \times 10^{-4}$
vacuum pressure	$\leq 1 \times 10^{-10}$ mbar

Table 1: Typical parameters of the SIS electron cooling device for ion beam accumulation.

intermediate energy (between 55 and 65 MeV/u) will allow rebunching at the second harmonic of the revolution frequency for generation of high density ion bunches.

The complete electron cooling system was assembled at GSI and tested with electron beam outside the synchrotron before installation in the ring tunnel [3]. The typical parameters of the electron cooling device for operation at the injection energy of the synchrotron, which requires an electron energy of 6.3 keV, are listed in Table 1.

The control hardware for the electron cooling system has been prepared for ramped operation synchronized with the acceleration cycle. Since the cooler has been used for beam accumulation at the injection energy to date operation with static magnetic field and constant electron energy and current was sufficient for commissioning in the synchrotron.

3 SYNCHROTRON OPERATION WITH ELECTRON COOLER

For the operation of the electron cooler in one straight section of the synchrotron additional corrections of the closed orbit had to be implemented. A small dipole magnet at both ends of the cooler and the correction coils in the adjacent main dipole magnets correct the horizontal kick introduced by the toroids and allow an adjustment of the ion beam displacement and the beam direction in the cooling section. The coupling of horizontal and vertical phase space due to the longitudinal field of the cooler is not corrected. For optimum injection the ring tune and the setting of the injection beam line have to be fine tuned after powering of the cooler magnetic field and of the closed orbit corrections. Multiturn injection with the cooler magnetic fields presently results in about 65 % of the standard multiturn gain factor.

For beam accumulation with cooling the amplitude of the orbit bump in the injection section is slightly reduced. Thus free space between the closed orbit and the electrostatic septum is provided for the cooled circulating beam to pass by the septum when new beam is injected. Beam accumulation starts when the electron beam is switched on with the electron velocity matched to the ion velocity after injection. Additional fine adjustment of the spatial and angular alignment between electron and ion beam minimizes the transverse cooling time as well as the emittance of the cooled beam. The intensity of the ion beam can be increased by more than one order of magnitude after proper setting of all cooler and ring parameters (Fig. 1).

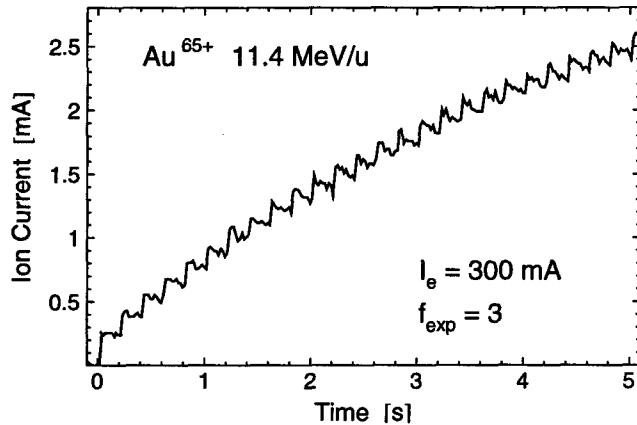


Figure 1: Accumulation of 1×10^9 Au^{65+} ions in less than 5 s. The ion beam was cooled at the injection energy with a 300 mA electron beam expanded by a factor of 3.

4 BEAM ACCUMULATION

For high average beam intensity from the synchrotron the accumulation rate, i.e. the intensity filled into the synchrotron per unit of time divided by the current in the injection beam line, has to be maximized. Systematic variations of the injection and cooler parameters were performed to find the optimum accumulation conditions. Figure 2 shows the influence of the electron beam current for three different electron beam expansion factors on the accumulation rate for optimized injection rate. An expansion factor of three and typical electron currents of 0.3–0.5 A are usually applied for beam accumulation. Higher electron currents result in slightly faster accumulation, but the recombination losses also increase and limit the maximum intensity (see Sect. 5).

The variation of the accumulation rate with the time between successive injections exhibits a maximum for rather short time intervals (Fig. 3). A time of about 200 ms is required for transverse cooling, for larger time intervals the additional cooling time will not accumulate the beam more efficiently and the accumulation rate decreases proportional to the injection rate.

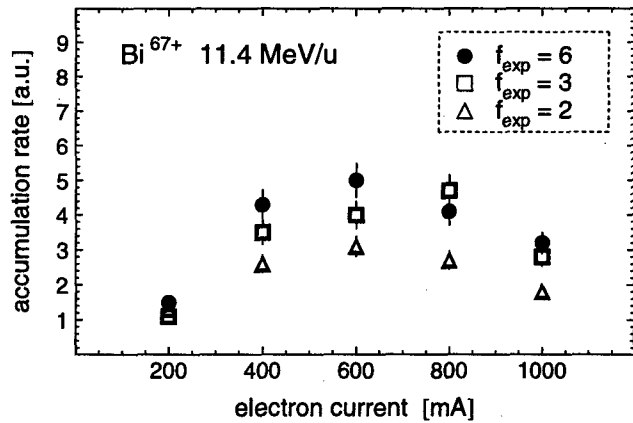


Figure 2: Accumulation rate as a function of the electron current for different expansion factors.

The maximum intensity of the ion beam usually saturates on a certain intensity level after some ten injections. Two diverse processes which limit the beam intensity have been observed. For light ions which can be injected with higher intensity from the injector (more than 10^8 ions after a single multiturn injection) beam instabilities arise due to the high phase space density of the ion beam. A maximum intensity of 7×10^9 Kr^{34+} (7 mA) has been achieved [4]. The ion beam approaches the space charge limit, but also coherent transverse oscillations may be excited by interaction with transverse impedances. A transverse feedback system is presently designed for damping of coherent oscillations.

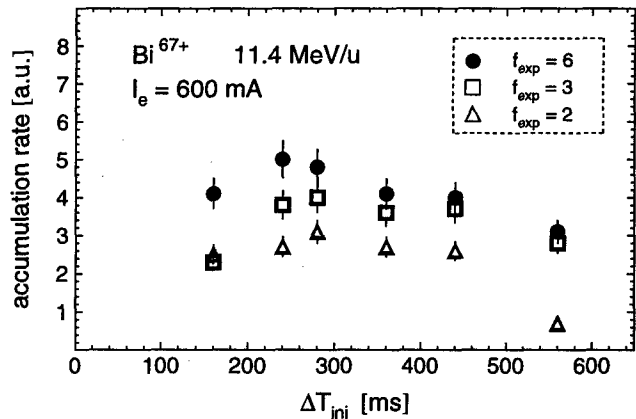


Figure 3: Accumulation rate versus the time interval between successive injections.

With highly charged heavy ions the limitation of the maximum beam intensity unambiguously is related to beam losses by recombination with free electrons in the cooling section which have been studied in more detail.

5 RECOMBINATION OF HIGHLY CHARGED IONS

Before injection into the synchrotron the ions are usually stripped at the injection energy 11.4 MeV/u in order to reach the highest final energy. At the injection energy heavy ions are produced with 10–20 bound electrons in largest abundance.

The recombination rate for two species of highly charged ions was studied experimentally for the various charge states available after the injection line stripper. The recombination rate was evaluated from the exponential decrease of the ion current when injection was stopped and the ion beam continued to circulate at the injection energy. Measurements of the beam lifetime for different electron currents allowed to distinguish between losses due to recombination with electrons in the cooler and the losses caused by interaction with the residual gas. The recombination rate with electrons showed a linear increase with electron density and for fixed electron current a scaling inversely proportional to the square root of the expansion factor as expected [5].

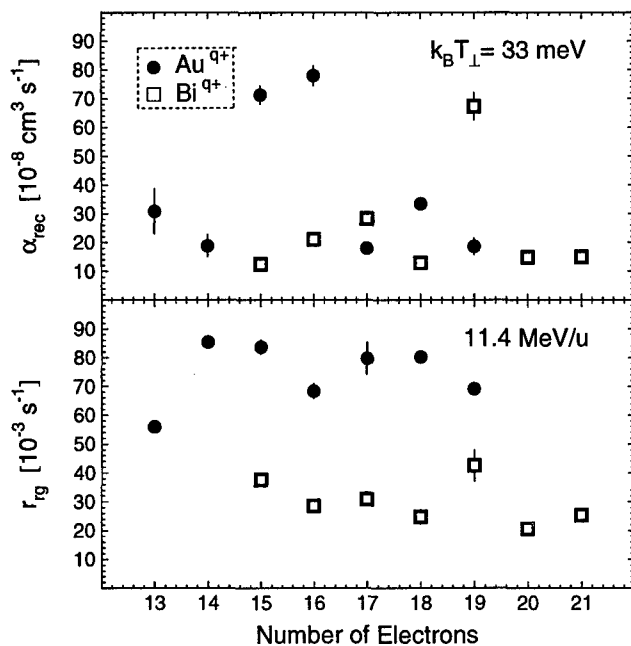


Figure 4: Rate coefficient α_{rec} for recombination with free electrons and recombination rate in the residual gas r_{rg} measured for the electron configurations of Au and Bi ions available at the synchrotron injection energy 11.4 MeV/u.

The results of measurements of the rate coefficient for recombination with free electrons and the recombination rate in the residual gas for Au and Bi charge states with the various numbers of bound electrons that are available after the stripper in the SIS injection line is shown in Fig. 4. The loss rate in the residual gas can be reasonably explained by recombination with bound electrons of the gas constituents which is the dominant charge changing process at SIS en-

ergies. The difference between Au and Bi is likely to be caused by changes in the vacuum pressure and the composition of the residual gas between the two experiments.

The recombination rate in the electron beam is in disagreement with calculations of radiative electron capture which is expected to be the dominant recombination process. Neither the absolute value of the rate coefficient nor the variations with the charge state which can amount up to a factor of five are comprehensible assuming radiative electron capture only. The recombination rate maxima for the two ions are not correlated with the electronic configuration. Resonant electron capture at small relative energy, e.g. by dielectronic recombination, could be an explanation for the enhanced recombination rates and the strong variations with the charge state which have been reported previously [6].

The charge states with high recombination losses must be avoided if accumulation of the maximum beam intensity is aimed at. Even for the more favorable charge states the beam lifetime due to recombination losses with free electrons is below 10 s for the typical electron densities of $3 - 5 \times 10^7 \text{ cm}^{-3}$, the lifetime due to the residual gas is on the order of some 10 s depending on the vacuum conditions. Therefore for the heaviest ions a careful choice of the most favorable charge state with respect to recombination is mandatory to take greatest advantage of beam accumulation. After selection of the most favorable charge state Au^{65+} the number of ions in a SIS pulse could be increased to 1.5×10^9 which is a factor of 15 higher than the maximum intensity achieved ever for gold beams.

6 REFERENCES

- [1] K. Blasche, B. Franzke, Proceedings of the 4th European Particle Accelerator Conference, London, 1994, edited by V. Suller and Ch. Petit-Jean-Genaz (World Scientific, Singapore, 1994) 133.
- [2] M. Steck, K. Blasche, W. Bourgeois, B. Franzke, L. Groening, N.S. Dikansky, V.I. Kudelainen, V.V. Parkhomchuk, A.I. Sharapa, A.V. Shemyakin, B.M. Smirnov, Proceedings of the 5th European Particle Accelerator Conference, Sitges, 1996, (World Scientific, Singapore, 1996) 1185.
- [3] L. Groening, M. Steck, T. Winkler, V.I. Kudelainen, V.V. Parkhomchuk, A.I. Sharapa, A.V. Shemyakin, B.M. Smirnov, Proceedings of the 6th European Particle Accelerator Conference, Stockholm, 1998, (Institute of Physics Publishing, 1998) 1034.
- [4] K. Blasche, H. Eickhoff, B. Franzak, B. Franzke, L. Groening, M. Steck, T. Winkler, V.I. Kudelainen, V.A. Dolgashev, V.V. Parkhomchuk, Proceedings of the 6th European Particle Accelerator Conference, Stockholm, 1998, (Institute of Physics Publishing, 1998) 550.
- [5] L. Groening, PhD Thesis, GSI DISS. 98-20.
- [6] J. Bosser, J. Broere, C. Carli, M. Chanel, C. Hill, R. Maccaferri, S. Maury, D. Möhl, G. Molinari, S. Rossi, E. Tanke, G. Tranquille, M. Vretenar, Proceedings of the 6th European Particle Accelerator Conference, Stockholm, 1998, (Institute of Physics Publishing, 1998) 253.

DESIGN OF ANTIPROTON ELECTRON COOLING IN THE RECYCLER

A. Burov, J. MacLachlan, J. Marriner and S. Nagaitsev, FNAL, Batavia, IL

Abstract

A conceptual design of electron cooling of 9 GeV antiprotons for the Tevatron is discussed. Analytic and numeric calculations of the cooling process determine the basic requirements of the cooler.

1 PURPOSE

During a Tevatron store, emittances of the colliding bunches grow and the luminosity decreases. For RUN II, the luminosity is calculated to drop by a factor of 2 after 6-7 hours [1], so the beams should be renewed after this time. The purpose of the Recycler storage ring is to accept the unspent antiprotons (\bar{p}) from the Tevatron, to recool them transversely and longitudinally, and to redeliver them to the collider. The Recycler must also accept fresh antiprotons from the Accumulator, and this process requires longitudinal cooling too. For RUN II, the stochastic cooling system is thought to be adequate; an example of simulations for the transverse cooling is shown in Fig. 1.

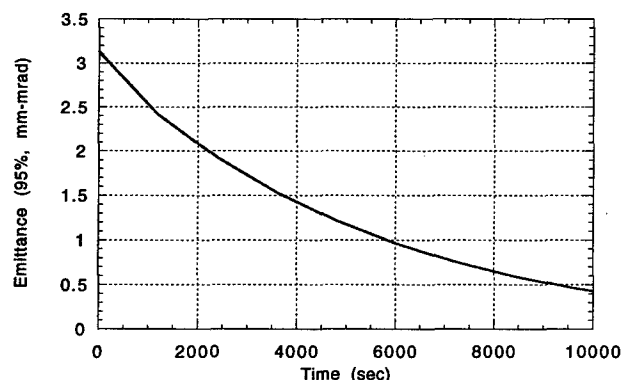


Figure 1: Evolution of the (unnormalized) emittance of $5 \cdot 10^{12}$ particles in the Recycler with the full momentum spread $\pm 2 \cdot 10^{-3}$ during stochastic cooling with 2-4 GHz bandwidth.

However, the efficiency of the stochastic cooling decreases with intensity of the cooled beam, which could make it insufficient for the future TeV 33 program. Electron cooling might be a good supplement to stochastic cooling because of its independence on the beam intensity. On the other hand, electron cooling is much more efficient if the beam is already precooled. Thus, a hybrid cooling scheme could be used in the Recycler, with stochastic cooling for the first stage and electron cooling for the second.

2 SCENARIO

A possible scenario for the periodic cooling-stacking process in the Recycler could be following:

- $t = 0$: 100 bunches of (hot) antiprotons leave the Tevatron, are decelerated in the Main Injector, and arrive at the Recycler, sharing its circumference with already cooled antiproton beam. Then, the cold portion is transferred to the Main Injector, releasing the phase space for the hot beam with $N = (2.5 - 10) \cdot 10^{12}$ \bar{p} 's occupying $\mathcal{A} = 400$ eVs of the longitudinal phase space and 30π mm mrad of the normalized 95% emittance. Transverse stochastic precooled starts.
- Every quarter of an hour, a fresh pbar batch arrives from the Accumulator. Its population is 10^{11} in 10eVs and 15π mm mrad (normalized 95%). It is adjoined longitudinally to the whole stack by means of the barrier-bucket technique [2].
- $t = 1-2$ h: Stochastic precooled finishes; beam emittance is 15π mm mrad. Electron cooling begins.
- $t = 3 - 8$ h: Electron cooling finishes producing a beam with 10 π emittance and 150 eVs or less of the longitudinal phase space. The cycle is then repeated.

3 SIMULATION RESULTS

To simulate electron cooling processes, a multi-particle C++ code has been written. This code tracks the time evolution of an ensemble of cooled particles, optimizes the cooling process under various conditions and finds the tolerances on imperfections.

In distinction to usual situation in low-energy coolers, relative velocities between the cooled particles and the electrons are supposed here to be determined by the cooled particle (\bar{p}) velocities. Electron velocities are assumed to be low enough not to depress the cooling rates. In this case, the longitudinal and transverse cooling rates λ_{\parallel} and λ_{\perp} are strong functions of the \bar{p} longitudinal and transverse velocities in the beam frame v_{\parallel} and v_{\perp} [3]:

$$\lambda_{\parallel} \propto (v_{\perp}^2 v_{\parallel})^{-1}, \quad \lambda_{\perp} \propto v_{\perp}^{-3} \quad \text{for } v_{\parallel} \leq v_{\perp}.$$

The smaller the \bar{p} velocity is, the faster it decreases. Thus, electron cooling tends to shape a narrow core of supercooled particles inside the distributions. For flat pbar distributions, i.e., $v_{\parallel} \ll v_{\perp}$, the longitudinal rates are higher than the transverse and the longitudinal core is created first. Actual size of this core is determined by an equilibrium between cooling and IBS diffusion which is calculated separately (see section 5). The evolution of the recycled \bar{p} 's from the initial state is shown in Figs. 2 and 3.

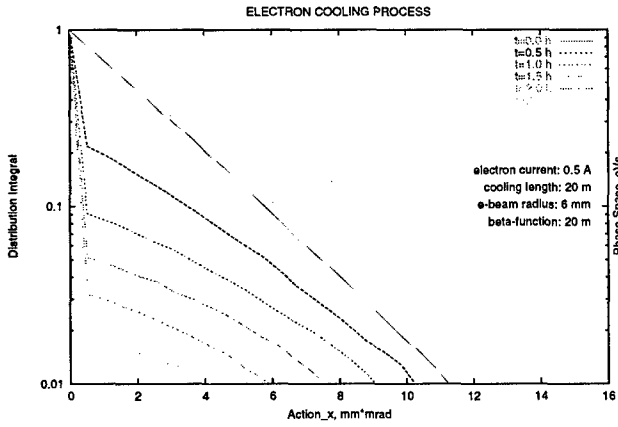


Figure 2: Evolution of the transverse \bar{p} distribution from the initial Gaussian one with the rms normalized emittance 2.5 mm mrad.

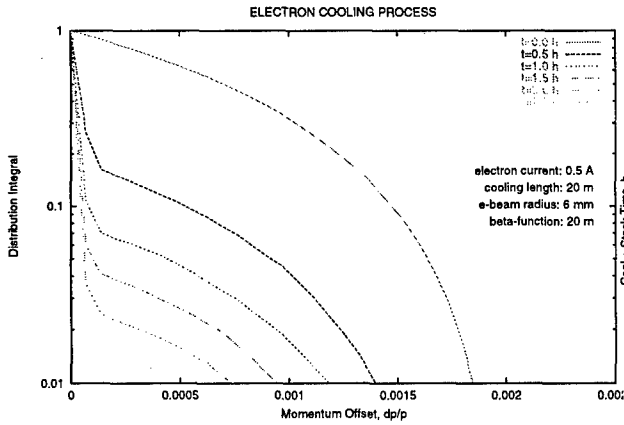


Figure 3: Evolution of the \bar{p} momentum distribution from an initial parabolic one.

The conclusion from the simulations is that transverse cooling of the recycled \bar{p} 's from $\epsilon = 15\pi$ mm mrad to $\epsilon = 10\pi$ mm mrad requires 0.9 Ampere \times hour (Ah) of (cooler length) \times (cooling time), for a 20 m cooling section. For beam from the Accumulator, this value is 0.7 Ah.

The longitudinal phase area \mathcal{A} shrinks with a rate $r_0 \approx 1.2 \text{ A}^{-1}\text{h}^{-1}$ over the whole interesting interval $150 \text{ eVs} < \mathcal{A} < 400 \text{ eVs}$. This approximate rate is used in the stacking model discussed below.

4 COOLING-STACKING PROCESS

The phase space evolution in the cooling-stacking process can be described as:

$$\dot{\mathcal{A}} = -r_0\mathcal{A} + f_s\mathcal{A}_b + f_s\Delta_s\mathcal{A}$$

where f_s is the stacking frequency, the number of injections per hour, \mathcal{A}_b is the batch phase area, and Δ_s is the fractional

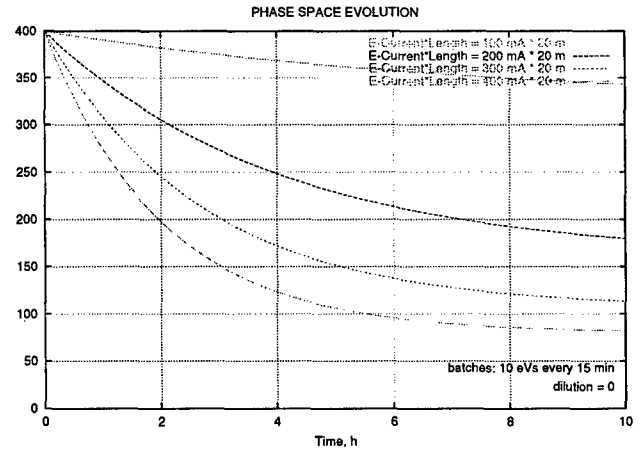


Figure 4: Evolution of the longitudinal phase space area in the cooling-stacking process

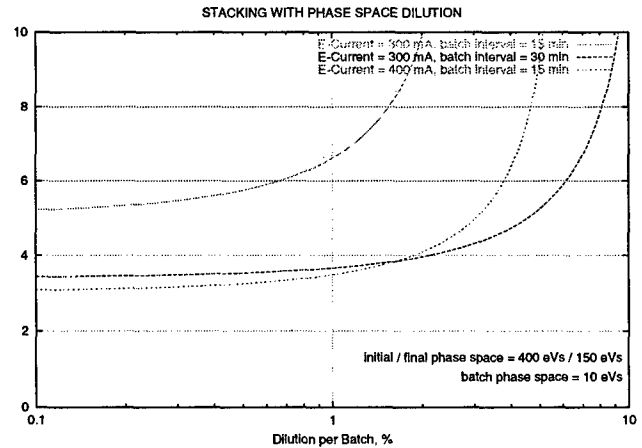


Figure 5: Tolerances on the longitudinal phase space dilution due to the stacking imperfection.

phase area dilution due to the stacking imperfection. The solution reads:

$$\begin{aligned} \mathcal{A}(t) &= \mathcal{A}(\infty) + (\mathcal{A}(0) - \mathcal{A}(\infty)) \exp(-(r_0 - f_s\Delta_s)t) \\ \mathcal{A}(t) \rightarrow \mathcal{A}(\infty) &= \mathcal{A}_b f_s / (r_0 - f_s\Delta_s) \end{aligned} \quad (1)$$

The asymptotic phase space area $\mathcal{A}(\infty)$ is related to an equilibrium between factors which tend to increase the phase space (stacking, dilution) and the factor tending to shrink it (cooling). The phase area evolution is presented in Fig. 4, a tolerance for the dilution can be found from the results shown in Fig. 5. The conclusion is that for the injection frequency $f_s = 4\text{h}^{-1}$ and dilution $\Delta_s < 1\%$, the current $I_e = 300 \text{ mA}$ is sufficient for antiproton accumulation.

5 INTRA-BEAM SCATTERING OF ANTIPROTONS

Intra-beam scattering (IBS) calculations are simplified by assuming that first, the longitudinal \bar{p} velocities are smaller than transverse (typical for hadron beams), and second, beam envelope variations are small enough (about 30% in the Recycler) to apply the smooth approximation.

Under these assumptions, IBS is reduced to a heat transfer from the hot transverse degrees of freedom to the cold longitudinal one which can be described as a diffusion in the longitudinal degree of freedom. The diffusion imposes a limit on the width of the longitudinal distribution: it cannot be smaller than the one determined by the cooling-diffusion equilibrium. If the equilibrium width is smaller than the design value, IBS can be neglected; otherwise, IBS puts a limit on the final width of the distribution.

Conventionally, the IBS diffusion coefficient is calculated as a single number for the whole distribution. This number results from an averaging of the local diffusion coefficient, which depends on actions of the scattered particle, over the distribution. However, to derive the equilibrium distribution with a good accuracy, a knowledge of the average diffusion is not sufficient; more detailed information contained in the local diffusion dependencies is required. The diffusion coefficient D as a function of velocity amplitudes v_x, v_y of the given particle which scatters on other particles distributed with rms velocity v_\perp is calculated from the Landau collision integral [3]. For a Gaussian transverse distribution

$$D = \frac{4\pi n_{\bar{p}} r_p^2 L_{\bar{p}}}{\gamma^2 \beta^2 v_\perp} \mathcal{I}, \quad v_\perp = \sqrt{\frac{\gamma \epsilon_n}{\beta_f}}$$

$$\mathcal{I} = \frac{2}{\pi} \frac{v_\perp^3}{\sqrt{(v_x^2 + v_y^2 + 2v_\perp^2/\pi)(v_x^2 + 2v_\perp^2/\pi)(v_y^2 + 2v_\perp^2/\pi)}} \quad (2)$$

where $n_{\bar{p}}$ is the pbar density at the beam axis, $L_{\bar{p}}$ is the IBS Coulomb logarithm and ϵ_n is the normalized rms emittance. The calculated diffusion is consistent with the average diffusion coefficient reported in [4] to an accuracy better than 10%; it is also consistent with numerical calculations of the average diffusion that are free from the above simplifications [5].

The evolution of the longitudinal distribution is described by the Fokker-Planck equation:

$$\frac{\partial f}{\partial t} = \frac{\partial}{\partial w} \left(Ff + \frac{D}{2} \frac{\partial f}{\partial w} \right); \quad w = \delta p/p. \quad (3)$$

Here

$$F = \frac{8(I_e/e)r_e r_p \eta L_{\parallel}}{\pi \beta^2 \gamma^2 a^2 v_x v_y} \quad (4)$$

is the cooling force independent in this case of the value of the longitudinal velocity w , with I_e as the electron current, a as the electron beam radius, η as the circumference fraction occupied by the cooler and L_{\parallel} as the Coulomb logarithm for the longitudinal cooling [3].

The Fokker-Planck equation (3) with the diffusion coefficient (2) and the cooling force (4) can be analytically resolved for the equilibrium distribution:

$$f = \exp(-w/\bar{w})/\bar{w}, \quad \bar{w} = D/2F,$$

yielding the equilibrium longitudinal phase space (95%) averaged over the transverse distribution

$$\mathcal{A} = \frac{1}{4} \frac{I_{\bar{p}}}{\eta I_e} \frac{r_p}{r_e} \frac{L_{\bar{p}}}{L_{\parallel}} \frac{a^2}{a_{\bar{p}}^2} E T_0.$$

This phase space is sufficiently small; for $N_{\bar{p}} = 1 \cdot 10^{13}$ and $I_e = 300$ mA, $\mathcal{A} = 30$ eVs. As long as the desired phase space area is larger than this equilibrium, the IBS may be neglected.

The main parameters of the electron cooling in the Recycler for the 100 bunch scenario are summarized in Tab. 1.

Table 1: Electron Cooling for 100 Bunches

Parameter	Value
Circumference	3319.4 m
Pbar momentum	8.9 GeV/c
Number of pbars, total	$(5 - 10) \cdot 10^{12}$
Init. long. area recycled pbars	400 eVs
Fin. long. 98% area, goal	150 eVs
Init. norm. 95% emittance	30π mm mrad
Fin. norm. 95% emittance	10π mm mrad
Batches per hour	$4 h^{-1}$
Batch area	10 eVs
Batch norm. 95% emittance	15π mm mrad
Cooling length	20 m
Beta-function in the cooler	20 m
Electron current	300 mA
Time of cool-stack cycle	7 hour
Electron beam radius	0.6 cm
Electron angle	$\leq 80 \mu\text{rad}$
Electron temperature	≤ 1 eV
Electron momentum spread	$\leq 5 \cdot 10^{-5}$

The authors are thankful to Ya. S. Derbenev and V. V. Parkhomchuk for fruitful discussions.

6 REFERENCES

- [1] G. Jackson, ed. "Fermilab Recycler Ring, TDR", Apr. 1996.
- [2] J. Griffin et al., IEEE Trans Nucl. Sci. **NS-30**, p. 3502 (1983).
- [3] A. Burov, J. MacLachlan, "Optimization of Electron Cooling for a Medium Energy Accumulator Ring", submitted to NIM A.
- [4] V. Lebedev et al., "Single and Multiple Intrabeam Scattering in a Laser Cooled Beam" NIM A **391**, p. 176 (1997).
- [5] P. Colestock, private communication.

SUPPRESSION OF TRANSVERSE BUNCH INSTABILITIES BY ASYMMETRIES IN THE CHAMBER GEOMETRY*

A. Burov, FNAL, Batavia, IL and V. Danilov, ORNL, Oak Ridge, TN

Abstract

The wake forces produced by a beam bunch can be reduced by making the vacuum chamber cross-section axially asymmetric. Furthermore, the asymmetry results in a betatron tune shift for particles in the tail of the bunch. As a result, transverse instabilities of the bunch should be significantly suppressed for an asymmetric vacuum chamber.

1 INTRODUCTION

The net effect of wake fields is determined by integrating the force over a structure period of the vacuum chamber L . The integrated transverse force \mathbf{F} caused by a slight offset \mathbf{r}_0 of the leading particle from the chamber axis is conventionally expressed in terms of the wake function [2]:

$$\int_L \mathbf{F} ds = -q^2 \mathbf{r}_0 W(z), \quad (1)$$

where q is the particle's charge and z is the distance between head and tail particles.

However, the linear approximation for the wake force (1) contains generally an additional term, proportional to the tail offset \mathbf{r} [3], which vanishes for round chambers. It means that, for round chambers, all the particles in the bunch are in resonance with each other. For axially asymmetric structures, however, the wake fields not only drive the oscillations of the tail particles but also detune them from the resonance with the driving force. Similar electrodynamic properties of external RF fields in asymmetric structures were used in Ref. [4], where it was proposed to utilize simultaneous accelerating and focusing to provide the acceleration and BNS damping [5] in linacs.

The importance of the betatron tune spread along a bunch in a storage ring was shown in Ref. [6]. It was demonstrated that this spread, introduced by means of an RF quadrupole, has a stabilizing role for the transverse bunch oscillations. It is natural to suppose that the tune spread produced by the wake fields is a stabilizing factor as well. If so, the detuning part of the wake may increase the thresholds of bunch transverse instabilities.

2 DRIVING AND DETUNING WAKES

The transverse wake forces are regular functions of the transverse offsets of the leading and trailing particles, \mathbf{r}_0 and \mathbf{r} and can be expanded in terms of these offsets [3]. Assuming for simplicity mirror symmetry for at least one transverse axis and neglecting the nonlinear terms, the

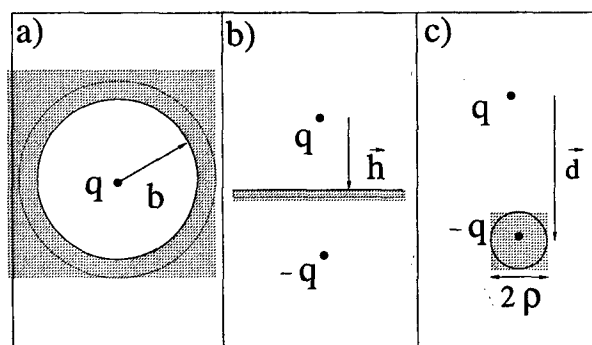


Figure 1: Three types of beam surroundings.

forces can be presented as follows:

$$\begin{aligned} \int_L F_x ds &= -q^2 x_0 W_x(z) + q^2 x D(z) \\ \int_L F_y ds &= -q^2 y_0 W_y(z) - q^2 y D(z), \end{aligned} \quad (2)$$

where insignificant constant terms are omitted. The first terms on the right hand sides describe the forces caused by the offsets of the leading particle; the functions $W(z)$ can be referred to as the driving wake functions. The second terms are responsible for the tune shifts of the tail particle; the function $D(z)$ can be called the detuning wake function. Due to the mirror symmetry, the detuning terms for x and y axis are described in Eqs.(2) by the single function $D(z)$. As follows from the form of Eqs.(2), there is no detuning for chambers invariant over a 90° rotation; $D(z) = 0$ in this case. To give examples, wake functions caused by the wall resistivity are presented below for three simplified cases, namely, for a round chamber, then, for an infinite plane and finally, for a small cylinder. The three cases are sketched at Figs. 1a, 1b and 1c.

For the first case of the round vacuum chamber the wake functions can be found in Ref. [2]:

$$W_x(z) = W_y(z) = -\frac{2}{\pi b^3} \sqrt{\frac{c}{\sigma z}} L, \quad D(z) = 0, \quad (3)$$

where c is a velocity of light, b is the vacuum chamber radius, and σ is a wall conductivity.

For the single resistive plane, the transverse wake functions follow:

$$W_x(z) = W_y(z) = D(z) = -\frac{L}{2\pi h^3} \sqrt{\frac{c}{\sigma z}}, \quad (4)$$

where $h = |\mathbf{h}|$ is the distance from the beam to the plane. This geometry demonstrates the possibility for the detuning wake to be equal to the driving wake.

The final example treats the case of the beam passing along a small resistive cylinder, Fig. (1c); the detuning

wake is shown to dominate here. Taking into account that the image charge is located at the position $\mathbf{r}' = \mathbf{r}\rho^2/r^2$ and assuming the cylinder radius ρ to be much smaller than the distance between the beam and the cylinder, $\rho \ll r_0 = |\mathbf{d}| = d$, the longitudinal electric field is:

$$E_s = -\frac{2\zeta q}{\rho} \left(1 + \frac{\rho^2 \mathbf{r} \mathbf{r}_0}{r^2 r_0^2} \right) + C \ln(r/\rho), \quad (5)$$

which includes an arbitrary constant C . The small dipole term in the brackets reflects a weak dependence of the fields on the source position \mathbf{r}_0 . To find the constant C , it can be assumed that this system is bounded by a conducting cylinder with the radius $R \gg r_0$. Then the constant C is found by equating the expression for the monopole part of E_s to zero at this remote surface, giving $C = \frac{2\zeta q}{\rho \ln(R/\rho)}$.

Then, one can obtain the integrated transverse force and finally the wakes:

$$D(z) = -\frac{L}{\pi d^2 \rho \ln(R/\rho)} \sqrt{\frac{c}{\sigma z}} \quad (6)$$

$$W_x(z) = W_y(z) = -\frac{L\rho}{\pi d^4} \sqrt{\frac{c}{\sigma z}}. \quad (7)$$

Introducing the detuning factors $\kappa_x = D(z)/W_x(z)$, $\kappa_y = D(z)/W_y(z)$, the results for the various geometries are expressed as $\kappa_x = \pm 1$ for the single plane, $\kappa_x = \pm d^2/(\rho^2 \ln(R/\rho))$ for the small cylinder, and $\kappa_x = 0$ for the round chamber.

The driving wake function $W(z)$ for the small cylinder (7) is a factor $\propto \rho/d \ll 1$ smaller than the wake functions of the round chamber (3) or parallel plates (4) with the same aperture. This result demonstrates how the transverse instability can be suppressed by the decrease of the driving wake function. The detuning wakes work in the same direction; they damp the instability even more.

Finally, note that the plane wall result $\kappa_x = \pm 1$ is valid not only for the resistive wall wake. It applies as well to the wake generated by a longitudinal variation of the chamber cross-section, when the cross-section is a significantly elongated figure such as a rectangle or ellipse.

3 COHERENT STABILIZATION BY THE DETUNING WAKE

The detuning wake modulates the betatron frequencies along the bunch. Such a modulation introduced by means of an RF quadrupole was studied in Ref. [6]. It was shown there that the transverse instabilities can be strongly damped in this case because the particles are kept out of resonance with each other. Following Ref. [6], the numerical results for the influence of the detuning wake on the transverse mode coupling instability are presented below.

Assuming the bunch to consist of particles with the same synchrotron amplitude a and a homogeneous distribution over the synchrotron phase (the so-called *air-bag model*

[2]), the transverse equation of motion is written

$$\begin{aligned} \frac{d^2 x(\phi)}{d\phi^2} + \omega_b^2 x(\phi) &= F_x(\phi) \\ F_x(\phi) &= -\frac{Nq^2}{2\pi\gamma m L} \int_{-\phi}^{\phi} |W(z)x(\phi') - D(z)x(\phi)| d\phi' \end{aligned} \quad (8)$$

Here ϕ is the synchrotron phase, ω_b and ω_s are the betatron and the synchrotron frequencies, and N is the number of particles in the bunch. An expansion of the deviation $x(\phi)$ over the synchrotron harmonics

$$x(\phi) = e^{-i\omega_b t} \sum_{n=-\infty}^{+\infty} x_n e^{-i\alpha\omega_s t + in\phi}, \quad (9)$$

reduces Eq. (8) to a set of algebraic equations for the eigenvector components x_n and the eigenvalues α :

$$x_n(\alpha - n) = K \sum_{m=-\infty}^{+\infty} x_m K_{nm}, \quad K = \frac{Nq^2}{2\pi^2 \gamma m \omega_b \omega_s L}$$

$$K_{nm} = \frac{\int_0^\pi \cos(n\phi) d\phi \int_0^\phi W(z) \cos(m\phi') d\phi' - \int_0^\pi \cos((n-m)\phi) d\phi \int_0^\phi D(z) d\phi'}{\int_0^\pi \cos((n-m)\phi) d\phi \int_0^\phi D(z) d\phi'}, \quad (10)$$

where the influence of the coherent interaction is taken to be small in a comparison with the transverse focusing, $\alpha\omega_s \ll \omega_b$. To resolve such equations, the sum has to be truncated to a finite number of the modes. In the numerical calculations, five modes were taken initially; then, the results were compared with nine- and fifteen-mode truncations. All the resistive wall wake functions have the following form:

$$W(z) = -Q/\sqrt{z}, \quad D(z) = -\kappa Q/\sqrt{z},$$

where Q is the geometry factor. The examples for the detuning factor κ are given above.

Figure 2 presents plots for dimensionless eigenvalues α as functions of the dimensionless intensity parameter

$$I = KQ/\sqrt{a} \quad (11)$$

at various detuning factors κ . The dependence of the mode behavior on this factor is seen to be significant.

The mode coupling instability threshold is least for the symmetric case, $\kappa = 0$. At $\kappa = 1$, coupling and decoupling thresholds merge (degenerate case) and the beam is stable for any current. This result is valid for any mode truncation, so it appears to be an exact property. A small coupling-decoupling instability area appears again at higher κ .

Fig. (3) shows the threshold behavior versus coefficient of asymmetry κ for the five, nine and fifteen modes calculation. The instability threshold has its minimum for the symmetric chamber, $\kappa = 0$. Then it increases with the absolute value of the detuning factor and has two asymmetrical maxima at $\kappa \approx -1.5$ and $\kappa \approx 2$.

The results shown in this figure should be interpreted carefully, taking into account that an asymmetry not only introduces the detuning wake but also changes the driving wake. For instance, the thresholds for the resistive wall, examples a) and b) (Fig. 1) with $h = b$, differ approximately by a factor of $4 \times 1.5 = 6$, where the factor 4 is related to the driving wake damping and the factor 1.5 is the benefit due to the detuning for $\kappa = -1$, according to the Fig. (3).

4 CONCLUSIONS

Only one kind of wake function, called here the driving wake function, has been conventionally taken into account for the beam stability analysis. It has been shown that this conventional approach can lead to significant underestimation of the beam stability thresholds for non-round vacuum chambers. For asymmetric vacuum chamber elements, which are usual in practice, the detuning wake function must be taken into account; conventional codes like MAFIA need to be improved accordingly. For all of the examples here, an asymmetry-driven increase of the detuning wake combines with a decrease of the conventional wake; both of these factors favor beam stability. These properties of asymmetric cross-sections look promising for design of future accelerators.

The authors are grateful to Bruno Zotter, Sam Heifets and Vladimir Shiltsev for interesting discussions. Our special thanks are to Jim Maclachlan and Jeff Holmes for their numerous stylistic corrections of the manuscript.

5 REFERENCES

- [1] * See also A. Burov and V. Danilov, Phys. Rev. Lett., **82**, p. 2286 (1999).
- [2] A. Chao, *Physics of Collective Beam Instabilities in High Energy Accelerators*, John Wiley & Sons, Inc., 1993.
- [3] S. Heifets, A. Wagner, B. Zotter, "Generalized Impedances and Wakes in Asymmetric Structures", SLAC/AP110, 1998
- [4] W. Schnell, "Microwave Quadrupoles for Linear Colliders", CLIC Note 34, CERN-LEP-RF/87-24, 1987.
- [5] V. Balakin, A. Novokhatsky and V. Smirnov, *Proc. 12th Int. Conf. High Energy Accel.*, (Fermilab, Batavia, 1983), p. 119.
- [6] V. Danilov, "On possibility to increase the TMCI threshold by RF quadrupole", Fermilab TM-2033 (1997); Phys. Rev. ST Accel. Beams, **1**, 041301 (1998).

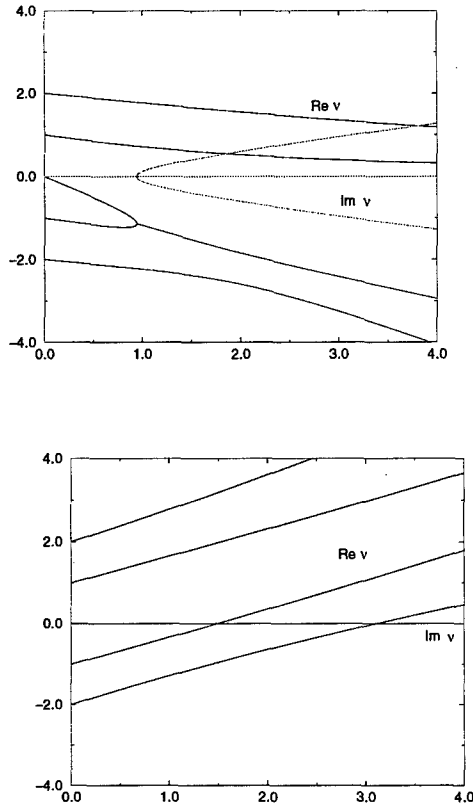


Figure 2: Eigenvalues α versus the intensity parameter I for various detuning factors $\kappa = 0$ (top) and $\kappa = 1$ (bottom).

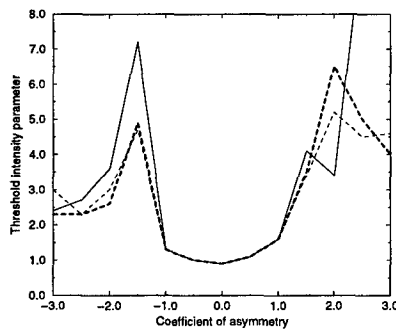


Figure 3: Intensity threshold of the transverse mode coupling instability I versus the detuning factor κ for the 5-mode (solid line) 9-mode (thick dash line) and 15-mode (thin dash line) truncations.

SLOTTED WAVEGUIDE SLOW-WAVE STOCHASTIC COOLING ARRAYS*

D. McGinnis[#], FNAL, Batavia, IL

Abstract

The slotted waveguide slow-wave stochastic cooling arrays are an integral part of the 4-8 GHz Debuncher Upgrade at FNAL. Unlike the standard array of stripline electrodes, these structures are designed to work when the beam pipe can support many microwave modes. The design theory and beam measurement results of this new type of pickup structure will be presented in this paper.

1 INTRODUCTION

In previous collider runs at Fermilab, all of the stochastic cooling pickup and kicker arrays consisted of stripline or planar loop electrodes. The signals from these electrodes are combined with a binary combiner tree formed by microstrip or stripline transmission lines. With a binary combining scheme, there must be no waveguide modes traveling down the beam pipe that would provide an alternate signal path in parallel to the binary combiner tree.

The nominal Debuncher transverse aperture is 30π -mm-mrad (95% un-normalized). To account for closed-orbit variations, the design aperture of the cooling arrays was set at 40π -mm-mrad. With lattice beta functions on the order of 10 meters, the transverse dimensions of the beam pipe will be about 40 mm which will propagate waveguide modes above 4 GHz. The presence of travelling waveguide modes in the beam pipe will limit the workable fractional bandwidth of the cooling arrays.

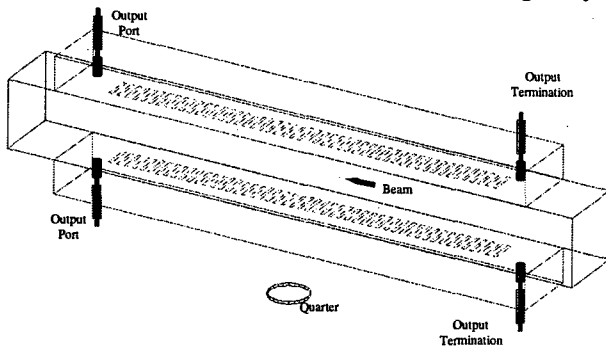


Figure 1: Conceptual drawing of a slow wave pickup

The solution was to divide the 4-8 GHz bandwidth into 4 narrower bands with each band having a bandwidth of about 1 GHz. The cooling arrays are built with slot coupled "slow-wave" waveguide structures as

shown in Figure 1. The structure consists of two rectangular waveguides that are coupled to a rectangular beam pipe by a series of slots. The transverse signal is derived from the difference between the two waveguides and the momentum signal is derived from the sum of the two waveguides.

The image current that flows along the walls of the beam pipe due to a charged particle beam travelling in the center of the beam pipe excites electromagnetic magnetic waves in the slots which in turn excite travelling waveguide modes in the side waveguides and beampipe. Since the phase velocity of the unperturbed waveguide modes is faster than the beam velocity, the slots also act to "slow down" the waveguide modes by multiple reflections so that the phase velocity of the waveguide modes along the structure matches the beam velocity.

2 MOMENT METHODS

The structure can be analyzed using the moment method technique.[1] Using the equivalence principle[2], the slots in the sides of the waveguides can be replaced with metal walls and an equivalent magnetic current source as shown in Figure 2. The magnetic current source is derived from the tangential electric field in the slot. The magnetic field in Region I is:

$$\vec{H}_t^{(1)} = \vec{H}_t^{(inc)} + \vec{H}_t^{(1)}(\vec{E}_t \times \hat{y}) \quad (1)$$

where the first term on the RHS of Eqn. 1 is the magnetic field as if the slot did not exist and the second term is the field due to the magnetic current source inside the slot. The magnetic field across the slot must be continuous:

$$\vec{H}_t^{(inc)} - \vec{H}_t^{(inc)} = \vec{H}_t^{(1)}(\vec{E}_t \times \hat{y}) + \vec{H}_t^{(2)}(\vec{E}_t \times \hat{y}) \quad (2)$$

This is the key equation of the moment method. Since $\vec{H}^{(inc)}$ is known, this equation can be inverted to determine \vec{E}_t in the aperture. Because Eqn. 2 is an integral equation, it is best solved by numerical methods. Let the tangential electric field in the aperture be given by:

$$\vec{E}_t = \hat{x} \sum_n E_{x_n} \theta_n(x, z) + \hat{z} \sum_n E_{z_n} \psi_n(x, z) \quad (3)$$

where $\theta_n(x, z)$ and $\psi_n(x, z)$ are a set of orthogonal functions. If the slots are very narrow in the z direction, the x component of electric field can be neglected. Equation 2 can be turned into a matrix equation by multiplying it by a set of orthogonal weighting functions $\phi_m(x, z)$ and integrating over the entire x - z plane.

* Work supported by the United States Department of Energy under contract No. DE-AC02-76CH03000

[#] Email: mcginnis@fnal.gov

$$\begin{aligned} & \langle \phi_m | H_x^{(inc)} | \rangle - \langle \phi_m | H_x^{(inc)} | \rangle_2 \\ & = \sum_n \left(\langle \phi_m | H_x^{(1)} | \psi_n \rangle + \langle \phi_m | H_x^{(2)} | \psi_n \rangle \right) E_{zn} \end{aligned} \quad (4)$$

where:

$$\langle \phi_m | H_v^{(k)} | \psi_n \rangle = \iint_{x,z} \left(\phi_m(x,z) H_v^{(k)}(\hat{x} \psi_n(x,z)) \right) dx dz \quad (5)$$

and:

$$\langle \phi_m | H_v^{(inc)} | \rangle = \iint_{x,z} \left(\phi_m(x,z) H_v^{(inc)}(x,z) \right) dx dz \quad (6)$$

Equation 4 forms a set of linear equations, which can be inverted to find the electric field coefficients E_{zn} . If the electric field expansion functions, ϕ and ψ , are chosen to be as close to the actual solution as possible then only a few terms of the expansion will be needed and the size of the matrix to be inverted will be minimized.

The electromagnetic fields leaving a region of sources as shown in Figure 3, can be expanded in terms of waveguide modes:

$$\bar{E}^{\pm} = \sum_n C_n^{\pm} (\hat{e}_{tn} \pm \hat{e}_{zn}) e^{\mp j\beta_n z} \quad (7)$$

$$\bar{H}^{\pm} = \sum_n C_n^{\pm} (\pm \hat{h}_{tn} + \hat{h}_{zn}) e^{\mp j\beta_n z} \quad (8)$$

where e_n and h_n are the waveguide modes. Using Lorentz reciprocity, the mode coefficients C_n are given as[3]:

$$C_m^{\pm} = \frac{1}{4P_m} \iiint_v \left((\hat{e}_{tm} \mp \hat{e}_{zm}) \cdot \bar{J} - (\mp \hat{h}_{tm} + \hat{h}_{zm}) \cdot \bar{M} \right) e^{\pm j\beta_m z} dv \quad (9)$$

where

$$P_m = \frac{1}{2} \iint_{S_t} (\hat{e}_{tm} \times \hat{h}_{tm}) \cdot \hat{z} dS \quad (10)$$

For example, the magnetic field in a waveguide due to a charged particle beam travelling in the +z direction located at x_b, y_b :

$$\bar{J}(x, y, z) = \hat{z} \frac{ib}{2} \delta(x - x_b) \delta(y - y_b) e^{-jkz} \quad (11)$$

is given as:

$$\begin{aligned} & H_x^{inc}(x, y, z) = \\ & -\frac{ib}{2} \sum_n \frac{e_{zn}(x_b, y_b)}{4P_n} \frac{2j\beta_n}{\kappa^2 - \beta_n^2} h_{xn}(x, y) e^{-jkz} \end{aligned} \quad (12)$$

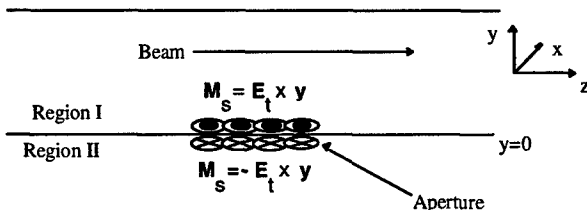


Figure 2: Equivalent magnetic source in slots.

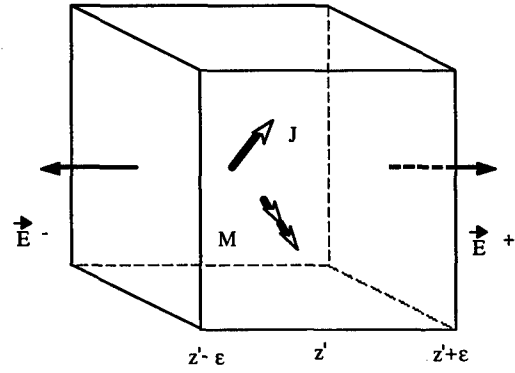


Figure 3: Elemental volume in waveguide containing sources

3 ARRAY IMPEDANCE

For the transverse mode, the pickup impedance of the array is derived from the relationship between the difference in power excited in opposing output waveguides as a function of beam current and beam position traveling through the array:

$$\frac{1}{2} P_{\Delta total} = \frac{1}{2} Z_{\Delta pu} \left(\frac{ib}{2} \right)^2 \left(\frac{y}{d/2} \right)^2 \quad (13)$$

The kicker impedance of the array is derived from the relationship between the transverse change in beam momentum as a function of input power supplied to opposing input waveguides:

$$P_k = \frac{1}{2} \frac{\left(\frac{\Delta pc}{q} \right)^2}{Z_k} \quad (13)$$

where

$$\frac{\Delta pc|_y}{q} = \int_{-\infty}^{\infty} (E_y - \eta H_x) e^{-jkz} dz \quad (14)$$

for a beam travelling in the -z direction. Since the ends of the array are not well defined, the limits of this integral are difficult to evaluate numerically.

Another way to evaluate the integral is to use Lorentz reciprocity on the geometry shown in Figure 4. The fields for the pickup case and the kicker case are related by:

$$\begin{aligned} & \oint_{S_0} (\bar{E}^p \times \bar{H}^k - \bar{E}^k \times \bar{H}^p) \cdot \hat{n} dS \\ & = \iiint_v (\bar{H}^k \cdot \bar{M}^p - \bar{E}^k \cdot \bar{J}^p) dv \end{aligned} \quad (15)$$

where the k indicates the kicker fields and sources and the p indicates pickup fields and sources. If the absorber kills the pickup and kicker fields at ports 2 and 4 and only the fundamental waveguide mode propagates in ports 1 and 3, then the left hand side of the reciprocity integral of Eqn. 14 is zero for ports 2, 3, and 4. The integral is non-zero only at port 1. If a current distribution:

$$\bar{J}^p = \hat{y} \frac{i_b}{2} \delta(x - x_b) \delta(y - y_b) e^{-jkz} \quad (16)$$

$$\bar{M}^p = \hat{x} \eta \frac{i_b}{2} \delta(x - x_b) \delta(y - y_b) e^{-jkz} \quad (17)$$

(which is unphysical) is substituted into Eqn. 14 and a pickup impedance of the following form is defined:

$$\bar{P} = \frac{1}{2} \left(\frac{i_b}{2} \right)^2 \bar{Z}_{\Delta p} \quad (18)$$

then the kicker impedance defined in Eqn 13 is given as:

$$2\bar{Z}_{\Delta p} = Z_{\Delta k} \quad (19)$$

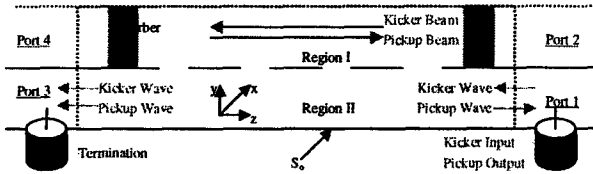


Figure 4: Slow wave array showing surface for reciprocity integral

4 MEASUREMENTS

A vertical slow wave pickup centered at 6 GHz was installed in the Debuncher ring. The pickup consisted of 50 slots. The length of each slot was 17.5 mm and the width was 2mm. The metal spacing between each slots was 3mm. The height of the output waveguide was 20 mm and the width was 40mm. The width and the height of the beam pipe were 40 mm.

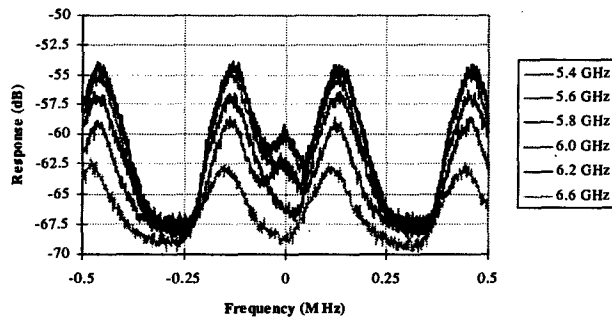


Figure 5. Narrow-band signal of the slow wave pickup in the difference mode at several microwave frequencies

Unbunched, coasting beam was injected into the Debuncher and stored. The beam was transversely excited with RF noise until the beam filled the transverse aperture. The power spectrum was measured with a spectrum analyzer at several frequencies as shown in Figure 5. The transverse aperture could be varied by means of a mechanical beam-scraping device (scraper). The transverse beam distribution was determined by measuring the amount of beam current remaining as a function of scraper position.

The impedance of the array was determined by measuring the power spectral density with a spectrum analyzer with and without beam. The resolution bandwidth of the spectrum analyzer was set much

greater than the revolution frequency of the Debuncher so as to average over the momentum distribution of the beam. The sum mode impedance is:

$$Z_{\Sigma} = (g-1) \frac{N_f S_{\text{therm}}}{e I_{dc}} \quad (20)$$

The difference mode impedance is

$$Z_{\Delta} = (g-1) \frac{N_f S_{\text{therm}}}{2e I_{dc} \left(\frac{\sigma}{d} \right)^2} \quad (21)$$

where N_f is the noise figure of the pre-amplifier, S_{therm} is the power spectral density of white thermal noise (which is equal to -174 dBm/Hz at room temperature), I_{dc} is the beam current, σ is the r.m.s transverse size of the beam, and d is the transverse size of the beam pipe. The quantity "g" is defined to be the ratio of the power per revolution band when there is beam in the machine to when there is no beam in the machine:

$$g = \frac{P_{\text{beam}} + P_{\text{noise}}}{P_{\text{noise}}} \quad (22)$$

The results are shown in Figures 6 and 7. The calculated impedance had to be adjusted by 4 dB to account for the measured cable and hybrid loss between the array and pre-amplifier.

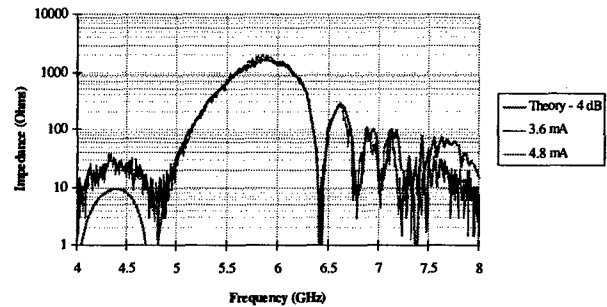


Figure 6. Difference response of the slow wave pickup.

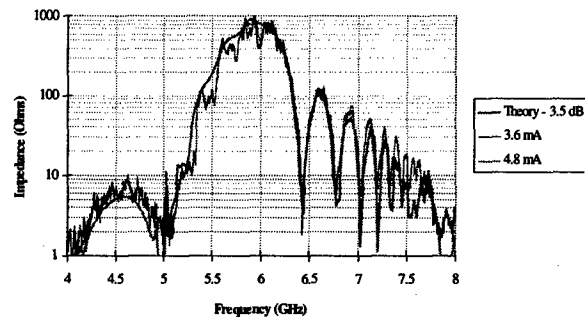


Figure 7. Sum response of the slow wave pickup.

5 REFERENCES

- [1] R.F. Harrington, "Matrix Methods for Field Problems," Proceedings of the IEEE, Vol. 55, No.2, February 1967, pg 136-149
- [2] R. F. Harrington, Time Harmonic Electromagnetic Fields, McGraw Hill, 1961, pg 106-109
- [3] R.E. Collin, Foundations for Microwave Engineering, McGraw-Hill, 1966 pg 184-185.

MODELING THE MUON COOLING CHANNEL USING MOMENTS*

B. A. Shadwick[†] and J. S. Wurtele, Department of Physics, UC Berkeley
A. M. Sessler, C. M. Celata, and P. B. Lee, Center for Beam Physics, LBNL

Abstract

Using a moment formalism [1, 2] we model beam transport in the muon collider cooling channel. This model contains much of the physics we believe to be relevant to muon cooling such as ionization energy loss and multiple scattering. Space-charge forces are currently neglected but can, in principle, be added to the model. Previously, this model has been shown to closely agree with particle tracking [1] while being significantly less computationally intensive. Presently our simulation is limited to the six-dimensional dynamics of the transverse cooling section. A matrix representation of an emittance exchange section is presented. This formulation of emittance exchange can either be ideal (conserving 6-d emittance) or can include energy loss and heating representative of the effects expected in a realistic emittance exchange section. These elements should give our model sufficient generality to enable the preliminary, yet realistic, design of a complete muon cooling channel.

1 INTRODUCTION

A significant technological challenge in the design of a high-luminosity $\mu^+\mu^-$ collider is the cooling of the muon beam. When the muons are produced the initial beam occupies such a large volume in phase space that efficient acceleration is impractical. The successful reduction of the initial phase-space of the muon beam by a factor of 10^5 – 10^6 is necessary to reach the luminosity goals demanded by high-energy physics applications [3]. Furthermore, this cooling must take place on a time scale that is set by the muon lifetime. Thus, cooling mechanisms such as synchrotron radiation, microwave stochastic cooling and sympathetic beam cooling are all too slow. Of several possible rapid cooling mechanisms, ionization cooling appears to be the most attractive technologically [3]. The basis physics of ionization cooling is well understood [4, 5] but detailed simulations are necessary for the design of a realistic cooling channel.

The design process necessarily entails exploration of a large parameter space. The initial stages of the design essentially amount to rejecting unsuitable configurations and identifying promising candidates for further study. Performing this task *via* particle tracking is laborious. We present a moment description [1, 2] of the cooling process that is significant less computationally intensive than full

tracking but still contains much of the physics relevant to ionization cooling. While this approach is useful in identifying promising designs, particle tracking [6, 7] remains an essential step to fully validate and optimize such preliminary designs.

2 MOMENT MODEL

Details of a formalism for describing beam dynamics by moments of arbitrary order is given in Ref. [2]. Here, we study transverse cooling considering only moments up to second order. In this model, the centroid is acted upon by the full nonlinear Lorentz forces while the quadratic moments are subjected to forces linearized about the centroid position. For simplicity, we restrict to the case where the beam centroid deviates little from the axis of the channel.¹ This results in a reduced model where the transverse centroid motion is eliminated and we follow the evolution of $\langle z \rangle$, $\langle p_z \rangle$, $\langle \delta x^2 \rangle$, $\langle \delta y^2 \rangle$, $\langle \delta z^2 \rangle$, $\langle \delta p_x^2 \rangle$, $\langle \delta p_y^2 \rangle$, $\langle \delta p_z^2 \rangle$, $\langle \delta x \delta p_x \rangle$, $\langle \delta y \delta p_y \rangle$, $\langle \delta x \delta y \rangle$, $\langle \delta x \delta p_y \rangle$, $\langle \delta y \delta p_x \rangle$, and $\langle \delta p_x \delta p_y \rangle$, where $\langle \cdot \rangle$ denotes an average over the beam distribution and $\delta x \equiv x - \langle x \rangle$ etc.

The lowest-order effects of multiple-scattering (MS) are incorporated into the moment equations as

$$\left. \frac{d\langle \delta p_x^2 \rangle}{dt} \right|_{\text{MS}} = \langle p_z \rangle^2 \frac{d\langle z \rangle}{dt} \frac{d\theta_0^2}{ds}, \quad (1)$$

$$\left. \frac{d\langle \delta p_y^2 \rangle}{dt} \right|_{\text{MS}} = \langle p_z \rangle^2 \frac{d\langle z \rangle}{dt} \frac{d\theta_0^2}{ds}, \quad (2)$$

where θ_0 is the (energy dependent) width of the Molière distribution as given by Lynch and Dahl [8]. Ionization energy loss (EL) enters the single particle equations as a frictional force in the direction of the particle momentum and subsequently enters the moment equations of motion as

$$\begin{aligned} \left. \frac{d\langle p_z \rangle}{dt} \right|_{\text{EL}} &= \frac{\langle \delta p_x^2 \rangle + \langle \delta p_y^2 \rangle}{2\langle p_z \rangle} \left[\frac{dE'}{ds} (\langle p_z \rangle) - \frac{dE}{ds} (\langle p_z \rangle) \right] \\ &+ \frac{dE}{ds} (\langle p_z \rangle) + \frac{\langle \delta p_z^2 \rangle}{2} \frac{dE''}{ds} (\langle p_z \rangle) \end{aligned} \quad (3)$$

$$\left. \frac{d\langle \delta p_x^2 \rangle}{dt} \right|_{\text{EL}} = 2 \frac{\langle \delta p_x^2 \rangle}{\langle p_z \rangle} \frac{dE}{ds} (\langle p_z \rangle) \quad (4)$$

$$\left. \frac{d\langle \delta p_z^2 \rangle}{dt} \right|_{\text{EL}} = 2 \langle \delta p_z^2 \rangle \frac{dE'}{ds} (\langle p_z \rangle) \quad (5)$$

*Supported by the U. S. DoE Division of High Energy Physics under grant No. DEFG-03-95ER-40936 and contract No. DEA-AC03-76SF0098

[†]email: shadwick@beams.lbl.gov

¹This assumption is consistent with ICOOL results of simulating the nominal cooling channel [3].

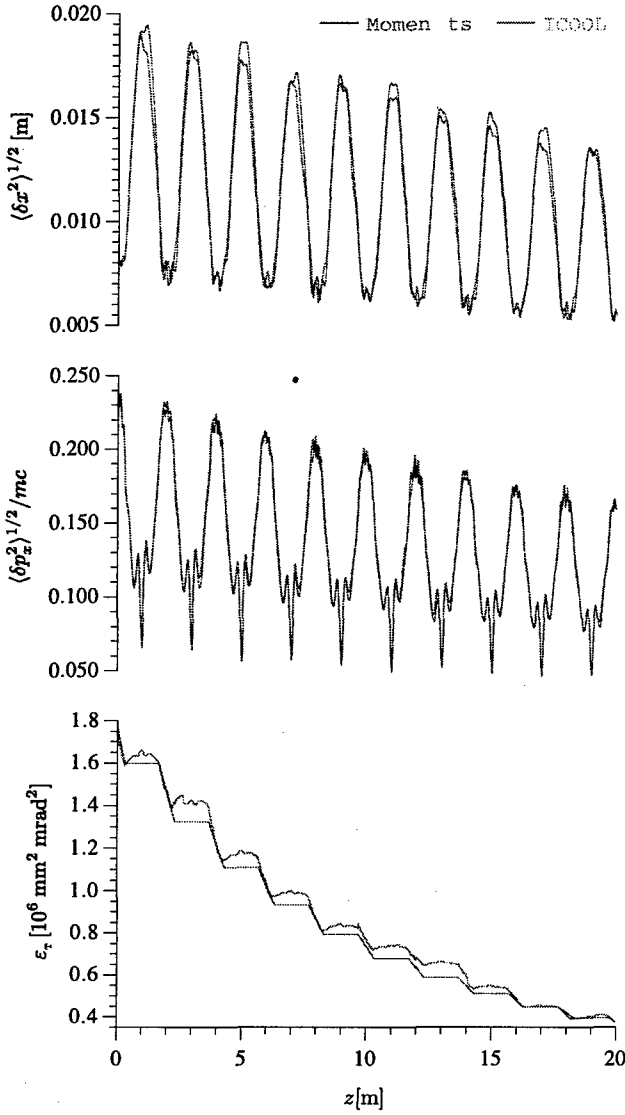


Figure 1: Results of the moment model compared with particle tracking neglecting the longitudinal spread of the beam.

$$\left. \frac{d\langle \delta p_x \delta x \rangle}{dt} \right|_{\text{EL}} = \frac{\langle \delta p_x \delta x \rangle}{\langle p_z \rangle} \frac{dE}{ds} (\langle p_z \rangle) \quad (6)$$

$$\left. \frac{d\langle \delta p_x \delta y \rangle}{dt} \right|_{\text{EL}} = \frac{\langle \delta p_x \delta y \rangle}{\langle p_z \rangle} \frac{dE}{ds} (\langle p_z \rangle) \quad (7)$$

$$\left. \frac{d\langle \delta p_z \delta z \rangle}{dt} \right|_{\text{EL}} = \langle \delta p_z \delta z \rangle \frac{dE'}{ds} (\langle p_z \rangle) \quad (8)$$

$$\left. \frac{d\langle \delta p_x \delta p_y \rangle}{dt} \right|_{\text{EL}} = 2 \frac{\langle \delta p_x \delta p_y \rangle}{\langle p_z \rangle} \frac{dE}{ds} (\langle p_z \rangle) \quad (9)$$

where dE/ds is the average energy loss due to ionization as given by the Bethe-Bloch model and equations for $\langle \delta p_y^2 \rangle$, $\langle \delta p_y \delta y \rangle$, and $\langle \delta p_y \delta x \rangle$ are given by the obvious substitutions. Energy (Landau) straggling has been neglected but its inclusion, in a statistically averaged sense, is planned for the future.

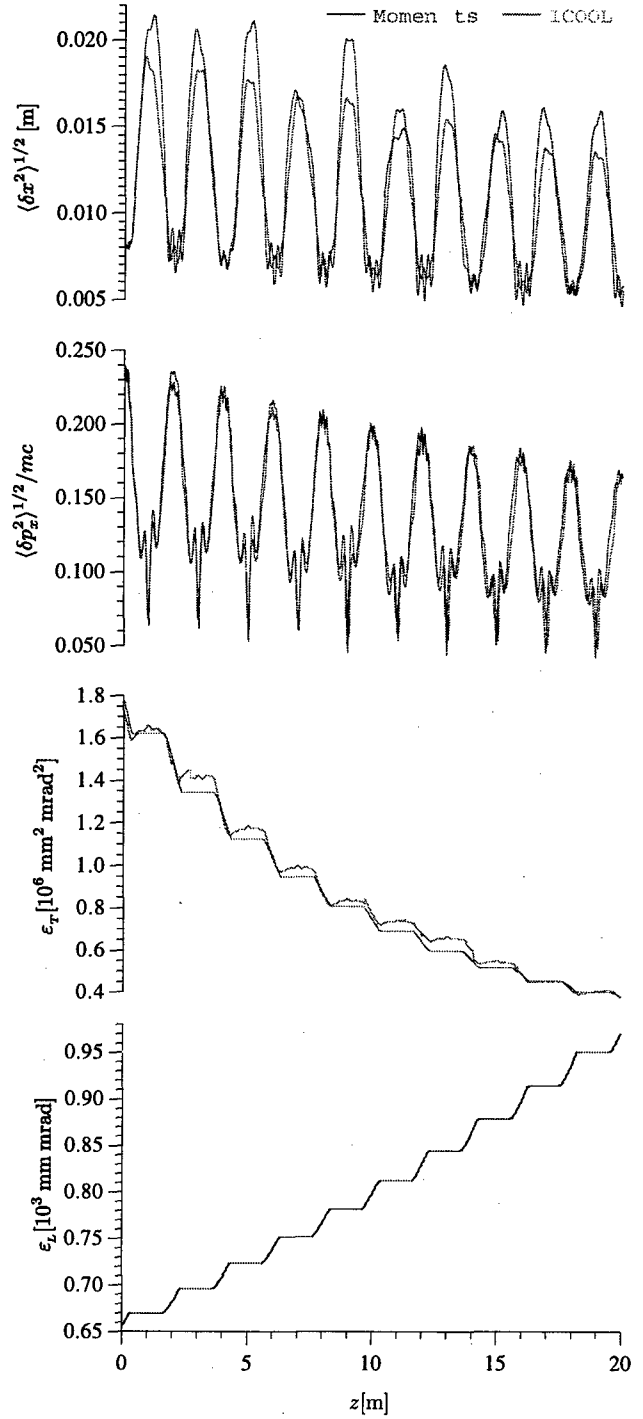


Figure 2: Results of the moment model compared with particle tracking including full longitudinal dynamics.

3 RESULTS

We present results from two variants of our model. In the first, shown in Fig. 1, we approximate the initial beam as having no longitudinal extent and use a simple constant gradient model for the linac. Even with this idealization, we obtain excellent agreement with ICool tracking results and the only discrepancies can be attributed to dif-

ferences in the linac models. As can be seen, the normalized transverse emittance (defined as the determinant of the second-order transverse covariance matrix) is constant except where the beam passes through the absorbers. Note even the high-frequency oscillations in $\langle \delta p_x^2 \rangle$ and $\langle \delta x^2 \rangle$ are reproduced by the moment model. In the second variant, shown in Fig. 2, the full longitudinal dynamics, as discussed above, are included and the linac is modeled as a traveling wave structure. Here again good agreement with ICOOL is obtained in the transverse dynamics. The longitudinal agreement is less perfect, with the moment model showing a factor of 1.5 increase in longitudinal emittance compared with the ICOOL prediction of 2.1. Possible sources of this discrepancy are differences in the linac model (most notably an absence of Beryllium windows in the traveling wave linac) as well as incompleteness in our treatment of the material interaction.

4 EMITTANCE EXCHANGE

As the beam proceeds through the transverse cooling section, not only is the transverse emittance reduced but the longitudinal emittance is increased due to Landau straggling as well as to the dependence of the ionization energy loss on the beam energy. To prevent the longitudinal emittance from growing without bound it is necessary to periodically exchange emittance between the longitudinal and transverse dimensions. For a preliminary design we feel that it is sufficient to represent this exchange process in a simplified form. One such simplification is shown in Fig. 3. The combination of dispersion and phase rotation has overall effect of converting a beam with large spread in δp_z and small δx into one with a small spread in δp_z and correspondingly larger δx .

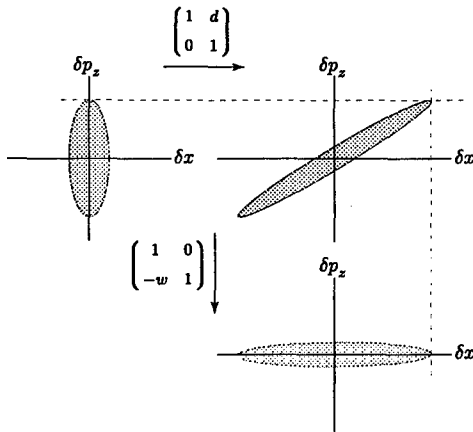


Figure 3: Exchanging emittance between x and z .

In terms in the single particle phase space, this action can be expressed as:

$$W = \begin{pmatrix} 1 & d \\ -w & 1 - dw \end{pmatrix}. \quad (10)$$

The second order moments of interest are $M_2 = \langle \mathbf{z} \mathbf{z}^T \rangle$, where $\mathbf{z}^T = (\delta x, \delta p_z)$. The effect on the moments is then

$M_2 \rightarrow M'_2 = W M_2 W^T$. Choosing w so that $\langle \delta x \delta p_z \rangle'$ is zero leads to ideal exchange:

$$\begin{pmatrix} \langle \delta x^2 \rangle & 0 \\ 0 & \langle \delta p_z^2 \rangle \end{pmatrix} \rightarrow \begin{pmatrix} \langle \delta x^2 \rangle + d^2 \langle \delta p_z^2 \rangle & 0 \\ 0 & \frac{\langle \delta p_z^2 \rangle \langle \delta x^2 \rangle}{\langle \delta x^2 \rangle + d^2 \langle \delta p_z^2 \rangle} \end{pmatrix} \quad (11)$$

A similar matrix can be used to in the $y - p_z$ plane completing the transverse-longitudinal exchange. This formulation can be easily extended to reflect the heating and energy loss that occurs in the wedge absorbers of the actual exchange section.

5 CONCLUSIONS

We have demonstrated that a moment description of muon cooling contains sufficient physics to yield results equivalent to particle tracking insofar as the average transverse dynamics are concerned. With regard to the longitudinal dynamics the degree of agreement is harder to judge due to the differences in accelerator geometry as well as to physics missing from the moment model. Further work towards understanding the source of the discrepancy with particle tracking results is underway. We are also working to improve the material interactions model in the simulation. The inclusion of an analytic expression for emittance exchange, as discussed above, in the simulation allows for the design a full cooling system.

6 REFERENCES

- [1] C. M. Celata, A. M. Sessler, P. B. Lee, B. A. Shadwick, and J. S. Wurtele, "A Moment Equation Approach to a Muon Collider Cooling Lattice," in *Proceedings of the Sixth European Particle Accelerator Conference*, Stockholm (IOP, Bristol, 1998), pp. 1058-1060.
- [2] B. A. Shadwick and J. S. Wurtele, "General Moment Model of Beam Transport," paper #THA130, this proceedings.
- [3] C. M. Ankenbrandt *et al.*, "Status of Muon Collider Research," submitted to PRST-AB.
- [4] D. Neuffer and A. Van Ginneken, "Simulation Studies of Ionization Cooling," Nucl. Instr. and Meth. A **403**, 1 (1998).
- [5] A. N. Skrinsky, "Ionization Cooling and the Muon Collider," in *Proceedings of the 9th Advanced ICFA Beams Dynamics Workshop. Beam Dynamics and Technology Issues for $\mu^+ \mu^-$ Colliders*, Montauk, NY (AIP, NY, 1996), No. 372.
- [6] R. Fernow, J. Gallardo, H. Kirk, R. Palmer, J. Norem, D. E. Alwinn, and A. Skrinsky, "Ionization Cooling in the Muon Collider," Technical Report No. BNL-63615, BNL, 1996.
- [7] R. Fernow, J. Gallardo, H. Kirk, and R. Palmer, "Transverse Cooling in the Muon Collider," Technical Report No. BNL-65698, BNL, 1998.
- [8] G. R. Lynch and O. I. Dahl, "Approximations to Multiple Coulomb Scattering," Nucl. Inst. and Meth. B **58**, 6 (1991).

TRANSVERSE INSTABILITY DUE TO THE SPACE CHARGE DURING THE ELECTRON-COOLING BUNCHING OF ION BEAMS

M. Takanaka, T. Katayama, RIKEN, Wako, Japan

Abstract

A beam-tracking simulation has been done for study of the electron-cooling bunching of ion beams around a few hundred MeV/u. In the simulation, the field due to the space charge of a beam in a round vacuum chamber is calculated from the charge distribution of macro-particles and the image particles due to the macro-particles. The simulation results show that the bunched beams meet a transverse instability more easily than coasting beams.

1 INTRODUCTION

Collision experiments with ion-electron beams and ion-ion beams are planned at the Double Storage Ring of RIKEN RI-beam factory project. Ion-beam bunching under electron cooling has been investigated by using a beam-tracking simulation for realization of the bunched beams required for the experiments. The previous-simulation results for the case of a 150-MeV/u U_{238}^{92+} -ion beam of 3.4 mA [1] have shown that 1) the beam has wide incoherent-tune spreads longitudinally and transversely, 2) the beam is not trapped into resonances due to the nonlinear fields of magnets, and 3) the beam is stable longitudinally under the longitudinal broad-band impedance of $|Z_L^{bb}/n| = 5 \Omega$ based on the broad-band impedance model.

The transverse space-charge impedance for a circle type of dipole charge distribution is described as follows;

$$Z_T^{sc} = i \frac{Z_0 R}{\beta^2 \gamma^2} \left(\frac{1}{a^2} - \frac{1}{b^2} \right), \quad (1)$$

where Z_0 is the free space impedance, R the mean radius of a ring, $a \sqrt{2} \times \text{rms}$ beam size, and b the inner radius of a round vacuum chamber. Such a type of impedance becomes no cause of instability, as the force induced through the impedance is proportional to the transverse beam position from the chamber center. There is a question whether the description is applicable to the cases of the space-charge-dominated beams or not, or a question whether a transverse space-charge force induced through the vacuum chamber becomes a cause of instability or not. For the sake of answering the question, the field due to the space charge in a round vacuum chamber is calculated from the charge distribution of the macro-particles and the image particles due to the macro-particles in the simulation on the assumption that the longitudinal component of the field is negligible.

Besides the above calculation of the field, in the simulation where coupled-bunch phenomena are not dealt, forces

induced through the transverse broad-band impedance Z_T^{bb} and the transverse resistive wall impedance have newly been taken into account as forces acting on ions. The notation Z_{LT}^{bb}/n is used just for parameterizing Z_T^{bb} ;

$$Z_T^{bb} = \frac{2R}{b^2} \frac{Z_{LT}^{bb}}{n}. \quad [2] \quad (2)$$

The transverse broad-band impedance of $|Z_{LT}^{bb}/n| = 50 \Omega$ has been used on the assumption of the broad-band impedance model. The ring and the beam input parameters to the simulation have been listed in [1]. The longitudinal and transverse cooling times for a zero-current beam are 5 ms and about 20 ms in the simulation, respectively. The following simplification has been done in the simulation.

1) The vacuum chamber has a round cross section of inner radius b around the ring. 2) The β functions along the ring are equal to the average ones, and α functions equal to 0. 3) The transverse position displacement of an ion due to the momentum difference is neglected in order that the instability described later is seen to have no relation with the displacement. 4) The effects of nonlinear fields of the magnets on beams are neglected because of the authors' focus just on the instability. 5) The transverse field due to the space charge is calculated from the transverse charge distribution that is made vertically symmetry by counting half a macro-particle at the coordinates (x, y) located at $(x, -y)$. Otherwise, the instability can occur in the horizontal and the vertical directions, and the analysis of the beam behavior becomes more complicated.

2 SMALL VACUUM CHAMBER

In the vacuum chamber of $b = 40$ mm, a 150-MeV/u U_{238}^{92+} -ion coasting beam of 3.4 mA is initially electron-cooled to $6 \times \text{rms}$ momentum spread of 5×10^{-4} , and is bunched by applying a fundamental RF (harmonics no., or $h = 87$) voltage. Every RF bucket is filled with the beam. The bunch spacing is 3.0 m. The RF voltage is increased gradually with the momentum-spread kept constant in order that the bunch length is made short.

Such a process was simulated with results as shown in Fig 1. The amplitude of the horizontal beam position becomes increased a synchrotron period after applying the RF voltage. After then, the horizontal emittance is blown up ten-times large within two synchrotron periods. The maximum instantaneous current at 5.1 ms is 10 mA at the bunch center. The horizontal phase-space distribution at 5.1 ms is shown in Fig 2. The instability is seen to be of the transverse dipole mode. The betatron-oscillation-phase differ-

ence from the head to the tail of the dense bunch 1.5 m long is about $1/2\pi$. The difference ϕ_b is understood in terms of the slippage factor η , the chromaticity ξ , and the bunch length l_b ;

$$\phi_b = \frac{\xi l_b}{\eta R}. \quad (3)$$

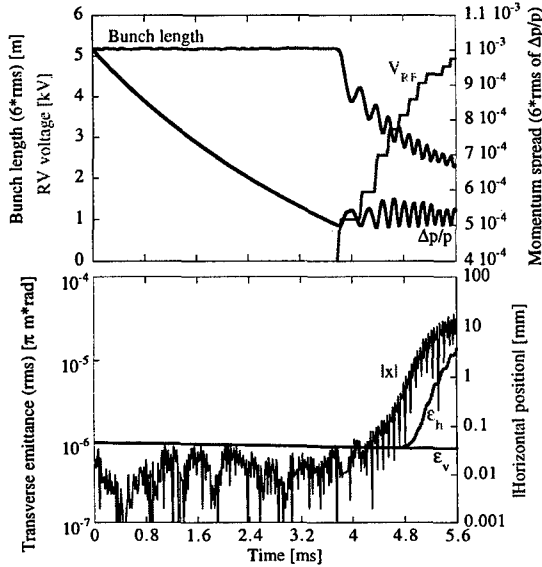


Figure 1: Instability in the vacuum chamber of 40 mm inner radius during the electron-cooling bunching.

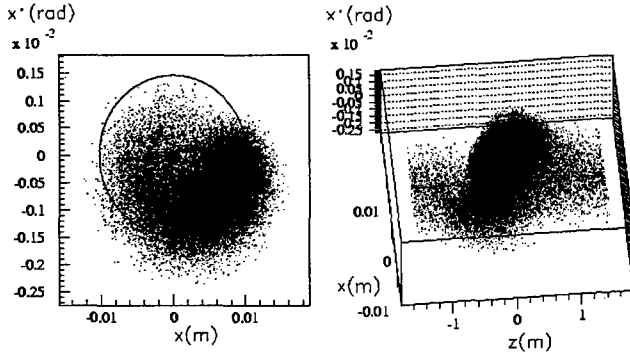


Figure 2: Horizontal phase-space distribution. The ellipse is for a reference.

3 COHERENT TRANSVERSE OSCILLATION

The dipole moment of a coherent transverse oscillation (transverse displacement $\times I \equiv I_1$) is Fourier-expanded as follows;

$$I_1(t, s) = \sum_{\Omega, n} A(\Omega, n) \exp\left(-i\Omega t + i\frac{ns}{R}\right), \quad (4)$$

where A is the component amplitude, t the time, s the longitudinal position, Ω the coherent frequency, and the integer n the oscillation number around a ring. ω_0 , described later, is the revolution frequency.

Figure 3 shows the spectrum of the horizontal dipole moment around 5.2 ms. There is no remarkable different spectrum between the fast waves with $n > 0$ and the slow waves with $n < 0$. A single peak of the major structure of the signal along $\Omega/\omega_0 - nh \approx p + 0.38$ (the integer p =fixed, the integer n =variable) means that the head-tail mode of the instability is the so-called rigid-bunch mode. The signal has synchrotron satellites on the both sides, as shown in two lower of Fig.3. The fractional coherent tune is read 0.3733 and 0.3867 from peak's coordinates of the signals with $p \geq 0$ and $p < 0$, respectively, while the fractional incoherent tune is estimated at 0.380 ± 0.005 from an FFT analysis.

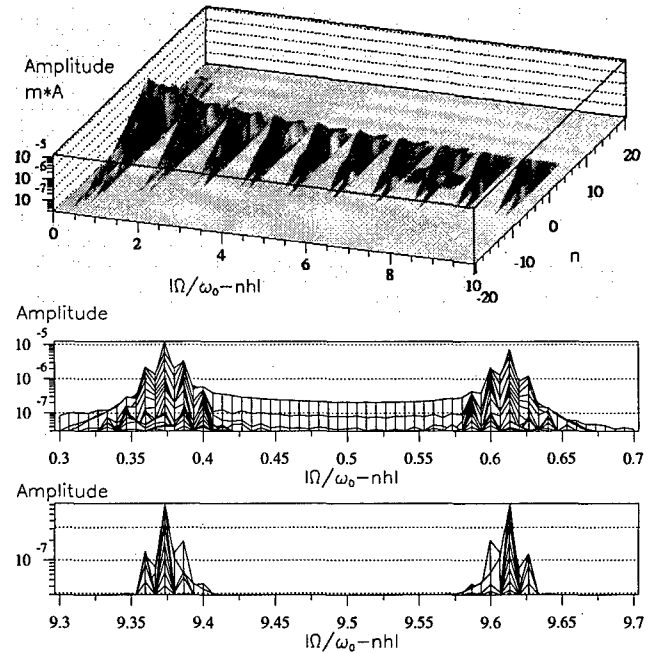


Figure 3: Spectrum of the dipole mode of coherent transverse oscillation which has low-level signals cut away.

4 LARGE VACUUM CHAMBER

The simulation was done on the same condition as described in Section 2 except for the double-sized vacuum chamber of $b = 80$ mm. The simulation results show that the beam is as stable as in the previous case[1] up to on the way. After the beam is bunched by applying the fundamental RF voltage 20 kV and becomes shorter than 1 m to the degree that the third harmonic RF voltage can be applied, the bunching is prompted by applying the third harmonic RF voltage. The beam meets the instability when the $6 \times \text{rms}$ bunch length reaches 0.6 m. Figure 4 shows the emittance blowing-up on two impedance conditions; the one being the broad-band impedance of $|Z_{LT}^{bb}/n| = 50 \Omega$ and the resistive wall impedance, and the other no broad-band impedance nor the resistive wall impedance. The maximum instantaneous currents at 38.5 ms and 39.5 ms are 37 mA and 39 mA at the bunch center, respectively. The instability threshold is seen to be dependent not only

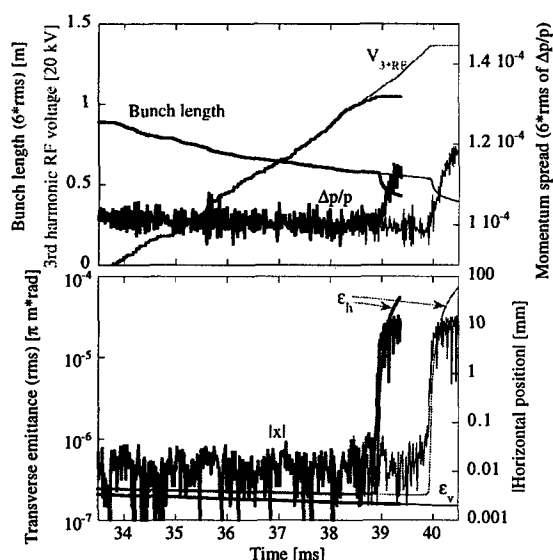


Figure 4: Instability in the vacuum chamber of inner radius $b=80$ mm during the electron-cooling bunching. The Thick curves are for the high impedance condition, and the thin curves for no-impedance condition.

on the inner radius of the vacuum chamber but also on the transverse broad-band impedance.

It is preferable from the viewpoint of the instability cure that the inner sizes of the vacuum chamber surroundings around the ring are designed to be as wide as possible to the degree that the broad-band impedance of the ring does not increase so high.

5 COASTING BEAMS

For the sake of checking whether the instability described in Section 2 is merely due to the increase of the instantaneous beam current or not, the simulation was done of higher-current coasting beams under the electron cooling in the small chamber of $b = 40$ mm.

The simulation results, as shown in Fig. 5, show that the coasting beam is stable even in the case where the coasting-beam current of 70 mA is 7 times higher than the maximum instantaneous current of the bunched beam. This means that the increase of the current is the necessary condition for the instability of the bunched beams but not the sufficient condition.

6 COHERENCY OF TRANSVERSE OSCILLATION

In the case of a coasting beam, even if the beam has coherent transverse oscillation on some account, when the electromagnetic interaction between the beam and the vacuum chamber surroundings are negligibly small, the coherent oscillation is diluted to disappear for the following reason. Localized ions spread around the ring and spread azimuthally 2π on the transverse phase planes in time owing to the momentum difference.

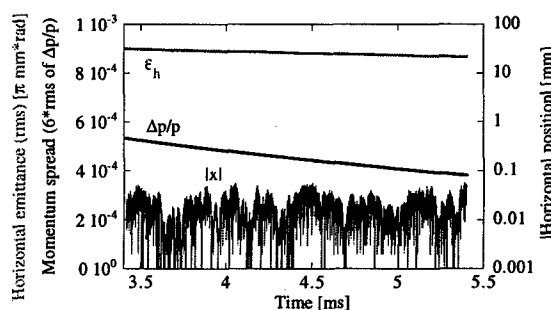


Figure 5: 70 mA coasting beam electron-cooled in the vacuum chamber of inner radius $b=40$ mm.

In the case of a bunched beam, the coherent transverse oscillation is not diluted for the following reason. Localized ions synchrotron-oscillate and remain localized in the RF separatrix, although ions localized near the boundary of the separatrix spread along the boundary in time owing to the non-linearity of the synchrotron frequency. There is a limitation on the betatron-oscillation-phase difference between an ion and the synchronous particle. The variation of the difference is described in the term of the longitudinal distance z_i to the ion from the synchronous particle by Eq. (3) in which l_b is replaced with $-z_i$. Therefore, the distribution of the phase difference of the beam is periodic at the synchrotron frequency.

It can be said from the above that coherency of the transverse oscillation is very low for a coasting beam and high for a bunched beam. Such high coherency is considered to be one of causes that make the bunched beams meet the instability more easily than coasting beams.

7 CONCLUSIONS

A beam-tracking simulation of the electron-cooling bunching of ion beams showed the following results. The space-charge dominated beams meet a transverse instability when they are bunched by using an RF system and an electron cooler. The instability is due to the transverse field induced through the vacuum chamber by the space charge of the beam, or through the transverse space-charge impedance. The instability has the dipole mode as the transverse mode and the rigid-bunch mode as the head-tail mode. The bunched beams meet the instability more easily than coasting beams at least by 7 times in the regard of the instantaneous beam current.

Coherency of the transverse oscillation is higher for the bunched beams than for coasting beams. Such high coherency is considered to be one of causes that make bunched beams meet the instability more easily than coasting beams.

8 REFERENCES

- [1] M. Takanaka, T. Katayama: Proc. of PAC'97, 1807(1997).
M. Takanaka, T. Katayama: Proc. of EPAC'98, 1014(1998).
- [2] B. Zotter, F. Sacherer: CERN 77-13, 175(1973).

DEVELOPMENT OF MUSES-ACR ELECTRON COOLER

T. Tanabe^{*}, T. Rizawa⁺, K. Ohtomo^{*}, and T. Katayama, RIKEN, Saitama, JAPAN

Abstract

An electron cooler (EC) device for the Accumulator Cooler Ring (ACR) in the MUSES project [1] is currently under development. The electron beam energy is varied from 30 keV to 250 keV with a maximum current of 4.1 A. An axial magnetic field of 0.2 T in a 3.6 m solenoid is chosen to satisfy the magnetization condition for the lightest ions and the expansion factor of 20 corresponds to the field of 4 T in the gun section. The details of the design and technological issues are discussed.

1 INTRODUCTION

The design of the ACR-EC has been modified since it was first reported at EPAC98 [2] due to various reasons. One of the main concerns is the vacuum level near the gun cathode which is to be operated under severe conditions. The maximum acceleration voltage has been reduced from 300 to 250kV, and the maximum magnetic field at the gun section has been decreased from 5 to 4T. The collector is partially based upon TARN-II collector [3] with a number of modifications. The design of the gun section is described in Sec. 2 and that of the collector is given in Sec. 3. Effects of the troidal section on the electron beam are examined in the following section before discussion.

2 GUN SECTION

2.1 Cathode/Anode and Acceleration Tube

The initial design of the gun had a magnetic field of 5T and acceleration voltage of 300kV. After careful examination of the design, we have concluded that the reduction of expansion factor from 25 to 20 gives only small degradation of the performance in terms of lowest achievable electron transverse energy [4]. The maximum nominal energy of the injected ion beam from the SRC ring is 400MeV/u which corresponds to the electron kinetic energy of 219.4 keV. Therefore, 250 kV is deemed to be sufficient.

The cathode diameter is increased from 10 to 12.7 mm in order to reduce the maximum voltage gradient in the vicinity of the cathode/anode from 50 to 36 kV/cm, while maintaining the same anode/cathode voltage (30kV) as before.

The maximum emission current density is also reduced from 5.1 to 3.15 A/cm². We plan to use an Ir-coated dispenser cathode produced by Toshiba Co. At one point, a fair amount of effort was made to reduce the diameter of the accelerator tube to make the bore size of a superconducting solenoid smaller. However, it turns out that the vacuum level near the cathode could never be satisfactory due to poor vacuum conductance of the small apertures of diaphragms in the original design (26 mm). This estimate assumes the outgassing rate from cold surfaces, so it would be worse under more realistic circumstances. Hence, the idea of small tube was abandoned for larger vacuum conductance. Figure 1 shows a result of EGUN simulation with the current design.

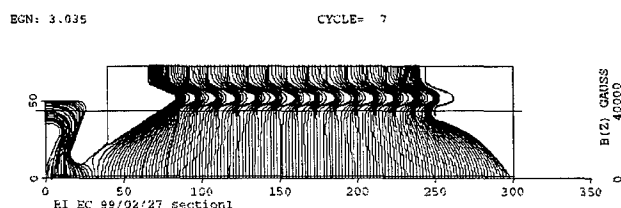


Fig. 1: EGUN simulation of the electron gun section

2.2 Magnetic Shielding

The design of the magnetic shielding at the gun section was optimized by SAM [5]. A schematic picture of the configuration of a superconducting solenoid, a warm solenoid and a correction coil and a magnetic shielding is delineated in Fig2. The magnetic field distribution and the adiabatic parameter is shown in Fig. 3.

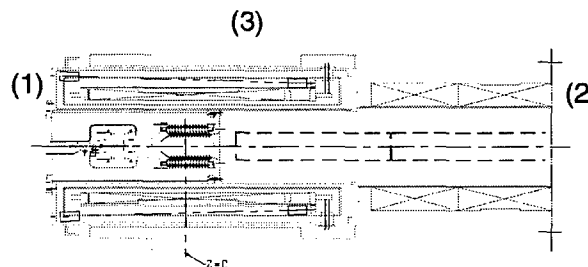


Fig. 2: Layout of (1) a superconducting solenoid, (2) a warm solenoid and (3) a magnetic shielding.

^{*} Email: ttanabe@postman.riken.go.jp

⁺ On leave from Toshiba corporation. ^{*} On leave from Sumitomo Heavy Industries.

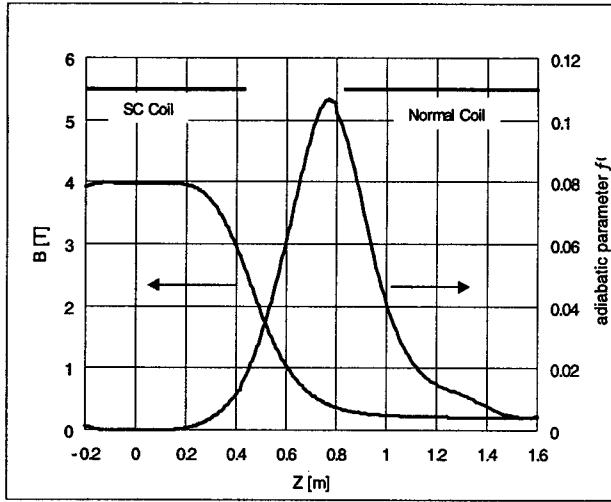


Fig. 3: The longitudinal magnetic distribution and the adiabatic parameter.

3 COLLECTOR SECTION

The initial design of the ACR collector was based upon the TARN II collector. Various improvement has been incorporated during the past year. The geometry of the new collector section is given in the Fig. 4. The collector consists of a deceleration tube, a repeller electrode, a collector electrode and two permanent magnetic coils. The collector electrode is a Faraday cap.

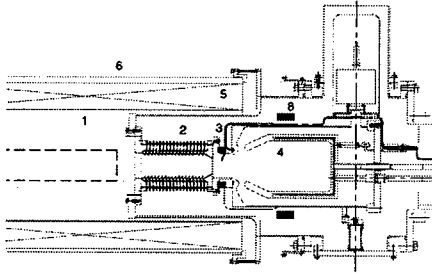


Fig. 4: The design of the collector. 1 is the drift chamber, 2 deceleration tube, 3 repeller, 4 collector electrode, 5 the solenoid of electron cooling, 6 magnetic shielding, 7 a permanent magnet coil placed on the collector entrance, and 8 is a permanent magnet coil placed on the collector surface.

The ratio of the current density of the reflected secondary electrons that escape a collector to that of the incoming beam is proportional to [6];

$$\frac{j_{ref}}{j} \approx \frac{\sigma_e}{\pi} \left(\frac{\varphi_{min}}{U_{col}} \right)^2 \frac{B_{col}}{B_{\varphi_{min}}}, \quad (1)$$

where j is the incoming beam current, $\sigma_e \approx 1$ is the secondary emission coefficient, B_{col} is the magnetic field on the collector surface, and $B_{\varphi_{min}}$ is the magnetic field in the region of minimum potential value.

Types of modifications applied are as follows:

- The collector diameter is increased to reduce the magnetic field on the collector surface, B_{col} .
- To increase $B_{\varphi_{min}}$, the permanent magnet coil is placed inside the repeller electrode with the magnetic field of 2 kG.
- A permanent magnet coil is placed on the collector surface to reduce B_{col} .
- The collector radius is reduced at the entrance to shift the position of the virtual cathode to the region in higher magnetic field.

The collector perveance is estimated as $P_{col} = I / U_{col}^{3/2} \approx 25 \sim 30 \mu A / V^{3/2}$. As a result, the current loss was reduced by an order of magnitude compared to the old design.

4 TORIODAL SECTION

The electrons obtain additional perturbation, when they pass through the EC toroidal section. This perturbation is observed for electrons which are displaced from the equilibrium axial trajectory. The guiding longitudinal magnetic field in toroidal section depends on the radial co-ordinate x .

$$B = B / (1 + x / R) \quad (2)$$

where R is the radius of the axial electron trajectory in the toroidal section. The transverse bending magnetic field used for compensation of the electron drift motion in the toroidal magnet is equal to

$$B_y = p / eR, \quad (3)$$

where p is the electron momentum. The drift motion caused by the centrifugal force $F_s = \gamma m v^2 / (R + x)$ is not entirely compensated by the transverse bending magnetic field B_y for the electrons whose trajectories are shifted from beam axis on the distance x . As a result, when the electrons pass through toroidal magnet, the additional drift velocity appears;

$$v_{dr} = \frac{\gamma m v^2 x}{Re B R} = v \frac{\rho x}{R R}, \quad (4)$$

where $\rho = v / \omega_B$ is the larmor radius. The transverse temperature corresponding to this drift velocity is equal to

$$T_{dr} = \frac{m v_{dr}^2}{2} = \frac{m v^2}{2} \left(\frac{\rho x}{R R} \right)^2. \quad (5)$$

Discontinuity of the magnetic field at the entrance/exit of toroidal magnets significantly increase the transverse temperature. This increase strongly depends on the radius of curvature, R as is shown in Eq. (5). It has been increased from 1.2 to 1.5 m to make this contribution comparable to the initial temperature even in case of abrupt field change.

5 DISCUSSION

Table 1 shows the latest parameters of the device and cross-sectional view of the whole EC system is shown in Fig. 5.

Table 1: Parameters of ACR-EC

Acceleration Voltage	30 ~ 250 kV
Magnetic Field (gun/cooling)	4 T / 0.2 T
Field Uniformity (gun/cooling)	$2 \times 10^{-3} / 5 \times 10^{-5}$
Cathode Diameter	12.7 mm
Maximum E-Beam Current	4 A
Gun Perveance	0.79 μ P
Anode-Cathode Voltage	30 kV
Main Solenoid length	3.6 m
Toroidal Angle / Radius	90° / 1.5 m
Collector Efficiency	> 99.98 %

In the initial plan, the EC is supposed be installed in one of the short straight sections in the ACR. However, insertion of correction solenoids in the adjacent cells lead to unnecessary complex in terms of beam dynamics [7]. Therefore, the device is likely to be installed in one of long straight section in a modified lattice of ACR. The modification is currently underway.

ACKNOWLEDGMENTS

The authors wish to thank Dr. Evgeny Syresin and Dr. Igor Meshkov of Joint Institute of Nuclear Research in Russia for their advice, and Mr. Akira Yamashita of Toshiba Co. for his assistance.

6 REFERENCES

- [1] T. Katayama, *et al.*, "MUSES Project of RIKEN RI Beam Factory", p. 529, proceedings of EPAC'98.
- [2] I. Watanabe, *et al.*, "Electron Cooling at ACR in MUSES Project", p. 2258, proceedings of EPAC'98.
- [3] T. Tanabe, *et al.*, "Electron Cooling Experiments at INS", NIM A 307 (1991), p.7.
- [4] E. Syresin, *et al.*, "Simulation and Design of an Electron Cooling System for ACR," RIKEN internal report.
- [5] M. Tiunov, *et al.*, Preprint INP, Novosibirsk, pp. 85-159.
- [6] E. Syresin, "The Parameters of the Secondary Electrons in the Electron Cooling System", NIM A, 391 (1997), p. 114.
- [7] T. Tanabe, *et al.*, "Development of ACR Electron Cooler," RIKEN Accel. Prog. Rep. (1998), to be published.

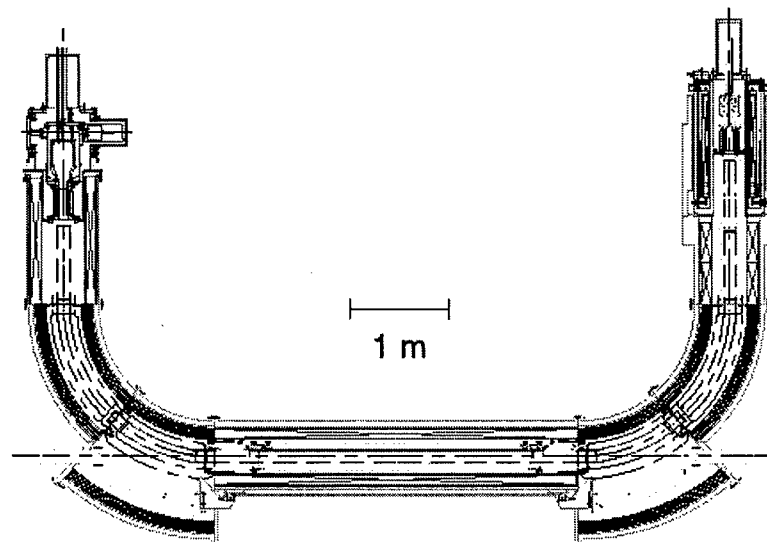


Fig. 5 Cross-sectional view of the MUSES-ACR EC

THE LONGITUDINAL HIGH-FREQUENCY IMPEDANCE OF A PERIODIC ACCELERATING STRUCTURE*

K. Yokoya, KEK, Tsukuba, Japan

K.L.F. Bane, SLAC, Stanford, CA

Abstract

In many future collider and FEL designs intense, short bunches are accelerated in a linear accelerator. For example, in parts of the Linac Coherent Light Source (LCLS) a bunch with a peak current of 3.4 kA and an rms length of 30 microns will be accelerated in the SLAC linac. In such machines, in order to predict the beam quality at the end of acceleration it is essential to know the short range wakefields or, equivalently, the high frequency impedance of the accelerating structure. R. Gluckstern[1] has derived the longitudinal, high-frequency impedance of a periodic structure, a solution which is valid for a structure with a small gap-to-period ratio. We use his approach to derive a more general result, one that is not limited to small gaps. In addition, we compare our results with numerical results obtained using a field matching computer program.

1 INTRODUCTION

Let us consider the infinitely periodic, cylindrically symmetric structure depicted in Fig. 1. R. Gluckstern has derived the high frequency behavior of the impedance of such a structure, to order $(kg)^{-1/2}$ relative to the leading term, with k the wave number and g the gap, as[1]

$$Z_L(k) = \frac{iZ_0}{\pi ka^2} \left[1 + (1+i) \frac{\alpha L}{a} \sqrt{\frac{\pi}{kg}} \right]^{-1}, \quad (1)$$

with $\alpha = 1$. Note that Z_L is the average impedance per unit length (averaged locally over frequency to give a smooth function, and averaged over a distance in the structure large compared to the period L), $Z_0 = 120\pi\Omega$, and a is the iris radius. Gluckstern's result was meant to be valid for $g/L \ll 1$. In this report, following Gluckstern's method, we will show that Eq. 1 is still valid in the general case g/L not small, but with α a function of g/L .

Other authors have investigated the high frequency behavior of the same structure. Their results agree in the leading order term ($iZ_0/\pi ka^2$), but not in the constant α in the higher order term. E. Keil, describing the so-called Sessler-Vaynshtein optical resonator model of high frequency impedance, obtains a constant $\alpha = 0.67$ [2] and S. Heifets and S. Kheifets give $\alpha = 8/\pi \approx 2.55$ [3]. G. Stupakov, considering the limiting case of a structure with infinitesimally thin irises (i.e. $g/L = 1$), finds that, in this case, $\alpha \approx 0.46$ [4].

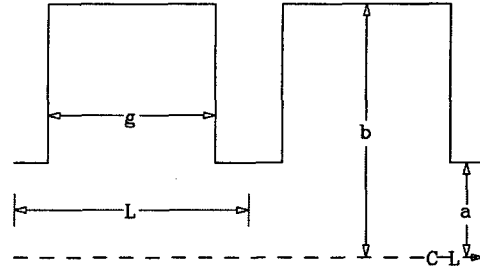


Figure 1: Two cells of the geometry under consideration.

2 ANALYTICAL STUDY

Let us begin by briefly summarizing Gluckstern's method: He divides the geometry of Fig. 1 into two regions, the pipe region ($r \leq a$) and the cavity region $r \geq a$. The fields are expanded in terms of Bessel functions in the pipe region and in term of the cavity eigenfunctions in the cavity region with the (perfectly conducting) metallic boundary condition on the iris surface $r = a$. He obtains a relation (Eq. 2.14 in the first of Ref. [1]) between the azimuthal magnetic field and the axial electric field along $r = a$. Then, by matching the fields in the pipe and cavity regions along $r = a$, he obtains an integral equation for the axial electric field along $r = a$ (normalized by $Z_0 I_0 / ka^2 e^{-ikz}$, with I_0 the arbitrary driving current), $F(z)$ (we follow his notation):

$$\int_0^g dz' \left[\hat{K}_c(z, z') + \sum_{m=-\infty}^{\infty} \hat{K}_p(mL + z' - z) \right] F(z') = -i. \quad (2)$$

The kernels in this equation are those of the cavity region \hat{K}_c and of the pipe region \hat{K}_p , with the \hat{K}_c term and the $m = 0$ term involving \hat{K}_p giving the contribution to the impedance of the cell that includes the point z , and the $m \neq 0$ terms giving the contribution of the other cells. Once we know $F(z)$ the impedance is simply given by

$$Z_L(k) = \frac{Z_0}{ka^2 L} \int_0^g dz F(z). \quad (3)$$

For our purposes we do not need to know the details of the kernels \hat{K}_c and \hat{K}_p , but only their high frequency behavior. Gluckstern found that the high frequency behavior of the cavity kernel \hat{K}_c is independent of the details of the cavity shape, and is given by

$$\hat{K}_c(z, z') = -\frac{(1+i)\sqrt{\pi}}{a\sqrt{k(z-z')}} \Theta(z-z'), \quad (4)$$

where $\Theta(z)$ is the step function (0 for $z < 0$ and 1 for $z \geq 0$). The kernel in the pipe region \hat{K}_p is given by

* Work supported by Department of Energy contract DE-AC03-76SF00515.

$$\hat{K}_p(z) = -\frac{2\pi i}{a} e^{ikz} \sum_{s=1}^{\infty} \frac{1}{b_s} e^{ib_s|z|/a}, \quad (5)$$

$$b_s = (k^2 a^2 - j_s^2)^{1/2}, \quad [\Im(b_s) \geq 0],$$

with j_s the s -th zero of the Bessel function J_0 . Gluckstern shows that, at high frequencies, the $m = 0$ pipe kernel, $\hat{K}_p(z' - z)$, is equal to the cavity kernel $\hat{K}_c(z, z')$, as given in Eq. 4. As for the $m \neq 0$ terms in \hat{K}_p , Gluckstern points out, that those with $m > 0$ oscillate rapidly at high k , and therefore do not contribute to the average impedance. The sum over negative m gives

$$K_s(v) \equiv \sum_{m=-\infty}^{-1} \hat{K}_p(mK + z' - z)$$

$$= \frac{2\pi i}{a} \sum_{s=1}^{\infty} \frac{1}{b_s} \frac{e^{i(\theta - \phi_s)v}}{1 - e^{i(\theta - \phi_s)v}}, \quad (6)$$

with $v = (z' - z)/L$, $\theta = kL$, $\phi_s = b_s L/a$. Noting that up to order $k^{-1/2}$, $(\theta - \phi_s)$ can be replaced by $j_s^2 L/2ka^2$, this becomes

$$K_s(v) = -\frac{4\pi}{L} \sum_{s=1}^{\infty} \left[\frac{1}{j_s^2} - \frac{iL}{2ka^2} \left(\frac{e^{ij_s^2 v L/2ka^2}}{1 - e^{ij_s^2 v L/2ka^2}} + \frac{2ka^2}{ij_s^2 L} \right) \right]. \quad (7)$$

The first term in square brackets can be summed: $\sum 1/j_s^2 = 1/4$; the second term can be approximated by an integral: $\sum_{s=1}^{\infty} f(j_s) \approx (1/\pi) \int_0^{\infty} f(x) dx$, for $k \rightarrow \infty$. Thus, we obtain

$$K_s(v) = -\frac{\pi}{L} \left[1 + \sqrt{\frac{2L}{\pi ka^2}} e^{\pi i/4} G_0(v) \right], \quad (8)$$

with

$$G_0(v) = \frac{2}{\sqrt{\pi}} \int_0^{\infty} dx \left[\frac{e^{x^2 v}}{e^{x^2} - 1} - \frac{1}{x^2} \right]$$

$$= \sum_{n=1}^{\infty} \left[\frac{1}{\sqrt{n-v}} - \frac{1}{\sqrt{n}} \right] + \zeta\left(\frac{1}{2}\right), \quad (9)$$

where ζ is the Riemann zeta function ($\zeta(1/2) = G_0(0) = -1.460$). Note that it is the second term in the brackets of Eq. 7 that Gluckstern has let go to zero, which will account for the difference in his final result and ours.

The original integral equation, Eq. 2, thus becomes

$$\frac{(1-i)}{\sqrt{\pi k L}} \int_0^{g/L} dv' \bar{G}(v' - v) F(v')$$

$$- \frac{ia}{L} \int_0^{g/L} dv' F(v') = \frac{a}{\pi L}, \quad (10)$$

with

$$\bar{G}(v) = \frac{2\Theta(-v)}{\sqrt{-v}} + G_0(v). \quad (11)$$

This equation can be rewritten in the form

$$\int_0^{g/L} dv' \bar{G}(v' - v) F_0(v') = 1, \quad (12)$$

with

$$F_0(v) = F(v)/A, \quad (13)$$

$$A = \frac{\sqrt{\pi k L}}{(1-i)} \left[\frac{a}{\pi L} + \frac{ia}{L} \int_0^{g/L} dv F(v) \right]. \quad (14)$$

Note that Eq. 12, with $F_0(v)$ the unknown, contains only one parameter $\gamma \equiv g/L$. The equation for the impedance, Eq. 3, becomes

$$Z_L(k) = \frac{Z_0}{ka^2} A \int_0^{\gamma} dv F_0(v). \quad (15)$$

Finally, the solution to this equation is an impedance of the form Eq. 1, with

$$\alpha(\gamma) = \frac{\sqrt{\gamma}}{\pi} \left[\int_0^{\gamma} dv F_0(v) \right]^{-1}, \quad (16)$$

a result that can be verified by substitution.

We find that for small γ , $\alpha = 1 + G_0(0)/\pi\sqrt{\gamma} + O(\gamma^{3/2})$, and for $\gamma = 1$, $\alpha \equiv \alpha_1 = -G_0(0)/\pi \approx 0.4648$. The numerical solution of Eq. 12 gives α in general (see Fig. 2). A polynomial fit in $\sqrt{\gamma}$

$$\alpha(\gamma) = 1 - \alpha_1 \sqrt{\gamma} - (1 - 2\alpha_1)\gamma, \quad (17)$$

given by the dashes in Fig. 2, agrees to within 1.5% with the numerical result. Note that $\alpha(0)$ is in agreement with the result of Gluckstern, and $\alpha(1)$ with that of Stupakov.

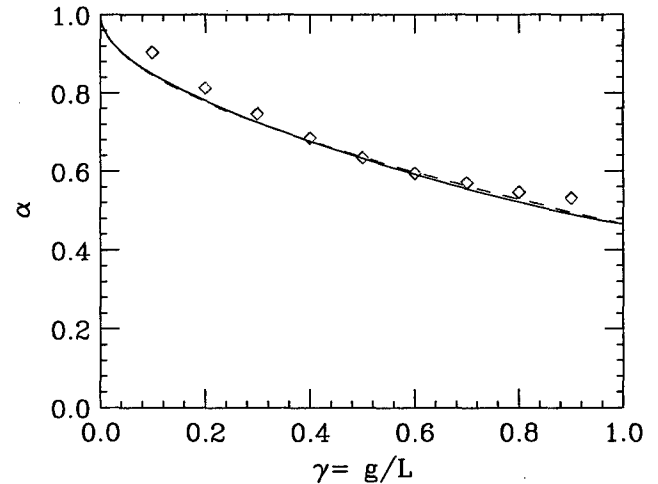


Figure 2: The coefficient $\alpha(\gamma)$. The dashed curve gives the analytical fit, Eq. 17. The plotting symbols are numerical results discussed in the next section.

3 NUMERICAL COMPARISON

To confirm these results numerically we have used a field matching computer program working in the frequency domain[5] (see also Ref. [6]). For the geometry of Fig. 1 and for a given k , this program matches the tangential fields at $r = a$, and then performs normalizing integrals. The result is an infinite dimensional matrix equation that is truncated and inverted to obtain $Z_L(k)$. In order to better study the asymptotic behavior, the program calculates the impedance along a path slightly shifted off the real k axis, which has the effect of averaging and smoothing out the many narrow impedance spikes otherwise found at high frequencies. (Note that to obtain the short-range wakefield from this impedance, after performing the inverse Fourier transform, the result must also be multiplied by the factor $\exp[\text{Im}(k)s]$, with s the distance between driving and test particles.) As example geometry we consider that of a typical cell of the NLC accelerating structure known as the damped, detuned structure (DDS)[7]. One simplification in our model, however, is that the irises are not rounded, unlike those in the real structure. The dimensions are $a = 4.924$ mm, $g = 6.89$ mm, and $L = 8.75$ mm (note that for the average, high-frequency impedance neither the cavity radius b , nor the coupling manifolds that couple through slots at $r = b$ in the DDS, play a role).

The numerical results, giving the real (R_L) and imaginary (X_L) parts of the impedance Z_L , when $\text{Im}(k) = 0.5 \text{ mm}^{-1}$, are given in Fig. 1 (the solid curves). We note that this impedance is indeed a relatively smooth function of $\text{Re}(k)$ (on the real axis, R_L would be a collection of many infinitesimally-narrow spikes). We should point out, however, that with this method, to get good convergence in the solution at high frequencies, the size of the matrix that needs to be solved becomes very large: at $k_R = 200 \text{ mm}^{-1}$ its size is $\sim 600 \times 600$. In Fig. 3 the dashed curves give the analytical result, Eq. 1 with $\alpha = 0.52$. We see that agreement is good for frequencies $ka \gtrsim 1.5$.

The impedance was calculated for several values of g/L with the field matching program, keeping the other dimensions fixed. The results, for fixed $\text{Im}(k)$, become bumpier as g/L decreases, due to the shorter reflection time $2g/c$ of a wave between irises; and for the calculations we let $\text{Im}(k) \sim 2/g$. Then to obtain α , the numerically obtained $\text{Re}(1/Z_L)$ was fit to the form $f(k) + \alpha g(k)$ (with f and g known functions taken from Eq. 1). The results of the fit are given in Fig. 2 (the plotting symbols). The agreement is relatively good, though, due to residual bumpiness in the impedance curve, the accuracy of the fit to the numerical result is limited to $\sim 10\%$.

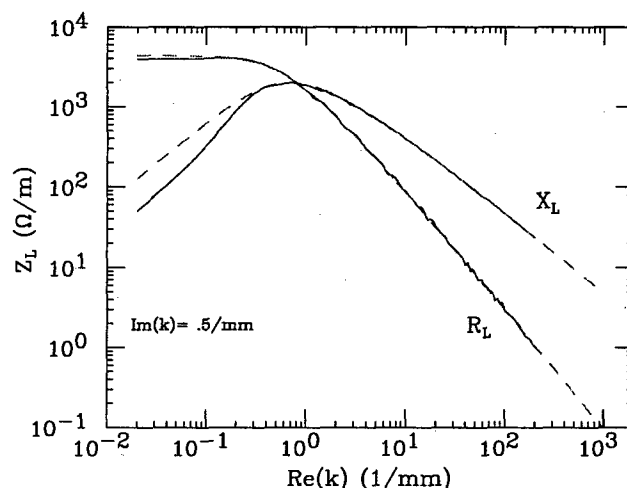


Figure 3: The real (R_L) and imaginary (X_L) parts of the impedance for the dimensions of the average NLC cell, as obtained by field matching (solid lines). The dashes represent Eq. 1 with $\alpha = 0.52$.

4 CONCLUSIONS

We have extended R. Gluckstern's analytical result for the high-frequency, longitudinal impedance of a periodic accelerating structure, a result valid for small gaps, to one valid for all gap to period ratios. We have, in addition, performed numerical calculations and obtained results that confirm the analytical result to an accuracy of $\sim 10\%$.

5 REFERENCES

- [1] R. Gluckstern, *Phys. Rev. D* **39**, 2773 (1989); and R. Gluckstern, *Phys. Rev. D* **39**, 2780 (1989).
- [2] E. Keil, *Nucl. Instr. Meth.* **100**, 419 (1972).
- [3] S. Heifets and S. Kheifets, *Phys. Rev. D* **39**, 960 (1989).
- [4] G. Stupakov, Proc. of IEEE Part. Acc. Conf., Dallas, 1995, p. 3303.
- [5] K. Yokoya, KEK Report 90-21, September 1990, p. 142-150.
- [6] K. Bane, *et al*, "Calculations of the Short Range Longitudinal Wakefields in the NLC Linac," Presented at ICAP'98, Monterrey, CA, Sept. 1998, and SLAC-PUB-7862(Revised), Nov. 1998.
- [7] "Zeroth-Order Design Report for the Next Linear Collider," SLAC Report 474 (1996).

OBTAINING THE BUNCH SHAPE IN A LINAC FROM BEAM SPECTRUM MEASUREMENTS

K.L.F. Bane, F.-J. Decker, F. Zimmermann, SLAC, Stanford, USA*

1 INTRODUCTION

In linacs with high single-bunch charge, and tight tolerances for energy spread and emittance growth, controlling the short-range wakefield effects becomes extremely important. The effects of the wakefields, in turn, depend on the bunch length and also on the bunch shape. It was shown in the linac of the Stanford Linear Collider (SLC), for example, that by shaping the bunch, the final rms energy spread could be greatly reduced, compared to for the standard Gaussian bunch shape[1]. Therefore, in machines with high single-bunch charge, a method of measuring bunch shape can be an important beam diagnostic.

In a linac with low single-bunch charge, the longitudinal bunch shape can be obtained relatively easily from a single measurement of the beam's final energy spectrum, provided that the final to initial energy ratio is large. One merely shifts the average phase of the beam, so that it rides off-crest sufficiently to induce an energy variation that is monotonic with longitudinal position. Then, by knowing the initial and final energies, the rf wave number, and the average beam phase, one can directly map the spectrum into the bunch shape. In a linac with high single-bunch charge, however, due to the effect of the longitudinal wakefield, this method either does not work at all, or it requires such a large shift in beam phase as to become impractical.

In earlier work[2],[3] it was shown that, even when wakefields are important, if one measures the final beam spectrum for two different (properly chosen) values of beam phase, then one can again obtain the bunch shape, and—as a by-product—also the form of the wakefield induced voltage; this method was then illustrated using data from the linac of the SLC. These SLC measurements, however, had been performed with the machine in a special configuration, where the current was low; in addition, the noise in the data was low and the measured spectra were smooth distributions. Under normal SLC conditions, however, the currents were higher, and it was difficult to get the required separation in phase for the two measurements (the required separation increases with current); and the measured spectra were not smooth functions. Under such conditions, the above method works poorly or fails.

If we know the Green function wake of the linac, however, we can still obtain the bunch shape from beam spectrum measurements. In this report, we present two such methods. One requires one spectrum measurement and involves the solution of a Volterra integral equation. The other requires a knowledge of upstream beam and transport properties and involves a least squares minimization

to simulated spectra. We then apply these methods to data from the SLC.

2 THEORY

Consider a bunch of charged particles that are accelerated in a linac from initial energy E_0 to final energy E_f . Let us assume that $E_f/E_0 \gg 1$, so that we can ignore the component of energy variation that is uncorrelated with longitudinal position. Then the relative energy of a particle at position z within the bunch (we take the convention that a more negative value of z is more to the front) at the end of the linac becomes

$$\delta(z) = [E_0 + E_a \cos(kz + \phi) + eV_{ind}(z)]/E_f - 1, \quad (1)$$

with E_a the total peak energy gain, k the rf wave number, and ϕ the average beam phase; with $V_{ind}(z)$ the induced voltage, given by

$$V_{ind}(z) = -eNL \int_0^\infty W_z(z') \lambda_z(z - z') dz' \quad , \quad (2)$$

where N is the bunch population, L the total length of accelerating structure in the linac, W_z the Green function wakefield, and λ_z the bunch shape. If the final energy E_f is fixed, as in the SLC with energy feedback on, E_a is also an unknown given by

$$E_a = [E_f - E_0 + eNLk_{tot}]/\langle \cos(kz + \phi) \rangle \quad , \quad (3)$$

with $k_{tot} = -\langle V_{ind} \rangle / (NL)$ the loss factor[†].

By knowing both $\lambda_z(z)$ and $\delta(z)$ over the bunch length we can compute the energy distribution $\lambda_\delta(\delta)$. Conversely, if we know $\lambda_\delta(\delta)$ and $\delta(z)$, we can calculate $\lambda_z(z)$, provided $\delta(z)$ is monotonic over the bunch. Let us assume that this is the case. Then

$$\lambda_z(z) = \lambda_\delta(\delta(z)) |\delta'(z)| \quad (4)$$

Suppose now that we know E_0 , E_f , k , and ϕ . Without knowing the induced voltage we cannot, in general, obtain λ_z from λ_δ , since δ depends also on V_{ind} . Only if eV'_{ind} is small compared to $\delta' E_f$ over the bunch does a single measurement of λ_δ suffice to give λ_z .

We now describe three possible solution strategies for the case when the wakefields cannot be neglected. The most suitable one in a given situation depends upon what is known and on properties of the data.

[†]In Ref. [3], the term $\langle \cos(kz + \phi) \rangle$ in Eq. 3 was replaced by $\cos(\phi)$, an approximation that did not affect the result greatly, except that the area under λ_z in the solution was found not to equal 1.

*Work supported by Department of Energy contract DE-AC03-76SF00515.

2.1 Both W_z and λ_z are Unknown

Suppose we measure the bunch spectrum twice: with the beam at phase ϕ^a we obtain λ_δ^a , and then with the beam at ϕ^b we obtain λ_δ^b . We assume the phases are chosen so that $\delta(z)$ is monotonic for both measurements. For the first measurement Eq. 4 becomes

$$\lambda_z(z) = \lambda_\delta^a [E_a^a k \sin(kz + \phi^a) - eV'_{ind}(z)] / E_f, \quad (5)$$

and a similar equation, with superscript b replacing superscript a , holds for the second measurement. Combining these two equations we obtain

$$eV'_{ind}(z) = k \frac{[E_a^a \lambda_\delta^a \sin(kz + \phi^a) \pm E_a^b \lambda_\delta^b \sin(kz + \phi^b)]}{\lambda_\delta^a \pm \lambda_\delta^b} \quad (6)$$

In Eq. 6 (and below) the upper symbol of \pm applies if the sign of $\delta'(z)$ is different for the two measurements, otherwise the lower symbol applies. The right hand side of Eq. 6 is a function both of z and—through the argument of λ_δ —of $V_{ind}(z)$. Eq. 6 is therefore a first order non-linear differential equation which we can solve numerically for the unknown $V_{ind}(z)$. As initial condition we take V_{ind} at the front of the bunch to be zero. Once V_{ind} is known we obtain λ_z using

$$\lambda_z(z) = k \lambda_\delta^a \lambda_\delta^b \frac{[E_a^a \sin(kz + \phi^a) - E_a^b \sin(kz + \phi^b)]}{E_f |\lambda_\delta^a \pm \lambda_\delta^b|} \quad (7)$$

We begin by setting $V_{ind} = 0$, $k_{tot} = 0$, and $\langle \cos(kz + \phi) \rangle = \cos(\phi)$. Then we solve, in order, Eqs. 3, 1, 6, and 7, and then iterate. We have the correct answer when the area under λ_z is 1. We see from Eq. 7, that for accuracy in λ_z we want two measurements from opposite sides of the rf crest. One problem with this, especially at higher currents, however, is that for the $\phi > 0$ measurement one may need to go way off-crest (which may not be possible) in order that λ_δ at the front of the beam—where the calculation begins—be monotonic.

2.2 W_z is Known, λ_z is Unknown

If we assume that $W_z(z)$ is known, and again that the total voltage is monotonic, then one measurement $\lambda_\delta(\delta)$ suffices for obtaining $\lambda_z(z)$. Eq. 5 can be written as

$$\lambda_z(z) = \frac{\pm \lambda_\delta}{E_f \mp e^2 N L W_z(0) \lambda_\delta} \left[E_a k \sin(kz + \phi) + e^2 N L \int_{-\infty}^z W_z(z - z') \lambda_z(z') dz' \right], \quad (8)$$

where the upper(lower) symbols represent the case of $\phi > (<) 0$. Eq. 8 is a Volterra integral equation of the second kind, which can be readily solved numerically.

As a measurement, we prefer one with $\phi < 0$, where the front of the beam is not near the rf crest. Our method of solving for λ_z is as follows: Initially we let $V_{ind} = 0$,

$k_{tot} = 0$, and $\langle \cos(kz + \phi) \rangle = \cos(\phi)$. We solve Eq. 3, then Eq. 1, then Eq. 8. Having obtained a first estimate of $\lambda_z(z)$, we can then obtain a first estimate of $V_{ind}(z)$ (using Eq. 2), k_{tot} , and $\langle \cos(kz + \phi) \rangle$. The process is then iterated until the area under λ_z equals 1.

2.3 Least Squares Fitting Method

If $\delta(z)$ is not monotonic the above methods fail. In such a case, however, we can use a least squares approach. In many linacs the longitudinal distributions of the beam at some position upstream of the linac are known, and the transport from this position to the linac is also well known. In the example of the SLC linac, the bunch shape and energy distribution in the damping rings is fairly well known, as are properties of the compressor section leading from the ring to the linac. We can simulate the development of longitudinal phase space from the known position to the end of the linac. Note that to do this we need to know W_z in the linac. We can define an objective function:

$$y = \int [(\lambda_\delta)_{meas} - (\lambda_\delta)_{calc}]^2 d\delta, \quad (9)$$

with $(\lambda_\delta)_{meas}$ and $(\lambda_\delta)_{calc}$, respectively, the measured and calculated energy distributions. We minimize the objective function by varying parameters in the system that we know imperfectly. If the fit is good, we can believe the calculated bunch shape. This method can work well if there are few unknowns, and if these unknowns have orthogonal effects (a subject which we have not systematically studied). Note that even though the least squares method does not require a monotonic $\delta(z)$, to obtain accurate results we still need a widened spectrum measurement.

3 APPLICATION

The measurements that we analyze come from the SLC linac. They were performed on July 7, 1997 with a wire monitor (with a dispersion of 70 mm) in the BSY region on the north side (the electron side). The parameters were $N = 1.9 \times 10^{10}$, $E_0 = 1.19$ GeV, $E_f = 46$ GeV, $k_{rf} = 60 \text{ m}^{-1}$, and $L = 2733$ m; the peak rf voltage of the damping ring was 800 kV; the bunch compressor voltage was set to $V_c = 41.8 \text{ MV}^\dagger$. The linac phase knob was first calibrated. Then for several phase settings the beam spectrum was measured, all the while keeping the feedback in final energy on. The measured rms energy spread, σ_δ , and the full-width-at-2-max/3.59, $\tilde{\sigma}_\delta$, are shown in Fig. 1, and six representative spectra are shown in Fig. 2 (the plotting symbols).

First we apply the least squares method. In the SLC the beam leaves a damping ring, goes into a bunch compressor, and then enters the linac. In the damping ring the bunch shape can be described as a tilted Gaussian in z , given by

$$\lambda_z \approx \frac{1}{\sqrt{2\pi}\sigma_z} \exp \left[\frac{-z^2}{2\sigma_z^2(1 \pm \epsilon)^2} \right], \quad (10)$$

[†]The reading was actually 5% higher, but historically this compressor has been known to read low by this amount.

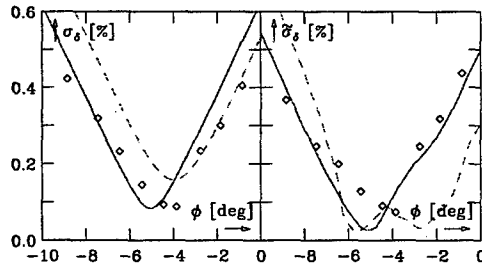


Figure 1: The rms energy spread (left) and full width at 0.2max/3.59 (right) of the measured spectra (the plotting symbols). Simulation results for $\phi_c = 90^\circ$ (dashes) and $\phi_c = 102^\circ$ (solid curves) are also given.

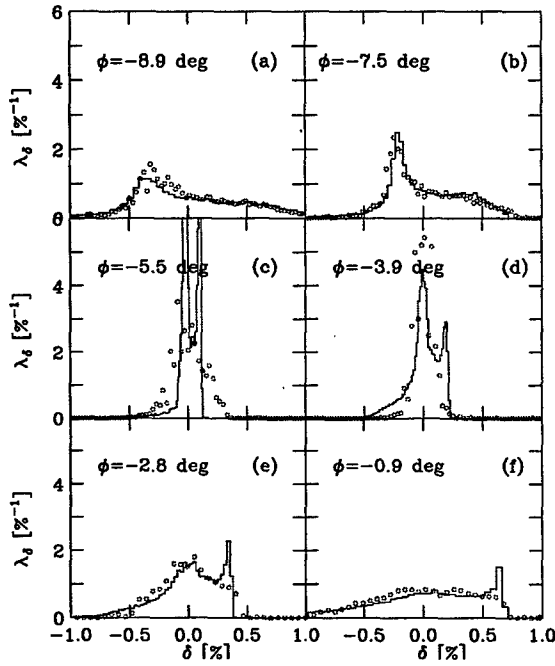


Figure 2: Six representative measured spectra (symbols); and simulation results for $\phi_c = 102^\circ$ (histograms).

with parameters rms length σ_z and asymmetry factor ϵ ; and a Gaussian in δ , with rms σ_δ . In this case we take $\sigma_z = 5.75$ mm, $\epsilon = .27$, and $\sigma_\delta = .085\%$ [4]. The wakefield for the SLAC linac is found in Ref. [5]. In the transport to the end of the linac, we know E_0 and E_f well, which leaves us with three parameters: the compressor voltage V_c , the compressor phase ϕ_c , and the linac phase ϕ . In our analysis we let these three parameters vary to minimize the objective function, Eq. 9. We obtained the expected result for V_c and ϕ ; however, the optimal ϕ_c was 102° , not the expected 90° . Simulation results for $\phi_c = 102^\circ$ and 90° are given by the curves in Fig. 1; and for the case $\phi_c = 102^\circ$, by the histograms in Fig. 2. Since these fits are good, we can believe the calculated bunch shape. The calculated bunch shape and spectrum for the optimum case are given in Fig. 3 (the solid curves) and compared with those for the case $\phi_c = 90^\circ$. We see that the latter case cannot possibly be correct (compare with Fig. 2b). For the optimized case, $z_{rms} = 1.2$ mm and $z_{FWHM} = 2.8$ mm.

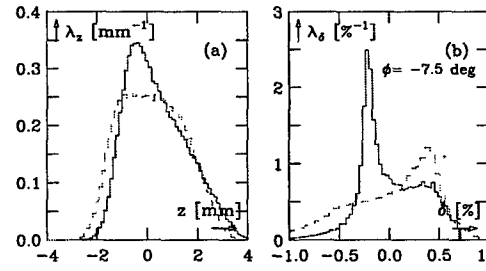


Figure 3: Bunch shape and spectrum obtained by the least squares method, with $\phi_c = 102^\circ$ (the solid curves). The results with $\phi_c = 90^\circ$ are also shown (the dashes).

Finally, we apply the Volterra integral equation method to the data of Fig. 2a and 2b (see Fig. 4). Note that the two results give almost the same bunch shape and induced voltage, and that the bunch shape agrees well with the result of the least squares method (Fig. 3a, the solid curve).

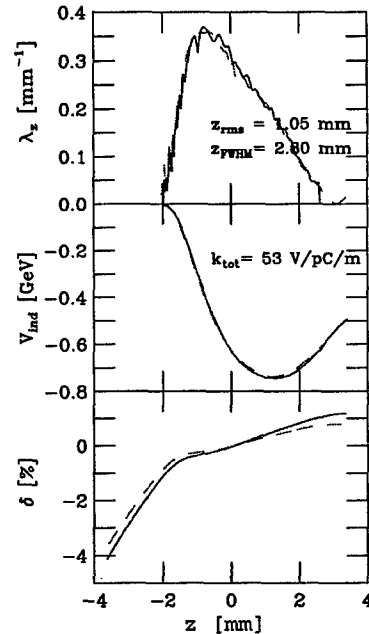


Figure 4: Results of the Volterra integral equation method, using data of Fig. 3a (solid curves) and 3b (dashes).

4 ACKNOWLEDGEMENTS

The authors thank M. Minty, P. Raimondi, and J. Seeman for having contributed to data taking on this topic.

5 REFERENCES

- [1] F.-J. Decker, *et al*, Proc. of LINAC94, Tsukuba, 1994, p. 47.
- [2] K. Bane, SLAC/AP-80 (1990).
- [3] K. Bane, *et al*, Proc. of IEEE Part. Acc. Conf., Vancouver, Canada, 1997, p. 1876.
- [4] R. Holtzapple, SLAC-R-0487, PhD Thesis, June 1996.
- [5] K. Bane and P. Wilson, Proc. of the 11th Int. Conf. on High-Energy Acc., CERN, 1980, p. 592.

DYNAMICS OF SPACE-CHARGE DOMINATED ELECTRON BEAMS IN CROSSED $E \times B$ -FIELDS *

A. V. Agafonov[†], Lebedev Physical Institute, Moscow, Russia

Abstract

Problems of nonlinear dynamics of space-charge dominated electron beams in crossed $E \times B$ -fields are discussed. The review of the results of computer simulations of an electron clouds formation due to nonlinear azimuthal instability inside magnetically isolated coaxial diodes (magnetron guns) under the condition of strong nonuniform secondary self-sustaining emission and pure thermionic emission is given. Emphasised is the dominant influence of a feedback on dynamics of electron beam modulation and on arising of a leakage current to an anode across an external magnetic field. A scheme of storage and capture of electron beams in crossed $E \times B$ -fields due to transient processes is proposed.

1 INTRODUCTION

Theoretical and experimental investigations of the dynamics of space-charge dominated rectilinear beams considered as a new physics subject, are receiving more and more attention in recent years. At the same time, a similar but more complex subject, space-charge dominated beams in crossed $E \times B$ -fields, finds practical applications and has been investigated over a long period of time but without notable success in theory. Suffice it to note that there does not yet exist a clear theoretical description even of the pre-generation operation of a classical (low-voltage) magnetron or the regime of magnetic insulation disturbance in high-current coaxial diodes. The physics of instruments with crossed fields is complex due to the strong nonlinearity of the processes and the necessity to take into account nonstationary effects.

2 PHYSICAL PROCESSES IN DEVICES WITH CROSSED FIELDS

The physical characteristics of the processes under consideration are partially presented in works [1 – 6].

Usually, to describe electron flow in so-called magnetron diodes (MD), one uses stationary models of Brillouin flow, in which it is not possible to describe the escape of particles from an emitting surface, or kinetic dual-velocity flow, in which it is possible [1]. For system in which extraction of the electron beam in the axial direction is absent, the applicability of such analytical models is complicated by the influence of the pre-history of flow formation. In particular, we can immediately note that for such systems the increase of voltage on the MD should lead to capture

of some of the emitted particles in acceleration gap which circulate around the cathode without returning to it. Hence, the value of the radial electric field on the cathode surface depends not only on emission current but on the magnitude of accumulated circulating charge in the acceleration gap.

Dividing the flow into two components, namely, one circulating during many turns and maintaining information on possible nonuniformities, and the other emitting from the cathode and returning to the cathode during a time of the order of a period of cyclotron rotation, leads to conditions arising for the development of azimuthal instability of the flow. However, without the provision of a number of additional conditions, this instability causes only weak azimuthal modulation of the flow and is not accompanied by the development of leakage current at the anode across an external magnetic field exceeding the threshold value for magnetic insulation.

Strong azimuthal modulation of flow accompanied by the development of leakage current at the anode, i.e., passing over of azimuthal instability to a strongly nonlinear regime in which an exchange of energy and momentum occurs between particles and the rotating self-consistent crossed $E \times B$ -field, can occur in two cases. First, if emission current is not too large and information about the developing structural flow is not carried to the cathode by the returning flow of electrons. Second, if feedback exists on the emitting surface of the cathode providing proper phasing of emitted particles that increases the degree of azimuthal variation of flow and, accordingly, discards part of the emitted particles not in proper phase.

Instability is saturated at a level of leakage currents at the anode which can amount to several percent of I_{CL} (Child-Langmuir current). Then, electron flow constitutes a self-organizing, regular (in the azimuthal direction), rotating structure of dense electron bunches. Such a structure rotates with approximately the same angular velocity and exists for a long time. Dynamic equilibrium is established between the current of emitted particles and return current to the cathode and current to the anode. The special feature of this dynamic equilibrium is the long presence of emitted particles in the acceleration gap, which considerably exceeds the period of cyclotron rotation [1 – 4].

Feedback on the emitting surface, promoting the development of strong azimuthal instability, is particularly effective when using a cathode with secondary emission of electrons. The sharp nonuniform character of secondary emission, depending in turn on flow structure, leads to the formation of alternating radial electric field at a given cathode azimuth due to rotation of the modulated flow as a whole. The average radial electric field at the cathode can be close

* Work supported by RFFI under grant 99-02-17590.

[†] Email: agafonov@sci.lpi.ac.ru

to zero. At the same time, the emission of particles in improper phases is simply suppressed by the negative value of the field, and the emission of particles in proper phases is sharply increased due to boundary effects [5].

The type of operation of an MD with a secondary-emission cathode depends on the maximal voltage and rate of voltage rise on the gap. For low voltages, characteristic for classical magnetrons, a regular azimuthal structure of flow arises on the flat top of a pulse and is maintained over a long period of time.

For higher voltages (above approximately 100 kV), the regular structure is formed on the long leading edge of the voltage, and when passing over to the flat top there begins a debunching of the original structure and formation of a new one, with a different number of azimuthal variations, if the voltage does not exceeds a certain maximal value. Exceeding this maximum in the process of rising voltage results in disruption of the self-maintenance regime of secondary emission. The physical feature of such a regime is that, at high voltage and accumulation of a large space charge in dense bunches, the energy spectrum of electrons returning to the cathode is significantly shifted in the direction of larger energies and exceeds that is optimal for maximal yield of secondary electrons. The sharp drop in secondary emission current leads to elimination of the "mismatched" part of the electron flow, and the particles remaining in the gap form, in the main, captured circulating flow. Such a regime is realized if primary current of low intensity is switched off after entering the regime of self-maintenance of secondary emission.

Practically, such systems represent a new class of flows — flows with a variable number of particles. The growth of azimuthal instability in such a system is possible only under conditions when accumulated information in the flow is not carried to the electrodes. In particular, for uniform emission of a primary beam with current comparable with the current of secondary emission, instability develops weakly.

A demonstrative example is the development of instability in pure primary beam emitting uniformly in azimuth. The results of computer simulations show that in a regime of current limited by space charge, azimuthal instability does not develop at all. However, it does become strong and accompanied by significant leakage current if it turns out that the cathode is operating in a regime of saturation. Then, the normal component of the electric field at the cathode differs from zero and the development of weak azimuthal instability increases as in the case of nonuniform secondary emission due to proper phasing of emitted particles. The difference will respect to the case of nonuniform secondary emission is only that the radial electric field at the cathode surface is not alternating, i.e., there is no direct suppression of emission from the cathode. However, large oscillation of field due to azimuthal bunching of beam promotes bunching of some of the electrons with proper phases relative to the rotating $E \times B$ -field, which are in the gap for a long time. It also promotes the return of electrons in improper phases (and, accordingly, not matched with the

field) back to the cathode in significantly less time. In the case of uniform space-charge limited emission, information about the development of weak instability comes to the cathode by returning particles. The density of those close to the cathode is high and only a small number of them can exist in the flow for a long time.

3 CAPTURE AND ACCUMULATION OF BEAM IN CROSSED FIELDS

The conditions for possible interruption of secondary emission current for the aforementioned reasons or, for example, by increasing the external voltage, which is accompanied also by the initial discarding of a part of the flow and its subsequent detachment from the cathode, require special attention. This is because they permit to realize a process of accumulation and capture of electron beam in crossed fields which circulates so that electrons cannot return to the cathode nor reach the anode.

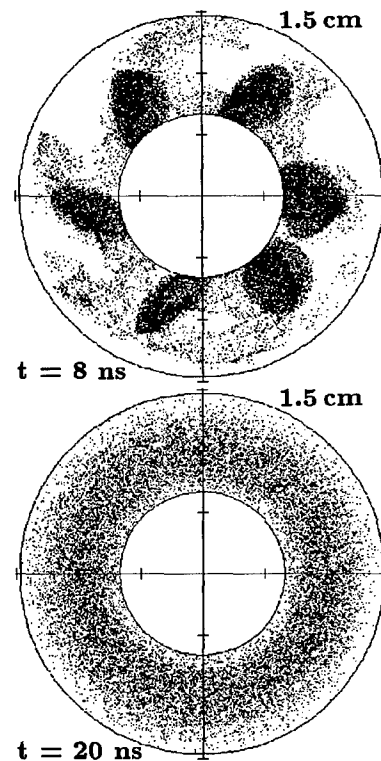


Figure 1: Configurations of flow at $t = 8$ ns and $t = 20$ ns.

The number of particles in a captured circulating beam can be sufficiently large for possible subsequent acceleration, including with high-frequency cycles, for example, in betatron-type systems. Such systems can also be used as injectors for classic accelerators.

Below, examples are given which illustrate the possibility of accumulating an electron flow having a number of particles at the level of 10^{12} per centimeter of length axially in a compact system with crossed fields. In this case, the lateral dimensions are several centimeters, the voltage is at

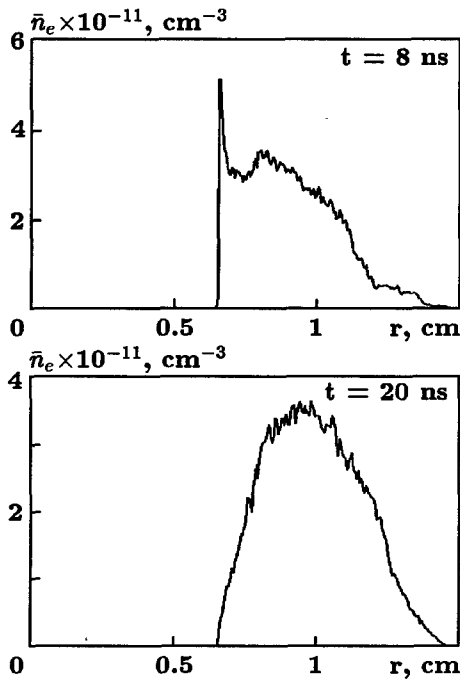


Figure 2: Averaged densities at $t = 8$ ns and $t = 20$ ns.

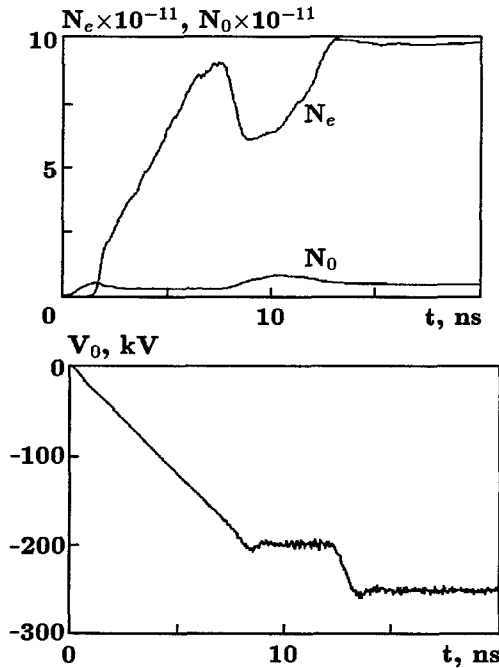


Figure 3: Dynamics of accumulation of secondary electrons $N_{e,s}$ and the form of the voltage.

the level of 100 – 200 kV and the external magnetic field is about of 3 kGs.

Computer simulations were performed using electromagnetic PIC-code KARAT [7] in two-dimensional $r - \theta$ geometry. Examples of calculations demonstrating physical features of processes in 2D and 3D-geometries are presented in an accompanying report [6]. For subsequent ac-

celeration of captured flow, one can use a betatron field and cut electrodes that do not hinder the formation of electron flow nor the penetration of the external longitudinal magnetic field.

The main idea consists in the following. After formation in an MD of electron flow with regular structure, total charge in the system still remains less than the limiting value and can be increased by raising the voltage on the MD. Growth of voltage leads to re-bunching of flow and change of azimuthal structure due to feedback disruption. During this process, azimuthal modulation of flow disappears and the flow becomes close to uniform in azimuth. Significant momentum spread of particles has a stabilizing effect on the existence of such a flow. A further increase in voltage results in the detachment of the flow from the cathode. The return bombardment of the cathode ceases, secondary emission current disappears, and leakage current at the anode is practically absent, i.e., there forms between the electrodes of the MD a captured circulating flow with a large number of particles.

Fig. 1 shows azimuthal structures of flows at different instants. The distribution of density along the radius, averaged over the azimuth, is presented in Fig. 2 for these two instants. The dynamics of accumulation of particles and voltage profile are shown in Fig. 3.

4 CONCLUSION

Problems of nonlinear dynamics of space-charge dominated electron beams in crossed ExB-fields are discussed from the point of view of the investigation of schemes of intense electron beam formation for compact cyclic accelerators and for high-efficiency relativistic magnetrons. The review of the results of computer simulations of an electron clouds formation due to nonlinear azimuthal instability inside magnetron is given. A scheme of electron storage and capture of electron beams in crossed fields is proposed.

5 REFERENCES

- [1] Agafonov A.V., Voronin V.S. Proc. of 1997 Particle Accelerator Conf., Vancouver, Canada. 1997, v. 2, 1302 – 1304.
- [2] Agafonov A.V., Fedorov V.M., Tarakanov V.P. Ibid., v. 2, 1299 – 1301.
- [3] Agafonov A.V., Krastelev E.G. Ibid., v. 3, 3141 – 3143.
- [4] Agafonov A.V., Fedorov V.M., Tarakanov V.P. Proc. of 12th International Conference on High-Power Particle Beams, Haifa, Israel, 1998.
- [5] Agafonov A.V., Lebedev A.N., Voronin V.S. Proc. of the 1995 Particle Accelerator Conf., Dallas, USA. 1995, v. 5, 3269 – 3271.
- [6] Agafonov A.V., Fedorov V.M., Tarakanov V.P. Proc. of 1999 Particle Accelerator Conf., New-York, USA. Report TUP109.
- [7] Kotetashwily P.V., Rybak P.V., Tarakanov V.P. Institute of General Physics, Moscow, Preprint N 44, 1991.

SELF-SUSTAINING SECONDARY EMISSION IN MAGNETRON GUNS, BEAM MODULATION AND FEEDBACKS *

A. V. Agafonov[†], Lebedev Physical Institute, Moscow, Russia

V. M. Fedorov, V. P. Tarakanov, High Energy Density Research Center, IVTAN, Moscow, Russia

Abstract

Problems of magnetic insulation violation inside a vacuum coaxial diode with dense electron flow are considered. The numerical model of nonstationary nonuniform secondary electron emission provoked by primary low-intensity beam from a cathode was developed. The results of computer simulations of electron cloud formation due to nonlinear azimuthal instability under the condition of strong nonuniform secondary self-sustaining emission are described. The existence of an instability with transverse quasistationary leakage current of a few percent of Child-Langmuir current and rotating states of electron flow has been shown under conditions of conservation of full power and full momentum of the system. Emphasised is the dominant influence of a feedback on dynamics of electron beam modulation and on arising transverse leakage current to the anode across the external magnetic field exceeding the critical magnetic field of magnetic insulation. Strong azimuthal instability exists if the current of primary beam is much less than the secondary emission current. If these currents are comparable, the instability is weak and decays in time due to the absence of strong azimuthal inhomogeneity of secondary emission current. In the case of the emission of primary beam alone (secondary emission absent), deep modulation and leakage current arises only if the condition of saturated regime of a cathode is satisfied. Such behaviour is conditioned by a feedback on the emitting surfaces similar to the case of nonuniform secondary emission which provides additional correct azimuthal modulation of electron flow by rotating crossed $E \times B$ -field and amplifies the instability. No azimuthal instability is observed if the current of primary beam is space-charge limited. The results of 2.5-D and 3-D computer simulations are presented.

1 INTRODUCTION

This paper reports on computer simulations of an electron cloud formation inside a smooth-bore magnetron. Preliminary results were published in [1 – 3]. Computer simulations have been performed using 2.5D and 3D electromagnetic PIC code KARAT [4] for the magnetron diode (MD) with parameters close to experimental [5], and with an external voltage source $V_0(t)$ connected to MD via an RL-circuit. The yield of secondary electrons from the cathode takes into account the dependence of the yield on the ener-

gy of electrons and the angle between the direction of electron velocity and the perpendicular to the cathode surface, and also the threshold of secondary emission.

2 DYNAMICS OF SELF-SUSTAINING SECONDARY EMISSION BEAM IN MD

The main parameters of MD are: radius of the anode $r_A = 0.53$ cm, radius of the cathode $r_K = 0.33$ cm; external longitudinal magnetic field $B_0 = 2.5$ kG ($B_0/B_{cr} \approx 1.15$, $\omega_{ec}/2\pi = 7$ GHz, period of cyclotron rotation 0.14 ns); the voltage rise time to maximum value of $V_{0m} = 12$ kV was varied from 2 to 10 ns; maximum emission current of the primary beam $I_{em} = 3$ A. For given voltage and geometry of MD the Child-Langmuir current through the MD without a magnetic field equals approximately $I_{CL} \approx 200$ A (here and below currents and charge densities correspond to linear values per cm of length in the longitudinal direction). Electrotechnical parameters are $\tau_{L/R} = 0.25$ ns, $\tau_{RC} = 0.24$ ns, where C is the capacitance of MD. Drift velocity of electrons in crossed fields is $\bar{v}_{e\theta} = cE_0/B_0 = 2.4 \times 10^9$ cm/s, if the electric field is estimated as V_{AK}/d_{AK} .

The process of electron cloud formation inside an axisymmetrical MD under the condition of homogeneous initial emission of low current primary beam from a cathode starts due to inevitable presence of electric field fluctuations in rotating flow of electrons stored inside the gap for the time of the growth of the external voltage. Weak azimuthal instability is amplified by nonuniform secondary emission and a feedback on the surface of the cathode. Under conditions of conservation of full energy and momentum a part of the electrons lose energy under the action of the field and drifts to larger radii towards the anode. Another part of the electrons increases its energy and returns to the cathode with an energy exceeding the threshold value for secondary emission. In view of indicated reasons, the emission of secondary electrons is nonuniform. This effect leads to an intensification of the cathode back-bombardment process and to fast and effective growth of secondary electrons inside MD. The secondary-emission current exceeds the primary-beam current by more than an order of magnitude and subsequently exerts a determining action on the operation of the MD. The MD passes over to a condition of self-sustaining emission and the primary beam could be switched off. After the transient process, a stable formation consisting of several bunches is formed in this geometry. Electron clouds rotate as a whole with

* Work supported by RFFI under grant 99-02-17590.

[†] E-mail: agafonov@sci.lpi.ac.ru

approximately constant angular frequency.

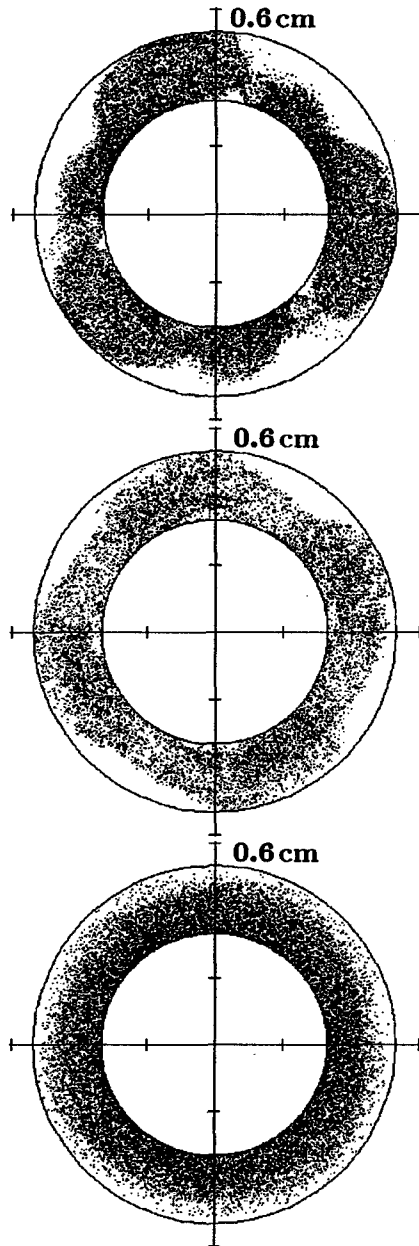


Figure 1: Stable configuration of secondary emission flow (top), primary flow in saturated working regime of the cathode (middle) and primary space-charge limited flow (bottom).

The feedback on the surface of the cathode exerts the dominant influence on the growth of the instability and on arising of a transverse leakage current to the anode across the external magnetic field exceeding the critical magnetic field of magnetic insulation. This feedback is conditioned by right phasing of a part of secondary emitted electrons by rotating crossed $E \times B$ -field. These electrons are captured inside rotating modulated electron flow and stay inside the gap for many revolutiones around the cathode, maintaining its azimuthal and time structures. Another part of sec-

ondary emitted electrons can stay inside the gap only for a small time comparable with the period of cyclotron motion because they are forced to return to the cathode by the radial component of rotating crossed $E \times B$ -field, which changes its direction during the rotation of the flow as a whole.

The regime of self-sustaining secondary emission in MD is characterized by the average radial component of electric field on the cathode surface, which is close but not equal to zero. At given azimuth of the cathode surface it oscillates with a frequency equal to the average rotating frequency of the flow as a whole times the number of bunches, and with amplitudes varying from -10 up to 30 — 40 kV/cm.

Note that strong azimuthal instability occurred only if the current of primary beam is small in comparison with the full current of self-sustaining secondary emission.

Fig. 1 (top) shows stable configuration of electron flow inside the MD with secondary emission cathode.

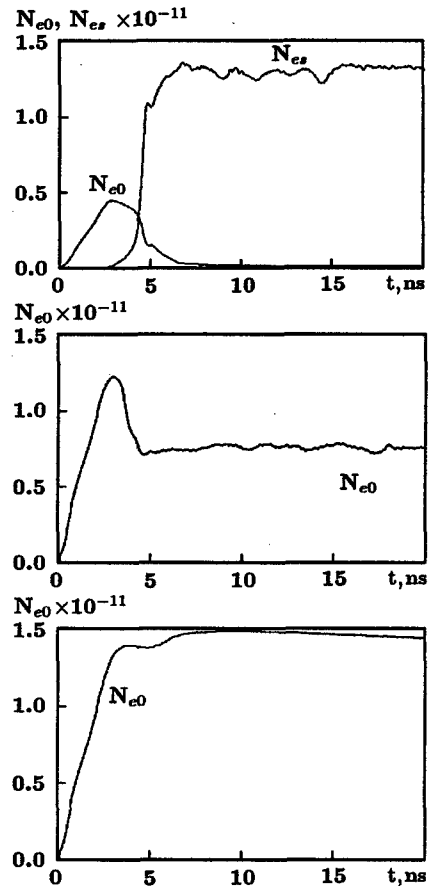


Figure 2: Dynamics of store of electrons inside the gap for the above mentioned cases.

Fig. 2 (top) shows dynamics of store of primary N_{e0} and secondary N_{es} electrons inside MD. The time behaviour of radial electric field near the surfaces of the cathode is shown in the top of Fig. 3.

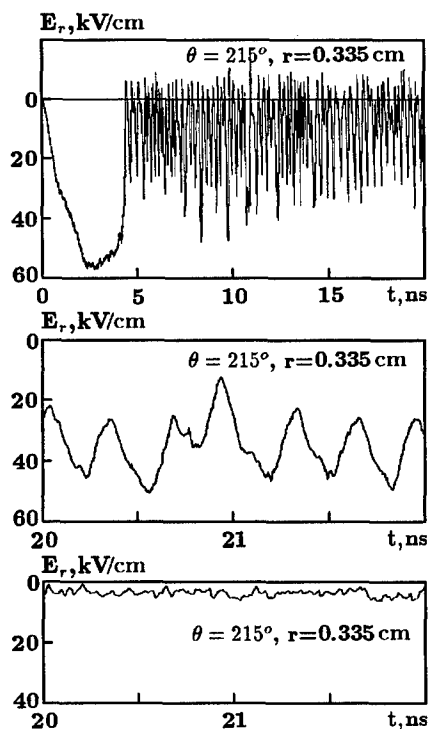


Figure 3: Behaviour of the radial electric field near the surface of the cathode for the aforementioned cases.

3 DYNAMICS OF PRIMARY BEAM AND OF MIXED SECONDARY AND PRIMARY BEAMS IN MD

Investigation of an instability of pure primary beam of different currents up to space-charge limited current homogeneously emitted from a cathode of MD (an MD with a thermionic cathode without secondary emission) shows that under condition of space-charge limited current no azimuthal instability occurs. Deep azimuthal modulation of the flow and leakage current to the anode arises only if the condition of saturated regime (normal component of electric field does not equal zero) of a cathode is satisfied. The behaviour is conditioned by the same feedback on the emitting surface providing additional correct azimuthal modulation of emitted particles similar to the case of secondary emission. The difference is that the radial electric field does not change its direction on the surface of the cathode, but oscillates with large amplitude. In the middle of Fig. 1 stable configuration of the flow of primary electrons inside the MD without secondary emission and the cathode operating in the saturated regime are shown. The bottom figure shows stable configuration for the case of space-charge limited current of primary electrons. In the middle and in the bottom pictures of Fig. 2 dynamics of store of primary N_0 inside MD are shown for aforementioned cases. The time behaviour of radial electric field near the surfaces of the cathode for aforementioned cases is shown in Fig. 3.

In the case when the current of primary beam is comparable with the current of secondary-emission beam the be-

haviour of the electron flow for later time is similar to the case of space-charge limited primary beam. The charge of primary beam emitted homogeneously from the cathode influenced the character of secondary emission and smoothes over a nonuniformity of secondary emission due to additional suppression of radial electric field on the cathode surface. Secondary-emission current increases initially and then drops to a value which provides the fall of radial electric field on the cathode surface to close to zero. Azimuthal modulation of the flow and leakage current to the anode do not exist in this case. However, they arise for a time if the current of primary beam decreases approximately by an order of its initial value.

4 3D COMPUTER SIMULATION

Presented above results obtained for 2-dimensional $r - \theta$ geometry of the system. Results of 3D calculations have confirmed all main physical mechanisms and conclusions of 2D calculation. The transverse leakage current drops sharply when $B_0/B_{cr} \geq 1.4$ and longitudinal leakage current prevail.

5 CONCLUSION

Emphasised is the dominant influence of a feedback on dynamics of electron beam modulation and on arising transverse leakage current to the anode across the external magnetic field exceeding the critical magnetic field of magnetic insulation. The instability arises due to an energy and a momentum exchange between particles and rotating crossed azimuthally modulated $E \times B$ -fields. Strong azimuthal instability exists if the current of primary beam is much less than the secondary emission current. If these currents are comparable, the instability is weak and decays in time due to the absence of strong azimuthal inhomogeneity of secondary emission current. In the case of the emission of primary beam alone deep modulation and leakage current arises only if the condition of saturated regime of a cathode is satisfied. Such behaviour is conditioned by a feedback on the emitting surfaces which provides additional correct azimuthal modulation of electron flow by rotating crossed $E \times B$ -field and amplifies the instability.

6 REFERENCES

- [1] Agafonov A.V., Fedorov V.M., Tarakanov V.P. Proc. of 1997 Particle Accelerator Conf., Vancouver, Canada. 1997, v. 2, 1299 – 1301.
- [2] Agafonov A.V. Proc. of the 2nd Sarantsev's seminar. Dubna, JINR, 1998. D9-98-153, 105 – 109.
- [3] Agafonov A.V., Fedorov V.M., Tarakanov V.P. Proc. of the 12th Intern. Conference on High-Power Particle Beams. Israel, Haifa, 1998.
- [4] Kotetashwily P.V., Rybak P.V., Tarakanov P.V. Institute of General Physics, Moscow, Preprint N 44, 1991.
- [5] Jepsen R.L. and Muller M.V. J. Appl. Phys. 1951, v. 22, 1196 – 1207.

MERGING BEAM-BEAM INTERACTION

Yuri K. Batygin and Takeshi Katayama

The Institute of Physical and Chemical Research (RIKEN), Saitama, 351-01, Japan

Abstract

New type of particle collisions is considered. In merging collisions two comoving beams intersect each other at small angle to provide low collision energy required for nuclear fusion experiments. Expression for luminosity is obtained. It is shown, that luminosity has a maximum value depending on particle velocity.

1 INTRODUCTION

Merging beam collisions is a new technique for study nuclear fusion processes [1]. Merging two radioactive isotope beams deliver low energy collisions just above the Coulomb barrier threshold that is difficult to be realized in other experimental methods. In this paper we analyze luminosity of merging beam-beam collision as a function of ring parameters and find optimal conditions to obtain maximum value of luminosity.

2 LUMINOSITY OF MERGING BEAM-BEAM COLLISIONS

Consider two bunched beams with particle densities ρ_1, ρ_2 and beam velocities $\vec{\beta}_1 = \vec{v}_1/c, \vec{\beta}_2 = \vec{v}_2/c$, crossing each other with angle 2φ (see Fig. 1). Assume beams have a Gaussian space charge density distributions

$$\rho_1 = N_1 \frac{\exp \left[-\frac{x_1^2}{2\sigma_{x1}^2} - \frac{y_1^2}{2\sigma_{y1}^2} - \frac{(z_1 - v_1 t)^2}{2\sigma_{z1}^2} \right]}{(2\pi)^{3/2} \sigma_{x1} \sigma_{y1} \sigma_{z1}}, \quad (1)$$

$$\rho_2 = N_2 \frac{\exp \left[-\frac{x_2^2}{2\sigma_{x2}^2} - \frac{y_2^2}{2\sigma_{y2}^2} - \frac{(z_2 - v_2 t)^2}{2\sigma_{z2}^2} \right]}{(2\pi)^{3/2} \sigma_{x2} \sigma_{y2} \sigma_{z2}}, \quad (2)$$

where N_1, N_2 are number of particles per each bunch, $\sigma_{xi}, \sigma_{yi}, \sigma_{zi}, i = 1, 2$ are root-mean square (rms) bunch sizes. Luminosity is defined as a ratio of interaction rate dN/dt to cross section σ of particle interaction $L = (1/\sigma) (dN/dt)$. According to invariant cross section formula [2], number of collisions δN in the volume dV during time dt is

$$\delta N = \sigma \sqrt{(\vec{v}_1 - \vec{v}_2)^2 - \frac{[\vec{v}_1 \times \vec{v}_2]^2}{c^2}} \rho_1 \rho_2 dV dt. \quad (3)$$

After two bunches crossed each other, total number of collisions, ΔN , is obtained via integration of Eq. (3) over volume of interacted bunches and time of interaction. In a ring N_b bunches collide per turn during time $T=1/f_0$, where f_0 is a particle revolution frequency. Therefore, luminosity of particle collider, $L = (1/\sigma) (\Delta N/T)$, is

$$L = N_b f_0 \sqrt{(\vec{v}_1 - \vec{v}_2)^2 - \frac{[\vec{v}_1 \times \vec{v}_2]^2}{c^2}} \int_V \int_t \rho_1 \rho_2 dx dy dz dt. \quad (4)$$

Transformation of coordinate system of every bunch $(x_i, y_i, z_i), i=1, 2$ into laboratory coordinate system (x, y, z) is given by (see Fig. 1):

$$\begin{cases} z_1 = z \cos \varphi + x \sin \varphi \\ x_1 = -z \sin \varphi + x \cos \varphi \end{cases}, \begin{cases} z_2 = z \cos \varphi - x \sin \varphi \\ x_2 = z \sin \varphi + x \cos \varphi \end{cases}. \quad (5)$$

Substitution of coordinate transformation (5) into Eq. (4) gives the following expression for luminosity:

$$L = G \frac{N_b f_0 c N_1 N_2}{(2\pi)^3} \sqrt{\beta_1^2 + \beta_2^2 - 2\beta_1 \beta_2 \cos 2\varphi - \beta_1^2 \beta_2^2 \sin^2 2\varphi}, \quad (6)$$

where integral over volume and time of interaction is

$$G = \int_{-\infty}^{\infty} \int_{-\infty}^{\infty} \int_{-\infty}^{\infty} \int_{-\infty}^{\infty} \frac{1}{\sigma_{x1} \sigma_{y1} \sigma_{z1} \sigma_{x2} \sigma_{y2} \sigma_{z2}} \cdot \exp \left\{ -x^2 \left[\frac{\cos^2 \varphi}{2} \left(\frac{1}{\sigma_{x1}^2} + \frac{1}{\sigma_{x2}^2} \right) + \frac{\sin^2 \varphi}{2} \left(\frac{1}{\sigma_{z1}^2} + \frac{1}{\sigma_{z2}^2} \right) \right] - \frac{y^2}{2} \left(\frac{1}{\sigma_{y1}^2} + \frac{1}{\sigma_{y2}^2} \right) - z^2 \left[\frac{\sin^2 \varphi}{2} \left(\frac{1}{\sigma_{x1}^2} + \frac{1}{\sigma_{x2}^2} \right) + \frac{\cos^2 \varphi}{2} \left(\frac{1}{\sigma_{z1}^2} + \frac{1}{\sigma_{z2}^2} \right) \right] - z t \cos \varphi \left(-\frac{v_1}{\sigma_{z1}^2} - \frac{v_2}{\sigma_{z2}^2} \right) - \frac{t^2}{2} \left(\frac{v_1^2}{\sigma_{z1}^2} + \frac{v_2^2}{\sigma_{z2}^2} \right) + x [z \sin \varphi \cos \varphi \left(\frac{1}{\sigma_{x1}^2} - \frac{1}{\sigma_{x2}^2} - \frac{1}{\sigma_{z1}^2} + \frac{1}{\sigma_{z2}^2} \right) - t \sin \varphi \left(\frac{v_1}{\sigma_{z1}^2} - \frac{v_2}{\sigma_{z2}^2} \right)] \right\} dx dy dz dt. \quad (7)$$

Assume, that collide bunches have the same longitudinal sizes $\sigma_{z1} = \sigma_{z2} = \sigma_z$ and same velocities $\beta_1 = \beta_2 = \beta$, but different transverse sizes $\sigma_{x1} \neq \sigma_{x2}, \sigma_{y1} \neq \sigma_{y2}$. Calculation of luminosity, Eqs.(6-7) results in expression

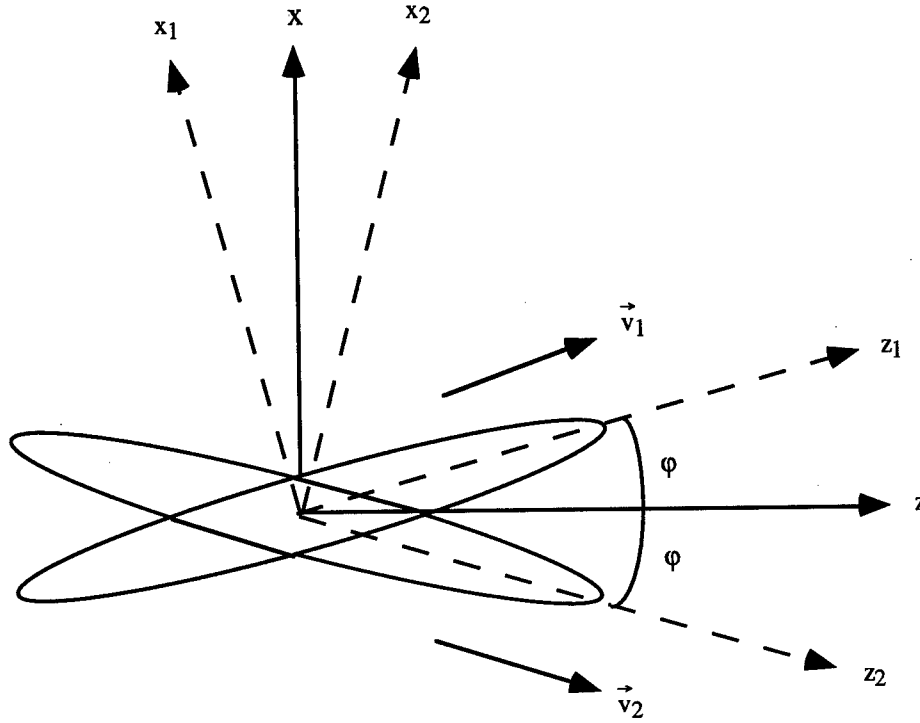


Fig. 1. Merging beam-beam interaction.

$$L = \frac{N_b f_0 N_1 N_2}{2\sqrt{2}\pi \sqrt{\sigma_{y1}^2 + \sigma_{y2}^2} \sigma_z \cos \varphi} \sqrt{\frac{1 - \beta^2 \cos^2 \varphi}{1 + \tan^2 \varphi \left(\frac{\sigma_{x1}^2 + \sigma_{x2}^2}{\sigma_z^2} \right)}} \quad (8)$$

Formula (8) is derived assuming $\varphi \neq 0, \pi/2$. For typical parameters in the interaction point, $\varphi \ll 2\pi$, $\sigma_{x1,2} \ll \sigma_z$, the denominator factor in Eq. (8) can be neglected as a product of two small values:

$$\tan^2 \varphi \left(\frac{\sigma_{x1}^2 + \sigma_{x2}^2}{\sigma_z^2} \right) \ll 1 \quad (9)$$

Luminosity, Eq.(8), is inversely proportional to longitudinal beam size, σ_z , and vertical beam size, $\sigma_{y1,2}$, and practically independent on horizontal beam sizes in the plane of particle collision, $\sigma_{x1,2}$.

Let us take into account, that revolution frequency of particle motion in a ring is given by $f_0 = \beta c / C_r$ where $C_r = 2\pi R$ is a circumference and R is a mean radius of the ring. Therefore, luminosity as a function of particle velocity is:

$$L = \frac{c N_b N_1 N_2}{2\sqrt{2}\pi \cos \varphi \sqrt{\sigma_{y1}^2 + \sigma_{y2}^2} \sigma_z C_r} \beta \sqrt{1 - \beta^2 \cos^2 \varphi} \quad (10)$$

Taking derivative of luminosity over particle velocity,

$$\frac{\partial L}{\partial \beta} = \frac{c N_b N_1 N_2}{2\sqrt{2}\pi \cos \varphi \sqrt{\sigma_{y1}^2 + \sigma_{y2}^2} \sigma_z C_r} \frac{(1 - 2\beta^2 \cos^2 \varphi)}{\sqrt{1 - \beta^2 \cos^2 \varphi}} = 0 \quad (11)$$

the maximum luminosity, L_{\max} , is obtained at the following optimal values of particle velocity, β_{opt} , and particle energy, γ_{opt} :

$$\beta_{\text{opt}} = \frac{1}{\sqrt{2} \cos \varphi}, \quad \gamma_{\text{opt}} = \frac{\sqrt{2} \cos \varphi}{\sqrt{2 \cos^2 \varphi - 1}} \quad (12)$$

$$L_{\max} = \frac{c N_b N_1 N_2}{4\sqrt{2}\pi \cos^2 \varphi \sqrt{\sigma_{y1}^2 + \sigma_{y2}^2} \sigma_z C_r} \quad (13)$$

In Fig. 2 luminosity as a function of particle velocity for angle $\varphi = 0.087$ is presented. Since the value of φ is small and $\cos \varphi \approx 1$, the maximum luminosity is obtained for $\beta_{\text{opt}} \approx 1/\sqrt{2}$, $\gamma_{\text{opt}} \approx 1.41$. At relativistic energies, $\beta \approx 1$, luminosity is

$$L(\beta \rightarrow 1) = \frac{c N_b N_1 N_2}{2\sqrt{2}\pi \sqrt{\sigma_{y1}^2 + \sigma_{y2}^2} \sigma_z C_r} \tan \varphi \quad (14)$$

Therefore, reduction of luminosity at relativistic particle energies $\gamma \gg \gamma_{\text{opt}}$ with respect to maximum value of luminosity is

$$\frac{L(\beta \rightarrow 1)}{L_{\max}(\beta_{\text{opt}})} = \sin 2\varphi \quad (15)$$

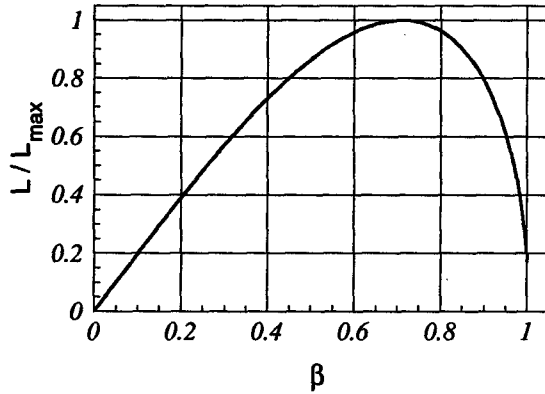


Fig. 2. Luminosity of merging beam-beam collisions for angle $\varphi = 0.087$ as a function of particle velocity.

3 COMPARISON WITH LUMINOSITY OF CROSSING ANGLE COLLISIONS

Let us compare maximum luminosity at merging collisions, Eq. (13) with that for head crossing angle collision with the same value of φ . Expression for luminosity with head crossing angle collision is obtained from general expression, Eqs. (6), (7), by change of \vec{v}_2 for $-\vec{v}_2$ [3]:

$$L = \frac{N_b f_0 N_1 N_2 \sqrt{1 - \beta^2 \sin^2 \varphi}}{2\pi \sqrt{\sigma_{y1}^2 + \sigma_{y2}^2} \sqrt{2\sigma_z^2 \sin^2 \varphi + \cos^2 \varphi (\sigma_{x1}^2 + \sigma_{x2}^2)}}. \quad (16)$$

Ratio of two values of luminosity is:

$$\frac{L_{\text{merge max}}}{L_{\text{cross angle}}} = \frac{\sqrt{\sigma_{x1}^2 + \sigma_{x2}^2}}{2\sqrt{2}\sigma_z \beta \cos \varphi} \sqrt{\frac{1 + \tan^2 \varphi \frac{2\sigma_z^2}{(\sigma_{x1}^2 + \sigma_{x2}^2)}}{1 - \beta^2 \sin^2 \varphi}} \approx \frac{\sigma_x}{2\sigma_z}. \quad (17)$$

For typical ring parameters $\varphi \approx 0$, $\beta \approx 1$, ratio of luminosity is of the order $\sigma_x/\sigma_z \approx 10^{-3}$. That means, that in merging collisions, achievable value of luminosity is several order of magnitude less than that in encountered crossing angle collisions, because merge beams are almost parallel to each other.

4 LUMINOSITY OF COMOVING BEAM COLLISIONS

From the previous section it is clear that merging collision is characterized by small value of luminosity. V.V.Parhomchuk (BINP, Novosibirsk) pointed out [4]

that, if collisions is performed on-axis, luminosity does not depend on particle velocities. Consider two bunched beams, which move in the same direction with different velocities $v_1 \neq v_2$. Luminosity of such comoving collisions is obtained from general formulas (6), (7) by change of \vec{v}_2 for $-\vec{v}_2$ and assuming $\varphi = 0$:

$$L = \frac{N_b f_0 c N_1 N_2}{(2\pi)^3} \frac{|\beta_1 - \beta_2|}{\sigma_x^2 \sigma_y^2 \sigma_z^2} \cdot G, \quad (18)$$

$$G = \int_{-\infty}^{\infty} \int_{-\infty}^{\infty} \int_{-\infty}^{\infty} \int_{-\infty}^{\infty} \exp \left[-\frac{x^2}{\sigma_x^2} - \frac{y^2}{\sigma_y^2} - \frac{z^2}{\sigma_z^2} - \frac{t^2}{2} \left(\frac{v_1^2 + v_2^2}{\sigma_z^2} + z \cdot t \frac{(v_1 + v_2)}{\sigma_z^2} \right) \right] dx dy dz dt. \quad (19)$$

After evaluation of integral (19), the value of luminosity is:

$$L = \frac{N_b f_0 N_1 N_2}{4\pi \sigma_x \sigma_y}. \quad (20)$$

Eq. (20) gives the same result as luminosity of head-on collision. Integration in Eq. (19) is performed in the infinite limits. It means, that bunches of both beams have to pass through each other completely. Bunch length is $l \approx 4\sigma_z$. To perform interaction, collision region, l_{coll} , has to be as long as [4]

$$l_{\text{coll}} = l \cdot \frac{\beta_2}{|\beta_1 - \beta_2|}. \quad (21)$$

Typical value of ratio in Eq. (21) is $\beta_2/\Delta\beta \approx 10$. To obtain the same value of luminosity in comoving collisions as that for head-on collisions, it is necessary to provide long interaction region with short bunches [4]. Merging beam collisions deliver smaller value of luminosity with short interaction region.

5 REFERENCES

- [1] T.Katayama, Y.Batygin, N.Inabe, K.Ohtomo, T.Ohkawa, M.Takanaka, M.Wakasugi, S.Watanabe, Y.Yano, K.Yoshida, J.Xia, Y.Rao and Y.Yuan, Nuclear Physics A626 (1997), 545-560.
- [2] L.Landau and E.Lifshitz, The Classical Theory of Fields, Pergamon Press, 1975.
- [3] Y.Batygin and T.Katayama, Luminosity of particle collider, RIKEN-AF-AC-10, 1998.
- [4] V.V.Parhomchuk, Private communication, 1998.

TEST PROBLEMS FOR VALIDATION OF SPACE CHARGE CODES

Yuri K. Batygin

The Institute of Physical and Chemical Research (RIKEN), Saitama, 351-01, Japan

Abstract

Particle-in-cell codes for intense beam dynamics study with space charge include parameters defined by user: number of modeling particles, number of grid points and integration step. Combination of that parameters has to provide the most accurate calculation of beam dynamics during reasonable computing time. Analytical solutions for intense beam dynamics problems with space charge allow comparable runs of codes with controlled accuracy of calculations. In present paper test problems using PIC code BEAMPATH are given.

1 INTRODUCTION

Self-consistent solutions for beam distribution function serve as test problems for verification of beam space charge codes. Most of the solutions are obtained for beam with linear space charge forces. Large number of tests are available utilizing KV equations for beam envelopes. Here we consider drift of uniform beam in free space (Section 2). Problem of beam drift is generalized for non-uniform beam as well (Section 3). Number of tests for both uniform and non-uniform beams are available for beam equilibria with space charge (Section 4). Several tests (drift of uniformly charged ellipsoid, Section 5 and beam bunching, Section 6) include longitudinal space charge forces.

2 DRIFT OF UNIFORM BEAM IN FREE SPACE

Spread of round uniform beam with current I , emittance ϵ , velocity β and energy γ in free space is described by KV equation for beam envelope R [1]:

$$\frac{d^2 R}{dz^2} - \frac{\epsilon^2}{R^3} - \frac{2I}{R(\beta\gamma)^3 I_c} = 0, \quad (1)$$

where $I_c = 4\pi\epsilon_0 mc^3/q$ is a characteristic value of beam current. For space charge dominated beam $\epsilon \approx 0$, Eq. (1) has a solution [2]:

$$\frac{R}{R_0} = 1 + 0.25 Z^2 - 0.017 Z^3, \quad Z = \frac{z}{R_0} \sqrt{\frac{4I}{I_c \beta^3 \gamma^3}}. \quad (2)$$

In Fig. 1 results of beam envelope evolution utilizing 10^4 particles on the grid 256×256 are presented. Deviation from analytical solution (2) is less than 10^{-4} .

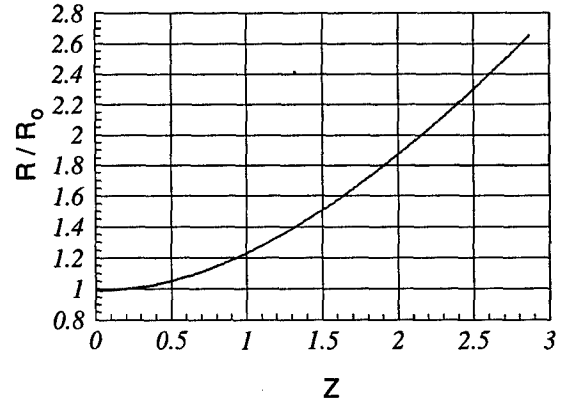


Fig. 1. Drift of uniform beam in free space.

3 DRIFT OF GAUSSIAN BEAM IN FREE SPACE

If beam is not uniform, its density profile as well as beam sizes are changed in drift space. Evolution of Gaussian beam with zero emittance in drift space under self non-linear space charge forces is described by expression [3]:

$$\rho = \frac{\rho_0 \exp(-2\xi_0^2)}{a_0 + a_1 F + a_2 F^2 + a_3 F^3 + a_4 F^4 + a_5 F^5 + a_6 F^6}, \quad (3)$$

where the following notations are used:

$$\xi_0 = \frac{r_0}{R_0}, \quad F = \sqrt{\frac{1 - \exp(-2\xi_0^2)}{\xi_0^2}}, \quad \eta = \frac{4I}{I_c \beta^3 \gamma^3} \frac{Z^2}{R_0^2}, \quad (4a)$$

$$a_0 = 1 + \eta \exp(-2\xi_0^2), \quad a_1 = -0.102 \eta^{3/2} \exp(-2\xi_0^2), \quad (4b)$$

$$a_2 = \frac{1}{4} \eta^2 \exp(-2\xi_0^2), \quad (4c)$$

$$a_3 = 0.017 \eta^{3/2} - 0.0425 \eta^{5/2} \exp(-2\xi_0^2), \quad (4d)$$

$$a_4 = 1.734 \cdot 10^{-3} \eta^3 \exp(-2\xi_0^2) - \frac{1}{16} \eta^2, \quad (4e)$$

$$a_5 = 0.01275 \eta^{5/2}, \quad a_6 = -5.78 \cdot 10^{-4} \eta^3. \quad (4f)$$

In Fig. 2 results of evolution of 35 MeV, 4.7 A, D^+ beam with initial Gaussian distribution and initial radius of $R_0 = 1.3$ cm are presented. Simulations with 10^4 particles on the grid 256×256 indicate good agreement with theory.

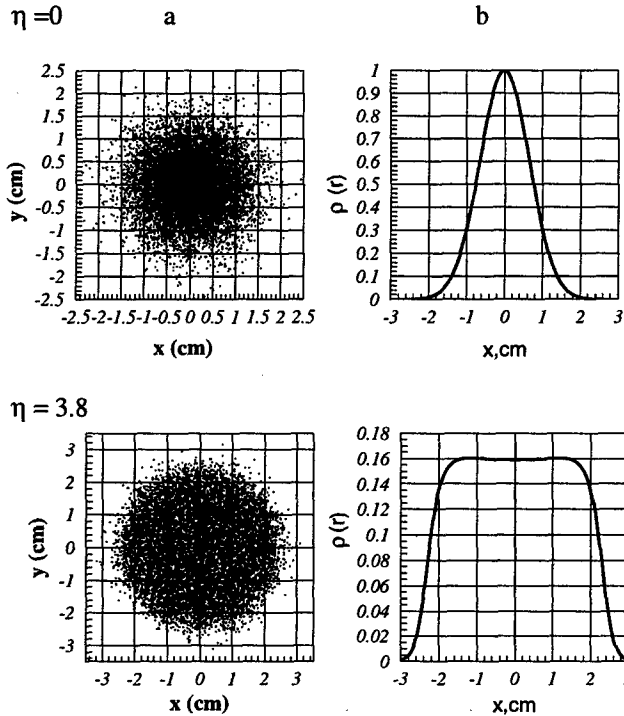


Fig. 2. Redistribution of Gaussian beam in drift space: a - PIC simulation, b - calculated from Eq. (3).

4 BEAM EQUILIBRIUM WITH SPACE CHARGE

If beam distribution function $f(x, y, p_x, p_y)$ is conserved in time-independent focusing field, beam is in equilibrium with external field. Stationary self-consistent beam distribution function is a solution of Vlasov-Poisson's equations:

$$\left\{ \begin{array}{l} \frac{1}{m\gamma} \left(\frac{\partial f}{\partial x} p_x + \frac{\partial f}{\partial y} p_y \right) - q \left(\frac{\partial f}{\partial p_x} \frac{\partial U}{\partial x} + \frac{\partial f}{\partial p_y} \frac{\partial U}{\partial y} \right) = 0 \\ \frac{1}{r} \frac{\partial}{\partial r} \left(r \frac{\partial U_b}{\partial r} \right) = - \frac{q}{\epsilon_0} \int_{-\infty}^{\infty} \int_{-\infty}^{\infty} f(x, p_x, y, p_y) dp_x dp_y \end{array} \right. \quad (5)$$

where $U = U_b + \gamma^2 U_{ext}$ is a total potential of the structure, U_b is a space charge potential and U_{ext} is an external focusing potential. General treatment of the problem (5) for arbitrary distribution function was given in [4]. In Table 1 self-consistent solutions for different beam distributions are given.

5 DRIFT OF UNIFORMLY CHARGED ELLIPSOID IN FREE SPACE

All mentioned problems dealt with transverse particle motion. Several tests are available including longitudinal space charge forces. Consider uniformly populated spheroid with charge Q and a, b , as longitudinal

and transverse semi-axes, respectively. Potential of the uniformly populated ellipsoid in free space is given by

$$U = - \frac{\rho}{2\epsilon_0} \left[\left(\frac{1-M_z}{2} \right) r^2 + M_z z^2 \right], \quad \rho = \frac{3}{4\pi} \frac{Q}{b^2 a}, \quad (6)$$

$$M_z = \frac{1-\epsilon^2}{\epsilon^2} \left[\frac{1}{2\epsilon} \ln \left(\frac{1+\epsilon}{1-\epsilon} \right) - 1 \right], \quad \epsilon = \frac{\sqrt{a^2 - b^2}}{a}. \quad (7)$$

Space charge forces inside ellipsoid are

$$E_r = \frac{3}{8\pi\epsilon_0} \frac{Q}{b^2 a} (1-M_z) r, \quad E_z = \frac{3}{4\pi\epsilon_0} \frac{Q}{b^2 a} M_z z. \quad (8)$$

Due to linear space charge forces, ellipsoid remains uniformly populated in drift space. Equations for evolution of ellipsoid boundaries are

$$\frac{d^2 a}{dt^2} = \frac{3}{4\pi} \frac{q}{m\epsilon_0} \frac{Q M_z}{b^2}, \quad \frac{d^2 b}{dt^2} = \frac{3}{8\pi} \frac{q}{m\epsilon_0} \frac{Q (1-M_z)}{a b}. \quad (9)$$

In Fig. 3. numerical results for ellipsoid with $Q = 3$ nK utilizing $2 \cdot 10^4$ particles on the grid 128×512 are presented. Initial ellipsoid with ratio of semi-axes $a/b = 3$ is transformed into ellipsoid with ratio of $a/b = 1.55$ (analytical solution $a/b = 1.62$). General treatment of ellipsoid drift in free space including finite value of beam emittance is given in [5].

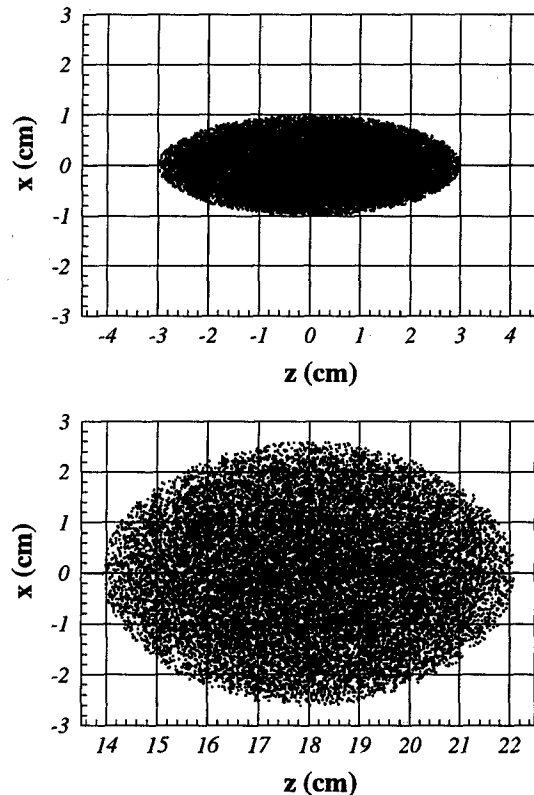


Fig. 3. Drift of uniformly populated ellipsoid in free space.

Table 1. Self-consistent beam equilibrium with space charge.

Distribution function	Definition	Required focusing field
KV	$f = f_0 \delta \left(\frac{p_x^2 + p_y^2}{(\epsilon/R)^2} + \frac{x^2 + y^2}{R^2} - H_0 \right)$	$E(r) = -\frac{mc^2}{qR} \frac{1}{\gamma} \left[\left(\frac{\epsilon}{R} \right)^2 + 2 \frac{1}{\beta \gamma I_c} \right]$
Gaussian	$f = f_0 \exp \left(-2 \frac{p_x^2 + p_y^2}{(\epsilon/R)^2} - 2 \frac{x^2 + y^2}{R^2} \right)$	$E(r) = -\frac{mc^2}{qR\gamma} \frac{r}{R} \left[\frac{\epsilon^2}{R^2} + \frac{4I}{\beta \gamma I_c} \frac{(1 - \exp(-2r^2/R^2))}{2(r^2/R^2)} \right]$
Water bag	$f = f_0, \quad \frac{2}{3} \left(\frac{x^2 + y^2}{R^2} + \frac{p_x^2 + p_y^2}{(\epsilon/R)^2} \right) \leq 1$	$E(r) = -\frac{mc^2}{qR^2\gamma} \frac{r}{R} \left[\frac{\epsilon^2}{R^2} + \frac{8I}{3I_c \beta \gamma} \left(1 - \frac{r^2}{R^2} \right) \right]$
Parabolic	$f = f_0 \left(1 - \frac{x^2 + y^2}{2R^2} - \frac{p_x^2 + p_y^2}{2(\epsilon/R)^2} \right)$	$E(r) = -\frac{mc^2}{qR^2\gamma} \frac{r}{R} \left[\frac{\epsilon^2}{R^2} + \frac{3I}{I_c \beta \gamma} \left(1 - \frac{r^2}{2R^2} + \frac{r^4}{12R^4} \right) \right]$
Extended Gaussian	$f = f_0 \exp \left(-2 \frac{p_x^2 + p_y^2}{(\epsilon/R)^2} - \frac{(x^2 + y^2)^2}{R^4} \right)$	$E(r) = -\frac{mc^2}{qR\gamma} \left[\left(\frac{\epsilon}{R} \right)^2 \frac{r^3}{R^3} + \frac{2I}{I_c \beta \gamma} \left(\frac{R}{r} \right) \operatorname{erf} \left(\frac{r^2}{R^2} \right) \right]$

6 BEAM BUNCHING

One-dimensional problem of beam bunching with space charge has an approximate analytical solution [6]. Consider non relativistic beam of energy qU_0 with fixed radius R propagating in a tube of radius a . Injected beam passes through the gap of length d with applied voltage $U(t) = U_1 \sin \omega_0 t$. In drift space particles are bunched which is characterized by the value of first harmonic of induced current I_1 as a function of bunching parameter X

$$\frac{I_1}{I} = 2 J_1(X), \quad X = \left(\frac{U_1 M_1}{2 U_0} \right) \left(\frac{\omega_0 z}{v} \right) \left[\frac{\sin \left(\frac{\omega_q z}{v} \right)}{\left(\frac{\omega_q z}{v} \right)} \right], \quad (10)$$

where $J_1(X)$ is a Bessel function, M_1 is a coupling coefficient of the beam with modulation gap:

$$M_1 = \frac{\sin(\theta/2)}{\theta/2}, \quad (11)$$

$\theta = \omega_0 d/v$ is a transit time angle trough the gap, $\omega_q = \sqrt{F} \omega_p$ is a reduced plasma frequency of the beam, $\omega_p = 2(c/R) \sqrt{I/(\beta I_c)}$ is a plasma frequency for an unbounded beam and F is a form factor of reduction of plasma frequency due to finite radius of the beam and tube:

$$F = 2.56 J_1^2(2.4 \frac{R}{a}) / [1 + 5.76/\theta_R^2], \quad \theta_R = \omega_0 R/v. \quad (12)$$

Numerical value of the first harmonic of bunched beam is calculated as follow:

$$\frac{I_1(z)}{I} = \frac{2}{N} \sqrt{\left[\sum_{n=1}^N \cos \omega_0 t_n(z) \right]^2 + \left[\sum_{n=1}^N \sin \omega_0 t_n(z) \right]^2}, \quad (13)$$

where $t_n(z)$ $i = 1, \dots, N$ is a time of reaching of the particle with number n of point z . Numerical example of bunching of 150 keV, 1 A, $R/a = 0.8$ proton beam represented by 10^4 particles on the 256×256 grid is given in Fig. 4.

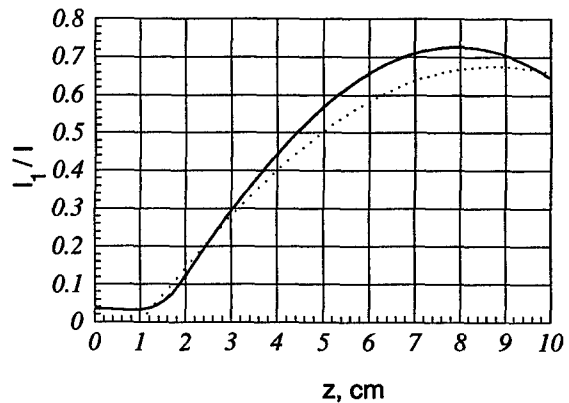


Fig. 4. Beam bunching: dotted line - analytical solution, Eq. (10); solid line - numerical values.

7 REFERENCES

- [1] I.M.Kapchinsky, Theory of Resonance Linear Accelerators, Harwood, Chur, 1986.
- [2] S.I.Molokovsky, A.D.Sushkov, Intense Electron and Ion Beams, Energoatomizdat, Moscow, 1991 (in Russian).
- [3] D.L.Bruhwiller and Y.K.Batygin, Proceedings of the PAC95, Dallas, (1995) 3254.
- [4] Y. K.Batygin, Phys. Review E, 53, 5358, (1996).
- [5] A.S.Chikhachev, Sov. Phys. Tech. Phys. 29 (9), 1984, p.990.
- [6] Yu.A.Katsman, Microwave Devices, Moscow, 1973 (in Russian).

TRANSVERSE PHASE SPACE PAINTING FOR SNS ACCUMULATOR RING INJECTION*

J. Beebe-Wang, Y. Y. Lee, D. Raparia, J. Wei
Brookhaven National Laboratory, Upton, NY 11973

Abstract

The result of investigation and comparison of a series of transverse phase space painting schemes for the injection of SNS accumulator ring [1] is reported. In this computer simulation study, the focus is on the creation of closed orbit bumps that give desired distributions at the target. Space charge effects such as tune shift, emittance growth and beam losses are considered. The results of pseudo end-to-end simulations from the injection to the target through the accumulator ring and Ring to Target Beam Transfer (RTBT) system [2] are presented and discussed.

1 INTRODUCTION

At Brookhaven National Laboratory work is in progress for the design and construction of SNS accumulator ring system [1]. The system consists of a 1MW, expandable to 2MW, accumulator ring [3] and two transfer lines. High-Energy Beam Transport line (HEBT) [4] brings beam from the end of linac to the injection bump of the ring, and Ring to Target Beam Transport line (RTBT) [2] brings beam from the extraction kicker of the ring to the target.

At the target, the proton beam must meet stringent specifications, as listed in Table 1, in consideration of the stress and lifetime of the target. The proton distribution at the target is crucially determined by the beam distribution in the ring. Furthermore, a proper proton distribution in the ring is critically dependent on the 6-dimensional phase space injection/stacking method. Therefore, in order to obtain the desired proton distribution at the target, one must create a set of suitable closed orbit bumps at the injection that provide a proper phase space painting.

In the current H⁻ charge exchange injection design [5], the horizontal and vertical bumps are formed by sets of four pulsed dipoles. The strengths of the dipoles, in each direction, can be programmed as functions of time during the injection to provide phase space painting. As a part of design study, we ask: (1) can the bumps, as in the current design, satisfy the beam requirements at the target? (2) if can, what are the prescriptions of the bumps as functions of time during the injection? (3) are these prescriptions technically achievable? To answer these questions, we investigated and compared a series of transverse phase space painting schemes by realistic computer simulations.

*Work performed under the auspices of the U. S. Department of Energy.

Table 1 : Beam requirements at the target [6]

Beam horizontal dimension	200 mm
Beam vertical dimension	70 mm
Time-averaged beam current density over beam footprint	$\leq 0.091 \text{ A/m}^2$
Beam power within target and outside nominal spot	$< 5\%$
Peak time-averaged beam current density over 1 cm^2	$\leq 0.182 \text{ A/m}^2$
Peak 1-pulse density over 1 cm^2	$1.89 \times 10^{16} \text{ proton/m}^2$

2 COMPUTER SIMULATIONS

Three computer simulation codes are used in this study: ACCSIM [7] and SIMPSONS [8] for beam tracking in the accumulator ring, and PARMILA [9] for the RTBT line. Both ACCSIM and SIMPSONS are capable of tracking a large number of macro-particles through the ring lattice, in the presence of space charge and beam to wall interactions, in full 6-dimensions. In addition to the common features, ACCSIM provides wide range of injection simulation options such as foil specifications, 6-D phase space painting and injected particle distributions. On the other hand, SIMPSONS is a powerful tool for extensive study of space charge effect. So, in this study, phase space painting is investigated with ACCSIM and space charge effect is done with SIMPSONS. Presently, efforts are been made [10] in BNL to integrate various codes onto a common platform that accommodates 6-D painting and space charge effects together with magnet field error and misalignment analysis, magnetic fringe field mapping, and beam collimation.

All the physical quantities used in the simulations are chosen to be as close as possible to the specifications in the current design. The lattice functions and other salient parameters used in the simulations are listed in Table 2.

Table 2 : Design parameters used in the simulation study

Beam Kinetic Energy	1 GeV
Beam Average Power	1.0-2.0 MW
Proton Revolution Period	0.8413 μsec
Ring Circumference	220.688 m
Number of Turns Injected	1225
Beam Emittance $\epsilon_{x,y}$	120 $\pi\text{mm-mr}$
Tunes ν_x / ν_y	5.82 / 5.80
Max. $\beta_x / \text{max. } \beta_y$	19.2 / 19.2 m
Dispersion X_p (max/min)	4.1 / 0.0 m

3 PHASE SPACE PAINTING

Since the beam is injected into the ring at a dispersion-free region [5], beam phase-space painting in the transverse direction is conveniently de-coupled from the longitudinal beam manipulation [11]. Furthermore, painting in the horizontal and vertical direction can be adjusted independently. The injection system is designed to accommodate both x - y correlated and x - y anti-correlated painting schemes, illustrated in Fig. 1.

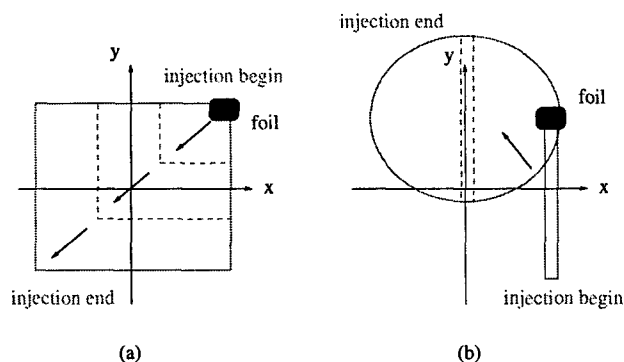


Figure 1: Basic painting scenarios. (a) x - y correlated painting, (b) x - y anti-correlated painting.

The most easily achievable bumps are the ones moving the closed orbit monotonically as an exponential function of time with a reasonably long time constant. With a x - y correlated bump setting, as shown in Fig. 2, phase spaces in both dimensions are painted from small to large emittances. Ideally, the resulting rectangular transverse profile, Fig. 3, can easily meet the target requirements.

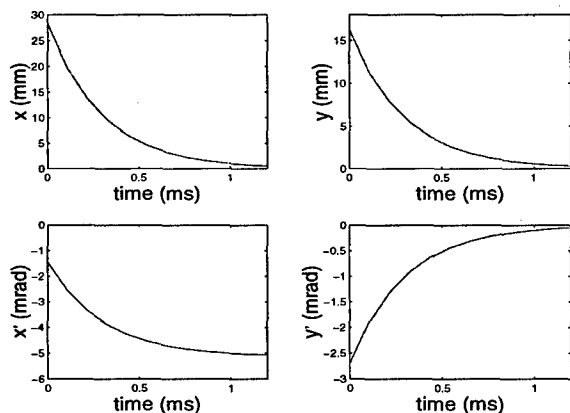


Figure 2: Orbit bump setting for a x - y correlated painting.

However, such a beam profile is susceptible to transverse coupling due to magnet misalignment and space charge forces, which in turn results in an effective doubling of the maximum emittance in both directions. On the other hand, with the x - y anti-correlated scheme the total transverse emittance is approximately constant during the injection. The resulting oval beam profile achieved by x - y anti-correlated painting, fig. 4, is immune to the transverse coupling. Table 3 compares the two painting schemes.

Table 3: Comparison of x - y correlated and anti-correlated phase space painting scenarios

painting scenarios	correlated	anti-correlated
Foil hitting rate	1 : 2	
Aperture clearance @ inj.	1 : 1.5	
Susceptibility to coupling	yes	no
Capability to KV painting	no	yes

In both painting examples, shown in Fig. 3 and 4, the time constants of the bumps were 0.3 ms or longer in consideration of eddy current effect in the vacuum chamber. Since painting is adopted in both directions without steering of the injecting beam the minimization of foil hitting and the design of downstream beam line and beam dump for the un-stripped beam become straightforward.

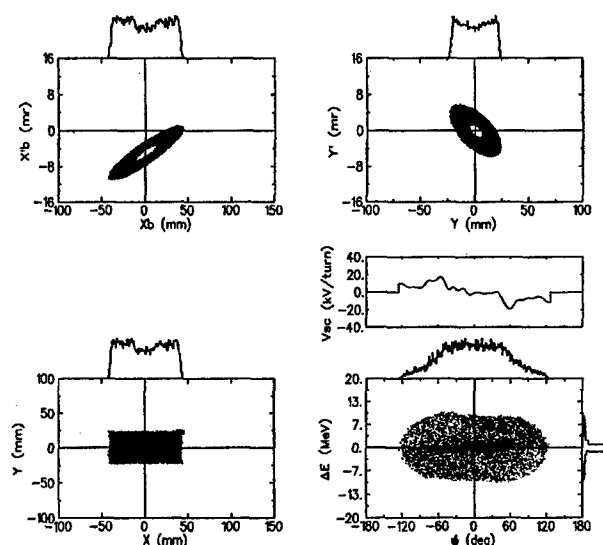


Figure 3: Phase space distribution at the end of injection achieved by a x - y correlated phase space painting.

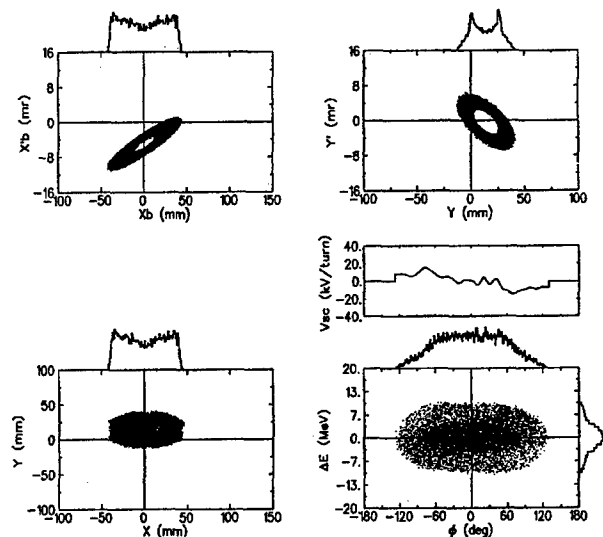


Figure 4: Phase space distribution at the end of injection achieved by a x - y anti-correlated phase space painting.

4 SPACE CHARGE EFFECT

We compare space charge effects between the beams in the current design of FODO nominal tune lattice and in an alternative design of FODO split tune lattice [12] developed recently as part of design studies in BNL. 10^5 macro particles, with transverse phase space distribution similar to the one shown in Fig. 4 were tracked in the two lattices for 100 turns by SIMPSONS 2D code. Space charge effect in beams with peak current 0-100A, corresponding to the proton accumulation of 0-2MW, was investigated. The rms emittance growth and tune shift due to space charge as functions of peak current are shown in Fig. 5 and Fig. 6 respectively. The lattice functions and space charge effects in 2MW beams in the two lattices are compared in Table 4. With the split tune lattice, the vertical beam envelope variation ($\beta_{\max}/\beta_{\min}$) is significantly reduced. Correspondingly, the vertical emittance and beam tail/halo generation is also dramatically reduced.

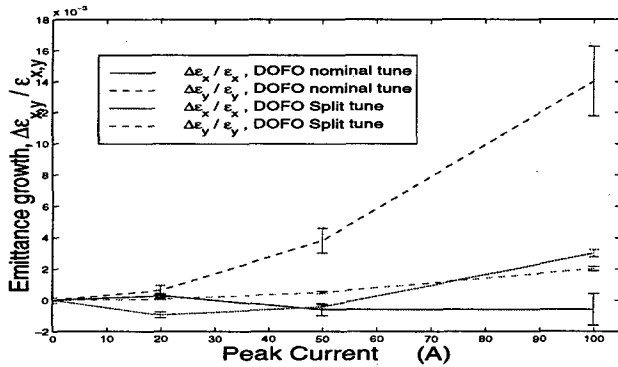


Fig. 5 RMS emittance growth as function of peak current.

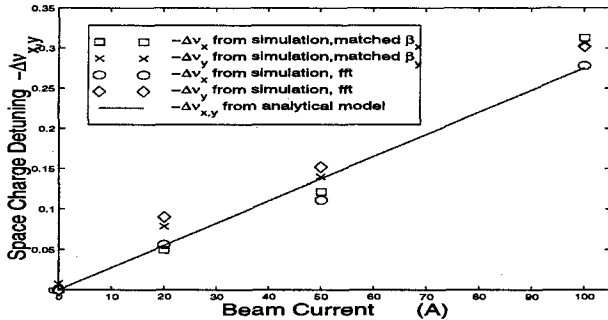


Figure 6: Maximum space charge tune shifts.

Table 4: Lattice comparison

LATTICE	Unsplit	Split
Tune v, (x/y)	5.82 / 5.80	5.82 / 4.80
Max. / min. β -function, (m)	19.2 / 1.4	19.4 / 2.6
Max. $ D_x $, (m)	4.0	3.9
$\beta_{\max}/\beta_{\min}$	13.7	7.5
Max. B_{SESD} (at 10cm), (kG)	3.0	3.2
Max. tune shift, Δv , (x/y)	0.2 - 0.3	0.2 - 0.3
SC β growth $\Delta\beta/\beta$, (x/y)	0.10 / 0.16	0.12 / 0.06
Emittance growth, $\Delta\epsilon/\epsilon$, (x/y)	~ 0 / .014	.003 / .002
Tail/halo rate, x/y ($10^5/\text{turn}$)	1.1 / 1.7	1.2 / 0.1

5 PSEUDO END TO END SIMULATION

Driven by searching for suitable painting schemes, injections with various bump settings were simulated in the accumulator ring. Then particle distribution obtained from the ring simulations were tracked to the target through the RTBT line with PARMILA. PARMILA was modified to include scattering effect of a 4mm thick inconel window, which is about 2 meter from the target. Then the current distributions are checked against the beam requirement at the target. (Table 1). It was found that, in a 2-D plan of time constant and bump strength, there is a nice-sized region in which all the bump settings give satisfactory distributions. Fig. 7 shows one example of satisfactory distribution at the target that was achieved by the bump settings shown in Fig. 2. Complete end-to-end simulations, from the ion source to the target through linac, HEBT, accumulator ring and RTBT is in progress.

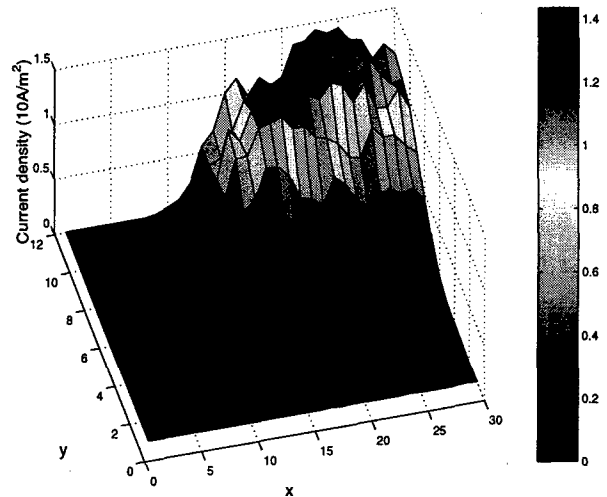


Fig. 7 Current density distribution at the target in units of 10 A/m^2 . One quadrant of the beam footprint is shown.

6 ACKNOWLEDGEMENT

The authors would like to thank F. Jones and S. Machida for developing ACCSIM and SIMPSONS and making them available. They would also like to thank A. Luccio and N. Malitsky for helping to set-up the codes in BNL.

7 REFERENCES

- [1] W.T. Weng *et al*, Proc. of PAC'97, p.972, (1997).
- [2] D.Raparia *et al*, these proceedings.
- [3] C.J. Gardner *et al*, Proc. of PAC'97, p.962, (1997).
- [4] D.Raparia *et al*, Proc. of PAC'97, p.162, (1997).
- [5] L.N. Blumberg *et al*, Proc. of PAC'97, p.159, (1997).
- [6] SNS Collaboration, "Spallation Neutron Source Design Manual", p.5.12-1, June 1998.
- [7] F. W. Jones, "User's Guide to ACCSIM", TRIUMF Design Note TRI-DN-90-17, June 1990 (and later additions).
- [8] S. Machida, "The Simpsons User's Manual", Dallas, 1992.
- [9] G. Boicort *et al*, "Parmila User's Manual", LA-UR-90-127.
- [10] N. Malitsky *et al*, these proceedings.
- [11] J. Beebe-Wang, "Study of Longitudinal Injection/stacking in the SNS Accumulator Ring", these proceedings.
- [12] C.J. Gardner *et al*, these proceedings.

PERFORMANCE OF THE AGS TRANSITION JUMP SYSTEM*

L.A. Ahrens, J.M. Brennan, J.W. Glenn, T. Roser, W.K. van Asselt[#], BNL, Upton, NY

Abstract

The transition jump system has been indispensable to the high intensity proton operation of the AGS complex. Nevertheless, transition crossing remains one of the major hurdles as the accelerator complex intensity is pushed upward. To enhance the performance of the system 'quadrupole pumping' in the Booster is used to minimize the necessary longitudinal dilution of the beam on the AGS injection porch. During the transition jump sextupole correctors at strategic locations are pulsed to minimize the effects of the chromatic non-linearity of the jump system. The available instrumentation for diagnosing the performance of the system will be described, along with performance at the recent record beam intensities.

1 INTRODUCTION

The gamma jump system at the AGS is in operation since 1994. It consists of three quadrupole doublets positioned symmetrical around the ring. When these quadrupoles are powered, they produce lattice perturbations resulting in a change of the transition energy. During acceleration of the beam in the AGS these quadrupoles are slowly ramped as the beam nears the transition energy of the unperturbed machine. The beam remains below transition in this way for a longer period. When the beam energy is well above the transition energy of the unperturbed machine, the currents in the quadrupoles are crowbarred to produce a fast change of the transition energy of the lattice and therefore an effective fast crossing of transition. Since the time constant of this crowbar is proportional to the inductance of the load each quadrupole magnet has its own charging supply and crowbar circuit. A more detailed description of the system can be found in [1,2] and references cited there.

The large distortion to the machine lattice inherent to the jump implies that the beam momentum spread, hence longitudinal emittance, is the critical beam parameter near transition.

The following will outline the strategies, which have been employed during the high intensity proton running period for the High Energy Physics program of FY98 and FY99. The first involves RF gymnastics in the Booster aimed at

reducing the longitudinal emittance of the beam in the AGS. The second involves powering sextupoles using newly installed hardware to counter the non-linear effects of the transition jump system.

2 REDUCTION OF THE BEAM DILUTION IN THE AGS

Optimizing beam intensity in the AGS involves a compromise between conflicting needs to create the most stable conditions on the long injection porch, and to produce a beam with minimal momentum spread for the transition jump. Beam properties relevant to front porch stability issues include the peak beam current, the momentum spread as well as transverse dilution. The beam has been longitudinally mismatched upon transfer from the Booster to the AGS in previous years and an RF cavity with a frequency about forty times that of the accelerating RF has been used, which smooths and speeds filamentation of the beam increasing the longitudinal emittance and the beam stability [3,4]. At transition this results in increased beam losses, because the beam size increases so much, which is a

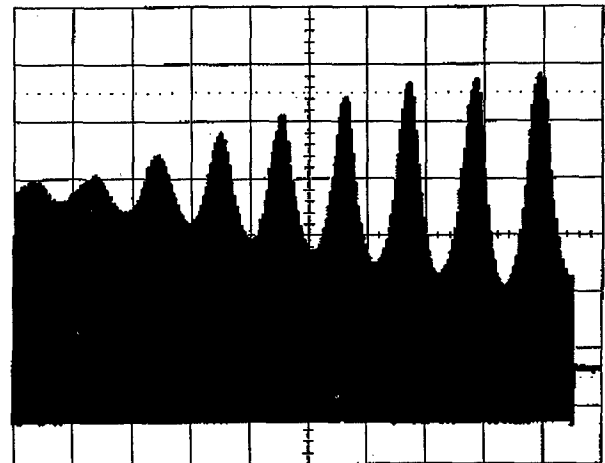


Figure 1: The wall current monitor signal showing the peak current density variations in the Booster before transfer to the AGS. Horizontal scale is 1 ms/s

* Work performed under the auspices of the U.S. Department of Energy

Email: vanasselt@bnl.gov

Result of the large modulation of the dispersion function during the pulsing of the transition jump quadrupoles [1,2]. For this running period the peak bunch intensity and momentum spread of the bunches transferred from the Booster to the AGS has been reduced by so-called quadrupole pumping, a process where the RF voltage is modulated before the beam transfers to the AGS. In this way the lower peak densities can be obtained in the AGS without the emittance increase associated with the dilution of the high frequency cavity. Figure 1 shows the wall current monitor signal in the Booster during the last 10 ms before transfer to the AGS. It is seen that the peak density is reduced to approximately 60% from the value before the quadrupole pumping process started.

However, operation of the highest intensity beams have been obtained with a significant longitudinal mismatch intentionally present between the Booster and the AGS, implying that some momentum spread increase was needed on the injection porch.

3 NON-LINEAR EFFECTS OF THE TRANSITION JUMP SYSTEM

The second order γ -jump scheme used in the AGS significantly distorts the machine lattice. In [5] Wei et al. described measurements and simulations of the large chromatic non-linearity, which accompanies the powering of the transition jump quadrupoles. Wei proposed the use of a current of about 100 A in the twelve superperiod symmetric horizontal chromaticity sextupoles in the AGS to minimize the nonlinear effects of the jump system. Subsequent measurements, using a longitudinally very small beam, confirmed this prediction [6].

However, attempts to implement this plan using the high intensity beam over the past several years have consistently resulted in increased beam losses at transition even for sextupole currents well below 100 A.

Although this is not rigorously understood, it is known that the beam equilibrium orbit is significantly offset from the sextupole centers. The resulting distortions may be responsible for the increased losses, which motivated attempting to reduce the number of sextupoles involved in the correction. Closer investigations of the effect of the sextupoles with the computer simulation code MAD showed that by choosing only three of the twelve sextupoles, those located near maxima of the distorted dispersion function inherent to the jump (B13, F13 and J13), an equally effective reduction in the nonlinearity could be achieved. Figure 2 shows some results of these simulations. The transition energy is plotted as a function of the momentum error of the beam in the AGS for various currents in these three sextupoles. These simulations also revealed some ill effects of the sextupole correction. Figure 3 shows the

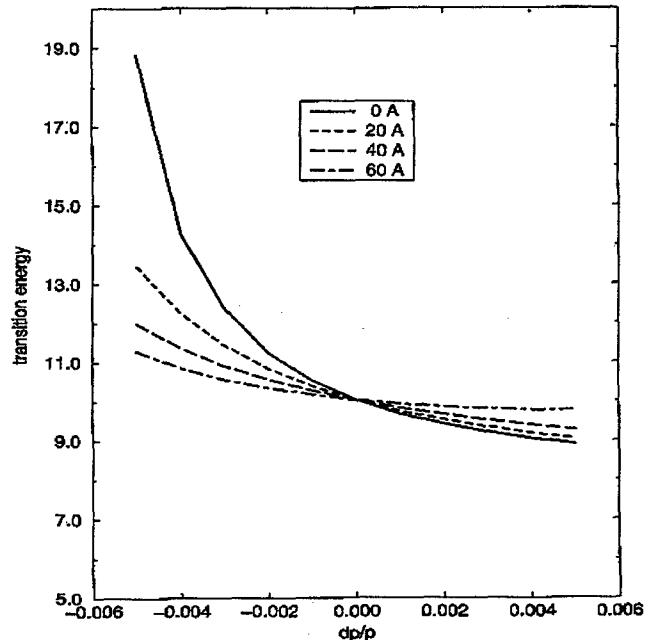


Figure 2: The transition energy versus momentum with the sextupole current as parameter

maxima in the horizontal beta function as a function of the momentum error for various values of the currents in the horizontal sextupoles.

To introduce sextupole correction near transition with minimal effect on the orbit and independent of the regular chromaticity correction, additional (floating) power supplies

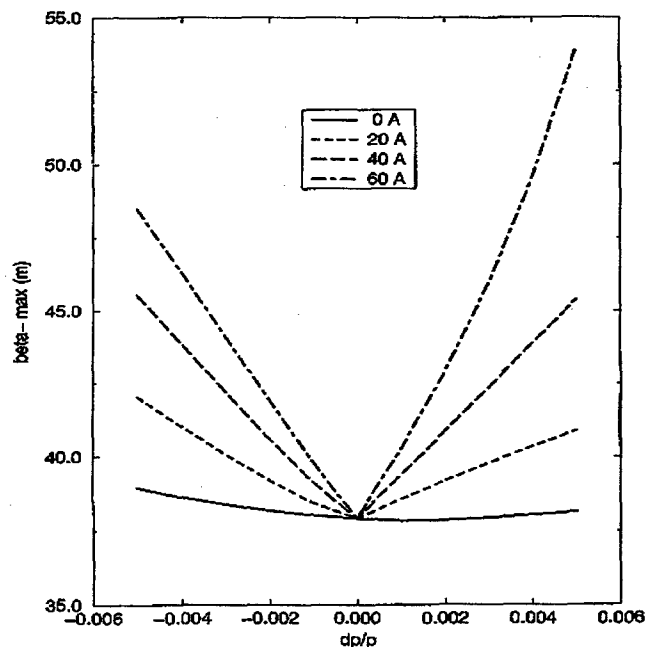


Figure 3: The maximum horizontal beta function versus momentum for different sextupole settings

have been installed for each of the three sextupoles at B13, F13 and J13 in the AGS ring. In pulsed mode the supplies are able to output 100 A.

4 DISCUSSION

During the recent high intensity proton run the AGS complex has reached record intensities above 70×10^{12} proton per cycle (70 TP). Details of how this has been achieved are described in a separate contribution [7]. Although tuning of transition can not be done independent of injection and extraction parameters, issues specific to the operational aspects of crossing of the transition energy will be described here.

The machine complex was turned on with quadrupole pumping in the Booster. The high frequency cavity is still being used, but the resulting dilution is smaller because of the reduced phase mismatch of the beam with respect to the RF in the AGS. As in previous years the gap volts have been reduced during the ramping of the transition quadrupoles to minimize the momentum spread, which is estimated $\Delta p/p = \pm 0.6\%$ at the time the transition jump occurs. Further the three sextupoles were powered with a current ramp similar to the ramp function in the transition quadrupoles. Because of the anticipated momentum spread the maximum current for this ramp was set at 35 A.

In previous years dipole and quadrupole magnets have been moved to minimize the effect of the jump system on the orbit [2]. Before this run the sextupole magnet at J13 was moved because beam loss data from the previous run had shown excessive beam loss at this location. At another location, downstream of the D20 RF cavity, where a similar problem existed a backleg winding bump was installed. Despite all these efforts the optimum tuned machine was one where the orbit excursions at the maximum of the ramp of the transition quads were intentionally not minimized and included deviations as large as 10 mm. Although beam losses downstream of the D20 cavity have been reduced, they are still problematic.

When the machine was routinely running above 60 TP it was observed that the transition losses were varying from cycle to cycle from ~ 2 to ~ 4 TP. A wall monitor mountain range program was modified such to provide integration of the individual bunch areas during the period around transition. This application revealed that most of the varying beam loss occurred on the last transfer from the Booster. Possible explanation for this behaviour is the fact that the last transfer has the highest intensity and the shortest exposure time to the high frequency cavity.

The performance of the transition jump system has improved during the recent run over previous years. On average beam losses have been reduced, while running at higher intensities. Because of the complexity of tuning the machine to the high intensities, it is not possible to identify, which of the new strategies has contributed most, but both, described in the above sections, will be pursued in coming runs.

The creation and evolution of the transition jump scheme has been driven by high intensity proton operation. The sextupole correction, in combination with the jump system, will also be explored further, when the AGS will be used as injector for RHIC, because of the desired low emittance for collider operation.

REFERENCES

- [1] M.J. Syphers, et al., 'The AGS γ -jump system', BNL Report 60824
- [2] W.K. van Asselt, et al., Proc. IEEE 1995 Particle Accelerator Conference, 95CH35843, 3022
- [3] L.A. Ahrens, et al., Proc. 1994 EPAC, 485
- [4] M. Blaskiewicz, et al., Proc. IEEE 1995 Particle Accelerator Conference, 95CH35843, 383
- [5] J. Wei, et al., Proc. IEEE 1995 Particle Accelerator Conference, 95CH35843, 3334
- [6] C. Ankenbrandt, et al., Phys. Rev. ST, Accelerators and beams 1(1998)030101
- [7] L.A. Ahrens, et al., High intensity performance of the Brookhaven AGS, These Proceedings.

OBSERVATIONS AND SIMULATIONS OF PARTICLE-DENSITY OSCILLATIONS IN AN APERTURED, SPACE-CHARGE DOMINATED ELECTRON BEAM*

S. Bernal[†], R. A. Kishek, M. Reiser,

Institute For Plasma Research, University of Maryland, College Park, MD

I. Haber, Naval Research Laboratory, Washington, D.C.

Abstract

Experiments and particle-in-cell (PIC) simulations in connection with the University of Maryland Electron Ring [1] demonstrate the appearance and evolution of transverse space-charge waves in a space-charge dominated electron beam. The waves are observed regardless of the focusing system, although the strength of the focusing affects their onset and evolution. An aperture induces the perturbation in the particle distribution in an initially freely-expanding beam. Simulations show that the effect of the aperture can be modeled approximately by a beam with an initially semi-Gaussian particle distribution with a temperature profile. Furthermore, simple tracking of test particles initially near the aperture's edge reproduce well the onset of the perturbation. For the parameters investigated, simulations further indicate that the perturbation damps out over a few plasma periods without causing any emittance growth.

Detailed understanding of the effects of space charge in the transport of intense beams is important in all areas of research and applications where beam quality is crucial. A rarely discussed aspect concerns the evolution of beams from the source to equilibrium, if any, including the role of source errors or aberrations, apertures and other factors that affect the initial particle distribution in phase space. The initial density profile of a beam has long been recognized as an important factor in determining its evolution (i.e., emittance growth, instabilities, etc.) [2]. A less appreciated influence on the dynamics is the initial temperature profile of the beam. For the Kapchinskij-Vladimirskij (K-V) distribution [3], Gluckstern [4, 5] has derived transverse kinetic oscillation modes that involve an exchange between the temperature and density profiles. However, since the K-V distribution is highly idealized, the Gluckstern modes, which can become unstable, have been thought not to exist for a physical beam. Using a warm-fluid model, Lund and Davidson [6] have rederived the Gluckstern modes and extended them to an arbitrary equilibrium distribution. Further, recent computer simulations by Lund et al. [7], relating to experiments at Lawrence Berkeley National Laboratory, exhibit density oscillations similar to Gluckstern modes, in a beam whose initial temperature or density pro-

files are perturbed. Despite the important insights provided by these studies, no clear connection has been established in either experiments or simulations between the physical cause(s) of the initial beam perturbation, the resulting phase-space distribution, and the long term evolution of this distribution.

This paper [8] presents concrete experimental evidence, augmented by self-consistent particle-in-cell (PIC) computer simulations, for the occurrence of wave-like transverse density oscillations in an electron beam. The beam is perturbed by an aperture near the source, giving rise to an initial distribution that is far from equilibrium around the beam's edge. Two transport experiments over a distance of about one meter and with similar overall focusing strengths (as given by the zero-current phase advance in the corresponding matched beams) demonstrate the onset and evolution of the beam perturbation.

Figure 1 shows the schematics of a transport experiment with three short solenoids of the type employed extensively at Maryland. The second experiment uses a solenoid and five printed-circuit (PC) air-core quadrupoles similar to the lenses introduced recently for the University of Maryland Electron Ring [1].

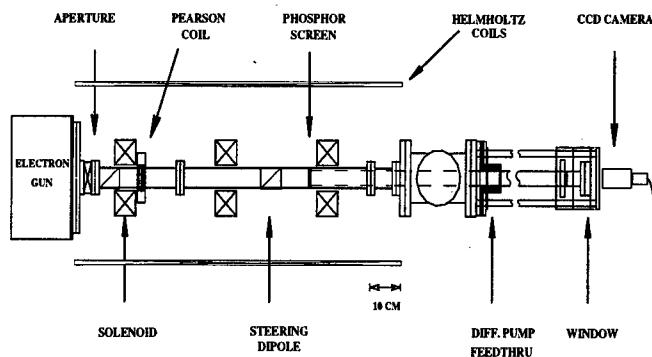


Figure 1: Three-solenoid experiment setup.

* Work supported by the U.S. Department of Energy.

[†] Email: saberni@glue.umd.edu

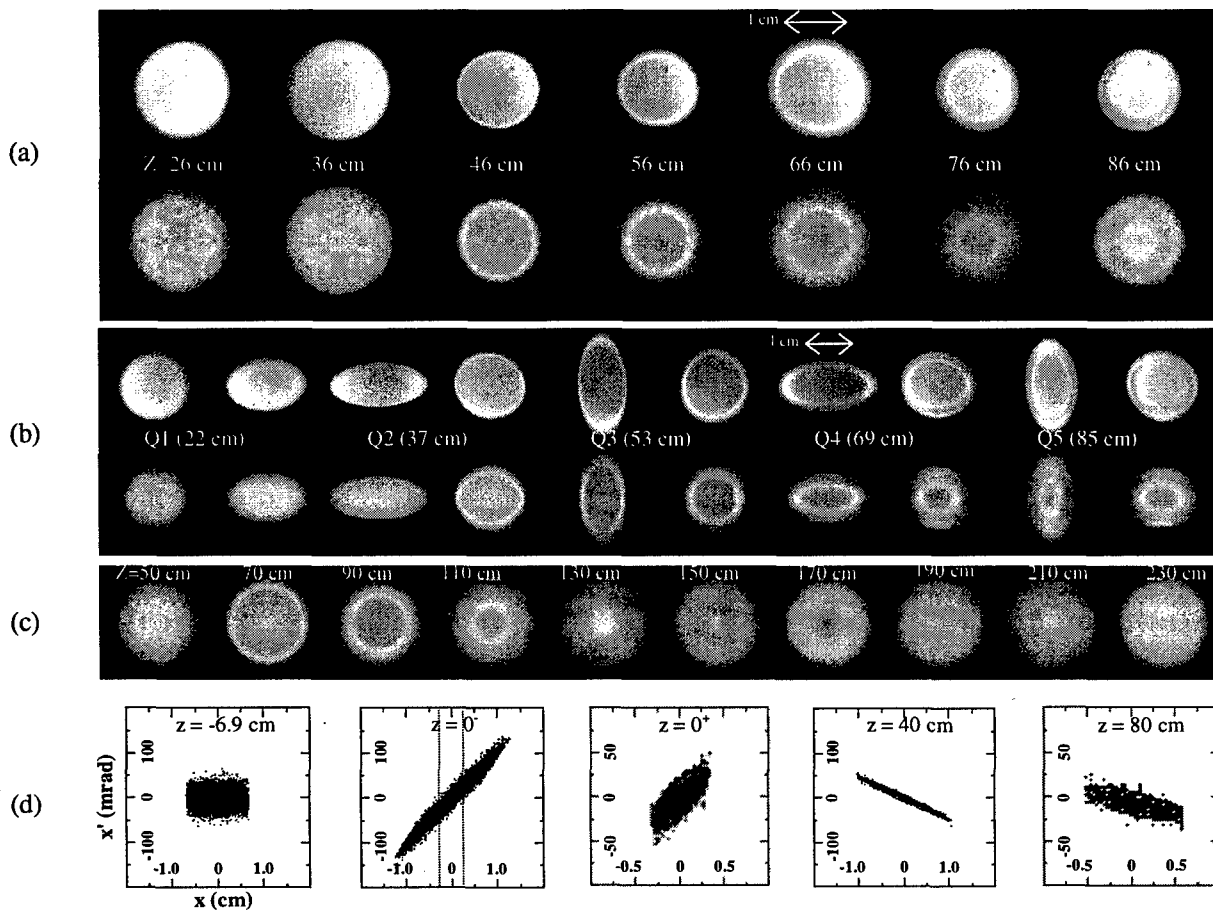


Figure 2: Summary of experiments and simulations: (a) three-solenoid experiment - phosphor screen pictures (top), and PIC simulations (bottom); (b) solenoid-five PC quadrupole experiment - phosphor screen pictures (top), and PIC simulations (bottom); (c) simulation of uniform focusing case, where the (matched) beam size is constant (0.8 cm in radius); and (d) horizontal projection of phase-space at (from left to right): the beam waist, the upstream plane of the aperture - the dashed lines indicate the 0.32 cm (radius) aperture - , the downstream plane of the aperture; the last two plots correspond to the solenoid-five quadrupole case. The strengths of focusing elements in both (a) and (b) (top parts) are adjusted for a zero-current phase advance $\sigma_0 = 85^\circ$ in the matched beams. In all cases, $z=0$ is the location of the aperture plane.

The electron gun, a Pierce-type source, produces 4 keV, 175 mA pulses ($5 \mu\text{s}$) at a rate of 60 Hz. An aperture, 6.4 mm in diameter, is placed 12.4 cm from the cathode; the aperture size is roughly 1/3 the full beam size at that plane and results in an almost uniform, 17 mA beam entering the transport pipe. The beam diagnostics is a 2.54 cm (diameter) phosphor screen that can be moved from the aperture out to a distance of nearly one meter. The beam pictures are captured with a charge-coupled device (CCD) camera and then digitized and displayed using associated hardware and software.

Figures 2(a)-(b), top parts, show the fluorescent screen pictures from typical experiments. The beam is fairly uniform over a distance of about 30 cm downstream from the aperture; the density perturbation is first seen in the form of a bright ring roughly 10 cm from the first beam waist in the three-solenoid case

[Fig. 2(a)], and near the plane between quadrupoles 2 and 3 in the solenoid-quad lattice, also about 45 cm from the aperture [Fig. 2(b)]. Further downstream, the ring moves inwards relative to the beam's edge, and a second ring emerges around 85 cm from the aperture. To aid in understanding the experiment, we have conducted 2-D and 3-D PIC simulations using the code WARP [9]. Details of the numerics and modeling of focusing elements are described thoroughly elsewhere in connection with simulations of the Maryland Electron Ring [10] and prototype injector experiments [11]. As is evident from Figs. 2(a)-(b) (bottom), the rings are also observed in the simulations, and agreement between the simulation and the experiment is good, although a difference in the phase of the perturbation is seen.

The simulations especially address the role of initial conditions. The phase of the perturbation is sensitive to the

temperature profile, so starting the simulations at the beam waist upstream from the aperture [Figure 2(d)], and fully modeling the latter, yields the best agreement with experiment. Alternatively, a semi-Gaussian distribution with a parabolic temperature profile right after the aperture produces similar results.

We gain additional insights for understanding the density perturbation when we replace the truncated distribution in the simulation with an rms equivalent equilibrium distribution, such as a K-V. In that case, no rings appear whatsoever, and the beam distribution remains K-V for the rest of the channel. This leads us to believe that the wave-like perturbation is the result of a large force imbalance or lack of equilibrium in a sheath at the beam edge, right after the aperture. As seen in Fig. 2(d), middle plot, the phase space is trapezoidal and tilted, with anomalous particle populations with relatively large velocities near the beam edge. In addition, the distribution lacks the spatial tails of an equilibrium thermal distribution (Maxwell-Boltzman), which are of the order of a Debye length [12]. In our case, the Debye length is 0.74 mm, which is non-negligible when compared to the beam radius near (and downstream of) the aperture, so the fraction of "missing" particles in a sheath one Debye length is significant. In summary, the truncated distribution is not only a non-equilibrium distribution, but also one where the departure from equilibrium is confined to the beam edge. As a consequence, the beam edge particles experience space-charge forces that are very different from those affecting the particles in the bulk of the beam. The resulting beam evolution in simulations of the solenoid-quadrupole case can be seen in the last two phase-space plots of Fig. 2(d).

Tracking of test particles moving near a model K-V beam (i.e. assuming the space charge forces arise from a uniform density beam with a sharp edge) reproduces correctly the onset of the perturbation in all experiments. In the model, test particles leave the beam near the edge of the aperture and are focused back into the beam. These results suggest that an electron flow component exists that explains the appearance of the first ring; the second ring, however, is most likely the result of a perturbation induced by the initial flow.

Finally, to examine the long term evolution of the beam, simulations were done in a uniform focusing channel over a distance of 20 m. The simulations are a "smooth approximation" version of the three-solenoid case, i.e. the beam has the same generalized perveance, and it's matched so its radius is constant, comparable to the average beam size in the experiments. As seen in Figure 2(c), the perturbation appears at a distance of about 70 cm from the aperture, and the oscillations persist for a few plasma periods ($\lambda_p \sim 1$ m in this case) and eventually diminish in amplitude as the beam evolves into equilibrium. Over the extent of the simulations, we observe no emittance growth associated with the perturbation, unlike other relaxation mechanisms [12]. Instead, the emittance oscillates slightly about its initial value, then levels off as the perturbation damps

out.

Since collimation is used in many systems, the phenomenon described here may be fairly universal and worth of additional studies. First, a wider range of parameters and conditions (generalized perveance, emittance, aperture size and location, external focusing, etc.) in both experiment and simulations has to be explored to answer important questions about scaling, stability of the oscillations and emittance growth. Secondly, the suggestion that the collective phenomena involves two components must be further studied to understand the extent of the particle-flow component and how it gives rise to a transverse wave.

REFERENCES

1. M. Reiser et. al., these Proceedings.
2. T. P. Wangler et al., in IEEE Trans., NS-32, 2196 (1985).
3. I.M. Kapchinskij and V.V. Vladimirkij, in Proceedings of the international Conference on High Energy Accelerators, Geneva, 1959 (CERN, Geneva, 1959), p. 274.
4. R. L. Gluckstern, in Proceedings of the Linac Conference, Fermilab, 1970, p. 811.
5. R. C. Davidson, Physics of Nonneutral Plasmas, Addison-Wesley, Reading, MA, (1990).
6. Steven M. Lund and Ronald C. Davidson, Phys. Plasmas **5**, 3028 (1998).
7. S. M. Lund, J. J. Barnard, G. D. Craig, A. Friedman, D. P. Grote, H. S. Hopkins, T. C. Sangster, W. M. Sharp, S. Eylon and T. J. Fessenden, E. Henestroza, S. Yu, and I. Haber, Nucl. Instrum. Methods Phys. Res., A **345** (1998).
8. S. Bernal, R. A. Kishek, M. Reiser and I. Haber, "Observations and simulations of transverse density waves in a collimated space-charge dominated electron beam", to appear in Phys. Rev. Lett., Spring, 1999.
9. A. Friedman, D. P. Grote, and I. Haber, Phys. Fluids B **4**, 2203 (1992).
10. R. A. Kishek, S. Bernal, M. Venturini, M. Reiser, and I. Haber, to appear in Proc. ICAPS'98 (1999).
11. S. Bernal, P. Chin, R. A. Kishek, Y. Li, M. Reiser, J. G. Wang, T. Godlove, and I. Haber, Phys. Rev. ST Accel. Beams **4**, 044202 (1998).
12. M. Reiser, Theory and Design of Charged-Particle Beams, Wiley & Son, New York (1994).

HIGH FREQUENCY BEHAVIOR OF TRANSVERSE IMPEDANCE FOR A CAVITY IN A BEAM PIPE *

A.V. Fedotov[†], R.L. Gluckstern, and M. Venturini

Physics Department, University of Maryland, College Park, MD 20742

Abstract

The interest in short bunches in many accelerator applications requires good understanding of the high frequency behavior of the interaction between the beam and its environment. In this paper we report an analytic calculation for the high frequency limit of the transverse impedance for both a single and periodic array of cavities in a beam pipe.

1 INTRODUCTION

The acceleration of charged particles in periodic structures leads to wakefields which are capable of interacting adversely with particles in the same bunch, or in following bunches. The conventional method of describing these limitations in the current that can be accelerated involves the longitudinal and transverse coupling impedances of the structure. With the increasing use of short bunches, it becomes necessary to evaluate these coupling impedances at high frequencies (wavelength of the order of the bunch length). This has been done for the longitudinal impedance of small periodic obstacles in an azimuthally symmetric structure [1], where we have derived an integral equation for the axial electric field at the inner bore radius. In this paper we address the corresponding problem for the transverse coupling impedance at high frequency. In particular, we first derive the integral equation for the electric field at the bore radius of the structure and obtain the result for the transverse impedance of a single small obstacle at high frequency by way of the high frequency limit of the kernels. The problem is more complicated than it was for the longitudinal impedance, since both TM and TE waveguide modes are present, which requires matching two components of the magnetic field at the boundary between the waveguide and the obstacle. As we shall eventually see, however, in the high frequency limit, the TM contribution dominates for a single obstacle, but the TE contributions must be included in the periodic case. Nevertheless, we find the same relation between the longitudinal and transverse impedances as exists for the resistive wall impedances of a beam pipe.

We now consider a point charge Q traveling in the z -direction at $(x, y) = (\Delta_x, 0)$. We start with the definition of the x component of the transverse coupling impedance

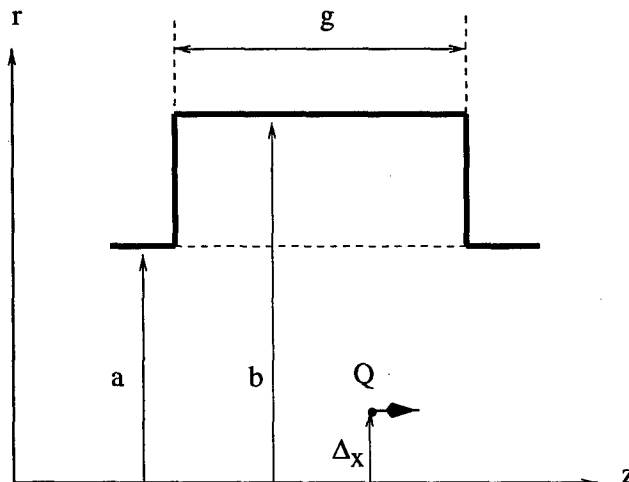


Figure 1: The layout of geometry for a single cavity.

as a function of $k = \omega/c$. In the limit of small Δ_x we have

$$Z_x(k) = \frac{j}{Q\Delta_x} \int_{-\infty}^{\infty} dz e^{jkz} \left[E_x(z; k) - Z_0 H_y(z; k) \right]_{x=0, y=0} \quad (1)$$

in units of $[\Omega/m]$ (of transverse displacement). Here $Z_0 = \sqrt{\mu_0/\epsilon_0} = 120\pi [\Omega]$ is the impedance of free space. We then use

$$\frac{\partial E_x}{\partial z} - \frac{\partial E_z}{\partial x} = -jk Z_0 H_y \quad (2)$$

to obtain the alternate expression [2]:

$$Z_x(k) = -\frac{1}{Q\Delta_x k} \int_{-\infty}^{\infty} dz e^{jkz} \frac{\partial E_z}{\partial x} \Big|_{x=0, y=0}, \quad (3)$$

where we use the time dependence $\exp(j\omega t)$.

The general technique consists of expanding fields in both the pipe ($r \leq a$) and cavity ($a \leq r \leq b$) regions into a complete set of functions. At the common interface (shown on Fig. 1) the fields have to be matched, yielding equations for the expansion coefficients.

2 INTEGRAL EQUATIONS AND SOLUTION FOR IMPEDANCE

We first consider a single cavity of radius b and axial length g . Matching of the azimuthal and longitudinal components

* Work supported by the U.S. Department of Energy

[†] fedotov@physics.umd.edu

of the magnetic field at the pipe radius $r = a$ for $0 \leq z \leq g$ (see Fig. 1), leads to the integral equations

$$1 = \int_0^g dz' [\mathcal{P}_{11}(z, z') + \mathcal{Q}_{11}(z, z')] e_z(z') + \int_0^g dz' \mathcal{Q}_{12}(z, z') e_\theta(z'), \quad (4)$$

$$0 = \int_0^g dz' \mathcal{Q}_{21}(z, z') e_z(z') + \int_0^g dz' \tilde{\mathcal{Q}}_{22}(z, z') \frac{de_\theta(z')}{dz'}, \quad (5)$$

where

$$\mathcal{P}(z, z') = \mathcal{P}^p(z - z') + \mathcal{P}^c(z, z'), \quad (6)$$

$$\mathcal{Q}(z, z') = \mathcal{Q}^p(z - z') + \mathcal{Q}^c(z, z'), \quad (7)$$

and $\tilde{\mathcal{Q}}_{22}(z, z') = -\int dz' \mathcal{Q}_{22}(z, z')$. In Eqs. (4) and (5) we defined

$$E_z(z) \equiv \frac{Q \Delta_x Z_0}{\pi a^2} e^{-jkz} e_z(z), \quad (8)$$

$$E_\theta(z) \equiv \frac{Q \Delta_x Z_0}{\pi a^2} e^{-jkz} e_\theta(z). \quad (9)$$

The kernels denoted by $\mathcal{P}(u)$ come from TM modes and those denoted by $\mathcal{Q}(u)$ come from TE modes. We use the superscript p for the pipe kernels and the superscript c for the cavity kernels.

Our next task is to compute the high frequency (large k) limit for the kernels after averaging over fast oscillations. The details are contained in [3]. All kernels vanish for $u = z - z' \leq 0$. For $u > 0$ the leading terms in the high k limit are:

$$\begin{aligned} \mathcal{P}_{11}^p(u) + \mathcal{Q}_{11}^p(u) &= \mathcal{P}_{11}^c(u) + \mathcal{Q}_{11}^c(u) \\ &\cong -(1+j)\sqrt{k/(4\pi u)}, \end{aligned} \quad (10)$$

$$\begin{aligned} \mathcal{Q}_{12}^p(u) &= \mathcal{Q}_{21}^p(u) = \mathcal{Q}_{12}^c(u) = \mathcal{Q}_{21}^c(u) \\ &\cong (1-j)/\sqrt{4a^2\pi k u}, \end{aligned} \quad (11)$$

$$\tilde{\mathcal{Q}}_{22}^p(u) = \tilde{\mathcal{Q}}_{22}^c(u) \cong (1-j)/\sqrt{\pi k u}. \quad (12)$$

Remarkably, the corresponding pipe and cavity kernels are identical for large k after smoothing. The same situation prevailed in our earlier calculation for the smoothed longitudinal coupling impedance at high frequency for a single obstacle with only TM modes being considered [1]. Thus the integral equations become:

$$1 = -(1+j)\sqrt{\frac{k}{\pi}} \int_0^g \frac{dz' e_z(z')}{\sqrt{z-z'}} + \frac{1-j}{a\sqrt{\pi k}} \int_0^g \frac{dz' e_\theta(z')}{\sqrt{z-z'}}, \quad (13)$$

$$0 = \frac{1-j}{a\sqrt{\pi k}} \int_0^g \frac{dz' e_z(z')}{\sqrt{z-z'}} + \frac{2(1-j)}{\sqrt{\pi k}} \int_0^g \frac{dz'}{\sqrt{z-z'}} \frac{de_\theta}{dz'}. \quad (14)$$

From Eq. (14) we see that, for large k ,

$$e_z(z') \cong -2a \frac{de_\theta}{dz'}. \quad (15)$$

The term involving $e_\theta(z')$ in Eq. (13) is therefore of order $1/(ka)$ compared with the term in $e_z(z')$ and can consequently be neglected. The solution for $e_z(z')$ is then [4]:

$$e_z(z') \cong -\frac{(1-j)}{2\sqrt{\pi k z'}}. \quad (16)$$

In order to obtain the impedance, defined in Eq. (3), we use the equation for the axial electric field in the pipe region

$$E_z(r, z; k) = \int_{-\infty}^{\infty} dq A(q) \frac{J_1(\kappa r)}{J_1(\kappa a)} e^{-jqz}, \quad (17)$$

to show that

$$\left. \frac{\partial E_z}{\partial x} \right|_{r=0} = \int_{-\infty}^{\infty} \frac{\kappa}{2} \frac{dq A(q)}{J_1(\kappa a)} e^{-jqz}. \quad (18)$$

Here $\kappa^2 \equiv k^2 - q^2$ and the contour in the complex q plane goes below the poles at $J_1(\kappa a) = 0$ (TM propagating modes) on the negative q axis and above the poles on the positive q axis. Equation (3) then becomes

$$Z_x(k) = -\frac{q}{Q \Delta_x k} \int_{-\infty}^{\infty} \frac{\kappa dq A(q)}{2 J_1(\kappa a)} \int_{-\infty}^{\infty} dz e^{j(k-q)z}. \quad (19)$$

The integral over z in Eq. (19) is $2\pi\delta(q-k)$, leading to

$$Z_x(k) = -\frac{2\pi A(k)}{Q \Delta_x k a} = \frac{-1}{Q \Delta_x k a} \int_0^g dz E_z(z) e^{jkz}. \quad (20)$$

Finally, by using Eqs. (8) and (16) in Eq. (20), we find

$$\frac{Z_x(k)}{Z_0} = \frac{-1}{\pi k a^3} \int_0^g dz' e_z(z') \cong \frac{(1-j)}{a^3} \sqrt{\frac{g}{\pi^3 k^3}}. \quad (21)$$

We note that the high frequency dependence of the transverse impedance for a single cavity arises essentially from the TM cavity and pipe kernels. Furthermore, we see that

$$\frac{Z_x(k)}{Z_0} \cong \frac{2}{ka^2} \frac{Z_{||}(k)}{Z_0}, \quad (22)$$

where $Z_{||}(k)$ is the high frequency limit for the longitudinal impedance of a single cavity [1], a relation which also applies to a lossy beam pipe [5]. In fact, in the high-frequency limit for a single cavity, simple arguments of diffraction theory can be used to obtain the same factor $2/(ka^2)$ as in Eq. (22) [6]. Here we used a more rigorous treatment and showed that TE modes give only next order frequency corrections, ensuring that only TM modes will govern the high-frequency behavior of the transverse impedance of a single cavity and providing the factor $2/(ka^2)$.

3 PERIODIC ARRAY OF CAVITIES

We are now ready to extend the calculation of the transverse impedance to a periodic array of identical cavities. In the geometry of the system considered, g is the length of each cavity and L is the axial distance (center to center) between two adjacent cavities.

We obtain the integral equations satisfied by the fields using the same steps as we followed for the case of a single cavity. The only difference is that in doing the field matching in each cavity one has to take into account the contributions to the fields coming from all the other cavities. These contributions determine the appearance of the coupling kernels in the integral equations. As for the case of a single cavity we find that in the high frequency limit we can reduce the original system of two integral equations to a single equation for the unknown axial component of the electric field e_z . This integral equation has the same form as the one in the calculation of the longitudinal impedance [1]. Therefore, for the transverse impedance of a periodic structure at high frequency we finally obtain [3]:

$$Z_x(g/L) = \frac{2}{ka^2} Z_{||}(g/L). \quad (23)$$

The problem is then reduced to calculating $Z_{||}$ from the solution of the integral equation for e_z . Although it was not explicitly stated in the paper, the final form for the integral equation in [1] was correct only in the limit $g/L \ll 1$, because of the way the coupling kernels were approximated. Recently, Yokoya [7] pointed out that one can treat the case of a general g/L by retaining an extra term of order $k^{-1/2}$ compared with the coupling kernel [1]. The resulting integral equation can be approximately solved [3], [7] with the following result for the impedance per period $Z_{||}(g/L)$:

$$\frac{Z_{||}}{Z_0} = \frac{-jL}{\pi ka^2} \left[1 + (1-j) \frac{L}{a} \sqrt{\frac{\pi}{kg}} \lambda(g/L) \right]^{-1}, \quad (24)$$

with

$$\begin{aligned} \lambda(\xi) \cong & 1 + \frac{\alpha_0}{\pi} \xi^{1/2} - \frac{\alpha_1}{3\pi} \xi^{3/2} + \frac{13\alpha_2}{45\pi} \xi^{5/2} \\ & + \frac{8\alpha_1^2}{45\pi^2} \xi^3 - O(\xi^{7/2}), \end{aligned} \quad (25)$$

where $\alpha_0 = \zeta(1/2)$, $\alpha_1 = \zeta(3/2)/2$, $\alpha_2 = 3\zeta(5/2)/8$, and ζ denotes the Riemann zeta function. In the limit $g \ll L$ we have $\lambda = 1$, and one recovers our earlier expression for the longitudinal impedance [1]. In the case $g/L = 1$ it is possible to obtain an exact analytic result, using diffraction theory, as was shown by Stupakov [8]. In our notation Stupakov's result is $\lambda(1) = -\zeta(1/2)/\pi \cong 0.464845$ [8], in agreement with Yokoya's numerical solution [7].

Equations (23)-(25) provide an analytic description of the transverse and longitudinal impedance at high frequency for an infinite array of periodic cavities. These expressions are valid when $NL \gg ka^2$, where N is the number of cavities. For $ka^2/L \geq N \gg 1$ there is a transition to the result valid for a finite number of cavities, and

one needs to use a different expression for the longitudinal impedance [9].

4 SUMMARY

In this paper we address the question of the transverse coupling impedance at high frequency. The problem is more complicated than for the longitudinal impedance, since both TM and TE waveguide modes are present, which requires matching two components of the magnetic field at the boundary between the waveguide and the obstacle. We show that, in the high frequency limit, the TM contribution dominates for a single obstacle, while the TE contribution must be included in the periodic case. Nevertheless, we find the same relation between the longitudinal and transverse impedances as exists for the resistive wall impedance of a beam pipe. Validity of the factor $2/(ka^2)$ between the longitudinal and transverse impedances allows simple estimates of the transverse impedance at high frequency.

5 ACKNOWLEDGMENT

We are grateful to K. Yokoya for sharing his notes with us and for making several useful comments. We also wish to thank S. Kurennoy for helpful comments.

6 REFERENCES

- [1] R.L. Gluckstern, Phys. Rev. D **39**, 2773 (1989); *ibid.*, 2780.
- [2] See, for example, R.L. Gluckstern, Phys. Rev. A **46**, 1106 (1992).
- [3] A.V. Fedotov, R.L. Gluckstern and M. Venturini, Transverse Impedance of a Periodic Array of Cavities, submitted for publication in Phys. Rev. ST Accel. Beams, 1999.
- [4] We note at this point, that the behavior of $e_z(z')$ near $z' = 0$ is expected to be $(kz')^{-1/3}$ for $kz' \ll 1$ (z' small compared with the wavelength $2\pi/k$). Thus $(kz')^{1/2}$ in the denominator of Eq. (16) should be replaced by $(kz')^{1/2} + \text{const } (kz')^{1/3}$, where const is $O(1)$. Nevertheless, the dominant region for the integration over z' in Eq. (21) is for $kz' \sim kg \gg 1$, and thus $(kz')^{1/2} \gg (kz')^{1/3}$. It is for this reason that Eq. (16) does not accurately reflect the behavior for values of $kz' \ll 1$, but this has no effect on the final result in Eq. (21).
- [5] A. Chao, *Physics of collective beam instabilities in high energy accelerators* (Wiley, New York, 1993).
- [6] K. Bane and M. Sands, Part. Accel., **25**, 73 (1990).
- [7] K. Yokoya, private communication; also K.L.F. Bane and K. Yokoya, The High-Frequency Impedance of a Periodic Accelerator Structure, these Proceedings.
- [8] G. Stupakov, In Proceedings of the 1995 Particle Accelerator Conference, Dallas, TX (IEEE, Piscataway, NJ, 1996), p. 3303.
- [9] R.L. Gluckstern, In Proceedings of the 1989 Particle Accelerator Conference, Chicago, IL (IEEE, Piscataway, NJ, 1989), p. 1157.

COULOMB SCATTERING WITHIN A SPHERICAL BEAM BUNCH IN HIGH CURRENT LINEAR ACCELERATORS *

A.V. Fedotov[†] and R.L. Gluckstern

Physics Department, University of Maryland, College Park, MD 20742

Abstract

Beam halo formation issues are important for the design of high current linear ion accelerators. Various mechanisms can potentially cause beam halo. Some recent studies have suggested that Coulomb collisions in the beam bunch can contribute significantly to beam bunch growth and halo development in linear accelerators. Despite the general belief that collisions are not important, it is clear that a rigorous treatment of this question is needed. In an effort to explore this issue in detail we have undertaken an analysis of the effects of Coulomb scattering between ions in a self-consistent spherical bunch.

1 INTRODUCTION

During the last several years, interest has grown in the design of high current linear ion accelerators for a variety of important applications. Since the beam bunch spends a very short time in a linac, compared with a circular machine or a storage ring, the general expectation is that collisions between individual ions will take place on too long a time scale to be important. However, there have been some recent numerical studies which suggested that small angle single Coulomb scattering may not be negligible for spheroidal bunches in a linac. Thus, the concern has arisen with regard to the possibility that Coulomb collisions between ions may contribute significantly to emittance growth and/or halo formation. It is clear that, because of the importance of this question for the design of high current linear ion accelerators, a more rigorous treatment of the effect of single Coulomb collisions is needed. In an effort to explore this issue in detail we have undertaken an analysis of the effects of Coulomb scattering between ions in a self-consistent [1] spherical bunch.

2 GENERAL CONSIDERATIONS

Our quantitative study of non-stationary distributions [2] shows that the parameters of halo formation are more or less the same as those caused by mismatches of an otherwise self-consistent phase space distribution.

We therefore start with our family of self-consistent, equipartitioned phase space distributions [1]:

$$f(\mathbf{r}, \mathbf{v}) = \begin{cases} N(H_0 - H)^n & , \quad H < H_0 \\ 0 & , \quad H > H_0 \end{cases}, \quad (1)$$

where the Hamiltonian is

$$H(\mathbf{r}, \mathbf{v}) = m\mathbf{v}^2/2 + k\mathbf{r}^2/2 + e\Phi_{sc}(\mathbf{r}), \quad (2)$$

and use

$$G(\mathbf{r}) \equiv H_0 - k\mathbf{r}^2/2 - e\Phi_{sc}(\mathbf{r}), \quad (3)$$

with k being the smoothed restoring force gradient. We choose the space charge potential $\Phi_{sc}(\mathbf{r})$ which vanishes at $r = \infty$, H_0 is a constant, the external forces are linear, and $f(\mathbf{r}, \mathbf{v})$ is normalized such that

$$\rho(\mathbf{r}) = Q \int d\mathbf{v} f(\mathbf{r}, \mathbf{v}), \quad \int d\mathbf{r} \rho(\mathbf{r}) = Q, \quad (4)$$

where Q is the total bunch charge.

The probability per unit time (in the coordinate system of the bunch) for a Coulomb collision between ions with velocity \mathbf{v}_1 and \mathbf{v}_2 , is then

$$\begin{aligned} \frac{dP}{dt} &= \int d\mathbf{r} \int d\mathbf{v}_1 f(\mathbf{r}, \mathbf{v}_1) \\ &\times \int d\mathbf{v}_2 f(\mathbf{r}, \mathbf{v}_2) |\mathbf{v}_1 - \mathbf{v}_2| d\Omega_s \frac{d\sigma}{d\Omega_s}, \end{aligned} \quad (5)$$

where $d\sigma/d\Omega_s$ is the classical differential Rutherford cross section.

3 HALO EXTENT

Using Eqs. (1) and (3) we find

$$\rho(\mathbf{r}) = QN \int_0^{v_0} 4\pi v^2 dv [G(\mathbf{r}) - mv^2/2]^n, \quad (6)$$

where $v_0^2 = 2G(\mathbf{r})/m$. We then examine the kinematics of the Coulomb collision [3]. Clearly the ions which travel to the largest radius before turning back are the ones which have the largest possible velocity at a given r and where, after the collision, one is left at rest and the other travels radially with all the kinetic energy. Such a collision can only conserve energy and momentum when the colliding ion velocities are at 90° to one another. With the maximum velocity before the collision given by $mv^2/2 = G(\mathbf{r})$, the maximum energy after the collision is

$$\frac{mv_{\max}^2}{2} = 2G(\mathbf{r}). \quad (7)$$

The maximum radius R then satisfies

$$2G(\mathbf{r}) + \frac{k\mathbf{r}^2}{2} + e\Phi_{sc}(\mathbf{r}) = \frac{kR^2}{2} + e\Phi_{sc}(R), \quad (8)$$

* Work supported by the U.S. Department of Energy

[†] fedotov@physics.umd.edu

where $r < a$, $R > a$. We then have

$$\frac{k(R^2 - a^2)}{2} - \frac{eQ}{4\pi\epsilon_0} \left(\frac{1}{a} - \frac{1}{R} \right) = G(r). \quad (9)$$

We proceed further in this analysis for $n = -1/2$, where

$$G(r) = \frac{3k}{\kappa^2} \left[1 - \frac{i_0(\kappa r)}{i_0(\kappa a)} \right]. \quad (10)$$

Here

$$\kappa^2 = \frac{eQ}{4\pi\epsilon_0 \int_0^a r^2 dr G(r)} \quad (11)$$

and

$$i_0(w) = \frac{\sinh w}{w}. \quad (12)$$

From Eq. (9) it is clear that outermost particles are those which start near the bunch center. We then rewrite Eq. (9) as

$$u^3 + \left[-\frac{12}{\kappa^2 a^2} + \frac{6(1+c)}{\kappa a s} - 3 \right] u + 6(1 - \kappa \frac{c}{s}) / \kappa^2 a^2 + 2 = 0, \quad (13)$$

where $u = R/a$, $s = \sinh(\kappa a)$, $c = \cosh(\kappa a)$. For large κa , Eq. (13) can be easily solved, and we obtain

$$\begin{aligned} \frac{R-a}{a} &\simeq \frac{\sqrt{3}-1}{\sqrt{\kappa^2 a^2 + 15/2}} \\ &\rightarrow \frac{\sqrt{2}(\sqrt{3}-1)}{\sqrt{15}} \eta_{\text{rms}} \simeq 0.27 \eta_{\text{rms}}, \end{aligned} \quad (14)$$

where η_{rms} is an rms tune depression [3].

An interesting consequence of Eq. (14) is that the thickness of the shell populated by the scattered ions decreases as the beam becomes more space charge dominated. We remind the reader that Eq. (14) was obtained for the self-consistent equipartitioned distribution with $n = -1/2$. In his report [4] on numerical studies for distributions which were not self-consistent, Pichoff observed a similar dependence on tune depression.

At first glance this thin shell does not resemble our earlier description of a halo [1, 2]. However, the shell thickness given by Eq. (14) was obtained for an equipartitioned beam. We now use Pichoff's definition of the equipartitioning factor $\chi = v_z/v_x$. The maximum possible velocity after the collision can be rewritten as $mv_{\text{max}}^2/2 = (1+\chi^2)G$, and we obtain for the shell thickness

$$\frac{R-a}{a} \simeq \frac{\sqrt{1+2\chi^2}-1}{\sqrt{15/2}} \eta_{\text{rms}}. \quad (15)$$

Clearly, when the beam is non-equipartitioned or the beam with the stationary distribution is rms mismatched, the thickness of the shell can be significantly larger, depending on the equipartitioning factor. Such an increased shell thickness can then easily resemble the typical halo extent [1, 2]. Thus, in order to understand whether scattering can

contribute to the halo formation we need to calculate the rate at which this shell becomes populated.

We note that solutions given by Eqs. (14)-(15) can be used with good accuracy only for large values of κa ($\kappa a > 4$) corresponding to tune depressions $\eta < 0.6$, which covers our range of interest [5]. For $\eta \geq 0.6$ a better solution of Eq. (13) should be used. For completeness, we present below some values based on numerical solution of Eq. (13). For equipartitioned beam ($\chi = 1$), the shell extent becomes $R/a = 1.41, 1.37, 1.32, 1.27, 1.22$ for $\eta = 1, 0.9, 0.8, 0.7, 0.6$, respectively. Similar values for the shell thickness were obtained by Pichoff for the distribution functions used [4]. In fact, in the limit of zero space-charge, the shell thickness becomes independent of the distribution, and, from Eq. (8), is simply given by $R/a = \sqrt{1+\chi^2}$ (see also [4]).

4 COULOMB SCATTERING RATE

The heart of our calculation is the evaluation [3] of the 11 dimensional integral in Eq. (5) over the range of r, v_1, v_2, Ω_s which enables particles to leave the bunch. The detailed analyses are presented in [3]. Here we just present an order of magnitude estimate of Eq. (5), assuming a spherical bunch of radius a . We use $|v_1| \sim |v_2| \sim v$ and $\int dv f(r, v) \sim 1/a^3$ and assume all integrals are finite to obtain the estimate

$$\frac{dP}{cdt} \sim \frac{r_p^2}{\epsilon_N^3}, \quad (16)$$

where the classical radius of the ion is given by

$$r_p = \frac{e^2}{4\pi\epsilon_0 mc^2}, \quad (17)$$

and where the (projected) normalized emittance of the bunch is

$$\epsilon_N \simeq av/c. \quad (18)$$

For a proton bunch with $r_p = 1.5 \times 10^{-18}$ [m] and $\epsilon_N \simeq 1 \times 10^{-6}$ [m rad], Eq. (16) yields

$$\frac{dP}{cdt} \sim 10^{-15}/\text{km}, \quad (19)$$

clearly negligible for a linac.

The problem with the foregoing estimate is that it ignores the divergence of the Coulomb cross section at $\theta_s = 0$, as well as the possible divergence of the distribution $f(r, v)$ near $mv^2/2 = G(r)$ for values of $n < 0$ in Eq. (1). We address these issues and present evaluation of the 11 dimensional integral given by Eq. (5) in [3].

After rigorous calculation [3] we finally find that the fraction of ions which leave the beam (and form a spherical layer around the bunch) per unit length is

$$\frac{dP}{cdt} \sim \begin{cases} r_p^2/\epsilon_N^3, & n > 0 \\ (r_p^2/\epsilon_N^3) \ell n(\epsilon_N^2/r_p a), & n = 0 \\ (r_p^2/\epsilon_N^3) (\epsilon_N^2/r_p a)^n, & -1 < n < 0 \end{cases}, \quad (20)$$

where, for the distributions with $0 \geq n > -1$, we assume that the Coulomb force between ions is screened at the Debye length λ_D . Using $r_p = 1.5 \times 10^{-18}$ [m], $\epsilon_N \cong 10^{-6}$ [m rad] and $a \cong 10^{-2}$ [m], we then have

$$\frac{dP}{cdt} \sim \begin{cases} 10^{-15}/\text{km} & , \quad n > 0 \\ 10^{-14}/\text{km} & , \quad n = 0 \\ 10^{-11}/\text{km} & , \quad n = -0.5 \\ 10^{-8}/\text{km} & , \quad n = -0.9 \end{cases} \quad (21)$$

5 EFFECT OF MULTIPLE COLLISIONS

The shortcoming of the approach in Section 4 is that it does not take into account the effect of a large number of small scattering angle Coulomb collisions. For this purpose we also examine the evolution of the phase space distribution in time due to Coulomb collisions by starting with the Boltzmann equation for an otherwise equipartitioned beam bunch. For our self-consistent distribution, the Boltzmann equation, which accounts for the scattering of particles into and out of regions of velocity space, can be written as

$$\begin{aligned} \frac{\partial f(u_1)}{\partial t} &= K n_D \int du_2 |u_1 - u_2| \\ &\times \int d\Omega_s \left[\frac{d\sigma}{d\Omega_s}(u'_1, u'_2 \rightarrow u_1, u_2) f(u'_1) f(u'_2) \right. \\ &\left. - \frac{d\sigma}{d\Omega_s}(u_1, u_2 \rightarrow u'_1, u'_2) f(u_1) f(u_2) \right] \end{aligned} \quad (22)$$

Here n_D is the ion particle density, and $d\sigma/d\Omega_s$ is the Coulomb scattering cross section for the initial and final states. Apart from constants, which are absorbed in K , $f(u)$ is $(1 - u^2)^n$, where we renormalized all velocities as $v^2 = [2G(r)/m]u^2$.

We now calculate the rate of change of $\langle u_1^2 \rangle$ and $\langle u_1^4 \rangle$ and find [3] that $d\langle u_1^2 \rangle/dt = 0$ and that the lowest non-vanishing power occurs for $d\langle u_1^4 \rangle/dt$:

$$\frac{d\langle u_1^4 \rangle}{dt} = \frac{4\pi^2}{18} K n_D \left[\ell n \left(\frac{1}{\theta_{\min}} \right) - 1 \right] \quad (23)$$

It is possible to calculate the rate of change of the expectation value of $(1 - u_1^2)^n$ for all values of n , with the same result as in Eq. (23), except for a numerical factor of order 1. In fact, the results obtained suggest the expected rounding of the $n = 0$ distribution near $u = 1$.

We therefore expect that multiple scattering simply leads to a generalization of our previous result in Section 4 with logarithmic behavior:

$$\frac{1}{c} \frac{dP}{dt} \sim \frac{r_p^2}{\epsilon_N^3} \ell n \left(\frac{1}{\theta_D} \right), \quad (24)$$

where θ_D is minimum angle corresponding to Debye length impact parameter. If so, the rate of scattering due to multiple collisions is only slightly higher than the rate for single encounters for the distributions with $n > 0$. For the same parameters as those used in Section 4 the rate becomes clearly negligible with $dP/cdt \sim 10^{-14}/\text{km}$.

6 SUMMARY AND CONCLUSIONS

In Sections 3-4 we have calculated the effect of single Coulomb scattering of a self-consistent 6-D distribution for a spherical beam bunch. In this calculation we find:

- Single collisions are capable of populating a thin spherical shell around the beam bunch.
- When the beam is non-equipartitioned or the beam with the stationary distribution is rms mismatched, the thickness of the shell can be significantly larger, depending on the equipartitioning factor.
- For the relatively singular distribution with $n = -1/2$, a bunch with a normalized emittance $\epsilon_N \sim 10^{-6}$ [m rad] and a radius of 1 [cm] will populate the shell with a probability of 10^{-11} per kilometer of linac.
- For distributions with $n > 0$, this rate of population is further reduced by a factor 10^{-4} .

Our conclusion is that effect of single Coulomb collisions on halo development in high current ion linear accelerators is not important.

In Section 5 we related our analysis to diffusion caused by many small angle Coulomb collisions, with the conclusion that the effect of multiple Coulomb collisions in halo development in high current ion accelerators is also expected not to be important.

7 ACKNOWLEDGMENT

We thank T. Wangler, R. Ryne and S. Habib for frequent valuable discussions. In addition we are indebted to R. Davidson and I. Hofmann for their helpful comments. We are grateful to N. Pichoff for sharing his manuscript with us and for making several useful comments about our calculations and manuscript. We also wish to thank Andy Jason and the LANSCE1 group for its hospitality during some of these studies.

8 REFERENCES

- [1] R.L. Gluckstern, A.V. Fedotov, S.S. Kurennoy and R.D. Ryne, Phys. Rev. E **58**, 4977 (1998).
- [2] A.V. Fedotov, R.L. Gluckstern, S.S. Kurennoy and R.D. Ryne, Phys. Rev. ST Accel. Beams, **2**, 014201 (1999).
- [3] R.L. Gluckstern and A.V. Fedotov, Coulomb Scattering Within a Spherical Beam Bunch in a High Current Linear Accelerator, Univ. of Maryland Physics Department Preprint 99-056; submitted for publication in Phys. Rev. ST Accel. Beams (1999).
- [4] N. Pichoff, DAPNIA/SEA Report 98-46, France (1998).
- [5] APT Conceptual Design Report, Los Alamos Report No. LA-UR-97-1329 (1997).

PIC CODE SIMULATIONS OF COLLECTIVE EFFECTS IN THE SPACE-CHARGE-DOMINATED BEAM OF THE UNIVERSITY OF MARYLAND ELECTRON RING (UMER)

R. A. Kishek[#], S. Bernal, Y. Li, M. Reiser, and M. Venturini,

University of Maryland, College Park, MD

I. Haber, Naval Research Laboratory, Washington, DC

T. F. Godlove, FM Technologies, Fairfax, VA

Abstract.

Numerical simulation using particle-in-cell codes is a powerful tool in understanding the nonlinear dynamics of space-charge-dominated beams. The University of Maryland Electron Ring (UMER) will explore the transport of beams with intensity previously inaccessible to circular machines. The ring will also function as a testbed for accelerator codes. Applications such as heavy ion fusion and colliders require the preservation of beam quality during transport over large distances. This need for low beam emittance and small particle losses constrains the design and fabrication of the lattice and the injector. Furthermore, the non-zero energy spread leads to dispersion in the circular lattice. Simulations using the WARP code address these issues: the magnets, including the fringe field nonlinearities, are modeled realistically; dispersion matching is attempted; and effects of lattice and beam errors are examined. The simulations aid in understanding experimental results, such as the transverse density waves observed in the injector.

1. INTRODUCTION

Many applications of accelerators are emerging that require high intensities and good beam quality. Heavy ion inertial fusion, for example, requires transporting and accelerating a high current beam and focusing it onto a tiny spot. Spallation neutron sources and high intensity colliders also require good beam quality, although the intensities needed may be somewhat lower. Furthermore, most of these applications involve some bending of the beam, and some can benefit from the concept of a recirculator to save space and costs. The University of Maryland Electron Ring (UMER) [1], which is currently in its early construction stages, is a scaled experiment designed to investigate the physics of space-charge dominated beams in a circular geometry. A key advantage of the project is its low cost, through the use innovative features such as printed-circuit magnets [2] and modularity in design.

With a nominal 100 mA at 10 keV and 50 mm-mrad emittance, the UMER beam operates with a tune depression (v/v_0) of 0.14, placing it in an extremely

space-charge-dominated regime, especially for a circular machine. The intensity of the beam and the circular geometry combine to generate complications such as resonances and dispersion. Mismatches and some lattice and alignment errors play a bigger role as the beam intensity increases, especially since the compact printed-circuit magnets introduce large fringe fields that may degrade the beam quality. Image forces play a role that cannot be neglected, especially since the beam fills a large cross-section of the pipe. Finally, bunch-end effects and longitudinal confinement of the intense beam in the ring is yet another complication.

Self-consistent computer simulations are necessary because of the nonlinear nature of these effects. In the ongoing process leading up to the commissioning of the ring, the numerical simulations using the WARP code [3] are benchmarked against any experimental measurements available, some of which may be unexpected. For example, simulation has been a successful tool in understanding the radial density waves seen in a prototype injector experiment [4]. Because of its low cost and versatility, UMER will provide a valuable testbed for computer codes to be used in designing larger machines.

Since the simulation work permeates all aspects of the ring design, we have only enough space to briefly address a few of the issues listed above, directing the reader to other publications for more involved discussions.

2. BACKGROUND

The nominal beam current is 100 mA at 10 keV, resulting in a generalized perveance of 0.0015. A nominal (unnormalized 4σ) emittance of 50 mm-mrad and nominal average beam radius of 10.2 mm (for $\sigma_0 = 76^\circ$, $v_0 = 7.6$) results in a tune depression (v/v_0) of 0.14. A future phase is planned where the beam is to be accelerated to 50 keV. Moreover, the ring is designed to run at lower beam currents, allowing us to explore a wide range of tunes.

Figure 1 displays a schematic of the ring lattice, which consists of 36 FODO cells around the 11.52 m circumference ring. Each cell is therefore 32.0 cm long and contains two evenly-spaced printed-circuit quadrupoles [2] and, in between those, a printed-circuit

* <http://www.ipr.umd.edu/~ebte/ring>

ramiak@ebte.umd.edu

dipole which bends the beam by 10° . The quadrupole gradient is about 0.078 Tesla/m, while the bending dipole peak field is about 0.00154 Tesla. Three induction gaps used for longitudinal confinement are evenly distributed around the ring, while the remainder of the spaces are occupied by diagnostics and pumping ports.

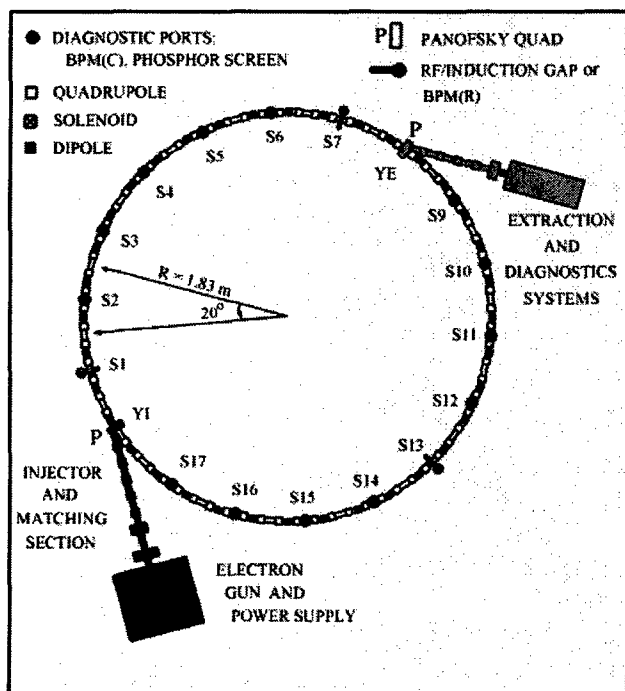


Figure 1. Schematic of ring design [1].

In the simulations described herein, we rely primarily on the WARP particle-in-cell (PIC) code [3], which has been developed at Lawrence Livermore National Laboratory (LLNL) for heavy ion fusion applications. An important feature of the WARP code is its ability to efficiently track a space-charge-dominated beam along bends. The particle orbits are integrated self-consistently under the applied fields and the self-fields. The simulations have the following characteristics: (a) the magnet nonlinearities, including those arising from the fringe fields, are fully included; (b) the numerics have been checked for convergence; and (c) although most simulations were performed using the 2d3v "slice model", certain key simulation were tested using the full 3d code. Ref. [5] contains further details.

3. SIMULATION RESULTS AND DISCUSSION

3.1 Magnet nonlinearities

Despite large fringe fields, the printed-circuit magnets were designed to be linear when integrated parallel to the magnet axis. Simulations with the quadrupoles that include the fringe fields exhibit no emittance growth,

confirming the designed linearity of the integrated fields [5]. Including the fringe fields of the bending dipoles, however, results in some non-numerical emittance growth (about 30 % in 10 turns or 360 dipoles). The question arises as to why the dipoles, which were also designed to be linear in the integrated sense, lead to more emittance growth than the quadrupoles. The difference is that the individual particles in the beam follow a curved trajectory inside the dipole, whereas the dipole fields were designed to be linear when integrated along z , the dipole axis. Extensive simulations [partially discussed in ref. 5] link the observed growth in emittance to the field inhomogeneities seen by the beam over its curved trajectory.

Although the emittance growth is relatively small, it can become significant if we wish to operate for > 25 turns. A remaining question currently being explored is therefore whether a dipole redesign can alleviate the long-term emittance growth by minimizing the nonlinearities integrated over the self-consistent particle orbits.

3.2 Dispersion Matching

Since a beam, in general, has a non-zero energy spread, propagation in bends leads to dispersion, i.e., particles at different energies oscillate around different reference trajectories. If not explicitly matched for dispersion, the beam experiences a dispersion mismatch as it enters the ring from the straight injector, or as it leaves it to the extraction section. For a space charge dominated beam, this dispersion mismatch leads to emittance growth, as confirmed earlier by theory and simulation [5-6]. It is possible to use the generalized envelope equations developed by Venturini and Reiser [6] to design a matching section that matches both the envelopes and the dispersion function for a space-charge-dominated beam. There remain questions, however, about the applicability of the theory as the beam attempts to relax to a state of equilibrium.

We applied numerical simulations with the WARP code to evaluate the results of employing dispersion matching at both injection and extraction. The results are discussed in ref. [7] and generally indicate that proper dispersion matching can help reduce the emittance growth. Indeed, the simulations indicate that a significant component of the emittance growth from a dispersion mismatch is reversible, meaning that it can be recovered by proper matching at extraction. However, dispersion matching using the generalized envelope equations becomes more difficult at higher currents because relaxation processes develop earlier downstream, and henceforth the predictions of these equations depart from the simulation results.

3.3 Errors, Mismatches and Misalignments

Table 1 is a summary of the error analyses conducted so far. The dipole nonlinearities have been included in the

error studies. By themselves, the nonlinearities contribute 31 % emittance growth over 10 turns. It is clear that reasonable errors in injection or mispowering do not affect the emittance growth beyond that. These studies show that as long as the beam centroid remains confined within 1 mm of the pipe axis, there is negligible change in the emittance growth.

A mismatched beam experiences an additional emittance growth as the free energy in the beam is converted to thermal energy. However, after 10-15 turns the emittance growth due to the mismatch diminishes as the mismatch oscillations damp out and the beam reaches a new equilibrium. A glance at Table 1 reveals that the beam is very sensitive to errors from quadrupole rotations (skew quads), thus imposing tight tolerances on the rotation angles. This subject is treated in more detail in ref. [8].

Table 1: Summary of multi-particle error studies.

Description	Error Magnitude (in 10 Turns)	$\Delta\epsilon/\epsilon$	Centroid Offset (mm)	Particle Losses
No Errors				
Linear	-	8%	0	0
Magnet Nonlinearities	Fringe Fields	31%	0.2 mm	0
Mismatches				
x	0.5 mm	41%		0
x and -y	0.5 mm	46%		0.1%
		(84% / 20T)		
Injection Errors				
within 1 mm or 4 mrad		33.5%	1 mm	0
2 mm or 8 mrad		45%	2 mm	0
Mispowering				
Dipoles				
Single Magnet	1.0%	38%	0.3 mm	0
Systematic	-2.5%	27%	1 mm	
	-5.0%	38%	2 mm	
Quadrupoles				
Single Magnet	1.0%	42%		0
	0.5%	35.5%		0
	0.2%	35%		0
Rotation				
Quadrupoles (random)	0.1 deg	40%		0
	0.2 deg	60%		

3.4 Other Issues

We have also applied the code to other situations, which are described more fully elsewhere. The code has played a role in designing the injector [9], especially the inflector bend, and in testing the effects of the Panofsky quad used in injection [10]. The simulations have reproduced radial density waves observed in a prototype injector experiment [4], and played a major role in linking this phenomena to the initial particle distribution at the aperture.

4. CONCLUSION

In this paper we have touched upon the magnet nonlinearities, dispersion matching, and error analyses, among others. In all cases, the simulation is proving to be a valuable tool in exploring complex physical phenomena that are not easily tractable by analytic means. The future plan of the simulation effort is to move towards full 3D simulation in order to (a) understand the end effects and longitudinal confinement, and (b) simulate the electron gun so as to get a better model of the initial beam distribution. As experimental data becomes available in the forthcoming commissioning process of UMER, it will be interesting to compare with the WARP predictions.

ACKNOWLEDGEMENTS

We wish to thank our colleagues D. P. Grote, J. J. Barnard, A. Friedman, S. Lund, and J.G. Wang for many fruitful discussions. We also thank K. Danylevich for assistance with presentation. The code runs on computers provided by the National Energy Research Scientific Computing Center (NERSC). This research is sponsored by the U. S. Department of Energy (DOE) under contract DE-FG02-94ER40855.

REFERENCES

- [1] M. Reiser, et. al., "The Maryland Electron Ring for Investigating Space-Charge Dominated Beams in a Circular FODO System," these proceedings, TUCR3.
- [2] T. F. Godlove, S. Bernal, and M. Reiser, Proc. 1995 Particle Accelerator Conference, 2117 (1995); also W. W. Zhang, "Magnetic Field Measurement of Printed-Circuit Quadrupoles and Dipoles," these proceedings, THP170.
- [3] D. P. Grote, et. al., Fus. Eng. & Des. 32-33, 193-200 (1996).
- [4] S. Bernal, R. A. Kishek, M. Reiser, and I. Haber, "Observations and Simulations of Transverse Density Waves in a Collimated, Space-Charge-Dominated Electron Beam," accepted in Phys. Rev. Lett (1999); also these proceedings, TUP115.
- [5] R. A. Kishek, et. al., "Unique Features of the University of Maryland Electron Ring and the Necessity of PIC Code Simulation," proc. ICAPS98, Monterey, CA, in print (1999); and references therein.
- [6] M. Venturini and M. Reiser, "rms Envelope Equations in the Presence of Space Charge and Dispersion," Phys. Rev. Lett., 81, 96 (1998);
- [7] M. Venturini, et. al., "The problem of dispersion matching in space charge dominated beams," these proceedings, THP134.
- [8] R. Kishek, et. al., "Effects of Quadrupole Rotations on the Transport of Space-Charge-Dominated Beams: Theory and simulations Comparing Linacs with Circular Machines," these proceedings, TUP119.
- [9] T. Godlove, et. al., "The 10 keV Injector for the University of Maryland Electron Ring Project," these proceedings, WEA36.
- [10] Y. Li, et. al., "Design, simulation and test of Panofsky quadrupole," these proceedings, THP169.

EFFECTS OF QUADRUPOLE ROTATIONS ON THE TRANSPORT OF SPACE-CHARGE-DOMINATED BEAMS: THEORY AND SIMULATIONS COMPARING LINACS WITH CIRCULAR MACHINES

R. A. Kishek, IPR, University of Maryland, College Park, MD,
J. J. Barnard and D. P. Grote, Lawrence Livermore National Lab, CA

Abstract

PIC-code simulation results are presented where a space-charge-dominated beam is transported in a lattice with quadrupole rotation errors. Two examples are studied in detail: the circular lattice for the University of Maryland Electron Ring (UMER) and the straight lattice from an early design of a proposed heavy ion inertial fusion (HIF) research experiment known as the Integrated Research Experiment (IRE). Reasonably small errors have little effect. However, the dependence on the strength of the errors is nearly quadratic. Slightly larger errors, therefore, can cause deterioration in beam quality, as manifest by a large increase in beam emittance and formation of a halo, leading eventually to particle losses. The simulations are accompanied by the moment equations for such a system in the presence of beam acceleration.

1 INTRODUCTION

Many applications, from heavy ion inertial fusion to high energy colliders, are relying increasingly on high brightness, space-charge-dominated, beams. To maintain the brightness of the beam during transport, it is important to control lattice errors so as to minimize emittance growth. Accelerator lattice errors may give rise to envelope mismatches and mismatches provide a source of free energy which, if thermalized, can result in emittance growth and hence brightness degradation. Quadrupole rotation errors are an interesting class of accelerator element misalignments, because the two transverse (x and y) equations of motion become coupled at linear order in the coordinates.

We perform simulations using the WARP code [1] to investigate emittance growth under the presence of quadrupole rotation errors. Two generalized emittances (defined below) give a measure of the phase space occupied by the beam and so give a measure of inherent beam-quality that would be ultimately achievable after compensating skew (rotated) quadrupoles undo the cumulative effects of small random rotation errors of the focusing quadrupoles. The simulations address issues such as reversibility of emittance growth, dependence on space charge, role of nonlinearities, periodicity of errors, and acceleration. For this paper, we will use simulations performed on two machines: the University of Maryland Electron Ring (UMER) [2] and the Integrated Research Experiment in heavy ion fusion (IRE) [3].

2 GENERALIZED EMITTANCE

When quadrupole rotation errors are present, the x and y normalized emittances are not conserved, even for a beam with an initial Kapchinskij-Vladimirskij (K-V) distribution with a linear space charge force profile propagating under linear external forces. However, if the equations of motion result from linear forces and are derivable from a Hamiltonian system, constants of the motion may be obtained analogous to the normalized x and y emittances [4]. Further, the K-V distribution has been generalized [5] to distributions in which the principal axes do not align with the x and y axes, and moment equations have been derived [6] that assume the space-charge profile remains linear, consistent with the assumption of the KV-like distribution of ref. [5]. In ref. [6], a drifting, non-relativistic beam was assumed, and a conservation constraint was derived that is equivalent to the first of the conservation constraints in ref. [4].

In this section, we generalize slightly the moment equations of ref. [6] to include acceleration, and we evaluate both the first and second independent emittance-like conservation constraints of ref. [5]. In the presence of non-linearities, either from space-charge or the external focusing field, the underlying assumption of a linear force profile is violated, and therefore the derived constraints will evolve (usually increasing) along the accelerator. For simplicity we consider non-relativistic beams. We assume the space charge force can be calculated from that of a beam with elliptical symmetry but that is rotated with respect to the z (longitudinal) axis. Using the same notation as ref. [6] the transverse (x and y) equations of motion are:

$$\begin{aligned} d^2x/dz^2 &= K_{qxx}x + K_{qxy}y + K_{sxx}(x - \langle x \rangle) \\ &\quad + K_{sxy}(y - \langle y \rangle) - (d \ln \beta_z / dz) x' \\ d^2y/dz^2 &= K_{qyy}y + K_{qxy}x + K_{syy}(y - \langle y \rangle) \\ &\quad + K_{sxy}(x - \langle x \rangle) - (d \ln \beta_z / dz) y' \end{aligned} \quad (1)$$

Here $\beta_z c$ is the longitudinal velocity, and K with leading subscript q is associated with external focusing from quadrupoles whereas K with leading subscript s result from space charge (cf. ref. 6.)

As in ref. [6], we may derive a set of ten first order equations for the quadratic moments of the distribution, here generalized slightly from ref. [6] to include acceleration (the operator $\Delta \equiv \langle ab \rangle - \langle a \rangle \langle b \rangle$):

$$d\Delta x^2 / dz = 2\Delta x x'$$

$$\begin{aligned}
 d\Delta x' / dz &= \Delta x'^2 + K_{xx}\Delta x'^2 + K_{xy}\Delta xy - (d \ln \beta_z / dz)\Delta x' \\
 d\Delta x'^2 / dz &= 2K_{xx}\Delta x' + 2K_{xy}\Delta xy - 2(d \ln \beta_z / dz)\Delta x'^2 \\
 d\Delta y'^2 / dz &= 2\Delta yy' \\
 d\Delta yy' / dz &= \Delta y'^2 + K_{yy}\Delta y'^2 + K_{xy}\Delta xy - (d \ln \beta_z / dz)\Delta yy' \\
 d\Delta y'^2 / dz &= 2K_{yy}\Delta yy' + 2K_{xy}\Delta xy - 2(d \ln \beta_z / dz)\Delta y'^2 \\
 d\Delta xy / dz &= \Delta xy' + \Delta x' y \\
 d\Delta x' y / dz &= \Delta x' y' + K_{xx}\Delta xy + K_{xy}\Delta y'^2 - (d \ln \beta_z / dz)\Delta x' y \\
 d\Delta xy' / dz &= \Delta x' y' + K_{yy}\Delta xy + K_{xy}\Delta x'^2 - (d \ln \beta_z / dz)\Delta xy' \\
 d\Delta x' y' / dz &= K_{xx}\Delta xy' + K_{xy}\Delta yy' + K_{yy}\Delta x' y + K_{xy}\Delta xx' \\
 &\quad - 2(d \ln \beta_z / dz)\Delta x' y' \quad (2)
 \end{aligned}$$

Here $K_{xx}=K_{qxx}+K_{sxx}$, $K_{xy}=K_{qxy}+K_{sxy}$, and $K_{yy}=K_{qyy}+K_{syy}$. Using the procedures in ref. [4] we obtain the following invariants which we denote as

$$\begin{aligned}
 \epsilon_{ng}^2 &= \frac{1}{2}(\epsilon_{nx}^2 + \epsilon_{ny}^2) + 16\beta^2(\Delta xy\Delta x' y' - \Delta xy' \Delta x' y) \\
 \epsilon_{nh}^2 &= (\epsilon_{nx}^2 \epsilon_{ny}^2 + (4\beta)^4 [(\Delta xy\Delta x' y')^2 + (\Delta xy' \Delta x' y)^2 \\
 &\quad - \Delta x'^2 \Delta y'^2 (\Delta x' y')^2 - \Delta x'^2 \Delta y'^2 (\Delta x' y)^2 \\
 &\quad - \Delta x'^2 \Delta y'^2 (\Delta xy')^2 - \Delta x'^2 \Delta y'^2 (\Delta xy)^2 \\
 &\quad - 2\Delta xy\Delta xy' \Delta x' y\Delta x' y' + 2\Delta xx' \Delta y'^2 \Delta xy\Delta x' y \\
 &\quad - 2\Delta xx' \Delta yy' \Delta xy\Delta x' y' - 2\Delta xx' \Delta yy' \Delta xy' \Delta x' y \\
 &\quad + 2\Delta x'^2 \Delta yy' \Delta xy\Delta xy' + 2\Delta x'^2 \Delta yy' \Delta x' y\Delta x' y' \\
 &\quad + 2\Delta xx' \Delta y'^2 \Delta x' y' \Delta xy')^{1/2} \quad (3)
 \end{aligned}$$

Here, $\epsilon_{nx}^2 \equiv 16\beta^2(\Delta x'^2 \Delta x'^2 - [\Delta xx']^2)$ and $\epsilon_{ny}^2 \equiv 16\beta^2(\Delta y'^2 \Delta y'^2 - [\Delta yy']^2)$ are the squares of the usual x and y normalized emittances. Note that the square of the generalized emittances ϵ_{ng}^2 and ϵ_{nh}^2 reduce to the arithmetic and geometric mean of ϵ_{nx}^2 and ϵ_{ny}^2 , respectively, in the absence of cross-correlations (i.e. $\Delta xy = \Delta x' y = \Delta xy' = \Delta x' y' = 0$), and so form two independent quantities.

3 SIMULATIONS

Of particular interest is the response of actual machines, such as UMER and the IRE, to quadrupole rotation errors. Early injector experiments at the University of Maryland, for example, indicated a high sensitivity to quadrupole rotations. UMER is a circular machine consisting of 36 FODO cells and 36 bending dipoles. The nominal operating point of 10 keV and 100 mA results in a generalized perveance of 0.0015. With a normalized emittance, ϵ_{nx} of 10 mm-mrad, this places the beam in the highly space-charge-dominated regime, with a tune-depression (v/v_0) of 0.14. The average beam size is about 1.0 cm. For the moment, we have explored only the case of a drifting beam. The IRE on the other hand is an induction linac. A number of K⁺ ion beams are injected at 1.6 MeV into a strong-focusing lattice and then accelerated in parallel to 200 MeV. The generalized perveance at injection is similar to that of UMER

(0.0015). The quantity ϵ_{nx} is 1.0 mm-mrad, placing it further than UMER in the space-charge-dominated regime. The average beam size is 1.5 cm. Please see refs. [2-3] for further detail. For the simulations, we used the 2d3v version of WARP, with a resolution of 256 cells across the beam pipe (~125 cells across the beam). In most cases we ran with 20,000 particles, and Gaussian filtering to reduce numerical collisions. We chose a semi-gaussian initial distribution in most cases so as to model a physical beam, although we occasionally used a K-V distribution to compare against the theory.

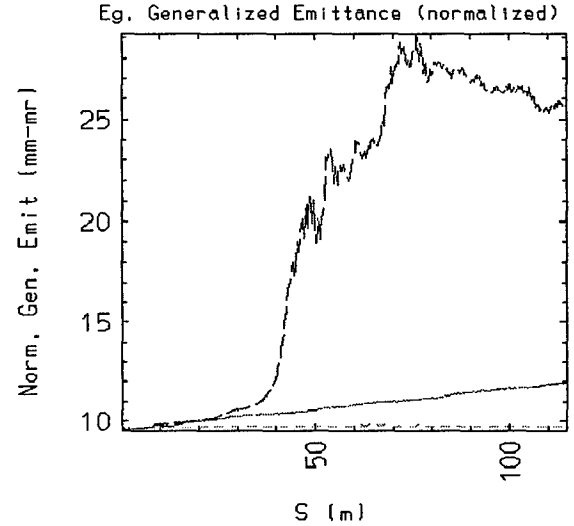


Figure 1: ϵ_{ng} along 10 turns in UMER; low current (lower); nominal current, straight (upper) and periodic (middle curve).

The simplest cases simulated are those of a drifting beam in a straight lattice with linear magnets. To isolate the effect of space charge, we compared our simulation to an equivalent emittance-dominated beam obtained by reducing the current and increasing the emittance to maintain the same beam size, while keeping the external forces unchanged. To both cases, we applied the same random distribution of errors, with an rms width of 0.2° (~ 4 mrad). As shown in the bottom curve in Fig. 1, the low-current beam exhibited almost no growth in the generalized emittance. The x and y rms emittances oscillated about their initial values. The beam rotation angle performs a random walk yet remains constrained within 3° (rms) from upright. Increasing the space charge to the nominal parameters of UMER results in markedly different behavior. The beam responds to the same set of errors by "wobbling" more violently, with the beam rotation angle exceeding 5° and continuing to increase in amplitude of oscillation. These large rotation angles translate into rms mismatches in x and y, with associated growth of the generalized [top curve of Fig. 1]. The rate of growth is slow initially, but experiences a sudden boost as a halo forms, then levels off as the beam-halo system reaches a new equilibrium.

A drifting beam in a ring (as in UMER) experiences random errors that repeat periodically every turn. This periodicity could introduce resonances that will further degrade the beam. Imposing this periodicity on our UMER simulation, however, resulted in remarkably different behavior. The periodicity of the errors imposes a periodicity on the beam rotation angle, preventing it from growing uncontrollably. Thus the rms mismatch in our case does not grow to a sufficient level to induce a halo. Therefore, the generalized emittance [middle curve, Fig. 1] grows steadily, but does not experience the abrupt growth during the 4th turn. Note that we have only explored one set of parameters. It may be possible to see different behavior if we operate near a resonance.

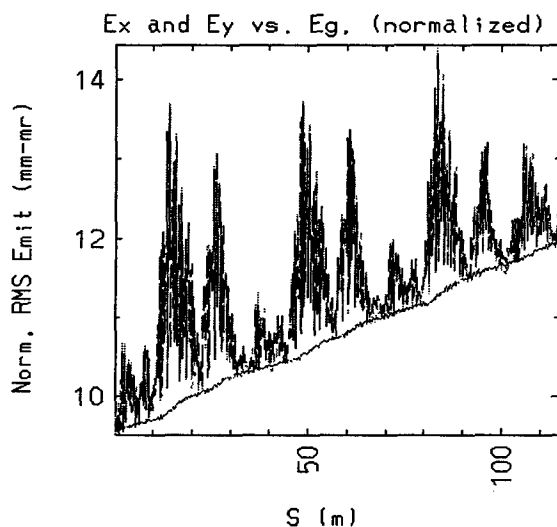


Figure 2: ϵ_{nx} , ϵ_{ny} (dotted) and ϵ_{ng} (solid) for 10 turns of UMER.

The emittance shown in Fig. 1 is the generalized emittance, ϵ_{ng} . The standard ϵ_{nx} and ϵ_{ny} follow a different behavior. Figure 2 compares ϵ_{nx} with ϵ_{ng} for the case of periodic errors shown in Fig. 1. Whereas the generalized emittance grows secularly and gradually, the standard x emittance oscillates wildly. The oscillations are due to the fact that the beam is wobbling, and some of the apparent emittance growth is reversible. Note that ϵ_{ng} acts as a lower bound for ϵ_{nx} , thus representing the nonreversible part of the emittance growth.

The beam rotation angle, as well as the emittance growth, depends sensitively on the magnitude of the errors. Figure 3 displays the evolution of ϵ_{nh} in the IRE for 2 values of errors. In both cases, an abrupt transition occurs at the point where halo formation takes place. In the case with larger errors, the halo formation is more severe (i.e., a larger fraction of the particles form the halo). It is evident that for smaller errors and prior to the halo formation, the generalized emittance is more nearly constant. The case with no errors is included to mark the numerical growth. By improving the numerics, we can obtain near zero emittance growth for the error-free case. Note that the dependence on the numerics can change in

the presence of errors, as preliminary evidence seems to indicate. Hence we are pursuing the matter further.

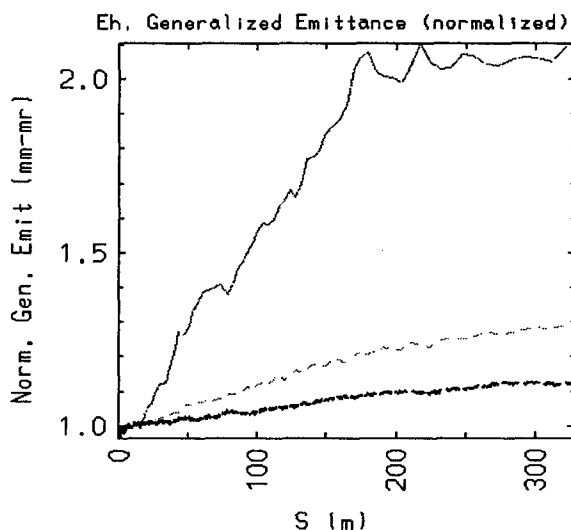


Figure 3: ϵ_{nh} along the IRE for an rms error of 0.2° (upper), 0.1° (middle) and no error (lower curve).

4 CONCLUSIONS

As we find from the simulations presented here, quadrupoles with small random rotations have a larger impact on higher intensity beams. We presented an analytic derivation of a generalized emittance, which is conserved in linear systems. With the introduction of nonlinearities in the space charge distribution as the beam evolves, these generalized emittances are found to grow, sometimes dramatically if a halo is formed. An interesting effect is observed if the errors are periodic, as in a beam drifting in a ring, where the beam's response to the errors appears to be periodic and bounded.

5 ACKNOWLEDGEMENTS

We wish to acknowledge the assistance of both the Maryland Electron Ring Team, especially M. Reiser, P. O'Shea, and S. Bernal, as well as the IRE simulations working group, especially A. Friedman and R. Bangerter. Thanks especially to I. Haber who belongs to both groups. Thanks also to K. Danylevich for assistance.

Research Supported by Department of Energy under contracts DE-FG02-92ER54178, DE-FG02-94ER40855, and W-7405-ENG-48.

6 REFERENCES

- [1] D. P. Grote, et. al., Fus. Eng. & Des. 32-33, 193-200 (1996).
- [2] M. Reiser, et. al., these proceedings, TUCR3; also R. A. Kishek, et. al., these proceedings, TUP118.
- [3] A. Friedman, et. al., these proceedings, TUP144.
- [4] Dragt, A.J., Neri, F., and Rangarajan, G., Phys. Rev. A, 45, 2572, (1992.)
- [5] Sacherer, F.J., Ph.D. Thesis, Univ. of California, Berkeley, UCRL-18454 (1968).
- [6] Barnard, John J., Proc. 1995 PAC Conf. (Dallas, TX) 5, p. 3241, (1996)

THE MAIN REGULARITIES OF CORE-HALO FORMATION IN SPACE CHARGE-DOMINATED ION BEAM*

B.I.Bondarev[#], A.P.Durkin, I.L.Korenev, I.V.Shumakov, S.V.Vinogradov,
MRTI, Moscow, Russia

Abstract

The laws that govern the charge redistribution in space charge dominated (SCD) beam during its transport is considered. Physical mechanisms of halo production and establishment of steady distribution inside core for matched beams are described. The image-based computer codes were generated and charge density redistribution process in the beam with concurrent phenomena was described. The main regularities of SCD-beam transporting were carried out. High-density core and low-density halo with particle active interchange are established in every case. Most of core particles are "ex-halo" or "coming-halo" ones which income from halo in previous instant of time or will emerge from core in next instant of time. Final steady states are ones with Coulomb field minimal potential energy. The transition from the SCD-beam initial state into a final steady state is accompanied by particle kinetic energy increasing and emittance growth. A steady state with constant transverse sizes of core can be established. Such beam state would be nominated as matched one.

1.INTRODUCTION

Growing needs in high-current CW ion linac aggravate both problems of beam losses and radiation purity. It turned out that acceptable beam loss standard is very tight. Linac designers were obliged to study beam physics mechanisms that lead to emittance growth and core-halo formation. Computational methods were widely used because analytical approaches are effective only in limited idealized cases (for example, K-V distribution). SCD beam study in linear transport and accelerator channels as well as computer code generation were performed and published by authors starting from 1986 [1-5]. The general results were obtained such as: (a) formation of quasi-uniform core and rarefied halo; (b) core oscillation damping with concurrent emittance growth; (c) beam matching using information of input beam distribution in phase space; (d) minimization of the space charge potential energy and concurrent emittance growth; (e) impossibility of halo stripping by diaphragm and so on. These results are agreed very closely with ones published by different researchers later.

In recent years works on convenient in operation computer codes for space SCD beam physics study were developed using modern image-based computer technology. The new code tools make calculations with

higher then formerly accuracy. They are adopted for education and training. In

recent report a lot of numerical experiments are discussed in order to clear out the main regularities of core-halo formation in SCD ion beam. The results were obtained in the frame of longitudinal and transverse uniform focusing. Solenoids were used directly as focusing elements. This relatively simple focusing gives a possibility to clear demonstration of all essential SCD-beam effects.

2. MATCHING INJECTION

The solution of the above task is well studied only for K-V distribution [6]. For more real (but not too exotic) distributions authors proposed the matching injection procedure based on rms parameters of the distribution. The procedure despite the fact that it gives only approximate matching offers practically steady state for beam with not very high beam current (tune depression $\eta \approx 0.8$) during further beam transport. A fast formation of beam halo takes place for beam distributions limited in space (such as uniform or waterbag). In all cases beam simulations extend to some tens of core oscillations. For large currents ($\eta \approx 0.2$) beam injection with distributions limited in transverse directions does not lead to emittance growth and beam is practically stabilized at once. For Gaussian transverse distribution there are both fast emittance growth up to 50% and core oscillation damping with further stabilization.

If a beam evolves to equilibrium state the charge distribution with the quasi-uniform central region in transverse coordinate plane is established. This distribution is very similar to stationary self-consistent analytical solution of Maxwell-Boltzmann type. But exact radial dependence in the region of the distribution "tail" remains in reality unknown.

Let us note that in spite of frequent using of term "beam core" nowhere the size of the beam core was defined. Following the work [1] we define core size as a distance between beam axis and the point where the maximum value of the space charge field is achieved. Physical sense of the definition is evident for the beam with elliptical cross section and uniform charge density - the core size coincides with the beam size. For Gaussian charge distribution in transverse plane the core radius is 1.12 of rms radius.

3. MISMATCHED BEAM INJECTION

Beam calculations with initial mismatch factor 1.5 were performed in order to study of effects of unequilibrium beam relaxation after its injection in focusing channel. For

*Work supported by International Science & Technology Center

[#]E-mail: lidos@aha.ru

low currents ($\eta \approx 0.8$) there is a damping of the core radius oscillations on the length of $15+20$ oscillation periods with simultaneous emittance growth up to $30+40\%$. The results fall into a pattern of filamentation phenomena due to nonlinear betatron frequency spread. The halo formation in the cases of distributions limited in transverse directions is followed by phase contours of nonlinear parametric resonance-2 (look below).

For the large beam currents ($\eta \approx 0.2$) a role of initial mismatch factor considerably increases. For various initial distributions the core oscillations caused by initial mismatching do not damp practically and emittance growth by factor of 2 or 3 on the length of $30+40$ oscillations takes place. The core oscillations lead to fast halo formation particularly for limited distributions. The phase trajectories of particles follow by phase contours of resonance-2 (look below). Indeed the time of halo formation may be evaluated taking into account the period of phase oscillations in near resonance region.

The absence of the core oscillation damping for large currents does not have satisfactory explanations so far. Maybe space charge strong nonlinearity would enhance a process of beam filamentation. It is possible that quasi-uniform beam core formation converges the distribution to KV type. It is necessary the further study of the problem.

4. HALO FORMATION

The simple (but effective) model of the halo particle dynamics reduces the problem to analysis of the sole particle behavior under linear focusing force and nonlinear force of space charge field. The own field of halo particles is supposed as negligible small. The analytical calculations [2] show that energy of external particle increases when it crosses the compressing uniform beam core and vice versa: particle energy decreases when core extends. R.L.Gluckstern [7] studied the halo particle dynamics in periodically alternating field of mismatched beam core. He has found the conditions of nonlinear parametric resonance. The particle amplitude can enhance considerably in the frequency band of the resonance. The resonance is often named as "resonance-2" because the particle oscillation frequency is 2 times less than core frequency. The convenient visual image of the resonance was used in work [8] by means of so called Poincare mapping. The pictures of phase contours in near resonance region allow to evaluate the maximum amplitudes of halo particles. For low currents the individual phase contours are clearly separated. The typical duration of resonance phenomena is characterized by the oscillation periods along the phase contours. For large currents the resonance separatrix is destroyed and near the core region arose island regions of high order resonances. Overlapping of the resonances and destroyed separatrix are formed the stochastic layer. As the beam current more as the layer broader. The halo formation is now caused by the particle diffusion along the layer.

Curves of the maximum radial size versus mismatching factor for resonance separatrix are shown on Fig.1 for various tune depression values.

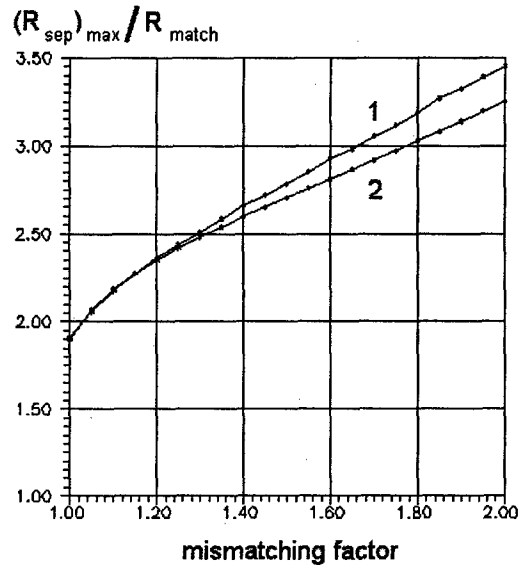


Fig.1: Resonance-2. Maximum radial size of separatrix:
1 - $\eta = 0.82$; 2 - $\eta = 0.24$.

In many of our PIC simulations the particle ejection along phase contours of the resonance-2 are observed (Fig.2). They are seen particularly clear if the initial distribution do not possessed the extended halo. Possible sources of halo particles in the initially bounded distributions are discussed in work [9] and more completely in review [10].

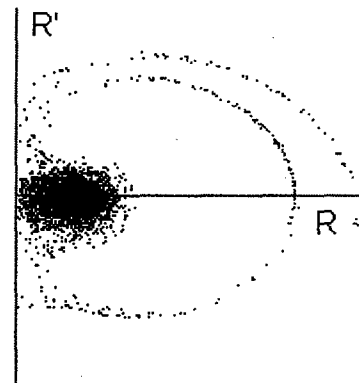


Fig.2: Phase trajectories of resonance-2 as result of PIC simulation.

Hence for many of the beam transport simulations the resonance-2 model gives satisfactory qualitative explanation of halo formation and possibility of its scale evaluation. But all approaches described above concerning resonance-2 do not give a reliable quantitative algorithm to calculate the transverse distribution of halo particles that must be the main goal of halo researches. Only the knowledge of distribution function opens the opportunity to receive the based data about the probable particle losses.

5. ADIABATIC TRANSFORMATIONS

The heating of halo particles due to compressing core (look [2]) may cause the halo extension in the time of adiabatic growth of the focusing field. We have made corresponding calculations. The effect of halo heating tells on the relatively less halo compression comparatively with the core. The behavior of halo particle having the initial radius double the radius of uniform core is shown on Fig.3.

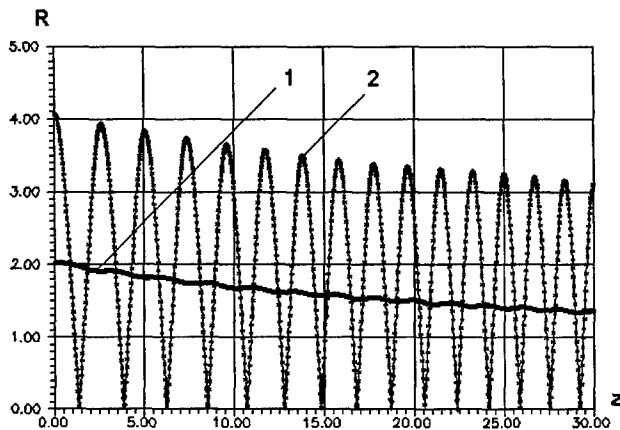


Fig.3. Adiabatic compression of beam: (1) – core radius; (2) – halo particle. Focusing grows $\sim (1 + 0.044z)$.

Analogously in the time of adiabatic beam extension the halo extends in the less degree than the beam core.

6. CODE PACKAGE DEVELOPMENT

The package is creating for visual study of the physical processes accompanying high current beam transport and bunching. The first part of the package is used for transverse beam dynamics describing. This part contains two tools that are used for beam simulations by analytical model and by PIC model respectively. The analytical model describes the motion of halo particles in collective field of the external focusing and oscillating uniform core. The PIC-model calculates the beam transport in solenoid or quadrupole channels. The space charge forces are resulted as digital solution of Poisson equation at the circular or square boundaries. Parameters of beam and channel are input either in generalized dimensionless form or in form of physical units. Initial distributions of the three types are used: Waterbag, Gauss or Uniform. By means of the last two ones it is possible to get distributions on coordinates and velocities independently. The visual information about beam cross-section and phase portraits (for various pairs of the dynamical variables) may be received as well as an evolution of distribution moments and of space charge field energies. Both intermediate and final visual images may be kept for consequent comparison of variants. Two

previously saved variants may be displayed simultaneously

The second part allows to calculate the high current beam bunching under the constant transverse characteristics ("frozen beam"). The periodical charge distribution in longitudinal dimension is supposed. The visual information showing charge redistribution phenomena and the evolution of harmonic spectrum of the longitudinal distribution are presented.

The last part of the code package combines two above ones describing together the longitudinal and transverse dynamics of high current ion beam.

7. CONCLUSION

One of the main problems in our opinion remains a reliable quantitative evaluation of the halo size or more exactly the distribution function for the halo particles. It is only way for correct calculations of the particle losses in the beam transport. The existing halo models do not solve the problem. We proceed a work to construct the algorithms for those calculations based on the beam PIC simulation data.

The most interesting are the time scales of the relaxation processes. According to our PIC simulations for the tune depression $\eta \leq 0.5$ the core oscillation do not damp on the channel lengths measured by many tens oscillation periods. Accuracy of the calculation results is confirmed by the clear view of Poincare mappings for that lengths.

We shall proceed the HALO-KERN code package design and the ion beam studies for more complicate configurations.

7. REFERENCES

- [1] Bondarev B.I., Durkin A.P. "The Space Charge Beam Equilibria in Longitudinal Magnetic Field". Zh.Techn.Phys., USSR, vol. 56, N 11, pp.2132-2138, 1986 (in Russian).
- [2] Bondarev B.I., Durkin A.P., Murin B.P., Jameson R.A. "Emittance Grow and Halo Formation in Charge-Dominated Beams". Int. Conf. on Acc.-Driv. Transm. Technologies and Applications, Las-Vegas, 1994, AIP proc. 346, pp 377-382.
- [3] Bondarev B.I., Durkin A.P. "SCD-Beam Main Regularities in Beginning Part of High-Current Proton Linac", Computational Accelerator Physics, Williamsburg, 1996, AIP proc. 391, pp 173-178.
- [4] Bondarev B.I., Durkin A.P., Murin B.P. "Intense Ion Beam Transport and Space Charge Redistribution", XVIII Int. Lin. Acc. Conf. LINAC96, Geneva, 1996, pp 208-209.
- [5] Durkin A.P., Bondarev B.I., Murin B.P., "Study of Space Charge-Dominated Beam Bunching", ibid, pp 210-212.
- [6] Kapchinskij I.M., Vladimirovskij V.V., "Limitations of Proton Beam Current in a Strong Focusing Linear Accelerator Associated with the Beam Space Charge", Proc. of Int. Conf. on High En. Acc., CERN, Geneva, 1959, pp 274-288.
- [7] Gluckstern R.L., Phys.Rev.Lett., vol.73, 1994, pp 1247-1249.
- [8] Lagniel J.-M., "Chaotic Behavior Induced by Space Charge", IV Europ. Part. Acc. Conf. EPAC94, London, 1994.
- [9] Gluckstern R.L., Cheng W.-H., "Stability of a Breathing K-V Beam", Int. Conf. on High-Energy Acc., vol.5,Dallas, 1995, pp 3179-3181.
- [10] Lagniel J.-M. "Halos and Chaos in Space-Charge Dominated Beams", V Europ. Particle Acc. Conf. EPAC96, Barcelona, 1996, pp 163-167.

HALO FORMATION OF BUNCHED BEAMS IN PERIODIC FOCUSING SYSTEMS

A. Letchford, RAL, UK, K. Bongardt, M. Pabst, Forschungszentrum Jülich, Germany

Abstract

A very critical design issue for high intensity proton linacs is to keep particle loss below 1 W/m at the high energy end and allow unconstrained hand on maintenance. Particle loss is caused by a small number of particles outside the dense beam core, called the beam halo. Halo formation of bunched beams in a periodic focusing channel is driven by mismatch, high space charge and temperature anisotropy. Unstable particles oscillate in all 3 phase space planes. Mode overlap due to large mismatch amplitudes can lead to a halo much larger than seen in uniform focusing systems. Resonance crossing due to acceleration is a possibility for designing high intensity linacs.

1 SINGLE PARTICLE - ENVELOPE RESONANCE

For realistic particle distributions, with nonlinear space charge forces, particles inside the beam core have different tunes. Parametric particle - envelope resonances can occur between the single particle tune and the frequency of the mismatch of the oscillating beam core.

For a bunched beam the frequencies of the three eigenmodes are approximately given by [1]

$$\sigma_{env,Q} = 2\sigma_t$$

for the pure transverse **quadrupolar mode** and by

$$\sigma_{env,H}^2 = A + B, \sigma_{env,L}^2 = A - B$$

with

$$A = \sigma_{to}^2 + \sigma_t^2 + \frac{1}{2}\sigma_{to}^2 + \frac{3}{2}\sigma_t^2$$

and

$$B = \sqrt{\left(\sigma_{to}^2 + \sigma_t^2 - \frac{1}{2}\sigma_{to}^2 - \frac{3}{2}\sigma_t^2\right)^2 + 2(\sigma_{to}^2 - \sigma_t^2)(\sigma_{to}^2 - \sigma_t^2)}$$

for the **high** and **low mode** which couple the transverse and longitudinal directions. The mismatch modes are expressed by the full and zero current transverse and longitudinal tunes σ_t , σ_{to} , σ_l and σ_{lo} . For the quadrupolar mode one has for the relative mismatches

$$\frac{\Delta a_x}{a_{xo}} = -\frac{\Delta a_y}{a_{yo}}, \frac{\Delta b}{b_o} = 0.$$

Here only anti-phase transverse mismatches is present. In case of the high and low mode one has

$$\frac{\Delta a_x}{a_{xo}} = \frac{\Delta a_y}{a_{yo}} = g_{H/L} \frac{\Delta b}{b_o}.$$

with

$$g_{H/L} = \frac{\sigma_{to}^2 - \sigma_t^2}{\sigma_{env,H/L}^2 - 2(\sigma_{to}^2 + \sigma_t^2)}.$$

g_H is always positive and g_L always negative.

The analytical expressions are derived for a uniform focusing channel with linear external and space charge forces. The derivatives of the formfactors are neglected. Numerical simulations of a periodic bunched beam transport line with spherical bunches ($b/a \sim 1$) or elongated bunches ($b/a \sim 3$) have shown that all three eigenmodes can be excited by using the above stated amplitude ratios.

Due to nonlinear space charge forces, particles have tunes distributed between the full current and zero current tune. The condition for exciting a parametric resonance either transversely or longitudinally is given by

$$\frac{\sigma_{t,l}^p}{\sigma_{env}} = \frac{m}{n} = \frac{1}{2}, \frac{1}{3}, \dots$$

with

$$\sigma_t \leq \sigma_t^p \leq \sigma_{to},$$

$$\sigma_l \leq \sigma_l^p \leq \sigma_{lo}$$

where σ_{env} is one of the three envelope tunes of the mismatched radii and $\sigma_{t,l}^p$ the single particle tune.

Fig. 1 shows the halo formation excited by the quadrupolar mode with 20% initial mismatch. Results are derived from Monte Carlo simulation of an almost spherical bunched beam in a periodic focusing system [1]. All calculations discussed below were done with at least 10000 particles which interact fully in 3d. A 6d waterbag distribution is used as input. Clearly visible is the onset of halo formation and its leveling afterwards. Above 1% of the particles are outside $10 * \epsilon_{rms}$, compared to 0.1% for the not shown matched case. The halo is limited to about $30 * \epsilon_{rms}$ in phase space. Similar results have been reported from Monte Carlo simulations for selfconsistent equipartitioned bunched beams in a uniform focusing channel [2]. For spherical bunches the halo formation is similar in the transverse and longitudinal directions.

2 UNSTABLE PARTICLE MOTION IN A PERIODIC FOCUSING CHANNEL

In a periodic focusing channel additional resonances and instabilities, which don't exist in an uniform channel, can influence single particle motion. One is the envelope - lattice instability which occurs for a bunched beam if the high mode frequency is nearly 180° . The instability leads to an increase of the rms beam envelope. Other important resonances can occur between single particles and the periodic

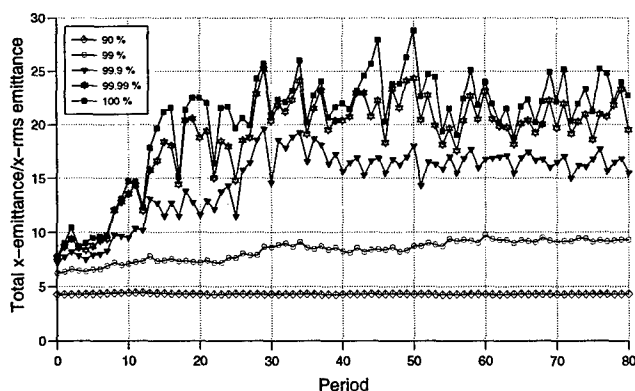


Figure 1: Transverse emittance ratio along a mismatched bunched beam transfer line

lattice if for dc [3] or bunched beams [4] the tune depressions are below 0.4 and the full current tunes below 60° .

Beside these instabilities other particle - lattice resonances can be excited either by temperature exchange or by mismatch. Even if all above mentioned instabilities are avoided large mismatch amplitudes can create unstable particle motion.

2.1 Unstable Particle Motion due to Resonance Overlap

In a periodic focusing system a parametric particle - lattice resonance is excited if the zero current tune is above 90° . If a particle - envelope resonance, excited by mismatch, is nearby a particle - lattice resonance, then particles can be driven by the envelope resonance into lattice resonance. This is called resonance overlap which can lead to unstable particle motion with large amplitudes.

In Fig. 2 unstable behaviour of a few particles in the longitudinal phase space is shown for an equipartitioned bunched beam by exciting a pure 20% transverse, 30% longitudinal high mode with an analytical phase advance of 166° . The transverse and longitudinal tune depressions are 0.77. The longitudinal zero current tune is about 90° and the transverse zero current tune is about 85° . The bunch is almost spherical. No unstable behaviour has been observed in the transverse planes. The tune of the most unstable particle is shown in Fig. 3. Its value is close to 90° after 50 periods.

Both transverse emittances of the longitudinally most unstable particles are close to the transverse rms emittances. Similar correlations for transversely outermost particles have been observed at the end of the ESS linac [5]. Comparing Fig. 2 with Fig. 1 the difference between an envelope resonance and unstable behaviour due to resonance overlap is evident. Few particles are expelled to very large emittance values when their tune is close to 90° .

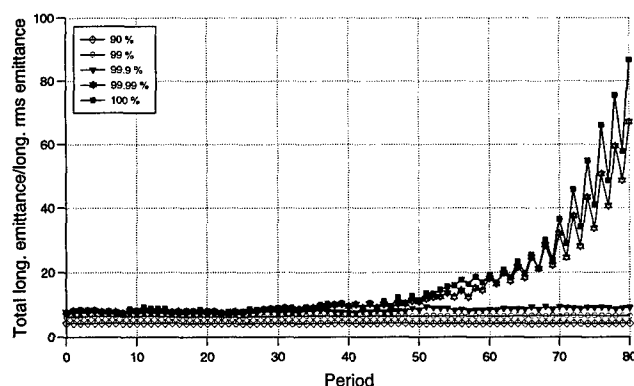


Figure 2: Longitudinal emittance ratio along a mismatched bunched beam transferline

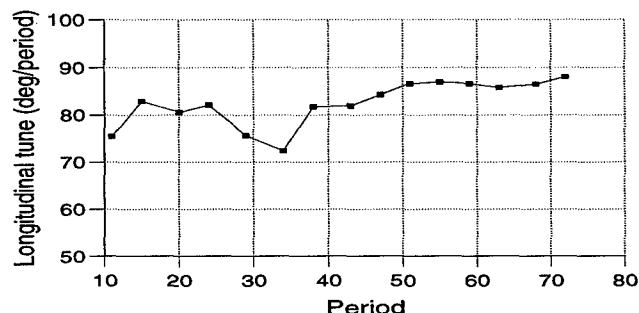


Figure 3: Single particle tune of the most unstable particle which is close to 90° after 50 periods

2.2 Unstable Particle Motion due to Temperature Exchange

In the design of high intensity linear accelerators substantial differences between transverse and longitudinal temperatures should be avoided [6,7].

In Fig. 4 the development of unstable particle motion due to temperature exchange and leading to the 90° particle - lattice resonance is shown for a matched beam. The longitudinal to transverse temperature ratio is 3 and the zero current transverse tune is 92° . The not shown rms emittances are oscillating due to temperature exchange. Clearly visible is the unstable motion of particles leading to very large emittances in the horizontal phase plane. No unstable behaviour is seen in the longitudinal plane. The single particle tune of 90° , as shown in Fig. 5, for the least stable particle, is in resonance with the periodic focusing, leading to the strong increase in its emittance value. Before the particle becomes unstable in one transverse plane, energy transfer between the longitudinal and the transverse plane is observed.

2.3 Unstable Particle Motion due to Large Mismatch Amplitudes

By avoiding temperature exchange, the 90° single particle - lattice resonance and high tune depression, mismatch amplitudes smaller than 30% lead to a superposition of 3

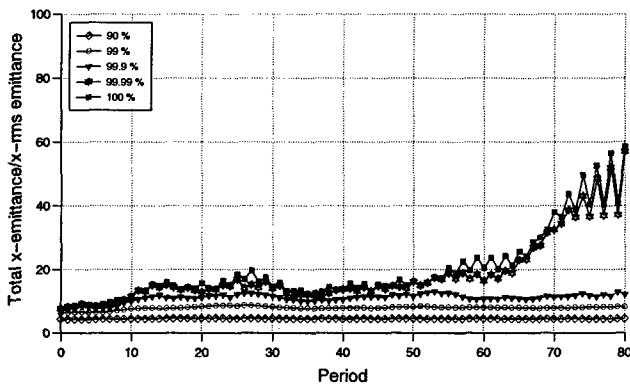


Figure 4: Transverse emittance ratio along a matched transfer line with temperature exchange

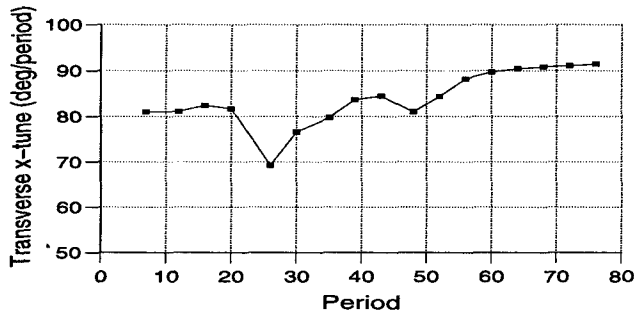


Figure 5: Single particle tune of the most unstable particle which is close to 90° after 50 periods

bunched beam eigenmodes.

The situation can be different for mode excitations with large amplitudes. For the layout of the periodic focusing system in Fig. 1, a 20% 'pseudo' high mode (equal mismatch amplitudes in all three directions) excitation leads to neither transverse nor longitudinal halo formation. By 50% pseudo high mode excitation however, mode overlap occurs and leads to unstable particle motion in all three planes after 40 periods. The periodic focusing system enlarges the maximal halo extent compared to an uniform focusing channel.

3 MONTE CARLO SIMULATION OF THE ESS LINAC

All the results above are for a bunched beam transfer line with no acceleration. The conclusions are also valid for the design of a high current linac. As an example a 50000 particle Monte Carlo simulation result is shown for the 214 mA ESS coupled cavity linac which accelerates the beam from 70 MeV up to 1.334 GeV [8]. The injection parameters at 70 MeV are about the same as for the discussed transfer-line in Fig. 4. The ratio between full and zero current tunes is greater than 0.7 both transversely and longitudinally, all along the linac. The transverse zero current tune is 92° at injection.

The ratio between the transverse and longitudinal tem-

perature in the rest system is 0.36 at injection and at linac end. The maximum value of 0.5 is reached about 360 MeV.

For the matched case there are no particles outside $15 * \epsilon_{rms}$ either transversely or longitudinally and the rms emittances change by about 20% due to temperature exchange. Fig. 6 shows the halo formation due to exciting a pure high mode with 20% transverse and 20% longitudinal mismatch.

As the 90° particle - lattice resonance is crossed transversely together with increasing the transverse temperature, halo formation due to mismatch is visible in the horizontal plane. Much weaker halo formation is seen in the longitudinal phase plane as expected from the high mode excitation.

These results are very much consistent with the results for a bunched beam in a periodic focusing channel. The unstable particle motion in the transverse plane however is much less dominant compared to similar periodic transport line of Fig. 4, because the very dangerous parameter combination of temperature ratio of 0.37 together with $\sigma_t^0 = 92^\circ$ is crossed quite fast due to acceleration. Fast crossing of the 90° particle - lattice resonance therefore is a possibility for designing high intensity linacs if equipartitioning would lead to strong tune depression.

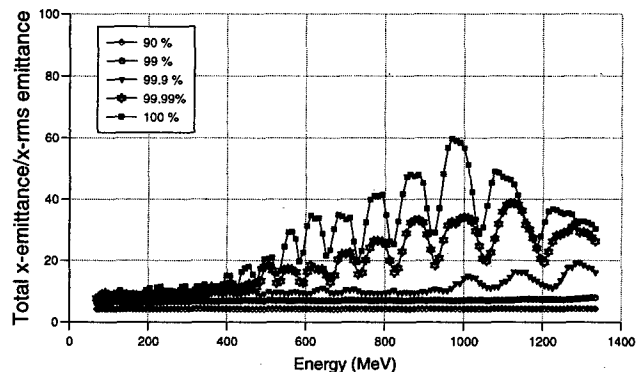


Figure 6: Transverse emittance ratio along the ESS linac for 20% high mode excitation

4 REFERENCES

- [1] M. Pabst et al., "Progress on Intense Proton Beam Dynamics", Proc. EPAC 1998, Stockholm, Sweden, p. 146
- [2] R. L. Gluckstern et al. Phys. Rev. E 58, 1994, p. 4977
- [3] J. Struckmeier et al., Part. Acc., vol. 15, p. 47, 1984
- [4] K. Bongardt et al., "Halo Formation by Mismatch for High Intensity Bunched Beams", Proc. LINAC 1998, Chicago, USA
- [5] M. Pabst et al., Proc. PAC 1997, Vancouver, Canada, p. 1846
- [6] M. Reiser, "Theory and Design of Charged Particle Beams", John Wiley, New York, 1994
- [7] R. A. Jameson, Fusion Eng. Design, 32-33, p. 149, 1996
- [8] "The European Spallation Source Study", Vol. 1-3, march 1997

STABILITY OF IONS IN THE ELECTRON BEAM WITH A GAP *

E. Bulyak [†], NSC KIPT, Kharkov, Ukraine

Abstract

A gap in the bunch train is one of methods to remove ions from the beam circulating in electron storage rings. Self-consistent theory of the ion stability in the bunch train with a gap is developed out. As is shown, stability of ions increases with the increase in the ion core density. Under certain conditions that have been determined, the stability islands become overlapping. Therefore, the beam clearing may not be achieved. It is proved that the maximum charge neutralization of the circulating current reaches in the continuous beams, any gap decreases stable density of ions. The stable density of the ion core decreases with number of the ion oscillation within the bunch train increases.

1 INTRODUCTION

Positive ions produced by an electron beam from the residual gas being confined within the beam, can demolish the beam performance. For the most electron storage rings, these ions have to be extracted from the beam. A gap in the bunch train is one of methods to remove ions from the beam circulating in electron storage rings. The essence of this method is as follows. Injection of a beam is performed in a way that leaves a number of consecutive RF buckets empty. Thus, the ions experience periodic attractive (the force of partially neutralized electron macrobunch) and repulsive (the self force of the ion core) forces. Length of the empty part of a beam is chosen to provide unstable ion motion within the operating intensity of a beam. The stability of a single ion (the ion core of zero density) was estimated in [1, 2]. As it was shown, the stability of an ion in the beam of a definite geometry is determined by the ion mass and the beam density. A real beam could confine the dense ion core before reaching the unstable conditions. The beam could trap the ions during the beam injection (when the beam density is below the unstable limit) or in operating cycle (when due to losses the beam enters the stable region from the above). Thus, during operation, the beam usually crosses the regions of ion stability. Therefore, of much importance is to establish the stable region border in the plane of beam density vs. ion core density.

2 MODEL

Let us consider the ions moving within the beam, as these only ions affecting the beam particles. This assumption allows to simplify the task with least losses in generality. The following model is chosen (see Fig 1). The train of bunches (macro bunch) of the radius a , length L_t , and the longitudinal electron density N_t are filled with ions of density N_i (the train neutralization factor is $\eta_t \equiv N_i/N_t$).

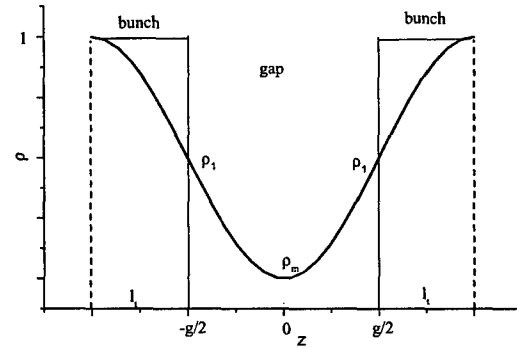


Figure 1: The model

We mean the bunch being long if an ion radius is changed significantly while the bunch passes by. The density limit of ion core provides that the clearing gap $G(\eta)$ between consecutive macrobunches causes the ion motion unstable.

From the physical point of view it follows that the phase volume of ion core decreases when the density is risen, therefore the core at the edge of equilibrium possess zero phase volume. The ions in this case move similarly (laminary). So, we can consider just dynamics of the boundary ions that are remaining in the border if the core is at the instability threshold.

The electrical field strength of the uniformly charged round rod of radius r in its surface is:

$$E_r(r' = r) = \frac{N_i e}{2\pi\epsilon_0 r}. \quad (1)$$

The corresponding potential function reads as

$$U_i(r) = -\frac{N_i e^2}{2\pi\epsilon_0} \ln \frac{r}{a} = -2N_i R_0 M c^2 \ln \frac{r}{a}, \quad (2)$$

* Work supported by the STCU, Project 855

[†] Email: bulyak@kipt.kharkov.ua

where a is the initial core radius, M is the ion mass; R_0 is the classical ion radius.

An attractive force acting on ions from the bunch space charge should be added to the repulsive force (1) of the core self-charge. Its potential is:

$$U_b = N_b R_0 M c^2 \left(\frac{r}{a} \right)^2. \quad (3)$$

Thus, we can write a (nonrelativistic) Hamilton function for the ion core border motion

$$\begin{aligned} H &= \frac{p^2}{2M} + U(x) \\ &= \frac{p^2}{2M} + R_0 M c^2 \left[\theta N_b \left(\frac{r}{a} \right)^2 - N_i \ln \left(\frac{r}{a} \right)^2 \right] \end{aligned} \quad (4)$$

Here we denote $\theta = 1$ within the bunch, and $\theta = 0$ outside (in the gap between consecutive bunches).

As we consider the bunch being long, the ion core can undergo a few oscillation while the bunch is passing by. The pulsation period can be derived from (4) put $p(r = a) = 0$. The hamiltonian (4) becomes:

$$H = E = \text{const} = N_b R_0 M c^2. \quad (5)$$

At the loser crossover, $p(r = r_m) = 0$, we have

$$\rho^2 - \eta_t \ln \rho^2 = 1 \quad (6)$$

where $\rho \equiv r/a$.

Equ. (6) has the root at $\rho = 1$, the second root $\rho_* < 1$ exists if the neutralization factor does not exceed unity: $\eta_t < 1$. Taking this into account, from (4) we get an expression for the period T of the border ion oscillation within the bunch:

$$T_i = \frac{a}{c} \sqrt{\frac{2}{N_i R_0}} \int_{\rho_*}^1 \frac{d\rho}{\sqrt{1 - \rho^2 + \eta \ln \rho^2}}. \quad (7)$$

As $\rho_m = \rho_m(\eta)$ (see (6)), we can denote

$$\Psi(\eta) \equiv \int_{\rho_m(\eta)}^1 \frac{d\rho}{\sqrt{1 - \rho^2 + \eta \ln \rho^2}}, \quad (8)$$

The pulsation length $\lambda = cT_i$ is dependent on the bunch radius and density, as well as on the ion mass and the neutralization factor.

Due to symmetry or the considered system, the core envelope reaches its minimal crossover ρ_m ($\rho_m \geq \rho_*$) just in the middle of the clearing gap between bunches (see Fig 1).

The trajectory of the border ions is described implicitly as

$$\begin{aligned} z &= z_0 + \frac{a}{\sqrt{2N_e R_i}} \int_{\rho_1}^1 \frac{d\rho}{\sqrt{1 - \theta \rho^2 + \eta_t \ln \rho^2}} \\ &= z_0 + \frac{a}{\sqrt{2N_e R_i}} \psi_\theta(\rho_1, \eta_t). \end{aligned} \quad (9)$$

Let define formally the reversed to $\psi(\rho, \eta)$ function:

$$x = \psi_p(\rho, \eta) \rightarrow \rho = \psi_p^{-1}(x, \eta). \quad (10)$$

Finally, after matching the trajectory within the bunch to that in the gap, we get the following conditions for the system to be periodic:

$$\begin{aligned} \frac{g}{2} &= \frac{a}{\sqrt{2N_i R_0}} [\psi_0(\rho_1, \eta) - \psi_0(\rho_m, \eta)]; \\ l_t &= \frac{a}{\sqrt{2N_e R_i}} \psi_1(\rho_1, \eta); \\ \lambda &= \frac{2a}{\sqrt{2N_e R_i}} \psi_1(\rho_*, \eta), \\ 2l_t &= L_t - n\lambda; \quad n = 0, 1, 2, \dots \\ \rho_* &= \exp \left[\frac{\rho_1^2 - 1}{2\eta_t} \right]; \\ \rho_1 &= \psi_1^{-1} \left(\frac{l_t}{a} \sqrt{2N_e R_i}, \eta_t \right). \end{aligned} \quad (11)$$

It can be seen that for the limiting case $\eta_t \rightarrow 0$ the stability conditions [1, 2] are deduced from (11).

3 COMPUTATION OF THE CORE STABILITY LIMITS

As it may be seen from the expressions obtained, the boundary lines of the stability islands can not be presented in an explicit analytical form. Then, a computer code was written for calculation of the limits of ion stability for both the case of round beam (considered above) and flat beam (derivation of the stability border for this case is similar to the round one). The reason is that for an actual beam of elliptic cross section, the stability bound must lay somewhere in between the flat and round ones.

Bunch intensity was presented with dimensionless parameter ν :

$$\begin{aligned} \nu_{\text{round}} &= \left(\frac{L_t}{a} \right)^2 \frac{2N_i R_0}{\pi^2}; \\ \nu_{\text{flat}} &= \left(\frac{L_t}{a} \right)^2 \frac{2N_i R_0}{\pi} \frac{a}{b}. \end{aligned}$$

where b is the width of a flat bunch.

The train neutralization factor η_t , and the relative bunch (train) length g/L_t were the other two parameters.

Computed stability islands are presented in Figs 2–3 where numbers in line brakes show the relative gap length g/L_t . As is seen from the figures, stability limits are shifted toward higher beam densities with increase in the ion core density. Then, projections of the islands into the abscissae are wider then for $\eta = 0$ and can overlap each other. Thus, the gap length shorter than some g_{01} is not provided clearing.

4 RESULTS

The analytical and computational study on the self-consistent stability of the ion core in the pulsed electron beam was carried out. As is yielded from the theory, relative core density reaches its maximum in the uniform, continuous beam. Any inhomogeneity in the longitudinal

- [2] Y. Miyahara, "Parametric Resonance of Trapped Ions in Electron Storage Rings," *NIM A* 366 p 221 (1995)
- [3] E. Bulyak, "Capturing and Confinement of Ions by the Beam Circulating in an Electron Storage Ring", *Sov. Physics JTF* vol. 56, p. 72 (1986)
- [4] E. Bulayk, "Ion Clearing Methods for the Electron Storage Rings", *Proc. EPAC-96* (Barcelona, Spain) p. 1078 (1996)

Also it is worth to take into account that the space between the stable islands is increased with its number. Thus, the gap in bunch train is effective for removing of ions from the intense electron beams circulating in the storage ring with large circumference.

1772

Frequency map analysis for beam halo formation in high intensity beams.

A. Bazzani, Dept. of Physics Univ. of Bologna and INFN sezione di Bologna, Italy,
M. Comunian, A. Pisent INFN Laboratory Nazionali di Legnaro, Italy

Abstract

The Frequency Map analysis is applied to the Particle-core model of an intense bunched beam in a focusing channel with cylindrical symmetry. The coupled longitudinal-radial motion is analyzed.

1 INTRODUCTION

The control of beam losses down to a very small percentage is one of the main challenges for the new generation of high power linacs. These losses are associated with the presence of a beam halo, populated by very few particles but with a radius significantly larger than the beam rms (root mean square) radius up to the bore hole. In previous papers we have applied the Frequency Map Analysis (FMA) [1][2] to the 2D case of a mismatched beam propagating in a FODO channel[3]; in this case it exists a self-consistent solution of the Vlasov-Poisson problem, the KV distribution, and we studied how the non linear resonances, driven by the space charge, can push a test particle to large amplitudes. The importance of the envelope oscillations and the advantage of a careful choice of the working point result clearly from this analysis.

Unfortunately in a linac the particle dynamics is intrinsically 3D, since the three tunes are close each other. The space charge can be in this case estimated assuming an ellipsoid uniformly populated, even if this does not correspond to a regular self-consistent solution of Vlasov problem. In this paper we move a first step toward the 3D problem, by considering a beam moving in a solenoid channel, interrupted by an RF gap (working with -90 deg synchronous phase). The envelope periodic solution (Fig. 1) and the three envelope modes are calculated. This problem is very similar to a linac with smooth quadrupole focusing and same focusing strength in the two transverse planes; the understanding of the coupled longitudinal and transverse motion in this case is important for the halo formation problem. We therefore analyzed the 2D motion of particles without angular momentum respect to beam axis; in this way we could apply the FMA and the stability criteria elaborated for the transverse case.

The extension of the FMA to the complete 3D case will be our next step.

2 PARTICLE-CORE MODEL

We assume that the particles are uniformly distributed into ellipsoidal bunches, defined by the equation

$$\frac{x_1^2}{a_1^2} + \frac{x_2^2}{a_2^2} + \frac{x_3^2}{a_3^2} = 1 \quad (1)$$

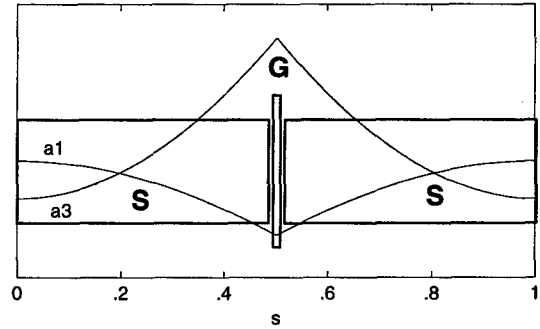


Figure 1: FODO Period with $a_1 = a_2$

where (x_1, x_2) are the transverse coordinates and x_3 is the longitudinal coordinate. The semi axis a_i are functions of position s . We compute the potential of the charge distribution according to

$$\Phi = \frac{3Ne}{16\pi\epsilon_0} \int_{\chi}^{\infty} \frac{\left(\frac{x_1^2}{a_1^2} + \frac{x_2^2}{a_2^2} + \frac{x_3^2}{a_3^2} - 1\right) du}{\sqrt{(a_1^2 + u)(a_2^2 + u)(a_3^2 + u)}} \quad (2)$$

where N is the total number of particle and the variable χ is set equal to 0 if the point (x_1, x_2, x_3) is internal to the ellipsoid (1), and is otherwise defined as the positive solution of the equation

$$\frac{x_1^2}{a_1^2 + \chi} + \frac{x_2^2}{a_2^2 + \chi} + \frac{x_3^2}{a_3^2 + \chi} = 1 \quad (3)$$

In order to simplify the problem we assume a rotational symmetry ($a_1 = a_2$). In such a case the integral (2) can be computed using elementary functions and the transverse and the longitudinal electric fields determine the single particle equations: ($j = 1, 2$)

$$\begin{aligned} x_j'' + K_j x_j - \frac{\mu(1 - f(p))}{2(a_1^2 + \chi)\sqrt{a_3^2 + \chi}} x_j &= 0 \\ x_3'' + K_3 \frac{\beta\lambda}{2\pi} \sin \frac{2\pi}{\beta\lambda} x_3 - \frac{\mu f(p)}{(a_1^2 + \chi)\sqrt{a_3^2 + \chi}} x_3 &= 0 \end{aligned} \quad (4)$$

where $\mu = 3Ne^2/4\pi\epsilon_0 m\gamma^3 v^2$, γ and β are relativistic factors, λ is the wavelength and the ' denotes the derivative with respect to s , $p = \sqrt{a_3^2 + \chi}/\sqrt{a_1^2 + \chi}$

$$f(p) = \frac{1}{p^2 - 1} - \frac{p \log(p + \sqrt{p^2 - 1})}{(p^2 - 1)^{3/2}} \quad (5)$$

is the form factor defined for $p \in \mathbb{R}^+$ by extending the log and the square root functions to complex values. Since a_j depends on s , the equations (4) are time-dependent canonical equations. Therefore in order to integrate eqs. (4) we

have solved the envelope equations which follow from the rms envelope equations using the relations $\langle x_i^2 \rangle = a_i^2/5$

$$\begin{aligned} a_j'' + K_j(s)a_j - \frac{\mu(1-f)}{(a_1+a_2)a_3} - \frac{\epsilon_j^2}{a_j^3} &= 0, \\ a_3'' + K_3(s)a_3 - \frac{\mu f}{a_1 a_2} - \frac{\epsilon_3^2}{a_3^3} &= 0 \end{aligned} \quad (6)$$

where $\epsilon_i = 5\sqrt{\langle x_i^2 \rangle \langle x_i'^2 \rangle} - \langle x_i x_i' \rangle^2$ $i = 1, 2, 3$ are the emittances. If we choose the periodic solution of the envelope equations, then it is possible to introduce the Poincaré map for the system (4) (matched case); otherwise in the generic case $a_i(s)$ are only quasi-periodic and the Poincaré map cannot be used to plot the phase space of the test-particle.

3 ENVELOPE MODES

If the deviations δ_i with $i = 1, 2, 3$ from the periodic envelope are small, they can be calculated from the linearization of (6), giving rise to envelope modes that enter single particle dynamics. In particular if the focusing is smooth ($\nu_i \ll 1/4$), one can directly calculate the equilibrium envelopes $a_i = \sqrt{\frac{\epsilon_i L}{2\pi\nu_i}}$, and the zero space charge tunes:

$$\nu_{0j} = \sqrt{\nu_j^2 + \frac{\mu}{4\pi^2} \frac{L^2(1-f)}{(a_1+a_2)a_j a_3}}. \quad (7)$$

$$\nu_{03} = \sqrt{\nu_3^2 + \frac{\mu}{4\pi^2} \frac{L^2 f}{a_1 a_2 a_3}}. \quad (8)$$

The envelope modes are solution of the system:

$$\delta_i'' + \sum_{l=1}^3 H_{il} \delta_l = 0. \quad (9)$$

where in the case $a_1 = a_2$, the matrix H_{il} has the form:

$$A = H_{11} = H_{22} = \nu_{01}^2 + 3\nu_1^2 + \frac{\mu(1-f)}{8a_1^2 a_3} - \frac{\mu f'}{4a_1^3},$$

$$B = H_{33} = \nu_{03}^2 + 3\nu_3^2 - \frac{\mu f'}{2a_3^3},$$

$$C = H_{12} = H_{21} = \frac{\mu(1-f)}{8a_1^2 a_3} - \frac{\mu f'}{4a_1^3},$$

$$D = H_{31} = H_{13} = H_{32} = H_{23} = \frac{\mu(1-f)}{2a_1 a_2^2} + \frac{\mu f'}{2a_1^2 a_3},$$

with $f' = df(p)/dp$. The eigen-frequencies are:

$$\alpha_0 \approx \sqrt{A - C} \quad (10)$$

$$\alpha_{\pm} = \sqrt{\frac{A+B+C}{2} \pm \sqrt{\left(\frac{A-B+C}{2}\right)^2 + 2D^2}} \quad (11)$$

and the corresponding eigen-vectors are:

$$\vec{\delta}_0 = (-1/\sqrt{2}, 1/\sqrt{2}, 0) \quad (12)$$

$$\vec{\delta}_- = (-\sin \phi/\sqrt{2}, -\sin \phi/\sqrt{2}, \cos \phi) \quad (13)$$

$$\vec{\delta}_+ = (\cos \phi/\sqrt{2}, \cos \phi/\sqrt{2}, \sin \phi) \quad (14)$$

with

$$\phi = \frac{1}{2} \arctan \left(\frac{2\sqrt{2}D}{A-B+C} \right). \quad (15)$$

This is the mode mixing angle. In particular, if radial and longitudinal focusing strength are equal, the mixing angle is $\pi/4$. On the contrary if the difference in focusing strength is large the mixing angle tends to zero. The lattices of practical interest are smooth enough so that the three modes calculated in smooth approximation can be recognized.

For numerical simulations we have chosen a lattice with $a_1 = a_2$ and with $\epsilon_1 = \epsilon_3 = 10^{-6}$ m, $K_1 = K_2 = 1.5$ m $^{-2}$, $K_3 = 0.9$ m $^{-2}$, $L = 3\beta\lambda = 1$ m, $\mu = 2 \cdot 10^{-9}$ m. In this case the frequencies in smooth approximation are: $\nu_{01} = 0.16$, $\nu_{03} = 0.16$, $\nu_1 = 0.13$, $\nu_3 = 0.12$ and the envelope modes are: $\alpha_0 = 0.27$, $\alpha_- = 0.26$, $\alpha_+ = 0.30$ with a mix angle of $\phi = 0.51$ rad.

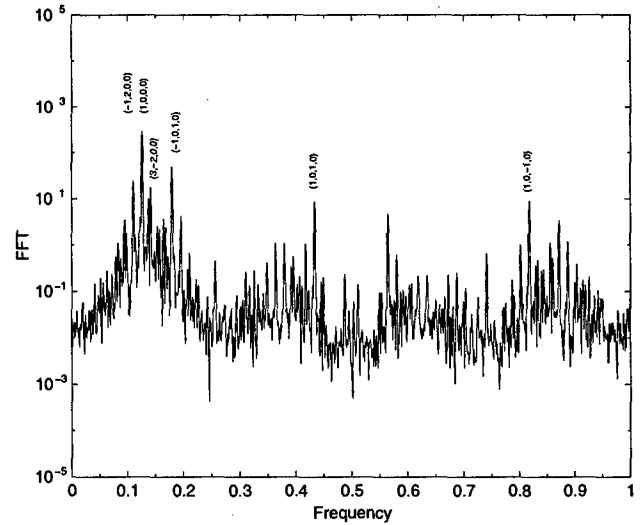


Figure 2: Fourier analysis of the mismatched case; (n_1, n_2, n_3, n_4) corresponds to $n_1\nu_1 + n_2\nu_3 + n_3\alpha_+ + n_4\alpha_- = 0$. Numerically $\nu_1 = .1247$, $\nu_3 = .1169$, $\alpha_+ = .3077$, $\alpha_- = .2657$

4 FREQUENCY-MAP ANALYSIS

The FM analysis is a useful tool to represent the phase space of a symplectic map of 2 or more degrees of freedom, which can be applied also to quasi-periodic time dependent maps. The basic idea is to compute the main frequencies associated to the invariant tori (regular orbits) and to study the regularity of the map (i.e. the FM) between the space of the invariant tori and the frequency space. According to the K.A.M. theory, in the regions of the phase space mostly filled by regular orbits the main frequencies associated to the invariant tori change smoothly from one torus to another, whereas in the resonant regions the frequencies are locked to the resonant values.

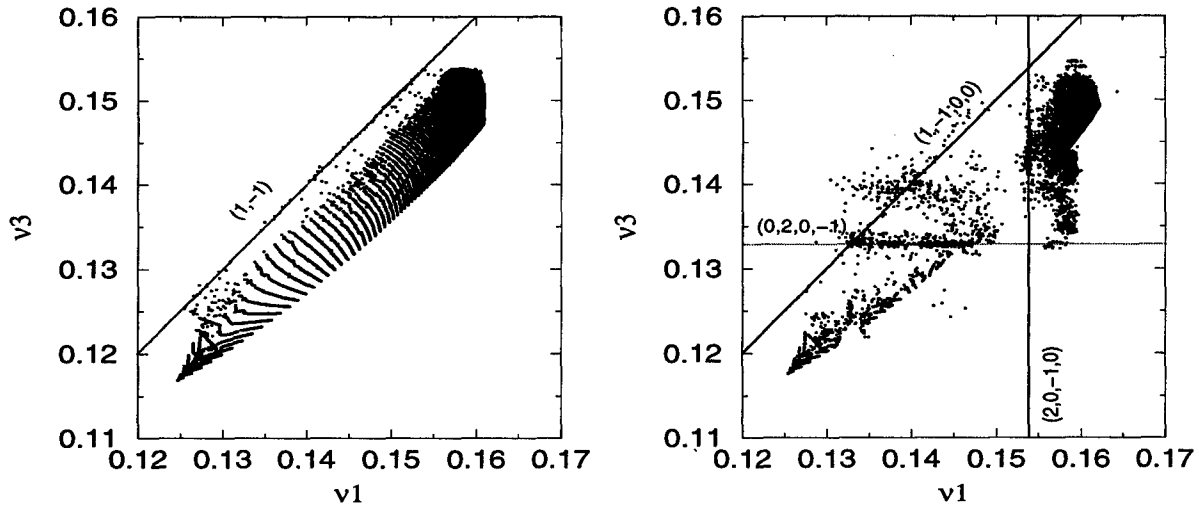


Figure 3: FMA in the matched and mismatched case: a $\delta_1 = 0.2a_1$ of mismatch is inserted in the envelope solutions: the low order resonances are indicated and the appearance of a chaotic region due to resonances overlapping for the mismatched case is clear.

In the case of the system (4), we numerically compute the transfer map for the FODO line and for a given initial condition we consider a fixed number of iterations. Then we project the orbit on the planes (x_i, x'_i) $i = 1, 2, 3$ and we compute the betatron and the synchrotronic frequencies by using an algorithm based on the Hanning filter.

In the figure 2 we show the FFT of a regular orbit for a test particle projected in a transverse plane when the beam envelopes are 20% mismatched. Even if the Fourier spectrum is very rich, due to the appearance of the integer combinations between the betatron and synchrotronic frequencies and the envelope frequencies, we observe that the highest peak still corresponds to the betatron frequency. This is in general true for the orbits of the system (4).

In order to study the regularity of the FM, we consider an uniform grid of initial conditions in the $(x_1 = x_2, x_3)$ plane (fig. 4). In the regular regions the initial grid of points is only smoothly deformed by the FM (fig. 3). In the resonant regions the points are mapped in a resonant line so that a dense straight line of points at the center of an empty channel is shown in the frequency space. In the chaotic regions the results of the FM changes strongly from one point to another and the fuzzy cloud of points appears.

5 CONCLUSION

We have shown the possibility to use the FMA the longitudinal-radial coupled motion for high intensity bunched beam. The FMA provides information on the regular, resonant and chaotic regions in the phase space and allows to define a dynamic aperture by using the border of the regular regions around the beam core. In the mismatched case the FM analysis for the P-C model points out the role of the resonances between the single particle and the enve-

lope frequencies for the stability of the orbits, through the mechanism of resonance overlapping.

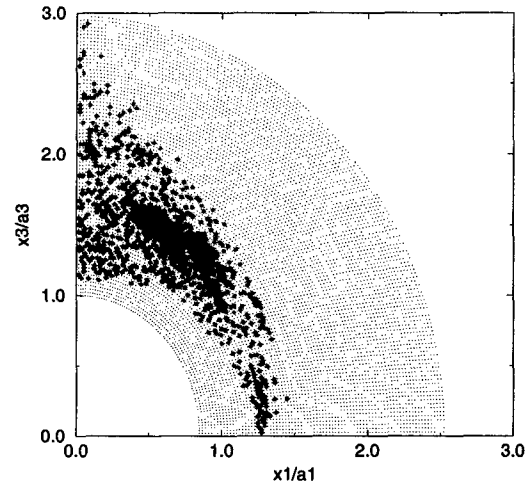


Figure 4: Initial condition corresponding to mismatched case (fig. 3 right side). The initial conditions corresponding to the two overlapping resonances $(2, 0, -1, 0)$ and $(0, 2, 0, -1)$ are indicated with thicker markers

6 REFERENCES

- [1] J.Laskar, *Physica D*, **67**, p. 257 (1993)
- [2] R.Bartolini, A. Bazzani, M.Giovannozzi, W.Scandale, E.Todesco, *Particle Accelerators* **52**, p. 147, (1996)
- [3] Bazzani A., Comunian M., Pisent A., "Frequency Map Analysis of an intense mismatched beam in a FODO channel", to be published on *Particle Accelerators*.

A MULTIGRID-BASED BEAM DYNAMICS CODE FOR HIGH CURRENT PROTON LINACS

Paolo Pierini[†], Giovanni Bellomo and Carlo Pagani,
INFN Milano LASA, Via Fratelli Cervi, 201 I-20090 Segrate (MI) Italy

Abstract

A beam dynamics code has been developed for the design assessment of a superconducting high current proton linac for the ENEA/INFN TRASCO Project (intended for nuclear waste transmutation in a subcritical reactor). The code deals with the dynamics of a moderate energy (above tens of MeV) and high current proton beam in a beamline composed of elliptical superconducting cavities and quadrupoles. A 3D Poisson solver based on multigrid techniques has been chosen for the space charge calculations. The simulation results for the reference linac design, with a particular care to emittance growth and halo generation, are here reported.

1 GENERAL FEATURES OF THE CODE

The code[1] has been specifically developed for the simulation of high current proton beams in a superconducting linac that uses "elliptical" cavities, as is the case for TRASCO[2]. The beam is advanced along the linac in phase steps (where the phase is defined as $\phi = \omega_{rf}t$, and ω_{rf} is 2π the frequency of the linac). In case a particle crosses an element boundary during a timestep, a substep is performed up to the element end and the step is then continued in the following element. Particles crossing an element boundary where output is desired are collected in buffers for disk storage.

The beamline is composed of a sequence of elements of different types: quadrupoles, drift spaces and cavities. An "ideal" 3D uniform focussing element can also be used for analytical checks of the code.

For the propagation in the quadrupoles and drifts analytical maps are used (which include chromatic effects for the quadrupole), whereas for the RF cavities a direct integration in the cavity field is performed. A cavity is described either with an analytical field shape of an "ideal" reduced β cavity or by an on-axis field map (provided by any cavity electromagnetic code). Off-axis expansion, to second order, of the electric and magnetic fields is computed for particle tracking.

Space charge is computed in multiples of the particle tracking phase steps. The space charge kicks can be evaluated either using a direct point to point method or with a fast 3D Poisson solver in the reference particle rest frame, based on a multigrid algorithm.

1.1 RF Cavities Modeling

The codes used for the design of the TRASCO linac replace the elliptical RF cavities with a properly chosen "ideal" cavity with an analytical field given by:

$$E_z(z,t) = 2E_{acc} \sin(\omega_{rf}t + \phi_c) \sin\left(\frac{\omega_{rf}z}{c\beta_c}\right)$$

where E_{acc} is the accelerating field, β_c the cavity synchronous velocity and ϕ_c the phase. Both E_{acc} and β_c are defined so that the cavity gives the same energy gain of the "real" cavity (as designed by a program as Superfish[3]) in all the energy range of the linac where the cavity is used. Note that β_c does not depend from the inner cell length, it rather comes from a "dynamical" equivalence of a real cavity with an ideal sine-like cavity.

This equivalence has been tested against a much simpler (although much quicker in terms of computational costs) model of a cavity: the RF gap. The transfer matrix elements for the longitudinal phase space ($\Delta\phi, \Delta E$) are plotted in Figure 1 for three cavity models: the direct integration in the E_z field, the sine-like approximation defined above and the RF gap equivalence, where the whole 5 cell cavity is replaced by a single RF gap, giving the right energy gain and phase advance at each energy. The plots were computed for the β range corresponding to the first section of the TRASCO linac (100-190 MeV).

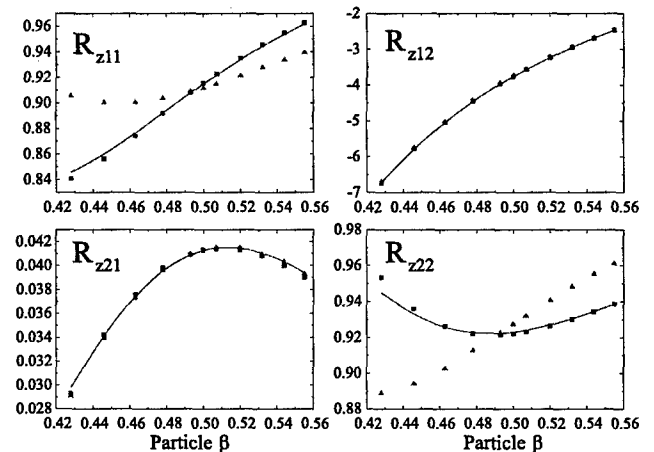


Figure 1: Longitudinal transfer matrix elements for the three cavity models: direct integration (solid line), sine-like equivalent (squares, see text) and RF gap (triangles). Phase space units are deg and MeV. $\phi_s = -30$ deg.

[†] Email: Paolo.Pierini@mi.infn.it

The transfer matrix of the transverse plane ($x, dx/ds$) is shown in Figure 2, for the same cavity models of Figure 1.

It is worth noting that the largest errors are found on the elements on the main diagonal of the transverse and longitudinal transfer matrices, where the sine-like equivalent has an error of 10^{-3} - 10^{-4} , whereas the RF gap gives a difference of the order of 10^2 .

In both the transverse and longitudinal matrix cases, when the cavity is operated near its nominal velocity (here $\beta=0.5$) the three models give approximately the same values for the elements (to few parts in 10,000).

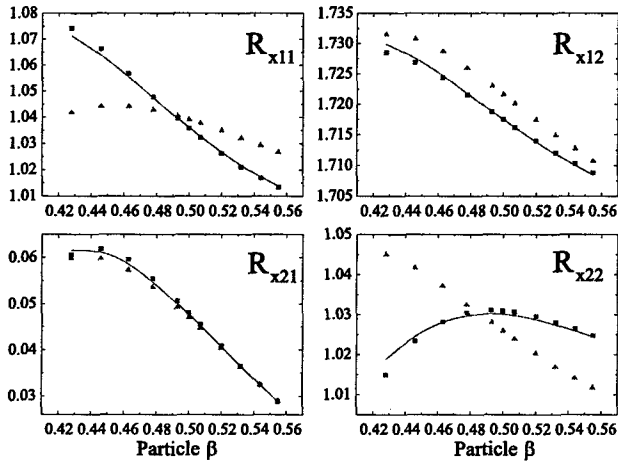


Figure 2: Transverse transfer matrix elements for the three cavity models: direct integration (solid line), sine-like equivalent (squares, see text) and RF gap (triangles). Phase space units are mm and mrad. $\phi_s = -30$ deg.

1.2 The Space Charge Multigrid Algorithm

Since the code advances in time (phase), when the space charge calculation is needed the particle coordinates are Lorentz-transformed to the rest frame of the reference particle, the charge distribution is evaluated using a cloud in cell (CIC) assignment scheme and the 3D Poisson equation is solved.

The fields computed from the solution potential are then transformed back in the laboratory frame and the force is interpolated on the particle position using trilinear interpolation[4].

The Poisson equation is solved iteratively using a multigrid solver[5], a fast iterative method that uses standard relaxation algorithms (in our case we chose the Gauss-Seidel) and combines it with the discretization of the problem on a series of nested grid levels (in our case obtained by step doubling of the finest level).

The code implements both the V-cycle and the full multigrid[5] cycling strategies, but the V-cycle allows to make use of the potential map computed at a previous space charge computation in order to start from a better estimate for the solution potential. This strategy leads to a speed up of the space charge calculations (reducing the time by a typical factor of 30%), in order to achieve the specified convergence[1].

The restriction operator (needed to transfer quantities to a coarser mesh level) is the trilinear averaging of the 27 neighboring nodes and the prolongation operator (needed to transfer the solution to a finer mesh level) is the trilinear interpolation.

The space charge routine based on the multigrid solver has been thoroughly tested, both with a comparison with the point to point space charge calculation (which, however, is limited to a small number of interacting particles, due to the time scaling with the squared number of particles) and with simple analytical cases. A report of the tests can be found in Reference 1.

Typical TRASCO simulations are performed with 10^4 - 10^5 particles, a phase step of a few (2-4) RF degrees, a space charge step every 5-15 phase steps using a mesh of $33 \times 33 \times 33$ points, extending to ± 5 -6 rms beam sizes. The whole linac runs in a few hours on a desktop system.

2 THE TRASCO LINAC SIMULATIONS

The 352 MHz superconducting linac accelerates a 25 mA proton beam from 100 MeV to a maximum energy of 1.6 GeV. The linac is divided in three sections, with five cell cavities designed for a synchronous β of 0.5, 0.65 and 0.85, grouped in cryostats containing 2, 3 and 4 structures each. The focussing is provided by a periodic array of quadrupole doublets between the cryostats and the lattice cells are 8.03, 11.152 and 15.34 meters each.

Beam dynamics studies of the TRASCO linac using the code described here, with a number of simulation particles ranging from few thousands to 10^5 , has been already reported in Refs. 6 and 7.

In Figure 3 we present the rms and 90% beam normalized emittances along the linac. The rms emittance growth is less than 4% in all planes. The beam distribution is well matched along the linac, as shown by the nearly constant behavior of the 90% emittance curves. No sign of particle drifting away from the beam core can be seen from the phase space plots.

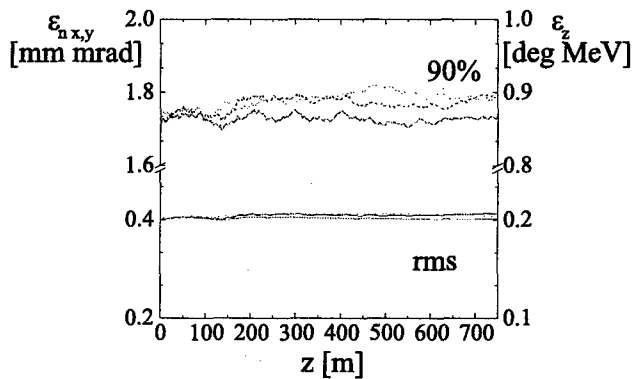


Figure 3: Normalized emittances along the linac. Bottom lines rms values, upper lines 90% beam emittance. The x plane is the solid line, the y plane is the dashed line and the z plane (on the right axis) is the dotted line. The simulation was performed with 10,000 particles.

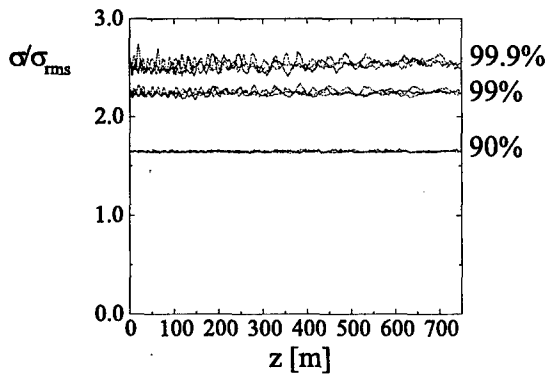


Figure 4: Ratio of the sizes containing different particle populations (including, from bottom to top 90%, 99% and 99.9% of the beam, respectively) to the rms beam size.

Another sign of the absence of beam tail formation can be seen from Figure 4, where we plot the ratio of the size containing 90%, 99% and 99.9% of the beam to the rms beam size. This beam size fraction is approximately constant (averaging the numerical noise due to the poor statistics on the higher values of beam size fractions) along the linac, and confirms that particles are not drifting to the tails of the distribution, as would be the case for a charge redistribution process, that could give rise to a large beam halo.

The matched beam conditions at the linac input and the matching between the three focussing sections of the linac have been determined with the linear dynamics code, TRACE3-D[8]. The matching between the sections is obtained using the gradients of two quadrupole doublets and the synchronous phase of the cavities in two cryomodules at the section interface. RF cavities are modeled in TRACE3-D with a modified tank element (type 13), consistently with the multiparticle simulations.

The phase advances per cell are always lower than 90 deg in all linac sections. The phase advances per meter, as computed by the beam dynamics code from the rms beam parameters, can be seen in Figure 5.

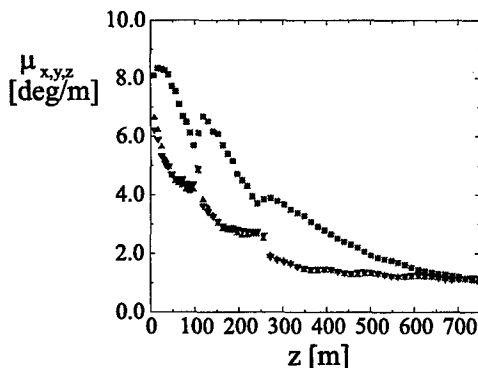


Figure 5: Phase advances per meter (up triangles: x, down triangles: y, squares: z) along the linac, as computed from the rms beam during the simulation. The cell lengths of the three sections are 8.03 m, 11.152 m and 15.34 m, respectively.

The rms beam envelopes plotted in Figure 6 show a discontinuity of the beam sizes at the interfaces, and a small transverse mismatch in the third linac section (visible also as oscillations in Figure 5 and due to the approximations of the TRACE3-D matching). However, no evident emittance growth is produced by these discontinuities and by the beam mismatch.

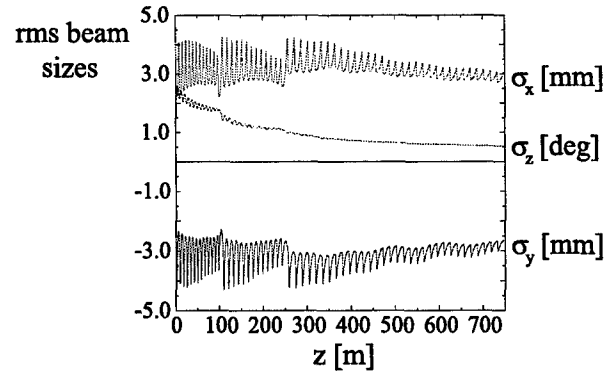


Figure 6: rms beam sizes in the TRASCO linac.

3 CONCLUSIONS

A multiparticle space charge code has been developed for high current superconducting proton linacs with elliptical cavities. The code uses an accurate cavity modeling, that reproduces the cavity behavior in the large velocity region in which the cavities are effectively used. Space charge is included with a 3D iterative Poisson solver, based on multigrid methods.

The code has been successfully used since two years to assess the design of the TRASCO linac.

4 ACKNOWLEDGEMENTS

We thank N. Pichoff (CEA/Saclay) for the many discussions and his help in the multigrid algorithm testing.

5 REFERENCES

- [1] P. Pierini, "A Multigrid-Based Approach to Modeling a High Current Superconducting Linac for Waste Transmutation", in *Proceedings of the 1998 Int. Computational Acc. Physics Conf.*, September 14-18 1998, Monterey, CA.
- [2] C. Pagani, D. Barni, G. Bellomo, R. Parodi, P. Pierini, "Status of the INFN High Current Proton Linac for Nuclear Waste Transmutation", in *Proceedings of the XIX International Linear Accelerator Conference*, August 23-28 1998, Chicago, IL.
- [3] J.H. Billen and L.M. Young, "Poisson Superfish", LA-UR-96-1834, Los Alamos, NM, revised 1999.
- [4] "Computer Simulations Using Particles", by R.W. Hockney and J.W. Eastwood, Adam Hilger, New York, NY 1988, ISBN 0-85274-392-0.
- [5] "A Multigrid Tutorial", by William Briggs, SIAM, Philadelphia, PA 1987, ISBN 0-89871-222-1.
- [6] G. Bellomo, P. Pierini, "Beam Dynamics In A Proposed 350 MHz SC Linac For Nuclear Waste Transmutation And Energy Production", in *Proceedings of the 1998 European Particle Accelerator Conference*, Stockholm, June 21-26 1998.
- [7] G. Bellomo, P. Pierini, "Beam Dynamics in a High Current SC Proton Linac for Nuclear Waste Transmutation", in *Proceedings of the XIX International Linear Accelerator Conference*, August 23-28 1998, Chicago, IL.
- [8] K. Krundall, D. Rushtoi, "TRACE3-D Documentation", LA-UR-97-886, Los Alamos, NM, 1987.

DAMPING EFFECT IN THE BEAM ENVELOPE AMPLITUDE OSCILLATIONS IN MISMATCHED HIGH INTENSITY ION BEAMS

T. Clauser, V. Stagno, Dipartimento di Fisica di Bari,
V. Variale, INFN sez.di Bari, Via Amendola 173 Bari 70126, Italy

Abstract

Space-charge dominated beams can induce chaotic behavior on particle trajectories leading to halo formation on the beam spot. This causes particle losses along the beam transportation that must be minimized. The fractional losses must be kept below $10^{-7}/m$. This is a very low threshold to check with standard multiparticle codes. To study this kind of problems a new particle simulation approach will be proposed in this paper in analogy with the single particle to core interaction model which is the most used calculation technique applied in these kind of phenomena. In particular, a damping effect in the amplitude oscillations of the beam envelope, for high intensity beam mismatched with a FODO cell, will be shown and discussed.

1 INTRODUCTION

In these last years, growing interest has been addressed, from the international scientific community, on the possible applications of high intensity ion beams. Among them, just as examples, we can mention the energy amplifier proposed by C. Rubbia [1] and the transmutations of radioactive waste [2]. However high intensity beam transport poses problems those need to be faced and solved. In particular, a halo formation has been observed around high intensity beams, during the transport, that leads to particle losses. For high current and energy beams the lost particles produce radio activation in the structures and the related radiation can damage the accelerator components. Furthermore the radioactivation makes the accelerator maintenance very difficult and expensive. Because of these problems, it becomes very important to study halo formation mechanism in the beam.

Multiparticle codes could be very helpful to this aim but it is very difficult to study this kind of phenomena by using the standard multiparticle codes because the lost particle fraction, along the transport, must be kept below $10^{-7}/m$ [3]. This means that the code should use a number of particles of the order of 10^6 , in the simulations, to appreciate this kind of lost fractions. This number is very high and very powerful calculators are needed to handle them. In fact, in these kinds of simulations, the space charge force effect, because of the high intensity beam used, becomes a very important issue.

A new calculation technique, called Particle Core Model (PCM) [4], has been introduced to study the halo formation without using of very powerful computers.

The PCM solves the beam envelope (or rms) equation for a continuous beam that is used as a model for the core of the beam. The core can be mismatched so that its radius, taken at the exit of the transport period cell, will oscillate. The halo particles are represented by test particles, which oscillate through the core, influenced by linear external focusing field and the non-linear space charge fields of the core. The model allows one to study the dynamics of the test particles.

Although the PCM calculations allow studying the halo formation, this is done by assuming some approximations and then their influence on the PCM results should be checked.

For that reason, a comparison test between the PCM results and the simulations of the multiparticle code PARMT, modified to allow a more direct comparison with the results of PCM calculations, has been carried out in ref. [5].

In that reference, a continuous beam has been transported through hundreds of FODO periodic cells. The comparison of the simulation results obtained either with the multiparticle code and PCM led to the following conclusions. PCM calculations seem unsuitable to study test particles taken near the beam core region in the case of high beam current. The discrepancies found between the multiparticle code and PCM results were mainly due to the following reason.

In PARMT simulations, the breathing mode oscillations, due to the mismatch of the input beam with the periodic cells, damp very quickly when the space charge is strong. In PCM calculations, a constant amplitude oscillation of the beam envelope is, instead, considered.

In this paper, an attempt to better understand the mechanism causing the fast damping of the beam breathing mode oscillations observed in ref. [5] will be done. Moreover, further simulations on the chaotic behavior originating, in some cases, in the test particle trajectories will be also shortly shown and discussed.

2 SIMULATIONS

The multiparticle code PARMT is a Monte Carlo program that can transport an ion beam through a system of optic elements by using the matrix method [6]. Being simulated a very high number of particles, PARMT uses a

'Fast Poisson Solver' (FPS) technique to compute the space charge electric field of the ion beam.

To compare directly the PCM with the PARMT results some modifications have been carried out in the PARMT code. Mainly, two new features have been introduced in the program: 1) an input file with the initial test particles coordinates that can be read, if required, by the main program; 2) N output files (with N number of test particles), where the test particle phase space coordinates along the transport in the periodic cells (Np) are stored.

The main input file parameters, used in the PARMT simulations of ref. [5], are here recalled. In that simulations we used FODO cell periods of length $L=80$ cm; transverse rms emittances, $\epsilon_x=\epsilon_y=0.25 \times 10^{-6}$ m-r; single particle phase advance $\sigma_0=60.7^\circ$ and space charge parameter (as defined in ref [7]) $\xi=4 \times 10^{-6}$ (corresponding to $I=95$ mA and $\beta=0.145$).

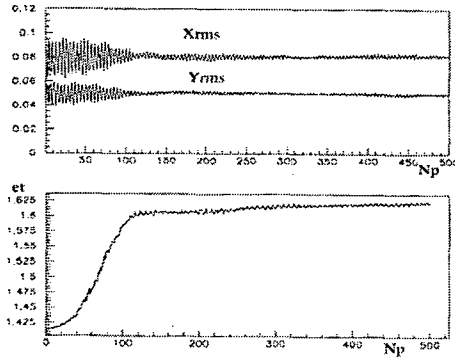


Fig.1 Transverserms beam size values vs cell period numbers (Np) for the case $\sigma/\sigma_0=0.55$.

Moreover an odd mismatching of about 20% has been added on the initial beam size, in all the simulations.

The fast oscillation damping of the beam breathing mode found in ref.[5] is presented in fig.1. In that figure the related total emittance variation et , defined as $et=(\epsilon_x^2/\epsilon_{x0}^2+\epsilon_y^2/\epsilon_{y0}^2)^{1/2}$, is also shown.

We think that the damping effect of the fig.1 can be ascribed to the Landau mechanism of stabilization that can occur when a very large number of oscillators, which are the same but for their natural frequency, are excited by an external force.

This mechanism is already used in accelerator physics to explain the Keil-Schnell stability criterion [8]. In fact, if one injects a very cool beam in accelerator machine, the microwave instability develops. The beam momentum spread blows up to a point when Landau damping gets strong enough to stabilize the unstable motion. The Keil-Shnell criterion gives the minimum energy spread, that is betatron frequency spread, for stability. The Landau damping is a stabilizing effect connected with the frequency spread [9].

To clarify, shortly, the Landau damping mechanism, consider a set of oscillators, with a frequency distribution $f(\omega_\beta)$, coupled to a harmonic excitation of frequency ω .

The response of the set to the excitation can be seen by the center-of-charge velocity of the set [10]:

$$\langle \dot{y} \rangle = \hat{G} e^{-i\omega t} \left[\pi f(\omega) - iPV \int \frac{f(\omega)}{\omega_\beta - \omega} d\omega_\beta \right] \quad (1)$$

where PV means Principal Value integral and \hat{G} is the amplitude of the harmonic excitation.

This response has a real part for which the velocity and the excitations are in phase and an imaginary part, where they are out of phase, indicating no energy exchange. The real part term indicates that the beam absorbs energy from the exciting signal. Since the beam particles absorb energy this can lead to the damping of the coherent oscillation that is often called Landau damping. From the equation (1) it can be noticed that the real term is proportional to the density of the frequency distribution, $f(\omega_\beta)$, in the region of the excitation frequency ω . Then a condition to obtain an effect of Landau damping is that the exciting frequency lies inside the incoherent frequency distribution. Furthermore, we have to add from ref. [10], that the equation (1) is only correct if the excitation has lasted for a long time. How long this time has to be depends on the shape of the frequency distribution $f(\omega_\beta)$ considered. If this distribution does not change significantly over a frequency range of $\Delta\omega_\beta$, around ω , it is sufficient to excite for a time $\tau \gg 1/\Delta\omega_\beta$. This means that all the oscillators with frequency inside $\Delta\omega_\beta$, in the time τ , are still responding positively to the exciting force. Then to have a large period of interaction between the exciting force and the oscillators we need a large $\Delta\omega_\beta$. In conclusion, the Landau damping mechanism applies only if we have oscillators with an enough large frequency spectrum that cover the exciting frequency.

To interpret the behavior of fig.1 we need to make some preliminary considerations.

The beam particles, in the reference particle system, can be seen as a set of oscillators that oscillate with their betatron frequency because of the focusing forces. When the beam particles have a certain momentum spread, because of the chromaticity, they will have also a betatron frequency spread. In general, this frequency spread tends to be very small, but when we have a space charge dominated beam ($Kr^2/4\epsilon \gg 1$ [11], see below for the symbol meaning) it enlarges very much. The space charge tune depression σ/σ_0 in the case of the simulations shown in fig.1 was 0.55. This means that the most inner beam particles will still have a phase advance σ_0 of 60.7° , that is, a betatron frequency ω_β of about 58 MHz, while the most external beam particles, filling the whole space charge force, will have a phase advance $\sigma=0.55(60.7^\circ)=33.4^\circ$, that is $\omega_\beta=31.6$ MHz. On the other hand, when a space charge dominated beam is mismatched with the focusing periodic cell, the beam itself starts to oscillate in a breathing mode with the plasma frequency ω_p :

$$\omega_p = (K\beta^2 c^2 / 2r^2)^{1/2} \text{ where } K = \frac{qI}{2\pi\epsilon_0\gamma^3\beta^2 mc^3}$$

and r is the beam radius. In the case simulated, in fig.1 ω_p is about 51MHz. In these conditions Landau damping can occur. In fact, there is a harmonic excitation given by the breathing mode oscillation of the beam envelope and a large set of oscillators, the beam particles oscillating with a large betatron frequency spectrum. From that figure, it can be noticed that the coherent oscillation energy is transferred to the incoherent oscillations of the beam particles. During the damping of the breathing oscillation there is a slight increase of the total emittance variation. At the end, we can say that the energy involved in this process is dissipated from a coherent motion to the very high number of degrees of freedom of the system. When this damping process is finished, the beam reaches the matched size and no further increase of emittance is observed.

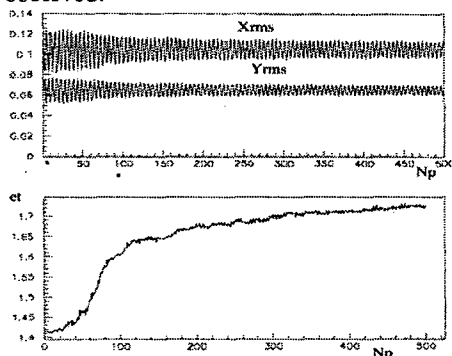


Fig.2 Transverse rms beam size values vs cell period numbers (Np) for the case $\sigma/\sigma_0=0.29$ ($I=200\text{mA}$).

In fig.2 are shown simulation results with an increased space charge tune depression, $\sigma/\sigma_0=0.29$. In this case, it can be noticed that only some part of the beam particles is involved in the Landau damping process. In fact, now the plasma frequency is about 56 MHz and the lowest betatron frequency is about 16 MHz. For this reason the part of the beam particles that have betatron frequencies too far from the plasma frequency interact very weakly with the coherent oscillation and then the breathing mode oscillation is only partly damped. In fig.3 is shown the case of emittance dominated beam ($Kr^2/4\epsilon \ll 1$) where no energy exchange occurs between the breathing mode and the betatron oscillations and emittance remain constant.

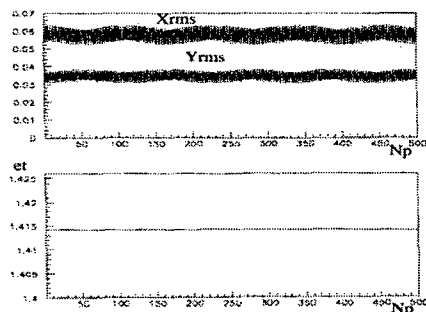


Fig.3 Transverse rms beam size values vs cell period numbers (Np) for the case $\sigma/\sigma_0=0.89$ ($I=0.5\text{mA}$).

The test particle trajectories considered in ref.[5] to detect the chaotic motion which is responsible of beam halo generation, showed only coupling between the transverse planes but remained confined inside their original positions. Those test particles started from near the beam core, where rms oscillations, due to mismatching, occur but through the damping the beam readjusted itself at matching conditions very soon. Maybe, considering, in those simulations, a larger number of test particles some chaotic trajectories had could be found.

Chaotic motions have been found in the test particle trajectories considered for the case of a space charge dominated beam with $\sigma_0 > 90^\circ$ where envelope instabilities occur [11]. In fig.4 are shown trajectory results for those test particles starting from near the beam core at a position around $x=0.2\text{cm}$ (the same of ref.[5]). It can be noticed that, although the shown test particles initial conditions differ only of few microns they have completely different phase trajectories (chaotic behavior). Furthermore the chaotic test particles oscillate between 0.2-0.5 cm originating a beam halo size greater than 0.5 cm.

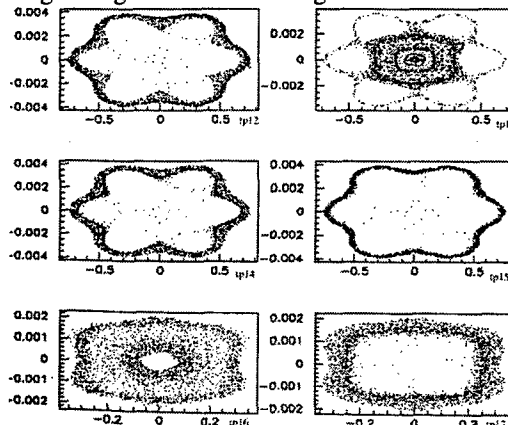


Fig.4 Chaotic test particle trajectories in phase space xx' .

3 CONCLUSIONS

The fast damping of the breathing mode oscillation occurring in mismatched beam space charge dominated can be ascribed to a Landau damping mechanism of stabilization. No test particle with chaotic motion has been found when fast damping of mismatched oscillation occurred.

4 REFERENCES

- [1] C. Rubbia et al., CERN/AT/95-44(ET)
- [2] C. Rubbia et al., CERN/AT/95-53(ET)
- [3] R. A. Jameson, G. P. Lawrence and S. O. Schriber, Proc. PAC'93
- [4] J. Lagniel, NIM in Phys. Res. A345 (1994) 405.
- [5] V. Variale, submitted to NIM in Phys. Res. A
- [6] J. Struckmeier, GSI-ESR-03 report.
- [7] J. L. Laclare, CAS CERN85-19, Vol. II
- [8] J. Landau J. Phys. USSR, 10, 25, 1946
- [9] A. Hoffmann, CAS CERN95-06, Vol. I
- [10] T. P. Wangler, AIP Conf. Proc. 377
- [11] I. Hofmann, App. Char. Part. Optics 13C, ed. A. Septier (1983)

SPACE CHARGE EFFECT ON EMITTANCE EXCHANGE BY SKEW QUADRUPOLES

G. Franchetti*, I. Hofmann, GSI, Darmstadt, Germany

Abstract

For high current synchrotron SIS it is crucial to improve the multiturn injection efficiency. We study active emittance exchange due to a second order (skew quadrupole) difference resonance which is modified by the presence of space charge. We start from an analytical expression for the coherent tune shift of this resonance and compared it with computer simulation for the SIS synchrotron lattice including self-consistent space charge calculation. The critical issue is the ratio of incoherent space charge tune shift and resonance width. We apply the results of simulation to the horizontal multiturn injection process with space charge and find an improvement of the injection efficiency from 65 % to 84 % (with a correspondent increase of the vertical emittance) in a typical example.

1 SPACE CHARGE EFFECTS IN THE LINEAR COUPLING

One limitation of multiturn injection schemes is the loss of particles hitting the vertical septum and vertical acceptance. A skew quadrupole couples the transverse planes exciting a difference resonance. When the bare tune is on such a resonance, horizontal oscillation energy is transferred to the vertical plane and the horizontal amplitude of the injected particle will diminish during the few revolutions of the multiturn injection. This effect can be exploited to move particles away from the septum, thereby improving the injection efficiency. As reported in [1] for a single particle case, if the bare tunes are on a difference resonance $q_{x_0} - q_{y_0} = 1 - \delta$ with $\delta \ll 1$ and if the initial vertical emittance is zero, then the emittance exchange is described by the formula

$$\epsilon_x = \epsilon_{x_0} - \frac{4Q_c^2 \sin^2 \Theta}{\delta^2 + 4Q_c^2} \epsilon_{x_0} \quad (1)$$

Here, $\Theta = 2\pi N_t \sqrt{\delta^2/4 + Q_c^2}$ and $\epsilon_x + \epsilon_y = \text{const}$ with initial values ϵ_{x_0} and $\epsilon_{y_0} = 0$, where ϵ_x, ϵ_y are the instantaneous Courant Snyder invariants, $Q_c = \sqrt{\beta_x \beta_y j / (4\pi)}$, N_t is the number of turns, and j is the integrated strength of the skew. We can define the bandwidth δ_b of the resonance as the δ where the number of turns for a complete exchange is half of the number of turns n_t needed for an exchange in the center of the resonance. It is straightforward to find $\delta_b = \sqrt{3}/n_t$ correspondent to the maximum exchange of $\epsilon_{x_0}/4$.

1.1 Coherent Effect

A crucial issue is the effect of the space charge on the particle dynamics. The linear coupling produces, when the resonance condition is satisfied, a coherent effect on the beam which exchanges the two beam sizes. When space charge is present it excites a coherent tilting eigenmode with eigenfrequency ω . This corresponds to $q_{x_0} - q_{y_0}$ in the absence of space charge in which case the resonance condition is $\omega = q_{x_0} - q_{y_0} = 1$. Keeping $\omega = 1$ as the resonance condition we can write for finite space charge by introducing a coherent tuneshift $\Delta\omega$

$$\omega = q_x - q_y + \Delta\omega = 1 \quad (2)$$

where $q_x = q_{x_0} - \Delta q_x$ and $q_y = q_{y_0} - \Delta q_y$ with $\Delta q_x, \Delta q_y$ the incoherent tuneshifts. By using the definitions $\sigma_p \equiv \omega_p/\nu_x$, $\alpha \equiv \nu_y/\nu_x$, $\eta \equiv a/b$ where ω_p is the "beam plasma frequency" and a, b are the semiaxis of the confining ellipse, the eigenfrequency of the tilting mode is characterized by the dimensionless coherent frequency $\sigma \equiv \omega/\nu_x$ which results in the dispersion relation [2]

$$\frac{\sigma_p^2}{2} \left(\frac{(1-\alpha)(1-\eta^2/\alpha)}{(1-\alpha)^2 - \sigma^2} + \frac{(1+\alpha)(1+\eta^2/\alpha)}{(1+\alpha)^2 - \sigma^2} \right) + (1+\eta)^2 = 0. \quad (3)$$

We compared the prediction of the theory with simulations for the frequency of the eigenmode using for few revolutions the skew quadrupole to excite the tilting eigenmode. A coasting beam under the action of a skew kick tuned to exchange in 40 turns has been tracked for five turns and afterwards the skew was turned off to stop the exchange while the simulation continued. The coasting beam has been tracked for 274 turns, each cell of the SIS has been

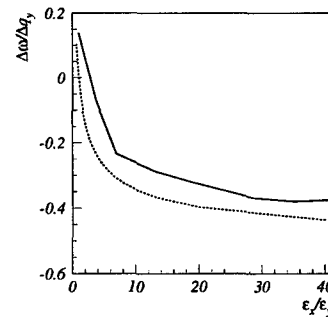


Figure 1: Comparison between analytical model (dashed-line) and simulations (solid-line).

* Email: G.Franchetti@gsi.de

divided in 20 steps of space charge calculation, the horizontal emittance has been kept constant to $\epsilon_{x0} = 200$ mm mrad and the current of the beam was $I = 140$ mA. At each step the quantity \overline{xy} , typical for the skew rotation, has been calculated and Fourier analyzed to determine ω . In Fig. 1 we plot the theoretical prediction according to Eq. 3 (dashed-line) and the results from simulation (solid line) for the quantity $\Delta\omega/\Delta q_y$ showing reasonably good agreement. In order to understand the effect of the space charge we split the eigenfrequency $\omega = \omega_l + \delta\omega_{sc}$ in a lattice component $\omega_l = q_{x0} - q_{y0}$ and in a space charge component $\delta\omega_{sc} = -\Delta q_x + \Delta q_y + \Delta\omega$. Analogous to the single particle theory we define the shift from the resonance as $\delta = 1 - \omega$. However since the space charge component $\delta\omega_{sc}$ changes according to the emittance exchange the relevant quantity which describes the dynamical regime of the beam evolution is $\delta\omega_{sc}/\delta_b$. Considering at the time $t = 0$ $\omega = 1$ we can distinguish the evolution of the beam between a weak space charge regime if $\delta\omega_{sc}/\delta_b \ll 1$ and a strong space charge regime $\delta\omega_{sc}/\delta_b \gg 1$ where the fast change of $\delta\omega_{sc}$ drives oscillations of δ up to the border of the resonance limiting the exchange. The maximum fluctuation of $\delta\omega_{sc}$ is expected to be of the order of $2\delta_b$.

1.2 Strong Space Charge Regime

In a strong space charge regime the dynamics of the exchange is strongly nonlinear. We simulate this case for a beam with $\epsilon_x = 195$ mm mrad, $\epsilon_y = 4$ mm mrad and a current $I = 160$ mA. Using the results of Fig. 1, according to the previous definition, the initial space charge eigenfrequency component is $\delta\omega_{sc} = 0.12$ and since $\delta_b = 0.02$ we find $\delta\omega_{sc}/\delta_b \sim 6$. We expect consequently a strong deviation in the emittance exchange described by Eq. 1. We investigated this effects repeating the same simulation with identical initial condition but different q_{y0} , changing in this way the initial resonance condition. We distinguish between the initial eigenfrequency below the resonance ($\delta < 0$) and above the resonance ($\delta > 0$). According to the condition $\omega = 1$ the center of the resonance is expected to be at $q_{y0} = 3.41$, but Fig. 2 shows that the exchange is strongly affected whether the resonance is reached from below or above. When the resonance is approached from below, Fig. 2b shows the existence of two regimes: one of small oscillations of ω and small exchange; and, for slightly higher working point ω sweeps through the whole stopband consistently with a much bigger emittance exchange. In this case the evolution of the exchange is not the same as described in Eq. 1 because of the dynamical change of the resonance condition. Figs. 2c-f show a slow decrease of the exchange for increasing values of q_{y0} that we interpret as a reduction of the swept area by ω in the bandwidth. The asymmetry of the exchange with respect to the case $\delta = 0$ is the stronger the bigger is the initial ratio $\delta\omega_{sc}/\delta_b$.

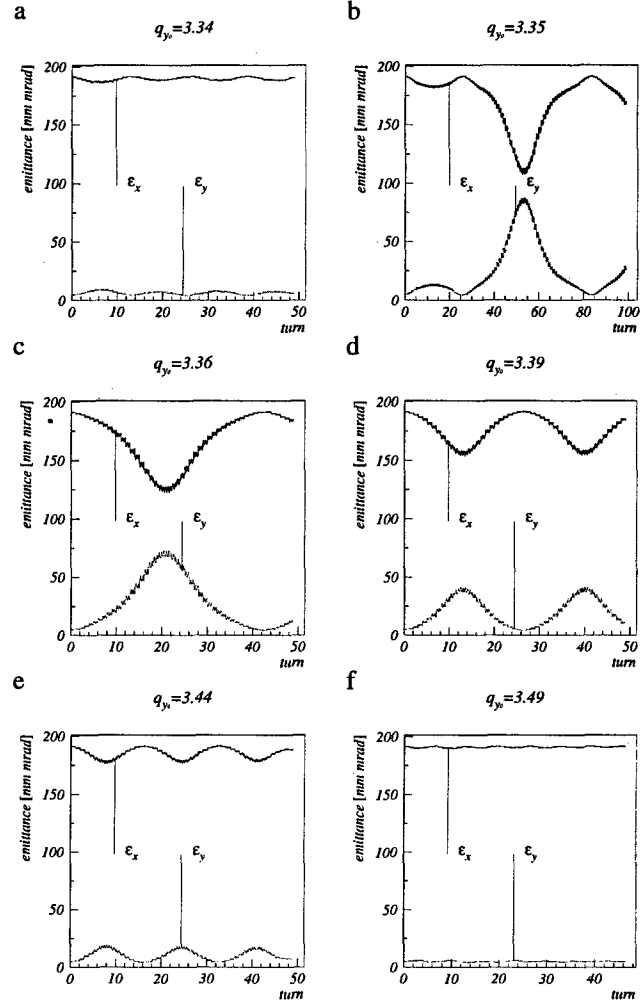


Figure 2: Strong space charge regime for $I=160$ mA. a)-f) show the emittance exchange for increasing q_{y0} . b) has been tracked for 100 turns to show the deviation of the exchange from the single particle theory Eq. 1.

2 MULTITURN INJECTION SIMULATIONS

In this section we present a study on the multiturn injection with skew. We model the SIS injection under somewhat idealized condition assuming the injection where $\alpha_x = 0$, reducing in such a way the septum losses. The multiturn injection scheme is modeled by a shift of the septum correspondent to the distance between septum and bumped orbit. At each turn the septum has been shifted outward by the amount $\Delta x = \sqrt{\epsilon_{x,max} \hat{\beta}_x} / N_t$, therefore its position at the n th turn with respect to closed orbit is $x_{sept.} = \Delta x n$. The septum scrapes all the particles satisfying the condition $x > x_{sept.}$. The acceptance is also simulated removing all the particles satisfying $x^2/A^2 + y^2/B^2 > 1$, where $A = 50.5$ mm and $B = 26$ mm. The multiturn injection takes place in 40 turns, each beamlet injected has $\epsilon_x = \epsilon_y = 4$ mm mrad with a current of $I = 4$ mA. The ions used have $Z = 28$, $A = 238$ and are injected

at 11.4 MeV/u. In the simulation each beamlet is described by $N_b = 100$ macroparticles and the space charge is calculated in a model of ellipsoidal symmetry [3]. Figs. 3a,b show the emittance increase for $q_{x0} = 4.29, q_{y0} = 3.29$ and $n_t = 8$. Here n_t is a dimensionless measure for the strength of the skew. It is defined as the number of turns required for a complete exchange of ϵ in the center of the resonance. Fig. 3c shows for the same setting the efficiency of the injection $N/(N_b n)$, the losses on the septum, and on the acceptance, (N is the number of macroparticles inside the ring). The losses up to 20 % on the septum after 4 turns (change in the slope of ϵ_x in Fig. 3a) can be explained by the initially small distance between septum and closed orbit. After ~ 20 turns, due to the high strength of the skew, losses on the acceptance begin (in Fig. 3b ϵ_y stops its growth). At the 10th turn $I = 32$ mA, $\delta\omega_{sc} = 0.024$ which leads to the shift from the resonance of $\delta = -0.024$. By using Eq. 1 the maximum exchange is $\delta\epsilon/\epsilon_{x0} = 0.96$ which is obtained in 4 turns and 10th beamlet would be lost on the acceptance if $\epsilon_{x0} = 51$. Because $\epsilon_{x0} = 50$ mm mrad the beginning of the acceptance losses at 22 turns instead of 15 must be attributed at the correction to Eq. 1 which is hold only for $\epsilon_{y0} = 0$. Fig. 3d shows the multturn injection for $q_{x0} = 4.4$ and $n_t = 8$. In this case space charge reduces the exchange. Let's consider again the beamlet injected after 10 turns, the closer to the resonance line which has $\epsilon_{x0} = 50$ mm mrad. Repeating the previous calculation we find that it is lost if $\epsilon_{x0} = 105$ mm mrad and since this emittance gap cannot be provided by the finite horizontal emittance, the acceptance losses are not present. The drawback is the increase of the septum losses since the skew is insufficient to keep the injected beamlet away from the septum. Fig. 3e shows a contour plot of the efficiency of multturn injection for different horizontal tunes and skew strength and no space charge. We only plot the working points with integrated efficiency exceedings 65 % (outer boundary), where each contour line corresponds to an increment of 1.7 %. Note that the efficiency region exceeding 65 % disappears with n_t exceeding 30. The efficiency maximum of 84 % is centered at $q_x = 4.4, n_t = 8$, where the emittance transfer horizontal to vertical just matches the vertical acceptance. Fig. 3f shows the effect of the space charge. The 84% efficiency in $q_x = 4.4, n_t = 7$ is close correspondent peak in Fig. 3e since the bandwidth $\delta_b = 0.21$ is very large and $\delta\omega_{sc} \sim 0.09$, so $\delta\omega_{sc}/\delta_b \sim 0.42$. In $n_t = 18$ this ratio become 1, hence the space charge shift on the optimum working point must be taken into account. Fig. 3e suggests that the off-resonance value $\omega \sim 1.1$ is without space charge. Maintaining the same condition with space charge requires shifting q_{x0} by -0.1 , which agrees roughly with the estimate of section 1.1.

3 OUTLOOK

From the discussion on the coherent space charge effect we find that in the multturn injection a gain up to 19 % is still possible, with space charge, if an appropriate skew

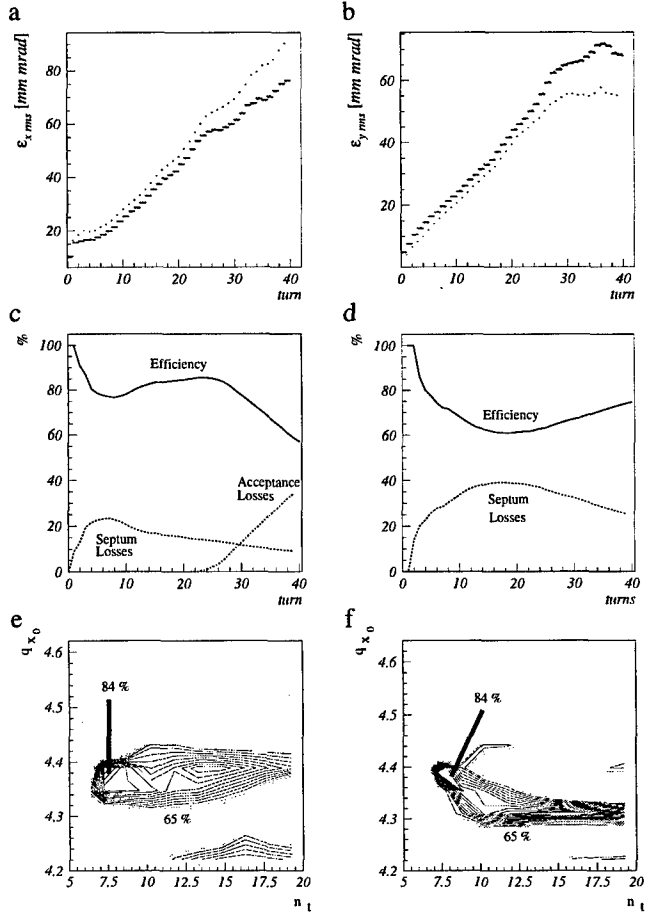


Figure 3: Multiturn injection simulations for SIS with skew quadrupole. a),b) horizontal and vertical emittance with an $q_{x0} = 4.29, q_{y0} = 3.29$ and skew strength correspondent to $n_t = 8$; in c) injection efficiency for the same settings in a),b); d) Integrated efficiency for $q_{x0} = 4.4, q_{y0} = 3.29$ and $n_t = 8$; e) Integrated efficiency after 40 turns in absence of space charge for $q_{y0} = 3.29$; f) Efficiency as in e) but with space charge.

strength and shift of the working point are applied. These results should be further optimized with a more accurate space charge calculation for detailed injection conditions.

4 REFERENCES

- [1] K. Schindl and P. Van der Stock, *Increase of Betatron Stacking Efficiency via linear Coupling in AG Proton Synchrotrons ("Skew Injection")*. Application to the CERN PS Booster. CERN/PS/BR 76-19.
- [2] I. Hofmann, *Phys. Rev. E*, **57**, 4713 (1998).
- [3] G. Franchetti, I. Hofmann, and G. Turchetti *AIP Conf. Proc.* **448**, 233 (1998); ed. A.U.Luccio and W.T. Weng.

Simulations of Axial Bunch Compression in Heavy Ion Rings for Plasma Physics Applications at GSI*

S.M. Lund^a, O. Boine-Frankenheim^b, G. Franchetti^b, I. Hofmann^b, P. Spiller^b

^a Lawrence Livermore National Laboratory (LLNL), Livermore, CA 94550, USA

^b Gesellschaft für Schwerionenforschung (GSI), D-64220 Darmstadt, Germany

Abstract

Simulations of axial bunch compression in heavy-ion rings have been carried out as part of a feasibility study for generating intense beams in a facility at GSI. The compression is implemented by a fast rotation of the longitudinal (\parallel) phase space and results in greatly increased transverse (\perp) space-charge strength while the bunch is compressed in a dispersive ring from an initial prebunch with a \parallel momentum spread of $\Delta p/p \sim 10^{-4}$ (full half-width) to a final spread of $\Delta p/p \simeq 1\%$ at the final focus optic. The need to maintain beam quality during the compression results in numerous issues that are explored with PIC simulations.

1 INTRODUCTION

Plasma physics experiments at GSI are being designed to produce dense, large-volume plasmas with heavy-ion beams for use in general scientific research and in exploring target issues in Heavy-Ion Fusion. These applications require high beam intensity on target with small focal spots and short pulse durations. Overall system configurations under consideration to achieve the needed parameters are discussed in a related paper¹. Here, we examine the final \parallel bunching needed to achieve such high intensities. Economic considerations dictate that the bunching is best carried out in a ring using a fast rotation of the \parallel phase-space. Parameters for 18 T-m and 100 T-m compressor rings (CR-18 and CR-100), which represent a range of bunching options, are summarized in Table 1. Bunching rings with similar compression physics are also under development at RIKEN and ITEP. The bunching waveforms needed for these options are consistent with conventional, low-frequency magnetic alloy RF "cavities" or new, high repetition rate induction cells developed at LLNL². For cavity/cell superpositions that approximate ideal, linear bunching waveforms, little difference is expected in the physics of bunching implemented by RF and induction technologies². Thus, here we assume linear RF bunching.

2 SIMULATIONS

A hierarchy of simulations with increasing model detail has been developed to investigate the compression of a bunch of N particles of rest mass m and charge q moving in a ring of radius R about a coasting, synchronous particle with \parallel kinetic energy $\mathcal{E}_s = (\gamma_s - 1)mc^2$. Here, c is the speed of light in vacuo, and $\gamma_s = 1/\sqrt{1 - \beta_s^2}$, where $\beta_s c$ is the \parallel velocity of the synchronous particle.

2.1 Envelope Simulations

Parametric changes associated with ideal bunch compressions are first analyzed with a simple envelope model. In this model, continuous bending (ring radius R) and \perp and \parallel focusing are assumed along with linear particle equations of motion consistent with a \parallel Neuffer

Table 1: Ring parameters and envelope model results.

Parameter	CR-18	CR-100
Ion	U_{238}^{+28}	U_{238}^{+4}
Ring Radius, R [m]	34.49	157
Ring Lattice Periods, M	12	60
Pipe Radius, r_p [cm]	10	10
\perp Tunes, Q_{0x}, Q_{0y}	4.2, 3.4	10.8, 9.7
Particle K.E., \mathcal{E}_s [MeV/u]	200	127
Particle Number, N	2×10^{11}	8.5×10^{12}
\perp Emittances, $\epsilon_x = \epsilon_y$ [mm-mr]	10	20
\parallel Emittance, ϵ_z [m-mr]	16.8	20.7
Envelope Model Results		
RF Voltage ($h = 1$), V [kV]	560	3000
Laps for Compression	59.475	49.412
Prebunch, 1/2 Ring, Mid-Pulse		
Tune Depression, σ/σ_0	0.978,	0.994,
Momentum Spread $\Delta p/p$	5×10^{-4}	1.1×10^{-4}
Full Compression, Mid-Pulse		
Pulse Duration τ_p [ns]	32	39
Tune Depression, σ/σ_0	0.652	0.592
Tune shift, ΔQ	-1.32	-4.18
Momentum Spread $\Delta p/p$	0.01	0.01

distribution and a \perp matched, KV distribution. The line-charge density within the bunch is parabolic with $\lambda \propto 1 - (\delta z/r_z)^2$, where δz is the \parallel coordinate relative to the synchronous particle and the \parallel bunch radius r_z evolves according to the envelope equation

$$r_z'' + k_{0s}^2 r_z - \frac{K_{\parallel}}{r_z^2} - \frac{\epsilon_z^2}{r_z^3} = 0. \quad (1)$$

Here, primes denote d/ds , where s is \parallel propagation distance of the bunch, k_{0s} is the synchrotron wavenumber in the linear RF approximation, K_{\parallel} is the space-charge perveance (dimension length), and $\epsilon_{\parallel} = \text{const}$ is the rms emittance. More explicitly, $k_{0s}^2 = qVh|\eta|/(2\pi R^2 \gamma_s \beta_s^2 mc^2)$ for an RF cavity operating on harmonic h (h = number of bunches) with a maximum voltage gain per turn of V , $K_{\parallel} = 3\bar{g}q^2 N|\eta|/(2\gamma_s^3 \beta_s^2 mc^2)$ where \bar{g} is an average of the geometric factor $g = 1/2 + 2\ln(r_p/r_b)$ (r_p and r_b are the \perp pipe-radius and bunch radius of the matched KV beam; \bar{g} includes weak \perp/\parallel coupling²), and $\epsilon_{\parallel} = |\eta|r_z \Delta p/p = \text{const}$ where $\Delta p/p$ is the half-width of the \parallel distribution in the fractional particle off-momentum $\delta p/p$. Here, $\eta = 1/\gamma_t^2 - 1/\gamma_s^2 < 0$ is the "slip factor" with transition gamma $\gamma_t \simeq Q_{0x}$ [Q_{0x} and Q_{0y} are the horizontal (x -plane) and vertical (y -plane) undepressed tunes].

The envelope equation (1) is integrated from an initial ($s = 0$) prebunch to estimate parametric changes due to a compression induced by a sudden increase in RF voltage V . Results are shown in Fig. 1 as a function of ring laps [$s/(2\pi R)$] for CR-18 parameters, a single bunch ($h = 1$), and a half-ring prebunch ($r_z = \pi R/2$). Results of this compression and an analogous one for CR-100 are summarized in Table 1. The compression corresponds to a 90°

* Research performed by LLNL, US DOE contract W-7405-ENG-48.

rotation of the initial phase-space ellipse and takes place in 59.475 laps [$59.475 > (1/4)/(Rk_{\beta 0}) = 59.147$ due to space-charge]. As the full-width pulse duration $\tau_p = 2r_z/(\beta_s c)$ decreases, the \perp space-charge becomes stronger as measured by the decrease in σ/σ_0 (σ and σ_0 are the phase advance per lattice period of \perp particle oscillations with and without space-charge) or the increase in tune shift $\Delta Q = (1 - \sigma/\sigma_0)k_{\beta 0}R$, where $k_{\beta 0} = (Q_{x0} + Q_{y0})/(2R)$. This increase in space-charge strength occurs rapidly over the final phase of the rotation and is accompanied by a large increase in the momentum-spread width of the distribution, $\Delta p/p$. This spread contains a coherent component, $(\Delta p/p)|_c = (r'_z/|\eta|)(\delta z/r_z)$, that nulls at full compression (upright phase-space ellipse with $r'_z = 0$) and an incoherent component, $(\Delta p/p)|_{ic} = \pm[\epsilon_{||}/(|\eta|r_z)]\sqrt{1 - (\delta z/r_z)^2}$, associated with the increasing local thermal spread. These spreads vary along bunch axis, ranging from all incoherent at mid-pulse ($\delta z = 0$), to all coherent at the bunch ends ($\delta z = \pm r_z$), and both coherent and incoherent in-between (plotted at $1/4$ pulse, $\delta z/r_z = 1/2$). The compression is timed such that, shortly before full compression, the bunch is extracted from the ring into an extraction line for transport to the target. The RF voltages V are set for mid-pulse $(\Delta p/p)_{ic} = 1\%$ at full compression, corresponding to the chromatic focusing limit of the final focus optic. Since this envelope model is only consistent with linear focusing, the linear RF voltage V must be interpreted in terms of harmonic cavity superpositions (requiring additional RF voltage) sufficient to suppress nonlinear phase-space wrapping consistent with the prebunch extent in the phase of the fundamental RF harmonic².

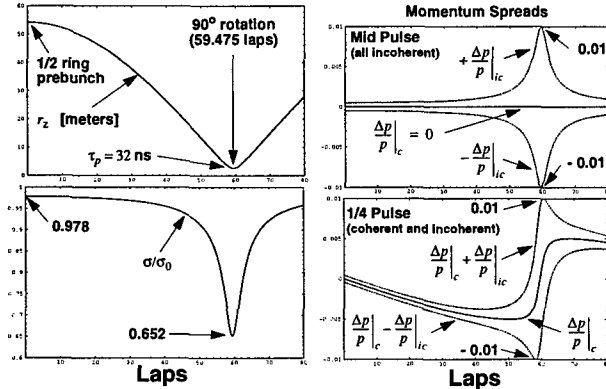


Figure 1: Envelope model of bunch compression (CR-18).

2.2 PIC Simulations

The combination of strong \perp space-charge and large momentum spread in the ring/extraction line lead to issues in maintaining \perp beam focusability (limiting emittance growth) that are being explored with 2d and 3d electrostatic PIC simulations based on the WARP code of LLNL³ and several GSI codes. These simulations include lattices with varying levels of detail, a proper treatment of dispersion, and self-consistent space-charge fields. Presented here are \perp 2d mid-pulse ($\delta z = 0$) simulations with a symmetric FODO lattice for \perp focusing (occupancy of quadrupoles and dipoles are 25% and 15% of the lattice period, respectively, with tunes $Q_{x0} \approx Q_{y0}$ equal to the mean of those in

Table 1), and compression implemented by continuously adjusting the particle weights and momentum deviations consistent with the envelope model. The initial prebunch is modeled by loading an rms matched \perp semi-Gaussian (uniform density and temperature) and a \parallel Gaussian momentum spread (rms Neuffer equivalent) distributions and then advancing the coasting beam many laps to allow relaxation of the loaded distribution due to weak space-charge and dispersive effects in the ring. These mid-pulse simulations model the region of strongest space-charge and momentum spread, and are structured to explore physics issues as opposed to detailed design evaluations.

The rms emittance ($\epsilon_x = 4[\langle x^2 \rangle \langle x'^2 \rangle - \langle xx' \rangle^2]^{1/2}$, etc.) evolution is shown in Fig. 2 for a 180° phase-space rotation in the CR-18 lattice with zero (small N) and full current. At peak compression (90° , 59.475 laps), the in-bend-plane x -emittance undergoes a large increase, whereas the out-of-bend y -emittance undergoes a smaller, nonlinear space-charge driven increase. The thickness of the x -emittance trace indicates the amplitude of emittance oscillations at the lattice and betatron frequencies that result from dispersion and the distribution being dispersion mismatched due to the bunch compression, respectively. To better understand this, the x -particle equation of motion is well approximated by

$$x'' + \left(\frac{1}{\rho^2} \frac{1-\delta}{1+\delta} + \frac{\kappa_q}{1+\delta} \right) x = \frac{\delta}{1+\delta} \frac{1}{\rho} - \frac{q \partial \phi / \partial x}{m \gamma_s^2 \beta_s^2 c^2}, \quad (2)$$

where $\delta = \delta p/p$, ρ is the local bend radius, $\kappa_q = (\partial B_y / \partial x) / [B \rho]$ is the \perp focusing strength of the magnetic quadrupoles, and ϕ is the self-field potential. Neglecting space-charge, chromatic effects [$\kappa_q/(1+\delta) \rightarrow \kappa_q$], and higher-order dispersive effects, $d\epsilon_x^2/ds = (32/\rho)[\langle x^2 \rangle \langle x' \delta \rangle - \langle x x' \rangle \langle \delta \rangle]$, showing that the emittance evolves primarily in the bends. For an uncorrelated initial distribution ($\langle x \delta \rangle = 0$, etc), it can be shown that $\epsilon_x^2(s) = \epsilon_x^2(0) + F(s)\epsilon_x(0)\langle \delta^2 \rangle$, where $F(s)$ is a function (constant out of bends) depending only on the lattice. This oscillation can be understood by examining a group of particles with off-momentum δ . If the closed orbit of this particle group is shifted from the \perp phase-space center of the group (from dispersion and dispersion mismatch), then the particles will betatron-rotate about the shifted orbit which oscillates according to the dispersion function. Hence, the phase-space ellipse bounding all off-momentum groups ($\sim \epsilon_x$) will oscillate with components at the betatron frequency (wavenumber k_β) and at the frequency of dispersion function oscillations ($2\pi/k \sim$ lattice period). The pumped momentum spread of the applied compression acts to increase the average and amplitude of the emittance oscillation. In this context, the emittance increase is a dispersion induced distortion that is reversible, and can be corrected in the extraction line with appropriate, compensating bends. However, this distortion influences the \perp bunch size, and thereby the \perp aperture and extraction. Moreover, nonlinear space-charge, chromatic, and higher-order dispersive effects can produce amplitude dependences that phase-mix (thermalize) part of these reversible emittance oscillations causing uncorrectable, "irreversible" growth.

Such growth must be limited, since it can also interfere with the correction of larger, reversible growth components. A measure of the irreversible growth is obtained in full 180° phase-space rotations, since these recover the initial momentum spread and emittance in the absence of irreversible effects. Small chromatic and dispersive terms prevent exact recovery in the zero current simulation shown. The emittance growth of these full-current simulations are qualitatively comparable with 180° rotation experiments⁴.

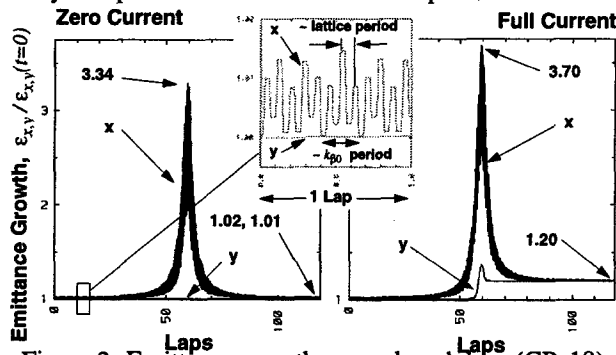


Figure 2: Emittance growth versus bunch laps (CR-18).

The dominant source of irreversible emittance growth appears to be nonlinear forces associated with space-charge modes launched during the compression. This is demonstrated by the simulations in Fig. 3, where the compression in Fig. 2 was carried out in a straight lattice ($\rho \rightarrow \infty$). Rapid growth occurs when σ/σ_0 becomes sufficiently depressed and remains when the compression is reversed. Negligible growth occurs for zero current, and space-charge instability induced growth can be reduced by adjusting \perp focusing for $\sigma_0 < 90^\circ$ to eliminate envelope and suppress higher-order collective modes. Little change was induced by varying the compression rate by factors of 2, suggesting fast instability saturation. Although these space charge instabilities are modified in a ring due to the \perp dispersive broadening weakening space-charge forces, the $\sigma_0 < 90^\circ$ criteria appears sufficient for rings. Reduced σ_0 also decreases envelope flutter, reducing sensitivity to focusing errors and problems associated with large envelope excursions combined with large momentum spread in bending dipoles. Unfortunately, this criteria is also inconsistent with long, low-dispersion straight sections (for bunch insertion/extraction, RF cavities, e^- cooling, etc.), since this requires high phase-advance through bends (with small superperiod number, M). However, in the presence of compression, strong space-charge, and large s -varying momentum spread, the conventional definition of a dispersion function D [$D = x/\delta$, where x is the closed orbit solution to Eq. (2) for δ small and $\phi \rightarrow 0$] carries little meaning. Large, s -varying space-charge strength and momentum spread in the compression result in a shift of D , complicating lattice design. From this perspective, the better approach appears to be a symmetric lattice with a large M ($\Rightarrow M = \text{cell number}$), where the zero-current fluctuations of D are as small as possible. This minimizes reversible emittance growth at peak compression, reducing consequences of correction errors and irreversible growth.

Chromatic focusing effects and possibly other higher-

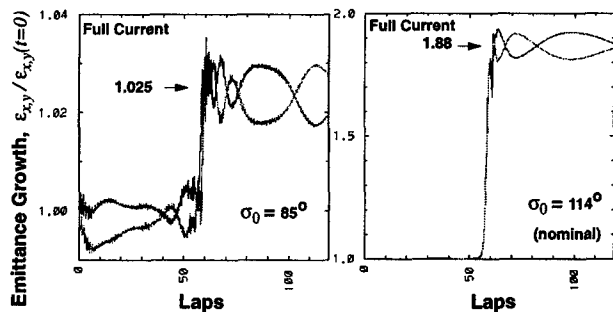


Figure 3: Emittance growth with no bends (CR-18).

order dispersive terms can phase-mix otherwise reversible distribution distortions into irreversible growth. Although these effects are typically weaker than space-charge induced nonlinearities, compensations should be considered. Also, since a momentum deviation δ is equivalent to all dipoles and quadrupoles having the same field error, tune values $Q_{x0} = Mk/2$ ($k = 1, 2, \dots$) should be avoided. However, in a symmetric ring ($M = \text{cell number}$) the $\sigma_0 < 180^\circ$ phase-advance limit for a valid \perp bunch envelope preclude such resonances and likewise, low-order resonances due to systematic field errors. Resonances from construction errors are not regarded as troublesome due to the limited number of laps in the compression and detuning due to varying space-charge strength as the particles change \parallel position in the bunch. This can be checked with full 3d simulations of distributions with realistic incoherent tune spreads. Finally, although results of 3d simulations with continuous, linear RF bunching differed little from the reduced 2d model presented, this must be re-evaluated for discrete RF cavities. The finite kick in δ provided by a discrete cavity leads to an instantaneous shift of the closed orbit of each group of off-momentum particles, which can lead to irreversible emittance growth when a series of kicks are applied. This can be properly evaluated in 3d simulations with realistic distributions of RF cavities.

3 CONCLUSIONS

This joint GSI/LLNL study is investigating the use of fast bunch rotation to compress a large number of particles in heavy-ion rings. The combination of large momentum spread and strong space charge in a ring creates challenges in limiting \perp emittance growth. Simulations have distinguished and characterized reversible (correctable) growth due to dispersion induced distribution distortions and irreversible (uncorrectable) growth due to various effects. Tentative design criteria were developed to mitigate these growths. Tradeoffs between these constraints and practical considerations will be made in more optimal ring designs.

References

- [1] P. Spiller, K. Blasche, O. Boine-Frankenheim, M. Emmerling, B. Franzcak, I. Hofmann, S. Lund, S. Lund, and U. Ratzinger, these proceedings.
- [2] S. Lund, I. Hofmann, O. Boine-Frankenheim, and P. Spiller, to appear, GSI internal report (1999).
- [3] D. Grote, Ph.D. Dissertation, Lawrence Livermore Laboratory, publication UCRL-LR-119363 (1994).
- [4] R. Capii, R. Garoby, D. Möhl, J.L. Vallet, and E. Wildner, in Proceeding of the 1994 European Particle Accelerator Conference, London, 27 June - 1 July, p. 279.

GENERATION OF HIGH POWER HEAVY ION BEAMS AT GSI

P. Spiller, K. Blasche, O. Boine-Frankenheim, M. Emmerling,
B. Franczak, I. Hofmann, S. Lund (*), U. Ratzinger

GSI - Gesellschaft für Schwerionenforschung, D-64220 Darmstadt, Germany

(*) LLNL - Lawrence Livermore National Laboratory, Livermore, CA94550, USA

Abstract

Besides laser- and light ion beams, short pulse duration bunches of intense heavy ion beams are attractive to deposit high specific power in experimental targets. Such volume heated matter is transformed into a plasma state that is characterized by its high density. The GSI accelerator facility offers a unique possibility for the generation of such a solid state density plasma. After the installation of the new high current injector, intense beams of low charge state uranium ions (U^{28+}) will be available. To achieve high target power densities with these beams, a strong longitudinal compression has to be performed. For this purpose, a new type of RF compressor cavity has been developed for the heavy ion synchrotron SIS. In the framework of a machine development program, first tests of the required bunch manipulations have been done with the available SIS cavities.

1 INTRODUCTION

Short pulse duration ion bunches can easily be produced by means of a high revolution frequency, or equivalently, high beam energy. However, the most interesting beam energy for plasma physics experiments is defined by the ion range in the target and the focal spot radius. Thus, for solid state density targets, 100-300 MeV/u is an appropriate range of energy for heavy ions. However, at 200 MeV/u the revolution time in the SIS is about $1.3\mu s$, which is far too long for optimal target heating. Taking into account the hydrodynamic target response, the ion pulse length has to be shortened by a factor of 20 or more.

Furthermore, optimum plasma generation with the present range of achievable total beam energies requires a single bunch of ions. Due to an insufficiently low minimum frequency of the SIS cavities, a minimum of harmonic 4 can be used for acceleration of U^{28+} . Thus, at least four ion bunches must be merged into one before final bunching is carried out with a new low-frequency cavity.

2 RF-MANIPULATIONS AND LONGITUDINAL COMPRESSION

In March 1997, the first attempt of single bunch generation in the SIS was carried out [1]. The method used is based on adiabatic debunching, followed by a rebunching on the first harmonic. In adiabatic compression the final bunch length l_f is determined by: $l \propto V^{1/4}$. With a maximum available RF voltage of $V = 14$ kV per cavity and a typical momen-

tum spread of $dp/p = \pm 5 \cdot 10^{-4}$ a coasting beam of Ar^{11+} ions could be captured in a single bunch with a pulse duration of 550 ns. No particle losses were observed at this process.

For the final compression of the single bunch, we consider a fast compression with a 90 degree rotation of the longitudinal phase space. This concept was tested in the Experimental Storage Ring ESR [2] and has been applied in experiments in the SIS since November 97 [3] [4]. The phase space rotation in fast compression is initiated by a fast jump of the RF-voltage amplitude.

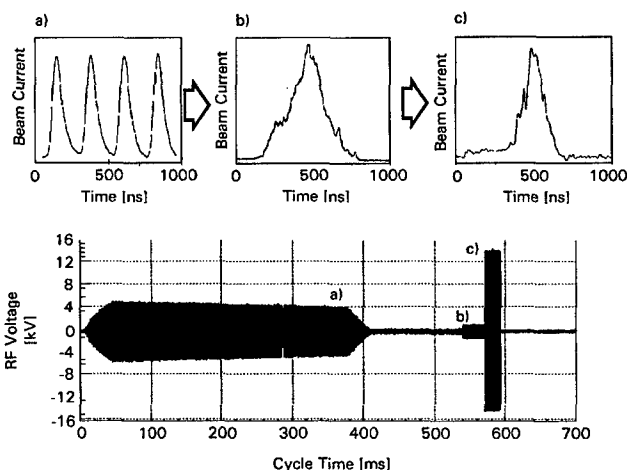


Figure 1: Measured bunch current signals at different stages of the acceleration cycle together with the measured RF gap voltage over the modified acceleration process. Shown is a) the typical four-bunch structure after acceleration with $h=4$, b) a single bunch profile after adiabatic debunching and rebunching at $h=1$ and c) a single bunch after fast bunch compression.

The rise time of the voltage must be much shorter than the synchrotron period of longitudinal particle oscillations. The measured rise time of the SIS cavities is $150\mu s$ which is sufficiently short relative to a typical synchrotron period of about 1 ms. Measurements of the full cycle of acceleration, adiabatic debunching and rebunching, and final fast bunch rotation are illustrated in Fig. 1.

However, measurements have shown that phase stability is essential for a stable compression. Figure 2 shows the beam current signal in the SIS, measured with a capacitive pick-up probe, over several synchrotron periods after the

RF voltage jump. Due to small RF phase instabilities coherent oscillations of the bunch are excited. The observed phase instability is due to a dependence of the ferrite permeability μ on the voltage amplitude. The varying permeability leads to a change of the eigenfrequency of the cavity. Although the RF phase is stabilized after the jump, these oscillations can be observed over many periods. These oscillations may dilute the longitudinal bunch emittance, limiting compression for a given final momentum spread.

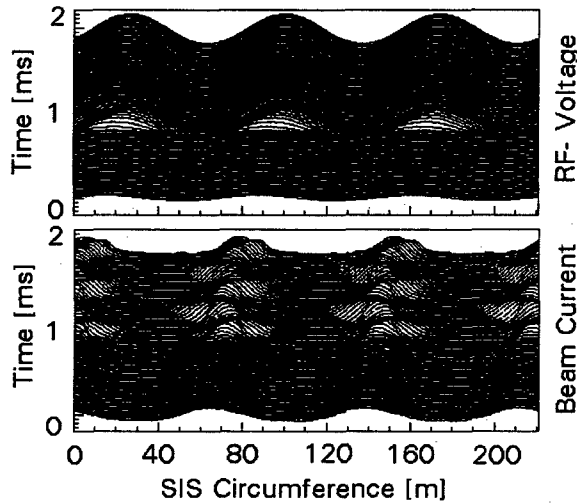


Figure 2: Evolution of the RF gap voltage and the beam current during fast compression. Strong coherent bunch oscillations are visible. These oscillations are excited by RF phase variations of about 15° at the fast voltage jump.

The strongest compression factor can be achieved with rather small prebunching amplitudes, according to: $l_f \propto \sqrt{A/q(V_i/V_f)} \cdot (dp/p)_i$. Here A is the mass number, q is the charge state and the subscripts i and f denote initial and final values. This equation assumes an initial stationary bunch, matched to the RF bucket and linear bunching. In case of smaller prebunching amplitudes, distortions of the longitudinal phase space occur due to the nonlinearity of the RF-voltage seen by the mismatched bunch.

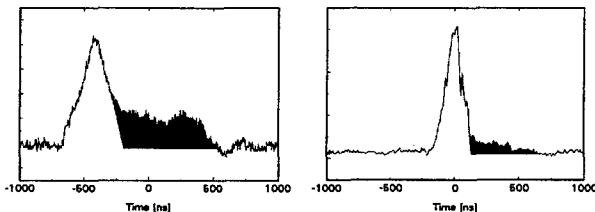


Figure 3: Bunch signal after extraction without (left) and with 1kV (right) prebunching. The shaded areas indicate the offset and tail depending on the amount of prebunching.

The nonlinear RF-voltage causes an S-shaped phase space

wrapping with associated nonlinear pulse lengthening. In an experimental program using an A_{r11+} -beam the influence of the prebunching amplitude on the final longitudinal distribution was studied. Fig. 3 shows the longitudinal profile of an extracted bunch for no prebunching and with 1 kV prebunching. A final pulse duration of 350 ns could be achieved. Table 1 shows results of 1D PIC simulations of a fast compression of a weak prebunched 200 MeV/u U^{28+} -beam. The fraction N_B/N of particles captured in the RF bucket is calculated for different levels of prebunching. Furthermore, the mid-pulse current gain factor I/I_0 which indicates the peak power of the bunch is listed. The final RF amplitude was assumed to be 100 kV.

Table 1: Current gain factor I/I_0 , fraction of captured particles N_B/N , and final bunch lengths z_f for different prebunching amplitudes.

V_i [kV]	z_f [m]	τ_f [ns]	I/I_0	N_B/N	$(dp/p)_f$ [%]
0	7	36.7	10.7	0.46	≈ 0.5
1	10.5	55.1	12	0.78	≈ 0.5
2	11.5	60.3	11.5	0.82	≈ 0.5
3	12.0	63	11.4	0.84	≈ 0.5
5	14.0	73.5	10.7	0.92	≈ 0.5

For a fixed prebunching amplitude of 2 kV the influence of beam loading on the cavity is studied for different impedances. Table 2 shows the degradation of the final beam parameters with increasing impedance.

Table 2: The filamentation of the phase space by space charge interaction with the cavity impedance degrades the achievable peak current. For an assumed prebunching voltage of 2 kV the same parameters as in Table 1 are listed.

R_s [k Ω]	z_f [m]	τ_f [ns]	I/I_0	N_B/N	$(dp/p)_f$ [%]
0	11.5	60.3	11.5	0.82	≈ 0.5
1	11.5	60.3	11.5	0.82	≈ 0.5
3	11.5	60.3	11.3	0.81	≈ 0.5
4	11.5	60.3	11	0.78	≈ 0.5
5	11.5	60.3	10.5	0.74	≈ 0.5
10	10	52	7	0.43	≈ 0.5

A significant drop of the peak current is visible starting from a total impedance of about 5 k Ω .

Further detailed simulations on the compression process in a dispersive ring lattice and the effect on the transverse emittance are presented in a corresponding paper [7].

3 THE COMPRESSOR CAVITY STUDY

The highest energy deposition in a target will be achieved with an intense U^{28+} -beam [5]. With the new high current injector [6], $2 \cdot 10^{11}$ uranium ions will be available at the end of 1999. Accelerated up to the maximum rigidity of 18

Tm, a total beam energy of 2 kJ can be produced for experiments. When focused onto a small spot ($R \leq 1\text{mm}$) on the target [8], a specific energy deposition of up to 50 kJ/g is expected. At this level of energy deposition the characteristic heating time, which is determined by the sound velocity of the plasma, is about 50 ns. A bunch with a matched pulse duration can only be generated with the installation of a dedicated bunch compressor cavity. Such cavities have been studied by the GSI RF group [9], using magnetic alloy technology. For compression of 100% of the beam particles down to a pulse duration of 50 ns, a total RF-voltage of 200 kV is required. This voltage must be produced at a fixed frequency of about 0.8 MHz for less than 100 μs (1/4 of the synchrotron period).

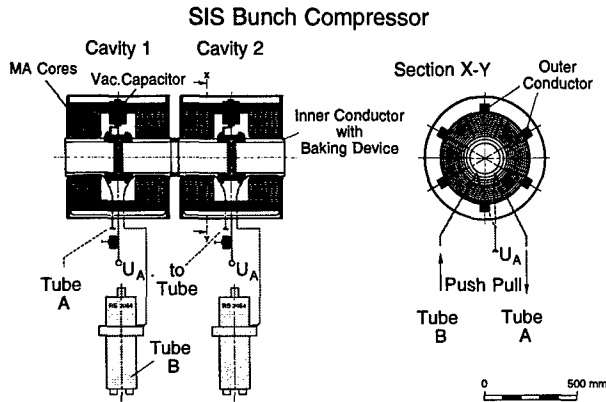


Figure 4: Schematic of a SIS bunch compressor cavity based on magnetic alloy cores. Shown are two out of six cavities. Each cavity is driven by a final stage in push-pull operation.

Table 3: Comparison of the technical parameters of the existing SIS ferrite loaded cavities and of the proposed MA compressor cavity.

	SIS Cavity	Compressor
Inductive Load	Ferrites	Magnetic Alloy
Frequency tuning range [MHz]	0.85-5.4	0.8
Peak RF-voltage [kV]	16	40
Length [m]	2.9	0.7
Pulse duration [μs]	cont.	100
Duty cycle [%]	100	0.01
Voltage rise time [μs]	150	≤ 30
Power dissipation - Peak [kW]	40	500
Power dissipation Mean [kW]	40	0.05
Cooling of cores	water	air
Gap impedance [k Ω]	2.5	0.68

The inductive load of the new cavity type consists of cores from amorphous metallic alloys (MA core). VITROVAC 6030F from Vacuumschmelze, is found to be an appropri-

ate material. This material has a high saturation flux density of 0.82 T and the $\mu Q f$ product is constant over a wide range of RF-voltage. Therefore the observed phase instabilities at a fast voltage jump, as shown in figure 2, will not occur with the MA cavity. The MA material is available with a ribbon thickness of only 17 μm and with a 2 μm thick interlaminar insulation. Proposed are 6 individual cavities, each capable of 40 kV in an axial length of about 0.7 m. Each cavity contains 2x 6 VITROVAC discs. Air cooling of the discs is sufficient because of the low duty factor of 0.01 %. The cavities are inductively coupled to the power amplifier by the anode supply cable guided around the MA cores (Fig. 4). In order to minimize the total impedance in the synchrotron, the gap will be short-circuited when the cavity is not in operation. For the low duty cycle operation an adequate RF tube is the Siemens RS 2054. The peak power per cavity is on the order of 500 kW. The gap impedances shown in table 3 are without fast feed back controls around the final amplifier. These controls are in the design stage.

With the high current injector and the new bunch compressor cavity we expect to achieve the beam and target parameters summarized in table 4.

Table 4 : Beam and target parameters for the currently available RF-voltages and beam intensities of Ar^{11+} -ion beams and future operation with U^{28} ion beam.

Ion species	Ar^{11+}	U^{28+}
N_B	$2 \cdot 10^{10}$	$2 \cdot 10^{11}$
ϵ_i [GeV]	12	47
E_0 [kJ]	0.04	2
τ_f [ns]	350	50
P_f [GW]	0.11	40
J_s [TW/cm ²]	0.029	1.25
J_m [TW/g]	0.0014	0.5
$\rho \cdot l$ [g/cm]	13.04	1.5
ϵ_m [kJ/g]	0.47	26

Acknowledgment : We thank P. Moritz, P. Kainberger and the plasma physics group for supporting the measurements.

4 REFERENCES

- [1] GSI Scientific Report 1997, (1998)163
- [2] G. Kalisch, GSI Report, GSI-94-05, (1993)
- [3] S. Stöwe et.al., Nucl. Instr. and Meth. in Phys. Res. A (1998)61-67
- [4] K. Blasche et.al., Proceedings of the 6th EPAC, (1998)1347
- [5] R.W. Müller and P. Spiller, GSI Report, GSI-96-07, (1996)
- [6] U. Ratzinger, Proc. of the 1996 Linac Conf., Geneva, Vol.1 (1996)288
- [7] S.M. Lund, et. al. these proceedings
- [8] M. Stetter et. al., Il Nuovo Cimento, Vol.106 A, N. 11(1725)
- [9] M. Emmerling et. al. GSI Internal Report Nr. SIS29019STR

BEAM-BEAM EFFECT AND DYNAMIC APERTURE OF THE MUON COLLIDER*

M. A. Furman[†], Center for Beam Physics, LBNL, Berkeley, CA, USA

Abstract

We consider the combined effects of the beam-beam interaction and the lattice nonlinearities for one specific design of the muon collider ring. The beam-beam interaction is represented by a thick gaussian lens, and the ring is described by a 9th-order Taylor map. At the single-particle level we compare the tune footprints and the dynamic aperture with and without the beam-beam effect. At the multiparticle level, using a "weak-strong" description of the beam-beam interaction, we compare the time evolution of the rms beam sizes with a linear lattice map and with the full nonlinear map.

1 INTRODUCTION

The desire to have a muon collider with high luminosity combined with the instability of the muon places serious constraints on the lattice design of this machine. In particular, lattice nonlinearities are severe, and the beam-beam interaction has a strength comparable to a mature e^+e^- collider [1]. Traditionally, the beam-beam interaction and lattice dynamics have been studied separately. It is likely that the muon collider will be the first machine in which these two pieces of dynamics, along with wakefield effects, may have to be studied in combination. In this note we present an initial step in this direction, improving upon a previous study [2] with linear lattices, by carrying out single-particle and multiparticle tracking calculations for one specific design of the muon collider whose relevant parameters are listed in Table 1. We represent the lattice by a 9th-order Taylor map obtained from the program COSY INFINITY [3], and the beam-beam interaction by a thick lens. We present our results in three cases: (a) linear part of the map plus beam-beam, (b) full 9th-order map without beam-beam, and (c) full 9th-order map plus beam-beam. We compute beam footprints, dynamic aperture plots and time evolution of the rms beam sizes.

There are several limitations in this investigation which we expect to improve upon in the future: (1) the beam-beam interaction is represented only in weak-strong mode, albeit in thick lens approximation (*i.e.*, nonzero bunch length effects included) assuming a tri-gaussian density distribution, (2) the longitudinal beam-beam forces are wholly neglected, and (3) the 9th-order map does not incorporate RF cavities.

* Work supported by the US Department of Energy under contract no. DE-AC03-76SF00098.

[†] E-mail address: mafurman@lbl.gov

Table 1: Selected muon collider parameters.

Circumference, C [m]	345
Beam energy, E [GeV]	50
Relativistic factor, γ	473.2
No. of particles per bunch, N	4×10^{12}
Beta function at the IP, β^* [cm]	4
Normalized emittance, ϵ_N [$\mu\text{m-rad}$]	85
RMS beam size at the IP, σ_0 [μm]	84.76
RMS bunch length, σ_z [cm]	4
Relative momentum spread, σ_p/p	1.2×10^{-4}
Nominal beam-beam parameter, ξ	0.051
Tunes, ν_x/ν_y	0.862/0.639

2 CALCULATION

In Table 1, the four beta functions at the interaction point (IP) are equal, as are the four emittances. The beam-beam element consists of a static trigaussian thick lens implemented by dividing the bunch into 5 kicks whose weights and longitudinal positions follow the "equal-weight" prescription [4]. The beams collide head-on at the IP. The longitudinal beam-beam force is wholly neglected. The transverse force from each of the 5 kicks is computed from the well-known expression of the electric field of a round gaussian beam. A particle from the dynamical beam is consecutively kicked by each of these 5 kicks; in between successive kicks, the particle undergoes simple drifts.

The lattice is represented by a 9th-order Taylor expansion of the 6-dimensional one-turn map at the IP, obtained from COSY INFINITY [3]. It does not include RF cavities. The beta functions and tunes listed in Table 1 are extracted from the linear part of the map, which also has $\beta' = 0$ at the IP. The action of the map on each particle of the dynamical beam is expressed by the polynomial

$$z'_i = \sum_{\ell=0}^L \sum_{\{n_k\}_\ell} C_i^{(\ell)}(n_1, n_2, n_3, n_4, n_5, n_6) \times z_1^{n_1} z_2^{n_2} z_3^{n_3} z_4^{n_4} z_5^{n_5} z_6^{n_6} \quad (1)$$

where z_i , with $i = 1, \dots, 6$, represents the (suitably defined [3]) i -th coordinate of the particle at turn t , z'_i is the coordinate at turn $t + 1$, ℓ is the order of the expansion, with maximum order $L = 9$, and $\sum_{\{n_k\}_\ell} (\dots)$ stands for a summation over all possible combinations of the n_k 's such that $\sum_k n_k = \ell$ with $n_k \geq 0$. The map is described by the full set of $C_i^{(\ell)}$'s; in the particular case we study, there are 5040 nonzero such coefficients. Eq. 1 is applied to every

particle in the dynamical beam.

In single-particle mode we track one particle in the dynamical beam with given initial coordinates x_0 and y_0 . By successively letting x_0 and y_0 take on values in a rectangular grid we can generate a tune footprint. We extract the tunes by numerically integrating the phases of the particle over 500 turns. To determine the dynamic aperture, we track the particle for 1000 turns. In all cases the initial values of the remaining coordinates (x' , y' , z and Δp) are set to 0. In order to avoid numerical overflow problems, we specify the criterion that a particle is outside the dynamic aperture if at any turn it is outside a sphere in x , y , z about the bunch center with radius 1 m.

In multiparticle mode we start from an initial 6D gaussian beam distribution of particles centered at the origin with the σ 's specified in Table 1 or extracted from these parameters. In all cases we choose 10,000 representative particles. We then track this distribution for 1000 turns and compute and record the rms values at every turn.

In all cases we take the muon to be a stable particle. There are no physical apertures in the calculation. Radiation and quantum excitation are ignored, as are the mutual interactions of the particles within the bunch.

3 RESULTS

3.1 Footprints

Footprints are shown in Fig. 1. We tracked 100 particles whose initial conditions were on a 10×10 grid with x_0/σ , $y_0/\sigma = 0.1, 1, 1.5, 2, 2.5, 3, 3.5, 4, 4.5, 5$. It is seen that resonances do not cause any distortion of the footprint in the case of linear map + beam-beam. There are severe distortions for the case of full map with or without beam-beam presumably due to island trapping.

3.2 Dynamic aperture

Figure 2 shows the dynamic aperture plots for the case of nonlinear map with and without beam-beam (the dynamic aperture for the case of linear map + beam-beam is obviously infinite). It can be seen that the beam-beam interaction has a slight effect on dynamic aperture.

3.3 Beam size evolution

Figure 3 shows the time evolution over 1000 turns of the normalized beam sizes, σ_x/σ_0 and σ_y/σ_0 . It is seen that the cases with beam-beam, with a linear map or with a full map, are very similar to each other. This implies that the map has little effect on beam-beam performance. Even though the beam starts out with $\sigma_x = \sigma_y$, the dynamical beam sizes quickly become different. This is due to the dynamical beta function effect [5] which implies $\sigma_x \neq \sigma_y$ whenever $\nu_x \neq \nu_y$.

In the absence of the beam-beam element, the beam sizes are also unequal, but in this case the difference is due purely to a " \sqrt{N} " fluctuation of the initial particle distribution.

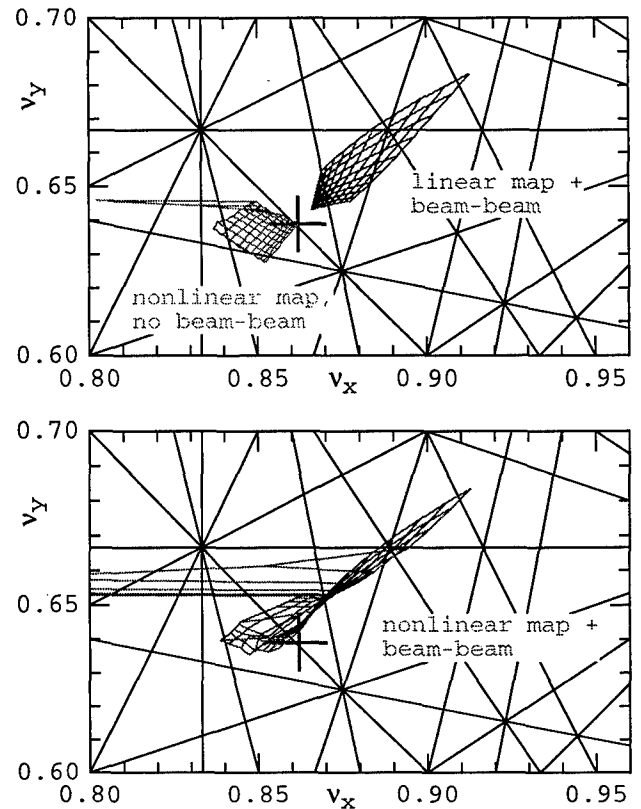


Figure 1: Tune footprints of the beam. Top: linear map + beam-beam and nonlinear map without beam-beam. Bottom: nonlinear map + beam-beam. The cross is at the working point defined by the map. Resonance lines up to 6-th order are shown.

4 DISCUSSION

The results presented here are to be taken only as an initial step in a more systematical examination of beam dynamics in the muon collider. It is desirable to study maps that better describe the machine, including RF cavities. It is also desirable to improve the beam-beam element so that it includes longitudinal forces, which have recently shown to be important when the momentum spread of the beam is very small [6].

Although preliminary, the present results confirm the generally accepted belief, derived from theory and experiment with e^+e^- colliders, that lattice nonlinearities do not affect the beam-beam dynamics significantly near the beam core. It is gratifying that this is the case even in this design, whose dynamic aperture is markedly smaller than in typical e^+e^- machines. We conclude that the luminosity performance will not be detrimentally affected by nonlinearities. We expect this conclusion to remain valid as long as the dynamic aperture is at least a few σ 's.

On the other hand, we expect that nonlinearities will have a significant effect on the large-amplitude tails of the beam, whose dynamics is quite different from the beam core. This issue remains to be studied.

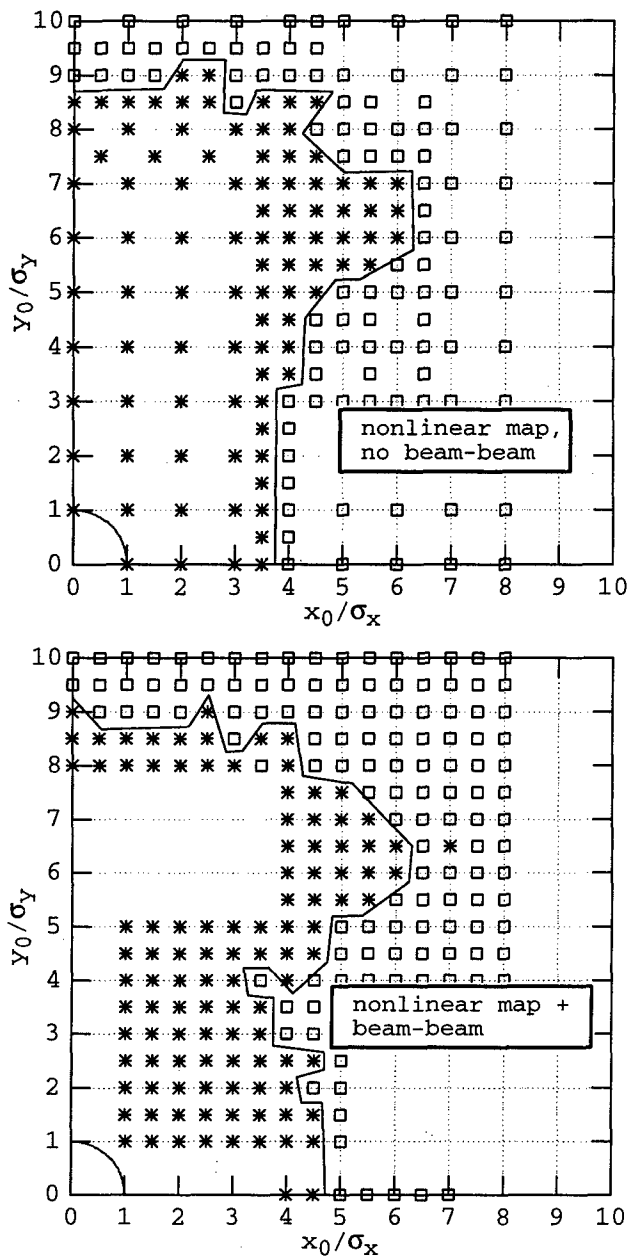


Figure 2: Top: dynamic aperture for the map without beam-beam. Bottom: map + beam-beam. Crosses indicate particles that survived for 1000 turns, boxes those that did not. The hand-drawn polygon is meant to guide the eye along the dynamic aperture boundary. The quarter-circle at the lower left corner is the $1 - \sigma$ beam profile.

5 ACKNOWLEDGMENTS

I am grateful to C. Johnstone and W. S. Wan for providing me with a COSY INFINITY map, to R. Palmer for discussions and clarification of machine parameters, and to NERSC for supercomputer support.

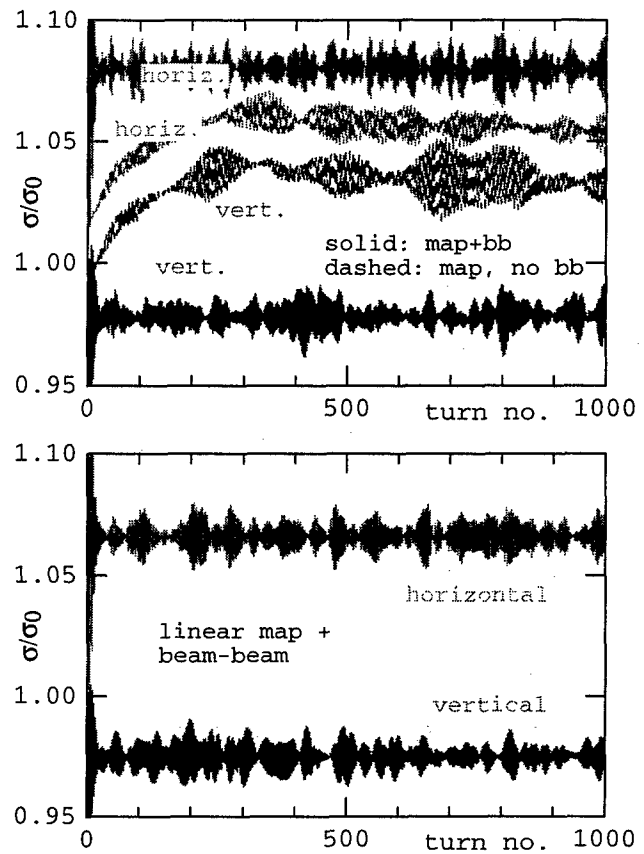


Figure 3: RMS beam size evolution. Top: nonlinear map with and without beam-beam. Bottom: linear map + beam-beam.

6 REFERENCES

- [1] "Status of Muon Collider R&D and Future Plans," BNL-65-623/Fermilab-PUB-98/179/LBNL-41935, Sept. 1998.
- [2] M. A. Furman, "The Classical Beam-Beam Interaction for the Muon Collider: A First Look," $\mu^+\mu^-$ Collider: A Feasibility Study, BNL-52503/Fermi Lab-Conf-96-092/LBNL-38946, July 1996, sec. 8.6; Proc. 1996 Snowmass Workshop *New Directions for High-Energy Physics*; http://www.lbl.gov/~miguel/mucoll_snowmass96.pdf.
- [3] M. Berz, "COSY INFINITY v8 User's Guide and Reference Manual," Nov. 7, 1997.
- [4] M. A. Furman, A. A. Zholents, T. Chen and D. Shatilov, "Comparisons of Beam-Beam Simulations," Proc. Seventh Advanced ICFA Workshop on Beam Dynamics, JINR, Dubna, Russia, 18-20 May, 1995, pp. 123-142; <http://www.lbl.gov/~miguel/BBcompICFA.pdf>.
- [5] M. A. Furman, "Beam-Beam Tune Shift and Dynamical Beta Function in PEP-II," Proc. EPAC94, London, England, June 27-July 1, 1994, p. 1145, http://www.lbl.gov/~miguel/epac94_dynbeta_LBNLrep.pdf.
- [6] E. S. Kim, A. M. Sessler and J. Wurtele, "Control of energy spread due to the beam-beam interaction in a 50 GeV \times 50 GeV muon collider ring," in preparation.

INCOHERENT EFFECTS DRIVEN BY THE ELECTRON CLOUD*

M. A. Furman[†] and A. A. Zholents, Center for Beam Physics, LBNL, Berkeley, CA, USA

Abstract

As a result of the synchrotron radiation from a positively-charged beam, an electron cloud is expected to develop in the vacuum chamber from the combined effects of the photoelectric and secondary emission processes [1–3]. We provide here a first estimate of the electron-cloud effect on individual particles of the beam. We focus on the space-charge tune spread, the distortion of the beta function and the dispersion, and synchro-betatron coupling. We illustrate the effects with numerical applications to the PEP-II positron ring [4]. We conclude that the magnitude of the effect is not negligible, although it is not large either. However, the present calculations can only be considered as a first estimate, since they do not include details of the electron cloud formation in different regions of the ring.

1 METHOD AND APPROXIMATIONS

We assume that an electron cloud has been established in the vacuum chamber of a positively-charged beam of closely spaced bunches. Although our analysis can be applied to any case with similar conditions, we will choose as an example the PEP-II low-energy ring (LER), which contains the positron beam.

Numerical simulations for the pumping straight chambers in the arcs of the PEP-II LER for a photon reflectivity $R \simeq 1$, photoelectric yield $Y' = 1$ and secondary electron yield corresponding to TiN, show that the electron cloud density is approximately uniform near the center of the chamber [3]. Indeed, the density on axis is $d \simeq 6.5 \times 10^5$ electrons/cm³, while its average value is $\bar{d} \simeq 4.1 \times 10^5$ electrons/cm³. For the purposes of this article we will make the approximation that the electron cloud density is uniform throughout the chamber and we will focus on the details of the electron cloud *within a positron bunch* as it traverses this uniform cloud. For vacuum chamber regions within a dipole magnetic field, the uniform-density approximation is not a good one, and a more detailed calculation is required. For the PEP-II LER, however, the pumping straight chambers account for $\sim 93\%$ of the arc length and $\sim 62\%$ of the ring circumference; hence our results, though incomplete, are meaningful.

When a bunch travels through the cloud, its head sees a density \bar{d} ; trailing positrons within the bunch sample different values of the density as the electrons are pulled in. The local electron density d is characterized by a dimensionless function $\rho(z)$ of the longitudinal coordinate z such that $d = \bar{d}\rho(z)$ with $\rho(z)$ normalized such that $\rho(z) = 1$

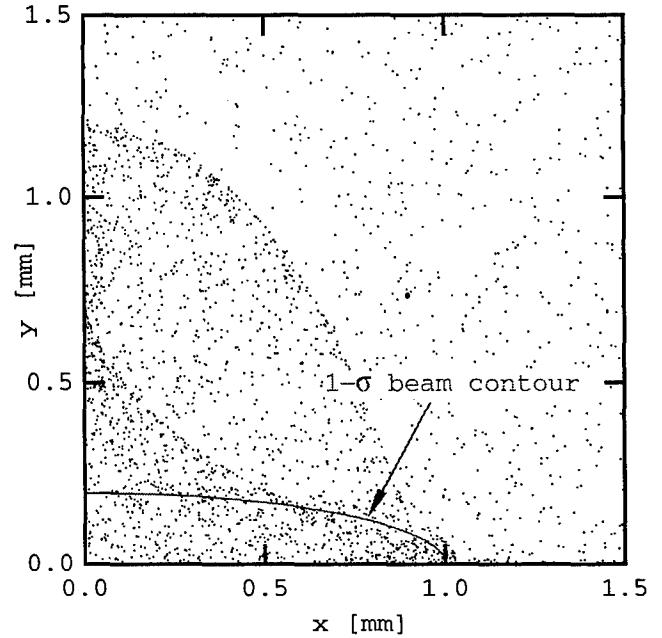


Figure 1: The electron distribution just after the bunch tail has passed. In this case, we used a sample of 100,000 static electrons initially distributed uniformly in a disk of radius 10 mm about the beam axis.

at the head of the bunch. Making the approximation that the chamber cross-section is a perfect ellipse of semi-axes a and b , the average linear density $\bar{\lambda}$ is given, in terms of the average bulk electron density \bar{d} , by

$$\bar{\lambda} = -e\pi ab\bar{d} \quad (1)$$

while its local density is $\lambda(z) = \bar{\lambda}\rho(z)$.

In our simulations aiming at determining $\rho(z)$, we divide the bunch longitudinally into a certain number of kicks such that the “head” and “tail” kicks are located at $z = \pm z_h$. Experience shows that adequate numerical convergence is achieved with 51 equally-spaced kicks whose weight are gaussian in z with rms σ_z such that $z_h = 3\sigma_z/2$. The simulation proceeds by “injecting” a bunch into a uniform cloud of static¹ electrons, and we extract the electron density at all kick locations z . As an example, Figure 1 illustrates the transverse particle distribution just after the tail of the bunch has passed.

For the purposes of determining $\rho(z)$ we count only those electrons within the one-sigma ellipse about the bunch axis; the value of $\rho(z)$ is then the ratio of electrons at kick location z relative to the number of electrons at the

* Work supported by the US Department of Energy under contract no. DE-AC03-76SF00098.

[†] E-mail: mafurman@lbl.gov.

¹ We have verified that $\rho(z)$ is not very sensitive to the initial electron-cloud average energy, up to 400 eV.

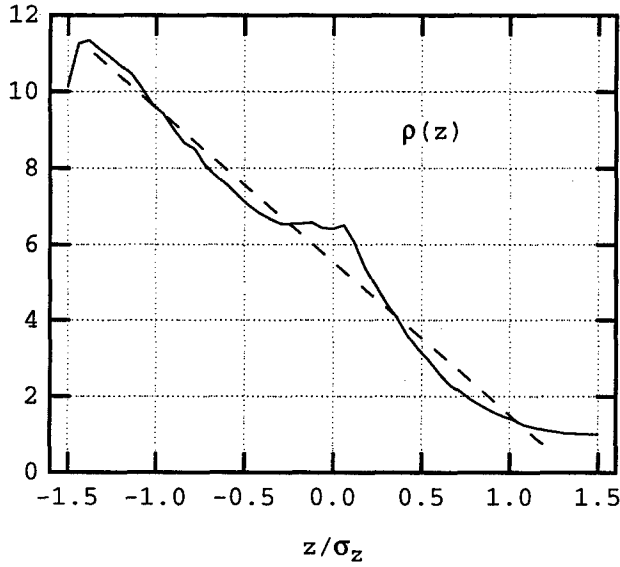


Figure 2: The electron density enhancement function $\rho(z)$ for the PEP-II LER pumping sections. The normalization is $\rho(3\sigma_z/2) = 1$. The straight line is a free-hand first-order approximation.

head of the bunch. Fig. 2 shows the result. PEP-II parameters used in the simulation are listed in Table 1.

The approximate linearity of $\rho(z)$ is a consequence of the parameter values used in the simulation. For higher values of N the electrons get pulled in more quickly into the bunch and remain temporarily trapped, leading to oscillatory behavior of $\rho(z)$. An analytic approach to this problem is described in Ref. 5.

2 TUNE SHIFT

The electric field \mathbf{E}_e from the cloud leads to a neutralization tune shift $\Delta\nu^{(n)}$ which adds to the direct space-charge tune shift $\Delta\nu^{(0)}$. A simple estimate of $\Delta\nu^{(n)}$ can be obtained by making the approximation that the transverse electron-cloud density is uniform within the bunch, as it can be qualitatively seen in Fig. 1. Our simulations show that, for nominal conditions, the kinetic energy does not exceed $\sim 8 \times 10^4$ eV, hence the electrons can be sensibly considered nonrelativistic. Thus the force on any given positron due to the electron cloud is approximately transverse and purely electric, and it is given by [6]

$$\mathbf{F}_e = e\mathbf{E}_e = \frac{4\bar{\lambda}\rho(z)}{a+b} \left(\frac{x}{a}\mathbf{i} + \frac{y}{b}\mathbf{j} \right) \quad (2)$$

where z is the longitudinal position of the positron. Inserting Eqs. 1–2 into the standard expression [7] for a tune shift yields

$$\Delta\nu_x^{(n)}(z) = \frac{r_e L \bar{\beta}_x b \bar{d}}{\gamma(a+b)} \rho(z) \quad (3)$$

where $r_e = e^2/mc^2 \simeq 2.82 \times 10^{-15}$ m is the classical electron radius, L is the aggregate length of the pumping

Table 1: Selected PEP-II parameters.

Circumference, C [m]	2200
Beam energy, E [GeV]	3.1
No. of particles per bunch, N	5.63×10^{10}
Aver. beta functions, $\bar{\beta}_x = \bar{\beta}_y$ [m]	16
Aver. hor. beam size, $\bar{\sigma}_x$ [mm]	1
Aver. ver. beam size, $\bar{\sigma}_y$ [mm]	0.2
RMS bunch length, σ_z [cm]	1
Synchrotron tune, ν_s	0.03
Chamber semi-axes, (a, b) [cm]	(4.5, 2.5)

sections, $\bar{\beta}_x$ is the average beta function and γ is the usual relativistic factor assumed $\gg 1$. A corresponding expression for $\Delta\nu_y^{(n)}$ is obtained from the above by the simultaneous substitutions $a \leftrightarrow b$ and $x \leftrightarrow y$.

Choosing the central particle ($z = 0$) as a reference, using parameter values from Table 1, setting $L = 1373$ m and $\bar{d} = 4.1 \times 10^5$ cm $^{-3}$ (obtained from separate simulations [3]) and setting $\rho(0) = 5.5$ from the linear fit in Fig. 2, we obtain

$$\left. \begin{aligned} \Delta\nu_x^{(n)} &= 8.3 \times 10^{-3} \\ \Delta\nu_y^{(n)} &= 1.5 \times 10^{-2} \end{aligned} \right\} \text{central particle} \quad (4)$$

for the contribution from the pumping sections. Here the bar over ν is meant to emphasize that this tune shift, which pertains to the central particle, also represents an average tune shift over the bunch, on account of the approximate linearity of $\rho(z)$.

The neutralization tune shift of the particle at the head of the bunch, which we denote with the subscript “h,” is obtained from Eq. (3) by setting $\rho(z_h) = 1$,

$$\left. \begin{aligned} \Delta\nu_{h,x}^{(n)} &= 1.5 \times 10^{-3} \\ \Delta\nu_{h,y}^{(n)} &= 2.7 \times 10^{-3} \end{aligned} \right\} \text{head particle} \quad (5)$$

The above expressions and numerical values should be compared with the direct space-charge tune shift of the central particle,

$$\Delta\nu_x^{(0)} = -\frac{r_e \bar{\beta}_x N C}{(2\pi)^{3/2} \gamma^3 \sigma_z \bar{\sigma}_x (\bar{\sigma}_x + \bar{\sigma}_y)} \quad (6)$$

where $\bar{\sigma}_x$ and $\bar{\sigma}_y$ are ring-averages of the rms beam sizes and N is the number of particles per bunch. A corresponding expression for $\Delta\nu_y^{(0)}$ is obtained from the above by the replacement $x \leftrightarrow y$. Substituting values from Table 1 we obtain

$$\left. \begin{aligned} \Delta\nu_x^{(0)} &= -1.3 \times 10^{-4} \\ \Delta\nu_y^{(0)} &= -6.6 \times 10^{-4} \end{aligned} \right\} \text{central particle} \quad (7)$$

3 SYNCHROBETATRON COUPLING

The z -dependence of the betatron frequency, given by

$$\omega_\beta(z) = \omega_{\beta,0} \left(1 + \Delta\nu^{(n)}(z) \right) \quad (8)$$

leads to synchrobetatron coupling. Here $\omega_{\beta,0}$ is the nominal betatron frequency, and we have neglected $\Delta\nu^{(0)}$ vis à vis $\Delta\nu^{(n)}$. For simplicity of the analysis we use a linear fit, $\rho(z) = \rho(0) - (\rho(0) - 1)z/z_h$. Setting $z = z_0 \sin \omega_s t$ we obtain a shifted and modulated betatron frequency, $\omega_\beta(t) = \omega'_\beta (1 - \epsilon \sin \omega_s t)$, where

$$\omega'_\beta = \omega_{\beta,0} \left(1 + \Delta\nu^{(n)} \right) \quad (9a)$$

$$\epsilon = \frac{z_0(\rho(0) - 1)\Delta\nu_h^{(n)}}{z_h(1 + \Delta\nu^{(n)})} \quad (9b)$$

The synchrotron angular frequency ω_s is expressed in terms of the synchrotron tune via $\nu_s = \omega_s/\omega_{\beta,0}$. Thus the betatron equation for the horizontal motion of a given positron is, in the smooth- β approximation,

$$\ddot{x} + \omega_\beta'^2 (1 - \epsilon \sin \omega_s t)^2 x = 0 \quad (10)$$

We have numerically integrated Eq. (10). The Fourier spectrum of $x(t)$, $\tilde{x}(\omega)$, exhibits characteristic peaks separated by $\Delta\omega = \omega_s$, as shown in Fig. 3. We assumed $\Delta\nu_h^{(n)} = 2.7 \times 10^{-3}$, $z_0/\sigma_z = 1$, and $\rho(0) = 5.5$.

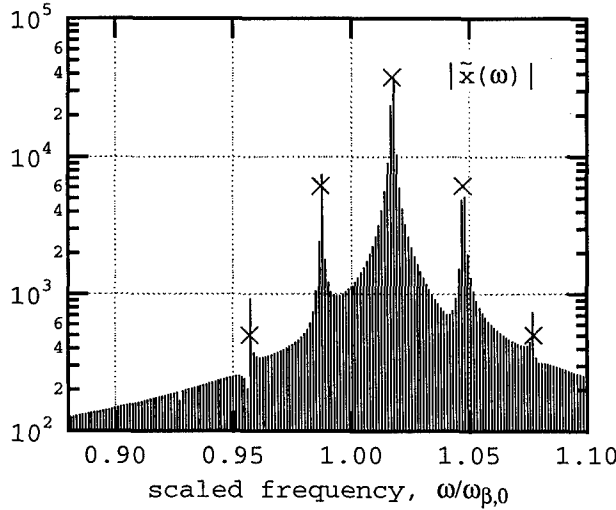


Figure 3: Unnormalized absolute-value spectrum $|\tilde{x}(\omega)|$. The frequency shift of the central peak is given by Eqs. (4)–(9a), and the sidebands are spaced by $\nu_s = 0.03$. The crosses are the values of $|J_k(\chi)|$ scaled to the main peak.

The relative height of the peaks in Fig. 3 can be understood from an approximate analytic solution [8] of Eq. (10). To order $\epsilon\omega_s/\omega'_\beta$, the spectrum is a series of delta functions at $\omega = \pm\omega'_\beta + k\omega_s$ for all integers k , with amplitude proportional to $J_k(\chi)$, where $J_k(\chi)$ is the ordinary Bessel function of order k and

$$\chi = \frac{\epsilon\omega'_\beta}{\omega_s} = \frac{z_0(\rho(0) - 1)\Delta\nu_h^{(n)}}{\nu_s z_h} = 0.32 \quad (11)$$

4 DISCUSSION

Eq. (4) represents only the contribution from the pumping sections; other regions of the ring will add to these numbers. In particular, the straight section IR2 and the wiggler section, although relatively short compared to the circumference, may develop a significant electron cloud density.

The electron cloud effectively provides a distortion of the guide field in the ring, and hence of the optics. The beta-function distortion and dispersion distortion scale as $\Delta\beta \sim \beta\Delta\nu^{(n)}/\sin 2\pi\nu$ and $\Delta\eta \sim \eta\Delta\nu^{(n)}/\sin \pi\nu$, respectively [7]. Hence these effects are small unless the tune ν is close to an integer or half-integer.

The density function $\rho(z)$, shown in Fig. 2, has higher-order components beyond the linear, as evidenced by the bump at the center. Therefore the synchrobetatron spectrum will, in general, be more complicated than what is discussed above.

When a train of bunches is injected into the ring the electron cloud has vanishing density at the head of the train and maximal density towards the tail. Therefore the tune shift $\Delta\nu^{(n)}$ will have a bunch-to-bunch variation along the train, which will introduce further complications in the synchrobetatron spectrum.

A more complete analysis describing the bunch average of the single-particle spectrum shown in Fig. 3, including the broadening effect from radiation damping, will be presented elsewhere [9].

5 ACKNOWLEDGMENTS

We are grateful to NESRC for supercomputer support.

6 REFERENCES

- [1] M. Izawa, Y. Sato and T. Toyomasu, Phys. Rev. Lett. **74**(25), 5044 (1995).
- [2] K. Ohmi, Phys. Rev. Lett. **75**(8), 1526 (1995).
- [3] M. A. Furman and G. R. Lambertson, KEK Proc. 97-17, MBI-97, Tsukuba, 15–18 July 1997, p. 170 (Y. H. Chin, ed.); <http://www.lbl.gov/~miguel/ECI-MBI97-PEPII.pdf>.
- [4] LBL-PUB-5379/SLAC-418/CALT-68-1869/UCRL-ID-114055/UC-IIRPA-93-01, June 1993.
- [5] J. S. Berg, LHC project note 97, 1 July 1997.
- [6] M. A. Furman, Am. J. Phys. **62**(12), 1134 (1994) and references therein; <http://www.lbl.gov/~miguel/ellEfield-art.pdf>.
- [7] E. D. Courant and H. S. Snyder, Ann. Phys. **3**, 1 (1958).
- [8] G. V. Stupakov and A. W. Chao, Proc. PAC95 and ICHA, Dallas, Texas, May 1–5, 1995, p. 3288.
- [9] M. A. Furman and A. A. Zholents, to be published.

Simulations of Transport and RF Power Production in a 35-GHz Relativistic Klystron*

S.M. Lidia, LBNL, Berkeley, CA 94720 USA

J. Gardelle, T. Lefevre, J.L. Rullier, CEA/CESTA, BP 2, 33114 Le Barp, France

J.T. Donohue, CENBG, BP 120, 33175 Gradignan, France

P. Gouard, CEA/CIF, BP 12, 91680 Bruyeres-le-Chatel, France

Abstract

A current experiment is underway to study beam dynamics and rf production in a 35-GHz relativistic klystron using a 1-kA, 7-MeV electron beam produced by the PIVAIR accelerator. We present simulations of transport in the PIVAIR accelerator, modulation from a free-electron laser interaction, post-wiggler solenoidal transport, and interaction with two rf cavities. These simulations are performed with a suite of various codes. Steady-state and transient effects are discussed. The calculated transverse and longitudinal profiles of the beam are compared with experimental diagnostic measurements.

1 INTRODUCTION

An experiment to produce a 35 GHz modulated beam by a FEL, and to subsequently extract power from this beam in a resonant cavity has been performed at CESTA. This work is in support of the study of two beam accelerators based on relativistic klystrons, and has been executed jointly by groups at LBNL, CEA/CESTA, and CERN. One of the aims of this current experiment is to validate and benchmark our simulation codes.

For the design of the experiment and the analysis of its results, we have relied upon four distinct codes: an envelope code for basic transport studies; PARMELA [1] for more detailed examination of the transverse phase space evolution; SOLITUDE [2] for the study of 3D, steady-state FEL interactions; and RKS [3] to study the time-dependent, 3D bunch evolution and power production in output microwave cavities. A brief description of the experiment is given elsewhere in these proceedings [4].

2 TRANSPORT IN PIVAIR

The simulation begins with a description of the transport from the cathode to the experiment. For this the envelope code is solely used. A plot of the magnetic field and beam edge radius is given in Figure 1.

The currents in the two final solenoids and dipole coils are adjusted for proper matching into the wiggler. A Rogowski coil placed at the entrance to the wiggler measured the beam current; 800 A were obtained in the current experiment.

* Work performed at LBNL was supported under the auspices of the U.S. Department of Energy under Contract No. AC03-76SF00098.

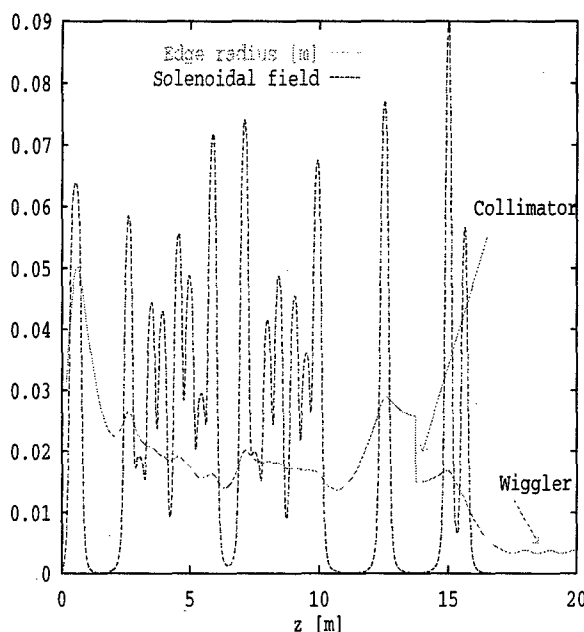


Figure 1: Transport in PIVAIR.

Wiggler period	20 cm
Resonant field	1650 G
Total no. periods	32
Total length	6.4 m
Input signal frequency	35.04 GHz
Input signal power	5 kW
DC current at entry	1000 A

Table 1: FEL parameters.

3 TRANSPORT THROUGH THE FEL

The main FEL parameters are listed in Table 1. SOLITUDE has been run to obtain fair agreement with the preliminary results of the current experiment, ie. 40 MW of FEL power and 250 A of current at the wiggler exit. Besides the basic parameters of the beam distribution (current, radius, emittance) and the input microwave power, SOLITUDE has a few additional 'knobs' with which to tune the resultant interaction. These allow the simulation to place the entry of the beam centroid at any radius and polar angle in the entry plane, and with two independent angles with respect to the normal of the entry plane. Sensitivity studies have shown that for small variations from normal,

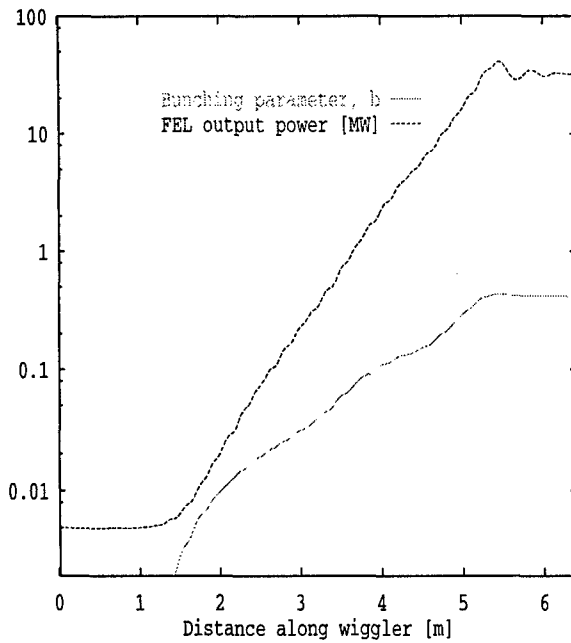


Figure 2: Evolution of FEL power and bunching.

on-axis injection, it is the azimuthal angle (angular divergence from the wiggler axis) of the centroid motion which has the largest effect on overall FEL performance. In particular, we have found that an azimuthal angle of ~ 33 mrad at the entrance plane generates trajectories within the FEL region that lead to the observed 40 MW of output power and 250 Amps of current at the exit current monitor. The bunching parameter at the FEL exit is given by SOLITUDE as $b \sim 0.4$. The evolution of the output power and of the bunching parameter as calculated by SOLITUDE is shown in Figure 2. The output data generated by SOLITUDE include the detailed particle distribution in the horizontal and vertical phase spaces, as well as the distribution in particle energy and arrival time for a given bunch. These data provide an indication of the initial conditions for simulations of the downstream region.

4 DOWNSTREAM TRANSPORT AND CAVITY INTERACTION

After a short drift space, the bunched beam is focused by a solenoid module (peak axial field ~ 0.27 T) into one of two Ka-band standing-wave RF output cavities. These cavities were designed using standard electromagnetic codes, and were built by the CLIC group at CERN. The measured parameters¹ of these cavities are shown in Table 3.

The transport from the end of the wiggler through the cavities has been studied with PARMELA, the envelope code, and RKS. The initial conditions generated by SOLITUDE have been used in the envelope simulation. In the case of the RKS code, on the other hand, we have slightly

¹These shunt impedance values have not been directly measured, but have been inferred from the beam interaction and the measured power.

Resonant frequency [GHz]	35.0	35.6
Quality factor, Q_{Loaded}	60	271
Shunt impedance [R/Q] [Ω]	76.	76.
DC current in cavity [A]	120	120
Measured output power [MW]	12	0.69

Table 2: RF cavity parameters.

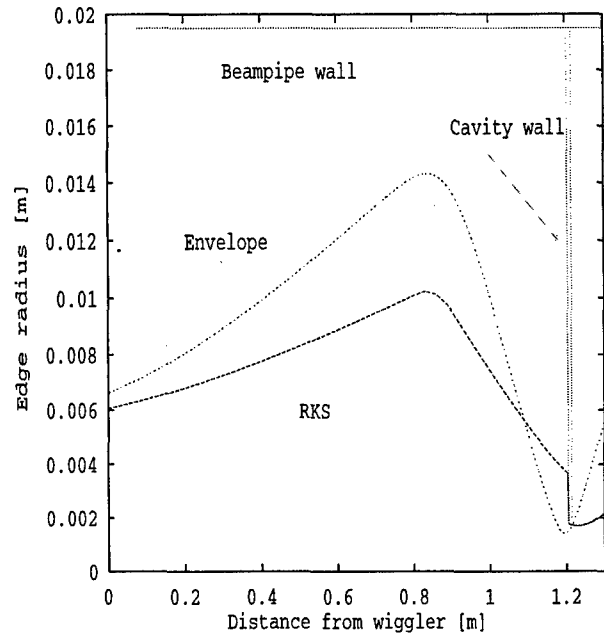


Figure 3: Beam edge radius evolution.

adjusted the initial conditions to obtain fair agreement with the experimentally measured beam spot sizes, and the incident and transmitted beam currents through the cavities. The trajectories calculated by the envelope code and RKS are shown in Figure 3.

The differences between the two codes are an indication of the effects of the detailed statistics of the transverse dynamics. The envelope code assumes an on-axis beam described by a transverse KV and a longitudinally uniform distribution, while the RKS code uses a semi-Gaussian distribution for the transverse phase space and a Gaussian distribution for the longitudinal phase space. The 'edge' radius in this case is twice the rms radius. These different models present slightly different modes of evolution, while showing fair agreement on the measured parameters at the end points. RKS reproduces good agreement with experiment in predicting a 4mm spot size radius at the cavity plane.

Measurements of the FEL output power give an indication of the bunching parameter of the beam at the FEL exit. This can be measured experimentally [5]. Subsequent measurement of the cavity output power and beam current allows us to indirectly measure the cavity shunt impedances. The steady-state output power from the cavities follows

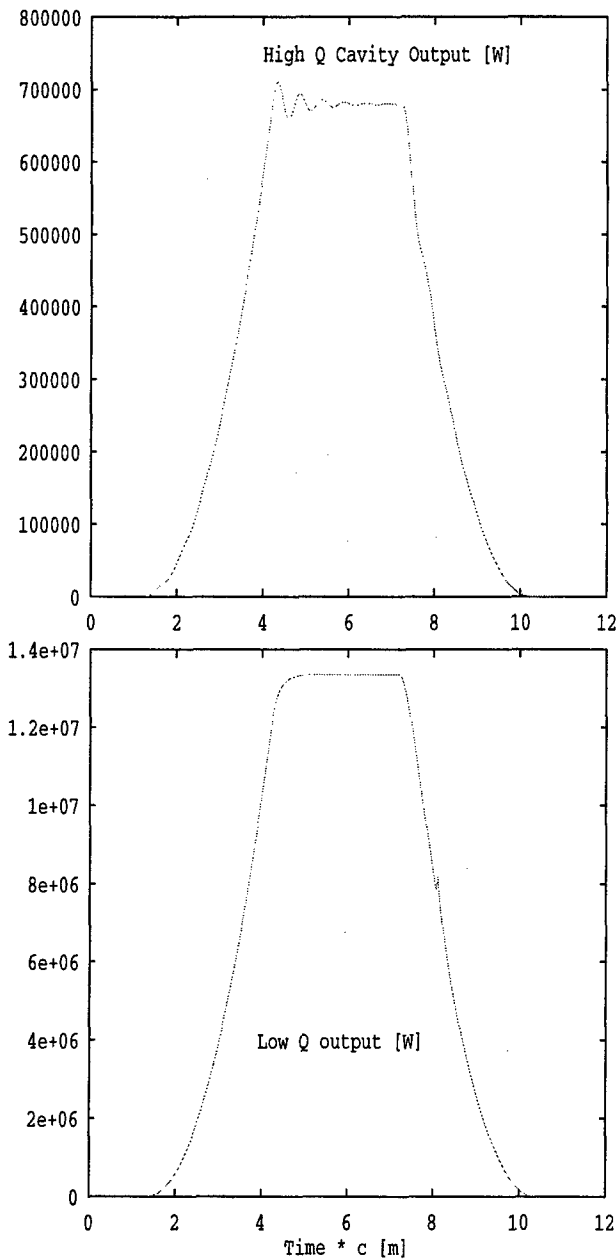


Figure 4: Temporal power development in the two cavities.

from the relation

$$P_{out} = I_{dc}^2 b^2 Q_{Loaded} \left[\frac{R}{Q} \right] \cos^2 \psi,$$

where b is the bunching parameter, and ψ is the cavity tuning angle [6]. The temporal evolution of the output cavity power is calculated by the RKS code. The output from the low- and high-Q cavities is shown in Figure 4. The temporal evolution of the power and phase in the output cavities is calculated by an equivalent circuit equation coupled to the detailed beam dynamics [7].

5 CONCLUSIONS

We have presented a suite of calculations that demonstrate the physics modelling of beam dynamics in a complex experiment. Good agreement has been reached between the codes and the experimental measurements. In particular, the codes have reproduced the experimentally observed output powers of 12 MW and 0.7 MW to very good agreement. More definitive measurements of the bunching parameter may increase the agreement between the code predictions and experiment.

6 ACKNOWLEDGMENTS

One of the authors (SML) would like to express his gratitude toward the CEA/CESTA and CENBG for their hospitality during his stay.

7 REFERENCES

- [1] Parmela. Maintained by the Los Alamos Accelerator Code Group.
- [2] J. Gardelle et. al. Free-electron laser simulations: Effects of beam quality and space charge. *Phys. Rev. E*, 50:4973, 1994.
- [3] S. Lidia. Relativistic klystron simulator. Unpublished, 1999.
- [4] T. Lefevre et. al. Results on the interaction of an intense bunched electron beam with resonant cavities at 35 ghz. In *these proceedings*, 1999.
- [5] J. Gardelle et. al. Direct observation of beam bunching produced by a high power microwave free electron laser. *Phys. Rev. E*, 79:3905, 1997.
- [6] J.C. Slater. *"Microwave Electronics"*. D. Van Nostrand Company, Inc., 1950.
- [7] S. Lidia. Single-mode beam-cavity interaction in relativistic klystrons. In *these proceedings*, 1999.

STABILITY OF MODULATED BEAM TRANSPORT IN RELATIVISTIC KLYSTRON TWO-BEAM ACCELERATORS*

S.M. Lidia, S.S. Yu, Lawrence Berkeley National Laboratory, Berkeley, CA 94720 USA

Abstract

We discuss the stability of the drive beam in a relativistic klystron two-beam accelerator (RK-TBA). Simulations are presented for the main extraction section of an RK-TBA. Longitudinal and transverse equilibria are discussed. Beamline parameters are chosen which correspond to the RTA experiment.

1 INTRODUCTION

The relativistic klystron two beam accelerator (RK-TBA) concept [1] is actively being pursued by experimental and theoretical programs at LBNL [2], and CEA/CESTA [3]. The LBNL effort is concerned with building a prototype, the RTA [4], to physics, engineering, and costing issues in a full-scale device from the source and injector, accelerator, modulator, and power extraction sections. The RTA is designed to produce ~180-200 MW/m of microwave power from standing wave rf cavities in the main extraction section. Kinetic energy in the beam is replaced by the use of highly efficient induction acceleration modules. Transverse focusing is provided by a permanent magnet FODO lattice. Longitudinal focusing is provided by inductively detuning the rf output structures. The FODO lattice is designed to produce a half-betatron oscillation between adjacent rf cavities, to minimize the effects of a cumulative dipole BBU mode associated with the cavities. A schematic of a single period of the main extraction section is shown in Figure 1.

In this paper, we discuss the beam dynamics in the main extraction section of the RTA. In particular, we examine the results of numerical simulation using the 3-D, time-dependent RKS code [5]. We have modeled the beam dynamics and the evolution of the cavity fields from initial transients into the steady-state regime. The main parameters of the simulation are given in Table 1.

2 EVOLUTION IN LONGITUDINAL PHASE-SPACE

The longitudinal dynamics of the rf bunches constitute the heart of any RK-TBA. The energy extracted from the bunches in the rf cavities must be replaced by the induction modules. The detuning of the cavity introduces a nonlinear correlation between energy and phase for particles within the bunch. This induces the bunch to rotate in longitudinal

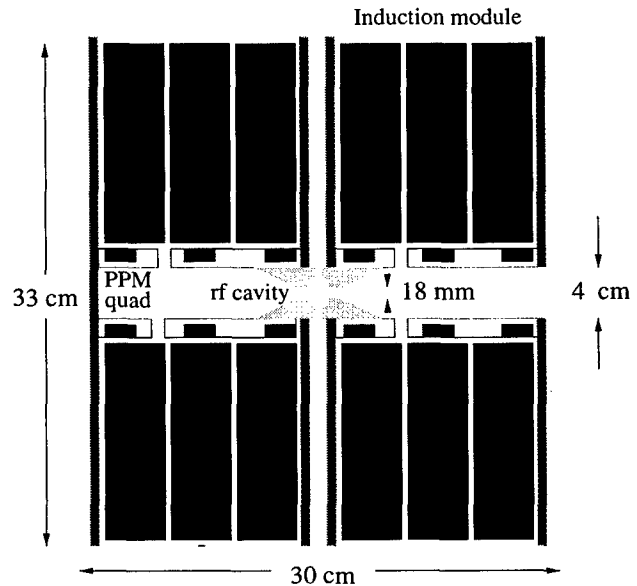


Figure 1: One period of the main RTA extraction section.

Nominal beam energy	3 MeV
Beam current, dc	600 A
ϵ_{edge} , normalized	800π mm mr
Bunching parameter	0.84
FODO cell length	10 cm
Phase advance/cell	60 deg.
Induction gap voltage	45 kV
Modulation frequency	11.424 GHz
Rf cavity frequency	11.55 GHz
Q_{loaded}	56
[R/Q]	10 Ω
Total simulation length	6 m

Table 1: Simulation parameters.

* This work supported under the auspices of the U.S. Department of Energy by LBNL under Contract No. AC03-76SF00098.

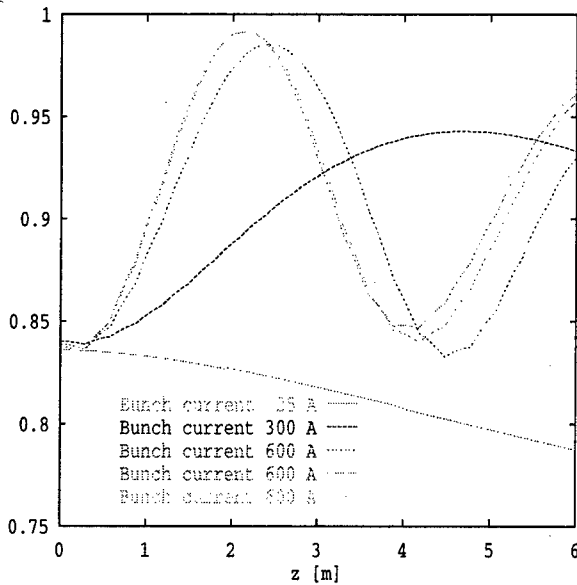


Figure 2: Bunching parameter variation along beamline.

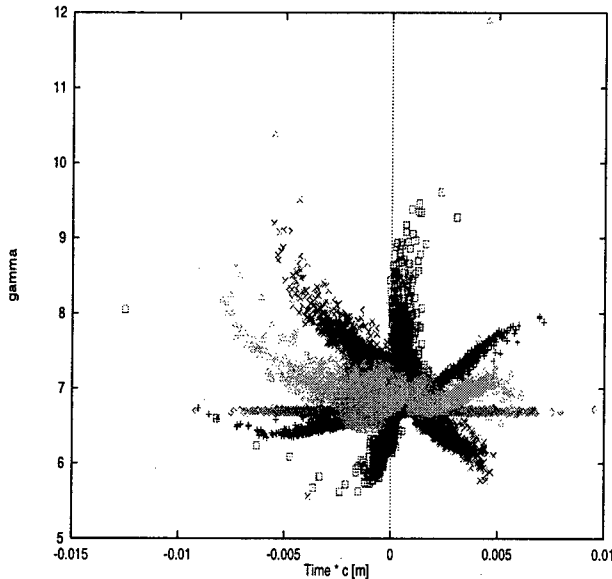


Figure 3: Bunch rotation along the beamline.

phase space. The re-acceleration in the induction modules is weakly dependent upon the dc beam current, but the rf cavity field excitation is strongly dependent upon both the dc current and the bunching parameter, $b (\simeq \frac{1}{2} I_{rf} / I_{dc})$. In our simulations, we see that while the dc current carried by a given bunch remains relatively constant, the bunching parameter varies significantly along the beamline, as well as temporally during the initial current ramp of the beam head. In Figure 2, we show the variation of the bunching parameter along the beamline, for bunches of lower dc current in the beam head through bunches in the main body of the beam. This clearly shows the synchrotron oscillation that follows the bunch rotation, shown in Figure 3.

We also see another effects of inductive detuning. Low

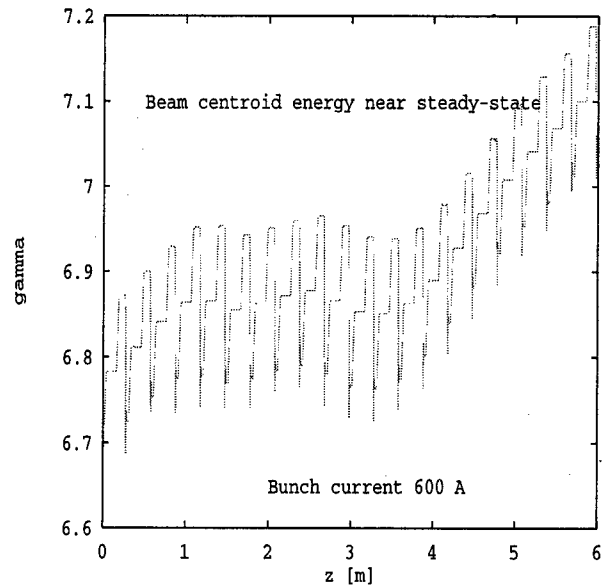


Figure 4: Variation of bunch centroid energy along beamline.

current, moderately compressed bunches resonantly excite cavity modes that react upon later bunches, which become more highly compressed. Due to their smaller bunch length, these later bunches will excite stronger fields in cavities further down the beamline, losing more energy as they do so. This is shown in Figure 4.

Later along in the synchrotron oscillation, these later bunches have a longer bunch length and deposit less energy into the cavity modes. Hence, they lose less energy in traversing a cavity. Inductive detuning thus has two manifestations in the bunch dynamics: a rotation in the longitudinal phase space of the bunch; and an oscillation in the bunch centroid energy. These oscillations affect the coupling of the bunch to the rf cavities, resulting in an oscillation along the beamline of the output power levels of the cavities, shown in Figure 5.

3 EVOLUTION IN TRANSVERSE PHASE-SPACE

The behavior of the bunches in longitudinal phase space effect the transverse dynamics as well. In particular we notice that an initially matched transport system, loses that feature as the bunch compresses and the bunch energy spread increases. The effect of bunch compression is to enhance the peak radial, defocusing self-fields in the presence of the conducting beampipe, while the enhanced energy spread introduces lower energy particles into the transport lattice. These two effects can, in principle, be dealt with by appropriately adjusting the strength of the quadrupoles along the beamline. In our studies we have maintained a constant parameter FODO lattice. In Figure 6 we show the evolution of the two transverse rms envelopes along the beamline for bunches in the center of the beam.

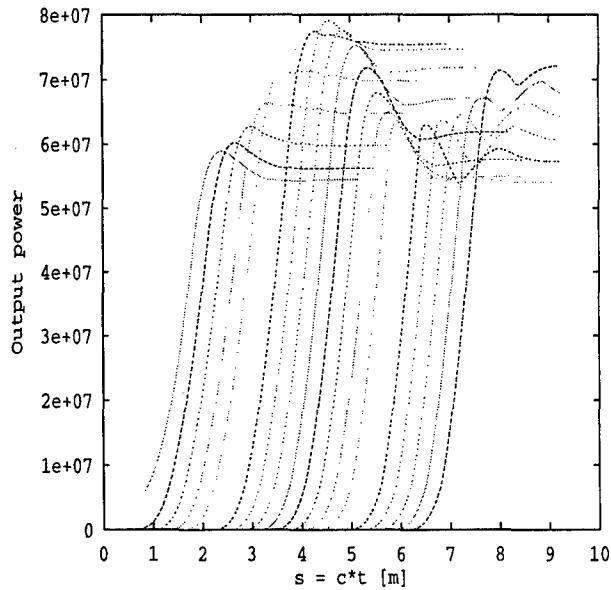


Figure 5: Power output from 20 rf cavities.

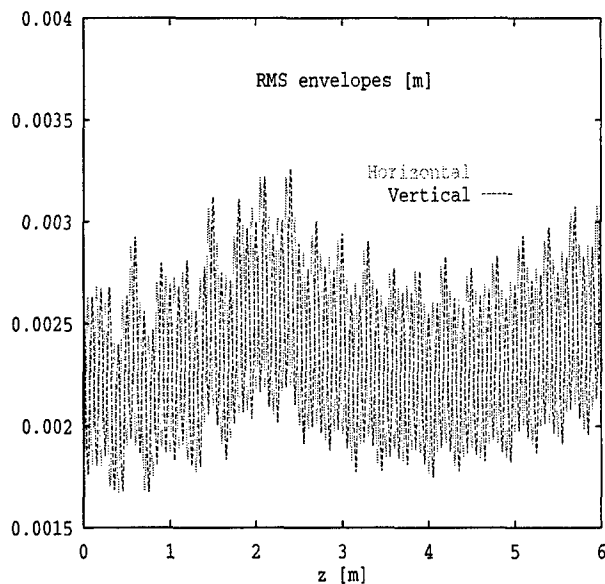


Figure 6: Evolution of transverse rms envelopes .

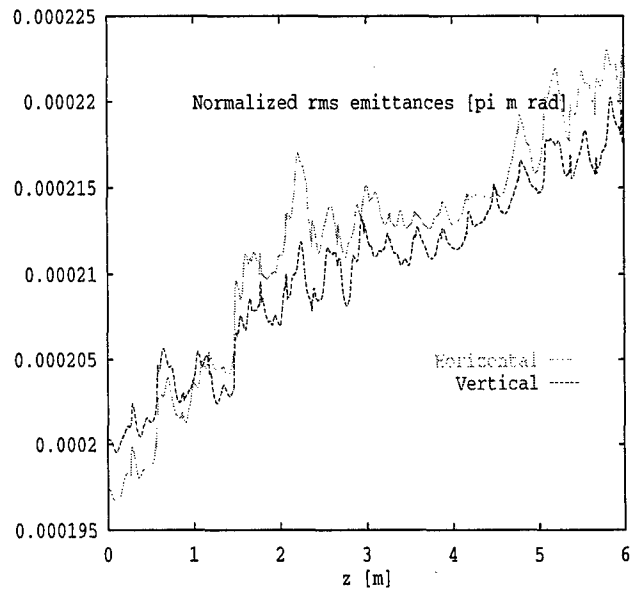


Figure 7: Evolution of transverse emittance.

In Figure 7, we show the evolution of the normalized rms transverse emittance. These simulations do not include the influence of transverse dipole modes in the induction modules or rf cavities. Thus, we have not included the important BBU instabilities that have shown to limit current transport in RK-TBA's. However, this simulation shows that pure rf monopole modes, 3-D space charge effects, and quadrupole transport do not significantly increase the transverse emittance in the beam. On average, we see these effects contributing an increase of $\sim 0.5\%$ /TBA period.

4 CONCLUSIONS

We have presented simulations of beam transport and the evolution in longitudinal phase space in an RK-TBA system. Longitudinal stability has been shown to result from inductively detuning the output rf structures. The coupling between longitudinal and transverse phase spaces has been shown to result in only a modest growth rate of the transverse emittance.

5 REFERENCES

- [1] A. Sessler and S. Yu. Relativistic klystron two-beam accelerator. *Phys. Rev. Lett.*, 54:889, 1985.
- [2] T. Houck et. al. Prototype microwave source for a relativistic klystron two-beam accelerator. *IEEE Trans. Plasma Sci.*, 24(3):938, 1996.
- [3] T. Lefevre et. al. Results on the interaction of an intense bunched electron beam with resonant cavities at 35 ghz. In *these proceedings*, 1999.
- [4] S. Lidia et. al. Initial commissioning results of the rta injector. In *these proceedings*, 1999.
- [5] S. Lidia. Relativistic klystron simulator. Unpublished, 1999.

EFFECTS OF MISALIGNMENTS ON SPACE-CHARGE-DOMINATED HEAVY ION BEAMS IN AN IRE

C.M. Celata and M.J.L. de Hoon, LBNL, Berkeley, CA, USA
J.J. Barnard, LLNL, Livermore, CA, USA

Abstract

Preliminary designs for the next large accelerator experiment envisioned for the Heavy Ion Fusion program, the IRE (Integrated Research Experiment) use an induction linac to accelerate multiple space-charge-dominated ion beams to an energy of several hundred MeV, and focus them at a target. This paper examines the effect of beam and quadrupole misalignments on beam emittance in the IRE. The dependence of the centroid orbit on the scaling of focusing parameters with z is analyzed. PIC simulations including misalignment give acceptable emittance growth for present IRE designs.

1 INTRODUCTION

The Heavy Ion Fusion program is in the process of designing the Integrated Research Experiment (IRE), a multi-beam induction linac which would accelerate space-charge-dominated driver-scale K^+ beams to a few hundred MeV and focus them onto a target. Preliminary linac designs consist of acceleration to ~ 8 MeV using electrostatic quadrupole focusing (IRE Section 1), followed by 2 sections of magnetic quadrupole focusing (IRE Sections 2 and 3). The phase advance per lattice period without space charge, σ_0 , and beam radius are kept constant throughout the machine in order to maximize transportable current and minimize cost. This requires different scaling of focusing parameters in different sections. In Section 1, L/v , η , and $K=qE'/m$ are constant (L =lattice half period length, v =longitudinal (i.e., z) velocity, η =quadrupole length, and E' =quadrupole gradient). In IRE Section 2, the beams are compressed longitudinally with line charge density, $\lambda, \propto v$. Here $L \propto v^{1/2}$, and η and $K=qvB'/m$ are constant. In IRE Section 3, λ , L/v , and magnet length are held constant, while quadrupole field gradient scales as $1/(1-2\eta/3)^{1/2}$ in order to keep σ_0 constant. In this paper we examine the effect of random misalignments of quadrupoles and initial misalignment of the beam on emittance growth. Centroid motion and its dependence on the above scaling are calculated for the present IRE design FODO lattice in Section 2 of the paper. In Section 3 a smooth approximation is used to elucidate the results of Section 2. Section 4 shows the emittance growth due to the misalignments in the presence of image forces and magnet fringe fields, as calculated by PIC simulations.

2 ALTERNATING GRADIENT MODEL

We consider the motion of the centroid of a transverse slice of the beam, and follow the treatment of L. Smith[1]. A good approximation to the centroid orbit for the present IRE design can be obtained by neglecting image forces and other nonlinearities. Then linearity implies that if the centroid is initially on axis with no transverse velocity, its position at the center of the N th quadrupole, x_N , is the sum of the individual perturbations from offsets of the upstream quadrupoles, so that [1]

$$x_N = 2 \sqrt{\frac{\beta_{+N}}{v_{+N}}} \sum_{n=1}^N \{ d_{+n} C_{+n} \sin[(N-n)\sigma_0] - d_{-n} C_{-n} \sin[(N-n)\sigma_0 - \frac{\sigma_0}{2}] \}. \quad (1)$$

Here subscripts $+n$ and $-n$ refer to evaluation at the n th focusing and defocusing quadrupole, respectively. d_{+n} is the n th focusing quad x offset. $C_{+n} = (\beta_{+n} K_{+n} / v_{+n})^{1/2} \sin(\theta_{+n}/2)$, $\theta_{+n} = K_{+n}^{1/2} \eta L_{+n} / v_{+n}$ and $C_{-n} = (\beta_{-n} K_{-n} / v_{-n})^{1/2} \sinh(\theta_{-n}/2)$. β is the betatron function. We assume that x and y are decoupled, so that the same description holds for the y dimension. We are interested in random quadrupole misalignments caused by physical limits on fabrication and alignment, so we assume no correlation between the offsets, and look at statistical behavior of centroid motion averaged over many sets of quad displacements for the lattice (average denoted by " $\langle \rangle$ "), with the rms " d " for each quad equal to d_{rms} . Then

$$\langle x^2 \rangle_N = 4 \frac{\beta_{+N}}{v_{+N}} d_{rms}^2 \sum_{n=1}^N \langle C_{+n}^2 \rangle \sin^2[(N-n)\sigma_0] + \langle C_{-n}^2 \rangle \sin^2[(N-n)\sigma_0 - \sigma_0/2]. \quad (2)$$

In IRE Section 1, only $\sin^2[(N-n)\sigma_0]$ in Eq. (2), and $\sin^2[(N-n)\sigma_0 - \sigma_0/2]$, are n -dependent, so the sum is easily done. For $N \gg 1$ the dependence of $x_{N,rms} = (\langle x^2 \rangle_N)^{1/2}$ on σ_0 is negligible, and we find that

$$x_{N,rms} \approx \zeta_1 d_{rms} \sqrt{N}, \quad (3)$$

Thus the centroid motion is to a good approximation (a few percent for $N > 5$) a random walk. $\zeta_1 \equiv \theta_{+10} [2K_{+10}(\beta_{+10} + \beta_{-10})]^{1/2}$, where the subscript " 0 " refers to an initial value in IRE Section 1. For present IRE design parameters, ζ_1 is 3.77, giving 1 mm centroid offset at the end of the 123 Section 1 lattice periods, for $d_{rms} = 0.0254$ mm (1 mil).

In IRE Section 2, the accelerating gradient, V_2' , increases as v^2 . We can approximate the gradient as constant over each half lattice period, and equal to the average of the gradient over that length, since $\Delta E/E \ll 1$,

*Work supported by the U.S. Department of Energy under contracts DE-AC03-76SF00098 (LBNL) and W-7405-ENG-48 (LLNL).

where ΔE is the energy increase in a period. Then it is easy to show that v increases exponentially with z . Using the fact that $L \propto v^{1/2}$, one can show that $v_n \propto (1 - n g_2 L_{20})^{-2}$ and $(K_n \beta_{n+1})^{1/2} \propto v^{1/2}$, with $g_2 = q V_2' / (m v^2)$. This determines the n dependence of all quantities in Eq. (1). The sum can then be done quite accurately if we expand to 2nd order in g_2 , since $g_2 \approx 0.01$. For $N \gg 1$, and no original offset or angle in IRE section 2, this gives

$$x_{N,rms} \approx \zeta_2 d_{rms} \sqrt{N(1 + \frac{c_2 N}{2} + \frac{c_2^2 N^2}{3})(1 - c_2 N)}. \quad (4)$$

N here is the number of lattice periods traversed in Section 2, and $c_2 = g_2 L_{20}$. $\zeta_2 = 3.48$ for the present design. Note that the growth of centroid displacement is considerably slower than $N^{1/2}$. This is due to the decrease of β , which $\propto v^{-1/2}$. Further insight on this result follows in Section 3.

In similar fashion, using $q V_3' / (m v^2) \ll 1$, $\theta_n \ll 1$, we find for section 3:

$$x_{N,rms} \approx \zeta_3 d_{rms} \sqrt{N - 1 - \frac{1}{3} \eta_{30} Z N^2 + \frac{2}{9} \eta_{30} Z^2 N^3}. \quad (5)$$

Here $Z = g_3 L_{30} / 2$. For the present design, $\zeta_3 = 3.48$ and $Z = 0.004$ m.

The above results have been derived assuming no initial offset or angle, in order to see the scaling for a particular section. They can easily be combined to calculate rms centroid orbit through the accelerator, using the fact that $x'_{N,rms} = x_{N,rms} / \beta_{N+1}$ for each section, and using the betatron formalism to carry the final offset and angle for IRE Sections 1 and 2 through the rest of the machine. Results agree with computer calculations to about 5%.

3 SMOOTH APPROXIMATION MODEL

The calculation of centroid offset in Section 2 is useful for making accurate estimates of centroid evolution. However, it is often useful for accelerator designers to have an even simpler formula that gives more physical insight and is amenable to incorporation into accelerator systems codes. To that end we have used the smooth approximation to represent the centroid orbit, but use the matrix representation of the momentum impulse to calculate the change in amplitude of a particle undergoing kicks from displaced quads. In the absence of quadrupole errors, the x-equation of motion in the smooth approximation is:

$$d^2 x / dt^2 = -v_z^2 k_{\beta 0}^2 x \quad (6)$$

Here $k_{\beta 0} \equiv \sigma_0 / 2L$. Letting j denote the number of betatron periods from $z=0$, then $dj/dz = k_{\beta 0} / 2\pi$. Transforming to j as the independent variable, we find

$$d^2 x / dj^2 + (d \ln \omega_{\beta 0} / dj) dx / dj + 4\pi^2 x = 0 \quad (7)$$

Here $\omega_{\beta 0} \equiv k_{\beta 0} v_z$ is the temporal betatron frequency. From Eq.(7) it is clear that if $\omega_{\beta 0}$ increases with z , the amplitude of the betatron motion decreases (in the absence of displacement errors.) We define the amplitude A through the equation $A^2 \equiv x^2 + x'^2 / k_{\beta 0}^2$. It follows that

$$dA^2 / dj + (1/2\pi^2)(d \ln \omega_{\beta 0} / dj) (dx / dj)^2 = 0 \quad (8)$$

We now consider the change in the amplitude arising from randomly displaced quads. The difference in position δx and angle $\delta x'$ between the centroid position with and without quad displacement after a focusing quad and drift is

$$\delta x = d_{-n}(1 - \cos \theta + (1/\eta - 1) \sin \theta) \text{ and}$$

$$\delta x' = d_{-n} \theta \sin \theta / (\eta L) \quad (9)$$

and after a defocusing quad and drift is:

$$\delta x = d_{+n}(1 - \cosh \theta - (1/\eta - 1) \sinh \theta)$$

$$\delta x' = -d_{+n} \theta \sinh \theta / (\eta L) \quad (10)$$

The resulting change in amplitude when averaged over different distributions of quad errors is given by $\langle \delta A^2 \rangle = \langle \delta x^2 \rangle + \langle \delta x'^2 / k_{\beta 0}^2 \rangle$, where terms linear in δx and $\delta x'$ average to zero. Averaging Eq.(8) over error distributions and adding effects from Eqs.(9), (10) yields the following evolution equation for the average amplitude squared:

$$\frac{d}{di} \langle A^2 \rangle = - \langle A^2 \rangle \frac{d}{di} \ln \omega_{\beta 0} + f(\sigma_0, \eta) \langle d_{\pm}^2 \rangle \quad (11)$$

Here i is a half lattice period (one quad and drift) and $f(\sigma_0, \eta) \equiv (1/2)[(1 - \cos \theta + (1/\eta - 1) \sin \theta)^2 + (1 - \cosh \theta - (1/\eta - 1) \sinh \theta)^2 + (2\theta/\eta \sigma_0)^2 (\sin^2 \theta + \sinh^2 \theta)]$. $\theta = [6\eta^2(1 - \cos \sigma_0)/(3 - 2\eta)]^{1/4}$ (ref. [2]). Since $f(\sigma_0=0, \eta) = 12/(3 - 2\eta)$ and variation due to σ_0 is small relative to that from η , for some purposes the $\sigma_0=0$ value of $f(\sigma_0, \eta)$ is adequate.

In order to compare the results from integrating Eq. (11) to the results obtained from transfer matrices, we need to evaluate the "smooth" component from each AG orbit. This is accomplished by averaging over the lattice period using the following procedure. We assume that the actual position after i half-lattice periods may be expressed as $x(i) = A \cos(\sigma_0 i / 2 + \phi) + x_L \cos(\pi i)$. We define the quantities $\bar{x}(i) \equiv (1/4)[x(i-1) + 2x(i) + x(i+1)]$ and $\bar{x}'(i) \equiv (1/4)[x'(i-1) + 2x'(i) + x'(i+1)]$. The smooth amplitude is then given by

$$A^2(i) = 4(\bar{x}(i)^2 + \bar{x}'(i)^2 / k_{\beta 0}^2) / (1 + \cos(\sigma_0 / 2))^2 \quad (12)$$

We compare integration of Eq. (11) with the numerical amplitude found using Eq. (12) in figure (1).

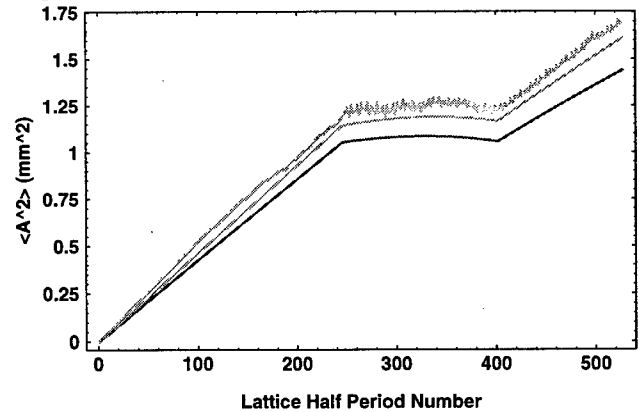


Figure (1): $\langle A^2 \rangle$ vs. half-lattice number i , calculated using Eq.(12) (upper), Eq. (11) (middle), and using the $\sigma_0=0$ value of $f(\sigma_0, \eta)$ (lower).

From Eq. (11) it is apparent that increasing $\omega_{\beta 0}$ with z helps to damp out betatron oscillations and the question arises as to whether advantage can be taken of this in accelerator design. We note that consideration of the smooth envelope equation places the constraint that $\omega_{\beta 0}$ is proportional to λ/a^2 and for designs in which the beam radius a is constant $\omega_{\beta 0}$ varies directly with the line charge λ , suggesting that damping will generally accompany bunch compression. Apertures and bunching schedules should be chosen bearing in mind this relation.

4 PIC SIMULATION RESULTS FOR OFF-AXIS BEAMS

Simulations using the 2d (transverse) version of the WARP particle-in-cell code were done to investigate the behavior of initially aligned and misaligned beams in the IRE for the case of random quad misalignments. In order to incorporate the effects of image charges on the beam, the presence of conducting boundaries in the three sections of the accelerator was included in the simulation. The aperture of the accelerator was 2.86 cm in IRE Section 1, and was increased to 3.36 cm in IRE Sections 2 and 3. In IRE Section 1, the focusing field is generated by four perfectly conducting electrostatic quadrupole rods with a radius of 3.27 cm. The distance from the axis of the accelerator to the tip of the quadrupoles was equal to the aperture of 2.86 cm. The boundary in the drift spaces between the quadrupoles was a square conducting box, 12.26 cm on a side. In Sections 2 and 3, instead of four quadrupole rods, a circular conducting boundary of 3.36 cm was used both in the quadrupoles and in the drift spaces.

A beam of K^+ ions was accelerated from 1.6 MeV to 200 MeV. σ_0 was set equal to 70° , average radius was 1.5 cm, and the perveance was 1.4×10^{-3} .

The rms random quadrupole offset was 0.0254 mm for each of the transverse directions. In the simulations in which the beam was initially misaligned, it was initially off axis by 0.8 mm in one of the transverse directions at the beginning of the first drift space. This resulted in an initial beam centroid oscillation of 2 mm in amplitude.

In real AG focusing systems, since the quadrupole field strength changes near the magnet ends, pseudo-octupole and pseudo-dodecapole fringe fields there will act nonlinearly on the beam [3]. These fringe fields were included in a subsequent simulation, assuming that the quadrupole field strength decreases smoothly near the magnet edge with a fall-off length of 4.5 cm. This length fills most of the drift space in the first few lattice periods, but avoids overlap of the fields from one quad to the next.

If the fringe fields are included in the simulation, the emittance growth is still small. Since the stepsize has to be much smaller in order to resolve the fringe fields, the simulation needed a much longer running time (67,500 user CPU seconds on a Cray J90).

The results of simulations using 80,000 particles on a 256×256 grid are shown in Table 1 and Figure 2. The

emittance behavior was alike in both transverse directions, due to coupling by nonlinearities. Maximum centroid offset was approximately 1.5 mm, which is consistent with the results of Sections 2 and 3 of this paper.

Table 1: PIC simulation results

Case	Particles lost	Emittance growth
Misaligned quads, no fringe fields (a)	3	4.1%
Misaligned beam, no fringe fields (b)	5	4.8%
Misaligned beam, with fringe fields (c)	3	5.2%
Misaligned quads, misaligned beam, no fringe fields (d)	42	5.9%

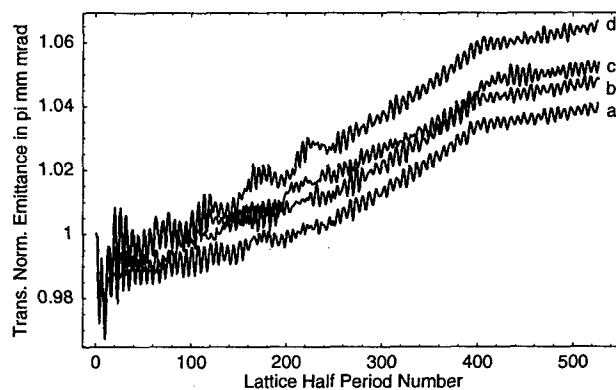


Figure 2: Increase in the normalized transverse emittance in case of misalignments in the IRE.

We conclude that moderate misalignments in the IRE do not lead to any significant emittance growth. These are encouraging results for beam stability in the IRE.

5 CONCLUSIONS

We have derived very accurate formulas for the statistical behavior of the beam centroid, given various practical scalings of lattice parameters, and shown that increasing λ/a^2 with z can produce damping of the centroid offset. These results can be used as design guidance, and to estimate necessary aperture, given fabrication and alignment tolerances. PIC simulations for a preliminary IRE design show very small emittance growth ($\sim 5\%$) due to beam and quadrupole misalignments for rms quad displacement of 0.0254 mm.

6 REFERENCES

- [1] L. Smith, "Effect of Random Quadrupole Misalignments in MBE", HI-FAN-251, July 1984, unpublished.
- [2] E.P. Lee, T.J. Fessenden, and L. J. Laslett, "Transportable Charge in a Periodic Alternating Gradient System," IEEE Trans Nucl. Science, NS-26, 2489 (1989).
- [3] E. P. Lee, "Field Calculation for a $\cos(2\theta)$ Quadrupole Magnet Without Iron", HI-FAR-464, July 1996, unpublished.

EFFECTS OF PHASE NOISE IN HEAVILY BEAM LOADED STORAGE RINGS *

J. M. Byrd†

Lawrence Berkeley National Laboratory, One Cyclotron Road, Berkeley, California 94720

Abstract

Synchrotron oscillations in a storage ring can be driven by noise in the storage ring RF system. For phase noise in the master oscillator, which falls off exponentially with frequency, we show that beam oscillations can become significant in cases of moderate to heavy beam loading. We derive the transfer function for generator phase to beam phase and calculate the beam motion using the measured phase noise in several master oscillator sources. This is compared with measurements of the beam noise made at the Advanced Light Source, a 1.5–1.9 GeV electron storage ring.

noise, and beam measurements. Conclusions are given in section 4.

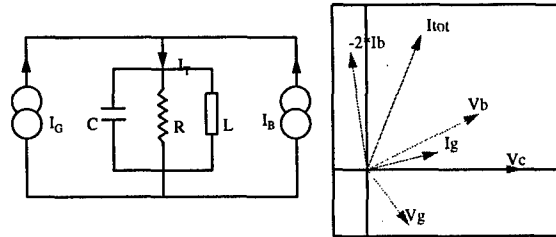


Figure 1: Phasor diagram for steady-state beam loading and the cavity equivalent circuit. The generator and beam are represented as equivalent current sources.

1 INTRODUCTION

In the summer of 1998, scientists using the infrared synchrotron light beam line at the Advanced Light Source (ALS) reported observations of beam motion in the frequency range of 4 to 10 kHz, variable with total beam current. Our investigations linked the beam motion to energy oscillations of the beam at a point of dispersion in the lattice. These oscillations were found to be driven by phase noise in the RF master oscillator (MO), which eventually was replaced with a lower noise MO. This paper describes the model used to calculate the effect of the phase noise on the beam and compares calculations with measurements of beam motion.

The dynamics of the interaction of a radiofrequency (RF) cavity with the beam, known as the Robinson effect[1], are well understood as are the regions of stability in the interaction. Although a storage ring RF system is always configured to Robinson stable, the effect of noise in the RF system can be significant[2], particularly in cases of moderate to heavy beam loading, where the Robinson frequency shift is large enough that the beam couples to low frequency noise sources. In this paper, we determine the beam motion driven by phase noise in master oscillator in the RF source in the limits of heavy beam loading. In particular, we are concerned with energy oscillations of the beam. Calculations of the effects are compared with beam measurements made on the Advanced Light Source, a 1.5–1.9 GeV electron storage optimized for producing synchrotron radiation.

Section 2 reviews the beam-cavity interaction using the Pedersen small-signal model the find the transfer functions between the generator phase and beam phase and energy. Section 3 presents measurements of master oscillator phase noise, calculations of the beam noise using the measured

2 PEDERSEN MODEL OF BEAM-CAVITY INTERACTIONS

The Pedersen model[3, 4] is a convenient model for finding the stability of the beam-cavity interaction as well as describing the transmission of small signal deviations of the RF variables, such as the generator voltage or phase to other parameters such as the beam amplitude or phase. An equivalent circuit for the beam-cavity interaction and a phasor diagram of the relative currents and voltages is shown in Fig. 1. Transmission of small signal variations of generator, cavity, and beam amplitude and phase can be represented in a scalar signal flow diagram as shown in Fig. 2. a_G , p_G , a_B and p_B , are small amplitude variations of the generator and beam amplitude and phase, respectively. The transfer functions from total current, I_T to cavity voltage V_C are given in general by

$$G_{pp}(s) = G_{aa}(s) = \frac{1}{2} \left(\frac{Z(s + j\omega_{rf})}{Z(j\omega_{rf})} + \frac{Z(s - j\omega_{rf})}{Z(-j\omega_{rf})} \right) \quad (1)$$

$$G_{pa}(s) = -G_{ap}(s) = \frac{j}{2} \left(\frac{Z(s + j\omega_{rf})}{Z(j\omega_{rf})} - \frac{Z(s - j\omega_{rf})}{Z(-j\omega_{rf})} \right) \quad (2)$$

where the frequency $s = j\omega$ and the subscripts refer to phase-to-phase or phase-to-amplitude modulations. $Z(s)$ is the cavity impedance given by

$$Z(s) = \frac{2\sigma R s}{s^2 + 2\sigma s + \omega_R^2} \quad (3)$$

R is the cavity shunt impedance, ω_R is the cavity resonant frequency, $\sigma = \omega_R/2Q$ is the damping rate of the cavity amplitude and Q is the quality factor. The superscript on

* This work was supported by the U.S. Dept. of Energy under Contract No. DE-AC03-76SF00098.

† jmbyrd@lbl.gov

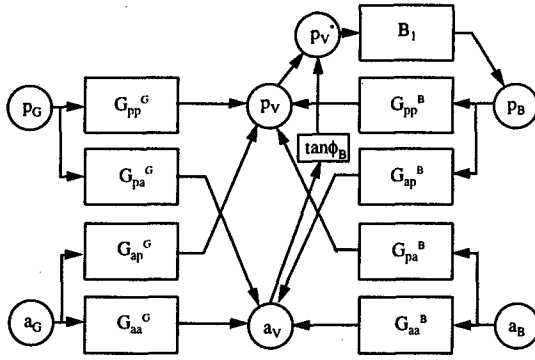


Figure 2: Scalar signal flow diagram using the Pedersen model of linear beam cavity interaction.

Parameter	Description	Value
E	Beam energy	1.9 GeV
f_{rf}	RF frequency	499.664 MHz
V_{rf}	total RF voltage	1.08 MV
h	Harmonic number	328
N_c	Number of cells	2
R	unloaded shunt imp.	5.3 M Ω
Q	unloaded quality factor	43000
β	coupling beta	2.4
ϕ_L	loading angle	-0.2 rad
U_0	rad. loss/turn	337 keV
f_s	synch. frequency	10.2 kHz
η	Momentum compaction	1.6×10^{-3}
τ_{rad}	rad. damping time	13.5 msec

Table 1: Nominal ALS RF parameters.

the current to voltage transfer functions represents modulations of either the generator or beam and are given by the projections of the generator or beam current onto the total current as shown in Fig. 1.

The transfer function from generator phase modulation to beam phase modulation is given by

$$\frac{p_B}{p_C} = \frac{(G_{pp}^G + \tan \phi_B G_{pa}^G) B_1}{1 - B_1 (G_{pp}^B + \tan \phi_B G_{pa}^B)} \quad (4)$$

where B_1 is the beam phase transfer function and is given by

$$B_1(s) = \frac{\omega_s^2}{s^2 + 2\sigma_B s + \omega_s^2} \quad (5)$$

where σ_B is the radiation damping rate. The beam energy transfer function is given by

$$\delta(s) = \frac{\omega_s s}{\omega_{rf} \alpha} B_1(s) \quad (6)$$

where α is the momentum compaction.

The transfer functions for the beam phase and energy, computed for the nominal ALS beam current range are shown in Fig. 3. For example, the phase transfer function shows a downward frequency shift as well as an initial damping. These are the Robinson frequency shift and

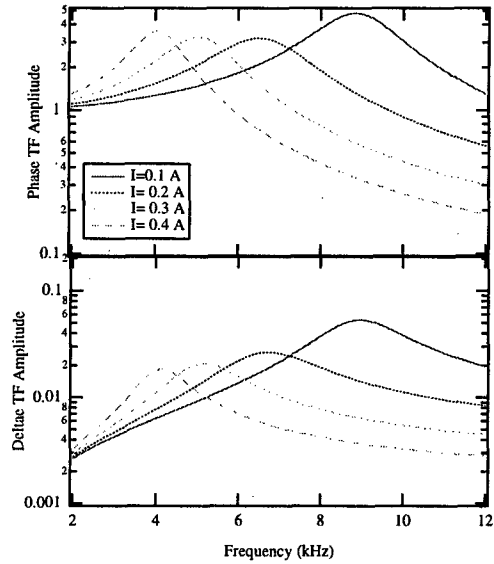


Figure 3: Computed beam phase and energy transfer functions using cavity parameters as a function of total current.

damping, respectively. To compute the total beam motion, one simply integrates the product of the noise spectrum and the transfer function. If the noise had a flat frequency distribution (i.e. white noise), the spectrum of the phase motion would be proportional to the transfer function. However, if the noise spectrum fell off exponentially at higher frequencies, as is the case with phase noise in the master oscillator, the beam would be more strongly excited at higher current with a larger Robinson frequency shift. The next section shows measurements made at the ALS confirming this.

3 MEASUREMENTS

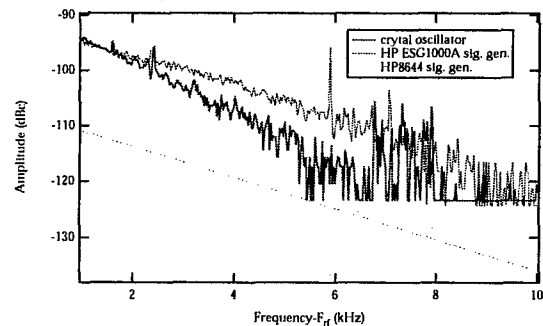


Figure 4: Phase noise from the three master oscillator sources express in dB from the carrier in a 1 Hz bandwidth. The values for the crystal oscillator and HP ESG1000A are measured and the noise for HP8644B is derived from values from the manufacturer.

The ALS presently has three MO sources: a crystal oscillator with a ± 5 kHz tuning range, an HP ESG1000A signal generator which has the feature that the frequency can be changed without interruption to the RF signal, and

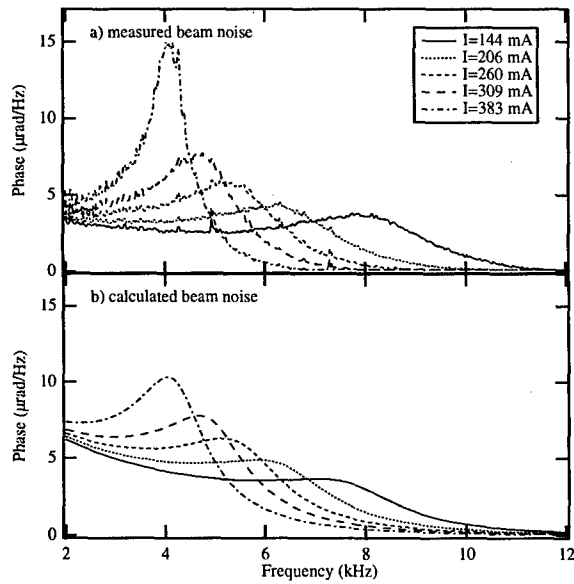


Figure 5: a) Measured beam phase noise vs. total beam current using the HP8644B signal generator as the MO. b) Calculated phase noise at the same beam currents.

an HP8644B low phase noise signal source, which was purchased when the source of the phase noise was identified. To determine the amount of beam motion driven by the phase noise in the MO, we measured the phase noise by simply observing the spectrum of phase modulation sidebands generated on a spectrum analyzer. This is shown in Fig. 4 in units of dBc per Hz from the 500 MHz carrier. Unfortunately, the noise for the HP8644B is too low to be measured in this way and thus only the catalog values are shown.

Beam phase measurements were made by recording the frequency spectrum of the sum of four beam position monitors (BPMs). The synchrotron oscillations phase modulate the beam signal, following a simple relation between the modulation sideband and the carrier. Measurements were made at a center frequency of 1499 MHz ($3 * f_{RF}$) to be more sensitive to phase oscillations. Shown in Fig. 5 are measurements of the spontaneous beam motion over the nominal range of beam current using the HP8644B as MO. The calculated motion shows fairly good agreement with the measured motion, particularly at lower beam current. The disagreement at high current may be due to the response of the coupled-bunch feedback system which has been neglected in calculations of the transfer function.

The effect of reducing the MO phase noise is shown in Fig. 6 which shows the spectrum of beam motion using the HP ESG1000A and HP8644B. The beam motion is reduced by the ratio of the noise in the two MOs.

4 CONCLUSIONS

We have identified phase noise in the 500 MHz master oscillator as a source of driven synchrotron oscillations in

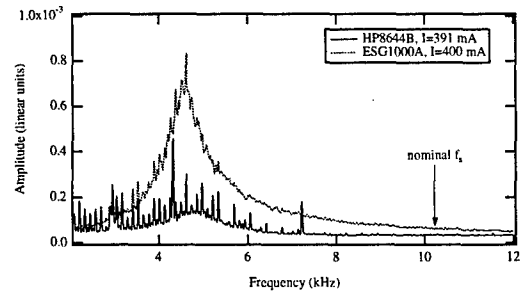


Figure 6: Measured beam noise using the two HP synthesizers described above. The reduction corresponds to the expected reduction in phase noise. Harmonics of the klystron power supply are visible with the reduced phase noise.

the ALS. The combination of the Robinson effect and the phase noise increases the coupling of the phase noise to the beam for increasing beam loading. Calculations of the beam motion from the measured MO phase noise show fairly good agreement with beam measurements. This effect can be serious for heavily loaded electron storage rings, necessitating consideration of the master oscillator design or possibly RF feedback to reduce the problem.

The author would like to thank Drs. F. Pedersen and M. Minty for many useful discussions.

5 REFERENCES

- [1] K. Robinson, CEA report CEAL-1010, 1964.
- [2] M. Sands, Orsay report 2-76 (1976).
- [3] F. Pedersen, IEEE Trans. Nucl. Sci., **NS-32**, 2138, (1985).
- [4] F. Pedersen, IEEE Trans. Nucl. Sci., **NS-22**, 1906, (1975).
- [5] M. Minty, R. H. Siemann, Nucl. Inst. Meth. A **376**, 301 (1996).

SINGLE BUNCH LONGITUDINAL INSTABILITIES IN PROTON STORAGE RINGS

J. Gao, LAL, B.P. 34, F-91898 Orsay cedex, France

Abstract

In this paper we try to explain the single bunch energy spread increasing in a proton storage ring. Different from an electron machine, the random motions of some particles of a bunch are caused by the nonlinear synchrotron oscillations perturbed by the short range longitudinal wakefield. An analytical single bunch threshold current formula has been established to indicate the beginning of the longitudinal random motions. By using kinetic descriptions one shows that the energy spread of the particles which execute random motions will increase, and the energy spectrum width of the random motions will be enlarged with increasing bunch current.

1 INTRODUCTION

The problem of the longitudinal instabilities in a proton storage ring is quite different from that in an electron one where the synchrotron radiation plays an important role [1]. It is observed experimentally that below an apparent threshold bunch current the bunch length increases with increasing current while the bunch energy spread remain unchanged, and the mechanism of this bunch lengthening is explained quite well by the potential well distortion theory. When the bunch current surpasses the threshold value the energy spread of the bunch increases also. In this paper, we try to explain the mechanism of the single bunch energy spread increasing in a proton storage ring and establish an analytical formula for the threshold current.

2 LONGITUDINAL MOTION PERTURBED BY SHORT RANGE WAKEFIELD

In a circular proton storage ring a non-synchronous particle will oscillate around the the synchronous one under the rf focusing in the longitudinal direction, and its phase ϕ with respect to the rf accelerating potential is determined by the following differential equation [2]:

$$\frac{d^2\phi}{dt^2} + \frac{\Omega_s^2}{\cos\phi_s} (\sin\phi - \sin\phi_s) = 0 \quad (1)$$

and

$$\Omega_s^2 = \frac{e\hat{V}h\eta\omega_s \cos\phi_s}{2\pi R_s p_s} \quad (2)$$

where \hat{V} is the peak accelerating voltage, h is the harmonic number, $\eta = 1/\gamma^2 - \alpha$, γ is the normalized particle energy, α is the momentum, R_s is the average radius of the ring, $\omega_s = c/R_s$, p_s and ϕ_s are the momentum and the phase of the synchronous particle. For the convenience in the later

mathematical treatment, we approximate eq. 1 by the following differential equation

$$\frac{d^2\Delta\phi}{dt^2} + \Omega_s^2 \sin\Delta\phi = 0 \quad (3)$$

where $\Delta\phi = \phi - \phi_s$. For the stationary bucket eq. 1 and eq. 3 are equivalent. It is obvious that $\Delta\phi$ oscillates as a pendulum. The deviation of a particle with respect to the synchronous one in terms of energy is expressed as follows:

$$\Delta E = -\frac{R_s p_s}{h\eta} \frac{d\Delta\phi}{dt} \quad (4)$$

By defining $P = \frac{d\Delta\phi}{dt}$ and $Q = \Delta\phi$, eq. 3 can be derived from an Hamiltonian $H(Q, P, t)$ expressed as

$$H(Q, P, t) = \frac{1}{2}P^2 - \Omega_s^2 \cos Q \quad (5)$$

where P and Q are canonical. Let us change P and Q to the action-angle variables, I and θ . By introducing two variables (\tilde{N} and ξ)

$$\tilde{N}^2 = \frac{1}{2} \left(1 + \frac{H}{\Omega_s^2} \right) \quad (6)$$

and

$$\tilde{N} \sin \xi = \sin \frac{Q}{2}, (\tilde{N} \leq 1) \quad (7)$$

one gets [3]

$$I(H) = \frac{8}{\pi} \Omega_s \left(E\left(\frac{\pi}{2}; \tilde{N}\right) - (1 - \tilde{N}^2) F\left(\frac{\pi}{2}; \tilde{N}\right) \right), (\tilde{N} \leq 1) \quad (8)$$

$$\theta = \frac{\partial S(Q, I)}{\partial I} \quad (9)$$

with

$$S(Q, I) = 4\Omega_s \left(E(\xi; \tilde{N}) - (1 - \tilde{N}^2) F(\xi; \tilde{N}) \right), (\tilde{N} \leq 1) \quad (10)$$

where $F(\xi; \tilde{N})$ and $E(\xi; \tilde{N})$ are the first and second kind elliptical integrals, respectively. The frequency of this nonlinear oscillator can be obtained easily as

$$\Omega(H) = \frac{dH(I)}{dI} = \frac{\pi\Omega_s}{2F(\frac{\pi}{2}; \tilde{N})}, (\tilde{N} \leq 1) \quad (11)$$

It is obvious that on the separatrix ($\tilde{N} = 1$) one has $H = H_c = \Omega_s^2$, and $\Omega(H_c) = 0$. Due to the interaction between the charged particles and the environment, after each turn a bunch will loss energy $W = e^2 N_p^2 \mathcal{K}_{//}^{tot}(\sigma_z)$, where N_p is the number of particles in the bunch, $\mathcal{K}_{//}^{tot}(\sigma_z)$ is the total longitudinal loss factor of one turn, and σ_z is the bunch

length (here we assume that particles are relativistic, otherwise, $\mathcal{K}_{//}^{tot}(\sigma_z)$ will depend on the particle velocity, and space charge forces should be taken into account). This energy loss will be compensated by the rf cavities. Since the short range longitudinal wakefield varies within the bunch and the synchrotron oscillation period is much longer than that of one revolution, the additional energy variation of a particle due to the short range wakefield after each turn can be reasonably expressed as

$$dE = U_w \cos \theta = e^2 N_p \mathcal{K}_{//}^{tot}(\sigma_z) \cos \theta \quad (12)$$

Obviously, averaging over one synchrotron period one has $\langle dE \rangle = 0$. Taking into account this additional energy variation after each revolution and the fact that this happens at instants t_k with constant interval T_0 (T_0 is the revolution period), a new Hamiltonian can be represented in the form:

$$\begin{aligned} H(I, \theta, t)^* &= H(I) + \frac{1}{2} \Delta P^2 T_0 \sum_{k=-\infty}^{\infty} \delta(t - kT_0) \\ &= H(I) + \frac{(dE)^2 h^2 \eta^2}{2R_s^2 p_s^2} T_0 \sum_{k=-\infty}^{\infty} \delta(t - kT_0) \\ &= H(I) + \frac{U_w^2 h^2 \eta^2 \cos^2 \theta}{2R_s^2 p_s^2} T_0 \sum_{k=-\infty}^{\infty} \delta(t - kT_0) \end{aligned} \quad (13)$$

where we have omitted the crossing term coming from eq. 4 and eq. 12 since both quantities are statistically independent. Eq. 13 can be simplified as

$$\begin{aligned} H(I, \theta, t)^* &= H(I) + \Delta H T_0 \sum_{k=-\infty}^{\infty} \delta(t - kT_0) \\ &= H(I) + \frac{U_w^2 h^2 \eta^2 \cos 2\theta}{4R_s^2 p_s^2} T_0 \sum_{k=-\infty}^{\infty} \delta(t - kT_0) \end{aligned} \quad (14)$$

where a constant term has been dropped, and

$$\Delta H = \Delta H_0 \cos 2\theta = \frac{U_w^2 h^2 \eta^2}{4R_s^2 p_s^2} \cos 2\theta \quad (15)$$

Consequently, one has

$$\frac{dI}{dt} = -\frac{\partial \Delta H}{\partial \theta} T_0 \sum_{k=-\infty}^{\infty} \delta(t - kT_0) \quad (16)$$

$$\frac{d\theta}{dt} = \Omega(I) + \frac{\partial \Delta H}{\partial I} T_0 \sum_{k=-\infty}^{\infty} \delta(t - kT_0) \quad (17)$$

Since the kicks on the pendulum $H(I)$ repeat after constant time interval T_0 , and between the kicks the motion is known, one can replace eqs. 16 and 17 by a so-called *universal mapping*:

$$I_{n+1} = I_n - T_0 \frac{\partial \Delta H}{\partial \theta} \quad (18)$$

$$\theta_{n+1} = \theta_n + \Omega_s T_0 + \Omega' I_{n+1} T_0 \quad (19)$$

where $\Omega' = d\Omega/dI$. We transform then the universal mapping into *standard mapping* which is expressed as

$$J_{n+1} = J_n + K_0 \sin \Psi \quad (20)$$

$$\Psi_{n+1} = \Psi_n + J_{n+1} \quad (21)$$

where $\Psi = 2\theta$, $J = 2T_0 \Omega' I$, $K_0 = 4\Omega' T_0^2 \Delta H_0$, and a constant term has been omitted from eq. 21. At this stage we can discuss the condition on which there starts to have chaotic motions. To this end we can use the Chirikov criterion [4] which shows that when

$$|K_0| \geq 1(0.97) \quad (22)$$

the Kolmogorov-Arnold-Moser (KAM) invariant tori will be broken and the particles which satisfy this condition will move in a *random* way. From eq. 22 one gets the threshold bunch current of the onset of the stochastic motion

$$I_{b,th} = \frac{R_s p_s}{e \sqrt{|\Omega'| T_0^2 h |\eta| \mathcal{K}_{//}^{tot}(\sigma_z)}} \quad (23)$$

Taking advantage of our simplifying the longitudinal motion of a particle to a pendulum, we can have the analytical expression for Ω' . When a particle moves near the separatrix, one gets

$$|\Omega'| = \frac{1}{\pi^4 |1 - H_b/H_c|} \left(\ln \frac{32}{|1 - H_b/H_c|} \right)^3 \quad (24)$$

where

$$\frac{H_b}{H_c} = \left(\frac{\delta E_b}{\delta E_{max}} \right)^2 = \frac{\pi h |\eta| E_s}{\beta^2 e \hat{V} G(\phi_s)} (\delta E_b)^2 \quad (25)$$

$$G(\phi_s) = 2 \cos \phi_s - (\pi - 2\phi_s) \sin \phi_s \quad (26)$$

H_b and δE_b are the maximum Hamiltonian value and the relative energy spread of the bunch, δE_{max} is the maximum acceptance of the rf bucket in terms of relative energy spread, β and E_s are the normalized velocity and the energy of the particle, respectively.

3 ENERGY SPREAD INCREASING

For those particles which have already executed chaotic motions a kinetic description of them will be appropriate. We will lose, certainly, some detailed information on the particle trajectories, this method, however, will help us to get useful physical results. When the random motion occurs eqs. 20 and 21 can be regarded as a Markov process, and in consequence, the possibility distribution function $F(t, I)$ is described by the Fokker-Planck equation:

$$\frac{\partial F}{\partial t} = -\frac{\partial (\mathcal{A}F)}{\partial I} + \frac{1}{2} \frac{\partial^2 (\mathcal{D}F)}{\partial I^2} \quad (27)$$

where \mathcal{A} and \mathcal{D} are defined as follows:

$$\mathcal{A} = \frac{1}{2\pi T} \int_0^{2\pi} \Delta I d\theta \quad (28)$$

$$\mathcal{D} = \frac{1}{2\pi T} \int_0^{2\pi} \Delta I^2 d\theta \quad (29)$$

where T is a small time interval. The legitimation of making average over the phase θ is based on the fact that the particle which moves randomly will mix its phase in the phase space. For our specific case described by eqs. 18 and 19 with $T = T_0$, one has

$$\mathcal{A} = 0 \quad (30)$$

$$\mathcal{D} = \frac{e^2 N_p^2 \mathcal{K}_{//}^{tot}(\sigma_z)^2 h^2 \eta^2}{2R_s^2 p_s^2} T_0 \quad (31)$$

Putting $\mathcal{A} = 0$ and \mathcal{D} into eq. 27, one gets

$$\frac{\partial F}{\partial t} = \frac{1}{2} \mathcal{D} \frac{\partial^2 F}{\partial I^2} \quad (32)$$

From eq. 32, one finds that stochastic heating occurs in the following way:

$$\langle I^2 \rangle = I_0^2 + \mathcal{D}t \quad (33)$$

where $\langle I^2 \rangle = \int_0^\infty I^2 F dI$. Similarly, one finds

$$\langle \Delta E^2 \rangle = \Delta E_0^2 + \mathcal{D}_e t \quad (34)$$

$$\mathcal{D}_e = \frac{U_w^2}{2T_0} \quad (35)$$

Obviously, the amplitude of the energy deviations of those particles executing random motions will increase with time. From eq. 35 it is evident that the resistive part of the impedance of the machine determines the diffusion coefficient instead of the reactive part. The relevant effect of the interaction between the charged particles with the reactive part impedance is the potential well distortion which results in the reduction of the area of the rf bucket.

The distinction between an electron and a proton storage rings is that there exists always a stable (cold) core in the bunch of proton particles around the synchrotron particle where no energy spread increasing occurs.

4 THE POWER SPECTRUM OF THE RANDOM MOTIONS

As shown in section 2, when the bunch current surpasses the threshold current $I_{b,th}$, some particles in the bunch will execute random motions, and the longitudinal positions of these particles will be random variables. When $I_b \gg I_{b,th}$, the autocorrelator of these random motion has the form [3]

$$\mathcal{R}(t) = \mathcal{R}_0 \exp\left(-\frac{t}{\tau_c}\right) \quad (36)$$

$$\begin{aligned} \tau_c &= \frac{2T_0}{\ln K_0} \\ &= \frac{T_0}{\ln\left(\frac{\sqrt{\Omega^2 T_0 e^2 N_p \mathcal{K}_{//}^{tot}(\sigma_z) h \eta}}{R_s p_s}\right)} \end{aligned} \quad (37)$$

By virtue of Wiener-Khintchine theorem, we know that the spectral power density of the random variable is the Fourier transform of its autocorrelation function, and we have then

$$\begin{aligned} S(\omega) &= \frac{1}{2\pi} \int_{-\infty}^{\infty} \exp(i\omega t) \mathcal{R}(t) dt \\ &= \frac{1}{\pi} \mathcal{R}_0 \frac{\tau_c}{1 + \omega^2 \tau_c^2} \end{aligned} \quad (38)$$

The power spectrum $S(\omega)$ falls off rapidly when

$$\omega > \omega_c = \frac{1}{\tau_c} \quad (39)$$

The variation of ω_c with respect to the bunch current can be measured experimentally, and apparently, one has $\omega_c \propto \ln(I_b)$.

5 DISCUSSION ON THE BUNCH LENGTHENING

In a proton machine, a bunch suffers from potential well distortion induced bunch lengthening just like what happens in an electron storage ring. When $I_b \geq I_{b,th}$ some particles in the bunch will execute random motions and the synchrotron oscillation amplitudes of these particles will increase (but not those of the particles in the stable core). In a global point of view, the bunch length increases much more quickly with respect to the increasing bunch current compared with when $I_b < I_{b,th}$. Since not all particles participate the random motions, it is much more difficult to get some simple formulae or equations to describe the global bunch lengthening and the energy spread increasing for the whole bunch current range as what has been done in ref. 1 for the electron storage rings.

6 CONCLUSION

In a proton storage ring, it is shown that the nonlinear longitudinal motion perturbed by the short range longitudinal wakefield can change the regular synchrotron motions of some particles in a bunch into random ones. An analytical formula of the threshold current for the onset of the random motion is established. The particles which execute random motions will be heated and their energy spread will increase. The width of the energy spectrum of the random motions is proportional to $\ln I_b$.

7 REFERENCES

- [1] J. Gao, "Bunch lengthening and energy spread increasing in electron storage rings", *Nucl. Instr. and Methods*, A418 (1998), p. 332.
- [2] J. Le Duff, CERN 85-19, p. 125.
- [3] R.Z. Sagdeev, D.A. Usikov, and G.M. Zaslavsky, "Nonlinear physics from the pendulum to turbulences and chaos", Contemporary concepts in physics, harwood academic publishers, 1988.
- [4] B. Chirikov, Phys. Reports, Vol. 52, No. 5 (1979), p. 263-379.

ANALYTICAL INVESTIGATION ON THE HALO FORMATION IN SPACE CHARGE DOMINATED BEAMS

J. Gao, LAL, B.P. 34, F-91898 Orsay cedex, France

Abstract

It is assumed that Fermion particles, such as electron and proton, in a matched beam follow Fermi-Dirac statistics in the equilibrium state. Parametric resonances, chaotic motion, and halo formation in transverse direction of motion are investigated analytically. The analytical expressions for the parametric resonances and the maximum transverse position deviation, above which chaotic motion starts to occur due to transverse beam envelope oscillation, are derived. Analytical formula for the current loss rate is established.

1 INTRODUCTION

Recently, high power ion beams are more and more demanded in the related possible applications such as thermonuclear energy production, transmutation of radioactive wastes, the production of tritium and the special materials, and the conversion of plutonium. One of the major challenges on the linac is to keep the machine maintenance hand-accessible which can be roughly quantified by a rule-of-thumb of the average particle loss rate $< 1 \text{ nA/GeV/m}$ [1]. The lost particles are mainly from the halo which surrounds the beam core. Among others, the particle-core model proposed by O'Connell, Wangler, Mills, and Crandall [2] is the simplest and the most explored, which illustrates many important features of the dynamics of the particles which constitute the halo with the assumption that the core has a uniform density and zero emittance. A good summary of what we know about the halo formation in linacs is given in ref. 3. The problem with the existing models, however, is that it is not obvious to predict the particle loss rate. In this paper we try to explain analytically the halo formation processes in detail, and try to estimate the halo current loss rate analytically.

2 PARTICLE DENSITY DISTRIBUTION

Kapchinskij and Vladimirskij derived the envelope and single particle transverse motion differential equations for a continuous beam as follows (we limit ourselves to round and continuous beams) [4]:

- Envelope equation:

$$\frac{d^2 R}{dz^2} + \omega_0^2 R - \frac{K}{R} - \frac{\epsilon^2}{R^3} = 0 \quad (1)$$

where R is the beam envelope in a continuous solenoid focusing channel, $K = 2(I_b/I_0)/(\beta\gamma)^3$, $\pi\epsilon$ is the beam unnormalized transverse emittance, γ and β are the normalized particle's energy and velocity (v/c), respectively, I_b is the beam current, and $I_0 = 4\pi\epsilon_0\pi m_0 c^3/q$ with m_0/q being the mass charge ratio of the particle ($I_0 = 3.1 \times 10^7 \text{ A}$ for

proton).

- Single particle equations:

$$\frac{d^2 x}{dz^2} + \left(\omega_0^2 - \frac{K}{R^2} \right) x = 0 \quad (2)$$

when $x < R$, and

$$\frac{d^2 x}{dz^2} + \omega_0^2 x - \frac{K}{x} = 0 \quad (3)$$

when $x > R$. Since the KV envelope equation is derived from a specific microcanonical distribution, the validity for the other kinds of distribution is not automatic. According to Lapostolle [5] and Sacherer [6], one can use the same form of envelope equation for any possible particle distributions provided that the envelope and the emittance are defined as

$$R^2 = 4\overline{x^2} \quad (4)$$

$$\epsilon = 4\sqrt{\overline{x^2 x'^2} - \overline{x x'}^2} \quad (5)$$

From now on the form of the envelope equation expressed in eq. 1 is regarded as particle density distribution independent. Now we distinguish two cases: the matched and mismatched beams. Considering now a continuous focusing channel, for the first case one means:

$$\omega_0^2 R - \frac{K}{R} - \frac{\epsilon^2}{R^3} = 0 \quad (6)$$

and

$$\frac{d^2 x}{dz^2} + \omega_p^2 x = 0 \quad (7)$$

for $x < R$, where $\omega_p^2 = \epsilon^2/R^4$. For the matched case, apparently, when $\epsilon = 0$ the motions of particles within the beam envelope can be equivalent to those of particles in collision free gas of zero temperature (in this paper we consider only Fermion gas such as electron and proton which have half-integral spins). For the zero emittance matched beam envelope radius, R_0 , one finds $R_0 = \sqrt{K}/\omega_0$. When $\epsilon \neq 0$ the stationary envelope radius will become $R = R_0 + \delta R$. Putting this expression into eq. 1, for $\delta R \ll R$, one finds

$$\delta R = \frac{\epsilon^2}{2\omega_0^2 R_0^3} \quad (8)$$

From eq. 1 one knows that if R deviate a little bit from R_0 at zero emittance limit the envelope oscillates approximately like an harmonic oscillator:

$$\frac{d^2 \delta R}{dz^2} + \omega_R^2 \delta R = 0 \quad (9)$$

where $\omega_R = \sqrt{2}\omega_0$ which is called the envelope oscillation frequency. Now we are at the stage to estimate the equilibrium particle density distribution function, $n(x)$. As noted above we regard the particles in the matched beam as the particles in a Fermion gas, and in consequence, the density distribution follows Fermi-Dirac statistics:

$$n(E) = \frac{n_{E=0}}{1 + \exp((E - \mu)/kT)} \quad (10)$$

where E is the particle's transverse oscillation energy, μ is the chemical energy of the gas, k is the Boltzmann constant, and T is the temperature of the gas. The transverse oscillation energy of a particle is proportional to the square of its plasma oscillation amplitude and kT is proportional to the square of Debye length, λ_D . One rewrites eq. 10 as

$$n(x) = \frac{n_{x=0}}{1 + \exp((x^2 - R_0^2)/\lambda_D^2)} \quad (11)$$

where λ_D is estimated as follows:

$$\lambda_D^2 = \frac{v_{thermal}^2}{\omega_p^2} = \frac{\delta R^2 \omega_R^2}{\omega_p^2} = \frac{1}{2} \frac{\epsilon^2}{\omega_0^2 R_0^2} \quad (12)$$

or

$$\frac{\lambda_D}{R_0} = \frac{\omega_p}{\omega_R} \quad (13)$$

Now we look at a more general situation when the beam is not matched with $R = R_0 + \Delta R$ and $\Delta R \ll R_0$. In analogy with δR we know that ΔR oscillates with envelope frequency, ω_R also. In the equilibrium state (there is no diffusion process exists) particles are assumed to follow Fermi-Dirac statistics as in the case of matched beam. The general expression for λ_D is obtained as:

$$\lambda_D^2 = \frac{v_{thermal}^2}{\omega_p^2} = \frac{(\delta R^2 + \Delta R^2) \omega_R^2}{\omega_{\Delta R}^2 + \omega_p^2} \quad (14)$$

where $\omega_{\Delta R}^2 = 2\omega_0^2 \Delta R / R_0$, ΔR and δR are statistically independent. When $\Delta R = 0$ eq. 14 reduces to eq. 12. In the case where the contribution from the definite emittance can be neglected eq. 14 can be simplified as:

$$\left(\frac{\lambda_D}{R_0}\right)^2 \approx \frac{\Delta R}{R_0} \quad (15)$$

To study single particle dynamics we assume that for $x < R_0 - \lambda_D$ and $x > R_0 + \lambda_D$ the particle transverse motions are described by eqs. 2 and 3, respectively.

3 INSTABILITY DUE TO PARAMETRIC RESONANCE: ARNOL'D TONGUES

In this section a mismatched beam in a continuous focusing channel is considered since for a matched periodic focusing channel the procedure to treat the problem is the same. From eq. 2 it is found that if the beam envelope is modulated from the matched radius, R_0 , by $\Delta R_c(z)$, the differential equation of motion reads:

$$\frac{d^2 x}{dz^2} + \left(\omega_p^2 + \frac{2K}{R_0^3} \Delta R_c(z)\right) x = 0 \quad (16)$$

where $\Delta R_c(z) = \Delta R_c(z + L_c)$, and L_c is the envelope modulation period. If $\Delta R_c(z)$ is expressed as a sinusoidal function of longitudinal position, z , the stability region of x will be determined by Mathieu equation. Not sticking to the mathematic rigor we assume that $\Delta R_c(z)$ is approximated by: $\Delta R_c(z) = \Delta R_{c0}$ when $0 \leq z < L_c/2$ and $\Delta R_c(z) = -\Delta R_{c0}$ when $L_c/2 \leq z < L_c$. Defining

$$\omega_p' = \frac{L_c}{2\pi} \omega_p \quad (17)$$

and

$$\varpi = \left(\frac{L_c}{2\pi}\right)^2 \frac{2K\Delta R_{c0}}{R_0^3} \quad (18)$$

one gets the stable and the parametric resonance regions described by the functions [7]:

$$\omega_p' \approx n \pm \frac{\varpi^2}{\sqrt{8}n^3}, n = 1, 2, 3, \dots \quad (19)$$

and

$$\omega_p' \approx k/2 \pm \frac{2\sqrt{2}\varpi}{\pi k^2}, k = 1, 3, 5, \dots \quad (20)$$

For $k = 1$ we obtain the result obtained by Gluckstern [8] that when the particle frequency is about one half the core frequency the parametric resonance occurs. In this paper we generalize this particular conclusion to a more general one: *when the particle frequency is about an integer times one half the core frequency the parametric resonance occurs.*

4 THE ONSET OF HALO DUE TO NONLINEAR RESONANCES AND STOCHASTIC MOTIONS

As we have assumed in section 2 the trajectory of a particle located in the nonuniform density region is determined by eq. 3. If we define $x = R_0 + \Delta x$, where $\Delta x \ll R_0$, one finds Δx satisfies the following nonlinear differential equation:

$$\begin{aligned} & \frac{d^2 \Delta x}{dz^2} + \omega_0^2 \Delta x + \frac{K}{R_0} \Delta x \\ & - \frac{K}{R_0} \left(\left(\frac{\Delta x}{R_0}\right)^2 - \left(\frac{\Delta x}{R_0}\right)^3 + \left(\frac{\Delta x}{R_0}\right)^4 - \dots \right) = 0 \end{aligned} \quad (21)$$

It has been shown numerically that the solution of Δx is stable and periodical [2]. Now let's consider the case when there is an envelope modulation, ΔR , around R_0 due to either periodic focusing or mismatching. The differential equation governing the particle motion near R_0 turns out to be:

$$\begin{aligned} & \frac{d^2 \Delta x}{dz^2} + \omega_0^2 \Delta x + \frac{K}{R_0} \Delta x - \frac{K}{R_0} \left(\left(\frac{\Delta x}{R_0}\right)^2 - \left(\frac{\Delta x}{R_0}\right)^3 + \dots \right) \\ & + \frac{K\Delta R}{R_0^2} \left(\frac{\Delta x}{R_0}\right)^2 - \dots = 0 \end{aligned} \quad (22)$$

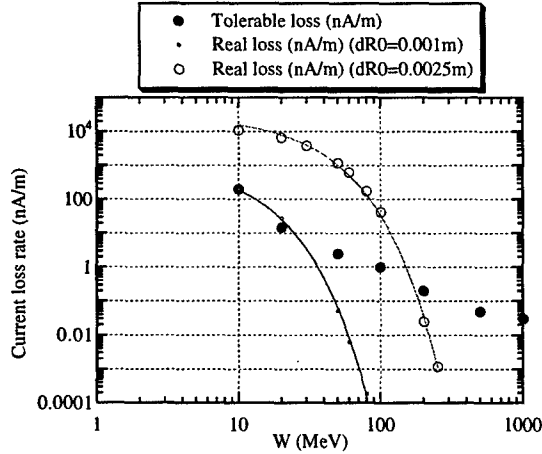


Figure 1: The current loss rates vs the energy of a proton beam of $I_b = 1\text{A}$, $R_0 = 0.005\text{m}$, $R_m = 10R_0$, $f = 0.1$, $L = 5\text{m}$, and $\beta(z) = 8\text{m}$.

For the matched case ΔR_{match} has the same period as that of the periodic focusing lattice, L . In this section we discuss only the matched periodic focusing channel, and denote $\Delta R_{match} = \Delta R_0$. To simplify the mathematics treatments we assume that $\Delta R_0(z)$ is represented by a periodic delta function of period L and amplitude ΔR_0 . It is shown (see ref. 10) that under the periodic envelope oscillation perturbation if the amplitude of a particle's deviation Δx is larger than some limit, say Δx_{max} , the motion of this particle will become chaotic, and Δx_{max} is analytically expressed as follows [10]:

$$\Delta x_{max} = \left(\frac{16R_0^8}{9L^2 K^2 \Delta R_0 \beta(z)^2} \right)^{1/3} \quad (23)$$

where $\beta(z)$ is the beta function of the focusing channel.

5 ESTIMATION OF BEAM CURRENT LOSS RATE

According to the discussion given above one knows that the particles located near R_0 ($x = R_0 + \Delta x$) with $\Delta x \geq \Delta x_{max}$ will diffuse outwards into the focusing-dominated region and contribute to the halo.

Now we discuss the average beam loss rate on the mechanical boundary of the beam transport system, and we may make a rough estimation in the following way. It is known that the particles located in $\Delta x \geq \Delta x_{max}$ will diffuse outwards, and the current, I_d , which participates this diffusion process can be calculated as:

$$I_d = \frac{I_b}{R_0^2} \int_{x=R_0+\Delta x_{max}}^{x=\infty} \frac{1}{1 + \exp\left(\frac{x^2 - R_0^2}{\lambda_D^2}\right)} dx^2 \quad (24)$$

One can imagine that a uniform halo disk is formed around the beam core started from $x = R_0 + \Delta x_{max}$. Due to the beam envelope oscillation the dimension of the disk, which extends to the radius, R_m , of the mechanical aperture of the

transport system, oscillates with $x = R_m \pm \Delta R_0$. Obviously, the particles located in $R_m \leq x \leq R_m + \Delta R_0$ are lost, and this loss will be filled through the diffusion process. If the particle re-distribution distance, or the so-called relaxation distance $\lambda_p/4$, ($\lambda_p = 2\pi R_0/\sqrt{3K}$) [3], is shorter than the envelope oscillation period, the beam current loss rate, \mathcal{R} (A/m), can be estimated as the $\mathcal{R} = I_d(\Delta R_0/R_m)^2/L$, where $R_m \gg R_0$. If, however, the relaxation distance is longer than L , one has $\mathcal{R} = 4I_d(\Delta R_0/R_m)^2/\lambda_p$. To summarize, we give a simplified beam current loss rate formula as follows:

$$\mathcal{R} \approx I_b f \frac{\Delta R_0^3}{\mathcal{L} R_0 R_m^2} \ln \left(\frac{1 + \exp(2\Delta x_{max}/\Delta R_0)}{\exp(2\Delta x_{max}/\Delta R_0)} \right) \quad (25)$$

where $\mathcal{L} = L$ when $L \geq \lambda_p/4$, $\mathcal{L} = \lambda_p$ when $L \leq \lambda_p/4$, and f is the ratio of the average beam current with respect to the peak bunch current. In Fig. 1 we give an example to show how one can use eqs. 23 and 25 to estimate the current loss and how this current loss varies with beam parameters, where we choose $R_0 = 0.005\text{m}$, $I_b = 1\text{A}$, $f = 0.1$, $L = 5\text{m}$, $\beta(z) = 8\text{m}$, $\Delta R_0 = 0.0025\text{m}$ and $\Delta R_0 = 0.001\text{m}$, respectively. In the figure the tolerable current loss rate [9] is presented by the dark dots, and it is obvious that in this case ΔR_0 should be less than 0.001m .

6 CONCLUSION

It is assumed that at the equilibrium state the transverse beam density distribution of a matched beam follows Fermi-Dirac statistics (for Fermion particles). The conditions for the particles' transverse motions to have parametric resonances and nonlinear force induced stochastic motions are derived analytically. Finally, the analytical loss rate formula is established.

7 ACKNOWLEDGEMENTS

The author thanks J. Le Duff and N. Pichoff (Saclay) for the clarifying discussions and their critical comments.

8 REFERENCES

- [1] R.A. Jameson, PAC93 (1993), p. 3926.
- [2] J.S. O'Connell, et al., PAC93 (1993), p. 3657.
- [3] T. Wangler, "Principles of rf linear accelerators", John Wiley and Sons, Inc. (1998).
- [4] I. Kapchinskij and V. Vladimirkij, Proceedings of the II Int. Conf. on High Energy Accel. CERN 1959, p. 274.
- [5] P.M. Lapostolle, Proceedings of the VII international conference on high energy accelerators, August (1969), p. 205.
- [6] F.J. Sacherer, IEEE Trans. Nucl. Sci. **18** (1971) 1105.
- [7] J.L. McCauley, Physica Scripta, **T20** (1988).
- [8] R. Gluckstern, Phys. Rev. Letters, **73** (1994) 1247.
- [9] A.P. Fedotov and B.P. Murin, Proceedings of the 1976 Linear Accelerator Conference, p. 377.
- [10] J. Gao, LAL/RT 98-04, 1998.

ANALYTICAL INVESTIGATION ON THE DYNAMIC APERTURES OF CIRCULAR ACCELERATORS

J. Gao, LAL, B.P. 34, F-91898 Orsay cedex, France

Abstract

In this paper by considering delta function sextupole and octupole perturbations and using difference action-angle variable equations, analytical formulae for the dynamic aperture of circular accelerators are derived based on the Chirikov criterion of the onset of stochastic motions.

1 INTRODUCTION

One of the preoccupations of the circular accelerator designers is to estimate the influence of nonlinear forces on the single particle's motion. Even though the nonlinear forces compared with the linear ones are usually very small, what is observed in reality, however, is that when the amplitudes of the transverse oscillation of a particle are large enough, the transverse motions might become unstable and the particle itself will finally be lost on the vacuum chamber. In the following sections we will show how the nonlinear forces limit the dynamic apertures and what is the relation between them.

2 DYNAMIC APERTURES DUE TO NONLINEAR RESONANCES AND STOCHASTIC MOTIONS

In this section a necessary distinction will be made between two essentially different cases: a proton machine and an electron one. The reason is simple. In the first case there is no dissipative forces (which is generally true) and the particle's motion can be described in the frame of Hamiltonian system. In the second case, however, one has to take into account of the synchrotron radiation damping effect.

2.1 Proton storage ring

To start with we consider the linear horizontal motion of a particle assuming that the magnetic field is only transverse and there are no screw fields. The Hamiltonian can be expressed as

$$H = \frac{p^2}{2} + \frac{K(s)}{2} x^2 \quad (1)$$

where x denotes normal plane coordinate, $p = dx/ds$, and $K(s)$ is a periodic function satisfying the relation

$$K(s) = K(s + L) \quad (2)$$

where L is the circumference of the ring. The solution of the deviation, x , is found to be

$$x = \sqrt{\epsilon_x \beta_x(s)} \cos(\phi(s) + \phi_0) \quad (3)$$

where

$$\phi(s) = \int_0^s \frac{ds}{\beta_x(s)} \quad (4)$$

As an essential step towards further discussion on the motions under nonlinear perturbation forces, we introduce action-angle variables and the Hamiltonian expressed in these new variables [1]:

$$\Psi = \int_0^s \frac{ds'}{\beta_x(s')} + \phi_0 \quad (5)$$

$$J = \frac{\epsilon_x}{2} = \frac{1}{2\beta_x(s)} \left(x^2 + \left(\beta_x(s)x' - \frac{\beta'_x x}{2} \right)^2 \right) \quad (6)$$

$$H(J, \Psi) = \frac{J}{\beta_x(s)} \quad (7)$$

Since the $H(J, \Psi) = J/\beta_x(s)$ is still a function of the independent variable, s , we will make another canonical transformation to freeze the new Hamiltonian:

$$\Psi_1 = \Psi + \frac{2\pi\nu}{L} - \int_0^s \frac{ds'}{\beta_x(s')} \quad (8)$$

$$J_1 = J \quad (9)$$

$$H_1 = \frac{2\pi\nu}{L} J_1 \quad (10)$$

Before going on further, let's remember the relation between the last action-angle variables and the particle deviation x :

$$x = \sqrt{2J_1\beta_x(s)} \cos \left(\Psi_1 - \frac{2\pi\nu}{L}s + \int_0^s \frac{ds'}{\beta_x(s')} \right) \quad (11)$$

Having well prepared we start our journey to find out the limitations of the nonlinear forces on the stability of the particle's motion. To facilitate the analytical treatment of this complicated problem we consider at this stage only sextupoles and octupoles (no screw terms) and assume that the contributions from the sextupoles and octupoles in a ring can be made equivalent to a point sextupole and a point octupole. The perturbed Hamiltonian can be thus expressed:

$$\begin{aligned} \mathcal{H} = & \frac{p^2}{2} + \frac{K(s)}{2} x^2 + \frac{1}{3!B\rho} \frac{\partial^2 B_z}{\partial x^2} x^3 L \sum_{k=-\infty}^{\infty} \delta(s - kL) \\ & + \frac{1}{4!B\rho} \frac{\partial^3 B_z}{\partial x^3} x^4 L \sum_{k=-\infty}^{\infty} \delta(s - kL) \end{aligned} \quad (12)$$

where ρ is the radius of curvature. Representing eq. 12 by action-angle variables (J_1 and Ψ_1), and using

$$B_z = B_0(1 + x b_1 + x^2 b_2 + x^3 b_3) \quad (13)$$

one has

$$H = \frac{2\pi\nu}{L} J_1 + \frac{(2J_1\beta_x(s_1))^{3/2}}{3\rho} b_2 L \cos^3 \Psi_1 \sum_{k=-\infty}^{\infty} \delta(s-kL) \\ + \frac{(J_1\beta_x(s_2))^2}{\rho} b_3 L \cos^4 \Psi_1 \sum_{k=-\infty}^{\infty} \delta(s-kL) \quad (14)$$

where s_1 and s_2 are just used to differentiate the locations of the sextupole and the octupole perturbations. By virtue of Hamiltonian one gets the differential equations for Ψ_1 and J_1

$$\frac{dJ_1}{ds} = -\frac{\partial \mathcal{H}}{\partial \Psi_1} \quad (15)$$

$$\frac{d\Psi_1}{ds} = \frac{\partial \mathcal{H}}{\partial J_1} \quad (16)$$

$$\frac{dJ_1}{ds} = -\frac{(2J_1\beta_x(s_1))^{3/2}}{3\rho} b_2 L \frac{d \cos^3 \Psi_1}{d\Psi_1} \sum_{k=-\infty}^{\infty} \delta(s-kL) \\ - \frac{(J_1\beta_x(s_2))^2}{\rho} b_3 L \frac{d \cos^4 \Psi_1}{d\Psi_1} \sum_{k=-\infty}^{\infty} \delta(s-kL) \quad (17)$$

$$\frac{d\Psi_1}{ds} = \frac{2\pi\nu}{L} + \frac{2\beta_x^2(s_2)}{\rho} J_1 b_3 L \cos^4 \Psi_1 \sum_{k=-\infty}^{\infty} \delta(s-kL) \\ + \frac{\sqrt{2}J_1^{1/2}\beta_x(s_1)^{3/2}}{\rho} b_2 L \cos^3 \Psi_1 \sum_{k=-\infty}^{\infty} \delta(s-kL) \quad (18)$$

Now it is the moment to change this differential equations to the difference equations which is *suitable* to analyse the possibilities of the onset of stochasticity [2][3]. Since the perturbations have a natural periodicity of L we will sample the dynamic quantities at a sequence of s_i with constant interval L assuming that the characteristic time between two consecutive adiabatic invariance breakdown intervals is shorter than L/c . The differential equations in eqs. 17 and 18 are reduced to

$$\bar{J}_1 = \bar{J}_1(\Psi_1, J_1) \quad (19)$$

$$\bar{\Psi}_1 = \bar{\Psi}_1(\Psi_1, J_1) \quad (20)$$

where the bar stands for the next sampled value after the corresponding unbarred previous value, or explicitly,

$$\bar{J}_1 = J_1 - \frac{(2J_1\beta_x(s_1))^{3/2}}{3\rho} b_2 L \frac{d \cos^3 \Psi_1}{d\Psi_1} \\ - \frac{(J_1\beta_x(s_2))^2}{\rho} b_3 L \frac{d \cos^4 \Psi_1}{d\Psi_1} \quad (21)$$

$$\bar{\Psi}_1 = \Psi_1 + 2\pi\nu + \frac{\sqrt{2}\beta_x(s_1)^{3/2}J_1^{1/2}}{\rho} b_2 L \cos^3 \Psi_1 \\ + \frac{2\beta_x(s_2)^2}{\rho} J_1 b_3 L \cos^4 \Psi_1 \quad (22)$$

Eqs. 21 and 22 are the basic difference equations to study the nonlinear resonance and the onset of stochasticities considering sextupole and octupole perturbations. By using trigonometric relation

$$\cos^m \theta \cos n\theta = 2^{-m} \sum_{r=0}^m \frac{m!}{(m-r)!r!} \cos(n-m+2r)\theta \quad (23)$$

one has

$$\cos^3 \theta = \frac{2}{2^3} (\cos 3\theta + 3 \cos \theta) \quad (24)$$

$$\cos^4 \theta = \frac{1}{2^4} (\cos 4\theta + 4 \cos 2\theta + \frac{4!}{((4/2)!)^2}) \quad (25)$$

Apparently, the right hand sides of eqs. 21 and 22 contain sinusoidal functions of phases, Ψ_1 , $2\Psi_1$, $3\Psi_1$, and $4\Psi_1$. If the tune ν is far from the resonance lines $\nu = m/n$, where m and n are integers ($n=1, 2, 3$, and 4 for this specific problem), the invariant tori of the unperturbed motion are preserved under the presence of the small perturbations by virtue of the Kolmogorov-Arnold-Moser (KAM) theorem. If, however, ν is close to the above mentioned resonance line, the situation is getting complicated and under some conditions the KAM invariant tori can be broken. Taking the third order resonance, $m/3$, for example, we keep only the sinusoidal function with phase $3\Psi_1$ in eq. 21 and the dominant phase independent nonlinear term in eq. 22, and as the result, we have eqs. 21 and 22 reduced to

$$\bar{J}_1 = J_1 + A \sin 3\Psi_1 \quad (26)$$

$$\bar{\Psi}_1 = \Psi_1 + B \bar{J}_1 \quad (27)$$

with

$$A = \frac{(J_1\beta_x(s_1))^{3/2}}{\sqrt{2}\rho} b_2 L \quad (28)$$

$$B = \frac{3\beta_x(s_2)^2}{4\rho} b_3 L \quad (29)$$

where we have dropped the constant phase in eq. 22. It is helpful to transform eqs. 28 and 29 into the form so-called *standard mapping* [3] expressed as

$$\bar{I} = I + K_0 \sin \theta \quad (30)$$

$$\bar{\theta} = \theta + \bar{I} \quad (31)$$

with $\theta = 3\Psi$, $I = 3BJ_1$ and $K_0 = 3AB$. By virtue of the Chirikov criterion [3] it is known that when $|K_0| \geq 0.97164$ [4] stochastic motions will appear and the diffusion will occur. Therefore,

$$|K_0| \leq 1 \quad (32)$$

can be taken as a natural criterion for the determination of the dynamic aperture of the machine. Putting eqs. 28 and 29 into eq. 32, one gets

$$|K_0| = \frac{9}{4\sqrt{2}} |b_2 b_3| \beta_x^2(s_2) \beta_x^{3/2}(s_1) J_1^{3/2} \frac{L^2}{\rho^2} \leq 1 \quad (33)$$

and consequently, one finds maximum J_1 corresponding to $m/3$ resonance

$$J_1 \leq J_{max,m/3} = \left(\frac{4\sqrt{2}\rho^2}{9|b_2b_3|\beta_x^2(s_2)\beta_x(s_1)^{3/2}L^2} \right)^{2/3} \quad (34)$$

The dynamic aperture of the machine is therefore

$$A_{dyn,m/3} = \sqrt{2J_{max,m/3}\beta_x(s)} = \left(\frac{16\rho^2\beta_x(s)^{3/2}}{9|b_2b_3|\beta_x^2(s_2)\beta_x(s_1)^{3/2}L^2} \right)^{1/3} \quad (35)$$

Eq. 35 gives the dynamic aperture of a sextupole and octupole strength determined case which is believed to be true for the most small emittance electron storage rings. Obviously, the dynamic aperture scales with the one third power of the sextupole and the octupole strength, respectively. If in a storage ring the perturbation from the sextupoles can be omitted, in a similar way one finds the maximum J_1 corresponding to $m/4$ resonance mode

$$J_1 \leq J_{max,m/4} = \frac{2\rho}{\sqrt{3}\beta_x(s_2)^2L|b_3|} \quad (36)$$

and the corresponding dynamic aperture

$$A_{dyn,m/4} = \sqrt{2J_{max,m/4}\beta_x(s)} = \left(\frac{4\rho\beta_x(s)}{\sqrt{3}\beta_x(s_2)^2L|b_3|} \right)^{1/2} \quad (37)$$

From eq. 37 one reads that the dynamic aperture, $A_{dyn,m/4}$, is proportional to the square root of the octupole strength. Usually, one has $A_{dyn,m/3} < A_{dyn,m/4}$.

Now I would like to spend some inks on the scenario of those particles whose motions do not satisfy the condition given by eq. 32. Once a particle begins to execute stochastic motion the phase mixing occurs, and the mapping given by eqs. 30 and 31 can be regarded as a Markov process [5], and in consequence, the possibility distribution function $\mathcal{F}(s, I)$ satisfies the Fokker-Planck equation:

$$\frac{\partial \mathcal{F}}{\partial s} = -\frac{\partial(\mathcal{A}\mathcal{F})}{\partial I} + \frac{1}{2} \frac{\partial^2(\mathcal{D}\mathcal{F})}{\partial I^2} \quad (38)$$

where $\mathcal{A} = \langle\langle \Delta I \rangle\rangle / L$, $\mathcal{D} = \langle\langle (\Delta I)^2 \rangle\rangle / L$, and the notation $\langle\langle \rangle\rangle$ denotes the average over phase θ . From eq. 30 one knows $\Delta I = K_0 \sin \theta$, and obviously, one has $\mathcal{A} = 0$ and $\mathcal{D} = K_0^2 / (2L)$. Due to the diffusion, needless to say, the amplitude of the particle's motion is increasing with the distance and finally the particle is lost on the vacuum chamber wall.

2.2 Electron storage ring

In an electron storage ring the physical picture is more complicated due to the synchrotron radiation damping. To treat this problem let's resort to the so-called *standard dissipative mapping* [2] which is different but similar to the standard mapping shown in eqs. 30 and 31, and expressed as

follows:

$$\bar{I} = \exp(-\Gamma)I + K_0\mu \sin \theta \quad (39)$$

$$\bar{\theta} = \theta + \bar{I} \quad (40)$$

where $\Gamma = \frac{2L}{\tau_x c}$, τ_x is the damping time of the betatron oscillation in the horizontal direction, and $\mu = (1 - \exp(-\Gamma)) / \Gamma$. Apparently, when $\Gamma \rightarrow 0$, eqs. 39 and 40 return to the standard mapping given by eqs. 30 and 31. The criterion for avoiding the onset of the stochastic motion in the dissipative system is given by

$$|\mu K_0| \leq 1 \quad (41)$$

The expressions for the dynamic apertures of the electron storage rings corresponding to the two expressions for the proton ones derived in the previous subsection are

$$A_{dyn,m/3} = \sqrt{2J_{max,m/3}\beta_x(s)} = \left(\frac{16\rho^2\beta_x(s)^{3/2}}{9\mu|b_2b_3|\beta_x^2(s_2)\beta_x(s_1)^{3/2}L^2} \right)^{1/3} \quad (42)$$

and

$$A_{dyn,m/4} = \sqrt{2J_{max,m/4}\beta_x(s)} = \left(\frac{4\rho\beta_x(s)}{\sqrt{3}\beta_x(s_2)^2L\mu|b_3|} \right)^{1/2} \quad (43)$$

Eq. 42 has been compared with the numerical dynamic aperture simulation results of ALLADIN [6] and KEK Photon Factory [7], and the satisfactory comparison results are shown in ref. 8.

3 CONCLUSION

Considering delta function sextupole and octupole perturbations, analytical expression for the dynamic aperture of a circular machine is obtained by using the Chirikov criterion. It is shown that when the dynamics aperture is sextupole and octupole strength determined which is true for the most cases the dynamic aperture inversely scales with the one third power of the sextupole and octupole strength, respectively. The author thanks J. Le Duff for discussions.

4 REFERENCES

- [1] R. Ruth, AIP conference proceedings, No. 153, p. 150.
- [2] R.Z. Sagdeev, D.A. Usikov, and G.M. Zaslavsky, "Nonlinear Physics, from the pendulum to turbulence and chaos", hardwood academic publishers, 1988.
- [3] B.V. Chirikov, Physics Reports, Vol. 52, No. 5 (1979), p. 263.
- [4] J.M. Greene, J. Math. Phys. 20 (1979), p. 1183.
- [5] R.L. Stratonovich, "Topics in the theory of random noise", Vol. 1, Gordon and Breach Science Publishers Inc., 1963.
- [6] J. Bridges, et al., *Particle Accelerators*, Vol. 28 (1990), p. 1.
- [7] Y. Kobayash, et al., Proceedings of PAC93 (1993), p. 215, see also: M. Katoh, *Particle Accelerators*, Vol. 28 (1990), p. 17.
- [8] J. Gao, LAL/RT 98-03.

PARTICLE-CORE ANALYSIS OF BEAM HALOS IN A SYNCHROTRON

M. Ikegami, JAERI, Tokai-mura, Naka-gun, Ibaraki-ken 319-1195, Japan
S. Machida and T. Uesugi *, KEK-Tanashi, Midori-cho, Tanashi-shi, Tokyo 188-8501, Japan

Abstract

A simple particle-core model for circular accelerators has been constructed assuming that dispersion effects are relatively weak. This model is applicable to a large class of high-intensity rings designed for modest density applications such as spallation neutron sources. Applying this model to isotropic beams in a smooth ring, halo formation processes in the presence of dispersion are investigated. In the analysis, it is found that dispersion matching is essentially important to suppress horizontal beam widening in injection. With dispersion matching, a halo is formed by the particle-core resonance, and its width is a little narrower than that in a straight channel. Dispersion effect on halo formation in high-density situations is also discussed.

1 INTRODUCTION

Recently, high intensity proton synchrotrons or storage rings have been proposed to be used for various applications such as bunch compression for spallation neutron sources. As uncontrollable beam losses due to halo formation is often considered as a main concern in these machines, increasing attention has recently been given to the beam halo problem in circular accelerators [1]. While the particle-core approach [2] has already been adopted in some of these studies, we propose an alternate particle-core model for beams in circular accelerators in this paper.

In this paper, we consider the simplest situation to clearly bring out the dispersion effect on halo dynamics, namely; we consider a coasting beam circulating in a smooth ring where both the bending and focusing fields are constant (smooth approximation). The emphasis is put upon situations with modest beam density where tune depression, or ratio of depressed tune to undepressed one, is well larger than 0.9, while halo formation in higher density cases is also discussed.

2 PARTICLE-CORE MODEL

The first basis of the particle-core analysis is envelope equations which describe the time-evolution of core envelope. Recently, envelope equations which include effects of dispersion and space charge were derived by Venturini and Reiser [3]. They found that the usual

horizontal rms emittance $\epsilon_x^2 = \langle x^2 \rangle \langle p_x^2 \rangle - \langle xp_x \rangle^2$ is not an invariant of motion in the presence of dispersion. Instead, the generalized emittance ϵ_{dx} defined as follows is conserved:

$$\epsilon_{dx}^2 = (\langle x^2 \rangle - D^2 \Delta^2)(\langle p_x^2 \rangle - D'^2 \Delta^2) - (\langle xp_x \rangle - DD' \Delta^2)^2, \quad (1)$$

where $\Delta = \sqrt{\langle (\delta p/p)^2 \rangle}$ is the rms momentum spread. The independent variable s is the longitudinal distance along the design orbit, and the prime indicates the derivative with respect to s . The dispersion function D obeys the equation

$$D'' + \left[\kappa_x - \frac{K}{2a(a+b)} \right] D = \frac{1}{\rho}, \quad (2)$$

where $a = \sqrt{\langle x^2 \rangle}$ and $b = \sqrt{\langle y^2 \rangle}$ are the rms beam widths, and ρ is the average radius of curvature. The generalized perveance K is a measure of the beam density, and κ_x is a constant which represents the external focusing field strength in the horizontal direction. Note here that κ_x includes the horizontal focusing effect of the dipole magnets.

The envelope equations with dispersion can be written as

$$a'' + \kappa_x a - \frac{K}{2(a+b)} - \frac{\Delta^2}{a} \left(\frac{D}{\rho} + D'^2 \right) - \frac{\epsilon_{dx}^2 - a'^2(a^2 - D^2 \Delta^2) + (aa' - DD' \Delta^2)^2}{a(a^2 - D^2 \Delta^2)} = 0, \quad (3)$$

and

$$b'' + \kappa_y b - \frac{K}{2(a+b)} - \frac{\epsilon_y^2}{b^3} = 0, \quad (4)$$

where ϵ_y and κ_y are, respectively, rms emittance and external focusing field strength in the vertical direction. As easily seen in Eq. (3), the emittance term is modified by adopting the generalized emittance, and the dispersion term is added compared to envelope equations for a straight channel. Simultaneously solving Eq. (2) to Eq. (4), we can obtain the time-evolution of core envelope.

To construct a particle-core model for beams with finite momentum spread, we need to know the matched beam width and coherent tune of these beams. The presence of dispersion causes changes of matched beam size and coherent tune. In the following, we examine these changes due to dispersion considering isotropic situations, namely $\kappa_x = \kappa_y$ and $\epsilon_x = \epsilon_y$.

* Also, University of Tokyo, Hongo, Bunkyo-ku, Tokyo 113-0033, Japan

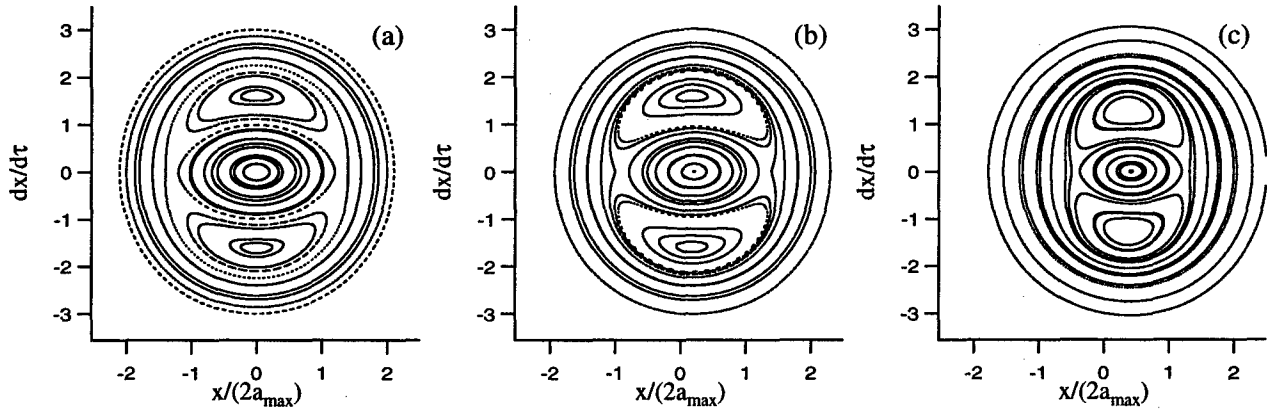


Figure 1: Poincaré plots for test particles in modest density cases with $\eta_x = 0.9$, $\mu = 1.1$ and $\xi = 0.15$. Test particle position scaled by the maximum beam boundary width $2a_{max} = 2a(0)$ is taken as the abscissa. Three different Λ , i.e., (a) $\Lambda = 0$, (b) $\Lambda = 2$, and (c) $\Lambda = 4$ are considered.

Considering situations where dispersion effect is modest, the matched beam widths are obtained [4] as

$$a_0 = \hat{a}_0 \left[1 + \frac{\hat{\eta}_x^2(3 + 5\hat{\eta}_x^2)}{4(1 + \hat{\eta}_x^2)(1 + 3\hat{\eta}_x^2)} \hat{\xi}^2 \right], \quad (5)$$

and

$$b_0 = \hat{a}_0 \left[1 - \frac{\hat{\eta}_x^2(1 - \hat{\eta}_x^2)}{4(1 + \hat{\eta}_x^2)(1 + 3\hat{\eta}_x^2)} \hat{\xi}^2 \right], \quad (6)$$

where \hat{a}_0 and $\hat{\eta}_x$ are, respectively, the matched beam width and tune depression of the corresponding zero-momentum-spread beam. The parameter $\hat{\xi} = \Delta/(\hat{a}_0 \rho \hat{\eta}_x^2 \kappa_x)$ is a measure of the strength of dispersion effect. As $\hat{\xi}^2$ is typically a few percent in modest-density circular accelerators [5], fourth or higher order terms of $\hat{\xi}$ are neglected in the derivation of Eq. (5) and Eq. (6).

In mismatched situations, core envelope and dispersion function oscillate around the matched solution. These coherent tunes can be obtained [4] as

$$\nu_b^2 = \left[2(1 + \eta_x^2) - \frac{2 + 14\eta_x^2 + 15\eta_x^4 - 7\eta_x^6}{(2 + \eta_x^2)(1 + 3\eta_x^2)} \xi^2 \right] \nu_x^2, \quad (7)$$

for breathing mode and

$$\nu_q^2 = \left[1 + 3\eta_x^2 - \frac{1 + 14\eta_x^2 + 30\eta_x^4 + 3\eta_x^6}{2(1 + 2\eta_x^2)(1 + 3\eta_x^2)} \xi^2 \right] \nu_x^2, \quad (8)$$

for quadrupole mode, where $\nu_x = \sqrt{\kappa_x} \rho$ is the horizontal bare tune. Although one additional mode arises due to coupling with dispersion function, its contribution to envelope oscillation is generally small. The tune depression η_x is related to $\hat{\eta}_x$ as

$$\eta_x^2 = \left[1 + \frac{(1 - \hat{\eta}_x^2)(1 + 2\hat{\eta}_x^2)}{(1 + \hat{\eta}_x^2)(1 + 3\hat{\eta}_x^2)} \hat{\xi}^2 \right] \hat{\eta}_x^2. \quad (9)$$

The parameter ξ is another measure of the strength of dispersion effect defined by $\xi = \Delta/(a_0 \rho \eta_x^2 \kappa_x)$. The

relation between ξ and $\hat{\xi}$ is easily obtained by using Eq. (5) and Eq. (9).

The second basis of the particle-core analysis is the equation of motions of test particles. Assuming that cores have the KV distribution [6] in the transverse phase space and that test particles have zero angular momentum, equation of motion for test particles initially located on the horizontal plane ($y = y' = 0$) can be written as [7]

$$x'' + \kappa_x x - \frac{K}{2a(a+b)} x - \frac{\Lambda \Delta}{\rho} = 0, \quad (10)$$

inside the core ($|x| \leq 2a$) and

$$x'' + \kappa_x x - \frac{K}{x^2 + |x|\sqrt{x^2 + 4(b^2 - a^2)}} x - \frac{\Lambda \Delta}{\rho} = 0, \quad (11)$$

outside the core ($|x| > 2a$), where relative momentum deviation $\Lambda = (\delta p/p)/\Delta$ is a particle-dependent constant. The maximum value of Λ typically ranges from two to four, while it is distribution-dependent.

3 NUMERICAL RESULTS

Applying the particle-core model described in the preceding section, we examine halo formation in the presence of dispersion. In this section, we concentrate on the cases where breathing mode oscillation is selectively excited. To start with, we consider a modest density beam with $\eta_x = 0.9$ and $\xi = 0.15$. Poincaré surface of section plots for test particles are shown in Fig. 1. In this figure, test particles with three different Λ have been considered, while the mismatch factor $\mu = a(0)/a_0$ is fixed to 1.1. As readily seen in Fig. 1(a), the width of 2:1 resonance island is a little narrower than that of the corresponding zero-momentum spread beam because of a decrease of coherent tune. As Λ is increased, dispersion effect gives a shift of fixed point

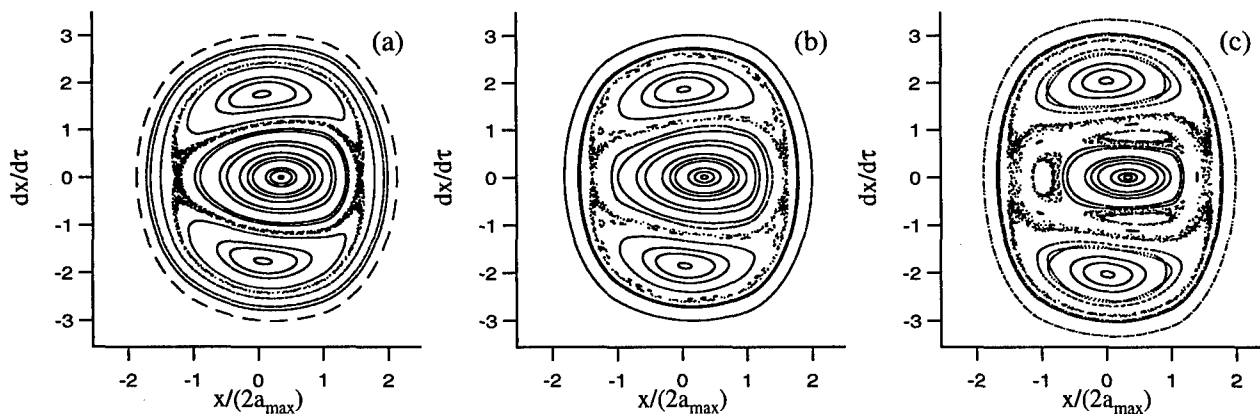


Figure 2: Poincaré plots for test particles in high density cases with $\mu = 1.1$, $\Lambda = 4$ and $\xi = 0.15$. Beams with three different densities, i.e., (a) $\eta_x = 0.5$, (b) $\eta_x = 0.4$, and (c) $\eta_x = 0.3$ are considered.

locations. At the same time, the width of 2:1 particle-core resonance decreases. As easily seen in Fig. 1, dispersion matching is essential if the maximum value of Λ is larger than a certain value, namely; particles with large momentum must be injected into outer side of the core. Without dispersion matching, the shift provides a transport mechanism by which particles initially located inside the core can escape from the core and become halos.

In particle-core analyses for straight channels, only particles which are trapped by the 2:1 particle-core resonance are considered to be halo particles, because particles initially located in the vicinity of the core can not go beyond the separatrix of the resonance. Obviously, this criteria is valid in estimating halo width in the presence of dispersion only in cases where the diffusion due to dispersion mismatch is suppressed. Applying this method, the halo width in the presence of dispersion is found to be a little narrower than that in a straight channel, and typically 1.8 times the maximum core width.

Although this particle-core model is constructed assuming modest density beams, it is applicable to high density cases provided that ξ is small. Poincaré plots for high density beams are shown in Fig. 2, where three different beam densities have been assumed. In increasing beam density keeping ξ to 0.15, some additional islands of higher order resonances appear around the central stable point. Weak chaosity is observed in all three cases in Fig. 2, which may increase halo intensity.

4 SUMMARY

We have constructed a simple particle-core model for beams in circular accelerators, neglecting fourth or higher order contribution of ξ . Although this model is efficient only in cases where ξ is small, it is applicable to a large class of circular accelerators designed

for modest-density applications and it provides us useful information on halo dynamics in these machines. Especially, this model is sufficient for halo studies in most rings designed as a bunch compressor for spallation neutron sources.

5 REFERENCES

- [1] S. Machida and M. Ikegami, in *Workshop on Space Charge Physics in High Intensity Hadron Rings*, Edited by A. U. Luccio and W. T. Weng, AIP Conference Proceedings No. 448, (AIP, New York, 1998), p. 73; J. A. Holmes, J. D. Galambos, D. K. Olsen, and S. Y. Lee, *ibid.*, p.254; in *Proceedings of the Sixth European Particle Accelerator Conference*, (IOP, London, 1998), p. 279; J. A. Holmes, J. D. Galambos, D. K. Olsen, J. H. Whealton, M. Blaskiewicz, A. Luccio, and J. Beebe-Wang, *ibid.*, p. 1109.
- [2] T. P. Wangler, K. R. Crandall, R. Ryne, and T. S. Wang, *Phys. Rev. ST-AB* **1**, 084201 (1998), and references therein.
- [3] We have adopted envelope equations derived in, M. Venturini and M. Reiser, *Phy. Rev. Lett.* **81**, 96 (1998), as the starting point of our analysis, while an alternative form of envelope equations is derived in, S. Y. Lee and H. Okamoto, *Phy. Rev. Lett.* **80**, 5133 (1998).
- [4] M. Ikegami, S. Machida, and T. Uesugi, in preparation.
- [5] For example, $\xi = 0.15$ for the proton storage ring proposed as an option in Nutron Science Project at JAERI. See for detailed design parameters of this ring, M. Kinsho, J. Kusano, M. Mizumoto, and F. Noda, in *Proceedings of the Sixth European Particle Accelerator Conference*, (IOP, London, 1998), p. 844.
- [6] I. M. Kapchinskij and V. V. Vladimirkij, in *Proceedings of International Conference for High Energy Accelerators*, (CERN, Geneva, 1959), p. 274.
- [7] See for example, O. D. Kellog, *Foundation of Potential Theory*, Frederick Ungar Publishing Company, New York, 1953, Chap. IV.

OBSERVATION OF QUADRUPOLE MODE FREQUENCY AND ITS CONNECTION WITH BEAM LOSS

T.Uesugi*, S.Machida, Y.Mori, KEK-Tanashi, Midori-cho, Tanashi-shi, Tokyo 188-8501, Japan
M.Ikegami, JAERI, Tokai-mura, Naka-gun, Ibaraki-ken 319-1195, Japan
S.Ninomiya, A.Mochihashi, T.Oki, S.Hidaka, RCNP, Ibaraki, Osaka 567-0047, Japan
D.Arakawa, T.Toyama, KEK 1-1 Oho, Tsukuba-shi, Ibaraki-ken 305-0801, Japan
and K.Noda, NIRS, Anagawa, Inage-ku, Chiba-ken 263-8555, Japan

Abstract

Recent Simulation results imply that the number of particles in a high intensity synchrotron is limited by the resonance crossing of coherent mode oscillations, not by the incoherent one. In order to verify it, we measured the tune shift of quadrupole mode oscillations in HIMAC at National Institute of Radiological Sciences (NIRS) to show the connection with beam loss. In this paper, we discuss signals observed in a coasting beam. We also presents the numerical calculation of envelope motion for a bunched beam.

1 INTRODUCTION

It is believed that space charge effects limit the number of particles in a high intensity synchrotron. However, the detailed mechanism of beam loss is not clear. One model tells that the incoherent tune of an individual particle is reduced by the space charge field to a major resonance line, and resonate with lattice field errors. Another model, proposed by Sacherer in 1960's[1], is that the coherent mode oscillations of a beam resonate with lattice field errors. The incoherent model is not self-consistent because it neglects the time evolution of distribution due to the space charge force.

Recent simulation results seem to support the latter model[2]. In order to verify this, we planned to measure the tune shifts of coherent mode oscillations and their connection with beam loss. We observed coherent mode signals in a coasting beam in HIMAC synchrotron. To start with, we discuss the three dimensional envelope equations, where it is shown that the envelope oscillation frequencies in a bunched beam do not differ much from that in a coasting beam. Then, we report our measurements.

2 ENVELOPE OSCILLATIONS IN A BUNCHED BEAM

2.1 3D envelope equations

For a bunched beam, envelope oscillations occur in three dimensions. Sacherer studied three dimensional envelope equations and found that they depend only on rms beam size, as far as the distribution has ellipsoidal symmetry [3]. They are

$$\begin{aligned}\frac{d^2\bar{x}}{d\phi^2} + \left(\nu_{0x}^2 - \frac{Nr_0R^2}{\beta^2\gamma^2} \lambda_3 g(\bar{x}, \bar{y}, \gamma\bar{z}) \right) \bar{x} &= \frac{(R\epsilon_x)^2}{\bar{x}^3} \\ \frac{d^2\bar{y}}{d\phi^2} + \left(\nu_{0y}^2 - \frac{Nr_0R^2}{\beta^2\gamma^2} \lambda_3 g(\bar{y}, \gamma\bar{z}, \bar{x}) \right) \bar{y} &= \frac{(R\epsilon_y)^2}{\bar{y}^3} \\ \frac{d^2\gamma\bar{z}}{d\phi^2} + \left(\nu_{0z}^2 - \frac{Nr_0R^2}{\beta^2\gamma^2} \lambda_3 g(\gamma\bar{z}, \bar{x}, \bar{y}) \right) \gamma\bar{z} &= \frac{(R\epsilon_z)^2}{\bar{z}^3}\end{aligned}\quad (1)$$

where ϕ is the azimuth along the circumference of a synchrotron, R is the ring average radius, ν_{0x} is bare tune, and the geometric factor g is elliptic integral,

$$g(a, b, c) = \frac{3}{2} \int_0^\infty \frac{ds}{(a^2 + s)^{3/2} (b^2 + s)^{1/2} (c^2 + s)^{1/2}} \quad (2)$$

and λ_3 is about $1/5\sqrt{5}$, which very weakly depends on details of distribution. In the parenthesis of the left hand side of eq.1 corresponds to a square of depressed tune ν_x^2 when $(\bar{x}, \bar{y}, \gamma\bar{z})$ is the matched beam size. Differentiating eq.1 and use $\epsilon_x = \nu_x \bar{x}_0^2/R$, we have

$$\begin{aligned}\frac{d^2}{d\phi^2} \Delta\bar{x} + 4\nu_x^2 \Delta\bar{x} &= \frac{\lambda_3 Nr_0 R^2}{\beta^2 \gamma^2} \bar{x}_0 \Delta g|_{\bar{x}_0, \bar{y}_0, \gamma\bar{z}_0} \\ \frac{d^2}{d\phi^2} \Delta\bar{y} + 4\nu_y^2 \Delta\bar{y} &= \frac{\lambda_3 Nr_0 R^2}{\beta^2 \gamma^2} \bar{y}_0 \Delta g|_{\bar{y}_0, \gamma\bar{z}_0, \bar{x}_0} \\ \frac{d^2}{d\phi^2} \gamma \Delta\bar{z} + 4\nu_z^2 \gamma \Delta\bar{z} &= \frac{\lambda_3 Nr_0 R^2}{\beta^2 \gamma^2} \gamma \bar{z}_0 \Delta g|_{\gamma\bar{z}_0, \bar{x}_0, \bar{y}_0}\end{aligned}\quad (3)$$

where the subscript "0" denotes matched solutions. The equations above can not be solved analytically because of elliptic integral. One way to solve them is to take some approximations[4] and substitute arithmetic function for g . Here, we employ numerical integration.

2.2 Numerical solution

We solved eigen equations of eq.3 numerically, for a given focusing force, emittance and beam intensity. It is expected that, in the limit of long bunch and low synchrotron frequency, the behavior of envelope motion will be similar to that of a coasting beam.

In solving eq.3, matched beam size $(\bar{x}_0, \bar{y}_0, \gamma\bar{z}_0)$ was calculated by eq.1 with $d^2/d\phi^2 = 0$ and elliptic integral

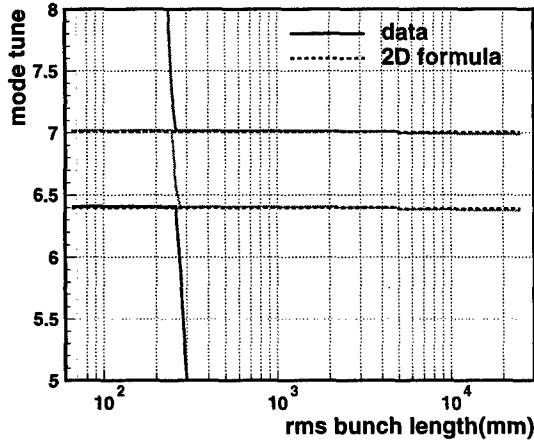


Figure 1: Bunch length dependence of eigen mode frequencies with the parameters of table 1.

is evaluated with a numerical package available [5]. We chose parameters in Table 1. In order to study bunch length dependence, we varied longitudinal focusing force, and adjusted beam intensity simultaneously so that transverse incoherent tune remains constant.

At first, we show in Fig.1 the eigen frequencies of envelope oscillations, together with the one calculated by a 2D formula.

$$\begin{aligned} \nu_{\pm}^2 &= \frac{\tilde{x}_0 + \tilde{y}_0}{2\tilde{y}_0} \frac{\nu_x}{\nu_{0x}} \pm \sqrt{(2\nu_{0x}^2 - 2\nu_{0y}^2)^2 - (\nu_{0x}\Delta\nu_x)^2} \\ &= 7.01^2, 6.39^2. \end{aligned} \quad (4)$$

In each region except $\gamma\tilde{z}_0 \sim 250\text{mm}$, two of calculated modes agree with the values estimated by eq.4. Eigen vectors, shown in Fig.2, prove that these modes are pure horizontal, vertical and longitudinal one. At around $\nu_{0z} \sim \nu_{0x}, \nu_{0y}$, the oscillations form two coupled modes, i.e. breathing(even) mode with higher frequency and quadrupole(odd) mode with lower frequency. This behavior is similar to the coupled phenomena of a single particle.

In conclusion, the coupling of transverse and longitudinal envelope oscillations due to space charge force seems negligible for a synchrotron where the synchrotron oscillation frequency is much less than betatron oscillation. More detailed discussion could be found in Ref.[6]

Table 1: Parameters used in envelope mode calculation.

particle	6MeV/u He ²⁺ ($\gamma = 1.006$)
bare tune	$(\nu_{0x}, \nu_{0y}) = (3.6, 3.3)$
	$\nu_{0z} = 0.00978$ @ $\gamma\tilde{z} = 5000\text{mm}$
100% emittance	$\epsilon = (10, 10, 55000)\pi\text{mm-mrad}$
beam intensity	$1 \times 10^{10}\text{ppp}$ @ $\gamma\tilde{z} = 5000\text{mm}$

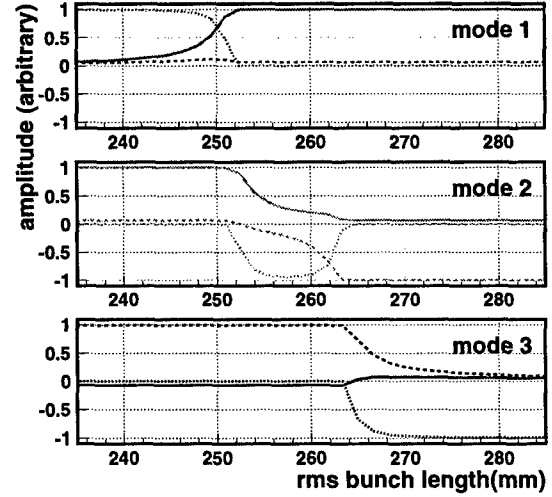


Figure 2: Amplitude ratio of eigen modes in x(solid line), y(broken line) and z(dot line). Mode 1, 2 and 3 is of the highest, middle and the lowest frequency.

3 MEASUREMENTS IN HIMAC

3.1 The HIMAC tune shifts

We chose a flatbase operation (no acceleration) with a He²⁺ beam to obtain the largest tune shift. Machine parameters are same as Table 1 except horizontal emittance of $264\pi\text{mm-mrad}$ and maximum beam intensity of $1 \times 10^{11}\text{ppp}$. That is due to multi-turn injection. The incoherent tune shift of vertical oscillation is calculated as $-0.0446/10^{11}\text{ppp}$. The coherent ones are $-0.00216/10^{11}\text{ppp}$ for dipole mode and $-0.0590/10^{11}\text{ppp}$ for quadrupole mode.

3.2 Quadrupole monitor

Among coherent mode oscillations, the tune shifts of quadrupole mode is dominant. Therefore, we installed a quadrupole pickup monitor in HIMAC in the summer of 1998. It is an electrostatic type pickup with four electrodes(Fig.3). The amplitude of quadrupole mode can be seen in a quadrupole channel output, which is subtracting the sum of vertical two electrodes signal from that of horizontal. The difference between opposite two electrodes are used to observe dipole mode oscillations. The estimated magnitude of output signal for a 6MeV/u He²⁺ beam is around $15\text{mV}/10^{11}\text{ppp}$ in each channel, and a quadrupole component is about the order of $(x/a)^2$ lower than that, where a is the radius of pickup electrodes.

3.3 Spectrum and tune shifts

We observed beam spectrum of a coasting beam of $3 \times 10^{10}\text{ppp}$ with a real time spectrum analyzer. We used RFQ[7] in order to excite quadrupole mode oscillations. Fig.4 shows the beam spectrogram around 4 times of revo-

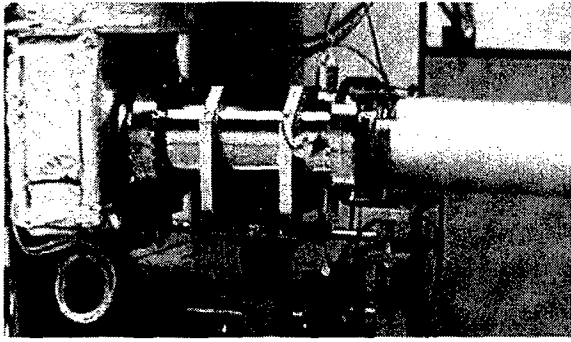


Figure 3: Quadrupole monitor in HIMAC.

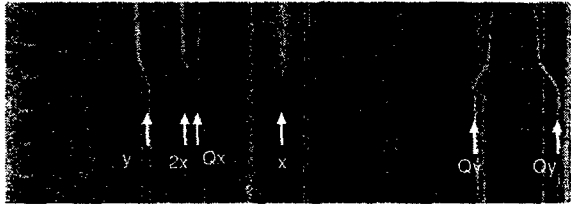


Figure 4: Spectrogram of coasting beam.

lution frequency. Quadrupole mode and dipole mode oscillations in horizontal and vertical space can be seen. Some of them are shifting in frequency as the beam current decreases at $\sim 1000\text{msec}$ after injection.

We estimated the space charge tune shift of each mode by plotting frequency versus beam current seen by a slow current transformer. Fitted value of tune shifts for quadrupole mode is about $-0.082/10^{11}\text{ppp}$, which is not in good agreement with theoretical value. A part of the discrepancy can be attributed to uncertainty of emittance. We are continuing measurements at other operation points.

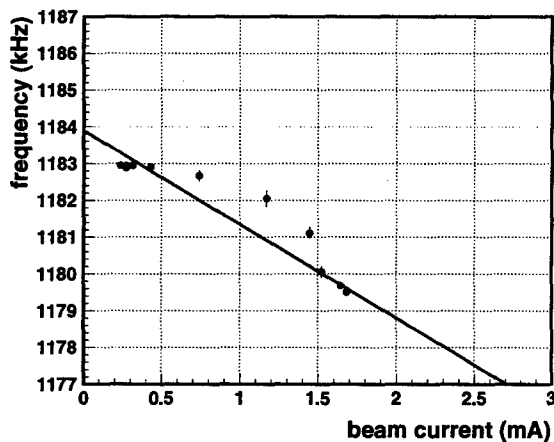


Figure 5: Tune shift vs circulating current.

3.4 Resonance crossing

Finally we show in Fig.6, where the operating point is moving gradually by varying defocusing field. As the current of defocusing magnet goes down, the quadrupole mode frequency approaches to revolution frequency. At

2500msec after beam injection, it finally meets $2\nu_y=7.0$ resonance line and beam disappears rapidly. The tune shift of coherent quadrupole mode oscillations at the beam current just before the resonance is so small that it is difficult to determine if the resonance occurs by coherent mode oscillation or incoherent one.

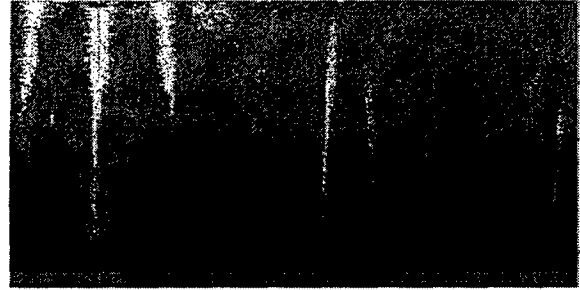


Figure 6: Half integer resonance. Frequency span is 200kHz centered at 1.64MHz . Time scale is 3000msec from top (beam injection) to bottom.

4 SUMMARY

First, we solved 3D envelope equations numerically, and found that the coupling between transverse and longitudinal motion due to space charge force is negligible in synchrotrons. Therefore, the mode frequencies in a coasting beam are fairly good approximations of that in a bunched one except one longitudinal mode.

Secondly, we presented our experiment in HIMAC synchrotron. We identified the coherent mode signals. The tune shift is not so good agreement with the expected value, at this moment. However, a part of the discrepancy can be attributed to uncertainty of emittance. We are carrying on the experiments to reveal the connection between tune shifts and beam loss.

5 ACKNOWLEDGEMENT

We would like to thank the staff of Accelerator Engineering Company for the help of our experiment in HIMAC.

6 REFERENCES

- [1] F.J.Sacherer, Ph.D.Thesis(1968).
- [2] S.Machida, Proceeding of EPAC'98(1998).
- [3] F.J.Sacherer, IEEE Trans.Nucl.Sci, 18(3)(1971).
- [4] M.Pabst and K.Bongardt, Proceeding of EPAC'98(1998).
- [5] For example, Numerical Recipe.
- [6] T.Uesugi *et.al.*, in preparation.
- [7] K.Sato, Proceeding of EPAC'98(1998).

BEAM COUPLING IMPEDANCE OF FAST STRIPLINE BEAM KICKERS*

B. R. Poole¹, G. J. Caporaso, Y. J. (Judy) Chen, S. D. Nelson, LLNL, Livermore, CA

Abstract

A fast stripline beam kicker is used to dynamically switch a high current electron beam between two beamlines. The transverse dipole impedance of a stripline beam kicker has been previously determined from a simple transmission line model of the structure [1]. This model did not include effects due to the long axial slots along the structure as well as the cavities and coaxial feed transition sections at the ends of the structure. 3-D time domain simulations show that the simple transmission line model underestimates the low frequency dipole beam coupling impedance by about 20% for our structure. In addition, the end cavities and transition sections can exhibit dipole impedances not included in the transmission line model. For high current beams, these additional dipole coupling terms can provide additional beam-induced steering effects not included in the transmission line model of the structure [2], [3].

1 INTRODUCTION

The stripline kicker is designed to spatially separate a high current electron beam for transport into two separate beam lines. This system is used in conjunction with a static magnetic dipole septum to provide an additional angular kick to the beam. This allows the two beamlines to diverge sufficiently fast as to incorporate additional focusing elements for further downstream transport. This system is shown schematically in Fig. 1.

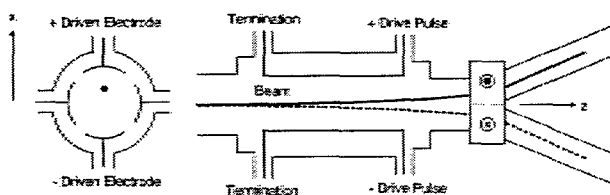


Figure 1: Stripline kicker and septum configuration

A high voltage pulse is applied to the downstream ports of the kicker and the beam is kicked by the electric and magnetic fields associated with the TEM waves propagating on the strip transmission lines. The beam is then directed into the septum magnet with opposite polarity dipole fields on either side of the plane separating the two downstream beamlines. All the upstream ports

and the two downstream ports in the non-kick plane are terminated in a matched load impedance for the dipole transmission mode on the structure.

2 KICKER TEM FIELDS

To steer the beam in x , opposite polarity high voltage pulses are applied to the downstream ports in the $y=0$ plane. The potential within the kicker plates ($r < b$) is given by

$$V = \frac{4V_p}{\pi} \sum_{n=odd} \left(\frac{1}{n} \right) \sin\left(\frac{n\phi_0}{2}\right) \cos(n\phi) \left(\frac{r}{b}\right)^n \quad (1)$$

where b is the interior radius of the kicker plates, ϕ_0 is the angle subtended by each kicker plate, and V_p is the kicker plate voltage giving a total steering voltage of $2V_p$. The solution is determined by solving for the potential in the interior region subject to the boundary condition that the applied potential at $r=b$ is given by the appropriate applied plate voltages and the potential in the gaps between the plates is zero. The $n=1$ term in Eq. 1 represents the transverse dipole force which provides the beam steering. The beam deflection due to the combined TEM electric and magnetic dipole forces is given by

$$\Delta x = \frac{4V_p}{\pi b} \sin\left(\frac{\phi_0}{2}\right) \left(\frac{q}{\beta \gamma m c^2} \right) \ell^2 \quad (2)$$

where ℓ is the length of the kicker.

3 DIPOLE WAKE IMPEDANCE AND BEAM-INDUCED STEERING

For intense beam applications, the beam current is sufficiently large as to induce substantial voltages and currents on the strip transmission lines. These TEM fields are introduced on the transmission lines as the beam traverses the upstream and downstream gaps as well as from changes in the dipole return current as the beam is deflected. These fields can then interact with the beam to cause beam-induced steering. In the limit of ultra-relativistic stiff beams the strength of this interaction is related to the dipole wake impedance.

3.1 Dipole Impedance

The $n=1$ transverse dipole wake impedance for the structure with an ultra-relativistic stiff beam centroid transported through the kicker structure offset from the z axis by an amount x_0 is given by [1]

*This work was performed under the auspices of the U.S. Department of Energy by the Lawrence Livermore National Laboratory under contract No. W-7405-Eng-48.

¹ Email: poole1@llnl.gov

$$Z_{\perp}(\omega) = \frac{8cZ_k}{\pi^2 b^2} \sin^2\left(\frac{\phi_0}{2}\right) \left(\frac{1}{\omega}\right) \left[\sin^2\left(\frac{\omega\ell}{c}\right) + j \sin\left(\frac{\omega\ell}{c}\right) \cos\left(\frac{\omega\ell}{c}\right) \right] \quad (3)$$

A kicker has been designed and installed on the Experimental Test Accelerator (ETA-II). The ETA-II kicker has the following set of parameters: $b=12.86$ cm, $R_0=19.5$ cm, $\phi_0=78^\circ$, $Z_k=50 \Omega$, and $\ell=160$ cm where R_0 is the outer vacuum chamber radius. The structure was modelled using the LLNL 3-D time domain electromagnetic code, TIGER [4] to determine the dipole impedance. Figures 2 and 3 show a comparison of the real and imaginary parts of the dipole impedance as calculated from Eq. 3 with the numerical results from the 3-D electromagnetic code.

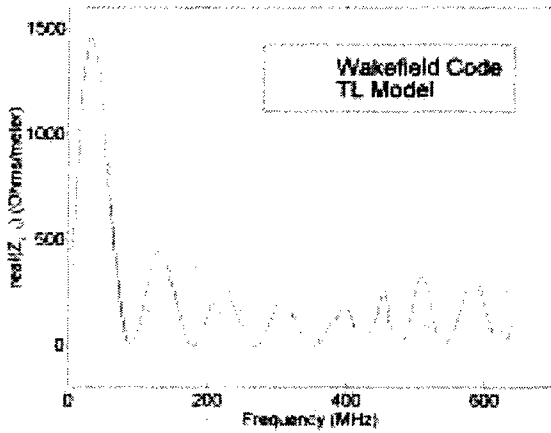


Figure 2: Real part of dipole impedance

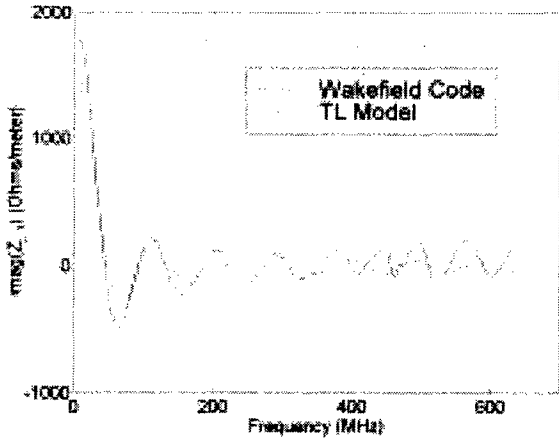


Figure 3: Imaginary part of dipole impedance

As can be seen in Figures 2 and 3, there is a good agreement between the transmission line model and the 3-D code results in the low frequency regime. The differences become more pronounced at higher frequencies as the end cavity transition sections associated with the feeds to the external 50 Ω coaxial

ports play a more significant role in the coupling. More will be discussed about this in section 4.

3.2 Beam Induced Steering

A detailed model of beam-induced steering has been previously described [2], [3]. The centroid motion of the beam in the kicker is given by [5]

$$\left(\frac{\partial}{\partial z} + \frac{s}{c}\right)^2 x(z) = \frac{V_p}{V_0} e^{-\frac{s}{c}(\ell-z)} + \frac{2I_b}{I_c \ell^2} \left[x(z) - 2 \frac{s}{c} e^{\frac{s}{c}z} \int_0^z x(z') e^{-\frac{s}{c}z'} dz' \right] \quad (4)$$

where s is the Laplace transform variable, $\partial/\partial t \rightarrow s$, and I_b is the beam current. The critical current, I_c is given by

$$I_c = \frac{\pi}{16} \left(\frac{b}{\ell}\right)^2 \frac{Z_0}{Z_k} \frac{\gamma\beta^2 I_0}{\sin^2(\phi_0/2)} \quad (5)$$

and the characteristic voltage, V_0 is defined as

$$V_0 = I_c Z_k \frac{\ell}{2\pi b} \sin\left(\frac{\phi_0}{2}\right) \quad (6)$$

where $I_0=17$ kA and $Z_0=377 \Omega$. Equation 4 can in principle be solved numerically for a particular set of conditions. Of particular interest is the case of an initially offset beam entering the kicker structure parallel to the beamline axis without any applied voltage since this solution can be related to the dipole wake impedance. It has been shown previously [3], that the asymptotic beam deflection for an initially offset beam has the form

$$x(z=\ell, t \rightarrow \infty) = x_0 \cosh\left(\sqrt{\frac{2I_b}{I_c}}\right) \quad (7)$$

where x_0 is the injection offset of the beam. For sufficiently small beam currents the asymptotic deflection is related to the dipole wake impedance by

$$x(z=\ell, t \rightarrow \infty) \approx x_0 \left[1 + \left(\frac{2\pi\ell}{\gamma\beta^2 I_0 Z_0} \right) I_b Z_{\perp 0} \right] \quad (8)$$

where $Z_{\perp 0} = \text{Im}[Z_{\perp}(\omega=0)]$. By numerically integrating Equation 4 it is possible to find a temporal solution for the beam displacement of the beam leaving the kicker. Consider an ETA-II electron beam with 6 MeV energy and a 2 kA beam current with a 1 cm initial offset. For these parameters, the critical current, I_c is about 4.2 kA and the asymptotic deflection given by Eq. 7 is $1.51x_0$. Figure 4 shows the temporal evolution of the beam displacement leaving the kicker from numerical integration of Eq. 4. Figure 4 shows a quite dramatic beam-induced steering effect for a high current beam. The time scale for reaching the asymptotic value is on the

order of the round-trip transit time of the structure, $2\ell/c \sim 10.6$ ns.

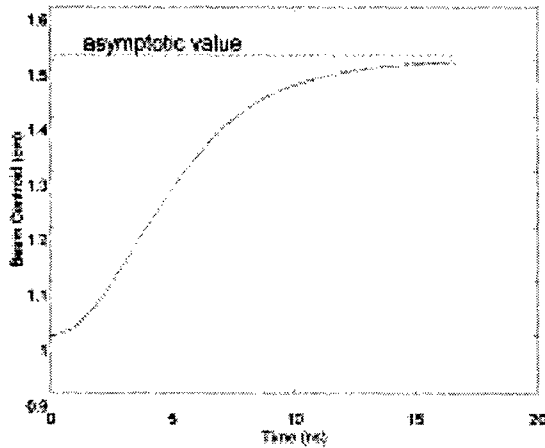


Figure 4: Temporal variation of beam centroid exiting ETA-II kicker for initial offset of 1 cm

4 CORRECTIONS TO THE DIPOLE IMPEDANCE FROM THE CAVITY TRANSITION SECTIONS

The 3-D code results show that the simple transmission line model underestimates the low frequency dipole wake impedance. Measurements of the kicker impedance show that the structure is not very well matched over a wide band of frequencies. In an effort to obtain a correction to the impedance at low frequencies, a simple inductance was incorporated as a model of the transition section connecting the strip transmission lines to the external coaxial ports. It was found that a 40 nH inductor would give an input impedance consistent with the experimental data. Figure 5 shows a plot of the experimental data and the projected low frequency input impedance.

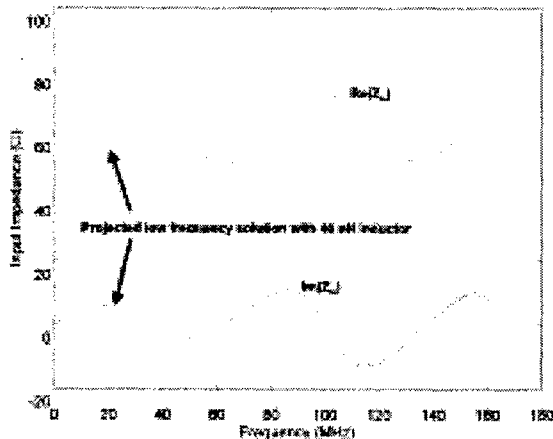


Figure 5: Kicker input impedance

The kicker dipole impedance is calculated including the series inductors to model the transition sections. Figures 6

and 7 show the real and imaginary parts of the dipole impedance for low frequencies.

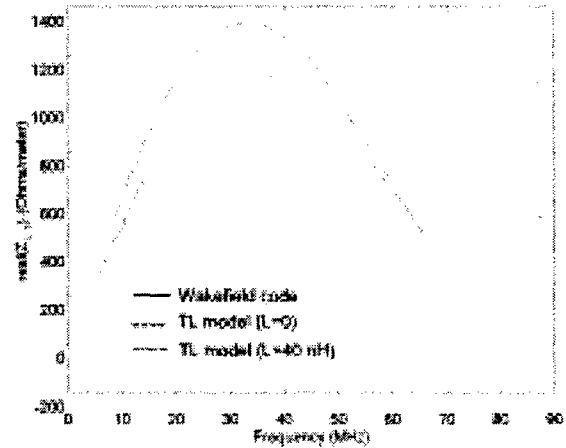


Figure 6: Real part of wake impedance with transition

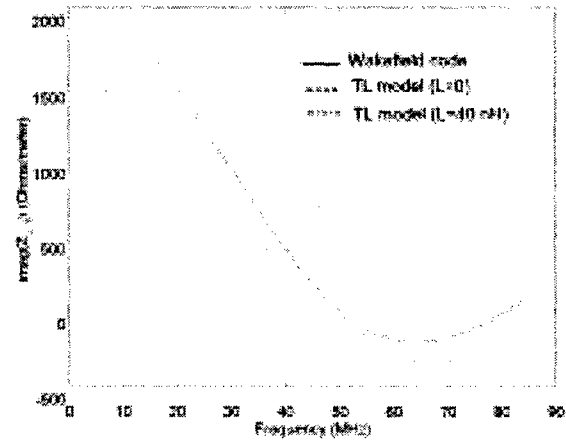


Figure 7: Imaginary part of dipole impedance with transition

As can be seen the transitions can modify the dipole wake impedance of the structure. In principle, additional reactive elements can be incorporated to extend the model to higher frequencies.

5 REFERENCES

- [1] K. Y. Ng, "Impedances of Stripline Beam-Position Monitors," *Particle Accelerators* **23**, 93-102 (1988)
- [2] G. J. Caporaso, Y. J. Chen, B. R. Poole, "Transmission Line Analysis of Beam Deflection in a BPM Stripline Kicker," 1997 Particle Accelerator Conference, Vancouver, B. C. Canada, May 12-16, 1997
- [3] B. R. Poole, G. J. Caporaso, Y. J. Chen, L. F. Wang, "Analysis and Modelling of a Stripline Beam Kicker and Septum," XIX International Linac Conference, Chicago, Ill, USA, August 23-28, 1998
- [4] D. Steich, J. Kallman, J.B. Grant, D. Mayhall, B. Poole, K. Kunz, H. Brand, G. Laguna, "TIGER: An Object Oriented Time-Domain Electromagnetics Simulation Code," LLNL Thrust Area Report, Computational Electronics and Electromagnetics, sec. 1., pp. 13-20, UCRL-ID-125470, 1997
- [5] Y. J. Chen, "Fast Kicker for High Current, Continuous Beams," To be published

DARHT2 X-RAY CONVERTER TARGET SYSTEM COMPARISON*

Yu-Jiuan Chen[†], Paul M. Bergstrom, Jr., George J. Caporaso, Darwin D.-M. Ho, James F. McCarrick, Philip A. Pincosy, and Peter W. Rambo, LLNL, Livermore, CA

Abstract

Four short current pulses with various pulse widths and spacing will be delivered to the x-ray converter target on the second-axis of the Dual-Axis Radiographic Hydrodynamic Test (DARHT-II) facility.[1] To ensure that the DARHT-II multi-pulse target will provide enough target material for x-ray production for all four pulses, the target needs either to survive the strike of four electron pulses or to accommodate target replenishment. A distributed target may survive hitting of four electron pulses. For target replenishment, two types of target configurations are being considered: stationary target systems with beam repositioning and dynamic moving target systems. We will compare these three target systems and their radiographic performance.

1 INTRODUCTION

Four 20 MeV, 2-4 kA current pulses with various pulse lengths and separations will be focused to sub-millimeter spots on DARHT-II x-ray converter targets. Maintaining a tight spot (a) and producing the required x-ray dose present the principal challenges for target design. To produce the required dose, each beam pulse needs to pass through enough target material. Three target concepts are considered. The first one is to reposition each pulse on a static target so that there is fresh target material for each pulse. The radiographic axis is not preserved, and its performance is affected. The second one is to move the target so that the subsequent pulse will strike a fresh target. The third is to distribute the static target material over a larger volume so that the energy density deposited by the beam decreases and target plasma expansion slows down. Thus, there may be enough target material around for the subsequent pulses.

Several effects may impact the spot size on the target. The target plasma created by preceding pulses may expand into the incoming beam's path. The charge neutralization effects produced by target plasma could change the final focus. Thus, the DARHT-II target system needs to provide means to control target plasma expansion. Furthermore, there may be a backstreaming ion problem [2] when the strong electric field created by the electron beam pulls ions in from an adjacent target plasma plume and the target surface. These ions could form an ion channel and change the final focus of the beam. Thus, the DARHT-II target system must also provide for mitigation of the backstreaming ion problem.

In Sections 2 and 3, we will discuss the backstreaming ion problem, target plasma and their mitigation. We will compare the beam repositioning, static target configuration and the dynamic, single axis, target configuration in Section 4. In Section 5, we will present a distributed target configuration for the 2 kA beam,

DARHT-II radiographic requirements. A summary will be given in Section 6.

2 BACKSTREAMING IONS AND MITIGATION

A high current beam, impinging on the x-ray converter target with a sub-millimeter spot size, will heat the target and ionize the target material and/or the surface contaminants. Ions can be extracted by the axial space charge field (\sim a few MV/cm) on the target, and charge neutralize the electron current. The electron beam is then prematurely focused in front of the target and subsequently overfocused at the target. Depending on the charge neutralization factor (f_i) and q/m of the ions, the spot size grows in time, as the ions move upstream, from a few tenths of a millimeter to several centimeters within \sim 40-60 ns. Regardless of whether there is enough ionization to cause the backstreaming ion problem during a single pulse, the backstreaming ion effect is a concern for a multiple pulse system since by the preceding pulses would have already ionized the target material.

The mitigation being considered for the DARHT-II target is to trap ions within a distance shorter than the 2-3 cm of disruption length, $L_D \approx a(\pi\gamma\beta^2 I_0/f_i I)^{1/2}$ where I and I_0 are the beam current and Alfvén current, either by a voltage barrier: an inductive ion trap [3] (Fig. 1) or a resistive ion trap [4], or by a physical barrier: a foil.[5] Simulations indicate that using a voltage barrier can control the DARHT-II beam spot size (Fig. 2a) and maintain the collimated x-ray dose effectively over the entire beam pulse (Fig. 2b). We have chosen the inductive ion trap as the DARHT-II baseline and the foil barrier as the backup plan for ion mitigation.

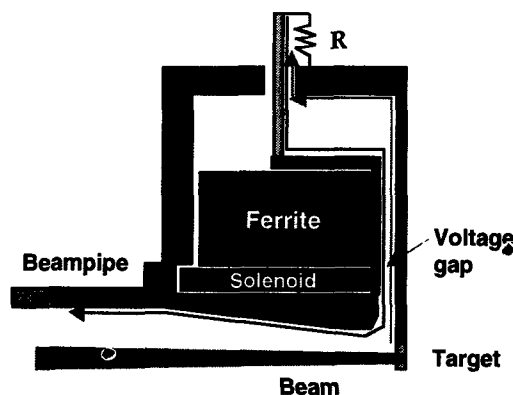


Fig.1 An inductive ion trap self-biases the target by the beam loading effect

* The work was performed under the auspices of the U.S. Department of Energy by LLNL under contract W-7405-ENG-48.

[†] chen6@llnl.gov

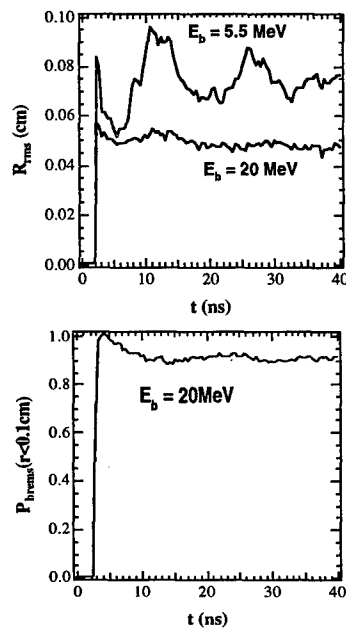


Fig. 2 (a) The R.M.S. spot size and (b) the normalized collimated x-ray dose as a function of time. The ion trap voltage is 370 kV, and the ion trap gap is 2 cm.

3 TARGET PLASMA AND MITIGATION

Hydrodynamic simulations [6] of a 2-4 kA, 20 MeV, 0.5 mm radius, 60 ns electron beam striking a 1-mm Ta target show that the target material is generally fully ionized immediately and that the target plasma expands at 1-2 cm/ μ s axially and ~ 1 cm/ μ s radially. The plasma electrons' number density varies from 10^{23} cm $^{-3}$ near the target surface to 10^{12} cm $^{-3}$ at the plasma edge which drops to zero within 1-2 mm. The plasma temperature is a few eV at the onset of the subsequent pulse. The magnetic diffusion time is much shorter than the electron pulse length. Thus, the plasma could only neutralize the space charges of the beam but not the beam current. Finally, the target plasma channel in the DARHT-II target region is too short to support growth of the ion hose instability.

The plasma channel's disruption length is about 2-3 cm. The plasma channel may be too long for the fourth pulse at the end of 2 μ s to maintain a small spot size if the plasma expansion velocity is large. Slowing target plasma expansion and reducing plasma production can minimize the beam-plasma interaction. Distributing the target material over a large volume decreases the energy deposition per unit volume, and hence reduces the initial plasma expansion velocity.[7] The scattered electrons in a distributed target may form a larger cone and deposit energy into more atoms. A smaller energy deposition per unit mass leads to a slower asymptotic plasma expansion. A lower energy deposition per unit mass at the downstream of the target may prevent the downstream target from turning into a plasma. Hence, less plasma is created. Moving the target transversely to the beam axis while the electron beam strikes the target also makes electrons deposit energy in a larger area and in more target atoms. Therefore, using a dynamic target also yields less plasma and slower plasma expansion.

4 REPOSITIONING TARGET AND DYNAMIC TARGET

The initial DARHT-II radiographic specifications require delivering four 4 kA, 20 MeV, 60 ns long pulses on the converter with the beam axis to be within 5 mm radius of the radiographic axis. To provide target replenishment, we have investigated two target configurations: a repositioning target and a dynamic (single axis) target. Both target configurations consist of a distributed target and an inductive ion trap. The repositioning target configuration's beamline is different from the single axis beamline [8] only in the few meters before the final focusing lens.

4.1 Repositioning Target Configuration

A 4-way kicker system (with a 4-way septum) or a fast deflector system is needed before the final focusing lens. Transport through these systems is difficult. The electron beam's nominal incident angle on the target is 1.36 $^\circ$ which would reduce the forward x-ray by 10 % compared with

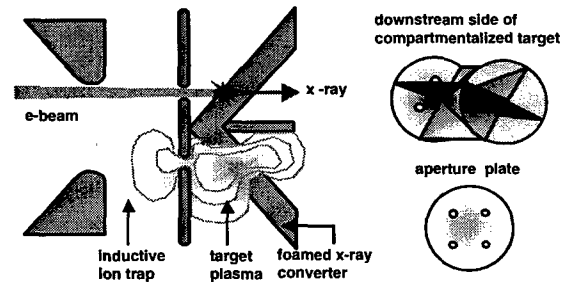


Fig.3 A repositioning target configuration

the x-ray production by a beam with zero incident angle. A compartmentalized, repositioning target configuration (Fig. 3) was proposed by Prono [9] to minimize the beam-plasma interaction. To accommodate four repositioned beams, the upstream aperture of the ion trap is large. This results in a larger required gap voltage and a longer ion trap channel length. Hydrodynamic simulations show that the electron pulses near the end of the 2 μ s would travel through up to 2.5 cm (\sim plasma disruption length) of plasma (Fig. 4) [6].

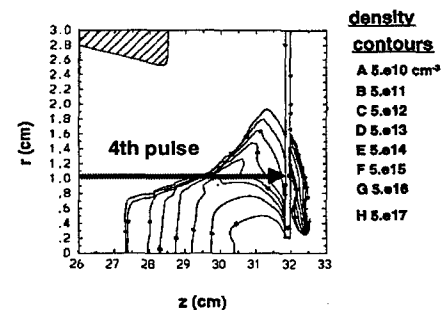


Fig. 4 Static Ta target's plasma density contours at 2 μ s. The target plasma is created by a 4 kA DARHT-II pulse at the beginning of 2 μ s.

4.2 Dynamic Target Configuration

The obvious advantages of using a single axis, dynamic target are preservation of the radiographic axis and ease

of beam transport without any beam repositioning optical elements. There are also other benefits. For a 0.6 mm radius beam striking a dynamic target moving at 1 cm/ μ s, reduction in energy deposition per unit mass over a 60 ns pulse would be 25 %, and reduction in the asymptotic plasma expansion velocity is 13 %. Also, a dynamic target moves the target plasma inertially away from the beam axis. Simulations show that none of four 4-kA current pulses will travel through the target plasma if the target is moving faster than 8 mm/ μ s (Fig. 5) [6]. Three options, a gas gun, shaped charge and flywheel, are available for the dynamic target. They all have difficulties to interface with a target chamber. Dynamic targets tend to be not very clean. However, cleanliness of the dynamic target should not be a concern for a multiple pulse system since an ion trap will be used to confine any target ions and contaminant ions.

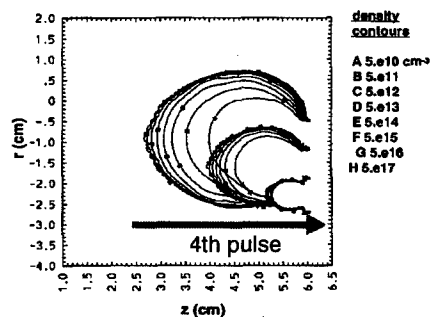


Fig. 5 Target plasma density contours at 2 μ s for a Ta target moving at 1 cm/ μ s. Three plasma plumes created by the first three 4 kA DARHT-II pulses separated by 630 ns are shown.

5 DISTRIBUTED TARGET

The DARHT-II radiographic specifications for the 2 kA, 20MV beam require the last beam pulse to generate an x-ray dose at 650 R @ 1m and the first three beam currents to generate three much lower dose x-ray pulses. The initial 4-pulse target consists of an ion trap and a static, distributed target that has ~ 20 thin 0.05 mm tungsten sheets distributed over 1 cm and separated by vacuum gaps. The sheets are held within a tungsten cylinder that provides radial confinement of the target. The single pulse, 2-3 kA, 16 MeV FXR experiment using a similar distributed target [7] demonstrated that the downstream side of target foils remained intact, and that the measured x-ray dose and spot size for the distributed foil target was the same as for a solid target as predicted by simulations. We have modeled the distributed target with the 2 kA DARHT-II current pulse format. For each pulse, the calculations include three types of modeling. First, a Monte Carlo calculation, using a given beam spot size, emittance and envelope slope, was done to calculate the beam scattering in the target and x-ray production. A hydro calculation was then carried out to characterize the target plasma. Finally, beam transport through the expanding plasma, including scattering and neutralization of target plasma and energy deposition by electrons, was modeled to determine the next pulse's spot size, emittance and envelope angle. These procedures were repeated

again for the subsequent pulse. To save computation time, the distributed foil target was modeled as a low density, foamed target. The calculations indicate that the configuration of distributed Ta foils within a Ta cylinder can radially confine the target material (Fig. 6). All four electron pulses will travel through the target with a line density equivalent to the line density of a Ta foil thicker than 0.25 mm. Therefore, it permits all four pulses using the same target material to produce the similar x-ray dose for photons within 2-6 MeV energy range.

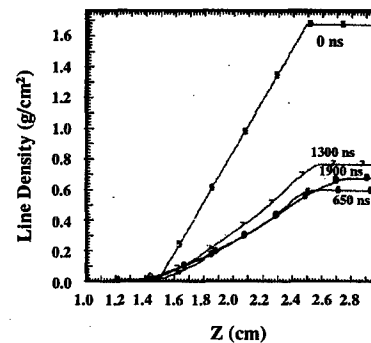


Fig. 6 Target line density for foamed target.

6 SUMMARY

We are developing the multiple pulse target system for the second axis of DARHT. Several configurations have been investigated. The baseline for the initial DARHT-II target configuration will consist of an ion trap and a distributed, static target that has ~ 20 thin 0.05 mm tungsten sheets distributed over 1 cm inside a tungsten cylinder and separated by vacuum gaps. The calculations indicate that no target replenishment is needed. However, the target density is the least for the most demanding dose requirement (the 4th pulse). We need experimental verification of target survivability through four pulses. Whether the quality of x-ray produced by all four pulses satisfy the radiographic also needs further investigation.

7 ACKNOWLEDGEMENTS

The authors like to thank many valuable discussions with T. P. Hughes, B. V. Oliver, and D. R. Welch.

8 REFERENCES

- [1] M.J. Burns, et al., "DARHT Accelerators Update and plans for Initial Operation," proceedings of this conference.
- [2] D. R. Welch & T. P. Hughes, "Effect of Target-Emitted Ions on the Focal Spot of an Intense Electron Beam," *Laser and Particle Beams* (1998), 2, pp.285-294.
- [3] J. McCarrick & T. L. Houck, "The Effects of Trapped Backstreaming Ions on Beam Focus in Radiographic Accelerators," proceedings of this conference.
- [4] T. J. T. Kwan, "Electron Beam-Target Interaction in X-ray Radiography," LA-UR-98-4802, submitted to *Physics of Plasma*, 1998.
- [5] T. P. Hughes, "Target Calculations for ITS Short-Focus Experiment," MRC Report MRC/ABQ-N-589, September 25, 1997.
- [6] D. D.-M. Ho, et al., "Hydrodynamic Modeling of the Plasma Plume Expansion from the Targets for X-ray Radiography," proceedings of this conference.
- [7] P. A. Pincosy, "Distributed Target for FXR," The Second Jointed Target Workshop, Livermore, CA May 21, 1998.
- [8] A. C. Paul, et al., "The Beamline for the Second Axis of the Dual Axis Radiographic Hydrotest Facility," proceedings of this conference.
- [9] D. S. Prono, private conversation.

BEAM DYNAMICS STUDIES FOR HEAVY ION FUSION DRIVERS*

A. Friedman*, J. J. Barnard, C. M. Celata, G. D. Craig, M. J. L. de Hoon, A. Faltens, D. P. Grote, E. P. Lee, W. M. Sharp, and E. Sonnendrucker†, LBNL/LLNL VNL for Heavy Ion Fusion
I. Haber, NRL
R. A. Kishek, University of Maryland

Abstract

A quantitative understanding of space-charge-dominated beam dynamics issues is essential to the development of a cost-effective driver for heavy-ion beam-driven inertial fusion energy (Heavy Ion Fusion, or HIF). A multi-laboratory "working group" is collaborating to develop such an understanding via detailed computer simulations, benchmarked versus experiments where possible. This work is motivated by the need to plan for an "Integrated Research Experiment" (IRE) facility to be proposed for construction, and for magnetic quadrupole beam transport experiments planned for the very near term. We began by identifying the issues which must be addressed; developing a model IRE design; and conducting "baseline" transverse WARPxy-code simulation studies of the central nominal-energy portion of the beam, for an ideal error-free version of that design. Current work is examining the effects of a wide spectrum of mismatches (including head-to-tail effects), errors, and imperfections, which establish the allowable tolerances and ultimately constrain the design. We are beginning to employ WARP3d to perform integrated time-dependent 3-D simulations from the source through the end of the machine.

1 INTRODUCTION

A successful HIF driver must produce a set of beams with the intensity, brightness, and pulse shape dictated by target requirements. This implies constraints on the ultimate transverse and longitudinal beam emittance. The beam phase space evolves as the beam moves down the accelerator, under the influence of applied-field, space-charge, and image nonlinearities, and of collective modes. Furthermore, it is necessary to minimize beam loss. This translates into limits on the allowable beam halo. Finally, the cost of the accelerator must be minimized, and so the beam must fill as much of the channel as possible. Thus a quantitative understanding of the dynamic aperture and its scaling with beam and accelerator parameters is essential.

Available experimental data is limited, so this effort must make heavy use of simulations and analytic theory, while planning for near-term full-scale magnetic transport experiments. The dynamics issues in a full-scale driver and a next-step IRE are very similar, except that issues associated with the highest beam kinetic energy arise only in the former. Detailed design is more urgently needed for IRE than it is for a driver, and simulations for a shorter system are more readily performed. Thus we are following a balanced approach whereby most calculations are being carried out in the IRE context.

Aspects of this work are presented in more detail in other papers at this conference; please see [1,2,3,4,5].

2 PRELIMINARY ACTIVITIES

As preliminary activities, we first identified a list of issues that must be addressed. These include mismatches and nonlinearities, machine errors, low-energy issues, collective modes, multi-beam and high-energy effects, and required diagnostics. We then developed "an" IRE design to use as the initial object of our studies. This is a "straw person" and is not "the" IRE design; however, a fairly complete "physics design" was needed. Finally, we began simulating a baseline "perfect IRE" accurately and efficiently, at first using a set of 2-D "slice" simulations of the center, head, and tail of the pulse, and most recently in full 3-D. It was deemed important to validate these simulations via convergence studies.

We sought a representative IRE design that would be credible, straightforward, and relatively easy to simulate. The design we developed is similar to an earlier "HTE Update" concept [6], but does not employ beam merging, since a detailed design for a magnetic merging section is not yet available. Relative to the earlier design, the initial pulse is twice as long, and the final kinetic energy is twice as great, so that the same total energy is achieved. This design is embodied in stand-alone scripts (versions using Basis and Python exist), which produce input that can be read by various codes, in particular the WARPxy and WARP3d PIC models, and SLV, a semi-Lagrangian Vlasov model. Some parameters are: initial line charge density $\lambda_1 = 0.25 \mu\text{C/m}$, pulse duration $\tau_1 = 7.33 \mu\text{s}$, 32 beams, 30 kJ total, phase advance $\sigma_0 = 70^\circ$, tune depression $\sigma/\sigma_0 = 0.1$, beam radius $a = 1.5 \text{ cm}$. Other features of this design are summarized in Table I.

These parameters set requirements on numerical resolution; the sheath at the edge of the beam falls off over 2-3 mm, so the maximum usable cell size is about 1 mm. With four-fold symmetry, we typically employ

*Work performed under the auspices of the U.S. DoE by LLNL, LBNL, NRL, and U. Md. under contracts W-7405-ENG-48, DE-AC03-76SF00098, DE-AI02-93ER40799 / DE-AI02-94ER54232 and DEFG0292ER54178.

#Email af@llnl.gov

†On leave from C.N.R.S., IECN – Projet Numath, Université Nancy 1, France.

	l_{beam} (m)	L_{hlp} (m)	I (A)	quad occ.	accel grad.	foc gradient
$V_0 = 1.6$ MeV	20.6	0.23	0.7	0.6	31	1.5×10^8 V/m ²
elec focusing accelerator: load- and-fire	const	$\propto V^{1/2}$	$\propto V^{1/2}$	0.6	$\propto V$	1.5×10^8 V/m ²
$V_1 = 8.3$ MeV	20.6	0.5	1.54	jump	148	jump
mag focusing accelerator 1: compression	$\propto V^{-1/2}$	$\propto V^{1/4}$	$\propto V$	0.33	$\propto V$	40 T/m
$V_2 = 52$ MeV	7.9	0.81	10.4	0.33	1000	40 T/m
mag focusing accelerator 2: const. accel	const	$\propto V^{1/2}$	$\propto V^{1/2}$	$\propto V^{-1/2}$	const	slow variation
$V_3 = 200$ MeV	7.9	1.59	20.4	0.17	1000	37 T/m

Table I. Parameters of reference IRE design

128 zones along each coordinate axis, then apply spatial filtering to minimize grid "aliasing" (this is important only for beams colder than those studied here); use of 32 zones unfiltered gives roughly similar results. Crude runs in (x,y) geometry require 5000-20,000 particles. Simulations of the baseline case also aided our learning to run WARPxy efficiently; we use the FFT Poisson solver, obtaining a round pipe via the capacity matrix method. We take the same number of steps across each half-lattice period. (HLP). HLP's start and stop at zero-length accelerating gaps, and the step size is changed at those points. We began by using sharp-edged elements and the code's "residence correction" capability which preserves second-order accuracy when the applied fields are so non-smooth. Numerical convergence tests show that with 80,000 particles and 128 cells there is emittance growth only in the second section; with 5000 particles, numerical collisionality causes some spurious growth of about 20%, but even this much is tolerable in the design, and less than that caused by undesirable physical effects, *e.g.*, mismatching of the off-nominal-energy parts of the beam.

3 ISSUES AND PROJECTS

Mismatch effects are associated with: transitions in the lattice period and element dimensions (does use of a small number of element designs lead to more emittance growth than a continuous variation, which may be harder to manufacture?); head-to-tail variations arising from acceleration and compression; and dispersion in bends, primarily in the injector, drift compression, and final focus sections. Nonlinearities of concern are associated with electric-quadrupole applied fields and images; magnetic quadrupole fields, including higher multipoles, and fringe fields (is it sufficient to design magnets that have zero integrated unwanted multipoles, or must cancellation be more local?); accelerating gap fields; and space charge, associated with nonuniform charge density.

We are beginning to examine (or re-examine) all of these areas; for example we employ both capacity-matrix methods (crude) and subgrid-scale boundary conditions (precise, but more expensive) to obtain electrostatic quadrupole fields and image effects. We also are comparing runs using axially-integrated fringe fields (lumped into an element one moderate Δs step long) against runs which resolve the fringing using small steps.

A key goal is the development of tolerance requirements with respect to errors in: beam alignment; magnet strength; magnet position and angle; accelerating waveforms (systematic, ripple and jitter); "ear" waveforms; and sensing / steering. The simulations in Figure 1 show the effect of various magnet errors on the normalized x emittance. Each color is an overlay of five runs with differing errors (obtained by varying the random number "seed").

Table II lists the RMS errors included in each set of runs (and notes whether the pseudo-octupole term is included in the magnet description); from top to bottom the rows in the table correspond to the shaded areas of the plot. The large fluctuations in the upper two plots with rotated quads appear because ϵ_{Nx} , rather than a generalized emittance, is shown.

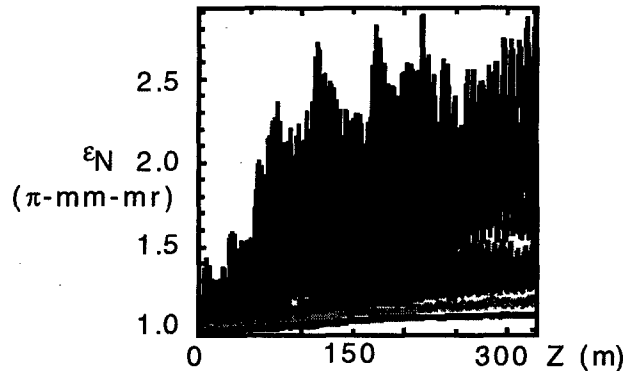


Figure 1. Effects of errors (see text and Table II).

Pseudo-octupole	Offset RMS	Strength RMS	Angle RMS
yes	25 μ	0.1%	0.2°
yes	25 μ	0.1%	0.1°
yes	25 μ	0	0
no	25 μ	0	0

Table II. Errors included in runs in Figure 1.

Low energy issues include: the initial longitudinal capture of the injected beam, using shaped accelerating pulses, and the initial acceleration program (a variant of "load and fire" is currently assumed, but may not be optimal); the competition between longitudinal "accelerative cooling" and collective modes which couple transverse thermal energy into longitudinal thermal energy

when the former exceeds the latter; and the relaxation of initial inhomogeneities via the phase-mixing of transverse oscillations. We are learning how to use a fixed computational grid in WARP3d to simulate the injection process, and then when the beam has been fully injected, setting the grid to act as a moving window so that it continually overlays the beam (zones are discarded from the "rear" of the mesh and inserted at the front; the alignment of the computational grid lines with the accelerator remains fixed). It is most rigorous to begin with an injected beam for all runs. However, for convenience it is desirable to learn how to begin simulations at downstream stations, and we are studying how best to do this; for example, we may be able to inject a Maxwell-Boltzmann beam at a "waist" (with correction for envelope convergence/divergence).

Collective mode issues include interactions of the beam with the walls and accelerating modules, especially: proper treatment of effects of voltage-divider shielding plates; longitudinal instability driven by module impedance (there has been much past work on this); and effects of the "beam break-up" mode (BBU). Transverse-longitudinal thermal energy coupling in the main accelerator needs to be better understood; does the seed amplitude matter, or is the beam always "marginally stable" with respect to this mode? If the seed amplitude matters, where does it come from, how big is it, and what are the implications with respect to machine design?

Multi-beam and high-energy issues include assessing the degree to which the separate beams must be kept "identical," understanding the deflections induced by neighboring beams, and the effects of the beam-induced magnetic field. This field can be important in a driver even when $v/c \leq 0.3$ because the self-electric field from neighboring beams may be well-shielded while the self-B is not; thus the "g-factor" which relates E_z to $\partial\lambda/\partial z$ can be driven negative, and space-charge waves may behave in an unfamiliar manner. The implications for longitudinal stability need to be understood. Furthermore, it is likely to be important to treat inductive effects with enough fidelity; to this end we are investigating magnetoinductive (Darwin) models, as well as simplified models motivated by the fact that (to a good approximation) the beam produces only a longitudinal current.

An early assessment of the required diagnostics will be important to the upcoming experiments; we must determine how often to measure the beam, in both the IRE (a research tool which must afford detailed knowledge of beam behavior through extensive diagnostics) and a driver (which needs just those diagnostics required for machine operation). Techniques for diagnosing beams at high kinetic energy must be developed.

4 DISCUSSION

We must refine the model IRE design. At the electric-to-magnetic transition, there is a jump in focusing strength

experienced by the "off-energy" head and tail of beam, so we may take out the velocity "tilt" in advance, and then reintroduce a larger tilt to initiate longitudinal bunch compression; alternatively, we can perhaps achieve "matching" via time-varying quadrupoles. Our near-term goal is to simulate the IRE in full 3D, including detailed accelerating waveforms and a realistic beam.

To properly model a fusion system it will be essential to perform integrated calculations. We must carry the particle distribution coming out of each accelerator section into the subsequent section, because the beam already has internal structure as it emerges from the injector, and disturbances can propagate long distances. Furthermore, the beam must have a particular pulse shape on target; hence it has a time-varying energy distribution and transverse distribution function, and the optical aberrations will be time-varying. Time-varying currents in the chamber affect the focusing, and must be modeled consistently with partial neutralization and other effects. Links have been made between WARP runs; linkages to the chamber code BIC, and thence to the target code LASNEX, exist, but have yet to be employed. It will also be desirable to establish links between the long-time beam transport calculations and detailed simulations studying instabilities, halo formation, and other effects. We believe that source-to-target simulation of a driver is within reach on upcoming "terascale" computers. A schematic for such simulations is depicted in Figure 2.

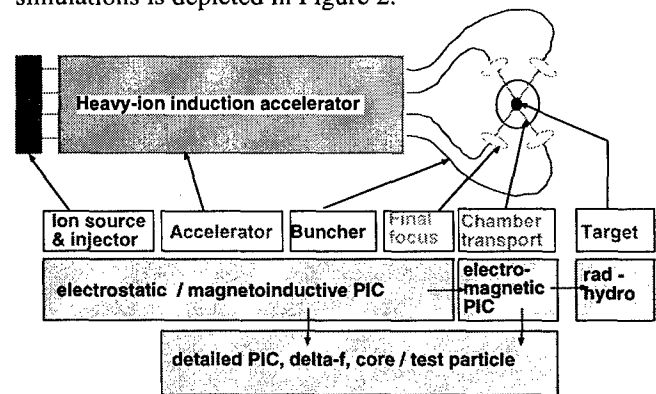


Figure 2. Schematic of driver and computational models.

5 REFERENCES

- [1] C. M. Celata, J. J. Barnard, and M. J. L. de Hoon, "Effects of Misalignments on Space-Charge-Dominated Heavy Ion Beams in an IRE," paper TUP133, this conference.
- [2] R. A. Kishek, J. J. Barnard, and D. P. Grote, "Effects of Quadrupole Rotations on the Transport of Space-Charge-Dominated Beams: Theory and simulations Comparing Linacs with Circular Machines," paper TUP119, this conference.
- [3] W. M. Sharp, D. P. Grote, and D. L. Judd, "Shaping and Focusing of High-Current Pulses for Heavy-Ion Fusion," paper TUP145, this conference.
- [4] D. P. Grote, et. al., "3-D Simulations Studies of IRE designs," paper THA61, this conference.
- [5] E. Sonnendruker, A. Friedman, and D. P. Grote, "Progress toward simulations of heavy ion beams for Inertial Fusion Energy based on a Darwin model field solver," paper THA64, this conference.
- [6] A. Faltens, "HTE Update," LBNL note HIFAR 468, May 3, 1996.

ACCELERATION SCHEDULES FOR A RECIRCULATING HEAVY-ION ACCELERATOR*

W. M. Sharp and D. P. Grote, LLNL, Livermore, CA

Abstract

The recent development of miniature inductive adders has made it feasible to design programmable high-repetition-rate pulsers with a substantially higher voltage than is possible using a conventional field-effect transistor architecture. Prototype pulsers using the new technology are being developed as part of a series experiments at Lawrence Livermore National Laboratory (LLNL) to test the concept of a recirculating induction accelerator. Preliminary numerical work is reported here to determine what effects the higher-voltage pulsers would have on the beam quality of the LLNL small recirculator.

1 INTRODUCTION

A series of scaled experiments is underway at the Lawrence Livermore National Laboratory (LLNL) to test the concept of a recirculating induction accelerator or "recirculator." The pulsed-power circuitry used to drive the induction modules on this "small recirculator" attains the needed precision and repetition rate by using a parallel array of field-effect transistors (FETs), which currently have a voltage limit of about 500V. Due to this limit, the original design required an induction modules or "cells" in each available half-lattice period (HLP) to meet the goal of doubling the beam velocity over fifteen laps. The pulsers for these modules constitute about half of the projected hardware cost of the small recirculator.

Recently, a project has been carried out jointly by the LLNL heavy-ion fusion group and First Point Scientific, Inc. (FPSI) to design prototype high-voltage pulsers for the small recirculator using the miniature inductive adders developed by FPSI. If successful, the new pulsers might lower the cost of the small recirculator by substantially reducing the number of acceleration modules.

The possible use of higher-voltage pulsers raises the question of whether applying stronger but less-frequent acceleration and control fields will seriously degrade beam quality in the LLNL small recirculator. In this paper, we report preliminary numerical work to compare the effects of using between five and thirty-four pulsers, using several acceleration schedules for each configuration.

2 METHOD

Acceleration schedules are examined here with the fast-running beam-dynamics code CIRCE [1], which combines an envelope description of transverse dynamics with a fluid-like treatment of longitudinal dynamics. For each acceleration schedule, the electric potential $V(t)$ across

induction modules is set up by a two-step calculation. A modified version of an approach developed by Kim and Smith [2] is used to generate acceleration fields for self-similar compression in the absence of the longitudinal space-charge field. Longitudinal-control fields or "ears" are then added to balance the longitudinal force due to the beam space charge.

As originally formulated, the Kim-Smith approach assumes that beam slices have ballistic trajectories between induction cells, so the velocity between the n th cell, centered at longitudinal position s_n , and the next one at s_{n+1} is

$$\beta_{n+1}^i c = \frac{s_{n+1} - s_n}{t_{n+1}^i - t_n^i} \equiv \frac{\delta s_n}{\delta t_n^i}, \quad (1)$$

where the slice arrival times t_{n+1}^i are chosen so that the beam current I_b at s_{n+1} is self-similar to that at s_n . When that the cell length is negligible, the voltage V_n^i needed in the n th cell at time t_n^i is then given approximately by

$$V_n^i \approx \frac{\tilde{\gamma}_i^3 M c^2}{2q e} [(\beta_{n+1}^i)^2 - (\beta_n^i)^2], \quad (2)$$

where q and M are the charge state and mass of beam ions, and $\tilde{\gamma}_i$ is the Lorentz factor associated with $\tilde{\beta}_i \equiv \frac{1}{2}(\beta_n^i + \beta_{n+1}^i)$.

The velocity estimate in Eq. (1) is suitable for a beam in a straight lattice, in which the design orbit coincides with the beam-pipe axis. In a circular accelerator like a recirculator, however, the head-to-tail velocity variation or "velocity tilt" needed for beam compression causes the lower-energy beam head to have a trajectory inside the design orbit, and the higher-energy tail has a trajectory outside it. This centroid displacement alters the path length of a slice in a bend and must be accounted for Eq. (1). A simple calculation using the approximation of continuous focusing shows that, for electric sector bends, each with an occupancy η_b , a radius ρ , and a mean radius $\bar{\rho} \equiv \rho/\eta_b$, the beam displacement X in the accelerator plane, averaged over the alternating-gradient flutter motion, is

$$\bar{X} \approx \frac{1}{\frac{\sigma_0^2}{4L^2} - \frac{K}{R^2} + \frac{2}{\bar{\rho}}} \frac{2 \Delta p}{p}. \quad (3)$$

Here, R is the beam-pipe radius, L is the half-lattice period, and σ_0 is the betatron phase advance over a full lattice period $2L$ in the absence of space charge. The "momentum error" $\Delta p \equiv p - p_0$ is difference between the local beam momentum $p \equiv \gamma \beta M c$ and the design momentum $p_0 = [q e \gamma M E_{bx} \rho]^{1/2}$, which is the value for which an ion will stay on the design orbit in a sector bend with a radius ρ and field strength E_{bx} . For a magnetic sector bend with a field strength B_{by} , the design momentum becomes $p_0 = q e \gamma M B_{by} \rho$, but the \bar{X} expression corresponding to Eq. (3) differs only in the factor $2/\bar{\rho}$ being replaced by $1/\bar{\rho}$. The phase-advance depression caused by

* Work performed under the auspices of the U. S. Department of Energy by Lawrence Livermore National Laboratory under Contract No. W-7405-ENG-48.

the beam space charge is accounted for by the term proportional to the perveance $K \equiv 2qeI_b/[4\pi\epsilon_0(\beta\gamma)^3Mc^3]$. To lowest order in \bar{X}/ρ , the added path length due to bends can be accounted for in Eq. (1) by the substitution

$$\delta s_n \rightarrow \delta s_n + \sum_{m=1}^{m_b} \frac{L_{bm}}{\rho_m} \bar{X}_i(s_{bm}), \quad (4)$$

where L_{bm} , ρ_m , and s_{bm} are respectively the length, bend radius, and axial location of m_b bends between the induction cells. Since \bar{X}_i depends on β_{n+1}^i directly through $\Delta p/p$ and γ_i , and indirectly through σ_0 and I_b , Eq. (1) becomes a transcendental equation for β_{n+1}^i and must be solved iteratively.

To calculate the full waveforms for acceleration and longitudinal-control, the modified Kim-Smith method is first used to generate waveforms for acceleration and compression only, ignoring the longitudinal component of the beam space-charge field. CIRCE is then run using these fields but with the longitudinal space-charge field artificially turned off, mimicking perfect longitudinal control. Finally, the beam current profile from this run is used to calculate the optimal ear field in each acceleration gap.

3 RESULTS

A large number of CIRCE runs have been carried out to study the effects of using higher-voltage cells in the LLNL small recirculator. This exploratory work uses simple acceleration schedules and a somewhat idealized lattice, ignoring fringe fields and errors, and employing sector bends instead of the more complicated "flat-plate" bends actually built. Nominal parameters of the small-recirculator are given in Table 1, and a detailed description of the lattice is found in Ref. [4]. With the nominal low-voltage pulsers, induction cells are required in thirty-four of the forty half-lattice periods. Three HLPs without acceleration are needed to insert the beam into the ring and to extract it, and a three-HLP extraction section is planned halfway around the ring. For this nominal case, the specified four-to-one reduction of the beam duration is obtained by imposing a velocity tilt as rapidly as possible, consistent with a maximum pulser voltage of 500V. The mid-point beam energy is taken to increase linearly with s except in the insertion/extraction sections, and the beam duration is specified so the first thirteen waveforms on the first lap are approximately triangular, with small deviations that account for the transverse space-charge field, and the remaining ones are nearly flat-topped.

After the final lap, centroid displacement X at the ends is about ± 0.3 cm, which is in fair agreement with the analytic estimate of Eq. (3). However, the plot in Fig. 1 of beam-head displacement for this case during the final lap shows substantial betatron oscillation, and the beam tail shows a similar betatron amplitude. This betatron motion arises because each pulse with a head-to-tail voltage increase ΔV causes an abrupt change in the momentum tilt $\Delta p/p$ without significantly changing X . From Eq. (3), we expect the centroid to be mismatched by an amount $\delta X \sim \delta(\Delta p/p)$, and a simple calculation using Eq. (2)

Table 1 Parameters of the LLNL small recirculator

beam parameters		
ion charge state	q	1
ion mass	M	39 amu
beam current	I_b	2 \rightarrow 8 mA
kinetic energy	$(\gamma_0 - 1)Mc^2$	80 \rightarrow 320 MeV
duration	Δt	4 \rightarrow 1 μ s
lattice parameters		
circumference	s_{\max}	14.4 m
half-period	L	36 cm
pipe radius	R	3.5 cm

shows that

$$\delta \left(\frac{\Delta p}{p} \right) \approx \frac{qe\Delta V}{2\bar{\gamma}_{mid}\bar{\beta}_{mid}^2 Mc^2}, \quad (5)$$

where $\bar{\beta}_{mid}$ is the average of β_{mid} before and after the cell and $\bar{\gamma}_{mid}$ is the corresponding Lorentz factor. The mismatches introduced in successive cells should add in a Markovian sense because the betatron wavelength of centroid motion is typically uncorrelated with the cell spacing. Therefore, if N pulses are used to give a specified energy increase and velocity tilt, so that $\Delta V \sim N^{-1}$, we expect the accumulated betatron amplitude to have the approximate scaling

$$\delta X \sim N^{\frac{1}{2}} \Delta V \sim N^{-\frac{1}{2}}. \quad (6)$$

3.1 Effects of pulser number

Comparing cases with from five to thirty-four cells per lap but with the same acceleration schedule, we find that the peak betatron amplitude at the beam ends approximately doubles going from thirty-four to eighteen cells, but then drops significantly for the ten-cell case, as seen in Fig. 1. This improvement results from the periodic spacing of cells that is possible in the ten-cell case. The two insertion/extraction sections prevent equal cell spacing in the lattices with eighteen and thirty-four cells, but when cells are added to these sections to make periodic lattices with respectively twenty and forty cells, the betatron motion at the beam ends becomes very similar to that for the ten-cell case. For the eight-cell and five-cell cases, the betatron oscillations are progressively worse due to the larger ΔV in the triangular pulses, effectively prohibiting the use of triangular waveforms in these lattices.

3.2 Effects of pulser waveforms

The mismatch of the beam ends caused by head-to-tail voltage variation can be reduced by using a smaller ΔV in a correspondingly larger number of induction cells. For the same overall compression, each lattice studied shows a reduction in beam-end betatron motion when a schedule with triangular pulses is replaced by one using a larger number of trapezoidal pulses. The minimum betatron amplitude is seen when trapezoidal pulses are used on all

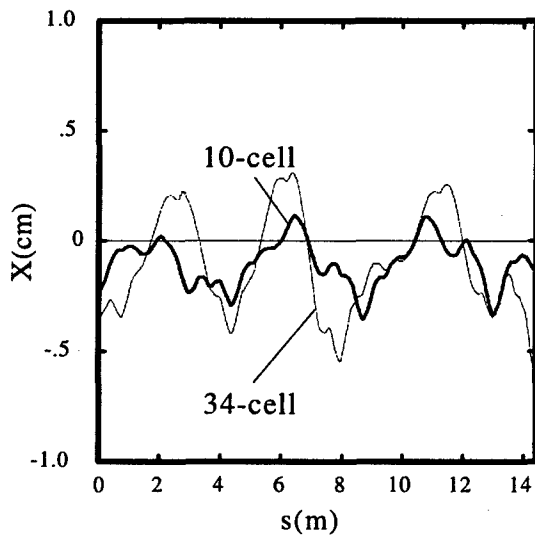


Fig. 1 Beam-head centroid displacement during the final lap in lattices with ten and thirty-four cells, with velocity tilt imposed rapidly during the first lap.

fifteen laps, as illustrated in Fig. 2. In lattices with regular cell spacing, we find that betatron motion introduced at the beam ends by a voltage tilt becomes negligible when $\Delta p/p$ changes in a cell by less than about 0.1%. Using Eq. (5), this criterion can be written to lowest order in β_{mid}^2 as

$$\frac{qe\Delta V}{\frac{1}{2}\beta_{mid}^2 Mc^2} \lesssim 0.004, \quad (7)$$

where $\frac{1}{2}\beta_{mid}^2 Mc^2$ is the beam kinetic energy in the non-relativistic limit. Nonperiodic cell spacing introduces an additional mismatch, leading to the fluctuations seen in Fig. 2 for thirty-four cells.

Another result of applying a reduced ΔV in more cells is that the maximum displacements of the beam head and tail increase. As the velocity tilt is applied more gradually, $\Delta p/p$ reaches its maximum of about 3% later in the acceleration sequence, and since σ_0 decreases roughly like β^{-1} for magnetic focusing, the average displacement at this point is larger, as seen from Eq. (3). Optimizing the acceleration schedule for a recirculator entails balancing this increased displacement against the reduced betatron amplitude found with a more gradual introduction of velocity tilt. The velocity tilt should therefore be introduced as rapidly as possible without initiating betatron oscillations at the beam ends, as determined by Eq. (7).

3.3 Emittance growth

The 3-D particle-in-cell code WARP3d [3] has been used to corroborate selected CIRCE results and to study emittance growth. In these comparisons, WARP3d used acceleration and ear fields generated by CIRCE and the same idealized lattice elements. As in CIRCE runs, WARP3d simulations using trapezoidal waveforms on all fifteen laps show substantially higher betatron amplitude in cases with thirty-four cells per lap than with ten. However, the amplitude is noticeably higher in both cases than in the corresponding CIRCE runs, evidently due to a poorer initial

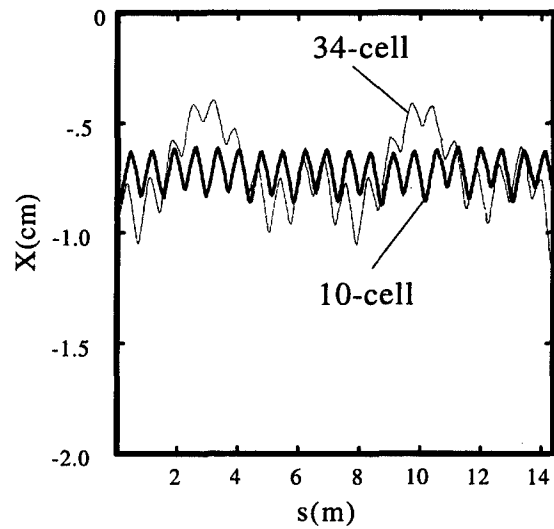


Fig. 2 Beam-head centroid displacement during the final lap in lattices with ten and thirty-four cells, with velocity tilt imposed gradually during all fifteen laps.

match. The particle simulations with thirty-four cells also show a larger and denser ‘halo’ of unconfined particles near the ends than the ten-cell simulations, resulting in a higher x -emittance near the ends. For both cases, the normalized emittance near the mid-point increases about 68% during the fifteen laps, but the increase is greater than 165% at two maxima near the ends for thirty-four cells, whereas no emittance growth above the mid-point value is seen the ten-cell case. The enhanced loss of ions near the beam ends in the thirty-four cell case appears to be another effect of nonperiodic cell spacing, since it is not seen in WARP3d runs in lattices with twenty or forty cells per lap.

4 CONCLUSIONS

The CIRCE and WARP3d simulations here indicate that beam in the LLNL small recirculator can be accelerated and compressed using as few as five acceleration cells per lap, provided that the velocity tilt is added gradually enough to avoid initiating betatron oscillations near the beam ends. A layout having ten uniformly spaced cells, with trapezoidal pulses used on perhaps the first five of the fifteen laps, appears optimum. This schedule produces acceptably small betatron oscillations at the beam ends, while keeping the centroid displacement less than 0.7 cm.

5 REFERENCES

- [1] W. M. Sharp, J. J. Barnard, D. P. Grote, S. M. Lund, and S. S. Yu, ‘Envelope Model of Beam Transport in ILSE,’ in *Proc. of the 1993 Computational Accelerator Physics Conference*, 22-26 February 1993, Pleasanton, CA, p. 540-548.
- [2] C. H. Kim and L. Smith, ‘A Design Procedure for Acceleration and Bunching in Ion Induction Linac,’ Lawrence Berkeley Laboratory Rpt. LBL-19137 (1985).
- [3] D. P. Grote, A. Friedman, I. Haber, and S. S. Yu, *Fusion Engineering and Design* 32-33, 193 (1996).
- [4] J. J. Barnard, et al., *Fusion Engineering and Design* 32-33, 247-258 (1996).

TIME-RESOLVED INVESTIGATION OF THE COMPENSATION PROCESS OF PULSED ION BEAMS

A. Jakob, H. Klein, A. Lakatos, O. Meusel, J. Pozimski

Abstract

A LEBT system consisting of an ion source, two solenoids, and a diagnostic section has been set up to investigate the space charge compensation process due to residual gas ionization [1] and to study experimentally the rise of compensation. To gain the radial beam potential distribution time resolved measurements of the residual gas ion energy distribution were carried out using a Hughes Rojanski analyzer [2,3]. To measure the radial density profile of the ion beam a CCD-camera performed time resolved measurements, which allow an estimation the rise time of compensation. Further the dynamic effect of the space charge compensation on the beam transport was shown. A numerical simulation under assumption of selfconsistent states [4] of the beam plasma has been used to determine plasma parameters such as the radial density profile and the temperature of the electrons. The acquired data show that the theoretical estimated rise time of space charge compensation neglecting electron losses is shorter than the build up time determined experimentally. An interpretation of the achieved results is given.

1 INTRODUCTION

Magnetic low energy beam transport (LEBT) systems enable space charge compensated transport of high perveance ion beams in comparison to electrostatic focussing systems, which suffer from the high beam

energy and the influence of the space charge forces on the beam. The magnetic LEBT suffers from the rise time of space charge compensation of pulsed ion beams.

Varying space charge forces of a pulsed ion beams lead to a shift of the focus and therefore to a mismatch of the following accelerator section. To investigate the effects of the rise time of compensation on the transport of ion beams a LEBT section with non-destructive diagnostics was set up in Frankfurt [5].

2 EXPERIMENTAL SETUP

Fig 1 shows the experimental set up at the Institut fuer Angewandte Physik (IAP) to investigate the behaviour of an ion beam (i.g. 10 keV) transported through a LEBT section. The LEBT has a length of approximately three meters and consist of an ion source, a first small diagnostic section, to measure the beam current directly behind the extraction system, two solenoids ($B_{max} = 0.8$ T) and a following diagnostic section with different diagnostic tools, to investigate the development of the compensation process. In the first step of the investigation of the compensation process the ion source was run in DC mode and the ion beam was decompensated in pulsed mode by a decompensation electrode electrode, which was biased at 350V, with a repetition rate of 1kHz, a decompensation time of 150 μ s (decompensation biased at 350V) and a compensation time of 850 μ s (grounded electrode).

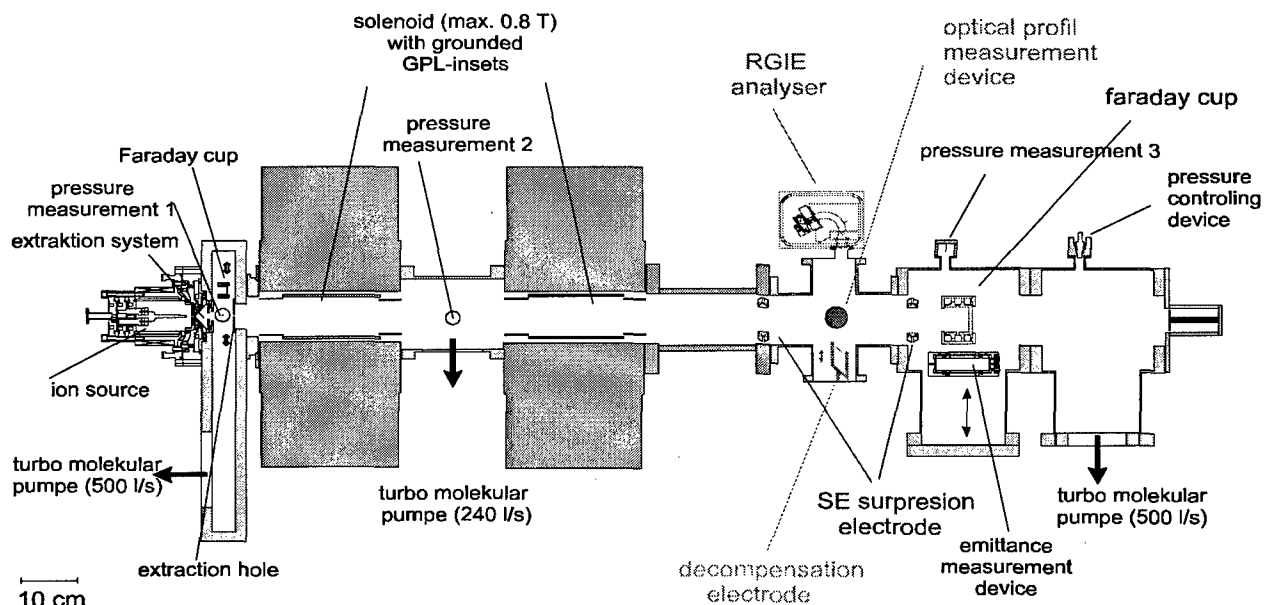


Figure 1: Frankfurt Low Energy Beam Transport (LEBT) section

As decompensation electrode a moveable wire was used. Thus it was possible to move the electrode to an definite place, which can be observe by the CCD camera, therefore we can be sure that the beam does not touch the wire, which has a strong effect on the compensation process by the production of secondary electrons. In the second step the ion source was run in pulsed mode, with a repetition rate of 1kHz and a duty cycle of 90 %. To observe the rise time of the ion source, the current measurements by the second Faraday cup in the LEBT (fig.1) were done using an oscilloscope. Fig.2 shows the result of such a measurement.

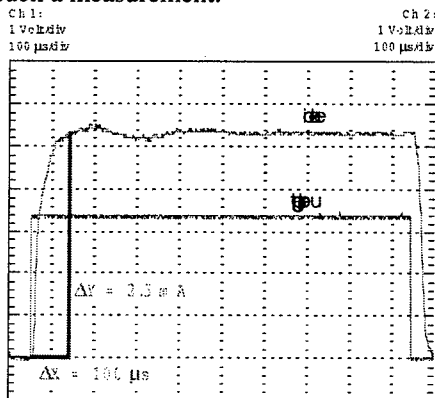


Figure 2: Beam current measurement of a pulsed ion beam

For a good comparability of the measurements all used diagnostics were placed at the same area, the CCD camera and the time-resolving residual gas ion energy analyser (RGIEA) were arranged orthogonally and the Faraday cup a few cm behind. The decompensation electrode also was placed orthogonally to the diagnostic devices to reach a local decompensation right at the region of interest. To find a better understanding of the data measured at the pulsed ion beam, the measurements at a pulsed decompensated DC ion beam were used as reference.

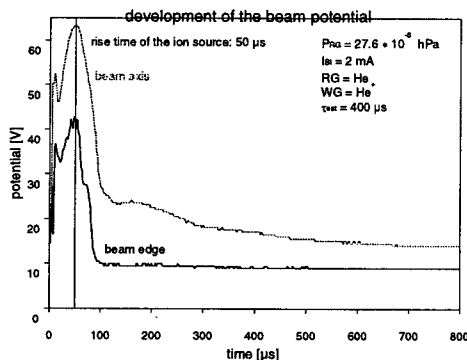


Figure 3: Temporal development of potentials of beam axis and beam edge.

The residual gas ions (RGI) produced by the interaction of beam ions and residual gas are expelled radially by

the self field of the beam. Under assumption of neglectable start energy, the kinetic energy of the RGI corresponds to the beam potential at the point of production. The energy distribution of the residual gas ions contains information on the radial beam potential distribution and thereby on the degree of compensation. For the time-resolving investigation of the build-up time of space charge compensation a RGIEA with an inserted single particle detector (channeltron) [5] was used. The time resolution was limited by the data acquisition to 2 µs.

3 MEASUREMENTS

Fig.3 shows the development of the beam potentials using pulsed beam operation obtained by the intersection point of the dynamic energy spectra and the 5% baseline (5% threshold) corresponding to the potential at the beam axis and the beam edge.

The CCD camera was used to observe the light emitted by the residual gas excited by the interaction of the beam ions with the residual gas molecules. Therefore one get the time development of the beam ion density under the assumption that the intensity of the emitted light is strongly correlated to the beam ion density. From the Abel transformation of the data gained from CCD measurements one can obtain the density profile of the ion beam. Fig 5 shows the development of the radius of the ion beam estimated from the 20 % threshold of the measured beam ion density profiles.

Fig.2 shows, that the ion source needs approximately 100 µs to reach a state of constant ion generation, then a current of 2 mA was measured. At 50 µs nearly 80% of the maximum current is reached, after 50 µs the current increases substantially slower. This can also be read off from fig.3. The potential increases up to 50 µs, then it decreases due to the compensation of the space charge forces of the ion beam.

In the first 50 µs the rise of the ion beam density dominates the development of the potential of the beam, due to the increasing ion production rate. Afterwards the compensation process dominates the potential development, which yields to a continuous potential depression. Fig.4 shows the development of the beam potential for a pulsed decompensated He⁺ (10kV, 2mA) DC ion beam under same conditions (residual gas pressure, beam current, duty cycle).

In comparison to the potential development of a pulsed ion beam, the potential depression starts just at the time when the compensation process begins. The maximum potential is by a faktor 1.5 higher in comparison to the pulsed operation mode. Both measurements (fig.2 and fig.4) show that after approximately 500 µs the process of potential depression is completed. Fig.5 also shows that after 500 µs the development of the beam radius,

obtained from the CCD profile measurements, is completed, no further shrinking can be ascertain. The comparison of both measurements shows, that in case of a pulsed ion beam the compensation process runs faster than in the case of a pulsed decompensated DC beam.

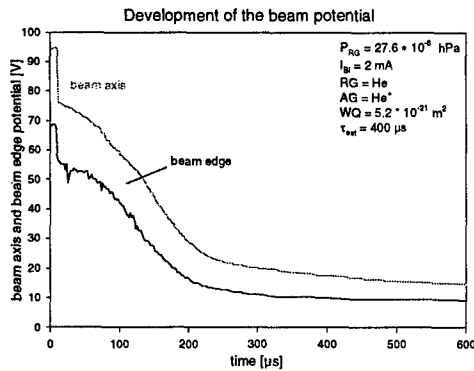


Figure 4: Temporal development of beam potential
In case of DC operation mode the potential drop inside the ion beam at the beginning of the compensation process has a substantially higher value in comparison to the pulsed operation mode of the ion source. Due to this effect two processes occur.

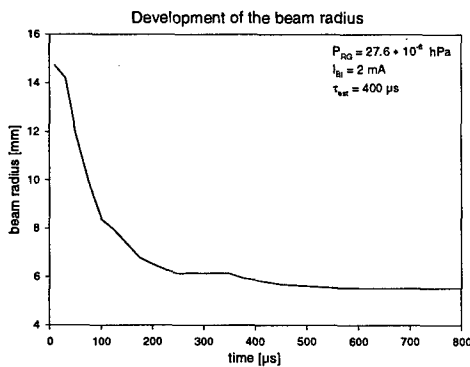


Figure 5: Temporal development of beam radius of a DC ion beam, which was decompensated in pulsed mode.
The compensation electrons produced at the beginning of the compensation process are trapped in the potential well. Due to the deeper potential drop in case of DC operation mode electrons of higher energy can be trapped. In case of pulsed mode faster electrons instantly get lost. The fast electrons increase the temperature of the trapped electrons. Due to the higher temperature it becomes harder for the decreasing beam potential to trap the electrons, which yields to a prolongation of the compensation process. Secondly the trapped electrons are accelerated in the potential gradient and therefore gain more kinetic energy in case of DC operation mode than in comparison to the pulsed operation mode, which yields to a higher average energy of the trapped electron ensemble and therefore again to a prolongation of the compensation process. In the present status of the analysis we do not know which process dominates. This

needs further studies and a precise investigation of the results of the self consistent simulations.

Fig 6 shows the development of the radius of a pulsed ion beam. It shows the same behaviour like in fig.5. (The fluctuation of the beam radius belongs to fluctuation of the measured data in combination with the data evaluation.)

The present considerations shows, that the process of space charge compensation of a pulsed as well as of a periodically decompensated DC He⁺ (10 keV, 2 mA) ion beam is finished after approximately 500 μ s. The rise time of compensation can be estimated [1] to 400 μ s assuming constant electron production rate and neglecting electron losses.

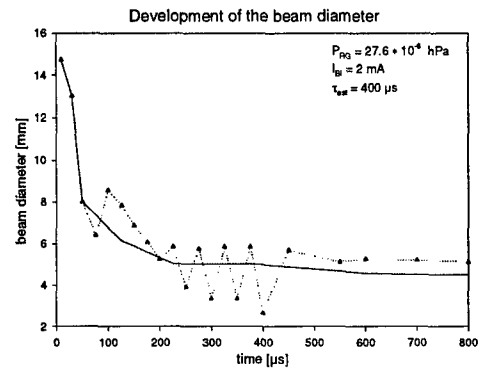


Figure 6: Temporal development of the beam radius of a pulsed ion beam, obtained from measured data (dotted line) and smoothed curve (full line).

4 FUTURE WORK

To get a precise estimation of the rise time of compensation, we have to await the results of the data evaluation using self consistent numerical simulation, which is in process. Furtheron the time-resolved measurements will be performed on a pulsed ion beam of other ion species and ions of higher energy.

The time development of the kinetic and potential energy of the compensation electrons will be analyzed using the numerical results of the simulation. The achieved particle and energy balance leads to a better understanding of particle loss processes, which is important for the investigation of the compensation processes.

5 REFERENCES

- [1] A.J.T. Holmes, Theoretical and experimental study of space charge intense ion beams., Phys. Rev. A 19 (1979), p 389
- [2] A.L. Hughes, V. Rojanski, On the analysis of electronic velocities by electrostatic field, Phys. Rev. 34 (1929) 291
- [3] R. Dölling, Raumladungskompensation driftender intensiver Strahlen niederenergetischer Ionen und Techniken zu ihrer Vermessung, Dissertation, IAP, JWG-University, Frankfurt, 1994
- [4] J. Pozimski et.al., „Determination of Electron Temperature in Partial Space Charge Compensated High Perveance Ion Beams“, Proc. International Symposium on Heavy Ion Inertial Fusion, II Nuovo Cimento 106A N.11, Frascati, Italy, May 1993, pp.1713
- [5] A.Jakob, Study of compensation process of ion beams, Proc XIX LINAC Conf. Chicago 1998

NEW LONGITUDINAL SPACE CHARGE ALGORITHM

Shane Koscielniak, TRIUMF, 4004 Wesbrook Mall, Vancouver, B.C., Canada

Abstract

We describe a new, improved longitudinal space-charge electric field calculation for particle beams with periodic modulation of the charge density. Whereas the usual method assumes long bunches with constant transverse cross-section, the new algorithm applies to long or short bunches with arbitrary binomial transverse distribution and incorporates dynamical corrections to the usual static approximation. The algorithm has been coded in Fortran and been made an option of the particle tracking program LONG1D. Based on tracking studies, it is concluded that these improvements to the physics model are most important for short bunches with high synchrotron frequency and high-order longitudinal multipole content.

1 INTRODUCTION

When simulating[6, 7] the longitudinal dynamics of a charged particle beam, it is customary to adopt a one-dimensional model that ignores the transverse coordinates and where each macro-particle is considered as a transverse slice or disc. The internal forces due to mutual Coulombic repulsion of like charges are called 'space-charge'. It is a common procedure to model longitudinal 'space charge' by forming the spatial derivative of the longitudinal charge density[4]. When this density is represented by a Fourier series, taking the derivative becomes particularly simple: each harmonic component is multiplied by its corresponding wave number (i.e. spatial frequency). This practice involves three assumptions:

- the beam bunches are long compared with the vacuum pipe cross-sectional radius
- the beam cross-section has constant charge density
- the field can be obtained (in the beam frame) from electrostatics.

1.1 Long bunches

The first assumption allows one to adopt a two-dimensional model for calculation of the transverse electric fields based on line charges (i.e. infinitely long filaments). This practice is inevitably dubious at the head and tail of the bunch. If one considers a moving point charge, with relativistic energy $\gamma m_0 c^2$, the longitudinal electric field is reduced by $1/\gamma^2$ and the field lines are 'compressed' into a transverse toroid that is coaxial with the motion. Hence it is clear that the assumption of line charges is best fulfilled by ultra-relativistic particles; but this is also the regime where longitudinal space charge is least important.

More realistic models that do not assume long bunches are available and have been used in computer simulations

– but not widely so. The simplest such model is that of Morton[1] (see also Refs.[3, 5]) in which the geometric factor g_0 is made to roll off with increasing spatial frequency. A more elaborate model is that of Lebedev[2], and we shall follow a similar procedure below.

1.2 Beam cross section

The field distribution depends on the transverse charge density distribution. It is also influenced by the proximity of the vacuum pipe which is taken to be a perfectly conducting cylindrical wall concentric with the beam. Further, the longitudinal electric field varies over the beam cross section and must be ensemble-averaged (transversally) so as to obtain values that are representative. All of these effects taken together are usually rolled into a single geometric factor g_0 . For example, for a uniform beam of radius a inside a pipe of radius b the on-axis geometric factor is $g_0 = 1 + 2 \ln(b/a)$ and the ensemble-average geometric factor is $g_0 = 0.5 + 2 \ln(b/a)$. These issues of transverse charge distribution and ensemble averaging have been addressed by Baartman[8], and will be pursued below.

1.3 Dynamics versus statics

Starting from the wave equation one may find an exact expression for the space-charge force in the frequency domain. Using this solution in a time-domain particle-tracking program leads to the following contradiction: the fields at each time step are calculated assuming the charge distribution is static and in equilibrium; however we also expect the beam distribution to be changing turn-by-turn in the synchrotron, or else there is little point performing a simulation. This contradiction is usually dismissed because "the effect is small"; the error incurred in the field estimate is of order the change in the beam distribution multiplied by the pipe radius and divided by the longitudinal distance moved in the time step. However, for machines with high synchrotron frequency and longitudinal distributions with significant high-order multipole content, changes in the distribution could be large. Moreover, at a fundamental philosophical level it is unsettling in a dynamical problem to use fields calculated for a statics problem.

2 NEW SPACE-CHARGE ALGORITHM

2.1 Field calculation

Let the electric field strength vector be \mathbf{E} , the charge density per unit volume be ρ . Suppose that the beam accelerates slowly. Let $s = ct$ where c is the speed of light and t

is the time coordinate. Let \mathbf{e} be a unit vector and \parallel denote the longitudinal axis. The electric field obeys the equation:

$$[\nabla^2 - \partial^2/\partial s^2] \mathbf{E} = (1/\epsilon_0) [\mathbf{e}_{\parallel} \beta_{\parallel} \partial/\partial s + \nabla] \rho. \quad (1)$$

Let r and z be the radial and longitudinal coordinates respectively, and $i = \sqrt{-1}$. Under the assumption that the charge distribution is longitudinally periodic and cylindrically symmetric, we may expand charge and field in Fourier series that contain a radial dependence for the coefficients:

$$\rho = \sigma(r) \sum_k \lambda^k(s) e^{ik(z-\beta s)\nu}, \quad \mathbf{E} = \sum_k \mathbf{E}^k(r, s) e^{ik(z-\beta s)\nu}. \quad (2)$$

Here k is the integer wave number and $\nu = h/R_s$ is the ratio of harmonic number h to the synchronous orbit radius R_s . Under the assumption that modulation frequencies are much smaller than the carrier frequencies, $\omega_k = k \times (\nu \beta_{\parallel} c)$, we may approximate the temporal field derivative as

$$\frac{\partial^2}{\partial s^2} \mathbf{E} \approx \sum_k - \left[(k\beta\nu)^2 \mathbf{E}^k + 2i(k\beta\nu) \frac{\partial}{\partial s} \mathbf{E}^k \right] e^{ik(z-\beta s)\nu}. \quad (3)$$

We substitute expressions (2, 3) into the wave equation to obtain a relation for each Fourier component

$$\begin{aligned} [\nabla_{\perp}^2 - (k\nu)^2/\gamma^2] E_z^k + 2i(k\nu\beta)(E_z^k)' \\ = \frac{\sigma(r)}{\epsilon_0} [i(k\nu)\lambda^k/\gamma^2 + \beta_{\parallel}(\lambda^k)'], \end{aligned} \quad (4)$$

where the superfix prime ($'$) denotes partial derivative w.r.t. s and ∇_{\perp}^2 is the transverse part of the Laplacian operator.

Let us suppose the transverse charge distribution of radius a is given by the (unity-normalized) binomial form

$$\sigma(r) = [1 - (r/a)^2]^{\mu} 2(\mu + 1)/a^2. \quad (5)$$

Because there is no transverse multipole content, we expand each of the field coefficients in terms of the zeroth order Bessel function basis:

$$E_z^k(r, s) = \sum_j a_{kj}(s) J_0(\alpha_j r). \quad (6)$$

To fulfil the boundary condition of a conducting wall at $r = b$ we take $J_0(\alpha_j b) = 0$ are consecutive zeros of the Bessel function. To find the time-dependent coefficients a_{kj} we make use of the orthogonality relation[11] between Bessel functions, leading to

$$\begin{aligned} (b^2/2) J_1^2(\alpha_j b) \{ [-\alpha_j^2 - (k\nu/\gamma)^2] a_{kj} + 2i(k\nu\beta) a_{kj}' \} \\ = (1/\epsilon_0) [i k \nu \lambda^k + \beta_{\parallel} (\lambda^k)'] B(\mu, \alpha_j a) \end{aligned} \quad (7)$$

where the function

$$B(\mu, x) \equiv (\mu + 1)! 2^{(\mu+1)} J_{\mu+1}(x)/x^{(\mu+1)}. \quad (8)$$

The longitudinal electric field is given by

$$E_z(r, z, s) = \sum_k e^{ik(z-\beta s)\nu} \sum_j a_{kj}(s) J_0(\alpha_j r). \quad (9)$$

To find the effective longitudinal field for a one-dimensional particle simulation, we must ensemble average over the transverse distribution; and this leads to

$$\langle E_z \rangle(z, s) = \sum_k e^{ik(z-\beta s)\nu} \sum_j a_{kj}(s) B(\mu, \alpha_j a). \quad (10)$$

If the charge density does not change then we may find an explicit expression for the complex coefficients a_{kj} ; and the static field is given by $\langle E_z \rangle(z, s) =$

$$\frac{1}{\epsilon_0} \sum_k e^{ik(z-\beta s)\nu} \sum_j \frac{-ik\nu \lambda^k B^2(\mu, \alpha_j a)}{(b^2/2) J_1^2(\alpha_j b) [(\alpha_j \gamma)^2 + (k\nu)^2]}. \quad (11)$$

For the case $k\nu \ll \gamma\alpha_j$ and $\mu = 0$ this expression leads to field values identical with the simple theory involving $g_0 = (1/2) + 2 \ln(b/a)$.

2.2 Discretization

If the line charge coefficients λ^k are time dependent then Eqn. (7) must be solved numerically using a suitable scheme that discretizes the time steps and replaces the derivatives by finite difference representations. In the computer program LONG1D[9] we have chosen a scheme that is consistent with the leap-frog algorithm for integrating particle motion under space charge and also does not require any more evaluations of λ^k than does a naive scheme assuming static fields. Essentially, the field coefficients are propagated from old to new values by using the replacements:

$$2a_{kj} \Rightarrow a_{kj}^{new} + a_{kj}^{old} \quad (12)$$

$$\Delta s a_{kj}' \Rightarrow a_{kj}^{new} - a_{kj}^{old} \quad (13)$$

$$2\lambda^k \Rightarrow \lambda_{new}^k + \lambda_{old}^k \quad (14)$$

$$\Delta s (\lambda^k)' \Rightarrow \lambda_{new}^k - \lambda_{old}^k \quad (15)$$

in Equation (7) with $\Delta s = c\Delta t$. In such a scheme one needs a "start-up procedure" and the simplest is to assume that $\lambda_{new}^k = \lambda_{old}^k$ before the first time step.

3 EXAMPLES AND TESTING

As an initial test of these formulae, we took a bunch in a machine with parameters similar to the original PS Booster at 50 MeV. We took line density $\lambda(\phi) = [1 - (\phi/L)^2]^3$ with $\phi = \nu z$ and $L = 1$ radian and transverse parameters $\mu = 0$, $a = 6$ cm in a pipe of radius $b = 10$ cm.

3.1 Short bunches

Under the assumption of statics, the field distribution was calculated according to equations (7) and (10) for harmonic numbers $h = 5$ and $h = 500$ and bunch lengths 10 m and 10 cm, respectively. The result is sketched in Figure 1.

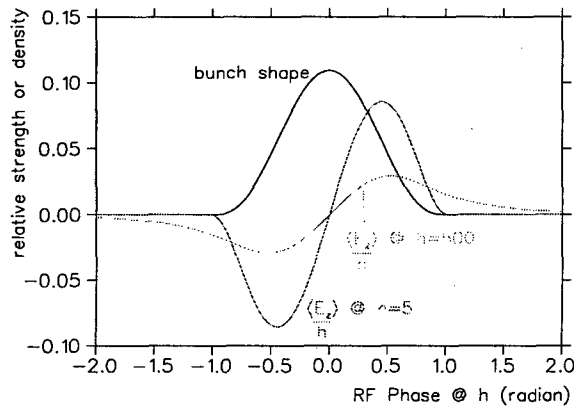


Figure 1: Comparison of $\langle E_z \rangle$ for long ($h = 5$) and short ($h = 500$) bunch lengths.

3.2 Statics versus dynamics

In order to see the dynamical correction to the static field approximation, the bunch was displaced 0.1 radian during a time step of one turn (so as to imitate part of a dipole oscillation) and the field calculated with and without the correction. The relative fractional error incurred by ignoring dynamical effects is presented as a mountain range plot in Figure 2. It is clear that the errors are worst at the head and tail of the bunch, and this is confirmed in the transverse ensemble-average, Figure 3, with peak errors of about 10% in narrow regions. However, these are the regions with fewest particles and so there is probably little impact on the beam dynamics of dipole oscillations.

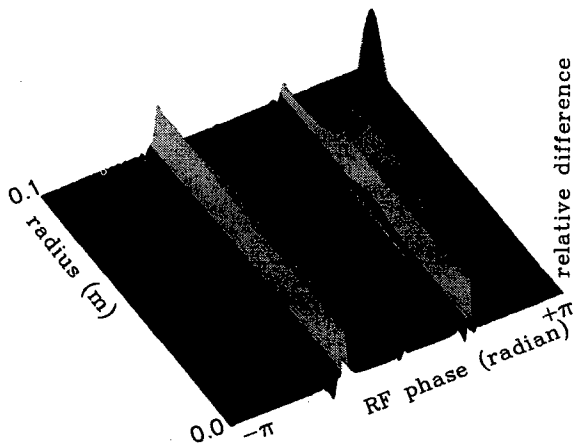


Figure 2: Comparison of relative fractional difference of $E_z(r, z)$, computed with and without dynamical corrections to the static approximation, versus cylindrical coordinates r, z . Vertical scale runs from -0.02 to +0.24.

3.3 Particle tracking

As a final test, the new space-charge algorithm was installed in the computer program LONG1D[9]. The evolution of a proton bunch in the TRIUMF KAON Accumulator ring mis-matched so as to give both dipole and quadrupole oscillations was tracked for 0.5 ms (about 4000

space-charge time steps) with and without the dynamical correction. The 450 MeV A-ring has $R_s = 34$ m and $h = 45$. Tracking of 5×10^4 macro-particles showed ensemble characteristics for the two cases to differ by only 1-to-2 parts in 10^4 .

4 CONCLUSION

We have described a new, improved longitudinal space-charge electric field calculation[10] for particle beams with periodic modulation of the charge density. The algorithm has the following features:

- correct for short or long bunches
- general binomial transverse density distribution
- transverse ensemble averaging
- field is solution of electrodynamics problem with time varying longitudinal charge density.

The algorithm has been coded in Fortran and been made an option of the particle tracking program LONG1D. In early trials, with accumulator and booster-type ring parameters, the dynamical corrections seem to be of little importance for dipole and quadrupole mode oscillations.

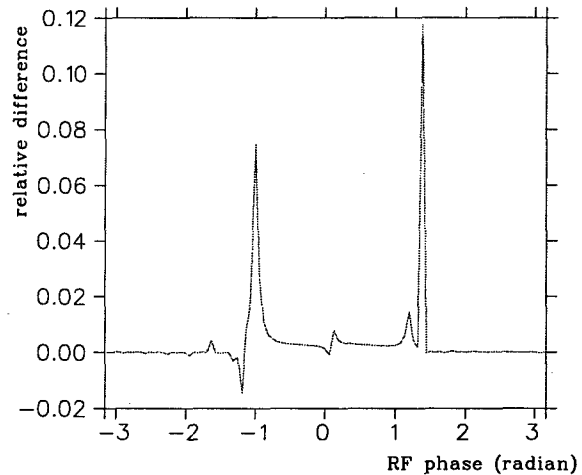


Figure 3: Comparison of relative fractional difference of $\langle E_z \rangle(z)$ computed with and without dynamical corrections.

5 REFERENCES

- [1] P. Morton: Rev Sci Inst, **36**, p.429, 1965.
- [2] A.N. Lebedev & E.A. Zhilkov: N.I.M. **45** pp.238-244, 1966.
- [3] W. Hardt: Proc. HEACC-IX, Stanford, 1974, p.434.
- [4] A. Hofmann: CERN 77-13, pp.141-145.
- [5] J. Laclare: CERN 85-19, pp. 381-384.
- [6] S. Koscielniak: Proc. EPAC88, Rome, 1988, pp 743-745.
- [7] J. Wei et al: Particle Accelerators, **23**, 1989.
- [8] R. Baartman: TRI-DN-92-K206.
- [9] S. Koscielniak: TRI-DN-97-12.
- [10] S. Koscielniak: TRI-DN-98-13.
- [11] M. Gradshteyn & I. Ryzik: *Tables of integrals, series and products*, Academic Press, 1964.

SIMULATIONS, EXPERIMENTS, AND ANALYSIS OF BEAM TARGET INTERACTION

Thomas J. T. Kwan, David C. Moir, and Charles M. Snell
Los Alamos National Laboratory, Los Alamos, NM

Abstract

The onset of the growth of the electron beam spot due to partial charge neutralization by ions extracted from the target plasma has been predicted by theory and simulation. The concept of an electrically self-biased target was developed to control the length of the ion column and experiments were fielded on the Integrated Test Stand (ITS) for the Dual Axis Radiographic Hydro Test (DARHT) facility at Los Alamos National Laboratory. The experimental results confirmed the stability of the spot size when the target is self-biased at a potential of 350 kV. Our analyses and quantitative comparison between computer simulations and experiments show that the ions generated by the electron beam were from target materials and that the delay for onset of the spot growth was governed by the time needed for the ionization of target material and formation of the ion column with sufficient length.

1 INTRODUCTION

The Dual Axis Radiographic Hydro Test (DARHT) machine uses an intense electron beam of 4 kA and 20 MeV to produce high dose radiation with small spot size for radiography of dense dynamic objects. However, this combination of high current in a small area leads to undesirable effects such as intense local energy deposition from the high intensity electron beam causing vaporization of the bremsstrahlung target. The hot plasma thus generated provides a copious source of positive ions that are rapidly accelerated into the negative potential well of the incoming electron beam. As the ions propagate upstream, they partially charge neutralize the electron beam. The carefully designed stable propagation of the electron beam to the target is disrupted, and its spot size at the target begins to increase. As the ions move further upstream, they neutralize an ever-increasing length of the electron beam, causing its spot size to diverge [1,2]. For the last two years, the important physics of the stability of the radiation spot size of the DARHT facility has been under intensive study. In 1997 the concept of an electrically self-biased target was developed by Kwan and his colleagues [3,4] to limit the length of the charge neutralizing ion column, which leads to the increase of the electron beam spot on the target plane. Shortly thereafter a target chamber based on the self-biased target concept was designed and fielded on the Integrated Test Stand (ITS) at Los Alamos National Laboratory [5]. The experimental results clearly confirmed the validity of the theoretical concept and the

utility of the design to achieve stable radiographic spot throughout the electron beam pulse. At the same time, the data also revealed several important and intriguing phenomena. It is the purpose of this paper to provide an interpretation of our experiments through detailed analysis and quantitative comparison to simulations. The conclusions from our study show that the ions which cause partial neutralization and subsequently lead to the increase of beam spot size on the target plane are predominantly coming from the target material itself and not from foreign contaminants. In other words, the ions are singly-charged ions with large atomic masses. Furthermore, the delay for the onset of growth of the spot size observed in the experiments was the time for the electron beam to deposit enough energy to cause ionization of target materials and the subsequent growth of the ion column to sufficient length for strong focusing of the electron beam.

2 EXPERIMENTAL ANALYSIS

The target experiments were fielded on the ITS, which is the injector for DARHT. It has an electron beam of

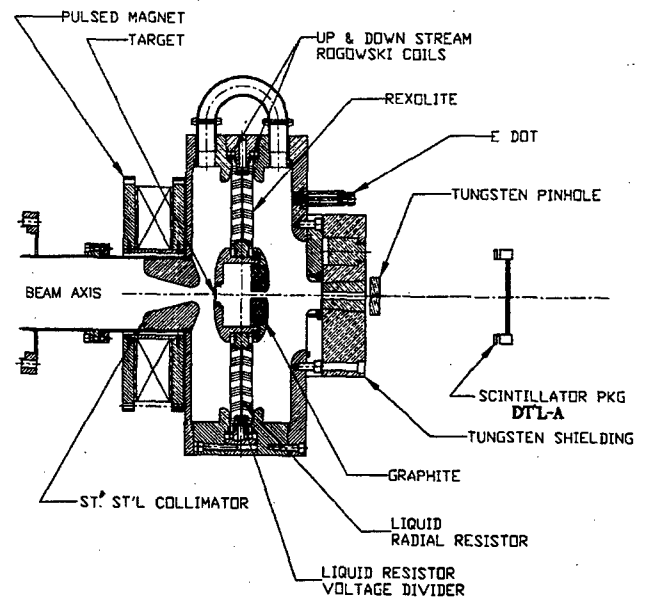


Figure 1: Experimental layout of the self-biased target chamber

energy 5.6 MeV and current up to 4 kA. The target chamber is shown in Fig. 1. For a given electron beam current, the magnitude of the self-biased target voltage can be chosen by selecting a desired resistance of the liquid radial resistor within the Rexolite. The electrical

resistance can be readily varied with the change of the salt concentration of the sodium thiosulphate of the resistor. Consequently, the charge deposited by the electron beam in the target assembly would establish a bias potential between the target and the collimator. An emittance filter was used in the beam line to reduce the electron current to 3.0 kA. The resistance of the liquid resistor was set at 145 ohms and 6 ohms for two experiments, respectively. The experimental results of the time behavior of the bias potential and electron current in the resistor are shown in Fig. 2. For a resistance value of 145 ohms, a bias potential of approximately 350 kV was developed to trap the ions and limit their axial excursion from the target. The upper part of Fig. 2 shows the electron current in the liquid resistor during the experiment.

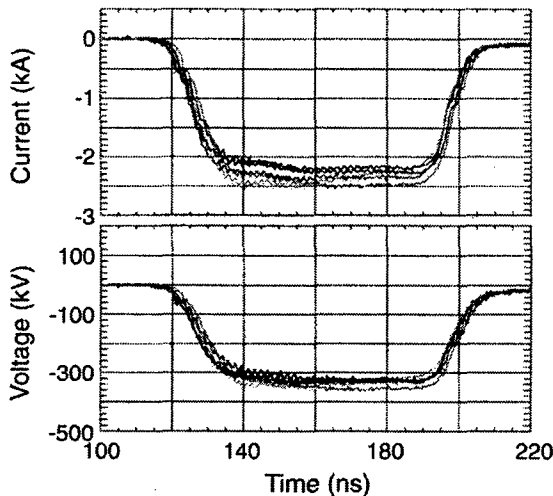


Figure 2: Experimental results of the electron current and voltage through the 145 ohms resistor. The multiple traces show the reproducibility of the experiment.

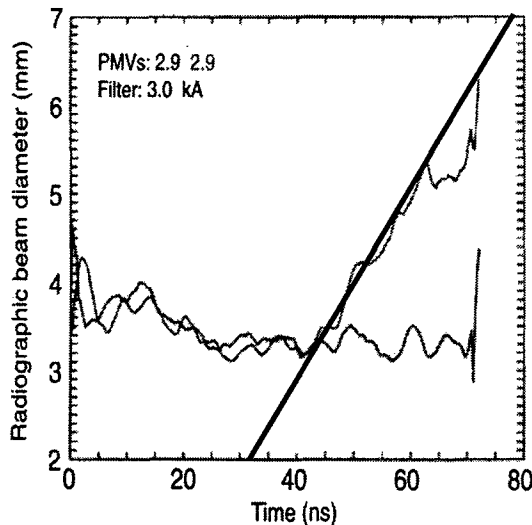


Figure 3: Radiation spot size obtained from the experiment. The slope gives the radial expansion velocity of 1.08×10^{-2} cm/ns.

In Fig. 3, we show the experimental results of the time dependence of the radiation spot size. The converter target was copper and had a thickness of 0.76 mm. We note that the radiation spot size stayed constant throughout the beam pulse in the presence of the bias potential. However, the other experiment with the resistor set to a very low value of 6 ohms produced a negligibly small bias potential and the radiation spot started to increase after about 40 ns into the beam pulse. More importantly, the rate of expansion of the electron beam spot size on the target plane is directly related to the velocity of the ions moving upstream. Comparison with simulations with different species of ions allows us to infer the particular ion species present in the experiment.

3 COMPARISON WITH COMPUTER SIMULATIONS

We have simulated the interaction of the electron beam with the converter targets in the ITS experiments using the two-dimensional, self-consistent, fully electromagnetic, relativistic particle code Merlin. The radial resistor was modelled in the r-z simulations as a vacuum diode with resistance corresponding to different magnitudes of bias voltage generated by the electron beam to confine the ions. The root-mean-square (rms) radius of the electron beam on the target plane was monitored during simulation. Neglecting the diffusion of beam spot due to electron scatterings in the converter target, one can relate the rms radius of the electron beam to the diameter of the Los Alamos radiation spot size by a factor of 3.76 [6]. Different species of ions were used in simulations to obtain the effect on the growth of the radiation spot size when the target is not biased. Figure 4 shows the time evolution of the radiation spot from the simulations with hydrogen ions with and without the buildup of the bias potential at the target. The bias potential is found to adequately stabilize the spot size whereas the spot increases in size without the bias. Figure 5 shows the temporal dependence of the bias potential from the simulation, which attains a steady value of 350 kV after the rise of the electron beam current. The good agreement between simulation and experiment confirms the concept and the design of a bias target for high dose radiographic applications.

In the absence of a bias potential, the ion column continues to expand and therefore, the beam spot size on the target increases. The radial expansion velocities of the radiographic spot can be obtained from experiment (Fig. 3) and simulation (Fig. 4). The electric potential, which accelerates the ions upstream, is determined by the space charge of the electron beam. Consequently, the ratio of

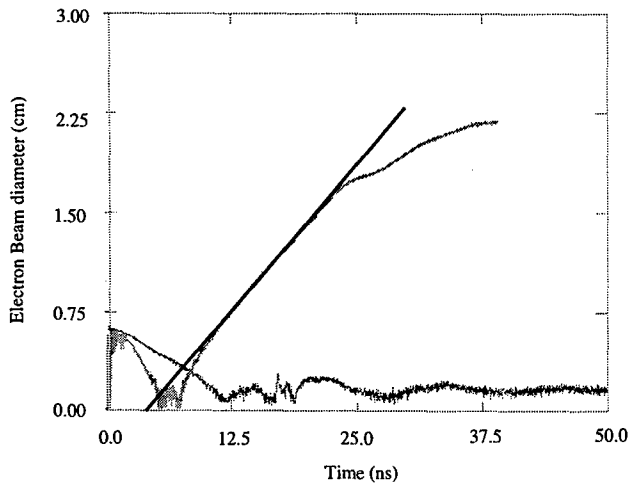


Figure 4: The electron beam diameter on the target plane from simulations with hydrogen ions.

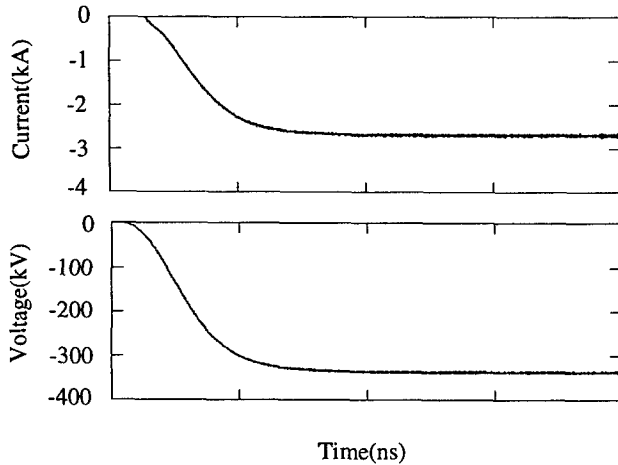


Figure 5: Bias Potential and electron current in the resistor as obtained from the simulation.

the velocities of different species of ions is inversely proportional to the ratio of the square root of the masses. Hence, we have $(M_1/M_2)^{1/2} = V_2/V_1$, where M_1 and M_2 denote the masses the ions species. For simplicity, one can rewrite the equation in terms of their atomic masses, $(A_1/A_2)^{1/2} = V_2/V_1$. The radial expansion velocities from the simulations with different ion species are tabulated in Table 1. The last column in Table 1 gives the atomic mass of the ions in the experiment as inferred from the simulations. The prediction is consistent with the target, which was copper in the experiment.

Table 1: Radial expansion velocities and ion masses

	$V_{sim}(cm/ns)$	A_{sim}	A_{expt}
H^+	8.67×10^{-2}	1	64.5
C^+	2.46×10^{-2}	12	62.3
O^+	2.18×10^{-2}	16	65.2
Cu^+	1.14×10^{-2}	64	70.5

The experimental data in Fig. 3 show the onset of the increase of the spot size occurred at 40 ns. This delay time is due in part to the time for vaporization to occur at the target spot and in part to the time for the target ions to form a column more than a quarter of the betatron wavelength of the electron beam near the target. The fractional pulse length τ of the electron beam needed to deposit enough energy to create sufficient ionization can be calculated according to $\tau = sT_b a / (d\epsilon/dx) I_b$, where s and T_b are the specific heat and the boiling temperature of the target material, respectively, a is the area of beam spot, I_b is the beam current, and $d\epsilon/dx$ is the energy loss of incident electrons in the target. For the ITS experiment, τ is found to be 14 ns, and the time for the ion column to reach 3 cm is about 28 ns. The delay time is then estimated to be 42 ns, which is consistent with the experiment.

4 CONCLUSIONS

A self-biased target fielded on the ITS experiments demonstrated the validity of concept and utility of the design. A self-biased potential of 350 kV was observed and a stable spot was confirmed in the experiment. Good agreements with the simulations have been obtained. Furthermore, comparisons between simulations and experiments show that the ions present in the experiments were from the target material, and that the delay time for the onset of the spot size growth was due to the time needed for target ionization and the formation of an ion column of sufficient length.

5 ACKNOWLEDGEMENTS

The authors wish to thank T. Hughes, D. Prono, L. Thode, and D. Wolkerstorfer for valuable discussions. This work is supported by the U.S. DOE.

6 REFERENCES

- [1] Thomas J. T. Kwan, John C. Goldstein, and Barbara G. DeVolder, "Influence of Ions on Electron Beam Spot Size in ITS/DARHT," Los Alamos National Laboratory Research Note, XPA-RN(U)97-021 (June 1997).
- [2] Dale R. Welch and Thomas P. Hughes, "Effect of Target-Emitted Ions on the Focal Spot of an Intense Electron Beam," *Laser and Particle Beams*, Vol. 16, no. 2, pp.285-294, 1998.
- [3] T. J. T. Kwan and C. M. Snell, "Stabilization of Radiographic Spot Size via Self-Biasing Targets," Los Alamos National Laboratory Research Note, XPA-RN(U)97-048 (November 1997).
- [4] Thomas J. T. Kwan and Charles M. Snell, "Electron Beam Spot Size Stabilization for Radiographic Applications," *Proceedings of 1998 International Congress on Plasma Physics*, Prague, Czech Republic (July 1998).
- [5] T. J. T. Kwan, D. C. Moir, B. G. DeVolder, C. M. Snell, M. Kang., "Design Simulation for Spot Size Stabilization of ITS/DARHT," *Proceedings of LINAC98 Conference*, Chicago, IL, Aug. 23 - 28, 1998.
- [6] K. H. Mueller, "Measurement and Characterization of X-Ray Spot Size," *Proceedings of the 1989 Flash Radiology Topical Conference*, American Defense Preparedness Association, pp383-391 (1989).

Email: tjtk@lanl.gov

BEAM HALO STUDIES USING A 3-DIMENSIONAL PARTICLE-CORE MODEL*

J. Qiang[†], R. D. Ryne, S. Habib, LANL, Los Alamos, NM

Abstract

In this paper we present a study of beam halo based on a three-dimensional particle-core model of an ellipsoidal bunched beam in a constant focusing channel. For an initially mismatched beam, three linear envelope modes – a high frequency mode, a low frequency mode and a quadrupole mode – are identified. Stroboscopic plots are obtained for particle motion in the three modes. With higher focusing strength ratio, a 1:2 transverse parametric resonance between the test particle and core oscillation is observed for all three modes. The particle-high mode resonance has the largest amplitude and presents potentially the most dangerous beam halo in machine design and operation. For the longitudinal dynamics of a test particle, a 1:2 resonance is observed only between the particle and high mode oscillation, which suggests that the particle-high mode resonance will also be responsible for longitudinal beam halo formation.

1 INTRODUCTION

The physics of beam halo has been extensively studied through analytical theory and multi-particle simulations[1, 2, 3, 4, 5, 6, 7, 8, 9, 10]. In these studies, the so-called particle-core model has been frequently used. This model provides insight into the essential mechanism of halo formation and enables estimates of the extent of beam halo. In this paper, we will use a three-dimensional particle-core model with a nonlinear rf field to study beam halo formation in a mismatched ellipsoidal bunched beam. Three envelope modes will be identified and their effects on the formation of beam halo through a parametric resonance with test particles will also be studied for the given physical parameters.

Bunch Current (A)	0.1
Proton Energy (MeV)	471.4
Synchronous Phase (degrees)	-30
rf Frequency (M Hz)	700
Accelerating gradient (MV/m)	5.246
Transverse Phase Advance (degrees)	81
Lattice Period (m)	8.54
Transverse RMS Emittance (π -mm-mrad)	0.2319
Longitudinal RMS Emittance (π -deg-MeV)	0.42

The physical parameters of the beam and the accelerator are given in Table 1[11]. The organization of this paper

* Work supported in part by DOE Grand Challenge in Computational Accelerator Physics.

[†] Email: jiqiang@lanl.gov

is as follows: the particle-core model is described in Section 2, the linear envelope modes are discussed in Section 3, the test particle dynamics under three envelope modes is presented in Section 4, and the conclusions are drawn in Section 5.

2 THREE-DIMENSIONAL PARTICLE-CORE MODEL

In the three-dimensional particle-core model, the beam consists of a core and test particles. The core, which contains most particles, is modeled by the rms envelope equations. The test particles contain a small fraction of the beam and are subject to the effects of external forces and space charge forces due to the core. The effects of test particles on the core and the mutual Coulomb interactions among test particles are neglected. The bunched core is assumed to have a uniform charge density distribution. Under the smooth approximation, the envelope equations for the bunched beam including nonlinear rf focusing are:

$$r_x'' + k_{x0}^2 r_x' - I_x(r_x, r_y, r_z, 0)r_x - \frac{\epsilon_x^2}{r_x^3} = 0(1)$$

$$r_y'' + k_{y0}^2 r_y' - I_y(r_x, r_y, r_z, 0)r_y - \frac{\epsilon_y^2}{r_y^3} = 0(2)$$

$$r_z'' + k_{z0}^2 f(r_z)r_z' - I_z(r_x, r_y, r_z, 0)r_z - \frac{\epsilon_z^2}{r_z^3} = 0(3)$$

with

$$I_i(r_x, r_y, r_z, s) = C \int_s^\infty \frac{dt}{(e_i^2 + t)\sqrt{(r_x^2 + t)(r_y^2 + t)(\gamma^2 r_z^2 + t)}} \quad (4)$$

where the semi-axes r_i are related to the RMS beam sizes a_i by $r_i = \sqrt{5}a_i$, $e_i = r_x, r_y, \gamma r_z$ ($i = x, y, z$), and $C = \frac{1}{2} \frac{3}{4\pi\epsilon_0} \frac{q}{mc^2} \frac{I}{f_{rf}\beta^2\gamma^2}$. Here, ϵ_0 is the vacuum permeability, q is the charge, mc^2 is the rest energy of the particles, c is the vacuum light speed, I is the beam average current, f_{rf} is the rf bunch frequency, $\beta = v/c$, v is the bunch speed, and $\gamma = 1/\sqrt{1-\beta^2}$. The quantities k_{x0} and k_{y0} are the transverse betatron wave numbers at zero current, which are defined as $k_{i0} = \sigma_{i0}/L$, $i = x, y$, under the smooth approximation for a periodic quadrupole focusing element. Here, σ_{i0} is the zero-current transverse phase advance per focusing period L . The longitudinal synchrotron wave number at zero current, k_{z0} , is defined as $k_{z0} = \sqrt{2\pi q E_0 T \sin(-\phi_s) / \gamma^3 \beta^3 mc^2 \lambda}$, where $E_0 T$ is the accelerating gradient, ϕ_s is the synchronous phase, and λ is the rf wavelength. The function $f(r_z)$ in the envelope

equation is a nonlinear rf focusing factor defined in Ref. 9. In the above envelope equations, we have used a continuous sinusoidal wave to represent the average effect of the synchronous rf space harmonics in the rf gap and neglected the acceleration of the rf field. The emittances, ϵ_x , ϵ_y , and ϵ_z , are five times the corresponding RMS emittances.

The equations of motion for a test particle in the presence of a uniformly charged core and external focusing fields are

$$x'' + k_{x0}^2 x - I_x(r_x, r_y, r_z, s)x = 0 \quad (5)$$

$$y'' + k_{y0}^2 y - I_y(r_x, r_y, r_z, s)y = 0 \quad (6)$$

$$\Delta z'' + k_\xi(\cos(k_\eta \Delta z + \phi_s) - \cos(\phi_s)) - I_z(r_x, r_y, r_z, s)\Delta z = 0 \quad (7)$$

where $k_\xi = qE_0 T / mc^2 \beta^2 \gamma^3$, and the parameter s is zero for a particle inside the core and is determined from the root of the equation

$$\frac{x^2}{r_x^2 + s} + \frac{y^2}{r_y^2 + s} + \frac{\Delta z^2}{r_z^2 + s} = 1 \quad (8)$$

for a particle outside the core. These coupled nonlinear ordinary differential equations are solved numerically using a leap-frog algorithm.

3 LINEAR ENVELOPE MODES

The steady state solution of the envelope equations has three components which define the stationary core size. For a mismatched beam three linear eigenmodes of the core envelope will be excited. From linear perturbation theory, we can find the eigenmodes of a mismatched core oscillation. For the physical parameters given in Table 1, we get the normalized wave number 1.945 for the high frequency mode, 1.641 for the low frequency mode, and 1.456 for the quadrupole mode.

To investigate the possible resonance between the test particle and the mismatched core oscillation, we calculated the evolution of the ratio of the possible test particle wave numbers to the mismatched mode wave number as a function of current with all the other physical parameters given in the Table 1 fixed. The results for the transverse betatron motion is given in Fig. 1. It shows that a 1:2 resonance be-

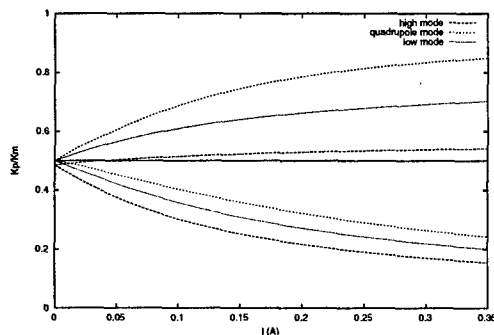


Figure 1: The ratio of particle betatron wave number to mode wave number as a function current

tween the test particle and low mode and quadrupole mode is always excited. For the high mode, the 1:2 resonance is excited when the current exceeds 40 mA. At a current of 100 mA, as in the present APT design, the 1:2 resonance between the betatron motion of test particles and all three mismatch-modes is excited. Fig. 2 shows the evolution of the ratio between the wave number of the particle synchrotron motion and the wave number of the high mode and low mode. Here, the 1:2 resonance between the test

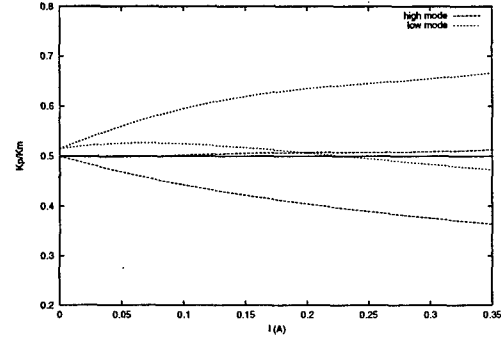


Figure 2: The ratio of particle synchrotron wave number to mode wave number as a function current

particle and high mode is excited with current greater than 60 mA. The 1:2 resonance between the particle and the low mode is only excited with a current greater than 230 mA.

4 TEST PARTICLE DYNAMICS UNDER THREE ENVELOPE MODES

For the mismatched core, three linear modes can be excited. When the ratio of the test particle wave number to the core envelope mode wave number is rational, the resonance between the test particle and core will be excited. Among these resonances, the 1:2 resonance is what we are most interested in. This is because this low order resonance will have the large oscillation amplitude and is generally believed to be responsible for the presence of beam halo. To understand the potential effects of these envelope modes on the test particle dynamics and beam halo formation, we use stroboscopic map to study the test particle dynamics with only one envelope mode excited each time. Fig. 3 (a) shows the stroboscopic plot of test particle dynamics in the $x - p_x$ plane under high mode envelope oscillation with 20% initial transverse mismatch. Fig. 3 (b) shows a similar plot of test particle dynamics in the $x - p_x$ plane under the low mode. Fig. 3 (c) shows the same plot for the quadrupole envelope oscillation. The peanut structure in the $x - p_x$ plane suggests that the 1:2 resonance between the test particles and the core envelope oscillation could be excited for all three modes. In Fig. 4 (a) and (b), we show the stroboscopic plots of the resonance between the synchrotron particle motion and the high envelope mode and low envelope mode in the longitudinal $\Delta z - \Delta p_z$ plane. In this case, the 1:2 resonance is present only for the high mode in the

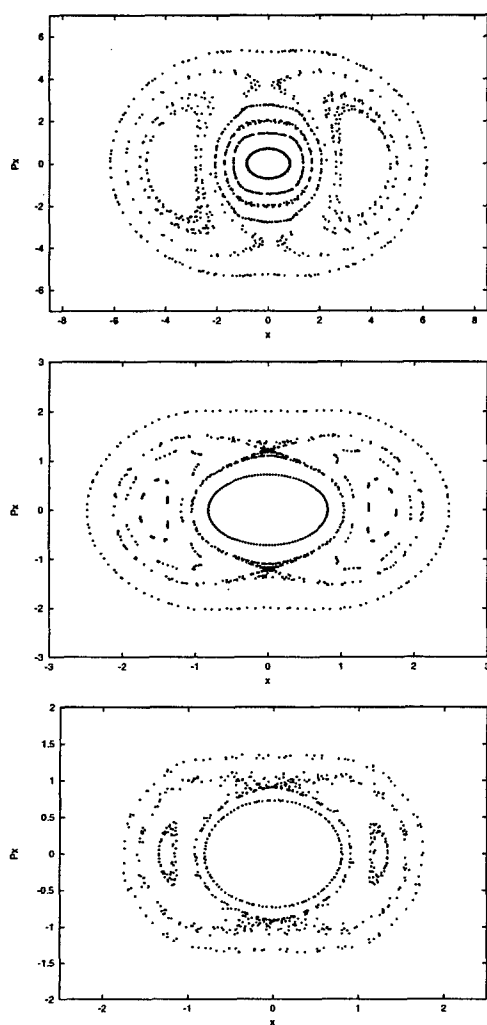


Figure 3: Stroboscopic plot of $x - p_x$ for high mode, low mode and quadrupole mode with 0.2 mismatch.

longitudinal phase space.

5 CONCLUSIONS

In the above study, we have used a three-dimensional particle-core model to study beam halo in a mismatched ellipsoidal bunched beam. Three linear envelope modes, a high frequency mode, a low mode and quadrupole mode, are identified. The 1:2 transverse resonances are present between the test particle and all three envelope modes. Among the three transverse particle-core resonances, the high mode presents the greatest potential danger for the machine design and operation due to its large transverse resonance amplitude. The high mode resonance also dominates the longitudinal 1:2 resonance which contributes to the formation of longitudinal beam halo.

6 ACKNOWLEDGMENTS

We are grateful to Drs. T. Wangler and J. Barnard for fruitful discussions. This work was performed on SGI Origin

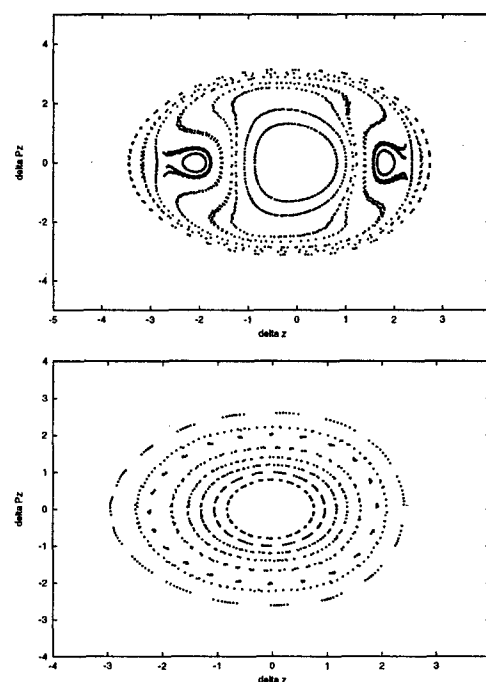


Figure 4: Stroboscopic plot of $\Delta z - \Delta p_z$ for high mode and low mode with 0.2 mismatch.

at the Los Alamos Advanced Computing Laboratory and T3E at the National Energy Research Scientific Computing Center.

7 REFERENCES

- [1] R. L. Gluckstern, Phys. Rev. Lett. **73**, 1247 (1994).
- [2] R. A. Jameson, Los Alamos Report No. LA-UR-94-3753.
- [3] J. Lagniel, Nucl. Instrum. Methods Phys. Res. A **345**, 46 (1994).
- [4] R. D. Ryne and S. Habib, Part. Accl. **55**, 365 (1996).
- [5] H. Okamoto and M. Ikegami, Phys. Rev. E **55**, 4694 (1997).
- [6] R. L. Gluckstern, A. V. Fedotov, S. S. Kurennoy, and R. D. Ryne, to appear in Phys. Rev. E, (1998).
- [7] T. P. Wangler, K. R. Crandall, R. Ryne, and T. S. Wang, Phys. Rev. ST Accel. Beams **1**, 084201 (1998).
- [8] J. J. Barnard and S. M. Lund, in Proceedings of the 1997 Particle Accelerator Conference, Vancouver, Canada (unpublished).
- [9] K. Bongardt, M. Pabst, and A. Letchford, in LINAC 98 conference, Chicago, 1998.
- [10] M. Ikegami, Phys. Rev. E **59**, 2330 (1999).
- [11] Private communications, 1999.

A PARTICLE-CORE STUDY OF HALO FORMATION FOR A MISMATCHED BEAM IN A PERIODIC-FOCUSING SYSTEM

Tai-Sen F. Wang** and Thomas P. Wangler, LANL, Los Alamos, NM

Abstract

This work is an attempt to explore possible techniques to graphically display the dynamics of halo particles for a mismatched beam in a periodic-focusing lattice. It is found that by using the particle-core model and a suitable change of the phase-space variables, stroboscopic plots similar to those made for the uniform-focusing channel can be created by strobing at the frequency of the core oscillation. This method does not require any smooth approximation to reduce the flutter due to the periodic focusing, and it is not limited by the constraint that the core-oscillation frequency has to be a subharmonic of the focusing frequency. The discussion will cover the applications to both the axisymmetric and the quadrupole-focusing channels. It is also found that, similar to the continuous-focusing system, the motion of halo particles, although focused by the externally applied periodic field, is strongly influenced by a parametric resonance.

1 INTRODUCTION

The particle-core model has successfully explained the dynamics of particles in the beam halo of a mismatched beam propagating through a uniform-focusing channel.[1-12] The simplicity of the model makes it possible to mathematically analyze the motion of a particle in the beam halo and provides a graphic picture using the stroboscopic plot made on the phase plane of a test particle. However, when attempting to apply the same model and method to a beam propagating through a periodic-focusing channel, one encounters difficulties both in mathematical analyses and in making the stroboscopic plots. The main cause of these difficulties is the flutter in the beam envelope and the particle orbit introduced by the varying focusing field.

In this paper, we will show that by using appropriate phase-space variables and by strobing at the frequency of the core oscillation, the flutter due to the periodic focusing can be greatly reduced. This method works best when the beam current is not very high, but it is also applicable to a wide range of parameter values. We will first introduce the new phase-space variables; then we will present the method and discuss the application of this new approach to

a quadrupole-focussing system. Numerical examples will be given for a core with a Kapchinskij-Vladimirskij (KV) distribution of beam particles. The emphasis in this paper is to introduce the method. More studies using this approach will be reported in other publications.

2 THE PARTICLE-CORE MODEL

We consider a theoretical model which has a test particle and a continuous beam (the core) propagating in a periodic-focusing channel. We consider a core with a KV distribution of particles. The linear transverse focusing force is assumed to vary in the axial direction (the z -direction) according to $GF(kz)$ where G is the maximal gradient of the focusing (or defocusing) strength, $F(kz)$ is a periodic function of z , and k is the wave-number of the periodic-focusing system. The maximum of $|F(kz)|$ is assumed to be one.

We consider the axisymmetric focusing case first. Using the variable $\tau = kz$, the equations of motion for the beam envelope and the test particle are:

$$\frac{d^2 X}{d\tau^2} + Q^2 X F(\tau) - \frac{\eta}{X} - \frac{1}{X^3} = 0, \quad (1)$$

and

$$\frac{d^2 x}{d\tau^2} - \frac{L^2}{x^3} + Q^2 x F(\tau) = \begin{cases} \eta x / X^2, & \text{for } x \leq X, \\ \eta / x, & \text{for } x > X, \end{cases} \quad (2)$$

respectively, where $x = x_r \sqrt{k/\epsilon}$, $X = X_r \sqrt{k/\epsilon}$, x_r is the transverse displacement of the particle from the symmetry-axis of the beam, X_r is the beam envelope, $Q^2 = qG/(m_0 \gamma v^2 k^2)$, $\eta = qI/(2\pi\epsilon_0 m_0 \gamma^3 v^3 k \epsilon)$, and $L = L_r/(m_0 \gamma v \epsilon)$; q , m_0 , and L_r are the charge, the rest mass, and the angular momentum of the test particle, respectively; γ is the relativistic mass factor, v is the axial speed of beam particles, I is the beam current, ϵ_0 is the permittivity of free space, and ϵ is the unnormalized total beam emittance.

We now introduce a set of new variables defined by

$$u = x/X, \quad (3)$$

$$w = X^2(du/d\tau) = X(dx/d\tau) - x(dX/d\tau), \quad (4)$$

and

$$u_e = X_m/X, \quad (5)$$

$$w_e = X^2(du_e/d\tau) = X(dX_m/d\tau) - X_m(dX/d\tau), \quad (6)$$

where the subscript m is for a matched core. Rewriting Eqs. (1) and (2) using these new variables, we find that these equations then depend explicitly on X instead

*Work supported by Los Alamos National Laboratory, under the auspices of the US Department of Energy.

** Email: TWANG@LANL.GOV

of $F(kz)$. Results from both numerical experiments (see Fig. 1 below) and perturbation calculations show that the flutter in u and w is smaller than that in x and $dx/d\tau$. One can also prove that the change of variables from $(x, dx/d\tau)$ to (u, w) is a canonical transformation, and for particles inside the phase-space ellipse of the beam core, the new Hamiltonian is a constant of motion with respect to the time s (defined by $ds = d\tau/X^2$). For particles outside the ellipse, the Hamiltonian is time-dependent and is non-integrable.

The proposed approach here is to study the particle dynamics in the phase space of (u, w) and to make the stroboscopic plot by taking snapshots of the particle's phase space at a certain fixed value, say, the maxima or the minima, of u_e . Numerical results have shown that the oscillation frequency of u_e is not constant in the periodic-focusing case, and strobing at constant period creates larger spread of points in the stroboscopic plots. Note that in Eqs. (3) and (4), one can also choose to normalize to X_m in place of X to minimize the flutter in u and w .

In quadrupole-focussing channels, the equations of the beam envelope and particle motion in the x -direction are

$$\frac{d^2 X}{d\tau^2} + Q^2 X F(\tau) - \frac{2\hat{\eta}}{X+Y} - \frac{\epsilon_x^2}{X^3} = 0, \quad (7)$$

and

$$\frac{d^2 x}{d\tau^2} + Q^2 x F(\tau) = \frac{2\hat{\eta}x}{\Xi_x(\Xi_x + \Xi_y)}, \quad (8)$$

respectively, where $X = X_r\sqrt{k}$, $Y = Y_r\sqrt{k}$, X_r and Y_r are the beam envelopes in the x - and y -directions, respectively, $x = x_r\sqrt{k}$, x_r is the displacement of the beam particle in the x -direction from the beam axis, $\hat{\eta} = qI/(2\pi\epsilon_0 m_0 \gamma^3 v^3 k)$, ϵ_x is the beam emittance in the x -direction, $\Xi_x = \sqrt{X^2 + \xi}$, $\Xi_y = \sqrt{Y^2 + \xi}$, $\xi = 0$ when the particle is inside the beam, and ξ is given by the solution of the equation $(x/\Xi_x)^2 + (y/\Xi_y)^2 = 1$, when the particle is exterior to the beam, $y = y_r\sqrt{k}$, and y_r is the excursion of the beam particle in the y -direction from the beam axis. The equations for the beam envelope and particle motion in the y -direction are similar. To generalize our method developed for axisymmetric systems to a quadrupole-focussing system, one can use the variables defined according to $u_x = x/X$, $w_x = X(dx/d\tau) - x(dX/d\tau)$, $u_{ex} = X_m/X$, $w_{ex} = X(dX_m/d\tau) - X_m(dX/d\tau)$, and similar definitions for the y -direction variables. Since both the beam envelope and the test particle now have two degrees of freedom, only the stroboscopic plots made for some special cases can be deciphered easily. Thus, we have to consider the x - and y -motion of the particle separately by setting one of the coordinates to zero, e.g. $y = 0$ and $dy/d\tau = 0$. Besides, in addition to the breathing mode, the beam envelope can now also

oscillate in a quadrupole mode. Since the frequencies of these two modes are very close, even when the test particle is limited to have only one degree of freedom, it still may resonate with either one or a combination of these two envelope modes.

3 NUMERICAL EXAMPLES

Figure 1 presents an example of a periodic-focusing channel showing that the flutter is less in u than in x . The case studied is an axisymmetric focusing channel with $F(\tau) = \cos \tau$, and $Q^2 = 0.31966$. At zero beam current, the betatron phase advance of a beam particle is 90° per period. At full beam current, $\eta = 0.206$ corresponding to a depressed phase advance of 60° per period for particles inside of the matched core. The initial values are: $u = 1.23491$, $X = 3.34883$, $u_e = 1/0.9$, $w = dX/d\tau = 0$, and $L_r = 0$.

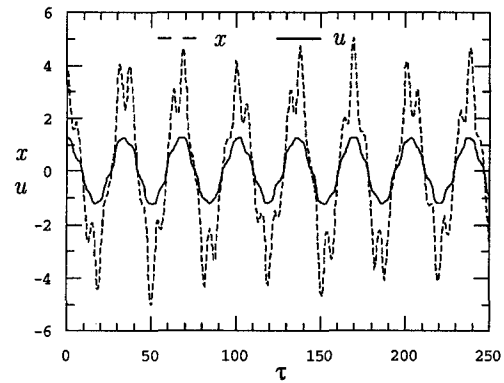


Fig. 1. The orbit x and the quantity u of a particle in a mismatched beam. The parameter values are described in the text.

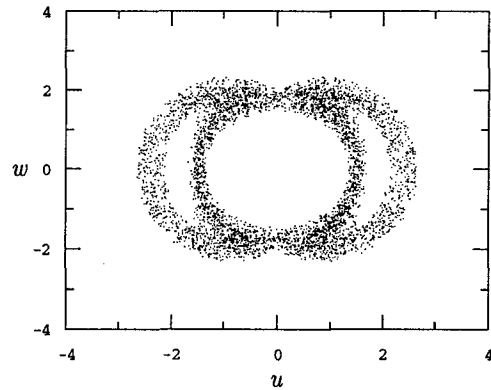


Fig. 2. The stroboscopic plot of the particle's position on the phase plane of u and w , where the same parameter values considered in Fig. 1 were used in the computation.

Figure 2 shows a typical stroboscopic plot for one particle constructed by strobing at every local minimum of u_e , where the same focusing channel and beam conditions in Fig. 1 are considered. The initial position of the test particle is $(u, w) = (1.28776, 0)$ in

the phase space. In the figure, we see points scattered near an invariant curve in the Poincaré plot for the smoothed uniform-focusing channel. Figure 2 suggests that in this particular case, the averaged particle motion is in resonance with the core oscillation, and the orbit of the particle could be quasi-periodic or almost-periodic. The scattering of points is a general feature for particles outside the phase-space ellipse of the beam core. This is because a stroboscopic plot made for a particle in the periodic-focusing system is actually the projection of a higher dimensional "plot" onto the two-dimensional plane.[13] As the particle approaches toward to the beam ellipse, the dispersion of the strobed points decreases. For a particle inside the phase-space ellipse of the core, the strobed points fall exactly on an invariant circle as expected.

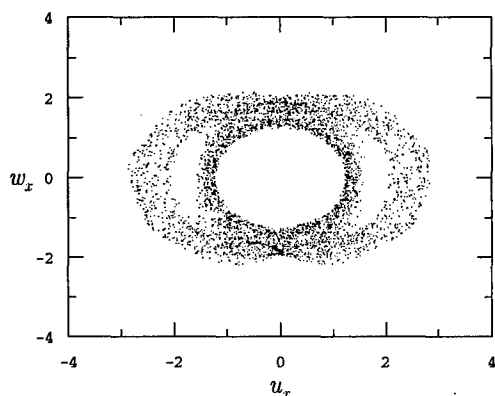


Fig. 3. Stroboscopic plot showing the resonance of a halo particle with the breathing mode oscillation of the beam envelope in a quadrupole-focusing channel.

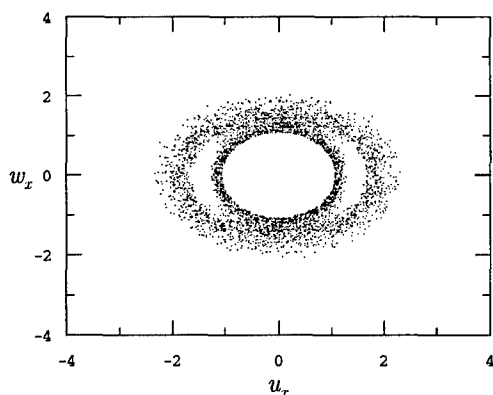


Fig. 4. Stroboscopic plot showing the resonance of a halo particle with the quadrupole mode oscillation of the beam envelope in a quadrupole-focusing channel.

Examples of stroboscopic plots for a quadrupole-focusing channel are shown in Figs. 3 and 4 for a particle in resonance with the breathing mode and the quadrupole mode of the envelope oscillation, respectively. The focusing and the beam parameters considered in these examples are: $F(\tau) = \cos(\tau)$, $\epsilon_x = \epsilon_y = \epsilon = 1$, $Q^2 = 3.198$, and $\hat{\eta}/\epsilon = 0.2502$. These

parameter values correspond to a tune depression from 90° to 70° for a particles inside the matched beam. The initial conditions used are: $u_{ex} = u_{ey} = 0.9$, $u_x \approx 1.26004$, for Fig. 3, and $u_{ex} = 0.9$, $u_{ey} = 1.1$, $u_x \approx 1.08235$, for Fig. 4; $w_{ex} = w_{ey} = w_x = u_y = w_y = 0$ for both figures.

4 CONCLUSIONS

A new method has been developed to use the particle-core model for studying the dynamics of halo particles in a mismatched continuous-beam propagating through a periodic-focusing channel. It was shown that by applying appropriate transformations of phase-space variables and by strobing at the frequency of the core oscillation, one is able to create stroboscopic plots similar to the Poincaré plots made for particles in a uniform-focusing channel. This method is applicable to a wide range of parameter values without using any smooth approximation, and it is not limited by the constraint that the frequency of core oscillation must be commensurable with that of the focusing lattice. Numerical examples were given to illustrate the method by considering a beam with a KV distribution and an axisymmetric cosine transverse-focusing force. We have discussed the possibility of extending this method to some limited cases in periodic quadrupole-focusing systems. It was also shown that, in spite of the complications brought in by the non-linear oscillations of the system, the motion of a halo particle is still strongly influenced by the resonance between motions of the particle and the core.

5 REFERENCES

- [1] R. Jameson, Los Alamos Report LA-UR-93-1209 (1993).
- [2] J. S. O'Connell, T. P. Wangler, R. S. Mills, and K. R. Crandall, Proc. of 1993 Particle Accelerator Conf., p. 3657 (1993).
- [3] T. P. Wangler, Los Alamos Report LA-UR-94-1135 (1994).
- [4] J. Lagniel, Nucl. Instrum. Meth., A345, 46 (1994); A345, 405 (1994).
- [5] R. Gluckstern, Phys. Rev. Lett., 73, 1247 (1994).
- [6] C. Chen, and R. C. Davidson, Phys. Rev. Lett., 72, 2105 (1994); Phys. Rev. E, 49, 5679 (1994).
- [7] S. Y. Lee, and A. Riabko, Phys. Rev. E, 51, 1609 (1995).
- [8] C. Chen, and R. A. Jameson, Phys. Rev. E, 52, 3074 (1995).
- [9] T. P. Wangler, R. W. Garnett, E. R. Gray, R. D. Ryne, and T.-S. Wang, Proc. of XVIII Intl. Linear Accelerator Conf., 1996, CERN report CERN 96-07, p. 372.
- [10] H. Okamoto, and M. Ikegami, Phys. Rev. E, 55, 4694 (1997).
- [11] M. Ikegami, Phys. Rev. E, 59, 2330 (1999). M. Ikegami, and M. Mitsumoto, Proc. of XIX Intl. Linear Accelerator Conf., Chicago, 1998, (in press).
- [12] T. P. Wangler, K. R. Crandall, R. Ryan, and T.-S. Wang, Phys. Rev. ST-AB, Vol. 1, No. 8, (1998).
- [13] F. C. Moon and W. T. Holms, Phys. Lett., 111A, 157 (1985).

HALO STUDIES IN SPACE CHARGE DOMINATED BEAMS

A. Piquemal

CEA/DIF/DPTA-B.P. 12, 91680 Bruyères-le-Châtel (France)

Abstract

We studied bounded thermal equilibrium of Vlasov-Maxwell in space charge dominated beams. These meta-equilibrium, which have a life time smaller than the short-range collision time and are in the region of the transit time in a Linac, can be used efficiently to avoid or to control the halo generation. Therefore, it is fundamental to understand their inner structure, and to analyze the basic mechanisms which can drive the beams to such equilibrium, or explain the way some known processes can contribute to their destruction.

1 INTRODUCTION

In the development of new accelerators requiring intense ion beams (40-150 mA), for the industrial production of tritium (APT, TRISPAL), for the generation of neutron intense sources (ESS) or the nuclear waste transmutation, the activation problem of the structures is crucial.

It is generally admitted that beam losses must be below 1 ppm, and comes from a peculiar profile of the radial beam density which goes very far and arrives to touch the walls; this profile is called "halo", to give the precise idea of a central core, surrounded by a diffuse tail [5].

For a better understanding of the halo formation, we limited our study to a continuous beam, and to the part of the machine where the beam can effectively activate the walls (5-1000 MeV); this part going from the DTL entrance to the CCL output, is represented by an axisymmetric focusing channel.

In these conditions, where the vacuum is good (10^{-5} - 10^{-7} torr), the beam is governed by the Vlasov-Maxwell system of equations which has theoretically a lot of mathematical solutions, like the Maxwellian which is not bounded, or some Meta-equilibria [1] which depend of the Hamiltonian and are bounded in the phase-space.

This propriety is interesting because we can hope that if the beam has not a maxwellian profile at the DTL entrance, it might be transported with a bounded profile.

But things begin to be wrong, when we try to determine if the beam converges really to one of these probable equilibrium states.

Firstly, in the absence of a residual gas, beam particles do not undergo elastic and inelastic binary collisions which could give them a thermal component.

Secondly, it is easy to verify that the Hamilton-Maxwell equations which govern the particle motion are deterministic and apparently invariant with time reversibility.

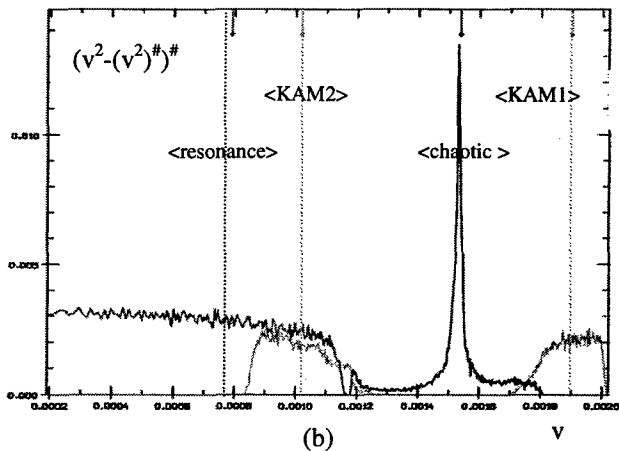
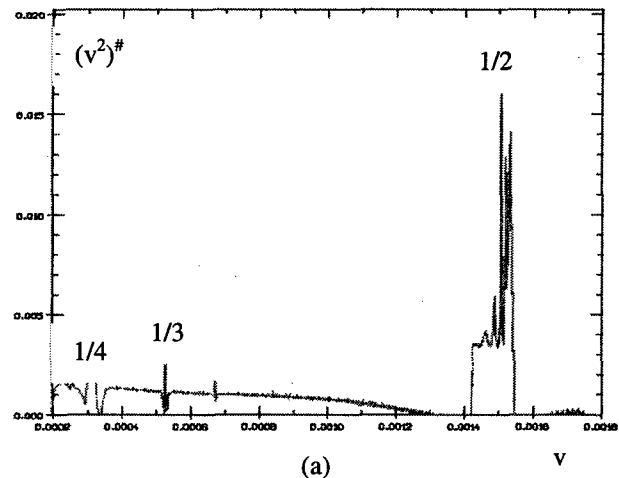


Figure 1 : ergodicity test with parameters $r_0=3\text{mm}$, $\eta=0.6$, $\mu=0.88$, $N=20$; fig 1.a represents $(v^2)^{\#}$ for the whole beam and fig 1.b represents $(v^2 - (v^2)^{\#})^{\#}$ for the resonance basin $1/2$.

In these conditions is it reasonable to imagine or to hope that the beam can relax to a macroscopic equilibrium following an irreversible way?

This is a forty years old discussion [1-2-3], and answers to this question are not straightforward, because in the absence of binary collisions, the non-linearities become predominant in the Vlasov-Maxwell or Hamilton-Maxwell equations, and complicate considerably the analyze of the problem.

In the following sections, we present some ideas which could help to clarify the discussion about topics like beam "irreversibility", "ergodicity", "mixing", and finally "stability".

2 IRREVERSIBILITY

Practically, the time reversibility of a dynamical system is not trivial to obtain without a large energy expense: the charged particle number is so large that it is out of mind to achieve the motion control of each particle at microscopic level, and then to proceed a reversible flash-back of the beam to its previous macroscopic state.

Therefore, the beam evolution is really time irreversible, even if the particle motion is deterministic; now, we have an indication of the time irreversibility, but we do not know, if the dynamical system is chaotic or if it can be described by a macroscopic state which verifies the statistic laws and more, if the dynamical system converges to a unique macroscopic equilibrium state.

Krillöv [10-11] studied this problem and concluded that, for the rapid establishment of any macroscopic state the system must be "ergodic", but for the relaxation to a unique macroscopic state the system must be "mixing".

3 ERGODICITY

The concept of ergodicity is introduced each time it is tried to split a system in sub-domains independent from the dynamic viewpoint.

In each sub-domain, we must verify the ergodic theorem proposed by Birkhoff [11] : the time average $\langle G \rangle^{\#}$ of any defined observable is equal to the space average $\langle G \rangle$ of the same observable; in fact, there is a less restrictive version of this theorem, which shows that in general the time average exists nearly anywhere in the concerned sub-domain and is distributed around the space average.

We verified the ergodicity concept using a PCM[4] code, and calculating the time average of the squared velocity $\langle v^2 \rangle^{\#}$ of the sampled particles, during N core oscillations.

We find first in fig 1.a that the beam is not ergodic as a whole, but it can be split in separated sub-domains which correspond exactly to the resonances $1/2, 1/3, 1/4, \dots$ [6].

In any sub-domains, the phenomena are blurred by the periodic motion associated to the core-breathing; this problem can be easily avoided by calculating the time average of an observable like the temperature $\langle v^2 - \langle v^2 \rangle^{\#} \rangle^{\#}$.

In each basin of resonances ($1/2$ for example), the phase space sub-domain is limited by bundles of invariant torus (KAM1 and KAM2 - figure 2.a); the complementary part contains stochastic particles and resonances and its size increases with the perturbation.

The results (see figure 1.b) are very surprising, because we find that all the components of the resonance basin are ergodic : these results are in accord with the PCM code, but are not realistic, and might be considered with care; even if the PCM code helps greatly in this analyze, we touch there one of the limits of this code : the Landau damping is not reproduced.

Therefore, the results are true for the KAM surfaces and the chaotic particles, but are false for the resonances which carry the energy of perturbation and might disappear with time, by Landau damping.

Now, if we forget the resonances, figure 1.b gives an exact description of the ergodic components in each basin of attraction; the beam is split in ergodic and embodied sub-domains, which are limited by KAM surfaces and contain chaotic particles...

4 MIXING

The mixing is generally very difficult to prove rigorously, but it is often associated with non-linear interactions which transform the phase space as a "backer rolling"; thus the Vlasov-Maxwell and Hamilton-Maxwell equations have two important proprieties :

- an extrem sensibility versus weak perturbations of the forces or small changes in initial conditions, and even the existence of parametric instabilities,
- quasi-periodical and ellipsoidal trajectories in the phase space which still increase the mixing rapidity, since the same particle can travel alternatively in the core and in the tail of the beam.

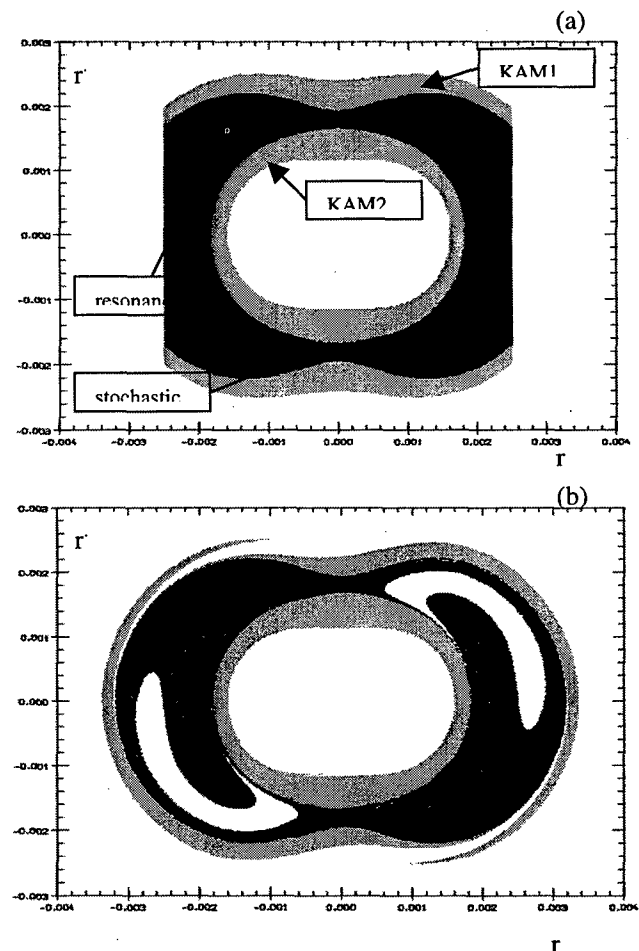


Figure 2 : mixing test with parameters $r_0=3\text{mm}$, $\eta=0.6$, $\mu=0.88$; fig 2.a represents the initial perturbation and fig 2.b gives $(r-r')$ for $N=20$.

We verified the mixing propriety in the resonance basin $1/2$; the initial perturbation is a violent cutoff of the phase space done by a scraper and is represented in figure 2.a. We can observe in figure 2.b, the rapid reconstruction of the sub-domain and we must conclude that a local equilibrium exists in this sub-domain; this could be verified for all sub-domains, and we would find the same result for each of them. Therefore, the beam does not relax to a unique equilibrium state, but it is continuously in balance between local and self-similar equilibrium which are very stable and strong.

5 DISCUSSION

From the preceding studies about ergodicity and mixing, two classes of organized structures appeared :

- the static structures, or KAM surfaces, which limit self-similar sub-domains in the phase space,
- the dynamical structures, or the resonances, the hyperbolic fixed points,..., which exist potentially in each sub-domain, and depend directly of the space charge η and the perturbation μ parameters [5].

This drives finally to very simple notions :

- a charged particle beam can be described by a balance between many self-similar local equilibrium,
- these local equilibrium have a fractal structure that we can find in the phase space, position and Fourier spaces,
- the fractals are governed by scale invariants which depend directly from the system parameters.

From these considerations, scale invariants and density profiles were calculated analytically, at equilibrium ($\mu=1$) and as a function of the space charge η (figure 3).

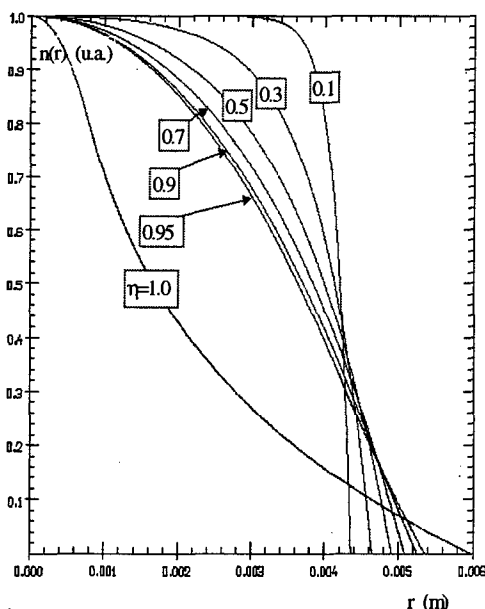


Figure 3 : radial density profiles calculated as a function of the space charge parameter η .

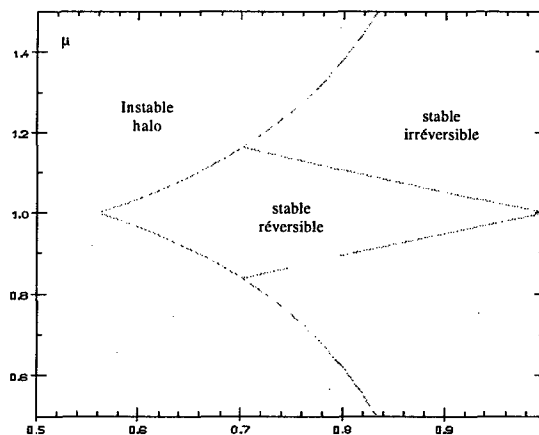


Figure 4 : stability graph as a function of the space charge η and the mismatch μ parameters.

Now, we know that these local equilibrium are strong and rapidly constituted and we can calculate their stability domain (figure 4).

As long the beam stays in its stability domain, the balance between local equilibrium is respected, and all is right; but this does not signify that the balance is indestructible!

If we try to transport the beam in conditions which are out of its stability domain, this one will try to reorganize itself to achieve a new balance of local equilibrium :

- if this new situation exists in the machine, the beam will suffer an emittance growth, but it's all !
- if this new situation does not exist, the beam will try to reorganize itself continuously, and will touch finally the walls of the machine.

The author would like to thank S.Joly, J.L.Lemaire and M.Promé for their constant interest in this work.

REFERENCES

- [1] N.A.Krall and A.W.Trivelpiece, "principle of plasma physics", McGraw-Hill book company (1973)
- [2] J.D.Lawson, Clarendon Press, Oxford (1988)
- [3] H.Reiser, Wiley series in beam physics and accelerator technology, New-York (1994)
- [4] J.S.O'Connell, T.P.Wangler, R.S.Mills and K.R.Crandall, PAC Washington (1993) 3657
- [5] T.Wangler, LA-UR-94-1135.
- [6] J.M.Lagniel, Nucl. Instr. Meth. Phys. Res. A345 (1994) 46-53 and A345 (1994) 405-410
- [7] J.M.Lagniel, A.Piquemal, LINAC Tsukuba, 529 (1994)
- [8] A.Piquemal, proceedings, EPAC (1996)
- [9] R.L.Gluckstern, Wen-Hao Cheng, S.S.Kurennoy, Huenchan Ye, Phys. Rev. E, (1996)
- [10] A.J.Lichtenberg, M.A.Lieberman, Springer Verlag (1991), «Regular and chaotics dynamics».
- [11] A.Dahan Dalmedico, J.L. Chabert, K.Chemla, «Chaos et déterminisme», éditions du seuil, (1992)

UNIFIED TREATMENT OF COLLECTIVE INSTABILITIES AND NONLINEAR BEAM DYNAMICS

K. Y. Ng¹ and S. Y. Lee^{2†}

¹FNAL *, Batavia, IL 60510, ²Physics Dept., Indiana University, Bloomington, IN 47405

Abstract

Nonlinear dynamics deals with parametric resonances and diffusion, which are usually beam-intensity independent and rely on a particle Hamiltonian. Collective instabilities deal with beam coherent motion, where the Vlasov equation is frequently used in conjunction with a beam-intensity dependent Hamiltonian. We address the questions: Are the two descriptions the same? Are collective instabilities the results of encountering parametric resonances whose driving force is intensity dependent? The space-charge dominated beam governed by the Kapchinskij-Vladimirskij (K-V) envelope equation [1] is used as an example.

1 INTRODUCTION

Traditionally, the thresholds of collective instabilities are obtained by solving the Vlasov equation, the dynamics of which comes from a wakefield-dependent Hamiltonian. The unperturbed beam distribution is computed using the unperturbed part of the Hamiltonian H_0 , which takes care of the mean field and potential-well distortion. The perturbation distribution is obtained by solving the Vlasov equation that involves the perturbation Hamiltonian ΔH_1 . The Vlasov equation is often linearized so that the modes of collective motion can be described by a set of orthonormal eigenfunctions and the corresponding complex eigenvalues give the initial growth rates. ΔH_1 may have a time-independent component, for example, the part involving the nonlinear magnetic fields, that gives rise to the dynamical aperture limitation. It may also have a time-dependent component, which includes the effects of wakefields and produces coherent motion of beam particles. The harmonic content of the wakefields depends on the structure of accelerator components. If one of the resonant frequencies of the wakefields is equal to a fractional multiple of the unperturbed tune of H_0 , a resonance is encountered and coherent particle motion is introduced. This may result in a runaway situation such that collective instability is induced.

Experimental measurements indicate that a small time dependent perturbation can create resonance islands in the longitudinal or transverse phase space and profoundly change the bunch structure [2]. For example, a modulating transverse dipole field close to the synchrotron frequency can split up a bunch into beamlets. Although these phenomena are driven by beam-intensity independent sources, they can also be driven by the space-charge force and/or the wakefields of the beam which are intensity dependent. Once perturbed, the new bunch structure can further enhance the wakefields inducing even more perturbation to

the circulating beam. Experimental observation of hysteresis in collective beam instabilities seems to indicate that resonance islands have been generated by the wakefields.

For example, the Keil-Schnell criterion [3] of longitudinal microwave instability can be derived from the concept of bunching buckets, or islands, created by the perturbing wakefields. Particles in the beam will execute *synchrotron* motion inside these buckets leading to growth in the momentum spread of the beam. In fact, the collective growth rate is exactly equal to the angular synchrotron frequency inside these buckets. If the momentum spread of the beam is much larger than the bucket height, only a small fraction of the particles in the beam will be affected and collective instabilities will not occur. This mechanism has been called Landau damping.

As a result, we believe that the collective instabilities of a beam can also be tackled from a particle-beam nonlinear-dynamics approach, with collective instabilities occurring when the beam particles are either trapped in resonance islands or diffuse away from the beam core because of the existence of a sea of chaos. The advantage of the particle-beam nonlinear dynamics approach is its ability to understand the hysteresis effects and to calculate the beam distribution beyond the threshold condition. Such a procedure may be able to unify our understanding of collective instabilities and nonlinear beam dynamics. Here, the stability issues of a space-charge dominated beam in a uniformly focusing channel are considered as an example [4].

2 COLLECTIVE-MOTION APPROACH

Gluckstern *et al.* [5] have studied the collective beam stabilities of a space-charge dominated K-V beam in a uniformly focusing channel. They showed that the (1,0) mode is stable for any amount of envelope mismatch and tune depression η . The (2,0) mode becomes unstable at zero mismatch when $\eta < 1/\sqrt{17} = 0.2435$ and also when the mismatch is large. This is plotted in Fig. 1 with the stable region enclosed by the red solid curve. The stability regions of the (3,0) and (4,0) modes, enclosed by the blue dashes and the magenta dot-dashes, respectively, are also shown. These latter two modes become unstable at zero mismatch when the tune depressions are less than 0.3859 and 0.3985, respectively. They found that the modes become more unstable as the number of radial nodes increases. Among all the azimuthals, they also noticed that the azimuthally symmetric modes ($\ell, 0$) are the most unstable.

3 PARTICLE-BEAM APPROACH

We want to investigate whether the instability regions in Fig. 1 can be explained by nonlinear parametric resonances. The particle Hamiltonian describing an azimuthally symmetric oscillating beam core of radius R is [6]

* Operated by the Universities Research Association, under contract with the US Department of Energy. † Work supported in part by US Department of Energy and the National Science Foundation.

$$H_p = \frac{1}{4\pi} p_y^2 + \frac{\mu^2}{4\pi} y^2 - \frac{2\mu\kappa}{4\pi R^2} y^2 \Theta(R - |y|) - \frac{2\mu\kappa}{4\pi} \left(1 + 2 \ln \frac{|y|}{R}\right) \Theta(|y| - R). \quad (1)$$

where y and p_y are the particle's transverse coordinate and canonical momentum, $\mu/(2\pi)$ the unperturbed particle's betatron tune, and κ the normalized space-charge permeance, which is related to the tune depression by $\eta = \sqrt{1+\kappa^2} - \kappa$. Here, only the situation of zero angular momentum is discussed [4]. For a weakly mismatched beam, the envelope radius can be written as $R = R_0 + \Delta R \cos Q_e \theta$, where Q_e is the envelope tune and θ the 'time'. The particle Hamiltonian can be expanded in terms of the equilibrium envelope radius R_0 , resulting in $H_p = H_{p0} + \Delta H_p$, where the unperturbed Hamiltonian H_{p0} is the same as H_p with R replaced by R_0 . Thus, for a matched beam, $\Delta H_p = 0$.

4 PARAMETRIC RESONANCES

For a mismatched beam, particle motion is modulated by the oscillating beam envelope. The perturbation Hamiltonian ΔH_p , obtained from Taylor's expansion, can be expanded as a Fourier series in the action-angle variables [6]. Parametric resonances occur when the phase is stationary. Focusing on the $n:m$ resonance, we perform a canonical transformation to the resonance rotating frame (I_p, ϕ_p) :

$$\langle H_p \rangle = E_p(I_p) - \frac{m}{n} Q_e I_p + h_{nm}(I_p) \cos n\phi_p, \quad (2)$$

with the effective κ -dependent resonance strength given by

$$h_{nm} = \frac{(m+1)M^m \mu \kappa}{2\pi R_0^2} |G_{nm}(I_p)|, \quad (3)$$

where $M = 1 - R_{\min}/R_0$ is the envelope mismatch. The n stable and unstable fixed points can be found easily. Because particles are affected only by resonances when they are just outside the envelope core, their tunes are essentially the tune inside the beam envelope. At zero mismatch, the threshold for the $n:m$ resonance can therefore be derived by equating the ratio of particle to envelope tunes to m/n , i.e.,

$$\kappa \geq \frac{1}{2\sqrt{2}} \left[\left(\frac{n}{m} \right)^2 - 4 \right] \left[\left(\frac{n}{m} \right)^2 - 2 \right]^{-1/2}. \quad (4)$$

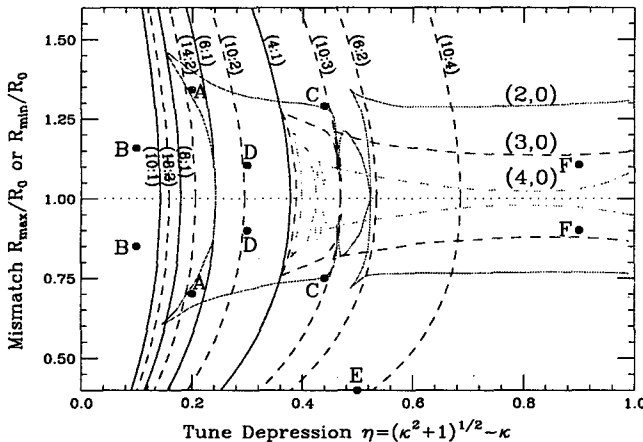


Figure 1: Beam stability versus particle tune depression and envelope mismatch: stability region for Gluckstern's (2,0) mode enclosed by red solid curve, the (3,0) and (4,0) modes by blue dashes curve and magenta dot-dashes. Overlaid are first-order resonances shown as solid and second- and higher-order resonances as dashes.

In particular, for the 6:1 resonance, $\kappa \geq 8/\sqrt{17} = 1.9403$, or tune depression $\eta \leq 1/\sqrt{17} = 0.2425$, which agrees with Gluckstern's instability threshold for the (2,0) excitation.

Trackings have been performed for particles outside the envelope core using the 4th-order symplectic integrator [7]. The Poincaré surface of section are shown in Plots A, B, C, D, E, F of Fig. 2 corresponds to Points A, B, C, D, E, F in Fig. 1. The innermost torus is the beam envelope. The sections are taken every envelope oscillation period when the envelope radius is at a minimum. In Plot A, with $(\eta, M) = (0.20, 0.30)$, particles that diffuse outside the beam envelope, will encounter the 6:1 resonance, which is bounded by a very thin layer of tori. This region is therefore on the edge of instability. However, the last good torus will be broken if η is further decreased, which corresponds to Plot B, a close-up plot with $(\eta, M) = (0.10, 0.15)$. Particles that diffuse outward from the beam core will wander easily towards the 2:1 resonance along its separatrix. This region, where $\eta \lesssim 0.2$, is therefore very unstable. This explains the front stability boundary of the (2,0) mode of Gluckstern, *et al.* Particles in Plot C with $(\eta, M) = (0.44, 0.25)$ see many parametric resonances, first 10:3, then 6:2, 8:3, 10:4 and after that a chaotic layer going towards the 2:1 resonance. These resonances are separated by thin layers of good tori. This region is on the edge of instability. Plot D with $(\eta, M) = (0.30, 0.10)$ shows the 6:2 resonance well separated from the 10:4 resonance with a wide area of good tori. Note that the 2:1 unstable fixed points and separatrices are not chaotic at all. This region will be very stable. Plot E, with $(\eta, M) = (0.50, 0.60)$, is at very large mismatch although the tune depression is moderate. The 2:1 unstable fixed points and separatrices are very chaotic, and are very close to the beam core. Thus particles can easily diffuse towards the 2:1 resonance, making this region unstable. Finally, Plot F, with $(\eta, M) = (0.90, 0.10)$, is with small space charge and small mismatch. The beam envelope is surrounded by good tori far away from the 2:1 separatrices. This region is very stable.

Since the 4:1 resonance is a strong one, its locus explains the front stability boundaries of Gluckstern's (3,0) and (4,0) modes also. The deep fissures of the (2,0) mode near $\eta = 4.7$ and 5.3 are probably the result of encountering the 10:3 and 6:2 parametric resonances. The width of the fissures should be related to the width of the resonance islands, which can be computed in the standard way. In general, a first-order resonance island, like the 4:1, is much wider than a higher-order resonance island, like the 6:1.

We tried very hard to examine the region between the 4:1 and 10:3 resonances with a moderate amount of mismatch. We found this region very stable unless it is close to the 10:3 resonance. We could not, however, reproduce the slits that appear in the (4,0) mode of Gluckstern, *et al.*

5 CONCLUSIONS

We have now an interpretation of the collective instabilities in the plane of envelope mismatch and tune depression through the particle-beam nonlinear-dynamics approach.

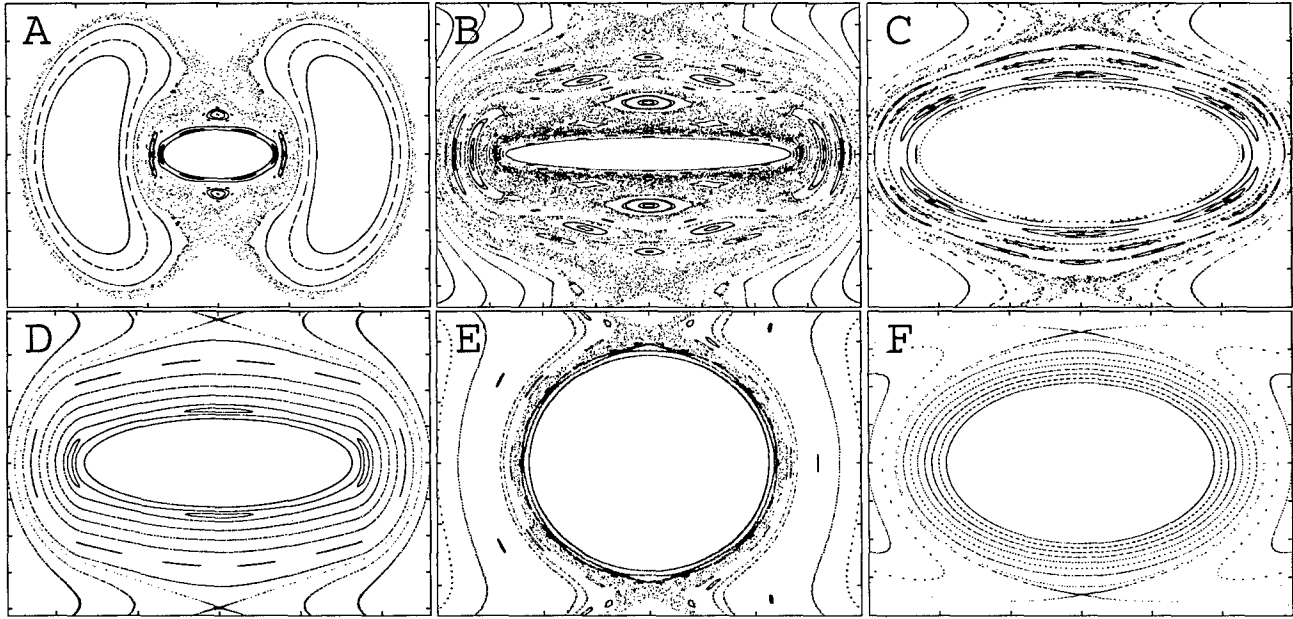


Figure 2: Poincaré surface of section in particle phase space (y, p) . Plot A is with $(\eta, M) = (0.20, 0.30)$, Plot B $(0.10, 0.15)$, Plot C $(0.44, 0.25)$, Plot D $(0.30, 0.10)$, Plot E $(0.50, 0.60)$, Plot F $(0.90, 0.10)$, corresponding, respectively, to Points A, B, C, D, E, F in Fig. 1. The last 5 are close-up plots, showing only up to the unstable fixed points and internal separatrices of the 2:1 resonance.

Because of the existence of noises of all types in the accelerators and the K-V equation is far from realistic, some particles will diffuse away from the K-V distribution. Although these particles may encounter parametric resonances once outside the beam core, an equilibrium will be reached if these resonances are bounded by invariant tori. It may happen that the island chains outside the beam envelope are so close together that they overlap to form a chaotic sea. When the last invariant torus breaks up, particles leaking out from the core diffuse towards the 2:1 resonance, which is usually much farther away from the beam envelope, to form beam halos. As particles escape from the beam envelope, the beam intensity inside the envelope becomes smaller and the equilibrium radius of the beam core shrinks. Thus more particles will find themselves outside the envelope. As this process continues because no equilibrium can be reached, the beam eventually becomes unstable.

So far, we have been able to explain the results of Gluckstern, *et. al* qualitatively. However, there are differences quantitatively. To the lowest order, the Vlasov equation studied by Gluckstern, *et. al.* does involve the perturbation force induced by the *perturbation* distribution via the Poisson's equation. In our nonlinear-dynamics approach, the particle that escapes from the beam envelope core, always sees the Coulomb force of the *entire unperturbed beam core*, independent of any variation of the core distribution due to the leakage of particles. This is mainly due to the fact that we have been treating the envelope Hamiltonian and the particle Hamiltonian separately. This leads to a dependency of the particle equation of motion on the envelope radius, but not the dependency of the equation of motion of the envelope radius on the particle motion. This is a shortcoming in our approach, which we need to improve. We believe that this is also the reason why we have not been able

to compute the growth rates of the instabilities.

It is possible that many collective instabilities can be explained by the particle-beam nonlinear dynamics approach. The wakefields of the beam interacting with the particle distribution produce parametric resonances and chaotic regions. Collective instabilities will be the result of particles trapped inside these resonance islands. The perturbed bunch structure further enhances the wakefields to induce these collective particle instabilities.

6 REFERENCES

- [1] I.M. Kapchinskij and V.V. Vladimirkij, Proc. Int. Conf. on High Energy Accelerators, CERN, Geneva, 1959, p.274.
- [2] D.D. Caussyn, *et. al.*, Phys. Rev. **A46**, 7942 (1992); M. Ellison, *et. al.*, Phys. Rev. Lett. **70**, 591 (1993); M. Syphers, *et. al.*, Phys. Rev. Lett. **71**, 720 (1993); D. Li, *et. al.*, Phys. Rev. **E48**, R1638 (1993); D.D. Li, *et. al.*, Phys. Rev. **E48**, 3 (1993); H. Huang, *et. al.*, Phys. Rev. **E48**, 4678 (1993); Y. Wang, *et. al.*, Phys. Rev. **E49**, 1610 (1994); Y. Wang, *et. al.*, Phys. Rev. **E49**, 5697 (1994); S.Y. Lee, *et. al.*, Phys. Rev. **E49**, 5717 (1994); M. Ellison, *et. al.*, Phys. Rev. **E50**, 4051 (1994); L.Y. Liu, *et. al.*, Phys. Rev. **E50**, R3344 (1994); D. Li, *et. al.*, Nucl. Inst. Meth. **A364**, 205 (1995).
- [3] E. Keil and W. Schnell, CERN Report SI/BR/72-5, 1972; D. Boussard, CERN Report Lab II/RF/Int./75-2, 1975.
- [4] K.Y. Ng and S.Y. Lee, "Particle-Beam Approach to Collective Instabilities—Application to Space-Charge Dominated Beams," Proc. 16th Advanced ICFA Beam Dynamics Workshop on Nonlinear and Collective Phenomena in Beam Physics, Arcidosso, Sep. 1-5, 1998.
- [5] R.L. Gluckstern, W-H. Cheng, and H. Ye, Phys. Rev. Lett. **75**, 2835 (1995); R.L. Gluckstern, W-H. Cheng, S.S. Kurennoy, and H. Ye, Phys. Rev. **E54**, 6788 (1996).
- [6] S.Y. Lee and A. Riabko, Phys. Rev. **E51**, 1609 (1995).
- [7] E. Forest and M. Berz, LBL Report LBL-25609, ESG-46, 1989.

PARTICLE DISTRIBUTIONS FOR BEAM IN ELECTRIC FIELD*

O.I.Drivotin, D.A.Ovsyannikov[†] St.-Petersburg State University, St.-Petersburg, Russia

Abstract

In the present report an approach for determination of particle distribution density in analytical form for beam in electric field is presented. It was applied previously for beams in magnetic fields [1]. The purpose of the report is to extend this approach on beams in electric field. For low current beam, the expressions for particle density are obtained in various cases. For intense beam, the integral equation for particle density in the space of first integrals of motion equations is proposed. The well known KV distribution is one of its solutions.

1 ERMAKOV SYSTEMS AND THEIR INTEGRALS

Consider stationary beam of charged particles in RF electric field, transverse components of which E_x, E_y are linear functions of the corresponding coordinates:

$$E_x = k_x x, \quad E_y = k_y y. \quad (1)$$

Let assume that in each cross-section of the beam all particles have the same longitudinal velocity \dot{z} . This assumption is realized, for example, for beam in initial part of RFQ channel.

Further we will consider distribution of particles of some infinitely thin layer moving along z -axis with the velocity \dot{z} and restricted by two infinitely closed planes moving with the same velocity. Let us assume that initially (in the beginning of the channel) particles fill ellipsoid in four-dimensional space:

$$X^* B_0 X = 1, \quad X^* = (x, \dot{x}, y, \dot{y}), \quad (2)$$

B_0 is diagonal matrix, $B_0 = \text{diag}(a_{x0}, c_{x0}, a_{y0}, c_{y0})$. As the equations of motion are linear:

$$\frac{d^2 x}{dt^2} = Q_x x, \quad \frac{d^2 y}{dt^2} = Q_y y, \quad Q_{x,y} = k_{x,y}/m, \quad (3)$$

in each subsequent moment particles fill ellipsoid, and envelopes on x, y satisfy the equations

$$\frac{d^2 R_x}{dt^2} = Q_x R_x + \frac{E_x^2}{R_x^3}, \quad (4)$$

$$\frac{d^2 R_y}{dt^2} = Q_y R_y + \frac{E_y^2}{R_y^3}, \quad (5)$$

where $E_x = a_{x0} c_{x0}$, $E_y = a_{y0} c_{y0}$. Here $R_{x,y}$ are beam envelopes. The equations (3) and (4,5) represent two pairs

of Ermakov systems [2]. They have well known Ermakov integrals

$$I_x^2 = (x\dot{R}_x - \dot{x}R_x)^2 + \frac{E_x^2}{R_x^2} x^2, \quad (6)$$

$$I_y^2 = (y\dot{R}_y - \dot{y}R_y)^2 + \frac{E_y^2}{R_y^2} y^2. \quad (7)$$

Assume that the beam cross section is bounded by the ellipse:

$$x^2/R_x^2 + y^2/R_y^2 \leq 1, \quad (8)$$

and find such set of I_x and I_y that this assumption would be true. Maximal value of the coordinate x is reached when the first term in (6) turns to zero:

$$x_{\max}^2 = I_x^2 R_x^2 / E_x^2.$$

Similarly,

$$y_{\max}^2 = I_y^2 R_y^2 / E_y^2.$$

The point (x_{\max}, y_{\max}) must lie inside the ellipse $x^2/R_x^2 + y^2/R_y^2 = 1$ and we get

$$\frac{I_x^2}{E_x^2} + \frac{I_y^2}{E_y^2} \leq 1, \quad I_x \geq 0, \quad I_y \geq 0. \quad (9)$$

So, the set of admissible values of I_x, I_y is bounded by the ellipse (9) and coordinate axes.

2 DISTRIBUTIONS IN THE SPACE OF INTEGRALS

Let us consider particle distribution of the moving infinitely thin layer introduced above. Taking into account that the thickness of the layer dz varies when the layer moves along z -axis, we normalize all densities dividing them by conserving value dz/\dot{z} .

We will denote the density of distribution on the variables a, b, \dots by $DN/D(a, b, \dots)$. For example, the phase density in this notation is $n = DN/D(x, \dot{x}, y, \dot{y})$. Assume that the phase density depends only on values of the integrals I_x and I_y . Under this condition the particle distribution is determined only by I_x and I_y , and, hence, we can introduce the density of distribution on values of the integrals I_x and I_y $f(I_x, I_y) = DN/D(I_x, I_y)$. Note, that setting of $f(I_x, I_y)$ as function of I_x, I_y is more correct procedure then setting of phase density n as function of I_x, I_y because we set density as function of the variables to which it is related as a density. In particular, we can correctly use generalized function as particle densities.

Let us express the phase density and the density in the configuration space through the density $f(I_x, I_y)$. Introduce the variables

$$q_x = x/R_x, \quad q_y = y/R_y,$$

* This work is supported by Russian Foundation for Fundamental Researches, project 99-01-00678

[†] E-mail: Dmitri.Ovsyannikov@pobox.spbu.ru

$$s_x = (x\dot{R}_x - \dot{x}R_x), \quad s_y = (y\dot{R}_y - \dot{y}R_y).$$

Then we have

$$\frac{DN}{D(q_x, q_y, I_x, I_y)} = 4 \frac{DN}{D(q_x, q_y, s_x, s_y)} \left| \det \frac{\partial(s_x, s_y)}{\partial(I_x, I_y)} \right| =$$

$$\frac{4I_x I_y}{|s_x s_y|} \cdot \frac{DN}{D(q_x, q_y, s_x, s_y)} = \frac{4I_x I_y}{|s_x s_y|} \cdot \frac{1}{R_x^2 R_y^2} \times$$

$$\frac{DN}{D(q_x, q_y, \dot{q}_x, \dot{q}_y)} = \frac{4I_x I_y}{|s_x s_y|} \cdot \frac{1}{R_x^2 R_y^2} \cdot \frac{DN}{D(x, y, \dot{x}, \dot{y})} \times$$

$$\left| \det \frac{\partial(x, y, \dot{x}, \dot{y})}{\partial(q_x, q_y, \dot{q}_x, \dot{q}_y)} \right| = \frac{4I_x I_y}{|s_x s_y|} \cdot n(I_x, I_y).$$

The factor 4 arises because there are four combinations of s_x, s_y which give the same values of I_x, I_y . To find the relation between $f(I_x, I_y)$ and $n(I_x, I_y)$ we must integrate last equality on q_x, q_y because

$$f(I_x, I_y) \equiv \frac{DN}{D(I_x, I_y)} =$$

$$\int_0^{q_{x, \max}} \int_0^{q_{y, \max}} \frac{DN}{D(q_x, q_y, I_x, I_y)} dq_x dq_y.$$

Integrating and taking into account that

$$|s_x| = \sqrt{I_x^2 - E_x^2 q_x^2}, \quad |s_y| = \sqrt{I_y^2 - E_y^2 q_y^2},$$

we get

$$f(I_x, I_y) = \pi^2 \frac{I_x I_y}{E_x E_y} n(I_x, I_y). \quad (10)$$

For density in configuration space we have

$$\varrho(x, y) = \frac{4}{R_x R_y} \int_{\Omega} \frac{DN}{D(q_x, q_y, I_x, I_y)} dI_x dI_y$$

or

$$\varrho(x, y) = \frac{4}{R_x R_y} \int_{\Omega} \frac{I_x I_y n(I_x, I_y) dI_x dI_y}{\sqrt{I_x^2 - E_x^2 q_x^2} \sqrt{I_y^2 - E_y^2 q_y^2}}. \quad (11)$$

Integration domain Ω is the set defining by the inequalities

$$I_x^2 \geq E_x^2 q_x^2, \quad I_y^2 \geq E_y^2 q_y^2, \quad \frac{I_x^2}{E_x^2} + \frac{I_y^2}{E_y^2} \leq 1.$$

Substituting the density $f(I_x, I_y)$ into the expression (11), one gets

$$\varrho(x, y) = \frac{4E_x E_y}{\pi^2 R_x R_y} \int_{\Omega} \frac{f(I_x, I_y) dI_x dI_y}{\sqrt{I_x^2 - E_x^2 q_x^2} \sqrt{I_y^2 - E_y^2 q_y^2}}. \quad (12)$$

Introducing the variables

$$\tilde{I}_x = \sqrt{(I_x/E_x)^2 - q_x^2}, \quad \tilde{I}_y = \sqrt{(I_y/E_y)^2 - q_y^2},$$

we can transform the expression (11) to simpler form

$$\varrho(x, y) = \frac{4E_x E_y}{R_x R_y} \times$$

$$\int_{\tilde{\Omega}} n(E_x \sqrt{\tilde{I}_x^2 + q_x^2}, E_y \sqrt{\tilde{I}_y^2 + q_y^2}) d\tilde{I}_x d\tilde{I}_y, \quad (13)$$

where $\tilde{\Omega}$ is determined by the inequalities $\tilde{I}_x^2 + \tilde{I}_y^2 \leq 1 - q_x^2 - q_y^2$, $\tilde{I}_{x,y} \geq 0$.

From this expression one can obtain particle distributions in configuration space.

3 EXAMPLES OF DISTRIBUTIONS

In the simplest case the phase density is constant: $n = n_0$. Substituting it to (13) and integrating, we have

$$\varrho(t, x, y) = \frac{\pi E_x E_y}{R_x(t) R_y(t)} n_0 \left(1 - \frac{x^2}{R_x^2(t)} - \frac{y^2}{R_y^2(t)} \right).$$

Other simple examples can be easily obtained if we take phase density (or density $f(I_x, I_y)$) as function of expression $1 - I_x^2/E_x^2 - I_y^2/E_y^2$. Let phase density has the form $n(I_x, I_y) = n_0 (1 - I_x^2/E_x^2 - I_y^2/E_y^2)^p$. Substituting to (11) we get

$$\varrho(t, x, y) = \frac{\pi E_x E_y}{R_x(t) R_y(t)} (1 - q_x^2 - q_y^2)^{p+1} \times$$

$$\int_0^{\sqrt{1-q_x^2-q_y^2}} \left(1 - \frac{\tilde{I}^2}{1-q_x^2-q_y^2} \right)^p \frac{\tilde{I}}{\sqrt{1-q_x^2-q_y^2}} \times$$

$$d\frac{\tilde{I}}{\sqrt{1-q_x^2-q_y^2}} = \frac{\pi E_x E_y}{(p+1) R_x(t) R_y(t)} (1 - q_x^2 - q_y^2)^{p+1},$$

$p \neq -1$, where $\tilde{I} = \sqrt{\tilde{I}_x^2 + \tilde{I}_y^2}$. For example, if n is proportional to $(1 - I_x^2/E_x^2 - I_y^2/E_y^2)^{-1/2}$, then ϱ is proportional to $(1 - q_x^2 - q_y^2)^{1/2}$. In both examples particle density falls down to zero on the border of the beam. It can be seen that for all $p > -1$ this property take place.

An interesting distribution we get taking the density $n(I_x, I_y)$ in a form

$$n(I_x, I_y) = n_0 e^{-\left(\frac{I_x^2}{E_x^2} + \frac{I_y^2}{E_y^2}\right)/\alpha^2}.$$

Then we have

$$\varrho(t, x, y) = \frac{\pi E_x E_y}{R_x(t) R_y(t)} n_0 \alpha^2 \times$$

$$\left(e^{-\frac{x^2/R_x^2(t) + y^2/R_y^2(t)}{\alpha^2}} - e^{-\frac{1}{\alpha^2}} \right).$$

If α is small, then the density is determined by the first term and represents Gauss distribution on transverse coordinates.

4 INTEGRAL EQUATION FOR DENSITY

Another problem of great interest is self-consistent distributions for intense beam. Consider stationary beam in RF electric field, transverse components of which are linear functions of coordinates and have form (1). As above, assume that initially particles fill ellipsoid (2) in phase space of transverse motion, and that in each cross section of the beam all particles have the same longitudinal velocity and fill ellipse (8). Under assumption that particles are uniformly distributed in beam cross section, the particles dynamics equations take the form [3,4]

$$\frac{d^2x}{dt^2} = Q_x x + \frac{\lambda x}{R_x(R_x + R_y)}, \quad (14)$$

$$\frac{d^2y}{dt^2} = Q_y y + \frac{\lambda y}{R_y(R_x + R_y)}, \quad (15)$$

and the envelope equations are

$$\frac{d^2R_x}{dt^2} = Q_x R_x + \frac{\lambda}{R_x + R_y} + \frac{E_x^2}{R_x^3}, \quad (16)$$

$$\frac{d^2R_y}{dt^2} = Q_y R_y + \frac{\lambda}{R_x + R_y} + \frac{E_y^2}{R_y^3} \quad (17)$$

The equations (14), (16) and (15), (17) represent two pairs of systems analogous to the Ermakov system and have the same integrals (6), (7) as systems (3), (4), (5). Moreover, all expressions for density $\rho(x, y)$ (11-13) obtained above are valid in this case. Taking into account the expression for density (11) we have integral equation for density $f(I_x, I_y)$:

$$E_x E_y \int_{\Omega} \frac{f(I_x, I_y) dI_x dI_y}{\sqrt{I_x^2 - E_x^2 q_x^2} \sqrt{I_y^2 - E_y^2 q_y^2}} = \pi^2 R_x R_y \rho_0. \quad (18)$$

The problem is to find such function $f(I_x, I_y)$ that result of the integration is independent on q_x, q_y (though the integrand is depend on them).

The well known KV distribution [3,4] is the solution of the equation (18):

$$f = f_0 I_x I_y \delta(1 - I_x^2/E_x^2 - I_y^2/E_y^2). \quad (19)$$

5 CONCLUSION

The approach for determination of particles distributions in electric field proposed in the present report allows modeling of nonuniform distributions for low intensity beams, which can be represented in analytical form along accelerating and focusing channel. In particular, these distributions can be widely used in various optimization problems of beam dynamics with the account of particle density distribution in configuration space [5,6].

Another result of this work is integral equation for density $f(I_x, I_y)$ for intense uniform charged beam. On the base of this equation the problem of finding of self-consistent distributions can be examined.

6 REFERENCES

- [1] O.I.Drivotin, D.A.Ovsyannikov, "New Classes of Uniform Distributions for Charged Particles in Magnetic Field," PAC'97, Vancouver, B.C., Canada, 1997. Proc. of the 1997 Part. Accel. Conf. Pp.1944-1945.
- [2] V.P.Ermakov, Univ.Izv.(Kiev), **20** (9), 1-25 (1880).
- [3] I.M.Kapchinsky, Particles Dynamics in Resonant Linear Accelerators Atomizdat, Moscow, 1966.
- [4] M.Reiser, Theory and Design of Charged Particle Beams, John Wiley & Sons, New York, 1994.
- [5] D.A.Ovsyannikov, "Mathematical Methods of Optimization of Charged Particles Beam Dynamics," EPAC'96, Sitges(Barcelona), 10-14 June 1996. Proc. of the 5th Europ.Part.Accel.Conf. Vol.2. Pp. 1382-1384.
- [6] O.I.Drivotin, D.A.Ovsyannikov, Yu.A.Svistunov, M.F.Vorogushin, "Mathematical Models for Accelerating Structures of Safe Energetical Installation," EPAC'98, Stockholm, 22-26 June 1998. Proc. of the 6th Europ.Part.Accel.Conf. Pp. 1227-1229.

AN ANALYTICAL APPROACH TO THE POISSON EQUATION IN 3-DIMENSIONAL SPACE CHARGE PROBLEMS

S. Valero*, P. Lapostolle**, A.M. Lombardi***, N. Pichoff*, E. Tanke***

* CEA-DSM-SEA, Saclay, F-91191 Gif-sur-Yvette Cedex, France

** Consultant, PS Division, CERN, CH-1211 Geneva 23, Switzerland

*** PS Division, CERN, CH-1211 Geneva 23, Switzerland

Abstract

The problem of electrostatics repulsion between charged particles in a bunch is a classical mixed Dirichlet-Neumann problem. In this paper, an analytical solution of this problem is described. The approach proposed here can be extended to other problems in mathematical physics.

1 INTRODUCTION

In an accelerator a bunched beam consists of an arbitrary system of charged particles embedded in a finite volume. The surface separating this system of particles from the environment possesses often a complicate form difficult to define. Moreover the density (number of particles per unity of volume) does not generally follow the usual mathematical statistics laws. However the forces acting on the particles are well-known and the behaviour of the system of particles can be in principle deduced from its distribution. knowing the position of these particles, the effects of the electrostatic repulsion between the particles can be calculated. The problem could be simplified in finding appropriate solutions of the Poisson equation $\Delta U = -\rho/\epsilon_0$ where ρ is the electric charge density, and U the electrostatic potential.

2 THE ELECTROSTATIC PROBLEM OF THE BUNCH

Summarising the more general problem in electrostatics for a system of particles embedded in a finite volume V , one obtains a mixed Dirichlet-Neumann problem. The solution of this problem requires the conditions prescribed on the boundary S of a finite region within V . When the system of charged particles is arbitrary, these conditions cannot be easily defined, and one substitutes the following problem:

- i) $\Delta U = -\rho/\epsilon_0$
- ii) U and its partial derivatives are null at ∞ (1)
- iii) ρ is continuously null outside a finite region

The density ρ will be obtained from the system of charged particles. For a system of particles lying in a closed volume, this problem can be considered identical to the Dirichlet-Neumann problem[1].

3 BEST-APPROXIMATION OF THE DENSITY FUNCTION WITH 3-D SERIES

The density function must be expressed in a suitable analytical form, allowing to compute the potential. To do so, the density is expanded in a series of 3-dimensional orthogonal functions. As the limits of the system of particles are not well-known, only 3-d orthogonal functions requiring no strict boundary limits must be retained. Periodic orthogonal functions (as Fourier series, for example) are complicated since they introduce image effects resulting of the periodicity. A good candidate, satisfying the conditions $\rho=0$ at ∞ can be obtained by a generalisation in 3-d of the Hermite functions.

One defines :

$$\delta_{lmn}(x, y, z) = \Psi_l(x) \Psi_m(y) \Psi_n(z), \quad (2)$$

where $\Psi_l(x)$ are the Hermite orthogonal functions generated from the following defining relation :

$$\Psi_l(x) = (-1)^l d^l (e^{-x^2/2}) / dx^l = H_l(x) e^{-x^2/2}, \quad (3)$$

where $H_l(x)$ are the orthogonal Hermite polynomials[2,4] of degree l , forming a complete sequence of orthogonal functions in the functional space $L^2(\mathbb{R}^3)$ of the functions measurable with the following Lebesgues-measure [3]:

$$d\omega = e^{-(x^2+y^2+z^2)/2} dx dy dz. \quad (4)$$

One endows this functional space with a scalar product :

$$\langle f, g \rangle = \iiint_{\mathbb{R}^3} f(x, y, z) g(x, y, z) d\omega. \quad (5)$$

The density ρ , being null outside a finite region, belongs to this functional space. One can then expand the density in the complete basis:

$$\rho(x, y, z) = \sum_{l=0}^{\infty} \sum_{m=0}^{\infty} \sum_{n=0}^{\infty} \frac{\langle \rho, \delta_{lmn} \rangle}{\langle \delta_{lmn}, \delta_{lmn} \rangle} \delta_{lmn}(x, y, z) \quad (6)$$

Let's consider now a finite sequence $\{\delta_{lmn}\}$ with $0 \leq l, m, n \leq l_1, m_1, n_1$. This sequence generates a functional space $X(l_1, m_1, n_1)$ endowed with the scalar product defined in Eq. 5. The finite sequence $\{\delta_{lmn}\}$ constitutes a complete basis of orthogonal functions, and any function in this space can be expanded in this basis. One can prove [3] that there exists one element and only one element $S_1(\rho)$ in $X(l_1, m_1, n_1)$, such that the following distance:

$$D = \left| \iiint_{\mathbb{R}^3} (\rho(x, y, z) - S_1(\rho)) dx dy dz \right| \quad (7)$$

is minimum. This element is the projection of the density ρ in the functional space $X(l_1, m_1, n_1)$. Expanding this projection with the basis one obtains :

$$S_1(\rho) = \sum_{l=0}^{l_1} \sum_{m=0}^{m_1} \sum_{n=0}^{n_1} \frac{\langle \rho, \delta_{lmn} \rangle}{\langle \delta_{lmn}, \delta_{lmn} \rangle} \delta_{lmn}(x, y, z). \quad (8)$$

One can show [3] that, contemplating a system of N charged particles, one has :

$$\frac{\langle \rho, \delta_{lmn} \rangle}{\langle \delta_{lmn}, \delta_{lmn} \rangle} = \frac{1}{(2\pi)^{3/2} l! m! n!} \sum_{i=1}^N H_l(x_i) H_m(y_i) H_n(z_i), \quad (9)$$

where x_i, y_i , and z_i are the co-ordinates of the particles.

One also proves [2,3] that the distance D given in Eq.7 is bounded, and one has :

$$D \leq C \frac{l_1! m_1! n_1!}{(2l_1)!(2m_1)!(2n_1)!}, \quad (10)$$

where C is a constant depending of the density.

The general expression of the field components is given by :

$$E_x(x, y, z) = \frac{1}{\epsilon_0} \iiint_{\mathbb{R}^3} \frac{\xi \rho(x+\xi, y+\mu, z+\zeta)}{(\xi^2 + \mu^2 + \zeta^2)^{3/2}} d\xi d\mu d\zeta. \quad (11)$$

The density ρ being positive or null in a finite region, from the first theorem of the average[4], the truncation error introduced in the potential or in the field components, when the density ρ is replaced by $S_1(\rho)$, could be deduced from the distance D .

4 ANALYTICAL SOLUTION OF THE POISSON EQUATION

In the problem (1), the density ρ can be replaced by its approximation $S_1(\rho)$ and one considers separately each term in the series in Eq. (8) :

$$\Delta U^*(u, v, w) = -\frac{1}{\epsilon_0} \frac{\langle \rho, \delta_{lmn} \rangle}{\langle \delta_{lmn}, \delta_{lmn} \rangle} \delta_{lmn}(u, v, w). \quad (12)$$

These u, v and w are the normalised co-ordinates obtained in scaling the co-ordinates along the principal axes relative to the r.m.s. dimensions a, b and c of the bunch. Applying a Fourier transformation to Eq. (12), one obtains an expression of the field component :

$$E_x^*(u, v, w) = (-i)^{l+m+n+1} (2\pi)^{-3/2} \frac{\langle \rho, \delta_{lmn} \rangle}{\epsilon_0 \langle \delta_{lmn}, \delta_{lmn} \rangle} \times \int_{-\infty}^{\infty} \int_{-\infty}^{\infty} \int_{-\infty}^{\infty} \frac{\hat{u}^{l+1} \hat{v}^m \hat{w}^n}{\hat{u}^2 + \hat{v}^2 + \hat{w}^2} e^{\frac{\hat{u}^2 + \hat{v}^2 + \hat{w}^2}{2}} e^{i(\hat{u}u + \hat{v}v + \hat{w}w)} d\hat{u} d\hat{v} d\hat{w}. \quad (13)$$

An analytical solution of this 3-d complex integral can be found by separating it into three 1-d complex integrals. This process leads to very sizeable analytical calculations [3], whom one only gives here the principle. One considers for instance in the 3-d integral above, the following integral function :

$$I_1(\hat{v}, \hat{w}) = a^2 \int_{-\infty}^{\infty} \frac{\hat{u}^{l+1}}{-\hat{u}^2 + \frac{a^2}{b^2} \hat{v}^2 + \frac{a^2}{c^2} \hat{w}^2} e^{-\hat{u}^2/2} e^{i\hat{u}u} d\hat{u}. \quad (14)$$

From the Cauchy residue theorem and from an integral representation of the probability function, one obtains an analytical expression of $I_1(\hat{v}, \hat{w})$ in terms of Hermite functions. Introducing this expression in the 3-d integral in Eq. (13), one has to calculate a new integral function :

$$I_2(\hat{w}) = \int_{-\infty}^{\infty} \hat{v}^m e^{-\hat{v}^2/2} I_1(\hat{v}, \hat{w}) e^{i\hat{v}v} d\hat{v}. \quad (15)$$

The Cauchy residue theorem and the properties of the Hermite functions, allow to obtain an other analytical expression in terms of Hermite functions. This expression introduced in Eq. (13), enable to obtain an analytical expression of the 3-d integral.

Further, in the aim to save computer time, integrals above could be calculated through expansions around specific positions in the bunch.

5 EXAMPLES

Figures 1-5 illustrate an estimation of the influence of the truncation error, done when the density ρ is replaced by its truncated series developments defined in Eq. (8), on the potential or on the field components calculated with the same 3-d Gauss numerical integration on a sphere. This numerical integration has been used in place of the analytical method explained in this paper, because this can only be applied to the series developments. The "noise" observed on the curves is induced by the numerical integration.

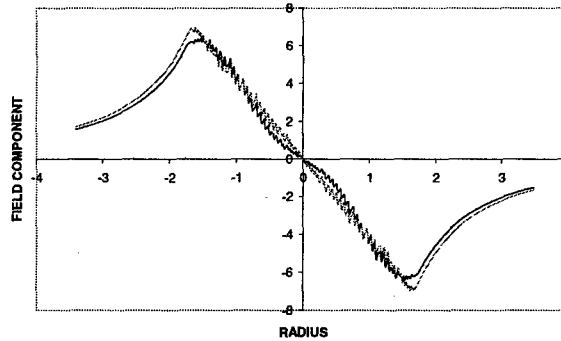


Figure 1: The radial field component along a diameter of a sphere for which the density $\rho(x, y, z) = 1$ is compared with the same component as calculated by series developments with l_1, m_1 and $n_1 = 12$. Due to the symmetry, only the terms in the series with even l, m and n are not null.

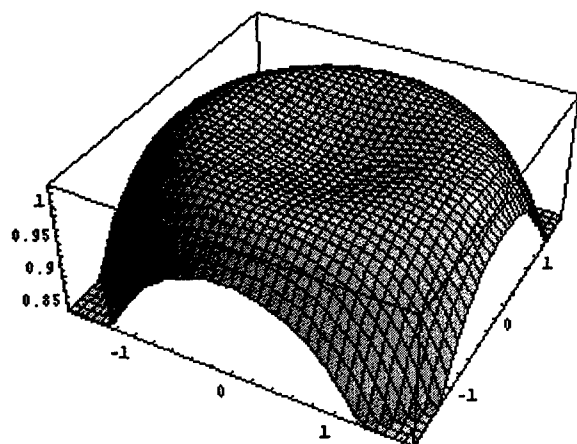


Figure 2: The density is a 4th order spherical function, represented here at $z = 0$.

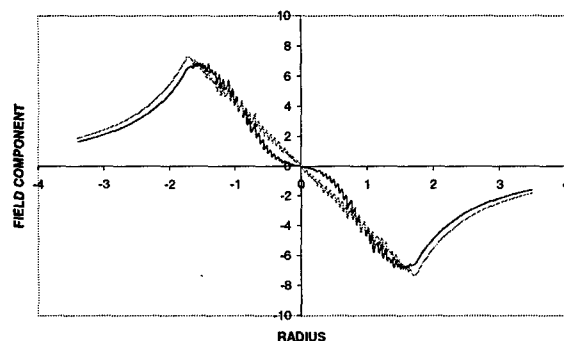


Figure 3: The field component E_x deduced from the density given in fig. 2 is compared with this obtained from the truncated series with l_1, m_1 and $n_1 = 6$. The difference vanishes when increasing this values to 12 (see fig. 1).

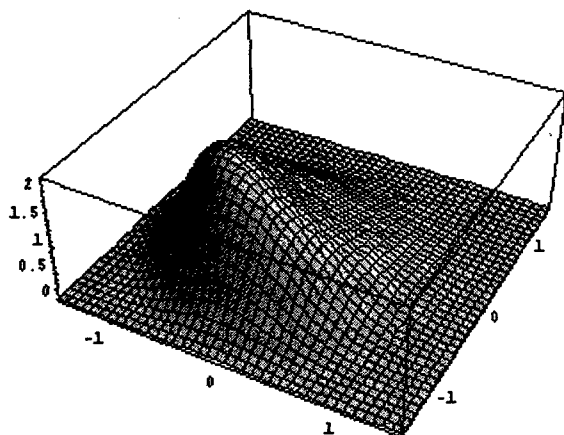


Figure 4: The density is a non-symmetrical function represented here at $z = 0$.

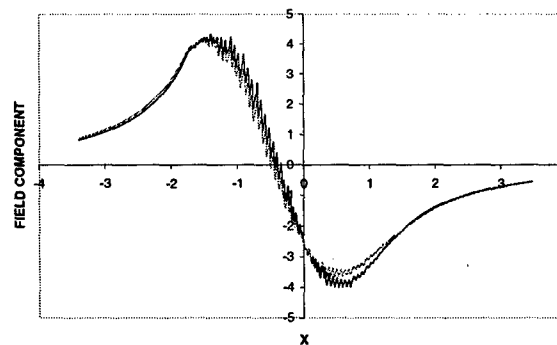


Figure 5: Field component E_x along x -axis with a beam density given in fig.4, compared with this calculated from series developments with l_1, m_1 and $n_1 = 7$. Here the terms in the series, with odd and even l, m and n are used. As in the practical cases, the density is here continuous at the boundary of its defining area, contrary to previous example (fig.2).

6 CONCLUSION

The present work suggest a new type of approach leading to an analytical solution of a classical Dirichlet-Neumann problem in 3-dimensions. It is particularly suitable for an arbitrary system of charged particles without symmetry, when the limits of the system are not well-known. It can be extended to other problems in mathematical physics. A new routine is being developed solve space-charge effects in accelerators. It could become a good tool helping in the estimation of tolerances necessary for the design and operation of high intensity linacs. Some possible refinements of the present method are still being studied. This process might also be used for cyclotrons.

7 ACKNOWLEDGMENTS

We thank B. Aune and J. M. Lagniel from Saclay and H. Haseroth and W. Pirkl from CERN for their interest and support.

8 REFERENCES

- [1] Ian Sneddon. *Elements of Partial Differential Equations, Chapter 4*. McGraw-Hill Kogakusha (1957).
- [2] A.M. Cohen. *Numerical Analysis, Chapter 1,2*. McCraw-Hill book Co., (1973).New York
- [3] *An Analytical Approach to the Solution of the Poisson Equation in 3-dimentional Electrostatics Problems*. To be published by the authors.
- [4] G.Valiron. *Théorie des Fonctions, Chapitre IV*. Masson et C^{ie} Paris(1955).

BEAM STABILITY IN THE DRIVE-BEAM DECELERATOR OF CLIC USING STRUCTURES OF HIGH-ORDER SYMMETRY

A. Millich, A. Riche, D. Schulte, CERN, 1211 Geneva, Switzerland

Abstract

The RF power necessary to accelerate the main beam of the Compact Linear Collider (CLIC) is produced by decelerating a high-current drive beam in Power Extraction and Transfer Structures (PETS). The reference structure is not cylindrically symmetric but has longitudinal waveguides carved into the inner surface. This gives rise to a transverse component of the main longitudinal mode which can not be damped, in contrast to the transverse dipole wakefield. The field is non-linear and couples the motion of the particles in the two planes. Limits of the stability of the decelerated beam are investigated for different structures.

1 INTRODUCTION

The CLIC study investigates a possible future linear collider based on acceleration with a frequency of 30 GHz [1]. The necessary power is produced by decelerating a high-current, low-energy beam which runs parallel to the main beam. This is done in 20 consecutive drive beam decelerators per main linac each of which is fed with a new beam [2]. During the deceleration the beam develops a large energy spread of a factor ten and is subject to transverse deflections due to wakefields. For reliable operation the beam stability in the decelerator is critical since the beam contains a large energy per pulse. In addition, the down-times of the 40 decelerators add to the total down-time.

2 DECELERATOR MODEL

The decelerators are on average 767 m long and consist of 550 PETS [3]. The layout of the drive beam decelerator is strongly coupled to that of the main beam accelerator. It consists of a simple FODO lattice with a constant quadrupole spacing of 1.115 m. Between each pair of consecutive quadrupoles a power extraction structure is placed. It feeds two accelerating structures in the main linac. The gradients of the quadrupoles are varied along the beam line to achieve a constant phase advance of about 88° per FODO cell for the lowest energy particles. The envelopes of the particles with higher energies will then automatically be smaller than those with lower energies [4].

3 STRUCTURE MODEL

The active length of the power extraction structures is 0.8 m; longer structures would lower the main linac fill fac-

tor. The inner bore of the structure is cylindrically symmetric except for the longitudinal waveguides that are cut into the surface. Here four structures are considered with four, six and eight waveguides, respectively, and a circularly symmetric one. Their main properties are listed in Table 1. The longitudinal and transverse wakefields can be well represented by a single mode each, with a frequency of 30 GHz for the longitudinal and 24 MHz less for the transverse mode. The group velocities of the wakefields are close to the speed of light, e.g. $\beta_{\perp} \approx \beta_{\parallel} = 0.441$ for the four waveguide structure.

The power the structure extracts from the beam has to be 512 MW. This is simply given by the product of average deceleration of the beam particles times the current. The longitudinal wakefield W_{\parallel} is a function of the structure radius a , $W_{\parallel} \propto a^{-3}$ for the four-waveguide structure. So one can in principle choose a high-energy, low-current beam in a small aperture structure or vice versa. Simulations of the transverse wakefield have shown that the best beam stability in a given decelerator using four waveguide structures is achieved by choosing the highest beam current possible. The injector complex is expected to allow for bunch charges q of up to $q = 20$ nC.

The high group velocity leads to a concentration of longitudinal and transverse wakefields at the end of the structure. In the simulation, the passage of a particle through the structure is therefore simulated in a number of steps. During each step the longitudinal and transverse field is assumed to be constant. But from step to step, the fields vary according to the field profiles in the structure. The transverse wakefields not only drain out of the structure but are damped with a quality factor $Q \approx 50$ [5].

Since the structure is not cylindrically symmetric, the longitudinal field varies with the transverse position.

$$E_{\parallel}(r, \phi) = \sum_{i=0}^{\infty} 2k_i \frac{r^{m_s i}}{a^{m_s i}} \cos(2\pi s/\lambda) \cos(m_s i \phi).$$

For the number of waveguides $m_s \neq 0$ this corresponds to a transverse field which can be written as

$$E_{\perp}(r, \phi) = \sum_{i=0}^{\infty} 2k_i m_s i \frac{r^{m_s i-1}}{a^{m_s i}} \frac{\lambda}{2\pi} \sin(2\pi s/\lambda) [-\vec{e}_r \cos(m_s i \phi) + \vec{e}_{\phi} \sin(m_s i \phi)]. \quad (1)$$

Here, $\phi = 0$ lies in a symmetry plane in the centre of a waveguide. In contrast to the transverse wakefield, this effect also plays a role if the beam is perfectly centred in the structures.

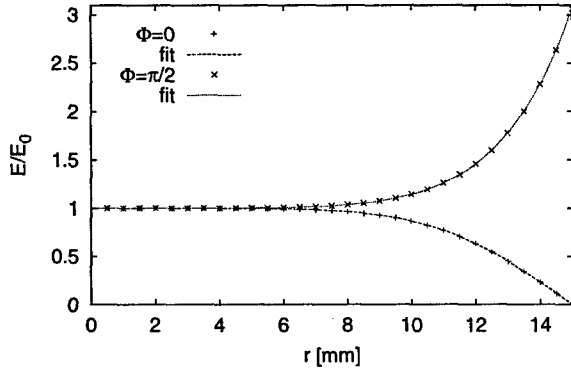


Figure 1: Fit of the field non-uniformity in the six waveguide structure.

Table 1: Parameters of the different power extraction structures used in the simulations. R'/Q is given in linac ohms. The last structure is circularly symmetric

m_s		4	6	8	∞
a	[mm]	13	15	16	12
R'/Q	[Ω/m]	41	50.8	49.0	292.6
\hat{W}_\perp	[V/pC/m ²]	225	250	260	3170
β_\parallel		0.441	0.59	0.64	0.78
q_b	[nC]	16.1	16.7	17.7	8.0
E_0	[GeV]	1.34	1.29	1.22	2.76
\hat{G}/G		4.3	3.0	2.5	1.0
k_1/k_0		1.8	1.6	1.4	—
k_2/k_0		1.0	0.65	0.21	—

For the six and eight waveguide structures the coefficients can be determined easily. Figure 1 shows the result of the fit in the two planes $\Phi = 0$ and $\Phi = \pi/2$ using eight coefficients. Only the first two are important, the others are quite small. In the case of the four waveguide structure, the fit is less reliable since the curves are not smooth due to the mesh used in the computations with MAFIA. Also in this case the first two coefficients are taken, even so the following ones are not much smaller. The most important effect is however expected from the lowest orders.

4 BUNCH TRAIN

The bunch train used to produce the RF power consists of four parts. In the main part, the flat top, the charge does not vary from bunch to bunch. It is used to produce the power during the passage of the main beam. It is preceded by a number of bunches in which the charge is increasing from bunch to bunch. This ramp is necessary to compensate the main linac beam loading by providing a field profile as if the first bunch of the main linac pulse had been preceded by others. An additional ramp of charge preceding the one described may be necessary if the drive beam injector cannot achieve the sudden change in charge. It is neglected in the following since its length and shape still have to be investigated. After the flat top, another ramp with decreas-

ing charges will follow which is needed for beam loading compensation in the drive-beam accelerator, see [6].

The bunch length is assumed to be $\sigma_z = 400 \mu\text{m}$, the transverse emittances $\gamma\epsilon_x = \gamma\epsilon_y = 150 \mu\text{m}$. During the deceleration, particles can lose up to the 90 % of their initial energy, while the first bunches will be hardly decelerated.

5 ADDITIONAL ENERGY LOSS

Due to the non-uniformity, off-axis particles can be decelerated more or less than on-axis. If the deceleration is too large these particles will be lost since they are over-focused by the quadrupoles. For a four-waveguide structure, the additional energy loss ΔE can be estimated as

$$\Delta E = G \frac{3}{8} c_0 \int_0^L \frac{\langle r^4(z) \rangle}{a^4} dz.$$

Here, L is the linac length, $\hat{r}(z)$ the maximum amplitude at position z and the factor $3/8$ is due to the integration over the betatron motion. For the lowest energy particles the beta-function is constant, so the integration leads to

$$\frac{\Delta E}{E_0 - E_f} = \frac{3}{8} c_0 \frac{\hat{r}^5 - \tilde{r}^5}{5(\hat{r} - \tilde{r})a^4} \frac{E_0}{E_f}.$$

Here, \hat{r} and \tilde{r} are the minimal and maximal amplitudes in the first FODO cell. If $\Delta E/E_f \approx 0.3$ the lattice will be over-focusing. Assuming $k_1/k_0 = 3.3$ in the four waveguide structure (attributing the full amplitude of the non-uniformity to this value) a particle can be lost if it has an initial offset of about 8σ . Simulations confirm this value.

If consecutive structures are rotated by π/m_s the lowest order term of the non-uniformity will about cancel. This will allow the particles to have even larger initial amplitudes without being lost.

6 TRANSVERSE EFFECTS

In order to stabilise the beam, it is useful to rotate every second structure by $\Phi = \pi/m_s$ [3]. Since the beta-function is significantly longer than the structures, the kick due to the lowest order in (1) averages out over a short distance. In Fig. 2, the maximum envelopes along the decelerator are shown for all three structures. A damping with $Q = 50$ and $Q = 200$ is assumed, the beam is offset by one sigma initially and has a size of $4\sigma_x$ and $4\sigma_y$. The envelope is normalised to the half-aperture. Even with $Q = 200$ the beam is sufficiently stable in all structures. The ones with six and eight waveguides are better than the one with four due to the larger aperture and the smaller non-uniformity.

7 AZIMUTHAL DEPENDENCE

The kick a particle experiences due the field non-uniformity is purely radial in a symmetry plane, but elsewhere also has an azimuthal component. To investigate the different effects, a four sigma beam is used, containing test particles with Courant-Snyder Invariants $A_x =$

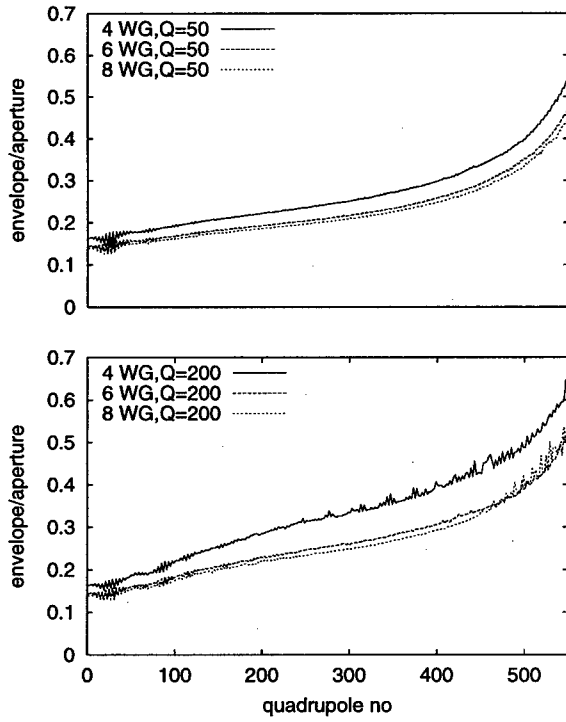


Figure 2: The normalised envelopes for the different structures with waveguides, the upper graph is for the expected damping $Q = 50$, the lower for $Q = 200$.

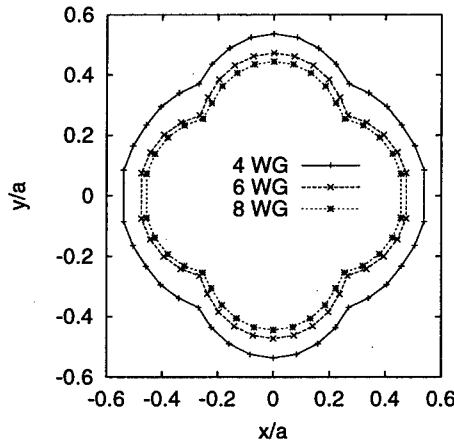


Figure 3: The envelopes in the different angles ϕ_0 .

$16 \cos^2(\phi_0) \epsilon_x$, $A_y = 16 \sin^2(\phi_0) \epsilon_y$. The beam has an initial offset in the direction of this plane of one sigma: $\Delta_x = \cos(\phi_0) \sigma_x$, $\Delta_y = \cos(\phi_0) \sigma_y$. Figure 3 shows the maximal excursion of any particle for the different angles. The variation is essentially due to the optics only.

8 CIRCULARLY SYMMETRIC STRUCTURE

The circularly symmetric structure has no field inhomogeneities. Its transverse wakefield as well as its impedance

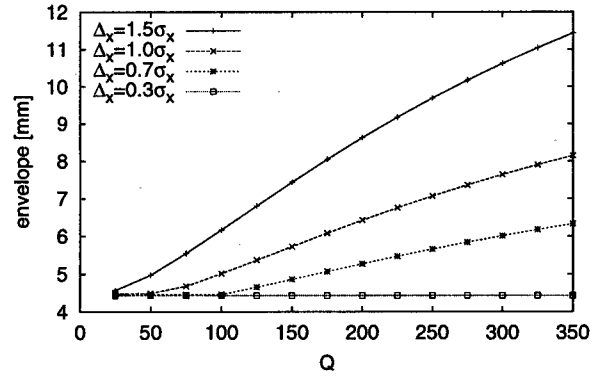


Figure 4: The beam envelopes for the circularly symmetric structure for damping with different Q .

are high. While it therefore seems natural to use a structure with larger diameter, it is very difficult to achieve a low group velocity in this case. Already at $r = 12$ mm, it is very high: $\beta_g = 0.78$. The initial energy of the beam is very high and its current significantly lower than in the former cases, see Table 1. In this case, it is more difficult to damp the transverse modes than in the former ones. First measurements indicate $Q \approx 150$ [7]. Figure 4 shows the maximal amplitudes of a four-sigma beam with different initial offsets for different values of Q . While the structure is clearly not excluded, the wakefield effect seems to be significantly stronger than in the previous ones.

9 CONCLUSION

Calculations of the beam stability in the drive beam decelerator have been performed for new transfer structures. The longitudinal and transverse effect of the non-uniformity of the longitudinal field have been included together with the usual wakefield effects. The stability improves compared to the previous case. Especially with the six and eight waveguide structures almost no effect of the non-uniformity is visible.

10 REFERENCES

- [1] J.-P. Delahaye and 30 co-authors, "CLIC a 0.5 to 5 TeV Compact Linear Collider." *EPAC 1998* and CERN-PS-98-009-LP.
- [2] H. Braun and 14 authors, "A new method of RF power generation for two-beam linear colliders." *EPAC 1998* and CERN-PS-98-014-LP.
- [3] A. Riche and D. Schulte, "The drive beam decelerator of CLIC". *LINAC 98* and CERN-PS-98-043-LP
- [4] A. Riche, "Maximum energy transfer efficiency in CLIC drive beam". *CLIC-Note 266* (1994).
- [5] L. Thorndahl. Private Communication.
- [6] D. Schulte, "The drive beam accelerator of CLIC". *LINAC 1998* and CERN-PS-98-042-LP.
- [7] G. Carron and L. Thorndahl. Private communication.

HALO FORMATION AND CONTROL

S.N.Andrianov*, N.S.Edamenko, SPbSU, S.Petersburg, Russia

Abstract

In this report we suggest some approaches to very intricate problem of the halo formation process. It is known that this process leads to the formation of a sufficiently compact core and a spreading cloud - halo, which surrounds the core. Our approach to this problem is based on two main objects: initial distribution functions and matrix formalism for Lie algebraic tools for time evolution of particle beam. Usage of the matrix formalism allows to investigate the influence of different forms of starting model distributions. All calculations are based on symbolic representation of necessary mapping generated by space charge forces and external control fields. This allows us to formulate the basic requirements which are necessary for halo formation, that gives us a possibility to control this process.

1 INTRODUCTION

It is known that usually the evaluation of space charge effects on the beam dynamics requires intensive numerical calculation. That is why there are innumerable publications, which devoted to modeling of space charge dynamics for concrete machines. The most of papers concentrate upon an numerical analysis of the influence of the beam line characteristics for matched or/and unmatched beams. Nevertheless the problem of the influence of beam distribution characteristics keep through our study. But it is impossible to obtain total presentation of, for example, halo problem without thorough investigation of different kind of conditions which affect halo formation. Most recent publications have dealt with either the KV-distribution or several simple distributions. In the paper [1] a very interesting approach to halo production is presented. The authors suggest new concepts for halo description which allows, in particular, to solve problems of halo control. All approaches to this problem have ultimately depended upon the calculation techniques that can be applied. To understand halo formation process, in this work we consider the evaluation of the phase-space distribution in terms of matrix representation for Lie transformations [2]. This allows us to use computer algebra methods and codes to reduce the real time needed for the numerical calculations. The external forces are assumed radial and periodical, as in solenoid channels. This force model can be also applied to quadrupole focusing if the phase advance is not too large. The focusing force as the space-charge forces are considered upto aberrations of the third order. In this paper we use the model of long beams with an elliptical cross-section in the transverse phase-space. Some models of phase-space distribution functions are described [3].

The Ferrer's integrals technique is used for calculation of space-charge forces in a symbolic form. Note if we neglect space-charge forces the motion equation for Lie transformation have linear operator form, but if the space-charge forces are included in our investigation the corresponding equation become nonlinear as the generating vector field depends on beam characteristics. Nonlinear nature of these equations leads to a necessity to use the successive approximations method. Obtained convergence conditions and algorithms give opportunity to estimate a current step value in advance and to create necessary software for modeling [4]. The truncated matrix equations (up to third order) are solved with the use of the matrix formalism for Lie algebraic tools with necessary simplification procedure [5]. As a result of this work, there are a number of computer experiments that show us what kind of both beam and beamline characteristics have to be taken in account. The necessary software was created using the dynamic modeling paradigm [6].

2 A SPACE CHARGE DESCRIPTION

2.1 The Initial Space Charge Distributions

The initial space-charge distribution in the phase-space can be written in the general form $f_0(X) = \sum_{k=0}^{\infty} f_k^0 X^{[k]}$ or in the case of elliptical symmetry

$$f_0(X) = \sum_{k=0}^{\infty} a_k^0 \kappa^{2k} = \sum_{k=0}^{\infty} a_k^0 (X^{[k]})^* \mathbf{A}_0^{\{k\}} X^{[k]}, \quad (1)$$

where $X^{[k]} = \underbrace{X \otimes \dots \otimes X}_{k\text{-times}}$ is the Kronecker power

of the phase vector $X = (x, p_x, y, p_y)^*$, $\dim X^{[k]} = \binom{k+3}{k}$, $\mathbf{A}_0^{\{k\}}$ is the symmetrical Kronecker power of the initial form matrix $\mathbf{A}_0 : \kappa^2 = X^* \mathbf{A}_0 X$:

$$(\mathbf{A}^{\{k\}})_{il} = b_i(k) (\mathbf{A}_0^{\{k\}})_{il},$$

$$i, l = 1, \binom{n+k-1}{k}, \quad b_i(k) = k! / k_1! \dots k_n!$$

2.2 The Self-Field of the Space Charge

Using the Ferrer's integrals technique we calculate the desired space-charge forces in symbolic forms for some modelfunction of space-charge distributions. In particular, we obtain the components of the vector of self-electrical field in the form

$$E_{\xi, \eta} = E_{\xi, \eta}^0 + \Delta E_{\xi, \eta}, \quad E_{\xi}^0 = \frac{4\pi\rho_0}{\epsilon_0} \frac{ab}{a(a+b)} \xi,$$

* Serge.Andrianov@pobox.spbu.ru

$$E_\eta^0 = \frac{4\pi\rho_0}{\epsilon_0} \frac{ab}{b(a+b)}\eta.$$

where ξ, η are local coordinates in which the transverse cross-section has the form of a canonical ellipse. The values of $\Delta E_\xi, \Delta E_\eta$ are calculated with the help of *MAPLE* codes. Note that for the KV distribution we have $\Delta E_\xi = \Delta E_\eta = 0$. Besides, if the arbitrary distribution $\rho(x, y) = \rho_0 \Phi(\kappa_1^2)$ is a polynomial of n -th order with respect to the variables κ_1^2 the functions ΔE_ξ and ΔE_η are polynomials of $(2n+1)$ -th order with respect to the variables ξ and η . Then we can return to the coordinates x, y referenced to a beamline system.

3 THE MOTION EQUATION

3.1 The Motion Equation for a Particle

For a nonbunched beam (the longitudinal self-electric field is missing) the motion equation for single particle can be written in the following matrix form

$$\frac{dX}{ds} = \sum_{k=1}^{\infty} \{ \mathbf{P}_{ext}^{1k}(s) + \mathbf{P}_{self}^{1k}(s) \} X^{[k]}.$$

The matrices \mathbf{P}_{ext}^{1k} and \mathbf{P}_{self}^{1k} describe the external and space-charge fields correspondingly [4].

3.2 Transfer Map in the Presence of the Space-Charge

It is known that the Lie algebraic tools is very valuable tools to studying beam dynamics without space-charge. The Lie map satisfies to the following linear operator equation

$$\frac{d\mathcal{M}(s|s_0)}{ds} = \mathcal{L} \circ \mathcal{M}(s|s_0), \quad (2)$$

where $\mathcal{M}(s|s_0)$ is a time-displacement operator (Lie map) between moments s_0 and s :

$$\mathcal{M}: X_0 \rightarrow X = \mathcal{M}(s|s_0) \cdot X_0.$$

and \mathcal{L} is a Lie operator associated with a generating vector field. If the beam is an ensemble of noninteracting particles then the operator \mathcal{L} depend only on beamline parameters. If we have to take into account the space-charge forces the Lie operator will depend on beam characteristics and as result it will depend on the Lie map. In this case we use nonlinear motion equation for Lie map already:

$$\frac{d\mathcal{M}(s|s_0)}{ds} = \mathcal{L}(\mathcal{M}) \circ \mathcal{M}(s|s_0). \quad (3)$$

In the frame of the matrix formalism [2] we can represent this map in the form $\mathcal{M}: X_0 \rightarrow X = \mathcal{M}(s|s_0) \cdot X_0$,

3.3 The Matrix Formalism for Lie Map

According to the matrix formalism [2] we can write

$$X = \mathcal{M}(s|s_0) \cdot X_0 = \sum_{k=1}^{\infty} \mathbf{M}^{1k}(s|s_0) X_0^{[k]}, \quad (4)$$

where \mathbf{M}^{1k} are matrices which can be calculated with the help of the matrix formalism tools.

According to our suggestions the beam particles occupy some elliptical cross-section \mathfrak{M}_0 in an initial state:

$$\mathfrak{M}_0 = \{ X_0 : X_0^* \mathbf{A}_0^{11} X_0 \leq 1 \}.$$

As we mention above in the presence of the space-charge the motion equation for the map \mathcal{M} assume a nonlinear form. For the solution of this equation in this paper we propose the method of step-by-step approximations. The basic idea of this method in our case is to calculate the distribution function according to the algorithm described in [4].

From the known properties of Lie maps we can write for an arbitrary function of an initial distribution $f_0(X) = f(X, s_0)$: $f(X, s) = f_0(\mathcal{M}^{-1}(s|s_0) \cdot X)$. In our case we have $\mathcal{M}^{-1}(s|s_0) \cdot X = \sum_{k=0}^{\infty} \mathbf{T}^{1k}(s|s_0) X^{[k]}$, where $\mathbf{T}^{10} = -\mathbf{M}^{10}$, $\mathbf{T}^{11} = (\mathbf{M}^{11})^{-1}$ and other matrices \mathbf{T}^{1k} for $k > 1$ can be calculated with the help of the recurrent generalized Gauss's algorithm using the matrices \mathbf{M}^{1k} . It is worthy to note that according to this algorithm one should inverse only the matrix \mathbf{M}^{11} and then use only matrix operations for calculation the necessary matrices \mathbf{T}^{1k} up to the desired order. So after some calculations we can obtain the following equation

$$\begin{aligned} f(X, s) &= f_0(\mathcal{M}^{-1} \cdot X) = \\ &= a_0^0 \sum_{k=1}^{\infty} a_k^0 (\mathcal{M}^{-1} \cdot X^{[k]})^* \mathbf{A}_0^{\{k\}} (\mathcal{M}^{-1} \cdot X^{[k]}) = \\ &= a_0^0 + \sum_{k=1}^{\infty} a_k^0 \sum_{l=k}^{\infty} \sum_{j=k}^{\infty} (X^{[l]})^* \mathbf{B}_k^{lj} X^{[j]}, \\ \mathbf{B}_k^{lj} &= (\mathbf{T}^{kl})^* \mathbf{A}_0^{\{k\}} \mathbf{T}^{kj}. \end{aligned}$$

For the test of the convergence of our approximations methods the following condition can be used

$$\begin{aligned} &\|f(\mathcal{M}_{k+1}^{-1} \circ X) - f(\mathcal{M}_k^{-1} \circ X)\| \leq \\ &\leq \beta \|f(\mathcal{M}_k^{-1} \circ X) - f(\mathcal{M}_{k-1}^{-1} \circ X)\| \end{aligned}$$

for $\beta < 1$, k - is an iterative loop number. The constant of this method β can be calculated as a function of the initial beam characteristics and the beamlines parameters. The condition $\beta < 1$ allows the limitations on the step values $|s_k - s_{k-1}| = \Delta s_k$ to be calculated which guarantee the fulfilment of the inequality $\beta < 1$.

4 COMPUTER EXPERIMENTS

The approach discussed above was used for some practical problems: the halo formation problems. The corresponding computer experiments was developed both in symbolic (with the help of *MAPLE* codes) and in numerical modes.

The symbolic investigation was carried out with main purpose to understand what parameters have the sufficient influence on halo production. For this task we studied the images of an initial beam state (in the distribution function terms) and used the concepts of virtual scrapers for investigation of what parts of the initial beam give the basic contribution to halo formation. According to this approach we transform the aperture boundaries of virtual scrapers with the help of inverse maps from some current sections to the initial point. Changing the aperture values one can select "tails" part of the initial distribution. This approach demonstrated its advantages and flexibility. As an example on the Figure.1 the initial and current phase distribution functions are demonstrated. On the pictures a)—d) one can see the images of the initial function for some moment: on the part a) — the image of total distribution function, on the part b) — the image of tails particles and on the part c) — the image of the intermediate particles, on the part d) — the image of the central core particles. We should note that for most distribution function the core particles give the corresponding contribution to halo. The most extreme particles from the tail part remain in halo if they reach it once. One can see on the presented pictures different phases of halo formation for two parts of initial beam state: the first is evaluated from central part which is small enough and the second is evaluated from particles which form so-called "tail" of distribution function which can be defined using the virtual scraper concept.

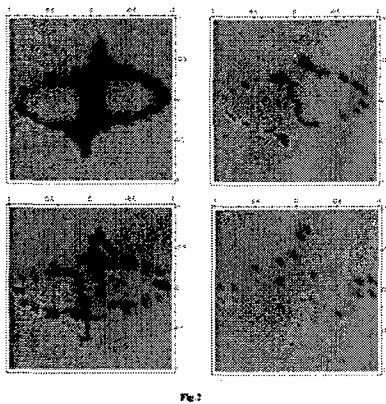
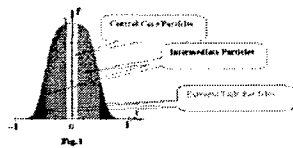


Figure 1: The initial model distribution function and 3D-contourplots for different parts of the initial distribution

5 REFERENCES

- [1] W.Lysenko, Z.Parsa *Beam Matching and Halo Control*. Preprint LA-UR-97-1712,
- [2] Andrianov S.N. *A Matrix Representation of the Lie Algebraic Methods for Design of Nonlinear Beam Lines*, Proc.

- of the 1996 Comput. Acc. Phys. Conf. — CAP'96, Sept. 24–27, Williamsburg, Virginia, USA, eds. J.J.Bisognano, A.A.Mondelli, AIP Conf. Proc. **391**, NY, 1997, pp.355–360.
- [3] Andrianov S.N. *Nonlinear Dynamics of Particle Beams with Space Charge*, in: Proc. of the 9th Intern. Conf. "Computational Modelling and Computing in Physics", September 16–21, 1996, D5, 11-97-112, pp.55–60, Dubna, 1997.
- [4] Andrianov S.N., *High-Order Optics with Space Charge: Analytical Approach*, Proc. of the Sixth European Part. Acc. Conf. — EPAC-98, Stockholm, 22–26 June 1998, Inst. of Phys. Publ., Bristol, UK, pp.1091–1093.
- [5] Andrianov S.N., Edamenko N.S. *Some Problems of Halo Formation in Beamlines*, Abstrs. of the Fifth Intern. Workshop on Beam Dynamics & Optimization — BDO'98, St.Petersburg, 29 June – 3 July 1998, p.12.
- [6] Andrianov S.N. *Dynamic Modeling Paradigm and Computer Algebra*, Proc. of the Int.Conf. on Comput. Modeling and Computing in Physics, Dubna, Russia, 16–21 Sept., 1996, Dubna, 1997, pp.60–64.

TRANSVERSE NONLINEAR FOCUSING OF NONSTATIONARY SPACE CHARGE DOMINATED BEAMS*

A.I.Borodich⁺, ISIR, Minsk

Abstract

The general analytical and numerical scheme to calculate the parameters of high intensity beam being transported is considered. Nonlinearities of external fields and space charge are taken into account. The matching conditions for a beam and focusing system aren't required. Lie algebraic technique was applied to derive the dynamic and the field equations selfconsistently. The distribution function and the macroscopic parameters of a beam at any transport channel cross-section were calculated in the framework of the Heisenberg picture in statistical mechanics. The computer code was carried out and verified. Test results are represented.

1 INTRODUCTION

To calculate the main dynamic parameters of the continuous relativistic high-current beam, being focused, at any cross-section of the transport channel one should operate with altering distribution function of transverse coordinates and momenta of charged particles. For chosen temporal and spatial scales interaction between particles inheres in collective behavior, charged plasma assumes to be collisionless. Therefore, firstly, one may consider a beam, submitted to the electromagnetic fields of focusing elements, as the Hamiltonian system. Secondly, to calculate the macroscopic parameters of a beam we may evaluate one particle distribution function $g(x, y, p_x, p_y; z)$ that satisfies the Vlasov equation.

For the realistic transport channels operations with a small parameter and linearized selfconsistent equations are not valid. One should implement nonperturbative methods to step forward. In [1] to apply Lie algebraic techniques were proposed and stationary case was examined. Nonstationary focusing was considered in [2] on the basis of the quasi-stationary plasma model by the algebraic methods. In this paper the general solution of nonlinear focusing of nonstationary space charge dominated beam is discussed.

2 TRANSFER MAP CALCULATION

Let's consider 4D-phase space of transverse canonical conjugated coordinates and momenta of the continuous charged particle beam. The actions of the transfer map M , which brings about the symplectic manifold

automorphisms, on the phase variables vector $\xi(x, y, P_x, P_y)$ and on the dynamic function $u(\xi)$ are defined as $\xi(z) = M\xi$ and $u(\xi, z) = Mu(\xi)$. An independent variable z is the coordinate along the reference trajectory. It is essentially, that the transfer map implementation allows operating with one-particle Hamiltonian. If the initial coordinates and momenta values of an arbitrary particle are known at $z = 0$, i.e. at the start point of the transport channel, using the operator M one may calculate them at any z , i.e. at any cross-section of the transport channel.

One-particle Hamiltonian $H(\xi, z)$, that governing the continuous beam transverse dynamics, may be expressed with sufficient accuracy as a finite sum of m-forms. This is legitimate provided that the transverse energy of an arbitrary particle is considerably less then its oriented motion energy. The number of the m-forms depends on the accuracy required. Without the loss of generality we will be concerned with

$$H(\xi, z) = H_2 + H_3 + H_4 \quad (1)$$

Here $H_2(\xi, z) = 1/2 \cdot S_{ij}(z)\xi_i\xi_j$,

$$H_3(\xi, z) = T_{ijk}(z)\xi_i\xi_j\xi_k,$$

$$H_4(\xi, z) = L_{ijkl}(z)\xi_i\xi_j\xi_k\xi_l.$$

Summation over repeated indexes is implied. Matrixes $S_{ij}, T_{ijk}, L_{ijkl}$ are symmetric for any pair of indexes and depend on z .

Taking into consideration (1) it is reasonable to find out the transfer map M structure according to the Dragt-Finn factorization theorem [3]:

$$M = \exp(:f_4:) \exp(:f_3:) \exp(:f_2:),$$

where $:f_m:$ is the Lie operator associated with the homogeneous polynomial of degree m .

The dynamic equations for the transfer map factors were received in [3]. After algebraic manipulation they are casted into the matrix form:

$$\begin{aligned} M_{ij}^{\&} &= J_{ia} S_{ab} M_{bj} \quad , \\ F_{ijk}^{\&} &= -T_{abc} M_{ai} M_{bj} M_{ck} \quad , \end{aligned} \quad (2)$$

$$\begin{aligned} G_{ijkl}^{\&} &= -L_{abcd} M_{ai} M_{bj} M_{ck} M_{dl} - \\ &- 9/2 \cdot F_{dij} T_{abc} M_{ar} M_{bk} M_{cl} J_{dr} \quad . \end{aligned}$$

* Work supported by the FFR of Republic of Belarus, grant M96-065

+ Email: bor@isir.minsk.by

Here $M(z) = \exp(:f_2:)$, $f_3 = F_{ijk}(z)\xi_i\xi_j\xi_k$, $f_4 = G_{ijkl}(z)\xi_i\xi_j\xi_k\xi_l$. Matrixes M_{ij} , F_{ijk} , G_{ijkl} are also symmetric for any pair of indexes and essentially dependent on z . The unitary symmetric and skew-symmetric matrixes are denoted as I_{ij} and J_{ij} . The differential equations (2) have to be solved subject to $M_{ij}(z=0) = I_{ij}$, $F_{ijk}(z=0) = 0$, $G_{ijkl}(z=0) = 0$.

If the explicit form of the transfer map M is known, one may calculate changed in time values of a phase variable vector ξ according to

$$\xi(z) = M\xi + (:f_3:)\xi + \left(\frac{:f_3:}{2}\right)M\xi + (:f_4:)\xi, \quad (3)$$

a dynamic function $u(\xi)$ - according to

$$u(\xi(z)) = u(M\xi) + u(:f_3:)\xi + u\left(\left(\frac{:f_3:}{2}\right)M\xi\right) + u(:f_4:)\xi, \quad (4)$$

a beam macroscopic parameter $U(z)$ - according to

$$U(z) = \int dx \int dy \int dp_x \int dp_y \times u(\xi(z))g(x, y, p_x, p_y). \quad (5)$$

The last formula assumes that averaging the microscopic dynamic function over an ensemble of particles implies the Heisenberg picture in statistical mechanics.

To evaluate the dynamic equations (2) one should know the z -dependence of the S, T, L matrixes. A nontrivial question is to evaluate the electromagnetic terms in the Hamiltonian (1). The electromagnetic forces acting on a beam particle are due to the external fields of focusing elements and to the interaction of a particle with its environment.

3 FOCUSING SYSTEM POTENTIALS

If in particular the magnetic focusing system is used to transport high-current relativistic beam, we have $\phi^{\text{field}}(x, y; z) = 0$. As for the vector $\mathbf{A}^{\text{field}}(x, y; z)$, its components are calculated analytically in 3 stages for each focusing element.

1) Solve the Laplace equation for the magnetostatic potential $U(x, y, z)$ taking into account the boundary conditions implied by the magnetic field symmetry.

2) Calculate the components of the magnetic induction $\mathbf{B}(x, y, z)$ from $\mathbf{B}(x, y, z) = \text{grad}U(x, y, z)$.

3) Obtain the vector potential $\mathbf{A}(x, y, z)$ projections from $\text{rot}\mathbf{A}(x, y, z) = \mathbf{B}(x, y, z)$.

4 SPACE CHARGE POTENTIALS

To calculate $\phi^{\text{beam}}(x, y; z)$ one should solve the Poisson equation. Its solution at an arbitrary point (x_0, y_0) of the beam cross-section at some z is

$$\phi^{\text{beam}}(x_0, y_0; z) = -\frac{1}{\epsilon_0} \frac{I}{v_0} \int dx' \int dy' \int dp'_x \int dp'_y \times G(x_0, y_0, x', y')g(x', y', p'_x, p'_y), \quad (6)$$

where I is a beam current, v_0 is a reference particle velocity, ϵ_0 is a dielectric permittivity of free space. And $G(x_0, y_0, x', y')$ denotes the Green's function.

It should be noted that the limits of integration over x', y', p'_x, p'_y are unknown. In general case one must substitute the initial variables x, y, p_x, p_y for transformed variables x', y', p'_x, p'_y in the integral, that should be of the form (5). As a result we conclude, that integration involves the inverse transfer map M^{-1} .

But if the initial distribution $g(x, y, p_x, p_y)$ is the Gaussian, transformed distribution $g(x', y', p'_x, p'_y)$ will be the Gaussian too. Moreover, if variables in $g(x, y, p_x, p_y)$ are not coupled, the same is valid for variables in $g(x', y', p'_x, p'_y)$. And for that distribution we may establish the limits of integration in (6) through the values $\sigma'_x = \sqrt{\langle x'^2 \rangle}$, $\sigma'_y = \sqrt{\langle y'^2 \rangle}$ and $\lambda'_x = \sqrt{\langle p_x'^2 \rangle}$, $\lambda'_y = \sqrt{\langle p_y'^2 \rangle}$ according to the "3 sigma" rule.

After integrating over momenta (6) takes the form

$$\phi^{\text{beam}}(x_0, y_0; z) = -\frac{1}{\epsilon_0} \frac{I}{v_0} \int_{-3\sigma'_x}^{3\sigma'_x} dx' \int_{-3\sigma'_y}^{3\sigma'_y} dy' \times \frac{G(x_0, y_0, x', y')}{(2\pi)\sigma'_x\sigma'_y} \exp\left(-\frac{1}{2}\left[\frac{x'^2}{\sigma_x'^2} + \frac{y'^2}{\sigma_y'^2}\right]\right) \quad (7)$$

Variable substitution $x' \rightarrow x'/\sigma'_x$, $y' \rightarrow y'/\sigma'_y$ allows choosing $G(x_0, y_0, x', y')$ as the Green's function of the inner Dirichlet problem for a circle [4].

When the explicit form of the transfer map M is known, we integrate (7) numerically at the knots of a spatial net, which covers the cross-section of a beam.

Hence, to calculate the transfer map factors, firstly, we should represent $\phi^{\text{beam}}(x', y'; z)$ as a finite sum of m-forms according to (1). Secondly, we should establish the z -dependence of the coefficients of the m-forms.

To satisfy the first requirement we consider $\phi^{\text{beam}}(x', y'; z)$ as a function of 2 variables x', y' and

1 parameter z . It is substantial, that the function is defined within the circle. Using the Chebyshev polynomials as a complete set of orthogonal functions we decompose $\varphi^{\text{beam}}(x', y'; z)$ on the polynomials of x', y' up to the 4-th degree. Coefficients $C_{ij}(z)$ of an approximation are calculated by the least squares method. Due to the elliptic symmetry we evaluate only 5 of them. As the result should be expressed in variables of (7), after the inverse substitution $x' \rightarrow \sigma'_x \cdot x', y' \rightarrow \sigma'_y \cdot y'$ we have

$$\varphi^{\text{beam}}(x', y'; z) = C_{20}(z)x'^2 + C_{02}(z)y'^2 + C_{40}(z)x'^4 + C_{04}(z)y'^4 + C_{22}(z)x'^2 y'^2.$$

To satisfy the second requirement we consider $\varphi^{\text{beam}}(x', y'; z)$ as a function of 1 variable z and 2 parameters x', y' . It is substantial, that any $C_{ij}(z)$ is a monotonous function within some focusing element. So one may construct the empiric formula with 2 parameters for each $C_{ij}(z)$ within each focusing element. We use the modified method of averages to establish the type of a formula and compute its parameters.

To calculate $\mathbf{A}^{\text{beam}}(x', y'; z)$ we solve the vector Poisson equation in the same manner. If there is no a shift of the beam centroid, one may use $A_x = A_y = 0$,

$$A_z^{\text{beam}}(x', y'; z) = \frac{V_0}{c^2} \varphi^{\text{beam}}(x', y'; z). \text{ In general}$$

case, the decomposition of functions and the construction of formulas lead to

$$\mathbf{A}^{\text{beam}}(x', y'; z) = \mathbf{D}_{20}(z)x'^2 + \mathbf{D}_{02}(z)y'^2 + \mathbf{D}_{40}(z)x'^4 + \mathbf{D}_{04}(z)y'^4 + \mathbf{D}_{22}(z)x'^2 y'^2.$$

5 FRINGE QUADRUPOLES FOCUSING

As an example we consider nonlinear focusing of an electron nonstationary space charge dominated Gaussian beam in a fringe magnetic quadrupole channel. The algebraic approach discussed above was implemented to the computer code LIE_HEI written in Fortran-90.

Let a beam current is $I = 100$ A, a reference particle energy is $E_0 = 1$ MeV, initial centroid parameters are $\bar{x}(0) = 0.375 \times 10^{-10}$ m, $\bar{y}(0) = -0.575 \times 10^{-9}$ m, initial sizes are $\tilde{x}(0) = 0.25 \times 10^{-2}$ m, $\tilde{y}(0) = 0.25 \times 10^{-2}$ m, initial divergences are of 1%.

Let a quadrupole channel is of the total length 1.25 m and consists of 3 lenses with lengths 0.375, 0.5, 0.375 m respectively. Each lens has the same values of the gradient $g = 0.025$ T/m and its second derivative $g'' = 0.001$ T/m³.

In that case of small nonlinearities the moments approach may be used to treat the example [4].

Figures 1 and 2 depict the transverse beam sizes and the beam centroid parameters respectively as functions of z in SI units. The solid curves concern the moments method [4] and the dashed ones concern the algebraic approach. It is clear, that results of different methods are in complete agreement with each other.

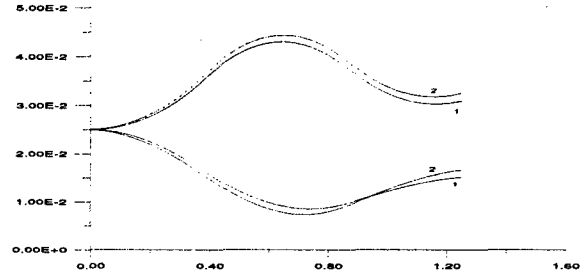


Figure 1: Transverse beam sizes variations.

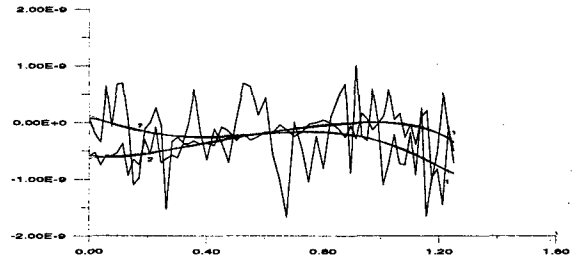


Figure 2: Beam centroid parameters variations.

6 CONCLUSION

The analytical approach to solve the problem of nonstationary nonlinear focusing of a high-current beam was developed. It uses the most general equations that govern a beam dynamics. And it means that the method may have various applications in charged particle beam physics and accelerator science.

Also it should be noted, that using in particular the Heisenberg picture allows to solve the dynamic equations and calculate the beam parameters, including its emittance and brightness, in the same manner and without a concern about the distribution evaluation.

7 REFERENCES

- [1] R.D.Ryne, A.J.Dragt, "Lie Algebraic Treatment of Space Charge", Proceedings of the 1987 IEEE PAC, pp.1063-1065, (1988).
- [2] A.I.Borodich, V.I.Stolyarsky, A.A.Khrutichinsky, "The Description of High Current Beam Dynamics Using the Lie Algebraic Methods", Proceedings of the 1995 IEEE PAC, pp.3232-3234, (1996).
- [3] A.J.Dragt, E.Forest, "Computation of Nonlinear Behavior of Hamiltonian Systems Using Lie Algebraic Methods", J. of Mathematical Physics, vol. 24, pp.2734-2744, (1983).
- [4] A.I.Borodich, I.A.Volkov, "High Current Relativistic Electron Beam Transport by Magnetic Multipoles", J. of Engineering Physics And Thermophysics, vol.70, pp.776-782, (1997).

OPTIMAL TRANSPORT OF NONSTATIONARY HIGH INTENSITY BEAMS*

A.I.Borodich⁺, ISIR, Minsk, I.A.Volkov, BSU, Minsk

Abstract

The problem to determine focusing field configuration that provides the minimal transverse emittance growth of an intense continuous beam at the end of the transport channel is considered. Nonlinear terminal Mayer problem of optimal control related with nonstationary space charge dominated beam transport by fringe magnetic quadrupoles was formulated. Then it was reduced to the quadrupoles parameters optimization. Squared transverse rms emittance of a beam was casted as the quality criteria. Matrix differential equations [1] for the transfer map factors together with the integral equations [1] for space charge potentials were evaluated. The solutions of the optimization problem were received by the Nelder-Mead method combined with the penalty functions. The computer code was carried out and verified. Test results are represented.

1 INTRODUCTION

The design of focusing systems provide the minimal transverse emittance growth of an intense relativistic beam has been one of the central challenges in charged particle beam physics and accelerator science for some decades. From the mathematical viewpoint minimizing the emittance is a problem of the optimal control theory [2]. It is formulated for a system of differential equations that govern the dynamics of an object under a control in order to find out the minimum of some functional, for example, the transverse rms emittance.

Considerable difficulties will emerge often in the optimal control theory while the minimum of a functional is calculated. Therefore, when some physical process is under the examination, one should reduce the optimal control problem to the problem of optimization, i.e. to find out the minimum of the function of many variables. For this purpose it is recommended [3] to approximate the control function by a set of independent polynomials and to use the conjugated variables for calculating the quality criteria gradient.

2 OPTIMIZATION SCHEME

We consider continuous nonstationary high-current beam with the Gaussian distribution as initial. The matrix differential equations for the transfer map factors

together with the integral equations for space charge potentials are used in frame of the algebraic approach for transverse nonlinear focusing [1]. Calculation of beam macroscopic parameters, including the transverse rms emittance, implies the Heisenberg picture in statistical mechanics. Notations of physical values, that are involved, are the same as in [1].

Let the focusing system consists of the magnetic quadrupoles cascading axially. Also the drifts may be inserted between the lenses. Scalar potential is $\phi^{field}(x,y;z) = 0$, and the components of vector potential $A^{field}(x,y;z)$ including the fringe fields are

$$\begin{aligned} A_x^{field}(x,y;z) &= \frac{1}{4} g'(z)(x^3 - xy^2), \\ A_y^{field}(x,y;z) &= \frac{1}{4} g'(z)(-y^3 + x^2y), \\ A_z^{field}(x,y;z) &= \frac{1}{2} g(z)(y^2 - x^2) - \\ &\quad - \frac{1}{12} g''(z)(y^4 - x^4), \end{aligned}$$

where $g(z)$ is the gradient of a single magnetic quadrupole lens, $g'(z), g''(z)$ are its derivatives with respect to an independent variable z .

The Mayer's problem of optimal control is stated as: determine physical parameters of magnetic quadrupoles (magnitudes of gradients, values of the first and the second derivatives of gradients) as functions of the longitudinal coordinate z , which provide the minimal transverse rms emittance of an intense continuous beam at the end of the transport channel.

This is nonlinear terminal problem of optimal control as the total length of the transport channel is fixed. It is reduced in the standard manner [3] to the problem of optimization of parameters of the quadrupoles and drifts.

The quality criteria (the objective functional or merit functional) is squared transverse rms emittance of a beam

$$\begin{aligned} Q = & \langle x^2 \rangle \langle p_x^2 \rangle - \langle xp_x \rangle^2 + \\ & + \langle y^2 \rangle \langle p_y^2 \rangle - \langle yp_y \rangle^2, \end{aligned}$$

where the angular brackets mean averaging the physical values over an ensemble.

* Work supported by the FFR of Republic of Belarus, grant M96-065

⁺ Email: bor@isir.minsk.by

Each quadrupole possesses 4 parameters: the length of a lens, the magnitude of gradient, the value of the first derivative of gradient, the value of the second derivative of gradient. Each drift possesses 1 parameter: the length of free space.

The assumption we make is that the action of each lens is independent of the others. It means we neglect the fields of one lens tend to leak into the region of any adjacent lenses [4]. Also we model the action of each lens using the "hard-edge" approximation. But both linear and nonlinear focusing forces of a lens are taking into account.

As a result of optimization 4 parameters (3 physical and 1 geometrical) for each lens plus the lengths of all drifts should be determined. The total number of parameters of optimization is $n=4m+m-1$, where m is the number of quadrupoles. We employ the Nelder-Mead method to compute the optimal values. It is the regular search method of the zero order and uses the simplex in n -dimensional space of the parameters of optimization.

The general calculated scheme to obtain the optimal focusing system parameters for a transport of an intense continuous beam with the initial Gaussian distribution on coordinates and momenta looks as it follows.

1. Define the initial configuration of focusing fields, which is determined by n parameters, and make the initial simplex.

2. Compute the transfer map, having the dynamic equations for its factors, from the start point z^{ini} to the end z^{fin} of the transport channel.

3. Compute the second moments as the average physical values in the Heisenberg picture, using the known transfer map factors, at the end of the transport channel z^{fin} .

4. Calculate the terminal meaning of the quality criteria, which corresponds to the initial configuration of focusing fields.

5. Make an advanced simplex, according to the Nelder & Mead idea to move it toward the optimum, and define the advanced configuration of focusing fields.

Then we repeat actions following steps 2-5 until obtain the minimum of the quality criteria as a function of n parameters with prescribed accuracy.

Three main operations are used to transfer the simplex with $(n+1)$ vertices in n -dimensional space. The coefficients of reflection, stretching and compression are $\alpha = 1$, $\beta = 0.5$, $\gamma = 2$, as it is recommended in [5].

Also the additive penalty function are implemented in the optimization. It provides the beam "effective" transverse size ($\sim 3\sigma'_x, \sim 3\sigma'_y$) is no greater than the transport channel aperture as well as the beam "effective" transverse momentum ($\sim 3\lambda'_x, \sim 3\lambda'_y$) never exceeds the longitudinal one.

It was the outer cycle implies the regular search for the quality criteria function minimum. There is also two inner

cycles to compute the transfer map in selfconsistent manner together with the space charge calculation.

The transport channel consists of the focusing elements. And every focusing element is conditionally divided with respect to the z variable onto 5 sections (6 calculated points). Data received are stored for statistics to construct the empiric formulas for unknown functions $C_{ij}(z)$ and

$D_{ij}(z)$ within each focusing element. We use the modified method of averages to establish the type of each empiric formula and calculate its 2 parameters. The transfer map from z^{ini} to z^{fin} is computed into 2 stages.

In the first stage we deal with the sections. Every time we calculate the transfer map from the start point z_i to the end z_{i+1} of the current section ($z_0 = z^{ini}$, $z_1 = z^{fin}$). All the coefficients C_{ij} and D_{ij} are constant, and we derive the dynamic equations for the current section transfer map factors. So, the transfer map from z^{ini} to z^{fin} is a consequence of transfer maps from z_i to z_{i+1} .

In the second stage we deal with the elements. Every time we calculate the transfer map from the start point z_k to the end z_{k+1} of the current element ($z_0 = z^{ii}$, $z_K = z^{fn}$). All the coefficients $C_{ij}(z)$ and $D_{ij}(z)$ are known functions of z , and we derive the dynamic equations for the current element transfer map factors. So, the transfer map from z^n to z^{fn} is a consequence of transfer maps from z_k to z_{k+1} .

3 FRINGE QUADRUPOLES OPTIMIZATION

The optimization scheme discussed above is an algorithm for computer code LIE_OPT written in Fortran-90. Matrix differential equations are computed by the Runge-Kutta-Merson method of the 4-th order. Four-dimensional integrals, used to calculate the beam macroscopic parameters, are executed by the Monte-Carlo method. Two-dimensional integrals, used to calculate space charge potentials values, we evaluate by the Gauss method for hyper-rectangles.

As an example we consider the optimization of a fringe magnetic quadrupole channel without drifts.

Let an electron Gaussian beam current is $I = 100$ A, a reference particle energy is $E_0 = 1$ MeV, initial centroid parameters are $\bar{x}(0) = 0$, $\bar{y}(0) = 0$, initial sizes are $\bar{x}(0) = 0.25 \times 10^{-2}$ m, $\bar{y}(0) = 0.25 \times 10^{-2}$ m, initial divergences are of 1%.

Let a quadrupole channel consists of 10 lenses of the same length.

The goal is to obtain the optimal values of the gradient g and its second derivative g'' for each lens.

To facilitate our task we require each quadrupole produces the same fringe field. It means that additional constraints should be included in the penalty function.

Figure 1 depicts the initial and optimal gradient values of each quadrupole in SI units. Solid line specifies the initial focusing field configuration as a quadrupole super triplet. Corresponding variations of the beam envelopes along the transport channel in SI units is shown on figure 2 also in solid. Dashed lines on the figures 1 and 2 concern the optimal quantities.

At the end of a transport channel the initial value of squared transverse rms emittance of a beam is $Q^0 = 2.65 \times 10^{-7} \text{ m/rad}^2$, and the optimal one is $Q^{opt} = 1.87 \times 10^{-7} \text{ m/rad}^2$. The optimal meaning of fringe fields is specified by $g'' = -0.2 \text{ Tl/m}^3$. They are responsible for the partial compensation of space charge nonlinearities. It leads to some reduction of the rms emittance growth.

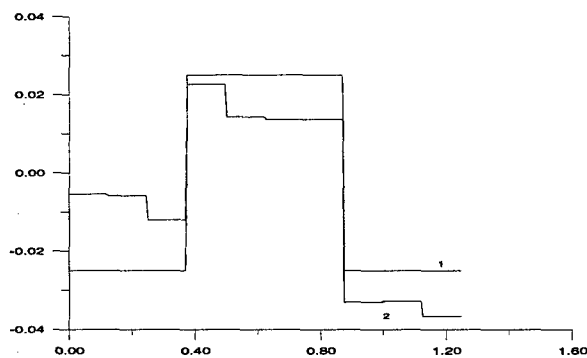


Figure 1: Arrangements of quadrupoles and their gradient values. .

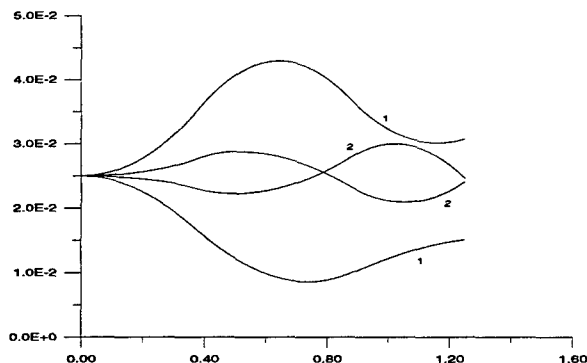


Figure 2: Beam envelopes variations.

We should also mark another nontrivial result, that follows from the solution of the optimal transport of high-current continuous beam. It is possible to minimize the transverse rms emittance growth without any increase of

the beam sizes while using in particular the fringed magnetic quadrupoles.

4 CONCLUSION

The optimization technique described here may be used in computer simulations for high-current continuous beam transport to provide the minimal emittance growth.

The major advantage of this approach is that it uses the most general equations that govern the dynamics of nonstationary space charge dominated beam. Also it is important that focusing field nonlinearities may be included in the group of controls.

The major drawback is that technique searches only local minimum. Therefore in future work the procedure of picking a starting point in the space of parameters will be adjusted.

5 REFERENCES

- [1] A.I.Borodich, "Transverse Nonlinear Focusing of Nonstationary Space Charge Dominated Beams", (this Proceedings).
- [2] N.N.Moiseev, "Numerical Methods in Theory of Optimal Systems", Moscow, (1971), (in Russian).
- [3] A.A.Kuraev, "Powerful Microwaves Devices: Methods of Analysis and Optimization of Parameters", Moscow, (1986), (in Russian).
- [4] C.K.Allen, S.K.Guharay, M.Reiser, "Optimal Transport of Low Energy Particle Beams", Proceedings of the 1995 IEEE Particle Accelerator Conference, pp.2324-2326, (1996).
- [5] B.D.Bunday, "Basic Optimization Methods", Edward Arnold, (1984)

ANALYSIS OF PHASE SPACE STRUCTURE FOR MATCHED INTENSE CHARGED-PARTICLE BEAMS IN PERIODIC FOCUSING TRANSPORT SYSTEMS*

Renato Pakter,¹ Chiping Chen¹ and Ronald C. Davidson²

¹MIT Plasma Science and Fusion Center, Cambridge, MA 02139, USA

²Princeton Plasma Physics Laboratory, Princeton, NJ 08543, USA

Abstract

Test particle motion is analyzed for a matched intense charged-particle beam in a periodic focusing solenoidal magnetic field to assess the effects of beam intensity on inducing chaotic particle motion and halo formation.

1 INTRODUCTION

Halo formation and control in intense charged-particle beams has been the subject of recent vigorous theoretical, computational and experimental investigations [1]. It is of fundamental importance in the development of next-generation high-intensity accelerators for basic scientific research in high-energy and nuclear physics as well as for a wide variety of applications ranging from heavy ion fusion, accelerator production of tritium, accelerator transmutation of nuclear waste, spallation neutron sources, and high-power free-electron lasers. In these high-intensity accelerators, beam halos must be controlled in order to minimize beam losses and activation of the accelerator structure.

2 THEORETICAL MODEL

We consider a thin, continuous, intense charged-particle beam propagating in the z -direction with characteristic axial velocity $\beta_b c$ and kinematic energy $\gamma_b mc^2$ through the periodic focusing solenoidal magnetic field

$$\mathbf{B}^{sol}(\mathbf{x}) = B_z(s)\mathbf{e}_z - \frac{1}{2}B'_z(s)(x\mathbf{e}_x + y\mathbf{e}_y). \quad (1)$$

Here, \mathbf{e}_x and \mathbf{e}_y are unit Cartesian vectors perpendicular to the beam propagation direction, $s = z$ is the axial coordinate, $x\mathbf{e}_x + y\mathbf{e}_y$ is the transverse displacement from the beam axis at $(x, y) = (0, 0)$, the superscript 'prime' denotes d/ds with $B'_z(s) = dB_z(s)/ds$, and the axial component of magnetic field satisfies

$$B_z(s + S) = B_z(s), \quad (2)$$

where S is the axial period of the focusing field.

To determine the self-electric and self-magnetic fields consistently, we make the following assumptions: (a) the

Budker parameter $\nu = N_b q^2 / mc^2$ for the beam is small compared with γ_b ; (b) the axial momentum spread of the beam particles is small in comparison with $\gamma_b m \beta_b c$; (c) the beam is axisymmetric ($\partial/\partial\theta = 0$); and (d) the beam is perfectly matched into the focusing field with uniform density profile over the beam cross section,

$$n_b(r, s) = \begin{cases} N_b / \pi r_b^2(s), & 0 \leq r < r_b(s), \\ 0, & r > r_b(s). \end{cases} \quad (3)$$

In Eq. (3), $r = (x^2 + y^2)^{1/2}$ is the radial coordinate, $r_b(s) = r_b(s + S)$ is the outer envelope of the beam, and $N_b = 2\pi \int_0^\infty n_b r dr = \text{const.}$ is the number of particles per unit axial length. The periodic outer beam envelope $r_b(s) = r_b(s + S)$ corresponds to a special solution of the beam envelope equation [2,3]

$$\frac{d^2 r_b}{ds^2} + \kappa_z(s)r_b - \frac{K}{r_b} - \frac{\varepsilon_T^2}{r_b^3} = 0, \quad (4)$$

where $K = 2q^2 N_b / \gamma_b^3 \beta_b^2 mc^2$ is the normalized perveance, $\kappa_z(s) = [qB_z(s) / 2\gamma_b \beta_b mc^2]^2 = [\Omega_c(s) / 2\beta_b c]^2$ is the focusing parameter, $\varepsilon_T = \text{const.}$ is the total unnormalized emittance, q and m are the particle charge and rest mass, respectively, and c is the speed of light *in vacuo*. The transverse phase-space distribution that self-consistently generates the density profile in Eq. (3) is the rigid-rotor Vlasov equilibrium distribution with angular rotation velocity ω_b [2].

In cylindrical coordinates (r, θ) in the Larmor frame, the equations of motion transverse to the direction of beam propagation can be derived from the normalized Hamiltonian

$$H_\perp(r, P_r, P_\theta, s) = \frac{1}{2} \left(P_r^2 + \frac{P_\theta^2}{r^2} \right) + \frac{1}{2} \kappa_z(s) r^2 + \psi(r, s), \quad (5)$$

where the normalized self-field potential $\psi(r, s)$ is defined by

$$\psi(r, s) = \begin{cases} \frac{K}{2} [1 - r^2 / r_b^2(s)] + K \ln[r_w / r_b(s)], & 0 \leq r < r_b(s), \\ K \ln[r_w / r], & r_b(s) < r \leq r_w. \end{cases} \quad (6)$$

3 ANALYSIS

In this section, we analyze the particle motion in the Larmor frame described by Eq. (5). For present purposes, the Hamiltonian in Eq. (5) is expressed as

$$H_\perp(r, P_r, P_\theta, s) = H_0(r, P_r, P_\theta) + H_1(r, P_r, P_\theta, s), \quad (7)$$

* This research was supported by Department of Energy under Grant No. DE-FG02-95ER-40919 and Contract No. DE-AC02-76-CH0-3073, and by Air Force Office of Scientific Research under Grant No. F49620-97-1-0325. The research by R. Pakter was also supported by CAPES, Brazil.

where

$$H_0 = \frac{1}{2}P_r^2 + V_0(r, P_\theta)$$

$$\equiv \frac{1}{2}P_r^2 + \frac{1}{2}\bar{\kappa}_z r^2 + \frac{P_\theta^2}{2r^2} + \psi(r, s)|_{r_b(s)=\bar{r}_b}, \quad (8)$$

$$H_1 = \frac{1}{2}[\kappa_z(s) - \bar{\kappa}_z]r^2 + \psi(r, s) - \psi(r, s)|_{r_b(s)=\bar{r}_b}. \quad (9)$$

In Eqs. (7)-(9), $\psi(r, s)$ is defined in Eq. (6), and the effective mean beam radius \bar{r}_b is defined by

$$\bar{r}_b = (\varepsilon_T S / \sigma)^{1/2}, \quad (10)$$

where $\sigma = \varepsilon_T \int_s^{s+S} ds / r_b^2(s)$ is the space-charge-depressed phase advance for the rigid-rotor Vlasov equilibrium. The effective mean focusing parameter $\bar{\kappa}_z$ occurring in Eqs. (8) and (9) is defined by

$$\bar{\kappa}_z = \frac{K}{\bar{r}_b^2} + \frac{\varepsilon_T^2}{\bar{r}_b^4}. \quad (11)$$

Physically, the Hamiltonian H_0 provides a good approximate description of the (slow) betatron oscillations, whereas the perturbation H_1 describes nonlinear resonances induced by the (fast) oscillations in $\kappa_z(s)$ and $r_b(s)$.

To determine the betatron oscillation frequency, we employ the Hamilton-Jacobi method and perform a canonical transformation from (r, P_r) to the action-angle variables (ϕ, J) . Let $W(r, J)$ be the characteristic function satisfying the partial differential equation

$$\frac{1}{2} \left(\frac{\partial W}{\partial r} \right)^2 + V_0(r, P_\theta) = H_0 = \text{const.} \quad (12)$$

As discussed below, the dependence of W on J is uniquely determined because of the one-to-one correspondence between H_0 and J [see Eq. (16)]. A formal expression for the angle variable ϕ is given by

$$\phi = \partial W / \partial J. \quad (13)$$

The action variable J can be expressed as

$$J = \frac{1}{2\pi} \oint P_r dr = \frac{1}{\pi} \int_{r_-}^{r_+} \{2[H_0 - V_0(r, P_\theta)]\}^{1/2} dr, \quad (14)$$

where the turning points r_\pm solve the algebraic equation

$$H_0 = V_0(r_\pm, P_\theta), \quad (15)$$

and $r_+ > r_-$ is assumed. Because the action variable J increases monotonically with increasing H_0 , Eq. (14) can be inverted to yield a Hamiltonian of the form

$$H_0 = H_0(J, P_\theta). \quad (16)$$

The betatron oscillation frequency can then be expressed as

$$\omega_\beta(J, P_\theta) = \partial H_0 / \partial J, \quad (17)$$

which, in general, must be evaluated numerically.

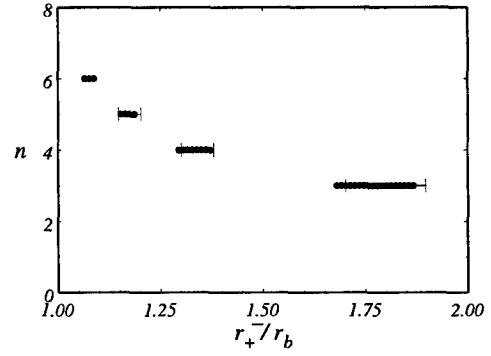


Figure 1: Locations and full widths of the primary resonances of order $n = 3$ to 6.

Under the influence of the perturbation H_1 , a variety of nonlinear resonances occur due to the coupling of the (slow) betatron oscillations and the (fast) oscillations in the focusing parameter $\kappa_z(s)$ and associated modulation in the beam envelope $r_b(s)$. The locations and widths of the nonlinear resonances are analyzed.

Making use of the action-angle variables (ϕ, J) , we express the total Hamiltonian H formally as

$$H(\phi, J, P_\theta, s) = H_0(J, P_\theta) + H_1(\phi, J, s). \quad (18)$$

Expanding H_1 in a Fourier series representation in ϕ and s , we obtain

$$H_1 = \sum_{n=-\infty}^{\infty} \sum_{l=-\infty}^{\infty} a_{nl}(J) \exp[i(n\phi + 2l\pi s/S)], \quad (19)$$

where the Fourier coefficients $a_{nl}(J)$ are determined numerically. Of particular interest in the present analysis are the primary nonlinear resonances that satisfy the resonance condition

$$n\omega_\beta(J_n, P_\theta) = 2\pi/S, \quad (20)$$

where J_n determines the location of the primary resonance of order n in the phase space (ϕ, J) , i.e., at $J = J_n$. The full width of the n th-order primary resonance is estimated to be

$$\Delta r_n = \left(\frac{\partial r}{\partial J} \right)_{P_\theta, J=J_n} \left[\frac{32|a_{n,-1}(J_n)|}{(\partial \omega_\beta / \partial J)_{J=J_n}} \right]^{1/2} \quad (21)$$

in the radial coordinate.

Figure 1 shows the locations and full widths of the primary resonances of order $n = 3$ to 6 obtained for the choice of system parameters corresponding to $\sigma_v = 80^\circ$ ($S^2 \bar{\kappa}_z = 8.712$), $\eta = 0.2$, $\sigma = 26.2^\circ$ ($SK/\varepsilon_T = 3.8$), $\omega_b = 0$ and $P_\theta = 0$. Here, a step-function lattice is used, and η is the filling factor. In Fig. 1, the solid lines correspond to the analytical estimates given in Eq. (21), whereas the dotted lines are obtained by integrating Eq. (5) numerically.

Use is made of the Poincaré surface-of-section method to examine extensively the phase-space structure described

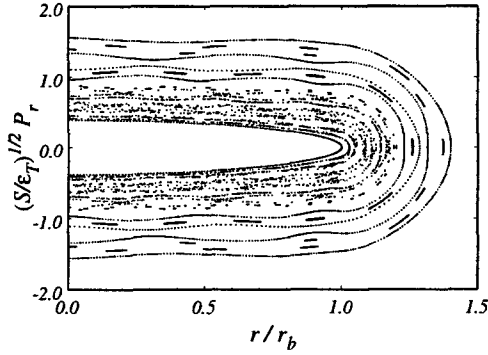


Figure 2: Poincaré surface-of-section plots in the phase space (r, P_r) for 15 test particle trajectories moving through the periodic step-function lattice from $s/S = 0.5$ to 1000.5. Here, the parameters are: $\sigma_v = 80^\circ$, $\eta = 0.2$, $\sigma = 11.4^\circ$ ($SK/\varepsilon_T = 10$), $\omega_b = 0$, and $P_\theta/\varepsilon_T = 0$.

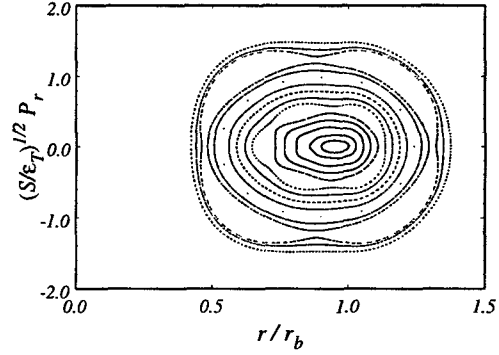


Figure 3: Poincaré surface-of-section plots in the phase space (r, P_r) for 15 test particle trajectories moving through the periodic step-function lattice from $s/S = 0.5$ to 1000.5. Here, the parameters are: $\sigma_v = 80^\circ$, $\eta = 0.2$, $\sigma = 11.4^\circ$ ($SK/\varepsilon_T = 10$), $\omega_b = 0.9$, and $P_\theta/\varepsilon_T = -0.9$.

by the Hamiltonian H in Eq. (5). Of particular interest are the nonlinear resonances and chaotic particle motion of test particles outside the boundary of the phase space occupied by the interior beam particles making up the rigid-rotor Vlasov equilibrium distribution f_0 [2]. The phase-space boundary of the rigid-rotor Vlasov equilibrium is a closed surface in the three-dimensional phase space (r, P_r, P_θ) at any given axial distance s . A projection of such a boundary onto the phase space (r, P_θ) can be determined from

$$\left[\frac{P_\theta r_b(s)}{\varepsilon_T r} + \omega_b \frac{r}{r_b(s)} \right]^2 + (1 - \omega_b^2) \frac{r^2}{r_b^2(s)} = 1 - \omega_b^2, \quad (22)$$

where the parameter ω_b ($|\omega_b| < 1$) is a measure of beam rotation in the Larmor frame. For a KV equilibrium distribution, $\omega_b = 0$.

Detailed results of the phase-space analysis are discussed in [4], and are summarized in Sec. 4. Here, we only illustrate the effect of beam rotation on beam dynamics in Figs. 2 and 3. For both cases shown in Figs. 2 and 3, the value of P_θ is chosen such that the boundary of the equilibrium distribution extends to $r = r_b$ [Eq. (22)]. It is evident in Figs. 2 and 3 that, for comparable choices of system parameters, the phase space structure for a nonrotating KV equilibrium distribution ($\omega_b = 0$) exhibits more pronounced chaotic behavior than that for a rigid-rotor Vlasov equilibrium distribution (with $\omega_b = 0.9$).

4 CONCLUSIONS

Test particle motion has been analyzed for matched intense charged-particle beam propagating through a periodic solenoidal magnetic field. The betatron oscillations of test particles in the average self fields and applied field were analyzed, and the nonlinear resonances induced by periodic modulations in the self fields and applied field were determined. It was found [4] that the phase-space structure changes significantly as the canonical angular momentum

(P_θ), beam intensity (as measured by SK/ε_T or σ/σ_v), vacuum phase advance σ_v , or beam rotation (ω_b) is varied. For an intense beam with nonrotating KV equilibrium distribution ($\omega_b = 0$), it was shown that the chaotic regions approach the phase-space boundary of the equilibrium distribution as the canonical angular momentum P_θ decreases in magnitude. For an intense beam with a rigid-rotor Vlasov equilibrium distribution ($\omega_b \neq 0$), it was found that the presence of beam rotation reduces the degree of chaotic behavior in phase space. Finally, for $\sigma_v < 80^\circ$, the test-particle analysis showed that at very high beam intensities, the chaotic layers associated with the separatrices of nonlinear resonances are still divided by the remaining invariant (KAM) surfaces and do not overlap completely to form an extended chaotic region.

5 REFERENCES

- [1] American Institute of Physics Conf. Proc. **377**, edited by S. Y. Lee (1996).
- [2] C. Chen, R. Pakter, and R. C. Davidson, Phys. Rev. Lett. **79**, 225 (1997).
- [3] R. C. Davidson and C. Chen, Part. Accel. **59**, 175 (1998).
- [4] C. Chen, R. Pakter, and R. C. Davidson, submitted to Phys. Rev. E (1998).

ENHANCING THE PERFORMANCES OF ECR ION SOURCES*

G. D. Alton, Y. Liu

Physics Division, ORNL, Oak Ridge, TN

Abstract

The performances of ECR ion sources can be enhanced in the spatial domain by tailoring the central magnetic field so that it is uniformly distributed over a large plasma volume and is of magnitude so as to be in resonance with single frequency microwave radiation. Analogously, the performances of conventional minimum- B ECR ion sources can be enhanced in the frequency domain by injecting multiple discrete frequency or broadband microwave radiation into their plasma volumes. In this report, examples of both the spatial-and frequency-domain techniques will be given. For example, the design aspects of an all permanent-magnet "volume-type" (spatial-domain) ECR ion source will be described and the effects of injecting multiple frequencies (frequency-domain) on the charge-state-distributions extracted from a conventional minimum- B ECR ion source will be presented.

1 INTRODUCTION

Electron-cyclotron-resonance (ECR) ion sources are being widely used for the production of highly charged ion beams for heavy ion accelerator based fundamental and applied research. In recent years, considerable progress has been made in ECR ion source technology in terms of their capabilities for generating high-charge-state ion beams as well as total beam intensities. In conventional minimum- B ECR ion sources, narrow bandwidth, single frequency microwave radiation produces thin annular, ellipsoidal-shaped ECR surfaces which constitute a small percentage of the plasma volume and consequently, the efficiency of RF power coupling is limited by the sizes of their ECR surfaces. It has been suggested that the performances of ECR ion sources can be significantly improved by tailoring the central region of the magnetic field so that it is resonant with single frequency microwave radiation (spatial-domain) [1-3] or by injecting multiple-discrete or broadband microwave radiation into conventional minimum- B ECR ion sources (frequency-domain) [3,4].

The spatial-domain technique employs a magnetic field configuration with an extended central flat region, tuned to be in resonance with single-frequency microwave radiation. Because of the large resonant plasma volume, significantly more RF power can be coupled into the plasma, resulting in heating of electrons over a much larger volume than possible in conventional ECR ion sources. The ability to ionize a larger fraction of the

particles in the plasma volume effectively reduces the probability of resonant and non-resonant charge exchange, thereby increasing the residence time of an ion in a given charge state and for subsequent and further ionization. All other parameters being equal, the "volume" ECR source should result in higher charge-state distributions, higher beam intensities, and improved operational stability [1-3]. This concept has been recently validated by Heinen, et al., who used the technique to improve the charge states for Ar^{q+} ($q>5$) by factors of 20 to 100 over those from a conventional minimum- B ECR ion source [5] and through the record proton intensities generated with the "flat" field source by Wills, et al. [6]. We are presently fabricating a compact, all-permanent-magnet "volume-type" ECR ion source that incorporates the flat-field concept for high charge-state ion beam generation.

With multiple discrete frequency microwave radiation simultaneously launched into a minimum- B ECR ion source, one can generate multiple, separated and nested ECR heating surfaces. These techniques have been validated at LBNL by increasing the high charge-state population and intensities within a particular charge state of Bi and U by injecting two frequencies into their AECS source [7] and at ORNL by increasing the charge states and intensities within a particular charge state for Ar^{q+} and Xe^{q+} by injecting three frequencies [8] into the ORNL Caprice ECR ion source [9].

The design details of an all permanent-magnet "volume-type" ECR ion source for multiply charged ion beam generation and the results derived from the three multi-frequency plasma heating experiments will be described in this report.

2 DESIGN FEATURES OF AN ALL-PERMANENT MAGNET VOLUME ECR ION SOURCE

A compact, all-permanent magnet, single-frequency ECR ion based on a novel magnetic field configuration has been designed and is presently under construction [10]. The source is designed to achieve a large, on-axis ECR "volume," which allows ECR power to be efficiently coupled along and about the axis of symmetry. A schematic representation of the source is illustrated in Fig. 1 and the axial magnetic field is displayed in Fig. 2. As noted, the axial magnetic field profile is flat (constant mod- B) in the center which extends over the length of the central field region along the axis of symmetry and radially outward to form a uniformly distributed ECR plasma "volume". This magnetic field design strongly

* Research supported by the U.S. Department of Energy under contract DE-AC05-OR22464 with the U.S. Department of Energy.

contrasts with those used in conventional ECR ion sources where the central field regions are approximately parabolic and the consequent ECR zones are "surfaces". According to computational studies [1] the new configuration will result in dramatic increases in the absorption of RF power, thus enabling the heating of electrons over a much larger volume, thereby increasing the electron temperature and "hot" electron population in the plasma. The axial mirror field is produced by two, 50-mm thick, annular NdFeB permanent magnets radially magnetized in opposite directions and separated by ~ 150 mm. Specially designed and positioned iron cylinders are used to create the flat central field region between the mirror magnets. The source is designed to operate at a central frequency of ~ 6 GHz and the flat magnetic field region can be adjusted by mechanical means to tune the source to the resonance condition within the limits of 5.6 to 6.9 GHz. The plasma confinement magnetic field mirror has a ratio B_{max}/B_{ECR} of slightly greater than two.

Since the radial magnetic field distribution is proportional to $B = B_0 r^{N/2-1}$ where N is the number of cusps and r is the radial distance from the center of the device to the tip of the magnet, a high-order multicusp field for confining the plasma in the radial direction can increase the resonant volume in the radial direction. Therefore, instead of a sextupole field, commonly used in conventional minimum- B ECR ion sources, a 12-pole multicusp field was designed for the source. Twelve NdFeB bar magnets, equally spaced in an alternating polarity arrangement around the circumference of a 57.2-mm diameter, water cooled Cu magnet holder, are used to produce the desired field for radial confinement, as shown in Fig. 3. In combination with the axial mirror field, a magnetic field strength of 5.1 kG, approximately equal to that of the axial mirror field, is generated at the inner wall of the plasma chamber. For comparison, the radial field profile for a sextupole configuration ($N = 6$) is also plotted in Fig. 3. As noted, the region over which the field region is uniform is much greater for the $N = 12$ multicusp field.

The cylindrical cavity plasma chamber is made of Al and is 15.6 cm in length and 5.4 cm in diameter. Computational design studies were performed for several different RF injection schemes, using the finite element code ANSYS [11]. A broadband RF injection system was then designed for the ion source. It is a long, precisely

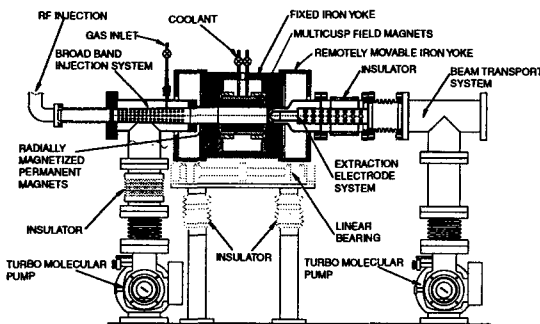


Fig. 1. Schematic view of the flat- B ECR ion source.

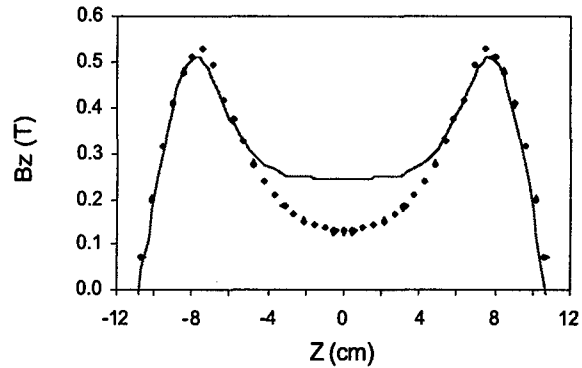


Fig. 2. Axial magnetic field profiles of the volume" (solid line) and conventional minimum- B configuration on "surface" (dotted line) ECR ion sources.

tapered rectangular-to-circular transition section, starting from a rectangular WR137 waveguide and ending with a circular diameter that matches the dimension of the plasma chamber. The transition from rectangular to circular is very smooth so that it has excellent voltage standing wave ratio (VSWR) while converting the rectangular waveguide TE_{10} dominant mode to the dominant circular waveguide TE_{1np} eigenmodes with the RF power concentrated near the axis of the resonant plasma volume and the E -vector oriented perpendicular to the magnetic field direction for efficient electron heating. The mechanical design of the source is very flexible in that it can be converted from a "volume" source to a "surface" source and vice-versa by simply adding/removing a Fe ring to/from the central region between the mirror magnets. The resulting minimum- B axial magnetic field profile, after adding the Fe ring, is also shown in Fig. 2. The multicusp field can also be changed to an $N = 6$ field distribution when the source is

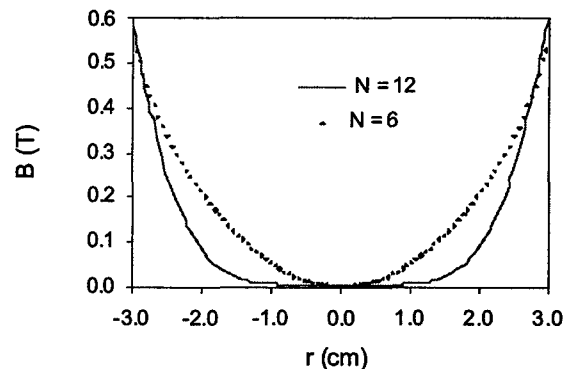


Fig. 3. Comparison of $N = 6$ and $N = 12$ cusp radial magnetic field profiles. The effect of increasing the number of cusps from $N = 6$ to $N = 12$ is apparent: the lower order multiple field results in a much smaller resonant plasma volume.

configured as a conventional "surface" source. Comparisons will be made of the performances of the "volume" and conventional single-frequency "surface" ECR sources in terms of the charge-state distributions and intensities within a particular charge-state for each configuration.

3 MULTI-FREQUENCY MICROWAVE PLASMA HEATING

We have conducted comparative studies to assess the relative performance of the conventional minimum-*B* ORNL Caprice ECR ion source [9] for the production of multiply charged ion beams when excited with one, two and three-frequency microwave radiation [8]. In order to simultaneously inject three frequencies into the plasma chamber of the source, it was found necessary to design and fabricate an appropriate waveguide/injection system to avoid cross coupling of the radiation in the waveguide system. The ORNL Caprice source, equipped with the new three-frequency injection module, is shown in Fig. 4. Microwave radiation between 10 and 14 GHz can be injected into the source. The studies were conducted with the existing 10.6 GHz, 1 kW, klystron power supply and two TWT-based microwave power supplies with rated powers of 80 and 200 W, respectively.

One, two and three-frequency heating experiments were conducted with Xe feed gas with 10.6 GHz (290 W), 10.6 GHz (290 W) + 11.57 GHz (40 W) and 10.6 GHz (290 W) + 11.57 GHz (40 W) + 12 GHz (52 W) microwave power. Fig. 5 shows the resulting charge-state distributions derived from these studies. It is clear that, with the addition of the second and third frequencies, the most probable Xe^{qt} charge state moves to higher values by one unit and the intensities for the high-charge states are increased by ~ 3 over those for the saturated, single-frequency 10.6 GHz (290 W) case. Our results clearly illustrate that the performance of conventional geometry ECR ion sources can be significantly improved by use of multiple-discrete frequency plasma heating.

4 REFERENCES

1. G. D. Alton, and D. N. Smithe, *Rev. Sci. Instrum.* **65** (1994) 775.
2. G. D. Alton, and D. N. Smithe, *Physica Scripta* **T71** (1996) 66.
3. G. D. Alton, Proc. of the 14th Int. Conference on Cyclotrons and their Applications, ed. J. C. Cornell (Capetown, South Africa, October 8-13, 1995), World Scientific, Singapore, p. 362.
4. G. D. Alton, *Nucl. Instr. and Meth. A* **382** (1996) 276.
5. A. Heinen, et al., *Rev. Sci. Instrum.* **69** (1998) 729.
6. J. S. C. Wills, R. A. Lewis, J. Diserens, H. Schmeing, and T. Taylor, *Rev. Sci. Instrum.* **69** (1998) 65.
7. Z. Q. Xie, and C. M. Lyness, in Proc. of the 12th Int. Workshop on ECR Ion Sources (Wakoshi, Japan, April 25-27, 1995), eds. M. Sekiguchi and T. Nakagawa, INS-J-182 (1995) 24.
8. G. D. Alton, F. W. Meyer, Y. Liu, J. R. Beene, and D. Tucker, *Rev. Sci. Instrum.* **69** (1998) 2305.
9. F. W. Meyer, M. E. Bannister, C. C. Havener, O. Woitke, and Q. Yan, in Proceedings of the Thirteenth International Workshop on ECR Ion Sources, edited by D. May, Texas A&M University, February, 1997, p. 102.
10. Y. Liu, G. D. Alton, G. D. Mills, C. A. Reed, and D. L. Haynes, *Rev. Sci. Instrum.* **69** (1998) 1311.
11. ANSYS is a finite element code marketed by ANSYS, Inc., Cannonsburg, PA 15317, USA.

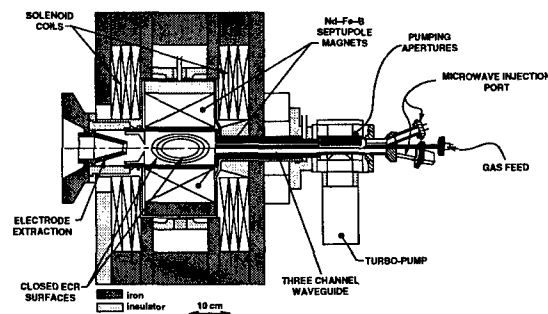


Fig. 4. Schematic drawing of the ORNL Caprice ECR ion source [9] equipped with a three-frequency microwave injection system.

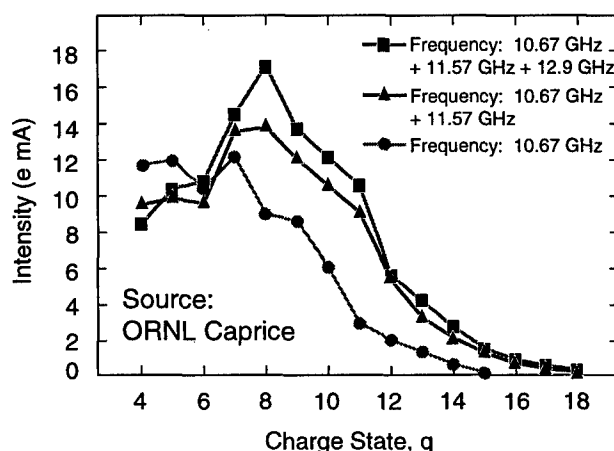


Fig. 5. Charge-state distributions for Xe ion beams extracted from the ORNL Caprice ECR ion source [9] equipped with a three-frequency microwave injection system; lower curve: 290 W of 10.6 GHz klystron power (optimized); middle curve: 290 W of 10.6 GHz klystron power (optimized) and 40 W of 11.59 GHz TWT power (nonoptimized); and upper curve: combination of 290 W of 10.6 GHz klystron power (optimized), 40 W of 11.57 GHz TWT power (nonoptimized), and 52 W of 12.9 GHz TWT power (nonoptimized) [8].

A HIGH-TEMPERATURE, "VOLUME-TYPE", ECR ION SOURCE FOR RIB GENERATION*

G. D. Alton, T. Zhang[†], Y. Liu, C. A. Reed[‡], C. Williams[‡],

Oak Ridge National Laboratory, P. O. Box 2008, Oak Ridge, TN 38731-6368 USA

Abstract

A high temperature, low-charge-state, "volume-type" source has been designed for use in the nuclear physics and nuclear astrophysics research radioactive ion beam (RIB) programs at the Holifield Radioactive Ion beam Facility (HRIBF). The source utilizes electromagnetic coils to generate a large and uniformly distributed central magnetic field with magnitude (875 G) chosen to be in electron-cyclotron-resonance (ECR) with single-frequency (2.45 GHz) microwave radiation. Among the features of the source include: a variable mirror-ratio at ion extraction as required for optimizing low-charge state ion beam generation; a right-hand, circularly-polarized RF injection system to overcome the relatively-low, cutoff-density, ($n_c = 7.4 \times 10^{10}/\text{cm}^3$) associated with the use of 2.45 GHz microwave radiation; and a high temperature, Ir- or Re-coated-Ta plasma chamber to reduce the residence times of radioactive species that are adsorbed on the walls of the chamber. No provisions are made for radial plasma confinement due to the sensitivity of permanent magnets to degradation by the large fluxes of neutrons incumbent during target irradiation, routinely used for this purpose. Aspects of the design features of the source are described in this report.

1 INTRODUCTION

Chemically active species, diffused from target materials for use at ISOL-based radioactive ion beam (RIB) research facilities, often arrive at the ionization chamber of the source in a variety of molecular forms. Since hot-cathode sources, such as the CERN-ISOLDE electron-beam-plasma ion source, presently used at the HRIBF, do not efficiently dissociate and ionize the atomic constituents of such carriers, the species of interest are often distributed in a variety of side-band ion beams with different masses and thereby, their intensities are diluted. Since intensity is at a premium for nuclear physics and astrophysics research with RIBs, it is important to concentrate the species of interest into a single mass-channel. ECR ion sources are particularly effective means for simultaneously dissociating molecules and ionizing their atomic constituents. While these sources

are most frequently used for generating multiply charged ion beams for which the plasma confining magnetic field must be optimized at high field values, the magnetic field can also be customized to accentuate low charge-state ion beam generation as required for radioactive ion beam (RIB) generation at the HRIBF. The present source design is predicated on recent advances in ECR ion source technology effected by designing the magnetic field so that the central magnetic field is uniformly distributed over a large volume with magnitude chosen to be resonant with 2.45 GHz microwave radiation [1-4]. By enlarging the ECR zones, the performances (molecular dissociation and ionization efficiencies) can be enhanced over those of conventional minimum- B geometry sources.

In this report, we briefly describe, the mechanical design features, magnetic field design attributes, ion extraction optics and the RF injection system for the source.

2 MECHANICAL DESIGN FEATURES

An isometric representation of the source is illustrated in Fig. 1. The source assembly consists of a tubular Ta plasma chamber (inner diameter: 75 mm; length: ~265 mm) to which is welded tubular Ta production beam entry and target chambers, positioned at right angles with respect to the plasma chamber axis. The production beam will pass through the center of the plasma chamber, at a right-angle with respect to the axis of symmetry of the source, where it will interact with target material, located in a target chamber diametrically opposed to the entry port, before coming to rest in a C-beam-stop. The plasma and target chambers will be coated with Ir or Re because of their low enthalpies for adsorption of many electronegative members of the periodic chart to reduce the residence times of RIB species that strike the plasma chamber walls. The end flanges of the plasma chamber, production beam entry port, and target chamber ports will be made of stainless steel, fusion-bonded to Ta. These flanges will be equipped with knife-edge-type metal-to-metal vacuum seals. Target materials will be heated to temperatures exceeding 2000 °C by resistively heating a Ta-heater that surrounds the target material reservoir. The plasma chamber will be independently heated up to ~1500 °C by Ta wrap-around heaters. The large conductance target chamber is close-coupled to the plasma chamber of the source in order to efficiently transport radioactive species to the plasma chamber of the source.

*Research sponsored by the U.S. Department of energy under contract De-AC05-96OR22464 with Lockheed Martin Energy Research Corp.

[†]On leave from China Institute of Atomic Energy (CIAE), Beijing.

[‡]Oak Ridge Institute of Science and Engineering (ORISE), Oak Ridge, TN 37831-6368.

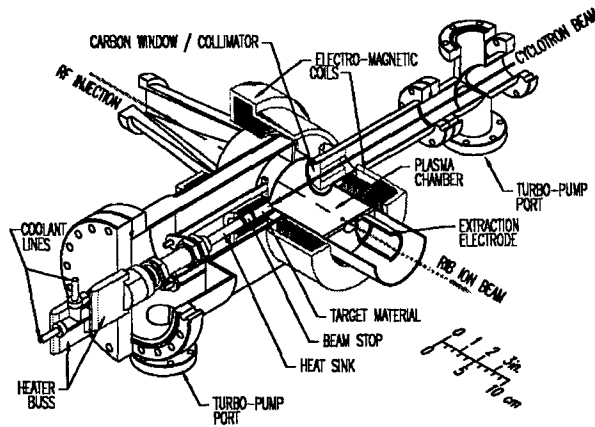


FIG. 1. Schematic representation of the high-temperature, low-charge-state ECR source

3 MAGNETIC FIELD DESIGN

For the source to perform according to the underlying principals, it is quintessential that the central field region be uniformly distributed (flat) along the axis of symmetry of the source with magnitude commensurate with the value required for excitation with single-frequency, 2.45 GHz microwave radiation ($B_{ECR} = 875$ G). The magnetic-field distribution, shown in Fig. 2, was computationally designed to achieve this objective by use of the simulation code Poisson [5]. The required flat central resonant field region is generated with two sets of primary and trim coil systems (inner coil diameters: $\Phi 122$ mm) located at each end of the plasma chamber; each coil system is housed in a magnetic flux return yoke (outer diameter: $\Phi 254$ mm). The axial magnetic field is designed with a fixed, high mirror ratio at the RF injection end and a variable mirror ratio at the

extraction end of the source, as required to optimize the efficiencies for dissociation of molecular carriers and ionization of their atomic constituents. While the mirror coils serve to confine the plasma in the axial direction, no analogous provisions are made for radial plasma confinement due to the sensitivity of permanent magnets to degradation by the large fluxes of neutrons incumbent during target irradiation, routinely used for this purpose. As noted, the field is designed to be uniform over a length of ~ 75 mm. In order to produce a central field distribution with the desired uniformity, high permeability, cylindrical geometry Fe shunts, located between the trim coils, are also required. The parameters of the magnetic field system are listed in Tables 1 and 2.

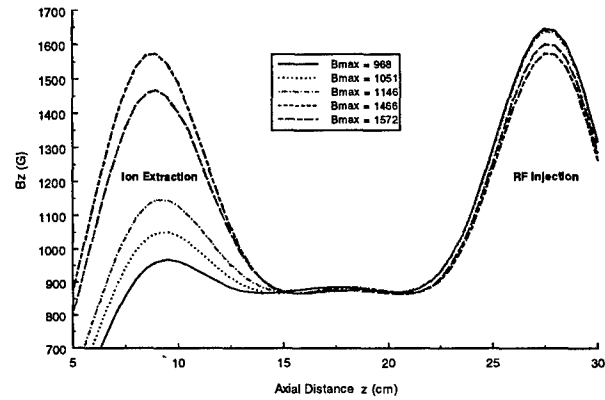


FIG. 2. Axial magnetic field profile for the low-charge-state ECR ion source.

TABLE 1. Mirror ratios of the axial magnetic field

RF injection end :	$B_{max}/B_{ECR} \approx 2/1$
Ion extraction end:	$B_{max}/B_{ECR} = 1.1/1$ to $1.8/1$

TABLE 2. Magnetic field intensity and uniformity values for the magnetic field distribution

Peak Value: Extraction end (G)	Peak Value: RF injection end (G)	Flat-B Region (cm)	Flat-B Uniformity (%)	Bmax (G)	Bmin (G)	Primary Coil: RF injection end (A.Turns)	Primary coil: Extraction end (A.Turns)	Trim Coil: RF injection End (A.Turns)	Trim Coil : Extraction End (A.Turns)
968	1646	8.5	± 1.0	884	867	18700	7700	2500	-2800
1051	1644	8.0	± 1.0	883	866	18650	8810	2000	-2800
1146	1638	7.5	± 1.0	884	866	18550	10030	1520	-2800
1466	1600	7.5	± 1.3	886	863	18170	15500	-1540	-2900
1572	1572	7.5	± 1.0	884	866	17800	17800	-2900	-2900

4 EXTRACTION OPTICS

In order to ensure beams with good transport properties and minimise aberration effects imparted to the beam during extraction, a series of simulation design studies for space charge limited extraction from the source were performed with the simulation code, PBGuns [6]. The following formula was used initially in choosing initial values for certain parameters such as the extraction gap, d , radius, r_c , of the aperture in the first extraction electrode (cathode), and extraction voltage, V , for space-charge limited flow through the system [7]:

$$I = P_p \left(1 - 1.6 \frac{d}{r_c} \right) \cdot V^{3/2} \quad (1)$$

$$P_p = \frac{4}{9} \epsilon_0 \left(\frac{2q}{M} \right)^{1/2} \frac{\pi a^2}{d^2}$$

in Eq.1, q is the charge, M the mass of the ion, and a is radius of the extraction aperture. Table 3 provides a list of species, intensities, RMS emittances and extraction voltages for the three-electrode extraction system under space-charge-limited conditions. The axial mirror fields are taken into account during the simulations. An example of beam transport of a 1.62 mA beam of $^{40}\text{Ar}^+$

through the three electrode extraction system is shown in Fig. 3.

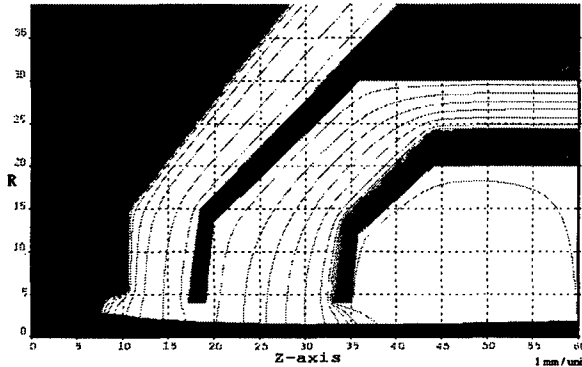


FIG. 3. The beam profile of a 1.62 mA $^{40}\text{Ar}^+$ beam extracted from the "volume-type" ECR ion source

From the figure, it can be seen that the spherical-sector plasma-electrode plays an important role in focusing the beam; the field gradients between the focus electrode and first and second extraction electrodes form a smooth extraction field, resulting in transportable beams with good emittance characteristics. This electrode system can also be used for extraction and transport of highly space-charge-dominated proton beams. In this situation, only the first electrode is used for extraction; the second electrode is biased negatively by ~ -1 kV to repel secondary electrons generated by ion impact with beam transport components and residual gas atoms that would otherwise be accelerated to the source. The result of these studies suggest that a 200 mA proton beam can be extracted from an 8-mm-diameter aperture at 55 kV. The RMS emittance for this case was found to be: $\varepsilon_n \sim 5 \times 10^{-2} \pi$ mm mrad.

TABLE 3. Simulation results for different species extracted from the "volume-type" ECR ion source

Species	Intensity (mA)	RMS Emittance (π mm mrad)	V_{ex1} (kV)	V_{ex2} (kV)
^{12}C	1.62	4.549×10^{-4}	7.0	20
^{16}O	1.62	3.995×10^{-4}	8.0	20
^{40}Ar	1.62	4.768×10^{-4}	8.0	20
^{84}Kr	1.62	2.978×10^{-4}	10.6	20
^{132}Xe	1.62	4.567×10^{-4}	12.8	20
^{209}Bi	1.13	6.149×10^{-4}	12.0	20

5 RF INJECTION SYSTEM

The microwave RF injection system features a right-hand circular polarizer to avoid the relatively-low cut-off density limit ($n_c = 7.4 \times 10^{10} \text{ cm}^{-3}$) associated with the use of 2.45 GHz microwave radiation. The microwave injection system consists of a 2.45 GHz, 2 kW magnetron power supply, circulator, directional coupler, WR-340 wave guide, stub-tuner, a right-hand circular polarizer, a rectangular-to-circular wave-guide converter and a circular plasma chamber. The microwave radiation travels along the rectangular wave-guide in the TE_{10} mode; this mode is then converted to a TE_{11} mode in a

rectangular-to-circular transition wave-guide section. The finite element code ANSYS [8] was used in determining the length of the converter that would minimize reflected power. Fig. 4 illustrates the dependence of reflected power on the length of the rectangular-to-circular transition section. The results of this studies also show that the forward power possesses the frequency independent character of the RF injection system. Fig. 5 shows that the electric field distribution is concentrated near the axis of the uniformly distributed magnetic field, in keeping with efficient coupling of the RF power to the plasma.

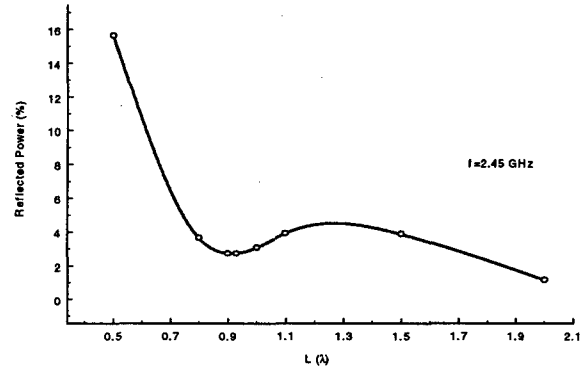


FIG. 4. Reflected power versus frequency for the RF injection

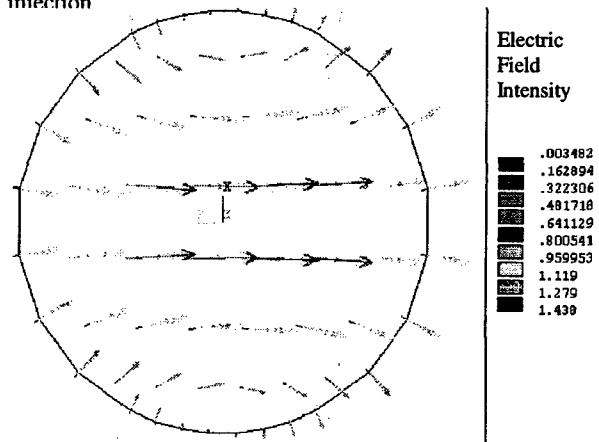


FIG. 5. The electric field distribution in the plasma chamber

6 REFERENCES

1. G. D. Alton and D. N. Smithe, *Rev. Sci. Instrum.* **65** (1994) 775.
2. G. D. Alton, in *Proceedings of the 14th International Conference on Cyclotrons and their Applications*, edited by J. C. Cornell, Capetown, South Africa, 8-13 October, 1994, (World Scientific, Singapore), p. 362.
3. G. D. Alton, F. W. Meyer, Y. Liu, J. R. Beene, D. Tucker, *Rev. Sci. Instrum.* **69** (1998) 2305.
4. A. Heinen, et. al., *Rev. Sci. Instrum.* **69** (1998) 729.
5. Poisson is a two-dimensional code for the simulation of magnetic fields developed at the Los Alamos National Laboratory, LA-UR-87-126(1987).
6. PBGu is an electron/ion optics simulation code, developed by Thunderbird Simulations, Garland, TX.
7. G. D. Alton, *Applied Atomic Collision Physics*, ed. S. Datz, Vol. 4, Ch. 2, Academic Press, New York, 1983, pp163.
8. ANSYS is a finite element code developed by ANSY Inc. Canonsburg, PA.

Design of a Permanent Magnet Electron-Cyclotron Resonance (ECR) Ion Source

Wayne D. Cornelius, *Scientific Solutions, PO Box 500207, San Diego CA 92150*

Abstract

A design for a permanent magnet electron cyclotron resonance (PM-ECR) ion source is presented. This PM-ECR ion source was originally designed to substitute for the electromagnet ECR source in the LEDA injector system at Los Alamos National Laboratory and was designed to duplicate, as much as was practical, the parameters of that ion source as detailed in recent publications. To maximize the utility of this ion source for producing other positive ion beams, this particular design is very flexible. The plasma chamber, the beam formation aperture, and the rf feed system are field-replaceable to facilitate the specific requirements of different ion beams. The design of the permanent magnet solenoid is quite flexible as well. The baseline magnetic field profile is set during fabrication by adjusting permanent magnet strengths to optimize the field shape for a particular range of ion species. Further, the magnetic field can be adjusted on-line (within certain limits) to optimize the performance of the ion source for a particular ion species. The permanent magnet eliminates all requirements for active components at high voltage. The only connections that cross the high-voltage boundary are the rf waveguide and the source gas feed lines.

1. PMECR SOURCE DESIGN FEATURES

The design of the PM-ECR ion source is quite flexible. The next two sections discuss the standard features of the baseline ion source. The following section illustrates the flexibility of the design by discussing various other features, additions, and modifications that are supported by this design.

1.1 Magnetic Field Profile Design

The solenoidal magnetic field of the PM-ECR ion source is produced by permanent magnets rather than electromagnets. The important differences between conventional electromagnet ECR sources and this permanent magnet (PM) version are 1) the absence of a high-current power supply, magnetic coils, and associated cooling system and 2) the potential to significantly reduce magnetic field intensity at the beam formation aperture.

Stokes Law requires that the integral of magnetic field around any closed contour be equal to the current enclosed within that contour. Since a permanent magnet solenoid contains no current, such an integral must be identically

zero. Hence the magnetic field must change sign near both ends of a permanent magnet solenoid such that the integral of the magnetic field external to the solenoid precisely cancels the integral of the internal field. Figure 1 compares the magnetic field of a PM solenoid with the field of an electromagnet solenoid.[1] Note the field reversal near the plasma aperture in the right-hand side of the figure. This field-reversal feature allows us to locate the beam formation electrode in the low-field regions, possibly resulting in reduced beam emittance compared with electro-magnet ECR sources.

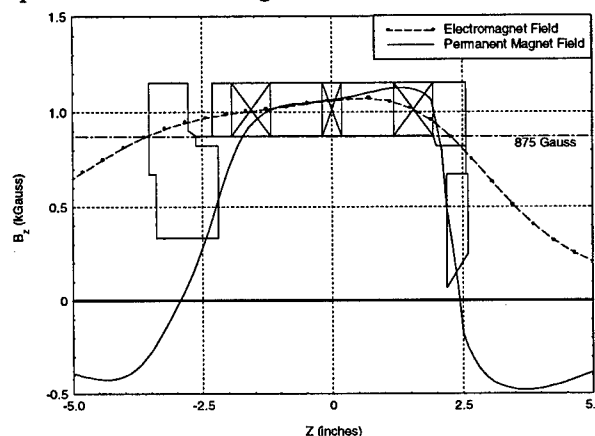


Figure 1. Comparison of magnetic fields of a PM solenoid and an "equivalent" electromagnet. The magnetic components of the PM-ECR source are illustrated by the thin outline. The permanent magnets are denoted by components with internal crossed lines.

The magnetic field profile of the PM-ECR source is comprised of three field "bumps" provided by three rings of permanent magnets. The lengths and strengths of these rings in the shell of the PM solenoid are variables in the baseline design that can be adjusted to tailor the solenoidal field profile. This baseline field profile can be further fine-tuned, without interrupting the operation of the ion source, by mechanically adjustable field shunts. Figure 2 shows the tuning range available in the baseline field of figure 1 when using these shunts. This combination of baseline field profile and field variability provided by the field shunts provides magnetic field versatility. In addition, substitution of various non-magnetic (magnetic) parts with their corresponding magnetic (non-magnetic) equivalents provides another mechanism of coarse-tuning the magnetic field profile that is generally unavailable with electromagnet solenoids because of Stokes Theorem.

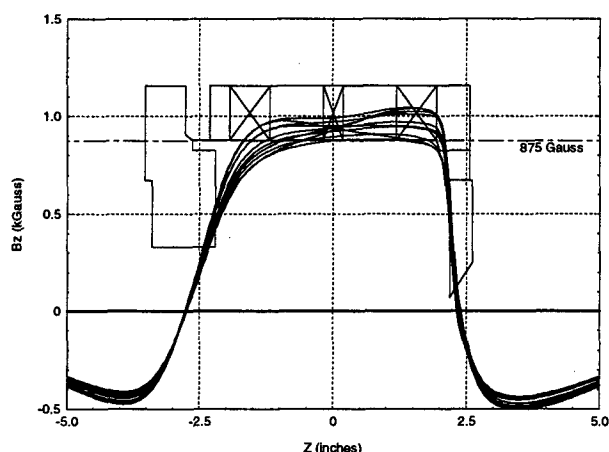


Figure 2. Illustration of the tuning range of the solenoidal magnetic field profile available via shunt tuners. The magnetic fields produced with the two shunts in a variety of different positions are shown by the collection of dark lines. As in figure 1, the permanent magnet shell and end-caps of the ion source are illustrated by the thin outline and the permanent magnet rings are denoted by the components with internal crossed lines.

1.2 Mechanical Design Features

The PM solenoid assembly is completely independent of the vacuum system. Hence the PM-ECR source can easily be adapted to mate with existing systems simply by substituting flanges. Also the ECR plasma chamber was designed to be removable from the ion source without affecting the high-voltage alignment or the permanent magnet solenoid. This design promotes easy replacement of ion source components 1) for maintenance, 2) to replace the plasma chamber to enable different ion beams that may require different plasma chamber characteristics, 3) to replace components that modify the magnetic field profile for different ions or ion beam requirements, and 4) to adjust the position or profile of the beam-formation aperture relative to the magnetic field profile to facilitate different ion beams or to optimize the beam characteristics for particular ion species.

The input waveguide can also be replaced easily by substituting either the waveguide end-flange of the ion source or by replacing an insert within that flange. In this manner the ion source can be coupled directly from a WR-284 waveguide and rf window. Alternatively this PM-ECR ion source design supports alternative waveguide configurations that may prove beneficial to the performance and/or to the long-term reliability of the PM-ECR source.[2]

1.3 Design Special Features

In addition to the features of the baseline design discussed above, the following features are also available, either as a

simple modification to the baseline design or by adding or enabling optional features in that design.

The magnetic field profile shown in figures 1 and 2 illustrate the profile that has been shown to be efficient in the production of low charge-state ions.[3],[4] To facilitate the production of ions with a higher mean charge-state, the baseline magnetic field profile can be modified to produce the classical double-humped mirror field. Some of this adjustment can be made through the addition of a third field-shunt. The third shunt reduces the strength of the center magnet and provides a magnetic mirror field configuration with small mirror ratios. Alternatively, the center magnet ring can be modified during fabrication to produce a mirror field configuration with mirror ratios of up to 2:1 (figure 3). In the former case, the fixed shunt can always be removed to reconfigure the magnetic field back into the low charge-state configuration. In the latter case, the mirror ratio becomes a permanent feature of the magnetic field. In either case, the two adjustable field shunts remain active to provide fine-tuning of the magnetic field during operation.

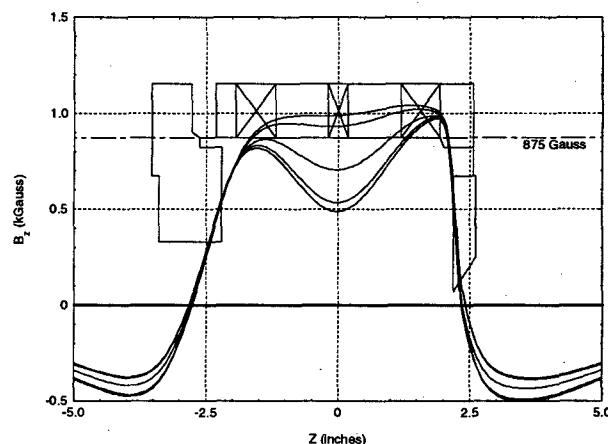


Figure 3. Field plot of a PM-ECR source showing the range of mirror field profiles available. As in figure 1, the permanent magnet shell and end-caps of the ion source are illustrated by the thin outline. The permanent magnet rings are denoted by the components with internal crossed lines.

2. ECR ION SOURCE DESIGN DETAILS

The high-current configuration of the PM-ECR source is illustrated in figure 4. This figure shows the ion source from the circular waveguide input end. Visible in the figure are the two shunt tuners with their screw-drive and drive belt assemblies, the waveguide endflange with its circular rf aperture, and the two end-flanges.

Fine-tuning the magnetic field profile is accomplished by sliding the magnetic shunts back and forth over the rings of permanent magnets using two sets

of ball-screws. In the neutral position, these shunts have little effect on the magnetic field profile. In the maximum shunt position, a substantial portion of the magnetization of the permanent magnets is short-circuited and the local magnetic field magnitude is decreased.

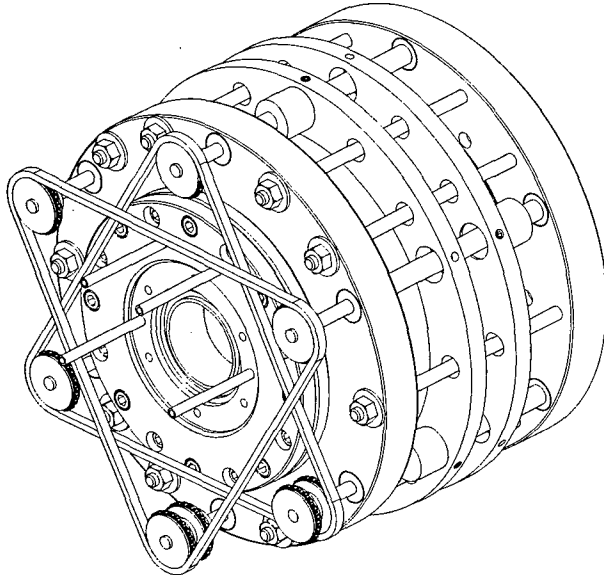


Figure 4. View of PM-ECR ion source assembly from the circular waveguide input end. The two magnetic field shunts are adjusted by rotating the three ball-screw supports for each ring via the two drive belts shown in the figure.

In the baseline design, the magnetic field magnitude increases monotonically from the rf window towards the beam aperture end. Alternate magnetic field configurations can be supplied with the more conventional mirror profiles (figure 3), however the simple ramp configuration of figure 1 has demonstrated superior performance in the production of low charge-state ions.[4],[5],[6]

The plasma chamber of the PM-ECR source was designed to be removable without disturbing the mounting or alignment of the ion source. This feature 1) facilitates maintenance, 2) enables different ion beams that may require different plasma chamber characteristics, 3) facilitates replacement of components that modify the magnetic field profile for different ions or ion beam requirements, and 4) allows adjustment of the position or profile of the beam-formation aperture relative to the magnetic field profile to facilitate different ion beams or to optimize the beam characteristics for particular ion

species. All of these activities can be performed by simply swapping one plasma chamber insert for another without affect the alignment of the electrodes and can be performed with minimal interruption of service.

3. CONCLUSION

This PM-ECR ion source design has many unique features that promote flexibility in providing solutions to ion source problems. The permanent magnet assembly represents a significant improvement over electromagnet sources by eliminating many trouble-prone components. Specific features unique to PM solenoids provide magnetic field design flexibility unmatched by electromagnet systems. The baseline magnetic field is variable over a wide range of profiles. The shunt-tuners provide fine-tuning of magnetic fields to facilitate differing requirements of different ion beams and allow on-line fine tuning to accommodate long-term changes in ion beam characteristics due to plasma sputtering and aging or wearing of components.

The flexible mechanical design of the PM-ECR ion source provides adaptability to virtually any ion beam system simply by replacing the end-flanges. The plasma chamber can be removed and/or replaced easily 1) for maintenance, 2) to enable different ion beams that may require different plasma chamber characteristics, 3) to replace components that modify the magnetic field profile for different ions or ion beam requirements, and 4) to adjust the position or profile of the beam-formation aperture relative to the magnetic field profile to facilitate different ion beams or to optimize the beam characteristics for particular ion species.

4. REFERENCES

- [1] J. D. Sherman, G. O. Bolme, L. D. Hansborough, D. J. Hodgkins, M. E. Light, E. A. Meyer, J. D. Schneider, H. V. Smith, Jr., M. W. Stettler, R. R. Stevens Jr., M. E. Thuot, T. J. Zaugg, and R. Ferdinand, in Proc. of the 1996 International Linac Conf, CERN 96-07, Geneva, Switzerland, (1996), p. 701
- [2] W. D. Cornelius, "Waveguide Assembly and Circular Polarizer for 2450 MHz ECR Ion Sources", these proceedings
- [3] T. Taylor and J. F. Mouris, Nucl Instr & Meth A336(1993)1
- [4] T. Taylor and J. S. C. Wills, Nucl. Instr. & Meth. A309(1991)37
- [5] T. Taylor, Rev. Sci. Instr. 63(1992)2507
- [6] J. Sherman, D. Hodgkins, P. Lara, J. D. Schneider, and R. Stevens, Jr., in proc. 1995 Particle Accelerator Conference, Dallas TX, p 867

Waveguide Assembly and Circular Polarizer for 2450 MHz ECR Ion Sources

Wayne D. Cornelius, *Scientific Solutions, PO Box 500207, San Diego CA 92150*

Abstract

Proper coupling of the rf power to the plasma in an electron-cyclotron resonance (ECR) ion source is probably the most important factor in achieving satisfactory performance of overdense plasmas in high-current ECR sources. Poor coupler design can lead to a variety of undesirable effects such as high reflected power, low plasma density, unstable operation, and poor performance. Scientific Solutions has produced an alternative rf waveguide feed assembly for 2450 MHz ECR ion sources currently being used in the community. This new waveguide assembly converts from standard WR-284 waveguide into dielectric-loaded circular waveguide whose transverse dimensions are substantially smaller than the original waveguide. The benefits of this transition assembly are reduced dimensions of the rf window and opening into the plasma chamber, greater freedom in the design of the rf/plasma interface, concentration of the rf energy on the axis of the plasma chamber, a choice of using circularly polarized rf waves, and improved protection of the rf source from reflected rf energy. This assembly is a direct replacement for the WR-284 waveguide and rf window assemblies used in ECR sources and should improve the performance and efficiency of the rf feed system in those sources.

1. BACKGROUND

Proper coupling of the rf power to the plasma in an electron-cyclotron resonance (ECR) ion source is the most important factor in achieving satisfactory performance of such sources. Poor coupler design can lead to a variety of undesirable effects such as high reflected power, low plasma density, unstable operation, and poor performance. Because the electrons circulate only in a particular direction with respect to the applied magnetic field, only that component of the rf field that rotates in the same sense as the electrons is strongly absorbed by the electron-cyclotron resonance. For aligned magnetic field and rf Poynting vectors, only right-hand circular (RHC) polarization is absorbed whereas for antialigned vectors, only left-hand circular (LHC) polarization is absorbed. Since the linearly polarized rf in the waveguide is comprised of equal parts of RHC and LHC polarization, only half of the rf energy can couple to plasma via the ECR resonance.

The maximum electron density achievable by rf excitation of an unmagnetized plasma is given by the classical relationship: $m_e \omega_p^2 = 4\pi e^2 n_e$, where m_e is the electron mass, ω_p is the rf frequency, and n_e is the plasma density. This relationship yields a maximum electron density of $\sim 7.5 \times 10^{10} \text{ cm}^{-3}$ for 2450 MHz rf—far below the density necessary for an efficient, high-current ion source. Hence some other mechanism is needed to increase the

plasma density to more than $50n_e$, a value typical of efficient high-current ECR sources.

The magnetic field permeating the plasma provides the additional modes of interaction between the rf and the plasma. Of particular importance is the so called upper hybrid (or whistler) mode. A discussion of this and other modes in a magnetized plasma can be found in references [1] and [2]. Note however that the whistler mode also depends on rotation in a particular sense relative to the applied magnetic field. Hence the rf coupling through this mode is also strongly dependent on the polarization of the rf wave.

Stevens et al.[3] develop a model for the impedance of the plasma and provide a discussion of matching that impedance to the rf waveguide. From a comparison of their model with experimental data, Stevens et al. postulate that “*various parameters...which have been noted to affect the efficiency of plasma production, may in fact be related more to the microwave coupling properties of the ER device.*” This conclusion is also supported by the results of Shimada, et al.[4].

Finally some benefit has also been noted for concentrating the rf energy on the axis of the plasma chamber. Taylor and Mouris [5] utilized a tapered, double-ridged waveguide segment to couple the rf into their ECR source. LANL also uses this waveguide section in the APT ion source.[6]

2. DESIGN FEATURES

In an attempt to take advantage of the three features described above, Scientific Solutions has implemented an rf feed system for 2450 MHz ECR sources. This feed system starts with a conventional WR-284 waveguide and transforms the rf energy through 1) a rectangular waveguide transition assembly, 2) a rectangular-to-circular waveguide transition assembly, 3) a circular polarizer, and 4) an rf vacuum window/coupler assembly. The ECR ion source rf feed configuration may utilize one or more of these devices in sequence. Each device has particular advantages in the rf feed system and are discussed separately below.

2.1 Rectangular Waveguide Transition Assembly.

The rectangular waveguide transition assembly (Figure 1) transforms the rf energy from a standard WR-284 waveguide into a rectangular WR-137 waveguide filled with boron-nitride ($\epsilon \approx 4.5$). This configuration substantially reduces the transverse dimensions of the waveguide and concentrates the rf energy into a smaller volume. This reduction in transverse dimensions reduces the size of the opening into the plasma chamber

and the corresponding dimensions of the rf vacuum window.

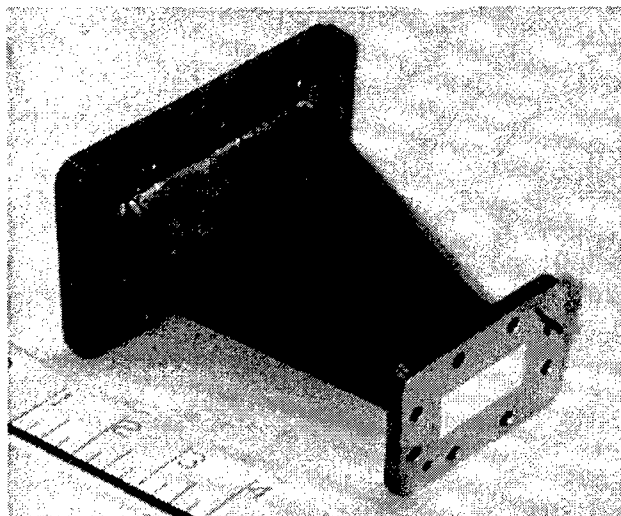


Figure 1. Rectangular waveguide transition assembly. This assembly converts from standard WR-284 waveguide to dielectric-filled WR-137 waveguide.

Another advantage of this configuration is that the rf vacuum window can be positioned well back from the ion source plasma chamber and protected from backstreaming electrons. In ECR ion sources with coaxial rf waveguide, electrons generated by ionization of the residual gas in the high-voltage column are accelerated into the ion source and can damage the rf window. Some ECR installations protect the rf window by placing a thin slab of boron-nitride immediately in front of the window to absorb the energy of the backstreaming electrons. Sputter erosion of this slab by backstreaming electrons limits the operational lifetime to a few hundred hours. The thickness of this slab cannot be increased substantially without incurring increased rf energy reflection from the impedance mismatch between the air-filled waveguide ($\epsilon \approx 1$), rf vacuum window ($\epsilon \approx 9$), boron-nitride protector ($\epsilon \approx 4.5$), and the plasma.

By moving the rf window behind several inches of boron-nitride, the impedance step can be moved to an upstream location where the impedances on both sides of the window are more easily controlled. The boron-nitride also blocks the plasma from expanding into the waveguide. Additionally, using this rectangular waveguide transition should improve the rf efficiency because of the increased rf energy density on the axis of the plasma. Finally note that the reduced dimensions of the waveguide input allows relocating the rf input penetration off the axis of the plasma chamber and out of the path of the backstreaming electrons.

Another potential benefit of the dielectric-loaded waveguide system is that the coupling of the rf to the plasma might be enhanced by extending the boron-nitride dielectric beyond the end of the metal waveguide surfaces. This "dielectric waveguide" can protrude into the plasma volume and the rf coupling to the plasma can be optimized

by modification of the shape and extended length of the dielectric protruding from the end of the waveguide.

2.2 Circular Waveguide Transition Assembly.

The second component of the rf input apparatus is a rectangular-to-circular waveguide transition. This device starts with the boron-nitride filled WR-137 waveguide. While maintaining constant impedance, the rectangular cross section of the waveguide is transformed into a circular 1.61" ID tube that is also filled with boron-nitride. This transition assembly matches the rectangular waveguide geometry to the cylindrical symmetry typical of ECR ion sources. All of the operational advantages noted above for the dielectric-filled rectangular waveguide also apply to the circular waveguide assembly. However an important additional feature of cylindrically symmetric waveguide is that it transports circularly polarized rf waves.

2.3 Circular Polarizer Assembly.

The third component of the waveguide apparatus is the circular polarizer. Using the appropriate sense of circular polarization potentially doubles the efficiency of the rf in producing the plasma and eliminates the destabilizing influence of the LHC polarization. Stevens et.al. [3] used a hybrid coupler and phase shifter to generate the circularly polarized rf wave directly in the plasma chamber. SSolutions has simplified this process by converting from the rectangular waveguide into a circular waveguide and employing a simple vane polarizer.[7] The vane polarizer is analogous to the quarter-wave plate commonly used in laser optics

An rf quarter-wave plate is formed by the introduction of a rectangular dielectric vane across the center of the circular waveguide (figure 2). The propagation velocity of the rf wave with the electric field parallel to this vane differs from the velocity of an rf wave with a perpendicular electric field. Circular polarization results when the phase delay between these two components equals $\pm 90^\circ$. If the dielectric vane is rotated to $+45^\circ$ relative to the input polarization plane, RHC polarization is the result. If the vane is rotated to -45° , LHC polarization is the result. Hence one can change between RHC and LHC polarizations simply by rotating the quarter-wave polarizer. Note also that positioning the polarizer at either 0° or 90° passes the linear polarization of the input waveguide. Hence one can directly compare the relative performance of linear and circular polarization simply by rotating the polarizer.

2.4 Virtual Isolator

An important additional benefit of the vane polarizer is the creation of a virtual rf isolator. This virtual isolator concept for ECR sources is most easily described by using the quarter-wave-plate analogy introduced above. In laser optics a "photon diode" is created by using a

quarter-wave plate in conjunction with a linear polarizer. The laser light passes unaffected through the polarizer when the polarization axis of the light is parallel to the axis of the polarizer. A quarter-wave plate downstream of the polarizer converts the linear polarization into RHC or LHC polarization as discussed above. The important feature of this particular configuration involves the interaction of circularly polarized light reflected back towards the laser from downstream of the quarter-wave plate. In passing back through the quarter-wave plate, the reflected circularly polarized light is converted back into linearly polarized light. However the polarization plane is now perpendicular to the initial polarization axis and the light is not passed by the polarizer. Hence the laser is protected from reflected photons by the quarter-wave plate/polarizer combination.



Figure2. Isometric view of the circular polarizer assembly.

The vane polarizer assembly works in an analogous manner. In the rf case, the reflected circularly polarized rf wave is transformed into a linearly polarized rf wave. However the new polarization axis is now aligned with the "wide" axis of the rectangular waveguide and cannot couple into the waveguide. Hence the reflected rf energy is again reflected at the rectangular waveguide interface back towards the plasma, passing through the circular polarizer a third time. Any rf energy reflected a second time from the plasma passes again through the circular polarizer and the polarization axis is returned to the initial orientation. Note however that the rf must interact with the plasma at least twice before escaping back towards the rf source. For any reasonable absorption of rf energy by the plasma, the reflected energy is reduced compared with direct coupling of the waveguide without a circular polarizer. Hence the circular polarizer assembly also acts as an isolator and protects the rf source from direct reflection of rf energy from the plasma.

2.5 Plasma Coupler

Experience has suggested the importance of concentrating the rf energy in the center of the ECR plasma. Achieving such a concentration of rf energy is difficult with 2450 MHz ECR plasmas because the transverse dimensions of the plasma chamber are usually comparable to the dimensions of the WR-284 waveguide. Both Chalk River and Los Alamos concentrated the rf energy by using a ridge-loaded, half-height waveguide and have claimed improved performance as a result.[5],[6] The waveguide assemblies described above provide such concentration of rf energy because the transverse dimensions of the waveguide are reduced substantially compared with their air-filled counterparts. In addition, the transverse and longitudinal dimensions of the boron-nitride dielectric can be tailored to optimally match the rf energy into the plasma chamber as discussed in reference [3]. The dielectric-loaded waveguide assemblies provide a great deal of flexibility in optimizing the rf coupler because the dielectric constant can be decreased as well as increased to optimize the rf coupling to the plasma.

3. CONCLUSION

The 2450 MHz rf feed system described in this paper provides a number of specific advantages over conventional rectangular waveguide systems. Use of this waveguide system should promote better rf coupling to the plasma, more stable plasma operation, and isolation of the rf power system from reflected rf power. These benefits should translate directly into improved performance, greater stability of the ion source parameters (ion current, species ratio, etc.), improved rf efficiency, and protection of the rf power system from reflected rf energy. In addition the user can directly compare differences in ion source performance between operation with linear, RHC, and LHC polarizations by simply rotating the circular polarizer. Tests to verify the benefits of this system are scheduled to take place later this year.

4. REFERENCES

- [1] Stix, *Theory of Plasma Waves*, McGraw-Hill, New York, 1962
- [2] Allis, Buchsbaum, and Bers, *Waves in Anisotropic Plasmas*, MIT Press, Cambridge MA, 1963
- [3] J. E. Stevens, J. L. Cecchi, Y. C. Huang, and R. L. Haerecki, Jr., *J. Vac. Sci. Tech A*9(1991)696
- [4] M. Shimada, I. Watanabe, and Y. Torii, J. E. Stevens, J. L. Cecchi, Y. C. Huang, and R. L. Haerecki, Jr., *J. Vac. Sci. Tech A*9(1991)707
- [5] T. Taylor and J. F. Mouris, *Nucl Instr & Meth A*336(1993)1
- [6] J. D. Schneider and J. D. Sherman, LANL, private communication
- [7] A. J. Baden Fuller, *Microwaves*, 3rd Edition, Pergamon Press, New York, 1990, p.147

MONTE CARLO MODEL OF CHARGE-STATE DISTRIBUTIONS FOR ELECTRON CYCLOTRON RESONANCE ION SOURCE PLASMAS*

D. H. Edgell⁺, J. S. Kim[#] and S. K. Wong, FARTECH, Inc., San Diego, CA
R. C. Pardo and R. Vondrasek, ANL, Argonne, IL

Abstract

A computer model for an Electron Cyclotron Resonance Ion Source (ECRIS) plasma is under development that currently incorporates non-Maxwellian distribution functions, multiple atomic species, and ion confinement due to the ambipolar potential that arises from fast electrons. Atomic processes incorporated into the model include multiple ionization and multiple charge-exchange with rate coefficients calculated for non-Maxwellian distributions. The electron distribution function is calculated using a Fokker-Planck code with an ECR heating term. The Monte Carlo method is used to calculate the charge-state distribution (CSD) of the ions. The Monte Carlo ion tracking is verified by CSD comparison with a conventional 0-D fluid model, similar to Shirkov's[1]. The Monte Carlo method is chosen for future extension to a 1-D axial model. Axial variations in the plasma parameters could affect confinement, CSD and extraction. The electron Fokker-Planck code is to be extended to 1-D axial by bounce-averaging.

1 INTRODUCTION

The complete understanding and optimization of an ECRIS is complicated with many issues to consider, such as plasma confinement, neutrals, multiple atomic species, and microwave resonances. Optimization for higher charged states and higher current with low emittance is challenging. A typical optimization is by trial and error because there are few suitable numerical tools available, none with a comprehensive modeling capability.

Current ECRIS modeling is typically a 0-D fluid model such as Shirkov's "Classical Model of Ion Confinement and Losses in ECR Ion Sources"[1]. Here the ion charge-state-distribution (CSD) is determined by solving a set of coupled fluid equations. Plasma parameters are assumed to be uniform over the plasma volume and no spatial effects are considered. Confinement is determined from a simple potential and magnetic box/well model. This 0-D fluid modeling has several drawbacks, in particular neglecting the electron distribution function and spatial effects.

1.1 Electron Distribution Function

Due to ECR heating and mirror confinement, the electrons in an ECRIS are expected to be highly non-Maxwellian and non-isotropic. The electrons in most ECRIS models are typically treated as two separate species, cold or warm Maxwellian electrons and hot perfectly confined collisionless electrons whose temperatures need to be input. The electron confinement usually ignores the potential between the plasma and the wall despite evidence that it is comparable to the cold electron energy[2]. Also, the hot electrons are obviously not perfectly confined. Their loss rate must balance the rate at which they are created by ECR heating.

The actual electron distribution, f_e , would be better modeled by a single continuous non-Maxwellian, non-isotropic distribution function. A Fokker-Planck code would allow f_e to be calculated taking into account RF heating and both magnetic and potential confinement. This would also eliminate the electron temperature as a fixed input to the model. Ideally, an ECRIS model should require as input parameters, only experimental knobs such as the magnetic field, gas inlet, rf power etc.

1.2 Spatial Effects

Usually, all effects of spatially varying parameters are ignored in ECRIS models. Confinement is modeled by assuming the magnetic field and potential can be treated as a uniform box/well. Inside the well, all plasma parameters are assumed to be constant. However, an ECRIS can have complex spatially varying asymmetric magnetic fields and potentials. In addition, the plasma parameters are not expected to be uniform. Higher charge-states are expected to be confined deeper in the potential well. The average electron, ion and neutral densities, they interact with, will be different than those seen by lower charge states. In particular, the varying conditions the ions must travel through between the main plasma and the extraction point should be considered.

Due to the high electron mobility, the electron spatial effects can be accounted for by a bounce-averaged Fokker-Planck code. In a typical ECRIS, however, the ion bounce frequency is much smaller than the ion collision frequency and a bounce-averaged treatment is inappropriate. Extending a fluid model axially may also be inappropriate as the plasma near the extraction point will be less dense and thus less collisional than in the center of the plasma and the fluid approximations may not apply. The Monte Carlo method is better suited for determining the ion

*Work supported by the U.S. DOE-SBIR Grant Number DE-FG03-97ER82381

⁺ Email: edgell@far-tech.com

[#] Email: kimjs@far-tech.com

spatial effects. This method can handle both highly collisional and collisionless regimes with smoothly varying and non-symmetric magnetic fields and potentials, resulting in better estimates of the true ion confinement. A Monte Carlo model would also be better suited for the possible future addition of ICRH and the resultant ion distribution anisotropy.

2 GENERIC ECRIS MODEL

In this paper, we present the initial results of the Generic ECRIS Model (GEM) code which attempts to improve ECRIS modeling by using an electron Fokker-Planck code and including Monte-Carlo ion modeling.

Collisional processes incorporated into the model so far include the single, double and triple electron impact ionization cross-sections, σ^I , of Lotz[3],[4] and Müller et. al.[5],[6], along with single, double, triple and quadruple charge-exchange cross-sections, σ^{CX} , from Müller and Salzborn[7]. For simplicity, we will include only single-step collision terms in all of the equations to follow.

2.1 0-D Fluid Model

For comparison, initial modeling results have also been obtained using a 0-D fluid model similar to Shirkov's [1].

Neutral Modeling: The neutral density inside the plasma is determined from the neutral density outside the plasma and the rate at which neutrals are converted into ions inside the plasma volume.

Ambipolarity: Radial transport is assumed to be negligible compared to axial endloss. Thus, the endloss currents must be ambipolar or balance.

$$\frac{n_e}{\tau_e} - S_e^{ext} = \sum_j \sum_{q=1}^{A_j} \frac{q n_{j,q}}{\tau_{j,q}^p}$$

where S_e^{ext} is the external electron source.

The confinement time for an ion of atomic species j and charge q , in a confining potential, is given by[8]

$$\tau_{j,q}^p = \left[RL \left(\frac{\pi m_j}{2k_B T_i} \right)^{1/2} + \frac{Gx^2}{(x + \frac{1}{2})(v_{j,q}^o + v_{j,q}^i)} \right] \exp(x)$$

where

$$x = \frac{qe\phi_o}{T_i} \quad \text{and} \quad G = \frac{\sqrt{\pi}(R+1)\ln(2R+2)}{2R}$$

and ϕ_o is the ion confining well potential, R is the mirror ratio and L is the length of the core plasma.

Ion Power Balance: The ion temperature is determined by solving the ion power balance

$$\frac{d}{dt} \left(\frac{3}{2} T_i \sum_j n_j \right) = \sum_j (p_j^o + p_j^{\Delta\phi} + p_j^e + p_j^{CX} + p_j^{loss})$$

where the terms on the right account for, respectively, the initial energy of the ionized neutrals, energy due to ionization inside a potential well, electron collisional heating, energy lost due to charge exchange and energy lost due to the ion endloss. All ion species are assumed to have the same temperature. Model test runs with separate ion temperatures for different atomic species have verified

that ion thermal equilibration is fast and all ion species will have nearly identical temperatures.

Ion CSD Modeling: The ion CSD is arguably the most important result desired from an ECRIS model. Traditionally, ECRIS models have determined the CSD by solving a coupled set of fluid equations for multiple atomic species j ...

$$\begin{aligned} \frac{dn_{j,q}}{dt} = & (n_{j,q-1} \langle \sigma_{j,q-1}^I v_e \rangle - n_{j,q} \langle \sigma_{j,q \rightarrow q}^I v_e \rangle) n_e \\ & + n_{j,q+1} \sum_h \langle \sigma_{j,q+1 \rightarrow j_h}^{CX} v_j \rangle n_{j_h,0} - n_{j,q} \sum_h \langle \sigma_{j,q \rightarrow j_h}^{CX} v_j \rangle n_{j_h,0} - \frac{n_{j,q}}{\tau_{j,q}} \end{aligned}$$

In the above set, there is one equation for each charge-state of each atomic species.

2.2 Fokker-Planck Electron Model

The electron distribution function, $f_e(v, \theta)$, can be determined by solving the Fokker-Planck equation

$$\frac{\partial f_e}{\partial t} + \vec{v} \cdot \frac{\partial f_e}{\partial \vec{x}} + \frac{\vec{F}}{m_e} \cdot \frac{\partial f_e}{\partial \vec{v}} = \left(\frac{\partial f_e}{\partial t} \right)_{coll} + S_e(v, \theta) + S^\perp(v, \theta)$$

where $(\partial f_e / \partial t)_{coll}$ is the Fokker-Planck collisional operator, S_e is the cold electron source and S^\perp is the perpendicular diffusion ECRF heating term:

$$S^\perp = \frac{1}{v_\perp} \frac{\partial}{\partial v_\perp} \left(v_\perp D_\perp \frac{\partial f_e}{\partial v_\perp} \right)$$

$$D_\perp = D_o \exp\left(-v^2 / 2c^2\right)$$

$$P_\perp = 2n_e m_e D_o V_p$$

The nonlinear multispecies code FPPAC94[9] has been incorporated into the model. The Fokker-Planck modeling also determines the e-i collisional energy exchange and the electron confinement.

As the electron distribution function is highly non-Maxwellian and non-isotropic, the reaction-rate coefficient should be calculated explicitly from distribution functions of the two colliding species.

$$\langle \sigma v \rangle = \frac{1}{n_a n_b} \int dv \int dv' f_a(v) f_b(v') \sigma(|v-v'|) |v-v'|$$

The model incorporates a routine[10] to compute the reaction-rates for arbitrarily shaped distribution functions. The routine can employ a non-uniformly spaced velocity-distribution, suitable to an ECRIS, where the electrons, ions and neutrals can have average velocities orders of magnitude apart.

2.3 Monte Carlo Ion Model

As discussed in Section 1.2, a Monte-Carlo model could incorporate the effects of spatially varying parameters on the ion confinement and CSD. A Monte Carlo code has several advantages. The Monte Carlo method is a powerful tool that enables the inclusion of complex geometries, energy distribution functions, and detailed atomic processes. The ion confinement, CSD and distribution function could be calculated axially using axially varying

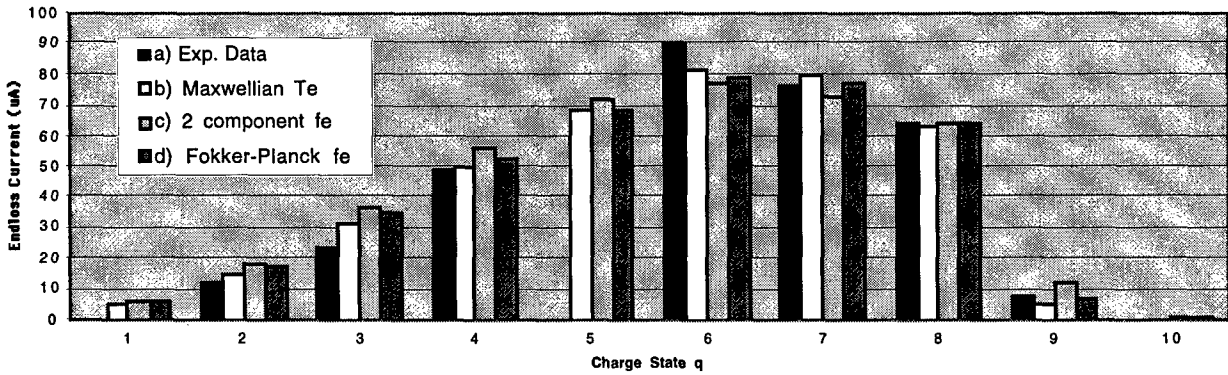


Figure 1: Comparison of Modeling results with ANL ECR-II Faraday cup measurements

plasma parameters such as the potential. A full 1-D axially Monte Carlo ion model is planned for this model.

As a first step, the Monte Carlo method has been incorporated in the code to calculate the 0-D multi-species ion CSD.

3 RESULTS

3.1 Electron Modeling

To investigate the validity of the model, comparisons have been made with Faraday cup measurements from ECR-II at Argonne. Due to an air leak the plasma ions had four major atomic species: He, N, O and Ne ions. The experimental data are shown as plot a in Figure 1.

The need for Fokker-Planck electron modeling is demonstrated by plots b and c in Figure 1. Plot b was produced by a Maxwellian electron distribution ($T_e=2$ keV) while plot c results from a combining collisionless hot electrons (100keV) with a very small amount (~0.3%) cold electrons (70eV). Clearly, one can match the experimental data using very different assumed electron distributions.

To eliminate this arbitrariness, the electron distribution should be determined by solving the Fokker-Planck equation. The predictions of the Fokker-Planck electron modeling are given as plot d of Figure 1. The Fokker-Planck electron modeling produces a good match to the experimental data with less arbitrariness.

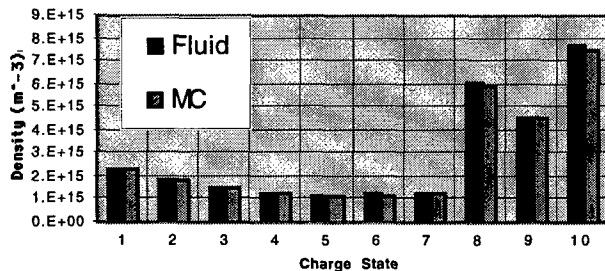


Figure 2: Comparison of Monte Carlo and fluid predictions for the ion densities in a pure Neon plasma

3.2 Ion CSD Modeling

Sample results of the initial CSD Monte Carlo modeling in comparison with the fluid ion modeling are shown in Figure 2 for a pure Neon plasma. They give nearly identical predictions, indicating the Monte Carlo modeling is tracking the ion charge state correctly.

4 DISCUSSION

To be predictive, the model should rely on measured experimental "knobs" only. Even with Fokker-Planck modeling of the electrons, some quantities such as the core plasma length and the electron confining potential still need to be arbitrarily input to the model. By extending the modeling spatially to 1-D axially, one should be able to determine these quantities from the plasma confinement.

The ion Monte-Carlo code must be extended to spatially track the ions and determine their profiles and confinement in addition to their CSD.

The electron Fokker-Planck code should be bounce-average to account for the localization of the ECR resonant surface and also the spatially varying potential and magnetic field. The electron distribution function modeling could also be improved further by including energy losses due to radiation and relativistic effects.

5 REFERENCES

- [1] G. Shirkov, Nuc. Instr.&Meth. in Phys. Res. Vol. A322, p.161, 1992
- [2] K. S. Golovanivsky and G. Melin, Rev. Sci. Inst., Vol. 63, No. 4, p. 2886, Apr. 1992.
- [3] W. Lotz, Z. Phys., Vol. 206, p. 205-211, (1967).
- [4] W. Lotz, Z. Phys., Vol. 216, p. 241-247, (1968).
- [5] A. Müller, et. al., J. Phys. B, Vol. 13, p. 1877, 1980.
- [6] A. Müller and R. Frodl, Phys. Rev. Lett., Vol. 44, No. 1, p. 29, Jan. 7 1980.
- [7] A. Müller and E. Salzborn, Phys. Lett., Vol. 62A, No. 6, p. 391, Sept. 19, 1977.
- [8] T. D. Rognlien and T. A. Cutler, Nuc. Fusion, Vol. 20, No. 8, p. 1003, Aug. 1980.
- [9] A. A. Mirin, et. al., Comp. Phys. Comm., Vol. 81, p. 403, 1994.
- [10] A. A. Mirin and M. G. McCoy, Comp. Phys. Comm., Vol. 51, p. 369, (1988).

Design of a Compact ECR Ion Source with Ku Band *

C. S. Lee[†], Y. K. Kwon, Chung-Ang University, South Korea
E. Tojyo, M. Oyaizu, S. C. Jeong, KEK-IPNS, Japan

Abstract

The electron cyclotron resonance (ECR) ion sources are increasingly popular for producing highly charged ions. With worldwide proposals to build the Isotope Separator On-Line (ISOL) facility being at hand, it becomes important to design a high efficiency ion source as a charge breeder for the secondary beam. A novel type of ECR ion source based on a flat magnetic field configuration has been proposed by Alton et al. [1, 2] This source provides a large, on-axis electron cyclotron resonance region, "ECR-volume". Due to a larger ECR zone, absorptivity of microwave power into plasma is much increased, thereby electron becomes so hot. And hot electron population of the plasma could result in higher charge states and higher beam intensity. Two solenoids are used to produce axial mirror magnetic field. Twelve permanent magnets (NdFeB) are designed for confining the hot electrons in the radial direction. Moreover, specially designed iron yokes are added to create the flat central field region. The single injected microwave frequency is tunable in the range of 6.45 to 14 GHz covering the range of the Ku band. We shall present the design report concerning the field mapping obtained by POISSON and OPERA-3D together with and mechanical design.

1 INTRODUCTION

ECR ion source (ECRIS) was first proposed by R. Geller and H. Postma in late 1960's for fusion plasma studies. Since then, ECRIS has improved continuously in many fields of science. Specially, The ECRIS is a very efficient tool providing highly charged ions for atomic and nuclear research, material science, and surface physics. The most important factors in ECRIS are the electron density, the electron temperature and the confinement time of plasma to produce highly charged ions. In a conventional ECRIS, the magnetic mirror makes a parabolic shaped field and the ECR zones are ellipsoidal-shaped surfaces which occur when microwave frequencies have the same value with electron cyclotron frequencies. There have been various attempts to increase beam intensity and charge state. The multi-frequency heating has proved an effective way to increase both the number and width of the ECR zone [3]. Wall coating [4] in the inner wall of plasma chamber was attempted in order to supply more electrons. The after-glow effect drastically improved beam intensity by one order of magnitude through injection of a pulsed microwave

[5]. Despite of these attempts, the only small fraction of the whole plasma still participates in the resonance of microwaves and electrons in this case. Therefore, electrons can be accelerated only in this ECR zone. In addition, because the size of ECR zone is smaller than that of plasma volume, that is, $n_e/n_0 < 1$ [6], it has a small ionization volume, and therefore, the absorptivity of microwave is limited by the size of ECR zone. To produce more highly charged ions, first of all, the ECRIS is preferred to have a larger ECR zone. The volume type ECRIS proposed by Alton et al. [1, 2] is a very efficient means for enlarging the size of ECR zone. In present work, we use two solenoid coils for mirror field and iron return yoke for producing flat magnetic field in the central region of plasma chamber. Simultaneously we tried to minimize the amount of electrons which are intended to escape into the wall of plasma chamber, with twelve NdFeB permanent magnets in a multicusp magnetic field.

2 MAGNETIC SYSTEM DESIGN

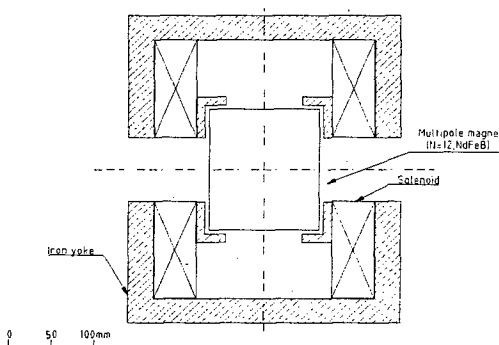


Figure 1: Schematic view of magnetic system

2.1 Axial mirror field

In this ECRIS, we use two solenoid coils (inner radius 40 mm, outer one 160 mm, thickness 50 mm) to make a variable mirror magnetic field. The schematic view of magnetic system is shown in Fig.1. There is also an added 30 mm-thick return yoke in order to reduce power consumption and to produce a flat magnetic field inside the plasma chamber. The ratio of a maximum and a minimum magnetic field, mirror ratio, is $B_{max}/B_{min} \sim 2.4$ at 14 GHz microwave. This large ECR volume is able to heat more electrons distributed throughout the whole area of plasma. And the population of hot electrons can produce

* Work supported by the Joint Research Program under the Korea-Japan Basic Scientific Promotion Program (KOSEF-JSPS 1988) and in part by the Nuclear R&D Program (Ministry of Science and Technology 1998).

[†] Email: cslee@cau.ac.kr

more highly charged ions. Fig. 2 and Fig. 3 are the results of simulation using by the POISSON code [7].

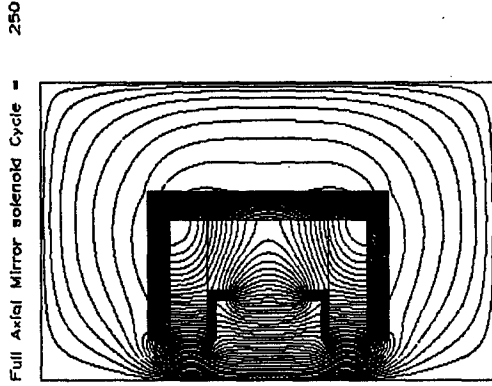


Figure 2: Simulated result of the full axial mirror magnetic field distribution

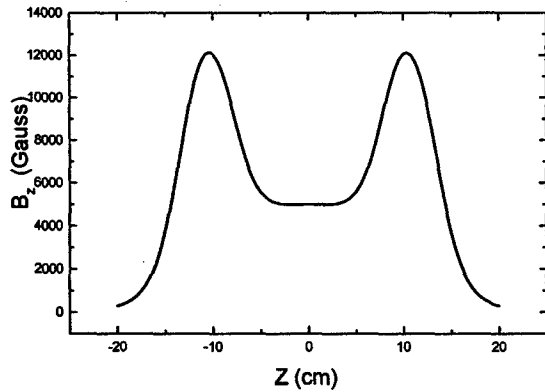


Figure 3: Simulated result of axial mirror magnetic field along the symmetric axis

2.2 Radial magnetic field

Twelve permanent magnets (NdFeB) are employed to make the volume type realized, instead of the hexapole field, which is composed of six permanent magnets usually used in conventional ECRIS for plasma confinement along the radial direction. As is well known, the magnetic field along the radial direction is expressed $B_r = B_0 r^{N/2-1}$ [8]. Thus, the magnetic field can be produced flat as the number of magnets is increased. Then, the ECR volume along the radial direction gets easily attained. The magnets comprise twelve NdFeB-its horizontal and vertical size are 14 mm and 30 mm, respectively. Fig. 4 and 5 is a three dimensional field distribution and cross-sectional field obtained by OPERA-3D[9], respectively.

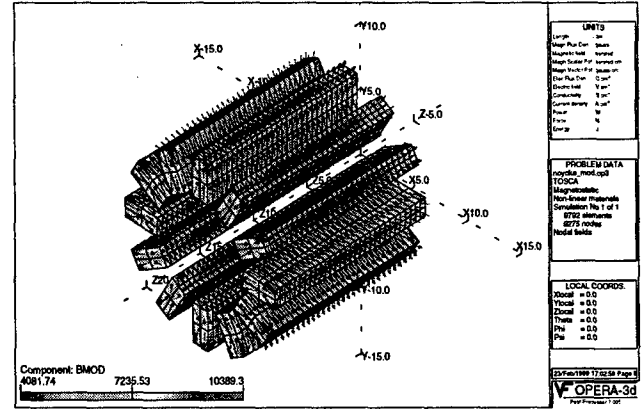


Figure 4: Magnetic field distribution of radial multicusp magnets

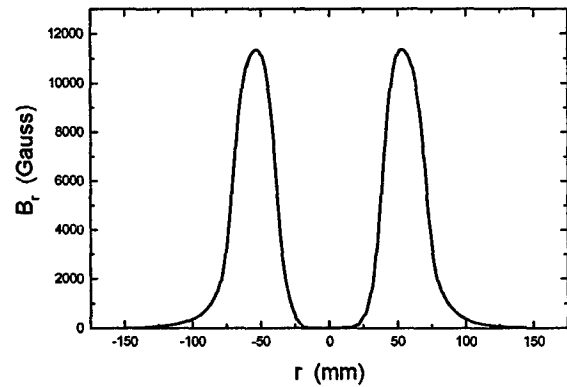


Figure 5: B_r along the radial direction

3 MICROWAVE SYSTEM

The microwave system is designed to be variable in the range of 6.45 to 14 GHz with a single injection port along the axial direction. With the present magnetic system shown in Fig. 1, the flat ECR region can be maintained for this range of microwave frequency. Fig. 6 shows axial magnetic fields corresponding to the microwave frequencies, where the relation that $\omega_{ce} = eB/m = \omega_{rf}$ leads to a simple expression as $f_{ce} = 2.8B_{ecr}$ (GHz) with B_{ecr} in units of kilogauss.

4 DISCUSSION

To extend the size of the ECR zone is a very efficient method for producing highly charged ions. Multi-frequency heating, broadband frequency [2] and volume type ECRIS are used for this purpose. In future work, we will construct the volume type ECRIS which successfully worked out by Alton et al. [2] and Heinen et al. [10] In addition two solenoids are used for varying flat magnetic fields. In the present work, we carried out the mechanical

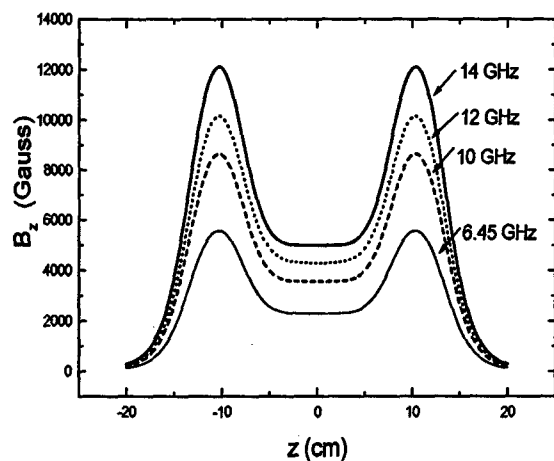


Figure 6: Various axial magnetic fields

design and simulated magnetic fields.

5 REFERENCES

- [1] G. D. Alton and D. N. Smithe, *Rev. Sci. Instrum.*, **65**, 775 (1994)
- [2] G. D. Alton, *Nucl. Instrum. Methods Phys. Res. A*, **382**, 276 (1996)
- [3] Z. Q. Xie and C. M. Lyneis, *Rev. Sci. Instrum.*, **66**, 4218 (1995)
- [4] M. Litvin, M. Vella, and A. Sessler, *Nucl. Instrum. Methods*, **198**, 189 (1982)
- [5] T. Nakagawa et. al., *Jpn. J. Appl. Phys.*, **35**, L1124 (1996)
- [6] R. Geller, *Electron Cyclotron Resonance Ion Sources and ECR Plasmas* (IOP, Bristol, 1996), p. 80
- [7] Reference Manual for POISSON/SUPERFISH Group of cords, LA-UR-87216
- [8] Y. Liu, G. D. Alton, G. D. Mills, C. A. Reed, and D. L. Haynes, *Rev. Sci. Instrum.*, **69**, 1311 (1998)
- [9] Reference Manual for OPERA3D, VF-07-96-D2
- [10] A. Heinen et al., *Rev. Sci. Instrum.*, **69**, 729 (1998)

SOME REMARKS TO CONSTRUCTION OF ECR ION SOURCE HEXAPOLES¹

J. Pivarč, J. Pivarč (Jr.)* and M.N. El-Shazly**

Institute of Physics, Slovak Academy of Sciences, Dúbravská cesta 9, SK-842 28 Bratislava
Slovak Republic

This paper gives performance data for construction of suitable hexapoles for Electron Cyclotron Resonance Ion Sources (ECR IS). Permanent magnets are made from Nd-FeB magnetic material. The main attention is given to hexapoles with inner diameters of ϕ 3.6 cm at different hexapole thicknesses of 1.3 - 6 cm. Some remarks on construction of type hexapoles are presented.

1 INTRODUCTION

About 30-year history of Electron Cyclotron Resonance Ion Sources (ECR IS) [1-2], which are based on the ECR has already shown that the ECR IS is an ideal tool for the production of multicharged ion states. The highly charged heavy ions are very useful not only for the ion source accelerators, but also for the investigations of the ion collision process as well as for various applications to material science.

Recently a compact ECR IS, so called "Compact 10 GHz ECR IS" [3], composed of permanent magnet structure has been developed at University in Giessen, Germany, for atomic physics experiments. This type of ECR IS is very simple and easy for operation and maintenance without powerful electric supplies and cooling systems for getting strong magnetic field without using of coils.

By considering this, we construct ion irradiation system using ECR IS so called "NANOGUN-10B" at Bratislava.

2 MAGNETIC FIELD CALCULATIONS OF HEXAPOLES

The plasma in the ECR IS is kept together by a magnetic field inside magnetic bottle. The field consists of a longitudinal one, made by coils or permanent magnets and a transversal one, made by hexapole compound of permanent magnets. The magnetic bottle is the region surrounded by a closed surface of constant magnetic field B so that $|B| e = m_e \omega_{rf}$, where B is the average value of the magnetic field in the region where the plasma is, e the charge of the electron, m_e the mass of

the electron and ω_{rf} the microwave frequency matching the electron cyclotron frequency ω_c . For $\omega_c = 10$ GHz we need $|B| = 0.36$ T and $|B| = 0.50$ T for $\omega_c = 14$ GHz. The magnetic field inside the plasma region is lower than that on the surface of the magnetic bottle. The stronger is the magnetic field inside the magnetic bottle the higher

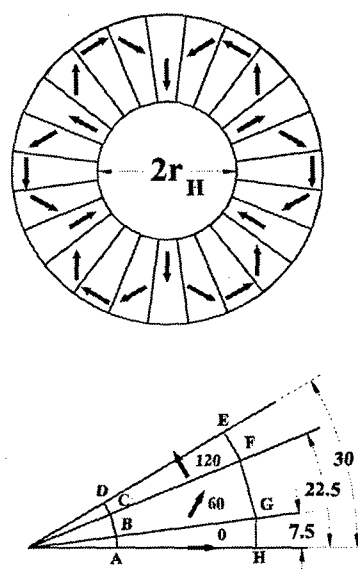


Figure 1: Cross section view of the hexapolar structures. Here, r_H is radius and ABCDEFGH characteristic segment of hexapole.

is the rf frequency of the resonance electrons. We thus can obtain larger plasma density that results in larger ionization possibility.

The computer program PANDIRA [4] was used at the calculations. The program calculates magnetic field on a grid in a 2-dimensional space. Permanent magnets, iron, currents and other anisotropic and isotropic materials can be defined by the user in several regions.

We have investigated 22 hexapoles with the thicknesses of $H = 1.4$ cm and the inner radii of hexapoles $r_H \in \{1.3, 6\}$ cm. Hexapole magnets are made of NdFeB with a remanence of 1.1 T and a coercivity of 800 kA/m. Each calculated hexapole consists of 24 trapezoidal segments where the angle of magnetization varies by 60° from one segment to the next one. Fig. 1 shows cross section view of hexapolar structures.

A detailed description of this hexapole geometry is

¹ Work supported by the VEGA L3 Ltd. firm, Záhradnícka 21, SK-821 74 Bratislava, Slovak Republic.

* Working-place address: Martin-Luther-University, Dept. of Physics, NMR Group, Friedemann-Bach-Platz 6, D-06108 Halle/Saale, Germany.

** Working-place address: Joint Institute for Nuclear Research, FLNR, 141980 Dubna, Moscow region, Russia.

given elsewhere [5]. With this hexapole geometry

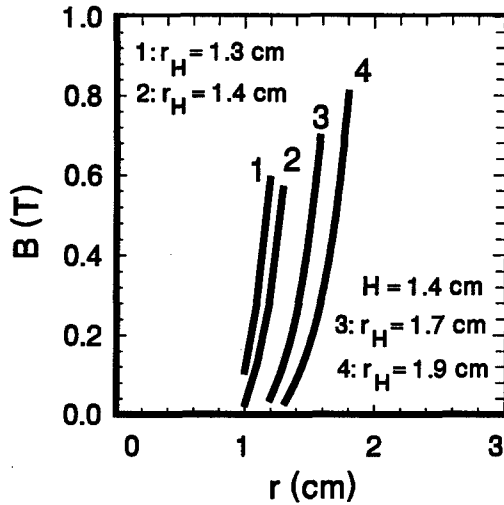


Figure 2: Magnetic field B inside hexapole where $B_{min} = 0$ for $0.9 \text{ cm} < r_{min} < 1.3 \text{ cm}$. Here, r_H , H and r are inner radius, thickness and cylindrical coordinate of hexapole, respectively.

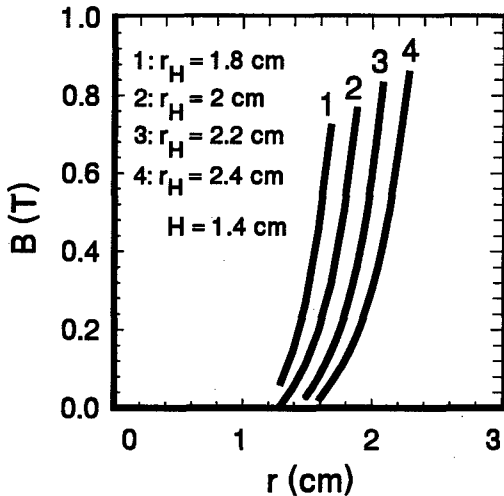


Figure 3: Magnetic field B inside hexapole where $B_{min} = 0$ for $1.1 \text{ cm} < r_{min} < 1.6 \text{ cm}$. Here, r_H , H and r are inner radius, thickness and cylindrical coordinate of hexapole, respectively.

a magnetic field of 1 T is obtained at the inner radius of hexapole $r_H = 5.2 \text{ cm}$ (the thickness of hexapole $H = 1.4 \text{ cm}$). This value corresponds to a ratio of $B_{max}/B_{ECR} = 2.77$ at the resonance magnetic field of $B_{ECR} = 0.36 \text{ T}$ corresponding to a cyclotron frequency of 10 GHz.

The calculations were done in the segment that is 1/12 of the total hexapole in which both the mirror and the rotational symmetries are assumed. The boundary conditions were also fixed. The results of the calculations are summarized

in Figs. 2 to 7. Figs. 2 to 4 show magnetic field B inside a hexapole as a function of a cylindrical coordinate r . These values correspond to the different cylindrical coordinates r_{min} at which is the magnetic field $B_{min} = 0$, mainly $r_{min} \in \langle 0.9, 2.1 \rangle \text{ cm}$. Figs. 5 to 7 show a magnetic field of B inside a hexapole as a function of a cylindrical coordinate r . These values correspond to the different average quantities $\Delta r_a = \sum_i \Delta r_i / n$ for $\Delta r_a \in \langle 0.133, 1.26 \rangle \text{ cm}$, where $\Delta r_i = (r_H - r)_i$, n is the number of Δr_i , r_H the inner radius of hexapole and r the cylindrical coordinate. Only one value of Δr_i is considered for the given calculation of the magnetic field of hexapole.

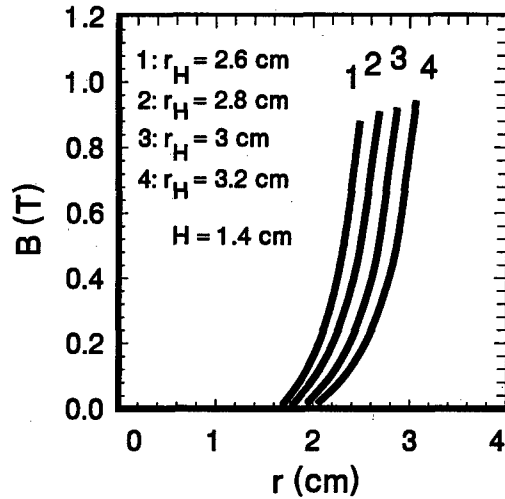


Figure 4: Magnetic field B inside hexapole where $B_{min} = 0$ for $1.6 \text{ cm} < r_{min} < 2.1 \text{ cm}$. Here, r_H , H and r are inner radius, thickness and cylindrical coordinate of hexapole, respectively.

3 RESULTS

We have chosen the thickness of hexapole $H = 1.4 \text{ cm}$ for NANOGUN-10B to find the maximum of the magnetic field B_{max} in the region of $r_H \in \langle 1.3, 6 \rangle \text{ cm}$. Suitable radius of hexapole can be taken from the region $r_H \in \langle 1.7, 3.2 \rangle \text{ cm}$ for the ECR IS NANOGUN-10B. An increasing of magnetic field at the surface of hexapole has also been found of $\Delta B = 0.24, 0.14$, and 0.06 T in the regions of $r_H \in \langle 1.3, 1.9 \rangle \text{ cm}$, $r_H \in \langle 1.8, 2.4 \rangle \text{ cm}$, and $r_H \in \langle 2.6, 3.2 \rangle \text{ cm}$, respectively.

To understand the influence of parameter Δr_a on $B(r)$ distributions, we have shown Figs. 5 to 7. The higher is the parameter Δr_a the lower is the magnetic field B for the given coordinate r . A saturation of the magnetic field B_s ($B_s = 1.09; 0.8; 0.65$, and 0.55 T) at the parameters $\Delta r_a \in \langle 0.133, 0.44 \rangle \text{ cm}$ can be seen. Therefore the magnetic field at the ECR IS plasma chamber surface is 0.45 T for hexapole of $r_H = 1.8 \text{ cm}$ and for the plasma chamber thickness of 1.77 mm .

A well-known rule of plasma physics says that the

higher is the mirror ratio of a magnetic trap, the smaller is the number of the particles lost from the confined plasma. The confining trap in the ECR IS is formed by the superposition of a mirror field and a hexapolar field. The higher is the hexapolar field, the higher is the confining trap and the ratios $B_{max}/|B|$ and B_{max}/B_{min} that are also important for ECR heating.

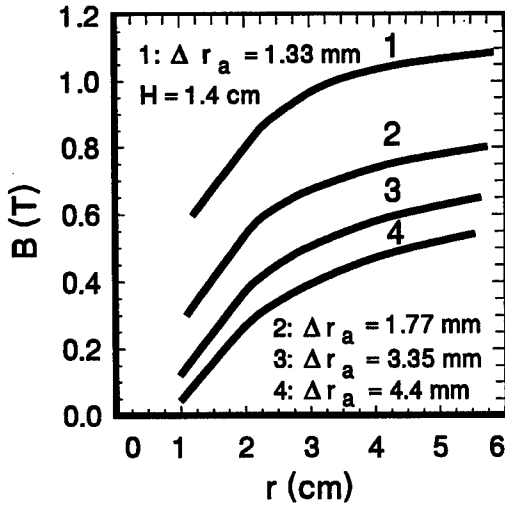


Figure 5: Magnetic field B inside hexapole where Δr_a , H and r are parameter, thickness and cylindrical coordinate of hexapole, respectively.

parameters Δr_a on B(r). It has been shown that the higher is the parameter Δr_a the lower is the magnetic field B for the given coordinate r. The thickness of hexapole $H = 1.4$ cm for NANOGUN-10B has been chosen to find a maximum of the magnetic field B_{max} in the region of $r_H \in \langle 1.3, 6 \rangle$ cm. We have shown that the best results are obtained with hexapole shape where $r_H \in \langle 1.4, 2.4 \rangle$ cm.

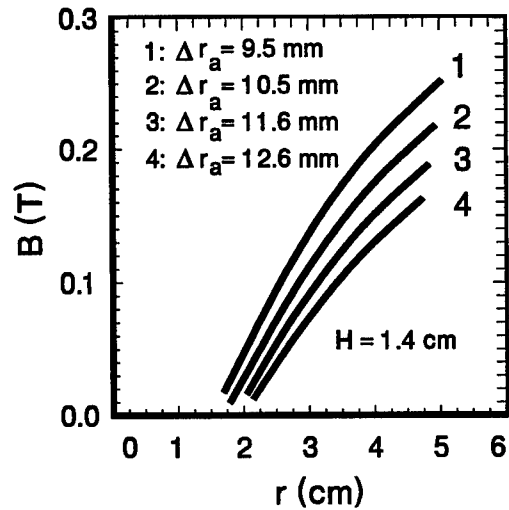


Figure 7: Magnetic field B inside hexapole where Δr_a , H and r are parameter, thickness and cylindrical coordinate of hexapole, respectively.

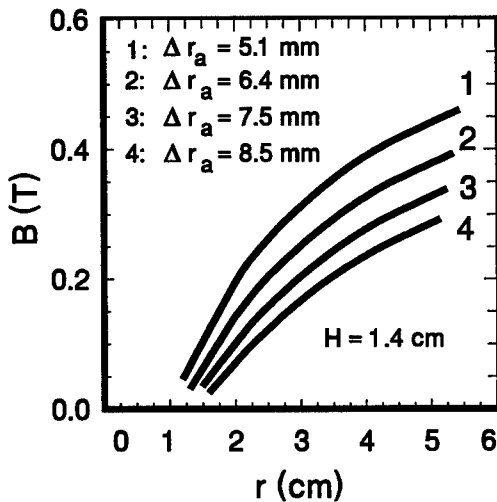


Figure 6: Magnetic field B inside hexapole where Δr_a , H and r are parameter, thickness and cylindrical coordinate of hexapole, respectively.

4 CONCLUSIONS

The magnetic field inside hexapole with thickness of $H = 1.4$ cm have been calculated, as well as influence of

5 ACKNOWLEDGEMENTS

The authors wish to thank E. Běták for his understanding in this work and for his help concerning the language correction of the paper. They are also indebted to P. Bandžuch and J. Zrubcová for helpful discussions. The work has been partially supported by VEGA grant No. 2/5122.

6 REFERENCES

- [1] J. Pivarč, A.N. Lebedev, J. Pivarč (Jr.), Production of Ion Beams with the Use of ECR Ion Source, Report E13-97-285, Publishing Dept., JINR Dubna, 141980 Dubna, Moscow region, Russia, 1997, p. 1-16.
- [2] B. Martin, M. Grether, R. Köhrbrück, U. Stettner and H. Waldmann, The Berlin 14.5 GHz ECR IS and its Testbench, KVI Report 996, Proc. of the 11th ECR IS Workshop, Groningen, May 6-7, 1993. Ed. A.G. Drentje, University of Groningen, The Netherlands, p. 188.
- [3] R. Trassl, F. Broetz, M. Pawlowsky, P. Hathiramani, M. Schlapp, J.B. Greenwood, R.W. McCullough and E. Salzborn, Status Report of a Compact 10 GHz ECR IS, Proc. of the 13th Int. Workshop on ECRIS, 26-28 Febr., 1997, Texas A&M University, Texas, USA, p. 143-145.
- [4] POISSON/SUPERFISH Reference Manual: Report LA-UR-87126, Los Alamos, New Mexico, USA.
- [5] K. Halbach, Nucl. Instr. and Meth. 169 (1980) 1.

RESULTS OF THE RECONSTRUCTED MEDEBIS

R. Becker, H. Hoeltermann, M. Kleinod

Institut fuer Angewandte Physik,

J.W.Goethe-Universitaet, D-60054 Frankfurt/Main

Abstract

The electron beam ion source (EBIS) can deliver sufficiently short and intense pulses of fully stripped light ions for single turn injection into a dedicated synchrotron for hadron therapy. The technology of such a MEDEBIS resembles travelling wave tubes used in satellites and can also be designed for lifetimes up to ten years. In a first setup using a normal conducting solenoid of 0.75 T and a trap length of 0.25 m the source delivered high charge states of light ions like O^{6+} , O^{7+} , O^{8+} and C^{6+} , C^{7+} [1]. The fast ion extraction in less than $2\mu s$ is realised through a special electrostatic structure providing a pulsed extraction potential gradient along the axis of the whole ion trap. The first results were very promising, but the residual gas pressure in the ionisation region was too high to make use of a sufficiently long confinement time in order to reach full abundance of bare nuclei. For the reconstructed MEDEBIS the inner two windings of the solenoid were drilled out to allow for a vacuum tube of about twice the diameter with better conductance. Together with the implementation of NEG getter material the residual gas pressure should be lowered sufficiently to reach the required yield of the fully stripped ions. Iron disks of high permeability have been added at both ends of the solenoid to increase the homogeneity of the magnetic field as well as to reduce the field in the gun and collector regions for a higher focussed current density in the trap region. The new MEDEBIS is under test and new experimental results will be presented.

1 INTRODUCTION

Treating cancers with heavy ions is a very promising kind of therapy for cases in which local control of tumors with conventional therapy fails. Conventional radiation such as bremsstrahlung, electrons or γ -rays show an exponential decrease of deposited energy while penetrating deeper into tissue. Ions in contrary deposit most of their energy in a narrow region, the bragg peak, at the end of their track, so healthy tissue in the tumor's vicinity will not be radiated. The first approaches to this kind of therapy have taken place since 1994 using large research accelerator centers i.e. Berkeley, United States, Chiba, Japan or GSI, Germany. Their aim is to give proof-of-principle while the realisation of hospital based therapy will need smaller machines dedicated only to clinical purposes. This is the

point where an electron ion beam source (EBIS) comes into consideration. An EBIS yields a short, but very intense ion-pulse of fully stripped ions. Using an EBIS gives sufficiently current of bare nuclei so the ion source alone combined with a low duty cycle RFQ is all what is needed as an injection line for a synchrotron[2]. Even the time structure of the ion pulse is well suited for single turn injection, leading to a less complex synchrotron. Advantageously, the lifetime of an EBIS, resembling travelling wave tubes in satellites, can easily reach ten years since it has no consumable parts. A setup like this wouldn't need a linac besides a RFQ and a stripper[3].

2 THE MEDEBIS PRINCIPLE

At the Institut fuer Angewandte Physik, Goethe-Universitaet, Frankfurt/Germany we assembled last year a reconstructed prototype of such an medically dedicated EBIS, named MEDEBIS. To reduce complexity and costs we use a normal conducting solenoid of 0.8 T for magnetic focussing of the electron beam. The electron gun and collector are magnetically shielded by iron cylinders of high permeability. Within the electron beam gas atoms of the feed gas like oxygen or carbon (methane) are getting ionised due to electron impact. Ions will be trapped radially in the space charge of the electron beam while they are confined on a length of 0.25m due to the positive potential of barrier electrodes around the axis. For the extraction a potential gradient will be applied to the ion trap, provided by a combination of two reverse slitted electrostatic structures on different radius. The slits have a parabolic shape resulting in an adjustable linear gradient while having different potentials on each electrode. The rise of the gradient allows a pulse compression down to $2\mu s$, what has already been proofed[4]. The confinement time of the ions is dependent on the charge state and number of bare nuclei, so ion species and current can be adjusted by the frequency of pulsing. A very important fact for the EBIS principle is the vacuum condition inside of the ion trap. As most of the currently used EBIS devices base on a cryogenic environment we had to deal with the higher desorption rates of a warm solenoid. So far we installed a larger vacuum tube in which NEG getter material has been introduced to provide an active pumping surface.

The expected ion current being trapped in the electron beam is limited by the space charge density ρ of the beam. Experience so far has shown that the number of extracted ion charges cannot exceed the number of electrons in the trap region. With N^- the number of electrons in a cylindrical electron beam of the length l , perveance P and the energy $e \cdot U_0$, the number of storeable ions N^+ is equal or less than the number of electrons:

$$N^+ \leq \frac{N^-}{q} = \sqrt{\frac{m_e}{2e^3}} \cdot \frac{P \cdot l \cdot U_0}{q} \approx \frac{10^{13}}{q} \cdot P \cdot l \cdot U_0 \quad (1)$$

Tab. 1: Actual MEDEBIS parameters:

Geometry	
Length of ion trap	0.25 m
Magnetic field	0.8 T
Electron beam	
Energy	3 keV
Electron current	300 mA
Current density	~250 A/cm ²
Extraction	
C ⁶⁺ particles per spill*	2.2*10 ¹⁰
Shortest extraction time	2μs
Ion current C ⁶⁺ *	1.5 mA
Extraction gradient	0-3kV/m

* Calculated by (1) for maximum of storeable charges at 2μs extraction time at present working parameters. Not yet being observed !

3 MEASUREMENTS AND RESULTS

Due to the extensive use of passive magnetic elements such as iron discs enclosing the electron gun and the main solenoid two important improvements have been done. First of all the magnetic field along the ion trap shows a more constant behaviour over a broader length than before, which is equal to a constant high compression in this area.

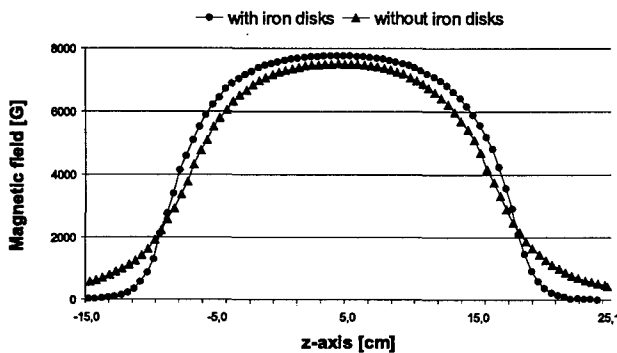


Fig 1.: MEDEBIS magnetic field along the ion trap

Secondly a higher beam compression right after the cathode leads to an more intensive electron beam. The electron current which could be obtained up to now is 300 mA, 80% more than in the first setup. Ionisation measurements at 65mA allow to deduce a current density of 50 A/cm², what leads to the conclusion that with the unchanged parameters of the main solenoid and given apperture of the barrier electrodes we have now current densities around 250 A/cm². Measurement of the actual current density through charge state breeding is already in process. The whole setup has been constructed for currents up to 800mA and current densities in the region of 600 A/cm², leading to particle spills of 3*10¹⁰ C⁶⁺ or an ion current equivalent to ~2 mA. During the ramp up of the electron beam it has been observed, that a dynamic reconfiguring of the magnetic fields especially at the end of the ion trap is necessary, while increasing the beam current. This can be interpreted as a change of the beam spreading due to its increasing space charge at constant magnetic focussing which needs a different magnetic field to be counteracted.

Loss of electron current on some of the electrodes could be minimized through the steerable iron shielding discs as well as through a reconfigured magnetic field. The new developed collector designed for suppressing of x-rays leading to desorption as well as to cope with a 4kW electron beam has already collected 96% of the 1kW electron beam, which is currently under test. During all experiments a pressure of 10⁻⁹ mbar in the electron gun and collector recipients is maintained.

4 BEAM PURITY

The medical application of the ion beam makes beam impurity an important issue. Different ion species will cause unwanted shaping of spread out bragg peaks resulting in different biological effects. All ion sources usually deliver an ion spectrum with a mixture of charge states and species. This is especially a problem using ions of the same charge to mass ratio. At the GSI proposed facility[5] magnetically selected C⁴⁺ ions will be accelerated up to the injection energy of the synchrotron where they will pass a stripper to remove the final two electrons. By this procedure bare nuclei of nitrogen or oxygen are not accepted simultaneously by the synchrotron, resulting in a very low impurity admixture. Of course an EBIS could also be operated at lower confinement time or current density delivering now a spectrum of ions peaking at C⁴⁺. The lower relative abundance necessitates a higher loading of the source capacity which could be counteracted by a higher electron current, which is easy at lower current density. Another possibility would be the use of isotopes like C¹³⁺, neglecting the use of PET for in-situ monitoring, or the implementation of ion cyclotron resonance[6] for ion separation during breeding of higher charge states.

REFERENCES

- [1] O.Kester, R. Becker and M. Kleinod, Rev. Sci. Instrum. 67, 1165 (1996)
- [2] R. Becker, M. Kleinod, A. Schempp, E.D. Donets, and A.I. Pikin, Rev. Sci. Instrum. 63 (1992) 2812
- [3] R. Becker, H. Hoeltermann, M. Kleinod, A. Schempp, B. Zipfel, Proc. EPAC 98, Stockholm 22-26 Juni 98, to be publ.
- [4] M. Kleinod, R. Becker, H. Hoeltermann, M. Muecke, R. Rao, M. Weidenmueller, and B. Zipfel Rev. Sci. Instrum. 69 (1998) 718
- [5] Proposal for a dedicated ion beam facility for cancer therapy, GSI Darmstadt/Germany, September 1998
- [6] B. Zipfel, R. Becker, M. Kleinod, and R. Rao Proc. 3 rd Euroconference on Atomic Physics with Stored Highly Charged Ions, Ferrara, Italy, 22-26 Sept. 1997, Hyperfine Interactions 115 (1998) p. 193-200

RESULTS OF BEAM TESTS ON A HIGH CURRENT EBIS TEST STAND*

E. Beebe^{*}, J. Alessi, S. Bellavia, A. Hershcovitch, A. Kponou, R. Lockey, A. Pikin, K. Prelec,
Brookhaven National Laboratory, Bldg. 930, Upton, NY 11973, USA

G. Kuznetsov, M. Tiunov

Budker Institute of Nuclear Physics, 630090, Novosibirsk, Russian Federation

Abstract

At Brookhaven National Laboratory there is an R&D program to design an Electron Beam Ion Source (EBIS) for use in a compact ion injector to be developed for the relativistic heavy ion collider (RHIC). The BNL effort is directed at developing an EBIS with intensities of 3×10^9 particles/pulse of ions such as Au^{35+} and U^{45+} , and requires an electron beam on the order of 10A. The construction of a test stand (EBTS) with the full electron beam power and 1/3 the length of the EBIS for RHIC is nearing completion. Initial commissioning of the EBTS was made with pulsed electron beams of duration < 1ms and current up to 13 A. Details of the EBTS construction, results of the pulse tests, and preparations for DC electron beam tests are presented.

1 INTRODUCTION

The program at the BNL has as its objective the development of a heavy ion source of the EBIS type that would satisfy present and possible future requirements of RHIC. Implementation of such an EBIS has been discussed elsewhere, [1] and a summary of the pertinent parameters is given in Table 1. The experimental program to be completed preceding the design of the RHIC EBIS consists of 4 phases. The first phase of this program was based on experiments at the BNL TestEBIS (based on the Sandia National Laboratory's SuperEBIS), while the subsequent phases utilize an electron beam test stand (BNL EBTS) that has been constructed to serve as a proof-of-principle device for the final EBIS for RHIC. During phase 1, an electron beam current of 1.1 A pulsed and 0.5 A d.c. has been achieved. Narrow charge state

Table 1: Parameters for an EBIS meeting RHIC requirements

Parameter	RHIC EBIS
Electron beam current	10 A
Electron beam energy	20 keV
Ion trap length	1.5 m
Trap capacity (charges)	1.1×10^{12}
Yield positive charges	5.25×10^{11}
Yield Au^{35+} , design value	3×10^9 ions/pulse
Yield U^{45+} , design value	2×10^9 ions/pulse

*Work performed under the auspices of the U.S. Department of Energy.

*Email: beebe@bnl.gov

spectra of sodium (peak 7+), argon (peak 14+) and thallium (peak 41+) ions have been produced, demonstrating the ability to produce sufficiently high charge to mass ratio ions of varied species. Furthermore, the heavy ion spectra of Xenon with peak charge state Xe^{27+} has been produced with a d.c. electron beam current above 0.4A and electron beam neutralization degree above 50%.[2] Encouraging results from these experiments led to the decision to proceed with phase 2, the design, construction, and commissioning of an electron beam test stand with parameters given in table 2.

Table 2: Nominal EBTS Parameters

Parameter	EBTS
Electron beam current	10 A
Electron beam energy	20 keV
e-beam current density	400 A/cm ²
e-beam pulse duration	~100 ms
ion trap length	0.5 m
trap capacity (charges)	4×10^{11}

This test stand will be used to develop technologies and study the physics aspects of a high intensity EBIS. This phase has been completed with the propagation of a 13 A, 50 μs pulsed electron beam, more than an order of magnitude improvement over the TestEBIS beams. Phase 3 will continue with high current electron beam formation and launching studies for long pulses and d.c. beams. Assembly is nearing completion and tests will begin this Spring. The fourth phase will concern extraction of ions, the main goal being production of 1/3 the final RHIC EBIS intensity. Also of interest is the development of primary ion injection into the trap, the study of ion formation in and loss from a high current electron beam, and the study of fast ion extraction. A successful operation of this device will be followed by the design of the full scale EBIS, together with the rest of the injector.

2 ELECTRON BEAM TEST STAND

As seen from tables 1 and 2, the EBTS is a full electron beam current and power prototype of the RHIC EBIS with one third the ion trap length. In an EBIS, high charge state ions are created by successive ionization by electron impact and are confined by the radial space charge of a high density electron beam.[3] The ion

confinement time necessary to reach the charge state of interest imposes the minimum electron beam pulse duration for a given current density. There is considerable flexibility in these nominal parameters and increased performance in one parameter may lead to relaxation of another. For example, for a given magnetic field configuration, an increase in electron beam current may result in an increase in both electron beam current density and trap capacity. This reduces both the ion confinement time necessary to reach a given charge state (and hence, electron beam pulse duration) and the length of the trap region. A schematic of the electron beam test stand is given in figure 1.

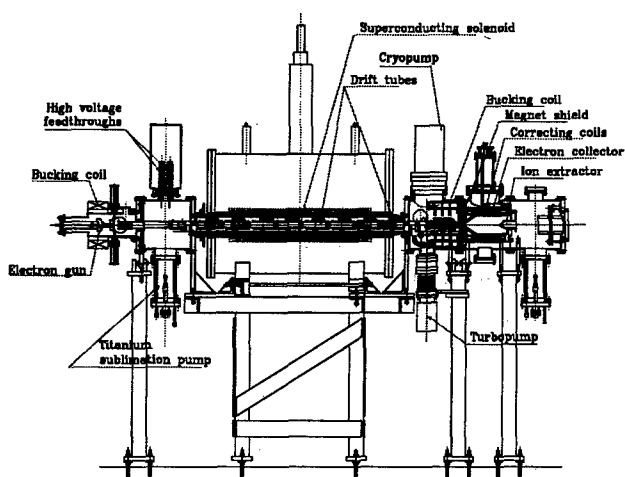


Figure 1: Layout of the electron beam test stand

Due to the low average power associated with pulsed electron beams, we were able to begin tests before all components necessary for the d.c. tests were available. Table 3 gives nominal parameters for major EBTS components. In the next section we will describe the

Table 3: EBTS Components and Parameters

EBTS Item	Parameters
Electron Gun	10 A, 50 kV; 8.2mm LaB ₆
Gun Solenoid	0.2 Tesla
Main Solenoid	5 Tesla, 1 meter long
Collector Solenoid	0.05 Tesla
Electron Collector	50 kW
Transverse Coils	15 Gauss
Vacuum System	1×10^{10} Torr

configuration during the pulsed electron beam tests, and note how the installation differs from the final test stand. Details of the complete test stand design and specifics concerning the electron gun and collector design have been given previously. [4,5,6]

2.1 Pulsed Electron Beam Configuration

In order to verify the basic EBTS design, pulsed electron beams of low average power were used. This allowed testing to begin before final versions of all elements of the test stand were installed. A simplified drift tube structure with two long drift tubes of 32 mm inner diameter in the trap region was used. A pulsed solenoid capable of producing 2 kG fields was used with the electron gun rather than a D.C. entrance solenoid. The electron beam was collected on electrically isolated segments of an electrode assembly, figure 2, which allowed us to measure both beam intensity and position information. The electron collector exit solenoid necessary for confining the electron beam at the source exit was not installed. As a result, some electron beam was incident on the exit aperture of the last drift tube.

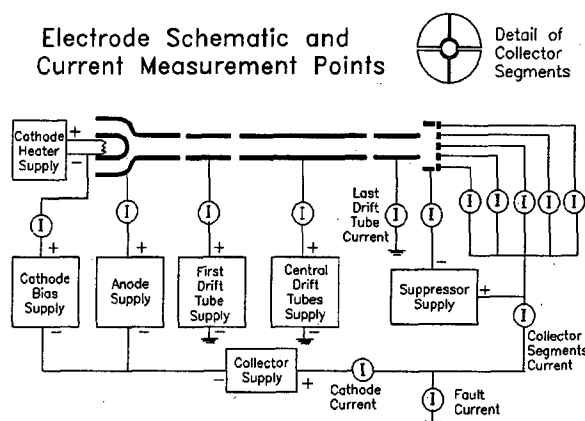


Figure 2: Electrode and current measuring schematic for pulsed electron beam tests at the BNL EBTS.

Electrically, the electrode configuration is as follows: The electron gun platform is held at approximately -10 kV with respect to the electron collector which is nominally held at ground through a single low impedance current measuring device. This arrangement allows us to measure sub-milliamp level current losses from the 10 A electron beam circuit and also avoids the expense of a 100 kW, 30 kV isolation transformer. Drift tube supplies were referenced directly to laboratory ground and were stabilized during these tests by capacitors ~20nf and facilitated measurement electron beam current losses on the drift tubes during the pulse.

The use of transverse coils has been important in our program and was first implemented on the TestEBIS[2], resulting in a doubling of electron beam current. The coils are especially easy to install in the case where iron shielding is not used to shape the magnetic field since the coils can reside outside the vacuum chamber. We use transverse fields of up to 15 Gauss to empirically adjust the magnetic field; thereby reducing unintentional asymmetries and introducing asymmetry at the collector where it is useful to reduce backstreaming electrons.

2.2 Experimental Results

Figure 3 shows some of the earliest results using a Trek 30 kV, 10mA anode supply at 9 kV to launch a 1.2 A electron beam. Note the 200 μ s slow time of the rising and falling edges. The transverse coils were adjusted to

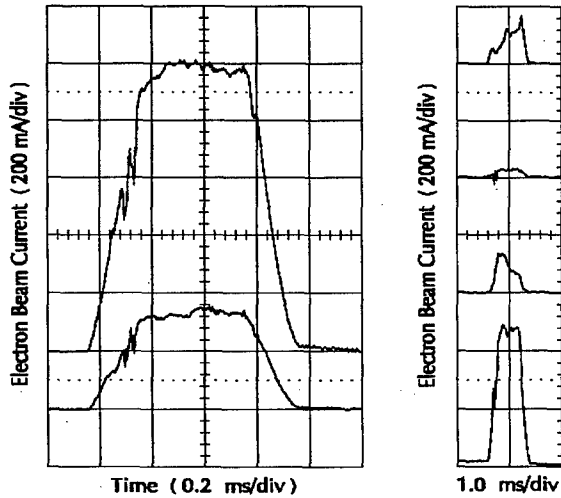


Figure 3: Electron beam current intercepted by various segments of the collector assembly shown in fig. 2: Sum current on 5 segments (upper left trace), central segment current (lower left trace), and 4 outer segment currents (right traces).

provide a rather asymmetric current distribution on the collector segments, thereby minimizing backstreaming current on the first drift tube. First drift tube losses were 30mA, giving a transmission factor of 97.5%. (A 170 mA current incident on the last drift tube is included in the total collector current). The Trek anode supply was used at 30 kV to propagate 7 A electron beams. In this case the slew times to and from flat top were $\sim 600 \mu$ s, causing considerable loading on the electrodes and giving pressures $\sim 1 \times 10^{-7}$ mBar at a 0.5 Hz repetition rate.

A fast anode supply, developed in our laboratory and based on Belke 65 kV solid state switching modules was used during the remainder of the tests. Figure 4 shows a 13A, 50 μ s electron beam pulse that was obtained with a 45 kV anode pulse and a 5 Tesla main field. The potential difference between the cathode and trap region electrodes was 36 kV and the entrance field was 2.4 kG. For a trap region comprised of four 15 cm long drift tubes, this gives an electron beam current density of $\sim 750 \text{ A/cm}^2$ and a trap capacity of 4.3×10^{11} charges, surpassing the objectives given in table 2. The fast anode supply has lowered transient times to 10 μ s, thereby reducing beam loading. During these tests a gun region pressure of $\sim 4 \times 10^{-8}$ mBar was maintained at a pulse repetition rate of 2 Hz. A transmission efficiency of greater than 99.5% was achieved and it is expected that introduction of the 50 kW electron collector will further reduce the losses.

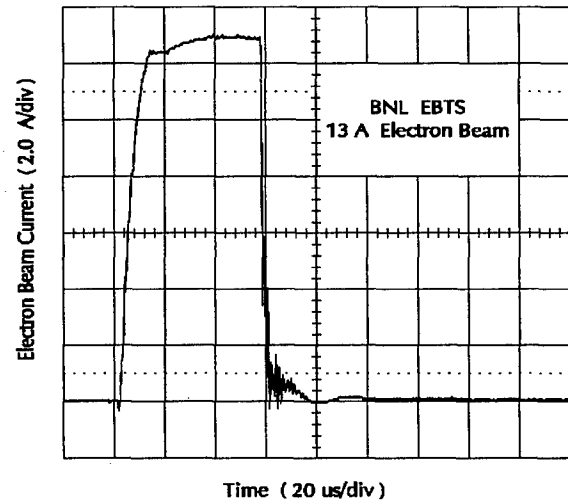


Figure 4: 13A, 50 μ s electron beam pulse at the EBTS

3 SUMMARY

The Electron Beam Test Stand has been operated successfully with pulsed electron beams. A 13A, 50 μ s electron beam was transmitted. This is more than a factor of 10 increase over electron beams produced on the TestEBIS used previously. Electron beam current density, total current, and trap capacity requirements were exceeded. Final assembly is underway for long pulses and DC electron beam operation. Continuous and high duty factor electron beams will be tested with current up to 10A and pulse duration at least 100 ms.

4 ACKNOWLEDGMENT

We would like to thank David Boeje, Walter Hensel, Bob Horton, Tim Lehn, Dan McCafferty, Wally Shaffer, Paul Stein, and Werner Tramm for their ongoing assistance on this project.

5 REFERENCES

- [1] H. Haseroth and K. Prelec "Possible Application of an EBIS in Preinjectors for Large Heavy Ion Colliders", *Physica Scripta* T71, 23 (1997).
- [2] E. Beebe, J. Alessi, A. Herscovitch, A. Kponou, A. Pikin, K. Prelec, P. Stein, and R.W. Schneider, "Experimental Results from the Brookhaven National Laboratory Test Electron beam Ion Source", *Rev. Sci. Instrum.* 69, 640 (1998).
- [3] E.D. Donets in "The Physics and Technology of Ion Sources", edited by I.G. Brown (Wiley, New York 1989), Chap.12.
- [4] A. Pikin, J. Alessi, E. Beebe, A. Kponou, K. Prelec, and L. Snydstrup, "Brookhaven National Laboratory Electron Beam Test Stand", *Rev. Sci. Instrum.* 69, 697 (1998).
- [5] J. Alessi, E. Beebe, A. Herscovitch, A. Kponou, A. Pikin, K. Prelec, L. Snydstrup, and G. Kuznetsov, "Design and Initial Results of a High Current EBIS Test Stand", EPAC'98, Stockholm, (1998)
- [6] A. Kponou, E. Beebe, A. Pikin, G. Kuznetsov, M. Batazova, and M. Tiunov "Simulation of 10A Electron Beam Formation and Collection for a High Current Electron Beam Ion Source", *Rev. Sci. Instrum.* 69, 1120 (1998).

FIRST TESTS OF THE TRAPPED ION SOURCE

V. Variale, V. Valentino, INFN sez. di Bari

G.Brautti, A. Boggia, A. Raino', Dipartimento di Fisica e INFN sez. di Bari

Abstract

Recently the detailed design and the construction problems of a Trapped Ion Source (TIS) have been presented in ref.[1,2]. In practice, TIS can be seen as a modified version of an Electron Beam Ion Trap (EBIT) or of an Electron Beam Ion Source (EBIS). The main new feature of TIS, with respect to an EBIS (or EBIT), is the transverse ion confinement given by a quadrupole field instead of the electron beam space charge. One can foresee that TIS could overcome some drawbacks of the EBIT and EBIS making it a more flexible device. In this paper a detailed discussion on the radio frequency containment of high charge state ions with the first rf containment test will be presented.

1 INTRODUCTION

TIS is a new type of source capable, in principle, of producing very highly charged ions and, at the same time, it is a radio frequency (rf) quadrupole linear trap suitable to study the interaction of the trapped ions (or charged microparticles) with electrons, high energy particles or laser beams. In practice, it is a modified version of an Electron Beam Ion Source (EBIS). TIS, in fact, is an EBIS where an rf quadrupole field has been added to contain transversally the ion produced by the electron beam.

Recently some proposals to use EBIS type sources as charge state breeder for radioactive ion beams extracted as singly charged ions with the isotope separator on-line (ISOL) technique have been suggested [3]. In fact, for efficient acceleration by compact linear accelerators, ions with typical mass ratios of 1/9 are required. However, after the high charge state ions have been produced, a mass separator is required before the ion beam acceleration. In this case, the use of TIS instead of an EBIS, could allow to accelerate radioactive ion beams directly at the exit of the TIS source. In fact, having TIS a selective ion containment given by the rf quadrupoles, it is, at the same time, an ion source and an ion mass separator.

Among the goal of TIS, other than the production of highly charged particles, it can be foreseen ion cooling studies, analysis of macromolecules and, also, "dust targets" for high energy accelerators. The status report of the project with a detailed discussion on the rf ion containment system will mainly be presented.

2 TIS DESIGN

TIS design has already presented in ref. [1,2], but here, for clarity sake, its main features will be recalled. In fig.1 a cutaway drawing of the ion source mechanical design and its operation scheme is shown. From the fig.1b) it can be seen the electron gun that generates the electron beam needed to ionize the atoms. Since an electron gun designed and built for another experiment is intended to use for TIS experiment a couple of iris are been used to match the electron beam emittance to the acceptance of the TIS transport channel.

The transport channel that drives the electron beam until to the collector is made of two 90 degree bending magnets (BM) and several quadrupole doublets of new design as shown in more details in ref. [2]. The main new feature of TIS, with respect to an EBIT (or EBIS), is the adding of radial ion confinement of the rf quadrupoles to the potential well of the eb space charge when it is on. When the eb is off (the eb will be pulsed) only the desired ions will remain trapped.

In the longitudinal direction the containment is obtained by two repelling electrodes placed at the edges of the quadrupole electrodes. These electrodes can be pulsed to pull-out the trapped ions for external use (e.g. acceleration).

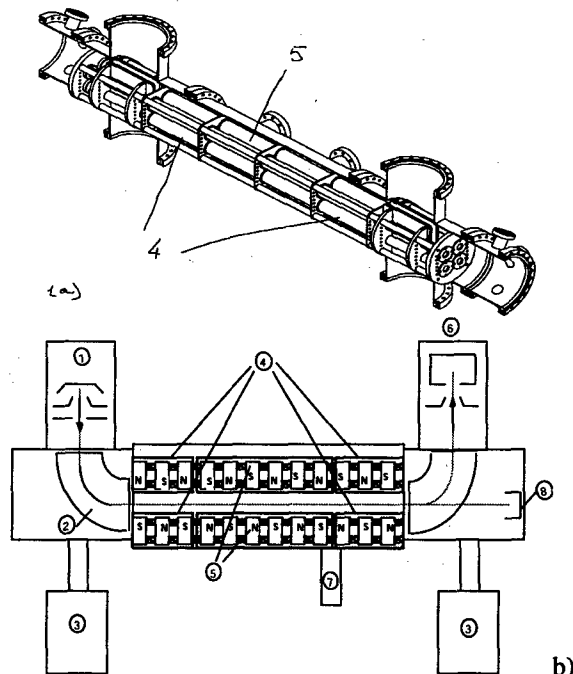


Fig.1a) cutaway view of the TIS mechanical design; 1b) Operation scheme of TIS: 1) electron gun, 2) bending

magnet, 3) vacuum pump, 4) static potential electrodes U_0 for longitudinal ion trapping, 5) rf quadrupole electrodes with inside the focusing magnetic quadrupoles, 6) electron collector, 7) gas-inlet, 8) ion collector.

In its normal operation, the electron beam pulse is injected transversally (see fig 1b) in the trap and then bent in the axial direction. Transversally too, in the center of the trap, vapor or powder can be injected, by a valve gas jet, that it is ionized and confined by the rf quadrupole field.

3 RADIO FREQUENCY CONTAINEMENT

The TIS eb transport line has been described in detail in ref [2]. In this paper we will present the rf system utilized to contain, transversally, the wanted ions with different charge states produced by the electron beam.

In a EBIS, the ion containment in the transverse planes is obtained by the potential well due to the space charge of the ionizing electron beam and longitudinally from the potential set by the electrodes placed on the edges of the ionization region. In these conditions the residual gas ions being in the vacuum chamber can be trapped together the wanted ions. For this reason EBIS sources require very high vacuum (about 10^{-11} Torr) and at the same time very dense energetic electron beams [3]. Furthermore the cold electrons coming from the ionization can be trapped by the ion space charge increasing, in this way, the probability of the recombination process. In TIS, to avoid those drawbacks, the adding of the rf quadrupole field is provided by 4 cylindrical shaped electrodes, see fig.1). Although, infinite hyperbolically shaped electrodes are needed for a pure quadrupole field, an appropriate chose of the ratio between the electrode cylinder radius and their distance from the symmetry axis can be chosen for a very good optimization of the quadrupole field. In ref. [1] we have found a very good optimization for a cylinder radius of 2.2 cm and a distance from the symmetry axis of 2 cm. In fact these parameters give a quadrupole Fourier coefficient, normalized to the sextupole coefficient which is the higher among the other multipole coefficients of 2.7×10^4 .

The equations of motion, at the presence of the potential given by these electrodes, in the transverse planes, can be written in Mathieu's equation form:

$$\frac{d^2 X}{d\theta^2} + (a - 2q \cos 2\theta)X = 0$$

$$a = \pm \frac{8eU}{mr_0^2 \omega^2}$$

$$q = \mu \frac{4eV}{mr_0^2 \omega^2}$$

and where: $X \rightarrow x, y$; $\theta \rightarrow \omega t/2$, and the upper and lower signs correspond to differential equations in x and y , respectively. The applied voltage has a dc component U plus an rf voltage V with the driving frequency ω .

The Mathieu equation solution can be stable or unstable. Whether stability exists depends only on the parameters a and q and not on the initial parameters of

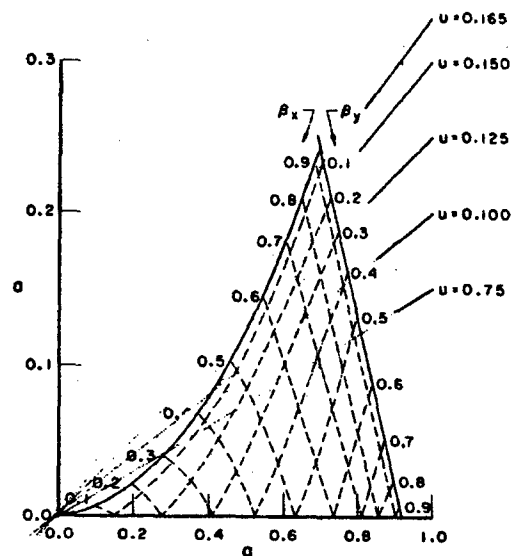


Fig.2 The a - q stability diagram. The positions of various operating lines $U/V = \text{Const.}$ are also indicated.

the ion motion. In fig.2 is shown the region of simultaneous stability in both the transverse planes x and y . It can be noticed that a given set of applied voltages U and V uniquely determines the relative values of a and q in the stability diagram. If we Define $u = |U|/|V| = a/2q$ a typical straight line $a = 2qu$ can be drawn as shown in fig.2. The portion of this line passing through the stable region of the diagram determines the range of ionic e/m values which will have stable trajectories through the quadrupole field. As the U/V ratio is increased, the intersected stability region becomes narrower and narrower, so that the device becomes more highly mass selective, but at the same time the x and y acceptances of the trap become smaller. Furthermore, it must be noticed that, for a chosen U/V ratio, the ions with stable e/m values can be scanned by varying the magnitude of both U and V simultaneously or by varying the applied frequency ω .

The operating point in the stability diagram a - q can be chosen in such a way to satisfy the required charge state on the output ion. In some cases it could not be necessary the e/m scanning as mentioned before. As an example we consider the case of using TIS to produce Ar^{+4} , which is the element we are using in our first tests. If we choose a line (see fig.2) with a low U/V ratio, renouncing to a large e/m resolving power, will have a large range of stability. Let us choose as lower q (the q value given by the interception of the line $a = 2qu$ with the left part of

stability triangle) the value 0.2, from the definition of q and using $V=1$ kV we obtain the rf frequency $\nu=1.7$ MHz. The corresponding a value is (see fig.2) 0.02 then $u=a/2q=0.05$. Following the operation line $a=2qu$, the higher q value 0.82 is intercepted on the stability diagram and at this point an $A/Z=10$ (Ar^{+4}) will also have a stable trajectory in TIS. In conclusion, with the choice of the above parameters we have stable trajectories from Ar^{+1} to Ar^{+4} . In these conditions of low resolving power, we expect that other elements with e/m inside the stability diagram could be trapped with wanted ions. The other elements present with Ar in the vacuum tank are, in general, the component of the residual gas. The tank residual gas has been analyzed and was mainly composed by N_2 ($A=28$), water ($A=18$), O ($A=16$), N ($A=14$), H_2 ($A=2$). By using the above parameters ($\nu=1.7$ MHz, $V=1$ kV, $U=50$ V) we have found that also the e/m of N_2^{+1} , N_2^{+2} , H_2O^{+1} and N^{+1} are in the stable region while the other e/m values lead to unstable trajectories.

The preliminary rf test done on TIS have had the aim to check the ion containment capability and the quadrupole symmetry of the potential well. In fig.3 is shown the residual gas plasma containment of the rf cylindrical shaped electrodes. The parameters used has been: $\nu=2.5$ MHz, $V=0.6$ kV and $U=50$ V giving stability for ions with $A>2$.

From fig.3, it can be seen a slight deformation of the quadrupole symmetry caused by a defect in feeding the rf electrodes. In fact, we did not have the exact same voltage, in opposition of phase, on the adjacent electrodes. We are correcting this defect with a better matching circuit having a more balanced transformer.

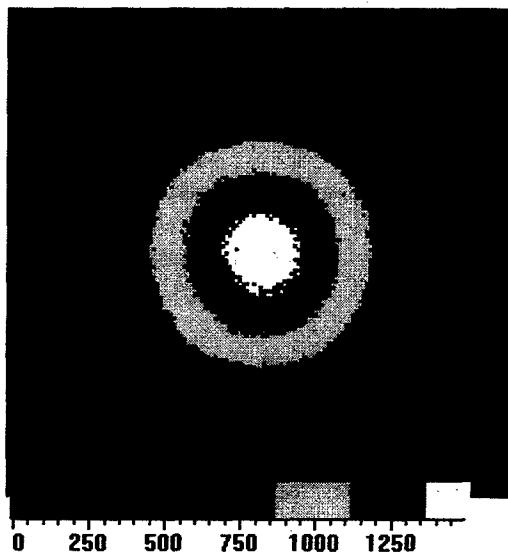


Fig.3 Plasma containment of the rf quadrupole electrodes as seen by a CCD camera placed at the end of the quadrupole axis. The intensity (ion density) levels are shown in the lower left corner.

3 STATUS OF THE PROJECT AND CONCLUSION

The mechanical design and the computer simulations of the device has been concluded. The electron gun test has been carried out at low voltage and, by measuring the electron current with a Faraday cup, a perveance of about $0.2 \mu\text{P}$ has been found..

The construction and the test of all the quadrupole doublets needed for the eb focusing have been done. The 90° bending magnets are also been constructed and tested.

Steering coils with Beam Position Monitor (BPM) has been placed behind the first and at the entrance of the second bending magnet. The system to excite the quadrupole doublet coils inside the rf cylindrical electrodes (as shown in ref.2) are also been tested. The vacuum chamber has also been tested and the cylinder shaped electrodes for the rf quadrupole field are also been tested.

In conclusion, we need only of the voltage pulser to drive the electron gun that will be available in the next month. After that we will be ready for the test of the electron beam transport from the gun to the collector and then for the ion productions and their trapping.

REFERENCES

- [1] G. Brautti, A. Boggia, A. Rainò, V. Valentino, V. Viale "Trapped Ion Source", Proc. of PAC'97 Vancouver (1997).
- [2] G. Brautti A. Boggia, A. Rainò, V. Valentino, V. Viale "Study of a Trapped Ion Source" proc. of EPAC98 Stockholm (1998)
- [3] U: Köster, O. Kester and D. Habs, Rev. of Sci. Inst., Vol. 69, N.3 (1998), 1317.
- [4] P. H. Dawson, Applied Charged Particle Optics, 13B, ed. A. Septier, pag. 173, Academic Press (1980)

EXTRACTOR CONFIGURATIONS FOR A HEAVY ION FUSION VOLUME SOURCE*

O. A. Anderson[†], LBNL, Berkeley, CA 94720, USA

Abstract

In order for volume sources to deliver the current (e.g., 0.8 A of Ar⁺ per module) and brightness necessary for heavy ion fusion (HIF), they must operate at high current density. Conventional extractor designs for 1 to 2 MeV run into voltage breakdown limitations and cannot easily produce the required current rise time (about one microsecond). We discuss two systems that can overcome these volume-extraction problems. Each uses multichannel preaccelerators followed by a single channel main accelerator. Fast beam switching is done in the low energy beamlet stages. A new design, utilizing concentric ring preaccelerators, was recently described for another application [2]. A more conventional design uses a large number of small round beamlets. In either case, the merging beamlets are angled toward the axis, a feature that dominates other focusing. By suitable adjustment of the individual angles, beam aberrations are reduced. Because of the high current density, the overall structure is compact. Emittance growth from merging of beamlets is calculated and scaling is discussed.

1 INTRODUCTION

For extraction of large currents with low emittance for Heavy Ion Fusion (HIF), we consider an arrangement originally proposed for a laser ion source extractor of very high perveance [2]. As shown in Figs. 1 and 2, the beamlets from a system of concentric preaccelerators are angled toward the axis. The inward momentum produces a powerful focusing effect, allowing the main MeV accelerator column (Fig. 1) to operate at low gradient. The angling at various radii can be adjusted to compensate for the aberrations typically present in high perveance extractors.

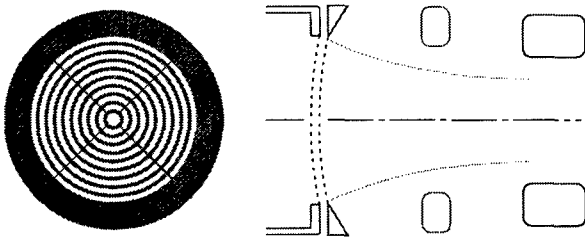


Fig. 1. Sketch of axial and cross-section views of preaccelerator grids and two-gap main extractor grids. In practice, more stages would be used in both sections.

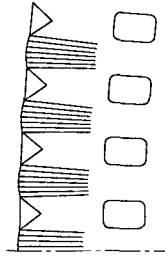


Fig. 2. Detail of preaccelerators.

The present paper studies extraction of HIF beams from conventional gas sources. The 0.75 A beams of Ar⁺ are to be injected at ~1.5 MeV into an array of ESQ channels spaced about 7 cm in both directions. The proposed system is compact and should fit within these dimensions.

As an alternative, we also consider an older arrangement [3] using pencil beams. Figures 3a and 3b compare axial views (before merging) for the old and new designs. In Fig. 3(a) the beamlets are arranged in idealized circular arrays to facilitate the calculations that follow.

Section 2 calculates free field energy and asymptotic emittance for both cases; it also compares transparency and brightness. Aberration control and general design considerations are discussed in section 3.

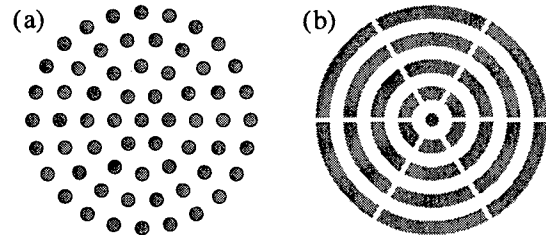


Fig. 3. Axial view of beamlets emerging from (a) beaded ring and (b) solid ring preaccelerators. Occupancy $\eta = 50\%$, number of rings $M = 4$.

2 EMITTANCE FROM MERGING

With X and V_x the rms values of position and velocity, we define the nonrelativistic normalized rms emittance $\epsilon_x^2 \equiv 16\beta^2 X^2 (V_x^2 - X'^2)$; $\epsilon_x = 4\beta X V_x$ for a matched beam. Under standard conditions [4], the asymptotic emittance ϵ_{xf} is then given by $\epsilon_{xf}^2 \rightarrow \epsilon_{xi}^2 + \epsilon_{xm}^2$ with

$$\epsilon_{xm} = \beta X_i (2Q U_n)^{1/2}; \quad (1)$$

ϵ_{xi} and X_i are initial quantities. The emittance due to merging ϵ_{xm} thus adds in quadrature to the initial emittance $\epsilon_{xi} = 4\beta X_i V_{xi}$. Q is the normalized perveance and U_n is the initial normalized free field energy (beam shape factor) discussed in reference [4].

2.1 Round Arrays of Round Beamlets

In the type of array shown in Fig. 3(a), the total number N of pencil beamlets is $N = 3M^2 + 3M + 1$, where M is the number of beaded rings. When N is large [4],

*This work is supported by the Office of Fusion Energy Science, US DOE under contract No. DE-AC03-76SF00098.

[†]Email: OAAAnderson@LBL.gov; also affiliated with Particle Beam Consultants, 2910 Benvenue Ave., Berkeley, CA 94705.

$$U_n^P \rightarrow \frac{4}{N} \left[\frac{3}{4} - \ln 3 - \ln \eta + \frac{3}{8} \eta^2 \right] \equiv \frac{f(\eta)}{N}. \quad (2)$$

The superscript P indicates *pencil* beamlets. The occupancy $\eta < 1$ is defined as the pencil beam diameter divided by the radial spacing. Some values of $f(\eta)$ are

η	0.9	0.7	0.5	0.3	0.1
$f(\eta)$	0.24	0.77	1.75	3.56	7.83

The approximation for U_n is accurate to about 1% for 3 or more rings with $\eta = 0.5$ but becomes less accurate as $\eta \rightarrow 1$. For $\eta \approx 1$, unless N is very large, it is better to use the tables or graphs in Ref. [4].

Exact values of U_n as a function of the number of rings M are given for $\eta = 0.5$ in Table 1. These values are represented with 1% accuracy by

$$U_n^P(\eta=0.5) = \frac{0.59}{M^2(1+1.2/M)} \quad (3)$$

over the practical range $3 \leq M \leq 12$.

2.2 Arrays Of Concentric Tubular Beamlets

We only have room here to discuss the case of parallel propagation where the self field E_s is radial. For tubular beamlets, we use Gauss's law to relate E_s to $\lambda_r(r)$, the line charge within radius r , and integrate E_s^2 . The normalized free field energy U_n within outer radius a is

$$U_n^T = 4 \int_0^a \lambda_r^2(r) / \lambda_r^2 dr - 1 + 4 \ln(2 X_i / a).$$

For the geometry of Fig. 3(b), the integrals are simplified by assuming a constant density within all tubes. (Note: the diameter of the central beamlet equals the thickness of the tubes.) We consider three values for the occupancy η : 1/2, 2/3, and 1 with the results shown in the table.

Table 1: Free field energy comparison

Beaded Rings			Solid Rings		
M	Un eta=1	Un eta=1/2	Un eta=1	Un eta=2/3	Un eta=1/2
1	0.0116	0.2070	0.0	0.0627	0.0897
2	0.0064	0.0882	0.0	0.0156	0.0289
3	0.0034	0.0466	0.0	0.0070	0.0142
4	0.0020	0.0285	0.0	0.0040	0.0085
5	0.0013	0.0192	0.0	0.0026	0.0056
6	0.0009	0.0138	0.0	0.0018	0.0040
8	0.0005	0.0081	0.0	0.0011	0.0023
10	0.0003	0.0053	0.0	0.0007	0.0015
12	0.0002	0.0037	0.0	0.0005	0.0011

For $\eta = 0.5$, the ratio U_n^P/U_n^T tends toward 3.5, which implies the emittance for pencil beams is larger by a factor ~ 1.87 . Some of the values from the table for $\eta = 0.5$ are plotted in Fig. 4. The useful approximation

$$U_n^T(\eta=0.5) = \frac{0.166}{M^2(1+0.9/M)} \quad (4)$$

is accurate to 1% for $2 \leq M \leq 40$.

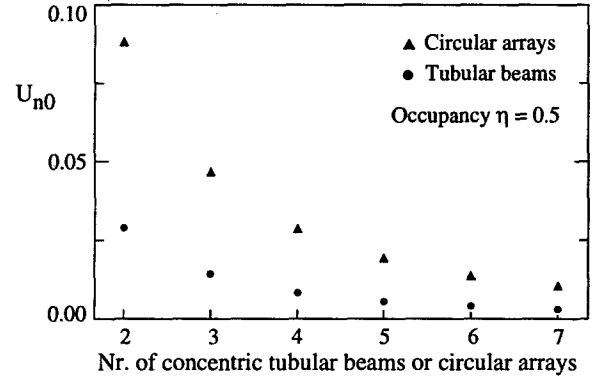


Fig. 4. Normalized free field energy U_n for the two configurations of Fig. 2.

2.3 RMS Beam Size

The maximum radius a_{\max} is defined as the largest radius in Fig. 3 (a) or (b). The rms size X_i as a function of a_{\max} , occupancy η , and number of rings M is easily calculated for beaded rings; see Ref. [4]. For solid rings, we have evaluated X_i for the cases $\eta = 1/2$ (5a) and $\eta = 2/3$ (5b):

$$\frac{4X_i^2}{a^2} = 1 + \frac{2}{m} - \frac{3}{m^2} + \frac{2}{m^2(m^2+2m-1)}; \quad m = 4M+1 \quad (5a)$$

$$\frac{4X_i^2}{a^2} = 1 + \frac{1}{\mu} - \frac{1.5}{\mu^2} + \frac{3}{\mu^2(\mu^2+\mu-0.5)}; \quad \mu = 3M+1. \quad (5b)$$

For the case $M = 4$ illustrated in Fig. 3, the values are $X_i(\eta=1/2) = 0.5a_{\max}(1+0.05)$ and $X_i(\eta=2/3) = 0.5a_{\max}(1+0.03)$. Of course, $X_i(\eta=1) = 0.5a_{\max}$, the usual value for a uniform beam. The corrections are just a few percent and may be neglected for purposes of estimation. For beaded rings, as well, it usually suffices to write $X_i \approx 0.5a_{\max}$.

2.4 Merge Emittance

Equation (1) with (3) and (4) gives approximately

$$\epsilon_{xm}^P(\eta=0.5) \approx \frac{a_{\max}}{M} \frac{\beta}{\sqrt{2}} \left[\frac{0.59Q}{1+\epsilon_p} \right]^{1/2} \quad (6a)$$

$$\epsilon_{xm}^T(\eta=0.5) \approx \frac{a_{\max}}{M} \frac{\beta}{\sqrt{2}} \left[\frac{0.166Q}{1+\epsilon_t} \right]^{1/2} \quad (6b)$$

with correction terms $\epsilon_p = 1.2/M$ and $\epsilon_t = 0.9/M$. For constant current I , $Q \sim I/\beta^3$ and $\epsilon_{xm} \sim \beta^{-1/2} \sim V^{-1/4}$. Omitting ϵ_p , ϵ_t and the corrections to X_i in Eq. (5) gives the rough scaling for large M (SI units, ϵ in π -m-rad):

$$\epsilon_{xm}^P(\eta=0.5) \approx C \frac{Z^{1/4}}{A^{1/4}} \frac{a_{\max}}{M} \frac{I^{1/2}}{V^{1/4}}$$

$$\epsilon_{xm}^T(\eta=0.5) \approx 0.53 C \frac{Z^{1/4}}{A^{1/4}} \frac{a_{\max}}{M} \frac{I^{1/2}}{V^{1/4}}$$

with Z and A the ion charge and mass numbers. The constant $C = 0.02$ with $\eta = 0.5$. For other occupancies, ϵ_{xm}^P can be adjusted using Eq. (2), the table below it, or

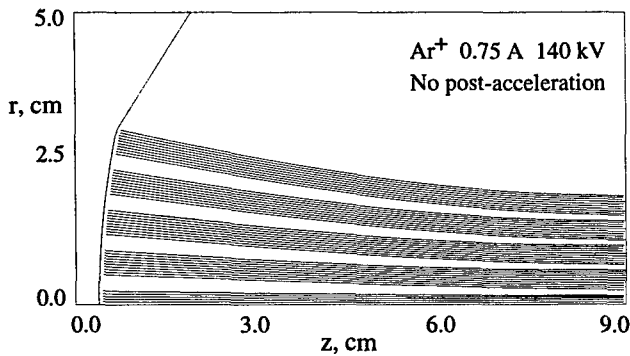


Fig. 5. Beam simulation to check emittance growth from free field energy in merging beams.

the information in Ref. [4]. For ϵ_{xm}^T , one can use Table 1 which, incidentally, indicates that the ratio $\epsilon_{xm}^P/\epsilon_{xm}^T$ becomes even larger than 3.5 as η increases.

2.5 Checking Against Particle Codes

Using WARPxy, the normalized emittance growth term ϵ_m^P for the merging pencil beam case was simulated for uniform transport using parameters representative of injection into an HIF ESQ channel [5]. The result, 0.4π -mm-mr, agreed well with the prediction of Eq. (6a). A typical initial thermal emittance ϵ_{xi} of 0.3π -mm-mr would then give a combined value ϵ_{xf} of 0.5π -mm-mr.

Using a different code [6], tubular beams were simulated as shown in Fig. 5. This case, somewhat different from that analyzed above, studied radial compression in drifting beams; ϵ_{xm}^T was predicted by (6b) to be roughly 0.6π -mm-mr. Fig. 6 shows the exit emittance diagram at the waist. The value 0.41 for emittance is reasonable since the beamlets are not yet completely merged at this point.

2.6 Other Differences

Pencil beams and tubular beams differ in other ways than emittance growth. The extraction hardware may be easier to fabricate in the first case. But a tubular beam design has the advantage that the essentially 1-D radial geometry precludes non-linear field distortion from neighboring

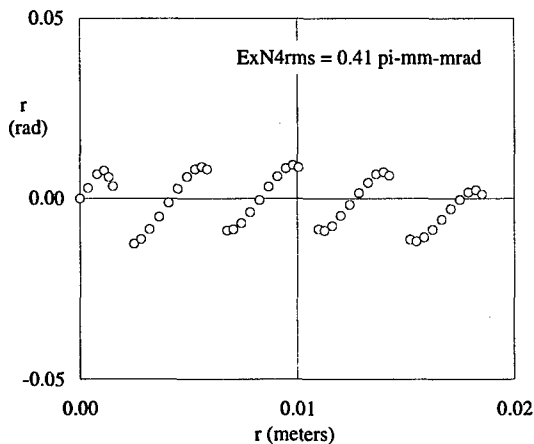


Fig. 6. Emittance phase plot at exit of Fig. 5.

beamlets that may occur with pencil beams before merging begins. Also, for a given occupancy η , the transparency for tubular beams is higher by the factor $4/\pi\eta$, increasing the brightness for cases of fixed current density.

3 EXTRACTOR SYSTEMS

In some high perveance designs for HIF, the high-voltage portion may produce beam aberrations. In the two-stage system of Figs. 1 and 2 the preaccelerator beamlets can be steered to reduce these aberrations. Figure 7 shows phase plots at the exit for a laser plasma extractor design with 40 A of Xe^{+8} . The main extractor gap was smaller than the diameter of the preaccelerator array, producing the overfocusing of outer beamlets seen on the left side of Fig. 7. Beam steering removed most of the aberrations.

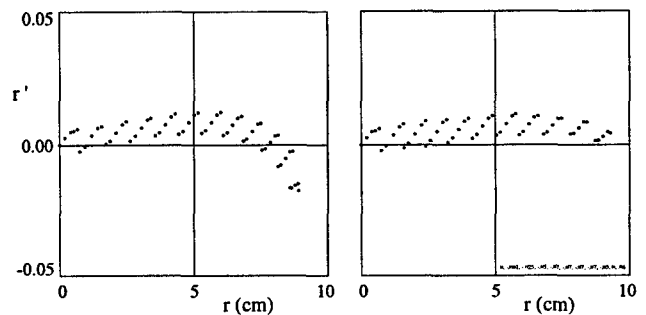


Fig. 7. Aberration control by pre-steering of beamlets: uncorrected (left), corrected (right).

The preaccelerators and the main accelerator channel for extraction from a conventional Ar^+ source have been studied separately. Using the above analysis, we find that the number of rings M required to produce an acceptable emittance is not so large that the individual units become impracticably small. The ring-to-ring spacing will be typically ~ 0.7 cm so that construction should not be difficult. The electric field for the preaccelerator cases studied is well under 100 kV/cm.

The length of the main column is controlled by the curvature of the preaccelerator exit array seen in Fig. 1. Preliminary simulations show that it should be possible to accelerate the beam to 1.5 MeV and compress it to the required diameter while maintaining an acceptable field gradient. Further studies are in progress.

4 REFERENCES

- [1] E.P. Lee, et al., *Fus. Eng. Des.* **32-33**, 323 (1996).
- [2] O.A. Anderson and B. Grant Logan, "Low Emittance Beam Extraction from Laser-Driven Multicharged Ion Sources," *Proc. 6th EPAC Conf.*, Stockholm, 1998.
- [3] O.A. Anderson, proceedings of US-Japan Workshop on Negative Ion Beams, JAERI, Japan, Nov. 14-17, 1988.
- [4] O.A. Anderson, "Emittance Growth from Merging Arrays of Round Beamlets," *Fusion Eng. and Design* **32-33**, 209-217 (1996).
- [5] David P. Grote, personal communication, LBNL, March 1999. The parameters were provided by J. W. Kwan.
- [6] S. Humphries, *J. Comput. Phys.* **125**, 488 (1996).

HIGH-CURRENT, HIGH-DUTY-FACTOR EXPERIMENTS WITH THE H⁺ ION SOURCE FOR THE SPALLATION NEUTRON SOURCE*

M.A. Leitner[#], D.W. Cheng, R.A. Gough, R. Keller, K.N. Leung,
S.K. Mukherjee, P.K. Scott, M.D. Williams; LBNL, Berkeley, CA

Abstract

The ion source for the 1 MW Spallation Neutron Source (SNS) is required to provide 35 mA of H⁺ beam current at 6% duty factor (1 ms pulses at 60 Hz) with a normalized rms emittance less than 0.15π mm mrad. The H⁺ beam will be accelerated to 65 keV and matched into a 2.5 MeV RFQ. The ion source is expected to ultimately produce 70 mA of H⁺ at 6% duty factor when the SNS is upgraded to 2 MW of power. For this application, a radio-frequency driven, magnetically filtered multicusp source is being developed at Berkeley Lab. The design of this new ion source is directed towards operation at the required high duty factor. Experimental results of the ion source operated in pure volume production mode (without cesium) and in hybrid mode (with cesium released into the source) are compared. An improved cesium dispensing system will be presented.

1 ION SOURCE DESIGN

A schematic of the SNS R&D #1 H⁺ ion source [1] is shown in figure 1. The ion source is mounted inside a reentrant cylinder to move the ion source into the vacuum vessel. This enhances the vacuum pumping of the extraction gap. The source plasma chamber (10-cm-long by 10-cm-diam.) is made out of a copper cylinder with a back plate at one end and an outlet electrode at the other end. The plasma is confined by the longitudinal line-cusp fields produced by 20 rows of water-cooled, samarium-cobalt magnets that surround the source chamber and transverse magnets on the back flange.

The hydrogen plasma is produced inductively by up to 65 kW of pulsed 2 MHz RF power. RF coupling is accomplished via a 2 1/2-turn, porcelain-coated (water-cooled copper tubing) antenna connected to a matching network that matches the impedances of RF amplifier and

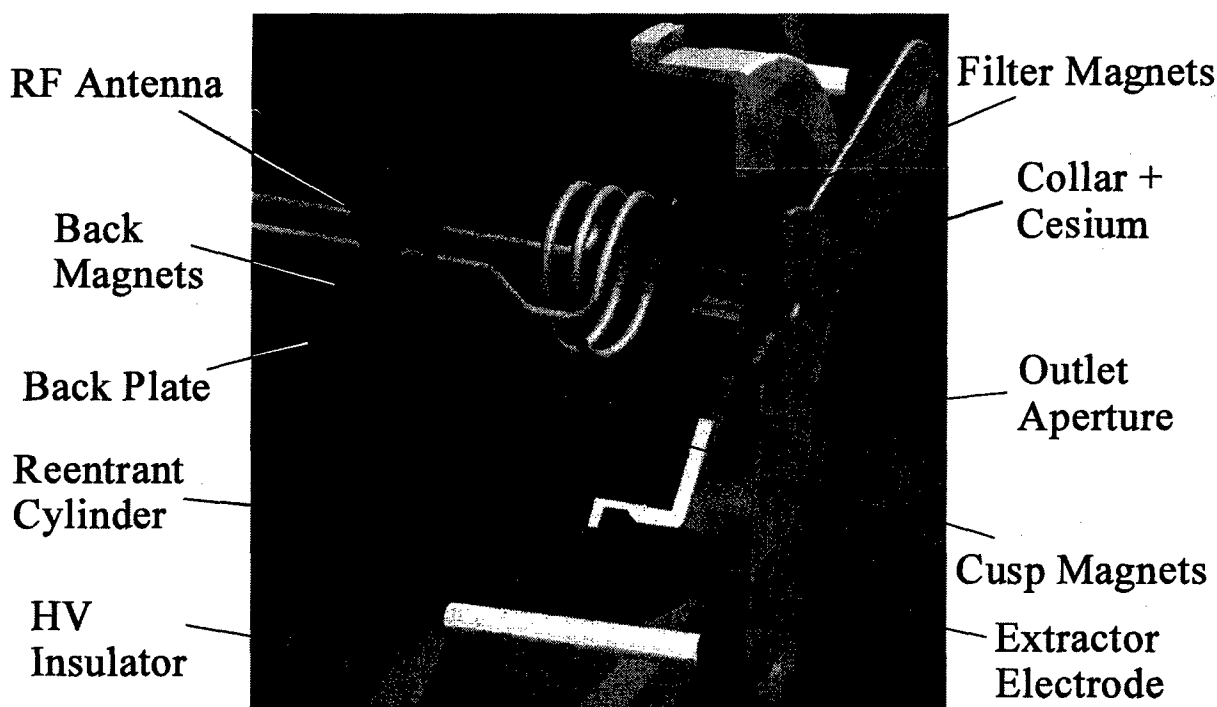


Figure 1: Schematic view of SNS R&D #1 H⁺ ion source.

Work supported by the Director, Office of Science, Office of Basic Energy Sciences, of the US Department of Energy under Contr. No. DE-AC03-76SF00098.

* Email: MLeitner@lbl.gov

plasma. To minimize RF noise interference, the amplifier and matching-unit are installed on the ion source high voltage (65 kV) platform, and are completely enclosed by a copper-plated steel shielding box.

Electrons supplied by a hairpin tungsten filament installed at the source back-flange assist starting of the ion source pulses. For cleaner discharge conditions, the filament can be replaced by an UV flash lamp or an inexpensive UV laser light system to produce primary photoelectrons.

A pair of water-cooled permanent magnet filter rods placed near the outlet electrode creates a narrow region of transverse magnetic field (200 G) that divides the source chamber into the ("hot-plasma") discharge region and the ("cold-plasma") H⁺ extraction region. The purpose of the hot plasma region is to produce excited H₂⁰(v") molecules, which can diffuse freely through the magnetic filter field. Hot electrons, which could easily destroy H⁺ ions, are deflected by the magnetic filter field. Therefore, they cannot reach the extraction area.

Cold electrons are trapped, diffuse through the filter field, and produce H⁺ ions in the outlet region by dissociative attachment to the excited H₂⁰(v") molecules. The removal of hot electrons is enhanced by installing a collar in front of the extraction hole. The deflected electrons are captured in this area. The optimum dimensions of the collar have been determined experimentally (15-mm-diam., 15-mm-long) for the 200 G filter field.

The RF-driven source is operated at a continuous hydrogen gas flow of 20-30 sccm. Beam is extracted at 35-65 kV across a single extraction gap and collected in a water-cooled double Faraday cup, which allows one to independently measure the H⁺ current and electron content in the beam. The Faraday cup has been calibrated by using helium as the discharge gas. Since He⁺ ions are extremely difficult to form, no current should be measured in the H⁺ Faraday cup. This was verified with an extracted electron beam of several amperes of current.

2 OPERATION WITHOUT CESIUM

More than 36 mA of H⁺ ion current can be extracted from the SNS R&D #1 ion source if no cesium is added. With proper tuning of the RF matching-section the e⁻-to-H⁺ current ratio can be reduced to about 27 at the highest H⁺ current levels, but it can be as high as 50. Due to the high electron current (0.9 to 2 A) in pure volume production mode, the duty factor is limited by the extraction power supply. If the power supply cannot deliver the beam power, the extraction voltage decreases during the beam pulse. As a result, the ion beam impinges on the extractor electrode because of perveance mismatch, and spark-downs occur.

Table 1 summarizes the peak performance of the ion source:

Table 1: SNS R&D #1 ion source performance without cesium.

H ⁺ current	36 mA
e ⁻ current	960 mA
e ⁻ /H ⁺ ratio	>27
RF power	63 kW
Duty factor*	< 0.25 %
Extraction voltage	27 kV
Extraction gap	4 mm
Extraction hole	3.5 mm radius
Gas flow through extraction hole	12 sccm

* Imposed by extraction power supply

3 OPERATION WITH CESIUM

Installing a collar around the outlet aperture can reduce the electron portion in the extracted beam. In such an arrangement, a small cylinder (15-mm-diam., 15-mm-long) is mounted on the outlet electrode, facing the plasma side (see Fig. 1). This collar can also be used to accommodate (inside radial grooves) tiny cesium getter-

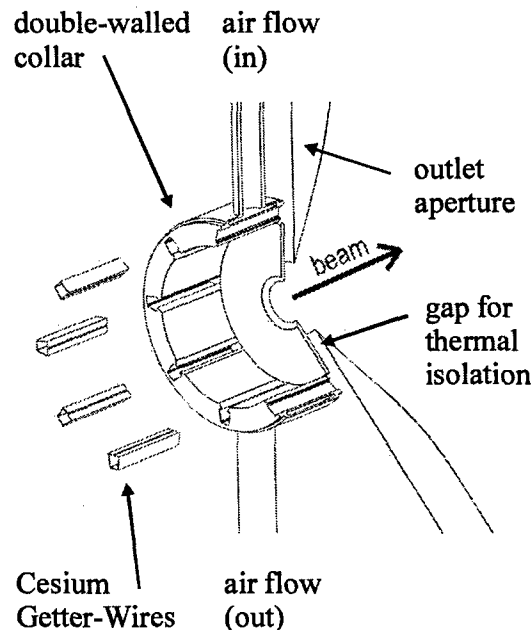


Figure 2: View of the new SNS H⁺ ion-source collar arrangement. Eight getter containers which slide into the slots located in the double-walled collar release a trace amount of cesium into this region.

containers [2]. Such a configuration has been developed for the SNS H⁺ ion source, and is shown in figure 2.

The stainless-steel double-walled collar is thermally insulated from the rest of the ion source. Active cooling or heating - depending on the source duty factor - is possible by passing a temperature-regulated airflow through the collar jacket. The collar is massive enough to maintain a uniform temperature distribution along its inner surface. Cesium coverage of the collar surface lowers the work function, thus increasing the H⁺ ion density in the plasma by surface production mechanism. The best source performance can be achieved at a surface temperature of around 200 degrees Celsius.

Uncooled, the new collar reaches a temperature of ~400 degrees Celsius at 50 kW RF input power at 12% duty factor. If cooled by pressurized air, the collar temperature could be reduced to 30 degrees Celsius. We have installed a heating element around the air input-line (outside the vacuum) to allow adjustment of the collar temperature independent from plasma heating (i.e. source duty factor).

This new cesium dispensing system allows very flexible source operation, which is not achievable with a cesium oven alone. In addition, since only trace amounts of cesium are dispensed into the ion source, no high-voltage spark-down problems occur in the extraction gap or in the downstream accelerator components.

After mounting the cesium dispensers inside the collar, maximum, stable source-performance can be achieved after only 1/2 hour of source operation without special conditioning procedures. If the source is restarted up after previous operation (i.e. without breaking the vacuum) this time is reduced to ~15 minutes. As shown in figure 3, 43mA of H⁺ have been achieved at 12% duty factor (1 ms pulse width)

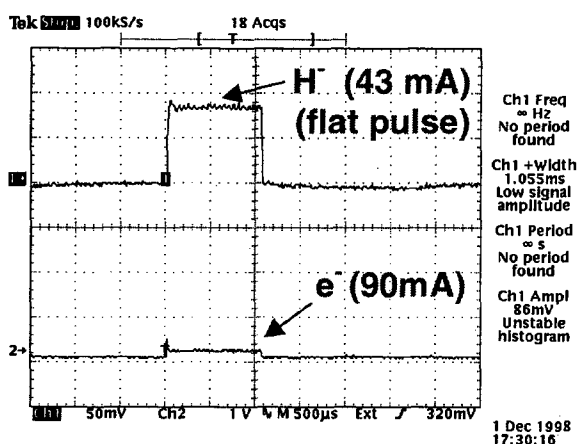


Figure 3: 43mA of H⁺ have been produced at 12% duty factor (1 ms pulse width) with trace amounts of cesium released into the ion source. At the same time, the extracted electron current has been reduced to 90 mA. The ion beam pulse uniformity is within 1.2% (~0.50 mA), the pulse-to-pulse reproducibility within 0.6% (~0.25 mA).

pulse length, 25kW RF input power, 25 sccm hydrogen gas-flow, extraction hole: 3.5 mm radius) with the described collar configuration. The ion beam pulse uniformity is within 1.2% (~0.50 mA), the pulse-to-pulse reproducibility within 0.6% (~0.25 mA). At the same time the extracted electron current has been reduced to 90 mA, lowering the e⁻/H⁺ ratio to a value of 2. (During these experiments, the outlet aperture was electrically connected to the ion source body.) Only traces of cesium have been released into the ion source, since the collar always stayed below the temperature (~500 degrees Celsius) needed to start evaporation of the cesium getter wires.

4 CONCLUSION

Figure 4 compares the SNS R&D source peak-performance without and with cesium released into the plasma chamber. By releasing cesium into the plasma chamber, the SNS ion-source requirements can be achieved at much lower RF input power. Furthermore, the extracted electron current is drastically reduced. Source start-up could be significantly simplified by introducing an improved collar design.

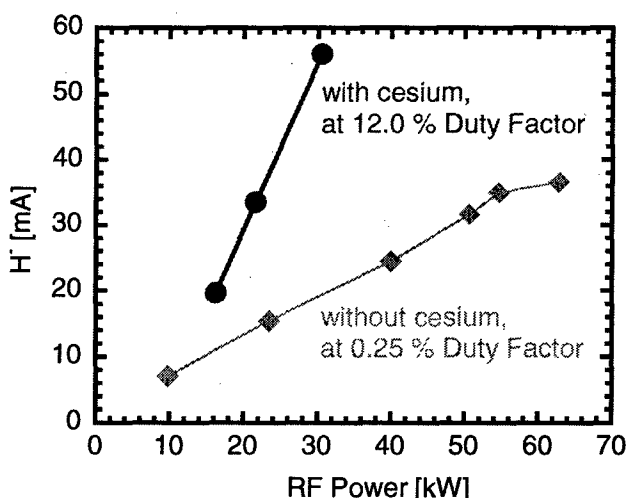


Figure 4: Comparison of SNS R&D #1 source performance without and with cesium released into the plasma chamber. In pure volume production mode the source duty factor is limited by the extraction power supply.

5 REFERENCES

- [1] M.A. Leitner, R.A. Gough, K.N. Leung, M.L. Rickard, P.K. Scott, A.B. Wengrow, M.D. Williams and D.C. Wutte, "Development of the radio frequency driven H⁺ ion source for the National Spallation Neutron Source", Rev. Sci. Instrum. **69**, 962 (1998)
- [2] SAES Getters U.S.A., Inc., 1122 E. Cheyenne Mt. Blvd., Colorado Springs, CO 80906 (<http://www.saesgetters.com>)

MECHANICAL DESIGN OF THE PROTOTYPE H⁻ ION SOURCE FOR THE SPALLATION NEUTRON SOURCE*

S. K. Mukherjee, D. Cheng, M. A. Leitner, K. N. Leung, P.A. Luft, R.A. Gough, R Keller,
M. D. Williams, LBNL, Berkeley, CA

Abstract

The mechanical design of the prototype H⁻ ion source for the Spallation Neutron Source (SNS) is presented. Experience obtained in the ongoing SNS R&D program is being utilized in the current design. The physics design parameters require a 2 MHz RF-driven multicusp ion source operated at 50kW, pulsed (6% duty factor) RF-power. The four major components (plasma-generator, cesium collar, outlet electrode, the source tilt mechanism) of the mechanical packaging of the ion source will be presented in details. The mechanical design has the unique capability of tilting the ion source in one plane in order to compensate the H⁻ ion beam deflection caused by a strong magnetic field across the outlet aperture. This B- field deflects electrons in the extracted beam back to the outlet electrode. An articulating strut system will provide accurate control over the adjustable tilt angle. This new ion source design will provide easy serviceability of maintenance parts like the RF-antenna and the cesium dispensing system.

1 INTRODUCTION

Experiments [ref.1] performed with an existing volume H⁻ source helped establish the design requirements for the prototype ion source for the SNS project. A plasma chamber size of 11.5 cm in diameter and 11.5cm in length has been found to be an optimum size for the prototype ion source. Installation of a cesium collar near the outlet electrode proved the advantage of reduced extracted electron current together with a significant increase in the H⁻ output. The optimum operating temperature of the collar was found to be 300° C. The location of the filter-magnet from the center of the outlet electrode was optimized to 15 mm. The above-mentioned results, helped establishing the base line design parameters.

2 MAJOR COMPONENTS

The modular design approach of the prototype source is meant to provide easy access to serviceable components with minimum changeover time.

*This research is sponsored by the Lockheed Martin Energy Research Corporation under the U.S. Department of Energy, Contract No. DE-AC05-96OR22464, through the Lawrence Berkeley National Laboratory under contract No. DE-AC 03-76SF00098.

Email: skmukherjee@lbl.gov

There are four major sub-assemblies in this design: (1) The plasma chamber and cusp magnet assembly, (2) The outlet electrode assembly, (3) The back flange assembly and (4) The tilt mechanism. Each sub-assembly has its cooling system for removing the heat generated by the plasma particles hitting the chamber wall. Figure 1 shows the general arrangement of the prototype source.

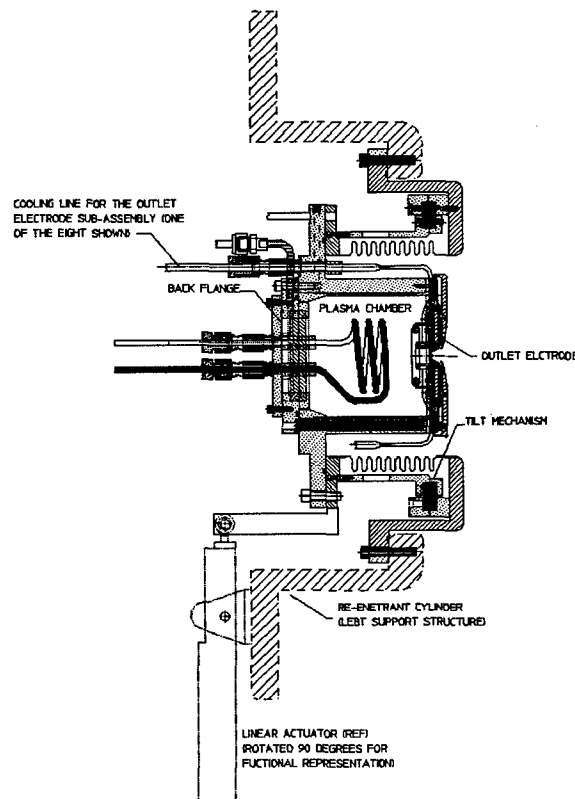


Figure-1 Ion source general layout

2.1 Plasma Chamber

The plasma chamber is machined out of 316L stainless steel and welded with another concentric chamber that holds the twenty NbFeB cusp magnets. The thin annular space between these two bodies is utilised as a cooling jacket. There are four cooling circuits for uniform heat removal from the twenty rows of magnets. The back flange and the outlet electrode at the two ends terminate the plasma

2.2 Outlet Electrode

The outlet electrode sub-assembly (see figure-2) consists of the outlet electrode itself, the electron deflection magnets, the electron dump electrode and the cooling channels for each area. The filter magnet and the cesium collar assemblies are also mounted from the outlet electrode. Eight cooling lines are oriented azimuthally and they come out through the corresponding vacuum feed-through on the main flange of the plasma chamber assembly. This design allows us to remove the outlet electrode sub-assembly from the source in one package and it provides easy service of the cesium collar. The alignment of the electrode with respect to the plasma chamber is critical. Use of an accurate fixture during mounting the pre aligned electrode assembly will enable us to reach the alignment target described in section 4.

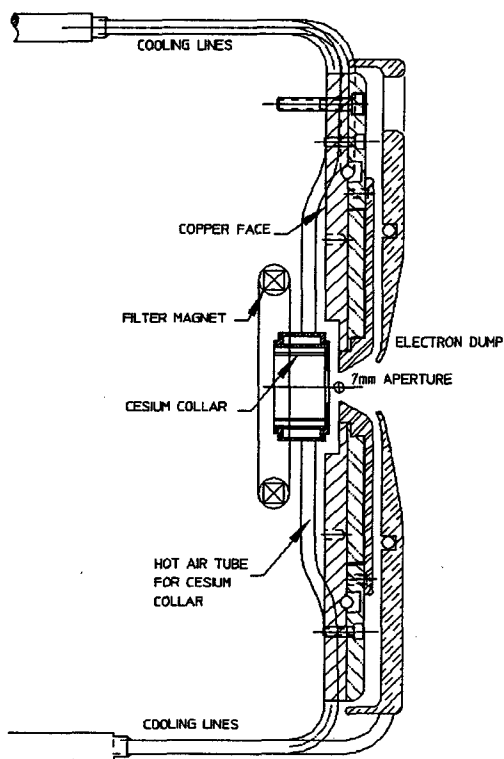


Figure-2 Outlet Electrode Layout

2.3 Back Flange Assembly

The back flange (see figure-3) has four magnet slots and a cooling passage machined in the 304 stainless body. A hidden O-ring serves as vacuum seal between the plasma chamber and the back flange. The RF antenna is mounted through another smaller flange, which facilitates easy

repair of feed through components. The two flanges are vacuum-sealed by o-ring. There are two -quartz-window flanges, welded on the back flange. They are needed for laser beam for plasma starting. The back flange sub-assembly is attached with the main flange of the plasma chamber. By removing the back flange section, the RF antenna can be replaced without disturbing the alignment of the ion source.

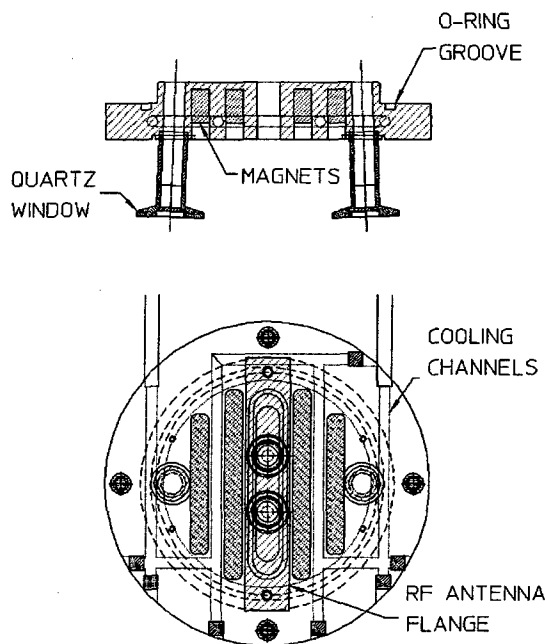


Figure-3 Back Flange Layout

2.4 Tilt Mechanism

To compensate for the deflection of the H^+ ion beam due to the strong magnetic field across the outlet electrode, the source has to be tilted. The maximum tilt range is 0 to 6 degrees. This is achieved by mounting the whole assembly on two flexural pins and a bellows connection that will allow the outer support cylindrical structure of the source assembly to articulate in the horizontal plane. The movement of the stainless steel bellows is limited to three degree. The bellows is adjusted to three degree at the neutral position. A stepper motor controlled actuator can rotate the rear end of the source assembly through the required travel. Figure-4 shows the three positions of tilt of the ion source. The resolution of the actuator movement is accurate enough to articulate the source in very small increments to suit the operating criteria of the source. The source is prevented from tilt past the zero position by a physical stop in addition to the limit switches.

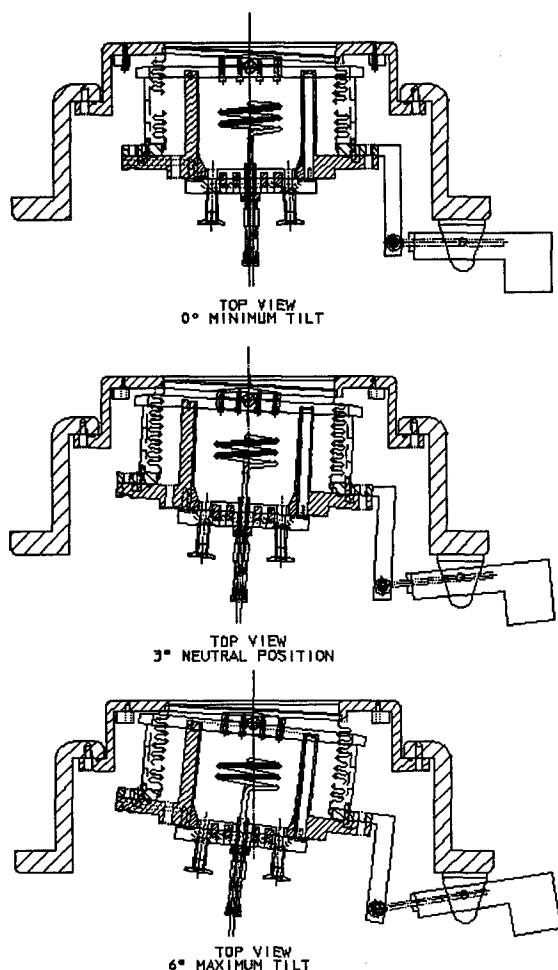


Figure-4 Ion source tilt position 0-6 degrees range

3 COOLING SYSTEM

The heat to be removed from the plasma chamber is approximately equal to the RF power consumption of the source (50 kW at 6% duty factor). The plasma chamber is bombarded by the hot-electrons at the locations of the cusp permanent magnet. This heat load is removed by the water jacket surrounding the whole plasma chamber. Similarly, the magnets in the back flange are cooled by the water channels machined in the body of the flange. Heat is also added in the form of hot air flow to the cesium collar from outside. This collar is maintained at the optimum operating temperature of 300° C. The hot-collar radiates heat to the outlet electrode inside face. To prevent the radiation heat transfer from the cesium collar, a gap is maintained between the collar and the electrode plate. In addition, the copper surface of the outlet electrode sub-assembly has a cooling line for removal of heat produced by deflected electrons from the filter magnets. The electron dump electrode also has its individual cooling line. These cooling lines are accessed through the insulated vacuum feed through in the main flange of the ion source.

4 ALIGNMENT

The ion source positional accuracy is critical for ion beam optics in the low energy beam transport (LEBT) section. Figure-5 shows ion beam deflection in the SNS LEBT if one of the electrostatic lenses is shifted transverse to the beam direction (calculated by the 3D optics code KOBRA).

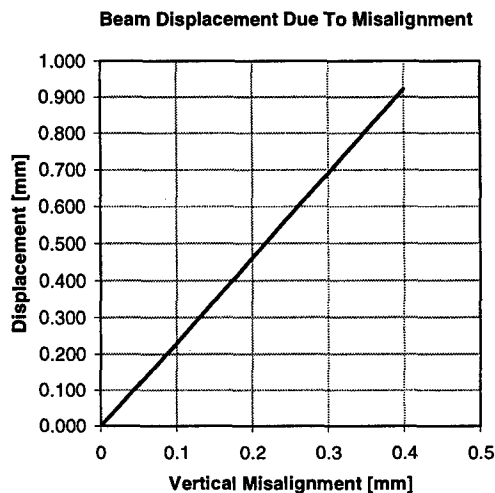


Figure-5 Effect of lens misalignment

As shown in the graph a lens-transverse-misalignment of .05mm would result in a beam deflection of .1mm out of the center position. The alignment target $\pm .05$ mm in X and Y planes, (perpendicular to the beam direction), is achieved by using a common axis reference between the source and the LEBT. The source tilt mechanism is kept on axis by the precision flexural pins and the position accuracy between the removable flanges is controlled by the use of precision dowel pins.

This new H ion source is being fabricated and testing is scheduled to start in June, of this year. Results of the source operation will be reported in the near future.

5 REFERENCES

- [1] M. A. Leitner, D.W. Cheng, J. Greer, K.N. Leung, S. K. Mukherjee, P.K. Scott, M.D. Williams, "High-Current, High-Duty-Factor Experiments with the RF driven H Ion Source for the Spallation Neutron Source", these proceedings.
- [2] D.W. Cheng, M.D. Hoff, M. A. Leitner, J.W. Staples, M.D. Williams, R. A. Gough, R. Keller, K.N. Leung "Design of the prototype Low Energy Beam Transport Line (LEBT) for the Spallation Neutron Source", these proceedings

Measurements on the LANSCE Upgrade H-Source*

R. Thoma^{*}, R. Gough, R. Keller, K. Leung, D. Meyer[†], M. Williams, Lawrence Berkeley National Laboratory, O. Sanders, W. Ingalls, B. Prichard, R. Stevens, Los Alamos National Laboratory

Abstract

For the upgrade of the Los Alamos Neutron Science Center (LANSCE) Facility, the Lawrence Berkeley National Laboratory is developing an H⁻ ion generator that can deliver the required beam. The output current has to be 40 mA at a repetition rate of 120 Hz and a pulse length of 1 ms (12 % duty factor), and the normalized emittance must be less than 0.1π mm mrad. During the last years, we improved the so-called surface-conversion source for the generation of higher H⁻ currents. Experiments with magnetic filter fields have shown that the output current increases linearly with the discharge power in contrast to saturation when operating without a filter. In the latest source configuration, the filter field is generated by the cusp magnets itself, resulting in a simple and reliable setup. In this paper we present measurements on the output current as a function of discharge power. We discuss operation conditions of the source at the required 40 mA output current. Furthermore, preliminary results using 2 MHz RF power with an antenna for plasma generation will be described.

1 INTRODUCTION

The requirement for higher intensity H⁻ ion beams for the upgrade of the Los Alamos Neutron Science Center (LANSCE) Facility necessitated the development of a new ion source. Lawrence Berkeley National Laboratory has been contracted by Los Alamos National Laboratory to develop an H⁻ ion source, which can deliver the required beam parameters, demanded by the LANSCE upgrade. In particular the output current has to be increased from 16 to 40 mA, whereby the beam emittance may not increase. Furthermore, the source must operate reliably at the prescribed 12 % duty factor (1 ms pulse length at 120Hz).

The Ion Beam Technology (IBT) Program at LBNL is developing the so-called surface converter source for the generation of negative ions for a number of years. This type of source was chosen as a candidate for the LANSCE upgrade because it is known as a very effective and

[†]Present Address: KVI, Atom Physics Group, Zernikelaan 25, 9747 AA Groningen, The Netherlands

reliable source. Although this principle was expected to have an intrinsic current limit, experimental studies at LBNL demonstrated that the output current can be increased linearly with discharge power when a magnetic filter field is applied, which prevents energetic electrons reaching the converter region [1]. Covering the converter surface with a thin layer of cesium can increase the efficiency of the source.

2 EXPERIMENTAL SETUP

The multicusp surface conversion source is under investigation at LBNL for a long time [2,3]. It is primarily composed of a plasma chamber and a negatively biased converter. The ions present in the hydrogen plasma (H⁺, H₂⁺, H₃⁺) are accelerated towards the converter surface. H⁻ can be formed either through a back scattering process or a sputtering process when the positive ions collide with the converter surface.

The LANSCE upgrade source consists of a cylindrical stainless steel plasma chamber, in which the converter is mounted along the axis. The diameter and length of the chamber are 250 mm and 230 mm, respectively. Outside the chamber 18 columns of magnets provide the cusp field. Fig. 1 shows a 3-D cutaway picture of the source.

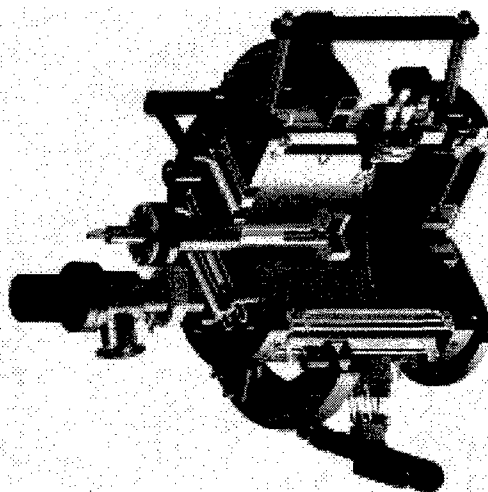


Figure 1: The LANSCE upgrade source. Shown here is the plasma chamber with the magnets and the filaments. The converter is mounted to the end plate. In the front

*This Work was supported by Los Alamos National Laboratory and the Department of Energy under Contract No. AC03-76SF00098.

^{*} Email: rwthomae@lbl.gov

plate a collar with two magnets is used to deflect the electrons.

The position and length of the filaments are arranged in such a way that their tips are surrounded by a magnetic field of approximately 30 Gauss. This is sufficient to prevent energetic electrons to reach the converter and extraction regions. The filaments are biased at 70 V negative with respect to the source body. They are heated by 5 V and 100 A each. The potential of the converter is varied in between -200 to -400 V. Cesium is brought into the plasma chamber by heating the oven and the valve to 200° to 300° C. During operation, the converter current, the repeller current, and the Faraday cup current are monitored. More detailed information on the design and construction of the source can be found in reference [4]. Fig. 2 shows a photograph of the source in the test stand.

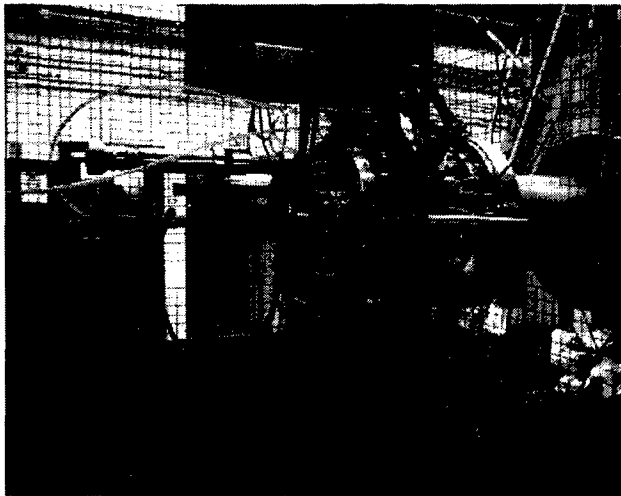


Figure 2: Photo of the source in the test stand.

3 EXPERIMENTAL RESULTS AND DISCUSSION

After assembling the source has to be conditioned for at least 10 hours. Conditioning is done by heating the source with filaments and plasma discharge. Then cesium is injected into the source chamber via a nozzle by means of heating the reservoir and oven valve. For an optimum oven temperature, the H^- output current is enhanced by more than a factor of 10. The cesium from the oven covers the surface of the plasma chamber and the converter surface. During the discharge pulses, the positive ions, which are present in the plasma, are accelerated across the plasma sheath formed in front of the converter surface. They can sputter a portion of the cesium coverage. The amount of cesium coverage on the converter surface is especially important for efficient H^- generation. It is therefore substantial to control this parameter. There are 3 different ways:

- i) A Change of the duty factor, either pulse length or repetition rate, influenced the amount of sputtered cesium. Increasing the duty factor can reduce the thickness of the cesium layer.
- ii) A change in converter voltage can modify the ion energy and therefore the sputter coefficient. A higher converter voltage reduces the thickness of the cesium layer.
- iii) A change of the converter surface temperature can influence the cesium coverage. Increasing the converter surface temperature (e.g. by reducing the cooling water flow) can reduce the thickness of the cesium layer.

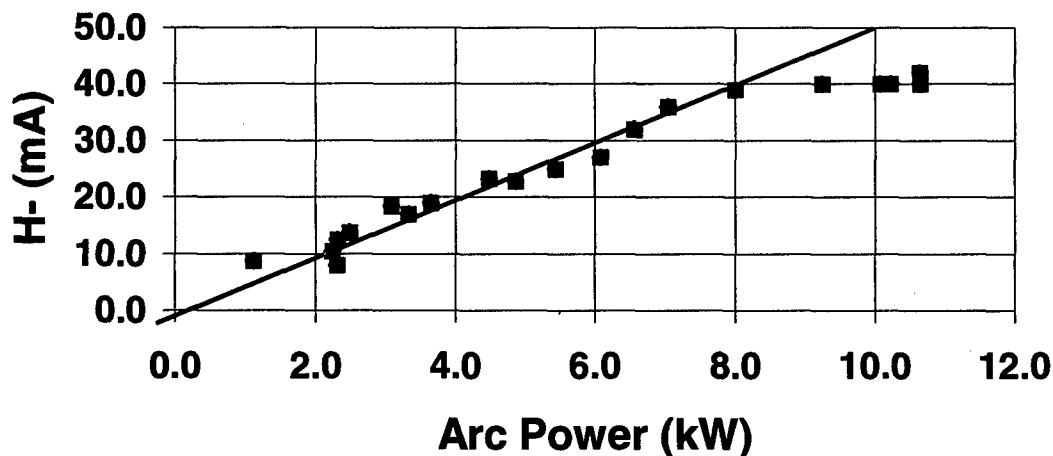


Figure 3: H^- current as a function of discharge power. The arc and converter voltages are 70 and 300 V, respectively. The pulse length and repetition rate are kept constant at 1.2 ms and 100 Hz (12% duty factor), respectively. The cesium coverage is optimized by adjusting the converter surface temperature.

For LANSCE operation the duty factor is fixed and only ii) and iii) can be applied. Because the converter voltage is limited by arcing towards the plasma, we believe that iii) is the best approach for adjustment of the converter surface cesium coverage.

In Fig. 3 the H^- current (measured in a Faraday cup, placed 3 cm behind the outlet electrode) is shown as a function of the discharge power. The arc and converter voltages are 70 and 300 V, respectively. The pulse length and repetition rate are kept constant at 1.2 ms and 100 Hz (12% duty factor), respectively. The cesium coverage is optimized by adjusting the converter surface temperature. It is clear from the figure that the current increases linearly with the discharge power from 10 mA at 2 kW to 40 mA at 8 kW. For larger values of discharge power the current saturates. We believe that this is due to the fact that at higher power levels more impurities are present, which has also been observed with a residual gas analyzer.

In Fig. 4 the pulse shape is plotted for an H^- current of 44 mA. The discharge power amounts to 8.6 kW. In this example the cesium coverage on the converter was optimized via the repetition rate, which is 190 Hz at a pulse length of 1.2 ms (duty factor 23%). The peak at the beginning of the pulse indicates a slightly overcesiated converter.

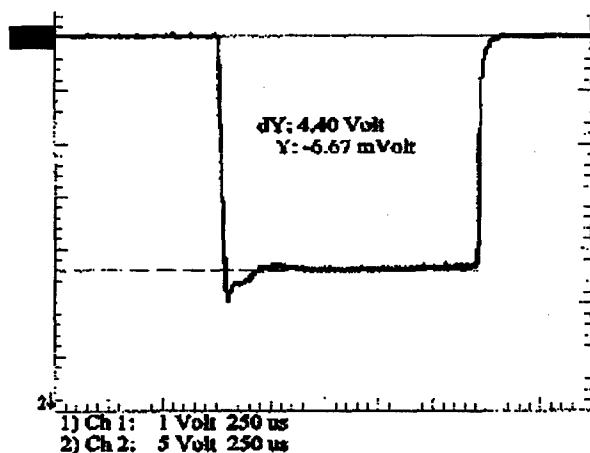


Figure 4: Pulse shape of a 44 mA H^- beam. The arc power amounts to 8.6 kW at a pulse length of 1.2 ms and a repetition rate of 190 Hz.

Recently we try to improve the overall efficiency of the source by using RF power to generate the plasma. Therefore, the filaments have been removed and are replaced by a quartz antenna as shown in fig. 5. The antenna is connected to a 2 MHz power supply via a

matching network. In contrast to the operation with filaments the power load of the source for RF operation is reduced by at least a factor of two.



Figure 5: The endplate of the source with the quartz RF antenna. Note that a silver plated copper wire is inside the quartz tube. The antenna is water-cooled. Also shown is the converter.

First operation without cesium injection shows that plasma generation is possible. However, the neutral gas pressure has to be increased compared to operation with filaments. Work is still in progress to optimize the source operation with RF discharges.

4 ACKNOWLEDGMENTS

We would like to thank S. B. Wilde, P. J. Rosado, T. A. McVeigh, P. Wong, L. W. Mills, and P. Kozy for their technical assistance.

5 REFERENCES

- [1] C.F.A. van Os, K. N. Leung, and W. B. Kunkel Appl. Phys. Lett. 57 (9), 27 Aug. 1990.
- [2] K. W. Ehlers and K. N. Leung, Rev. Sci. Instrum. 51, 721 (1980).
- [3] K. W. Ehlers and K. N. Leung, Rev. Sci. Instrum. 53(6), 803 (1982).
- [4] M. Williams, R. Gough, K. Leung, R. Low, C. Matuk, R. Thomae, S. Wilde, this proceedings

DESIGN OF ION SOURCE FOR LANSCE UPGRADE*

M. Williams, R. Gough, K. Leung, R. Low, C. Matuk, R. Thomae, S. Wilde
E. O. Lawrence Berkeley National Laboratory, Berkeley, CA 94720

Abstract

The upgrade of the Los Alamos Neutron Science Center (LANSCE) Facility will require high intensity H^- beams. Lawrence Berkeley National Laboratory (LBNL) has been contracted by Los Alamos to develop an H^- ion generator that will meet the LANSCE upgrade requirements. H^- current is to be increased from the present 18 mA to 40 mA. The current LANSCE ion source uses surface conversion process and extracts ions radially. Two tungsten filaments are used as cathodes. The ion source designed by LBNL is also a surface conversion type source but the ions are extracted axially. This design allows six or more tungsten filaments to be installed radially so that the magnetic field of the permanent magnets on the cylindrical wall provides a magnetic filter field. This filter field prevents energetic electrons from entering the central plasma region where they could strip the H^- ions. The LBNL designed ion source has been operated successfully at the design parameters, 40 mA H^- at 12 % duty factor with 1 msec pulses. This paper describes the design and fabrication of the ion source.

1. INTRODUCTION

The next generation spallation neutron sources, such as the upgrade of the Los Alamos Neutron Science Center (LANSCE) Facility will require high intensity negative hydrogen (H^-) beams. Lawrence Berkeley National Laboratory has been contracted by Los Alamos National Laboratory to develop an H^- ion generator that can meet the upgrade LANSCE neutron source requirement. Specifically, the output current of the new H^- ion source has to increase from 16 to 40 mA. In addition, source emittance, reliability, and availability will need to be improved. All of which must be achieved while operating under the facility's prescribed 12% duty factor (1 ms pulse at 120 Hz).

In order to meet the LANSCE source requirement, the Ion Beam Technology (IBT) Program at LBNL chose the surface-conversion multicusp ion source as the base candidate. The present LANSCE H^- source is also a surface-conversion source, however the H^- output current does not increase much beyond 20 mA with higher discharge power.¹ Previous experimental study at LBNL demonstrated that if the surface-conversion source is operated with a magnetic filter, the H^- output current generated by a barium converter can increase without saturation with increased discharge power.² Based on this study, a prototype ion source has been developed to utilize the multi-cusp magnet arrangement as a filter. Cesium is

used to lower the work function of the converter and therefore enhance the H^- yield.

2. ION SOURCE CONFIGURATION

LBNL has been developing multicusp surface conversion ion sources for many years.^{3,4} The typical multi-cusp H^- surface conversion source consists of a plasma chamber and a negatively-biased converter electrode as illustrated in Figure 1.

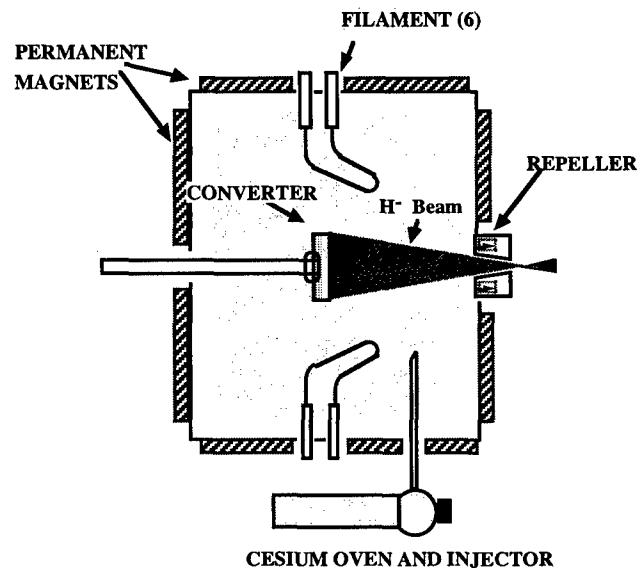


Figure 1: Schematic of the surface conversion ion source.

The positive ions present in the hydrogen plasma (H^+ , H_2^+ , H_3^+) are accelerated across the plasma sheath formed along the converter surface. H^- ions are formed on the surface and extracted back across the sheath. The spherical surface of the converter focuses the negative ions through the extraction aperture. The converter is coated with a low work-function material such as cesium to enhance negative ion conversion.

The current LANSCE ion source has a cylindrical body and the negative ions are extracted radially. The two filament cathodes are located on the cylinder end flanges. The new LANSCE H^- ion source is also of cylindrical design, however, the converter is installed along and parallel to the cylindrical axis as shown in Figure 2. Negative ions are extracted along the cylindrical axis. Six filaments are installed radially between the cylindrical wall cusp magnets, Figure 3. The magnets provide a filter field, which reduces the number of energetic electrons in the main plasma volume. This reduces the negative ion stripping due to energetic electrons. A converter of twice

the area of the current converter is also used. The radius of curvature is increased to maintain the same projection angle. The axial position of the converter was optimized for maximum H^- output.

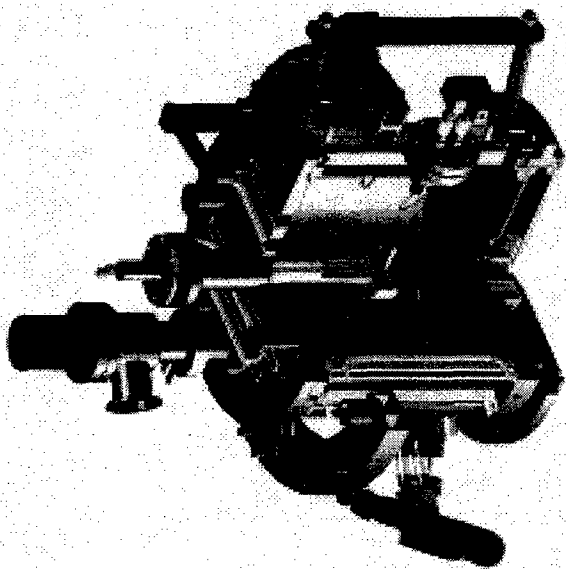


Figure 2: 3-D cutaway rendering of the LBNL designed ion source for LANSCE. Note that the filaments are placed radially and the converter is mounted along and parallel to the cylindrical axis.

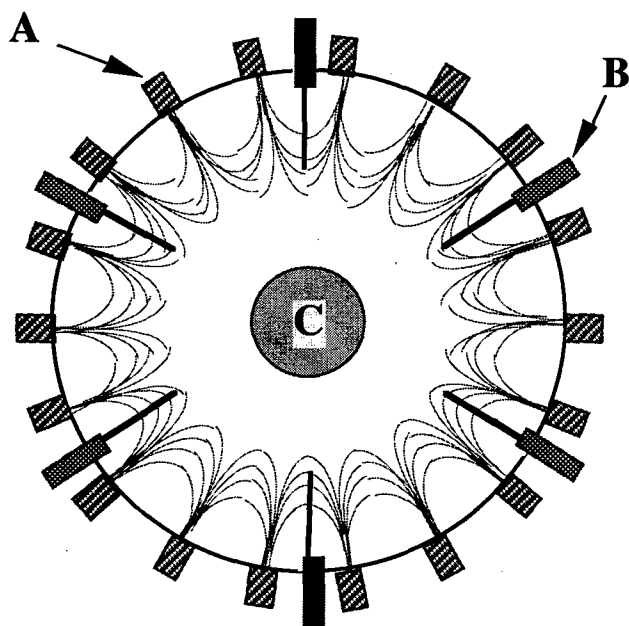


Figure 3: Magnet and filament configuration. (A) Wall cusp magnets (18 columns). (B) Filaments (total 6). The filament tips are placed at approximately the 25 gauss region. (C) Converter installed on the cylindrical axis.

A repeller similar to one used on the current LANSCE source is utilized in the new design to prevent electrons from being extracted and accelerated along with the

primary H^- beam, Figure 1. This is an electrically isolated, conical collimator installed in front of the outlet aperture. The collimator is biased slightly positive with respect to the ion source body. This repels positive ions. The lack of positive charge in the region will prevent plasma electrons from entering. Two magnets form a cusp field within the collimator to deflect energetic electrons from the converter to the conical wall.

Cesium is injected into the source from a heated oven. The oven is mounted on the cylindrical wall with an injection tube penetrating the This arrangement enables one to inject cesium into the central plasma region. Cesium forms a thin layer on the converter, which enhances H^- conversion. The operating temperature is typically between 200 and 300 C° .

3. ION SOURCE CONSTRUCTION

The ion source body is constructed of stainless steel. It is cylindrical with plasma confinement provided by samarium cobalt magnets placed on all source walls. The cylindrical sidewall has 18 line cusps parallel to the source axis. The rear flange has four line cusps placed on parallel chords. The front flange has 18 radially arranged magnets. A space is provided in the center of the radial array for installation of the repeller assembly. The wall and back flange magnets are installed in copper boats to provide cooling. The front flange magnets are mounted on a low carbon steel plate, which is brazed to a copper plate. The copper plate is in turn attached to the main water-cooled flange.

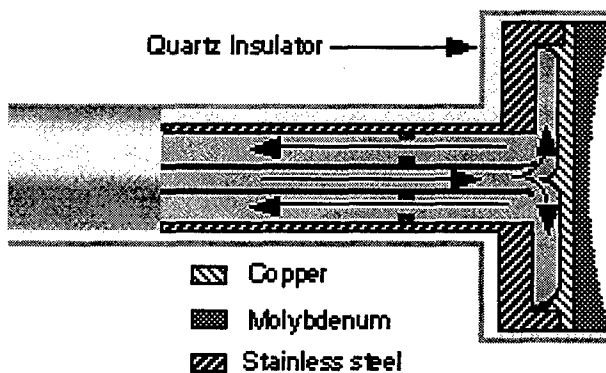


Figure 4: Cross-section schematic of the converter showing construction and water flow.

The converter is installed through the rear flange. An insulating flange is used to provide electrical isolation from the source body. Figure 4 is a schematic of the converter construction. The converter surface is machined to a spherical shape from molybdenum. The molybdenum plate is vacuum brazed to a copper interface piece to provide good thermal contact and conductance to the cooling channel. The cooling channel is machined from stainless steel and is vacuum brazed to the copper. Coaxial stainless steel tubing is welded to the cooling channel

plate. Water is supplied through the inner tube and returned through the outer. A quartz cover is provided for the rear and side surfaces of the converter assembly. The cover isolates the areas which face the plasma. Only the spherical surface is exposed to the plasma.

Six filament feedthroughs are provided. They are arranged radially around the cylindrical wall. Cooling is provided by squirt tubes inserted in each feedthrough leg. The filaments are fabricated from 1.5-mm diam. tungsten rod. The filaments are inserted into and held firmly by a molybdenum and copper chucks.

A cesium oven connected to a commercial high temperature valve is installed radially on the cylindrical wall. A molybdenum tube is used to transport cesium vapor into the central region of the ion source. A heating block is mounted on the oven. It is heated by a 250 Watt cartridge heater.

4. CONCLUSION

Two ion identical ion sources have been fabricated. Figures 5 and 6 are photographs of one of the sources. One has been delivered to LANSCE for testing on their test stand. The second source is being tested on the LBNL test stand.

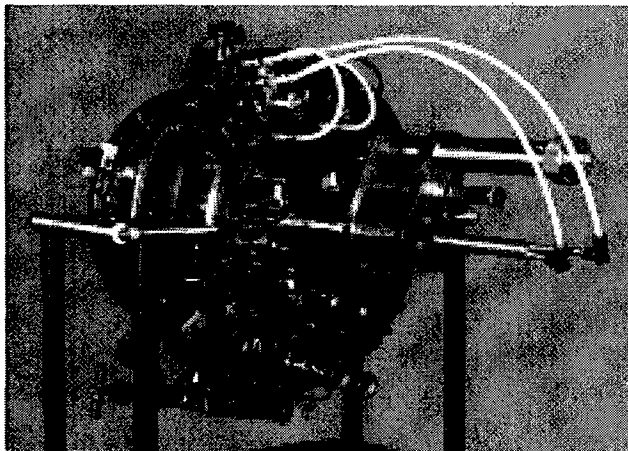


Figure 5: Photograph showing the back flange of the ion source. The linear manipulator is for test purposes only. It will be used to optimize the converter position for optimum current and emittance.

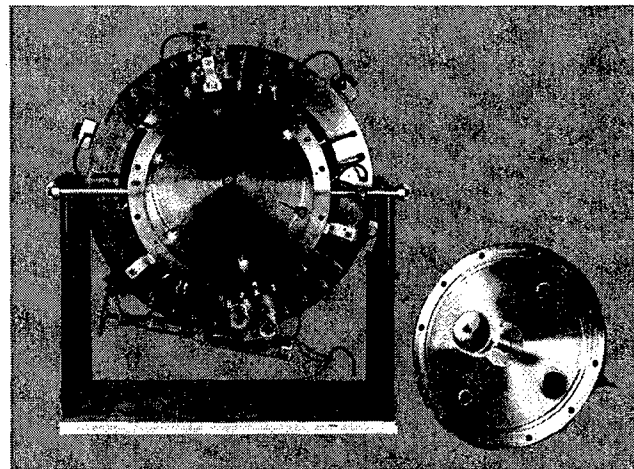


Figure 6: Photograph showing inside of the ion source. The converter can be seen on the removed end flange. Notice the six radially positioned filaments.

5. ACKNOWLEDGMENTS

We would like to thank S. B. Wilde, P. J. Rosado, T. A. McVeigh, P. Wong and L. W. Mills for their technical assistance.

* This work was supported by Los Alamos National Laboratory and the U.S. Department of Energy under Contract No. AC03-76SF00098

6. REFERENCES

- [1] R. R. Stevens Jr., R.L. York, R. Kendarian, Proceedings of the 1984 Linear Accelerator Conference.
- [2] C.F.A. van Os, K. N. Leung, and W. B. Kunkel Appl. Phys. Lett. **57** (9), 27 Aug. 1990.
- [3] K. W. Ehlers and K. N. Leung, Rev. Sci. Instrum. **51**, 721 (1980).
- [4] K. W. Ehlers and K. N. Leung, Rev. Sci. Instrum. **53**(6), 803 (1982).

STATUS OF THE H⁻ INJECTOR DEVELOPMENT PROGRAM AT LANSCE**

W. Ingalls, B. Prichard, Jr., O. Sander, J. Stelzer, R. Stevens, Jr., J. Wieting, T. Zaugg, LANL, Los Alamos, NM, R. Keller, K. Leung, M. Williams, LBNL, Berkeley, CA

Abstract

The H⁻ injector at Los Alamos National Laboratory (LANL) is being upgraded to provide a 12% duty-factor, 40-mA, 80-keV H⁻ beams, which will enable 200- μ A operation of the Los Alamos Neutron Scattering Center (LANSCE) proton storage ring (PSR). An improved version of the LANSCE operational surface-conversion ion source and a new accelerating column have been developed in collaboration with the Lawrence Berkeley National Laboratory (LBNL) for this application [1]. We report here the results of the initial tests at LANL on a proof-of-principle (POP) ion source built at LBNL and on modeling studies. The POP ion source has been operated at the 40-mA design beam current, and the beam emittance of the 80-keV extracted beam has been measured both at the exit of the accelerating column and in the 80-keV low-energy beam transport (LEBT) line. Significant, current-dependent, emittance growth was observed in the LEBT. Experimental investigations of this growth are described.

1. INTRODUCTION

A goal of the Short Pulse Spallation Source (SPSS) Enhancement Project [1] at LANL is to upgrade the existing facilities at LANSCE to reliably produce 200 μ A for the Manuel Lujan Neutron Scattering Center target. To achieve this SPSS goal, a significant increase in beam current from the H⁻ injector is required. Higher peak current will reduce the fill time of PSR and reduce the stored-beam losses, and higher peak current allows an increased gap in the chopped beam, which could improve beam stability at high currents. A minimum of 20 mA is essential; a beam current of 40 mA is the desired goal. Our present H⁻ injector produces 16-17 mA of beam with a normalized beam emittance equal to 1.0 π mm-mrad for 95% of the beam. A reduction in beam emittance is also required; smaller emittance should reduce beam losses in the linac. A normalized beam emittance of 95% of the beam should be less than 0.8 π mm mrad, whereas 0.4 is our desired goal. To limit the demand on resources, we will continue using the present 80-keV LEBT and plan to achieve the injector improvements via source and column upgrades.

2. THE EXPERIMENTAL SETUP

2.1 The Ion Source Test Stand (ISTS)

The ISTS was built to develop the necessary injector improvements without interfering with LANSCE

operations. We designed the ISTS to duplicate the H⁻ 80-keV beam transport inside the LANSCE 750-kV injector dome. The ISTS has additional emittance diagnostics to better characterize the beam behavior. They are located at end of column (EM01) and at the location of the entrance to the 670-kV accelerating column (EM03). The EM02 diagnostic is located between the two solenoids as in the LANSCE injector. Reference [2] give a detailed description of the ISTS. Figure 1 shows an 80-kV dome LEBT schematic.

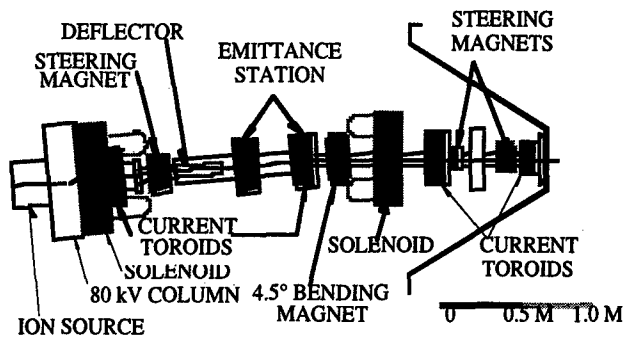


Figure 1 Line Drawing of the Dome LEBT

2.2 New 80-keV Column Design

The present 80-kV column has shortcomings when operated with high currents in our present LEBT. During normal operations we limit emittance growth in the column, typically, by perveance matching in the column. To prevent the formation of aberrations in the first LEBT solenoid, we must produce a beam at the column exit with relatively small beam size and with small divergence so not to fill the aperture of the first solenoid. Using the present column, we cannot simultaneously maintain a perveance-matched beam and control the beam size in the LEBT. This inability becomes unacceptable at high-beam currents. The new-column design addresses the above problems. It uses an asymmetric Einsel lens and provides perveance matching and independent beam focussing for a range of high currents. Simulations show that this column can produce sufficiently small beam sizes at high currents. In addition, the new column includes an ion trap to stop back-streaming positive ions, thereby, reducing their damage to the ion source and enhancing the beam neutralization in the downstream LEBT. Figure 2 shows the new column design. The new column has been

* Work supported by the U.S. DOE

installed but not tested. All following results were made with the operations-type column.

3. EXPERIMENTAL RESULTS

3.1 Operations Source

As reported earlier [2,3] concerning the operations source, we found that the beam at EM02 had the same emittance as measured in the LANSCE injector. Using the additional emittance station, EM01, we also observed that the beam had the emittance equal to the expected source admittance.

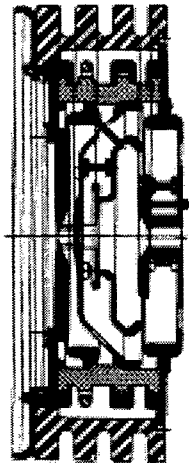


Figure 2 Line drawing of the new 80-keV column design

Because the emittance at EM02 is significantly larger than EM01, all the observed emittance growth occurs in the first 104 cm of the LEBT.

3.2 POP Source

Initially the POP source produced significantly less beam than observed at LBNL. Simulations of the source and column showed that significant beam current loss occurred on the 1-cm plasma aperture. We enlarged this aperture to 1.6 cm, obtained 40 mA of H^- current, and confirmed the previous LBNL measurement [4]. With the 1.6-cm aperture the beam current increased linearly with arc current as it reached 40 mA; however the LANSCE operations source saturated at 28 mA. An interesting but unexplained observation is that for a given arc current the operations-source beam current increased by only 10% when the aperture was enlarged; however, the POP-source current increased by a factor of two. Nonetheless, increasing the plasma aperture did increase the maximum current from the operation source.

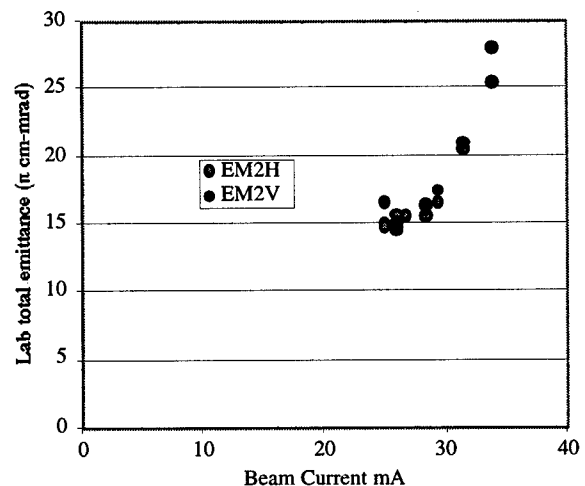
3.3 Emittance measurements and growth

We were unable to obtain a complete set of EM01 measurement at the exit of the column. However, two EM01 measurements showed that the normalized rms emittance was 0.014 and 0.018 π cm-mrad with the POP and operations sources respectively. These emittance areas, with the enlarged plasma aperture, are again similar

to the admittance (0.014 π cm-mrad) of the source and predictions of PBGUNS [5]. The POP source supplied 24.5 mA, and the operations source supplied 15 mA during these measurements.

Using the 1.6-cm plasma electrode aperture, we continued to observe significant growth between column exit and EM02. Using the operations source we observed that the normalized total emittance at EM02 increased from 0.25 to 0.31 π cm-mrad emittance (a 25 % increase) as the beam current increased from 8 to 24 mA. Using the POP source we measured a normalized total emittance increase from 0.20 to 0.29 π cm-mrad (a 45% increase) as the current increased from 24 to 34 mA. Above 28 mA of beam current the EM02 emittance increases rapidly with increasing beam current, but below 28 mA the rate of increase is significantly less. See figure 4. PBGUNS simulations show that for beam currents above 28 mA, the beam size in the first solenoid becomes sufficiently large so that the solenoid will begin causing significant aberrations to the beam. We observe that the rms emittance, which is determined using a moments analysis, increases even more rapidly with beam current than the total emittance. This result supports our conclusion that part of the increasing emittance growth is caused by beam aberrations from the solenoid. It should be noted that when both sources were producing the same amount of current, 24 mA, the beam emittance with the POP sources was 33% smaller than that with the operations source.

Figure 3. Horizontal and vertical emittance at EM02 with the 1.6 cm plasma electrode aperture.



As we increased the beam current from the sources, we did not obtain a complete set of EM01 measurements to compare with all the EM02 measurements. However, where the comparison can be made and when the beam emittance should not be affected by solenoid aberrations, the emittance growth between EM01 and EM02 is greater than a factor of two. At higher beam currents where solenoid aberrations are also important, the emittance growth is significantly greater. To explore this emittance growth, we modeled the beam dynamics between EM01 and EM02 using the codes SCHAR [6] and SOLEN [7]

and used three different initial beam distributions, the 4-volume, the KV and the Gaussian distributions. The initial beam distribution was constrained to have the Courant-Snyder [8] parameters and rms emittance of the measured beam. Figure 4 shows the simulated dependence of EM02 emittance on beam current and beam distribution. Of the three distributions, only the Gaussian distributions produced the observed emittance

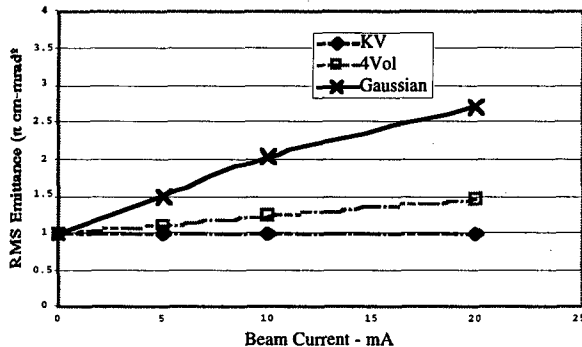


Figure 4. Rms Emittance at EM02 as a function of effective beam current for various assumed beam distribution

growth. Our beams appear to have a Gaussian distribution because we found that the total emittance (E) has the dependence

$$E(F) = K \times \ln(1/(1-F))$$

where F is the beam fraction contained within the area E and K is equal to twice the rms emittance value. Such dependence is indicative of a Gaussian distribution [9]. See figure 5.

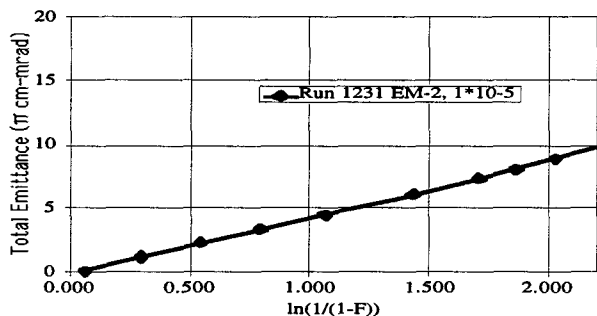


Figure 5. Total Emittance versus fraction of beam enclosed

We suggest that emittance growth was the result of beam space charge effects due to an incompletely neutralized beam. To test this hypothesis we added argon gas to the LEBT and measured the EM02 emittance versus gas pressure in the LEBT. Because we were seeking a qualitative result, we did not attempt to uniformly distribute the argon in the LEBT, but only added gas at one point. We observed 15% decrease in emittance that varied approximately linearly with gas pressure.

4. CONCLUSIONS AND FUTURE PLANS

We confirmed that the POP source can meet the SPSS beam-current goal; the POP produced more beam than the operations source. We observed that the emittance at EM01 was smaller using the POP source compared to using the operations source at the same beam current. Significant emittance growth occurs between the column exit and the mid-point of the 80-keV LEBT; the growth is at least a factor of two. Initial measurements indicate that the emittance growth was in part due to space charge effects that can be reduced with the addition of a neutralizing gas. Beam-dynamics simulations indicated that beams with Gaussian distributions could exhibit the kind of emittance growths that we observe. Furthermore, the measured emittance dependence on beam fraction is consistent with a Gaussian distribution.

Because the present beam emittance at the mid-point of the LEBT does not meet the SPSS requirements we must develop methods to reduce the emittance growth in the LEBT. To support our development, we will examine the following topics: Can we limit the emittance growth between EM01 and EM02 by more uniformly adding neutralizing gases in the LEBT? Does the new column perform as designed? Does emittance growth occur between EM02 and EM03? What are the beam production characteristics of the final version of the LBNL source and do they meet the SPSS requirements?

5. REFERENCES

- [1] "Los Alamos Neutron Science Center Short Pulse Spallation Source Enhancement Project Execution Plan", LAUR-98-4172, Los Alamos National Laboratory (1998)
- [2] W. I. Ingalls, M. W. Hardy, B. A. Prichard, Jr., O. R. Sander, J. E. Stelzer, R. R. Stevens, Jr., K. N. Leung, M. D. Williams, "Status of the H⁻ Injector Development Program at LANSCE", Proc. 1998 Linear Accel. Conf. (1998)
- [3] R. R. Stevens, Jr., W. Ingalls, O. Sander, B. Prichard, Jr., J. Sherman, "Beam Simulations for the H⁻ Injector Upgrade at LANSCE", Proc. 1998 Linear Accel. Conf. (1998)
- [4] M. Williams et al., "Ion Source Development for the LANSCE Upgrade", Proc. 1998 Linear Accel. Conf. (1998)
- [5] Jack E. Boers, Proc. 1995 Particle Accel. Conf. (1995) 2312
- [6] R. J. Hayden and M. J. Jakobson, "The Space Charge Computer Program SCHAR", IEEE Transactions on Nuclear Science NS-30 (1983) 2540
- [7] R. Ryne et al, "The U.S. DOE Grand Challenge in Computational Accelerator Physics", Proc. 1998 Linear Accel. Conf. (1998)
- [8] E. D. Courant and H. S. Snyder, "Theory of the Alternating Gradient Synchrotron", Ann. Phys. 3,(1958) 1-48
- [9] P. W. Allison, "Some Comments on Emittance of H⁻ Ion Beams", 4th International Symposium on the Production and Neutralization of Negative Ions and Beams, Upton, New York (October, 1986)

A VERSATILE COLUMN LAYOUT FOR THE LANSCE UPGRADE.*

R. Keller, J. M. Verbeke, P. Scott, M. Wilcox, L. Wu, and N. Zahir
E. O. Lawrence Berkeley National Laboratory, Berkeley, CA

Abstract

An upgrade program for the LANSCE facility at Los Alamos National Laboratory [1] aims at generating and transporting a 40-mA H^- beam with 80 keV energy and minimal emittance increase over the value currently measured with a 16-mA beam. Within a collaboration between the two laboratories, LBNL has built a new ion source [2] that allows the extraction of a 40-mA beam. However, there are strong indications that a new layout of the extraction system/LEBT is needed to efficiently deliver a low-emittance beam with this increased beam current. An additional requirement for the new system is its adaptability to a range of beam currents between 20 and 40 mA. The design of this new system, based on extensive simulations with the code IGUN [3], is described in this paper.

1 INTRODUCTION

The LANSCE facility at Los Alamos National Laboratory is currently operating with a 16-mA H^- ion beam obtained from a surface-production ion source [4]. A project to improve the neutron output of the facility is now underway and aims at an ion-beam current-increase of a factor of two. Beam simulations [1], however, clearly indicate that the available 80-kV column that incorporates the extraction system and the initial, electrostatic, part of the LEBT will be unable to transport beams of this intensity through the subsequent magnetic LEBT.

Members of the Ion Beam Technology Program at Berkeley Lab were already engaged in providing a 40-mA ion source [2] for the LANSCE upgrade project, and the work presented in this paper was undertaken to develop a viable modification to the existing 80-kV column. One main constraint for this work was the condition that the existing insulators be preserved in order to keep this project within budget and schedule. Another condition was imposed by the magnetic LEBT whose first solenoid aperture of 38-mm diameter was not to be illuminated to more than 50%.

2 BASIC CONSTRAINTS

2.1 80-kV Column

The existing 80-kV column in the LANSCE injector re-

presents a modified Pierce extraction system [5] with two intermediate electrodes between source outlet potential and ground. The electrode contours are shaped according to Pierce's design, but the voltage in the first gap had to be considerably reduced to avoid frequent high-voltage breakdown. In addition, the aperture in the first intermediate electrode was widened from 10 to 22 mm which moved the column parameters even further away from a true Pierce system. A trap is added on the downstream side of the column electrodes to keep space-charge neutralizing, positive, ions within the transported H^- beam.

The column insulator is shown in Fig. 1, already fitted with the new electrodes that will be discussed later on. It consists of two concentric ceramic tubes enclosing a space that can be filled with an insulating gas. With this construction, high-voltage breakdown in air is totally avoided up to a total voltage of 80 kV. The inner tube carries corona rings on its outer perimeter which are connected to feed-throughs that pass through this insulator and connect to the inner electrodes. Small recesses on the inner perimeter of this tube serve as indices for the installed electrodes.

2.2 Ion Source

Both, the old and the new ion source are of the surface-production type with internal, cesium-covered converter [2]. The converter bias of -250 V with respect to the outlet-electrode potential already accelerates the H^- ion beam within the plasma generator and helps to overcome problems arising from high space-charge density at thermal ion velocities usually encountered with other ion sources. An arrangement of permanent magnets inside the plasma electrode significantly reduces the amount of electrons that are extracted together with the H^- ions.

2.3 IGUN simulations

The beam-trajectory simulation code IGUN [3] is capable of handling positive ions extracted from a plasma or "injected" into a system under study as an external input file. Our rationale in using IGUN as a design tool for the LANSCE column upgrade was that we did not intend to study the fundamental processes of H^- beam formation but rather build on an existing system and investigate the effects caused by the higher space-charge density of the envisaged 40-mA beam. For this purpose, assuming a proton beam with inverted electrode potentials was judged to be adequate.

*Work supported by the Director, Office of Science, Office of Basic Energy Sciences, of the US Department of Energy under Contr. No. DE-AC03-76SF00098.

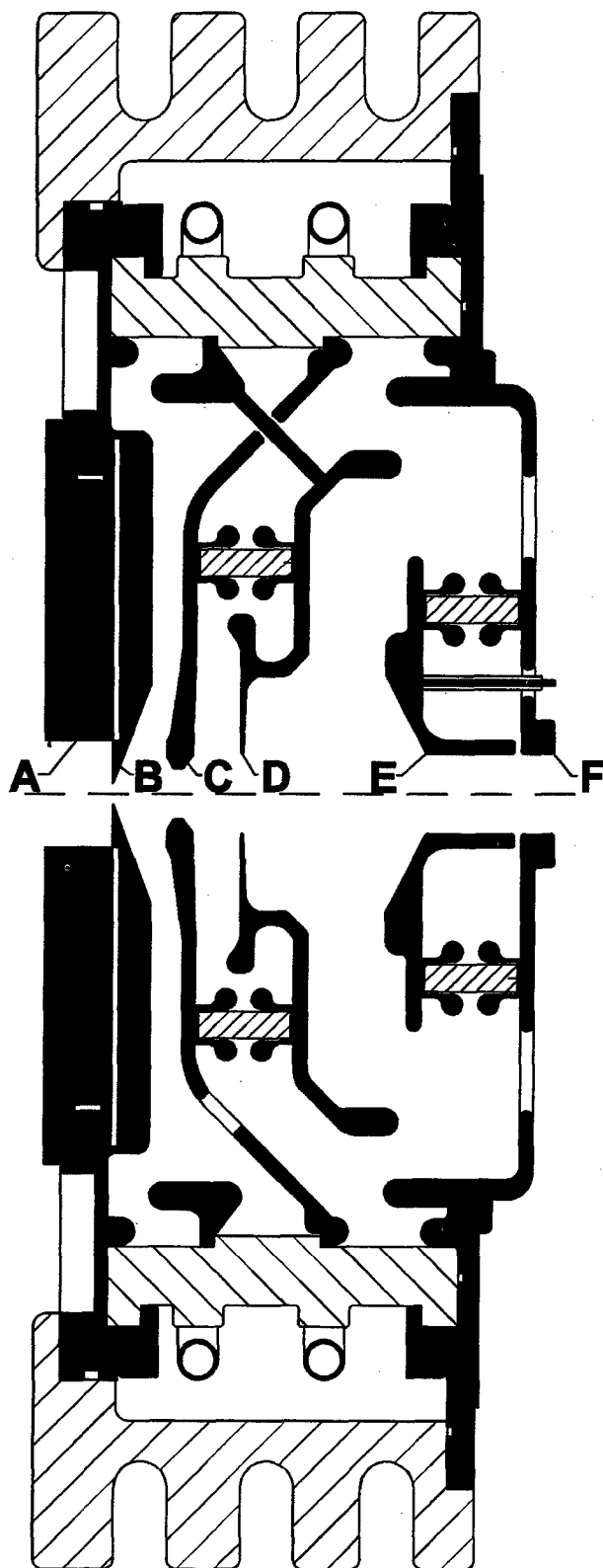


Figure 1. New 80-kV column for the LANSCE injector. A, ion-source plasma-electrode. B, outlet ("Pierce") electrode on -80 kV. C, extractor electrode (-50 kV). D, lens (-75 kV). E, ion trap (+8 kV). F, ground electrode. All potentials apply to negative ions.

The simulations had the goal of creating an electrostatic LEBT as first part of the existing hybrid LEBT capable of accommodating a wide range of beam currents, between 15 and 40 mA, and with minimized aberrations to keep the effective beam emittance as low as possible.

In most of the simulations performed for this study, a longitudinal energy of 375 eV was assigned to the ions within the ion-source plasma. The exact value of this energy, down to 250 eV, proved to have only a weak influence on the resulting beam parameters. Because of the fact that reduction of aberrations was a primary goal in this study, most of the calculations were performed for vanishing ion temperature, but for emittance evaluations, ion temperatures of 1 eV were assumed.

As stated above, the existing LEBT relies on space-charge compensation for the ion beam drifting between its electrostatic (column) and magnetic parts. To simplify our simulation work and significantly cut down on the CPU times, we did not calculate complete beam trajectories over the full drift length but confined the range of calculations to the column itself, with the implicit assumption that the ion trajectories remain straight after passing the first equipotential on slightly negative potential from the downstream side (the sign convention here applies to a positive ion beam).

To adequately judge the simulation results, however, trajectories were traced to the entrance plane of the first magnetic solenoid lens, 300 mm downstream of the column entrance plane. Up to 19 mm beam radius in this plane was regarded as acceptable. Once we arrived at a viable design we split the simulation problem into two parts, performing the calculations near the outlet electrode at twice the resolution applied to the remaining part.

3 NEW COLUMN DESIGN

As a first approach to developing the new column, we pursued the idea of a "compound system" [6] which consists of a low-voltage extraction gap followed by an electrostatic einzel lens and the main gap that determines the final beam energy. We soon realized, however, that such a system would occupy more longitudinal space than the existing insulator could accommodate and therefore decided to integrate two of the functions, i. e. those of lens and main gap, into one element which is labeled as 'D' in Fig. 1.

Another condition we imposed was to keep the extractor electrode, C, at least as far away from the outlet electrode and the system axis as the first intermediate electrode of the existing column has been, ensuring that the risk of high-voltage breakdown caused by stray particles coming from the source is not increased in the new design. We did, however, raise the voltage in the gap between the outlet and first intermediate electrode, B and C, because we felt this voltage had been chosen with extreme conservatism and did not by itself actually contribute to sparking.

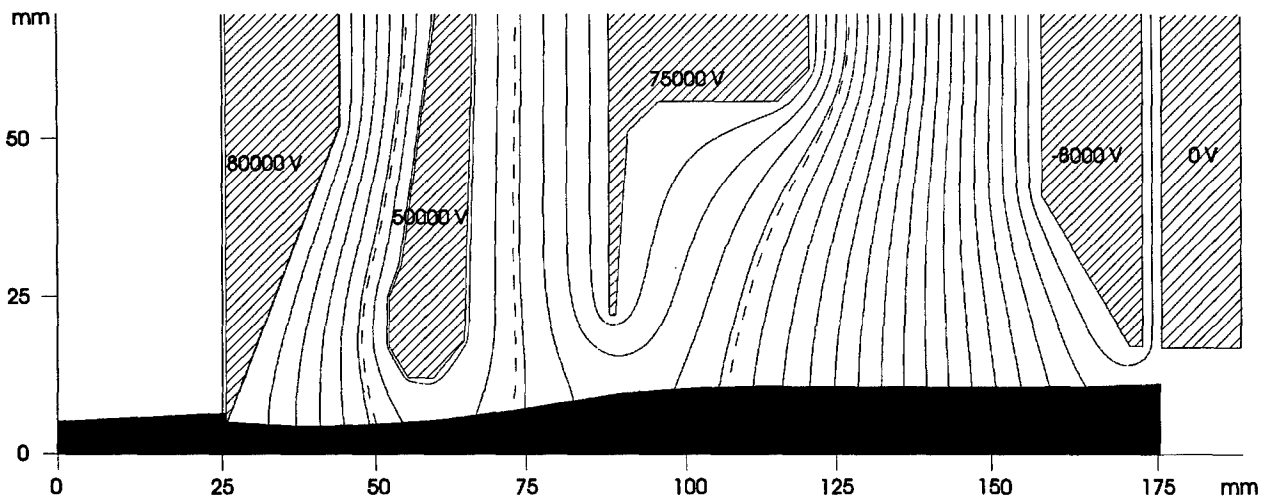


Fig. 2. Simulated beam in the optimized electrode configuration. Electrode potentials as marked in this figure apply to a positive ion beam. The contour of the ground electrode on the right has been graphically added to the contours actually used in the IGUN runs. The second dashed equipotential line, between the 50- and 75-kV electrodes, marks the transition surface for split calculations as described in the text.

After we gained some experience with the intricacies of this design we substantially modified the contour of the lens, D, from a cylinder to the bell shape shown in Fig. 1. We also shortened the length of the ion trap electrode, E, because it contributes to the path length the ion beam has to traverse under the influence of its full space charge, increasing its radial growth. This change is not shown in Fig. 1, but rather in the integral trajectory plot in Fig. 2.

4 RESULTS

Emittance plots for the first and second parts of the optimized configuration are given in Fig. 3. The first gap of the new column is virtually aberration-free, whereas the main gap produces a faint distortion, only visible in the zero-temperature condition.

After the new electrodes were assembled within the insulator the system could be immediately conditioned to the design voltage of 80 kV [7].

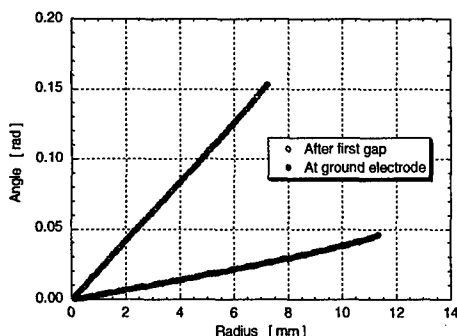


Fig. 3. Emittance plots for the optimized configuration.

5 ACKNOWLEDGMENTS

The authors thankfully acknowledge the contributions by K.-N. Leung, Berkeley Lab, who initiated this collaboration with the LANSCE group and by R. R. Stevens Jr., Los Alamos Nat. Lab., for frequent exchange of technical information and suggestions how to improve the column design. The mechanical design of the new column configuration was carried out by C. Matuk, Berkeley Lab.

6 REFERENCES

- [1] R. R. Stevens, W. Ingalls, O. Sander, B. Prichard, and J. Sherman, "Beam Simulations for the H- Upgrade at LANSCE," Proc. 1998 Linac Conf., Chicago, IL.
- [2] M. Williams, R. Gough, R. Keller, K. Leung, D. Meyer, A. Wengrow, O. Sander, W. Ingalls, B. Prichard, and R. Stevens, "Ion Source Development for LANSCE Upgrade," Proc. 1998 Linac Conf., Chicago, IL.
- [3] R. Becker, "New Features in the Simulation of Ion Extraction with IGUN," Proc. EPAC 98, Stockholm, Sweden (1998)
- [4] R. L. York and Ralph R. Stevens, Jr., "Third International Symposium on Production and Neutralization of Negative Ions and Beams," Brookhaven National Laboratory, 1983, p. 410.
- [5] J. R. Pierce, "Theory and Design of Electron Beams," Van Nostrand, Toronto, 1954, pp. 177 - 181.
- [6] R. Keller, "Ion Extraction," in I.G. Brown, ed., "The Physics and Technology of Ion Sources," John Wiley, New York, 1989.
- [7] R. R. Stevens, Jr., private communication (1999).

COMPARISON OF BEAM SIMULATIONS WITH MEASUREMENTS FOR THE LEDA LEBT H⁺ BEAM[†]

H. Vernon Smith, Jr., Terry Figueroa, Lash D. Hansborough, Margye Harrington, Kenneth Johnson, Debora Kerstiens, Subrata Nath, Joseph D. Sherman, Ralph R. Stevens, Jr., Michael Thuot, Lloyd M. Young, and Thomas J. Zaugg
Los Alamos National Laboratory, Los Alamos, NM 87545

Adrian H. Arvin, A. S. Bolt, and Mitchell C. Richards
Westinghouse Savannah River Corporation

James H. Kamperschroer
General Atomics Corporation

Abstract

The Low-Energy Demonstration Accelerator (LEDA) injector is designed to provide 75-keV, 110-mA, proton beams for the LEDA RFQ. After testing the LEDA injector using a 1.25-MeV, CW RFQ, we shortened the low-energy beam transport (LEBT) to 2.69 m, replaced the first LEBT solenoid with one that has a shorter length but the same focusing power, and installed and operated the LEDA injector in the beam tunnel. In this paper we use the TRACE, SCHAR, and PARMELA computer codes to model the proton beam for the as-installed LEBT and we compare the results of these simulations with the LEBT beam measurements. We use the computer code PARMTEQM to transport the SCHAR- and PARMELA-generated beams through the RFQ so that we can compare the predicted RFQ performance with the measured RFQ performance. For a 100-mA, 0.239- π -mm-mrad input beam, PARMTEQM predicts the LEDA RFQ transmission will be 92.2%.

1 INTRODUCTION

The LEDA injector [1] was tested under operating conditions by altering the ion-source extraction system from a tetrode at 75 keV to a triode at 50 keV [2] and injecting the hydrogen beam into a 1.25-MeV, CW RFQ [3]. The LEDA microwave-driven source beam (50 keV, 70-100 mA, $\approx 90\%$ H⁺ fraction) was matched to that RFQ using the two-solenoid, gas-neutralized low-energy beam transport (LEBT) [4] described in Ref. [2]. Two steering-magnet pairs provided the desired beam centroid position and angle at the RFQ match point. Beam neutralization of 95-99% occurred in the LEBT residual hydrogen gas [5]. The RFQ accelerated the beam to 1.25 MeV and a simple HEBT transported that beam to a beamstop. The RFQ transmission and spatial profiles were measured as a function of injected current and LEBT solenoid excitations [2]. The expected beam performance was calculated using the computer codes TRACE [6] and SCHAR [7] to model the LEBT [8], PARMTEQM [9] to model the RFQ, and PARMELA [10] to model the HEBT. Excellent agreement between the simulations and the measurements was obtained (see Table 2 of [11]).

The LEDA injector is now installed in the beam tunnel [12] and connected to the LEDA RFQ [13]. Low-current, pulsed-beam commissioning of this 6.7-MeV RFQ has commenced [14, 15]. Changes in the LEBT since the work reported in [11] include reconfiguration of the ion-source extraction system to a tetrode at 75 keV and replacement of the first LEBT solenoid with one that has a shorter length but the same focusing power.

Ultimately we will compare the beam measurements with simulations of the LEDA LEBT, RFQ, and HEBT. In this paper we report the first step toward obtaining these end-to-end simulations — comparison of the as-installed LEDA LEBT measurements with simulations. We also report predictions for the RFQ transmission using the simulated beam as input. Our procedure is as follows. The hydrogen beam is first characterized using the Emittance-Measuring Unit (EMU), Fig. 1. We use these results and the TRACE code to get the input parameters for the SCHAR code. We iterate on the input parameters until SCHAR reproduces the measured phase space. Then the LEBT beam line, from the extractor to the RFQ match point (Fig. 1), is simulated and the resulting SCHAR-generated beam is transported through the RFQ using PARMTEQM to predict the RFQ performance. A preliminary study of the LEDA LEBT is reported in [8].

2 INPUT PARAMETERS

The input H⁺ beam parameters are determined from phase-space measurements of the LEDA injector beam

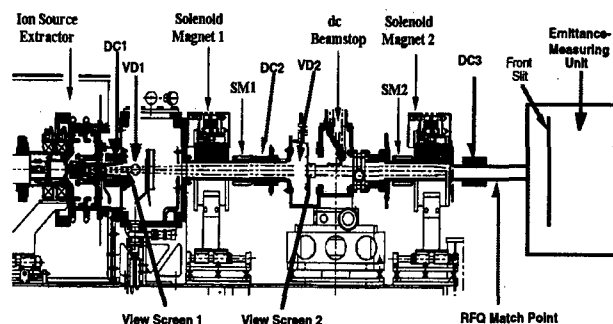


Fig. 1. The LEDA injector with the EMU. The positions of the RFQ match point, and the beam-line components, are indicated and discussed in the text.

[†] Work supported by the US DOE, Defense Programs.

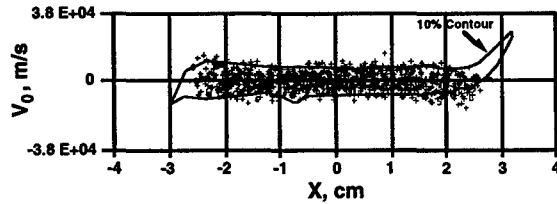


Fig. 2. The SCHAR-calculated phase space (crosses) at the EMU for the 100-mA H^+ beam in the LEDA LEBT (Fig. 1). The solid line is the 10% phase-space contour measured with the EMU.

using the EMU (Fig. 1). Beams with 50-, 80-, and 111-mA total current are characterized using the EMU. Assuming the proton fraction is $\approx 90\%$, the resulting H^+ currents are 45-, 72-, and 100 mA, respectively. Using TRACE [6], with the rms normalized emittance ϵ_N and Twiss parameters α and β at 10% threshold as input, the beam is drifted back along the LEBT, 3.28 m from the front slit of the EMU to the ion source, as a function of the un-neutralized current. The un-neutralized current that gives the predicted H^+ beam size closest to that of the 8.6-mm-diam ion source emitter is noted, and the resulting α and β , as well as ϵ_N , are used as input to the first round of the SCHAR simulations.

3 LEDA LEBT SCHAR SIMULATIONS

The LEBT, in both the EMU and the RFQ configuration, is simulated with the non-linear space-charge computer code SCHAR. These simulations use a 4-volume distribution and the line mode with 999 lines. The LEBT dimensions are extractor to solenoid 1, 87.7 cm; solenoid 1 to solenoid 2, 140.4 cm; solenoid 2 to EMU, 100.1 cm; and solenoid 2 to RFQ match point, 40.7 cm (Fig. 1). Beam neutralizations of 95-99% are used [5], depending upon the results of the TRACE-backs. In all cases SCHAR predicts no proton beam loss in the LEBT.

SCHAR Input Parameter Determination

Using the TRACE parameters as SCHAR* [7] input, and scaling them using $\alpha_{\text{new}} = \alpha_{\text{old}}[\epsilon_{\text{old}}/\epsilon_{\text{new}}]$ and $\beta_{\text{new}} = \beta_{\text{old}}[\epsilon_{\text{old}}/\epsilon_{\text{new}}]$, gives the measured ϵ_N at the EMU to within 0.1%, usually within two iterations. The resulting SCHAR-predicted input beams (Table 1) have ϵ_N lower than that measured at the EMU because of predicted emittance growth in the LEBT transport (primarily arising from aberrations in the LEBT solenoid lenses). When SCHAR transports the beam parameters in Table 1 3.28 m through the LEBT, the approximate phase-space shapes at the 10% contour and beam profiles at the video

Table 1. SCHAR input H^+ beam parameters for the three input beams. For these cases, $v_0 = 3.790 \times 10^6$ m/s.

I_{H^+} (mA)	r_{12}	X_{max} (mm)	$V_{x \text{ max}}$ ($\times 10^6$ m/s)	I_{eff} (mA)	ϵ_N (π mm mrad)
45	0.8027	2.394	13.13	0.5	0.1032
72	-0.2288	5.124	6.137	2.0	0.1714
100	-0.2701	5.171	7.049	5.5	0.1955

* $v_0 = [2E/m_p c^2]^{1/2} c$, $r_{12} = -\alpha/[1+\alpha^2]^{1/2}$, $x_{\text{max}} = [\beta\epsilon(6\text{rms})]^{1/2}$, $v_{x \text{ max}} = [\gamma\epsilon(6\text{rms})]^{1/2} v_0$

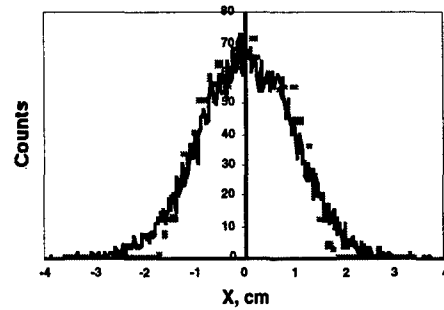


Fig. 3. Profile for the 100-mA H^+ beam 152.6 cm from the source measured with a video camera (line) and predicted by SCHAR (squares).

diagnostics are reproduced. The agreement between the SCHAR-predicted phase space at the EMU and the measured phase space is shown in Fig. 2 for the 100-mA H^+ input beam. The agreement between the SCHAR prediction and the videocamera data 42.2 cm from the source (VD1 in Fig. 1) is typically good at moderate microwave power levels (Fig. 2 of Ref. 11) and poor at high microwave power levels (Fig. 5 of Ref. 11). The agreement between the SCHAR prediction and the videocamera data 152.6 cm from the source (VD2 in Fig. 1) is usually good (example for the 100-mA H^+ beam is shown in Fig. 3). The centroid and amplitude of the videocamera data in Fig. 3 have been normalized to display the match to the SCHAR-predicted profile.

SCHAR Simulations of the LEDA LEBT

Using the input data from Table 1, SCHAR is used to predict the best match to the RFQ for the 2.69-m-long LEBT. The sample in Fig. 4 is for the 100-mA input beam with $B_{\text{sol } 1} = 3052$ G and $B_{\text{sol } 2} = 3650$ G, giving $\epsilon_N = 0.238 \pi$ mm mrad at the RFQ match point. Our previous experience [11] is that the actual $B_{\text{sol } 1}$ setting is close to the SCHAR prediction whereas the actual $B_{\text{sol } 2}$ setting is 10% higher than the SCHAR prediction. The $B_{\text{sol } 2}$ setting is underestimated because of the absence in the SCHAR model of the un-neutralized section of beam transport just in front of the RFQ. Most of the SCHAR-calculated emittance growth is due to spherical aberrations in solenoid #1 and solenoid #2 (Table 2). SCHAR predicts that the non-linear, space-charge-induced emittance growth in the LEBT is low compared to the

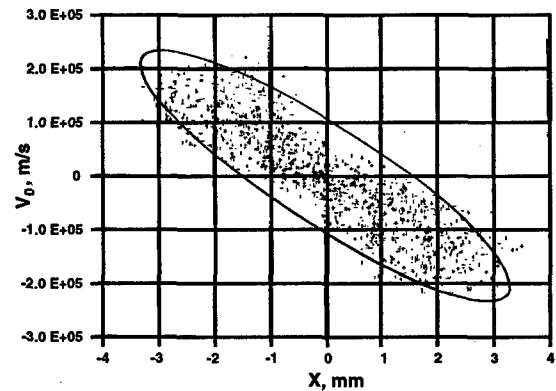


Fig. 4. SCHAR-calculated phase space (crosses) at the RFQ match point for the 100-mA input beam. The curve is the RFQ acceptance for 110 mA and 0.02π cm mrad.

overall emittance growth — 2.1% vs. 57.2% for the 45-mA beam, 1.4% vs. 13.7% for the 72-mA beam, and 3.7% vs. 21.7% for the 100-mA beam.

4 LEDA RFQ PARMTEQM SIMULATIONS

The SCHAR output files are used to generate 5,000 particle input beams for the PARMTEQM computer code to calculate the RFQ transmission and output ϵ_N . The proton fraction can be as high as 95% [16], but typical values are ~90%. We use the measured DC2 [DC2 is a dc parametric current transformer] current (Fig. 1), multiplied by 0.9, for the PARMTEQM input current. The result for the 100 mA beam (111 mA at DC2) is transmission = 92.2% and output $\epsilon_N = 0.232 \pi$ mm mrad (Fig. 5, Table 2) at the design RFQ intervane voltage. The predicted LEDA RFQ transmissions and output beam emittances for the other input beam currents are given in Table 2.

5 DISCUSSION

There is good overall agreement between the simulation for 100 mA reported here and that for 110 mA reported in Ref. [8]. This is striking because the input parameters for the simulations in [8] were obtained for a prototype LEBT in which the two solenoid magnets were placed next to each other, with no separation (see Fig. 3 of Ref. 1). The large emittance growth in solenoid #1 for the 45-mA beam (Table 2) arises from the large divergence of the 45-mA beam from the ion source extraction system. This extraction system is designed for 110-mA H^+ beams — at 50 mA there is a large perveance mismatch, with a cross-over in the extraction gap. This accounts for the large divergence, and small beam size, for the 45-mA case (Table 1).

In the initial LEDA accelerator commissioning stage, we are injecting pulsed low-current (10-20 mA), low-duty-factor (~1%) beams into the RFQ to allow us to gain understanding of the system operation without damaging components. To produce these low-current pulsed beams,

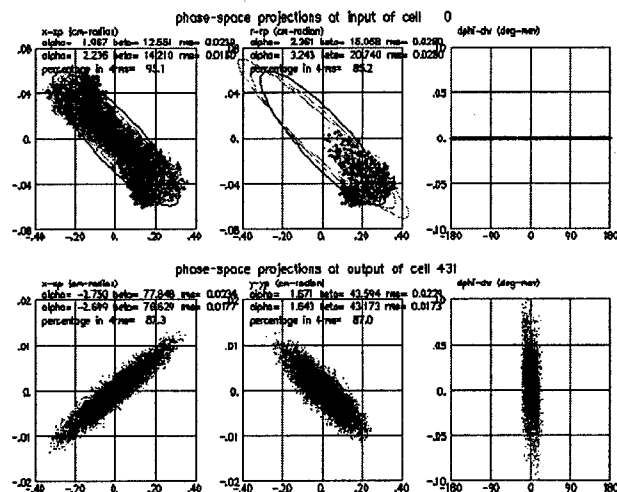


Fig. 5. PARMTEQM-calculated RFQ input (top) and output (bottom) phase space for the 100-mA beam.

Table 2. Results of the LEDA LEBT and RFQ simulations with SCHAR and PARMTEQM, respectively.

ϵ	ϵ	SCHAR	PARM-	PARM-	
growth	growth	RFQ	TEQM	TEQM	RFQ
in	in	ϵ_{in}	RFQ	RFQ	trans-
I_{H^+}	Sol#1, Sol#2,	π mm	ϵ_{in}, π	ϵ_{out}, π	mission
mA	%	mrad	mm mrad	mm mrad	%
45	31.1 17.5	0.162	0.164	0.173	96.6
72	0.5 11.6	0.195	0.195	0.206	96.5
100	5.2 11.6	0.238	0.239	0.232	92.2

we have installed a 5.0-mm-diam aperture in place of the 8.6-mm-diam aperture used for the measurements and simulations reported in this paper. Also, a variable beam iris has been installed just in front of solenoid #1. In our initial tests, 40 mA of hydrogen ions are extracted from the source, and the iris used to aperture out 50-75% of the beam current. We simulated the low-current beams from the 5-mm-diam emission-aperture based extraction system with PARMELA [10]. Using the PARMELA LEBT results as input to PARMTEQM, we find good agreement between the PARMTEQM RFQ simulations and the initial RFQ measurements [14]. After we have demonstrated good operation of the RFQ with the 5-mm-diam extraction system at its full current (~50 mA), we will install the 8.6-mm-diam extraction system to test the LEDA RFQ up to its full design current of 100 mA.

REFERENCES

- [1] J. Sherman *et al.*, "Status Report on a dc 130-mA, 75-keV Proton Injector," Rev. Sci. Instrum. **69** (1998) 1003-1008.
- [2] J. Sherman *et al.*, "Development and Test Results of the Low-Energy Demonstration Accelerator (LEDA) Proton Injector on a 1.25-MeV CW Radio Frequency Quadrupole," Proc. 1998 LINAC Conf. [Chicago, 24-28 August 1998] (in press).
- [3] G. M. Arbique *et al.*, "Beam Parameter Measurements on the CW RFQ1-1250 Accelerator," Proc. 1992 LINAC Conf. (AECL-10728, November, 1992) 55-57.
- [4] R. R. Stevens, Jr., "High-Current Negative-Ion Beam Transport," AIP Conf. Proc. No. 287 (1994) 646-655.
- [5] R. Ferdinand, *et al.*, "Space-Charge Neutralization Measurement of a 75-keV, 130-mA Hydrogen-Ion Beam," Proc. PAC97 (Vancouver, 12-16 May 1997) 2723-5.
- [6] K. R. Crandall "TRACE: An Interactive Beam-Transport Program," Los Alamos Scientific Laboratory report LA-5332 (October, 1973).
- [7] R. J. Hayden and M. J. Jakobson, "The Space-Charge Computer Program SCHAR," IEEE Trans. Nucl. Sci. **NS-30** (1983) 2540-2.
- [8] H. V. Smith, Jr. *et al.*, "Simulations of the LEDA LEBT H^+ Beam," Proc. PAC97 (Vancouver, 12-16 May 1997) 2746-8.
- [9] K. R. Crandall *et al.*, "RFQ Design Codes," Los Alamos National Laboratory report LA-UR-96-1836 (revised February 12, 1997).
- [10] L. M. Young, "PARMELA," Los Alamos National Laboratory report LA-UR-96-1835 (revised May 11, 1998).
- [11] H. V. Smith, Jr., *et al.*, "Comparison of Beam Simulations With Measurements for a 1.25-MeV, CW RFQ," Proc. 1998 LINAC Conf. [Chicago, 24-28 August 1998] (in press).
- [12] H. V. Smith, Jr. and J. D. Schneider, "Status Update on the Low-Energy Demonstration Accelerator (LEDA)," Proc. 1998 LINAC Conf. [Chicago, 24-28 August 1998] (in press).
- [13] D. Schrage *et al.*, "CW RFQ Fabrication and Engineering," Proc. 1998 LINAC Conf. [Chicago, 24-28 August 1998] (in press).
- [14] K. F. Johnson *et al.*, "Commissioning of the Low-Energy Demonstration Accelerator (LEDA) Radio-Frequency Quadrupole (RFQ)," this conf.
- [15] J. D. Schneider, "Operation of the Low-Energy Demonstration Accelerator: the Proton Injector for APT," this conf.
- [16] J. H. Kamperschroer *et al.*, "Doppler-shift Proton Fraction Measurement on a CW Proton Injector," Proc. 1998 LINAC Conf. [Chicago, 24-28 August 1998] (in press).

MULTIBEAM RF ION SOURCE WITH GROUNDED RF GENERATOR FOR HIGH CURRENT ACCELERATORS AND NEUTRON GENERATORS

B. Bogdanovitch¹, N. Gavrilov, V. Zubovsky, A. Nesterovitch,
S. Ostrikov, S. Stepanov, MEPhI, Moscow, Russia

Abstract

A multibeam RF ion source with grounded meter range RF generator was developed and experienced in MEPhI [1]. The source, besides direct assignment, can be used for the ion implantation, for manufacture of solar batteries etc. For example, during a target irradiation in neutron generators with a deuteron beam, target longevity essentially (in some times) increases due to dispersion uniformity rising.

1. SOURCE DESIGN

The scheme of source design is shown on Figure 1. The facility consists of the vacuum container 1 and a cylindrical $\lambda/2$ spiral loaded RF resonator 2 mounted on insulator 3 by means of holder 4. The resonator operating frequency is defined by the spiral length and can be chosen in (35+150) MHz range. High voltage on resonator makes up to 130 kV. The dielectric (quartz glass) cylindrical discharge chamber 5 with a diameter of 45 mm and length of 60 mm is placed inside the spiral.

An ions are extracting from plasma through the holes in extracting electrode 6 which is fixed by means of insulator 7 to holder 4. High voltage is supplied to resonator and extraction electrode through partition insulator 8. The difference between resonator U_R and electrode 6 U_e potentials makes extraction voltage U_{extr} .

To rise plasma density a ring-shaped permanent magnet 9 is placed inside of resonator and holes in electrode 6 are supplied with special insets, which are fabricated from magnetic steel. All another metallic elements of source are fabricated from nonmagnetic materials (stainless steel and copper). Beam parameters measurement were performed by means of beam control system 10.

Distinctive features of the source design are insulated RF power input unit 11 and system of working gas filling 12 into the chamber. In this case RF generator has a potential of ground, that allows to simplify the generator and gas filling system design and to increase RF power in the resonator up to some tens of kW. Use of the resonator provides practically complete absorption of RF power by plasma, increasing a degree of its ionisation and density.

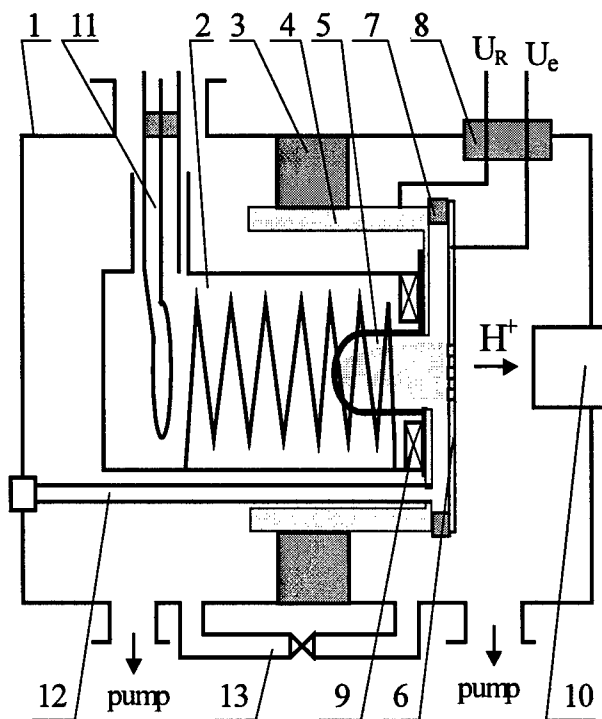


Figure 1 : The scheme of source design (see text)

An insulated RF power input unit 11 constitute coaxial design with circle coupling loop at the end.

A system of working gas filling 12 is fabricated from Teflon pipe. It's length was chosen proceeding from the highest electrical strength.

An insulator 3 divides vacuum container 1 into two independent vacuum compartments. At the back section (with resonator) working vacuum is not worse than 10^{-4} Pa, and in the forward section - not worse than 10^{-2} Pa. The pumping of sections is carried out by means of sputter-ion pump and turbo-pump correspondingly. At the stage of preliminary pumping pass-by system 13 is used.

Main units of source have following sizes:

resonator: diameter - 170 mm, length - 260 mm;

container: diameter - 520 mm, length - 500 mm.

Container is installed on the turbo pump module with sizes 1m x 1m x 1m.

¹ E-mail: bogdan@uni.mephi.ru

2 EXPERIMENTAL RESULTS

In experiments the extracting electrode had 6 holes with a diameter of 2 mm placed over the circle with a diameter of 30 mm and 1 hole at centre. The following results were obtained. In a continuous mode: ion energy (defined by resonator potential) $W_{H^+} = 7$ kV, extraction voltage $U_{extr} = 5$ kV, ion current $I_{H^+} = 5$ mA. In a pulse mode: $W_{H^+} = 70$ kV, $U_{extr} = 3$ kV, $I_{H^+} = 40$ mA. Working gas was hydrogen, particles - H^+ ions. The average RF power level in resonator was about 70 W in both cases (continuous RF generator was used). In comparison with similar devices RF ion source developed has the increased durability, gas profitability and power efficiency[2].

3 REFERENCES

- [1] Abramenko N.I. et al, *Proceedings of the II European Particle Accelerators conference EPAC - 90*, Nice, June 12 - 16, 1990, Vol. 1, p.p. 595 - 596.
- [2] Stepanov S.S., in *"Radiative accelerating arrangements"*, Moscow, Energoatomizdat, 1991, p.p. 3 - 10 (in Russian).

Abstract

We will present the beam-head dynamics calculations as well as the solenoid design and preliminary feasibility test results.

1 INTRODUCTION

2 THE 3.2 MV ELECTRON DIODE

[illegible]

Figure: 1 Main components of a 3.2 MV electrostatic injector.

In order to have a reliable machine the diode design has to minimize breakdown risks. This requirement translates into a design with maximum current extraction for a given maximum field stress. From final focus requirements at the end of the machine, the beam quality has to be controlled and the normalized emittance be maintained under 1000 pi-mm-mr.

For a given field stress limit, maximum current extraction is obtained from cathodes surrounded by a flat shroud as compared to diodes incorporating Pierce electrodes. On the other hand, the beam quality is better controlled by a Pierce electrode; flat shrouds produce hollow beams whose normalized emittance grow as being transported and accelerated along the induction linac. A compromise between the two conflicting requirements is to design the diode with a Pierce electrode assuming the maximum voltage holding capability that can be obtained using special surface handling procedures.

For the 2 kA case, this peak field is around 120 kV/cm on the cathode side of the diode and around 150 kV/cm on the anode side. For the 4 kA case the peak field is around 165 kV/cm on the cathode side of the diode and above 200 kV/cm on the anode side. For these designs the emittance at the end of the diode is under 1000 pi-mm-mr as calculated by EGUN.

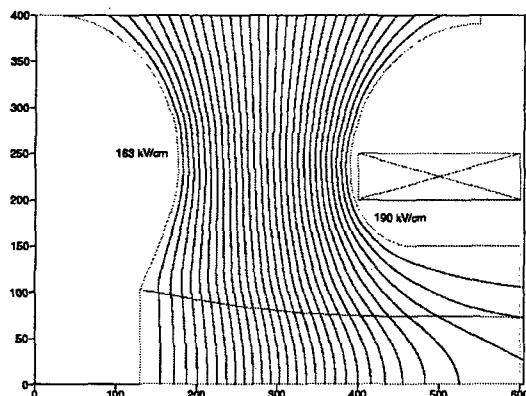


Figure: 2 Electron beam envelope and field equipotential lines as calculated by EGUN..

3 BEAM DYNAMICS IN THE INJECTOR

A two-dimensional particle-in-cell (PIC) slice (x-y) code [4] has been used to study the transverse beam dynamics of the electron beam generated at the diode as it is transported and accelerated along the first induction-accelerator section. This section consists of 8 induction cells each providing 200 kV of acceleration. Each cell contains a solenoid used to focus the electron beam.

Figure 3 shows the beam envelope for various off-energy components (beam-head) during the 400 ns energy rise time for the 2 kA case. The magnetic tune was chosen to confine the beam envelope within 60% of the aperture thus avoiding beam spillage on the pipe. Calculation for the 4 kA case show containment of the beam-head within 90% of the aperture leading to a possibility of beam spillage. To reduce the risk of beam spillage, we are considering shaping the focusing field during the beam rise time by using a time-dependent magnetic field.

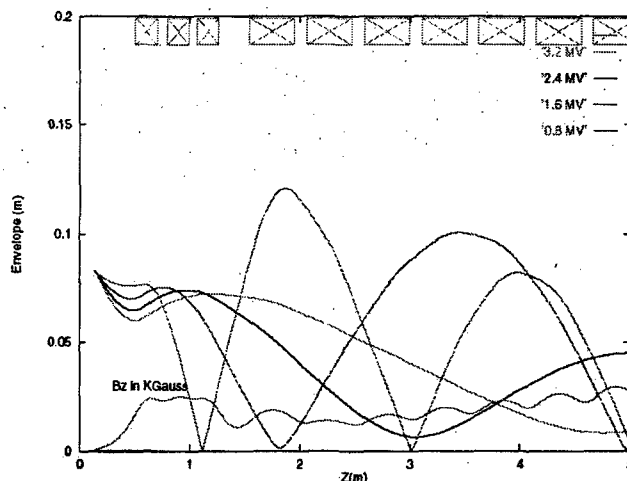


Figure: 3 EGUN simulation of the electron beam from source to the end of the first acceleration section (7 cells)

4 TIME-VARYING MAGNETIC FIELD SOLENOID

The additional focusing field, $B_z(t)$, for the 4kA case, is applied during the beam rise-time (400ns) to contain the beam envelope at lower energies and eliminate beam spillage. The required $B_z(t)$ field profile goes down from around 400 Gauss to 0 Gauss within 400ns, overlapping the beam rise time.

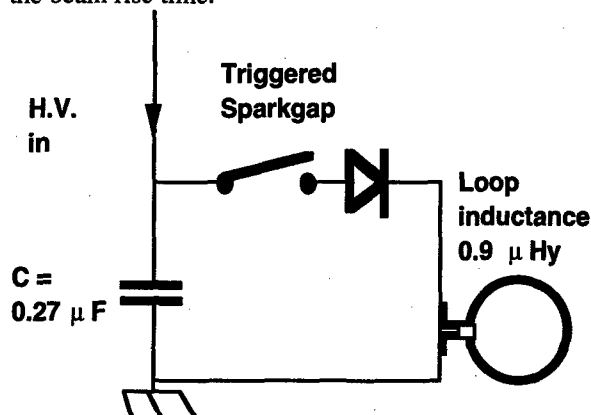


Figure: 4 $B_z(t)$ solenoid driver schematics.

The solenoid that generates the time-varying field, which consists of a single loop coil 10.5" in diameter, is placed in the beam tube under the anode shroud. The solenoid is driven by a simple 6kA, 1μs half sine wave current pulse. The solenoid driver (Figure 4) consists of an L Cringing-discharge circuit. An up to 30kV spark gap switch is turned-on at 600ns before the beam turn-on time. The current waveform (Figure 5) will be limited to a half cycle, so that it will not interfere with the main body of the beam, by using high current (1.5kA), high voltage (10kV) semiconductor diodes. We measured the effect of the beam tube walls on the $B_z(t)$ for various solenoid diameters. Following the measurements results we limited the solenoid diameter to 60% of the beam tube diameter where the tube wall effect on $B_z(t)$ is negligible.

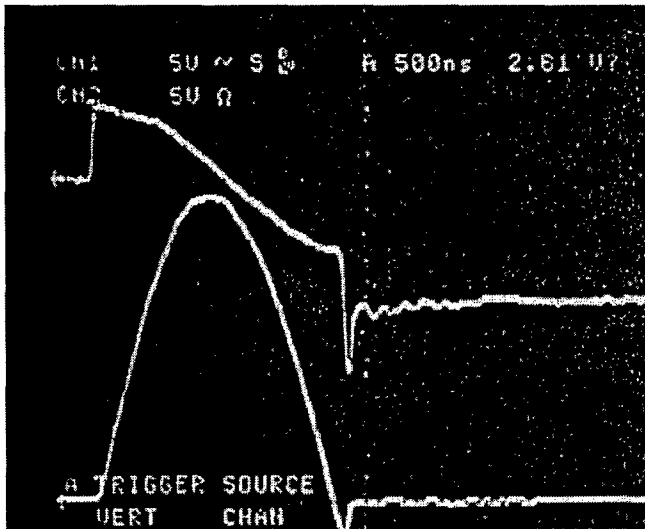


Figure: 5 Waveform of the 3kA current (bottom curve) driving the time-varying solenoid.

5 DIODE DESIGN SUPPORT EXPERIMENTS

Scaled experiments are under construction to support the DARHT-II injector design.

The LBNL RTA 1MV, 1kA, 300 ns injector[3] diode configuration allows the extraction of a high quality, high density beam. The injector AK gap, cathode shroud material and shape were designed to allow the study of vacuum breakdown issues in the diode in the presence of a beam.

The RTA thermionic source heat management and support stability were tested. Thermocouples can be placed along the source support to map the temperature and evaluate flow in the cathode assembly. Furthermore the gap between the source and cathode shroud was monitored during the source heating experiment. This gap has to be small (<5mm) to insure a high quality beam. Initial measurements using a hot wire pyrometer, performed on the RTA 3.5" diameter source at a cathode surface temperature of 1060 °C showed a temperature uniformity within 5°C. A temperature of 30°C was measured using a thermocouple at the cathode assembly input flange showing a good heat management. A gap around 24 mils between the source surface and the cathode shroud was observed using a survey telescope looking at the source through a front window.

Initial breakdown experiments were performed with a long duration (8 μs discharge time constant) 200 kV, 0.5 kJ pulser. Using machine-polished stainless steel, molybdenum and copper electrodes we measured breakdown fields above 400 kV/cm in a 3 mm gap. Figure 3 shows that the breakdown field is independent on vacuum pressure within a range of 10(-8) to 10(-4) Torr. We observed more damage on the copper and stainless steel electrodes and no difference in the breakdown voltage between stainless steel, copper and molybdenum electrodes.

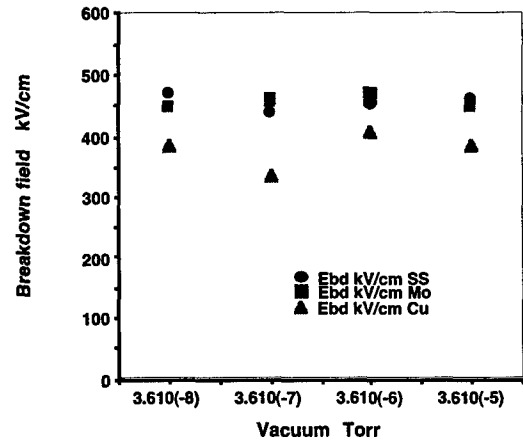


Figure: 6 Breakdown field dependence on vacuum pressure and electrode material.

6 ACKNOWLEDGEMENTS

This work was performed under the auspices of the U.S. Department of Energy under contract AC03-76SF00098. We thank Dr. D. Spreyn and his colleagues at SLAC for fruitful discussions on breakdown issues.

7 REFERENCES

- [1] E Henestroza, "Injectors for Heavy Ion Fusion", invited talk, 11th International Workshop on Laser Interaction and Related Plasma Phenomena, Monterey, CA, October 25-29, 1993. AIP Conference Proceedings 318, Ed. G.H. Miley, pp 577-582.
- [2] W.B. Herrmannsfeldt, "EGUN- An electron optics and gun design program," SLAC-Report-331, 1988.
- [3] S. Lidia et al., "Initial Commissioning Results of the RTA Injector", this conference.
- [3] B. Carlsten, "The PIC-xy 2-DSLICE code", private communication.

A MULTIPLE-BEAM INJECTOR FOR HEAVY ION INERTIAL FUSION*

J. W. Kwan, O. A. Anderson, D.N. Beck, F. M. Bieniosek, C. F. Chan, A. Faltens, E. Henestroza, S. A. MacLaren, P. A. Seidl, LBNL, Berkeley, CA; L. Ahle, D. P. Grote, E. Halaxa, C. T. Sangster, LLNL, Livermore, CA; W. B. Herrmannsfeldt, SLAC, Stanford, CA

Abstract

In a typical heavy ion fusion driver design, the induction linac requires a multiple beam injector. We present a conceptual design for an 84-beam injector system with each beam channel carrying 0.5 A of beam current. Each channel starts with a 10-cm diameter surface ionization source followed by a 1.7 MV electrostatic Einzel lens-type preaccelerator and an electrostatic quadrupole (ESQ) matching section. The preaccelerator and matching section are 0.7 m and 5.0 m long respectively. The array has an overall diameter of 3.0 m at the ion source end and 1.0 m diameter at the exit.

1 INTRODUCTION

For heavy ion driven inertial fusion, the primary approach in the US is the induction linac [1]. Typical beam energy delivered to the target is ~5 MJ with a pulse length of ~10 ns and a particle kinetic energy ~5-10 GeV. Thus the total beam charge is ~0.5-1.0 mC. This beam charge is supplied by the injector, although the pulse length here is typically less than 20 μ s long, based on the volt-sec limitation of the induction cores. The total beam current output from the injector is therefore expected to be in the order of 50 A. Typical ions of interest are those of Bi, Pb, Hg, Cs, Xe, Rb, K, Ar, and Ne, generally singly charged, but higher charge states are also of interest in some driver designs. Some lighter ions such as K, Ar and Ne are included because at the early stages of driver development they provide an opportunity to do experiments at driver-scale ion velocities on a medium length accelerator facility.

There are two main reasons for producing the 50 A beam current using many beams of smaller current (e.g., less than 1 A each). First, multiple beams provide better target illumination symmetry. This is an important requirement for high gain direct-drive targets. Second, heavy ion beams have significant space-charge effects, so the current per beam is limited by the focusing capabilities of the beam extraction and transport systems. Our goal is to design an injector that will produce an array of parallel beams feeding into the channels of a multiple-beam induction linac.

* This work is supported by the Office of Fusion Energy Science, US DOE under contract No. DE-AC03-76SF00098 (LBNL) and W-7405-ENG-48 (LLNL).
Email: jwkwan@lbl.gov

2 OPTIMIZING CURRENT DENSITY

Beam focussing in an induction linac can be achieved by using either electrostatic quadrupoles (ESQ) or magnetic quadrupoles. At the front end where the ion velocity is still low, ESQs are more effective and economical than magnetic quadrupoles. By considering the line charge density in ESQ beam transport, one can determine the average beam current density J_{ave} for an array of beams [2]. For a given total beam current, higher J_{ave} means smaller induction cores and therefore lower cost.

Since the voltage spark down threshold scales favorably with small ESQs, the optimum J_{ave} occurs at a point when the ESQ size cannot be further reduced in order to allow enough beam clearance for possible electrode alignment and beam steering errors. For example, in the ILSE/Elise design [2], the ESQs at the beginning of the induction linac (2 MeV energy) have a bore radius of 2.33 cm which corresponds to a conservative clearance of 1.0 cm. In this case, the required beam current in each channel is 0.8 A of K^+ ; with an average beam radius of 1.0 cm, and a current density of 254 mA/cm² in the channel. Since the ESQ electrodes are round rods with a radius 8/7 times the bore radius, the current density averaged over the entire array is only 16.5 mA/cm². A more aggressive design using smaller clearance will result in less beam current per channel but a higher J_{ave} .

At first look, it appears that the injector will require an array of ion sources that can provide the above J_{ave} . However, the actual critical component is the preaccelerator ion gun, which is responsible for accelerating the beam to a suitable energy and focussing the beam envelope before injecting into the ESQ matching section. In our earlier attempt to design a 2 MV ion gun using the conventional Pierce type column, we found that the beam current was well below 0.5 A at the sparkdown limit. There are two ways to deal with this problem: either reduce the gun to a simple Pierce diode by starting the ESQ section at a lower energy or optimize the gun performance (by using an accel-decel scheme) to reach an acceptable current limit. The previous ILSE/Elise injector was constructed according to the first method. Its 750 kV Pierce diode extracted 0.8 A K^+ . Since the ESQ dimensions scale inversely with beam energy (for the same current), J_{ave} at the ESQ entrance was reduced to ~1.0 mA/cm². In the following sections, we present an injector design using the second method. It is based on a 1.7 MV ion gun capable of transporting 0.5 A K^+ current.

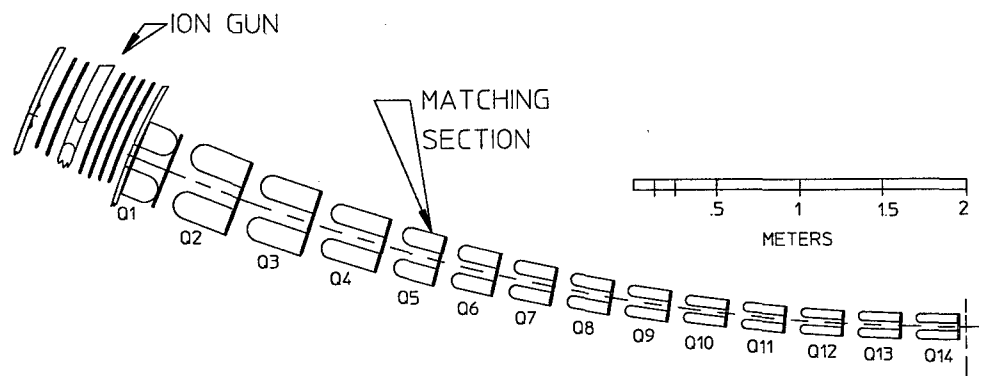


Figure 1: Schematic diagram of a single beamline at the edge of the injector array.

3 THE PREACCELERATOR AND ESQ MATCHING SECTION

According to our past experience in building the ILSE single beam injector [3], an injector that allows each beam to occupy an independent focussing channel and vacuum housing will be unacceptably large and costly. Therefore it is essential to arrange multiple beams in an array by sharing common electrodes, supporting structures, power supplies and vacuum systems.

Each beamline of the multiple-beam injector array consists of a gun and a matching section. Figure 1 shows a schematic diagram of a single beamline at the edge of the array. The gun is composed of a 200 kV diode extracting 500 mA of K^+ from a 10-cm diameter source aperture, followed by an Einzel lens column that focuses and accelerates the beam to 1.7 MV. The peak electric field stress in the gun is kept below 100 kV/cm to avoid electrical breakdown. Under this restriction, a standard Pierce-column (beam energy increases monotonically) cannot produce a converging beam. Our solution is to use Einzel lens (accel-decel) to provide extra beam focusing without exceeding the breakdown limit.

The matching section will simultaneously compress the beam envelopes and transform a round beam into an elliptical shape in order to match the alternating-gradient (AG) focusing lattice in the induction linac. As shown in Fig. 1, the ESQ electrodes in the matching section gradually decrease in size, thus a multiple beam array has the shape of a funnel. In order to avoid a sharp bend at the linac, the beam trajectories are deflected by a small angle at each ESQ module in the matching section. Eventually, the beams are brought together into parallel channels just before injecting into the downstream lattice.

In an ideal quadrupole, the transverse electric field gradient is constant within the aperture, thus an off-center beam will experience a combination of quadrupole and dipole fields; the dipole field will steer the beam centroid. In most parts of our design, the required beam displacement is small compared to the beam aperture. The beam envelope has a maximum excursion at the 2nd quadrupole (Q2), therefore the overall size of the array (and the required bending angle) is dictated by the required bore

diameter at Q2. In the present case, the ion guns are straight and the ion sources are separated by 30.5 cm. A surface ionization source can meet the specifications in beam current and low emittance (normalized edge $\epsilon < 1$ pi-mm-mr) [4]. As long as Q2 is dominating the size requirement, higher J_{ave} at the ion source is not needed.

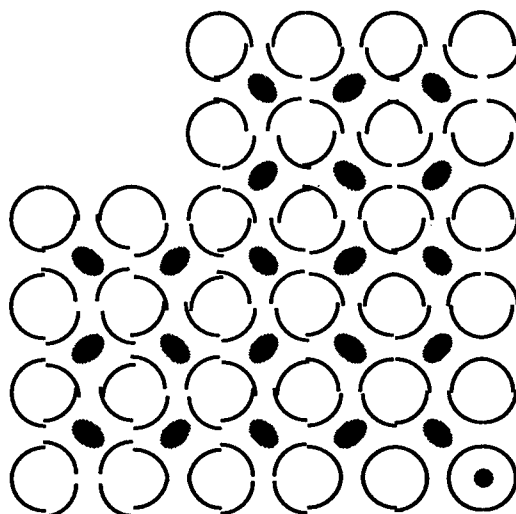


Figure 2: Cross section view of 1/4 of an 84-beam array.

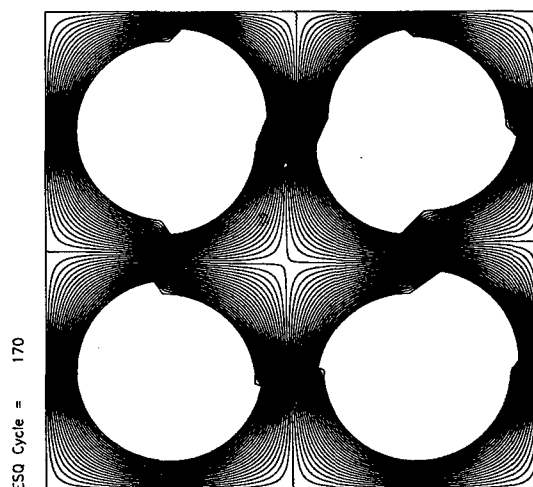


Figure 3: POISSON field calculation of a modified ESQ.

3.1 Multiple-beam array

The beamline on the edge of the array (as shown in figure 1) has an angle of 333 mr. There is no bending at the first 2 quads where the beam envelopes are large. Q3 and Q4 each provides about 33 mr bending, while the remaining angle is equally divided among Q5-Q14. In bending the beam, Q3 and Q4 are offset by ~9 mm but the offset gradually reduces down to 1.5 mm at the final quad.

One advantage of packing multiple beams in an array is to share electrodes between beams. However the bending requirement complicates matters significantly because neighboring beams bend by different angles. In addition, there is a polarity change between adjacent quadrupoles such that the required offsets are in opposite directions. Figure 2 is a cross section view of 1/4 of the array at the 4th quadrupole plane. It shows how the electrode surfaces need to be altered (from a perfect circular pattern) in order to bend the beams through the desired arcs.

A simple ESQ geometry using round rods has a good field aperture of nearly 80% of the mechanical aperture. However here the ESQ electrodes are divided into 4 sections, each facing a given beamlet and with a fixed horizontal and vertical offset. Figure 3 shows the result from POISSON field calculation of the worse case (ESQ at the edge of the array). It confirms that aberrations are introduced by the distortions in the electric field structure. These aberrations reduce the effective aperture of the quadrupoles (possibly by as much as 50%). Thus in order to avoid introducing emittance growth, we may consider lengthening the ESQ section or enlarging the ESQ array transversely.

Figure 4 is a drawing of an ESQ electrode. Typically the surfaces are at a slight angle, ~2° with respect to the electrode axis, in order to produce the funneling effect. The electrodes are hollow for minimizing weight. They must be fabricated and mounted onto a spherical support plate with a positioning tolerance of about 0.1 mm. Based on preliminary price quotes, the most cost-effective way in machining these ESQ electrodes is to use wire electrical discharge machining (EDM). An initial bid for fabricating these ESQ electrodes was priced at \$1500 each.

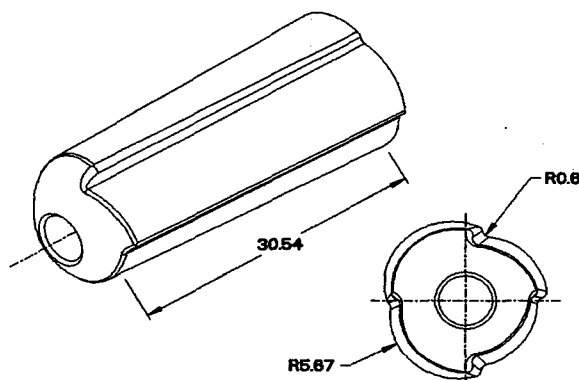


Figure 4: Drawing of a Q4 electrode near edge of array (nominal radius is 5.5 cm).

One other way to funnel many beams without using offset electrodes is to slowly shrink the quadrupoles. In this case, one-half of the beams in the array at any given quadrupole plane will be bending in the wrong direction, but over any two successive quadrupole planes the net bending will be correct for all beams (similar to AG focusing). In order to avoid excessive space charge expansion in the z-direction, the matching section can not be arbitrary long. Preliminary simulation result indicated that a 50-m length is probably acceptable. At this point, it is not clear which method is more cost effective: a 50 m matching section with simple round rod electrodes or a 5 m matching section with specially shaped electrodes.

3.2 Multi-aperture extraction and preacceleration

Although the present design has already reduced the overall size of a multiple-beam injector compared with those in the previous designs using separate beamlines, the array is still very large at the source end. At present, we are developing an alternate concept that will produce a significantly smaller injector—one that possibly does not require a funnel-shaped geometry. The basic idea of this concept is to use miniature beamlets to overcome the beam transport problem mentioned in section 2. A multi-aperture grid at the ion source can obtain high current density beamlets. Since the apertures are small, each beamlet will have a current of only a few mA and can be focused while accelerating to ~1.7 MV. After preacceleration, the beamlets are merged together to form beams of 0.5 A each, ready for injecting into an ESQ channel. There will be emittance growth from beam merging, however the effect can be minimized by using a large number of beamlets and high grid transparency. Our preliminary estimation indicates that an injector system based on this principle is promising but requires further studies.

4 SUMMARY

In our conceptual design for an 84-beam injector system for HIF, the beamlines are arranged in an array that has the shape of a funnel. Each beamline consists of an ion source, a 1.7 MV ion gun and an ESQ matching section. Beam steering is done by displacing the ESQ electrodes. We are also continuing to explore alternate concepts that are either more compact or more cost effective.

5 REFERENCES

- [1] R.O. Bangerter, Proc. of Inter. Symp. on Heavy Ion Inertial Fusion, Frascati, Italy, May 25-28, 1993, Nuovo Cimento 1445 (1993).
- [2] J. W. Kwan, et al, Proc. of Inter. Symp. on Heavy Ion Inertial Fusion, Princeton, New Jersey, USA, Sept 6-9 (1995); Fusion Engineering and Design, 32-33, p299, (1996).
- [3] S. Eylon, E. Henestroza, W.W. Chupp, and S. Yu, Proc. of Inter. Symp. on Heavy Ion Inertial Fusion, Frascati, Italy, May 25-28, 1993, Nuovo Cimento 1509 (1993).
- [4] J. W. Kwan, W.W. Chupp, and S. Eylon, Proc. Particle Accelerator Conf., Vancouver, May, (1997).

OPERATION EXPERIENCE OF CYCIAE30 INJECTOR

Cengjie Chu, Tianjue Zhang, Mingwu Fan

China Institute of Atomic Energy, P. O. Box 275, Beijing 102413, P. R. China

Abstract

A 30 MeV compact cyclotron, CYCIAE 30 has been working as a supplier of medium and short live time radioactive isotopes for more than four years. To meet the increasing requirements of medical isotopes, it is asked that the machine should continuously run at a high level of beam intensity. But last September, it was difficult to get the beam more than 100 μA . Some troubles came from the injector were found in the injection system. In this paper, the injection system and the existing problem will be described briefly and the proposal to improve the injection system is given.

1 INTRODUCTION

CIAE medical cyclotron is a fixed-field, fixed-frequency isochronous machine. Maximum energy of accelerating H- ions is up to 30 MeV and extracted beam intensity of more than 350 μA has been archived. Low power consumption less than 100 kW is suitable for industrial use. Design of the machine was reported elsewhere [1,2,3].

An external multicusp ion source is used for CYCIAE 30. The H- beam produced from the ion source is injected into the central region axially. The injection line consists of steering magnet, Einzel lens, buncher, solenoid and electrostatic deflector, a high voltage electrostatic field channel. Through the channel the beam will enter the machine horizontally away from vertical direction. The channel should keep spiral shape since the particle affected simultaneously by magnetic field in the central region. The beam will be further accelerated by the RF field once the particles leave the injector channel and enter the magnet gap. Simulation of the beam dynamics

were done to keep the beam loss as less as possible in the central region [4]. Fig 1 shows the central region of CIAE 30 MeV cyclotron.

Four years after the machine put into operation, the injection system works at a reasonable efficiency. The machine usually worked with the beam more than 200 μA according the isotopes production purpose until last September when the machine had a hard time to get 100 μA beam. Two positions damaged were found by beam when the central region of the cyclotron was checked. One spot is inside the deflector, a part of the electrostatic channel. That is easy to be understood since the beam pass through that channel. But another damaged place is located on the wall of RF shielding wall. Thus the further study for the injector was carried out as shown following.

2 ELECTROSTATIC FIELD FORMED BETWEEN THE DEFLECTOR AND RF SHIELDING PARTS

The beam dynamics study did when the machine designed was based on an assumption that the ion after the deflector effected by two field forces only: magnetostatic field and RF field from Dee puller. Before that the electrostatic field between the two electrodes of the deflector would change the beam direction from vertical to horizontal.

From the damaged spot on the wall of the RF shielding parts, we suppose that there is another field exists in the region between the deflector electrode and RF shielding wall. The field is estimated by a three dimensional finite different code. The geometry used in the calculation is shown in Fig. 1. And the potential distribution is given in Fig. 2. The maximum electric field in the interested region is as high as a half of those inside the deflector channel. In fact, another deflection channel is formed between a deflector electrode and RF shielding wall. This field will make the injected beam expand and part of beam will enter this extra deflection channel. It would be more serious once the current of the steering magnet is not set properly. The beam would be deflected into the shielding parts by this field. That is the reason why the RF shielding parts was damaged. A new deflector is used to replace the old one now. The machine seems work well for months.

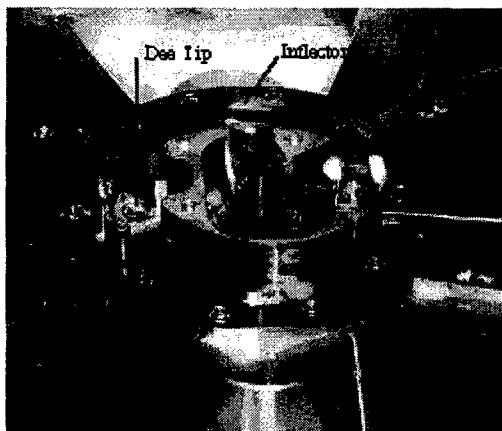


FIG. 1. Central Region of CIAE 30 MeV Cyclotron

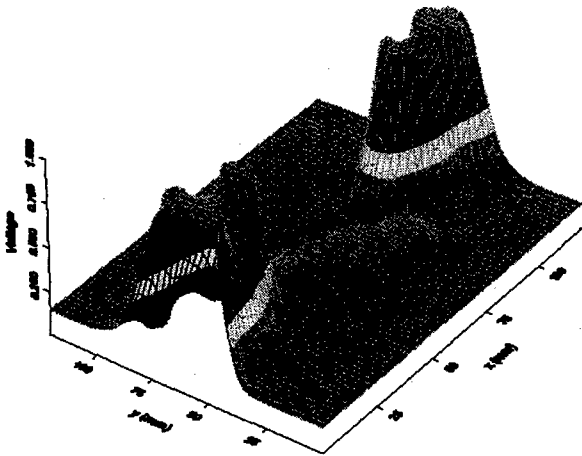


FIG. 2. The potential distribution in the central region of CYCIAE 30

3 OPTICS CALCULATION OF INJECTION LINE

The beam damages the deflector wall since beam divergence inside the deflector channel. Some stripped copper skin is sometimes found during the operation caused by beam loses on the electrodes' wall. Time after time the gap between the electrode increases. Then higher deflecting voltage would be required since the gap becomes bigger. Also the damaged spot destroy the channel shape that would make injection even more difficulty.

The operation records of the cyclotron show that the focus of the beam line is not strong enough since the measured beam becomes higher with the lens current increasing. The injection line is shown in Fig 3 (the solenoid is inside the magnet of the cyclotron). To improve the injection, the beam spot should be limited to smaller size. Several schemes have been tried to provided the better focus of the beam line and smaller beam envelope inside the deflector.

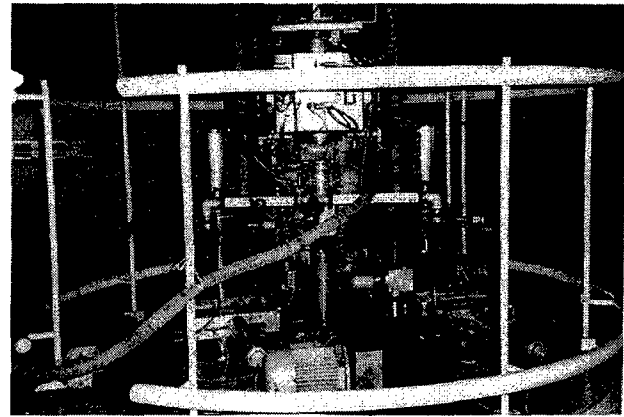


FIG. 3. The injection line of CYCIAE 30

- One triplet is used to replace the solenoid (E&T).
- Two triplets are used. One replaces the solenoid and the other one replaces the Einzel lens (T&T).
- One triplet is used to replace the Einzel lens (T&S).

The simulation results show that One triplet is used to replace the Einzel lens is quite competent to control the beam profile at a better level. The spot at the 8 mm width inlet of the deflector is smaller than 5 mm. The required current of the solenoid is relatively lower. The comparison of the results calculated by TRANSPORT [5]

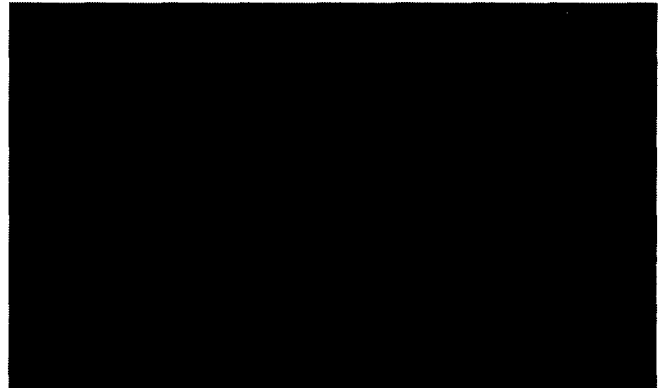


FIG. 4. The Envelope calculated by TRANSPORT is listed in table 1. And the envelope is shown in Fig 4.

TABLE 1 The Results Comparison of Different Schemes

	Rmax (outside the main magnet)	Rmax (inside the main magnet)	Xmax on target	Ymax on target	Magnetic Field of the Solenoid
E&S	0.95 cm	0.96 cm	0.24 cm	0.24 cm	2.2 kG
E&T	0.95 cm	1.37 cm	0.42 cm	0.63 cm	
T&T	1.63 cm	1.10 cm	0.57 cm	0.21 cm	
T&S	2.33 cm	1.21 cm	0.25 cm	0.25 cm	1.8 kG

4 THE QUADRUPOLE MAGNET DESIGN

Quadrupole magnet is widely used for beam focus, such as in storage ring and beam transportation system. In the past, quadrupole pole face designed parabolized since conform algorithm used for the field simulation. In the case, the infinite permeability of iron is assumed to keep the constant field gradient in the beam area. But parabola pole face brings following shortcomings: machining difficult, assembling difficult. Besides, the field distribution is not expected constant, but distorted since iron saturation is not considered when the magnet performance computed. The numerical simulation techniques are used to design this kind of magnet. The shape of pole can be chosen freely according to the real requirements and simple machining procedure. According to the magnetic field gradient of a quadrupole for the injection line, The quadrupole magnets are designed and shown in Fig 5. The pole face is broken line shaped. The inner diameter is $\Phi 78$ mm. The good field region is about 80 %. The magnetic field gradient from the design is linear. They are shown in Fig 6.

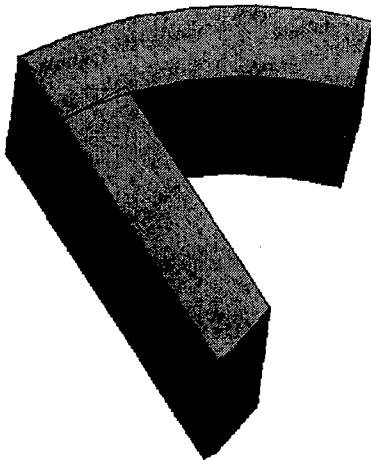


FIG. 5. The Geometry of Quadrupole Magnet with Broken Line Profile Pole Tip

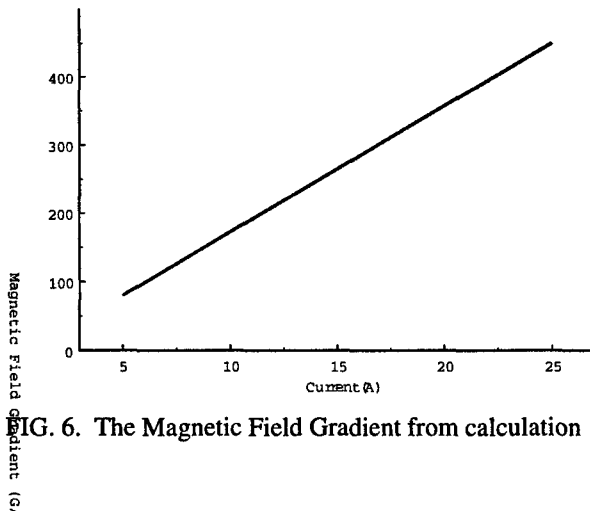


FIG. 6. The Magnetic Field Gradient from calculation

5 CONCLUSION

Injection system is an important part for CYCIAE type cyclotron. From our experience the machine works well once the injector system work well. To improve the machine some R & D job must be taken. A better ion source and a better designed injection line are to get higher beam intensity. Some experiences have been proved that the bottleneck of the machine is ion source and injection system since the magnet quality has ensured very little beam loss when the ion accelerated inside the cyclotron.

6 REFERENCES

1. Mingwu Fan and Tianjue Zhang, Proc. Of PAC'97, 0-7803-4376-X/98, 1998, IEEE, pp3834-3836.
2. Mingwu Fan et al, Proc. of International Conference on Electromagnetic Field Problems and Applications, Wuhan, China, 1996.
3. Mingwu Fan et al, Proc. of PAC'93, 0-7703-1203-1/93, 1993 IEEE, pp2841-2843.
4. Tianjue Zhang and Mingwu Fan, Proc. of The 6th CHINA-JAPAN Joint Symp. on Accelerators for Nuclear Science and Their Applications, Chengdu, 1996
5. TRANSPORT-PC is a PC version of TRANSPORT maintained by CIAE.

MULTICUSP ION SOURCE FOR INDUCTION LINAC APPLICATIONS*

J. Reijonen[†], M. Eardley, R. Keller, J. Kwan, K. N. Leung, D. Pickard[‡], R. Thomae
and M. D. Williams, LBNL, University of California, Berkeley, CA 94720, USA

Abstract

At LBNL we are investigating the use of gaseous ion sources for induction linac applications such as heavy ion inertial fusion. Typical requirements for the ion source is to produce 20 μ s pulses with a rise-time of 2 μ s. The current density should be greater than 100 mA/cm² at a duty cycle of 10 Hz [1]. Noble gases such as krypton, neon and xenon will be used. The source used for the measurements described in this paper was a standard 10 cm in diameter multicusp source with RF-discharge. Current densities of more than 400 mA/cm² at RF-power levels of 20 kW using neon discharge were demonstrated. With heavier elements such as Ar, Kr and Ne, current densities of 200 - 300 mA/cm² were obtained at the same extraction voltage of 20 kV. By using a starter filament, the rise-time has been reduced from 20 μ s to 5 μ s. Beam emittance was measured using a pepper-pot device. An argon beam showed that the normalized emittance is of the order of 0.1 π mm-mrad.

1 INTRODUCTION

For some years there have been studies to produce energy by Heavy Ion Fusion (HIF). There are proposals to accelerate heavy ions in a multi-channel induction linac. At LBNL, the Plasma and Ion Beam Technology Group has been investigating the use of a gaseous ion source for production of the heavy ion beam. RF-multicusp sources [2] have been reported to deliver high current density of positive and negative ions [3]. The advantage of the RF-driven plasma is the use of various different gases and metallic elements for ion production at high current density. In this paper we present measurements on inert gas elements Ne, Ar, Kr and Xe.

2 EXPERIMENTAL SETUP

2.1 Source setup

The RF-amplifier is a pulsed 65 kW supply with maximum duty factor of 0.5% (100 μ s, 50 Hz) at frequency of 2 MHz. The RF-power is delivered through a 50 Ω coaxial transmission line to the impedance matching network. The purpose of the matching network is to match the 50 Ω impedance of the amplifier to the impedance of antenna immersed to the plasma. To aid starting the

plasma, a negatively biased tungsten filament, with respect to the source body is used.

All experimental measurements were carried out using a standard 10 cm multicusp source, shown in Fig 1. The plasma chamber has an inner diameter of 10 cm and is surrounded by 20 SmCo magnet columns. Two pairs of magnets in the source back plate enhance the cusp confinement. Plasma is generated by a two-turn quartz-antenna. The gas is introduced to the plasma chamber through a needle valve and the absolute pressure in the source is measured by a capacitance manometer. A small starter filament was used to feed seed electrons to the source.

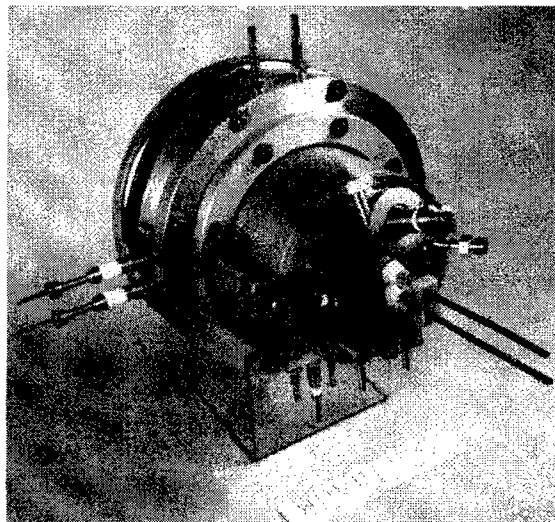


Figure 1. RF driven 10 cm in diameter multicusp ion source with starter filament.

The extraction system consists of a plasma electrode with an aperture of 3 mm for current density measurements and an aperture of 5.5 mm for emittance measurements. This is to simulate the proposed hole size of the HIF source. The faraday cup was located 5 cm from the grounded second electrode. The faraday cup is magnetically shielded to suppress the secondary electrons.

The beam emittance was determined using a "pepper-pot" measurement device. This device consists of a discriminator and a film holder plate. The discriminator is a thin plate with small holes drilled to form a certain pattern. Tantalum was used as a discriminator material.

* Work is supported by a LBNL LDRD grant and by US DOE under contract No. DE-AC03-76SF00098

[†] Email: reijonen@mh1.lbl.gov

[‡] Permanent address: Department of Applied Physics, Stanford University

The hole diameter and the thickness of the plate was 200 μm . The film is placed at a distance of 2 cm from the discriminator. Different film materials like kapton, tantalum, stainless steel, mylar and aluminium coated mylar were used. It was found that for our beam parameters a mylar film was the most advantageous.

3 EXPERIMENTAL RESULTS

3.1 Current Density Measurement

The ion current was measured using four different gases: Ne, Ar, Kr and Xe. The current was measured as a function of acceleration voltage. In Fig 2 the results for the krypton beam is shown. From this result the saturation current is determined.

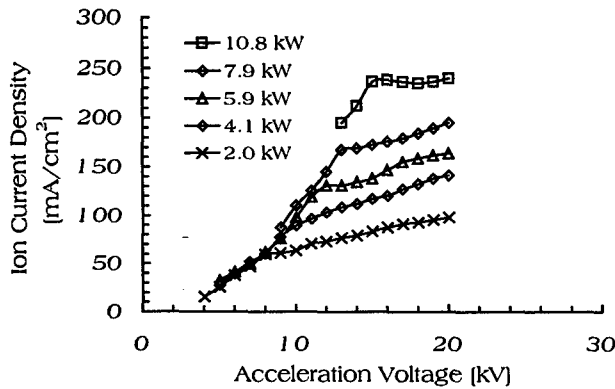


Figure 2: Extracted krypton beam current as a function of acceleration gap voltage. The saturation current is determined from this graph.

In Fig. 3 the current density as a function of RF-power for the four elements is shown. The pressure is selected so that it gives the maximum ion current. The current density is calculated from the measured saturation current values. In these measurements, it is found that the neon gas required higher pressure to sustain stable plasma.

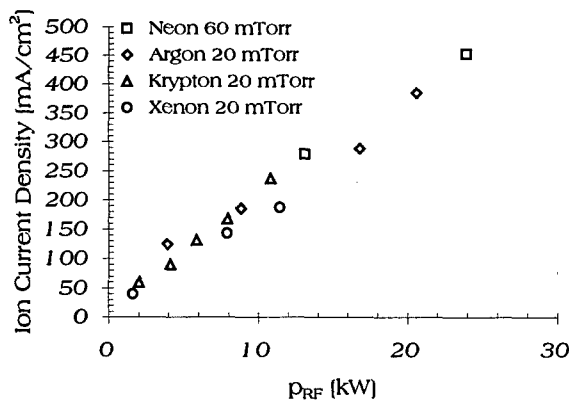


Figure 3: Current density as a function of RF-power for different elements.

3.2 Rise-time measurement

The rise-time of the pulses is measured using 80 μs discharge pulse. Two gases were used, namely Neon and Krypton. The measured rise-times are displayed in Fig 4. For the rise-time measurement the starter filament position was optimized to achieve stable plasma at the low source pressure.

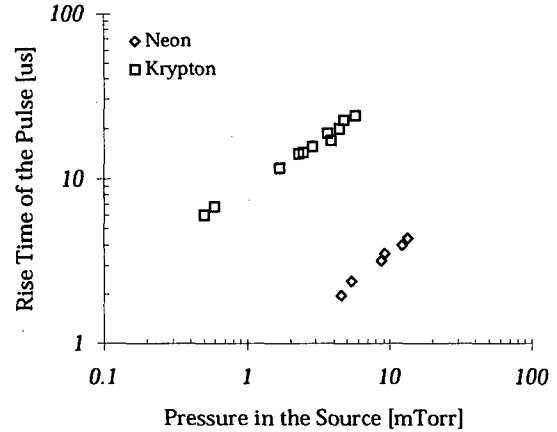


Figure 4: Rise-time of discharge pulses with two different gases as a function of source pressure. In the case of neon gas the rise-time is order of magnitude smaller compared to krypton. The shorter rise-time may be due to the higher mobility of neon ions.

3.3 Emittance measurement

The beam emittance was measured using a "pepper-pot" device. This device consists of a discriminator, which is a thin plate where tiny holes are drilled. Behind the plate is a film, where beamlets form a pattern. From the film patterns the emittance can be determined. For this purpose the patterns were measured by means of a microscope. An ellipse was fitted around the measured data points. The equation [4] for an ellipse is

$$r' = \pm \frac{B}{A} \sqrt{A^2 - r^2} + Cr$$

Where A, B and C are variables that must be fitted to the measured points in the r - r' phase space. The r and r' are the radius of the beamlet from the beam axis and the angle of the beamlet respectively. The emittance in the r - r' plane is then calculated using A and B simply

$$\epsilon = \pi A \cdot B$$

In Fig 5 an example of such a fit is shown for an argon beam.

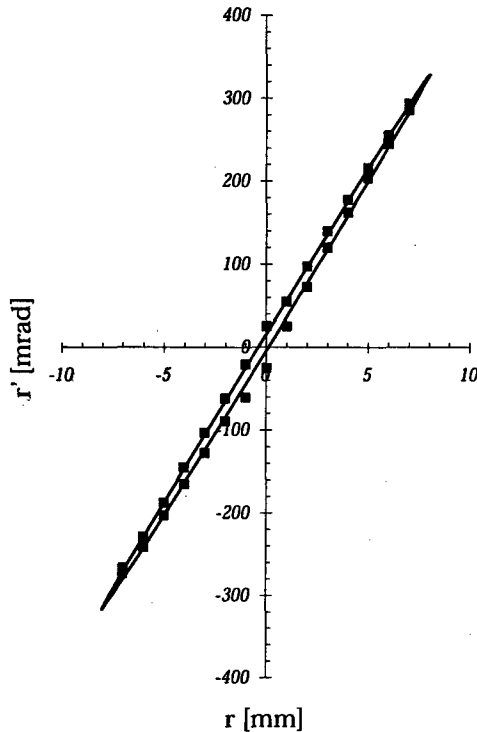


Figure 5. The emittance plot of a 20 kV argon beam at 0.2% duty factor.

The normalised emittance for 20 kV argon beam is of the order of 0.1π -mm-mrad and for 20 kV krypton beam, 0.08π -mm-mrad.

4 DISCUSSION

We have demonstrated that it is possible to generate current density of 100 mA/cm^2 at a RF-power level of 5 kW for all gases. The current density increases linearly in the measured power range, i.e. even higher current densities can be achieved using higher RF-power. Furthermore in the multicusp ion source, the plasma is known to be uniform in large area in the extraction region, which allows one to use a multiaperture extraction system for high current applications like HIF.

For the current density measurements presented, the pressure in the source was fairly high (order of few tens of mTorr). This can be reduced significantly by optimising the starter filament position and current. The higher pressure, in the case of neon (compared to krypton, argon and xenon) is due to the low ionisation cross-section of neon

In the rise-time measurements, the chemically etched tip of the filament was positioned behind the RF-antenna coil in cusp field free region. This enables the operation of the source at lower pressure. The difference in the rise-times

between neon and krypton can be explained because of the higher mobility of the neon as a lighter element.

The emittance of the pulsed (0.2% duty factor) 20 kV argon beam was measured to be 105π -mm-mrad, which corresponds to a normalised emittance of 0.1π mm-mrad. The krypton beam emittance (80π mm-mrad) is slightly smaller.

5 REFERENCES

- [1] J. W. Kwan, "Ion Sources for Heavy Ion Fusion Induction Linacs", 12th Inter. Symp. on Heavy Ion Inertial Fusion, Heidelberg, Germany, Sept. 1997
- [2] K. N. Leung et. al., Rev. Sci. Instrum. 69 (2), 962 (1998)
- [3] K. N. Leung et. al. NIM B74, 291-294 (1993)
- [4] R. Keller et. al. IEEE Trans. Nucl. Sci NS-32, p. 2579 (1985)

HALF-POWER TEST OF A CW PROTON INJECTOR WITH A 1.25-MeV RFQ*

G. Bolme, L. Hansborough, T. Hardek, D. Hodgkins, D. Kerstiens, E. Meyer, J. D. Schneider, J. Sherman[#], H. V. Smith, Jr., M. Stettler, R. R. Stevens, Jr., M. Thuot, L. Young, T. Zaugg [Los Alamos National Laboratory, Los Alamos, NM], A. Arvin, A. S. Bolt, M. Richards [Savannah River Site, Aiken, SC], P. Balleyguier [CEA-Bruyeres le Chatel, France], J. Kamperschroer[General Atomics, San Diego, CA]

Abstract

A 75-keV, 110-mA cw proton injector capable of pulsed operation has been developed for testing the LEDA 6.7-MeV cw radio frequency quadrupole (RFQ). Part of the preliminary development of this injector included operation of a 1.25-MeV cw RFQ at beam currents up to 100 mA. The 75-keV LEDA injector was modified to operate at 50 keV for these tests. We report here on the operational experience of the 1.25-MeV RFQ where 50-mA beam current was accelerated through the RFQ with 90% transmission. This half-power operation is of interest because (1) the injector beam current monitoring was more reliable, and (2) sufficient rf power was available to ensure the design cavity fields. These two features simplify the comparison of injector-RFQ performance with design codes. The information obtained from these studies will be applied to the 75-keV injector during the LEDA 6.7-MeV RFQ commissioning.

1 INTRODUCTION

Commissioning and startup of high-power cw RFQs[1] and cw accelerators[2] require initial operation at lower beam powers with pulsed and/or lower dc current beams. This lower-power operation allows insertion of diagnostic devices, which would otherwise be destroyed by the beam. Beam power can then be ramped up by guidance from design codes, previous experience, and careful attention to cw beam monitoring.

A 75-mA, 1.25-MeV cw RFQ[3] tested at Los Alamos[4] was commissioned by using a half-power injector beam operating in dc mode. In this paper we will discuss the injector design considerations for the half-power 1.25-MeV RFQ commissioning, and then will present the measured transmission results through the RFQ. This work confirms earlier design calculations[5] which predicted the 1.25 MeV RFQ transmission would be 90% at 50-mA accelerated RFQ current. A motivating factor for this work was injector development for the commissioning of a 6.7-MeV, 100-mA RFQ[6]. We refer to 50-mA operation as "half-power" because previous

measurements[7,8] have obtained 100-mA beam current (25 mA greater than design) from the 1.25-MeV RFQ.

2 THE 50-KEV INJECTOR

A 75-keV injector based on a microwave proton source [9], has been designed, fabricated, and tested for the Low-Energy Demonstration Accelerator (LEDA) project. For the 50-keV tests the ion source beam extractor was modified from a tetrode to a triode system[8]. The two triode extraction geometries for the 50 and 100-mA 1.25 MeV RFQ operation are summarized in Table 1.

Table 1. Summary of the triode extraction systems used in the 1.25-MeV RFQ commissioning (50 mA) and highest power operation (100 mA).

1.25 MeV RFQ output current (mA)	50	100
Emission aperture radius (mm)	2.5	3.4
Extraction aperture radius (mm)	3.4	3.4
Extraction gap (mm)	9.3	8.1

Figure 1 shows the line drawing for the 50-keV injector used in these measurements. The ion source

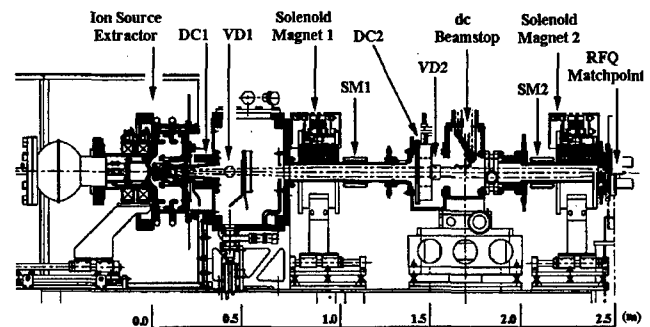


Figure 1. Line drawing of 50-keV injector used on the 1.25 MeV RFQ.

beam current, i_b , is measured in a dc current toroid labeled DC1 in Fig. 1. The source produced $i_b = 58$ mA accelerated through the 2.5-mm emission aperture radius (r_e) with 1270 W forward power at 2.45 GHz. This corresponds to an ion emission current density of $j_i =$

*Work supported by the US DOE, Defense Programs

[#]Email: jsherman@lanl.gov

$i_p/(\pi r_c^2) = 295 \text{ mA/cm}^2$. The proton fraction was not measured while the injector was operating with the RFQ, but earlier proton fraction data acquired at 50 keV as function of the ion source microwave power are shown in Fig. 2. Proton fractions > 90% are observed for 900 W, and we therefore assume the ion source proton current is > 52 mA. At 900 W, within measurement accuracy of

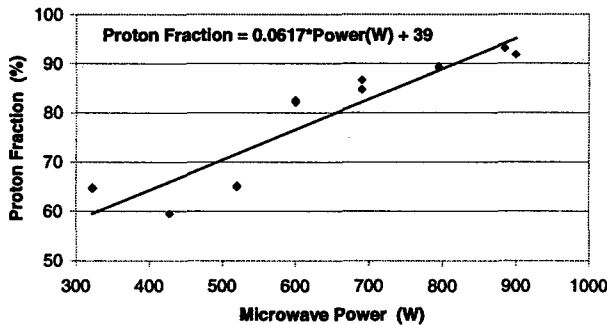


Figure 2. Proton fraction as a function of 2.45 GHz microwave power. The diamonds are measurements while the line is a linear least squares fit to the data.

1%, the remaining 10% of the beam is H_2^+ .

Beam emittance was not measured for the 50-mA extraction system (cf Table 1). An estimate of the ion source beam emittance, however, may be made by use of the PBGUNS code[10]. This code includes a Maxwellian

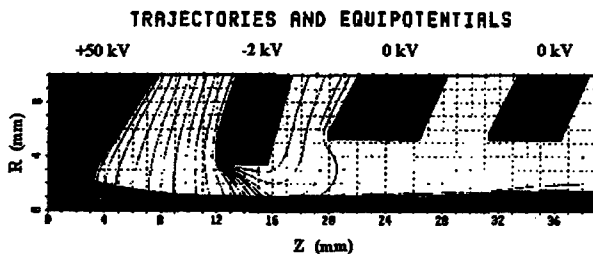


Figure 3. Simulation of the 50-keV beam using the PBGUNS code.

ion temperature, kT_i . Figure 3 shows the trajectory and equipotential plot for the 50-mA triode geometry summarized in Table 1 for $kT_i = 1 \text{ eV}$. Predictions for the ion source rms normalized emittance, E_{rms} , are shown in Fig. 4 as function of kT_i . The PBGUNS code emittance prediction, shown as diamonds connected with solid line, is about 0.1 ($\pi\text{mm-mrad}$) for $kT_i = 1 \text{ eV}$. This ion temperature may be a reasonable estimate for plasma ion temperatures in a microwave plasma source[11,12]. For comparison, the squares connected with the broken line are calculated from the temperature model formula, $E_{rms} = (r_c/2)(kT_i/mc^2)^{1/2}$ [13]. The code emittance prediction is greater than the temperature model because the PBGUNS code also includes ion-optical extraction aberrations and space-charge effects. The PBGUNS prediction is close to other ion-source emittance measurements[14].

3 RFQ BEAM MATCHING AT 50 MA

RFQ beam transmission measurements were made using the 2.5-mm emission aperture radius shown in Table 1. The LEBT solenoid magnets 1 and 2 were set at

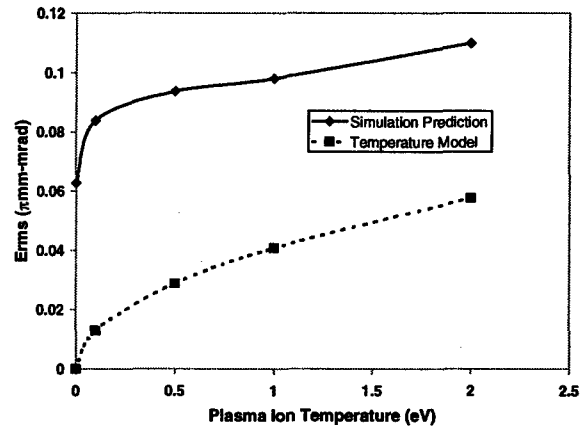


Figure 4. Prediction for the ion source normalized rms emittance from the PBGUNS code and the temperature model.

varying currents, and the transmission through the RFQ was measured. RFQ transmission is defined in per cent as $100(\text{DC3}/\text{DC2})$. DC3 refers to a dc current toroid located at the exit of the RFQ[15]. Beam transmission measurements are shown as contours in Fig. 5 where the horizontal and vertical axes are the LEBT solenoid magnets 1 and 2 current excitation, respectively.

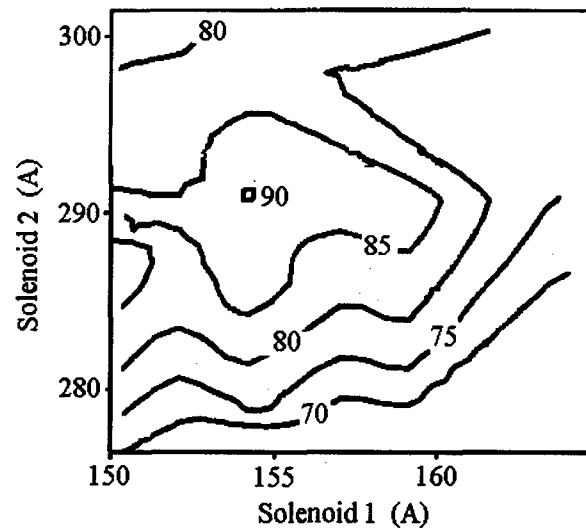


Figure 5. RFQ beam transmissions are plotted as contour labels.

The 90% contour corresponds to the RFQ half-power operation of 50 mA. Minimal steering magnet excitation (cf. Fig. 1, SM1, SM2) was required during these measurements.

First-order low-energy beam transport (LEBT) calculations using the TRACE code[16] were done using

the PBGUNS predictions for the Courant-Snyder $\{\alpha, \beta\}$ parameters and the magnetic field strengths corresponding to the 90% transmission solenoid currents shown in Fig. 5. The TRACE beam envelopes for the $\{\alpha, \beta\}$ parameters corresponding to $kT_i = 0$ and 1 eV are shown in Fig. 6.

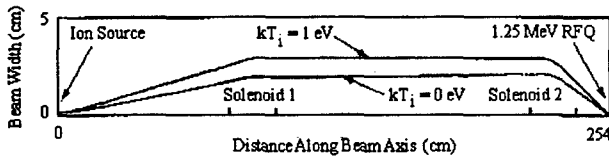


Figure 6. TRACE beam envelope calculations for the $\{\alpha, \beta\}$ parameters deduced from the $kT_i = 0$ and 1 eV PBGUNS simulations.

They give a good qualitative description of the RFQ-matched beam; a more quantitative description of this matching process requires use of a higher-order LEBT code [15]. The process of using the PBGUNS and TRACE codes together is a first-order method used for designing and commissioning the 50-keV injector on the 1.25 MeV RFQ.

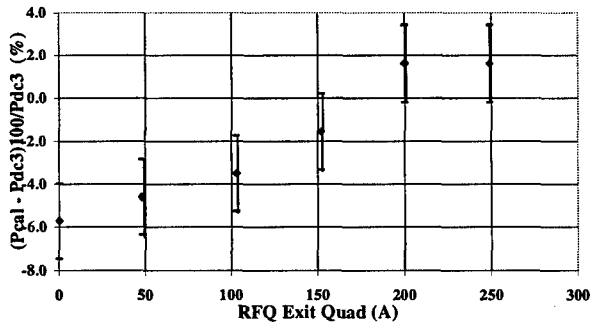


Figure 7. Calorimetric measurement beam power check on the DC3 beam current monitor.

A check was made on the RFQ output beam power and current monitor (DC3) by measuring the water temperature increase in the cw RFQ beam stop [17]. The difference of the measured calorimetric and beam power - based on the DC3 current measurement assuming acceleration to RFQ design energy - is chosen as a figure of merit. These difference data are shown in Fig. 7 plotted vs. the excitation of the RFQ exit quadrupole singlet. These measurements were made for an RFQ beam current of 74 mA with 1.3 l/s water flow. The equilibrium water temperature increase was 19°C. The error bars were calculated based on uncertainties in the temperature and water flow measurements. Some dependence is observed on the exit quadrupole excitation, but the calorimetry confirms the RFQ beam toroid current measurement.

4 ACKNOWLEDGMENTS

We thank Chalk River Laboratories for technical support in completing the work reported here.

References

- [1] K. F. Johnson, et. al., "Commissioning of the Low-Energy Demonstration Accelerator (LEDA) Radiofrequency Quadrupole (RFQ)", these conference proceedings.
- [2] M. Olivo, E. Mariani, and J. Sherman, "The PSI 870 keV High-Intensity Cockcroft-Walton Preinjector", Rev. Sci. Instrum. 63(4), (1992), 2714.
- [3] B. G. Chidley, F. P. Adams, G. E. McMichael, T. Tran Ngoc, and T. S. Bhatia, "New Vanes for RFQ1", Proceedings of the 1990 Linear Accelerator Conference, Los Alamos Report LA-12004-C, (Sept. 1990), 42.
- [4] J. D. Schneider, J. Bolme, V. Brown, M. Milder, G. Neuschaefer, D. Rees, P. Schafstall, J. Sherman, R. R. Stevens, Jr., T. Zaugg, G. E. McMichael, J. Sheikh, and T. Taylor, "Installation of a cw Radiofrequency Quadrupole Accelerator at Los Alamos", Proceedings of the 1994 International Linac Conference, Tsukuba, Japan (Aug. 1994), 149.
- [5] G. M. Arbiue, B. G. Chidley, G. E. McMichael, and J. Y. Sheikh, "Beam Parameter Measurements on the cw RFQ1-1250 Accelerator", 1992 Linear Accelerator Conf. Proc., Ottawa, Ontario, Canada, AECL-10728, (Aug. 1992), 55.
- [6] J. David Schneider, "Operation of the Low-Energy Demonstration Accelerator: the Proton Injector of APT", these conference proceedings.
- [7] J. Bolme, et. al., "A dc Proton Injector for Use in High-Current cw Linacs", Proc. of the 1998 European Particle Accelerator, Stockholm, Sweden, (June, 1998), to be published.
- [8] J. Sherman, et. al., "Development and Test Results of the Low-Energy Demonstration Accelerator Proton Injector on a 1.25 MeV cw Radio Frequency Quadrupole", XIX International Linac Conference Proc., Chicago, Illinois, (Aug. 1998), to be published.
- [9] J. D. Sherman, et al., "Status Report on a dc 130 mA, 75 keV Proton Injector" Rev. Sci. Instrum. 69(2), (1998), 1003.
- [10] Jack E. Boers, "An Interactive Version of the PBGUNS Program for the Simulation of Axisymmetric and 2-D, Electron and Ion Beams and Guns", Proceedings of the 1995 Particle Accelerator Conference, Dallas, Texas, IEEE Catalog Number 95CH35843, (May, 1995), 2312.
- [11] R. Geller, Electron Cyclotron Resonance Ion Sources and ECR Plasmas, Institute of Physics Publishing, (1996), 267.
- [12] A. J. T. Holmes and M. Inman, "Development of a High-Brightness Ion source", Proc. of the 1979 Linear Accelerator Conference, Montauk, NY, BNL 51134, (Sept. 1979), 424.
- [13] Paul Allison, Joseph D. Sherman, and H. Vernon Smith, Jr., "Comparison of Measured Emittance of an H Beam with a Simple Theory", unpublished Los Alamos Report, LA-8808-MS.
- [14] Terence Taylor and Jozef F. Mouris, "An Advanced High-Current Low-Emittance dc Microwave Proton Source", Nuclear Instrum. And Methods in Phys. Res., A 336 (1993), 1.
- [15] H. Vernon Smith, Jr., et. al., "Comparison of Beam Simulations with Measurements for a 1.25-MeV, CW RFQ", XIX International Linac Conference Proc., Chicago, Illinois, (Aug. 1998), to be published.
- [16] K. R. Crandall and D. P. Rusthoy, Los Alamos National Lab Report LA-UR-90-4146 (1990).
- [17] David W. Doll, "Three Beam Stops for APT", Bull. Of the Amer. Phys. Soc., 43(2) (1998), 1105.

A NON-INTERRUPTING ELECTRON BEAM DIAGNOSTIC USING COHERENT OFF-AXIS UNDULATOR RADIATION

C.P. Neuman*, W.S. Graves, Brookhaven National Laboratory, Upton, NY
P.G. O'Shea, University of Maryland, College Park, MD

Abstract

We propose a technique for measuring the length of an electron bunch from a linear accelerator without interrupting the electron beam. Bunch lengths are measured by observing off-axis undulator radiation. The wavelength of undulator radiation increases with the angle of emission. At angles as large as 10 degrees, the wavelength may be longer than the electron bunch, and as a result coherence effects emerge. As the angle of observation increases and the radiation becomes coherent, the intensity may change by up to a factor of 10^9 . The angle at which this change occurs is related to the bunch length. Thus the bunch length may be obtained by observing the change in intensity of the radiation with respect to the angle of observation. This electron beam diagnostic does not interrupt the electron beam and would be useful for single-pass FELs. Electron bunches could be characterized while the FEL is operating, and thus the FEL could be optimized in real time. In this paper, we develop the theory of coherent off-axis undulator radiation (COUR), including near-field effects, and we discuss future experimental efforts to observe this radiation and to use it to characterize electron bunches.

1 THEORY

1.1 Introduction

In most descriptions of undulator radiation, the discussion is limited to small angles of observation, particularly angles less than $\frac{1}{\gamma\sqrt{N_w}}$ radians [1], where N_w is the

number of periods in the undulator. In our study we explore the radiation outside the narrow $\frac{1}{\gamma\sqrt{N_w}}$ cone.

The peak wavelength of undulator radiation increases with angle:

$$\lambda_0(\theta) = \frac{\lambda_w}{2\gamma^2} \left[(1 + a_w^2) \cos \theta + 2\gamma^2 (1 - \cos \theta) \right], \quad (1)$$

where θ is the angle of observation, λ_w is the undulator period, a_w is the undulator parameter, and γ is the relativistic factor of the electron beam. Typical values of λ_0 , for $\lambda_w = 4$ cm and $\gamma = 400$, are 250 nm on-axis, and 1.3 mm for $\theta = 15^\circ$. Note that for γ large and θ greater than a few degrees, Eq. 1 becomes

$$\lambda_0(\theta) \approx \lambda_w (1 - \cos \theta)$$

which is independent of the electron beam energy.

For small angles, the radiation typically has a wavelength that is much shorter than a bunch length. Here, the electrons radiate incoherently, and the intensity of the radiation scales linearly with the number of electrons. For a large enough angle, the wavelength may be much larger than the bunch length. In this case, the electrons radiate coherently, and the intensity of the radiation scales with the square of the number of electrons. As the angle of observation is increased and the radiation becomes coherent, the intensity will jump by a factor equal to the number of electrons, which is typically on the order of 10^9 . The angle at which this large jump occurs depends on the electron bunch length. Thus, relative bunch length measurements may be performed by observing undulator radiation from a range of angles [2].

1.2 Energy Calculations for Single Electron

We calculate the total energy and the spectral energy of the emitted undulator radiation using a straightforward approach derived from Liénard-Wiechert potentials [3]. The geometry for the calculation is shown in Fig. 1.

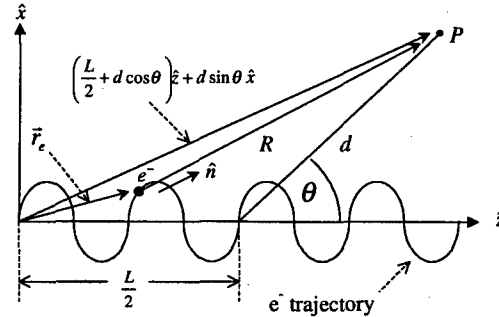


Figure 1: Geometry for energy calculations. P is the point of observation, \vec{r}_e is the instantaneous position of the electron, R and \hat{n} are the distance and direction, respectively, from the electron to the point of observation, and d is the distance from the center of the undulator to the point of observation.

The total power per unit solid angle radiated by an accelerating electron, in the electron's time, is given by

$$\frac{dP(t')}{d\Omega} = R^2 \vec{S} \cdot \hat{n} (1 - \hat{n} \cdot \vec{\beta}) = c\epsilon_0 E^2 R^2 (1 - \hat{n} \cdot \vec{\beta}),$$

where \vec{S} is the Poynting vector associated with the radiation. The total energy per unit solid angle is obtained

* Corresponding author. Neuman@bnl.gov.

by integrating over time. The electric field \vec{E} can be derived from Liénard-Wiechert potentials:

$$\vec{E} = \frac{q^2}{4\pi\epsilon_0} \left\{ \frac{1}{\gamma^2 R^2} \frac{\hat{n} - \vec{\beta}}{(1 - \hat{n} \cdot \vec{\beta})^3} + \frac{1}{cR} \frac{\hat{n} \times [(\hat{n} - \vec{\beta}) \times \dot{\vec{\beta}}]}{(1 - \hat{n} \cdot \vec{\beta})^3} \right\} \quad (2)$$

The first term represents the velocity field, which does not radiate and is thus disregarded in this study. The second term represents the radiating acceleration field and depends on both the velocity and acceleration of the electron. Thus, the energy per unit solid angle is:

$$\frac{dW}{d\Omega} = \frac{1}{4\pi\epsilon_0} \frac{q^2}{4\pi c} \int_0^L \frac{\left| \hat{n} \times [(\hat{n} - \vec{\beta}) \times \dot{\vec{\beta}}] \right|^2}{(1 - \hat{n} \cdot \vec{\beta})^5} dt \quad (3)$$

To calculate the energy spectrum, we begin with an expression for the energy per unit solid angle:

$$\frac{dW}{d\Omega} = \int_{-\infty}^{\infty} |\vec{A}(t)|^2 dt = \int_{-\infty}^{\infty} |\vec{A}(\omega)|^2 d\omega,$$

where $\vec{A}(t)$ is defined as

$$\vec{A}(t) \equiv \sqrt{\epsilon_0 c R} \vec{E},$$

and $\vec{A}(\omega)$ is the Fourier Transform of $\vec{A}(t)$:

$$\vec{A}(\omega) = \frac{1}{\sqrt{2\pi}} \int_{-\infty}^{\infty} \vec{A}(t) e^{i\omega t} dt$$

The total energy per unit solid angle can be expressed as

$$\frac{dW}{d\Omega} = \int_0^{\infty} \frac{d^2W}{d\omega d\Omega} d\omega,$$

where

$$\frac{d^2W}{d\omega d\Omega} \equiv 2|\vec{A}(\omega)|^2$$

is the energy radiated per unit solid angle per unit angular frequency. Using Eq. 2, the spectral energy becomes:

$$\frac{d^2W}{d\omega d\Omega} = \frac{\epsilon_0}{c\pi} \frac{q^2}{(4\pi\epsilon_0)^2} \left| \int_0^L e^{i\omega \left(t + \frac{R}{c}\right)} \frac{\hat{n} \times [(\hat{n} - \vec{\beta}) \times \dot{\vec{\beta}}]}{(1 - \hat{n} \cdot \vec{\beta})^2} dt \right|^2 \quad (4)$$

The total energy and spectral energy are related to the respective energies per unit solid angle by

$$W = \frac{1}{d^2} \left(\frac{dW}{d\Omega} \right) \Delta A \quad (5)$$

$$\frac{dW}{d\omega} = \frac{1}{d^2} \left(\frac{d^2W}{d\omega d\Omega} \right) \Delta A$$

where d is the distance of the detector from the center of the undulator, and ΔA is the area of the detector entrance aperture.

To evaluate Eqs. 3 and 4, the normalized acceleration and velocity of the electron are needed, along with the approximation $z \approx \bar{\beta}_z ct$. These are calculated by applying the Lorentz force equation to the periodic undulator field, yielding the following well-known expressions:

$$\dot{\beta}_x = \frac{-a_w \sqrt{2}}{\gamma} \sin(k_w z) k_w \bar{\beta}_z c \quad (6)$$

$$\dot{\beta}_z = \frac{a_w^2}{\gamma^2} \sin(2k_w z) k_w \bar{\beta}_z c$$

$$\beta_x = \frac{a_w \sqrt{2}}{\gamma} \cos(k_w z) \quad (7)$$

$$\beta_z = \bar{\beta}_z - \frac{a_w^2}{2\gamma^2} \cos(2k_w z), \quad \bar{\beta}_z \equiv 1 - \frac{1}{2\gamma^2} (1 + a_w^2)$$

1.3 Bunch Form Factor for N_e Electrons

The energy for N_e electrons is related to the energy for a single electron by [4]:

$$W_{N_e \text{ electrons}} = W_{1 \text{ electron}} [N_e + N_e(N_e - 1)f(\omega)], \quad (8)$$

where $f(\omega)$ is the bunch form factor:

$$f(\omega) = \left| \iint dy dz S_y(y) S_z(z) e^{-i\frac{\omega}{c} y \sin \theta + i\frac{\omega}{c} z \cos \theta} \right|^2 \quad (9)$$

$S_y(y)$ and $S_z(z)$ are the transverse and longitudinal electron bunch densities, respectively. In this study we use Gaussian-shaped bunch densities. Eqs. 8 and 9 include the coherence effects described above: for ω large $f(\omega) \approx 0$, and $W \propto N_e$; for ω small $f(\omega) \approx 1$, and $W \propto N_e^2$.

The form factor depends on both the length and width of the electron bunch. In this study we only consider the effects of the bunch length since the length is a critical quantity in many beam physics and FEL applications.

1.4 Near-Field Effects

Near-field effects are introduced by accounting for the fact that \hat{n} and R change as the electron passes through the undulator (see Fig. 1). The vector $R\hat{n}$ can be expressed as

$$R(t)\hat{n}(t) = \left(\frac{L}{2} + d \cos \theta \right) \hat{z} + d \sin \theta \hat{x} - \vec{r}_e(t), \quad (10)$$

where $\vec{r}_e(t)$ is the electron trajectory. \vec{r}_e is calculated by integrating Eqs. 7 with the approximation $z \approx \bar{\beta}_z ct$:

$$r_x = \frac{a_w \sqrt{2}}{\gamma k_w \bar{\beta}_z} \sin(k_w \bar{\beta}_z ct) \quad (11)$$

$$r_z = \bar{\beta}_z ct - \frac{a_w^2}{4\gamma^2 k_w \bar{\beta}_z} \sin(2k_w \bar{\beta}_z ct)$$

Thus, $R(t)$ is obtained by taking the magnitude of Eq. 10, and $\hat{n}(t)$ by dividing Eq. 10 by $R(t)$. The consequences of including near-field effects are discussed below.

1.5 Results

Eqs. 3 and 4 are evaluated numerically. A plot of the total energy radiated versus angle of emission is displayed in Fig. 2. The two traces correspond to two different bunch lengths. It can be seen that the bunch length determines

the angle at which the intensity of the radiation increases dramatically. This characteristic of COUR may allow us to measure relative bunch lengths by observing COUR at a range of angles.

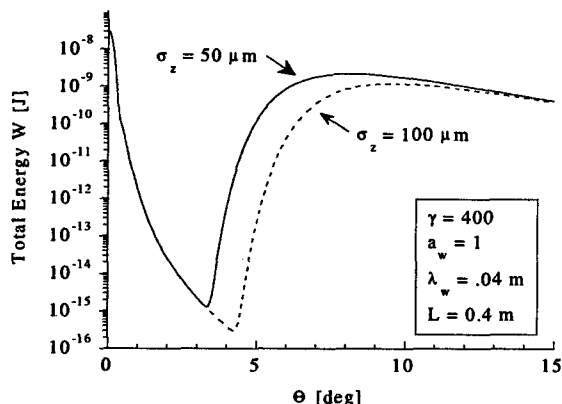


Figure 2: The effect of bunch length on COUR. σ_z is the rms bunch length divided by $\sqrt{2}$, as defined in [4].

Calculations reveal that near-field effects have a significant effect on the energy spectrum for detector distances of less than 1 m (see Fig. 3). The fundamental peak is shifted to higher frequencies and is broadened. Without near-field effects, the spectrum displays the

expected $\text{sinc}^2\left(N_w \pi \frac{\Delta\omega}{\omega_0}\right)$ behavior on-axis, and slight

variations of this behavior off-axis, as seen in Fig. 3. This behavior is disturbed in the near-field calculation. As the detector distance becomes large, greater than 1 m in this case, the near-field and far-field calculations begin to have similar behavior.

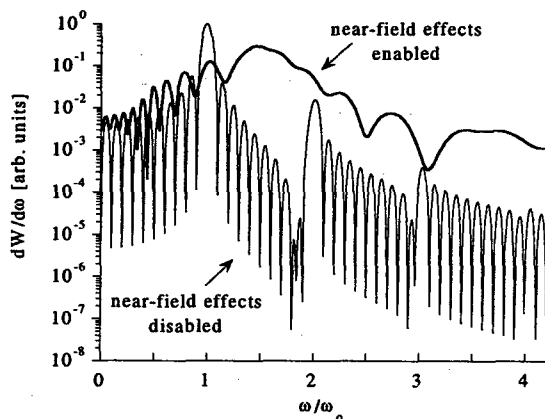


Figure 3: Effect of near-field effects on energy spectrum for a single electron. $\theta = 5^\circ$, detector distance $d = .5$ m. All other parameters are the same as in Fig. 2.

3 EXPERIMENT

The goals of a COUR experiment are to observe COUR and to measure relative bunch lengths using COUR.

A COUR experiment is planned for the DUV-FEL facility, a new priority for BNL designed to produce a coherent light source in the ultraviolet range [5]. The

linear accelerator will produce 210 MeV electrons. The undulator for the COUR experiment is a 13 period prototype of the 10 m NISUS undulator, now installed at the DUV-FEL. The NISUS prototype has an undulator parameter of up to 1.44 and an undulator period of 3.89 cm [6].

A liquid helium-cooled bolometer detector will be used to detect energy levels as low as 10^{-12} J. A spectrometer will be used to determine the spectral content of the radiation. Radiation will exit the beamline through an aperture with a diamond window, after being reflected away from the beamline by a small mirror (see Fig. 4).

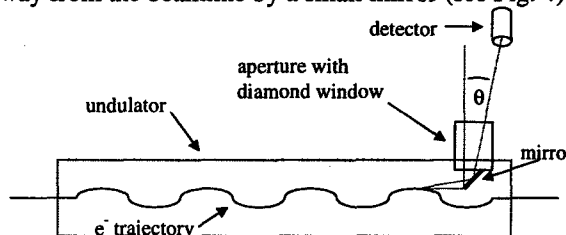


Figure 4: COUR experiment.

The COUR experiment is one of a series of beam diagnostics experiments planned for the DUV-FEL [7]. The various diagnostic techniques will be compared and will be used in conjunction with each other.

4 CONCLUSION

We have shown that a promising technique for measuring electron bunch lengths is to observe coherent off-axis undulator radiation (COUR). Our technique is non-interrupting and thus will be useful for single-pass FELs, where bunch lengths could be measured while an FEL is operating. Calculations including near-field effects show the expected energy levels and energy spectra. An experiment at the DUV-FEL facility at BNL will verify the calculations and will demonstrate the use of COUR to measure electron bunch lengths.

5 ACKNOWLEDGEMENTS

The authors wish to thank Larry Carr and Jim Murphy of BNL for helpful discussions on detection and electromagnetic theory, respectively. Computational support, in the form of Cray computer time, was provided by the North Carolina Supercomputing Center. This work was supported, in part, by a U.S. Army AASERT grant to the Duke University FEL Lab.

6 REFERENCES

- [1] S. Krinsky et al, from E.E. Koch, ed., *Handbook on Synchrotron Radiation*. Amsterdam, North Holland, 1983, 152.
- [2] C.P. Neuman et al, *Proc. of FEL98 Conference*.
- [3] J.D. Jackson, *Classical Electrodynamics*. New York: Wiley, 1975, 662-70.
- [4] E.B. Blum et al, *Nucl. Instr. and Meth. A* 307 (1991), 568-76.
- [5] I. Ben-Zvi et al, *Proc. of SPIE*, 2988 (1997), 15-19.
- [6] D.C. Quimby et al, *Nucl. Instr. and Meth. A* 285 (1989), 281.
- [7] W.S. Graves et al, *Proc. of IEEE PAC99*.

DEVELOPMENT OF AN ^{14}O ION BEAM AT THE 88" CYCLOTRON

D. Wutte, J. Burke, B. Fujikawa, P. Vetter, S.J. Freedman, R.A. Gough, C. M. Lyneis, Z. Q. Xie,
LBNL, Berkeley, CA

Abstract

At the 88" Cyclotron at the Lawrence Berkeley National Laboratory we are developing an intense ($3 \cdot 10^7$ pps), low energy ^{14}O ion beam to measure the shape of the beta-decay spectrum. The ^{14}O half-life of 71 seconds requires on-line production of the isotope. ^{14}O is produced in the form of CO in a high temperature carbon target using a 20 MeV $^3\text{He}^+$ beam from the LBNL 88" Cyclotron via the reaction $^{12}\text{C}(^3\text{He},n)^{14}\text{O}$. In order to minimize the background radiation for the planned experiment, the ^{14}O atoms must be separated from the other radioactive isotopes produced in the carbon target and implanted into a thin carbon foil.

For this purpose, we have developed an experimental set-up including the target, a transfer line, an ion source, and a low energy ion beam transport line. The major components of this set-up are described. The release and transport efficiency for the CO molecules from the target through the transfer line was measured for various target temperatures. Experimental results of ionization efficiencies for carbon and oxygen using a multicusp and an ECR ion source are presented

1 INTRODUCTION

At the Lawrence Berkeley National Laboratory we have commissioned an ion source test stand for radioactive ion beam development [1] (see figure 1). The primary goal of this test stand is the on-line production of a $^{14}\text{O}^+$ ion beam to measure the shape of the ^{14}O beta-decay. The ^{14}O half-life of 70 seconds requires producing the isotope on-line at the 88" Cyclotron. ^{14}O is generated in the form of CO in a high temperature carbon target using a 20 MeV $^3\text{He}^+$ beam from the LBNL 88" Cyclotron via the reaction $^{12}\text{C}(^3\text{He},n)^{14}\text{O}$.

The ^{14}O atoms must be then separated from the other radioactive isotopes produced in the carbon target and implanted into a thin carbon foil in order to:

- minimize the radiation background
- maximize the signal in the beta spectrometer by concentrating the ^{14}O sample size.

For this purpose, an 8 m stainless steel transfer line

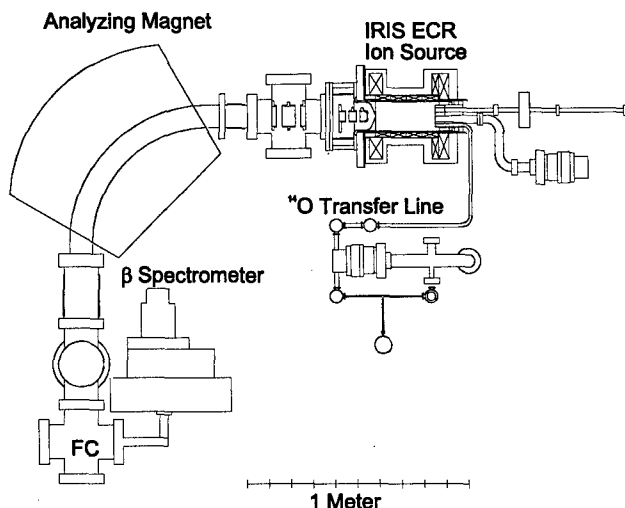


Figure 1: Schematic of the new exotic ion beam test stand and the ^{14}O experiment.

connects the target chamber to an ECR ion source through a turbo molecular pumping stage. Thus, the turbo pump separates the target vacuum chamber from the ion source. The gas coming from the turbo pump is fed into the ion source and ionized, extracted at energies of 20 to 30 keV and mass separated. To achieve a small sample size for the beta spectrometer, it is planned to implant the $^{14}\text{O}^+$ ions in a 2 mm spot on a thin carbon foil. This sample will then be transferred to the beta-spectrometer. The three major experimental requirements for the ion source are:

1. To achieve the necessary ^{14}O particle current of $1\text{-}2 \cdot 10^7$ pps at the implant target, the ion source should be able to provide 10 % ionization efficiency for $^{14}\text{O}^+$.
2. At the estimated implantation rate of $1\text{-}2 \cdot 10^7$ pps the expected continuous run of the experiment will be at least 150 hours. Therefore, the ion source should continuously operate for at least 200 hours.
3. The gas hold up time in the ion source must be less than one ^{14}O half-life.

In order to fulfill these demands, a RF multicusp ion source [2] and the AECR-U [3] were tested off-line with respect to ionization efficiency and gas hold-up times. The presented efficiencies Table 1 and 2 quote the overall system efficiencies (ion source and transport line).

Because the experimental requirements could not be met with the cusp source and because of the promising results measured on the AECR-U, the cusp ion source has been replaced by the compact IRIS ECR ion source.

This work was supported by the Director, Office of Energy Research, Office of High Energy Physics and Nuclear Physics Division of the U.S. Department of Energy under contract No. DE-AC03-76SF00098.

2 EXPERIMENTAL SETUP

2.1 Hot Carbon Target

An all carbon target was constructed using a high porosity carbon material[1]. The target is resistively heated and bolted to water-cooled copper electrodes. Graphite and boron nitride heat shields were then added concentrically around the target.

At 1720 °C and 2 μ A cyclotron beam current on the target $3 \cdot 10^7$ pps of ^{14}O have been measured at the exit of the turbo pump (at the entrance to the ion source). Figure 2 shows the production rate as a function of target temperature. Therefore at 20 μ A primary beam current a production rate of $3 \cdot 10^8$ pps of ^{14}O can be expected. Using the assumed thick target production rate of $2 \cdot 10^8$ pps/ μ A, an efficiency of 7.5 % for this target set-up has been achieved.

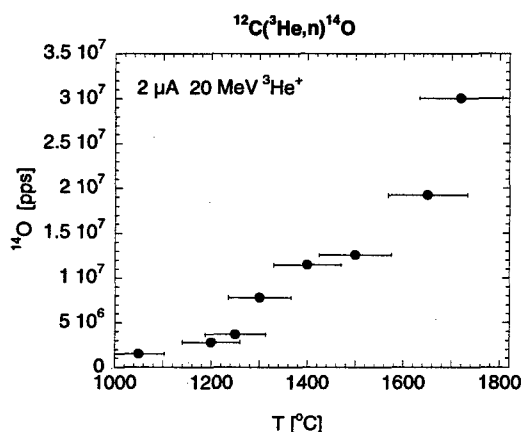


Figure 2: Production rate as a function of target temperature as measured at the end of the transport line.

2.2 Beam-line Layout

The ion beam transport line has been designed around an existing double focusing 90°-sector magnet from the former HILAC injector line at LBNL. It has a bending radius of 54 cm, edge angles of 30 degrees, and a gap width of 3.8 cm. The horizontal waist is located about 43 cm downstream from the vertical waist. Therefore, the ion beam has an elliptical shape after the sector magnet. An additional focusing element will be needed to achieve the required beam spot size of 2mm diameter at the implant foil. The 30 kV extraction system and the following electrostatic transport line consist of an accel-decel extraction system and two sets of einzel lenses. It was optimized with the ion trajectory code IGUN [4]. The use of two einzel lenses allows limited independent control over both beam size and divergence at the magnet entrance. Therefore, the ion optics can be adjusted over a

wide range of extraction voltages and current densities (3 mA/cm² to 60 mA/cm², corresponding to a total extracted current of 100 μ A to 2 mA), as verified experimentally. The extraction system and the two einzel lenses are mounted on a single flange to ensure a proper alignment.

3 OFF-LINE ION SOURCE TESTS

3.1 Multicusp Ion Source

A detailed description of the RF driven multicusp ion source used in this study, together with its basic characteristics can be found elsewhere [2]. The main concerns with this type of ion source with respect to the production of radioactive ion beams are the relative high operation pressure as well as the reliability of the ion source.

Ionization efficiencies were measured off-line for singly charged argon, oxygen, carbon, and carbon monoxide ions using calibrated leaks. The maximum ionization efficiencies for all measured species are summarized in Table 1. The experimental gas hold up time is described by the exponential fit $A \cdot \exp(-t/\tau_{\text{fast}}) + B \cdot \exp(-t/\tau_{\text{slow}})$. The fast component describes the holdup time of the ions in the plasma, the slow component is related to the wall sticking time. The signal drops to about 70 % within the time τ_{fast} .

Table 1: Ionization efficiencies and hold up times for singly charged oxygen and carbon produced by RF driven cusp ion source.

ion	calibrated leaks			
	CO %	τ_{fast} (sec)	O ₂ %	τ_{fast} (sec)
O ⁺	0.7	42	0.7	36
C ⁺	0.33	13		
CO ⁺	1	17		
Ar ⁺				
			26.3	6

Whereas a promising ionization efficiency of up to 26.3% and a gas hold-up time of 6 seconds have been measured for argon, the ionization efficiencies for CO⁺ and O⁺ are much lower. With the cusp source the best efficiencies achieved have been 1 % for CO⁺, 0.7 % for O⁺ and 0.33 % for C⁺. In general rather long ion hold-up times have been observed, the longest has been measured for O⁺.

The discrepancy between the argon efficiencies and the carbon or oxygen efficiencies may be explained by the differences in the plasma wall sticking probabilities. Noble gases can be recycled into the plasma, explaining the high efficiency for argon. On the contrary, carbon and oxygen tend to stick at the plasma chamber wall, leading to low source efficiencies in the cusp ion source. The average ion source lifetime for the above mentioned performance tests was about 15 hours, limited by the failure of the porcelain-coated copper antenna.

3.2 AECR-U Ion Source

A detailed description of the AECR-U ion source (Advanced Electron Cyclotron Resonance-upgrade) can be found elsewhere [3]. The source is optimized for production of high charge state ions. Ionization efficiencies and gas hold-up times for high charge state ions have been measured with the LBNL AECR-U ion source for various gases [5].

Listed in Table 2 are the ionization efficiencies and decay times of various high charge state ion beams from CO, CO₂ and O₂. These gases may react with or stick to the plasma chamber surface made of aluminum. Nevertheless efficiencies of up to 25% were achieved for C⁴⁺, 33% for O⁶⁺ and more than 10% for C⁵⁺ and O⁵⁺. The shortest gas hold up time has been measured for ions produced from CO, which behaves as a noble gas prior to dissociation.

Table 2: Ionization efficiencies and hold up times for selected charge states of oxygen and carbon produced by the LBNL AECR-U ion source.

ion	calibrated leaks					
	CO %	τ_{fast} (sec)	CO ₂ %	τ_{fast} (sec)	O ₂ %	τ_{fast} (sec)
O ³⁺					3.9	
O ⁴⁺					8	
O ⁵⁺	11.5	3.2	12.5		11.3	4.7
O ⁶⁺	26.3	3.2	33	7.1	16.0	
O ⁷⁺	7.5	3.2	7.44		5.6	
C ⁴⁺	23.7	2.9	23.4	5.6		
C ⁵⁺		2.9	15.4			

4 IRIS ECR ION SOURCE

A compact ECR ion source IRIS (Ion source for Radioactive ISotopes) shown in Figure 3, has been installed on the radioactive ion beam test stand, replacing the multicusp ion source. An existing 2.45 GHz ECR ion source [6] was upgraded for 6.4 GHz microwave operation. The mirror field was improved to reach a maximum field of 0.7 Tesla at the injection and 0.4 Tesla at the extraction. At the plasma chamber-wall the sextupole-field strength reaches 0.32 Tesla.

The ion source consists of one plasma stage only. The microwaves are launched through an off-axis wave-guide terminated at a bias plate in the injection region. The aluminum plasma chamber has a diameter of 13.5 cm and the mirror length is 28.3 cm, providing a relatively large plasma volume of 5 liters. The plasma chamber is double-walled to accommodate cooling water.

IRIS is expected to start operation in the beginning of April.

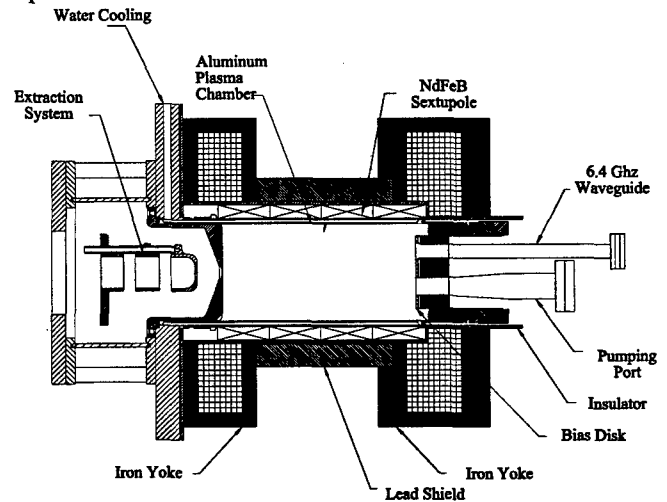


Figure 3: An elevation view of the IRIS ECR ion source.

5 REFERENCES

- [1] D. Wutte, J. Burke, B. Fujikawa, P. Vetter, S.J. Freedman, R.A. Gough, C. M. Lyneis, Z. Q. Xie, Development of a radioactive ion beam test stand at LBNL, Proceedings of the Heavy Ion Accelerator Technology Conference (HIAT'98), Argonne National Laboratory, Illinois, USA, 5-10 October 1998
- [2] Wutte D.C., S. Freedman, R.A. Gough, Y. Lee, M. Leitner, K. N. Leung, C.M. Lyneis, D.S. Pickard, M. D. Williams, Z. Q. Xie, NIMB 42 (1998)
- [3] Z. Q. Xie and C. M. Lyneis, Proceedings of the 13th International Workshop on ECR Ion Sources, Texas A&M, College Station, USA, 16 (1997).
- [4] R. Becker, W. B. Hermannsfeldt, RSI 63, 2756 (1991)
- [5] Z. Q. Xie, D. Wutte, C. M. Lyneis, to be published
- [6] D. C. Wutte, M. A. Leitner, M. D. Williams, K. N. Leung, R. A. Gough, RSI 69, 712 (1998)

STATUS OF THE REX-ISOLDE PROJECT*

R. von Hahn[†], M. Grieser, H. Podlech, R. Repnow, D. Schwalm
Max-Planck-Institut für Kernphysik, Heidelberg, Germany
H. Bongers, D. Habs, O. Kester, T. Sieber, K. Rudolph, P. Thirolf
LMU München, Garching, Germany

A. Schempp, Universität Frankfurt, Frankfurt, Germany
F. Ames, G. Bollen, I. Deloese, CERN, Geneva, Switzerland
U. Ratzinger, GSI, Darmstadt, Germany

L. Liljeby, K.G. Rensfelt, F. Wenander, Manne Siegbahn Institute of Physics, Stockholm, Sweden

P. van Duppen, Instituut voor Kern- en Stralingsfysica, Leuven, Belgium

G. Walter, Université Louis Pasteur, Strasbourg, France

A. Richter, TU Darmstadt, Germany

A. Ostrowski, A. Schotter, University of Edinburgh, Great Britain
and the REX-ISOLDE collaboration

Abstract

The Radioactive beam Experiment REX-ISOLDE, a pilot experiment testing a new concept of post acceleration of radioactive ions at ISOLDE/CERN is in progress. Singly charged radioactive ions delivered by the online mass separator ISOLDE are accumulated in a Penning trap (REX trap), charge bred in an electron beam ion source (EBIS), separated from the residual gas in a mass separator and then accelerated in a Linac with output energies between 0.8 and 2.2 MeV/u.

The REX trap is in operation, a first test beam was already injected. The design phase of the EBIS is finished and the construction has been started. The superconducting magnet is delivered.

The Linac consists of a radio frequency quadrupole (RFQ) accelerator, an interdigital IH-structure and 3 seven gap resonators to vary the final energy. The RFQ is assembled and vacuum tested, a beam test for the RFQ is in preparation. The vacuum tank of the IH-structure is machined, the assembly of the resonator has started. The first 2 seven gap resonators of the high energy section are finished and ready for power tests, the last one is ready for assembly.

1 INTRODUCTION

The Radioactive beam Experiment (REX-ISOLDE) at ISOLDE/CERN [1, 2, 3] is under progress, first hardware components are completed and some tests of the components were performed. In the experiment the radioactive ions of charge 1+ from the on-line mass separator ISOLDE will be cooled and bunched in a Penning trap (REX trap), charge bred in an electron beam ion source (EBIS), separated from the residual gas ions and finally accelerated in a short LINAC to a target energy between 0.8

and 2.2 MeV/u. The LINAC consists of a radio frequency quadrupole (RFQ) accelerator, which accelerates the ions up to 0.3 MeV/u, an interdigital H-type (IH) structure with a final energy between 1.1 and 1.2 MeV/u and three seven gap resonators, which allow the variation of the final energy. All components of the experiment are either in production or undergo first test measurements. The lay-out of REX-ISOLDE is shown in fig. 1.

2 REX TRAP

The Penning trap is fed from the ISOLDE main beam line where the beam axis is 1.27 m above the floor. The Penning trap is fully assembled on a 60 kV high voltage platform including the differential pumping stages which ensure good vacuum conditions in the beam line. High tension tests with the equipment and first tests of ion injection into the trap have been carried out in order to investigate the injection optic [4]. The electrode structure consisting of gold plated copper rings isolated by ceramic spacers is assembled and installed in the solenoid bore. The central field strength is 3 T and the gas pressure inside the trap 10^{-3} mbar for rest gas cooling. A plasma ion source has been installed to test the ion capture with a stable 60 keV $^{40}\text{Ar}^+$ beam. These capture tests were done in the beginning of 1999 and the first ions were trapped. A new shielding due to charging of the insulators are installed and will be tested in the near future. The singly charged ions will be extracted from the trap with a typical bunch length of 10 μs every 20 ms and accelerated to 60 keV.

3 EBIS

In the EBIS the ions are bombarded by a 0.5 A, 5 keV electron beam with a current density of about 200 A/cm² [5]. In the EBIS the ions will be charge bred in about 15 ms to a charge to mass ratio between 0.22 and 0.34, which is well suited for the mass separator and the LINAC. After several

* Work supported in part by the German Federal Ministry for Education, Science, Research and Technology (BMBF) under contract No. 06HD802I and No. 06LM868I(2).

[†] Email: robert.von.hahn@mpi-hd.mpg.de

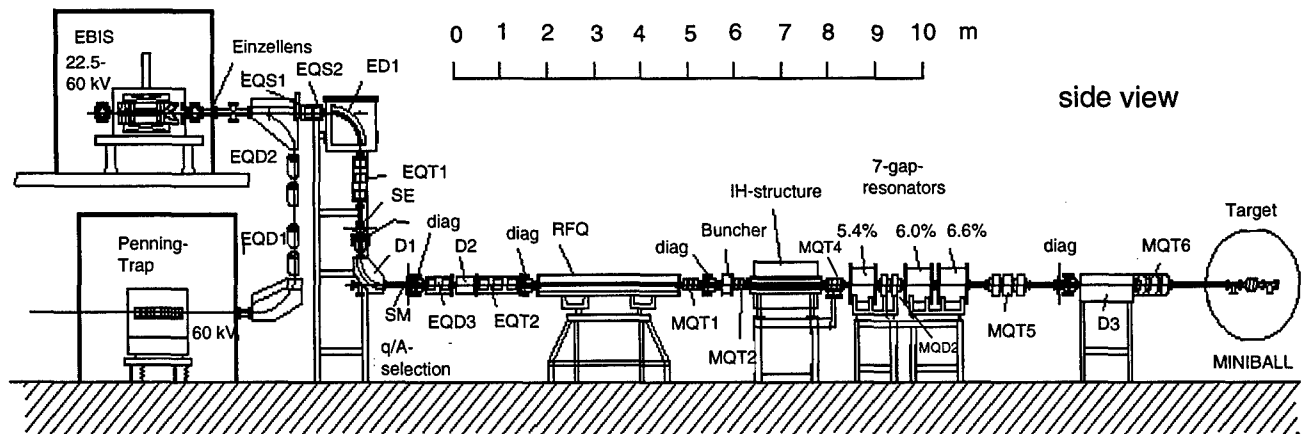


Figure 1: Lay-out of the REX-ISOLDE experiment

repairs of the REX-EBIS solenoid by the manufacturer due to damages occurring during quench tests, the EBIS magnet is now back at CERN and ready for operation. The vacuum system is completed and being assembled at Stockholm. The electron gun, the collector and the electrode system are completed and will be shipped to CERN. As shown in fig. 1 the EBIS rests on a platform above the trap. This platform has been completed and the high voltage platform for the EBIS has been mounted on top of that support.

4 MASS SEPARATOR

The S-shaped beam line between the EBIS and the LINAC consists of a mass separator [6] to separate the few highly-charged radioactive ions from ions originating from the residual gas. The deflecting magnet has been ordered and the construction of the electrostatic elements has been completed. The electrostatic lenses are now in production. The massive ridge which carries the electrostatic deflector and the vertical beam line of the separator (fig. 1) will be mounted to the same concrete tower which carries the trap-EBIS transfer beam line.

5 LINAC

The RFQ is the first structure of the LINAC [7]. It is now fully assembled, which means the water cooled ground plates, the stems and the mini-vane like quadrupole electrodes are mounted in the tank and the capacitive plungers are installed, cabled and tested. The vacuum system has been installed and first vacuum tests have been performed. Low level frequency tuning and flatness measurements have been done. Alignment of the electrodes, final adjustment of the voltage flatness and the installation of the in-coupling loop are presently being performed.

The IH-structure of REX-ISOLDE [8] is a short version of the IH-tank1 of the CERN LINAC III [9] and consists of a center frame which carries the drift tubes and two half

shells carrying cooling jackets. The first acceleration section is followed by an inner tank quadrupole triplet lens, which has been delivered and will be installed after some test measurements and the delivery of the IH-vacuum tank. The drift tubes and the stems are completed and are now being copper plated together with the IH-vacuum tank. The piston tuners are in production. The change of the final energy of the IH-structure via the piston tuners has been examined once more by a detailed MAFIA model of the power resonator. The calculations are in very good agreement with measurements taken from the vacuum tank of the power resonator and show the required tuning by changing the half shell height [10].

The production of the three seven gap spiral resonators forming the back part of the LINAC [11] is almost finished. The design velocities of the resonators were fixed to 5.4%, 6.0% and 6.6% of the velocity of light and the field optimization at the operation frequency of the power amplifiers ($f=101.28$ MHz) of the three down scaled models resulted in an achievable resonator voltage of 1.75 MV at 90 kW in-coupled rf power. The 5.4% and 6.0% power resonators are finished and ready for high power rf and beam tests. Fig. 2 presents a view inside the resonator. The resonance structure is connected to the tank via three stems, in which the copper hollow profiles for the cooling of the arms and the drift tubes are brazed together. Fine tuning is done with a tuning plate. With segments connected on the half shell the so called rough tuning to 101.28 MHz is done. The resonator is seen here on a test bench where the low level rf measurements were done.

The 6.6% resonator is assembled, the tuning to the amplifier frequency of 101.28 MHz is presently done.

So far low level RF measurements have been performed with the 5.4% and 6.0% resonator yielding parameters shown in table 1. In particular, these measurements show that a resonator voltage of 1.9 MV can be expected with a rf power of 90 kW, which is safely above the design voltage of 1.75 MV. As the first out of three rf power amplifiers

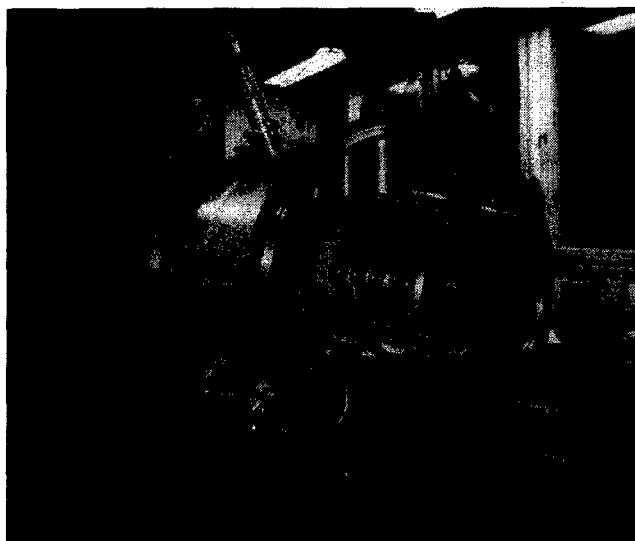


Figure 2: The 5.4% power type resonator

providing 100 kW with a duty factor of 10% has been delivered in December 1998, high power and beam tests have now been started. The second rf amplifier is in production and will be delivered directly to Munich. The residual three rf power amplifiers will be completed until end of 1999 and delivered directly to CERN.

The set up of the fully tested 7-gap-resonators at CERN is planned to take place in autumn 1999.

parameter	5.4% resonator	6.0% resonator
f [MHz]	101.28	101.28
Q-value	5620 ± 50	5420 ± 50
Z [M Ω /m]	71 ± 6	68 ± 5
U_0 [MV]	1.9 ± 0.1	1.9 ± 0.1

Table 1: Measured parameters of the 5.4% and 6.0% power type resonators, f = frequency, Z = shunt impedance, U_0 is the expected resonator voltage reached with an rf power of 90 kW.

6 TARGET

The MINIBALL γ -detector array [12] consists of a new generation of Ge-detectors with large full-energy peak efficiency to make an optimum use of the expensive radioactive beams. With its compact arrangement it is mainly suited for detecting events with small γ -ray multiplicities. In the final system the array will consist of 14 clusters with 3 individually encapsulated 6-fold segmented Ge-detectors. A prototype has been tested and have shown resolutions around 2.1 keV at 1.33 MeV γ -energy. 6 Clusters are expected to be operational when REX-ISOLDE starts operation. The electronics for MINIBALL will be purchased from the company XIA; in contrast to former Ge-detector electronics, all analog circuits are replaced by digital electronics using

flash ADC's and DSP's. The target chamber is completed and has been vacuum tested. Prototypes of the particle detectors (double sided silicon strip detector DSSSD) have been produced and tested with an alpha-source.

7 REFERENCES

- [1] D. Habs et al., Nucl. Phys.A616199729c
- [2] D. Habs et al., Nucl. Instrum. and Meth.B1261997218
- [3] D. Habs et al., Nucl. Instrum. and Meth.B1391998128
- [4] F.Ames, G. Bollen, G. Huber and P. Schmidt, "REXTRAP, an Ion Buncher for REX-ISOLDE", presented at the ENAM98, Michigan, USA, June 1998
- [5] F. Wenander, Ph.D. thesis, Chalmers University of Göteborg 1998
- [6] R. Rao et al., "Beam optics Design of the REX-ISOLDE q/m-Separator", to be published in NIM A
- [7] T. Sieber et al., this report p.xxx
- [8] S. Emhofer et al., contribution to LINAC98
- [9] D. Warner et al., "CERN Heavy-Ion Facility Design Report" CERN 93-011993
- [10] H. Bongers et al., contribution to LINAC98
- [11] H. Podlech et al., Nucl. Instrum. and Meth.B1391998447
- [12] P. Reiter et al., contribution to LINAC98

DESIGN OF THE PROTOTYPE LOW ENERGY BEAM TRANSPORT LINE FOR THE SPALLATION NEUTRON SOURCE*

D.W. Cheng[†], R.A. Gough, M.D. Hoff, R. Keller, M.A. Leitner, K.N. Leung,
J.W. Staples, M.D. Williams,
Ernest Orlando Lawrence Berkeley National Laboratory, Berkeley, CA 94720

Abstract

The design of the Spallation Neutron Source (SNS) prototype low-energy beam transport (LEBT) system is discussed. This LEBT must transfer 35 mA of H^- current from the ion source outlet aperture to the entrance of the radio-frequency quadrupole (RFQ). The plasma generator is a radio frequency-driven multicusp source, operated at 6% duty factor (1 ms, 60 Hz). The entire LEBT configuration is electrostatic, with a high-voltage extraction gap followed by two sets of einzel lenses. The second einzel lens will be split into four quadrants to permit the application of transverse steering and beam chopping fields. The H^- ion source emits a gas flow into the LEBT that must be efficiently pumped to reduce stripping losses of the H^- ions. Therefore, an efficient electrode design is incorporated to reduce the gas pressure between the electrodes. Alignment requirements and related issues will also be discussed.

1 INTRODUCTION

The Spallation Neutron Source front end systems, being built at the Lawrence Berkeley National Laboratory (LBNL), must supply a 2.5 MeV, 28 mA H^- beam at 6% duty factor to a 1 GeV linac that injects into an accumulating ring. This ring then delivers a 1 MW average beam power to a neutron production target at 60 Hz. This paper discusses the design of the low energy beam transport (LEBT) line of the front end accelerator system.

2 REQUIREMENTS

The LEBT is designed to transport 35 mA of a 65 keV H^- beam from an rf-driven source to the RFQ, operating at a 6% duty factor. It must match the beam to the RFQ entrance with a normalized emittance of less than 0.15π mm•mrad and Twiss parameters, $\alpha = 1.6$, and $\beta = 6.5$ cm. The entire LEBT is electrostatic, with a high-voltage (~80 kV) extraction gap and an einzel lens configuration with beam chopping and steering capabilities incorporated into the second (G5) lens electrode. The entire package is approximately 10 cm in length. Figure 1 shows a cross-

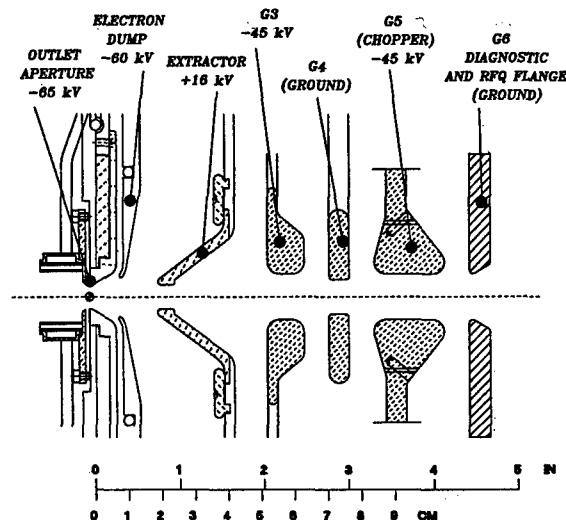


Figure 1. Cross section of the LEBT electrodes, with the ion source outlet aperture, electron dump, and RFQ endwall.

section of the lens configuration. Because of the limited space, voltage holding and creepage length along the surface of insulators must be taken into consideration. Table 1 summarizes the design parameters used. In addition, alignment for these electrodes must be held to a ± 0.05 mm tolerance in the radial direction, and ± 0.1 mm in the z (beam) direction.

Table 1. Criteria for voltage holding used.

*units of d are cm, units of U are kV

	in Vacuum	in Air
Gap:	* $d = (0.0141U^{3/2})/10$	10 kV/cm
Insul. Surface:	15 kV/cm	8 kV/cm

3 ELECTRODE DESIGN

3.1 Extractor Electrode

The extractor electrode consists of three sub-parts: the main stainless-steel "spider-arm", a retainer ring, and the aperture insert held in place by the ring (see Figure 1). The aperture insert is replaceable in case of accidental damage by hitting of the beam particles. Therefore, the aperture is designed to be accessible and replaceable without affecting the alignment of the entire LEBT assembly. We will use copper, as opposed to stainless steel, for the insert material because of its excellent thermal conductivity. We will also consider other

*This research is sponsored by the Lockheed Martin Energy Research Corporation under the U.S. Department of Energy, Contract No. DE-AC05-96OR22464, through the Lawrence Berkeley National Laboratory under contract No. DE-AC03-76SF00098.

Email: dwcheng@lbl.gov

materials, such as a 70%/30% tungsten-copper sintered material, which combines tungsten's structural integrity with copper's thermal properties.

3.2 G3 and G5 Einzel Lenses

The LEBT matching section consists of two "pseudo"-einzell lenses: the aperture G3 and the split G5 lens. G5 is used for fast beam chopping[1]. The inner diameter of this lens has to be very narrow in order to achieve sufficient beam deflection with the available chopper power supplies. This contradicts the general rule that a small lens filling-factor (beam diameter/inner lens diameter) is required for good ion optics. Ion optics simulations have been performed to minimize beam emittance-growth due to aberrations caused by the lens configuration[2]. Figure 2 shows a SimIon 3D simulation of the H⁺ beam passing through the LEBT. We have used the ion optics codes KOBRA 3D, IGUN[3] and AXCEL to optimize the LEBT lens arrangement.

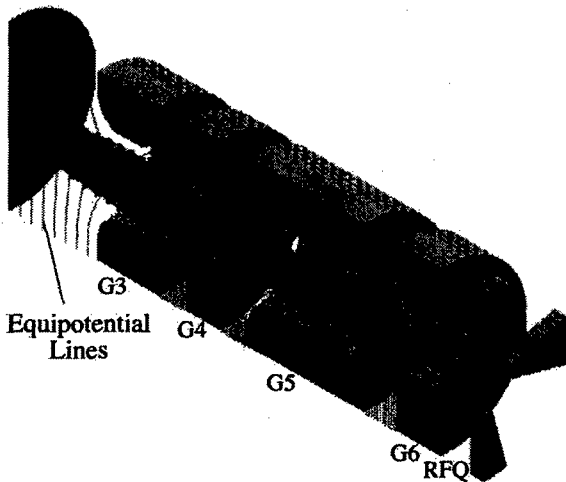


Figure 2. SIMION 3D simulation of the beam passing through the LEBT to the RFQ.

To allow beam chopping as well as beam steering in the *x*- and *y*-directions lens G5 has been designed as a four-segmented aperture. It will be fabricated as a single piece with alignment holes drilled prior to wire-edm machining into the four segments. The pieces are then pinned with ceramic standoffs for voltage holding of 5 kV max. A further discussion of its function can be seen in [1].

3.3 Ground Electrode

The electrode G4 has been designated as the main support structure, since it is fixed at ground potential. All other electrodes will be bench-mounted and pre-aligned to it. This whole, monolithic LEBT package facilitates easier alignment to the RFQ and ion source since now only one single component has to be adjusted. Figure 3 shows a blow-up assembly of the LEBT electrodes.

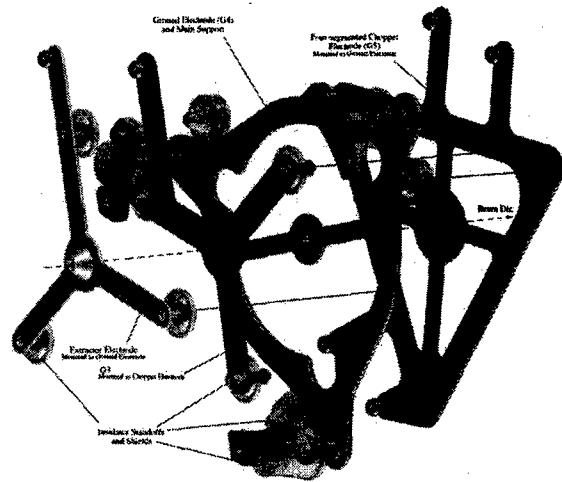


Figure 3. Blow-apart view of the LEBT electrode assembly.

4 THE ELECTRODE ASSEMBLY

The whole LEBT assembly is mounted to the ion source re-entrant cylinder as shown in Figure 4a. A three-point mounting scheme is employed with ceramic insulator posts standing between the ion source re-entrant cylinder biased at -65 kV and the electrode G4 on ground potential. Each electrode is held in place by using similar three ceramic post standoffs. Each standoff is shielded from a direct line of sight to the ion beam in order to prevent coating of, or sputtering on the insulator surfaces.

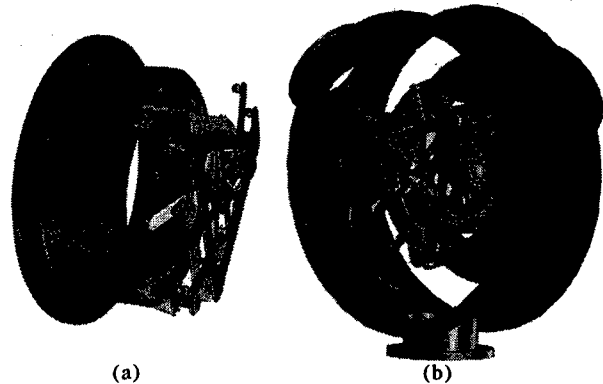


Figure 4. (a) LEBT assembly mounted to the source re-entrant cylinder, and (b) in a conceptual vacuum vessel.

The stainless-steel shields are glued to the ceramic standoffs with epoxy. The electrodes are then screwed to the metal shields. 2 mm shims are used in some locations to compensate for misalignment during the fabrication process.

Tests were conducted on two critical standoffs: the main standoff from the -65 kV source potential to the ground (G4) lens, and the standoff from ground to the -55 kV chopper lens (G4 to G5), see Figure 5. The inside geometry of the shields was fabricated and each assembly was hi-potted. Both tests were successful: the standoffs

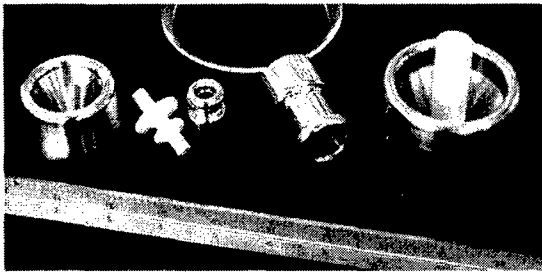


Figure 5. Insulator standoffs prior to testing. Shown are (left) the chopper to ground (G5-G4) insulators, and (right) the main insulator (main support to -65 kV source potential)

held 15% more than their design voltages after minimal conditioning.

5 VACUUM VESSEL

A noticeable departure of this design from traditional LEBT structures is the lack of gradient rings and stacked insulators. The main insulator will be a cast silica-filled epoxy structure, insulating the ion source re-entrant cylinder at -65 kV from the ground potential of the vacuum vessel. Its cross-sectional shape is similar to a horizontal "S" and is shown in Figure 6. Besides reducing the length of the ion-source re-entrant cylinder, this design also provides a wider-open geometry for improved pumping.

Triple-point protection consists of a brass screen that is cast into the epoxy, allowing the thread inserts for the mounting bolts to remain in a field-free region at the source re-entrant cylinder flange. The flange at ground potential is of a Kofoid design[4]. ANSYS finite element simulations verified electrical potentials and gradients, and RASNA finite element runs have been used to determine the structural loading. Deflection tests will also be performed on this insulator under vacuum loading to determine the amount of shim necessary for correct alignment of the LEBT assembly.

The vacuum vessel consists of a 3/16" thick stainless-steel chamber, 28" diameter by 9" deep, with three 10" pumping ports and high-voltage feedthroughs for the

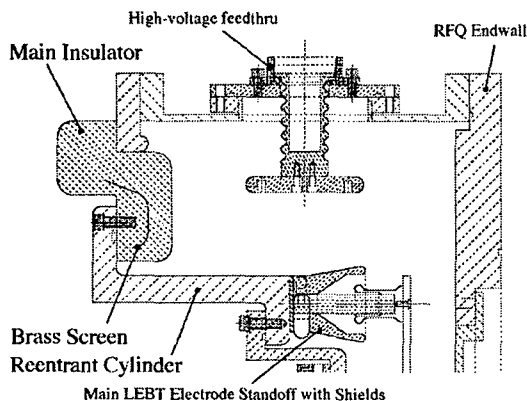


Figure 6. The LEBT assembly in a conceptual view of the vacuum vessel.

LEBT electrodes. See Figure 4b for a conceptual view of the vessel containing the LEBT.

The main LEBT-assembly flange is movable under vacuum load. This allows on-line alignment of the ion source and the LEBT as an entire package to the RFQ entrance aperture. Screw-jacks will be mounted to the main insulator flange in the x- and y-directions, and will be manually actuated with long shafts. The movement under vacuum load is accomplished by using an O-ring seal and friction-free teflon-impregnated pads upon which the flange rests. The weight of the ion source/LEBT package is held by flange bolts mounted on Belleville washers, which are tightened to a degree that allows movement without loosening the bolts.

6 FABRICATION

Detail design of the LEBT components is in progress; fabrication will start in the beginning of April 1999. The LEBT is scheduled to come on-line along with the ion source and a prototype section of the RFQ for testing in the summer of 1999.

7 ACKNOWLEDGMENTS

The authors would like to thank Russell Wells and Gary Koehler for their expertise, and Sam Mukherjee, Peter Luft, and John Pruyn for their design effort. Additional thanks go to Alessandro Ratti, Jim Greer, and Bill Abraham for their input, and their challenge of making a huggable LEBT become a reality.

8 REFERENCES

- [1] J.W. Staples, J.J. Ayers, D.W. Cheng, J.B. Greer, M.D. Hoff, A. Ratti, "The SNS Four-Phase LEBT Chopper", these proceedings.
- [2] M.A. Leitner, D.C. Wutte, K.N. Leung, "Simulation of the Low Energy H- Injector into the National Spallation Neutron Source Radio Frequency Quadrupole Accelerator", Rev. of Sci. Instrum., 69, 965 (1998).
- [3] R. Becker and H. Hermannsfeldt, Rev. Sci. Instrum. 63, 2756 (1992).
- [4] Kofoid, M.J., "Effect of metal dielectric junction phenomena on high-voltage breakdown over insulators", AIEE Trans. Power Apparatus and Systems, 79, 999-1004 (Dec. 1960).

THE SNS FOUR-PHASE LEBT CHOPPER*

J. W. Staples, J. J. Ayers, D. W. Cheng, J. B. Greer, M. D. Hoff, A. Ratti
Ernest Orlando Lawrence Berkeley National Laboratory
University of California, Berkeley, CA 94720, USA

Abstract

The Spallation Neutron Source front end incorporates a beam chopper in the LEBT that will remove a 295 ns section of beam at a 1.118 MHz rate (65% transmission) with less than 50 ns rise/falltime. The H^- beam pulse length is one ms at a 60-Hz rate (6% duty factor). The LEBT is all-electrostatic, and the chopper incorporates four 3-kV solid-state switches driving an einzel lens, split into quadrants, with a 4-phase chopping waveform. The suppressed beam is targeted on a four-segment Faraday cup which provides on-line intensity and steering diagnostics. Results of proton beam tests will be reported.

1 BEAM REQUIREMENTS

The Spallation Neutron Source (SNS) comprises a 1-GeV H^- linac injecting a storage ring with a 1 ms injection time and single-turn extraction, operating at 60 Hz[1]. During the 1 ms injection into the ring, approximately 1200 turns are accumulated. To reduce the activation of the extraction Lambertson septum magnet, a 295 ns notch is introduced in the injected beam by two sets of choppers, operating at the ring revolution frequency of 1.188 MHz.

2 IMPLEMENTATION

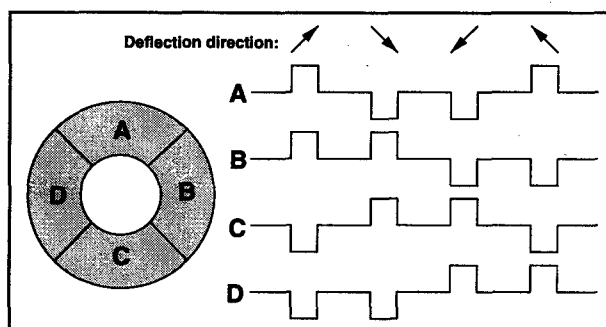


Figure 1: Waveforms to Deflector

The first chopper stage is at the end of the 65-keV all-electrostatic LEBT[2], followed by a fast-rise clean-up chopper at 2.5 MeV. The LEBT chopper is included as a modification of the second LEBT einzel lens, which is split azimuthally into four quadrants. A four-phase chopping

waveform on the four segments deflects the beam sequentially in four directions, shown in Figure 1, creating the 295 ns gaps in the 1 ms beam pulse. The four electrode segments are each independently pulsed to ± 3 kV by solid-state switches, deflecting the beam sequentially along each of the 45 degree diagonals. The solid-state switches have active pull-up and pull-down, providing a less-than 50 ns chopping transitions.

Figure 2 shows an early version of the split einzel electrode.

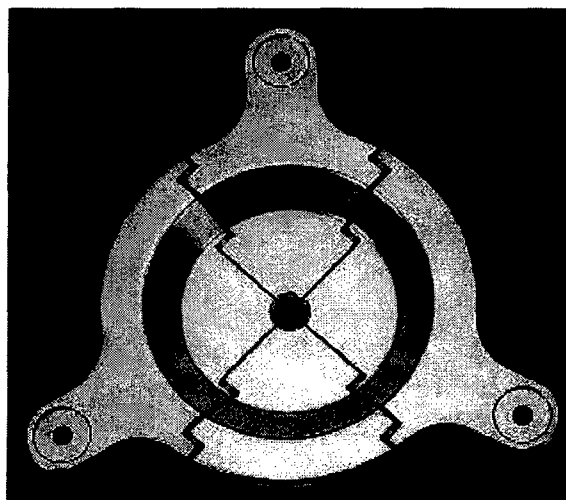


Figure 2: Split Chopper Electrode

The beam is targeted onto a diagnostic plate, split along the diagonals similar to the chopping electrode itself, in the wall common to the end of the LEBT and the start of the RFQ. The four segments of the target electrode are electrically isolated and water cooled, serving as a beam current diagnostic and a beam steering diagnostic. For a 65 keV, 35 mA H^- beam with a 65% duty factor and with 35% of the current removed by the 1.188 MHz chopper, the total average power dissipated on the target is 48 watts.

Angular beam steering is provided by a symmetric d-c bias on each segment of up to ± 1 kV. Beam position steering is provided by physically moving the entire ion source and LEBT relative to the RFQ and the diagnostic plate on a sliding vacuum seal.

3 ELECTRONICS

The key electronic component of the LEBT chopper system is the solid-state ± 3 kV bipolar switch. This switch is

* This research is sponsored by the Director, Office of Energy Research, Office of Basic Energy Sciences, of the U. S. Department of Energy, under Contract No. DE-AC03-76SF00098.

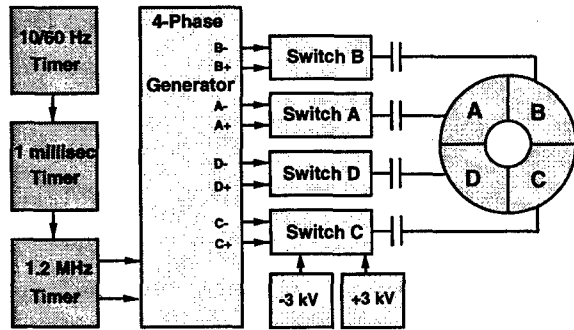


Figure 3: Chopper Block Diagram

a modified version of a standard product from Directed Energy Inc.[3]. The DEI design provides rise and fall times of less than 60 ns and a duty cycle of up to 12% at 60 Hz for up to a 2 ms burst. The switch design is protected against load faults (sparking) and mis-timed or incorrect gating of the positive and negative gate inputs.

The major internal power dissipation of the solid-state switches occurs at the voltage transitions. The average power dissipation is less than 450 watts per switch at a 12% duty cycle.

Figure 3 shows the control logic used during the test phase. Figure 4 shows a detail of the actual equipment: two of the four DEI bipolar solid-state switches, topped by a four-phase waveform generator.

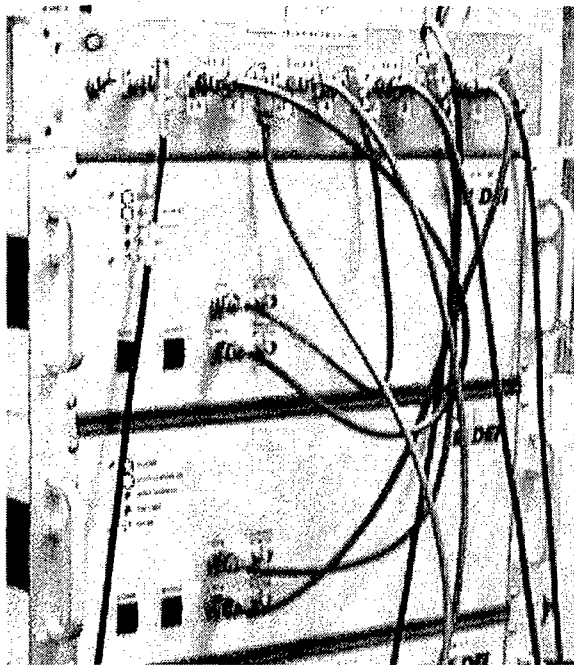


Figure 4: Chopper Switches and Driving Electronics

The electronics used during the test phase includes a series of delay/gate generators and a 4-phase generator that drive the inputs of the DEI switches. The high-voltage bipolar output is delivered to the electrodes via coupling capacitors, allowing the switches to be at ground potential,

isolated from the steering offset and accelerating potentials. The rise and fall times are specified for a load capacitance of 100 pf along with a four-foot length of coax interconnect cabling of an additional 100 pf.

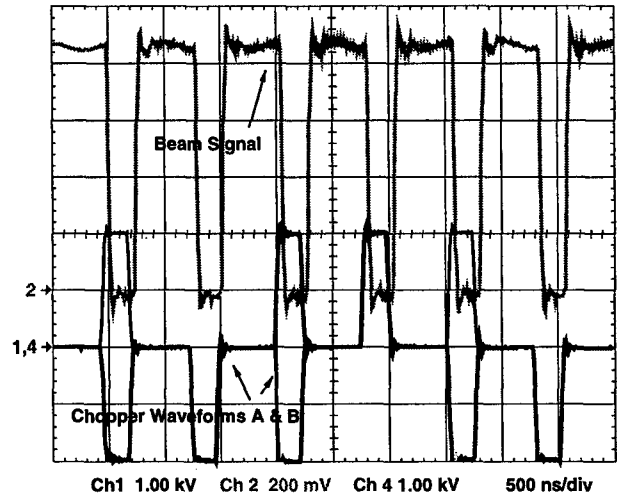


Figure 5: Deflection Waveforms, Beam Current, 500 ns/div

4 PROOF OF PRINCIPLE

A proof-of-principle test has been conducted on a 40 keV proton injector that includes all the elements in the SNS source/LEBT design: an r.f.-driven multicusp ion source and a two-einzel lens all-electrostatic LEBT. The LEBT is followed by an aperture plate and a fast 50-ohm Faraday cup.

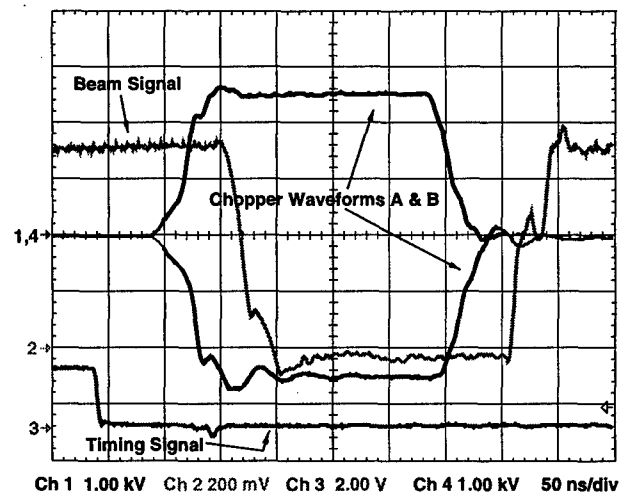


Figure 6: Deflection Waveforms, Beam Current, 50 ns/div

Figure 5 shows the beam current (upper trace) and the chopping potentials on two adjacent chopper segments (lower traces) at 500 ns/div. The peak deflection voltage is ± 2 kV and the pulse period is 0.75 microseconds. In Figure 6, the time scale is expanded to 50 ns/division and the chopping voltage increased to ± 2.5 kV, showing the

risetime (center) is less than 50 ns, and the beam rise and falltime also less than 50 ns. The transit time of the beam through the last einzel electrode is 12 ns, which sets a lower limit of the chopping transition time.

Note in Figure 5 that the chopped beam time structure exhibits no subharmonic of the chopping frequency, even though the beam is sequentially chopped in four directions. For a lower chopping voltage where the beam is only partially chopped, the subharmonic amplitude of the partially chopped current is a sensitive indication of beam missteering on the chopping aperture.

5 SNS CHOPPER CONFIGURATION

Figure 7 shows a cross-section of the LEBT electrodes, starting at the plasma generator at the left [4],[5], [6] and continuing to the diagnostic plate (RFQ endwall) at the right, spanning a 10 cm total length. The last electrode (G5) before the RFQ endwall is the split deflection electrode that also acts as the second einzel focusing electrode.

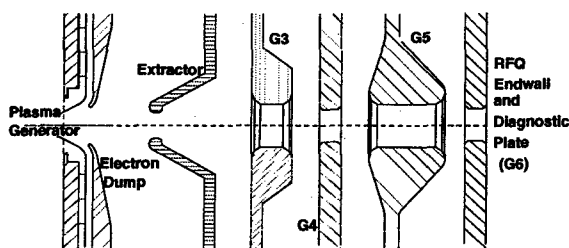


Figure 7: LEBT Electrode Configuration

Figure 8 shows a three-dimensional simulation (SimIon) of the beam deflection by the chopper electrode, deflected toward the chopping aperture plate (G6) and the following RFQ[7]. In the final configuration, the aperture plate hole radius is equal to the envelope radius of the beam passing through it. With this aperture radius, 85% of the deflected beam will be lost on the diagnostic plate, and the remaining 15% of beam will be deflected *between* the RFQ vanes and will not be accepted for acceleration by the RFQ.

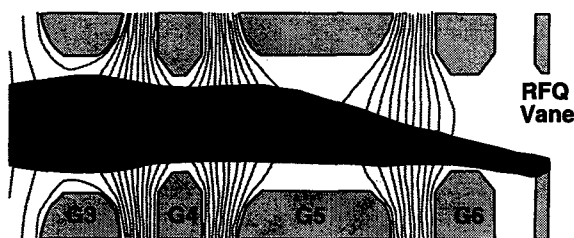


Figure 8: Deflected Beam Profile (From SimIon Plot)

Figure 9 shows the diagnostic plate detail with the pick-up electrodes sandwiched between the LEBT ground plane and the RFQ end plate. The diagnostic plate is constructed of layers of metal and thermally conducting epoxy, one millimeter thick. The pick-up electrodes comprise two brazed-

together layers of OFE copper and contain water cooling passages (not shown) surrounded by an air guard.

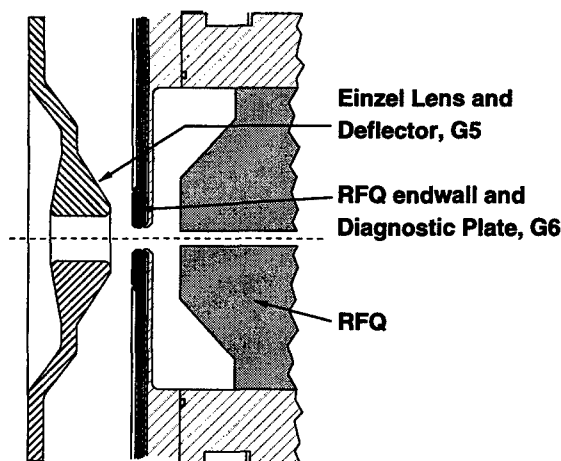


Figure 9: Deflecting Electrode, Diagnostic Plate

The fully operational version of the ion source, LEBT and chopper are currently being manufactured and will be tested by the end of Summer 1999.

6 ACKNOWLEDGMENTS

The authors acknowledge the pioneering SNS leadership by Bill Appleton of ORNL, the LBNL SNS leadership team of Rick Gough and Roderich Keller, and the superb development of the SNS ion source by Matthaeus Leitner and Ka-Ngo Leung.

7 REFERENCES

- [1] R. Keller et al., "The SNS Front-End Systems", Int. Topical Meeting AccApp 98, Nuclear Applications of Accelerator Technology, Gatlinburg, 1998
- [2] John Staples, Daniel Cheng, Martin Fong, James Greer, Matthew Hoff, Roderick Keller, Kurt Kennedy, Matthaeus Leitner, Robert MacGill, Daryl Oshatz, Alessandro Ratti, Justin Remais, Steve Virostek, "The SNS Front End Accelerator Systems", 1998 Linac Conference Proceedings, Chicago
- [3] DEI, Inc., Fort Collins, Colo. (www.dirnrg.com)
- [4] D. W. Cheng et al., "Design of the Prototype Low Energy Beam Transport Line for the Spallation Neutron Source", Paper WEA31, 1999 Particle Accelerator Conference, New York
- [5] M. A. Leitner et al., "High-Current High-Duty-Factor Experiments with the RF-Driven H⁻ Ion Source for the Spallation Neutron Source", Paper WEA13, 1999 Particle Accelerator Conference, New York
- [6] S. K. Mukherjee et al., "Mechanical Design of the Prototype H⁻ Ion Source for the Spallation Neutron Source", Paper WEA14, 1999 Particle Accelerator Conference, New York
- [7] Private Communication, Matthaeus Leitner, LBNL.

DESIGN OF A 35 keV LEBT FOR THE NEW HIGH INTENSITY OPPIS AT BNL

J. Alessi, M. Okamura[#], D. Raparia, T. Roser, BNL, NY, U. S. A.
 C. D. P. Levy, A. Zelenski⁺, TRIUMF, Vancouver, Canada
 T. Takeuchi, Konan Univ., Kobe, Japan
 Y. Mori, KEK, Tsukuba, Japan

Abstract

As a part of the RHIC Spin project, the KEK optically pumped polarized ion source (OPPIS) is being upgraded at TRIUMF, and will then be installed at BNL. This new source will deliver > 100 times more current than the existing BNL polarized H⁺ source. In order to transport and accelerate this more intense polarized beam efficiently, a new 35 keV low energy beam transport (LEBT) line has been designed. Each beamline element has been designed to minimize aberrations using 2D and 3D-field analysis. Spin motion and beam optics were tracked from the ionizer cell in the source to the 200 MHz RFQ, including 3D-field effects.

1 INTRODUCTION

The KEK OPPIS is being upgraded at TRIUMF, and has now produced 1.0 mA of H⁺ beam with DC mode. Also duration of a pumping laser has reached 200 μ s [1 - 3]. At BNL, a new beamline was designed to match from this source into the 200 MeV linac. The expected beam emittance from this OPPIS is much larger than that of existing atomic type polarized source, and the beam should be matched to the acceptance of the existing RFQ without depolarization. Therefore, this beamline must be designed carefully.

2 SCHEME OF THE LEBT

The normalized beam emittance determined empirically from similar OPPIS is about 2π mm mrad, while a calculation discussed later in this paper predicts a value of 2.35π mm mrad (100%). This is approximately ten times of the emittance from the existing atomic beam polarized H⁺ source now being used for AGS, and also larger than the emittance of the ≈ 100 mA unpolarized H⁺ beam. The beam from the new source will be merged to the existing high intensity beam line and injected into the RFQ, which has an acceptance which is almost the same as the emittance from the OPPIS.

When designing the LEBT for a polarized beam, not only the beam optics but also spin motion must be considered. Beam leaving the OPPIS has longitudinal polarization, and should be rotated to the vertical direction before

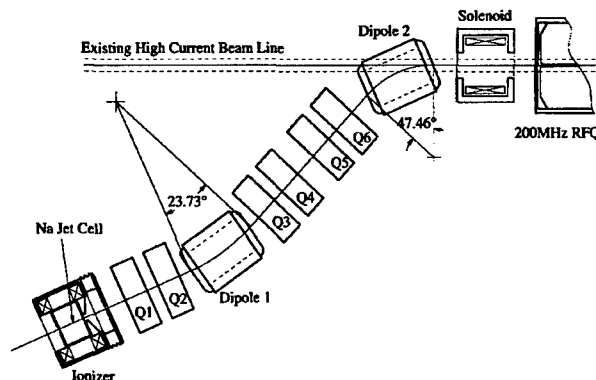


Figure 1: The LEBT for the new OPPIS

injection into the booster synchrotron. Figure 1 shows the planned beam line before the RFQ. First the beam from the source is accelerated to 35 keV in the extraction gap, goes through a quadrupole doublet, and is deflected by 23.73 degrees in Dipole 1. In this dipole, the spin direction is rotated by 90°, making it perpendicular to the beam direction and in horizontal plane. The beam then goes through two more quadrupole doublets and is then merged to the existing beamline by using 47.46° bending magnet. This dipole will be pulsed, to allow switching between polarized and unpolarized H⁺ beam on a pulse-to-pulse basis. In this dipole the spin direction is rotated by 180°, so is still perpendicular to the beam direction and in the horizontal plane. After this, the beam is focused strongly by a pulsed solenoid magnet and injected into the RFQ. At the same time, the spin rotates more than one revolution in the transverse plane. The exact rotation is not determined because the field strength of the solenoid will be adjusted to maximize transmission through the RFQ. After acceleration from 35 keV to 750 keV, the beam then goes through another pulsed solenoid, added to 750 keV beam, and there are sufficient quadrupoles existing in this line to allow flexibility in matching to

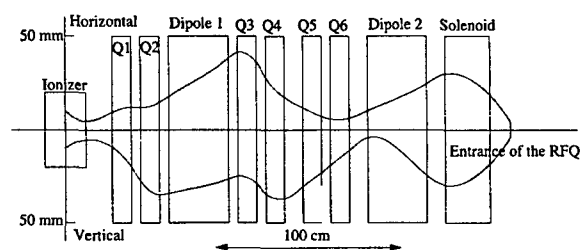


Figure 2: The beam envelope at the LEBT

[#] Visitor from RIKEN okamura@bnl.gov

⁺ Visitor from INR

the 200 MeV allow one to rotate the spin to the vertical direction. This solenoid has minimal effect on the transverse optics of the Alvarez linac. The beam envelope for the 35 keV line, calculated using TRANSPORT, is shown in Fig. 2.

3 BEAM EMITTANCE FROM THE OPPIS

To start designing the LEBT, the beam emittance of the OPPIS had to be investigated. Figure 3 shows a schematic of the OPPIS.

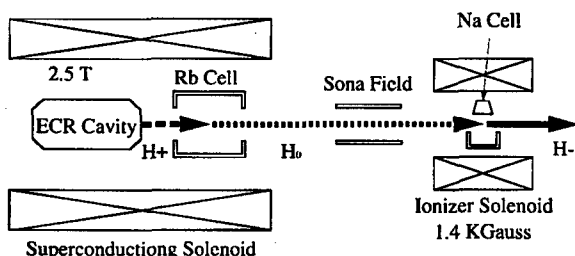


Figure 3: Schematic of OPPIS

The OPPIS consists of two solenoid magnets, a 2.5 T super-conducting magnet, which includes an ECR cavity and Rb vapor cell, and a 1.4 kGauss ionizer solenoid that has the Na vapor cell. H^+ ions are produced in the ECR cavity and extracted at 3.5 keV. The protons pick up a polarized electron in the Rb cell, to become neutral. The neutralized H beam drifts without effect from the magnetic fields to the Na cell, where it picks up an electron to become H^- . The H^- beam then leaves the OPPIS under the influence of fringing field of ionizer solenoid. The initial emittance of the OPPIS depends on where the neutralized beam becomes H^- , and how the fringing field of the solenoid affects the H^- beam. The emittance has been calculated using Monte Carlo for the charge exchange process, and Runge Kutta for particle tracking through electric and magnetic field maps created using OPERA-2D. Spin motion was calculated by the Runge Kutta method, and the effect of the fringing field of the ionizer was analyzed. In this new OPPIS, a jet type Na cell, which has been recently developed at TRIUMF, will be used. We hope that with this new Na cell, the extraction voltage, accelerating from 3.5 keV to 35 keV, can be achieved by biasing only the ionizer at high voltage, due to much less flow of Na vapor to outside. The electric field of the beam extraction was optimized to produce a waist in the beam at the center of the fringing region of the solenoid, so the effect of transverse magnetic fields to the spin motion can be minimized. As a result, calculations predict that depolarization due to the fringe field will be reduced by about 3%. Figure 4 and Fig. 5 show the electric and magnetic fields calculated by OPERA-2D and the projection of the H particles respectively. The distribution of Na vapor was assumed to be Gaussian and σ was set to 20 mm. The total gas thickness was assumed to be 1.5×10^{15} atoms/cm². Only

two process were considered, $H^0 \rightarrow H^-$ and $H^- \rightarrow H^0$, as charge exchange process between H and Na atoms, with cross sections of

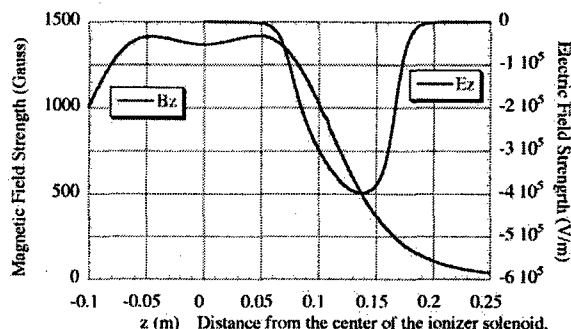


Figure 4: Field distribution of the Ionizer solenoid.

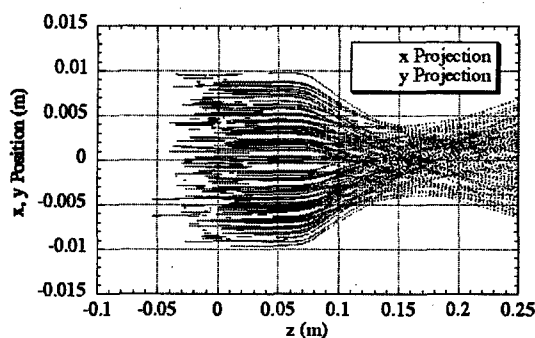


Figure 5: Projection of H^- particles

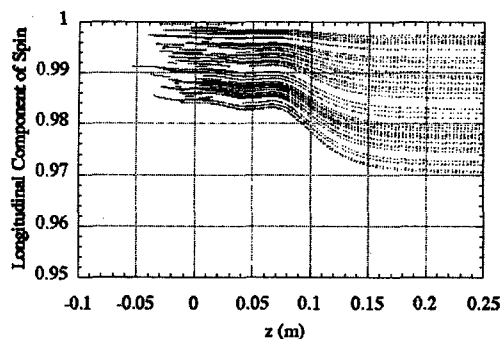


Figure 6: Spin motion at the ionizer cell

0.03×10^{-14} cm² and 0.30×10^{-14} cm² respectively. At this beam energy, other charge exchange cross sections are negligible. Five thousand neutral protons were created uniformly within a circle of 10 mm radius and 1.0 mrad of divergence, and were tracked from 20 cm upstream of the center of the solenoid. The yield of H^- ions was 9.0%. The predicted beam emittance 35 cm downstream from the center of the solenoid are given in Table 1. The calculated spin motion is shown in Fig. 6. Assuming 100 % initial longitudinal polarization of the beam, a polarization of

98.49% was calculated after passing through the fringing field.

Table 1: Twiss parameters of the beam from the OPPIS

ϵ (100%)	270.4 mm mrad
α	3.81
β	0.903 mm/mrad
γ	17.2 mrad/mm

4 COMPONENTS OF THE LEBT

Each device in the beamline was designed to minimize spin aberrations. The six quadrupoles in this line will be electrostatic. In this section, only the dipole and solenoid magnets are discussed. Again, the Runge Kutta method was used in particle tracking with field maps created using OPERA-2D and 3D (TOSCA).

4.1 Dipole Magnets

To maintain the existing high current beam line, Dipole 2 (47.46°), shown in Fig. 2, has to have at least 10 cm of aperture and be less than 30 cm in length. The bending angle of Dipole 1 is only 23.73° , but the identical design

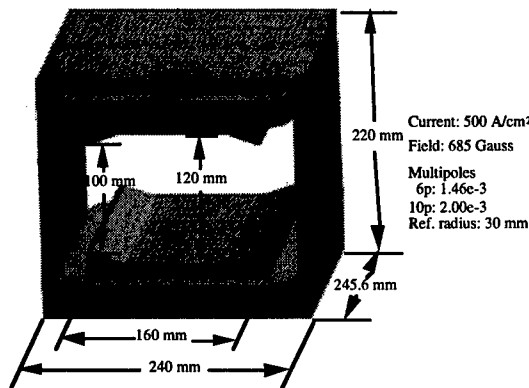


Figure 7: Over view of the Dipole magnet

Table 2: Effect of dipole magnets

Magnet	Dipole 1	Dipole 2
Hor. emit. growth (rms)	7.9 %	6.7 %
Ver. emit. growth (rms)	2.4 %	4.2 %
Conserved spin	99.96 %	99.82 %

as Dipole 2 was applied due to large divergence from the OPPIS. In order to minimize spin aberrations, a rectangular shape was adopted so each particle sees almost the same integral of magnetic field, so has almost the same spin rotation. There is strong edge focussing of the beam in the vertical direction. An overview of the dipole design is shown in Fig. 7. The calculated emittance

growth, using rms emittance, and conserved spin component are shown in Table 2.

4.2 Solenoid

The solenoid lens is the best focusing element for matching of the high current (100 mA) H^- beam into the RFQ. However, we must pay careful attention to the spin motion for the polarized beam, since the spin axis rotates around the magnetic axis of the solenoid. As mentioned above, the spin rotation angle will vary due to fine adjustment of the solenoid field strength for focusing. Therefore, there will be another solenoid after the RFQ to align the spin direction vertically. Figures 8 shows the spin motion of an on-axis particle. The calculated remaining spin component is 99.6%. The aperture and length of the solenoid magnet are 108 mm and 241.3 mm respectively, and the calculated effective length is 205.8 mm. This magnet will be operated at ≈ 3.3 kGauss at the center of the magnet to match to the acceptance of the RFQ.

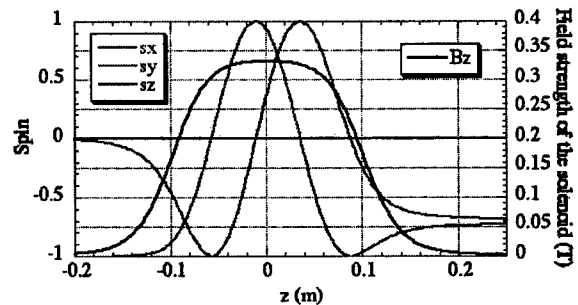


Figure 8: Spin motion in the solenoid magnet.

4 CONCLUSION

The LEBT for the new BNL OPPIS was designed considering 3D field effects (except quadrupoles), and spin depolarization. The expected total conserved polarization is calculated to be better than 97.8% from the source ionizer to injection into the RFQ. The emittance growths for both planes through the line are less than 28%, and the predicted RFQ transmission is 70%.

5 REFERENCES

- [1] M. Kinsho, et al., "Production of Polarized Negative Deuterium Ion Beam with Dual Optical Pumping" Review of Scientific Instruments, Vol. 67-3, 1362-1364 (1996)
- [2] A. N. Zelenski, et al., "Optically Pumped Polarized H^- Ion Sources for RHIC and HERA Colliders" These Proceedings.
- [3] C. D. P. Levy, et al., "Development of High-Current Polarized H^- Ion Sources at TRIUMF", EPAC'98, TUO028B, Stockholm, (1998)

STUDIES OF SLOW-POSITRON PRODUCTION USING LOW-ENERGY PRIMARY ELECTRON BEAMS

E. Lessner, D. Mangra, J. G. Power, P. Schoessow, M. White

Argonne National Laboratory, Argonne, IL 60439

Abstract

Slow-positron beams produced from negative-work-function solid-state moderators have found numerous applications in condensed matter physics. There are potential advantages in using low-energy primary electron beams for positron production, including reduced radiation damage to single-crystal moderators and reduced activation of nearby components. We present numerical calculations of positron yields and other beam parameters for various target-moderator configurations using the Argonne Wakefield Accelerator (AWA) [1] and Advanced Photon Source (APS) [2] electron linacs [3] as examples of sources for the primary electron beams. The status of experiments at these facilities is reviewed.

1 INTRODUCTION

Slow positrons are valuable tools in atomic physics, materials science, and solid state physics research. They can be used to probe defects in metals, to study Fermi surfaces and material surfaces and interfaces, and to obtain detailed information about the electronic structure of materials. Positrons can be used to gain information complementary to that acquired by other means such as x-ray and neutron scattering. Slow positrons can be obtained either by moderating positrons emitted by some radioactive sources or produced when an accelerated electron beam hits a high-Z target.

In both cases the positron beam occupies a much larger phase-space volume than is useful and some kind of cooling is required. Damping rings can be used at high-energy accelerators, but for the eV-scale positron kinetic energies used in condensed matter physics experiments, a more appropriate technique is the use of solid state moderators. The moderators are typically single-crystal metal films or solid noble gases and are made of materials that possess a negative work function for positrons. Positrons thermalize near the moderator surface and are eventually ejected with a kinetic energy equal to the work function.

The moderation efficiency is low due to competition between the thermalization process and the annihilation of positrons with electrons in the moderator. The geometry of the moderator is relevant as well; a moderator structure with a large surface-to-volume ratio will provide the best chance for the positrons to stop near the surface and be ejected [4]. The moderator material quality is also an issue. Polycrystalline materials contain crystal defects and grain boundaries that can provide

potential wells in which positrons can be trapped, thereby further reducing moderation efficiency.

Since the positron production rate is proportional to beam power, the required beam power is generally achieved using high-energy electron beams. There is a possible advantage in using a low-energy, high-intensity primary electron beam for positron production. The raw positron yield decreases with the electron energy. The softer positron energy spectrum should improve the yield of moderated positrons, due to the shorter time required for the positron energy to be reduced by dE/dx losses in the moderator. Additionally, use of low-energy positrons should reduce radiation damage to the moderator crystal lattice, and also result in lower activation of the target, moderator, and nearby beamline materials. At the 14-MeV incident electron beam energy with which we are primarily concerned, photoneutron production rates are very low [5,6].

In this paper we report on a planned experiment to study the efficiency and yield of slow positrons produced by the low-energy intense electron beam from the AWA drive linac. We discuss simulations, experimental configurations, and instrumentation. Possible future directions will also be mentioned.

2 POSITRON YIELD CALCULATIONS

The EGS4 electromagnetic shower Monte-Carlo code [7], together with a C-language user interface code [8], was used to optimize the production target thickness for maximum positron yield. Phase-space coordinates of positrons exiting the target were taken as input to beam optics codes used for design of the spectrometer and detector. The incident electron beam energy was taken as 14 MeV, corresponding to the beam energy from the AWA drive linac. The production target is made of tungsten.

Raw positron yield was studied at various energies as a function of target thickness [9]. The maximum yield of ~ 0.005 e^+e^- occurs at around 2.5 mm; this thickness will be used subsequently in this paper. In the simulations, the incoming electron beam energy is represented by a Gaussian distribution whose mean and standard deviation are 14 MeV and 0.7 MeV, corresponding to the measured AWA average beam energy and energy spread. The beam size is similarly represented by a Gaussian distribution of zero mean and standard deviation equal to an rms beam radius of 1.5 mm. The beam is normal to the target. Positrons exiting the target are distributed over a broad

range of angles and energies. The positron energy spectrum is shown in Figure 1. The spectrum exhibits a broad peak at an energy of 2 MeV and standard deviation of ~ 2 MeV. The positron radial distribution right after the target is shown in Figure 2. The positron angular distribution with respect to the z axis is shown in Figure 3, where only the positive angles are plotted. The distribution is peaked around 0° , the small angles correspond to the high-energy particles, and the distribution is symmetric with respect to the z axis. The angular distributions around both the x- and y- axes are uniform. An insert in Figure 3 shows the coordinate system used in the analysis.

Only a small fraction of the positrons produced will actually be transported to the test chamber due to their large angular divergence and energy spread. The PARMELA code [10] was used to calculate the acceptance of the spectrometer and diagnostic chamber. We estimate that 8.75×10^6 positrons per 40 nC of incident 14-MeV electrons will arrive at the test chamber.

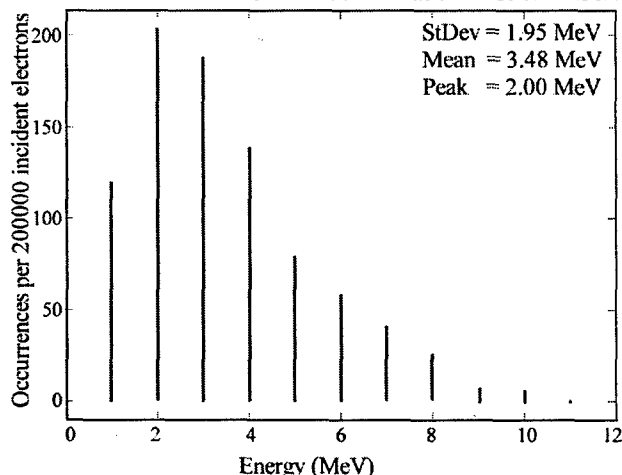


Figure 1: Energy spectrum of positrons from 14-MeV electrons impinging on a 2.5-mm-thick tungsten target.

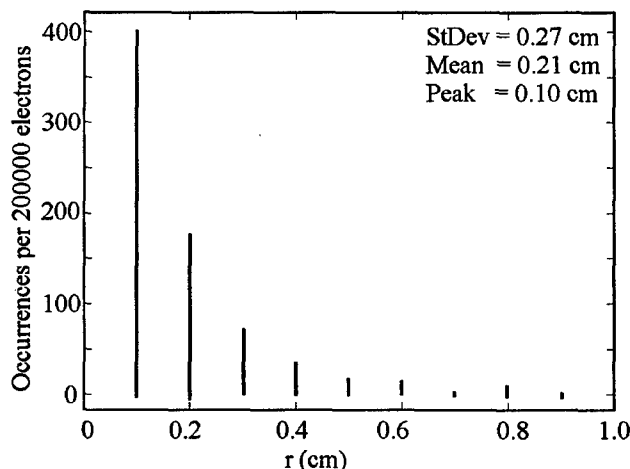


Figure 2: Radial distribution of positrons right after the target from 14-MeV electrons impinging on a 2.5-mm-thick tungsten target.

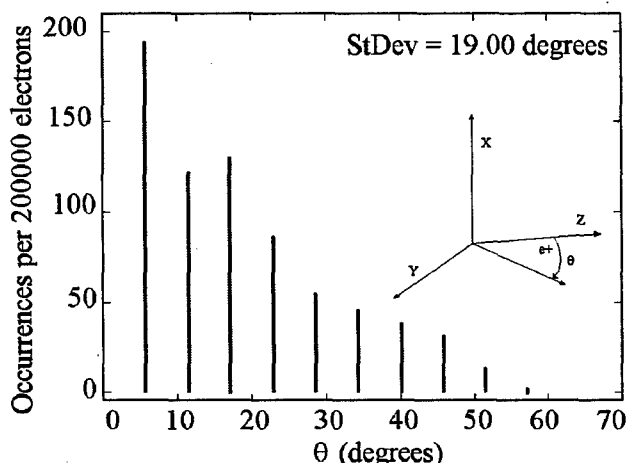


Figure 3: Positron Z angular distribution from 14-MeV electrons impinging on a 2.5-mm-thick tungsten target. The distribution is symmetric with respect to the z axis. Only positive values are shown.

3 EXPERIMENTAL CONFIGURATION

The AWA drive linac is a photoinjector-based machine that can provide 30-ps-long electron pulses containing more than 40 nC/pulse at 14 MeV. The electron beam will be focused to a ≤ 1 -cm-diameter spot at the 2.5-mm-thick tungsten target. The target is located directly upstream of a dipole magnet that acts as a spectrometer to measure the positron energies and as a charge separator to dump secondary electrons. The electron (negative bend) side of the vacuum chamber is lined with 2.5 cm of graphite to absorb secondary electrons while minimizing x-ray background due to bremsstrahlung in the chamber walls. Figure 4 is a plan view showing the target, spectrometer, and diagnostics.

Positrons are bent by the spectrometer into a diagnostic chamber. The path of the positrons as they are bent toward the screen is indicated in Figure 4. Initial experiments involve measurement of raw positron yields under various conditions of energy and target thickness in order to calibrate the Monte Carlo calculations. Instrumentation consists of a phosphor screen viewed by a CCD camera and a Faraday cup. A 10-mm-thick (about 3 radiation length) tungsten plate is located upstream of the Faraday cup. The plate has a 1-mm slit to define the momentum slice accessible to the Faraday cup for a given spectrometer field setting. Sweeping the spectrometer current permits a measurement of the positron energy spectrum. Reversing the spectrometer current bends electrons into the diagnostic chamber for tuning and calibration purposes. Construction of the vacuum equipment is nearing completion and we anticipate being able to make measurements shortly.

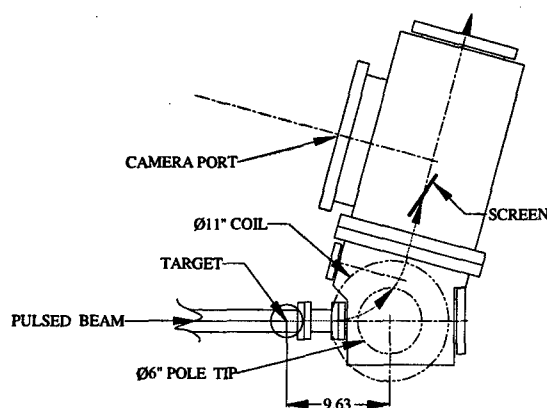


Figure 4: Plan view of the target, spectrometer, and diagnostics, showing the beam path as the positrons are bent toward the screen.

4 FUTURE PLANS

After the positron yield has been fully understood, the Faraday cup/phosphor assembly will be replaced by tungsten sheet moderators and eventually also by thin single-crystal tungsten moderator foils. The moderation efficiency as a function of moderator type and incident beam energy will be studied using a pair of NaI counters to measure the back-to-back 511-keV gamma rays from positron annihilation at rest in the moderator. A solenoid will be installed immediately downstream of the target and tested to assess its effect on capture and transport efficiency as compared to simulation.

A low-field solenoidal beamline will be constructed to transport the slow positrons to a secondary moderator and experimental chamber. Yield from the secondary moderator will be measured using micro-channel plates.

Several of the envisaged experiments require short-pulse beams with good timing resolution. A trap capable of collecting positrons from the entire beam macropulse and expelling them as a short pulse will then be required.

The 30-ps pulse length from the AWA photocathode gun can be shortened to several ps using a fairly simple magnetic chicane. The resulting positrons can be energy selected and used to perform positron lifetime studies in bulk materials.

Previously, computer simulations and beam studies were performed using the APS linac and determined that it is well suited as a slow-positron-source driver [11,12]. The APS linac is being reconfigured to drive an FEL in addition to its normal duties as the APS injector. The DC thermionic gun has been replaced by a photoinjector. Spent beam from the FEL is a source of high-energy, few-ps electron pulses that could be directed into a slow-positron target instead of to a beam dump. The DC thermionic gun can then be reconfigured to drive a high-intensity (70nC/30ns pulse), low-energy positron source as well.

5 ACKNOWLEDGMENTS

The authors would like to acknowledge D. Haid for graphics support and C. Eyberger for editorial assistance. This work was supported by the U.S. Department of Energy, Office of Basic Energy Sciences and Division of High Energy Physics, under Contract No. W-31-109-ENG-38.

6 REFERENCES

- [1] URL <http://www.hep.anl.gov/awa/awa/awahome.htm>
- [2] URL <http://www.aps.anl.gov/welcome.html>
- [3] M. White et al., "Construction, Commissioning and Operational Experience of the Advanced Photon Source (APS) Linear Accelerator," XVIII Intl. Lin. Acc. Conf. Proc., pp. 315-319 (1996).
- [4] P. Schoessow, J. Simpson, "Accelerator-Based Cold Positron Beams," in *Linear Collider BB Factory Conceptual Design*, Proc. of the UCLA Workshop, D. H. Stork, Ed., 26-30 Jan 1987.
- [5] S. S. Dietrich and B. L. Berman, "Atlas of Photoneutron Cross Sections Obtained with Monoenergetic Photons," LLNL Report UCRL-94820, June 1986, Preprint.
- [6] Marion M. White and Eliane S. Lessner, "A Low-Neutron-Background Slow-Positron Source," 8th Int'l. Workshop on Slow Positron Beam Techniques for Solids and Surfaces (SLOPOS8), Cape Town, South Africa, 6-12 September, 1998, to be published.
- [7] R. Nelson, H. Hirayama, D. W. Rogers, "The EGS4 Code System," SLAC-265 (1985).
- [8] L. Emery, private communication.
- [9] E. Lessner, M. White, "Bremsstrahlung Pair-Production of Positrons with Low Neutron Background," Proc. of the XIX Int'l. Linac Conf., Chicago, IL, USA, 23-38 August 1998, pp. 306-308.
- [10] L. Young, J. Billen, LANL Internal Report LA-UR-96-1835, 1996.
- [11] E. Lessner and M. White, "Concepts for a Slow-positron Target at the Advanced Photon Source," 1997 Particle Accelerator Conference, May 10-17, 1997, Vancouver, Canada, pp. 327-329 (1998).
- [12] M. White and E. Lessner, "Slow Positron Target Concepts for the Advanced Photon Source (APS) Linear Accelerator," Positron Annihilation ICPA-11, Proceedings of the 11th International Conference on Positron Annihilation, Material Sciences Forum Volumes 255-257, pp. 778-780 (1997).

THE 10 KEV INJECTOR FOR THE UNIVERSITY OF MARYLAND ELECTRON RING PROJECT*

T. Godlove, P. Haldemann, and D. Kehne, FM Technologies, Inc., S. Bernal, P. Chin, R. Kishek, Y. Li, M. Reiser, M. Venturini, J.G. Wang, W.W. Zhang, Y. Zou, UMD, and I. Haber, NRL

Abstract

The 10 keV, 100 mA, Pierce-type electron gun and injector for the University of Maryland Electron Ring (UMER) Project are described. Using a pulsed control grid located 0.15 mm from the 4-mm radius cathode, 100-ns bunches are generated. The A/K gap is variable, producing beam currents ranging from 50 to 160 mA. A rotatable aperture plate is included to allow six different masks, including a pepperpot. Beam current after the aperture plate is measured with a built-in Rogowski coil. The injector line consists of a solenoid lens, five printed-circuit quadrupoles, and two in-line diagnostic chambers. A separate, multi-purpose chamber is placed at the end of the injector line during gun characterization studies for emittance, profile, and energy analysis.

1 INTRODUCTION

A model electron ring is being built at the University of Maryland to investigate the effects of space charge in bending systems, heavy-ion recirculators and rapid-cycling rings with a limited number of turns [1]. For this research a space-charge-dominated, low emittance, relatively low energy (nonrelativistic) beam is desired. In this paper we describe the design of the injector, a key component of the electron ring. The injector consists of an electron gun, means for matching the beam into a quadrupole lattice, and pulsed elements for injecting the beam into the ring. The pulsed elements include a pulsed dipole and two Panofsky quadrupoles, one for the injected beam and the other for the recirculating beam [2].

The beam parameters were chosen to be 10 keV and 100 mA, corresponding to generalized perveance of 0.0015, to model large accelerators with similar space-charge effects and to keep the cost in line with university research. Here the generalized perveance is $K = 2(I/I_0)(m/M)(\beta)^{-3}$, where I is the beam current, $I_0 = 10^7 \text{ mc/e} = 17 \text{ kA}$, m and M are the mass of an electron and the particle in question, respectively, and β are the usual normalized velocity and total energy of the particle. For $K=0.0015$, the space charge forces are similar, for example, to a 100-MeV, 2.5 kA proton beam or a 1-GeV, 5 kA mass-200 beam. While such ion currents have not been achieved, nevertheless the space-charge forces put the 10-keV beam in an important new regime of study which is important for a number of applications.

2 ELECTRON GUN

The electron gun is similar to a 2.5 keV gun used at the University of Maryland for some years [3]. It employs a conventional Pierce geometry and has a control grid located at 0.15 mm from an 8-mm diameter dispenser cathode. The electrode boundaries are shown in Fig. 1. While the gun is designed using EGN for an optimum current of 100 mA, a variable A/K gap is included to provide currents from 60- to 140 mA. A rotatable aperture plate, located near the beam waist, allows 6 different masks to be moved into the beamline.

The primary aperture, having a diameter twice that of the

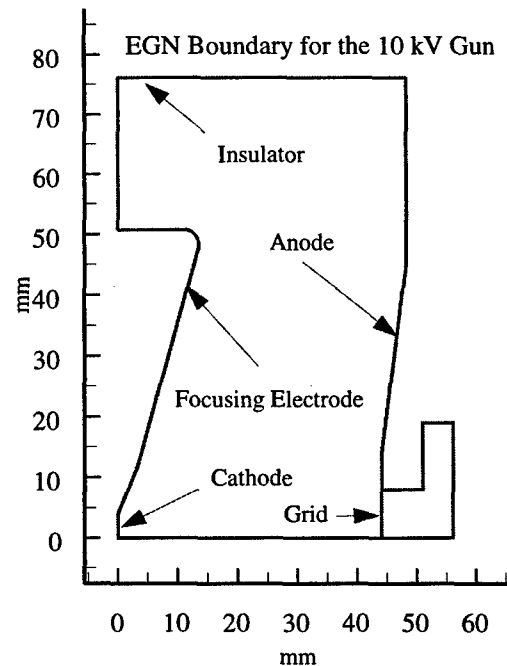


Fig. 1 Boundaries used in EGN gun design.

beam, allows full beam transport. Three round intercepting apertures provide currents of 0.5%, 15%, and 55%. A "pepperpot" mask is included for emittance measurements, and the final mask employs a 5-beamlet distribution to enable detailed comparison with PIC simulations.

* Supported by the US Department of Energy.

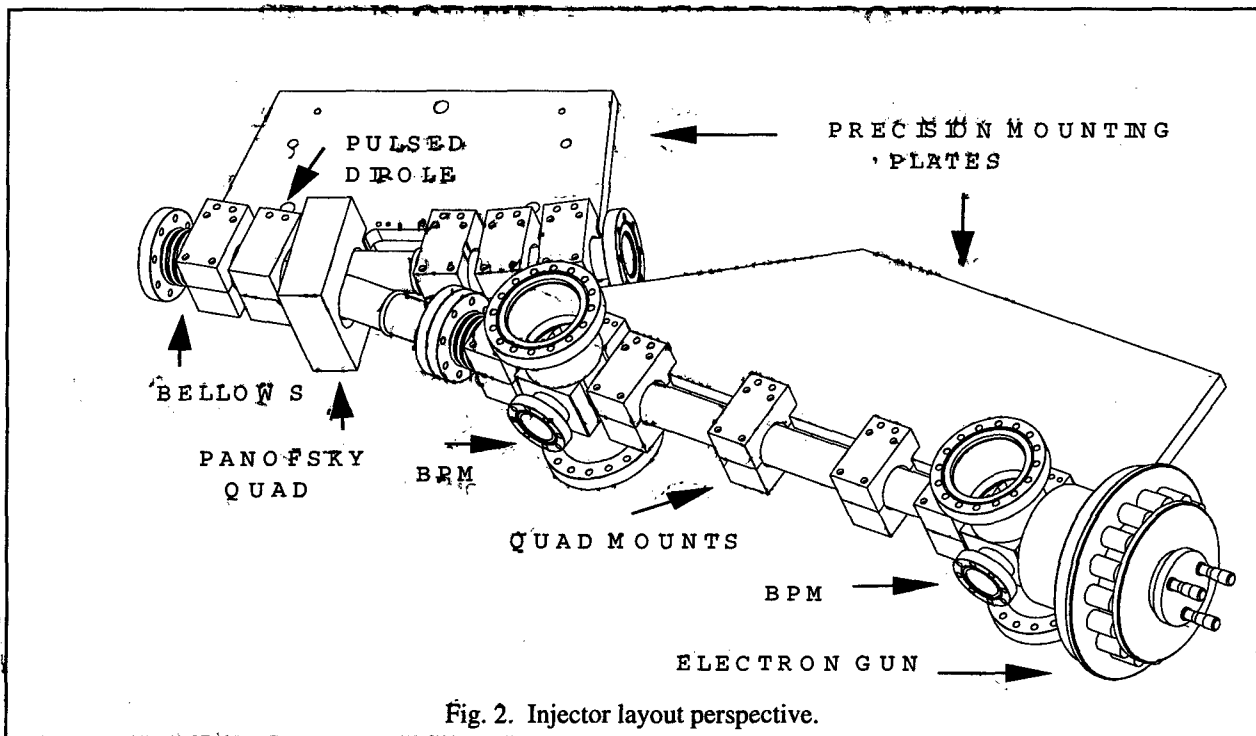


Fig. 2. Injector layout perspective.

Beam current is measured after the aperture plate with a built-in Rogowski coil. A gate valve is included to allow isolation from the remainder of the vacuum system. EGN simulations locate an 8-mm diameter waist at 1.2 cm downstream from the anode grid. The 4x rms normalized thermal emittance of the cathode is calculated to be 3.5 mm-mrad. EGN predicts negligible growth above this. Analytic calculation of grid effects produces a total expected emittance of 4 mm-mrad. While previous experience with the 2.5-keV gun indicates emittance growth of up to 80% [3] above the thermal emittance, the specification for the 10-keV injector allows for emittance growth of up to 280%. This should be easily achievable.

The entire gun is bakeable to 250° C. An 8 l/s ion pump mounted below the front face of the gun is sufficient. The field from the pump is <0.1 G at the cathode.

A large, multi-purpose, bakeable diagnostic chamber is under construction to characterize the electron gun both before and after it is mounted on the injector line.

Diagnostics include: (1) a fluorescent screen which is movable along the axis for transverse profile and envelope measurements; (2) a Faraday cup used as a beam stop and current monitor; (3) a slit-and-wire system for emittance measurements and (4) a retarding-field analyzer to measure the energy homogeneity. The last two diagnostics are mounted on flanges transverse to the beam axis so that they may be accurately inserted and retracted using remotely controlled precision motor drive.

Beam characterization will be performed in several steps: first with the gun alone, then with the injector line to study

the lattice optics, then with dc injection elements, and finally with the pulsed dipole and Panofsky quadrupoles.

3 INJECTOR LINE

The injector line, shown in Fig. 2, has one solenoid and five printed-circuit quadrupoles [4] plus the Panofsky quadrupole. This enables matching the beam into the lattice as well as providing considerable freedom of adjustment of the parameters. Two diagnostic chambers are included in the injector line similar to those in the ring. Each houses a capacitive pickup beam position monitor (BPM), a fluorescent screen, and a 4-inch pumping port.

The injection angle is 10°, with the injection point located at one of the normal 10° ring bends, enabling a 20° angle between the two adjacent straight sections.

Because of the strong space charge, the quadrupoles in the ring are spaced with a half-lattice separation of 16 cm. However, the cramped quarters near the injection point preclude such close spacing. For this reason the design uses two Panofsky quadrupoles (one shown in Fig. 2), one for the entering beam (which is turned *off* before the beam completes one turn) while the other serves as a normal ring quadrupole and must be turned *on* before the beam completes the first turn. With a circulation time of 200 ns, the bunch length is expected to be 50-75 ns. The rise and fall time of the pulsed elements is expected to be ~30 ns [2]. Since the two Panofsky quadrupoles overlap slightly, the mutual interaction is of some concern and is being studied with bench models.

The injection Y-shaped chamber will be glass, with a thin metallic coating on the inside to prevent charge buildup but allow fast field penetration.

Figure 3 shows a calculation using the K-V envelope code SPOT [5] based on a configuration without the bend. The position and strength of the solenoid and printed-circuit quadrupoles were adjusted based on the mechanical constraints noted above as well as optimum match to the FODO lattice. Orbit steering corrections will be accomplished with a combination of Helmholtz coils and thin discrete dipoles located in the injector line.

The 3-D PIC code, WARP [6], is being used for more detailed calculations of the beam dynamics, including the 10° bends. Results to date indicate that emittance growth is reasonably small for 25 turns in the ring. One particularly sensitive tolerance is rotation of the printed-circuit quadrupoles about the beam axis. WARP calculations specific to the injector dynamics agree well with the SPOT results noted above, provided that initial runs were done to determine the optimum lattice conditions just before the inflector bend.

Transport of a 4-keV beam in a 1-m long FODO lattice with five printed-circuit quadrupoles has been studied recently [7]. Results indicate good agreement with both SPOT and WARP. This study provides an excellent foundation for the present design.

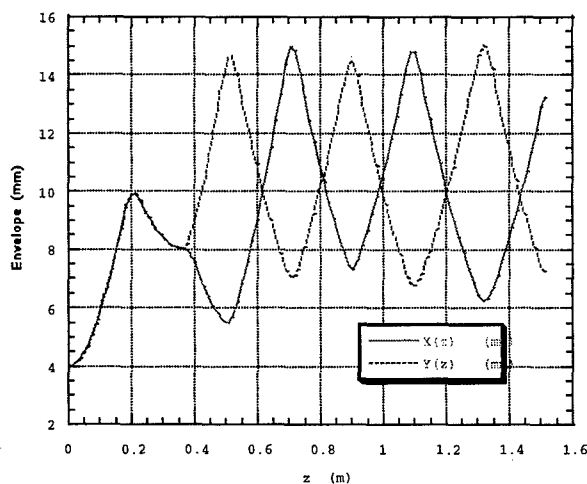


Fig. 3. Envelope calculation using SPOT.

4 ELECTRONICS

The pulser for the electron gun is similar to that used in the existing UMD 2.5-keV gun. It consists of a high-voltage deck which houses a filament transformer, a grid bias supply, a 200-V pulser supply and the 100-ns pulse generator. The pulse generator uses a charged coaxial

cable for the pulse network and a fast (~ 1 ns) avalanche transistor switch.

Power is supplied through an isolation transformer, and pulses are supplied to the deck via a fiber-optic link. A trigger pulser has been built and tested which produces pulses from 1 Hz to 120 Hz. The pulser is synchronized to the AC line and has delay capability up to 8 msec for setting the trigger to coincide with zero AC fields at the cathode.

5 CONCLUSION

A complete injection system has been designed and is under construction for the University of Maryland electron ring. It is capable of delivering a high quality, matched beam to the ring with dynamics ranging from emittance-dominated to space-charge-dominated, satisfying the needs of the experimental program. Initial tests of the gun are scheduled for the summer of 1999. Full installation and tests of the injector are planned to be completed by December 1999.

6 REFERENCES

1. M. Reiser *et al*, "The Maryland Electron Ring for Investigating Space-Charge Dominated Beams in a Circular FODO System" TUCR3, these proceedings.
2. Y. Li *et al*, "Design, Simulation and Test of Pulsed Panofsky Quadrupoles" THP169, these proceedings.
3. J.G. Wang, D.X. Wang and M. Reiser, Nucl. Inst. and Methods in Phys. Res. **A316**, 112 (1992).
4. T.F. Godlove, Santiago Bernal and Martin Reiser, Proc. 1995 Particle Accel. Conf., 2117 (1996).
5. C.K. Allen, S.K. Guharay, and M. Reiser, Proc. 1995 Particle Accel. Conf., 2324 (1996).
6. D.P. Grote *et al*, Fus. Engr. & Des. 32-33, 193 (1996); R. Kishek *et al*, "Simulations of Collective Effects in the Space-Charge-Dominated Beam of the University of Maryland Electron Ring" TUP118, these proceedings; R. Kishek *et al*, "Effects of Quadrupole Rotations on the Transport of Space-Charge-Dominated Beams: Theory and Simulations Comparing Linacs with Circular Machines" TUP119, these proceedings.
7. S. Bernal *et al*, Phys. Rev. ST, Accel. & Beams **4**, 044202 (1998).

SECONDARY EMISSION MAGNETRON INJECTION GUN IN LONG PULSE MODE

S. A. Cherenshchikov, G.M. Ivanov, L.A. Makhnenko, KIPT, Kharkov, Ukraine.

Abstract

The Secondary Emission Magnetron Injection Gun (SEMIG) is relatively a new cold-cathode electron gun [1]. The advantages of the SEMIG in long pulse operations are more obvious when we apply it for power radio-frequency sources and electron linacs. Experimental facility and a method of emission excitation in the SEMIG are described. The method consist of the secondary emission multiplication on the trailing edge of the voltage pulse. The SEMIG is operated with the extern pulse-driver. Similar method is known for magnetrons. The electron beam with pulse duration up to 3000 μ s and repetition rate up to 50 Hz (duty factor up to 15%) is obtained.

1 INTRODUCTION

The main direction of accelerator development is increasing its lifetime and efficiency. The new cold cathode electron gun gives us this possibility. The gun is known as the Secondary Emission Magnetron Injection Gun (SEMIG) [1]. It is based on a new principle: self-supported secondary emission in crossed fields. The gun may be used as injector in electron linacs [2] and radio-frequency power sources [3-6] for accelerators.

The field of gun application may be large if it could produce high current relatively long pulses of electron beam at high current. Conveniently, all high current linacs and power sources use solenoid as magnetic field sources. If the duty factor of device increases then full efficiency increases too, because solenoid feed power is constant. This shows the great importance of increasing pulse length because duty factor is in proportional of pulse length. The possibility of obtaining a long pulse in cold cathode magnetron was shown earlier [7]. Now we describe the long pulse mode in SEMIG.

2 THE PULSE DURATION LIMITATIONS

The limit of the current density J depends on pulse length τ and cathode material. The estimation is made on the base of Kovalenko's understanding [8] of the physical processes in vacuum tube. The current density J is estimated as:

$$J = \frac{const}{\sqrt{\tau}} \quad (1)$$

where for copper: $const=260 [A \cdot cm^{-2} (\mu s)^{1/2}]$; for tungsten: $const=860 [A \cdot cm^{-2} (\mu s)^{1/2}]$. Maximum current I may be estimate as

$$I=JL\pi d \quad (2)$$

where L - cathode length, d - cathode diameter. In our data I is equal to 45 A. The current is more large then one from conventional thermoionic cathode for the accelerator [8].

3 THE CONDITION OF SECONDARY EMISSION EXCITATION

The SEMIG consists of a hollow tube anode and coaxial finger-like secondary emission cathode inside it [1]. Correspondence between value of magnetic field and apply voltage pulse is chosen in order to make electrons to return the cathode (Hell's cut off relation). The start of electron multiplication occurs at the fall of the negative high voltage pulse applied to the cathode [10,11]. After initiation the electron emission continues at the top of the following part of the pulse [12].

The cause of secondary emission is additional energy of returned electrons from the turbulent electron flow in cross-field gap due to increasing electron space charge. Near the cathode edge the electron space charge gives axial component of the electric field. The axial component is the cause of electron injection and produces the annual electron beam.

For emission excitation the amplitude of voltage pulse and the magnetic induction must be large enough. Figures 1,2 show theory [10] and experimental boundaries [12] of excitation region in coordinates "voltage-induction".

4 EXPERIMENTAL FACILITY

The auxiliary firing pulse amplitude for pure-metallic cathodes is high enough even when the magnetic field is optimal [12]. The attempts to start the secondary emission with the help of the existing submodulator was made to do it by the in previous tests and experiments were unsuccessful. That's why the decision was made to do it by the main modulator pulse which in our previous experiments ensured firing with the sufficiently high voltage decrease. The submodulator forming circuits and its pulse transformer didn't ensure producing of pulses with the microsecond range. So, the scheme of experiment was chosen as shown in Fig. 3. By this scheme the pulse from main pulse modulator 1 was used as exciting one. Position 2 is the matched cable, and position 3 is the pulse step-up transformer, put in tank 4 filled with oil. The

pulse was fed to vacuum volume through high-voltage insulator 5, and reached the cathode 6. The cathode 6 was situated coaxially inside the anode 7 which simultaneously worked as passing pipe. The isotropic magnetic field along the axis of cathode 6 and anode 7 was produced by solenoid 8. The magnetic field induction could be tuned in the interval 0 - 0.3 T by changing the current in the solenoid 8. The beam formed by the gun 6, 7 was falling on the collector 9. The beam current value and the pulse duration were obtained from oscillograph 10 of type C4-74, using the synchronization system 11 of Universal Injecting Complex (UIC) [9]. The long beam current pulse was formed by accumulating condenser 12. To avoid the rectifier diodes damage in the case of gun spark-over the resistor 13 with low resistance was included in series into the gun circuit. The choke 15 was the short circuit defense of the gun. The voltage of the accumulating condenser 12 was tuned by autotransformer in limits of 0-20kV.

5 RESULTS

After the pulse from modulator 1 is guided to the gun cathode 6, relatively the grounded passage tube 7 at the fall of the pulse begins the secondary emission multiplication [10,11]. If the multiplication is large enough at the end of the pulse, self-supporting secondary emission mode is established. After the pulse ends generation of the beam is continuous due to the discharge of accumulating capacity 12. If the pulse duration increases the beam current decreases. Experiments have shown that it is possible to increase the duration of the pulse to 3,000 μ s at the magnetic field of 0.13 T and the value of capacity 12 is 0.1 μ F.

All modes are shown in the table

Number the mode	of Magnetic field, T	Pulse duration, μ s	Beam current, A
1	0.130	200	0.05
2	0.154	400	0.10
3	0.138	3,000	0.005

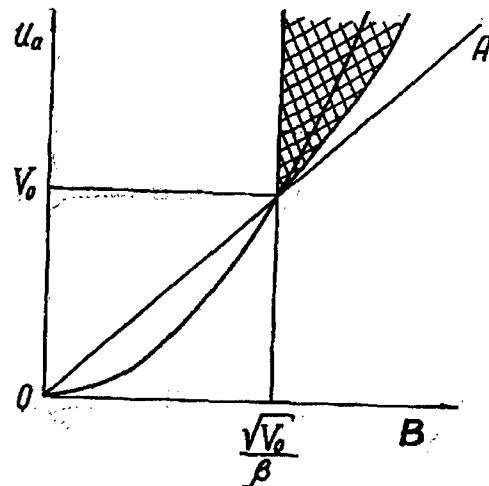


Fig.1 The theory region of secondary emission cross-field excitation [10] (xxx)

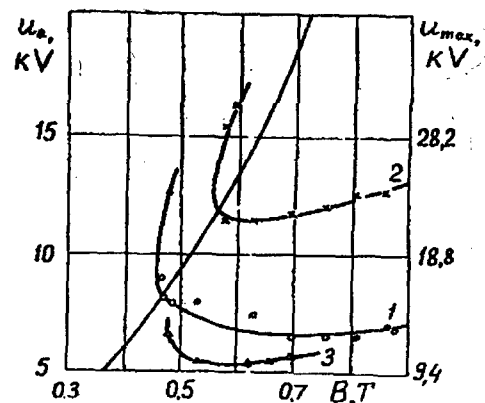


Fig.2 The experimental excitation boundaries in the magnetron [12].

At the left the pulse modulator voltage is shown. At the right the amplitude exciting pulse is shown.

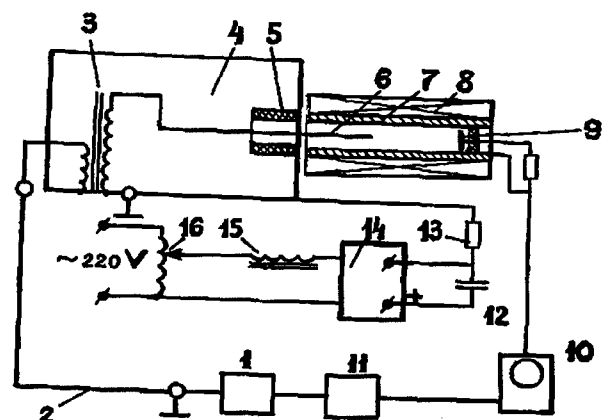


Fig.3 The scheme of experimental facility:

1- main pulse modulator; 2-coaxial cable; 3- pulse transformer; 4- oil tank; 5- main insulator; 6- secondary emission cold cathode; 7- anode- (drift-tube); 8- solenoid; 9- collector (Faraday cup); 10- oscillograph; 11- synchronization system; 12- accumulating condenser; 13- defense resistor; 14- gun power source (submodulator); 15- defense choke.

6 ACKNOWLEDGEMENT

The author expresses his gratitude to Dr.A.Opanasenko for useful discussion of the obtained results and his assistance in the preparation of these reports.

7 REFERENCES

- [1] S.A. Cherenshchikov et al. // AIP Conference Proceeding. 1994. Vol. 337. P. 350-359.
- [2] S.A. Cherenshchikov, G.M. Ivanov, L.A. Makhnenko, A.N. Opanasenko. Secondary Emission Magnetron Injection Gun as Injector for Linac. (Poster report WEA-38 of this conference)
- [3] S.A. Cherenshchikov, A.N. Opanasenko, "Secondary Emission Magnetron Injection Gun for RF-Sources", // Abstract for V European Particle Accelerator Conference (Barcelona, 10-14 June 1996).
- [4] S.A. Cherenshchikov, A.N. Opanasenko, "Concept of Employing SEMIG in RF-Sources for Future Linear Colliders", // Abstract for V European Particle Accelerator Conference (Barcelona, 10-14 June 1996).
- [5] S.A. Cherenshchikov, A.N. Opanasenko, Prospects of Increasing Life Time and Efficiency of New Generation RF Sources by Path of Application Secondary-Emission Unheated Metallic Cathodes, Abstract for XVII Particle Accelerator Conference PAC'97, Vancouver, Canada.
- [6] S.A. Cherenshchikov, G.M. Ivanov, L.A. Makhnenko, A.N. Opanasenko, "About Possibility of Thermoionic Gun Substitution at Power Klystron Amplifier for Secondary Emission Magnetron Guns" // Voprosy Atomnoy Nauki i Tekhniki. Seriya: Yadernofiz. Issled. (Kharkov) 4,5 (31,32), pp. 40-42, 1997.
- [7] S.A. Cherenshchikov, V.D. Naumenko, "Investigation of the Magnetron Start with a Cold Secondary-Emission Cathode at the Trailing Edge of the Voltage Pulse", Izvestija Vuzov "Radiofizika", vol. 27, pp. 250-256, February, 1984.
- [8] V.F. Kovalenko. Thermal Physics Processes and Electron Vacuum Devices. Sov. Radio. Moscow. 1975.
- [9] S.A. Cherenshchikov, G.M. Ivanov, V.I. Kurilko, L.A. Makhnenko, A.N. Opanasenko, P.M. Ryabka, and, "Experimental Investigations of Electrodynamics Characteristics of Accelerating Structure STRUM-90". Journal of Technical Physics, Vol. 64, No. 4, 1994, (p.115-123)
- [10] S.A. Cherenshchikov, "About the Magnetron Start with a Cold Cathode at the Trailing Edge of the Voltage Pulse", Elektronnaja Tehnika - Ser. Elektronika SVCh, 1 6, pp. 20-28, June, 1973
- [11] S.A. Cherenshchikov. "Secondary-Emission Multiplication at Magnetically Insulated Discharge in a Variable Field", Izvestija Vuzov "Radiofizika", vol.27, pp.1331-1337, October, 1984.
- [12] S.A. Cherenshchikov, V.D. Naumenko, "Investigation of the Magnetron Start with a Cold Secondary-Emission Cathode on the Trailing Edge of the Voltage Pulse", Izvestija Vuzov "Radiofizika", vol. 27, pp. 250-256, February, 1984.

SECONDARY EMISSION MAGNETRON INJECTION GUN FOR LINAC

S.A.Cherenchchikov, G.M.Ivanov, L.A.Makhnenko,
A.N.Opanasenko, KIPT, Kharkov, Ukraine

Abstract

The experimental research results for operation of the cold cathode magnetron injection gun in the linear traveling wave accelerator are described. The mechanism of the gun operation is connected with the current secondary electronic increase and the establishment of a self-supported secondary emission. The comparison of the beam passage conditions for a thermionic gun points on the fact, that the characteristics of the magnetron gun are acceptable for the purposes of injection in the rf accelerator.

1 INTRODUCTION

The development of the accelerator engineering and of associated powerful rf sources put the new requirements to the appropriate sources of powerful electron beams. Thus it is more and more necessary to consider the alternatives to the traditional sources based on thermionic cathodes. One of such alternatives in the case of the necessity to achieve simultaneously a high current density and a long service life it can be the magnetron injection gun in the secondary emission mode [1]. The long service life of the cathode creates new opportunities in the accelerating engineering. For example, the manufacturing of the steamed off industrial accelerator modules instead of the existing vacuum pumped ones. Besides, the magnetron gun with the cold cathode, as will be shown below, is capable to form short (nanoseconds) current pulses with the help of the rather long voltage pulses on the gun. It has the essential practical importance for creation of the high current short pulse accelerators, as it facilitates formation of a high voltage to feed the gun. Moreover it is supposed, that the magnetron gun with cold cathode will be steady to back bombardment by the electrons reflected from the accelerating structure [2], and the last can limit the pulse recurrent frequency and the service term of the thermionic cathodes. The magnetron gun has a number of peculiarities, which can affect the gun operation in the rf linacs. First it is the cathode not magnetic screened and the tubular form of beam. To estimate the operation peculiarities of such a gun in the rf linacs was the purpose of the researches presented below.

2 EXPERIMENTAL EQUIPMENT

The Universal Injector Complex (UIC) of the accelerator, LA-300 MeV [3] was used for the experiments. UIC was intended for expansion of LA-300MeV opportunities to accelerate high current short pulse beams in a mode of rf

energy accumulation. UIC consist of a threode thermionic gun; two cavity buncher placed in focusing solenoids; injector and two accelerating sections, which are supplied by a system of rf power recuperation. To carry out the experiments, described below, the thermionic gun was demounted and on its isolator a secondary emission magnetron injection gun (SEMIG) was mounted. The circuit of experiment is shown on Fig. 1. SEMIG consists of two cylindrical coaxial electrodes placed inside the solenoid of the buncher (SG). The internal electrode serving as a cathode (C) is a metal rod established on high-voltage isolator (I) in the transit channel, the walls of which are the anode (A). The cathode feeder of a short pulse voltage consists of the coaxial cable serving secondary winding of the high-voltage pulsed transformer (PT). The signal of the gun current is transferred through this cable from the high-voltage circuits to the oscillograph (IO).

3 THE GUN TESTING

After feeding the high voltage pulses on the cathode, and turning on the solenoid creating the magnetic field in the gun area the cathode current pulses with the amplitude up to 20 • were obtained. Their duration changed from 20 ns up to 0.5 microsec depending on the mode. For this gun the C-V characteristic, submitted on Fig. 2, is close to a square law. The use of a cathode material identical to the cathode material of the earlier investigated gun [4], allows to compare their parameters on the basis of the similarity theory [1]:

$$I = C \frac{U^2}{BD_c \ln^2 \left(\frac{D_a}{D_c} \right)} \quad (1)$$

Where I is the beam current emitted from SEMIG; D_a , D_c are diameters of the cathode and anode accordingly; C is a constant depending on emission properties of the cathode; U is the gun voltage; B is the magnetic induction of the solenoid.

The comparison shows the increase of the current in our case. It is probably explained by stronger magnetic field. It agrees with dependence of the beam current on the magnetic field [5] measured later on.

3 HIGH CURRENT ACCELERATION MODE

After feeding the rf power to the accelerating sections and tuning the passage beam system, at the gun current about

12 A and the gun voltage about 45 kV, the current of the accelerated electrons about 0.5 A was obtained at the exit of UIC. The small value of the beam capture factor is probably caused by the low injection energy of electrons, determined by the low gun voltage. Comparison of the measured capture factors represented on the fig. 3 for the beams injected by both the traditional thermionic gun and SMIG shows that this capture factors represented on the fig. 3 are practically equal when the gun voltages are equal. The pulse duration of the relativistic electrons at the accelerator exit was about 20 ns. The duration of the current pulses and voltage on the gun was essentially more and was accordingly 50 ns and 1 microsec. The reduction of the beam duration observed at the Faraday's cylinder is determined mainly by two factors: by the small (down to 1 ns) time of the excitation of secondary emission in the gun at peak gun voltage and by the mode of accumulated energy when feeding the gun and the accelerating structures. The front of the beam pulse is formed due to fast excitation of secondary emission. The beam duration is increased with increasing the level of the accumulated energy and is decreased with increasing the gun current.

At testing SEMIG only the grouping and accelerating sections were turned on. The second section was without rf feeding and the focusing solenoid. Moreover, this section had the small effective shunt impedance [3], therefore at the current achieved in our case the influence of the induced fields to the movement of the beam particles can be neglected. Thus the second section played only the role of a long pipe collimator with known aperture.. In this case with the length, L and the diameter, d one can estimate the beam emittance [6] as

$$\varepsilon \leq \frac{d^2}{\pi L} \quad (2)$$

Substituting numerical meanings of the aperture $d=3.0$ cm and the length $L=200$ cm, we receive the estimation of the emittance not exceeding $\varepsilon \leq 140$ mm mrad.

4 CYCLOTRON RESONANS MODE

During tests of SEMIG in the structure of UIC, we have detected that feeding the rf power to the buncher cavity influences the excitation of the gun current. The gun was located near to the buncher in a magnetic field as is represented in a fig. 1. Probably the fringing field region at the end of the buncher cavity achieved the area of the gun cathode. Originally it was detected the current from the cathode which was not seized in the mode of the acceleration. The current was during almost the whole gun voltage pulse (about 1 microsecond, 60 kV). The current from the cathode arisen in a narrow interval of the magnetic fields close to 136-140 mT and achieved of 1 A. By tuning of the buncher phase it was possible to receive 20. mA current of the accelerated electrons with energy

over several MeV at the exit of UIC. The pulse duration of the current corresponded to the pulse duration of the gun voltage. The typical oscillograms of the current pulses are represented in the fig. 4. The rf pulse duration exceeded the pulse duration of voltage on the gun (about 2 ms), and the synchronization system was adjusted so that during the voltage pulse the rf power it would be a constant. Thus to obtain the accelerated beam it is necessary simultaneous feeding the voltage on the gun and feeding of the rf power for the certain magnitude of the magnetic field at the cathode and for the certain ratio of phases of the buncher and the accelerating sections. The typical oscillograms of the current pulses are represented in the fig. 4. The rf pulse duration exceeded the pulse duration of voltage on the gun (about 2 ms), and the synchronization system was adjusted so that during the voltage pulse the rf power it would be a constant. Thus to obtain the accelerated beam it is necessary simultaneous feeding the voltage on the gun and feeding of the rf power for the certain magnitude of the magnetic field at the cathode and for the certain ratio of phases of the buncher and the accelerating sections.

Because of above we may assume that the researched gun operates in the mode of the resonance cyclotron. Let us estimate the magnitude of the frequency of cyclotron oscillations. The transit time of an electron starting from the cathode and back we determine in the correspondence with [9]. Let's note the equation of radial motion of electron in the gun:

$$\frac{d^2 r}{dt^2} = -\frac{d\Pi}{dr} \quad (3)$$

$$\Pi(r) = \frac{e}{m} \frac{U}{\ln\left(\frac{b}{a}\right)} \ln \frac{r}{a} + \frac{\Omega^2}{8} \left(r - \frac{a^2}{r} \right)^2 \quad (2)$$

Where r is the radial coordinate of an electron; e , m are the charge and mass of the electron accordingly; a , b are the radiuses of the anode and cathode respectively. $\Omega = eB/m$ is the cyclotron frequency. This equation has the solution in quadratures:

$$\tau = \int_a^r \frac{dr}{\sqrt{-2\Pi(r)}} \quad (4)$$

The period of motion was calculated as the double time of the motion up to the maximum radius. By inserting in the integral expression (4) the numerical meanings of the geometrical sizes of the gun: $a=0.15$ cm, $b=1.5$ cm and the experiment data: $B=138$ mT, the average meaning of the magnetic field taking from the interval in which there is the secondary emission excitation; $U=30$ kV, the gun voltage; we find the meaning of the cyclotron frequency, $f_c=2.967$ GHz. We see that the calculated frequency coincides with the sufficient accuracy with the meaning of the accelerator frequency, $f=2.797$ GHz. It point out

on the fact that the gun works in the mode of the cyclotron resonance.

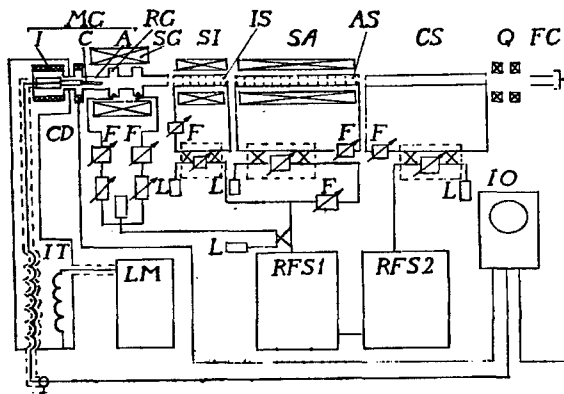


Fig.1 The experimental circuit of SEMIG in structure of Universal Injector Complex (UIC).

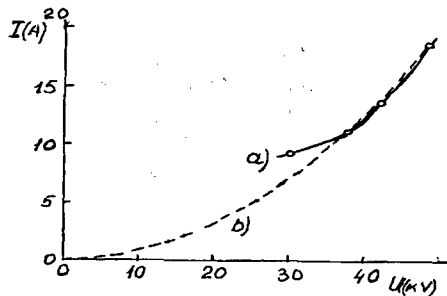


Fig.2 C-V characteristic of SEMIG.

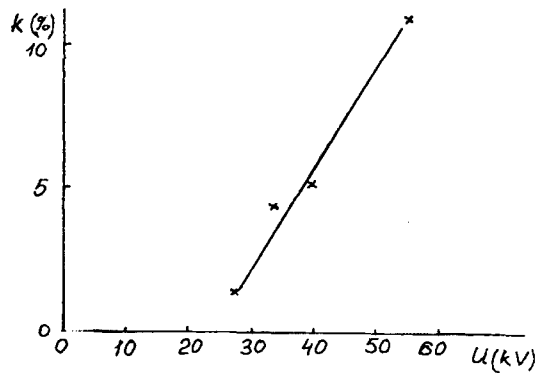


Fig.3 The capture factors v.s. the gun voltage. The markers corresponds to the beam injected by SEMIG; the line corresponds to the conventional thermionic gun.

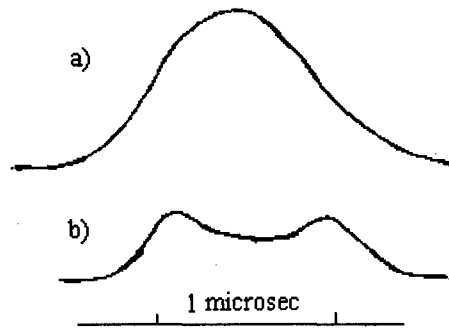


Fig.4 The typical oscillograms. The curves (a) and (b) correspond to the pulses of the gun voltage and the beam current respectively.

5 REFERENCES

- [1] Cherenshchikov S.A. et al. // AIP Conference Proceeding. 1994. Vol. 337. P.350-359.
- [2] Antropov G.P., Arkhangelov N.A., Bekhtev B.V. et al. // Voprosy Atomnoy Nauki i Tekhniki, 1985. # 2(23). pp. 3-5.
- [3] Ivanov G.M., Kurilko V.I., Makhnenko L.A. et al. // Zh. Tekh. Fiz. 64, 115 (1994) [Sov. Phys.Tech.Phys.]
- [4] Cherenshchikov S.A. // Proc. 13th All-Union Conf. on Charged Particle Accelerators [in Russian], Dubna, October 13-15, 1992. Äóäâ, Dubna (1993) Vol. 2, pp. 142-144.
- [5] Cherenshchikov S.A. et al // Bulletin of the American Physical Society. 1995. Vol. 40. N 3. P.1166-1167.
- [6] Moskalev V.A., Sergeev G.I., Shestakov V.G. // Izmerenie parametrov puchkov variatsionnykh chastits. Moscow, Atomizdat, 1980.
- [7] Gallagher W.J. // Proc. IEEE.1969. Vol.57. N 1. P. 94-95.
- [8] Lebedev I.V. // Tekhnika i pribory sverkhvysokikh chastot. Tom. 2. Elektrovakuumnye pribory SVCh. Moscow, "Vysshaya shkola", 1972.
- [9] Vaynshteyn L.A., Solntsev V.A. // Lektsii po sverkhvysokochastotnoy elektronike. Moscow, "Sov. Radio", 1973.

A HOT-SPARE INJECTOR FOR THE APS LINAC*

J.W. Lewellen[†], K. Thompson, J. Jagger, S.V. Milton, A. Nassiri, M. Borland, D. Mangra
Advanced Photon Source, Argonne, IL

Abstract

Last year a second-generation SSRL-type thermionic cathode rf gun was installed in the Advanced Photon Source (APS) linac. This gun (referred to as "gun2") has been successfully commissioned and now serves as the main injector for the APS linac, essentially replacing the Koontz-type DC gun. To help ensure injector availability, particularly with the advent of top-up mode operation at the APS, a second thermionic-cathode rf gun will be installed in the APS linac to act as a hot-spare beam source. The hot-spare installation includes several unique design features, including a deep-orbit Panofsky-style alpha magnet. Details of the hot-spare beamline design and projected performance are presented, along with some plans for future performance upgrades.

1 INTRODUCTION

In the coming months the APS linac will be supporting a much broader range of uses than those for which it was originally intended. It will be required to support not only APS user operations with once-per-day fills, but also to support storage-ring top-up mode operation [1] and next-generation light source research such as the APS low-energy undulator test line (LEUTL) project [2].

The LEUTL and other next-generation light source experiments require low-emittance, high-charge single bunches delivered to the end of the linac; and, as this is in support of an experiment and not storage ring operations, injector availability is not as strong of a concern as beam quality. The current injector of choice for LEUTL operations, therefore, is a Brookhaven/SLAC-style photoinjector rf gun using a copper cathode and a frequency quadrupled Nd:glass laser to generate the photoelectrons. This injector is due for installation into the APS linac in March '99 and will take the place of the DC gun at the head of the linac.

The removal of the DC gun would leave the APS linac with only one high-availability injector, and this has been deemed to be an unacceptable risk to APS operations. Therefore, a hot-spare injector, based on a first-generation SSRL-style thermionic cathode gun [3] ("gun1"), has been installed into the APS linac to serve as a backup injector.

This paper details the design requirements of the gun1 injector system, reviews the lattice design used for the gun1 injector, reports on first beam from gun1 into the

APS linac system, and describes possible upgrades to the primary injection systems of the APS linac.

2 UPGRADE REQUIREMENTS

2.1 Portions of beamline available for injectors

The APS linac already has an injector located in-line with the first 3-meter SLAC-type structure in the linac line (presently a DC gun, to be replaced by the photocathode gun in March '99). There is a 2.5-meter gap between the first and second linac sections of the APS linac; the gun2 injector alpha magnet is located approximately 1.4 meters upstream of the entrance to the second linac section in the APS linac [4]. The only reasonable location for a hot-spare injector would be in this same gap between the first and second linac sections, upstream of the gun2 injector alpha magnet. Other open spaces along the APS linac would either interfere with photocathode gun operation (if located upstream of the first linac section) or would physically not fit into the linac tunnel.

2.3 Required performance

Any backup injector for the APS will eventually be required to have the same performance as the standard injector in terms of APS operation: delivered charge to the end of the APS linac, injection efficiency from the linac into the rest of the APS injector system, and availability. It will not be required to serve as a backup or alternate injector for experiments such as LEUTL, and the sole criterion on beam quality is that it be "good enough" to be accepted by the APS linac and downstream injection systems. These criteria should be easily met by a first-generation SSRL-style thermionic cathode rf gun.

3 BEAMLINE DESIGN AND CONSTRUCTION

As mentioned above, there are strict constraints on the possible placement of a backup injector in the APS linac line. In addition to fitting an injector into the allowed space, other goals of the design process were to keep the rf gun beamlines as similar as possible, to reduce requirements on spare parts stores, and to reduce training required for maintenance and operation.

The previously installed gun2 beamline is a fairly standard thermionic-cathode rf gun beamline, using an alpha magnet for bunch compression and for injecting

* Work supported by the U.S. Dept. of Energy, Office of Basic Energy Sciences, under Contract No. W-31-109-ENG-38.

[†] email: lewellen@aps.anl.gov

beam into the linac line. One unique feature is the use of a fast crossed-field kicker to limit the current injected into the APS linac line [4] [5]. The new gun1 beamline was made to mirror the gun2 beamline as closely as possible, including beamline component placement and rf flange arrangement, allowing a possible future update to both guns with a single new gun design.

A sketch of the gun1 and gun2 injector beamline layout is shown in Figure 1.

3.1 Power supply

Two high-power rf switches are used to provide power to the rf guns. The first switch in line determines whether the power from the first APS linac section exhaust is sent to a load or to the rf guns. A second switch determines whether rf power is directed towards gun1 or gun2. Since each switch has two input ports, the "spare" input port on the second switch is connected to a waveguide adapter, allowing a network analyzer to be used on whichever gun is not receiving high-power rf.

3.2 Required differences

Because the gun1 alpha magnet is located so far from the linac, the gun1 alpha magnet must considerably overcompress the beam from gun1. The beam then ballistically recompresses during the drift to the linac. This requires a deep-orbit alpha magnet, with a maximum penetration depth of approximately 21 cm. (This is in contrast to the gun2 system, which requires a maximum penetration depth into its alpha magnet of only 10 cm.)

For several reasons, a Panofsky-style alpha magnet was chosen for the gun1 beamline, as opposed to a more conventional parabolic pole-face geometry alpha magnet. The Panofsky geometry allows generation of the

large required "good field" region with relative ease. The Panofsky-style quads and alpha magnets operate using current sheets, so the actual magnet construction is rather simple; this allowed tight construction and installation schedules to be met. Finally, the Panofsky-style alpha magnet, even with its large good-field region, is actually rather compact, allowing it to readily fit into the beamline.

The crossed-field kicker design is the same for both beamlines; however, the pulsed power supply for the gun1 kicker is located outside the tunnel, in a shielded rack enclosure, rather than inside the tunnel as is the gun2 kicker supply. This was done not only to reduce the amount of equipment located in the tunnel (and thus less accessible for maintenance) but also to attempt to reduce the noise introduced onto the beam current monitors when the kicker fires.

3.3 Diagnostics

The gun1 diagnostics are similar to those used for gun2. A beam current transformer is located immediately downstream of the gun, allowing the total beam current pulse to be measured and integrated for current stabilization via feedback on the cathode heater. A Faraday cup, located on the straight-through trajectory, allows verification of kicker operation and beam transport efficiency. A second beam current transformer downstream of the alpha magnet allows verification of beam transport through the alpha magnet.

After the beam from gun1 has been injected into the APS linac, all of the standard APS linac diagnostics, including wall current monitors, beam position monitors, fluorescent screens, spectrometers, etc., are available as well.

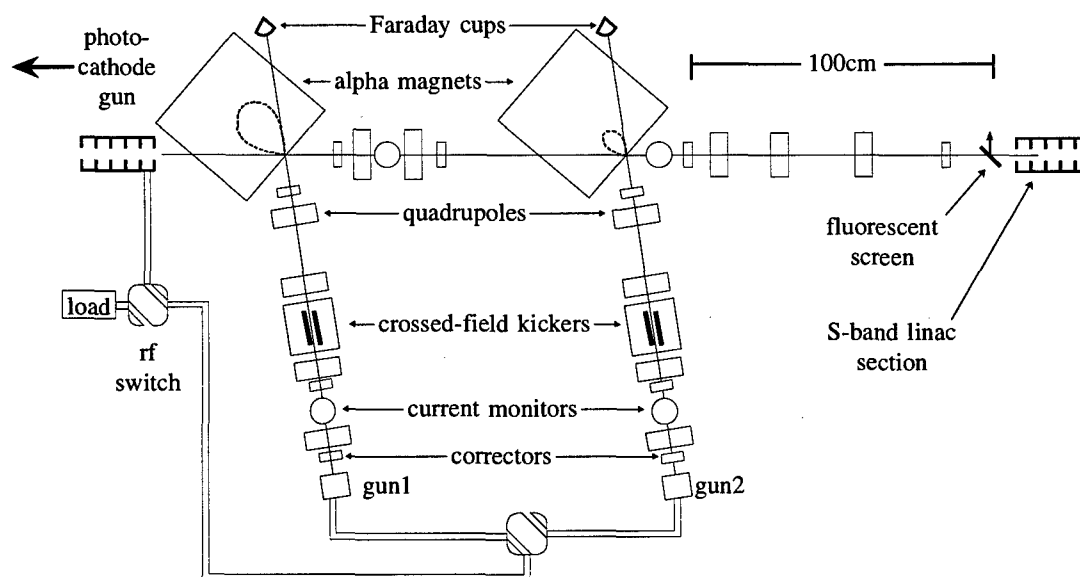


Figure 1: APS main injector layout. Trajectories in the alpha magnets are to scale.

4 PERFORMANCE TO DATE

4.1 Gun1 testing

Initial testing of gun1 consisted of cathode heater cycling, low-power rf measurements, and high-power rf conditioning. Once installed in the tunnel and fully rf conditioned, gun1 was used to generate a 1-A (macro-pulse average) beam current without difficulty.

4.2 Beamline components

The gun1 alpha magnet was tested before installation and found to have acceptable field quality inside the region to be traversed by the electron beam; in fact, its field quality is better than gun2's more traditional parabolic pole-face alpha magnet. Larger than anticipated external (stray) fields were measured, especially when operating the magnet at higher currents. This is due to the use of "back-leg"-style coils rather than saddle coils for the alpha magnet windings, a choice made in the interests of economy and fabrication time. The stray fields are not strong enough to overwhelm the available steering correction at the operating magnet currents, however.

The location of the crossed-field kicker supply outside of the linac tunnel has proved to be effective in reducing the noise introduced into the diagnostics signals.

4.3 Operation as an APS injector

Gun1 has successfully been operated as an injector for the APS, providing beam injection into the linac and through the APS injection system to the booster dump. Sufficient charge was delivered to allow a storage ring refill via gun1, should beam have been lost at that time.

Larger than anticipated beam current losses were encountered between gun1 and its alpha magnet; this does not appear to be related to the alpha magnet stray fields, as the losses are also encountered when running beam to the gun1 alpha magnet Faraday cup. Once through the alpha magnet, however, beam losses through to the end of the linac line and the remainder of the APS injection system were normal.

Commissioning of gun1 as an APS injector is continuing. As of this writing, the linac control software is being upgraded to automatically control either gun1 or gun2 as the APS primary injector.

5 POSSIBLE FUTURE UPGRADES

Although the gun1 injection system has been demonstrated to be operational, and control system integration is continuing, there are several possible future upgrades being considered.

5.1 Alpha magnet coil upgrade

As mentioned, the gun1 alpha magnet uses racetrack-style coils rather than saddle coils. This is a less effi-

cient design and is the most likely candidate for the cause of measured stray fields.

Pending additional commissioning studies and field measurements to determine requirements, a set of saddle coils for the gun1 alpha magnet could be complete and ready for installation during the December '99 - January '00 APS maintenance shutdown.

5.2 Magnetic field probes for fast turnover

Presently both gun1 and gun2 alpha magnets are solid-core magnets, and if not degaussed, exhibit relatively strong residual fields. In order to achieve good beam transport from the gun1 alpha magnet to the linac entrance, a relatively long degauss cycle must be completed on the gun2 alpha magnet. Both alpha magnets should be thoroughly degaussed when running the photocathode gun in order to help preserve beam emittance.

By including a magnetic field sensor such as a Hall probe inside both alpha magnets, the APS control system could be used to automatically adjust the alpha magnet trim supplies to zero the field completely without the need for a long degauss cycle. This would assist both in experimental operation of the photocathode gun and in the use of gun1 as a hot-spare injector, as presently the gun2 alpha magnet degauss is the longest task in the switchover process.

5.3 Diagnostics

Although beamline space in the main injector area is now limited, there is still room for additional diagnostics. In particular, a longitudinally thin wire scanner placed at the entrance of both alpha magnets would considerably aid in obtaining proper injection into the alpha magnets. Also, a beam position monitor could be placed immediately before the linac entrance aperture. This would allow automatic beam transport and steering optimization between either alpha magnet and the linac entrance.

5 ACKNOWLEDGEMENTS

We would like to thank Charles Doose, George Goepner, John Noonan, Stan Pasky, and Dean Walters for their assistance and support of the fabrication, installation, and commissioning of the gun1 injector system.

6 REFERENCES

- [1] L. Emery and M. Borland, "Top-Up Operation Experience at APS," these proceedings
- [2] S.V. Milton et al., "Status of the Advanced Photon Source Low-Energy Undulator Test Line," FEL '97, Beijing, (1997)
- [3] M. Borland, et al., "Performance of the 2 MeV Microwave Gun for the SSRL 150 MeV Linac," LINAC '90, Albuquerque, (1990)
- [4] J.W. Lewellen et al., "Operation of the APS RF Gun," LINAC '98, Chicago, (1998)
- [5] Y.W. Kang et al., "Beam Chopper for the Low-Energy Undulator Test Line (LEUTL) in the APS," PAC '97, Vancouver, (1997)

CERAMIC DISKS AS EFFICIENT AND ROBUST CATHODES

I. Boscolo

University and INFN, Dipartimento di Fisica via Celoria 16, 20133 Milano, Italy

Abstract

Electron emission from ceramic disks depends strongly on the shape of the front electrode. The common interconnected grid is not good for a stable emission. An electrode consisting of an ensemble of metal point-like islands within a metal ring leads to quite a stable emission. In the first case the sandwich of the continuous electrode (on one surface) and the grating (on the front surface) constrains the domain and the charge carriers to move within the zones covered by the stripes, whilst the quasi-open patchy surface allows the domain switching and in turn the electron flux over the whole area.

1 INTRODUCTION

The emission presented in the paper refers to energetic electrons expelled in a ceramic disk when excited by a fast high voltage pulse applied to the electrodes deposited on the two surfaces [1, 2]. The so-called relaxors and antiferroelectric ceramics with fast transition under the action of an electric field are suitable for electron emission [3]. Lead lanthanum zirconate titanate (PLZT) was used in the emission experiments, in proportions of 4/95/5 and 8/65/35, where the numbers refer respectively to the lanthanum, zirconium, and titanium atomic percentage. The two ceramics are in the antiferroelectric and ferroelectric (AFE-Fe) phase respectively at room temperature [3].



Figure 1: Sketch of the two electroding types of the front surface: the stripes are 200 μm with an interdistance of the same width.

The emission results erratic as a function of samples and decaying with the shot number when the conventional grating front electrode, fig.1, is used. The aging effect, which leads to segregation of spontaneous polarization switching under the metal strips and to the screening of the domains of the uncovered zones, can be accounted for that behavior [4]. These segregation processes are avoided substituting the grating with an electrode consisting of a pattern of unconnected patches contained within a ring. The experimental results and a possible interpretation are presented.

The application of a ≥ 10 kV/cm electric field through the samples induces not only spontaneous polarization switching within the crystal, but also plasma formation on the cathode surface [2]. Both processes generate electrons, but the former generates a group of energetic electrons (FE electrons), whilst the latter generates only nonenergetic electrons.

2 EXPERIMENTAL RESULTS

Different patterns of metallic islands (fig.1) were tested: a) deposition of a uniform 100-Å gold film (which auto-arranges in separate patches); b) a very thin silver paste film, which auto-arranges as a patchwork; c) a uniform filling of the surface holes (the material is porous) with a carbon paste; and d) Au evaporation with a mask of 50- μm -diam islands with an interdistance of 50 μm .

Samples without metal islands (with the external metal ring only) did not work; samples with a 50- μm interdistance between islands worked badly. All the others always emitted, but the shorter the interdistance between the islands the more stable the emission.

The repetition rate was around 10 Hz for 8/65/35 samples, it was, instead, about 1 kHz for 4/95/5 samples.

In the following, results obtained from hole filling and 8/65/35 samples are reported. Only unprepoled ceramic at room temperature was used.

Only the energetic ferroelectric electrons are collected at the anode Faraday cup when the accelerating voltage is zero.

a) Negative pulse at the rear electrode

The signal obtained with 8/65/35 material is reported in figure 2. First, the quite good stability is evident. The almost linear increase in the 8/65/35 signal is explained by the continuous spontaneous polarization switching all along the excitation pulse.

The relaxation process of spontaneous polarization is longer than its buildup because the latter is driven by the fast voltage pulse, while the polarized state is metastable.

b) Positive pulse at the rear electrode

The emission signal is shown in fig. 3. Note the good stability of the signals with positive excitation. In this case, emission occurs at the end of the pulse, i.e., at relaxation of spontaneous polarization P_s .

In fig. 4 signals obtained with the negative HV pulse applied to the GE (front) electrode on 8/65/35 is reported.

In this experimental configuration the negative pulse sets an acceleration field for the whole emission phenomenon.

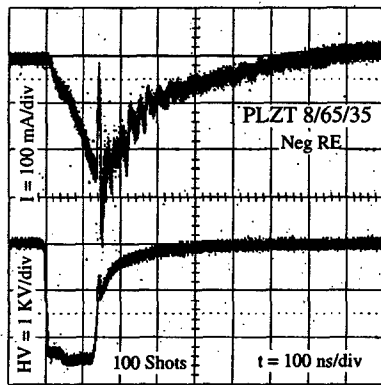


Figure 2: The superposition of 100 current signals, upper trace, and voltage signals, lower trace, is reported. The voltage pulse is applied to the rear electrode (RE), and the sample was a PLZT 8/65/35, as written in the frame, of 1 mm thickness.

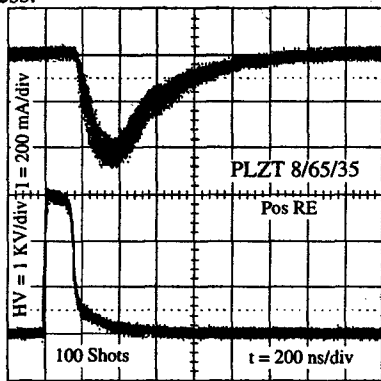


Figure 3: As in fig. 2 but with positive pulse to the rear electrode of a PLZT 4/95/5 sample.

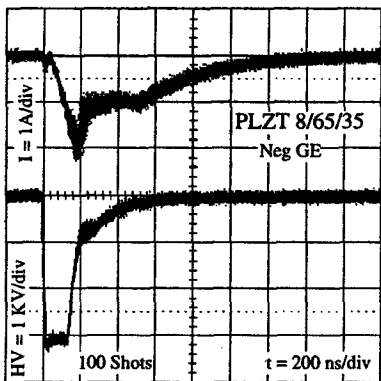


Figure 4: Superposition of 100 current signals, upper trace, and voltage signals, lower trace, are reported. The voltage pulse is applied to the front electrode (GE).

This explains the one order of magnitude higher amplitude of the current.

c) Negative pulse at the rear but with an accelerating field across the diode gap

The signals relative to 8/65/35 samples are presented in figs. 5, and 6. The scheme of the apparatus for these mea-

surements is shown in 2

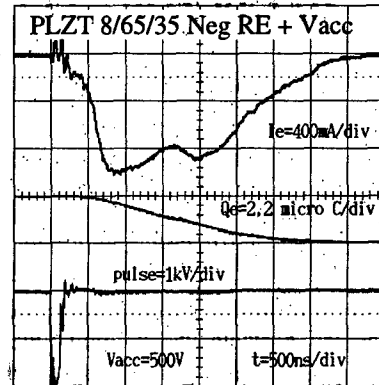


Figure 5: Signals of the current and of the charge with an accelerating voltage of 500 V.

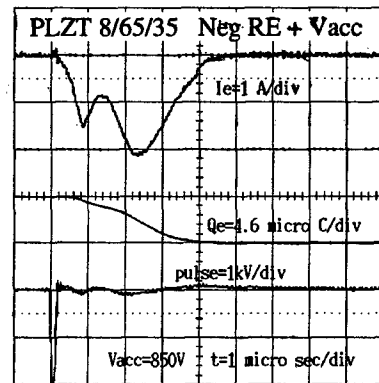


Figure 6: Ibidem as previous figure but with an accelerating voltage of 850 V

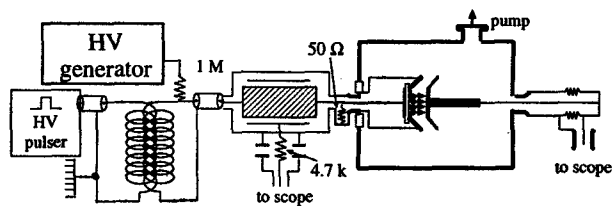


Figure 7: Sketch of the experimental apparatus used in tests with accelerating field

A probe tailored for the measurements of the high voltage pulse at the high voltage terminal has been developed.

The current signal has always two peaks: the first can be assigned to electrons emitted because of the ferroelectric switching, the second can be assigned to plasma produced electrons. The amplitude of the FE peak did not change doubling the accelerating voltage, in contrast with the plasma peak whose amplitude doubled. The emitted charge corresponds to the one stored in the buffer capacitors.

The signals were quite stable in shape and amplitude.

3 DISCUSSION

The experimental observations obtained with samples electroded with grating could be lumped together in the concept of the crystal aging process. The neat separation of the cathode material in two parts, one under the metal strips and the other outside could induce a process of switching limitation within the covered zones and passivation of the uncovered surface.

The patchy electrode made the front surface homogeneous, preventing the segregation of the electric field and polarization switching. Our phenomenological view of electron emission is that the front of the voltage pulse propagates as a wave to the front surface, the induced polarization switching co-propagates with it, and spontaneous polarization sets through the whole sample; this polarization causes strong electric stress at the surface, which, in turn, changes the electric property of the surface from non-conductive to substantially conductive. This conclusion is supported by two facts: i) the measured switching current dP/dt is the same as that obtained with samples having the surfaces completely metalized [3]; ii) in [6] a high mobility of the charge carriers within the stressed region was measured.

When the voltage excitation pulse is over, the charge carriers diffuse through the surface towards the external ring or through the bulk. The FE electron paths through the surface are not fixed because the surface state of a ferroelectric ceramic is dynamic and the surface is like a patchwork of pieces, whose properties [5] range from metallic to insulating. We recall that relaxors are in continuous evolution through metastable states, as in the spin-glass systems. Similar considerations also hold for antiferroelectric ceramics owing to the change of phase at each shot. It could also be possible that electrons traveling through the surface towards ground continuously rejuvenate the state of the surface.

The emission observed with an accelerating voltage tells that the switching activity has a time less than 1 microsecond. The amount of charge is of the order of $1 \mu C$. The time of the plasma formation results around $1 \mu s$. This matches with the time of its expansion over the surface (the diameter of the ring is about 6 mm) with the estimated plasma velocity of $1 \text{ cm}/\mu s$.

4 CONCLUSIONS

Stable copious emission of energetic electrons from a ferroelectric ceramic disk, under the application of a fast high-voltage pulse, was obtained when the electrode of the emitting surface was a uniform pattern of unconnected metal patches contained within a metallic ring. This kind of front electrode avoids the aging process because the surface behaves like an almost homogeneous sheet, and the charge carriers migrate from the external ring to the dispersed points of the surface and viceversa through continuously changing paths. These two phenomena prevent any segregation either of the electric field or of polarization, and the

material is continuously rejuvenated by the back and forth movements of the electrons through the surface and/or the bulk.

The plasma assisted emission can be exploited: the emitted charge is determined by the charge stored in the buffer capacitor.

5 REFERENCES

- [1] H. Gundel, J. Handerek, H. Riege, E.J.N. Wilson and K. Zioutas, *Ferroelectrics* 100,1,1989.
- [2] H. Riege, I. Boscolo, J. Handerek, U. Herleb, *J. Appl. Phys.* 84,1602, 1998.
- [3] G. Benedek, I. Boscolo, J. Handerek, A. Moscatelli, A. Scurati, *J. Appl. Phys.* 83,2776,1998.
- [4] I. Boscolo, A. Scurati, M. Stellato, "The ferroelectric emission with suitable electroding of ceramic disks" *J. Appl. Phys.* in publ.
- [5] K. Szot, W. Speier and W. Eberhardt, *Appl. Phys. Lett.* 60 (10), 1190-1192, 1992.
- [6] W. Mock, Jr. and W. H. Holt *J. Appl. Phys.* 50, 2740, 1979.

EFFICIENT PHOTOEMISSION FROM ROBUST FERROELECTRIC CERAMICS

I. Boscolo, University and INFN, Via Celoria 16, 20133 Milano, Italy

M. Castellano, L. Catani, M. Ferrario, F. Tazzioli, INFN-LNF,

Via E. Fermi, 00044 Frascati - Roma, Italy

L. Giannessi, ENEA-CRE, Via E. Fermi, 00044 Frascati - Roma, Italy

Abstract

Experimental results on photoemission by ferroelectric ceramic disks, with a possible interpretation, are presented. Two types of lead zirconate titanate lanthanum doped, PLZT, ceramics have been used for tests. 25 ps light pulses of 532 and 355 nm were used for excitation. The intensity ranged within the interval $0.1\text{--}3\text{ GW/cm}^2$. The upper limit of the intensity was established by the damage threshold tested by the onset of ion emission. At low value of the intensity the yield was comparable at the two wavelengths. At the highest intensity of green light the emitted charge was $1\text{ nC per } 10\text{ mm}^2$, but it was limited by the space charge effect. In fact, the applied field was only 20 kV/cm , allowed both by the mechanical design of the apparatus and the poor vacuum, 10^{-4} mbar . No surface processing was required. The measurement of the electron pulse length under way.

1 INTRODUCTION

Lead zirconate titanate lanthanum doped (referred as PLZT) ferroelectric ceramic showed interesting properties as photoemitter material [1, 2]: this type of photo-cathode showed an emissivity higher than that of metals, they were able to emit at any photon energy from green to UV and they were very robust, they did not need any processing and, furthermore, they did not require high vacuum condition.

An experimental program has been set at the LNF (Lab Nazionali Frascati-Roma) based on the fact that the properties of this material can be determined simply changing the compositional percentage and changing the polarization state. The physical state of the surface is strongly changed by prepoling and by setting a polarization state. In particular, it seems possible to set a polarization state such that the surface electrons are acted on by a repulsive force, or, alternatively, it is possible to set at the surface a very dense sheet of electrons[3].

The sketch of the experimental setup is shown in fig.1. Two incidence angles were used: 60° and 0° . In the latter case a hollow Faraday cup with a front grid was used. No variation of the yield was measured for the two configurations.

The experimental program started with the material good for emission with electric excitation [4, 5], that is PLZT 8/65/35 and 4/95/5, where the numbers refer to lanthanum

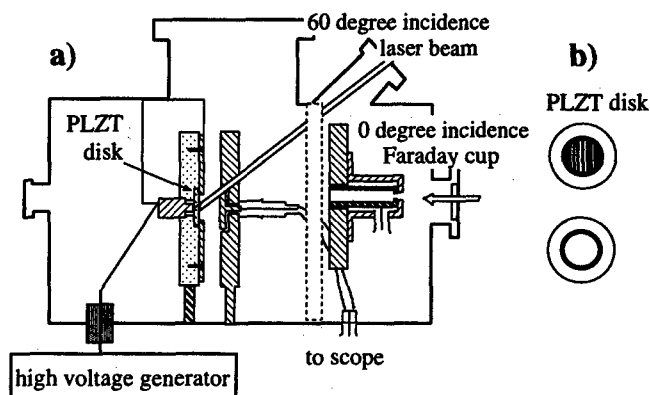


Figure 1: a) Sketch of the experimental apparatus used in the photoemission experiments: the two used Faraday cups are shown for simplicity on the same figure (one behind the other); they are interchanged depending on the incidence angle. b) Sketch of the cathode with the two front electrodes used in tests. The passively mode locked Nd-YAG laser provides some mJ of light at $\lambda = 532\text{ nm}$ for a pulse length of 25 ps. The illuminated area was about 10 mm^2

(in relation to lead), zirconium and titanium relative atom percentage. Samples without and with prepoling, at room temperature, were tested. Ceramic 8/65/35 is in ferroelectric phase, while 4/95/5 is in antiferroelectric phase. These materials have a high density of defects whose activation energy is about 1 eV [6]. The cathodes are disks of 16 mm diameter and 1 mm thickness, coated by a uniform metallic film at the back surface and by either an external ring or a grating at the front surface, see fig.1 b). The best results came with the ring front electrode and 8/65/35 unprepoled samples.

2 EXPERIMENTAL RESULTS

The emission in the log-log diagram from a PLZT 8/65/35 is shown in figs. 2 and 3. The emission was limited by the space charge effect in the case of green light shining, it was not in the case of violet light shining.

The damage threshold has been checked reversing the direction of the accelerating field. In fig. 4 it is shown that the energy at which the ion emission starts is farther than the beginning of the space charge effect.

From figs. 2 and 3 we notice: a threshold with green light, a yield of an angular coefficient nearby 4 for green light and nearby 3 for violet light. Extrapolating with an

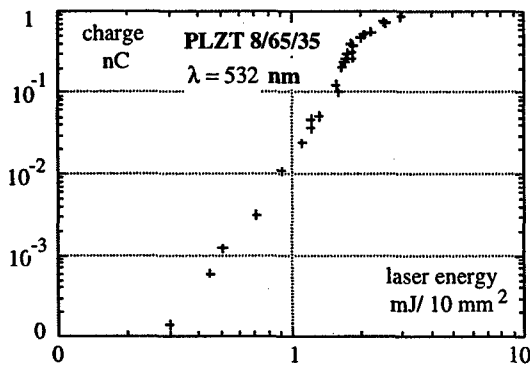


Figure 2: Emitted charge versus laser energy for PLZT 8/65/35 shined with green light in log-log frame. The line fitting the points scales as $Q \propto I^4$.

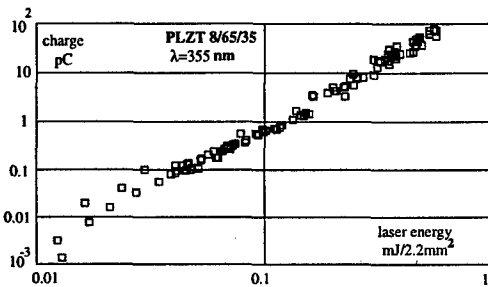


Figure 3: Emitted charge versus laser energy for PLZT 8/65/35 shined with violet light in log-log frame. The slope of the line is $Q \propto I^3$.

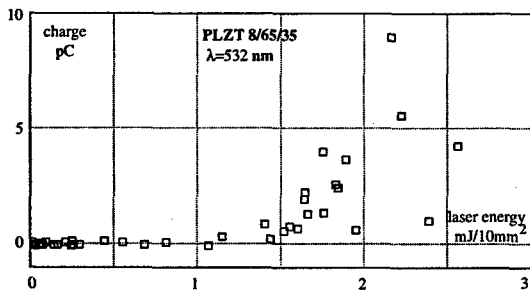


Figure 4: Starting of emission of ions versus laser energy with green light.

accelerating field high enough to avoid saturation effects, the emitted charge at 3 mJ of laser light would be 2 nC. The value of quantum efficiency results around 10^{-6} with both wavelengths.

With violet light we could shine with an energy up to 0.5 mJ only.

The experiments with the antiferroelectric material 4/95/5 and hard ferroelectric material *lead titanate* (PT) gave a much lower yield. The 4/95/5 material showed quite a high enhancement of the yield increasing the accelerating field in the gap as shown in fig. 5. It is notable that this antiferroelectric material shows an hysteretic behavior as function of the applied voltage.

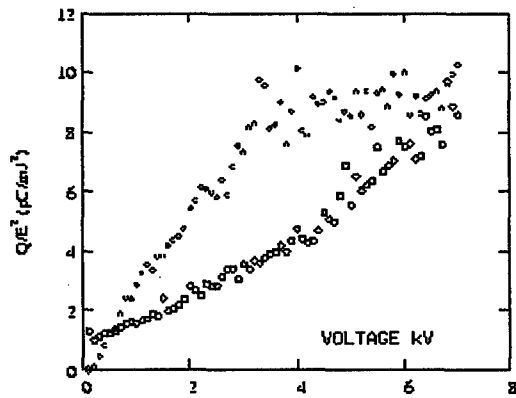


Figure 5: Emitted charge versus laser energy: the lower points are obtained at 7 kV of applied voltage, while the points of the upper curve are obtained in succession but after having reduced the voltage to 3.5 kV. The hysteretic behavior was not observed keeping constant the voltage.

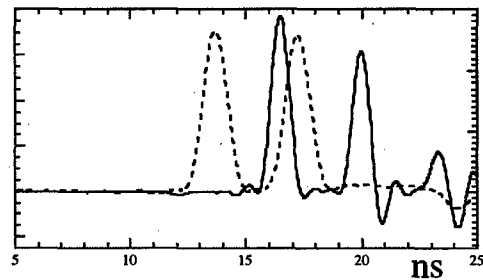


Figure 6: Succession of two electron pulses 2 ns apart

All the tested ceramics had the scaling law $Q \propto I^2$ at relatively low light flux for both wavelength.

We have tested the emission with two light pulses separated by 2 ns. The two emissions are substantially stable. The system seems able to provide pulse trains with nanosecond time separation.

The yield of the prepoled samples was higher than that of the unprepoled ones, but the damage threshold was considerably lower. They showed an emission law which was a bit faster than the two photon emission, but the relatively low damage threshold did not allow an efficient emission.

3 DISCUSSION

The two main characteristics of the strong emission are: a very low emission up to a laser intensity of about 0.5 GW/cm^2 and the high non-linearity starting from that point. In addition to this, the other notable fact is the change of the operational regime for the PLZT 4/95/5 sample when it is immersed in a relatively high electric field.

The energy diagram of the material shows a trap level at 1 eV from the conduction band and has an estimated electron affinity of 3 eV. The electron affinity E_a is not well defined because the surface state is un-defined: is like a

patchwork of pieces with different physical characteristics, which range from insulating to metallic [8]. A value of the potential barrier greater than 4 eV is a fairly crude approximation. The quadratic power law of the emission at both photon energy of 2.3 and 3.4 eV is congruent with the energy diagram.

Furthermore, our disk is immersed in the electric field applied through the diode gap, hence a counter field is created by the induced polarization. When the crystal is polarized, there is a band bending at the surfaces with a potential well for electrons at the positive side of the polarization.

The generalized Fowler-Dubridge theory [7] cannot explain these results. The emission at 2.3 eV and its non-linearity with a power equal or greater than 4 would envision the anomalous heating regime [9], cooperating with the Auger effect [3]. More generally, we should have the concurrence of different contributions: one and two-photon emission, thermally assisted and Auger emission.

The increase of the emission of 4/95/5 sample as a function of the applied field, together with its hysteretic behavior of fig. 5 tells that the polarization is very important: when the polarization builds up in the sample, the emission steps up, then the sample remains polarized when the electric field is reduced because of the hysteresis loop. The experiment with PT material says that the polarization by itself is not sufficient for obtaining strong emission, but a strong doping, that is a large number of defects, must be also present.

Assuming that the electron pulse length is strictly correlated to the light pulse length, that is $\approx 25ps$, since the illuminated area is about 10 mm^2 , the current density would be higher than 1 kA/cm^2 .

4 CONCLUSIONS.

A new very efficient configuration for ferroelectric photocathodes has been investigated. We got $1nC$ level of emission only because the charge was limited by space charge effect. Since the damage threshold of a ceramic is relatively high, a large amount of extracted charge can be foreseen.

The emission has shown to be very sensitive to the sample polarization. This fact allows to foresee a large enhancement of the quantum efficiency just increasing the polarization. This polarization increasing occurs naturally with the high electric field that are applied in electron guns.

The characteristics of these cathodes, are: a) strong robustness, they work in any kind of vacuum showing a long life; b) they do not require any particular processing; c) they can be operated with green light. In the next future the extracted electron beam will be characterized in terms of time structure. If the electron pulse duration is strictly related to the laser pulse duration, these cathodes promise to deliver current densities larger than 1 KA/cm^2 and to be valid competitors of both metallic and alkali cathodes.

5 ACKNOWLEDGEMENTS

We recognize the technical support given by R. Sorchetti and L. Cacciotti.

6 REFERENCES

- [1] K. Geissler, H. Gundel, H. Riege, J. Handerek, Appl. Phys. Lett. 56, 895, 1990.
- [2] K. Geissler, A. Meineke, H., Riege, S. DE Silvestri, N. Nisoli, O. Svelto, I. Boscolo, J. Handerek, Nucl. Instrum. Meth. Phys. Res.A 372, 567-571, 1996
- [3] G. Benedek, I. Boscolo, Appl. Phys. Lett. 72, 522, 1998.
- [4] G. Benedek, I. Boscolo, J. Handerek, A. Moscatelli, A. Scurati, J. Appl. Phys, 83, 2776, 1998.
- [5] I. Boscolo et al. Appl. Phys. Lett. 74, 859, 1999.
- [6] H. Gundel, J. Handerek, H. Riege, E.J.N. Wilson and K. Zioutas, Ferroelectrics 109, 137, 1990.
- [7] J.H. Bechtel, W.L. Smith, N. Bloembergen, Phys. Rev. B. 15, 4557, 1977.
- [8] K. Szot, W. Speier, J. Herion, Ch. Freiburg, Appl. Phys. A 64, 55, 1997.
- [9] J. P. Girardeau-Montaut, C. Girardeau-Montaut, Phys. Rev. 51, 13560, 1995.

SUPERLATTICE PHOTOCATHODES FOR ACCELERATOR-BASED POLARIZED ELECTRON SOURCE APPLICATIONS*

J. E. Clendenin[#], T. Maruyama, G. A. Mulhollan, SLAC, Stanford, CA
Yu. A. Mamaev, A. V. Subashiev, Yu. P. Yashin, SPTU, St. Petersburg, Russia

Abstract

A major improvement in the performance of the SLC was achieved with the introduction of thin strained-layer semiconductor crystals. After some optimization, polarizations of 75-85% became standard with lifetimes that were equal to or better than that of thick unstrained crystals. Other accelerators of polarized electrons, generally operating with a much higher duty factor, have now successfully utilized similar photocathodes. For future colliders, the principal remaining problem is the limit on the total charge that can be extracted in a time scale of 10 to 100 ns. In addition, higher polarization is critical for exploring new physics, especially supersymmetry. However, it appears that strained-layer crystals have reached the limit of their optimization. Today strained superlattice crystals are the most promising candidates for better performance. The individual layers of the superlattice can be designed to be below the critical thickness for strain relaxation, thus in principle improving the polarization. Thin layers also promote high electron conduction to the surface. In addition the potential barriers at the surface for both emission of conduction-band electrons to vacuum and for tunneling of valence-band holes to the surface can be significantly less than for single strained-layer crystals, thus enhancing both the yield at any intensity and also decreasing the limitations on the total charge. The inviting properties of the recently developed AlInGaAs/GaAs strained superlattice with minimal barriers in the conduction band are discussed in detail.

1 INTRODUCTION

The polarization of electrons extracted from III-V semiconductor crystals has a theoretical upper limit of 50%. In 1991 it was first demonstrated that growing a thin crystalline layer on a substrate having a slightly different lattice constant could raise this limit [1]. The lattice mismatch introduces a strain in the epilayer that removes the degeneracy of the heavy-hole (hh) and light-hole (lh) valence bands. Polarizations on the order of 80% are routinely achieved from these strained-layer cathodes, which simultaneously exhibit quantum yields, Y , of >0.1%. Such a cathode, consisting of 100-nm of GaAs grown on a GaAsP substrate, became the standard for the SLC polarized electron source, eventually accumulating ~20,000 hours of operating time for the SLC program, making possible the single-most precise measurement of the electro-weak mixing angle, $\sin^2 \theta_W^{eff}$.

Future colliders will require both higher polarization and more charge. Higher polarization will not only increase the effective luminosity of a collider, but if $\geq 95\%$ will also significantly increase the physics reach, especially in the exploration of supersymmetry [2]. For JLC/NLC, the required charge per 100-ns macropulse is ~300 nC at the gun, which is an order of magnitude greater than produced for SLC. The problem is that the maximum steady-state current in a long macropulse that can be produced from an SLC-type cathode is on the order of 0.2 A cm^{-2} , which would require an impractical cathode diameter of 4 cm to meet the collider charge requirement. The maximum current of an SLC-type cathode can probably be increased by an order of magnitude simply by increasing the dopant density from the mid 10^{18} cm^{-3} range to the low 10^{19} cm^{-3} range. However, both experimental and theoretical efforts to date point to a limitation of the polarization of the strained-layer cathode at the 85-90% level [2].

A major source of depolarization for the strained-layer cathodes is the relaxation of the strain as the distance from the heterojunction increases beyond the critical thickness, h_c , for maintaining perfect strain, thus decreasing the average hh-lh separation. Typically h_c is ~10 nm, whereas the optimum epilayer thickness to maintain both high polarization and high charge is ~100 nm. This problem is overcome in principle using the superlattice (SL) structure, in which the hh-lh degeneracy is removed by the localization of holes in quantum wells. Since the overall critical thickness, H_c , for a short-period SL can be considerably larger than h_c , the total thickness of the SL can be on the order of 100 nm without relaxation of the strain.

SL structures were shown to produce >50% polarization in 1991 soon after the first strained-layer results, but the path to simultaneously high polarization and high Y has taken longer. Recently however, polarizations approaching 90% with Y within an order of magnitude of that of the SLC cathodes have appeared [3,4].

2 SUPERLATTICE WITH ZERO CONDUCTION BAND OFFSET

In previously used $\text{Al}_x\text{Ga}_{1-x}\text{As}/\text{GaAs}$, $\text{In}_x\text{Ga}_{1-x}\text{As}/\text{GaAs}$ and $\text{Al}_x\text{Ga}_{1-x}\text{As}/\text{In}_y\text{Ga}_{1-y}\text{As}$ SL, the hole miniband splitting was accompanied by the building of high barriers for electrons as a result of the high value of the ratio of the conduction-band offset ΔE_c to the valence-band offset ΔE_v ($\Delta E_c/\Delta E_v \approx 2$) at the heterointerface. The necessity for the electrons to tunnel through the SL barriers results in a lower electron diffusion rate along the SL axis

*Work supported by the U.S. Department of Energy contract DE-AC03-76SF00515, the U.S. Civilian Research and Development Foundation Award No. RP1-351, the Russian State Program Project 2.6.99, and the Russian State Programs "Physics of Solid State Nanostructures" under grant 97-1091.

[#]Email: clen@slac.stanford.edu

accompanied by growth of the spin relaxation rate. Therefore the spin diffusion length restricts the thickness of the active layer for these structures.

The main advantage of the $\text{Al}_x\text{In}_y\text{Ga}_{1-x-y}\text{As}/\text{GaAs}$ SL proposed here comes from the band line-up between the semiconductor layers of the SL. The Al content determines the formation of a barrier in the conduction band, while adding In leads to conduction band lowering, so the conduction band offset can be completely compensated by appropriate choice of x and y , while barriers for the holes remain uncompensated. Therefore the use of superlattices with the optimized quaternary alloy composition can provide a high vertical electron mobility and simultaneously a small spin relaxation rate while also maintaining a sufficiently large valence-band splitting.

We have studied an $\text{Al}_{0.20}\text{In}_{0.18}\text{Ga}_{0.62}\text{As}/\text{GaAs}$ SL consisting of 17 pairs of GaAs (4 nm) and AlInGaAs (4 nm) Be doped with density $4 \times 10^{17} \text{ cm}^{-3}$ except the top layer, GaAs, with $4 \times 10^{18} \text{ cm}^{-3}$. The dopant density was maintained low in the bulk to minimize depolarization but high at the surface to increase the negative affinity. The sample was grown by molecular beam epitaxy (MBE) by the Ioffe Physico-Technical Institute in St. Petersburg [4]. A protective As coating was added as the final step.

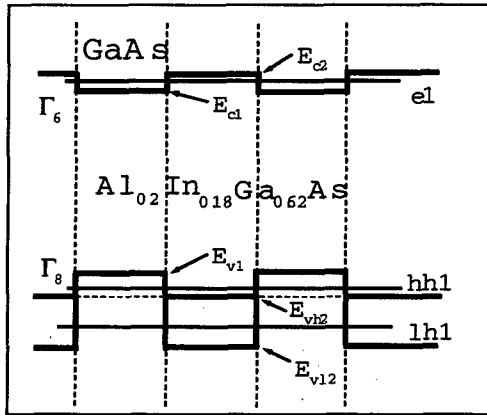


Fig. 1. Energy band diagram of $\text{Al}_x\text{In}_y\text{Ga}_{1-x-y}\text{As}/\text{GaAs}$ SL. The minibands (thin lines) are identified by notation e1 and hh1, lh1 for electrons and holes respectively.

The miniband spectrum of the SL is determined by the band offsets at the heterointerfaces. In the case of a heterointerface with lattice matched ternary solid solution (e.g., $\text{Al}_x\text{Ga}_{1-x}\text{As}/\text{GaAs}$) the conduction-band offset ratio, Q_{c1} , is defined as $Q_{c1} = \Delta E_c(x)/\Delta E_{g1}(x)$, where ΔE_{g1} is the difference in the band gaps of the contacting crystals so that the valence band offset ratio, Q_v , is $Q_v = 1 - Q$. For an $\text{In}_y\text{Ga}_{1-y}\text{As}/\text{GaAs}$ interface the offset is modified by the strain distribution in the contacting layers. For the structure with a thin $\text{In}_y\text{Ga}_{1-y}\text{As}$ layer grown on a thick GaAs substrate all the strain is assumed to accumulate in the InGaAs layer. For this case, ΔE_c is given by:

$$\Delta E_c(y) = Q_{c2,def} \times (\Delta E_{g2}(y) + \delta E_{g2}^{def}(y)),$$

where $Q_{c2,def}$ is the conduction-band offset ratio for the strained $\text{In}_y\text{Ga}_{1-y}\text{As}$ layer, while $\delta E_{g2}^{def}(y)$ is the change of

the band gap induced by strain that can be expressed through interpolated deformation potentials, elastic constants, and the lattice constant mismatch. For the case of the $\text{Al}_x\text{In}_y\text{Ga}_{1-x-y}\text{As}/\text{GaAs}$ SL, a linear interpolation between the values for $\text{Al}_x\text{Ga}_{1-x}\text{As}/\text{GaAs}$ and $\text{In}_y\text{Ga}_{1-y}\text{As}/\text{GaAs}$ interfaces should be valid for small x and y . We have found that interpolation starting with the unstrained value of the band offset for the $\text{In}_y\text{Ga}_{1-y}\text{As}/\text{GaAs}$ heterointerface gives band-gap values that are far from the experimental data obtained from emission spectra. Using the band offset value for the strained $\text{In}_y\text{Ga}_{1-y}\text{As}/\text{GaAs}$ interface, we get:

$$\Delta E_c(x, y) = Q_{c1} \times \Delta E_{g1}(x) + Q_{c2,def} \times (\Delta E_{g2}(y) + \delta E_{g2}^{def}(y)).$$

The schematic of the position of the band edges for $x=0.20$, $y=0.18$ is shown in Fig. 1. Taking $Q_{c1}=0.66$ and $Q_{c2,def}=0.7$, we have found that the conduction band offset appears to be minimized for $x=1.1y$.

The calculated positions of the band edges of the layers in the strained SL sample are given in Table 1. It is seen that the conduction band offset does not exceed 20 meV. For the thermalized electrons at room temperature the influence of the resulting periodical potential should be negligible. Besides, as a result of the conduction-band line up, the 4-nm barriers for the electrons in the SL are transparent. Thus the changes of electron mobility and spin relaxation rate should be small compared to pure GaAs.

It is seen from Fig. 1 and the data of Table 1 that the strain of the $\text{Al}_x\text{In}_y\text{Ga}_{1-x-y}\text{As}$ layers produces barriers for both heavy and light holes, the barrier for the light holes being 75 meV higher, which leads to additional hole-miniband splitting favorable for the electron optical orientation.

Table 1. The positions (in eV) of the band edges at room temperature in an $\text{Al}_{0.20}\text{In}_{0.18}\text{Ga}_{0.62}\text{As}/\text{GaAs}$ SL sample.^a

E_{vh2}	E_{vl2}	E_{c1}	E_{c2}	E_{g1}	E_{g2}
-0.056 ^b	-0.138	1.423	1.445	1.422	1.501

^a 1- GaAs, 2- $\text{Al}_x\text{In}_y\text{Ga}_{1-x-y}\text{As}$ layer.

^b Zero energy is at valence-band edge of the GaAs layer.

The choice of the layer thickness is dictated by the need to split the hole minibands. The splitting grows when barriers are broad enough and wells are narrow and deep. Still the thickness of the strained $\text{Al}_x\text{In}_y\text{Ga}_{1-x-y}\text{As}$ layer should be less than the critical thickness $h_c(y)$. The overall critical thickness for the superlattice with alternating layers of equal thickness can be estimated as $H_c = h_c(y/2)$. The thickness of a single $\text{Al}_x\text{In}_y\text{Ga}_{1-x-y}\text{As}$ layer was taken to be 4 nm (to be less than the calculated $h_c(y)$), and in accordance with X-ray data the chosen thickness of the SL sample (0.136 μm) exceeded H_c much less than in the case of a cathode structure with one strained GaAs layer.

A model-dependent calculation of the hole miniband energies yields absolute values of $E_{hh1} = 13 \text{ meV}$ and $E_{lh1} = 54 \text{ meV}$. For a small conduction-band offset the electronic band can be taken as the average of the conduction-band energies of the contacting layers. Thus the band gap, E_g , can be estimated as:

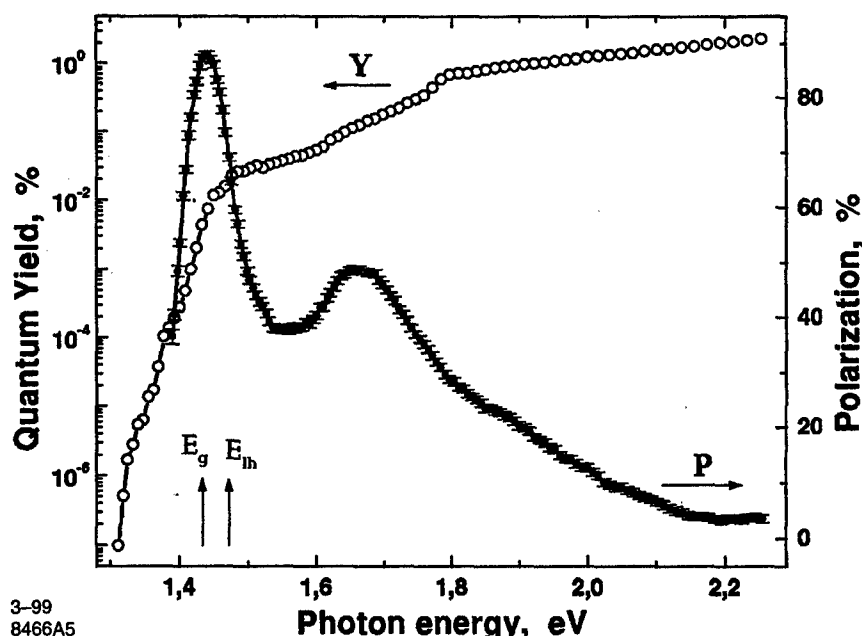


Fig. 2. Electron spin polarization and quantum yield as a function of excitation energy at room temperature for the $\text{Al}_{0.20}\text{In}_{0.18}\text{Ga}_{0.62}\text{As}/\text{GaAs}$ SL sample (SPTU data). The band gap energy E_g and the light hole excitation energy E_{lh} are indicated by arrows.

$$E_g = E_{g1} + E_{hh1} + (E_{c2} - E_{c1})/2,$$

which is in line with experiment.

3 EXPERIMENTAL RESULTS

The Mott analysers both at St. Petersburg Technical University (SPTU) and at the Stanford Linear Accelerator Center (SLAC) were used to measure the spin polarization, P , of photoelectrons.

In Fig. 2 the polarized emission and quantum yield data measured at SPTU are shown as a function of the optical excitation energy. The maximum polarization obtained was 86% and the corresponding quantum yield was $7.5 \times 10^{-3}\%$. The yield for the excitation energy at the polarization maximum is sensitive to the activation procedure and the vacuum in the setup. At SLAC, $P=82.7\%$ with $Y=9.4 \times 10^{-2}\%$ was obtained for a crystal obtained from the same wafer. For another sample (not shown), in which the time lapse between the two sets of measurements was very short, the polarization results were found to be similar despite the somewhat different techniques of sample preparation, activation, and vacuum. Due to better vacuum conditions in the SLAC apparatus, the values of Y measured there were regularly higher than those measured at SPTU.

The maximum current density that can be extracted from the SL samples similar to the one described above have yet to be determined. Initial measurements at SLAC gave anomalously low values, perhaps because the surfaces were being heat-cleaned at 600°C exactly as for the SLC strained-layer cathodes. Other SL structures—all of which were produced in Japan—that have been studied for charge limit have shown normal emission after removal of the As cap at low ($\sim 400^\circ\text{C}$) temperature [5,6].

There is now strong evidence that the SCL can be overcome by using extremely high dopant density ($\geq 4 \times 10^{19} \text{ cm}^{-3}$) in at least the surface layer [6]. This greatly reduces the barrier to holes tunneling to the surface, which are responsible for neutralizing the surface charge. It may also be necessary to increase the negative affinity at the surface by using a large band gap and also possibly a large offset of the conduction miniband. All of these parameters are easily controlled for an MBE-grown SL structure with compensated conduction band as described here.

4 CONCLUSIONS

Electron spin polarization as high as 86% has been obtained at room temperature from strained $\text{Al}_x\text{In}_y\text{Ga}_{1-x-y}\text{As}/\text{GaAs}$ superlattice with minimal conduction band offset. Modulation doping of the SL provides high polarization and high quantum yield. The position of the polarization maximum can be easily tuned to an excitation wavelength by choice of the SL composition. Further improvement of the emitter parameters can be expected with additional optimization of the SL structure parameters.

5 REFERENCES

- [1] R.A. Alley et al., Nucl. Instrum. and Meth. A 365 (1995) 1, and references therein.
- [2] A.V. Subashiev et al., Phys. Low-Dim. Struct. 1/2 (1999) 1, also issued as preprint SLAC-PUB-8035 (1998).
- [3] T. Nakanishi et al., Proc. of Low Energy Polarized Electron Workshop, St. Petersburg (1998) 118; also Polarized Gas Targets and Polarized Beams, AIP Conf. Proc. 421 (1998) 300.
- [4] A.V. Subashiev et al., Proc. of Low Energy Polarized Electron Workshop, St. Petersburg (1998) 55, also issued as preprint SLAC-PUB-7995 (1998).
- [5] Y. Kurihara et al., Jpn. J. Appl. Phys. 34 (1995) 355.
- [6] K. Togawa et al., Nucl. Instrum. and Meth. A 414 (1998) 431.

A LOAD-LOCKED GUN FOR THE JEFFERSON LAB POLARIZED INJECTOR*

W.J. Schneider[#], P. Adderley, J. Clark, A. Day, B. Dunham[†], J. Hansknecht, P. Hartmann, J. Hogan, R. Kazimi, D. Machie, M. Poelker, J.S. Price[†], P.M. Rutt, K. Ryan, C.K. Sinclair and M. Steigerwald
Thomas Jefferson National Accelerator Laboratory, Newport News, VA

Abstract

Construction is underway at Jefferson Lab on a load-locked polarized electron source. The design incorporates all of the essential features of the existing non load-locked gun and improves on the designs of existing load-locked guns operating at other labs. When complete, we expect the new load-locked gun to enhance the versatility of the JLAB polarized injector.

1 INTRODUCTION

Historically, load-locked guns have been constructed as a means of circumventing seemingly insurmountable obstacles that have prevented labs from delivering reliable polarized beam to physics end-stations. For example, at SLAC, prior to the construction of their load-locked gun, full cathode activation in the main gun chamber caused high voltage breakdowns. It is believed that the high voltage breakdowns were associated with cesium deposition on the cathode electrode during the initial activation [1]. Once this process (i.e., initial full activation of the photo cathode) was performed in the preparation chamber of their load-locked gun, the high voltage incidents ceased. At MAMI, short cathode lifetimes (~ hours) necessitated frequent cathode replacement, a situation that prevented reliable beam delivery to nuclear physics users during a typical months-long experiment [2]. The load-locked gun at MAMI now allows the accelerator staff to change photo cathodes with minimal delay (few hours) to the nuclear physics program.

At Jefferson Lab, we have demonstrated that a load-locked gun is not essential to meet the demanding requirements of the Jefferson Lab nuclear physics program. For example, unlike SLAC, we do not have any high voltage problems associated with doing cathode activation in the gun proper and, unlike MAMI, our cathode life at high current is excellent. Over the past two years, we have identified a number of mechanisms that contribute to the decay of photo cathode quantum efficiency. Understanding these decay mechanisms has allowed us to implement design changes to our non-load-locked gun that have resulted in exceptional lifetime (1/e lifetime > than 100 H at 100 μ A, > 1000 H at 10 μ A) [3].

With our present non-load-locked gun, 10's of Coulombs can be delivered to Users before intervention (i.e., re-ciesiation or heat treatment followed by full activation) is required. Such polarized source performance means that intervention can occur during a scheduled-maintenance day, (every other week at JLAB) with no impact on the physics program.

Still, the obvious disadvantage of the present non-load-locked gun is that a bake-out is required when photo cathode replacement is necessary. We have reduced the entire replacement process (photo cathode replacement, bake-out and gun re-commissioning) down to fifty-two hours beam to beam - albeit small, but still a delay. Although we do not expect to improve the inherent performance of the non-load-locked gun, we believe a load-locked gun will greatly enhance the *versatility* of the polarized injector. With a load-locked gun, we could rapidly change photo cathodes to meet changing demands of the nuclear physics program, and during biannual facility development periods; we could change photo cathodes quickly to conduct photo cathode research using the superb diagnostics in the injector.

Before making specific design plans, we outlined the basic features of the Jefferson Lab load-locked gun. These features are based on our experiences at JLAB and the experiences of our colleagues at other Labs. They include:

- Installation of the photo cathode from air to the gun chamber must take less than six hours.
- The load-lock vacuum chamber must be at ground potential and there must be no moving parts at high voltage.
- The gun and bend magnet must produce beam in the horizontal plane; the bend magnet must not deflect the beam more than 15 degrees.
- There will be four chambers; a) main gun chamber, b) cathode preparation chamber, c) heat cleaning chamber, and d) atomic hydrogen cleaning chamber where samples are inserted into the load-lock mechanism and cleaned with atomic hydrogen
- A fifth chamber may be added for storage of photo cathodes or cleaned wafers ready for activation.
- Gun features that have proven to be essential on the non-load-locked gun (superb vacuum, electrodes designed specifically for Jefferson Lab beam current requirements, electron optics that minimize stray electrons hitting vacuum chamber walls, etc.) must be incorporated into the load-locked gun design.

*Work supported by U.S. Department of Energy DE-AC05-84-ER40150

[†]Email: schneide@jlab.org

[#]Now at GE Medical Systems Milwaukee, WI

A brief description follows of the load-locked gun being assembled with specific detail on the major points of interest.

2 MAIN GUN CHAMBER

The gun design (figure 1) is a novel one as it makes use of the better electron optics of a horizontal configuration, has no moving parts at HV and has all adjacent chambers at ground potential. Low base pressure (with and without beam extraction) and wise choice of materials is thought to be the most important ingredient for long photo cathode lifetimes. The main gun chamber is manufactured from a standard six-way stainless steel cross. It has one 220 l/s ion pump and three GP 500 MK 2, SORB-AC SAES cartridge pumps symmetrically located around the photo cathode. The non evaporable getter (NEG) pumps are well suited for pumping CO, CO₂ and greatly enhance the pumping speed (~ 4000 l/s) for hydrogen, the dominant gas species in the vicinity of the photo cathode. Pressure in the gun chamber is further reduced, because all cathode preparation is done in a separate chamber. We have achieved pressures below 1×10^{-12} Torr with a similar gun [4] pumped by a massive NEG array. That was measured by an extractor gauge with a measurement limit claimed to be 1×10^{-12} by the manufacturer.

A stainless steel tee supports the cathode electrode which has a shape designed for high current operation and is made of titanium alloy (Ti-6Al-4V). The titanium exhibits better high voltage performance (ie conditioning, low field emission current at full gun fields, etc.) [5]. The ceramic, to isolate the 100 kV (120 kV peak) high potential, is located vertically so that photo cathode preparation is performed at ground potential. A molybdenum puck, which carries the cathode wafer, is similar in concept to the SLAC design. The puck is held in place inside the tee supporting the cathode with a stem spring holder and sapphire rollers. The electrode holder, triple point protectors and internal surfaces of the six-way cross are electropolished while the electrodes are metallographically polished with diamond paste. The anode, also manufactured of titanium alloy, is mounted on a stainless steel spider with a large open area to increase vacuum conductance from the gun proper through a 2.5-inch beam line. A channel cesiator is provided behind the anode for in situ "touch-up". Alignment of the electrodes relative to the beam axis was accomplished to better than a 1/2 mm.

A Surface Interface (SI) manipulator [6], on the beam axis which can both translate and rotate, is used to move the puck between the preparation chamber and the gun (figure 2). A silver plated stainless steel adapter, mounted on the manipulator engages a set of transfer ears inside the puck to allow attachment and release of the puck. Movement of the puck into and out of the gun has worked smoothly although we have not yet baked out the entire apparatus. Isolation between the gun and the cathode

preparation chamber is accomplished through a 1.5-inch ultra high vacuum metal sealed VAT valve [7].

3 CATHODE PREPARATION CHAMBER

The cathode preparation chamber contains all of the components to produce negative electron affinity (NEA) photocathodes: a stainless steel chamber with eight ports placed around the circumference. Two ports are used for the SI manipulators, the others ports are for a 40 l/s sputter ion pump, a GP 100 SAES NEG, a channel cesiator, a NF3 oxidizer, an optical window with a mirror for light and a ring anode. In addition, a SRA [8] residual gas analyzer (RGA) and an extractor gauge have been added for vacuum diagnostics. On beam axis of the chamber is the SI manipulator, previously mentioned, that transfers the puck into the gun. The puck is transferred from the on axis to the transverse manipulator via an aluminum clamp that attaches to the molybdenum puck. This transfer from gun manipulator to load lock manipulator has also worked smoothly; again we have not baked. Pressure in the cathode preparation chamber is maintained at better than 1E^9 Torr. At some point, we may add a storage area to the preparation chamber that will allow us to activate a number of wafers during an accelerator maintenance day and store them for future use. Separating the cathode preparation chamber from the next chamber - heat-cleaning chamber is a 2.5-inch VAT ultra high vacuum metal sealed valve.

4 HEAT CLEANING CHAMBER

Heating the photocathode samples is accomplished in a separate chamber in a manner that differs from techniques used at other labs. The heat-cleaning chamber is fabricated from two six-way stainless steel crosses and one water-jacketed spool piece where the heating takes place. A SI manipulator allows transfer of the puck between the load-locked or the cathode preparation chambers into the heat-cleaning chamber. A Research Inc. model 4085 infrared spot heater, powered by a Chromolox Port-12221 control system is used to heat the wafer to ~ 600 C at a ramp rate up and down of 1 degree C per second. The chamber is also equipped with active cooling. The heater is capable of 750 W although we have found that 375 W appears to be sufficient and have limited the power supply. A thermocouple in the IR beam is presently used for control of the heater. We are in the process of developing the parameters (rates of heating, thermocouple location, pressure rise, etc.) for the heat-cleaning chamber. Separating the cathode preparation chamber from the heat-cleaning chamber is a 2.5-inch VAT ultra high vacuum metal sealed valve. We hope to maintain ultra high vacuum using a combination of a 40 l/s ion pump and a GP100 SAES NEG to minimize the pressure rise during the heating cycle and to remove the hydrogen which is desorbed from the wafer due to the hydrogen cleaning process. A similar 2.5-inch

VAT ultra high vacuum metal sealed valve separates the heat cleaning chamber from the atomic hydrogen cleaning chamber.

5 ATOMIC HYDROGEN CLEANING AND LOAD LOCK CHAMBER

The primary function of this chamber is to introduce a number of different wafers on pucks and store them for eventual processing. Processing that takes place in the load lock is atomic hydrogen cleaning which is now the only cleaning method used to prepare photo cathodes at JLAB [9]. To maximize quantum efficiency we have incorporated an in situ atomic hydrogen cleaner. The highest quantum efficiencies achieved at JLAB have been wafers that were cleaned in situ in a low voltage test chamber. Similar efficiencies have been achieved when samples obtained in a portable cleaning chamber were transferred through air and installed in a gun. A Balzer model TMU-071 turbo-pump is used during atomic hydrogen cleaning where typical values for temperature and pressure near the sample are 350 C and 1×10^{-5} Torr respectively. The load lock makes use of the identical infrared heater presently used in the heat-cleaning chamber to raise sample temperature for atomic hydrogen cleaning. It is anticipated that in situ atomic hydrogen cleaning will provide a means to clean exotic photo cathode materials for which wet chemistry techniques are incapable; for example, chalcopyrites that contain silicon.

6 CONCLUSIONS

In summary, we have discussed the design of the polarized electron gun and its associated processing chambers. We have developed a 100 kV photoemission electron source, which currently supports the delivery of highly, polarized, high average current CW electron beams with long cathode operational lifetime. The new load-locked source incorporates the capability of exchanging, cleaning (both atomic hydrogen and heat) and activating (co-deposition of cesium and NF_3) the photo cathodes without breaking the necessary ultra high vacuum. The gun chamber proper is separated from the preparation, heating and cleaning load lock chambers so that it is capable of reaching the extreme high vacuum regime to obtain long cathode lifetimes.

7 REFERENCES

1. J.E. Clendenin, "Polarized Electron Sources", IEEE 0-7803-3053, (1996).
2. E. Reichert; Nucl. Inst. Meth. A, Vol. 391, Pg 498-506, (1997).
3. M. Poelker et al, LE 98 Workshop, St. Petersburg, Russia, (1998).
4. C.K. Sinclair, invited paper this conference.
5. R. Latham, *High Voltage Vacuum Insulation*, Academic Press, (1995)
6. Surface Interface Inc., 110 Pioneer Way, Suite D, Mountain View, CA 94041, (415) 965-8205.
7. VAT Inc., 500 W. Cummings Pk, Woburn, MA 01801, (617) 935-1446.
8. Stanford Research Systems, SRS, 1290 D Reamwood Ave., Sunnyvale, CA 94089, (408) 744-9040
9. C.K. Sinclair, et al, Atomic Hydrogen Cleaning of Semiconductor Cathodes PAC '97 Proceedings, Vancouver, B.C., (1997).

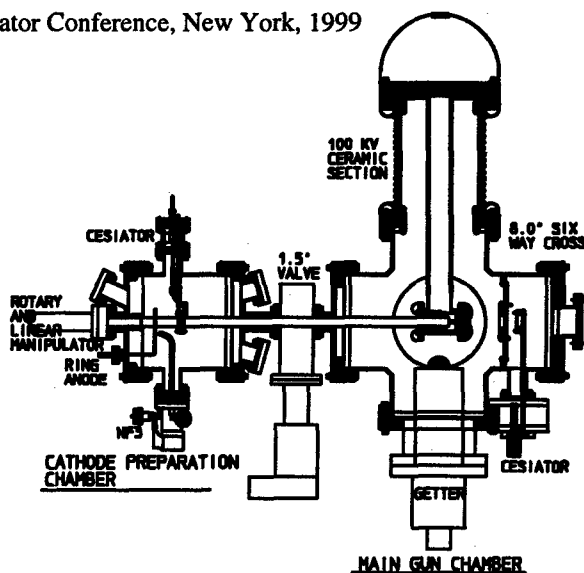


Fig. 1

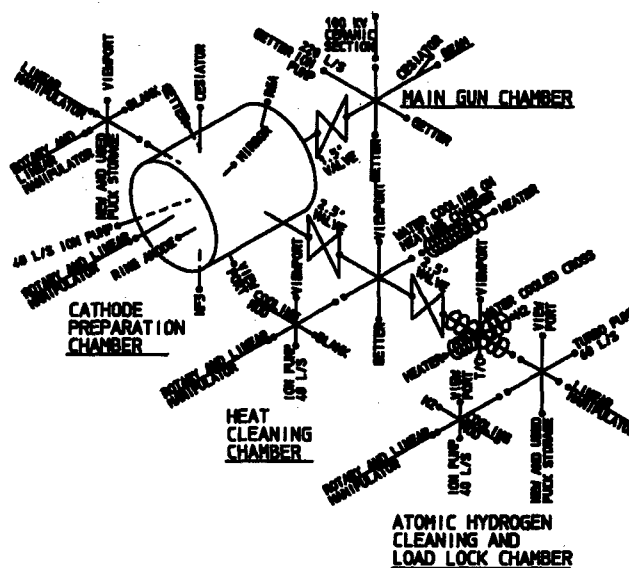


Fig. 2

KEK ATF INJECTOR UPGRADE*

A. D. Yeremian[#], D. J. McCormick, M. C. Ross, SLAC, Stanford, CA

H. Hayano, T. Naito, KEK, Tsukuba, Japan

Abstract

The main goal at the Accelerator Test Facility (ATF) at the KEK laboratory in Japan is to develop the technology that can stably supply the main linac with an extremely flat multi-bunch beam. The injector for this accelerator was upgraded to produce greater than 2×10^{10} in electrons a single bunch at 80 MeV in a very narrow bunch.

1 INTRODUCTION

The ATF accelerator consists of an injector up to 80 MeV, the main S-band linac up to 1.3 GeV and a Damping Ring [1]. The injector consists of a thermionic gun, two 357 MHz subharmonic bunchers, an S-band buncher, a 3-m accelerator structure, many solenoids and diagnostics. The injector was upgraded to produce more than 2×10^{10} electrons in 20 ps of a single bunch and with the potential for greater than 80% charge transmission from the gun to the end of the linac.

2 BEAMLINE MODIFICATIONS

The modified beam line is shown in figure 1. The main

aspects of the modification include relocation of the existing subharmonic bunchers for improved bunching thus the potential for a small energy spread at the end of the linac and redistribution of the solenoids for smaller beam size and better transmission through the injector 3-m accelerator structure. Additionally some beam-pipes were replaced to allow for larger apertures, and some steering coils were added to allow for more adiabatic steering correction in the solenoid region. One of the considerations during the design of the upgrade was to use as much of the existing hardware as possible to save costs. Figure 1 shows a diagram of the modified injector beam line. All the major components, the gun, the bunchers, the 3-m accelerator section and all but one of the solenoids are the original hardware on the ATF injector beam line.

Almost all the diagnostics in the modified injector came from the old injector [2] except for an external bunch length monitor cavity [3] between the S-band buncher and the accelerator section. This monitor as well as one solenoid, some steering coils and some power supplies came from SLAC.

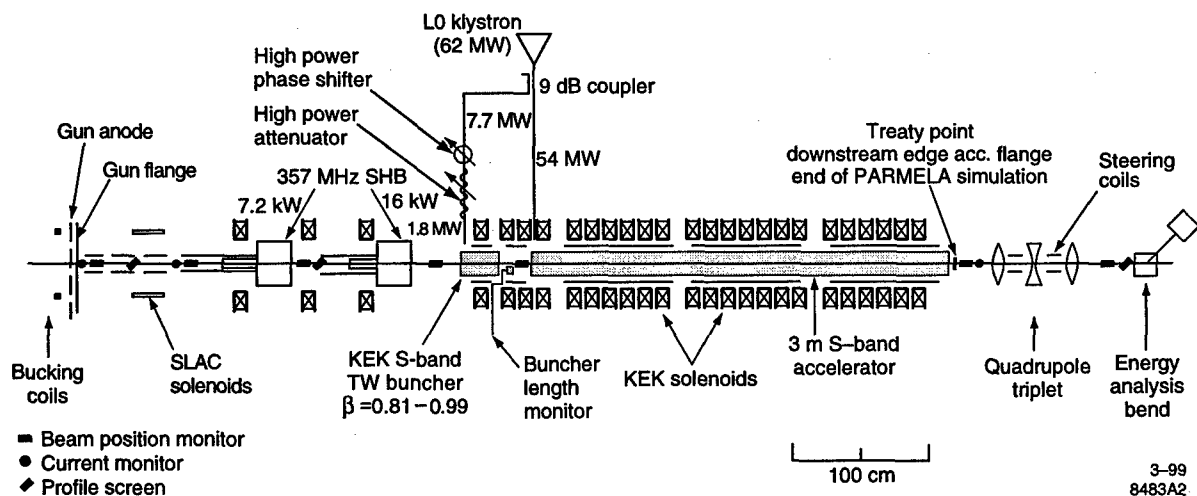


Figure 1. Schematic diagram of the new KEK ATF injector beam line.

*Work supported by DOE contract DE-AC03-76SF00515.

Email: anahid@slac.stanford.edu

3 SIMULATION

Simulations for the beam line upgrade were conducted using PARMELA. As input to PARMELA the simulated beam parameters of the existing gun [4] and the simulated and measured parameters of the existing bunchers [5] were used. The locations and strengths of the bunchers were optimised for best bunching and the locations of solenoids and their strengths were optimised for optimum beam spot size in the bunching and acceleration region up to 80 MeV. After the ideal locations were determined, we found that it was impossible to fit some of the solenoids near the subharmonic bunchers exactly where we wanted them to be on the beam line because of physical obstacles that would be too costly to remedy. Thus, we did the best we could on the beam line and ran the simulations again with the actual locations of the solenoids. We found that this only cost us a few percent in transmission in the simulation, but it also reduced the margin between the beam envelop and the aperture at the entrance to the S-band buncher.

Figure 2 shows the axial magnetic field profile from the gun up to the end of the accelerator section at 80 MeV, known as the treaty point where the injector ends and the linac begins. Simulations downstream of the treaty point are conducted using codes which do not take into account space charge forces and are not the subject of this paper. The gun anode tip is at $Z=0$, the S-band buncher spans from 287 cm to 314 cm, and the accelerator spans from 339 cm to 646 cm. The axial magnetic field is about 100 Gauss from the gun to the S-band buncher and rises rapidly to about 1.7 KG on the accelerator section.

Figure 3 shows the simulated beam envelop from the gun up to the treaty point. The solid lines represent the physical apertures in the beam pipe, the subharmonic bunchers, in the S-band buncher, and in the accelerator

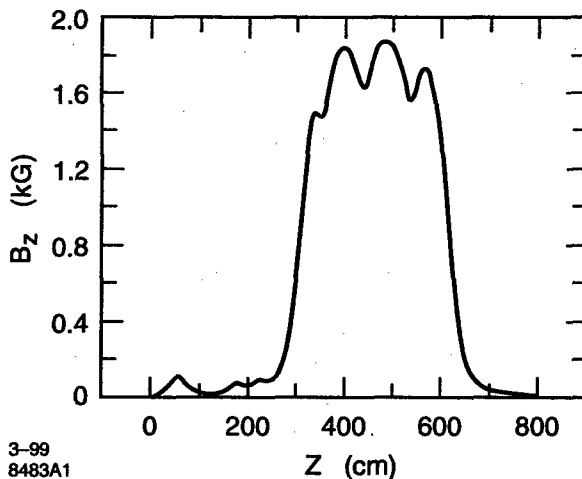


Figure 2. Simulated axial magnetic field profile from the gun to the end of the injector.

section. As it can be seen in the figure, the smallest margin between the beam envelop and the aperture is at the entrance to the S-band buncher.

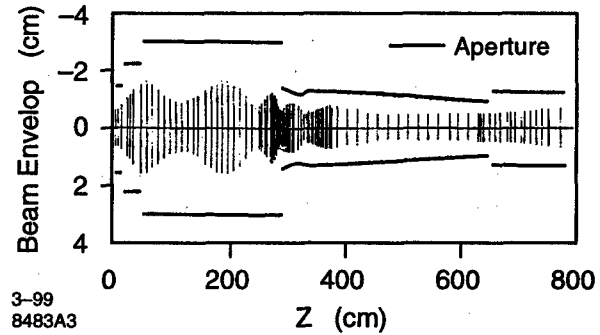


Figure 3. Simulated beam envelop from the gun to the end of the injector.

Figure 4 shows the beam parameters at the end of the 3-m accelerator section (treaty point) where the beam energy is 78.3 MeV.

In the simulations 96% of the charge from the gun reaches the treaty point, but only 83% is in the 20 ps constituting the main bunch. The rest of the charge is in the low energy tail or in satellite bunches. Most of the low energy particles are lost in a real beam line where steering is required to minimise the deviation of the bunch orbit from the centre line. The steering is optimised for

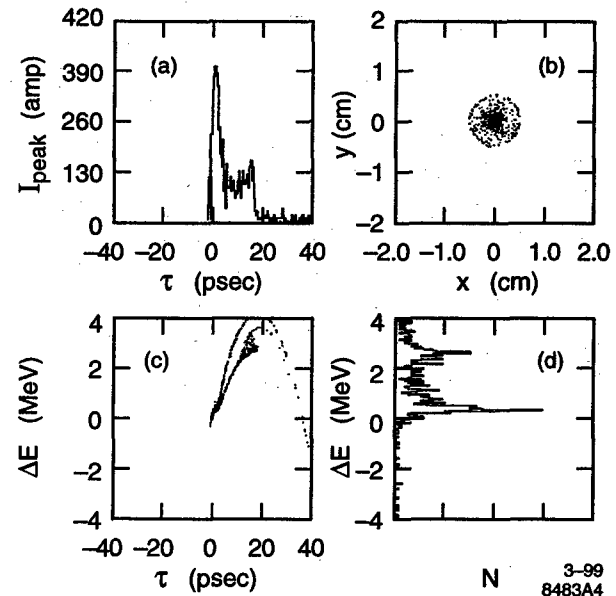


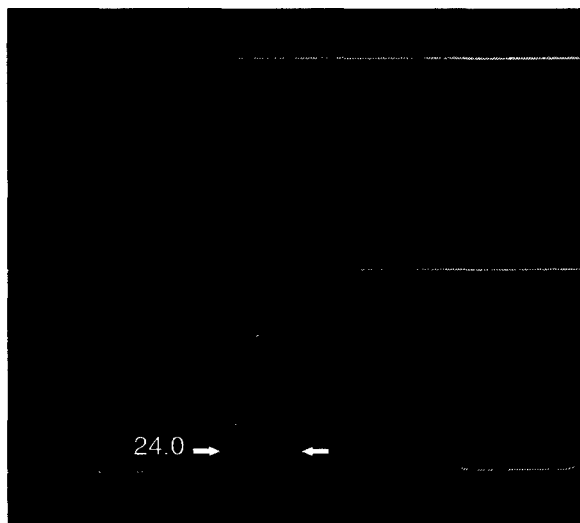
Figure 4. Simulated electron beam parameters at the end of the injector at nominal 80 MeV. a) temporal distribution, b) X-Y space, c) longitudinal phase space, d) energy distribution,

the main bunch energy and particles with much lower energy tend to be intercepted by the beam line aperture. The total energy spread is about 4 MeV or about 5%. Since the first portion of the accelerator structure contributes to the bunching process this energy spread is inevitable. However since this energy spread is correlated with bunch length, it can be taken out in the next accelerating structure by phasing it such that the bunch rides slightly behind the crest of the RF. The transverse beam profile shows that there is a dense, 3mm diameter core and a halo that spans out to 10 mm in diameter. The halo is mainly composed of the low energy particles.

4 INITIAL COMMISSIONING

Once the physical beam line modifications were complete and systems were checked out, we spent about 4 shifts to commission the new beam line. We set the amplitudes of the bunchers and the strengths of the solenoids to the simulated values and adjusted the phases of the bunchers to minimise the bunch length at the streak camera screen at the end of the injector accelerator section. In addition we adjusted a few of the solenoid strengths very slightly and steered the beam.

Figure 5 shows a photograph of one of the streak camera signals for a bunch with 2.2×10^{10} electrons in 24 ps at the end of the first accelerator section (the treaty point). In this case we set the gun for 2.7×10^{10} electrons per bunch.



3-99
8483A5

Figure 5. Streak camera picture of the bunch length at the end of the injector for 2.2×10^{10} electrons.

Table 1 shows the simulated and achieved beam parameters. All the parameters are in good agreement with respect to the simulations except for the energy spread which was higher than the simulated 5.8%. This value was very difficult to measure and even more

Table 1: Simulation and Experimental Electron Beam parameters at the end of the injector (treaty point)

	Simulation	Experimental results
At the Gun		
Charge, 10^{10} e-	2.7	2.7
PW _{edge} , ns	1.2	1.2
Energy, KeV	180	180
End of Injector		
Total Charge, 10^{10} e-	2.6	2.2
Charge in 20°, 10^{10} e-	2.2	2.2
PW _{edge} , ps	20	24
Satellite bunches, no.	2	0
Emittance, mm-mrad	17	
Energy, MeV	78.3	81
$\Delta E/E_{edge}$, %	5.8	>5.8

difficult to set. One of the complications is that in order to adjust the phase of the first accelerator structure, one has to adjust the phase of the klystron which feeds both the buncher and the accelerator and then readjust the buncher. While adjusting these two knobs one has to look at a myriad of diagnostics – minimise bunch length, minimise energy spread, maximise beam transmission and minimise beam orbit.

One cause of the additional energy spread could be that in the first accelerator section the beam does not slip to the crest at the same rate as it does in the simulation. One remedy for this would be to slightly change the temperature of the accelerator structure, thus changing the its frequency. The effect is the adjustment of the phase slippage rate of the beam with respect to the RF in the accelerator.

As expected the total transmission from the gun to the treaty point is less than the simulations results, but the bunch charge and width are very close to the predictions. We were able to accelerate 2.2×10^{10} electrons in a 24 ps FW bunch with 82% transmission from the gun to the end of the injector.

5 REFERENCES

- [1] J. Urakawa et. al, "KEK/ATF Damping Ring", PAC97, <http://www.triumf.ca/pac07/papers/pdf/5B005.PDE>
- [2] H. Hayano, "ATF Linac Commissioning", 18th International Linear Accelerator Conference proceedings, p 547, Geneva, 1996.
- [3] R. H. Miller, "Proposed Bunch Monitor, SLAC TN-63-65, 1963
- [4] T. Naito, "EGUN calculation of ATF Thermionic Gun" ATF Internal Memorandum, 1995.
- [5] T. Asaka, "Development of High-gradient High-current Pre-injector", Master Thesis, Tohoku-Gakuin University, 1995.

A 90 GHZ PHOTOINJECTOR*

D. T. Palmer* and M. J. Hogan, SLAC, Stanford, CA
M. Ferrario and L. Serafini, INFN-Frascati/INFN-Milan, Milan Italy

Abstract

Photocathode rf guns depend on mode locked laser systems to produce an electron beam at a given phase of the rf. In general, the laser pulse is less than $\sigma_z = 10^\circ$ of rf phase in length and the required stability is on the order of $\Delta\phi = 1^\circ$. At 90 GHz (W-band), these requirements correspond to $\sigma_z = 333$ fsec and $\Delta\phi = 33$ fsec. Laser system with pulse lengths in the fsec regime are commercially available, the timing stability is a major concern. We propose a multi-cell W-band photoinjector that does not require a mode locked laser system. Thereby eliminating the stability requirements at W-band. The laser pulse is allowed to be many rf periods long. In principle, the photoinjector can now be considered as a thermionic rf gun. Instead of using an alpha magnet to compress the electron bunch, which would have a detrimental effect on the transverse phase space quality due to longitudinal phase space mixing, we propose to use long pulse laser system and a pair of undulators to produce a low emittance, high current, ultra-short electron bunch for beam dynamics experiments in the 90 GHz regime.

1 INTRODUCTION

In this paper we present a detailed rf and beam dynamics design of an 90 Ghz electron source for use as a source of unpolarized electrons for a switched matrix accelerator [1]. RF simulations in both the frequency and time domains were conducted using GdfidL [2]. The beam dynamics simulations were conducted using HOMDYN [2] and ITACA [3]. The design parameters of this injector are listed in Table 1.

2 THEORY

The scaling of a S-band design up to W-band following scaling laws [4] for RF guns brings to on cathode emissivity which are well present state of the art. In fact, since bunch sizes scale like RF wavelength as well as for the bunch charge, that implies that bunch peak current scales invariant while current density scales like the square of the frequency. This leads to a current density in excess of a few MA/cm² if the BNL/UCLA/SLAC [5] gun design is scaled up to 91 GHz (see Table 1). Furthermore, the cathode RF peak field, as well as the solenoid peak field, scale like the frequency leading to a peak field in excess of 3 GV/m and a solenoid peak field of several

Teslas. Because of the tight requirements imposed by a pure scaling, together with the requirement of a laser phase-jitter less than 30 fs, we abandon the conventional scheme for RF guns and adopt a different lay-out.

We follow the scheme presented in [6], where a laser pulse longer than the rf period is sent onto the photocathode surface in order to extract a long electron bunch, typically a quarter of the rf wavelength, carrying a modest current, around 20 A. There is no need for phase stability of the laser in this case, not even phase-locking: the accelerating rf field sets up the time structure for the beam. The scaling up to W-band of the lay-out presented in [6] at 1.3 GHz requires a 1.5 GV/m peak field at the cathode and an 11 ps laser pulse generating 170 pC at the cathode surface, of which only 40 will be extracted from the gun. Since the cathode spot size is 120 microns and the extracted current 10 A, the cathode current density is limited to 20 kA/cm².

	Nominal S-band Parameters	Scaled W-band Parameters	Scaled W-band Long Pulse Parameters
Gradient [GeV/m]	0.140	4.5	1.5
Solenoid Peak Field [T]	0.23	7.3	2.5
Charge [nC]	1	0.032	0.166 (see 1/6)
Laser Pulse Length [ps]	10	0.3	11
Laser rf Phase Jitter [fs]	1000	30	Anything
Cathode Spot Size [μm]	1000	30	100
Current Density [A/cm ²]	2×10^4	$>10^6$	3×10^4

Table 1: Nominal S-band operating scaled to W-band for both a pure scaling and the proposed long pulse scaling.

The HOMDYN and ITACA simulations shown in Section 4 show that the linear energy-phase correlation at the front part of the bunch (i.e. the first 30 RF deg), can be transformed into a phase compression using a undulator, achieving a current in excess of 600 A in a sharp peak a few RF degrees long.

3 DESIGN AND MECHANICAL FABRICATION

This rf gun is basically a 1.6 cell BNL/SLAC/UCLA S-Band rf gun scaled to 91.324 GHz. Power is symmetrically feed into the full cell which also has

*Work supported by USDOE DE-AC03-76SF00515

*Email: dtp@slac.stanford.edu

symmetrical tuners, as does the half cell. The gun is shown in Figure 1.

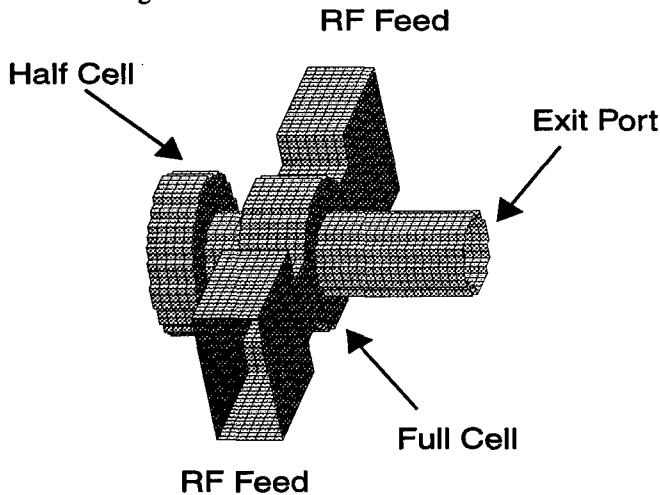


Figure 1: A schematic of the 1.6 cell W-band electron source.

The waveguide to full cell coupling slot is the full height of the full cell. This was decided upon to facilitate the wire EDM manufacturing process. The waveguide feed in the body of the gun is not standard WR-10. The waveguide cutoff dimension is still 2.54 mm or 60 GHz. The waveguide height is slightly smaller at 1.016 mm versus 1.27 mm for standard WR-10 waveguide. This decision was determined by our manufacturing technique of wire EDM and our assembly process of high temperature bonding at the high rf current joints. The gun is manufactured out of 5 layers of Glidcop AL-15 [3] to prevent distortion of the cell to cell and rf coupling iris during the thermal cycle necessary for the bonding. The first of these five layers consists of a cathode plate. A half cell plate, which is the thickness of the half cell which is wired EDM. The third plate is the cell to cell iris. The full cell plate which is slightly thinner than the narrow dimension of WR-10 waveguide. It should be noted that the symmetric waveguide feed does not extend to the boundary of the material. Only after these five layers are bonded does the waveguide extend to the outer body of the gun. This is to facilitate the alignment and assembly of the gun. The last layer is the exit port of the gun. This layer has the same ID as that of the cell to cell iris. The individually layers of the gun are produced out of a single piece of Glidcop Al-15, in which alignment pin hole are first bored in to the block. A section of this block is sliced off to produce the cathode plate with its alignment pins. A wire start hole is popped through the remaining block. The cell to cell iris is wired into the block and then a section of the block is cut off. This section will be used to manufacture the cell to cell iris and the exit port of the gun. One of the blocks is then sliced into thin section a little thicker than the required cell to cell iris thickness. These will be diamond fly cut flat and parallel to facilitate diffusion bonding. Next the other half of the original block will be cut in half and the full cell cavity and waveguide profile will be wired and sliced as was the case of the half cell. These in turn are also diamond fly cut. The assembly is then cleaned and diffusion bonded. At

this point the outer body of the gun is cut to expose the WR-10 waveguide.

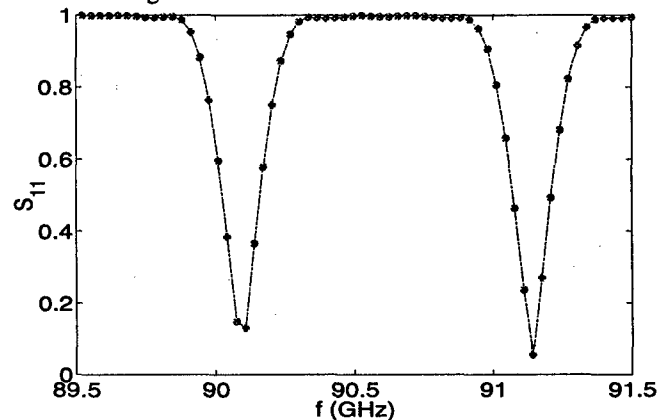


Figure 2: Smith chart representation of Gdfidl simulations of S_{11} .

The rf simulation code Gdfidl was utilized to produce an $S_{11} = 1.00$ with equal fields at the cathode and in the middle of the full cell (see Figure 2). A Smith Chart representation of this match is shown below in Figure 3.

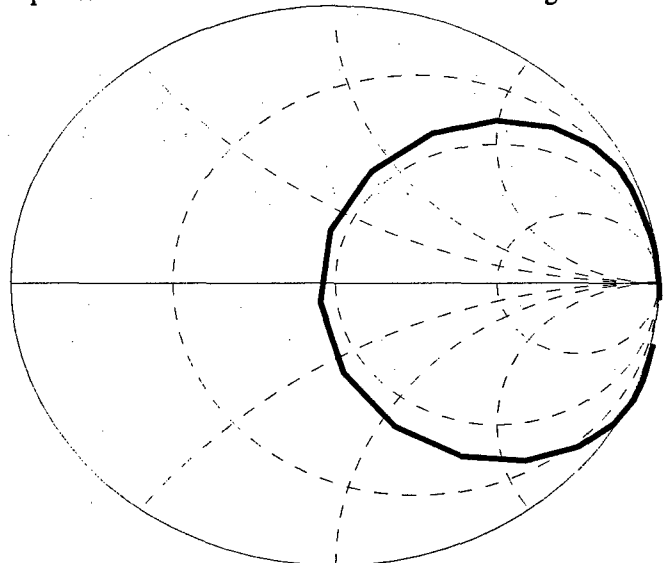


Figure 3: S_{11} of both the 0 and pi-modes.

Using the Shunt impedance calculated from Gdfidl we find that the required power from a W-band rf source will be in excess of 1 GW.

4 SIMULATIONS

In this section we present a possible configuration for a W-band injector based on a preliminary study of beam dynamics in a system consisting of a 1.5 cell W-band gun, followed by a solenoid lens, a SW 8 cell booster linac and a short undulator. The gun is 2.5 mm long, the drift up to the booster is 17.5 mm, the booster is 13 mm, the drift up to the undulator is 12 mm and the undulator is 160 mm (8 periods with 2 cm period length).

In order to achieve a nice phase focusing in the gun we have to use a low value for α (0.8), resulting in 1.5 GV/m peak field at the cathode. The solenoid lens, located

6.3 mm from the cathode (at $z=0$), must provide a 2.5 T peak field. The booster linac is run at 500 MV/m accelerating gradient, while the undulator requires a peak field of 0.5 T.

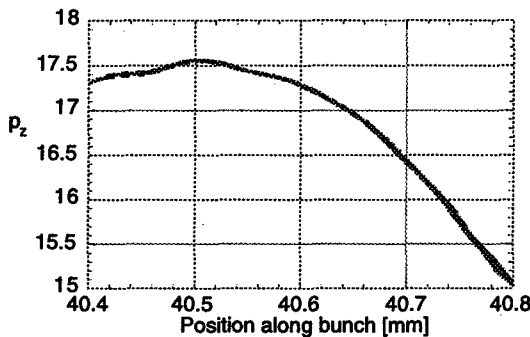


Figure 4: Correlated head of bunch at booster exit.

A bunch charge of 166 pC is produced at the photocathode surface during the illumination of a 11.1 ps laser pulse (as long as the RF period): because of the low α , only the first 65 RF degrees are successfully extracted from the gun, i.e. the first 2 ps of laser pulse lasting from the 0 cathode-field time (0 RF deg) until the 65 RF deg time. The rest of the electrons are either back-accelerated onto the cathode after leaving the cathode surface (those between 65 and 180 RF deg) or not even extracted because of the wrong sign in the applied field (those between 180 and 360). The nominal current in the extracted electron bunch is 15 A (30 pC in 2 ps), implying a cathode current density of 33 kA/cm² at a cathode spot size of 120 microns (as was used in the simulations). The bunch is then focused by the solenoid lens, which is needed to overcome the RF defocusing kick, and injected almost collimated into the booster, which brings up its energy to 7.8 MeV (at the gun exit 1.8 MeV). As a result of the huge phase spread, the energy spread is but nicely linearly correlated in the head part of the bunch (the first 20 RF degrees from $z=40.65$ to $z=40.8$, the bunch has just exited the booster). The effect of phase-focusing, achieved thanks to the operation at low α , brings a density compression in the head part of the bunch, as shown in Figure 4, plotting the local current carried by the bunch, which is much larger than the nominal value in the head part while much lower in the tail: because of the phase-focusing one obtains peak currents around 70 A, a factor 4 larger than the nominal value.

The beam is further injected into an undulator (no other focusing lenses were used in the short drift to the undulator) that acts like a dispersive medium boosting the phase compression mechanism which would take place anyway even in a simple drift, because of the negative correlation in the energy-phase correlation of the bunch (head particles less energetic than tail particles).

In summary, using a long laser pulse and a suitable gradient alleviates the severe restrictions imposed by a

pure scaling on laser-rf phase jitter and cathode current density.

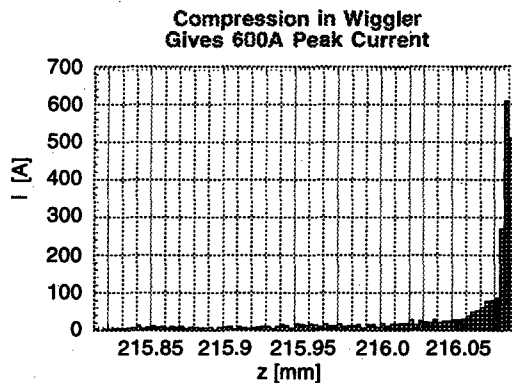
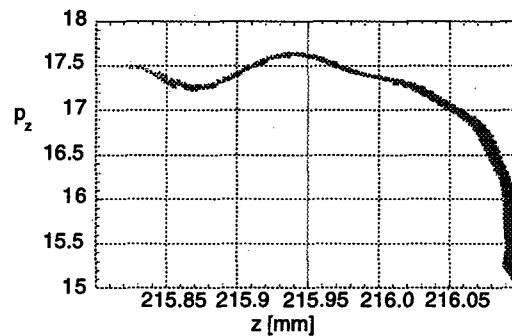
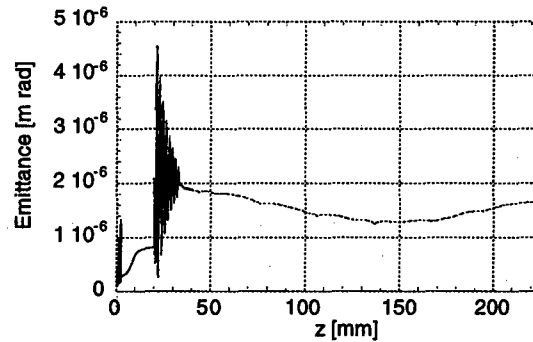


Figure 5: ITACA output of Gun, booster and undulator showing: the beam emittance, longitudinal phase space, and peak current.

5 REFERENCES

- [1] David H. Whittum and Sami G. Tantawi, SLAC-PUB-7848.
- [2] M. Ferrario, *et al.* Proc. Of EPAC98, , Ed. S. Myers, IoP Publ., Bristol, 1998, p.1271.
- [3] L. Serafini and C. Pagani, Proc. of I EPAC, Rome, 1988 (ed World Sci., Singapore), p.866.
- [4] J. Rosenzweig, E. Colby, AIP 335 (1995) 724
- [5] D. T. Palmer, The Next Generation Photoinjector, Ph.D. Thesis, Stanford University.
- [6] N. Pioella et al., Proc. of EPAC98, Ed. S. Myers, IoP Publ., Bristol, 1998, p.1465.

RESULTS FROM THE SECOND X-BAND RF GUN*

C. H. Ho^{*}, T. T. Yang, W. K. Lau, M. J. Horny, J. Y. Hwang, M. S. Yeh, Y. L. Tsai, SRRC
F. V. Hartmann, E. C. Landahl, H. A. Baldis, N.C.Luhmann, Jr., A. L. Troha, UC Davis

Abstract

A collaborative research effort between the Synchrotron Radiation Research Center (SRRC) and the UC Davis (UCD) is being put to improve the design and performance of the X-band (8548 MHz) rf gun. The fabrication and cold test will be performed at SRRC. The high power test will be conducted at UC Davis. The cold test results are presented.

1 INTRODUCTION

A collaborative research effort for the development of the X-band photoinjector system has been formed between UC Davis and SRRC. Both the design and fabrication procedures have included separate verification from both groups [1]. The first X-band rf gun was fabricated, cold tested and brazed at SRRC and was delivered to UC Davis at the Lawrence Livermore National Laboratory (LLNL) site in April, 1997. The gun was installed and characterized by the research personnel from both groups [2], [3].

The first brazed X-band rf gun in 1997 had a few problems. The brazing joints between the various cavity components failed between the water cooling channel and the inner surface of the RF cavity. All cavity leaks were sealed with vacuum epoxy. External cooling was applied in the form of heat sink and copper tubing wound around the body of the accelerator cavity. Furthermore, the peak field ratio between the half cell and the full cell is out of balance. Fortunately, critical coupling of the Klystron signal corresponded to half-cell coupling. Critical coupling allowed the accelerator to be safely used as a resonant load from the Klystron despite this non-optimized condition. In addition, since the half-cell was energized, high-energy photoelectron production is still possible.

Therefore our goal for the second X-band rf gun is aiming for correcting above deficiencies.

*Work supported in part by the National Science Council (Taiwan) under contract No. NSC88-2112-M-213-007, as well as by MURI (USA) under contract F49620-95-1-0253, by ATRI (USA) under contract F30602-94-2-0001, and by DoE (USA) under contract DE-FG03-95ER54295.

*Email: chh@srcc.gov.tw

2 DESIGN AND FABRICATION

Figure 1 shows the assembly drawing of the second X-band rf gun. Most of the design is the same as the first gun, except the cathode assembly.

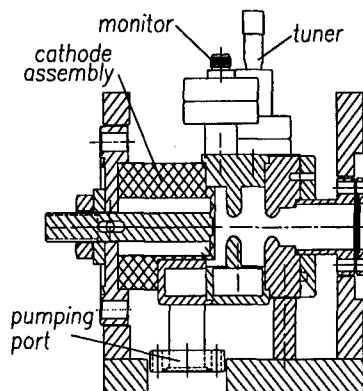


Figure 1: Assembly drawing of the gun system.

The cathode in the first gun is a choke type plunger with a large diameter of 20 mm to reduce the arcing problem from the gap between the cathode plug and cavity wall [1]. But it was found from the operation experience of the first gun that the resonant frequency becomes very sensitive to the cathode position. Therefore we prefer to braze a copper plate of 27.79mm diameter to cover the end of the half cell (27.63mm diameter) and just use this plate as a fixed-position cathode. Figure 2 shows the drawing of the cathode assembly.

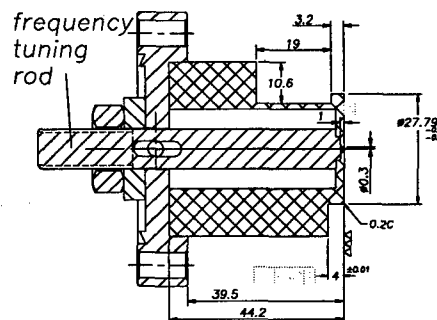


Figure 2: Drawing of the cathode assembly.

From our previous brazing experiences, the resonant frequency may shift a lot and can not be corrected back by only using the tuner. Therefore we also brazed a frequency-tuning rod to the back of the cathode plate. The cathode plate can be deformed a little bit by the movement of tuning rod using a 2-arm gear puller. We certainly don't like to deform the cathode plate if not really necessary. This option will just save us from discarding the whole-brazed cavity set without any new experimental effort from high power test.

The cavity inner diameter was first enlarged to a little bit higher resonant frequency than the target frequency of 8548 MHz. Then the rf coupling irises are gradually enlarged to get close to the critical coupling. The final dimension of the cavity inner diameter is 27.63mm. The sizes of the two elliptical rf coupling irises on the half cell and the full cell are 3.0mm×8.4mm and 4.5mm×8.4mm respectively.

There is a frequency tuner and a field monitor on each cell. The tuner is a copper rod with 2.37mm diameter. The maximum tuning range of the tuner is around +30 MHz. The field monitor is a loop type monitor. It is made of a loop (50/50 Au/Cu alloy) attached to a commercial SMA coaxial feedthrough (ISI P/N 9252003). A Desktop Laser Welder EDW-25 (made by Equilasars Inc.) was used to weld the loop onto the SMA coax. The monitor is mounted on the cavity wall with a hole, which was gradually enlarged to 2mm diameter for an appropriate transmission (S_{21}) signal (around -60dB during cold test).

3 COLD TEST RESULTS

The experimental arrangement for the bead pull measurement is shown in Fig. 3.



Figure 3: Bead pull measurement setup.

Two lab's jacks were used to support and adjust the height of the gun body. One translator stage was used for the horizontal alignment and the other translator stage was used to move the gun body so that we were able to position the bead at any position along the longitudinal axis of the cavity. The movement resolution of the translator stage is 0.01mm, while we only move the gun body along the longitudinal axis in steps of 0.5mm.

Since the minimum mode separation between the π -mode and O-mode is around 6 MHz according to the URMEL-T prediction, the frequency perturbation from the bead should not be too large to break the coupling of both modes. A 0.83mm length, 0.53mm diameter metal cylinder, made from a section of a hypodermic needle was used as the perturbing bead, which gives around 1.5 MHz perturbation. An example bead pull measurement is shown in Figure 4 for a balanced field case.

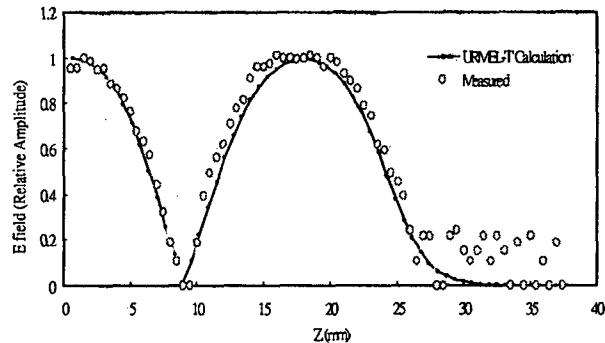


Figure 4: Longitudinal E-field distribution on axis.

The measured data also shows a good agreement with the URMEL-T calculation. We noticed the E-field goes to null at the beam iris position, which agrees with the distinct feature of the π -mode. The phase from field monitor (S_{21} transmission signal) is also measured to look for 180 degrees phase difference, corresponding to the π -mode. Figure 5 shows the reflected signal when the peak field ratio is 1.03.

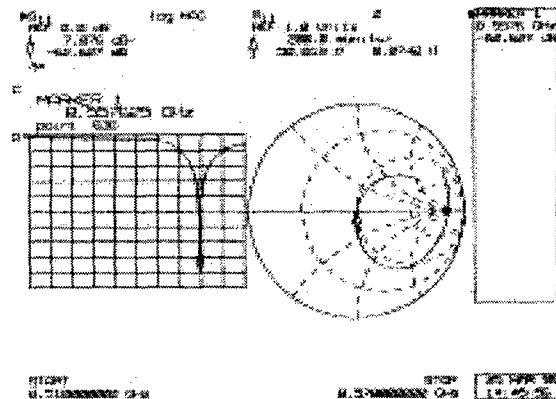


Figure 5: Reflection coefficient for the field ratio of 1.03.

4 SUMMARY

An OFE copper cavity has been fabricated at SRRC for the second X-band rf gun. The dimensions of the cavity were optimized. The cold test results showed a promising balanced field case. All the cavity components had been fine polished and are going to be brazed very soon. We expect to begin the installation and high power test at UC Davis in late April, 1999.

5 REFERENCES

- [1] C. H. Ho, W. K. Lau, T. T. Yang, J. Y. Hwang, S. Y. Hsu, Y. C. Liu, G. P. Le Sage, F. V. Hartemann, and N. C. Luhmann, Jr., "The Design and Fabrication of an X-Band RF Gun", AIP Conf. Proc. 398 for the Seventh Workshop on Advanced Accelerator Concepts (Lake Tahoe, California, 1996), p. 705.
- [2] C. H. Ho, W. K. Lau, T. T. Yang, S. S. Chang, J. Y. Hwang, Y. C. Liu, G. P. Le Sage, F. V. Hartemann, and N. C. Luhmann, Jr., "The Construction and Initial high power test of an X-band rf gun", Proc. 1997 Particle Accelerator Conf. (Vancouver, B. C., Canada, 1997), p. 2858.
- [3] E. C. Landahl, F. V. Hartemann, G. P. Le Sage, W. E. White, H. A. Baldis, C. V. Bennett, J. P. Heritage, N. C. Luhmann, Jr., and C. H. Ho, "Phase Noise Reduction and Photoelectron Acceleration in a High-Q RF Gun", IEEE Transactions on Plasma Science, Special Issue on High Power Microwave Generation, Vol. 26, No. 3, pp. 814-824 (June 1998).

A PERMANENT-MAGNET FOCUSED X-BAND PHOTOINJECTOR

D. Yu, D. Newsham, P. Wilson, J. Zeng, *DULY Research Inc.*

J. Rosenzweig, X. Ding, *UCLA*

F. Hartemann, E. Landahl, *ILSA/UCD*

Abstract

A Plane-Wave-Transformer (PWT), integrated photoinjector operating at an X-band frequency (8.547GHz) is being developed by DULY Research Inc. in a DOE SBIR project, in collaboration with UCLA and UCD/ILSA. Upward frequency scaling from an S-band PWT photoinjector would result in a compact photoinjector with unprecedented brightness. Challenging technological innovations are required at X-band. In particular, water cooling capacity, mechanical support strength, and materials properties do not scale linearly with frequency. Instead of using large solenoids, we have successfully designed the required focusing for an X-band PWT using a compact, permanent magnet system. Also described in this paper is a system design of the X-band photoinjector, including the RF system and the cooling/support of the PWT structure.

1 INTRODUCTION

This paper reports an ongoing research project in which DULY Research Inc. develops a compact, high-brightness, 8.547-GHz, 20-MeV photoinjector using a plane-wave-transformer (PWT) design for the standing-wave accelerating structure (Figure 1). The motivation for a high-frequency photoinjector lies in the great enhancement of beam brightness in a much smaller footprint, important for many commercial applications. Our design directly integrates the photocathode into a PWT linac. The integrated X-band PWT photoinjector has a designed beam brightness of 10^{15} A/m², an order of magnitude higher than an earlier S-band version, being constructed and now near completion in a DULY/UCLA collaboration [1,2].

2 BEAM BRIGHTNESS SCALING

The beam brightness, by natural frequency scaling, is defined as:

$$B \equiv 2I / \varepsilon^2 \propto Q / \sigma_z \varepsilon^2 \propto \lambda^{-2},$$

where I is the beam current, or charge (Q) per bunch per unit time, ε is the emittance, σ_z is the rms bunch length, and λ is the RF wavelength. It is apparent from this expression that there is much to be gained by operating RF photoinjectors at high frequency. One can also show that including emittance dilution due to space charge, RF chromatic contribution and other field asymmetry effects, and keeping the charge density constant, the beam

brightness for an X-band photoinjector is better than that achieved at S-band by roughly an order of magnitude.

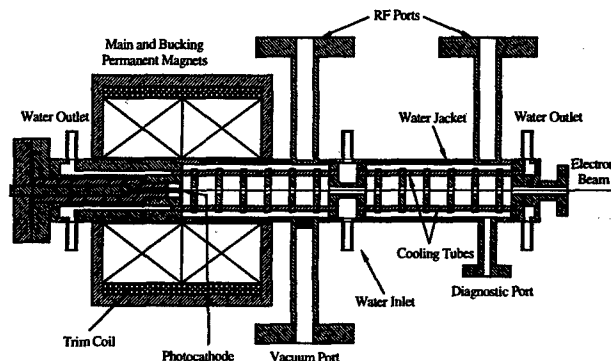


Figure 1: X-band PWT photoinjector schematic.

3 PERMANENT MAGNET FOCUSING SYSTEM

A prescribed magnetic field profile, following the principle of emittance compensation [3], is a key ingredient of success for the focusing and propagation of a small electron beam through the X-band PWT linac. The longitudinal magnetic field on axis must vanish at the photocathode, rise sharply to 3-4 kG in the first full cell or thereabouts, and then taper down to zero in a few more cells. The radial and azimuthal components of the magnet fields should be small. Such a magnetic field configuration assures not only that the beam emittance is preserved for the entire length of the accelerator, but also that the beam can be focused beyond to a spot sufficiently far away, where the first set of quadrupole magnets are located. Using solenoids to obtain the necessary magnetic field profile for the X-band PWT would require large

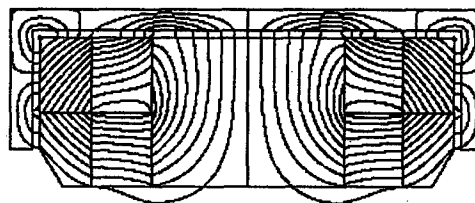


Figure 2: Field lines of permanent magnet.

coils, leaving little room for other essential, auxiliary structures of the linac such as the RF and vacuum ports.

DULY Research has proposed, and designed a hybrid, permanent magnet focusing system using the POISSON and PANDIRA codes. Figures 2 and 3 show the field profile due to the focusing magnets. The main and bucking magnets in this system are identical, but with

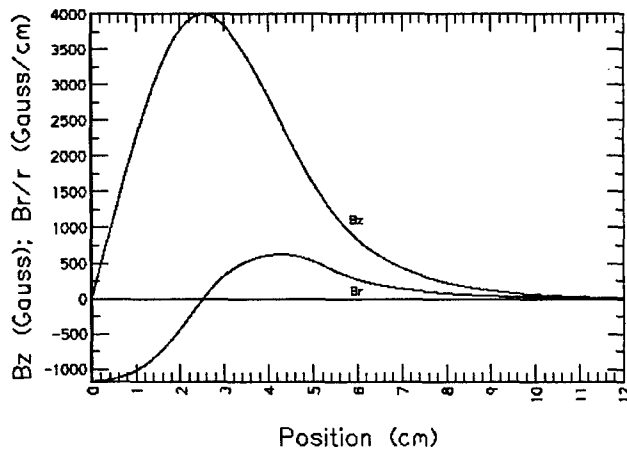


Figure 3: Field strength of permanent magnet.

opposite polarizations. An 80-turns, one-eighth-inch square trim coil is included for final adjustment of the null position of the longitudinal magnetic field at the cathode. A small current of 50A (or 4000 Ampere-turns) in the trim coil can move the axial position of the magnetic null by 1.4 mm. The footprint of this system is quite small (about 6" diameter), and fits well over the PWT linac, as shown in Figure 1.

4 RF SYSTEMS

The main RF power supply for the X-band photoinjector linac will be a 8.547 GHz, SL3 klystron at ILSA/UCD which produces square RF pulses at power levels in excess of 15 MW at 30 Hz repetition rate, with a pulse duration of 2 μ s, and an amplitude ripple <2%. The phase stability of the klystron is currently measured at $\pm 10^\circ$ over the pulse duration, and will be brought down to $\pm 1^\circ$ by using a phase stabilisation feedback loop. The 2-kW TWTA input drive to the klystron will be synchronised to the laser oscillator, using a phase-locked dielectric resonance oscillator to upconvert the laser oscillator output frequency to the desired X-band drive frequency.

We have designed a RF system using the SL3 klystron power supply to provide sufficient energy to accelerate an electron beam in the X-band PWT photoinjector to 20 MeV. Since the PWT is a standing-wave structure, some RF power may be reflected during startup and conditioning. To prevent the reflected power from damaging the klystron, we use a 3 dB power splitter to divide the main RF into two feeds with 90° phase difference (Figure 4a). The PWT linac structure is also split, and the two linac sections are fed by the two feeds from the power splitter. Thus, no reflected power will get back to the klystron (assuming the two linac sections have the same coupling coefficient and are both tuned to resonance); and no high-power isolator is needed.

Because the SL3 klystron RF pulse is long (2 μ s) compared with the filling time of the PWT linac (292 ns), a SLED pulse compression system [4] may be optionally

installed between the klystron and the aforementioned power splitter (Figure 4b) to increase the linac energy gain. SLED stores some of the pulse energy, which would otherwise be wasted, and delivers it to the structure. Calculations show that an additional 30% energy gain for the electrons in the standing-wave PWT linac may be achieved with SLED.

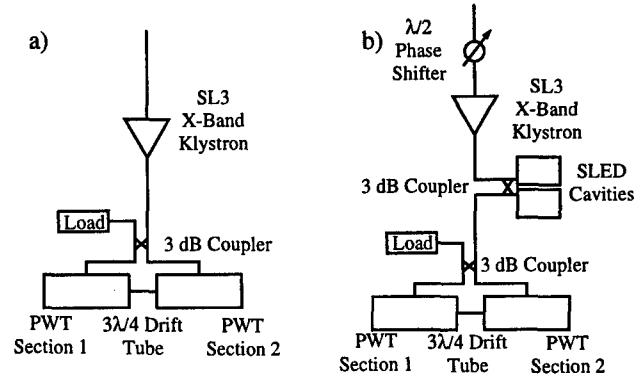


Figure 4: a) Schematic for RF feed to X-band PWT.

b) Same system with SLED pulse compression.

5 PWT ACCELERATING STRUCTURE

To compensate for the phase difference between the feeds, the two linac sections are connected by a short drift tube having a length equal to $3\lambda/4$. In this case, the RF phase of the second section is *ahead* of that of the first section by 90° . The photocathode is inserted through a demountable flange and integrated into the center of the end plate of the first PWT linac section. The linac consists of a series of suspended disks which are supported and cooled by water-carrying tubes. Two inlets, through the center divider of the two linac sections, feed water into eight tubes in parallel, four in each section; and the water outlets are located outside the end plates at the far ends of the linac sections. No internal cooling channels inside the disks are needed.

The RF properties for the X-band PWT linac are calculated using the 3D electromagnetic code GdfidL, and are shown in Table 1 for the accelerating mode, for the cases with 1) no cooling rod, 2) four cooling rods with a diameter of 0.83", scaled from the S-band version, and 3) four rods with a larger diameter of 0.125". The RF degradation for the case with larger rods is not overwhelming compared with the smaller rods. The case with no rods has the best RF properties. This can be implemented with disks supported by synthetic diamond washers as proposed by DULY Research [5].

The X-band PWT linac has a good frequency separation between the accelerating mode and the nearest 0-mode, i.e. 1043 MHz and 612 MHz, respectively, for the configurations with four thin and thick rods. The dipole and quadrupole modes are insignificant for these cases.

Based on the available klystron power and the RF properties of the linac, the structural parameters, expected

accelerating gradients, and energy gains are shown in Table 3, for several RF/linac configurations (Table 2). The variations are the length of the linac, and whether or not a SLED pulse compression is used. We have used the values of Q , r/Q and r of the 4-thin-rod PWT linac (Table 1) to calculate the linac parameters shown in Table 3. Using larger rods (0.125" diameter), the shunt impedances are lower by 6-7%, and the corresponding energy gains and gradients by only 3-4%. Including waveguide losses (about 1.5%/m at 8.5 GHz) the actual energy gains and gradients may be about 10% less than the values shown on Table 3.

 Table 1: RF Properties of π -Mode for the PWT Linac

	r/Q (Ω/m)	Q	r (M Ω/m)
No Rod	6,488	21,657	140.5
4 Thin Rods	7,578	15,717	119.1
4 Thick Rods	8,510	13,052	111.1

Table 2: X-Band Linac Configurations

Case	RF Pulse Compression	No. of Sections	No. of cells in each section
1	None	2	5 full + 2 half
2	None	2	7 full + 2 half
3	SLED	2	5 full + 2 half
4	SLED	2	7 full + 2 half

Table 3: X-Band PWT Linac Parameters

	Case 1	Case 2	Case 3 (SLED)	Case 4 (SLED)
Section length (cm)	10.53	14.04	10.53	14.04
Cells per section	5+2/2	7+2/2	5+2/2	7+2/2
Filling time (ns)	293	293	167	167
Shunt impedance (M Ω)	12.54	16.72	12.54	16.72
Energy gain/section (MeV)	9.70	11.20	12.61	14.56
Final energy (MeV)	19.40	22.40	25.22	29.12
Linac length (cm)	21.06	28.08	21.06	28.08
Gradient (MV/m)	92.10	79.76	119.7	103.6

6 BEAM DYNAMICS SIMULATIONS

We have performed simulations of the split injector configuration for Case 1 (2 sections, each having 5 full + 2 half cells), and Case 2 (2 sections, each having 7 full + 2 half cells). The PARMELA simulations use as input files the full magnetic field profile (longitudinal and transverse), obtained with POISSON and PANDIRA, and the electrical field profile, with SUPERFISH. The beam charge, spot size and bunch length, as well as the computed emittances and rms radius for the two cases are summarized in Table 4 and Figures 5a-d. Both cases yield a high beam brightness (0.8×10^{15} A/m²), and the longer structure (Case 2) results in a higher energy gain, as expected. The peak gradients shown in Table 4 are consistent with the available RF power. The average gradients are 95 MV/m and 82 MV/m, for cases 1 and 2. The normalized beam emittance (1 mm-mrad) and energy spread (0.2%) are low, proving the validity of the principle of emittance compensation in the X-band PWT

linac. Effects of the RF octupole due to the rods on the accelerating mode have been estimated in a companion PAC99 paper [6] and are small for charge less than 2 nC.

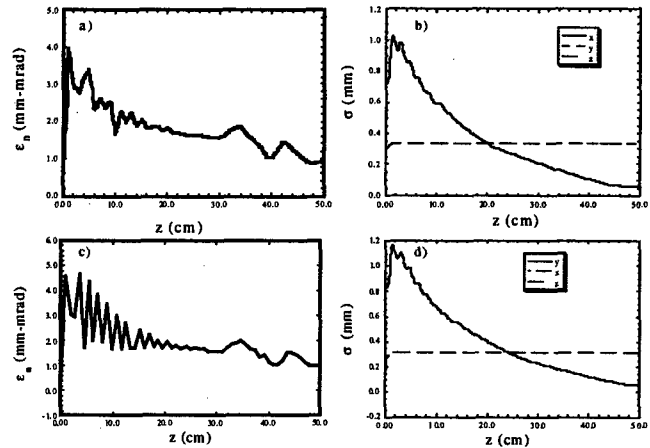


Figure 5: Results of PARMELA simulations. a) and b) are emittance and rms radius for Case 1. c) and d) are emittance and rms radius for Case 2.

Table 4: Summary of PARMELA Calculations

	Case 1	Case 2
Active linac length (cm)	21	28
Number of cells	$2 \times (5+2/2)$	$2 \times (7+2/2)$
Peak magnetic field (Gauss)	3315	2965
Charge per bunch (nC)	1.0	1.0
Bunch Length (mm)	0.36	0.33
RMS transverse beam size (at cathode) (mm)	0.70	0.84
Emittance (mm-mrad)	0.95	1.00
Energy spread (%)	0.2	0.2
Final Energy (MeV)	20	23
Peak gradient (MV/m)	156	180
Beam brightness (A/cm ²)	0.8×10^{15}	0.8×10^{15}

7 CONCLUSIONS

We have demonstrated the feasibility of a high-brightness, X-band photoinjector by design and simulations. In the next phase of project, we will fabricate and test the X-band photoinjector upon DOE approval.

*Work supported by DOE SBIR DE-FG03-98ER82566.

*Email: duly@technologist.com

- [1] D. Yu et al., Proc. of Particle Accelerator Conf., Vancouver, B.C. Canada, May 1997, p. 2802.
- [2] X. Ding et al., these proceedings.
- [3] L. Serafini and J. Rosenzweig, Phys. Rev. E, 55, 6B, p.7565-90, 1997. and B.E. Carlsten, Proc. of Particle Accelerator Conf., Chicago, IL, March 1989, p. 313.
- [4] Z.D. Farkas, H.A. Hogg, G.A. Loew, P.B. Wilson, SLAC-PUB-1453, June 1974.
- [5] D. Yu and T. Lee, Patent pending.
- [6] J. Rosenzweig, S. Anderson, X. Ding, D. Yu., these proceedings.

COMMISSIONING OF THE NEPTUNE PHOTOINJECTOR*

S. Anderson[#], J. Rosenzweig, K. Bishofberger, X. Ding, T. Holden, A. Murokh,
C. Pellegrini, H. Suk, A. Tremaine, UCLA Physics Dept., Los Angeles, CA
C. Clayton, C. Joshi, K. Marsh, P. Muggli, UCLA Dept. of Electrical Engineering,
Los Angeles, CA

Abstract

The status of the commissioning of the rf photoinjector in the Neptune advanced accelerator laboratory is discussed. The component parts of the photoinjector, the rf gun, photocathode drive laser system, booster linac, rf system, chicane compressor, beam diagnostics systems, and control system are described. This injector is designed to produce short pulse length, high brightness electron beams. Experiments planned for the immediate future are described. Initial measurements of various beam parameters are presented.

1 THE NEPTUNE LABORATORY

The primary goal of the Neptune laboratory is the acceleration of a high brightness, relativistic electron beam in a plasma beatwave accelerator (PBWA), while maintaining the initial phase space density. [1] To this end, the main components of the lab are the high power, short pulse, two-frequency Mars CO₂ laser [2], and the rf photoinjector.

2 THE PHOTOINJECTOR

The Neptune photoinjector consists of many components. The most important of which are described below.

2.1 Accelerator Sections

The accelerator is a split system consisting of a photocathode gun, a drift space, and a booster linac. The gun is a 1.625 cell π -mode standing wave cavity produced by a BNL-SLAC-UCLA collaboration. [3] The gun has been conditioned up to an input power of 6.5 MW which corresponds to the planned on-axis peak field of 100 MV/m. The booster linac is a 7 and 2/2 cell π -mode standing wave structure. The linac design is that of a plane-wave transformer (PWT) which benefits from strong cell-to-cell coupling and large mode separation. [4] The linac has been conditioned up to the nominal operating power of 13 MW.

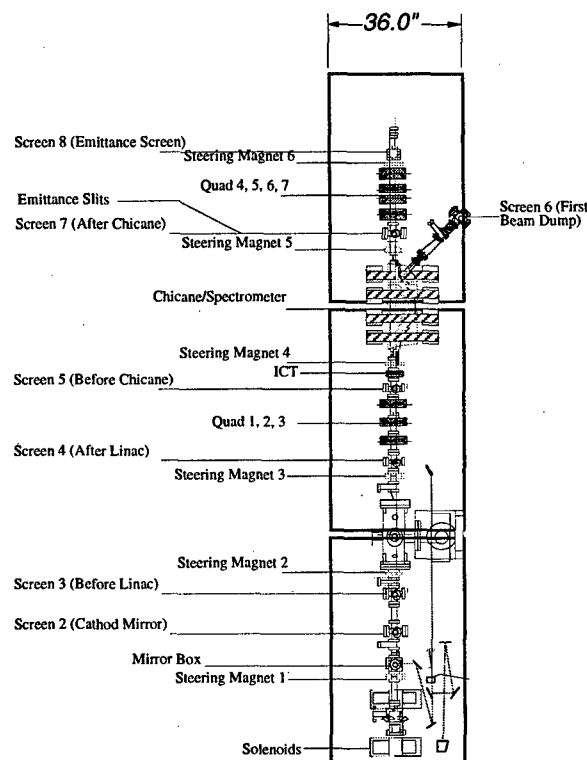


Figure 1: The Neptune Photoinjector Beamline

2.2 RF System

Low level rf is produced by a 38.08 MHz signal which is frequency multiplied 75 times up to S-band. After passing through a phase shifter, the signal is raised to over 400 W by a pulsed solid state amplifier. This signal is then used as the rf input to a SLAC XK-5 klystron. The klystron is pulsed by a modulator with a pulse length currently set to 4 μ sec. The modulator was designed to produce a flat-top pulse, when fired by an SCR-triggered thyatron timed to the klystron rf input, impedance matched to the klystron at high voltage. [5] The klystron has output 22 MW pulses to the wave guide system on a consistent basis.

The rf power distribution system consists of vacuum wave guide separating power manipulating elements. The first of these is a circulator which protects the klystron from reflected power due to the impedance mismatch at the standing wave structures at the beginning and end of an rf pulse. The power is then split by a 4.77 dB divider sending two thirds into the PWT. After the split there are

*Work supported by U.S. Dept. of Energy grant DE-FG03-92ER40693.

[#] Email: anderson@physics.ucla.edu

high power attenuators to control the power delivered to each accelerator. In addition the linac wave guide has a phase shifter to control the relative phase of the two structures.

2.3 Photocathode Drive Laser

The drive laser system begins with a 1064 nm mode-locked Nd:YAG laser which is matched into a 500 m long fiber to lengthen the pulse and yield a frequency chirp. The chirped pulse is then sent to a regenerative amplifier that increases the signal by a factor of one million. The chirp correlation is then removed and the pulse compressed by a grating pair. Adjustments to the grating pair allow control over the pulse length which is currently set at 3 psec (FWHM). At this point the pulse is frequency doubled by a BBO doubling crystal. The green laser light is then transported approximately 40 meters to the next BBO crystal which frequency doubles again to produce 266 nm light. The pulse energy in UV has been measured reproducibly at 130 μ J.

Due to the long transport length, a vacuum transport system has been constructed to hold beam optics and to combat fluctuations in transverse position. To handle long time scale (≥ 10 sec) beam drift, a feedback system consisting of motorized mirror mounts and segmented photodiodes functions in the transport system. This system is computer automated by iteratively reading the position of a beacon laser with the photodiodes (beam position monitor) and adjusting the motorized mirror accordingly.

2.4 Chicane Compressor

The compressor installed at Neptune was designed in part by scaling an L-band compressor designed for the TESLA Test Facility (TTF)[6]. As shown in figure 2, it consists of four dipole magnets which can be configured either as a compressor or a spectrometer. In compressor mode a negative correlation in longitudinal phase space caused by running off-crest in the PWT is removed by the difference in path length of particles of different momentum. The problem of excessive vertical focusing in the chicane has been addressed by adjusting the initial and final edge angles to approximately equalize horizontal and vertical focusing in the device. By switching off the first two dipoles, the second two are used as a spectrometer. The chicane in spectrometer mode has been used for preliminary beam energy measurements.

2.5 Beam Diagnostics

The main diagnostic used at Neptune for beam transport, spot size, and profile measurements is the phosphor screen. For this device phosphor is deposited on the downstream side of an aluminum foil mounted normal to the incident beam. A 45° mirror then directs light produced by the phosphor out to a CCD camera. From

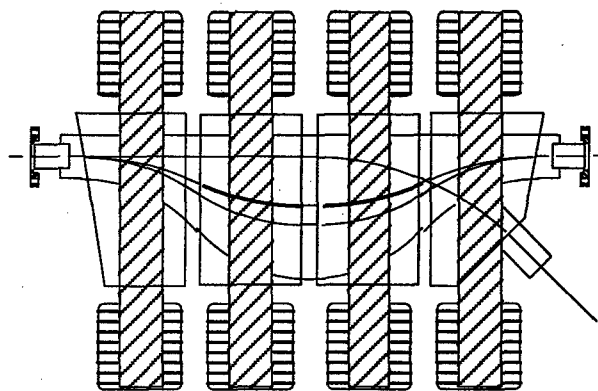


Figure 2: Chicane Compressor/Spectrometer

there the video data is digitized by a computer and analysis is preformed on the image. In addition to phosphor, beam spot screens using YAG crystals, which offer higher resolution and better vacuum properties, are active at Neptune.

To measure charge non-destructively we employ an integrating current transformer (ICT). This device produces data on a shot-to-shot basis and has been used at UCLA to measure charges from 10 pC to 5 nC [5]. For destructive bunch charge measurements Faraday cups mounted as beam dumps are used. The Faraday cups have been used for initial charge measurements at Neptune.

Transverse emittance measurements will be made using a slit based system [7]. In this system collimating slits are used to separate the beam into many beamlets whose intensity after propagation in a drift can be used to determine the phase space distribution of the initial beam.

To measure the longitudinal profiles produced at Neptune (< 1 psec after compression), a technique using coherent transition radiation (CTR)[8] will be employed.

2.6 Control System

The photoinjector control system begins with an Apple Macintosh computer. The computer has a video digitizing card which allows real time analysis such as dark current subtraction, spot size calculation, and emittance slit image analysis. Also, the computer is equipped with a GPIB interface which is used to import oscilloscope traces, and communicate with a GPIB controlled CAMAC crate. The CAMAC crate contains modules responsible for phosphor screen insertion, steering and quadrupole magnet control and read-back, chicane control, and rf attenuators and phase shifters.

3 PLANNED EXPERIMENTS

Before the PBWA experiment is ready to proceed, there is an opportunity to do experiments in the area of high brightness beam physics. Investigations in this domain will include parametric studies of the emittance compensation process, comparison of emittance

measurement techniques, and studies on the compressibility of pulses in the chicane as well as emittance growth in the chicane due to space charge effects.

3.1 Emittance Compensation Studies

Recent theoretical work has given a prescription for producing a minimum in transverse emittance in RF photoinjectors [9]. By varying the key parameters in this process, i.e. beam aspect ratio, solenoid field strength, and bunch charge, we plan to experimentally check this theory.

3.2 Emittance Measurement Techniques

The space charge dominated behavior of high brightness beams produced at Neptune can be seen through examination of the RMS envelope equation for a beam in a drift.

$$\sigma_x'' = \frac{\epsilon_n^2}{\gamma^2 \sigma_x^3} + \frac{4I}{\gamma^3 I_0 (\sigma_x + \sigma_y)} \quad (1)$$

Here the ratio of the space charge to emittance terms determines the character of the electron beam.

$$R = \frac{2I\sigma_0^2}{I_0 \gamma \epsilon_n^2} \quad (2)$$

For typical Neptune parameters $R \gg 1$ indicating a space charge dominated beam. Thus, any emittance measurement scheme based on beam propagation in a drift must take this ratio into account.

In the slit based measurement we see that the function of the slits is to produce beamlets for which this ratio is drastically reduced. For a uniform beamlet formed by a slit of width d , this ratio becomes

$$R_{\text{beamlet}} = \sqrt{\frac{2}{3\pi}} \frac{I}{\gamma_0} \left(\frac{d}{\epsilon_n} \right)^2 \quad (3)$$

For the slits installed at Neptune $d = 50 \mu\text{m}$ and $R_{\text{beamlet}} \ll 1$.

This emittance measurement system will be compared with the quadrupole scanning technique. In the quad scan procedure, the beam spot size is measured as a function of quadrupole field gradient. A purely emittance dominated beam under these conditions will behave such that the mean square beam size varies quadratically with the inverse focal length of the quadrupole lens. The transverse emittance is then calculated from the fit parameters of this curve.

We see from simulation how a space charge dominated beam can mimic the behavior of an emittance dominated beam in the quad scan procedure. Figure 3 shows this effect. At Neptune we plan to study this phenomenon and compare the results with an analytical model currently being developed.

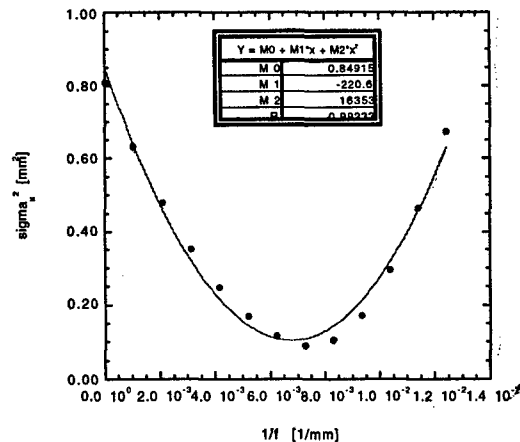


Figure 3: PARMELA simulation of a quad scan performed on a space charge dominated beam. The apparent emittance calculated from the quad scan is 4 mm mrad. The RMS emittance of the beam is actually 1.6 mm mrad.

3.3 Compressor Studies

In addition to basic studies on the compressibility of electron pulses, we plan to investigate the phenomenon of emittance growth in bends. Experiments in this area will be complimented by simulations using a three-dimensional code based on Lienard-Wiechart potentials [10].

4 INITIAL COMMISSIONING

The Neptune photoinjector was commissioned and photoelectrons were observed in early March 1999. The beam was accelerated by both structures and the chicane was used to measure an initial energy of 12 MeV.

5 REFERENCES

- [1] C. Clayton, *et al.*, *Nucl. Instr. Methods A* **410** (1998).
- [2] C. Clayton, *et al.*, *Phys. Rev. Lett.* **54**, 2353 (1985).
- [3] D. T. Palmer, *et al.*, *Proc. 1997 Particle Accelerator Conf.*, 2846 (IEEE, 1997).
- [4] R. Zhang, *et al.*, *Proc. 1995 Particle Accelerator Conf.*, 1102 (IEEE, 1995).
- [5] J. Rosenzweig, *et al.*, *Nucl. Instr. Methods A* **410** (1998).
- [6] E. Colby, *et al.*, *Proc. 1995 Particle Accelerator Conf.*, 1445 (IEEE, 1995).
- [7] J. Rosenzweig, *et al.*, *Nucl. Instr. Methods A* **341**, 379 (1994).
- [8] A. Murokh, *et al.*, *Nucl. Instr. Methods A* **410** (1998).
- [9] L. Serafini, *et al.*, *Proc. 1997 Particle Accelerator Conf.*, 2876 (IEEE, 1997).
- [10] F. Ciocci, *et al.*, *Nucl. Instr. Methods A* **393**, 434 (1997).

THE STATUS OF S-BAND RF GUN SYSTEM AT SRRC*

C. H. Ho*, S. S. Chang, J. P. Chiou, M. J. Horny, K. T. Hsu, S. Y. Hsu,
J. Y. Hwang, K. K. Lin, Y. L. Tsai, SRRC, Hsinchu, TAIWAN

Abstract

An S-band rf gun system is being developed at SRRC (Synchrotron Radiation Research Center), Taiwan. An XK-5 klystron (2856 MHz) and a TH2100A klystron (2998 MHz) will be used as the microwave sources. The modulator systems for both klystrons are being constructed at SRRC. The status of the rf gun and modulator systems are reported.

1 INTRODUCTION

Through the international collaboration on the X-band rf gun research project between SRRC and UC Davis [1-2], SRRC had acquired a lot of high power S-band rf components, including the XK-5 klystron (2856 MHz), TWT driver, and PFN components. For the short-term goal, we are going to assemble these components for delivering approximately 16 MW rf power by the end of year 1999. For the long-term goal, we are constructing a high power modulator similar to that for the SRRC booster linac system (2998 MHz), which is able to deliver 35 MW rf power. The completion date is set to be sometime in the year 2000. On successful commissioning of this home made modulator, it means our maintenance ability for the booster linac will be highly improved and the high power technology at SRRC be elevated to a new level. This in turn will definitely reduce the possibility for down time of our booster linac. On the other hand, it could also serve as the high power rf source for the rf gun research project when the booster is in normal operation. The main application of the rf gun at SRRC aims for the IRFEL. (Infra Red Free Electron Laser) in the near future. For a quick start, we are going to build a single cell S-band (2856 MHz) thermionic rf gun first. We expect to commission this gun with the XK-5 klystron modulator system very soon.

2 COLD TEST OF THE RF GUN

We have designed a single cell S-band (2856 MHz) rf gun using the code URMEL [3]. The cavity is a simple pill box type with 80.36mm diameter and 32.50mm cell length. A flat copper cathode with 15.50mm diameter was used for test purpose. A prototype copper cavity had been fabricated and brazed. Figure 1 shows the assembly drawing of the prototype gun. Three stages of vacuum brazing corresponding to three different melting

temperatures of brazing alloys (from WESGO company) were used to allow the fabrication of various components.

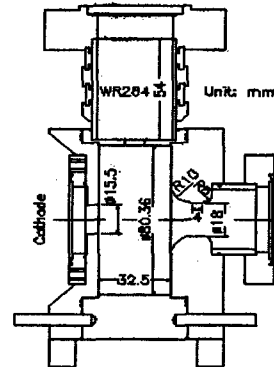


Figure 1: Assembly drawing of the gun cavity.

The first stage used 35/65 Au/Cu (35% Gold and 65% Copper) as the brazing alloy (melting temperature: 1010 °C) to braze the following three items: (1) WR 284 OFHC waveguide and SUS 304 Meridian flange (female), (2) Copper cathode plate and 35 CF flange (SUS 304), and (3) Copper plate and SUS 304 straight vacuum tube (1.5" O.D.) for electron beam exit. The second stage used 50/50 Au/Cu as the brazing alloy (melting temperature: 970 °C) to braze the following two items: (1) WR 284 waveguide and the surrounding enforcement copper bars (to prevent the waveguide deformation when evacuated), and (2) Cavity body, cathode plate, and beam exit plate. The last stage used Palcusil 15 (65% Ag, 20.3%Cu and 14.7%Pd) as the brazing alloy (melting temperature: 900 °C) to braze the cavity body and WR 284 waveguide together. After brazing, the cavity was vacuum tested using a Helium leak detector and found to be Helium leak tight to better than 10^{-9} standard c.c./sec.

The experimental arrangement for the bead pull measurement is shown in Fig. 2. A machineable ceramic (Aluminium Oxide) bead with 2 mm diameter was used as an axial cavity perturbation. The bead was drilled using an Nd:Yag laser, and supported by a nylon string with 0.1mm diameter. Two lab jacks were used to support and adjust the height of the gun body. One translator stage was used for the horizontal alignment and the other translator stage was used to pull the gun body so that we were able to position the ceramic bead at any position along the longitudinal axis of the cavity. The movement resolution of the translator stage is 0.01mm, while we only move the gun body along the longitudinal axis in

* Work supported in part by the National Science Council (Taiwan) under contract No. NSC88-2112-M-213-007.

* Email: chh@srcc.gov.tw

steps of 0.5mm. The bead-pull measurement result is shown in Fig. 3. We also show the consistency of the measured data with an URMEL calculation.

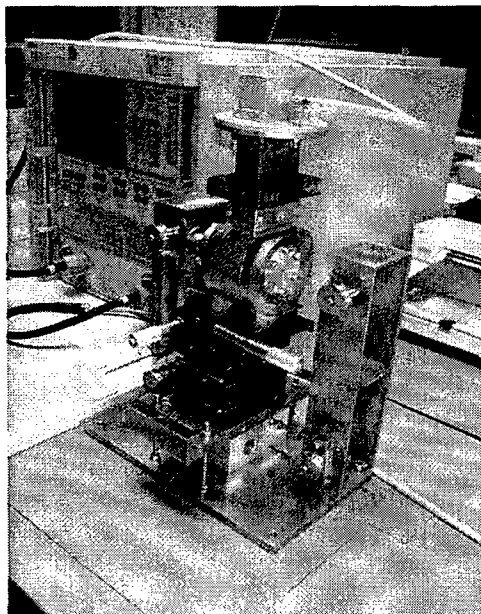


Figure 2: Bead - pull measurement setup.

An elliptical rf coupling iris was gradually enlarged to the length of the major semi-axis being 13.25 mm and the minor semi-axis being 4.90 mm before brazing. The coupling coefficient was found to shift from 0.8 (before brazing) to 2.1 (after brazing). The measured unloaded quality factor is 6740 after brazing.

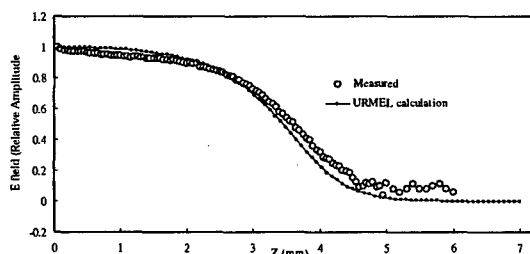


Figure 3: Longitudinal E - field profile on axis.

3 THE PFN TEST STAND

In order to provide necessary rf power in feeding the 2856 MHz rf gun cavity, a modulator was designed and built to power the XK-5 SLAC klystron. The circuit diagram of this S-band klystron modulator is given in figure 4.

The Spellman SR-6 DC charging power supply (PS) is used for testing purpose and is capable of delivering 0.2 A output current at 30 kV and up to 50 kV at smaller current. The CX1154 thyatron switch holds the high voltage at capacitors of pulsed forming network (PFN).

Protection of the DC PS and thyatron is accomplished with a charging inductor and diodes. PFN inductors are made of copper tube with 6 mm in diameter. Inductance tuning at nominal charging voltage is done by adjusting the position of short circuit clamp associated with every

inductor. The match resistor reduces power reflected from the circuit load. As the thyatron is triggered, the pulsed current from the PFN is fed into XK-5 klystron such that the low power driving rf signal can be amplified up to 16 MW [4]. Calculated current pulse from the PFN is optimized for the indicated load resistor and is shown in figure 5. Table 1 gives the technical specification of the designed modulator.

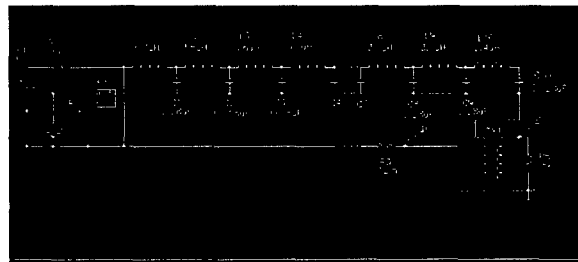


Figure 4: The circuit diagram of this S-band klystron modulator. It consists of 10 sections of LC circuit. Every individual inductor is tuned to obtain the required flattop pulse.

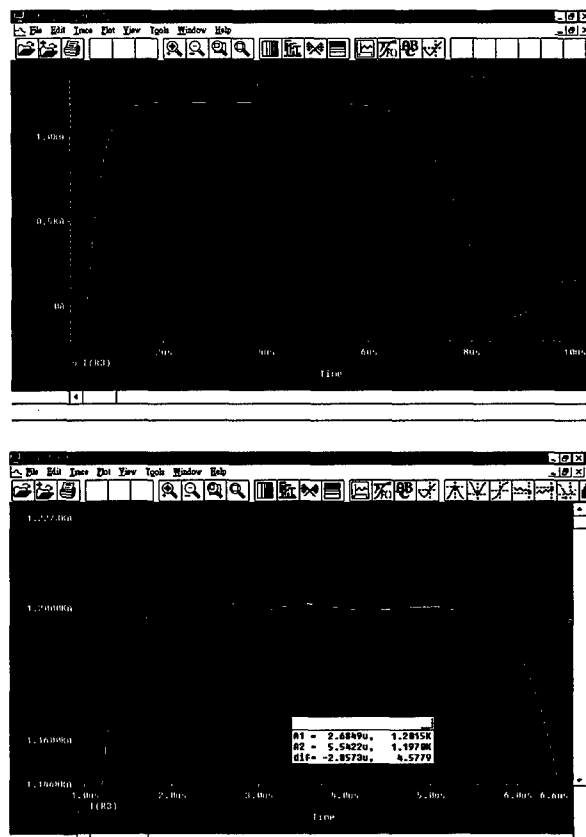


Figure 5: On top of the figure, the calculated current pulse from the PFN is optimized for the indicated load resistor. The expanded view of the flattop region is shown in the lower part. It indicates that a flattop with 0.5 % amplitude variation over 3 μ sec is estimated.

Figure 5 shows the PFN current feeding into the XK-5 klystron. The top of the figure gives the current pulse and the bottom shows its flatness is 0.5 % over 3 μ sec range.

Table I. Technical specification of S-band modulator

Design parameter		
PFN charging voltage (nominal)	30	kV
Output voltage (nominal)	15	kV
Repetition rate (nominal)	10	Hz
Pulse width (50%)	7	μsec
Rise time (10 – 90%)	< 1	μsec
Fall time (10 – 90%)	< 2	μsec
Pulse flatness (for 3 μsec)	< 0.5	%
Number of sections	10	

A preliminary test run of the constructed PFN system is given in figure 6. It gives the voltage pulse shape at the load resistor. This test run was done at charging voltage of 10 kV. Considering the flatness requirement, further adjustment of individual inductance at every section is necessary to improve the flatness of the pulse. It also indicates that adjusting the match resistor is needed to reduce the bump signal at the pulse tail.

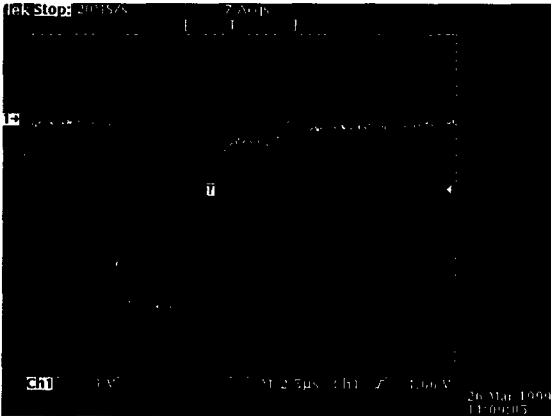


Figure 6: Preliminary test result of the PFN output voltage pulse at the load resistor. The charging voltage of this test is 10 kV.

4 SUMMARY

An S-band rf gun system is being developed at SRRC. Both 2856 MHz and 2998 MHz systems are considered. The rf cavity and the associated klystron modulator are under construction and fine tuning. The measured results on cavity E - field profile and modulator output pulse shape are compared with the calculation expectation. Tuning of each subsystem in further optimizing their performance is expected.

5 REFERENCES

- [1] C. H. Ho, W. K. Lau, T. T. Yang, J. Y. Hwang, S. Y. Hsu, Y. C. Liu, G. P. Le Sage, F. V. Hartemann, and N. C. Luhmann, Jr., "The Design and Fabrication of an X-Band RF Gun", AIP Conf. Proc. 398 for the Seventh Workshop on Advanced Accelerator Concepts (Lake Tahoe, California, 1996), p. 705.
- [2] E. C. Landahl, F. V. Hartemann, G. P. Le Sage, W. E. White, H. A. Baldis, C. V. Bennett, J. P. Heritage, N. C. Luhmann, Jr., and C. H. Ho, "Phase Noise Reduction and Photoelectron Acceleration in a High-Q RF Gun", IEEE Transaction on Plasma Science, Special Issue on High Power Microwave Generation, Vol. 26, No. 3, pp. 814-824 (June 1998).
- [3] U. Laustroer, U. van Rienen and T. Weiland, "URMEL and URMEL-T User Guide," DESY M-87-03 (1987).
- [4] S. Park and G. LeSage, private communication.

A LASER TRIGGERED ELECTRON SOURCE FOR PULSED RADIOLYSIS

H. Monard*, J.C. Bourdon, J. Le Duff, T. Garvey, B. Mouton, J. Rodier, Y. Thiery,
Laboratoire de l'Accélérateur Linéaire, Université de Paris-Sud, IN2P3 - CNRS, Orsay, France.
M. Gaillard,

Laboratoire de Photophysique Moléculaire, Université de Paris-Sud, IN2P3 - CNRS, Orsay, France.

Abstract

We present the design of a photo-injector based accelerator for pulsed radiolysis applications. This machine is destined to meet the needs of the physical chemistry community at the Université de Paris XI. A 4 MeV electron pulse of a few picoseconds duration and with a charge in the range of 1 to 10 nC is produced from a Cs₂-Te photocathode. The photocathode is placed in the half cell of a 1-1/2 cell, 3 GHz RF gun, whose design is based on the gun used for the drive beam of the CERN CLIC Test facility. A 4 cell "booster" cavity is then used to accelerate the beam to an energy of 9 MeV. The transport system consists of a quadrupole triplet downstream of the booster, two rectangular, 30 degree bend, dipoles with a pair of quadrupoles between them and a second triplet downstream of the second dipole. Energy dependent path length effects in the two dipoles allow the possibility of magnetic bunch compression depending on the phase-energy correlation of the bunch exiting the booster cavity. The beam envelope and the bunch length have been calculated through the transport line using TRACE-3d and PARMELA. These codes allow us to verify the required beam parameters at the experimental areas. We will discuss the adjustment of the optics, aimed at producing the minimum electron bunch length at the experimental targets.

1 INTRODUCTION

The project ELYSE aims to provide the physical chemistry community with a tool to study rapid chemical reaction dynamics. Chemical samples will be irradiated by a fast, high charge electron pulse and the resulting reactions will be analysed using a laser pulse synchronised with the electron beam. The necessity for both a laser and electron beam to perform such 'pump-probe' experiments suggests the use of a photoinjector for the electron beam, as the laser to be used as a probe can also be employed to produce the electron beam. The beam requirements necessary for ELYSE are given in table 1. Although the nominal charge per bunch is set to 1 nC one hopes to be able to produce more intense pulses (up to 10 nC) with similar pulse widths. In addition to these conditions there is a need to reduce the charge from the dark current arriving at the experimental samples to a level of < 1% of the charge of the primary beam. As the RF pulse width is

of the order of 3 μ s the dark current must not exceed a few microamperes.

Table 1: ELYSE beam specifications

Energy	4 - 9 MeV
Bunch charge	> 1 nC
Bunch duration	< 5 ps (FWHM)
Energy spread	< 2.5 % (RMS)
Normalised emittance	< 60 mm-mr (RMS)
Beam size on target	2 - 20 mm

2 THE ACCELERATOR

The layout of the accelerator, chosen to satisfy the ELYSE requirements, is shown in figure 1.

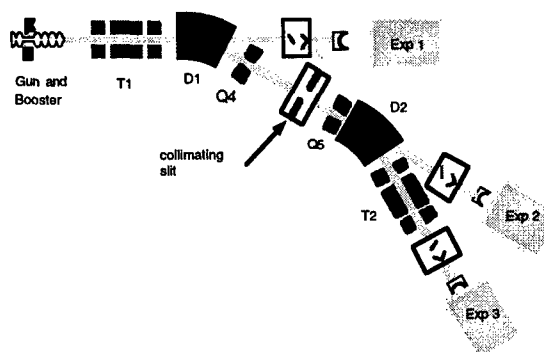


Figure 1. The accelerator layout.

It consists of a 1-1/2 cell RF gun, followed by a four cell "booster" cavity and a magnetic transport line to deliver the beam to one of three experimental areas (EA). The choice of the gun is based on the design used at CERN for the CLIC Test Facility [1]. The 1-1/2 cell gun will provide a beam of approximately 4 MeV while the booster cavity will allow further acceleration to 9 MeV. A solenoidal magnet is placed at the exit of the gun to focus the beam through the booster. The design of the transport line is chosen with two objectives in mind. The use of the two dipoles allows the dark current from the source to be filtered out before arriving at EA2 or EA3. If necessary, the collimating slit can further reduce the dark current but at the expense of losses in the primary beam. Secondly, the correlated phase-energy dependence of the

* Email : monard@lal.in2p3.fr

beam leaving the booster can be exploited to provide temporal compression of the bunches due to energy dependent path length effects in the transport line [2]. This will help to compensate space-charge effects which will tend to lengthen the pulse duration, particularly on EA1.

3 SIMULATIONS

2.1 The electron gun

As stated above, the electron gun is based on the design used at the CTF. Nevertheless, we have made slight modifications to allow operation of the gun at lower cathode gradients (65 MV/m) with the aim of reducing the dark current while still allowing transport of the high charge through the booster. Optimisation of the gun was performed with SUPERFISH. The calculated field distribution was then used as input for PARMELA calculations of the beam envelope. The magnetic field of the solenoid was calculated with POISSON.

2.2 The transport line

The design and calculated settings of the transport line were made bearing in mind that the most important parameter, for the experimental targets is the bunch length. The layout of the line is rather classical. The beam exiting the booster encounters a first quadrupole triplet followed by two dipoles with a pair of quadrupoles between them and, finally, a second triplet. The machine has a point of symmetry centered between the pair of quadrupoles. This means that the dipoles, quadrupoles and triplets are identical as are the lengths of the corresponding drift spaces

The RMS beam parameters at the exit of the booster, calculated using PARMELA, were used to provide input Twiss parameters for TRACE-3d in each of the phase spaces (x, x') , (y, y') and (ϕ, E) . TRACE-3d has the advantage of allowing quadrupole fitting procedures and permits one to quickly check on the transport. On the other hand, only the linear part of the space charge field is taken into account. For this reason, we used PARMELA to calculate the envelope through the entire machine with the quadrupole settings found using TRACE-3d. No major discrepancies are seen when comparing the transverse RMS beam envelopes. However, the final bunch length calculated with PARMELA appears to be slightly longer than that calculated with TRACE-3d. The difference may be due to the inclusion of the non-linear space charge fields when using PARMELA.

Now let us discuss the transport setting from the exit of the booster up to EA3. The phase space coordinates at the exit of the transport line, x_i , are related to those at the entrance, x_{0j} , by the transfer matrix R_{ij} using the equation,

$$x_i = \sum_{j=1}^6 R_{ij} x_{0j} \quad (i = 1, 2, \dots, 6),$$

where $x_i \equiv (x, x', y, y', \delta z, \delta p/p)$. First, we find the correct settings for the pair of quadrupoles (Q4 and Q5) in order to have the transport matrix elements $R_{51} = R_{52} = 0$. This setting makes the bunch compression independent of the geometric terms at the exit of the booster cavity. Moreover, it is also the correct setting for a first-order achromatic transport (neglecting space charge effects). The fields of the first triplet are then adjusted to give a reasonable value for the horizontal beam size between the two dipoles. Finally, the second triplet is set to deliver the required beam size, at EA3. It is then necessary to re-adjust Q4 and Q5 to maintain $R_{51} = R_{52} = 0$. If the gun and booster are adjusted to provide the required phase-energy correlation then bunch length compression occurs after the beam traverses the two dipoles.

2.3 The dipoles

The dipoles were designed with the 2D-codes POISSON and OPERA [3]. We have chosen to use rectangular, C-type magnets, with a 30° bend angle, and a bending radius of 500 mm. The main windings were calculated to produce a maximum magnetic field of 0.1 T. A secondary winding allows one to cancel remanent fields of the order of 20 G, in order to deliver the beam to experimental areas 1 & 2 when required.

2.4 Results

The initial conditions for the PARMELA calculation assume an RMS laser pulse, $\sigma_t = 1$ ps, truncated at $\pm 2.5 \sigma_t$. Figure 2 shows the phase-energy correlation at the exit of the booster for a 1 nC beam at 9 MeV. Even for the highest charge and lowest energies of interest, the beam exiting the booster meets the user requirements.

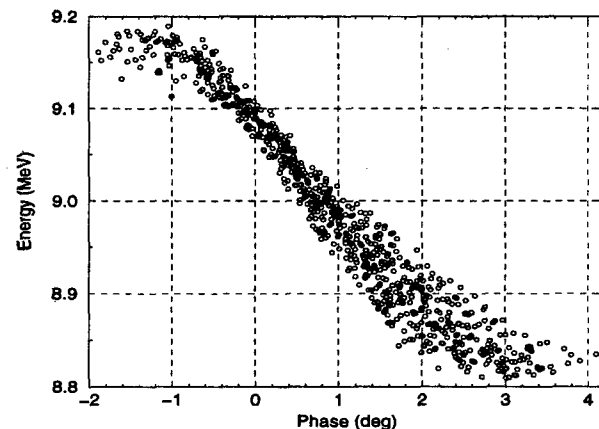


Figure 2. Energy-phase correlation at the booster exit.

The envelope of the same beam transported from the booster exit to EA3 is shown in figure 3. The calculated bunch compression in this case is 28% although we have shown that 50% can be achieved. At 9 MeV and 1 nC the

desired pulse length is obtained (see Table 2, figure 3). At the lower energy of 4 MeV we still manage to transport 1 nC to EA3 but we see that the space charge effects lead to a longer pulse.

Table 2. Parameters at EA3 for 1 nC charge.

Energy	4 MeV	9 MeV
σ_z	3.7 ps	0.8 ps
$\delta E/E$	3.6%	2.3%
RMS norm. emitt.	51 mm-mr	70 mm-mr

In contrast, we note that the charge of 10 nC cannot be transported without some loss in the second dipole. We continue to perform calculations to optimise the transmission at 10 nC.

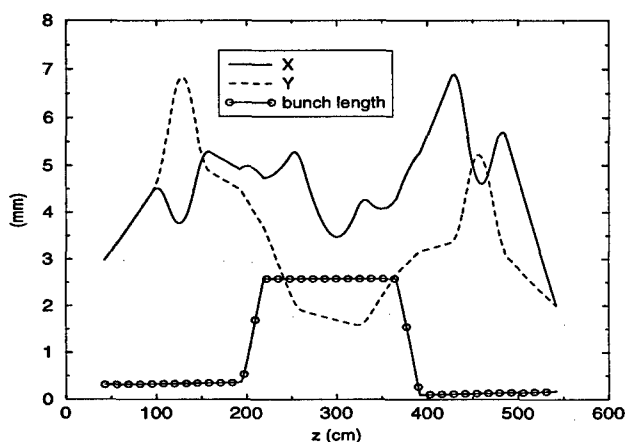


Fig. 3. The RMS values of the transverse and longitudinal dimensions of the beam through the transport line as calculated using TRACE-3d.

4 THE PREPARATION CHAMBER

As we aim to extract high charges (~ 10 nC) with a laser energy of ~ 50 μ J at 266 nm we choose to use a caesium-telluride photocathode. These cathodes, as well as having a high quantum efficiency ($>1\%$), are now known to have a long lifetime, of the order one month [4] and exhibit low dark current [1]. However, the choice of such a cathode requires the use of a dedicated preparation chamber. We plan to install a simplified preparation chamber based on the design of a new chamber currently being installed at CERN for the CLIC Test Facility probe beam [4].

5 PROJECT STATUS

In this paper we have mainly discussed the simulation work aimed at verifying that the desired beam performance can be obtained. In parallel with these calculations we have been making progress on the construction of the machine. Low level measurements have been performed on a prototype RF gun to fix the dimensions of the gun.

We will use a booster structure which already exists. The entire RF network for feeding the gun and booster has been ordered from industry as has the klystron. The modulator will be built in-house. The quadrupoles and solenoid are under construction in industry and the dipoles are out to tender. Once delivered they will be tested using the facilities at LURE. The magnet power supplies will also be built by a group from the LURE laboratory. Position and intensity instrumentation is being developed at LAL. The control system has been contracted to industry and is well in progress. The vacuum system has been designed and many components are already on site with others ordered. The LAL drawing office is working on the design of many of the mechanical components (vacuum chambers, diagnostic ports, supports etc.). ELYSE will use an entirely commercial laser which has already been delivered.

The facility will be housed in an existing building which is currently being renovated. Installation and 'first beam' are foreseen for the summer of the year 2000.

6 ACKNOWLEDGEMENTS

We are pleased to acknowledge the aid of R. Bossart and J.C. Godot of CERN for helpful discussions on the RF gun as well as G. Suberluq (CERN) for advice on the preparation chamber. We thank M. Corlier (LURE) for assistance in the specification of all the magnetic elements of ELYSE, and in particular for her aid in the dipole calculations. Finally, we thank H. Borie (LAL) for the preparation of the technical specifications for ELYSE components. Funding for ELYSE is provided by the CNRS, the MENRT, the Université de Paris-Sud, the Conseil Regional Ile-de-France and the Conseil General de l'Essone.

7 REFERENCES

- [1] R. Bossart et al., "Modular electron gun consisting of two RF sections and an intermediate focusing solenoid", Nucl. Inst. and Meth. A, Vol 340, pp 157-163 (1994)
- [2] M. Uesaka et al., "Precise measurements of a sub-picosecond electron single bunch by the femtosecond streak camera", Nucl. Inst. and Meth. A, Vol 406, pp 371-379 (1998).
- [3] H. Monard, "Etude des Dipôles pour l'accélérateur d'ELYSE", Internal Report, LAL/SERA, 99-30 (1999).
- [4] E. Chevallay et al., "Photocathodes for the CERN CLIC Test Facility", Proceedings of The 19th International Linear Accelerator Conference (Chicago), 1998.

INITIAL RESULTS OF RF GUN EXPERIMENT

H. Abe, T. Asaka, H. Hanaki, A. Mizuno, S. Suzuki, T. Taniuchi*, K. Yanagida,
SPRING-8, Hyogo 679-5198, JAPAN

Abstract

A photocathode RF gun was built and it has been operated for beam measurement at SPRING-8. The cavity was tested by using high power RF up to 18 MW. The electric field gradient on the cathode reached 127 MW/m. After RF conditioning, a laser pulse was irradiated on a copper cathode and the photo-emitted beam was accelerated up to 2.9 MeV. An effective quantum efficiency of the cathode was obtained by changing laser power and field gradient.

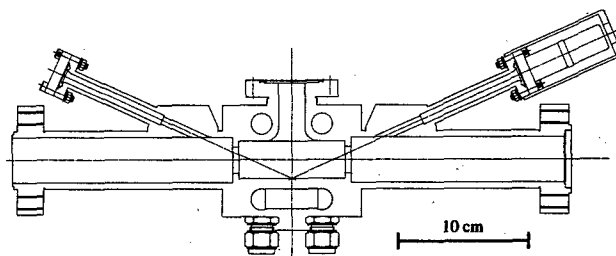


Figure 1: Schematic drawing of gun cavity.

1 INTRODUCTION

A photocathode RF gun is promising as an optional injector for the SPRING-8 linac since a much lower emittance than that of the present thermionic gun system is expected. This feature can enable such future applications of the linac as a single-pass FEL based on SASE, which requires lower emittance and shorter bunch length.

For the optimization of a realistic gun system, an experimental and a simulation[1] study are being conducted in parallel. The purposes of this experiment were to develop a reliable simulation code by comparison with experimental results, to confirm stable operation of the RF cavity under a high gradient field environment, and establish the effectiveness of surface treatment for the reduction of dark current. Furthermore, technical problems with operating an RF gun system were revealed. In this paper, the initial results of the experiment are described.

2 EXPERIMENTAL SET UP

2.1 Gun Cavity

A single-cell RF cavity[2, 3] was designed by using MAFIA[4]. The field distribution of a single-cell cavity is considered to be simpler than that of multi-cell cavities and preferable for comparison with the simulation results. The accelerating gap length was determined by TS2 simulation to minimize the emittance, and the dimensions such as coupling hole size and cell radius were obtained by a 3D solver. A schematic drawing of the cavity is shown in Fig. 1.

A cavity wall made of OFHC copper was used as a photocathode. Two quartz windows for laser injection were located with an angle of 24° from the cathode plane. Two couplers in this cavity were adopted to improve the field symmetry and shorten the filling time. The displacement of the field center from the geometrical center of the cavity was thus 0.13 mm, while it was 0.55 mm for the single coupler case. By connecting a dummy load to the output

coupler, the Q value of the cavity was reduced and the filling time was shortened. A shorter filling time enables a higher field gradient, more stable operation and reduction of dark currents. A higher gradient is needed to check the simulation results. The parameters of the cavity are summarized in Table 1.

Table 1: Parameters of high power model cavity.

Frequency	MHz	2856
Number of cells		Single
Accelerating gap	mm	28
Bore diameter	mm	20
Intrinsic Q value		13000
External Q value for output port		3684
External Q value for input port		2786
Loaded Q value		1414
Filling time	μsec	0.31
Shunt impedance (for $\beta=1$)	M Ω	1.16
$E_{\text{max}} / E_{\text{cathode}}$		1.09
Laser injection angle	[deg]	90 / 24

2.2 Laser

The seed laser used in this experiment was a cw mode-locked Nd:YLF laser (Lightwave Model 131) with a repetition rate of 178.5 MHz. A single IR pulse sliced by a Pockels cell was amplified by flash-lamp-pumped regenerative amplifiers at a repetition rate of 10 Hz. Then fourth harmonic photons were generated by two BBO crystals. A UV pulse with a wavelength of 262 nm and a pulse duration of 10 ps was transferred into the radiation-shielded area and focused on the gun cathode. The maximum energy of the laser pulse is about 2mJ at 262nm.

*Email: taniuchi@spring8.or.jp

2.3 RF System

A block diagram of the high power RF system is shown in Fig. 2. A 35 MW klystron was installed at the RF gun test area located in the Machine Laboratory Building next to the 1 GeV linac. RF power generated from the klystron is divided into two waveguides, and one is fed into the gun cavity while the other is fed into a dummy load. The RF power divider consists of a Magic Tee, a phase shifter and a 3 dB coupler and can divide power in an arbitrary ratio. There is an RF window between the waveguide system and the cavity. The vacuum pressure in the cavity is kept lower than 10^{-5} Pa by a 100 l/sec sputter ion pump. The RF power can be monitored through the directional couplers (DC1~5) shown in Fig. 2.

The klystron drive frequency of 2.856 GHz is generated by a 178.5 MHz RF signal from the seed laser.

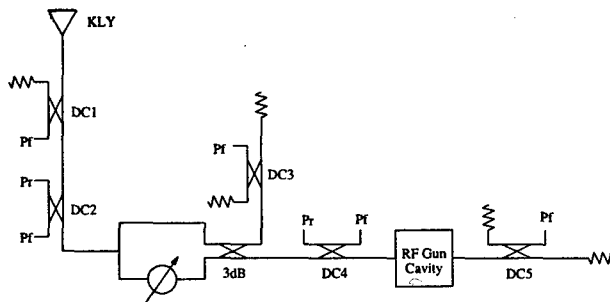


Figure 2: Block diagram of high power RF system.

2.4 Beam Diagnostic System

As shown in Fig. 3, the beam transport line consists of two solenoid magnets, two pairs of X-Y slits, a wall current monitor, two screen monitors, an energy analyzing magnet and a Faraday cup. All components are mounted on an optical table. We do not use a return yoke plate for the solenoid magnets, because the field distribution of such a coil can be solved easily and included into the simulation code. These magnets are only used to transport the beam with appropriate beam size but not optimized to minimize emittance. Two pairs of X-Y slits are used for emittance measurement.

During measurements mentioned below, it was found that the field distribution of solenoid magnets was distorted by the optical table made of magnetic material. As a result, a horizontal deflection of beam occurred. A steering magnet was installed to compensate the beam deflection due to the solenoid field. This optical table will be replaced by non-magnetic one.

3 HIGH POWER TEST OF GUN CAVITY

The RF conditioning of the cavity was performed with a pulse duration of 1 μ sec and a repetition rate of 10 Hz. The vacuum in the cavity was kept lower than 1×10^{-4} Pa

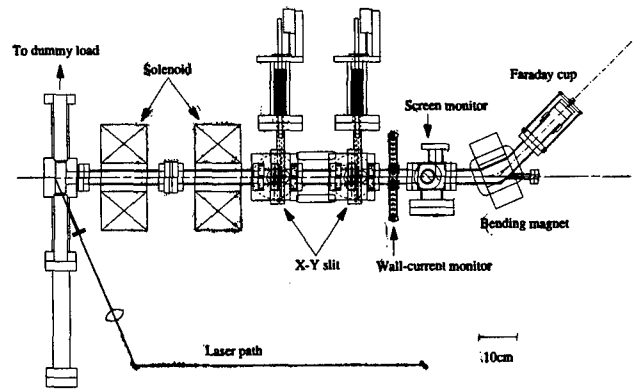


Figure 3: Top view of beam diagnostics system.

during the conditioning. The RF power fed into the cavity reached up to 18 MW after 6 hours operation. The maximum RF power was limited due to klystron problems.

Fig. 4 shows typical RF wave forms at the upstream and downstream of the gun cavity. The electric field strength in the cavity saturated within 1 μ sec, although some reflection effects could be seen on the wave forms due to the lack of an RF circulator. The pulse duration could be shortened during a single bunch mode to reduce dark currents and achieve more stable operation in a higher field gradient.

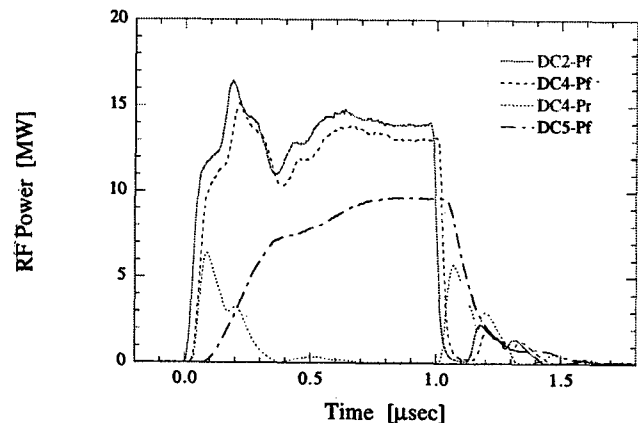


Figure 4: Typical RF waveforms observed by directional couplers shown in Fig. 2.

The dependence of the dark current on the field gradient is shown in Fig. 5. Dark currents were measured by using a Faraday cup directly connected to the cavity. The peak current increased exponentially with increasing the field gradient. It reached up to 10 mA when the field gradient was 121 MV/m. The dark current will decrease largely along the transport line with solenoid fields.

Since continuous RF breakdowns and beam loading effects on reflection and transmitted RF power from the cavity could not be seen at this power level, the field gradient could be further increased.

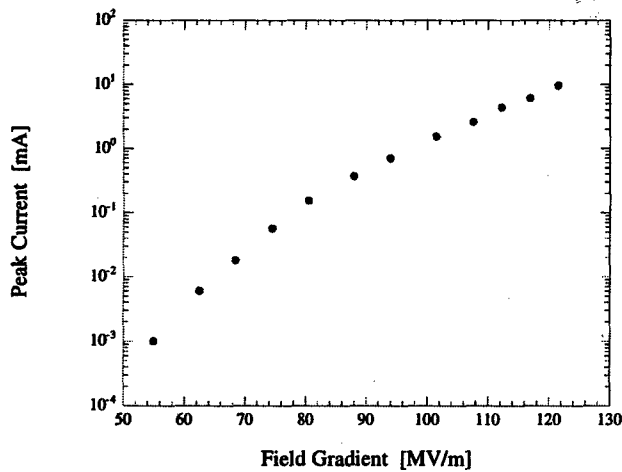


Figure 5: Dark current as a function of field gradient on cathode.

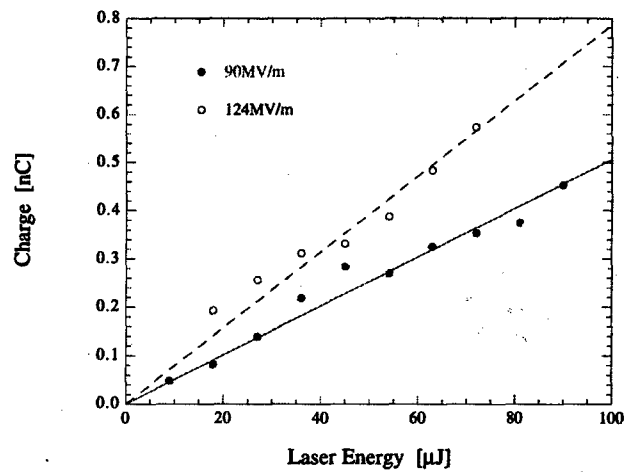


Figure 6: Beam charge per bunch as a function of irradiated laser energy.

4 BEAM MEASUREMENTS

4.1 Energy

After RF conditioning of the cavity, a laser pulse was irradiated on the cathode and the photo-electrons were accelerated. The center beam energy was 2.6 MeV and energy spread was about $\pm 10\%$ when the input RF power was 18 MW. The field gradient on the cathode reached 127 MV/m. These results agreed with the simulation results. A dependence of beam energy and energy spread on RF phase could not be obtained because of an asymmetry of solenoid field.

4.2 Quantum Efficiency

The effective quantum efficiency was measured by connecting a Faraday cup directly to the cavity. A pulsed signal of the current was flattened by an RC filter with a time constant of 1.7 second. The contribution of dark currents was subtracted. Fig. 6 shows the bunch charge as a function of irradiated laser energy when the field gradients were 90 and 124 MV/m. The RF phase was adjusted to obtain a maximum charge. From the slope of these data, the effective quantum efficiency for 90 MV/m case was found to be 2.4×10^{-5} . It was enhanced to 3.7×10^{-5} in the case of 124 MV/m by Schottky effect. Though laser power was enough to produce a charge of more than 1 nC at this condition, it could not be possible to transport whole charge against the space charge force without solenoid magnets. In order to improve the quantum efficiency, a laser cleaning of the cathode and change of laser polarizing angle will be effective.

5 CONCLUSIONS

The fabricated gun cavity has shown the expected performance in experiments conducted so far. The dependences among the field gradient, charge, RF phase, laser power and so on should be further studied and compared with the

simulation results. In order to investigate the beam characteristics in a higher field gradient, klystron power needs to be increased up to 35 MW. At this power level, the field gradient becomes about 180 MV/m. Measurement of the transverse emittance and bunch length will be major activities in the next phase of this experiment. Furthermore, another two cavities will be evaluated to confirm the effectiveness of surface processing on the reduction of dark current.

6 REFERENCES

- [1] A. Mizuno, et al., "Simulation for an rf gun test apparatus in the SPring-8 Linac", this conf., NY, (1999).
- [2] T. Taniuchi, et al., "Study of an RF Gun for the SPring-8 Linac", FEL conf., Rome, (1996).
- [3] T. Taniuchi, et al., "Design of High Power Model Cavity for RF Gun", FEL conf., Beijing, (1997).
- [4] M. Bartsch et al., Computer Physics Communications 72 , 22-39 (1992).

A High-duty 1.6 Cell s-Band RF Gun Driven By a psec Nd:YAG Laser*

Y. Aoki[#], J. Yang, M. Yorozu, Y. Okada, A. Endo /SHI, Yato, Tanashi, Japan/
T. Kozawa, Y. Yoshida, S. Tagawa /ISIR, Osaka Univ., Mihogaoka, Ibaragi, Japan/
M. Washio /RISE, Waseda Univ., Ohkubo, Shin-juku, Japan /
X.Wang, I. Ben-Zvi /ATF, BNL, Upton, NY/

2 RF GUN SYSTEM

Abstract

The performance tests were done for a 1.6 cell s-band BNL-type photocathode RF electron gun, GUN-IV, under a condition of 1.5MW RF power input and 266nm Nd:YAG laser pulse irradiation. As a result, the maximum energy and the maximum charge/ bunch were obtained as 1.6 MeV and 120 pC/bunch, respectively. In addition, a sinusoidal behavior of current with the polarization angle of laser light were measured. Furthermore, the change in current as a function of laser injection phase was measured and reasonably reproduced by a numerical calculation.

1 INTRODUCTION

Recently, photocathode RF electron guns are being vigorously developed by several groups for free electron laser, laser- and plasma- accelerations, laser Compton scattering experiments etc., since this kind of gun has several advantages. First, ultra-low emittance beam can be realised. And then, any bunching section is not necessary in an accelerator, energy spread can be largely suppressed, bunch length can be controlled by the pulse width of laser, the synchronization can be easily achieved with laser pulse, and so on.

A new BNL-type photocathode RF gun (GUN IV) was designed and constructed under the BNL/KEK/SHI international collaboration in 1997[1], based on the design of BNL-GUN III[2]. Here, the second generation of the GUN IV is introduced, which was manufactured by SHI for ultra-short X-ray pulse generation through the inverse Compton scattering [3,4].

In this paper, some results from the performance tests of this gun, such as the electron energy and the dependence of the beam characteristics on the parameter of laser injection, are shown. Though the designed peak power of RF pulse is 7MW, only 1.5MW power was fed into the gun due to the limitation of experimental setup. However, the results show the gun can be operated satisfactorily by such low RF power.

*This work was partially performed under the management of the Femtosecond Technology Research Association (FESTA) supported by the New Energy and Industrial Technology Development Organization Japan.

[#] Email: yss_aoki@shi.co.jp

Our gun system has almost the same structure as the first generation[1] and can be separated into a gun cavity (1.6 cell), a single emittance compensation solenoid magnet[5], a pair of dipole magnet and a vacuum pumping unit. The gun cavity has two s-band cells made of oxygen-free highly pure copper (class 1), called "half cell"(0.6 cell) and full cell (1.0 cell). These cells are directly-coupled. The half cell ended with the photocathode and have two optical ports for laser injection whose angle is 67.5° to the normal of the photocathode. On the other hand, the full cell has the beam exit and is connected with the waveguide for RF power input. Furthermore, this gun has three water cooling channels for the higher repetition rate in operation (high-duty).

The solenoid magnet is ca. 230mm long including yoke plates and directly connected with the gun at one-side. The magnetic field along the central axis of the solenoid coil was measured to be homogeneous over 100 mm in z-direction and at least 30 mm in the radial direction. The maximum field strength was 3 kG at 200A.

The dipole magnets for x- and y- direction are located in the hole of the solenoid magnet and have the common central axis in z-direction with the solenoid. The straight section of the coil is 100mm long and can give homogeneous field. The field strength shows a linear relationship with the current and 40G was measured at the current of 1A.

The gun cavity was directly pumped out by an ion pump (150 l/s) and the base pressure was achieved to about 1×10^{-6} Pa. An auxiliary turbo molecular pump system is set in the down stream of the solenoid coil. It is used only for starting up evacuation of the system.

3 ELECTRON BEAM GENERATION

The performance tests were done in the LINAC facility of ISIR, Osaka University. The power of input RF was measured through a directional coupler to be 1.5 MW. The laser which drives the gun was a 15 picosecond Nd:YAG laser which is developed especially for RF guns by Time Bandwidth Products (TBP) and Sumitomo Heavy Industries (SHI)[6].

The profile of electron beam was monitored by the combination of a phosphor plate, which is made of sintered Al_2O_3 doped with Cr, and a CCD camera (screen

monitor). Fig. 1 shows the optimal beam profile in the form of the cross sectional views along x axis(left) and y axis(right) obtained after the solenoid. The fitting of the profile with a gaussian curve resulted in the beam size of about $1.5\text{mm}\phi$ ($2\sigma_x=1.48\text{mm}$ and $2\sigma_y=1.53\text{mm}$).

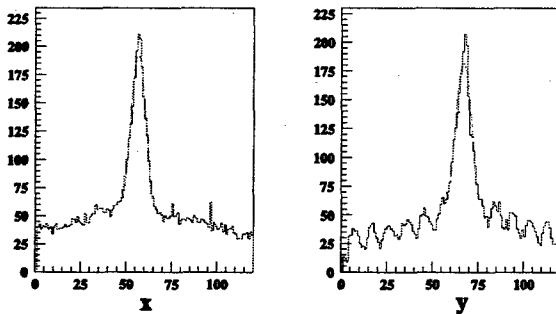


Fig. 1 The cross-sectional view of the optimal beam profile (x-axis:left, y-axis:right), observed on the screen monitor after the solenoid magnet. The dimension is described in unit of pixels (1pixel=0.287mm). The oscillation at low level in the right figure might be some back-ground frequency noise on measurement.

4 ENERGY MEASUREMENT

The energy of electron beam was measured by the steering action of the magnetic fields on the beam. In the measurement, the dipole(x) field was set and fixed to the appropriate value and the distance of the center in the beam profile from the original one ($B_{\text{dipole}(x)}=0$) was measured. Then, changing the solenoid field, the distance was measured. The results are seen in Fig. 2 with three simulation curves. The beam trajectory was calculated based on a simple Lorentzian eq. in the simulation for the electron beam energy of 1.5-1.7MeV.

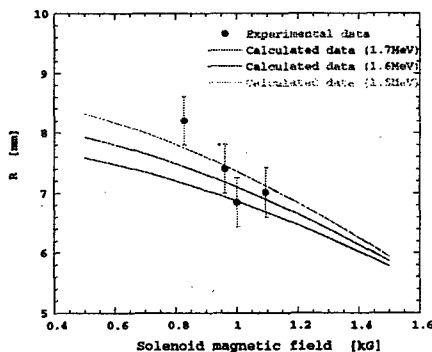


Fig. 2 The radial distance of the beam position from the original one, observed on the screen monitor. The solenoid field was changed while the dipole field was fixed. The simulation curves are for 1.5, 1.6 and 1.7MeV electron beams.

From this figure, in the case of 1.5 MW power input, approximately 1.6 MeV of beam energy was obtained.

At this energy, emission intensity was not so sufficient in the measurement then the data are relatively scattered. The error bars in Fig. 2 show the resolution of the CCD camera (1 pixel).

On the other hand, the maximum acceleration field in the gun is calculated to 17MV/m, using the RF power of 1.5MW. This acceleration field can give the energy of about 1.9 MeV which is not so different from the experimentally estimated above.

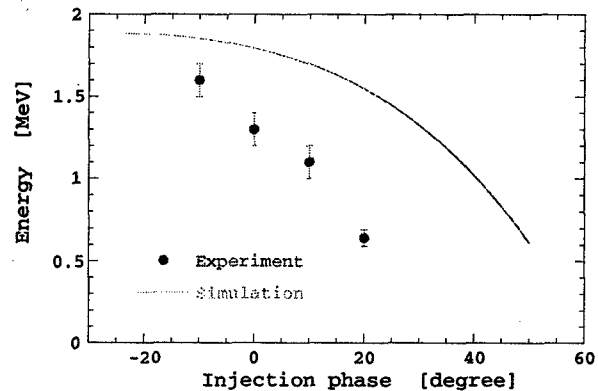


Fig. 3 The dependence of the electron energy on the laser injection phase. Error bars indicate the resolution of the CCD camera.

The dependence of the energy on laser injection phase was also measured. The trend of change in energy is similar to the curve from simulation which was done with the calculated acceleration field. The curve indicates that acceleration efficiency become lower by the phase change. The difference between the measured values and the simulated curve seems enhanced with increase in phase. It may come from scattering effects by residual gas, because the RF conditioning is not sufficient yet.

4 CHARGE MEASUREMENT

Current of the output beam was measured with a thick copper electrode ($10\text{mm}\phi$) with impedance-matched to 50 ohm which is located at 730mm from the photocathode. The charge of the bunch was estimated from the current, considering the repetition rate of 10 Hz and subtracting the dark current.

In Fig. 4, the measured charge is plotted as a function of laser injection phase. The simulated curve which is normalized at the maximum point is also shown in the figure. The maximum current was obtained at the phase somewhat before that giving the maximum field (phase =0). It is the same situation as in the case of energy, seen in Fig. 3. Over 30 degree in Fig. 4, a small peak appears. This may be because the RF power of 1.5 MW was used instead of the designed power of 7MW. It is suspected

that electron beam might have a complicated trajectory between the half cell and full cell.

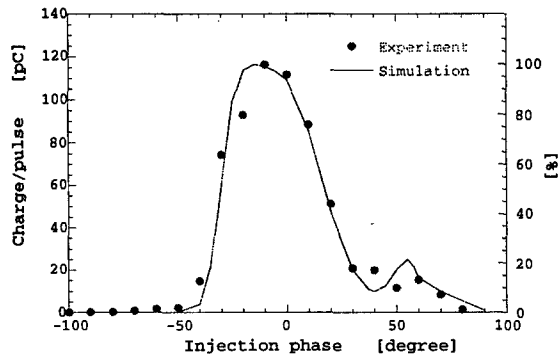


Fig. 4 The charge measurement as a function of the laser injection phase and the simulation curve.

The effect of polarization angle of laser light on the charge was measured by using a $1/\lambda$ plate. As shown in Fig. 5, sinusoidal change in charge was obtained. As Sakai et al. pointed out[1], since we inject laser pulse onto the photocathode, one directional component of the field of laser light may affect much largely on the photoemission process at the cathode. The maximum effect should be obtained at p-type polarization.

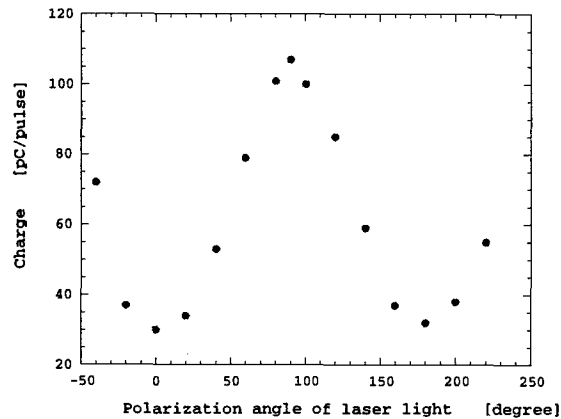


Fig. 5 The change in charge /pulse with the laser injection phase.

After a series of performance tests described above, we have got the optimum parameters for the solenoid field and for the laser injection to get the maximum electron charge from the gun. Finally, the maximum charge was recorded 120 pC/pulse at the solenoid field of 0.6 kG and the laser injection phase of -10 degree, while the dark current was 60 pC/RF pulse. As discussed on Fig. 4, the insufficient RF conditioning can make the gun performance worse. The relatively high dark current may come from this condition. In future, using high power RF,

the performance test including the emittance measurement and the bunch length measurement will be done and our project on ultra-short X-ray generation through the inverse Compton scattering will be proceeded.

5 CONCLUSION

The performance test of the second generation of GUN-IV was done with RF power of 15MW and Nd:YAG laser. The maximum energy and the maximum charge/pulse were 1.6MeV and 120pC/pulse, respectively. One of the most important advantage of RF gun is ultra-low emittance beam generation based on the large acceleration gradient ($>100\text{MV/m}$) induced by high power RF. Next step, we should perform this kind of experiment. But here, in other words, we demonstrated that the gun works well even with such low power RF (1.5MW).

6 ACKNOWLEDGEMENTS

The authors would like to thank Mr. Yamamoto and Mr. Saeki for their helpful, technical support in the performance tests.

7 REFERENCES

- [1] F. Sakai et al., The proc. 11th Symp. Acc. Sci. Tech., Harima, pp.473-475 (1997).
- [2] X. Wang et al., The proc. PAC '93 pp.3000-3002 (1993).
- [3] M. Washio et al., The proc. 7th China-Japan Bilateral Symp. Radiat. Chem., Chengdu, China (1996).
- [4] J. Yang et al, The proc. 6th EPAC, Stockholm, pp.1082-1084 (1998).
- [5] D.T. Palmer et al., The proc. PAC '97, Vancouver, pp.2843-2845 (1998).
- [6] F. Sakai et al., PAC '99, New York (1999).

THE DEVELOPMENT OF S-BAND PLANE WAVE TRANSFORMER PHOTOINJECTOR*

X. Ding, C. Pellegrini, J. Rosenzweig, S. Telfer, A. Tremaine, W. Vernon
Department of Physics and Astronomy, UCLA, LA, CA90095-1547

D. Yu, D. Newsham, J. Zeng, T. Lee, J. Chen
DULY Research Inc.

Abstract

An integrated S-Band RF photoinjector based on the plane wave transformer (PWT) is being built in the Particle Beam Physics Laboratory at UCLA in collaboration with DULY Research. This novel structure integrates a photocathode directly into a PWT linac [1] making the structure simple and compact. Due to the strong coupling between each adjacent cell, this structure is relatively easy to fabricate and operate [2]. This photoinjector can provide high brightness beams at energies of 15 to 20 MeV, with emittance less than 1 mm-mrad at charge of 1 nC [3]. These short-pulse beams can be used in various applications: space charge dominated beam physics studies, plasma lenses, plasma accelerators, free-electron laser microbunching techniques, and SASE-FEL physics studies [4]. It will also provide commercial opportunities in chemistry, biology and medicine. The present status of the PWT photoinjector including fabrication and cold test to characterise the structure is described. RF system and photocathode drive laser system are also discussed.

1 INTRODUCTION

The photoinjector concept was first proposed and experimentally tested at Los Alamos in mid-80s. Photoinjectors have proven their ability to produce very bright electron beams. The high brightness beams have several applications, such as self-amplified spontaneous emission free-electron lasers (SASE-FEL), Compton scattering sources, wake-field accelerator drivers, and linear collider sources of polarized electrons.

The conventional BNL/SLAC/UCLA 1.625 cell photocathode RF gun has been proved to be a reliable high brightness beam source [5], but the beam energy of this type of gun is relative low (4~5 MeV), it usually needs additional accelerating sections to get relative high energy. And due to its small cell-to-cell coupling and small mode separation (3 MHz), it is hard to make.

A new S-band photoinjector design is pursued by a UCLA/DULY Research collaboration. A novel compact standing wave RF structure (PWT) is integrated with a removable photocathode. This structure has great coupling between the accelerating cells. The mechanical tolerances for the PWT gun is much higher than those for

the BNL/SLAC/UCLA type gun, making it much easier to fabricate.

The S-band PWT photoinjector is a Small Business Innovation Research (SBIR) project proposed by DULY research Inc. teaming up with UCLA to develop a novel photoelectron linear accelerator. The goal of this project is to accelerate a short pulse (~5 ps), low emittance (~1 mm-mrad), high charge (1 nC) electron beam in a compact (~33 MeV/m), low-cost linear accelerator. The compact linac will have broad commercial and research applications.

A schematic of the PWT photoinjector is shown in Fig. 1. The structure consists of a cylindrical tank and an array of disks. There are totally 10 full cells and 2 half cells in the whole structure. The disks are connected together by 4 metal rods parallel to the axis. The disks are separated from the cylindrical tank, so they are like a centre conductor to support a TEM-like plane wave between the tank and disks. The field within the region of the disk is similar to a TM₀₁ mode, which can accelerate electrons on the axis. This structure transforms a transverse plane wave field into a field having a longitudinal electric component for acceleration of electrons. The feature causes the PWT structure to have the advantages of high shunt impedance and strong coupling between each cell. The PWT also provides good vacuum conductance and easy fabrication. But this structure also raises the concern about the field asymmetry caused by the four supporting/cooling rods. Our simulation and cold test shows this effect is negligible.

In this paper, we describe the RF structure design, focusing solenoid design, beam dynamics study, RF system, laser system and current status of the PWT gun.

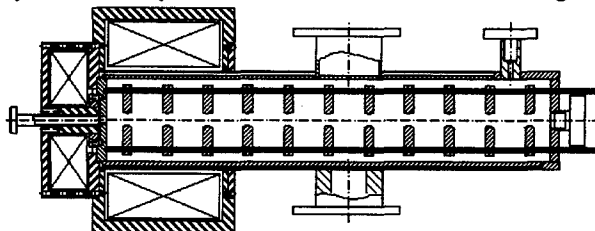


Figure 1: Schematic view of the PWT photoinjector.

*Work supported by U.S. DOE grants DE-FG03-98ER45693 and SBIR DE-FG03-96ER82156.

2 ELECTROMAGNETIC STRUCTURE DESIGN

The PWT structure is simulated by using both SUPERFISH and GDFIDL. The SUPERFISH code is a 2D electromagnetic field solver; it is helpful in finding dimensions of PWT for a given frequency. However, the metal rods cannot be included because the code is lack of ability to solve 3D problem. Therefore, the 3D code GDFIDL has been used to obtain a more complete picture of the RF field and it gives a more precise value of the properties of the RF structure.

Figure 2(a) shows a field plot from SUPERFISH and GDFIDL, a clear plane wave (TEM-like) pattern is shown between the outer tank and the disk assembly. The acceleration electric field distribution (TM01-like) is shown at the centre of the disk irises. Figure 2(b) shows the feature of electric field contours on the transverse cross-section at the centre of the full cell. It should be noted that the rods (not shown on Figure) only produce a minor on-axis perturbation on the field distribution for this operation mode. Especially for the field closed to the beam centre, this perturbation is negligible. A detailed study of this perturbation is shown in another conference paper by J.Rosenzweig et al [6].

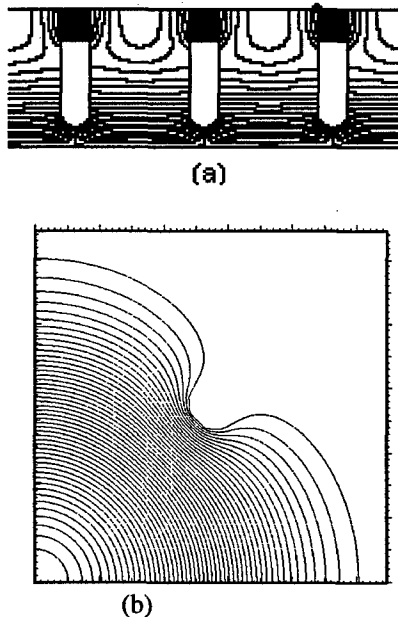


Figure 2: (a) Plots of the Electric field distribution of the operating mode at the on-axis cross-sections. (b) The feature of axial direction electric field contour.

In the beam dynamics simulation, we first make an electric field map from SUPERFISH and GDFIDL and a magnetic field map from POISSON. Then we run PARMELA to get a good electron beam simulation. This design is subject to the following constraints:

- Relatively high shunt impedance;
- Minimizing higher spatial harmonic content;
- Cell number and gradient appropriate to deliver 20MeV beam;
- Good coupling and high mode separation;
- Low transverse multipole content;
- Relatively low Q to allow for structure filling;
- Relatively small outer diameter to allow compact focusing solenoid;

Given all of these constraints, we have chosen an inner radius of the tank wall to be 5.5cm. Disks have donut shapes with ID irises of 1.6cm, which can minimize higher spatial harmonic content and provide 55MΩ/m shunt impedance. According to a recent analytical theory of emittance compensation, the solenoid magnetic field should start focusing as early as possible, and the emittance compensation prefers a relatively low field gradient. In our case we choose the on-axis maximum field to be 60MV/m. With a 24MW input power, we decide to use 10+2/2cells (57.75cm) structure to obtain 20MeV electrons. The coupling coefficient is mainly dictated by the distance from the outer radius of the disks and the inner radius of the tank. For the parameters we have chosen, the coupling was quite strong, with 0 and π mode separation about 400 MHz, 10/11 π and π mode over 8MHz. The quality factor Q is around 20,000. That allows for the structure filling time less than 4 μ s. A solenoid field map is shown in Figure 3.

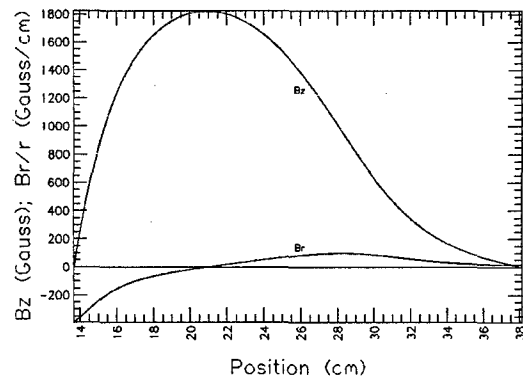


Figure 3: Magnetic field distribution along the axis.

3 BEAM DYNAMIC STUDY

The beam optics design is closely related to the RF structure design and the focusing solenoid design. The purpose of the beam dynamics design is for obtaining the highest brightness beam with minimal emittance. The basic technique for the beam dynamics design is experimenting with different electron input and electromagnetic fields layout, using code such as PARMELA to get the best beam output. Based on the Serafini and Rosenzweig (SR) theory, we can get good

emittance compensation if the beam profile follows the *invariant envelope*, which has the form:

$$\sigma = \frac{2m_e c^2}{E} \sqrt{\frac{I}{3I_0 \gamma(z)}} \quad (1)$$

where E is the average acceleration field, I is the rms current, and $I_0=17\text{kA}$. The theory prefers a low gradient (60MV/m) and a nominal launch phase $\phi_0=32^\circ$ to match the invariant envelope. Besides considering this matching, we also have other constraints in our beam dynamic design: beam charge 1nC to be ideal for FEL experiment, frequency 2856MHz to match the RF power provided by S-Band klystron, pulse length 9.8psec FWHM by availability of the laser source. Figure 4 displays the evolution of the rms beam size and emittance from the PARMELA simulation and invariant envelope equations.

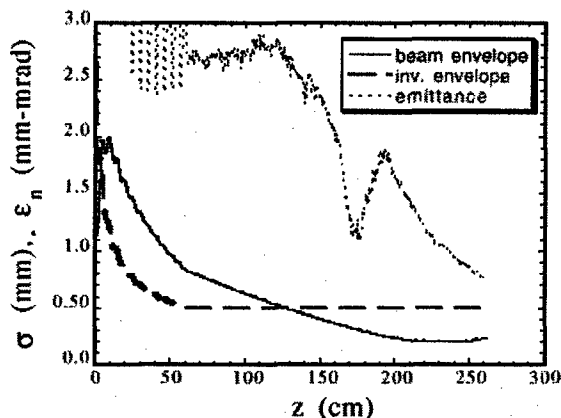


Figure 4: Comparison of beam envelope, emittance from PARMELA and invariant envelope from equation (1).

According to a scaling theory of RF gun design, this injector can also run at low charge (15pC), ultra-low emittance (0.06mm-mrad) mode, which can be used as an injector for the plasma beatwave acceleration and optical acceleration experiments.

4 THE COLD TEST RESULTS

To test what we found in the numerical simulation, a cold test piece that characterises the PWT structure was made. The test piece consists of 2 half cells shown in Figure 5. All measurements were done with a HP network analyser. The on-axis electric field distribution is measured by a bead-pull perturbation technique. To reduce the system error in the measurements, the room temperature has to be regulated with very small fluctuation. The π mode frequency from the cold test is 2856.556MHz. The GDFIDL simulation gives us 2855.820MHz for the chosen dimensions. The difference is less than 0.03%. We also measured the mode separation between the π mode and 0 mode which is over 400MHz. The real PWT structure has been machined and copper plated on the tank inner surface and metal rods. The whole structure (10 full cells and 2 half cells) will be brazed together and be tested soon.

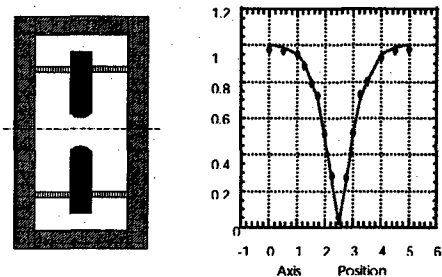


Figure 5: (a) Schematic of test piece (b) Electric field distribution on axis, line value from simulation, dot value from bead pull measurement.

5 SUPPORT SYSTEMS

5.1 RF Systems

The RF system supplies the power to drive the PWT gun. A 2856MHz low-level signal (~mW) is generated by the laser/timing system and amplified by a solid state amplifier to 300W. A SLAC XK5 type klystron driven by a modulator uses this signal to produce up to 24MW RF powers in a 4μs pulse. The output power is controlled by adjusting the high voltage supplied to the modulator. A high power isolator and a RF window are installed between the gun and the klystron to protect the klystron.

5.2 Laser System

A new Lightwave 131 laser with all-diode pumped Nd:YLF regenerative amplifier was developed and installed at UCLA, in collaboration with Lightwave electronics. This system provides 10ps FWHM pulses without CPA. Doubling crystals are available to provide UV conversion. We can get 300μJ UV (wavelength 263nm) pulse, more than enough energy to make the PWT gun to yield over 1 nC of charge from a copper photocathode.

6 REFERENCES

- [1] R. Zhang, R. Cooper and C. Pellegrini, "Study of a Novel Compact Standing Wave RF Linac", in course of publications in Nuclear Instruments and Methods in Physics Research, Section A (1996)
- [2] D.Yu, et.al. Proc. of the 1997 particle accelerator conf., 2802 (1997)
- [3] J. Rosenzweig, et.al. Proc. of the 1997 particle accelerator conf., 1968 (1997)
- [4] M.Hogan, et.al, Phys. Rev. Lett. 80, 289 (1998)
- [5] D.T.Palmer, et al., Proc. 1997 Part. Accel. Conf. 2687 (1998)
- [6] J. Rosenzweig, et al. Field Asymmetry Study, this proceeding

THE OPERATION OF THE BNL/ATF GUN-IV PHOTOCATHODE RF GUN AT THE ADVANCED PHOTON SOURCE*

S.G. Biedron*, G.A. Goepfner, J.W. Lewellen, S.V. Milton, A. Nassiri, G. Travish, X.J. Wang†, N.D. Arnold, W.J. Berg, M. Babzien†, C.L. Doose, R.J. Dortwegt, A. Grelick, J.N. Galayda, G.M. Markovich, S.J. Pasky, J.G. Power††, B.X. Yang

Advanced Photon Source, Argonne National Laboratory, Argonne, Illinois USA

† Accelerator Test Facility, Brookhaven National Laboratory, Upton, New York USA

†† Argonne Wakefield Accelerator, Argonne National Laboratory, Argonne, Illinois USA

Abstract

At the Advanced Photon Source (APS) at Argonne National Laboratory (ANL), a free-electron laser (FEL) based on the self-amplified spontaneous emission (SASE) process is nearing completion. Recently, an rf photoinjector gun system was made available to the APS by Brookhaven National Laboratory/Accelerator Test Facility (BNL/ATF). It will be used to provide the high-brightness, low-emittance, and low-energy spread electron beam required by the SASE FEL theory. A Nd:Glass laser system, capable of producing a maximum of 500 μ J of UV in a 1-10 ps pulse at up to a 10-Hz repetition rate, serves as the photoinjector's drive laser. Here, the design, commissioning, and integration of this gun with the APS will be discussed.

1 INTRODUCTION

The Advanced Photon Source (APS) at Argonne National Laboratory (ANL) is currently commissioning a free-electron laser (FEL) based on the self-amplified spontaneous emission (SASE) process [1]. This project, referred to as the APS SASE FEL, is designed to achieve saturation in the visible, UV, and ultimately VUV wavelengths. To assist in producing the beam required for saturation in the shortest possible distance, the APS has installed an on-loan copy of the Brookhaven National Laboratory/Accelerator Test Facility (BNL/ATF) high-brightness photoinjector, GUN-IV, at the head of its linac. This paper will discuss the gun design, drive-laser, integration with the APS systems, commissioning, and future plans.

2 RF GUN DESIGN

A performance enhanced version of the traditional BNL/ATF 1.6-cell 2856-MHz photocathode rf gun system [2] will be used. These enhancements include symmetrization of the rf fields [3] and an upgrade to

insure performance at high repetition rates [4]. The solenoidal field is used to control transverse emittance dilution [5].

3 THE APS DRIVE LASER

The drive-laser system consists of a mode-locked, diode-pumped Nd:Glass oscillator coupled to a Nd:Glass regenerative amplifier. The 119-MHz oscillator can produce 260 fs FWHM bandwidth-limited pulses centered at 1053 nm. The repetition rate of the oscillator is the 24th subharmonic of the accelerating field. The oscillator average output power is approximately 100 mW and is timing stabilized to < 1 ps rms. The regenerative amplifier is capable of producing 5 mJ in the IR and, after frequency quadrupling, ~500 μ J in the UV. During the amplification, some bandwidth is lost; therefore, the shortest pulse produced by the amplifier is roughly 1.5 ps FWHM. This is sufficiently short, based on the requirements of the photoinjector, and can be easily lengthened if so desired. The amplifier is capable of operating at up to 5 Hz, with a best effort repetition rate of 10 Hz.

4 PHOTOINJECTOR SYSTEM

Figure 1 shows the layout of the photoinjector at the APS. A copper cathode is used, since the energy output of the drive laser is capable of producing sufficient quantum efficiency with this metal. In addition, copper will reduce the amount of time dedicated to laser cleaning and cathode replacement, and, since it is robust compared to other commonly used cathode materials, such as yttrium (Y) and magnesium (Mg), will also reduce the risk of cathode damage. The gun is driven by the UV laser beam at near normal incidence from an input mirror just after the solenoid magnet as opposed to the more difficult 70° incidence through two available laser ports. This input mirror is mounted on a rotatable *in vacuo*, micrometer, which provides the vertical positioning of the mirror as well as the horizontal positioning of the laser.

*Work supported by U.S. Department of Energy, Office of Basic Energy Sciences, under Contract No. W-31-109-ENG-38.

* Email: biedron@aps.anl.gov

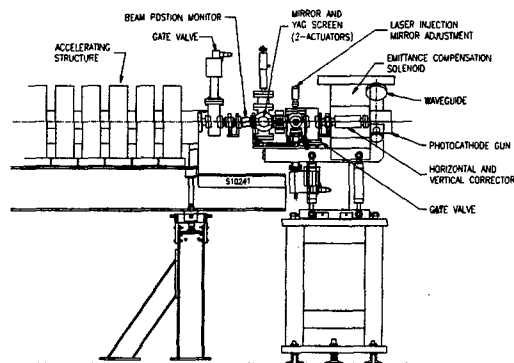


Figure 1: The photoinjector as installed in the APS linac

There is a vacuum pump on the gun itself, the waveguide, and immediately following the solenoid magnet. There are two gate valves: one just after the solenoid exit and one immediately following the beam position monitor. This allows for easy maintenance of the beamline components between the gun and the rest of the linac when needed.

Since the drive laser is not entering the gun via either of the 70° laser ports, the ports are instead used for a cathode inspection light and cathode imaging in the visible and UV. There are three corrector magnets: one inside the bore of the solenoid assembly, one immediately after the exit of the solenoid, and one just after the laser injection port. Just before this injection port is an integrating current transformer, and just downstream lies a two-way actuator assembly. One arm contains a YAG screen and the other maintains a mirror for additional cathode inspection. After the actuator assembly is a stripline BPM. Additional diagnostics include thermocouples for monitoring the gun and waveguide temperatures, rf power readbacks, and a heliax cable from the gun's rf pick-up loop for on-line cavity tuning.

6 RECENT RESULTS, PROGRESS, AND FUTURE PLANS

The BNL/ATF 1.6-cell 2856-MHz photocathode rf gun was fully conditioned with rf power in four days in December 1998 in a recently constructed rf test area. First photoelectrons were achieved with $\sim 25 \mu\text{J}$ in the UV (263 nm) on March 8, 1999, with 8 MW forward power at the gun. This translates into nearly 102 MV/m and 5.0 MeV electrons. Figure 2 shows the first captured image on the YAG screen of such photoelectrons. Many of the diagnostics listed above, other than the YAG screen, were not available in this rf test area, since they were being prepared for the photoinjector installation into the linac. The charge, therefore, was unfortunately not available in conjunction with these first electrons to compare with the total input photon energy. It was, however, estimated as $\sim 50 \text{ pC}$, derived from the work

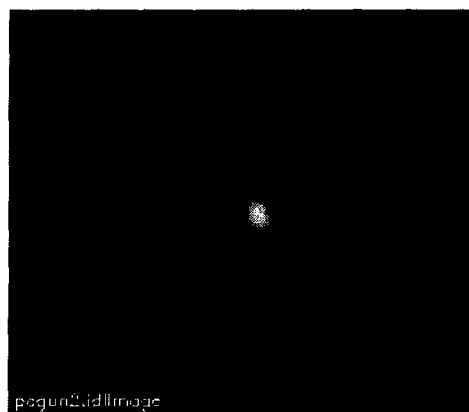


Figure 2: First photoelectrons; March 8, 1999

function of copper and a previously proven quantum efficiency of $\sim 1 \times 10^{-5}$, based on the preparation of this copper cathode [6]. The dark current was barely observable on the YAG screen. The purpose of this run in the rf test area run was to prove the operational readiness of the photocathode rf gun before installation into the linac.

The photoinjector system was installed at the head of the APS linac on March 12, 1999, replacing the original source, a thermionic DC gun, pre-buncher, and buncher. Here, the photocathode rf gun has a water flowrate of 6.1 liters/minute (1.6 gallons/minute) at a temperature of $50 \pm 0.1^\circ\text{C}$. The four water channels, which provide water to the cathode, half cell, full cell, and gun waveguide, respectively, have separate flow regulation to assist in maintaining the desired temperature stability. Additional thermal insulation has been installed around the gun. The solenoid is cooled to a temperature of $32 \pm 1^\circ\text{C}$. With respect to the waveguide system, there is a water-cooled rf window isolating the gun from the rest of the rf delivery system. Just after this window is a 3-dB hybrid that helps to reduce excess reflected power to the klystron. The modulator and klystron assembly are capable of providing 35-MW forward power with repetition rates up to 30 Hz and rf pulses ranging from 0.1-10 μs , which is well above the $\sim 8 \text{ MW}$ at 5-10 Hz in 1-3 μs required for optimal operation.

Before the waveguide between the gun's isolation window and the rest of the run were connected, a launcher was attached onto the isolation window. Two microwave measurements were then taken to insure the tune in the gun's cavities was correct after being moved and reinstalled. A 10-W amplifier was used to drive the gun through the launcher. The network analyzer measurements of the reflection (S_{11}) and transmission (S_{21}) were obtained and are shown in Figures 3 and 4, respectively. From these and previous measurements, we found a loaded Q of 5700 and, assuming a coupling beta close to one, yields an unloaded Q of ~ 11400 . The 0- and π - mode separation is 3.40 MHz.

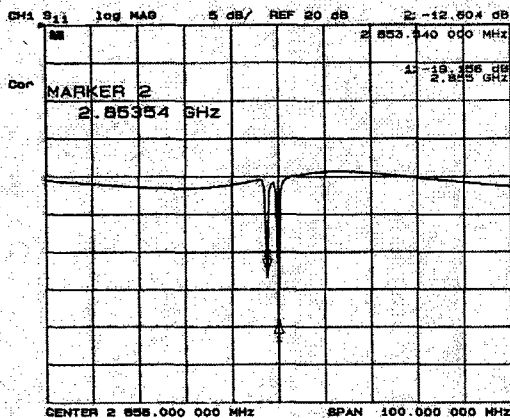


Figure 3: Reflection measurement

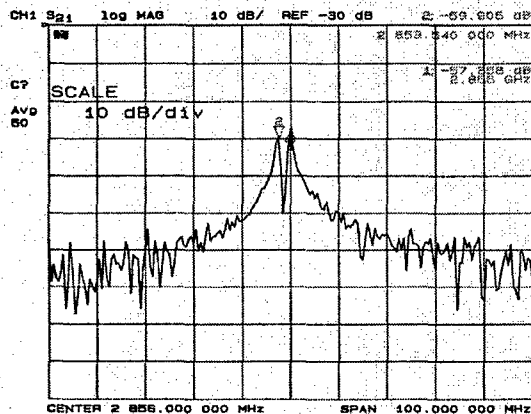


Figure 4: Transmission measurement

Previous to the photocathode gun installation at the head of the linac, two thermionic rf guns with corresponding alpha magnets were fully integrated into the linac. Their location is just downstream of the first SLAC-type, 3-m accelerating structure. They now serve as the primary injectors for the APS [7]. The second thermionic rf gun, nearest to the second downstream accelerating structure, was used to commission the APS SASE FEL beamline in February 1999. Although this thermionic rf gun will continue to be used in further APS SASE FEL commissioning, the BNL/ATF photoinjector will serve as the main injector for this project, since it is capable of producing the high-brightness, low-emittance, low-energy spread, and high peak current electron beam required to best satisfy the SASE theory [8]. The parameters of these two guns to be used with the APS SASE FEL may be found in Table 1.

Table 1: Expected photocathode rf and measured thermionic rf gun parameters

Parameter	Photocathode	Thermionic
Energy [gun exit]	5 MeV	5 MeV
Repetition rate	1-5 Hz	1-10 Hz
Emittance	3π mmmrad	10π mmmrad
Peak current	300 A	150 A
Energy spread	0.1%	0.5%

Preliminary alignment of the drive laser to the cathode center was performed during the March 1999 general maintenance period. The photocathode rf gun system verification and check-out is underway, and full commissioning of the linac and APS SASE FEL beamline with this new injector is expected to begin in April 1999.

6 ACKNOWLEDGEMENTS

The authors wish to thank all of the additional personnel at the APS, Argonne Wakefield Accelerator (AWA), ANL Chemistry, BNL, Positive Light, UCLA shops, and SLAC who contributed to the success of the integration of this system into the APS linac. This includes all engineering, laser, design, and technical support as well as secretarial assistance.

7 REFERENCES

- [1] S.V. Milton et al., "FEL Development at the Advanced Photon Source," Proceedings of Free Electron Laser Challenges II, SPIE, January 1999, to be published; S.V. Milton et al., "The APS SASE FEL: Initial Commissioning Results," these proceedings.
- [2] X.J. Wang et al., "Design and Construction of a Full Copper Photocathode Gun," Proc. 1993 Part. Accel. Conf. (1993) p. 3000.
- [3] D.T. Palmer, X.J. Wang, et al., "Beam Dynamics Enhancement due to Accelerating Field Symmetrization in the BNL/SLAC/UCLA 1.6 Cell S-Band Photocathode RF Gun," Proc. 1997 Part. Accel. Conf. (1997) p. 2846.
- [4] F. Sakai, X.J. Wang et al., "Development of High Duty Factor Operation RF Photoinjector," BNL-65003, Proceedings of the 11th Symposium on Accelerator Science and Technology, Spring-8, Hyogo, Japan, October 21-23, pp. 473-475 (1997).
- [5] B.E. Carlsten, NIM in Phys. Res. A285 (1989) 313-319.
- [6] T. Srinivasan-Rao, J. Yu, and X.J. Wang, "Study on the Sensitivity of Quantum Efficiency of Copper Photocathodes on Sample Preparation," BNL-62626 (1996).
- [7] J.W. Lewellen, S. Biedron, A. Lumpkin, S.V. Milton, A. Nassiri, S. Pasky, G. Travish, M. White, "Operation of the APS RF Gun," Proceedings of the XX International Linear Accelerator Conference, Chicago, Illinois, August 23-28, 1998, to be published; J.W. Lewellen, K. Thompson, J. Jagger, S.V. Milton, A. Nassiri, M. Borland, D. Mangra, "A Hot-Spare Injector for the APS Linac," these proceedings.
- [8] M. Babzien, I. Ben-Zvi, P. Catravas, J.-M. Fang, T.C. Marshall, X.J. Wang, J.S. Wurtele, V. Yakimenko, and L.-H. Yu, Phys. Rev. E 57, 6039, 1998

FIRST RESULTS OF THE FERMILAB HIGH-BRIGHTNESS RF PHOTOINJECTOR

J.-P. Carneiro, R. A. Carrigan, M. S. Champion, P. L. Colestock, H. T. Edwards,
J. D. Fuerst, W. H. Hartung, K. P. Koepke, M. Kuchnir, J. K. Santucci, L. K. Spentzouris
Fermi National Accelerator Laboratory,* Batavia, Illinois 60510 USA
M. J. Fitch, A. C. Melissinos P. Michelato, C. Pagani, D. Sertore
Univ. of Rochester, Rochester, New York INFN-Milano-LASA, Milano, Italy
N. Barov, J. B. Rosenzweig
University of California at Los Angeles, Los Angeles, Ca.

1 INTRODUCTION

A collaboration has been formed between FNAL, UCLA, INFN Milano, the University of Rochester, and DESY to develop the technology of an RF photoinjector, followed by a superconducting cavity, to produce high bunch charge (8 nC) with low normalized emittance ($< 20 \text{ mm} \cdot \text{mrad}$) in trains of 800 bunches separated by $1 \mu\text{s}$. The activities of the collaboration fall into two categories:

1. the development of Injector II for the TeSLA/TTF accelerator [1]. This photoinjector (*TTF RF Gun*) was tested at Fermilab in September and October 1998 and installed at DESY in November 1998.
2. the installation at the A0 Hall of Fermilab of a modified version of the TTF photoinjector, for photoinjector R&D and to study novel applications of high-brightness, pulsed electrons beams. This photoinjector (*A0 RF Gun*) produced its first beam in March 1999.

This paper presents a summary of the tests done at Fermilab on the TTF Injector II and the first results obtained on the new Fermilab photoinjector.

2 EXPERIMENTAL LAYOUT

The photoinjector consists of an RF gun with a high efficiency photocathode, driven by a Nd:YLF laser, followed by a 9-cell superconducting cavity and a magnetic chicane, composed of four dipoles, to compress the bunches. At the end of the beam line, a spectrometer magnet is used to measure the energy. The electrons are accelerated to 4-5 MeV in the gun and further accelerated to 14-18 MeV in the 9-cell superconducting cavity. The parameters of the photoinjector are summarized in Table 1. The upstream portion of the beam line is shown in Fig. 1.

2.1 RF Gun

The high duty cycle (1%) RF gun [2] consists of a standing wave structure with a one-and-a-half-cell cavity resonating in the π mode at a frequency of 1.3 GHz. The gun was designed to be operated at a nominal RF power of 4.5 MW for $800 \mu\text{s}$ at 10 Hz, which corresponds to an average power

*Operated by the Universities Research Association under contract with the U. S. Department of Energy.

Table 1. Injector II Parameters.

<i>Before compression</i>	
Bunches per macropulse	800
Macropulse spacing	100 ms
Bunch spacing	$1 \mu\text{s}$
Bunch charge	8.0 nC
Laser pulse length FWHM	28 ps
Beam radius at cathode	3.0 mm
Peak field on cathode (nominal)	35 MV/m
Beam total energy	18 MeV
Transverse emittance (normalized)	$11 \text{ mm} \cdot \text{mrad}$
Longitudinal emittance (100 % RMS)	$820 \text{ deg} \cdot \text{keV}$
Momentum spread	4.2%
Bunch Length	4.3 mm
Peak Current	276 A
<i>After compression, from theory</i>	
Transverse emittance (normalized)	$15 \text{ mm} \cdot \text{mrad}$
Bunch Length	1.0 mm
Peak Current	958 A

dissipation of 36 kW. The gun is cooled via channels machined into the walls, with 4L/s of water flow. In order to obtain a high brightness and low emittance beam, the emittance growth due to mainly linear space charge must be reduced. To reduce the linear space charge, a high gradient is used ($E_c=50\text{MV/m}$ at 4.5MW and 35MV/m at 2.2MW) and, as required by the Carlsten emittance compensation scheme [3], a focussing solenoid (divided into a primary and a secondary solenoid) surrounds the gun, as shown in Fig. 1.

2.2 Laser

A Cs_2Te photocathode [4] located in the first half-cell of the gun produces photoelectrons when illuminated by a 263 nm wavelength light (fourth harmonic of the Nd:YLF laser). The laser [5] was designed to produce a train of up to 800 equal amplitude, $10 \mu\text{J}$ UV pulses spaced by $1 \mu\text{s}$ at 1 Hz repetition rate. The laser pulse length is adjustable to 1-20ps FWHM at Fermilab and to a longer length at DESY.

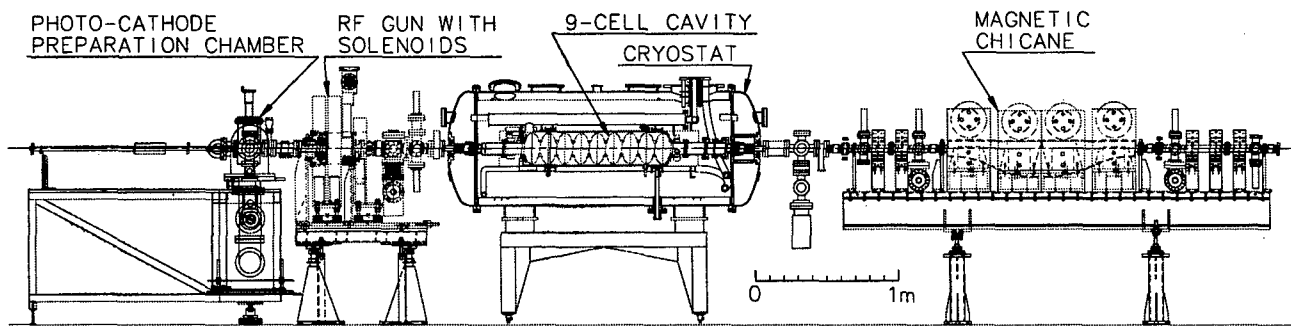


Figure 1. A0 beam line layout.

2.3 Nine-cell Cavity

The superconducting accelerating cavity is a 9-cell Nb structure [1]. Sub-systems include a high-power coaxial input coupler ($Q_{ext} = 10^6$ to $9 \cdot 10^6$), a cold tuner (range $\approx \pm 400$ kHz), and 2 coaxial higher-order mode couplers. The cavity is a prototype fabricated by industry for TTF. It was etched, rinsed, heat treated, and tested with RF at DESY. The cavity is one of a batch with low quench field (13 MeV/m in CW for this cavity), attributed to contamination in the electron beam welds at the equator. The horizontal cryostat was designed at Orsay [6] for the TTF capture cavity and built by industry. The cavity and cryostat were assembled at Fermilab, cooled to 1.8 K, and tested with RF, as well as beam [7].

3 TTF RF GUN

Using a molybdenum cathode, the TTF RF gun was conditioned with an RF pulse of 3.4 MW (the maximum power available from the klystron) for 100 μ s at 1 Hz repetition rate, providing an RF field of 44 MV/m on the cathode. At 800 μ s, the peak power was limited to 2.8 MW at 1 Hz due to trips. Dark current associated with field emission was observed with a Faraday cup on an actuator located about 40 cm from the exit of the gun. The integrated Faraday cup signal indicated 0.4 mA of dark current with an electric field of 40 MV/m on the cathode. With a Cs_2Te photocathode, the gun was operated at 3 MW with 100 μ s at 1 Hz. RF trips limited the power to 2.2 MW at 800 μ s and 1 Hz. However, measurements with the Faraday cup showed a decrease of the dark current: 0.08 mA at 40 MV/m on the Cs_2Te photo-cathode.

The dark current was significantly smaller for the TTF gun than the first prototype gun [8]. The decrease may be explained by careful cleaning of the TTF gun and the installation in the beam line under a HEPA filtered laminar flow and by the use of a different type of spring around the photocathode.

Electron beam measurements were made at Fermilab on the TTF RF gun. Pulse trains of 800 bunches at 1 Hz with 0.3-0.4 nC per bunch were accelerated, as shown in Fig. 2. Other experiments with 1-10 bunches per train at 1-10 nC per bunch were carried out to characterize the gun. Phase scans of the gun showed a phase acceptance of 100° . The energy measurements were done with 35 MV/m on the cathode, producing electrons with a total energy of 4.3

MeV (according to the PARMELA code [9]); the 9-cell had an accelerating gradient of 14.5 MV/m. Electrons of total energy of 19.3 MeV were expected and measured at 18.5 MeV. The uncertainties in the measurement of the electric field and in the calibration of the spectrometer are sufficient to account for this difference.

4 AO RF GUN: FIRST RESULTS

After the modulator and the TTF gun were sent to DESY, the A0 RF gun was installed in its place, following the same procedures as for the TTF RF gun. A new modulator was installed at A0, with a maximum RF pulse length of 600 μ s and 1 Hz repetition rate. It was operated with pulse lengths of up to 400 μ s.

Thus far, we have been able to power the A0 RF gun with the maximum output of the klystron, i.e 3 MW, at 400 μ s and 1 Hz. Dark current measurements were done with a Faraday cup at the same location as for the TTF RF gun. At 37 MV/m on the cathode (2.44 MW of forward power), a current of 0.05 mA and 0.06 mA was measured with the molybdenum and the Cs_2Te cathodes, respectively. The values of the dark current for the A0 RF gun are thus comparable to those of the TTF RF gun.

Preliminary measurements with beam in the A0 RF gun have been done. Phase scans were made, measuring the charge in the Faraday cup versus the phase of the RF relative to the laser. Results showed a phase acceptance of 100° . The phase that gave the maximum amount of charge was chosen for operation. Once the gun phase was fixed, we measured the energy of the beam versus the phase of the 9-cell (Fig. 3), with 35 MV/m on the gun and 7.8 MV/m of accelerating gradient in the superconducting cavity. The total energy of the beam was expected to be 12.4 MeV and we measured 13.7 MeV. As for the TTF RF gun, uncertainties in the calibration of the spectrometer and in the measurement of the field level are enough to explain this difference.

5 FUTURE EXPERIMENTS

5.1 Tests on the A0 RF Gun

Beam dynamics studies will be done on the A0 RF gun. The transverse emittance will be measured via emittance slits located after the quadrupole triplet. A quadrupole scan emittance measurement will also be carried out. A 2 ps streak camera will be used to measure the longitudinal emittance of the beam and the longitudinal compression of

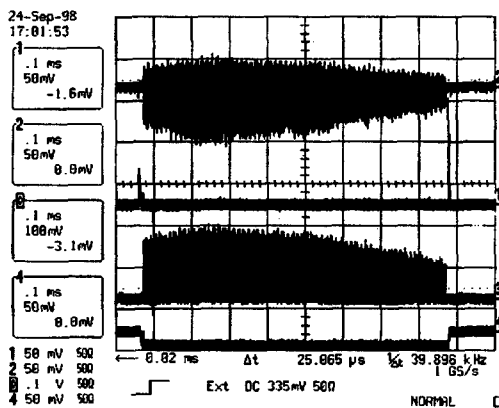


Figure 2. Scope traces for 800-bunch operation of the TTF RF gun, showing the laser photo-diode signal (channel 3) and the Faraday cup signal (channel 2).

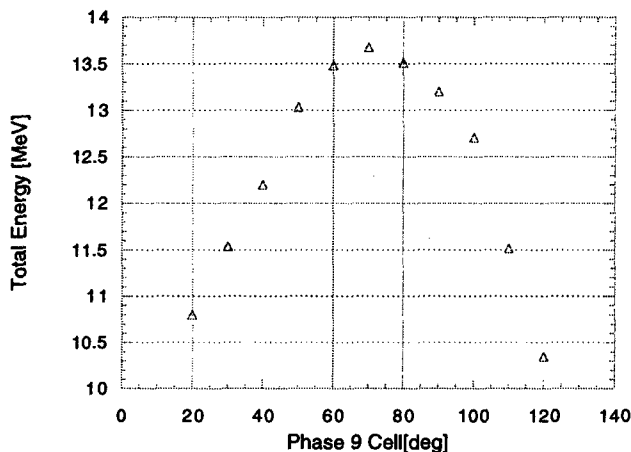


Figure 3. Energy of the beam versus phase of the superconducting cavity.

the chicane. These quantities will be measured as a function of beam parameters, charge, and solenoid strength, among others.

5.2 Bunch Length Measurement by Electro-Optic Sampling

The electro-magnetic field of a 10 nC electron bunch will be detected using the electro-optic effect [10]: the polarization of a picosecond IR probe laser pulse is modulated as the laser pulse and the beam field propagate collinearly in a LiTaO₃ crystal. By scanning the relative delay, the bunch length and temporal profile can be obtained.

5.3 Plasma Wake Field Acceleration

The photoinjector will be used to carry out a test of plasma wake-field acceleration. In this acceleration scheme, a high brightness relativistic electron beam is injected into a underdense plasma (having density less than the density of the beam). The plasma electrons are ejected from the beam's path to form an ion channel. A second bunch is injected at the correct time to be accelerated by the plasma wave, typically 1 ps after the drive beam pulse. In an under-

dense plasma, the plasma focuses and accelerates the second bunch. Gradients up to 1 GeV/m are expected.

5.4 Crystal Channeling Experiment

While gaseous plasma acceleration gradients can be very large, gradients from solid state plasmas could be even larger, in the range of 10 GeV/m. Solid state plasma acceleration conditions can be reached with the A0 beam. However, at the plasma densities required for acceleration, there are severe limitations. Crystal channeling has been discussed as a method to mitigate the problems associated with the solid state plasmas and also introduce focussing [11]. There have been no studies of the channeling process under these conditions. A Darmstadt-Fermilab group is preparing an experiment to observe channeling at A0 under conditions required for solid state acceleration. This experiment will look for quenching of channeling radiation as the bunch intensity is increased. If the initial experiment is successful, solid state acceleration may be attempted in a later stage.

6 REFERENCES

- [1] D. A. Edwards, Ed., "TeSLA Test Facility Linac—Design Report," TeSLA 95-01, DESY (1995).
- [2] Eric R. Colby, Ph. D. Thesis, UCLA (1997).
- [3] B. E. Carlsten, *NIM*, **A285**, 313 (1989).
- [4] A. Fry *et al.*, "Experience at Fermilab with High Quantum Efficiency Photo-Cathodes for RF Electron Guns", presented at the 1998 Linac Conference.
- [5] Alan R. Fry, Ph. D. Thesis, University of Rochester (1996).
- [6] S. Buhler *et al.*, in *Proc. of the 7th Workshop on RF Superconductivity*, CEA/Saclay 96 080/1 (1996), p. 689-693.
- [7] W. Hartung *et al.*, "Beam Test of a Superconducting Cavity for the Fermilab High-Brightness Electron Photo-Injector," these proceedings.
- [8] J.-P. Carneiro *et al.*, TM-2067, Fermilab, to be published (1999).
- [9] B. Mouton, "The Parmela Program, V5.03", SERA/97-85, LAL/Orsay (1997).
- [10] M. J. Fitch *et al.*, "Picosecond electron bunch length measurement by electro-optic detection of the wakefield", these proceedings.
- [11] P. Chen and R. Noble, in *Advanced Accelerator Concepts*, S. Chattopadhyay, J. McCullough and P. Dahl, Eds., AIP Press C398, New York (1997), p. 273.

DESIGN AND CONSTRUCTION OF A HIGH CHARGE AND HIGH CURRENT 1 - 1/2 CELL L-BAND RF PHOTOCATHODE GUN*

M.E. Conde⁺, W. Gai, R. Konecny, J.G. Power and P. Schoessow

Argonne National Laboratory, Argonne, IL

Abstract

The Argonne Wakefield Accelerator has been successfully commissioned and used for conducting wakefield experiments in dielectric loaded structures and plasmas. Although the initial wakefield experiments were successful, higher drive beam quality would substantially improve the wakefield accelerating gradients. In this paper we present a new 1-1/2 cell L-band photocathode RF gun design. This gun will produce 10 - 100 nC beam with 2- 5 ps rms pulse length and normalized emittance less than 100 mm mrad. The final gun design and numerical simulations of the beam dynamics are presented.

1 INTRODUCTION

High current short electron beams have been a subject of intensive studies [1]. One of the particular uses for this type of beam is in wakefield acceleration applications. High current (kA) short electron beam generation and acceleration did not materialize until the advent of RF photoinjector technology[2]. Although most photocathode RF gun development has been concentrated on high brightness, low charge applications such as free electron laser injectors, there have been several relatively high charge rf photocathode based electron sources built and operated[3,4,5]. In general, there are two approaches to attaining high peak current. One approach is to generate an initially long electron bunch with a linear head-tail energy variation that is subsequently compressed using magnetic pulse compression. The advantage of magnetic compression is that it is a well-known technology and can produce sub-picosecond bunch lengths. However, due to strong longitudinal space charge effects, this technology is limited to relatively low charges (<10 nC).

Another approach is to directly generate short intense electron bunches at the photocathode and then accelerate them to relativistic energies rapidly using high axial electric fields in the gun [3]. The advantage of this approach is that it can deliver very high charges, for example, 100 nC if one uses an L-band gun. This would satisfy the requirements of most electron driven wakefield experiments for both plasma and dielectric structures, if the pulse length is short enough (< 10 ps FWHM). So far,

the Argonne Wakefield Accelerator (AWA) has demonstrated the capability of producing 100 nC, 25 — 35 ps (FWHM) electron beams at 14 MeV. This unprecedented performance was obtained using a half cell photocathode gun cavity and two standing wave iris-loaded linac sections [6]. The AWA machine has reached its design goal and has been used for dielectric wakefield [7] and plasma [8] experiments. The initial results are encouraging [9]. Achieving higher gradients in wakefield experiments would require the drive electron pulse to be even shorter and have a lower emittance. In this paper, we discuss the design of a new RF photocathode gun with the capability of producing 10 - 100 nC with 2 - 5 ps (rms) pulse lengths.

2 DESIGN CONSIDERATIONS

In order to generate high charge and short bunch lengths from a photocathode RF gun, the electric field on the cathode surface has to be very intense. In this way the electrons leaving the cathode surface are quickly accelerated to relativistic velocities, minimizing the bunch lengthening and the emittance growth that the space charge forces produce [10,11]. There is also bunch lengthening and transverse emittance growth at the exit iris of the gun cavity due to the defocusing forces of the RF fields. Thus, this effect also calls for high accelerating gradient and high beam energy at the exit of the gun. It is therefore desirable to have a multicell gun with high accelerating gradient. Practical considerations (mainly a finite amount of RF power) limit the design to 1 - 1/2 cells. The choice for our new gun design is a Brookhaven type 1- 1/2 cell cavity [12] scaled up to L band operation. This gun will be followed by one of the present linac tanks that exist at the AWA facility.

A detailed numerical study [13, 14] of this gun was performed with the computer codes SUPERFISH and PARMELA [15]. Table 1 summarises the parameters used in the simulations. These extensive numerical simulations showed a strong dependence of bunch length and emittance with respect to the accelerating gradient in the gun cavity. Based on these studies, it was decided that an accelerating gradient of 80 MV/m on the cathode surface was a good operating point. This requires 10 MW of RF power to be coupled into the gun cavity, which still leaves enough power to run one of the linac tanks. This accelerating gradient yields good values of emittance and bunch length, while still not high enough to make the RF conditioning of the gun a challenging task. (In fact, we

* This work is supported by the Department of Energy, High Energy Physics Division, Advanced Technology Branch under the Contract No. W-31-109-ENG-38.

⁺ Email: conde@hep.anl.gov

recently conditioned a duplicate of the present AWA gun up to a gradient of 125 MV/m [16].)

TABLE 1. The gun design parameters as calculated using SUPERFISH

Inner Radius of the Cell, b (cm)	9.03
Radius of the iris, a (cm)	2.75
Width of the iris, d (cm)	1.5
Aperture of the exit (cm)	2.5
Operating frequency (GHz)	1.3
Initial beam radius (cm)	1
Quality factor, Q	26008
Shunt impedance (M Ω /m)	36.47

3 REALIZABLE GUN DESIGN

In order to reach a design that can actually be built, one has to take into account all the other constraints besides the optimization of the electron beam parameters. There must be enough space around the gun to allow for a waveguide to couple RF power into the cavity. Space must also be available for tuning plungers, RF pickup probes, vacuum pumping and cooling channels. All these space requirements limit the size and constrain the location of the solenoids. Certainly one must also be careful not to

drive the solenoid steel into saturation.

Figure 1 shows a drawing of the complete gun and solenoids design. Two solenoids are exactly next to each other, with the photocathode plane as their plane of symmetry. This maximizes the space available for the RF power coupler over the full cell of the gun. The tuning plunger in the full cell is located diametrically opposite to the RF coupler, both being at the equator line of the full cell. An RF pickup probe is located half way along the circumference of the full cell between the RF coupler and the tuning plunger. The half cell has both the tuning plunger and the RF pickup probe on the back plate of the cell. This breaks the symmetry of the half cell, but it is acceptable in our L-band size cavity. The perturbation of the field lines over the relatively small size cathode area is negligible. The tuning plungers and RF pickup probes will allow us to verify and, if necessary, to adjust the parameters of the two cells, in order to achieve the right resonance frequency for the π mode and field balance in the cavity. The cooling channels are drilled along the cylindrical wall of the gun, and also run over part of the back and front plates of the cavity.

Numerical simulations of this final design yield values for the emittance and bunch length that are slightly worse than the ones obtained in reference [13, 14]. This results from the fact that the location and dimensions of the solenoids are not dictated only by the optimization of the beam parameters, but also by other physical constraints.

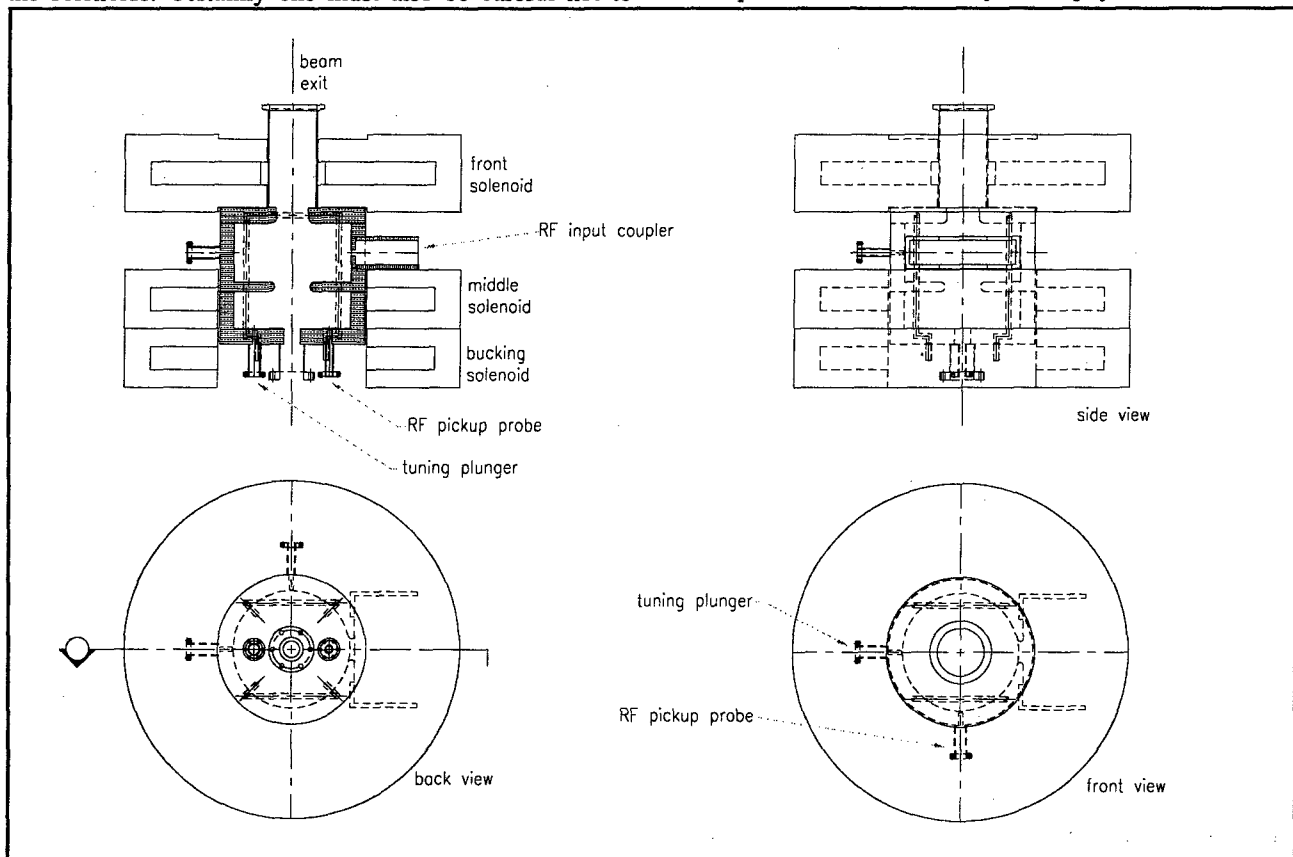


Figure 1: Photocathode RF gun

The degradation is however very small, and the gun is still expected to generate very short bunches with low emittance. Results of numerical simulations with PARMELA are shown in Fig. 2. These plots show emittance, bunch length, energy and radial coordinate as a function of the longitudinal coordinate along the accelerator for a bunch charge of 40 nC. At the exit of the linac the code predicts a normalized rms emittance of 66 mm mrad and an rms bunch length of 3.7 ps.

4 DISCUSSION AND SUMMARY

We have reached a final design for the new AWA photocathode RF gun. This gun will dramatically improve the capabilities of our program to study wakefield acceleration in dielectric loaded structures and plasmas. The electron beam produced by this gun is expected to excite wakefields in plasmas with accelerating gradients in excess of 1 GeV/m with a plasma density of $\sim 10^{14}/\text{cm}^3$.

In dielectric loaded structures, this beam will also make a significant improvement over present attainable gradients. One can use this beam to directly demonstrate collinear wakefield acceleration gradients in excess of 50 MV/m corresponding to 200 MW of RF power generated in 30 GHz dielectric structures.

It is worth pointing out that the present AWA photocathode RF gun has achieved unprecedented values of charge per bunch, and has allowed us to advance the understanding of wakefield acceleration in plasmas and in

dielectric structures. However, the present gun was designed when only a very limited amount of RF power was available for the experiment (2 MW). Thus, the beam parameters, namely, bunch length and emittance, suffered serious limitations due to this relatively low level of RF power. The newly designed gun will take advantage of the higher level of RF power now available in the facility, yielding better beam parameters and, consequently, higher accelerating gradients in the wakefield acceleration experiments.

5 REFERENCES

1. C. Travier, Proceedings of Advanced Acceleration Concepts Workshop, Edited by P. Schoessow, AIP Proceedings, No. 335, p.57, 1994.
2. J. Fraser *et al.*, IEEE Trans. Nucl. Sci., NS-32, p.1719 (1985).
3. P. Schoessow *et al.*, Proceedings of Particle Accelerator Conference, p.976, 1995.
4. B. Carlsten, *et al.*, Proceedings of Particle Accelerator Conference, p.985, 1995.
5. E. Colby *et al.*, Proceedings of Particle Accelerator Conference, p.967, 1995.
6. M.E. Conde *et al.*, Proceedings of Particle Accelerator Conference, p.1996, 1997.
7. P. Schoessow *et al.*, Proceedings of Particle Accelerator Conference, p.639, 1997.
8. N. Barov, M.E. Conde, W. Gai, J. Rosenzweig, Phys. Rev. Lett., Vol. 80, No. 1, p.81, 1998.
9. P. Schoessow *et al.*, Journal of Applied Physics, Vol. 84, No. 2, p.663, 1998.
10. K.J. Kim, Nuclear Instrumentation and Methods, A275, p.201, 1989.
11. L. Serafini, J. Rosenzweig, Physical Review E, Vol. 55, No. 6, p.7565, 1997.
12. K. Batchelor *et al.*, Proceedings of European Particle Accelerator Conference, p.541, 1990.
13. W. Gai *et al.*, Nucl. Instr. and Meth. A 410, p.431, 1998.
14. W. Gai *et al.*, Proceedings of Advanced Acceleration Concepts Workshop, Baltimore, 1998.
15. SUPERFISH and PARMELA, Los Alamos National Lab. Report LA-UR-96-1834, 1997 and LA-UR-96-1835, 1996.
16. C.H. Ho *et al.*, Proceedings of Linac98 Conference, Chicago, 1998.

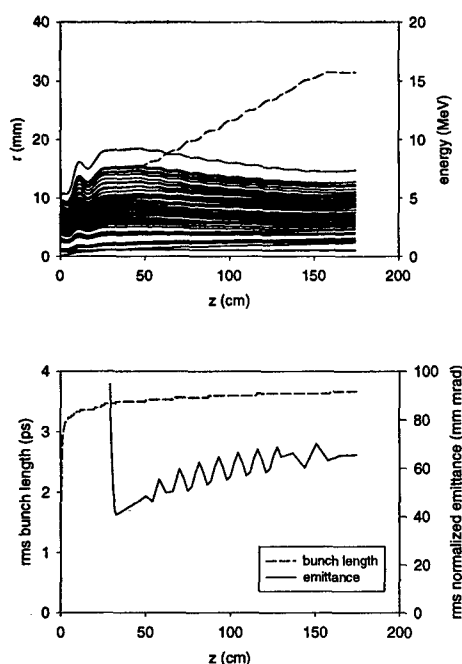


Figure 2: Numerical simulations of the beam along the gun and linac structures: (a) energy and trajectories in the transverse plane; (b) bunch length and emittance.

A SUPERCONDUCTING RF GUN CURRENT STATUS OF THE DROSSEL COLLABORATION

D. Janssen^{*}, FZ Rossendorf, Germany

Bushuev, M. Karliner, S. Konstantinov, J. Kruchkov, O. Myskin, V. Petrov, I. Sedlyarov,

A. Tribendis, V. Volkov, BINP, Russia

P. vom Stein, H. Vogel, ACCEL Instruments, Germany

A. Matheisen, M. Pekeler, DESY, Germany

W. Sander, I. Will, MBI, Germany

Abstract

The Drossel collaboration [1] was established for the development a low emittance, high average current, cw electron injector [2] suitable for the ELBE project [3,4]. The injector is based on a photocathode rf gun with a superconducting cavity. A half-cell 1.3GHz superconducting niobium cavity incorporated with a normal conducting cathode unit was designed and produced to check the basic design concepts. Cold rf tests of the cavity at T=2K were successfully carried out at DESY TTF. Now preparation of the necessary components for the beam tests is in progress.

1 INTRODUCTION

The Drossel collaboration between FZR and BINP started in 1996. Recently more organisations joined the collaboration. The basic idea of the project is to combine high brightness of an rf gun with low rf losses of a superconducting cavity. A design of a 1.3GHz, 3+1/2 cell rf gun was worked out. The geometry of the 3 full cells is based on the TESLA design [5] to simplify the production. The shape of the half cell is optimised. A Cs₂Te photocathode placed at the half cell back wall will be activated by an ultraviolet laser. The photolayer will be deposited on the tip of an OHFC copper stem in a special preparation chamber. The stem can be then transferred to the cavity by a manipulator. It will require neither any vacuum break nor cavity warm up to change the cathode.

2 HALF CELL PROTOTYPE

A prototype of the gun based on a half cell niobium cavity was developed to test the design solutions and to prove the compatibility of a photocathode and a sc cavity.

2.1 Design Considerations

The half cell cavity (fig. 1) is somewhat simplified compared to the optimum one in order to use an available

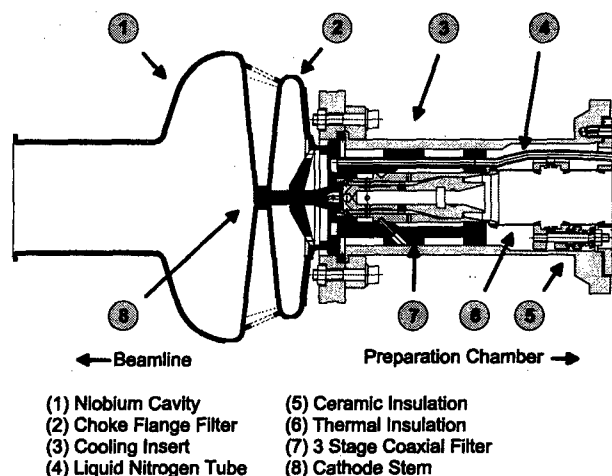


Fig. 1. Draft of 1/2 cell prototype.

TESLA endcup. Some parameters of the prototype cavity are listed in table 1.

Table 1. Prototype cavity parameters.

Material	
Cavity	Niobium (RRR > 250)
Cathode Stem	OHFC Copper
Operating Temperature	
Cavity	2K
Cooling Insert	77K
RF Parameters	
Frequency	1300MHz
Geometry Factor	187.7Ohm
R/Q*	120.5Ohm
H _{peak} /E _{cath}	2.84mT/(MV/m)
E _{peak} /E _{cath}	1.37

$$* R/Q = U_{gap}^2 / (2 \cdot P_{diss} \cdot Q)$$

A key part of the design is a special cathode support structure. The photolayer deposited on a copper stem will operate at 77K. All the power dissipated in the cathode will be removed by LN₂ neat exchanger attached to the cathode holder. The cathode holder is thermally and electrically isolated from the sc cavity and so causes only minimum additional heat load to the cavity and He bath.

* Email: janssen@fz-rossendorf.de

Rf power leakage from the cavity to the cathode holder is prevented by a niobium choke flange filter accompanied with a normal conducting coaxial filter which is a part of the cooling insert.

2.2 Cavity Preparation and Test Results

A few micrometers was etched away from inner and outer surfaces of the welded cavity at BINP. Then the cavity received a rough chemical treatment at FZR. Approximately 100Å was removed from the inner surface. The final preparation of the cavity to the tests, including baking at 800°C, light 1:1:2 BCP, high pressure rinsing and clean room assembling, was done at DESY. Two cold tests were carried out at DESY up to date. In the first run the cavity was tested without the cathode in it to evaluate the achievable gradient. A maximum surface field of 36.1MV/m was reached limited by field emission (fig. 2). Because of a very weak coupling during the first test the emitter could not be processed. Prior to the second test the cavity received a light BCP and a high pressure rinsed again. An uncoated copper cathode stem

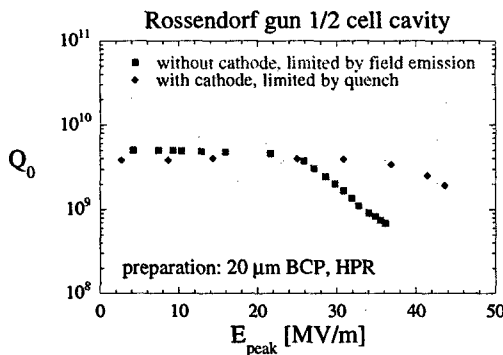


Fig. 2. Vertical test results.

was mounted directly to the cavity back flange using a special holder. In the second test the cavity reached a peak surface field of 43.6MV/m which corresponds to a cathode field of 31.8MV/m. This time the maximum field was limited by a thermal break down (quench) at a peak magnetic field of 90.3mT. The difference between the low field unloaded Q values is quite small, $5 \cdot 10^9$ to $4 \cdot 10^9$, which proves a very good performance of the choke flange filter.

3 PREPARATION CHAMBER

A photocathode preparation chamber has been designed and manufactured at BINP. First Cs_2Te photolayers were prepared and tested with this chamber at FZR. The layers reached a quantum efficiency of 9% at a wavelength of 260nm. The light source was a Xenon lamp with a monochromatic filter. The initial value of the quantum efficiency decreased to 6% within 2 days and then kept unchanged for the following weeks.

4 LASER

Currently a pulsed laser system for activation of the photocathode is under construction at MBI, Berlin. The laser is a frequency quadrupled Nd:YLF laser operating in the ultraviolet range at 263nm. The laser shall provide a full synchronisation to the cavity rf with a time jitter of less than 3 ps. A pulse length of 4 to 7ps is projected. The laser is optimised for a quasi continuous operation. The average output power is 1 to 2W. The pulse repetition frequency can be chosen between 46.4MHz and the next two subharmonics.

5 BEAM TESTS

The next step is to prepare all the necessary equipment for the beam tests. The test set-up is shown in fig. 3.

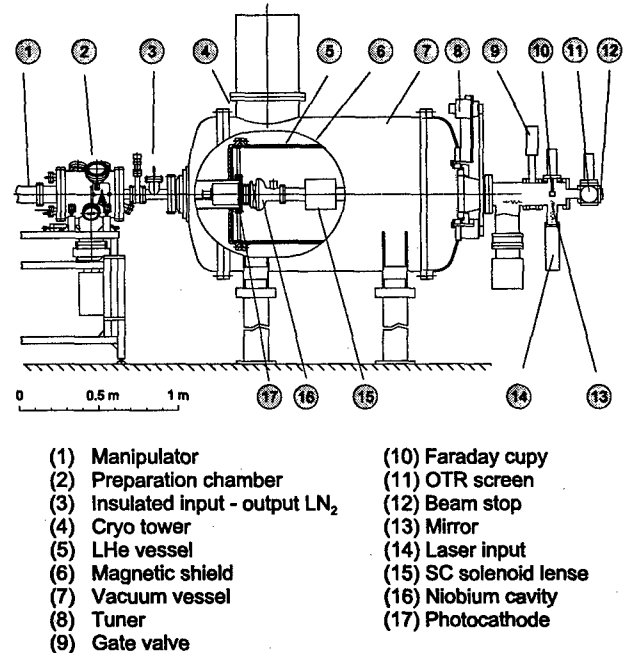


Fig. 3. Layout of the beam test set-up.

A horizontal cryostat is available from Stanford University. It is quite suitable for our needs after some modifications which will be made with help of ACCEL. The rf power source will be provided by FZR. The other parts, such as manipulator and gate valves, are commercially available. The beam tests are scheduled to the middle of the next year.

6 ACKNOWLEDGEMENTS

We are pleased to thank the many colleagues who supported our work with their advice and helped us in our experiments. Special thanks to our colleagues from DESY for providing the vertical tests of our cavity. Also we wish to thank colleagues from TU Dresden for their help in cryogenic questions.

7 REFERENCES

- [1]D. Janssen et al., Proc. PAC 1997, p. 2838
- [2]V. Volkov et al., Proc. PAC 1997, p. 2799
- [3]F. Gabriel ed., FZR Internal Design Report, Dresden, 1995
- [4]D. Janssen and P.vom Stein, Nucl. Instr.&Meth., A380, 1996, p. 497
- [5]D. Edwards, Tesla Test Facility – Design Report, DESY, Hamburg, 1995

ALL-SOLID-STATE PICOSECOND LASER SYSTEM FOR PHOTOCATHODE RF GUN*

F. Sakai, M. Yorozu, Y. Okada, A. Tsunemi, Y. Aoki, J. Yang, A. Endo
Sumitomo Heavy Industries, Ltd.
2-1-1 Yatocho, Tanashi, Tokyo, 188-8585, Japan

Abstract

A compact diode-pumped picosecond laser was developed for the illumination of the photocathode of RF guns. Nd:YLF and Nd:YAG were selected as the active medium and the laser stability was the main interest during the development. Achieved performances were 0.5ps timing jitter in the oscillator, 1-% UV pulse energy fluctuation and 5 μ rad beam pointing stability.

1 INTRODUCTION

A reliable and compact picosecond UV light source is the key requirement for the stable operation of RF guns. The improvement of the beam quality may benefit the ultra-short pulse X-ray generation by Thomson scattering [1]. As the high brightness electron source and the high peak power laser develop, the laser Thomson X-ray source becomes more realistic [2]. We have been developing a photocathode RF gun [3] and an all-solid-state picosecond compact laser for the photocathode [4]. The laser stability, e.g., energy stability, timing stability and the pointing stability, was requested stringently during the course of the research. A compact and stable laser system was developed by a joint project with Sumitomo Heavy Industries, Ltd and Time-Bandwidth Products Ltd.

In this paper, the research and the system performance are reported on the Nd:YLF all solid state picosecond laser. Additionally to the laser system, a pulse compression and an oblique incidence optical system are also reported.

2 LASER SYSTEM

The laser system, which was shown in Fig.1, was composed of a passive mode-locked oscillator with a timing stabilizer, a regenerative amplifier and a frequency conversion part. Some photo-diodes were equipped for diagnostics and monitors. Optical elements were fixed on a breadboard of Invar plate with 1000x600mm dimension, to avoid thermal misalignment. A controller box, which was composed of power supplies for diode-lasers, high voltage circuits for Pockels Cells, timing stabilizer circuits and so on were installed near the laser box.

2.1 Oscillator

The seeding laser was a passive mode-locked laser with a semiconductor saturable absorber mirror (SESAM). Repetition rate of the mode-locked pulse was determined by the length of the cavity. 79.34MHz-repetition rate was equal to 1/36 of 2856MHz S-band radio frequency, which was used for the photocathode RF gun. The cavity length was controlled to be synchronised with 79.34MHz repetition frequency. The timing stabilizer measured the phase and the frequency offset between the laser pulses, which was detected by a photo-diode, and the reference RF signal, and adjusted the cavity length to maintain the constant phase relation between two signals. The system adjusted the cavity length with a piezoelectric transducer for a small cavity length change, and with a motor moving stage to cover 0.1 MHz wide range change.

2.2 Regenerative Amplifier

A Pockels Cell captured a single seed laser pulse to increase the pulse energy from sub-nano-Joule to mJ range, and released the amplified single pulse from the regenerative amplifier cavity. The temperature change of the Pockels Cell crystal was the main source of the amplitude fluctuation. Water cooling of the Pockels Cell was introduced to achieve the pulse energy stability.

2.3 Harmonics Generator

This component converted the fundamental output to the 4-th harmonics, which was necessary for the illumination of the photocathode, with KTP and BBO crystals. The temperature of crystals was also controlled to stabilize the frequency conversion efficiency. The net conversion efficiency was close to 10% from the fundamental to the 4-th harmonics. The UV energy was obtained up to 200 μ J depending on the choice of the operational condition. The UV output energy was controlled with a rotational half wave plate and a thin film polarizer by a remote controller to change the emission electron charge from the RF gun.

3 LASER PERFORMANCE

3.1 Energy and Pulse length

The UV pulse energy, which was quadrupled from the fundamental of 1053nm wavelength, was measured to be around 200 μ J. The energy on the cathode surface was requested to be around 50 μ J to obtain 1nC bunch charge in the condition of the quantum efficiency of 1×10^{-4} . There could be energy delivery loss in the laser injection optical system where laser beam was shaped by an iris and reflected by a grating, but the UV pulse energy seemed enough for the requirement after accounting the delivery loss. The pulse duration of the fundamental part was measured as 12 ps by a single scan auto-correlator. The UV pulse duration was estimated as around 6ps.

3.2 Stability

UV energy stability was measured for 10,000 shots and over hours. Energy was detected by a photo-diode for 10,000 shots and by a power meter for over hours, respectively. The histogram of energy deviation from the mean value was shown in Fig.2. Energy fluctuation was estimated to be 0.55 %rms. Long term UV pulse energy stability over hours was also measured. As a result, UV averaging energy was stable within $\pm 2\%$, except 2-5 minutes of warming time from the switch-on.

The timing jitter of the laser oscillator was estimated from the output of the phase detector in the feedback loop [5]. A phase detector measured the phase difference between the fast photodiode signals of laser pulse and the reference RF signal, and generated an "error signal". This phase difference was related to the timing jitter between the laser phase and the reference RF phase. The timing jitter of the oscillator was estimated as 0.39ps rms.

The pointing stability of UV output pulse was measured by a CCD camera. UV beam profiles were measured on a diffuser plate at 1.5m away from the laser output port. Beam profile was shown in Fig.3. Pointing stability of the beam centroid was estimated to be 5 μ rad rms.

The specification and the laser performance are listed on Table 1.

4 OPTICAL SYSTEM

4.1 Pulse compression

The duration of the fundamental pulse was about 12ps. We have developed a pulse compression device to obtain shorter pulse duration from the laser system. The pulse compression system was composed of a single-mode optical fiber of 450m length and a pair of gratings with 1800G/mm groove density. As the first step, the output from the fiber was compressed directly with the gratings without an amplifier to evaluate the optical fiber characteristics. A Nd:YLF oscillator with longer pulse

length of 24ps was used for this experiment. The relation between the input energy to the fiber and the pulse duration was measured. The pulse length measured by a scanning auto-correlator is shown in Fig.4.

4.2 Delivery system of oblique injection

In many cases, the laser beam was injected onto the cathode surface at an oblique angle with p-polarization, because the quantum efficiency was known to be enhanced by a factor of three in comparison with one at normal incidence. There are two problems in this configuration, namely the prolonged beam shape and the arrival time difference between the beam edges on the cathode surface. We designed a correction beam delivery system. Laser beam was cut to be flat top shape with an iris. Image at the iris was translated to the cathode surface by an image relay method. In this optical system, the transverse beam shape was made to be ellipse with four littrow prisms and the longitudinal beam shape was made to be tilt with a grating. In this way, beam shape was circle with near flat top and beam pulse duration was kept to be the same as one of laser output at the cathode surface. The beam profile measurement by a CCD camera was carried out, and the image relay system was confirmed to work as was designed. We have a plan to check the longitudinal beam shape with a streak camera.

5 CONCLUSION

The all-solid-state picosecond UV source has been developed based on the laser diode pumping, the passive mode-locked oscillator with SESAM and the feedback timing stabilizer. Invar breadboard and water cooling of thermal components prevented thermal misalignment of optical components. The laser performance was quite stable for the reliable photocathode RF gun operation.

This work was supported by the New Energy and Industrial Technology Development Organization (NEDO) in Japan.

6 REFERENCES

- [1] R.W.Schoenlein, et al. "Femtosecond X-ray Pulses at 0.4A generated by 90 Thomson Scattering: A Tool for Probing the structural Dynamics of Materials", Science, Vol.274, 236(1996)
- [2] A. Endo "Femtosecond X-ray Pulse Generation by using a Low Emittance Electron Beam and a High Brightness Laser", Proc. of 4th International Workshop on Femtosecond Technology, Feb. 13-14, Tsukuba, Japan, 58(1997)
- [3] F. Sakai, et al. "Development of High Duty Operation RF Photoinjector, Proc. of 11th Symp. on Acc. Sci. and Tech., Oct. 21-23, Harima, Japan, 473(1997)
- [4] F. Sakai, et al. "All Solid State Picosecond UV Source for RF Photoinjector" Proc. of Lasers'97, New Orleans, 63(1997)
- [5] M. R. Walker, D.W. Crust, et al. "Reduction of phase noise in passively mode-locked lasers" IEEE J. Quantum Electron., Vol. 28, 289(1992)

Table.1 Laser Performance

Wavelength(UV)	263nm
Oscillator Frequency	79.34MHz
Oscillator Frequency Adjustable Range	0.01MHz
Energy(UV)	0.2mJ
Repetition rate	1-100Hz
Pulse width (fundamental)	12ps
Timing jitter for oscillator	0.39ps rms.
Beam profile	TEM ₀₀
Pointing stability	5 μ rad
Energy stability(UV, hours)	<2%
Energy Stability(UV,10000shots)	0.55%rms

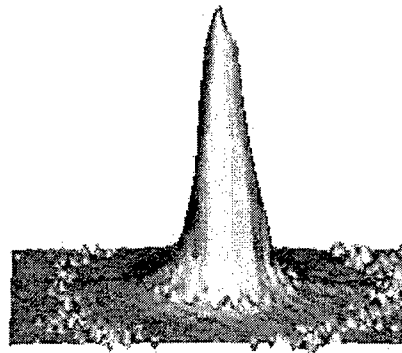


Fig 3 Beam profile of UV pulse
Beam diameter is about 3.5mm at FWHM

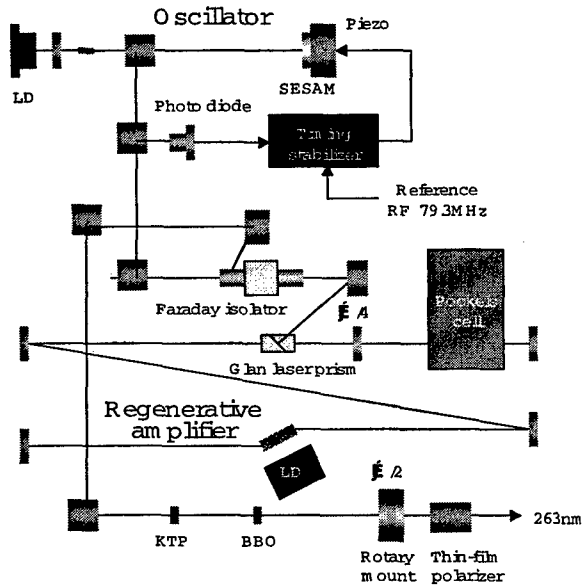


Fig.1 Layout of the Picosecond Nd:YLF laser system

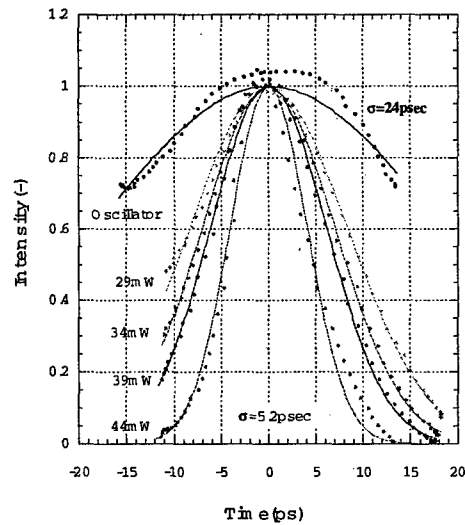


Fig.4 The relation between the input energy to the fiber and the pulse length

The output from the fiber was compressed directly with gratings without amplifier. These data were measured by a scanning auto-correlation.

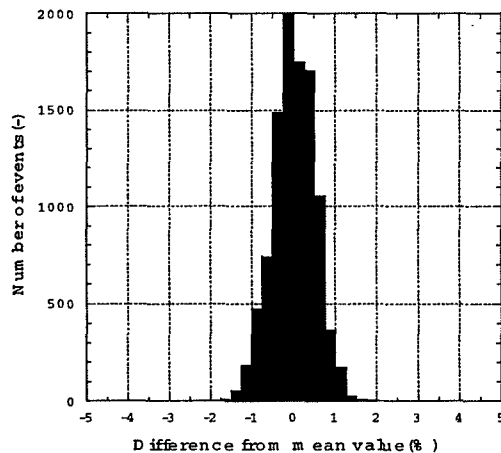


Fig.2 Histogram of UV energy fluctuation for 10000 shots
($\sigma=0.55\%$)

A COMPARISON BETWEEN THE PERFORMANCE OF SPLIT AND INTEGRATED RF PHOTOINJECTORS*

J. B. Rosenzweig, S. Anderson, X. Ding, and L. Serafini[†]

UCLA Department of Physics and Astronomy,
405 Hilgard Ave., Los Angeles, CA 90095

Abstract

RF photoinjectors, the present source of choice for production of ultra-high brightness electron beams, have two basic design types: split, in which a short, high gradient rf gun is followed by a drift and a booster linac, and a lower gradient integrated photoinjector, in which the linac acceleration is connected directly to the gun. The first type is represented at UCLA by the Neptune photoinjector, the second by the newly constructed S-band PWT photoinjector. We examine, through simulation and theory, the relative merits of each type of injector, both from the point of view of the beam physics (ability of the source to produce high currents and low emittances), and of relative technical advantages.

1 PHOTOINJECTOR TYPES

The rf photoinjector is a photoelectron source embedded in a high-gradient rf accelerating cavity system which produces high peak current, low emittance, short pulse electron beams. These beams find application in radiation production (SASE FELs, Compton-scattering sources), as well as advanced accelerator applications (linear collider development, ultra-low emittance test beams, high current drivers for wake-field accelerators).

The photocathode "gun" region is followed by a transverse focusing element (usually a solenoid), which aids in beam size and emittance control. It additionally must be post-accelerated to bring the beam to a usable energy, and to mitigate space-charge effects. This acceleration is accomplished in a booster linac, which may be physically separated, or integrated into the same rf structure as the gun. These two configurations, termed *split* and *integrated* photoinjectors, are displayed in Figs. 1 and 2, respectively. The two devices shown are both in use at UCLA.

The first is the Neptune photoinjector[1], a device dedicated fundamental beam physics, as well as injection into advanced short-wavelength accelerator experiments, such as the plasma beatwave accelerator[2]. The Neptune photoinjector consists of a 1.6 cell high gradient 2856 MHz rf gun[3] derived from a family of guns developed originally at BNL, followed by 90 cm of drift and a post-acceleration plane-wave transformer (PWT) linac[4]. Because ultra-short pulses are at a premium in this lab, a magnetic chicane[5] for pulse compression is added after

the acceleration in the PWT linac from 5 to over 15 MeV. Pulse compression of this sort, albeit at higher energies, is a common feature of ultra-short wavelength SASE FEL designs.

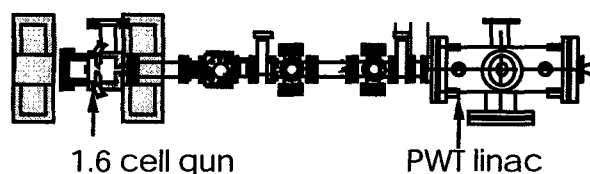


Figure 1. The UCLA Neptune photoinjector with 1.6 cell gun, focusing solenoids, 5 MeV transport section and PWT linac.

The integrated photoinjector, which can be recognized as the original LANL design archetype, is represented at UCLA by the PWT photoinjector, a $10+2/2$ cell 2856 MHz device shown in Fig. 2. It operates at roughly the same acceleration gradient (60 MV/m peak) as the PWT linac in the Neptune injector, which is one-half the acceleration gradient of the 1.6 cell gun at Neptune. Thus the PWT injector can be considered a relatively low gradient device.

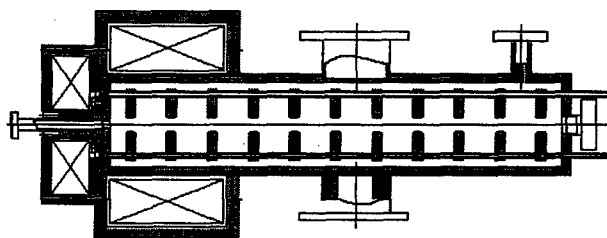


Figure 2. The UCLA/DULY PWT photoinjector, showing rf structure and compact focusing solenoid.

Both of the UCLA devices have been proposed as ultra-high brightness injector candidates for driving the LCLS x-ray FEL. While a number of copies of the 1.6 cell gun have been fabricated and are now being employed, its ultimate performance is not known. Likewise, the PWT photoinjector is only now approaching commissioning, with no experimental data to verify its utility as a high brightness injector. Since we cannot rely on experimental studies to evaluate the prospects for each of these sources, we undertake here a critical computational and theoretical comparison of the expected performances of the devices.

2 PHOTOINJECTOR BEAM PHYSICS

The analysis and design of rf photoinjector sources for peak brightness — short pulse, high charge, and low emittance — entail a working understanding of many aspects of beam physics. We now give a cursory discussion of the physics of these beams, which are dominated by space-charge and violent acceleration effects.

The longitudinal dynamics in an rf photoinjector are characterized by violent acceleration. This is due to two effects: the need to mitigate detrimental space-charge effects, and the requirement that the beam be captured in the rf wave within the initial cell of the standing wave rf cavity. This can be quantified by defining a unitless parameter which must exceed approximately unity[6]

$$\alpha \equiv \frac{eE_0}{2k_{RF}m_e c^2} = \frac{\gamma'}{k_{RF}} > 1 \quad (1)$$

This parameter allows a classification of injector types: high gradient injectors have $\alpha \approx 1.5 - 2.5$, whereas the lowest gradient injectors operate with $\alpha \approx 1$. In split injectors, beams will typically suffer degradation in the inter-accelerator drift unless they are run at high gradient ($\alpha \approx 2$ at Neptune). On the other hand, the space-charge dynamics of beams in integrated photoinjectors is optimized for low gradients ($\alpha \approx 1$ for PWT).

The peak current at injection (leaving the cathode surface) is $I = Q/\sqrt{2\pi\sigma_t}$. This current tends to be enhanced by the longitudinal focusing of the rf gradient at injection, and be diminished by the longitudinal defocusing due to space-charge. Both of these effects are asserted only close to the cathode. A one-dimensional Hamiltonian theory has been recently developed to analyze these effects, with the result that the pulse compression/expansion factor is expected to be

$$\frac{d\phi_f}{d\phi_0} = \frac{2\sin(\phi_0) - \phi_0 \cdot [\cos(\phi_0) - \delta']}{1 + \sin(\phi_0)} \quad (2)$$

Here ϕ_0 is the phase at injection, and

$$\delta' = \frac{4\pi r_e n_b}{eE_0 k_{RF}} = \frac{1}{\alpha} \left[\frac{k_p}{k_{RF}} \right]^2, \quad (3)$$

with n_b defined as the beam density expected with no phase compression or expansion.

Note that for low α , ϕ_0 is smaller, as the bunch slips more in phase while accelerating to a final optimum phase $\phi_0 = \pi/2$, which Eq. 2 indicates tends to compress the bunch. On the other, hand Eq. 3 predicts that the pulse lengthening due to space-charge is enhanced by running at for low α . In order to understand how these effects

compete, we must first examine the role of the plasma wave-number k_p in photoinjectors.

Violent acceleration carries with it large transverse forces, which for an accelerator cavity terminate on a conducting (cathode) plane, gives a net first order kick to an off-axis accelerating particle. Further, this kick is rf phase dependent, and thus for a finite pulse length beam, an effective “rf” emittance is[6]

$$\epsilon_{RF} \propto \gamma k_{RF}^2 \sigma_r^2 \sigma_z^2 \propto \alpha k_{RF}^3 \sigma_r^2 \sigma_z^2. \quad (4)$$

The first order rf kick can be thought of as originating at the end of the structure. All other irises in the rf structure have a balance in first order inward/outward kicks, but have a second order alternating gradient focusing (of strength $\propto \gamma'^2$)[7]. The combined effect of the rf focusing can be included in envelope and matrix treatments of the beam dynamics. The analytical model has been recently verified experimentally[8].

The rf emittance is much more of a problem in the split injector than in the integrated case, because the rf kick giving rise to this effect occurs when the beam is large, at the end of the second cell, where the solenoid has not yet focused the beam. In the integrated case, the beam is generally small at the structure exit, and therefore the rf kick is diminished and the emittance contribution is negligible.

Photoinjector beams are generally space-charge dominated, meaning that the envelope dynamics are driven by space-charge forces, and not emittance “pressure”. The space-charge effects give rise to plasma oscillations about an externally imposed (solenoid and rf focused) equilibria (the invariant envelope[9]). This plasma behavior in turn gives rise to emittance oscillations due to the fact that different longitudinal “slices” of the beam oscillate about different equilibria. After an integer number of plasma oscillations, the beam slices are realigned in phase space, and the emittance is “compensated”.

The plasma picture of the beam dynamics has allowed the development of laws for taking an optimized photoinjector design and scaling it to a different charge or rf wavelength[10]. Since we are comparing two different devices at the same rf wavelength, we only need to discuss here the charge scaling at a given rf wavelength. In this case, we simply require that the beam n_b density is constant, and thus the beam dimensions scale as $\sigma_i \propto Q^{1/3}$. This dependence gives emittance scaling as

$$\epsilon_n = \sqrt{aQ^{4/3} + bQ^{8/3}}. \quad (5)$$

where the first term is due to space-charge, with constant a proportional to $k_p^{4/3}/\alpha^3$, and the second term is due to rf and chromatic effects. The highest brightness beams are created at lowest charge, where the emittance is mainly due to space-charge, and thus $\epsilon_n \propto k_p^{2/3}/\alpha^{3/2}$.

All dependences of brightness can thus be understood when we assert that the plasma wave-number must scale

as the acceleration rate, $k_p \propto \alpha$. For a given charge Q this implies that the relative pulse lengthening is diminished for low α . Also, at a constant Q , the emittance will scale as $\epsilon_x \propto \alpha^{-5/6}$.

These predictions were tested in scaling comparisons of both optimized performance of the Neptune and PWT photoinjectors using the simulation code PARMELA. The behavior of the final rms bunch length is shown for these cases in Figs. 3 and 4, along with the "launched" rms bunch length cT , and the predictions of Eq. 2. The PARMELA results show excellent agreement with theory. It is seen that, while the beam launched beam is longer in the PWT (9.8 psec FWHM) than in Neptune (6 psec), that the beam compresses in the low α PWT, while expanding in the 1.6 cell gun, leaving the achievable current in both cases nearly identical. The expansion in the split injector is potentially troublesome (it can be enhanced by the cathode emission nonuniformities), and has been observed in initial 1.6 cell gun tests at BNL.

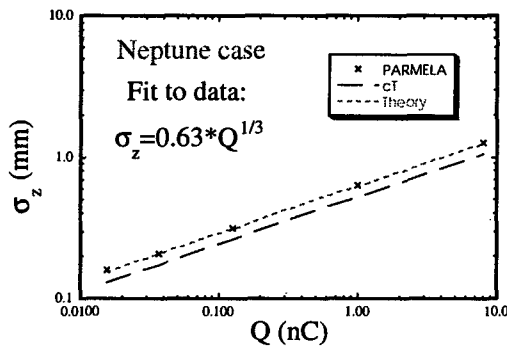


Figure 3. Neptune photoinjector bunch length vs. charge.

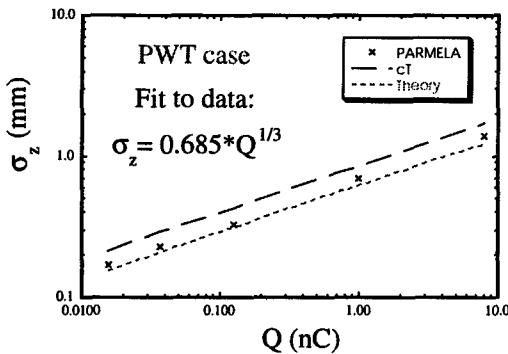


Figure 4. PWT photoinjector bunch length vs. charge.

The simulated behavior of the beam emittances as a function of charge are shown in Figs. 5 and 6 for our two cases. It can be seen that for the high α split photoinjector that both the contribution to the emittance due to space-charge and rf effects is smaller than for the integrated case. At one nC, the Neptune photoinjector is expected to give normalized (rms, using 90% of the beam) $\epsilon_x = 0.62$ mm-mrad, while the PWT injector is expected to give $\epsilon_x = 1.16$ mm-mrad, which is a ratio of 1.87, which compares well with the predicted scaling ratio of 1.78. Thus we conclude that for the nominal application of

creating an ultra-high brightness beam that the split photoinjector is better at 1 nC in S-band by a factor of 3.

These conclusions are modified by practical considerations if one allows a different choice of rf wavelength in the design. It has been shown that the brightness of a source scales as k_{RF}^2 , which implies that one should scale the photoinjector to higher rf frequency. This can't, due to engineering constraints, be done for the split injector, and thus recent work on ultra-high brightness high k_{RF} sources has focused on integrated systems.

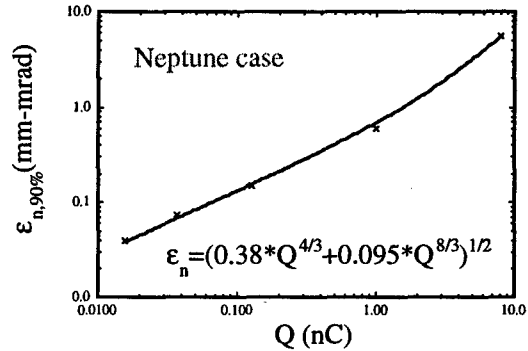


Figure 5. Neptune photoinjector emittance vs. charge.

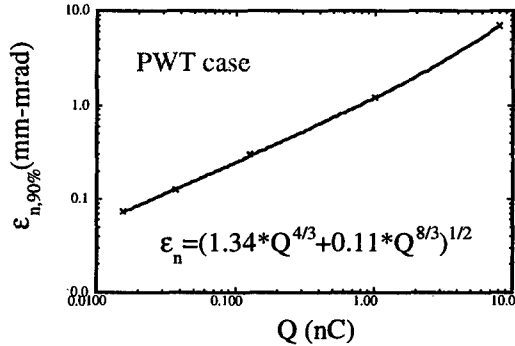


Figure 6. PWT photoinjector emittance vs. charge.

*Work supported by US DoE DoE Contracts DE-FG03-92ER40693 and DE-FG03-98ER45693.

*Email: rosenzweig@physics.ucla.edu

+INFN-Milano, Univ. Milan..

5 REFERENCES

1. J. Rosenzweig, et al., NIM A **410**, 437 (1998).
2. C. Clayton, et al., NIM A **410**, 437 (1998).
3. D.T. Palmer, et al., Proc. PAC'97, 2687 (IEEE, 1998)
4. R. Zhang, et al., Proc. of the 1995 PAC (IEEE, 1996)
5. J.B. Rosenzweig, N. Barov and E. Colby, IEEE Trans. Plasma Sci. **24**, 409 (1996).
6. K.J. Kim, NIM A **275**, 201 (1989).
7. J. Rosenzweig and L. Serafini, Phys. Rev. E **49**, 1499 (1994).
8. S. Reiche, et al., Phys. Rev. E **56**, 3572 (1997).
9. Luca Serafini and James Rosenzweig, Phys. Rev. E **55**, 7565 (1997).
10. J. Rosenzweig, and E. Colby, Proc. 1995 Advanced Accelerator Concepts Workshop 337 (AIP, 1996).

THE EFFECTS OF RF ASYMMETRIES ON PHOTOINJECTOR BEAM QUALITY *

J. B. Rosenzweig, S. Anderson, X. Ding, and D. Yu⁺
UCLA Department of Physics and Astronomy,
405 Hilgard Ave., Los Angeles, CA 90095

Abstract

A general multipole-based formalism to study the effects of RF asymmetries on the production of ultra-high brightness beam is presented, which employs both analytical and computational techniques. These field asymmetries can cause the degradation of beam emittance due to time dependent and nonlinear focusing effects. Two cases of interest are examined: the dipole asymmetry produced by a coupling slot in a standard high gradient rf gun, and the higher multipole content introduced by the support/cooling rods in a PWT structure. Practical implications of our results, as well as comparison to cold test and beam-based experimental tests, are discussed.

1 RF FORCE-DERIVED EMITTANCE

In a high gradient rf photoinjector, the necessity of using violent longitudinal acceleration also implies the existence of large transverse forces. These forces are time-dependent, and may be nonlinear or non-axisymmetric as well. All of these attributes can give rise to transverse emittance growth. Time dependent monopole[1] and dipole[2] fields can cause correlations between the beam's transverse and longitudinal phase spaces, which, while not contributing to the so-called slice emittance, (the transverse emittance of a narrow longitudinal slice of the beam), can increase the total projected transverse emittance. We shall discuss the relationship between these emittance contributions and the Panofsky-Wenzel theorem, as well as observations verifying the conclusions we reach from this analysis.

Nonlinear fields have typically been considered in the context of the axisymmetric, non-synchronous spatial harmonics of the rf field. In this paper, we examine the contribution to synchronous rf multipole fields to the emittance, and analytically estimate the amplitude of these multipoles for rf structure types of interest. We compare the analytical estimates with experimental evidence and computer simulations.

2 PANOFSKY-WENZEL THEOREM

As cavities are designed first and foremost to accelerate, it is of interest to relate the longitudinal acceleration which is imparted to a given particle. This is accomplished by an updated version of the Panofsky-Wenzel theorem[3], in which we take into account the fact that the electrons which are accelerated from rest starting from a point (a photocathode) where the field is not zero. The Panofsky-Wenzel theorem explicitly assumes in its derivation that

the particle experiencing Lorentz forces in the rf cavity environment moves parallel to the axis at constant velocity. The approximation of constant velocity is as badly violated as can be close to the photocathode, but in this region there are few transverse forces. Thus the application of the theorem is still reasonable in this case.

Our version of the Panofsky-Wenzel theorem gives the integrated transverse and longitudinal momentum "kicks" in terms of the components of the rf vector potential \vec{A}

$$\Delta \vec{p}_\perp = \frac{q}{c} \left[\int_{z_i}^{z_f} \frac{\partial \vec{A}_\perp}{\partial \zeta} dz + \int_{z_i}^{z_f} \vec{\nabla}_\perp A_z dz \right], \text{ and} \quad (1)$$

$$\Delta p_z = \frac{q}{c} \left[\int_{z_i}^{z_f} \frac{\partial A_z}{\partial \zeta} dz \right], \text{ with } \zeta = z - ct. \quad (2)$$

The first term in Eq. 1 vanishes because it is a perfect differential, and the transverse components of the vector potential vanish at the cathode, and outside of the cavity. Thus we have the relation

$$\frac{\partial(\Delta p_\perp)}{\partial \zeta} = \vec{\nabla}_\perp(\Delta p_z). \quad (3)$$

We consider a multipole standing wave field with a sinusoidal dependence of the phase on distance away from the power coupler,

$$E_z = E_0 \sin(\alpha x - \kappa_y y + \theta_0) \cos(kz) \sum_{n=0}^{\infty} a_n r^n \cos(n\phi) \quad (4)$$

The asymmetry term inside of the sine function is the phase asymmetry due to power flow (finite Q effect), and the series expansion is the multipole content of the mode fields. The vector potential associated with Eq. 4 is

$$A_z = \frac{E_0}{k} \cos(\alpha x - \kappa_y y + \theta_0) \cos(kz) \sum_{n=0}^{\infty} a_n r^n \cos(n\phi). \quad (5)$$

3 POWER FLOW EFFECTS

To isolate the transient power flow component of the acceleration, we use only the lowest multipole component field, to arrive at longitudinal momentum gain in a gun of length L_g of approximately

$$\Delta p_z = \frac{eE_0 L_g}{2c} \cos(k\zeta - \kappa_y y)$$

$$\equiv \frac{eE_0 L_g}{2c} \left[1 - \frac{(\Delta\phi)^2}{2} - \frac{(\kappa_y y)^2}{2} \right], \quad \Delta\phi = k\Delta\zeta. \quad (6)$$

The transient power flow wave number can be estimated as $\kappa_y \equiv k/Q$, where Q is the unloaded quality factor, which is of order 10^4 . Thus for reasonable beam size parameters, the effect of the power flow can be neglected.

4 MULTIPOLE FIELDS

4.1 Monopole effects

For the monopole component of the field, with normalization $a_0 = 1$, the acceleration is independent of transverse offset (e.g. y), and the transverse emittance growth for a beam with a uniform density distribution propagating near the peak acceleration phase is

$$\varepsilon_{ny} = \bar{\gamma} \sqrt{\langle y^2 \rangle \langle y'^2 \rangle - \langle yy' \rangle^2}$$

$$= \sqrt{\frac{13}{20}} \frac{eE_0}{2m_e c^2} \sigma_y^2 (k\sigma_z)^2. \quad (7)$$

This is the rf emittance contribution first analyzed by Kim[1], and can be mitigated by keeping the beam sizes small.

4.2 Dipole effects

The lowest significant order asymmetry has traditionally arisen from the existence of a coupling slot on one side (in y) of the cavity. In the first 1.5 cell BNL designed S-band gun, the coupling was in both cells, and thus initial condition on the transverse vector potential is $A_y = 0$, giving a transverse momentum kick of

$$\Delta p_y = \partial_y \int \Delta p_z d\zeta = \frac{eE_0}{2c} \frac{a_1}{k} L_g \sin(k\zeta)$$

$$\equiv \frac{eE_0}{2c} a_1 L_g \zeta \quad (8)$$

This phase dependent dipole kick gives rise to an effective projected emittance

$$\varepsilon_{n,y} = \frac{eE_0}{2m_e c^2} a_1 L_g \sigma_y \sigma_z. \quad (9)$$

According to the Panofsky-Wenzel theorem, the transverse momentum kick is accompanied by an acceleration which is dependent on the offset of the electron in y ,

$$p_z(y)c \equiv eE_0 L_g (1 + a_1 y/k). \quad (10)$$

If one measures this asymmetry, then one can determine a_1 , and the expected emittance growth due to dipole kicks can be estimated. This was done on a 1.5 cell gun obtained from BNL at UCLA[4], with a view of the momentum spectrometer shown in Fig. 1. Here the particles at larger y (actually at large x in the gun, as the focusing solenoid provides a nearly 90 degree rotation) are seen to have a smaller momentum in the spectrometer.



Figure 1. Electron beam (green) image in focal plane of spectrometer, with smaller energy electrons at larger y .

From this image, and knowledge of the bunch size and length, it was deduced that the gun dipole asymmetry contributed 3.5 mm-mrad to the normalized rms emittance. The low charge vertical emittance in this gun was measured to be 5 mm-mrad, most of which came not from the more familiar monopole effects, but from rf dipole components. This is partially due to the overcoupling of the device ($\beta = 1.6$); the coupling slots were anomalously large, and the dipole component of the rf field was larger than necessary.

4.3 Higher multipole effects.

In the next-generation rf guns[Palmer,Colby] beyond the 1.5 cell BNL style model, several design innovations were implemented, including the coupling of external power only through the full cell, and the use of a dummy slot opposite to the coupling slot for dipole symmetrization. These schemes worked well, and have additionally been supplemented by the use of a race-track outer wall geometry[5] to eliminate the quadrupole components of the field left after dipole symmetrization.

In the new PWT photoinjector structure, under development by a UCLA/DULY Research collaboration, the structure is based on disks which are not connected to

the outer wall, but are supported by four rods (the cross-sections of two are shown in Fig. 2). The cell-to cell coupling in this device is obtained through the annular region between the disks and the outer wall, and can be very strong, leading to excellent mode separation. The external coupling is through the outer wall, and is so far from the axis that it does not give rise to significant dipole components of the field. In fact, the rods, which are relatively close the axis, give rise to a dominant octupole field perturbation.

We have examined this perturbation both analytically and through field simulations. The rods effect lasts for the entire structure, just as the dipole component, and so the normalized emittance in such a long device may be impacted more severely than in a short gun. All of the higher multipole components which have a strong effect on the beam will have a speed-of-light phase velocity, and thus have a transverse field profile which obeys the equation $\nabla_{\perp}^2 E_z = 0$ with solutions as in Eq. 4. The boundary conditions for the situation with the rods may be approximated as the field being constant at the rod offset radius ρ , but dropping to zero in the region of the rods (which have radius b). Fourier analysis of this rectangular profile in ϕ gives the ratio of the octupole to monopole components of the field,

$$\frac{a_4}{a_0} \equiv \frac{2 \sin(4b/\rho)}{\rho^4((4b/\rho) - \pi)} \quad (11)$$

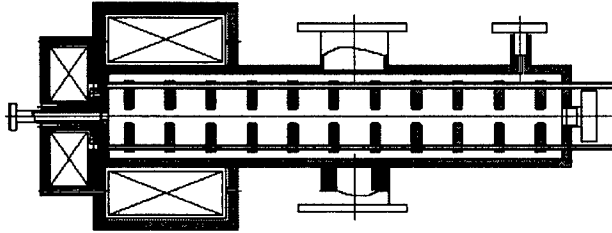


Figure 2. S-band PWT photoinjector cross-section, with 2 support/cooling rods showing.

For the S-band PWT linac, Eq. 11 gives $a_4/a_0 \equiv 10^{-3} \text{ cm}^{-4}$, while the GdfidL 3-D field simulations shown in Fig. 3 give $a_4/a_0 \equiv 1.3 \times 10^{-3} \text{ cm}^{-4}$, which is good agreement for so rough of a model.

The effect of the octupole component on the emittance in this device can be estimated as

$$\varepsilon_{n,y} = \frac{\sqrt{3}}{14} \gamma_f a_4 \sigma_y^4 \sigma_z, \quad (12)$$

where we have written it as proportional to the final energy $\gamma_f m_e c^2$ to emphasize that the emittance is linearly dependent on the length of the structure. For the 20 MeV S-band PWT photoinjector at UCLA, $\sigma_z = 0.7 \text{ mm}$, $\sigma_y \equiv 1.5 \text{ mm}$, and the expected octupole contribution to

the emittance is $\varepsilon_{n,y} \equiv 2.3 \times 10^{-8} \text{ m-rad}$, which is almost two orders of magnitude smaller than the expected emittance due to monopole rf and space-charge effects.

On the other hand, for the proposed X-band PWT photoinjector[6] under study by a DULY/UCLA/LLNL collaboration, the rods must expand by a factor of 50% relative to the disk size in order to provide adequate cooling water flow. In this case Eq. 11 gives $a_4/a_0 \equiv 0.15 \text{ cm}^{-4}$, while the beam, for 1 nC operation (as in S-band), is smaller by a factor of $\sqrt{3}$ in all dimensions. In this case, the expected octupole contribution to the normalized emittance is $\varepsilon_{n,y} \equiv 2.1 \times 10^{-7} \text{ m-rad}$. This is now significant, as it is roughly 20% of the design monopole emittance. In addition, it implies that it would be unwise to raise the charge Q significantly in this device, as this would result octupole-induced emittance scaling[8] as $Q^{5/3}$.

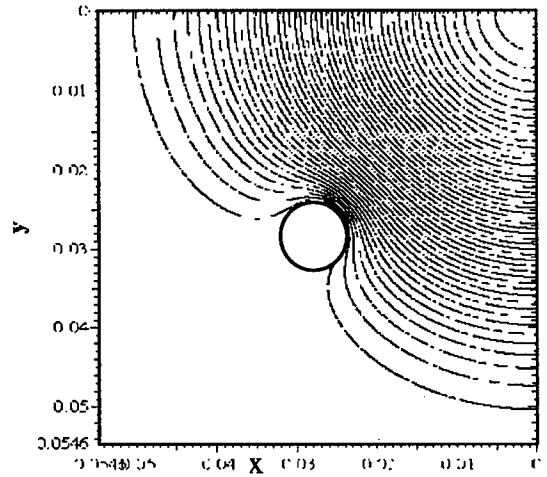


Figure 3. Calculated contours of constant E_z in S-band PWT at mid-cell, from GdfidL simulation.

*Work supported by US DoE Contracts DE-FG03-92ER40693 and DE-FG03-98ER45693.

* Email: rosenzweig@physics.ucla.edu

+Duly Research.

5 REFERENCES

1. K.J.Kim, *Nucl. Instr. Methods A* **275**, 201 (1988)
2. D.T.Palmer, et al., *Proc. PAC'97*, 2687 (IEEE,1998)
3. W. K. H. Panofsky and W. A. Wenzel, *Rev. Sci. Inst.* **27**, 967 (1956).
4. J.B. Rosenzweig, et al., *NIMA* **341**, 379 (1994).
5. J. Haimson, private communication.
6. J.B. Rosenzweig, et al., *Proc. PAC'97*, 1968 (IEEE, 1998)
7. D. Yu, et al., *Proc. PAC'97*, 2806 (IEEE, 1998)
8. J.B. Rosenzweig and E. Colby, *Advanced Accel. Concepts*, 724 (AIP Conf. Proc. 335, 1995).

OPTIMAL SCALED PHOTOINJECTOR DESIGNS FOR FEL APPLICATIONS*

J. B. Rosenzweig, S. Anderson, X. Ding, C. Pellegrini and G. Travish⁺
UCLA Department of Physics and Astronomy,
405 Hilgard Ave., Los Angeles, CA 90095

Abstract

Much of the research and development surrounding the effort to create X-ray FELs based on the SASE process has centered on the creation of ultra-high brightness electron beam sources. The sources for existing short wavelength FEL designs, which employ RF photoinjector technology, have all been specified to contain 1 nC of charge. We show, by scaling existing designs, that this constraint causes the maximum beam brightness to be found when the rf wavelength is shortened to X-band. If, instead of holding the charge constant, we assume a certain RF wavelength device and then scale the charge, notable improvements in the beam brightness, and thus the FEL performance, are found. Charge scaling assumes that the density and aspect ratio of the beam stays constant as the charge is changed. If we relax the requirement of a constant aspect ratio in order to maximize the beam current and brightness by shortening the beam pulse, we find that the pulse lengthening due to space charge eventually brings this effort to a stop. The results of this investigation and their impact on SASE FEL design is discussed.

1 PHOTOINJECTOR SCALING LAWS

The optimization of rf photoinjector performance can be understood most straightforwardly by the scaling, in frequency, and in charge, of the beam dynamics – beams are simply brighter when produced in the short rf wavelength, high field environment. A strict scaling of photoinjector design parameters has been developed by Rosenzweig and Colby[1], allowing the understanding of systematic variations of both charge and wavelength. The scaling laws for maintaining optimum operation of an rf photoinjector while changing the rf wavelength λ in the design are summarized as follows:

- 1) The accelerating and focusing field amplitudes must scale as the inverse of the wavelength,

$$E_0 \propto \lambda^{-1}, B_0 \propto \lambda^{-1}. \quad (1)$$

- 2) In this change, the natural scaling of the beam parameters is then

$$\sigma_i \propto \lambda, Q \propto \lambda. \quad (2)$$

This scaling rigorously produces (including all space-charge, rf, chromatic and thermal effects), an emittance which scales as

$$\epsilon_n \propto \lambda. \quad (3)$$

Note that this “natural” wavelength scaling implies that at shorter wavelength, the charge and the bunch length both scale downward as λ , yielding a design current which is independent of λ . Thus the beam brightness scales naturally as

$$B \equiv \frac{2I}{\epsilon_n^2} \propto \lambda^{-2}. \quad (4)$$

If one constrains the charge Q needed for a given application, however, one may not use natural scaling alone, one must rescale the charge to re-obtain the initial charge after first scaling naturally in wavelength. This is accomplished by keeping the beam density (proportional to the beam plasma frequency squared) constant,

$$\sigma_i \propto Q^{1/3}. \quad (5)$$

Under these circumstances, current scales as $I \propto Q^{2/3}$, the space charge contribution to the emittance follows $\epsilon_{sc} \propto Q^{2/3}$, while the rf/chromatic contribution scales as $\epsilon_{rf} \propto Q^{4/3}$. Assuming these two sources of emittance are independent (which is approximately valid), the full emittance then scales in charge as

$$\epsilon_n = \sqrt{aQ^{4/3} + bQ^{8/3}}. \quad (6)$$

2 SCALING OF SPECIFIC DEVICES

The coefficients a and b in Eq. 6 are properties of a given type of device. At UCLA[2], we have developed two types of high-brightness rf photoinjectors, a split photoinjector consisting of a high-gradient 1.6 cell gun[3] followed by a drift and a low gradient plane-wave transformer (PWT) post-acceleration linac[4], and an integrated, low gradient device, the 10+2/2 cell PWT photoinjector[5]. A direct comparison of the advantages and disadvantages of these designs is given in Ref. 6.

As scaling to short rf wavelength implies high fields (according to Eqs. 1), the high gradient gun and its focusing scheme cannot easily be scaled. Thus we

concentrate on the PWT photoinjector in this paper, which is now proposed as a serious candidate for development at short rf wavelength.

The characteristics of the PWT photoinjector have been investigated by computer simulation scans of charge[6]. It is found that for this 2856 MHz ($\lambda = 10.49$ cm) device

$$\epsilon_n = \sqrt{1.34 \cdot \tilde{Q}^{4/3} + 0.11 \cdot \tilde{Q}^{8/3}}, \quad (7)$$

with charge \tilde{Q} in nC and rms normalized emittance in mm-mrad. To obtain a full scaling of the expected performance for arbitrary charge and rf wavelength, therefore, we write the emittance as

$$\epsilon_n = \tilde{\lambda} \sqrt{1.34 \cdot \left(\frac{\tilde{Q}}{\tilde{\lambda}}\right)^{4/3} + 0.11 \cdot \left(\frac{\tilde{Q}}{\tilde{\lambda}}\right)^{8/3}} \quad (8)$$

where \tilde{Q} is again in nC and $\tilde{\lambda} = \lambda(\text{cm})/10.49$. This expression implies that the emittance is optimized for a certain charge at a given rf wavelength, as at very short wavelength, the rf emittance asserts itself very strongly, and the advantages of running at high accelerating gradient are lost. Differentiation of this expression with respect to $\tilde{\lambda}$

$$\frac{\partial \epsilon_n}{\partial \tilde{\lambda}} = 0 \rightarrow \tilde{\lambda} = 0.286 \quad (8)$$

gives an optimum PWT operating wavelength of 9.97 GHz for 1 nC operation, which is the benchmark charge for SASE FEL designs.

The simulations also give the scaling of the bunch length with charge at S-band,

$$\sigma_z = 0.69 \cdot \tilde{Q}^{1/3} \text{ (mm)}, \text{ or } \sigma_t = 2.3 \cdot \tilde{Q}^{1/3} \text{ (psec)}. \quad (9)$$

We thus can arrive at a final expression for the brightness

$$B(\text{A/m}^2) = \frac{347 \cdot \tilde{Q}^{2/3}}{\tilde{\lambda}^2 \left(1.34 \cdot \left(\frac{\tilde{Q}}{\tilde{\lambda}}\right)^{4/3} + 0.11 \cdot \left(\frac{\tilde{Q}}{\tilde{\lambda}}\right)^{8/3} \right)} \quad (10)$$

Since the current is not an explicit function of the wavelength, the brightness for a constant charge is optimized at the same point as the emittance.

3 X-BAND INJECTOR OPTIMIZATION

The PWT photoinjector was first proposed as a good candidate for a scalable type of high-brightness source several years ago[7]. In the intervening time, a UCLA/DULY Research/LLNL-UCD collaboration has

been investigating the physics and engineering issues associated with this scaling. One of the issues surrounding this project is the choice of rf frequency between 3 and 4 times the S-band PWT (8.56 and 11.42 GHz), set by the availability of high power rf sources. Note that the brightness is optimized, according to Eq. 9, at a frequency is directly between the two X-band frequencies we have considered for development.

In order to illuminate the possible differences between the two choices of λ , as well as the superiority of short versus long wavelength operation, we plot of these dependences are shown for 2.856 GHz, 8.6 GHz, and 11.4 GHz operation below. The emittances and brightnesses shown in Figs. 1 and 2 also include a small contribution of emittance growth due to multipole field errors in the PWT (due to cooling/disk-support rods)[8].

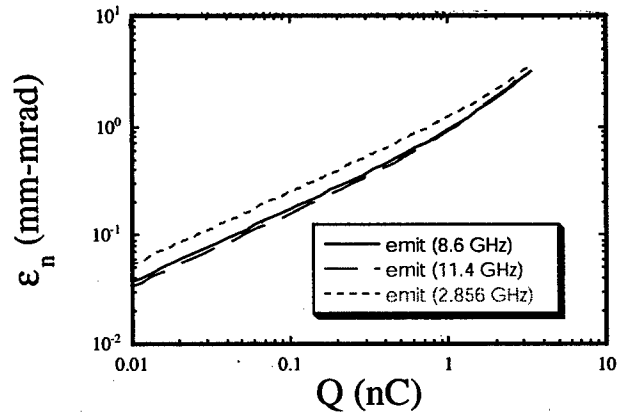


Figure 1. Emittances for scaled PWT photoinjectors as a function of charge.

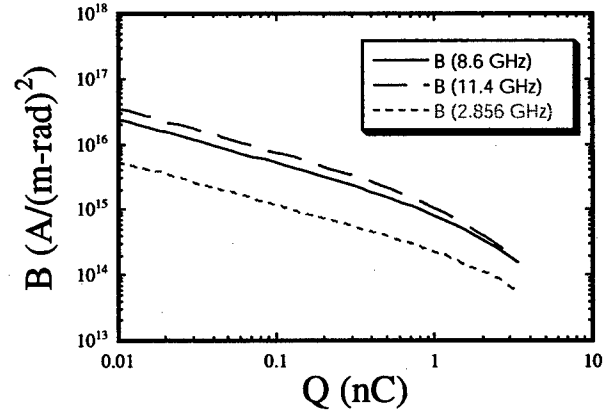


Figure 2. Beam brightness for scaled PWT photoinjectors as a function of charge.

It can be seen that the 8.6 and 11.4 GHz results are nearly identical for 1 nC operation. Also, the beam brightness in both X-band cases is better than that achieved at S-band by roughly an order of magnitude. Since the engineering problems (scaling of the solenoid field, cooling rods, rf power needs, dark current intensity at large accelerating fields, etc.) associated with operation at 8.6 GHz are smaller than those at 11.4 GHz[9], the

UCLA/DULY/LLNL development collaboration has decided to proceed with work at 8.6 GHz.

It should be duly noted that the operation of the device is better in X-band all cases regardless of charge for any high brightness beam case. It would perhaps be better to run very high charge, low emittance beams (e.g. for wake-field accelerator drivers) at long rf wavelength, meaning S- or even L-band. This is in fact the case for the facilities which demand this type of beam (ANL at L-band, CLIC at S-band). For high brightness, lower charge (< 2 nC) beams, however, these scaling studies have pointed towards X-band as the most promising direction.

4 X-BAND INJECTOR DEVELOPMENT

The UCLA/DULY/LLNL collaboration has completed a Phase I SBIR project, which has analyzed the feasibility of constructing an ultra-high brightness 8.6 GHz photoinjector based on the PWT design principle. In this study[9], the problems of scaling the magnetic field (solved by use of a permanent magnet design) and the cooling rod geometry (the effects of induced multipole fields were understood) were addressed. In addition, the cold testing of an 11.424 GHz, $10+2/2$ cell device was undertaken to show the robustness of the cavity design (the mode separation between the π -mode and the $10\pi/11$ -mode was shown to be 18 MHz), and good comparison to the results of the 3D EM field simulation program GdfidL was demonstrated. In the PWT design, in order to solve the problem of reflected power from the standing wave structure during filling, a split structure which allows cancellation of reflected power has been proposed. For more information on this program, see Ref. 9.

In addition, UCLA and SLAC has been exploring a hybrid design based on a standing wave 1.5 cell gun "married" to a travelling-wave section, with external coupling accomplished through the joining cell. This design would eliminate both the cooling rods (and their associated engineering problems) as well as the reflected power associated with a pure standing wave structure.

With these possible methods of scaling integrated photoinjector technology to X-band operation, it seems likely that beam brightnesses which are significantly higher than those found in today's sources can be achieved. The X-band photoinjector would be an important component of the proposed[10] ultra-short wavelength SASE FELs currently under development[11].

5 REFERENCES

1. J.B. Rosenzweig and E. Colby, *Advanced Accel. Concepts*, 724 (AIP Conf. Proc. 335, 1995).
2. J. Rosenzweig, *et al.*, *NIM A* **410** 437 (1998)
3. D.T. Palmer, *et al.*, *Proc. PAC'97*, 2687 (IEEE, 1998)
4. R. Zhang, *et al.*, *Proc. of the 1995 PAC* (IEEE, 1996)
5. X. Ding, *et al.*, these proceedings (#WEA58)
6. J.B. Rosenzweig, *et al.*, these proceedings (#WEA64)
7. J.B. Rosenzweig, *et al.*, *Proc. PAC'97*, 1968 (IEEE, 1998)
8. J.B. Rosenzweig, *et al.*, these proceedings (#WEA65)
9. D. Yu, *et al.*, these proceedings (#WEA65).
10. C. Pellegrini, *et al.*, *NIM A* **331**, 223 (1993)
11. M. Hogan, *et al.*, *Phys.Rev.Lett.* **81** 4867 (1998).

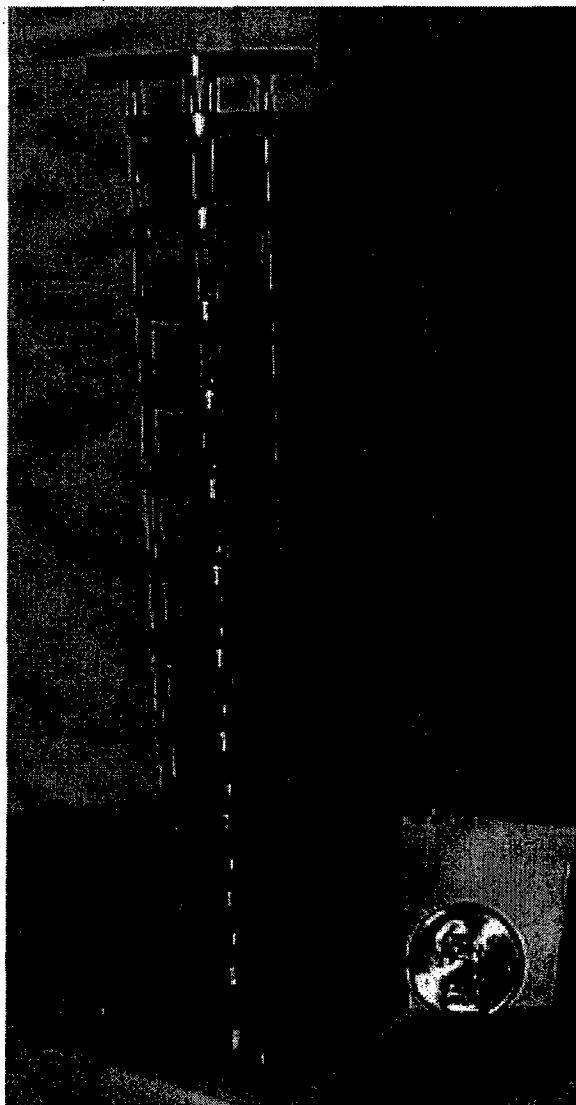


Figure 3. Cold test model (with outer wall removed) of 11.424 GHz, $10+2/2$ cell PWT photoinjector.

*Work supported by US DoE Contracts DE-FG03-92ER40693 and DE-FG03-98ER45693.

* Email: rosenzweig@physics.ucla.edu

+ Argonne National Laboratory.

A CLOSED ORBIT MEASUREMENT WITH THE NSRL BPM SYSTEM*

J. H. Wang[#], Y. Yin⁺, J. Y. Li, Z. P. Liu, B. G. Sun, G. C. Wang, J. H. Liu
NSRL, USTC, Hefei, Anhui 230029, P.R.China

Abstract

The beam position monitor system (BPM) of NSRL electron storage ring have a resolution of 10 microns with an accuracy of 50 microns, which is adequate for beam position measurement and the closed orbit correction. The paper describes both of the BPM system and the closed orbit measurement.

1 INTRODUCTION

The electron storage ring of NSRL of the University of Science and Technology of China at Hefei, P.R.China is a special synchrotron radiation facility. It operates with the energy of 800 MeV and the beam current of 100-300mA. As known to all that the BPM system is one of key measuring equipment for advancing the quality of beam current and insuring the machine in normal operation. And the BPM system of NSRL has constructed early and its electronics have been modified now. The signals to noise ratio and the dynamic range of the measurement have been greatly increase after the modified electronics. The accuracy and the reliability of the system have been improved, which have the accuracy of 50 μ m and a resolution of 10 μ m. With the help of the system we have finished the commission of insertion devices of NSRL storage ring [1]. The experiments prove that is adequate measurement of beam position and closed-orbit correction [2].

2 THE BPM SYSTEM AND ITS SIGNAL PROCESSING

2.1 The BPM system and Calibration

The circumference of the NSRL electron storage ring is 66 meter. The ring contains 12 dipole magnets and 48 quadrupole magnets, with 27 BPM. Each BPM has four button type pick-ups mounted in a skew manner as shown in Figure 1. The diameter of the button is 25mm. Each BPM button is welded to a BNC vacuum feedthrough, which then is welded to beam pipe. The beam pipes are 1.8 meter long with BPMs on both ends. The calibration has been done for each BPM. A wire

goes through the centre of the pipe to simulate the beam.

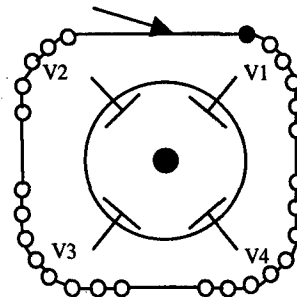


Figure 1: Distribution of BPM along ring and Single construction of BPM

The wire can be moved inside the beam pipe. A home-made electronics circuit detect the induce voltage from each pick-up for each position of the wire. In the way, two BPMs at the both ends of beam pipe can be Calibrated simultaneously. A computer recorded the voltage readings, and calculates the offset between the electronic and mechanical centre.

For the 25 mapped data, a least square method is used to calculate the coefficients A_n . The calculation is shown below [3]:

$$U = (v_2 - v_1 + v_3 - v_4) / (v_1 + v_2 + v_3 + v_4)$$

$$V = (v_1 - v_4 + v_2 - v_3) / (v_1 + v_2 + v_3 + v_4)$$

$$X_I = \sum_{i=0}^N \sum_{j=0}^i a_{i-j,j} (U_I - U_0)^{i-j} (V_I - V_0)^j, U_0 = U_I|_{x=0}, I = 1, \dots, 25$$

$$Y_I = \sum_{i=0}^N \sum_{j=0}^i b_{i-j,j} (U_I - U_0)^{i-j} (V_I - V_0)^j, V_0 = V_I|_{y=0},$$

make $N=3$

$$X \text{ or } Y = A_1 + A_2(U_I - U_0) + A_3(V_I - V_0) + A_4(U_I - U_0)^2 + A_5(V_I - V_0)^2 + A_6(V_I - V_0)(U_I - U_0) + A_7(U_I - U_0)^3 + A_8(U_I - U_0)^2(V_I - V_0) + A_9(U_I - U_0)(V_I - V_0)^2 + A_{10}(V_I - V_0)^3 \quad (1)$$

2.2 The performance of the signal processing electronics

The BPM system has total 108 output signals. The distribution of BPM in storage ring and the structure of a single BPM can be see Fig.1. The storage ring is divided into four quadrants. Each quadrant has 5-8 BPMs, which provide up to 32 output signals. The multiplexer system has three levels. Each quadrant has a sub-multiplexer (100c1423 relay switch) system. Each sub-multiplexer system has 5-8 multiplexer, which acquires 4 pick-up

*Work supported by China Academy of Science contract KJ85

[#] Email: wjhua@ustc.edu.cn

⁺Present address: Y.Y.Labs, Inc., P.O.Box 597, Fremont, CA 94537-0597, USA

signals (total 16 for 4 quadrants). These 16 signals are then delivered to the central control room to a higher lever 4-multiplexer system via a long cable about 50 meters. Each time, the higher level system acquires 4 signals. Finally, one multiplexer processes these 4 signals. The rf cavity of the storage ring has frequency of 204 MHz, therefore a narrow bandwidth filter, which has a centre frequency of 204MHz with only 10MHz bandwidth, is used as first stage. This 204MHz single frequency signal then is sent to a linear amplifier. The signal again goes through a low-pass filter and an A to D converter. The DC voltage reading is finally collected by computer. The 10MHz narrow band filter has greatly increased the accuracy and reliability of the system. The block diagram of the signal electronics circuit is shown in Figure 2.

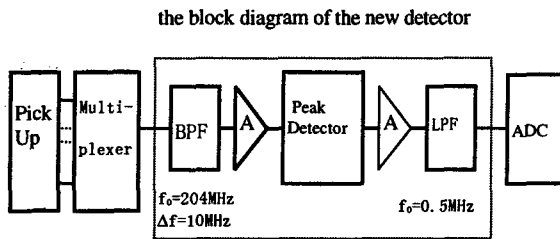


Figure2: The signal processing electronics

2.3 Specification of the electronics

In order to characterise the electronics system, we use a HP-8648A digit signal generator and a HP-3456 digit voltmeter for the measurement. The results indicate that S/N of new electronics circuit is as larger than 50db. The system has dynamic range of 33db. The non-linearity is less than 1% in the dynamic range. The input/output and the stability of the gain of the electronics are plotted in Figure3 (a) and (b).

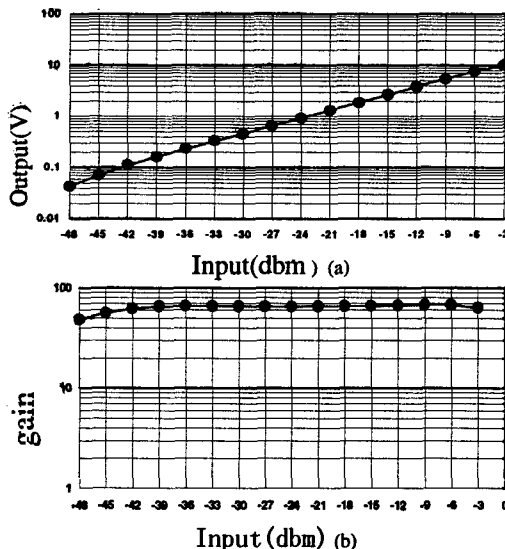


Figure 3: Character curve of I/O and Stability of gain

3 ANALYSIS OF THE MEASURING RESULT TO THE BPM SYSTEM

3.1 Experiment Result

We have done a lot of testing regarding the repeatability and reliability of the BPM system. The test results show that the BPM readings are reproducible in 30μm and the biggest deviation of beam position (*x* and *y*) was below 50μm with beam current reducing from 150mA to 68mA during 10 hours. This also shows that it has little dependent on beam intensity see Figure 3.

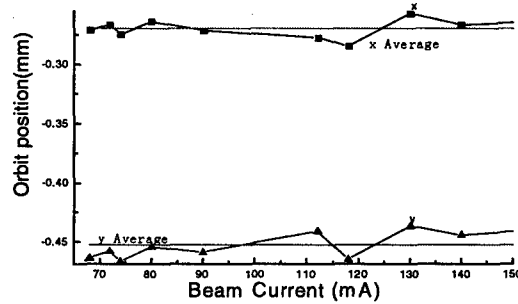


Figure 4: Deflect of the orbit with current

The system resolution can be expressed with the following formula:

$$R = 3N_{RMS} \times 1/S \quad (2)$$

Where, N_{RMS} is mean square root noise level, S is the system sensitivity. The measured value is close to the one calculated based on this formula, which is about 10μm, the resolution of the BPM system.

3.2 Closed orbit measurement

On the other hand, we use the induced signals on the button electrodes to determine the reliability of the system. The peak voltage detected by BPM button electrode can be calculated by the following formula [4]

$$V_{1,2,3,4} = \frac{d^2}{8a} \cdot \frac{R\bar{I}c}{\sqrt{2\pi\sigma^2 f_0 \sqrt{e}}} \cdot F(\delta, \theta_{1,2,3,4}) \quad (3)$$

Where $F(\delta, \theta_{1,2,3,4})$ is a beam position function, a is BPM geometric radius and d is BPM pickup radius.

If the button electrodes are working properly, $(V_1 + V_3)$ and $(V_2 + V_4)$ should be roughly equal for beam position change at *x* direction, the similar with *y* direction.

Therefore, $(V_1 + V_3) - (V_2 + V_4)$ should be close to zero. Since all the BPM sees the same beam current, the deviation of the sum signal of each BPM can be used to

indicate the system reliability. The following are the described formula:

$$S = \frac{\sum_{j=1}^4 V_j}{V_A} \approx 1, \quad D = \frac{(V_1 + V_3) - (V_2 + V_4)}{V_A} \approx 0$$

$$V_A = \left(\sum_{j=1}^4 V_j \right)_{\text{average for all BPM}} \quad (4)$$

In our case, the measurements showed that S is inside 1 ± 0.2 and Deviation is no bigger than 0.01 for most of BPMs. Beam orbit measurements have been done with orbit change induced by the use of the magnetic correctors[5]. The measurements supported the predicted orbit changes based on the machine physics calculation, see Figure 5, Figure 6.

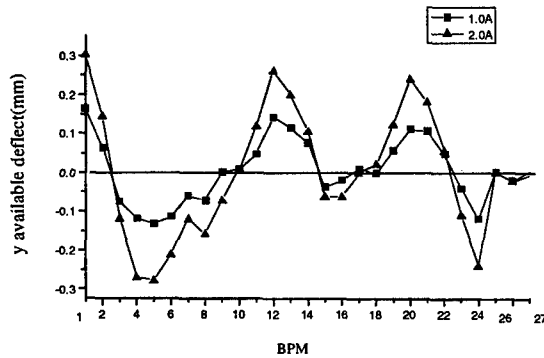


Figure 5: Relation curve of position deflect and Correct current

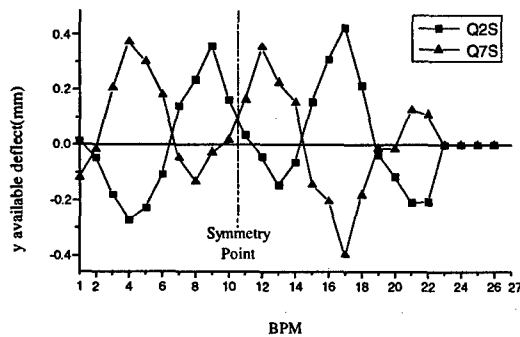


Figure 6: The analysis for system symmetry (Q2S and Q7S been separately charged)

The subsystem of the BPM for each quadrant also showed similar orbit shifts with phase difference between the quadrants when the corresponding magnetic correctors in each quadrant were in operation. The detail is shown in Figure 7.

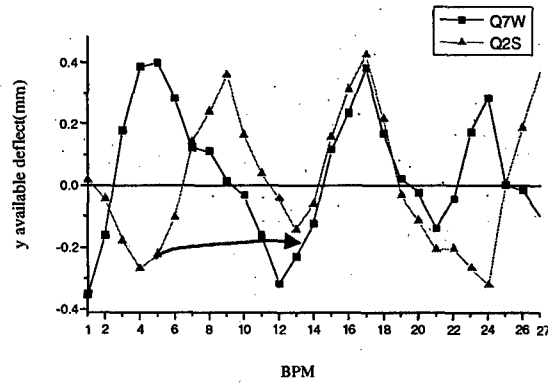


Figure 7: the analysis for system period (Q2S and Q7W been separately charged)

4 CONCLUSION

The beam position monitoring system of the NSRL storage ring basically satisfies the requirements of machine operation and studies of storage ring. The short-term reproducibility of measurement is better than $10\mu\text{m}$. The measurement time for scanning all 27 BPMs is about 15 seconds. Absolute beam position with respect to the magnetic centre of the adjacent quadrupole magnet will be determined directly with the beam in the near future.

5 ACKNOWLEDGEMENTS

We would like to thank Prof. C.Y. Yao of APS, Mr. Y.G. Zhou and many colleagues of NSRL, who made contributions to this work. The first author especially thanks Dr. Takao IEIRI of KEK and Prof. L. Ma of BEPC for their fruitful discussion.

6 REFERENCE

- [1] H.N. Xu, closed-orbit correct, Paper of Doctor of NSRL, 1998.
- [2] J.Y. Li, Z.P. Liu., and J.H. Wang, High power Laser and Particle Beams, Vol.10 No.2(1998), P291.
- [3] Y. Yin, J. S. Fan, The proceeding of the International Conference on Synchrotron Radiation Application. (May 9-12, 1989), P270.
- [4] Ma Li, BPM measurement, The Symposium of Science and Technology of BEPC.
- [5] M. Sands, The Physics of Electron Storage Ring, An introduction, SLAC-121 (1970).

REDUCTION OF X-BPM SYSTEMATIC ERRORS BY MODIFICATION OF LATTICE IN THE APS STORAGE RING*

G. Decker, O. Singh H. Friedsam, J. Jones, M. Ramanathan, and D. Shu, ANL, Argonne, IL

Abstract

With recent developments, X-ray beam position monitors (BPMs) are capable of making accurate photon position measurements down to the sub-micron level. The true performance of X-ray beam position monitors when installed on insertion device beamlines is, however, severely limited due to the stray radiation traveling along the beamline that contaminates the insertion device photons. The stray radiation emanates from upstream and downstream dipole magnet fringe fields, from steering correctors, and from sextupoles and quadrupoles with offset trajectories. While significant progress has been made at the APS using look-up tables derived from translation stage scans to compensate for this effect, performance of ID X-BPMs to date is at the 10 to 20 micron level. A research effort presently underway to address this issue involves the introduction of a chicane into the accelerator lattice to steer the stray radiation away from the X-ray BPM blades. A horizontal parallel translation of the insertion device allows only ID photons and radiation from two nearby correctors to travel down the beamline, simplifying the radiation pattern considerably. A detailed ray tracing analysis has shown that stray radiation gets displaced by up to 2 cm horizontally at the X-BPM locations so that it can be easily masked. Results from such a modified lattice, implemented for one of the insertion devices, are reported here.

1 INTRODUCTION

During the design of the APS, much consideration was given to the requirement for micron-scale beam position stabilization. To this end, a very careful mechanical design for photoemission gold-plated diamond blade-based X-ray beam position monitors was executed [1]. As described elsewhere [2], a method has been developed at the APS for reducing stray radiation background signals from X-ray beam position monitors on insertion device beamlines. This radiation originates not only from the fringe fields of the dipole magnets located upstream and downstream of the insertion device source point, but also from collinear steering corrector magnets and off-axis particle beam trajectories through quadrupole and sextupole magnets in the straight section. By realigning girders in the two sectors straddling the insertion device, one can eliminate all of the stray radiation with the

exception of that emanating from two corrector magnets located immediately upstream and downstream of the insertion device.

Figure 1 illustrates the concept of displacing accelerator girders in such a way that stray radiation is directed away from the X-ray BPM field of view. The strength of the dipole magnets on either side of the insertion device is decreased by 1 mrad, while two corrector magnets located immediately upstream and downstream of the insertion device are powered to compensate for this 1-mrad loss of bend angle in the main dipoles. With these changes in magnet strengths comes an accompanying displacement in the girders and an approximately 6-mm parallel horizontal displacement of the insertion device.

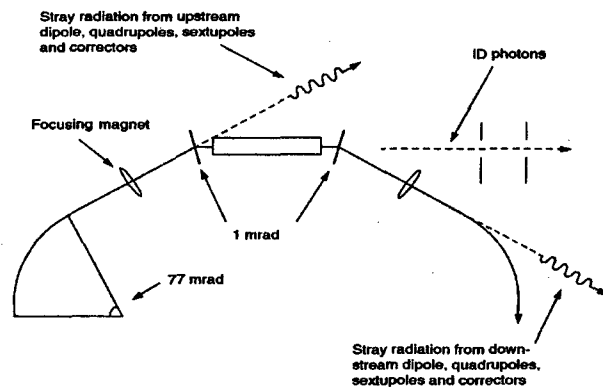


Figure 1: X-BPM stray radiation realignment concept

Because there are many insertion device beamlines in operation at the APS, an alternative concept was implemented that was less disruptive to users. Rather than displacing the insertion device outboard, the two adjacent accelerator sectors were displaced inboard, leaving the insertion device and its associated front-end and beamline components undisturbed. This required changing the strengths of four main dipole and four corrector magnets and realignment of ten girders (each APS sector is composed of five girders in addition to an insertion device).

2 IMPLEMENTATION

The lattice modification just described required a significant planning and analysis effort over a period of 15 months prior to its implementation in the APS storage ring. Among the tasks undertaken was an extensive program of computer-aided design ray tracing to ensure that no uncooled interior vacuum chamber surfaces would be struck by X-rays, both with standard particle beam steering and in the presence of large but physically

*Work supported by the U.S Department of Energy, Office of Basic Energy Sciences, under Contract No. W-31-109-ENG-38.

possible beam misalignment conditions. Shown in Figures 2 and 3 are plots indicating some results of this ray tracing effort.

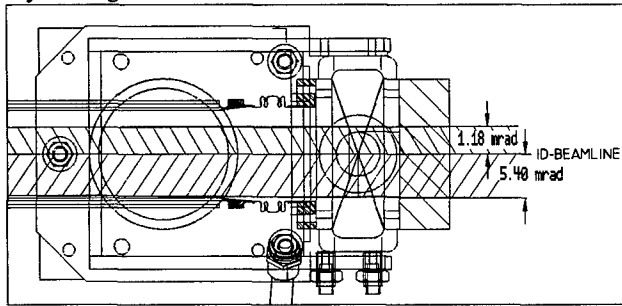


Figure 2: Insertion device exit port ray tracing result

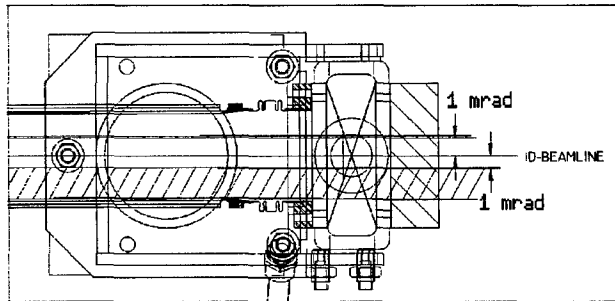


Figure 3: Ray tracing results showing separation of bending magnet radiation (crosshatched areas) relative to insertion device beamline axis after lattice change

The crosshatched areas in Figures 2 and 3 indicate the regions where bending magnet radiation, streaming from left to right, is present at the insertion device beamline exit port. The region above the beamline axis represents bending magnet radiation emanating from the downstream fringe fields of the dipole bending magnet located upstream from the insertion device, while the lower crosshatched area corresponds to bending magnet radiation emanating from the upstream end of the downstream dipole magnet.

In Figure 3, notice the separation between the dipole “fans” and the insertion device centerline resulting from the girder realignment. Note that only a sliver of radiation from the upstream dipole fan survives, with the majority of it having been occluded by an upstream radiation absorber. The downstream dipole fan is not displaced inboard by as much as the upstream fan has been displaced outboard, a consequence of the relative distances to the associated source points.

3 EXPERIMENTAL CONFIRMATION

Figure 4 gives the approximate geometry for the two X-ray beam position monitor blades installed in all standard APS beamline front ends. The views shown are taken from inside the accelerator looking out along the beamline, with the center of the accelerator on the right-hand side. The geometry was chosen such that the upstream assembly would not shadow the downstream blades and to avoid strong radiation background from

dipole radiation lying in the plane of the particle beam trajectory.

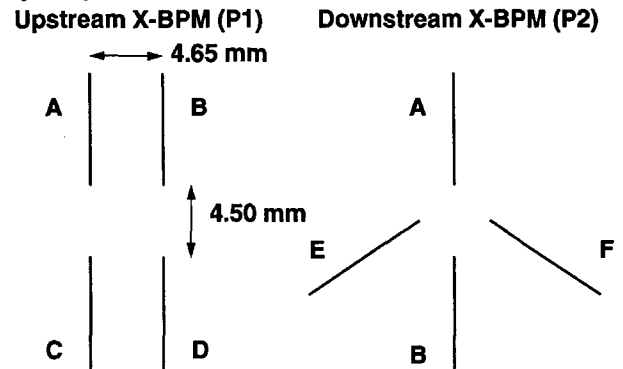


Figure 4: APS X-BPM blade geometry

Figure 5 shows plots of the blade sum signal for each of two X-BPMs located along two different beamlines, as a function of insertion device gap. One of them, beamline 1-ID, is a standard configuration, while the second, 34-ID, has undergone the “alternative” lattice modification described in the text following Figure 1 above.

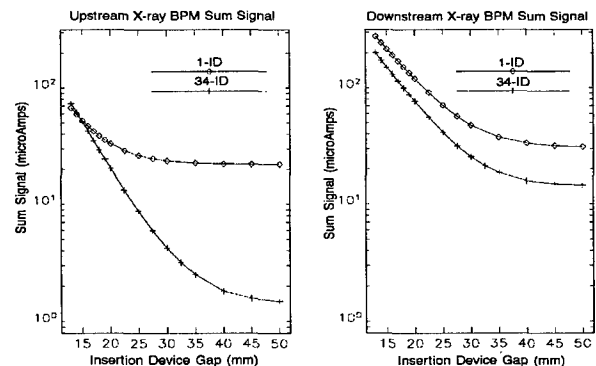


Figure 5: X-BPM sum signals vs. insertion device gap

Notice for the upstream X-BPM in the left-hand figure that the 34-ID background signal seen with the gap open (approaching 50 mm) is more than a factor of ten reduced in comparison to the signal from 1-ID. A factor of more than two improvement is seen for the downstream X-BPM.

While these results are encouraging, it is important to understand the characteristics of the remaining background signals. While radiation from the main dipole bending magnets should have been all but eliminated, keep in mind that the 1-mrad corrector magnets are themselves sources of synchrotron radiation. Because this radiation is predominantly off-axis horizontally, one would expect that the “E” and “F” blades would be strongly affected by it. As reported elsewhere [2], this is, in fact, the case. By steering vertically with the gap open, one sees a rapid variation of the signals on these two blades.

One fascinating observation was that the response of the P1 blade signals to local vertical steering with the insertion device gap open was almost perfectly symmetric. The top two blades tracked each other and were mirror images of the response of the bottom two blades. This raises the possibility of using the corrector magnet radiation itself as a position diagnostic. One would expect this radiation to show a peak value at a location 0.5 mrad horizontally off-axis from the insertion device beamline centerline. A blade monitor design similar to P1 and located 0.5 mrad off-axis would hold promise as a gap-independent X-ray position monitor.

Shown in Figure 6 are insertion device gap scans for the individual blade signals of the upstream (P1) X-BPM on beamline 34-ID, after the lattice modification.

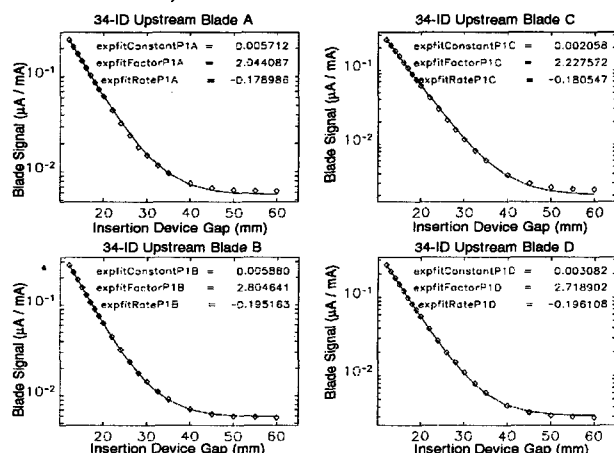


Figure 6: Normalized 34-ID X-BPM blade signals vs. gap

The data plotted are normalized by dividing the blade photocurrent signals in microamperes by the total stored beam current in milliamperes. Each blade signal was fit to a function of the form

$$\text{Signal} = \text{Constant} + \text{Factor} * \text{Exp}(-\text{Rate} * \text{Gap}),$$

which is shown by the solid lines in Figure 6. The data is indicated by diamond-shaped symbols, and the fit parameters are shown on each plot.

An important aspect of the data in Figure 6 is that the slopes of the four curves (i.e., the "rates" for the fit) are significantly different from blade to blade. Whatever the cause, this phenomenon has serious consequences if one is interested in using these blade monitors as gap-independent position diagnostics. Suspecting a nonlinear electronics effect to be responsible for the observed differences in slope in Figure 6, the cables were swapped so that the top blades' electronics were connected to the bottom blades, and vice versa. The effect was observed to move with the blades and not the electronics, thus exonerating the electronics as the culprit.

Shown in Figure 7 are plots showing the variation of the "factor" and "rate" fit coefficients as functions of horizontal and vertical beam position at the P1 blade monitor location resulting from a local orbit distortion at

the insertion device source point. The transverse beam positions were computed by an extrapolation from rf beam position monitors employing capacitive pickup electrodes mounted on opposite ends of the insertion device vacuum chamber.

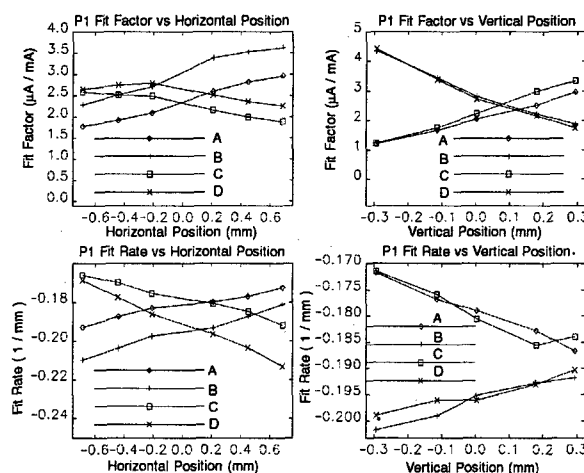


Figure 7: Gap scan fit coefficients vs. position

One possible explanation for the behavior seen in Figure 7 is that it is a result of detailed fabrication differences from blade to blade, for example, small variations in blade rotation angle. While in principle it may be possible to compensate for this effect, it is unlikely that the beam can be stabilized at the sub-micron level long enough to determine the coefficients to the required accuracy to support submicron level compensation.

4 CONCLUSIONS

A technique to substantially reduce stray radiation background levels from insertion device X-ray beam position monitors has been implemented at the APS. While use of these devices as a submicron-stable position diagnostic remains a challenge, it appears that a device sensitive to corrector magnet synchrotron radiation may hold the potential to be a stable gap-independent X-ray position diagnostic.

5 ACKNOWLEDGEMENTS

This work is the result of a cross-divisional effort, with significant contributions from members of both the Accelerator Systems and Experimental Facilities Divisions.

6 REFERENCES

- [1] D. Shu, et al., Nucl. Instr. Meth. A, **319**, p. 56 (1992).
- [2] G. Decker, O. Singh, "A Method for Reducing X-ray Background Signals from Insertion Device X-ray Beam Position Monitors," Phys. Rev. ST-AB (to be published).

CONTROL AND DATA PROCESSING OF THE DISTRIBUTED 500 MHz NARROWBAND BEAM POSITION MONITOR SYSTEM OF ELSA

J. Dietrich*, J. Keil** and I. Mohos*

*Institut für Kernphysik, Forschungszentrum Jülich, Germany

**Physikalisches Institut, Universität Bonn, Germany

Abstract

The preservation of the polarization level during acceleration of the electron beam is currently the main topic at the Electron Stretcher Accelerator (ELSA) of the University of Bonn. It can be improved by a good correction of the closed-orbit relative to the magnetic quadruple centres using the method of beam-based alignment. Beam position monitor electronics, developed in the Forschungszentrum Jülich/IKP for ELSA are integrated to form the 28 BPM orbit measurement equipment. The deviation of the closed orbit measured by the BPM system was reduced to an rms-value of 140 μm .

1 INTRODUCTION

The 3.5 GeV Electron Stretcher Accelerator (ELSA) at Bonn University was recently upgraded for the acceleration of polarized electrons [1]. During the energy ramp several strong depolarizing resonances have to be crossed. The strengths of one type of resonances connected with the vertical closed orbit distortions can be reduced by steering the beam through the magnetic quadrupole centers of ELSA. A common technique to determine the magnetic axis of a quadrupole relative to the axis of the beam position monitors (BPM) is the method of beam-based alignment [2]. To make use of this method a BPM system with a good resolution and long term stability is required, which is also able to be used at low currents of some mA.

2 SYSTEM ARCHITECTURE

The new BPM electronics forming a 28 BPM orbit measurement equipment are integrated in the control system of ELSA. The control system of ELSA is organised hierarchically in three layers with distributed intelligence. The presentation level is based on HP9000/700 workstations running HP-UX as the operating system. Its purpose is to display the status of the machine and to hold the distributed data base. The process level is used for preprocessing data from devices using VME processors running the VxWorks real-time operating system on Motorola 68K CPUs. The lowest level is the fieldbus level for the direct communication with the devices. A dedicated VME crate for the BPM system uses a serial communication board based on the

MC68360 communication controller and a MC68060 CPU for high level data processing. The front-end devices are connected with four fieldbus lines to the communication controller. The communication between the two processors is done over the VME backplane using mailbox interrupts (Fig. 1).

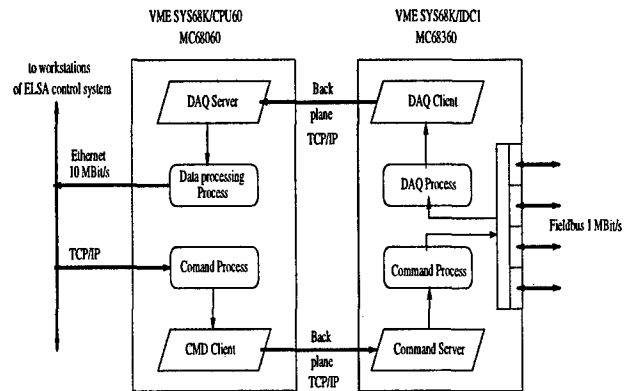


Figure 1: Architecture of the high level data acquisition system.

The data communication between the VME processors and the workstations is done via a fibre optics link using TCP and UDP protocols with 10 MBit/s. The orbit data and BPM status information is displayed on workstations running a GUI based on the X-Window system and OSF/Motif.

3 FRONT-END ELECTRONICS

Front-end electronics each consisting of an rf narrow-band signal processing unit and a data acquisition and control unit with data processing capability are placed close to the four-button monitor chambers [3]. The monitor stations arranged in four subgroups are connected via galvanically decoupled serial fieldbuses to the host.

3.1 Analog Electronics

Narrowband superhet rf electronics (Fig. 2) process the fundamental components of the button signals. At the input analog rf multiplexer with programmable button sequence scans the four buttons. Low noise narrowband preamplifier ($B=5$ MHz) amplifies the signal of the selected button. For high signal levels a switched 30dB attenuator can be inserted. Mixer transposes the desired

frequency range to the intermediate frequency, where narrowband filters reduce the bandwidth to ~200 kHz and amplifier with controlled gain enhances the signal level appropriate for demodulation.

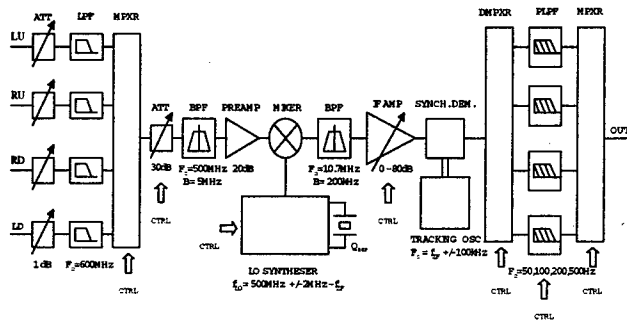
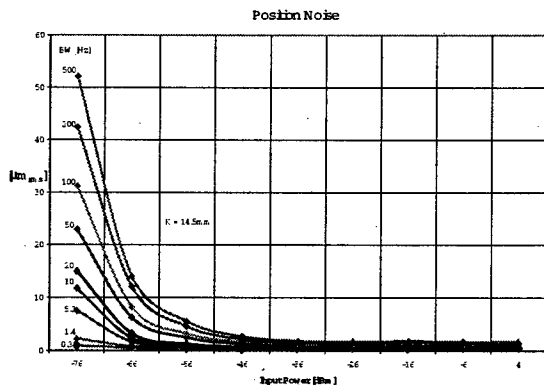


Figure 2: Block diagram of the rf signal processing module.

On-board remote controlled synthesizer generates the LO signal applied to the mixer. Its frequency determines the band-center frequency of the signal processing. Frequency changes within the IF bandwidth will be automatically tracked by the demodulator in real time.

Band-center frequency adjustments can be achieved in the range of 500MHz \pm 2MHz with 50kHz steps. The output signal of the linear synchronous demodulator is proportional to the rms value and carries level changes with frequencies up to 500 Hz. The gain control range of the processing chain is about 100 dB. Signal level dynamic



between -80dBm and +10dBm is allowed. The typical equivalent beam position noise is $<0.5 \mu\text{m}_{\text{rms}}$ @ $P_{\text{in}} = -46 \text{ dBm}$, $B=10 \text{ Hz}$ and $K=14.5 \text{ mm}$ (Fig. 3).

Figure 3: Equivalent rms position noise.

3.2 Data Acquisition

The Data Acquisition Unit (Fig. 4) consists of a 8bit microcontroller with 8kbyte EPROM and 32kbyte RAM and built-in timer, half-duplex 1 Mbit/s asynchronous serial interface with galvanic isolated twisted-pair

transceiver for data communication, 12 bit ADC for digitizing of the demodulated electrode signals and 12 bit DAC for gain control, several bits for timing and bandwidth control and a 3-wire serial interface for synthesizer control.

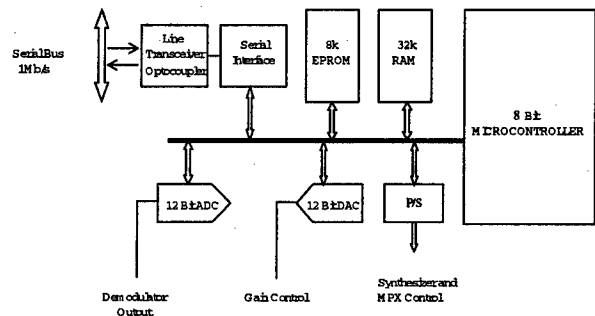


Figure 4: Block diagram of the data acquisition and control module.

The timer of the microcontroller controls the rf multiplexer and the timing phases of the acquisition. The sampling rate can be set by means of remote command between 1-256ms corresponding to the selected lowpass filter.

4 DATA PREPROCESSING

The built in firmware of the front-end daq unit performs some basic computing tasks. After digitizing of the button signals the horizontal and vertical positions are computed. In automatic gain control mode the measured values are compared with a reference and a gain correction value will be prepared for the next cycle. The scan timing and the step gain control are synchronised. Four button signals will be measured in each cycle with the same gain, therefore consistent data are used for position computing. Subsequently a digital lowpass filter algorithm reduces the signal bandwidth. Its cutoff frequency is programmable in 14 steps. The overall bandwidth can be reduced down to 0.1Hz. On request of the host the acquired and preprocessed data will be transferred in real time, or can be buffered in the 4kS RAM for slower read or later use.

5 HIGH LEVEL DATA PROCESSING

In the free run mode the data acquisition of all BPM stations is triggered in regular intervals by the fieldbus host computer. The BPM stations send as a response on the trigger the measured values as a sequence of data blocks on the four fieldbus segments to the host. The complete data block of 28 BPMs is passed over to the BPM controller CPU using a TCP/IP network connection. A second process with a lower priority sends periodically the actual status and BPM settings to the control system. Commands for settings and changing of hardware parameters of the BPM stations are passed over to the server process using a second TCP/IP connection.

The BPM controller CPU corrects first for unequal electrode attenuations [4] and linearizes the nonlinear response of the electrode configuration using a combination of a look-up table and a two-dimensional local polynomial approximation of second degree. Closed orbit data is transferred to the workstations and can be displayed and analyzed. Several different orbit correction algorithms like harmonic correction, least square fit, MICADO, and local bumps are available.

Furthermore data traces with the signals of all BPMs can be acquired and saved to disc for off line analysis. The sampling interval can be up to 1 ms covering 4096 positions.

6 CALIBRATION

The strengths of the imperfection resonances depend on the correction of the vertical closed orbit during resonance crossing. The technique of beam-based alignment [4] was used to determine the magnetic centers of the quadrupoles which define the zero positions of the nearby BPMs. To locate the magnetic axis of the quadrupole with the beam, a small change of the focusing strength ($\approx 1\%$) with an additional power supply was applied. The orbit was moved to different positions using a local four corrector bump. If the beam passes through the magnetic center of the quadrupole, the position shift due to the change of the focusing strength vanishes at the 28 BPMs. An example of a measurement is shown in Fig. 5.

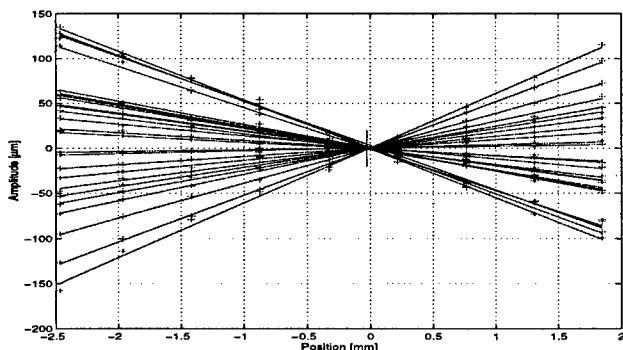


Figure 5 : Shift in position due to a 1 % change of the gradient in quadrupole QD15 for different beam bump amplitudes.

The zero position of the BPM is determined from the analysis of all zero crossings of the BPMs weighted with the errors from a linear regression for each BPM. The reproducibility of the zero positions of the BPMs determined by this method is approximately 100 μm mainly due to statistical fluctuations.

7 ORBIT CORRECTION

Before orbit correction the orbit distortion in the vertical plane was reduced by a good alignment of the quadrupole and dipole magnets. For the closed orbit correction 20 horizontal and 18 vertical steerer magnets were used. The

uncorrected orbit with $x_{\text{rms}} = 2.46\text{ mm}$ and $z_{\text{rms}} = 0.93\text{ mm}$ was reduced after five iterations to values of $x_{\text{rms}} = 0.126\text{ mm}$ and $z_{\text{rms}} = 0.141\text{ mm}$ using a least-square orbit correction algorithm based on the singular value decomposition. The uncorrected and corrected orbit is shown in Fig. 6.

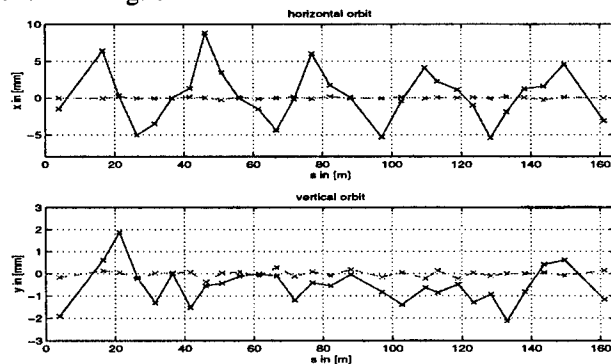


Figure 6: Uncorrected (solid) and corrected (dashed) closed orbit.

First measurements with polarized electrons showed, that after the orbit correction the polarization at the first strong imperfection resonance at 1.32 GeV could be almost completely preserved without additional means like harmonic correction.

8 CONCLUSIONS

The close placing of the rf and data acquisition electronics to the pick-up buttons reduces effectively the rf interference and allows to utilize the remarkable noise performance of the front-end unit. The galvanically decoupled fieldbus eliminates the disturbances caused by the potential difference between the monitor chambers and the host and enhances the reliability of the data transfer. Software development on the user's side is not necessary for the low-level acquisition control and preprocessing. The distributed and time-overlapped data processing improves the overall system performances.

It was possible with the new BPM system to correct the closed orbit of ELSA up to rms values of 140 μm in both planes.

9 REFERENCES

- [1] C. Steier et al.: „Acceleration of Polarized Electrons in ELSA“, EPAC 98.
- [2] P. Rösler: „A beam position measurement system using quadrupole magnets magnetic centres as the position reference“, Nucl. Inst. and Meth., A343 (1994) 374.
- [3] I. Mohos and J. Dietrich: „500MHz Narrowband Beam Position Electronics for Electron Synchrotrons“, AIP Conf. Proc. No. 451
- [4] Y. Chung, G. Decker: „Offset Calibration of the Beam Position Monitor Using External Means“, AIP Conf. Proc. No. 252

BEAM POSITION MONITORS FOR THE CORNELL ELECTRON SYNCHROTRON*

R. Holtzapple, G. Dugan, and R. Littauer

Laboratory of Nuclear Studies, Cornell University, Ithaca, NY 14853 USA

Abstract

The Cornell 10-GeV Electron Synchrotron, built in 1968 for fixed-target physics, has served since 1979 as injector to the storage ring CESR. In this mode, which calls for a sparse fill pattern (45 bunches at most), the original beam position monitors are ineffective. An improved system, now under construction, is described.

1 INTRODUCTION

Originally, the Cornell Electron Synchrotron accelerated a "continuous" beam (all 700 MHz RF buckets filled); its beam detectors used ferrite-core current transformers that could not resolve individual bunches. The cores carried auxiliary differential windings that served as rudimentary beam position monitors (BPMs). However, with the widely spaced bunches called for by CESR, these windings no longer deliver useful signals. New BPMs are being installed as part of a general improvement program.

With cost and downtime as major constraints, we decided that the new BPM system should fit into the present vacuum enclosures and work through the existing cable system. Analog signals representing intensity, horizontal, and vertical position are brought to the control room through three 75 Ω cables that encircle the synchrotron (~756 m circumference). These cables, similar to RG59/U but triaxially shielded, have an uncomfortably long risetime ($t_r \approx 70$ ns, maximum).

The BPM signals, after treatment by local preamplifiers, are multiplexed into the cables via small relays that are energized one at a time. Taking data for the complete ring requires stepping sequentially through all the relays.

BPMs for the synchrotron, as opposed to the storage ring, must deal with some special features: (1) The beam is about three orders of magnitude smaller—only a few times 10^8 particles per bunch—and it is not steady. (2) The orbit errors change during the acceleration cycle because remanent fields and eddy currents, important at injection time, become insignificant at high energy: orbit measurement must thus take place in a selected short time interval within the 8 ms acceleration cycle. (3) Coherent beam oscillations, caused principally by injection errors, remain significant throughout the acceleration cycle: the BPM signals must be averaged over several turns to locate the equilibrium orbit.

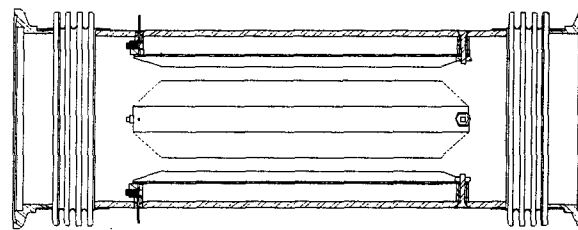


Figure 1. Vertical section through the stripline beam detector. e^- travel from right to left in this diagram, delivering at the downstream end of the stripline a pulse doublet with initially positive excursion. (e^+ moving in the opposite direction produce a similar signal.)

2 BEAM PROBES

Short beam probes (pickup "buttons" or loops) have capacitive or inductive source impedances. When loaded by a resistance R , such probes pseudo-differentiate the bunch signal. The time constants ($\tau = RC$ or L/R) come out well below 1 ns when $R \approx 50 \Omega$. Since this is comparable to the duration of the bunch, the output signal becomes a short, bipolar pulse *doublet*. When such a doublet encounters a long risetime t_r , the output amplitude goes as $1/t_r^2$. In our case the signal would be reduced almost to the noise level. We avoid this by immediately converting the probe signal into a longer, monopolar pulse, using peak rectification by a fast diode.

A strip-line probe is better than a short probe in this mode of operation. Instead of pseudo-differentiating, the line adds a delayed, inverted reflection from its far end (shorted). The resulting doublet spacing can be large—twice the propagation time of the line. To fit into the available space, our lines are 0.15 m long, yielding a doublet spacing of 1 ns.

Between the 96 pairs of synchrotron magnets mounted on I-beams there are drift spaces (usually 0.28 m long) that alternately accommodate pump ports and corrector coils. The latter, assembled on a tube of 43 mm inner radius, leave enough clearance for BPM signal feed-throughs. The lattice functions β_x and β_y are approximately equal (~12 m) at these locations, giving similar sensitivities to the BPMs in both planes. The betatron tunes are $Q_x = 10.65$, $Q_y = 10.77$; we expect to install about 50 BPMs, spaced roughly by quarter-wavelengths.

Figure 1 shows one BPM consisting of four strip lines placed in symmetrical pairs on opposite sides of the beam in each dimension, horizontal (x) and vertical (y).

* Work supported by the National Science Foundation

The strip, spaced 9.5 mm from the wall of the tube, is 38 mm wide, yielding $Z_0 \approx 100 \Omega$. (The strips are lightly folded longitudinally to conform to the curvature of the tubular wall.)

3 SIGNAL PROCESSING

To first order, the amplitudes from the two probes of a pair are, respectively,

$$a_+ = qk_+ \left(1 + \frac{x}{x_0} \right) \quad \text{and} \quad a_- = qk_- \left(1 - \frac{x}{x_0} \right),$$

where q is the bunch charge, k_+ , k_- are gain factors, x is the bunch displacement from center, and x_0 is a scale length. [Similarly for y .] In the ideal case we have $k_+ = k_-$; then

$$x = \frac{\Delta a}{\Sigma a} x_0,$$

with $\Delta a \equiv a_+ - a_-$ and $\Sigma a \equiv a_+ + a_-$. To ensure that a null Δ -signal correctly indicates $x = 0$, we evidently need to maintain $k_+ = k_-$ over an adequate dynamic range.

Unfortunately, pulse stretching (by peak rectification) cannot be done *after* the Δ -signal is formed, since this signal may have either sign. The two line signals must therefore be rectified individually, with the two rectification yields entering separately into k_+ and k_- . As illustrated in Fig. 2, the main feature of diode rectification is a threshold intercept, governed by the diode's cut-in voltage.

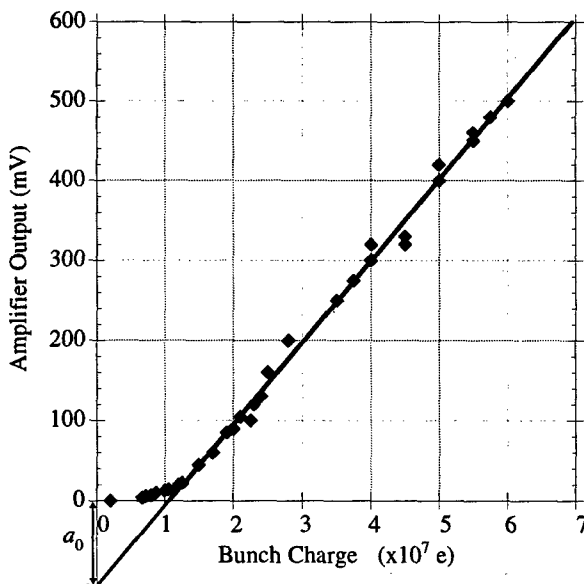


Figure 2. Amplifier output as a function of bunch charge. A linear fit to the data above threshold is shown.

With our particular strip lines and diodes (Hewlett-Packard HP5082-2835 in the prototype), this threshold corresponds to $\sim 10^7$ particles per bunch; above threshold the

rectification yield is substantially linear. We will use matched pairs of diodes for each pair of strip lines; when the intercepts are equal a null Δ -signal still correctly indicates $x = 0$. To calculate a nonzero bunch displacement from the stretched signals we use

$$x = \frac{\Delta a}{\Sigma a + 2a_0} x_0,$$

where a_0 is the threshold intercept projected onto the pulse amplitude axis (see Fig. 2).

If a small gain mismatch does remain, suppose that

$$k_+ = (1 + \epsilon) k_- \quad [\epsilon \ll 1].$$

A centered bunch then yields $\Delta a / \Sigma a \approx \epsilon / 2$, giving a false indication

$$x_E \approx (\epsilon / 2) x_0.$$

With $x_0 \approx 21$ mm, to hold $x_E \leq 1$ mm—adequate for our purposes—we need only maintain $|\epsilon| \leq 9\%$.

4 CIRCUITS

Figure 3 shows the arrangement of stretchers and amplifiers for forming Δa and Σa and driving the coaxial cables. Figure 4 shows the Δ -signal observed through the coaxial cable. A high-pass time constant of 0.4 μ s, well below the 2.5 μ s revolution period, ensures that the signal returns to zero between pulses. (Orbit measurements will be made with only a single bunch of e^- circulating.)

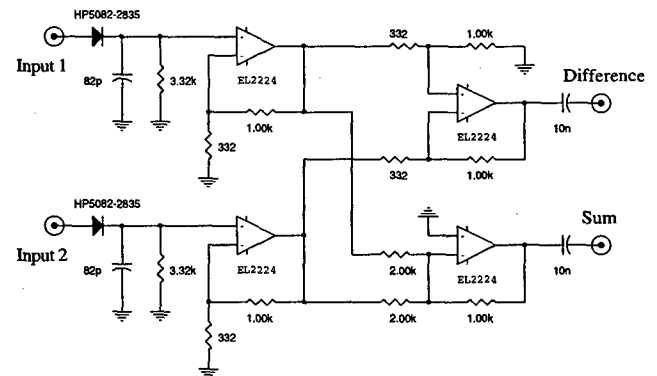


Figure 3. Schematic of prototype stretchers, sum, and difference amplifiers for one pair of striplines. (To avoid reaching the amplifier's output current limit, the sum channel has a lower gain than the difference channel.)

Starting at the desired time in the acceleration cycle, BPM pulses from a selected group of turns must be integrated to obtain the *average* bunch position (in the presence of oscillations). This is illustrated, for 5 turns, in Fig. 5. The burst of 5 gate signals is timed so as to exclude the reverse-polarity excursion of each BPM pulse. The gate output is applied to an operational integrator, which is reset before the burst but allowed to hold its accumulated voltage until read out by a computer.

and Gerry Codner for helpful advice and valuable discussions on the design of the electronics.

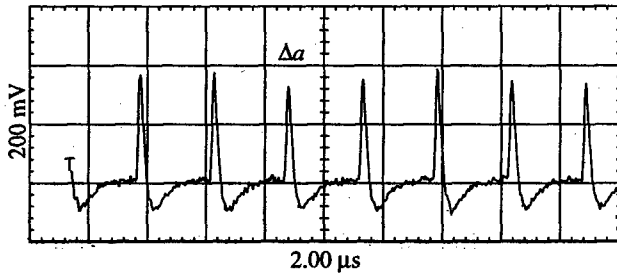


Figure 4. Delta-signal from a vertical pair of striplines, seen ~ 4 ms into the acceleration cycle. A substantial offset of the equilibrium orbit is indicated, as well as some bunch oscillations.

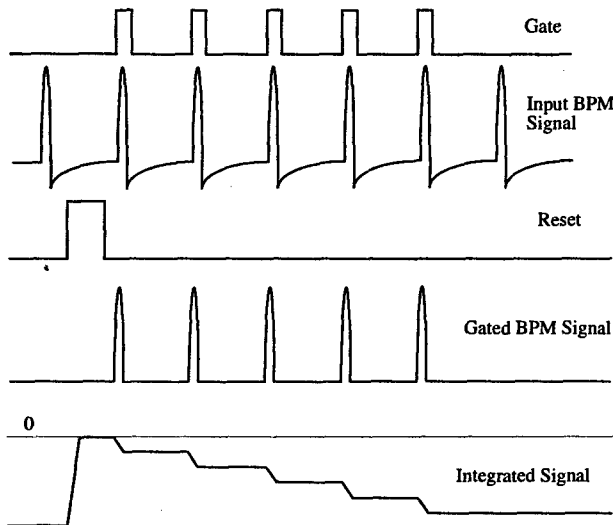


Figure 5. Timing diagram for the gated integrator circuit. (The integrator reverses the signal polarity.)

5 CALIBRATION

A rough estimate for x_0 (≈ 21 mm) was obtained in bench measurements, using a short pulse sent down a movable conductor to simulate the beam. A more appropriate calibration will be obtained, in due course, during studies of the orbit-correcting procedures themselves.

6 CONCLUSION

A stripline BPM, together with its signal processing circuits, has been designed and tested with good results. Slight modifications to these designs will be made, but a suitable system is close to reality. During the 1999 summer shutdown, in preparation for CESR Phase III high-current running, the synchrotron will be completely outfitted with this BPM system.

7 ACKNOWLEDGMENTS

The authors thank Yulin Li and Tobey Moore for designing and building the stripline detector, and John Sikora

A NEW APPROACH TO PHOTON BEAM POSITION MONITORING AT ELETTRA

A. Galimberti¹, C. J. Bocchetta, A. Gambitta, G. Paolucci, SINCROTRONE TRIESTE
G. Paolicelli, INFN UNITA' ROMA TRE
G. Stefani, UNIVERSITA' DI ROMA TRE AND INFN UNITA' ROMA TRE

Abstract

In the latest generation of SR sources, local bump orbit feedback systems are under development for improving the stability of the delivered radiation. Photon Beam Position Monitors (PBPM) are being built as detectors of beam movements and as references for feedback systems. A new generation of PBPM's for Undulator beamlines is being designed at ELETTRA. Detectors based on the use of electron energy analysers will drastically reduce the contamination of dipole magnet radiation on the PBPM to less than 0.1%. A detector prototype has been designed and is currently under construction. A full description of the detector layout, its working principle and the expected behaviour obtained by computer simulations are presented.

1 INTRODUCTION

For the latest generation of SR sources, local bump orbit feedback systems are being developed for the improvement of the stability of the delivered radiation [1].

The conventional approach to a PBPM system for a high brightness beamline from an Insertion Device (ID) is to provide a pair of detectors based on four blades that intercept the fringes of the beam and photoemit electrons. The positions of the beam centre in the vertical and horizontal planes and the angles of emission are then computed from the eight photocurrents measured. At ELETTRA, in all the front-ends of the ID beamlines, a PBPM system is installed [2]. Because of our storage ring configuration, a significant part of the radiation from the upstream and downstream dipoles is superimposed to the ID beamline radiation [3]. This fact inhibits the application of any feedback algorithm based on the PBPM measurements.

2 DETECTOR LAYOUT

Even if the peak intensity of the Undulator radiation is much higher than the Bending Magnet (BM) contribution, the integrated intensity seen by a conventional PBPM, can be comparable. A drastic reduction of the contribution of dipole magnet radiation down to less than 0.1% can be achieved by selecting the energy of the photoelectrons. The Undulator energy spectrum is peaked within a narrow bandwidth around a particular value, which changes with the K parameter and the harmonics. The energy range of the BM radiation is wide and goes from few eV to 20KeV with a photon flux at 2GeV of about 10^{13} [photons/s/mrad²/0.1%BW]. Furthermore, only the fringe fields of the dipole contribute to the contamination of the

PBPM, so the effective BM photon flux seen is expected to be some order of magnitude smaller.

On the other hand, the first harmonic photon flux of, for example, the Elliptical Wiggler (section 4.2) working in the Plane Undulator Mode at $K_1=1.1$ is about 1×10^{16} [photons/s/mrad²/0.1%BW] at a photon energy of 112eV. Therefore, we have designed a new detector that selects the contribution to the spectrum at a given photon energy, with a bandwidth comparable to the Undulator linewidth. It will thus take advantage of the flux difference between BM and ID contribution at the positions of the harmonics.

A first prototype is under development and its layout is depicted in fig. 1. It is designed for position detection on a single plane and is composed of two parts: the photoemissive blades and a pair of electron energy analysers. The electron analysers are composed by an input lens and a hemispherical dispersing element. Each analyser is aligned with a blade and it collects the electrons, with an angular acceptance of a tenth of mradian, photoemitted by the blade.

The geometric position of the electrostatic lens and its polarisation ensure that each system (analyser & blade) is independent of the other. Tuning the analyser at the proper energy, depending on the Undulator spectrum and the photoemission line of the blade, we are able to reject most of the BM contribution to the signal.

The detector is energy tuneable from few eV to some keV. Therefore, it is suitable, for every Undulator device. Moreover it may be set easily and quickly for any working gap of the Undulator.

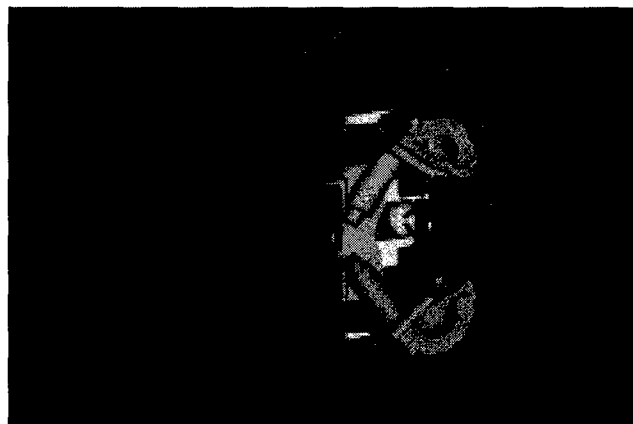


Figure 1: The New PBPM prototype layout. The flange of the manipulator supports the detector. The main active elements are visible: the couple of blades and the hemispherical analysers that collect and filter the photoemitted electrons.

¹ galimberti@elettra.trieste.it

3 DETECTOR WORKING PRINCIPLE

3.1 The Electron Analyser

The new PBPM utilises the electrostatic hemispherical analyser [4] developed and used, by the *Aloisa* and *Gas-Phase* beamlines at ELETTRA; to perform angle resolved time coincidence photoemission experiments. This analyser is characterised by a compact hemispherical dispersing element ($R_0 = 33$ mm), an electrostatic lens with a cylindrical symmetry formed by four elements and a system of selectable input and exit slits. All these features have been fully exploited on the experimental end stations at ELETTRA.

The dispersing element, composed of a pair of concentric hemispheres with fixed input and exit slits, selects electrons of a particular energy E_p proportional to the voltage difference between the hemispheres ($E_p = k_1 \Delta V$). It is characterised by a constant relative energy resolution $\Delta E/E = k_2$ [5]. The dimension of the internal and external hemisphere determines the constant k_1 , which is fixed for a given spectrometer. The constant k_2 is inversely proportional to the mean radius R_0 and directly proportional (in first order approximation) to the slit width so the relative resolution can be varied by changing the settings of the slits set when the experimental chamber is in air. Energy spectra can be performed in two ways: changing the kinetic energy of the analysed particle to match the fixed value selected by a constant applied voltage on the hemispherical sector or moving the applied potential on the hemisphere according to proportional factor k_1 . With the help of an input electrostatic lens, we can work in both conditions preserving optimised efficiency. The first operation mode is used to keep constant the energy resolution. The lens focuses electrons from blade to the hemisphere and changes, in a controlled way, their kinetic energy E to a fixed value to reach constant energy resolution ($\Delta E = k_2 E_p$). The lens transmission changes during the energy scan because angular magnification and linear magnification vary

($M_L \cdot M_\alpha = \sqrt{\frac{E}{E_p}}$). The second operation mode is

characterised by a constant lens transmission because the lens is used just to focus electrons and eventually to change their energy by a fixed proportional factor

($\frac{E}{E_p} = \text{Retarding Ratio} = R$). Since in the present

application, the essential point is not energy resolution but a controlled and possibly, constant transmission of the spectrometer for different analysed energy ranges, we plan to work in the second operation mode called Constant Relative Resolution. The intrinsic relative resolution k_2 has been estimated by computer simulation considering second order angular terms. Imposing a slit width of 2 mm, it results to be of the order of $3.5 \cdot 10^{-2}$. So it is comparable to the relative bandwidth of Undulator harmonics $\Delta E/E = (1 \text{ to } 5) \cdot 10^{-2}$. To achieve a fine tuning of the overall analyser relative bandwidth with respect to the Undulator line shape we have optimised the optical system for a *Retarding Ratio* ranging from 1 to 5.

As an example we may consider a lens system working at $R=2$; the overall behaviour results:

$$\frac{\Delta E}{E} = \left(\frac{\Delta E}{E_p R} \right) = \left(\frac{\Delta E}{E_p} \right) \frac{1}{R} = \frac{3.5}{2} \cdot 10^{-2} \approx 2 \cdot 10^{-2}$$

3.2 The Data Acquisition System

The instrumentation set-up of this detector is more complex than for a standard PBPM. Firstly, each electrode of the electron analysers and their electrostatic lenses is controlled by a set of low ripple programmable HV power supplies. Secondly, at each electron analyser exit an electron multiplier, that increases the signal level, has to be biased to some kV for its proper functioning. Two different ways of data acquisition are needed: counting mode and current mode. Each mode has a dedicated electronics: the former detects the fast pulse train coming out from the analyser and counts them. The latter integrates, with a configurable time constant, the signal. Then in both cases the data is processed in order to find the vertical beam centre.

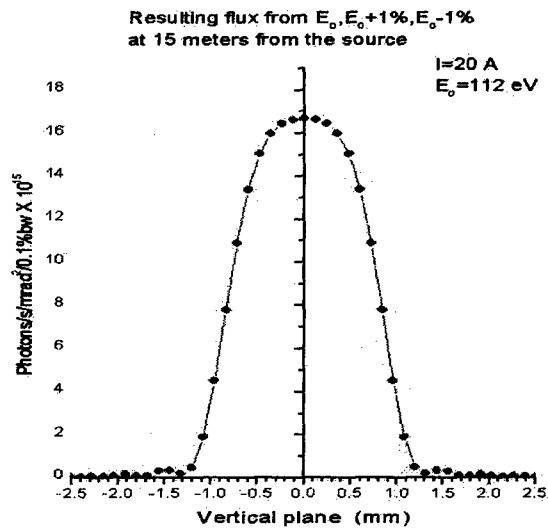


Fig. 2

Figure 2: Photon flux spatial distribution for the insertion device ID4 tuned at 112eV within an energy bandwidth of $\pm 1\%$ (@ 15m from the source)

Moreover, the two photocurrents of the blades are also acquired for alignment purposes. The acquisition in current mode is performed by custom floating picoammeters to decouple the biasing HV.

4 SYSTEM SIMULATION

The behaviour of the analyser has been studied by an electron ray-tracing simulation [6]. In particular we have made an effort to evaluate the spectrometer Field of View (or better the spatial transmission function at fixed analysed energy). In fact, the convolution of this curve with the photon flux spatial distribution (Fig. 2) determines the sensitivity of our system to beam motion. The result of the simulation is shown in fig. 3 for an

analyser configuration characterised by $\Delta E/E=2\%$. A grid of emission points, placed at the blade surface, has been utilised (0.1x0.5 mm spacing). Each point emits electrons in two orthogonal planes both perpendicular to the blade surface with a symmetric emission angle of $\pm 6^\circ$ (the lens geometrical acceptance angle). All the electrons have the same kinetic energy and lens and hemisphere voltages are tuned for this energy. The green colour scale represents the fraction of trajectories that reaches the exit slit of the hemisphere.

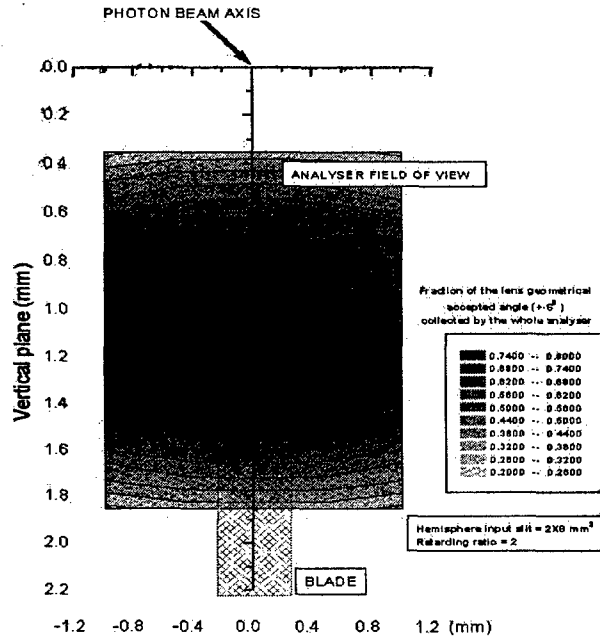


Figure 3: A simulation of the spectrometer transmission function with a $\Delta E/E=2\%$.

The electron beam orbit stability has to achieve 0.1% intensity constancy of the delivered radiation. Therefore, the Synchrotron light sources have stability goals from 10% to 1% of the photon beam size and divergence [7]. At 15m from the source it means a detector sensitivity of about 10 μm .

In order to estimate the sensitivity we consider that measured signal will be proportional to the convolution of spectrometer transmission function (fig.3) with the photon beam distribution (fig.2). We have calculated this curve along the vertical plane for a centred beam and for a 10 μm beam displacement. The result indicates a relative difference between the two signals of the order of 4%. The estimated current signal at the exit of the analyser is about 1nA. So a current measurement with the accuracy of 10pA is able to achieve a beam position sensitivity better than 10 μm . The electronics allow an accuracy of 1pA and so it would be possible to reach a sensitivity of 1 μm .

8 THE UHV CHAMBER AND TEST MEASUREMENTS

An UHV test chamber for PBPM testing will be placed along the Circular Polarisation Beamline immediately

after the front-end and before any optical element. A white beam is available at this location 15 meters from the source. An X-Z manipulator will provide the translations of the detector on an orthogonal plane with respect to the beam. In addition each pair of blade and analyser is mounted on a movable support that allows change the distance between the two blades. Therefore it is possible to change the working position of the detector with respect to the photon beam. The chamber has to be built as a compact experimental chamber with particular attention paid to the magnetic shielding.

6 PRESENT STATUS

Currently all the mechanical components are under construction. Delivery is planned for this summer. The control system and the instrumentation have been designed and are in construction. The first measurements with the detector are planned for the end of the year.

7 CONCLUSIONS

A new possible solution to photon beam position monitoring for Undulator beamlines has been presented. The simulations confirm that it is possible to obtain good sensitivity and to reduce drastically the contamination from BM radiation. The design allows a great flexibility and a large operative range. The measures will confirm if it is also completely compatible with the strictly requirements for the orbit stability feedback controls.

8 ACKNOWLEDGEMENTS

The authors would like to thank B. Diviacco for his scientific suggestions and C. Fava for his technical skill and friendly collaboration.

REFERENCES

- [1] C. J. Bocchetta et al.: 'The Design of the ELETTRA Fast Local Feedback System', Proc. 17th PAC, Vancouver, Canada, 1997.
- [2] A. Galimberti et al.: 'Photon Beam Position Monitors suitable for a Local Feedback System at ELETTRA', Proc. 5th EPAC, Sitges, Spain, 1996.
- [3] A. Galimberti and C. Scafuri: 'A Preliminary Study on High Precision Photon Beam Position Monitor Design for Local Feedback Systems', Proc. 6th EPAC, Stockholm, Sweden, 1998.
- [4] G. Stefani, M.V. Marabello: 'The Electron Spectrometer for the ALOISA Beamline', INFN, Internal report, 1991.
- [5] E.H.A. Granneman and M.J. Van der Wiel: 'Transport, Dispersion and Detection of Electrons, Ions and Neutrals' in Handbook of Synchrotron radiation, Vol. 1, Ed.by E.E. Koch North Holland 1983.
- [6] SIMION 3D code by David A. Dahl, Idaho National Engineering Laboratory, 1995.
- [7] H. Winick: 'Synchrotron Radiation Sources', World Scientific, 1994.

TURN-BY-TURN ANALYSIS OF PROTON AND GOLD BEAMS AT INJECTION IN THE AGS BOOSTER*

C. Gardner, L. Ahrens, N. Williams, BNL, Upton, NY 11973, USA

Abstract

In this paper we describe the latest version of a program we have used for several years to acquire and analyze turn-by-turn data from pick-up electrodes in the AGS Booster during injection. The program determines several parameters of the injected beam including the tunes and the position and angle of the incoming beam. Examples are given for both proton and gold injection.

1 INTRODUCTION

Several years ago we developed a computer program called "PIP" [1] to acquire and analyze turn-by-turn data from PUEs (Pick-Up Electrodes) in the AGS during injection. Originally, the turn-by-turn data were generated by a half-turn pulse of beam (some $2.4 \mu\text{s}$ long) that was injected and allowed to pass turn-by-turn through a given PUE. The resulting signals were digitized and the digital data were processed to yield the position of the beam on each pass through the PUE. A several-parameter function was then fitted to the position-versus-turn data yielding, among other things, the tune and the position and angle of the injected beam. Recently we developed another method for generating the turn-by-turn data in which a half-turn gap or "hole" (typically 1 to $10 \mu\text{s}$ wide) is chopped out of a long beam pulse before the pulse is injected into the synchrotron. When the "hole" enters the machine and passes turn-by-turn through a PUE, it produces a signal similar to that of a single half-turn of beam. The advantage of this technique is that it neither interrupts the machine-physics processes occurring during the injection stacking nor (on a more practical level) does it interrupt the normal delivery of beam to the Physics programs. This has been particularly useful for studying the injection of gold and other heavy ions in the AGS Booster [2].

The program originally employed stand-alone digitizers. These were eventually replaced with multi-channel digital oscilloscopes which perform the necessary digitization and storage of data and at the same time provide an instantaneous picture of the signals to be analyzed; this makes setup and verification of the signals very easy. The program is now also able to analyze the coupling between the horizontal and vertical planes. This is essential for detailed studies of heavy ion injection in the Booster where coupling is used to enhance the injection efficiency [2]. Following is a detailed description of the most recent version of the program, now used primarily to study and monitor the injection of protons and heavy ions in the Booster.

2 DATA COLLECTION

Before digitization, the signals from the plates of a given PUE assembly are combined to produce a SUM signal proportional to the total charge inside the PUE and a DIFFERENCE signal proportional to the horizontal or vertical displacement of the beam in the PUE. The SUM and DIFF signals are piped from the Booster ring to the MCR (Main Control Room) where they are connected to a multi-channel digital oscilloscope. We are currently using LeCroy 9304A (Quad 200 MHz) or 9414 (Quad 150 MHz) oscilloscopes for this purpose. The digitized data are transferred from the oscilloscopes to Sun work stations in the MCR via a National Instruments GPIB-ENET IEEE 488 controller. A LabView program collects the data. Figures 1 and 2 show typical digitized SUM and DIFF signals generated by a half-turn of protons injected into the Booster and observed for some 40 turns. (The revolution period here is $1.2 \mu\text{s}$.)

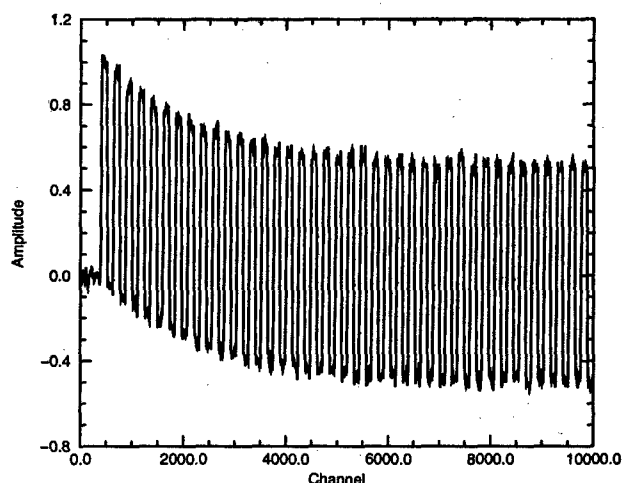


Figure 1: Digitized PUE SUM Signal.

3 DATA ANALYSIS

The digitized SUM and DIFF signals collected from the oscilloscope are analyzed by a collection of Fortran subprograms. The analysis begins with the SUM data which serve as a set of markers for the times when beam enters and exits the PUE. Specifically, the well-defined "edges" in the SUM signal allow one to determine precisely when beam enters and exits the PUE on each turn around the machine. This eliminates the need for any synchronization of the digitization with the revolution period. Moreover, it allows one

* Work supported by the U.S. Department of Energy.

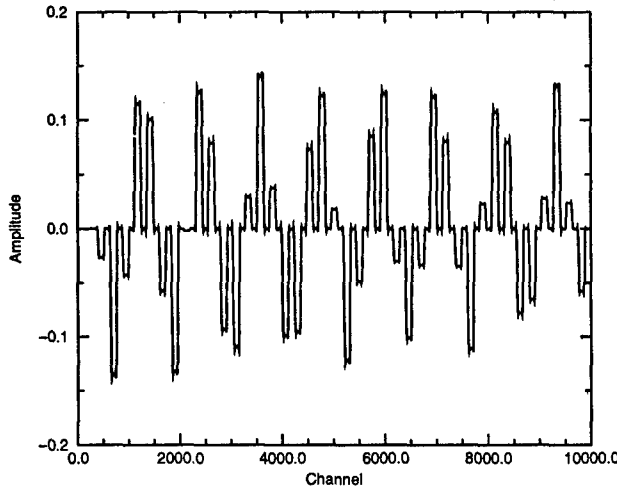


Figure 2: Digitized PUE DIFF Signal.

to establish local baselines for determining the signal amplitude for each pass through the PUE. For each turn then, the digitization sample numbers (labeled "Channel" in Figures 1 and 2) corresponding to the interval of time when beam is inside the PUE are located and the average value of the SUM signal (with respect to the local baseline) is computed over those sample numbers. The value of the DIFF signal (with respect to its local baseline) is averaged over the *same* sample numbers for each turn. In this way one obtains an average SUM and an average DIFF value for each turn. The position, X_n , of the beam in the PUE on the n th turn is then just a constant (which depends only on the geometry of the PUE) times the DIFF value divided by the SUM value for that turn. We have found this treatment of the SUM and DIFF data to be particularly robust; even DIFF signals with rather poor signal-to-noise ratios yield surprisingly good position-versus-turn data.

A Fast Fourier Transform [3] of the position-versus-turn data gives the tune and initial phase of the betatron oscillations at the PUE. Using these as starting values, a function of several parameters is fitted [4] to the data. For the case in which there is no coupling between the horizontal and vertical planes, the fitting function is [1]

$$X_n = C + Dn + Ae^{-f(n)} \cos \psi(n) \quad (1)$$

where

$$f(n) = \{n\pi\Delta Q\}^2/2, \quad (2)$$

and

$$\psi(n) = 2\pi n\{Q_0 + n\delta Q/2\} + \phi. \quad (3)$$

Here the seven parameters, C , D , A , Q_0 , ϕ , ΔQ , and δQ are, respectively, the position of the closed orbit at the PUE; the change in the closed orbit position per turn; the amplitude, tune and phase of the betatron oscillations; the tune-spread of the beam; and the tune-shift per turn. Figure 3 shows the position-versus-turn data and fitted curve obtained from the SUM and DIFF signals of Figures 1 and 2.

The corresponding FFT is shown in Figure 4. The values of the fitted parameters are given in Table 1.

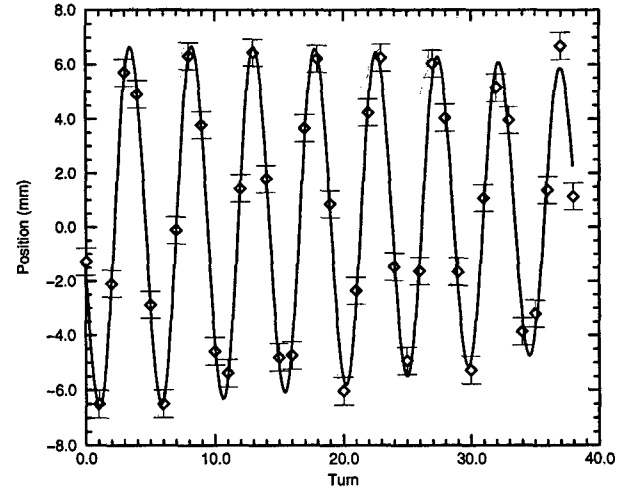


Figure 3: Position-vs-Turn Data and Fitted Curve.

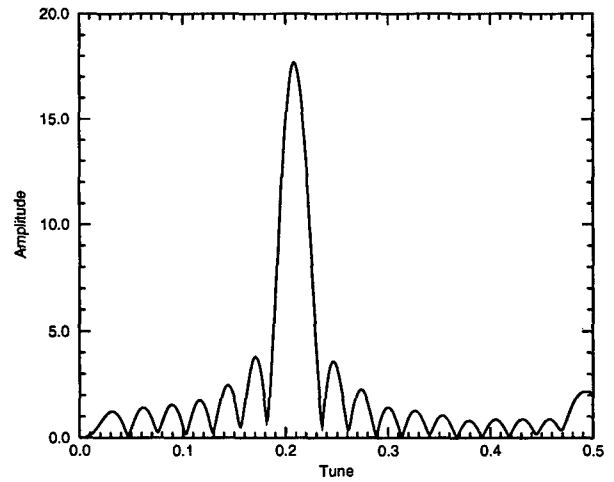


Figure 4: FFT of Position-vs-Turn Data.

Table 1: Fitted Parameters (Uncoupled Case)

C	0.0(2)	mm
D	0.02(1)	mm/turn
A	6.6(2)	mm
Q_0	4.792(1)	tune
ϕ	$0.283(8) \times 2\pi$	radians
ΔQ	0.006(1)	tune-spread
δQ	-0.00002(5)	tune/turn

The initial position and angle, X_p and X'_p , of the beam at the PUE are given by

$$X_p = A \cos \phi \quad (4)$$

$$X'_p = -(A/\beta)\{\alpha \cos \phi + \sin \phi\} \quad (5)$$

where A and ϕ are the fitted amplitude and phase, and α and β are the Courant-Snyder lattice parameters at the PUE. The transfer matrix from the PUE to the point of injection then gives the initial position and angle of the beam at injection. The lattice parameters and transfer matrix are obtained from the MAD [5] code.

For the case in which there is coupling between the planes, the fitting function is taken to be

$$X_n = C + Dn + A_1 \cos \psi_1(n) + A_2 \cos \psi_2(n) \quad (6)$$

where

$$\psi_1(n) = 2\pi nQ_1 + \phi_1, \quad \psi_2(n) = 2\pi nQ_2 + \phi_2. \quad (7)$$

Here we assume that the tune-shift per turn and the loss of coherence due to tune-spread are negligible. The six parameters A_1 , A_2 , Q_1 , Q_2 , ϕ_1 , ϕ_2 are the amplitudes, normal-mode tunes, and initial phases of the coupled betatron oscillations. Figure 5 shows the position-versus-turn data and fitted curve obtained for gold ions in the Booster with linear coupling introduced during injection. The corresponding FFT in Figure 6 clearly shows the two normal-mode tunes. The values of the fitted parameters are given in Table 2. As with the uncoupled case, the program calcu-

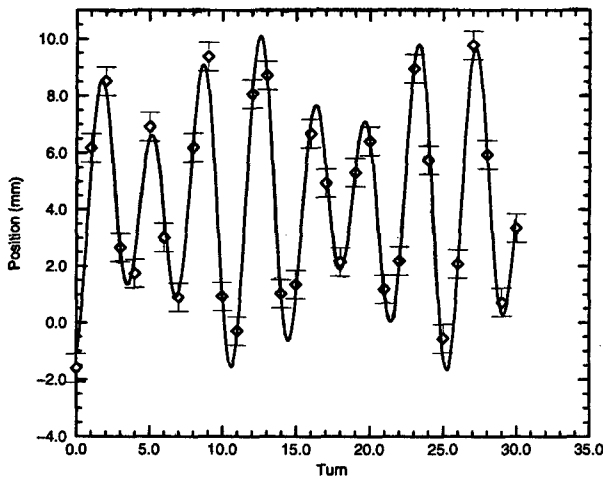


Figure 5: Position-vs-Turn Data and Fitted Curve.

Table 2: Fitted Parameters (with Coupling)

A_1	4.2(1)	mm
A_2	1.8(1)	mm
Q_1	4.726(1)	tune
Q_2	4.800(1)	tune
ϕ_1	$0.58(1) \times 2\pi$	radians
ϕ_2	$0.44(2) \times 2\pi$	radians

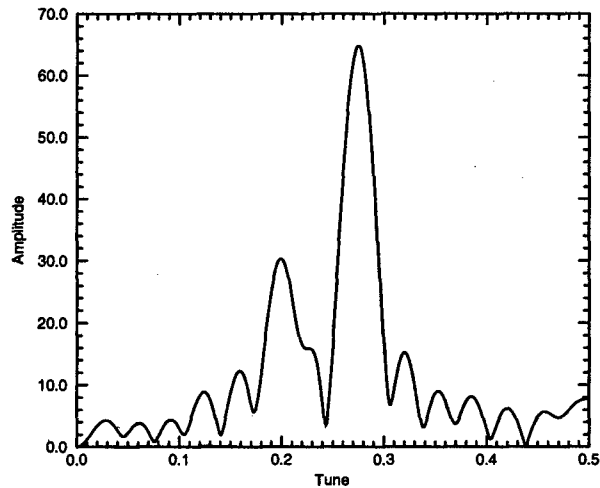


Figure 6: FFT of Position-vs-Turn Data.

using the fitted parameters and the lattice parameters at the PUE. The explicit formulae used are given in Ref. [6]. The transfer matrix from the PUE to the point of injection then gives the initial position and angle of the beam at injection.

4 REFERENCES

- [1] C. Gardner and L. Ahrens, IEEE Transactions on Nuclear Science, Vol. NS-32, No. 5, October 1985, pp. 1888-1890.
- [2] C. J. Gardner, "Injection of Gold Ions in the AGS Booster with Linear Coupling", Proceedings of the 1999 Particle Accelerator Conference.
- [3] W. H. Press, et. al., *Numerical Recipes in Fortran*, 2nd edition, Cambridge University Press, (1992), pp. 498-508
- [4] W. H. Press, et. al., pp. 678-682
- [5] H. Grote and F. C. Iselin, "The MAD Program Version 8.4 User's Reference Manual", CERN/SL/90-13 (AP), 27 August 1991.
- [6] C. J. Gardner, "Formulae for the PIP Analysis of Linear Coupling", AGS/AD/Tech. Note No. 476, March 30, 1998.

lates the initial position and angle of the beam at the PUE

THE ONLINE CHARACTERIZATION OF THE MAIN INJECTOR BPM

A. A. Hahn, Fermi National Accelerator Laboratory, Batavia IL, 60510*

Abstract

The design of the Main Injector beam position monitor (BPM) was driven by the desire to minimize its beam impedance and longitudinal space requirements. The resulting BPM consists of four striplines inset into a section of Main Injector Beam pipe. The striplines are combined in pairs to form either a horizontal or a vertical BPM by switches located nearby in the tunnel. The BPM response is decidedly non-linear and furthermore shows sensitivity to the beam position on the orthogonal axis. This paper presents the method in which consecutive measurements in both planes are used to derive the actual (x, y) position in an online environment.

1 INTRODUCTION

The Fermilab Main Injector (FMI) was designed as a high intensity medium energy (150 GeV) injector into the Tevatron to replace the original Main Ring Accelerator. In addition the FMI can operate as a 120 GeV Fixed Target Accelerator and antiproton production facility. In either modes the anticipated particle intensities are expected to be high ($>3 \cdot 10^{13}$). In order to avoid beam instabilities it was desired to reduce any sources of beam impedance. The resulting BPM [1, 2, 3] consists of four striplines inset into a section of Main Injector Beam pipe, which to the beam appears as nearly as possible as just another section of beam pipe. The striplines are grounded at one end and a sheet metal vacuum enclosure is welded over the inserts.

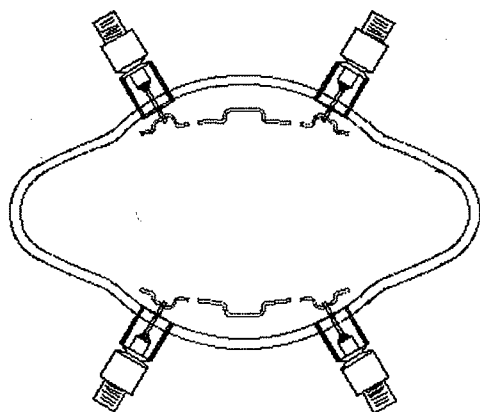


Figure 1. Schematic drawing of MI BPM.

A front-view diagram is depicted in figure 1. The design was also guided by the desire to minimize non-magnetic space, so the entire BPM can be inserted into one end of a quadrupole magnet.

*Operated by Universities Research Association under contract with the U.S. Department of Energy

The four striplines are combined in pairs to provide either horizontal or vertical BPM's. This summing of the individual plates is accomplished by an external switching box located in the tunnel next to the BPM. Whether a BPM operates as a horizontal or a vertical pickup can be changed from the control room. However the slow nature of the switches (relays) prevents the simultaneous measurement of both planes. The two summed signals are cabled to the Service Building. This scheme was implemented as a cost saving method, as two cabling runs per BPM were eliminated and the old Main Ring processing electronics could be reused. The disadvantage of this scheme is due to the particular characteristics of these BPM's. Not only do the BPM's exhibit a non-linear response, but they are also relatively sensitive to the beam position in the orthogonal plane. Since we can read only a single plane at a time during the acceleration cycle, two acceleration cycles are needed to capture both horizontal and vertical measurements. The assumption is that the two cycles are (nearly) identical. The default configuration of the BPM system is such that horizontally focusing quads have horizontal BPM configurations, and horizontally defocusing quads have vertical BPM configurations. This is called the (normally) "ON" configuration. The switched configuration is referred to as the (normally) "OFF" configuration (vertical BPM in horizontally focusing quad and horizontal BPM in horizontally defocusing quad).

2 CHARACTERIZATION OF THE BPM RESPONSE

Figure 2 shows the response of a particular BPM that was measured by the stretched wire method [4]. The wire was moved on an x-y grid with 5 mm gridlines between $|x| \leq 25\text{mm}$, and $|y| \leq 15\text{mm}$. The horizontal (and vertical) positions are plotted as a function of the voltage output (V_{π}) by the processing electronics RF module [5]. The family of curves is the result for the wire at different vertical (horizontal) positions. The dots are the actual data points, while the curves are the result of fitting the data with the function, $\text{Position}(V_{\pi}) = a_0 + a_1 \cdot V_{\pi} + a_2 \cdot V_{\pi}^3$. As one can see the fit is reasonably accurate over the range of the data. However it can be noticed that a_0 , a_1 , and a_2 , are themselves functions of the orthogonal coordinate of the wire.

The coefficients, a_0 , a_1 , and a_2 , for a particular BPM are plotted as a function of the orthogonal coordinate in figure 3. The shape of the curves for a_1 and a_2 vs. the orthogonal coordinate is similar to a gaussian and in actual fact, we have fit this data to a gaussian function with a pedestal as a way to characterize the functional dependence of the

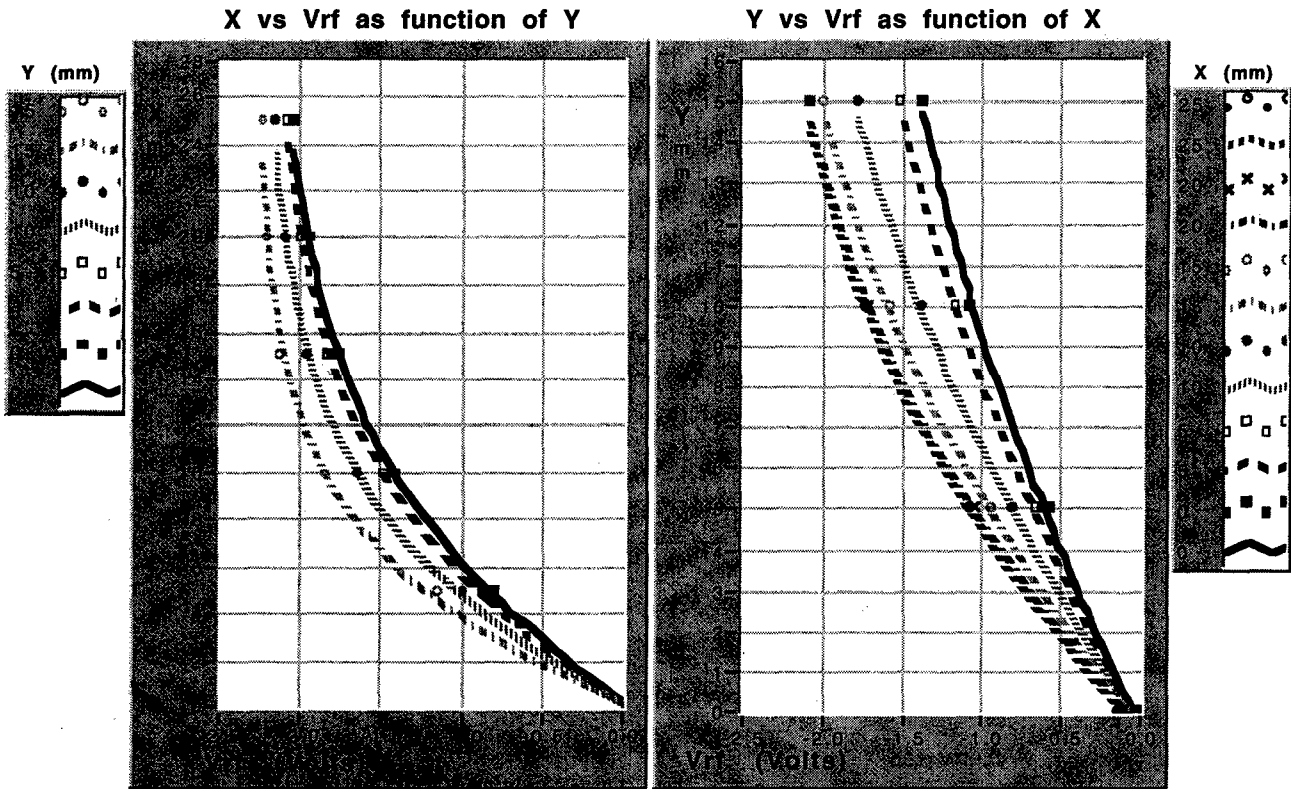


Figure 2. The Position vs. V_{rf} for a particular MIBPM as a stretched wire is moved on a x-y grid (5mm spacing). The left (right) plot is that BPM configured as a horizontal (vertical) BPM. Only the positive positions are shown for reasons of plot legibility.

coefficients on the orthogonal coordinate. When all BPM's are put through this analysis, the average parameterizations for a_1 and a_2 represent the BPM's adequately.

Only a_0 tends to defy parameterization. One reason is that this coefficient is very sensitive to actual electrical and mechanical aspects of the BPM construction, whereas the linear and cubic terms are more representative of the electric field map (which in any case would contain only odd powers of V_{rf}). The actual a_1 and a_2 were taken from the entire BPM ensemble average. The choice for a_0 was the value found by averaging a_0 over the orthogonal coordinate for each individual BPM. The final result is that each BPM has a unique a_0 , but all BPM's share a common a_1 and a_2 , or

$$x(V_{rf}, y) = a_0^x + a_1^x(y)V_{rf} + a_2^x(y)V_{rf}^3$$

$$y(V_{rf}, x) = a_0^y + a_1^y(x)V_{rf} + a_2^y(x)V_{rf}^3$$

where,

(1)

$$a_{(1,2)}^x(y) = A_{(1,2)}^x e^{-\frac{1}{2}(y/\sigma_{(1,2)}^x)^2} + B_{(1,2)}^x,$$

and similarly for $a_{(1,2)}^y(x)$.

The values for A , σ , B are given in table 1 for a_1 and a_2 . The algorithm for calculating the actual beam positions, x and y , is as follows (for a particular BPM).

1) Using the measured V_{rf} from the "On" and "Off" BPM configurations, the zeroth order positions are calculated assuming the orthogonal measurement is zero, i.e.

$$x(V_{rf}, 0) = a_0^x + a_1^x(0)V_{rf} + a_2^x(0)V_{rf}^3$$

$$y(V_{rf}, 0) = a_0^y + a_1^y(0)V_{rf} + a_2^y(0)V_{rf}^3.$$

2) Using these values for x and y , the equation is iterated.
3) When the change of x and y is below some threshold (e.g. 0.1 mm) or after a maximum number of iterations, the iteration stops. Typically this is less than 7 iterations for positions $< \pm 10$ mm.

Table 1. Parameterization of coefficients $a_{1,2}$ on the orthogonal plane position. The function is a gaussian of amplitude A , rms width σ , and pedestal B . See equation 1.

Horizontal Coefficients			
	A	σ	B
$a_1(y)$	6.07e-1	10.5	0.459
$a_2(y)$	1.16e-3	12.0	-2.81e-4
Vertical Coefficients			
	A	σ	B
$a_1(x)$	7.19e-1	8.18	0.915
$a_2(x)$	2.27e-3	3.79	-4.31e-4

Using this prescription, the data from the wire measurements of all the BPM's were fed back into the analysis. For positions within ± 10 mm of the BPM center, the rms error over the BPM ensemble is less than 0.33 mm. The residual difference between the actual position and the parameterized curve is less than 1.0 mm

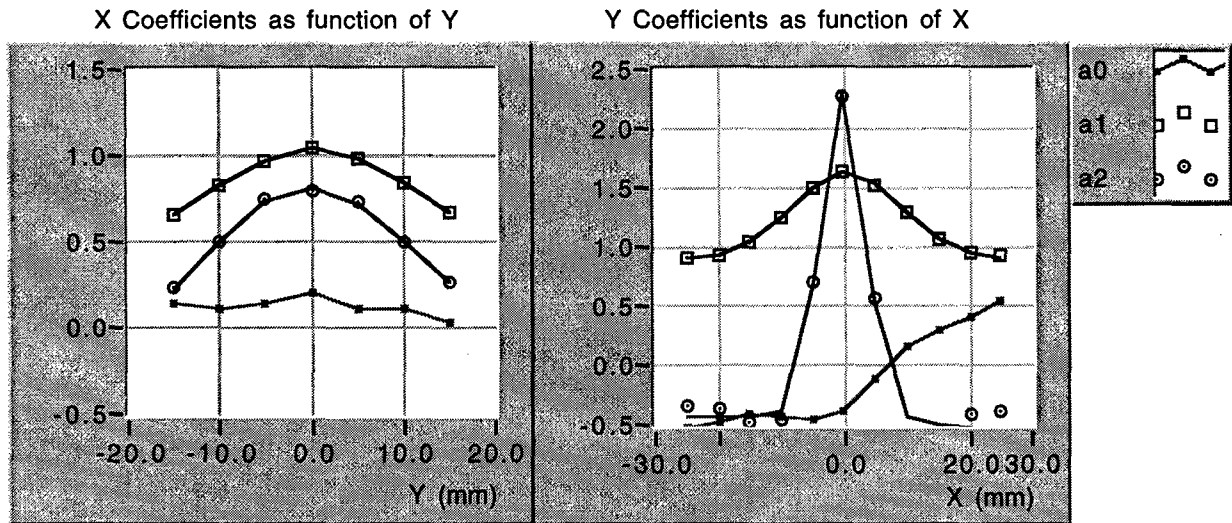


Figure 3. The variation of the coefficients a_i as a function of the orthogonal plane position. The points were derived from the fitted curves of figure 2, while the lines (for a_1 and a_2) are derived from fitting the points to a gaussian function (see text). In the case of a_0 , the line simply connects the points. It should be noted that a_2 has been multiplied by 1000 for display purposes on this plot.

rms. This level of absolute accuracy is adequate as the smallest beam rms size will typically be ~ 1.0 mm at extraction). Precision use of the bpm system is usually confined to lattice studies. Since under these circumstances, only orbit differences matter, the precision will be much better.

3 CONCLUSION

It is possible to parameterize the response of the MI BPM system, even though the behavior of the pickups is non-linear and exhibits a significant cross plane coupling. During Main Injector Commissioning, it has been possible to ignore the cross plane effect and use the system as a "normal" BPM system (as of this writing, the implementation of remote switching of the tunnel switch boxes has been delayed due to other considerations). Once we begin to systematically study the MI, the higher precision needed will require the use of the cross plane knowledge to correct the BPM response.

Currently the algorithm (iteration scheme) has been written and installed in the Console Application written for the MI BPM system. Since the BPM digitizer is only an 8-bit system, it is possible to implement the algorithm as a 65k element x-y lookup array. As future hardware would most likely use a higher bit ADC, it has not seemed worthwhile to make this change (in addition modern processors make the iterative method very fast).

4 ACKNOWLEDGEMENTS

It must be noted that all actual measurements of the MIBPM's were made by members of Beams Division RFI department and not this author.

5 REFERENCES

- [1] P.J.Chou, 'Theoretical Study of Stripline Beam Position Monitors', unpublished, 4/17/92
- [2] Barsotti, E., Crisp, J., 'Preliminary design of the Beam Position Detectors for the Fermilab Main Injector', Proceedings of the Particle Accelerator Conference, IEEE, 1993
- [3] Fitzgerald, J., Crisp, J., 'A Compact BPM for the Fermilab Main Injector', Proceedings of the Particle Accelerator Conference, IEEE, Vancouver, 1997
- [4] Fitzgerald, J.A., Crisp, J., McCrory, E., Vogel, G., 'BPM Testing, Analysis, and Correction', Proceedings of the Beam Instrumentation Workshop, Stanford, May 98
- [5] Vogel, G., 'MI BPM RF Module Test Results', Main Injector Note 0226, unpublished, 1/16/98

TURN-BY-TURN BPM ELECTRONICS BASED ON 500 MHz LOG-RATIO AMPLIFIER

K.H. Hu, Jenny Chen, C. H. Kuo, K.T. Hsu, T. S. Ueng

Synchrotron Radiation Research Center

No 1, R&D Road VI, Hsinchu Science-Based Industrial Park, Hsinchu, Taiwan, R.O.C.

Abstract

Log-ratio processor working at 500MHz applied to turn-by-turn beam position measurement was implemented. The processor circuit consists of two logarithmic amplifiers and a subtraction circuit. The output value is proportional to beam position. Before, the upper usable frequency of logarithmic amplify is lower than 500MHz. At present, several manufacturers support higher upper usable frequency of logarithmic amplifiers. In this paper, we will present the performance test result of the 500MHz log-ratio processor applied to turn-by-turn BPM electronics.

1. INTRODUCTION

Wells and Gilpatrick et al. [1,2] have mentioned log-ratio processor working at 100 MHz to 500 MHz. Most of the log-ratio processors need down converter to translate interested frequency to this working intermediate frequency (100KHz~100MHz). Electronics working at bunch-crossing frequency can reduce the complexity of signal processing chain. Benefited from the promising progress in wireless communication recently, low cost wide bandwidth logarithmic amplifier is available. The BPM electronics based upon this complete multistage log-amplifier is highly interesting due to its low cost and simple. The bunch-crossing rate of SRRS storage ring is 500 MHz. The turn-by-turn beam position signal processed by using log-ratio processor directly working at 500MHz is reported here. This system is working at single bunch or multi-bunch operation mode. Two versions of amplifiers have been tested. One is a commercial log-amplifier module, another is using complete multistage log-amplifier chip. The preliminary test result is presented here.

2. LOG-RATIO ELECTRONICS FOR TURN-BY-TURN BEAM POSITION DETECTION

The logarithmic amplifier feature includes large input dynamic range, bandwidth 500MHz or more, easy to use, low cost, and so on. The detection signal at RF frequency provide a simple solution compared with difference-over-sum or AM/PM conversion approaches. Normally, logarithmic amplifier applied to a very wide range IF and RF power measurement. The logarithmic amplifier and a subtraction circuit (sum, difference, ...etc) have been applied to beam position / intensity measurement module [2][3]. A logarithmic amplifier function is expressed as equation (1).

$$V_{OUT} = V_{SLOP} \log (P_{IN} / P_O). \quad (1)$$

where:

V_{OUT} is the demodulated and filtered output.

V_{SLOP} is the logarithmic slop (V/dB).

P_{IN} is input power.

P_O is the logarithmic intercept.

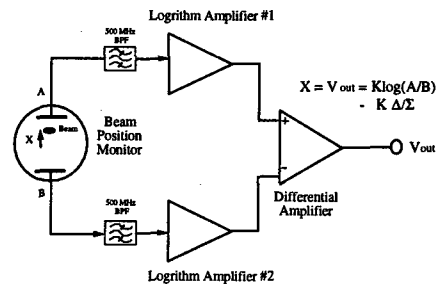


Figure1: 500MHz log-ratio processor.

The 500MHz log-ratio processor consists of the 500 MHz band-pass filter and two logarithmic amplifiers and a differential amplifier as show in Fig. 1. Log-ratio processor output direct proposition to normalize beam position X is expressed in equation (2).

$$X = K (\Delta / \Sigma) \cong K \log (A/B) = V_{OUT} \quad (2)$$

The revolution of storage ring is 2.5MHz. BPMs, hybrid junctions, 500MHz band-pass filters (15MHz bandwidth) and log-ratio processor make up the turn-by-turn measurement system.

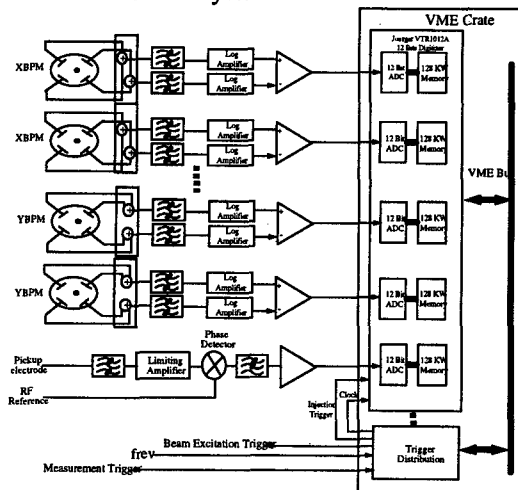


Figure 2: Block diagram of the turn-by-turn BPM system.

The button electrode of BPM is mounted on skew position. Hybrid junctions were used to transform the BPM as horizontal or vertical direction BPM. The stored beam induces an impulse like doublet at button electrode. After the hybrid junctions, the output of BPF is impulse response with 500 MHz center frequency. The electron beam signal induced by the BPM buttons to pass through hybrid junction and the log-ratio processor to VME based transient digitizer. The clock of the transient digitizer is the revolution clock. The digitizer records the turn-by-turn beam position. The system is useful for studying the nonlinear beam dynamics. In this report we attempt to use two versions of logarithmic amplifiers. One is a commercial log-amplifier module, which was made by discrete components. Another is to use the log-amplifier chip. Results of both versions of log-ratio processors are similar.

3. PRELIMINARY BEAM TEST RESULTS

Implement the turn-by-turn BPM electronics by using 500 MHz log-ratio processor is the goal of this study. The preliminary beam test was done to evaluate the performance of log-ratio processor. The turn-by-turn beam position measurement of a stable beam was used to estimate resolution of processing electronics. Fig.3 shows the beam position data is scattered in a small region. The resolution of electronics is estimated about 100 μm when beam current is 10 mA. The processor can keep its resolution with the stored beam down to 1 mA. For a routine use, the further improvement is needed.

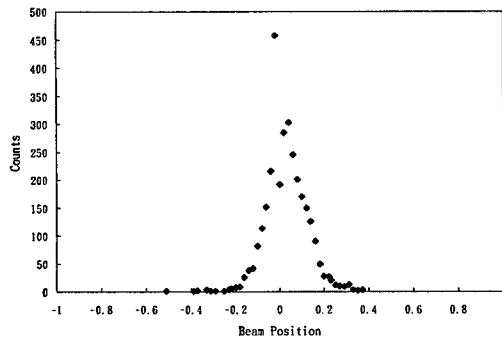


Figure3: Histogram of the beam position reading when beam is stable.

One of an injection kicker was used to excite horizontal betatron oscillation of the stored beam, the kick angle is about 1 mrad, and the beam will undergo damped oscillation as shown in Fig. 4. The horizontal tune at measurement is 7.196. The damping is strong which is lattice dependent. From the measured data, it confirms that the system is working well in turn-by-turn BPM signal processing at the bunch crossing frequency.

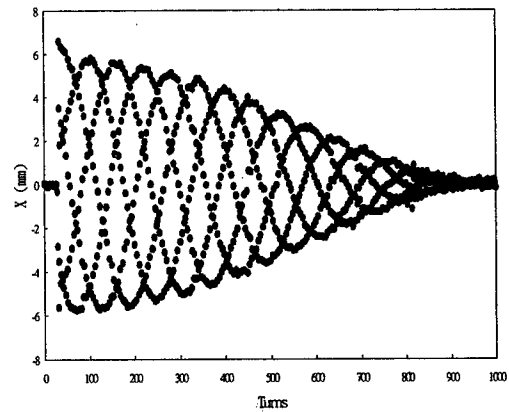


Figure 4: Horizontal turn-by-turn beam position, $v_x=7.196$

To explore more depth, we set the tune near fourth order resonance ($4v_x=29$). The turn-by-turn beam position and the phase space plot are shown in Fig. 5 and Fig. 6. The kick strength is about 1.5 mrad in this measurement. The spiral like arm damp rapidly. De-coherence and re-coherence is observed from the turn-by-turn beam position data.

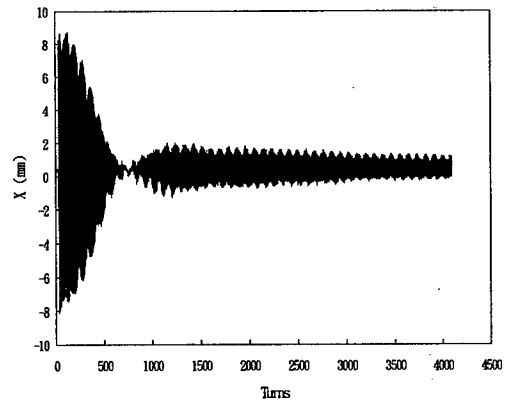


Figure 5: Horizontal turn-by-turn beam position, near $4v_x=29$ resonance.

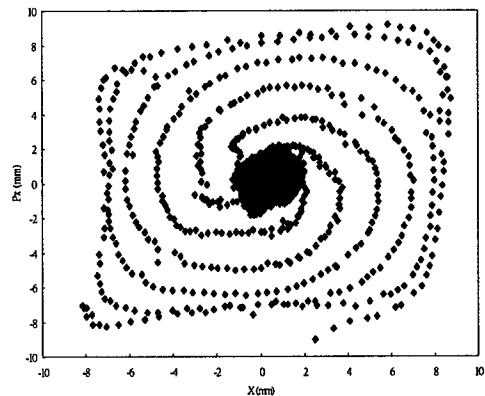


Figure 6: Phase space plot, near $4v_x=29$ resonance.

4. PERFORMANCE TEST OF LOG-AMP CHIPS

Various measurements are performed to familiarize the behavior of log-amplifier chips working at 500 MHz [5]. The output voltage as a function of input power is shown in Fig. 7. The slope is 20 mV/dB. The log linearity of the chip working at 500 MHz is shown in Fig. 8. The output linearity is less than ± 0.5 dB without correction. The linearity is acceptable for BPM signal processing. Over 70 dB dynamic range (-70dBm ~ 10dBm) is also applicable in BPM application.

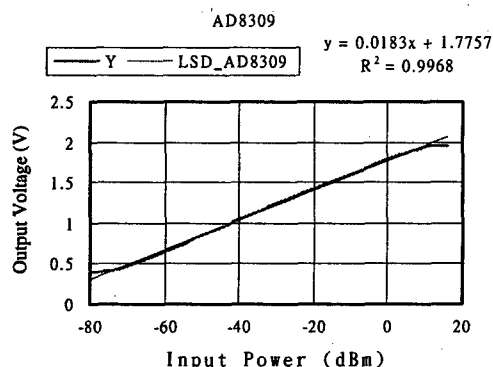


Figure 7: Output vs. input power, Frequency for 500MHz, Single-Ended Input.

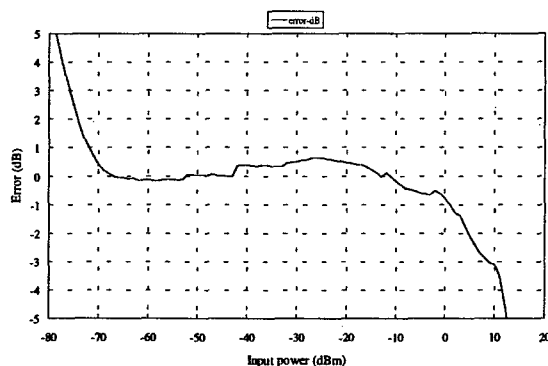


Figure 8: Log linearity of logarithmic amplifier output vs. input power, at frequency of 500 MHz.

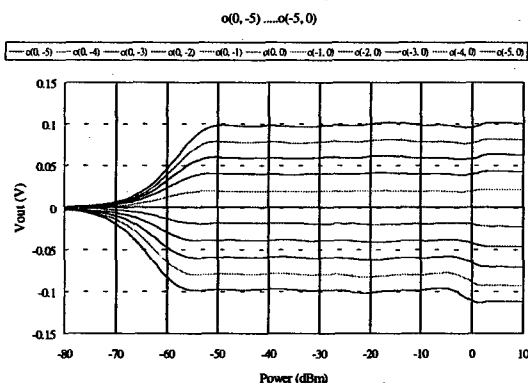


Figure 9: The output voltage offset of the Log-ratio processor when difference input power.

The preliminary test of log-amplifier chip (AD8309) based log-ratio processor was used for this test. The corrected data is shown in Fig. 9. The vertical scale is in voltage, and the horizontal scale is in dBm. The input RF signals to both channels are offset by -5dBm to 5dBm. Important characteristics to note in the graph of Fig. 8 is that the curve exhibit the dynamics range of the test. For a properly performing log-ratio system, the line will be centered about zero offset and be flat. The performance will be improved after a special care during the layout.

5. SUMMARY

This paper presents a log-ratio processor working at 500 MHz for a turn-by-turn beam position measurement that eliminates the need of down-converter. Preliminary results showed 100 μ m resolution was achievable with simple electronics. Commercial logarithmic amplifier chips (e.g. AD8309) which could work at 500 MHz directly are highly interested. The test of usability of AD8309 for 500MHz application was also performed. The new electronics for the beam position monitor on the booster-to-storage ring transport line will be installed with dedicated log-ratio processors soon.

6. REFERENCES

- [1] F. D. Wells, et al., "Beam Position Monitoring in the 100 MHz to 500 MHz Frequency Using the Log-Ratio Technique", PAC'93, Washington, 2316 (1993).
- [2] J. D. Gilpatrick, et al., "LEDA & APT Beam Position Measurement System: Design and Initial Tests", LINAC'98, Chicago, IL, August 23-28, 1998.
- [3] C. R. Rose, et al., "Description and Operation of the LEDA Beam Position /Intensity Measurement Module", PAC'97, Vancouver, BC, Canada, June 1997.
- [4] C. R. Rose, et al., "Test Results of the LEDA Beam Position /Intensity Measurement Module", BIW'98, Stanford, CA, May 4-7, 1998, pp 423-427.
- [5] Data sheet of AD8309, Analog Devices, Inc., 1998.

CLOSED ORBIT MEASUREMENT SYSTEM FOR THE BOOSTER SYNCHROTRON IN SRRC

K.H.Hu, Jenny Chen, K.T.Hsu, T. S. Ueng, S. Y. Hsu

Synchrotron Radiation Research Center

No 1, R&D Road VI, Hsinchu Science-Based Industrial Park, Hsinchu, Taiwan, R.O.C

Abstract

The booster of SRRC is a 1.3 GeV synchrotron with 10 Hz repetition rate. Electron beam from 50 MeV accelerates to 1.3 GeV within 50 msec. It serves as the injector for 1.3~1.5 GeV storage ring of Taiwan Light Source (TLS). To reduce heat related problem in the machine and beamline optics, 1.5 GeV full energy injection is scheduled in near future. The closed orbit measurement system of booster synchrotron consists of 23 set of BPMs, multiplexes, 500MHz receivers, timing control electronic and VME bus transient digitizer. The closed orbit is sampled every 150 μ sec, 600 orbits acquired while the energy ramping. The closed-orbit is observed as function of energy. The orbit change due to imperfection of lattice and slow pulse magnet is easily observed. This system is expected to provide us abundant information to improve the operation efficiency, trouble shoot of booster.

1. INTRODUCTION

In the SRRC booster synchrotron, dipole and quadrupole are drive by White circuit working in resonance excitation. To achieve high performance of the magnet system operation condition is crucial. Closed-orbit measurement is helpful to optimization conditions of the magnet system, which includes excitation level, phasing of individual magnet family, and tracking between different family of magnet. The closed-orbit system to provide useful information of energy dependent in closed-orbit are related with tracking condition of magnet excitation, lattice error and correctors setting, optimized these injection and extraction elements condition. Booster energy is expected upgrade from 1.3 GeV to 1.5 GeV on October 1999. Major power supply will replace due to present equipment's have not enough rating to run in 1.5GeV. At that time the beam closed-orbit can to become useful re-commingling tool.

Several years ago, a simple standalone closed orbit measurement system has been setup [1]. In order to, understand more about the booster and its beam dynamic behavior, a new design was established. The new system will be integrated with the control system of the machine. An advanced graphical user interface will also be installed to aid machine physicists and operators.

2. SYSTEM DESCRIPTIONS

In the SRRC booster synchrotron, the beam position monitor (BPM) are locate in upstream and downstream of dipole magnets as shown in Fig. 1, except one location is reserved as synchrotron radiation diagnostic port (location 12 of BPM). There are 23 BPMs mounted around the ring totally for closed-orbit measurement.

The system use two stages 500 MHz RF multiplexer to eliminate high cost matter, the multiplexes. The first stage RF multiplexes are similar with ESRF booster RF

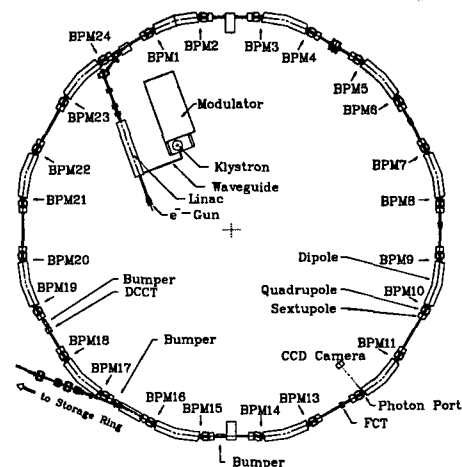
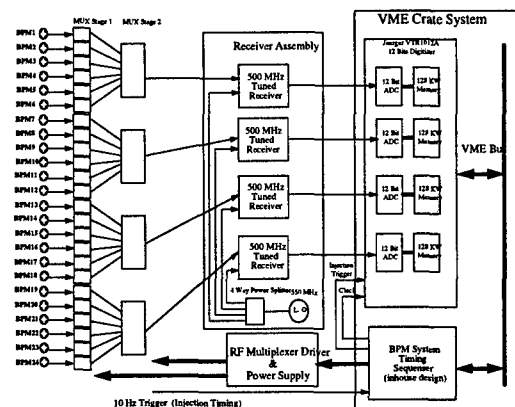


Figure 1: BPM layout in Booster synchrotron.



Booster Synchrotron BPM Electronics - Block Diagram
Figure 2: Closed Orbit measurement system.

MUX. The ESRF version work at 352 MHz while SRRC work in 500 MHz. One BPM accompany with one 4-to-1 RF multiplexer. The second are also 4-1 RF MUXs off-the-shelf products. All multiplexes driver and power supply are mounted on a distribution box.

The schematic diagram of the closed orbit

measurement is shown in Fig. 2. It uses 23 sets (BPM12 is dummy BPM) of electron beam position monitor. The BPMs divided into four-measurement group and parallel process to reduce the orbit acquisition cycle time. Each button takes $6 \mu\text{sec}$ to acquire the signal from the electron beam. One processing channel handle 6 BPMs (24 buttons plus 1 reserved), But BPM12 is dummy. The acquisition time for each closed orbit need to $150 \mu\text{sec}$. Four heterodyne receives are used in this system. The dynamic range of signal processing chain is about from -60 dBm to 0 dBm , which corresponds to beam current 0.1 to 10 mA .

The timing sequence generator provides the clock for digitizer and the scan sequence of RF multiplexes. As the timing system receives enable and 10Hz trigger signal, the data acquisition system and multiplexes system are immediately switched on. The signals picked up by the buttons of electrodes pass through the multiplexes and receiver to arrive the VME-based digitizer for further processing.

3. SOFTWARE STRUCTURE

The development of software for this closed orbit measurement system is divided into the low level data acquisition and the GUI presentation in the console. The low data acquisition software utilizes a VME based electronics system. It is responsible for setting parameters of the data acquisition module, calculating beam position from raw data, arranging the data acquisition, and uploading data to the console workstation. The function of software on workstation includes data request, user interface, and data presentation. The console display will show the beam position vs. energy, the closed orbit at different energy, the closed orbit difference between different energy, ...etc. Machine physicists and operator can easily to use the presentation to understand the condition of the booster.

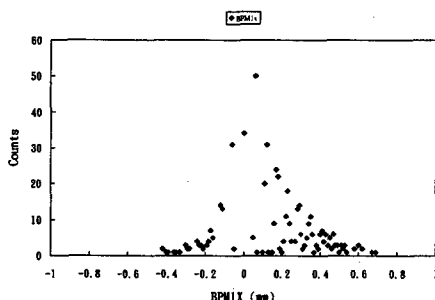


Figure 3: Histogram of beam position resolution, standard deviation $1\sigma = 200 \mu\text{m}$.

4. BEAM TESTS AND APPLICATION

To verify performance of the system, various beam tests have been performed. Histogram of a typical beam position reading is shown in Fig. 3, the standard deviation is about $200 \mu\text{m}$ which is the resolution of

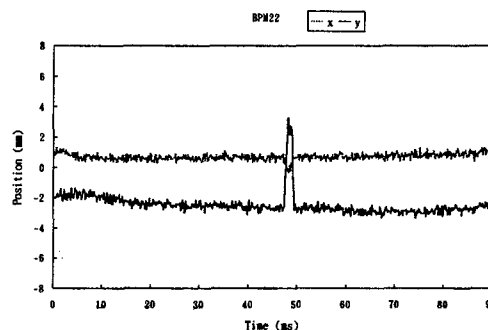
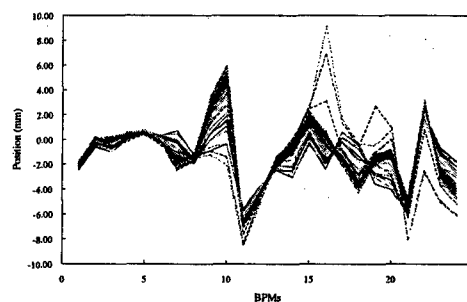


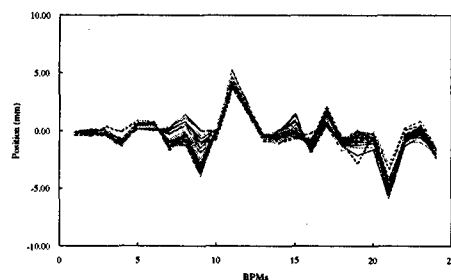
Figure 4: Typical beam position reading of BPM22 vs. time (energy).

BPM signal processing chain. That resolution can keep for the operating current range from 0.5 to 5 mA in multi-bunch operation mode.

The orbit displacement of electron beam in booster as a function of ramping energy is expected large, which is dependent on tracking of magnet excitation and error of lattice. Figure 4 shows the beam position varied as function of ramping time (energy). The electron beam is injected into the booster with energy of 50 MeV at 0 msec . It increases gradually to 1.3 GeV within 50 msec , then, decreases when passing 50 msec . Figure 4 shows that the beam position is changing at low energy side and approaches a steady state as beam energy rises higher enough. The spike shown in the beam position reading is due to the turn-on of extraction bumpers during the data taking.



(a) Horizontal.



(b) Vertical.

Figure 5: $50 \text{ MeV} \sim 1.3 \text{ GeV}$ closed orbit variation.

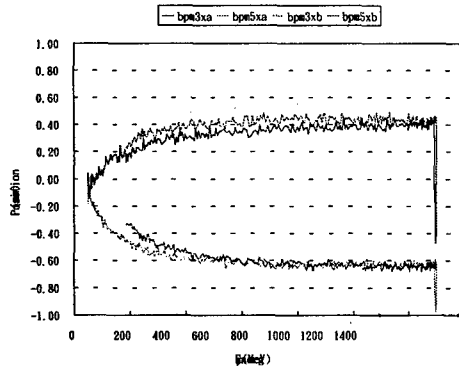


Figure 6: Beam position evolution of two BPMs vs. energy.

The energy dependence in closed orbit is related with tracking condition of magnet excitation, lattice error and corrector settings. To optimize these operating parameters, the closed orbit measurement at various beam energies is helpful. With an exaggerated tracking condition, the orbits displacement from 50 MeV to 1.3 GeV at each BPM position are shown in Fig. 5. The actual displacement between these energies is small. The typical energy dependent position change of SRRS booster is shown in Fig. 6. In the figure, it is shown that the beam energy reaches 1.3 GeV and decreases again, but the beam position does not follow the ramp up route. This phenomenon may be the result of tracking characteristics and hysteresis properties of magnet. As for which one is the major contributor, a further study should be performed.

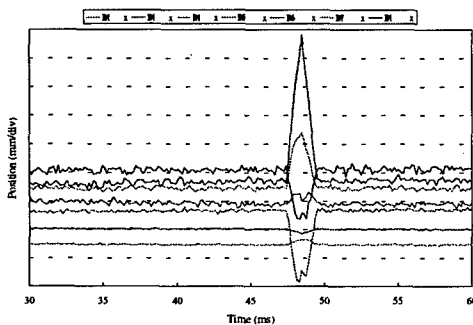


Figure 7: Beam position at serial BPMs, the bump occurs near 50 msec is due to excitation bump turn on.

The extraction scheme of the booster synchrotron is to use one kicker, three extraction bumpers and one septum. Three extraction bumpers produce a 2 msec half-sine bump to aid the extraction process. During the routine operation, the extraction condition seems not so critical to the beam extraction. However, the optimization of the extraction condition to improve the extraction efficiency and minimize the radiation loss is needed. It is clear that a non-closed bump was created

between the first bumper and third bumper, seven BPMs (BPM 1,5,9,13,16,17,21) are selected for display purpose. BPM16 and BPM17 are located inside the bump. The bump occurs at about 50 msec after the electron beam injected into the booster. All data have been added with different offset for display purpose. The optimization of bumper condition can be done easily by the closed orbit measurement system.

The condition of extraction septum is related to the extraction efficiency of the booster. During last several years, the short circuit of the extraction septum happened several occasions due to the electron beam hitting directly the structure of septum and the heat melted part of the structure. The beam position reading at upstream and downstream of extraction septum will be useful to assure the trajectory of stored beam and prevent electron beam from hitting the septum directly.

5. SUMMARY

We have set up a beam position acquisition system to acquire the closed orbit of SRRS booster synchrotron. The orbit acquisition time is 150 μ sec. Its performance was evaluated by beam tests. The energy-dependent behavior of beam position was observed clearly. The bump produced by extraction bumpers was also studied [2,3]. The system will be useful to optimize the operation condition, such as tracking condition of magnet excitation, extraction bump, preventing electron beam from striking the septum, ...etc. A closed orbit measurement system will be also useful for the re-commissioning of 1.5 GeV booster synchrotron in the near future. Further study on the orbit response is planned [4]. The booster can also be operated at low currents (<10 mA), low energy (<800 MeV), and short lifetime storage mode for various machine test in near future. At present, the rating of magnet power supplies, injection scheme and vacuum condition limit it. The closed orbit measurement system is expected to be useful for this mode of operation.

6. REFERENCE

- [1] T. S. Ueng et al., "The Closed Orbit Measurement of SRRS Booster During Ramping", Proceedings of the 1995 Particle Accelerator Conference, 2497-2499 (1995).
- [2] R. Bakker, et al., "Fast Flexible BPM-System: Valuable Commissioning Tool for BESSY II", Proceedings of the 6th European Particle Accelerator Conference, Stockholm, 1482 (1998).
- [3] M. Abo-Bakr, et al., "Commissioning of the BESSY II Booster Synchrotron", Proceedings of the 6th European Particle Accelerator Conference, Stockholm, 436 (1998).
- [4] R. Bakker, et al., "Orbit Response Measurements in the Commissioning of the BESSY II Booster Synchrotron and Storage Ring", Proceedings of the 6th European Particle Accelerator Conference, Stockholm, 900 (1998).

MICROWAVE CHARACTERIZATION OF THE WAVEGUIDE BPM

T. Kamps*, R. Lorenz, DESY Zeuthen, Zeuthen, Germany
S. deSantis†, LBNL, Berkeley, USA

Abstract

For electron beam orbit observation at the TESLA Test Facility FEL one undulator module will be equipped with ten waveguide-type beam position monitors having a design frequency of 12 GHz. Since the operation of this waveguide BPM is related to microwave concepts, a precise characterization of its microwave behaviour is necessary to describe and optimize the system performance. The purpose of this paper is to summarize the theory, different simulations and measurements of the device. Calculations and MAFIA simulations are presented for the coupling into the ridged waveguide as well as for the design of the waveguide-to-coax transition. Beside that the resonant frequencies of trapped modes inside a waveguide are estimated. Finally, back reactions on the electron beam in terms of wakefields are estimated by numerical simulations and by a simple analytical model.

1 MOTIVATION

The Free Electron Laser (FEL) at the TESLA Test Facility (TTF) [1] is designed for a radiation in the spectral band from VUV to soft X-rays. To ensure the overlap between photon and electron beam, the undulator modules will be equipped with beam position monitors (BPM) and correctors. For the BPMs, the realization of two different system concepts with small vertical dimension is under way [2]. Beside that, diagnostic ports between two adjacent modules are foreseen. A BPM system consists of a transducer close

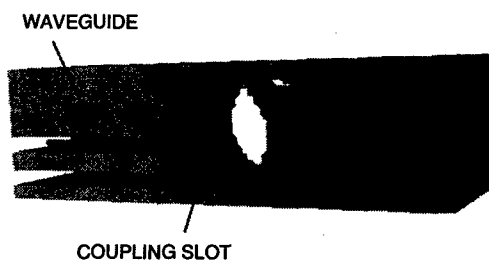


Figure 1: One BPM plane with two waveguides.

to the beam, transmission lines, signal processing electronics, and control software. This paper concentrates on the

* Email: tkamps@ifh.de

† Supported in part by Department of Energy contract DE-AC03-76SF00098

microwave components close to the beam realizing the coupling to the magnetic field, and the transmission to the 50 Ω system outside the vacuum chamber. Fig.1 shows the first part of the transmission line for two waveguide channels.

2 GENERAL BPM CONCEPT

Because of limited space in vertical direction and due to short-bunch operation, a microwave concept was considered for a BPM system. With four slots and waveguides a position sensitive signal from the electro-magnetic field of the electron beam will be detected. Because of space limits one BPM consists of two waveguide pairs grouped in planes separated in beam direction. One BPM channel with the objects discussed in this paper is sketched in Fig.2. The

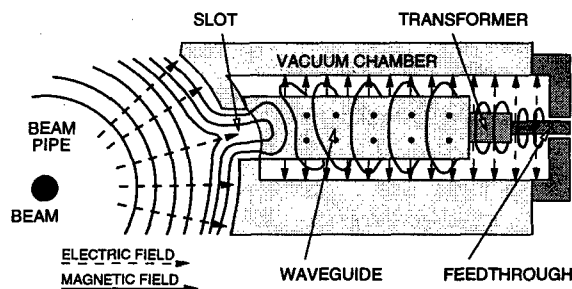


Figure 2: Zoom into vacuum chamber with one BPM channel and electro-magnetic field distribution.

magnetic field penetrates through a slot into the waveguide. The amplitude of the excited fundamental mode is directly proportional to beam offset. To enable a good coupling to the vacuum feedthrough a short rectangular coaxial line follows the waveguide, forming an impedance transformer.

3 MICROWAVE DESIGN ASPECTS

For the design, the whole structure was divided into two parts: The one which determines the coupling to the beam - and, hence, the induced signal strength - and the adapter to the 50 Ω coaxial cable system. Technological aspects were taken into account in all design steps.

First it is important to estimate the signal, which will be down-converted and detected in a heterodyne receiver.

3.1 Slot coupling

Intuitively the slot coupling mechanism can be described in terms of perturbed wall currents. As the slot cuts the way of the wall currents, energy by means of magnetic field can penetrate into the region behind the slot. For good BPM

performance, a coupling of 1% was sighted to obtain a reasonable compromise between signal to noise ratio and interference with the beam. Driving parameters for the coupling are geometry as well as slot size and location in the waveguide profile. Transmission from beam pipe to one waveguide port was simulated using the MAFIA package [3], and the model is shown in Fig.1.

As computer simulations are time consuming an attempt was made to describe analytically the slot coupling by using Bethe's theory [4]. To evaluate the coupling impedance it is necessary to calculate the fields induced in a vacuum chamber for a given current distribution. First, one finds the fields produced by the current distribution without the slot. Then, these fields are considered as an electromagnetic wave on the slot. In the next step it is obvious to find the fields diffracted by the slot into the waveguide. These diffracted fields bear a resemblance with fields radiated by equivalent electric or magnetic dipoles, whose moments are proportional to the normal electric field and the tangential magnetic field of the incident wave. After comparing these fields one obtains the coupling impedance. As a first step a simple structure, where a rectangular waveguide is positioned with its longitudinal axis normal to a cylindrical beam pipe surface (see Fig.3), has been investigated using a modified Bethe theory [5]. According to this the ratio of the magnetic fields of the fundamental mode H_x and of the beam H_ψ is

$$\left| \frac{H_x}{H_\psi} \right| = \frac{2\tilde{\alpha}_m \frac{k_z}{ab}}{\sqrt{1 + \left(2\tilde{\alpha}_m \frac{k_z}{ab} \right)^2}} \quad (1)$$

where a and b are waveguide dimensions and k_z wave vector pointing downwards the waveguide. To include the effect of the coupling aperture thickness T , the thick wall polarizability $\tilde{\alpha}_m$ is needed, given by

$$\tilde{\alpha}_m = 0.67\alpha_m \exp\left(-\frac{\pi}{w}T\right) \quad \text{with} \quad \alpha_m = \frac{\pi}{16}lw^2 \quad (2)$$

for the magnetic polarization of a rectangular slot with edge lengths l and w . A comparison between MAFIA simulations for S_{21} and field ratio calculations according to Eqs. 1 and 2 is shown in Fig.3, for a standard X-band waveguide coupling via a 4 mm \times 4 mm slot to a beam pipe. For frequencies above the waveguide's cut-off the deviation between MAFIA and theory is less than 5%. Further studies will investigate the BPM case with its ridged waveguide.

3.2 Ridged waveguide

Transverse space limitations and the vacuum constraints of no extra material inside the vacuum chamber required special interest for the waveguide design.

The waveguide has been made ridged to reduce its size. In addition, the hammer-like shape concentrates the magnetic field lines at the location of the coupling slot, so that they are parallel to the magnetic field of the beam over the entire slot.

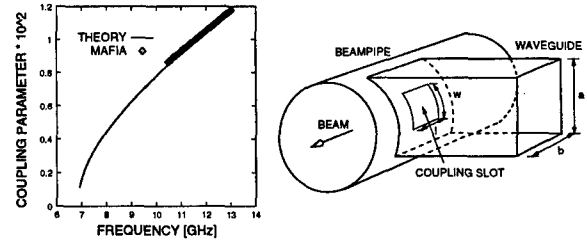


Figure 3: Left: Comparison chart for MAFIA S_{21} simulations against analytical calculations. Right: Geometry used for calculations.

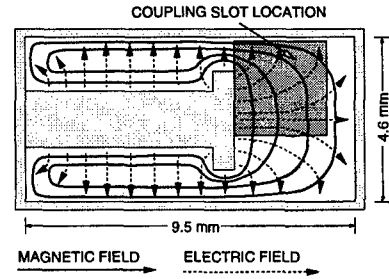


Figure 4: Profile cut of the waveguide with electromagnetic field distribution of the fundamental mode.

The working frequency was limited because of the H_{10} cut-off frequency treating the beam pipe as a circular waveguide. Keeping this in mind, the working frequency and thus the frequency for the first stage of the signal processing electronics was set to $\nu_w = 12$ GHz. Commercially available electronics components from satellite technology in the X-band can be used for signal processing. Size and shape of the waveguide (see Fig.4) have been optimized for a coupling of about 1%. With the present design it is possible to extrude the waveguide structure in one step by electro-discharge machining (EDM).

3.3 Waveguide-to-coax transition

The signal excited in the waveguide has to be coupled into a 50 Ω coaxial cable to be detected. An ultra-high vacuum microwave feedthrough by KAMAN Corp. (SMA connector, part #853872) was foreseen for this purpose. In a first design an electrical coupling was chosen. The resulting adapter was very narrowband, difficult to be tuned to 12 GHz, and the welding into special flanges caused problems. In a new design a smooth transition from the waveguide into the feedthrough has been realized by a $\lambda/4$ -transformer, formed by a rectangular coaxial line. This new geometry shown in Fig.5 for prototype II results in a closer spacing of both planes in beam direction, has larger bandwidth (no tuning problems), and is better for fabrication and installation. The design realized in the vacuum chamber follows the idea sketched for prototype II.

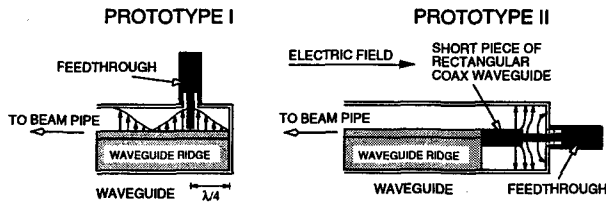


Figure 5: Waveguide-to-coax transitions, first and improved design.

4 INTERFERENCES

4.1 Resonances inside the Detector

Resonances of trapped modes inside the waveguide close to the working frequency enhance the signal amplitude, but due to fabrication problems it would be difficult to tune and stabilize all waveguides to the same resonance frequency.

Waves beyond $\nu_c = 8.99$ GHz can propagate into the waveguide and excite resonant modes there. Every waveguide of length l , which is not perfectly matched at the both ends, has q longitudinal resonances according to

$$\nu_r^2 = \nu_c^2 + \frac{c_o^2}{4} \left(\frac{q}{l} \right)^2 \quad (3)$$

Two different prototypes and one undulator vacuum chamber with ten BPMs were built.

Tab. 1 compares calculated and measured modes for the second prototype and for the undulator vacuum chamber. The length of both structures estimated from the design are 44.9 mm and 20.6 mm, respectively. Since it is difficult to include the wall curvature and the electrical length of the adapter into the resonance condition, measured values deviate slightly from calculated ones using Eq.3.

Mode #	Resonance [GHz]			
	Prototype II		Vacuum chamber	
	Estimate	Measure	Estimate	Measure
1/2	11.23	11.32	17.17	17.72
1/3	13.47	13.30	above cut-off	
2/1	13.67	13.60	15.14	15.32
2/2	14.84	14.65	above cut-off	

Table 1: Estimated and measured resonances. Mode # designates the cut-off number and the parameter q ; values for the vacuum chamber are averaged over all BPMs.

4.2 Wakefields

The coupling slot act as a discontinuity in the beam pipe and will therefore excite transversal and longitudinal wakefields. Although energy is radiating into the slot, the diffraction model [6] can be used to estimate the longitudinal peak wake potential. Fig.6 shows the longitudinal wake

potential for a bunch length of $\sigma = 250 \mu\text{m}$, and values for the peak wake potential for different bunch lengths. Both were simulated using MAFIA.

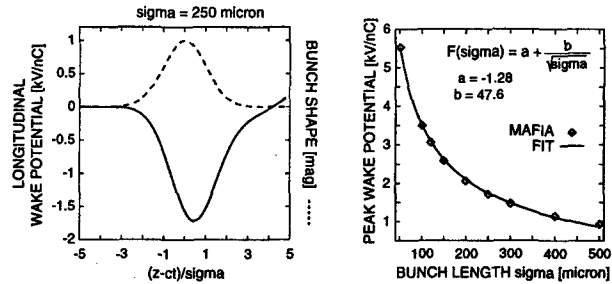


Figure 6: Left: Wake Potential simulated using MAFIA. Right: Diffraction model fitted to simulations for different bunch lengths.

5 CONCLUSION

Several attempts have been followed to describe the microwave properties of the waveguide BPM. Simulations using MAFIA in comparison with theoretical models have been proven useful to qualify and optimize the system performance.

6 ACKNOWLEDGEMENTS

The authors would like to thank U.Hahn, G.Schmidt and the TESLA group at Zeuthen for many fruitful discussions.

7 REFERENCES

- [1] A VUV Free Electron Laser at the TESLA Test Facility Linac - Conceptual Design Report, DESY Hamburg, TESLA-FEL 95-03, 1995
- [2] R. Lorenz, T. Kamps and M. Wendt, *Beam Position Measurement Inside the FEL-Undulator at the TESLA Test Facility Linac*, presented at the DIPAC97, Frascati, 1997
- [3] R. Klatt et al., *MAFIA - A Three-Dimensional Electromagnetic CAD System for Magnets, RF Structures and Transient Wake-Field Calculations*, IEEE Proceedings of the LINAC 86, p. 276
- [4] H.A. Bethe, *Theory of diffraction by small holes*, Phys. Rev., Vol.66, No.7 and 8, 1944, pp.163-182
- [5] S. deSantis, *Radiation effects of slots and coupling holes in the vacuum chamber of particle accelerators*, PhD thesis, University of Rome 'La Sapienza', 1998
- [6] K.L.F. Bayne, M. Sands, *Wakefields of Very Short Bunches in an Accelerating Cavity*, SLAC-PUB-4441, 1987

EXPERIENCE WITH THE BEAM POSITION MONITOR SYSTEM OF THE BESSY II STORAGE RING*

P. Kuske[#], R. Bakker, F. Falkenstern, R. Görgen, D. Krämer, J. Kuszynski, R. Müller
BESSY, Berlin, Germany

Abstract

The beam position monitor (BPM) system has been developed at BESSY and operates in 3 different modes: the closed orbit, the single turn, and the diagnostics mode. Details of the BPM system are presented together with the result of some bench tests. The commissioning of the system was done primarily with beam-based techniques and is described in more detail. First measurements of fast and slow beam motions are presented. From the very beginning the BPM system was used successfully for the optimisation of the storage ring.

1 INTRODUCTION

Stability of the beam position in a third generation light source like BESSY II [1] is essential in order to achieve and guarantee the high brilliance of the photon beams produced by insertion devices. Usually a lot of care is taken in the construction of the facility and in the design of the hardware to prevent beam motion from environmental or other sources. In any case a fast and accurate measurement of the orbit is required for monitoring beam motion or use the measurements in order to improve the short and long term position stability with local or global feedback systems. Aside from these more user driven requirements, the measurement of orbits and their variation as other storage ring parameters are changed, i. e. steering magnets for the determination of the response matrix or individual quadrupole magnets for beam-based alignment, are very important for understanding the storage ring hardware, the optics and for improving the performance of the storage ring as a light source. Accelerator physicists usually expect in addition to the precise orbit measurements a turn-by-turn capability or in the case of BESSY a diagnostics mode of operation.

2 TECHNICAL BPM DESIGN

The general technical layout of the BPM system [2] chosen for the BESSY II storage ring is shown in Fig. 1. The basic operating principle for closed orbit measurements has been developed at the NSLS storage ring [3]. The four pickup signals are attenuated and

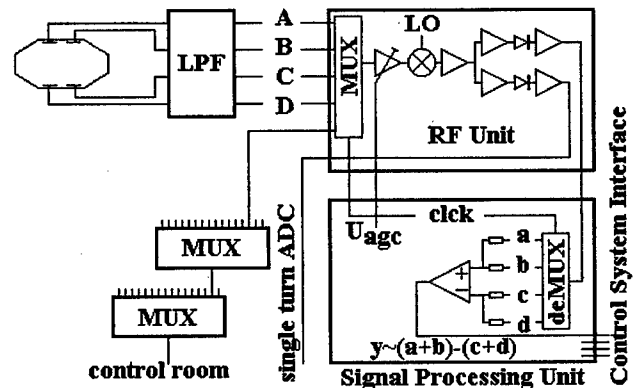


Figure 1: Layout of the BESSY II BPM system.

filtered in the low-pass filter (LPF) located close to the sensor and switched at a rate of 4 kHz sequentially to the tuned receiver contained in the RF unit. The rectified output of the super heterodyne receiver is processed in the signal processing unit by purely analog means. This is indicated in Fig. 1 for the vertical position of the beam. Finally both positions, the gain control voltage, U_{agc} , which is used to keep the sum signal constant, and an error signal proportional to $(A-C)-(B-D)$ are available in analog form. All signals are digitised at a rate of 10 kS/s with 16 bit resolution. Usually each input is sampled over 100 ms and then averaged. Mean values, standard deviations, and status bits are available in the control system. A new orbit can be displayed every second. The receiver has a second demodulated output with much larger bandwidth of 1.5 MHz which is used for turn-by-turn measurements. 64 such signals are digitised over 32 thousand turns with 12 bit resolution. This is repeated for each pickup signal at 100 ms intervals in synchronism with the injection system running at 10 Hz. The position of the beam is calculated by a computer. Displayed orbits on a pre-selected turn are updated every 2 seconds. Alternatively, in the diagnostics mode, the signal of a particular pickup electrodes can be switched to the control room through a chain of 16-to-1 multiplexers (MUX).

3 DEBUGGING AND COMMISSIONING OF THE BPM SYSTEM

Prior to installation all units and pieces of equipment relevant for the precise and stable operation of the BPM systems were carefully checked on the bench whenever reasonable. In addition strong emphasis was put on the

*Work supported by the Bundesministerium für Bildung, Wissenschaft, Forschung und Technologie and by the Land Berlin

[#] Email: Kuske@bii.bessy.de

commissioning of the complete system with beam-based techniques.

3.1 Bench tests

For example the test of the short connection between the pickup electrodes and the LPF box with high quality semi rigid SMA-cables were impossible since their installation had to be done just before the vacuum chamber was lowered into the half-opened magnets and finally fixed to the girders. During that moment of time careful RF measurements with a network or spectrum analyser were impossible. Later on it turned out, that 5 out of the 112 BPMs could not be used, because of faulty connections of that type. During the last shut down period 3 of them could be fixed. In the two other cases the vacuum feed through of the pickup would have to be replaced, which is, at least in principle, possible since the pickups are welded into demountable flanges. For the time being the beam positions at these locations are determined from only 3 pickup signals by a small modification to the signal processing electronics.

The results of the bench tests can be summarised as follows: in the closed orbit mode the position of the beam can be measured over a very large range of intensities spanning more than 4 orders of magnitude. The measurements are insensitive to the beam intensity over a range of nearly 3 orders of magnitude at the few micron level even for beams being off-centre by ± 5 mm. At nominal beam currents, above 50 mA, the resolution is better than 1 μ m in a 1 ms time interval. Fast transverse beam oscillations up to 250 Hz can be observed. In the single turn mode the resolution at low intensity is ≈ 1 mm. With the expected large excursions of the injected beam and without correction the non-linear contributions from the vacuum chamber geometry and the arrangement of the pickup electrodes is much larger than the resolution. In the diagnostics mode the filtered pickup signals in the control room are attenuated by approximately 20 dB due to the losses in the LPF, insertion losses of the chain of multiplexers, and cable losses.

3.2 System tests without beam

Unexpectedly difficulties arose with the local oscillator due to a poor quality inductor and subsequently the coil had to be replaced in nearly all oscillators. In this debugging phase all components of the BPM system were already installed and the diagnostics mode could be used for trouble shooting: In the control room a 500 MHz signal at 0 dBm from the master oscillator was fed into the output of the chain of RF multiplexers. The BPM system was set to run in the closed orbit mode and with the finite isolation of the last GaAs-switch the selected unit should work properly showing a nicely centred beam position. The procedure was automated and for each BPM the signals to the control system were recorded. Thus at

the same time the proper operation of the BPM system including the control system interface was checked.

3.3 Commissioning with beam

During the first 24 hours of the storage ring commissioning an electron beam could be stored without using the turn-by-turn mode only with the support of 9 fluorescent screens distributed around the circumference of the ring. Due to the large dynamic range of the BPM electronics, orbits could be measured at currents above 50 μ A which is achievable with single shot injection. Thus a lot of the final commissioning of the BPM system running in the closed orbit mode was done with stored beam. In the beginning with closed orbit distortions of up to ± 10 mm the error signal was very helpful in order to find missing connections and interchanged cables. In this way a couple of inoperable BPMs could be excluded for example from the closed orbit correction algorithm or the analysis of collected orbit data.

Another very helpful tool is the analysis of measured response matrices [4]. At BESSY II this matrix contains 112 times 145 elements. Each element is the orbit variation measured at one of the 112 BPMs as the 145 steering elements are changed by a small amount. The lattice and the arrangement of hardware is of 8-fold symmetry. Thus every eighth column should contain very similar information. These 8 columns can be displayed superimposed if the numbering is shifted correspondingly. Individual hardware errors show up as large deviations from the average. In this way the gain error of one of the signal processing boards could be detected.

Total BPM offset errors with respect to the centres of nearby quadrupole magnets have been obtained with an iterative procedure developed and tested at BESSY I [5]. Additional windings on the 144 quadrupole magnets of the BESSY II storage ring allow to change the gradient in each magnet. The resulting closed orbit perturbations are proportional to the actual offsets of the orbit relative to the axis of the magnet. This information has been used to redefine the targets for the closed orbit correction. In the horizontal plane a few iterations were required in order to achieve a centred beam in all quadrupoles. Finally the beam is on average only off by $\sigma_y = 0.13$ mm and $\sigma_x = 0.15$ mm relative to these magnets. The resulting distributions of the total BPM offset errors have mean values of -0.02 mm and 0.28 mm and standard deviations of 0.24 mm and 0.43 mm in the horizontal respectively in the vertical plane. This spread is in agreement with expectations based on the bench measurements and reasonable assumptions for the precision of the mechanical adjustments of the pickup sensors and the limitations of the steering concept based on 64 vertical and 80 horizontal corrector magnets. The significant mean offset in the vertical plane indicates that the vacuum chambers have been mounted too low.

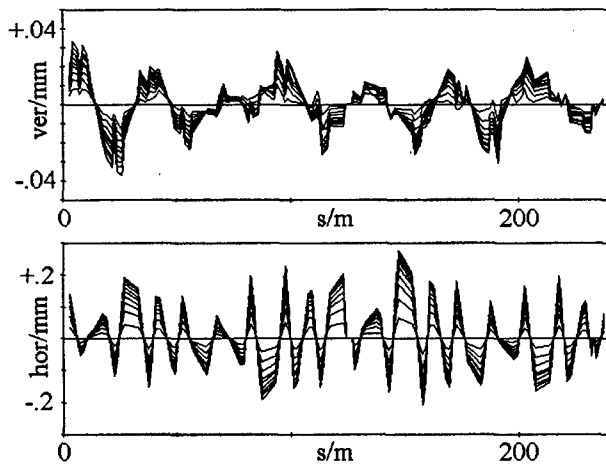


Figure 2: Slow orbit drifts in the vertical (top) and horizontal plane (bottom) relative to the orbit just after a beam of 200 mA was accumulated.

4 OPERATIONAL EXPERIENCE

As expected the most important mode of operation is the measurement of the closed orbit. Single turn data has only been used a few times early during the commissioning of the storage ring and was helpful to give the integer part of the tunes [2]. Until now the diagnostics mode has only been applied for trouble shooting the BPM system.

Software tools have been developed in order to collect orbit data at a rate of 1 orbit per second while other parameters are varied. Examples are the above mentioned beam-based determination of the position relative to the quadrupole magnets or the measurement of the response matrix. Both measurements take 1 to 2 hours depending on the degree of averaging chosen. These and similar tools have been extremely helpful for the smooth and fast commissioning of the BESSY II storage ring [6].

Slow and intensity dependent orbit drifts can be observed in both planes during the daily operation of the ring. In the case shown in Fig. 2 the beam was accumulated within less than 2 minutes from 10 mA to nearly 200 mA. The orbits have been taken just after the injection in 1 minute intervals. During the injection the beam motion was small. Drifts are much larger horizontally and an equilibrium is reached after approximately 10 minutes. This and the repetition of the pattern of the orbit distortion after each refill is an indication that they are induced by thermal effects. In routine operation the drifts can be compensated for by running the global orbit correction permanently.

Fast oscillations of the closed orbit can not be observed directly since the presently installed control system interface is too slow. Additional buffered outputs are available for the off-line analysis at each signal processing unit. In Fig. 3 the FFT of the horizontal beam motion at a location with high dispersion is shown. The observations were made at high and low beam currents, before and after the modification of the horizontal steering magnet power supplies and the installation of

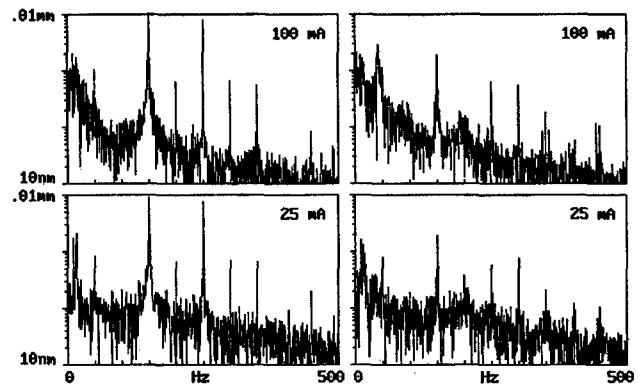


Figure 3: Fast beam motion in the horizontal plane before (left) and after hardware modifications. The top traces are taken at around 100 mA and the lower traces at 25 mA.

damping antennas in all 4 cavities. The impact of the synchrotron running at 10 Hz and eigen modes of the storage ring girders at around 15 Hz are visible at low intensities. At high beam currents longitudinal instabilities produce a broad low-frequency noise floor which does not appear in the vertical plane.

5 SUMMARY

The BPM system of the BESSY II storage ring has been in operation from the very beginning of the commissioning. In addition to bench tests further debugging took place with beam-based techniques. In the closed orbit mode beam positions are measured fast, accurate, insensitive to changing beam currents, and over a very large dynamic range of intensities. 64 out of the 112 BPMs have a limited turn-by turn capability and the diagnostics mode can be used for the analysis of the 500 MHz component of the beam spectrum by special equipment in the control room. The system is in full operation now and has led to substantial progress already.

6 ACKNOWLEDGEMENT

The support of the BESSY staff in the operation of the facility and in the acquisition of the data is gratefully acknowledged.

7 REFERENCES

- [1] W. Anders, et. al. "Status And Commissioning-Results Of BESSY II", this conference
- [2] R.J. Bakker, et. al. "Fast And Flexible BPM-System: Valuable Commissioning Tool for BESSY II", EPAC'98, Stockholm, p. 1482, (1998)
- [3] R. Biscardi, J.W. Bittner, "Switched Detector For Beam Position Monitor", PAC'89, Chicago, Vol. 3, p. 1516, (1989)
- [4] W.J. Corbett, et. al., "Debugging Real Accelerators", Particle Accelerator, 1997, Vol. 58, p. 193
- [5] P. Kuske, K. Ott, "Beam-Based Alignment At BESSY, EPAC'96, Sitges (Barcelona), Vol. 2, p. 887, (1986)
- [6] P. Bakker, et. al., "Experiences With Commissioning Software Tools At BESSY II, this conference

SELF TRIGGERED, SINGLE TURN BEAM POSITION MONITOR FOR ELECTRON STORAGE RINGS*

J. Rothman^{*}, R. Michta, R. Nawrocky, BNL, Upton, NY

A. Batrakov, V. Shilo, BINP, Novosibirsk, Russia

S. Kuznetsov, Kurchatov Institute, Moscow, Russia

Abstract

A VME based single turn beam position monitor has been developed to improve diagnostics for the NSLS UV ring. A monopulse network processes the PUE pulses, generating the sum and difference signals. An analog processing board amplifies, rectifies, and holds the signals. A digital board then digitizes and stores the data. The system can measure 32,000 turns of bipolar PUE signals from button type electrodes (1nS per lobe) at a 170nS repetition rate, with bunches separated by 18.9nS. The system makes useful measurements over a 40dB dynamic range of beam current. At full current the resolution is 50 microns.

1 INTRODUCTION

The ability to measure beam position on a turn by turn basis allows operators to increase the injection efficiency and reduce radiation levels by optimizing the injection process. It also enables the measurement of non-linear beam dynamics through phase space tracking. These measurements are particularly difficult when using the button type pickup electrodes (PUEs) commonly found in light sources. The signals are bipolar with no delay between the two 1nS wide lobes (figure 3 trace A). This makes the direct use of commercial sample and hold amplifiers impossible and the use of integrators difficult. Synchrotron oscillations can introduce substantial jitter in the arrival time of PUE signals with respect to the ring timing system, making externally gated rectifiers impractical. The analog front end described in this paper accurately samples the amplitude of the PUE pulse in the presence of timing jitter

2 SYSTEM DESIGN

One unit of the system is shown in figure 1. Monopulse networks are used to generate sum and difference signals from the PUE pulses. The sum and difference signals are then rectified, stretched, and held by the analog boards. The outputs from two analog boards are processed by each digital board. Once digitized, the CPU calculates the beam position and transmits the data to the control system via ethernet.

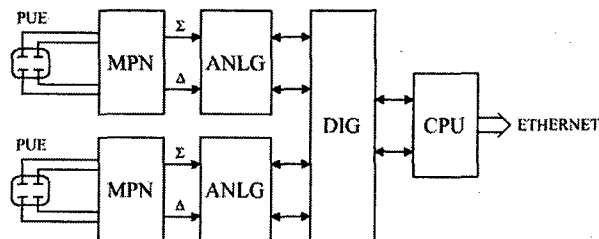


Figure 1: Simplified system block diagram

2.1 Analog Board

A simplified block diagram of the analog board is shown in figure 2.

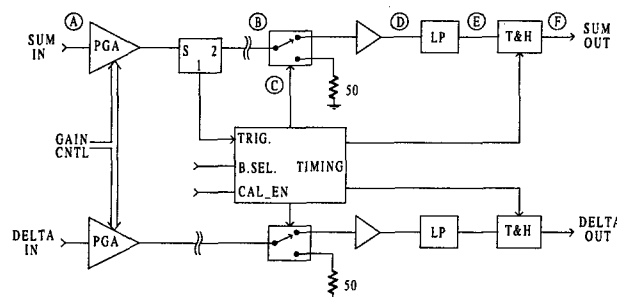


Figure 2: Analog board block diagram

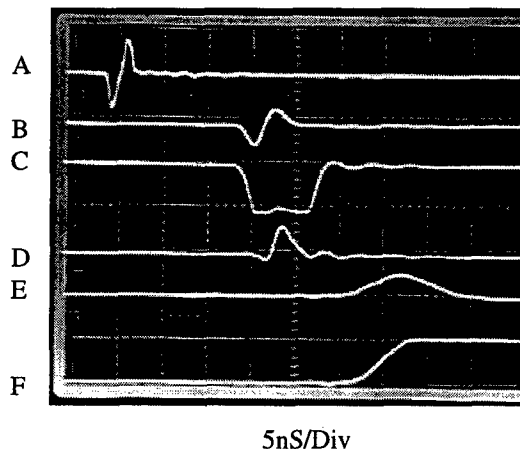


Figure 3: Analog board waveforms

* Work performed under the auspices of the U.S. Department of Energy.

* Email: jrothman@bnl.gov

The associated waveforms are shown in figure 3. The sum input (trace A) is amplified by the programmable gain amplifier (PGA) and split two ways. The PGA consists of two GaaS FET multiplexers, two amplifiers, and 1 attenuator. The selectable gains are -6dB, +12dB, and +24dB and are controlled by the digital board via the P2 backplane. Splitter output 1 triggers the timing circuit and splitter output 2 is routed to a SPDT GaaS FET switch via a coaxial delay line. The delay line compensates for delays in the timing circuit so the gate arrives at the switch at the correct time to rectify the sum signal (traces B and C). When the gate drops low the positive going lobe passes through the switch (trace D). A 50 MHz gaussian lowpass filter then stretches the pulse (trace E), allowing the track and hold amplifier to accurately sample the signal (trace F). The delta signal is processed similarly.

The digital board drives the bunch select (B. Sel.) input with a 10nS pulse, selectively enabling the timing circuit only for the chosen bucket. A PUE sum signal arriving during the 10nS window triggers the timing circuit, generating control signals for the GaaS FET switches and the track and hold amplifiers.

The output offset voltage can be measured with no beam in the ring by pulling the CAL. EN. bit high and applying pulses to the B. Sel. input. This generates the same timing signals that would normally be produced by the PUEs. This is useful for measuring and correcting

drift in the electronics. The linearity of the analog board at three different gain settings is shown in figure 4.

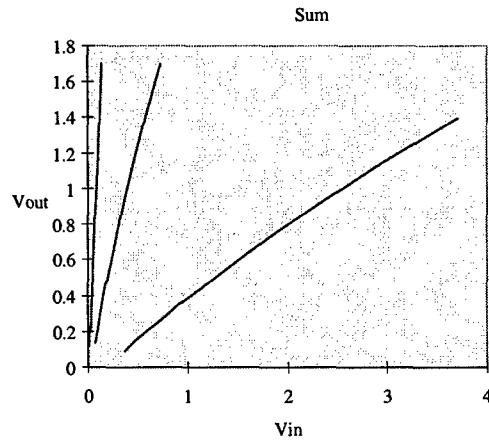


Figure 4: Analog board linearity

2.1 Digital Board

The digital board (figure 5) is a four channel transient digitizer with 12 bit resolution, 8MHz maximum sampling rate, and 32 Ksamples of buffer memory. Pretrigger and posttrigger timing modes have been implemented, allowing the trigger to appear at the beginning, middle, or end of the sampled data.

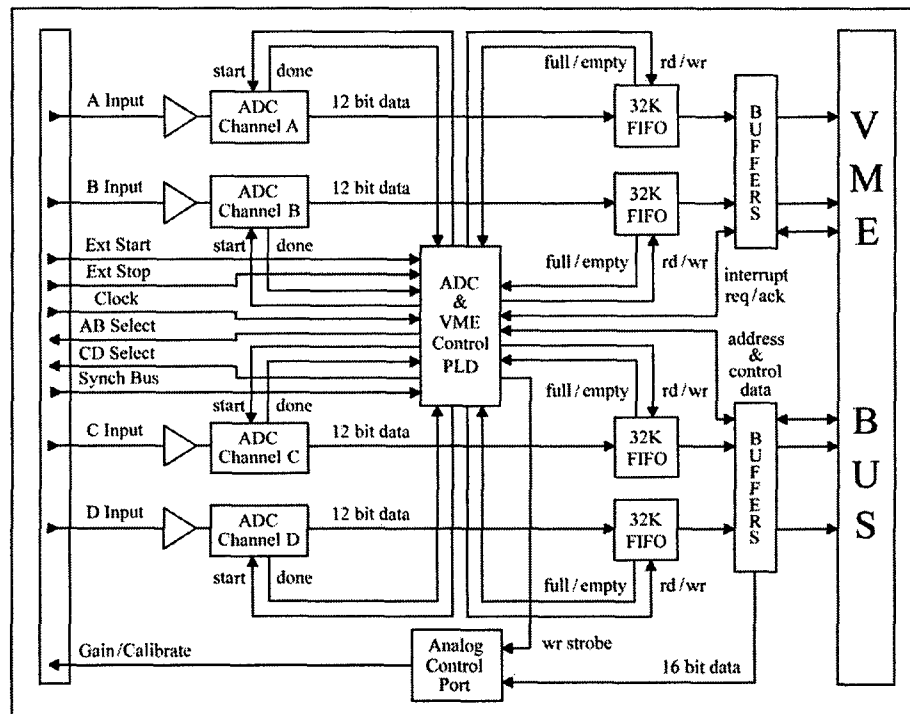


Figure 5: Digital board block diagram

Triggering and halting the data acquisition process can be accomplished either externally, or internally under software control.

The unit provides an independently delayed bunch select pulse (AB Select and CD Select) for each analog board. Each delay generator has a range of 150nS with a resolution of 0.3nS. External timing signals that are locked to the beam rotation period (Clock and Synch bus) drive the state machine and delay generators. A 16 bit TTL port on the P2 backplane (Gain/Calibrate) controls the PGA gain on the analog boards.

The VME interface provides slave functions with standard A(24)D(32) single and block data transfer modes. Interrupt level and interrupt vector ID can be defined by the application software.

3 PERFORMANCE

Turn by turn beam position measurements in the NSLS UV ring are shown in figures 6 and 7. Only the first 200 turns are shown for clarity. The graphs show the horizontal orbit distortion to stored beam resulting from the injection kicker magnets. The bump is not closed and a large residual betatron oscillation results. Prior to turn 47 the beam is undisturbed and the noise floor is visible. The noise is 0.1mm RMS at 750 mA and 2mm RMS at 25 mA. Note in figure 7 the noise is periodic, and probably due to RF pickup. Improved shielding in the production version of the analog board should improve the noise performance. The noise floor measured on the bench is 50 μ m.

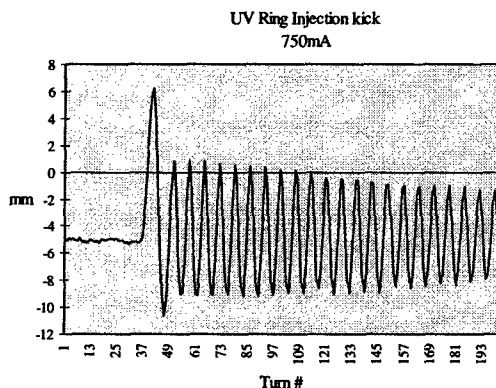


Figure 6

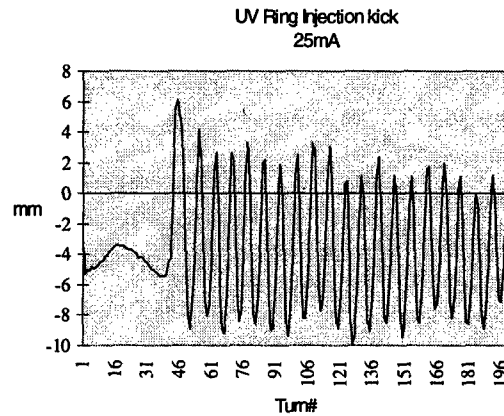


Figure 7

4 ACKNOWLEDGEMENTS

The authors would like to thank Jack Tallent for his assistance breadboarding and prototyping this system.

Analog board layout by 4DI, Inc. 97 Marcus Blvd., Hauppauge, NY 11788.

5 REFERENCES

- [1] <http://www.nsls.bnl.gov/Systems/SingleTurn/singleturn.htm>

DETECTION OF THE POSITION OF TWO BEAMS WITH A COMMON BPM

Kotaro SATOH, KEK, Tsukuba, Ibaraki, Japan

Abstract

This paper proposes a method of detecting the position of two beams with a common BPM, the method which is useful even if the bunch time-spacing between the two beams is too small to separate each beam signal with fast switches. The method is based on the idea that unknown beam parameters can be estimated if the number of BPM electrodes is greater than that of the parameters, and if the signals are independent of each other. Since the number of unknown parameters of the two beams is 6, consisting of 4 positions and 2 intensities, an 8-electrode BPM, whose signals are detected in the frequency domain, is expected to play the role. The method is to be applied to measuring beam positions near the interaction point of the two-ring collider KEKB, where the bunch spacing is only 2 ns in each ring. The independence of the signals is insured by a finite orbit separation at the common BPM.

1 INTRODUCTION

In a two-ring collider like the KEKB orbit stabilities at the interaction point are essential for keeping stable beam collisions. Near the interaction point the orbit separation is so small that the two beams travel through common pipes and common BPMs, if inserted. If position measurements are required with the common BPM, it has been believed that the bunch separation, in the time domain, between the two beams must be sufficiently large for separating beam signals with fast switches. In the KEKB, however, the bunch spacing is too small to apply the above method. It should be pointed out that, although the present case has not a sufficient separation in the time domain, here exists a finite orbit separation between the two beams. Providing a finite orbit separation in the transverse space, the paper discusses a possibility of detecting the beam position of each ring with a common BPM having many electrodes. The present method is an extension of that in the previous papers[1][2].

2 OUTPUT SIGNAL MODEL

One of the common BPMs, analyzed here, is 55 mm in diameter, and has 8 electrodes, as shown in Fig.1. The ideal orbits of the two rings, $(-7.5,0)$ for the positron LER and $(6.26,0)$ for the electron HER, are shown in the same figure. The horizontal orbit separation at the BPM is 13.8 mm. The output signal is detected with a narrow-band detector at 1017.16 MHz, two times the accelerating frequency.

The output signal can be represented well with a phaser. The phaser output of the i -th pickup button \tilde{V}_i is given by

$$\tilde{V}_i = g_i e^{i\phi_i} (pF_i(x, y) + qF_i(u, v) e^{i\theta}), i = 1, \dots, 8,$$

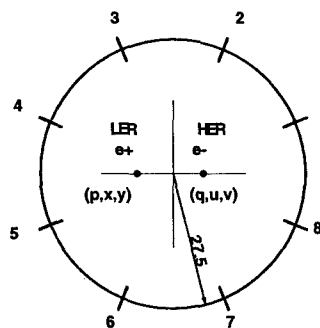


Figure 1: Geometry of the model BPM and the design orbits.

where g_i , ϕ_i and $F_i(x, y)$ are the gain, the phase shift and the response function of the i -th electrode, (p, x, y) , (q, u, v) are the charge and position for positron and electron beams, and θ their phase difference.

The detector measures the peak value V_i of the phaser ,

$$V_i = g_i \sqrt{(pF_i(e+))^2 + (qF_i(e-))^2 + 2pqF_i(e+)F_i(e-)\cos\theta}.$$

The gains can be calibrated with beams, as a later section shows. The response function is calculated from the BPM geometry. The phase difference θ must be constant and can be calculated from the distance between the BPM and the interaction point, or can be estimated with beams as shown later. For each measurement are 6 unknown parameters (p, x, y, q, u, v) . Since the number of unknown parameters is less than that of the BPM electrodes, the parameters are determined by nonlinear fitting. It should be pointed out here that, if the phase were included into fit parameters, the phase resolution would be very poor and would degrade the other resolutions accordingly. By analyzing the covariant matrix associated with the fitting procedure, we can estimate the errors of fit parameters for given measurement errors. The expected error of the i -th parameter σ_i is given by the i -th diagonal element of the covariant matrix $C(i, j)$. Text books show

$$\sigma_i^2 = C(i, i) \times \sigma_0^2,$$

where σ_0 is the absolute measurement error of signals.

The position response function used here is derived from a simple BPM model having very small electrodes. More realistic response functions can be used, if needed. The response functions are expanded with harmonic functions of positions up to the 4-th order terms, and are given by

$$F_i(X, Y) = 1 + \sum_{k=1}^4 R^k(a_i(k) \cos k\varphi + b_i(k) \sin k\varphi),$$

Table 1: Fit parameters

j	p	x	y	q	u	v
1	2.29	-7.50	.00	-1.00	6.26	.00
2	2.29	-5.50	.00	-1.00	6.26	.00
3	2.29	-7.50	2.00	-1.00	6.26	.00
4	2.29	-9.50	.00	-1.00	6.26	.00
5	2.29	-7.50	-2.00	-1.00	6.26	.00
6	2.29	-7.50	.00	-1.00	8.26	.00
7	2.29	-5.50	.00	-1.00	8.26	.00
8	2.29	-7.50	2.00	-1.00	8.26	.00
9	2.29	-9.50	.00	-1.00	8.26	.00
10	2.29	-7.50	-2.00	-1.00	8.26	.00
11	2.29	-7.50	.00	-1.00	6.26	2.00
12	2.29	-5.50	.00	-1.00	6.26	2.00
13	2.29	-7.50	2.00	-1.00	6.26	2.00
14	2.29	-9.50	.00	-1.00	6.26	2.00
15	2.29	-7.50	-2.00	-1.00	6.26	2.00
16	2.29	-7.50	.00	-1.00	4.26	.00
17	2.29	-5.50	.00	-1.00	4.26	.00
18	2.29	-7.50	2.00	-1.00	4.26	.00
19	2.29	-9.50	.00	-1.00	4.26	.00
20	2.29	-7.50	-2.00	-1.00	4.26	.00
21	2.29	-7.50	.00	-1.00	6.26	-2.00
22	2.29	-5.50	.00	-1.00	6.26	-2.00
23	2.29	-7.50	2.00	-1.00	6.26	-2.00
24	2.29	-9.50	.00	-1.00	6.26	-2.00
25	2.29	-7.50	-2.00	-1.00	6.26	-2.00

Table 2: Diagonal elements of the covariant matrix

j	p	x	y	q	u	v
1	2.5	13.6	9.8	7.9	2373.3	418.6
2	4.2	19.9	16.0	11.8	4543.2	789.9
3	2.2	13.1	9.6	7.0	2095.0	404.3
4	1.5	11.7	6.7	4.9	1313.2	252.8
5	2.2	13.1	9.6	7.0	2095.1	404.3
6	3.1	13.5	8.0	10.0	2782.5	171.7
7	6.1	15.1	10.5	17.5	5762.0	272.7
8	2.5	13.0	8.1	8.2	2252.4	168.1
9	1.5	12.1	6.1	5.4	1383.1	121.7
10	2.5	13.0	8.1	8.2	2252.4	168.1
11	1.5	13.6	10.5	4.9	1384.9	497.3
12	2.3	18.7	20.4	7.4	2581.4	1162.5
13	2.0	13.2	10.5	6.6	1875.4	524.6
14	1.0	11.7	6.8	3.3	834.0	267.4
15	1.1	13.0	9.9	3.7	983.3	447.3
16	2.7	15.9	16.3	8.2	2904.2	1127.6
17	3.9	33.6	39.7	11.3	5637.0	2555.6
18	2.5	15.0	15.1	7.7	2672.5	1070.1
19	1.8	11.7	8.5	5.7	1657.1	557.2
20	2.5	15.0	15.1	7.7	2672.5	1070.1
21	1.5	13.6	10.5	4.9	1385.0	497.3
22	2.3	18.7	20.4	7.4	2581.2	1162.4
23	1.1	13.0	9.9	3.7	983.3	447.3
24	1.0	11.7	6.8	3.3	834.0	267.4
25	2.0	13.2	10.5	6.6	1875.4	524.6

where $X = R \cos \varphi$, $Y = R \sin \varphi$, and

$$a_i(k) = 2 \cos(k(2i-1)\frac{\pi}{8}), b_i(k) = 2 \sin(k(2i-1)\frac{\pi}{8}).$$

The function is normalized by $F_i(0,0) = 1$, and the position is measured from the BPM center, not from the ideal orbit.

3 SIMULATION

Simulation was done for a case where the position of each beam is on the ideal orbit, or shifted by ± 2 mm at each measurement. Measurement is done 25 times with different position combination. The phase difference θ is $\pi/4$. The nominal charge of each ring is $p=2.29$ for LER and $q=-1.0$ for HER. The optimum charge ratio is determined by the energy ratio of two rings, 3.5 GeV and 8.0 GeV.

The objective of the simulation is not only the demonstration of measuring the two beam positions, but also the derivation of the covariant matrix to estimate the position resolution. Fit parameters for 25 measurements are listed in Table 1, and the diagonal elements of the covariant matrix are shown in Table 2. Assuming a relative signal measurement error of 3×10^{-4} and knowing of a typical signal magnitude of 3, the absolute measurement error σ_0 is about 1×10^{-3} . The worst case for the position resolution is at the 17-th measurement, where the orbit separation is the minimum value. The worst position resolution is

$$\sigma_x = 6\mu m, \sigma_y = 6\mu m, \sigma_u = 75\mu m, \sigma_v = 51\mu m.$$

4 EFFECT OF PHASE DIFFERENCE ERROR

The relative phase difference θ between the two beams is determined by the distance between the interaction point

and the BPM, and must be kept constant for stable collisions. Even though the BPM is installed at the designed position within a few mm, the relative phase may differ from the design value by several degrees. Simulation studies show that a major effect of the phase error is movement of the position reading in the horizontal direction. Figure 2 shows the position reading of two rings when each beam stays at the design position and the phase difference is changed around the nominal phase of $\pi/4$. The phase error effect is more harmful in HER than in LER. If the position displacement is required to be less than 0.5 mm the phase error must be kept less than 1 degree.

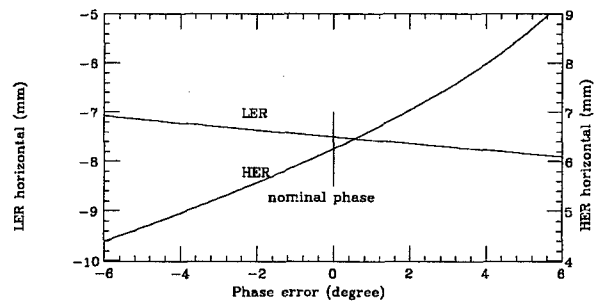


Figure 2: Position reading of two beams staying at the design orbit when the phase changes from the nominal value.

If the relative phase error exists, the position readings are also moved as the beam current changes. This fact helps finding the true phase difference. The position reading of HER is shown in Fig.3 for the case where the phase error is ± 1 degree, each beam stays at the design orbit, and the electron charge of HER is increased from 0 to -1.6 while the positron charge of LER is fixed at 2.29, the nominal value. If the closed orbit of HER at the BPM is stable within 0.5 mm in real beam operations, we can find the

true phase with a resolution of less than 0.5 degrees.

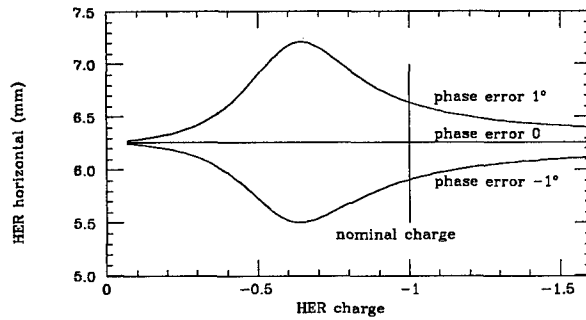


Figure 3: Position reading of HER when the phase error exists and the HER charge is changed.

The other effects of the phase error are deformation of the position sensitivity and the coupling, in which the position reading of one beam is moved when the other beam moves. These are analyzed by a simulation where one beam is fixed at the design orbit and the other beam is displaced from the design orbit within 2 mm in both the horizontal and vertical directions, and the phase error is 0.5 degrees. The two effects are shown in Fig.4 when the HER orbit is fixed, and in Fig.5 for the other case. The grid indicates the ideal position reading including the displacement shown in Fig.2 due to the phase error, and helps observe the deformation of the sensitivity. The crosses in the smaller box show the position reading of the fixed beam, and their distribution measures the coupling. The simulation shows that both effects are small, compared with the beam size at the BPM, particularly in the vertical direction. This fact favors the operation condition that the orbit stability is required in the vertical direction rather than in the horizontal direction.

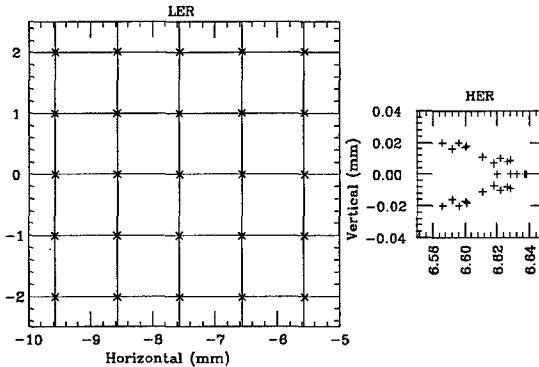


Figure 4: Position reading of two beams when the HER orbit is fixed and the other LER orbit is shifted.

5 GAIN CALIBRATION

So far the gains have been set unity in the paper. The gains of the real BPM are not equal to unity, and must be calibrated. Otherwise the monitor center would be shifted and

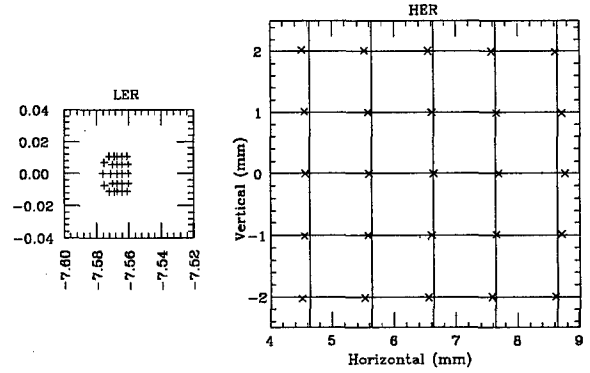


Figure 5: Position reading of two beams when the LER orbit is fixed and the other HER orbit is shifted.

the position sensitivity would be deformed. The gain calibration can be done with beams by another nonlinear fitting. The BPM has 8 electrodes and the number of unknown gains, normalized by the first electrode gain, is 7. The gain calibration was studied under the condition that measurements are done 6 times with a single beam, 3 times for one beam and 3 times for the other. At each measurement the beam is on the design orbit, or displaced by 2 mm in the vertical direction. Beam measurement parameters and their covariant matrix elements together with elements for 7 relative gains are shown in Table 3. Assuming the relative detection error of 3×10^{-4} , we find that the gain error is less than 0.1%, and the position resolution is less than $4 \mu\text{m}$ in both directions.

Table 3: 6 beam positions and the diagonal elements of the covariant matrix for the gain fitting.

i	p	x	y	C(p)	C(x)	C(y)	
1	1.10	-7.50	-2.0	2.3	159	153	
2	1.10	-7.50	0	2.2	165	158	
3	1.10	-7.50	2.0	2.2	159	152	
4	1.05	6.26	-2.0	1.1	172	164	
5	1.05	6.26	0	1.0	178	170	
6	1.05	6.26	2.0	0.9	172	165	
C(g)	g ² 0.9	g ³ 1.8	g ⁴ 3.7	g ⁵ 4.7	g ⁶ 3.1	g ⁷ 2.4	g ⁸ 1.1

6 REFERENCES

- [1] K. SATOH and M. TEJIMA, Proceedings of the 1995 Particle Accelerator Conference, Dallas, 2482.
- [2] K. SATOH and M. TEJIMA, Proceedings of the 1997 Particle Accelerator Conference, Vancouver, 2087.

BPM SYSTEM FOR THE SWISS LIGHT SOURCE

M. Dehler, A. Jaggi, P. Pollet, T. Schilcher, V. Schlott R. Ursic, PSI, Switzerland

Abstract

The layout of the SLS beam position monitor (BPM) system is presented. Since sub-micron position data in normal closed orbit and feedback mode as well as turn by turn information are required, the SLS BPM electronics pursues a new digital approach. The self calibrating four channel system consists of a RF front end, a digital receiver and a DSP controller. The whole system is integrated in the EPICS control system, which allows to select between different operation modes, so that the same BPM electronics applies to all the sections of the machine, namely linac, transfer lines, booster and storage ring. Mechanical drifts will be monitored by an independent measurement system and taken into account, when processing the final electron beam position.

1 INTRODUCTION

One of the challenges of the SLS project is to ensure the beam quality needed for the production of high brilliance synchrotron radiation requiring a wide range of beam diagnostics measurements. Therefore, the beam position monitor system has to provide a variety of operation modes.

One extreme (in terms of requirements) is the mode used for the closed orbit feedback. Since the feedback has to reduce the electron beam jitter to less than $\sigma/10$ of the vertical beam size in the ID sections, the corresponding measurements require sub micron precision at a bandwidth of a few kHz. The other extreme is to take a snap shot of the beam orbit in turn-by-turn mode, a high speed measurement requiring an bandwidth of about 0.5 MHz. An overview of the technical specifications and the measurement modes is given in table 1.

2 MECHANICAL ALIGNMENT

At SLS, the BPM stations, six per ring sector (layout see figure 1), are rigidly attached to the girders and serve as supports for the vacuum system. The mechanical prealignment gives a relative position deviation of the BPM center with respect to the adjacent quadrupole axis of less than $\pm 25 \mu\text{m}$. A more precise alignment to less than $10 \mu\text{m}$ can subsequently be obtained with the stored electron beam, applying the method of beam based alignment BBA [1]. A complete BBA cycle will take about 15 minutes and will be performed after every start-up of the machine.

During operation, thermal effects lead to mechanical drifts of the BPM chamber, which have been simulated to be in the order of $2 \mu\text{m/K}$ for SLS. This is already critical for the transverse closed orbit feedback system. Therefore, the mechanical drifts of the BPMs with respect to

Table 1: Digital BPM system specifications.

Parameter	Specification
Dynamic range by mode:	
Multi Bunch	1 - 500 mA (avg.)
Single Bunch	1 - 20 mA (avg.)
Pulsed and First Turn	1 - 10 mA (peak)
Position Measuring Radius	5 mm
Resolution (2 kHz bandwidth)	$< 1 \mu\text{m}$
Beam Current Dependence	
1-400 mA	$< 100 \mu\text{m}$
1 to 5 relative	$< 5 \mu\text{m}$
RF and IF frequencies	
Carrier RF	500 MHz
Carrier IF	36 MHz
Pilot RF	498.5 MHz
Pilot IF	34.5 MHz
Max. data acquisition rate	$f_{\text{revolution}}$
Feedback mode throughput	4000 x & y pos./s
Modes of operation	Pulsed Booster Turn-by-turn Tune Closed orbit

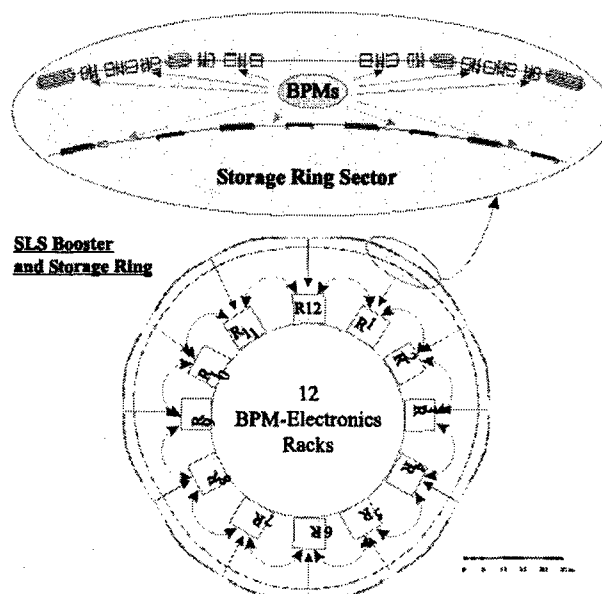


Figure 1: BPM positions including layout of the electronics and feedback architecture.

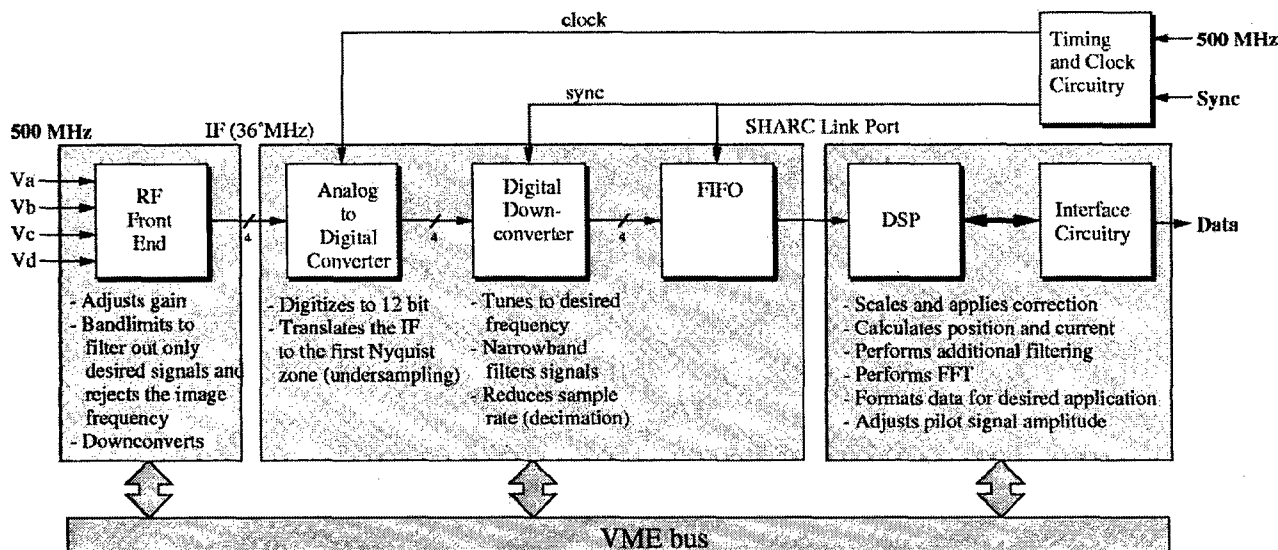


Figure 2: Block diagram of the digital BPM electronics

the adjacent quadrupole magnets are monitored via a set of absolute linear encoders, which are rigidly clamped to the quadrupoles. The system resolution is less than $1 \mu\text{m}$ within a measuring range of $\pm 2.5 \text{ mm}$. The position information from the encoders is continuously recorded by the control system and used to correct the BPM readings.

As a position sensor, the most promising candidate is a linear encoder, which has been jointly developed by former PSI Zürich [2] and Baumer Electric AG [3]. It was originally developed for use in machining tools, handling systems and robotics and offers the required resolution and range. Preliminary tests are currently under way at the SLS test stand as well as at Sinchrotrone Trieste (ELETTRA) in order to examine radiation resistance and to validate the measurement principle.

3 BPM ELECTRONICS

The SLS BPM electronics represents a departure from conventional BPM system design insofar, as the same setup delivers high speed/medium precision and low to medium speed/high precision measurements.

The electronics is a four-channel system. The button signals enter the RF front end, where they get mixed to the intermediate frequency of 36 MHz and then pass through a low cost 5 MHz wide Surface Acoustic Wave (SAW) filter. At the input of the digital receiver, the signals are then sampled at 31.25 MHz in case of Storage Ring BPMs (27.78 MHz in case of Booster BPMs). This means that the 36 MHz signal, which lies in the third Nyquist zone, is aliased down to 4.75 MHz (8.22 MHz). More about this under sampling concept can be found in [4]. For the A/D conversion we selected the AD9042 analog-to-digital converter (ADC) available from Analog Devices. It is a 12 bit ADC which has 41 MHz maximum sampling rate and 100 MHz analog bandwidth. The remainder of the processing is done in a digital way. Four digital down converters (DDC) first translate the signals to baseband and then filter and deci-

mate the data streams. The latter two processes are very important: filtering defines system bandwidth which in turn affects measurement fluctuation; decimation, a reduction of the output data rate with respect to the input, significantly reduces the downstream digital signal processing requirements. We have selected HSP50214 DDC integrated circuit from Harris. It is one of the more sophisticated and flexible programmable down converters available on the market today. In the last stage, digital signal processors (DSP) calculate the beam positions, apply correction factors and do further post processing like FFTs. The second task for the DSPs is the real time calculation of corrector settings via the singular value decomposition algorithm, which is used for the closed orbit feedback loop. To that effect, additional communication links to DSPs in the adjacent storage ring sectors are provided [5].

The problem associated with drifting gains of one channel with respect to the others is avoided by a separate pilot signal with a frequency that is 1.5 MHz lower than the RF. Four pilot signals are added to the inputs that are later on demodulated in the DDC and used to keep the gain of the four RF/IF channels matched within the dynamic range. The problem of nonlinearities associated with demodulation is avoided by direct IF sampling. Since all the processing downstream the ADC is done digitally in a DDC, it is the ADC that defines the nonlinearity. The specification for the AD9042 integrated circuit is:

Differential non-linearity : $\pm 0.30 \text{ LSB}$ or $\pm 7.3 \cdot 10^{-5} \text{ FS}$
 Integral non-linearity : $\pm 0.75 \text{ LSB}$ $\pm 1.8 \cdot 10^{-4} \text{ FS}$

The effective resolution of the complete system is determined by the following. The analog to digital conversion using a 12 bit ADC in itself would restrict the resolution to an order of $3 \mu\text{m}$. The subsequent reduction in measurement fluctuation is due to an improvement in the signal-to-noise ratio gained through the oversampling (with respect to the band of interest) and digital filtering. It is the ratio

of the passband to the Nyquist bandwidth expressed in dB. This process recovers the missing precision such, that for beam current above 50 mA and the output sample rate of 4 kHz, which is critical for the closed orbit feedback, beam movements smaller than $0.1 \mu\text{m}$ can be measured. A graph of expected resolution versus current and sampling rate is shown in figure 3.

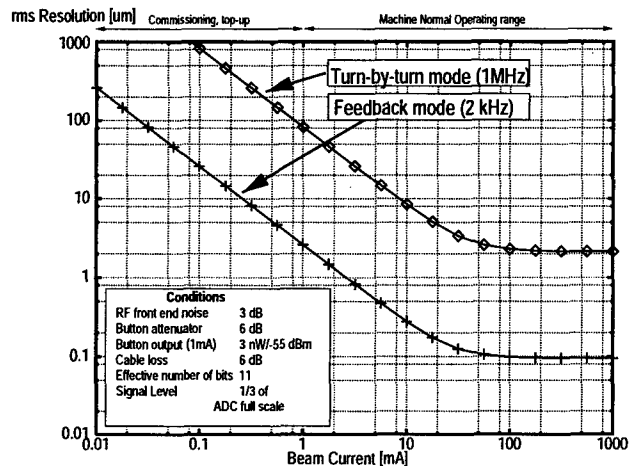


Figure 3: BPM resolution versus current for different operation modes and bandwidths.

4 CONCLUSION

For the SLS beam position monitoring system, a wide range of measurement modes, from high speed/medium resolution to low speed/high resolution, is required. To cover these, only one type of system will be used, which provides the flexibility to adapt to different measurement types by the use of programmable digital down converters. The DSP back end allows further high level post processing like FFT and an implementation of the closed orbit feedback algorithm as an integral part of the BPM electronics. Compared to more conventional solutions, the approach is cost advantageous, it offers the required sub micron resolution and programmable bandwidth, including turn-by-turn capability at a cost lower than that of two separate electronic systems to perform the same set of functions. As a nearly free feature, the closed orbit feedback is integrated into the BPM system.

The BPM stations are going to be prealigned with respect to the adjacent quadrupole magnet. This setting are updated and refined at each new run using the method of beam based alignment. Drifts occurring during operation will be monitored by absolute linear encoders, whose readings are used to recalibrate the BPM center position.

An evaluation of the electronic system using an experimental setup of commercial ADC, digital down converter and digital signal processor boards very similar to the proposed system has shown the validity of the approach. A first prototype is in work, first tests with beam are planned in the first half of this year at the synchrotron light facility

ELETTRA in Trieste/Italy.

5 ACKNOWLEDGEMENTS

We would like to thank the controls and instrumentation groups at the synchrotron light facility ELETTRA/Italy for the support in a fledgling collaboration and for giving us the possibility for various tests using their accelerator facility.

6 REFERENCES

- [1] P. Röjssel, "BPM System for Storage Rings, Measuring Beam Position against Quadrupole Magnets Magnetic Center", proc. EPAC'94, pp 1557, (1994)
- [2] K. Engelhard and P. Seitz, "Absolute High-Resolution Optical Position Encoder", Appl. Optics, Vol. 35, No.1, 201-208, (1996).
- [3] LHKK 016B03S01.XXX, "Absolute Position Encoders", Baumer Electric AG, Frauenfeld, Switzerland.
- [4] R. Ursic, "Digital receivers offer new solutions for beam instrumentation", this conference.
- [5] M. Boege, M. Dehler, T. Schilcher, V. Schlott, R. Ursic, "Fast Closed Orbit Control in the SLS Storage Ring", this conference.

CVD-DIAMOND-BASED POSITION SENSITIVE PHOTOCONDUCTIVE DETECTOR FOR HIGH-FLUX X-RAYS AND GAMMA RAYS

Deming Shu, P. K. Job, Juan Barraza, Tim Cundiff, and Tuncer M. Kuzay,
Advanced Photon Source, Argonne National Laboratory,
9700 S. Cass Av. Argonne, IL 60439, U.S.A.

Abstract

A position-sensitive photoconductive detector (PSPCD) using insulating-type CVD diamond as its substrate material has been developed at the Advanced Photon Source (APS). Several different configurations, including a quadrant pattern for a x-ray-transmitting beam position monitor (TBPM) and 1-D and 2-D arrays for PSPCD beam profilers, have been developed. Tests on different PSPCD devices with high-heat-flux undulator white x-ray beam, as well as with gamma-ray beams from ^{60}Co sources have been done at the APS and National Institute of Standards and Technology (NIST). It was proven that the insulating-type CVD diamond can be used to make a hard x-ray and gamma-ray position-sensitive detector that acts as a solid-state ion chamber. These detectors are based on the photoconductivity principle.

A total of eleven of these TBPMs have been installed on the APS front ends for commissioning use. The linear array PSPCD beam profiler has been routinely used for direct measurements of the undulator white beam profile. More tests with hard x-rays and gamma rays are planned for the CVD-diamond 2-D imaging PSPCD. Potential applications include a high-dose-rate beam profiler for fourth-generation synchrotron radiation facilities, such as free-electron lasers.

1 INTRODUCTION

Natural diamonds as photoconductive radiation detectors (PCDs) have been studied since 1956 [1], and only certain diamonds, those with low impurity concentrations (specifically nitrogen), were found to be suitable for use as radiation detectors [2]. Natural diamonds have been used as PCDs for soft x-ray detection with a laser-produced plasma soft x-ray source and a synchrotron radiation source [3]. Insulating type (type IIa) synthetic diamonds (from a high-pressure cell) used as solid-state ionization-chamber radiation detectors have been studied for biological applications with alpha particles and gamma radiation [4]. Compared with other photoconductors, diamond is a robust and radiation-hardened material with high dark resistivity and a large

breakdown electric field; diamond is also sensitive to hard x-rays [5].

The working principle of a position-sensitive photoconductive detector (PSPCD) can be described as follows: a thin CVD-type diamond disk is patterned on both surfaces with a thin layer of electrically conductive material, such as aluminum, etc. These coated patterns are individually connected to a biased current-amplifier circuitry through an ohmic contact. When the electrically biased CVD disk is subjected to either monochromatic or white x-ray beam, the photons activate the impurities in the CVD diamond causing a local conductivity change, then a local current change through the contact points. The amount of the generated current is a function of the photon flux.

2 PSPCD TESTED AT THE APS WITH X-RAYS

A compact filter/mask/window assembly has been designed for undulator beamline commissioning activity at the APS beamlines [6]. The assembly consists of one 300- μm graphite filter, one 127- μm CVD diamond filter and two 250- μm beryllium windows. A water-cooled Glidcop fixed mask with a 4.5 mm X 4.5 mm output optical aperture and a 0.96 mrad X 1.6 mrad beam missteering acceptance is a major component in the assembly. The CVD diamond filter is mounted on the downstream side of the fixed mask and is designed to also function as a transmitting hard x-ray beam position monitor. It has a quadrant pattern configuration. From the test results, we have learned that, compared to a photoemission-type TBPM, the beam position signal from a photoconductive-type TBPM has less undulator gap dependence [7].

A x-ray-transmitting beam profiler system using two linear-array PSPCDs has been designed for Advanced Photon Source (APS) undulator beamline commissioning [8]. The same insulating-type CVD diamond disk was used as for the linear array substrate. On each disk, sixteen 0.2- μm -thick, 175- μm -wide aluminum strips were coated on one side, and an orthogonal single 175- μm -wide strip was coated on the other side. Hence looking through the disk, a linear array of sixteen pixels was created as the

photoconductive sensor elements, with $175\ \mu\text{m} \times 175\ \mu\text{m}$ pixel size.

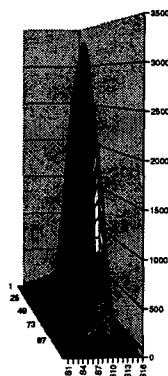


Fig. 1. A typical profile of APS undulator white beam directly measured by a 16-pixel linear-array PSPCD.

During the measurement, two sets of 16-pixel linear array PSPCDs are placed perpendicular to each other into the hard x-ray beam. The two arrays read out the beam's vertical and horizontal profile information simultaneously. To obtain a complete beam 2-D profile, one can scan across the beam. Fig. 1 shows a typical profile of an APS undulator white beam directly measured by a 16-pixel linear-array PSPCD scanning across the beam with the undulator magnet gap setting equal to 15 mm. A 12.7-mm-thick aluminum filter was used for these measurements to eliminate most of the soft x-rays.

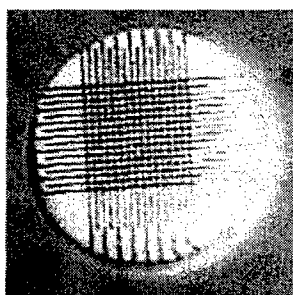


Fig. 2. Sixteen aluminum strips are coated on both sides of the CVD-diamond disk creating a 16×16 pixel two-dimensional array with $175\ \mu\text{m} \times 175\ \mu\text{m}$ pixel size.

A prototype of a 2-D imaging PSPCD has been built at the APS. As shown in Fig. 2, sixteen aluminum strips are coated on both sides of the CVD-diamond disk creating a 16×16 pixel two-dimensional array with a $175\ \mu\text{m} \times 175\ \mu\text{m}$ pixel size. The CVD-diamond disk was mounted on a water-cooled base with a couple of

ceramic connector-interface disks. Preliminary tests proved that a 2-D hard x-ray beam profile image could be read out by a multichannel current amplifier with pulsed bias electronics.

Fig. 3 shows the schematic of the readout electronics for the prototype of 2-D imaging PSPCD. Two sets of multichannel analog switches are synchronized by a clock, which also provides the triggering signal for the computer data acquisition system. For each scanning position, one of the vertical strips was pulsed by a bias-voltage, and the 16-channel current amplifier then read out the current signal from the identical column of the imaging pixels on the CVD-diamond disk. A 16×16 LED array was used as an imaging screen. The scanning rate was 300 – 3000 columns per second. A steady 2-D image was observed with the APS undulator white beam.

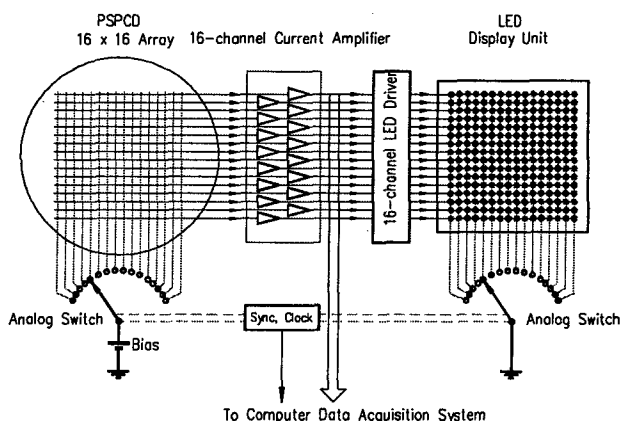


Fig. 3. Schematic of the readout electronics for the prototype of the 2-D imaging PSPCD.

We have tested the single-pixel response of this 2-D imaging PSPCD using undulator white beam with a $150\ \mu\text{m} \times 150\ \mu\text{m}$ aperture. It was found that the pixels in this 2-D array PSPCD do not cross talk. Fig. 4 shows different images observed on the LED array with variant beam condition and slit settings. We have also studied several different CVD-diamond products from different vendors with different manufacturing process. We found that, only certain CVD-diamonds, those with low impurity concentrations (specifically nitrogen and graphite), are suitable for use as imaging detectors.

3 TESTS OF THE PSPCD WITH GAMMA RAYS

We have started study of the CVD-diamond-based position sensitive detector with high-dose-rate gamma-ray beams. Preliminary experimental results with a ^{60}Co source at a NIST radiation laboratory show that it is

feasible to use CVD-diamond as an imaging detector for high-dose-rate gamma rays.

The high-flux ^{60}Co vertical-beam source, which we used at the NIST, has 33.0 Gray/hour or 1.45×10^9 photons/cm²/sec photon flux with 1.2 MeV photon energy.

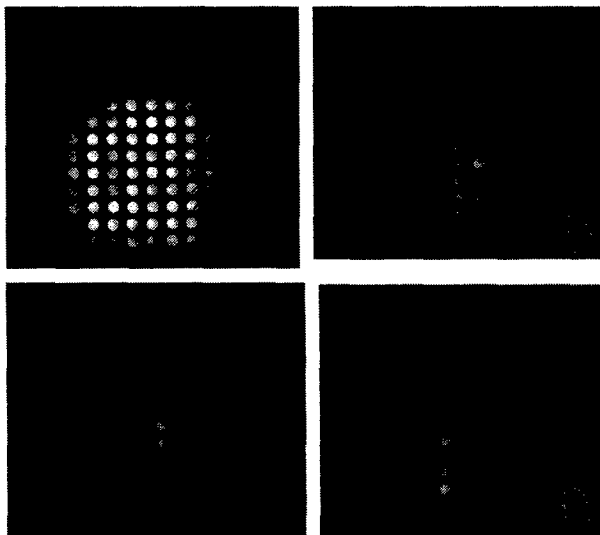


Fig. 4. Different images observed on the LED array with various undulator gap sizes and slits settings.

A 20-mm-thick tungsten slit was applied to form a narrow test beam 2.9-mm wide. The PSPCD sample was mounted on a precision stepping-motor-driven stage with linear encoder. The distance from the ^{60}Co source to the PSPCD was 480 mm. The PSPCD test sample demonstrated a 0.059 nA/mm positioning sensitivity on a 10 mm x 10 mm single element with 6 volts bias. Fig. 5 shows the PSPCD time response to the gamma-ray photon shutter. The PSPCD readout rise time was limited by the shutter speed and the system capacitance.

4 SUMMARY

We have developed a novel position-sensitive photoconductive detector using free-standing insulating-type CVD diamond as its substrate material. Several different configurations, including 1-D and 2-D arrays as imaging detectors for beam profilers, have been developed. Tests on different PSPCD devices with high-heat-flux undulator white beam, as well as with a high-flux gamma-ray source, have been done at the APS and NIST. It was proven that the insulating-type CVD diamond can be used to make a hard x-ray position-sensitive detector based on the photoconductivity principle and that acts as a solid-state ion chamber.

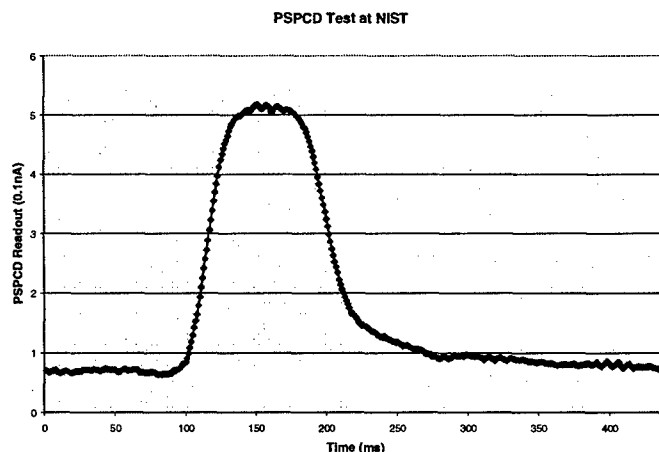


Fig. 5. PSPCD time response to the photon shutter motion during the test at the NIST high flux ^{60}Co gamma ray source.

5 ACKNOWLEDGEMENTS

The authors would like to thank Rogelio Ranay, Michel Lehmuller from the APS, and James Puhl from the NIST for their help in the PSPCD experiment. This work was supported by the U.S. Department of Energy, BES-Materials Science, under contract W-31-109-Eng-38.

REFERENCES

- [1]. Cotty W. F., (1956), *Nature* 177 1075-6.
- [2]. Kozlov S. F., Stuck R., Hage-Ali M., and Siffert P., (1975), *IEEE Trans. Nucl. Sci.*, NS-22 160-170.
- [3]. Kania D. R., Pan L., Kornblum H., Bell P., Landen O. N., and Pianetta P., (1990), *Rev. Sci. Instrum.* 61 (10) 2765.
- [4]. Keddy R. J., Nam T. L., and Burns R. C., (1987), *Phys. Med. Biol.*, Vol.32, No. 6, 751-759.
- [5]. Kozlov S. F., Bachurin A. V., Petrusev S. S., and Fedorovsky Y. P., (1977), *IEEE Trans. Nucl. Sci.*, NS-24 240-241.
- [6]. D. Shu, and T.M. Kuzay, (1996), *Rev. Sci. Instrum.* 67(9).
- [7]. D. Shu, J. Barraza, T. M. Kuzay, G. Naylor, and P. Elleaume, *Proceedings of the 1997 International Particle Accelerator Conference*, 2210 – 2213.
- [8]. D. Shu, T. M. Kuzay, Y. Fang, J. Barraza, and T. Cundiff, (1998), *Journal of Synchrotron Radiation*, 5, 636-638.

COMMISSIONING RESULTS OF THE NARROW-BAND BEAM POSITION MONITOR SYSTEM UPGRADE IN THE APS STORAGE RING

O. Singh, C. Doose, J. Carwardine, G. Decker, F. Lenkszus and R. Merl

Advanced Photon Source, Argonne, IL 60439 USA

Abstract

When using a low emittance storage ring as a high brightness synchrotron radiation source, it is critical to maintain a very high degree of orbit stability, both for the short term and for the duration of an operational fill. A fill-to-fill reproducibility is an additional important requirement. Recent developments in orbit correction algorithms have provided tools that are capable of achieving a high degree of orbit stability. However, the performance of these feedback systems can be severely limited if there are errors in the beam position monitors (BPMs). The present orbit measurement and correction system at the APS storage ring utilizes 360 broad-band-type BPMs that provide turn-by-turn diagnostics and an ultra-stable orbit: < 1.8 micron rms vertically and 4.5 microns rms horizontally in a frequency band of 0.017 to 30 Hz. The effects of beam intensity and bunch pattern dependency on these BPMs have been significantly reduced by employing "offset compensation" correction. Recently, 40 narrow-band switching-type BPMs have been installed in the APS storage ring, two in each of 20 operational insertion device straight sections, bringing the total number of beam position monitors to 400. The use of narrow-band BPM electronics is expected to reduce sensitivity to beam intensity, bunch pattern dependence, and long-term drift. These beam position monitors are used for orbit correction/feedback and machine protection interlocks for the insertion device beamlines. The commissioning results and overall performance for orbit stability are provided.

1 INTRODUCTION

The third-generation synchrotron light sources, such as the Advanced Photon Source (APS) storage ring, must meet very tight orbit stability requirements needed for low-emittance charged particle beams. These requirements get even tighter as the beam size reduces further. The orbit stability work at APS is at the forefront in many ways; here, we will discuss results of recently commissioned narrow-band switching-type beam position monitors (NBBPMs), connected to the insertion device chambers.

This type of BPM, first developed in the late 1980s [1], was followed by several design improvements [2,3], particularly a significant increase in the input dynamic range. The bulky chassis-type package has been reduced to a single height Euro-type module with several practical built-in features. Such a unit now is commercially

available. Forty of these units have been integrated together with the existing 360 broad-band-type or monopulse beam position monitors (MPBPM). Front-end upgrade work on the MPBPM system is also in progress, which will enhance the global orbit stability performance [4].

Two orbit correction systems – "fast" [5] and "slow" [6] – that correct the orbit up to about 50 Hz have been employed at the APS storage ring. Both systems make orbit correction only for the long spatial wavelength motions, taking great statistical advantage of a large number of BPMs, thus not responding to local artificial effects that may be exhibited by individual BPMs. The "offset compensations," based upon "scrape down" fitted data [6], are made to the raw BPM data. This reduces a large number of systematic errors, such as intensity/bunch pattern dependency and thermal effect in the data, presented to the orbit correction algorithms.

The bench data for NBBPMs show that the beam intensity dependence is less than 2 microns in the upper 40 dB of the power range, but it is challenging to make similar claims in the storage ring. Uncertainty in the orbit itself and the thermally induced chamber motion are some of the culprits that contaminate the measurements. The high performance x-ray-type beam position monitors (XBPMs) [7] have been routinely used as a reliable reference, but only for the bending magnet (BM) sources. However, recent work done by modifying the lattice [8] for one insertion device may hold the key to future use of XBPMs as a reference for ID sources as well.

2 INSTALLATION/COMMISSIONING

There are ten Eurocrates installed around half the ring, each housing NBBPM modules for two sectors. The NBBPM output signals are sent to a digitizing beam position limit detector (DBPLD) for machine protection [9]. The response time requirement of 350 microseconds for a beam deflection of ± 1 mm is easily met. A 300-Hz anti-aliasing filter module is used to provide input to a 16-bit orbit measurement digitizer that samples at the orbit feedback rate of 1.6 kHz. This sampled data is fed to the real-time feedback system and to an averager that then passes data to the "slow" correction system. The NBBPM calibrations for the 8-mm chamber are 3V/mm and 5V/mm for vertical and horizontal planes, respectively.

The MPBPM electronics had previously been connected to the small gap chamber's buttons (P0 buttons), which were moved earlier from the nearby standard chamber

buttons (P1 buttons), as the insertion device chambers were installed. Since the NBBPM electronics were to be connected to P0 buttons, the MPBPM electronics had to be moved back to P1 buttons. This exchange was done in several stages, by swapping electronics for only a few insertion device chambers at a time. Careful procedures were followed to ensure the user orbit was restored as closely as possible. After the swap, standard practice was to perform an orbit correction without using the swapped BPMs, followed by enabling these BPMs and generating new offset values based on the newly measured orbit. In some cases, further alignment was required at a user's request.

3 BENCH MEASUREMENT DATA

The rms noise and linearity error were measured in a bench setup; data is shown in Fig. 1. A continuous wave (CW) signal from an rf source at 351.927 MHz together with a 1-4 power splitter were used to simulate button signals. The power level was varied such that a range of -10 dBm to -70 dBm was achieved at the input of NBBPM electronics. Note that 100 mA in the APS storage ring generates about -30 dBm power at 351.927 MHz (with centered beam), when measured at the NBBPM electronics. The measurement in Fig. 1 shows that the noise and linearity for the full range vary up to 22 microns, but for a normal user run (about -30 dBm to -40 dBm), these variations are only between 1 to 2 microns.

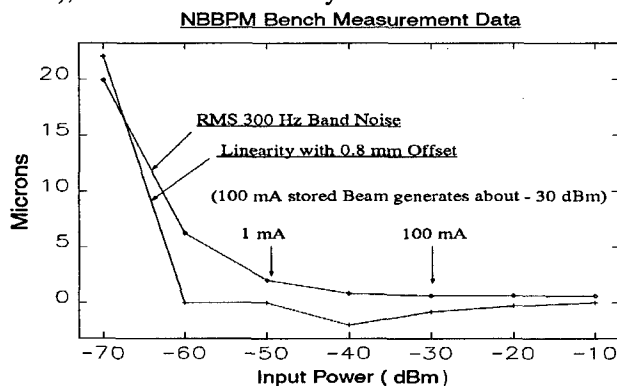


Figure 1: Noise and linearity data vs. input power

As also seen in Fig. 1, the "good" range of -10 to -30 dBm is not used due to the low power level of the stored beam. To boost the power levels, preliminary work has shown that, with minor modifications, an rf matching network, developed for the MPBPM upgrade [4], boosts the power level by 8 to 10 dBm. These matching networks will be installed in the near future at all P0 buttons.

Measurements were also made to characterize the narrow-band filter that rejects the revolution harmonics around the rf frequency. These harmonics, at 271.5 kHz away, were only about 25 dB down from the center frequency amplitude. This could have an impact on the bunch pattern dependency and further studies are needed.

4 STORAGE RING DATA

All NBBPMs have been commissioned for the slow orbit correction system, increasing the total number of available BPMs to 400. Work is in progress to include NBBPMs for the real-time feedback system. To quantify the overall performance of NBBPMs in the storage ring is rather difficult, but data show that there are significant improvements both in the intensity and in the bunch dependency. We also make use of XBPM data to compare some results.

The scrape down data shown in Fig. 2 indicate that there is a reduction in the offset compensation by almost a factor of 2. This data is taken in a controlled set of conditions where the orbit is believed to be as stable as possible, as the storage ring current is scraped from 100 mA to 40 mA in about 20 minutes. The MPBPM data were taken in early 1998 when all ID chamber buttons were connected to MPBPM electronics. The NBBPM data were taken in early 1999 when same ID chamber buttons were connected to NBBPM electronics. It is believed that a smaller amount of systematic errors should provide a better estimate for orbit correction.

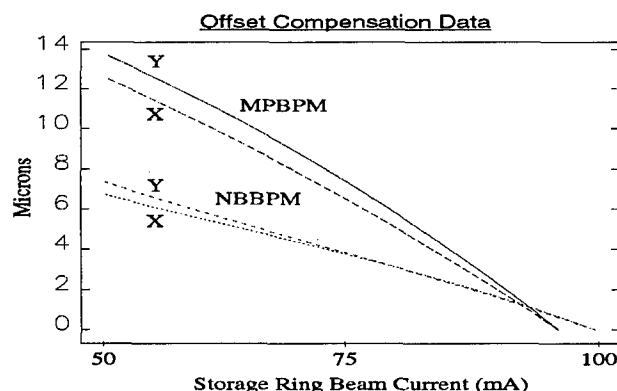


Figure 2: Scrape down data for MPBPMs and NBBPMs

We performed an experiment where we did almost the opposite of scrape down. The storage ring was filled at about two-minute intervals from 50 mA to 100 mA. The data in Fig. 3 shows that orbit drift, as measured by all NBBPMs, is less than 3.5 microns for both planes as compared to seven microns measured during scrape down. In this experiment, all designated bunches were filled except those used by the MPBPMs, making the MPBPM system insensitive to the intensity changes (not the case during scrape down), and thus perhaps providing a better orbit control. Note that horizontal drift cannot be observed in the bottom trace due to a higher orbit noise level exhibited in the horizontal plane. However, it can safely be concluded that the intensity/bunch dependency effects in NBBPMs are less than 3.5 microns for a fill of 50 to 100 mA.

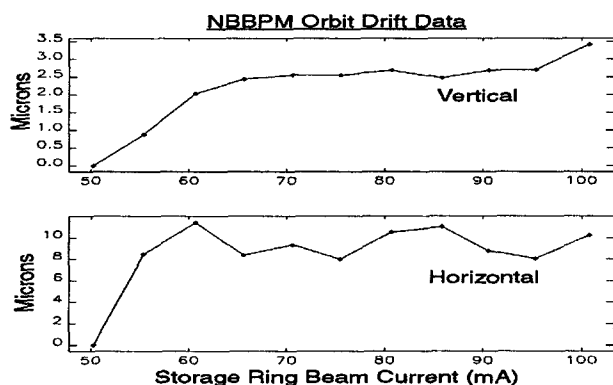


Figure 3: Orbit drifts as measured by NBBPMs

The NBBPMs can measure submicron level changes. The top trace in Fig. 4 is horizontal XBPM data shown for a period of about seven hours during a user run; it shows a downward motion. This XBPM is located ~ 15 m away from the ID source and therefore has an angular advantage of ~ 12 over NBBPMs. The bottom trace is a computed signal (called forward-mapped) at the XBPM location derived from NBBPMs straddling the ID source. This trace shows a combination of a downward motion overlapped with a periodic motion that is about 33 minutes long. Since the similar periodic motion is not seen on the XBPM, it is apparently not a real orbit motion. The observed periodic motion in NBBPMs is probably due to submicron level motion of the chambers to which these BPMs are attached, and is caused by a correlated periodic variation that has been observed in the chamber cooling water temperature. It is noteworthy to point out that the orbit correction system does not respond to such variations, as it only corrects for long spatial wavelength orbit changes.

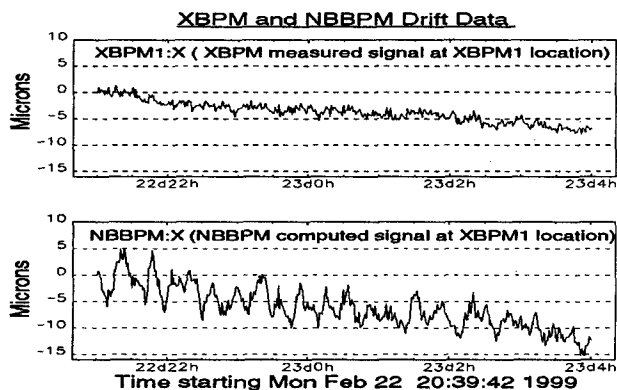


Figure 4: X-ray BPM and rf BPM forward-mapped data

The NBBPM also provides signals for the digitizing beam position limit detector (DBPLD), an interlock that detects beam missteering conditions. This system works well for stored beam, but has not yet been commissioned for top-up operation. The vertical BPM sensitivity (V/mm) for the small-gap insertion device chambers has a strong dependence on horizontal beam position. This was evident during injection when several mm horizontal orbit

transient occurred, inducing a false vertical transient. It was also observed that this coupling showed a minimum as DC vertical orbit was varied. The vertical position where minimum is observed probably indicates the vacuum chamber's geometric center. Further work is in progress, so that the DBPLD can be used in the near future. Presently, the older system (BPLD) connected to P2 buttons is used to protect the machine.

5 CONCLUSIONS

Data from the bench and storage ring show improvements in orbit measurement by the NBBPM system. The intensity and bunch dependence effects are smaller. Further work is in progress to characterize these BPMs more precisely utilizing XBPMs.

6 ACKNOWLEDGEMENTS

We would like to thank L. Emery and M. Borland for their support in commissioning NBBPMs into the operational orbit control system. This work is supported by the U.S. Department of Energy, Office of Basic Energy Science, under Contract No. W-31-109-ENG-38.

7 REFERENCES

- [1] R. Biscardi and J.W. Bittner, "Switched Detector for Beam Position Monitor," Proc. 1989 IEEE Particle Accelerator Conf., Chicago, IL, Vol. 3, pp. 1516-1518 (1989).
- [2] J. A. Hinkson and K. B. Unser, "Precision Analog Signal Processor for Beam Position Measurements in Electron Storage Rings," Proc. of the European Workshop on Beam Diagnostics and Instrumentation for Particle Accelerators, Travemunde, Germany, pp. 124-126 (1995); also published as DESY Technical Report DESY-M-95-07.
- [3] K. Unser, "New Generation Electronics Applied to Beam Position Monitors," AIP Proc. No. 390, Proc. of the Seventh Beam Instrumentation Workshop, Argonne, IL, pp. 527-535 (1996).
- [4] R. Lill and G. Decker, "Advanced Photon Source Monopulse RF Beam Position Monitor Front-End Upgrade," Proc. of the Eighth Beam Instrumentation Workshop, Palo Alto, CA, AIP Proc. No. 451, pp. 318-324 (1999).
- [5] J. A. Carwardine and F. R. Lenkszus, "Real-Time Orbit Feedback at the APS," Proceedings of the Eighth Beam Instrumentation Workshop, Palo Alto, CA, AIP Proc. No. 451, pp. 125-144 (1999).
- [6] L. Emery and M. Borland, "Advancements in Orbit Drift Correction in the Advanced Photon Source Storage Ring," Proc. of the 1997 Particle Accelerator Conference, Vancouver, Canada, pp. 742-744 (1997).
- [7] D. Shu, B. Rodricks, J. Barraza, T. Sanchez and T. M. Kuzay, Nucl. Instr. Method. A, 319, p. 56 (1992).
- [8] G. Decker, O. Singh, H. Friedsam, J. Jones, M. Ramanathan, and D. Shu, "Reduction of X-bpm Systematic Errors by Modification of Lattice in the APS Storage Ring," these proceedings.
- [9] R. Merl, G. Decker, "Design of the Digitizing Beam Position Limit Detector," Proc. of the Eighth Beam Instrumentation Workshop, Palo Alto, CA, AIP Proc. No. 451, pp. 575-582 (1999).

ELECTRON BEAM POSITION MONITOR (EBPM) DIAGNOSTICS FOR DIAMOND

M J Dufau, D M Dykes, R J Smith
CLRC Daresbury Laboratory, Warrington, UK

Abstract

This paper presents a global view of the proposed diagnostic systems for DIAMOND, but discusses in greatest detail the EBPMs, including data acquisition and control. Details of Total Current Monitor systems, and an active, beam position based interlock system for protecting ID vessels against thermal damage, by beam mis-steer, are also included.

1 INTRODUCTION

The DIAMOND light source project is proposed as the replacement for the Synchrotron Radiation Source (SRS) machine currently situated at Daresbury Laboratory. This accelerator source will consist of a main ring and most likely a gun, linac or microtron, and booster pre-injection system. These combined components will be capable of providing full energy injection and allow 'top up mode' running if required.

The Electron Beam Position Monitoring (EBPM) and ancillary diagnostic systems for DIAMOND will be extensive, comprehensive and complex. A fully instrumented pre-injector system is envisaged, complemented by high specification installed monitors in the main machine, to achieve the demanded performance.

Table 1: Machine Parameters

Lattice	20 Cell, DBA
Energy [GeV]	3.0
Accelerating Frequ. (MHz)	500
Circumference [m]	396.8
Max length for IDs [m]	16 x 4.76; 4 x 8.14
Injection energy [GeV]	3.0
Beam current [mA]	300
Source size (fwhm) [μm^2]	
Low beta straight; h x v	78 x 14
High beta straight; h x v	335 x 12
Long straight; h x v	331 x 23
Number of EBPMs	140 (7 per cell)
Accuracy (H & V)	1 μm
Stability Required (H & V)	10% beam size

All areas of beam transport, ramping and storage will be equipped with EBPMs and other diagnostic systems to provide position control, feedback and protection where necessary. Since the storage ring is the most critical with regards to operational stability and performance, it is

possible to describe a reasonable installation scheme for the EBPMs associated with this, and other principal areas including the pre-injection stages. A review of the main storage ring parameters that directly concern the diagnostic systems are shown in Table 1.

2 PRE-INJECTION DIAGNOSTICS

2.1 Beam Position Transport Diagnostics

Beam extracted from the electron source will be produced with an RF structure at the machine frequency of 500MHz. Bunched beam current pulses, after extraction at rates between 5 and 10Hz, will pass through an accelerating stage to the booster ring and then to the storage ring. The RF structure, relativistic nature and sufficiency of beam current allows the use of capacitive button type pickup EBPM heads to be located appropriately along the flight paths. For efficiency, it is hoped to rationalise the EBPM head to a single standard four button 'on axis' type giving two fully isolated measurements for each plane.

Since beam production is pulsed, the detection electronics will be of the single shot type. The processing detector electronics for such a system will be required to resolve beam position to the order of 200 μm . This can be achieved using synchronous homodyning detector systems[1] located in an adjacent accessible areas. Two pre-processing 180° hybrids mounted local to the EBPM heads will be used to provide sum and difference outputs. These will be switched into the detector electronics to provide alternate readings from consecutive gun pulses of horizontal and vertical beam position. The output of these detectors will be fed into local analogue to digital conversion/digital signal processing (ADC/DSP) systems for quantisation then input into the control system to provide graphical mimic displays and steering feedback.

In keeping with the intended policy of integrating comprehensive diagnostics aids into all areas of DIAMOND, it is likely that some form of pulse-beam monitoring will be included in both transport lines. This will be designed around commercial devices, and will include an integrating beam charge monitor located after the gun to monitor gun efficiency. Fast AC current transformers may also be included at the ends of both transport lines to provide indications of pre-injector efficiency.

2.2 Booster Synchrotron Diagnostics

Beam captured in the booster synchrotron will be accelerated to the storage ring energy at a frequency upto 10Hz. Four-button on-axis EBPM pickups will be installed at regular intervals around the circumference; position resolutions of 200 μ m should be adequate. As is the case for the beam transport system, the beam will be present only for a short time and so a single shot detector will also be suitable for application here. A high speed horizontal and vertical switching system and associated ADC/DSP system will allow readings to be taken from all EBPMs, in both planes, during the beam fill time, enabling feedback to be applied as required. Figure 1 shows a schematic arrangement of such a system. This is similar to that which would be fitted to the transport lines.

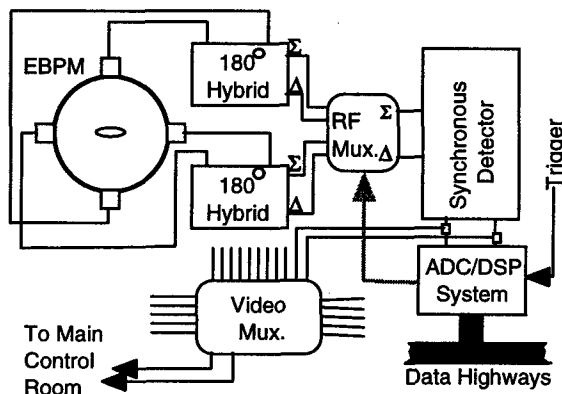


Figure 1: Basic Booster/Beam Transport EBPM System.

A delayed storage ring trigger pulse is used to arm the DSP for data collection. This will be used to gate out unwanted artefacts from the injection pulse.

Additionally a commercially available Total Current Monitor (or Parametric Current Transformers, PCT), plus, one on axis, quarter wavelength strip-line vessel will be installed within the booster. The strip-line will provide high sensitivity 'clean' signals direct to the Main Control Room (MCR). A suitable coaxial multiplexer will be used to provide processing to allow tune measurements to be made via a further synchronous detector and digital oscilloscope.

3 STORAGE RING DIAGNOSTICS

3.1 Storage Ring Main EBPM System

The storage ring main EBPM system will consist of 140 EBPMs, with at least 7 heads incorporated within each cell of the machine. Straights containing insertion devices will have heads that are fixed onto highly stable mounts to reduce mechanical movement, the greatest source of beam stability problems. These 'golden' EBPMs will share the same type of processing electronics as the remainder of the EBPMs, but with their improved

mechanical stability, should provide the storage ring with known stable beam position alignment references. Again for efficiency, the pickup heads will be of a single rationalised design. A prototype design for the pickup head is shown in Figure 2.

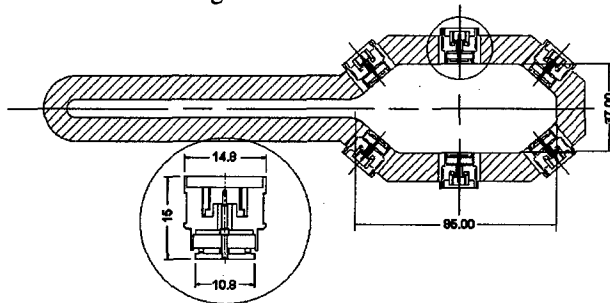


Figure 2: Typical Storage Ring EBPM Head vessel Design and capacitive button pickup.

Daresbury modified, ESRF type, capacitive button pickups are used for the EBPM head. These have reduced capacitance, which allows scanning wire bench calibration of the pickup head at low frequency (5 MHz). Electrostatic finite element analysis of the EBPM head has been carried out in both planes using QuickField™. This has shown an adequate horizontal response but poor vertical response from the four buttons. This can be compensated for by the inclusion of separate on-axis buttons for the vertical plane, with the added advantage of completely de-coupling vertical beam movements from those in the horizontal plane. The electrical response for this configuration, shown in Figure 3 gives calibration factors near the centre of less than 12.5 for each plane.

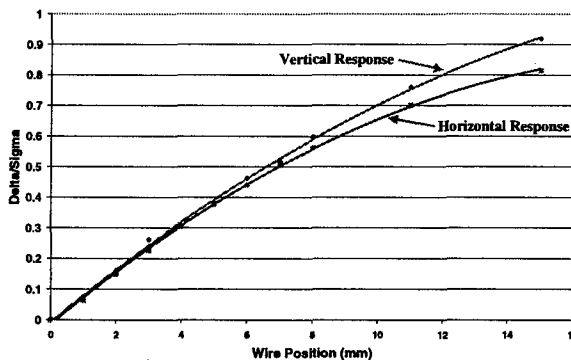


Figure 3: Horizontal and Vertical Calibration Curves.

Signal processing for these EBPMs will be done at several accessible marshalling points around the storage ring, using precision commercial detector electronics[2]. These detectors offer an improvement over the current Daresbury type detectors in that they have faster update rates (up to 2.5kHz) and are more cost effective. The output of these detectors will pass into a DSP system for quantisation and presentation to the controls/positional feedback system. Once again, the same electronic systems will be applied to all EBPMs to standardise. The combination of the proposed small beam dimension and operating current specification of the detectors means that

the system will heavily rely on mechanical stability to achieve its specification. A separate, dedicated single turn detector will be included on the 'golden' EBPM pickups to assist with machine operations and accelerator physics. Figure 4 below shows a typical detector system.

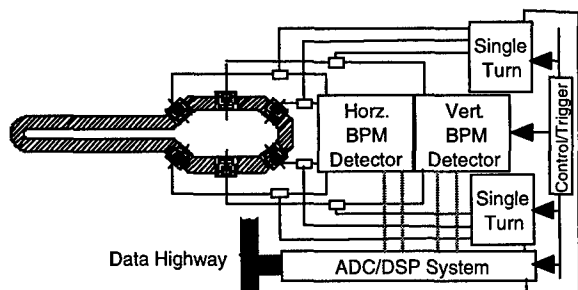


Figure 4: Typical Storage Ring 'Golden' type EBPM

Additionally, a commercial PCT will be installed, along with an on axis diagnostic quarter wavelength strip vessel for basic beam diagnostics. A 45° strip-line vessel will also be fitted to provide a beam tickler drive and pickup.

3.1 Machine Protection and ID EBPMs

For each of the IDs installed in the proposed source, an active electronic interlock system will be required, to protect the associated narrow-gap vessel from potential thermal damage, that would result from mis-steered beam. It is intended that the same successful philosophy of operation, as employed in both vessel protection systems currently operational in the SRS, will be applied to these future systems[3].

The two primary interlock inputs will be beam displacement information for the vessel, and temperature of the vessel walls and flanges, either of which will be capable of tripping off the machine RF at potentially damaging levels. As in the SRS, monitoring of the beam position will be designed around commercially available processing electronics operating from EBPMs within the ID vessel itself, while a thermocouple array interfaced via a Programmable Logic Controller, will monitor the temperature of the vessel walls. Because reliability is paramount, the integrity of all electronic hardware both primary and secondary, and also of that hardware providing support signals, will be monitored.

Since the application of this philosophy to the SRS vessel protection has led to a flexible design of satisfactory result, it is likely that the design will be applied en bloc to the requirements of DIAMOND. However local variations in the distribution of EBPMs may be required depending on specific vessel geometry.

During the period that the model for future vessel protection has been installed in the SRS, operational experience has highlighted the desirability for an integrated development enhancement offering diagnostic information regarding beam position, immediately prior to tripping the RF. Figure 5 shows a schematic,

illustrating the proposal.

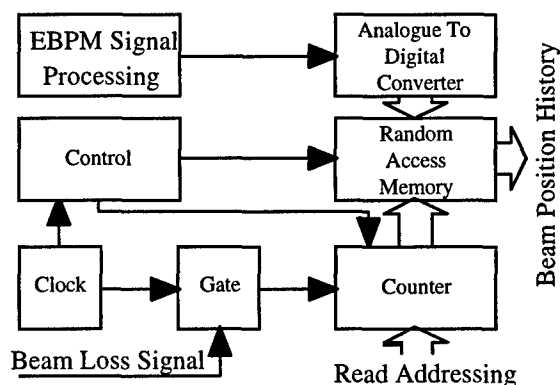


Figure 5: Beam Loss Data Recording System From Ids

Samples of the digitised beam position signal are stored in Random Access Memory (RAM) locations during read mode. A cyclic counter whose serial input is fed from a clock source provides the addressing for the locations. On beam loss the address counter is 'frozen' when the clock is inhibited, capturing in digital form the recent history of beam position. Addressing the locations via the parallel input of the counter can access the stored samples when the RAM is set to the write mode. Accessed samples could be read digitally or converted to analogue form.

4 CONCLUSIONS

This overview of proposed DIAMOND diagnostics presents realisable solutions for the major EBPM systems of the facility. At the present time, the systems discussed for the pre-injection stages would utilise old technology for the detectors, requiring extensive in-house development to produce an economically viable design of wide application. However, a suitable commercial unit is at present under development, and will probably be employed when available.

When active development of data processing systems commences, for economic reasons, it is intended that the DSP based data handling system, be of maximum versatility, with application to the full range of DIAMOND diagnostics.

5 ACKNOWLEDGEMENTS

Acknowledgements to M. Collier and C. Hill of the Daresbury Laboratory design office for providing engineering drawing.

6 REFERENCES

- [1]T. Ring, "Beam Position Monitors For The High brightness Lattice", Internal Daresbury Lab. Technical Memorandum RING-85/134, (1985)
- [2]J. A. Hinkson, K. B. Unser., "Precision Analogue Signal Processor for Beam Position Measurements in Electron Storage Rings", Proceedings, 2nd DIPAC, Travemunde, Germany, (May 1995)
- [3]D. M. Dykes et al., "The SRS Multipole Wiggler Vacuum Vessel Protection System", Proceedings, 6th EPAC, Stockholm, (1998)

BEAM POSITION MONITORS FOR DUKE FEL STORAGE RING*

P. Wang#, N. Hower, V. Litvinenko, M. Moallem, O. Oakeley, G. Swift, Y. Wu
Duke University, Free Electron Laser Laboratory, Department of Physics, NC27708

Abstract

The Duke FEL storage ring is a 1Gev electron ring, which is designed for driving UV-VUV free electron lasers. The ring has been in operation since November of 1994 [1] but the beam position monitors (BPMs) were connected and operated just recently. The BPM pick-ups are 4 stripline electrodes. In order to reduce the higher-order-mode loss excited by the stored beam at the BPM pick-up area, the BPM vacuum chamber is designed with 4 grounding strips between the electrodes that have the same diameters as the electrode. This design allows the electron beam to see a much smoother vacuum chamber at the BPM area. The pick-up signals are processed by Bergoz's electronic modules, which give X/Y outputs directly. Each BPM has its own process module and 34 modules have been connected to the EPICS control system. The beam orbit now can be displayed and corrected through EPICS in the control room. The system performance and the test data will be presented in this paper.

1 INTRODUCTION

The Duke FEL storage ring has two arc sections with 6.7-meter radii and two long straight sections (34-meter each). The stored beam has a bunch length FWHM (Full Width Half Maximum) of 10-30 mm. The stripline electrode BPM has been developed and installed. Since the vacuum chamber in the arc sections has a much smaller diameter than in the straight sections, two types of BPM electrodes are designed to fit the vacuum chamber size in these areas. A special design effort of adding four grounding strips, which are parallel to the pick-up electrode, has reduced the chamber impedance further. There are 36 BPMs installed on the arc sections, one BPM per arc quadrupole magnet, and 18 BPMs in the straight sections. The signal processing system works at 178.5 MHz, which is the fundamental ring RF frequency. A total of 34 BPMs have been connected to the EPICS control system. The system has been in operation since September 1998. Detailed mechanical design, calibration procedure and system performance will be presented in the following sections.

2 MECHANICAL DESIGN

Both types of BPMs utilize short stripline-style electrodes,

*Work supported by U. S. Air Force Office of Scientific Research Grant F49620-93-1-0590 and U. S. Office of Naval Research Grant N00014-94-1-0818

#Email: wang@fel.duke.edu

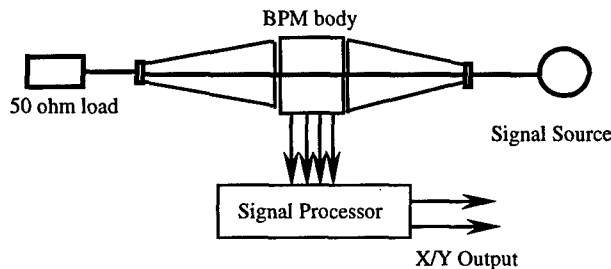
electrically grounded at one end by either welding or brazing to the outer vacuum envelope, and at the other end separated from making electrical contact by the presence of a physical gap of 0.5-mm width. At the end closest to this gap, a ceramic-to-metal electrical feedthrough is affixed by a lightly welded contact, and the signal induced on the electrode by the passing electron bunch is carried through the vacuum wall to a SMA coaxial connector. The lengths of these striplines (from their grounded end to the center of the electrical feedthrough pin at the other end) are 21.64 mm for the arc BPM and 30.53 mm for the straight section BPM. Longer striplines usually are preferred but the available physical space limits it. The inner radii of the striplines in both cases is the same as that of the adjacent vacuum chamber wall, R17.78 mm for the arc BPM and R47.75 mm for the straight section BPM. To further enhance the impedance matching, the four electrodes are interleaved with four parallel and otherwise geometrically identical striplines, dubbed by us as "grounding strips", which are brazed or welded to the adjacent tube wall at both ends. The modules are rotated at installation so that the electrode strips are centered at 45 degrees above and below the horizontal orbital plane of the electrons, so as to avoid being struck directly by synchrotron radiation.

A prototype electrode ring with grounding strips was machined from aluminium and the impedance of striplines was measured. With adding of grounding striplines, the impedance is much smaller than the one calculated from a parallel stripline with the same width and space (32-ohm instead of 50-ohm). Adjustments were deduced on the body radii with the goal of achieving 50-ohm impedance in each case. The final electrode/grounding strip pieces were machined from one-piece stainless steel cylindrical shells, slit lengthways over part of their length. The critical dimensions on all units were machined to within .001 to .002 inch of their nominal values. Fig. 1 is a photograph of both BPMs.

3 BENCH CALIBRATION

After the BPMs were assembled and welded together, they were serialized and individually calibrated. Two kinds of calibrations were performed. One is to measure the offset between the electrical center and the mechanical center. This has been done for every single BPM body and is a very good way of quality control for manufacturing. Another calibration we did is to measure the sensitivity of the electrode to beam motion. This is done for each type of BPM. A bench test set has been

fabricated to perform these jobs. The test set has a V-block fixture to hold the BPM body. To simulate the beam, an antenna rod carries the electronic signal going through the BPM chamber to a dummy load. The BPM becomes part of a coaxial transmission line where the rod is the central conductor and the BPM body is the outer conductor. Two tapered cones connected at both ends of the BPM chamber are made to reduce the effects of the impedance mismatch. The output signals from 4 pick-ups are used to get the position of the antenna rod relative to the electrical center of the BPM. The test set is sketched as below:



The offset between the electrical center and the mechanical center can be derived from the test data measured with rotating the BPM body. The mechanical center is referred to the outer surface of the BPM body, which has four tooling balls for alignment purposes. We measured about 60 BPM pick-ups of the arc sections and 25 of the straight sections; the offset for most of them is less than 100 micrometers. The sensitivity coefficient is measured with the antenna's displacement near the center. The test results is:

$$S_x = S_y = 6.67\%/mm, \text{ for the arc section}$$

$$S_x = S_y = 2.8\%/mm, \text{ for the straight section}$$

The beam position is determined by the following equations:

$$X = k * (V_a - V_b - V_c + V_d) / (V_a + V_b + V_c + V_d)$$

$$Y = k * (V_a + V_b - V_c - V_d) / (V_a + V_b + V_c + V_d)$$

Where V_a , V_b , V_c , and V_d are detected signals from the pick-up electrodes and $k = 1/S_x$.

At the time we did the calibration, the BPM electronics for processing the pick up signals was not available. A short pulse signal generated from the snap diode is used to simulate the bunched beam. The signal's FWHM is around 100ps, which corresponds a bunch length of 30 mm for a relativistic beam. A fast digital scope, Tektronix DSA-602, is used to record the output signals from each pick-up electrode. Now with a signal processing electronics working at 178.5 MHz, we plan to

recheck the sensitivity with a 178.5 MHz CW signal in the near future. The available electrostatic analysis program also will be used to get the sensitivities at larger displacement from the center. By doing so, the pin-cushion-like distortion can be compensated. According to Jim Hinkson at LBL, the calculated sensitivities have very good agreement with his bench test data [2].

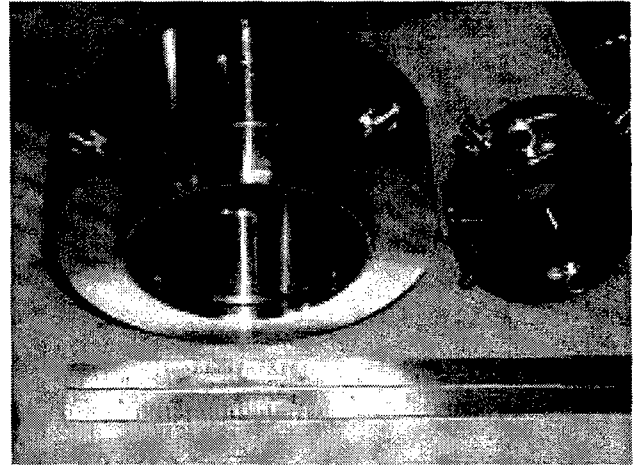


Fig. 1

4 SIGNAL PROCESSOR

The signal processor we used is simple and straightforward. The commercially available BPM electronic modules from a company named Bergoz [3] are employed. Each module is a 4"x6" printed circuit board, which accepts the 4 pick-up signals and gives the X/Y output directly. Each BPM has its own electronic module. The amplifier gain of this module is set at 0.2V output for 1% of tested signal difference. The 54 BPMs around the storage ring are divided into 4 divisions: Northwest, Southwest, Northeast, and Southeast. There are four crates located at each corner inside of the ring. Each crate is 17 inches wide, 11 inches high and 9 inches deep. The crate can hold up to 16 modules. High quality coaxial cables are used to connect each BPM pick-up electrode to the signal input at the crate. The 1/4" Heliac coaxial cables were selected to connect the straight section BPM because of its low loss (2.4dB/100ft at 200MHz) and good shielding, since the straight section BPM has lower sensitivity and the cables are longer. The relatively shorter cables for arc BPM are RG223 for economy reasons. Among the 54 BPMs, 34 of them have been connected to Bergoz electronic modules. From each Bergoz's module, there are 3 output signals (X, Y and sum) sent to a VME crate for computer readout. The VME crate is located at west-center of the ring where the EPICS system is connected.

5 SYSTEM PERFORMANCE

The whole BPM system started to operate in September 1998. At the beginning, all the beam position data were fluctuated over a range of 5-15%. Observations revealed that the X/Y output signals had strong AC components and some of them were 60 HZ related AC noises. It was contributed mainly by the magnet power supplies. The signal conditioning boards purchased from VMIC Company have been added to reduce the AC noises. Its function is to provide a low pass filter with a bandwidth of 3dB attenuation at 4 HZ. With the conditioning boards, the fluctuation has been reduced to ± 25 micrometers over a short period (a few minutes) of time.

The system has a beam current resolution of about 1mA. When stored beam currents are below 1mA, the beam position data becomes current dependent. However, most of our ring operations are not at the low current region and we do not expect this to be a significant problem for us. The beam position data are currently delivered at a rate of 2 HZ. A sophisticated display tool (ADT) from APS is used for beam orbit displaying.

Overall, our BPM system is still in the process of being commissioned. Our future goals are:

- 1) Using the beam to calibrate the BPM offset related to nearby magnet
- 2) Using the beam position data to correct beam orbit (locally and globally)
- 3) Developing a slow orbit feedback system to correct the orbit drifting
- 4) Establish a fast (up to 120 HZ) beam orbit control feedback system.

6 ACKNOWLEDGEMENT

Authors would like to thank J. L. Pellegrin at SLAC and Jim Hinkson at LBL for the constructive discussions. The consulting with them has been very helpful for the work we did here.

7 REFERENCES

- [1] V. N. Litvinenko, et al., "Commissioning of the Duke Storage Ring", Proceedings of 1995 Particle Accelerator Conference, Dallas, TX May 1-5, V. I, P. 213.
- [2] J. Hinkson, "Advanced Light Source Beam Position Monitor", Conference Proceedings NO. 252, Accelerator Instrumentation Third Annual Workshop, Newport News, VA 1991 P. 21.
- [3] Klaus B. Unser, "New Generation Electronics Applied to Beam Position Monitors", Bergoz Precision Beam Instrumentation, F-01170 Crozet, France.

DEVELOPMENT OF A PROTOTYPE CAPACITIVE BPM FOR THE UNIVERSITY OF MARYLAND ELECTRON RING*

Y. Zou[#], J.G. Wang⁺, Paul Chin, Y. Li, S. Bernal, M. Reiser

Institute for Plasma Research, University of Maryland, College Park, MD 20742

Abstract

Work has been performed at the University of Maryland by the electron beam physics group to design and develop a prototype capacitive Beam-Position-Monitor (BPM) for an electron ring project. Extensive theoretical work and PSPICE simulation of the equivalent circuit of the BPM have been conducted to fully understand the behaviour of the capacitive BPM. This BPM has 4 pieces of electrostatic pickups around a beam pipe of 2-inch diameter. The capacitance between the electrode and the beam pipe is approximately 0.55nF, which results in a time constant long enough to reproduce the current waveform faithfully. A bench test of this prototype BPM has been completed. The test shows that the capacitive BPM has a very fast response to the beam current with high sensitivity. Also, the BPM can measure the beam centroid displacement with adequate accuracy. In addition, this BPM can measure the total beam current by appropriate calibration.

1 INTRODUCTION

Both capacitive and resistive BPMs are widely used in charged particle accelerators and beam lines. At the University of Maryland, a compact electron ring (UMER) [1-3] is being built for the study of the physics of space-charge-dominated beams. Because the beam has relatively low energy (10 keV), it is very easy for it to go off-center due to stray magnetic fields (the earth's field and other stray fields due to the presence of metal), misalignments, etc. To guarantee the success of the UMER, the beam centroid motion has to be measured very accurately and the information from the BPMs must be provided to a beam steering system to steer the beam back to the central orbit. Both resistive wall BPMs and capacitive BPMs will be used in the UMER. This paper will discuss the theory and design of the capacitive BPM. The resistive wall BPM has been discussed in the pervious paper.[5]

2 BASIC PRINCIPLE

Figures 1 and 2 are the schematics of a capacitive BPM and its equivalent circuit. In Figure 1, there are four electrodes inside the beam pipe forming four capacitors. In Figure 2, C is the capacitance between the electrode and beam pipe while R_1 is the bleeder resistor to avoid excess charge accumulation on the electrodes. The R_1C time constant must be long enough to be able to reproduce the beam profile faithfully. I_s is a frequency dependent current source. The formula to calculate I_s is

$$I_s = \frac{dQ}{dt} = \frac{\Phi L}{2\pi v_0} \frac{dI_b(t)}{dt} \quad (1)$$

Here, L is the electrode length, v_0 is the beam velocity and Φ is the electrode angle width.

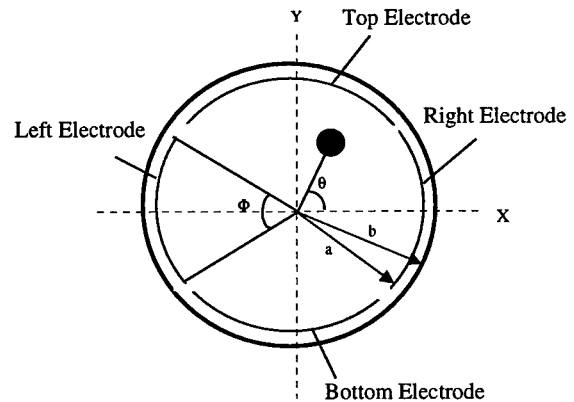


Figure 1. BPM schematic drawing.

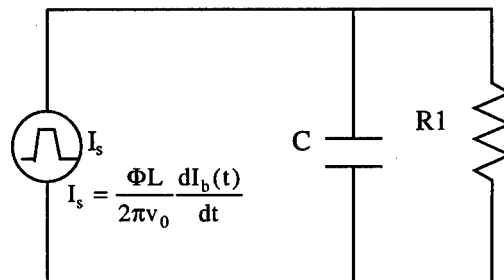


Figure 2. BPM equivalent circuit.

* Work supported by DOE.

Email: yunzou@glue.umd.edu

+ Current Address: ORNL and Visiting at BNL.

If the beam is centred, the four pick-up signals are the same. When the beam is off-centred, the signals from four electrodes are different. The ratio of the signals from the two opposite electrodes will give us the beam position information. The formula is as following [4]

$$20 \log(V_R / V_L) = \frac{160}{\ln 10} \frac{\sin(\Phi/2)}{\Phi} \frac{x}{b} + \frac{20}{\ln 10} \left[\frac{8 \sin(3\Phi/2)}{3\Phi} - 16 \frac{\sin(\Phi)\sin(\Phi/2)}{\Phi^2} + \frac{128 \sin^3(\Phi/2)}{3\Phi^3} \right] \frac{x^3}{b^3} + \left[-8 \frac{\sin(3\Phi/2)}{\Phi} + 16 \frac{\sin(\Phi)\sin(\Phi/2)}{\Phi^2} \right] \frac{xy^2}{b^3} + \dots \quad (2)$$

If x/b is small enough, we can take the first term, which is the linear term. The formula is as follows:

$$20 \ln(V_R / V_L) = \frac{160}{\ln 10} \frac{\sin(\Phi/2)}{\Phi} \frac{x}{b} \quad (3)$$

Here, b is the pipe radius and x is beam displacement. The coefficient of the linear term is called the sensitivity of the BPM, the parameter that we are most interested in. The coefficient of the second term tells us the nonlinearity of the BPM. We can compensate this term by calibrating the BPM on the x or y axis. The third term, which depends on both x and y displacements, is called the coupling between the x and the y direction.

The coefficient of each term only depends on the electrode angular width Φ . Both the sensitivity and the nonlinear term are greater than zero if Φ is between zero and 90° . The coupling term, however, could be positive or negative, depending on Φ . We could let it be zero by using an appropriate electrode width Φ .

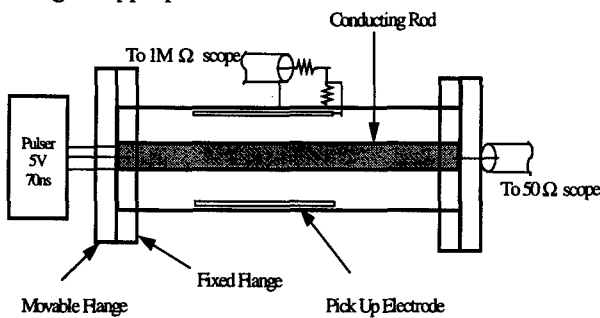


Figure 3. Bench test set up.

3 DESIGN AND BENCH TEST

A prototype capacitive BPM has been designed and built to test our theory of the capacitive BPM. There are four electrodes inside the pipe. The electrodes are insulated from the grounded wall by mylar, which has a dielectric constant of $2.9\epsilon_0$. Each electrode is connected to a bleeder resistor R . For the bench test, a conducting cylindrical bar was built to simulate the beam. The bar and pipe are a co-axial structure with 50Ω impedance. The

bar can move freely in the radial direction inside the pipe. A pulser provides a 100 mA current pulse on the bar and the pulse is terminated by a 50Ω load. Figure 3 shows the set up of this bench test. The parameters of the prototype BPM are listed in Table 1.[7]

Table 1. BPM parameters

Pipe inner radius	Electrode radius	Electrode angle
23.6 mm	23.5 mm	83°
Beam Current	Capacitance	Resistance
100 mA	0.55 nF	3 k Ω

Figure 4 is a typical BPM signal from one electrode when the beam current is a rectangular waveform. This figure shows that the BPM output can reproduce the beam signal faithfully.

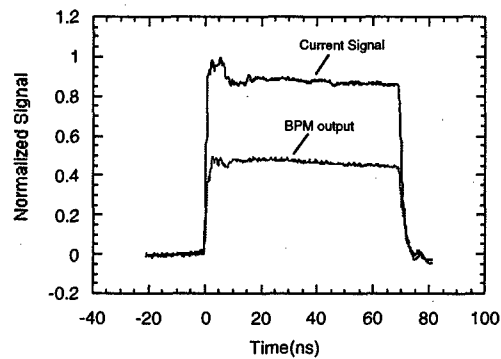


Figure 4. Typical BPM output signal.

As the beam moves off-centre, the voltage from the four electrodes are different. By calculating the voltage ratio

from two opposite electrodes we can find the displacement in the X and Y directions from Eq. 3. However, in practice, in order to get accurate beam position measurement, the BPM has to be calibrated. Figures 5 and 6 are two calibration curves on both X and

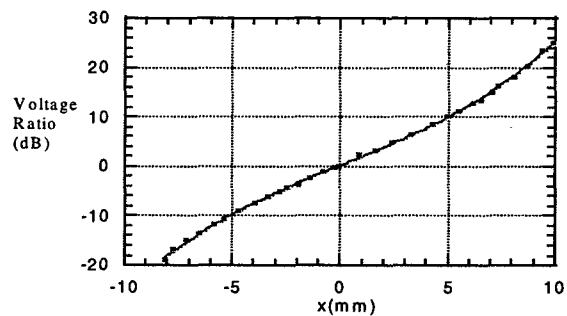


Figure 5. Calibration on X axis.

Y axes. In each figure, the horizontal axis is either x or y offset, and the vertical axis is the corresponding voltage ratio of two opposite electrodes. By using the two

calibration curves, we assume that the voltages from the X and Y direction are not coupled, otherwise we have to calibrate the BPM on the whole X-Y plane, which is very tedious.

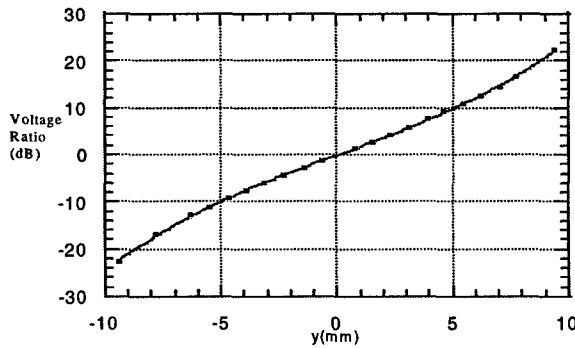


Figure 6. Calibration on Y axis.

To test the performance of this BPM, we have done a bench test. We set the conducting rod at different radial positions, and measured the beam positions based on the BPM signal. Then we compared the measurement and the mechanical position. Figure 7 shows the results of this measurement. In the figure, crosses are the mechanical positions and dots are BPM measurements. Within a 3-mm displacement, measurements agree with the mechanical position pretty well (error smaller than 0.2mm). But at 6 mm, there is a rather large difference between them (about 0.8mm). We think this is due to the coupling between X and Y electrodes. Because of the existence of the coupling term, the voltage ratio in the x direction depends on both x and y off-centring. We expect this systematic error will be much smaller when we optimise the electrode angle.

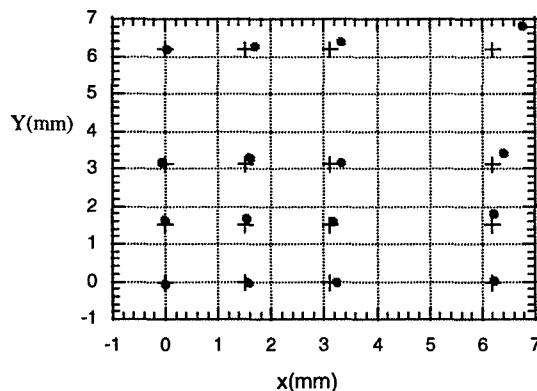


Figure 7. Comparison between the set up and measurement. (Cross: set up, Dot: measurement)

4 CONCLUSION

A prototype capacitive BPM has been designed and bench tested. The results show that our understanding of the capacitive BPM is correct and the performance of the BPM can meet our design objectives. A real BPM will be built and tested for electron ring.

5 REFERENCES

- [1] M. Reiser et al, Fusion Engineering and Design, 32-33,292(1996).
- [2] M. Reiser et al, Proceedings of this Conference.
- [3] J.G. Wang et al., Proc. of PAC97, p. 1855 (1997).
- [4] Robert E. Shafer, Beam Position Monitoring, workshop on Accelerator Instrumentation, BNL,1989.
- [5] H. Suk et al., Proc. of PAC97, p. 2143 (1997).
- [6] M. Reiser, Theory and Design of Charged Particle Beams, 1994, John Wiley & Sons, INC. , New York.
- [7] UMER web page, <http://www.ipr.umd.edu/ebte/ring>.

VIBRATING WIRE SCANNER FOR BEAM PROFILE MONITORING

Arutunian S.G., Dobrovolski N.M., Mailian M.R., Sinenko I.G., Vasiniuk I.E.
Yerevan Physics Institute, Br. Alikhanian St. 2, 375062 Yerevan, Armenia

Abstract

Method of beam transverse profile measurement in accelerators by scanning wire is wide-spread in accelerator technology [1-6]. In this work vibrating wire is proposed to use as a scanning wire. In such way the system of radiation (or secondary particles) extraction and measurement can be removed. Dependence of oscillations frequency on beam scattering is determined by several factors. Our estimations show that influence caused by wire heating will dominate.

1 INTRODUCTION

A beam of charged particles affects on vibrating wire frequency in several ways: mechanical transverse influence caused by transferred pulse of the beam, influence of beam magnetic field, radiation affect of the beam on the wire material, heating of the wire. The last effect is dominating, since for typical currents of accelerator beams the wire of μm diameter heats over 1000 K [2, 3].

Authors have accumulated a certain experience in development of tension gauges on the basis of vibrating wire. Frequency long-time relative stability $\sim 10^{-5}$ at relative resolution $\sim 10^{-6}$ is obtained. As a result of frequency multiplication its measurement become much more accurate. We have used such pickups for measurement of spatial distribution of magnetic field [7].

2 EQUILIBRIUM TEMPERATURE

Consider a long thin round wire, strained along the y axis. Wire ends are kept at constant temperature T_0 . "Thin" and "long" mean that the wire diameter d , its length l and part of the wire irradiated by the beam σ_y satisfy the condition $d \ll \sigma_y \ll l$. Beam propagates along the z axis, the wire scans the beam in transverse x direction.

Equilibrium temperature of an immobile wire in vacuum under beam is defined by the

balance between the power $\Delta E/\Delta t$ brought to it by the beam and two factors of heat removal: thermal radiation through the surface W_1 and thermoconductivity of the wire material through its ends W_2 .

The power released on the wire can be estimated by formula:

$$\frac{\Delta E}{\Delta t} = k \left(\frac{dE}{dz} d \right) (p(x) \sigma_y d), \quad (1)$$

where dE/dz is the ionisation loss of beam particles in wire material, $p(x)$ is local flux density of beam particles, k is the coefficient characterising the part of scattered beam energy working on wire heating. In works [3, 4] k is set equal to 1/3.

The thermal radiation W_1 is determined by the formula:

$$W_1 = S_{\text{side}} \sigma (T^4 - T_0^4), \quad (2)$$

where S_{side} is the side surface of the wire, σ is the constant of Stefan-Boltzmann, T is the absolute temperature of the wire.

Heat loss through the wire ends approximately is equal

$$W_2 = 2SK(T - T_0) / l, \quad (3)$$

where S is the wire cross section, K is the thermal conductivity of wire material.

Fig. 1 shows calculated curves W_1, W_2 and $W_1 + W_2$ ($\sigma_y = 1 \text{ mm}$).

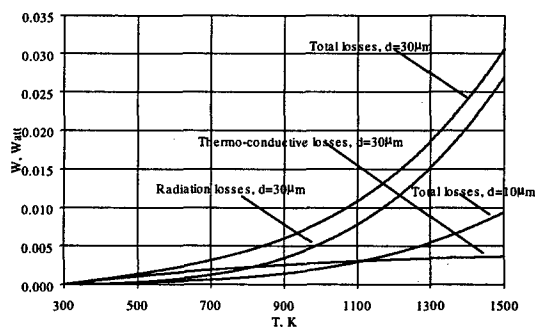


Fig. 1. Energy losses for tungsten wire, $d_1=30 \mu\text{m}$, $d_2=10 \mu\text{m}$, $l=40 \text{ mm}$, $\sigma_x=3 \text{ mm}$, $\sigma_z=1 \text{ mm}$.

The equilibrium temperature of the wire is determined from the equation of balance:

$$W_1 + W_2 = \Delta E / \Delta t. \quad (4)$$

Solution of this equation with respect to T at different distances of the wire from the beam centre are presented in Fig. 2.

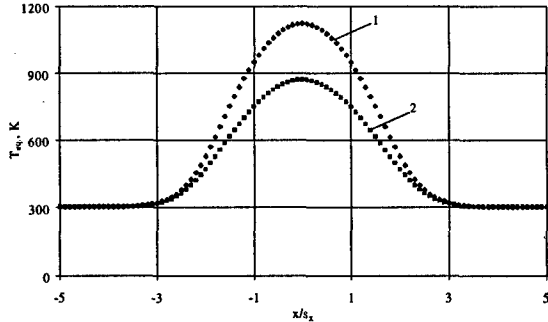


Fig. 2. Wire equilibrium temperature, $d=30 \mu m$ (1), $d=10 \mu m$ (2).

Time of thermalisation $\tau \equiv E_{store}/W$ also is an important parameter for the scanning, where E_{store} is the thermal energy stored in the wire. Calculations show that the thermalisation time is minimal in the beam centre and is 2 and 3 seconds respectively for tungsten wires of diameters $10 \mu m$ and $30 \mu m$. In the beam periphery this time is approximately doubled.

Note when scanning consecutively the total time of scanning is much more less than the sum of thermalisation times of individual points, because of the wire temperature changes insignificantly at passing from one point to another.

3 MODEL EXPERIMENT

Influence of the wire temperature on its natural oscillations frequency is determined by its elongation:

$$\Delta f/f = -(1/2) \Delta l/l = \alpha_b \Delta T, \quad (6)$$

where ΔT is the temperature variation. Coefficient α_b for metals varies from few units of $10^{-6} K^{-1}$ up to $10^{-5} K^{-1}$ (steels, bronzes, brasses, aluminium alloys).

However, for the rigidly fixed wire more essential is the influence of temperature changes on wire tension arising from inequality of coefficients of thermal expansion of wire α_s and the base α_b :

$$\frac{\Delta f}{f} = \frac{1}{2} \frac{\Delta F}{F} \approx \frac{ES}{F} (\alpha_b - \alpha_s) \Delta T, \quad (7)$$

where E is the Young's modulus, F is the wire tension. In formula (7) a large dimensionless factor ES/F is separated out. Thus, for the wire with

rigidly fixed ends the dominating factor is the influence of the temperature on wire tension.

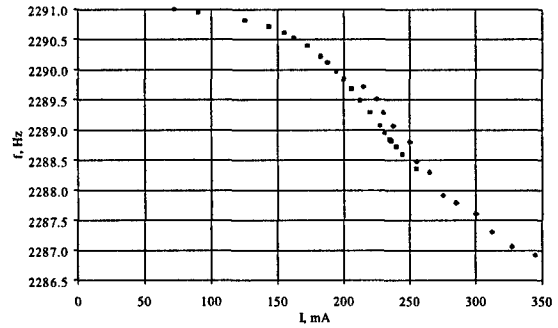


Fig. 3. Frequency dependence on current.

Heating of the scanning wire was modelled by passing of direct currents through the wire. Wire natural oscillations were generated in two modes: with one free end and with fixed ends of the wire.

Results of two series of measurements for tungsten wire of diameter $70 \mu m$ are presented in Fig. 3. The first series (squares) was carried out for currents from 75 mA up to 250 mA (glow appeared at 235 mA) and from 215 mA up to 345 mA. In first series the current was changed stepwise. In second case between two consequent values the current was nullified. In second series the frequency had restored well at each switching on for currents up to 345 mA. Yellow glow ($T \approx 1000 K$) appears for currents more than 300 mA.

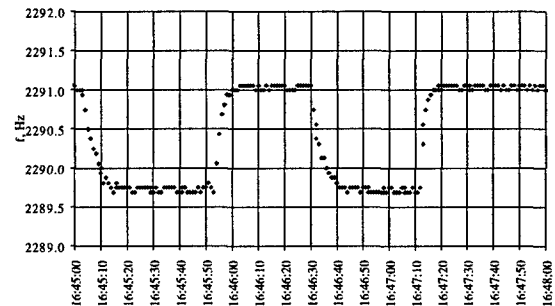


Fig. 4. Transient characteristics of wire with a free end, $I=215 mA$.

Fig. 4 shows the transient characteristics at switching on/off for the current 215 mA. One can see that the frequency exceeds its steady-state value during a few seconds. One can take this value for estimate of the thermalisation time τ . Cooling down processes are depicted without destruction, because after switching on it takes some time for current to reach its steady-state.

5 THERMALISATION TIMES

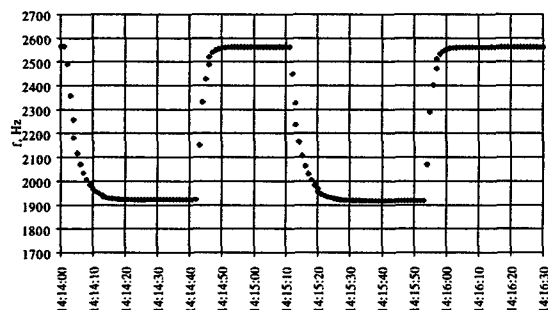


Fig. 5. Transient characteristics of wire with rigidly fixed ends, $I=215\text{mA}$.

Similar experiments were done for wires with rigidly fixed ends. As it was mentioned above, the frequency changes interval was much more wider. Fig. 5 shows the transient characteristics at switching on/off of the current 215 mA.

Restoration of the frequency in both cases were good enough, i.e. heating of the wire up to 1000 K does not lead to irreversible changes of wire parameters.

4 MAGNETIC FIELD

There are two possibilities in scheme of vibrating wire scanner: to use a scheme with own magnet or use the accelerator magnetic fields (dipole magnets, quadrupole lenses). In developed by the authors pickups natural oscillations of the wire were excited in autogeneration scheme. Exciting action on the wire arises as a result of interaction between the current through the wire and magnetic field of the samarium cobalt magnet, the field being localised in an magnet operating gap of the length 10 mm. The characteristic field induction inside the gap was about 8 kGs.

To keep the transverse effective square of the wire with respect to on-going bunch, separation of oscillations along the bunch axis is desirable.

Fields of dipole magnets are strong enough, however, they fix the horizontal movement of the wire. It is also possible to use the fields of quadrupole lenses. Scanning can be done in vertical, horizontal or under the angle 45° directions.

Usage of vibrating wire scanners with own magnets located in accelerators free spaces is also possible. In so doing it is preferable to intersect the bunch at $1/4$ of wire length, the magnetic circuit being located symmetrically with respect to wire centre, in such way providing generation of the second harmonic. In this case the magnetic field outside the gap is to be carefully screened.

Stability with respect to wire heating is one of the main problems in developed wire scanner technologies. To solve this problem, the scanning was done at a high speed, up to $\approx 10\text{ m/sec}$. [3, 4], i.e. the wire passes across the mm size bunch during 10^{-4} seconds. Such times are too small for thermalisation of the wire. Note, the estimate of τ can be lowered, because in real movement from one point to another will result in less temperature jumps. However, one cannot expect thermalisation times less than 10^{-2} s at temperatures, where long time exploitation of wire is possible.

It is possible that problem of thermalisation time can be solved by improvement of wire fixing system, which now is essentially simplified in comparison with similar wire scanning systems.

6 CONCLUSION

Indubitable advantage of proposed method is the compactness of the whole system and the elimination of the unit of radiation receivers. The peripheral monitoring of the bunch by proposed method also can be interesting.

Authors would like to thank R.Reetz and A.Ts.Amatuni for helping support.

7 REFERENCES

1. Suwada T. et al. First beam test result of a prototype wire scanner for the KEKB injector linac and BT lines. - KEK Preprint 97-184, 1997.
2. Steinbach Ch. Emittance measurements with the CERN PS wire scanner. - CERN/PS 95-04(OP).
3. Agoritsas V. et al. The first wire scanner of the CERN PS, - CERN/PS 95-06 (BD/OP).
4. Fulton R. et al. A high resolution wire scanner for micron-size profile measurements of the SLC. - SLAC-PUB-4605, 1988.
5. Field C. The wire scanner system of the Final Focus Test Beam. - SLAC-PUB-6717, 1994.
6. McCormick D. et al. Measuring micron size beams in the SLC Final Focus, - SLAC-PUB-6615, 1994.
7. Arutunian S.G. et al, Magnetic field distribution measurement by vibrating wire strain gauge.- PAC'99.

THE FIRST RESULTS OF OPTICS MATCHING USING WIRE SCANNERS FOR THE KEKB BEAM TRANSPORT LINE

Naoko Iida, Yoshihiro Funakoshi, Mitsuo Kikuchi, Kotaro Satoh, Tsuyoshi Suwada, and Takashi Kawamoto, KEK, 1-1 Oho, Tsukuba-shi, Ibaraki-ken 305-0810, Japan

Abstract

In the beam transport lines from the injector linac to KEKB rings, four wire scanners were installed for each of positron and electron line. The vibrations and non-linearities of the wire holders were suppressed to be small enough for beam size measurements. Optics matchings were made using the wire scanners. Better transmission from the linac to the rings was obtained. By detecting shower due to Bremsstrahlung near the detector, the beam sizes were successfully measured without any beam tunings dedicated for background.

1 INTRODUCTION

In the KEKB the electrons(positrons) accelerated in the linac up to 8GeV(3.5GeV) are transported to the main rings through beam transport(BT) lines whose length are about 500m. At the BT, electron and positron lines have a double-decked structure in the first part of tunnel of 350m long and fed into separated tunnel in the rest part. In order to maintain high luminosity, a well-controlled operation transport line is required for minimizing tuning time and a stable operation. A wire scanner(WS) for monitoring beam profiles non-destructively is useful for these purposes. Beam tests of a prototype for WS have been done at KEKB injection linac so far[1][2]. We produced improved wire scanners as an actual model; more compact, less expensive but with smaller wire vibrations. Especially we took care of the wire positioning which leads directly the systematic error. In order to study this effect two prototypes with cantilever supports had been produced. One had linear guides in vacuum which can suppress wire vibrations most effectively since the cantilever was very short. Another had linear guide outside the vacuum chamber. We measured the wire positioning for both of them[3]. As a result, both types were feasible but we adopted the type with one linear guide for its easier handling in maintenance and lower cost. We installed ten wire scanners in total to the BT lines, for all of which wire positionings had been measured before installation.

In the entrance of BT lines, at least three WS's are needed to determine beam emittance and Twiss parameters in the optics matching. For redundancy, we adopted four wire scanners are mounted in each line. By using a photomultiplier tube(PMT) with plastic scintillator, we detected shower occurred near the PMT due to Bremsstrahlung emitted from the wire crossing a beam. The PMT's were set at a wide angle(65°) to the beam lines. By this setting beam background from the upstream was effectively shut off and high S/N ratio was obtained without any dedicated

beam tunings. In this paper, the first results of beam-size measurement and optics matching in the positron BT line are presented.

2 PRODUCTION OF WIRE SCANNERS

2.1 A structure of the wire scanner

The schematic view of the wire scanner is shown in Fig. 1. A thin thread of tungsten of $100\mu\text{m}$ in diameter is stretched between three pins on the wire holder so as to form three(X-, U- and Y-) wires perpendicular to the beam. The holder is attached on one side of long shaft, while another side of which is fixed, in a cantilever style, to a stainless block mounted on the Linear Guide. The block is moved with a pulse-motor through a screw shaft. The Linear Guide rails are tightly bolted on the thick base plate, which also support the total weight of the mover. The holder and its support shaft is in vacuum. The conversion ratio of rotation with pulse motor to linear motion is $4\mu\text{m}/\text{pulse}$. The linear motion is monitored through a potentiometer with a resolution of $50\mu\text{m}$. The vacuum chamber has a window of stainless steel of $50\mu\text{m}$ in thickness which allows low-energy knock-on electrons(δ -ray) to pass the window. We detected the δ -ray at the window and also high energy γ -rays at the downstream using a PMT(Hamamatsu/R329-02) with a $40 \times 50 \times 10\text{mm}^3$ plastic scintillator.

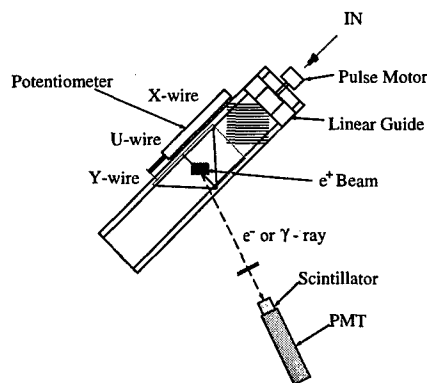


Figure 1: Schematic view of the wire scanner.

2.2 Measurement system of displacements of wire holder

Since we adopted a cantilever to support the wire holder, a vibration in the direction perpendicular to linear motion and to the beam was a serious concern. We have measured a static displacement (non-linearity) and also a vi-

bration during linear motion. The layout of measuring system is shown in Fig. 2. A laser displacement-meter, KEYENCE/LC2430, was placed at the side of the wire holder. The LC2430 measures the distance from the surface reflecting the emitted laser light, using a built-in position-sensitive detector (PSD). The resolution is $0.02\mu\text{m}$. As a reflector, we attached a block gauge with flatness of less than $0.1\mu\text{m}$ and with area of $30\times 10\text{mm}^2$ on the one side of the holder. We measured the displacements for all of ten WS's to be installed within the area of the block gauge. The linear motion was monitored with a magnescale. The measurement was done without a vacuum vessel. The pulse rate of the pulse motor was 1kHz. The results were: maximum amplitude of non-linear displacement was $\pm 8\mu\text{m}$ in peak-to-peak, maximum amplitude of vibration was $\pm 10\mu\text{m}$ in peak-to-peak. These are sufficiently small for the present beam size.

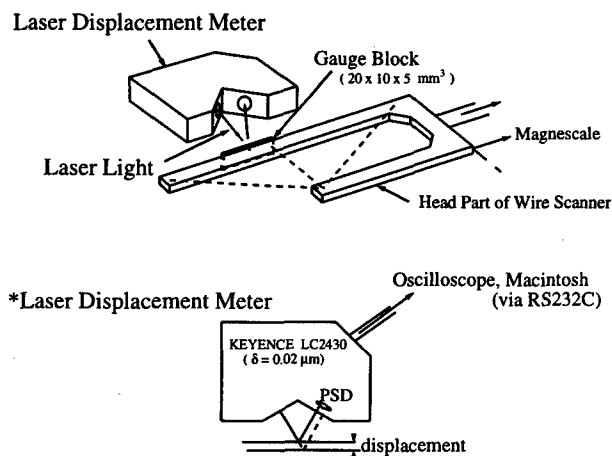


Figure 2: Schematic view of vibration measurement system.

3 OPTICS MATCHING

3.1 Arrangement of the wire scanners

The four wire scanners were placed at the downstream of quadrupole magnets for each of the positron and electron line. The arrangement of WS's in the positron line is shown in Fig 3. Two detectors (PMT's with plastic scintillators) were set for the four wire scanners: One PMT located near the C-wire detects high energy particles emitted from wires of "A" and "B", while another PMT near the D-wire detects particles emitted from wires of "C" and "D". For electron line, all detectors sit on in the same manner as "D" detector. The PMT was placed just downstream of the window with 65° in angle to the beam line. The detectors were surrounded by lead shield of 66mm in thickness in all direction, while to the upstream side the thickness was 166mm. The signal from PMT was put into the CAMAC ADC/2249W, LeCroy. The data were taken by a VME system via CAMAC serial highway.

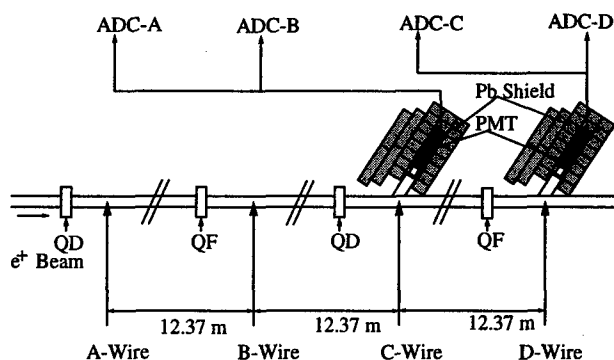


Figure 3: The arrangement of WS's in the positron line

3.2 Beam optics in the wire scanners

The four wire scanners were placed at a regular section of long straight, where the phase advance is $\pi/2$ for both of the horizontal and vertical planes. At the region, there is no dispersion in the design. A- and C-(B- and D-) wire scanners were placed at the downstream of the defocusing(focusing) quadrupole magnets. A matching of Twiss parameters to the linac was done by using all quadrupole magnets upstream the wire scanners, under the condition that the dispersion is to be closed and beta functions at some points not exceed some maximum values.

3.3 Measurement of beam sizes

The typical results of beam-size measurements are shown in Fig. 4 and 5 for electron(C-wire) and positron(A-wire) line, respectively. The horizontal axis is a position of wire holder along the scanning direction and the vertical axis is ADC count of the signal. We can clearly see three peaks corresponding to the Y, U and X wires crossing the beam. Each peak was fitted to an asymmetric Gaussian shape. The beam sizes of Y and X were obtained from peak with divided by $\sqrt{2}$. The typical S/N ratio was about 45 and 7.5 for electron and positron. For A, B, C wire scanners, we observed high S/N ratios almost independent on the beam condition. This is because the background from beam halo was almost completely shielded with the lead blocks of 166mm (30 radiation length). On the other hand, the signal from electromagnetic shower occurred at the beam pipe near the detector, which was generated by Bremsstrahlung γ -rays from the upstream wire. Although the detector sits at the wide angle (65°), huge amount of Bremsstrahlung γ -rays emitted in extremely small angle gives high S/N ratio. For D-wire scanner as shown in Fig 6, however, the PMT detects the small δ -ray as the signal, while the background comes from the shower produced in front of the detector by beam halo. We needed some dedicated beam tunings in order to decrease the background.

3.4 Matching

We have made optics matching at the positron line. The beam sizes at the four wire scanners were used to ob-

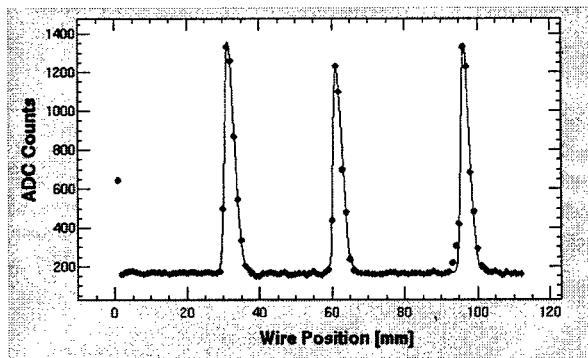


Figure 4: Typical transverse beam distributions(C-wire) in electron line. The left, middle and right peaks correspond to Y-, U- and X-wires, respectively.

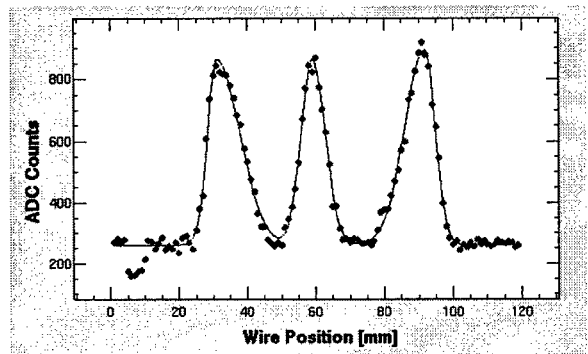


Figure 5: Typical transverse beam distributions(A-wire) in positron line.

tain Twiss parameters at the A-wire. In the phase space, we can draw two ellipses, one from measured parameters(S1) and another from design ones(S2). An additional ellipse(S3) can be drawn that it circumscribes the ellipse S1 and is similar to S2. Here Bmag means a ratio of an area of ellipse(S3) to that of ellipse(S2). It is given by[4]; $Bmag = [\beta_2/\beta_1 + \beta_1/\beta_2 + \beta_1\beta_2(\alpha_1/\beta_1 - \alpha_2/\beta_2)^2]/2$. The subscripts 1 and 2 mean measured and design values, respectively. When measured twiss parameters are the same as design ones, Bmag becomes unit. The obtained emittances and Bmag's are summarized in Table 1. Although in the horizontal direction Bmag was not changed so much, in the vertical direction, it became smaller and the products of emittance and Bmag decreased after matching. This means that the transmission of the transport line becomes better.

4 CONCLUSION

We developed wire scanners for the BT line from the injector linac to KEKB rings. Since a cantilever support for a wire holder was adopted for easier maintenance and lower cost, we carefully designed them to suppress vibration and non-linear motion of the wire. Bench measurements showed that they were negligibly small for beam size measurements.

By using the wire scanners, the first trial for optics matching in the positron line has been successfully done.

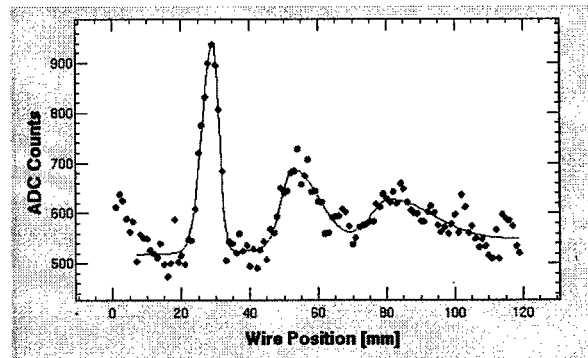


Figure 6: Transverse beam distributions of D-wire in positron line.

Table 1: The obtained emittances and Bmag's of positron line before and after matching.

	Before matching	After matching
ϵ_x [m]	1.09×10^{-6}	7.30×10^{-7}
Bmag _x	1.16	1.62
$\epsilon_x \cdot Bmag_x$ [m]	1.26×10^{-6}	1.18×10^{-6}
ϵ_y [m]	2.58×10^{-7}	2.33×10^{-7}
Bmag _y	6.54	2.04
$\epsilon_y \cdot Bmag_y$ [m]	1.69×10^{-6}	4.75×10^{-7}

Better transmission was obtained in the line. Emittances as well as Twiss parameters obtained in the optics matching process gave useful information for a tuning of the injector linac.

5 ACKNOWLEDGMENTS

The authors gratefully acknowledge the KEKB commissioning group who helped preparation of the measurement.

6 REFERENCES

- [1] T. Suwada et al.: "FIRST BEAM TEST RESULT OF A PROTOTYPE WIRE SCANNER FOR THE KEKB INJECTOR LINAC AND BT LINES", Proceedings of the 11th Sympo. on Accelerator Science and Technology, 1997, Hyogo, Japan, KEK Preprint 97-184, 1997
- [2] Y. Funakoshi et al.: "BEAM TESTS OF A WIRE SCANNER FOR THE KEKB INJECTOR LINAC AND BEAM TRANSPORT LINE", Proceedings of the APAC98
- [3] N. Iida et al.: "A METHOD FOR MEASUREING VIBRATIONS IN WIRE SCANNER BEAM PROFILE MONITORS", Proceedings of the APAC98
- [4] J. T. Seeman et al.: SLAC-PUB-5705 Aug. 1992

BEAM PROFILE MEASUREMENT AT 30 GEV USING OPTICAL TRANSITION RADIATION*

P. Catravas,[†] W. P. Leemans, E. Esarey and M. Zolotorev, LBNL, Berkeley, CA 94720
D. Whittum, R. Iverson, M. Hogan, and D. Walz, SLAC, Stanford, CA 94309

Abstract

We present results of measurements of spot size and angular divergence of a 30 GeV electron beam through use of optical transition radiation (OTR). The OTR near field pattern and far field distribution are measured as a function of beam spot size and divergence at wavelengths of 441, 532, and 800 nm, for both the single and double foil configurations. Electron beam spot sizes of 50 μm rms have been resolved, demonstrating the utility of OTR for measurement of small beam spot sizes of high energy (30 GeV) electron beams. Two-foil interference was clearly observed and utilized to extract electron beam angular divergences of $\sim 100 \mu\text{rad}$.

1 INTRODUCTION

The theory of transition radiation was first introduced by Frank and Ginzburg in the first half of the century [1] and was further developed in the late 1950's by Garibyan [2] and others. Transition radiation has been widely used in high energy physics for particle identification, as well as for diagnosis in accelerator research. A comprehensive body of experimental work in the area of accelerator beam diagnosis currently covers a large range of beam energies, from 10's to 100's of MeV for visible transition radiation [3, 4], while most work at multi-GeV energies shifts to the X-ray portion of the spectrum [5]. Only recently, work has been performed in the visible wavelengths at energies up to 3.2 GeV and detailed discussions of the spatial resolution of OTR have been presented (see for example [6]-[9]).

In this paper, results are presented of the diagnostic implementation of optical transition radiation for a 30 GeV electron beam. Spot sizes as low as 50 μm rms have been resolved using radiation at 532 nm and beam divergences on the order of $\sim 100 \mu\text{rad}$ have been obtained using the double foil configuration. Spot size resolution is consistent with what is expected from the collection angle of the optical imaging system.

2 CONCEPT

Diagnostic spatial resolution, d , is determined by diffraction: $d \sim \lambda/\theta$, where λ is the radiation wavelength and θ is the collection angle. Typically, radiation from highly relativistic electrons is concentrated in a cone of width $1/\gamma$,

which makes it difficult to measure spots of high γ beams with sufficient spatial resolution. In contrast, while the angular distribution of OTR photons does peak at the angle $1/\gamma$, the intensity falloff outside the $1/\gamma$ cone is much slower than, for example, that of synchrotron radiation. The fraction of energy inside the $1/\gamma$ cone drops with increasing energy, giving OTR utility for beam diagnosis at ultra-relativistic energies. The OTR angular distribution from a single electron for a metal foil is

$$\frac{d^2 W_1(\theta)}{d\omega d\Omega} \sim \frac{\theta^2}{(\gamma^{-2} + \theta^2)^2} \approx \frac{1}{\theta^2}, \quad \frac{1}{\gamma} \ll \theta \ll 1, \quad (1)$$

which is valid for both backward and forward OTR if the photon energy is smaller than ~ 10 eV, the typical energy corresponding to the plasma frequency of metallic foils.

While beam divergence can in principle be obtained from the far field pattern of a single foil, the two foil interferometer, as developed by L. Wartski [3], is often preferred as it provides increased sensitivity to beam divergence [4]. Furthermore, the two-foil interferometer provides control over the angular resolution, unlike the single foil configuration, for which the resolution is fixed at each beam energy. In the two-foil interferometer, forward radiation from an upstream foil combines with backward radiation from a second foil located a distance L downstream, yielding an addition of phases of $1 - \exp[-j\pi(\gamma^{-2} + \theta^2)L/\lambda]$. The interference term depends on the formation length, $L_f = (\lambda/\pi)(\gamma^{-2} + \theta^2)^{-1}$ (written for vacuum, $\gamma \gg 1$ and $\theta \ll 1$) [2, 3]. The angular intensity distribution [3] for the two foil interferometer for large angles ($\theta \gg 1/\gamma$) becomes

$$\frac{d^2 W_2(\theta)}{d\omega d\Omega} \sim \frac{1}{\theta^2} \sin^2 \left(\frac{L}{2L_f} \right), \quad (2)$$

where $L_f \simeq \lambda/(\pi\theta^2)$. After convolution of the two-foil interference pattern for a single electron with a Gaussian electron beam distribution of angular width σ_θ , the angular intensity distribution can be written,

$$\frac{d^2 W_2(\theta, \sigma_\theta)}{d\omega d\Omega} = 2 \frac{d^2 W_1(\theta)}{d\omega d\Omega} G, \quad (3)$$

where

$$G = [1 - \exp(-2\pi^2 L^2 \sigma_\theta^2 \theta^2 / \lambda^2) \cos(\pi L \theta^2 / \lambda)]. \quad (4)$$

* Work supported by the U.S. Department of Energy under contract No. DE-AC-03-76SF0098.

[†] Email: PECatras@lbl.gov

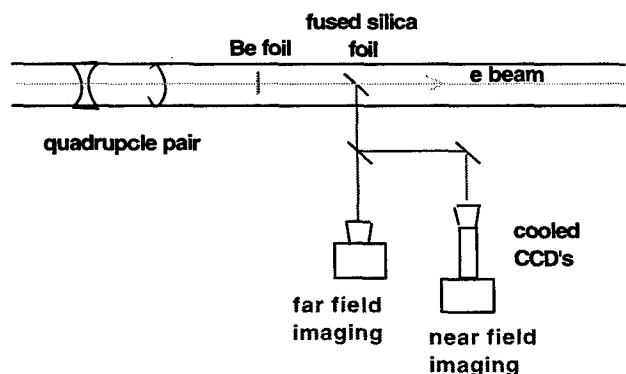


Figure 1: Experimental setup.

3 EXPERIMENTAL SETUP

The experiments were performed in the FFTB beamline at SLAC. The experimental setup is shown in Fig. 1. An aluminum coated fused silica substrate ($150\mu\text{m}$ thick) was located 0.56 m downstream from a retractable, $25\mu\text{m}$ thick Beryllium foil. The backward reflected OTR was split by a pellicle beamsplitter between two cooled CCD cameras, 16 bit and 12 bit, providing simultaneous images of the near and far field, respectively. The near field resolution was determined using a resolution target and was $10\mu\text{m}$ or better. This is consistent with the collection angle of 0.1 rad . The available field of view was approximately 3 mm . Far field resolution was set at $6/\gamma$ radians per pixel. For this experimental run, the beam energy was 28.5 GeV , and single microbunches with about 1.5×10^{10} particles with normalized vertical and horizontal emittances of $0.47 \times 10^{-5}\text{ m-rad}$ and $6.5 \times 10^{-5}\text{ m-rad}$ were used.

4 RESULTS

4.1 Spot size measurement

Results from near field imaging of the OTR from a single foil (fused silica inserted, Be removed from the beam path) are shown in Fig. 2. Quad scans were performed in the vertical and horizontal axes, and OTR images were recorded as the scans passed through and beyond a waist at the foil location. The series of five images shown in Fig. 2 are near field images recorded by the cooled CCD during the horizontal and vertical quad scans. The accompanying plots contain the complete set of extracted rms beam sizes as a function of quadrupole strength. Beam spot sizes of $50\mu\text{m}$ were resolved in both axes in a single shot measurement.

Beam spot size resolution and photon yield were compared with and without the addition of the second foil (Be at 0.56 m upstream). No difference was observed in either the measured spot size or the number of collected photons. This observation is consistent with the depth of focus of the near field imaging of our setup, which was small compared with the foil separation; only the photons from one foil were well imaged onto the CCD chip.

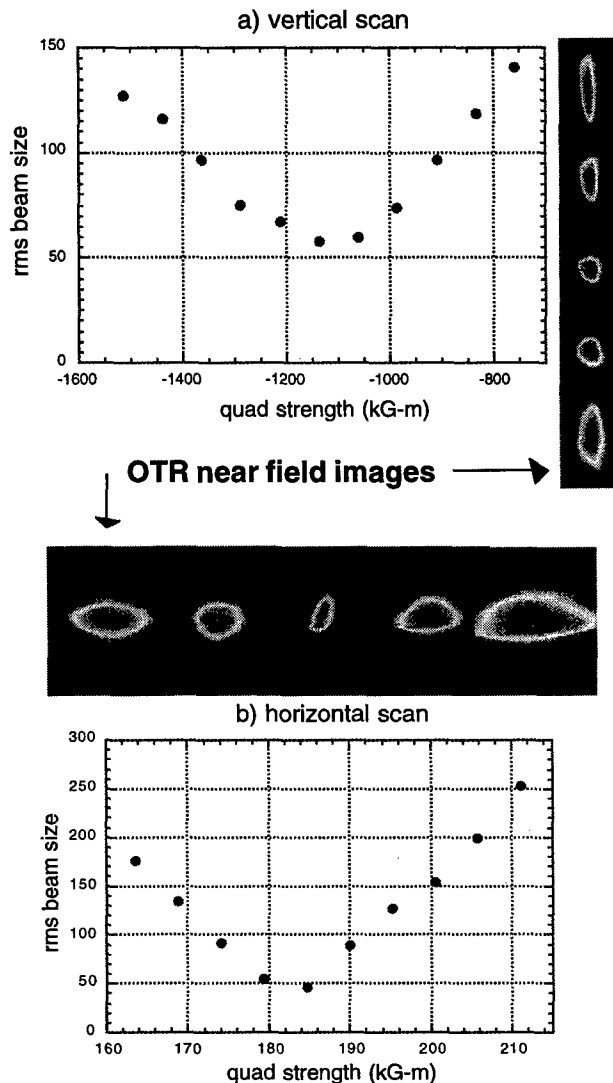


Figure 2: Spot size measured with OTR and near field images for vertical and horizontal quadrupole scans.

4.2 Angular divergence measurement: two-foil interferometry

Interference patterns were recorded from the two-foil interferometer at a variety of wavelengths: 441, 532, 632, 800, and 1064 nm. The appearance of the intensity maxima is well described by Eq. (2) both as a function of angle and as a function of wavelength. In Fig. 3, two-foil interference patterns centered at 441 and 800 nm display the expected increase in peak separation with wavelength. At 28.5 GeV , $\lambda = 532\text{ nm}$, and foil separation $L \sim 0.6\text{ m}$, the first interference maximum is expected and observed at angle of $50/\gamma$. Note that if one wishes to set the first interference maximum near $1/\gamma$, then the required foil separation length, $\lambda\gamma^2/2\pi$, is on the order of a km, which is comparable to the total length of the SLAC linac.

Foil separation L is chosen only according to the range of divergence one wishes to diagnose. From Eqs. (3)-(4), one can see that the angular resolution (minimum resolv-

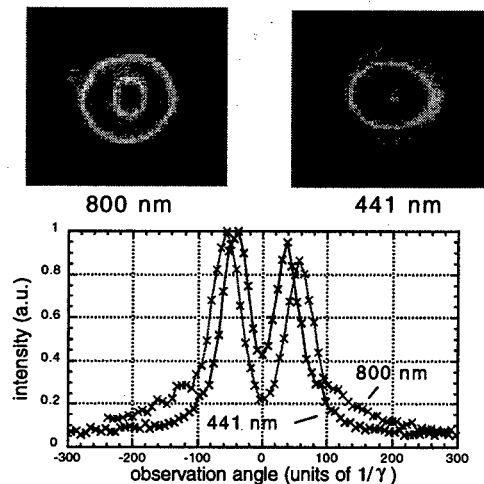


Figure 3: Comparison of two-foil interference at 441 and 800 nm shows expected wavelength dependence.

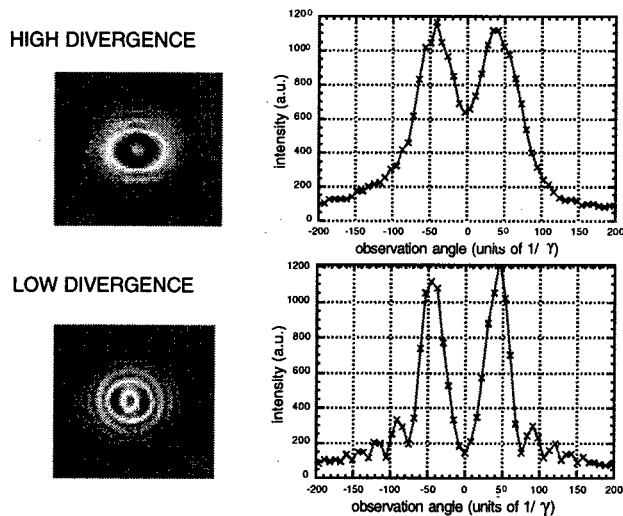


Figure 4: Two foil interference during a quadrupole scan evolves from no modulation to full modulation, indicating that realistic beam parameters can be diagnosed.

able divergence) is $\sigma_{res} = d/L$. For the far field imaging, the effective collection angle was considerably smaller than for the near field imaging, and was approximately 3 mrad, corresponding to $d = 30 \mu\text{m}$. Choosing a foil separation L of 0.6 m gives an angular resolution of $50 \mu\text{rad}$. Note also that from the practical point of view, the spatial and angular resolution become independent of the beam energy.

Sensitivity of the far field pattern to changes in beam divergence was studied by performing a quadrupole scan to vary the divergence. The resulting profiles (Fig. 4) shifted from nearly full modulation to no modulation as the divergence was increased. Furthermore, in Fig. 4(a), an absence of modulation in the horizontal axis was observed while clear modulation was present in the vertical axis. This is consistent with known difference in vertical and horizontal emittance at the FFTB. Divergences of $\sigma_\theta \sim 100 \mu\text{rad}$

were extracted from the data using Eq. 3 and 4.

The described techniques were developed in support of the E157 experiment [10] at the FFTB at SLAC, which will study the interaction of the 30 GeV beam with a long plasma column. In effect, the OTR foils have been designed into the setup in such a way that they serve a double purpose. One of the foils will separate a plasma volume from an ultra-high vacuum section of beam pipe; the other doubles as an Excimer incoupler. Viewing OTR in this compact fashion will provide non-destructive diagnostic information for the E157 experiment as close as possible to the interaction region. OTR will be collected both at the oven entrance and exit to determine beam parameters directly at the experiment entrance as well as after interaction with the plasma. Because this interaction is expected to produce large changes in the beam spot size and divergence which are time varying, streaking the OTR at the oven exit is planned.

5 CONCLUSIONS

Measurements of transition radiation in the visible wavelengths have been performed at nominally 30 GeV at the FFTB beamline at SLAC. Spot sizes on the order of $50 \mu\text{m}$ have been measured with OTR at this energy and wavelength. Beam divergences of approximately $100 \mu\text{rad}$ have been calibrated with a two-foil interferometer.

6 ACKNOWLEDGMENTS

The authors thank Leon Archambault, Scott DiMaggio and Jim Dougherty for their technical assistance.

7 REFERENCES

- [1] V.L. Ginzburg and I.M. Frank, Sov. Phys. JETP 16, 15 (1946).
- [2] G.M. Garibyan, Sov. Phys. JETP 6, 1079 (1958); *Ibid.*, Sov. Phys. JETP 10, 372 (1960).
- [3] L. Wartski et al., J. Appl. Phys., 46, 3644-3653 (1975).
- [4] D.W. Rule, Nucl. Instr. & Meth., B24/25, 901 (1987); *Ibid.* et al., Nucl. Instr. & Meth. A 296, 739 (1990); A.H. Lumpkin et al., Nucl. Instr. & Meth. A, 296, 150 (1990); R.B. Fiorito et al., 1991 PAC Proc., 2, 1204, (1991); A.H. Lumpkin (Ed.), Proc. 1996 Beam Instrum. Workshop, AIP Conf. Proc. 390 (1997); W.P. Leemans et al., Phys. Rev. Lett. 77, 4182 (1996); A.H. Lumpkin, Nucl. Instr. & Meth. A 393, 170 (1997).
- [5] L.C.L. Yuan et al., Phys. Rev. Lett., 25, 1513-1515 (1970).
- [6] P. Piot et al., Proc. 1996 Beam Instrumentation Workshop, AIP Conf. Proc. 390, 298 (1997).
- [7] X. Artru et al., Nucl. Instr. & Meth. A 410, 148-158 (1998).
- [8] D.W. Rule, R.B. Fiorito, AIP Conf. Proc. 229, 315 (1991).
- [9] M. Castellano and V. A. Verzilov, Phys. Rev. Special Topics, 1, 062801-1 (1998).
- [10] R. Assman et al., these Proceedings, FRA113.
- [11] P. Muggli et al., these Proceedings, FRA115; S. DiMaggio et al., these Proceedings, FRA138

THE RHIC IONIZATION BEAM PROFILE MONITOR

P. Cameron, R. Connolly, R. Michnoff, V. Radeka, W. Ryan, T. Shea,
R. Sikora, D. Stephani, S. Tepikian, and N. Tsoupas
Brookhaven National Lab, Upton, NY
L. Woodworth
Raytheon Electronic Systems Div., Sudbury, MA

Abstract

Four ionization beam profile monitors (IPM's) have been installed in RHIC to measure vertical and horizontal profiles in the two rings. Each IPM collects and measures the distribution of electrons in the beamline resulting from residual gas ionization during bunch passage. The electrons are swept transversely from the beamline and collected on strip anodes oriented parallel to the beam axis. At each bunch passage the charge pulses are amplified, integrated, and digitized. The system is designed to measure single-bunch profiles with up to 120 bunches in each ring.

1. INTRODUCTION

The Relativistic Heavy Ion Collider (RHIC) at Brookhaven National Lab will accelerate and store beams of ions ranging from protons to gold nuclei [1]. Transverse beam profiles will be obtained by measuring the distribution of free electrons formed by beam ionization of the residual gas [2,3]. The electrons are swept from the beamline by a transverse electric field, amplified by a microchannel plate (MCP), and collected on a circuit board with strip anodes oriented parallel to the beam axis. A uniform magnetic field, parallel to the sweep electric field, counters the defocusing effects of space charge and recoil momentum.

The RHIC IPM detector is a close copy of the prototype, ref. 2, which was tested in the AGS-RHIC transfer line in 1997. However the prototype measured bunches separated by several seconds so it was adequate to use slow charge-sensitive amplifiers ($\tau \sim 4\mu\text{s}$), track-and-hold amplifiers, and slow digitizers. The RHIC monitors are intended to digitize individual bunches spaced 107ns apart. This requires faster preamplifiers and digitizers. Also much of the ground plane on the collector board is removed to lower capacitance. Finally a test pulse input was added to the detector to make it possible to determine gain and offset corrections for all 64 channels in a single measurement.

This paper describes the detector, digitizers and data-collection systems. The kinematics of electron confinement by the magnet field is discussed in ref. 2.

2. DESIGN CONSIDERATIONS

RHIC will accelerate and store many different beams and the IPM's are located 50m from an interaction point where the lattice optics varies with the requirements of the experiment. Depending on energy, ion species and i.p. optics the rms width of the beam can vary from 0.7mm to 6.5mm. The channel spacing has to be small enough that a reasonable measurement can be made on the most narrow beam but the collector has to be wide enough to see the largest beam with some allowance for missteering and betatron oscillations.

The compromise chosen was to build a collector with 64 channels spaced 0.6 mm apart. Only 6σ of the widest beam fits on the collector and 6σ of the narrowest beam fits on only 7 channels. However the measurement of a Gaussian beam of $\sigma = 0.7\text{mm}$ with a collector 0.6mm wide yields a rms width less than 4% larger than the true width.

RHIC has superconducting magnets so the residual gases are helium and hydrogen. The measured primary ionization rate for minimally ionizing protons in these two gases at atmospheric pressure is about 5.5 ion pairs/cm and the cross section is proportional to Z^2 [4]. A gold bunch with 10^9 ions in a vacuum of 10^{-8}torr will create about 4,000 ion/electron pairs in one passage. An MCP has a detection efficiency for 1.5kV electrons of 36% so about 1,400 electrons will be detected per bunch [5]. Monte Carlo simulations show that the variance of a Gaussian parent distribution can be obtained to within $\pm 2.2\%$ by sampling 1000 points.

A bunch of 10^{11} protons will produce only ~ 20 detected electrons. In the beginning proton-beam profiles will be generated by summing up 50 or more single bunch signals. This can either be done with all bunches or by looking at the same bunch on consecutive turns. Single proton bunches can only be measured if a pressure bunch is added.

3. DETECTOR

Figure 1 is a cross section of the IPM from the perspective of looking along the beamline. The detector vacuum chamber is made from 10x15cm rectangular 304 stainless steel tubing. A detector port is formed by welding a short section of this tubing into the side with a

10" conflat flange attached. The detector (fig. 2) is mounted entirely on a mating flange.

Two 30-cm long 'C' permanent dipole magnets producing 0.14T are placed 30 cm apart along the chamber. One is centered on the detector to focus the electrons and the second corrects the beam deflection caused by the first. The magnet pole tips are shaped to produce parallel field lines within an area of 38mm parallel to the collector by 63mm perpendicular to it. Within this collection area the maximum field-line transverse runout is 0.034mm or 6% of a channel width.

The collector board is alumina metallized with gold. There are 64 anodes which are 91mm long and spaced 0.6mm apart. Plated-through holes connect the anodes to traces on the back of the board which bring the collected charge to the edge. Short alumina coated wires are soldered to pads on the board and are attached to two 35-pin feedthroughs with push-on connectors. A chevron 8x10cm microchannel plate detector [6] is screwed directly to the board with a kapton gasket providing electrical insulation. The transverse sweep field is generated with an electrode and secondary-electron suppression grid on the other side of the beam.

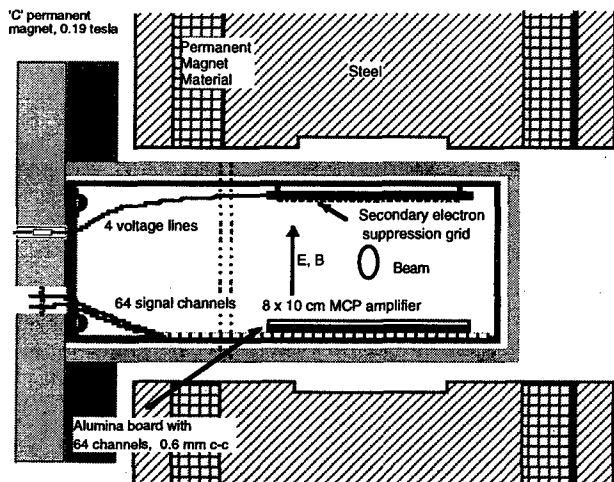


Figure 1. Cross sectional view of IPM. View is looking along the beamline. In this orientation the IPM would measure horizontal profiles.

Taut-wire beam-coupling measurements showed that the collector board needed to be shielded from the beam and that the MCP electrodes did not provide good rf shielding. The board is enclosed in a phosphor bronze shield and the input of the channel plate is covered with copper mesh with ~90% OAR. Capacitors soldered around the edge of the mesh provide bypassing and the structure is grounded to the vacuum chamber with rf finger stock.

Four high-voltage lines bias the MCP input and output and the sweep electrode and suppression grid. The sweep voltage power supply floats on the MCP input

voltage so the sweep field remains a constant 3.0kV as the MCP bias is adjusted. The MCP bias voltage is the only gain control 'knob' in the system. MCP bias is adjusted until the channel with the largest signal approach the dynamic ceiling of the electronics.

The detector flange has four 2.75" conflat ports. Two are for signal feedthroughs and one is for the high voltage feedthrough. The top port in fig. 2 has a quartz window for illuminating the MCP with UV light. Although the illumination across the plate is not uniform, it will provide a method to baseline the new MCP. The current illumination pattern can be compared to the baseline to tell when the plate ages and the gain drops in the center channels.

Each collector anode capacitively couples to the output electrode of the MCP by about 1.3pF. A step pulse delivered to the MCP output drives all 64 channels with pulses that only vary by the small differences in anode areas, differences which also affect the beam signals. The bias line to the MCP output is a parallel transmission line with $Z \approx 105\Omega$. This pulse input will be used to calibrate each detector to compensate in software for channel-to-channel variations in gain and offset.

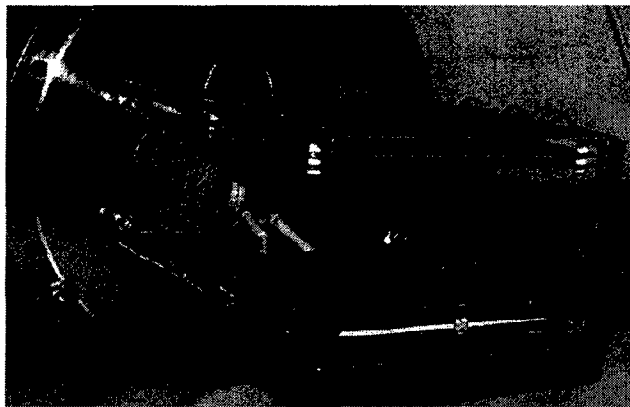


Figure 2. Photograph of detector. The MCP and anode board are on the bottom.

4. ELECTRONICS

Each bunch passage will deliver charge pulses to the anodes. Individual pulses are integrated and shaped by charge-sensitive, hybrid preamplifiers and hybrid shapers both designed by BNL Instrumentation Division. The preamplifier has a charge sensitivity of 0.6V/pC and a decay time constant of 20ns, and the shaper has a voltage gain of 10. Bench tests done by injecting signal directly into the prototype IPM measured a noise floor for the system of 2-3fC. The shaper output is amplified by a AD811 op amp [7] set to a gain of 2, and coupled into a 100Ω balanced line via a 1:1 pulse transformer.

Every channel also has a low-pass-filtered output which rolls off at about 100kHz. These channels provide dc coupling to measure beam profiles with unbunched

beams. After filtering the signals are amplified by OP-37 op amps and coupled into twisted-pair cables through SSM2142 balanced-line drivers [7].

Eight preamp circuits are on a 15x15cm board. Four of these boards are mounted in a chassis box which is attached to the vacuum feedthrough to minimize signal lead length. The pulse outputs are connected to VME digitizers installed in racks beneath the beamline to minimize cable lengths. The filtered signals are brought out of the tunnel to the instrumentation control room (ICR) on twisted pair cable and digitized with a RHIC general purpose A/D converter [8]. All eight pulse channels on each preamp board are summed together into one signal which is brought back to the ICR on coaxial cable for diagnostic purposes.

The fast pulses have a base width of 100ns and a frequency of 9.4MHz with 120 bunches in a ring. They are digitized by Hytec VTR2535 8-channel VME digitizers [9]. Each digitizer channel has a dedicated AD9220 12-bit, 10MSPS ADC [7] backed with 128k words of memory. The digitizers are triggered by a V124 trigger module synchronized to the beam-sync clock [10]. During beam measurement the data are written into memory on the digitizer cards. Acquisition is then stopped and the data are read by the front end computer in the VME chassis and sorted into profiles.

4. CONTROL PROGRAM

During the commissioning of RHIC the IPM will be an experimental device which is operated manually from the ICR. The power supplies for both the MCP bias and the sweep field will be controlled from their front panels although they will be interlocked to vacuum gauges. Early commissioning will be done with only a few bunches in the ring so neither gain depletion or saturation is a concern. Eventually the measurement application will control these voltages.

The control application allows the operator to select a bunch and to select the number of turns to be collected. When the selected number of profiles are acquired, the program sums the data into one average profile. It fits a Gaussian to the profile and displays both the measured profile and the center and variance of the fit. If desired this can be repeated at a selected interval. After each data set is collected the new profile and width are displayed. The last profile is added to a mountain-range display and the values of the width and center are added to a strip-chart display. In this manner we can follow the beam profile during the energy ramp.

5. SUMMARY

Four IPM's are installed in RHIC to measure horizontal and vertical beam profile in both rings. The design is based on a prototype which measured single-bunch profiles in the AGS-RHIC transfer line. We expect to be able to measure single-bunch profiles of gold beams and averaged profiles of proton beams. Single-bunch profiles of proton beams will only be possible with a pressure bump.

6. ACKNOWLEDGMENTS

We thank Phil Cerniglia for supervising the cable installation and John Cupola for assembling much of the hardware. Doug Hunter and Pedro Solano assembled the magnets and John Daddario terminated most of the cables. Also thanks to Animesh Jain for mapping the magnet and Chau Lac for designing the magnet stands. Jim Zagel alerted us to the problem of rf coupling through the MCP. This work was done under the auspices of the U.S. Department of Energy.

7. REFERENCES

1. <http://www.rhichome.bnl.gov/RHIC/index.html>
2. R. Connolly, P. Cameron, W. Ryan, T.J. Shea, R. Sikora, and N. Tsoupas, "A Prototype Ionization Profile Monitor for RHIC," Proceedings of the 1997 Particle Accelerator Conference, Vancouver, BC.
3. W.H. DeLuca, "Beam Detection Using Residual Gas Ionization", IEEE Trans. Nucl. Sci., NS-16, 813 (1969).
4. F. Sauli, "Principles of Operation of Multiwire Proportional and Drift Chambers," CERN 77-09 (1977).
5. J. Wiza, "Microchannel Plate Detectors," Nucl. Instr. Meth. 162 (1979) 587-601.
6. Galileo Electro-Optics Corp., Sturbridge, MA 01566.
7. Analog Devices, Norwood, MA 02062-9106.
8. Michnoff, R. "The RHIC General Purpose Multiplexed Analog-to-Digital Converter System", Proceedings of the 1995 Particle Accelerator Conference, Dallas, TX.
9. Hytec Electronics Ltd., Reading, Berks. RG20JT, UK.
10. H. Hartmann and T. Kerner, "RHIC Beam Synchronous Trigger Module," these proceedings.

The RHIC Tune Measurement System

P. Cameron, R. Connolly, J. Cupolo, A. Drees, W. Ryan, T. Shea,
R. Sikora, D. Trbojevic, and N. Tsoupas
Brookhaven National Lab, Upton, NY 11973

Abstract

Each of the four fractional betatron tunes of RHIC (two planes, two rings) is measured with a transverse beam kicker and dedicated beam position monitor (BPM). A 1-5kV pulse is generated by a fast FET switch, passed through a stripline kicker, attenuated, and returned to the instrumentation control room (ICR) for monitoring. When pulsed at 3kV, the four-meter long kicker gives a gold beam at injection ($\gamma=12.6$) an angular kick of $11\mu\text{rad}$ resulting in a betatron amplitude of 0.8mm at the BPM ($\sigma_{\text{beam}}=4.3\text{mm}$). A single bunch is kicked a few times and then measured for several hundred turns. A fast Fourier transform (FFT) of the position data gives the tune.

1. INTRODUCTION

The Relativistic Heavy Ion Collider (RHIC) at Brookhaven National Lab consists of two synchrotrons which intersect at six points around the 3.8km circumference [1]. Ion beams from protons to fully-stripped gold will be accelerated and stored. Both rings are designed to have horizontal tunes of 28.19 and vertical tunes of 29.18. Each fractional tune will be measured by exciting a betatron oscillation in a single bunch with a transverse beam kicker and measuring the transverse position on subsequent turns with a BPM [2].

Each ring has two kicker modules with four 2m-long striplines to allow both horizontal and vertical kicks. Two kickers are installed in a ring so one can be used with pulsed power for kicks and the other can be driven proportionally with rf amplifiers for transverse damping. For early operation of RHIC only pulsed power will be used and the two kickers are connected in series to provide 4m of stripline kicker. Additionally only one stripline in each plane will be powered and the opposing stripline will be terminated on both ends.

In this paper we describe the kicker and the BPM. We describe the timing which allows the selection of the same bunch for the kicker and BPM. Finally results are given of simulations done to determine the measurement accuracy possible considering the RHIC tune spread and BPM resolution.

2. KICKER AND BPM

Figure 1 shows one section of kicker in the assembly area set up for electrical measurements. Four 2m-long, stainless steel striplines are mounted on ceramic standoffs

spaced 1m apart. Each subtends an angle of 70° and the aperture is 7cm. Electrical connectors are type HN feedthroughs. The assembly is designed to give 50Ω impedance when opposing lines are driven in the difference mode. With three lines terminated the impedance of a single line is 55Ω .

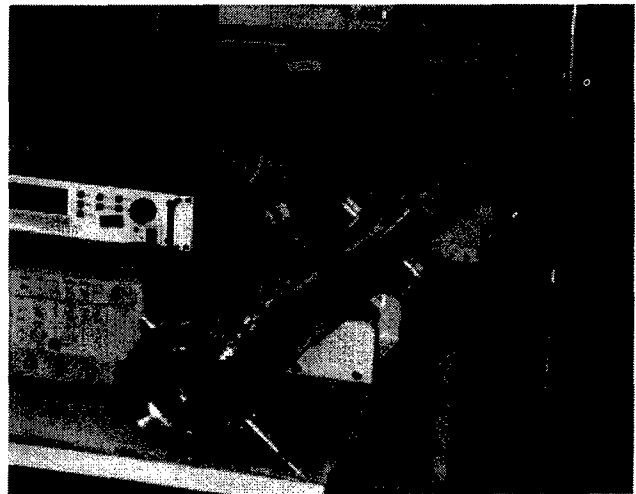


Figure 1. One section of kicker in assembly area.

One channel of the kicker system is shown in fig. 2. The kick pulses are generated by fast FET switches made by Behlke [3]. Pulse current is supplied by capacitors on the switch input which are charged by a 5kV power supply. The switches for all four measurement planes are mounted in one chassis box and powered by a single power supply. One switch is triggered at a time by TTL pulses from the timing system.

The RHIC acceleration system operates at harmonic number 360. Speed limitations of the injection kicker require that at least two empty buckets be between adjacent bunches. Therefore bunches cannot be closer together than about 110ns. The FET switch which fires the tune kicker gives a pulse length of 140ns which will be centered on the measured bunch, fig. 3. Also shown are the coupled pulses from both the 180° line and one of the 90° lines. This shows that there is a flat region of about 70ns where the beam will be affected only by the pulsed line.

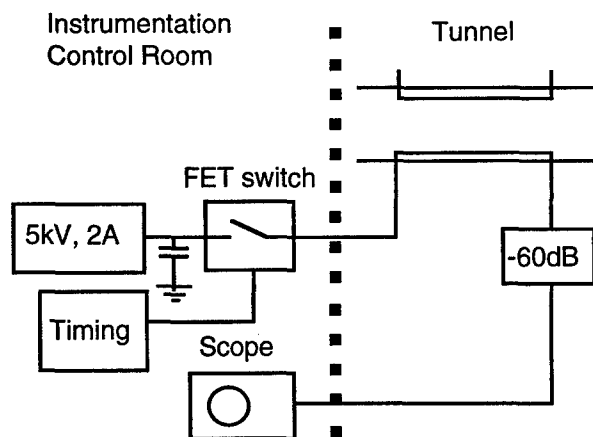


Figure 2. Electrical block diagram of kicker.

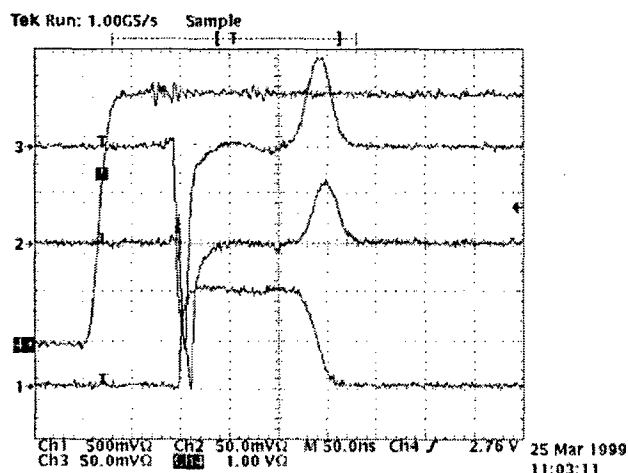


Figure 3. Oscilloscope display of trigger signal (4), output pulse (1), and coupled pulses from the 180° line and one 90° line (2,3). The trigger delay here is 80ns and the pulse is about 130ns long. A 1kV pulse returns as a 1V pulse after -60dB of attenuation.

A ring has 161 BPM's for each plane. These are 23cm-long 50Ω striplines with one end shorted and the other end connected to high-speed, peak-sampling integrated processing electronics. The system is described in ref. 4. In principle any of the BPM's can be used for the measurement and one is chosen where the β -function is large.

A single kick of a gold beam at injection will cause a deflection of 11μrad giving a betatron amplitude of 780μm at the BPM we plan to use. The expected BPM noise floor for single bunch measurements 50μm. Also there is a movable dual-plane BPM located near each kicker. These can be positioned to null out the closed

orbit signal therefore possibly increasing the resolution to around 1μm.

3. TRIGGERING

The FET switch is triggered by a TTL pulse from a modified BPM module. This module receives and decodes the beam synchronous event link, fig. 4. This is a timing and event channel which delivers both a revolution tick synchronous with the beam and encoded event triggers.

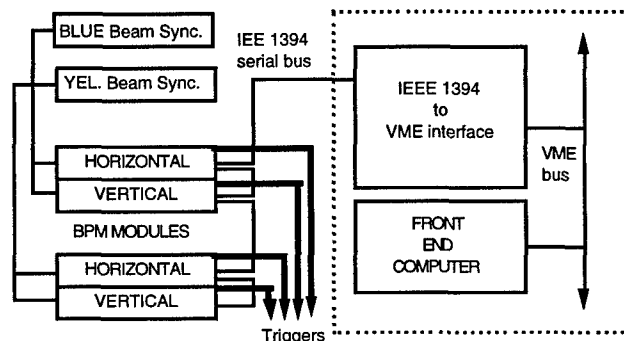


Figure 4. Block diagram of kicker timing. This is same as BPM data acquisition.

In the case of the kicker, the 'turn-by-turn data acquisition of the BPM' event will trigger a sequence of one or more kicks. The kicker trigger is supplied by the enable gate output which normally triggers data acquisition by the BPM. Each BPM and the kicker module has the appropriate delay so, on turn-by-turn acquisition, the same bunch will be kicked and observed on all BPM's. For most tune measurements the data from a single BPM per plane in each ring will be used.

All of the BPM's are connected to VME via IEEE 1394 serial bus interface. In the case of the kicker the connection will be used to read a time-stamped history of kicks for correlation to the time-stamped position measurements. Also kick delay will be adjusted over this bus.

4. SIMULATION RESULTS

In early operation of RHIC the tune will be measured by kicking a single bunch with one or more kicks to build up a betatron oscillation. The transverse position of this bunch will be measured on consecutive turns with one dedicated BPM at a location with a high beta function. Also being considered is white noise excitation of the beam by applying random kicks to the bunch during the entire measurement process and continuous low-level excitation via a phase-lock loop.

A Monte Carlo simulation was done to estimate the possible measurement accuracy and to test the performance of application software. A sinewave multiplied by a

calculated Gaussian-shaped envelope [5] is analyzed by performing a fast Fourier Transformation (FFT) on the position data for 1024 turns. In the simulation a coupling of 90% between horizontal and vertical betatron motion has been assumed. The fractional tunes with a tune spread of 0.001 each were set to be 0.01 apart. White noise with various rms amplitudes was added to simulate the anticipated noise floor of the BPM. Noise filter algorithms are implemented in the application software to enhance fit results.

Figure 5 shows a smoothed FFT spectrum with simulated data at a signal-to-background ratio of 0.7. The solid lines correspond to the fitted horizontal and vertical tune signals. The FFT, noise filtering and fitting were performed on a set of input signals (q_{inp}) superimposed by white noise at signal-to-background ratios from 0.1 to 1.0.

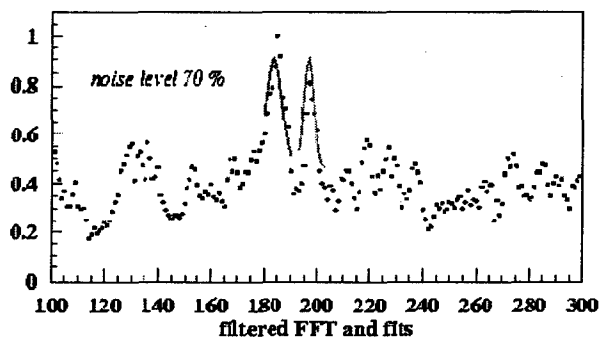


Figure 5. Smoothed FFT spectrum with simulated data with a signal-to-noise ratio of 0.7.

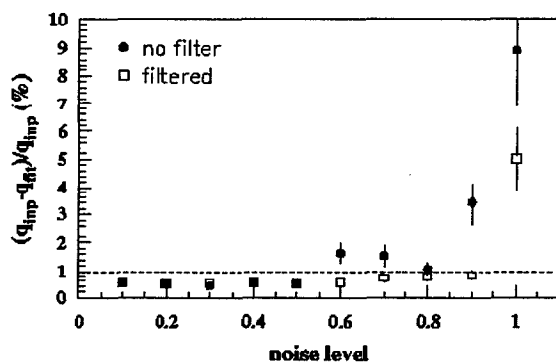


Figure 6. Measurement error ($\Delta q/q$) plotted as a function of noise amplitude for filtered and unfiltered data.

Figure 6 shows the deviation of the fitted tune (q_{fit}) from the input value as a function of noise level for both filtered and unfiltered FFT spectra. It can be seen that while using a noise filter the average deviation from the real value stays below 1% up to a noise level of 90%.

This value corresponds to an accuracy of the order of 10^{-3} which is required for the tune measurement. For the anticipated BPM noise level at RHIC start up, i.e. 50%, we expect a measurement accuracy of 1×10^{-3} .

5. DISCUSSION

The RHIC tune system has been described. Two kicker sections in each ring will be connected in series at first and transverse kicks will be delivered to the beam via fast FET switches. For early operation tune will be measured by giving a single bunch one or more kicks to build up a betatron oscillation and following this bunch with a BPM in the turn-by-turn mode. Simulations indicate that fractional tune can be measured with an uncertainty of $<0.5\%$.

6. ACKNOWLEDGMENTS

We thank Phil Cerniglia for coordinating the cable installation. Also several of the authors had very helpful discussions with Hermann Schmickler. This work was done under the auspices of the U.S. Department of Energy.

7. REFERENCES

1. <http://www.rhichome.bnl.gov/RHIC/index.html>
2. P. Cameron, R. Connolly, A. Drees, T. Ryan, H. Schmickler, T. Shea, D. Trbojevic, "ARTUS: A Rhic TUne monitor System," http://www.rhichome.bnl.gov/AP/ap_notes/index.html
3. Behlke Electronic GmbH, <http://www.eurotek.com/>
4. T. Shea, P. Cameron, P. Cerniglia, J. Cupolo, C. Degen, J. Mead, R. Olsen, W. Ryan, T. Satogata, and R. Sikora, "The RHIC Position Monitor System," these proceedings.
5. R. Connolly, "Decoherence of Betatron Oscillations in RHIC," AD/RHIC/RD-118, Brookhaven National Lab, Upton, NY 11973.

Optical Beamlines for the KEK B-Factory Synchrotron Radiation Monitors*

J. W. Flanagan[†], S. Hiramatsu, T. Mitsuhashi, KEK, Tsukuba, Ibaraki Japan

Abstract

We have designed and constructed two optical beamlines for the KEK B-Factory synchrotron radiation monitors, one for each ring. Each beamline transports the SR beam 30-40 meters to an external optics hutch along two parallel paths. One path is used for direct imaging with adaptive optics[1], the other is used for transverse beam size measurements via SR interferometer[2] and longitudinal profile measurements via streak camera. We designed and installed relay lens systems for the adaptive optics paths. We also provide remote alignment control for components which are inaccessible during beam operation (14 mirrors and 2 pairs of lenses total), with monitoring provided by a set of remote-controlled optical screen monitors. We describe the design of the relay lens and alignment systems along with performance results.

1 INTRODUCTION

The KEK B-Factory is an asymmetric electron-positron collider with two intersecting storage rings: the High Energy Ring (HER) for storing 8 GeV electrons, and the Low Energy Ring (LER) for storing 3.5 GeV positrons. Each ring has a complete, independent SR monitor system, consisting of a 5 mradian bend SR source magnet, water-cooled beryllium extraction mirror, closed optical beamlines and above-ground optical hutch. The beamline for the LER is shown in Fig. 1; the HER beamline is similar, except for having one less bend in the tunnel. The beamline is split into two paths soon after the extraction mirror. One path, the imaging line, contains two pairs of relay lenses which are used to transport the SR wavefront at the extraction mirror to a deformable mirror in the optics hutch for wavefront correction prior to imaging. The other path, the direct beamline, has no focusing optics.

The mirrors for both imaging and direct beamlines are custom ground and coated with aluminum for a surface flatness of $\lambda/10$.

2 OPTICAL PATH DESIGN

2.1 Imaging Beamline

The principle features of the imaging beamline are shown in Fig. 2. The optical path begins at an SR extraction point on the beam line, reflects from a beryllium extraction mirror in the beam pipe, and then passes to an optical hutch aboveground outside the tunnel, where the im-

age is captured via camera and processed. The surface of the beryllium mirror is deformed by heating from the X-ray component of the synchrotron radiation. The deformation, which varies as a function of the SR beam intensity, introduces a corresponding wavefront distortion in the SR beam. The surface deformation of the mirror will be continuously monitored in the tunnel with a Shack-Hartmann wavefront measurement system to be installed during the machine shutdown for physics detector roll-in, and the wavefront distortion corrected by the use of a deformable mirror (CILAS BIM31) in the optical hutch. This adaptive optics system[3] should permit the wave front distortion to be corrected to within $\lambda/10$ in RMS.

Because of the distance between the hutch and the beamline, the optical path between the two mirrors is constrained to be at least 30 meters. A set of relay lenses is used to transport the SR wavefront from the extraction mirror to the deformable mirror, which is located at the conjugation point of the relay lens system.

2.2 Relay Optics Design

The requirements for the relay lenses are:

- Provide plane-to-plane focusing for the extraction and correction mirrors: each mirror sits at a conjugation point of the relay lens system, to map the surface of the extraction mirror onto that of the correction mirror;
- Match the active area of the correction mirror to that of the extraction mirror: the 15x15 mm usable surface of the extraction mirror needs to be magnified by a factor of 2 to make the most effective use of the clear aperture (active area) of the 5 cm diameter correction mirror;
- Minimize aberrations at the wavelengths of interest; a bandpass filter in the optical path sets this range to $550 \text{ nm} \pm 5 \text{ nm}$;
- Use commercially available lenses where feasible.

The basic design uses two pairs of doublet lenses. Each pair consists of a concave lens and a convex lens with focal lengths of equal magnitude but opposite sign, which minimizes the dependence of focal length on errors in focal lengths of the two lenses. The convex lenses are common, commercially available lenses (Melles-Griot achromatic doublets). Concave lenses are not commercially common, so they have been custom ordered.

To reach the factor of two magnification between the front focal plane (extraction mirror surface) and the rear focal plane (correction mirror surface), the focal length of the first pair of lenses is taken as $1/3$ of the total distance

* Work supported in part by the Japan Society for the Promotion of Science.

[†] Email: john.flanagan@kek.jp

SR Monitor relay optics path (LER)

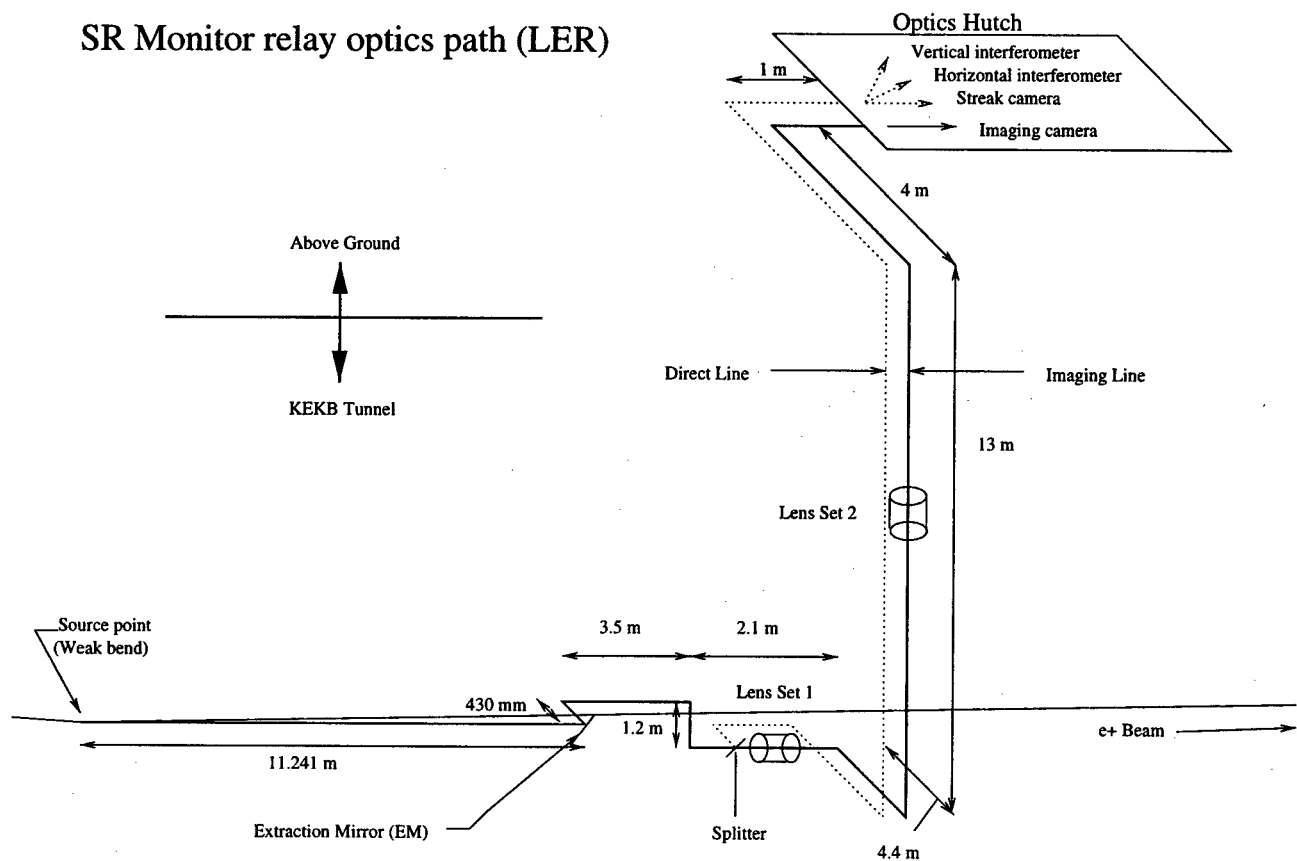


Figure 1: SR Monitor optical beamlines (LER)

between the mirrors (5100 mm), while that of the second pair is taken as 2/3 of the distance (10200 mm). The resulting set of design parameters is shown in Table 1.

Table 1: Relay Lens Specifications

Pair/ Lens	Eff. Foc. Len. (mm)	Edge Dia. (mm)	Thick- ness (mm)	Pair Foc. Len. (mm)	Lens Sep. (mm)
Pair 1: Convex (Melles Griot LAO366)	1000	80	10	5100	187
Concave (custom)	-1000	80	10		
Pair 2 Convex (Melles Griot LAO379)	2000	150	23.27	10200	373
Concave (custom)	-2000	150	23		

As a starting point, the concave lenses are specified as being identical to the convex lenses, but with opposite radii of curvature. The glasses used in the custom lenses are then changed to more common types (BK7 crown and F2 flint), and optimized for the required focal lengths. Commercially available lenses are optimized for minimum aberrations at infinite conjugate ratios; the curvatures of the custom lenses were optimized with the use of optical design software (Zemax) for minimum aberrations in combination with the commercial convex lenses at the finite conjugate ratios needed and at the required magnification on the surface of the correction mirror.

In addition to the above, an additional MG LAO366 is used after the correction mirror to bring the image to a final focus at the video camera input. This final focus lens is added to the simulated system, and the spacings between lens pairs in the end-to-end design re-optimized.

The resulting design shows a wavefront distortion of $\lambda/10$.

2.3 Direct Beamline

In addition to the imaging beamline described above, a direct (non-imaging) optical beamline is split off from the imaging beamline before the first lens, and proceeds parallel to the imaging beamline into the optical hutch. This direct beamline is used for precise transverse beam size mea-

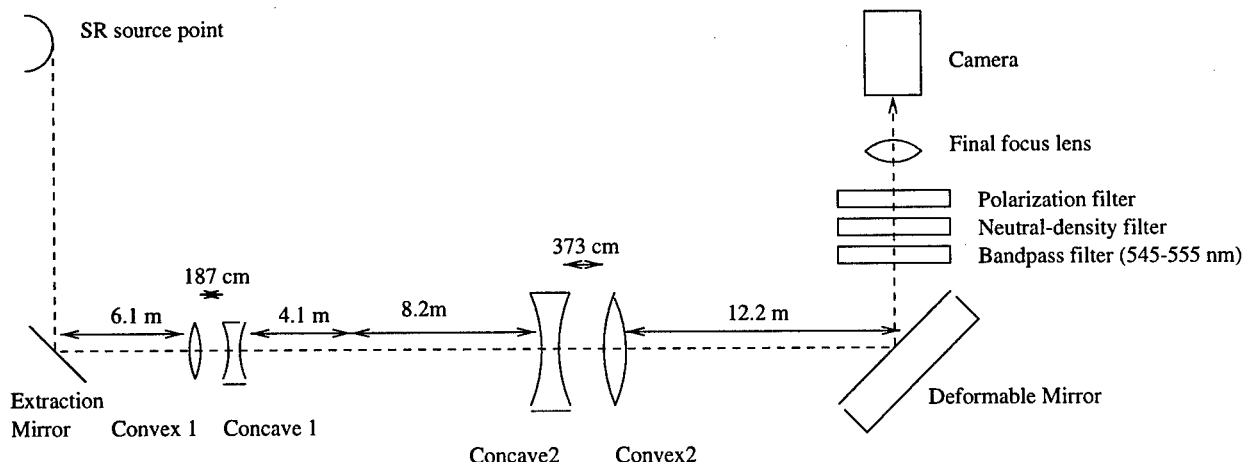


Figure 2: Relay lens optics. Extraction and deformable mirrors sit at conjugation points of the lens system.

surement via interferometry, as well as for longitudinal profile measurement via streak camera. The direct beamline contains no focusing optics between the SR source point and the hutch, only mirrors, in order to preserve both the spatial coherence for the SR interferometer and the temporal structure for the streak camera.

3 MECHANICAL DESIGN

All mirrors which are below ground (8 in the LER ring and 6 in the HER ring) are movable in two degrees of freedom with pulse motors. The pulse motors are remotely controlled from the optical hutches to permit alignment while the rings are in operation, by both manual control and GPIB interface.

In addition to the mirrors, the second set of lenses in each SR beamline are remotely movable as well, to adjust the focal length and magnification of the mapping of the surface of the extraction mirror onto the surface of the correction mirror. The alignment of the beamlines before particle beam commissioning was carried out using a laser auto-collimation method: a laser beam is sent down the beamline from the optics hutch, and the mirrors adjusted sequentially to deliver the beam to the SR extraction port, where a temporary mirror reflects the beam back up both beamlines.

For alignment with the SR beam itself, when the laser auto-collimation method can not be used, a set of "optical screen monitors" were designed and installed in the system at several locations in each beamline. These monitors consist of remotely operable guillotine-like semi-opaque screens, which are monitored via cameras from the optics hutch to facilitate optical path alignment using the SR beam.

To reduce image fluctuations due to air currents, the beamline is closed with a minimum diameter of 200 mm. Some fluctuations are still visible and further work remains to be done in this area, but the system works successfully for streak camera measurements and for beam profile mea-

surements using both the imaging and direct lines. An measurement output example is shown in Fig. 3.

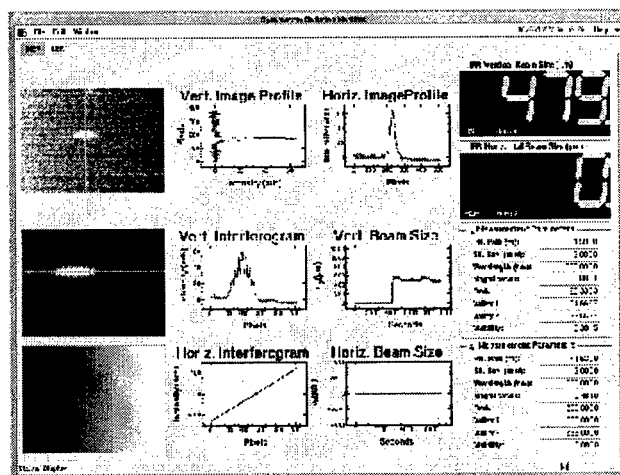


Figure 3: Example of SR measurement system output. Beam size (LER, vertical only in this example) is monitored continuously.

4 RESULTS

The direct and optical beamlines for the LER and HER have been designed, installed and commissioned, and are working well to deliver initial SR beams for imaging, interferometry, and streak camera use. Refinements to the measurement methods are underway, and commissioning of the adaptive optics components is scheduled to begin shortly.

5 REFERENCES

- [1] N. Takeuchi et al., Tech. Digest of Nonastronomical Adaptive Optics (NAAO'97), (1997) p. 26.
- [2] T. Mitsuhashi et al., Proc. EPAC 1998, p. 1565.
- [3] T. Mitsuhashi et al., Proc. APAC 1998, p. 698.

CRYSTALLINE CHROMIUM DOPED ALUMINUM OXIDE (RUBY) USE AS A LUMINESCENT SCREEN FOR PROTON BEAMS*

K. A. Brown, D. M. Gassner*

Brookhaven National Laboratory, Upton, NY 11973, USA

Abstract

In our search for a better luminescent screen material, we tested pieces of mono-crystalline chromium doped aluminum oxide (more commonly known as a ruby) using a 24 GeV proton beam. Due to the large variations in beam intensity and species which are run at the Alternating Gradient Synchrotron (AGS), we hope to find a material which can sufficiently luminesce, is compatible in vacuum, and maintain its performance level over extended use. Results from frame grabbed video camera images using a variety of neutral density filters are presented.

1 INTRODUCTION

A study of luminescent properties of four test materials mounted on a variable position plunged actuator was conducted. The flag materials were installed at a 45° angle to the beam. The light emitted from the flag leaves the vacuum enclosure through a transparent quartz port, then reflected 90° by a mirror to the video camera which was mounted parallel to the beam path.

2 HARDWARE

2.1 Flag materials

Two of the materials tested were poly-crystalline aluminum oxide pieces, one doped with Cr_2O_3 , the other undoped. These were supplied by Morgan Matrox Inc. commercially called Chromox (Al_2O_3 99.4%, Cr_2O_3 0.5%), average grain size 10-50um. Chromox and radlin (zinc cadmium sulfide, 40% cadmium by weight, by MCI Optonix, commercial name Optex PFG) are the present flag materials used for diagnostics in the slow extracted beam lines, and the upstream portion of the fast extracted beam line.

The other two pieces were mono-crystalline aluminum oxide (ruby) doped with different amounts of Cr_2O_3 . Union Carbide Corporation Crystal Products provided the 0.22% doped piece (1.5 mm thick), and Crystal Optics Research, Inc. supplied the 0.05% piece (1 mm thick).

* Work performed under auspices of the U. S. Department of Energy.

* Email: gassner@bnl.gov

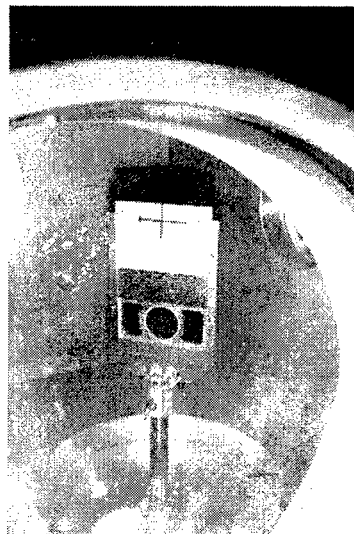


Figure 1: The picture above is the view looking into the vacuum chamber (typical transport vacuum is 10 microns or 10^{-2} torr) at the four test materials. From top to bottom: doped aluminum oxide, undoped aluminum oxide, ruby 0.22% doped, and a round ruby 0.05% doped. The location of the test assembly is 157 feet from the AGS ring. The beam travels left to right.

These commercially available laser grade rubies were manufactured using the Czochralski production technique. The ruby price and availability is attractive due the popular use of ruby lasers in industry. In fact, the majority of the cost is for cutting and polishing of the surfaces.

2.2 Video camera

We used the Dage-MTI Inc. 70R video camera. The camera head (with 1" vidicon tube) is separate from the camera control unit, it is specifically designed for use in high radiation environments. For linearity purposes the automatic gain control was disabled, and the auto black compensation had a negligible effect due to the presence of a reference near absolute black in the image.

A remote control neutral density filter assembly is mounted between the camera lens and vidicon tube. It has four filters (0.5, 1, 1.5, 2) which can supply attenuation variations up to 100,000.

2.3 Framegrabber

The VME based framegrabber is the Modular Vision Computer (MVC) by Imaging Technology Inc. which operates at 40 MHz with a pipeline processing configuration.

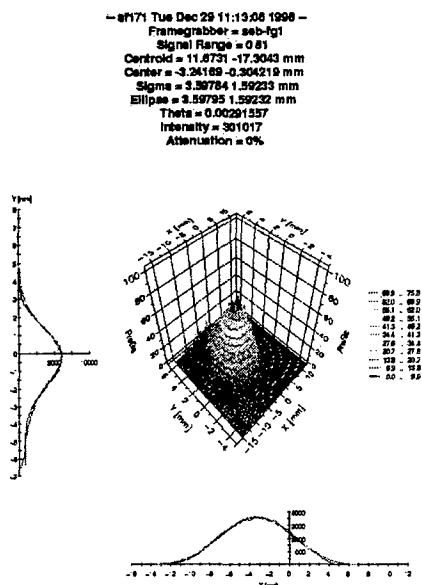


Figure 2: Sample data from framegrabber application.

An onboard modular histogram processor produces the horizontal and vertical projections. The image was displayed via an application written for our Sun Solaris controls system. The digitised image (512 X 480) pixel values can range from 0-255 (8 bits).

3 TEST TECHNIQUE

The flag materials were individually positioned into the path of the 24 GeV slow extracted proton beam from the AGS. The beam was spilled out at rate of 14 tera-protons/sec. (for 2.5 sec.) or average current 2.2 microamps. One set of data was acquired at 0.2 pa, which was our typical intensity during a polarized proton run.

Data from the framegrabber was analysed by determining the value of the peak pixels in the center of the beam spot. Neutral density filters were remotely inserted until the peak pixel values were in the lower half of the full response range. This was done to avoid saturation and stay in the linear response of the system.

4 RESULTS

The data in table 1 shows the peak pixel values for the camera's response to the chosen combinations of test materials and neutral density filters.

Table 1: Data from flag material study.

ND Filter Atten.	Beam Current	Ruby .05%	Ruby .22%	Al ₂ O ₃ Undoped	Al ₂ O ₃ Doped
1/3160	2.2 ua	32	30	0	18
1/1000	2.2 ua	96	85	0	51
1/31.6	2.2 ua	sat.	sat.	55	sat.
None	0.2pa	20	17	0	<5

The undoped poly-crystalline aluminum oxide produced about 30 times less light than the doped version. The emitted light from the polished ruby was less dispersed than the other materials.

The mono-crystalline material produced roughly twice more light than the poly-crystalline.

5 SUMMARY

A factor of two more light is emitted from mono-crystalline rubies verses the poly-crystalline material. Slightly higher peak levels from the polished ruby due to less scattering of the emitted light.

We intend to use the mono-crystalline ruby (which is more compatible in a vacuum environment) as an alternative to radlin which will out gas under vacuum.

ACKNOWLEDGMENTS

We acknowledge the contributions of the AGS Beam Components & Instrumentation Group, Jon Hock, Larry Hoff, Steve Tepikian, James C. Smith (Crystal Optics Research, Inc.), and Colin Johnson (CERN).

DEVELOPMENT OF FILM-MODE WALL CURRENT MONITOR AND ITS APPLICATION IN HLS

Wang Guicheng*, Leng Yongbin, Fang Zhigao, Wang jihong, Zhao Feng, Tao Xiaoping, NSRL
Liu Guangjun, Li Guangyeng, Fang Lei, Anhui Institute of Optics and Fine Mechanics, Hefei

Abstract

A film-mode wall current monitor was developed in NSRL in cooperate with Anhui Institute of Optics and Fine Mechanics, Academia Sinica. It is in an advantageous position of continuity and uniformity of the film and used on line with success in HLS. The beam current toroids used in the LINAC of HLS are just employed for measuring the μ s bunch beam current, it is limited by band width of toroid and preamplifier. We embed a film-mode resistor inside of every toroid to respond to ns wall current, diagrams of structure of the film-mode wall current monitor and cross section of film-mode resistor are given in this paper.

1. THE PRINCIPLE AND STRUCTURE OF WALL CURRENT MONITOR

The non-interaction monitor is related to the use of the wall image current induced by relativistic particle bunch.

1.1 Principle of Current Monitor

The principle of current monitor is shown in Fig.1

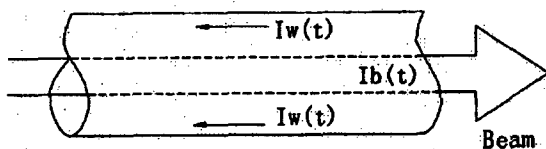


Fig1 The particle beam and it's induced image current

Making Assume:

* Particle-beam with $\gamma > 10$;

* Metallic chamber is perfectly conducting or with skin depth \ll wall thickness.

From continuity equation

$$\frac{\delta p}{\partial t} + \nabla J = 0$$

We have: $i_w(t) = -I_b(t)$

Therefor the induced image current and its azimuthal distribution can be used to monitor the beam intensity (see Fig1).

1.2 Structure of Current Monitor

As an original model, ceramic ring of 1cm in length is inserted into the vacuum tube, with 20 inductance-less resistors, of 1 kilo ohm each, welded across the ring and evenly distributed to allow the wall current to pass (see Fig2).

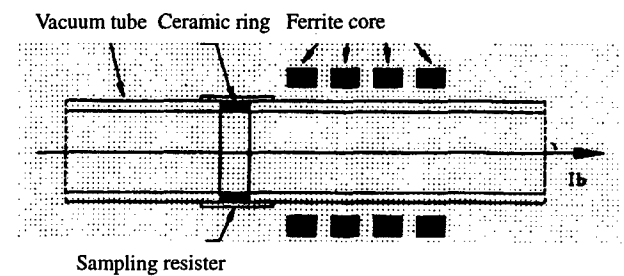


Fig.2 Structure of wall current monitor

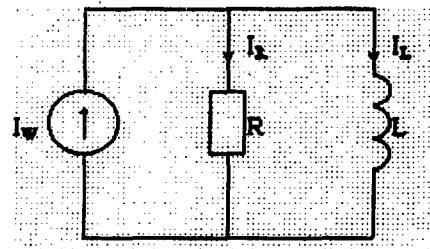


Fig.3 Equivalent circuit of wall current monitor

From the equivalent circuit of the wall current monitor (see Fig3) we can get:

$$\begin{cases} i_R R = L \frac{di}{dt} \\ i_w = i_R + i_L \quad (\text{when } t=0, i_L=0) \end{cases}$$

Where, i_w - Wall current

R - Sampling resistor

L - Inductance between sampling point

And ground

Thus we obtained:

$$i_R = i_w \cdot \exp\left(-\frac{t}{\tau}\right)$$

i_R (the current passing through sampling resistors) is an

exponentially decay of the wall current with time constant τ . When the beam current pulse width is 2ns, and if $\tau=10\text{ns}$, $R=50\Omega$, then $L=0.05\mu\text{H}$. This is a small inductance, can be formed by vacuum tube itself, it means that under the condition of beam current pulse width is 2ns we can use the film resistor as wall-current sampling resistor without the ferrite core for enhancing the inductance L . Finally, we mount the film resistor into the gap between surface of vacuum tube and coil (Tor) used for monitoring \square s pulse beam current (see Fig4).

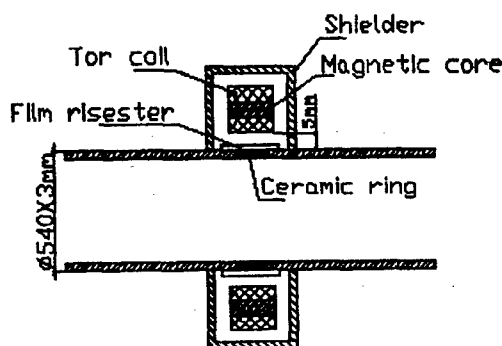


Fig.4 structure of film-mode wall current monitor

2. STRUCTURE OF FILM RESISTOR

A cross section of film-mode resistor with length of 20cm and width of 7cm is shown in Fig5. Both conductor-bands and resistor-band are carried by a PET-film of 200nm in thickness. The resistor-band is made of high purity Nickel located at the center of 2cm in width and 40-60nm in thickness. One SiO_2 layer of 100nm in thickness is evaporated on the resistor-band for protecting it from decline. Resistance of resistor-band is controlled in around 5Ω - 10Ω . On the surface of four conductor-bands, each of both of front and back side has tow bands, they are gold-plated to take form an output band.

Pay attention to clean the surface of PET film and keep the material of Ni in high purity for preventing the resistance of resistor-band from decline.

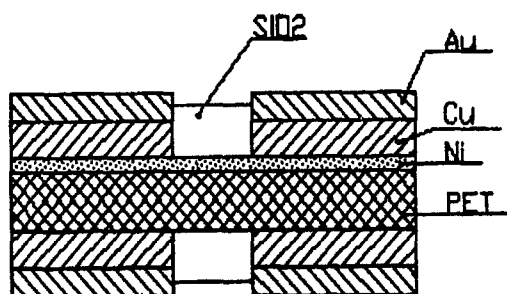


Fig.5 Diagram of cross section of film-mode resistor

3. APPLICATION IN HLS

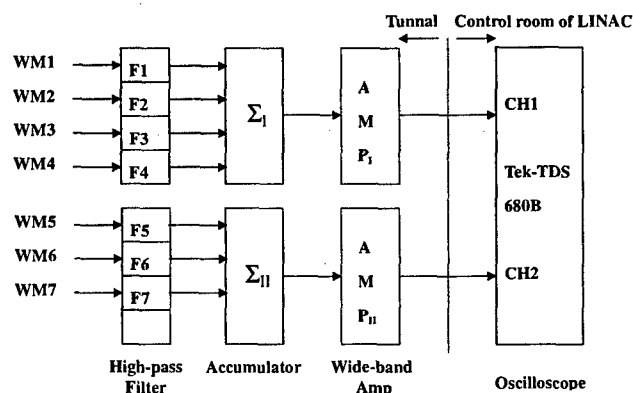


Fig.6. Diagram of wall current monitor

There are 7 sets of film-mode wall current monitors in the LINAC of HLS. They are Divided into tow groups one includes 4 sets another 3 sets. The signals from one group are feed together to one accumulator, then to an APM, to one channel of oscilloscope. See Fig.6.

In fact, much noise are picked up by the film-mode resistor which connect immediately with the wall of vacuum tube of LINAC. Main peaks of spectrum of noise concentrate at around 1MHz in frequency domain. High-pass filters, with 10MHZ cut-off frequency, employed for suppressing the low frequency noise are fixed in the front of accumulators [2].

The cables from monitors to filters are cut out for different length in proper order, such as WM1-F1 is 5m; WM2-F2 is 10m; WM3-F3 is 15m and so on. At the end one can make a pulse packet including four wall current pulses to be displayed on a sweep line of Tek-TDS680B. Usually, one can spread out any one of pulse by turning time delay and changing the time base, see the Fig.

4. CALIBRATION OF SYSTEM

The calibration of whole system has been done with calibration set [3], see Fig.7. In our case for ns beam current the sampling resistor is film-mode used without the ferrite core. The wall current and input signals are shown in Fig.8. As a result, the efficiency of this calibration set is 70%. Adjusting the amplification of preamplifier one can keep the whole gain from out of toroid to input of oscilloscope at 6dB.

Finally, the calibration coefficients of every film-mode wall current monitor are listed in table 1.

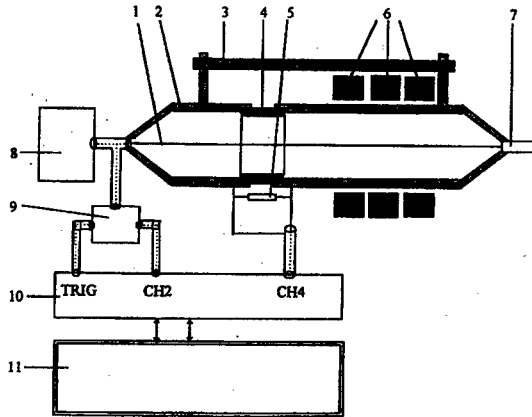


Fig.7 Diagram of calibration system

Annotations on the Fig.7:

- 1-Signal wire through inside of vacuum tube;
- 2-Vacuum tube;
- 3-Metal pole;
- 4-Ceramic ring;
- 5-Sampling resistor (film-mode for ns signal);
- 6-Ferrite core;
- 7-Terminal load for matching;
- 8- Pulse generator (HP8082A);
- 9-Power divider(HP11667B);
- 10.-Probe (HP54121A, 20GHZ test set);
- 11- Oscilloscope (HP54120B).

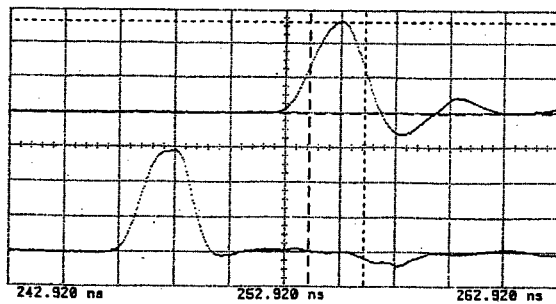


Fig.8 Calibration signal and sampling output

In Fig.8:

- Up-line: output signal from sampling resistor;
Down-line: Calibration signal.

Table 1 Calibration coefficients of film-mode wall current monitors

Monitor No.	Resister	Efficiency
1	10.5Ω	14.7 ma/mv
2	10.0Ω	14.7 ma/mv
3	10.5Ω	14.7 ma/mv
4	11.5Ω	16.1 ma/mv
5	5.0Ω	7.0 ma/mv
6	50.0Ω	70.0 ma/mv
7	10.0Ω	14.0 ma/mv

5. REFERENCES

- [1] J.Borer and R.Jung. European Organization for Nuclear Research, LEP-Division, Geneva, October 1984
- [2] Fang Zhigao, Li Hui, Leng Yongbin, Nuc. Sci. & Tech. Jan. 1998, 79-83
- [3] Fang Zhigao Thesis for the master, NSRL,USTC, Hefei, july, 1996 36-40

A Flying Wire System in the AGS*

H.Huang[†], W. Buxton, G. Mahler, A. Marusic, T. Roser,
G. Smith, M. Syphers, N. Williams, R. Witkover
Brookhaven National Laboratory, Upton, NY 11973, USA

Abstract

As the AGS prepares to serve as the injector for RHIC, monitoring and control of the beam transverse emittance become a major and important topic. Before the installation of the flying wire system, the emittance was measured with ionization profile monitors in the AGS, which require correction for space charge effects. It is desirable to have a second means of measuring profile that is less dependent on intensity. A flying wire system has been installed in the AGS recently to perform this task. This paper discusses the hardware and software setup and the capabilities of the system.

1 INTRODUCTION

The primary method for measuring the beam profile in the AGS has been through the use of an Ionization Profile Monitor (IPM).[1] Another method which has been used with some success in the AGS Booster is one in which the RF is turned off and the beam is allowed to spiral inward as the magnetic field is varied; the beam intercepts a scraper and the beam loss is measured versus time.[2] Analysis of this data can also give the beam profile. However, this scheme only works for measuring horizontal beam distributions.

Since the optical properties of the AGS are fairly well understood, a measurement of the beam profile with the IPM monitors can give information about the emittance of the beam. In the vertical, this is a direct measurement. However, in the horizontal, one must fold in the spread in beam size due to the spread in momentum of the beam particles and the non-zero dispersion of the ring. Moreover, the IPM measurements require space charge corrections, which makes the measurement sensitive to beam intensity. Such corrections can be implemented but require frequent calibration of the system high voltage to obtain accurate measurements.

Flying wires ("wire scanners") have been widely used to measure the transverse beam profile at many other proton accelerators such as CERN PS and SPS, KEK, FNAL and LANL. A flying wire system consists of a thin wire which traverses the beam with constant speed and a detector which measures the scattering of the beam caused by the wire. Since the scattering is proportional to beam intensity at a particular wire position, the detected scattering versus the wire position gives the transverse beam profile.

Placement of a flying wire profile monitor in the AGS

allows for a non-destructive, independent means of measuring the transverse beam size and cross-calibrating the AGS IPM. Since the AGS accelerates protons and heavy ions, it is desired that the flying wire measures emittance for both scenarios. For heavy ion beams, because of the stripping that can occur as the wire intercepts the beam, it obviously would not be unobtrusive. For proton beams, however, especially high intensity beams where the space charge effects of the IPM are questioned, the wire could prove beneficial. However, wire survival may be compromised with high intensity beams due to wire heating.

1.1 Heating of the Wire

To estimate the temperature rise in the wire, we assume that the particles lose energy in the wire due to ionization losses and that some fraction e_h of that energy remains in the wire. This implies that the temperature rise will be approximately

$$\Delta T \approx \frac{e_h \frac{dE}{dx} N_p f_0}{\sqrt{2\pi} \sigma_y \rho c_s v},$$

where dE/dx is the energy loss per unit length due to ionization, N_p is the number of particles in the ring, σ_y is the rms beam dimension in the direction along the wire, ρ is the density of the wire material and c_s is the specific heat of the wire material.

Measurements have been made at CERN[3] to determine a value for e_h and its value was found to be roughly 0.3. Their measurements also showed that the wire would break due to beam heating at speeds less than about 1 m/s for total beam intensities of 2×10^{13} protons. If a similar wire system were used in the AGS, then the speed below which the wire would break at intensities of 7×10^{13} would be approximately

$$v \approx (1\text{m/s}) \times \frac{7 \times 10^{13}}{2 \times 10^{13}} \times \frac{0.5\text{mm}}{2\text{mm}} \times \frac{6200\text{m}}{807\text{m}} \\ \approx 7\text{m/s},$$

where a Gaussian beam with emittance $\epsilon_N = 50\pi$ mm-mr beam in the AGS is assumed. This speed is easily within the range of present systems. In reality, the AGS beam size is estimated about $\epsilon_N = 100\pi$ mm-mr. If one anticipates higher intensities, then a system which can attain 10 m/s wire speeds is in order.

Radiative cooling also helps in this regard. As the wire heats up, it will radiate as an inefficient "black-body." Suppose a wire with the same parameters as the CERN wire

* Work supported in part by the U.S. Department of Energy.

[†] Email: huanghai@bnl.gov

system is used in the AGS at a location where the amplitude function is $\beta_x = \beta_y = 15$ m. At the highest AGS momentum 29 GeV/c, the temperature rise in the center of the wire for the passage through a Gaussian beam with emittance $\epsilon_N = 100\pi$ mm-mr at speed of $v = 7$ m/s is about 2100K.

1.2 Emittance Dilution Estimates

Due to Coulomb scattering, passing a wire of diameter d will increase the emittance of the beam. The amount of emittance increase can be estimated by considering the wire to pass through the beam with speed v at a location where the amplitude function has value β_0 . Then, the increment in emittance due to a single scan of the wire is

$$\Delta\epsilon_N = \frac{6\pi\beta_0 d^2 f_0}{\beta^3 \gamma L_{rad} v} \left(\frac{15}{938} \right)^2$$

where f_0 is the revolution frequency, β and γ are the relativistic kinematic factors, and L_{rad} is the radiation length of the wire material. Inputting the AGS parameters used above, and assuming a $33\mu\text{m}$ carbon fiber, the emittance increase using a speed of 7 m/s would be approximately $\Delta\epsilon_N = 3.4\pi$ mm-mr at injection (1.9 GeV/c), and 0.2π mm-mr at 29 GeV/c.

Based on the analyses described briefly above, it appears that a $33\mu\text{m}$ diameter Carbon filament, traveling at speeds greater than above 7 m/s would survive crossing an AGS beam of 7×10^{13} protons with normalized transverse emittances of 100π mm-mr.

2 THE AGS FLYING WIRE SYSTEM CONFIGURATION

2.1 Flying Wire System

The AGS flying wire beam profile monitor system is located in a 10-foot straight section of the AGS, A20. One vacuum chamber hosts both the horizontal flying wire and the vertical flying wire, sitting upstream and downstream, respectively. A scintillator paddle installed down stream is used to measure the beam scattering due to the interaction with the wire. It can measure beam profile in horizontal and vertical directions, but only one direction can be measured at a time. The scintillator paddle is 1.2 m down stream from the vertical flying wire and 1.5 m down stream from the horizontal one.

Two rotary stepping motors are used to move the horizontal and vertical wires through the beam. Each motor rotates a shaft with two wires stretched between the ends. The angle between wires is 120 degrees. One of the wires on the same shaft is considered a spare. The motor takes the wire from its parked position outside the beam, accelerates it to desired speed, sweeps it through the beam, and decelerates it to a stop at the other side of the beam. There exists no mechanical interference between the wires in horizontal and vertical directions. The scattering caused by the

passage of any of the wires through the beam is measured with the same photo multiplier. Therefore only one wire can be moved through the beam at one time. The wires can rotate full rotation in 5000 steps. At their desired speed of 10 m/s, wires travel 0.2 mm in 20 us.

2.2 Detector and Readout

The detector for the flying wire is a scintillation counter. The scintillation material is Bicron, BC-408. The counter paddle has a circular cutout at its end so that the scintillator can straddle the vacuum pipe and intercept a 180 degree, one inch wide arc in the beam scattered in the forward direction. A light guide about one foot long is used to guide the light to an XP2203B ten stage photo multiplier tube. The whole assembly, tube base and all, is enclosed in a metal shield to provide for the best possible noise rejection. An LED was added in the light guide to provide for testing in place.

Discrete counting is not possible due to the beam bunching, therefore, the analog charge signal from the PMT must be used. The XP2203B has an S20 photo cathode assuring the largest signal and best overall linearity. A resistor divider in the tube base provides the tube bias to the dynodes. Two bases are available: one for high intensity, which uses five dynodes and takes the output from the sixth; the other for low intensities, which uses all ten dynodes taking the output from the anode. Much of the base and paddle design was fashioned after a design used in the FNAL flying wire system [4],[5] and we are grateful for their help.

Signals from the PMT are read differentially by a VME module. This module is a BNL design known as an MADC (Multiplexed Analog to Digital Conversion System). Running at full speed, this module provides digital signal samples to the AGS Control Computer.

2.3 Software and Controls

An Oregon Micro Systems VMEX-2E Motor Controller board is used for the control of the motors. It can control 2 axes of motion while monitoring their actual positions with the built in incremental encoder interface. The board has a Motorola 68000 processor which can be programmed to execute a wide variety of motion commands. A sync line is available to synchronize moves to external events and there is an auxiliary line for each axis which allows the control of external events. The start of flying wire movement is initiated by V102 Event Link Delay Module. Motion signals generated by the motor controller board, besides being used for motor control, are used as external scan trigger signals to MADC module.

All signals generated by or going to the motor controller board go through a transition module. The operation mode of the transition module is determined by the state of the motor controller X and Y auxiliary lines. When the auxiliary line for one of the axes is set to the high level, the transition module will allow that axis of motion to operate as the sync line becomes active. The transition module will

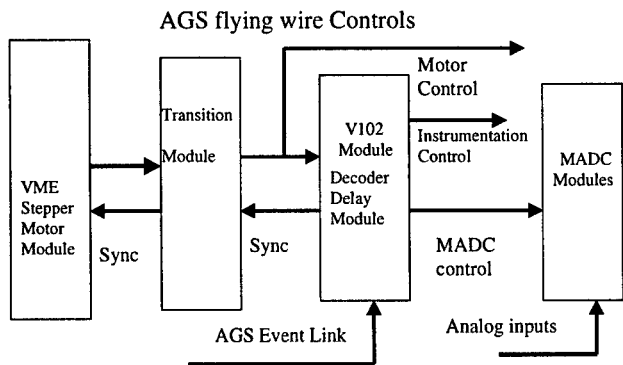


Figure 1: The AGS flying wire control sequence diagram.

also send signals to the MADC to take data. When both auxiliary lines are set high then the transition module will only send signals to the MADC and not allow either motor to move. The purpose of this mode of operation is to take background measurements.

The control sequence is shown in Figure 1. Beginning with the sync signal, the V102 decodes an event from the AGS event link and delays a programmable amount of time and then generates the sync pulse. When the VME stepper motor module receives the sync signal it begins to execute code that determines the direction of the appropriate motor and outputs the clock to step either the X or Y plane motor. The transition module passes the motor step clock and direction signals to the appropriate motor indexer and the step clock to the V102 module. The motor step clock is used by the V102 to generate programmable delayed signals which in turn control the instrumentation electronics and the MADC. The MADC digitizes the analog data on every step of the motor while the wire is in the beam. The VME stepper motor module automatically accelerates the motor to the correct velocity, runs the motor at a constant velocity through the beam and decelerates the motor after the wire leaves the beam.

3 PERFORMANCE AND FUTURE

The flying wire system has been tested during the AGS FY99 high intensity proton run. A horizontal beam profile measured with the AGS flying wire is shown in Figure 2. Due to the proximity of the detector to the AGS Ring, and the remote location of the electronics, noise pickup from the beam and other devices is a significant problem. A large fraction of the noise is rejected by the differential input of the MADC. The rest can be filtered effectively by proper DSP techniques.

The flying wire system in the AGS provides a simple

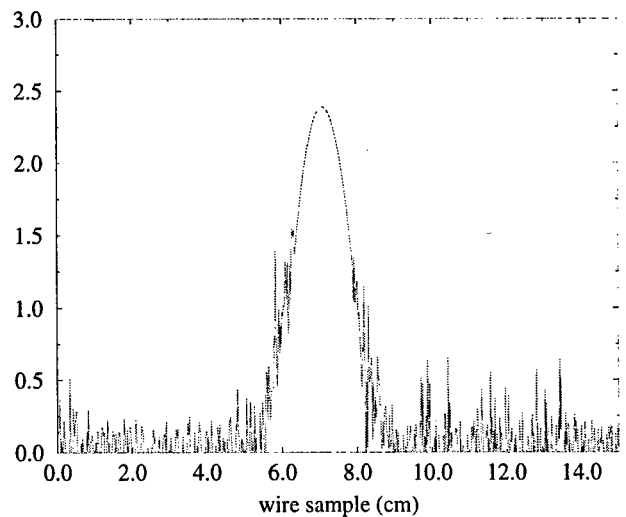


Figure 2: The horizontal beam profile measured with the AGS flying wire.

precise means of measuring beam profiles. We plan to run it utilizing other species such as heavy ion and low intensity polarized proton beam in the AGS in the future. It will become a valuable tool for AGS beam diagnostics.

4 REFERENCES

- [1] A. N. Stillman, R. Thern, and R. L. Witkover, *Rev. Sci. Instrum.* 63, 3412 (1992); A. Stillman and R. E. Thern, "Full Cycle Beam Diagnostics with an Ionization Profile Monitor," *Proc. 1993 IEEE Part. Accel. Conf.*, p. 2471.
- [2] K. Zeno, AGS Studies Report No. 314.
- [3] A. Burns, et al., "Wire Scanner News from the CERN-SPS," *Proc. 1989 IEEE Part. Accel. Conf.*, Chicago, p.1580(1989).
- [4] W. Blokland, et al., "New Flying Wire System for the Tevatron", *Proc. of the 1997 IEEE PAC*, pp. 2032-4, May 12-16 1997, Vancouver, B.C.
- [5] J. Zagel, et. al, "Upgrades to the Fermilab Flying Wire Systems," 1991 IEEE Part. Accel. Conf., 91CH3038-7,p.1174-6 (1991).

BEAM STUDIES IN DIAGNOSTIC BEAMLINE AT PLS*

J. Y. Huang^{*}, D. K. Seon, I. S. Ko, and T. -Y. Lee

Pohang Accelerator Laboratory, Pohang 790-784, Korea

Abstract

A diagnostic beamline has been operated in the PLS storage ring for the diagnostics of electron- and photon-beam properties. It consists of two optical imaging systems: a visible light imaging system and a soft x-ray imaging system. We measure transverse and longitudinal beam structure with a streak camera to study short-time beam dynamics from the visible light image. Accurate transverse beam size is measured with soft x-ray image to minimize diffraction error. In this paper, results of the beam studies and the measurement of beam parameters are summarized and discussed.

1 INTRODUCTION

The Pohang Light Source (PLS) is a third generation synchrotron light source dedicated to many scientific applications. The storage ring is equipped with various electron- and photon-beam diagnostic instruments such as the beam position monitor, beam current monitor, photon beam monitor, and the beam feedback system to stabilize photon beam. Photon beam diagnostics is an essential technique for the study of the small-scale electron beam structure as well as its temporal dynamics in short-time scale [1, 2]. For this purpose, a diagnostic beamline has been operated in PLS for the measurement of the transverse electron beam shape, beam position and the longitudinal structure of the bunch from the synchrotron radiation source.

Various machine parameters were measured in the diagnostic beamline with imaging systems at two different band of wavelengths: visible light and soft x-ray. Transverse beam position is monitored with a position-sensitive photodiode detector, and the beam-size is measured with a 2-dimensional CCD camera or with two linear photodiode-arrays. Time-averaged bunch length is measured with a fast photodiode in conjunction with a fast sampling oscilloscope. A synchroscan streak camera is used for the study of the transient beam structure with 2 ps resolution. On the other hand, more precise beam size is measured with x-ray optics.

In this paper we describe the status of the PLS diagnostic beamline, and various beam diagnostics and result of beam studies being conducted using synchrotron radiation.

*Work supported by the Ministry of Science & Technology and POSCO

*Email: huang@postech.ac.kr

2 DIAGNOSTIC BEAMLINE

The diagnostic beamline extracts the source light from the bending magnet located at the center of the triple-bend arc sector. From the bending magnet radiation, 8 mrad is used for the visible light imaging system and 2 mrad is used for the x-ray imaging system. Designed beam size at the sector symmetry point is $\sigma_x=185\text{ }\mu\text{m}$, and $\sigma_y=59\text{ }\mu\text{m}$, and the design value of the emittance is 12.1 nm-rad. The source point is 2.9° behind the symmetry point of the bending magnet where the beam size and the divergence is slightly different from the center of the magnet. Since the visible light image has large diffraction error ($R_s = (\rho\lambda^2)^{1/3}$ where ρ is bending radius and λ is wavelength) in the low emittance source due to the very small radiation angle [2], an x-ray imaging system is used for the precise measurement of the spatial beam structure with the minimum diffraction error. Diffraction error of the imaging system with 440 nm (2.8 eV) visible light is around 100 μm vertically, but is less than 10 μm with 284 eV soft x-ray. The visible light imaging system is mainly used for study of the temporal beam structure and transient beam dynamics in the picosecond regime. A layout of the diagnostic beamline is shown in Fig. 1 and more description on the beamline refers to Ref. [3].

2.1 Visible Light Optics

The visible light imaging optics consists of a water-cooled copper mirror inside the vacuum tank, a remote controlled beam-steering mirror outside the vacuum and two achromatic lenses. An 1:1 image is formed by two achromatic lenses of 3 m focal length, and is delivered onto the optical table mounted with various detectors inside a dark room. Two imaging lenses are located with a mirror-symmetry. The first focusing lens is located at 7.5 m from the source point and the second mirror is located at 7.5 m from the final image point. Total distance from the source to the image is 25 m.

2.2 X-ray Optics

The x-ray imaging system consists of a flat deflecting mirror, two spherical mirrors arranged as a Kirkpatrick-Baez optics [4] for horizontal and vertical focusing, and a 5 μm carbon foil to cut off the low energy photons. Vertical and horizontal focusing mirrors are located at 10.581 m and 10.911 m from the source point and the image is formed at 21.492 m from the source.

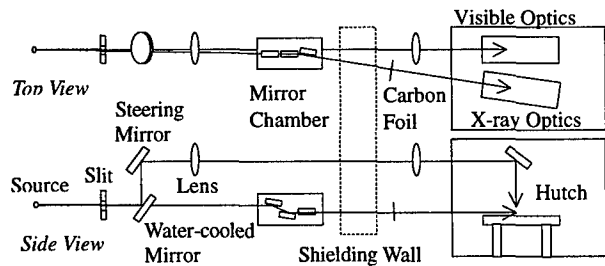


Fig. 1 Layout of the diagnostic beamline.

All three mirrors have 3° grazing incidence angle. A flat water-cooled mirror is made of nickel-plated Glidcop, and two spherical mirrors are made of single-crystalline Silicon. All the mirrors are coated with 250 nm thick nickel. The high energy photon above 0.8 keV is absorbed by the grazing incidence metal mirrors and the low energy photon below 200 eV is absorbed by the carbon foil. Since the carbon foil has the sharp absorption edge at 284 eV, the combination of all beamline components passes only 200 eV to 284 eV photons, forming a band-pass filter.

Ray tracing of the x-ray imaging optics has been performed with SHADOW program. Starting from the source point located 2.9° behind the center of the bend-magnet, including various conditions of the optical component errors, the ray tracing has shown the distortion or aberration error of the optics is acceptable to within the specification. Wave-front distortion or the image diffuse error by the carbon foil and the scintillation plate are not considered.

2.3 Detection Instruments

Transverse beam parameters are measured with the photo-diode detectors: two $25\mu\text{m} \times 512$ linear photodiode array, a CCD camera with $9.7\mu\text{m} \times 9.7\mu\text{m}$ pixels and a position-sensitive photodiode. We use a fast 20GHz optical-to-electrical (O/E) converter (New Focus 1437) plugged into a 20GHz sampling-oscilloscope (TEK CSA803A) for the measurement of the bunch length. Both components have 17ps input rise-time. The optical image is guided to the O/E input through a $4\mu\text{m}$ single mode optical fiber. Two 15 dB, 25 GHz amplifiers are used for the amplification of the O/E output signal.

To measure the transient bunch structure in time domain, a Hamamatsu streak camera(C5680) is installed on the optical table in the experimental hutch. Not only the picosecond-regime bunch-structure measurement in the time domain with fast-scan module but also the spatio-temporal measurement of the bunch train is possible with a slowscan and a synchroscan module.

Two kinds of beam position monitors are used in the diagnostic beamline. An x-ray position monitor made of

two gold plated electrodes measures the vertical beam position with vertical sensitivity of $0.4\%/ \mu\text{m}$ at the center of the monitor. A quadrant photodiode sensor measures beam positions with $0.1\%/ \mu\text{m}$ sensitivity using the visible light image.

3 BEAM MEASUREMENTS

In the diagnostic beamline, various beam parameters have been measured such as transverse beam size, beam emittance, and bunch length. The 'fast beam ion instability' [6] has been observed at the diagnostic beamline by increasing the residual gas pressure in the storage ring.

3.1 Beam Size and Emittance

We measure beam sizes from visible images as well as from x-ray images. True beam size is estimated from the measured value by subtracting the diffraction-limit error. The horizontal beam size σ_x is $303\mu\text{m}$ and the vertical beam size σ_y is $63\mu\text{m}$ when measured with a visible light image. The beam emittance obtained from this measurement is 40 nm-rad, which shows large difference compared to the design value of 12.1 nm-rad. Since it is an integrated beam image during the CCD exposure time around 100 ms, the measured beam size contains beam oscillation amplitudes induced by beam instabilities. The beam instability is mainly due to the higher order modes of the rf cavity. When the rf cavity temperature is adjusted carefully to an optimum condition to suppress the higher order cavity modes, the beam size is reduced to $182\mu\text{m}$ and the equivalent emittance is 11.3 nm-rad. Vertical beam size is still larger than the expected value, $\sim 40\mu\text{m}$ obtained from the coupling-ratio measurement [5]. In both cases, we have used the design values of the dispersion function and beta function to get the beam emittance.

In x-ray optics, an image is formed on a thin fluorescent crystal and we measure the beam size with negligible diffraction error. This image is monitored with a CCD camera through a micro-telescope. With $5\mu\text{m}$ carbon filter, we have obtained $43\mu\text{m}$ for vertical beam size and $186\mu\text{m}$ for horizontal beam size at 100mA. It gives 12nm-rad of beam emittance, implying that the storage ring has reached its design performance. Measured beam parameters are summarized in Table 1.

Table 1: Measured and designed beam parameters.

Beam parameters	Measured value	Design value
σ_x	$182\mu\text{m}$	$189\mu\text{m}$
σ_y	$40\mu\text{m}$	$59\mu\text{m}$
σ_z	21ps	17ps
ϵ_x	11.3 nm-rad	12.1nm-rad

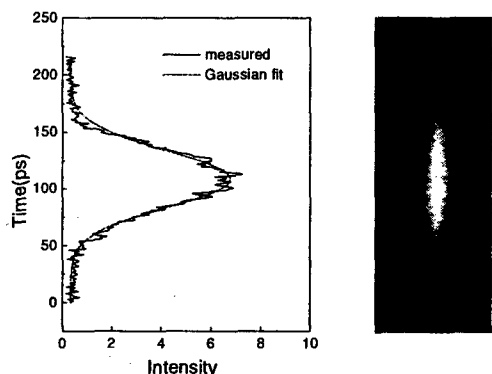


Fig.2 Bunch length measurement by Gaussian fitting of the profile from the streak camera image.

The x-ray imaging system has shown an unexpected intensity-dependence in the measurement of beam sizes. When we use 10 μ m carbon filter, beam size decreases to 33 μ m. Further investigation and refinement of the x-ray optics are planned for more precise measurement.

3.2 Bunch Length

Bunch lengths are measured by a fast sampling oscilloscope and a streak camera. Using a sampling oscilloscope, the synchrotron oscillation amplitude adds up to the signal. By subtracting the instrumental rise-time effect from the measured value, the true bunch length is 33 ps which is also very long compared to the design value of 17 ps due to the longitudinal beam instability. Using a streak camera, we have measured true single bunch lengths as shown in Fig. 2 and 3. Figure 3 shows the bunch length vs beam current. The estimated value with SPEAR-scaling is also drawn on the measured data for comparison. It shows reasonable agreement with calculated values but the onset of the instability starts at higher bunch current than expected. For the case of 0.1mA, 0.2mA, and 0.5mA, multibunch-length is used for the single bunch lengths at lower bunch current.

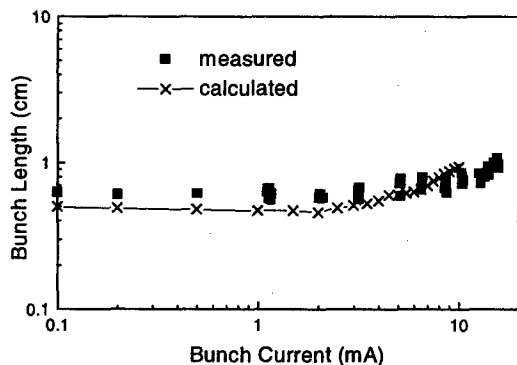


Fig.3 Bunch current vs bunch length.

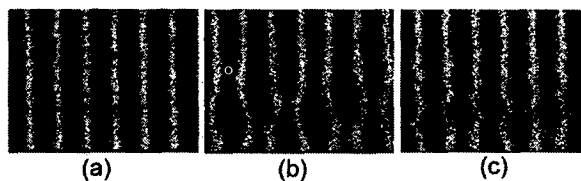


Fig.4 A fast-beam-ion-instability signal taken with streak camera: a) normal state, b) when ion pumps are turned off, bunch-train tail oscillates at CO-ion frequency, c) ion frequency increases with He injection. x: 25 μ s, y: 500ns.

3.3 Fast Beam-Ion Instability

The fast beam-ion instability (FBII) has been directly observed from the storage ring by injecting Helium gas to increase the growth time. Snapshots of the bunch train were taken by a streak camera and a single-pass beam position monitor. By measuring the amplitude of the beam oscillation, ion frequency, and the vertical bunch size along the bunch train, we have observed characteristic signals of the FBII: increase of the oscillation amplitude and the bunch size along the bunch train with expected beam-ion oscillation frequency. A beautiful visual evidence of the fast beam-ion instability is shown in Fig. 4 [7].

4 SUMMARY

A visible optics is under normal operation in PLS for the transverse and longitudinal beam profile measurements. Various instruments such as a CCD camera, photodiode arrays, position sensitive photodiodes, a synchroscan streak camera and a fast photodiode detector are equipped at the focal plane of visible optics. We could measure the transverse beam profiles, beam position and the longitudinal bunch structure in micrometer spatial-scale and the picosecond temporal-scale. In particular, we study the spatio-temporal beam properties of the electron beam with a streak camera. An x-ray image is used for the precise beam size measurement with a negligible diffraction error. However, the x-ray imaging system has shown an unexpected intensity-dependence in the measurement of beam sizes. Further refinement of the x-ray optics is planned for the precise measurement of the beam size and the beam emittance.

5 REFERENCES

- [1] E. Rossa, AIP Conf. Proc. 333, 148 (1994).
- [2] M. D. Wilke, AIP Conf. Proc. 333, 128 (1994).
- [3] J. Y. Huang and I. S. Ko, J. Synchrotron Rad. 5, 642 (1998).
- [4] P. Kirkpatrick, A. V. Baez, J. Opt. Soc. Am. 39, 766 (1948).
- [5] T. -Y. Lee and M. Yoon, Proc. of EPAC'96, 1423 (1997).
- [6] T. O. Raubenheimer, F. Zimmermann, Phys. Rev. E52, 5487 (1995).
- [7] J. Y. Huang, *et al.*, Phys. Rev. Lett. 81, 4388 (1998).

HIGH-BRIGHTNESS BEAM DIAGNOSTICS FOR THE APS LINAC*

A. H. Lumpkin, B. X. Yang, W. J. Berg, J. W. Lewellen and S. V. Milton
Advanced Photon Source, Argonne National Laboratory, Argonne, IL 60439 USA

Abstract

The Advanced Photon Source (APS) injector includes an S-band linac with the capability to accelerate beams to 650 MeV. The linac has recently been upgraded with the installation of an rf thermionic gun in addition to the standard DC thermionic gun. The rf gun is predicted to have lower emittance (5π mm mrad) and may be used to support the APS self-amplified spontaneous emission (SASE) experiments. The critical characterization of this gun's beam has begun with a beam diagnostics station at the end of the linac that can address beam transverse size, emittance, and bunch length (peak current). This station uses both an optical transition radiation (OTR) screen at 45° to the beam direction and a Ce-doped YAG single crystal normal to the beam with a 45° mirror behind it. The visible light images are detected by a Vicon CCD camera and a Hamamatsu C5680 synchroscan streak camera. Spatial resolution of about $30\text{ }\mu\text{m}$ (σ) and temporal resolution of 1 ps (σ) have been demonstrated. Examples of rf gun beam characterization at 220 MeV are reported.

1 INTRODUCTION

The ongoing interest in high-brightness particle beams has been "stimulated" by the potential applications to self-amplified spontaneous emission (SASE) free-electron laser experiments [1,2]. At the Advanced Photon Source (APS) the injector linac has recently been upgraded with the installation of an rf thermionic gun [3,4] and a laser-driven photocathode (PC) rf gun [5]. The rf gun is predicted to have lower emittance (5π mm mrad) and sufficient peak currents ($\sim 100\text{A}$) to be used in the APS SASE experiments [6]. The PC rf gun is expected to have even better brightness [5]. The capability to characterize such beams includes a beam diagnostic station with improved spatial and temporal resolution that can address beam transverse size, emittance, and bunch length (peak current). The station uses both optical transition radiation (OTR) and a Ce-doped YAG single crystal normal to the beam with a mirror behind it. The visible light images were detected by a charge-coupled device (CCD) camera and a dual-sweep streak camera. Spatial resolution of about $30\text{ }\mu\text{m}$ (σ) and temporal resolution of about 1 ps (σ) have been demonstrated in earlier studies [7,8]. Examples of beam measurements for the rf gun are reported.

2 EXPERIMENTAL BACKGROUND

The APS facility's injector system uses a 250-MeV S-band electron linac and an in-line 450-MeV S-band positron linac. The original electron gun was a conventional, gated DC thermionic gun. The diagnostics station was initially commissioned using this gun's beam [7]. More recently an rf thermionic gun was installed that is designed to generate low-emittance beams ($< 5\pi$ mm mrad). It is configured with an alpha magnet that allows beam injection just after the first linac accelerating section [3,4]. Both in-line linacs can be phased to produce 50- to 650-MeV electron beams when the positron converter target is retracted.

The predicted lower normalized emittance of beams from the rf thermionic gun and PC rf gun versus the DC gun results in correspondingly smaller beam spot sizes. We have addressed this at selected diagnostics stations by supplementing or replacing the standard Chromox screen, with its approximate $200\text{-}\mu\text{m}$ spatial resolution and 300-ms decay time, with the OTR and Ce-doped YAG screens. For the station at the end of the linac the OTR screen was a molybdenum mirror from Melles Griot and oriented so that its surface was at 45° to the beam direction. The doped YAG crystal of 0.5 mm thickness (obtained from Startec) was mounted with its surface normal to the beam direction with a Zerodur mirror at 45° to the beam just behind it.

An alignment laser was injected on-axis into the bore of the linac just after the first accelerating structure and used to assess the relative orientation of the two mirrors involved at the station. The laser was reflected into the optical transport line and then used to simulate the path of the visible light images. In the case of OTR, the direction of the path is particularly critical since OTR is emitted around the angle of specular reflection. The visible light was transported out of the linac tunnel to an optics table via two 150-mm-diameter achromat lenses and two mirrors. For these experiments the OTR or YAG:Ce light could be viewed by a Vicon CCD camera and/or a Hamamatsu C5680 dual-sweep streak camera. The synchroscan unit was phase-locked to 119.0 MHz, the 24th subharmonic of the 2856-MHz linac frequency. A low-jitter countdown circuit has been built using Motorola ECLIN PS Logic to generate the 24th subharmonics with sub-ps jitter [9]. The synchroscan unit was critical to the bunch length measurements due to the lower charge/micropulse in early experiments. The model M5677 slow-sweep unit was used in the measurement of the YAG-Ce response time, which was previously

*Work supported by the U.S. Department of Energy, Office of Basic Energy Sciences, under Contract No. W-31-109-ENG-38.

reported [10] as about 80 ns (FWHM). Although beam energies as high as 540 MeV have been used, one set of data is at 220 MeV, the energy that would be used for SASE experiments at 517 nm.

3 EXPERIMENTAL RESULTS

Preliminary results are reported in this section on rf gun beam transverse size, emittance, and bunch length. Additionally, the measurement of the YAG:Ce crystal response time is reported.

3.1 Beam Transverse Size

Recently measurements at 220 MeV were performed on the beam at the end of the linac. Beam images were obtained with both the YAG:Ce crystal and the OTR converter. Figure 1 shows an example of the beam vertical profile using OTR. The MAC-TA algorithm calculated a spot size of $\sim 170 \mu\text{m}$ (FWHM) that corresponds to about $72 \mu\text{m}$ (σ), assuming a Gaussian-shaped profile. The aspect ratio (H:V) was about 4:1 for this beam focus.

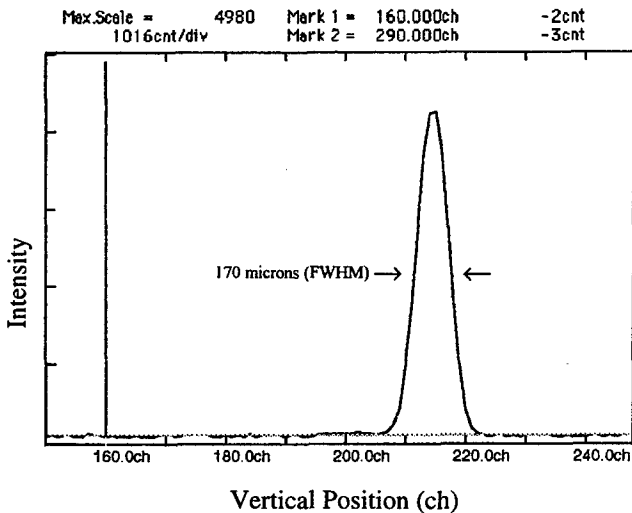


Figure 1: An example of the rf thermionic gun's vertical beam profile: 170 μm (FWHM).

3.2 Preliminary Emittance

Having obtained reasonable transport and focus of the beam, an evaluation of the beam emittance was performed by the standard tracking of beam size with the quadrupole field strength of an upstream magnet. In this screen position there were two quadrupoles that were available to be adjusted. A script developed by M. Borland was adapted that automatically stepped the fields and logged the measured beam sizes via the EPICS process variables [11]. As shown in Fig. 2, the horizontal beam size can be minimized by selecting a combination of fields from the linac-to-PAR magnets LTPQ9 and LTPQ10. The Max Video-20 digitized data were fit to Gaussian profiles in this case. An example of emittance data is shown in Fig.

3. The data are consistent with normalized emittances, $\epsilon_x = 8.8 \pi \text{ mm mrad}$ and $\epsilon_y = 9.5 \pi \text{ mm mrad}$ for a 25-mA macropulse current. Errors are estimated as 20-30%. Simulations of this particular rf gun setup with *elegant* [12] have reproduced the emittance asymmetry between the two planes. It is noted that the measured and computed emittance ratios are similar although the measured values are 60% higher. These measurements were made without an energy filter in the alpha magnet. As a result, the beam contains a trailing, low-energy component that is expected to significantly increase the projected (but not slice) emittance. Although this low-energy "tail" contains only a small fraction of the total charge (approximately 10% of the total bunch charge by the time the bunch reaches the end of the linac), it is the greatest contribution to the projected (longitudinal whole-beam) emittance. Considerably lower measured emittances are expected once the alpha magnet energy filter has been installed.

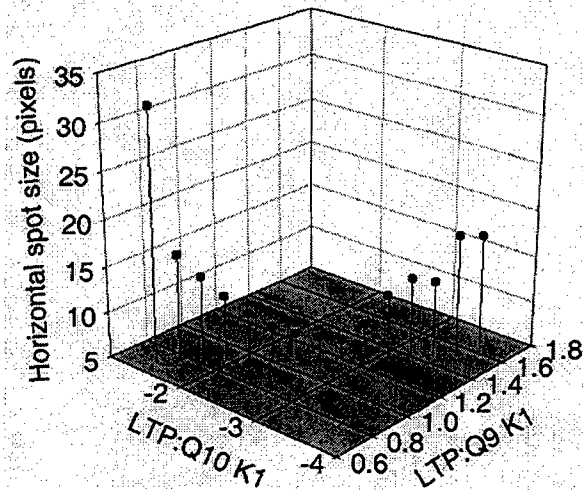


Figure 2: Variations of the observed horizontal beam size with the two upstream quadrupoles Q9 and Q10.

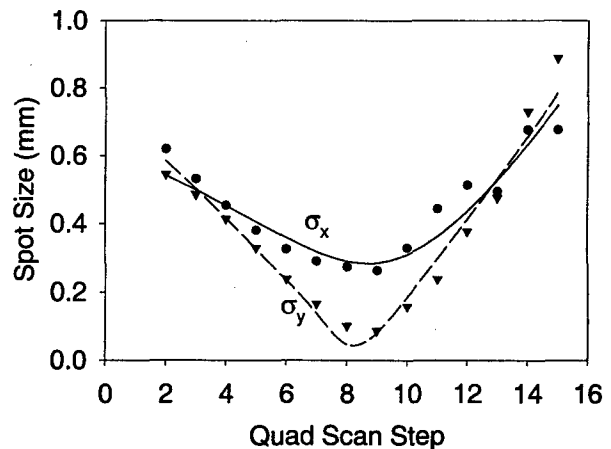


Figure 3: An example of the quadrupole field scan versus observed beam sizes: σ_x (circles) and σ_y (triangles). Emittances of $\epsilon_{x,y} < 10 \pi \text{ mm mrad}$ were determined from the fitted curves.

3.3 YAG:Ce Crystal Response Time

The rf gun's macropulse is typically 30 to 40 ns, shorter than the 80-ns (FWHM) response time of YAG:Ce reported by Graves et al. [10]. This would preclude any submacropulse imaging with this converter. We have used the slow sweep streak module operating at 1- μ s full range to assess the actual response times of our specific crystals. The electron-beam macropulse duration is not a delta function impulse to the system, but it is still sufficiently short that a reasonable measurement is possible. In these data we actually used the DC gun beam with a shortened macropulse of ~ 20 ns. As shown in Fig. 4, the measured YAG:Ce response is 105 ns (FWHM). A preliminary assessment of the 1/e time is also about 112 ns. The streak unit's calibration factor is based on the original factory calibrations.

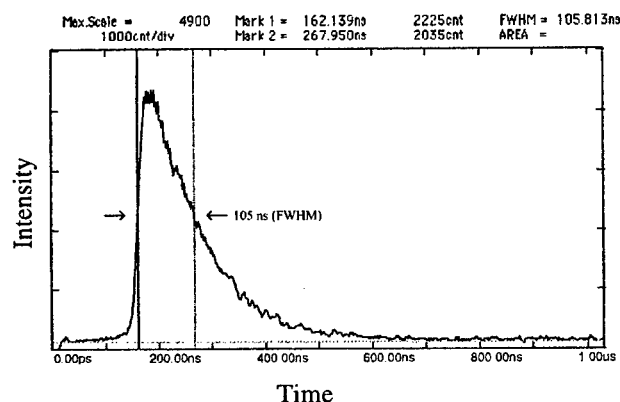


Figure 4: Streak camera data showing the response time of the YAG:Ce crystal to the incident 20-ns electron beam. The effective response is about 105 ns (FWHM). The horizontal axis spans 1 μ s.

3.4 Bunch Length Measurements

Assessments of micropulse-averaged bunch length using the synchroscan streak camera have begun. Preliminary results at 540 MeV and for macropulse currents of less than 150 mA are 3-4 ps (σ). Low signal levels required averaging over about 30 macropulses (few seconds) and so may involve some phase slew blurring the image and lengthening the apparent size. Measurements with the optimized gun and an optimized optical path at 220 MeV are planned. Use of a fifth-harmonic cavity signal to optimize bunch length was previously reported by Lewellen et al. [4].

4 SUMMARY

In summary, a diagnostics station that can support the characterization of bright electron beams at the end of the APS linac has been tested. It has also been used to attain preliminary data for the rf thermionic gun beam quality at low beam currents. Further experiments are planned this

year at high macropulse currents of the rf gun and on the PC rf gun.

5 ACKNOWLEDGEMENTS

The authors acknowledge M. Borland for adaptation of the on-line emittance software package for this linac case.

6 REFERENCES

- [1] Proceedings of the Workshop on Fourth Generation Light Sources, M. Cornacchia and H. Winick (Eds.), SLAC, Feb. 24-27, 1997, SERL 92/02 (1997).
- [2] Proceedings of the Workshop on Fourth Generation Light Sources, J. L. LaClare (Ed.), ESRF, Grenoble, France (1996).
- [3] M. Borland, "An Improved Thermionic Microwave Gun and Emittance Preserving Transport Line," Proc. 1993, PAC, Washington, D.C., May 17-20, 1993, IEEE, Vol. 4, pp. 3015-3017 (1993).
- [4] J. Lewellen et al., "Operation of the APS RF-Gun," Proc. of the 1998 Linac Conf., Chicago, IL, Aug. 18-22, 1998 (to be published).
- [5] S. G. Biedron et al., "The Operation of the BNL/ATF Gun-IV Photocathode RF Gun at the Advanced Photon Source," these proceedings.
- [6] S. V. Milton et al., Nucl. Inst. and Meth., **A407**, pp. 210-214 (1998).
- [7] A. H. Lumpkin et al., "Optical Techniques for Electron-Beam Characterizations on the APS SASE FEL Project," Proc. of the 1998 FEL Conference, Williamsburg, VA, Aug. 16-21, 1998, NIM (to be published).
- [8] A. H. Lumpkin et al., "Time-Resolved Imaging for the APS Linac Beams," Proc. of the 1998 Linac Conference, Chicago, IL, Aug. 18-22, 1998 (to be published).
- [9] R. Laird and F. Lenkszus, Argonne National Laboratory, private communication, April 1997.
- [10] W. S. Graves, R. D. Johnson, and P. G. O'Shea, "A High Resolution Electron Beam Profile Monitor," Proc. of the 1997 PAC, Vancouver, B.C., May 12-16, 1997, pp. 1993-1995 (1998).
- [11] M. Borland, Argonne National Laboratory, OAG Application Programs, Feb. 1999.
- [12] *elegant* code, On-line Users Manual at URL <http://www.aps.anl.gov/asd/oag/oagSoftware.shtml>

OBSERVATIONS OF "EFFECTIVE" TRANSVERSE BEAM-SIZE INSTABILITIES FOR A HIGH CURRENT PER BUNCH FILL PATTERN IN THE APS STORAGE RING*

A. H. Lumpkin, L. Emery and B. X. Yang

Advanced Photon Source, Argonne National Laboratory, Argonne, IL 60439 USA

Abstract

The x-ray pinhole camera diagnostics on the Advanced Photon Source (APS) storage ring have recorded an "effective" transverse beam size instability during operations with a sextuplet plus 22 singlets fill pattern. These instabilities were not observed with the sextuplet plus 25 triplets fill pattern that has been the standard fill pattern in FY'98. The instability threshold is at 82-85 mA with positrons. The features include an increased average (few seconds) transverse size both horizontally and vertically for stored currents above the threshold with a correlated effect on the beam lifetime. The horizontal transverse emittance is 25-30% larger at 100 mA than below the threshold. There is a related horizontal beam centroid motion as well, but this does not explain the vertical size change nor the lifetime effect. Complementary data were also taken with the diagnostic undulator, and a similar threshold effect on divergence was observed. The cross-comparison of the data and possible mechanisms will be presented.

1 INTRODUCTION

Operations of the Advanced Photon Source (APS) storage ring have included two fill patterns in the last year: one with a bunch sextuplet followed by 25 bunch triplets that were spaced by 102 ns and the other with the sextuplet followed by 22 singlets spaced 148 ns apart. In both cases the total stored current in the ring at the end of the fill is the nominal 100 mA, but in the singlets case the charge per bunch is about three times higher than in each bunch of the triplets. In the singlets-fill case our x-ray pinhole camera diagnostics were used to identify two instabilities that result in increases in averaged transverse beam sizes. One instability occurs only near the maximum beam current in the present conditions, and the horizontal beam size at the dispersive point is dramatically increased. The other is also present down to the threshold of 82-85 mA. Several cross-comparisons of results from both the dispersive and nondispersive bending magnet source points, the diagnostics undulator, and the streak camera bunch length data were used to separate the features of the two instabilities. These features are consistent with a transverse instability with the 82-85 mA threshold and a longitudinal instability at the top of the fill. The first is

sensitive to changes in the sets of sextupole currents (chromaticity) and the second to changes in the rf cavity temperature setpoints (HOMs). Representative examples of the different types of data will be presented. The observations were initially performed with stored positrons, but the basic features persisted with the change to electrons in October 1998.

2 EXPERIMENTAL BACKGROUND

The APS storage ring utilizes a 7-GeV positron or electron beam (since Oct. 1998) circulating in a 1104-m circumference ring. Normal stored beam currents are 100 mA with a natural emittance, $\epsilon = 7.9 \pm 1.1$ nm rad. The baseline vertical coupling was 10%, but we now generally run at the 1-2% level. The standard fill pattern involves a sextuplet (each of similar intensity) totaling 10 mA of stored beam current. The other 90 mA are distributed in 25 triplets spaced 102 ns apart in the ring. In a special user mode we have run ~15 mA in the sextuplet and 85 mA distributed in 22 singlets that are 148 ns apart. It is this latter fill pattern with about three times the charge per bunch that has exhibited the "effective" transverse beam size growth. These phenomena have been detected with photon diagnostics, rf BPMs, and the tune measurement system. This paper will concentrate on the photon diagnostics results.

The photon diagnostics are located in one of the 40 sectors of the APS [1-3]. We use radiation from bending magnets and a diagnostics undulator as shown in Fig. 1. For the dipole magnet source at a dispersive point in the lattice, both x-ray synchrotron radiation (XSR) and optical synchrotron radiation (OSR) techniques are used. An in-tunnel x-ray pinhole camera includes a remotely controlled four-jaw aperture at 9.1 m from the source, a CdWO_4 or YAG:Ce converter crystal at 17 m from the source, and a charge-coupled device (CCD) camera. Effective spatial resolutions of about 25 μm (σ) are estimated. The video is digitized by a Data Cube MaxVideo-200 (MV200) unit, and the digital results are identified as process variables (PVs) for the EPICS platform. Data logging of beam size, centroid, and emittance can thus be done on a 24-hour period. The OSR is transported out of the tunnel to an optics station where a CCD camera, a Stanford Computer Optics (SCO) Quik-05 gated camera, and a Hamamatsu C5680 dual-sweep streak camera are available. The synchroscan unit is phase locked to 117.3 MHz, the third subharmonic of the SR rf

*Work supported by the U.S. Department of Energy, Office of Basic Energy Sciences, under Contract No. W-31-109-ENG-38.

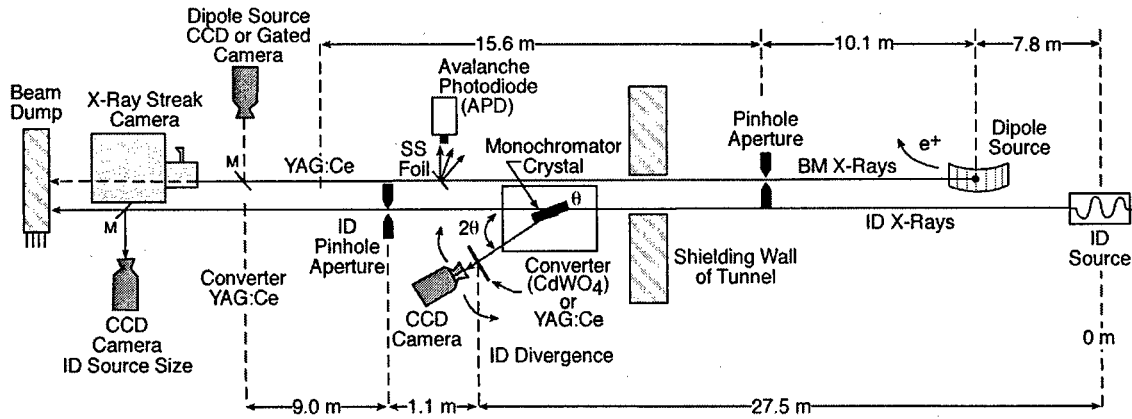


Figure 1: A schematic view of the dipole and diagnostics undulator beamline. On the undulator line the monochromator and pinhole are indicated. On the dipole source the aperture is in the tunnel, and the converter and camera are indicated.

master oscillator. In these studies the streak camera was used to monitor changes in average stored beam bunch length as a function of current. The streak images also were processed by a second MV200 and tracked.

Additionally, the nearby diagnostics undulator and low-dispersion-point dipole source beamline were used as warranted. As schematically shown in Fig. 1, the undulator radiation (UR) is used with the single-crystal monochromator for divergence information and the subsequent four-jaw aperture for horizontal beam-size information [4,5]. The divergence resolution is about $2.6 \mu\text{rad}$ (σ) and the pinhole resolution is about $60 \mu\text{m}$ (σ).

3 EXPERIMENTAL RESULTS AND DISCUSSION

In this section representative examples of results from the different sources and for the two principal instabilities will be presented. The EPICS data logger and a second MV200 allowed us to select different image sources while keeping the x-ray pinhole camera as a reference for each 12-hour stored beam decay period.

3.1 Transverse Instability

The basic observation in the x-ray pinhole data is the increased averaged horizontal beam size for some current levels. We attribute this size increase to both a measured centroid oscillation at the fractional betatron tune of 0.20 and an intrinsic size increase of some kind. In Fig. 2 the effects are plotted versus stored positron beam current. Both the horizontal beam size and emittance in Fig. 2a and 2b, respectively, are larger above ~ 85 mA. There is a correlated change in the slope of beam lifetime versus current also at ~ 85 mA as seen in Fig. 2c. In fact, the correlated change in lifetime seen in Fig. 2 is why we do not attribute only a centroid motion to the observed increase in transverse horizontal size. The only effect in the streak camera data was the expected gradual decrease in bunch length with decrease in single-bunch current.

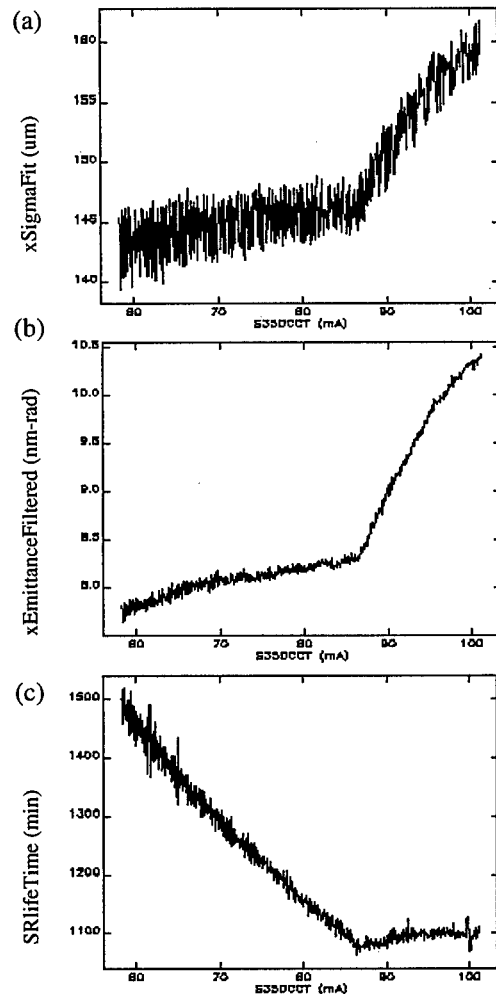


Figure 2: Plots of beam a) horizontal size (dispersive point) and b) horizontal emittance, and c) stored beam lifetime versus stored beam current. There is a correlated change in the respective slopes at ~ 85 mA of stored positrons.

During the stored electron beam runs in Dec. 1998 the x-ray pinhole camera data were compared to the ID divergence data, the ID pinhole data, lifetime data, and

the streak camera. Correlated changes were seen in the first two horizontal transverse sizes, as shown in Fig. 3, and also with the lifetime.

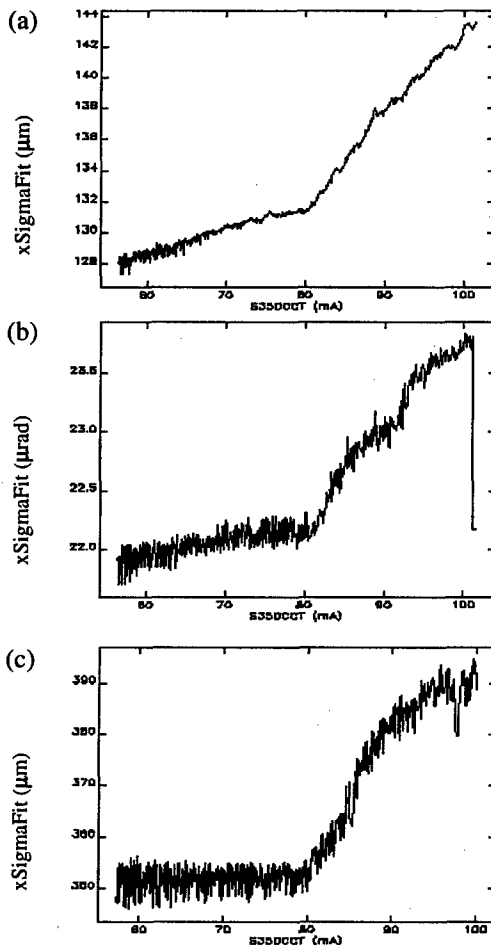


Figure 3: Plots of the variation with current of stored electron beam a) horizontal size at a dispersive point, b) horizontal divergence, and c) ID source point size. All have the increased values above 85 mA.

3.2 Longitudinal Instability

In this case at currents around 101 mA, the observed horizontal beam size shows growth from 140 to 260 μm as shown in Fig. 4a. In Fig. 4b the beam bunch length change from 35 ps to 70 ps is shown over the same 10-min period. An effect in longitudinal phase space is clearly supported.

Additionally, the nature of the bunch length blurring is related to a phase instability detected by a dual-sweep streak camera. A synchrotron oscillation can also develop over the many turns at 1.8 kHz. The superposition of the two effects gives the 30-ms averaged bunch-length change from 35 ps to 70 ps (σ).

The magnitude of this effect was sensitive to the rf cavity temperature and was reduced by changing the rf cavity temperature setpoint. It is suspected that the

higher-order modes (HOMs) are strongly temperature dependent and are contributors to the effects observed.

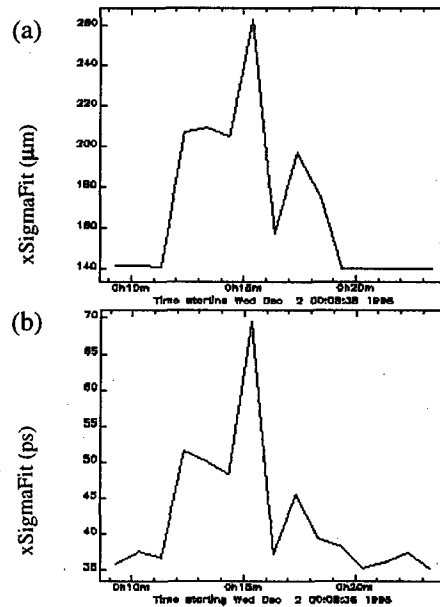


Figure 4: Plots of the correlated change in a) horizontal beam size at a dispersive point and b) the beam bunch length near 101-mA stored beam currents. These are consistent with a longitudinal instability.

4 SUMMARY

In summary, we have used the correlated observations of beam transverse size, beam divergence, and bunch length to sort the features of the two instabilities that cause an increase in effective beam size. The evidence is consistent with a transverse instability with a threshold at 80-85 mA that can be controlled with increased chromaticity. The longitudinal instability near 101 mA (at present) is controlled by rf cavity temperature setpoints. Further experiments with a gated camera to search for horizontal quadrupolar effects or energy centroid shifts may be of interest. We are now in position to provide a more stable singlets-fill beam for the users, and this was successfully done in March 1999.

5 REFERENCES

- [1] A.H. Lumpkin and B.X. Yang, "Status of the Synchrotron Monitors for the APS Facility Rings," Proc. of the 1995 PAC, IEEE, Vol. 4, p. 2470 (1996).
- [2] B.X. Yang and A.H. Lumpkin, "Initial Time-Resolved Particle Beam Profile Measurements at the Advanced Photon Source," SRI95, Rev. Sci. Instrum. 67, 1996.
- [3] A.H. Lumpkin et al., "Recent Observations on the APS Storage Ring Using Synchrotron Radiation Monitors," Proc. of EPAC'98, Stockholm, p. 1556 (1999).
- [4] B.X. Yang et al., "Status of the APS Diagnostics Undulator Beamline," Proc. of the 1997 PAC, IEEE, Vancouver, B.C., (1999).
- [5] B.X. Yang and A.H. Lumpkin, "Simultaneous Measurement of Electron Beam Size and Divergence with an Undulator," these proceedings.

SYNCHROTRON RADIATION MONITORING SYSTEM AT BEPC

L.Ma, Z.Zhao, D.Liu, J.Cao, L.Wang, K.Xue, S.Wang and H.Yu
Institute of High Energy Physics, Beijing 100039, China

Abstract

The synchrotron radiation by the relativistic particles is a useful and important diagnostic tool to obtain various beam parameters. The visible light of the synchrotron radiation emitted in a bending magnet of the BEPC storage ring is reflected through the window by a water-cooled mirror in the vacuum chamber and then directed by a remote controlled mirror onto the optical bench supporting the diagnostic instruments in the dark room. These instruments include a CCD camera providing the image of the beam transverse profile on a TV monitor, a lens system focusing the synchrotron light onto a solid state scanned photodiode arrays to obtain the beam height or width, a streak camera to measure the bunch length for a single pass, and a two-dimensional position sensing photo-detector to monitoring the drift of the beam position. This paper will give the detailed description of the synchrotron radiation monitoring system at BEPC.

1 GENERAL DESCRIPTION

The Beijing Electron-Positron Collider (BEPC) was built for the high energy physics experiment and the synchrotron radiation research. The BEPC has been in operation for around 10 years. The synchrotron radiation monitoring system has been put into operation since the startup of the BEPC. The characteristics of the electron and positron beams circulating in the ring, such as the transverse beam size, the bunch length and the beam position, can be measured with the system. Table 1 lists the designing values of some parameters related with the synchrotron radiation monitoring system. The vertical beam size in the table assumes an emittance coupling of 3%.

Table 1: Some parameters related with the synchrotron radiation monitoring system of BEPC

Parameters	Collid. mode	SR mode
Ring energy (GeV)	1.55 - 2.0	2.2
Revolution freq. (MHz)	1.247	
Natural emitt. (nm-rad)	406 - 666	76
H/V rms beam size at source point (mm)	1.32/0.42 - 1.69/0.54	0.58/0.26
Rms bunch length (ps)	360 - 470	255
Bending radius at source point (m)	10.34	
Distance from source point to first mirror (m)	1.75	
Natural open angle of light, $\lambda=491$ nm (mrad)	2.2	

Two BEPC primary flat and optically polished mirrors in the vacuum chamber, one each for the positron and electron beams, are made of Cu coating with gold. The visible part of the synchrotron light is reflected horizontally through the side window by the water-cooled mirror and then directed vertically by a remote controllable mirror to the optical building where contains an optical table, detector electronics, work space. The third mirror brings the light into the horizontal plane again and to the optical table supporting the optical components comprising the detector system. The newly-built optical table was put into use at the beginning of 1998. The surface area of the optical table is $1.81 \times 1.2 \text{ m}^2$ and is more than 5 times of the area of the original optical table.

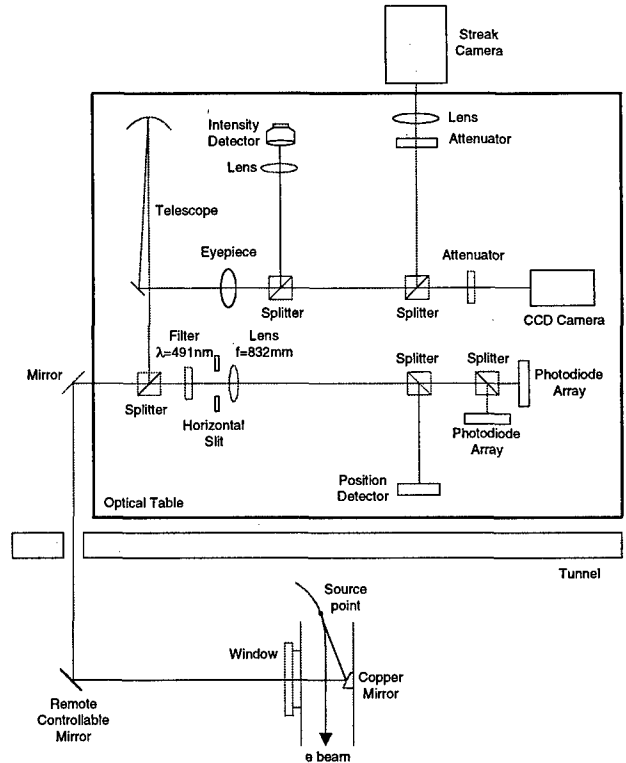


Figure 1: Setup of the BEPC synchrotron radiation monitoring system

Figure 1 shows the setup of the synchrotron radiation monitoring system at BEPC. As can be seen from the figure, a CCD camera provides the beam profile on a TV monitor. The image of the beam profile is also displayed in the center control room. The beam height and width are measured with a lens system focusing the synchrotron light onto two solid state scanned photodiode arrays. The bunch length for a single pass is measured with a streak camera only for the electron beam. The light beam posi-

tion is monitored with a position sensing photo-detector. Figure 2 shows a photo of the new optical table.

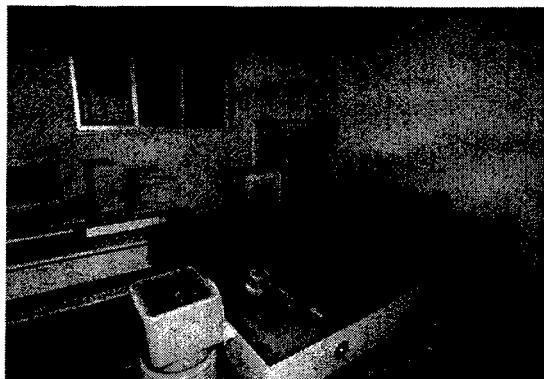


Figure 2: New optical table for the e^- beam

2 PHOTODIODE ARRAY

Two solid state self-scanning linear photodiode arrays of EG&G Reticon, Model RL0512S, have been used as the detectors for the transverse beam size measurements, one each for the horizontal and vertical planes. The array consists of a row of silicon photodiodes, each with an associated storage capacitor on which to integrate photocurrent and a multiplex switch for periodic readout via an integrated shift register scanning circuit. The photodiode array contains 512 diode sensor elements of $25\ \mu\text{m}$ centers, so the overall length of the array is 12.8 mm. The width of each sensor element is 2.5 mm giving each element a geometry with the 100:1 aspect ratio. The spectral response range for the quartz-windowed array is from 250-1000 nm with a peak response around 750 nm.

The synchrotron light with $\lambda = 491\ \text{nm}$ collected on a sensor area generates a charge which is proportional to the intensity of the incident light and to the integration period. Charges accumulated on the photodiodes are readout sequentially and processed by a sample and hold signal processing circuit. The resulting video output signal is sent to an oscilloscope and appears the sampled and held boxer waveform. The FWHM width of the waveform is then read by a PC with the GPIB interface card to obtain the rms half height and width of the beam.

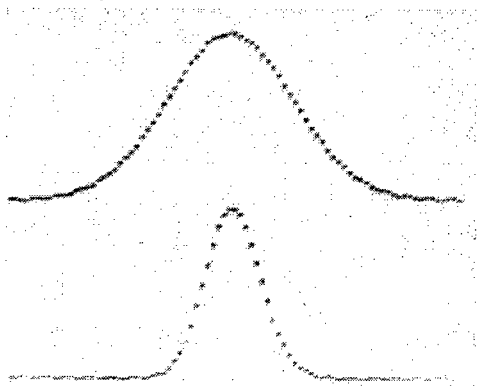


Figure 3: Horizontal (upper trace) and vertical (lower trace) beam profiles

It was decided to use a single focusing lens system for both transverse beam size and beam position measurements. The focus length and the diameter of the lens are 832 mm and 80 mm, respectively. Considering the object distance of 6800 mm and image distance of 948 mm, the magnification coefficient of the optics is 0.139.

Figure 3 shows a photo of the oscilloscope waveforms of beam profiles at 1.55 GeV. Taking account of the magnification 0.139 of the optics and various measurement errors such as curvature of the electron beam orbit, field depth and diffraction errors, the horizontal and vertical rms beam size at the source point can be derived.

3 STREAK CAMERA

A streak camera Model C5680-11 of the Hamamatsu Photonics has been used for the bunch length measurement since 1996. The streak camera can be divided into the main unit C5680, the synchroscan unit M5675 and the dual time axis expansion units M5679. The C5680 includes the input optics, the photocathode, the MCP, the CCD camera, and other image control system. The M5675 controls the vertical sweep by the signal synchronized to the incident light. It insures the image section of the device to keep up with the high-speed light, and also insures the high temporal resolution within 2 ps. The M5679 controls the horizontal sweep of the screen image and determines the acquisition time of every picture. The whole system also includes the delay unit C1097, a remote controller, a monitor, a pulse generator, a control computer and other auxiliary parts as shown in Figure 4.

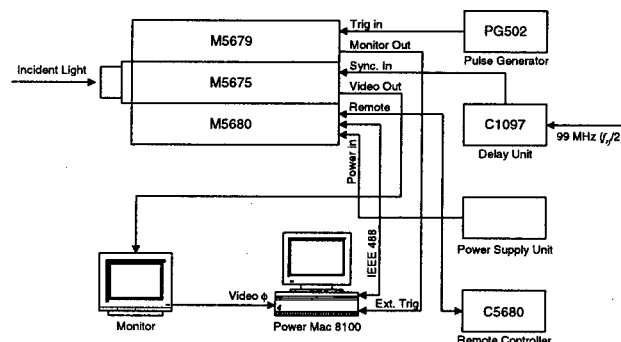


Figure 4: Configuration of the streak camera

The pulses of synchrotron radiation incident light being measured pass through the optics and enter the streak camera. The RF signal with the 99.76 MHz frequency (half the RF frequency of the ring) goes into the M5675 as the vertical sweep timing signal after passing through the C1097. At the same time the pulse signal from the pulse generator PG502 acting as the horizontal sweep timing signal is sent to the M5679. The streak camera can be operated from the Power Macintosh 8100 computer with an image processing board, an GPIB board and the streak camera control software U5565. It can also be operated from the remote control panel. The video signal of the bunch image is monitored by a monitor and can be captured by the PC.

The incident light pulses, only those bombard on the photocathode, are converted into electrons, and are effective for the streak camera measurement. The photocathode has an area of 150 μm in height and 6 mm in width. The diaphragm before the camera lens can be chosen from several holes with the diameters of 10 μm , 30 μm and 100 μm . Even if the diaphragm is opened completely, we must adjust the light being measured within the size of the photocathode. The light adjustment is one of the most important but difficult jobs for the bunch length measurement.

Figure 5 shows the bunch image of the BEPC storage ring we have obtained with only one electron bunch in the ring. The revolution period of the bunch in the storage ring is 801 ns and the horizontal sweep time of the streak camera is 5 ms, so 6 consecutive turns of the same bunch can be seen on the screen at a time.

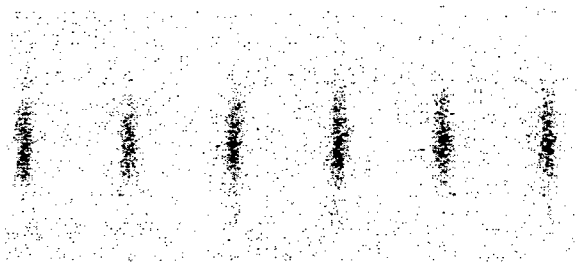


Figure 5: Beam image of 6 consecutive turns of the same bunch

The software U5565 gives the counts for each of 480 channels (or 480 time intervals) of the full scale. The rms bunch length σ is obtained by fitting these data.

4 POSITION SENSING PHOTO-DETECTOR

As mentioned in the previous section, the beam position is measured with a single focusing lens system. After reflection from the three mirrors and passage through an 832 mm focusing lens, the image of the electron beam cross section is formed on a position sensing photo-detector Model SC/10D of United Detector Technology (UDT). The SC/10D is the planer diffused construction PIN diode which provides the high performance and reliability with the low noise value for the 10 x 10 mm² active area.

For one of the two transverse planes, the two opposite output signals of the SC/10D are fed to a sum and difference amplifier Model 301B/AC of UDT. The sum and difference signals of the 301B/AC are digitized by a PC-based ADC card which fits into one ISA/EISA expansion slot in the backplane of an industry-standard compatible PC. The ADC has a 12-bit resolution and 25- μs AD conversion time. The range of the sum signal is around 1-10 volts when the beam intensity is 10-100 mA in the case of the dedicated synchrotron radiation operating mode with the beam energy of 2.2 GeV. The difference signal is divided by the sum signal in the computer to obtain the normalized position signal of the light beam.

The normalized position signal versus the image position is calibrated by moving the SC/10D with a micrometer. As shown in Figure 6, the sensitivity of the light beam position is 0.467 mm in the central 50% active area of the SC/10D. Considering the magnification coefficient 0.139 of the optics, the sensitivity of the electron beam position is 3.36 mm.

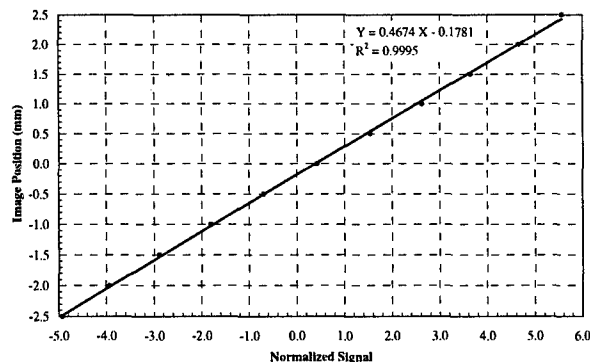


Figure 6: The sensitivity of the light beam position

Figure 7 shows a long term electron beam position drift of 60 hours. The data are stored in the BEPC archive database with the sampling time interval of 60 seconds.

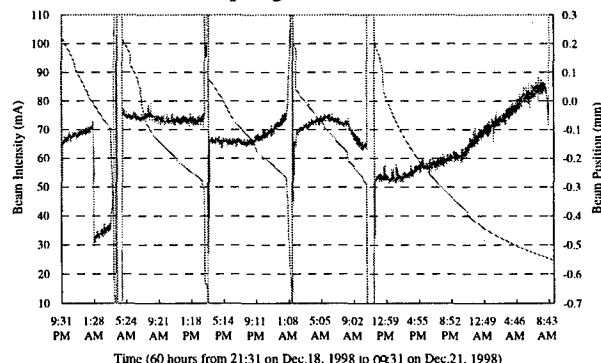


Figure 7: The beam position and beam intensity vs. time

5 SUMMARY

The synchrotron radiation monitor plays an important role in the BEPC beam diagnostic instrumentation system. Two new optical tables have been put into use and almost all measurement systems have been modified during the period from year 1996 to 1998. These modifications are very useful for overall machine operation and machine studies. The efforts are still carrying on to make measurements more accurate and reliable.

6 ACKNOWLEDGMENTS

The authors would like to thank all colleagues, especially Dr. Q.Zhang, who made contributions to build and upgrade the BEPC synchrotron radiation monitoring system.

REFERENCES

- [1] D.Liu, L.Ma and K.Xue, "The Bunch Length Measurement of BEPC with a Streak Camera", Proceedings of ICEMI'97, Beijing, October 1997

EMITTANCE MEASUREMENT AT KEK-ATF DAMPING RING

H.Hayano, K.Kubo, T.Mitsubishi, T.Naito, N.Terunuma, N.Toge, J.Urakawa,KEK
T.Okugi,Tokyo Metropolitan U., S.Kashiwagi, Graduate U. of Advanced Studies

Abstract

In order to achieve an extremely low emittance down to $\epsilon_y \sim 1 \times 10^{-11}$ m-rad, the beam development has been continued at KEK-ATF for future linear collider. The emittance measurement in the damping ring is a key point to confirm the low emittance beam. The beam size measurement is done by SR interferometer using visible light (~ 500 nm) at ATF damping ring. The measured beam sizes were already reached less than $14 \mu\text{m}$ (vertical) and $37 \mu\text{m}$ (horizontal), respectively. The beta function was also measured by applying a perturbation on the quadrupole magnet. The dispersion function was measured by means of rf frequency modulation method. Combining these measured values, the emittance was measured as $\epsilon_x = 1.8 \times 10^{-9}$ m-rad, $\epsilon_y = 6.1 \times 10^{-11}$ m-rad. The measurement technologies are described.

1 INTRODUCTION

To establish a low emittance beam is one of the significant milestone for the future linear collider. The ATF was designed to develop the low emittance beam, and its designed emittance is $\epsilon_y \sim 1 \times 10^{-11}$ m-rad and $\epsilon_x \sim 1 \times 10^{-9}$ m-rad[1]. The measurement of an emittance such a small beam is not easy by using the ordinal methods such as an imaging of Synchrotron radiation(SR). At the beginning of the ATF commissioning, the beam size monitor by means of the imaging of the SR was used for an observation of the damped beam size. The predicted beam size at source point is $6 \mu\text{m}$ for the vertical and $30 \mu\text{m}$ for the horizontal, however the diffraction limit of the imaging system is about $50 \mu\text{m}$. The resolution of the beam size measurement is limited by the diffraction in this monitor[2].

The SR interferometers for horizontal and vertical beam size measurements were installed to solve the problem of the resolution those can be measure down to $\sim 5 \mu\text{m}$ with $1 \mu\text{m}$ resolution[3]. The SR interferometer measures the degree of complex spatial coherence of visible-SR beam. Under the assumption of gaussian distribution of the electron beam profile, the absolute value of the degree of complex spatial coherence(visibility) is also gaussian. The beam size is easily obtained by a least squares fitting for the visibility curvature by using a beam size as the free parameter[3]. In practical, the measurement is done by observing the visibility through the intensity of the interferogram. The beta function and the dispersion function were also measured from the perturbation on the

quadrupole magnet and the rf frequency modulation method, respectively.

2 BEAM SIZE MEASUREMENT BY SR INTERFEROMETER

The set up of the SR interferometer is shown in Fig.1. The synchrotron light is split into four lines, 1)the line for the imaging system by using a fast gate camera for the observation of the damping phenomena, 2)the line for the streak camera for measurement of the bunch length, 3)the line for horizontal SR interferometer, 4)the line for the vertical SR interferometer.

The SR interferometer is basically a wavefront-division-type two-beam interferometer using a polarized quasi-monochromatic rays. A double slit assembly having a aperture size of 1mm (width) \times 3mm (height) which can be changed the separation of the slits. A diffraction limited doublet lens($f=600 \text{mm}$) is used as a objective to make the interferogram. A band-pass filter which has 80nm band width at 500nm and a polarization filter are used to obtain the polarized (select a σ -polarization) quasi-monochromatic rays. The interferogram is observed by the CCD camera(SONY SSC-M370) after the magnifier lens($\times 5$). The visibility is evaluated by using an image

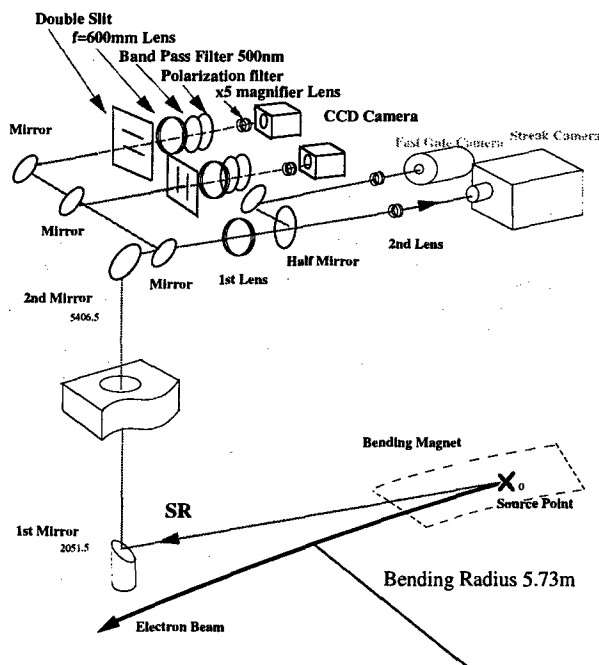


Fig.1 Layout of SR monitor - There is four monitor shared the synchrotron light, 1)Streak camera, 2)fast gate camera, 3)SR interferometer(H) and 4)SR interferometer(V).

processor.

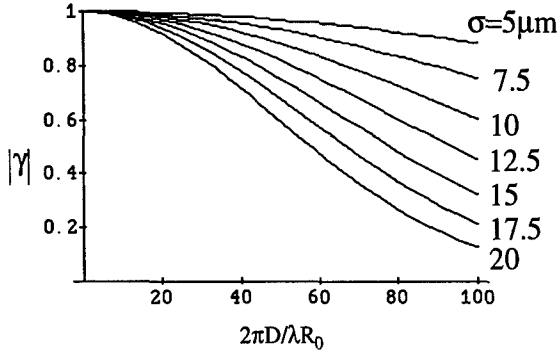


Fig.2 Calculation of the visibility at each beam size

2.1 Vertical Beam Size Measurement

With the assumption of gaussian beam profile, the visibility γ , as a function of spatial frequency ν , is given by the Fourier transform of beam profile f , as a function of position y_0 , as follows;

$$\gamma(\nu) = \int f(y_0) \cdot \exp\{-i2\pi\nu \cdot y_0\} dy$$

$$\nu = \frac{2\pi}{\lambda R_0} D$$

where R_0 is the distance between the object beam and the double slit, λ denotes the wave length and D is a slit separation. The observed interferogram is given by,

$$I(y_1) = I_0 \left[\sin c \left(\frac{2\pi a}{\lambda R_1} y_1 \right) \right]^2 \cdot \left[1 + |\gamma(\nu)| \cos \left(\frac{2\pi D}{\lambda R_1} y_1 + \varphi \right) \right]$$

where a denotes the half of slit height of the double slit,

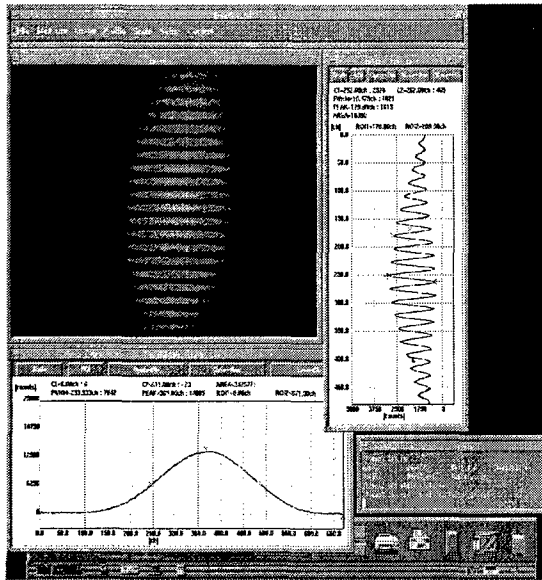


Fig.3 Example of the vertical interferogram. Double slit separation is 35mm.

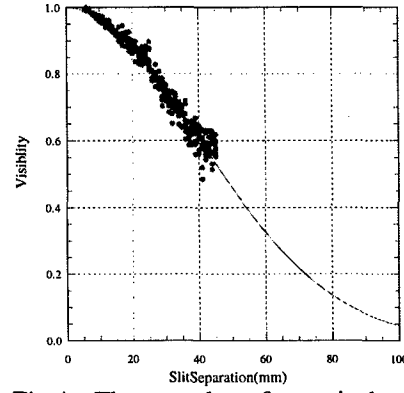


Fig.4 The result of vertical visibility. The horizontal axis is converted to the slit separation. Dotted line denotes measured visibility, and solid line is the best-fit value of 14.0μm

R_1 denotes distance between the interferogram and the back principle point of objective lens of the interferometer, and φ denotes the phase of the interference fringe.

To demonstrate the sensitivity of the interferometer, we make a simulation of the visibility curve in case of the beam size from 5μm to 20 μm by 2.5 μm step. The results are shown in Fig. 2. The useable slit separation is limited to 40mm due to the opening angle of the aperture of the vacuum duct. In case of 5 μm beam size, the visibility reduces by 6.1% at the slit separation 40mm. 1μm difference at the beam size of 5μm makes 2.8% difference in the visibility. Since we can measure easily the visibility better than 1%, the sensitivity and the resolution of the SR interferometer is sufficient for a small beam size measurement.

An example of measured interferogram is shown in Fig.3 and the visibility as a function of double slit separation is shown in Fig. 4. In this case, the vertical beam size is measured as 14.0μm by the least squares fitting.

2.2 Horizontal Beam Size Measurement

The horizontal visibility was measured in the same way as the vertical direction, except for the double slit assembly rotated by 90degrees. For horizontal measurement, the optical beam line of the SR was switched by a flat mirror manually. In the horizontal direction, including the effect of the field depth, the visibility γ is given by,

$$\gamma = \frac{\int \int \frac{2\sqrt{I_1(\psi) \cdot I_2(\psi)}}{I_1(\psi) + I_2(\psi)} f(x - \rho(1 - \cos(\psi))) \cdot g(\psi) \cdot \exp\left(-i \frac{2\pi D}{\lambda f} x\right) d\psi dx}{\int \int \frac{2\sqrt{I_1(\psi) \cdot I_2(\psi)}}{I_1(\psi) + I_2(\psi)} f(x - \rho(1 - \cos(\psi))) \cdot g(\psi) \cdot \exp\left(-i \frac{2\pi D}{\lambda f} x\right) d\psi dx}$$

where g is the angular distribution of the SR in the horizontal plane as a function of the observation angle ψ , I_1 and I_2 are intensity of the two modes of the SR at the double slit, f is the beam profile distribution, ρ is the bending radius[3].

The result of measured plot is shown in Fig. 5. In this case, the horizontal beam size is measured 36.8 μm by the least squares fitting.

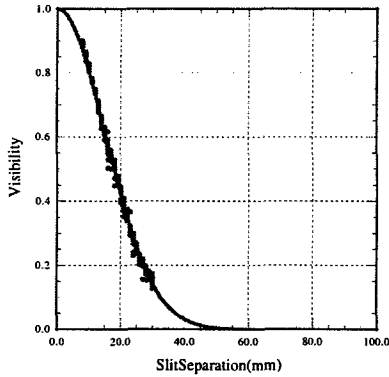


Fig.5 The result of horizontal visibility. Dotted line denotes measured visibility, and solid line is the best-fit value of 36.8 μm

3 BETA FUNCTION MEASUREMENT

Because there is no BPM at the source point, the β -function at the SR source point was obtained by measuring a shift of the betatron-tune during changing the magnetic fields of three quadrupole magnets located in the upstream and the downstream of the SR source point. The betatron tune was measured by the spectrum of the orbit oscillation due to injection error. The value of β -function was obtained by a fit of the β -function at each quadrupole magnet. The measured β -function is shown in

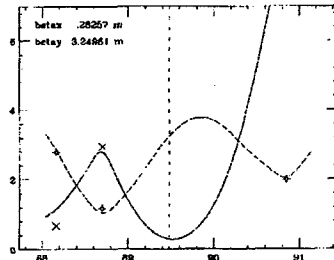


Fig.6 β -function plot near the SR source point (dotted line)

Fig. 6.

4 DISPERSION FUNCTION MEASUREMENT

The η -function at the SR source point is measured from the change of the closed orbit due to change of the rf frequency. The change of the closed orbit is measured at every BPM position. The η -function at the SR source point is obtained by the least squares fitting. The measured η -function is shown in Fig. 7. In order to reduce the vertical emittance, the vertical dispersion correction software has been developed[4].

5 CONCLUSION

The beam size measurement was performed in the ATF damping ring by the use of SR interferometer. We conclude the beam sizes reached less than 14 μm (vertical) and 37 μm (horizontal), respectively. The beta function

was also measured by applying a perturbation on the quadrupole magnets. The dispersion function was measured by means of rf frequency modulation method. Combining these measured values, we conclude the emittances are as $\epsilon_x=1.8 \times 10^{-9}$ m-rad, $\epsilon_y=6.1 \times 10^{-11}$ m-rad. From this conclusion, the vertical-horizontal emittance coupling is 3.4%.

The emittance of extracted beam was also measured by wire scanners at the extraction line[5]. The comparison of two emittance measurements are listed in table 1. The result of these two measurement is well agreed. The emittance tuning is underprogressing by using of SR interferometer.

Table 1: Comparison of the measured emittance with SR interferometer and with wire scanner

	SR interferometer	Wire Scanner
Vertical	$6.1 \pm 2.0 \times 10^{-11}$	$5.8 \pm 0.4 \times 10^{-11}$
Horizontal	$1.8 \pm 0.5 \times 10^{-9}$	$1.5 \pm 0.2 \times 10^{-9}$

6 ACKNOWLEDGMENT

Authors would like to express our thanks to Professors M.Kihara and K.Takata for their encouragement and their helpful discussion. We also wish to thank the ATF operation group for their support.

7 REFERENCES

- [1] F. Hinode et. al., 'ATF Design and Study report', KEK Internal 95-4, June(1995)
- [2] T.Naito et. al., "SR Monitor for the ATF Damping Ring", PAC'97, Vancouver, May 1997.
- [3] T.Mitsuhashi et. al., "Beam size measurement at ATF DR by the use of SR interferometer", EPAC'98
- [4] K.Kubo et. al., "OPTICS DIAGNOSTICS AND TUNING FOR LOW EMITTANCE BEAM IN KEK-ATF DAMPING RING" in this conference.
- [5] K.Okugi et. al., "VERTICAL EMITTANCE IN THE KEK ACCELERATOR TEST FACILITY" in this conference.

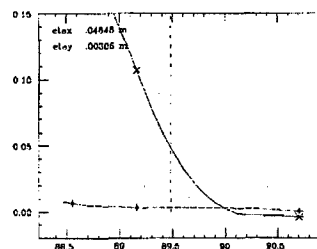


Fig. 7 η -function plot near the SR source point (dotted line)

THE RHIC WALL CURRENT MONITOR SYSTEM*

P.R. Cameron[#], R.C. Lee, T.J. Shea, J. van Zeijts, BNL, Upton, NY
E. Barsotti, J. Crisp, B. Fellenz, FNAL, Batavia, IL

Abstract

The RHIC Wall Current Monitor System will provide data which closely represents the longitudinal profile of bunches in the RHIC ring. This data will be available throughout the machine cycle, from injection through acceleration, transition, transfer to storage RF, and storage. Information which can be derived from this data includes fill pattern, synchrotron motion, longitudinal bunch profile, beam spectrum, and luminosity. The system is similar to that which has operated successfully at the Fermilab Tevatron and Main Ring[1,2,3]. The detectors[4] are broadband resistive wall current monitors. Their signals are sampled and digitized by a high-speed oscilloscope. A Macintosh computer running LabVIEW controls the scope via GPIB, controls system calibration, processes the data, and communicates to the VME-based RHIC Control System via a PCI/MXI/VME interface.

1 INTRODUCTION

The Relativistic Heavy Ion Collider (RHIC) at Brookhaven National Laboratory consists of two synchrotrons which intersect at six points around the 3.8 kilometer circumference[5]. Ion beams from protons to fully stripped gold will be accelerated and stored. The baseline design has 60 bunches of about 10^{11} charges, with an anticipated upgrade intensity of 120 bunches of 2×10^{11} charges. RMS bunch lengths will vary from about 2.5m for gold at injection energy to 7cm for protons at full energy.

2 SYSTEM HARDWARE

System Hardware is shown in Figure 1.

2.1 The Detectors

Detectors are installed near the 2 o'clock Intersection Point in each of the two RHIC rings. As shown in Figure 1, these detectors are fully integrated into the RHIC Control System. A third stand-alone detector has been installed at the 4 o'clock IP, where the signals from the counter rotating bunches will cancel. This detector will be useful for adjusting the collision point, especially during commissioning. Transfer impedance of the detectors is one ohm. Frequency response of this type of detector is typically flat within 3dB from a few KHz to 6GHz. The

detectors at the 2 o'clock IP are installed with microwave absorbing material on either side of the detector, to absorb energy propagating down the 7cm beam pipe above cutoff (2.5GHz and 3.3GHz for the lowest TE and TM modes). Signals travel about 70m over low-loss 7/8 inch heliax cable from the detectors to the digitizer in the Instrumentation Control Room.

2.2 Data Acquisition

Data is acquired by a LeCroy Model 584AL Digital Storage Oscilloscope controlled via GPIB by a Macintosh G3 computer running LabVIEW. The scope specifications include analog bandwidth of 1GHz, maximum sample rate of 8GS/sec, maximum retrigger rate in segmented mode of 30KHz, data transfer rates of several hundred KB/s through GPIB, and 8MB of waveform memory. This digitizer is the only one currently available which meets all requirements for our WCM system. In addition to the detector signals, the scope also digitizes the RF bucket clock for each ring, permitting the observation of synchrotron oscillations.

2.3 Interface to the Control System

Communication between the Macintosh and the VME-based Control System[6] is accomplished by a National Instruments PCI/MXI/VME interface. This interface provides 32MB of shared memory in VME, which is read and written to by both the Macintosh and the VME-based Front End Computer (FEC). Scope triggering is accomplished by a VME-based Beam Synchronous Trigger Module[7]. Timestamps are generated by a VME-based Utility Module and the Trigger Module. Communication with console level computers is accomplished via 100 Mbit/s Ethernet.

3 SYSTEM SOFTWARE

System Software resides in the locations shown in Figure 1.

3.1 The Application

Application programs running on Console Level Computers are the Control System's interface between the users (typically operators and accelerator physicists) and programs called Accelerator Device Objects (ADOs) which run in the FECs. The WCM user interface includes fields for setting data acquisition parameters and a graphic display to present the monitored profile data and bunch fill patterns. The application will be integrated with a logging system and will include an option for tomographic

*Work supported in part by the US Department of Energy.

[#] Email: cameron@bnl.gov

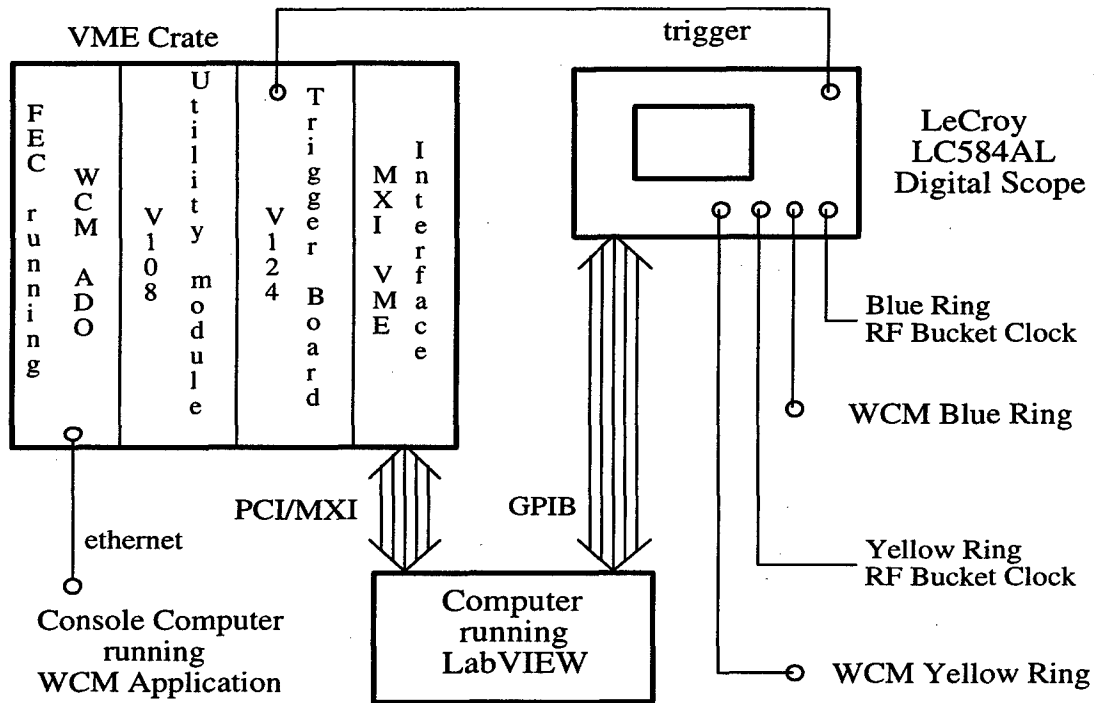


Figure 1: System Block Diagram

reconstruction of the longitudinal phase space using the TOMO package developed at CERN[8].

3.2 The ADO

ADOs are the Control System's interface to all accelerator equipment in RHIC. Application programs communicate with ADOs running in FECs. The FECs are VME based Power PC processors using the vxWorks real-time operating system. Data is transferred over 100 Mbit/s Ethernet using TCP/IP and RPC protocols.

The ADOs for the two WCMs (one for each of the two counter-rotating rings) communicate with the WCM computer through shared VME memory. The memory is divided equally for the two ADOs. The memory for each ADO is partitioned into four blocks - command, status, data control, and data blocks. The data blocks are circular buffers. Commands are sent to the WCM computer which in turn responds with status information. The data control block is used to define the dynamically allocated circular data buffers and to control writing by the WCM computer and reading by the ADO. Semaphores are used in all blocks to synchronize and prevent race conditions when the two computers access memory.

ADO parameters allow application programs to define the type of acquisition - sample rate, profile length, number of profiles, scope scale and offset, and trigger requirements. Beam-synch clock event decoder modules for each ring are set up by the ADO to provide triggers to the WCM scope. Timestamps associated with each

acquisition are provided by the ADO to aid data correlation with other accelerator events. Data is transferred to applications from the ADO either on demand or automatically when an acquisition is complete.

3.3 The LabVIEW Program

The possibility of controlling the scope in C++ directly from the ADO was considered and rejected based upon the need for calibration and the availability of existing calibration, instrument control, and analysis software.

Calibration of bunch intensities and width is based upon the system frequency response and the beam spectrum. The frequency response of the detector, cabling and connectors, and oscilloscope signal path is measured. The detector can be readily measured only before tunnel installation. The rest of the path can be measured periodically with a calibrated signal generator at relevant frequencies and gains, resulting in a transfer function with two dimensions, frequency and gain. An off-line simulation program then transmits an ideal gaussian representing beam through this transfer function to generate the intensity and width calibration factors.

There are instances where local processing of data either in the scope or in LabVIEW before transfer to the Control System is advantageous. Bunch fill patterns require only that a single number, the intensity of each bunch, be made available in the control room. Powerful scope-based timing and jitter analysis (which might ease analysis of synchrotron oscillations) is available, as are frequency domain transforms. LabVIEW has an extensive suite of

well-developed data analysis software. The balance between local and console level analysis is evolving.

3.4 Acquisition Modes

A variety of acquisition modes are necessary for RHIC acceleration and storage. Some of those which we intend to have available for day one operations are shown in the following table. With the RHIC 78KHz revolution frequency and the 30KHz maximum scope retrigger rate, the value for N in the table below must be 3 or greater.

Table 1: Acquisition Modes

Mode	No. of Samples	Sample Length [KB]	Record Length [KB]
Injection - digitize continuously for sample length	1	200 typically	200
Multi-turn - digitize 1 turn every N turns	N	20	20*N
Multi-bunch - digitize 1 bunch every N turns	N	0.1	0.1*N

4 OTHER POSSIBILITIES

The existence of a flexible and powerful data acquisition system at the commissioning of a new and unique machine opens new opportunities.

The unprecedented combination of beam current and particle charge present with gold beams in RHIC opens the possibility of broadband observation of the longitudinal Schottky signal. To the best of our knowledge, all previous observations of the Schottky signal have been with resonant detectors. A broadband Schottky monitor would be an excellent diagnostic for the mysterious 'micro-coherent' signal which has been seen at all other high energy accelerators[9], and which has frustrated efforts to implement stochastic cooling. With high pass filtering and perhaps some pre-amplification, the WCM system might provide broadband Schottky spectra.

Similarly, by utilizing a detector sensitive to transverse position, broadband observation of the transverse Schottky signal might be possible, perhaps with the data acquisition being the same. These broadband spectra might provide useful information about chromaticity. Such a system might also be useful for chromaticity measurements by observing the coherent betatron tune shift between the head and tail of the bunch[10].

5 CONCLUSIONS

Detectors have been fabricated and installed. A flexible and powerful data acquisition system has been assembled, and integration has been demonstrated from the scope through to the console level application. We await beam with eagerness and enthusiasm.

6 REFERENCES

- [1] C.D.Moore et.al., "Single Bunch Intensity Monitoring System Using an Improved Wall Current Monitor", Proc. 1989 PAC, P. 1513.
- [2] E.L. Barsotti, "A Longitudinal Bunch Monitoring System Using LabVIEW and High-speed Oscilloscopes", Proc. 1994 Beam Instrumentation Workshop, Vancouver, AIP 333, P.466.
- [3] an online description of the FNAL Sampled Bunch Display is available at <http://www-rfi.fnal.gov/SBD/systems.html>
- [4] R.C.Webber, "Longitudinal Emittance: An Introduction to the Concept and Survey of Measurement Techniques Including Design of a Wall Current Monitor", Proc. 1989 Beam Instrumentation Workshop, Brookhaven, AIP 212, P.85.
- [5] <http://www.rhichome.bnl.gov/RHIC/index.html>
- [6] T. S. Clifford, D. S. Barton and B.R. Oerter, "The Relativistic Heavy Ion Collider Control System", Proc. Int. Conf. on Accelerator & Large Experimental Control Systems (ICALEPCS '97), IHEP, Beijing, China, November 3-7, 1997, P. 12.
- [7] H. Hartmann and T. Kerner, "RHIC Beam Synchronous Trigger Module", these proceedings.
- [8] S. Hancock, P. Kanus, and M. Lindros, Tomographic Measurement of Longitudinal Phase Space Density, submitted to Elsevier Preprint.
- [9] D.A. Goldberg, private communication.
- [10] H. Schmickler, private communication.

OPTICAL DIAGNOSTICS ON ETA II FOR X-RAY SPOT SIZE*

R. A. Richardson, LLNL

Abstract

Gated and streak cameras have been used to look at a high current focused electron beam on a target, and the x-rays produced by that interaction. An optical camera images the optical transition radiation (OTR) from the beam hitting a carbon target to give focused beam profiles. Blackbody radiation from heavy metal targets is experimentally proven to be dominant. The roll bar technique is used as a thick knife edge to 'image' the x-ray spot produced by the beam-target interaction. The x-ray shadow is converted to visible photons using a scintillator and imaged using a gated optical camera. The scintillator thickness places a limit on the resolution of the diagnostic. Data will be presented from these techniques and compared to an x-ray pinhole camera.

1 INTRODUCTION

This diagnostic is used to measure the spot size of an x-ray source. A bar that is optically thick to x-rays is used to shadow the source, acting as a knife edge. This produces a shadow that is effectively the integral of the x-ray profile. We assume that the profile here is Gaussian in shape. The profiles are fitted to an erfc function, which is the integral of a Gaussian. The Gaussian assumption is verified using other diagnostics such as a x-ray pinhole camera.

The shadowed x-rays are then converted to visible photons for imaging using commercial cameras. The image is corrected for flat field using an image taken without the rollbar present. The image is averaged in the dimension orthogonal to the rollbar edge to increase photon statistics.

The full-width half maximum (FWHM) of the Gaussian (from the fitted erfc function), corrected for magnification, is reported as the spot size. The magnification of the rollbar is simply the distance from the rollbar to the x-ray image converter (scintillator) divided by the distance from the x-ray source to the rollbar (Fig. 3).

Limitations of this diagnostic are the blurring effects due to the finite thickness of the image converter. This can be reduced by increasing the magnification, but at a cost of reduced x-ray flux. The photon conversion efficiency is low, so that detection is marginal for short gate widths and large magnification.

*This work was performed under the auspices of the U.S. Department of Energy by the Lawrence Livermore National Laboratory under Contract No. W-7405-Eng-48.

The ultimate limiting resolution of the roll bar is set by the finite radius of the roll bar. While a flat surface would provide an ideal knife edge, a small misalignment of this edge degrades the resolution rapidly. This effect is reduced if the edge is a cylinder, Fig. 1. The resolution is calculated by assuming a photon takes a straight line geometric path from an ideal point source and is attenuated by the roll bar exponentially, $I=I_0 \cdot \exp(-\mu x)$, where x is the amount of high density material that the x-ray photon passes through, and μ is the 5.5 MeV extinction coefficient, taken as 81 m^{-1} for tungsten. This ignores any scattering effects and is only a lower limit calculation for the resolution. For the parameters in this paper, this calculation gives a limiting resolution of 0.09 mm, calculated from the FFT of the intensity plot in Fig. 2.

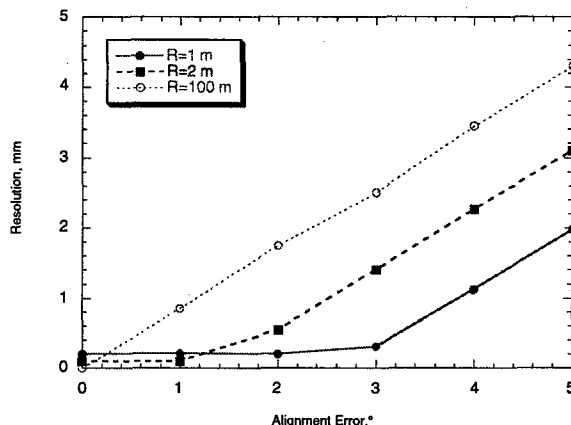


Figure 1: The ultimate resolution of the rollbar versus the alignment angle, the parallelism to the source. R is the rollbar cylinder radius.

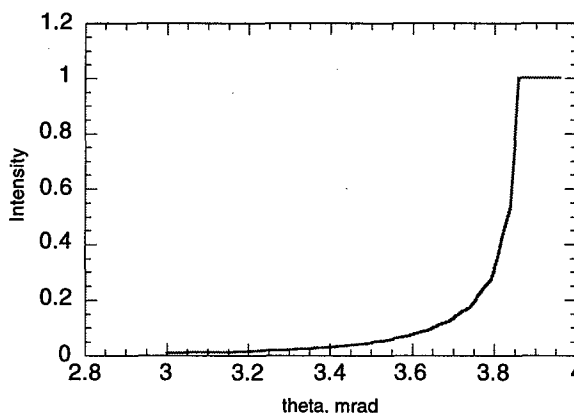


Figure 2: The calculated effect of a rollbar with radius of 1 m and alignment error of 1°. Theta is the angle of a photon from a point source.

2 EXPERIMENTAL SETUP

This diagnostic is used to measure the x-ray spot on the ETA II linear electron accelerator. The machine parameters are 5.5 MeV energy, 2 kA current, 50 ns pulse width. X-rays are created when the beam is focused on a (typically) 0.005" Tantalum target. The diagnostic setup (Fig. 3) consists of a heavymet (mostly Tungsten) rollbar, which is a 8x8x3 cm block with a 1 meter radius machined on one face. This bar is located a distance 108 cm from the target (x-ray source). Between the target and the rollbar is a 0.060" aluminum vacuum window. At a distance of 427 cm there is a 90x90x19 mm BC-400 scintillator. The magnification is therefore 3.95. We use a 0.010" tantalum sheet in front of the scintillator to convert the x-rays to electrons which are detectable by the scintillator. Black cloth between the tantalum and scintillator absorbs reflections.

The scintillator is imaged using a gated camera. We have used a Cohu SIT camera (10 ns gate) and a Princeton Instruments CCD camera (5 ns gate). Both cameras use a microchannel plate to intensify and gate the image.

Typically a short lead bar is placed directly in front of the scintillator-Tantalum stack orthogonal to the direction of the rollbar edge, partially blocking the x-rays. This is done to provide an edge that is representative of the blurring introduced by the scintillator and camera. The optical resolution is typically much less than the scintillator blur.

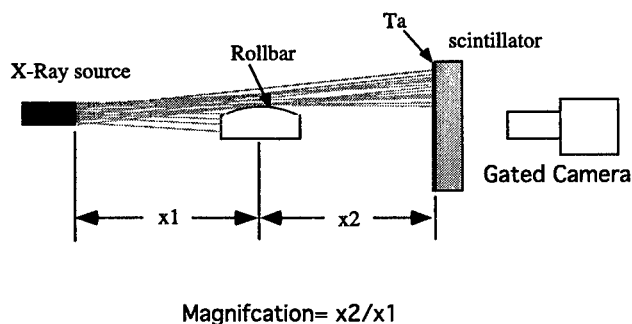


Figure 3: Diagnostic setup.

3 DATA

An example rollbar image is shown in Fig. 4. This is the raw scintillator image, uncorrected for flat field. The scintillator is imaged with the Princeton Instruments camera (ICCD-576). The 5 ns gate of the camera is timed to the middle of the accelerator pulse. The dark frame around the scintillator is clearly visible. The rollbar in this case is vertical, and an averaged lineout in the horizontal direction is analyzed to get the spot size of the x-ray source. The sharper horizontal shadow in the lower half of the image is due to a 0.25 inch thick lead bar placed immediately in front of the scintillator. Lineouts in

the vertical direction are analyzed to approximate the blurring due to x-ray and electron scattering in the scintillator and tantalum backing, as well as optical blurring.

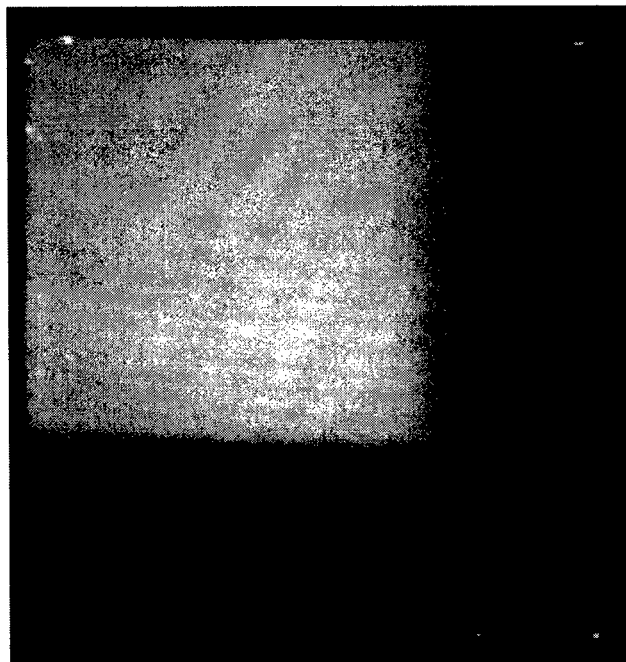


Figure 4: Scintillator image showing rollbar and edge blur x-ray shadows.

A horizontal lineout and erfc fit are shown in Fig. 5. This is the raw data, uncorrected for any blur. A lineout of the image in the vertical direction, which shows the shadow from the lead bar is shown in Fig. 6. An erfc fit is done on the data to quantify the blur produced. As expected, the fit is not perfect, but gives a representation of the spot size error, in this case around 1 mm.

The scintillator blur can be corrected for by deconvolution of the data with the blur. This is done using Fourier transforms of the data. First the data is smoothed and differentiated. The Fourier transform of the data is taken and normalized to give the modulation transfer function (MTF). The spot size can be obtained by finding the frequency (f_0) at which the $MTF = 0.5$. The equivalent Gaussian spot size is then $FWHM = 0.112/f_0$. The resulting transforms are shown in Fig. 7. The spot size of 2.5 mm when corrected for scintillator blur drops to 1.9 mm. Also plotted in Fig. 7. is the FFT of the calculated rollbar resolution limit of Fig. 2.

This method of spot size determination is more effected by noise. Note there is a slight difference in the uncorrected spot size when determined by FFT or erfc fit to the raw data (2.5 versus 2.4 mm).

4 RESULTS

The rollbar diagnostic is useful for final tuning of the accelerator. The image data is recorded real time electronically. The lineouts and fit can be done in a manner of minutes, and a tuning curve can be generated rapidly, Fig. 8.

The rollbar diagnostic is compared with data from a x-ray pinhole camera in Fig. 9. The scintillator blur for this data set limited the resolution of the rollbar to about 2 mm.

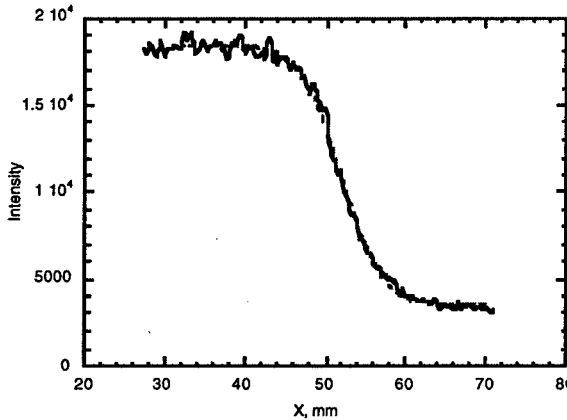


Figure 5: Rollbar data with erfc fit. Magnification=4, Gaussian FWHM = 2.4 mm.

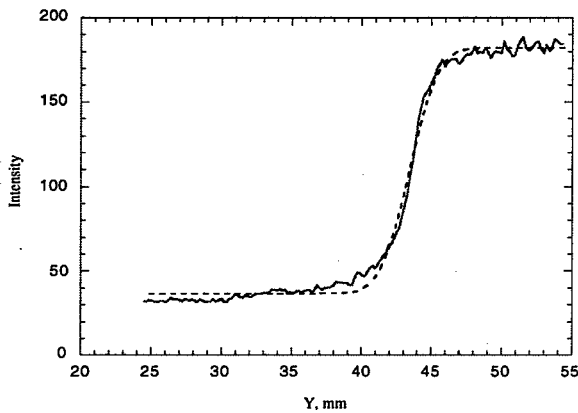


Figure 6: Scintillator blur with erfc fit. The equivalent spot size is 0.97 mm.

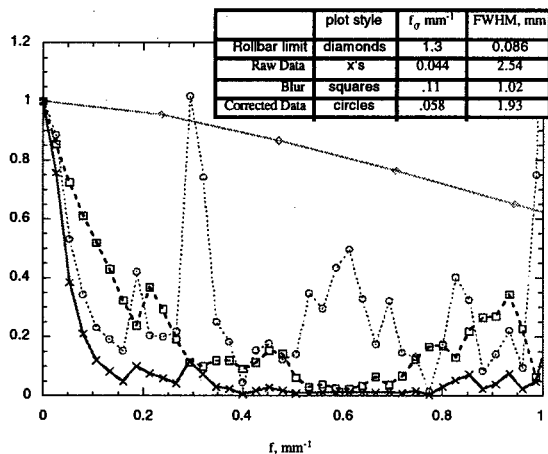


Figure 7: Fourier transforms of image lineouts, with corrected data.

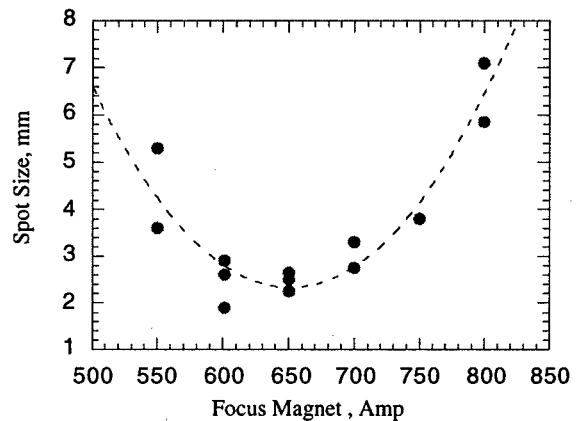


Figure 8: X-ray spot size (FWHM) tuning curve.

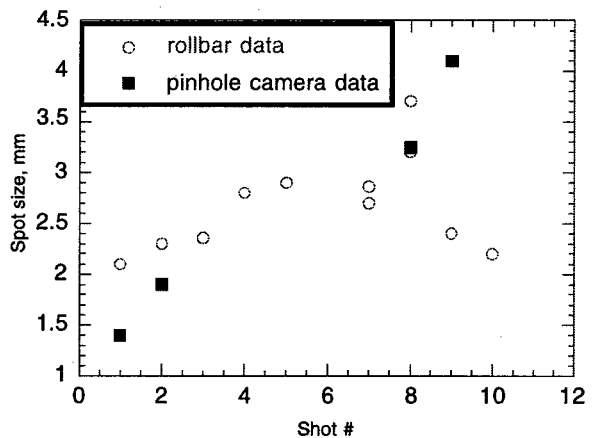


Figure 9: Rollbar calculated spot size and spot size calculated from the x-ray pinhole camera.

5 ACKNOWLEDGMENTS

The author wishes to thank the ETA II experimental staff for their support, and Tim Houck in particular, who initially designed this experiment.

A COMPACT RESIDUAL GAS IONIZATION PROFILE MONITOR (RGIPM) SYSTEM*

W. C. Sellyey and J. D. Gilpatrick, Los Alamos National Laboratory, Los Alamos, NM

Abstract

The Accelerator Production of Tritium (APT) and Spallation Neutron Source (SNS) accelerators will produce high power density beams, which cannot be observed using conventional intercepting beam profile devices. The beam produces electrons when it ionizes the residual gas in the beam tube. These electrons, when accelerated by a uniform electric field and guided by uniform parallel magnetic field, produce a projected image of the beam on a detector perpendicular to the fields. A particle tracking program shows that this can be done with a resolution better than the needed 100 μm . There are typically no dipoles available in these accelerators to produce the needed magnetic field. Triple dipole systems are being designed which will give no net trajectory change to the beam, but will produce the needed field for the diagnostic. Although the field is not completely uniform in the electron collection region, particle tracking calculations show that the resolution is not seriously degraded relative to a uniform field. Several ways of viewing the beam profile are considered. Radiation resistant and hardened materials needed for this are discussed.

1 INTRODUCTION

RGIPM has been implemented by detecting either the positive ions or the electrons that result from the beam ionizing the residual gas in the beam tube. Here we will consider only electrons. This paper will discuss design considerations for the space restricted, high radiation environment of a high power linac. It will also discuss various ways of imaging the profile information contained in the electrons coming from the ionized residual gas. These RGIPM are intended to observe 200 to 1700 MeV proton or H⁻ beams, with cw current up to 100 mA. The beam profiles will be non-Gaussian with dimensions down to 0.8 mm rms.

2 RESOLUTION LIMIT OF RGIPM METHOD

One method of implementing RGIPM is to use a strong magnetic field so that the resolution is determined by the Larmor radius of the electron. This will be one of the ways investigated here. A second method is to take advantage of the fact that the Larmor period of non-relativistic electrons depends only on the magnetic field

strength. In this case all electrons can be made to go through nearly one complete orbit in the magnetic field and the resolution can be much smaller than the Larmor radius [1]. Thus lower magnetic fields can be used. A Monte Carlo particle tracking code was used to investigate the achievable resolution [2]. It takes into account the beam space charge and the distribution of the initial electron velocities. A minor modification of the program enabled the calculation of the delta function response (particle distribution at the detector for electrons coming from a plane parallel to a plane defined by the beam direction and the magnetic field.) From this the resolution can be calculated.

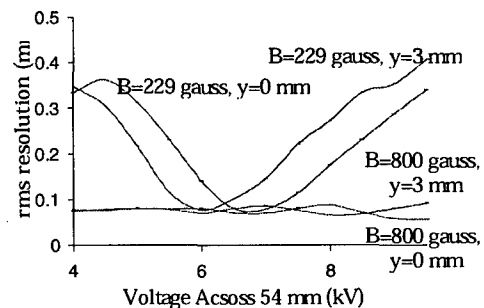


Figure 1. rms Resolution For Two B Fields

Figure 1 shows the calculated rms delta function response for a gap of 54 cm and a gap voltage range of 4 to 9.5 kV. Two curves are for a B-field of 229 gauss, and two are for 800 gauss. Within each pair, one is for the beam centered on the beam tube, and the second is with the beam displaced 3 mm towards the detector (beam width = 1 mm rms). This illustrates the main features of the two ways of generating the beam profile at the electron detector. With the 800 gauss field, the resolution is independent of beam position and electric field and is expected to vary in proportionally to the magnetic field. In the 229 gauss case, the needed field is much lower but the resolution depends strongly on the fields and beam position. In practice, the magnetic fields will not be uniform because short dipoles will be used.

3 MAGNET DESIGN

Triple dipoles are being designed using a commercial finite element code (Vector Fields, TOSCA). Both coil and permanent magnet driven designs are being investigated. Figure 2 shows one quadrant of a permanent magnet design for a 16 cm beam tube. The

* Work supported by the U. S. Department of Energy.

beam moves in the z direction and the ionization electrons drift in the y direction. The center of the magnet, marked by +, is 4 cm above the beam tube center (origin). The magnet extends ± 24 cm in the x direction. Figure 3 shows B_y along the y axis, and this is near where most of the observed electrons will be moving. It also shows B_y along a line parallel to the z -axis through the center of the magnet.

4 RADIATION FIELDS

A major challenge will be to use imaging devices which can survive the expected high radiation levels. Assuming that the average beam loss is 0.1 nA/m, the expected dose rate at 1 m from the beam line at 1.1 GeV will be 20 rad/h [3]. Beam line component activation calculations indicate that for the safety of personnel working on the beam line, dose rates will need to stay well below this level. Beam loss rates in LANSCE between 300 MeV and 800 MeV were measured to average about 0.2 nA/m [4].

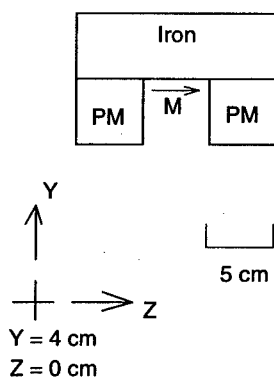


Figure 2. One quadrant of a triple dipole using permanent magnet (PM). The arrow points in the magnetisation (M) direction in the iron.

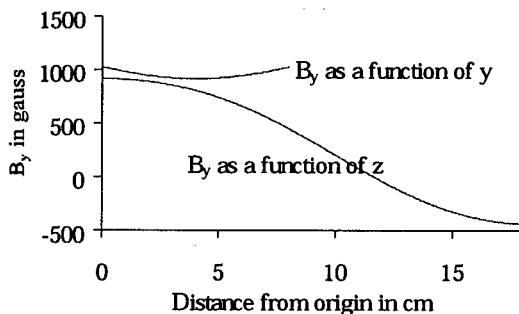


Figure 3. B_y along the y -axis and parallel to the z axis passing through the magnet center.

These losses were deemed excessive and would be too high for SNS and APT. Thus a maximum average of 20 rad/h at 1m will be assumed in this paper. This translates

into 0.175 Mrad/year at 1m and 7 Mrad/year at 2.5 cm from the beam.

5 RADIATION RESISTANT AND HARDENED ITEMS

Some of the radiation resistant materials and components under consideration for use are listed below:

Measurements have been made on the light attenuation caused by radiation damage to sapphire[5]. An initial darkening will happen in 75 hours under nominal operating conditions (assuming 10 krad/h γ 's). No further darkening due to γ 's will occur. It will take about $4 \cdot 10^4$ years for neutrons to cause a 50% light attenuation in a 1 cm thick sapphire 2.5 cm from the beam.

High OH content silica fibers 1m long will take 70 years to reduce transmission by 37% in the visible spectrum [6].

Cerium activated Yttrium Aluminum garnet (YAG:Ce) is a linear scintillator which has been measured to half its light output in 10000 h with a 10 keV electron beam of current density 71 nA/cm² [7]. Light output is about 18 photons/keV [8]. Resolution and electron depth penetration is 20 microns at 100 keV [9]. Thus at 5 keV these would be about 5 microns. It has been found that 0.2 mC of 15 MeV 5 mm diameter electron beam on 1 mm thick YAG produced no visible darkening [10]. From this one can estimate that it would take >40 Mrad to cause a 50% reduction in light transmission of a 0.1 mm thick piece of YAG.

Micro Channel Plates (MCP) have been exposed to 1 Mrad of Co-60 γ 's with no degradation in performance [11]. Thus one can estimate that MCP's will be useable with total dose >10 Mrad. Gains of several 1000 can be obtained with one MCP and over 10^8 with stacks of MCP's. Output currents for conventional 25 mm MCP is around 2 μ A. Advanced devices can output 20 μ A and have a life of 40 C/cm².

Channeltrons are electron multiplying tubes about 100 μ m across. They are made of the same material and in a similar fashion as MCP's and thus the radiation related life times are expected to be similar. Gains are up to 10^8 and output currents up to 5 μ A.

Resistive position sensing element are made by depositing a roughly rectangular, uniform thickness, resistive surface on alumina. The effect of accumulated dose on this element is expected to be unimportant.

A radiation hardened CID camera manufactured by CIDTEC is specified as operating to 1 Mrad without change in performance. It is a standard RS-170 camera. Noise is about 1400 electrons per pixel per frame.

Xyberon has combined an intensifier with the CIDTEC camera. The intensifier resolution is better than 88 μ m FWHM. One photo electron produces $2 \cdot 10^5$ photons at the intensifier output. There is a reduction of 1.46 by the fiber coupling and the quantum efficiency of the CID is about 20%. For the integrated count over all light

receiving pixels $S/N \approx 5$. This may allow the observation of a single photo electron generated at the photo cathode and the determination of its impact point. For high radiation use, the photo cathode and phosphor substrates and fiber coupling may need to be high OH silica.

Radiation hardened charge sensitive pre amplifiers that can withstand >100 krad are available. For these to survive several years, the radiation will be attenuated to 5 krad per year by placing them 2m away, 1m into the accelerator concrete shielding [12]. A possible choice for this amplifier is the Amptek A225 which is rated at 100 krad. Noise (rms) will be 1600 electrons with 3 m of cable on the input. Typical easily achievable count rates are $10^5/s$.

6 IMAGING SYSTEMS

Some candidates for imaging the electron current from the beam and associated considerations are:

The electrons hit a 0.1 mm thick YAG crystal, and form an image viewed by an intensified camera about 1 m away. At a pressure of 10^{-6} torr, a 1 GeV, 1 mm rms, 100 ma proton beam, will cause a YAG crystal to lose 10% of its light output in 6 years. The view port would probably be sapphire. At 10^{-8} torr, 1 mA beam will produce $5 \cdot 10^7$ photons/(s·cm). Assuming 50% transmission, a 2 in lens 1 m from the YAG would produce 4000 photons/(s·cm) on the intensifier. Assuming 20% quantum efficiency this would result in 800 events per second on the CID. Thus a good profile could be obtained in 1 to 10 seconds. Alternately, if the 2 in lens has a magnification of 0.5 and the beam rms width is 1 mm, the summed S/N for 1 cm of beam when imaged on the CID for one second will be about 80. The error in a Gaussian width would be 5%. Achromatic lenses made from sapphire and fused quartz or Cassegrain optics would be used to generate an image on the intensifier. Light collection efficiency 5 times larger than assumed here is probably achievable. The life of the system should be 5 years or greater.

A stack of three 18 mm MCP's would be places about 2.5 cm from the beam. The MCP output for each electron strike would land on a resistive sheet. Four outputs at the corners of the sheet would be amplified by radiation shielded charge sensitive amplifiers. Each output would produce about $2.5 \cdot 10^6$ electrons. The amplifier noise of 1600 electrons will be unimportant compared to the error caused by fluctuations in gain of MCP channels. The signals would be digitised and positions calculated with 70 μ m rms accuracy. This system would be purchased from a vendor. At a pressure of 10^{-10} torr (N_2) the peak electron flux for a 1 mm rms 100 mA proton beam is estimated to be $4 \cdot 10^6/(s \cdot cm^2)$. To reduce the count rate to 10000/s a mask with a 100 μ m slot will be placed in front of the MCP. The peak electron flux that a conventional MCP can handle in this type of position measuring device has been measured as

$10^7/(s \cdot cm^2)$ [13]. An advanced MCP may be able to handle ten times this rate. Thus an important consideration for this system will be the pressure in the beam line and a vacuum pump will probably need to be part of the system. Radiation damage may limit the life of this detector to a couple of years.

A Channeltron would be mechanically moved across the e-beam. It would have a mask cut with a 100 μ m by 300 μ m slot in front of it. A charge sensitive amplifier would be remotely placed and shielded and electrons would be individually counted. The Channeltron can handle MHz count rates and thus the count rate will be limited by the charge sensitive amplifier. At 10^{-10} torr the count rate would be about 1.2 kHz. Radiation damage may limit the life of this system to a couple of years. The mechanical drive and radiation hard position sensing system for this unit will need to be a couple of feet from the Channeltron, outside the magnetic field.

A 100 μ m optical fiber (silica or sapphire) would conduct light from a 100 μ m diameter, 100 μ m long YAG scintillator to a high gain photo multiplier tube a couple of meters from the beam tube. Typically 5 photons would reach the photo multiplier for every electron on the scintillator.

7 REFERENCES

- [1] Private communication, A. Jason, Los LANL, Los Alamos, N.M.
- [2] A. Hahn, FNAL, Batavia, IL
- [3] Private communication, Eric Pitcher, LANL, Los Alamos, N.M.
- [4] N. Bultman, A. Jason, E. Pitcher, G. Russel, W. Sommer, D. Weinacht, R. Woods, "Los Alamos Next-Generation Spallation Source Volume I", LANL Report LA-UR-95-4300, (1995) p. 2-81.
- [5] P. W. Levy, "Color Centers and Radiation-Induced Defects in Al_2O_3 ", Phys. Rev. 123, (1961) 1226.
- [6] D. W. Cooke, B. L. Bennett, E. H. Farnum, "Optical Absorption of Neutron-Irradiated Silica Fibers", Journal of Nuclear Materials 232 (1996) 214.
- [7] R. Autrata, P. Schauer, Jos. Kvapil, J. Kvapil, "Singel-Crystal Aluminates - A New Generation of Scintillators for Scanning Electron Microscopes and Transparent Screens in Electron Optical Devices", Scanning Electron Microscopy, 11 (1983) 489.
- [8] W. S. Graves, E. D. Johnson, S. Ulc, "A High Resolution Electron Beam Profile Monitor and its Applications", AIP Conference Proceedings, 451 (1998) 206.
- [9] M. Kotera, Y. Kamiya, "Computer Simulation of Light by High-Energy Electrons in YAG Single Crystals", Ultramicroscopy, 54 (1994) 293.
- [10] J. G. Power, N. Barov, M. E. Conde, W. Gai, R. Konecny, P. Schoessow, "Initial Characterisation of the YAG Crystal" AGN #32, Technical Report, Argonne National Laboratory (1997).
- [11] J. G. Timothy, R. L. Bybee, "Effects of 1-MeV Gamma Radiation on a Multi-Anode Microchannel Array Detector Tube", Rev. Sci. Instrum., 50 (1979) 743.
- [12] K. Tesch, "A Simple Estimation of the Lateral Shielding for Proton Accelerators in the Energy Range 50 to 100 MeV", Radiation Protection Dosimetry, 11 (1985) 165.
- [13] Private communication, M. R. Mellon, Quantar Technology Inc., Santa Cruz, CA.

Application Limit of SR Interferometer for Emittance Measurement

Y. Takayama*, T. Okugi, T. Miyahara, Tokyo Metropolitan University, Tokyo, Japan
S. Kamada, J. Urakawa, T. Naito, KEK, Tsukuba, Japan

Abstract

We investigate the application limit of the SR interferometer for emittance measurement at the KEK-ATF. We need to consider two important problems, which are the limitation of the availability of the van Cittert-Zernike theorem and the diffraction effect due to a narrow vertical aperture of the SR extraction line. The former problem is analyzed with the theory introduced in another paper [1]. The latter one is studied with the numerical calculation, where the narrow aperture is assumed to be an optical slit with an adequate vertical width. We show that these problems must be solved for the accurate measurement of the electron emittance, especially in the vertical direction.

1 INTRODUCTION

A measurement of the electron beam emittance is one of the most important theme for the accelerator physics. At the KEK-ATF damping ring, several attempts are performed to estimate the emittance. Especially, the SR interferometer which measures the spatial coherence (visibility) has some advantages compared with other methods [2]. The electron beam size can be obtained by performing the Fourier transformation of the spatial coherence, which is called as the van Cittert-Zernike theorem. However, it is not trivial whether this theorem is available for the bending magnet radiation. Recently, some conditions to judge whether this theorem is available or not for the bending magnet radiation were derived by the authors [1]. We investigate whether these conditions are satisfied for the SR interferometer at the ATF damping ring.

We need to consider another important problem, the effect of the narrow vacuum chamber at the SR extraction line. If the light is cut by this vacuum chamber, the spatial coherence at the downstream changes. For an extreme example, if the width of the vacuum chamber is much smaller than the wavelength of light, the spatial coherence at the downstream is perfect for any electron beam parameters. Therefore, in order to measure the electron beam size with the SR interferometer, we must investigate how the vacuum chamber affects the spatial coherence.

In this paper, we investigate above two points in detail and judge whether the SR monitor is available to measure the electron beam size at the ATF damping ring.

2 AVAILABILITY OF THE VAN CITTERT-ZERNIKE THEOREM

The Twiss parameters and dispersion at the position where the electron beam size is evaluated, and emittance in the horizontal and vertical directions are shown in the Table 1 [3]. Here, we assumed that there is no vertical dispersion and the coupling is 1 %. We investigate whether the van Cittert-Zernike theorem is available in the horizontal and vertical directions individually. The details of derivation of the conditions are shown in another paper [1].

Table 1: Design value of the ATF damping ring at the point where the SR interferometer is installed.

	horizontal (x)	vertical (y)
α	0.3590	-1.1690
β (m)	0.3796	2.8435
γ (1/m)	2.9739	0.8323
η	0.0491	0
η'	-0.1458	0
ε (nm-rad)	1.08	0.0108

2.1 Horizontal direction

In the horizontal direction, three conditions must be satisfied for the electron beam size σ_x in order to use the van Cittert-Zernike theorem, which are

$$\sigma_x \gg \frac{\rho \bar{\beta}_x \varepsilon_x}{L^2}, \quad (1)$$

$$\sigma_x \gg \frac{\rho \bar{\beta}_y \varepsilon_y}{L^2 \left(1 + \frac{\bar{\beta}_y \varepsilon_y}{\sigma_p^2}\right)}, \quad (2)$$

$$\sigma_x \gg \sqrt{\frac{\bar{\beta}_x}{\beta_x}} \frac{\rho \varepsilon_x}{L}, \quad (3)$$

where $L = 7.04$ m is the distance between the light source and double slit, $\rho = 5.73$ m is the bending radius. α , β , γ and ε are the Twiss parameters and emittance after integrating energy spread, respectively. $\bar{\beta}$ is defined as $\bar{\beta} = \beta - 2\alpha L + L^2\gamma$. σ_p and σ'_p are the beam size and beam divergence of the light at the waist in the vertical direction which is emitted by a single electron. $\bar{\sigma}_p$ is defined as $\sqrt{\sigma_p^2 + L^2 \sigma_p'^2}$. For the wavelength $\lambda = 500$ nm, σ_p and σ'_p are calculated as 19.4 μ m and 2.06 mrad, respectively.

Using the parameters in Table 1, we have $\sigma_x = 34.0$ μ m.

* Email: takayama@phys.metro-u.ac.jp

The conditions in (1), (2) and (3) are written as

$$\begin{aligned}\sigma_x &\gg 5.20 \times 10^{-2} \mu\text{m}, \\ \sigma_x &\gg 7.56 \times 10^{-5} \mu\text{m}, \\ \sigma_x &\gg 3.42 \times 10^{-2} \mu\text{m},\end{aligned}$$

respectively. These condition are well satisfied for the design value and the van Cittert-Zernike theorem is safely used to estimate the beam size in the horizontal direction.

2.2 Vertical direction

As same with the case of the horizontal direction, three conditions are necessary in order to use the van Cittert-Zernike theorem, which are

$$\sigma_y \gg \frac{\rho}{L^2} \sqrt{\frac{\varepsilon_x \varepsilon_y \bar{\beta}_x \bar{\beta}_y}{\left(1 + \frac{\bar{\beta}_y \varepsilon_y}{\bar{\sigma}_p^2}\right)}}, \quad (4)$$

$$\sigma_y \gg \frac{L \varepsilon_y}{\bar{\sigma}_p}, \quad (5)$$

$$\sigma_y \gg \frac{L}{2k \bar{\sigma}_p} \sqrt{\frac{\varepsilon_y \bar{\beta}_y}{\bar{\sigma}_p^2 + \varepsilon_y \bar{\beta}_y}}, \quad (6)$$

where $\sigma_y = 5.54 \mu\text{m}$ is the electron beam size in the vertical direction. There is an extra condition on the divergence of the light beam under which the light beam reaches at the observer points strongly enough, which is

$$\sigma_y > \frac{\sigma_p}{\sqrt{1 + \left(\frac{\sigma'_y}{\sigma_p}\right)^2}}, \quad (7)$$

where we put the electron beam divergence as $\sigma'_y = \sqrt{\varepsilon_y \gamma_y}$.

As for the conditions in (4), (5) and (6), we have

$$\begin{aligned}\sigma_y &\gg 1.98 \times 10^{-3} \mu\text{m}, \\ \sigma_y &\gg 5.25 \times 10^{-3} \mu\text{m}, \\ \sigma_y &\gg 2.41 \times 10^{-1} \mu\text{m},\end{aligned}$$

respectively. Therefore, these conditions are well satisfied. However, the condition (7) is written as

$$\sigma_y > 19.9 \mu\text{m},$$

which is not satisfied in this case. This means that the whole curve of the visibility can not be obtained due to the weak intensity of the light for large slit separation and the accurate measurement of the electron beam size is very difficult in the vertical direction.

3 EFFECT OF VERTICAL APERTURE

Between the light source and the double slit, there is a narrow space of the vacuum chamber in the vertical direction whose width is only $4 \sim 5 \text{ mm}$. It is important to investigate whether this narrow space affects the coherence in

the vertical direction. For this purpose, we suppose that the narrow space is equivalent with the vertical entrance slit with the width d , as shown in Figure 1. We put the distance between the light source and the entrance slit to be $L_1 = 0.56 \text{ m}$ and the distance between the entrance slit and the double slit to be $L_2 = 6.48 \text{ m}$, respectively.

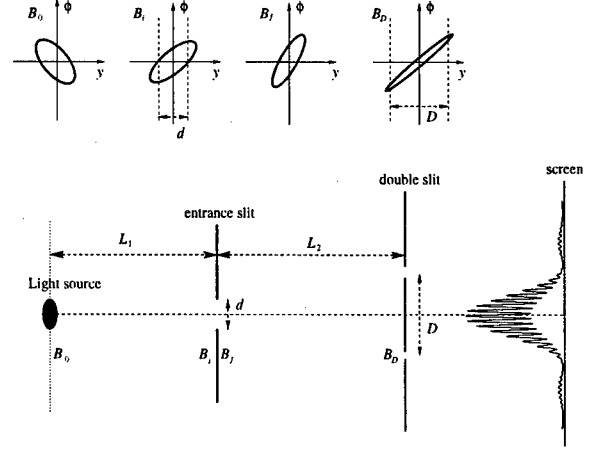


Figure 1: Transformation of the phase space of light.

If we denote the electric field on the entrance slit and on the double slit as $E_i(y)$ and $E_D(y)$, respectively, the correlation of the fields are related with the equation

$$\begin{aligned}\Gamma_D(y_1, y_2) &= \int dy_a dy_b T^*(y_a) T(y_b) \\ &\quad \Gamma_i(y_a, y_b) \frac{e^{-ik(r_{1a} - r_{2b})}}{r_{1a} r_{2b}},\end{aligned} \quad (8)$$

where the integration is performed on the entrance slit. k is the wave number of light and

$$\begin{aligned}\Gamma_i(y_1, y_2) &= \langle E_i^*(y_1) E_i(y_2) \rangle, \\ \Gamma_D(y_1, y_2) &= \langle E_D^*(y_1) E_D(y_2) \rangle, \\ r_{1a} &= \sqrt{L_1^2 + (y_1 - y_a)^2}, \\ r_{2b} &= \sqrt{L_2^2 + (y_2 - y_b)^2}.\end{aligned}$$

$T(y)$ is the transmittance function of the entrance slit. (8) is valid if the wavelength of the light is much smaller than the entrance slit. Intuitively, (8) means that the electric field on the double slit can be obtained by summing up the spherical wave emitted by the point sources on the entrance slit. The spatial coherence on the double slit is written as

$$\gamma(D) = \frac{\Gamma_D(D/2, -D/2)}{\sqrt{\Gamma_D(D/2, D/2) \Gamma_D(-D/2, -D/2)}},$$

where D is the separation of the double slit.

In order to calculate the spatial coherence, the correlation of the fields on the entrance slit is needed. This can be obtained by approximating the radiation field with the Gaussian beam. With this approximation, the brightness function is represented analytically. Since the brightness

function $B(y, \phi)$ and the correlation of the fields $\Gamma(y_a, y_b)$ are related with the Fourier transformation [4]. $\Gamma(y_a, y_b)$ is also obtained analytically. Using this property, the visibility is numerically calculated if we set the electron beam parameter at the emitting point [5].

3.1 Numerical calculation

We calculate the visibility with the formula discussed in the previous section. We put $\varepsilon_y = 0.01$ nm-rad. Figures 2, 3 and 4 are plots of the numerical calculations for $\sigma'_p = 1.0$ mrad, 2.0 mrad and 3.0 mrad, respectively. For each light divergence, four types of the entrance slits are used. In each figure, three curves are drawn. The curve with "relative intensity" is the plot of the intensity on the double slit normalized by that for $D = 0$. The curve with "without slit" is the curve of the spatial coherence without the entrance slit. The curve with " d mm slit", where $d = 2, 4, 5$ or 6, is the curve of the spatial coherence with the d mm entrance slit. The horizontal axis represents the separation of the double slit D , and the vertical axis represents the relative intensity or the spatial coherence.

Although the intensity distribution on the double slit is Gaussian, the behaviors of the relative intensity on the double slit are very complicated, especially for small entrance slit and large light divergence. It is due to the diffraction effect. The vibrations of the spatial coherence with the entrance slit are caused by the Fraunhofer diffraction. For the region where this vibration remarkably appears, the spatial coherence with the entrance slit has great discrepancy with that without the entrance slit. Fortunately, this discrepancy is hard to observe since the light intensity is extremely weak for such region.

As we pointed out in the previous section, it is difficult to obtain the exact curve of the coherence in the vertical direction, since the intensity decreases rapidly before the coherence decreases.

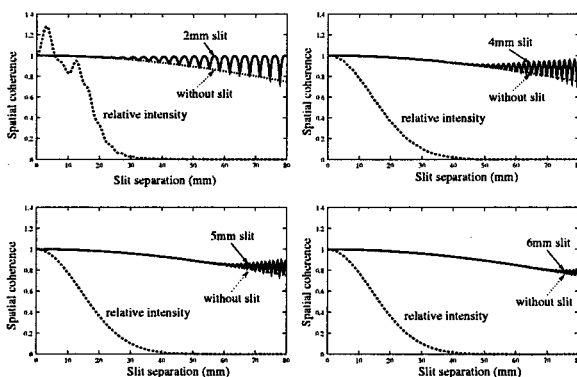


Figure 2: Calculation for $\sigma'_p = 1.0$ mrad.

4 CONCLUSION

The calculation in this paper shows that the electron beam size in the vertical and horizontal directions can be esti-

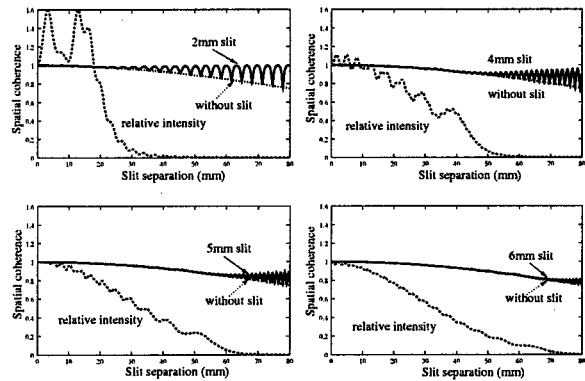


Figure 3: Calculation for $\sigma'_p = 2.0$ mrad.

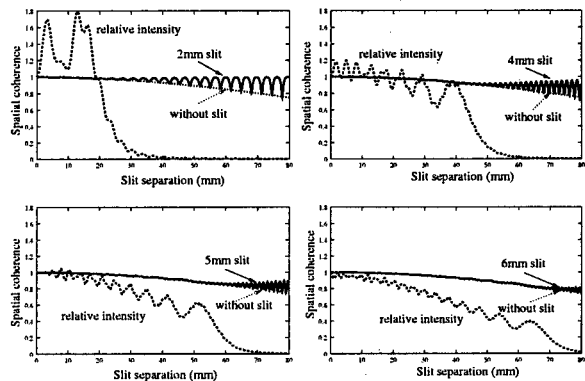


Figure 4: Calculation for $\sigma'_p = 3.0$ mrad.

mated by using the van Cittert-Zernike theorem at the ATF damping ring. There exists an experimental difficulty in the vertical direction because of the weakness of light intensity. This difficulty will be overcome by using the vertical bend as mentioned in another paper [1]. However, the vertical intensity distribution on the double slit might have a very complex form due to the vacuum chamber, which has a chance to improve the spatial coherence. Therefore, the measurement of the intensity distribution on the double slit is significant.

5 ACKNOWLEDGEMENT

The authors would thank to all members of the ATF collaboration to make available discussions and support this work.

6 REFERENCES

- [1] Y. Takayama and S. Kamada, Phys. Rev. E **59** Number 6, to be published (1999).
- [2] T. Naito et. al., "Emission Measurement at ATF Damping Ring", in this conference.
- [3] K. Kubo, "Beam Development In ATF Damping Ring", Proc. of EPAC'98, (1998).
- [4] K-J. Kim, Nuc. Instr. Methods **A246**, 71, (1986).
- [5] Y. Takayama et. al., J. Synchrotron Rad. **5**, 1187, (1998).

RECENT PROGRESS IN EMITTANCE CONTROL OF THE PHOTOELECTRON BEAM USING TRANSVERSE LASER SHAPE MODULATION AND TOMOGRAPHY TECHNIQUE*

M. Babzien, I. Ben-Zvi, R. Malone, X.-J. Wang, V. Yakimenko, BNL, Upton, NY 11973.

Abstract

A low emittance beam is very important for many applications, such as short-wavelength Free-Electron Lasers. A diagnostic that provides detailed information on the density distribution of the electron bunch in multi-dimensional phase-space is an essential tool for obtaining small emittance at a reasonable charge. Accurate phase space reconstruction and an analysis using a transport line with nine focusing magnets and techniques to control the optical functions and phases was demonstrated in previous publication. Relatively long time of measurements (approximately 30 minutes) was improved by installing Hall probes into each quadrupole magnet. This eliminated necessity to degauss all quadrupoles between each measurement points. Additional phase control of RF system and driving laser should also improve confidence in 5 dimensional phase space reconstruction.

1 INTRODUCTION

The determination of the electron beam density distribution in multi-dimensional phase-space is accomplished by the combination of two techniques: The slice-emittance measurement, which provides the longitudinal information, and transverse phase-space tomographic measurement that provides the density distribution in the four transverse dimensions of phase space. Measurement of a slice emittance has been achieved and provided a clear demonstration of the linear longitudinal emittance-compensation scheme [1]. Changing the laser pulse profile of a photocathode RF gun has been suggested as one way to achieve non-linear emittance compensation [2]. The tomographic reconstruction of the phase space was suggested [3] and implemented [4,5] using a single quadrupole scan. In the present work we give special attention to the accuracy of the phase space reconstruction and present an analysis using a transport line with nine focusing magnets and techniques to control the optical functions and phases. This high precision phase space tomography together with the ability to modify the radial charge distribution of the electron beam presents an opportunity to improve the emittance and apply non-linear radial emittance corrections.

2 TOMOGRAPHIC RECOVERY

Tomography is the technique of reconstructing an object from its projections. In the Physics of beams one can use tomographic techniques to reconstruct a beam density distribution in phase space using its projections in real space. In other words, the images of a beam on a phosphorescent screen (taken, for example, by a CCD camera) can be used to derive the phase-space density-distribution. In order to do that, we must be able to rotate the distribution in phase space to generate independent projections on the screen. Changing the beam transport matrix, using variable strength lenses does this.

In order to establish the quality of the tomographic recovery procedure, a special program based on Mathcad was developed. Some of the issues studied were the tolerances for angular and stretching errors in the focusing channel, the required number of measured projections, the effect of smoothening during recovery and more. We concluded that in order to recover features that are about one tenth of the distribution size we should measure 32 evenly space projections and the rotation phase and stretch errors should be of the order of 10% or less.

3 EXPERIMENTAL SETUP

The schematic layout of the ATF acceleration and transport lines that were used in the slice emittance measurement and the tomographic reconstruction is presented in Figure 1.

In the naming convention of ATF elements, the first letter designated a particular straight beam line between bending dipoles, followed by letter(s) designating the type of element, followed by a number, increasing along the beam direction. Thus the H beam line (between the linac and the first dipole HD1) had quadrupole lenses HQ1 through HQ9, pop-up phosphor screen beam distribution monitors HPOP-UP1 through HPOP-UP 2, etc. The beam is generated at the photocathode by a 10 ps long UV laser pulse. A linear emittance compensation solenoid is located right after the RF gun controls the phase space distribution of the electron beam. Two RF linac sections with independent phase control accelerate

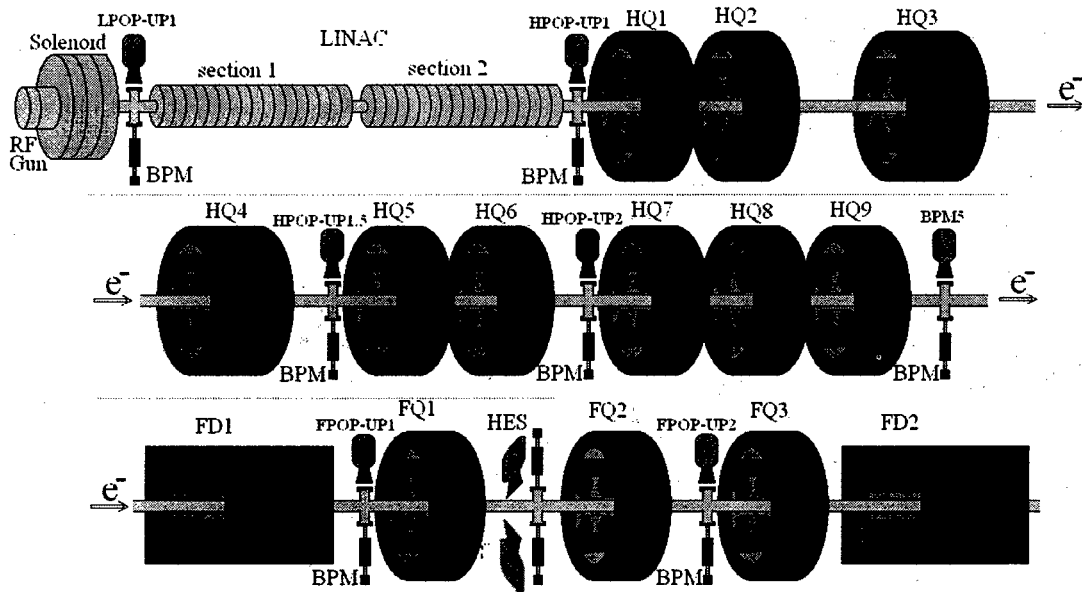


Figure 1. Schematic layout of the ATF accelerator system components used in the slice emittance measurement and the tomographic analysis.

beam from 5 MeV to approximately 50 MeV. The phase of the second section is controlled independently by a motor controlled phase shifter. The H straight line with nine quadrupoles (HQ1 to HQ9) was used to generate rotations (phase advance) without a change in the beam size (constant optical functions). A beam profile monitor (BPM5) was used to measure the projection. The tomographic recovery procedure determines the phase space distribution at HPOP-UP1. The high energy beam is bent horizontally by a 20 degrees dipole magnet and a small slice in energy may be selected by a variable aperture slit. Additional beam diagnostics, located downstream of the slit provide charge and profile information.

4 IMPLEMENTATION OF THE GAUSSMETERS

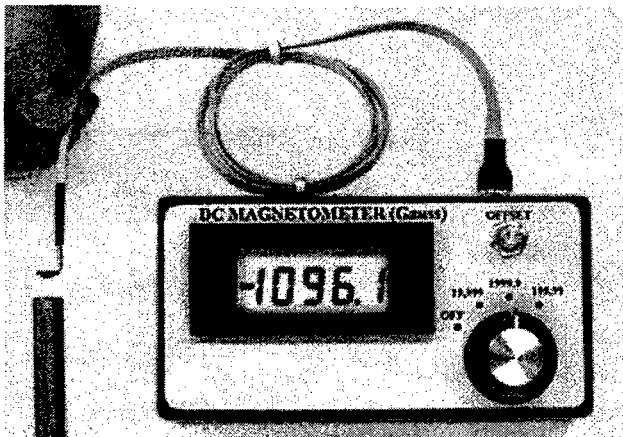


Figure 2. Photo of the DC gaussmeter.

DC gaussmeters were installed into each of the nine quadrupole magnets that we are using to control phase space rotation. This allows us set quadrupole current to desired value and measure actual gradient that effects the beam. Some problem occur during tests:

1. Noise from pulsed RF system was limiting the magnet field measurement accuracy. It was resolved by using rechargeable batteries to power hall probe.
2. The measured quadrupole field error was so far from calculated value that the resulting tune was unacceptable. The two solutions were used to address this issue: partial (fast) degaussing or second iteration for current setting.
3. The magnet power supplies noise limits accuracy of phase control. This problem is currently under investigation.

5 MEASUREMENT PROCEDURE

The tomographic measurement can be broken into a few steps [6].

1. The first step of the tomographic analysis is a measurement of the initial conditions of the electron beam at the linac's exit. The variation of the beam size as a function of current in the first triplet is used to match the optical functions in two directions. In the first step, the graphics window shows the beam size in the X and Y planes as a function of the triplet current. One can observe the fluctuations of the beam size and get a measure of the stability of the system.
2. In the second step, we calculate tunes for the just-measured initial conditions of the beam. A simplex method is used to match the required phase advance and keep the electron-beam conditions at the end of the transport line nearly constant. At this stage, the graphical window shows the variation of the optical functions vs. position along the transport line for each selected value of the phase advance.

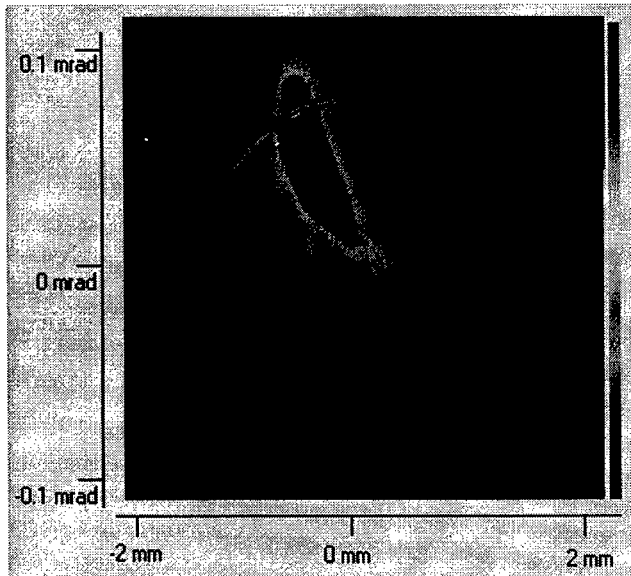


Figure 3. Typical image of the recovered vertical phase space.

3. The third step is to measure the beam projections for the tunes calculated in the previous step. The graphics output window shows the measured projections in the X and Y planes for a particular tune.

4. In the last step we reconstruct the phase space distribution from the measured projections. In this step the graphics window presents the recovered distribution in X-X' and Y-Y' phase spaces.

The tomographic reconstruction of transverse phase space may be combined with the measurement of a longitudinal slice [1], to produce the transverse phase space distribution of a longitudinal slice [5]. This leads to a measurement of the 5 dimensional phase space density distribution in (X, P_x, Y, P_y, Z) . For this purpose we

replace the quadrupole scan emittance measurement by a tomographic analysis of the slice. Tomographic measurements of a slice may be done at FPOP-UP2 in the Y-Y' plane, or in one of the experiment hall beam lines downstream of another dipole (e.g. FD2), which are dispersion free.

6 CONCLUSION

As result of implementation of hall probes the data acquisition for phase space reconstruction was reduced from half of a hour to approximately 5 minutes. It is necessary to further reduce this time to be able reliably recover 5 dimensional phase space. Optimisation of the computer communication procedure can decrease measurement time in our case and will be addressed in near future.

7 ACKNOWLEDGMENTS

This work was supported by Department of Energy Contract DE-AC02-76CH00016

8 REFERENCES

- [1] X. Qiu, K. Batchelor, I. Ben-Zvi and X.J. Wang, Phys. Rev. Let. **76** No. 20, 3723, (1990)
- [2] J.C. Gallardo, BNL Report 522246, (1990).
- [3] J.S. Fraser, IEEE Trans. Nucl. Sci. NS-26, No. 1, 1641 (1979)
- [4] C.B. McKee, P.G. O'Shea and J.M.J. Madey, Nucl. Inst. And Meth. In Phys. Res. **A358**, 264 (1995)
- [5] I. Ben-Zvi, J.X. Qiu and X.J. Wang, Proceedings of the 1997 Particle Accelerator Conference, Vancouver BC Canada, May 12-16, 1997
- [6] V. Yakimenko, M. Babzien, I. Ben-Zvi, R. Malone, and X.-J. Wang, Proceedings of the 1998 European Particle Accelerator Conference, Stockholm, Sweden, June 1998.

SIMULTANEOUS MEASUREMENT OF ELECTRON BEAM SIZE AND DIVERGENCE WITH AN UNDULATOR*

B. X. Yang and A. H. Lumpkin

Advanced Photon Source, Argonne National Laboratory, Argonne, IL 60439, USA

Abstract

We present the simultaneous measurement of beam divergence and source size based on the APS diagnostic undulator line. A 300- μm -thick Si(400) crystal monochromator is used to measure the divergence with a resolution down to 3 μrad (1 μrad with the third harmonic). X-rays transmitted through the crystal are simultaneously used by a pinhole camera to measure the beam size, at a resolution of about 40 μm . We demonstrate that this measurement of emittance is robust against fluctuations of lattice functions due to a partial cancellation of systematic errors present in each of the measurements.

1 INTRODUCTION

Synchrotron radiation imaging is widely used for the measurement of beam size in electron/positron storage rings [1]. With knowledge of lattice beta functions, one can further deduce the particle beam emittance [1-4]. Similarly, undulator measurement of the beam divergence can also be used [3]. Since both of these approaches depend on accurate knowledge of the lattice functions, attempts have been made to use pinhole scan or multi-pinhole aperture measurement with undulator radiation to obtain the emittance independent of lattice functions [5,6]. To date these methods still require long time for data collection or analysis.

In this work, we present theory and an experiment for a new approach also based on undulator radiation. A thin-crystal monochromator is used to measure the x-ray beam divergence while a x-ray pinhole camera is used downstream of the crystal to measure the beam size at the same time. We will demonstrate that the combined measurement of emittance is robust against fluctuations of lattice functions due to a partial cancellation of systematic errors present in each of the measurements.

2 THEORETICAL BACKGROUND

The fully damped, stored electron beam can be well approximated by a Gaussian distribution in the 6-dimensional phase space involving two transverse coordinates (x, y) and angles (x', y') , time, and energy. For an undulator located in a dispersion-free region, we will take a simplified picture where only transverse components are considered in Eq. (1):

$$\rho(x, x', y, y') = \frac{\exp\left\{-\frac{\gamma_x x^2 + 2\alpha_x x x' + \beta_x x'^2}{2\varepsilon_x}\right\}}{2\pi\varepsilon_x} \cdot \{x \rightarrow y\}, \quad (1)$$

where α, β, γ are Twiss parameters and ε is the emittance. In this paper, we will use the center of the undulator as the origin of our coordinate system.

2.1 Monochromatic Divergence Measurement

A single electron traveling through the center plane of the undulator ($z=0$) with transverse coordinates (x, x', y, y') generates a radiation pattern on a downstream detector screen located at $z = S_m$. The pattern centers on the point $(x_m, y_m) = (x + S_m x', y + S_m y')$. For energies at or slightly above the nominal resonance of the undulator, the distribution function can be approximated by a Gaussian-like function [7] with its width given by $\sigma_m = \sqrt{\lambda/2L}$, where L is the undulator length. Under this approximation, the two transverse dimensions are decoupled. Hence we will treat them separately. Multiplying the Gaussian response function with the distribution function of electrons in Eq. (1), and integrating over (x, x') , we get a Gaussian-shaped horizontal profile, with its width given by

$$S_m^2 \sigma_{x, \text{eff}}^2 = (S_m - Z)^2 \sigma_{x'}^2 + S_m^2 \sigma_m^2 + \sigma_{x0}^2. \quad (2)$$

Here the location of the electron beam waist is $Z = \alpha/\gamma$, the width of the beam waist is σ_{x0} , and the beam divergence is $\sigma_{x'}$. For $S_m - Z \gg \beta$, the divergence term dominates in this expression, while the beam size and undulator cone angle are just systematic errors to be corrected.

2.2 Pinhole Camera Source Size Measurement

If the monochromator crystal is thin, substantial high-energy x-ray flux will pass through it, enabling a pinhole camera to simultaneously record the source size. Again we will approximate the angular dependence of the photon beam with a Gaussian function (width σ_γ). For a pinhole located at a distance S from the undulator and S' from the detector screen, the geometrical optical approximation predicts that the image is a Gaussian function with a width, given in the source plane coordinates, of

$$\sigma_{x, \text{eff}}^2 = \frac{S^2 \left(\sigma_{x0}^2 + \sigma_\gamma^2 + \frac{Z^2}{\beta_0^2} \sigma_\gamma^2 \right)}{\sigma_{x0}^2 (S - Z)^2 + \sigma_\gamma^2 S^2 + \sigma_{x0}^2} \sigma_{x0}^2. \quad (3)$$

* Work supported by U. S. Department of Energy, Office of Basic Energy Sciences under Contract No. W-31-109-ENG-38

For a long undulator ($\sigma_y \ll \sigma_x$) and a centered beam waist ($Z = 0$), Eq. (3) predicts that the measured effective size is smaller than the actual beam, due to the high collimation of the undulator beams. While the electrons' angular distribution is independent of their positions at the beam waist, the farther off-axis the electrons, the fewer photons they generate will pass through the pinhole. This results in a systematic error of a smaller measured effective source size, as pointed out previously [2,3,5]. This expression, based on simple geometrical optics models, applies only to the horizontal direction, where the beam size is much larger than the width of the camera point-spread-function (PSF).

2.3 Horizontal Beam Emittance

The expressions for effective divergence and beam size both show strong dependence on β functions, as well as the location of the beam waist, thus making them susceptible to magnetic lattice fluctuations. The product of these two numbers, however, is less dependent on them,

$$\epsilon_{x,eff} = \sigma_{x,eff} \sigma_{x',eff}$$

$$= \epsilon \sqrt{\frac{\beta_0^2 + (S_m - Z)^2 + S_m^2 \frac{\sigma_m^2}{\sigma_{x'}^2}}{\beta_0^2 + (S - Z)^2 + S^2 \frac{\sigma_y^2}{\sigma_{x'}^2}}} \left(1 + \frac{\beta \sigma_y^2}{\beta_0 \sigma_{x'}^2} \right), \quad (4)$$

where β_0 is the β function value at the beam waist.

(1) When the pinhole camera and the divergence measurement are using x-rays of the same energy, we may choose the location of monochromator and x-ray slits to be at the same distance from the undulator, $S_m = S$. Equation (4) can be further simplified to

$$\epsilon \equiv \sigma_{x,eff} \sigma_{x',eff}, \quad (5)$$

with a small correction term (less than 1% for the APS diagnostics undulator, $\sigma_y \approx 2.6 \mu\text{rad}$ and $\sigma_{x'} \approx 20 \mu\text{rad}$).

(2) When the pinhole camera is operating with a broad-band x-ray beam, σ_y increases somewhat, but the correction to Eq. (5) is still expected to be small.

2.4 Fresnel Diffraction Broadening in y-Direction

The diffraction broadening of the pinhole image has been discussed by several authors [2,3], based on the hybrid model in which the geometric shadow of the pinhole and the Fraunhofer diffraction pattern were both approximated by Gaussian function, and the total broadening was assumed to be their convolution. Borland [5] appeared to be the first to point out the inadequacy of Fraunhofer diffraction and briefly discussed the effect of Fresnel diffraction. We have performed a detailed analysis of the PSF based on Fresnel diffraction. The PSF for monochromatic radiation for a pinhole aperture (width = d) can be written as the square of a Fresnel integral. It can be represented by an integral to allow analytical

convolution with a Gaussian source function and a Gaussian spectrum function (polychromatic PSF). The result can then be compared directly with experimentally measured profiles.

3 EXPERIMENT

The experiment was performed at the diagnostics beam line of the Advanced Photon Source. The set up is shown in Figure 1 with relevant parameters given in Table 1.

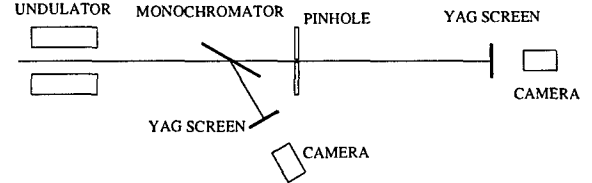


Figure 1: APS diagnostics undulator beamline

Table 1: Parameters for the APS undulator experiment

Undulator, period length, λ_u	18 mm
Undulator length, L	3.56 m
Undulator, fundamental photon energy	25.9 keV
Monochromator to undulator distance, S_m	27.47 m
Monochromator crystal	Si(400)
Monochromator crystal thickness	0.3 mm
Pinhole to undulator distance, S	28.56 m
Pinhole to x-ray camera distance, S'	9.13 m

3.1 Divergence Measurement

The Bragg reflection of a 300- μm Si(400) monochromator crystal was used for the divergence measurement. The crystal angle is chosen to be slightly lower than that for the resonance (10.13°). Integrated intensity profiles were obtained from digitized video images and fitted to Gaussian functions at video frequency (30 Hz). The data are logged at one-minute interval during user runs. Figure 2 shows such a log in a 12-hour run during December 1998. At high current in the fill, the horizontal beam size and divergence were high due to a subtle transverse instability [8]. As current decays, the divergences settle to values independent of the current,

$$\sigma_{x',eff} = 22.8 \pm 1 (\mu\text{rad}), \text{ and } \sigma_{y',eff} = 3.2 \pm 0.2 (\mu\text{rad}), \quad (7)$$

after correction for resolution (3 μrad).

3.2 Source Size from Pinhole Camera

The pinhole camera operates with a broad-band x-ray spectrum. The upstream 300- μm monochromator crystal at 10° grazing incidence angle is effectively a 1.73-mm thick silicon filter, which only allows photons above 15 keV to pass. The calculated angular distribution of the transmitted photons fits well to a Gaussian function ($\sigma_y = 20.3 \mu\text{rad}$). We also found that the measured horizontal intensity profile from the pinhole camera has

a nearly perfect Gaussian shape, giving an effective beam size $\sigma_{x,\text{eff}} = 360 \text{ } (\mu\text{m})$. Correction for instrument resolution is insignificant in this case.

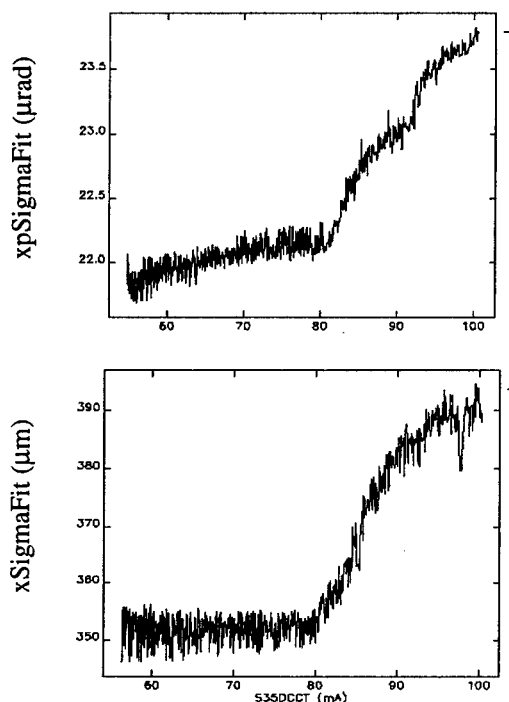


Figure 2: Beam data logged at 1-minute intervals. Upper panel: horizontal beam divergence (μrad); Lower panel: horizontal beam size (μm).

3.3 Horizontal Beam Emittance

Multiplying the effective beam divergence and size, we obtain the horizontal emittance $\epsilon_x = 7.9 \pm 0.5 \text{ (nm rad)}$. This agrees well with the measurement from the bending magnet sources.

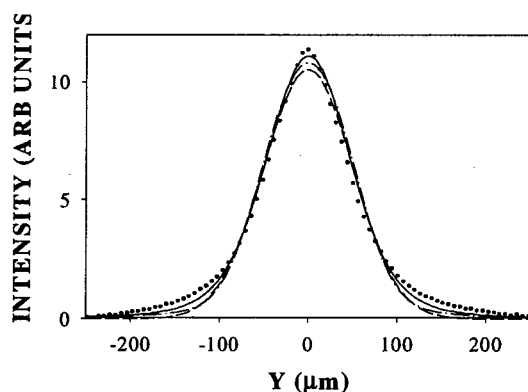


Figure 3: Integrated intensity profile in the vertical direction. (Dots) measured, (dashed line) Gaussian fit, (dash-dot) hybrid model fit with $\sigma_x = 24 \text{ } (\mu\text{m})$, and (solid line) Fresnel diffraction fit with $\sigma_x = 34 \text{ } (\mu\text{m})$.

3.4 Fresnel Diffraction in the Vertical Direction

Figure 3 shows the vertical intensity profile obtained from the pinhole image. Attempts to fit the profile with either a Gaussian function or a hybrid profile function failed due to the pronounced center peak and sidelobes. The polychromatic Fresnel model appears to improve the fit with an effective beam size of $\sigma_{y,\text{eff}} = 34 \pm 7 \text{ } (\mu\text{m})$. The vertical emittance is thus $\epsilon_y = 0.11 \text{ (nm rad)}$. This represents a vertical coupling of 1.4%, larger than that deduced from the measured beam size at the bending magnet source and measured beta functions.

4 SUMMARY

We reach the following conclusions from this work.

(1) By combining a thin monochromator crystal and a pinhole camera with a suitable undulator source, we have demonstrated experimentally that both electron beam divergence and size can be measured simultaneously. The current rate of measurement is limited by the speed of the camera/digitizer at about 30 Hz.

(2) While the lattice function and the properties of the undulator radiation can significantly affect either measured effective beam divergence or size, their product remains a good measure of emittance, robust against fluctuations of lattice α - and β -functions.

(3) We have presented experimental evidence showing that the Fresnel diffraction is valid and important in understanding x-ray pinhole camera data. Its introduction also pushes the fundamental resolution limit below that of the current, hybrid model by $\sim 30\%$.

We wish to acknowledge G. Goepfner, I.-C. Sheng, E. Rotela, and S. Sharma for their help in beamline construction; M. Borland and L. Emery for help with the storage ring experiment; and G. Decker and J. Galayda for their continued support for the project.

5 REFERENCES

- [1] A. Hofmann, "Beam Diagnostics and Applications," AIP Conf. Proc. **451** (3) 1998.
- [2] P. Elleaume, C. Fortgang, C. Penel, E. Tarazona, "Measuring Beam Sizes and Ultra-Small Electron Emittances Using an X-Ray Pinhole Camera," J. Synch. Rad. **2**, (209) 1995.
- [3] C. Zai et al., "Beam Size Measurement of the Stored Electron Beam at the APS Storage Ring Using Pinhole Optics," Rev. Sci. Instrum. **67**, (3368) 1996.
- [4] B. X. Yang and A. H. Lumpkin, "Particle-Beam Profiling Techniques on the APS Storage Ring," AIP Proc. **390** (491) 1997.
- [5] M. Borland, "A Method for Calculating emittance from Undulator Images," SSRL ACD-NOTES 60, 1989.
- [6] C. Zai et al., "Phase-space Measurement of Stored Electron Beam at the Cornell Electron Storage Ring Using a Combination of Slit Array and CCD Detector," Rev. Sci. Instrum. **66**, (1859), 1995.
- [7] K.-J. Kim, "Characteristics of Synchrotron Radiation," AIP Conf. Proc. **184** (565) 1988.
- [8] A. H. Lumpkin, L. Emery, and B. X. Yang, "Observations of 'Effective' Transverse Beam Size Instabilities for a High Current per Bunch Fill Pattern in the APS Storage Ring," these proceedings.

IMPROVEMENTS TO THE FERMILAB IONIZATION PROFILE MONITOR SYSTEMS *

J. R. Zagel, A. A. Hahn, J. L. Crisp, C. Jensen, FNAL, Batavia, IL

Abstract

The Ion Profile Monitor Systems have been studied in the Fermilab Tevatron, Main Injector, and Booster accelerators. These systems capture 64K samples of both horizontal and vertical profiles at a turn by turn sample rate. Some early results have revealed various systematic problems and where improvements in the present system can be accomplished. Identification of these systematics and improvements for these systems are described. An entirely new design is planned which incorporates a magnetic field and can collect electrons instead of ions. In addition, selective gating of the top microchannel plate in a 2-plate system will allow us to minimize saturation and charge depletion problems.

1 CURRENT INSTALLATIONS

Ionization Profile Monitors (IPM) are installed in the Fermilab Booster [1] and Main Injector. Two devices that were previously installed in the Main Ring [2] were removed, new microchannel plate (MCP) glass installed, and then placed in the new Main Injector.

The Booster system has an 8 kV clearing field and currently collects positive ions. The reworked Main Injector devices operate at 28 kV, also collecting positive ions.

2 SATURATION

The system is timed to observe about 1 μ sec of beam at a set time delay from each revolution marker. This time corresponds to just under 1 Booster batch. We would expect that the signal observed should be directly proportional to the number of ions collected. It was recognized that the area of the profile should be consistent throughout the acceleration cycle and proportional to the ionization produced by the fraction of beam current within our 1 μ sec integration time. [3] Area is defined as the sigma multiplied by the amplitude from a gaussian fit. When motion of the beam caused a change in position on the MCP, ions impinging on a different area of the MCP caused greater amplitude peaks for some number of turns. When additional batches are injected, a corresponding loss of signal occurs that is not consistent with any losses noted from the observed batch. Instead a much larger loss is noted in the beam-induced signal. An oscilloscope trace taken during a short run in the Tevatron also showed this behavior.

* Work supported by the U.S. Department of Energy under Contract No.DE-AC02-76CH03000

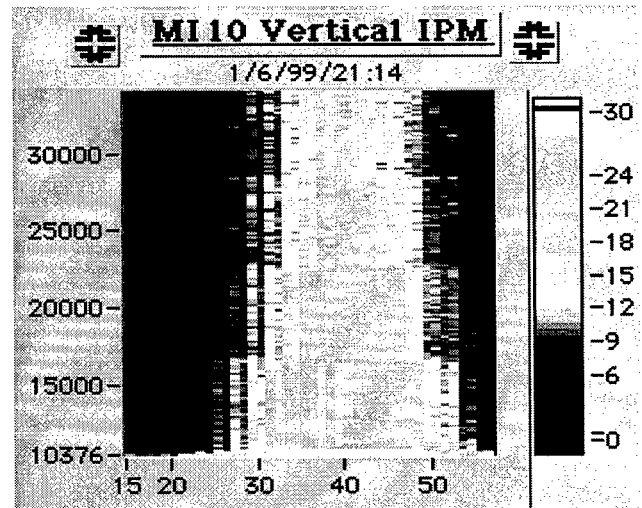


Figure 1. Injection effects on observed batch.

Figure 1 shows the intensity profile for the time period during which 4 Booster batches are injected into Main Injector. The intensity decrease noted after each batch is injected, approximately 6000 samples, is the result of charge depletion from the MCP not beam losses in the observed batch.

Three potential solutions to this problem are: 1. obtain an MCP with greater output current capability, 2. higher gain preamplifiers, or 3. use the dual chevron MCP configuration in a mode where the ion collection plate is used as a fast gate while the lower plate is used to provide gain. This mode of operation allows the signal producing plate to recharge during the off time of the gating plate.

2.1 High Output MicroChannel Plates

The MCP's used in these systems originate from Galileo Corporation. Extended Dynamic Range (EDR) glass is available that can provide a 4 to 10 times improvement in output current. Typically an MCP can provide 10 to 20% of the bias current as a linear output.

Table 1: MicroChannel Plate specifications

MCP Type	Bias Current 1000 Volts	Gain
Long Life	120 μ amps	$2.5 \cdot 10^4$
EDR	420 μ amps	$2.6 \cdot 10^4$

We have been using simple voltage dividers to provide bias voltages for the existing dual chevron plate assemblies. This will not provide the appropriate bias using the newer extended dynamic range glass, which

exhibits much lower impedance. Dual power supplies will be used to provide a separately adjustable bias for each plate. The top plate will then be pulsed to provide a gate consistent with the batch to be observed. For the Fermilab Main Injector the gate will be on for 1.6 μsec out of an approximately 11.1 μsec revolution period.

2.2 Gating MicroChannel Plates

To provide time gating of the micro channel plate, the first stage must be gated by applying a voltage pulse during the time of interest. The ultimate goal is to have this stage go from below threshold to above threshold in approximately 50 nsec (3 empty bunches between batches). The application requires a series of 1.6 μsec pulses to repeat for approximately 1 second and then have 0.5 seconds of off time. There are two approaches, each requiring a fast pulse generator and an isolation transformer: 1) keep the plate biased at below nominal operating voltage and then supply a 200 V pulse, or 2) keep the plate at 0 V and apply the full necessary voltage.

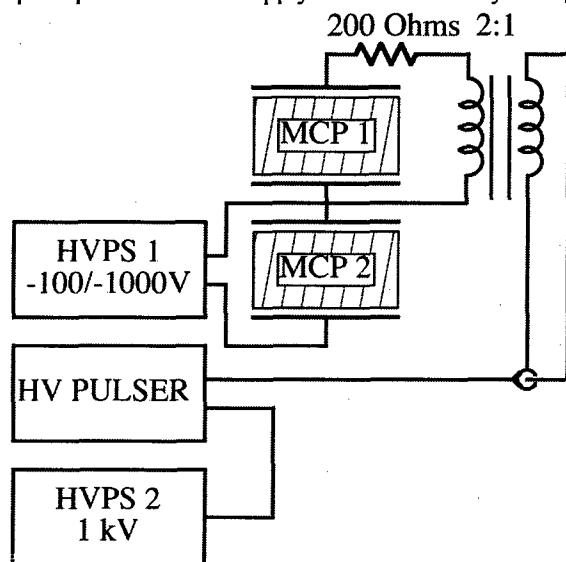


Figure 2: MCP Bias scheme.

The kicker group at Fermilab has developed a fast high voltage pulse generator for their work [4]. This can be used to generate a pulse of up to 800V with a rise time of 15 nsec into 50 Ohms. An additional power supply is needed to remotely control either the variable bias or to supply the variable pulse amplitude from the pulse generator. There is a tradeoff in how much power is dissipated in resistors. For the biased case, a DC blocking capacitor is required but this must be discharged otherwise the pulse current would overcharge it. For the full voltage case, the termination resistor will have a much higher power dissipation. The latter solution requires fewer components, and failures in the circuit tend to inhibit operation of the MCP instead of causing damage. There will be only passive components mounted in the tunnel, external to the vacuum system, connected via several hundred feet of 50 Ω cable.

3 SIGNAL CONDITIONING

When the Main Injector started to ramp we observed a potential difference in tunnel ground as referenced to the service building. The IPM has only a few microseconds to measure nanoamperes of current. Even small differences in ground can cause problems.

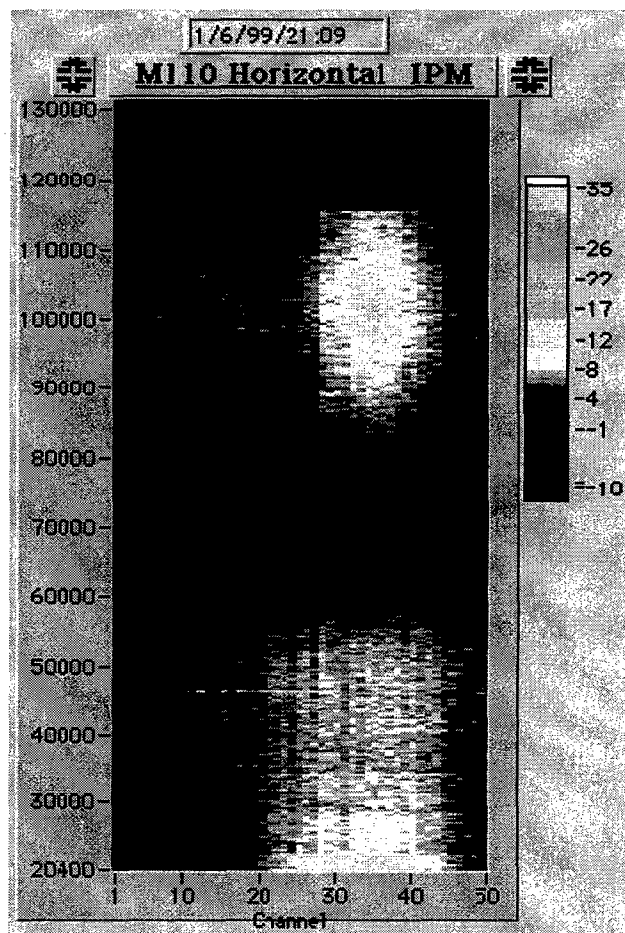


Figure 3: Signal variations through acceleration cycle.

The apparent loss of signal in figure 3, sample 62000 through 77000, is explained by the capacitive coupling of ramp currents into the beam pipe ground. Since the system software calculates a baseline in the fitting routines this does not affect the final profile information. However steps have been taken to capacitively decouple the grounds to prevent possible damage to the amplifiers.

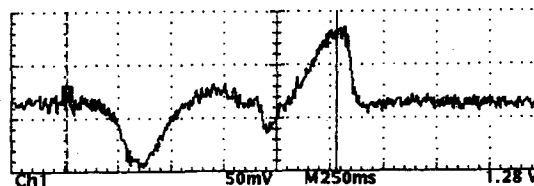


Figure 4: Shorted RG-58 signal as seen from upstairs.

The capacitance to ground in the main bend magnets allows bend bus voltage to induce currents along the beam pipe. As a power supply ramps up, the beam pipe closes the loop between capacitive coupling to ground through the magnets on both sides of the supply. The IPM's in the Main Injector are located 17 meters apart and a power supply feeds the bend bus half way between them. The measured ground potential between IPM's peaks at 150 millivolts and is proportional to dI/dt in the bend buss. Ohms law suggests 5 amps of current flows through the .0017 Ω/m stainless beam pipe separating the IPM's.

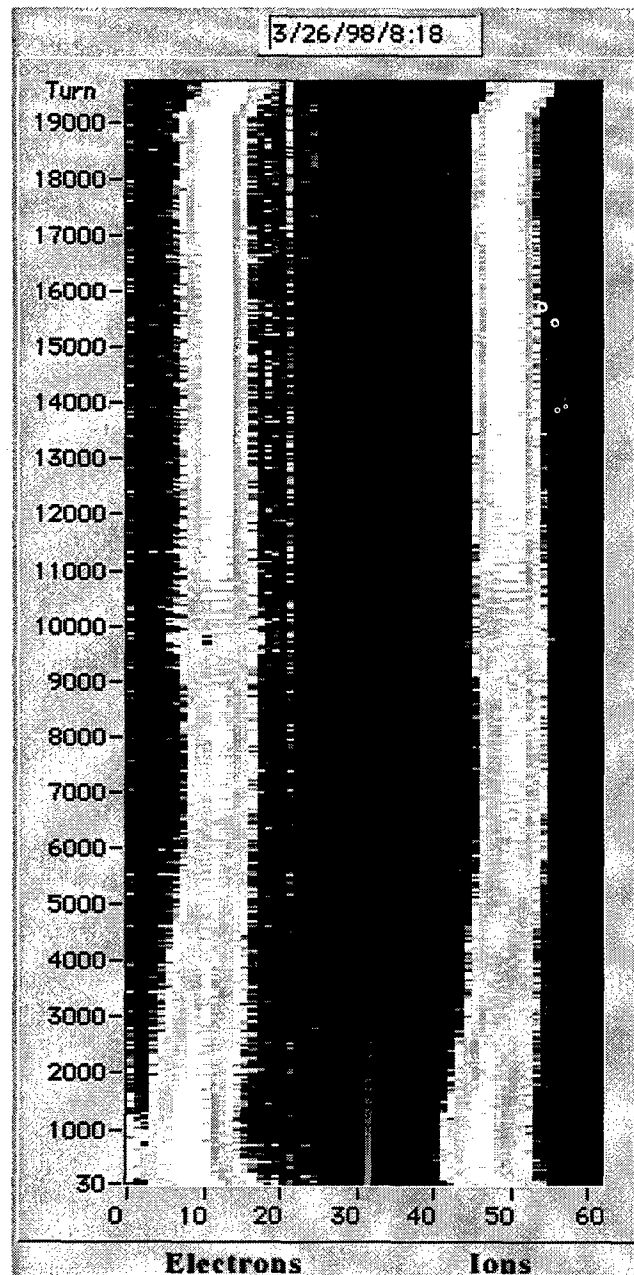


Figure 5: Electron collection test in Booster at 600 gauss.

4 THE CASE FOR ELECTRON COLLECTION

The collection of positive ions produced in the proton beam is problematic in that the space charge of the beam itself contributes to spreading those ions. The problem is exacerbated by the smaller beam sizes, in the Main Injector (1mm) and Tevatron (.5mm), where the spreading increases the measured profiles by up to 500% over the actual beam size. To eliminate this effect we are adding a magnetic field and switching the polarity of the clearing field to collect electrons. An experiment was done in the Fermilab Booster to determine the effects of placing a magnetic field around the IPM and collection of electrons. The conclusion is that electron collection is at least as good as with positive ions. In the Booster the expected ion spreading was at the 10% level at most. We were dominated by systematic effects due to saturation at these signal levels and could not decisively prove that the electron profiles were 10% smaller than the ion profiles. Calculations suggest that a magnetic field of 2000 Gauss for the Main Injector and 3000 Gauss for the Tevatron will be sufficient to contain electrons produced in the beam while they are accelerated toward the MCP. This field will reduce spreading to the 1 to 2% level.

5 WORK IN PROGRESS

High output glass has been installed into the Main Injector IPM's. We are now building the additional power pulsing devices to install for the next run. By using the top plate of the chevron configuration as a gate and the bottom plate for gain we hope to minimize the effects of saturation on the lower plate.

Design work is now being undertaken to produce a magnet and improved mounting scheme for the internal devices to allow us to capture electrons on the MCP's in the Main Injector and Tevatron Installations.

6 REFERENCES

- [1] Zagel, J. R., Chen, D., Crisp, J. L., "Fermilab Booster Ion Profile Monitor System Using LabVIEW", 1994 Beam Instrumentation Workshop, AIP Conference Proceedings 333, pp384-390.
- [2] J. R. Zagel, J. L. Crisp, A. H. Hahn, P.G. Hurh, "Main Ring Ion Profile Monitor System", 1997 Particle Accelerator Conference, IEEE Conference Proceedings 97CH36167, pp2166-2168.
- [3] Alan A. Hahn, and James R. Zagel, "Observation of Bethe-Bloch Ionization using the Booster Ion Profile Monitor", Paper THAR4 of this conference.
- [4] C. Jensen, D. Qunell, "A Thyatron Trigger with Low Jitter", Proceedings of 1997 Particle Accelerator Conference, IEEE Conference Proceedings 97CH36167, pp1281-1283.

NON-DESTRUCTIVE SINGLEPASS MONITOR OF LONGITUDINAL CHARGE DISTRIBUTION IN AN ULTRARELATIVISTIC ELECTRON BUNCH.

P.V. Logatchov, P.A. Bak, A.A. Starostenko, N.S. Dikansky, V.S. Tupikov, K.V. Gubin, V.M. Mishnev, M.B. Korabelnikov, M.G. Fedotov, BINP, Novosibirsk, Russia.

Abstract

We present here the first experimental test of a singlepass non-destructive method of monitoring of longitudinal charge distribution in an intensive relativistic electron bunch. This method is based on the scanning of a thin electron beam within the energy range 20-100 kV in the electromagnetic field of an intensive relativistic bunch.

The probe beam was injected across the path of primary relativistic bunch. This type of an electron beam probe is suitable for both circular or linear accelerators. The prototype results obtained at VEPP-3 storage ring are in good agreement with the calculations and give us a very high degree of confidence that this single bunch diagnostic tool can be very useful not only for accelerator tuning, but also for precise measurements.

1 THEORY

The thin probe beam moves along X axis, is orthogonal to the direction of the relativistic bunch motion (Z axis) with the offset parameter ρ (Fig.1).

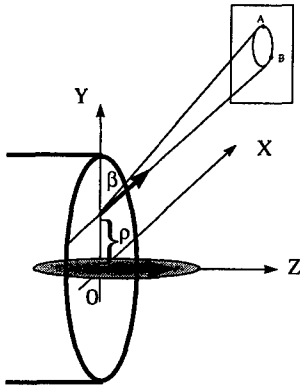


Fig. 1.

The results of scanning are monitored on the screen parallel to the Y-Z plane and positioned at the distance L from Z axis. Let the center of the relativistic bunch is located at the origin at time $t=0$ whereas the testing beam has the uniform density along X and the diameter $d \ll \rho$. Here, we assume ρ exceeds the typical transverse size of the relativistic bunch. At the time $t=0$ every testing beam particle is corresponded to the certain X-coordinate. The total deflecting angle in Y direction for every particle under the influence of the electric field of the relativistic bunch can be expressed as:

$$\theta_y(x) = \frac{2\rho r_e}{\beta} \int_{-\infty}^{+\infty} \frac{n(z) dz}{\rho^2 + (x + \beta z)^2} \quad (1)$$

where r_e is the classical electron radius, $\beta=v/c$ - the relative velocity of the testing beam, c - the velocity of light, x - the coordinate of testing beam particle at $t=0$, $n(z)$ - the relativistic bunch linear density along Z axis. The expression for the deflecting angle of the particle in Z direction due to magnetic field can be written as:

$$\theta_z(x) = 2r_e \int_{-\infty}^{+\infty} \frac{(x + \beta z) n(z) dz}{\rho^2 + (x + \beta z)^2} \quad (2)$$

As a result, the testing beam traces the closed curve on the screen. In assumption of the constant current I of the testing beam one can derive the simple correlation between the X-coordinate and the charge distribution $q(l)$ along the indicated curve on the screen from point A to point B (Fig. 1):

$$x = \frac{\beta c}{I} \int_A^B q(l) dl \quad (3)$$

Integrating the charge along the curve from point A up to point B (Fig.1) one can find the X-coordinate (3) and correspond to it the certain angles $\theta_z(x)$ and $\theta_y(x)$ at point B. Since the dependencies $\theta_y(x)$ and $\theta_z(x)$ are determined, it is possible using any of this functions to restore the dependence $n(z)$:

$$n(z) = \frac{\beta^2}{4\pi^2 r_e} \int_{-\infty}^{+\infty} \theta_y(k) e^{(ikz\beta + |k|\rho)} dk \quad (4)$$

$$\text{where } \theta_y(k) = \int_{-\infty}^{+\infty} \theta_y(x) e^{-ikx} dx.$$

It is necessary to emphasize that dependencies (1), (2) and (4) are valid only for ultra relativistic bunch with $\gamma \gg 1$ and for $\theta_Y^{MAX} \ll 1$ (5). The last condition gives a small perturbation of probe beam longitudinal motion by the electric field of relativistic bunch.

2 EXPERIMENTAL SETUP

The test of the electron beam probe was held at VEPP-3 storage ring at the bunch energy 350, 1200 and 2000 MeV. We placed the device in the straight section

of the ring between two RF cavities. The probe system was evacuated to a typical storage ring vacuum level of 10^{-9} Torr. The schematic diagram of the layout is shown in Fig. 2. The probe electron gun had a flat diode geometry with 0.2 mm diameter anode diaphragm. We used 4 mm dispenser cathode with emission ability 3 A/cm^2 . The maximum pulse current of the probe electron beam was 1 mA at the energy of 60 keV. Axial magnetic focusing lens formed a minimal transverse probe beam size as at the interaction region as on the screen. Transverse correction coils was installed to adjust the position of the probe beam on the screen. We used to direct the probe beam to the thin strip placed just before the Micro Channel Plate (MCP) of 20 mm diameter. It allowed to avoid the MCP saturation by 5 ns , 1mA probe beam and to measure its pulse current. We also measured probe beam energy. These two parameters gave us a possibility to restore the X value (3) or time from the charge distribution on the MCP entrance. The relativistic bunch duration was in the range of one nanosecond, so all voltages on MCP, screen and gun could be considered as constant during this time period. The shortest pulse on the MCP served as a gate pulse. It helped to make a single bunch picture on the phosphor screen (the revolution frequency of the bunch in the ring is 4.03 MHz). To digitise the screen image we used the conventional black and white CCD video camera and special ADC grabber of standard video signal with external start. Synchronous start of the camera is absolutely necessary to the brightness stability of the screen image from pulse by pulse for brightness to charge conversion.

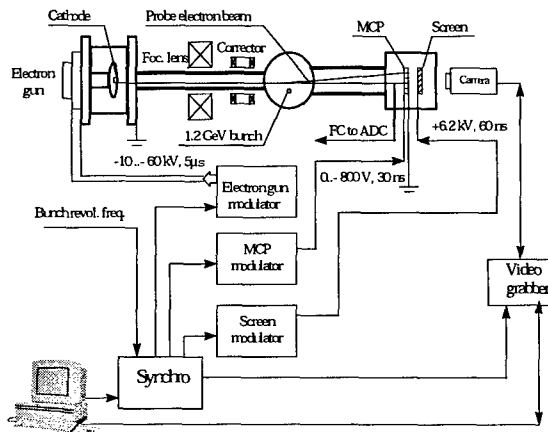


Fig. 2 The scheme of installation.

Since built-in brightness to charge calibration system was not ready at the first set of experiments we used for that purpose longitudinal charge distribution data obtained by dissector [2]. This stroboscopic device works properly for operation with a stable bunch at the time resolution level of 100 ps.

The maximum repetition rate for our system was limited by the screen luminescence time (5 ms) and video

data acquisition time (500 ms). So all presented measurements were made on 0.5 pps.

Probe beam focusing system, all modulators, video and synchronous start system was controlled by computer from the main control room.

3 EXPERIMENTAL RESULTS

At first we adjusted the synchronous start system and modulators to reach a reliable operation with good time stability (a maximum long time jitter was less than 1 ns). The pulse to pulse voltage stability at the moment of relativistic bunch passing was better than 2% for each modulator. Then we checked the surface uniformity of MCP-Screen-Camera conversion system. The nonuniformity less than 3% was detected. All presented measurements were made with 60 keV, 1 mA probe electron beam. The probe beam size was 0.5 mm at the interaction point and 1 mm on the screen. To restore the bunch shape according to (4) we need the ρ value. It was measured directly by moving the probe beam up to the crossing with relativistic bunch trajectory. One can recognise the crossing picture very clearly.

After that we fulfilled the calibration measurements with stable bunch in the ring in order to have a real longitudinal charge distribution in the bunch from the dissector (the longitudinal bunch shape is very close to the Gaussian). Using this data one can calculate the brightness to charge conversion coefficient, pentium-133 can process the image for the time period less than 1 second. Since the range of brightness changing was not so big in comparison with dynamic range of video signal (less than 10%) and MCP-Screen system can be considered as linear within our range of parameters it was possible to use that conversion coefficient for most of our measurements. Fig. 3 shows an example of calibration measurement with a stable bunch state at the energy of 1200 MeV.

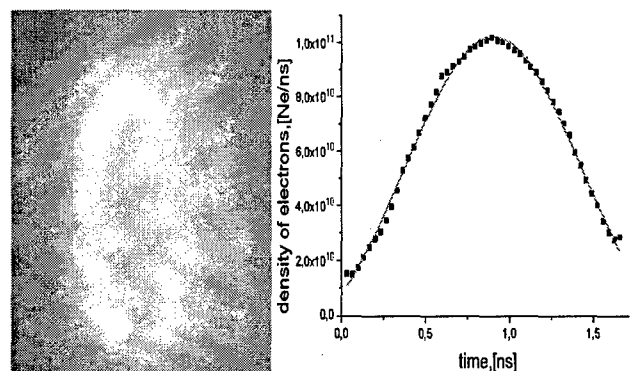


Fig.3 . The calibration measurement with dissector at a stable bunch state. The solid line is a result of the best Gaussian fitting to the dissector data. Dots correspond to our device measurement.

After calibration procedure we used our device to monitor the longitudinal bunch instability. In this case the signal from dissector was very wide and unstable and it had two peaks with flashing amplitudes. Fig.4

shows typical single bunch pictures for that instability at the energy of 1200 MeV.

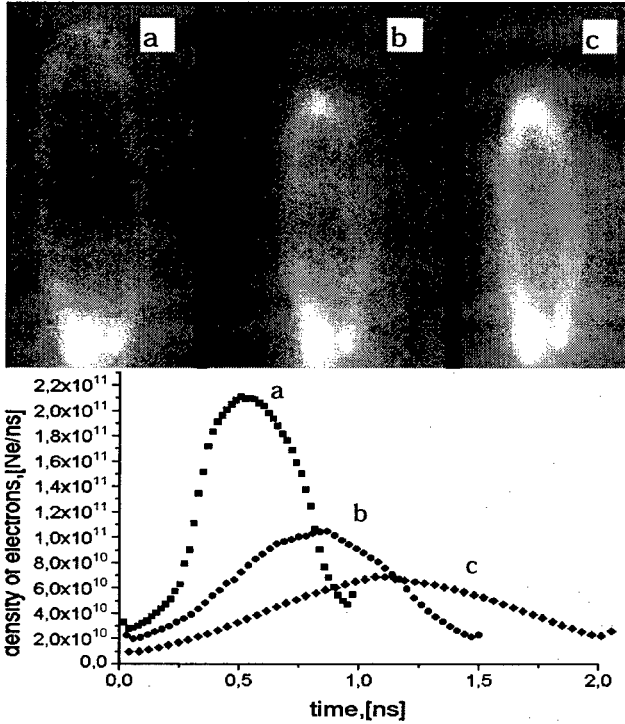


Fig. 4. Typical single bunch pictures for longitudinal instability: (a) - minimum bunch length, (c) - maximum, (b) - intermediate state.

This is just an example to show the ability of the method. But for detail instability analysis one need at least few pictures: for example after 10th, 20th, 30th turn and so on. Unfortunately at existing device we can not make this shot. It need some changes in modulators, additional horizontal scanning system and bigger MCP with screen. We plan all this changes this year as a next step.

4 DISCUSSION

The basic idea of this diagnostic looks simple, but one should be very careful evaluating the time resolution of this method. At first we have a finite angle resolution $\Delta\theta_y$ due to a probe beam size on the screen or spatial resolution of electron detecting system. An angle resolution can be recalculated to a time resolution as follows:

$$\Delta t_1 = \frac{\Delta\theta_y}{\left[\frac{d\theta_y(x)}{dx} \right]_{MAX}} \cdot \frac{1}{\beta c} \quad (6).$$

From the other side the modulation of longitudinal probe beam velocity due to X component of bunch electric field increase the time error value. Total time resolution is given by both effects. Assuming that

$$n(z) = \frac{Ne}{\sigma\sqrt{2\pi}} e^{-\frac{z^2}{2\sigma^2}},$$

we can evaluate time resolution τ in two occurrence:

$$\text{for } \frac{\sigma \cdot \beta}{\rho} \gg 1, \tau \approx \frac{r_e \cdot Ne \cdot \rho}{c \cdot \sigma \cdot \beta^3} + \frac{\Delta\theta_y \sigma^2 \beta^2}{c \cdot r_e \cdot Ne} \quad (6); \text{ and}$$

$$\text{for } \frac{\sigma \cdot \beta}{\rho} \ll 1, \tau \approx \frac{\Delta\theta_y \rho^2}{c \cdot r_e \cdot Ne} + \frac{2r_e \cdot Ne}{c\beta^2} e^{-\sqrt{\frac{\rho}{\beta\sigma\sqrt{2}}}} \quad (7).$$

Our experiment fits the first case, the expression (7) is suitable to linear accelerators. Taking into account the final size of the screen, one can evaluate (6) the time resolution value for our experiment (50 ps). To improve time resolution significantly we plan to rearrange optic and decrease the beam size on the screen. The maximum vertical size of the loop on the screen can be calculated for Gaussian bunch as follows:

$$h_{max} = \frac{Lr_e Ne \sqrt{2\pi}}{\beta^2 \sigma} e^{\frac{\rho^2}{2\beta^2 \sigma^2}} \left(1 - \text{erf} \left(\frac{\rho}{\beta\sigma\sqrt{2}} \right) \right) \quad (8)$$

where L is the distance between the interaction point and the screen. So you can not decrease probe beam energy to much in order to feed the image to the screen.

5 CONCLUSION

The design of the monitor essentially depends on the relativistic beam parameters. We just note the general useful qualities of the method:

1. Ability of simultaneous measurement not only longitudinal distribution of beam density, but the transverse position of its center of mass also [1] (two testing beams - above and below the relativistic beam).
2. Testing beam has practically no influence on the relativistic bunch, so its parameters don't get worse.
3. Small slots for testing beam transit in main vacuum chamber don't change its impedance.

In this year the monitor will be installed either in the (VEPP-4) storage ring and in the linear accelerator (VEPP-5 injector).

6 ACKNOWLEDGMENTS

The authors wish to thank Dr. A.V. Burov, Dr. D.V. Pestrikov and Dr. V.A. Kiselev of the Budker Institute of Nuclear Physics for very usefull discussions.

7 REFERENCES

1. John A. Pasour and Mai T. Ngo «Nonperturbing electron beam probe to diagnose charged-particle beams», Rev. Sci. Instrum. 63 (5), May 1992.
2. E.I. Zinin «Stroboscopic method of electro-optical picosecond-resolution chronography and its application in synchrotron radiation experiments», NIM, 208 (1983) 439-441.

Impulse magnet of positron source with adiabatic field decreasing.

R.M.Lapik P.V.Martyshkin

Budker Institute of Nuclear Physics, Novosibirsk, Russia

1 INTRODUCTION

Positrons produced by conversion target have a large transverse injection angles and wide energy distribution. To capture positrons a matching device which forms a strong magnetic field is used. This field may be achieved only by impulse operated device. This device is utilized to form strong magnetic impulse field (10 T) and uses a capacitor bank.

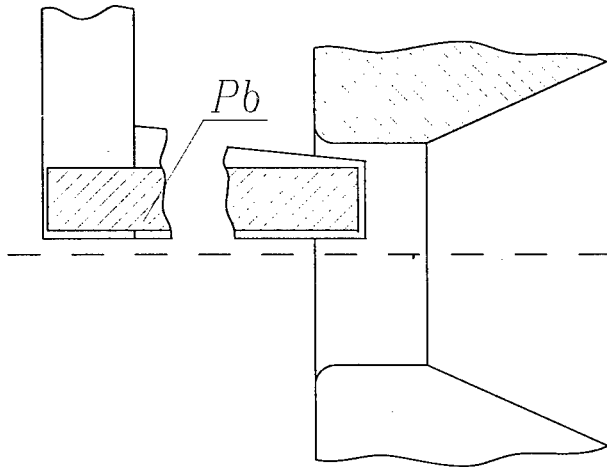


Figure 1: Sketch of capsule lead liquid target and its location relatively marching device.

Incident electron bunch with energy 300 MeV and energy spread $\pm 1\%$ is focused by a triplet on conversion target to beam spot size 1 mm. Electron bunch length is about 6 mm. The total target yield for positron after tungsten conversion target and the one radial angle and energy distributions had been calculated using the electromagnetic shower simulation provided by the GEANT code[1]. The total positron yield defined as the number of positron generated per one incident electron from such a target is about 0.8.

To avoid a thermal heating damage of conversion target is usually utilized a rotated tungsten target with water cooling [2]. To technical unloading of conversion system by a different elements was decided to use a lead liquid target of capsule type (fig.1). The melting of lead is a result of incident electron bunch energy deposition in target material. Application of this target allows to locate it into top magnetic field and doesn't require additional target cooling.

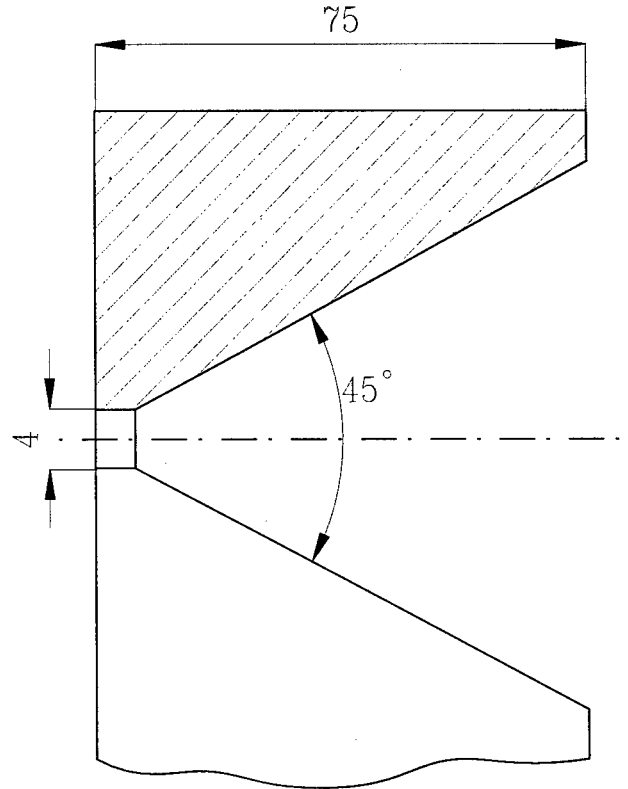


Figure 2: Cross section of pulsed magnet prototype .

2 IMPULSE MAGNET PROTOTYPE

Positron beam injected from conversion target occupies a large space volume and is wide distributed in energy (from several MeV to several dozen MeV). Impulse magnet forms adiabatically decreasing longitudinal magnetic field with required shape. Magnet is located after conversion target and acts as short focal length lens.

To measure a magnetic field of matching device the prototype has been fabricated as a single turn solenoid with a radial cut to center of conical hole. A cross section of pulsed magnet prototype is schematically shown in fig.2. The copper body of prototype is 75 mm along and internal cone angle is 45° . Minimal aperture d of magnet prototype is 4 mm.

The magnet prototype is powered by a sinusoidal shaped current pulse of 75 kA to produce a peak magnetic field of 10 Tesla at a conversion target. The longitudinal mag-

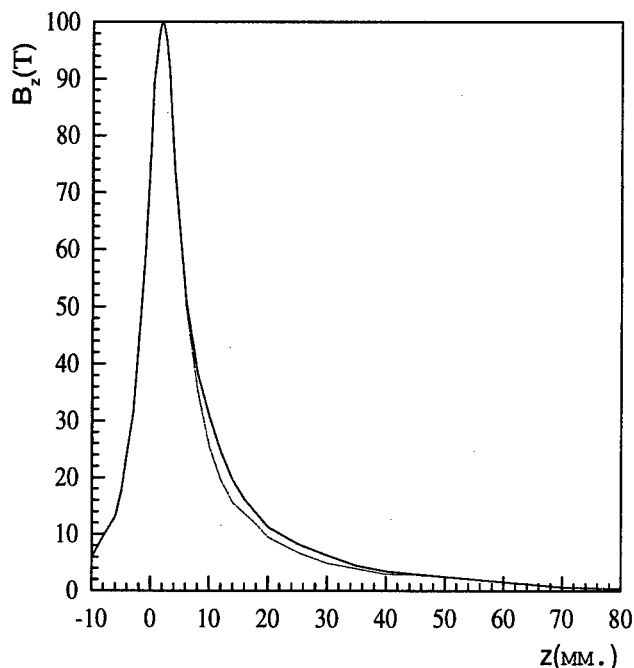


Figure 3: Magnetic field profile along longitudinal axes of prototype. Dashed line – 4 mm solid line 5 mm.

netic field along axis of prototype is presented in fig.3 by a dashed line. Energy deposition of magnetic field inside conical hole of device is about 10 J.

After several tests of a previous magnet prototype the minimal aperture d was increased up to 5 mm and the tests of a second prototype were repeated. The longitudinal field of a second magnet prototype is slight different (fig.3 solid line). To obtain a peak magnetic field strength of 10 Tesla a 100 kA current pulse was required that is increased 30% against of a first pulsed magnet prototype test. Magnetic field strength at rear plane of impulse magnet decreases to 0.1 Tesla for both magnet prototypes.

A current pulse of time length 20 μsec had been used for both test series of magnet prototype. Magnet had been placed on an air and its external body surface was cooled by a water flow. Temperature of magnet body was increased to $40 \div 50^\circ\text{C}$ in $2 \div 3$ hours of test with repetition rate 50 pps. Energy deposition of capacitor bank is triple large the energy deposition of magnetic field inside conical hole.

3 NUMERICAL SIMULATION

For numerical simulation of magnet prototype a special code based on final differences method had been written. This code allows to simulate magnetic impulse field of any magnet geometry with axial symmetry. Conversion target and accelerating structure location is also available to include into consideration.

Close located accelerating structure at rear plane of impulse magnet decreases strength of magnetic field. Fig.4 shows a behavior of magnetic field strength in front plane

of accelerating structure for different cases of structure and impulse magnet position. Minimum aperture of impulse magnet is 5 mm. Distance between structure and impulse magnet was chosen to be 10, 30, 50 mm. Location of magnet rear plane and accelerating structure are marked in fig.4. As one can see, magnetic field strength is decreased fast almost to zero value in front plane of accelerating structure.

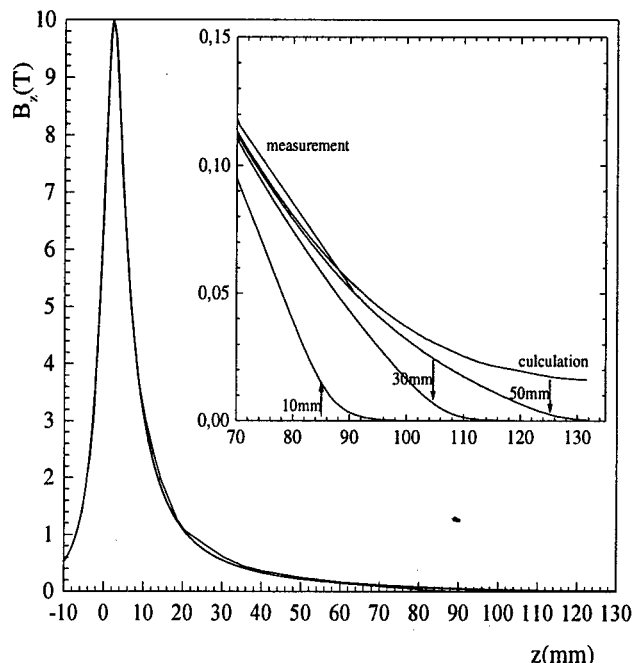


Figure 4: Numerical simulation of impulse magnet with closed location of accelerating structure.

4 CONCLUSIONS

The tests of both impulse magnet prototypes with conversion target demonstrated a technical realizations opportunity of this positron system design. It had been evident, during the operation time, that a 15 Tesla magnetic field strength is quite technically reliable for repetition rate 50 pps.

5 REFERENCES

- [1] GEANT—Detector Description and simulation Tool. CERN, Geneva 1993.
- [2] Stan Encklud Positrons for linear colliders. SLAC-PUB-4484, November 1987(M).

BUNCH LENGTH MEASUREMENTS USING A MARTIN PUPLETT INTERFEROMETER AT THE TESLA TEST FACILITY LINAC

B. Leissner, Ch. Berger, R. Siedling, M. Tonutti, RWTH Aachen, D-52056 Aachen
M. Geitz, G. Schmidt, P. Schmüser*, DESY, D-22603 Hamburg

Abstract

The longitudinal charge distribution of the electron bunches in the TESLA Test Facility linac has been determined using coherent transition radiation produced at a thin metal foil. The autocorrelation of the radiation pulse is measured with a Martin Puplett interferometer and then Fourier transformed to yield the coherent radiation spectrum and the bunch form factor. Several techniques, including a Kramers-Kronig analysis, have been applied to determine the longitudinal bunch charge distribution. Measurements with a thermionic electron gun and a radio-frequency photo injector are presented. The influence of frequency-dependent acceptance corrections is discussed.

1 INTRODUCTION

Future electron drive linacs for Free Electron Lasers in the VUV and X ray regime require the production and acceleration of bunches whose length is in the sub-picosecond regime [1]. Coherent Transition Radiation (CTR) emitted by the electron bunches upon crossing a thin aluminum foil can be used to determine the longitudinal charge distribution. The radiator is oriented at an angle of 45° with respect to the beam direction so that the radiation can be extracted at 90° through a quartz window. The spectral intensity emitted by a bunch of N particles consists of an incoherent and a coherent term

$$I_{tot}(\omega) = NI_1(\omega) + N(N-1)I_1(\omega)|f(\omega)|^2 \quad (1)$$

Here $I_1(\omega)$ is the intensity radiated by a single electron at the frequency ω and $f(\omega)$ is the bunch form factor [2, 3, 4], defined as the Fourier transform of the normalized charge distribution ρ . For a relativistic bunch whose transverse dimensions are small compared to the length the form factor becomes

$$f(\omega) = \int \rho(z) \exp(i\omega z/c) dz = \int c\rho(ct) \exp(i\omega t) dt \quad (2)$$

2 THE MARTIN PUPLETT INTERFEROMETER

The Martin Puplett interferometer used to measure the autocorrelation function of the radiation pulse is shown schematically in Figure 1. The interferometer has been fabricated at the physics institute of the RWTH Aachen according to optical standards and is rigidly mounted on a

* permanent adress: University of Hamburg, D-20146 Hamburg

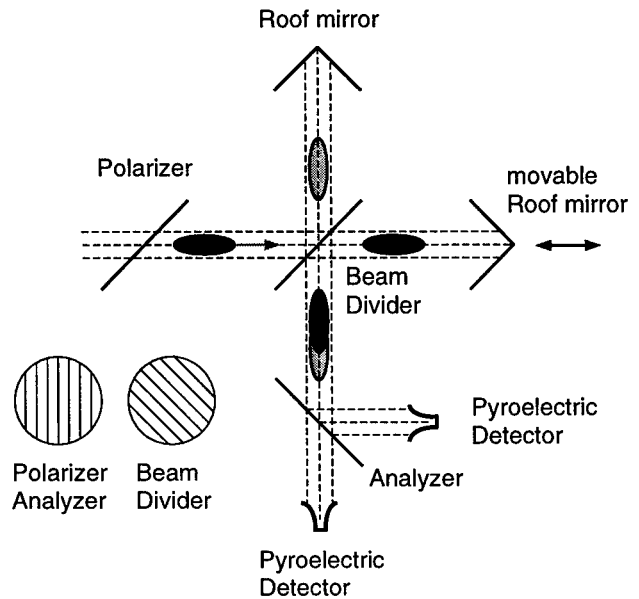


Figure 1: The Martin Puplett interferometer.

40 mm thick aluminum plate. Wire grids wound from $20 \mu\text{m}$ diameter thick gold plated tungsten wire with a spacing of $100 \mu\text{m}$ act as polarizer, beam splitter and analyzer. The incident radiation pulse is polarized horizontally by the first grid and then splitted by the beam divider into components of different polarization entering the two spectrometer arms. The polarization is flipped by the roof mirrors, hence the component first transmitted at the beam splitter is now reflected and vice versa. The recombined radiation is in general elliptically polarized, depending on the path difference in the two arms. The analyzing grid transmits one polarization component into detector 1 and reflects the orthogonal component into detector 2. Two pyroelectric detectors equipped with horn antennas are used as detection devices for the sub-millimeter wavelength radiation. Not shown in the schematic diagram are two parabolic mirrors of optical quality which transform the diverging beam leaving the CTR radiator into a parallel beam and focus the recombined beam onto the detectors.

The result of a scan is shown in Figure 2. Plotted is the response of the two detectors as a function of the time delay between the two spectrometer arms. Both detectors register an autocorrelation signal but with opposite sign. The sum of the two detector signals is a measure of the total radiation power entering the interferometer. The raw data show some fluctuations which occur simultaneously

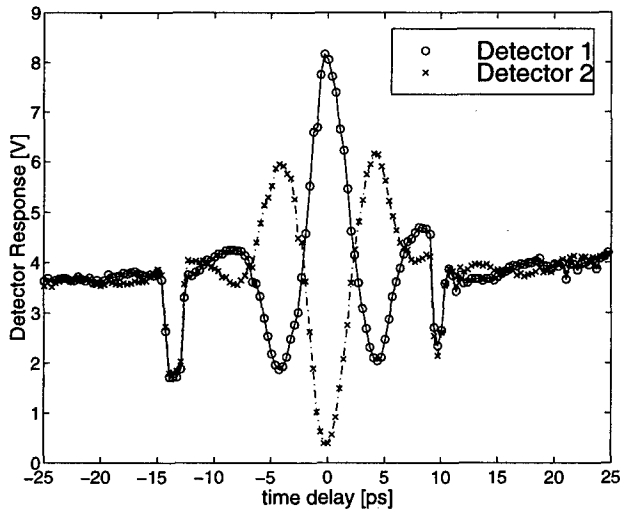


Figure 2: The signals of the two pyroelectric detectors (circles and crosses) as a function of the path difference in the two spectrometer arms. Note the anticorrelation in the interference signals. The correlated fluctuations at -13 ps and +9 ps are due to intensity fluctuations of the electron beam.

in both detectors and can be attributed to instabilities in the electron beam. Such correlated fluctuations can be eliminated by taking the difference of the two detector signals and normalizing it to the sum. The normalized difference interferogram, presented in Figure 3, shows in fact a very smooth behaviour. Remaining statistical fluctuations due to amplifier noise etc are within the size of the data points.

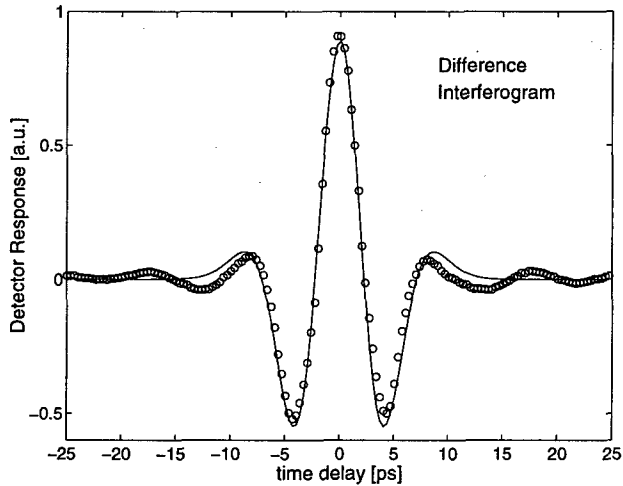


Figure 3: The difference of the signals of the pyroelectric detectors normalized to the sum (open circles). The solid curve is the result of a time domain fit explained in section 3.1. The data were taken with a thermionic cathode.

3 DATA ANALYSIS

The power spectrum of the coherent transition radiation is obtained by Fourier transformation of the autocorrelation

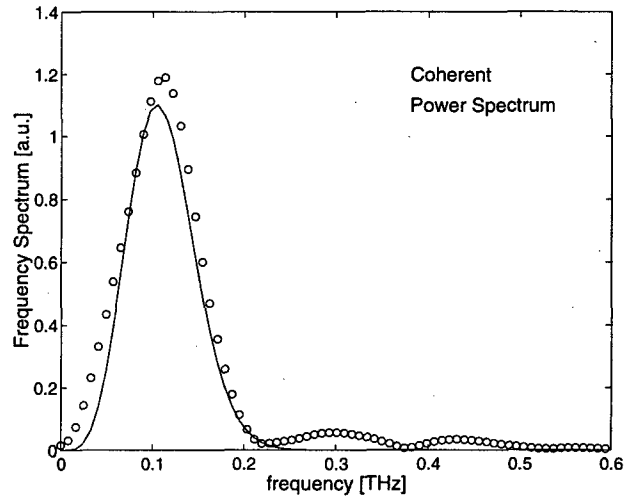


Figure 4: The power spectrum corresponding to the interferogram of Figure 3 (open circles). The suppression at low frequencies is due to the high-pass characteristics of the experimental setup. The solid curve is the frequency domain equivalent of the time domain fit explained in section 3.1.

function. The resulting power spectrum is shown in Figure 4. The power spectrum reveals one of the main limitations in the application of frequency-domain techniques for determining the bunch length: the low frequency part of the spectrum is strongly suppressed. Several effects contribute: diffraction losses due to the limited apertures in the interferometer, the finite size of the radiator foil which leads to a widening of the angular distribution of transition radiation and sensitivity of the detectors at long wavelengths. These systematic effects are still under study. In the following analysis they will be treated in an empirical way only, and the resulting bunch lengths have to be taken with some care.

3.1 Time Domain Fitting

The low frequency part of the power spectrum is suppressed by cutoff effects. Following Murokh et al. [5] we describe this in terms of a filter function

$$g(\omega) = 1 - e^{-\xi^2 \omega^2} \quad (3)$$

where ξ is an adjustable parameter. Assuming a Gaussian longitudinal charge distribution of variance σ , the measured power spectrum is expected to be

$$\tilde{S}(\omega) = e^{-\sigma^2 \omega^2} \left(1 - e^{-\xi^2 \omega^2} \right)^2 \quad (4)$$

Transforming to the time domain we obtain the expected autocorrelation curve

$$S(t) = \left(e^{-\frac{t^2}{4\sigma^2}} - \frac{2\sigma \cdot e^{-\frac{t^2}{4(\sigma^2 + \xi^2)}}}{\sqrt{\sigma^2 + \xi^2}} + \frac{\sigma \cdot e^{-\frac{t^2}{4(\sigma^2 + 2\xi^2)}}}{\sqrt{\sigma^2 + 2\xi^2}} \right) \quad (5)$$

The result of the fit of Equation (5) to the interferogram is presented as the continuous curve in Figure 3. The obtained rms bunch length is $\sigma = 2$ ps. The error of the analysis is dominated by the systematic low-frequency effects and is estimated to be in the order of 20% - 30%.

3.2 Kramers Kronig Analysis

A Fourier transformation of the autocorrelation function yields only the absolute magnitude $|f(\omega)|$ of the form factor. The Kramers-Kronig dispersion relation approach can be used to compute the phase. The so-called minimal phase ψ is given by [6]

$$\psi(\omega) = \frac{-2\omega}{\pi} \int_0^\infty \frac{\ln[|f(u)|/|f(\omega)|]}{u^2 - \omega^2} du. \quad (6)$$

The inverse Fourier transformation yields then the desired longitudinal charge distribution

$$\rho(z) = \int_0^\infty |f(\omega)| \cos(\psi(\omega) + \omega z/c) d\omega. \quad (7)$$

The Kramers Kronig technique will be applied to the interferogram in Figure 5. The low frequency attenuation of the frequency spectrum has been corrected for by smoothly extrapolating the form factor with a fourth order polynomial. The reconstructed bunch form, depicted in Figure 6, is trapezoidal with a FWHM of about 4 ps. It should be noted, however, that the result of the reconstruction depends strongly on the exact parametrization and the starting point and slope of the extrapolation. It is possible to obtain differences of up to 1 ps in FWHM and variations of the shape by varying the initial conditions and the parametrization of the extrapolation.

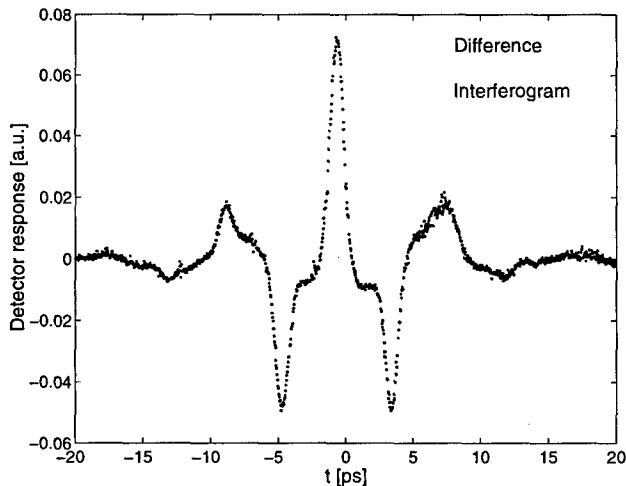


Figure 5: Normalized difference interferogram measured at the TTF linac equipped with an rf photo-cathode and a bunch compressor.

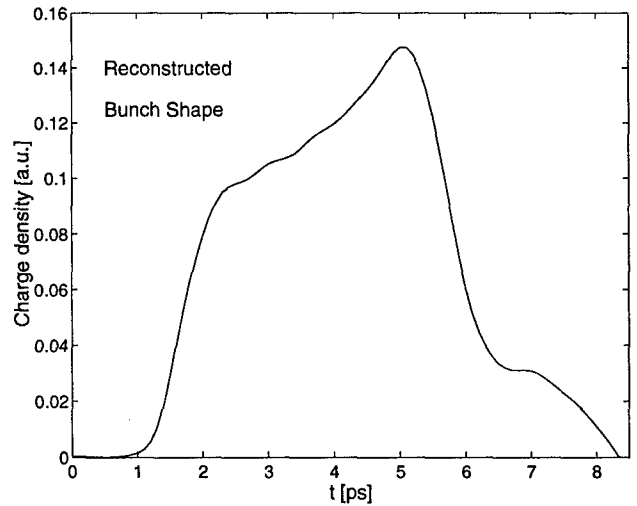


Figure 6: Longitudinal bunch profile as reconstructed by the Kramers Kronig technique.

4 CONCLUSION

A high precision Martin Puplett interferometer has become a standard device for bunch length measurements at the TESLA Test Facility linac. One useful side effect is that the signal amplitude of the pyroelectric detectors increases strongly with decreasing bunch length and can therefore be used as a fast monitor for optimizing the bunch compression in the linac. Bunch lengths and bunch shapes have been determined for various machine configurations. The main problem for precise measurements of picosecond bunches is the not-well known low frequency attenuation of the coherent radiation. Detailed investigations are in progress.

5 REFERENCES

- [1] TESLA - Collaboration, DESY-TESLA 95-01 (1995).
- [2] C. J. Hirschmugl et al., Physical Review A, Vol. 44, No. 2 (1991).
- [3] J. S. Nodvick, D. S. Saxon, Physical Review, Vol. 96, No. 1 (1954).
- [4] E. B. Blum, U. Happek, A. J. Sievers, Nucl. Instr. Meth. A307 (1991).
- [5] A. Murokh, J. B. Rosenzweig, U. Happek, M. Hogan, H. Suk, G. Travish, Phys. Rev. Lett., (1998).
- [6] R. Lai, A. J. Sievers, Nucl. Instr. Meth. A 397, (1997), 221 - 231.
- [7] B. Leissner, PITHA 99/4, (1999).
- [8] K. Hanke, DESY-TESLA 97-14, (1997).

PHASE SPACE TOMOGRAPHY AT THE TESLA TEST FACILITY LINAC

M. Geitz, G. Schmidt, P. Schmüser*, DESY, D-22603 Hamburg

Abstract

The transverse phase space distribution of an electron beam can be determined with a quadrupole scan by measuring the resulting beam profiles via optical transition radiation and applying a tomographic reconstruction method. Phase space tomography has been successfully used at the TESLA Test Facility (TTF) linac equipped with a radio frequency photo-injector. Measurements of phase space distributions and emittances will be presented.

1 INTRODUCTION

To be usable as a driver for an envisaged Free Electron Laser in the VUV regime the TTF electron linac will have to provide 500 MeV to 1 GeV bunches with a charge of 1 nC and a normalized emittance in the order of $1 - 2 \pi$ mm mrad. A laser-driven rf photocathode produces bunches with an rms length of 5 ps which are accelerated to about 5 MeV in a 1 1/2-cell rf cavity. The transverse phase space distribution and emittances of the electron beam are difficult to predict since they depend strongly on the density profile of the laser beam, on space charge forces and on the applied focusing by solenoid fields at the photo-injector. An experimental determination of the entire transverse phase space distribution can be accomplished by applying a quadrupole scan in combination with tomographic image reconstruction techniques [2]. For this purpose a set of quadrupoles is used to rotate the phase space distribution in well-defined angular steps between a reconstruction point z_0 in front of the quadrupoles and an observation point z_1 behind the quadrupoles. The transverse beam density distribution at the observation point is recorded by means of an optical transition radiation screen read out by a CCD camera. The horizontal and vertical beam profiles obtained at the different rotation angles allow to reconstruct the initial phase space distribution at z_0 .

2 PHASE SPACE TOMOGRAPHY

The beam transport from z_0 to z_1 is described by a 4×4 transfer matrix M whose elements are easily computed for given quadrupole settings. The measured horizontal charge density distribution can be expressed in terms of the horizontal phase space density ρ_1 at z_1 by the integral

$$\begin{aligned} p_1(x_1) &= \int \rho_1(x_1, x'_1) dx'_1 \\ &= \int \rho_1(x_1, x'_1) \delta(x_1 - \tilde{x}_1) d\tilde{x}_1 dx'_1. \end{aligned} \quad (1)$$

Using the beam transfer matrix M , equation (1) can be rewritten in terms of the phase space distribution ρ_0 at the reconstruction point z_0

$$p_{1,M}(x_1) = \int \rho_0(x_0, x'_0) \delta(x_1 - M_{11}x_0 - M_{12}x'_0) dx_0 dx'_0. \quad (2)$$

We have added the index M to $p_1(x_1)$ to indicate that the horizontal density distribution at z_1 depends explicitly on the transfer matrix M . In order to be compatible with the algorithms used in conventional computer tomography we introduce a "rotation angle" ϕ by the relations

$$\cos \phi = \frac{M_{11}}{\sqrt{M_{11}^2 + M_{12}^2}}, \quad \sin \phi = \frac{M_{12}}{\sqrt{M_{11}^2 + M_{12}^2}}. \quad (3)$$

This yields

$$\tilde{p}_{1,\phi}(u) = \int \rho_0(x_0, x'_0) \delta(u - x_0 \cos \phi - x'_0 \sin \phi) dx_0 dx'_0 \quad (4)$$

with $u = x_1 / \sqrt{M_{11}^2 + M_{12}^2}$ and $\tilde{p}_{1,\phi}(u_1) = \sqrt{M_{11}^2 + M_{12}^2} \cdot p_{z,M}(x_1)$.

Hence we arrive at the conventional Cartesian rotation by scaling the measured intensity profiles with $\sqrt{M_{11}^2 + M_{12}^2}$ and the x coordinate with $1/\sqrt{M_{11}^2 + M_{12}^2}$. The distribution $\tilde{p}_{1,\phi}(u)$ has to be determined at narrow equidistant angular steps covering at least 180° in order to permit a reconstruction of the distribution ρ_0 which is free from artifacts. In practice the full angular range is often not accessible and the step width may be too large. Interpolation and filtering techniques can be applied to improve the quality of such incomplete scans. A useful filter function is obtained by combining a frequency ramp function $|f|$ with a low-pass filter $L(f)$ [4]

$$w(u) = \frac{1}{8\pi^2} \int |f| L(f) \exp(iuf) df. \quad (5)$$

Here f is a spatial frequency. The filtered profiles are given by

$$p_\phi^F(x_1) = \int \tilde{p}_\phi(\tilde{x}_1) w(x_1 - \tilde{x}_1) d\tilde{x}_1. \quad (6)$$

The low-pass filter suppresses frequencies larger than the sampling frequency of the profiles and the ramp function enhances high spatial frequencies, i. e. profiles with strong curvature. The filtered profiles can now be backprojected to obtain the reconstruction $\rho_0^R(x_0, x'_0)$ using

$$\rho_0^R(x_0, x'_0) = \int_0^\pi p_\phi^F(x_0 \cos \phi + x'_0 \sin \phi) d\phi. \quad (7)$$

* permanent address: University of Hamburg, D-20146 Hamburg

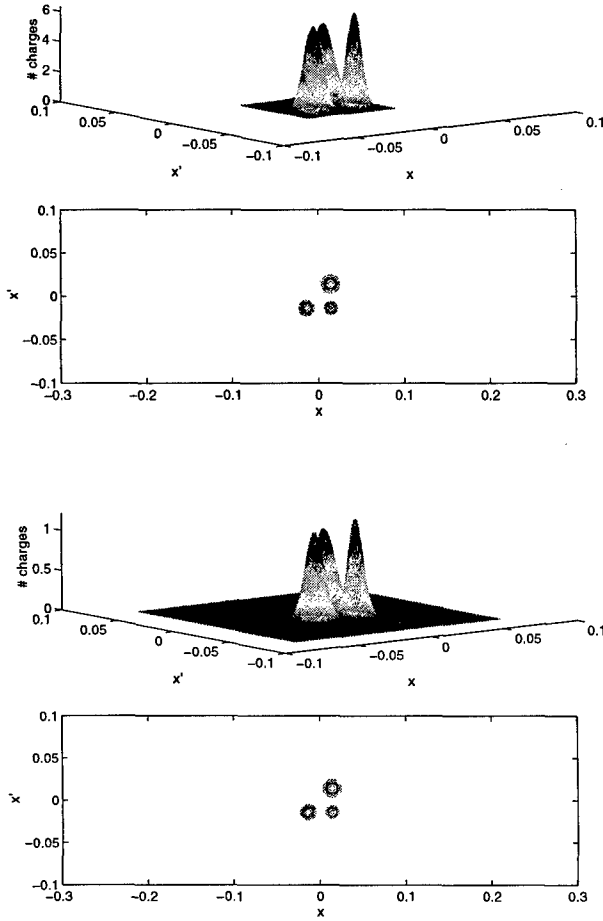


Figure 1: Result of a simulation using an asymmetric phase space distribution consisting of three peaks of different height and width. The agreement of the initial (upper graph) and reconstructed (lower graph) distribution is better than 1 %.

Figure 1 shows a simulation with an asymmetric phase space distribution consisting of three peaks of different height and width. The upper graph shows the initial distribution, the lower graph the reconstruction using 180 projections at a 1° angular spacing. The reconstruction agrees with the initial distribution to better than 1 %.

3 EMITTANCE AND OPTICS PARAMETERS

The emittance is defined in terms of the variances of x and x' by

$$\varepsilon = \sqrt{\langle x^2 \rangle \langle x'^2 \rangle - \langle xx' \rangle^2} \quad (8)$$

with

$$\langle x^2 \rangle = \frac{1}{N} \left(\sum_{i=1}^N x_i^2 \right) - \frac{1}{N^2} \left(\sum_{i=1}^N x_i \right)^2 \quad (9)$$

$$\langle x'^2 \rangle = \frac{1}{N} \left(\sum_{i=1}^N x_i'^2 \right) - \frac{1}{N^2} \left(\sum_{i=1}^N x_i' \right)^2 \quad (10)$$

$$\langle xx' \rangle = \frac{1}{N} \left(\sum_{i=1}^N x_i x_i' \right) - \frac{1}{N^2} \left(\sum_{i=1}^N x_i \sum_{i=1}^N x_i' \right) \quad (11)$$

where N denotes the total number of electrons of the beam. The optical functions α , β , and γ are given by

$$x_{rms}^2 = \varepsilon_{rms} \beta, \quad x_{rms}'^2 = \varepsilon_{rms} \gamma \quad \text{and} \quad (xx')_{rms} = \varepsilon_{rms} \alpha. \quad (12)$$

4 SPACE CHARGE

Linearized space charge forces are implemented into the beam transfer calculations. The lattice needed to compute the transfer matrix M is subdivided into intervals of about 1 mm. At these points, defocusing lenses are placed with

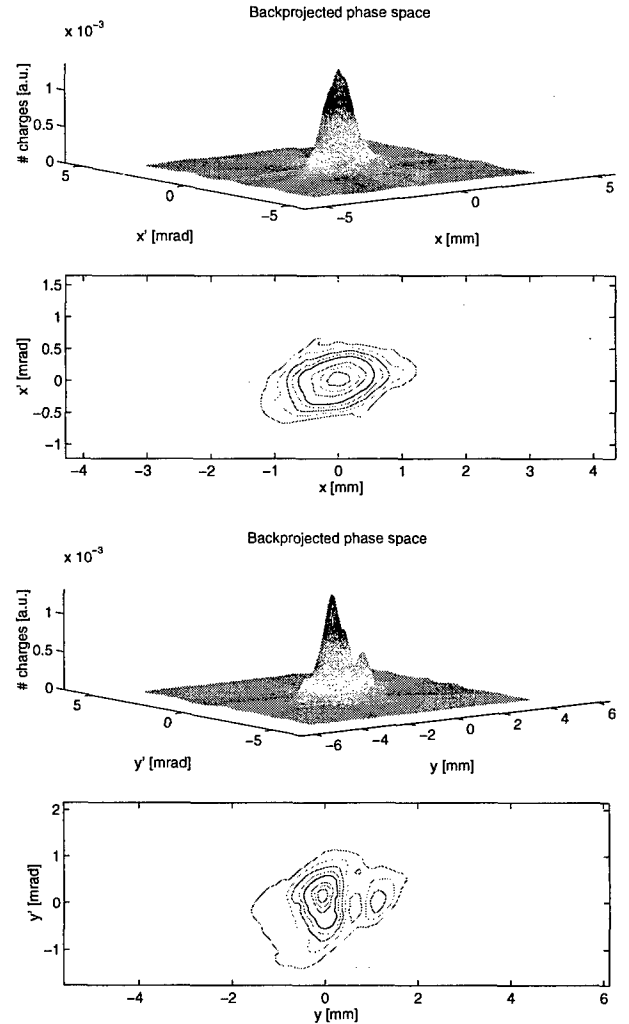


Figure 2: Reconstructed phase space density of the beam emitted by the photo injector, energy 16 MeV, charge 1nC.

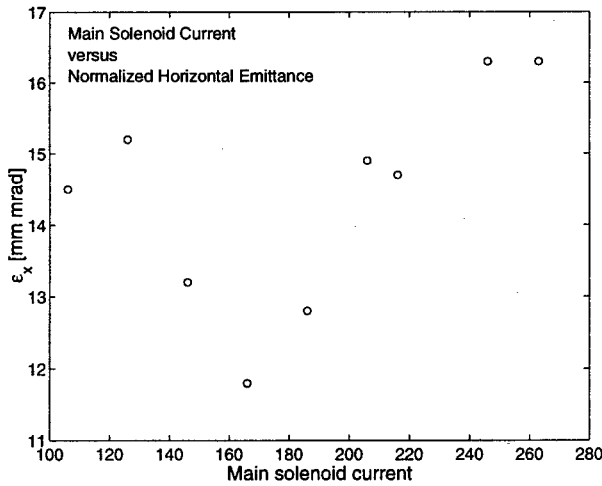


Figure 3: Normalized horizontal emittance versus the primary solenoid current. The secondary solenoid current is held at about 1/4 of the primary current. Note the emittance assumes its minimum of $\varepsilon_x = 11.8$ mm mrad at $I_{prim} = 166$ A, $I_{sec} = 41.5$ A. The systematic error of the emittance determination is about 30 %.

a strength

$$k_x = \frac{2Nr_e}{\sqrt{2\pi}} \frac{1}{\sigma_x(\sigma_x + \sigma_y)\sigma_z\gamma^3}$$

$$k_y = \frac{2Nr_e}{\sqrt{2\pi}} \frac{1}{\sigma_y(\sigma_x + \sigma_y)\sigma_z\gamma^3} \quad (13)$$

where γ denotes the Lorentz factor, r_e the classical electron radius, σ_x , σ_y , and σ_z the rms bunch dimensions. Gaussian-shaped bunches are assumed.

5 MEASUREMENTS AT THE TTF LINAC

A set of quadrupole scans has been performed behind the TTF photo injector and the capture cavity with a bunch charge of 1 nC and a beam energy of 16 MeV. Here, space charge effects cannot be neglected. They are included in the analysis in linear approximation using formulae (13). The horizontal and vertical phase space density of the TTF beam is shown in Figure 2. The normalized emittances measured are

$$\varepsilon_x = (5.5 \pm 2.5) \text{ mm mrad}, \quad \varepsilon_y = (9.5 \pm 3) \text{ mm mrad}.$$

The beam emittance has been determined as a function of the strength of the gun solenoids. A variation with the magnetic field strength has to be expected because of the space charge forces acting on the charge distribution. These intrinsic forces are counter-balanced by the solenoid fields and an optimum setting has to be found for every bunch charge. The horizontal emittance is plotted in Figure 3 for different currents in the primary solenoid [5]. An normalized emittance of $\varepsilon_x = 11.8$ mm mrad has been obtained during the scan of the primary solenoid current between

100 and 270 A. It should be noted that the emittance shown in Figure 2 is smaller because it was obtained after a careful optimization of all injector parameters [5].

6 CONCLUSION

The applicability of transverse phase space tomography has been demonstrated at the TTF electron linac. The technique permits a reconstruction of the transverse phase space distribution and allows the determination of the emittance and the optics parameters. Linearized space charge effects have been included in the beam transfer matrix.

7 REFERENCES

- [1] TESLA - Collaboration, DESY-TESLA 95-01 (1995).
- [2] O. R. Sander, G. N. Minerbo, R. A. Jameson and D. D. Chamberlin, Proc. of the Linear Accelerator Conference 1979, 1979.
- [3] C. B. McKee, P. G. O'Shea, J. M. J. Maday, Nucl. Instr. Meth. A 358, (1995), 264 - 267.
- [4] F. Natterer, The Mathematics of Computerized Tomography, Teubner, Stuttgart, 1996.
- [5] S. Schreiber, private communication.

A HILBERT TRANSFORM SPECTROMETER USING A HIGH- T_c JOSEPHSON JUNCTION FOR BUNCH LENGTH MEASUREMENTS AT THE TESLA TEST FACILITY LINAC

M. Geitz, K. Hanke*, P. Schmüser†, DESY, D-22603 Hamburg

Y. Y. Divin‡, U. Poppe, IFF, Forschungszentrum Jülich GmbH, D-52425 Jülich

V. V. Pavlovskii, V. V. Shirov, O. Y. Volkov, IRE, Moscow 103907, Russian Federation

J. Menzel, M. Tonutti, RWTH Aachen, D-52056 Aachen

Abstract

The longitudinal charge distribution of an electron bunch can be determined from the coherent transition radiation emitted when the bunch crosses a thin metal foil. A Josephson junction made from a thin film of $\text{YBa}_2\text{Cu}_3\text{O}_{7-x}$ on a bicrystal substrate is used as a detector for transition radiation in the millimeter and submillimeter range. The spectral intensity of the radiation and the longitudinal form factor of the bunch are derived by applying a Hilbert transformation to the radiation-induced modification of the current-voltage characteristic of the Josephson junction. The physical principles of a Josephson junction as a detector for submillimeter radiation are outlined and a first bunch length measurement is presented.

1 INTRODUCTION

Future electron-positron linear colliders as well as electron drive linacs for Free Electron Lasers (FEL) in the X-ray regime require the production and acceleration of bunches whose length is in the 50-100 μm range [1]. To determine the bunch length, frequency-resolved techniques are adequate such as far-infrared grating spectroscopy [2] or Fourier-transform spectroscopy [3, 4, 5]. If the wavelength exceeds the bunch length, all electrons in the bunch radiate coherently and the longitudinal charge distribution in the bunch can be obtained by Fourier transformation of the measured frequency spectrum. The spectrometers used for such measurements are usually equipped with mechanically movable elements like mirrors or gratings, hence the recording of the entire frequency spectrum may last several minutes and an average over many successive bunches has to be taken.

Hilbert-transform spectroscopy based on the ac Josephson effect offers the possibility of high-speed spectroscopy in the millimeter- and submillimeter-wavelength range [6]. This technique might even permit single-bunch measurements. The principle is to investigate the modification of the current-voltage characteristic of a Josephson junction due to incident radiation. Applying a Hilbert transforma-

tion the frequency spectrum of the radiation can be derived and, after Fourier transformation, the charge distribution in the bunch can be calculated. A Hilbert transform spectrometer has been tested at the TESLA Test Facility (TTF) linac. In a first stage the device is able to measure the average bunch length during a macropulse.

2 PRINCIPLE OF THE BUNCH LENGTH MEASUREMENT

Transition radiation is produced when relativistic charged particles pass the interface between two materials of different dielectric properties. By arranging the radiation, here a thin aluminum foil, at an angle of 45° with respect to the beam direction, the radiation is emitted at 90° and can easily be extracted from the vacuum chamber through a quartz window. The spectral intensity emitted by a bunch of N particles can be expressed as

$$I_{tot}(\omega) = I_1(\omega)\{N + N(N-1)|f(\omega)|^2\} \quad (1)$$

where $I_1(\omega)$ is the intensity radiated by a single electron at a given frequency ω and $f(\omega)$ is the bunch form factor [7, 8, 9], defined as the Fourier transform of the normalized charge distribution ρ . Neglecting the transverse charge distribution the form factor $f(\omega)$ becomes

$$f(\omega) = \int \rho(z) \exp\left(\frac{i\omega z}{c}\right) dz = \int c \cdot \rho(c \cdot t) \exp(i\omega t) dt. \quad (2)$$

For wavelengths in the order of the bunch length and longer, the form factor approaches unity. The emitted radiation is then coherent and permits a direct measurement of $|f(\omega)|^2$.

3 PRINCIPLE OF HILBERT TRANSFORM SPECTROSCOPY

A Josephson junction serves as a Hilbert transform spectrometer. The electric properties of a junction are determined by Cooper-pair tunneling which leads to the I-U characteristic shown as the dashed curve in Fig. 1. A dc current I_0 can be passed through the junction without observing a voltage drop as long as the current stays below a critical value I_c (dc Josephson effect). For currents

* present address: CERN, CH-1211 Geneva 23

† home address: Univ. Hamburg, D-20146 Hamburg

‡ home address: IRE, Moscow 103907, Russian Federation

above I_c a voltage drop across the junction is observed accompanied with an alternating current whose frequency is given by the relation $\omega = 2eU/\hbar$ (ac Josephson effect, $f_{Jos} = \omega/2\pi = 483.6$ GHz for $U = 1$ mV). When the

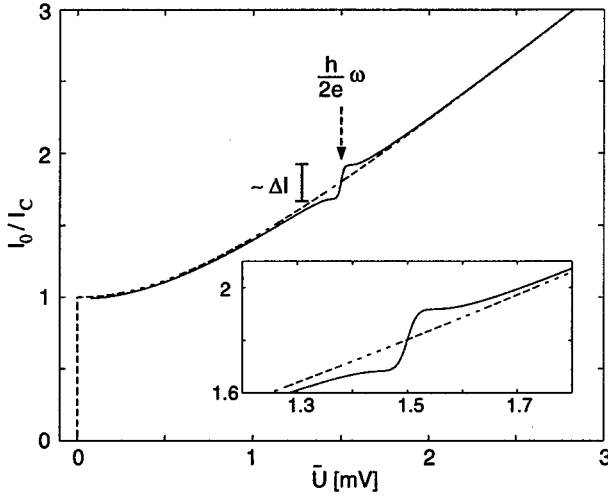


Figure 1: Dashed curve: voltage across the junction as a function of the dc bias current. Solid curve: modification of dc characteristic curve due to monochromatic incident radiation.

Josephson junction is exposed to monochromatic radiation of (angular) frequency ω the current-voltage characteristic acquires a current step ΔI at the voltage $\bar{U} = (\hbar\omega/2e)$, see Figure 1 (\bar{U} is obtained by averaging over the Josephson oscillation). Within the framework of the Resistively Shunted Junction (RSJ) model [11], and in small-signal approximation, the magnitude of this step is proportional to the power of the incident radiation. Hence the junction acts as a quadratic detector and can be used to measure the spectral intensity of a continuous radiation spectrum. For this purpose we define a characteristic function

$$g(\bar{U}) = \frac{8}{\pi} \frac{\hbar}{2e} \cdot \frac{\Delta I(\bar{U}) I(\bar{U}) \bar{U}}{R^2 I_c^2} \quad (3)$$

where R is the ohmic resistance of the junction. The spectral intensity is derived from g by an inverse Hilbert transform [6]

$$S(\omega) = \frac{1}{\pi} \mathcal{P} \int_{-\infty}^{\infty} \frac{g(\omega_0) d\omega_0}{\omega - \omega_0} \quad \text{where} \quad \omega_0 = \frac{2e}{\hbar} \bar{U}. \quad (4)$$

Here \mathcal{P} denotes the principal value of the integral.

To determine the function g the voltage-current characteristic of the Josephson junction is scanned with and without incident radiation, increasing the bias current I_0 in small steps. At each step the voltage \bar{U} and its modification ΔU due to the radiation are measured. ΔI is computed using the differential resistance $R_d = d\bar{U}/dI$ derived from the unperturbed I - U curve.

4 MEASUREMENT OF THE COHERENT SPECTRUM

High- T_c Josephson junctions were fabricated by epitaxial growth of $\text{YBa}_2\text{Cu}_3\text{O}_{7-x}$ on NdGaO_3 bicrystal substrates. A schematic view of the detector which incorporates the antennas for millimeter and submillimeter wave detection is shown in Figure 2. The grain boundary leads to a thin resistive barrier between the two superconductors, which then acts as a Josephson junction. Electrical connections to bias the junction with a dc current and to measure the potential difference across the junction are bonded to the antennas. The junction features a large dynamic range of

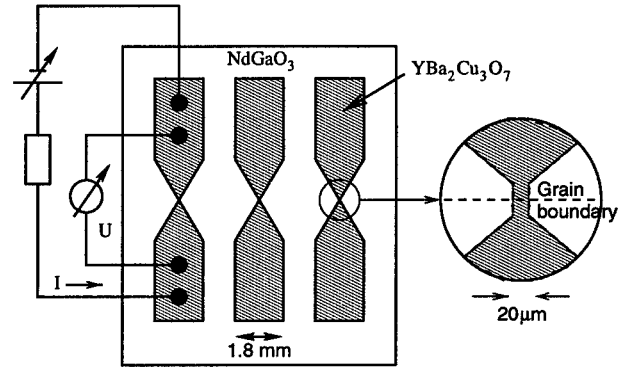


Figure 2: A schematic view of the Josephson junction used as a detector for millimeter and submillimeter wave radiation.

about 10^5 and a high sensitivity of $\approx 10^{-14}$ W/Hz $^{1/2}$ Noise Equivalent Power (NEP) to millimeter- and submillimeter radiation [13]. The resolution is around 1 GHz in the temperature range from 4 to 78 K [14].

The TTF linac was operated with a thermionic gun producing bunches with $2.3 \cdot 10^8$ electrons at a repetition rate of 216 MHz. The macropulse length was 30 μ s at a repetition rate of 2 Hz. Using the compression of a sub-harmonic buncher and a superconducting cavity an rms bunch length of $\sigma_t = 2$ ps was achieved [5, 12]. Fig. 3 shows the measured voltage response of the junction to incident transition radiation and the function $g(\bar{U})$ (as defined by Equation (3)). At small voltages \bar{U} the internal noise of the detector becomes large hence g is obtained in this region by a smooth extrapolation. The intensity spectrum is calculated using an algorithm of discrete Hilbert transform. Fig. 4 shows the evaluated coherent radiation spectrum. The spectrum is plotted in the frequency range between 60 and 260 GHz. Points below 100 GHz are marked by crosses and have to be treated with care. The decrease towards smaller frequencies is mainly due to the cut-off frequency (60 GHz) of the WR-10-type waveguide which guides the radiation to the junction.

The main systematic uncertainty of the present, preliminary, experiments originates from the wavelength-dependent acceptance of the transmission line guiding the

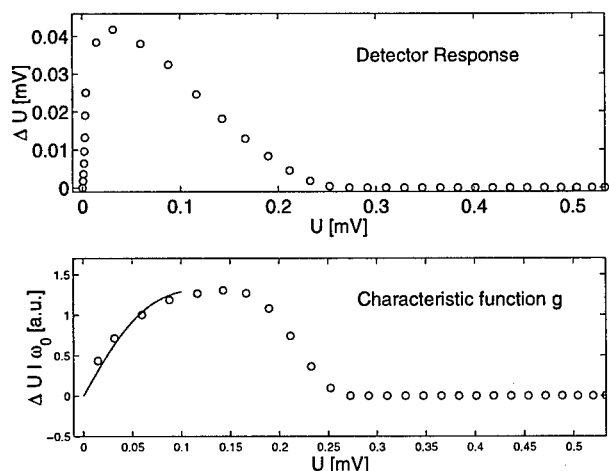


Figure 3: Upper graph: The detector response ΔU as a function of \bar{U} . Lower graph: The characteristic function g , as defined by Equation (3), plotted versus \bar{U} . The solid line shows an extrapolation of g for small \bar{U} .

radiation to the detector. The point-to-point errors are dominated by the read-out errors of the voltage response ΔU of the junction. These values were determined from a digital oscilloscope after averaging over 15 seconds. The present data are not accurate enough to determine the detailed shape of the longitudinal charge distribution. Therefore, a Gaussian shape has been assumed. The Gaussian fit applied to the data, shown as a solid line in Fig. 4, yields

$$\sigma_f = (78 \pm 12) \text{ GHz} \quad \text{or} \quad \sigma_t = (2.0 \pm 0.2) \text{ ps} \quad (5)$$

The error quoted is the statistical error of the fit. The systematic error of the analysis is dominated by the low-frequency attenuation of the coherent radiation spectrum.

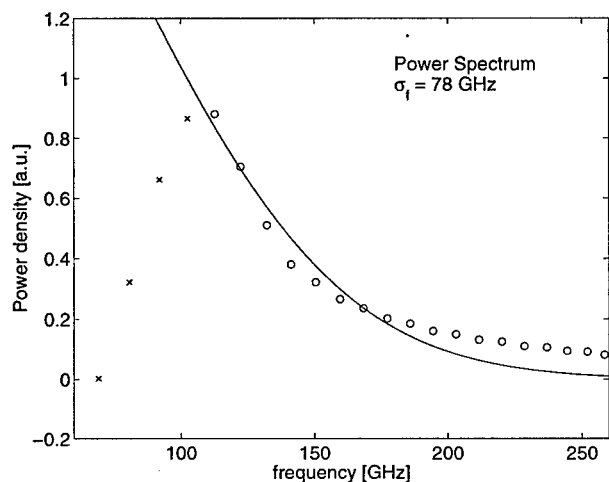


Figure 4: The coherent radiation spectrum as obtained from a discrete Hilbert transform of the characteristic function g . Solid line: Gaussian fit to the power spectrum.

It is estimated to be in the order of 20% - 30%.

5 CONCLUSION AND OUTLOOK

A Josephson junction has been successfully used as a frequency-selective detector for millimeter and submillimeter wave radiation and for a first bunch length measurement at the TESLA Test Facility Linac. It is planned to improve the detector by mounting it into a cryostat with direct optical coupling of the radiation onto the detector. The bandwidth of the read-out electronics will be enhanced to permit measurements of selected bunches within a macropulse.

6 REFERENCES

- [1] TESLA - Collaboration, DESY-TESLA 95-01 (1995).
- [2] T. Nakazato et al. , Phys. Rev. Lett. **63**, 1245 (1989).
- [3] T. Takahashi et al. , Phys. Rev. E **48**, 4674 (1993), and references therein.
- [4] H. Wiedemann, AIP Conf. Proc. 367, 293 (1996), and references therein.
- [5] K. Hanke, DESY-TESLA 97-19 (1997).
- [6] Y. Y. Divin, et al. , Sov. Tech. Lett. **6**, 454 (1980); Y. Y. Divin, et. al. , IEEE Trans. Magn. **19**, 613, (1983).
- [7] C. J. Hirschmugl et al. , Physical Review A, Vol. **44**, No. 2 (1991).
- [8] J. S. Nodvick, D. S. Saxon, Physical Review, Vol. **96**, No. 1 (1954).
- [9] E. B. Blum, U. Happek, A. J. Sievers, Nucl. Instr. Meth. A307 (1991).
- [10] M. Geitz et. al. , DESY-TESLA 98-10, (1998).
- [11] K. K. Likharev, *Dynamics of Josephson Junctions and Circuits*, New York, Gordon Breach, (1996).
- [12] A. Variola, LAL 98-01, (1998).
- [13] Y. Y. Divin et al. , Appl. Phys. Lett. **68** (11), (1996).
- [14] Y. Y. Divin et al. , Physica C **256**, 149 (1996).

PICOSECOND ELECTRON BUNCH LENGTH MEASUREMENT BY ELECTRO-OPTIC DETECTION OF THE WAKEFIELD.

M. J. Fitch^{*†}, A. C. Melissinos[‡], University of Rochester, Rochester, NY
P. L. Colestock[§], FNAL, Batavia, IL

Abstract

The longitudinal profile of an 10 nC electron bunch of a few picoseconds duration will be measured by electro-optic detection of the wakefield. The polarization of a short infrared probe laser pulse (derived from the photocathode excitation laser) is modulated in a LiTaO₃ crystal by the transient electric field of the bunch. The bunch profile is measured by scanning the delay between the laser and the bunch, and is sensitive to head/tail asymmetries. A single-shot extension of the technique is possible using a longer chirped laser pulse.

1 PICOSECOND BUNCH LENGTH MEASUREMENTS

The generation and manipulation of very short electron bunches is important for many applications including future linear colliders, free electron lasers (FELs), and plasma wakefield acceleration. Consequently, methods of measuring the bunch length and temporal profiles of charged particle beams on picosecond and sub-picosecond time scales have attracted great interest.

Notable recent efforts have used coherent radiation from an electron bunch. Coherent transition radiation (CTR) has been analyzed with far-infrared interferometry [1, 2] with impressive results. Since the measured signal is an autocorrelation, it is symmetric in time and insensitive to head-tail asymmetries. Cherenkov radiation has been examined with a 200-fs streak camera [3]. Below 1 ps, streak cameras are increasingly costly and inefficient. A Hilbert transform spectrometer employing a Josephson junction detector [4] can also be used to analyze the millimeter and submillimeter radiation from CTR.

Ideally, it is desirable to know the longitudinal phase space distribution function, not just the rms width (the bunch length) of this distribution. Frequency-domain techniques may suffer from the problem of missing phase information, though reconstructing the charge density from the form factor using Kramers-Kronig relations [5] may be an improvement. Time-domain techniques do not suffer from requiring *a priori* assumptions on the longitudinal bunch shape. A recent example of a time-domain study using an rf zero-phasing method is Wang, *et al.* [6]. The imposed

longitudinal momentum spread of the zero-phasing cavities is transformed into a horizontal position spread in a spectrometer bend. However, the intrinsic energy spread of the bunch must be small compared with the correlated energy spread from the zero-phasing cavities. This condition is well satisfied by the DC thermionic beam of Wang, *et al.*, and they achieve 100 fs resolution. For a high-brightness photoinjector beam, this condition seems difficult to satisfy.

For beams of high average power, such as the TESLA design [7], non-interceptive, minimally invasive measurement techniques are desired. Our current effort is to develop a time-domain longitudinal profile measurement based on electro-optic sampling at Fermilab's AØ Photo Injector (AØPI), made possible by the combination of a high-charge (10 nC) high-brightness electron beam and synchronized picosecond laser pulses.

2 ELECTRO-OPTIC SAMPLING

In a nonlinear optical crystal, an applied electric field modulates the polarization of light passing through the crystal. This electro-optic, or Pockels effect has wide-ranging applications.

The principle of electro-optic sampling (EOS) is to use a short laser pulse as a probe of the fields in the crystal by measuring a polarization change as the relative delay is scanned. Since the first studies of EOS on an electric field injected into a crystal [8, 9], EOS has been demonstrated in various materials to have multi-THz bandwidths [10, 11]. Electro-optic detection of field transients propagating in free space has been demonstrated in the far-infrared [12] and also in the mid-infrared [13].

The passage of a very short, high-charge, relativistic electron bunch is accompanied by a strong transient electric field—the wake field. In the lab frame, the electric field is relativistically flattened to a radial pancake. A simple estimation of the magnitude of the field may then be obtained using Gauss' law. Treating the electron bunch as a line charge ($Q = 10$ nC), the radial field is

$$\int_S \vec{E} \cdot d\vec{A} = \frac{q}{\epsilon_0} \quad (1)$$

$$|E_r| = \frac{q}{2\pi\epsilon_0 al} = 3 \text{ MV/m.} \quad (2)$$

where we have taken the bunch length to be $l = 3$ mm for a 10 ps bunch, and have evaluated the field at a radius $a = 2$ cm.

* Fermilab Beams Division Graduate Fellow

† Email: mjfitch@pas.rochester.edu

‡ Email: meliss@urhep.pas.rochester.edu

§ Email: colestock@adcon.fnal.gov

Calculating wake fields or the Fourier transform beam impedances [14] is an important research activity. A more accurate calculation including the boundary conditions of the beampipe walls can be made with various computer codes. For example, ABCI gives for the iris of the AØPI gun a field magnitude $|E_r| = 1.5$ MV/m.

2.1 The Photo Injector Beamline

Fermilab's AØPI is a TESLA prototype injector [15, 16] with a Cs₂Te photocathode in a 1.625-cell L-band Cu gun with a solenoid lens. A superconducting Nb 9-cell "capture" cavity [17] accelerates the beam to 18 MeV followed by magnetic compression in a dipole chicane.

The laser system is described elsewhere [18, 19]. Briefly, an actively modelocked Nd:YLF oscillator at 81.25 MHz is phase-locked to the rf with ~ 1 –2 ps rms jitter. These pulses are stretched and chirped in a 2 km single-mode fiber. A fast electro-optic pulse picker selects a 1 MHz pulse train for amplification in a chain of Nd:glass amplifiers. After grating compression to 1–2 ps FWHM, the 1054 nm infrared pulses pass through two BBO crystals, generating the second and fourth harmonics to green (532 nm) and UV (263.5 nm). Full charge operation requires 3–5 μ J UV per pulse for quantum efficiencies of order 1%, and the laser can provide 200 μ sec pulse trains adequate for full charge, and longer 800 μ sec trains at reduced charge.

After the harmonic generation crystals, a dichroic beam-splitter separates the colors: the unconverted infrared passes through a delay stage (with a stepper motor) and is expanded and transported to the beamline enclosure as a probe beam; the UV is expanded and transported to the cathode. Since the ~ 1 ps UV pulse is undesirably short, it will be temporally manipulated to a 10 ps quasi-flat-top by a pulse stacker. The pulse stacker is a compact arrangement of multiple delay lines arranged around a single UV beam-splitter [20] and this work in progress will be described separately. Both the infrared and UV beams share the same evacuated transport line, and so are combined and separated at either end with dichroic beamsplitters. From the first dichroic to the cathode, the UV transmission is measured to be $78 \pm 2\%$.

2.2 Expected Signal

We have chosen a crystal of lithium tantalate (LiTaO₃) based on the high electro-optic coefficient and good transparency at our infrared laser wavelength and at the millimeter waves of the transient field. The crystal is 7 mm \times 8 mm \times 1.5 mm, and is cut with the \vec{c} -axis (with extraordinary index of refraction n_e) parallel to the longest dimension, and the \vec{b} -axis the shortest dimension (ordinary index n_o for this and the \vec{a} -axis). See Fig. 1.

To avoid conductors which perturb the electric fields, the crystal is mounted in a vacuum cross with a machined Macor ceramic holder, and is just recessed into the cross to avoid being hit by the beam.

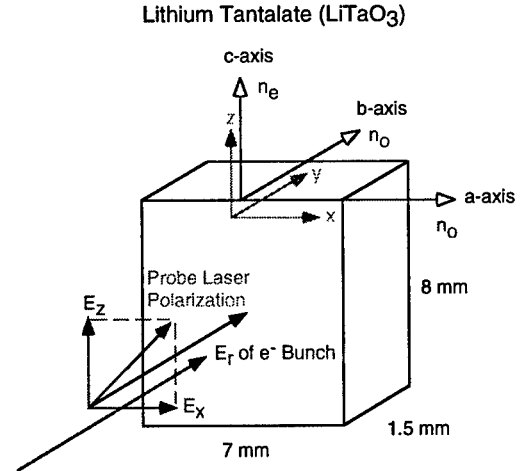


Figure 1: Electro-Optic Crystal: Detailed Axis Geometry

The probe laser is linearly polarized at 45° with respect to the ordinary and extraordinary optic axes. The laser and the transient pulse propagate colinearly in the y -direction, which coincides with the crystal \vec{b} -axis. Due to the static birefringence, the laser ($\hbar\omega$) becomes elliptically polarized:

$$\delta\phi_{nat} = \frac{\omega}{c}(n_e - n_o)\delta y, \quad (3)$$

An additional phase shift is acquired in the presence of the transient field:

$$\delta\phi_{tra}(T) = \frac{\omega}{c}n_o^3 r_{22} E_{tra}(T)\delta y. \quad (4)$$

where the appropriate electro-optic coefficient is $r_{22} = 1 \times 10^{-12}$ m/V and the index is $n_o = 2.154$, so that a 1 MV/m field accumulated over 2 ps ($ct = 0.6$ mm) gives a phase shift of 36 mrad, or $\sim 2^\circ$.

This phase shift is analyzed by a polarizing cube beam-splitter and two photodiodes (see Fig. 2). The static birefringence is compensated by a waveplate which balances the current in the two photodiodes. By detecting the difference current between the pair of photodiodes, small photomodulation depths can be observed, particularly with the signal averaging of a lock-in amplifier. While it may be possible to use a lock-in with our 1 MHz pulse trains, we have concentrated on single-shot difference current measurements. While 10^{-3} is adequate for the above estimate ($\sim 1\%$), and increased signal-to-noise ratio is greatly desired.

Group velocity mismatch between the probe laser and the transient field causes slippage, and degradation of the time resolution. The common approach is to use a very thin crystal, or a complicated geometrical phase matching.

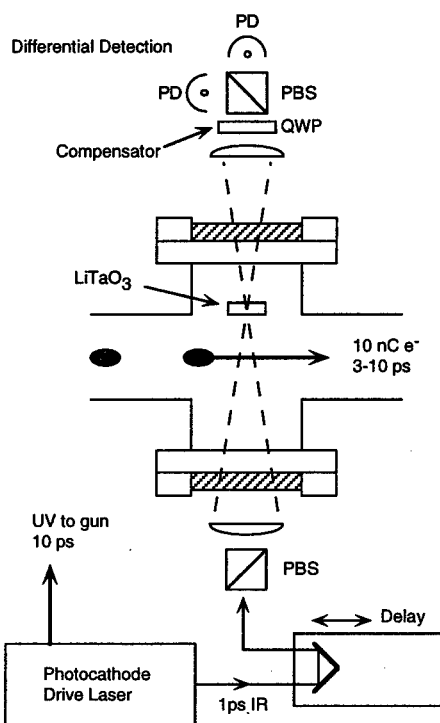


Figure 2: The probe laser passes completely through a vacuum cross with the LiTaO₃ crystal mounted in a Macor holder (not shown). The polarization change is analyzed by a polarizing beam splitter (PBS), balanced with a quarter-wave plate (QWP) and detected with a balanced pair of photodiodes (PD).

We have chosen a simple colinear geometry [21, 22] since for the large group velocity mismatch of LiTaO₃, the transient field is nearly stationary so that the laser sweeps over the entire portion of the waveform that is inside the crystal. The desired waveform is recovered by numerical differentiation.

3 EXPERIMENTAL PROGRAM

Once the issues of signal detection, timing, data acquisition, *etc.* are resolved, there are several interesting studies that can be done. A careful study of magnetic bunch compression in the dipole chicane would allow comparison of the bunch length (and profile) measured with electro-optic sampling to traces of a streak camera. Since the UV pulse length on the cathode has some degree of adjustability, the optimum can be found.

An extension of this scheme to a single-shot measurement using a longer chirped laser pulse and a grating spectrograph [23] is under consideration. In this case, the correlation of frequency versus time (the chirp) replaces the scanning delay, although the time resolution is broadened

due to a convolution effect. As the technology of picosecond semiconductor diode lasers improves [24], it may be possible to greatly reduce the size, cost, and complexity of the laser, so that a stand-alone electro-optic bunch length monitor might be realized.

4 REFERENCES

- [1] Pamela Kung, Hung-chi Lihn, Helmut Wiedemann, and David Bocek, *Phys. Rev. Lett.* 73 (1994), p967-970.
- [2] Y. Shibata *et al.*, *Phys. Rev. E* 50 (2-B) (1994) p1479.
- [3] Mitsuru Uesaka, Toru Ueda, Takahiro Kozawa, and Toshiaki Kobayashi, *Nucl. Instr. Meth. A* 406 (1998) p371-279.
- [4] M. Geitz *et al.*, DESY-TESLA 98-10, April 1998.
- [5] R. Lai, U. Happek, and A. J. Sievers, *Phys. Rev. E* 50 (1994), pR4294-R4297.
- [6] D. X. Wang, G. A. Krafft, and C. K. Sinclair, *Phys. Rev. E* 57 (1998) p2283-2286.
- [7] D. Edwards, editor, "TESLA Test Facility Linac - Design Report", DESY-TESLA 95-01 (1995).
- [8] J. A. Valdmanis, G. Mourou and C. W. Gabel, *Applied Physics Letters*, 41 (1982), p211-212.
- [9] J. A. Valdmanis, G. Mourou and C. W. Gabel, *IEEE J. of Quantum Electronics*, QE-19, (1983) p664-667.
- [10] Q. Wu and X.-C. Zhang, *Applied Physics Letters*, 70, (1997) p1784-1786.
- [11] Q. Wu and X.-C. Zhang, *Applied Physics Letters*, 71, (1997), p1285-1286.
- [12] Peter R. Smith, David H. Auston, and Martin C. Nuss, *IEEE J. of Quantum Electronics*, QE-24 (1988), p255-260.
- [13] Z. G. Lu and P. Campbell and X.-C. Zhang, *Applied Physics Letters*, 71, (1997), p593-595.
- [14] Alexander W. Chao, "Physics of collective beam instabilities in high energy accelerators", Wiley, 1993.
- [15] Eric R. Colby, Ph. D. Dissertation, UCLA, 1997.
- [16] J. P. Carneiro, *et al.*, these proceedings.
- [17] W. H. Hartung, *et al.*, these proceedings.
- [18] Alan R. Fry, Ph. D. Dissertation. Univ. of Rochester, 1996.
- [19] A. R. Fry, M. J. Fitch, A. C. Melissinos, B. D. Taylor, "Laser System for a High Duty Cycle Photoinjector" UR-1559. (1998) Accepted for publication in *Nucl. Instr. Meth. in Phys. Res. A*.
- [20] D. Reis and D. Meyerhofer, private communication. 1998. We have adapted their infrared design to the UV.
- [21] P. Uhd Jepsen *et al.*, *Physical Review E* 53, (1996) pR3052-R3054.
- [22] C. Winnewisser *et al.*, *Appl. Phys. Lett.* 70 (1997) p3069.
- [23] Z. Jiang and X.-C. Zhang, *Appl. Phys. Lett.* 72 (1998) p1945.
- [24] Peter Vasil'ev. *Ultrafast Diode Lasers*. Artech House, Boston, 1995.

BUNCH LENGTH MEASUREMENT AND ITS LENGTHENING IN HLS*

B. G. Sun[#], L. K. Chen⁺, J. H. Wang, Y. M. Jin, G. C. Wang, P. Lu

NSRL, USTC, Hefei, Anhui 230029, P.R.China

⁺Dept. of Applied Physics, ShenZhen University
Shenzhen 518060, P.R.China

Abstract

The paper discusses the method and principle of bunch length measured by HP54121T 20GHz digital sampling oscilloscope in Hefei Light Source (HLS) ring. The measurement results of the bunch length and the energy spread are given. The rms. bunch length is about 3.8 ~ 10.33cm. A new theory on the bunch lengthening is used to explain the experimental results. It is proved that the beam-cavity interaction is the most important factor to the multi-bunch lengthening of HLS.

1 INTRODUCTION

As bunch length and its lengthening have an influence on the machine performance in an electron storage ring, these measurements are very important. Several methods to measure the bunch lengths have been developed, for example, electronic measurement, optical measurement and optoelectronic measurement. We use a 20 GHz digital sampling oscilloscope to measure the bunch length and its lengthening. In this method, a bandwidth stripline electrode with a length of $L=30\text{cm}$ and an impedance of $Z_0=50\ \Omega$ is used for picking up beam signal.

There are two sorts of theories to explain the bunch lengthening and the energy spread widening, i.e. the potential well distortion and microwave instability. But, the existing theories are difficult to explain the experimental results. In the reference[1], the distribution function of the particles is gained with the statistical mechanics method for intense current. The theory unites the existing potential well distortion and microwave instability. The theory proves that the bunch lengthening is a multi-bunch effect in nature. So the theory points out the importance of the narrow-band impedance to the bunch lengthening.

2 MEASUREMENT PRINCIPLE

2.1 Stripline monitor

The stripline is an electrode with the characteristic impedance Z_0 , usually longer than the characteristic bunch length. By a suitable choice of the ratio between

the stripline width and distance from the vacuum pipe, the characteristic impedance is made $50\ \Omega$. The electrode is terminated at both ends via coaxial vacuum feedthrough into termination loads matched to Z_0 .

In principle we get a useful signal only at the up-stream terminal of the monitor. The voltage signal at the up-stream load resistor is a doublet of opposing polarity reproducing the longitudinal time distribution of the beam current and separated in time by an interval $\Delta t=2L/c$, where L is the stripline length. So, the time domain voltage signal of the matched stripline at the up-stream terminal for a centred beam [2] is

$$v(t) \approx \frac{Z_0}{2} \left(\frac{\alpha}{2\pi} \right) \left[i_b(t) - i_b\left(t - \frac{2L}{c}\right) \right] \quad (1)$$

Where, α is the opening angle of the stripline, $i_b(t)$ is the instantaneous beam current, $L=30\text{ cm}$.

The voltage signal of stripline at the up-stream pot on HP54121T 20GHz digital sampling oscilloscope is shown Fig.1. Here, the negative pulse is signal sensed on stripline by the beam $i_b(t)$. Therefore, the pulse width of the beam signal may be measured by the voltage signal of the stripline.

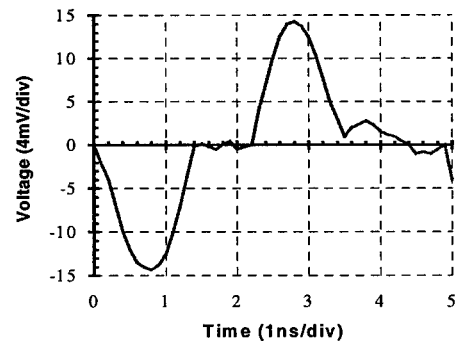


Figure 1: The voltage signal of the stripline on HP54121T

2.2 The relation between the bunch length and the FWHM of the time domain beam signal

We can assume that the bunch has a Gaussian longitudinal distribution in a ring. So, the beam current $i_b(t)$ can be expressed in the time domain as

$$i_b(t) = I_p \exp\left(-\frac{c^2 t^2}{2\sigma_s^2}\right) \quad (2)$$

* Work supported by Chinese Academy of Sciences contact KJ85-3

* Email: bgsun@ustc.edu.cn

Here, σ_s is the bunch length, I_p is the peak current of a bunch.

Because the pulse width of the beam signal can be expressed as the FWHM, we get

$$\sigma_s = c \times \text{FWHM} / 2.3548 \quad (3)$$

Therefore, the bunch length is got by measuring the FWHM of the beam signal.

3 THE SYSTEM COMBINATION

This bunch length measurement system consists of a stripline monitor, an attenuator, a 20GHz digital sampling oscilloscope HP54121T (Four Channel Test Set HP54121A and Mainframe HP54120B), a RF trigger system and a printer HP2225AB. A block diagram of this system is shown in Fig.2.

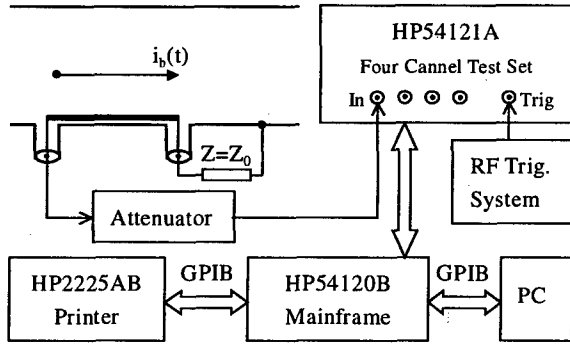


Figure 2: A block diagram of the bunch length measurement system

4 BUNCH LENGTHENING AND ENERGY SPREAD WIDENING

4.1 The measured result of the bunch lengthening and energy spread widening

We measure the FWHM of the beam signal with the bunch length measurement system in various beam currents[3]. The rms. bunch length is about 3.8 ~ 10.33 cm. The measured results are shown in Fig.3. I is the total current of forty five bunches.

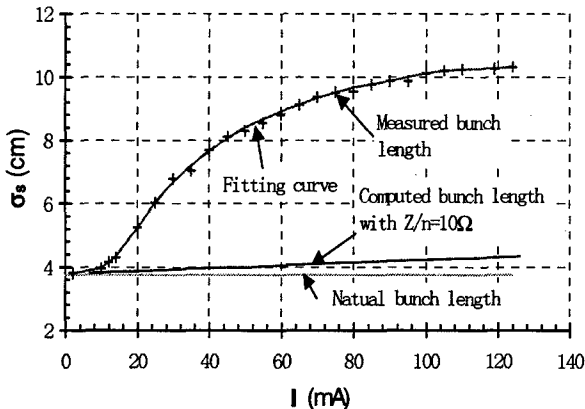


Figure 3: Bunch length vs. beam current

The energy spread is measured by decreasing the longitudinal acceptance via lowering the RF voltage until the longitudinal quantum lifetime becomes dominant. Then we can get the energy spread from measured quantum lifetime and the height of the RF bucket. The measured results are shown in Fig. 4

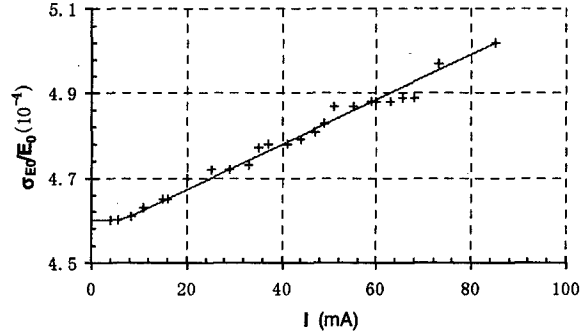


Figure 4: Energy spread vs. beam current

4.2 The new theory on bunch lengthening

The change of the particle energy in the interaction between the beam and the environment is written by[1]

$$U_w(\tau, \epsilon) = -U_{w0} + B\tau + 2T_0\alpha_s\epsilon \quad (4)$$

Where, U_{w0} , B , α_s are independent of τ and ϵ . α_s is the growth rate of longitudinal instability generated by the interaction of the beam and the environment.

So, the bunch lengthening and the energy spread widening have given by

$$\sigma_E = \sqrt{Q/4\alpha_r}, \quad \frac{\sigma_E}{\sigma_{E0}} = \sqrt{\frac{\alpha_r}{\alpha_r'}} \quad (5)$$

$$\text{Here, } Q = \frac{55h_r m_0 c^4 \gamma^7}{48\pi \sqrt{3} R^3}, \quad \alpha_r' = \alpha_r - \alpha_s$$

$$\frac{\sigma_s}{\sigma_{s0}} = \frac{\sigma_E}{\sigma_{E0}} \left(\frac{2\pi h e \hat{V}_{rf} |\cos \phi_s|}{2\pi h e \hat{V}_{rf} |\cos \phi_s| + BT_0} \right)^{\frac{1}{2}} \quad (6)$$

Where, α is the factor of damping, ϕ_s is the synchronous phase at zero current, ϕ_s' is the new synchronous phase under the interaction of the beam and the environment, h is the harmonic number, σ_{s0} is the natural bunch length, σ_{E0} is the natural energy spread. In HLS, $\sigma_{s0} = 3.76 \text{ cm}$, $\sigma_{E0}/E_0 = 4.6 \times 10^{-4}$

For the inductive wall model, U_{w0} , B_{in} and α_s in Eq. (4) respectively are

$$U_{w0} = 0, \quad B_{in} = -\frac{\sqrt{2\pi e R^2 c l_b} |Z_{11}|}{\sigma_s} \frac{1}{n_0}, \quad \alpha_s = 0$$

Where, R is the average radius of the machine, $|Z_{11}|/n_0$, the longitudinal impedance of the machine.

So, the effect of the inductive wall only generates the bunch lengthening, while the energy spread does not vary. The bunch lengthening is given by the following equation

$$\left(\frac{\sigma_s}{\sigma_{s0}}\right)^3 - \left(\frac{\sigma_s}{\sigma_{s0}}\right) - \frac{\sqrt{2\pi}I_b}{h\hat{V}_{rf}|\cos\varphi_s|} \left(\frac{Z_{11}}{n}\right)_0 \left(\frac{R}{\sigma_{s0}}\right)^3 = 0 \quad (7)$$

For the microwave instability model, $\alpha_s \neq 0$. So, the bunch lengthening and the energy spread widening are

$$\left(\frac{\sigma_E}{E_0}\right)^2 = \frac{eI_b}{\sqrt{2\pi}E_0\alpha_p} \left(\frac{R}{\sigma_s}\right) \left(\frac{Z_{11}}{n}\right)_{crit}, \quad \frac{\sigma_s}{\sigma_{s0}} = \frac{\sigma_E}{\sigma_{E0}} \quad (8)$$

Where, $|Z_{11}/n|_{crit}$ is the impedance at the threshold of the microwave instability.

If the inductive wall model and the microwave instability are regarded together, the bunch lengthening is given by the following equation

$$\left(\frac{\sigma_s}{R}\right)^3 = \frac{\sqrt{2\pi}I_b}{h\hat{V}_{rf}|\cos\varphi_s|} \left(\left(\frac{Z_{11}}{n}\right)_0 + \left(\frac{Z_{11}}{n}\right)_{crit} \right) \quad (9)$$

At the threshold of the microwave instability, the bunch length given the Eq. (7) should be equal to the bunch length by the Eq. (9). Then

$$\frac{\sigma_{sth}}{\sigma_{s0}} = \left(1 + \frac{\left(\frac{Z_{11}}{n}\right)_0}{\left(\frac{Z_{11}}{n}\right)_{crit}} \right)^{1/2} \quad (10)$$

For long bunch, we will assume that the frequency of the microwave instability is lower than the cut-off frequency. So, $|Z_{11}/n|_{crit} = |Z_{11}/n|_0$. Then,

$$\sigma_{sth} = \sqrt{2}\sigma_{s0} \quad (11)$$

$$I_{bth} = \left(\frac{\sigma_{s0}}{R}\right)^3 \frac{h\hat{V}_{rf}|\cos\varphi_s|}{\sqrt{\pi} \left(\frac{Z_{11}}{n}\right)_0} \quad (12)$$

$$= \frac{2\sqrt{\pi}\alpha_p E_0}{e \left(\frac{Z_{11}}{n}\right)_0} \left(\frac{\sigma_{s0}}{R}\right) \left(\frac{\sigma_{E0}}{E_0}\right)^2$$

Where, α_p is the momentum compact factor.

According to the parameter of the machine, we get

$$I_{bth} \left(\frac{Z_{11}}{n}\right)_0 = 103.1 \text{ mV}$$

If it is considered that $|Z_{11}/n|_0 = 10\Omega$, then $I_{bth} = 10.3 \text{ mA}$. That is, the total current is 463.5 mA .

Substituting Eq. (12) it into Eq. (7), we get

$$\left(\frac{\sigma_s}{\sigma_{s0}}\right)^3 - \left(\frac{\sigma_s}{\sigma_{s0}}\right) - \sqrt{2} \frac{I_b}{I_{bth}} = 0 \quad (13)$$

According to Eq. (13), the curve of the bunch lengthening computed by the inductive wall model is shown in Fig.3. So, the microwave instability does not occur in our experiment.

Now, we analyse that the narrow band impedance acts up on the bunch lengthening. When a narrow band impedance $Z(\omega)$ acts up on the beam, U_{w0} , B_c and α_s in Eq. (4) respectively are

$$U_{w0} = 2eI \sum_{K=1}^{\infty} e^{-K^2 M^2 \omega_0^2 \sigma_s / 2c^2} Z_R(KM\omega_0) \quad (13)$$

$$B_c = eI\omega_0 \sum_{K=1}^{\infty} e^{-(KM+\mu)^2 \omega_0^2 \sigma_s / 2c^2} [(KM+\mu)Z_i^+ + e^{-(KM-\mu)^2 \omega_0^2 \sigma_s / 2c^2} (KM-\mu)Z_i^- - 2e^{-K^2 M^2 \omega_0^2 \sigma_s / 2c^2} KMZ_i^-] \quad (14)$$

$$\alpha_s = \frac{\alpha_p e I \omega_0}{4\pi v_s E_0} \sum_{K=1}^{\infty} e^{-(KM+\mu)^2 \omega_0^2 \sigma_s / 2c^2} [(KM+\mu)Z_R^+ + e^{-(KM-\mu)^2 \omega_0^2 \sigma_s / 2c^2} (KM-\mu)Z_R^-] \quad (15)$$

Where, U_{w0} indicates the change of synchronous phase generated by $Z(\omega)$ so as to generate the bunch lengthening; B_c indicates the RF potential well distortion generated by $Z(\omega)$ so as to generate the bunch lengthening; α_s is the growth rate of longitudinal instability generated by $Z(\omega)$ so as to generated the energy spread widening.

The experiments have shown that the longitudinal instability occurs at a low current threshold of 10 mA (total current) in HLS[4]. Therefore, the beam-cavity interaction is the most important factor to the bunch lengthening of HLS.

5 CONCLUSION

According to the experimental results of the bunch lengthening and the energy spread widening in HLS, the conclusions are got as follows:

- (1). When the total current is lower than 10 mA , the bunch lengthening is generated by the inductive wall, while the energy spread basically maintained constant.
- (2). When the total current is greater than 10 mA , which is the threshold current of the longitudinal instability, it is obvious that the bunch lengthening and the energy spread widening. So, above 10 mA , except that the bunch lengthening is generated by the inductive wall, the bunch lengthening and the energy spread widening are mainly generated by the narrow band impedance.

On the base of the new theory, the experimental results of the bunch lengthening are explained reasonably.

6 REFERENCES

- [1] Longkang Chen, "Theoretical Study on the Bunch Lengthening", High Power Laser and Particle Beams, Vol.9, No.1, Feb. 1997
- [2] Mario Serio, Mikhail Zobov, "Measurement of Transverse and Longitudinal Spectra", Proceedings of the First European Workshop on Beam Diagnostics and Instrumentation for Particle Accelerators, May 1993
- [3] Baogen Sun, Junhua Wang et al. "Bunch length Measured by 20GHz Digital Sampling Oscilloscope", Atomic Energy Science and Technology, Vol.30, No.4, July 1996
- [4] Hengsheng Liu, Naiquan Liu et al. "Beam-cavity Interaction in HLS Storage Ring", Proceedings of the Workshop on Beam Instabilities in Storage Rings", July 1994

COMPARISON OF FEMTOSECOND ELECTRON BEAM DIAGNOSTIC METHODOLOGIES

I. Sugahara*, T. Watanabe, K. Yoshii, T. Ueda, M. Uesaka

Nucl. Eng. Res. Lab., Univ. of Tokyo, 2-22 Shirakata-Shirane, Tokai, Naka, Ibaraki, Japan

Y. Kondo

School of Eng., Tohoku Univ., Aoba08, Aramaki, Aoba-ku, Sendai, Miyagi, Japan.

Y. Shibata, K. Ishi, M. Ikezawa,

Res. Inst. Sci. Meas., Tohoku Univ., 2-2-1 Katahira, Aoba-ku, Sendai, Japan.

Abstract

Measurements of longitudinal pulse length of femtosecond electron beams have been performed by the three methodologies at the 35 MeV S-band twin liner accelerators at Nuclear Engineering Research Laboratory, University of Tokyo [1]. The methods we adopt are the femtosecond streak camera with a dispersionless reflective optics, the coherent transition radiation (CTR) Michelson interferometer [2] and the CTR polychromator. The results were compared with one another, and the reliabilities of the methods to diagnose femtosecond electron pulses have been discussed.

1 INTRODUCTION

Now it has become possible to generate femtosecond electron pulses, which are available for the ultrashort X-ray generation and the subpicosecond pulseradiolysis in our facility. In near future, we aim to produce and measure a 10 fs (FWHM) electron pulse which pulse length is shorter than the time resolution of the femtosecond streak camera (200 fs at FWHM). Therefore it is necessary to construct an alternative diagnostic system for the femtosecond electron pulse. As the alternative, there are two promising methods to evaluate the subpicosecond pulse shape, both of which use coherent transition radiation (CTR) emitted by the electron pulses in frequency domain. The first is the CTR Michelson interferometer, which utilizes an autocorrelation to obtain a CTR spectrum. The second is the CTR polychromator, which enables us to get a CTR spectrum directly by a single shot. It is very important to compare the results by these methods with that by the femtosecond streak camera in order to confirm the precision of the methods. In this paper, we describe the principle of pulse diagnostics by the methods and measure subpico- and picosecond electron pulses, which are longer than the time resolution of the streak camera.

2 DIAGNOSTICS BY CTR METHODS

2.1 CTR

Transition radiation is emitted when an electron passes the interface of two mediums of different dielectric constants. In case that the wavelength of the radiation is longer than the bunch length, the radiation becomes CTR. CTR emitted by electron pulses carries the information of bunch distribution and we can derive the longitudinal shapes of the electron bunch by analyzing the frequency information.

2.2 Michelson interferometer

From the interferogram, the power spectrum of the radiation $|E(v)|^2$ is given by the Fourier transformation as follows,

$$|\tilde{E}(v)|^2 = \frac{1}{4\pi c |RT|^2} \int_{-\infty}^{+\infty} S(\delta) e^{-i2\pi v \delta / c} d\delta, \quad (1)$$

where v is the wavenumber, $S(\delta)$ is the light intensity of the recombined radiation at the detector which expressed in the time domain with an additional time delay δ/c for the movable mirror minus the intensity at $\delta \rightarrow \pm \infty$ and R, T are the coefficients of reflection and transmission at the beam splitter, respectively. The longitudinal bunch form factor can be obtained by,

$$f(v) = \frac{\int_{-\infty}^{+\infty} S(\delta) e^{-i2\pi v \delta / c} d\delta}{4\pi c |RT|^2 N^2 I_e(v)}, \quad (2)$$

where N is the number of electrons in the bunch and $I_e(v)$ is the radiation intensity emitted from a single electron. The longitudinal bunch distributions can be deduced under an assumption of the asymmetric bunch distribution and then the Kramers-Kronig relation is used with the inverse Fourier transformation as follows,

$$h(z) = \int_{-\infty}^{+\infty} f_L(v) \exp[i(\phi_g(v) - 2\pi vt)], \quad (3)$$

$$\phi_g(v) = -2v \int_0^{+\infty} \frac{\ln[g(v') - g(v)]}{v'^2 - v^2} dv'. \quad (4)$$

Furthermore, we must choose theoretical distribution

* Email: jun@tokai.t.u-tokyo.ac.jp

functions of the electron bunch such as a Gaussian distribution or an exponential distribution. The results of these methods and the discussion appear in the following chapter.

2.3 Polychromator

Using the polychromator, we can get the spectrum of the radiation directly. From the spectrum, the bunch distribution can be deduced by the same procedure as that by the interferometry. This simplification of the analysis is one of the advantages of the polychromator method. Another advantage is that it enables us to diagnose the electron beam by a single shot. However, the information is very limited by the number of detectors (10 ch). Hence we must be careful in choosing theoretical extrapolation in the procedure of the reconstruction.

3 EXPERIMENT

3.1 Experimental setup

We performed this comparison at the 35L linac where the achromatic-arc-type magnetic pulse compressor was installed. In the experiment the longitudinal bunch distributions were controlled by tuning the energy modulation of the bunch in the accelerating tube for the magnetic pulse compression. We chose subpico- and picosecond pulse widths and performed the comparison among the femtosecond streak camera, the Michelson interferometry and the polychromator measurement as shown in Fig. 1. We measured the transition radiation in the far-infrared region emitted by an electron bunch at the Al-foil put in the air after the 50 μm -thick Ti window at the end of the 35L linac. We used liquid-He-cooled Si bolometer as a detector for the far-infrared radiation. The major beam parameters are as follows: the energy was 34 MeV, the pulse length is from about 600 fs to 8.0 ps (FWHM) and the electron charge per bunch is controlled to be 10 to 100 pC avoiding the over-scale of the detectors.

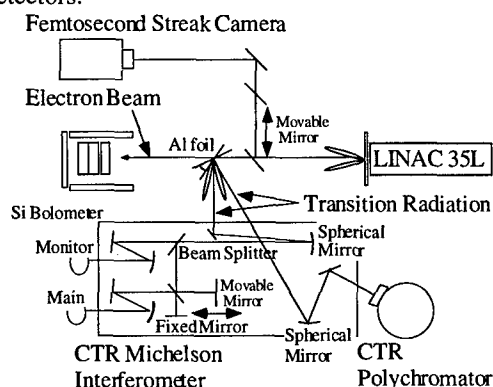


Fig.1 Experimental setup

3.2 Procedure of analysis

On the bases of the procedure of analysis in Ch 2, the longitudinal distribution is evaluated. The longitudinal bunch form factors obtained by the two methods were rather limited because of the nonuniform transparency of the 100 μm -thick Mylar beam splitter in the Michelson interferometer and measurement region which depends on the grating pitch (1.0 mm) installed in the polychromator. Therefore we have to adopt theoretical extrapolation assuming the Gaussian or exponential distributions out of the range, referring to the pulse shape measured by femtosecond streak camera.

4 RESULTS AND DISCUSSION

The CTR spectrum calculated from the interferogram and by the polychromator are shown by the solid curves and the transparency of a 100 μm -thick Mylar-type beam splitter by dashed curve in Fig.2. From the figure, we decided to use the experimental data in the range of 9.5 to 18.0 cm^{-1} for the analysis in the interferometry, while the measurable range of the polychromator was already determined from 12.2 to 26.2 cm^{-1} discretely by the 1mm grating pitch.

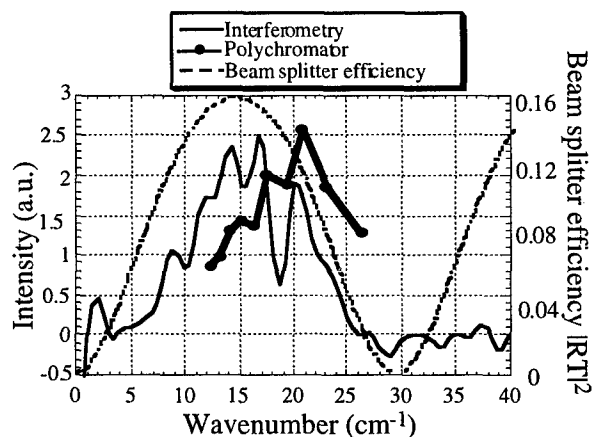


Fig.2. Spectrum of CTR

The experimental results of the longitudinal bunch form factor by the interferometry and by the polychromator are shown by the solid curves and that of theoretical by dashed curve in Fig.3. In the figure, we chose the Gaussian distribution as the theoretical curve, since the exponential distribution has unphysical long tails in both sides. The simultaneous observation of the bunch shapes by the streak camera indicates that the Gaussian distribution is closer to the real bunch distribution. We used the measured bunch form factor in the range that had been described in advance and the theoretical bunch form factor out of the range for the analysis. In the case of the interferometry, we adopt and extrapolate 650 fs (FWHM) bunch length for the subpicosecond pulse and 1.6 ps [FWHM] for the picosecond one, respectively. In the case

of the polychromator, we chose 1.0 ps for the subpicosecond pulse and 1.4 ps for the picosecond one, respectively.

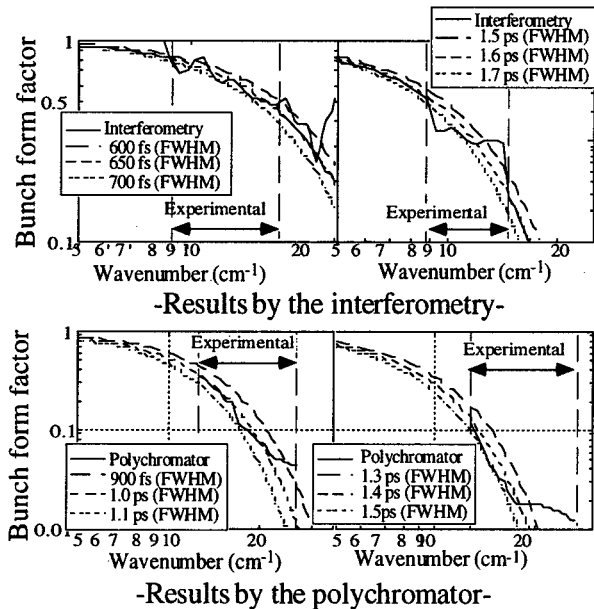


Fig.3 Measured longitudinal bunch form factors with the Gaussian fittings

In both cases, the extrapolation for the subpicosecond pulse was more suitable than that for the picosecond one. The reason is that the range of the CTR spectrum measured is more appropriate for the subpicosecond pulse. The longitudinal bunch form factors calculated from the results measured by the streak camera are shown in Fig.4. The important range of the longitudinal bunch form factor to get the coherent effect moves to the larger wavenumber range, as the pulse becomes shorter. We can see that only the bunch form factor of the 1.0 ps or less pulses become smooth in the measurement range, while those of the longer pulses are fluctuated and noisy.

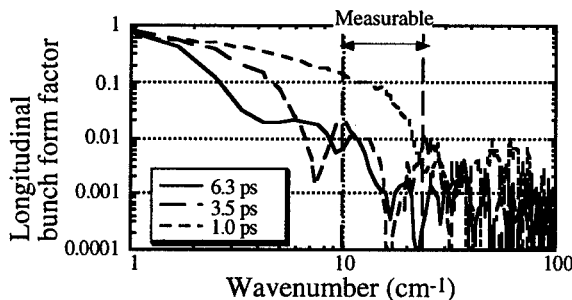


Fig.4 Bunch form factor by the streak camera

Finally, we reconstructed the longitudinal bunch distributions after using Kramers-Kronig relation to derive the phase information. The result of the subpicosecond pulse measurement by the interferometry

and that by the polychromator were 650 fs and 1.0 ps at FWHM as shown in Fig.5. Typical result by the streak camera is also shown in the same figure. Here we have got reasonable agreement and confirm the enough reliability of the diagnostics methods by the CTR measurement.

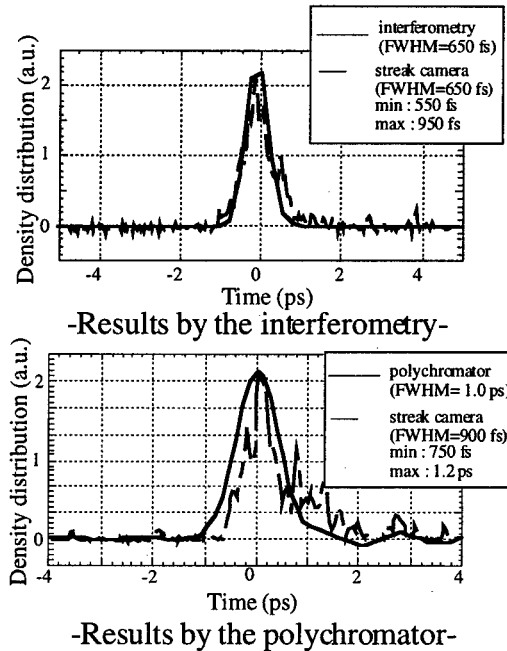


Fig.5 Bunch distributions by the three methods

With the choice of a thinner beam splitter or a grating with a narrower pitch, we expect the CTR methods are promising for the shorter electron beam (< 200 fs) with better resolution because the spectrum shifts from the far-infrared region to the infrared region where the sensitivity of the detector becomes better. Especially, the polychromator can be expected to the most useful methodology because of the advantage of diagnostics by a single shot.

5 CONCLUSION

From the comparison of the results, the reliability of the methods utilizing the CTR to measure subpicosecond electron pulses was confirmed. And we suggested the validity of the femtosecond streak camera for subpicosecond (≥ 200 fs) measurement and possibility of the polychromator to measure pulses shorter than the resolution of femtosecond streak camera (< 200 fs) in the future.

6 REFERENCES

- [1] M. Uesaka et al., *Nucl. Instr. and Meth.* A406 (1998) 371-379.
- [2] T. Watanabe, M. Uesaka et al., submitted to *Nucl. Instr. and Meth.*

LIMITATIONS AT SHORT BUNCH LENGTH MONITORING

Alexander Tron*, MEPHI, Kashirskoe sh. 31, 115409 Moscow, Russia

Abstract

Analysis of main limitations on time resolution inhering in techniques for bunch length or bunch phase distribution monitoring with resolution in subpicosecond range, and also expressions for longitudinal aberrations of main optical elements in technique like a streak camera will be presented. Possibility of realization of the last with the resolution of about 0.01ps and less is discussed.

1 INTRODUCTION

Bunch phase distribution (BPD) monitoring with resolution in femtosecond range, that is required for the next linear collider, X-ray FELs, is a challenging problem for decision of which in the paper a new approach is proposed and validated through consideration of some basic limitations inhering in well-known techniques.

The monitoring implies a use of coherent or incoherent bunch radiation that, at present, corresponds to measurement technique operating in frequency- or time-domain respectively. The first limitation follows at once from the radiation wave length that is considered below. We note at once also that the name "coherent" is not very correct one because the BPD retrieving from its frequency spectrum demands the measurement in the entire domain of the BPD-spectrum including its incoherent part too.

2 TIME CONVERTING TECHNIQUE

The principle of coherent technique operation in the frequency-domain consists in retrieving the BPD from the square of its Fourier transformation $F(\omega)$ that in turn is determined from the well-known expression [1]

$$P_c(\omega) = P(\omega)[N + N(N-1)F(\omega)],$$

where $P_c(\omega)$ - measured frequency spectrum of power radiation and $P(\omega)$ - the power spectrum emitted by a single electron and defined in the domain of the F -function. Consideration of the technical problems of the P_c -measurement one can find anywhere [2], but here we touch the basic problem dealt with the P -determination.

If P_c is the spectrum at the entrance of a spectrometer then P represents itself a transfer function of a vacuum chamber with a radiator.

To determine $F(\omega)$ correctly the function P has to be uniform over the entire spectrum of a bunch. It can be only in an idealized case. In the case of transition radiation, for example, it could correspond to the perfectly conducting and infinite screen, absence of another boundary conditions and movement of an electron beam with infinitesimal transverse sizes along its infinite emission length. In reality, it is not so and, moreover, it is impossible to determine the function P correctly by experimental way or through calculation.

In the general case, the measured spectrum P_c is too far from the power spectrum F . In a specific device we always have, for example, a finite emission length L . In the case, considering P as a function of L through the term $[1 - \cos(L/Z)]$ [3] only, where the formation zone $Z \sim \gamma^2/\omega \sim \gamma^2\lambda$, we obtain that $P(\omega) \sim \omega^2$ at $L/Z \ll 1$ and, as consequence, the broadening of the measured spectrum P . The last may lead to considerable compression of a retrieved BPD in comparison with real one. This effect is demonstrated in the papers [4,5] where the retrieved bunch length was nearly by an order less one obtain from to some extent idealized simulation of beam dynamics. In the paper [2] for specific measurement scheme, equipment and beam condition the spectrum P measured in very narrow band was divided by to fit the retrieved BPD obtained by "coherent" technique and more precise one together.

Hence, the "coherent" technique requires another one and may serve as an indicator for an accelerator maintenance in a specific regime.

To avoid the mentioned above frequency dependence of the P -spectrum we have to satisfy the condition $L/Z \gg 1$, i.e. $\lambda \ll L/\gamma^2$. In reality, for relativistic beam (for example, $\gamma > 100$, $L \sim 100\text{mm}$) it leads us to use the radiation in the frequency domain of about visible light and higher. then we will have to use another time converting technique based on use of device like a streak camera.

In the case, taking the transition radiation as an example for consideration, the scheme of the monitoring could look as the following: the beam radiation from a foil-mirror passes through lens and is focused on the surface of photocathode of a streak camera. Impact of chromatic and spherical aberration on the focusing of ultrashort light pulses by lenses was researches rather well in the papers [6,7] where it was shown that the pulse broadening can be less than 10fs. Then the main limitation in this scheme of the monitoring will be defined by the resolution of a streak camera.

* Email: tron@plasma.mephi.ru

Below, it will be shown how can create the device, like a streak camera but realizing new principle of construction, with the resolution of 10fs and less.

3 TRANSIT TIME SPREAD

Using the method [8] for precise integration of motion equation one can obtain the following expressions for the chromatic aberration of the h-distance gap (being under the U_0 -accelerating voltage) caused by an initial photoelectron energy spread, for example, from W_{01} to W_{02} for two cases: marked as 1 - for two electrode system formed by a cylindrical emitter with an optional radius R and plane electrode; 2 - the coaxial system with the internal electrode as the emitter

$$\Delta t_i \equiv \frac{t_0}{k_i} \left\{ \sqrt{W_2} - \sqrt{W_1} - \left[1 + a_i \left(1 - \frac{1}{\sqrt{1 - \xi_i}} \right) \right] \frac{W_2 - W_1}{2} \right\},$$

where $i=1,2$; $t_0 = (2h/c)\sqrt{W_0/2U_0}$ - time of flight the h-distance in uniform field; k_i - coefficient of the field enhancement on the emitter in comparison with the uniform field and, respectively, equaled $k_1 = \sqrt{m(m+2)}/\ln(m+1+\sqrt{m(m+2)})$, $k_2 = m/\ln(m+1)$;

$W_1 = W_{01}/U_0$; $W_2 = W_{02}/U_0$; a_i equaled respectively $a_1 = m/2$ and $a_2 = m$; $\xi_1 = 2(k_1-1)/m$ and $\xi_2 = (k_2-1)/m$; $W_0 = 0.511 \cdot 10^6$ eV; c - speed of light.

The main parameter here is $m = h/R$. Taking $m > 10$ one can enhance the field, decrease the effective length of the electron transit and, as consequence, decrease the aberration up to several fs and less for $W_{02} = 1$ eV, $W_{01} = 0$ and $h = 1$ mm at $U < 8$ kV.

4 DIAPHRAGM ABERRATION

The hole of a diaphragm restricting the gap disturbs the accelerating field that in turn courses additional transit time spread of the photoelectrons. This diaphragm aberration in the unit of t_0 as a function of the h-distance in the unit of semi-width of a slit or radius of a circular hole (Δx) is shown in Fig.1 for the following cases: 1 - the aberration taking a spherical one into account for the slit in the field of the cylindrical emitter with $m = 100$; 2 - id., but $m = 10$; 3 - the slit diaphragm in the field of a plane electrode; 4 - the circular diaphragm in the field of a plane electrode; 5 - the slit diaphragm in the field of the cylindrical emitter for $m = 100$, but without the spherical aberration.

The dependencies have been determined as the FWHM of the transit time distribution of the electrons with uniform density of escaping along the emitter surface and for the diaphragm with infinitesimal thickness. Confidence probability for $h/\Delta x > 10$ was more 0.8.

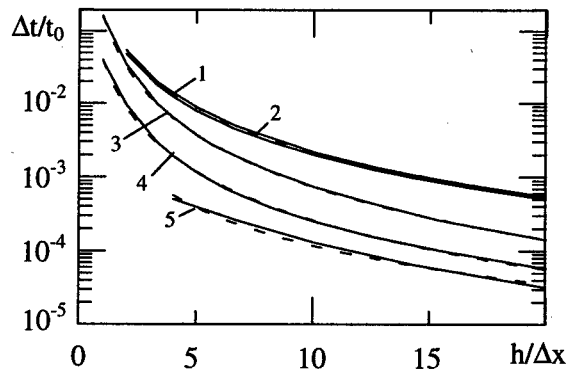


Figure 1: Diaphragm aberration as a function of the h-distance of the gap.

Approximating dependencies shown by the dashed line here are determined by the formula

$$\frac{\Delta t}{t_0} = \frac{A}{(h/\Delta x)^\alpha}$$

where values of A and α for the mentioned above cases are: 1 - $A = 0.2186$, $\alpha = 2.0$; 3 - $A = 0.1640$, $\alpha = 2.35$; 4 - $A = 0.0406$, $\alpha = 2.2$; 5 - $A = 0.006084$, $\alpha = 1.71$.

Taking the coaxial geometry of the gap we eliminate the spherical aberration completely. In the case diaphragm aberration can be reduced to the negligible one.

5 RF-GAP

In the device for the BPD-monitoring the action of the rf-gap has to be independent of the photoelectron transverse position. For rf-deflector this basic requirement is not satisfied in principle, and, as consequence, there is an optimum field of the rf-deflector for the best resolution, i.e. the rf-field is restricted on its maximum magnitude here. It is quite different situation in the case of the longitudinal rf-modulation.

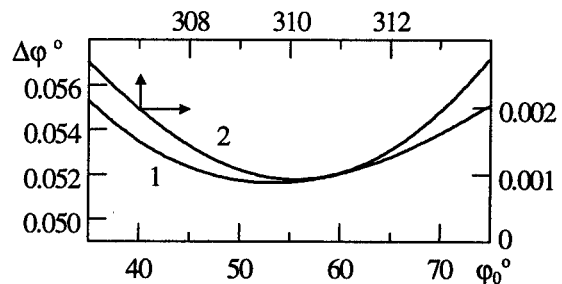


Figure 2: Phase resolution of coaxial resonator vs. ϕ_0 .

The phase resolution of the rf-resonator in the case of the longitudinal modulation is defined as $\Delta\phi = |P(W_{02}) - P(W_{01})|/(dP/d\phi_0)$, where the photoelectron momentum $P(W_{01})$ with its initial energy W_{01} is determined at the resonator output, ϕ_0 - the initial phase at the electron

start. The resolution as a function of ϕ_0 for the coaxial resonator is shown in Fig.2 for two cases: 1 - amplitude of the rf-voltage $U = 3\text{kV}$, accelerating voltage $U_0 = 4\text{kV}$, $h = 1\text{mm}$; 2 - $U = 8\text{kV}$, $U_0 = 8\text{kV}$, $h = 10\text{mm}$. All dependencies were determined for $W_{02} = 1\text{eV}$, $W_{01} = 0$, $R = 0.01\text{mm}$ and $f = 2.998\text{GHz}$.

6 CAMERA

Combining the electrostatic accelerating field and the electron modulating rf-field in the coaxial resonator, where its internal conductor is the photocathode (or as a secondary electron emitter for SEM-monitor of the BPD-measurement can be used) one can get ultra-fast camera for the BPD-monitoring (so named, maybe, for simplicity "troncamera" to retain the name "streak camera" for conventional one) if after the resonator a spectrometer operating in the regime of a spectrography will be installed. To get the resolution of about 100fs, 10fs or 1fs the camera will need the spectrometer with the relative momentum resolution equaled, respectively, 10^{-3} , 10^{-4} or 10^{-5} . For the spectrometer with uniform magnetic field (it is shown in Fig.3) its well-known resolution is $\Delta x/2R_m = \alpha^2/2$ that allows us to get the camera resolution of 100fs and less. For getting the 10fs-resolution we will have to use, for example, an electrostatic prism with installation of a transaxial lens at its entrance and exit; for the 1fs-resolution one may use the magnetic spectrometer with its field index $n = 3/7$.

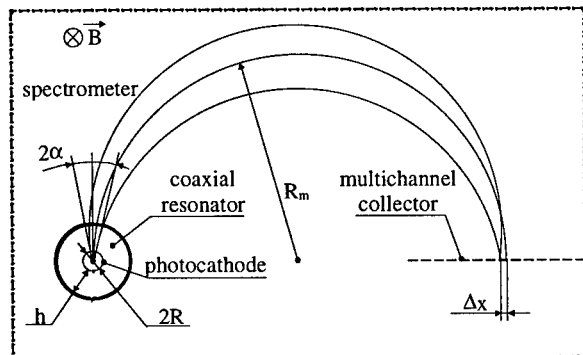


Figure 3: Scheme of camera

7 TIME EXPANDER

In Figure 4 the scheme of another device (tronexpander so named) for the BPD-monitoring is represented where the same coaxial resonator and instead of the spectrometer the l-space free of field are used. The principle of its operation follows from its name directly. After the longitudinal rf-modulation the electrons fly within the angle $\pm\alpha$. The time expansion is defined here by the derivative

$$\frac{dt}{d\tau} = \frac{360^\circ f \cdot l}{c \cdot \beta^2 \gamma^2 w} \cdot \frac{d(pc)}{d\phi_0},$$

where t - the time of arrival at the collector for the electron with its time departure from the resonator τ ; w - relativistic energy of the electron.

For $l = 100\text{mm}$, $f = 3\text{GHz}$, kinetic energy of the electron 1.8keV the magnitude of this derivative will be 10^4 at $d(pc)/d\phi_0 = 1 \cdot 10^5\text{ eV/deg}$. The last derivative can be obtained, for example, at $U_0 = 0.5\text{kV}$, $U = 10\text{kV}$, $h = 10\text{mm}$, $R = 0.01\text{mm}$.

It means that by taking the recorder channel including the collector with entire frequency band of about 1GHz one can measure the BPD with the 100fs-resolution. It should be noted that for the same parameters mentioned above the estimation of the error of this method gives 1fs.

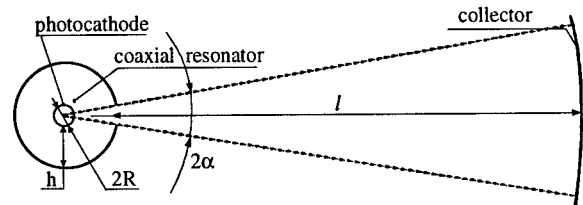


Figure 4: Scheme of expander.

8 CONCLUSION

Proposed camera and expander face the limitations now following from the time spread of the photoelectron escaping and quantum mechanics, but all of them lay below 10fs here.

When a measuring system represents itself the tandem from the expander and the camera, i.e. when at the exit of the expander instead of its collector a plane rf-gap (close to that) with the transit hole for the electron and after that the spectrometer are installed, the resolution of the tandem will be determined through the time expansion in the expander and the time resolution of the camera so that entire resolution can reach $10^{-18} \dots 10^{-20}\text{ s}$. for solitary electron going from the photocathode.

9 ACKNOWLEDGMENTS

Author thanks I.G. Merinov for his codes and help to get the paper ready.

Work supported in part by the Russian Foundation for Basic Research

10 REFERENCES

- [1] J.S. Nodvick and D.S. Saxon, Phys. Rev. 96 (1954) 180.
- [2] Gi. Schneider, et al., Nucl. Instr. and Meth. A396 (1997) 283.
- [3] I.E. Tamm, J. Phys. USSR 1 (1939) 439.
- [4] P. Kung, et al., Phys. Rev. Lett. 73 (1994) 967.
- [5] Y. Shibata, et al., Phys. Rev. E49 (1994) 785.
- [6] E.M. Gordeev, S.D. Fanchenko, in book "Physical Electronics", "Nauka", Moscow, 1976.
- [7] M. Kempe and W. Rudolph, Opt. Lett. 18 (1993) 137.
- [8] A. Tron, J. Teh. Phys. Lett., Vol. 25, 8 (1999) 17.

EFFECTS OF DIFFRACTION AND SCREEN SIZE ON CTR BASED BUNCH LENGTH MEASUREMENTS

M. Castellano, A. Cianchi, V. A. Verzilov * INFN-LNF, G. Orlandi INFN-Roma2

Abstract

Coherent transition radiation (CTR) is now well established as one of basic tools to measure electron bunches on a sub-picosecond scale. However, a series of experiments has demonstrated that suppression of CTR spectra at low frequencies, occurring in practice, leads to a great uncertainty in the bunch length determination. In addition to known sources of suppression, it was recently found [1, 2] that the size of a screen used to produce transition radiation (TR) can be a factor strongly affecting the spectrum. In this paper we calculate TR spectra emitted by a relativistic electron from a finite-size metallic screen and influenced by diffraction on apertures in environment and collecting optics.

1 INTRODUCTION

Operating with subpicosecond bunches is crucial to the new generation of e^+e^- colliders and FELs for reaching their final goals, which are respectively high luminosity and high peak current. To obtain this result, much depends on the ability to monitor bunch dimensions on such a small scale.

Coherent transition radiation (CTR) is now intensively used for ultra-short bunch length measurements due to its simplicity of implementation and small perturbations produced to the beam.

In this technique the bunch longitudinal dimension can be extracted from the measured CTR spectrum if the incoherent TR spectrum is precisely known [3]. In practice, however, there is a number of experimental factors, such as the limited bandwidth of the detector and diffraction effects due to finite apertures in the radiation transport channel, which cause hardly evaluated losses of the low frequency part of measured spectra, thus leading to a considerable uncertainty in the bunch length and shape determination [4].

Furthermore, the proper role of the size of the target in modifying the power spectrum of incoherent TR was shown [1, 2] recently. It was found that the TR spectrum from a finite target is a complex function of the beam energy, target extensions, frequency and angle of emission, i.e., very different from the flat spectrum given by the Frank formula, that has been used so far. The effect occurs when the parameter $\gamma\lambda$, where γ is the relativistic factor of the beam and λ is the radiation wavelength, exceeds the transverse dimensions of the target.

2 EFFECTS OF DIFFRACTION AND TARGET SIZE ON TR SPECTRA

In the pioneering works [1] the treatment of the problem was performed for a thin layer of matter and TR emitted in the forward direction. As a consequence, the resulting picture of the effect includes interference between TR, the particle field and diffraction radiation and, therefore, is rather complex.

In the present analysis, we rely on the Kirchhoff diffraction theory to describe the propagation of the field generated by a charged particle on the boundary between the vacuum and a perfect conducting material [5]. TR is considered to emerge in the backward directions with respect to the momentum of the particle crossing the boundary at normal incidence. Three different schemes of measurement, which are simplified models of those typically encountered in practice, are investigated.

2.1 Spectrum of TR filtered by a finite aperture

The first scheme considered is characterized by the presence of a circular diaphragm between the emitting screen and the detector. For ease of calculation we assume a cylindrically symmetric geometry. A circular screen with a radius r made of a perfect metal is placed at a distance a from the diaphragm, while b is the distance between the diaphragm and the detector having a diameter $2d$ (Fig. 1a). The incident particle with charge q and velocity v hits the screen at the center. Emerging TR propagates in the z direction. Let us introduce three different sets of coordinates $(x_s, y_s), (\xi, \eta)$ and (x, y) for the screen, diaphragm and detector planes, respectively.

In cylindrical coordinates we have:

$$\begin{Bmatrix} x_s \\ y_s \end{Bmatrix} = \rho_s \begin{Bmatrix} \cos \varphi \\ \sin \varphi \end{Bmatrix}, \quad \begin{Bmatrix} x \\ y \end{Bmatrix} = \rho \begin{Bmatrix} \cos \chi \\ \sin \chi \end{Bmatrix}, \quad (1)$$

Then the TR field components at an arbitrary point $P(x, y)$ in the detector plane in the first order Fresnel approximation of the diffraction theory, and neglecting phase constants, are found to be

$$E_{x,y}(P, \omega) = \frac{q}{2\pi^2 v} \frac{k^2}{ab} \int d\rho_s \rho_s \int dk_{\perp} \frac{k_{\perp}^2 J_1(k_{\perp} \rho_s)}{k_{\perp}^2 + \alpha^2} \times e^{i(k/2am)\rho_s^2} \int d\varphi \begin{Bmatrix} \cos \varphi \\ \sin \varphi \end{Bmatrix} e^{-i(k/am)\rho\rho_s \cos(\varphi-\chi)} \mathcal{L}(p), \quad (2)$$

where k_{\perp} is the projection on the xy plane of the photon wave vector $k = \omega/c$, $\alpha = \omega/v\gamma$, $m = 1 + b/a$, J_1 is the Bessel function of the first kind and

$$\mathcal{L}(p) = 2\pi e^{i(k/2bm)p^2} \int_0^D d\zeta \zeta e^{i(km/2b)\zeta^2} J_0(k\zeta p/b), \quad (3)$$

* Email: verzilov@lnf.infn.it

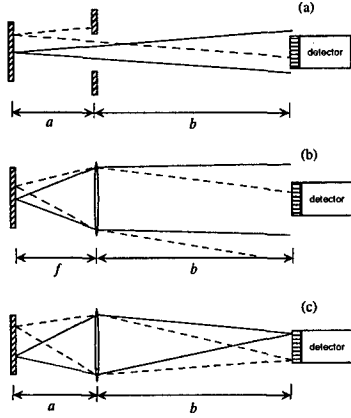


Figure 1: Three schemes of measurements under consideration.

$$p = \sqrt{\rho^2 + (b^2/a^2)\rho_s^2 + 2(b/a)\rho\rho_s \cos(\varphi - \chi)},$$

As follows from Eq. (2), the field in P is built up by a coherent summation of the waves emitted by all points of the source and so it depends on both the shape and the size of the screen. The function \mathcal{L} , mainly determined by the integral over the diaphragm surface, gives a contribution from the standard diffraction by the aperture. The above integral is well known (see, e.g., [6]) and is expressed in terms of the Lommel functions.

Thus, Eq. (2) includes effects given by both the size of the screen and the diffraction produced by the diaphragm. The latter is well known to produce, basically, a low frequency spectrum cutoff, almost entirely defined by the diaphragm aperture and angular acceptance. Hence, from this point on, we found it reasonable to focus our study on that of the screen size. To this end we formally let D tend to ∞ .

In terms of the theory of radiation, the phase factor quadratic in ρ_s in Eq. (2) specifies first order corrections to the so-called wave zone (or radiation zone) approximation due to the extension of the source and the sphericity of wave fronts at the point P.

For a finite-size screen these corrections are noticeable if

$$\frac{r^2}{am} \geq \lambda \geq \frac{am}{\gamma^2}. \quad (4)$$

and their effect is, in last instance, to reduce the "effective" size of the screen.

It should be noted that these corrections are relevant even for an infinite screen causing it to act like a finite-size one with an "effective" dimension depending on the wavelength and the distance to the observation point, if TR is observed at distances

$$\lambda\gamma^2 \geq z. \quad (5)$$

In the far-infrared region, that represents our main interest, the wave-zone condition can be well fulfilled by adjusting the distance between the target and detector, thus

allowing to approximate the aforementioned phase factor by 1.

As a consequence of simplifications made, the total spectrum of TR from the finite-size screen, integrated over the detector aperture, in the wave zone is found from Eq. (2) upon a change of variable $\rho = am \sin \theta$:

$$S_\omega = \frac{2q^2 k^2}{\pi c \beta^2} \int_0^{\theta_m} d\theta \sin \theta \cos \theta \Phi^2(r, \alpha, k, k \sin \theta), \quad (6)$$

where $\theta_m = \arcsin(d/am)$ is the angular acceptance of the detector and

$$\begin{aligned} \Phi(r, \alpha, k, \delta) = & \frac{\delta}{\alpha^2 + \delta^2} - \frac{\alpha r}{\alpha^2 + \delta^2} [\delta K_1(\alpha r) J_0(\delta r) \\ & + \alpha J_1(\delta r) K_0(\alpha r)] - \int_0^r d\rho_s J_0(k\rho_s) J_1(\delta\rho_s). \end{aligned} \quad (7)$$

Here K_n is the modified Bessel function of the n-th order.

Figures 2 and 3 show the spectra calculated by using Eq. (6) for parameters and frequency ranges typical for bunch length measurements, and normalized to the corresponding spectra from an infinite screen.

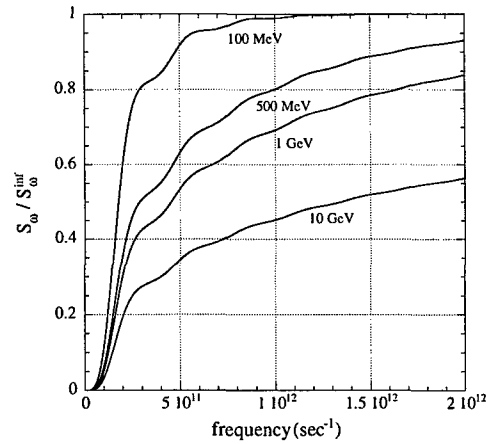


Figure 2: Spectra S_ω of TR in the first scheme of measurements, for a screen with radius of 20 mm and a detector angular acceptance of 0.05 rad.

2.2 Spectrum of TR from a screen in the focal plane of a lens

The second scheme under consideration (Fig. 1b) is a simplified geometry normally used in autocorrelation interferometric measurements, when the screen is placed in the front focal plane of a converging lens (parabolic mirror) to produce, behind the lens, a quasi-parallel photon beam.

The analysis performed for a thin lens with diameter $2D$ and focal length f results in the expression for the field identical to Eq. (2) and (4) if one puts $a = f$ and $m = 1$. The power spectrum, in the infinite lens approximation, is, therefore, given by Eq. (6) with

$$\theta_m = \arcsin(d/f). \quad (8)$$

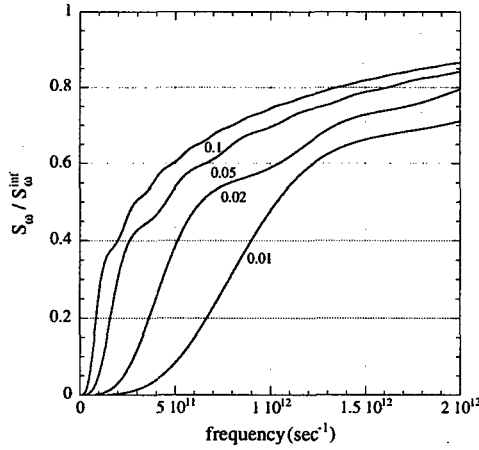


Figure 3: Spectra of TR S_ω in the first scheme of measurements for a screen radius of 20 mm and beam energy of 1 GeV. Numbers next to the curves are detector angular acceptances in radians.

The similarity between the first and second schemes can be seen by simple ray tracing: the effect of the lens is basically to "draw" the detector towards the screen, resulting in an increase of the angular acceptance of the system.

2.3 Spectrum of TR in the screen's image plane

Here the diaphragm of the first scheme is replaced by a lens of the same size and a and b are chosen such that the condition $1/a + 1/b = 1/f$ is satisfied (Fig. 1c). In this geometry the screen is simply imaged onto the detector. The expression for the field is given by

$$E_{x,y}(P, \omega) = \frac{q}{2\pi^2 v} \frac{k^2}{ab} \int d\rho_s \rho_s \int dk_\perp \frac{k_\perp^2 J_1(k_\perp \rho_s)}{k_\perp^2 + \alpha^2} \times e^{i(k/2a)\rho_s^2} \int d\varphi \begin{Bmatrix} \cos \varphi \\ \sin \varphi \end{Bmatrix} \mathcal{L}(p), \quad (9)$$

where, as before, \mathcal{L} is the pattern resulting from the diffraction on the lens, that in this case is given by the well-known expression

$$\mathcal{L}(p) = \frac{2\pi a D}{k p} J_1\left(\frac{k D}{a} p\right), \quad (10)$$

$$p = \sqrt{\varrho^2 + \rho_s^2 + 2\varrho\rho_s \cos(\varphi - \chi)},$$

with $\varrho = \rho/M$, where $M = b/a$ is the lens magnification.

For the infinite lens and neglecting the phase factor, the total power spectrum can be given in the form

$$S_\omega = \frac{2q^2}{\pi c} \frac{1}{\beta^2} \int_0^{d/M} d\varrho \varrho \left[\alpha K_1(\alpha\varrho) - \frac{J_0(k\varrho)}{\varrho} \right]^2. \quad (11)$$

In Eq. (11) we imply that $d/M \leq r$, while generally one should integrate from 0 to $\min\{d/M, r\}$.

We want to attract attention to the identical role of the screen and detector dimensions in affecting the spectrum. In fact, since the intensity distribution in the image plane

is just a "magnified" image of that in the source plane, both screen and detector are equivalent in producing restrictions on the transverse region over which the power spectrum must be calculated; namely, the spectrum is only determined by the minimum values of d/M and r .

3 EFFECT OF THE SCREEN SIZE IN CTR BASED BUNCH LENGTH MEASUREMENTS

Considering a low-frequency distortion of the TR spectrum due to a finite-size screen in the context of bunch length measurements one can expect that its effect on the accuracy of the bunch information retrieval may be sufficiently small as long as the corrupted portion of the spectrum is negligible compared to the frequency content of the bunch structure represented by the bunch form-factor. For the gaussian-shaped beam the following qualitative criterion can be used to estimate whether for a given bunch length σ_z the effect of the screen size is important

$$\sigma_z < c/\sqrt{2}\omega_{ch}. \quad (12)$$

Here ω_{ch} is a characteristic cutting frequency of the spectrum due to the effect. If, as usual for such kind of problems, one defines the cutting frequency as a 10% dropoff of spectra from the high-frequency plateau, simple approximate relations for ω_{ch} may be obtained by analyzing Eqs. (11) and (6), respectively

$$\omega_{ch}(\text{sec}^{-1}) = 3.3 \cdot 10^9 E^{0.87}(\text{MeV}) / \sqrt[4]{\theta_m(\text{rad})} \quad (13)$$

and

$$\omega_{ch}(\text{sec}^{-1}) = 8.3 \cdot 10^{10} E^{0.87}(\text{MeV}) / d(\text{mm}). \quad (14)$$

4 REFERENCES

- [1] N.F.Shul'ga and S.N.Dobrovol'skii, Pis'ma Zh. Eksp. Teor. Fiz. 65 (1997) 581 [JETP Lett. 65 (1997) 611]. N.F.Shul'ga, S.N.Dobrovol'skii and V.G.Syshchenko, Nucl.Instr. and Meth. in Phys. Res. B 145 (1998) 180.
- [2] A.P.Potylitsin, Nucl. Instr. and Meth. in Phys. Res. B 145 (1998) 169.
- [3] W.Barry, AIP Conference Proceedings 390 (1997) 173; Proc. of the 7th Beam Instrumentation Workshop, Argonne, May 1996.
- [4] A.Murokh, J.B.Rosenzweig, M.Hogan, H.Suk, G.Travich and U.Happek, Nucl. Instr. and Meth. in Phys. Res. A 410 (1998) 452.
- [5] M.Castellano and V.A. Verzilov, Phys. Rev. ST- Accel. Beams 1 (1998) 062801.
- [6] M.Born and E.Wolf, *Principles of Optics* (Pergamon Press, New York, 1965).

TIME RESOLVED ENERGY MEASUREMENT OF THE TESLA TEST FACILITY BEAM THROUGH THE ANALYSIS OF OPTICAL TRANSITION RADIATION ANGULAR DISTRIBUTION

M. Castellano, A. Cianchi, V. Verzilov INFN-LNF CP 13 00044 Frascati (Italy)
L. Catani, G. Orlandi INFN-Roma 2

Abstract

The study of the energy stability along the macropulse of the TESLA Test Facility Linac (TTFL) [1] was obtained by the measurement of the angular distribution of the Optical Transition Radiation (OTR). This technique does not require a dispersive section and can be performed at any point of the beam line.

Measurements have been performed with different settings of the RF low level control and at different values of the beam current. An energy variation along the macropulse was observed in a good agreement with the measured energy spread of the whole macrobunch.

The analysis of the OTR angular distribution pattern allows also, to some extent, to evaluate the beam angular spread.

1 INTRODUCTION

The energy stability along the macropulse of the TESLA Test Facility Linac (TTFL) [1] is the result of an accurate timing between the RF pulse and the beam injection to compensate for the beam loading. A digital feedback and feedforward algorithm takes care of fast and slow fluctuations. A measurement of the energy stability is required for a fine tuning of the algorithm parameters.

Typically, energy and energy spread measurements are performed in the dispersive section at the end of the transport line, where a dipole magnet bends the beam by 20° and drives it to the dump.

Energy variation along the macropulse can be measured by means of the strip-line beam position monitor available in the same dispersive section, but the large beam width, of the same order or larger than the linear range of the monitor, strongly reduces the accuracy of the measure.

Instead, we used the angular properties of the Optical Transition Radiation (OTR) emitted by the beam crossing a thin aluminum foil, to realize a time resolved energy measure. This measure does not require a dispersive section and can be done, in principle, at every section of the accelerator.

A sensor is placed in the focal plane of a thin achromatic lens to allow the imaging of the OTR angular distribution.

The radiation is emitted in a cone of semiaperture $1/\gamma$, γ being the relativistic factor of the incident particles.

In our case the sensor is the cathode of an intensified CCD camera that has several advantages with respect to a normal CCD. It provides the possibility of a fast controlled gate (down to 200 ns), allows a 12 bits dynamics and has a high signal to noise ratio.

We integrated the signal over 1 microsecond. Delaying the gate by steps of 1 microsecond, we could follow the whole macrobunch evolution. To ensure the bunch to bunch stability we repeated the measure several times.

2. RESULTS

We performed two different measures at different stages of the commissioning of TTF.

The first one was realized with the so-called injector I delivering a beam current of 6 mA at a repetition rate of 216 MHz, with a single accelerating module in operation.

A 45° beam splitter was used to perform in the same time the measure of both the beam energy (with the ICCD) and the spot size (with a normal CCD). The reflectivity of the beam splitter depends on the radiation polarization, resulting in a different intensity in the horizontal and vertical planes (see Fig.1.)

We used a thin achromatic lens of $f = 200$ mm focal length. Peak positions, and hence the beam energy, were found by applying a fit to the profile obtained from the OTR image along the vertical line crossing the center.

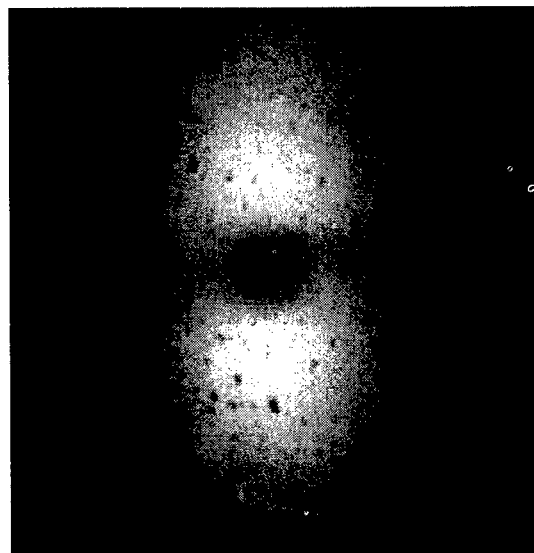


Fig 1 An image of the OTR angular distribution. The difference between horizontal and vertical planes is due to the use of a beam splitter

Fig.2 displays the results of the measurement for two different beam energies.

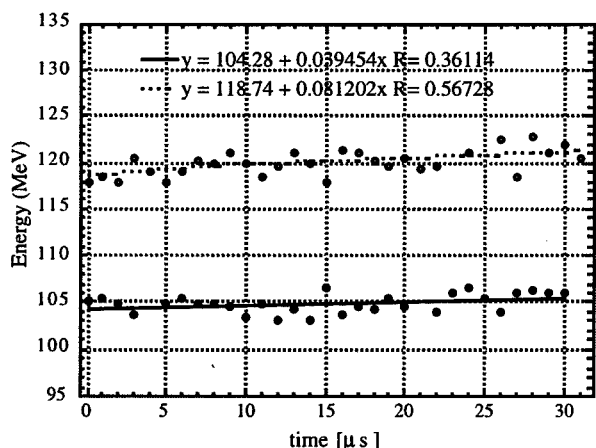


Fig 2 - Variation of the beam energy along the macropulse for two different RF gradients.

In the case of the higher energy, that is the usual working point, the total energy variation along the macropulse is of the order of 2.5%. This result is in a good agreement with the measure made in the dispersive section, which gives a rms energy spread of about 1% over the whole macrobunch.

At a second stage of the commissioning, we operated with the injector II, which supplies a different pulse time structure. The repetition frequency is 1 MHz, so that the integration over 1 microsecond allows the detection of a single micropulse. For these measurements we used a beam current of 1 mA, equivalent to 1 nC of charge for each micropulse, as required for the FEL operation [2].

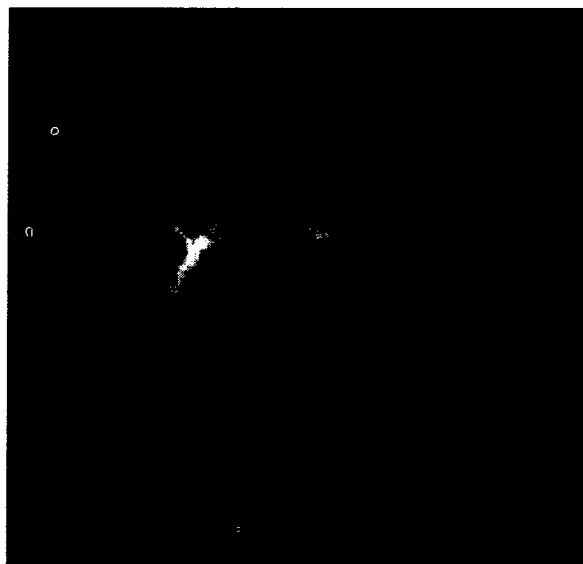


Fig 3 - A typical image of the OTR angular distribution with the injector II

In addition, the installation of a second accelerating module increased the energy of about a factor of 2. In Fig.3 a typical image recorded in this condition is shown.

We performed measurements for three different values of the loop gain in the low-level RF feedback control system for the accelerating modules. This is an important

parameter for the control of the gradient during the RF flat top and, thus, of the energy stability along the macropulse. Fig.4 shows the results for the loop gain equal to 44, 36 and 27, respectively.

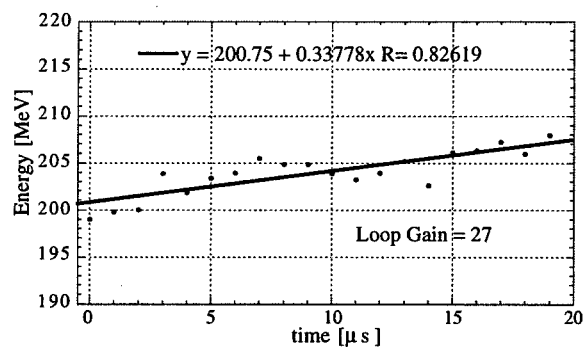
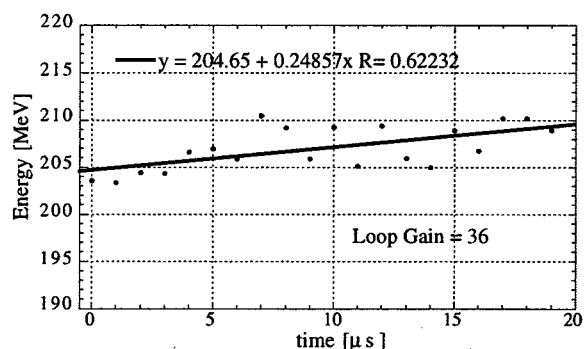
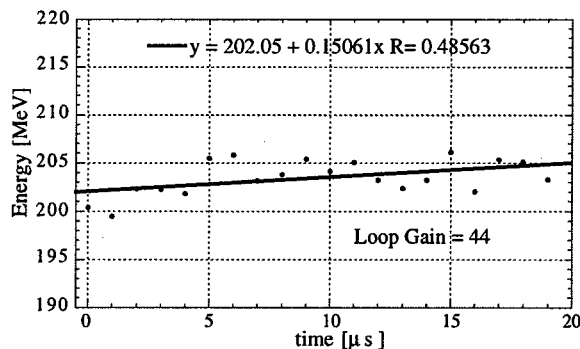


Fig. 4 - Energy variation in the macropulse with three different setting of the RF loop gain

Although the statistical fluctuation of the points is rather large, it is possible to conclude that the energy stability is better at larger values of the loop gain.

A more accurate and systematic work is required in order to determine the best setting for the low-level RF control, and it will be performed in the next run this Summer.

As a by-product of our measurements, we found that an information about the beam angular spread could be obtained by the analysis of the OTR angular distribution profiles.

In Figs. 5 and 6 an example of the vertical profile is presented.

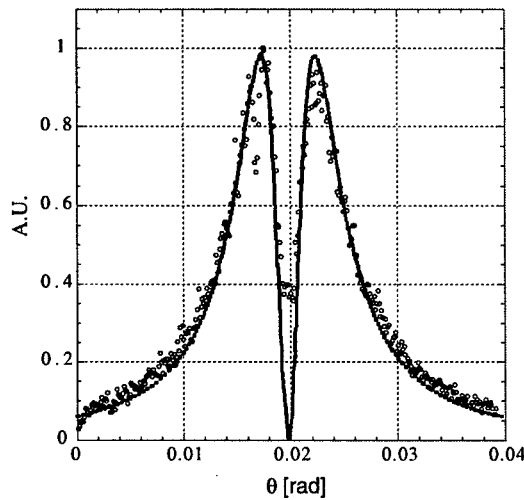


Fig 5 - A profile for the vertical plane of the OTR angular distribution and fitting curve for a parallel beam

The solid line in Fig. 5 is a fit according to the theoretical prediction for a zero divergence beam.

The fit in Fig 6 takes into account the beam divergence and reveals a better agreement with the experimental data.

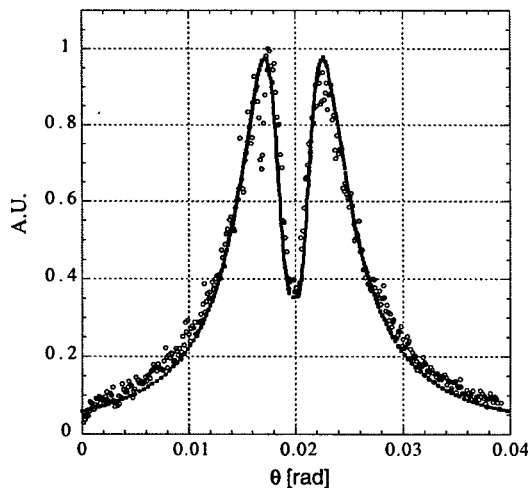


Fig. 6 - Profile of the OTR angular distribution with a fitting function taking into account the beam angular divergence.

A rms angular spread of 0.7 mrad is obtained in this case. Unfortunately, for this data set, in order to avoid the distortion introduced by the beam splitter, we were not able to measure simultaneously the beam spot size. Nevertheless, a spot size value of about 200 μm could be obtained, for the same conditions, from the emittance measurements performed just before. According to this value, a normalized emittance of about 60 mm mrad can be estimated. This is fully consistent with the measured values that ranged from 50 to 100 mm mrad, depending on beam transport conditions.

3. CONCLUSION

We used the properties of the OTR to monitor the energy variation along the macropulse of TTF beam.

Two different measures were performed at different stages of the commissioning, and in both cases we found an increase of the energy along the macropulse.

We have proven that the loop gain value of the low-level RF control can affect the time energy dependence, and that the correct value for this parameter must still be found. A more accurate measurement is needed to explore better this point.

A preliminary analysis shows that it is possible to obtain from the same data also the beam angular divergence, that, together with the measure of the spot size, can give an independent emittance measurement.

To improve the measure accuracy, we plan to use a lens with a longer focal length. A higher number of images for each setting point is also needed in order to reduce the statistical fluctuations.

4 REFERENCES

- [1] D. Edwards (editor), TESLA Test Facility Linac – Design Report, DESY TESLA 95-01 (1995)
- [2] A VUV Free Electron Laser at the TESLA Test Facility at Desy – Conceptual Design Report DESY TESLA-FEL 95-03 (1995)

THE ISIS SYNCHROTRON BEAM CONTROL AND STUDY PROGRAMME

D.J.Adams, K.Tilley, C.M.Warsop, Rutherford Appleton Laboratory, Oxfordshire, UK.

Abstract

Progress on the beam control and study programme for the 800 MeV High Intensity Proton Synchrotron of the Spallation Neutron Source ISIS, is outlined. Recent hardware upgrades to diagnostics, instrumentation and computing have increased the amount, accuracy and availability of beam information. The measurement methods employed and their planned applications for beam control, optimisation and study are described. Work includes detailed study of longitudinal and transverse dynamics at high and low intensity. Results obtained so far and future plans are summarised.

1 INTRODUCTION

1.1 Background

This paper summarises progress on the beam control and study programme, which was detailed in an earlier paper [1]. Here, recent experimental results from the upgraded hardware are summarised, along with their application to machine control.

The ISIS Synchrotron [2] accelerates 2.5×10^{13} protons per pulse at 50 Hz (200 μ A). The high intensity beam is established via charge exchange injection over 120 turns. Beam is then bunched and accelerated from 70-800 MeV in 10 ms, extracted in a single turn and transported to the target.

Extensive use is made of low intensity 'diagnostic' beams [1]. These provide additional, detailed information which complements high intensity measurement. On ISIS suitable beams are produced by 'chopping' the injection pulse from the normal 120 turns to less than 1 turn. Such beams can be interleaved with normal 50 Hz high intensity pulses; typical 'chopping' at 1 pulse in 128 has minimal effect on operational beam.

1.2 Synchrotron Diagnostics Upgrades

The diagnostics hardware upgrade is based on the addition of many fast digitising channels to make full use of the existing instrumentation. Twenty 100 MS/s digitisers allow turn by turn beam position measurements at 10 monitors simultaneously. Two 1 GS/s digitisers allow the acquisition of longitudinal profiles. Position monitor electronics upgrades enable measurements with both high and low intensity beams.

A dedicated DEC Alpha work station linked to the control system allows extensive hardware control, thus facilitating automated measurement. The increased

computing power enables the use of high level data analysis software and graphical user interfaces, which simplify correction procedures significantly.

2 CLOSED ORBIT MEASUREMENT AND CORRECTION

2.1 Closed Orbit Correction and Lattice Model

Closed orbit data is now readily acquired and processed on the new systems. Closed orbit correction and manipulation is based on the solution to the linear equation:

$$x_i = A_{ij} \cdot b_j \quad (1)$$

The elements of steering matrix A_{ij} give the closed orbit deviation x_i at monitor i due to an angular kick b_j at corrector j . Optimal corrections are found by reducing A_{ij} using Singular Value Decomposition and solving Eq.1 for b_j .

A synchrotron lattice model has been developed to calculate linear lattice parameters and track particle trajectories. The model is very effective for manipulation and correction of closed orbits, by generating the steering matrix A_{ij} and solving Eq.1.

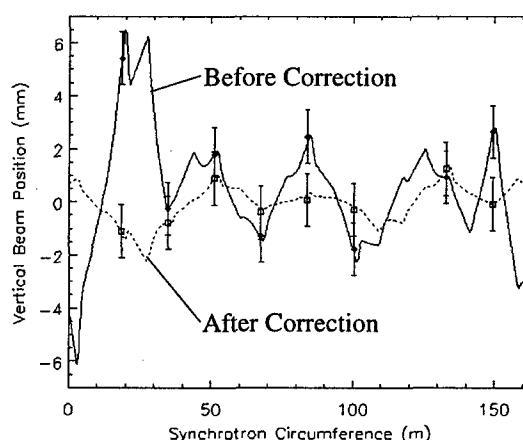


Figure 1: Vertical C.O. measured before and after correction, with modelled trajectory.

Figure 1 shows an example of the measured high intensity vertical closed orbit before and after correction with the lattice model. The model optimises kicks at 7 steering magnets, to fit measured closed orbit errors. As would be expected from the well optimised set of

correctors, calculated orbits can be seen to fit measurements very well (rms difference <1 mm). Application of the calculated kicks typically reduces the peak closed orbit errors from ~6 mm to ~1 mm in three iterations. The correction could be improved further by using a measured steering matrix, which will be possible when automated magnet control becomes available.

The correction technique has now been incorporated in the machine set-up schedule. The time to correct, or re-establish empirically optimised 'Golden Orbits', throughout acceleration has been reduced from days to hours. Planned automation should reduce this to minutes.

2.2 Further Closed Orbit Work

Correction of closed orbits at injection will be much improved with the use of chopped beams, where AC coupled monitors and the unbunched beam prevents reliable high intensity orbit measurements. More sophisticated uses of the measurements and models are envisaged, including the location of alignment and field errors. Good models of beam trajectories and closed orbits, at high and low intensity, will be useful for aperture studies and beam loss collector set-up.

3 BETA FUNCTION

3.1 Multi-turn Position Measurements

Measurement of turn by turn, coherent transverse motion at a given monitor allows numerous ring parameters to be extracted by fitting a suitable function [3]. Most important are centroid betatron amplitude (b), closed orbit, betatron Q and phase. Measurements are possible at high and low intensity but the most accurate results come from the latter. Here low intensity measurements at injection are presented; the injection painting process conveniently provides the coherent motion. Future developments will allow measurements throughout the machine cycle, using a fast kicker to excite the beam.

Multiple digitisers and suitable monitors now allow simultaneous measurement of the above parameters at 10 points around the ring. This allows reconstruction of closed orbit, phase advance and beta functions. Below, first measurements on beta functions are summarised.

3.2 Beta Function Measurements

The betatron amplitude (b) at ~10 monitors is measured on the same pulse. The relation to the local beta function (β_i) is $b_i = \sqrt{\beta_i \epsilon_c}$, where the centroid emittance (ϵ_c) is identical at all monitors for a given pulse. In comparing measurements sets, variation of ϵ_c from one pulse to another has to be accounted for.

To demonstrate the validity of the basic measurements a set of b_i were measured first with the synchrotron in a

normal configuration, and then with a deliberate gradient error introduced by switching off one trim quadrupole. The theoretical change in the beta function due to such perturbations is known and gives an envelope oscillation at 2Q, given by the following formula:

$$\frac{\Delta\beta(s)}{\beta(s)} = \mp \frac{1}{2 \sin 2\pi Q} \oint \Delta k(\sigma) \beta(\sigma) \cos 2[\mu(\sigma) - \mu(s) - \pi Q] d\sigma \quad (2)$$

where the notation is standard [4]. The data was then brought into the above form using both measurement sets, and the optimal least squares fit determined. To simplify interpretation, only measurements at equivalent lattice positions in the 10 superperiods (where the β_i are ideally identical) were considered. The results are plotted in Figure 2.

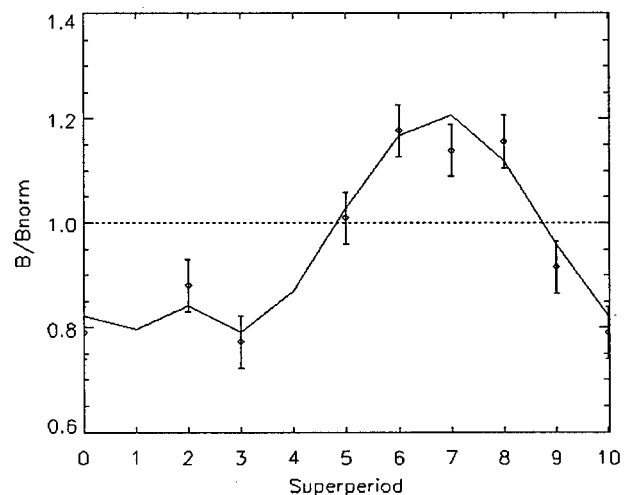


Figure 2: Perturbation in Relative Beta due to Gradient Error in Superperiod 2; Measurement and Theory.

Agreement between the functional forms is good and gives confidence in the measurements. A fuller theoretical comparison is being developed.

3.3 Further Applications

An obvious application for these measurements is to correct beta function perturbation by applying appropriate harmonics to the 20 trim quadrupoles. Measurements could also be used to locate single large gradient errors. Use of two monitors separated by a drift space, to deduce (y, y') on a turn by turn basis, should allow measurement of absolute beta at one monitor; this combined with the above provides beta at all monitors. Absolute beta at each trim quad can also be calculated by measuring the change in Q as a function of quadrupole current [1]. Collectively these measurements would yield the beta function at 30 points per plane.

4 LONGITUDINAL MEASUREMENTS

4.1 Basic Measurements

These measurements are based on digitising the longitudinal bunch shapes from a capacitive monitor over thousands of turns. Some processing, making use of the digitised RF voltage, yields the instantaneous beam intensity as a function of RF phase on every turn. Moments analysis of the turn by turn longitudinal distributions then provides the bunch centroid phase and bunch length on each turn. Using these techniques the dynamics of both high and low intensity beams can be studied. Early results are shown below.

4.2 High and Low Intensity Measurements

Examples of bunch length measurements for a high intensity beam are given in Figure 3. This shows bunch lengths at various percentages of the peak instantaneous current. The 95 % contour follows the theoretical (zero intensity) RF bucket length in the expected manner, with high bucket occupancy during trapping which then decreases through acceleration. Oscillation at the synchrotron frequency is also visible.

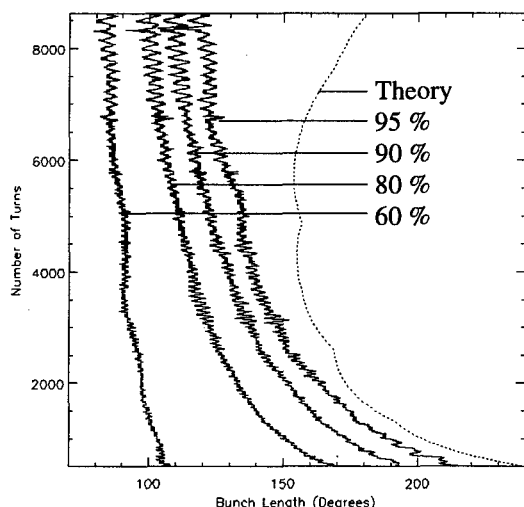


Figure 3: High Intensity Bunch Length Measurement compared with theoretical RF Bucket Length.

The injection and acceleration of chopped beams, occupying less than one turn, reveal details of longitudinal motion. Depending on the bunch length, and relative phase of the injected beam with respect to the RF, dipole and bunch length oscillations of various amplitudes can be set up. From this, using the processing described above, the FFT of first and second moments of the longitudinal distribution over thousands of turns allows extraction of the synchrotron tune Q_s . Figure 4 shows good agreement with theory.

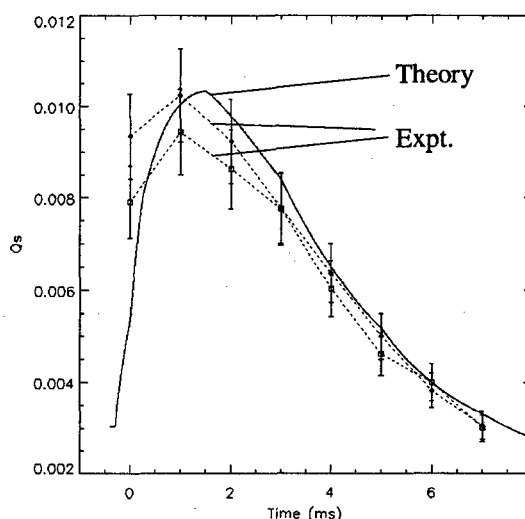


Figure 4: Synchrotron Tune (Q_s) through the machine cycle; Low Intensity Measurements and Theory.

4.3 Further Studies

The above results represent the first stage of measurement development. More sophisticated studies are planned. These will include detailed investigation of phase stable regions, Q_s , and effects of RF loops. The longitudinal diagnostics are particularly important in light of the expected Dual Harmonic RF upgrade [5], which is designed to increase intensity by 50 %. Phase space distributions and dynamics may be reconstructed from longitudinal profiles using 2D tomographic techniques [6]. Comparisons with results from space charge codes are also planned.

5 CONCLUSIONS

Upgrades to the diagnostics are providing much valuable and detailed information on most aspects of beam dynamics. The challenge now lies in making full use of low and high intensity measurements to understand and optimise high intensity performance.

6 REFERENCES

- [1] Development of the ISIS Synchrotron Diagnostics, D J Adams et al, Proc. EPAC 98.
- [2] Spallation Neutron Source, B Boardman, RAL Report RL-82-006.
- [3] Low intensity and Injection Studies on the ISIS Synchrotron, C M Warsop, Proc. ICANS XII, RAL Report RAL 94-025.
- [4] Circular Accelerators and Storage Rings, P Bryant, K Johnsen.
- [5] A Possible Upgrade for ISIS, M Harold et al, Proc. PAC 97.
- [6] Tomographic Measurements of Longitudinal Phase Space Density, S Hancock et al, Proc. EPAC 98

TUNE MEASUREMENT FOR THE CERN PROTON SYNCHROTRON BOOSTER RINGS USING DSP IN VME

A. Chapman-Hatchett, V. Chohan, T. E. d'Amico, CERN, Geneva, Switzerland

Abstract

The CERN PS Booster (PSB) consists of 4 superposed rings supplied with protons from a 50 MeV Linac. The proton beam is then accelerated to 1 GeV and sent either to the 26 GeV Proton Synchrotron (PS) or to the ISOLDE facility. This is carried out in a multi-cycle mode every 1.2 s. For high-intensity beams, the working-point in the tune diagram needs to be changed considerably during acceleration from 50 MeV to 1 GeV and the repeated measurement of the tunes throughout the cycle is an important requirement. Up to now, tune values were obtained through calculations based on quadrupole currents. However, practical experience has shown the need for a direct tune measurement system. For this purpose, a classical kick technique is used. A fixed amplitude kick of duration equal to one revolution period excites coherent betatron oscillations. For fast treatment, a Digital Signal Processing (DSP) module in a VME-standard crate was selected. It carries out the Fast Fourier Transform (FFT) analyses of signals from position-sensitive pickups in both planes and evaluates the tunes. These measurements are carried out every 10 ms during the 450 ms acceleration ramp. The paper presents the novel features of this system, particularly the beam-offset signal suppression as well as the peak-search algorithm which yields the tune values.

1 INTRODUCTION

The PSB was constructed as an injector for the 26 GeV PS and started running in 1972. In the early days, the PSB had a very elaborate measurement system to measure the tune values [1],[2],[3] in both planes for all 4 Rings. The system was based on inducing coherent betatron oscillations by the excitation of a 'Q-kicker' for a fraction of the revolution period. However, around 1976, it was proposed to calculate the tune values based on the measurement of various magnet currents in the rings [4],[5],[6]. This meant that the Q-kicker method was progressively disused and finally abandoned in the eighties. In parallel, the current acquisition approach has been considerably refined over several generations of the control systems, to become the principal method of evaluating the tunes in PSB rings to date. In recent years, particularly in the light of LHC beam requirements, it was decided that a tune measurement system using a Q-kicker was again necessary for the PSB. With DSP possibilities in a modern VME environment,

such measurements every 10 ms during acceleration seemed feasible. This approach was adopted, as in the PS [7], and forms the basis of the system described here.

2 SYSTEM DESCRIPTION

The PS control system is based on the VME standard. DBV96 modules, which use the Motorola 96001 DSP chip, were purchased for the PSB Q measurement System. The VME system provides the interface to the rest of the control system and permits the down-loading of the DSP software. To perform a measurement, one needs to excite betatron oscillations, at the requested times in the machine cycle. Timing pulses are generated at these times, gated with the revolution frequency. To ensure coherence, the revolution frequency is obtained from another VME crate which generates the radio frequency signals for the PSB. The gated signal is sent to the pulser, which generates a one-turn pulse to drive the kicker. The same pulses are used to trigger the ADC, starting the process of putting the 1024 data points into memory, ready for the DSP. When the data has been acquired, the DSP commences the processing. Fig. 1 shows the main units of the system.

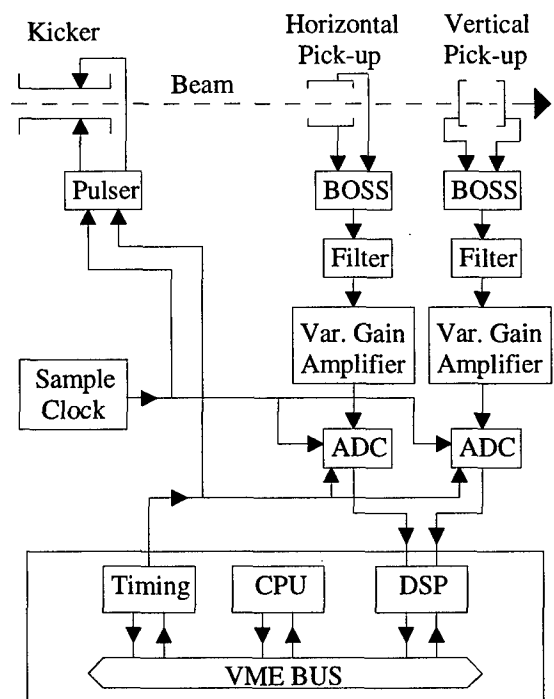


Figure 1 : System block diagram

3 HARDWARE

The layout of one acquisition channel is illustrated in Fig. 1. The PSB type-A electrostatic pick-up (PU) has 4 identical electrodes. The voltage induced on each electrode is proportional to the beam intensity and to the distance of the beam from the PU centre. The electrodes are transformer-matched to 50 Ω coaxial cables, which bring the signal from the ring up to the BOSS units. Opposite pairs of electrodes are used for the horizontal and vertical measurements, which are then processed in identical analogue signal channels.

3.1 Beam Offset Signal Suppressor(BOSS)

During the acceleration cycle the beam position can move significantly away from the centre of the vacuum chamber. Typically this can be between 5 to 10 mm. The amplifiers in front of the Analogue to Digital Converter (ADC) must have their gain set so that they do not saturate, at any point in the machine cycle. The Q measurement pulser applies a 500 V pulse to the kicker which gives an oscillation amplitude of ~ 0.1 mm. Therefore, the measured signal is typically of the order of one hundredth of the ADC's input range. To improve the signal-to-noise ratio, one could augment the amplitude of the pulse but this has two undesirable consequences. The pulser becomes costly and difficult to maintain and kicking many times along the cycle causes beam blow-up.

The BOSS unit has an input amplifier for each electrode of a plane. The internal feedback system acts on the gain of the two input amplifiers, to give identical output voltages. These two voltages are then subtracted to obtain the betatron signal. The frequency response of the feedback loop is chosen so that it is fast enough to act on the relatively slow changes of the closed orbit position. The betatron frequencies are higher and therefore, are not attenuated.

3.2 Filter

The PSB revolution period is 1.67 μ s at injection and 0.54 μ s at extraction. There are fixed cable delays between the sample clock generator and the pickup signal of the order of 1 μ s. This makes it difficult to control the phase between the bunch signal and the sample clock. At present, the sample clock is at twice the revolution frequency. The beam can have a bunching factor of down to 0.4. These conditions can result in the ADC taking a block of data, sampled between the bunch signals. This effect can be clearly seen on the trace of the raw signal without BOSS, as short "drop-outs" of the signal. In an ideal case, the filter cut-off frequency should follow the revolution frequency. However, by choosing a filter with a cut-off frequency sufficiently low to stretch the bunch signal at injection, but high enough not to attenuate the betatron frequencies too much at extraction, one can use a

fixed cut-off frequency filter. In the future, these filter trade-off effects will be minimised by sampling at four times the revolution frequency.

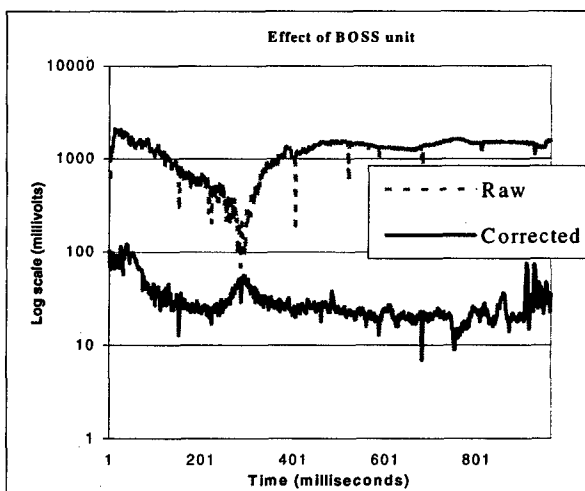


Figure 2 : Effect of the BOSS unit on the pickup signal

3.3 Variable Gain Amplifier & ADC

This uses a voltage programmable amplifier followed by a fixed gain buffer. Its gain range is -20 dB to $+60$ dB. At present, the gain is set by a front panel potentiometer but, this could be controlled by a DAC. For routine operation, the gain is set so that there is no saturation with the highest beam intensity. The system then measures over a range of 1×10^{12} to 3×10^{13} protons per pulse. A 12-bit resolution, 1×10^6 samples/s ADC is used, giving a 80 dB dynamic range in the power spectrum.

3.4 Pulser

To carry out a tune measurement, betatron oscillations are excited by pulsing a kicker in each ring. The amplitude of the kick had to be chosen based on the criteria that it must be large enough to produce reliable measurements, but small enough to avoid blowing up the beam [4]. The present pulser is a device of the utmost simplicity. It is driven by a 5 V logic signal which is gated to equal one revolution period. The pulse is isolated by an opto-coupler and further gated by two monostable multivibrators. These limit the maximum pulse length to 2 μ s, and the maximum repetition frequency to 200 Hz. The pulse is then amplified to 15 V to drive the output stage. This consists of two power MOSFETS wired as 10 A current sources. These are connected in parallel to an isolating transformer, which drives the kicker. The transformer permits ground isolation between the pulser and the kicker. It also permits an output pulse of either polarity, without recourse to floating power supplies.

4 SIGNAL PROCESSING & SOFTWARE

The filtered PU signal is digitised by an ADC sampling at twice the revolution frequency in a synchronised manner. The time series obtained consists of 1024 samples. This time series is manipulated by DSP programs in order to extract the information needed, i.e. the machine fractional tune. The first tasks (applying a 72 dB Blackman-Harris window [8], FFT transforms, power spectrum computation and peak search) are coded in assembler language to achieve the required speed. A peak search algorithm was developed to find all the frequencies corresponding to the first peaks in the power spectrum which are above a given noise level. It consists of two phases : the coarse search and the fine tuning. The former is based on first order differences which generate a three-levels function : 0 if at least one of the values is below the noise level, -1 if the first order difference is negative and +1 if it is positive.

The required frequencies $f^{(1)}$ are those at which the value of this auxiliary function jumps from +1 to -1. A simple algorithm sorts the obtained maxima in descending order. It is well known that the effect of the finite duration of the time series is to convolute the spectral estimate with a kernel which depends on the chosen window. This "leakage effect" introduces a small error (less than the frequency sampling interval Δf) in the computation of the frequency of the maximum. One may assume that the square root of the power spectrum $z(f)$ is well approximated by a parabola in the neighbourhood of the maximum for most types of windows by :

$$z(f) \approx z_{\max} [1 - a (f - f_{\max})^2]$$

where z_{\max} , f_{\max} and a are the square root of the power spectrum maximum, the corresponding frequency and the frequency spread respectively. If z_0 , z_{-1} , z_1 are the values $z(f^{(1)})$, $z(f^{(1)} - \Delta f)$ and $z(f^{(1)} + \Delta f)$, simple algebra gives the following second estimate of f_{\max} :

$$f^{(2)} = f^{(1)} - \frac{z_{-1} - z_1}{2(z_{-1} - 2z_0 + z_1)} \Delta f$$

The program checks if the fraction in this expression is less than 1 in absolute value to ensure the validity of the second estimate. It is not usually the case when z_{-1} and z_1 are below the noise level.

A program written in C language computes the machine fractional tunes in the DSP board and subsequently delivers them in the correct format to the control system. Display programs at the console provide the operator with the complete behaviour of the fractional tune along the machine cycle (Fig. 3). Facilities are available to observe

all the data including the raw ADC samples and the FFT Spectra.

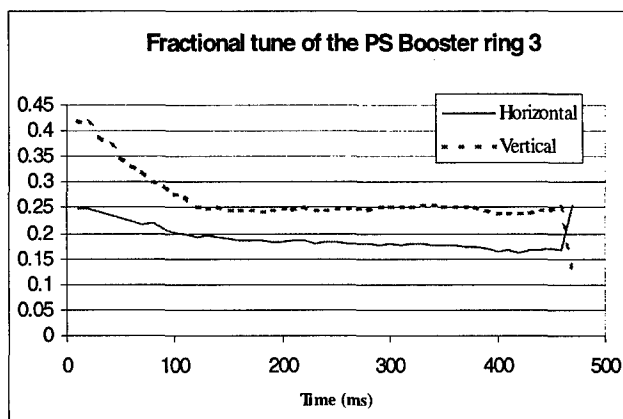


Figure 3. Display of the measured horizontal and vertical fractional tune in the PS Booster ring 3.

5 CONCLUSIONS

The PSB tune measurement system is evolving rapidly; considerable modifications are underway to permit measurements in all 4 rings by multiplexing the treated source signals to the ADC and DSP chain. A new ADC board and a timing burst generator are also to be added together with a more powerful, controllable pulser to augment the kick strength. With the rapid evolution in DSP technologies, a more modern DSP Board in VME will also have to be considered in the near future; this would permit identical hardware configurations for the PSB and PS Rings.

6 ACKNOWLEDGEMENTS

The hardware development for the beam offset Signal suppressor was carried out by L. Soby and O. Marquersen. The help of P. Pepin and M. LeGras, essential for this system's controls development and integration, is gratefully acknowledged.

7 REFERENCES

- [1] H.Kozioł, "Q Measurement for the PS Booster", MPS/Int.BR/74-14, (1974)
- [2] H.Kozioł, "Beam Observation For the Booster", SI/Int.DL/68-4, rev1, (1968)
- [3] C. Carter, "A Tunable BandPass Filter", CERN/SI/Int.DL/70-7, (1970)
- [4] G.Baribaud, J.Donnat, M.Lelaizant, K.Schindl, "Calcul de Q a partir des Courants, Specifications du materiel et du logiciel", PS/BR Note 76-6, (1976)
- [5] C.Metzger, "Calcul de Q: Description du Programme en Fortran", PS/BR/Note/79/18, (1979)
- [6] G.Baribaud, J.Donnat, H.Schönauer, "Specifications du Systeme pour le calcul de Q du PSB", PS/BR Note/80-2, (1980)
- [7] J. González, S. Johnston, E. Schulte, "Fast Q Measurement for the PS by FFT analysis", CERN/PS 94-12 (BD), & Proc. 4th EPAC, London, pp. 1734 (1994)
- [8] F. J. Harris, "On the Use of Windows for Harmonic Analysis with the Discrete Fourier Transform", Proc. IEEE, vol. 66, no. 1, (1978)

MEASUREMENT OF BEAM CHARACTERISTICS OF PLS LINAC*

J.-Y. Choi[#], H. S. Kang, S. H. Nam, S. S. Chang

Pohang Accelerator Laboratory, POSTECH, Pohang 790-784, Korea

Abstract

The PLS (Pohang Light Source) linac has been operated routinely as the injection linac for PLS, a third-generation synchrotron light source. The transverse electron beam emittance was measured at the pre-injector end of the PLS linac, where the beam energy is about 100 MeV. The emittance was measured using a quadrupole magnet and a fluorescent target. We used a progressive scan CCD camera with an asynchronous random trigger shutter to obtain precise beam sizes. The beam image analysis was made with a PC equipped with a frame grabber. Bunch length was also measured at the pre-injector end using a streak camera to observe transition radiation emitted from a radiator inserted into the beam path. The measurement system and the results are described in detail.

1 INTRODUCTION

The PLS (Pohang Light Source) linac has been operated as the full energy injection linac for the PLS, a third generation synchrotron light source storage ring [1,2]. It provides electron beams to the PLS storage ring twice a day. In the regular injection mode, the electron beams from the gun has a pulse width of less than 1 ns (FWHM), beam current of 1.7 A, and repetition rate of 10 Hz.

Just after the completion of the linac and during the commissioning period in 1994, beam parameters were measured and reported [1]. To further improve the beam quality and the operation stability of the linac, we are again measuring the electron beam parameters at the linac.

In this paper we describe some preliminary results on the emittance and bunch length measurements done at the pre-injector of the linac. The pre-injector includes the bunching system and two accelerating columns. The prebuncher is an S-band standing-wave type cavity, and the buncher has a traveling-wave structure with four cavities. The pre-injector is powered by the first klystron-modulator module, and accelerates the electron beam to 100 MeV.

Figure 1 shows typical electron beam transmission efficiency along the linac, under the usual beam acceleration condition for normal injection into the

storage ring. The first wall current monitor (WCM) is located near the exit of the electron gun and the second WCM is located at the end of pre-injector. The electron beam loss occurs mainly during the bunching process and the first acceleration stage, and the transmission efficiency at the pre-injector is about 60%. After the pre-injector, the electron beam is transmitted to the linac end with small beam loss. The results reported in this paper refer to this beam condition unless otherwise stated.

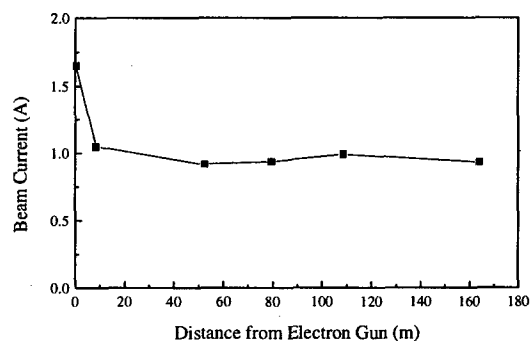


Figure 1: Beam current transmission efficiency along the linac measured by wall current monitors.

2 EMITTANCE MEASUREMENT

The transverse electron beam emittance was measured at the pre-injector using a quadrupole magnet (QM) and a beam profile monitor (BPRM) utilizing a fluorescent screen.

In order to measure the exact electron beam spot sizes on the BPRM screen, we used a frame grabber (LBA-300PC, Spiricon Inc.) and an asynchronous CCD camera (CV-M10, Costar Ind.), in which the camera shutter timing can be controlled by the beam trigger. To have a good resolution the camera was operated in the progressive scan mode during the measurements.

Although we have one set of a QM and a BPRM in the drift space of the pre-injector, the distance between the QM and the BPRM is too short to observe an appreciable change of the beam spot size with the change of the QM excitation current. Instead, we measured the beam size at a BPRM located in the beam energy analyzing station. Since the horizontal beam size can be affected by the dispersion function of the bending magnet, it is

* Work supported by Ministry of Science and Technology and POSCO

[#] Email: choij@postech.ac.kr

necessary to isolate its contribution from the observed horizontal beam size.

The beam spot sizes in the vertical direction are shown in the Fig. 2 as a function of the QM excitation current. The emittance was calculated from these measured beam sizes by the relationship on the beam radius and beam matrix elements [3]. The calculated emittance value was about 80π -mm-mrad. While the beam intensity profiles were Gaussian shapes in the vertical direction, the horizontal beam sizes varied largely from pulse to pulse. Therefore, no reliable data about beam spot sizes were obtained in the horizontal direction during the preliminary measurement. This pulse-to-pulse beam size variation is believed to be caused by beam energy jitters, probably due to the temporal instability of the modulator and other components. We are planning to continue the emittance measurement at the pre-injector after reducing the energy jitters.

The energy spread of the electron beams at the pre-injector was measured from the horizontal beam sizes in the beam analyzing station using the frame grabber. The observed energy spread at the pre-injector was about $\pm 0.27\%$, and this energy spread varied from ± 0.24 to $\pm 0.3\%$ from pulse to pulse.

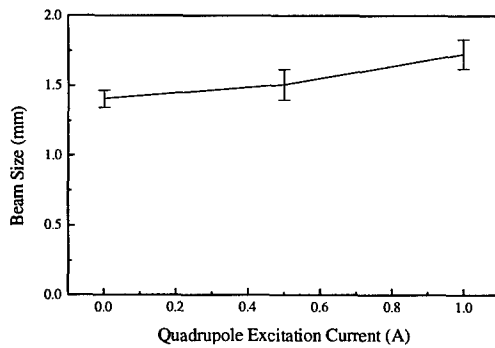


Figure 2: Variation of the vertical beam spot size with the current of the focusing quadrupole magnet.

3 BUNCH LENGTH MEASUREMENT

Bunch lengths were measured using the optical transition radiation (OTR) emitted from a metal target when accelerated electron beams impinged on the target. The bunch monitor system utilizing OTR has favorable characteristics to accurately measure the bunch shape and the bunch length, and is widely used in electron linacs [4,5]. The schematic layout of the measurement system is shown in Fig. 3.

The target is made of stainless steel 2.6 mm thick, and its surface was polished to the roughness less than $0.1 \mu\text{m}$ in Ra value. The target chamber was installed at the pre-injector end where the electron energy is 100 MeV. The emitted OTR is guided to the gallery via optical components such as lenses and mirrors. To block stray light and to have better S/N ratio, the optical

components were surrounded by a light-shielding structure. The guided OTR was measured by a streak camera (Hamamatsu Photonics K. K. Co.) with a fast single sweep unit. Since the beam intensity was not high enough, the alignment of the optical components was critical in the measurement. We aligned the optical components with a He-Ne laser. The optical path from the target to the streak camera is about 10 m long. The time resolution of the streak camera is less than 2 ps, which is a sufficiently small value for S-band linac bunch length measurement. To keep better time resolution the slit width of the streak camera was kept as narrow as $20 \mu\text{m}$.

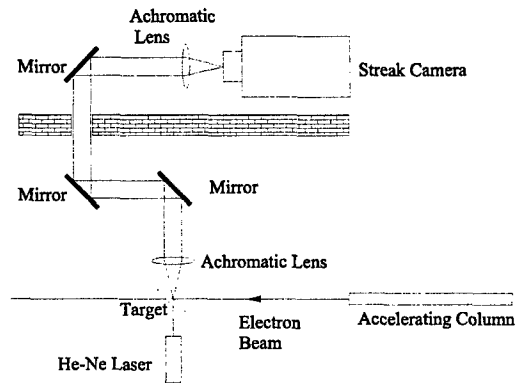


Figure 3: Layout of the bunch length measurement system.

Figure 4 shows two examples of the streak camera image of the bunch train contained in one electron beam pulse. The electron beam has a pulse width less than 1 ns (FWHM) and a beam current of about 1 A. Five bunches are observed in one beam pulse.

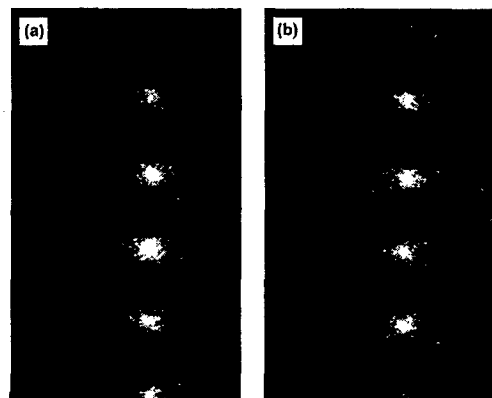


Figure 4: Streak camera images of the bunch train contained in one beam pulse of 1 ns. The vertical direction corresponds to time axis and in this case time range is 2 ns.

As is clear in Fig. 4(a), the bunch lengths were different from bunch to bunch. The length of a bunch

with more charge content tends to be larger. In addition, the charge distributions among the bunches show different pattern from pulse to pulse. On the other hand, Fig. 4(b) shows relatively uniform bunch lengths. These phenomena can be explained qualitatively by two facts; the time structure of the electron charge emitted from the electron gun has a triangular shape due to a short pulse length, and the electron beam and RF phase of the bunching system do not have definite synchronization in our linac.

The effects of RF parameters of the bunching system on bunch length have been investigated. Measurements were done for the beam of 2-ns pulse length to reduce the above-mentioned bunch length variation from bunch to bunch and from pulse to pulse. Figure 5 shows the bunch image and intensity profile for the case where RF parameters of the bunching system were not optimally adjusted. The bunch lengths in this case were more than 17 ps. On the other hand, Fig. 6 shows the bunch image and intensity profile after RF parameters were adjusted. Bunch lengths were reduced to less than 12 ps by the adjustment of the RF parameters of the bunching system.

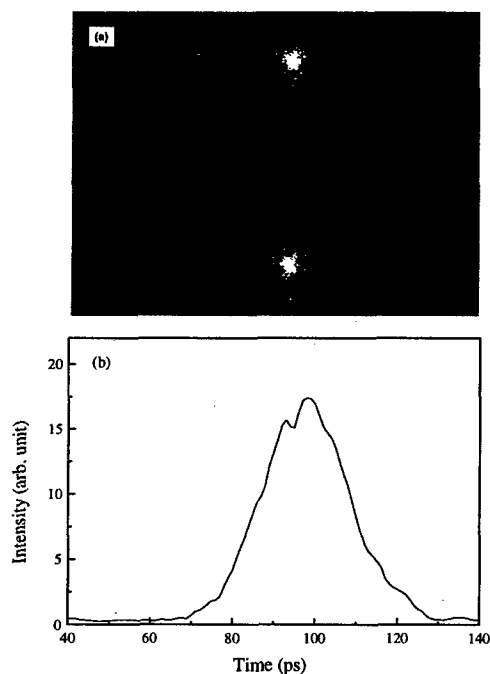


Figure 5: (a) Bunch image and (b) intensity profile of bunch before RF parameters of the bunching system were adjusted. In (a) the vertical axis corresponds to streak time whose range is 500 ps, and the intensity profile of the lower bunch is plotted in (b).

4 SUMMARY

We have been measuring electron beam parameters at the pre-injector of the PLS linac. The measured beams have the same condition as the beam injected to the

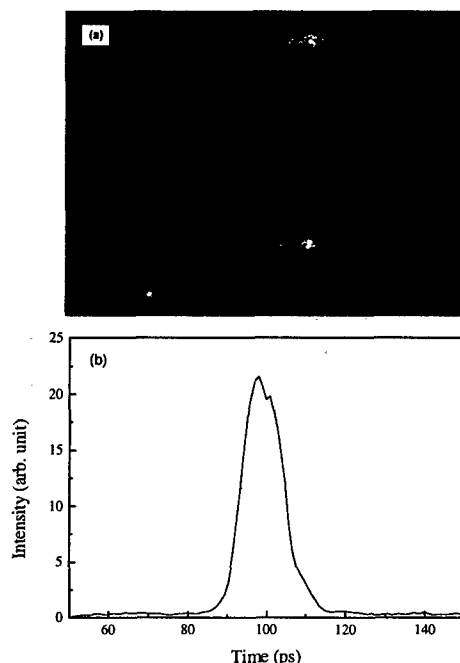


Figure 6: (a) Bunch image and (b) intensity profile of the bunch after RF parameters of the bunching system were adjusted. The intensity profile represents the lower bunch shown in (a).

storage ring. The transverse emittance in the vertical direction was measured. Preliminary measurement results were presented. We are planning to continue the bunch length and emittance measurement at the pre-injector after reducing the pulse-to-pulse energy jitters. The beam parameter measurements at the linac end are now in progress.

5 REFERENCES

- [1] W. Namkung, "PLS 2.0-GeV LINAC", Proceedings of the 1994 International Linac Conference, August 21-26, 1994, Tsukuba, Japan
- [2] S. H. Nam, K. R. Kim, Y. J. Han, Y. C. Kim, and S. S. Chang, "Status of PLS 2-GeV Electron Linac", in these proceedings
- [3] H. Wiedemann "Particle Accelerator Physics", p. 157, Springer-Verlag (1993)
- [4] M. Jablonka, J. Leroy, X. Hanus and L. Wartski, "Beam diagnostic using transition radiation produced by a 100 MeV electron beam", DPhn Saclay 91-32, 1991.
- [5] Y. Ogawa, J.-Y. Choi, T. Suwada, T. Kamitani, T. Urano, K. Furukawa, S. Ohsawa, A. Enomoto and I. Sato, "Beam Monitor Utilizing Transition Radiation" 1993 Proceedings of the 1993 Particle Accelerator Conference, May 17-20, Washington, D. C., USA, 1993

DESIGN OF AN ELECTROSTATIC ENERGY SEPARATOR FOR THE ISIS RFQ TEST STAND

J. Duke, A. Letchford, RAL, Chilton, Didcot, UK

Abstract

It is planned to replace the 665 keV Cockroft Walton set of the ISIS spallation neutron source in the UK with a four rod RFQ. Before this replacement is made, the performance of the RFQ will be extensively assessed on a test stand. One of the quantities we hope to measure is the proportion of accelerated (trapped) beam at the exit of the RFQ for various H⁺ ion source currents and rod voltages. In order to do this it is necessary to separate the untrapped beam which is largely at the ion source extraction energy of 35 keV from the trapped beam which has an energy centred on 665 keV. This paper describes the design process for an instrument to perform this separation using parallel electrostatic plates to bend away the low energy beam while allowing all the higher energy beam to pass through, therefore measuring directly the fraction of trapped beam, and by implication the fraction of untrapped beam.

1 THE DESIGN PROCESS

The aim of the investigation was to find a method of removing the low energy component from the beam while retaining the high energy component for long enough that its current could be measured. Initially, extensive studies were performed to discover if it was possible to use the chromaticity of a series of quadrupoles to over focus the low energy beam and cause it to hit the beam pipe while retaining the high energy beam. (For the purposes of this paper, 'high energy' is defined as 0.665 ± 0.1 MeV and low energy is anything less than this). Solutions were found, but due to the highly divergent beam from the RFQ the beam size grows large very quickly, making it necessary to have very large bore quadrupoles in order not to lose any high energy beam. The size, weight and cost of these quadrupoles caused us to look for another way of separating the two energy groups. The fact that the untrapped beam is at such low energy and that there is a wide gap between the two energy groups caused us to think of using an electrostatic method of separating the groups.

Studies were performed to investigate the feasibility of using two parallel high voltage plates of opposite polarity to deflect the low energy beam more than the high energy beam. These were done by tracking a 'large' distribution of quasi-particles which had been generated by an RFQ simulation program written by A. Letchford. The final optimisation was performed using an initial

distribution of 95351 quasi-particles, of which 89349 were 'high energy' and 6002 of lower energy, which corresponds to fractions of 93.7% and 6.3% respectively. Particle tracking was performed with Parmila [1] throughout, and various Fortran routines were written to perform tasks such as counting the proportions in the two energy groups at various stages of the device, calculating the trajectories of all the particles as they pass through the electric field and calculating the distribution of particles hits on the plate which the particles are bent towards.

The parallel plate device was to be situated in the second half of a diagnostics box of outside length 430 mm, the first half of which will contain an emittance scanner. The entrance port of the box ends 163 mm after the end of the RFQ rods. At this point the low energy beam is already being lost on the 70 mm diameter beam pipe, and all components of the beam are diverging. At the entrance port to the box, the high energy component is quite round with a radius in both transverse directions of about 8 mm. By the middle of the box, e.g. after 253 mm from the port, the beam looks transversely like Figure 1.

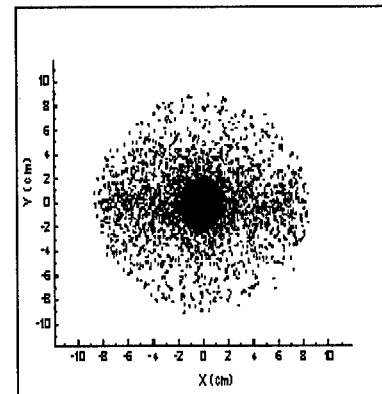


Fig. 1

Transverse distribution of all remaining particles at position of beginning of parallel plates, if there were *no* aperture plate

The radius in the x direction of the high energy beam only at the same point in the box is about 1.5 cm. This means that if nothing else were done the low energy beam would have to be bent $\sim (1.5 + 8.0)$ cm more than the high energy beam to be spatially separated.

For this reason an aperture plate was added to the middle of the box, 217 mm after the entrance port, to crop the low energy component as tightly around the high energy

component as possible without losing any high energy particles. The aperture was chosen to be of radius 35 mm which was a little larger than the radial co-ordinate of any high energy particle.

As shown by Figure 2, the beam after the aperture plate has a considerable spread of energies intermediate to the two main groups. Although not clearly visible on Fig. 2, the energy distribution also contains some fine structure caused by the way particles in the RFQ are more likely to be lost at particular places in the r.f. bucket and hence cluster around certain energies.

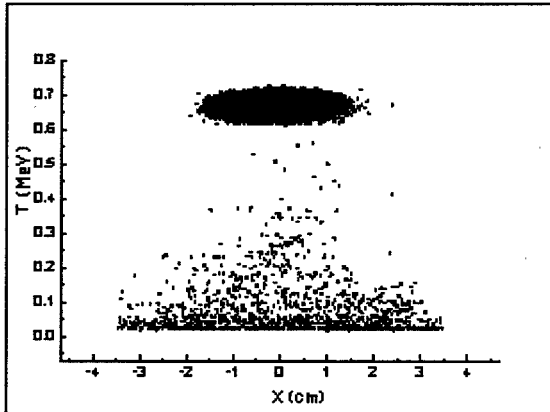


Fig. 2

Plot of x versus kinetic energy T for all remaining particles at the start of the parallel plates, with the aperture plate

The voltage to be used on the parallel plates was decided by setting the separation of the plates to be large enough that the high energy beam would not strike them even after being bent, and then trying different voltages in the program written to calculate the effect of the bending field. The final current was to be measured with a beam toroid, whose accuracy was estimated to be no better than 1%, so the system only had to be designed to separate the low energy particles to the order of 1% of the total number of particles. Using a 45 mm final aperture throughout, 100% of high energy particles survived. The results for the low energy particles are in Table 1 below: *

Table 1

Plate Voltages (\pm kV)	% of original low energy particles remaining	Low energy particles % of total
20	6.486	0.699
25	4.906	0.529
30	3.933	0.424

Plate voltages of ± 25 kV were chosen because this gives an error in the high energy beam of less than 1%.

Using ± 25 kV on the parallel plates with a separation of 70 mm, split left and right 33 and 37 mm respectively (non-symmetrical to maintain the highest field while still allowing for the small bending of the high energy component), the bending effect of the plates on the particles was calculated. Plates 140 mm long were used, because these were as long as possible in the space available while leaving good clearance at either end to avoid sparking between the parallel plates and the aperture and end plates. The clearances were 26 mm to the aperture plate and 30 mm to the endplate. In all later calculations, the particles are shown being bent to the right, but this was an arbitrary choice. Figure 3 shows the transverse positions of particles at the toroid if they could pass through the parallel plate without being stopped. Figure 4 shows the calculated distribution of hits on the right hand parallel plate. From this plot the height of the plate from the centre line was chosen to be 60 mm. The nine particles plotted at $x = -1$ have been reflected by the potential barrier they encountered between the plates.

1.1 Temperatures of the parallel plate and the aperture plate

Using this distribution of hits and the distribution of hits on the front face of the aperture plate to estimate the peak number density and hence the peak power density being absorbed by the plates, estimates were made for the maximum temperatures reached by these components in normal operation at 50 mA (the maximum expected peak operating current) for both 1% and 10% duty cycles. On the basis of heat loss by radiation only, the maximum temperatures at 10% Duty Cycle and 50 mA beam current were 307°C for the parallel plate and 233°C for the aperture plate. The aperture plate is to be made of 10 mm Stainless Steel and the parallel plates and their supporting rods have already been made from Copper. The plates are 4mm thick.

These estimated temperatures are comfortably below the melting points of these materials.

Figure 5 shows the way the particles of lower energy have been bent to the right and lost on the final aperture. The particles which cannot be separated and which have x values within the high energy group can also be seen.

* The figures in Table 1 are different to those in Table 2 because the calculation in Table 1 did not include the effect on the particles' energies of entering and leaving the region of high potentials between the plates, from and to the region outside, which has zero potential. All other calculations in this paper do include this effect, which was found later in the investigation to be non-negligible.

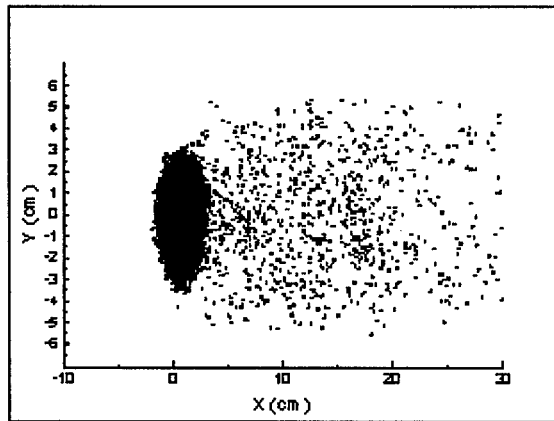


Fig. 3

Transverse distribution of particles just before toroid using ± 25 kV 140 mm long plates, if no particles were intercepted by the parallel plates

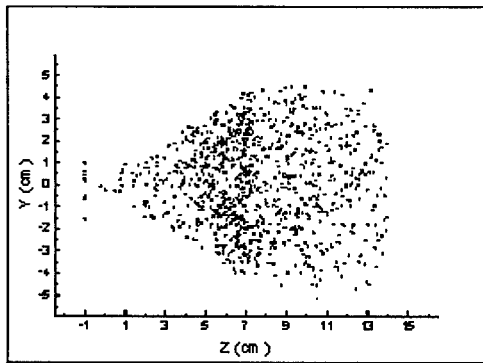


Fig. 4

The distribution of hits on the parallel plate

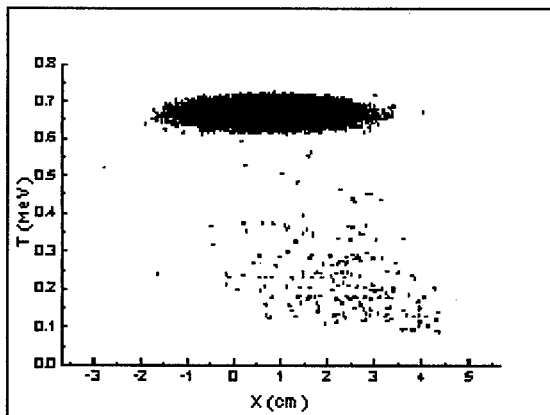


Fig. 5

Plot of x versus energy T after being bent and passing through an aperture of radius 45 mm at the exit of the diagnostics box

2 RESULTS

Below in Table 2 are shown the fractions of high and low energy particles remaining at the position of the final toroid which surrounds the exit port of the device for two different exit port radii. If :

N_H = Number of high energy quasi-particles at end of the device,

ΔN_H = Change from original number of high energy particles,

N_L = Number of low energy quasi-particles at end of device,

ΔN_L = Change from original number of low energy particles, and

$N_T = N_H + N_L$ = original total number of quasi-particles, then:

Table 2

Aperture (mm)	N_H (ΔN_H)	% high remaining	N_L (ΔN_L)	% low remaining	$\frac{N_L}{N_T}$ (%)
35	89316 (-33)	99.96	212 (-5790)	3.66	0.22
45	89349 (+0)	100	286 (-5716)	4.77	0.30

3 CONCLUSIONS

Simulations indicate that the energy separator system as specified above, i.e. a 35 mm radius aperture 26 mm before two parallel plates 140 mm long, separated by 70 mm, with ± 25 kV on them, followed by a drift of 30 mm and an end aperture of radius 45 mm, should be able to reduce the initial number of low energy particles to 4.8 % of their original number. This represents 0.30 % of the total particle numbers, which is comfortably below the expected accuracy of the toroid which will be used to measure the exit current. This system will produce peak temperatures for 10% Duty Cycle and 50 mA beam current, the maximum power that can be envisaged being used, on the parallel plate of about 307°C, and on the aperture plate of about 233°C, in the most likely estimate. This system is expected to draw about 0.73 mA from the power supplies for the parallel plates.

4 ACKNOWLEDGEMENTS

My thanks go to Chris Bailey for useful ideas and suggestions, and to Graeme Murdoch for advice on the practical engineering realities and getting the plans drawn up.

5 REFERENCES

- [1] PARMILA Linac Design Code written by Harunori Takeda, LANL.
- [2] 'Matching solutions between the ISIS RFQ and Tank 1' - ISIS paper no. ISIS/RFQ/PHYS/JPD/98-2
- [3] 'The first order design of the ISIS RFQ Test Stand Spectrometer' - ISIS paper no. ISIS/RFQ/PHYS/JPD/98-1

FERMILAB MAIN INJECTOR INSTRUMENTATION*

Ed Barsotti, Wim Blokland, Jim Crisp[#], Brian Fellenz, Jim Fitzgerald, Gianni Tassotto, Greg Vogel, and Jim Zagel, FNAL, Batavia, IL

Abstract

An overview of the instrumentation installed in the Fermilab Main Injector is presented. Efficiency, beam loss, average intensity, bunch intensity, position, betatron and synchrotron oscillation frequency, as well as transverse and longitudinal profiles are measured. Systems such as the Beamline Tuner and the Ionization Profile Monitor track changes through the accelerating cycle and analyze their rate of change.

1 INTENSITY MONITORS

1.1 DC Current Transformers

The DC current transformer (DCCT) used in Main Injector was designed at Fermilab for the Main Ring [2]. The device measures the second harmonic content from excitation windings to control a bucking current through magnetic cores surrounding the beam. The circuit is carefully balanced to maintain no net magnetic flux in the cores by making the bucking current exactly cancel the beam current. The bucking current is then a measure of the DC beam current. A careful balance of transformer coupling provides bandwidth from DC to several kilohertz.

A commercial current monitor was purchased for the Recycler ring (Bergoz, Crozet France). The unit has 100 kilohertz bandwidth, 7 decades of dynamic range, and .05% accuracy [3].

1.2 Torroids

Torroids (Pearson Electronics Inc., Palo Alto California) provide an inexpensive method of measuring beamline intensities and thus transfer efficiency. These devices are transformer coupled to the beam current and have no DC response. Their bandwidth is 40 hertz to 7 megahertz and they produce 1 volt per amp. A gated integrator is used to measure the total charge. Cable loss and matching, beam structure, limited bandwidth, and finite integration time result in 2% absolute accuracy. Relative accuracy is about ten times better. The calibration is adversely affected when secondary particles created by beam losses strike the torroid.

2 LOSS MONITORS

The same argon filled ion chamber (Troy-onics Inc., Kenil, NJ) is used for Main Injector, beamline, and Tevatron loss monitors [4]. The sensitivity is $7e-8$ coulombs per rad. The maximum signal is 100 rads "instantaneous dose rate" or $7e-6$ coulombs of collected charge. Electronic noise limits the dynamic range to 6 decades.

2.1 Main Injector Loss Monitor Integrator

The daughter card used for the 250 Main Injector loss monitors has two channels. One channel provides a resettable integrator with a full scale output of 0.14 rads. An 8 bit A/D converter provides about 2 decades of dynamic range. The second channel provides a complicated decay integrator output to the MADC for time plotting. It has selectable gain advertised as .014 or 1.4 rads full scale. The response depends heavily on the time structure of the losses. Between 100 and 1000 hertz for example, the low gain setting produces full scale for 140 rads/second.

2.2 Beamline Loss Monitor Integrator

A new daughter card was designed and built for the 106 beamline loss monitors. It uses a "decaying integrator" circuit with a logarithmic response and a 1 decade per 30 msec decay time. The log amplifier has a 6 decade dynamic range. For losses shorter than 1 msec (as in the beamlines), 1 rad will produce the full scale output. For dc losses, the full scale output is 1000 rads/sec.

3 POSITION MONITORS

3.1 Position Detectors

To conserve tunnel space and maintain the beam pipe shape and minimize beam impedance, new detectors were designed that fit inside the downstream end of every quadrupole [5]. The 208 detectors measure 4 positions per betatron wavelength in both the horizontal and vertical planes.

The detector has four striplines that can be combined in pairs to measure either horizontal or vertical position at each quad. The plate width, position, and length were selected for best linearity and signal amplitude to match the Main Ring rf modules. The Main Injector bpm's provide about 0.7 db/mm for the ratio of A to B.

The four plate structure exhibits a pin cushion error which mirrors the field lines produced between the plates and the beam charge. This distortion couples the horizontal and vertical measurements for positions far off axis. Each detector was mapped with a set of 50 wire measurements at 5 mm spacing. This data was collected into a database and can be used to correct orbits with data from the orthogonal plane [6].

The Recycler ring uses a split tube design with separate horizontal and vertical geometry. Positions are

* Work supported by the U.S. Department of Energy under Contract No. DE-AC02-76CH03000

[#] Email: crisp@fnal.gov

measured at 438 locations. The detector design allows a 500 volt clearing field to be applied to the bpm plates. Larger aperture detectors are required at 24 locations near injection and extraction points.

3.2 Position Electronics

The electronics from Main Ring were re used in the Main Injector. The system employs the AM to PM conversion technique to measure the relative amplitudes of the A and B detector signals and thus the beam position. The multibus system used to digitize the results are lacking in processing power, particularly by today's standards. However, a substantial savings was realized.

New position electronics using log amplifiers were developed for the Recycler [7]. Preamps are required in the tunnel in order to measure the position of unbunched beam using the rising and falling edges of the beam signal. Four positions are measured with a single CAMAC card. The log amp design is inexpensive but has ± 5 mm errors that depend on intensity and position. VME based computers and commercial digitizer cards with memory collect and process the data.

4 PROFILE MONITORS

4.1 Multiwires

A new paddle was designed for Main Injector multiwires with horizontal and vertical grids to allow simultaneous measurement of both planes. Each grid consists of 48 .003 inch diameter gold-tungsten wires with either 1 or 2 mm spacing. The distribution of charge is measured with a 96 channel integrator designed by the controls group for use in the Switchyard beamlines [8]. The central wire collects about 24 picocoulombs of charge for 5e11 protons.

4.2 Flying Wires

The Main Injector Flying Wires measure the transverse size of the particle beam used to calculate emittance [9], [10]. At separate horizontal and vertical locations, the system passes a 33 micron carbon monofilament (the 'wire') through the beam at speeds up to 10 m/s. Particles collide with the wire as it moves through the beam producing a cascade of secondary particles proportional to beam density. The secondary particles are measured with a scintillator paddle and photo multiplier tube. A 14-bit resolver measures the wire position with 0.022 degree angular resolution. The beam profile is a plot of photo multiplier tube output versus wire position. A non-linear fit is performed and the resulting summary data is made available to the accelerator network (ACNET) for use in calculating beam emittance.

4.3 Ionization Profile Monitors

The Main Injector and Recycler Ion Profile Monitors capture horizontal and vertical profiles at a once-per-turn sample rate [11], [12]. Microchannel plates are used to amplify the charge produced when the beam passes

through the residual gas in the normal accelerator vacuum. The distribution of charge collected on a grid of conductors matches the beam profile. Current analysis include position, emittance (or sigma), 2D color intensity plot of raw data, single turn profiles for any turn during the cycle, and fourier transforms of bunch centroid (or tune).

An amplifier in the tunnel is required to convert the 140 nanoamp signal to the 0 to 5 volt 50 Ω input of the A/D cards located in the equipment gallery. Sixty anode strips with 1.5 mm spacing are used to measure the transverse profile of the proton beam. Because the profile can be measured every Main Injector turn, each strip requires a dedicated amplifier and digitizer.

5 OTHER SYSTEMS

5.1 Sampled Bunch Display

The Sampled Bunch Display (SBD) is used to measure bunch intensities and longitudinal lengths of beam bunches. A wide band (3 kHz-6 GHz) longitudinal signal comes from a dedicated Resistive Wall Current Monitor. The signal is digitized by a LeCroy 9384L scope (4 GSamples/sec, 1 GHz analog bandwidth, 4 MByte segmentable memory with 100 usec re-arm time). A Macintosh computer running LabView does the processing and ACNET interface. Versatile, programmable acquisition timing is provided with a CAMAC 177 (TCLK-decoding) and a Kinetic Systems 3660 (programmable clock generator).

5.2 Fast Bunch Integrator

A real time intensity measuring system known as a Fast Bunch Integrator (FBI) was developed to determine the efficiency of this process and monitor when losses occur [13]. This system measures the intensity of both the original batch and the final individual bunch by using wide and narrow gated integrators [14]. A comparison of these two measurements provides the capture efficiency and indicates how much beam remained in adjacent RF buckets.

The FBI is a VME based system using a Motorola MVME-162LX embedded computer. The system supports fast time plots, snapshot plots and data logging of bunch intensity for all bunches as well as sums of bunch intensities for use as transfer qualifiers. The narrow gates provide the integrated intensity for individual bunches while the wide gates provide the integrated intensity for an adjustable sized batch centered on each narrow gated bunch.

5.3 Beamline Tuner

The Main Injector Beam Line Tuner (MIBLT) samples the integrated signals of vertical and horizontal beam position pickups using a Kinetics V440 60MHz digitizer. A LabView program analyzes the turn-by-turn position data and calculates the tunes, amplitudes and phase of the injection oscillation. The program has the

capability to automatically make corrections for the next transfer. The integration of the pickup signal can be done using a low bandwidth RF module (batch resolution) or a high-bandwidth Fast-Integrator module (bucket resolution).

6 SPECIAL DEVICES

6.1 Wide Band Striplines

The Institute for High Energy Physics, near Moscow Russia, designed and built four stripline beam detectors for use at Fermilab [15]. A round geometry with two stripline plates allows installation as either horizontal or vertical detectors. Electrical feedthroughs at both ends of the 1.4 meter long striplines allow measurement of both proton and antiproton signals. The 1 gigahertz bandwidth and 9.3 nsec doublet separation allow measurement of high frequency structure within the beam bunches. The detectors are for general purpose use, two in the Main Injector and two in the Recycler.

The 60 degree wide plates intercept and carry about 1/6 of the beam image current. The peak amplitude on the 50 Ω plates is 10 volts for 6e10 protons in a 3 nsec sigma gaussian bunch. A plate length of 1.4 meters (1/4 wavelength at the rf frequency of 53 MHz) is used to maximize the doublet separation. In the time domain, this allows observation of the bunch shape and changes in position along it's length. In the frequency domain, zero's in transmission occur when the plate is a multiple of 1/2 wavelengths long. This occurs at even harmonics of the rf frequency.

6.2 Resistive Wall Monitor

Resistive Wall Monitors were designed and built for the Fermilab Main Injector project [16]. These devices measure longitudinal beam current from 3 KHz to 4 GHz with a 1 ohm gap impedance. The new design provides a larger aperture and a calibration port to improve the accuracy of single bunch intensity measurements. Microwave absorber material is used to reduce interference from spurious electromagnetic waves traveling inside the beam tube. Several types of ferrite materials were evaluated for the absorber. Inexpensive ferrite rods were selected and assembled in an array forming the desired geometry without machining.

6.3 Schottky Detectors

A split tube detector is resonated through an inductor to provide a signal to the schottky receiver. The signal to noise ratio goes as the square root of the detector impedance which is proportional to it's Q. A Q of 300 is achievable, provides sufficient impedance, is reasonably stable with temperature, and has sufficient bandwidth. A center frequency of 21.4 MHz was chosen because of readily available crystal filters. The detected signal is dominated by coherent oscillations, not schottky noise as the name suggests.

7 REFERENCES

- [1] <http://ahse30.fnal.gov/home.html>, RF&Instrumentation home page
- [2] Webber, R.C., "Charged Particle Beam Current Monitoring Tutorial", Beam Inst. Workshop, Vancouver Canada, Oct. 1994.
- [3] Unser, K.B., "The Parametric Current Transformer", AIP Acc. Instr. Conf. Proc., No. 252, 1991.
- [4] Johnson, M., "Loss Monitors", AIP Acc. Instr. Conf. Proc. No. 212, 1989.
- [5] Fitzgerald, J., Crisp, J. "A Compact BPM for the Fermilab Main Injector" IEEE PAC, 97CH36167, May 1997.
- [6] Fitzgerald, J., Crisp, J., McCrory, E., Vogel, G. "BPM Testing, Analysis, and Correction", Beam Instrumentation Workshop, AIP Conf. Proc. No. 451, May 1998.
- [7] Barsotti, E., Lackey, S., McClure, C., Meadowcroft, R., "Beam Position Monitors for the Fermilab Recycler Ring", Beam Instrumentation Workshop, AIP Conf. Proc. No. 451, May 1998
- [8] Kissel, W., Lublinsky, B., Franck, A., "New SWIC Scanner/Controller System", presented at ICALEPCS 95, Chicago, IL, Oct. 1995.
- [9] Vogel, G., Dey, J., "Flying Wires", IEEE PAC, 97CH36167, May 1997.
- [10] Gannon, J., Crawford, C., Finley, D., Flora, R., Groves, T., "Flying Wires at Fermilab", IEEE PAC, 1989
- [11] Zagel, J., Crisp, J., Hahn, A., Hurh, P. :Fermilab Main Ring Ion Profile Monitor System. 1997 IEEE Part. Acc. Conf. 2166-8. May 1997.
- [12] Zagel, J., Chen, D., Crisp, J. :Fermilab Booster Ion Profile Monitor System Using LabView. Beam Instrumentation Workshop. AIP Conf. Proc. 333. 384-90. October 1994.
- [13] Utterback, J., Vogel, G., "Fast Bunch Integrator, A System for Measuring Bunch Intensities in Fermilab's Main Ring", presented at ICALEPCS 95, Chicago, IL, Oct. 1995.
- [14] Vogel, G., Fellenz, B., Utterback, J., "A Multi-Batch Fast Bunch Integrator for the Fermilab Main Ring", Beam Instrumentation Workshop. AIP Conf. Proc. 390. 375-80. May 1996.
- [15] Crisp, J., Gubrienko, K., Seleznev, V. :Stripline Detectors for Fermilab Main Injector. Proc. National 16th Conf. on Accelerators. Protvino, Russia. October 1998.
- [16] Crisp, J., Fellenz, B. :An Improved Resistive Wall Monitor. Beam Instrumentation Workshop, AIP Conf. Proc. No. 451, May 1998.

LOW ENERGY DEMONSTRATION ACCELERATOR (LEDA) BEAM INSTRUMENTATION: RFQ-ACCELERATED BEAM RESULTS*

J. D. Gilpatrick, D. Barr, J. Power, W.C. Sellyey, R. Shurter, M. Stettler, LANL, Los Alamos, NM
J. Kamperschroer, D. Martinez, General Atomics, Los Alamos, NM
J. O'Hara, AlliedSignal Inc., Los Alamos, NM

Abstract

Beam diagnostic instrumentation is being developed for the LEDA, a 6.7-MeV, 100-mA-cw proton accelerator, presently being commissioned at the Los Alamos National Laboratory (LANL). This instrumentation will be the basis for much of the Accelerator Production of Tritium and the Spallation Neutron Source linac. Located in the LEDA injector and the high energy beam transport (HEBT) this initial instrumentation suite's purpose is to verify the RFQ pulsed and cw operation. The instrumentation include a series of DC, pulsed- and bunched-beam current measurements from which RFQ beam-transmission efficiency will be determined. Ionization-chamber beam loss measurements are mounted above the HEBT and provide input signals to a fast equipment protection system. Central beam phase and energy measurements provide RFQ longitudinal performance information. Beam position measurements provide information to properly center the beam within the HEBT beam pipe. Finally, two types of transverse profile measurements including a slow wire scanner and a video fluorescence monitor provide beam width and projection information in the LEDA HEBT. This paper will discuss these measurements developed for LEDA and summarize how they performed during RFQ verification experiments.

1 INTRODUCTION

The LEDA RFQ has been installed and, as of March 16, 1999, has accelerated beam [1]. Beam instruments located in a simple HEBT were developed, fabricated, and installed to initially verify 100-mA RFQ operation [2]. To minimize the risk to the HEBT beamline equipment from beam impingement damage, the RFQ has been initially operated with a beam repetition rate, pulse length, and peak current to 10 Hz, 3 ms, and 40 mA, respectively. Therefore, the beam instrumentation has been required to operate during both pulsed and cw beam operation.

2 INSTRUMENTATION LOCATION

Most of the diagnostics instrumentation is located in the HEBT [3], pictured in Figure 1. The DC and pulsed beam-current measurements are placed near the RFQ's entrance and exit to determine the RFQ total beam transmission. A third set of beam current measurements

is placed near the entrance to the beamstop to determine the HEBT beam transmission.

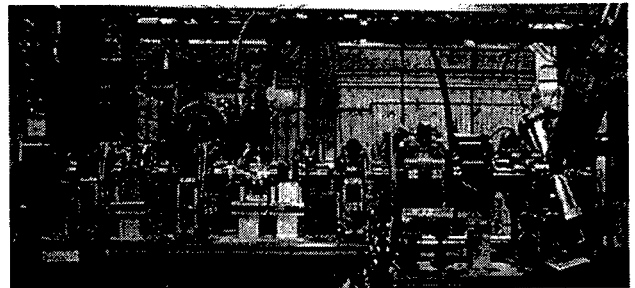


Figure 1: This picture shows the assembled HEBT including magnetic transport elements (i.e., four quadrupole and two steering magnets) and beam instrumentation.

Ionization chamber loss measurements are placed at the RFQ exit, at the middle of the HEBT, and at the entrance to the beamstop. These chambers, located at the beamline's elevation but approximately 1 meter from the beamline, provide fast beamline-equipment protection and additional beam transport tuning information.

Three capacitive probes detect the beam's central phase and energy. Beam energy is calculated by detecting the flight time for a bunch to travel between two probes. The first two probes, located approximately 0.5 m from the RFQ exit, are separated by approximately 0.1 m and provide approximate beam energy information. The first and third probes are separated by approximately 1 m and provide the more accurate energy information. The central phase is acquired by measuring the phase between an RFQ field sample probe and the first capacitive probe.

Five beam position monitors (BPM) are located throughout the HEBT. These micro-stripline BPMs are at locations sensitive to beam position variations due to changes in beam angle at the RFQ exit and the two HEBT steering magnets. BPMs #4 and #5 are located after the final quadrupole magnet for monitoring the beam's final trajectory to the beamstop. In addition, each BPMs' four-electrode signals are summed to provide bunched beam current information [4]. Since the RFQ's 6.7-MeV beam is captured within the 350-MHz RF bucket, the bunched beam current amplitude provides a reliable measure of the relative accelerated-beam current.

* Work supported by the US Department of Energy.

A slow wire scanner is positioned just in front of the beamstop to assess the expanded beam's size at the end of the beamstop and to measure the emittance of the beam using a "quadrupole scan" technique [5]. In the near future, a background gas-fluorescence beam-profile measurement will be placed at this same longitudinal HEBT location to measure cw beam profiles.

3 MEASUREMENT DISCUSSION

3.1 Pulsed Beam Current

The pulsed beam current measurements use a single toroidal transformer core with two sets of secondary windings: one set for beam current detection and another set for an in situ calibration [6]. The current detection-winding signals are initially processed using a simple analog feedback amplifier to increase the innate transformer L/R time constant, therefore, reducing the droop of the transformer signal. The low-droop signals from two transformers (e.g., RFQ entrance and exit) are digitized and are manipulated in digital signal processing (DSP) circuitry to produce a 200-kHz-bandwidth differential-current measurement. This digital difference signal is then integrated for approximately 2 millisecond and compared to a fast protection lost-charge value. If the lost charge is greater than this value, the fast protection system is initiated and discontinues beam operation.

3.2 Central Beam Phase and Energy

Since these electronics processors are still being fabricated, the phase and energy measurements were initially performed with only the installed capacitive probes, phased stabilized RF cables, a down converter, and an oscilloscope. The down converter transfers the 350-MHz phase information from the capacitive probes to 2 MHz where phase may be more accurately converted to time. Because the distance between probes is known, the energy can then be accurately calculated.

3.3 Beam Loss (Ionization Chambers)

Beam loss measurements use ionization chambers to detect the interaction between lost protons and beamline components [7]. Electron signal currents created and collected from the result of gamma-radiation ionizing the N₂ chamber gas. These electron signal currents are then amplified and integrated and are compared to a fast protection lost-charge value. If the integrator signals are greater than this value, the fast protection system is initiated and discontinues beam operation. These three chamber integrated signals are also monitored to provide beam tuning information.

3.4 Beam Position and Bunched Beam Current

Since the BPM electronics processors are also still being fabricated, we used only the analog front end (AFE) circuitry from the DSP-based BPM electronic processors.

The AFE circuitry filters, amplifies, and detects BPM electrode signals in such a way as to provide a logarithmic amplitude of the 350-MHz electrode signals. For these initial RFQ beam measurements, the individual signal amplitudes were quantified using an oscilloscope and subtracted to provide an approximate measure of beam position using the log ratio technique. The AFE circuitry also acquires bunched beam current by summing the four-electrode processed signals.

3.5 Beam Profiles

The slow wire scanner consists of an actuator that is mounted with a 45-degree angle with respect to the vertical and horizontal axes. SiC 0.1-mm-diameter fibers are mounted on the actuator "fork". Two fibers are used as bias to optimize the secondary electron coefficient of the fiber and the remaining fiber senses the beam. The wires traverse from one tine of the fork to the other vertically, then turn 90 degrees and traverse back. With such a system, horizontal and vertical beam profiles may be acquired in a single sweep. The beam charge-density information is acquired by measuring the beam-induced secondary electrons emitted from the fiber. Beam charge density data and fiber position are both acquired and controlled with LabVIEW™ software [8].

4 INITIAL RESULTS

The pulsed current measurements at the RFQ exit and entrance to the HEBT beamstop show good agreement with theory and are consistent with each other and their in situ calibration hardware. Their 200-kHz bandwidth precision and accuracy are measured to be <0.1 mA and <0.25 mA, respectively. However, under certain beam conditions, the RFQ-entrance current measurement appears to have an error during beam operation that is not present during the in situ calibration procedure. This error results in a higher than expected beam transmission through the RFQ. This error is presently being investigated and will be corrected. Figure 2 displays a partial LabVIEW™ screen that reports the pulsed beam current data with data.

Preliminary loss measurement observations performed during wire-scanner profile measurements indicate that the ionization chambers beam loss precision is approximately 0.2 mA.

Beam energy was measured with both a short and long drift distances between capacitive probes. For the long-drift-distance energy measurements, the initial measurement precision and accuracy are <1 keV and <10 keV, respectively. Figure 3 displays both energy measurements and the results from simulating the transport and the acceleration of the beam through the RFQ. The two measurements appear to be consistent and agree well with the RFQ simulations.

The wire scanner measurements also performed as expected. With amplifier gains set so that the peak of the

charge distribution is below their saturation limits, the ratio of fiber signals acquired at the distribution peak and tails was measured to be $> 500:1$. The combination of this large signal-to-noise ratio and the small 0.1-mm diameter fiber widths will allow this profile measurement to acquire valid profile data beyond 3 rms widths.

The final two beam position measurements have been shown to be consistent with each other, steering magnet currents, and the nearby wire scanner profile measurement.

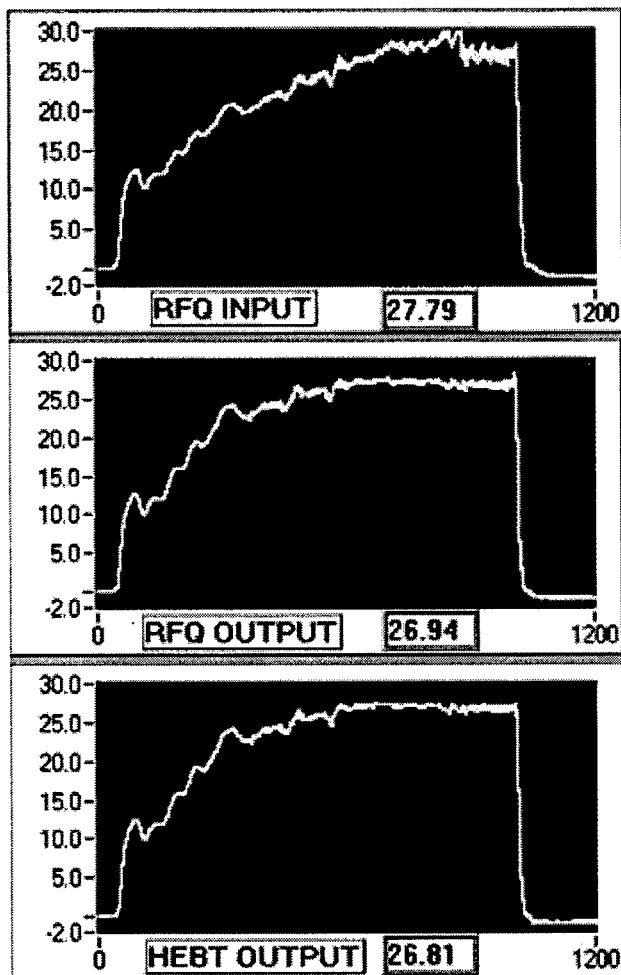


Figure 2: This picture shows the pulsed beam current at the entrance and exit of the RFQ and at the entrance of the HEBT beamstop. The abscissa and ordinate units are μs and mA, respectively. The values in the three smaller boxes under each waveform are beam currents typically averaged during the final 300 μs of the macropulse.

5 CONCLUSIONS

During the past 9 days of initial LEDA RFQ operation, most of the beam diagnostic measurements have been preliminarily tested with beam. With a few exceptions, most appear to be operating as expected. With additional beam commissioning time, the beam instrumentation will be fully commissioned and ready for further RFQ studies.

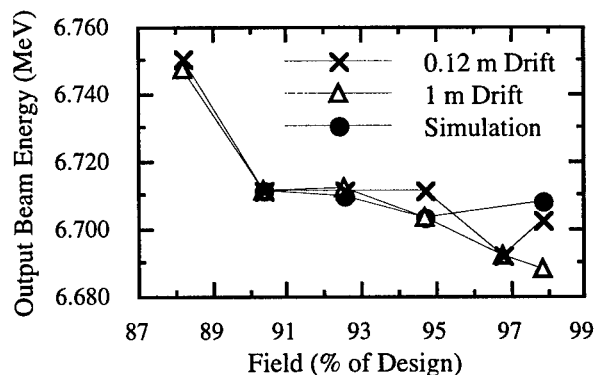


Figure 3: This graph illustrates the RFQ measured output-beam energy as a function of the percent of the RFQ designed field. Within measurement error, the two energy measurements are consistent and compare favorably with the simulation.

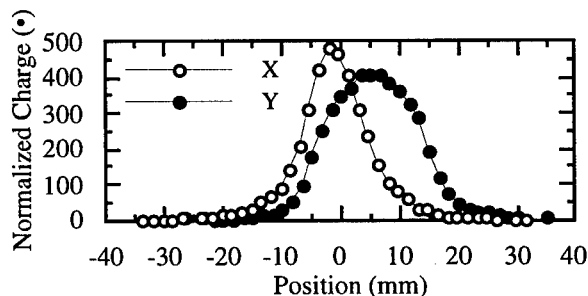


Figure 4: The above graph shows typical data acquired from the wire scanners located approximately 2.8 m from the LEDA RFQ exit. The horizontal beam location and rms width and the vertical beam location and rms width are -0.9 , 6.2 , 5.9 , and 6.8 mm, respectively.

6 REFERENCES

- [1] J. D. Schneider, et al., "Operation of the Low-Energy Demonstration Accelerator: the Proton Injector for APT," these proceedings.
- [2] J. D. Gilpatrick, et al., "LEDA and APT Beam Diagnostics Instrumentation," PAC '97, Vancouver, BC, Canada, June, 1997.
- [3] W. Lysenko, et al., "High Energy Beam Transport Beamline for LEDA," XIX International Linear Accelerator Conference, August 23-28, Chicago, IL, 1998.
- [4] J. D. Gilpatrick, et al., "LEDA & APT Beam Position Measurement System: Design and Initial Tests," XIX International Linear Accelerator Conference, August 23-28, Chicago, IL, 1998.
- [5] W. P. Lysenko, private communication (1998).
- [6] J. Power, et al., "Beam Current Measurements for LEDA," these proceedings.
- [7] J. D. Gilpatrick, et al., "Experience with the Ground Test Accelerator Beam Measurement Instrumentation," in AIP Conference Proceedings 319, (Santa Fe, NM, August, 1993), p. 154.
- [8] LabVIEW™ is commercial software sold by National Instruments, Inc.

A TECHNIQUE FOR MEASURING THE RELATIVE CESR BEAM ENERGY*

S. Henderson[†], V. Boisvert, K. Finkelstein, D. Rice, J. White, Cornell University, Ithaca, NY

Abstract

The beam energy at the Cornell Electron Storage Ring must be maintained within 1 MeV of the $\Upsilon(4S)$ resonance peak. The beam energy is determined on a run-by-run basis by calculation based upon machine parameters. As a test of the energy calculation we have explored a technique for determining the relative CESR beam energy using synchrotron radiation. We describe the technique and present a status report on our experimental investigations.

1 INTRODUCTION

The Cornell Electron Storage Ring (CESR) operates on and just below the $\Upsilon(4S)$ resonance ($\sqrt{s} = 10.58$ GeV) providing e^+e^- collisions for the CLEO experimental detector. The resonance peak is traditionally found by performing lengthy beam energy scans. Following such a scan the CESR beam energy is determined on a run-by-run basis by calculation based upon the machine parameters (RF frequency, measured dipole field, corrector strengths, electrostatic separator voltages, etc.) while taking into account the magnetic history. For maintenance of the beam energy over the course of many months we rely on the energy program to properly predict the relative energy changes. In order to maximize the physics event rate and to simplify data analysis, it is necessary to maintain the CESR beam energy within 1 MeV of the resonance peak (the $\Upsilon(4S)$ resonance width is 10 MeV).

We seek a method for verifying the beam energy calculation under actual operating machine conditions which include pretzel orbits, detector solenoid and compensation, and a rippled vertical orbit. If such a method were realizable and capable of functioning at full CESR beam currents, we would envisage incorporation of the measurement technique into routine operations, although our primary motivation at present is to provide verification for the energy calculation. Thus we seek a non-invasive, rapid measurement technique with relative precision of $\sim 2 \times 10^{-4}$.

The traditional method of beam energy measurement at electron storage rings is that of resonant depolarization [1], which provides quite accurate energy calibration with relative precision of $\sim 10^{-5}$. Resonant depolarization was used at CESR to determine the $\Upsilon(1S)$ mass [2]. Another class of measurement techniques which have been proposed utilize synchrotron radiation (SR) in one way or another. A solid-state detector was used at BESSY to measure the SR spectrum directly for determination of the critical energy [3]. Several proposals based on synchrotron radiation have

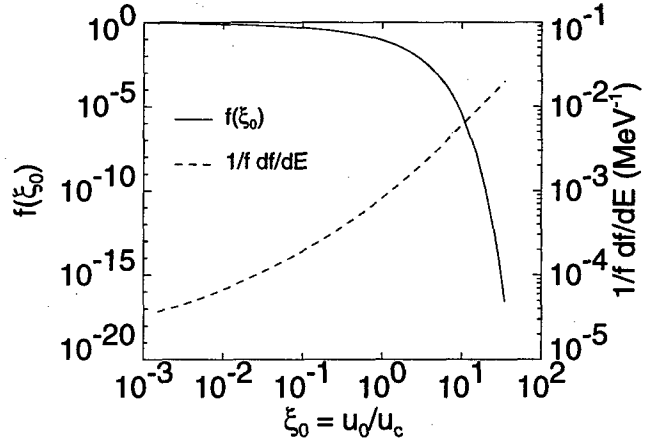


Figure 1: Integrated synchrotron radiation spectrum, f , and the sensitivity, $1/f df/dE$ as functions of the cutoff energy ξ_0 . The sensitivity assumes $E = 5.290$ GeV.

been described for measurement of the TJNAF electron beam energy [4]. We describe a technique for measuring relative beam energy changes based on synchrotron radiation and present our preliminary findings.

2 METHOD

The method that we present exploits the very steep energy dependence of the SR spectrum at x-ray energies, u , several times the critical energy, u_c . Define the fraction of SR photons above a given energy $u_0 = \xi_0 u_c$ as

$$f(\xi_0) = \int_{\xi_0}^{\infty} \frac{d\bar{N}}{d\xi} d\xi \quad (1)$$

where $d\bar{N}/d\xi$ is the normalized SR energy spectrum and $\xi = u/u_c$. Because of the steep energy dependence of the SR spectrum, the integrated SR flux $f(\xi_0)$ is quite sensitive to the cutoff energy, u_0 , for $u_0 \gg u_c$ as shown in Figure 1.

The fractional change in SR flux above the cutoff energy for a given change in energy $\Delta\xi_0$ is

$$\frac{1}{f} \frac{df}{d\xi_0} \Delta\xi_0 = -\frac{1}{f} \frac{d\bar{N}}{d\xi}(\xi_0) \Delta\xi_0, \quad (2)$$

or in terms of the beam energy E ,

$$\frac{1}{f} \frac{df}{dE} = \frac{1}{f} \frac{df}{d\xi_0} \frac{d\xi_0}{dE} = \frac{3\xi_0}{E} \frac{1}{f} \frac{d\bar{N}}{d\xi}(\xi_0) \quad (3)$$

If the integrated SR flux above a given energy u_0 could be measured, then for a beam energy change ΔE , the fractional change in integrated flux is $1/f df/dE \Delta E$. This

* Work supported by the National Science Foundation.

[†] Email: sdh9@cornell.edu

quantity is displayed in Figure 1, and shows the sensitivity of such a beam energy measurement technique as a function of cutoff energy ξ_0 . For example, at $u_0 = 10u_c$, a 1 MeV change in beam energy changes the integrated flux by 0.57%. Clearly, if one could monitor the SR flux above $\sim 10u_c$ with accuracy 0.1%, then one could measure relative beam energy changes rather accurately.

As a way of "integrating" the SR flux above a given energy, we use the K -edge of a high- Z material selected so that the edge energy $E_K \gg u_c$. x -rays with energy above the K -edge are (primarily) photoabsorbed, and a fraction of those x -rays produce characteristic K -shell x -ray fluorescence emission. The flux of characteristic x -ray emission measured with an x -ray detector is proportional to the SR flux above the K edge, which depends on the beam energy. To be precise, the rate of K -shell emission is given by the integral of the SR spectrum folded with the energy dependent photoabsorption cross-section which at falls like $u^{-7/2}$; this varies more slowly than the SR spectrum which at high energies falls like $e^{-\xi}/\sqrt{\xi}$. As a result, the observed sensitivity will be somewhat different from that shown in Figure 1.

Since the K -shell emission counting rate is beam current dependent and also depends on details of the SR source, target and detector geometry, a normalization is required. In addition to K -shell emission, the target also emits L -shell characteristic x -rays from photoabsorption of SR photons having energies between the L and K edges. The L -shell emission makes an ideal normalization since it is measured simultaneously with the K -shell emission in the same detector. Problems associated with combining measurements from two detectors having different stability and gains are avoided. The L -shell emission will also depend on beam energy, but since typically $E_L \simeq 1/6 E_K$, the dependence is much smaller than the K emission dependence, as shown in Figure 1.

3 EXPERIMENTAL SETUP

The measurements reported in this paper were performed at the Cornell High Energy Synchrotron Source (CHESS) facility at one of the dipole bending magnet stations. The experimental layout is shown in Figure 2. A white SR beam of critical energy 10.4 keV from a bending magnet ($\rho = 31.7$ m) was collimated horizontally with a Pb mask and filtered with a 0.25 in Al plate. The Al filter hardens the SR spectrum in order to reduce the flux of L x -rays to tolerable levels. All adjustable vertical slits were retracted to avoid intercepting the beam which would modify the spectral distribution at low energies. The SR beam is then brought into the experimental station where the intensity is monitored with an ion chamber. The beam strikes a 125 μ m gold foil placed 45° to the incident beam. The SR source to target distance is 13.5 m. The gold K edge is 80.7 keV ($7.8u_c$) and the L edges are ~ 13 keV ($1.3u_c$). The foil has attenuation factors μt of 2.9 at the K edge and 61 at the L edge. At 90° to the beam direction a Ge solid-state

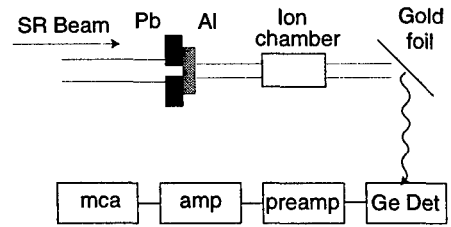


Figure 2: Experimental Layout

detector views the gold foil. Standard x -ray spectroscopy instrumentation is used to amplify and shape the pulse and the signal is then digitized in a multi-channel analyzer.

Figure 3 shows a typical x -ray spectrum obtained with this setup. The lines near ~ 70 keV are the characteristic K -shell emission and the lines near ~ 10 keV are the L -shell lines. The energy resolution of the system is 0.3 keV at 69 keV (Au $K\alpha_1$). Generally, the beam current was limited to less than 0.5 mA so that the detector counting rate remained below ~ 5 kHz in order to minimize pulse pileup. As is evident, the spectrum is remarkably clean; K and L lines are easily identified and virtually free of background from other scattering sources.

We define a K to L counting rate ratio as follows:

$$R_{K/L} = \frac{N_{K\alpha} - B_{K\alpha} + N_{K\beta} - B_{K\beta}}{N_L - B_L} \quad (4)$$

where $N_{K\alpha}$ is the sum of counts in both $K\alpha$ peaks, $N_{K\beta}$ is the sum of counts in both $K\beta$ peaks, N_L is the sum of counts in all L peaks, and the B 's are background count rates contained in separate background subtraction windows.

4 RESULTS AND DISCUSSION

To model the sensitivity of this method, an x -ray scattering Monte-Carlo simulation which includes Compton scattering, Rayleigh scattering, photoabsorption and K and

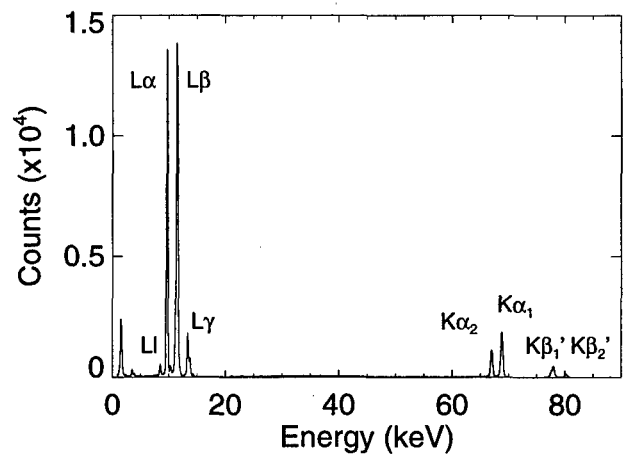


Figure 3: A typical x -ray spectrum from the gold foil.

L shell emission was employed. This simulation predicts that $R_{K/L}$ increases with beam energy at the rate of 0.21%/MeV (for $E \approx 5290$ MeV) for the basic experimental conditions described above. We therefore require a combined statistical and systematic precision in $R_{K/L}$ of better than 0.2%. Since we need a technique which will reliably measure relative energy changes regardless of how they arise, we need to verify that this method is insensitive to changes in SR source position, angle and size. An obvious concern is the source magnet field uniformity. The CESR dipoles have uniformity $\sim 10^{-4}$ over ± 2 cm about the center, resulting in a beam energy error of only ~ 0.25 MeV over the full range. A more significant effect is clipping of the SR beam on apertures in the x -ray beamline which has the potential to modify the spectral distribution. Other concerns arising from changes in SR source angle include the thickness uniformity of the gold target and Al filter. In our efforts to date, we have tested the viability of this technique by exploring several of these factors.

Figure 4 shows measured ratios $R_{K/L}$ (taken during a single machine studies period) plotted versus run time, where individual runs correspond to various changes in machine conditions. The data were obtained by collecting spectra for 8 minutes per point. The error bars are due to counting statistics. The first three data points were taken under identical conditions, and constitute the "reference" conditions. The remaining points show the effect of changes relative to these reference conditions. The next two data points show the effect of a vertical angle bump at the source ($\pm 40 \mu\text{rad}$) corresponding to ± 0.4 mm motion on the target. We conclude that we were not "clipping" on vertical apertures in the x -ray beamline. For the next point the electrostatic horizontal separators were turned off, changing the horizontal angle at the SR source by ~ 2 mrad. The next two points correspond to the reference conditions but with smaller and larger beam currents. In the following run, the vertical beamsize was increased by more than a factor of two. Despite rather significant changes in source angle, size and beam current, the ratio $R_{K/L}$ remains constant within statistical errors, except perhaps for the latter data point.

Finally the CESR dipole field was increased by 1 G (from nominal $B = 2010$ G), and the measured ratio increases by 0.97 ± 0.19 %. By changing the dipole field, the beam energy is increased by the factor $\Delta B/B$ (giving $\Delta E = 2.6$ MeV), but the field at the source magnet is also increased so that the SR critical energy is increased by $\Delta u_c = 3u_c \Delta B/B$ (whereas for a beam energy change alone, $\Delta u_c = 2u_c \Delta E/E$). The measured value is in good agreement with the simulation prediction of 0.83%.

The results of another dipole field dependence measurement are shown in Figure 5, along with the slope predicted by the simulation. Again, the data show good agreement with expectations.

In other machine studies sessions, the data were not always as reproducible as shown in Figure 4. It is thought that this may be due to clipping of the x -ray beam on ver-

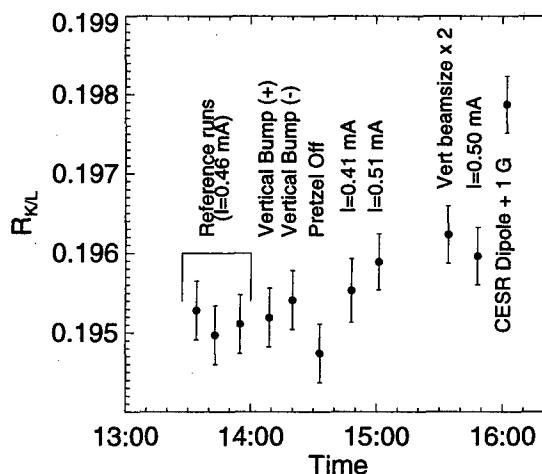


Figure 4: Measured $R_{K/L}$ for various machine conditions.

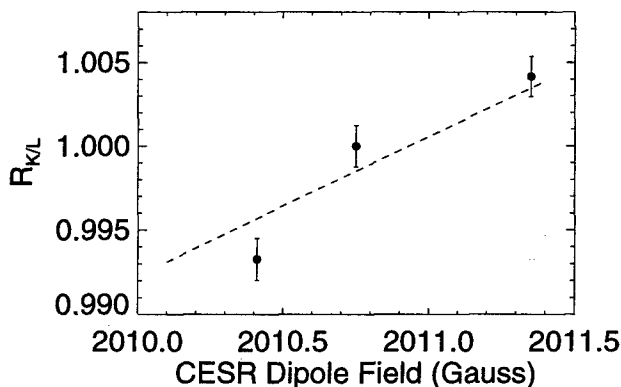


Figure 5: Measured $R_{K/L}$ (normalized to the middle point) versus CESR dipole field. The slope predicted by the simulation is overlaid.

tical apertures which would affect the spectrum, although this effect is still under investigation.

5 SUMMARY

The SR-based method that we describe for measuring relative beam energy changes shows promise. We are able to measure energy changes consistent with expectations. Our efforts in the near future will center on understanding the various factors that limit the reproducibility of the measurements and on increasing the count rate capability.

6 REFERENCES

- [1] A.A. Sokolov and I.M. Ternov, Sov. Phys. Dokl. 8, 1203 (1964).
- [2] W. W. MacKay et. al., Phys. Rev. D29 (1984) 2483.
- [3] E. Tegeler and G. Ulm, NIM A266 (1988) 185.
- [4] I.P. Karabekov, D.L. Egikian and C. Yang, NIM A286 (1990) 37; I.P. Karabekov and R. Rossmanith, NIM A321 (1992) 18; I.P. Karabekov and George R. Neil, NIM A356 (1995) 181.

RECENT DEVELOPMENTS ON BEAM OBSERVATIONS AT SRRC

Ian C. Hsu, G. H. Luo, and K. T. Hsu

Department of Nuclear Science, National Tsing-Hua University and
Synchrotron Radiation Research Center,
Hsinchu, 300 Taiwan

Abstract

In this paper, we will present some recent developed methods of beam observations and their experimental results. These methods including: beam energy measurement by laser Compton scattering, investigating electron beam orbit sensitivities on the flux of the photon beam line, beam lifetime investigation in storage rings.

1 INTRODUCTION

We have been trying to utilize the known principles of Beam physics and the existing Photonics knowledge and devices to investigate or to perform new methods of beam observations. In this paper, we will present some recent developed methods of beam observation and their experimental results. These methods including: beam energy measurement by laser Compton scattering, investigating electron beam orbit sensitivities on the flux of the photon beam line, beam lifetime investigation in storage rings. Only brief description and results are presented in this review. References are provided for more detail information for each individual study. All of the experiments are performed on the electron beam in the storage ring of Taiwan Light Source(TLS) of Synchrotron Radiation Research Center(SRRC), Taiwan.

2 BEAM ENERGY MEASUREMENT BY LASER COMPTON SCATTERING[1],[2]

The method of Compton scattering to measure the electron beam energy in the storage ring or to produce quasi-monochromatic γ -rays is characterized by excellent signal-to-noise ratio. To acquire a high γ -ray flux, a pulsed CO_2 laser with up to 2.67MW peak power is employed. Owing to the fact that the background radiation from Bremsstrahlung is extremely high (about 1200 counts/sec at 20mA electron beam current), how to effectively subtract the background radiation is a relevant concern. In this study, we developed the method of synchronous measurement to resolve the above problem. The synchronous measurement used a gate to periodically allow the signals to pass from the detector to the counting system. Since the scattered photons were produced after the laser pulse reached the interaction region, the laser could provide a trigger signal for the gate to open. The method proposed herein increases the signal to noise ratio

from 1.2 to 42.5. Figure 1 presents the entire system's schematic diagram. According to this figure, the laser photons pass through the optical system into the storage ring's straight section. After being scattered by relativistic electrons, the γ -rays pass through the lead collimator and is then detected by the HPGe detector. The signal processing instruments, then, acquire the back-scattered γ -rays' spectrum.

Considering that the highest energy of the back-scattered photons was around 3000keV, we chose ^{24}Na the standard source in energy calibration of the HPGe detector since the two characteristic energies of ^{24}Na were 1368.4keV and 2753.6keV. Those energies contributed to a sum-peak energy of 4122keV that could be applied to the interpolation method in energy calibration.

Figure 2 presents the spectrum of the Compton scattering with a collimator having an inner diameter of 3mm that corresponded to a half opening angle of 0.2241mrad. The background radiation's counting rate without the laser Compton scattering effect was around 0.82 counts/sec with gating. After the laser collided with the electron beams, the counting rate raised to 34.83 counts/sec. The S/N ratio was approximately 42.5.

The highest back-scattered γ -ray energy could be estimated from the sharp edge of the spectrum as shown in Fig. 2. For our latest experiment, it was $3054\text{keV} \pm 2.6\text{keV}$. According to the results, we can infer that the electron beam energy was $1.3058 \pm 0.0017\text{GeV}$. The relative energy measurement uncertainty of this experiment is 0.13%.

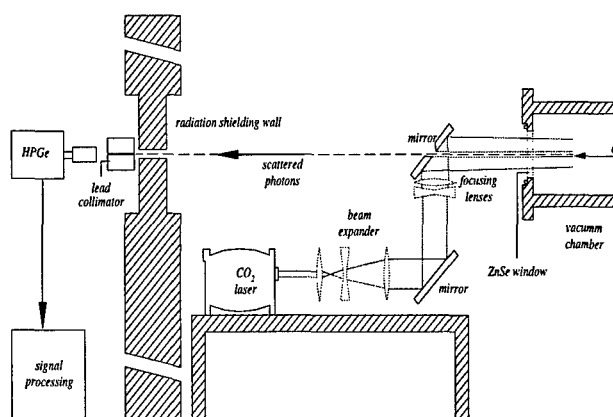


FIG. 1 Schematic diagram of the overall system: part of the vacuum chamber of the storage ring, optical system, detecting system, and signal processing system.

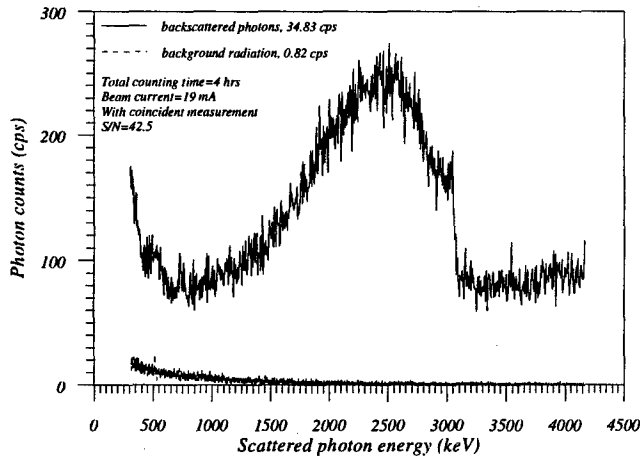


FIG. 2 γ -ray spectrum of Compton scattering with collimator of 3mm diameter under synchronous measurement. (electron beam current=19mA, counting time=4hrs., and S/N ratio =42.5.)

3 INVESTIGATING ELECTRON BEAM ORBIT SENSITIVITIES ON THE FLUX OF THE PHOTON BEAM LINE[3]

This study examines the beamline flux sensitivity due to an electron beam's positional and angular changes at the source point of the beamline. Beam experimental and numerical studies have been undertaken. It was performed by varying the size of either the electron beam's orbit local position bump or that of the local angular bump. Changes in the beamline flux are measured at the entrance slit downstream. Those two types of local bumps are created by four correction magnets. The strength of four correction magnets must adhere to a certain ratio to control the amplitude and slope of the electron beam's orbit at a given position in a ring. The experiments in this study are conducted on the 6m-HSGM (6 meter High energy Spherical Grating Monochromator)[4] beamline at TLS.

Results obtained from the beamline studied herein indicate that 10 μm vertical beam position displacement causes a relative photon flux change of $0.9 \pm 0.3\%$, as measured at the entrance slit downstream. This observation corresponds to the numerical results. In addition, a vertical beam angular change of 10 μrad causes a relative photon flux change of $1.2 \pm 0.4\%$. The above two values depend on the electron beam size, slit size as well as the beamline's optics. Figure 3 presents the measurement results for which only the position bump was varied. Horizontal axis denotes the beam position at the source point. The left vertical axis represents the relative photon flux fluctuation $(\Delta I_0/I_0)$ per unit beam position displacement at the source point. While varying the beam positions, the beam angle should remain unchanged. Due to the position bump's imperfection, the beam angle at the source point slightly changes. This

figure also plots the beam angle's value at each step on the right vertical axis, i.e. the X-X' correlation.

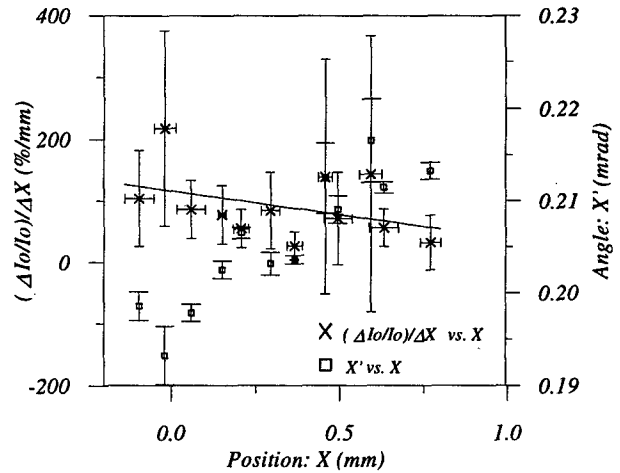


Fig. 3 The measurement results for which only the position bump was varied.

4 BEAM LIFETIME INVESTIGATION IN STORAGE RINGS[5]

As is generally known, the two unequal bunches method[6] can separate the beam lifetime contributions from these two effects. The beam current vs. time for each individual bunch was measured by the voltage signal of a broad band pickup. The lifetime of each individual bunch was then calculated. The calibration of the broad band pickup signal was done by a DC current transformer (DCCT) when a single bunch beam was stored. Figure 4 summarizes these results. The horizontal axis is the difference between the two bunch currents in mA. The vertical axis is the difference of the inverse of the bunch total lifetime. From the slope of the fitted line, the proportionality constant A can be obtained and the Touschek lifetime for a given bunch current can be calculated. Under the experimental conditions of the nominal transverse beam sizes ($\sigma_x = 180 \pm 9 \mu\text{m}$, $\sigma_y = 70 \pm 5 \mu\text{m}$), a total RF voltage of 700 kV and a bunch length of 100 ps, the results derived from Fig. 4 are:

$$\text{Touschek lifetime (min)} = (366 \pm 52) / (\text{single bunch current in mA})$$

In the following calculations, the above results are used to estimate the multibunch beam lifetimes. For a total beam current of 195 mA (filling 140 bunches), the single bunch current is 1.39 mA. The Touschek lifetime is 263 ± 38 min. The measured total beam lifetime at 195 mA with a multibunch mode by DCCT is 238 ± 1 min. Subtracting $1/(263 \text{ min})$ from $1/(238 \text{ min})$ yields the gas scattering lifetime as 2500 ± 1361 min. The reason of the large uncertainty was discussed in Ref[5].

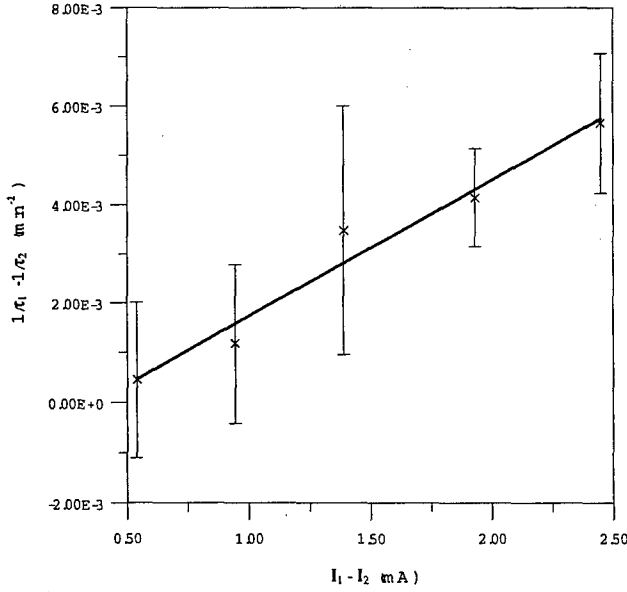


Fig. 4 The Touschek lifetime measurement by the two unequal bunch beam method. The horizontal axis is the difference between the two bunch currents in units of mA. The vertical axis is the difference of the inverse of the bunch total lifetime.

In the multibunch method, using the same total RF voltage, we first measured the total beam lifetime at the multibunch mode with the nominal transverse beam sizes ($\sigma_x = 180 \pm 9 \mu\text{m}$, $\sigma_y = 70 \pm 5 \mu\text{m}$). The beam current was 195 mA (filling 140 bunches) with a total beam lifetime τ_a of 238 ± 1 min. Next, the beam was driven into the difference resonance and the transverse beam area ($\sigma_x = 357 \pm 14 \mu\text{m}$, $\sigma_y = 353 \pm 16 \mu\text{m}$) was increased by a factor of 10. The beam current was 194.3 mA with a total beam lifetime τ_{10a} of 960 ± 1 min. If the difference between the beam current of 195 mA and 194.3 mA can be disregarded, the following two equations can be solved easily, yielding a Touschek lifetime τ_T of 285 ± 14 min and a gas scattering lifetime τ_{gas} of 1443 ± 280 min which includes the ion effects, if they exist.

$$1/\tau_a = 1/238 = 1/\tau_T + 1/\tau_{\text{gas}} \quad (1)$$

$$1/\tau_{10a} = 1/960 = 1/(10\tau_T) + 1/\tau_{\text{gas}} \quad (2)$$

The results obtained above are valid for estimating the beam lifetimes for the multibunch operation mode because all the measurements are taken in the multibunch mode.

According to the measurement results, the Touschek lifetime is longer when measured by the multibunch method (285 ± 14 min) than when measured by the two unequal bunches method (263 ± 38 min). The reason for this discrepancy is that in the two unequal bunches method, the Touschek lifetime was measured at the few bunches mode and in that mode, the bunch lengthening

effects, possibly caused by the couple bunch effects may not be as prevalent as those in the multibunch mode. For the estimation of the gas scattering lifetime of the operation mode i.e., the multibunch mode, in which the total lifetime was measured, we used the Touschek lifetime measured at the few bunches mode. This misuse caused the Touschek effect in the multibunch mode to be overestimated and consequently, underestimated the gas scattering effects in the multibunch mode. The Touschek lifetime is longer by 8% {i.e., $(285-263)/[(285+263)/2]$ } when measured by the multibunch method than when measured by the two unequal bunches method. The theoretical value of the Touschek lifetime at the corresponding parameters is 302 min. There is a 54% {i.e., $(2500-1443)/[(2500+1443)/2]$ } discrepancy of the gas scattering lifetime measured by the two methods. Besides the consequence of the overestimation of the Touschek effect as previously mentioned, a significant reason for this discrepancy is a possibility of the discounting of the effects of any trapped ions in the multibunch operation mode, when the lifetimes were estimated by the results of the two unequal bunches method.

5 ACKNOWLEDGMENTS

We would like to thank Prof. Y. C. Liu and Dr. G. L. Chen and the Operation group, the Vacuum group of SRRC for their help while we are doing the experiment. The support of SRRC and NSC, Taiwan was acknowledged.

6 REFERENCE

- [1] I. Hsu, C.-C. Chu, and C. I. Yu, *Phys. Rev., E* **54**(5), 5657 (1996).
- [2] I. Hsu, C.-C. Chu, S.-S. Chen, C.-L. Cho, and H.-C. Chen, *Nucl. Instrum. and Meth. A* **384**, 307(1997).
- [3] I. Hsu, *Phys. Rev., E* **55**(5), 6011 (1997).
- [4] S. C. Chung et al., *Rev. Sci. Instrum.* **66**(2), 1655 (1995).
- [5] I. Hsu, *Jpn. J. Appl. Phys.* **36**, 11 (1997).
- [6] J. C. Besson, P. Certain, A. Dael, P. Juan, A. Labeque, M. P. Level, P. C. Marin, J. Michaut, C. Monet-Descombey, P. Nghiem, M. Sommer, R. Souchet and H. Zyngier: ORSAY Rep. RT-88-01, France, 1980.

A MAGNETIC QUADRUPOLE PICK-UP FOR THE CERN PS.

A. Chapman-Hatchett, A. Jansson*[†], D.J. Williams
PS Division, CERN, CH-1211 Geneva 23, Switzerland.

Abstract

In the LHC era, there will be a need to monitor and correct betatron mismatch between machines in a non-destructive way. For this purpose, a quadrupole pick-up has been designed for the CERN PS. Originally, the PS was built for much larger beam sizes than now required when generating the LHC beam, but its large physical aperture should be maintained. Because of this large aperture to beam-size ratio, the quadrupole signal component in a standard pick-up design is strongly suppressed with respect to the common-mode signal, and thus demands a very high common-mode rejection in the signal processing. A magnetic quadrupole pick-up has been designed, in which the common-mode rejection is incorporated in the pick-up itself, by virtue of its geometry. The rejection is thus limited only by mechanical tolerances and can therefore be very large. Without the common-mode component, the dominating signal is dipolar, and small when the beam is centred in the pick-up. The dipole and quadrupole signals can thus be separated using a hybrid circuit with only moderate demands on common-mode rejection. Another advantage with a magnetic pick-up is the low output impedance, allowing the use of passive components when forming the quadrupole signal, which is highly desirable in the radiation environment of the PS ring. Simulations and tests of the pick-up and read-out electronics, as well as the first results with real beam are presented.

1 INTRODUCTION

1.1 Why a Quadrupole Pick-Up?

In the production of the LHC beam, the rms emittance blow-up at each inter-machine interface has to be kept lower than 10%. This is less than the absolute accuracy of any present diagnostic tool for emittance measurement [1]. Thus, a comparison of emittance measurements made in two consecutive machines along the injection chain is not enough. If the injection mismatch causing the blow-up can be measured directly, a higher sensitivity can be achieved since many error sources are eliminated.

A quadrupole pick-up measures the aspect ratio $Q = \sigma_x^2 - \sigma_y^2$ of the beam. At least two individual pick-ups are needed to estimate the horizontal and vertical beam emittances (if the beta function is known) and six pick-ups are needed to measure the emittance and Twiss parameters of the beam in both planes [2].

If the beam size is oscillating in one plane, for example due to optical mismatch at injection, the quadrupole pick-up signal will be modulated by twice the betatron frequency. Since the tune is generally different in the horizontal and vertical planes, the oscillations in the two planes can be separated in a Fourier transform of the signal. Therefore, a single quadrupole pick-up is useful as a diagnostic tool for beam optical matching between machines.

2 THEORETICAL CONSIDERATIONS

2.1 Electric Coupling

The traditional design of a quadrupole pick-up couples to the electric field of the beam. The electric potential $V(r, \theta)$ around an infinitely long beam is given by

$$V(r, \theta) = m_{00} \frac{1}{r} + m_{01} \frac{\cos \theta}{r^2} + m_{10} \frac{\sin \theta}{r^2} + m_{11} \frac{\cos 2\theta}{r^3} + (m_{20} - m_{02}) \frac{\sin 2\theta}{r^3} + \dots, \quad (1)$$

where the moments m_{ij} of the transverse charge distribution $\rho(x, y)$ are defined as

$$m_{ij} = \int \rho(x, y) x^i y^j dx dy, \quad (2)$$

and the order of each moment is $k = i + j$. If electrodes are positioned at $\theta = 0, \pi/2, \pi, 3\pi/2$, the quadrupole signal Q can be obtained by

$$Q = V(r_p, 0) - V(r_p, \frac{\pi}{2}) + V(r_p, \pi) - V(r_p, \frac{3\pi}{2}), \quad (3)$$

where r_p is the radius of the pick-up. The individual signals are dominated by the first term in (1), which is of the order $m_{0th}/r_p = \rho_{tot}/r_p$, whereas the quadrupole signal component in each signal is of the order $m_{2nd}/r_p^3 = \rho_{tot}\sigma^2/r_p^3$. Thus, there is factor σ^2/r_p^2 difference in signal strength. In the case of the LHC beam in the PS ring, where the beam size is much smaller than the aperture, this demands a very high common-mode rejection for the derivation of Q , since a difference between two large signals has to be taken.

2.2 Magnetic Coupling

The magnetic field around an infinite beam has two components. If the field is expressed in cylindrical coordinates, the θ -component B_θ is essentially given by (1) but with an extra factor $\mu_0/2\pi$ [3]. The B_r -component

$$B_r(r, \theta) = m_{01} \frac{\mu_0}{2\pi} \frac{\sin \theta}{r^2} + m_{10} \frac{\mu_0}{2\pi} \frac{\cos \theta}{r^2} + m_{11} \frac{\mu_0}{2\pi} \frac{\sin 2\theta}{r^3} + (m_{20} - m_{02}) \frac{\mu_0}{2\pi} \frac{\cos 2\theta}{r^3} + \dots \quad (4)$$

* CERN and Manne Siegbahn Laboratory, Stockholm, Sweden.

[†] Email: Andreas.Jansson@cern.ch

is more interesting. In this case, there can be no m_{00} component since this would violate Maxwells equation $\nabla \cdot B = 0$. The rest of the formula is similar, however. Therefore, if a pick-up is set up to measure only B_r , there is no intensity signal. Furthermore, if the beam is centred in the pick-up the dipole signal vanishes, and thus a magnetic pick-up coupling to B_r measures "only" the quadrupole signal. A coupling to the radial field component B_r is achieved by placing the coupling loops in the plane of constant r (in cylindrical coordinates).

2.3 Masking of the quadrupole oscillation signal due to dipole oscillation

A problem with all quadrupole pick-ups is that if the pick-up and beam centre do not coincide, the quadrupole signal gets an extra contribution proportional to the square of the displacement. If the displacement is large relative to the beam size, this will dominate the measured quadrupole signal. But, since this pick-up also measures the displacement of the beam, it should be possible to correct for the dipole component, providing the measurement is accurate enough.

3 PROTOTYPE PICK-UP DESIGN

3.1 Mechanical Design

A prototype pick-up coupling to the radial magnetic field of the beam has been built and installed in the PS machine during the 98/99 winter shutdown. The mechanical design of the prototype pick-up has been based on a spare ceramic vacuum chamber designed for the PS Booster position monitors, whose diameter of 145mm fits the physical aperture of the PS machine. The ceramic allows the coupling loops to be placed outside the vacuum, which saves vacuum feed-throughs and facilitates possible interventions once the pick-up is installed in the machine. The loops are placed directly on the outside of the ceramic, at radius $r_p = 80mm$. The θ -range covered by each loop was chosen to be 45° , which was found to be a good compromise. A wider angle would give larger coupling to the beam but also increase the inter-loop coupling. To avoid build-up of static charges, and to reduce the longitudinal impedance seen by the beam at higher frequencies [4], the inside of the ceramic chamber was coated with a few microns of titanium. For continuity of low frequency wall currents, and to protect against outside noise, the whole arrangement is housed in a metal cylinder of 300mm diameter. This shield also enhances the quadrupole signal relative to the dipole signal and reduces the inter-loop couplings.

3.2 Read-Out Electronics

The copper rods that make up the loops are connected to earth at one end, and connected in pairs to 1:15 transformers at the other end. The secondary side of each transformer is connected via 50 Ω cable to a hybrid circuit, which is

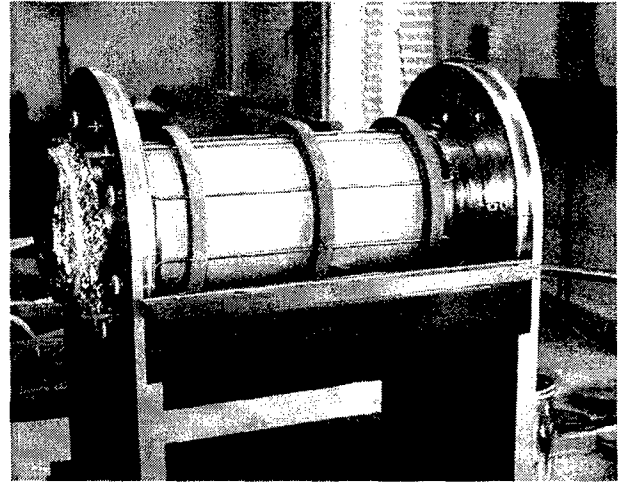


Figure 1: A picture of the pick-up before mounting the shield cylinder.

physically separated from the pick-up to facilitate modifications. The load seen by each antenna loop is thus only 225 $m\Omega$, which gives a low cut-off frequency of around 100 kHz.

The hybrid forms the four composite signals; quadrupole, the two dipoles, and the sum (which ideally should be zero). It can be bypassed using remotely controlled switches, in case the signals from the pick-up are to be measured individually. The hybrid outputs are fed to amplifiers, which are placed under the floor to protect them from radiation. These amplifiers have an amplification factor of 100, a bandwidth of 30 Mhz, and a noise level of 2.3 $nV/Hz^{-1/2}$.

4 TESTS AND MEASUREMENTS

4.1 Simulations

Simulations of the pick-up have been performed using the High Frequency Structure Simulator (HFSS) program, using a slightly simplified model for the pick-up geometry. The results show, as expected, that the sum signal is totally suppressed. The different couplings obtained from these simulations are shown in Table 1.

Moment	Dipole	Quadrupole
Analytic (w/o coating)	10 nH/mm	180 pH/mm ²
Simulation (w. coating)	1.5 nH/mm	32 pH/mm ²

Table 1: Coupling strengths from analytic approximation and simulation.

4.2 Test Bench Measurements

Test bench measurements have been performed, using a wire antenna to map the signal as a function of an-

tenna position in the x-y plane. The result is shown in Figures. 2 and 3. Typical output signals in time domain are shown in Figure. 4. Some ringing at the first resonance frequency of the cavity, formed by the shielding cylinder, was found at about 70 MHz. The signal is a common mode signal, and is therefore suppressed by the hybrid. It will also be filtered out by the limited bandwidth of the amplifiers. It was experimentally verified that, thanks to the titanium layer, the beam does not see a significant longitudinal impedance at the resonance.

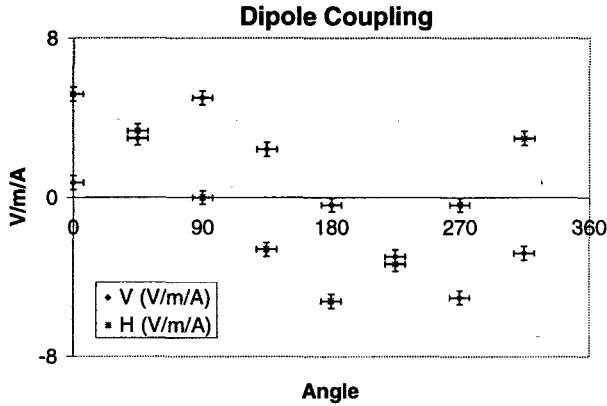


Figure 2: Output dipole signals versus azimuthal angle of antenna in the transverse plane. Antenna displacement from centre: 3 cm. Note the $\sin \theta$ and $\cos \theta$ structure, which is expected for the dipole signal.

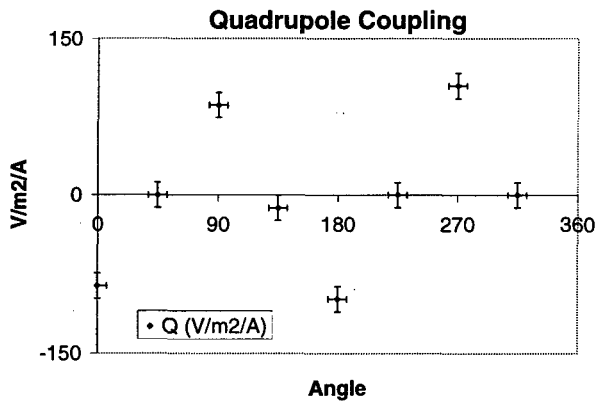


Figure 3: Output quadrupole signal versus azimuthal angle of antenna in the transverse plane. Antenna displacement from centre: 3 cm. Note the $\cos 2\theta$ variation, which signifies the quadrupole signal.

5 SUMMARY AND CONCLUSIONS

A quadrupole pick-up coupling to the radial magnetic field induced by the beam has been built and tested. This pick-up design has several advantages with respect to a 'traditional' design, such as:

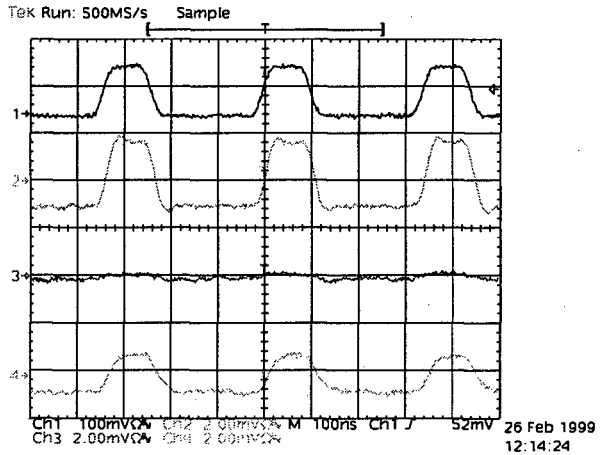


Figure 4: Output signals from the pick-up in time domain. Trace 1 is the input signal, traces 2 and 3 are the horizontal and vertical dipole signals respectively. Trace 4 is the quadrupole signal. The test was performed with a wire antenna displaced 3 cm horizontally.

- Suppression of the dominating sum signal, thus facilitating the signal treatment.
- No active electronic components needed in the radiation environment of the ring.
- No vacuum feed-throughs necessary.

The test bench measurements have shown that the pick-up works as expected. It will be thoroughly tested with beam during the coming year.

6 ACKNOWLEDGEMENTS

The authors would like to thank F. Caspers, J.M. Roux and L. Soby for practical help and interesting discussions.

7 REFERENCES

- [1] H. Koziol, K. Wittenburg, "Summary on Transverse Emittance Measurements and Instruments", Proceedings of the 4th ICFA Beam Dynamics Mini-Workshop on Transverse Emittance Preservation and Measurement, CERN, 1997, CERN/PS/DI/Note98-03, CERN Internal Note.
- [2] R.H. Miller, J.E. Clendenin, M.B. James, J.C. Sheppard, "Non-Intercepting Emittance Monitor", Proceedings of the XII High Energy Accelerator Conference, 1983.
- [3] A. Jansson, "The Measurement of Higher Order Moments of Beam Transverse Distribution Using a Magnetic Pick-Up.", 1998, CERN/PS/OP/Note98-27, CERN Internal Note.
- [4] C. Gonzalez, M. Morvillo, M. D'yachkov, "Impedance Measurements on the LHC Dump Kicker Prototype", LHC Project Note 151.

TOMOGRAPHIC RECONSTRUCTION OF TRANSVERSE PHASE SPACE FROM TURN-BY-TURN PROFILE DATA

S. Hancock, A. Jansson*[†], M. Lindroos

PS Division, CERN, CH-1211 Geneva 23, Switzerland.

Abstract

Tomographic methods have the potential for useful application in beam diagnostics. The tomographic reconstruction of transverse phase space density from turn-by-turn profile data has been studied with particular attention to the effects of dispersion and chromaticity. It is shown that the modified Algebraic Reconstruction Technique (ART) that deals successfully with the problem of non-linear motion in the longitudinal plane cannot, in general, be extended to cover the transverse case. Instead, an approach is proposed in which the effect of dispersion is deconvoluted from the measured profiles before the phase space picture is reconstructed using either the modified ART algorithm or the inverse Radon Transform. This requires an accurate knowledge of the momentum distribution of the beam and the modified ART reconstruction of longitudinal phase space density yields just such information. The method has been tested extensively with simulated data.

1 TOMOGRAPHY ALGORITHMS

1.1 The Inverse Radon Transform

The idea of tomography is to reconstruct a distribution from a large number of projections taken at different angles. There are many algorithms for tomographic reconstruction.

The (2D) Radon transform [1] $r(s, \theta)$ of a distribution $\rho(x, y)$ is defined as

$$r(s, \theta) = \int_{-\infty}^{\infty} \rho(s \cos \theta - u \sin \theta, s \sin \theta + u \cos \theta) du, \quad (1)$$

where $0 < \theta < \pi$. For a given θ it gives the projection of $\rho(x, y)$ onto a line through the origin at an angle θ . The inverse of the Radon transform is

$$\rho(x, y) = \int_0^\pi \tilde{r}(x \cos \theta + y \sin \theta, \theta) d\theta, \quad (2)$$

where $\tilde{r}(s, \theta)$ can be written in terms of the Fourier transform $R(\xi, \theta)$ of $r(s, \theta)$ as

$$\tilde{r}(s, \theta) = \int_{-\infty}^{\infty} |\xi| R(\xi, \theta) e^{i2\pi\xi s} d\xi \quad (3)$$

which is just r filtered with a filter whose frequency response is $|\xi|$. If a number of projections $r(s_i, \theta_j)$ are known from measurements, an approximation of $\rho(x, y)$ can be made using a discrete version of (2). However, since $|\xi| \rightarrow \infty$ in (3), high frequency noise is strongly amplified and thus, in practice, an additional low-pass filter is needed.

1.2 The Algebraic Reconstruction Technique

Algebraic Reconstruction Technique (ART) [2] is an iterative method. It exploits the fact that each point in a projection corresponds to a line in the reconstructed picture. The projections are thus "back-projected" in such a way that the value at each point in a projection is distributed along the corresponding line in the picture. This yields a crude approximation. The approximation is then projected down again, and each projection of the approximation is compared to the original projection. The difference between the two is back-projected again. In this way, the approximation is improved until it converges, and the iteration is terminated.

2 TOMOGRAPHY OF TRANSVERSE PHASE SPACE

2.1 The Problem of Dispersion

If higher order effects are neglected, transverse phase space density performs a rigid rotation in phase space for each turn in a circular machine. This is manifest in normalised phase space, where all particles follow circular trajectories, rotating at the betatron frequency. Thus, performing a tomographic reconstruction from a number of transverse profiles where the dispersion is zero is trivial. With a non-zero dispersion, it is not as obvious. Two possible solutions have been tested and the results are summarised below.

2.2 Modified ART with Dispersion

Recently, a modified ART algorithm has been used with great success to reconstruct particle density in longitudinal phase space [3], even when the motion is strongly non-linear. The algorithm is based on the tracking of test particles. By changing the tracking routine, the code was adapted to tackle the transverse case with dispersion. Dispersion was included by giving the test particles an extra degree of freedom (momentum) with a statistical distribution given by the beam momentum spread, which was assumed to be Gaussian. It was found, however, that this approach does not work. An ART reconstruction that includes dispersion in the tracking code cannot resolve details blurred by dispersion.

2.3 Deconvolution of Dispersive Effects

The dispersive blurring effect can be removed directly from the individual profiles, knowing that the physical beam pro-

* CERN and Manne Siegbahn Laboratory, Stockholm, Sweden

[†] Email: Andreas.Jansson@cern.ch

file is given by the convolution

$$\rho_\sigma(x) = \int \rho_\beta(z) \cdot \rho_D(x-z) dz, \quad (4)$$

where $\rho_\beta(x)$ is the pure betatronic profile, $\rho_D(x)$ is the dispersive spread and $\rho_\sigma(x)$ the measured profile. Since the profiles are measured in discrete points, the discrete equation

$$\rho_\sigma(x_i) = \sum_j \delta_D(x_{i-j}) \cdot \rho_\beta(x_j) \quad (5)$$

applies, which can be written in matrix form as

$$\bar{\rho}_\sigma = H \cdot \bar{\rho}_\beta \quad (6)$$

where H is a band matrix constructed from $\rho_D(x)$. Thus, the betatronic profile $\rho_\beta(x)$ can be recovered by inverting the matrix H . However, band matrices are known to be numerically ill-conditioned. Therefore, measurement errors and noise will be strongly amplified. In order to achieve a useful result, (6) has to be regularized in some way to make it numerically stable. Several schemes exist. The scheme which has been mainly used in this work is the so-called Hunt regularization method [4]. It is an extension of the well known least squares fit, where an extra term is added in the minimization function to control the second derivative of the result. If $\tilde{\rho}_\sigma$ denotes the noisy measured profile, the deconvolution result is the vector $\tilde{\rho}_\beta$ that minimizes the functional

$$J_\alpha(\rho_\beta) = (\tilde{\rho}_\sigma - \tilde{H} \cdot \rho_\beta)^T (\tilde{\rho}_\sigma - \tilde{H} \cdot \rho_\beta) + \alpha (C \cdot \rho_\beta)^T (C \cdot \rho_\beta) \quad (7)$$

for $\alpha > 0$. The parameter α is the regularization constant and the regularization function C is the matrix of the numeric second derivative

$$C = \begin{pmatrix} -2 & 1 & 0 & \cdots \\ 1 & -2 & 1 & \\ 0 & 1 & -2 & \\ \vdots & & & \ddots \end{pmatrix}. \quad (8)$$

The solution to the minimization problem can be written as

$$\tilde{\rho}_\beta = (\tilde{H}^T \cdot \tilde{H} + \alpha C^T \cdot C)^{-1} \cdot H^T \cdot \tilde{\rho}_\sigma. \quad (9)$$

The result is dependent of the value of α . As a rule of thumb, its value should be chosen so that

$$(\tilde{\rho}_\sigma - \tilde{H} \cdot \tilde{\rho}_\beta)^T (\tilde{\rho}_\sigma - \tilde{H} \cdot \tilde{\rho}_\beta) = (\tilde{\rho}_\sigma - \rho_\sigma)^T (\tilde{\rho}_\sigma - \rho_\sigma), \quad (10)$$

where the right hand side of the equation is just the rms error of the measured profiles, which can be estimated.

The Hunt regularization scheme is not the only possible one. An approximate solution of (6) can also be obtained for example by using singular value decomposition (SVD) techniques. The idea is to eliminate very small singular values from the matrix H before solving the equation by means of the least squares fit.

When the profiles have been deconvoluted, transverse phase space can be reconstructed using either ART or the inverse Radon transform.

2.4 How to Measure the Dispersive Spread?

In order to deconvolute the dispersive effect from the measured beam profiles, a very accurate measurement of the momentum distribution is needed. Attempts to use an assumed distribution (ie Gaussian or parabolic) with the right measured rms width have been made with little success due to the strong error amplification. However, using tomographic methods in the longitudinal plane an accurate picture of the longitudinal phase plane can be obtained. Projecting onto the energy axis gives the momentum spread. The expected accuracy, estimated from simulations, is better than 1%. The momentum distribution then has to be scaled by the dispersion at the transverse profile monitor to obtain the dispersive spread. This has to be done for each transverse profile, since in particular the dispersion can vary significantly between the first few turns after injection into a circular machine.

3 SIMULATION RESULTS

3.1 Simulation and Reconstruction Codes

Several pieces of code have been written to test the method. A simple 4D tracking code has been implemented, which produces both longitudinal and transverse mountain range data for the reconstructions.

For the longitudinal reconstruction, the code was readily available and tested [5].

The Hunt deconvolution has been implemented in *Mathematica*, as well as the inverse Radon transform for transverse reconstruction. A modified version of the longitudinal reconstruction code has been produced, which can handle the ART reconstruction in the transverse plane.

It was found that the inverse Radon transform and the ART code give similar results. However, the results from the inverse Radon transform tend to be noisier. Therefore, the ART code has been used mainly, with occasional cross-checks using the inverse Radon transform. ART also has the additional advantage that nonlinear transverse beam dynamics can be treated, although this has not been done here.

3.2 Reconstructions

For the simulations presented here, a parabolic energy-phase distribution was used. The momentum spread (2σ) was roughly 1.2×10^{-3} , and the dispersion at the profile measurement device 3.0m.

In the transverse plane, a test distribution with a doughnut shape was used to check the resolving power of the method. The distribution is shown in Fig. 1. To simulate noise and cut the simulation time, an insufficient number of test particles was used. Ideally, a larger number of particles should be tracked and noise added afterwards, but for a proof-of-principle this was considered sufficient.

To show the importance of handling the dispersion problem, a reconstruction of transverse phase space without

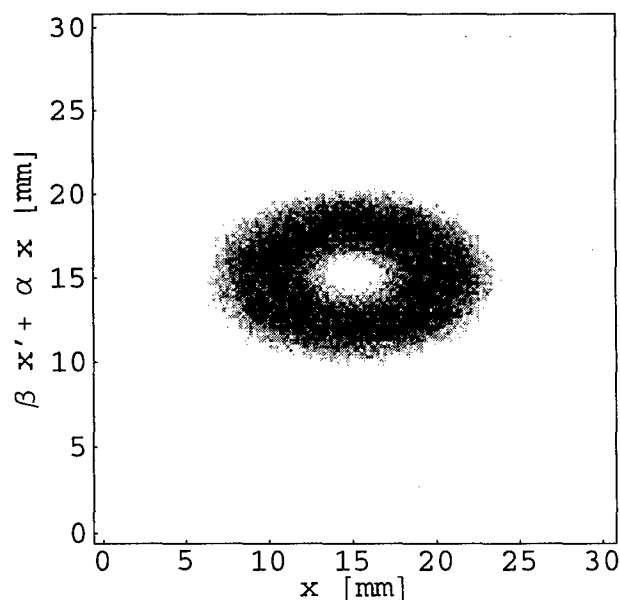


Figure 1: The test distribution in transverse phase space.

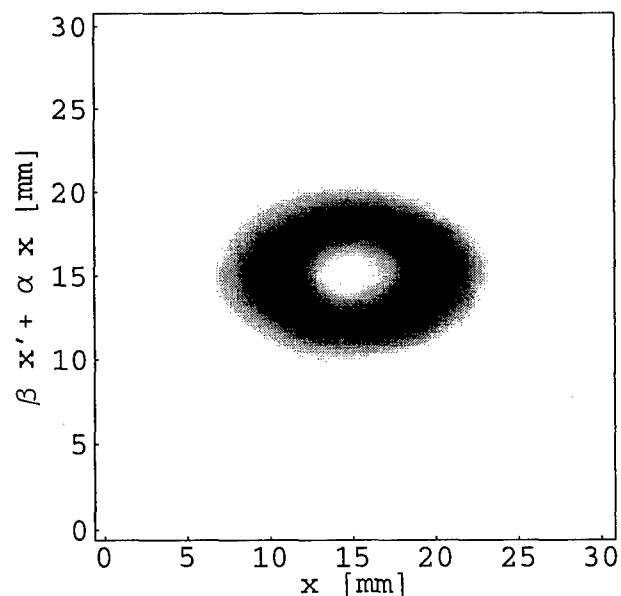


Figure 3: Reconstruction with ART, using dispersion correction.

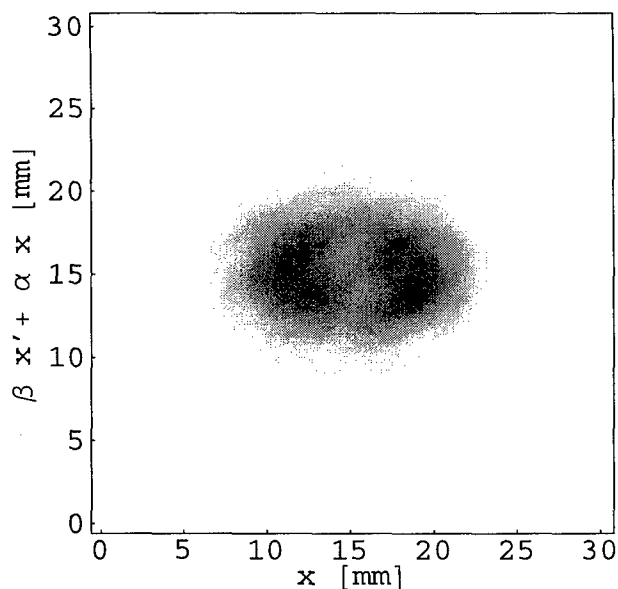


Figure 2: Reconstruction with ART, using no dispersion correction.

preceding deconvolution of the measured profiles is shown in Fig. 2.

With deconvolution of the dispersion effect, the picture is much more like the original (Fig. 3). Deconvolution using SVD also works and yields a very similar picture for the tested distribution.

4 CONCLUDING REMARKS

It has been shown that the transverse phase space distribution can be reconstructed using tomographic methods, even

in the presence of dispersion. The deconvolution of the dispersive effect requires very accurate input data, since any noise is strongly amplified. The final result depends on the momentum spread, the dispersion, and the accuracy of the measurement.

Tests of the method with measured data will be done in 1999, using a SEM-grid in the CERN PS and an OTR (Optical Transition Radiation) screen in the SPS for the acquisition of transverse profiles.

5 REFERENCES

- [1] J. Radon, "On the Determination of Functions from Their Integrals Along Certain Manifolds", Ber. Verh. Sächs. Akad. Wiss. Leipzig, Math.-Phys. Kl. 69, pp262-277 (1917).
- [2] R. Gordon, G.T. Herman, "Three Dimensional Reconstruction from Projections: a Review of Algorithms" Int. Rev. Cytol. 38, pp111-151 (1974).
- [3] S. Hancock, P. Knaus, M. Lindroos, "Tomographic Measurements of Longitudinal Phase Space Density", 1998, Proceedings of EPAC'98, Stockholm, Sweden.
- [4] M. Martini, M. Arruat, "Deconvolution of Momentum Distributions from Measured Beam Profile Data", CERN PS/PA Note 92-13, CERN Internal Note
- [5] S. Hancock, M. Lindroos, E. McIntosh, M. Metcalf, "Tomographic Measurements of Longitudinal Phase Space Density", 1998, Accepted for publication in Computational Physics Communications

Performance of the Electron Beam Diagnostics at Jefferson Lab's High Power Free Electron Laser*

P. Piot, G.A. Krafft, K. Jordan, A. Grippo, J. Song[†]

Thomas Jefferson National Accelerator Facility, Newport News, VA 23606 USA

Abstract

We describe the performance and current status of the electron beam diagnostic complement for Jefferson Lab's IR-FEL oscillator. In addition measurements for the driver-accelerator are presented. Beam diagnostics devices include optical transition radiation profile monitors, multi-slit beam emittance measurement, coherent transition and synchrotron radiation based bunch length monitors, both strip-line and button antenna BPM's and pick-up cavities for longitudinal transfer function measurement. All device are controlled via the EPICS control system.

1 OVERVIEW

Diagnostics in a high power FEL such as the JLab IR-FEL [1] were crucial to smoothly commission the driver-accelerator, measure and control the beam parameters. Among the parameters that must be thoroughly measured and controlled over the beam generation and transport, transverse emittance and longitudinal bunch length are probably the most important since their degradation can significantly affect the beam brightness and consequently degrade the laser gain. A generic diagnostic consists of a detector mounted on the beam line that is required to operate in the so-called "tune-up mode", a low duty cycle beam mode that can be used during machine setup without damaging any beamline components. The choice to perform most of the measurements at low duty signal is legitimate: in the Jefferson Lab's IRFEL the beam physics is dominated by single bunch effects (the inter-bunch distance cannot be smaller than $\simeq 4.02$ m). The signal from the detector is treated with a appropriate system (digitizer, ADC, etc...) and pre-processed on an input-output controller (IOC) operating under the VxWorks environment. The generated data are sent on the local network and can be accessed from any application running on one of our HP-9000 workstations connected to the local network. In parallel to the EPICS system it is possible to access some of the data using the Cdev protocol. For many purposes, especially during commissioning activities, we have developed high level applications based on the Tcl/Tk scripting language or the MATLAB package.

* This work was performed under the auspices of the US-DOE contract #DE-AC05-84ER40150, the Office of Naval Research, the Commonwealth of Virginia, and the Laser Processing Consortium.

[†] Now at Brookhaven National Laboratory

2 BEAM POSITION

The beam position monitoring system consists of two types of detector: stripline detectors that provide a low RF-impedance so that no beam degradation due to wakefield occurs and the button antenna detector which are used in large aperture vacuum chambers required in the resonator bypass chicanes and the recirculation arcs. Two different electronics are used for processing the signal: the 4-channel electronic is used since it offers a high reproducibility. This electronic consists of 4 detectors for each of the 4 antenna. In the wiggler region, the switched electrode electronic [2] is used: it switches the signal between each pair of the four antenna and offers a higher dynamics range compared to the 4 channels electronics. The most stringent requirement on the BPMs concern the six BPMs located in the wiggler insertion region: the demand on position measurement accuracy is $45 \mu\text{m}$. During the commissioning of the driver accelerator we have been able using saved value of the reading from the BPM's to routinely achieve a very reproducible orbit which significantly expedites the startup of the laser. It has also been used to test the lattice first order transfer matrix using the difference orbit method. The SEE electronics also provides a "B-scope" feature which consists of acquiring and recording for off-line analysis the beam position at higher frequency (e.g. 30 Hz). This feature enables the operator to quantify beam jitter and identify potential frequency dependent beam motion.

3 MOMENTUM COMPACTION & COMPRESSION EFFICIENCY

One must carefully set up the bunching elements to achieve ultrashort bunch length at the wiggler insertion. We characterize the compression efficiency of the lattice by measuring the transfer function $\langle \phi_{laser} | \phi_{out} \rangle$. The phase of the photocathode drive laser ϕ_{laser} is modulated and the output phase ϕ_{out} after a section of the transport is measured using a stainless pill-box cavity by detecting the fundamental mode TM_{010} . The signal is processed with a precise phase detector: the signal is phase shifted and mixed with the reference master oscillator signal. Before the measurement the phase shifter is set to insure the cavity is at zero-crossing. An example of measurement of $\langle \phi_{laser} | \phi_{out} \rangle$ transfer map is presented in figure 1. There are four pickup cavities in the driver-accelerator: located downstream of the 10 MeV cryomodule in the injector, at the linac front end, at the exit of the first and second recirculation Bates-type arcs. The three latter cavities are also used to measure

the $\langle \delta_{linac}, \phi_{out} \rangle$ where δ_{linac} is the energy variation at the linac exit. For such a measurement we modulate the gradient of the last cavity of the linac while measuring the time of arrival at the aforementioned cavities. Non-linear fit of these longitudinal transfer map, or alternative Tchebychev analysis [8], can be used to extract M_{55} , T_{555} , or M_{56} , and T_{556} first and second order transfer matrix coefficients and compare them with optics code. On the other hand, the transfer function pattern can also be used to set the machine in a reproducible way, i.e. by checking time to time whether these patterns are unchanged. They can also be compared to simulated transfer functions generated with particle pushing code such as PARMELA [3].

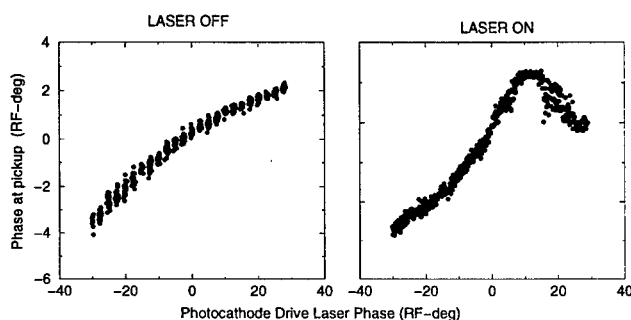


Figure 1: Effect of the laser on the $\langle \phi_{laser} | \phi_{out} \rangle$ transfer function.

4 BEAM TRANSVERSE ENVELOPES

Except in the 350 keV beam generation region, the beam transverse densities are measured exclusively by detecting the backward optical transition radiation produced at the surface of a 2 μm aluminum foil. The foil is imaged with an aberration-optimized optical system on a CCD array whose video output is digitized by the means of DATACUBE image processing board running on its own IOC. Beam 2D density, projection, centroid position and rms size are computed on the CPU of the dedicated IOC before being broadcasted on the local network. Because of the difficulty to observe OTR in the 350 keV region, we have instrumented this beam line with a highly sensitive wire scanner that can profile beam at the gun exit, after the first solenoidal lens, and with a fluorescent screen at the entrance of the 10 MeV accelerating structure to check beam transverse envelope. Along with (pure betatron) beam size measurement, some of the OTR monitors are located in high dispersion region, e.g. compressor and decompressor chicanes and recirculation arcs, to measure the beam energy spread. An example of energy spread distribution measured in the decompressor chicane located downstream the undulator is shown in figure 2. It is also planned to use synchrotron radiation to monitor the beam spot during cw operation. Unfortunately because of our bend curvature $\rho \simeq 0.6$ m the critical wavelength is of the order of $\lambda_c = 4\pi\rho/(3\gamma^3) \simeq 7$ μm which implies the use of very sensitive (and expensive) camera that will be installed once beam physics experiments are

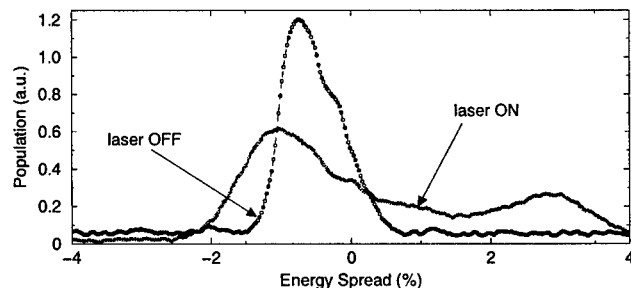


Figure 2: Example of energy spread distribution variation when the FEL is off or turned on.

completed (to avoid damaging them).

Two types of emittance measurement have been implemented: In the 10 MeV injection line, where the beam is space-charge-dominated, the transverse emittance is measured with a multislit [5] mask that can provide emittance, Twiss parameters at 1 Hz level and transverse trace-space isocontours at 0.5 Hz; an example of generated beamlets is shown in figure 3. In the 38+ MeV region, the emittance is measured using the standard beam envelope fitting technique, i.e., either quadrupole scan or multi-monitor methods. A Tcl/Tk application has been written to automate the measurement as much as possible and render it flexible by letting the user choose any quadrupole/profile monitor he/she desired to use for the measurement. Such automation is possible thanks to the use of the Artemis [10] modelserver, an online updated model of the beamline lattice capable of providing to any applications "real world" machine transfer matrices in real time. Based on quadrupole scan technique we have also implemented a transverse phase space tomographic reconstruction [9].

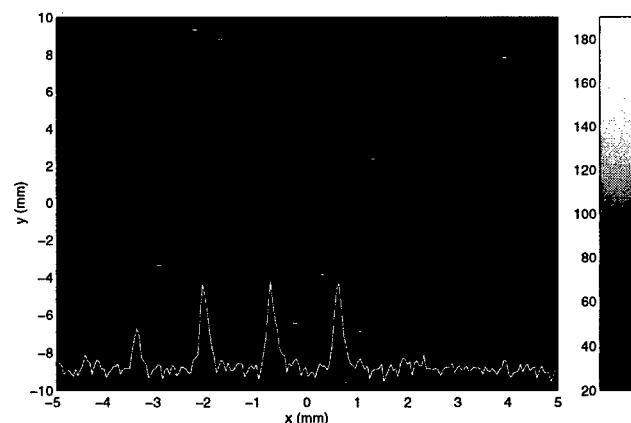


Figure 3: Example of beamlets pattern generated by the multislits mask from which the Twiss parameters and emittance are inferred.

5 BUNCH LENGTH

During the early stage of the commissioning of the driver accelerator we have experimented with bunch length mea-

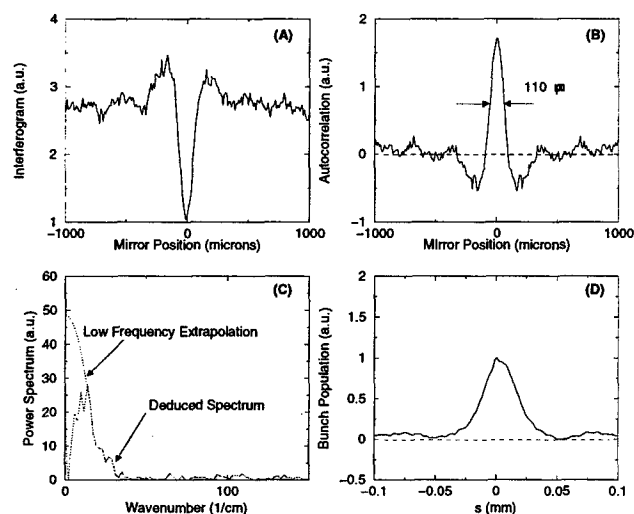


Figure 4: (A) raw data from the detector i.e. interferogram, (B) autocorrelation obtained from the interferogram, (C) energy spectrum obtained by fourier-transforming the autocorrelation, (D) bunch distribution obtained by hilbert-transforming the energy spectrum after low frequency extrapolation.

surement using zerophasing technique. This consists of inducing an energy ramp along the bunch by operating one or several cavities at the zero-crossing point and mapping the energy distribution into the horizontal plane with a spectrometer [4, 6]. Also this method enables the measurement of both bunch length and longitudinal phase slope; it is not practical for operation purposes compared to bunch monitor based on coherent radiation detection. The IRFEL has been instrumented with two of these latter monitors: one is located in the injector front end while the other in the wiggler region. From an interferogram measurement one can compute the bunch length, its frequency spectrum and reconstruct the longitudinal distribution as shown in figure 4. Currently only the interferometer located in the wiggler vicinity is fully commissioned: it has confirmed the ultra-short bunch length we were achieving of the order of $100 \mu\text{m}$ (RMS) [6]. In fact under routine operation to start up the laser, the interferogram is not measured, but the total CTR signal is maximized to ensure the bunch length is minimum at the undulator location, then fine adjustment of the linac phase is performed to compensate for the slippage effect, by measuring the output power of the laser and maximizing the FEL gain. The bunch length inferred from autocorrelation must be interpreted with care: during operation of the linac in overcompression mode, it could provide erroneous results as is shown in figure 5 where the simultaneous measurement of CTR power and bunch length (inferred from the interferogram) are presented versus the linac phase. One can see the discrepancy in the overcompression regime as the total CTR power decreases, yet the bunch length still decreases. This effect was traced back via numerical modeling and found to be due to tail formation in the bunch due to the space charge collective force.

These tails are present in the interferogram function but are so weak that they are part of the baseline. Therefore the bunch length computed is not characteristic of the whole bunch, but only of its core.

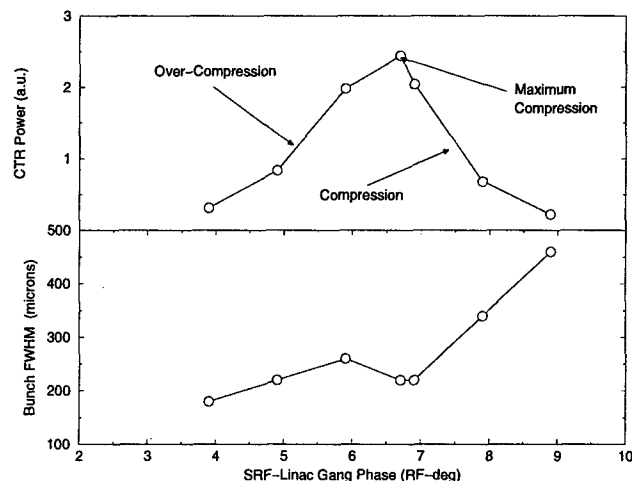


Figure 5: Limitation of CTR based bunch length measurement.

6 BEAM CURRENT AND CHARGE

There are two methods that can be used to measure the beam current. An averaging method consists in using the IRFEL dumps as Faraday cups which provide an absolute beam current measurement. A faster but relative method, capable of providing data at 10 kHz, consists in measuring the amplitude signal out of a pillbox cavity similar to the one used for the measurement of the longitudinal transfer functions described above. Such a method, after calibration, is used continuously to monitor the instantaneous beam current delivered at injector front end. Recently an integrator has been added so that we can measure the total charge delivered for a given period, typically between photocathode reciesation or wafer changes and monitor the photocathode performance.

7 REFERENCES

- [1] C.L. Bohn, et al., These Proceedings
- [2] T. Powers et al., AIP conf. proc. 390, 257-263 (1996)
- [3] P. Piot, et al., Proc. Eur. Acc. Conf. 98, 1327-1329 (1998)
- [4] D.X. Wang, G.A. Krafft, C.K. Sinclair, Phys. Rev. **E57**, 2283-2291 (1998)
- [5] P. Piot, et al., to appear in Proc. Linear Acc. Conf. 98 (1998)
- [6] G. A. Krafft, et al., Proc. Eur. Acc. Conf. 98, 1580-1582 (1998)
- [7] G. A. Krafft, AIP conf. proc. 367, 46-55 (1995)
- [8] G. A. Krafft, Proc. Acc. Conf. 97, 2268-2270 (1998)
- [9] C. K. Mc Kee, et al., Nucl. Inst. Meth. A **272**, 456-670 (1995)
- [10] B. Bowling, S. Witherspoon, unpublished

New Technique for Absolute Beam Energy Calibration in e^+e^- Accelerators.

G.Ya. Kezerashvili and N.Yu. Muchnoi*

Budker Institute of Nuclear Physics, Novosibirsk, Russia

Abstract

A new approach for absolute beam energy measurement with a use of the kinematic properties of the Compton backscattering is suggested. Under reasonable gamma-ray beam detector requirements, it possesses absolute accuracy for beam energy measurement up to the value of 10^{-4} .

1 INTRODUCTION

There are several approaches to measure the electron beam energy by use of Compton backscattering kinematic properties. The Compton backscattering kinematics is shown on Fig.1: a photon with energy ω_0 and wave vector \vec{k}_0 is incident on a high energy electron ($\varepsilon = |\vec{p}|$) with angle α . In the final state an energetic γ -quantum (ω, \vec{k}) is scattered by angle θ .

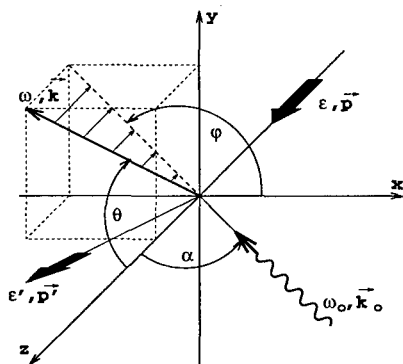


Figure 1: Compton backscattering kinematics

Main kinematic parameters of the Compton backscattering are coupled by the following formula [1]:

$$\omega = \varepsilon \frac{\lambda}{1 + \lambda + (\theta \varepsilon / m_e c^2)^2}; \quad \lambda = \frac{4 \varepsilon \omega_0}{(m_e c^2)^2} \cos^2 \frac{\alpha}{2} \quad (1)$$

Since that, one can measure the Compton energy spectrum for a couple or more laser wavelengths and then determine the electron beam energy ε from the relative positions of the energy spectrum edges ($\theta = 0$). Although these edges are very sharp and thus may be measured with a very high accuracy, one must exactly know the linearity of the energy scale of the detector used for the measurements to obtain the high accuracy for the electron beam energy calibration.

* Corresponding author. E-mail: muchnoi@inp.nsk.su

2 IDEA

The main idea of the current suggestion is an attempt to skip through the problem of having a perfect detector for direct Compton energy spectra measurements. As far as the laser-electron interaction is the interaction of two monochromatic beams, there is an unambiguous correlation between the scattered photon energy ω and its emission angle θ , described by equation (1). Thus one can measure the photon emission angle instead of its energy. If we use two laser lines to scatter on the electron beam: $\omega_1 = \omega_0$ and $\omega_2 = K \cdot \omega_0$ ($K > 1$), then for any monochromatic line ω in the backscattered photon energy spectra (below the backscattered photons energy spectrum edge for ω_1) we have the following equation:

$$\frac{\lambda}{1 + \lambda + (\theta_1 \varepsilon / m_e c^2)^2} = \frac{K \lambda}{1 + K \lambda + (\theta_2 \varepsilon / m_e c^2)^2}, \quad (2)$$

where θ_1 and θ_2 are the photon scattering angles for laser lines with the energies ω_1, ω_2 . This gives a possibility to determine the electron beam energy by measuring the θ_1 and θ_2 angles:

$$\varepsilon = m_e c^2 \sqrt{\frac{K - 1}{\theta_2^2 - K \theta_1^2}}, \quad (3)$$

To perform the calibration of the electron beam energy ε we suggest to obtain the Compton backscattering for two laser lines on the electron beam, and then to measure the backscattered photon energy and coordinates by the γ -quanta detector, situated at distance D from the interaction area along the photon beam propagation direction. The essential difference from the mentioned above idea of direct measurement of the Compton energy spectra edges is that the sense of the energy spectrometer in our case is only to select the same energy range for the backscattering photons from both initial laser photons energies.

First, let's assume that we have the γ -quanta detector with perfect energy and space resolution, and that the electron beam itself has zero transverse size and all electrons momenta are collinear. In this ideal case any monochromatic line ω in the energy spectra for ω_1 and ω_2 laser photons energies gives delta-function distributions over radius $R = D \tan(\theta)$ in the coordinate detector plane. The accuracy for the beam energy calibration is then given by the expression:

$$\frac{\delta\varepsilon}{\varepsilon} \simeq \frac{1}{D} \sqrt{\left(\frac{\varepsilon}{m_e c^2}\right)^2 \Delta R^2 + \Delta D^2}; \quad (4)$$

Where ΔR and ΔD are the accuracies for the radius R and detector distance D . From this expression we can mention that for the beam energy $\varepsilon = 5.0 \text{ GeV}$ and detector distance $D = 50 \text{ m}$ we need to measure the radius R with accuracy about $1 \mu\text{m}$ to have the $\simeq 10^{-4}$ accuracy for ε . The values of m_e , c and K are considered to be known with the accuracy of 10^{-8} and are treated as constants in the further discussion.

In real life this narrow R -distribution is smeared by the following parameters:

- the width of the choozen energy range in the backscattered photon energy spectrum;
- energy resolution of the spectrometer;
- space resolution of the coordinate detector;
- energy, coordinate and angular spreads in the electron beam.

3 RADIUS MEASUREMENT

We have to determine the radius that corresponds to the selected energy diapason in the backscattered photon spectra for both the ω_1 and ω_2 laser lines from the coordinate distributions of these photons on the coordinate detector. This section describes one of the possible approaches to solve the problem. We assume that the coordinate distribution of the backscattered photons is described by the following formula:

$$f(x, y) = \frac{1}{4\pi^2 \sigma_x \sigma_y R_0} \cdot \int_0^{2\pi} \exp \left[-\frac{(R_0 \cos \varphi - x)^2}{2\sigma_x^2} - \frac{(R_0 \sin \varphi - y)^2}{2\sigma_y^2} \right] d\varphi; \quad (5)$$

that is the convolution of the ring with radius R_0 with the two-dimensional Gaussian for coordinates x and y .

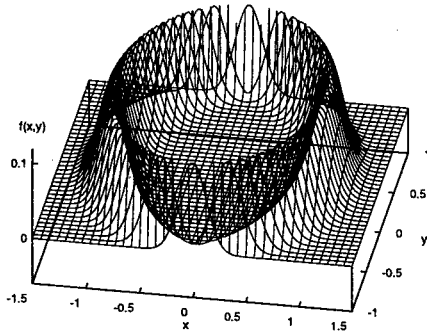


Figure 2: The $f(x, y)$ function

The ring with radius R_0 corresponds the angle θ for the backscattering photons of energy ω , and all the factors from

the list in the end of the previous section give the Gaussian dispersions σ_x and σ_y . By simple integration of the $f(x, y)$ function over x or y coordinates, we have the functions to fit the y and x coordinate distributions of the backscattered photons on the coordinate detector, and then determine the R_0 . The plot for the $f(x, y)$ function is given on Figure 2.

4 NUMERICAL EXAMPLE

The Monte Carlo simulations were performed to obtain the possible experimental accuracy of the electron beam energy measurement. The following parameters were set for the Compton backscattering process simulation:

- electron beam energy $\varepsilon = 5 \text{ GeV}$ (that is the case of VEPP-4M collider [2]);
- photon energies $\omega_1 = 1.165 \text{ eV}$ and $\omega_2 = 2.33 \text{ eV}$ that corresponds to the first and the second harmonics of Nd:YAG laser (this means $K = 2$);
- electron-laser beams interaction angle $\alpha = \pi/2$, that allows to obtain accurate knowledge of the electron-photon interaction area position;
- Gaussian dispersions for the electron beam transverse sizes $\sigma_y = 100 \mu\text{m}$, $\sigma_x = 200 \mu\text{m}$;

The backscattered photon energy spectra for two laser photon energies $\omega_1 = 1.165 \text{ eV}$ and $\omega_2 = 2.33 \text{ eV}$ are plotted on Figure 3. The dashed region (100 MeV width) was divided into 1 MeV intervals, for each of them the x and y coordinate distributions were simulated on the coordinate detector.

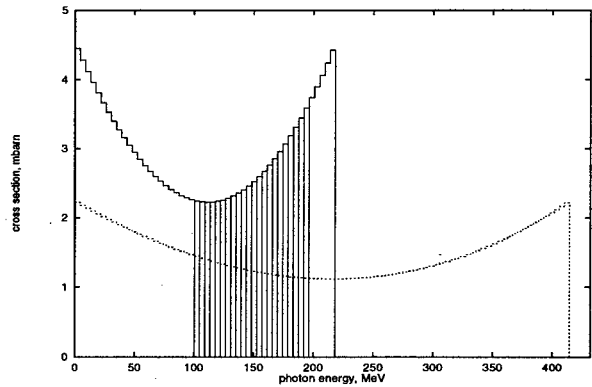


Figure 3: The backscattered photons energy spectra

Next set of simulation parameters describes the detector for the backscattered photons:

- The coordinate detector Gaussian dispersions for the space resolution $\sigma_y = 100 \mu\text{m}$, $\sigma_x = 100 \mu\text{m}$;
- The coordinate detector distance from the electron-photon interaction area and its accuracy $D \pm \Delta D = 7500 \pm 0.5 \text{ cm}$.

Coordinates and energy are measured in channels: one coordinate channel equals $100 \mu\text{m}$, one energy channel equals 0.1 MeV . The coordinate distribution of backscattered photons for one of the energy intervals is shown on Figure 4:

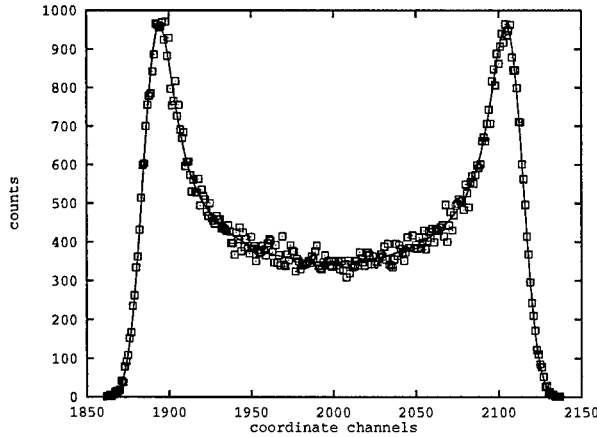


Figure 4: X-coordinate distribution of backscattered photons for $\omega_0 = 2.33 \text{ eV}$, $\varepsilon = 5 \text{ GeV}$. Energy interval fixed by the spectrometer is $139 - 140 \text{ MeV}$. Empty squares - result of Monte Carlo simulation, the fit was done as it was described in section 3. $\chi^2=1.047$

The dependence of the relative statistical error in radius measurement from the number of counts in histogram is given on Figure 5:

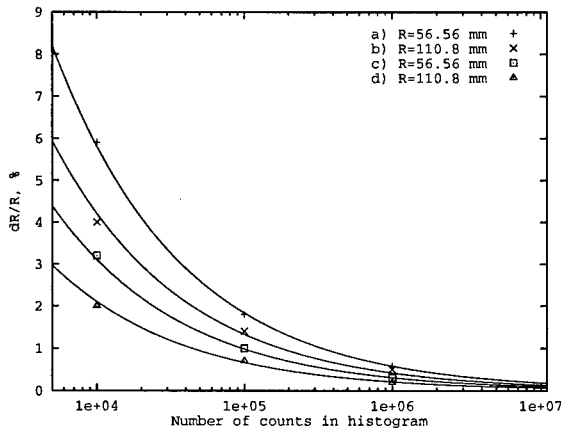


Figure 5: Dependence of the relative statistical error in radius measurement from the number of counts in histogram. The labels in the corner are in the same order (from top to bottom) as the lines and points on the plot. The Gaussian angular spread in the electron beam equals $0.2 \cdot 10^{-4} \text{ rad}$ for cases a), c) and $0.1 \cdot 10^{-4} \text{ rad}$ for cases b), d)

Figure 5 shows that the errors in radius measurement obey to the $1/\sqrt{N}$ law. Then we have to deal with a systematical error in ε measurement, originating from the width of each energy interval, selected by the spectrometer. The point is that we actually have two different energy spectra shapes for the two selected laser photon energies

ω_1 and ω_2 , as it was shown on Figure 3. The non-zero width of the selected interval gives the difference between the average energy (inside each interval) for these two spectra. The effective width of the interval is determined by the convolution of the selected range with the resolution of the spectrometer. Therefore there is no sense to select the intervals narrower than the spectrometer energy resolution. The dependence of the systematical beam energy shift on the spectrometer energy resolution is given on Figure 6:

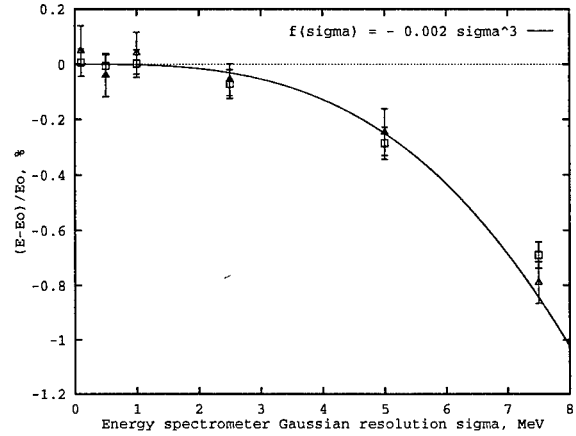


Figure 6: The dependence of the $(\varepsilon - \varepsilon_0)/\varepsilon_0$ on the σ_ω .

The absolute value of the electron beam energy on Figure 6 was determined by averaging the values, obtained from 20 energy intervals of 1 MeV width. The systematical shift must be taken into account for correct electron beam energy measurement.

5 DISCUSSION

A new approach to measure an absolute electron beam energy by the coordinate-sensitive detector has been suggested in this report. The statistical errors for radiuses determination could be minimized to the level of 10^{-3} or even better by increasing the experimental statistics to the value of 10^7 or more photons per histogram. A numerical estimations for the method accuracy at the electron beam energy $\varepsilon=5 \text{ GeV}$ shows that the main source of systematical errors is in the difference of the energy spectra shapes for two laser lines in the selected energy range. These systematical shift in the absolute beam energy calibration have to be significantly smaller for higher beam energies, cause the arbitrary energy resolution of the photon spectrometer will be much better for this case.

6 REFERENCES

- [1] V.B.Berestetsky, E.M.Lifshitz, L.P.Pitaevsky. Relativistic Quantum Theory, Moscow, 1968
- [2] G.Ya. Kezerashvili et al. Nucl. Inst. Meth. B 145 (1998) 40-48

HIGH PRECISION ELECTRON BEAM DIAGNOSTIC SYSTEM FOR HIGH CURRENT LONG PULSE BEAMS

Scott D. Nelson¹, Tom Fessenden, Yu Ju (Judy) Chen, Clifford Holmes, LLNL, Livermore, CA
Nicholas Selchow, RMC Corp., San Ramon, CA

Abstract

As part of the effort to develop a multi-axis electron beam transport system using stripline kicker technology for DARHT II [1] applications, it is necessary to precisely determine the position and extent of long high energy beams (6 - 40 MeV, 1 - 4 kA, 2 microseconds) for accurate position control. The kicker positioning system [2] utilizes shot-to-shot adjustments for reduction of relatively slow (< 20 MHz) motion of the beam centroid. The electron beams passing through the diagnostic systems have the potential for large halo effects that tend to corrupt measurements performed using capacitive pickoff probes. Likewise, transmission line traveling wave probes have problems with multi-bounce effects due to these longer pulse widths. Finally, the high energy densities experienced in these applications distort typical foil beam position measurements.

1 INTRODUCTION

The constraints dictated by these beam diagnostic requirements indicate a system that has the advantage of only measuring high energy beams (such that sensitivity to intensity can be small). On the other hand, positional accuracy needs to be sub millimeter in order to define the outer bounds of the beam for determination of the correct transport parameters. As a result, a low Q structure allows for a faster response time and different parts of the beam will not effect the measurement of the beam position during later times. The completed diagnostic system involves a high accuracy beam position detection system, a data acquisition system, a computer controlled feedback system (to control the stripline kicker pulser waveforms) and the kicker pulsers themselves.

The precision beam position monitors are utilized as part of the kicker beam deflection system [3] which requires precise beam control to successfully position the beam through the subsequent output divergent septum beampipe. Accuracies of 0.5 mm are desirable for use with the kicker system and accuracies of 0.1 mm are needed for the proposed target system [3].

2 BASELINE BUG TESTING

As part of the development effort, the existing beam position monitors (a.k.a. BPM's or beam bugs) were tested to evaluate their long pulse performance. Since evolution



Figure 1. The quad stripline kicker (left) in the Experimental Test Accelerator (ETA-II) beamline as part of the verification experiments [3]. Downstream of the kicker, the deflected beam passes through the septum magnet (right) and into the divergent beam lines.

of the existing BPM's has been an on-going process for many years, they were used as part of the baseline experiments to determine the feasibility of using this type of design for long pulse efforts. Other designs used in beam position measurements were examined but these designs have compatibility problems with long pulse beams, with beams with high degrees of halo, or suffer from charge build up problems over the course of the beam pulse.

To simulate the long pulse beam, a pulser capable of several microseconds and kilovolts was used to drive the test stand. The stand consists of a tapered coaxial section

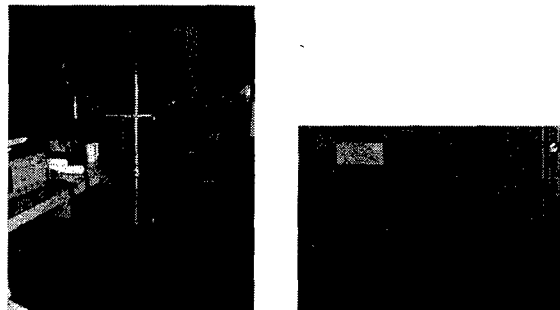


Figure 2. The beam position monitor test stand (left) used for measuring the accuracy and response of the various BPM's. The stand was driven by a variety of pulsers including a fast rise time pulser and a long pulse VelonexTM pulser with capabilities above one kilovolt and beyond six microseconds (left).

on each end of the test stand. This provides an impedance match to 50 Ω and exhibited excellent spectral uniformity agreeing to within 0.15 dB. These sections drive the straight section of beampipe which is offset to allow for displacing the current conductor with respect to the BPM. Displacements of up to one centimeter were examined.

¹Email: nelson18@llnl.gov

Displacements significantly beyond one centimeter cause higher order modes to be established due to the beam pipe discontinuity at the displacement points. Note that the center conductor is fixed with respect to the tapered coaxial sections and so displacement of the BPM causes the center conductor to get closer to one side of the BPM thus simulating the displaced beam. One drawback of the VelonexTM pulser is its characteristic requiring a total output waveform integrating to zero. Thus, for the unipolar pulse there is a long baseline tail on the data. In this case, the decay rate for this tail has a time constant of 94 μ s (its peak voltage is only 3% of the main pulse) but data beyond the main pulse should be ignored.

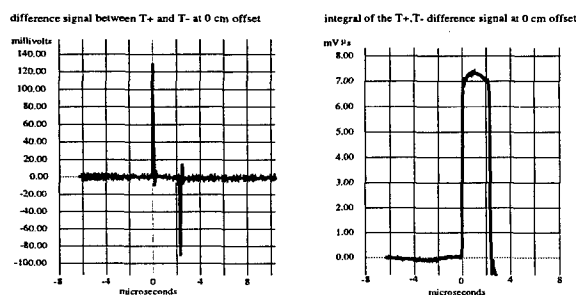


Figure 3. The waveform on the left shows the difference signal between two opposite output ports on the BPM when the current carrying conductor is on-axis. This allows the performance of each channel to be calibrated before displacing the current carrying conductor; thus allowing for greater precision. The waveform on the right shows the integral. In this case, it corresponds to the positional error of this BPM and can be unfolded from the final data. [The hash in the waveforms on the left in figures 3 and 4 is a graphing artifact and is not representative of the noise in the signal. The noise is 2 mV. ed.]

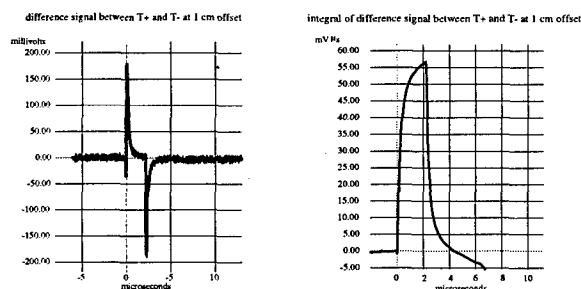


Figure 4. Two channels on opposite sides of the BPM are acquired with a displacement of one centimeter. The difference is then computed (left) and the position is found by integrating (right). Notice that the vertical scale in Figure 4 is significantly different than that of Figure 3.



Figure 5. The region between the leading and trailing edge is magnified here exposing the baseline offset between the leading and trailing edges of the pulse.

Figure 5 shows a close up view of the differential signal with a one centimeter offset of the current conductor. Observe the baseline shift in the waveform which is caused by preferential coupling to the port closer to the current conductor. Acquiring each channel from the beam position monitor separately allows for greater control of the unfolding of the data. In the cases shown in Figures 3 and 4, the total waveforms are represented by 15,000 points with 30 points defining the rise time of the pulse.

3 BPM DESIGN AND TEST

3.1 Drawbacks of Existing BPM's

The existing test stand generates a maximum of twenty amps and so the saturation of the ferrite material is not an issue. But at an operating point of 1 - 4 kiloamps for 2 μ s, a beam pulse would saturate the existing ferrite material simply due to the limited number of volt-seconds in the existing material. Likewise, the existing mechanical fabrication process for the BPM's involves several hand assembly steps as evident in the difference between on-axis signals shown in Figure 3. Although precise for a hand assembled component (appx. 1% position error due to assembly), greater precision between ports is desired in order to achieve the necessary beam position precision and to avoid extensive calibration unfolding after every data set.

As part of the effort, several other BPM concepts [4,5,6,7,8] were also considered. Although the test results for the existing beam position monitors in ETA-II looked encouraging, performance parameters for the long pulse beam test would saturate the ferrite material in the existing BPM's. Likewise, initial experimental evidence [9] indicates that thin films can survive direct exposure to 2 μ s beams for profile measurements.

3.2 Unfolding BPM Position Data

To determine the position of the beam from the waveforms generated by the BPM's, it is necessary to take into account the calibration of each port of the BPM (both time and amplitude correction) and to remove differences between the port responses. The early time coupling effect comes from [9] with voltage V produced at a port

$$V(\theta, \rho, t = 0) = I_b K \frac{1 - \rho^2}{1 - 2\rho \cos \theta + \rho^2}$$

with the beam at relative displacement $\rho = r/r_a$ from the centerline (r_a = beampipe radius) and at an angle θ with respect to the port in question (0° is directed toward the port). K is a calibration constant related to the resistance of the foil and may be determined using the on axis case, $\rho = 0$. The curves in figure 6 illustrate the variations for $t=0$; but expressions are available for general expressions in t .

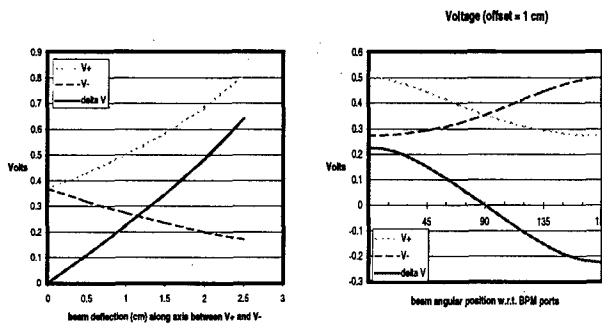


Figure 6. The various parameters of the received voltage are related to the position of the beam centroid in the beampipe. Note that the underlying equation assumes that the beam radius is small with respect to its displacement.

3.3 Design Parameters for Long Pulse BPM's

As a consequence, the design parameters for the long pulse high precision beam position monitors were determined to allow for a 2 μ s beam pulse [10] at 2 kA. Since the skin depth for materials such as nichrome and stainless steel is 6 μ m at 70 MHz, the thickness of the existing material can be expanded. 1 mil stainless steel foil, having a surface resistivity of 0.036 Ω /square, yields a bulk resistance, R , of 3.4 m Ω across the portion of the foil exposed to the flux in the BPM

$$R = \frac{1}{\sigma_s \delta_s} \left(\frac{V_m \sigma_n \delta_n}{V_p / Z_0} \right)$$

where σ_s , σ_n are the conductivities for stainless and nichrome respectively, δ_s , δ_n are the skin depths (in this case the material thicknesses dominate so $\delta_s = \tau_s$, $\delta_n = \tau_n$), V_m , V_p were the voltages during the coefficient determination (0.37V and 1 kV respectively). V_p was fed into the $Z_0 = 50\Omega$ transmission line that drives the test stand.

4 CONCLUSIONS

The precision required as part of the operation of the kicker and target systems dictates a high precision beam position monitor with an accuracy between 0.5 and 0.1 mm. In the case of the kicker system, these BPMs must also be able to withstand a 2 μ s long 2kA beam pulse. Initial results with the existing BPMs indicate that operation with a two microsecond beam at two kiloamps will be possible provided that:

1. Data is acquired from each BPM port separately. This allows the calibrations for each port to be unfolded from the data.

2. Measurements of the radiation effects on cables [11] indicate that several volts can be induced onto typical RF cables at high X-ray levels. However, for most applications there should be sufficient shielding around the various incidental X-ray sources.

3. Partition the vertical scale of the signal using multiple data acquisition systems. This may be necessary until

greater dynamic range (more than 8 bits) is available from commonly available high speed acquisition systems. The trade-off is signal-to-noise errors caused by the partitioning.

4. Time resolution from commonly available high speed acquisition systems is more than adequate for these applications. It is important to get sufficient resolution on the leading edge of the pulse such that the rise time of the integral is preserved. Self triggering on the received waveform reduces jitter in the measurement.

5. Signal cables should be of sufficient quality to preserve the leading edge of the pulse. More importantly, they should be matched and low in dispersion in order to avoid problems during the difference calculations.

6. Although the range of currents over which the BPM must operate is large, the necessary precision at each current level can be different. Thus the low current levels used in the calibration process do not have to be single-shot acquisitions. The benefits of laser welded foils, made possible by the move to 1 mil stainless, are expected to alleviate some of the existing error in the BPMs caused by hand welding the 0.2 mil nichrome foils

5 ACKNOWLEDGMENTS

Thanks go to Jim Dunlap for his efforts and assistance efforts in performing the beam bug measurements. This work was performed under the auspices of the U.S. Department of Energy by the Lawrence Livermore National Laboratory under contract No. W-7405-Eng-48.

6 REFERENCES

- [1] M. Burns, "DARHT Accelerators Update and Plans for Initial Operation," 1999 Particle Accelerator Conference (PAC99), New York, New York, USA, March 29 - April 2, 1999.
- [2] Y. J. (Judy) Chen, "Precision fast kickers for kiloampere electron beams," 1999 Particle Accelerator Conference (PAC99), New York, New York, USA, March 29 - April 2, 1999.
- [3] S. Sampayan, et. al., "Experimental investigation of beam optics issues at the bremsstrahlung converters for radiographic applications," 19th International Linear Accelerator (LINAC98) Conference, Chicago, IL, August 23-28, 1998, LLNL UCRL-JC-130417
- [4] A. Hofmann, "Beam Diagnostics and Applications," Beam Instrumentation Workshop '98, SLAC, Stanford University, California, U.S.A., included as part of the American Institute of Physics Conference Proceeding 451.
- [5] R. Lorenz, "Cavity Beam Position Monitors," Beam Instrumentation Workshop '98, SLAC, Stanford University, California, U.S.A., included as part of the American Institute of Physics Conference Proceeding 451.
- [6] R. Jung, "Image Sensor Technology for Beam Instrumentation," Beam Instrumentation Workshop '98, SLAC, Stanford University, California, U.S.A., included as part of the American Institute of Physics Conference Proceeding 451.
- [7] B. Fellenz and J. Crisp, "An Improved Resistive Wall Monitor," Beam Instrumentation Workshop '98, SLAC, Stanford University, California, U.S.A., included as part of the American Institute of Physics Conference Proceeding 451.
- [8] K. W. Struve, "Electrical Measurement Techniques for Pulsed High Current Electron Beams," Measurement of Electrical Quantities in Pulse Power Systems-II, National Bureau of Standards, Gaithersburg, Maryland, March 5-7, 1986, LLNL UCRL-93261
- [9] B. Carlsten, Los Alamos National Laboratory, THOR 2 microsecond facility used for DARHT component verification. Private communication.
- [10] T. J. Fessenden, "Beam Bugs - Asymptotic Response," Lawrence Livermore National Laboratory, Beam Research Memo 88-8, February 2, 1988.
- [11] M. Brubaker, "Optical Based Beam Position Monitor," Los Alamos National Laboratory, Private communication.

RECALIBRATION OF A WALL-CURRENT MONITOR USING A FARADAY CUP FOR THE KEKB INJECTOR LINAC

T. Suwada^{*}, S. Ohsawa, K. Furukawa, N. Akasaka, and K. Oide

Accelerator Laboratory, High Energy Accelerator Research Organization (KEK)

1-1 Oho, Tsukuba, Ibaraki 305-0801, Japan

Abstract

An absolute beam-charge measurement of single-bunch electron beams with a pulse width of 10 ps and short-pulsed electron beams with a pulse width of 1 ns was performed by the beam test for the KEKB injector linac using a Faraday cup. A wall-current monitor was directly recalibrated by the beam test with an error of $\pm 2\%$.

1 INTRODUCTION

The KEK B-Factory (KEKB) [1] is an asymmetric electron-positron collider comprising 3.5-GeV positron and 8-GeV electron rings. The KEKB injector linac [2] was upgraded in order to inject single-bunch positron and electron beams directly into the KEKB rings. The beam charges are required to be 0.64 nC/bunch and 1.3 nC/bunch for the positron and electron beams, respectively. High-current primary electron beams (~ 10 nC/bunch) are required in order to generate sufficient positrons. About seventy wall-current monitors (WCMs) have been newly installed in order to reinforce the beam-charge-monitoring system in the injector linac for the KEKB. A bench calibration for the WCMs was performed using fast test pulses with a width of nanoseconds, and the calibration coefficients were derived from the pulse-height response of the monitor, depending upon the pulse width [3]. It is, however, difficult to directly obtain the calibration coefficient for a single-bunch beam with a pulse width of about 10 ps, because the direct generation of such extremely fast test pulses is not very easy. One of the authors (T. Suwada) has tentatively derived calibration coefficients for a 10-ps pulse width from extrapolation based on the results of the bench calibration. It is, however, not sufficiently accurate to estimate them by this extrapolation method, because the WCM has a strong frequency response and a beam-position dependence for shorter pulses [4]. A recalibration of the WCM using a Faraday cup (FC) has been performed using beam tests. The purpose of this report is to give the results of precise measurements of the amount of an absolute beam charge for a single-bunch beam with a pulse width of 10 ps and a short-pulsed beam with a pulse width of 1 ns generated from the injector linac, and the recalibration for the WCM by a beam test.

^{*} Email: tsuyoshi.suwada@kek.jp

2 FARADAY CUP

A cross-sectional view of the FC is shown in Fig.1.

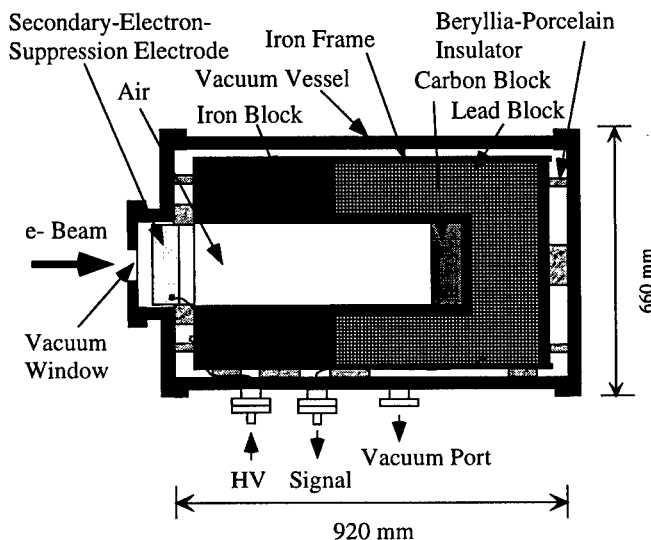


Figure 1: Cross-sectional view of the Faraday cup.

It was originally designed at the Laboratory of Nuclear Science of Tohoku University about thirty years ago. Since a detailed design report is available elsewhere [5], here, the geometry and a simple discussion about its design are briefly presented. The FC comprises a vacuum vessel made of iron, a lead block, an iron block and a carbon block with cylindrical symmetry. The FC dimensions are about 1 m in total length to the beam axis and about 660 mm in diameter; the total weight is about 1.8 t. The bottom thickness of the lead block is 190 mm, which corresponds to 34 radiation lengths, in order to perfectly absorb incident electron beams with an energy of less than 300 MeV. The FC can be separated by the vacuum vessel and a thin vacuum window with a thickness of 0.01 mm made of stainless steel (SUS304) from the beam line. The window thickness is required to be as thin as possible in order to suppress as much as possible any backscattering and multiplescattering of incident beams. A carbon block with a thickness of 80 mm is used to suppress any rapid increase of an electromagnetic shower cascade caused by incident beams in the lead block. An opening hole with a diameter of 200 mm and a depth of 600 mm in the central region needs to suppress the escape of secondary charged particles

generated by an electromagnetic shower cascade in the carbon block. A good vacuum condition needs to be maintained through a vacuum port in order to suppress the generation of ions caused in the residual air gas. The inner materials are sufficiently insulated to be larger than 1000 M Ω by several beryllia porcelains from the vacuum vessel, which is connected to a ground line. A negative electric potential with several hundred volts is typically applied to an electrode at the entrance of the monitor through a vacuum feedthrough in order to suppress the escape of directly backscattered charged particles as much as possible. The integrated beam charge is extracted from a signal port, which is connected to the lead block.

3 EXPERIMENTAL SET-UP

Figure 2 shows a schematic layout of the experimental set-up and the beam line at sectors A and B of the injector linac.

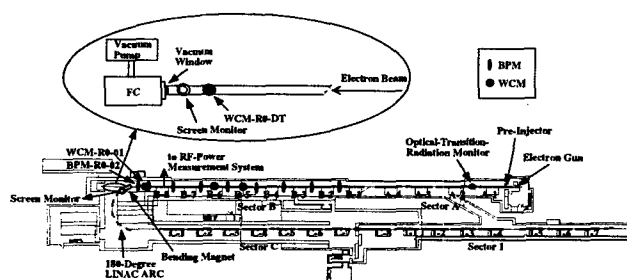


Figure 2: Schematic layout of the experimental set-up and the beam line for the sectors A and B at the injector linac.

Single-bunch electron beams can be generated by a new pre-injector [6], which is composed of two sub-harmonic bunchers, a prebuncher and a buncher. The electron gun can generate a beam charge of about 20 nC/pulse. The nominal beam energies are about 500 MeV and 1.5 GeV at the end of the sectors A and B, respectively. A longitudinal beam profile can be monitored using an optical transition-radiation monitor (OTR) with a streak-camera system [7] installed after the exit of the module A-1. The beam experiments were carried out using electron beams ejected from a straight line after the sector B. The FC was installed 2.3 m behind the first bending magnet, which guides the electron beams to the 180-degree arc section. The beam energies and the energy spreads were measured after the bending magnet using a screen monitor installed behind. The vacuum of the FC was separated from the beam line with a 10 μ m-thick vacuum window 30 mm ϕ in diameter made of stainless steel, and the vacuum pressure inside the FC was maintained at 1.1×10^{-4} Torr using a turbo-molecular vacuum pump. Twenty-two stripline-type beam-position monitors (BPMs) and twenty WCMs measure the beam positions and the beam charge in order to control them stable without any beam loss, respectively. Another WCM and a screen monitor were mounted just before the FC in order to observe the beam losses and the spatial beam sizes, respectively. A data-

acquisition (DAQ) system was constructed for the beam experiment. It comprises several front-end computers and a host computer, which control the BPMs and the WCMs, an electrometer (Keithley 617) used for the FC. All of the BPMs and the WCMs are controlled by digital sampling oscilloscopes (Tektronics TDS680B) and VME/OS-9-based front-end computers. The host computer and the front-end computers communicate with each other through a network system. Trigger-pulses synchronized with the linac beam are provided to all of the devices at 0.33 Hz. This rate is limited by the communication throughput between the front-end computer and each device through a GPIB line. A detailed report is available elsewhere [8].

4 BEAM TEST

4.1 Beam experiment

Two kinds of electron beams, single-bunch and short-pulsed beams with the energies of 1.5 GeV and 325 MeV, were tuned for the beam test. Single-bunch beams were generated using the two sub-harmonic bunchers; on the other hand, short-pulsed beams were accelerated without them. A single-bunch beam with the energy of 1.5 GeV is a nominal-injection beam for the KEKB ring. The other beams with the energy of 325 MeV were generated in order to reduce as much as possible any systematic error for the beam-charge measurement. The energy spread of the 325-MeV beam was 5.5%, which was greater than that (2%) of the 1.5-GeV beam due to the longitudinal beam spread caused by a deceleration at the sector B. The bunch length of the single-bunch beam and the envelope width of the short-pulsed beam were measured by the OTR to be 8.64 ps and 1 ns in FWHM, respectively. The beam orbits were carefully tuned for all of the beam modes by using the BPMs without any observational beam loss. The spatial beam size was measured to be about 6 mm in diameter in front of the FC by a screen monitor. The negative bias voltage applied to the secondary-electron-suppression electrode was chosen to be -1 kV by measuring the beam-charge reduction using single-bunch beams with the energy of 1.5 GeV by changing the applied voltage. Two background measurements were carried out before the beam-charge measurement. The first was a dark current generated from accelerator structures and the second was a dark current from the electron gun. The first background was estimated by the beam-charge reduction by disturbing the dark currents using a screen monitor in front of the FC with a "beam off" condition, which meant no high voltage applied to the electron gun. The second background was obtained by measuring the beam-charge increment with a "beam wait" condition, which meant no triggers were fed to the gun with a high voltage applied. The background contribution from the first one was negligibly small compared with the second one (0.3 nC/scan) which was corrected in the analysis. The beam-charge measurement was carried out by

changing the bias voltage applied to the gun four times, which were 172.8, 191.2, 209.6 and 228.4 V; the measured beam charge was about 1 to 3 nC for all of the beam modes.

4.2 Experimental results

It is important to carefully analyze the beam loss between the end of the module B-8 and the FC, any generation of secondary charged particles (shower) at the vacuum window, and the effect of a beam halo, because such phenomena may produce systematic errors. The first and second phenomena can be estimated by relating the ratios of the charge measured by the FC to that of the WCM-R0-01, and to that of the WCM-R0-DT depending upon the beam positions obtained by the BPM-R0-02 (see Fig.2). The systematic error analysis is given elsewhere in detail [9]. Figure 3 show the results after only a dark-current correction for a 1.5-GeV single-bunch beam. We can find beam losses slightly before the FC in the region of the horizontal beam-position displacement of less than zero. An analysis was performed after data reduction due to the beam loss and after rejecting data larger than $\pm 2\sigma$ obtained from a Gaussian-function fitting procedure for the charge-ratio distributions in order to exclude any noisy events caused by the klystron modulators. Figure 4 shows a linear relation of the beam charge of the WCM-R0-01 to that of the FC by using a least-squares fitting procedure after data reduction. The slope (a) corresponds to a recalibration coefficient of the beam charge for the WCM-R0-01. The errors in the figure give only statistical errors. For the other beam modes, the analysis was also performed in the same way after the data-reduction procedure while carefully taking into account the beam-loss and the shower events. Table 1 summarizes the analysis results for all of the beam modes and the combined recalibration coefficients for the single-bunch (s-b) beam, and for the short-pulsed (s-p) beam, respectively.

5 CONCLUSIONS

An absolute beam-charge measurement for single-bunch and short-pulsed electron beams was performed by using a Faraday cup at the KEKB injector linac. A wall-current monitor was recalibrated according to the analysis results; the recalibration coefficients were obtained to be $1.11 \pm 7 \times 10^{-4}$ (stat.) $\pm 2 \times 10^{-2}$ (syst.) for the single-bunch beam, and $1.04 \pm 2 \times 10^{-3}$ (stat.) $\pm 2 \times 10^{-2}$ (syst.) for the short-pulsed beam, respectively.

6 ACKNOWLEDGMENTS

We are grateful to Prof. T. Terasawa (Tohoku University, Japan) for allowing us the use of his group's Faraday cup.

7 REFERENCES

- [1] KEKB B-Factory Design Report:KEK Report 95-7 (1995).
- [2] Design Report on PF Injector Linac Upgrade for KEKB: KEK Report 95-18, 1996.
- [3] T. Suwada *et al.*, Nucl. Instrum. & Methods A396 (1997) p.1.
- [4] T. Suwada *et al.*, APAC'98, KEK, Tsukuba, Japan, 1998, p.528.
- [5] T. Ohama *et al.*, Mitsubishi Electric Advance 43 (5) p.739 (1969).
- [6] S. Ohsawa *et al.*, LINAC'96, CERN, Geneva, Switzerland, 1996, p.815.
- [7] Y. Ogawa *et al.*, APAC'98, KEK, Tsukuba, Japan, 1998, p.534.
- [8] T. Suwada *et al.*, APAC'98, KEK, Tsukuba, Japan, 1998, p.531.
- [9] T. Suwada, to be in preparation.

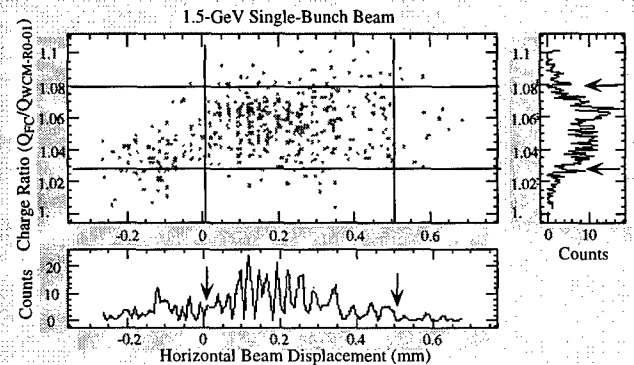


Figure 3: Scatter plots for the charge ratio ($Q_{FC}/Q_{WCM-R0-01}$) to the horizontal beam displacement measured for the 1.5-GeV single-bunch electron beam. The allows and lines indicate the data-reduction conditions.

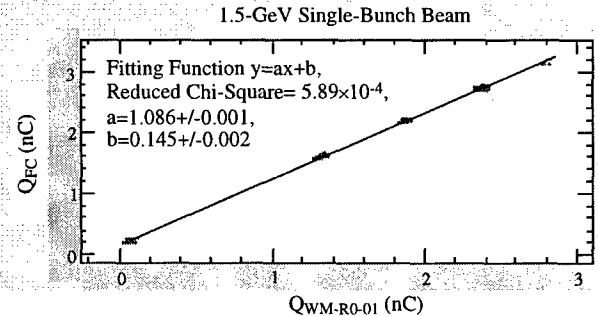


Figure 4: Linear relation of the beam charge measured by the WCM-R0-01 to the FC for the 1.5-GeV single-bunch electron beam.

Table 1: Results for the beam experiment. "a" and " δa " show the recalibration coefficient and its error, respectively.

Beam Mode	a	δa (stat., syst.)
1.5-GeV s-b beam	1.086	$\pm 1 \times 10^{-3} \pm 2 \times 10^{-2}$
1.5-GeV s-p beam	1.031	$\pm 2 \times 10^{-3} \pm 2 \times 10^{-2}$
325-MeV s-b beam	1.126	$\pm 1 \times 10^{-3} \pm 2 \times 10^{-2}$
325-MeV s-p beam	1.061	$\pm 3 \times 10^{-3} \pm 2 \times 10^{-2}$
Combined s-b beam	1.11	$\pm 7 \times 10^{-4} \pm 2 \times 10^{-2}$
Combined s-p beam	1.04	$\pm 2 \times 10^{-3} \pm 2 \times 10^{-2}$

BEAM CURRENT MEASUREMENTS FOR LEDA *

J. Power[†], D. Barr, J. Gilpatrick, D. Martinez, R. Shurter, and M. Stettler, LANL, Los Alamos, NM

Abstract

Beam diagnostics systems for the Low Energy Demonstrator Accelerator (LEDA) at Los Alamos include beam current measurements [1,2]. The LEDA machine operates in both pulsed and cw modes with a peak current of 100 mA. Two types of current sensors are employed. Some are dc- to 4-kHz-bandwidth modular parametric current transformer (MPCT) sensors from Bergoz® and the others are 10-Hz to 200-kHz bandwidth custom-designed transformers. Both ac and dc sensors are integrated into common shielding enclosures on the beam line. A VXI module has been developed to interface the analog sensors to the EPICS control system. The same VXI module can be used for either type of sensor and contains an on-board calibration system which provides a system absolute accuracy of $\pm 0.2\%$. The calibration, data processing, and general operation of the VXI module is controlled by two internal DSP modules. The performance of the system on the LEDA beam line is presented.

1 INTRODUCTION

The beam diagnostics systems for LEDA are primarily VXI-based instruments. While the control system will soon be fully implemented under EPICS, we are presently operating the diagnostics systems under LabVIEW®. The beam current measurements are divided into two types; "ac" or pulsed beam systems with a 10-Hz to 200-kHz bandwidth and "dc" systems with dc- to 4-kHz-bandwidth response. A single VXI motherboard is used as the backbone for both of these measurement types with different analog-front-end (AFE) electronics used depending on the requirements. We have chosen to use the modular parametric current transformer (MPCT) sensors and electronics modules from Bergoz® for the dc systems and custom transformers and AFE electronics for the ac systems.

2 BEAMLINE SENSORS

Both ac and dc sensors are enclosed in a common enclosure at each location on the accelerator. This enclosure is made of iron to provide some shielding from the various quadrupole magnet fields. A typical assembly is shown in Figure 1. Our present designs nest the ac toroidal core inside the dc sensor. Two sizes of Bergoz® sensors are used. We have 17.5-cm-o.d. and special-order 34-cm-o.d. units.

The ac sensors use 1-mil-thick Superalloy® tape

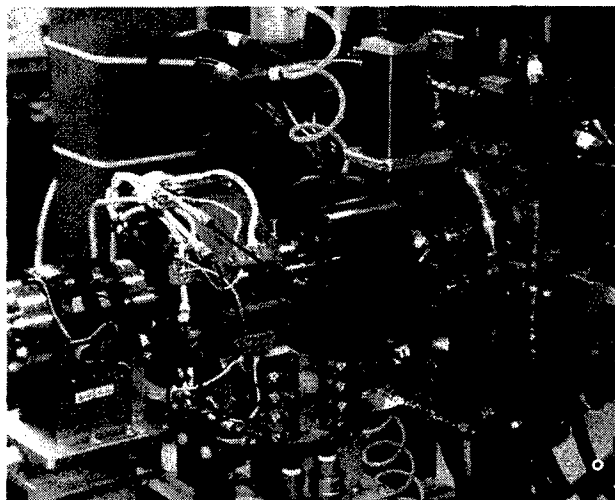


Figure 1: A typical beam current sensor assembly located at the exit of the RFQ. Both ac and dc sensors are contained in the same housing.

cores of an appropriate diameter to fit within the sensor housing. Each ac transformer has a 50-turn sense winding and two-turn calibration winding. The inductance of each sense winding is approximately 50 mH.

Both sensors are supported in the housing with felt material to help absorb vibrations on the beamline from the vacuum pumps.

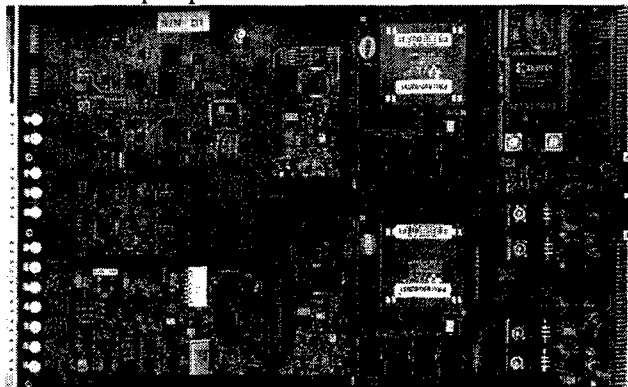


Figure 2: The VXI motherboard printed circuit shown with two ac AFE circuits installed in the middle of the motherboard. The 14-bit ADC circuits are at the top left, DAC and calibrator at the bottom left, and the DSP modules just right of center. The VXI interface and power supply components are on the right.

3 VXI MODULE DESIGN

A single VXI format motherboard was developed for both the ac and dc measurement systems. A modular approach allows for the replacement or revision of sub-circuits to avoid the expense and time required in fabricating a full

*Work supported by the U.S. Department of Energy

[†]Email: jpower@lanl.gov

VXI module (see Figs. 2 and 4). Various plug-on modules include the ac AFEs, dc Bergoz® AFEs, a wire scanner charge-integrating AFE, calibration current generator, dual output DAC circuit, two DSP modules, and the VXI interface circuit. Each motherboard supports two channels of beam current measurement. Electronics associated with the motherboard include various gate arrays for interfacing the modules, two 14-bit ADC channels, timing generation gate arrays, and power supply components.

Two commercial DSP modules (TMS320C40), one per channel, control the operation of the module. Functions provided by the DSPs include module calibration, fast-protect calculation, waveform array storage, and filtering. The most demanding feature of the DSP is the fast-protect output, which is tripped whenever the differential beam loss between to adjacent sensors exceeds a programmable level. The VXI motherboard design and DSP code is heavily influenced by this requirement.

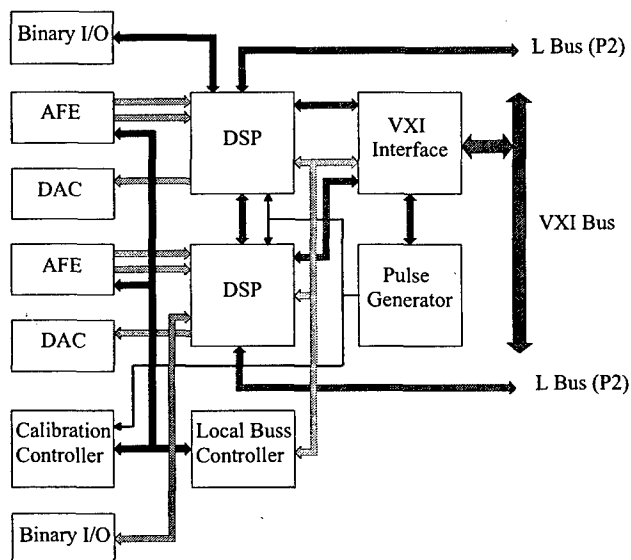


Figure 3: Block diagram of the ac/dc VXI module. Each measurement channel has a dedicated DSP module and DAC. Plug-on modules are controlled via a local buss.

Most of the plug-on modules are connected with an eight-bit buss whose purpose is to allow set-up, and control data to flow between them and either the DSP modules or the VXI interface. Separate dedicated busses control the flow of the realtime data streams. A block diagram of the VXI module is shown in Figure

The most significant difference between the implementation of the ac verses the dc systems is the size of the AFE electronics. The Bergoz® MPCT-E electronics modules are sufficiently large as to require a double-wide-module front panel for the two-channel design (see Fig. 4). Another interesting point is that ADC sampling rate required for the lower 4-kHz bandwidth of the dc system will leave more time available to the DSP modules to perform additional calculations such as additional filtering functions. The dc systems have not been fully implemented at this time, as the LEDA

accelerator is being commissioned with pulsed beam. These dc systems will be significantly easier to field than the faster ac systems, however.

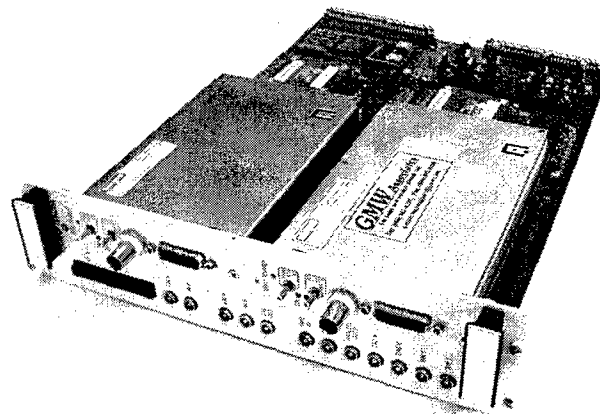


Figure 4: The dc beam current system double-wide VXI module. Two Bergoz® MPCT-E electronics modules are mounted to the front panel. Only the sensor cables need to be attached to the front panel connectors. The ac system uses a single-wide module with the same motherboard.

4 OPERATIONAL EXPERIENCE

As of this writing we have just completed the first two weeks of LEDA accelerator commissioning. This time has been sufficient to measure several important parameters of both the diagnostic systems as well as the accelerator operation.

As installed, the ac system has a current measurement range of ± 200 mA. In this configuration the noise floor of the current measurement is about $33 \mu\text{A}$ with a 200 kHz bandwidth. This is measured as the standard deviation of 1000 consecutive samples at 1 MSPS. The overall bandwidth of the three operating ac systems is 8.7 Hz to 200 kHz, worst case. The bandwidths vary slightly as all of the sensor cores are not of the same geometry.

Each VXI module generates a single calibration pulse that is looped between two adjacent sensors. The stability of this source needs testing over temperature, but is at least much better than the $\pm 0.2\%$ -absolute-accuracy specification of the diagnostic. Our present laboratory instrumentation measurement limit is $\pm 0.04\%$, absolute. Each beamline measurement system is calibrated to within ± 1 ADC count, or $\pm 0.02\%$ of the set points (gain and offset). The system has demonstrated a stability of on the order of ± 2 ADC counts over the two week run period, so far. It should be noted the temperature is fairly constant in the accelerator building this time of year. Overall, we are confident that the required $\pm 0.2\%$ measurement accuracy is met.

We are presently running the beam diagnostics systems under LabVIEW® while the EPICS-based control system is being completed. A single National Instruments VXIpc-850 controller in the ac beam current measurement VXI

crate handles the control, display, and data archiving functions of the system running LabVIEW® under Windows 95. The primary display is shown in Figure 5 with typical beam currents as seen during one of the first LEDA commissioning experiments.

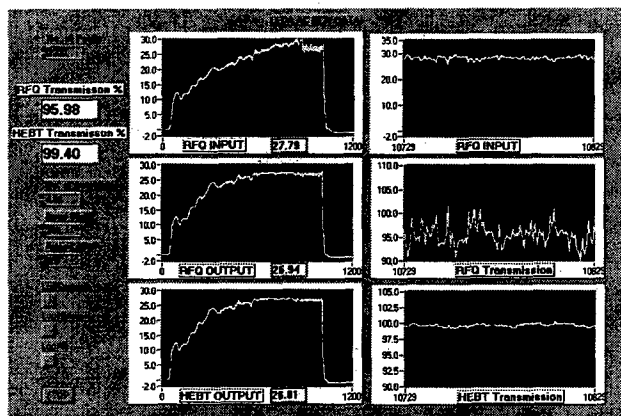


Figure 5: The LabVIEW virtual instrument front panel display for the ac beam current monitor system. The RFQ input, RFQ output, and HEBT output current waveforms are displayed on the left and the RFQ input current, RFQ transmission, and HEBT transmission charts are on the right.

5 CONCLUSION

New beam current diagnostics have been designed for the LEDA accelerator. The ac (pulsed beam) system has been installed, tested, and has provided the required performance needed to commission the accelerator. It is capable of measuring ± 200 -mA pulsed currents with an absolute accuracy of $< \pm 0.2\%$ with a resolution of about 33 μ A (without gain switching) and a 10-Hz to 200-kHz bandwidth. Both the ac and dc systems utilize DSP-based VXI modules, which provide high-performance and ease of use.

6 REFERENCES

- [1] J. D. Schneider, et. al., "Operation of the Low-Energy Demonstration Accelerator: the Proton Injector for APT," these proceedings.
- [2] J. D. Gilpatrick, D. Barr, J. Power, W.C. Sellyey, R. Shurter, J. Kamperschroer, D. Martinez, and J. O'Hara, "Low Energy Demonstration Accelerator (LEDA) Beam Instrumentation: RFQ-Accelerated Beam Results" these proceedings.

CHAMBER MOTION MEASUREMENTS AT THE NSLS X-RAY RING*

L. Solomon[#], D. Lynch, BNL; J. Safranek, SSRL; O. Singh, ANL

Abstract

Work has been ongoing at the NSLS to improve the orbit stability of the X-Ray Ring by accounting for the thermal motion of the vacuum chamber, which supports the electron beam position monitors (BPMs). In-situ contact measurements of the vacuum chamber motion have been carried out using support stands that have been designed and extensively tested to reduce errors associated with thermal changes in the stands themselves. Using this chamber motion as a correction to the orbit motion measured by the BPMs, the precise location of the radiation beam can be predicted. These predictions are compared with actual radiation beam measurements on the experimental floor, and with predictions based solely on BPM measurements of the electron beam position. This paper reviews this work including stand design and performance, chamber motion measurements, predictions based on these data, and results.

1 INTRODUCTION

In order to stabilize the electron beam position in the NSLS X-Ray Ring, pickup electrodes monitor the beam position and are used in the feedback system for stabilization. However, the temperature of the vacuum chamber is a function of time due to radiative heating, and therefore its motion is also a function of time. Thus, in order to stabilize the motion in a stationary coordinate system it is necessary that both the beam motion with respect to the chamber, and the chamber motion itself, are monitored and used in the feedback. Towards this end a) motion of the vacuum chamber has been measured and correlated to the motion of the radiation on the X-Ray Ring floor, and b) carbon fiber stands which are extremely stable and relatively insensitive to temperature changes within the ring have been designed and tested. This paper summarizes the results of this work to date.

2 BEAM MOTION

The motion of the beam at the source point of the X28 beamline was measured with a pinhole camera. The

beam position with respect to the vacuum chamber on two BPMs just upstream of X28 (BPM 33 and 34) and the first BPM downstream (BPM 35) was also measured, along with the horizontal vacuum chamber motion at the three BPM locations. For measurement of the vacuum chamber motion, linear voltage displacement transducers are mounted on stands and are used to monitor the horizontal motion. These transducers have a range of ± 0.125 inches, and with our readback electronics the digital resolution is 0.4 microns/count. Each of the LVDT devices was calibrated individually throughout its range of motion, with its cabling and circuitry.

The shift in the electron beam orbit at the X28 source point can be predicted given the measured change in beam position at nearby BPMs. This assumes that the orbit shift is caused by magnetic field changes elsewhere in the ring. The magnetic field changes between the BPMs and the source point must be small.

Three BPMs are needed to accurately predict horizontal motion at the source point, because horizontal orbit motion can be caused by a change in electron energy (δ) as well as in horizontal betatron phase space (x, x'). A significant fraction of the closed orbit shift over the course of a fill in the X-Ray Ring is associated with δ [1]. Given the 3x3 transfer matrices for x, x' and δ and the measured orbit shifts at the three BPMs, the orbit motion at X28 can be predicted.

Through the course of a 12 hour fill of the X-Ray Ring, the horizontal motion of the vacuum chamber at BPM 33, 34 and 35 location was about 30, 130, and 160 microns respectively. By comparing the chamber motion data with the BPM data, it is seen that the chamber motion is reflected in an apparent motion of the electron beam to varying degrees for the various locations. For example, at BPM 34 location, almost all of the electron beam motion is due to chamber motion.

In Figure 1, the measured horizontal motion of the radiation beam at the source point is compared with predictions based solely on the motion of the electron beam, and also on the movement of both the chamber and the electron beam with respect to the chamber. The prediction incorporating the motion of the vacuum chamber closely mimics the actual radiation beam motion. These results provide a strong impetus towards real-time measurement and incorporation of the vacuum chamber motion into the feedback as a means towards a significantly more stable beam.

*Work performed under the auspices of the U.S. Department of Energy

[#] Email: solomon@bnl.gov

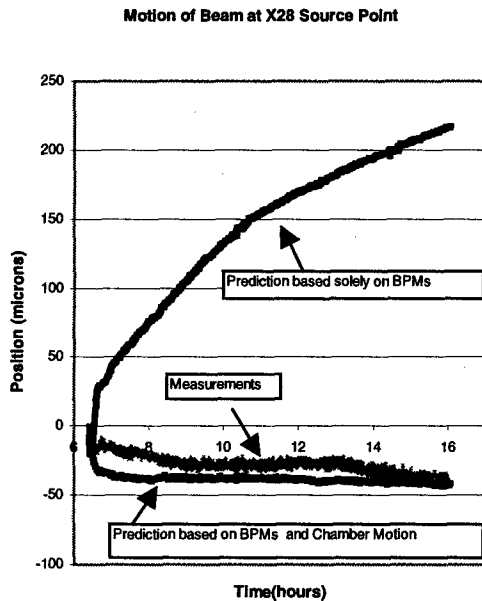


Figure 1 Motion of the Radiation Beam at the X28 Source Point at NSLS X-Ray Ring. The measurements, the predicted motion based solely on BPMs 33,34 and 35, and the predicted motion based on both the BPMs and the vacuum chamber motion at the location of the BPMs is shown.

3 TRANSDUCER SUPPORT STAND

In order to accurately measure the chamber motion it is imperative that the stands which support the LVDT devices be extremely stable over time, and temperature insensitive. In the X-Ray Ring, support stand temperature changes of a couple of degrees during a fill are seen. When making measurements on the micron scale, this can translate to unacceptably large motions due to thermal expansion of the LVDT support stand. Initially, to null motion associated with thermal changes, stands of alternating aluminum and steel telescoped sections were built and tested. Aluminum and steel expansion coefficients are approximately 24×10^{-6} and 18×10^{-6} inch/inch $^{\circ}\text{C}$, respectively. The relative proportion of each material was chosen for zero net thermal expansion. Though this strategy worked for equilibrium states and very slow temperature changes, it was inadequate during more rapid temperature changes. Subsequent to this, stands comprised entirely of carbon fiber tubing with a very low thermal expansion were fabricated and tested. In order to measure the carbon fiber expansion coefficient, a reference invar tube (thermal expansion $\approx 1 \times 10^{-6}$ inch/inch $^{\circ}\text{C}$) and the carbon tube to be measured were both mounted horizontally on a vertical steel tube, which was secured to the floor. The carbon tubing held the LVDT device, and measured horizontal motion with respect to a flat on the invar tubing. With this setup, floor or steel

motions do not affect the relative motion of the invar and the carbon tubes. These measurements yield a carbon fiber thermal expansion coefficient value of approximately 1×10^{-6} inch/inch $^{\circ}\text{C}$. This coefficient is sufficiently small that errors associated with thermal motion in the ring will be on the order of a couple of microns.

The support stand reported on here consists of a vertical member approximately 60" high, with a 3.25 inch outer diameter and 0.25" wall thickness. A horizontal member (clamped to the vertical tubing at ≈ 55 " off the floor) is approximately 25" long, with a 1.50 inch outer diameter and 0.25" wall thickness. At the end of the horizontal arm is a graphite piece which can hold two LVDT devices, one held in the vertical orientation for vertical motion measurements, and the other held in the horizontal orientation for horizontal motion measurements. The relative positions of these LVDT's are matched to the vacuum chamber dimensions of the X-Ray Ring at the NSLS. Two carbon stands were fabricated for testing. In order to measure their behavior as a function of temperature and time, motion with respect to a 4 inch diameter invar tube with machined flats was recorded. The stands were positioned on opposite sides of the invar tube, and bolted to a granite table. Measurements of the stand motions and air, stand and granite temperature were recorded during the room temperature changes resulting from the disabling of the heating and air conditioning controls. Air temperature changes of up to seven degrees were measured.

The results obtained by the aforementioned tests were complicated by the fact that the granite itself has a quite large thermal expansion coefficient, approximately ten times that of the carbon tubing. Thus, the behavior of the stands was largely a function of the granite temperature changes. This can be seen in Figure 2, where data taken over 6.5 days is compared with data taken over 11 days. The range in the horizontal and vertical stand motion roughly doubled, as the range of the granite temperature changed by 85% and the range of the air temperature changed by 16%. Thus, since the dependence on temperature should be linear, it appears that the behavior of the stands is dominated by the granite support to which the stands are bolted. A function to predict the stand motion was contrived, which assumes linear motion associated with temperature changes in the stand and the graphite separately, and assumes a fixed ratio between the thermal expansion coefficients. With this, the predicted behavior in the horizontal plane is within 10 microns of the actual behavior, which goes through a 70 micron range of motion during the 7° air temperature change. This agreement is quite good, given that the behavior of the materials is actually quite complex due to temperature gradients within the granite slab.

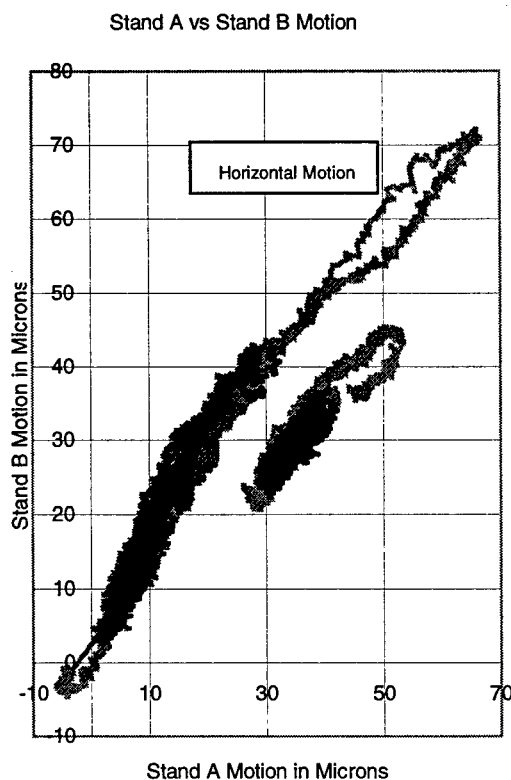


Figure 2 The horizontal and vertical motion recorded by one carbon fiber test stand compared with another carbon test stand. The upper data is the horizontal motion, and the lower data is the vertical motion. The lighter grey data was collected over an 11 day period, during which there was a 7° air temperature change, and a 4.8° temperature change in the granite. The darker data points represent 6.5 days of data, with a 5.6° air temperature change and a 2.8° temperature change in the granite.

Because of this large temperature effect associated with the granite table, the behavior of the two test stand motions were compared to each other to measure the stability of the stands as a function of temperature and time. Any undesirable behavior in the stability of the stands should not be simultaneously seen in both of the two tested stands. As can be seen in Figure 2, over the course of an 11 day period, the two stands tracked each other in both the horizontal and the vertical directions within ± 5 microns. This level of stability over such a long term (11 days) is excellent. Actually, the relevant time scale for actual use of these stands is the twelve hour fill period of the X-Ray Ring. Over this time, the stands track each other to within a couple of microns. Given these test results, current plans are to re-measure both vertical and horizontal ring movements at several locations with these improved stands, and test incorporation of this data into the feedback system during study periods at NSLS.

4 SUMMARY

In summary, measurements have been performed which indicate that significant improvement in the radiation beam stability can be expected when the motion of the vacuum chamber is accounted for. This is seen through comparison of beam motion predictions based on strictly BPM measurements, and on BPM and vacuum chamber motion measurements. Thus, very accurate chamber motion measurements are required. Stable support stands have been built and tested, with long term stability results on the order of several microns. Presently, measurement of the chamber motion with these improved stands, and utilization of the data in the orbit feedback system is being implemented in certain areas within the X-Ray Ring at NSLS.

5 ACKNOWLEDGEMENTS

The authors would like to thank M. Lehecka for his technical assistance throughout the course of this work, and S. Krinsky for guidance. This work performed under the auspices of the U.S. Department of Energy under contract DE-AC02-98CH10886

6 REFERENCES

- [1] J. Safranek, O. Singh, and L. Solomon, "Orbit Stability Improvement at the NSLS X-Ray Ring", 1995 Particle Accelerator Conference, Dallas, Texas.

RHIC BEAM LOSS MONITOR SYSTEM INITIAL OPERATION*

R. L. Witkover[†], R. J. Michnoff and J. M. Geller

Brookhaven National Laboratory

Upton, NY, USA 11973

Abstract

The RHIC Beam Loss Monitor (BLM) System is designed to prevent beam loss quenching of the superconducting magnets, and acquire loss data. Four hundred ion chambers are located around the rings to detect losses. The required 8-decade range in signal current is compressed using an RC pre-integrator ahead of a low current amplifier. A beam abort may be triggered if fast or slow losses exceed programmable threshold levels. A micro-controller based VME module sets references and gains and reads trip status for up to 64 channels. Results obtained with the detectors in the RHIC Sextant Test and the prototype electronics in the AGS-to-RHIC (ATR) transfer line are presented along with the present status of the system.

1 THE DETECTORS AND ELECTRONICS

It has been estimated that the RHIC superconducting magnets will quench for a fast (single turn) loss > 2 mJ/g or a slow (100 msec) loss > 8 mW/g. These correspond to a signal current range from 5.5 mA for fast loss at injection, and 17.6 nA for a slow loss at full energy. Allowing for studies, a dynamic range of 8 decades in detector current is required. The processed BLM signal is digitized at 720 Hz and continually compared to programmable fast and slow loss abort levels. An abort halts data acquisition providing a 10 second loss history. BLM parameters may be adjusted to set gains, fast and slow loss thresholds and abort mask bits on specific RHIC Event Codes.

The RHIC Ring BLM system uses 400 FNAL Tevatron type ion chambers [1] modified by using an isolated BNC to break the ground loop formed by the signal and HV cable shields. Rexolite rather than PTFE is used for the insulators in the BNC and SHV connectors to improve the radiation hardness. The ion chamber [2] consists of a 113 cc glass bulb filled with argon to about 725 milli-Torr. Each chamber is calibrated using a cesium-137 source. The mean sensitivity in the middle of the plateau (1450 Volts) is 19.6 pA/rad/h, with 95% within ± 1.5 pA/rad/hr of the mean. The high voltage is normally set to 1450 V with a 3000 V upper limit. Half of the ion chambers (198) are mounted on the quadrupole cryostats between the Rings using stainless steel "belly bands". Ninety-six

*Work supported by the US Department of Energy

[†]witkover@bnl.gov

BLMs are placed at insertion region quads. In the warm regions, 68 detectors are mounted on the beam pipe at sensitive loss points. In addition, 38 BLMs are available as re-locatable monitors.

Belden 9054, a low noise, non-tribo-electric RG-59 equivalent cable was used for signal transmission. The HV bias voltage is carried on red RG-59 cable which is daisy-chained from detector to detector. Two HV cables are used in each sector, picking up alternate BLMs to provide some redundancy in the event of a high voltage short. An RC network built into each ion chamber housing provides decoupling in the case of a short, noise filtering, and storage capability to handle large fast losses.

The analog electronics are packaged in VME modules, each of which interfaces to 8 BLMs. Up to 8 analog boards are managed by a micro-controller module which is independent of the crate front-end computer (FEC) once the event-driven write list values have been set through high level code. This insulates the real-time operations from the control system I/O, allowing the BLM system to operate during an FEC link failure. Commercial digital I/O and DAC modules control the HV power supplies. The electronics are located in service buildings at 2,4,5,7,8,10 and 12 o'clock, allowing access during beam storage. Standard VME crates were modified for the special needs of the BLM electronics. Tests indicated that the standard ± 12 Volt switcher power supplies were too noisy for the high sensitivity analog circuitry. On-board DC-DC converters were not used due to limited real estate and the possibility of oscillator noise. It was decided to incorporate a separate linear ± 15 Volts supply into the crate to power the analog modules. A piggy-back board across the last nine P2 connectors provides a dedicated bus between the micro-controller module and the 8 analog modules.

1.1 The Analog Module

Figure 1 shows a simplified schematic of one channel of the Analog Module. The input RC filter matches the magnet thermal time constant and integrates any fast loss, greatly reducing the dynamic range required, while providing a sufficient signal to protect against a fast loss quench. Back-biased matched low leakage diodes (DPAD-5) protect the amplifier input from high voltage spikes. The OPA627AU low current amplifier is rolled

off to a 10 μ sec rise time. To allow for BLM shielding differences, jumpers can set three alternate gains.

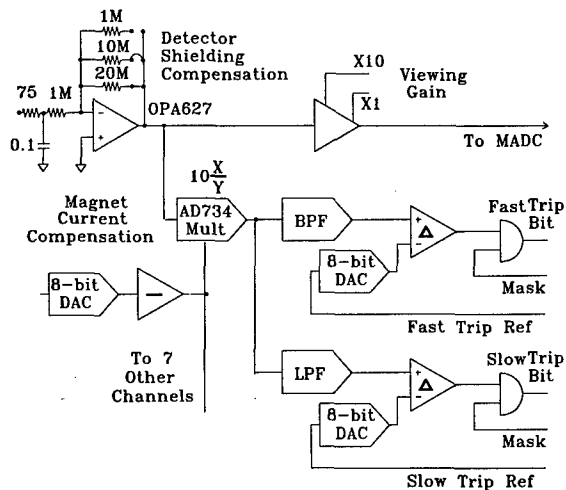


Figure 1. Schematic of a typical channel of the BLM Analog Module.

A second amplifier provides programmable gains of 1 or 10 in the signal acquisition path. The data is read at 720 Hz by a RHIC VME MADC [3] configured for ± 10 V, 13-bits, and stored in a 2 Mbyte on-board memory. An optional off-board 360 Hz anti-aliasing filter is available. Readings can be taken at additional times as required for specific applications. For the nominal jumper setting and a buffer gain of 10, one LSB represents 12.5 pA, comparable to the noise observed in beam tests. Offsets, typically a few LSBs at unity viewing gain, are not adjustable since these can be removed in the higher level processing.

The first stage output also goes to an AD734 analog multiplier which provides gain to compensate for the increased magnet quench sensitivity with current. An 8-bit DAC sets the gain for all multipliers on a board. A high pass (100 μ sec) and low-pass (20 msec) filter direct the signal to respective fast or slow loss comparators with independent programmable references. The gain provided by the multiplier cuts the dynamic range so 8-bit reference DACs are sufficient. Each comparator may be masked to prevent a bad BLM from inhibiting the beam or to allow special conditions. The gains, mask bits and trip levels may be changed by events on the RHIC Event Link. Any trip latches the state allowing the trip location to be determined. An Altera 7128 chip is programmed to perform all logic and communication functions with the BLM Micro-controller module via the dedicated bus on the VME P2 backplane.

1.2 The Micro-Controller Module

The RHIC Control System communicates with the Analog Modules via the BLM Micro-Controller [4].

Once the Micro-Controller receives the Write-list containing the array of set-points (gains, thresholds, masks, etc.) it completely controls the Analog Module, freeing the FEC for other controls tasks and allowing the BLM system to operate even in the event of a controls failure. A Microchip PIC16C64 micro-controller services the 256 byte registers on the BLM Analog modules. A 64k x 16 bit memory holds the Write-lists for 256 RHIC Event codes, each associated with up to 255 address/data values. On detection of a specific Event, the corresponding Write-list is sequentially executed with the data going to a particular register. Altera 9320 and 7128 gate arrays are used on the board.

2 BLM TEST RESULTS

Figure 2 shows the responses of the circuitry to 8 bunches of 2×10^{12} protons each, extracted at 30 Hz rate. The top trace is the analog output showing the signal rising rapidly due to the loss from each bunch transfer. It then decays with the 100 msec front-end filter time constant. The middle trace is the slow loss filter output clearly showing rejection of the fast losses. The bottom trace is the comparator output for a 2 Volt reference.

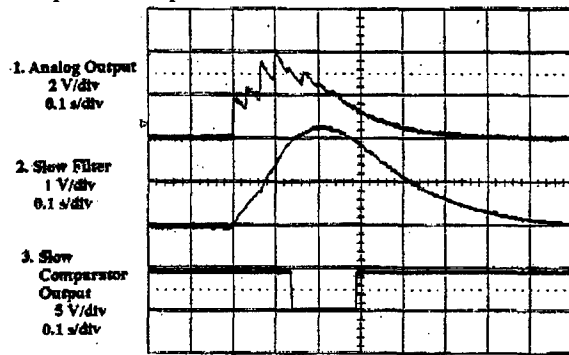


Figure 2. Losses from eight bunch 2×10^{12} protons/bunch transfer, Slow Filter and Comparator outputs

The top trace of Figure 3 is another cycle of 8 extracted proton bunches. The middle trace is the fast loss filter output, showing only the fast component of the signal. The

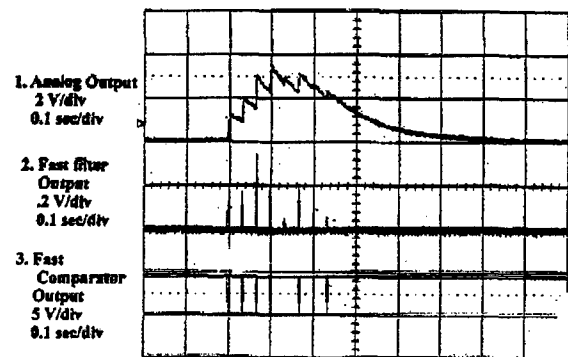


Figure 3. Losses from eight bunch 2×10^{12} protons/bunch transfer, Fast Filter and Comparator outputs

bunches did not have equal losses so the comparator did not trip for every transfer. It is clear that the circuit has the ability to discriminate between fast and slow losses.

In January 1997 single bunches of an Au^{+79} beam were injected into RHIC Sectors 4 and 5 of one ring of superconducting magnets. In this sextant BLMs were on the inside of the Ring carrying the beam. Since sufficient Ring electronics were not yet available, and the beam was single pass, AtR loss monitor electronics (low-leakage integrators) were used. For normal injection conditions the loss signals were easily observed even though the intensity of $1 \times 10^8 \text{ Au}^{+79}$ ions was an order of magnitude below the design value. A large loss was purposely created at S=600 meters. The data with the background loss signal subtracted is shown in Figure 4. With the BLMs located at the quads (about 15 meter interval) it can be seen from the data that there is sufficient spatial resolution and dynamic range to determine the direction of the beam causing the loss. The observed integrator noise was of the order of a few LSBs, consistent with results in the AtR line. Noise due to the injection kickers and RF was not noticeably greater.

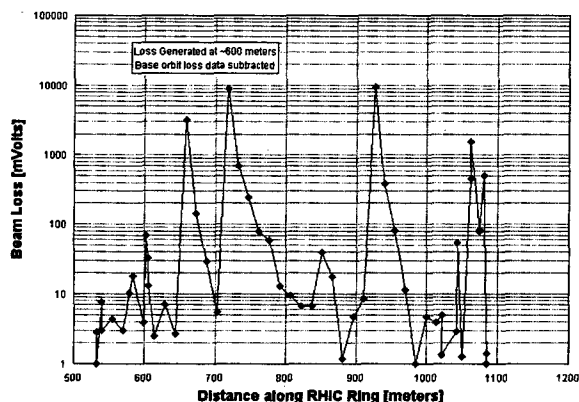


Figure 4. Beam loss along RHIC Sectors 5 and 4 due to test loss at 600 meters for $1 \times 10^8 \text{ Au}^{+79}$ ions, with the background loss signal subtracted

The data shown in Figure 4 covers a 4 decade range and was taken without switching gain. In other runs larger losses were purposely generated, requiring lowering the integrator gain. These results, and the low observed noise, indicated that the BLM system will have sufficient range to meet the design requirements.

3 SYSTEM STATUS

All eleven BLM VME crates have been installed in the service buildings around the RHIC tunnel. The crates were accessed through the RHIC Control System to calibrate the electronics. The calibration consisted of injecting signals from a precision current source at several different currents into each channel. The offset and gain data were

then entered in the system database. Cabling has been installed, terminated and tested. The system is ready for first beam to be circulated in RHIC.

4 ACKNOWLEDGEMENTS

Pat Thompson, as system commissioner, was a key figure in the system check out, siting of detectors and beam testing. He was also responsible for integrating the BLMs into the Contols database. Paul Ziminski was responsible for calibrating the detectors in the lab and, together with Ron Schroeder, the field calibration of the electronics. Much of the work on the electronics design was done by Emil Zitvogel. Barry Clay was responsible for setting up the LabView testing of the Analog Modules.

5 REFERENCES

- [1] Shafer, R. E., et al., "the Tevatron Beam Position and Beam Loss Monitoring Systems", Proc. The 12th Int'l. Conf. High Energy Accel., p609, 1983
- [2] Troy-Ionic Inc., 88 dell Ave, PO Box 494, Kenvil, NJ 07847
- [3] Michnoff, R., "The RHIC General Purpose Multiplexed Analog-to-Digital Converter System", Proc 95 Particle Accel. Conf., IEEE Cat. No. 95CH35843, p2229, 1995
- [4] Michnoff, R., see <http://www.rhichome.bnl.gov:80/Hardware/lossmon1.htm>

BEAM INSTRUMENTATION FOR THE SPALLATION NEUTRON SOURCE RING*

R.L. Witkover[‡], P.R. Cameron, T.J. Shea, R. C. Connolly and M. Kesselman
Brookhaven National Laboratory

Abstract

The Spallation Neutron Source (SNS) will be constructed by a multi-laboratory collaboration with BNL responsible for the transfer lines and ring. [1] The 1 MW beam power necessitates careful monitoring to minimize un-controlled loss. This high beam power will influence the design of the monitors in the high energy beam transport line (HEBT) from linac to ring, in the ring, and in the ring-to-target transfer line (RTBT). The ring instrumentation must cover a 3-decade range of beam intensity during accumulation. Beam loss monitoring will be especially critical since un-controlled beam loss must be kept below 10^{-4} . A Beam-In-Gap (BIG) monitor is being designed to assure out-of-bucket beam will not be lost in the ring.

1 THE SNS PROJECT

The SNS will be designed and built by a collaboration of ANL, BNL, LBL, LANL and ORNL for installation at ORNL in 2005. The design consists of a 1 GeV H-minus linac injecting into an accumulator ring at 60 Hz for an average power of 1 MW. Much of the design allows simple upgrade to a 2 MW beam. The H-minus beam from the linac will be transported via the HEBT line to the 220 m circumference ring where it will be stripped to protons. The injected beam will be accumulated over 1 msec with the RF system maintaining a compact bunch. At the end of the injection pulse the single half-microsecond bunch of 1×10^{14} protons will be extracted and transported down the RTBT line to a neutron conversion target.

2 BEAM LOSS MONITORS

Because of the very high average beam power, uncontrolled losses must be kept very low to allow machine maintenance. Controlled losses, such as from H-minus stripping and other expected sources will be intercepted on collimators designed to contain the resulting radiation. All other losses will result in component activation. The Beam Loss Monitor (BLM) system is designed to detect an uncontrolled loss of 1×10^{10} protons per pulse (1 part in 10^4 at 1 MW) over the full ring and provide a signal to inhibit further injection. Ion chambers will provide the interlock function and the basic, multi-turn loss data. Eight scintillator-photo-multipliers

*This work supported by the US Department of Energy

[‡] Witkover@bnl.gov

(SPM) will serve as fast beam loss monitors (FBLM) observing the losses within the bunch. These will be located in the injection and extraction areas and at high dispersion points. Ion chambers will be located at each quadrupole, at the collimators, and at key injection and extraction loss points. Several relocatable units may be placed local at hot-spots, for a total of 80 channels. The detectors will be mounted close to the beam pipe.

Tevatron type ion chambers [2] as modified for RHIC [3] will be used. The modifications included eliminating Teflon® in the connectors and using isolated BNCs to break ground loops of the cable shields through the BLM aluminum outer case. These BLMs are low cost and reliable, and have good reproducibility and long term stability and low maintenance. Nominal sensitivity is 70 nC/rad. Since the beam cycle is so short most of the signal will come from the electrons, cutting the sensitivity in half. The 10^{-4} loss limit can occur in a single turn or slowly over the entire cycle resulting in a 10^3 range in signal current. A similar problem in RHIC was solved by using a front-end capacitor to pre-integrate the potential current spike. Signals from the 48 BLMs at the quads will be summed to monitor the 10^{-4} total Ring loss requirement. Individual ADCs will acquire each BLM signal at the revolution rate. Several seconds of data will be stored locally and be available for replay in the event of a Beam Inhibit.

The FBLMs consist of photomultipliers immersed in liquid scintillator to reduce radiation darkening.[4] Unit-to-unit variation and radiation effects on the scintillator and window of the tube will require periodic re-calibration and individual HV power supplies. The signals will be integrated over the bunch length and read through digitizer channels clocked at the revolution frequency. In addition units may be selected through a wideband multiplexer to be read into a multi-channel fast digitizer (1 GSa/s) to observe losses within the bunch.

3 BEAM CURRENT MONITORS

The circulating current in the ring will be monitored using a Beam Current Transformer (BCM) designed to handle the 2×10^{14} protons which will be required for a 2 MW beam. In this case the peak current can reach 100 A so care must be taken to prevent saturation of the transformer core. The signal droop must be less than 0.1% during the 1 msec accumulation period, requiring a decay time

constant of about 1 second. The rise time is specified at 50 nsec. A Superalloy tape wound core with 9.5-inch ID, 3" width and 14" OD, will be used to fit over the 8-inch beam pipe. Tests on a similar, smaller core, indicate that a resistor-damped winding of 100 turns with a 1 Ohm load will meet these specification with acceptable ringing. The transformer signal will be processed by a switchable gain amplifier followed by a gated integrator. The output will be proportional to the charge in the ring on each revolution. This will be sampled and held for acquisition at the revolution frequency by an ADC. A second current transformer optimized for high frequency response will monitor the bunch current. Transformers are commercially available which will provide nano-second rise time with low droop over the 550 nsec bunch length, and will tolerate the high peak current. [5] The fast transformer signal will be processed by a gain switching amplifier and acquired by a dedicated channel of a very fast ADC (1 GSa/s).

4 BEAM IN GAP (BIG) MONITOR

Any beam present in the gap (out of the RF bucket) will be driven across the extraction magnet at the end of the cycle, representing a potentially large loss. This beam may have been a residual of poor chopping, or due to longitudinal dynamics in the Linac or Ring. Observing beam next to a 4 order-larger bunch is very difficult. It is unlikely that a BCM will be able to do this although the possibility of making a coarse measurement is being studied. This would utilize a transformer similar to the ring BCM but with overshoot <0.1% after 100 nsec. Compromise of rise time and droop would be required to meet this specification.

A second approach would measure the gap beam and also clean the gap, which would be important in meeting the loss specification. The gap beam would be kicked into a collimator where it would be observed with a gated FBLM. The rise time of the kicker must be much less than the 290 nsec gap width so a full aperture kicker is not practical. However, by resonantly kicking at the vertical betatron tune over many revolutions a much smaller kick is required. The hardware might be similar to that of the RHIC Damper [6] which uses commercially available MOSFET banks to supply 5 kV, 120 A, 10 nsec rise and fall pulses to a transmission line kicker. Burst frequency is greater than 1 MHz, permitting turn-by-turn kicking. Power dissipation limits the kicks to about 100 per msec at 60 Hz. The 5m straight section downstream of the extraction Lambertson magnet is available for the BIG kickers. For a 5m kicker and the above pulser, each kick gives about a half milliradian deflection, so the beam would hit the collimator in about 25 turns, fast enough at normal tune spread and machine chromaticity conditions.

5 BEAM POSITION MONITORS

Design goals for beam position monitor (BPM) system are shown in Table 1.

Table 1. BPM Design Goals

Parameter	Value
Lowest intensity	5×10^{10} protons
Highest intensity	2×10^{14} protons
Range of measurement	± 20 mm
Accuracy	± 1 mm
Stability of filtered orbit – long term	± 1 mm
Stability of filtered orbit – short term	± 0.15 mm
Resolution of filtered orbit	0.15 mm rms
Period of filtered orbit	100 turns
Resolution of turn by turn position – low intensity	1 mm rms
Depth of turn by turn buffer	>50 turns

For robust operation with the changing bunch shape, measurements should rely on signals at the fundamental and the lowest harmonics of the revolution frequency. The 402.5 MHz linac microstructure will be present only on the most recently injected bunches. Additional receivers could be added to a few channels to observe the injected beam in the presence of circulating charge, allowing parameters such as the space charge tune shift to be measured. A dual plane, shorted stripline electrode will be located at each of the 48 quadrupoles. The typical aperture at these locations is 200 mm. With a 250 mm length, the striplines will provide a signal that is sufficient at low intensity, yet not excessive at high intensity. They will also provide reasonable coupling to the 402.5 MHz linac bunching frequency and its next harmonic. Since the main quads trim windings are powered in families, beam based alignment is not practical, so the required position accuracy will be obtained by an initial calibration of the electrode alignment and on-line calibration for the electronics. The initial calibration could utilize the surveyed antenna technique developed for RHIC [7] while the online calibration could utilize signal injection into the orthogonal plane.

The signals from the electrodes will be carried on coaxial

cables to centrally located electronics. Low frequency noise will be rejected by high-pass filters with a corner frequency of a few hundred kHz. For measurement of the circulating beam, the passband of the electronics will extend to a few MHz and the signal will be digitized with at least 12 bit resolution well above the Nyquist frequency. The common mode dynamic range of over 60 dB will be handled by log amplifiers or by programmable gain amplifiers. Preliminary analysis has shown that this simple approach can meet the design goals. With a design that places high-speed digitizers early in the signal processing chain, the resulting data rates will be a concern. If the digitizer system contained onboard digital filtering, the data rate across VME could be significantly reduced. Turn by turn data would be delivered at a sustained rate of about 145 kbytes/s/digitizer and averaged orbit data would be delivered at 1.4 kbytes/s/digitizer. The local Controls processor will calculate position and apply corrections before delivering data to the console level applications.

6 DAMPER/TUNE MONITOR

While specific requirements for a damper have not been established, a 2 m section of beam pipe has been reserved for a tune meter/damper. A system similar to that in the AGS [8] will be installed. Signals from the BPMs will be used. The average orbit at the kicker will be subtracted to determine the bunch error and the required kick amplitude obtained from a look-up-table. The kick is delayed using a FIFO and applied to the bunch on a later turn. The digital acquisition and processing electronics for each beam position monitor has sufficient memory to store the position for the entire cycle. A spectral analysis of this data will be used to find the integer and fractional tune.

7 BEAM PROFILE MONITOR

The high beam current density in the ring makes the use of an ionization profile monitor (IPM) very attractive. An IPM measures the spatial distribution of ions or electrons freed by ionizing collisions of the beam with residual gas in the vacuum chamber. Similar devices in the past have collected ions but have suffered from space charge defocusing by high intensity beams. This problem can be reduced by collecting the electrons and embedding the device in a stabilizing magnetic field. The electrons will be swept from the beam pipe by a transverse electric field, amplified by an 8x10cm microchannel plate (MCP), and collected by a circuit board with strip anodes oriented parallel to the beam axis. A magnetic field, parallel to the sweep electric field, counters the defocusing effects of space charge and recoil momentum. For the 2 MW beam the maximum space-charge field will be about 10^5 V/m. In a magnetic field of 0.1 T, an electron subject to this field will travel parallel to the collector channels at 10^6 m/s with a gyration radius of 70 μ m. Profile broadening by the

space-charge field will be insignificant. An electric field of 150kV/m will remove electrons in under 10ns producing a maximum longitudinal drift of less than 1.0cm. The energy spectrum of recoil electrons extends to 3.0 MeV but over 95% will have energies <500 eV. The 0.1T field will confine a 500 eV electron to a Larmor radius of <0.8 mm which is 2% of the beam radius. For a field ≥ 0.1 T most of the electrons will be collected on the anodes over which they are formed. Three permanent magnet dipoles will be used to provide electron confinement without perturbing the beam orbit.

The 120 π mm-mrad full-beam (5σ) emittance (2 MW) gives a beam diameter at $\beta=10$ m of 35mm. The transverse profile is approximately rectangular due to the smoke-ring distribution in phase space. Collimators in the Ring restrict the 5σ emittance to 180 π mm-mrad and a maximum diameter of 84mm. The collector board will have 64 anodes 1.4mm wide and 74mm long, covering a width of 90mm. The full beam will produce signals in 50 channels. At 5×10^{-9} Torr, 2×10^{14} protons will produce 3.7×10^4 electrons (about 740 per channel). An MCP operated at a gain of 10^4 will deliver a current of 2 μ A to each channel, but to improve statistics in the tails the signals must be integrated over a number of turns. For beam studies early in the cycle the pressure will be raised locally and integration over more revolutions will be required.

8 REFERENCES

- [1] J. Alonso, et al, "The Spallation Neutron Source Project", These proceedings.
- [2] R. E. Shafer, et al., "The Tevatron Beam Position and Beam Loss Monitoring Systems", Proc. 12th Intl. Conf. On. H. E. Accel., p609 (1983)
- [3] T. J. Shea and R. L. Witkover, "RHIC Instrumentation", Proc. Beam Instr. Workshop, p145 (1998) AIP Conf. Proc. 451
- [4] M. Awschalom, et al., "An Inexpensive Loss Monitor for Use at NAL", FNAL Tech Rpt TM-274 Oct 1970
- [5] FCT manufactured by Bergoz, 01170 Crozet, France
- [6] Drees, A. et.al., "ARTUS: A Rhic Tune monitor System", RHIC/AP/98-156 (1998). (available at http://www.rhichome.bnl.gov/AP/ap_notes/index.html)
- [7] P. R. Cameron, et al., RHIC Beam Position Monitor Characterization", Proc. 1995 PAC p2458 (1995) IEEE Cat. No. 95CH35843
- [8] Smith, G. A., Castillo, V., Roser, T., Van Asselt, W., Witkover, R., Wong, V., "Digital Transverse Damper for the Brookhaven AGS," Proc. 1995 PAC p 2678 (1995) IEEE Cat. No. 95CH35843

DIGITAL RECEIVERS OFFER NEW SOLUTIONS FOR BEAM INSTRUMENTATION

R. Ursic, Instrumentation Technologies, Srebrnicev Trg 4a, 5250 Solkan, Slovenia
R. De Monte, Sincrotrone Trieste

Abstract

Digital receivers revolutionize today's telecommunication industry. In this article we examine the features, the applications and the opportunities of this new and promising technology from the beam instrumentation point of view.

1 INTRODUCTION

Since the invention of the superheterodyne receiver, radio architecture has remained remarkably unchanged. While it is true that development has not stood still - increasing integration, ever more sophisticated devices, and the use of digital circuitry to implement baseband functions are just some examples of technological advancements - it is also true, that none of these developments can be said to have revolutionized the original concept. It seems however, that such a revolution may already be in progress, in the guise of the so-called digital receivers or software radio. The purpose of a digital receiver is similar to that of his analog counterpart: to downconvert, filter and recover any analog signal, such as those signals with amplitude, frequency or any other kind of modulation. Its main advantage lies in its programmability which means that new functions, features and upgrades to the system do not necessitate hardware re-design, but rather the writing and loading of software code.

There are clearly many advantages of using digital receivers in telecommunications. The economy of scale of such a huge market and the unrelenting search for the holy grail of all things cheaper, faster and more versatile, make digital receivers also an attractive option for particle accelerator beam instrumentation.

2 THE DIGITAL RECEIVER CONCEPT

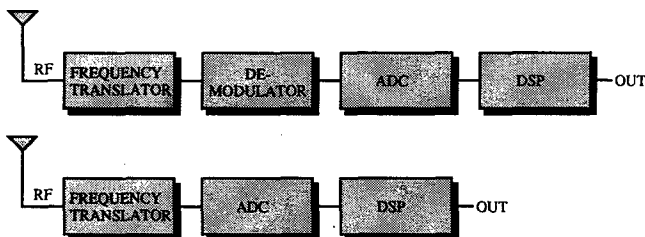


Figure 1: Block diagram of the analog (top) and the digital receiver (bottom) counterparts.

3 TECHNOLOGY DRIVERS

3.1 Analog to Digital Converter

Some of the key parameters in the specification of an analog-to-digital converter (ADC) for intermediate frequency (IF) digitization are: sampling rate, bandwidth, signal-to-noise ratio, and dynamic range. Much research and development is being carried out on faster ADCs, with wider bandwidths and larger dynamic ranges. Companies such as Harris Semiconductor and Analog Devices are producing the current state-of-the-art devices. An example of a low cost state of the art ADC for digital receiver applications is the AD9042 from Analog Devices. It is a 12 bit ADC, has 41 MHz maximum sampling rate and 100 MHz analog bandwidth.

3.2 Digital Signal Processing

With the wideband IF signal successfully digitized, at a reasonable sample rate, the next stage is the processing. It would be convenient at this point to simply transfer the digital data to one or more digital signal processor (DSP) chips, and implement all remaining functions in software. However, even a cursory look at the processing demands of digital receivers makes it apparent that this operation is not straightforward. The total processing requirements in such a receiver may add up to more than 10 GFLOPS (giga floating point operations per second). Clearly, to implement all the radio functions using DSP alone would require an impractical number of chips. The answer? A hybrid approach incorporating specialized digital hardware, a digital downconverter (DDC), which performs specific tasks (downconversion, filtering, sample-rate reduction, demodulation, amplification) to reduce considerably the load supported by the DSP.

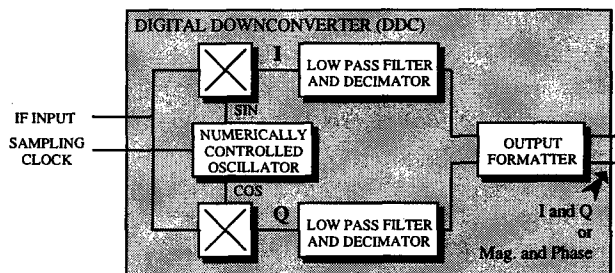


Figure 2: Functional block diagram of a DDC integrated circuit.

Companies such as Analog Devices, Graychip and Harris have developed a number of DDCs. Devices such as these are essential components of current digital receivers, and will be until DSP chips are developed that possess the

necessary horsepower to handle far higher bit rates than present technology allows.

3.3 RF Front End

The focus so far in this article has been on the digital (and analog/digital interface) hardware necessary for digital receiver implementation. However, such a receiver design also has implications for the RF front end circuitry, depending on the particular approach taken, and also depending on the particular application. In the RF front end, special filters, gain control schemes and very linear amplifiers (to provide a large dynamic range) may be required.

4. FEATURES AND PERFORMANCE OF DIGITAL RECEIVERS

In this paragraph we examine some of the features and performance of digital receivers that are of particular interest to beam instrumentation.

4.1 Linearity

Linearity of a conventional analog receiver is defined by the most nonlinear element in the processing chain, which is usually the analog demodulator. Digital receiver on the other hand implements digital demodulation, which shifts the source of non-linearity either to the RF front end or the ADC. With a careful RF front end design we can minimize non-linearity effects by driving all the active components well below the 1 dB compression point. As an example we can examine linearity characteristics of the AD9042 ADC:

Differential non-linearity ± 0.3 LSB or $\pm 7.3 \cdot 10^{-5}$ FS

Integral non-linearity ± 0.75 LSB or $\pm 1.8 \cdot 10^{-4}$ FS

A possibility to implement a simplified gain control scheme is just one of the possibilities offered by the excellent linearity of ADCs; one can easily imagine having a fixed gain RF front end for a system with a 40 dB dynamic range.

4.2 Temperature Stability

The AD9042 also offers excellent temperature stability. Its gain drift is guaranteed to -50 ppm/ $^{\circ}\text{C}$. To verify this parameter we have setup a measurement, where we applied two signals of approximately same amplitude to two AD9042 converters. The two ADCs resided on a single VME board, one on the top and the other on the bottom. The measurements were taken over a period of 16 hours, the ambient temperature changed for 5°C and the temperature of the two converters tracked each other within app. 1°C .

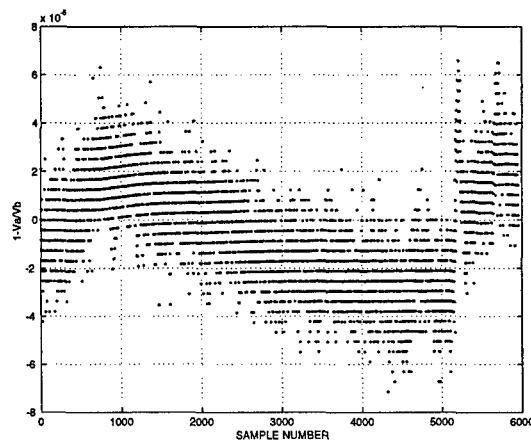


Figure 3: Deviation of the ratio between the readings from two AD9042 ADCs. V_a and V_b are readings from the two ADCs respectively.

4.3 Processing Gain

Processing gain is the improvement in the signal-to-noise ratio gained through the oversampling and digital filtering. It is the ratio of the passband to the Nyquist bandwidth expressed in dB. An important consequence of the processing gain is the effective increase in resolution. For example, if an IF signal is being sampled and digitized at 40 MHz (Nyquist bandwidth = 20 MHz) and we set the digital filter to 20 kHz the processing gain would be $-10 \times \log(0.02 \text{ MHz}/20 \text{ MHz})$ or 30 dB. In other words we gain 5 bits of resolution.

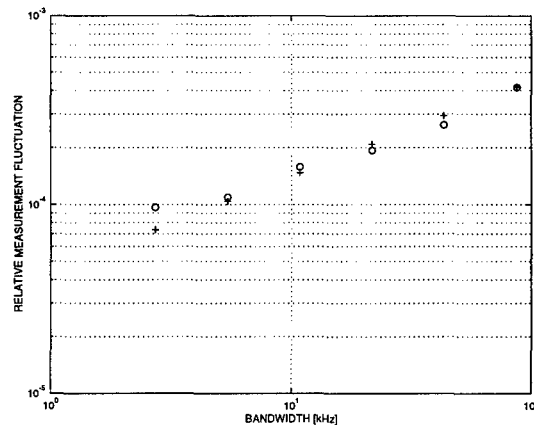


Figure 4: Processing gain shows up as decrease in measurement fluctuation. The graph shows measured (o) and predicted (+) measurement fluctuation for different bandwidth settings. The measurements were done with AD9042 ADC and GC1011 DDC from Graychip. The GC1011A is an all digital downconverter which can extract narrow band signals from wide band digitized sources.

4.4 Undersampling

Undersampling is a very attractive technique that has two important advantages. First, it drastically reduces the sample rate requirements. Second, it downconverts (aliases) a bandlimited IF signal close to the baseband.

The theory underlying the undersampling technique is that the Nyquist's theorem is met with respect to bandwidth, rather than the absolute frequency of a bandlimited IF signal. In other words sampling must occur at a rate of twice the bandwidth of the desired signal, resulting in the band of interest being aliased down to a frequency band close to dc. The result of the AD9042 undersampling performance test is shown in figure 5.

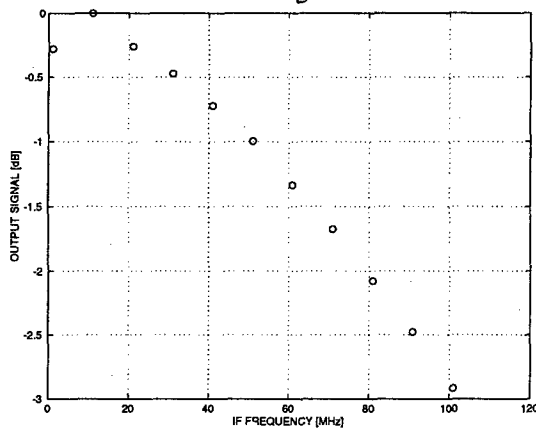


Figure 5: We cascaded an AD9042 ADC and a GC1011 DDC tuned to 1 MHz. Sampling frequency = 10 MHz. The graph above shows amplitude of the output signal for different input IF frequencies (1 MHz, 11 MHz, 21 MHz, up to 101 MHz) aliased to 1 MHz.

4.5 Multicarrier Receiver

High sampling frequencies delivered by today's state of the art ADCs allow a wide spectral input signal to be transferred to the DDC. This wide-band approach also offers a multi-channel advantage over a standard narrowband approach. The main advantage is that the RF front end does not need to be reduplicated in case we want to recover multiple carriers. We need only one DDC per channel or, in case the real time response is not required, we can use time multiplexing of a single DDC to recover multiple carriers.

5 SOME IMPLEMENTATION EXAMPLES AND OPPORTUNITIES

The new BPM system under development at the Paul Scherrer Institute for the Swiss Light Source implements digital receivers to measure the amplitude of individual pick-up button signals [1]. The digital receiver is built around Harris HSP50214 DDC integrated circuit interfacing to Analog Devices SHARC DSP. Set to low-bandwidth (10 kHz), the system offers high stability, accuracy and resolution. Set to wide-bandwidth (600 kHz), the system supports turn-by-turn and tune measurements.

An other opportunity for digital receiver technology are lock-in amplifiers. They are used to detect and measure very small AC signals up to approximately 100 kHz. They use a technique known as phase-sensitive detection to single out the component of the signal at a specific reference frequency and phase. Digital lock-in amplifiers,

which internal architecture resembles that of a digital receiver, have been successfully used for beam diagnostics in the past [2], [3]. Digital receivers based on fast ADCs and DDC integrated circuits look as a promising technology for building new generation lock-in amplifiers with wide frequency range spanning couple of tens of MHz.

The technique of controlling the in-phase (I) and the quadrature (Q) components is gaining in popularity with respect to standard amplitude (A) and phase (F) control loop approach in the field of low level RF control. Stability, excellent phase detection performance and programmability make digital receiver a promising technology for this application too.

6. CONCLUSION

Digital receivers are an exciting new technology that paves the ground for the development of new and innovative low-cost and high-performance beam instrumentation systems. The digital receiver building blocks are primarily designed for and used in the telecommunication industry. However, the few features and tests presented in this paper demonstrate that such components offer excellent building blocks for beam instrumentation devices. An other advantage that we can capitalize on is the economy of scale in the telecommunication industry that continuously pushes the prices down.

7 REFERENCES

- [1] M. Dehler et.al, " SLS Storage Ring BPM System", paper presented at this conference
- [2] B. Podobedov and R. Siemann, "New apparatus for precise synchronous phase shift measurements in storage rings", Physical review special topics - accelerators and beams, Volume 1, 072801
- [3] Rok Ursic et.al, "1 nA Beam Position monitoring system", Proceedings of the 1997 Particle Accelerator Conference, Vancouver, Canada

NUCLOTRON BEAM DIAGNOSTICS

V. Andreev, V. Gorchenko, A. Govorov, A. Kirichenko, A. Kovalenko, I. Kulikov, V. Mikhailov,
V. Monchinsky, S. Romanov, B. Sveshnikov, A. Tsarenkov, B. Vasilishin, M. Voevodin,
V. Volkov[#], JINR, Dubna, Russia

Abstract

The superconducting synchrotron Nuclotron [1] was put into operation in March 1993 at the Laboratory of High Energies, JINR in Dubna. The Nuclotron Control System (NCS) [2] provided an efficient support for the machine operation during all runs. The dedicated NCS subsystem for beam diagnostics in the injection transfer line and the Nuclotron ring is described.

1 INTRODUCTION

The Nuclotron is intended to accelerate nuclei and multicharged ions up to an energy of 6 GeV/u for the charge-to-mass ratio $q/A=0.5$. There are 96 dipole, 64 quadrupole, 32 correcting multipole SC-magnets in the Nuclotron magnetic ring with a circumference of 251.1m. The maximum value of the magnetic field is about 2T.

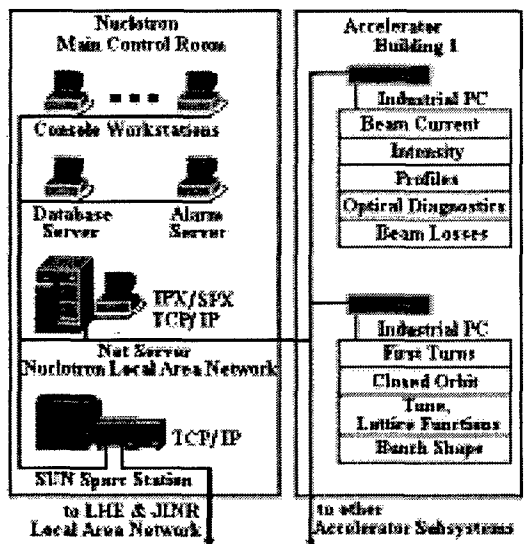


Figure 1: Fragment of the NCS structure.

The NCS consists of two physical levels: an Operator Control Level and a Front End Level. The first one supplies all appropriate man-machine tools for operators to run the accelerator. High performance workstations and server computers are used at this level.

[#] Email: volkov@sunhe.jinr.ru

The workstations act as operator consoles, while the servers provide a communication process, data storage, printing utilities, a common database, alarm service, a program library, and data exchange between the Nuclotron and the users. The Front End Level comprises both industrial PCs and intelligent CAMAC crate-controllers with embedded micro-PCs. The NCS is a distributed system. Its subsystems are geographically separated by as much as 500 m. The common backbone of the system is an Ethernet Local Area Network.

The beam diagnostics subsystem integrated into the NCS (Fig. 1) has been operating successfully since the beginning of the Nuclotron commissioning. The subsystem is based on the industrial rack-mountable PCs from ADVANTECH equipped with I/O and communication boards.

2 INJECTED BEAM TRANSFER LINE

The injector (Alvarez type linac) accelerates ions with a charge-to-mass ratio of $0.28 < q/A < 0.5$ up to 5 MeV/u and protons up to 20 MeV/u. The injected beam transfer line 30 m long includes 2 bending magnets, 12 quadrupole lenses, and 12 correctors. The equipment of single-turn injection comprises a superconducting septum magnet and kick electric plates. The injected beam pulse duration ($q/A=0.5$) is 8 μ s.

Several types of detectors are used for beam diagnostics: 2 Faraday cups, 1 multi-wire beam current monitor, 2 multi-wire profilometers, 2 destructive fluorescent screen monitors, and 1 screen monitor of 95% transparency. These instruments make beam parameter measurements available over a wide range of intensities.

The Faraday cups of 10^6 charge/pulse sensitivity are used for beam intensity measurements. The IN/OUT movements are remote-controlled by means of DC motor actuators.

The beam profile monitor consists of X- and Y-wire planes. Each plane assembled on a movable frame has 32 golden tungsten wires 0.1 mm in diameter separated by 2 mm. The charge-to-voltage converters (CV1...CV32, see Fig. 2) with adjustable sensitivity, sample-and-hold amplifiers (S/H1...S/H32) and a multiplexer (MPX) are placed close by the detector. A timer/synchronizer (T/S), a 40 kHz buffered ADC of a 10-bit resolution and a multiplying scaling DAC (MDAC) are arranged in the processing center at a distance of 50 m. The external

trigger is provided with the machine timing system, and it is the same pulse which is driving the injection elements. The sensitivity of the profilometer is about 10^8 charges/pulse.

The monitor used to measure the shape and duration of the injected beam pulse has one plane with 32 golden tungsten wires 0.05 mm in diameter separated by 2 mm and connected in parallel. A fast 50 MHz buffered ADC of a 8-bit resolution is used for beam pulse signal digitizing. The measured data together with the parameters of the septum magnet and kick electric plates (Fig. 4) are presented to the operator to tune the injection.

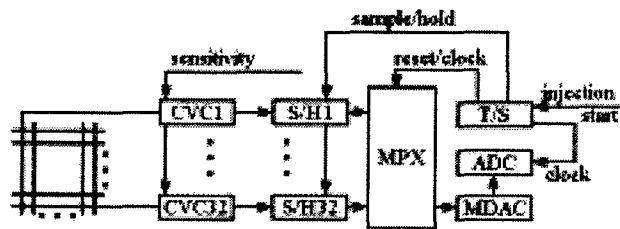


Figure 2: Profilometer block diagram.

The screen monitor of 95% transparency (wire grid assembly) is made of horizontal and vertical tungsten wires 0.1 mm in diameter separated by 5 mm with luminophor beads in the grid junctions. The observation station is equipped with an image amplifier and a photomultiplier to register a low intensity beam current, the profile and shape of the beam pulse.

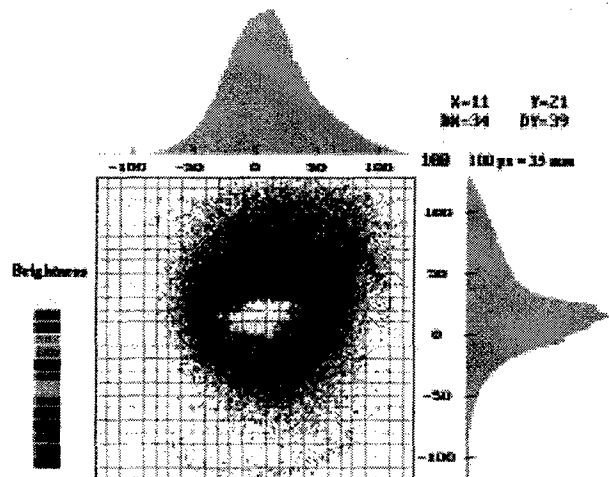


Figure 3: Beam image with X- and Y- profiles.

The image processing technique based on fluorescent screens, CCD cameras, and frame-grabbers ensures the following possibilities: screen selection and setting inside the beam, video tuning, background subtraction, pseudo-colour for displays, the ability to save and restore specific images, snapshot and live mode selection (Fig. 3).

3 NUCLOTRON RING

2.1 General

The Nuclotron ring diagnostics equipment is composed of 5 multi-wire profilometers, 20 electrostatic position pick-ups, 1 electrostatic intensity pick-up, 2 beam current transformers, 4 screen monitors, and 4 Faraday cups.

The ring profilometers have the same construction and parameters as described above. Two of the five profilometers are placed at the entrance and exit of the inflector magnet. The profilometers located at the end of the transfer line, at the inflector magnet entrance, and in the accelerator ring straight section permit one to measure the injected beam emittance and to adjust more exactly injected beam matching to the ring lattice.

The localization of beam losses around the accelerator ring facilitates machine tuning. Therefore, mounting beam loss monitors and developing data acquisition electronics are planned.

2.2 Intensity Monitors

The intensity and shape of the bunches (Fig. 4) are measured with a special-purpose electrostatic pick-up. The corresponding amplifier has a bandwidth of 30 MHz and a controllable gain within a range of 60 dB. The base line restorer insures the specified output level between bunch signals. This device covers a beam intensity from 10^9 to 10^{12} charges per pulse. The average beam intensity signal is digitized with a 12-bit ADC after analog processing.

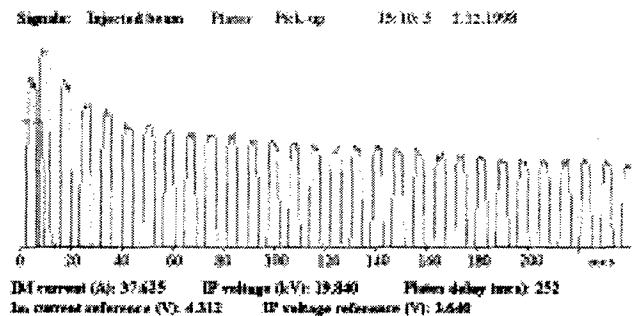


Figure 4: Example of the bunch intensity and shape measurement during first turns (RF off).

Additional opportunities for beam diagnostics are maintained by beam current transformers. To observe the longitudinal profile of the bunched beam, a fast current transformer (a frequency band of 50 kHz...10 MHz) is used. The transformer toroid core is made of thin (0.02 mm) high permeability alloy tape with an amorphous structure. There are one sense 30-turn winding connected to the amplifier and one 1-turn test winding allowing a calibration signal to be fed in. The measured beam current ranges from 0.1 to 10 mA.

The DC current transformer is employed for circulating beam average current measurements. It consists of 2 cores with 2 exciting, 1 measuring, and 1 calibration windings. The exciting frequency of the modulator is 25 kHz. A filter together with a demodulator and an integrator is used for signal second-harmonic selection and its conversion into a DC voltage. The sensitivity of the device is 200 V/A, and the frequency band is 0...60 kHz.

2.3 Beam Position Monitors

20 BPM electrostatic pick-ups in the form of diagonally cut 66(H)×132(W)×110(L) mm boxes are arranged in the Nuclotron ring for non-destructive measurements of the beam position along the machine. The BPM front end amplifiers are placed close by the pick-ups but outside the vacuum chamber and have a room temperature. The processing electronics are located in the centre of the ring so that the longest cable segment is smaller than 50 m. This allows us to have a precise signal matching and negligible attenuation with relatively inexpensive cable. The main purpose of the BPM hardware and software is to provide accurate information for the correction of orbit errors. Some results obtained with the BPM system are presented in Fig. 5. The dashed line is the original closed horizontal orbit without correction at the field of injection. The solid line is drawn after correction.

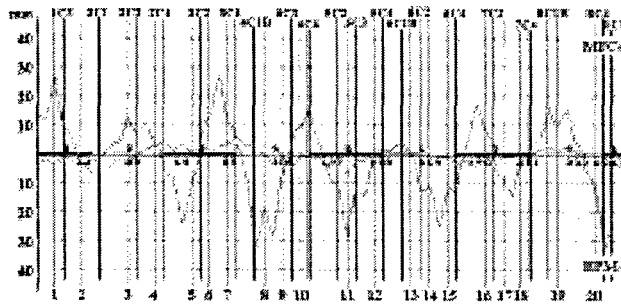


Figure 5: X-closed orbit before and after correction.

At present, we are redesigning the BPM electronics and post-processing software to extend functionality and to improve processing speed, dynamic range, and resolution. In accordance with specification, the BPM system has to function in a first turn (turns) mode and in a closed orbit mode. A substantial hardware upgrade enables one to acquire beam signals with turn-by-turn and bunch-by-bunch capabilities.

The distinguishing features of the new BPM system are outlined in Fig. 6. Each position monitor electrode has a 30 MHz amplifier with an adjustable gain of 46 dB for use with high and low intensity beams. A gain control loop keeps a maximum signal level to improve the signal-to-noise ratio. For cost reasons, the amplifier has one pair (X or Z) of remotely selected output signals.

The beam revolution frequency (f_{rev}) ranges from 125 kHz to 1.2 MHz. The accelerating frequency harmonic number is 5. The timer/synchronizer uses a B-train with a 0.1 Gs resolution and $f_{RF}=5f_{rev}$ as an external clock to synchronize with the main magnetic field and bunch signal. An ADC1...ADC40 sample rate of 50 MS/s ensures the required signal resolution over the band up to 500 kHz. A simultaneous sampling of all the BPM-stations with a 64 KB record length permits acquiring several hundred successive closed orbits. Waveform digitizers (DSO-2125 from CyberResearch) with a 256 KB onboard memory and a time-bin duration of 4 ns allow more than 1000 turns to be acquired under combined parallel/sequential sampling.

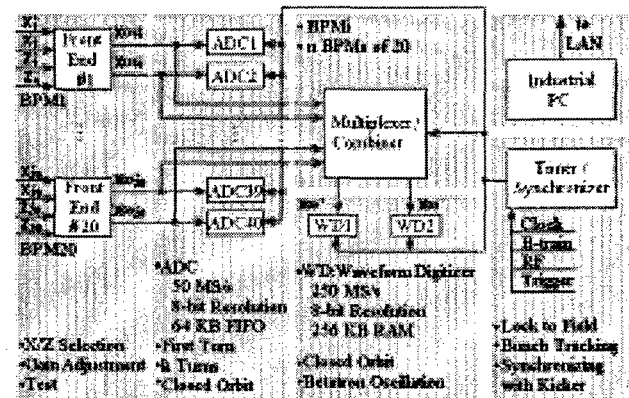


Figure 6: Structural model of BPM hardware.

The analysis of the acquired data is a very powerful tool to provide a reliable measurement of the tunes and lattice parameters of the real machine, such as beta values, or a phase advance between BPMs.

4 CONCLUSION

The beam diagnostics subsystem has been successfully used in all Nuclotron runs. It ensures reliable operating conditions for different operating modes of the accelerator. Several modifications are still under way in order to improve the beam diagnostics functionality. New information provided with the subsystem will be a significant aid to optimize the machine.

5 ACKNOWLEDGEMENTS

We would like to thank our colleagues who have contributed to the Nuclotron beam diagnostics development. The authors are grateful to L. Sveshnikova for her help in preparing this paper.

6 REFERENCES

- [1] A. D. Kovalenko, "Status of the Nuclotron", EPAC'94, London, (1994)
- [2] V. Andreev et al, "Nuclotron Control System", PAC'97 Vancouver, (1997)

Author Index

- Abe, Hiroshi 2015, 2749
 Aberle, Oliver 949
 Abo-Bakr, Michael 2385
 Acharya, R. 1393
 Adachi, Toshikazu 2271, 3348, 3752
 Adamenko, Stanislav V. 3269, 3271
 Adams, D.J. 2199
 Adderley, P. 1991
 Adolphsen, Christopher D. 253, 777, 3411, 3423, 3477
 Afonin, A.G. 53
 Agafonov, Alexey V. 1731, 1734
 Agematsu, Takashi 2259
 Ahle, Larry 1937, 3248
 Ahn, Hyo-Eun 875, 1255
 Ahrens, Leif A. 614, 1276, 1746, 2063, 2286, 2918, 3291, 3294
 Akagi, Hirofumi 3749
 Akai, Kazunori 440, 1132, 2731
 Akaoka, Nobuo 3546
 Akasaka, Nobumasa 1132, 2238, 2731, 3411
 Akemoto, Mitsuo 3414
 Akiyama, Atsuyoshi 343, 3158
 Akre, Ronald A. 2846
 Alai Tafti, A. 2722
 Alba, Rosa 2578
 Aleksandrov, A. 237, 3321
 Aleksandrov, Aleksander V. 78, 2948
 Aleksandrov, Vladimir S. 3501
 Alekseev, Nicolay N. 1479
 Aleshaev, Alexander N. 750
 Alessi, James G. 106, 614, 1297, 1902, 1964, 3300
 Alexahin, Yuri 1527
 Alford, Owen J. 2590, 3251
 Alimov, Andrey S. 2301, 2555
 Alonso, Jose 574
 Alton, Gerald D. 1878, 1881
 Alton, William J. 845
 Altuna, Xavier 2617
 Amano, Daizo 2403, 2689
 Amatuni, Andrey Ts. 3657, 3660
 Ambrosio, G. 174
 Ames, Friedhelm 1955
 Anderegg, Jim 1402
 Anders, W. 197, 2385
 Anderson, David E. 3390
 Anderson, Edwin B. 1686
 Anderson, James L. 571
 Anderson, Oscar 1908, 1937
 Anderson, Scott 217, 2006, 2039, 2042, 2045
 Andersson, Ake 2945
 Andreev, N. 174, 3194, 3197
 Andreev, Nikolai 154
 Andreev, V.A. 2256
 Andrianov, Serge N. 1866, 2701
 Anerella, Michael D. 185, 3161, 3170
 Anferov, Vladimir A. 392
 Anguelov, Vladimir 2289
 Anthouard, Philippe 3260
 Antoine, Claire 919
 Antonello, M. 1324
 Antonsen Jr., Thomas M. 360
 Aoki, Yasushi 2018, 2036
 Apel, Ruediger 812, 818
 Arakawa, Dai 1141, 1653, 1821
 Arakawa, Kazuo 2259
 Araki, Sakae 343
 Arapov, L. 237
 Arcan, T. 174, 3197
 Archambault, L. 325, 3705
 Arduini, Gianluigi 1282, 1285, 2617, 2996
 Argan, Andrea 1599
 Arimatea, Claudio 2617
 Arkan, T. 3194
 Arkan, Tug T. 3242
 Arnett, Don 1390
 Arnold, Ned D. 2024
 Aronson, A. 548
 Artoos, Kurt 154
 Arutunian, Suren G. 1468, 2105, 3657
 Arvin, Adrian H. 1444, 1447, 1929, 1946
 Arvin, Andy 349
 Asaka, Takao 2015, 2749, 3507
 Asano, K. 777, 3417, 3423
 Asaoka, Seiji 667, 670
 Aspenleiter, Jeffrey 1390, 2698
 Assadi, Saeed 711, 720, 1082, 1085, 2719
 Assmann, Ralph 330, 2996, 2999, 3002
 Aston, David 2990
 Atencio, Samuel J. 965
 Aune, Bernard 432
 Autin, Bruno 3071
 Autrey, Daryl 3248
 Avilov, Alexandr M. 2549
 Ayers, James J. 1961
 Baartman, Richard A. 128, 3534, 3537
 Babayan, Ruben A. 2424
 Baboi, N. 922
 Babzien, Marcus 2024, 2158, 2471, 2480, 3722
 Bach, H. 2427
 Backe, H. 165
 Badan, L. 1324
 Badea, V. 3767
 Bae, Young-Soon 3525
 Bai, Mei 387, 471, 2725, 3336
 Bailey, Roger 2617, 2996
 Bak, J. S. 1384
 Bak, Peter A. 2167
 Bakker, Rene J. 197, 726, 2078, 2379, 2382
 Baklakov, Boris 1387
 Balakin, Vladimir 461
 Balbekov, Valeri I. 315, 3062, 3146
 Baldis, Hector A. 2000
 Ball, M. 498, 1545, 1548
 Ball, Millicent J. 3245
 Ballarino, Amalia 1405
 Balleyguier, Pascal P. 1444, 1447, 1946
 Baltadoros, D. 1037
 Bane, Karl F. 3432, 3486
 Bane, Karl L.F. 1725, 1728, 2822, 3423, 3453, 3474, 3477
 Bangerter, Roger O. 3215
 Banks, Thomas I. 1686
 Banna, S. 3600, 3606, 3609
 Bannon, M. 3767
 Baptiste, Ken 1471, 3131
 Baranauskas, V. 2811
 Barber, D. P. 2635
 Bardy, Jacques 3260
 Barklow, Timothy L. 307, 3489
 Barlow, D. 3576
 Barnard, John J. 1761, 1803, 1830, 3248
 Barnes, C. 321
 Barnes, Michael J. 1509, 3378
 Barnes, Peter D. 2590
 Barnes, Phil 980
 Barnett, Ian 3743
 Barone Tonghi, L. 2578
 Barov, N. 2027
 Barr, Dean S. 2214, 2241
 Barraza, Juan 2090
 Barry, Walter C. 636, 1207
 Barsotti, E.L. 2146, 2211
 Bartolini, R. 1557
 Barzi, E. 174, 3330
 Bassalleck, B. 471
 Batchelor, Kenneth 75
 Batsikh, Gennady I. 2564
 Battle, Chris 2936
 Batygin, Yuri K. 1737, 1740
 Bauda, B. 197
 Bauer, P. 3194
 Baumann, C. A. 2659
 Bayanov, Boris F. 3086
 Bazhan, Anatoli 461
 Bazzani, Armando 1773
 Bechstedt, Ulf 1701, 2292
 Bechtold, Alexander 530
 Beck, David 1937, 2849
 Beck, U. 206
 Becker, R. 1899
 Becker, T. 197
 Becker, Ulrich 2951
 Beczek, Kevin J. 1378
 Beebe, E. 1902
 Beebe-Wang, Joanne J. 1743, 2843, 3143, 3185
 Beetham, C. Gary 765
 Behne, Dan 1333
 Beinbauer, Wolfgang 1647
 Bellavia, S. 1902
 Bellomo, Giovanni 1776
 Bellomo, Paul 206, 3429
 Belomestnykh, Sergey A. 272, 980, 1112
 Belousov, Ilja V. 750
 Belov, Victor P. 3086
 Ben-Zvi, Ilan 75, 2018, 2158, 2471, 2480, 2552, 3495, 3722
 Benabed, Karim 2990
 Benjamin, John 2277
 Benjegerdes, R. 3233
 Benson, S.V. 212, 2456
 Bent, Bruce 931
 Berg, Georg P. A. 2519
 Berg, J. Scott 3152
 Berg, Jeff 1333
 Berg, William J. 2024, 2134
 Berger, Christoph 2172
 Bergstrom, Paul M. 1827
 Bernal, Santiago 234, 1749, 1758, 1970, 2102, 3372
 Bernard, Michel 922
 Bertolini, Louis R. 2477, 3251
 Besnier, Gilbert 1192, 1195
 Besson, Jean-Claude 1569, 2686

- Bharadwaj, Vinod K. 3429, 3447, 3450
 Bhat, Chandra M. 114, 717, 3155
 Bhatia, Tarlochan S. 3585
 Biagini, Maria E. 1536
 Biallas, George 2456, 3306, 3312
 Bibber, Karl V. 2480
 Bickley, Matthew H. 732, 735, 741
 Biedron, Sandra G. 2024, 2471, 2483, 2486, 2945
 Bieler, Michael 554
 Bielicki, J. 1249
 Bieniosek, F. M. 1249, 1937
 Bienvenu, Gerard 913
 Billen, James H. 3570, 3585
 Billen, Ronald 2617
 Billing, Michael G. 410, 1112, 1115, 2975, 2978, 3221, 3501
 Birke, Thomas 197, 726, 2382
 Birx, D. 3257
 Biryukov, Valery M. 53, 1234, 1237, 1240, 3050
 Biscari, Caterina 131, 1536
 Bish, P. 3233
 Bishoffberger, Kip 2006
 Bisoffi, Giovanni 1324
 Blank, M. 1016
 Blas, Alfred 143
 Blasche, K. 527, 1704, 1788
 Blaskiewicz, Michael M. 109, 614, 857, 1611, 2280, 3185
 Blazhevich, Sergey V. 2584
 Blind, B. 611, 3582
 Blinov, Boris B. 392
 Bliss, Neil 2656
 Blokland, Wim 1085, 2211
 Blondel, Alain 2999
 Blosser, H. 1318
 Bluem, Hans 3570
 Blum, Eric B. 2304
 Bocchetta, Carlo J. 2060, 2313
 Boege, Michael 1129, 1542, 2430
 Boehnke, Michael 851
 Bogacz, S. Alex 738, 2897
 Bogart, S. Locke 603
 Bogdanovitch, Boris Yu. 1291, 1932, 2570, 2573
 Boggia, Antonio 1905
 Bogomolov, Guenrikh. D. 592
 Bohl, Thomas 2617
 Bohlen, Heinz P. 445
 Bohn, Courtlandt L. 2450, 2456
 Bohne, D. 2513
 Boine-Frankenheim, B. 1788
 Boine-Frankenheim, O. 1785
 Boisvert, Veronique 2217
 Boivinnet, Raynald 3260
 Bollen, Georg 1955
 Bolme, Gerald O. 1444, 1447, 1946
 Bolotin, Igor M. 1482
 Bolshakov, Timophei 1387
 Bolt, A. Scott 349, 1444, 1447, 1929, 1946
 Bonati, R. 3767
 Bondarev, Boris I. 1764, 2808
 Bongardt, Klaus 1767
 Bongers, Henning 3516
 Boni, Roberto 866
 Bonnafond, Christophe 1381, 3260
 Bonthond, J. 1228
 Booch, Rex 1506
 Bopp, Markus 795
 Borak, Thomas 2990
 Borburgh, Jan C. 2283
 Bordry, Frederick 3203, 3740
 Boriskin, V.N. 753
 Borland, Michael D. 200, 1587, 1644, 1979, 2319, 2939
 Borne, Jean-Luc 919
 Borodich, Andrei, I. 1869, 1872
 Borovina, Dan L. 786, 2772
 Borunov, Ivan E. 750
 Bosch, Robert A. 2388, 2394, 2397, 2659
 Boscolo, Ilario 1982, 1985
 Boscolo, M. 1536
 Bossart, R. 250
 Bossier, Jacques 465
 Bossert, R. 3194, 3197
 Botman, J.I.M. 759, 1539, 2825, 2864, 3266
 Bottura, Luca 154, 3179
 Boucham, Abdel 2990
 Bourdon, Jean-Claude 2012
 Bourque, Robert F. 2954
 Boussard, Daniel 946, 949
 Bousson, Sebastien 919
 Boutigny, D. 2990
 Bovet, Claude 465
 Bowden, Gordon B. 206, 824, 1390, 3423, 3426
 Bower, Gary 307
 Bowles, Edward 3755
 Bowling, Bruce A. 732
 Bowman, Jim 1333
 Boyce, Richard M. 206, 1363
 Boyd, John K. 3513
 Brabson, B. 1548
 Bracco, Roberto 2680
 Bradley III, Joseph T. 1010
 Bradshaw, David J. 2656
 Braeutigam, Werner 957, 959, 3549
 Brandt, Daniel 304, 3005
 Brandt, J. 3194, 3197
 Braun, Hans H. 250, 3402
 Brautti, Giulio 1905
 Breese, Mark 53
 Breidenbach, Martin 3384
 Brennan, Joseph M. 614, 857, 1746, 2280
 Brennan, Michale 1258
 Bressanutti, Raffaele 1120
 Bricault, P. 100, 450, 3540
 Briggs, R. 3257
 Brinkmann, Reinhard 16
 Bromberek, David J. 3095
 Brooksby, Craig A. 625
 Brouet, Michel 562
 Brovko, Oleg I. 2262
 Browman, Andrew A. 518, 998, 2790, 3582
 Brown, Bruce C. 714, 717, 3315, 3318
 Brown, C.N. 3324
 Brown, Kevin A. 614, 1258, 1267, 1270, 2123, 2722, 2725, 2728, 2918, 3291
 Brown, Terence F. 3381
 Brown, Winthrop J. 81, 833
 Bruenger, W.H. 2575
 Bruhwiler, David L. 369
 Brumwell, Franklin R. 2274
 Brunelle, Pascale 1569, 2686
 Brunet, Jean-Claude 1330, 1339
 Bruning, Oliver 40, 2629
 Bruno, Donald 3734
 Bruns, Warner 2767
 Bryan, David A. 732, 735
 Bryant, Phil 2957
 Buckles, Robert 1303
 Budnick, J. 1545, 1548
 Buerkmann, K. 197
 Buerkmann, Klaus 2385
 Bugrov, Vladimir P. 1312
 Bulfone, Daniele 1120
 Bullard, D. 3309
 Bullard, Donald 3306
 Bultman, Nathan K. 3591, 3594
 Bulyak, Eugene V. 1770, 3122, 3269, 3271
 Bunce, G. 471
 Burgess, Edward L. 617, 3257
 Burke, D.L. 3423
 Burke, Jason 1952
 Burkhardt, Helmut 2996, 3011
 Burla, Paolo A. 762
 Burn, Kenneth W. 2531
 Burns, Michael J. 617
 Burov, Alexey V. 521, 1088, 1201, 1608, 1707, 1710
 Bushuev, Alexander A. 2033
 Busse-Grawitz, Max Erick 986
 Butenko, Andrey V. 2262
 Buth, Gernot 2424
 Butterworth, Andy 2996
 Buxton, W. 2128
 Bychenkov, Valery Yu. 3716
 Byer, Robert L. 321
 Byers, B. 2990
 Bylinsky, Yuri V. 450, 893
 Byrd, John M. 382, 495, 1207, 1806, 2370, 3131
 Cai, Y. 296
 Calabretta, Luciano 2578, 3288
 Calame, J. 1016
 Calatroni, Sergio 949
 Callin, Richard S. 783
 Cameron, Peter R. 2114, 2117, 2146, 2250, 3185
 Campbell, B. 965
 Campbell, Billy M. 971, 1327, 2954
 Campbell, Lora P. 3722
 Campbell, Richard 1515
 Campisi, Isidoro E. 937, 1177, 1180, 2456
 Cao, Jianshe 2140
 Capista, David P. 714
 Caporaso, George J. 617, 622, 625, 1204, 1303, 1824, 1827, 3254, 3381
 Carathers, Jeremy R. 1447
 Carlier, Etienne 1509
 Carlson, Charles 2277
 Carlsten, Bruce E. 477, 617
 Carneiro, Jean-Paul 992, 2027
 Carr, G. Lawrence 134
 Carr, Roger 1390, 2477, 2698
 Carrigan, R.A. 2027
 Carron, Georges 250
 Carter, Anthony 3101
 Carwardine, John A. 2093
 Cary, John R. 369, 377, 2784
 Casas-Cubillos, Juan 3203
 Casey, Jeffrey A. 568, 1491
 Caspers, Fritz 1408, 2629
 Caspi, Shlomo 174, 2793, 3194, 3197, 3233, 3236
 Cassel, Richard L. 1494, 1500, 3429
 Cassinari, Lodovico 1168, 1569
 Castellano, Michele 1985, 2193, 2196, 2695
 Castillo, Vincent 490
 Castle, Mike 1040, 1046
 Castro, Maurizio 97
 Castro, Pedro 456
 Catani, Luciano 1985, 2196
 Catravas, Palmyra 325, 330, 2111, 3705
 Caussyn, D.D. 1548
 Celata, Christine M. 1716, 1803, 1830

- Celona, Luigi 97, 2578
 Cerny III, Joseph 533
 Chae, Yong-Chul 1644, 2486
 Chai, Jongseo 2265, 3137
 Chai, Xuedong 1453
 Champion, Mark S. 992, 2027
 Chan, C. F. 1937
 Chan, K.C.D. 1327, 2954, 3582
 Chan, Kwok-Chi D. 965, 968, 971
 Chang, Cheng-Hsiang 2671
 Chang, H.P. 2409
 Chang, J. H. 2593
 Chang, Lung Hai 1159
 Chang, Peace 2837
 Chang, S. S. 2009
 Chang, S.S. 679, 2205, 2501
 Chang, Shi-Hong 1375
 Chang, Suk S. 2418
 Channell, Paul J. 1629
 Chao, Yu-Chiu 738
 Chapelle, Sonja 3758
 Chapman-Hatchett, Arthur 2202, 2223
 Chargin, Anthony (Tony) K. 2590
 Charrier, Jean-Pierre 432, 919
 Chattopadhyay, Swapan 330, 2370
 Chavanne, Joel 2662, 2665
 Cheever, Dan 3101
 Chel, Stéphane 916
 Chen Y.-J. 617
 Chen, C.S. 682, 685, 2412
 Chen, Chien-Rong 1150
 Chen, Chiping 1875, 2752
 Chen, H.H. 2671
 Chen, J. 682, 2021
 Chen, J.R. 1605, 2409, 2415
 Chen, J.S. 682, 1450
 Chen, Jenny 685, 2069, 2072, 2412, 2671
 Chen, Jie 741, 747
 Chen, June-Rong 1150, 1375
 Chen, Longkang 2184
 Chen, Pisin 224, 330, 3648
 Chen, Senyu 209
 Chen, Szu-Yuan 3666, 3716
 Chen, W. 3345
 Chen, Y. J. 1824
 Chen, Yu Ju (Judy) 617, 622, 2235, 3254, 3381
 Chen, Yu-Juan 1204, 1210, 1303, 1827, 3254, 3257, 3513
 Chen, Zukun 3591, 3594
 Cheng, Daniel W. 1911, 1914, 1958, 1961
 Cheng, Hung-Ming 1150
 Cheng, W.H. 382
 Chepegin, V.N. 53
 Chepurmov, Alexander S. 2584
 Cherbak, Ernest E. 1019
 Cherenshchikov, S. A. 1973, 1976
 Cherepakhin, A. 1249
 Cherix, Jacques 418
 Cherniakin, Alexander D. 3086
 Chernin, David P. 360
 Cherwinka, Jeffrey J. 3221
 Chesnokov, Yuri A. 53, 1237
 Chesworth, Andrew A. 2433
 Chiaveri, Enrico 946, 949
 Chichili, Deepak R. 174, 3194, 3197, 3242
 Chin, Y.H. 1058
 Chin, Paul 234, 1970, 2102, 3369, 3372
 Chin, Yongho 633, 3414
 Chines, Franco 97
 Chiou, J.P. 1450, 2009
 Chishiro, Etsuji 3546
 Chitose, Norihisa 2602
 Chiurlotto, F. 1324
 Cho, M.H. 2593
 Cho, Yong-Sub 875, 1255, 3525
 Chohan, Vinod 2202
 Choi, B. H. 206
 Choi, Byung-Ho 875, 1255, 3525
 Choi, J. 1016
 Choi, Jae-Young 2205, 2501, 2593
 Choi, Jinhyuk 2418
 Chojnacki, Eric 845, 980, 2635
 Chong, Henry 2370, 2498
 Chou, Ping-Jung 1159, 2415, 2837
 Chou, W. 565, 3285
 Chow, Ken P. 171, 3233, 3236
 Christiansen, David W. 3573
 Christina, Vincent 780, 3306
 Chu, C.M. 392, 1545, 1548, 2286
 Chu, Chunjie 1940
 Chu, W. 2537
 Chung, Kie-Hyung 2558, 2561
 Chung, Sukmin 1357
 Chupyr, Andrei 1387
 Church, Michael D. 56
 Church, Roy A. 1013
 Cianchi, Alessandro 2193, 2196
 Ciavola, Giovanni 97, 2578
 Cimabue, Anthony G. 965
 Cinabro, David 3221
 Citver, G. 1420
 Clark, George S. 3378
 Clark, J. 1991
 Clark, John C. 3513
 Clark, Robert E. 2746
 Clark, William L. 965
 Clarke, James A. 2433, 2653, 2656
 Clauser, Tarcisio 1779
 Claverie, Joseph 2686
 Clayton, Christopher E. 330, 2006, 3651, 3654, 3708
 Clendenin, James E. 1988, 3384, 3447, 3450
 Clifft, Ben E. 524
 Cline, D. B. 2552, 3639, 3722
 Codner, Gerald W. 1115, 1441, 3221, 3224
 Cola, Mark J. 962
 Colby, E. 321
 Cole, M. 780
 Cole, Michael D. 3570
 Colestock, Patrick L. 114, 2027, 2181, 3155
 Collier, Michael 3594
 Collier, Paul 2617, 2996
 Collins, Ian R. 2629
 Collins, J.C. 673, 1548
 Comins, J.D. 3257
 Comunian, Michele 1773
 Conde, Manoel E. 2030, 3621
 Conkling Jr., Charles R. 699
 Connolly, Roger C. 2114, 2117, 2250
 Cooke, Simon J. 360
 Coosemans, W. 250
 Corbett, Jeff 206, 2355, 2358, 2364
 Corlett, John N. 296, 800, 896, 1207, 3149, 3429
 Corlier, Muriel 2686
 Cornacchia, Max 267, 2480
 Cornelis, Karel 1189, 2617, 2996
 Cornelius, W. D. 1884, 1887
 Cornuelle, J. 3423
 Corredoura, Paul L. 435, 800, 3429
 Corsini, Roberto 250, 3396
 Corstens, J.M. 2864
 Counsell, Joseph 1025
 Coupal, David 2990
 Cours, Alexander 1022
 Cousin, J.M. 1569
 Coutrakon, George 11
 Cozzolino, John 185, 3230
 Craddock, Michael 2620, 2623
 Craievich, P. 1123
 Craig, George D. 1830, 3248
 Crandall, K.R. 611, 3582
 Crandell, D.A. 392
 Crawford, A.C. 521
 Crawford, Curtis 237, 3321
 Crisp, J. L. 2164
 Crisp, Jim 2146, 2211
 Crist, Charles 1303
 Crockford, Guy 2617
 Crosbie, Edwin A. 1587, 2325
 Cruikshank, Paul 1330, 3203
 Ctcherbakov, Anatoliy M. 1482
 Cullen, J.R. 1267, 1270
 Cummings, Karen A. 881, 1396
 Cundiff, Tim 2090
 Cupola, J. 2117
 Cuttone, Giacomo 2578
 Czarnaski, Mark 360
 d'Amico, Tommaso E. 250, 1638, 2202, 3399
 D'Olando, Stefano 1120
 D'Ottavio, Theodore W. 693
 D'Yachkov, Mikhail 128, 1408
 DaCosta, Tony 1333
 Dahlerup-Petersen, Knud 3200, 3203
 Dai, Jianping 1453
 Dalesio, Leo R. 349, 652, 655
 Daly, E. T. 206, 1363
 Dambach, S. 165
 Danared, Håkan 1698
 Danby, Gordon T. 3185, 3333
 Danilov, Vyacheslav V. 109, 641, 1198, 1201, 1608, 1710, 3140, 3143, 3303, 3728
 Danly, B. 1016
 Danowski, G. 3767
 Darpentigny, Jacques 1168, 1569
 Date, Shin 2346
 Dattoli, Giuseppe 1219
 Datz, Sheldon 1671
 Davidson, Ronald C. 1518, 1623, 1626, 1629, 1875
 Davis, Brent 1506
 Davis, Jerry L. 1001
 Davis, Roger 557
 Day, T. 1991
 de Hoon, Michiel J.L. 1803, 1830
 de Loos, Marieke 2462, 3266
 De Monte, R. 2253
 De Ryck, C. 3212
 De Santis, Stefano 2075, 2873
 De Wit, F.F. 759
 Debeling A. 3248
 Debiak, Ted, W. 587
 Debus, J. 2513
 Decker, Franz-Josef 307, 330, 771, 774, 1252, 1728, 2846, 2987, 3384, 3648
 Decker, Glenn A. 2051, 2093, 3092
 Decking, Winfried 1581
 Decyk, V. K. 3672
 Degasper, Francisco T. 1366
 Degtyarev, I.I. 1321
 DeHart, Terrance E. 2668

- Dehler, Micha 1129, 2087
Dehning, Bernd 2999
Dejus, Roger J. 2486, 2489, 2492
Dekin, W. D. 2590
Delahaye, J.P. 250
DeLamare, Jeffery E. 1494
Delayen, Jean R. 925, 928, 934, 937, 940, 955, 1462, 3498
Dell'Orco, D. 206, 2355
Den Hartog, P.K. 1369, 2483, 2489
Deng, Jianjun 3263
Denker, A. 3519
Denz, Reiner 3200
Derbenev, Yaroslav S. 392
Derenchuk, V. 1548
Derrick, M. 2635
Deruyter, H. 590, 3423
Deryuga, Vyacheslav A. 2546, 2549
DeSantis, Stefano 382
Desforgues, Bernard 2617
Desmons, Michel 916
Despas, Claude 2617
Despe, Oscar 3773
DeStaebler, Herbert 2990
Detweiler, Gerald 2468
DeVan, W.R. 355
Devin, André 3260
Devmal, S. 2990
DeVries, Jan 162
Dewa, Hideki 3690, 3702
Dey, Joseph E. 869
Di Bartolo, Gaetano 2578
Diaczenko, Nick 2936
Dias, Joao M. 3725
Dickson, R. 646
Dietderich, D.R. 171, 3233, 3236
Diete, W. 957
Dietrich, J., 2054
Dietrich, Jürgen 1701, 2292
Dikansky, Nikolay S. 78, 2167, 2948
Dimaggio, S. 325
DiMaggio, S. 3705
DiMarco, Joseph 3194, 3197, 3318, 3327
Ding, Bainan 3263
Ding, X 2504
Ding, X. 2003, 2021, 2039, 2042, 2045
Ding, Xiaodong 2006
Dinkel, J. 1249
Dittmann, B. 197
Diviacco, Bruno 2680
Divin, Yuri Y. 2178
Diwan, Milind V. 3023
Dix, Brendon 1390
Dobbing, Gavin S. 2433, 2653
Dobrovolski, Nikolaj M. 1468, 2105
Dohlus, Martin 1650
Dolgashev, Valery 2822
Doll, D.W. 1393
Dombsky, M. 100
Dome, George 1408
Domer, Gregory A. 649
Donald, Martin H. 296, 1584
Dong, Xiaoli 1596
Donohue, John T. 1797, 3387
Dooling, Jeffrey C. 2274
Doolittle, Lawrence R. 768, 928, 934, 937, 940, 1462
Doose, Charles L. 2024, 2093
Dormiani, M. 206
Dortweg, Robert J. 1414, 2024
Dorskow, J. 471
Doss, J. Daniel 426
Douglas, David 1177, 1180, 2456, 3306, 3312
Douryan, Adnan 2471
Dovbnya, A. 3122
Doyle, Stephen 2424
Doyuran, Adnan 2480, 2942
Drago, Alessandro 131, 636
Dragt, Alex J. 1551, 1593, 2761
Drees, K. Angelika 2117
Dressler, Olaf 1279
Drivotin, Oleg I. 1857
Drozhdin, Alexandr I. 56, 1231, 1234, 2614, 3050
Drury, Michael 931
Ducimetière, Laurent 1228, 1509
Duda, Brian J. 3669
Duerr, Volker 2385
Duffau, Michael J. 2096
Duffy, Patrick 1390, 2477
Dugan, Gerald F. 48, 2057, 2632, 3221, 3224
Duke, Jonathan P. 2208
Dunbar, Ann 1100
Dunham, B. 1991
Dupaquier, Andre 3740
Dur, V. 197
Durkin, Alexander P. 1764, 2808
Dutto, Gerardo 106, 893
Dykes, Michael D. 1025, 2096
Eardley, Matthew 1943
East, G. 1548
Ecklund, Stan D. 296, 3450
Economou, A. 1037
Edamenko, N. S. 1866
Edgell, Dana 1043, 1890
Edwards, Helen T. 992, 2027
Egawa, Kazumi 3351, 3354, 3357
Egiazarian, Suren L. 1468
Ehrlich, Richard 980
Eichhorn, Ralf 2951
Eichner, John 1512
Eickhoff, Hartmut 527, 1704, 2513
Eilerts, S. 471
Einfeld, Dieter 806, 809, 1360, 2424, 2427, 3375
Eisert, D. E. 2659
El-Shazly, M.N. 1896
Elbakian, Sergey S. 3657, 3663
Elioff, T. 206
Elleau, Pascal 2662, 2665, 3119
Elliott, T. 780
Elliott, Tim 2936
Ellis, Gretchen G. 965
Ellison, M. 1548
Elmer, John 777
Elzhov, Artem V. 3393
Emamian, Mark 221, 2468
Emery, Louis 200, 401, 1644, 2137, 2319, 2939
Emhofer, Stephan 3516
Emma, Paul 3429, 3438, 3447, 3456
Emmerling, M. 1788
Endo, Akira 2018, 2036, 2552
Endo, M. 600
Engels, Oliver 3519
Enomoto, A. 1132, 2731
Eppley, Kenneth R. 2778
Erdmann, M. 1369, 2489
Erickson, John L. 3594
Eriksson, L. 3462
Eriksson, Mikael 2945
Ermakov, Dimitry I. 2555
Erokhin, Alexander 1387
Esarey, E. 330, 2111
Esarey, Eric 325, 3696, 3699
Escallier, John 3161
Eschenko, Viktor N. 3086
Esin, Sergei K. 3561
Etzkorn, Franz-Josef 851
Evans, I. 206
Evans, Jr., Kenneth 352, 744
Evans, Lyndon R. 21
Evans, R. 2456
Eyl, Patrick 3260
Eylon, Shmuel 1934, 3248, 3390
Eyssa, Y. 3227
Ezura, Eiji 413, 440
Faatz, B. 2486
Fabris, Alessandro 809, 1120, 1123
Fagan, M.J. 1327
Fahmie, Michael P. 756
Falabella, Steve 1303
Falkenstein, F. 2078
Fallmann, W. 2575
Faltens, Andris 1503, 1830, 1937, 2849, 2852, 3215, 3339
Fan, Kuanjun 1315, 1596
Fan, Mingwu 1940
Fan, T.C. 2671
Fang, J.M. 3627
Fang, Lei 2125
Fang, Shouxian 1695
Fang, Shuyao 890
Fang, Si 3761
Fang, Zhigao 2125
Fann, C.S. 1450
Fant, Karen 1435
Farkas, Zoltan David 771, 774, 3423
Farrell, J. Paul 75
Fartoukh, Stéphane 922
Farvacque, Laurent 3119
Faugier, Andre 2617, 2996
Faulbaum, D. 197
Fawley, William M. 1204, 1210, 1934, 3254, 3257
Fedorov, Vacheslav 1479, 1485
Fedorov, Vladimir M. 1734
Fedorova, Antonina 1614, 1617, 1620, 2900, 2903, 2906, 2909, 2912
Fedotov, Alexei V. 606, 1752, 1755
Fedotov, M. G. 2167
Fedotov, Yu.S. 53
Feher, Sandor 1420, 1426, 3191, 3194, 3197
Feigenbaum, Irv 2277
Feikes, Joerg 197, 1279, 2376
Feldl, Erich 928, 934
Fellenz, Brian 2146, 2211
Feng, Z.Q. 3345
Ferianis, Mario 1120
Fernow, Richard C. 3020, 3032
Ferracin, Paolo 3206
Ferrari, Antoine 2617
Ferrario, Massimo 1985, 1997, 2734
Fessenden, Tom 2235
Fieguth, Theodore 296, 2990
Field, R. Clive 296, 307
Fields, D. 471
Figueira, Goncalo 3725
Figueroa, Terry L. 1929
Filhol, Jean-Marc 2331, 2334, 3119
Filippas, A. V. 1037
Finkelstein, Ken D. 2217
Finley, David A. 3728

- Finocchiaro, Paolo 2578
 Fiorito, Ralph B. 487, 3722
 Firebaugh, J. 1246
 Firjahn-Andersch, Arne 530
 Fisch, Nathaniel J. 3675
 Fischer, Claude 465
 Fischer, Wolfram 702, 1261, 2716, 2725, 2921
 Fisher, Alan S. 296
 Fisher, M. V. 2659
 Fitch, Michael J. 2027, 2181
 Fitze, Hansruedi 418, 795
 Fitzgerald, Daniel H. 518, 1198, 1201
 Fitzgerald, Jim 2211
 Flanagan, John W. 1132, 2120, 2731
 Flechtner, D. 3600, 3606
 Fliflet, Arne W. 1049
 Flippo, Kirk 3716
 Floersch, D. 652
 Floersch, Richard H. 649
 Flora, R. H. 714
 Flottman, K. 3450
 Flynn, G. 1533, 1569
 Fong, Ken 450, 890
 Foose, R. 590
 Forest, Etienne 404
 Foster, G. William 182, 3324, 3327, 3330
 Fouaidy, Mohammed 913, 919
 Fournier, P. 103
 Fowkes, W.B. 3423
 Fowkes, William R. 783, 1432, 3426
 Fox, John D. 131, 636, 1207, 1213
 Franchetti, Giuliano 1782, 1785
 Franco, Jose G.S. 2421
 Franczak, B. 527, 1704
 Franks, R. Mark 800, 803
 Franzcak, B. 1788
 Franzke, B. 527, 1704
 Freedman, Stuart J. 1952
 Frei, Hans 418, 795
 Fresquez, M.G. 426
 Freund, Henry P. 2486
 Friedman, Alex 1830, 2758, 3248
 Friedsam, Horst 2051, 2635
 Friesel, Dennis L. 498, 1548
 Frigola, Pedro 217, 2480
 Frisch, Josef C. 253, 3447, 3450
 Fritz, A. 3248
 Frommberger, Frank 3098
 Fromowitz, Daniel B. 1632
 Fuerst, Joel D. 992, 2027
 Fugita, H. 3110
 Fujieda, Miho 413, 798, 857, 860, 863, 1007, 1653, 2271, 2280
 Fujikawa, Brian 1952
 Fujioka, M. 3348
 Fujiwara, Chikara 842
 Fukuda, Mitsuhiro 2259
 Fukuda, Shigeki 3414
 Fukui, Yasuo 3032
 Fukuma, H. 633, 1132, 2731
 Funahashi, Y. 777, 3423
 Funahashi, Yoshisato 2731, 3417
 Funakoshi, Yoshihiro 1132, 2108
 Fung, K.M. 1545, 1548, 2286
 Funk, L.W. 3582
 Furman, Miguel A. 1674, 1791, 1794
 Furst, Mitchell L. 2388
 Furukawa, Kazuro 1132, 2238, 2731
 Furuya, Takaaki 440
 Fuss, Brian 1390
 Futami, Y. 600
 Gaedke, Rudolph 2936
 Gahl, John M. 786, 2772
 Gai, Wei 2030, 3618, 3621
 Gaillard, Michel 2012
 Gaiser, H. 3552
 Galambos, John D. 109, 1198, 1201, 3140, 3143, 3303
 Galayda, John N. 2024, 2471
 Galdi, Vincenzo 2882
 Galimberti, Andrea 2060
 Gallardo, Juan C. 3032, 3722
 Gallo, Alessandro 131, 866, 1147
 Galstjan, Eugene A. 1477
 Galvin, J. 2537
 Gamba, Claudio 1120
 Gambitta, A. 2060
 Gammino, Santo 97, 2578
 Ganetis, George L. 3161, 3170, 3734
 Gao, Jie 1216, 1809, 1812, 1815, 3017
 Gardelle, Jacques 1797, 3387
 Gardner, Christopher J. 614, 1276, 2063, 3182, 3185
 Gardner, K. 2918
 Garnett, Robert 518
 Garren, A. 206
 Garren, Alper A. 2364, 2439, 3050, 3065, 3068, 3152
 Garven, M. 1016
 Garvey, Terrence 916, 2012
 Gassner, D. M. 2123
 Gassot, Huimin 919
 Gaudreau, Marcel P.J. 568, 1491
 Gautier, Cort 977, 1396
 Gavrilov, Nikolay M. 1932
 Gebel, Ralf 2292
 Gebre-Amlak, K. 3681
 Geer, S. 3062
 Geitz, Marc 2172, 2175, 2178, 2507
 Geld, T. 2990
 Gelfand, Norman M. 1677, 2861
 Geller, Joseph M. 2247
 Geng, Rong-Li 429, 980, 983
 Gentzlinger, Robert C. 962, 965, 968
 Georgsson, Mattias 2945
 Gericke, W. 197
 Ghebremedhin, Abiel 11
 Ghigo, Andrea 131, 1536
 Ghiorso, William 2849
 Ghosh, Arup K. 185, 3161, 3188, 3197, 3230
 Ghosh, Subhendu 952
 Giachino, Rossano 2617
 Giannessi, L. 1985
 Gibbins, Peter E. 1025
 Gies, Albert 2424
 Gillespie, George H. 1551, 2805
 Gilpatrick, John D. 2152, 2214, 2241, 3528, 3582
 Ginzburg, Naum S. 1055
 Gioia, Jack G. 977, 1396, 2954
 Giovannozzi, M. 1282
 Girault, F. 1569
 Gladkikh, P. 3122
 Glass, Henry D. 3318
 Glazov, Alim A. 2262
 Glenn, Joseph W. 614, 702, 1258, 1270, 1746, 2918, 3291
 Glover, Ernie 2370, 2498
 Gluckstern, Robert L. 606, 1752, 1755, 2876
 Gluskin, Efim 2489
 Godefroy, Jean-Marie 2686
 Godlove, Terry F. 234, 1758, 1970, 3369
 Godot, J.C. 250
 Goepfner, George A. 2024
 Goergen, R. 2078
 Goertz, D. 625
 Goethe, J.W. 3516
 Gold, Saul 1512
 Gold, Steven H. 1049, 1474
 Goldberg, J. D. 1043
 Goldenberg, Constantin A. 1055
 Golkowski, Cz. 3600, 3603
 Gomez-Costa, Jose Louis 3200
 Gonzalez, Carlota 474, 1408
 Goodenough, C. 2990
 Goodzeit, Carl L. 3245
 Gorbachev, A.M. 1474
 Gorchenko, V.M. 2256
 Gordon, Daniel 3684
 Gorev, V. V. 3711
 Gorski, Anthony J. 1411, 2635, 3342
 Goto, Akira 2268
 Goto, Y. 471
 Gottschalk, Stephen C. 2668, 2674, 2677, 3722
 Gouard, P. 1797
 Gough, Richard A. 884, 1911, 1914, 1917, 1920, 1952, 1958
 Gourlay, S. A. 171, 3236
 Govorov, A.I. 2256
 Graef, Hans-Dieter 2951
 Grafstrom, Per 1671
 Granatstein, Victor 1040, 1046
 Graves, Bill 2471
 Graves, Rossie M. 2388
 Graves, Williams S. 1949
 Green, Michael A. (LBL) 2439, 3149, 3227
 Green, Michael A. (SRC) 2391, 2659
 Greenler, Lee 2388
 Greenwald, Shlomo 3221
 Greenwald, Zipora 1300, 3221
 Greer, James B. 1961
 Gregoire, Guillaume 103
 Grelick, A. 2024
 Greninger, Paul 878, 3570, 3573
 Griep, B. 957
 Grieser, Manfred 1955, 3543
 Griesmayer, Erich 2957
 Griffin, James E. 1201, 3152
 Griffiths, Stephen A. 2960
 Grigorev, Yu. 2927, 3122
 Grimm, Terry L. 3719
 Grippo, A. 2229
 Grishin, Vladislav K. 2581, 2584, 2587
 Grishiu, V.N. 392
 Grobner, Oswald 1339
 Groening, L. 527, 1704
 Gromov, Roman G. 78, 750
 Gross, Dan 2936
 Grossberg, Phyllis 338
 Grote, David P. 1761, 1830, 1833, 1937, 2758, 3248
 Groöbner, Oswald 2629
 Gu, Shaoting 3716
 Gu, Sunhee 1357
 Gubin, Konstantin V. 750, 1456, 2167
 Guerra, Al 3306
 Guharay, S.K. 234, 1306
 Guidi, Vincenzo 2948
 Guiducci, Susanna 277, 1536
 Guignard, Gilbert F. 250, 1635, 1638, 3399
 Guler, Hulya 3026

- Guo, Fanqing 533
Guo, Zhiyuan 633
Gupta, Ramesh C. 171, 185, 3161, 3176, 3236, 3239
Gurd, David P. 355, 3528
Guthrie, Arthur 3594
Guy, F.W. 3531
Göetert, Jost 2424
Ha, Jangho 2265, 3137
Haagenstad, Harvey 965
Haber, Irving 234, 1749, 1758, 1830, 1970
Haberer, Th. 2513
Habib, Salman 366, 1845
Habs, Dietrich 3516
Haebel, Ernst 946, 949
Haeuser, Juergen 3519
Hafizi, Bahman 3687, 3693
Haga, Kaiichi 2310
Hagedoorn, H.L. 1539, 2825
Hagedorn, Dieter 3200
Hagel, Johannes 250, 1635
Hagelstein, Michael 2424
Hagenbuck, F. 165
Hagestedt, Andre 2424
Hahn, Alan A. 468, 1085, 2066, 2164
Hahn, Harald 1100, 1103
Hahn, Robert von 1955
Hahn, Ulrich 1369
Hairapetian, G. 3708
Halaxa, Ernie 1937, 3248
Halbach, K. 2301
Haldemann, Paul 234, 1970
Hama, Hiroyuki 592
Hambikov, Valeriy D. 1456
Hamilton, Andrew 2388
Hamilton, B. 498, 1545, 1548
Hammen, A.F.J. 759, 2825, 2864
Hammon, Duncan L. 965
Hammonds, J.P. 355
Han, Bum-Soo 3525
Han, D. H. 1079
Han, Jang-Min 875, 3525
Han, Qian 1228
Han, Y.J. 3345, 3504
Hanaki, Hirofumi 2015, 2749, 3507
Hancock, Steven 143, 2226
Hanke, K. 2178
Hanke, Klaus 1282, 1285, 2617
Hanks, Roy L. 625
Hanna, S. 3423
Hanna, Samy M. 2516
Hannaford, R. 3233
Hanni, Raymond 949
Hansborough, Lash D. 1444, 1447, 1929, 1946
Hansen, Gene 1336
Hansen, Jan 562
Hansen, Robert 1049
Hansknecht, J. 1991
Hanuska, S. 2635
Harada, Hisashi 848
Harada, Kentaro 2436
Harano, Hideki 2605
Hardek, Thomas W. 1444, 1447, 1946
Hardekopf, Robert A. 3597
Harding, David J. 3318
Hardy, L. 2331, 2334
Hargenrater, Thomas 1396
Harkay, Katherine C. 123, 1641, 1644
Harnden, W. 171, 3233
Harper, Mark 1333
Harrington, Margye P. 349, 1929
Harriott, Lloyd 595
Harris, Guy 1342
Harris, Neville 2656
Harrison, Michael A. 6, 3176, 3230
Hartemann, Frederic V. 2000, 2003
Hartill, Don 980, 2975, 2978
Hartman, N. 3149
Hartmann, H. 696
Hartmann, P. 1991
Hartouni, Edward P. 2590
Hartung, Walter H. 992, 2027
Harvey, A. 3576, 3579
Harwood, Leigh 3306, 3309
Hasan, A. 2990
Hasegawa, Kazuo 3546
Hasegawa, N. 3690
Haseroth, Helmut 103
Hashimoto, Yoshinori 860
Hassanein, A. 3062
Haustein, Peter 533
Hawkey, Timothy P. 568, 1491
Hawkins, Alonzo 1037, 1515
Hayano, H. 1994
Hayano, Hitoshi 256, 2143
Hayano, Hiroyoshi 3432
Hayashi, K. 3330
Hayashi, Y. 3600, 3606
Haynes, W. Brian 965, 977, 1396
Hayoshi, N. 471
He, P. 2552, 3639, 3722
He, Xiaoye 1315
Heese, Richard H. 2304
Heidenreich, G. 1360
Heifets, Samuel 1118, 1665
Heimann, Philip 2370, 2498
Helm, D. 259
Hemker, Roy G. 330, 3672
Hemmer, Michael 37
Henchel, Bill 2936
Henderson L. 296
Henderson, Stuart D. 410, 1351, 2217, 3221
Henderson, Tom 803
Hendrickson, Linda J. 307, 338, 3456
Henestroza, Enrique 1934, 1937, 2849, 2852, 3390
Henke, Heino 812, 815, 818, 1034
Henn, Kurt 1701, 2292
Henrist, Bernard 2629
Herbeaux, Christian 2686
Hermle, Stefan 1360, 2424
Hernandez, Kenneth 803
Heron, Mark T. 661
Herr, Werner F. 304, 3005
Herrmann, J. 2915
Herrmannsfeldt, William 1937
Herrup, David A. 1091
Hershcovitch, Ady I. 584, 1902
Hertel, N. 2427
Hess, Mark 2752
Hettel, R. 206
Hezel, T. 165
Hiatt, Thomas 1462, 3306, 3309
Hickman, Bradley C. 625
Hidaka, S. 1821
Hig 3423
Higashi, Yasuo 777, 3417, 3423
Higley, H. 3233
Higo, Toshiyasu 777, 3417, 3420, 3435, 3468, 3477
Hilaire, Alain 40
Hildreth, Mike 2999
Hill, Barrey W. 1551, 2805
Hill, Ed 2936
Hill, Jeremy M. 2480
Hill, M.E. 3612
Hill, Marc E. 545
Hill, R. 2456
Hilleret, Noel 2629
Himmel, Thomas M. 293, 296, 338
Hinson, William M. 3212
Hiramatsu, Shigenori 492, 633, 1132, 2120, 2731
Hiramoto, Kazuo 2528, 3366
Hirata, Kohji 1689
Hiraya, A. 2689
Hirose, Tachishige 256, 2552
Hirota, Jun'ichi 3366
Hirshfield, Jay L. 1049, 1052, 1474, 3627, 3630
Hitomi, Nobuteru 777, 3417
Ho, C.H. 1450, 2000, 2009
Ho, Darwin D.-M. 1827
Hoag, Harry 777, 3423
Hoberg, H. G. 197
Hockman, Jeffrey N. 2590
Hodgkins, David J. 349, 1444, 1447, 1946
Hodgkinson, Cheryl L. 2656
Hoellering, Frank 3519
Hoeltermann, H. 1899
Hoff, Lawrence T. 693, 1261
Hoff, Matthew D. 884, 1958, 1961
Hoffman, J.R. 3651
Hoffmann, Markus 3098
Hoffstaetter, George H. 407
Hofmann, A. 296
Hofmann, Ingo 137, 1782, 1785, 1788
Hogan, Bart 1046
Hogan, G. E. 579
Hogan, J. 1462, 1991
Hogan, John 934
Hogan, M. 217
Hogan, Mark J. 330, 1997, 2111
Holden, Travis 2006
Holder, David J. 2433
Holmes, Clifford 2235
Holmes, Jeffrey A. 109, 1198, 1201, 3140, 3143, 3303
Holmes, Stephen D. 43
Holstein, Friedrich 2424
Holtkamp, Norbert 896, 3062, 3149
Holtzapple, Robert L. 410, 2057, 2972, 2975, 2978
Homeyer, H. 3519
Homeyer, William G. 2954
Homma, T. 600
Homscheidt, M. 165
Honda, Tohru 2310
Horan, Douglas 1019, 1022
Hori, H. 3507
Hori, Toshitada 2298, 2400, 2403, 3702
Horioka, Kazuhiko 3690
Horny, M.J. 2000, 2009
Hosaka, Masahito 592
Hosokai, Tomonao 3690, 3702
Hosoyama, Kenji 440, 1132, 2731
Houck, Timothy L. 1210, 1303, 2755, 3257, 3390
Hourican, Michael D. 2283
Hovater, Curt 768, 1177
Howell, Joseph W. 3095
Hower, Nelson L. 221, 2099, 2468
Hoyer, Egon H. 162

- Hseuh, Hsiao-Chaun 557, 1345
Hsi, W.C. 1548, 2286
Hsiao, Ko-Ming 1375
Hsiung, Gao-Yu 1375, 1605
Hsu, Ian C. 2220
Hsu, Kuo Tung 682, 685, 1153, 1156, 1159, 1162, 1450, 1605, 2009, 2069, 2072, 2220, 2409, 2412, 2671, 2837
Hsu, S.Y. 1450, 2009, 2072
Hsu, Shen-Nung 1375
Hsu, Yao-Jane 1375
Hu, Hongliang 1596
Hu, Kuo Hwa 2412
Hu, Kwo Hwa 682, 1153, 1156, 2069, 2072
Hu, Shouming 1596
Huan, N. 1132
Huang, H. 471, 1548, 2128
Huang, Hong 633
Huang, Jung-Yun 1076, 2131, 2418
Huang, M.H. 2671
Huang, N. 2731
Huang, Nan 2963
Huang, Yen-Chieh 321
Huang, Zhirong 262, 1644, 2495
Hubbard, E. 3576, 3579
Hubbard, Richard F. 3687, 3693
Huelsmann, Peter 3405
Hughes, Thomas P. 2746
Hughey, Lanny R. 2388
Huhtinen, Mika . 1231
Humpert, Michael 806
Humphries Jr., Stanley 2737, 2772, 2778
Hundzinger, Denis 3743
Hunt, W. A. 676
Hunter, W. Ted 3576, 3594
Hurh, Patrick G. 1423
Husmann, Dirk 3098
Hutchins, S. 250
Huttel, Erhard 1360, 2424
Hwang, C.S. 1450, 2671
Hwang, J.Y. 2000, 2009
Iazzourene, Fatma 2707
Ichihara, Masahiro 3546
Ieiri, Takao 1132, 1135, 2731
Igarashi, Susumu 1141
Igolkin, Aleksandr G. 1456
Iida, Naoko 1132, 2108, 2731
Iino, Youshuke 842
Ikegami, Kiyoshi 1653
Ikegami, Masanori 62, 1818, 1821, 3546
Ikezawa, Mikihiro 2187
Ilg, Thomas 3594
Imai, K. 471
Ingalls, William B. 1917, 1923
Inoue, Makoto 1294, 2528, 3110
Irwin, John 259, 363, 3423, 3453, 3480
Isaev, V.A. 1474
Ishchanov, Boris S. 2584
Ishi, Kimihiro 2187
Ishi, Sadahiro 2271
Ishi, Yoshihi 1653
Ishibori, Ikuo 2259
Ishihara, M. 471
Ishkhanov, Boris S. 2555
Issinsky, Igor B. 2262, 2289
Ito, Takashi 3546
Ivanov, Alexander P. 3501
Ivanov, G. M. 1973, 1976
Ivanov, O.A. 1474
Ivanov, Yu.M. 53
Ivers, J.D. 3600, 3603, 3606
Iverson, R. 2111
Iverson, Richard H. 330, 1252, 2987, 3648
Iwasaki, H. 492
Iwashita, Y. 2280
Iwashita, Yasuhisa 3110
Iwashita, Yoshihisa 857, 1294, 2528, 3645
Izawa, Masaaki 633, 904
Jablonka, Marcel 922
Jackson, Alan 2641
Jackson, G.P. 3324
Jackson, John W. 3185, 3333
Jackson, Leslie T. 3257
Jacob, Jorn 1647
Jacobs, Kenneth D. 3101
Jaekel, Markus 2424
Jaeschke, E. 197
Jagger, Jack M. 1378, 1979, 2635
Jaggi, Andreas 2087
Jahnel, Lucia 2421
Jain, Animesh 185, 3161, 3170, 3173, 3176, 3179, 3188, 3336
Jaitly, Ray 1010
Jakob, Ansgar 1288, 1836
Jander, Donald R. 2668
Janssen, Dietmar 2033
Jansson, Andreas 2223, 2226
Jeanneret, Jean-Bernard 40, 2620, 2623
Jensen, C. 2164
Jensen, Erk 250, 1408
Jeon, D. 1545
Jeon, Dong-o 109, 1198, 1201, 3140, 3143, 3303
Jeong, S. C. 1893
Jeram, B. 658
Jericha, Erwin 2957
Jett, Nelson D. 649
Jia, Qika 2406
Jiang, Daoman 1315
Jin, Yuming 2184, 2406
Job, P.K. 2090
Jobe, R. Keith 253, 3411, 3429, 3447, 3453
Johnson, D. 1318
Johnson, David 518
Johnson, David E. 714, 717, 1243, 2647
Johnson, Erik D. 584, 2471, 2480
Johnson, Kenneth F. 1929, 3528
Johnson, Mark 2936
Johnson, Marty 2468
Johnson, Neil G. 3764
Johnstone, Carol J. 1677, 3050, 3065, 3068, 3071, 3152
Johnstone, John A. 1082
Joly, Jean-marc 922
Jones, Frederick W. 128, 2933
Jones, Justin 2051, 3095
Jones, Kevin H. 518, 3528
Jones, Roger M. 777, 3423, 3468, 3471, 3474, 3477
Jones, W.P. 1548, 2519
Jongewaard, Erik N. 783
Jonker, Michel 2617, 2996
Joosten, Rainer 533
Jordan, Kevin 2229, 2456
Joshi, Chad 931
Joshi, Chan 330, 2006, 3651, 3654, 3684, 3705, 3708
Jowett, John M. 1680
Judkins, J. 206
Juillard, Michel 432
Julian, James 1471, 3131
Julian, R.A. 2394
Jung, Roland 465
Jungmann, K. 1488
Junquera, Tomas 919
Juras, M. 658
Kabel, Andreas 1650, 2507
Kabeya, Zenzaburo 842
Kadantsev, S. 106
Kaganovich, Dmitri 3693
Kageya, Tsuneo 392
Kahn, S. 185
Kahn, Stephen A. 3023, 3026
Kai, Satoru 1309
Kaiser, Hartwig 2385
Kaiser, K.-H. 165, 2915
Kaji, M. 343
Kako, Eiji 432
Kalinichenko, Alexandr I. 2546
Kaltchev, Dobrin 2620, 2623
Kamada, Susumu 256, 2155, 3432
Kaminsky, Alexander A. 1055, 3393
Kaminsky, Alim K. 1055, 3393
Kamitani, T. 1132, 2731
Kamitsubo, Hiromichi 188
Kamiya, Yukihide 904, 1174, 2436, 3363
Kamperschroer, James H. 1444, 1447, 1929, 1946, 2214
Kamps, T. 2075
Kamykowski, Edward 587
Kanai, T. 600
Kanai, Y. 1653
Kanai, Yasumori 3348
Kanaya, Noriichi 664, 667, 670
Kanazawa, Mitsutaka 413, 600, 798, 863, 2271
Kando, Masaki 3690, 3702
Kaneda, T. 592
Kang, H.S. 2205, 2501, 2593
Kang, X. 1545
Kang, Yoon W. 168, 3092
Kaplan, Dannie M. 3032
Kaplan, Roger 980
Karabarbounis, A. 1037
Karantzoulis, Emanuel 1126, 2316
Karasuk, V. 3086
Karlner, Marlen M. 2033
Karn, Jeff 3306, 3309, 3312
Karnauchov, I.M. 2930, 3122
Karyotakis, Yannis 2990
Kashikhin, Vladimir 174, 182, 3327
Kashiwagi, Shigeru 256, 2143, 3432
Kaspar, Klaus 3552
Kasuga, Toshio 633, 2310
Katane, Mamoru 2528
Katayama, Takeshi 404, 1719, 1722, 1737, 3164
Kato, S. 1132, 2731
Katoh, Masahiro 664, 2307
Katoh, Tadahiko 343
Katonak, David J. 974
Katsouleas, Thomas C. 330, 3651, 3654, 3672, 3708, 3713
Katsumata, Tadasu 1309
Katsumura, Yosuke 2602
Kawachi, K. 600
Kawamoto, Takashi 343, 2108
Kaye, Robert A. 524
Kazacha, Vladimir I. 3393
Kazakov, S. 1058
Kazakov, Serguei 3414
Kazanskiy, Lev N. 1477
Kazarinov, Nikolai Yu. 3501

- Kazimi, R. 1991
 Keane, John 1028
 Kedzie, Mark 524, 955
 Keesee, Marie 747
 Keffeler, David R. 1444, 1447
 Kehne, David M. 234, 1970
 Keil, Eberhard 1408
 Keil, J. 2054, 3098
 Keller, L. 2990
 Keller, Roderich 87, 884, 1911, 1914, 1917, 1923, 1926, 1943, 1958
 Kelley, John P. 965
 Kelly, Eugene 185, 3161
 Kempkes, Michael A. 568, 1491
 Kenda, K. 658
 Kennedy, K. 206
 Kennedy, Kurt D. 884
 Kenney, S. 3227
 Kerby, J. 3194, 3197
 Kernel, Philippe 1192, 1195
 Kerner, Thomas M. 696, 699
 Kerstiens, Debora M. 349, 652, 655, 1929, 1946
 Kesselman, Martin 2250
 Kester, Oliver 3516
 Kewisch, Jorg 705, 708
 Kezerashvili, Guram Ya. 2232
 Khachatryan, Arsen G. 3663
 Khan, Sameen A. 2817, 3280
 Khan, Shaikat 197, 1144, 1147, 2831
 Khodyachikh, A. 3122
 Khodzhibagiy, Gamlet G. 2262
 Khomenko, S. 103
 Kiang, L.L. 1545
 Kikuchi, Mitsuo 1132, 2108, 2731
 Kikutani, Eiji 633, 1132, 1138, 2731
 Kikuzawa, Nobuhiro 2459
 Kim, Eun-San 3053, 3056
 Kim, G.N. 2593
 Kim, Han-Sung 2558, 2561
 Kim, Jin-Soo 1043, 1890
 Kim, Jong-Won 2268
 Kim, K.R. 3504
 Kim, Kwang W. 1384
 Kim, Kwang-Je 2495
 Kim, Mun-Gyung 2418
 Kim, Sang-Ho 2558, 2561
 Kim, Y.C. 3504
 Kim, Yong-Hwan 2558, 2561
 Kim, Young-Hwan 2558, 2561
 Kim, Yujong 1076, 1079
 Kim, Yuseok 3137
 Kimura, Wayne D. 487, 3722
 Kincaid, Brian 162
 Kindermann, Hans-Peter 946
 King, Bruce J. 318, 3035, 3038, 3041
 King, Quentin 762, 3743
 Kinkad, Allen K. 1049
 Kinoshita, Kenichi 2605
 Kinsho, Michikazu 3128, 3546
 Kirbie, Hugh C. 625
 Kirichenko, A.E. 2256
 Kirk, Harold G. 896, 3029, 3032, 3149
 Kishek, Rami A. 234, 1656, 1749, 1758, 1761, 1830, 1970, 3274, 3369, 3372
 Kishiro, Jun'ich 1141
 Kishiyama, Keith 1333, 1336, 1396
 Kitabayashi, Teruyuki 343
 Kitagawa, A. 600
 Kitazawa, Yasuji 592
 Klaffky, Roger 2304
 Klaisner, L. 206
 Kleev, Andrey I. 592
 Kleimenov, Victor 1339
 Klein, Horst 1288, 1836, 3405
 Klein, John 551
 Kleinod, M. 1899
 Klenov, V. 106
 Klette, Hallgeir 562
 Klingmann, Jeffrey 777
 Knapp, Edward A. 2301, 2555
 Kneisel, Peter 937, 943
 Kniegl, Gregor 3740
 Knobloch, Jens 980
 Knoch, Herbert 2424
 Knudsen, Helge 1671
 Knuth, Thomas 197, 1144, 1147
 Ko, In-Soo 1076, 1079, 2131, 2593, 3525
 Ko, Kwok 2822, 3423, 3480
 Koba, Kiyomi 1653, 2271
 Kobayashi, T. 3507
 Kobayashi, Yukinori 633, 2436, 3113, 3363
 Koehler, G. 800
 Koepke, Karl P. 992, 2027
 Koeth, Tim 995
 Koganeya, M. 3330
 Kohaupt, Rolf Dieter 1171
 Koiso, H. 1132, 2731
 Koizumi, Nozomi 343
 Kolbe, J. 197
 Kolysko, A.L. 1474
 Komada, Ichitaka 343
 Kondo, Shuji 3690, 3702
 Kondo, Yasuhiro 2187
 Kondrashev, S. 103
 Kondratenko, Anatoly 2289
 Konecny, Richard 2030, 3618, 3621
 Kononenko, S. 3122
 Konstantinov, Sergey G. 2033
 Koontz, Roland 1512
 Korabelnikov, Maxim B. 2167
 Korenev, Igor L. 1764
 Kornilova, Alla A. 1312
 Korolev, Aleksey 2567
 Koroliov, Alexander N. 2570
 Koscielniak, Shane R. 143, 1839
 Koseki, Shoichiro 3770
 Koseki, Tadashi 592, 2436, 3363
 Koseki, Takashi 904
 Kostas, Chris 360
 Kostial, Stephan 2740, 2951
 Kostin, Denis V. 910, 2301
 Kotaki, Hideyuki 3690, 3702
 Kotov, V.I. 53, 1237
 Kotseroglou, T. 3432, 3447
 Kotseroglou, Theofilos 3450
 Koupsidis, J. 2385
 Kourbanis, Ioanis 2840
 Koutchouk, Jean-Pierre 372
 Koutin, S.V. 392
 Kovalenko, Alexander D. 2256, 2289
 Kowalski, Ludwik 490
 Koyama-Itou, H. 600
 Kozanecki, W. 2990
 Kozanecki, Withold 296
 Kozawa, Takahiro 2018, 2596
 Kozioł, Heribert 465
 Kozyrev, Evgeny V. 1049
 Kponou, A. 1902
 Kraemer, Dieter 197, 2379
 Krawczyk, George 3761
 Krafft, Geoffrey A. 1177, 2229, 2448, 2456
 Kraft, G. 2513
 Krakauer, D. 2635
 Kramer, Stephen L. 134, 140
 Krasnopolsky, Vsevolod A. 1479
 Krasnykh, Anatoly 1512
 Kraus, David E. 490
 Krause, Herbert F. 1671
 Kravchuk, Leonid V. 2799, 3282, 3561
 Krawczyk, Frank L. 965, 977, 1396, 3588
 Kreischer, Kenneth E. 81
 Krejčík, Patrick 296, 3429, 3447, 3450
 Kresnin, Yuri A. 2546
 Krienen, Frank 3134
 Krietenstein, Bernd 3552
 Krinsky, Samuel 2304, 2471
 Krisch, Alan D. 392
 Krishnagopal, Srinivas 1674
 Krishnan, Mohan 3666
 Kriznar, I. 658
 Kroc, T. 521
 Krogh, Michael L. 1303, 2611
 Kroll, Norman M. 777, 830, 1432, 1435, 3423, 3468, 3471, 3474, 3477, 3612
 Kruchkov, Jaroslav G. 2033
 Kruessel, Alois 2424, 3375
 Krylov, Stanislav Y. 1479, 1485, 2567
 Krämer, D. 2078
 Kubantseva, Natalia 1423
 Kube, G. 165
 Kubo, Hiroshi 3770
 Kubo, Kiyoshi 256, 2143, 3432, 3435
 Kubo, Ta. 3158
 Kubota, Chikashi 1653
 Kuchnir, Moyses 992, 2027
 Kudinov, Valery V. 1291
 Kudo, Hirofumi 3363
 Kudo, Kikuo 343
 Kugler, Hartmut 103
 Kuhler, S. 197
 Kulikov, Artem V. 3447, 3450
 Kulikov, I.I. 2256
 Kumada, Masayuki 600, 2510
 Kumagai, Keiko 2337, 2343, 2346
 Kumagai, Noritaka 188, 2337, 2340, 2343, 2346, 2349, 2352
 Kuner, B. 197
 Kuno, Kazuo 3363
 Kuo, C.C. 2409, 2412, 2837
 Kuo, Chang Hor 685, 1153, 1156, 1159, 1162, 1165, 2069, 2409, 2412
 Kurennoy, Sergey S. 1399, 2867, 3588
 Kurita, Nadine R. 206, 1363
 Kurnaev, O. 1249
 Kuroda, Ryunosuke 2298
 Kuroda, T. 1306
 Kurokawa, S. 633
 Kurz, Stefan 2796
 Kusano, Joichi 3128, 3546
 Kusche, Karl P. 2552, 3722
 Kushin, Victor V. 3564
 Kusikov, S.V. 1474
 Kuske, Bettina 197, 2379, 2382
 Kuske, Peter 197, 2078, 2379, 2385
 Kustom, Robert L. 168, 518, 998
 Kuszynski, J. 2078
 Kuzay, Tuncer M. 2090
 Kuzminski, Joze 965
 Kuzminski, Jozef 968, 2954
 Kuznetsov, G. 237, 1902

- Kuznetsov, Yu. 106
 Kvasha, Adolf I. 893, 3561
 Kwan, Joe 1937, 1943, 2537
 Kwan, Thomas J.T. 617, 1842
 Kwiatkowski, K. 471
 Kwon, Hyeok-Jung 2558, 2561
 Kwon, Myeun 899, 902, 1076, 1079, 1357
 Kwon, Sung-il 1064, 1067, 1070
 Kwon, Y. K. 1893
 Kühnel, K.U. 3516
 Lach, Joseph 1387
 Laclare, Jean-Louis 1533
 Ladran, A. S. 2590
 Lager, Darrel L. 3513
 Lakatos, Andreas 1288, 1836
 Lalot, Michel 922
 Lamanna, Giuseppe V. 2948, 3522
 Lamarre, J.F. 1569
 Lambertson, Glen R. 1225
 Lambiasi, Robert F. 3734
 Lamm, Michael J. 3191, 3194, 3197
 Lamont, Michael 304, 2996, 3008
 Landahl, Eric C. 2000, 2003
 Lange, M. 2424
 Lange, R. 197
 Lange, Ralph 2382
 Lanting, T. 2990
 Lanza, Richard C. 584
 Lapik, Roman M. 2170
 LaPointe, Mike A. 3627
 Lapostolle, Pierre 1860
 Lapshin, V. 3122
 Larbalestier, David C. 177
 Larimer, Ruth-Mary 533
 Larrieu, Christopher A. 741, 747
 Larsen, Ray 636
 Larsen, Richard C. 490
 Latypov, Tomas A. 1485, 2567
 Lau, Wai Keung 1153, 1159, 1162, 1165, 2000, 2837
 Laurent, Jean-Michel 2629
 Lauth, W. 165
 LaVeigne, Joseph 134
 Lavery, Michael 890
 Lawrence, George P. 3567, 3582
 Lawson, Wesley 1040, 1046
 Lawton, Don 234
 Laxdal, Robert E. 893, 3534, 3537
 Lazarus, Donald M. 490
 Laziev, Eduard M. 3393
 Le Duff, Joel 913, 2012
 Le Sage, G.P. 2480
 Lebedev, Pavel 1387
 Lebedev, Valeri A. 646, 738, 1183, 2897
 Leblanc, G. 206
 LeBlanc, Greg 2945
 LeBon, Douglas J. 3758
 Lebrun, Paul 3032, 3062
 LeCocq, C. 1390
 Lee, Y.Y. 1267
 Lee, Bryan S. 625
 Lee, Chun Sik 1893
 Lee, Edward P. 1830, 3254
 Lee, Hyeyoung 3137
 Lee, J.C. 1602, 1605, 2837
 Lee, J.W. 679
 Lee, Jan Fung 1162
 Lee, Jinhyung 2784
 Lee, Kang-ok 2558, 2561
 Lee, P. B. 1716
 Lee, Peter J. 177
 Lee, Roger C. 557, 1348, 2146
 Lee, S. 3672
 Lee, S.H. 682
 Lee, S.Y. 109, 392, 1545, 1548, 1854, 2286
 Lee, Seung 330
 Lee, Seung C. 1384
 Lee, T. 2021
 Lee, Tae-Yeon 679, 1384, 2131, 2418
 Lee, W. Wei-Li 1623, 1626
 Lee, Yong Y. 1297, 1488, 1743, 3182, 3185, 3300
 Lee, Yvette 2540, 2575
 Leemans, Wim P. 325, 330, 2111, 3696, 3699, 3705
 Lefebvre, Daniel 2686
 Lefevre, Thibaud 1797, 3387
 Legan, Al. 56
 Lehrach, A. 1578
 Lehrach, Andreas 1701, 2292
 Lei, Ge 747
 Leissner, Boris 2172
 Leitner, Matthaeus A. 1911, 1914, 1958
 Lekston, J.M. 3387
 Len L. K. 70
 Leng, Yongbin 1315, 2125
 Lenkszus, Frank R. 333, 2093
 Leon, Asunción 2531, 2534
 Lepercq, Pierre 916
 Lepeule, Patrick 1339
 Lesjak, B. 658
 Lesrel, Jean 919
 Lessner, Eliane S. 1644, 1967, 2325
 Letchford, Alan P. 1767, 2208
 Lettry, J. 92
 Leung, Ka-Ngo 1911, 1914, 1917, 1920, 1923, 1943, 1958, 2540, 2575
 Leunissen, Leonardus H.A. 1557, 1683
 Level, Marie-Paule 1533
 Levush, Baruch 360, 1016
 Levy, C.D. Philip 106, 1964
 Lewellen, John W. 1979, 2024, 2134, 2483
 Lewis, B. 471
 Lewis, S.A. 355
 Li, C.D. 2671
 Li, Derun 382, 800, 896, 907, 1207, 1548, 3149
 Li, Guangyong 2125
 Li, Jingyi 2048
 Li, Nanyang 3339
 Li, Rui 118, 2456
 Li, Shaopeng 633
 Li, Weimin 2406
 Li, Yongjun 2406
 Li, Yulin 3221
 Li, Yun 234, 1656, 1758, 1970, 2102, 3369
 Li, Zenghai 2822, 3423, 3447, 3468, 3480, 3483, 3486
 Liaw, Chong-Jer 1345, 3300
 Libkind, Marcus A. 1390, 2477, 2590
 Lidia, Steven M. 1797, 1800, 2698, 2870, 3387, 3390
 Liebermann, Holger 530
 Lietzke, A. 171, 3233
 Likhachev, Sergey P. 2587
 Liljeby, Leif 1955
 Lill, Robert M. 1411
 Lima, Roberto R. 1366
 Limberg, Torsten 1650
 Limborg, Cecile G. 206, 2361, 3104, 3107
 Limon, Peter J. 174, 1420, 2644, 3194, 3197
 Lin, F.Y. 2671
 Lin, Ke Kang 682, 1450, 2009, 2409, 2412, 2415
 Lin, Tsai-Fu 1375
 Lin, Xintian E. 75, 1429, 3612
 Lindgren, Lars-Johan 2945
 Lindroos, Mats 143, 2226
 Linnecar, T. 2617
 Lira, Antonio C. 3125
 Lisi, Nicola 103
 Lisitsyn, A. 461
 Littauer, Raphael M. 410, 2057
 Litvak, A.G. 1474
 Litvinenko, Vladimir N. 221, 2099, 2468
 Liu, Chen-Yao 3776
 Liu, Dekang 633, 2140
 Liu, G. 2337
 Liu, Guangjun 2125
 Liu, H.C. 2671
 Liu, James 3450
 Liu, Jinhong 2048
 Liu, Kuo-Bin 3776
 Liu, Lin 2421, 2891, 2894, 3125
 Liu, Y. 2552, 3639, 3722
 Liu, Yuan 1878, 1881
 Liu, Zuping 2048, 2406
 Lo, C.C. 1471, 3131
 Lobo, Ricardo P.S.M. 134
 Lockey, R. 1902
 Loew, G.A. 3423
 Loewen, Roderick J. 3420, 3423, 3426, 3480
 Logan, B. Grant 3248
 Logatchov, Pavel V. 78, 237, 2167, 2948
 Loh, M. 3708
 Lohrmann, Erich 554
 Lombardi, Alessandra M. 103, 1860
 Lombardi, Augusto 1324, 3522
 Lonza, Marco 1120
 Lopes, Nelson 3725
 Lorenz, Ronald 2075
 Lorenzon, Wolfgang 392
 Loschner, H. 2575
 Losito, Roberto 946, 949
 Lou, G.H. 2220
 Lou, Weiran 1441, 3221, 3224
 Loulergue, Alexandre 1530
 Low, Raymond 1920
 Lozowski, B. 471
 Lu, Chang-guo 3026
 Lu, Ping 2184
 Lucas, Peter W. 1246, 2614
 Luccio, Alfredo U. 1578, 3143
 Ludwig, Hans 548, 3185
 Ludwig, B. 2537
 Luft, P. A. 1914
 Luhmann, Jr., Neville C. 2000
 Luiten, O.J. 3266
 Lujan, Richard E. 977
 Lumpkin, Alex H. 1644, 2134, 2137, 2161
 Lund, Steven M. 1785, 1788, 3248, 3381
 Lundah, Eric W. 3480
 Lunev, Pavel 461
 Luo, Xiaolan 2963
 Luo, Xuefang 1596
 Luo, Yun 633
 Luong, Michel 250, 821
 Lyles, John T. M. 998, 1001
 Lynch, Don 2244
 Lynch, Michael T. 453, 1061
 Lyneis, Claude M. 533, 1952
 Lyons, Mike B. 962
 Lysenko, Walter P. 3528

- Ma, Li 633, 2140
 Ma, Qing 1342
 Macek, Robert J. 518, 1198, 1201
 MacGill, R.A. 3149
 MacGill, Robert 884
 Machida, Shinji 62, 1653, 1818, 1821, 2271
 Machie, D. 1991
 MacKay, William W. 693, 702
 MacLachlan, J. 521, 1707
 MacLaren, Stephan A. 1937, 2849, 2852
 Madden, Robert P. 2388
 Madrid, Mike 1396
 Maeng, AeHee 1384
 Maerki, Max 418
 Maezawa, Hideki 667, 670
 Magerski, Andy W. 3573
 Magne, Christian 922
 Magurno, Benjamin 490
 Mahler, G. 2128
 Maier, Rudolf 851, 1701, 2292
 Mailian, M.R. 1468, 2105, 3657
 Majka, Richard 1258
 Makarov, A. 3327
 Makarov, K. 103
 Makdisi, Y. 471
 Makhnenko, L. A. 1973, 1976
 Makita, Yo 848
 Mako, Frederick M 70
 Maksimchuk, Anatoly 3666, 3716
 Malamud, E. 3330
 Malchow, Russell 2990
 Malitsky, Nikolay 2713, 3185
 Malone, Robert G. 2158, 2471, 2942
 Mamaev, Gennady L. 1479, 1482, 1485, 2564, 2567
 Mamaev, Sergey L. 1479, 1482, 1485, 2567
 Mamaev, Yuri A. 1988
 Mammosser, John 925, 934, 937, 955, 1462
 Manglunki, D. 1282
 Mangra, Danny 1967, 1979
 Manni, Mario 2277
 Mant, Geoff 3248
 Manwaring, Wm. 498, 673
 Manzo, Mario P. 965
 Mao, Stan 3429
 Mapes, M. 1345
 Marcellini, Fabio 131, 866, 1147
 Marchand, Patrick 986, 989
 Marcouille, Olivier 2686
 Marhauser, Frank 3405
 Marini, J. 919
 Markiewicz, Thomas W. 307, 3462, 3489
 Markovich, G. M. 2024
 Marks, Steve 162, 3429
 Marl, Ron 2656
 Marlats, Jean-Louis 2686
 Marletta, Salvo 97
 Marneris, Ioannis 2543, 3767
 Marone, Andrew 3161, 3170
 Marque, Sébastien 946, 949
 Marriner, John 641, 1707, 2638
 Marsh, Kenneth A. 330, 2006, 3651, 3705
 Marshall, Thomas C. 3627
 Marteau, Fabrice 2686
 Marti, F. 1318
 Martin, D. 206
 Martin, Edward 3309
 Martin, K. S. 714
 Martin, Michael C. 495
 Martin, Philip S. 31, 1082, 3318
 Martin, Siegfried A. 959, 3549
 Martinez, D. 2214
 Martinez, Derwin G. 2241
 Martinez, Felix A. 965
 Martinez, Horace J. 965
 Martini, M. 1282
 Martins, Marcos N. 1366
 Martlew, Brian G. 661
 Martono, Hendy 1551, 2805
 Martyshkin, Pavel V. 1456, 2170
 Marusic, A. 2128
 Marutsuka, Katumi 3360
 Maruyama, T. 3447
 Maruyama, Takahashi 3450
 Maruyama, Takashi 1988
 Marx, Michaela 2385
 Masahiro, Kaji 343
 Masaki, Mitsuhiro 2346
 Masi, M. 1324
 Masullo, Maria R. 1599
 Masunov, E. 2855, 2858
 Masuzawa, Mika 1132, 2731, 3351, 3354, 3357
 Matheisen, A. 2033
 Matheson, John 2999
 Mathis, Yves-Laurent 2424
 Matoba, Suguru 2271
 Matsufuji, N. 600
 Matsumoto, Hiroshi 536, 842, 3411
 Matsumoto, Shuji 3414
 Mattison, Thomas 2990
 Matuk, Charles 1920
 May, Michael P. 1423
 May, T.E. 2394
 Maymon, Jean-Noel 1168
 Mazaheri, G. 296
 Mazur, Peter O. 182, 3318, 3330
 Mazzitelli, Giovanni 1536
 McAllister, Brian 3101
 McAshan, M.S. 182
 McCandless, Brian 3480
 McCarrick, James F. 1303, 1827, 2755
 McCarthy, Michael P. 1061, 1402
 McChesney, David D. 3179, 3188
 McClellan, Jonathan T. 965
 McCormick, Douglas J. 253, 307, 1994, 3411, 3453, 3477
 McDaniel, Boyce 410
 McDonald, Kirk T. 310, 3026
 McGehee, Peregrine M. 652, 3528
 McGehee, Robert 688
 McGinnis, David 59, 854, 1713
 McGuire, David 1402
 McIntosh, Peter A. 1025
 McInturff, Alfred D. 171, 3197, 3233, 3236
 McIntyre, Gary T. 3336
 McIntyre, Peter 2936
 McKee, B.D. 3429, 3447
 McKemey, Adrian 2990
 McKinney, W. 495
 McMahan, Margaret A. 533
 McMichael, Gerald E. 2274
 McNeerney, A.J. 1267, 1270
 Mead, William C. 2790
 Meadow, B. 2990
 Meads, Phillip, F. 3549
 Meddahi, Malika 304, 2996, 3005
 Meier, Wayne R. 1503
 Meilunas, Ray 2599
 Meinke, Rainer B. 3212, 3215, 3245
 Mele, K. 658
 Melissinos, Adrian C. 2027, 2181
 Meller, Robert E. 1115
 Melnychuk, Stephan T. 587, 2599
 Mendonca, Jose T. 3725
 Menefee, Tina 3306
 Menegat, Al 824, 3420
 Menna, Mariano 2578
 Menshov, Alexander A. 893
 Menzel, Jan 2178
 Meot, Francois 2445
 Merl, Robert 2093
 Merle, Eric 3260
 Merminga, Lia 768, 1177, 1180, 2456
 Merrill, Frank 518
 Merte, Rolf 815, 818
 Mertens, Volker 40
 Meseck, Atoosa 554
 Meth, Marvin 3336
 Metral, G. 1282
 Meurdesoif, Y. 3387
 Meusel, Oliver 1288, 1836
 Mexner, Wolfgang 2424
 Meyer, Christophe 103
 Meyer, Dirk 1917
 Meyer, Earl 1946
 Meyer, H.O. 471
 Meyer, Ross K. 3594
 Meyer-ter-Vehn, Jurgen 3675
 Mezi, Luca 1219
 Mi, J.-L. 1488
 Michaut, Jean 2686
 Michelato, P. 2027
 Michizono, Shin-ichiro 1132, 2731, 3414
 Michnoff, Robert J. 693, 2114, 2247
 Michta, Richard J. 2081
 Middendorf, Mark E. 2274
 Miera, D.A. 426
 Miertusova, Jana 2316
 Migliorati, M. 131
 Migliorati, Mauro 1219
 Mikawa, Katsuhiko 3360
 Mikhailichenko, Alexander A. 2814, 3218, 3633, 3636
 Mikhailov, Vladimir A. 2256, 2262, 2289
 Miki, Miyako 2596
 Mikkelsen, Ulrik 1671
 Milardi, Catia 1536
 Milharcic, T. 658
 Millage, Kyle K. 3429, 3447, 3450
 Miller, J.R. 3227
 Miller, Roger H. 777, 3423, 3426, 3468, 3471, 3474, 3477, 3480, 3483, 3486
 Millich, Antonio 250, 1863
 Millo, Daniele 2680
 Millos, Gabriel 171, 3236
 Mills, Frederick E. 3152
 Milton, Bruce 587
 Milton, Stephen V. 1644, 1979, 2024, 2134, 2325, 2483, 2486
 Mimashi, T. 1132, 2731
 Minaev, Sergey A. 1291, 3552
 Minaev, Serguei 3555
 Mincer, Allen 1258
 Minehara, Eisuke J. 2459, 3546
 Minohara, S. 600
 Minty, Michiko G. 256, 296, 307, 338, 771, 800, 1207, 2846, 3384, 3432
 Mirabal, J.S. 426
 Mirochnik, E. 2567
 Mirzozan, Alexandr N. 3561

- Mischenko, Aleksandr V. 2564
Mishin, Andrey V. 590
Mishnev, V. M. 2167
Mishra, C. Shekhar 31, 2641, 2644, 2647, 2719, 3318
Mistry, Nariman B. 3221
Mitchell, John C. 965
Mitchell, Russell R. 965
Mitra, Amiya K. 450, 839, 893
Mitsubishi, Toshiyuki 492, 2120, 2143, 2307
Mitsumoto, Toshinori 2268
Mitsunobu, Shinji 440
Miyade, Hiroki 2403
Miyahara, N. 600
Miyahara, Tsuneaki 2155
Mizumoto, Motoharu 513, 3128, 3546
Mizuno, Akihiko 2015, 2749, 3507
Mizuno, Hajime 3414
Mizutani, Yasuhiro 2596
Moallem, M. 2099
Mocheshchnikov, N.I. 2924
Mochihashi, Akira 1821
Moeller, Shoren Pape 2295, 2427
Mohos, I. 2054
Moir, David C. 617, 1842
Moir, Ralph W. 1503
Mokhov, Nikolai V. 56, 1231, 1234, 2525, 2614, 3041, 3047, 3050, 3074
Molodkin, V. 3122
Molodozhentsev, Alexander 2522
Molvik, Arthur W. 1503, 3248
Monard, H. 2012
Monchinsky, V.A. 2256
Mondelli, Alfred A. 360
Montag, Christoph 1566
Montoya, Debbie I. 965
Montoya, Dennis R. 965
Moore, Elizabeth R. 2483, 2489
Moore, Christopher I. 3687, 3693
Moore, Craig D. 1246, 2614
Moore, D. 652
Moore, John M. 1551, 2805
Moore, T. L. 2590
Morcombe, Peter H. 221, 688
Moretti, Alfred 896, 3032, 3149, 3152
Morgan, Gerry H. 185, 3161, 3170
Mori, Warren B. 330, 3669, 3672, 3684
Mori, Yoshiharu 106, 413, 565, 798, 857, 860, 863, 1007, 1653, 1821, 1964, 2271, 2280, 3348, 3770
Morita, Akio 1294, 2528
Morpurgo, Giulio 2996
Morrison, L. 171, 3233
Morrison, M. 171, 3233
Morse, W.M. 1488
Mortazavi, Payman 1028
Morvillo, Michele 1408, 2629
Moser, Herbert O. 165, 2424
Moser, S. Scott 3041
Mosnier, Alban 628, 1533, 1662, 2834
Moss, Andrew J. 1025
Moss, James D. 965
Mostacci, Andrea 2873
Mouillet, Marc 3260
Mouton, Bernard 2012
Muchnoi, Nickolay Yu. 2232
Mueller, Roland M. 726, 2078, 2379, 2382, 2385
Mugge, Marshall 777
Muggli, Patrick 330, 2006, 3651, 3654, 3708
Mugnai, G. 2999
Mukherjee, Sam K. 1911, 1914
Mukugi, Ken 3546
Mulhollan, Gregory A. 1988, 3447, 3450
Mullacrane, I. D. 2656
Muller, Anke-Susanne 2885, 3011
Muller, Ralph 197
Mulvaney, J. Michael 568, 1491
Muneyoshi, T. 2689
Munoz, Marc 1542
Munro, Morrison H. 3429, 3447
Munson, D.V. 3257
Murakami, T. 600
Muramatsu, M. 600
Muramatsu, Ryosaku 413, 798, 860, 863, 1007, 2271
Murata, Hirohiko 2403
Muratore, Joseph F. 185, 3161, 3170
Murokh, Alex 217, 2006, 2480
Muroya, Yusa 2602
Murphy, James B. 134, 140, 1106
Musameci, Pietro 2480
Musson, John 768, 1183
Muto, Masayuki 565, 3348, 3770
Myakishev, Dmitry G. 2775
Myers, Stephen 299
Myskin, O. 2033
Mytsykov, A. 3122
Nadji, Amor 1168, 1533, 1569
Nagai, Ryoji 2459
Nagaitsev, Sergei 521, 1088, 1707
Nagaoka, Ryutaro 1192, 1195, 3119
Nagayama, Takahisa 848
Nahon, Laurent 2686
Naito, Takashi 256, 343, 1994, 2143, 2155, 3432
Naitoh, Takashi 492
Nakajima, Kazuhisa 2510, 3690, 3702
Nakajima, Mitsuo 3690
Nakajima, Tsukasa 3360
Nakamura, Eiji 1141
Nakamura, M. 471
Nakamura, Norio 1174, 2436, 3363
Nakamura, Shinsuke 3098
Nakamura, T. 1132, 2731, 3158
Nakamura, Takeshi 2346
Nakamura, Tatsuro 343
Nakamura, Yoshiteru 2259
Nakanishi, T. 3098
Nakayama, Hitoshi 413, 798, 1007
Nam, S.H. 2205, 2501, 3504
Namito, Yoshihito 3450
Namkung, W. 2593
Nantista, Christopher D. 1432
Napoly, Olivier 922
Nara, Takayuki 2259
Narang, R. 3708
Nasonov, Nikolay N. 2584, 2587
Nassiri, Alireza 1073, 1979, 2024, 2483
Nath, Subrata 611, 1929, 3528, 3582
Nation, J.A. 3600, 3603, 3606, 3609
Naumann, Olaf 1647
Navarro, G. 1324
Nawrath, Guenther 554
Nawrocky, Roman J. 2081
Neil, G. R. 2456
Nelson, Eric M. 360, 2778
Nelson, Scott D. 1824, 2235
Nelson, W. Ralph 253, 2990, 3450
Nemoshkalenko, V. 3122
Nesterovitch, Alexandre V. 1291, 1932, 2573
Neuffer, David V. 3062, 3080, 3083, 3152
Neugebauer, F. 2764
Neuman, Charles P. 1949
Neurath, R. 2611
Nevada, Bechtel 1506
Newman, Ernest W. 971
Newsham, D. 2003, 2021
Nezhevenko, Oleg A. 1049, 1052, 1474, 3492
Ng, Cho-Kuen 206, 800, 3423, 3426
Ng, King Y. 872, 1545, 1548, 1854, 3077
Nghiem, Phi 1533
Nguyen, Dinh C. 217, 2480
Nguyen, K. 1016
Nguyen, Minh N. 1494, 1497
Nguyen, Viet 780, 928, 931, 934, 1459
Niederer, James A. 1270, 1578, 2722
Nief, J.-Y. 2990
Niell, Fred M. 237, 1004
Nielsen, B.R. 2427
Niki, Kazuaki 3770
Nikiforov, Alexej A. 750
Nikitine, Iouri 1339
Ninomiya, Shiro 1821
Niquille, C. 2617
Nishi, Masatsugu 2528
Nishimori, Nobuyuki 2459
Nishimura, Hiroshi 203, 234
Nishiura, M. 1306
Nobrega, A. 3194, 3197
Noda, Akira 857, 1294, 2280, 2528, 3110
Noda, Fumiaki 3128, 3546
Noda, Koji 413, 600, 798, 863, 1309, 1821, 2271
Noda, Takashi 2352
Nogiec, Jerzy M. 1426, 3191
Noguchi, Shuichi 432
Nordberg, Emery 980, 3221
Norem, J. 1417, 2635, 3062
Norman, Eric B. 533
Normann, L. 2617
North, William 1037, 1515
Norum, W. Eric 3764
Nosochkov, Yuri 206, 2355, 2358, 2364, 3465
Novikov, Gleb A. 2301
Novikov, Vladimir N. 3716
Novikova, Tat'ana A. 2581
Novitski, I. 3194, 3197
Novokhatski, Alexander 2743, 2879
Nuhn, H. D. 2486
Nurushev, S. 471
Nusinovich, G. 1040
Nyman, M. 3257
O'Hara, James F. 2214
O'Neil, James 533
O'Shea, Patrick G. 234, 1949
Oakeley, Owen 221, 2099
Oakley, Owen 2468
Obina, Takashi 1135, 2310
Oerter, Brian R. 699
Ogata, Atsushi 3713
Ogawa, Y. 2731
Ogawa, Yujiro 1132, 2984
Ogitsu, T. 174, 3158, 3194
Oguri, Hidetomo 3546
Oguri, Yoshiyuki 3525
Oh, Saewoong 2265, 3137
Ohkuma, Haruo 2337, 2340, 2343, 2346, 2349, 2352
Ohmi, Kazuhito 633, 1132, 2731, 3113
Ohmori, Chihiro 413, 798, 857, 860, 863, 1007, 1653, 2271, 2280
Ohnishi, Y. 1132, 2731, 2981

- Ohnuma, S. 2590
 Ohsawa, S. 2731
 Ohsawa, Satoshi 1132, 2238
 Ohshima, Takashi 2346
 Ohtomo, Kiyotaka 1722
 Ohuchi, N. 1132, 2731, 3158
 Oide, Katsunobu 288, 1132, 2238, 2731, 3432
 Oishi, Masaya 2352
 Okada, Yasuhiro 2018, 2036
 Okamura, M. 3161
 Okamura, Masahiro 106, 471, 1964, 3164
 Oki, Toshiyuki 1821
 Okita, Shunsuke 2605
 Okugi, Toshiyuki 256, 2143, 2155, 3432
 Okumura, Susumu 2259
 Oliveira e Silva, Luis 3725
 Olsen, David K. 109, 1198, 1201, 3140, 3143, 3303
 Omori, Tsunehiko 2552
 Onda, Takashi 842
 Ongaro, Carla 2531, 2534
 Onillon, Emmanuel 1109
 Ono, Masaaki 432
 Op de Beeck, W.J. 3212
 Opanasenko, Anatoly N. 1976
 Oragiri, Jun-ichi 343
 Oren, Will 3309
 Orlandi, Gianluca 2193, 2196
 Ormond, Kern W. 1354
 Orris, Darryl F. 1420, 1426, 3191, 3194, 3197, 3318
 Orsini, Fabienne 2834
 Ostiguy, Jean-Francois 2710
 Ostojic, R. 1330, 2921
 Ostrikov, Sergey V. 1932
 Ostroumov, Petr N. 103, 893, 3282, 3561
 Otboev, Alexey 1524
 Ott, Klaus 197, 2385, 2608
 Otting, Donnie 803
 Ouchi, Nobuo 3546
 Overett, Trevor 1061, 3755
 Ovsyannikov, Alexander D. 2808
 Ovsyannikov, Dmitri A. 1857
 Owen, Hywel L. 2433
 Oyaizu, M. 1893
 Ozaki, K. 592
 Ozaki, T. 3158
 Ozelis, J.P. 174, 3194, 3197
 Pabst, Michael 1767
 Padamsee, Hasan S. 429, 980, 983
 Pagani, Carlo 1776, 2027
 Pagano, Oreste 3209
 Pai, Chien-Ih 1100, 1488
 Pakter, Renato 1875, 2752
 Palmer, Dennis T. 545, 1997, 3612
 Palmer, Robert B. 3023, 3032, 3062, 3149, 3152
 Palmieri, Vincenzo 541, 943
 Palumbo, Luigi 1219, 1599, 2873
 Pantell, R. H. 3722
 Panvier, Roger 916
 Paolicelli, Guido 2060
 Paolucci, Giorgio 2060
 Papaleo, R. 2578
 Papanicolas, N. 1037
 Papaphilippou, Yannis 1554, 1557, 1560
 Pappas, Chris 1494, 1500, 3429
 Pappas, G.C. 1488
 Paramonov, Valentin V. 893, 2799
 Pardo, R. C. 1890
 Parietti, L. 3591
 Park, Chongdo 1357
 Park, E.S. 2418
 Park, H. J. 899
 Park, I. S. 899, 902
 Park, S. 206, 2367
 Park, Seong Hee 221, 2468
 Parker, Brett L. 3336
 Parkhomchuk, Vasily V. 1387, 1704
 Parodi, Renzo 913
 Parsa, Zohreh 2820, 3044
 Pasky, Stanley J. 1414, 2024
 Pasotti, Cristina 809, 1123
 Pasquinelli, Ralph J. 1094
 Pasternak, J. W. 2590
 Pate, David 557, 1348
 Paterson, J.M. 3423
 Patterson, Janet L. 2468
 Paul, Arthur C. 1204, 3251, 3254, 3513
 Pavlovic, M. 2513
 Pavlovskii, V. V. 2178
 Payet, Jacques 1530
 Pearce, P. 250
 Pearson, Chris 777, 3423, 3426
 Pearsons, R. 3579
 Peaupardin, Philippe 2686
 Peck, Stuart B. 285, 980
 Pedeau, Dominique 1168
 Pedersen, Flemming 143, 474
 Pedrozzi, Marco 81
 Peggs, Stephen G. 705, 1572, 3176, 3179, 3336
 Pei, A. 1545
 Pei, X. 1548
 Pei, Yuanji 1315, 1596
 Peikert, Martin 815
 Peiniger, M. 957, 3510
 Pekeler, M. 245, 2033
 Pelaia, Thomas A. 1115
 Pellegrin, Eric 2424
 Pellegrini, Claudio 217, 2006, 2021, 2045, 2480, 2504, 3708
 Pellico, William A. 1097
 Pelzer, Wolfgang 3519
 Penn, Gregg 3059
 Peraire, Serge 40
 Perelstein, Elkuno A. 3393, 3501
 Perera, Lalith 3221
 Perevedentsev, Eugene 1521, 1524
 Perez, Francisco 806, 809, 2424
 Perko, M. 658
 Pershing, D. 1016
 Peskov, Nikolay Yu. 1055
 Pestrikov, D. 1132, 2731
 Petelin, M.I. 1474
 Peternel, M. 658
 Peters, Craig 3257
 Peterson, Edward 551
 Peterson, T. 1420, 3194, 3197
 Petillo, John J. 360, 2737, 2778
 Petit, Annie 2686
 Petitpas, Patrick 2990
 Petracca, Stefania 1689, 2882
 Petrak, Sibylle 2990
 Petree, Mark 2990
 Petrichenkov, Michael V. 3086
 Petrossian, Marzik L. 3657
 Petrov, Viktor M. 2033
 Pett, John G. 762, 3743
 Petukhov, Vladimir P. 2584
 Pfeffer, Howie 3761
 Pflüger, Joachim 157, 1369
 Phelps, R.A. 392
 Phillips, H.L. 1459
 Phillips, Lawrence 780, 934, 937, 1462
 Phinney, Nan 307, 338, 3384, 3447, 3456
 Piaszczyk, Christopher 1465
 Pichoff, Nicolas 1860, 3277
 Pickard, D. 1943
 Pico, Randolph E. 2590
 Picon, Jean-Claude 3260
 Pieck, M. 652
 Piekarz, Henryk 182, 3330
 Piel, C. 3510
 Pierini, Paolo 1776
 Pierret, Olivier 3260
 Pikin, A. 1902
 Pilat, Fulvia 37, 2716, 2728, 3179
 Pile, P.H. 1267
 Pile, Geoffrey 1022
 Pilipenko, Yuri 2289
 Pillai, Chandra 518
 Piller, C. 955
 Pinayev, Igor V. 221, 2468
 Pincosy, Philip A. 1827
 Pinto, Innocenzo 2882
 Piot, Philip 2229, 2456
 Pipersky, Paul 162
 Piquemal, Alain C. 1851
 Pirkel, Werner 103
 Pirozhenko, A. 2567
 Pirozhenko, Vitaly M. 2564
 Pisent, Andrea 1773, 3522
 Pitts, Cliff 3342
 Pivarc, J. 1896
 Pivarc, J., Jr. 1896
 Pivi, Mauro 2629
 Placidi, Massimo 296, 2999
 Plate, David 162, 803
 Platise, U. 658
 Plawski, Eugeniusz 3408
 Plesko, M. 658, 2424, 2424
 Plettner, Tomas 321
 Plotnikov, Sergey V. 3564
 Plum, Michael A. 518, 1198, 1201
 Podlech, Holger 1955, 3543
 Podlevskii, Vitaly V. 2802
 Podobedov, Boris 146, 1665, 2978
 Poelker, B.M. 1991
 Pogorelsky, Igor V. 2471, 2552, 3722
 Poirier, Roger L. 450, 839, 893, 3540
 Pollet, Patrick 2087
 Polozov, S. 2858
 Pomazan, Yu. V. 1291
 Poncet, A. 1330
 Pont, Montse 2424, 3375
 Poole, Brian R. 1824, 3381
 Poole, Michael W. 2433, 2656
 Pope, Rodd 777
 Popov, Gennadiy F. 2546, 2549
 Poppe, Uli 2178
 Porcellato, A.M. 1324
 Portante, Luciano 1366
 Portmann, Gregory, J. 2373
 Potier, J.P. 250
 Potukuchi, Prakash N. 952
 Poutchkov, Sergey N. 1479, 1482, 1485, 2567
 Powell, James 533
 Power, John F. 1399, 2214, 2241
 Power, John G. 1967, 2024, 2030, 3621
 Pozimski, Jürgen 1288, 1836
 Prabhakar, Shayam 131, 636

- Prabhaker, Shyam 1207
 Pradal, Franco 2316
 Praestegaard, L. 2427
 Prange, H. 197
 Prasuhn, Dieter 1701, 2292
 Preble, Joseph P. 780, 931, 934, 1459, 1462, 2456
 Prebys, Eric J. 3026
 Preger, Miro A. 131, 1536
 Prelec, K. 1902
 Prestemon, S. 3227
 Price, J.S. 1991
 Prichard, Benjamin A. 1917, 1923
 Prieto, Peter S. 1246
 Pritzkau, David P. 824
 Prodell, Albert 185, 3161, 3170
 Pronin, Oleg D. 3561
 Prono, Daniel S. 617
 Proudlock, Paul I. 1330, 3200, 3203, 3746
 Pruessner, Marcel 234
 Przeklasa, Roy 1010
 Przewos, B. 471
 Puitsin, Vadim I. 37, 702, 1575, 2716, 2921
 Puggli, P. 3705
 Pugh, M. J. 2656
 Pukhov, Alexander 3675
 Puntus, Vladimir A. 3561
 Pusterla, Modesto 3280
 Pérez, José 2531
 Qian, Zubao 872
 Qiang, Ji 137, 366, 1845
 Qin, Hong 1623, 1626, 1629
 Qin, Qing 633
 Qinggui, Lai 3263
 Quigley, Peter 980
 Quimby, David C. 2668, 2674, 2677, 3722
 Quintana, Bobby 349
 Quintana, Stephen W. 965
 Rabedeau, T. 206
 Radecke, F. 197
 Radeka, Veljko 2114
 Rago, C. E. 3447
 Raia, Guido 2578
 Raimondi, Pantaleo 307, 338, 2996, 3384
 Raino, Antonio 1905
 Rakowsky, George 1390, 2471, 2477, 2698
 Ramamoorthy, Susila 690
 Ramanathan, Mohan 2051
 Rambo, Peter W. 1827
 Ramos, H.J. 1306
 Ramsell, Christopher T. 3719
 Raparia, Deepak 1297, 1743, 1964, 3185
 Rasson, J. 800
 Rathjen, Eric 2424
 Rathke, J. 780
 Rathke, John 551
 Ratner, Larry G. 392
 Ratschow, S. 2915
 Ratti, Alessandro 884, 1961
 Ratzinger, Ulrich 1788, 1955, 3552, 3555
 Raubenheimer, Tor O. 240, 250, 253, 338, 800, 3423, 3429, 3438, 3441, 3444, 3447, 3453, 3456, 3462, 3465, 3474, 3483, 3486, 3489
 Rauch, Helmut 2957
 Ravello Alberto 2936
 Reass, William A. 426, 453
 Redin, Sergei I. 3167
 Redler, K. 1393
 Reece, C.E. 940
 Reed, C. 3062
 Reed, C.A. 1881
 Rees, Daniel E. 786, 881, 1010, 1061, 1402, 2772, 3528
 Regan, Amy H. 1061, 1064, 1067, 1070, 3528, 3582
 Reginato, Louis L. 2537, 3257
 Regler, Meinhard 2957
 Reiche, S. 2486
 Reichel, I. 296
 Reid, Ron J. 2656
 Reijonen, Jani 1943
 Reilly, John 980
 Reilly, Robert E. 56
 Reiman, Sergei I. 1312
 Reiser, Martin 234, 1040, 1046, 1656, 1659, 1749, 1758, 1970, 2102, 3274, 3369, 3372
 Reitze, David H. 134
 Rendon, Armando M. 965
 Rensfelt, K.G. 1955
 Repnow, Roland 1955, 3543
 Revol, Jean-Luc 1192, 1195
 Reymermier, Christian 1339
 Reyzi, Ingrid 1171
 Riabko, A. 1548
 Ribes, Jean-Bernard 765
 Rice, David H. 410, 2217, 2972, 3221
 Rice, John A. 3242
 Richards, Mitchell C. 349, 655, 1444, 1447, 1929, 1946
 Richardson, Roger A. 1303, 2149
 Riche, A.J. 250, 1863
 Richied, Donald, E. 2954
 Richter, Achim 2740, 2951
 Richter, D. 197
 Riddone, Germana 3203
 Ries, T. 3540
 Rieul, B. 1569
 Rifkin, Jeff 777, 3423
 Rifuggiato, Danilo 2578, 3288
 Rimmer, Robert A. 800, 803, 896, 907, 3131, 3429
 Rindfleisch, Ulrich 851
 Ringwall, A. 3462
 Rinkel, Tomas 392
 Rinolfi, I. 250
 Ristau, U. 2424, 2427
 Ritchie, Gary 2852, 3339
 Rizawa, Takahito 1722
 Roberts, L. 1488
 Roberts, Scott E. 1351, 3221
 Robin, David 203, 1581
 Robin, G. 2617
 Robinson, Kem E. 2668, 2674, 2677, 3722
 Robinson, Theodore G. 702
 Robl, Phil 2388
 Rodarte, Henry J. 3573
 Rode, Claus 3309
 Rodenas, Jose 2534
 Rodier, Jacques 2012
 Rodriguez-Mateos, Felix 154, 3200, 3203
 Roerich, V. 103
 Rogers, G. C. 2659
 Rogers, Joseph T. 1354, 1686
 Rohmig, P. 1330
 Rokni, Sayed 253, 330, 3429
 Romanov, G.V. 2799, 3561
 Romanov, S.V. 2256
 Roncarolo, Frederico 2999
 Root, Larry 3534
 Roper, R. 3540
 Ropert, Annick 2328
 Rosenberg, Richard A. 1641
 Rosenzweig, James B. 217, 2003, 2006, 2021, 2027, 2039, 2042, 2045, 2480, 2504, 3624, 3708
 Roser, Thomas 26, 614, 857, 1267, 1270, 1276, 1578, 1746, 1964, 2128, 2280, 2725, 3291, 3336
 Roshal, A. 2858
 Ross, Marc C. 253, 307, 800, 1994, 3411, 3429, 3432, 3447, 3453, 3477
 Rossmann, R. 165, 2424, 2427
 Rotela, E. 2635
 Rothmund, Karsten 2787
 Rothman, Jeffrey L. 2081
 Roudskoy, I. 103
 Rovelli, Alberto 482, 2578
 Rowe, Michael 533
 Roy, Ghislain 2617, 2996
 Roybal, William 1396, 1402
 Roódenas, José 2531
 Rubin, David L. 285, 410, 980, 1300, 3221
 Rudiger, H. 197
 Rudolph, Klaus 3516
 Rudychev, Vladimir G. 2549
 Ruegg, Roman 587
 Rueter, M. 1369
 Ruggiero, Alessandro G. 2590, 3731
 Ruggiero, Francesco 1408, 2626, 2629
 Ruland, Robert 1390, 2698
 Rule, Donald W. 487, 3722
 Rullier, Jean-Luc 1797, 3387
 Rusnak, Brian 965, 974, 977, 1396
 Russell, Steven J. 477
 Russenschuck, Stephan 154, 2796
 Ruth, Ronald D. 250, 262, 423, 777, 3423, 3468, 3480
 Rutkowski, Henry L. 617, 3257
 Rutt, P.M. 1991
 Ryan, K. 1991
 Ryan, W. 2114, 2117
 Rybalchenko, G.V. 2689
 Rybaryk, Lawrence J. 881, 3528, 3582
 Ryne, Robert D. 137, 366, 611, 1845
 Rödel, Volker 946
 Saban, Roberto 3203
 Sabbi, Gianluca 3179, 3194, 3197
 Sabjan, R. 658
 Sachleben, W. 928
 Saeki, Akinori 2596
 Saeki, Hiroshi 2352
 Saethre, Robert B. 625
 Saewert G. 237
 Safa, Henri 432, 919, 1396
 Safranek, James 206, 1584, 2244, 2304, 2364, 3101
 Sagan, David C. 410, 2966, 2969
 Sah, R.C. 2409, 2415
 Saito, Kenji 432
 Sajaev, Vadim V. 2471, 2942
 Saka, K. 592
 Sakai, Fumio 2036, 2298, 3702
 Sakai, I. 2271
 Sakai, Y. 592
 Sakaki, Horonao 3507
 Sakanaka, Shogo 904, 2310
 Sala-Ferrari, Paola 40
 Salakhutdinov, A.S. 2555
 Salazar, Gilbert A. 655
 Sampayan, Stephen E. 617, 1303, 2611
 Sampson, William B. 185, 3230
 Sandberg, J. 3767
 Sander, Oscar R. 518, 1917, 1923

- Sanders, David M. 1303, 2611
 Sanders, Ralph T. 1100, 1261, 1264, 1488, 3336
 Sandner, Wolfgang 2033
 Sandweiss, J. 3722
 Sangster, T. Craig 1937, 3248
 Sannibale, Fernando 131, 1536
 Santucci, James K. 237, 2027
 Sapp, W. 590
 Sarkisov, Gennady S. 3716
 Sasao, M. 1306
 Sassowsky, Manfred 3378
 Sato, H. 3098
 Sato, Hikaru 392, 2650, 3360, 3749, 3752
 Sato, Shigeru 664
 Sato, Yasuo 413, 600, 633, 798, 857, 860, 863, 1007, 2271, 2280
 Satogata, Todd J. 693, 705, 2722, 2728
 Satoh, Kotaro 1132, 2084, 2108, 2731
 Satoh, Masanori 1174
 Satov, Y. 103
 Satpute, Sharad 1402
 Sattarov, Dior 2936
 Savchenko, A.N. 753
 Sawada, Junichi 3546
 Sawamura, Masaru 2459
 Sazonov, Michael N. 3501
 Scandale, Walter 53, 3206, 3209
 Scanlan, Ronald M. 171, 3194, 3197, 3233, 3236
 Schachter, L. 3600, 3603, 3606, 3609
 Schaffner, Sally K. 729
 Scheer, Michael 2385
 Scheidenberger, Christoph 1671
 Schempp, Alwin 530, 1955, 3516, 3519
 Schep, T.J. 1539
 Schieler, H. 658, 2424
 Schilcher, Thomas 1129
 Schill, J. 75
 Schlabach, Phillip 3194, 3197, 3327
 Schlarb, Holger 2879
 Schleuter, Ross 3429
 Schlicher, Thomas 2087
 Schlitt, Bernhard 3555
 Schlott, Volker 1129, 2087
 Schlueter, Ross 162
 Schmalzle, Jesse D. 3170
 Schmickler, Hermann 465
 Schmidt, C.W. 521
 Schmidt, Frank 1557, 1560, 1563
 Schmidt, Gerald 2172, 2175, 2507
 Schmidt, Rüdiger 3200, 3203
 Schmierer, Eric N. 977, 1396
 Schmolke, Michael 1034
 Schmor, Paul W. 100, 106, 508
 Schmueser, Peter 2172, 2175, 2178
 Schnase, Alexander 851, 1701, 2292
 Schneegans, T. 197
 Schneider, Gerhard 1339
 Schneider, Herbert 1701
 Schneider, J. David 503, 1946, 3528
 Schneider, Th. 165
 Schneider, William J. 934, 1462, 1991
 Schnuriger, Jean-Claude 103
 Schoenlein, Robert 2370, 2498
 Schoessow, Paul 1967, 2030, 3621, 3624
 Scholfield, George 1010
 Schonauer, Horst O. 2933, 2957
 Schonberg, R.G. 590
 Schrage, Dale L. 965, 1333, 1399
 Schreiber, Siegfried 84, 922
 Schröder, Gerhard H. 1228, 1408, 1509
 Schuch, Reinhold H. 1671
 Schuett, Petra 2951
 Schug, Gebhard 3549
 Schulte, Daniel 250, 259, 1668, 1863, 3441
 Schultheiss, Carl M. 3737
 Schultheiss, Thomas 780, 3306
 Schultz, David C. 1252, 3447, 3450
 Schultz, Sheldon 830
 Schulze, Martin E. 3528, 3576, 3579, 3582, 3758
 Schwalm, Dirk 1955, 3543
 Schwandt, Peter 392
 Schwartz, Charles 1073
 Schwartzkopf, S. 545
 Schwarz, Heinz 206, 800, 3429
 Scorzato, Carlos 2421
 Scott, Benjamin 206, 1363
 Scott, Mike 1010
 Scott, Paul K. 1911, 1926
 Scrivens, Richard 103
 Sears, James 980
 Sebek, James J. 206, 2361, 3104, 3107
 Sedlyarov, Igor K. 2033
 Sedykh, Sergey N. 1055, 3393
 Seeman, John T. 1, 296
 Seidel, Mike 34, 554
 Seidl, Peter 1937, 2849, 2852
 Selchow, Nicholas 2235
 Seleznev, Igor B. 2567
 Sellyey, W. C. 2152, 2214
 Semenov, P.A. 392
 Semertzidis, Yannis K. 490, 1488
 Sen, T. 1677, 2635
 Senichev, Yuri V. 2442, 3549
 Senioukov, Victor A. 2570
 Senti, M. 3212
 Seon, Dong K. 2131
 Serafini, Luca 1997, 2039, 2734
 Sereno, Nicholas S. 1587, 1644, 2322
 Sergeev, Anatoly P. 1055, 3393
 Serio, Luigi 1405, 3203
 Serio, Mario 131, 636, 1536
 Serov, Valeri L. 3561
 Sertore, D. 2027
 Servranckx, Roger 2620
 Sery, Andrey 237, 3321, 3728
 Sessler, Andrew M. 1716, 3053, 3056
 Setzer, Stefan 2951
 Shabunov, Alexey V. 2262
 Shadwick, Bradley A. 1716, 2888
 Shafer, Robert E. 3758
 Shang, Clifford C. 3251
 Shang, Lei 1315, 1596
 Shank, Charles 2370
 Shapiro, Michael A. 81, 833, 836
 Shapiro, Stephen 2990
 Sharamentov, S.I. 3561
 Sharapa, Anatoly 237
 Sharkov, B. 103
 Sharma, Sushil K. 2635, 3095, 3342
 Sharonov, S. 3191
 Sharp, William M. 1830, 1833, 3248
 Shasharina, Svetlana G. 369, 377
 Shatilov, Dmitry 1536
 Shchepounov, V. 3288
 Shcherbakov, A. 3122
 Shea, Thomas J. 2114, 2117, 2146, 2250
 Sheehan, J. 3495
 Sheffield, Richard L. 217
 Shemyakin, Alexander 237, 521
 Shen, Stewart S. 1333, 1336, 1372, 1396
 Shepard, Kenneth W. 524, 952, 955
 Sheppard, John C. 3429, 3447, 3450, 3486
 Sherman, Joseph D. 349, 655, 1444, 1447, 1929, 1946, 3528
 Sheu, Jeng-Tzong 1450, 3776
 Shevchenko, Oleg A. 2492
 Sheynin, S. 3576, 3579
 Shibata, Yukio 2187
 Shibuya, S. 1653
 Shibuya, Takashi 3363
 Shiltsev, Vladimir 237, 641, 1387, 1608, 1692, 2638, 3321, 3728
 Shimbo, M. 600
 Shinn, M. 2456
 Shinoo, Kenji 3363
 Shintake, Tsumoru 3411
 Shinto, Katsuhiko 1653
 Shioya, Tatsuro 2683
 Shirai, Toshiyuki 1294, 2528, 3110
 Shirakabe, Y. 565
 Shirakata, Masashi 3360
 Shirasawa, K. 2689
 Shiroto, V. V. 2178
 Shishido, Toshio 432
 Shiyankov, Sergei V. 2948
 Shooee, Hamid 338
 Shoaff, Phillip V. 1336
 Shpak, A. 3122
 Shu, Deming 2051, 2090
 Shumakov Igor V. 1764
 Shuman, Derek 3339
 Shumshurov, A. 103
 Shurter, Robert B. 2214, 2241
 Shvedunov, Vasilii I. 910, 2301, 2555, 2584, 2915
 Shvets, Gennady 3675
 Sibley, Coles 3101
 Sidorov, Aleksey 1479, 1485
 Sidorov, Guennady 2522
 Sieber, Thomas 3516
 Siedling, Rolf 2172
 Siegel, Norbert 154
 Siemann, Robert H. 146, 321, 330, 545, 824, 3612, 3648
 Siemko, Andrzej 154
 Sigg, Peter K. 418
 Siggins, T. 2456
 Sikora, John P. 1115
 Sikora, Robert E. 2114, 2117
 Silbar, Richard R. 2790
 Silvestri, M. 2578
 Silvestrov, Gregory I. 3062, 3086, 3089
 Sim, James W. 1426, 3318
 Simmering, D. 197
 Simon, Rolf 2424
 Simonov, Karlo G. 2567, 2570
 Simos, Nikolaos 548
 Simrock, Stefan 922
 Sinclair, Charles K. 65, 1991
 Sinenko, Irina G. 1468, 2105
 Singatulin, Shavkat 1387
 Singh, Om 2051, 2093, 2244
 Sinjavski, A.V. 1468
 Sivers, Dennis W. 392
 Skarbo, Boris 237, 3321
 Skarita, John 2552
 Skaritka, John 1390, 2471, 2477, 2480, 3722
 Skarpass, Knut VIII 3384
 Skocic, Ante 2951
 Skoczen, Blazej 1339

- Skowbo, D. 590
 Skozen, Blazej 1330
 Skrinsky, Alexander N. 3089
 Slater, James 11
 Slaton, Timothy 3411, 3477
 Sloan, T. 498, 1545, 1548
 Smart, Loralie A. 557, 1348
 Smedley, John 75, 75
 Smimov, Alexei V. 3615
 Smith, Brian G. 977, 1396
 Smith, David R. 830
 Smith, Frank M. 965, 968
 Smith, G. 2128, 2286
 Smith, H. Vernon 1444, 1447, 1929, 3528
 Smith, Howard 2987
 Smith, John D. 355, 690, 2713
 Smith, Jr., H. Vernon 1946
 Smith, Kevin 2280
 Smith, Kevin S. 614, 857, 2725
 Smith, Peter D. 2954, 3573
 Smith, Robert J. 2096
 Smith, Susan L. 2433
 Smith, Terry L. 3755, 3758
 Smith, Todd I. 321
 Smithwick, J. 3233
 Smolej, M. 658
 Smolyakov, M. N. 2692
 Smolyakov, N.V. 2689
 Snell, Charles M. 1842
 Snodgrass, N. Leon 3594
 Snyder, Arthur 2990
 Sobenin, Nicolay P. 910, 2301
 Soga, F. 600
 Soika, Rainer 2936
 Sokoloff, M. 2990
 Solheim, Larry 1515
 Solomon, Lorraine 2244, 2471, 2698
 Solyak, Nikolay 461
 Solyga, Steffen 1034
 Someya, Hirohiko 3348, 3752
 Sommer, M. 1569, 2686
 Song, Jinhua 2229
 Song, Joshua J. 168, 789, 3092
 Sonnemann, Florian 154, 2999, 3200
 Sonnendruker, Eric 1830, 2758
 Soukas, A. 1264, 1267, 1270, 3767
 Sourkont, Konstantin V. 392
 Soutome, Kouichi 2337, 2340, 2343, 2346, 2349, 2352
 Souza, R. J. 2590
 Spalek, George 3573
 Spataro, Bruno 1147, 2873
 Spataro, Charles 3333
 Spence, William 1043
 Spencer, Cherrill M. 1252, 3429, 3447
 Spencer, James E. 321
 Spentzouris, Linda K. 114, 2027, 3155
 Spentzouris, Panagiotis 3062, 3083
 Sperisen, Franz 392
 Spiller, P. 1785, 1788
 Spinos, Frank 1333
 Spitz, Richard 857, 2280
 Sprangle, Phillip A. 3687, 3693
 Spyropoulos, Basile 2543
 Sredniawski, Joseph 587
 Srinivasan-Rao, Triveni 75, 490
 Staats, Joachim 2740
 Stagno, Vincenzo 1779
 Stanford, G. 100, 3540
 Staples, John W. 884, 1958, 1961
 Starling, W.J. 3531
 Starostenko, Alexander A. 2167
 Stassen, Rolf 1701, 2292
 Steck, M. 527, 1704
 Stedinger, M. 2978
 Stefani, Giovanni 2060
 Steier, Christoph 3098
 Steigerwald, M. 1991
 Steinhauer, Loren C. 3722
 Steinhof, A. 165
 Steininger, Ralph 2424
 Stella, A. 131
 Stelzer, James E. 1923
 Stengl, G. 2575
 Stepanov, A. 103
 Stepanov, Anatoli A. 3561
 Stepanov, Sergey S. 1932, 2573
 Stephani, Dmitri 2114
 Steski, Dannie B. 2277
 Stettler, Mathew W. 349, 652, 1946, 2214, 2241
 Stevens, Alan F. 1013
 Stevens, Alan J. 1237
 Stevens, Jr., Ralph R. 1444, 1447, 1917, 1923, 1929, 1946
 Stiliaris, E. 1037
 Stirbet, Mircea 946
 Stockhorst, Hans 851, 1701, 2292
 Stoner, J. M. 2590
 Stout, Daniel S. 3597
 Stover, Greg D. 636, 1213
 Strait, J. 2921, 3194, 3197
 Strasburg, Sean 1518
 Stratienco, Vladimir A. 3269, 3271
 Street, Richard W. 3755
 Streun, Andreas 1542, 2430
 Striganov, Sergei I. 2614
 Stroman, Charles R. 1115
 Stronisch, U. 197
 Strubin, Pierre M. 346, 562
 Stupakov, Gennady V. 382, 3444, 3453, 3474
 Subashiev, Arsen V. 1988
 Suberlucq G. 250
 Suda, M. 600
 Suemine, Shouji 2596
 Sueno, Takeshi 3360
 Suetake, M. 1132, 2731
 Suetsugu, Y. 633, 1132, 2731
 Sugahara, Jun 2187, 2602
 Sugimoto, Masayoshi 2459
 Sugimura, Takashi 1294, 3110
 Suk, H. 1659
 Suk, Hyyong 2006, 3708
 Sukhanova, Asiya K. 2262
 Sukhina, Boris 237, 3321
 Suller, Victor P. 2433
 Sullivan, Kevin 3306, 3309
 Sullivan, Michael K. 296, 2990
 Summers, Don 3149, 3152
 Sun, Baogen 2048, 2184, 2406
 Sun, Ding 854
 Sun, H. 913
 Sun, Yong 3480
 Sutton, Terry D. 3597
 Suwada, T. 1132
 Suwada, Tsuyoshi 2108, 2238, 2731
 Suzuki, Shinsuke 2015, 2749, 3507
 Suzuki, Shoji 664
 Suzuki, Toshikazu 777, 3417
 Suzuki, Yasuaki 2352
 Svandrik, Michele 809, 1120, 1123
 Sveshnikov, B.N. 2256
 Swenson, Donald A. 3531
 Swent, Richard L. 321
 Swift, Gary 221, 2099, 2468
 Sylvester, C. 1420
 Sylvestor, C. 3194
 Syphers, Michael J. 1578, 2128, 2632
 Syphers, Mike 2641
 Syrathev, I. 250
 Tadokoro, Masahiro 2528, 3366
 Taffarello, L. 1324
 Tafti, A. Alai 2728
 Tagawa, Seiichi 2018, 2596
 Tajima, Tsuyoshi 440
 Takada, Ei-ichi 600, 1309
 Takado, Hiroshi 3546
 Takagi, Akira 413, 565, 798, 860, 863, 1007, 1653
 Takagi, Makoto 343
 Takahashi, Hiroshi 1273
 Takahashi, Jiro 1366
 Takahashi, Takeshi 904
 Takaki, Hiroyuki 592, 2436, 3363
 Takanaka, Masao 1719
 Takano, M. 256, 3432
 Takano, Siro 2346
 Takao, Masaru 2337, 2340, 2343, 2346, 2349, 2352
 Takata, Koji 3414, 3417
 Takatomi, Toshikazu 777, 3417
 Takayama, Ken 1141
 Takayama, T. 592
 Takayama, Takeshi 2403, 2689
 Takayama, Yasuhiro 256, 2155
 Takeda, Harunori 3585
 Takeda, Osamu 3546
 Takeda, S. 3447
 Takeichi, N. 592
 Takeuchi, Takeshi 106, 1964
 Takiyama, Youichi 3363
 Talerico, Paul J. 426, 453
 Talman, Richard 410, 2713
 Tamura, Hiroyuki 2259
 Tamura, Kazuhiro 2346
 Tanabe, J. 206, 2355
 Tanabe, Toshiya 1722
 Tanaka, Hitoshi 2337, 2340, 2343, 2346, 2349, 2352
 Tang, Ch. 2769
 Taniguchi, Yoshiki 1007
 Taniuchi, Tsutomu 2015, 2749, 3507
 Taniuchi, Yukiko 2352
 Tanke, E. 1860
 Tanner, David B. 134
 Tantawi, S.G. 3423
 Tantawi, Sami G. 423, 783, 1432, 1435
 Tao, Xiaoping 2125
 Tarakanov, Vladimir P. 1734
 Tarasov, Sergej G. 2799
 Tartaglia, Michael A. 1420, 1426, 3191, 3194, 3197
 Tassotto, Gianni 2211
 Tatanov, V.I. 753
 Tavares, Pedro F. 2421, 2894, 3125
 Tavian, L. 1330
 Tawada, M. 1132, 2731
 Taylor, Brian 1471
 Taylor, C. 3233
 Tazzari, Sergio 2313
 Tazzioli, Franco 1985, 2734

- Tecchio, Luigi B. 2948, 3558
 Tecker, Frank A. 711, 720, 1082, 2719
 Tejima, M. 1132, 2731
 Telegin, Yu. 3122
 Telfer, S. 2021
 Temkin, Richard J. 81, 833, 836
 Temnykh, Alexander B. 410, 3221
 Tenenbaum, Peter G. 253, 338, 3453, 3456, 3459, 3462
 Teng, Lee C. 2635
 Tenishev, Vladimir 103
 Tenyakov, Igor E. 1479, 1485, 2567
 Tepes, Frank 3306
 Tepikian, Steven 37, 1575, 2114, 2728
 Terechkine, Iouri 174, 3242
 Terekhov, V.I. 53
 Terunuma, Nobuhiro 2143, 3432
 Teter, Dave F. 962
 Teytelman, Dmitry 131, 636, 1207, 1213
 Theuws, W.H.C. 759, 2825
 Thibus, Jan 530
 Thieberger, Peter 548, 2277
 Thiery, Yves 2012
 Thikim, M. 2659
 Thivent, Michel U. 2283
 Thomae, Rainer 1917, 1920, 1943
 Thomas, Catherine 913
 Thomas, Manfred 1028
 Thomas, Richard A. 3170, 3188
 Thompson, K. 3465
 Thompson, Kathleen A. 259, 307, 3423, 3489
 Thompson, Kenneth 1979, 2635
 Thompson, Pat 185, 3176
 Thorndahl, L. 250
 Thorson, I. 100
 Thuot, Michael E. 349, 1929, 1946
 Tichonchuk, Vladimir T. 3716
 Tiefenback, Michael G. 1183
 Tighe, Richard C. 800, 1438, 3429
 Tilley, K. 2199
 Timm, Martin 2879
 Ting, Antonio C. 3687, 3693
 Tisserand, Vincent 2990
 Tiunov, M. 1902
 Tkacik, G. 658
 Tobiyama, Makoto 633, 1132, 1138, 2731
 Toda, Makoto 413, 1007
 Todd, Robert 557
 Todesco, Ezio 3206, 3209
 Todosow, M. 548
 Toelle, Raimund 2292
 Toge, Nobukazu 777, 2143, 3414, 3417, 3432
 Tohyama, I. 592
 Tojyo, E. 1893
 Toki, Walter 2990
 Tokumoto, Shuichi 3414
 Tollestrup, Alvin V. 3032, 3062
 Tolmachev, Nikolay G. 3269, 3271
 Tolstun, Nickolay 603
 Tominaka, Toshiharu 3164
 Tomisawa, Tetsuo 3546
 Tommasini, Davide 154
 Tompkins, John C. 174, 3191, 3194, 3197, 3318
 Tonguu, Hiromu 1294, 3110
 Tonutti, Manfred 2172, 2178
 Tooker, Joseph F. 1061, 2954, 3567
 Toole, Loren 1402, 2772
 Torikoshi, Masami 600, 1309
 Toriyama, Minoru 3770
 Torrence, Eric 2999
 Tosi, Lidia 1120, 1126, 2316
 Tosin, Giancarlo 3125
 Tovo, E. 1324
 Towne, Nathan A. 1028, 1031, 2828
 Toyama, Takeshi 1141, 1653, 1821, 3098
 Trakhtenberg, Emil 1369, 2489
 Trautwein, T. Ann 206, 1363
 Travier, Christian 916
 Travish, Gil 2024, 2045, 2483
 Trbojevic, Dejan 37, 1237, 2117, 3176, 3336
 Tremaine, Aaron 217, 2006, 2021, 2480
 Tremblay, Kelly 3306, 3312
 Treps 2990
 Tribendis, Alexey G. 2033
 Trines, D. 245
 Trines, R.M.G.M. 1539
 Trofimov, A.V. 2704
 Trofimov, Nikolai 346
 Troha, Anthony L. 2000
 Tromba, G. 2316
 Trombly-Freytag, Kelley 3318
 Tron, Alexander 2190
 Tron, Wolfgang 986
 Tropea, Paola 3206
 Trower, W. Peter 910, 2301, 2555
 Troyanov, E. 53
 True, Richard 1049
 Trujillo, Marcos C. 965
 Trzeciak, Walter S. 2388, 2391, 2659
 Tsai, H.J. 1162, 2409
 Tsai, Y.L. 2000, 2009
 Tsai, Zone-Da 1150
 Tsang, Thomas 490
 Tsarenkov, A.P. 2256
 Tsoupas, Nicholas 702, 1100, 1267, 1270, 1578, 2114, 2117, 2722, 2725, 2918, 3182, 3185, 3291
 Tsubuku, Hideo 1309
 Tsuchida, Hiroyuki 848
 Tsuchiya, Kimichika 2683, 3158
 Tsukamoto, K. 633
 Tsukishima, Chihiro 848
 Tsunemi, Akira 2036, 2552
 Tsung, F. S. 3672
 Tsutsui, Hiroshi 1058, 3414
 Tuckmantel, Joachim 949
 Tung, Louann S. 1372
 Tuozzolo, Joseph E. 1100, 1264, 1267, 1270, 3300
 Tupikov, Vitaliy S. 2167
 Turner, James 256, 774, 1252, 3432, 3450
 Turner, William C. 1674, 3149
 Tölle, Reimund 1701
 Ueda, Toru 2187, 2602, 2605
 Ueng, Tzong-Shyan 1375, 1450, 2069, 2072, 2412
 Ueno, Ryuichi 2271
 Uesaka, Mitsuru 2187, 2602, 2605
 Uesugi, Tomonori 62, 413, 798, 860, 863, 1007, 1653, 1818, 1821, 2271
 Umezawa, K. 2271
 Umezawa, Masumi 2528, 3366
 Umstadter, Donald 3666
 Urabe, Osamu 2602
 Urakabe, E. 600
 Urakawa, Junji 256, 2143, 2155, 2552, 3432
 Urbanus, W.H. 2462
 Urita, K.K. 471
 Ursic, Rok 1120, 1129, 2087, 2253
 Usack, Victor 490
 Usher, Tracy 307, 3384
 Uythoven, Jan 1228, 2996, 2999
 Uzat, H. W. 450
 Uzunoglou, N. 1037
 v. Drachenfels, Wolther 3098
 Vaccaro, Vittorio G. 1599
 Vahsen, Sven E. 3026
 Vaillancourt, Kurt W. 3423, 3480
 Valdiviez, Robert 1333
 Valentini, Marco 250, 3402
 Valentino, Vincenzo 1905
 Valero, Saby 1860
 Valicenti, Raymond A. 971, 1327
 Valla, Arthur S. 2668
 van Asselt, Willem K. 1746
 van Bibber, Karl A. 777, 3447, 3450
 van der Geer, Bas 2462, 3266
 van der Wiel, M.J. 3266
 van Duppen, Piet 1955
 Van Eindhoven, S.J.L. 1539
 Van Ginneken, Andy 2525, 3074, 3080
 Van Hagan, T. 1393
 Van Rienen, U. 2764, 2787
 van Steenberghe, Arie 3722
 Van Vaerenbergh, Pierre 2662, 2665
 van Zeijts, Johannes 705, 732, 2146, 2722, 2725, 2728
 VanAsselt, W. 614, 3291
 VanBrocklin, Henry 533
 Vane, C. Randy 1671
 Vanecek, David L. 3390
 Vanenkov, Iouri 154
 Varela-Rodriguez, F. 103
 Variale, Vincenzo 1779, 1905
 Vascotto, Alessandro 2316
 Vasilishin, Bogdan V. 2256, 2262
 Vasiniuk, Ivan E. 1468, 2105
 Vasserman, Isaac B. 2471, 2489
 Vasyuchenko, Alexandr V. 3561
 Vella, Michael C. 3257
 Veness, Raymond J. 1339
 Vengrov, R. M. 3561
 Venturini, Marco 234, 1590, 1593, 1752, 1758, 1970, 3274, 3369, 3372
 Ver Planck, Peter 1491
 Verbeke, Jerome M. 1926, 2540
 Verdier, Andre 304, 398, 1557, 1563, 2623, 3005
 Verdu, Gumersindo 2534
 Verhoeven, A.G.A. 2462
 Vermare, C. 3387
 Vernon, W. 2021
 VerPlanck, Peter 568
 Verstovsek, I. 658
 Verzilov, Viktor A. 2193, 2196
 Veshcherevich, Vadim 980
 Vest, Robert E. 2388
 Veteran, J. 2686
 Vetter, Arthur M. 1186
 Vetter, Paul 1952
 Vier, David C. 830, 3612
 Vignola, Gaetano 131, 866, 1536
 Vikharev, A.L. 1474
 Vilakazi, Zebulon Z. 1671
 Villate, Denis 1381
 Vinciguerra, Domenico 2578
 Vinogradov, N. 2855
 Vinogradov, Stanislav V. 1764
 Vinokurov, Nikolai A. 2492
 Virostek, Steve 884
 Vlieks, Arnold E. 3420, 3423, 3447
 Voevodin, M.A. 2256

- Vogel, Greg 2211
 Vogel, Hans 957, 2033, 3510
 Vogel, Vladimir 461
 Vogt, S. 197
 Voigt, Siegfried 806, 809, 2424
 Volfbeyn, Paul 325, 330, 3696, 3705
 Volk, J.T. 182, 3324
 Volkov, Igor A. 1872
 Volkov, O. Y. 2178
 Volkov, V.I. 2256
 Volkov, Vladimir N. 2033
 vom Stein, Peter 957, 2033, 3510
 von Hahn, R. 3543
 von Hartrott, M. 197
 von Holtey, Georg 3008
 von Przewoski, Barbara 392
 Vondrasek, R. 1890
 Vorobiev, Leonid G. 234, 2781, 3116
 Vos, Lucien 304, 465
 Voss, Gustav A. 2385
 Vossenber, Eugene B. 1228, 1509
 Vsevolozhskaya, Tatiana A. 3062, 3086, 3089
 Vujic, Jasmina 2540
 Vysotskii, Vladimir I. 1312, 3642
 Wada, M. 1306
 Wagner, Stephen 2990
 Wahl, Dan 2388
 Wait, Gary D. 1509
 Wake, M. 174, 3330
 Walbridge, Dana G.C. 3318
 Walcher, Th 165
 Waldron, William L. 3257
 Walker, J. 548
 Walker, R. 182, 2456
 Walker, Richard P. 2313, 2680
 Wallen, Erik 2945
 Walters, Dean R. 1342, 1378
 Walther, R. 2424
 Walz, Dieter R. 253, 330, 2111, 3453
 Wan, Weishi 395, 1677, 2465, 3065, 3068, 3152
 Wan, Xiang 81
 Wanderer, Peter J. 185, 3161, 3170, 3173, 3176, 3230
 Wang, C.J. 682, 685
 Wang, Ch. 2409, 2671
 Wang, Changbiao 1052, 3630
 Wang, Chunxi 363
 Wang, D. X. 934
 Wang, Fuhua 3101
 Wang, Guicheng 1315, 1596, 2048, 2125, 2184
 Wang, Huacen 3263
 Wang, J.G. 1659, 1970
 Wang, J.M. 1106
 Wang, J.Q. 1058
 Wang, J.W. 3423, 3468
 Wang, Jian-Guang 234, 1656, 2102, 3369, 3372
 Wang, Jihong 2125
 Wang, Jiuqing 633, 3414
 Wang, Ju 3773
 Wang, Junhua 2048, 2184
 Wang, Juwen 777, 3420, 3426, 3477, 3480
 Wang, Lanfa 633
 Wang, Li-Fang 3381
 Wang, Lin 1315, 1596, 2140
 Wang, M.H. 1159, 1602, 1605, 2837
 Wang, P. 3600, 3603, 3606, 3609
 Wang, Ping 221, 2099
 Wang, S. 330, 1695, 3705
 Wang, S.T. 3227
 Wang, Sho Qin 3651
 Wang, Shuhong 633
 Wang, Shumei 2140
 Wang, Tai-Sen F. 1623, 1848, 2876
 Wang, X. 2018
 Wang, X.J. 229, 2024, 3495, 3627
 Wang, Xiangqi 1315, 1596
 Wang, Xijie 2158, 2471, 2480, 2942
 Wang, Yi-Ming 1064, 1067, 1070
 Wangler, Thomas P. 611, 1061, 1848, 3582
 Warburton, D. 1488
 Warner, A. 521
 Warren, David S. 349, 655
 Warsop, C.M. 2199
 Washio, Masakazu 2018, 2298, 2552
 Watanabe, Kowashi 2352
 Watanabe, Takahiro 2187, 2602, 2605
 Watanabe, Tamaki 1653
 Watanabe, Yuichi 777, 3417
 Watson, Scott A. 617
 Waynert, J.A. 977, 1327
 Webber, Robert C. 1097
 Weber, Robert 3740
 Weggel, Robert J. 3041, 3047
 Wei, Jie 548, 1575, 1743, 2713, 2921, 3176, 3179, 3182, 3185
 Wei, Wen-His 1375
 Weihreter, Ernst 197, 2385
 Weijers, S.R. 759
 Weiland, Thomas 2740, 2743, 2879, 2951
 Weindl, A. 658
 Weinrich, U. 2331, 2334
 Weir, John T. 622, 1303, 3513
 Weise, Hans 922, 2507
 Weiss, Daniel 557, 1348
 Weiss, M. 759
 Weisse, Eberhard 40
 Welch, James J. 1441, 3221, 3224
 Welsch, C. 3516
 Welz, J. 100
 Wen, Long 3263
 Weng, Wu-Tsung W. 1297, 3185
 Wenninger, Joerg 2885, 2996, 2999, 3011, 3014
 Werin, Sverker 2945
 Wermelskirchen, C. 206
 Westenskow, Glen A. 617, 1303, 3251, 3254, 3387, 3390
 Westphal, T. 197
 White, Jeff 2217
 White, Karen S. 729, 732, 735
 White, Marion M. 1414, 1967
 Whittum, David H. 330, 2111, 3612
 Wiedemann, Helmut 206, 321
 Wiemerslage, G. 1369
 Wienands, Hans-Ulrich 296, 1252, 2993
 Wieting, James 1923
 Wight, Geoff. W. 106
 Wilcox, Marc 1926
 Wilde, Stephen 1920
 Wildman, David W. 237, 869, 2840
 Will, Ingo 2033
 Wille, K. 206
 Willeke, Ferdinand 407, 554
 Willen, Erich 185, 3161, 3173
 Williams, C. 1881
 Williams, David J. 2223
 Williams, Malcom D. 1911, 1914, 1917, 1920, 1923, 1943, 1958, 2540, 2575
 Williams, Neville W. 2063, 2128, 2286
 Williams, Robert A. 2790
 Williams, Ronald L. 3681
 Wilson, Ian 250, 821
 Wilson, J. H. 2590
 Wilson, P. 2003
 Wilson, Perry B. 423, 3423
 Wind, D. 2936
 Wines, Robin 3309
 Winick, Herman 2385
 Winkler, Martin 2578
 Winkler, T. 527, 1704
 Winschuh, Erich 530
 Winter, W. R. 2659
 Wiseman, Mark 934, 3309
 Wisnivesky, Daniel 792
 Wissmann, Mark 768
 Witherspoon, R. 545
 Witherspoon, Sue D. 732
 Witkover, Richard L. 2128, 2247, 2250
 Wolcott, Chip 1037, 1515
 Wolf, Z. 1390
 Wolff, Dan 3761
 Wolfley, Rick 3306
 Wollnik, Hermann 2578
 Wolski, Andrzej 2433
 Wong, Seung 1043, 1890
 Wong, Tom 3618
 Wong, Victor K. 392
 Woodle, Martin 1028, 2471
 Woodley, Mark D. 256, 307, 3384, 3429, 3432, 3447, 3456
 Woods, Mike 3465
 Woodworth, Lee 2114
 Wright, R. 652
 Wright, Robert 3342
 Wrulich, Albin F. 192
 Wu, G. 714, 717, 1462
 Wu, Guozhong 2602
 Wu, Lydia K. 1926, 2540
 Wu, Xiaoyu 1318, 3116
 Wu, Ying 221, 688, 2099, 2468
 Wu, Yingzhi 282
 Wuensch, Walter 250, 821, 827, 3387
 Wuestefeld, Godehard 197, 2376, 2385
 Wurtele, Jonathan S. 1716, 2888, 3053, 3056, 3059
 Wutte, Daniela 533, 1952
 Wyss, Carlo 149, 3203
 Xavier, Jr., Ademir L. 2891
 Xiao, Meiqin 404
 Xie, Ming 3678
 Xie, Zu Qui 533, 1952
 Xu, Hongjie 209
 Xu, Hongliang 1315
 Xu, Jingwei 633
 Xu, S. 1369
 Xu, X.J. 533
 Xu, Z. 3600
 Xue, K. 2140
 Yadav, S. 174, 3194, 3197
 Yakimenko, Vitaly 461, 2158, 2471, 2552, 2942, 3495, 3722
 Yakovlev, Vyacheslav P. 1049, 2775, 3492
 Yamada, Hironari 592
 Yamada, R. 174
 Yamada, S. 600, 2271
 Yamaguchi, Seiya 1058, 3414
 Yamamoto, Masanobu 413, 798, 860, 863, 1007, 1653
 Yamamoto, N. 2731
 Yamamoto, Nobor 1132
 Yamamoto, Noboru 343

Yamamoto, Tamotsu 2596
 Yamamoto, Y. 492, 2271
 Yamashita, H. 600
 Yamauchi, Toshihiko 2459
 Yamazaki, Junichiro 592
 Yamazaki, Yoshishige 513
 Yan, Yiton T. 363
 Yanagida, Kenichi 2015, 2749, 3507
 Yanaoka, Eiichi 3348
 Yang, Bingxin 1644, 2024, 2134, 2137, 2161
 Yang, J. S. 902
 Yang, Jinfeng 2018, 2036, 2298, 3702
 Yang, Ming-Jen 711, 720, 723, 1082, 1085, 2719
 Yang, Tz Te 1159, 2000
 Yang, W.Y. 2265
 Yano, Yasushige 2268
 Yao, Chenggui 1596
 Yarba, V. 174
 Yashin, Yuri P. 1988
 Yazynin, Igor A. 1321
 Ye, Kairong 633
 Yeh, Meng Shu 1153, 1159, 1162, 2000
 Yen, Boris 1506
 Yeremian, A. D. 1994
 Yin, B.G. 3345
 Yin, Yan 2048
 Yip, Harry H. 1402
 Yokoi, Takeichiro 1653
 Yokomizo, Hideaki 3128, 3507, 3546
 Yokota, Watalu 2259
 Yokoya, Kaoru 633, 1725, 3435
 Yoon, Byung-Ju 3525
 Yoon, J.C. 679
 Yoon, Moohyun 2265, 3137
 York, Richard C. 234, 1318, 2781, 3116, 3719
 Yorozu, Masafumi 2018, 2036
 Yosh 2731
 Yoshida, H. 2689
 Yoshida, Katsuhisa 848, 848
 Yoshida, Mitsuhiro 3158, 3411
 Yoshida, Susumu 343
 Yoshida, Yoichi 2596
 Yoshida, Youichi 2018
 Yoshii, Jean 3654
 Yoshii, Kenji 343
 Yoshii, Koji 2187, 2602, 2605
 Yoshii, Masahito 413, 798, 857, 860, 863, 1007, 1653, 2280
 Yoshii, Masato 2271
 Yoshikawa, H. 3507
 Yotam, R. 206
 Young, Andrew 131, 636, 1213
 Young, Anthony 162
 Young, Lloyd M. 881, 1444, 1447, 1929, 1946, 3528, 3570, 3582
 Yourd, Roland 884
 Youssof, S.S. 392
 Yovchev, I. 1040, 1046
 Yu, D. 2042
 Yu, David 815, 2003, 2021
 Yu, H. 2140
 Yu, Li Hua 2471, 2474, 2942
 Yu, Simon S. 1800, 1934, 2746, 3257, 3390
 Yudin, Ivan P. 2704
 Yun, V. 3372
 Yunn, Byung C. 1177, 1180, 2453, 2456
 Zachariadou, Katerina 2990
 Zadorozhny, Vladimir 2820
 Zagar, K. 658
 Zagel, James R. 468, 2164, 2211
 Zahir, Nastaran 1926, 2540
 Zalateu, M. 2680
 Zaltsman, Alexander 857, 2280
 Zalyubovskiy, Ilya I. 2549
 Zangrando, Dino 2680
 Zanini, Alba 2531
 Zapasek, R. 1488
 Zaplatine, Evguenii N. 887, 959, 3549
 Zaugg, Thomas J. 349, 655, 1444, 1447, 1923, 1929, 1946
 Zavialov, V. 592
 Zeitlin, Michael 1614, 1617, 1620, 2900, 2903, 2906, 2909, 2912
 Zelazny, Michael S. 2987
 Zelenski, Anatoli N. 106, 1964
 Zelinsky, A.Yu. 2924, 2927, 2930, 3122
 Zeng, J. 2003, 2021
 Zeno, Keith L. 1276
 Zhabitsky, Vyacheslav M. 1222
 Zhang, Chuang 633, 1695
 Zhang, F.Q. 3348, 3752
 Zhang, Jinguo 1315
 Zhang, Jun 1273
 Zhang, Kaizhi 3263
 Zhang, Min 2769
 Zhang, S.Y. 614, 3185, 3294, 3297
 Zhang, T-B. 3627
 Zhang, T. 1881
 Zhang, Tiejue 1940
 Zhang, Wenwei 234, 1970, 3263, 3372
 Zhang, Wu 1261, 1264, 2406
 Zhang, Xiaolong 2629
 Zhao, Feng 1315, 2125
 Zhao, G.Y. 3345
 Zhao, Yongxiang 3149
 Zhao, Zheng 2140
 Zhao, Zhentang 209, 1453
 Zhogeev, Pavel 461
 Zholents, Alexander A. 1794, 2370, 2465, 2498
 Zhou, Anqi 2406
 Zhou, Feng 633, 2963
 Zigler, Arie 3687, 3693
 Ziggrosser, Douglas 557, 1348
 Zimmerman, Robert 1396
 Zimmermann, F. 1560, 2626
 Zimmermann, Frank 206, 256, 307, 382, 1728, 3432
 Zimmermann, Holger 530
 Zinchenko, Alexander 1692
 Ziomek, Chris D. 1064, 1070
 Zisman, Michael S. 293, 296
 Zlobin, Alexander V. 174, 3194, 3197
 Zbov, Mikhail 131, 1147, 1536
 Zolecki, Robert A. 2274
 Zolfaghari, Abbi 1037, 1515
 Zolotarev, Max S. 2111, 2370, 2498
 Zorko, B. 658
 Zotter, Bruno 1118, 1408
 Zou, Peng 3618
 Zou, Yong 3263
 Zou, Yun 234, 1659, 1970, 2102, 3369
 Zoubets, V. 106
 Zubovsky, Victor P. 1932
 Zumdick, John F. 2668
 Zuo, K. 206
 Zvonaryova, O. 2927



1999 PARTICLE ACCELERATOR CONFERENCE

Brookhaven National Laboratory, Bldg. 911B, P.O.Box 5000, Upton, New York USA 11973-5000 <http://pac99.bnl.gov/>

AT THE NEW YORK MARRIOTT MARQUIS

MARCH 29 - APRIL 2, 1999

Conference Chairman

W.T. Weng, BNL
Telephone: 516-344-2135
Fax: 516-344-5954
E-mail: weng@bnl.gov

Program Chairman

I. Ben-Zvi, BNL
Telephone: 516-344-5143
Fax: 516-344-3029
E-mail: ilan@bnl.gov

Organizing Committee

M. Allen, SLAC (NPSS)
J. Ball, ORNL
W. Barletta, LBNL
I. Ben-Zvi, BNL
Y. Cho, ANL
L. Costrell, NIST
M. K. Craddock, UBC & Triumf
W.K. Dawson, TRIUMF (IEEE)
D. Finley, FNAL
D. Friesel, IUCF
D. Hartill, Cornell U.
C. Joshi, UCLA
M. Kihara, KEK (APAC)
S. Krinsky, BNL
C. Leemann, TJNAF
J. Peoples, FNAL (DPB)
M. Reiser, U. Maryland
B. Ripin, APS
C. Roberson, ONR
S. Schriber, LANL
R. Siemann, SLAC
D. Sutter, DOE
S. Tazzari, U. Roma & INFN-LNF (EPAC)
W.T. Weng, BNL, Chairman
G. Westenkow, LLNL
R. York, NSCL

Conference Secretary

M. Campbell, BNL
Telephone: 516-344-5458
Fax: 516-344-5954
E-mail: pac99@bnl.gov

Local Committee, BNL

J. Becker, Treasurer
H. Kirk, Coordinator, Poster & Exhibits
J. Laurie, Printing
E. Lowenstein, BNL Tour
P. Lucas, Publishing (FNAL)
A. Luccio, Editor
W. MacKay, Editor
C. Ronick, Hotel Coordinator
J. Smith, Electronic Publishing
P. Yamin, Social & Spouse Activities

The
American
Physical
Society



BROOKHAVEN NATIONAL LABORATORY
BROOKHAVEN SCIENCE ASSOCIATES

DTIC

8725 John J Kingman Road
Ste. 0944
Ft. Belvoir, VA 22060-6218

February 23, 2000

Dear Sir,

The 1999 Particle Accelerator Conference (PAC'99) took place on March 29 - April 2, 1999 at the New York Marriott Marquis. We had approximately 1,195 registrants, 76 invited speakers and 1,528 abstracts covering all aspects of accelerator science, technology and applications. Among the registrants, approximately 2/3 were from the United States, 1/3 from abroad - truly an international conference in its scope and participation. Concurrent with the conference, there were 40 industrial firms participating in the exhibition.

The proceedings of PAC'99 were published and distributed in November 1999. Total published papers are 1,223 which are published in a 5 volume set with the total pages numbering 3,779.

The total amount of the ONR grant of \$10,000.00 was all used in the support of the expense of junior staff, graduate students, and scientists from the developing nations and former Soviet Union.

As requested form SF298 is enclosed, and shipped separately is one set of the PAC '99 proceedings.

I would like to express my sincere thanks to ONR for its support to PAC'99 which is a very effective vehicle for the development and communication in the accelerator profession.

Sincerely yours,

Wu-Tsung Weng
Chair, PAC'99

attachment: Form SF298

cc: K. Galuchie, IEEE
Grant Administrator - ONR

WTW:mc

A373870 Vol 5

A373874 Vol 1 / A373873 Vol 2 / A373872 Vol 3 / A373871 Vol 4

